Courses in Physics

Quantum Mechanics

for Atomic & Molecular Physics, Quantum & Atom Optics

Ph.W. Courteille
Universidade de São Paulo
Instituto de Física de São Carlos
30/05/2025

2

.

.

Part I

Quantum Mechanics

Preface

Developed at the beginning of the 20^{th} century, quantum mechanics is today the most fundamental and far-reaching theory in physics. It shaped our World more than any other science, as technologies based on quantum mechanical effects are the key to an industry representing today one third of the World's global domestic product. Boosted by the invention of the transistor and the laser, the industry today branches out in many areas including energy generation, electronics, optics, and photonics. Nevertheless and despite its long history and its incomparable success, quantum mechanics is far from being exhausted. The invention of novel techniques for quantum state manipulation and entanglement generation, awarded with various Nobel prizes in the past, and advances in information science during the past 25 years prepared the ground for a second wave of quantum-based technologies called Quantum Revolution 2.0. In terms of economic, military, and social advantages the stakes of this revolution are so important that they triggered a fierce international race for technological domination.

The course starts in chapter 1 with a thorough introduction into the conceptual and mathematical foundations of quantum mechanics, which are disruptive with classical mechanics and electrodynamics. The following Chps. 2 to 4 are organized according to the symmetries (separable in Cartesian space, isotropic, or periodic) underlying the studied systems.

This script represents a synthesis of several postgraduate courses given at the Institute of Physics of São Carlos (IFSC) of the University of São Paulo (USP). The courses are *Quantum Mechanics* (SFI5774), *Atomic and Molecular Physics* (SFI5814), *Quantum Mechanics B* (SFI5707), *Interaction of Light and Matter* (SFI5905), and *Atomic Optics* (SFI5887). The topics of the courses are, of course, closely intertwined. The purpose of this composite script is to emphasize the interconnection of topics and facilitate the understanding of how they are related. In part I we introduce the quantum mechanics, which represents the fundamental theory for the rest of the book. In the second part we focus on the structure of the atom. In the third and fourth part we study the properties of light, its interaction with individual atoms and atomic ensembles and how the interaction is influenced by cavities and surfaces. Finally, in part V we introduce the optics of matter wave.

The course is intended for masters and PhD students in physics. The script is a preliminary version continually being subject to corrections and modifications. Error notifications and suggestions for improvement are always welcome. The script incorporates exercises the solutions of which can be obtained from the author.

Information and announcements regarding the course will be published on the website:
http://www.ifsc.usp.br/ strontium/ $->$ Teaching $->$ Semester

The student's assessment will be based on written tests and a seminar on a special topic chosen by the student. In the seminar the student will present the chosen topic in 15 minutes. He will also deliver a 4-page scientific paper in digital form. Possible topics are:
- Observation of super- and subradiant spontaneous emission of two ions (Exc. 23.2.4.9),

- Squeezed states (Sec. 14.4),
- The Jaynes-Cummings model (Sec. 17.2),
- Quantum projection noise (Sec. 18.2.2),
- Quantum gates (Sec. 24.3),
- The method of quantum Monte-Carlo wavefunction simulation (Sec. 18.1.2),
- The quantum Zeno effect (Sec. 18.2.1),
- Bloch equations: derivation and interpretation (Sec. 16.3),
- The quantum jumps, its history and observation (Sec. 18.1.2),
- Schrödinger's cat (Sec. 18.1.1),
- The Einstein-Podolski-Rosen hypothesis and its experimental falsification (Sec. 24.1.1),
- Elitzur and Vaidman bomb testing problem (Sec. 18.1.3),
- Topological phases and the Aharonov-Bohm effect (Sec. 18.3),
- Quantum non-demolition measurements (Sec. 18.2.3),
- Calculation of photoelectric effect from Fermi's golden rule (Exc. 5.4.5.7),
- Quantum correlations and the experiments of Young and Hanbury-Brown-Twiss (Sec. 17.3.1),
- The Hartree-Fock method (Sec. 11.3.3),
- Temporal evolution of a free particle described by a Gaussian wave packet,
- The WKB approximation (Sec. 5.3),
- Rydberg atoms (Sec. 9.4.4),
- The helium atom (Sec. 11.2),
- The quadratic and the dynamic Stark effect (Sec. 10.3),
- The blackbody radiation-induced Stark effect (Exc. 5.4.5.9),
- The method of combining atomic orbitals (LCAO) (Sec. 12.1.4),
- Ultracold molecules,
- Efimov states (Sec. 13.3.8),
- Bose-Einstein condensation (Chp. 27.9).

The following literature is recommended for preparation and further reading:

Ph.W. Courteille, script on *Classical Mechanics: Dynamics of Point Masses and Rigid Bodies, Vibrations and Waves, Gravity* (2025)

Ph.W. Courteille, script on *Electrodynamics: Electricity, Magnetism, and Radiation* (2025)

Ph.W. Courteille, script on *Thermodynamics & Statistical Physics: applied to Gases and Solids* (2025)

Ph.W. Courteille, script on *Quantum Mechanics applied to Atoms and Light* (2025)

Ph.W. Courteille, script on *Optical Spectroscopy: A practical course* (2020)

W.R. Theis, *Grundzüge der Quantentheorie*, Teubner (1985)

H.J. Metcalf, P. van der Straten, *Laser Cooling and Trapping*, Graduate Texts in Contemporary Physics, Springer (1999)

J. Weiner and P-T. Ho, *Light-Matter Interaction: Fundamentals and Applications*, Springer-Verlag, Berlin (2003)

Ch.J. Foot, *Atomic physics*, (Oxford Master Series in Atomic, Optical and Laser Physics, 2005)

R. Loudon, *The quantum theory of light*, Oxford Science Publications, Oxford (1973)

Ch.C. Gerry and P.L. Knight, *Introductory Quantum Optics*, Cambridge University Press (2005)

P. Meystre and M. Sargent III, *Elements of Quantum Optics*, Springer-Verlag, Berlin (1990)

I.I. Sobelman, *Atomic Spectra and Radiative Transitions*, Springer Verlag, Berlin (1977)

M. Weissbluth, *Photon-Atom Interactions* (Academic Press, Boston, 1989)

C. Cohen-Tannoudji, B. Diu, F. Laloe, *Quantum mechanics, vol. 1*, Wiley Interscience

D.J. Griffiths, *Introduction to Quantum mechanics*, Pearson Education Limited (2014)

L.I. Schiff, *Quantum mechanics*, McGraw-Hill Book Company (1968)

J.J. Sakurai, J.J. Napolitano, *Modern Quantum Mechanics*, 2^{nd} ed., Springer (2011)

P.W. Atkins and R.S. Friedman, *Molecular Quantum Mechanics*, (3^{rd} ed. Oxford University (2001)

I.N. Levine, *Quantum Chemistry*, Allyn and Bacon, 7^{th} ed. Pearson (1983)

H.A. Bethe, R. Jackiw, *Intermediate Quantum Mechanics*, 3^{rd} ed. Taylor & Francis (1997)

J.I. Steinfeld, *Molecules and Radiation*, The MIT Press, Cambridge (2005)

A. Corney, *Atomic and Laser Spectroscopy*, Clarendon Press, Oxford (1977)

B.H. Bransden, C.J. Joachain, *Physics of Atoms and Molecules*, John Wiley & Sons (1983)

Philippe W. Courteille, São Carlos, January 2025

Content

Chapter 1

Foundations and mathematical formalism

This chapter traces briefly the historical conditions and the discoveries that led to the invention of quantum mechanics. The fundamental idea of quantum mechanics is the assumption that there are entities which can not be subdivided beyond a certain limit. Examples are the mass of a body, the speed of an electron orbiting an atom, or the intensity of a beam of light. This idea was first uttered by *Leucippus* 500 years a.c. and his student *Democritus*, who imagined matter being made of smallest particles which they called *atoms*. These atoms move freely, collide, combine, and separate: 'There is nothing else than atoms and free space' they claimed. The microscopic atoms would have the same characteristics as the macroscopic objects they form when they combine, for example, color and shape. The idea of the atom resurfaced and was refined in the course of the 18^{th} century (see Tab. 1.1 below). Today, we know that the basic idea was good, but reality is a little more complicated.

Table 1.1: *Historical time line of the quantization of matter.*

500 a.c.	Democritus	invention of the atom
1800	Avogadro, Dalton	reinvention of the atom
1897	Thomson	charge transport, raisin-in-a-cake model
1909	Rutherford, Geiger, Marsden	α-scattering, charge localized in nuclei
1911	Rutherford	planetary model
1913	Bohr	quantized orbitals
1923	de Broglie	matter has characteristics of waves
1927	Davisson, Germer, Stern	electron and atoms diffraction

Still, at the end of the 19^{th} century, the physical world seemed rather simple: matter and light was all that existed. Matter was made up of atoms and light was a wave. Therefore, to describe a real system, it was enough to calculate the trajectories of its elementary particles and the propagation of light between them. The way that light interacts with polarizable and magnetizable matter via electric and magnetic fields had been perfectly explained by laws discovered by Coulomb, Ampère, Faraday, and Maxwell.

However, new experimental observations, such as the ultraviolet divergence of

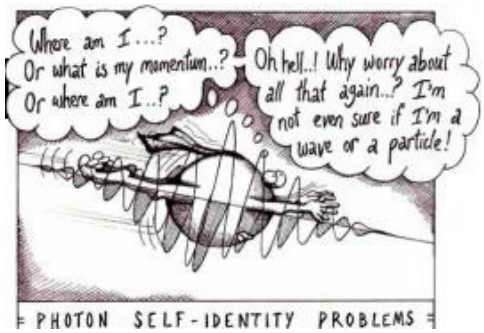

Figure 1.1: Particle-wave duality.

black-body radiation, that appeared in the late 19^{th} century, were incompatible with these traditional concepts. New ideas were pioneered by *Max Planck* who, in 1905, with a little help from Einstein quantized the electromagnetic field, and therefore the light, into small harmonic oscillators. This was the starting point for the development of a new theory called 'quantum mechanics'. Soon, this theory was applied to explain the photoelectric effect. The second important step was initialized by *Niels Bohr*, who quantized the hydrogen atom in 1913 into discrete excitation levels.

Table 1.2: *Historical time line of the quantization of light.*

1801	Young	light is diffracted like a wave
1860	Maxwell	unified theory of electrodynamics including light
1888	Hertz	detection of radio waves
$\sim$ 1890		accurate measurements of black-body radiation spectra
1900	Planck	quantum hypothesis: $E = h\nu$
1905	Einstein	photoelectric effect, light behaves like a particle

Nowadays we know that our universe is not as simple as classical mechanics suggested, and that atoms are also waves and light also behaves like particles. This *duality principle* is one of the fundamental ideas of quantum mechanics. The appearance of an object as a wave or as a particle depends on the situation in which it is observed. While the wave nature of light was well established in classical physics since a long time, Louis de Broglie was the first in 1924 to apply the duality principle also to massive particles and to predict that particles, under certain conditions, behave like waves the wavelengths of which increase as their velocity decreases. Each particle (or body) is delocalized along a distance corresponding to this 'de Broglie wavelength'. This feature of matter was soon discovered experimentally in electron beams and is still used today in commercial devices, for example in electron microscopes.

1.1 The discovery of the atom

1.1.1 Democrit's model

'The principles of reality are atoms and emptiness while other things are mere opinions.' This is a quotation from the Greek philosopher *Democritus* 400 years before Christ and before Socrates. Together with his teacher Leucippus, he formed the first idea of indivisible particles: atoms.

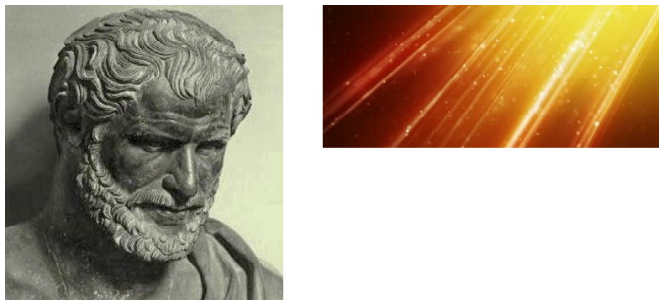

Figure 1.2: Democritus and dust in a sun ray.

Democritus' work only survived as second-hand accounts, the major part of it having been written down by *Aristotle*, who also, defending the idea of the continuum, was the greatest critic of Democritus' theory. Aristotle said that the reasoning that guided Democritus to affirm the existence of atoms was as follows. For a body to change its shape, it is necessary that its parts can move. This presupposes an emptiness (or vacuum) in which the matter moves. But if matter were divided infinitely into ever smaller parts, it would loose its consistency. Nothing could be formed because nothing could arise from the ever more infinitely deep dilution of matter into emptiness. Hence, he concluded that the division of matter can not be infinite, that is, there is an indivisible limit: the atom. 'There is only atoms and emptiness', he said.

Observing dust particles in a whirling motion within a ray of sunlight, Democritus was led to the idea that atoms would behave in the same way, randomly colliding, some crowding, others dispersing, others never yet joining with another atom.

The consistency of clusters of atoms, which makes something look solid, liquid, gaseous, or animated (which is the state of the soul) would then be determined by the shape of the atoms involved and their spatial arrangement. In this sense, water atoms are smooth and slippery; the atoms of steel have shapes with sharp edges that hold them solidly together; the atoms of salt, as their taste shows, are harsh and pointed; the atoms of air are small and little connected, penetrating all other materials; and the atoms of soul and fire are spherical and very delicate.

We know nowadays that Democritus' first theory of the structure of matter was very close to the truth: There really are indivisible particles called atoms composed of a nucleus and an electronic shell, and the space between the atomic nuclei is, in fact, quite empty.

The atomic hypothesis came to be reborn in the modern age with the scientists

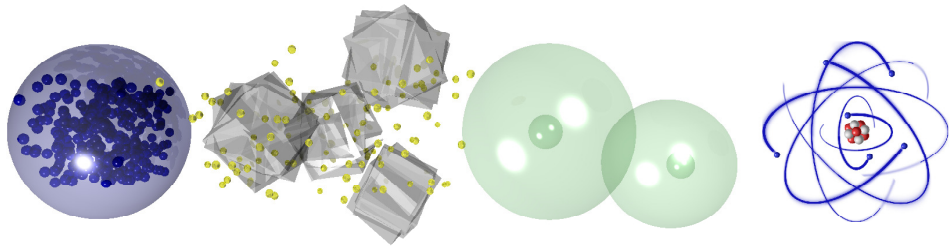

Figure 1.3: Atoms of steel and air, atoms of the soul, and Bohr's atom model.

Boyle, Clausius, Maxwell, and Boltzmann due to their successful explanations of the properties of gases based on the so-called kinetic theory, where they assumed a gas being constituted of identical molecules that collided elastically with each other and with the walls of the recipient containing them. The discovery of the atom through the *laws of proportions* in chemistry and the establishment of Avogadro's number considerably strengthened the atomic hypothesis. The hypothesis was definitely consecrated with the various experiments that established the charge of the electron and the mass ratio between electrons and protons.

By the beginning of the 19^{th} century the atomic nature of matter had definitely been established, and the basic composition of the atoms was already relatively well known. It was known, through experiments, that electrons could be removed from neutral atoms thus creating positively charged ions and that only a certain number of electrons could be removed from each atom. This number proved to be dependent on the atomic species and was called the atomic number Z. This information was fundamental for establishing the basic composition of atoms. The question that arose at this point concerned the dimensions and configurations of the atomic system. How would loads and masses be distributed in this entity?

1.1.2 Thomson's model and Rutherford's experiment

The internal structure of a body can be studied by throwing beams of small particles against it. The detection of the angular distribution of the scattered particles gives access to the structure factor of the body. In crystallography we throw X-rays into super-complicated molecules to learn the architecture e.g. of proteins. And in medicine, X-rays reveal the internal structure of the human body. Obviously, the scattering technique is an extremely powerful tool, used in many areas of modern physics.

In a series of experiments done before 1911, *Ernest Rutherford* analyzed the internal structure of gold atoms using α-particles, i.e., He^{2+} atoms. The experiments carried out by Geiger, Marsden, and Rutherford consisted of observing the deflection of particles from a collimated beam when scattered by a thin metallic sheet (gold of thickness $\sim 1\,\mu m$) carefully obtained by electroplating [see Fig. 1.4(cd)].

The atomic model proposed by *Joseph John Thomson* suggests a structure resembling a *pudding with raisins*: the electrons would be homogeneously distributed within an extended nucleus (size 0.1 nm) of positive charge thus compensating for the negative charge of the electrons. The α-particles would penetrate the gold nucleus,

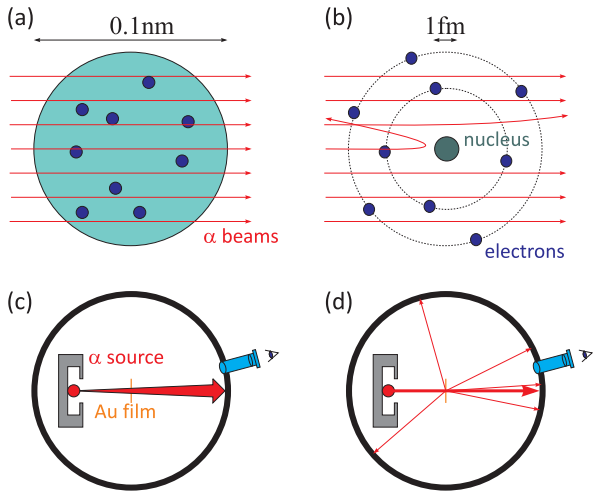

Figure 1.4: Comparison of Rutherford scattering by free electrons and electrons strongly bound to small nuclei. (a) Thomson's 'raisin-in-a-pudding' type atom; (b) Rutherford's 'planetary' atom. (c) Rutherford scattering by a raisin pudding atom and (d) by a planetary atom.

perceived as almost homogeneous, but would suffer multiple deflections due to collisions with the disordered electrons within the nucleus. Since electrons are very light, the angle of deflection θ would be small, even after many collisions. For this model we expect a Gaussian dependence of the particles' deflection angle given by the *scattering cross section* [see Fig. 1.4(a-b)],

$$\frac{d\sigma}{d\Omega} \propto e^{-\theta^2/\theta_0^2} \ , \tag{1.1}$$

where θ_0 is a small angle.

However, the measurements performed on this *Rutherford scattering* showed different results:

- For a fixed scattering angle, the amount of particles scattered into a solid angle element $d\Omega$ is proportional to the thickness of the metal foil.
- For a given fixed angle and a given metal sheet the amount of scattered particles in $d\Omega$ varies inversely with $E_{\rm kin}^2$, where $E_{\rm kin}$ is the kinetic energy of the α-particles.
- For a given energy and a given metal sheet, the number of particles scattered into $d\Omega$ is proportional to $(\sin\frac{\theta}{2})^{-4}$.
- For a given energy and sheet thickness, the number of particles scattered into $d\Omega$ in a given direction is proportional to $Z_{\rm tg}^2$, where $Z_{\rm tg}$ is the atomic number of the element that constitutes the sheet.

The extremely rare deflection of α-particles and their angular distribution can be understood by the assumption that the positive charge is concentrated in a very small

volume ($\sim 1\,\mathrm{fm}$, that is 10000 times less than the size of the atom itself). This volume is called the atomic nucleus, hence the denomination of *nuclear model*. Since most of the particles pass through the gold sheet without hindrance, there must be a large gap between the nuclei. The electrons, which move within a large (in comparison with the diameter of the nucleus) empty space (the vacuum) around the nucleus, shield the positive nuclear charge, so that the atom appears outwardly neutral.

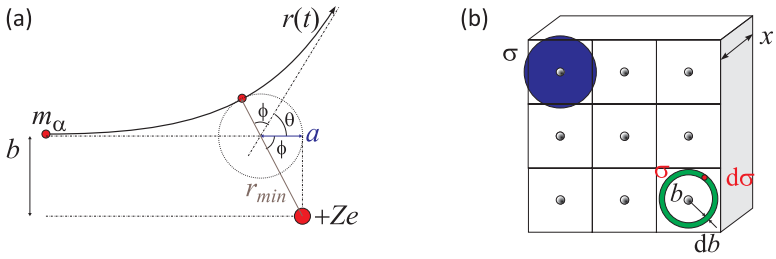

Figure 1.5: (a) Trajectory of an α-particle. (b) Illustration of the scattering cross section.

We now derive Rutherford's scattering formula from the hypothesis of a point-like nucleus. Due to the repulsive action of the Coulomb force,

$$F = \frac{Z_\alpha Z_{\mathrm{tg}} e^2}{4\pi\varepsilon_0 r^2} \ , \tag{1.2}$$

we have for the trajectory of the α-particle ($Z_\alpha = 2$) a hyperbola [see Fig. 1.5(a)]. The large half-axis of the hyperbola can be determined from the following ansatz,

$$E_{\mathrm{kin}} = \frac{Z_\alpha Z_{\mathrm{tg}} e^2}{4\pi\varepsilon_0} \frac{1}{2a} \ , \tag{1.3}$$

where $2a$ is the minimum distance of the particle α, when it collides with the nucleus in a central collision [1]. The distance a depends on the kinetic energy and can also be used for non-central collisions. The collision parameter b is the minimum distance of the α-particle to the nucleus, if it continued to fly in a straight line. In fact the α-particle will be deflected by an angle θ. From the geometry of the hyperbola, as $2\phi + \theta = 180°$, we obtain the following equation:

$$\tan\phi = \tfrac{b}{a} = \tan\left(90° - \tfrac{\theta}{2}\right) = \cot\tfrac{\theta}{2} \ , \tag{1.4}$$

and therefore

$$\cot\tfrac{\theta}{2} = \frac{b}{a} = \frac{8\pi\varepsilon_0 E_{\mathrm{kin}}}{Z_\alpha Z_{\mathrm{tg}} e^2} b \ , \tag{1.5}$$

replacing a with the formula (1.3). Taking the derivative of this latter formula, we obtain a relation between the width db of the hollow cone and the pertinent width $d\theta$ of the deflection angle θ,

$$-\frac{1}{2\sin^2\frac{\theta}{2}} d\theta = \frac{8\pi\varepsilon_0 E_{\mathrm{kin}}}{Z_\alpha Z_{\mathrm{tg}} e^2} db \ . \tag{1.6}$$

[1] In a central collision, when the α-particle reaches the minimum distance $2a$, its initial kinetic energy, E_{kin} is fully converted into potential energy.

Let $n_{\rm tg} = \frac{N_{\rm tg}}{V}$ be the density of the particles in the target ($N_{\rm tg}$ atoms per volume V) and x the film thickness. Then $\sigma = \frac{A}{N_{\rm tg}} = \frac{V/x}{N_{\rm tg}} = \frac{1}{n_{\rm tg}x}$ is the average cross-section per atom sensed by the α-particle on its way through the film. The probability $P(\theta)d\theta$ for the α-particle of being within a ring at distance b from the nucleus (whose area is $2\pi bdb$) and being scattered into the angle θ is then given by,

$$P(\theta)d\theta = \frac{2\pi bdb}{\sigma} = n_{\rm tg}x2\pi bdb \ . \tag{1.7}$$

These particles, i.e., dN of the N particles, are deflected into the hollow cone with the probability,

$$\begin{aligned}\frac{dN}{N} = P(\theta)d\theta &= n_{\rm tg}x2\pi\frac{Z_\alpha Z_{\rm tg}e^2}{8\pi\varepsilon_0 E_{\rm kin}}\cot\frac{\theta}{2}\cdot\frac{Z_\alpha Z_{\rm tg}e^2}{8\pi\varepsilon_0 E_{\rm kin}}\cdot\frac{1}{2\sin^2\frac{\theta}{2}}d\theta \\ &= n_{\rm tg}x\frac{Z_\alpha^2 Z_{\rm tg}^2 e^4}{64\pi\varepsilon_0^2 E_{\rm kin}^2}\cdot\frac{\cos\frac{\theta}{2}}{\sin^3\frac{\theta}{2}}d\theta \ ,\end{aligned} \tag{1.8}$$

where we replaced the parameters b and db with the expressions (1.5) and (1.6). The solid angle of the cone can be expressed by,

$$d\Omega = 2\pi\sin\theta d\theta = 4\pi\sin\tfrac{\theta}{2}\cos\tfrac{\theta}{2}d\theta \ . \tag{1.9}$$

Thus, the number dN of particles scattered to the solid angle $d\Omega$ remains,

$$\boxed{\frac{dN}{N} = n_{\rm tg}x\frac{Z_\alpha^2 Z_{\rm tg}^2 e^4}{256\pi^2\varepsilon_0^2 E_{\rm kin}^2}\cdot\frac{1}{\sin^4\frac{\theta}{2}}d\Omega} \ . \tag{1.10}$$

That is Rutherford's scattering formula. Often, the formula is expressed with the *differential* cross section $\frac{d\sigma}{d\Omega}$. We get,

$$\frac{dN}{N} = \frac{d\sigma}{\sigma} = n_{\rm tg}xd\sigma \ , \tag{1.11}$$

and therefore

$$\frac{d\sigma}{d\Omega} = \frac{dN}{Nn_{\rm tg}xd\Omega} = \left(\frac{Z_\alpha Z_{\rm tg}e^2}{4\pi\varepsilon_0\cdot 4E_{\rm kin}}\right)^2\frac{1}{\sin^4\frac{\theta}{2}} \ . \tag{1.12}$$

Here, we have to make some comments:

- The angle $\theta = 0$ is not defined, since there exists a minimum deflection angle $\theta_{\rm min}$. This angle is reached, when the α-particle moves at the distance $b = b_{\rm max}$ from the atom, that is, at the edge of the circular area of the cross section. For a greater collision parameter b, the α-particle traverses the field of the next neighboring atom, and the deflection angle increases again. We have:

$$\sigma = \frac{A}{N_{\rm tg}} = \pi b_{\rm max}^2 \qquad \text{and} \qquad \tfrac{\theta_{\rm min}}{2} \simeq \tan\tfrac{\theta_{\rm min}}{2} = \frac{Z_\alpha Z_{\rm tg}e^2}{8\pi\varepsilon_0 E_{\rm kin}\cdot b_{\rm max}} \ , \tag{1.13}$$

  simply by inverting the formula (1.5). For very large impact parameters, that is, when the α-particle passes the atom outside its electronic layer, the electrons of the atom shield the charge of the nucleus, an effect called *screening*.

- For very high energies, the distribution of the nuclear charge over a finite volume influences the scattering, calling for corrections in the Rutherford formula. Moreover, at short internuclear distances, nuclear forces appear additionally to the electromagnetic interaction.

- The integral over the probability distribution $P(\theta)d\theta$ is normalized,

$$\int_{\theta_{\min}}^{\pi} P(\theta)d\theta = 1 \ . \tag{1.14}$$

Similarly, we have for the surface integrals,

$$\int_{\theta \geqslant \theta_{\min}} \frac{d\sigma}{d\Omega} d\Omega = \sigma \ . \tag{1.15}$$

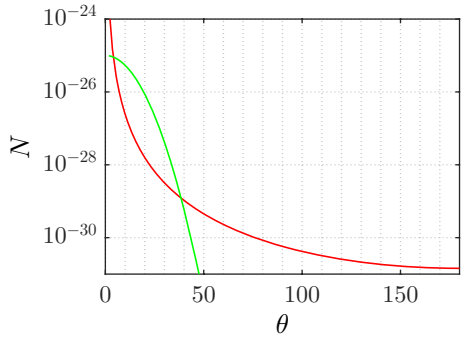

Figure 1.6: (code) Angular dependence of the cross-section corresponding to Thomson's (green) and Rutherford's (red) models.

Rutherford derived the formula (1.12) describing the scattering of α-particles within classical physics. A derivation from the laws governing quantum mechanics using the *Born approximation* shows that Rutherford's formula describes scattering correctly in first order, and that purely quantum effects present only minor corrections. We will review the Rutherford scattering in Excs. 1.1.6.1 and 1.1.6.2 and discuss the screening effect in Exc. 1.1.6.3.

1.1.3 Emission of radiation in the planetary model

The *planetary model* proposed by Rutherford suggests electrons spinning around a positively charged nucleus in circular orbits [2]. This motion of electrons should obey the laws of Maxwell's electrodynamic theory. Let us now calculate some consequences of this picture.

[2] This type of model had already been proposed by Jean Perrin in 1901 and by Hantaro Nagaoka in 1903, around the same time when Thompson developed his model. The planetary model was later on rescued by John William Nicholson in 1911.

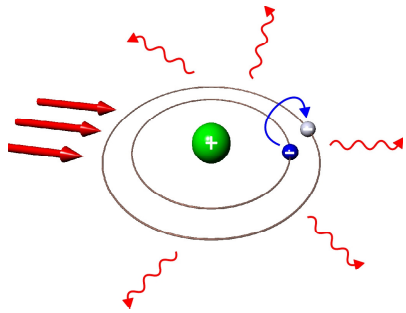

Figure 1.7: Light-induced transitions between orbits in the planetary model.

We now treat the atom as a rotor where the negative particle, the electron, orbits the positive particle. The dipole moment is,

$$p_0 = -er \ . \tag{1.16}$$

We calculate in the Exc. 1.1.6.4 the power emitted by the acceleration $a = \omega^2 r$ of the electron on its circular trajectory,

$$P = \frac{\mu_0 \omega^4 p_0^2}{12\pi c} \ . \tag{1.17}$$

The initial energy of the electron spinning around the nucleus (for a hydrogen atom $Z = 1$),

$$E = \frac{p^2}{2m_e} - \frac{e^2}{4\pi\varepsilon_0 r} = \frac{m_e \omega^2 r^2}{2} - \frac{e^2}{4\pi\varepsilon_0 r} \ , \tag{1.18}$$

is dissipated by radiation of the power (1.17), i.e.,

$$-P = \frac{dE}{dt} = m_e \omega^2 r \frac{dr}{dt} + \frac{e^2}{4\pi\varepsilon_0 r^2}\frac{dr}{dt} = 2m_e \omega^2 r \frac{dr}{dt} \ . \tag{1.19}$$

The latter equation supposes an equilibrium between the centrifugal force and the Coulomb force,

$$m_e \omega^2 r = \frac{e^2}{4\pi\varepsilon_0 r^2} \ , \tag{1.20}$$

allowing to link the revolution frequency ω to the instantaneous radius of the orbit $r(t)$. Resolving the Eq. (1.19) by $\dot{r}$ and replacing the power by the relation (1.17) and the frequency ω by the relation (1.20), we obtain,

$$\frac{dr}{dt} = -\frac{P}{2m_e \omega^2 r} = -\frac{\mu_0 \omega^2 e^2}{24\pi m_e c} r = -\frac{e^4}{96\pi^2 \varepsilon_0^2 m_e^2 c^3}\frac{1}{r^2} \ . \tag{1.21}$$

Integration of this equation gives,

$$t - t_0 = -\frac{32\pi^2 \varepsilon_0^2 m_e^2 c^3}{e^4}[r^3 - r^3(t_0)] \ . \tag{1.22}$$

Now inserting $t_0 = 0$ and assuming $r(t_0) = a_\mathrm{B}$, the time τ within which the loss of energy due to radiation emission decreases the radius of the electronic orbit to $r = 0$, is,

$$t = \tau = \frac{32\pi^2\varepsilon_0^2 m_e^2 c^3 a_\mathrm{B}^3}{e^4} \ . \tag{1.23}$$

Insertion of the numerical values gives the decay time $\tau \sim 10^{-10}\,\mathrm{s}$. This is the effect called *radiation collapse* of the classical atomic model.

1.1.4 Zeeman effect in the planetary model

The orbital motion of the electron generates a ring current $I = e/T = e\omega/2\pi$, which produces an *orbital magnetic moment* which, as shown in Exc. 1.1.6.5, can be calculated following the laws of electromagnetism,

$$\vec{\mu}_\ell = IA\hat{\mathbf{n}} = \frac{e\omega}{2\pi}\pi r^2\hat{\mathbf{n}} \ , \tag{1.24}$$

where $A = \pi r^2$ is the area of the trajectory. Introducing the angular momentum $\mathbf{L} = m_e\omega r^2\hat{\mathbf{n}}$ we get in vector notation,

$$\vec{\mu}_\ell = \frac{e}{2m_e}\mathbf{L} \ . \tag{1.25}$$

We now imagine this atom in the presence of a magnetic field $\vec{\mathcal{B}}$ oriented in the direction that we will call z. This results in a precession of the magnetic moment around the field (similar to the precession of a spinning top in the presence of a gravitational field) governed by the equation,

$$\frac{d\mathbf{L}}{dt} = \vec{\mu}_\ell \times \vec{\mathcal{B}} = \frac{e}{2m_e}\mathbf{L} \times \vec{\mathcal{B}} = -\mathbf{\Omega}_\mathrm{L} \times \mathbf{L} \ ,$$

with $\mathbf{\Omega}_\mathrm{L} = \frac{e}{2m_e}\vec{\mathcal{B}}$ representing the precession frequency and being called *Larmor frequency*. It is evident that the presence of the magnetic field considerably alters the state of the atom, even producing profound modifications in the frequency of the orbit of the electron ω_0 and therefore in the energetic state of the atom. This change is called *Zeeman effect*.

The Zeeman effect can be calculated by imagining that the field has an arbitrary direction with respect to $\mathbf{L}$. In this case, the equation describing the electronic motion as resulting from an equilibrium between the centrifugal force and the Coulomb force needs to be complemented by a Lorentz force,

$$m_e\ddot{\mathbf{r}} + m_e\omega_0^2\mathbf{r} = \mathbf{F}_\mathrm{L} = -e\mathbf{v} \times \vec{\mathcal{B}} \ . \tag{1.26}$$

where $m\ddot{\mathbf{r}}$ is the centrifugal force due to the circular motion of the electron and $m_e\omega_0^2\mathbf{r}$ the centripetal force due to the Coulomb attraction exerted by the nucleus. Assuming the direction of the magnetic field given by $\vec{\mathcal{B}} = \mathcal{B}\hat{\mathbf{e}}_z$ with $\mathcal{B} = 2m_e\Omega_\mathrm{L}/e$, the equations of motion can be decomposed into,

$$\begin{aligned} \ddot{x} + \omega_0^2 x + 2\Omega_\mathrm{L}\dot{y} &= 0 \\ \ddot{y} + \omega_0^2 y - 2\Omega_\mathrm{L}\dot{x} &= 0 \\ \ddot{z} + \omega_0^2 z &= 0 \ . \end{aligned} \tag{1.27}$$

The z-direction is not influenced. With the ansatz $x = ae^{\imath\omega t}$ and $y = be^{\imath\omega t}$ we obtain the system of equations,

$$\begin{aligned} a(\omega_0^2 - \omega^2) + 2\imath\Omega_{\mathrm{L}}\omega b = 0 \\ b(\omega_0^2 - \omega^2) - 2\imath\Omega_{\mathrm{L}}\omega a = 0 \ , \end{aligned} \tag{1.28}$$

which has a non-trivial solution for a and b only when the determinant of the coefficients of a and b vanishes:

$$0 = \begin{vmatrix} \omega_0^2 - \omega^2 & 2\imath\Omega_{\mathrm{L}}\omega \\ -2\imath\Omega_{\mathrm{L}}\omega & \omega_0^2 - \omega^2 \end{vmatrix} = \omega^4 - (2\omega_0^2 + 4\Omega_{\mathrm{L}}^2)\omega^2 + \omega_0^4 \ . \tag{1.29}$$

We get,

$$\omega = \omega_{1,2} = \sqrt{\omega_0^2 + 2\Omega_{\mathrm{L}}^2 \pm 2\Omega_{\mathrm{L}}\sqrt{\omega_0^2 + \Omega_{\mathrm{L}}^2}} = \omega_0 \pm \Omega_{\mathrm{L}} + \frac{1}{2}\frac{\Omega_{\mathrm{L}}^2}{\omega_0} + \dots \ , \tag{1.30}$$

or, as $\Omega_{\mathrm{L}} \ll \omega$, we get $\omega_{1,2} = \omega_0 \mp \Omega_{\mathrm{L}}$. The result is a splitting of the energy levels proportional to the magnetic field,

$$\Delta E = 2\hbar\Omega_{\mathrm{L}} = \frac{\hbar e}{m_e}\mathcal{B} = 2\mu_{\mathrm{B}}\mathcal{B} \ , \tag{1.31}$$

where the abbreviation $\mu_{\mathrm{B}} = e\hbar/2m_e \simeq 9.27 \cdot 10^{-24}\,\mathrm{JT}^{-1}$ is called the *magneton Bohr*.

Although the classical derivation shows quantitative deviations from experimental observations, it is quite interesting, as it illustrates several aspects which have a quantum mechanical equivalence.

Example 1 (*Stern-Gerlach experiment*): Among several historical experiments carried out to unravel the atomic structure, one of the most important is the experiment carried out by *Otto Stern* and *Walther Gerlach* in 1922 to measure the magnetic moment of atoms. The results of this experiment once again demonstrated the need for new concepts to explain the observations.
Using Bohr's quantization rule, $L = n\hbar$, within the formula (1.25) we get,

$$\vec{\mu} = -\mu_{\mathrm{B}}\frac{\mathbf{L}}{\hbar} \ .$$

In the presence of a magnetic field the dipole undergoes an interaction $W = -\vec{\mu}\cdot\vec{\mathcal{B}}$, and therefore a feels a force,

$$\mathbf{F} = -\vec{\mu}\cdot\nabla\vec{\mathcal{B}} \ .$$

By subjecting beams of atoms to the gradient of a magnetic field and detecting this force, Stern and Gerlach were able to measure the magnetic moment produced by the rotation of the electrons around the atomic nuclei.

1.1.5 Bohr's theory and its limitations

The classical model of the planetary atom provides a mechanical illustration of the microscopic world but fails to quantitatively explain experimental observations such as the discrete nature of atomic spectra.

The radiation emitted by hydrogen atoms is characterized by discrete, spectrally very thin lines. The observed lines are grouped in series named after Lyman, Ballmer and others,

$$\frac{1}{\lambda} = R_{\rm H}\frac{\mu}{m_e}\left(\frac{1}{m^2} - \frac{1}{n^2}\right) \ , \tag{1.32}$$

where m and n are integers. $R_{\rm H} = (1/4\pi\epsilon)^2(m_e e^4/4\pi\hbar^3 c)$ is the Rydberg constant and $\mu = m_e m_{\rm at}/(m_e + m_{\rm at})$ the reduced mass.

The discrete nature of spectral lines and the problem of the radiation collapse led *Niels Bohr* to formulate the following *postulates*:

1. There are specific stationary orbits, where electrons do not emit energy.

2. Each emission or absorption of radiation energy by electrons comes with a transition between stationary orbits. The radiation emitted during this transition is homogeneous.

3. The laws of mechanics can describe the dynamic equilibrium of electrons in stationary states, but fails to describe the transition of electrons *between* stationary orbits.

Thus, Bohr's model predicts the quantization of energy levels, known as *first quantization* of quantum mechanics. The radii of the possible orbits can be calculated from the postulate that the orbital angular momentum be quantized in units of $\hbar$, that is, the electrons form stationary de Broglie waves along the orbits [3]. We discuss Bohr's model in Excs. 1.1.6.6 and 1.1.6.7.

In the picture proposed by Bohr, the radiative decay happens as an abrupt transition of an electron between an outer (more energetic) orbit and an inner (less energetic) orbit. Since the energies of stationary orbits are very well defined, the emitted radiation is mono-energetic, i.e., the spectrum consists of discrete characteristic lines.

We note here that the picture of an abrupt transition of electrons between discrete states, called the *quantum jump*, did not receive Schrödinger's blessing. He rather imagined for electrons, within his theory of quantum wave mechanics, wave-shaped orbitals instead of planetary trajectories, thus avoiding the problem of radiation due to charge deceleration and the quantum jump concept. According to him, during a transition between electronic orbits, the energy is transformed into radiation *gradually* [4].

1.1.6 Exercises

1.1.6.1 Ex: Analysis of Rutherford scattering

a. What conclusions can be drawn from the observation that Rutherford's formula describes well the scattering of charged particles traveling through matter over a wide

[3] A generalization of Bohr's theory was provided by *Arnold Johannes Wilhelm Sommerfeld*. Assuming elliptical orbits for the electrons he managed to explain some features of the fine structure, provided the motion of the electron was treated relativistically. The basic premises were 1. stable orbits when the Coulomb attraction is balanced by the centrifugal force, 2. quantization of phase space $\int r_q dq = n_q\hbar$, and 3. quantization of angular momentum $\int L d\theta = n_\theta\hbar$.

[4] We note here, that quantum jumps were observed much later!

range of parameters?
b. Why do we see a deviation from Rutherford's formula for large energies?
c. The scattering of protons with energy E crossing a thin film of thorium is well described up to energies of $E = 4.3\,\mathrm{MeV}$ by Rutherford's formula. Estimate for this case the range of nuclear forces.
d. For small scattering angles θ we observe large deviations from Rutherford's formula. Explain why?
e. Assume the thorium atoms of item (c) to form a periodic crystal with the lattice constant $d = 10a_\mathrm{B}$. At which minimum angle θ Rutherford's formula loses its validity.

1.1.6.2 Ex: Rutherford scattering

a. A beam of α-particles with energy $E_\mathrm{kin} = 3\,\mathrm{MeV}$ and flux $I = 5\cdot10^3\,\mathrm{s}^{-1}$ impinges on a thick gold film $x = 1\,\mu\mathrm{m}$. Using Rutherford's formula, calculate how many particles are scattered in $\Delta t = 10\,\mathrm{minutes}$ in the range of angles $10° \leq \theta \leq 30°$.
b. Now, the gold film is replaced with an aluminum film of the same thickness. How many α-particles are scattered under equal circumstances?

1.1.6.3 Ex: Screening of electrons

Consider thin layer of charge $-Z_\mathrm{tg}e$ with radius R. This screening causes a scattering angle,

$$\tan\tfrac{\theta}{2} = \frac{D}{2b}\frac{\sqrt{1-(b/R)^2}}{1+D/2R}\ ,$$

with $D \equiv \frac{3Ze^2}{m_2v^2/2}$ for $b < R$. Verify how the screening changes the differential cross section $\frac{d\sigma}{d\Omega}$.

1.1.6.4 Ex: Radiation of an oscillating dipole

Calculate the angular distribution of the power radiated by an oscillating electric or magnetic dipole from expressions for the emitted electric and magnetic fields found in literature.

1.1.6.5 Ex: Magnetic moments

a. Derive from the expression $\vec{\mu}_L = \frac{1}{2}\int_{\mathbb{R}^3}\mathbf{r}\times\mathbf{j}(\mathbf{r}')d^3r'$ of classical electrodynamics and an appropriate parametrization of the current density $\mathbf{j}$ the relation between the magnetic dipole moment $\vec{\mu}$ due to the orbiting electron and the angular momentum $\mathbf{L}$.
b. The length of the angular momentum vector being given by $|\mathbf{L}| = \hbar$, calculate the magnetic moment for an electron and for a proton.

1.1.6.6 Ex: Bohr's atom

In 1913, Niels Bohr presented his atomic model adapting Rutherford's model to the quantization ideas proposed by Max Planck.
a. Impose the quantization rule for the angular momentum ($L = n\hbar$) of an electron

orbiting an atom of atomic number Z to find an expression for the radii of the allowed orbits.
b. According to Bohr's model, the transition between different orbits is accompanied by the emission (or absorption) of a photon. Determine the energy of a photon emitted during a transition between the first excited state and the ground state of a hydrogen atom.
c. Consider an electron trapped in an infinite one-dimensional box potential of width a. Determine an expression for the electronic energy levels.
d. What should be the width a of this potential, in terms of the Bohr radius, so to ensure that a photon emitted during a transition between the first excited state and the ground state equals that obtained in item (b)?

1.1.6.7 Ex: The hydrogen atom

The hydrogen atom can be seen as a point-like proton and an electron distributed over space with charge density $\rho = Ae^{-2r/a_B}$ around the proton that is in the center. Here, A is a constant and r is the distance from the center.
a. Calculate A considering the fact that the atom is electrically neutral.
b. Calculate the amplitude of the electric field at a radius $r = a_B$.

1.2 The discovery of the photon

The concept of the nature of light has a variable history. Newton proposed around ~ 1650 a corpuscular model to explain Snellius' law on the refraction of a light beam penetrating a crystal. Around the same time Huygens found a wave-based interpretation. The two models predicted different speeds of light within the dense medium. Newton found, that the speed of light is greater in the medium than outside, while Huygens found the opposite [5]. In the late 1800's the wave nature of light was established through observations of interference effects confirming Huygens' hypothesis. However, some observations made were incompatible with this simplistic ideas, for example, the spectrum of blackbody radiation, the Compton effect, the specific heat of the solid, the radiation pressure, and the photoelectric effect. All these observations are readily understood by assuming a corpuscular nature of the light [6].

Nowadays, knowing the theory of quantum mechanics, we are aware that both ideas have their range of validity and that the electromagnetic radiation is dual: In general, propagation and interference effects are best described by waves. However, when interacting with matter, light tends to localize into small energy packets that we call *photons*.

1.2.1 Radiation in a conductive cavity

In the age of lasers a classical treatment of the emission and absorption of light may seem an atavism. However, even with coherent and monochromatic radiation

[5] Note that until today there remain doubts about the correct value of the momentum of light in dielectric media [584].

[6] The corpuscular hypothesis is now called the second quantization of quantum theory or quantization of the electromagnetic field.

sources, the most commonly used physical picture is that of a classical optical field interacting with an atom or a molecule whose energetic structure is treated quantum mechanically. And even the atomic or molecular dipole is often treated like a classical oscillator. The exposition of such a dipole to simple boundary conditions prepares the analogous development of a quantum oscillator and provides a direct path to quantization of the radiation field.

Even if we rarely do experiments by throwing light into a small hole in a metallic box, the electromagnetic fields obtained by solving Maxwell's equation are particularly simple for boundary conditions, where the fields disappear on the inner surfaces of the box. Before discussing the physics of radiation in a perfectly conducting cavity, we have to introduce some basic relations between electromagnetic amplitudes, stored energy, and intensity.

The electric field of a plane wave oscillating with frequency ω and propagating through vacuum in the direction of propagation defined by the *wave vector*,

$$\mathbf{k} = \frac{2\pi}{\lambda}\hat{\mathbf{k}} \,, \tag{1.33}$$

can be written,

$$\vec{\mathcal{E}} = \vec{\mathcal{E}}_0 e^{\imath(\mathbf{k}\cdot\mathbf{r}-\omega t)} \,, \tag{1.34}$$

where $\vec{\mathcal{E}}_0 = \mathcal{E}_0\hat{\mathbf{e}}$ consists of an amplitude $\mathcal{E}_0$ and a polarization $\hat{\mathbf{e}}$. Since the field $\vec{\mathcal{E}}_0$ is transverse to the direction of propagation, the polarization has two components perpendicular to $\mathbf{k}$. The magnetic induction field associated with the wave is,

$$\mathcal{B}_0 = \tfrac{1}{c}\mathcal{E}_0 \,. \tag{1.35}$$

For a propagating wave $\vec{\mathcal{E}}$ and $\vec{\mathcal{B}}$ are in phase, while for a standing wave they are out of phase.

For a given cavity mode we can express the standing wave in this mode as,

$$\vec{\mathcal{E}} = \vec{\mathcal{E}}_0(\mathbf{r})e^{-\imath\omega t} \,. \tag{1.36}$$

The energy of the electromagnetic field of a standing wave, averaged over one oscillation of the frequency ω is,

$$\bar{U} = \frac{1}{2}\int\left(\frac{\varepsilon_0}{2}|\vec{\mathcal{E}}|^2 + \frac{1}{2\mu_0}|\vec{\mathcal{B}}|^2\right)dV \,. \tag{1.37}$$

Now, the *energy density* of the oscillating electromagnetic field is given by,

$$\boxed{\bar{u} = \frac{d\bar{U}}{dV} = \frac{1}{4}\left(\varepsilon_0|\vec{\mathcal{E}}|^2 + \frac{1}{\mu_0}|\vec{\mathcal{B}}|^2\right)} \,. \tag{1.38}$$

From the equation (1.35) we can see that the contributions of the electric and magnetic fields are equal. Therefore,

$$\bar{U} = \tfrac{1}{2}\int \varepsilon_0|\vec{\mathcal{E}}|^2 dV \qquad \text{and} \qquad \bar{u} = \tfrac{1}{2}\varepsilon_0|\vec{\mathcal{E}}|^2 \,. \tag{1.39}$$

Another important quantity is the *flux of electromagnetic energy* through a surface. The *Poynting vector* describing this flux is defined by,

$$\mathbf{I} = \tfrac{1}{\mu_0}\vec{\mathcal{E}} \times \vec{\mathcal{B}} \; . \tag{1.40}$$

Again using the equation (1.35), we find the value averaged over a time period,

$$\boxed{\bar{I} = \tfrac{1}{2}\varepsilon_0 c|\vec{\mathcal{E}}|^2} \; . \tag{1.41}$$

This quantity, called *intensity*, describes the fact that the flux is a density of energy multiplied with the velocity of propagation in vacuum,

$$\bar{u}c = \tfrac{1}{2}\varepsilon_0 c|\vec{\mathcal{E}}|^2 = \bar{I} \; . \tag{1.42}$$

The intensity can also be written,

$$\bar{I} = \frac{1}{2}\sqrt{\frac{\varepsilon_0}{\mu_0}}|\vec{\mathcal{E}}|^2 \; . \tag{1.43}$$

where the factor $\sqrt{\mu_0/\varepsilon_0}$ is called *impedance of free space*, because it has the unit of a resistance and the last equation has the same form as the power dissipated in a resistor,

$$W = \frac{1}{2}\frac{V^2}{R} \; . \tag{1.44}$$

1.2.2 Black body radiation

We now want to calculate the energy density inside the cavity before using the result to describe the interaction between light and a sample of two-level atoms located inside the cavity. The basic idea is to say that the electrons inside the conducting surface of the cavity oscillate because of thermal motion. The oscillation generates a dipolar radiation leading to stationary waves developing within the cavity. As the walls of the cavity are conducting, the electric field $\vec{\mathcal{E}}$ must disappear inside the wall and on its surfaces. The task is now twofold: first count the number of possible standing waves, which satisfy the boundary conditions as a function of frequency; second, determine the energy for each wave and then calculate the spectral distribution of the energy within the cavity.

The equations describing the radiated energy in free space are,

$$\nabla^2\vec{\mathcal{E}} = \frac{1}{c^2}\frac{\partial^2\vec{\mathcal{E}}}{\partial t^2} \qquad \text{and} \qquad \nabla\cdot\vec{\mathcal{E}} = 0 \; . \tag{1.45}$$

The stationary waves solutions separate into terms oscillating in time and in space. Now, respecting the boundary conditions for a three-dimensional box of length L, we have for the components of $\vec{\mathcal{E}}$ [7],

$$\begin{aligned}\vec{\mathcal{E}}(\mathbf{r},t) = e^{-\imath\omega t}[&\hat{\mathbf{e}}_x \cos(k_x x)\sin(k_y y)\sin(k_z z) \\ &+\hat{\mathbf{e}}_y \sin(k_x x)\cos(k_y y)\sin(k_z z) \\ &+\hat{\mathbf{e}}_z \sin(k_x x)\sin(k_y y)\cos(k_z z)] \; ,\end{aligned} \tag{1.46}$$

[7] See script on *Electrodynamics: Electricity, Magnetism and Radiation* (2025).

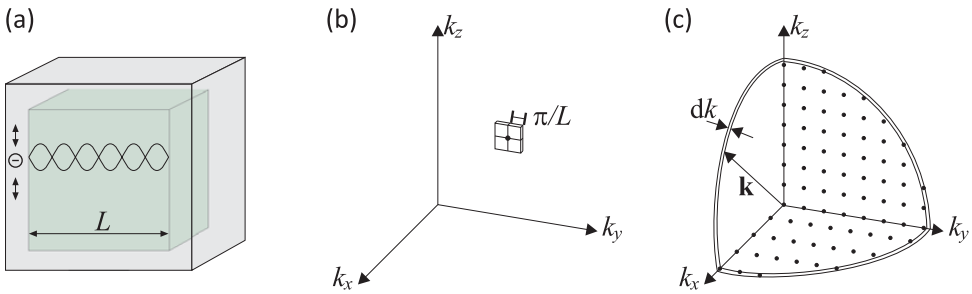

Figure 1.8: (a) Cavity in position space showing the thermal motion of the electrons inside the walls. (b and c) Density-of-states in a cavity in momentum space.

with the components,

$$k_x = \frac{\pi n_x}{L} \qquad \text{for} \qquad n_x = 0, 1, 2, ... \tag{1.47}$$

and similar for k_y and k_z. Note, that for each component $\mathcal{E}_{x,y,z}$ the transverse amplitudes disappear in 0 and L. By inserting this solution into Helmholtz's equation (1.45), we obtain,

$$k_x^2 + k_y^2 + k_z^2 = \frac{\omega^2}{c^2} \ . \tag{1.48}$$

The states $k_{x,y,z}$ (enumerated by integer numbers $n_{x,y,z}$) form a three-dimensional orthogonal lattice of points in space $\mathbf{k}$ separated by a distance along the axes k_x, k_y, k_z of $\frac{\pi}{L}$, as shown in Fig. 1.8. In principle, the number of states that can be placed within a sphere of radius k in the momentum space is,

$$N = \int_{\text{sphere}} dn_x dn_y dn_z \ . \tag{1.49}$$

However, the periodic boundary conditions for $|\mathbf{k}|$ limit the components k_x, k_y, k_z to positive values ($n \geq 0$), that is, the volume under consideration is limited to an octant. On the other hand, we must multiply the number of states by two because of the degeneracy of polarizations. Hence,

$$4N = \int_0^n 4\pi n^2 dn = \left(\frac{L}{\pi}\right)^3 \int_0^k 4\pi k^2 dk = \frac{4L^3}{\pi^2}\frac{k^3}{3} = \frac{4L^3\omega^3}{3\pi^2 c^3} \ . \tag{1.50}$$

With this, we obtain the *mode density*,

$$\frac{N}{L^3} = \frac{\omega^3}{3\pi^2 c^3} \ . \tag{1.51}$$

The *spectral density of modes* ϱ can be given in several units,

$$\int \varrho(n) dn = \int \varrho(k) dk = \int \varrho(\omega) d\omega = \frac{N}{L^3} \ , \tag{1.52}$$

such that,

$$\boxed{\varrho(n) = \frac{\pi n^2}{L^3} \qquad \text{or} \qquad \varrho(k) = \frac{k^2}{\pi^2} \qquad \text{or} \qquad \varrho(\omega) = \frac{\omega^2}{\pi^2 c^3}} \ . \tag{1.53}$$

The density of oscillating modes within the cavity grows like the square of the frequency. Now, the mean energy per mode in a sample of oscillators in thermal equilibrium is, following the equipartition law, equal to,

$$\bar{E} = k_{\mathrm{B}} T \ , \tag{1.54}$$

where k_{B} is the Boltzmann constant. We conclude that the *spectral energy density* $u_{\mathrm{RJ}}(\omega)$ in the cavity is,

$$\boxed{u_{\mathrm{RJ}}(\omega)d\omega = k_{\mathrm{B}} T \varrho(\omega) d\omega = k_{\mathrm{B}} T \frac{\omega^2}{\pi^2 c^3} d\omega} \ . \tag{1.55}$$

This law is known as the *Rayleigh-Jeans law* of *black-body radiation*. As seen in Fig. 1.9, this law suggests the physically impossible fact, called *ultraviolet catastrophe*, that the energy storage in the cavity grows without limits like the square of frequency.

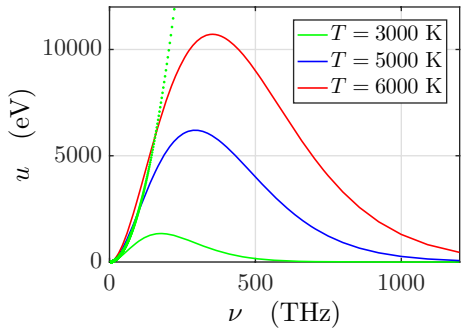

Figure 1.9: (code) Spectral energy density following Rayleigh-Jeans' and Planck's laws.

1.2.3 Planck's distribution of modes

We obtained the result (1.54) by multiplying the number of modes with the mean energy per mode. As there is no doubt about our method of counting the modes, the problem with the ultraviolet catastrophe can only root in the use of the equipartition principle for assigning energy to the oscillators.

Planck's idea to solve this problem was to first consider the probability distribution for exciting the modes (thermal states) for a sample of oscillators in thermal equilibrium at temperature T. This probability distribution p comes from mechanical statistics and can be written in terms of the *Boltzmann factor*, $e^{-E_n/k_{\mathrm{B}}T}$, and the partition function $q = \sum_{n=0}^{\infty} e^{-E_n/k_{\mathrm{B}}T}$ as,

$$p_n = \frac{e^{-E_n/k_{\mathrm{B}}T}}{q} \ . \tag{1.56}$$

Now Planck hypothesized that the energy be quantized, that is, it must be assigned in discrete portions, proportional to the frequency, such that,

$$\boxed{E_n = n\hbar\omega} \ , \tag{1.57}$$

where $n = 0, 1, 2, ..$ and the proportionality constant $\hbar$ is called *Planck's constant*. With the abbreviation $Z \equiv e^{-\hbar\omega/k_B T}$ and using the rule $\sum_{n=0}^{\infty} Z^n = (1-Z)^{-1}$, we find the average number,

$$\bar{n} = \sum_n n p_n = (1-Z)\sum_n n Z^n = (1-Z)Z\frac{\partial}{\partial Z}\sum_n Z^n = \frac{Z}{1-Z} = \frac{1}{e^{\hbar\omega/k_B T}-1} \ . \tag{1.58}$$

The probability of occupancy of state n is,

$$p_n = (1-Z)Z^n = \frac{\bar{n}^n}{(1+\bar{n})^{1+n}} \ , \tag{1.59}$$

and the average energy is,

$$\bar{E} = \sum_n E_n p_n = \sum_n n\hbar\omega e^{-n\hbar\omega/k_B T} = \frac{\hbar\omega}{e^{\hbar\omega/k_B T}-1} \ , \tag{1.60}$$

in contrast to the initial assumption (1.55).

Finally, we obtain Planck's expression for the energy density inside the cavity by replacing the energy (1.60) for the factor $k_B T$ in Rayleigh-Jeans' law (1.55),

$$\boxed{u_P(\omega)d\omega = \bar{E}\varrho(\omega)d\omega = \frac{\omega^2}{\pi^2 c^3}\frac{\hbar\omega}{e^{\hbar\omega/k_B T}-1}d\omega} \ . \tag{1.61}$$

This result, drawn in Fig. 1.9, is much more satisfactory, because now the energy density has an upper bound, and it coincides with the results of experiments. For high temperatures or low excitation energies, $\hbar\omega \ll k_B T$, Planck's distribution converges to that of Rayleigh-Jeans', $u_P(\omega) \to u_{RJ}(\omega)$.

Note, that the form of the expression for the energy depends on the parametrization and must be derived respecting $u(\omega)d\omega = u(\lambda)d\lambda$, etc.. Often the blackbody radiation is expressed in terms of the *spectral radiance*,

$$L(\omega) \equiv \frac{c}{4\pi}u(\omega) \ , \tag{1.62}$$

which can be understood as the (isotropic) energy flux into all directions of space. Solve the Excs. 1.2.9.1 to 1.2.9.7.

1.2.4 The corpuscular nature of the photon

1.2.4.1 The photoelectric effect

Light incident on a metallic surface can expel electrons. For this to occur, the light must have a *minimum frequency*. If the frequency is below this value, there is no point in increasing the light intensity: the electrons won't be expelled. The main experimental observations are: 1. Electrons are ejected without apparent delay, i.e. it is not necessary (and it doesn't help) to accumulate a certain amount of energy. 2. Higher light intensities increase the number of electrons, but not their kinetic energy after expulsion. 3. Red light does not eject electrons, even at high intensities. 4. Weak ultraviolet light only ejects few electrons, but with high kinetic energy.

These observations challenge the classical electromagnetic model according to which the Lorentz acceleration of the electrons should be proportional to the field *amplitude*. The observations were explained by Einstein's theory of the *photoelectric effect*, which assumes the light to be quantized (unlike Planck, who preferred to quantize the process of light absorption),

$$E = h\nu \ . \tag{1.63}$$

Assuming a fixed exit work A for the extraction of an electron, we can measure the constant $\hbar$:

$$h\nu = A + \tfrac{mv^2}{2} = A + eV \qquad \rightarrow \qquad h = \frac{eV}{\nu - \nu_{\mathrm{g}}} \ . \tag{1.64}$$

The energy of the fastest electrons is measured through the decelerating voltage by varying ν and I. We will discuss the photoelectric effect quantitatively later in the Exc. 5.4.5.7.

1.2.4.2 Bremsstrahlung and the Franck-Hertz experiment

Bremsstrahlung is, in a way, the inverse process of the photoelectric effect. Here, electrons are accelerated toward a cathode. Finding a target they are rapidly decelerated, a process in which they emit a continuous spectrum of X-rays (in addition to characteristic lines attributed to electronic transitions in the target atoms). For any given kinetic energy the spectra have a red threshold corresponding to photons that receive the entire energy of the electron.

In the *Franck-Hertz experiment* free electrons produced in a plasma are accelerated by a strong electric field. Having traveled a sufficiently long distance they have acquired enough kinetic energy to excite electronic transitions in the atoms of the plasma. When an excitation occurs, the electron suddenly loses all its energy and must be accelerated again, starting from rest, before it can excite another atom.

1.2.4.3 Radiative pressure and Compton scattering

When light is scattered from a particle, it transfers momentum to it called *photonic recoil*. This effect, known as *radiation pressure*, occurs for example in *Compton scattering*.

X-rays scattered by the electrons of a carbon target are red-shifted by an amount, which increases with the scattering angle. This is the *Compton effect*. The data are understood assuming a corpuscular nature of light and applying the laws of conservation of energy and momentum to the collision processes between photons and electrons. The scattered photon sees its energy reduced and therefore its wavelength increased.

In a material where there are free electrons, this effect will occur at all photon energies. In other materials, it is only observed with high energy photons. For high energy photons, exceeding the atomic binding energy, the electrons can be considered free such that, in the scattering process, the photon is able to eject the electron from its atom. The photon receives the remaining energy and is deviated, such that the overall momentum of the system is conserved. The loss of energy for the photon results in a spectral shift to the red during its passage through the material.

Photons of visible light, on the other hand, do not have enough energy to eject bound electrons. In this case, the mass in the Compton formula must be replaced by the atomic mass, such that the spectral displacement becomes much smaller. This limit, which involves bound electrons, is that of Thomson and Rayleigh scattering.

The relevance of this effect lies in the fact that it shows that light exhibits properties commonly attributed to corpuscles, since Thomson's scattering model, based on the classical theory of charged particles accelerated by electromagnetic fields, can not explain any spectral shift.

1.2.5 Einstein's transitions rates

Bohr's atom model explained for the first, time how light interacts with matter: Atoms have discrete excitation levels, and they absorb and emit discrete energy packets $\hbar\omega$. Unfortunately, Bohr's model can not predict transition rates. Here, Einstein helped out by developing a useful theory (see Fig. 1.10).

Figure 1.10: Bohr model and Einstein rate diagram.

We consider a two-level atom or a sample of atoms within a conducting cavity. We have N_1 atoms in the lower energy state E_1 and N_2 in the upper state E_2. Light interacts with these atoms through stimulated resonant absorption and emission. The rates, $B_{12}u(\omega)$ and $B_{21}u(\omega)$ are proportional to the energy spectral density $u(\omega)$ of the cavity modes. The central idea of Einstein is to postulate that atoms in the higher state can emit light spontaneously at a rate A_{21}, which depends only on the density of modes of the cavity, i.e. the volume of the cavity, but not the energy of the field of radiation. With the Einstein coefficients we can formulate valid rate equations in situations, where the spectral distribution of the radiation is wider than the spectral width of the atomic transition and where the spectral distribution of the light flux from the source, $\bar{I}(\omega)$, is weak compared to the saturation intensity of the atomic transition. Even if modern light sources generally have very narrow and intense spectral emission bands, Einstein's coefficients are often used in the spectroscopic literature to characterize the light-matter interaction with atoms and molecules.

The Einstein rate equations describe the energy flux between atoms and the optical modes of the cavity,

$$\begin{aligned} \frac{dN_1}{dt} = -\frac{dN_2}{dt} &= -R_{1\to 2} + R_{2\to 1} + \mathcal{S}_{2\to 1} \\ &= -N_1 B_{12} u(\omega) + N_2 B_{21} u(\omega) + N_2 A_{21} \ . \end{aligned} \tag{1.65}$$

$R_{1\to 2}$ is the *absorption rate*, $R_{2\to 1}$ the *stimulated emission rate* and $\mathcal{S}_{2\to 1}$ the *spontaneous emission rate*. The assumption of a third type of transition, called spontaneous

emission, is necessary, if $B_{12} = B_{21}$ but $N_1 > N_2$ in thermal equilibrium. In thermal equilibrium we have the condition of stationarity, $\frac{dN_1}{dt} = -\frac{dN_2}{dt} = 0$ for a given energy density value $u(\omega) = u_{th}(\omega)$, such that,

$$u_{th}(\omega) = \frac{A_{21}}{\left(\frac{N_1}{N_2}\right) B_{12} - B_{21}} \ . \tag{1.66}$$

The *Boltzmann distribution law* controlling the distribution of the number of atoms in the lower and upper states is given by,

$$\frac{N_1}{N_2} = \frac{g_1}{g_2} e^{-(E_1 - E_2)/k_{\rm B}T} \ , \tag{1.67}$$

where $g_{1,2}$ are the degeneracies of the lower and upper states and $E_2 - E_1 = \hbar\omega_0$. We find,

$$u_{th}(\omega) = \frac{A_{21}}{\frac{g_1}{g_2} e^{\hbar\omega_0/k_{\rm B}T} B_{12} - B_{21}} \ . \tag{1.68}$$

But this result must be consistent with Planck's distribution (1.61). Therefore, by comparing this equation with the equation (1.68), it must be that,

$$\frac{g_1}{g_2}\frac{B_{12}}{B_{21}} = 1 \ . \tag{1.69}$$

and also,

$$\frac{A_{21}}{B_{21}} = \frac{\hbar\omega_0^3}{\pi^2 c^3} \ . \tag{1.70}$$

This equation shows that, once we know one of the three transition rates, we can always calculate the others.

It is useful to compare the rate A_{21} with B_{21} from the equation (1.68) inserting the equation (1.69),

$$\frac{A_{21}}{B_{21} u_{th}(\omega)} = e^{\hbar\omega_0/k_{\rm B}T} - 1 \ . \tag{1.71}$$

This expression shows that, when $E_2 - E_1 \gg k_{\rm B}T$, that is, for optical, UV, or X-ray frequencies, spontaneous emission dominates. But in low-frequency regimes, that is, IR, microwave, or radio waves, stimulated emission is more important. Note that even when stimulated emission dominates, spontaneous emission is always present and plays an important role, for example, in processes ultimately limiting the emission bandwidth of lasers.

1.2.6 Absorption spectrum for a single atom

Every light source has a certain spectral width. Conventional light sources, such as incandescent bulbs or plasmas have relatively broad emission bands compared to atomic or molecular absorbers, at least when the latter ones are studied in dilute gases. Even when we use pure spectral sources, such as a laser tuned to the peak of a resonance, the transition line always exhibits an intrinsic width associated with the interruption of the phase evolution of the excited state. Phase interruptions such

as spontaneous or stimulated emission and collisions are common examples of line broadening mechanisms. The emission or absorption of radiation occurs within a frequency distribution centered about $\omega_0 \equiv \omega_2 - \omega_1$, and we must account for this spectral distribution in our calculation of the energy transfer.

On the other hand, as we will see in Sec. 16.1.3 and Sec. 16.4.1, spontaneous decay at a rate Γ of the excited level causes a finite linewidth for the atomic transition. Consequently, even perfectly monochromatic light will be absorbed according to a probability distribution given by the spectral absorption profile of the atomic transition. This profile is called the frequency-dependent *optical cross section* and reads [8],

$$\boxed{\sigma(\omega) = \frac{g_2}{g_1}\lambda^2 \frac{\Gamma}{2\pi} \frac{\frac{1}{4}\Gamma}{(\omega-\omega_0)^2 + \frac{1}{4}\Gamma^2} = \frac{g_2}{g_1}\lambda^2 \frac{\Gamma}{4}\mathcal{L}_\Gamma(\omega-\omega_0)\ ,} \tag{1.72}$$

where we defined the Lorentzian profile as,

$$\mathcal{L}_\beta(\Delta) \equiv \frac{\beta}{2\pi}\frac{1}{\Delta^2 + (\beta/2)^2} \qquad \text{with} \qquad \int_{-\infty}^{\infty} \mathcal{L}_\beta(\Delta)d\Delta = 1\ . \tag{1.73}$$

The total power P absorbed by a two-level atom with resonance frequency ω_0 from a radiation field with the spectral intensity distribution $I(\omega)$ and with the total intensity of the laser beam $\bar{I} = \int I(\omega)d\omega$ can now be expressed as the integral,

$$\boxed{P = \int \sigma(\omega) I(\omega) d\omega}\ , \tag{1.74}$$

Example 2 (*Limiting cases*): Let us analyze the two limiting cases when either one of the spectral distributions $I(\omega)$ or $\sigma(\omega)$ is much narrower than the other.

For a *narrow laser*, we may assume a δ-peaked spectral intensity distribution,

$$I(\omega) = \bar{I}\delta(\omega - \omega_{\rm las})\ . \tag{1.75}$$

When it drives a *broad transition* described by an optical cross section given by (1.72), the scattered power is,

$$P = \bar{I}\sigma(\omega_{\rm las})\ . \tag{1.76}$$

For a *narrow transition*, we may substitute the Lorentzian in (1.72) by a Dirac δ-function,

$$\sigma(\omega) \overset{\Gamma\to 0}{\longrightarrow} \frac{g_2}{g_1}\lambda^2\frac{\Gamma}{4}\delta(\Delta)\ . \tag{1.77}$$

When it is driven by a *broad laser*, for which we assume a spectral intensity distribution,

$$I(\omega) = \bar{I}\mathcal{L}_\beta(\omega-\omega_{\rm las}) \qquad \text{with} \qquad \bar{I} = \int I(\omega)d\omega = \frac{I(\omega_{\rm las})}{\mathcal{L}_\beta(0)} = \frac{\pi\beta}{2} I(\omega_{\rm las}) \tag{1.78}$$

we obtain for the scattered power,

$$P = \int \frac{g_2}{g_1}\lambda^2\frac{\Gamma}{4}\delta(\omega-\omega_0)\bar{I}\mathcal{L}_\beta(\omega-\omega_{\rm las})d\omega = \frac{g_2}{g_1}\lambda^2\frac{\Gamma}{4}\bar{I}\mathcal{L}_\beta(\omega_0-\omega_{\rm las})\ . \tag{1.79}$$

[8] At low saturation.

1.2.6.1 Broad laser driving a broad transition

Until now we assumed a fixed laser frequency $\omega_{\rm las}$ (with finite emission bandwidth) driving a fixed resonance frequency ω_0. What we call *absorption spectrum* is what we obtain when we tune either the laser frequency or when we (somehow) vary the resonance frequency, such that $\Delta \equiv \omega_{\rm las} - \omega_0$ is ramped. Assuming Lorentzian profiles with finite linewidths for both, $\bar{I}$ and σ, we get,

$$P(\Delta) = P(\omega_{\rm las} - \omega_0) = \int \sigma(\omega) I(\omega) d\omega = \int \frac{g_2}{g_1} \frac{\lambda^2 \Gamma}{4} \mathcal{L}_\Gamma(\omega - \omega_{\rm las}) \bar{I} \mathcal{L}_\beta(\omega - \omega_0) d\omega$$
$$= \frac{g_2}{g_1} \frac{\lambda^2 \Gamma}{4} \bar{I} \int \mathcal{L}_\Gamma(\omega' + \omega_0 - \omega_{\rm las}) \mathcal{L}_\beta(\omega') d\omega' \ . \tag{1.80}$$

That is, the absorption spectrum is obtained as a convolution of both profiles,

$$\boxed{P(\Delta) = \frac{g_2}{g_1} \frac{\lambda^2 \Gamma \bar{I}}{4} (\mathcal{L}_\Gamma \star \mathcal{L}_\beta)(\Delta)} \ . \tag{1.81}$$

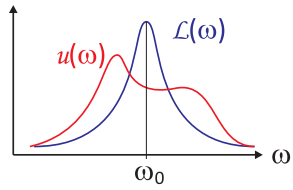

Figure 1.11: Absorption spectrum (blue) and spectral energy distribution of the source (red).

This result reproduces the two limiting cases discussed in the above example, since for narrow transitions, $\Gamma \to 0$, that is $\mathcal{L}_\Gamma \to \delta$, we recover the results (1.79), and for narrow lasers, $\beta \to 0$, that is, $\mathcal{L}_\beta \to \delta$, we recover (1.76). Obviously, this formula holds for other line profiles e.g. when the resonance is broadened by some perturbations [9].

1.2.6.2 Two-level atom in a blackbody radiation field

When considering a two-level atom interacting with a blackbody a radiation field, we describe the spectral intensity distribution by (1.61),

$$I(\omega) = \frac{\omega^2}{\pi^2 c^2} \frac{\hbar\omega}{e^{\hbar\omega/k_{\rm B}T} - 1} \tag{1.82}$$
$$\text{with} \qquad \bar{I} = \int I(\omega) d\omega = \frac{\hbar}{\pi^2 c^2} \left(\frac{k_{\rm B}T}{\hbar}\right)^4 \int_0^\infty \frac{x^3 dx}{e^x - 1} = \frac{\pi^2}{15 c^2 \hbar^3} (k_{\rm B}T)^4 \ .$$

[9] Let us here remind the following identities holding for Lorentzian and Gaussian line profiles:

$$(\mathcal{L}_\gamma \star \mathcal{L}_\beta)(\Delta) = \mathcal{L}_{\gamma+\beta}(\Delta) \qquad \text{and} \qquad (\mathcal{G}_\Gamma \star \mathcal{G}_\beta)(\Delta) = \mathcal{G}_{\sqrt{\gamma^2+\beta^2}}(\Delta) \ .$$

Since the width of the transition is negligibly small in comparison with the blackbody spectrum, $\Gamma \to 0$, we may evaluate the scattered power as,

$$P = \int \frac{g_2}{g_1}\frac{\lambda^2\Gamma}{4}\mathcal{L}_\Gamma(\omega-\omega_0)\frac{\omega^2}{\pi^2c^2}\frac{\hbar\omega}{e^{\hbar\omega/k_BT}-1}d\omega \tag{1.83}$$
$$\overset{\Gamma\to 0}{\longrightarrow} \frac{g_2}{g_1}\frac{\lambda^2\Gamma}{4}\frac{\omega_0^2}{\pi^2c^2}\frac{\hbar\omega_0}{e^{\hbar\omega_0/k_BT}-1} .$$

1.2.7 Absorption in a gas

We are often interested in the attenuation of the intensity of a beam of light traversing a dilute gas of resonant scattering atoms. The Einstein rate equation yields the *temporal* transition rates, but does not say how they relate to the *spatial* attenuation length of the light beam. Let us now generalize the previous results to a gas of two-level atoms. As long as the transition linewidth is narrow [case (1.77)], the power is removed from the system only by spontaneous emission; absorption only converts radiation into atomic excitation which, subsequently, can be returned to the radiation field by stimulated emission. At steady-state the Einstein rate equation (1.65) reads,

$$0 = -N_1B_{12}u(\omega_0) + N_2B_{21}u(\omega_0) + N_2A_{21} . \tag{1.84}$$

Using the result (1.69), we can write the amount of power removed from the system by spontaneous emission as,

$$P = N_2A_{21}\hbar\omega_0 = u(\omega_0)B_{12}(N_1 - \tfrac{g_1}{g_2}N_2)\hbar\omega_0 . \tag{1.85}$$

The second part of the equation describes the energy loss of the beam, i.e. the difference between energy removed by absorption and energy returned to the beam by stimulated emission.

On the other hand, the power absorbed from the radiation field $u(\omega_0)$ by atoms whose transition is described by the cross section (1.72), is given by,

$$P = \int (N_1 - \tfrac{g_1}{g_2}N_2)\sigma(\omega)I(\omega)d\omega . \tag{1.86}$$

Remembering $I(\omega) = cu(\omega)$ and assuming a *large radiation spectrum*, $I(\omega) \simeq I(\omega_0)$, a comparison of equations (1.85) and (1.86) yields,

$$\boxed{B_{12} = \frac{c}{\hbar\omega_0}\int \sigma(\omega)d\omega} . \tag{1.87}$$

1.2.7.1 Lambert-Beer law

In the expression (1.86) the absorption probability distribution $\sigma(\omega)$ is convoluted with the spectral energy distribution of the light source, $u(\omega) = d\bar{u}/d\omega$, which in turn is related to the energy *density* via, $\bar{U} = V\bar{u}$, where V is the mode volume of the light field. Considering a thin slab of the absorber with volume ΔV, we have $d\bar{U} = \Delta V d\bar{u}$. Assuming that the light propagates in z-direction across the absorber and converting the time dependence into a spatial dependence, we have on one hand,

$$P = -\frac{d\bar{U}}{dt} = -\frac{d\bar{u}}{dt}\Delta V = -c\frac{d\bar{u}}{dz}\Delta V = -\frac{d\bar{I}}{dz}\Delta V . \tag{1.88}$$

On the other hand, assuming that the light field be a *laser with narrow emission bandwidth*, $I(\omega) = \bar{I}\delta(\omega - \omega_{\rm las})$, we get from (1.86),

$$P = \int (N_1 - \tfrac{g_1}{g_2} N_2)\sigma(\omega) I(\omega) d\omega = \bar{I}(N_1 - \tfrac{g_1}{g_2} N_2)\sigma(\omega_{\rm las}) \ , \tag{1.89}$$

Now comparing both results,

$$\frac{d\bar{I}}{\bar{I}} = -\frac{N_1 - \frac{g_1}{g_2} N_2}{\Delta V}\sigma(\omega_{\rm las}) dz \simeq -n\sigma(\omega_{\rm las}) dz \ , \tag{1.90}$$

where the approximation holds for low saturation, that it, if $N_1 \gg N_2$. The solution of this differential equation is,

$$\boxed{\bar{I} = \bar{I}_0 e^{-\sigma(\omega_{\rm las}) n z}} \ . \tag{1.91}$$

Here, z is the total distance, over which absorption takes place. The last equation is the *Lambert-Beer law* for light absorption. It is very useful for measuring atomic densities in gas cells or of atomic beams [560, 530, 859]. Solve the Excs. 1.2.9.9 to 1.2.9.11.

1.2.8 Saturation

Strong driving of a transition leads to its saturation and causes line broadening. To see this, we go back to Einstein's rate equations in steady-state (1.65) additionally simplified by assuming $g_1 = 1 = g_2$, such that $B_{12} = B_{21}$. Resolving these equations by N_1 and N_2 and using $N_1 + N_2 = N$ and $N_1 - N_2 \equiv \Delta N$, we get,

$$N_1 = N\frac{B_{21}u(\omega) + A_{21}}{2B_{21}u(\omega) + A_{21}} \qquad \text{and} \qquad N_2 = N\frac{B_{12}u(\omega)}{2B_{21}u(\omega) + A_{21}} \ . \tag{1.92}$$

For vanishing pump rate we expect, $N_1 \overset{u\to 0}{\longrightarrow} N$ and $N_2 \overset{u\to 0}{\longrightarrow} 0$. In contrast, when the pump rate becomes much larger than the relaxation rates, $N_1, N_2 \overset{u\to\infty}{\longrightarrow} \frac{1}{2}$. This means that the absorption coefficient $\alpha = \sigma(N_1 - N_2)$ goes to zero, and the medium becomes completely transparent. The difference in the populations of the ground and excited states,

$$\Delta N = N\frac{A_{21}}{2B_{21}u(\omega) + A_{21}} = \frac{N}{1 + s(\omega)} \ , \tag{1.93}$$

can be expressed via a *saturation parameter*

$$s(\omega) \equiv \frac{2B_{12}u(\omega)}{A_{21}} \ , \tag{1.94}$$

which represents the ratio of pump rate to the relaxation rate. The pump rate due to a monochromatic wave with intensity $\bar{I}$ is obtained by comparing (1.85) with (1.89),

$$B_{12}u(\omega) = \frac{\sigma(\omega)\bar{I}}{\hbar\omega} \ . \tag{1.95}$$

We obtain for the saturation parameter,

$$s(\omega) = \frac{2\sigma(\omega)\bar{I}}{\hbar\omega A_{21}} \ . \tag{1.96}$$

According to (1.85) and (1.93) the power absorbed per unit volume on the transition by atoms with the populations $N_{1,2}$ in a radiation field with a broad spectral profile and spectral energy density $u(\omega)$ is,

$$P = \hbar\omega B_{12} u(\omega) \Delta N = \hbar\omega B_{12} u(\omega) \frac{N}{1 + s(\omega)} \ . \tag{1.97}$$

With (1.94) this can be written as,

$$P = \hbar\omega \frac{A_{21}}{2} \frac{N}{1 + s(\omega)^{-1}} \ . \tag{1.98}$$

Let us now remember that the absorption cross section (1.72) of a homogeneously broadened line is Lorentzian. This means that the saturation parameter (1.96) itself becomes Lorentzian. We can assume that the relaxation rate A_{21} is independent of ω within the frequency range of the line profile,

$$\boxed{s(\omega) = s(\omega_0) \frac{(\Gamma/2)^2}{\Delta^2 + (\Gamma/2)^2}} \ . \tag{1.99}$$

Substituting this into (1.98) yields the frequency dependence of the absorbed radiation power per unit frequency interval $d\omega$,

$$P = \hbar\omega \frac{A_{21} N}{2} \frac{s(\omega_0)(\Gamma/2)^2}{(\omega - \omega_0)^2 + (\Gamma/2)^2 [1 + s(\omega_0)]} = N \bar{I} \sigma(\omega_0) \frac{(\Gamma/2)^2}{\Delta^2 + (\gamma_{\rm sat}/2)^2} \ , \tag{1.100}$$

where we introduced the increased halfwidth of the Lorentzian profile,

$$\boxed{\gamma_{\rm sat} \equiv \Gamma \sqrt{1 + s(\omega_0)}} \ . \tag{1.101}$$

Apparently, the halfwidth of the saturation-broadened line increases with the resonant saturation parameter $s(\omega_0)$. If according to (1.94) the induced transition rate at resonance equals the total relaxation rate $A_{21}/2$, the resonant saturation parameter becomes $s(\omega_0) = 1$, which increases the linewidth by a factor $\sqrt{2}$, compared to the unsaturated linewidth Γ for weak radiation fields. Starting from (1.100) we can define a *saturated* absorption cross section,

$$\boxed{\sigma_{\rm sat}(\omega) = \sigma_{\rm sat}(\omega_0) \frac{(\gamma_{\rm sat}/2)^2}{\Delta^2 + (\gamma_{\rm sat}/2)^2} = \sigma(\omega_0) \frac{(\Gamma/2)^2}{\Delta^2 + (\gamma_{\rm sat}/2)^2} = \sigma(\omega) \frac{1}{1 + s(\omega)}} \ , \tag{1.102}$$

where the unsaturated absorption profile is,

$$\sigma(\omega) = \sigma(\omega_0) \frac{(\Gamma/2)^2}{\Delta^2 + (\Gamma/2)^2} \ . \tag{1.103}$$

This shows that the saturation decreases the absorption coefficient by the factor $1 + s(\omega)$. At the line center, this factor has its maximum value $1 + s(\omega_0)$, while it decreases to 1 for increasing $|\Delta|$, see (1.101), see Fig. 1.12. This is the reason why the line broadens.

From (1.96) we see, that unity saturation, $s(\omega_0) = 1$, corresponds to a light intensity of,

$$\bar{I}_{\text{sat}} \equiv \frac{\hbar\omega}{2\sigma(\omega_0)}\Gamma = \frac{2\pi^2 c\hbar}{3\lambda^3}\Gamma \ . \tag{1.104}$$

This intensity is called *saturation intensity*. Taking account of the degeneracies g_j of the levels the saturation intensity becomes [10],

$$\boxed{I_{\text{sat}} = \frac{g_1}{g_2}\frac{2\pi^2 c\hbar}{3\lambda_0^3}\Gamma} \ . \tag{1.105}$$

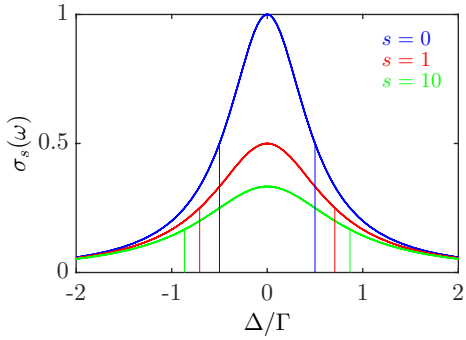

Figure 1.12: (code) Optical cross section for absorption at various saturation parameters. The reduction of absorption is understood by considerable depletion of the ground state at the profit of the excited state, $N_1, N_2 \overset{s\to\infty}{\longrightarrow} \frac{1}{2}$, in which case absorption is totally compensated by stimulated emission.

Finally, we anticipate that the resonant saturation parameter is basically a measure for the ratio between the stimulated population transfer rate, given by a quantity called *Rabi frequency* Ω, which will be thoroughly introduced in Secs. 5.4.3 and 16.3.2, and the spontaneous decay rate Γ,

$$s(\omega_0) = \frac{2\Omega^2}{\Gamma^2} \ . \tag{1.106}$$

We thus obtain the important relationship between laser intensity and Rabi frequency,

$$\boxed{\Omega^2 = \sigma(\omega_0)\frac{\bar{I}}{\hbar\omega_0}\Gamma} \ . \tag{1.107}$$

1.2.9 Exercises

1.2.9.1 Ex: Resistance of vacuum

Show that $\sqrt{\mu_0/\varepsilon_0}$ has the dimension of a resistance and the value of $376.7\,\Omega$.

[10] Some authors define the saturation for $s = 2$, as happens when $\Omega = \Gamma$.

1.2.9.2 Ex: The laws of Planck and Rayleigh-Jeans

Show that Planck's law reproduces the Rayleigh-Jeans law in the low-frequency limit.

1.2.9.3 Ex: The laws of Wien and Stefan-Boltzmann

a. Derive the parametrization of Planck's law in terms of frequency ν and wavelength λ.
b. Derive the law of *Stefan-Boltzmann* according to which the total power radiated per unit surface area of a black body across all wavelengths (also known as the blackbody radiant emittance) is given by σT^4, where $\sigma \equiv \pi^2 k_B^4/60c^2\hbar^3$ is called the Stefan-Boltzmann constant.
c. Derive *Wien's displacement law* according to which the maximum emission of a blackbody spectrum occurs at $\lambda_{max}T = 2.898\times10^{-3}\,\mathrm{Km}$ in the wavelength parametrization and $\nu_{max}/T = 0.0588\,\mathrm{THz/K}$ in the frequency parametrization. Determine the frequency of the maximum emission for the 2.7 K background radiation of the universe.

1.2.9.4 Ex: Radiometric thermometry

Modern radiometric thermometers measure the blackbody radiation emitted by a hot body. Calculate the variation of the blackbody radiant emittance of a person having fever (40° instead of 37° body temperature). How much does the maximum emission wavelength change? In which spectral range should the thermometer be sensitive?

1.2.9.5 Ex: Photons in a resonator

a. The light power emitted by a laser ($\lambda = 633\,\mathrm{nm}$) be $P = 1\,\mathrm{nW}$. How many photons does the laser emit per second? How many photons of the emitted laser beam are in a mode volume of $L = 10\,\mathrm{cm}$ length?
b. How many photons on average are inside an optical cavity having the same mode volume at ambient temperature, when there is no incident light?

1.2.9.6 Ex: Number of modes in a cavity

a. How many modes do fit into a cubical box of 10 cm size for a frequency interval of 1000 Hz centered at a wavelength of 500 nm?
b. How many photons are in the box supposing it has a temperature of $T = 300\,\mathrm{K}$, respectively, $T = 6000\,\mathrm{K}$?

1.2.9.7 Ex: Number of photons emitted from lasers and blackbodies

a. Calculate the total number of photons per area per unit time emitted by a blackbody at temperature T.
b. The linewidth of a helium-neon laser is $\Delta\nu = 1000\,\mathrm{Hz}$. The operating wavelength is $\lambda = 632.8\,\mathrm{nm}$, the power is $P = 1\,\mathrm{mW}$, and the beam size $w_0 = 1\,\mathrm{mm}$. How many photons are emitted per second?

c. What would be the temperature of a blackbody radiator emitting the same number of photons from an equal area and over the same frequency interval as the laser?

1.2.9.8 Ex: Number of photons per radiation mode

Assume the isotropic emission of a pulsed flashlamp with spectral bandwidth $\Delta\lambda = 100\,\text{nm}$ around $\lambda = 400\,\text{nm}$ amounts to $P_0 = 100\,\text{W}$ peak power out of a volume of $1\,\text{cm}^3$. Calculate the spectral power density $u(\nu)$ and the spectral intensity $I(\nu)$ through a spherical surface $r = 2\,\text{cm}$ away from the center of the emitting sphere. How many photons per mode are contained in the radiation field?

1.2.9.9 Ex: Atoms in an optical cavity

a. Consider a closed optical cavity at $T = 600°\,\text{C}$. The cavity has the shape of a $L = 1\,\text{m}$-long and $d = 3\,\text{cm}$-diameter tube. Calculate the total energy of the blackbody radiation inside the cavity.
b. Inside the cavity there is a gas with strontium atoms (1 fundamental level and 3 degenerate excited levels, $\lambda = 461\,\text{nm}$). Using the expression (1.67), assuming thermal equilibrium, calculate the number of excited atoms for a partial pressure of the strontium gas of $10^{-3}\,\text{mbar}$.
c. Calculate the optical density for a laser in resonance with the transition traversing the cavity along the symmetry axis.

1.2.9.10 Ex: Sodium atoms in an optical cavity

A sodium atom is placed in a cavity of volume $V = 1\,\text{cm}^3$ with walls at the temperature T, producing a thermal radiation field with spectral energy density $u_P(\nu)$. At what temperature T are the spontaneous and induced transition probabilities equal
a. for the transition $3P \to 3S$ with the transition wavelength $\lambda = 589\,\text{nm}$ and the excited state lifetime $\tau_{3P} = 16\,\text{ns}$;
b. for the hyperfine transition $3S$ $(F = 3 \to F = 2)$ with the transition frequency $\nu = 1772\,\text{MHz}$ and the excited state lifetime $\tau_{3F} \simeq 1\,\text{s}$?

1.2.9.11 Ex: Applying the Lambert-Beer law

The beam of a monochromatic laser passes through an absorbing atomic vapor with path length $L = 5\,\text{cm}$. If the laser frequency is tuned to the center of an absorbing transition $|i\rangle \to |k\rangle$ with absorption cross section $\sigma_0 = 10^{-14}\,\text{cm}^2$, the attenuation of the transmitted intensity is 10%. Assuming low saturation calculate the atomic density n_i in the absorbing level $|i\rangle$.

1.3 Basic notions

As we have seen in the precedent section, the important message of quantum mechanics is that matter propagates as a wave and light, when localized, only changes its energy in discrete units. Once we understand (or at least accept) this fact, a large part of quantum mechanics follows just as a corollary. The idea expressed by de Brogie, that matter would be a wave led to the first quantization. Interestingly, the concept

of light underwent a reverse evolution. Classically described as a wave, it was divided by Planck and Einstein into quantized corpuscles, today called 'photons'.

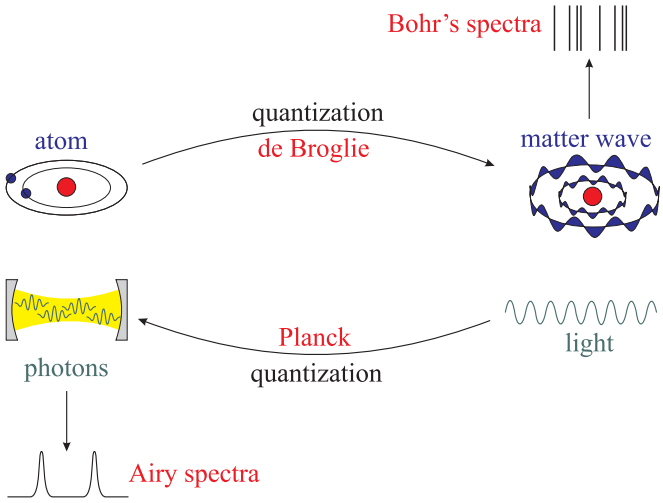

Figure 1.13: Illustration of particle-wave duality for matter and light.

In this chapter, we will introduce step by step the formalism of quantum mechanics by gradually increasing the degree of abstraction. Applications of the formalism will be shown in consecutive chapters (watch talk).

The aim of this section is to give 'feeling' for the new concepts introduced and used by quantum mechanics. We will first motivate the fundamental quantum equations of motion by linking them to classical dispersion relations and then spend some time to discuss the probabilistic concept proposed by Max Born.

1.3.1 Dispersion relation and Schrödinger equation

A fundamental problem in physics is the issue of the propagation of physical entities. On one hand, we have the light, whose propagation in the vacuum is described by the dispersion relation $\omega = ck$ or,

$$\omega^2 - c^2k^2 = 0 \ . \tag{1.108}$$

Since light is a wave, in the most general form, assuming the validity of the superposition principle, it can be described by a wave packet, $A(\mathbf{r},t) = \int e^{\imath(\mathbf{k}\cdot\mathbf{r}-\omega t)}a(\mathbf{k})d^3k$. It is easy to verify that the *wave equation*,

$$\frac{\partial^2}{\partial t^2}A - c^2\nabla^2 A = 0 \ , \tag{1.109}$$

reproduces the dispersion relation.

On the other hand, we have slow massive particles possessing kinetic energy,

$$E = \frac{p^2}{2m} \ . \tag{1.110}$$

With the hypothesis of de Broglie that even a massive particle has wave quality, we can try an *ansatz* [11] of a wave equation satisfying the dispersion relation (1.110). From Planck's formula, $E = \hbar\omega$, and the formula of *Louis de Broglie*, $\mathbf{p} = \hbar\mathbf{k}$, describing the particle by a wave packet $\psi(\mathbf{r},t) = \int e^{\imath(\mathbf{k}\cdot\mathbf{r}-\omega t)}\varphi(\mathbf{k})d^3k$ not subject to external forces, it is easy to verify that the equation,

$$\imath\hbar\frac{\partial}{\partial t}\psi = \left(-\frac{\hbar^2}{2m}\nabla^2\right)\psi \ , \tag{1.111}$$

reproduces the dispersion relation. If the particle is subject to a potential, its total energy is $E = \mathbf{p}^2/2m + V(\mathbf{r},t)$. This dispersion relation corresponds to the famous *Schrödinger equation*,

$$\imath\hbar\frac{\partial}{\partial t}\psi = \left(-\frac{\hbar^2}{2m}\nabla^2 + V(\mathbf{r},t)\right)\psi \ . \tag{1.112}$$

1.3.2 Relativistic particle waves

Despite the similarities between light particles and material particles, there are notable differences: The photon is a relativistic particle with no rest mass. How can we establish a relationship between such different objects?

To clarify this relationship we now consider particles that are similar to light in the sense that they have high velocities, that is, relativistic particles. From the relativistic principle of the equivalence of mass and energy, we obtain for a massive particle $E^2 = m^2c^4 + c^2p^2$ or,

$$\omega^2 - c^2k^2 = \frac{m^2c^4}{\hbar^2} \ . \tag{1.113}$$

This dispersion relation can be obtained from the differential equation,

$$\frac{\partial^2}{\partial t^2}A - c^2\nabla^2 A = -\frac{m^2c^4}{\hbar^2}A \ , \tag{1.114}$$

inserting, for example, the already proposed wave packet $A(\mathbf{r},t) = \int e^{\imath(\mathbf{k}\cdot\mathbf{r}-\omega t)}a(\mathbf{k})d^3k$, supposed not to be subject to external forces. The equation (1.114) is a wave equation called *Klein-Gordon equation*. For particles without rest mass, as in the case of photons, the equation is reduced to the wave equation of light (1.109).

Now, making the transition to non-relativistic velocities, $v \ll c$, we can expand the dispersion relation,

$$E = \sqrt{m^2c^4 + c^2m^2v^2} = mc^2\left(1 + \frac{v^2}{2c^2} + ..\right) \qquad \text{or} \qquad \hbar\omega \simeq mc^2 + \frac{\hbar^2k^2}{2m} \ . \tag{1.115}$$

In analogy with the Klein-Gordon equation we can derive the approximate dispersion relation (1.115) from a wave equation,

$$\imath\hbar\frac{\partial}{\partial t}A = \left(mc^2 - \frac{\hbar^2}{2m}\nabla^2\right)A \ . \tag{1.116}$$

[11] Trial, working hypothesis.

With the transformation $\psi = e^{-\imath mc^2 t/\hbar} A$, we rediscover the Schrödinger equation (1.111),

$$\imath\hbar \frac{\partial}{\partial t}\psi = -\frac{\hbar^2}{2m}\nabla^2\psi \tag{1.117}$$

as the non-relativistic limit of the Klein-Gordon equation.

It is interesting to note that in all cases discussed, obviously the dispersion relations and the differential equations can be interconverted by the substitutions,

$$E \longrightarrow \imath\hbar\frac{\partial}{\partial t} \qquad \text{and} \qquad \mathbf{p} \longrightarrow -\imath\hbar\nabla \ . \tag{1.118}$$

We will discuss this later in the context of Ehrenfest's theorem in Secs. 1.3.6, 1.3.7, and 1.6.6.

Example 3 (*Demystifying Quantum Mechanics 1.0*): The essence of quantum mechanics can be boiled down to the particle-wave duality. That is the fact that the building blocks of matter must be considered as de Broglie waves. Once this fact is understood and assimilated, quantum mechanics loses much of its mystery. For example delocalization of an atom, that is, the fact that it can be at two locations at the same time irritates us only as long as we try to imagine it as an indivisible solid block. In contrast we are not surprised to encounter the same ocean wave or tsunami in different continents.

The misconception is already rooted in the statement that *a quantum particle can be simultaneously in two places*. What we really mean when we say a particle is delocalized is, that the way it is embedded in space-time (which is the frame in which we can (or cannot) attribute locations and velocities to it) resembles a wave, and that the way this wave evolves or propagates in space is wave-like and described by a Schrödinger equation. Note that position-velocity is just one property that a particle can have. Spin is another one, and the appropriate space in which a spin is embedded is not necessarily position space, but can be an abstract configuration space. An atom can have an internal structure, whose dynamics is totally independent of how the atom moves as a whole. Thus, a particle IS not a wave, but PROPAGATES like one in space-time. Still, its evolution will follow a Schrödinger-type equation.

At first the Schrödinger equation seems weird, because it is complex and thus rules the behavior of an unphysical quantity, the wave function. But we should keep in mind the Schrödinger equation is the non-relativistic approximation of the Klein-Gordon equation, which resembles much more a classical wave equation, and applies also to particles propagating at velocities nearly as fast as light. With regard to these facts, a terminology that suits much better the features of quantum mechanics is simply wave mechanics, how Schrödinger termed it. This terminology also has the advantage of avoiding confusion with light wave effects erroneously attributed to quantum mechanics, such as light tunneling which is totally understood within Maxwell's theory.

We must however be aware that the simple wave picture is not sufficient to understand all of quantum mechanics. As we will see in the next sections, it is necessary to complement wave mechanics with a measurement theory, and phenomena genuine to what today is called Quantum Mechanics 2.0, in particular, entanglement are difficult to understand in wave mechanics.

1.3.3 Born's interpretation

The first part of this script is devoted to *individual particles* or systems of distinguishable *massive particles*, and we will only turn our attention to *light* and *indistinguishable particles* when discussing the (second) *quantization of fields*.

According to our current conviction, the complete reality (neglecting relativistic effects) on any system is contained in the Schrödinger equation (1.112). That statement does not make us smarter without having to explain the meaning of the *wavefunction* ψ. In an attempt to marry the concepts of particles and waves, *Max Born* proposed in 1926 the interpretation of the quantity

$$\int_V |\psi(\mathbf{r},t)|^2 d^3r \tag{1.119}$$

as probability of finding the particle inside the volume V.

If $|\psi(\mathbf{r},t)|^2$ has the meaning of a *probability density* or *probability distribution*, the square of the wavefunction must be integrable,

$$\|\psi(\mathbf{r},t)\|^2 \equiv \int_{\mathbb{R}^3} |\psi(\mathbf{r},t)|^2 d^3r < \infty \ . \tag{1.120}$$

This allows us to proceed to a *normalization* of the wave function,

$$\tilde{\psi}(\mathbf{r},t) \equiv \frac{\psi(\mathbf{r},t)}{\sqrt{\int_{\mathbb{R}^3} |\psi(\mathbf{r},t)|^2 d^3r}} \ , \tag{1.121}$$

such that $\|\tilde{\psi}(\mathbf{r},t)\| = 1$.

1.3.4 Continuity equation

In quantum mechanics we associate the wavefunction that describes a quantum system to a *probability wave*. As the Schrödinger equation describes a time evolution, in order to be useful, the wavefunction must allow for probability flows. We define the probability density and the probability flow by,

$$\rho(\mathbf{r},t) \equiv \psi^*(\mathbf{r},t)\psi(\mathbf{r},t) \ , \tag{1.122}$$

$$\mathbf{j}(\mathbf{r},t) \equiv \frac{\hbar}{2m\imath} \left[\psi^*(\mathbf{r},t)\nabla\psi(\mathbf{r},t) - \psi(\mathbf{r},t)\nabla\psi^*(\mathbf{r},t)\right] \ .$$

Starting from the Schrödinger equation we can easily derive the *continuity equation* (see Exc. 1.3.8.1),

$$\dot{\rho}(\mathbf{r},t) + \nabla\cdot\mathbf{j}(\mathbf{r},t) = 0 \ , \tag{1.123}$$

or in the integral form,

$$-\frac{d}{dt}\int_V \rho d^3r = \int_V \nabla\cdot\mathbf{j} d^3r = \oint_{\partial V} \mathbf{j}\cdot d\mathbf{S} \ , \tag{1.124}$$

using Gauß' law. With $I \equiv \int_S \mathbf{j}\cdot d\mathbf{S}$, the *probability current* which flows through the surface S delimiting the *probability charge* $Q \equiv \int_V \rho(\mathbf{r},t)d^3r$, we obtain,

$$-\dot{Q} = I \ . \tag{1.125}$$

The continuity equation is obviously similar to that of electromagnetism.

1.3.5 Distributions in space and time

So far we only spoke of spatial distributions, $\psi(\mathbf{r},t)$. But we could also consider velocity or moment distributions. In classical mechanics, a particle has a well-defined position and velocity. Knowing the position and velocity, Newton's equations allow predicting its coordinates at future times. Let us now investigate whether the Schrödinger equation allows this as well.

In the absence of an external potential the most general solution of the Schrödinger equation can be written as a superposition of plane waves $e^{\imath(\mathbf{r}\cdot\mathbf{k}-\omega t)}$ with frequencies $\omega = \mathbf{p}^2/2\hbar m$ and wave vectors $\mathbf{k} = \mathbf{p}/\hbar$. Each plane wave has an individual amplitude $\varphi(\mathbf{p})$, such that,

$$\psi(\mathbf{r},t) = \tfrac{1}{h^{3/2}} \int d^3p \varphi(\mathbf{p}) e^{\imath(\mathbf{r}\cdot\mathbf{k}-\omega t)} = \int d^3p \tfrac{1}{h^{3/2}} \varphi(\mathbf{p}) e^{\imath(\mathbf{r}\cdot\mathbf{p}/\hbar - \mathbf{p}^2 t/2m\hbar)} \ , \qquad (1.126)$$

with $h \equiv 2\pi\hbar$. At time $t = 0$, this expansion is nothing more than a Fourier transform,

$$\psi(\mathbf{r},0) = \tfrac{1}{h^{3/2}} \int d^3p \varphi(\mathbf{p}) e^{\imath\mathbf{r}\cdot\mathbf{k}} \ , \qquad (1.127)$$

that we can reverse,

$$\varphi(\mathbf{p}) = \tfrac{1}{h^{3/2}} \int d^3r \psi(\mathbf{r},0) e^{-\imath\mathbf{r}\cdot\mathbf{k}} \ . \qquad (1.128)$$

In the absence of forces the momentum distribution becomes stationary. We can now use the momentum distribution $\varphi(\mathbf{p})$ as coefficients of the expansion of the temporal wavefunction $\psi(\mathbf{r},t)$, as shown above. Thus, the expansion represents a general solution of the Schrödinger equation. The magnitude $|\varphi(\mathbf{p})|^2$ is the probability density in *momentum space*.

Example 4 (*Normalization of the wave function in momentum space*): It is easy to show that the probability density in momentum space is also normalized:

$$\begin{aligned}
\int |\varphi(\mathbf{p})|^2 d^3p &= \tfrac{1}{h^3} \int d^3p \int d^3r \psi^*(\mathbf{r}) e^{\imath\mathbf{r}\cdot\mathbf{k}} \int d^3r' \psi(\mathbf{r}') e^{-\imath\mathbf{r}'\cdot\mathbf{k}} \\
&= \int d^3r \int d^3r' \psi^*(\mathbf{r}) \psi(\mathbf{r}') \tfrac{1}{(2\pi)^3} \int d^3k e^{\imath\mathbf{k}\cdot(\mathbf{r}-\mathbf{r}')} \\
&= \int d^3r \int d^3r' \psi^*(\mathbf{r}) \psi(\mathbf{r}') \delta^3(\mathbf{r}-\mathbf{r}') = \int |\psi(\mathbf{r})|^2 d^3r = 1 \ ,
\end{aligned}$$

knowing that the Fourier transform of a plane wave is nothing more than the Dirac distribution.

Since the probability distributions $|\psi(\mathbf{r})|^2$ and $|\varphi(\mathbf{p})|^2$ are interconnected by Fourier transform, we already know that we can not localize [12] both simultaneously. If one is well localized, the other is necessarily delocalized. Do the Exc. 1.3.8.2.

[12] Localize: Restrict the distribution volume indefinitely.

1.3.6 Eigenvalues

We have already seen that the position and momentum distributions of a particle are spread. We calculate the mean values of these distributions, denoted by $\langle \mathbf{r} \rangle$ and $\langle \mathbf{p} \rangle$, as *first moments* of the respective distributions:

$$\langle \mathbf{r} \rangle = \int d^3r |\psi(\mathbf{r},t)|^2 \mathbf{r} \qquad \text{and} \qquad \langle \mathbf{p} \rangle = \int d^3p |\varphi(\mathbf{p},t)|^2 \mathbf{p} \ . \tag{1.129}$$

Using the expansions (1.126) and (1.127), we can calculate,

$$\begin{aligned} \langle \mathbf{p} \rangle = \int \varphi^*(\mathbf{p}) \mathbf{p} \varphi(\mathbf{p}) d^3p &= \int \tfrac{1}{h^{3/2}} \int \psi^*(\mathbf{r}) e^{\imath \mathbf{k}\cdot\mathbf{r}} d^3r \mathbf{p} \varphi(\mathbf{p}) d^3p \\ &= \tfrac{1}{h^{3/2}} \int \psi^*(\mathbf{r}) \int \varphi(\mathbf{p}) \mathbf{p} e^{\imath \mathbf{k}\cdot\mathbf{r}} d^3p d^3r \\ &= \tfrac{1}{h^{3/2}} \int \psi^*(\mathbf{r}) \tfrac{\hbar}{\imath} \nabla \int \varphi(\mathbf{p}) e^{\imath \mathbf{k}\cdot\mathbf{r}} d^3p d^3r = \int \psi^*(\mathbf{r}) \tfrac{\hbar}{\imath} \nabla \psi(\mathbf{r}) d^3r \ . \end{aligned}$$

This calculation shows that the expectation value, called *eigenvalue*, of the momentum can be expressed through an operator $\hat{p} \equiv (\hbar/\imath)\nabla$ acting on the wavefunction [13,14].

More generally, we can compute the eigenvalue of a function in $\mathbf{r}$ and $\mathbf{p}$ via,

$$\langle f(\hat{\mathbf{r}}, \hat{\mathbf{p}}) \rangle = \int d^3r \psi^*(\mathbf{r}) f(\mathbf{r}, \hat{\mathbf{p}}) \psi(\mathbf{r}) \ . \tag{1.130}$$

However, it is important to note that the operators $\hat{\mathbf{r}}$ and $\hat{\mathbf{p}}$ do not necessarily commute.

Example 5 (*Non-commutation of space and momentum*): Considering a one-dimensional motion, we verify,

$$\hat{p}_x x \psi = \frac{\hbar}{\imath} \frac{d}{dx} x\psi = \frac{\hbar}{\imath}\psi + x \frac{\hbar}{\imath} \frac{d}{dx}\psi \neq x \frac{\hbar}{\imath} \frac{d}{dx}\psi = x \hat{p}_x \psi \ .$$

1.3.7 Temporal evolution of eigenvalues

We now consider the temporal evolution of the position of a particle. We will use in the following the partial integration rule $\int_V \psi \nabla \xi = \oint_{\partial V} \psi\xi - \int_V \nabla\psi\xi = -\int_V (\nabla\psi)\xi$, assuming that at least one of the functions, ψ or ξ, disappears at the edge of the volume, which can be guaranteed by choosing the volume large enough. To begin with, we will concentrate on the x-component of the position, the time derivative of which is computed using the continuity equation (1.123),

$$\frac{d}{dt}\langle \hat{x} \rangle = \int d^3r \frac{d}{dt} |\psi|^2 x = -\int d^3r \ x \nabla \cdot \mathbf{j} = -\cancelto{0}{\int d\mathbf{S} \cdot \mathbf{j} x} + \int d^3r \ \mathbf{j} \cdot \nabla x = \int d^3r \ \mathbf{j}_x \ , \tag{1.131}$$

[13] From now on, the hat over a physical magnitude will denote quantum operators.

[14] We note here that the rules $\langle \psi | \hat{x} | \psi \rangle \leftrightarrow \langle \phi | - \frac{\hbar}{\imath} \nabla_p | \phi \rangle$ and $\langle \psi | \frac{\hbar}{\imath} \nabla_{\mathbf{r}} | \psi \rangle \leftrightarrow \langle \phi | \hat{p} | \phi \rangle$ from the Fourier transformation are useful for numerical simulations of the Schrödinger equation: Instead of calculating the spatial derivative $\left(\frac{\hbar}{\imath}\nabla\right)^2$ of the wavefunction, one makes a Fast Fourier Transform (FFT) to momentum space, multiplies with $\mathbf{p}$, and transforms back.

Generalizing to three dimensions, we can write,

$$\frac{d}{dt}\langle m\hat{\mathbf{r}}\rangle = m\int d^3r\ \mathbf{j} = m\int d^3r\frac{\hbar}{2mi}[\psi^*\nabla\psi - \psi\nabla\psi^*] \tag{1.132}$$
$$= \tfrac{1}{2}\int d^3r[\psi^*\hat{\mathbf{p}}\psi + \psi\hat{\mathbf{p}}\psi^*] = \int d^3r\psi^*\hat{\mathbf{p}}\psi = \langle\hat{\mathbf{p}}\rangle\ ,$$

since the eigenvalue of $\hat{\mathbf{p}}$ is a real quantity.

Now, we define the abbreviation:

$$\hat{H} \equiv -\frac{\hbar^2}{2m}\nabla^2 + V(\hat{\mathbf{r}},t)\ , \tag{1.133}$$

called the *Hamilton operator* or *Hamiltonian* and we calculate the second derivative of the position using the Schrödinger equation (1.112),

$$\frac{d}{dt}\langle\hat{\mathbf{p}}\rangle = \int d^3r\left[\left(\tfrac{1}{i\hbar}\hat{H}\psi\right)^*\hat{\mathbf{p}}\psi + \psi^*\hat{\mathbf{p}}\tfrac{1}{i\hbar}\hat{H}\psi\right] = \tfrac{i}{\hbar}\int d^3r\ \psi^*(\hat{H}\hat{\mathbf{p}} - \hat{\mathbf{p}}\hat{H})\psi = \tfrac{i}{\hbar}\langle[\hat{H},\hat{\mathbf{p}}]\rangle\ , \tag{1.134}$$

introducing the *commutator* $[\hat{a},\hat{b}] \equiv \hat{a}\hat{b} - \hat{b}\hat{a}$ as an abbreviation. After that,

$$\tfrac{i}{\hbar}\langle[\hat{H},\hat{\mathbf{p}}]\rangle = \tfrac{i}{\hbar}\langle[\hat{V},\hat{\mathbf{p}}]\rangle = \tfrac{i}{\hbar}\int d^3r\psi^*\left[\hat{V}\tfrac{\hbar}{i}\nabla\psi - \tfrac{\hbar}{i}\nabla(V\psi)\right] = -\int d^3r\psi^*\psi\nabla V = \langle\hat{\mathbf{F}}\rangle\ . \tag{1.135}$$

In summary, we found a law,

$$\langle\hat{\mathbf{F}}\rangle = \frac{d^2}{dt^2}\langle m\hat{\mathbf{r}}\rangle\ , \tag{1.136}$$

much like *Newton's law*, but instead of applying to localized particles, the law applies to the eigenvalues of probability distributions. Similar laws can be derived for angular momentum and energy conservation.

The observation made by *Paul Ehrenfest*, that in quantum mechanics the mean values follow the same laws of classical mechanics, is called *Ehrenfest theorem*.

1.3.8 Exercises

1.3.8.1 Ex: Conservation of probability

Demonstrate the conservation of local probability through the definitions of probability densities, $\rho(\mathbf{r},t)$, and probability current $\mathbf{j}(\mathbf{r},t)$.

1.3.8.2 Ex: Fourier theorem

The spatial distribution of a particle is given by a Gaussian function with the width Δx. Calculate the momentum distribution and its width Δp. Just consider one spatial dimension. Show that $\Delta x\Delta p = \hbar$ using the *rms* definition for the widths.

1.4 Postulates of quantum mechanics

In this section we will introduce the fundamentals and main methods of quantum mechanics. We will learn what are observables and get to know the postulates which establish the foundation of quantum mechanics, as well as Heisenberg's famous principle of uncertainty.

1.4.1 Superposition principle (1. postulate)

A physical system can be found in several states. For example, a particle may be at rest or in motion, an atom may be excited or deexcited. In quantum mechanics, every possible state is described by a *wavefunction* ψ. Wavefunctions can be functions of various types of coordinates, for example, of position $\psi = \psi(\mathbf{r})$, of momentum $\psi = \psi(\mathbf{p})$, or of energy $\psi = \psi(E)$. The choice of the coordinates is called *representation*.

One peculiarity of quantum systems is that they may be in a *superposition of states*. That is, if $\psi_1, \psi_2, ..., \psi_k$ are possible states with amplitudes c_k, automatically the functions,

$$\psi = \sum_k c_k \psi_k \qquad \text{or} \qquad \psi = \int dk\ c(k)\phi(k) \tag{1.137}$$

are possible states as well. This is called *superposition principle*, and means, for example, that a particle may be *simultaneously* in several places or that an atom may be *at the same time* excited and deexcited.

There are systems that can only exist in a *restricted number* of states, such as the two-level atom. Others may exist in an *infinite number* of states or even in a *continuous distribution* of states.

1.4.2 Interpretation of the wavefunction (2. postulate)

A *state function* (or wavefunction) characterizes a system of which we may calculate various properties. The function can adopt complex values devoid of immediate physical interpretation. In fact, the wavefunction is above all a mathematical construct. On the other hand, the norm $|\psi|^2$ has the meaning of a probability of the system to be in the state ψ. This is the famous interpretation of *Max Born* of the wave function (see Sec. 1.3.3).

If ψ_k with $k = 1, 2, \ldots$ are all possible states of a system, the interpretation as a probability requires,

$$\sum_k |\psi_k|^2 = 1\ . \tag{1.138}$$

Analogically, for a continuous distribution, for example, in spatial representation,

$$\int_{-\infty}^{\infty} |\psi(x)|^2 dx = 1\ . \tag{1.139}$$

That is, the probability needs *normalization*.

1.4.3 Dirac bra-ket notation and vector representation

In order to distinguish more easily the amplitudes (which are complex numbers) and the wavefunctions we will now use the Bra-Ket notation introduced by *Paul Dirac*. The functions are represented by *kets*,

$$|\psi\rangle = \sum_k c_k |k\rangle\ . \tag{1.140}$$

The complex transpositions of these states are represented by *bras*,

$$\langle\psi| = |\psi\rangle^\dagger = \sum_k c_k^* \langle k| \ . \tag{1.141}$$

But the notation has other advantages. For example, let us suppose that we know the three possible states of a system, $|1\rangle$, $|2\rangle$, and $|3\rangle$, which are linearly independent. Then we can define the states as vectors:

$$|1\rangle = \begin{pmatrix} 1 \\ 0 \\ 0 \end{pmatrix} \quad , \quad |2\rangle = \begin{pmatrix} 0 \\ 1 \\ 0 \end{pmatrix} \quad , \quad |3\rangle = \begin{pmatrix} 0 \\ 0 \\ 1 \end{pmatrix} \ . \tag{1.142}$$

These three states can be interpreted as the basis of a *vector space* representing the system. Now, each wavefunction can be expanded on this basis and expressed by a vector. An arbitrary ket state of this system will then be,

$$|\psi\rangle = \begin{pmatrix} c_1 \\ c_2 \\ c_3 \end{pmatrix} \ . \tag{1.143}$$

The corresponding bra state will be,

$$\langle\psi| = \begin{pmatrix} c_1^* & c_2^* & c_3^* \end{pmatrix} \ . \tag{1.144}$$

Now we can easily calculate the probability for a system to be in a state $|\psi\rangle$,

$$||\psi\rangle|^2 = \langle\psi|\psi\rangle = \begin{pmatrix} c_1^* & c_2^* & c_3^* \end{pmatrix} \cdot \begin{pmatrix} c_1 \\ c_2 \\ c_3 \end{pmatrix} = |c_1|^2 + |c_2|^2 + |c_3|^2 \ . \tag{1.145}$$

1.4.4 Observables (3. postulate)

The only way to get information about a system is to *measure* the values of characteristic quantities of the system, e.g. energy or linear momentum. In classical mechanics we have learned that a system can be completely characterized by a set of measurable physical quantities. For example, the motion of a rigid body of mass m and inertial moment $\mathbf{I}$ is defined by its position $\mathbf{r}$, its moment $\mathbf{p}$, and its angular momentum $\mathbf{L}$. In quantum mechanics we describe observable physical quantities by *operators* acting on the *Hilbert space* of wavefunctions, $|\psi\rangle \mapsto \hat{\mathbf{p}}|\psi\rangle$, where $\hat{p}$ would be the operator of the linear momentum. To better distinguish the observables, we decorate their symbols with a hat. We will see more ahead (see Sec. 1.5.5) that every quantum system is completely described by a complete set of observables.

To find the current values a_ψ of any *observable* $\hat{A}$ in a specific situation given by a wave function ψ, we need to solve an equation of eigenvalues,

$$\hat{A}|\psi\rangle = a_\psi|\psi\rangle \ . \tag{1.146}$$

We can rewrite the equation as $a_\psi = \langle\psi|\hat{A}|\psi\rangle$. The values a_n are real numbers, if the observable is a *Hermitian operator*, that is,

$$\hat{A} = \hat{A}^\dagger \quad \Longrightarrow \quad a_\psi = a_\psi^* \ . \tag{1.147}$$

We leave proof of this for the Exc. 1.4.9.1.

Thus, we postulate the substitution of the *dynamic variables* characterizing a classical system by abstract objects called operators. These operators can be understood as mathematical prescriptions, e.g., differential operators acting on a state of the system. The expectation value of any operator $\hat{A}$ characterizing a system in a state $|\psi\rangle$ is $a_\psi \equiv \langle\hat{A}\rangle_\psi \equiv \langle\psi|\hat{A}|\psi\rangle/\langle\psi|\psi\rangle$. Such operators are specific for a system, but independent of its state. The dynamical variables for a specific state are obtained as eigenvalues of the respective variable in that specific state. The temporal evolution of the operators or of the states is governed by equations of motion (see Sec. 1.6) [15].

1.4.5 Representation of operators as matrices

In the same way as we already represented wavefunctions by vectors, we can also represent operators by matrices,

$$\hat{A} \equiv \sum_{i,j} |i\rangle a_{ij} \langle j| = \begin{pmatrix} & \vdots & \\ .. & a_{ij} & .. \\ & \vdots & \end{pmatrix} = \begin{pmatrix} & \vdots & \\ .. & \langle j|\hat{A}|i\rangle & .. \\ & \vdots & \end{pmatrix} . \tag{1.148}$$

To extract components from a matrix we do, $\langle i|\hat{A}|j\rangle$, for example,

$$\langle 1|\hat{A}|1\rangle = \begin{pmatrix} 1 & 0 & .. \end{pmatrix} \cdot \hat{A} \cdot \begin{pmatrix} 1 \\ 0 \\ \vdots \end{pmatrix} = a_{11} . \tag{1.149}$$

Projectors are particular operators defined by,

$$\hat{P}_k \equiv |k\rangle\langle k| = \begin{pmatrix} 0 & \vdots & 0 \\ .. & 1 & .. \\ 0 & \vdots & 0 \end{pmatrix} . \tag{1.150}$$

The eigenvalue of a projector, $\langle\hat{P}_k\rangle = \langle\psi|\hat{P}_k|\psi\rangle = |\langle k|\psi\rangle|^2$, is nothing more than the probability of finding a system, whose general state is $|\psi\rangle$, in the particular state, since expanding as done in (1.140), we have,

$$\langle\hat{P}_k\rangle = \sum_{m,n} c_m^* c_n \langle m|k\rangle\langle k|n\rangle = |c_k|^2 . \tag{1.151}$$

Using the matrix formalism we can define other interesting operators and verify their properties. For example, choosing the basis,

$$|1\rangle = \begin{pmatrix} 1 \\ 0 \end{pmatrix} \quad , \quad |2\rangle = \begin{pmatrix} 0 \\ 1 \end{pmatrix} , \tag{1.152}$$

we find,

$$\begin{aligned} |1\rangle\langle 1| &= \begin{pmatrix} 1 & 0 \\ 0 & 0 \end{pmatrix} \quad , \quad |2\rangle\langle 2| = \begin{pmatrix} 0 & 0 \\ 0 & 1 \end{pmatrix} \\ |1\rangle\langle 2| &= \begin{pmatrix} 0 & 1 \\ 0 & 0 \end{pmatrix} \quad , \quad |2\rangle\langle 1| = \begin{pmatrix} 0 & 0 \\ 1 & 0 \end{pmatrix} \end{aligned} . \tag{1.153}$$

[15] Note that there are theoretical attempts to generalize the concept of observables to non-Hermitian operators [66, 67] only displaying $\mathcal{PT}$-symmetry.

Obviously, these matrices can be used to expand any 2×2 matrix. An equivalent set of matrices are the *Pauli spin matrices*,

$$\boxed{\mathbb{I} \equiv \begin{pmatrix} 1 & 0 \\ 0 & 1 \end{pmatrix} \quad , \quad \hat{\sigma}_x \equiv \begin{pmatrix} 0 & 1 \\ 1 & 0 \end{pmatrix} \quad , \quad \hat{\sigma}_y \equiv \begin{pmatrix} 0 & \imath \\ -\imath & 0 \end{pmatrix} \quad , \quad \hat{\sigma}_z \equiv \begin{pmatrix} -1 & 0 \\ 0 & 1 \end{pmatrix}} \, . \tag{1.154}$$

An important property of the Pauli matrices is their behavior under commutation and anti-commutation,

$$\begin{aligned} [\hat{\sigma}_k, \hat{\sigma}_m]_- &\equiv \hat{\sigma}_k \hat{\sigma}_m - \hat{\sigma}_k \hat{\sigma}_m = 2\imath \epsilon_{kmn} \hat{\sigma}_n \\ [\hat{\sigma}_k, \hat{\sigma}_m]_+ &\equiv \hat{\sigma}_k \hat{\sigma}_m + \hat{\sigma}_k \hat{\sigma}_m = 2\delta_{km} \ , \end{aligned} \tag{1.155}$$

with $x, y, x = m, n$.

Defining so-called ladder operators or rising, respectively, lowering operators, depending on the arrangement of the level system via,

$$\boxed{\hat{\sigma}^{\pm} = \tfrac{1}{2}(\hat{\sigma}_x \pm \imath \hat{\sigma}_y)} \, , \tag{1.156}$$

we may represent the matrices as,

$$\begin{aligned} |1\rangle\langle 1| &= \tfrac{1}{2}(\mathbb{I}_2 - \hat{\sigma}_z) = \hat{\sigma}^- \hat{\sigma}^+ \quad , \quad |2\rangle\langle 2| = \tfrac{1}{2}(\mathbb{I}_2 + \hat{\sigma}_z) = \hat{\sigma}^+ \hat{\sigma}^- \\ |2\rangle\langle 1| &= \tfrac{1}{2}(\hat{\sigma}_x + \imath \hat{\sigma}_y) = \hat{\sigma}^+ \quad , \quad |1\rangle\langle 2| = \tfrac{1}{2}(\hat{\sigma}_x - \imath \hat{\sigma}_y) = \hat{\sigma}^- \end{aligned} \, , \tag{1.157}$$

and write down the *Pauli vector* [16],

$$\hat{\vec{\sigma}} \equiv \begin{pmatrix} \hat{\sigma}_x \\ \hat{\sigma}_y \\ \hat{\sigma}_z \end{pmatrix} = \begin{pmatrix} \hat{\sigma}^- + \hat{\sigma}^+ \\ \imath(\hat{\sigma}^- - \hat{\sigma}^+) \\ [\hat{\sigma}^+, \hat{\sigma}^-] \end{pmatrix} \tag{1.158}$$

and the vector

$$\vec{\rho} \equiv \begin{pmatrix} \langle \hat{\sigma}_x \rangle \\ \langle \hat{\sigma}_y \rangle \\ \langle \hat{\sigma}_z \rangle \end{pmatrix} \, , \tag{1.159}$$

which is called *Bloch vector* [17,18]. The eigenvalue of the Bloch vector has a fixed length (see Exc. 1.4.9.2).

The representation of physical quantities by matrices is essential for the description of quantum superposition states.

[16] Note that other definitions of the Pauli matrices, e.g. $\hat{\sigma}_y \to -\hat{\sigma}_y$ and $\hat{\sigma}_z \to -\hat{\sigma}_z$ are also found in literature. They simply correspond to a change of basis $|1\rangle \leftrightarrow |2\rangle$.

[17] The Bloch vector is widely used in describing the interaction of a two-level system with a light field.

[18] Schrödinger invented the *wave mechanics* when he derived his wave equation from the dispersion relation for massive particles. Heisenberg invented a mechanics (detailed in later sections), which he called *mechanics of matrices*. Later, he showed the formal equivalence of both theories.

1.4.6 Correspondence principle (4. postulate)

Operators do not necessarily commute. We have already seen in Sec. 1.3.6, that in one dimension the position and the momentum operators do not commute. We can generalize to three dimensions via,

$$[\hat{p}_j, \hat{x}_k] = -\imath\hbar\delta_{jk} \qquad \text{and} \qquad [\hat{p}_j, \hat{p}_k] = 0 = [\hat{x}_j, \hat{x}_k] \ , \tag{1.160}$$

which is easily verified by replacing the operators with $\hat{x}_k = x_k$ and $\hat{p}_k = \frac{\hbar}{\imath}\nabla$ and allowing the commutators to act on a wavefunction $\psi(x)$.

Conversely, quantum mechanics follows from classical mechanics with the prescription, $A(q_k, p_k, t) \longrightarrow A(\hat{q}_k, \hat{p}_k, t) = \hat{A}$. Letting the smallest amount of energy possible go to zero, $\hbar \longrightarrow 0$, the commutator disappears and, as we will see later, discrete energy spectra become continuous, quantum noise disappears, and we recover classical mechanics.

1.4.7 Schrödinger equation and quantum measurements (5. postulate)

The time evolution is given by the Schrödinger equation,

$$\boxed{\imath\hbar\frac{\partial}{\partial t}|\psi\rangle = \hat{H}|\psi\rangle} \ . \tag{1.161}$$

A closed system, disconnected from the rest of the world (we will now call the rest of the world *reservoir*) is not subject to dissipation, i.e., it does not lose energy to the reservoir. Such a system is always described by a hermitian Hamiltonian. Unfortunately, this system also does not allow information leakage, that is, we can not measure the system. This is reflected in the fact that the Schrödinger equation does not allow to describe the process of a *quantum measurement*. This is because before the measurement, the system can be in several states or even in a superposition of states, while after the measurement we know exactly the state. This amounts to a reduction of entropy, which is not allowed in a closed system.

The famous *postulate* of *state reduction* or *projection of the wavefunction* formulated by *John von Neumann* describes the quantum measurement process as a sequence of two distinct steps [19]. In a first step, the measuring apparatus projects the measured operator $\hat{A}$ on an eigenvector basis. That is, if the measurement is compatible with the operator [20], we obtain a distribution of probability amplitudes of the results,

$$\hat{A} \quad \curvearrowright \quad \langle\hat{A}\rangle = \langle\psi|\hat{A}|\psi\rangle = \langle\psi|\hat{A}|\sum_k c_k|k\rangle = \sum_k a_k c_k\langle\psi|k\rangle = \sum_k a_k|c_k|^2 \ , \tag{1.162}$$

with $\langle\psi|\psi\rangle = \sum_k |a_k|^2 = 1$. Therefore, we can understand $|\langle k|\psi\rangle|^2$ as the probability of the system to be in the eigenstate $|k\rangle$. In other words, this first step of

[19] For simplicity, we only consider pure state, here.

[20] To understand the meaning of *compatible*, we must establish a more complete theory of measurement including the reservoir in the quantum description.

the measurement process removes in an irreversible manner all coherences from the observable,

$$\hat{A} \quad \curvearrowright \quad \sum_k |k\rangle\langle k|\hat{A}|k\rangle\langle k| \ . \tag{1.163}$$

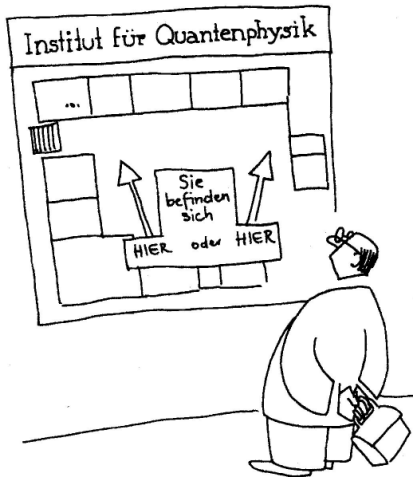

Figure 1.14: Superposition.

In a second step, the observing scientist will *read* the measuring device and note the result, which will necessarily be one of the possible a_k,

$$\langle\hat{A}\rangle \quad \curvearrowright \quad a_k \ . \tag{1.164}$$

If the state is stationary, it will never change any more. That is, each subsequent measurement will yield the same result. The Exc. 1.4.9.3 illustrates the process of quantum measurement at the example of a measurement of the excitation energy of a two-level atom.

1.4.8 Stationary Schrödinger equation

The general form of the Schrödinger equation in one dimension is,

$$\hat{H}\Psi(t,x) = \imath\hbar\frac{\partial}{\partial t}\Psi(t,x) \ , \tag{1.165}$$

with $\hat{H} \equiv \frac{\hat{p}^2}{2m} + V(x,t)$ and $\hat{p} \equiv -\imath\hbar\frac{\partial}{\partial x}$. If the potential is independent of time, $V(x,t) = V(x)$, we can do the following ansatz, $\Psi(x,t) \equiv \psi(x)f(t)$. Insertion into the Schrödinger equation yields,

$$\frac{1}{\psi(x)}\left(-\frac{\hbar^2}{2m}\frac{d^2}{dx^2} + V(x)\right)\psi(x) = \frac{\imath\hbar}{f(t)}\frac{d}{dt}f(t) = const. \equiv E \ . \tag{1.166}$$

The solution of the right-hand side of the equation is $\imath\hbar(\ln f - \ln f_0) = E(t - t_0)$. Hence,

$$f(t) = f(0)e^{-\imath E(t-t_0)/\hbar} \ . \tag{1.167}$$

Obviously, $|\Psi(x,t)|^2 = |\psi(x)|^2$.

Now, we can see that the stationary Schrödinger equation,

$$\hat{H}\psi(x) = E\psi(x) \ , \tag{1.168}$$

is nothing more than an eigenvalue equation. This means that the Schrödinger wave mechanics is equivalent to the mechanics of the Heisenberg matrices. The Excs. 1.4.9.4 and 1.4.9.5 are first simple calculations of the eigenvalues and eigenvectors of a two-level system.

1.4.9 Exercises

1.4.9.1 Ex: Reality of eigenvalues

Show that the eigenvalues of an observable are real.

1.4.9.2 Ex: Normalization of the Bloch vector

Calculate the expectation value of the length of the Pauli vector and the length of the Bloch vector (1.156).

1.4.9.3 Ex: Quantum measurement

Explain the idea of quantum measurement at the example of a measurement of the excitation energy of a two-level atom.

1.4.9.4 Ex: Two-level atom

Consider a two-level atom. The Hamiltonian is given by,

$$\hat{H} = \begin{pmatrix} 0 & 0 \\ 0 & \hbar\omega_0 \end{pmatrix} \ .$$

Using the stationary Schrödinger equation, calculate the eigenvalues and eigenvectors.

1.4.9.5 Ex: The ammonium molecule

Consider the two states $|1\rangle$ and $|2\rangle$ of the ammonium molecule outlined in the figure. Suppose they are orthonormal, $\langle i|j\rangle = \delta_{ij}$, and that only these two states are accessible to the system, so that we can describe it using the basis formed by $|1\rangle$ and $|2\rangle$. On this basis the Hamiltonian $\hat{H}$ of the system is given by,

$$\hat{H} = \begin{pmatrix} E_0 & -E_1 \\ -E_1 & E_0 \end{pmatrix} \ .$$

a. If the system is initially in state $|1\rangle$, will it remain in that state at a later time? How about if the initial state is $|2\rangle$?
b. Obtain the eigenvalues E_{I} and E_{II} and the respective eigenvectors $|I\rangle$ and $|II\rangle$ of

$\hat{H}$, expressing them in terms of $|1\rangle$ and $|2\rangle$.
c. What is the probability of measuring an energy $E_{\rm I}$ in the following state,

$$|\psi\rangle = \tfrac{1}{\sqrt{5}}|1\rangle - \tfrac{2}{\sqrt{5}}|2\rangle \ ?$$

d. Based on the above result, we can predict at least one possible electromagnetic radiation emission frequency for an ammonia sample. What is this frequency?

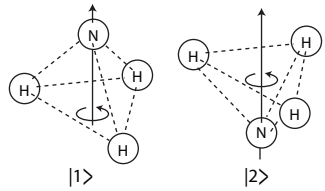

Figure 1.15: The two states of the ammonium molecule.

1.5 Abstract formalism of quantum mechanics

The formal development of quantum mechanics will be the subject of this section. We will learn how to find a complete set of observables characterizing a system, discuss the role of symmetries in quantum mechanics and show how to switch between several representations of the same system.

1.5.1 Lie algebra

The quantum mechanical operators form a *Lie algebra* $\mathcal{L}^2$. This means that $\mathcal{L}^2$ is at the same time a complex and linear *vector space* with respect to addition and scalar multiplication and a *non-commutative ring* with scalar internal product. In particular, $\mathcal{L}^2$ is unitary, normalized, and complete and acts on a *Hilbert space* of quantum states,

$$\begin{aligned}(\hat{A}+\hat{B})|\psi\rangle &= \hat{A}|\psi\rangle + \hat{B}|\psi\rangle, \\ (\alpha\hat{A})|\psi\rangle &= \alpha(\hat{A}|\psi\rangle)\ , \\ (\hat{A}\hat{B})|\psi\rangle &= \hat{A}(\hat{B}|\psi\rangle)\ .\end{aligned} \tag{1.169}$$

The properties of the Hilbert space are,

$$\begin{aligned}\hat{A}|\psi+\varphi\rangle &= \hat{A}|\psi\rangle + \hat{A}|\varphi\rangle\ , \\ \hat{A}|a\psi\rangle &= a\hat{A}|\psi\rangle\ .\end{aligned} \tag{1.170}$$

For a *Hermitian operator*, $\hat{A} = \hat{A}^\dagger$, we have $\langle\psi|\hat{A}|\psi\rangle = \langle\hat{A}\psi|\psi\rangle$ or $\langle\hat{A}\rangle \equiv \langle\psi|\hat{A}|\psi\rangle = \langle\hat{A}\rangle^*$, using the Dirac bra-ket notation,

$$\langle\psi|^\dagger \equiv |\psi\rangle\ . \tag{1.171}$$

There are identity and nullity operators,

$$\mathbb{I}|\psi\rangle = |\psi\rangle \qquad \text{and} \qquad \hat{0}|\psi\rangle = 0 \; . \tag{1.172}$$

We define the *(anti-)commutator* as,

$$[\hat{A}, \hat{B}]_{\mp} \equiv \hat{A}\hat{B} \pm \hat{B}\hat{A} \; , \tag{1.173}$$

which can be $\neq 0$. The sum of two Hermitian operators is Hermitian, but the product is not, since,

$$(\hat{A} + \hat{B})^\dagger = \hat{A}^\dagger + \hat{B}^\dagger = \hat{A} + \hat{B} \qquad \text{but} \qquad (\hat{A}\hat{B})^\dagger = \hat{B}^\dagger \hat{A}^\dagger = \hat{B}\hat{A} \neq \hat{A}\hat{B} \; . \tag{1.174}$$

On the other hand, the following relations of Hermitian operators are always Hermitian,

$$\hat{A}\hat{B} + \hat{B}\hat{A} \qquad \text{and} \qquad \imath(\hat{A}\hat{B} - \hat{B}\hat{A}) \; . \tag{1.175}$$

We define the *scalar product* as,

$$\langle\psi|\varphi\rangle \; . \tag{1.176}$$

Two states are called *orthogonal*, if $\langle\psi|\varphi\rangle = 0$. The norm is written as,

$$|\psi|^2 = \langle\psi|\psi\rangle \; , \tag{1.177}$$

the deviation is,

$$\Delta A \equiv \sqrt{\langle\hat{A}^2\rangle - \langle\hat{A}\rangle^2} \; . \tag{1.178}$$

A *unitary operator* is defined by,

$$\hat{A}^{-1} = \hat{A}^\dagger \; . \tag{1.179}$$

1.5.2 Complete bases

If it is impossible to find a set of amplitudes c_n,

$$\nexists\{c_n\} \quad \text{such that} \quad \sum_n c_n|n\rangle = 0 \; , \tag{1.180}$$

the functions are called *linearly independent*. A set of linearly independent functions may form a *basis*. The space opened by a set of linearly independent functions is called *Hilbert space*.

An operator $\hat{A}$ is completely characterized by its *eigenvalues* and *eigenfunctions*. If a set of eigenfunctions $|n\rangle$ is *complete*, every allowed state of the system can be expanded in these eigenfunctions,

$$|\psi\rangle = \sum_n c_n|n\rangle \qquad \text{and} \qquad \hat{A}|n\rangle = a_n|n\rangle \; . \tag{1.181}$$

To calculate properties of a specific system, we often want to find a matrix representation for the operator $\hat{A}$. For this, we solve the stationary Schrödinger equation,

that is, we calculate the eigenvalues and *eigenvectors*. When all eigenvalues are different, $a_n \neq a_m$, we know that the corresponding eigenvectors are orthogonal, $\langle n|m\rangle = 0$,

$$\hat{A}|n\rangle = a_n|n\rangle \quad , \quad \hat{A}|m\rangle = a_n|m\rangle \quad , \quad \forall\{n,m\}\ a_n \neq a_m \tag{1.182}$$
$$\implies \forall\{n,m\}\ \langle n|m\rangle = \delta_{m,n}\ .$$

Exc. 1.5.9.1 asks for demonstrating this.

Frequently, for example, in the case of a particle confined to a potential, there exist discrete eigenvalues (for $E < 0$) simultaneously with continuous eigenvalues (for $E > 0$). Assuming $\langle m|m'\rangle = \delta_{m,m'}$, $\langle m|\mathbf{k}\rangle = 0$ and $\langle \mathbf{k}|\mathbf{k}'\rangle = \delta^{(3)}(\mathbf{k}-\mathbf{k}')$, with a complete base,

$$\sum_m |m\rangle\langle m| + \int d^3k |\mathbf{k}\rangle\langle\mathbf{k}| = \mathbb{I}\ , \tag{1.183}$$

an arbitrary vector can be expanded on an orthogonal basis,

$$|\psi\rangle = \sum_m |m\rangle\langle m|\psi\rangle + \int d^3k\ |\mathbf{k}\rangle\langle\mathbf{k}|\psi\rangle\ . \tag{1.184}$$

This also applies to observables,

$$\hat{A} = \sum_{m,n} |m\rangle\langle m|\hat{A}|n\rangle\langle n| + \int d^3k d^3l\ |\mathbf{k}\rangle\langle\mathbf{k}|\hat{A}|\mathbf{l}\rangle\langle\mathbf{l}|\ , \tag{1.185}$$

and functions of observables,

$$f(\hat{A}) = \sum_{m,n} |m\rangle f(\langle m|\hat{A}|n\rangle)\langle n| + \int d^3k d^3l\ |\mathbf{k}\rangle f(\langle\mathbf{k}|\hat{A}|\mathbf{l}\rangle)\langle\mathbf{l}|\ . \tag{1.186}$$

1.5.3 Degeneracy

The eigenvectors form a natural basis for the Hilbert space. However, a problem arises in the case of *degeneracy*, that is, when some eigenvalues are equal, $a_n = a_m$. In this case, the eigenvectors that correspond to degenerate eigenvalues are not completely defined, and we have to construct a basis verifying that all constructed eigenvectors are orthogonal. For this, there exists the method of *orthogonalization by Schmidt*, which works like this: We assume that we have already solved the eigenvalue equation, that we found a degenerate eigenvalue, $\hat{A}|a_k\rangle = a|a_k\rangle$ for every $k = 1,..,g_k$, where g_k is the degree of degeneracy, and that we also found a complete basis of eigenvalues $|a_m\rangle$, but which is not orthogonal, that is, $\exists\{m,n\}$ with $\langle a_n|a_m\rangle \neq 0$. The task is to build another basis $|b_m\rangle$ satisfying $\langle b_n|b_m\rangle = \delta_{n,m}$.

The first vector of the orthogonal base can be chosen freely, e.g.,

$$|b_1\rangle \equiv |a_1\rangle\ . \tag{1.187}$$

Since the basis $\{|a_k\rangle\}$ is assumed to be complete, the second vector is necessarily a linear combination of vectors $|a_k\rangle$, that is, $|b_2\rangle = |a_2\rangle + \lambda|b_1\rangle$. With the condition $\langle b_1|b_2\rangle = 0 = \langle b_1|a_2\rangle + \lambda\langle b_1|b_1\rangle$ we can determine the parameter λ, and obtain for the second vector,

$$|b_2\rangle \equiv |a_2\rangle - |b_1\rangle\frac{\langle b_1|a_2\rangle}{\langle b_1|b_1\rangle}\ . \tag{1.188}$$

In the same way, we can derive for a third vector, $|b_3\rangle = |a_3\rangle + \mu|b_1\rangle + \nu|b_2\rangle$, the conditions, $\langle b_1|b_3\rangle = 0 = \langle b_1|a_3\rangle + \mu\langle b_1|b_1\rangle$ and $\langle b_2|b_3\rangle = 0 = \langle b_2|a_3\rangle + \nu\langle b_2|b_2\rangle$, and obtain,

$$|b_3\rangle \equiv |a_3\rangle - |b_1\rangle\frac{\langle b_1|a_3\rangle}{\langle b_1|b_1\rangle} - |b_2\rangle\frac{\langle b_2|a_3\rangle}{\langle b_2|b_2\rangle} \ . \tag{1.189}$$

An overall way of writing this down is,

$$|b_k\rangle \equiv \left(1 - \frac{|b_1\rangle\langle b_1|}{\langle b_1|b_1\rangle} - \frac{|b_2\rangle\langle b_2|}{\langle b_2|b_2\rangle} - \ldots - \frac{|b_{k-1}\rangle\langle b_{k-1}|}{\langle b_{k-1}|b_{k-1}\rangle}\right)|a_k\rangle \ . \tag{1.190}$$

In the Exc. 1.5.9.2 we practice the orthogonalization of a set of three linearly independent but non-orthogonal vectors, and in the Exc. 1.5.9.3 we find an orthogonal basis for a partially degenerate three-level system.

1.5.4 Bases as unitary operators

One way to formulate the eigenvalue problem is as follows: Let $|n\rangle$ be an orthonormal basis with the respective eigenvalues a_n of an operator $\hat{A}$:

$$\hat{A}|n\rangle = a_n|n\rangle \qquad \text{with} \qquad \langle n|m\rangle = \delta_{mn} \ . \tag{1.191}$$

We construct the matrices,

$$\mathcal{U} \equiv \begin{pmatrix} |1\rangle & |2\rangle & \cdots \end{pmatrix} \qquad \text{and} \qquad \hat{E} \equiv \begin{pmatrix} a_1 & 0 & \cdots \\ 0 & a_2 & \\ \vdots & & \ddots \end{pmatrix} \ . \tag{1.192}$$

With the definition of $\mathcal{U}^\dagger$ we have,

$$\mathcal{U}^\dagger = \begin{pmatrix} \langle 1| \\ \langle 2| \\ \vdots \end{pmatrix} \qquad \text{and} \qquad \mathcal{U}^\dagger\mathcal{U} = \begin{pmatrix} \langle 1|1\rangle & \langle 1|2\rangle & \cdots \\ \langle 2|1\rangle & \langle 2|2\rangle & \cdots \\ \vdots & \vdots & \ddots \end{pmatrix} = \mathbb{I} \ . \tag{1.193}$$

Therefore,

$$\begin{aligned} \mathcal{U}^\dagger\mathcal{U} = \mathbb{I} \quad &\Longrightarrow \quad \mathcal{U}^\dagger\mathcal{U}\mathcal{U}^{-1} = \mathbb{I}\mathcal{U}^{-1} \quad \Longrightarrow \quad \mathcal{U}^\dagger = \mathcal{U}^{-1} \\ \mathcal{U}^\dagger\mathcal{U} = \mathbb{I} \quad &\Longrightarrow \quad \mathcal{U}\mathcal{U}^\dagger\mathcal{U}\mathcal{U}^{-1} = \mathcal{U}\mathbb{I}\mathcal{U}^{-1} \quad \Longrightarrow \quad \mathcal{U}\mathcal{U}^\dagger = \mathbb{I} \ . \end{aligned} \tag{1.194}$$

An important property of unitary matrices is,

$$|\det\mathcal{U}| = 1 \ . \tag{1.195}$$

Also,

$$\boxed{\hat{A}|n\rangle = \hat{E}|n\rangle \qquad \text{and} \qquad \hat{A}\mathcal{U} = \mathcal{U}\hat{E}} \ . \tag{1.196}$$

That is, by knowing the *unitary matrix* (or *transformation matrix*) $\mathcal{U}$, we can solve the eigenvalue problem simply by $\hat{E} = \mathcal{U}^{-1}\hat{A}\mathcal{U}$.

Note, that this does not apply to a non-orthonormal basis. In this case, we need to do a Schmidt orthogonalization and use the condition $\det\mathcal{U} = 1$. We apply the technique detailed in this section to solve Excs. 1.5.9.4, 1.5.9.5, and 1.5.9.6.

1.5.5 Complete set of commuting operators

Even for simple systems, we can ask various types of questions (measurements). Considering, for example, a particle flying freely in space, we can gather its position or its velocity. Let a be the result of a measurement of the observable $\hat{A}$, that is, $a = \langle\psi_a|\hat{A}|\psi_a\rangle$. Due to the measurement we know that the system is in the state $|\psi_a\rangle$. Immediately after this first measurement we perform another measurement of *another* observable $\hat{B}$ giving $\langle\psi_a|\hat{B}|\psi_a\rangle$. The result of this measurement can only yield an eigenstate, $b = \langle\psi_a|\hat{B}|\psi_a\rangle$, if the operators commute, $[\hat{A},\hat{B}] = 0$. That is, *if two operators $\hat{A}$ and $\hat{B}$ commute, and if $|\psi\rangle$ is an eigenvector of $\hat{A}$, then $\hat{B}|\psi\rangle$ is also an eigenvector of $\hat{A}$ with the same eigenvalue*:

$$\begin{aligned} & [\hat{A},\hat{B}] = 0 \quad , \quad a = \langle\psi|\hat{A}|\psi\rangle \\ \Longrightarrow\ & \hat{A}(\hat{B}|\psi\rangle) = a(\hat{B}|\psi\rangle) \quad \text{and} \quad \langle\psi|\hat{B}|\psi\rangle \in \mathbb{R} \ . \end{aligned} \tag{1.197}$$

In addition, we observe that, if two operators commute, the orthonormal basis constructed for one of the operators is also orthonormal for the other. That is, *if two operators $\hat{A}$ and $\hat{B}$ commute and if $|\psi_1\rangle$ and $|\psi_2\rangle$ are two eigenvectors of $\hat{A}$ with different eigenvalues, then the matrix element $\langle\psi_1|\hat{B}|\psi_2\rangle$ is equal to zero:*

$$\begin{aligned} & [\hat{A},\hat{B}] = 0 \quad , \quad a_1 = \langle\psi_1|\hat{A}|\psi_1\rangle \neq \langle\psi_2|\hat{A}|\psi_2\rangle = a_2 \\ \Longrightarrow\ & \langle\psi_1|\hat{B}|\psi_2\rangle = 0 \ . \end{aligned} \tag{1.198}$$

Finally, we affirm that, *if two operators $\hat{A}$ and $\hat{B}$ commute, we can construct an orthonormal basis $\{|\psi_{a,b}\rangle\}$ with common eigenvectors of $\hat{A}$ and $\hat{B}$*:

$$\begin{aligned} & [\hat{A},\hat{B}] = 0 \\ \Longrightarrow\ & \exists\ \{|\psi_{a,b}\rangle\} \quad \text{tal que} \quad \hat{A}|\psi_{a,b}\rangle = a|\psi_{a,b}\rangle \quad \text{and} \quad \hat{B}|\psi_{a,b}\rangle = b|\psi_{a,b}\rangle \ . \end{aligned} \tag{1.199}$$

The statements (1.197) to (1.199) are verified in Exc. 1.5.9.7.

The fact that commuting operators have a common system of eigenvectors authorizing sharp eigenvalues can be used to construct and characterize a state.

Example 6 (*Measuring momenta in orthogonal directions*): For example, the obvious solutions of the eigenvalue equations,

$$\hat{p}_x|\psi_{p_x}\rangle = \frac{\hbar}{\imath}\frac{d}{dx}|\psi_{p_x}\rangle = p_x|\psi_{p_x}\rangle \quad \text{and} \quad \hat{p}_y|\psi_{p_y}\rangle = \frac{\hbar}{\imath}\frac{d}{dy}|\psi_{p_y}\rangle = p_y|\psi_{p_y}\rangle$$

are the plane waves $e^{\imath p_x x/\hbar}$ and $e^{\imath p_y y/\hbar}$. Therefore, the total state of the particle can be described by,

$$|\psi_{p_x,p_y,p_z}\rangle = |\psi_{p_x}\rangle|\psi_{p_y}\rangle = e^{(\imath/\hbar)(p_x x + p_y y)} f(z) \ .$$

However, these eigenfunctions are infinitely degenerate, since the linear momentum in z-direction is not specified. A third operator $\hat{p}_z|\psi\rangle = p_z|\psi\rangle$ commutes with the others,

$$[\hat{p}_k,\hat{p}_m] = 0 \ .$$

Hence,

$$|\psi_{p_x,p_y,p_z}\rangle = e^{(\imath/\hbar)(p_x x + p_y y + p_z z)} \ ,$$

is a possible state of the system.
On the other hand, choosing $\hat{p}_z^2 = -\hbar^2 \frac{\partial^2}{\partial z^2}$ as the third operator, giving the eigenvalues p_z^2, the state would have been,

$$|\psi_{p_x,p_y,p_z^2}\rangle = e^{(\imath/\hbar)(p_x x + p_y y)} \cos \tfrac{p_z z}{\hbar} \quad \text{or} \quad |\psi_{p_x,p_y,p_z^2}\rangle = e^{(\imath/\hbar)(p_x x + p_y y)} \sin \tfrac{p_z z}{\hbar} \,. \tag{1.200}$$

Therefore, there are two solutions with the same eigenvalues, p_x, p_y, p_z^2. To lift this degeneracy, we need to introduce yet another observable. This observable can be, for example, the *parity* $\hat{P}$, that is, the behavior of the wave function upon mirroring $z \longrightarrow -z$ in the x-y plane. The fact that the set of operators p_x, p_y, p_z on one hand and p_x, p_y, p_z^2, $\hat{P}$ on the other are equivalent, shows that the required number of observables for a complete characterization depends on their judicious choice.

Also, the number needed for a *complete set of commuting operators* (*CSCO*) depends on the number of *degrees of freedom* and the symmetry of the system. In the case of the free particle in one dimension it is enough to consider one observable only, for example, $\hat{x}$ or $\hat{p}$. In three dimensions, we already need at least three commuting observables. In Exc. 1.5.9.8 we will try to find a CSCO for a matrix with partially degenerate eigenvalues.

1.5.6 Uncertainty relation

We have already learned that observables that do not commute can not be measured with arbitrary precision. This principle can be quantified as follows: If $\hat{A}$ and $\hat{B}$ are two observables, then,

$$\boxed{\Delta\hat{A}\Delta\hat{B} \geq \tfrac{1}{2}|\langle[\hat{A},\hat{B}]\rangle|} \,. \tag{1.201}$$

This is Heisenberg's famous *uncertainty principle*. For example, $[\hat{p},\hat{x}] = -\imath\hbar$, and hence, $\Delta p \Delta x \geq \hbar/2$. We will see later (see Sec. 3.3.1), that $[\hat{l}_x,\hat{l}_y] = \imath\hbar\hat{l}_z$ such that $\Delta l_x \Delta l_y \geq \hbar|\langle l_z\rangle|/2$. More difficult to show, since time has no simple quantum operator, is $\Delta E \Delta t \geq \hbar/2$. In the Exc. 1.5.9.9 we will show the *Schwartz inequality*, and in the Exc. 1.5.9.10 we ask for a formal derivation of Heisenberg's uncertainty principle.

1.5.7 Representations

1.5.7.1 Spatial representation

A Hilbert space can be discrete or, as in the case of the momentum of a free particle, continuous. In this latter case, the eigenvalues are continuously distributed, since the equation,

$$-\imath\hbar\nabla_{\mathbf{r}}\psi(\mathbf{r}) = \mathbf{p}\psi(\mathbf{r}) \,, \tag{1.202}$$

has solutions for each value of E. The eigenfunctions are $\psi(\mathbf{r}) = ae^{\imath\mathbf{p}\cdot\mathbf{r}/\hbar}$. Eq. (1.202) clearly has the form of an eigenvalue equation, for which we have already introduced the Heisenberg matrix formalism. The question now is how these descriptions combine.

Observables that do not commute correspond to expansions on different bases and generate alternative representations. For example, we can represent quantum mechanics in *position space* or *linear momentum space*. If $|\mathbf{r}\rangle$ is a basis of the space of the particles' state,

$$\hat{\mathbf{r}}|\mathbf{r}\rangle = \mathbf{r}|\mathbf{r}\rangle \quad , \quad \langle\mathbf{r}'|\mathbf{r}\rangle = \delta^3(\mathbf{r}' - \mathbf{r}) \quad , \quad \int_{\mathbb{R}^3} |\mathbf{r}\rangle\langle\mathbf{r}| d^3r = \mathbb{I} \ , \tag{1.203}$$

we can expand the position operator on a position basis as,

$$\hat{\mathbf{r}} = \int_{\mathbb{R}^3} \mathbf{r}|\mathbf{r}\rangle\langle\mathbf{r}| d^3r \ , \tag{1.204}$$

and any state vector as,

$$\boxed{|\psi(t)\rangle = \int_{\mathbb{R}^3} |\mathbf{r}\rangle\psi(t,\mathbf{r}) d^3r} \ . \tag{1.205}$$

The quantities $\langle\mathbf{r}|\psi(t)\rangle = \psi(t,\mathbf{r})$ Schrödinger wave functions. We can also say that the wavefunctions are the coordinates of the state in the particular base $|\mathbf{r}\rangle$. Consequently,

$$\begin{aligned} \langle\mathbf{r}|\hat{\mathbf{r}}|\mathbf{r}'\rangle &= \mathbf{r}\delta^3(\mathbf{r} - \mathbf{r}') \\ \langle\mathbf{r}|f(\hat{\mathbf{r}})|\mathbf{r}'\rangle &= f(\mathbf{r})\delta^3(\mathbf{r} - \mathbf{r}') \ . \end{aligned} \tag{1.206}$$

It is also true that,

$$\boxed{\langle\mathbf{r}|\hat{A}|\psi(t)\rangle = \int_{\mathbb{R}^3} A(\mathbf{r},\mathbf{r}')\psi(t,\mathbf{r}') d^3r'} \ , \tag{1.207}$$

where the quantity $A(\mathbf{r},\mathbf{r}') \equiv \langle\mathbf{r}|\hat{A}|\mathbf{r}'\rangle$ is called *kernel* of the operator. The transition from Heisenberg's abstract mechanics to Schrödinger's wave mechanics is done by the substitutions $|\psi(t)\rangle \to \psi(t,\mathbf{r})$ and $\hat{A} \to A(\mathbf{r},\mathbf{r}')$.

1.5.7.2 Momentum representation

The uncertainty relation is symmetric in $\hat{\mathbf{r}}$ and $\hat{\mathbf{p}}$. Nothing prevents us from choosing as a basis,

$$\hat{\mathbf{p}}|\mathbf{p}\rangle = \mathbf{p}|\mathbf{p}\rangle \quad , \quad \langle\mathbf{p}'|\mathbf{p}\rangle = \delta^3(\mathbf{p}' - \mathbf{p}) \quad , \quad \int_{\mathbb{R}^3} |\mathbf{p}\rangle\langle\mathbf{p}| d^3p = \mathbb{I} \ , \tag{1.208}$$

in which we can expand the momentum operator on a momentum basis as,

$$\hat{\mathbf{p}} = \int_{\mathbb{R}^3} \mathbf{p}|\mathbf{p}\rangle\langle\mathbf{p}| d^3p \ , \tag{1.209}$$

with the wavefunctions,

$$\boxed{|\psi(t)\rangle = \int_{R^3} |\mathbf{p}\rangle\varphi(\mathbf{p},t) d^3p} \ , \tag{1.210}$$

where $\langle \mathbf{p}|\psi(t)\rangle = \varphi(t,\mathbf{p})$. The formulas are analogous to the ones in the spatial representation. In particular, in the momentum representation the position operator is $\mathbf{r} = \imath\hbar\nabla_{\mathbf{p}}$.

The representations follow from one another by Fourier transformation. Since $-\imath\hbar\nabla_{\mathbf{r}}\langle \mathbf{r}|\mathbf{p}\rangle = \mathbf{p}\langle \mathbf{r}|\mathbf{p}\rangle$, we know,

$$\boxed{\langle \mathbf{r}|\mathbf{p}\rangle = \tfrac{1}{h^{3/2}}\exp(\tfrac{\imath}{\hbar}\mathbf{r}\cdot\mathbf{p})}\,, \tag{1.211}$$

where the prefactor $\hbar^{-3/2}$ is introduced to take account of the unit of the states [21]. ψ and φ are different representations of the same quantum state related by,

$$\begin{aligned}\langle \mathbf{r}|\psi(t)\rangle &= \int_{\mathbb{R}^3}\langle \mathbf{r}|\mathbf{p}\rangle\langle \mathbf{p}|\psi(t)\rangle d^3p = \tfrac{1}{h^{3/2}}\int_{\mathbb{R}^3} e^{\imath\mathbf{r}\cdot\mathbf{p}/\hbar}\varphi(\mathbf{p},t)d^3p = \psi(\mathbf{r},t) \\ \langle \mathbf{p}|\psi(t)\rangle &= \int_{\mathbb{R}^3}\langle \mathbf{p}|\mathbf{r}\rangle\langle \mathbf{r}|\psi(t)\rangle d^3r = \tfrac{1}{h^{3/2}}\int_{\mathbb{R}^3} e^{-\imath\mathbf{r}\cdot\mathbf{p}/\hbar}\psi(\mathbf{r},t)d^3r = \varphi(\mathbf{p},t)\ .\end{aligned} \tag{1.212}$$

Normalization ensures that $\psi = \mathcal{F}^{-1}\mathcal{F}\psi$ with the relation,

$$\delta(x) = \lim_{t\to\infty}\tfrac{1}{2\pi}\int_{-t}^{t} e^{\imath kx}dk\ . \tag{1.213}$$

Using the wavevector $\hbar\mathbf{k} = \mathbf{p}$ we can also write,

$$\psi(\mathbf{r}) = \tfrac{1}{(2\pi)^{3/2}}\int_{\mathbb{R}^3} e^{\imath\mathbf{r}\cdot\mathbf{k}}\tilde{\varphi}(\mathbf{k})d^3k \qquad \text{and} \qquad \tilde{\varphi}(\mathbf{k}) = \tfrac{1}{(2\pi)^{3/2}}\int_{\mathbb{R}^3} e^{-\imath\mathbf{r}\cdot\mathbf{k}}\psi(\mathbf{r})d^3r\ , \tag{1.214}$$

defining the function $\tilde{\varphi}(\mathbf{k}) \equiv \hbar^{3/2}\varphi(\mathbf{p})$. Applying the Fourier transform to functions of operator we can calculate,

$$\begin{aligned}\langle \mathbf{r}|G(\hat{\mathbf{p}})|\mathbf{r}'\rangle &= \int d^3p\langle \mathbf{r}|G(\hat{\mathbf{p}})|\mathbf{p}\rangle\langle \mathbf{p}|\mathbf{r}'\rangle = \int d^3pG(\mathbf{p})\langle \mathbf{r}|\mathbf{p}\rangle\langle \mathbf{p}|\mathbf{r}'\rangle \\ &= \tfrac{1}{\hbar^{3/2}}\int d^3pG(\mathbf{p})e^{\imath\mathbf{k}\cdot(\mathbf{r}-\mathbf{r}')} = \tfrac{1}{\hbar^3}(\mathcal{F}G)(\mathbf{r}-\mathbf{r}')\ .\end{aligned} \tag{1.215}$$

In Exc. 1.5.9.11 we will show $\langle \mathbf{r}|\hat{\mathbf{p}}|\psi\rangle = (\hbar/\imath)\nabla_{\mathbf{r}}\langle \mathbf{r}|\psi\rangle$, thus justifying that we can understand an operator as a rule to determine what happens to a function. For example, the rule $\hat{p}_x$ asks for a derivation of the wavefunction by x.

1.5.8 Spanning a Hilbert space with several degrees of freedom

All systems analyzed up to this point were characterized by a single degree of freedom (e.g., energy, momentum, or angular momentum), which could have a continuous or discrete spectrum. Even when we treated systems exhibiting various degrees of freedom (motion of a particle in 3D space, electron orbitals in the hydrogen atom), we always found a way to separate the degrees of freedom into orthogonal Hilbert

[21] Note that the units of the wavefunctions are defined by normalization: $\langle \mathbf{r}'|\mathbf{r}\rangle = \delta^3(\mathbf{r}-\mathbf{r}')$. Introducing the parenthesis [...] to extract the unit of a physical quantity, we find, $[|\mathbf{r}\rangle] = [\psi(\mathbf{r})] = [r^{-3/2}]$ and $[|\mathbf{p}\rangle] = [\varphi(\mathbf{p})] = [p^{-3/2}]$. We do not assign a unit to the abstract state $|\psi\rangle$, that is, $[|\psi\rangle] = 1$.

spaces, which allowed us to treat the dynamics of the degrees of freedom separately. In this chapter, we will establish the theoretical foundations allowing us to analyze systems, where degrees of freedom can not be separated because they are entangled or interact. In particular, we will consider the system of two spins and the coupling of angular momenta in general.

1.5.8.1 Projection and internal sum

A *projector* is an operator which *reduces* the domain of an operator, originally acting on a Hilbert space $\mathbb{H}$ to the *subspace* defined by the projector. We consider an operator $\hat{A}$ with the matrix representation,

$$\hat{A} \equiv \sum_{\substack{i,j \\ |i\rangle,|j\rangle\in\mathbb{H}}} |i\rangle A_{ij}\langle j| = \begin{pmatrix} & \vdots & \\ .. & A_{ij} & .. \\ & \vdots & \end{pmatrix} , \tag{1.216}$$

acting on wavefunctions $|\psi\rangle \in \mathbb{H}$ which can be expanded on a basis $|i\rangle$ of $\mathbb{H}$. Now, we consider a subspace $\mathcal{R} \subset \mathbb{H}$ defined by the base $|k\rangle$. Then the projector $\hat{P}_{\mathcal{R}}$ can be represented by,

$$\boxed{\hat{P}_{\mathcal{R}} \equiv \sum_{\substack{k \\ |k\rangle\in\mathcal{R}}} |k\rangle\langle k| = \begin{pmatrix} 0 & 0 & 0 \\ 0 & \begin{pmatrix} 1 & & \\ & .. & \\ & & 1 \end{pmatrix} & 0 \\ 0 & 0 & 0 \end{pmatrix}} . \tag{1.217}$$

Applied to the operator $\hat{A}$,

$$\hat{A}_{\mathcal{R}} \equiv \hat{P}_{\mathcal{R}}\hat{A} = \hat{P}_{\mathcal{R}}\hat{A}_{\mathcal{R}} = \sum_{k,l} |k\rangle A_{kl}\langle l| = \begin{pmatrix} 0 & 0 & 0 \\ & \vdots & \\ 0 & \begin{pmatrix} .. & A_{kl} & .. \end{pmatrix} & 0 \\ & \vdots & \\ 0 & 0 & 0 \end{pmatrix} . \tag{1.218}$$

Applied to a state $|i\rangle$,

$$|\psi\rangle_{\mathcal{R}} = \hat{P}_{\mathcal{R}}|\psi\rangle = \hat{P}_{\mathcal{R}}|\psi\rangle_{\mathcal{R}} = \sum_k c_k|k\rangle = \begin{pmatrix} 0 \\ \begin{pmatrix} \vdots \\ c_k \\ \vdots \end{pmatrix} \\ 0 \end{pmatrix} . \tag{1.219}$$

We study an example in Exc. 1.5.9.12.

Consequently, we can understand the Hilbert space as the sum of its subspaces,

$$\hat{A} = \bigoplus_{\mathcal{R}} \hat{A}_{\mathcal{R}} \qquad \text{and} \qquad \bigoplus_{\mathcal{R}} \hat{P}_{\mathcal{R}} = \mathbb{I} . \tag{1.220}$$

The dimensions of the subspaces are additive,

$$\dim \hat{A} = \sum_{\mathcal{R}} \dim \hat{A}_{\mathcal{R}} \ .$$

Example 7 (*Projection for a three-level atom*): The Hamiltonian of a three-level atom with excitation of two transitions is given by,

$$\hat{H} = \begin{pmatrix} \omega_1 & \Omega_{12} & 0 \\ \Omega_{12} & \omega_2 & \Omega_{23} \\ 0 & \Omega_{23} & \omega_3 \end{pmatrix} \ .$$

The projector,

$$\hat{P} = \begin{pmatrix} 1 & 0 & 0 \\ 0 & 1 & 0 \\ 0 & 0 & 0 \end{pmatrix}$$

reduces the Hamiltonian to a two-level transition,

$$\hat{H}_{\mathcal{R}} = \begin{pmatrix} \omega_1 & \Omega_{12} & 0 \\ \Omega_{12} & \omega_2 & 0 \\ 0 & 0 & 0 \end{pmatrix} \ .$$

As another example we can cite the Jaynes-Cummings model introduced in Sec. 17.1.2 and describing the interaction between a single atom and a single light mode. In this model the total Hilbert space is constructed as a sum of orthogonal subspaces characterized by different fixed excitation numbers.

Obviously, the concatenation (1.220) only serves to increase the Hilbert space of a given degree of freedom described by a given observable, e.g., when we add one more level of energy to the spectrum of an atom described by a Hamiltonian. If, in contrast, we want to add another degree of freedom, we need the external sum or external product discussed below.

1.5.8.2 Tensorial product

We have previously worked with systems exhibiting more than one degree of freedom and therefore having to be characterized by more than one observable with its spectrum of eigenstates. One example are the electronic orbitals of the hydrogen atom $|n\ell m\rangle$, which need three quantum numbers to be labeled unambiguously. Obviously, each quantum number increases the dimensionality of the Hilbert space. Another example is the system $|\alpha\beta\rangle$ of two particles with spin $\frac{1}{2}$, each spin being defined on its respective space,

$$|\alpha\rangle = \begin{pmatrix} \alpha_1 \\ \alpha_2 \end{pmatrix} = (\alpha_i)_i \in \mathbb{H}_A \qquad \text{and} \qquad |\beta\rangle = \begin{pmatrix} \beta_1 \\ \beta_2 \end{pmatrix} = (\beta_k)_k \in \mathbb{H}_{\mathrm{B}} \ . \tag{1.221}$$

The combined state is,

$$|\alpha\beta\rangle \in \mathbb{H}_A \otimes \mathbb{H}_{\mathrm{B}} \qquad \text{with} \qquad \dim \mathbb{H}_A \otimes \mathbb{H}_{\mathrm{B}} = \dim \mathbb{H}_A \dim \mathbb{H}_{\mathrm{B}} \ . \tag{1.222}$$

The symbol $\otimes$ denotes the *outer tensorial product* of two vectors (states) [22]. Now, in order to represent the multidimensional space $\mathbb{H}_A \otimes \mathbb{H}_\mathrm{B}$ by a matrix, we use the fact that it is isomorphic to the space $\mathbb{H}_\mathbb{I} \otimes \mathbb{H}_{A\otimes B}$, that is, we proceed to a reorganization of the quantum numbers identifying,

$$|\gamma\rangle \equiv |\alpha\rangle|\beta\rangle = |\alpha\rangle \otimes |\beta\rangle = |\alpha\beta\rangle = \begin{pmatrix} \alpha_1|\beta\rangle \\ \alpha_2|\beta\rangle \end{pmatrix} = \begin{pmatrix} \alpha_1\beta_1 \\ \alpha_1\beta_2 \\ \alpha_2\beta_1 \\ \alpha_2\beta_2 \end{pmatrix} = (\gamma_m)_m \in \mathbb{H}_A \otimes \mathbb{H}_\mathrm{B} \ , \tag{1.223}$$

where $m = 1, 2, 3, 4$ is identified with $(i, k) = (1, 1), (1, 2), (2, 1), (2, 2)$. The new vector is element of the 4-dimensional vector space $\mathbb{H}_A \otimes \mathbb{H}_\mathrm{B}$. If $\{|\alpha\rangle_i\}$ and $\{|\beta\rangle_k\}$ are bases in their respective spaces $\mathbb{H}_A$ and $\mathbb{H}_\mathrm{B}$, then $\{|\gamma\rangle_m\}$ is a basis of the product space $\mathbb{H}_A \otimes \mathbb{H}_\mathrm{B}$.

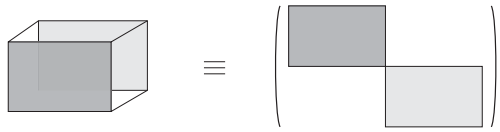

Figure 1.16: Illustration of the isomorphism between $\mathbb{H}_A \otimes \mathbb{H}_\mathrm{B}$ and $\mathbb{H}_\mathbb{I} \otimes \mathbb{H}_{A\otimes B}$ for matrices of rank 2.

For observables we proceed in the same way: The external product of two commutators spans a Hilbert product space with the dimension corresponding to product of the dimensions of the sub-spaces. Assuming that,

$$\hat{A} \equiv \sum\nolimits_{i,j} |i\rangle A_{ij} \langle j| \qquad \text{and} \qquad \hat{B} \equiv \sum\nolimits_{k,l} |k\rangle B_{kl} \langle l| \ . \tag{1.224}$$

[22] The tensorial product of two states should not be confused with other definitions of products, such as the inner (or scalar) product of two states,

$$\langle\alpha|\beta\rangle \equiv \alpha_1\beta_1 + \alpha_2\beta_2 \ ,$$

the outer product,

$$|\alpha\rangle\langle\beta| \equiv \begin{pmatrix} \alpha_1\beta_1 & \alpha_1\beta_2 \\ \alpha_2\beta_1 & \alpha_2\beta_2 \end{pmatrix}$$

$$\begin{pmatrix} A_{11} \\ A_{12} \\ A_{21} \\ A_{22} \end{pmatrix} \begin{pmatrix} B_{11} \\ B_{12} \\ B_{21} \\ B_{22} \end{pmatrix}^\dagger = \begin{pmatrix} A_{11}B_{11} & A_{11}B_{12} & A_{11}B_{21} & A_{11}B_{22} \\ A_{12}B_{11} & A_{12}B_{12} & A_{12}B_{21} & A_{12}B_{22} \\ A_{21}B_{11} & A_{21}B_{12} & A_{21}B_{21} & A_{21}B_{22} \\ A_{22}B_{11} & A_{22}B_{12} & A_{22}B_{21} & A_{22}B_{22} \end{pmatrix} \ ,$$

the exterior (cross) product,

$$|\alpha\rangle \times |\beta\rangle = \begin{pmatrix} \alpha_2\beta_3 - \alpha_3\beta_2 \\ \alpha_3\beta_1 - \alpha_1\beta_3 \\ \alpha_1\beta_2 - \alpha_2\beta_1 \end{pmatrix} \ ,$$

nor the point-wise or *Hadamard product*,

$$\hat{A} \circ \hat{B} \equiv \begin{pmatrix} A_{11} & A_{12} \\ A_{21} & A_{22} \end{pmatrix} \circ \begin{pmatrix} B_{11} & B_{12} \\ B_{21} & B_{22} \end{pmatrix} = \begin{pmatrix} A_{11}B_{11} & A_{12}B_{12} \\ A_{21}B_{21} & A_{22}B_{22} \end{pmatrix} \ .$$

then

$$\hat{A} \otimes \hat{B} \equiv \sum_{(ik)(jl)} |ik\rangle A_{ij} B_{kl} \langle jl| \ , \tag{1.225}$$

such that

$$\dim \hat{A} \otimes \hat{B} = \dim \hat{A} \dim \hat{B} \ .$$

For example, $|i\rangle\langle j| \otimes |k\rangle\langle l| = |ik\rangle\langle jl|$.

For two two-dimensional operators $\hat{A}$ and $\hat{B}$, the *tensorial external product* is defined by,

$$\hat{A} \otimes \hat{B} = \begin{pmatrix} A_{11}B_{11} & A_{11}B_{12} & A_{12}B_{11} & A_{12}B_{12} \\ A_{11}B_{21} & A_{11}B_{22} & A_{12}B_{21} & A_{12}B_{22} \\ A_{21}B_{11} & A_{21}B_{12} & A_{22}B_{11} & A_{22}B_{12} \\ A_{21}B_{21} & A_{21}B_{22} & A_{22}B_{21} & A_{22}B_{22} \end{pmatrix} \ , \tag{1.226}$$

and can be decomposed as,

$$\boxed{\hat{A} \otimes \hat{B} = (\hat{A} \otimes \mathbb{I})(\mathbb{I} \otimes \hat{B}) = \begin{pmatrix} A_{11} & & A_{12} & \\ & A_{11} & & A_{12} \\ A_{21} & & A_{22} & \\ & A_{21} & & A_{22} \end{pmatrix} \begin{pmatrix} B_{11} & B_{12} & & \\ B_{21} & B_{22} & & \\ & & B_{11} & B_{12} \\ & & B_{21} & B_{22} \end{pmatrix} .} \tag{1.227}$$

The concept (1.225) can be generalized to more degrees of freedom like,

$$\hat{A} \otimes \hat{B} \otimes \hat{C} \equiv \sum_{(ikm)(jln)} |ikm\rangle A_{ij} B_{kl} C_{mn} \langle jln| \ , \tag{1.228}$$

Obviously, the external product is associative $(\hat{A} \otimes \hat{B}) \otimes C = \hat{A} \otimes (\hat{B} \otimes C)$, but does not commute, even though the operators acting on different spaces do commute, $[\hat{A}, \hat{B}] = 0$. Nevertheless, we can reverse the order of the product of two operators using,

$$\hat{A} \otimes \hat{B} = \mathbb{S}(\hat{B} \otimes \hat{A})\mathbb{S} \qquad \text{with} \qquad \mathbb{S} \equiv \begin{pmatrix} 1 & & & \\ & 0 & 1 & \\ & 1 & 0 & \\ & & & 1 \end{pmatrix} \ . \tag{1.229}$$

The operator $\mathbb{S}$ is also called *SWAP-gate*.

We note, that it is important to distinguish from what space the vector came from. In our notation, the vector *before* the symbol of the tensorial product ($\otimes$) is belongs to the space $\mathbb{H}_A$, and the one *after* the $\otimes$ belongs to the space $\mathbb{H}_B$. With the definition (1.224) we can verify that the operators only act on their respective states:

$$(A \otimes B)(|\alpha\rangle \otimes |\beta\rangle) = A|\alpha\rangle \otimes B|\beta\rangle \ . \tag{1.230}$$

Example 8 (*Tensorial product*): We can check the relationship (1.230) by

the definitions (1.223) and (1.226) of the external product,

$$\left[\begin{pmatrix} A_{11} & A_{12} \\ A_{21} & A_{22} \end{pmatrix} \otimes \begin{pmatrix} B_{11} & B_{12} \\ B_{21} & B_{22} \end{pmatrix}\right]\left[\begin{pmatrix} \alpha_1 \\ \alpha_2 \end{pmatrix} \otimes \begin{pmatrix} \beta_1 \\ \beta_2 \end{pmatrix}\right] \tag{1.231}$$

$$= \begin{pmatrix} A_{11}B_{11} & A_{11}B_{12} & A_{12}B_{11} & A_{11}B_{12} \\ A_{11}B_{21} & A_{11}B_{22} & A_{12}B_{21} & A_{11}B_{22} \\ A_{21}B_{11} & A_{11}B_{12} & A_{22}B_{11} & A_{22}B_{12} \\ A_{21}B_{21} & A_{11}B_{22} & A_{22}B_{21} & A_{22}B_{22} \end{pmatrix} \begin{pmatrix} \alpha_{11}\beta_{11} \\ \alpha_{11}\beta_{21} \\ \alpha_{21}\beta_{11} \\ \alpha_{21}\beta_{21} \end{pmatrix}$$

$$= \begin{pmatrix} A_{11}B_{11}\alpha_{11}\beta_{11} + A_{11}B_{12}\alpha_{11}\beta_{21} + A_{12}B_{11}\alpha_{21}\beta_{11} + A_{11}B_{12}\alpha_{21}\beta_{21} \\ A_{11}B_{21}\alpha_{11}\beta_{11} + A_{11}B_{22}\alpha_{11}\beta_{21} + A_{12}B_{21}\alpha_{21}\beta_{11} + A_{11}B_{22}\alpha_{21}\beta_{21} \\ A_{21}B_{11}\alpha_{11}\beta_{11} + A_{11}B_{12}\alpha_{11}\beta_{21} + A_{22}B_{11}\alpha_{21}\beta_{11} + A_{22}B_{12}\alpha_{21}\beta_{21} \\ A_{21}B_{21}\alpha_{11}\beta_{11} + A_{11}B_{22}\alpha_{11}\beta_{21} + A_{22}B_{21}\alpha_{21}\beta_{11} + A_{22}B_{22}\alpha_{21}\beta_{21} \end{pmatrix}$$

$$= \begin{pmatrix} (A_{11}\alpha_1 + A_{12}\alpha_2)(B_{11}\beta_1 + B_{12}\beta_2) \\ (A_{11}\alpha_1 + A_{12}\alpha_2)(B_{21}\beta_1 + B_{22}\beta_2) \\ (A_{21}\alpha_1 + A_{22}\alpha_2)(B_{11}\beta_1 + B_{12}\beta_2) \\ (A_{21}\alpha_1 + A_{22}\alpha_2)(B_{21}\beta_1 + B_{22}\beta_2) \end{pmatrix}$$

$$= \begin{pmatrix} A_{11}\alpha_1 + A_{12}\alpha_2 \\ A_{21}\alpha_1 + A_{22}\alpha_2 \end{pmatrix} \otimes \begin{pmatrix} B_{11}\beta_1 + B_{12}\beta_2 \\ B_{21}\beta_1 + B_{22}\beta_2 \end{pmatrix} = \begin{pmatrix} A_{11} & A_{12} \\ A_{21} & A_{22} \end{pmatrix} \begin{pmatrix} \alpha_1 \\ \alpha_2 \end{pmatrix} \otimes \begin{pmatrix} B_{11} & B_{12} \\ B_{21} & B_{22} \end{pmatrix} \begin{pmatrix} \beta_1 \\ \beta_2 \end{pmatrix} .$$

Example 9 (*Mathematical definition of the tensor product*): If α belongs to the Hilbert space $\mathbb{H}_\alpha$ and β belongs to $\mathbb{H}_\beta$, then the equivalence class of (α, β) is denoted by $\alpha \otimes \beta$ and called the tensor product of α with β. This use of the $\otimes$-symbol refers specifically to the outer product operation. An element of $\mathbb{H}_\alpha \otimes \mathbb{H}_\beta$ that can be written in the form $\alpha \otimes \beta$ is called a pure tensor. In general, an element of the tensor product space is not a pure tensor, but rather a finite linear combination of pure tensors. For example, if α_1 and α_2 are linearly independent, and β_1 and β_2 are also linearly independent, then $\alpha_1 \otimes \beta_1 + \alpha_2 \otimes \beta_2$ cannot be written as a pure tensor. The number of pure tensors required to express an element of a tensor product is called the tensor rank. The rank should not be confused with the tensor order, which is the number of spaces one has taken the product of (in this case two), and which corresponds to the number of indices. For linear operators or matrices, thought of as $(1, 1)$ tensors (elements of the space $\mathbb{H}_\alpha \otimes \mathbb{H}_\alpha^*$), the tensor rank agrees with matrix rank.
Given bases $\{\alpha_i\}$ and $\{\beta_j\}$ for $\mathbb{H}_\alpha$ and $\mathbb{H}_\beta$ respectively, the tensors $\{\alpha_i \otimes \beta_j\}$ form a basis for $\mathbb{H}_\alpha \otimes \mathbb{H}_\beta$. Therefore, if $\mathbb{H}_\alpha$ and $\mathbb{H}_\beta$ are finite-dimensional, the dimension of the tensor product is the product of dimensions of the original spaces; for instance $\mathbb{R}^m \otimes \mathbb{R}^n$ is isomorphic to $\mathbb{R}^{nm}$.
The tensor product also operates on linear maps (called operators in quantum mechanics) between vector spaces. Specifically, given two linear maps $\hat{A} : \mathbb{H}_\alpha \to \mathbb{H}'_\alpha$ and $\hat{B} : \mathbb{H}_\beta \to \mathbb{H}'_\beta$ between vector spaces, the tensor product of the two linear maps $\hat{A}$ and $\hat{B}$ is a linear map,

$$\hat{A} \otimes \hat{B} : \mathbb{H}_\alpha \otimes \mathbb{H}_\beta \to \mathbb{H}'_\alpha \otimes \mathbb{H}'_\beta ,$$

defined by,

$$(\hat{A} \otimes \hat{B})(\alpha \otimes \beta) = \hat{A}(\alpha) \otimes \hat{B}(\beta) .$$

In this way, the tensor product becomes a bifunctor from the category of vector spaces to itself, covariant in both arguments. If $\hat{A}$ and $\hat{B}$ are both injective,

surjective or (in the case that $\mathbb{H}_\alpha$, $\mathbb{H}'_\alpha$, $\mathbb{H}_\beta$, and $\mathbb{H}'_\beta$ are normed vector spaces or topological vector spaces) continuous, then $\hat{A} \otimes \hat{B}$ is injective, surjective or continuous, respectively.
By choosing bases of all vector spaces involved, the linear maps $\hat{A}$ and $\hat{B}$ can be represented by matrices. Then, depending on how the tensor $\alpha \otimes \beta$ is vectorized, the matrix describing the tensor product $\hat{A} \otimes \hat{B}$ is the Kronecker product of the two matrices. For example, if $\mathbb{H}_\alpha$, $\mathbb{H}'_\alpha$, $\mathbb{H}_\beta$, and $\mathbb{H}'_\beta$ above are all two-dimensional and bases have been fixed for all of them, and $\hat{A}$ and $\hat{B}$ are given by the matrices,

$$\hat{A} = \begin{pmatrix} A_{11} & A_{12} \\ A_{21} & A_{22} \end{pmatrix} \quad , \quad \hat{B} = \begin{pmatrix} B_{11} & B_{12} \\ B_{21} & B_{22} \end{pmatrix}$$

respectively, then the tensor product of these two matrices is,

$$\begin{pmatrix} A_{11} & A_{12} \\ A_{21} & A_{22} \end{pmatrix} \otimes \begin{pmatrix} B_{11} & B_{12} \\ B_{21} & B_{22} \end{pmatrix} = \begin{pmatrix} A_{11} \begin{pmatrix} B_{11} & B_{12} \\ B_{21} & B_{22} \end{pmatrix} & A_{12} \begin{pmatrix} B_{11} & B_{12} \\ B_{21} & B_{22} \end{pmatrix} \\ A_{21} \begin{pmatrix} B_{11} & B_{12} \\ B_{21} & B_{22} \end{pmatrix} & A_{22} \begin{pmatrix} B_{11} & B_{12} \\ B_{21} & B_{22} \end{pmatrix} \end{pmatrix} .$$

The resultant rank is at most 4, and thus the resultant dimension is 4. Note that rank here denotes the tensor rank i.e. the number of requisite indices (while the matrix rank counts the number of degrees of freedom in the resulting array). Note $\mathrm{Tr}\ \hat{A} \otimes \hat{B} = \mathrm{Tr}\ \hat{A} \times \mathrm{Tr}\ \hat{B}$.
A dyadic product is the special case of the tensor product between two vectors of the same dimension.

1.5.8.3 Direct external sum

Using the nomenclature (1.224) we define the external direct sum by,

$$\hat{A} \oplus \hat{B} \equiv \sum_{(ik)(jl)} |ik\rangle (A_{ij} + B_{kl}) \langle jl| \ , \tag{1.232}$$

that is,

$$\hat{A} \oplus \hat{B} = \begin{pmatrix} A_{11} + B_{11} & A_{11} + B_{12} & A_{12} + B_{11} & A_{12} + B_{12} \\ A_{11} + B_{21} & A_{11} + B_{22} & A_{12} + B_{21} & A_{12} + B_{22} \\ A_{21} + B_{11} & A_{21} + B_{12} & A_{22} + B_{11} & A_{22} + B_{12} \\ A_{21} + B_{21} & A_{21} + B_{22} & A_{22} + B_{21} & A_{22} + B_{22} \end{pmatrix} . \tag{1.233}$$

It can be decomposed as,

$$\boxed{\hat{A} \oplus \hat{B} = \hat{A} \oplus \mathbb{O} + \mathbb{O} \oplus \hat{B} = \hat{A} \otimes \begin{pmatrix} 1 & 1 \\ 1 & 1 \end{pmatrix} + \begin{pmatrix} 1 & 1 \\ 1 & 1 \end{pmatrix} \otimes \hat{A} \ .} \tag{1.234}$$

Again, using the definition (1.229) of the unitary operator $\mathbb{S}$, we can reverse the order of the operator by,

$$\hat{A} \oplus \hat{B} = \mathbb{S}(\hat{B} \oplus \hat{A})\mathbb{S} \ . \tag{1.235}$$

Example 10 (*Direct external sum of two diagonal Hamiltonians*): As an example we consider a two-level atom excited by radiation and trapped in an external harmonic potential. We assume that the degrees of freedom do not interact. As the Hamiltonian of the HO is diagonal, the total Hamiltonian is organized into a diagonal matrix of quadratic subspaces,

$$\hat{H} = \hbar\omega(n+\tfrac{1}{2}) \oplus \begin{pmatrix} 0 & \hbar\Omega \\ \hbar\Omega & \hbar\Delta \end{pmatrix} = \begin{pmatrix} \frac{\hbar\omega}{2} & \frac{\hbar\omega}{2}+\hbar\Omega & 0 & 0 & \vdots \\ \frac{\hbar\omega}{2}+\hbar\Omega & \frac{\hbar\omega}{2}+\hbar\Delta & 0 & 0 & \vdots \\ 0 & 0 & \frac{3\hbar\omega}{2} & \frac{3\hbar\omega}{2}+\hbar\Omega & \vdots \\ 0 & 0 & \frac{3\hbar\omega}{2}+\hbar\Omega & \frac{3\hbar\omega}{2}+\hbar\Delta & \vdots \\ \cdots & \cdots & \cdots & \cdots & \ddots \end{pmatrix} .$$

It acts on the product state $|n\rangle|i\rangle$, where the first ket denotes the vibrational level and the second ket the electronic excitation of the atom.

Other examples are studied in Excs. 1.5.9.13 and 1.5.9.14.

1.5.8.4 Collective spins

Two spins $\hat{A}$ and $\hat{B}$ sum up according to the rule,

$$\hat{A}\otimes\mathbb{I}+\mathbb{I}\otimes\hat{B} = \begin{pmatrix} A_{11}+B_{11} & B_{12} & A_{12}+B_{12} & \\ B_{21} & A_{11}+B_{22} & & A_{12} \\ A_{21} & & A_{22}+B_{11} & B_{12} \\ & A_{21} & B_{21} & A_{22}+B_{22} \end{pmatrix} . \tag{1.236}$$

The procedure can be arbitrary extended to several spins, $\hat{A}\otimes\mathbb{I}\otimes\mathbb{I}+\mathbb{I}\otimes\hat{B}\otimes\mathbb{I}+\mathbb{I}\otimes\mathbb{I}\otimes\hat{C}$.

1.5.8.5 Trace

The *trace* of an operator over a subspace reduces its domain to the remaining dimensions (the $\cdot$ -symbol is a place holder for the dimension over which we do NOT want to trace):

$$\begin{aligned} \mathrm{Tr}_{\mathrm{B}}\hat{A}\otimes\hat{B} &= \sum_{(ik)(jl)(\cdot m)} \langle\cdot\, m|ik\rangle A_{ij}B_{kl}\langle jl|\cdot m\rangle = \sum_{(ik)(jl)(\cdot m)} |i\rangle A_{ij}B_{kl}\langle j|\delta_{km}\delta_{lm} \\ &= \sum_{(i)(j)(m)} |i\rangle A_{ij}B_{mm}\langle j| = \hat{A}\sum_m B_{mm} = \hat{A}\ \mathrm{Tr}_{\mathrm{B}}\hat{B}\ . \end{aligned} \tag{1.237}$$

For example, $\mathrm{Tr}_\rho\hat{A}\otimes\hat{\rho} = \hat{A}$. See the Excs. 1.5.9.15 and 1.5.9.16.

It can be shown,

$$\mathrm{Tr}\ \hat{A}\hat{B} = \mathrm{Tr}\ \hat{B}\hat{A}\ . \tag{1.238}$$

1.5.9 Exercises

1.5.9.1 Ex: Orthogonality

Show that two eigenvectors of a Hermitian operator associated with two different eigenvalues are orthogonal.

1.5.9.2 Ex: Orthonormalization

Orthonormalize the base $\langle a_1| = \begin{pmatrix}1 & -1 & 0\end{pmatrix}$, $\langle a_2| = \begin{pmatrix}0 & 1 & 0\end{pmatrix}$, $\langle a_3| = \begin{pmatrix}0 & 1 & 1\end{pmatrix}$.

1.5.9.3 Ex: Orthonormal base

Construct an orthonormal basis for the following operator describing a partially degenerate three-level system,

$$\hat{A} = \begin{pmatrix}1 & 1 & 1\\ 1 & 1 & 1\\ 1 & 1 & 1\end{pmatrix} .$$

1.5.9.4 Ex: Eigenvalue equation

Calculate the unitary matrix $\mathcal{U}$ transforming the Hamiltonian $\hat{H} = \begin{pmatrix}1 & -\imath\\ \imath & 1\end{pmatrix}$ into a diagonal matrix $E = \mathcal{U}^\dagger \hat{H} \mathcal{U}$.

1.5.9.5 Ex: Spin rotation operators

Prove the following relations for the spin rotation operator: $e^{-\imath\pi\hat{\sigma}_x/4}\hat{\sigma}_z e^{\imath\pi\hat{\sigma}_x/4} = -\hat{\sigma}_y$ and $e^{-\imath\pi\hat{\sigma}_x/4}\hat{\sigma}_y e^{\imath\pi\hat{\sigma}_x/4} = \hat{\sigma}_z$.

1.5.9.6 Ex: Eigenvalues and eigenvectors

Find the eigenvalues and -vectors of the operator $\hat{A} = \begin{pmatrix}1 & 1 & 1\\ 1 & 1 & 1\\ 1 & 1 & 1\end{pmatrix}$ and construct the unitary matrix which transforms this operator into a diagonal matrix.

1.5.9.7 Ex: Commuting operators

a. Show that if two operators $\hat{A}$ and $\hat{B}$ commute and if $|\psi\rangle$ is an eigenvector of $\hat{A}$, $\hat{B}|\psi\rangle$ also is an eigenvector of $\hat{A}$ with the same eigenvalue.
b. Show that if two operators $\hat{A}$ and $\hat{B}$ commute and if $|\psi_1\rangle$ and $|\psi_2\rangle$ are two eigenvector of $\hat{A}$ with different eigenvalues, the matrix element $\langle\psi_1|\hat{B}|\psi_2\rangle$ is equal to zero.
c. Show that if two operators $\hat{A}$ and $\hat{B}$ commute, we can construct an orthonormal basis of eigenvectors common to $\hat{A}$ and $\hat{B}$.

1.5.9.8 Ex: Eigenvalues

a. Find the eigenvalues and eigenvectors of the operator,

$$\hat{A} = \begin{pmatrix} 1 & 0 & 1 \\ 0 & \mu & 0 \\ 1 & 0 & 1 \end{pmatrix} \qquad \text{for} \qquad 0 < \mu < 2 \ .$$

b. Write down the unitary matrix $\mathcal{U}$ satisfying the eigenvalue equation: $\hat{A}\mathcal{U} = \mathcal{U}E_A$, where E_A is the matrix that has all eigenvalues of $\hat{A}$ in its diagonal.
c. Now consider the case $\mu = 0$. Find a complete set of commuting operators (CSCO). That is, calculate the components of a second operator $\hat{B}$, which commutes with $\hat{A}$, as a function of its eigenvalues λ_1, λ_2, and λ_3, and verify $[\hat{A}, \hat{B}] = 0$. Find the most general form of operator $\hat{B}$.

1.5.9.9 Ex: Schwartz inequality

Demonstrate the Schwartz inequality $|\langle u|v\rangle|^2 \leq \langle u|u\rangle\langle v|v\rangle$.

1.5.9.10 Ex: Heisenberg's uncertainty principle

Develop the formal derivation of Heisenberg's uncertainty principle.

1.5.9.11 Ex: Fourier transform

Show that $\langle \mathbf{r}|\hat{\mathbf{P}}|\psi\rangle = \frac{\hbar}{i}\nabla\langle \mathbf{r}|\psi\rangle$ reproduces the Schrödinger equation in position representation.

1.5.9.12 Ex: Projection of the motion of a particle

Project the Hamiltonian of the motion of a free particle onto the plane x-y at the position $z = z_0$ using the projection operator $\hat{P} = |z_0\rangle\langle z_0|$ and the trace defined in (1.232) generalized to continuous variables.

1.5.9.13 Ex: Complete system of commuting operators

Construct the Hilbert space of two independent two-level systems a and b. Consider observables $\hat{X}_a$ and $\hat{Y}_b$ acting on their respective systems. What will be their shapes $\hat{X}_{ab}$, respectively $\hat{Y}_{ab}$, in the total Hilbert space? Construct the expanded state $|\psi_{ab}\rangle$ from the basis of the individual systems. Verify $[\hat{X}_{ab}, \hat{Y}_{ab}] = 0$. Verify that the expanded observables obey the same eigenvalue equations as the original ones.

1.5.9.14 Ex: Liouville equation

Show that $\begin{pmatrix} 1 & 0 \\ 0 & 0 \end{pmatrix} \otimes \hat{A} + \begin{pmatrix} 0 & 0 \\ 0 & 1 \end{pmatrix} \otimes \hat{B} = \hat{A} \oplus \hat{B}$.

1.5.9.15 Ex: Liouville equation

Show at the example of a two-level system that the von Neumann equation, $\dot{\hat{\rho}} = -\frac{\imath}{\hbar}[\hat{H}, \hat{\rho}]$, can be written, $\dot{\vec{\rho}} = -\frac{\imath}{\hbar}(\hat{H} \otimes \mathbb{I} - \mathbb{I} \otimes \hat{H})\vec{\rho}$, using the definition of the external product and $\vec{\rho} \equiv \begin{pmatrix} \rho_{11} \\ \rho_{12} \\ \rho_{21} \\ \rho_{22} \end{pmatrix}$. **Help:** For this exercise the physical interpretation of $\hat{\rho}$ as the density operator does not matter. It may be regarded as a common observable.

1.5.9.16 Ex: Unitary transformation of singlet states

Consider two spins a and b that do not interact. Applying to each spin the same transformation to another base, show that the singlet state has in each base the following form: $|\psi\rangle = \frac{1}{\sqrt{2}}(|\uparrow\rangle_a|\downarrow\rangle_b - |\downarrow\rangle_a|\uparrow\rangle_b)$.

1.6 Time evolutions

Quantum systems may evolve in time, as predicted by the time-dependent Schrödinger equation (1.161). In this section we show different equivalent but complementary descriptions of the temporal evolution of quantum systems depending on whether the time dependence is attributed to the state function of to observables.

1.6.1 Unitary transformations

The best we can do to characterize a system is, obviously, to measure all its observables. However, neither the state functions nor the observables are fixed unambiguously, since defining a unitary operator, $\mathcal{U}^\dagger = \mathcal{U}^{-1}$, we can do,

$$\langle\psi|\hat{A}|\psi\rangle = \langle\psi|\mathcal{U}^\dagger\mathcal{U}\hat{A}\mathcal{U}^\dagger U|\psi\rangle = \langle\mathcal{U}\psi|\mathcal{U}\hat{A}\mathcal{U}^\dagger|U\psi\rangle \ . \tag{1.239}$$

That is, exchanging $|\psi\rangle$ by $\mathcal{U}|\psi\rangle$ and at the same time $\hat{A}$ by $\mathcal{U}\hat{A}\mathcal{U}^\dagger$, we obtain quantities describing the same physical reality, since the eigenvalues are unchanged. This allows us to choose the best mathematical representation for a specific problem. As an example, we will apply the temporal unitary transformation to solve the dynamics of a coupled two-level system in Exc. 1.6.7.1.

1.6.2 Schrödinger picture

Important examples of how the same system can be represented in different ways (related by unitary transformations) are the Heisenberg, Schrödinger, and interaction pictures.

The *Schrödinger picture*, denoted by the subscript S, is defined by the choice of a Hamiltonian,

$$\hat{H}_{\rm S} = \hat{H}(t, \hat{p}_{\rm S}, \hat{r}_{\rm S}) \qquad \text{with} \qquad \frac{d}{dt}\hat{p}_{\rm S} = \frac{d}{dt}\hat{r}_{\rm S} = 0 \ . \tag{1.240}$$

That is, the observables of the system $\hat{A}_{\rm S}(t,\hat{p}_{\rm S},\hat{r}_{\rm S})$ can only depend *explicitly* on time, but not via other operators, for instance $\hat{p}_{\rm S}$ and $\hat{r}_{\rm S}$, which are stationary,

$$\frac{d}{dt}\hat{A}_{\rm S} = \frac{\partial \hat{A}_{\rm S}}{\partial t} + \cancelto{0}{\dot{\hat{p}}_{\rm S}}\frac{\partial \hat{A}_{\rm S}}{\partial p_{\rm S}} + \cancelto{0}{\dot{\hat{r}}_{\rm S}}\frac{\partial \hat{A}_{\rm S}}{\partial r_{\rm S}} \ . \tag{1.241}$$

This is,

$$\boxed{\frac{d}{dt}\hat{A}_{\rm S}(t) = \frac{\partial}{\partial t}\hat{A}_{\rm S}(t)} \ . \tag{1.242}$$

In the context of a moving particle, this means that the Hamiltonian $\frac{1}{2m}\hat{p}_{\rm S}^2 + V(\hat{r}_{\rm S})$ is time-independent (unless the potential $V(\hat{r}_{\rm S},t)$ is itself time-dependent). In this case, the formal solution of the Schrödinger equation,

$$\boxed{\imath\hbar\frac{d}{dt}|\psi_{\rm S}(t)\rangle = \hat{H}_{\rm S}|\psi_{\rm S}(t)\rangle} \ , \tag{1.243}$$

can be written,

$$|\psi_{\rm S}(t)\rangle = e^{-(\imath/\hbar)\hat{H}_{\rm S}t}|\psi_{\rm S}(0)\rangle \equiv \mathcal{U}(t)|\psi_{\rm S}(0)\rangle \ . \tag{1.244}$$

Apparently, the temporal dynamics is completely within the wave functions.

Example 11 (*The time evolution operator*): Generalizing to an arbitrary initial time t_0 we write the temporal translation operator,

$$\mathcal{U}(t,t_0)|\psi(t_0)\rangle = |\psi(t)\rangle \ . \tag{1.245}$$

By the expression (1.244) we find immediately, with $t_0 < t_1 < t_2$,

$$\mathcal{U}(t_2,t_0) = \mathcal{U}(t_2,t_1)\mathcal{U}(t_1,t_0) \quad \text{and} \quad \mathcal{U}(t_0,t) = \mathcal{U}^\dagger(t,t_0) = \mathcal{U}^{-1}(t,t_0) = \mathcal{U}(t,t_0)^{-1} \ .$$

The conjugate operator of time evolution acts on the vector 'bra',

$$\langle\psi(t)| = \langle\psi(t_0)|\mathcal{U}^\dagger(t,t_0) \ .$$

1.6.3 Heisenberg picture

As unitary transformations do not change the physics, the system described by,

$$|\psi_{\rm S}(t)\rangle \longrightarrow \mathcal{U}(t)^\dagger|\psi_{\rm S}(t)\rangle \equiv |\psi_{\rm H}\rangle \quad \text{and} \quad \hat{A}_{\rm S}(t) \longrightarrow \mathcal{U}(t)^\dagger\hat{A}_{\rm S}(t)\mathcal{U}(t) \equiv \hat{A}_{\rm H}(t) \tag{1.246}$$

with the transformation defined by equation (1.244), is equivalent. The subscript H means the *Heisenberg picture*. In particular, we obviously have,

$$\hat{H}_{\rm S} = \hat{H}_{\rm H} \equiv \hat{H} \ . \tag{1.247}$$

Thus, the matrix element of the operator $\hat{A}_{\rm S}$ in Schrödinger's picture with the time-dependent base $\{|\psi_{\rm S}\rangle\}$ is equal to the matrix element of the operator $\hat{A}_{\rm H} = \mathcal{U}^\dagger\hat{A}_{\rm S}\mathcal{U}$

in Heisenberg's picture with the time-independent base $\{|\psi_{\rm H}\rangle\}$. In this picture the wavefunctions are independent of time,

$$\boxed{\frac{d}{dt}|\psi_{\rm H}\rangle = \frac{d}{dt}|\psi_{\rm S}(0)\rangle = 0}\,, \tag{1.248}$$

but the operators depend *im- and explicitly* on time,

$$\begin{aligned}\frac{d}{dt}\hat{A}_{\rm H}(t) &= \frac{d}{dt}\left(U(t)^\dagger \hat{A}_{\rm S}(t)\mathcal{U}(t)\right) = \frac{d\mathcal{U}^\dagger}{dt}\hat{A}_{\rm S}(t)\mathcal{U}(t) + \mathcal{U}(t)^\dagger \hat{A}_{\rm S}(t)\frac{d\mathcal{U}}{dt} + \mathcal{U}(t)^\dagger \frac{\partial \hat{A}_{\rm S}(t)}{\partial t}\mathcal{U}(t) \\ &= \frac{\imath}{\hbar}\hat{H}^\dagger U(t)^\dagger \hat{A}_{\rm S}\mathcal{U}(t) + \mathcal{U}(t)^\dagger \hat{A}_{\rm S}\frac{-\imath}{\hbar}\hat{H}\mathcal{U}(t) + \mathcal{U}^\dagger(t)\frac{\partial \hat{A}_{\rm S}(t)}{\partial t}\mathcal{U}(t)\,. \end{aligned} \tag{1.249}$$

That is,

$$\boxed{\frac{d}{dt}\hat{A}_{\rm H}(t) = \frac{\imath}{\hbar}[\hat{H}, \hat{A}_{\rm H}(t)] + \frac{\partial \hat{A}_{\rm H}(t)}{\partial t}}\,. \tag{1.250}$$

This so-called *Heisenberg equation*, which describes the temporal evolution of an operator acting on time-independent states in the Heisenberg picture, is equivalent to the Schrödinger equation, which expresses the temporal evolution of a quantum state in Schrödinger's picture.

According to equation (1.250), the rate of temporal variation of an operator in the Heisenberg representation is given by the commutator of that operator with the total Hamiltonian of the system. Note that if an operator representing a dynamic variable commutes with the Hamiltonian in the Schrödinger representation, it will also commute with the Hamiltonian in the Heisenberg representation and thus with the complete set of commutating observables,

$$[\hat{H}, \hat{A}_{\rm S}] = 0 \qquad \Longleftrightarrow \qquad [\hat{H}, \hat{A}_{\rm H}] = 0\,. \tag{1.251}$$

We will show this in the Exc. 1.6.7.2. Note that we could interpret Eq. (1.248) as a Schrödinger equation with a Hamiltonian $\tilde{H}_{\rm H} = 0$. That is, *the Hamiltonian used in the Schrödinger equation differs from the one used in the Heisenberg equation.* We will study this in more detail in Secs. 1.6.4 and 1.6.5.

Example 12 (*Position and momentum operators in the Heisenberg picture*): We know that in Schrödinger's picture (1.240), the operators $\hat{p}_{\rm S}$ and $\hat{r}_{\rm S}$ are stationary. Using this fact in derivation (1.249), we can show for example for the momentum operator,

$$\frac{\partial}{\partial t}\hat{p}_{\rm S} = 0 \qquad \Longrightarrow \qquad \frac{\partial}{\partial t}\hat{p}_{\rm H} = 0 \qquad \Longrightarrow \qquad \frac{d}{dt}\hat{p}_{\rm H} = \frac{\imath}{\hbar}[\hat{H}, \hat{p}_{\rm H}]\,.$$

In the Exc. 1.6.7.3 we will use the Heisenberg picture to derive the equations of motion for a particle confined to a potential.

1.6.4 Interaction picture

The *interaction picture* deals with problems where the total Hamiltonian is composed of a time-independent part and a time-dependent part,

$$\hat{H} = \hat{H}_0 + \hat{V}(t) \ . \tag{1.252}$$

Analogously to Eq. (1.244), we define a time evolution operator in terms of the *time-independent* part of the total Hamiltonian,

$$\boxed{|\psi_{\rm I}(t)\rangle = e^{\imath \hat{H}_0 t/\hbar}|\psi_{\rm S}(t)\rangle \qquad \text{and} \qquad \hat{A}_{\rm I}(t) = e^{\imath \hat{H}_0 t/\hbar}\hat{A}_{\rm S}e^{-\imath \hat{H}_0 t/\hbar}} \ . \tag{1.253}$$

Now we are interested in the temporal dependence of quantum states and operators in the interaction picture. Replacing the inverse function $|\psi_{\rm S}(t)\rangle = e^{-\imath \hat{H}_0 t/\hbar}|\psi_{\rm I}(t)\rangle$ in the Schrödinger equation (1.243) we immediately see,

$$\boxed{\hat{V}(t)|\psi_{\rm I}(t)\rangle = \imath\hbar\frac{\partial}{\partial t}|\psi_{\rm I}(t)\rangle} \ . \tag{1.254}$$

Apparently, in the interaction picture, only the perturbative term in Hamiltonian controls the temporal evolution. Taking the time derivative of both sides of the equation (1.253) transforming an operator from the Schrödinger to the interaction picture results in,

$$\boxed{\frac{d\hat{A}_{\rm I}}{dt} = \frac{\imath}{\hbar}[\hat{H}_0, \hat{A}_{\rm I}] + \frac{\partial \hat{A}_{\rm I}}{\partial t}} \ . \tag{1.255}$$

Therefore, we see that the time derivative can be expressed in the form of a commutator, resembling the Heisenberg equation (1.250), except that only the unperturbed term of the Hamiltonian appears in the argument of the commutation operator. As already state in Sec. 1.6.3, different Hamiltonians are used in the Schrödinger and in the Heisenberg equation.

> **Example 13 (*Schrieffer-Wolff transformation*):** The *Schrieffer-Wolff transformation* is a unitary transformation used to perturbatively diagonalize the system Hamiltonian to first order in the interaction. As such, the Schrieffer-Wolff transformation is an operator version of second-order perturbation theory. The Schrieffer-Wolff transformation is often used to project out the high energy excitations of a given quantum many-body Hamiltonian in order to obtain an effective low energy model. The Schrieffer-Wolff transformation thus provides a controlled perturbative way to study the strong coupling regime of quantum-many body Hamiltonians.
> Consider a quantum system evolving under the time-independent Hamiltonian operator $\hat{H}$ of the form $\hat{H} = \hat{H}_0 + \hat{V}$, where H_0 is a Hamiltonian with known eigenstates $|m\rangle$ and corresponding eigenvalues E_m, and where V is a small perturbation. Moreover, it is assumed without loss of generality that $\hat{V}$ is purely off-diagonal in the eigenbasis of $\hat{H}_0$, i.e.,
>
> $$\langle m|\hat{V}|m\rangle = 0 \tag{1.256}$$
>
> for all m. Indeed, this situation can always be arranged by absorbing the diagonal elements of $\hat{V}$ into $\hat{H}_0$, thus modifying its eigenvalues to,
>
> $$E'_m = E_m + \langle m|\hat{V}|m\rangle \ . \tag{1.257}$$

The Schrieffer-Wolff transformation is a unitary transformation which expresses the Hamiltonian in a basis (the 'dressed' basis) where it is diagonal to first order in the perturbation $\hat{V}$. This unitary transformation is conventionally written as:

$$\hat{H}' = e^{\imath S}\hat{H}e^{-\imath S} \ . \tag{1.258}$$

When $\hat{V}$ is small, the generator S of the transformation will likewise be small. The transformation can then be expanded in S using the Baker-Campbell-Haussdorf formula,

$$\hat{H}' = \hat{H} + [\imath S, \hat{H}] + \tfrac{1}{2}[\imath S, [\imath S, \hat{H}]] + \dots \ . \tag{1.259}$$

In terms of $\hat{H}_0$ and $\hat{V}$, the transformation becomes,

$$\hat{H}' = \hat{H}_0 + \hat{V} + [\imath S, \hat{H}_0] + [\imath S, \hat{V}] + \tfrac{1}{2}[\imath S, [\imath S, \hat{H}_0]] + \tfrac{1}{2}[\imath S, [\imath S, \hat{V}]] + \dots \ . \tag{1.260}$$

The Hamiltonian can be made diagonal to first order in $\hat{V}$ by choosing the generator S such that,

$$[\hat{H}_0, \imath S] = \hat{V} \ . \tag{1.261}$$

This equation always has a definite solution under the assumption that $\hat{V}$ is off-diagonal in the eigenbasis of $\hat{H}_0$. Substituting this choice in the previous transformation yields:

$$\hat{H}' = \hat{H}_0 + \tfrac{1}{2}[\imath S, \hat{V}] + O(\hat{V}^3) \ . \tag{1.262}$$

This expression is the standard form of the Schrieffer-Wolff transformation. Note that all the operators on the right-hand side are now expressed in a new basis 'dressed' by the interaction $\hat{V}$ to first order.
In the general case, the difficult step of the transformation is to find an explicit expression for the generator S. Once this is done, it is straightforward to compute the Schrieffer-Wolff Hamiltonian by computing the commutator $[S, \hat{V}]$. The Hamiltonian can then be projected on any subspace of interest to obtain an effective projected Hamiltonian for that subspace. In order for the transformation to be accurate, the eliminated subspaces must be energetically well separated from the subspace of interest, meaning that the strength of the interaction $\hat{V}$ must be much smaller than the energy difference between the subspaces. This is the same regime of validity as in standard second-order perturbation theory.

1.6.5 Hamiltonian under arbitrary unitary transformation

In the preceding section we have studied particular unitary transformations between the Schrödinger, Heisenberg, and interaction pictures. Let us now have a look at *arbitrary* unitary transformations.

We have seen that the unitary transformation,

$$|\psi_{\mathcal{U}}\rangle = \mathcal{U}^\dagger|\psi\rangle \qquad , \qquad \hat{A}_{\mathcal{U}} = \mathcal{U}^\dagger \hat{A}\mathcal{U} \ , \tag{1.263}$$

leaves the physics of a system unchanged. The question is now, how the Schrödinger equation,

$$\hat{H}|\psi\rangle = \imath\hbar\frac{d}{dt}|\psi\rangle \tag{1.264}$$

transforms into the new system, that is, what will the Hamiltonian $\hat{H}_{\mathcal{U}}$ look like in the transformed equation,

$$\hat{H}_{\mathcal{U}}|\psi_{\mathcal{U}}\rangle \stackrel{?}{=} \imath\hbar\frac{d}{dt}|\psi_{\mathcal{U}}\rangle \ . \tag{1.265}$$

We calculate,

$$\begin{aligned}\imath\hbar\frac{d}{dt}|\psi_{\mathcal{U}}\rangle &= \imath\hbar\dot{\mathcal{U}}^\dagger\frac{d}{dt}|\psi\rangle + \imath\hbar\dot{\mathcal{U}}^\dagger|\psi\rangle = (\mathcal{U}^\dagger\hat{H} + \imath\hbar\dot{\mathcal{U}}^\dagger)|\psi\rangle \\ &= (\mathcal{U}^\dagger\hat{H} + \imath\hbar\dot{\mathcal{U}}^\dagger)\mathcal{U}|\psi_{\mathcal{U}}\rangle = (\mathcal{U}^\dagger\hat{H}\mathcal{U} + \imath\hbar\dot{\mathcal{U}}^\dagger\mathcal{U})|\psi_{\mathcal{U}}\rangle = \hat{H}_{\mathcal{U}}|\psi_{\mathcal{U}}\rangle \ .\end{aligned} \tag{1.266}$$

Hence,

$$\boxed{\hat{H}_{\mathcal{U}} = \mathcal{U}^\dagger\hat{H}\mathcal{U} + \imath\hbar\dot{\mathcal{U}}^\dagger\mathcal{U}} \ . \tag{1.267}$$

We will apply this concept in Exc. 1.7.6.2 to a particle in the field of gravity.

Example 14 (*Interaction picture*): The above derivation is general and holds for any unitary transformation. We will now apply it to transform the Hamiltonian $\hat{H} = \hat{H}_0 + \hat{V}(t)$ into the interaction picture via the transformation $\mathcal{U} = e^{-(\imath/\hbar)\hat{H}_0 t}$. From

$$\dot{\mathcal{U}}^\dagger = \tfrac{\imath}{\hbar}\hat{H}_0 e^{(\imath/\hbar)\hat{H}_0 t} = \tfrac{\imath}{\hbar}\hat{H}_0\mathcal{U}^\dagger \tag{1.268}$$

we calculate,

$$\begin{aligned}\hat{H}_{\mathcal{U}} &= \mathcal{U}^\dagger\hat{H}\mathcal{U} + \imath\hbar\dot{U}^\dagger\mathcal{U} = \mathcal{U}^\dagger[\hat{H}_0 + \hat{V}(t)]\mathcal{U} + \imath\hbar\tfrac{\imath}{\hbar}\hat{H}_0 U^\dagger\mathcal{U} \\ &= \mathcal{U}^\dagger[\hat{H}_0 + \hat{V}(t)]\mathcal{U} - \hat{H}_0 = \mathcal{U}^\dagger\hat{V}(t)\mathcal{U} \ ,\end{aligned} \tag{1.269}$$

which confirms the validity of the Schrödinger equation (1.254) in the interaction picture, provided the Hamiltonian is taken to be the perturbation part $\hat{V}(t)$, only. In the Heisenberg picture $\hat{V}(t) = 0$, such that,

$$\hat{H}_{\mathcal{U}} = 0 \ , \tag{1.270}$$

which confirms Eq. (1.248).

1.6.6 Ehrenfest's theorem

For linear operators satisfying $[\hat{A}, \hat{B}] = \imath$ we can give a generalization of the commutation relation:

$$\boxed{[\hat{A}, F(\hat{A}, \hat{B})] = \imath\frac{\delta F(\hat{A}, \hat{B})}{\delta\hat{B}}} \ . \tag{1.271}$$

This can be verified by a Taylor expansion of $F(\hat{A}, \hat{B})$ by $\hat{B}$ around $\hat{B} = 0$, as will be shown in Exc. 1.6.7.4. An immediate consequence of $[\hat{p}, \hat{r}] = -\imath\hbar$ is,

$$[\hat{p}, F(\hat{r})] = -\imath\hbar\frac{\delta F(\hat{r})}{\delta\hat{r}} \ . \tag{1.272}$$

The momentum observable is not singularly defined by the commutation relation, because each unitarily transformed operator satisfies the relation as well. We

can expand a unitarily equivalent momentum as $\tilde{p} = \mathcal{U}p\mathcal{U}^\dagger = e^{\imath F(r)}pe^{-\imath F(r)} = p + \imath[F(r), p] + \frac{1}{2!}[F(r), [F(r), p]] + ...$ using the relation (1.272).

The observables in the Heisenberg picture follow the same equations of motion as the corresponding classical quantities. This *correspondence principle* is called *Ehrenfest theorem*. For example, when working with position and momentum variables $[\hat{r}, \hat{k}] = \imath$ and $\hat{H} = \frac{\hbar^2}{2m}\hat{k}^2 + V(\hat{r})$, we obtain,

$$[\hat{r}, \hat{H}] = \imath\hbar\frac{\delta\hat{H}}{\delta\hat{p}} \quad \text{and} \quad [\hat{p}, \hat{H}] = -\imath\hbar\frac{\delta\hat{H}}{\delta\hat{r}} \ , \tag{1.273}$$

and using the Heisenberg equation (1.250),

$$\dot{\hat{r}} = \frac{\delta\hat{H}}{\delta\hat{p}} \quad \text{and} \quad \dot{\hat{p}} = -\frac{\delta\hat{H}}{\delta\hat{r}} \ . \tag{1.274}$$

We will demonstrate this in Exc. 1.6.7.5 for the case of a harmonic potential.

In the Schrödinger picture the equation of motion for the eigenvalues of the observables takes the form,

$$\frac{d}{dt}\langle\hat{A}_\mathrm{S}\rangle = \langle\partial_t\psi|\hat{A}_\mathrm{S}|\psi\rangle + \langle\psi|\partial_t\hat{A}_\mathrm{S}|\psi\rangle + \langle\psi|\hat{A}_\mathrm{S}|\partial_t\psi\rangle = \frac{\partial}{\partial t}\langle\hat{A}_\mathrm{S}\rangle + \frac{\imath}{\hbar}\langle[\hat{H}, \hat{A}_\mathrm{S}]\rangle \ . \tag{1.275}$$

The eigenvalues behave as Heisenberg observables in Eq. (1.249), that is, they follow the laws of Hamilton's and Newton's mechanics.

The important result now is that the equations that govern the eigenvalues of the observables are identical in the both pictures, since from the Heisenberg picture we obtain with Eq. (1.249),

$$\frac{d}{dt}\langle\hat{A}_\mathrm{H}\rangle = \frac{\partial}{\partial t}\langle\hat{A}_\mathrm{H}\rangle + \frac{\imath}{\hbar}\langle[\hat{H}, \hat{A}_\mathrm{H}]\rangle \ . \tag{1.276}$$

1.6.7 Exercises

1.6.7.1 Ex: Coupled two-level atom

Calculate the time evolution of an atom with two levels coupled by a light field using the Hamiltonian,

$$\hat{H} = \begin{pmatrix} 0 & \frac{1}{2}\hbar\Omega \\ \frac{1}{2}\hbar\Omega & -\hbar\Delta \end{pmatrix} \ ,$$

where $\Delta = \omega - \omega_0$ is the detuning between the frequency of the light and the frequency of the transition and Ω the Rabi frequency. **Help:** Determine the matrix of the eigenvalues $\hat{E}$ and the unitary transformation $\mathcal{U}$ given by $\mathcal{U}^\dagger\hat{H}\mathcal{U} = \hat{E}$ and use the formal solution of the Schrödinger equation: $|\psi(t)\rangle = e^{-\imath\hat{H}t/\hbar}|\psi_0\rangle = e^{-\imath\mathcal{U}^\dagger\hat{E}\mathcal{U}t/\hbar}|\psi_0\rangle = \mathcal{U}^\dagger e^{-\imath\hat{E}t/\hbar}\mathcal{U}|\psi_0\rangle$.

1.6.7.2 Ex: Commutator in Schrödinger's and Heisenberg's picture

Show that operators which commute with the Hamiltonian in the Schrödinger picture also do it in the Heisenberg picture. Use the rule $[\hat{H}, \hat{A}\hat{B}] = \hat{A}[\hat{H}, \hat{B}] + [\hat{H}, \hat{A}]\hat{B}$.

1.6.7.3 Ex: Motion in Heisenberg's picture

Consider the Hamiltonian $\hat{H} = \frac{\hat{p}^2}{2m} + \frac{m}{2}\omega^2\hat{r}^2$. Using the relation $[\hat{p}, \hat{r}] = -\imath\hbar$ calculate in the Heisenberg picture the equations of motion for the observables $\hat{p}$, $\hat{r}$, and $\hat{p}\hat{r}$.

1.6.7.4 Ex: Commutator of a function of operators

Prove the relationship (1.271).

1.6.7.5 Ex: Ehrenfest's theorem

Compare the equations of Ehrenfest's theorem with those of Hamilton-Jacobi for a classical particle subject to a time-independent potential. Discuss the classical limit, that is, when the Hamilton-Jacobi equations approach those of Ehrenfest.

1.7 Symmetries in quantum mechanics

We already saw in Sec. 1.5.4 that, beyond observables, there is another category of operators that does not correspond to measurable physical quantities, but is very useful in the quantum formalism. These are the *unitary transformations*. In this section we will encounter some interesting examples.

1.7.1 Translation, rotation and momentum kick

1.7.1.1 Temporal translation operator

The temporal evolution of a system is described by the Schrödinger equation whose formal solution can be written as follows,

$$|\psi(t)\rangle = e^{-\imath\hat{H}t/\hbar}|\psi(0)\rangle \ . \tag{1.277}$$

With this we can define an *evolution operator* or temporal translation,

$$\boxed{\mathcal{U}_{\rm tp}(\tau) \equiv e^{-\imath\hat{H}t/\hbar} \qquad \text{such that} \qquad \mathcal{U}_{\rm tp}(\tau)|\psi(t)\rangle = |\psi(t+\tau)\rangle} \ . \tag{1.278}$$

The temporal evolution has already been discussed extensively in Sec. 1.6.

1.7.1.2 Spatial translation operator

In this section we look for a unitary *translation operator*,

$$\mathcal{T}_{\rm tr}\mathbf{r} \equiv \mathbf{a} + \mathbf{r} \ . \tag{1.279}$$

Before this, we need to derive the following calculation rule for commutators, which will be done in Exc. 1.7.6.1:

$$e^{\hat{A}}\hat{B}e^{-\hat{A}} = \hat{B} + [\hat{A}, \hat{B}] + \tfrac{1}{2!}[\hat{A}, [\hat{A}, \hat{B}]] + \ldots \ . \tag{1.280}$$

Applying this formula to the two operators $\hat{\mathbf{p}}$ and $\hat{\mathbf{r}}$ related by the commutation rule (1.160), we obtain,

$$e^{(\imath/\hbar)\mathbf{a}\cdot\hat{\mathbf{p}}}\hat{\mathbf{r}}e^{(-\imath/\hbar)\mathbf{a}\cdot\hat{\mathbf{p}}} = \hat{\mathbf{r}} + [(\imath/\hbar)\mathbf{a}\cdot\hat{\mathbf{p}},\hat{\mathbf{r}}] + \tfrac{1}{2!}\cancelto{0}{[(\imath/\hbar)\mathbf{a}\cdot\hat{\mathbf{p}},\mathbf{a}]} + ... = \hat{\mathbf{r}} + \mathbf{a}\ . \tag{1.281}$$

That is, the operator

$$\boxed{\mathcal{U}_{\rm tr}(\mathbf{a}) \equiv e^{(-\imath/\hbar)\mathbf{a}\cdot\hat{\mathbf{p}}}} \tag{1.282}$$

performs a spatial translation of the position operator. The operator is unitary,

$$\mathcal{U}_{\rm tr}(\mathbf{a})^{-1} = \mathcal{U}_{\rm tr}(\mathbf{a})^\dagger\ , \tag{1.283}$$

and forms a group since $\mathcal{U}_{\rm tr}(\mathbf{a})\mathcal{U}_{\rm tr}(\mathbf{b}) = \mathcal{U}_{\rm tr}(\mathbf{a}+\mathbf{b})$. Summarizing the impact of the translation on the operators of space,

$$\boxed{\mathcal{U}^\dagger_{\rm tr}(\mathbf{a})\hat{\mathbf{r}}\mathcal{U}_{\rm tr}(\mathbf{a}) = \hat{\mathbf{r}} + \mathbf{a} \quad , \quad \mathcal{U}^\dagger_{\rm tr}(\mathbf{a})\hat{\mathbf{p}}\mathcal{U}_{\rm tr}(\mathbf{a}) = \hat{\mathbf{p}}}\ , \tag{1.284}$$

where the second relation is obvious.

To demonstrate how the translation acts on a state, let us calculate,

$$\hat{\mathbf{r}}e^{(-\imath/\hbar)\mathbf{a}\cdot\hat{\mathbf{p}}}|\mathbf{r}\rangle = e^{(-\imath/\hbar)\mathbf{a}\cdot\hat{\mathbf{p}}}(\hat{\mathbf{r}}+\mathbf{a})|\mathbf{r}\rangle = (\mathbf{r}+\mathbf{a})e^{(-\imath/\hbar)\mathbf{a}\cdot\hat{\mathbf{p}}}|\mathbf{r}\rangle\ . \tag{1.285}$$

Hence,

$$\boxed{\mathcal{U}_{\rm tr}(\mathbf{a})|\mathbf{r}\rangle = e^{(-\imath/\hbar)\mathbf{a}\cdot\hat{\mathbf{p}}}|\mathbf{r}\rangle = |\mathbf{r}+\mathbf{a}\rangle}\ . \tag{1.286}$$

Therefore, if a particle is in an eigenstate $|\mathbf{r}\rangle$ of the position operator (i.e. located exactly at the position $\mathbf{r}$), then after $\mathcal{U}_{\rm tr}(\mathbf{a})$ acts on it, the particle is at the position $\mathbf{r}+\mathbf{a}$: The translation operator $\mathcal{U}_{\rm tr}(\mathbf{a})$ hence moves particles and fields by the distance $\mathbf{a}$.

Finally, we want to describe, how the translation operator acts on an arbitrary state $|\psi\rangle$ represented in position-space, remembering that the position-space wavefunction is obtained via $\psi(\mathbf{r}) \equiv \langle\mathbf{r}|\psi\rangle$, as already mentioned in Sec. 1.5.7. We get,

$$\psi'(\mathbf{r}) \equiv \mathcal{T}_{\rm tr}\psi(\mathbf{r}) \equiv \langle\mathbf{r}|\mathcal{U}_{\rm tr}(\mathbf{a})|\psi\rangle = \langle\mathcal{U}^\dagger_{\rm tr}(\mathbf{a})\mathbf{r}|\psi\rangle = \langle\mathbf{r}-\mathbf{a}|\psi\rangle = \psi(\mathbf{r}-\mathbf{a})\ . \tag{1.287}$$

This relation is easier to remember as $\psi'(\mathbf{r}+\mathbf{a}) = \psi(\mathbf{r})$, which can be read as: *The value of the new wavefunction at the new point equals the value of the old wavefunction at the old point.*

> **Example 15 (*Translation of spatial wavefunctions*):** Here is an example showing that these two descriptions (1.286) and (1.287) are equivalent. The state $|\mathbf{x}\rangle$ corresponds to the wavefunction $\psi(\mathbf{r}) = \delta^3(\mathbf{r}-\mathbf{x})$, while the state $\mathcal{U}_{\rm tr}(\mathbf{a})|\mathbf{x}\rangle = |\mathbf{x}+\mathbf{a}\rangle$ corresponds to the wavefunction $\psi'(\mathbf{r}) = \delta^3(\mathbf{r}-(\mathbf{x}+\mathbf{a}))$. These indeed satisfy $\psi'(\mathbf{r}) = \psi(\mathbf{r}-\mathbf{a})$.

Comparing the expansion of the translation operator,

$$\langle\mathbf{r}|\mathcal{U}_{\rm tr}(\mathbf{a})|\psi\rangle = \langle e^{(\imath/\hbar)\mathbf{a}\cdot\hat{\mathbf{p}}}\mathbf{r}|\psi\rangle = \left(1 + \frac{\imath}{\hbar}\mathbf{a}\cdot\hat{\mathbf{p}} - \frac{1}{\hbar^2}\frac{(\mathbf{a}\cdot\hat{\mathbf{p}})^2}{2!} + ..\right)\langle\mathbf{r}|\psi\rangle\ , \tag{1.288}$$

with the Taylor expansion of the wavefunction,

$$\langle \mathbf{r}+\mathbf{a}|\psi\rangle = \psi(\mathbf{r}+\mathbf{a}) = \left(1 + \mathbf{a}\cdot\nabla + \frac{(\mathbf{a}\cdot\nabla)^2}{2!} + ..\right)\psi(\mathbf{r}) \ . \tag{1.289}$$

we obtain

$$\hat{\mathbf{p}}|\mathbf{r}\rangle = \frac{\hbar}{\imath}\nabla|\mathbf{r}\rangle \ . \tag{1.290}$$

Finally, we note that the momentum operator can be defined via the translation operator,

$$\hat{\mathbf{p}} = \imath\hbar\ \nabla_{\mathbf{a}}\mathcal{U}_{\rm tr}(\mathbf{a})|_{\mathbf{a}=\mathbf{0}} \ . \tag{1.291}$$

1.7.1.3 Momentum kick operator

In this section we look for the unitary transformation into a frame moving a constant velocity $\mathbf{v}$,

$$\mathcal{T}_{\rm kc}\mathbf{p} \equiv \mathbf{p} + m\mathbf{v} \ . \tag{1.292}$$

As this transformation corresponds to a 'translation' in momentum space, the form of the unitary transformation operator and the way it acts on operators and states are easy to derive by analogy to the spatial translation operator, simply interchanging the roles of the conjugate operators of space and momentum. The corresponding unitary operator in the so-called *kick operator*,

$$\boxed{\mathcal{U}_{\rm kc}(m\mathbf{v}) = e^{(\imath/\hbar)m\mathbf{v}\cdot\hat{\mathbf{r}}}} \ . \tag{1.293}$$

where $m\mathbf{v} = \mathbf{p} = \hbar\mathbf{k}$ is the gain in momentum due to the kick.

A common situation where such a kick occurs is the photonic recoil that an atom receives upon absorption of a photon. Using the relationship (1.280) derived in Exc. 1.7.6.1 it is easy to verify the following expressions of the left-hand panel,

$$\boxed{\begin{aligned} e^{\imath\mathbf{k}\cdot\hat{\mathbf{r}}}|\mathbf{r}\rangle &= e^{\imath\mathbf{k}\cdot\mathbf{r}}|\mathbf{r}\rangle \\ e^{\imath\mathbf{k}\cdot\hat{\mathbf{r}}}|\mathbf{p}\rangle &= |\mathbf{p}+\hbar\mathbf{k}\rangle \\ e^{-\imath\mathbf{k}\cdot\hat{\mathbf{r}}}\hat{\mathbf{r}}e^{\imath\mathbf{k}\cdot\hat{\mathbf{r}}} &= \hat{\mathbf{r}} \\ e^{-\imath\mathbf{k}\cdot\hat{\mathbf{r}}}\hat{\mathbf{p}}e^{\imath\mathbf{k}\cdot\hat{\mathbf{r}}} &= \hat{\mathbf{p}}+\hbar\mathbf{k} \\ e^{-\imath\mathbf{k}\cdot\hat{\mathbf{r}}}\frac{\hat{\mathbf{p}}^2}{2m}e^{\imath\mathbf{k}\cdot\hat{\mathbf{r}}} &= \frac{(\hat{\mathbf{p}}+\hbar\mathbf{k})^2}{2m} \end{aligned}} \quad , \quad \boxed{\begin{aligned} e^{-\imath\mathbf{b}\cdot\hat{\mathbf{p}}/\hbar}|\mathbf{r}\rangle &= |\mathbf{r}+\mathbf{b}\rangle \\ e^{-\imath\mathbf{b}\cdot\hat{\mathbf{p}}/\hbar}|\mathbf{p}\rangle &= e^{-\imath\mathbf{b}\cdot\mathbf{p}/\hbar}|\mathbf{p}\rangle \\ e^{\imath\mathbf{b}\cdot\hat{\mathbf{p}}/\hbar}\hat{\mathbf{r}}e^{-\imath\mathbf{b}\cdot\hat{\mathbf{p}}/\hbar} &= \hat{\mathbf{r}}+\mathbf{b} \\ e^{\imath\mathbf{b}\cdot\hat{\mathbf{p}}/\hbar}\hat{\mathbf{p}}e^{-\imath\mathbf{b}\cdot\hat{\mathbf{p}}/\hbar} &= \hat{\mathbf{p}} \\ e^{\imath\mathbf{b}\cdot\hat{\mathbf{p}}/\hbar}V(\hat{\mathbf{r}})e^{-\imath\mathbf{b}\cdot\hat{\mathbf{p}}/\hbar} &= V(\hat{\mathbf{r}}+\mathbf{b}) \end{aligned}} \tag{1.294}$$

The rule implies $[e^{\imath\mathbf{k}\cdot\hat{\mathbf{r}}}, \hat{\mathbf{p}}] \neq 0 \neq [e^{\imath\mathbf{k}\cdot\hat{\mathbf{r}}}, \hat{H}]$. That is, we describe the kick by simply adding the corresponding momentum $\hbar\mathbf{k}$ to the system and adjusting the kinetic energy accordingly.

The right-hand panel of Eq. (1.294) summarizes rules for calculating with the spatial *displacement operator*, $\mathcal{U}_{\rm tr}(\mathbf{b}) = e^{-\imath\mathbf{b}\cdot\hat{\mathbf{p}}/\hbar}$, introduced in Sec. 1.7.1. By analogy we find $[e^{-\imath\mathbf{b}\cdot\hat{\mathbf{p}}/\hbar}, \hat{\mathbf{r}}] \neq 0 \neq [e^{-\imath\mathbf{b}\cdot\hat{\mathbf{p}}/\hbar}, \hat{H}]$ when the particle is subject to a potential. The (complex) eigenstates of the translation operator $e^{(-\imath/\hbar)\mathbf{a}\cdot\hat{\mathbf{p}}}$ are the momentum states $|\mathbf{p}\rangle$, and the eigenvalues $e^{(-\imath/\hbar)\mathbf{a}\cdot\mathbf{p}}$ are unitary. The (complex) eigenstates of the kick operator $e^{\imath\mathbf{k}\cdot\hat{\mathbf{r}}}$ are the position states $|\mathbf{r}\rangle$, and the eigenvalues $e^{\imath\mathbf{k}\cdot\mathbf{r}}$ are unitary.

The 'kick' will play a prominent role in the discussion of photonic recoil (see Sec. 2.6.2). Of course the assumption of an infinitely fast transition is an idealization and the ultimate reason for the non-conservation of momentum and energy by the system. In real situations, such as in the case of photonic recoil, the dynamics should be described by a collision process which conserves momentum and energy.

1.7.1.4 Periodic systems, quasi-momentum

Systems with potentials are generally not translationally invariant, since according to Eq. (1.294),

$$e^{(\imath/\hbar)\mathbf{a}\cdot\hat{\mathbf{p}}}V(\hat{\mathbf{r}})e^{(-\imath/\hbar)\mathbf{a}\cdot\hat{\mathbf{p}}} = V(\hat{\mathbf{r}}+\mathbf{a}) \neq V(\hat{\mathbf{r}}) \ . \tag{1.295}$$

An exception are precisely those potentials satisfying $V(\hat{\mathbf{r}}+\mathbf{a}) = V(\hat{\mathbf{r}})$, which are called periodic. The (complex) eigenstates $|\mathbf{q}\rangle$ of the translation operator, given by,

$$\mathcal{U}_{\rm tr}(\mathbf{a})|\mathbf{q}\rangle = e^{(-\imath/\hbar)\mathbf{a}\cdot\mathbf{q}}|\mathbf{q}\rangle \ , \tag{1.296}$$

are called *quasi-momenta*. In contrast to the continuous symmetries of homogeneity or isotropy, periodicity and parity represent discrete symmetries. We will study periodic systems state in detail in Chp. 4.

1.7.1.5 Rotation operator

In this section we look for the unitary transformation corresponding to the *rotation operator* [813],

$$\mathcal{T}_{\rm rt}\mathbf{r} \equiv e^{\vec{\alpha}\times}\mathbf{r} \ . \tag{1.297}$$

We calculate,

$$\begin{aligned} e^{\vec{\alpha}\times}\mathbf{r} &= \sum_n \frac{(\vec{\alpha}\times)^n}{n!}\mathbf{r} = \mathbf{r} + \vec{\alpha}\times\mathbf{r} + \tfrac{1}{2}\vec{\alpha}\times(\vec{\alpha}\times\mathbf{r}) + .. \\ &= \hat{\mathbf{e}}_\alpha(\hat{\mathbf{e}}_\alpha\cdot\mathbf{r}) + \hat{\mathbf{e}}_\alpha\times\mathbf{r}\sin\alpha - \hat{\mathbf{e}}_\alpha\times(\hat{\mathbf{e}}_\alpha\times\mathbf{r})\cos\alpha \ , \end{aligned} \tag{1.298}$$

as we will see in Exc. 1.7.6.4. We define the unitary rotational transformation by,

$$\boxed{\mathcal{U}^\dagger_{\rm rt}(\vec{\alpha})\hat{\mathbf{r}}\mathcal{U}_{\rm rt}(\vec{\alpha}) = e^{\vec{\alpha}\times}\hat{\mathbf{r}} \quad , \quad \mathcal{U}_{\rm rt}(\vec{\alpha})|\mathbf{r}\rangle = |e^{\vec{\alpha}\times}\mathbf{r}\rangle} \ . \tag{1.299}$$

To derive the explicit form of the rotation operator, we consider two rotations about the same axis $\vec{\alpha} = \lambda_1\hat{\mathbf{e}}_\alpha + \lambda_2\hat{\mathbf{e}}_\alpha$, such that

$$\mathcal{U}_{\rm rt}(\lambda_1\hat{\mathbf{e}}_\alpha)\mathcal{U}_{\rm rt}(\lambda_2\hat{\mathbf{e}}_\alpha) = \mathcal{U}_{\rm rt}(\lambda_1\hat{\mathbf{e}}_\alpha + \lambda_2\hat{\mathbf{e}}_\alpha) \ . \tag{1.300}$$

Calculating the derivative of this equation by λ_1 and then setting $\lambda_1 = 0$, we have,

$$\begin{aligned} & \tfrac{d\mathcal{U}_{\rm rt}(\lambda_1\hat{\mathbf{e}}_\alpha)}{d\lambda_1}\Big|_{\lambda_1=0}\mathcal{U}_{\rm rt}(\lambda_2\hat{\mathbf{e}}_\alpha) &=& \tfrac{d\mathcal{U}_{\rm rt}(\lambda_1\hat{\mathbf{e}}_\alpha+\lambda_2\hat{\mathbf{e}}_\alpha)}{d(\lambda_1+\lambda_2)}\Big|_{\lambda_1=0}\tfrac{d(\lambda_1+\lambda_2)}{d\lambda_1}\Big|_{\lambda_1=0} \\ \Longrightarrow\quad & \tfrac{d\lambda_1\hat{\mathbf{e}}_\alpha}{d\lambda_1}\Big|_{\lambda_1=0}\cdot\nabla_{\vec{\alpha}}U_{\rm rt}(\vec{\alpha})|_{\vec{\alpha}=0}\mathcal{U}_{\rm rt}(\lambda_2\hat{\mathbf{e}}_\alpha) &=& \tfrac{d\mathcal{U}_{\rm rt}(\lambda_2\hat{\mathbf{e}}_\alpha)}{d\lambda_2} \\ \Longrightarrow\quad & \hat{\mathbf{e}}_\alpha\cdot\tfrac{\hat{\mathbf{L}}}{\imath\hbar}\,U_{\rm rt}(\lambda_2\hat{\mathbf{e}}_\alpha) &=& \tfrac{d\mathcal{U}_{\rm rt}(\lambda_2\hat{\mathbf{e}}_\alpha)}{d\lambda_2} \end{aligned} \tag{1.301}$$

where we define the angular momentum operator,

$$\hat{\mathbf{L}} \equiv \imath\hbar\, \nabla_{\vec{\alpha}} \mathcal{U}_{\rm rt}(\vec{\alpha})|_{\vec{\alpha}=0} \ . \tag{1.302}$$

The solution of the last differential equation (1.301) is, with $\lambda_2 \hat{\mathbf{e}}_\alpha = \vec{\alpha}|_{\lambda_1=0}$,

$$\boxed{\mathcal{U}_{\rm rt}(\vec{\alpha}) = e^{(-\imath/\hbar)\hat{\mathbf{L}}\cdot\vec{\alpha}}} \ . \tag{1.303}$$

The explicit form of $\hat{\mathbf{L}}$ follows from its action on a state $|\psi\rangle$ projected into position space. In analogy with the derivation of the result (1.290), comparing the expansion of the operator (1.303),

$$\langle \mathbf{r}|\mathcal{U}_{\rm rt}(\vec{\alpha})|\psi\rangle = \langle e^{(\imath/\hbar)\vec{\alpha}\cdot\hat{\mathbf{L}}}\mathbf{r}|\psi\rangle = \left(1 + \frac{\imath}{\hbar}\vec{\alpha}\cdot\hat{\mathbf{L}} + ..\right)\langle \mathbf{r}|\psi\rangle \ , \tag{1.304}$$

with the Taylor expansion of the wavefunction,

$$\langle e^{\vec{\alpha}\times}\mathbf{r}|\psi\rangle = \psi(\mathbf{r} + \vec{\alpha}\times\mathbf{r} + ..) = [1 + (\vec{\alpha}\times\mathbf{r})\cdot\nabla_{\mathbf{r}} + ..]\,\psi(\mathbf{r}) \ , \tag{1.305}$$

we find,

$$\frac{\imath}{\hbar}\vec{\alpha}\cdot\hat{\mathbf{L}} = (\vec{\alpha}\times\mathbf{r})\cdot\nabla_{\mathbf{r}} = \vec{\alpha}\cdot(\mathbf{r}\times\nabla_{\mathbf{r}}) = \frac{\imath}{\hbar}\vec{\alpha}\cdot(\mathbf{r}\times\hat{\mathbf{p}}) \ , \tag{1.306}$$

that is,

$$\hat{\mathbf{L}} = \hat{\mathbf{r}}\times\hat{\mathbf{p}} \ . \tag{1.307}$$

Therefore, the observable $\hat{\mathbf{L}}$ is the *orbital angular momentum* of the particle producing the rotations.

Inserting the angular momentum expression (1.307) into the rotation operator (1.303) and using the rule (1.280) as well as the commutation relations for position and momentum operators, we can now verify the expression directly. Note also that the rotation transformation acts on the momentum operators and states in the same way as on position operators and states. This is not surprising, as the angular momentum operator is symmetric in $\mathbf{r}$ and $\mathbf{p}$.

1.7.2 Transformation to accelerated and rotating frames

1.7.2.1 Transformation to an accelerated frame

Transformation into a accelerated frame with acceleration $\mathbf{g}$ adds a homogeneous force term to the Hamiltonian. At non-relativistic velocities, the transformation can be performed via a unitary kick into a system instantaneously moving at velocity $\mathbf{g}t$,

$$\boxed{\mathcal{U}_{\rm ac}(\mathbf{g}) = e^{(\imath/\hbar)m\mathbf{g}t\cdot\hat{\mathbf{r}}}} \quad , \quad |\psi_{\rm ac}\rangle = \mathcal{U}_{\rm ac}(\mathbf{g})|\psi\rangle \ . \tag{1.308}$$

This operator removes the force field from the Hamiltonian, since the Schrödinger equation,

$$\imath\hbar\frac{d}{dt}|\psi\rangle = \hat{H}|\psi\rangle \qquad \text{with} \qquad \hat{H} = \frac{\hat{\mathbf{p}}^2}{2m} + m\mathbf{g}\cdot\hat{\mathbf{r}} \ , \tag{1.309}$$

transforms into the Schrödiner equation,

$$\begin{aligned} \imath\hbar\frac{d}{dt}|\psi_{\rm ac}\rangle &= \imath\hbar\frac{d}{dt}\left(e^{(\imath/\hbar)m\mathbf{g}t\cdot\hat{\mathbf{r}}}|\psi\rangle\right) \\ &= \imath\hbar e^{(\imath/\hbar)m\mathbf{g}t\cdot\hat{\mathbf{r}}}\frac{d}{dt}|\psi\rangle + \imath\hbar|\psi\rangle\frac{d}{dt}e^{(\imath/\hbar)m\mathbf{g}t\cdot\hat{\mathbf{r}}} \\ &= e^{(\imath/\hbar)m\mathbf{g}t\cdot\hat{\mathbf{r}}}\left(\frac{\hat{\mathbf{p}}^2}{2m}+m\mathbf{g}\cdot\hat{\mathbf{r}}\right)|\psi\rangle - m\mathbf{g}\cdot\hat{\mathbf{r}}e^{(\imath/\hbar)m\mathbf{g}t\cdot\hat{\mathbf{r}}}|\psi\rangle = \frac{\hat{\mathbf{p}}^2}{2m}|\psi_{\rm ac}\rangle\ . \end{aligned} \tag{1.310}$$

1.7.2.2 Transformation to a rotating frame

Transformation into a frame rotating at angular velocity $\vec{\omega}$ adds ... to the Hamiltonian. At non-relativistic velocities, the transformation can be performed via a unitary rotation transformation into a system rotated by an angle $\vec{\omega}t$,

$$\boxed{\mathcal{U}_{\rm ar}(\vec{\omega}) = e^{(\imath/\hbar)m\vec{\omega}t\cdot\hat{\mathbf{L}}}} \quad , \quad |\psi_{\rm ar}\rangle = \mathcal{U}_{\rm ar}(\vec{\omega})|\psi\rangle\ . \tag{1.311}$$

1.7.3 Composite transformations, Galilei boost

Some transformations are generated by several operators. The Galilei transform of a system into a moving frame, the displacement operator for coherent states (2.130), or the squeezing operator (14.104) are prominent examples. These transformations can be handled using Glauber's formula, which will be introduced below, before we turn our attention to the Galilei transform.

1.7.3.1 Glauber's and Baker-Campbell-Hausdorff's formulas

The *Baker-Campbell-Hausdorff formula* for operators $\hat{A}$ and $\hat{B}$ reads,

$$\ln(e^{\hat{A}}e^{\hat{B}}) = \hat{A}+\hat{B}+\tfrac{1}{2}[\hat{A},\hat{B}]+\tfrac{1}{12}[\hat{A},[\hat{A},\hat{B}]]-\tfrac{1}{12}[\hat{B},[\hat{A},\hat{B}]]+\ldots\ . \tag{1.312}$$

A useful special case called *Glauber's formula* follows when $\hat{A}$ and $\hat{B}$ commute with their commutator, i.e. $[\hat{A},[\hat{A},\hat{B}]]=[\hat{B},[\hat{A},\hat{B}]]=0$,

$$\boxed{e^{[\hat{B},\hat{A}]/2}e^{\hat{A}}e^{\hat{B}} = e^{\hat{A}+\hat{B}} = e^{[\hat{A},\hat{B}]/2}e^{\hat{B}}e^{\hat{A}}}\ . \tag{1.313}$$

Example 16 (*The Baker-Hausdorff formula*): In order to prove the Baker-Hausdorff formula, we consider the operator,

$$\hat{G}(\tau) \equiv e^{\tau(\hat{A}+\hat{B})}e^{-\tau\hat{B}}e^{-\tau\hat{A}}\ .$$

The derivative is,

$$\begin{aligned} \hat{G}'(\tau) &= (\hat{A}+\hat{B})e^{\tau(\hat{A}+\hat{B})}e^{-\tau\hat{B}}e^{-\tau\hat{A}} - e^{\tau(\hat{A}+\hat{B})}\hat{B}e^{-\tau\hat{B}}e^{-\tau\hat{A}} - e^{\tau(\hat{A}+\hat{B})}e^{-\tau\hat{B}}\hat{A}e^{-\tau\hat{A}} \\ &= e^{\tau(\hat{A}+\hat{B})}\left[\hat{A}e^{-\tau\hat{B}} - e^{-\tau\hat{B}}\hat{A}\right]e^{-\tau\hat{A}} = e^{\tau(\hat{A}+\hat{B})}\left[\hat{A}-e^{-\tau\hat{B}}\hat{A}e^{\tau\hat{B}}\right]e^{-\tau\hat{B}}e^{-\tau\hat{A}} \\ &= e^{\tau(\hat{A}+\hat{B})}\left[\hat{A}-\left(\hat{A}+[-\tau\hat{B},\hat{A}]+\tfrac{1}{2!}[-\tau\hat{B},[-\tau\hat{B},\hat{A}]]+..\right)\right]e^{-\tau\hat{B}}e^{-\tau\hat{A}}\ , \end{aligned}$$

using the formula (1.280). If now $[\hat{A},[\hat{A},\hat{B}]]=0=[\hat{B},[\hat{A},\hat{B}]]$, then,

$$\hat{G}'(\tau) = e^{\tau(\hat{A}+\hat{B})}\tau[\hat{B},\hat{A}]e^{-\tau\hat{B}}e^{-\tau\hat{A}} = -\tau[\hat{A},\hat{B}]e^{\tau(\hat{A}+\hat{B})}e^{-\tau\hat{B}}e^{-\tau\hat{A}} = -\tau[\hat{A},\hat{B}]\hat{G}(\tau)\ .$$

The solution of this differential equation is,

$$\hat{G}(\tau) \equiv e^{-(\tau^2/2)[\hat{A},\hat{B}]}\hat{G}(0) \ .$$

With $\hat{G}(0) = 1$ we obtain at the point $\tau = 1$,

$$e^{\hat{A}+\hat{B}} e^{-\hat{B}} e^{-\hat{A}} = e^{-(1/2)[\hat{A},\hat{B}]} \ .$$

1.7.3.2 Galilei and Lorentz boosts

The *Galilei transform* (or *Galilei boost*) is defined by,

$$\mathcal{T}_G \mathbf{r} = \mathbf{r} + \mathbf{v}t \qquad \text{and} \qquad \mathcal{T}_G \mathbf{p} = \mathbf{p} + m\mathbf{v} \ . \tag{1.314}$$

It describes the transformation of a system into a moving frame. Obviously, the Galilei transform must satisfy $\mathcal{T}_{\mathbf{v}_1}\mathcal{T}_{\mathbf{v}_2} = \mathcal{T}_{\mathbf{v}_1+\mathbf{v}_2}$, while this certainly does not hold for relativistic velocities.

In quantum mechanics we define,

$$\hat{\mathbf{G}} = \hat{\mathbf{p}}t - \hat{\mathbf{r}}m = \imath\hbar\nabla_{\mathbf{v}}\mathcal{U}_G(\mathbf{v})|_{\mathbf{v}=0} \ , \tag{1.315}$$

with the Galilei boost,

$$\boxed{\mathcal{U}_G(\mathbf{v}) = e^{(-\imath/\hbar)\mathbf{v}\cdot\hat{\mathbf{G}}}} \ . \tag{1.316}$$

We can simplify this unitary transform using Glauber's formula (1.313). To this end we first calculate the commutator,

$$[\mathbf{v}\cdot\hat{\mathbf{p}}, \mathbf{v}\cdot\hat{\mathbf{r}}] = -\imath\hbar\mathbf{v}^2 \ , \tag{1.317}$$

which does not depend on $\hat{\mathbf{p}}$ nor $\hat{\mathbf{r}}$, but may contribute a phase factors. With this we can rewrite the expression (1.316),

$$\begin{aligned}
\mathcal{U}_G(\mathbf{v}) &= e^{(-\imath/\hbar)\mathbf{v}t\cdot\hat{\mathbf{p}}+(\imath/\hbar)\mathbf{v}m\cdot\hat{\mathbf{r}}} \\
&= e^{(-\imath/\hbar)mt\mathbf{v}^2/2} e^{(\imath/\hbar)\mathbf{v}m\cdot\hat{\mathbf{r}}} e^{(-\imath/\hbar)\mathbf{v}t\cdot\hat{\mathbf{p}}} = e^{(\imath/\hbar)mt\mathbf{v}^2/2} e^{(-\imath/\hbar)\mathbf{v}t\cdot\hat{\mathbf{p}}} e^{(\imath/\hbar)\mathbf{v}m\cdot\hat{\mathbf{r}}} \\
\mathcal{U}_G^\dagger(\mathbf{v}) &= e^{(\imath/\hbar)\mathbf{v}t\cdot\hat{\mathbf{p}}-(\imath/\hbar)\mathbf{v}m\cdot\hat{\mathbf{r}}} \\
&= e^{(-\imath/\hbar)mt\mathbf{v}^2/2} e^{(-\imath/\hbar)\mathbf{v}m\cdot\hat{\mathbf{r}}} e^{(\imath/\hbar)\mathbf{v}t\cdot\hat{\mathbf{p}}} = e^{(\imath/\hbar)mt\mathbf{v}^2/2} e^{(\imath/\hbar)\mathbf{v}t\cdot\hat{\mathbf{p}}} e^{(-\imath/\hbar)\mathbf{v}m\cdot\hat{\mathbf{r}}} \ .
\end{aligned} \tag{1.318}$$

We apply these expressions to transform the position and momentum operators,

$$\boxed{\begin{aligned}
\mathcal{U}_G^\dagger(\mathbf{v})\hat{\mathbf{r}}\mathcal{U}_G(\mathbf{v}) &= e^{(\imath/\hbar)\mathbf{v}t\cdot\hat{\mathbf{p}}}\hat{\mathbf{r}}e^{(-\imath/\hbar)\mathbf{v}t\cdot\hat{\mathbf{p}}} = \hat{\mathbf{r}} + \mathbf{v}t \\
\mathcal{U}_G^\dagger(\mathbf{v})\hat{\mathbf{p}}\mathcal{U}_G(\mathbf{v}) &= e^{(-\imath/\hbar)\mathbf{v}m\cdot\hat{\mathbf{r}}}\hat{\mathbf{p}}e^{(\imath/\hbar)\mathbf{v}m\cdot\hat{\mathbf{r}}} = \hat{\mathbf{p}} + m\mathbf{v}
\end{aligned}} \ , \tag{1.319}$$

and consequently,

$$\begin{aligned}
\mathcal{U}_G^\dagger(\mathbf{v})\frac{\hat{\mathbf{p}}^2}{2m}\mathcal{U}_G(\mathbf{v}) &= \frac{[\mathcal{U}_G^\dagger(\mathbf{v})\hat{\mathbf{p}}\mathcal{U}_G(\mathbf{v})]^2}{2m} = \frac{(\hat{\mathbf{p}}+m\mathbf{v})^2}{2m} \\
\mathcal{U}_G^\dagger(\mathbf{v})V(\hat{\mathbf{r}})\mathcal{U}_G(\mathbf{v}) &= V(\mathcal{U}_G^\dagger[\mathbf{v}\hat{\mathbf{r}}\mathcal{U}_G(\mathbf{v})] = V(\hat{\mathbf{r}}+\mathbf{v}t) \ .
\end{aligned} \tag{1.320}$$

Setting $m = 0$ the Galilei boost simply reproduces a spatial translation by a vector $\mathbf{v}t$, and setting $t = 0$ the Galilei boost simply becomes the prescription for the momentum kick by an amount $m\mathbf{v}$.

Applying the Galilei boost expressions (1.318) to states, we find,

$$\boxed{\begin{array}{rcl} \mathcal{U}_G(\mathbf{v})|\mathbf{r}\rangle & = & e^{(\imath/\hbar)m\mathbf{v}\cdot(\hat{\mathbf{r}}+\mathbf{v}t/2)}|\mathbf{r}+\mathbf{v}t\rangle \\ \mathcal{U}_G(\mathbf{v})|\mathbf{p}\rangle & = & e^{-(\imath/\hbar)t\mathbf{v}\cdot(\hat{\mathbf{p}}+m\mathbf{v}/2)}|\mathbf{p}+m\mathbf{v}\rangle \end{array}} \ . \tag{1.321}$$

The prefactors do not shift the states, but only contribute irrelevant phase factors.

Finally, knowing the commutator of $\hat{\mathbf{p}}$ and $\hat{\mathbf{r}}$ we derive,

$$[\mathbf{G}\cdot\mathbf{a}, \mathbf{G}\cdot\mathbf{b}] = 0 \ , \tag{1.322}$$

for any vectors $\mathbf{a}$ and $\mathbf{b}$, and with that, using Glauber's formula (1.313), we verify,

$$\mathcal{U}_G(\mathbf{v}_1)\mathcal{U}_G(\mathbf{v}_2) = e^{(-\imath/\hbar)(\mathbf{v}_1+\mathbf{v}_2)\cdot\mathbf{G}-[\mathbf{v}_1\cdot\mathbf{G},\mathbf{v}_2\cdot\mathbf{G}]/2\hbar^2} = \mathcal{U}_G(\mathbf{v}_1+\mathbf{v}_2) \ . \tag{1.323}$$

Obviously, for very high velocities, the Galilei-boost should be replaced by the *Lorentz transform* (or *Lorentz boost*) [425]. Here, we only note, that the additivity of velocities expressed by equation (1.323) does not hold for non-collinear relativistic velocities [23].

1.7.4 Gauge transformations

We learn in electrodynamics [24], that the motion of a particle carrying the charge q and interacting with an electrical potential $\Phi(\mathbf{r},t)$ and a magnetic vector potential $\mathbf{A}(\mathbf{r},t)$ is governed by the electric and the magnetic field,

$$\vec{\mathcal{E}}(\mathbf{r},t) = -\nabla\Phi - \partial_t\mathbf{A} \qquad \text{and} \qquad \vec{\mathcal{B}}(\mathbf{r},t) = \nabla\times\mathbf{A} \ . \tag{1.324}$$

Also, we know that the fields are invariant under the substitution,

$$\Phi \to \Phi' \equiv \Phi - \partial_t\chi \qquad \text{and} \qquad \mathbf{A} \to \mathbf{A}' \equiv \mathbf{A} + \nabla\chi \ , \tag{1.325}$$

where $\chi(\mathbf{r},t)$ is a scalar field called *gauge field*.

In quantum mechanics the *gauge transform* defined by,

$$\boxed{\mathcal{U}_{\rm gg}(\chi) = e^{-\imath q\chi(\mathbf{r},t)/\hbar}} \tag{1.326}$$

obviously must keep the Schrödinger equation invariant. However, since the gauge field may depend on time, as shown in Sec. 1.6.5, the Hamiltonian is different in the transformed system. Transforming operators and wave functions as,

$$\hat{H} \to \mathcal{U}_{\rm gg}\hat{H}\mathcal{U}_{\rm gg}^{-1} \equiv \hat{H}_{\mathcal{U}} \qquad \text{and} \qquad |\psi\rangle \to \mathcal{U}_{\rm gg}|\psi\rangle \equiv |\psi_{\mathcal{U}}\rangle \ , \tag{1.327}$$

[23] See script on *Electrodynamics: Electricity, Magnetism and Radiation* (2025), Sec. 9.1.6.
[24] See script on *Electrodynamics: Electricity, Magnetism and Radiation* (2025).

we calculate for the energy,

$$\hat{H}_{\mathcal{U}}|\psi_{\mathcal{U}}\rangle = \mathcal{U}_{\rm gg}\imath\hbar\tfrac{d}{dt}\mathcal{U}_{\rm gg}^{-1}|\psi_{\mathcal{U}}\rangle = \mathcal{U}_{\rm gg}\imath\hbar\mathcal{U}_{\rm gg}^{-1}\tfrac{d}{dt}|\psi_{\mathcal{U}}\rangle + \mathcal{U}_{\rm gg}\imath\hbar\left(\tfrac{-\imath q}{\hbar}\mathcal{U}_{\rm gg}^{-1}\tfrac{d\chi}{dt}\right)|\psi_{\mathcal{U}}\rangle$$
$$= \imath\hbar\left(\tfrac{d}{dt} - \tfrac{\imath q}{\hbar}\tfrac{d\chi}{dt}\right)|\psi_{\mathcal{U}}\rangle\ , \tag{1.328}$$

in accordance with the transformation rule (1.267) for time-dependent unitary transformations. For the momentum, we get analogously,

$$\hat{\mathbf{p}}_{\mathcal{U}}|\psi_{\mathcal{U}}\rangle = \mathcal{U}_{\rm gg}(-\imath\hbar\nabla)\mathcal{U}_{\rm gg}^{-1}|\psi_{\mathcal{U}}\rangle = \mathcal{U}_{\rm gg}(-\imath\hbar)\mathcal{U}_{\rm gg}^{-1}(\nabla|\psi_{\mathcal{U}}\rangle) + \mathcal{U}_{\rm gg}(-\imath\hbar)\left(\tfrac{-\imath q}{\hbar}\mathcal{U}_{\rm gg}^{-1}\nabla\chi\right)|\psi_{\mathcal{U}}\rangle$$
$$= (-\imath\hbar)\left[\nabla - \tfrac{\imath q}{\hbar}(\nabla\chi)\right]|\psi_{\mathcal{U}}\rangle\ , \tag{1.329}$$

This corresponds to the substitutions [25],

$$\boxed{\mathcal{U}_{\rm gg}\imath\hbar\frac{d}{dt}\mathcal{U}_{\rm gg}^{-1} = \imath\hbar\frac{d}{dt} + q\frac{d\chi}{dt} \qquad \text{and} \qquad \mathcal{U}_{\rm gg}\hat{\mathbf{p}}\mathcal{U}_{\rm gg}^{-1} = \hat{\mathbf{p}} - q\nabla\chi}\ . \tag{1.330}$$

This shows that the gauge transformation applies to the *minimal coupling* rule (see Sec. 10.1.2),

$$\hat{H} = \hat{H}_{\rm kin} + q\Phi \overset{\mathcal{U}_{\rm gg}}{\curvearrowright} \hat{H}_{\rm kin} + q\Phi + q\partial_t\chi \quad \text{and} \quad m\hat{\mathbf{v}} = \hat{\mathbf{p}} - q\mathbf{A} \overset{\mathcal{U}_{\rm gg}}{\curvearrowright} \hat{\mathbf{p}} - q\mathbf{A} - q\nabla\chi\ , \tag{1.331}$$

confirming the rules (1.325). That is, the Hamiltonian of a particle carrying the charge q and interacting with an electric potential Φ and a magnetic vector potential $\mathbf{A}$ is,

$$\hat{H} = \tfrac{1}{2m}(\hat{\mathbf{p}} - q\mathbf{A} - q\nabla\chi)^2 + q\Phi + q\partial_t\chi\ . \tag{1.332}$$

1.7.5 Noether's theorem and conservation laws

The fundamental laws of physics are often expressed as symmetries. The knowledge of symmetries allows the characterization of a system and its behavior without the need to know its details. We can often deduce the differential equation of motion from the symmetries. The fundamental symmetries define the fundamental laws of physics. Following *Noether's theorem* each symmetry corresponds to a conserved quantity, that is, a quantities that remains invariant for all time. The invariance of a system under symmetry transformation represents a *conservation law*. For example, the homogeneity of space corresponds to the conservation of linear momentum.

In quantum mechanics, a *symmetry transformation* is defined by,

$$|\psi\rangle \longrightarrow \mathcal{U}|\psi\rangle \qquad \text{and} \qquad \hat{Q} \longrightarrow \mathcal{U}\hat{Q}\mathcal{U}^\dagger\ . \tag{1.333}$$

Therefore, to find a conservation law, i.e., an invariable observable (also called *constant of motion*), we must verify that the observable and the transformed wavefunctions simultaneously satisfy the same fundamental equations (that is, Schrödinger's or Heisenberg's equation) as the original observable and wavefunctions. For example,

[25] In quadrivetorial notation $\imath\hbar\partial_\mu \longrightarrow \imath\hbar\partial_\mu + q\partial_\mu\chi$.

if the wavefunction $|\psi\rangle$ satisfies the Schrödinger equation, the wave function $\mathcal{U}|\psi\rangle$ must do this too,

$$\hat{H}\mathcal{U}|\psi\rangle \stackrel{!}{=} \imath\hbar\frac{d}{dt}\mathcal{U}|\psi\rangle = \imath\hbar\frac{d\mathcal{U}}{dt}|\psi\rangle + \imath\hbar\mathcal{U}\frac{d}{dt}|\psi\rangle = \imath\hbar\frac{d\mathcal{U}}{dt}|\psi\rangle + \mathcal{U}\hat{H}|\psi\rangle \ . \tag{1.334}$$

Consequently, we obtain the relation,

$$[\hat{H},\mathcal{U}] = \imath\hbar\dot{\mathcal{U}} \ . \tag{1.335}$$

As shown in (1.275) and (1.276), an operator that commutes with the Hamiltonian does not explicitly depend on time, that is, it is *conserved*.

1.7.5.1 Temporal homogeneity

Temporal homogeneity means invariance under translation in time by a fixed time interval τ, that is, under the unitary temporal transformation,

$$\mathcal{U}(\tau) \equiv |\psi(\tau)\rangle\langle\psi(0)| = e^{(\imath/\hbar)\hat{E}\tau} \ . \tag{1.336}$$

Since $\frac{d}{dt}e^{(\imath/\hbar)\hat{E}\tau} = 0$, this means $[e^{(\imath/\hbar)\hat{E}\tau}, \hat{H}] = 0$, which implies conservation of energy $[\hat{E}, \hat{H}] = 0$. This will be verified in the Exc. 1.7.6.5.

> **Example 17 (*Homogeneity of time*):** We imagine the following mental experiment or *Gedankenexperiment*: We consider two attractive bodies that move away from each other until they reach the perihelia. At this point, before the bodies reapproach, we change the laws, for example, by modifying the force of attraction. As a consequence, when the bodies arrive at the initial point, the total energy is non-zero. Therefore, the conservation of energy indicates that the laws are invariant.

1.7.5.2 Temporal isotropy

The fundamental laws of classical physics and quantum mechanics are all symmetrical under *time reversal*. That is, they are remain invariant when we change the arrow of time, $t \to -t$.

1.7.5.3 Spatial homogeneity

Spatial homogeneity means invariance under spatial translation, that is, under the unitary translational transformation,

$$\mathcal{U}_{\rm tr}(\mathbf{a}) \equiv \int |\mathbf{r}+\mathbf{a}\rangle\langle\mathbf{r}|d^3r = e^{(-\imath/\hbar)\hat{\mathbf{p}}\cdot\mathbf{a}} \ . \tag{1.337}$$

This is equivalent to momentum conservation $[\hat{\mathbf{p}}, \hat{H}] = 0$ [26].

[26] Imagine that the forces attracting two bodies to each other are not equal: Contrary to Newton's third law, body A attracts body B, more than the body B attracts the body A. In that case after a while the two bodies have different momenta. With the unitary transformation $\mathcal{U}_{\rm tr}(\mathbf{a}) = e^{-\imath\hat{p}\cdot\mathbf{a}/\hbar} \simeq$

Example 18 (*Homogeneity of space*): Ehrenfest's theorem says $[\hat{\mathbf{p}}, H] = -\imath\hbar\frac{\partial H}{\partial \hat{\mathbf{p}}}$. Therefore, the commutator is not zero when there is a potential, $\hat{H} = \hat{\mathbf{p}}^2/2m + V(\hat{\mathbf{r}})$. This is obvious, because the potential introduces an energy inhomogeneity to a particle interacting with the potential. However, this does not mean that the space itself is inhomogeneous, because in order to verify the translational invariance of space, we must displace the entire system, that is, the particle together with the potential. For example, if the potential is generated by another particle we must consider the Hamiltonian $\hat{H} = \hat{\mathbf{p}}_1^2/2m_1 + \hat{\mathbf{p}}_2^2/2m_2 + V(\hat{\mathbf{r}}_1 - \hat{\mathbf{r}}_2)$.

1.7.5.4 Spatial isotropy

Spatial isotropy means invariance under rotation, that is, under rotational unitary transformation,

$$\mathcal{U}_{\rm rt}(\phi) \equiv e^{(-\imath/\hbar)\hat{\mathbf{L}}\phi} \ . \tag{1.338}$$

This is equivalent to the conservation of angular momentum $[\hat{\mathbf{L}}, \hat{H}] = 0$.

1.7.5.5 Parity conservation

Besides continuous symmetry transformations there exist discrete transformations. Discrete symmetries are important in elementary particle physics. The *parity conservation* means invariance to spatial reflection: $\mathbf{r} \to -\mathbf{r}$. A parity transformation is defined by the mirroring of the wavefunction through a point in space, for example $\mathbf{r} = 0$,

$$\hat{P}|\psi(\mathbf{r})\rangle \equiv |\psi(-\mathbf{r})\rangle \ . \tag{1.339}$$

with

$$\hat{P}^2 = \hat{P} \ . \tag{1.340}$$

We talk about *even* parity when $\hat{P}|\psi(\mathbf{r})\rangle = |\psi(\mathbf{r})\rangle$ and *odd* parity when $\hat{P}|\psi(\mathbf{r})\rangle = -|\psi(\mathbf{r})\rangle$. See Exc. 1.7.6.6.

1.7.5.6 Invariance to the velocity of the inertial system

The *Galilei boost* asks for *Galilei invariance* regarding the transformation,

$$\mathcal{U}_G(\mathbf{v}) \equiv \iint |\mathbf{r} + \mathbf{v}t, \mathbf{p} + m\mathbf{v}\rangle\langle \mathbf{r}, \mathbf{p}| d^3r d^3p \ , \tag{1.341}$$

that is, the equations of motion ruling the dynamics of the inertial system under consideration should not dependent on its velocity $\mathbf{v}$.

$1 - \imath\epsilon\mathbf{p}\cdot\mathbf{a}/\hbar + ...$ we have,

$$\mathcal{U}_{\rm tr} H|\psi\rangle = \mathcal{U}_{\rm tr} E_\psi|\psi\rangle = E_\psi \mathcal{U}|\psi\rangle = H|\psi(\mathbf{r}+\mathbf{a})\rangle =? = H|\psi(\mathbf{r}\rangle \ .$$

Since, $[H, \hat{p}] = 0$, Heisenberg's equation yields,

$$\frac{\partial}{\partial t}\langle\psi|\hat{p}\cdot\mathbf{a}|\psi\rangle = \frac{1}{\imath\hbar}\langle\psi|[\hat{p}\cdot\mathbf{a}, \hat{H}]|\psi\rangle = 0 \ .$$

1.7.5.7 Charge conservation

Let us consider again the gauge transform (1.325). We know that the Lagrangian density in free space is given in terms of the potentials by,

$$\begin{aligned}\mathcal{L}(x^\mu) &= \tfrac{1}{4\mu_0}F^{\mu\nu}F_{\mu\nu} - A_\mu j^\mu = \tfrac{\varepsilon_0}{2}\vec{\mathcal{E}}^2 - \tfrac{1}{2\mu_0}\vec{\mathcal{B}}^2 - A_\mu j^\mu \\ &= \tfrac{\varepsilon_0}{2}[\nabla\Phi + \partial_t\mathbf{A}]^2 - \tfrac{1}{2\mu_0}[\nabla\times\mathbf{A}]^2 - \Phi\rho + \mathbf{A}\cdot\mathbf{j}\ ,\end{aligned} \tag{1.342}$$

and the *action* is simply the four-dimensional integral,

$$S = \int \mathcal{L}(x^\mu)dVdt\ . \tag{1.343}$$

From the Lagrangian formulation, Maxwell's equations can be derived by requiring the action to be minimal, $\delta S = 0$, which yields the Euler-Lagrange equations. As the field equations do not change under gauge transformation, this implies that the action is also unchanged.

To find the relation with *charge conservation*, we simply have to compare the actions in different gauges. First, we express the Lagrangian transformed into the old gauge,

$$\begin{aligned}\mathcal{L}'(x^\mu) &= \tfrac{\varepsilon_0}{2}\{\nabla[\Phi - \cancel{\partial_t\chi}] + \partial_t[\mathbf{A} + \cancel{\nabla\chi}]\}^2 - \tfrac{1}{2\mu_0}\{\nabla\times[\mathbf{A} + \cancel{\nabla\chi}^{\,0}]\}^2 \\ &\quad - [\Phi - \partial_t\chi]\rho + [\mathbf{A} + \nabla\chi]\cdot\mathbf{j} \\ &= \mathcal{L} + (\partial_t\chi)\rho + \nabla\chi\cdot\mathbf{j}\ .\end{aligned} \tag{1.344}$$

With this result, we can calculate the difference between the actions under gauge transformation and recall, that they can not be different:

$$0 \stackrel{!}{=} S' - S = \int[(\partial_t\chi)\rho + \nabla\chi\cdot\mathbf{j}]dVdt = -\int\chi[\partial_t\rho + \nabla\cdot\mathbf{j}]dVdt\ , \tag{1.345}$$

using partial integration [27] and choosing volumes so large, that every charge is inside. This is the *continuity equation* derived from the global *gauge invariance* of the action. The calculation really is nothing more than an application of Noether's theorem from which we could have derived directly the continuity equation, $\partial_\mu j^\mu = 0$.

In summary, the conservation of charge means invariance with respect to gauge transformations,

$$\mathcal{U}_{cl}(\chi) \equiv e^{-\imath q\chi(\mathbf{r},t)/\hbar}\ , \tag{1.346}$$

where χ is the gauge field. We note that q and χ are conjugated observables. Therefore, if $[\chi, \hat{H}] = 0$, then the charge q is a conserved quantity.

Transformations can be combined. For example, we believe that nowadays all laws are invariant with respect to CPT transformation, that is, a combination of *charge conjugation*, *parity inversion*, and *θ-transform*.

1.7.6 Exercises

1.7.6.1 Ex: Calculus with commutator

Derive the rule (1.280) via a Taylor expansion of the operator $\hat{G}(\tau) \equiv e^{\tau\hat{A}}\hat{B}e^{-\tau\hat{A}}$.

[27] Think about the argument, because $\int\partial_t|\chi\rho dt = 0$!

1.7.6.2 Ex: Particle in a homogenous gravitational field

a. Consider a particle free to move along the axis of gravity. Derive the time-dependent unitary operator describing the transformation into the particle's rest frame and check, whether the transformation satisfies the expression (1.267).
b. Solve the Schrödinger equation and derive the Heisenberg equations for $\hat{x}$ and $\hat{p}$.
c. Calculate the phase shift due to gravity from the solution of the Schrödinger equation.

1.7.6.3 Ex: Phase shift in a Ramsey-Bordé interferometer

a. Calculate the time dependence of the dynamical phase accumulated by an atom in the field of gravity as a function of its initial momentum.
b. Derive the phase difference of a particle wavefunction passing through a *Ramsey-Bordé interferometer* [28].
c. Assuming that both free evolution periods of the Ramsey cycle have the same duration τ, generalize the result obtained under (b) allowing for an arbitrary initial velocity.

1.7.6.4 Ex: Rotation operator

Derive the rule $e^{\vec{\alpha}\times}\mathbf{r} = \sum_n \frac{(\vec{\alpha}\times)^n}{n!}\mathbf{r} = \hat{\mathbf{e}}_\alpha(\hat{\mathbf{e}}_\alpha \cdot \mathbf{r}) + \hat{\mathbf{e}}_\alpha \times \mathbf{r}\sin\alpha - \hat{\mathbf{e}}_\alpha \times (\hat{\mathbf{e}}_\alpha \times \mathbf{r})\cos\alpha$.

1.7.6.5 Ex: Constants of motion

Show at the example of energy conservation using the relation (1.335), that energy commutes with the Hamiltonian if $\dot{E} = 0$.

1.7.6.6 Ex: Parity

Show that the eigenfunctions of the Hamiltonian $\hat{H} = -(\hbar/2m)(d^2/dx^2) + V(x)$ have well-defined parity, i.e., parity is a *good quantum number* in cases where the energy is an even function of position, $V(x) = V(-x)$.

1.8 Further reading

W. Demtröder, *Atoms, Molecules and Photons: An Introduction to Atomic, Molecular, and Quantum Physics* [ISBN]

J. Weiner et al., *Light-matter interaction, Fundamentals and applications* [DOI]

R. Loudon, Oxford Science Publications, Oxford (1982), *The quantum theory of light* [ISBN]

Ph.W. Courteille (2020), *Script on Optical spectroscopy: A practical course* [http]

[28] A Ramsey-Bordé interferometer consists of a $\pi/2$-π-$\pi/2$ laser pulse sequence (similar to photon echo in NMR) of Bragg diffraction pulses leading to a splitting and recombination of an atomic wavefunction in momentum space. Assume that every pulse transfers one unit of photonic recoil, $\hbar k$, to the atomic center-of-mass, where k is the wavevector of the laser light.

Ph.W. Courteille (2020), *Script on Electrodynamics: Electricity, magnetism, and radiation* [http]

Ph.W. Courteille (2020), *Script on Quantum mechanics applied to atomic and molecular physics* [http]

W.R. Theis, Teubner (1985), *Grundzüge der Quantentheorie* [ISBN]

C. Cohen-Tannoudji, B. Diu, F. Laloe, Wiley Interscience, *Quantum mechanics, vol. 1,2* [ISBN]

L.I. Schiff, McGraw-Hill Book Company (1968), *Quantum mechanics* [ISBN]

J.J. Sakurai, J.J. Napolitano, 2^{nd} ed. Springer (2011), *Modern Quantum Mechanics* [ISBN]

H.A. Bethe, R. Jackiw, 3^{rd} ed. Taylor & Francis (1997), *Intermediate Quantum Mechanics* [ISBN]

D.J. Griffiths, *Introduction to Quantum Mechanics* [ISBN]

Photonics101, *How the Gauge Invariance of the Action implies Charge Conservation* [http]

Chapter 2

Linear motion / Separable potentials

We have seen in the last chapter that the motion of a particle is ruled by an interplay of kinetic and potential energy and can be characterized by solving the Schrödinger equation. For arbitrary potential landscapes the solution can be difficult to obtain. In contrast, the existence of symmetries can dramatically simplify the task. The present chapter is devoted to, potentials with separable Cartesian dimensions, the subsequent Chp. 3 to potentials with cylindrical or spherical symmetries, and Chp. 4 to periodic potentials. More specifically, we will analyze in the present chapter the translational and vibrational motion of a quantum particle and give special consideration to the rectangular potential and the harmonic oscillator.

2.1 Translational motion

In one dimension the Hamiltonian of a free particle is,

$$\hat{H} = -\frac{\hbar^2}{2m}\frac{d^2}{dx^2} \ . \tag{2.1}$$

Therefore, the general solution of the Schrödinger stationary equation,

$$\hat{H}\psi(x) = E\psi(x) \ , \tag{2.2}$$

is,

$$\psi(x) = Ae^{\imath kx} + Be^{-\imath kx} \qquad \text{with} \qquad k = \sqrt{\tfrac{2mE}{\hbar^2}} \ . \tag{2.3}$$

Note that the $e^{\imath kx}$ functions are not quadratically integrable, since $\int_{-\infty}^{\infty} |e^{\imath kx}|^2 dx = \int_{-\infty}^{\infty} dx \to \infty$. On the other side, they do not represent actual physical systems. In practice, we need to consider wave packets or specify a finite volume for the particle. Note also that the spectrum of eigenvalues is continuous. Do the Exc. 2.1.4.1.

2.1.1 Quadratic integrability

To allow for an interpretation as probability density we need to ask for quadratic integrability,

$$\int |\psi|^2 d^3r = 1 \ . \tag{2.4}$$

This means that the wavefunction can not be infinite inside a finite volume. But it can be infinite within an infinitely small volume. Also, since the Schrödinger equation contains the second derivative by position, the wavefunction must be continuous and have a continuous derivative.

2.1.2 Separation of dimensions

Frequently, a 3D potential can be written in the way,

$$V(x,y,z) = V_x(x) + V_y(y) + V_z(z) \ . \tag{2.5}$$

This is the case, for example, for a rectangular well with $V_x(x) = V_y(y) = V_z(z) = V_0/3$ inside the well and $V(x,y,z) = 0$ outside. It also holds for a harmonic potential,

$$V(\mathbf{r}) = \frac{m}{2}\left(\omega_x^2 x^2 + \omega_y^2 y^2 + \omega_z^2 z^2\right) \ . \tag{2.6}$$

In these cases, the following ansatz for the wavefunction is generally useful,

$$\psi(\mathbf{r}) = \psi_x(x)\psi_y(y)\psi_z(z) \ , \tag{2.7}$$

since inserting the ansatz into the Schrödinger equation,

$$\begin{aligned}&\left[-\frac{\hbar^2}{2m}\left(\frac{d^2}{dx^2} + \frac{d^2}{dy^2} + \frac{d^2}{dz^2}\right) + V_x(x) + V_y(y) + V_z(z)\right]\psi_x(x)\psi_y(y)\psi_z(z) \\ &= E\psi_x(x)\psi_y(y)\psi_z(z) \ ,\end{aligned} \tag{2.8}$$

the equation separates into three independent one-dimensional equations,

$$-\frac{\hbar^2}{2m}\frac{\psi_x''(x)}{\psi_x(x)} + V_x(x) = const. \equiv E_x \ , \tag{2.9}$$

and the same for y and z. Since, $E = E_x + E_y + E_z$ may have the same value for different combinations of E_x, E_y and E_z, multidimensional systems are often degenerate.

2.1.3 Homogeneous force fields, gravity

The behavior of a wavefunction in a homogeneous force field has been studied in Excs. 1.7.6.2 and 1.7.6.3.

2.1.4 Exercises

2.1.4.1 Ex: Trapped particle

Consider the problem of a particle of mass m forced to move in x-direction and completely confined to a box, with walls placed at the positions $x = 0$ and $x = a$.
a. The particle be in the ground state, what is its energy and its wavefunction?
b. Suppose the particle has the following wavefunction:

$$\psi_{\mathrm{I}}(x) = \tfrac{1}{\sqrt{7a}}\left[2\cos\left(\tfrac{\pi}{2a}(6x-a)\right) - 3\imath\sin\left(\tfrac{2\pi}{a}x\right) + \cos\left(\tfrac{\pi}{2a}(2x-a)\right)\right] \ ,$$

what is the probability that a measurement of the energy yields the result $E = \frac{2\pi^2\hbar^2}{ma^2}$?
c. Considering again the ground state of item (a), what is the probability distribution for the momentum of the particle in this state?
d. Still starting from the ground state, suppose we remove (instantaneously) the walls, leaving the particle free ($\hat{H} = \hat{p}^2/2m$). What is the energy of this free particle?
Formulae:

$$\int_0^L e^{\imath Bx} \sin\left(\frac{n\pi x}{L}\right) dx = \frac{n\pi L[1-(-1)^n e^{\imath BL}]}{n^2\pi^2 - B^2L^2} \qquad \text{for} \qquad n = 1, 2, 3, ...$$

$$\int_{-\infty}^{\infty} \frac{x^2}{(1-x^2)^2} \cos^2 \tfrac{\pi x}{2} dx = \tfrac{\pi^2}{4}$$

2.2 Rectangular potentials

The continuity equation (1.123) teaches us that the probability flux of a moving particle cannot make abrupt changes. That is, even if the particle encounters an obstacle represented by a smooth or abrupt variation of the potential depth, the wavefunction and its derivative must remain continuous, unless the potential step is infinitely high.

2.2.1 Box potential

Let us now place the particle into a rectangular potential well, such that the Hamiltonian is,

$$\hat{H} = -\frac{\hbar^2}{2m}\frac{d^2}{dx^2} + V(x) \qquad \text{with} \qquad V(x) = \begin{cases} 0 & \text{for} \quad x \in [0, L] \\ \infty & \text{for} \quad x \notin [0, L] \end{cases} . \tag{2.10}$$

As the potential barriers are high, the walls are hard, that is, the particle, even being a quantum particle, can not penetrate. The wavefunction and the possible energy values are,

$$\boxed{\psi(x) = \sqrt{\frac{2}{L}} \sin\frac{n\pi x}{L} \qquad \text{and} \qquad E_n = \frac{n^2\hbar^2\pi^2}{2mL^2}} . \tag{2.11}$$

The Exc. 2.2.5.1 asks to demonstrate the result (2.11) illustrated in Fig. 2.1.

Obviously the spectrum of eigenvalues is now discrete. They can be enumerated by an integer n called *quantum number*. Note that the energy levels are not equidistant.

> **Example 19 (*Localization energy*):** There is a minimal *energy* $E_1 = \frac{\hbar^2\pi^2}{2mL^2}$ which is called *zero point energy* or *localization energy*. This energy can be understood as a consequence of Heisenberg's *uncertainty principle*. We can make the following gross estimation of the zero point energy. Obviously, the particle is localized with an uncertainty lower than $\Delta x < L$. Hence, $\Delta p > \hbar/\Delta x > \hbar/L$. The average kinetic energy is,
>
> $$\frac{\langle p^2\rangle}{2m} = \frac{\langle p\rangle^2 + \Delta p^2}{2m} = \frac{\Delta p^2}{2m} > \frac{\hbar^2}{2mL^2} .$$
>
> The fact that the numerical value is different from the value calculated by the formula (2.11) comes from the particular geometry of the box potential.

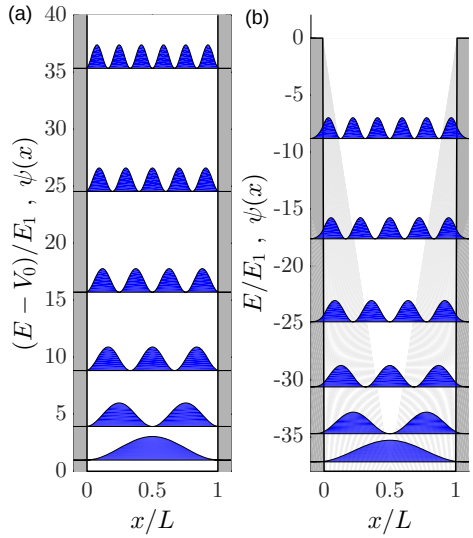

Figure 2.1: (code) (a) Wavefunctions and energies in the box potential. (b) The rectangular potential well with the reference energy set to the height of the well.

2.2.2 Multidimensional box potential

In a multidimensional well there can be degeneracy if the well exhibits symmetries. In the case of a 2D quadratic well $L_x = L_y$, the eigenenergies are doubly degenerate, since $E_{n_x,n_y} = E_{n_y,n_x}$. In the case of a 3D cubic well $L_x = L_y = L_z$, the eigenenergies are 6-fold degenerate, because $E_{n_x,n_y,n_z} = E_{n_y,n_z,n_x} = E_{n_z,n_x,n_y} = E_{n_z,n_y,n_x} = E_{n_y,n_x,n_z} = E_{n_x,n_z,n_y}$. The states and energies of the 2D well are calculated in Exc. 2.2.5.2.

2.2.3 Potentials with several sections of constant depths

To find the global wavefunction in potentials with several sections of constant depths, we solve Schrödinger's equations separately for each section labeled by $a = 1, 2, ..,$

$$\left(-\frac{\hbar^2}{2m}\frac{d^2}{dx^2} + V_a\right)\psi_a(x) = E\psi_a(x)\ . \tag{2.12}$$

The general solution for a section a with potential energy V_a is,

$$\boxed{\psi_a(x) = A_a e^{\imath k_a x} + B_a e^{-\imath k_a x}}\ , \tag{2.13}$$

where $k_a = \frac{1}{\hbar}\sqrt{2m(E-V_a)}$. If $E > V_a$, the wave is propagating. k_a is the Broglie wavevector of the wave. If $E < V_a$, the wave is evanescent. That is, the wave decays within a distance $\kappa_a = -\imath k_a$.

If the particle is confined, that is, if $E < V(x \to \pm\infty)$, the possible energy levels are quantized and the spectrum is discrete.

For every transition between two sections $a = 1$ and $a = 2$ we require the boundary conditions,

$$\psi_1(x) = \psi_2(x) \qquad \text{and} \qquad \psi_1'(x) = \psi_2'(x) \ . \tag{2.14}$$

Together with the normalization, $1 = \int_{-\infty}^{\infty} |\psi|^2 dx$, these conditions are sufficient to determine the wavefunction unambiguously.

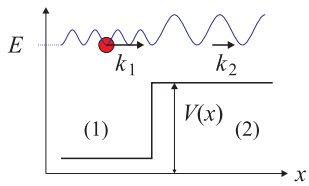

Figure 2.2: Scheme of a potential with several sections of constant depths.

2.2.4 Potential well

Consider a particle with energy E and a potential well of finite depth such that $V(x) = V_0 < 0$ for $-L/2 > x > L/2$ and $V(x) = 0$ otherwise, as illustrated in Fig. 2.3(a). The particle be confined, $E < 0$.

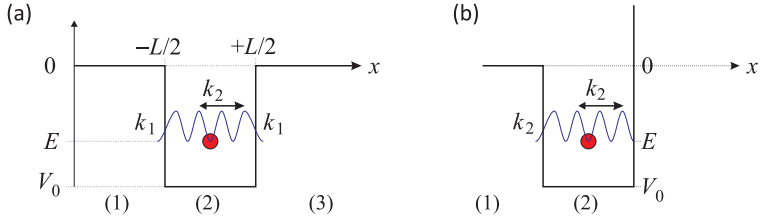

Figure 2.3: (a) Scheme of a two-sided and (b) one-sided potential well.

The wavevectors are

$$k_1 = k_3 = \tfrac{1}{\hbar}\sqrt{2mE} = \imath\tfrac{1}{\hbar}\sqrt{2m|E|} = \imath\kappa_1 \qquad \text{and} \qquad k_2 = \tfrac{1}{\hbar}\sqrt{2m(E - V_0)} \ . \tag{2.15}$$

with $\kappa_1 \in \mathbb{R}^+$. The boundary conditions yield,

$$\begin{aligned} A_1 e^{-\imath k_1 L/2} + B_1 e^{\imath k_1 L/2} &= A_2 e^{-\imath k_2 L/2} + B_2 e^{\imath k_2 L/2} \\ -\imath k_1 A_1 e^{-\imath k_1 L/2} + \imath k_1 B_1 e^{\imath k_1 L/2} &= -\imath k_2 A_2 e^{-\imath k_2 L/2} + \imath k_2 B_2 e^{\imath k_2 L/2} \\ A_2 e^{\imath k_2 L/2} + B_2 e^{-\imath k_2 L/2} &= A_3 e^{\imath k_1 L/2} + B_3 e^{-\imath k_1 L/2} \\ \imath k_2 A_2 e^{\imath k_2 L/2} - \imath k_2 B_2 e^{-\imath k_2 L/2} &= \imath k_1 A_3 e^{\imath k_1 L/2} - \imath k_1 B_3 e^{-\imath k_1 L/2} \ . \end{aligned} \tag{2.16}$$

For confined particles, $E < 0$, the problem is totally symmetric. In addition, the wavefunction must disappear for $x \to \pm\infty$. Therefore, we can simplify,

$$A_1 = 0 = B_3 \qquad \text{and} \qquad A_3 = B_1 \ . \tag{2.17}$$

The first two equations (2.16) now give,

$$B_1 e^{\imath k_1 L/2} = A_2 e^{-\imath k_2 L/2} + B_2 e^{\imath k_2 L/2} = \frac{k_2}{k_1}\left(-A_2 e^{-\imath k_2 L/2} + B_2 e^{\imath k_2 L/2}\right) . \tag{2.18}$$

We now consider the quotient B_2/A_2. Using the right part of equation (2.18),

$$\frac{B_2}{A_2} = \frac{e^{-\imath k_2 L/2}(k_2 + k_1)}{e^{\imath k_2 L/2}(k_2 - k_1)} = \frac{e^{-\imath k_2 L}(k_2 + \imath\kappa_1)^2}{k_2^2 + \kappa_1^2} . \tag{2.19}$$

Since the amplitudes are real, the imaginary part of the quotient (2.19) should disappear, which is the case when,

$$0 = \mathfrak{Im}\, e^{-\imath k_2 L}(k_2 + \imath\kappa_1)^2 = 2\kappa_1 k_2 \cos k_2 L + (\kappa_1^2 - k_2^2)\sin k_2 L \tag{2.20}$$
$$\implies \tan k_2 L = \frac{2\kappa_1 k_2}{-\kappa_1^2 + k_2^2} .$$

In order to construct graphically the values of the momenta k_2 of the particle associated with the allowed energy levels, we introduce a constant $\beta \equiv \hbar/(L\sqrt{2m|V_0|})$. Hence,

$$\tan k_2 L = \tan \frac{1}{\beta}\sqrt{1 - |E/V_0|} = \frac{2\sqrt{|E/V_0|}\sqrt{1 - |E/V_0|}}{1 - 2|E/V_0|} = \frac{2\kappa_1 k_2}{-\kappa_1^2 + k_2^2} . \tag{2.21}$$

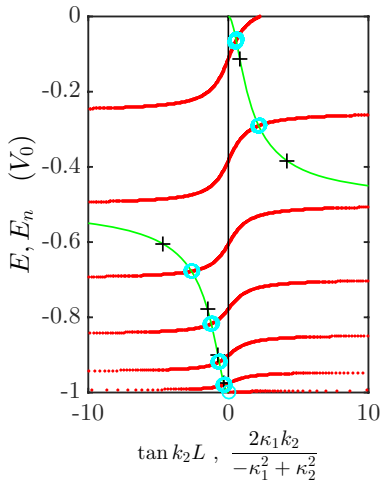

Figure 2.4: (code) Graphical solution for a finite bilateral potential well. The red dotted curves represent the tangents (left side of the equation (2.21)), the solid green curves the hyperbolas (right side of the equation), the circles in cyan are the eigenenergies. When $0 < E - V_0 \ll E$, they converge to the eigenenergies of the infinitely deep well (black crosses and vertical black line).

At the bottom of deep potentials, that is, when $0 < E - V_0 \ll E$, or equivalently, $E \simeq V_0$, we have $k_2 \ll \kappa_1$ and hence, $\tan k_2 L \to 0 \implies k_2 L = n\pi$. The energies are

then,

$$E - V_0 = \frac{\hbar^2}{k_2^2} 2m = \frac{\hbar^2 \pi^2}{2mL^2} n^2 \ . \tag{2.22}$$

Apply the notions obtained in this section to solve Excs. 2.2.5.3 and 2.2.5.4.

2.2.5 Exercises

2.2.5.1 Ex: Particle in a box

Obtain the wavefunctions and associated energy levels of a particle confined in a box, where $V(x) = 0$ for $0 \leq x \leq l$ and $V(x) = \infty$ outside.

2.2.5.2 Ex: Particle in a two-dimensional box

Obtain the wavefunctions and associated energy levels of a particle trapped in a two-dimensional box inside which the particle is confined to a rectangular surface with dimensions L_1 in x-direction and L_2 in y-direction, $V(x, y) = 0$ for $0 \leq x \leq L_1$ and $0 \leq y \leq L_2$ and $V(x, y) = \infty$ else.

2.2.5.3 Ex: Particle in a well

Obtain the energies of the bound states of a particle in the potential well in which $V(x) = \infty$ for $x < 0$, $V(x) = -V_0$ for $0 \leq x \leq L/2$ and $V(x) = 0$ to $x > L/2$. Compare the obtained values with those of the symmetrical well discussed in Sec. 2.2.4 and the well with infinitely high walls discussed in Sec. 2.2.1.

2.2.5.4 Ex: Least bound states and localization energy

Calculate, based on the discussion in Sec. 2.2.4, the minimum required potential depth V_0 of a three-dimensional finite rectangular well potential of size L to have a bound state capable of trapping an ^{87}Rb atom. Assuming a trap volume of $L = 10\,\text{nm}$, how deep should the trap be?

2.3 Potential barrier

The linear momentum of a particle described by $\psi(x, t) = Ae^{\imath kx}$ is,

$$\langle \psi | \hat{p} | \psi \rangle = \langle \psi | \frac{\hbar}{\imath} \frac{d}{dx} | \psi \rangle = \hbar k \ . \tag{2.23}$$

Therefore, this particle propagates towards $+\infty$. On the contrary, the particle $Be^{-\imath kx}$ propagates towards $-\infty$. Thus, the two solutions (2.13) of the Schrödinger equation (2.12) correspond to propagating particle waves. From here on we will use the letter A (B) to denote the amplitudes of waves propagating in direction ∞ ($-\infty$).

In locations where the potential changes abruptly, the particle can be partially reflected.

2.3.1 $\mathcal{T}$-scattering matrix

As we have already shown in the previous section, we can write the transformation of the amplitudes due to a potential step at position L as,

$$\begin{aligned} A_2 e^{\imath k_2 L} + B_2 e^{-\imath k_2 L} &= A_1 e^{\imath k_1 L} + B_1 e^{-\imath k_1 L} \\ \imath k_2 A_2 e^{\imath k_2 L} - \imath k_2 B_2 e^{-\imath k_2 L} &= \imath k_1 A_1 e^{\imath k_1 L} - \imath k_1 B_1 e^{-\imath k_1 L} \ . \end{aligned} \tag{2.24}$$

We can summarize these two equations in a matrix formalism,

$$\boxed{\begin{pmatrix} A_2 \\ B_2 \end{pmatrix} = \mathcal{T} \begin{pmatrix} A_1 \\ B_1 \end{pmatrix}} \ , \tag{2.25}$$

with the *scattering matrix* $\mathcal{T}$ for a particle with energy E (see Fig. 2.2),

$$\begin{aligned} \mathcal{T} &= \tfrac{1}{2} \begin{pmatrix} \left(1 + \frac{k_1}{k_2}\right) e^{\imath(k_1 - k_2)L} & \left(1 - \frac{k_1}{k_2}\right) e^{\imath(-k_1 - k_2)L} \\ \left(1 - \frac{k_1}{k_2}\right) e^{\imath(k_1 + k_2)L} & \left(1 + \frac{k_1}{k_2}\right) e^{\imath(-k_1 + k_2)L} \end{pmatrix} \\ &= \tfrac{1}{2} \begin{pmatrix} e^{-\imath k_2 L} & 0 \\ 0 & e^{\imath k_2 L} \end{pmatrix} \begin{pmatrix} 1 + \frac{k_1}{k_2} & 1 - \frac{k_1}{k_2} \\ 1 - \frac{k_1}{k_2} & 1 + \frac{k_1}{k_2} \end{pmatrix} \begin{pmatrix} e^{\imath k_1 L} & 0 \\ 0 & e^{-\imath k_1 L} \end{pmatrix} \ . \end{aligned} \tag{2.26}$$

If there are more zones with different depths, we may concatenate the scattering matrices. Denoting by $\mathcal{T}_{m \to n}$ the scattering matrix describing a transition at position $L_{m,n}$ of a potential of the depth V_m to another potential V_n, we write,

$$\mathcal{T} = \mathcal{T}_{2 \to 3} \mathcal{T}_{1 \to 2} \ . \tag{2.27}$$

2.3.2 $\mathcal{S}$-scattering matrix

Another common definition is the *scattering matrix* $\mathcal{S}$,

$$\boxed{\begin{pmatrix} A_2 \\ B_1 \end{pmatrix} = \mathcal{S} \begin{pmatrix} B_2 \\ A_1 \end{pmatrix}} \ . \tag{2.28}$$

To see how the scattering matrices are interconnected, we start with

$$\begin{pmatrix} A_2 \\ B_2 \end{pmatrix} = \mathcal{T} \begin{pmatrix} A_1 \\ B_1 \end{pmatrix} = \begin{pmatrix} \mathcal{T}_{11} A_1 + \mathcal{T}_{12} B_1 \\ \mathcal{T}_{21} A_1 + \mathcal{T}_{22} B_1 \end{pmatrix} \ , \tag{2.29}$$

Multiplying the first line with $\mathcal{T}_{22}$ and the second with $-\mathcal{T}_{12}$ and adding them,

$$\mathcal{T}_{22} A_2 - \mathcal{T}_{12} B_2 = \left(\mathcal{T}_{11} \mathcal{T}_{22} - \mathcal{T}_{12} \mathcal{T}_{21}\right) A_1 \ . \tag{2.30}$$

This equation resolved by A_2 along with the second equation (2.29) resolved by B_1 give,

$$\begin{pmatrix} A_2 \\ B_1 \end{pmatrix} = \mathcal{S} \begin{pmatrix} B_2 \\ A_1 \end{pmatrix} = \begin{pmatrix} \mathcal{T}_{12}/\mathcal{T}_{22} & \mathcal{T}_{11} - \mathcal{T}_{12}\mathcal{T}_{21}/\mathcal{T}_{22} \\ 1/\mathcal{T}_{22} & -\mathcal{T}_{21}/\mathcal{T}_{22} \end{pmatrix} \begin{pmatrix} B_2 \\ A_1 \end{pmatrix} \ . \tag{2.31}$$

The matrix $\mathcal{S}$ describes the causality of scattering process more adequately: The amplitude A_2 in region (2) results from the superposition of a wave B_2 being reflected by the barrier and a wave A_1 being transmitted by the barrier. The amplitude B_1 in region (1) results from the superposition of a wave A_1 being reflected by the barrier and a wave B_2 being transmitted by the barrier. Therefore, the matrix $\mathcal{S}$ is more appropriate for the description of the quantum reflection, as we will discuss in the next section. However, it has the disadvantage that it can not be concatenated in the same way as the $\mathcal{T}$ matrices.

Unlike the $\mathcal{T}$ matrix the $\mathcal{S}$ matrix is *unitary*, since

$$\det \mathcal{S} = \mathcal{S}_{11}\mathcal{S}_{22} - \mathcal{S}_{12}\mathcal{S}_{21} = -\frac{\mathcal{T}_{11}}{\mathcal{T}_{22}} = -e^{2\imath k_1 L} \ . \tag{2.32}$$

Also, it is possible to show,

$$\mathcal{S}^\dagger \mathcal{S} = \begin{pmatrix} \mathcal{S}_{11}^* & \mathcal{S}_{21}^* \\ \mathcal{S}_{12}^* & \mathcal{S}_{22}^* \end{pmatrix} \begin{pmatrix} \mathcal{S}_{11} & \mathcal{S}_{12} \\ \mathcal{S}_{21} & \mathcal{S}_{22} \end{pmatrix} = \begin{pmatrix} 1 & 0 \\ 0 & 1 \end{pmatrix} \ . \tag{2.33}$$

2.3.3 Quantum reflection at a potential step

The *quantum reflection* is a non-classical property of the motion of a particle. An example is the *reflection* of a quantum particle by an *attractive* potential. To study this effect, we consider a plane wave $e^{\imath k_1 x}$ propagating in region (1) ($E_1 > V_1$) encountering a potential step up or down at position $x = 0$ leading to another region (2). Using the S matrix formalism introduced in the previous section,

$$\mathcal{S} = \frac{1}{k_1 + k_2} \begin{pmatrix} k_2 - k_1 & 2k_1 \\ 2k_2 & k_1 - k_2 \end{pmatrix} \ , \tag{2.34}$$

we find that one part of the wave is reflected into the region (1), another is transmitted into the region (2),

$$\begin{aligned} \begin{pmatrix} A_2 \\ B_1 \end{pmatrix} = \mathcal{S} \begin{pmatrix} 0 \\ 1 \end{pmatrix} = \begin{pmatrix} \mathcal{T}_{11} - \mathcal{T}_{12}\mathcal{T}_{21}/\mathcal{T}_{22} \\ -\mathcal{T}_{21}/\mathcal{T}_{22} \end{pmatrix} = \begin{pmatrix} \frac{(1+k_1/k_2)^2 - (1-k_1/k_2)^2}{2(1+k_1/k_2)} \\ -\frac{1-k_1/k_2}{1+k_1/k_2} \end{pmatrix} \\ = \frac{1}{k_1 + k_2} \begin{pmatrix} 2k_1 \\ k_1 - k_2 \end{pmatrix} \ . \end{aligned} \tag{2.35}$$

We use $B_2 = 0$, since no wave comes from the side of region (2), and $A_1 = 1$, because it simplifies the formulas and does not affect the generality of the results. The interesting results are:

- Even when $E_2 < V_2$, the particle enters the classically prohibited region: $\psi_2(x) \propto e^{-\kappa_2 x}$ with $\kappa_2 = \frac{1}{\hbar}\sqrt{2m(V_2 - E_2)}$, i.e. the transmission is non-zero, $|A_2| > 0$.
- Even with $E_2 > V_2$, the particle has a probability of being reflected at the step, $|B_1| > 0$.

Example 20 (*Contrast of a partially reflected wave*): Defining $K_\pm \equiv \frac{1}{2}\left(\max|\psi_1|^2 \pm \min|\psi_1|^2\right)$, the *contrast* of the wavefunction in region (1) is given

by K_-/K_+. Writing the function as $\psi_1 = e^{\imath k_1 x} + B_1 e^{-\imath k_1 x}$ it is easy to show, that

$$|B_1| = \frac{\sqrt{K_+ + K_-} - \sqrt{K_+ - K_-}}{\sqrt{K_+ + K_-} + \sqrt{K_+ - K_-}} \simeq \frac{K_-}{2K_+} \ . \tag{2.36}$$

This formula can be understood as an analogue of *Fresnel formula* for matter waves [1].

In Exc. 2.3.7.1 we calculate the behavior of a Broglie wave passing through a potential step and entering a classically forbidden region. In Exc. 2.3.7.2 we investigate a model describing the collision between attracting or repelling particles via a partial reflection at a potential step.

2.3.4 Continuity of probability flow

The continuity equation (1.123) requires that the *probability flux* be preserved in stationary situations,

$$0 = \frac{dj}{dx} = \frac{d}{dx}\frac{\hbar}{2m\imath}\left[\psi^*\left(\frac{d}{dx}\psi\right) - \left(\frac{d}{dx}\psi^*\right)\psi\right] \ . \tag{2.37}$$

Applying this to a potential step separating the regions $n = 1, 2$, we find,

$$\begin{aligned} j_n &= \frac{\hbar}{2m\imath}\left[\psi^*\frac{d}{dx}\psi - \psi\frac{d}{dx}\psi^*\right] \\ &= \frac{\hbar}{2m\imath}\left[(A_n^* e^{-\imath k_n x} + B_n^* e^{\imath k_n x})(\imath k_n A_n e^{\imath k_n x} - \imath k_n B_n e^{-\imath k_n x})\right. \\ &\quad \left. - (A_n e^{\imath k_n x} + B_n e^{-\imath k_n x})(-\imath k_n A_n^* e^{-\imath k_n x} + \imath k B_n^* e^{\imath k x})\right] \\ &= \frac{\hbar k_n}{m}(|A_n|^2 - |B_n|^2) \ . \end{aligned} \tag{2.38}$$

Hence, $j_1 = j_2$ implies $k_1|A_1|^2 - k_1|B_1|^2 = k_2|A_2|^2 - k_2|B_2|^2$. Assuming that the particle comes from side 1 and $B_2 = 0$, we have,

$$1 = |B_1|^2 + \tfrac{k_2}{k_1}|A_2|^2 = R + T \ , \tag{2.39}$$

defining the *transmission* T and the *reflection* R as,

$$T \equiv \tfrac{k_2}{k_1}|\mathcal{S}_{12}|^2 = \tfrac{k_2}{k_1}|A_2|^2 \qquad \text{and} \qquad R \equiv |\mathcal{S}_{22}|^2 = |B_1|^2 \ . \tag{2.40}$$

2.3.5 Tunneling and quantum reflection at a potential well

Particles thrown with a kinetic energy E against potential barriers can cross them even if $V_0 > E$ or be reflected even when $V_0 < E$, as illustrated in Fig. 2.5(a). This can be verified by considering a particle propagating from $x = -\infty$ towards $x = +\infty$ through a potential well located at $x \in [0, a]$. We determine the concatenation $\mathcal{T} = \mathcal{T}_{2\to 3}\mathcal{T}_{1\to 2}$. Then we find the $\mathcal{S}$ matrix that corresponds to the $\mathcal{T}$ matrix and solve the

[1] In this sense light reflection at an optical interface (with typical losses of 4% for glass) can be interpreted as quantum reflection of light

problem in the same way as in the previous section. For example, we can calculate the transmission and reflection probabilities. The formula is derived in Exc. 2.3.7.3,

$$\boxed{R = 1 - T = \left(1 + \frac{16E/V_0(1 - E/V_0)}{(e^{\kappa L} - e^{-\kappa L})^2}\right)^{-1}}\,, \tag{2.41}$$

and sketched in Fig. 2.5(b). The phenomenon is called *tunneling*. Do the Exc. 2.3.7.4.

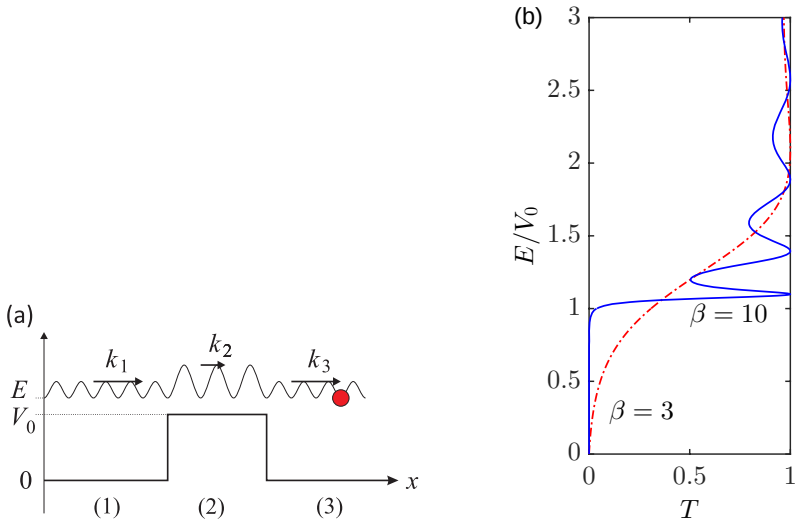

Figure 2.5: (code) (a) Tunnel effect and quantum transmission and reflection at a potential barrier. (b) Coefficients of transmission and reflection (horizontal) through the shown potential barrier as a function of the energy normalized to the height of the barrier E/V_0. The dashed red curve corresponds to a low barrier, $\beta \equiv \frac{1}{\hbar}L\sqrt{2mV_0} = 3$, the blue solid curve corresponds to a deep barrier $\beta = 10$.

2.3.6 The delta-potential

In quantum mechanics the δ-potential can be used to simulate situations, where a particle is free to move in two regions of space with a barrier in between. For example, an electron can move almost freely in a conducting material, but when two conducting surfaces are put close together, the interface between them acts as a barrier for the electron that can be approximated by a δ-potential. The δ-potential is a limiting case of the finite potential well when we decrease its width while maintained the product of its width and its depth constant. Here, for simplicity, we only consider a one-dimensional potential well, but the analysis can be expanded to more dimensions.

The time-independent Schrödinger equation for the wavefunction $\psi(x)$ of a particle in one dimension is,

$$-\frac{\hbar^2}{2m}\frac{d^2\psi(x)}{dx^2} + \alpha\delta(x)\psi(x) = E\psi(x)\,, \tag{2.42}$$

The potential is called a δ-potential well if α is negative and a δ-potential barrier if α is positive.

The potential splits the space in two parts ($x < 0$ and $x > 0$). In each of these parts the potential energy is zero, and the Schrödinger equation reduces to,

$$\frac{d^2\psi}{dx^2} = -\frac{2mE}{\hbar^2}\psi \ . \tag{2.43}$$

The solutions of this differential equation are linear combinations of $e^{\imath kx}$ and $e^{-\imath kx}$, where the wavenumber k is related to the energy by $k = \frac{\sqrt{2mE}}{\hbar}$. In general, due to the presence of the δ-potential in the origin, the coefficients of the solution need not be the same in both half-spaces:

$$\psi(x) = \begin{cases} \psi_1(x) = A_1 e^{\imath kx} + B_1 e^{-\imath kx} & \text{for } x < 0 \\ \psi_2(x) = A_2 e^{\imath kx} + B_2 e^{-\imath kx} & \text{for } x > 0 \end{cases} , \tag{2.44}$$

where, in the case of positive energies (real k), $e^{\imath kx}$ represents a wave traveling to the right, and $e^{-\imath kx}$ one traveling to the left. One obtains a relation between the coefficients by imposing that the wavefunction be continuous at the origin,

$$\psi(0) = \psi_1(0) = \psi_2(0) = A_1 + B_1 = A_2 + B_2 \ . \tag{2.45}$$

A second relation can be found by studying the derivative of the wavefunction. Normally, we could also impose differentiability at the origin, but this is not possible because of the δ-potential. However, if we integrate the Schrödinger equation around $x = 0$ over an interval $[-\epsilon, +\epsilon]$:

$$-\frac{\hbar^2}{2m}\int_{-\epsilon}^{+\epsilon} \psi''(x)dx + \int_{-\epsilon}^{+\epsilon} V(x)\psi(x)dx = E\int_{-\epsilon}^{+\epsilon} \psi(x)dx \ . \tag{2.46}$$

In the limit $\epsilon \to 0$ the right-hand side of this equation vanishes,

$$-\frac{\hbar^2}{2m}[\psi_2'(0) - \psi_1'(0)] + \alpha\psi(0) = 0 \ . \tag{2.47}$$

Substituting the definition of ψ into this expression, we obtain,

$$-\frac{\hbar^2}{2m}\imath k(A_1 - B_1 - A_2 + B_2) + \alpha(A_1 + B_1) = 0 \ . \tag{2.48}$$

The boundary conditions thus give the following restrictions on the coefficients,

$$\boxed{\begin{array}{rcl} A_1 + B_1 - A_2 - B_2 &=& 0 \\ A_1 - B_1 - A_2 + B_2 &=& \dfrac{2m\alpha}{\imath k\hbar^2}(A_1 + B_1) \end{array}} \ . \tag{2.49}$$

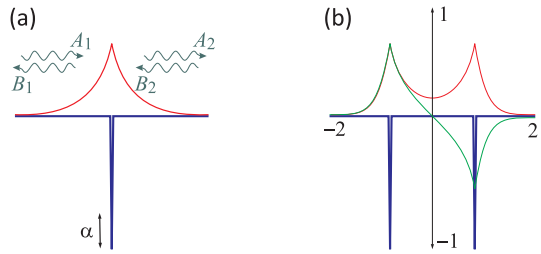

Figure 2.6: (a) The δ-potential (green) and the bound state wavefunction (blue). (b) Double δ-potential (green).

2.3.6.1 Bound states

The bound state wavefunction solution to the δ-function potential is continuous everywhere, but its derivative is not defined at $x = 0$.

In any one-dimensional attractive potential there will be a bound state. To find its energy, note that for negative energies, $E < 0$, the wavenumber $k = \imath\sqrt{2m|E|}/\hbar = \imath\kappa$ is imaginary and the wavefunctions are exponentially increasing or decreasing functions of x (see above). Requiring that the wavefunctions do not diverge at infinity eliminates half of the terms: $A_2 = B_1 = 0$. The wavefunction is then an evanescent wave,

$$\psi(x) = \begin{cases} \psi_1(x) = A_1 e^{\kappa x} & \text{for } x < 0 \\ \psi_2(x) = B_2 e^{-\kappa x} & \text{for } x > 0 \end{cases} . \tag{2.50}$$

From the boundary conditions and normalization conditions, it follows that,

$$A_1 = B_2 = \sqrt{\kappa} \qquad \text{and} \qquad \kappa = -\frac{m\alpha}{\hbar^2} , \tag{2.51}$$

from which follows that α must be negative, that is the bound state only exists for the well, and not for the barrier. The Fourier transform of this wavefunction is a Lorentzian function. The energy of the bound state is then,

$$E_\mathrm{b} = -\frac{\hbar^2\kappa^2}{2m} = -\frac{m\alpha^2}{2\hbar^2} . \tag{2.52}$$

The δ-potential well and its wavefunction are exhibited in Fig. 2.6(a).

2.3.6.2 Scattering

For positive energies, the wavefunctions are oscillating functions of x. That is, the particle is free to move in either half-space: $x < 0$ or $x > 0$, but it may be scattered at the δ-potential. The quantum case can be studied in the following situation: a particle incident on the barrier from the left side (A_1) may be reflected (B_1) or transmitted (A_2). To find the amplitudes for reflection and transmission for incidence from the left, we set in the equations (2.49) $A_1 = 1$ (incoming particle), $B_1 = r$ (reflection), $B_2 = 0$ (no incoming particle from the right), and $A_2 = t$ (transmission), and solve

for r and t,

$$t = \frac{1}{1 - \dfrac{m\alpha}{\imath\hbar^2 k}} \quad , \qquad r = \frac{1}{\dfrac{\imath\hbar^2 k}{m\alpha} - 1} \, . \tag{2.53}$$

Due to the mirror symmetry of the model, the amplitudes for incidence from the right are the same as those from the left. The result is that there is a non-zero probability,

$$R = |r|^2 = \frac{1}{1 + \dfrac{\hbar^4 k^2}{m^2\alpha^2}} = \frac{1}{1 + \dfrac{2\hbar^2 E}{m\alpha^2}} \, . \tag{2.54}$$

for the particle to be reflected. This does not depend on the sign of α, that is, a barrier has the same probability of reflecting the particle as a well. This is a significant difference from classical mechanics, where the reflection probability would be 1 for the barrier (the particle simply bounces back), and 0 for the well (the particle passes through the well undisturbed). The probability for transmission is,

$$T = |t|^2 = 1 - R = \frac{1}{1 + \dfrac{m^2\alpha^2}{\hbar^4 k^2}} = \frac{1}{1 + \dfrac{m\alpha^2}{2\hbar^2 E}} \, . \tag{2.55}$$

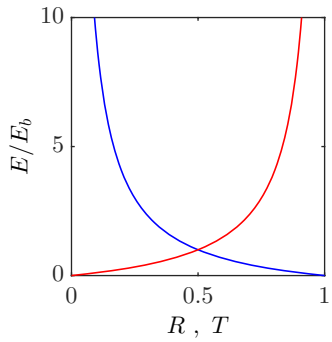

Figure 2.7: (code) Transmission (red) and reflection (blue) probability of a δ-potential well. The energy $E > 0$ is in units of $E_\mathrm{b} = m\alpha^2/2\hbar^2$.

An application example regards the interfaces between two conducting materials. In the bulk of the materials, the motion of the electrons is quasi-free and can be described by the kinetic term in the above Hamiltonian with an effective mass m. Often, the surfaces of such materials are covered with oxide layers or are not ideal for other reasons. This thin, non-conducting layer may then be modeled by a local δ-function potential. Electrons may then tunnel from one material to the other giving rise to a current.

Example 21 (*Double delta-potential*): The δ-function model is actually a one-dimensional version of the hydrogen atom. The model becomes particularly useful when applied to the hydrogen molecule ion, as shown in the following.

The double-well δ-function models a diatomic hydrogen molecule by the corresponding Schrödinger equation:

$$-\frac{\hbar^2}{2m}\frac{d^2\psi}{dx^2}(x) + V(x)\psi(x) = E\psi(x) \ ,$$

where the potential is now:

$$V(x) = -q\lambda\left[\delta\left(x+\tfrac{R}{2}\right) + \delta\left(x-\tfrac{R}{2}\right)\right]$$

where $0 < R < \infty$ is the 'internuclear' distance with δ-function (negative) peaks located at $x = \pm R/2$ (shown in brown in the diagram). Keeping in mind the relationship of this model with its three-dimensional molecular counterpart, we use atomic units and set $\hbar = m = 1$. Here $0 < \lambda < 1$ is a formally adjustable parameter. From the single well case, we can infer the 'ansatz' for the solution to be:

$$\psi(x) = Ae^{-d\left|x+\frac{R}{2}\right|} + Be^{-d\left|x-\frac{R}{2}\right|} \ .$$

Matching of the wavefunction at the δ-function peaks yields the determinant:

$$\begin{vmatrix} q-d & qe^{-dR} \\ q\lambda e^{-dR} & q\lambda - d \end{vmatrix} = 0 \quad \text{where} \quad E = -\frac{d^2}{2} \ .$$

Thus, d is found to be governed by the pseudo-quadratic equation:

$$d_\pm(\lambda) = \tfrac{1}{2}q(\lambda+1) \pm \tfrac{1}{2}\left\{q^2(1+\lambda)^2 - 4\lambda q^2[1-e^{-2d_\pm(\lambda)R}]\right\}^{1/2} \ ,$$

which has two solutions $d = d_\pm$. For the case of equal charges (symmetric homonuclear case), $\lambda = 1$ and the pseudo-quadratic reduces to:

$$d_\pm = q[1 \pm e^{-d_\pm R}] \ .$$

The '+' case corresponds to a wave function symmetric about the midpoint (shown in red in the diagram) where $A = B$ and is called gerade. Correspondingly, the '-' case is the wavefunction that is anti-symmetric about the midpoint where $A = -B$ is called ungerade (shown in green in the diagram). They represent an approximation of the two lowest discrete energy states of the three-dimensional H_2^+ and are useful in its analysis. Analytical solutions for the energy eigenvalues for the case of symmetric charges are given by:

$$d_\pm = q + W(\pm qRe^{-qR})/R \ ,$$

where W is the standard Lambert function. Note that the lowest energy corresponds to the symmetric solution d_+. In the case of unequal charges, and for that matter the three-dimensional molecular problem, the solutions are given by a generalization of the Lambert function (see section on generalization of Lambert function and references herein).

One of the most interesting cases is when $qR \leq 1$, which results in $d_- = 0$. Thus, one has a non-trivial bound state solution with $E = 0$. For these specific parameters, there are many interesting properties that occur, one of which is the unusual effect that the transmission coefficient is unity at zero energy.

2.3.7 Exercises

2.3.7.1 Ex: Tunneling

A rubidium-87 atom moves in free space (region 0) with velocity $v = 1\,\mathrm{cm/s}$ (see diagram). Suddenly it encounters a gap with depth $V_1 = -k_\mathrm{B} \cdot 1\,\mu\mathrm{K}$.
a. What is the particle's Broglie wavelength in region 1?
b. Now the atom encounters a barrier of height $V_2 = -V_1$. What is the probability that the particle will enter region 2?
c. What is the probability of finding the particle inside region 2 up to a depth of $x_2 = 10\,\mathrm{nm}$?

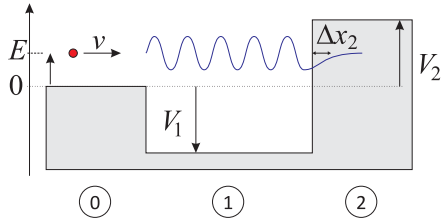

Figure 2.8: Particle in a potential landscape.

2.3.7.2 Ex: Collisions

A *collision* between attractive or repulsive particles can be described by the Schrödinger equation as a one-dimensional scattering,

$$-\frac{\hbar^2}{2m}\psi''(x) + \alpha\delta(x)\psi(x) = E\psi(x)\ .$$

The energy spectrum may be a discrete spectrum of bound states and a continuum of free states.
a. Calculate the transmission coefficient for the case of a particle with energy E thrown against the potential energy barrier $V(x) = \alpha\delta(x)$. Does the result change for the case when $V(x) = -\alpha\delta(x)$, with $\alpha > 0$?
b. For this last potential, find the energy of the bound state and its corresponding wavefunction.

2.3.7.3 Ex: Energy barrier

Consider a particle with energy E thrown (in the direction $\hat{\mathbf{e}}_x$) against a potential energy barrier of finite height and width, such that $V(x) = 0$ for $x < 0$ or $x > L$ and $V(x) = V_0$ for $0 \le x \le L$.
a. Obtain the reflection and transmission coefficients R and T for the case $E > V_0$. Discuss the result.
b. Do the same for the case $E < V_0$.

2.3.7.4 Ex: Wavepacket reflected at a potential barrier

Simulate the reflection of a Gaussian wavepacket at a potential barrier for various kinetic energies using the Julia programming language.

2.4 Numerical approaches for arbitrary potentials

In practice, many potentials are not box-shaped or harmonic, which renders an analytic treatment difficult or impossible. To some extend approximation methods can be used, as will be discussed in Sec. 5.5, but many problems can only be solved numerically. In Sec. 2.4.1 we will first show at the example of arbitrary one-dimensional potentials, how the Schrödinger equation can be solved numerically and how this allows one to determine the eigenenergies of bound states. In Sec. 2.4.2 we will introduce the very efficient Fourier grid method for calculating bound state energies and wavefunctions.

2.4.1 Calculation of free and bound states wavefunctions

Numerical routines or packages are available for solving ordinary differential equations (ODE). Generally it is advantageous to convert the one-dimensional second-order Schrödinger equation into two first-order differential equations via,

$$\varphi'(x) = \frac{2m}{\hbar^2}[E - V(x)]\psi(x) \qquad \text{and} \qquad \psi'(x) = \varphi(x)\ . \tag{2.56}$$

For free states, $E > V(x)$, we just solve equation (2.56) specifying the kinetic energy of the particle. The magenta curve in Fig 2.9(a) is an example of a collisional wavefunction in a Morse-type interatomic potential.

For bound states, we must additional satisfy the eigenvalue problem, since only specific discrete eigenenergies E are permitted. A possible procedure consists in guessing an eigenvalue E, calculating the associated wavefunction $\psi(x)$ using an ODE solver, check whether it diverges for $x \to \pm\infty$, and vary E until $\psi(x)$ no longer diverges. Then we repeat the procedure for are bound state energies, until we got them all. The red curve in Fig 2.9(a) shows the wavefunction of a vibrational state in a Morse-type potential obtained by solving the Schrödinger equation and adjusting the energy until the function stops diverging in the classically forbidden range. In this example the iteration process was stopped when the wavefunction diverged at around $R \approx 19a_\mathrm{B}$. In Exc. 2.4.4.1 we will practice this technique at the example of Hermite's differential equation, and in Exc. 2.4.4.2 we will study the case of a potential whose depth linearly increases with the distance from origin.

2.4.2 The Fourier grid method for bound states

The objective of the *Fourier grid method* is to analytically solve the 1D Schrödinger equation with an arbitrary potential $V(r)$ on a grid of $2N + 1$ equally spaced spatial points r_i, where $i = 0, \pm1, ..., \pm N$. That is, we assume the potential $V(r_i)$ to be given at these points. Skaling by the spatial coordinate r by $r/L = x/2\pi$, we get for the

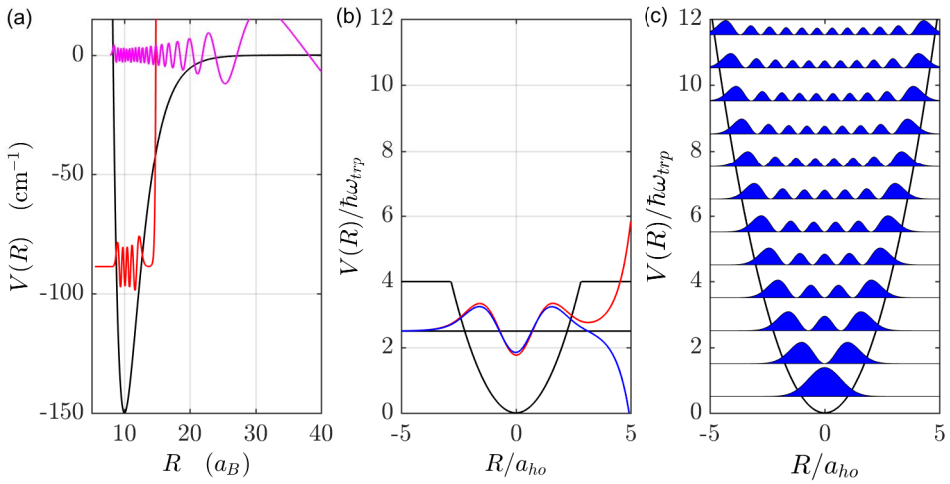

Figure 2.9: (code) (a) Free particle (magenta) and bound state wavefunction (red) calculated using a MATLAB ODE solver. (b) Bound state wavefunction of the harmonic oscillator calculated using a MATLAB ODE solver. For the red curve the eigenvalue has been slightly overestimated and for the blue curve underestimated. (c) Calculation of the harmonic oscillator energies and wave functions using the Fourier grid method.

dimensionless coordinate x the Schrödinger equation,

$$\left[-\frac{h^2}{2mL^2}\frac{d^2}{dx^2} + V(x)\right]\psi(x) = E\psi(x) \ , \tag{2.57}$$

with the grid given by,

$$x_i \equiv \frac{2\pi i}{2N+1} \ . \tag{2.58}$$

The main difficulty for numerically solving such eigenvalue equations is obviously the derivative. Numerical differentiation schemes can be cast into the following general form [575],

$$f'(x_i) = \sum_{j=-N}^{N} D_{ij} f(x_j) \ , \tag{2.59}$$

that is, they can be expressed as a multiplication of the discretized wavefunction represented as a vector $f(x_j)$ and a matrix D_{ij}. These schemes are usually based on interpolation polynomials and are the more accurate, the higher the order of these polynomials is chosen to be.

Example 22 (*Newton's derivation matrix*): For example the Newton method, which represents the lowest order interpolation polynomial, consists in approx-

imating the differentiation matrix by,

$$D_{ij}f(x_j) \simeq \frac{1}{\Delta x}\begin{pmatrix} \ddots & \ddots & & \\ & -1 & 1 & \\ & & -1 & \ddots \\ & & & \ddots \end{pmatrix}\begin{pmatrix} \vdots \\ f_{j-1} \\ f_j \\ \vdots \end{pmatrix} = \begin{pmatrix} \vdots \\ \frac{f_j - f_{j-1}}{\Delta x} \\ \frac{f_{j+1} - f_j}{\Delta x} \\ \vdots \end{pmatrix} \simeq \begin{pmatrix} \vdots \\ f'_{j-1} \\ f'_j \\ \vdots \end{pmatrix} .$$

Instead of using interpolation polynomials, one may consider over-all approximation of a function $f(x)$ by a Fourier series of N-th order, i.e. to assume,

$$f(x) = \sum_{k=-\infty}^{\infty} c_k e^{\imath kx} \simeq \sum_{k=-N}^{N} c_k e^{\imath kx} . \tag{2.60}$$

The highest harmonics of the Fourier expansion N is set by the distance between two grid points. The expansion coefficients are,

$$c_k = \frac{1}{2\pi}\int_0^{2\pi} f(x)e^{-\imath kx}dx \longrightarrow \frac{1}{2\pi}\sum_{j=-N}^{N} f(x_j)e^{-\imath kx_j}\Delta x = \frac{1}{2N+1}\sum_{j=-N}^{N} f(x_j)e^{-\imath kx_j} . \tag{2.61}$$

Now, substituting x by the discrete variable x_i, we take the derivative $f'(x_i)$ of the function (2.60), insert the expansion coefficients (2.61), and compare the resulting expression to the linear combination (2.59) of the functional values $f(x_j)$,

$$\begin{aligned} f'(x_i) &= \sum_{k=-N}^{N} \imath k c_k e^{\imath kx_i} = \frac{\imath}{2N+1}\sum_{k=-N}^{N} k \sum_{j=-N}^{N} f(x_j)e^{\imath k(x_i - x_j)} \\ &= \frac{2}{2N+1}\sum_{k=1}^{N} k \sum_{j=-N}^{N} f(x_j)\sin k(x_j - x_i) \equiv \sum_{j=-N}^{N} D_{ij}f(x_j) . \end{aligned} \tag{2.62}$$

From this we see, that the matrix elements D_{ij} are given by,

$$D_{ij} = \frac{2}{2N+1}\sum_{k=1}^{N} k \sin k(x_j - x_i) = \frac{2}{2N+1}\sum_{k=1}^{N} k \sin\frac{2\pi k(i-j)}{2N+1} . \tag{2.63}$$

The sum can be evaluated analytically, as shown in Exc. 2.4.4.3 [785],

$$D_{ii} = 0 \qquad \text{and} \qquad D_{i\neq j} = \frac{(-1)^{i-j}}{2\sin\frac{x_i - x_j}{2}} = \frac{(-1)^{i-j}}{2\sin\frac{\pi(i-j)}{2N+1}} . \tag{2.64}$$

We may proceed similarly for the second derivative,

$$\begin{aligned} f''(x_i) &= -\sum_{k=-N}^{N} k^2 c_k e^{\imath kx_i} = \frac{-1}{2N+1}\sum_{k=-N}^{N} k^2 \sum_{j=-N}^{N} f(x_j)e^{\imath k(x_i - x_j)} \\ &= \frac{-2}{2N+1}\sum_{k=1}^{N} k^2 \sum_{j=-N}^{N} f(x_j)\cos k(x_j - x_i) \equiv \sum_{j=-N}^{N} (D^2)_{ij}f(x_j) , \end{aligned} \tag{2.65}$$

yielding,

$$(D^2)_{ij} = \frac{-2}{2N+1}\sum_{k=1}^{N} k^2 \cos k(x_j - x_i) = \frac{-2}{2N+1}\sum_{k=1}^{N} k^2 \cos\frac{2\pi k(i-j)}{2N+1} \ . \tag{2.66}$$

Again, the sum can be evaluated analytically, as shown in Exc. 2.4.4.3 [785],

$$\boxed{(D^2)_{ii} = -\frac{N^2+2}{12} \qquad \text{and} \qquad (D^2)_{i\neq j} = -\frac{(-1)^{i-j}}{2\sin^2\frac{\pi(i-j)}{2N+1}}} \ . \tag{2.67}$$

With this scheme of differentiation, the set of difference equations representing the problem (2.67) is readily found to be [550, 250, 785],

$$\boxed{\hat{H}\psi = E\psi \qquad \text{with} \qquad \hat{H}_{ij} = -\frac{h^2}{2mL^2}(D^2)_{ij} + V(x_j)\delta_{ij}} \ . \tag{2.68}$$

This eigenvalue problem can easily be solved on a computer, see Fig 2.9(b).

2.4.2.1 Mapping coordinate grids to potentials

To properly describe the wavefunction of a particle it obviously takes a minimum number of points per de Broglie wavelength. Now, if the particle moves in a potential characterized by shallow and deep areas, the de Broglie wavelength suffers large variations. Numerical procedures evaluating the wavefunction on a grid of points then benefit from a flexible distribution of the points along the propagation axis: Where the potential is shallow less points are needed, while in deeper areas the grid is more dense.

The general procedure consists in rescaling the Schrödinger equation

$$\left[-\frac{\hbar^2}{2m}\frac{d^2}{dr^2} + V(r)\right]\psi(r) = E\psi(r) \tag{2.69}$$

by transforming the r-axis into an x-axis according to [477],

$$\boxed{r = f(x) \quad , \quad dr = J(x)dx \quad , \quad V_x(x) = V(r) \quad , \quad \psi_x(x) = \psi(r)} \ . \tag{2.70}$$

The function $f^{-1}(r)$ must now be designed as a function of the local potential depth such as to produce less grid points x in shallow areas of the potential. Applying the transform we find,

$$\left[-\frac{\hbar^2}{2m}\left(\frac{1}{J(x)^2}\frac{d^2}{dx^2} - \frac{J'(x)}{J(x)^3}\frac{d}{dx}\right) + V_x(x)\right]\psi_x(x) = E\psi_x(x) \ . \tag{2.71}$$

Introducing a new wavefunction via,

$$\boxed{\psi_x(x) = J^{-1/2}(x)\phi(x)} \tag{2.72}$$

we get,

$$\left[-\frac{\hbar^2}{2mJ^2}\frac{d^2}{dx^2} + \frac{\hbar^2 J'}{mJ^3}\frac{d}{dx} + V_x + \frac{\hbar^2}{2m}\left(\frac{1}{2}\frac{J''}{J^3} - \frac{5}{4}\frac{J'^2}{J^4}\right)\right]\phi = E\phi \ , \tag{2.73}$$

or introducing an effective potential,

$$\bar{V}_x \equiv V_x + \frac{\hbar^2}{2m}\left(\frac{7}{4}\frac{J'^2}{J^4} - \frac{1}{2}\frac{J''}{J^3}\right) , \tag{2.74}$$

we get,

$$\boxed{\left[-\frac{\hbar^2}{4m}\left(\frac{1}{J(x)^2}\frac{d^2}{dx^2} + \frac{d^2}{dx^2}\frac{1}{J(x)^2}\right) + \bar{V}_x(x)\right]\phi(x) = E\phi(x)} . \tag{2.75}$$

Finally, we apply the Fourier grid method to the mapped coordinate grid in the same way as in (2.68), however with the modified matrices,

$$\boxed{\begin{array}{lcl} (D^2)_{ii} & = & -\frac{N^2+2}{12}\frac{1}{J_i^2} \qquad \text{and} \qquad (D^2)_{i\neq j} = -\frac{(-1)^{i-j}}{2\sin^2\frac{\pi(i-j)}{N}}\left(\frac{1}{2J_i^2} + \frac{1}{2J_j^2}\right) \\ \bar{V}(x_j) & = & V(x_j) + \frac{1}{2m}\left(\frac{7}{4}\frac{J'^2}{J^4} - \frac{1}{2}\frac{J''}{J^3}\right) \end{array}} , \tag{2.76}$$

where $J(x) = f'(x)$, $J'(x)$ and $J'(x)$ are calculated numerically on the grid x_j.

In practice, to adapt the mapped grid to the rapidity of the de Broglie wave oscillations, we define an equidistant grid x and set,

$$x = f^{-1}(r) \equiv \frac{1}{\pi}\int_{r_i}^{r} k(r')dr' \qquad \text{with} \qquad k(R) = \sqrt{\tfrac{2m}{\hbar^2}[0 - V(r)]} . \tag{2.77}$$

Inverting this function we obtain the desired mapped grid,

$$r = f(x) . \tag{2.78}$$

Do the Exc. 2.4.4.4.

2.4.3 Steepest descent ot the ground state

The softwares 'Maple' or 'Mathematics' are useful for analytical calculations, that is, multiplying matrices or determining eigenvalues. For numerical calculations the softwares 'Matlab' or 'Python' are more adapted. For example, the time evolution of a Schrödinger equation,

$$|\psi(t)\rangle = e^{-\imath\hat{H}t/\hbar}|\psi(0)\rangle , \tag{2.79}$$

can be calculated in a single command line using the Matlab `expm` function.

When the system varies temporally, $\hat{H}(t)$, we may divide time into small units dt and propagate the wavefunction as,

$$|\psi(t+dt)\rangle = e^{-\imath\hat{H}(t)dt/\hbar}|\psi(t)\rangle \simeq |\psi(t)\rangle\left(1 - \imath\frac{\hat{H}(t)}{\hbar}dt\right) , \tag{2.80}$$

continuously reinserting the solution into the equation. This *Newton method* does not converge quickly (dt should be chosen small enough, when $\hat{H}(t)$ varies rapidly), but there are other more sophisticated methods like the *Runge-Kutta method*.

A variation of this method is called *steepest descent method*. This method is similar to the Newton Eq. (2.80), but replaces the time dt with an imaginary time.

Thus, the coherent temporal evolution of the Schrödinger equation is replaced by a dissipative evolution. The loss of energy automatically takes the system to the ground state. However, in order to preserve the normalization of the wavefunction, it must be renormalized at each iteration step,

$$|\psi(t+dt)\rangle \to \frac{|\psi(t+dt)\rangle}{\sqrt{\langle\psi(t+dt)|\psi(t+dt)\rangle}} \,. \tag{2.81}$$

The method also applies to more complicated equations than the Schrödinger equation, for example, the *Gross-Pitaevskii equation*. We will deepen this technique in Sec. 27.3.3.

As an example Fig. 2.10 shows the splitting of a quantum mechanical function (in this case a Bose-Einstein condensate with repulsive interatomic interactions) in the ground state of a quartic double-well potential calculated from the steepest descent method. In Exc. 2.4.4.5, using the Fourier grid method, we study the splitting of bound state energy levels due to tunneling in a *double-well potential*.

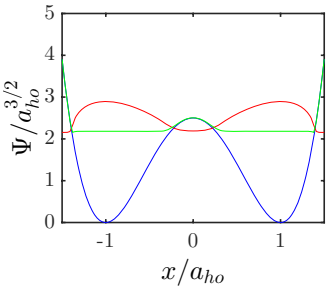

Figure 2.10: (code) Condensate wavefunction (red) in a double-well potential (blue) numerically calculated using the steepest descent method. Also shown is the chemical potential (green).

Another numerical method often used in quantum mechanics is the method called the quantum *Monte Carlo simulation* of the wavefunction [594]. This method simulates trajectories of quantum systems treating intrinsic quantum noise as random processes disrupting the uniformity of the trajectory. The advantage of this method is that it also applies to dissipative systems.

2.4.4 Exercises

2.4.4.1 Ex: Numerical resolution of the Hermite differential equation

Solve the Hermite differential equation (2.102) numerically for $n = 8$, e.g. using the `ode45` ordinary differential equation solver of Matlab, or similar. Plot the wavefunction of the 8-th vibrational level of a harmonic oscillator.

2.4.4.2 Ex: Numerical resolution of the Schrödinger equation

Paramagnetic atoms, such as rubidium, can be confined in quadrupolar magnetic traps, which are characterized by a linear increase of the magnetic field in any

direction of space. Let us consider one dimension of such a potential, given by $V(x) = \mu_B \partial_x B\ |x| - V_0$ wherever $V(x)$ is negative and $V(x) = 0$ else. Here μ_B is the Bohr magneton. Be $\partial_x B = 200\,\mathrm{G/cm}$ the magnetic field gradient and $V_0 = h\ 15\,\mathrm{kHz}$ the potential depth.
a. Calculate the energy and wavefunction of the lowest bound state of this potential by numerical integration of the stationary Schrödinger equation using Matlab or another software.
b. Obtain all bound state energies and wavefunctions using the Fourier grid method.

2.4.4.3 Ex: The Fourier grid method

Derive (a) the formula (2.64) and (b) the formula (2.67) for $N \gg 1$ using the formula (1.352) from [334].

2.4.4.4 Ex: Derivation of the Fourier grid method from the FFT

The Fast Fourier Transform (FFT) is defined by,

$$\begin{aligned} H_n &= \sum_{k=0}^{N-1} e^{-2\pi\imath nk/N} h_k \\ &= \sum_{k=0}^{N-1} e^{-2\pi\imath nk/(N/2)} h_{2k} + e^{-2\pi\imath k/N} \sum_{k=0}^{N/2-1} e^{-2\pi\imath nk/(N/2)} h_{2k+1} = even + odd\ . \end{aligned}$$

the inverse transform is,

$$h_k = \frac{1}{N} \sum\nolimits_{k=0}^{N-1} e^{2\pi\imath nk/N} H_n\ .$$

The sinus transform of a real vector s_k is,

$$S_n = \frac{2}{N} \sum\nolimits_{k=1}^{N-1} s_k \sin \pi nk/N\ .$$

Calculate the inverse transform of the matrix $T_{rs} = k_r^2 \delta_{rs}$.

2.4.4.5 Ex: Infinite rectangular double-well potential

a. Consider the rectangular double-well potential sketched in Fig. 2.11 and calculate the energy levels according to the procedure taught in Sec. 2.3.5.
b. For the same type of potential as in (a) prepare a numerical calculation of the wavefunctions, e.g. using the Fourier grid method introduced in Sec. 12.2.5, for ^{87}Rb using the following dimensions of the potential: $V_0 = h \times 15\,\mathrm{MHz}$, $L = 40\,\mathrm{nm}$, and $b = 3\,\mathrm{nm}$.

2.5 Harmonic oscillator

Many systems oscillate. Common examples are vibrations of atoms bound in a molecule or in a crystalline lattice, of particles trapped in applied electric or magnetic

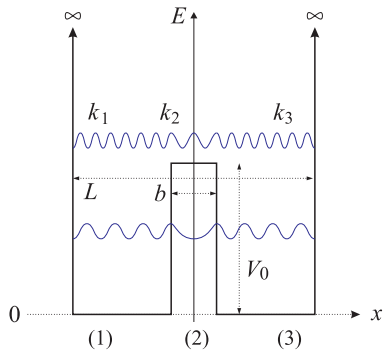

Figure 2.11: Scheme of the rectangular double-well potential.

fields, or light in an electromagnetic mode. Most periodic movements are approximately harmonic for small amplitude vibrations and can be treated in a way that we will detail now.

We start with the unidimensional *harmonic oscillator* (OH),

$$\left[\frac{-\hbar^2}{2m}\frac{d^2}{dx^2} + V(x) - E\right]\psi(x) = 0 \qquad \text{where} \qquad V(x) = \frac{m}{2}\omega^2 x^2 \ . \tag{2.82}$$

2.5.1 Factorization of the Hamiltonian and Fock states

Respecting the fact that the operators $\hat{p}$ and $\hat{x}$ do not commute, $\frac{\imath}{\hbar}[\hat{p},\hat{x}] = 1$, we can rewrite the Hamiltonian of the harmonic oscillator in the following way,

$$\begin{aligned}\hat{H} &= -\frac{\hbar^2}{2m}\frac{d^2}{dx^2} + \frac{m}{2}\omega^2\hat{x}^2 = \hbar\omega\left[\left(\sqrt{\tfrac{m\omega}{2\hbar}}\hat{x} - \imath\sqrt{\tfrac{1}{2m\hbar\omega}}\hat{p}\right)\left(\sqrt{\tfrac{m\omega}{2\hbar}}\hat{x} + \imath\sqrt{\tfrac{1}{2m\hbar\omega}}\hat{p}\right) + \tfrac{1}{2}\right] \\ &= \hbar\omega\left(\hat{a}^\dagger\hat{a} + \tfrac{1}{2}\right) \ ,\end{aligned} \tag{2.83}$$

with the abbreviation

$$\hat{a} \equiv \sqrt{\frac{m\omega}{2\hbar}}\hat{x} + \imath\sqrt{\frac{1}{2m\hbar\omega}}\hat{p} \tag{2.84}$$

and its Hermitian transposition $\hat{a}^\dagger$. Now let's try to find out the properties of the operators $\hat{a}^\dagger$ and $\hat{a}$. First of all, the commutator is,

$$\begin{aligned}[\hat{a},\hat{a}^\dagger] &= \left[\sqrt{\frac{m\omega}{2\hbar}}\hat{x} + \imath\sqrt{\frac{1}{2m\hbar\omega}}\hat{p}, \sqrt{\frac{m\omega}{2\hbar}}\hat{x} - \imath\sqrt{\frac{1}{2m\hbar\omega}}\hat{p}\right] = \frac{\imath}{2\hbar}\left[\hat{x}+\hat{p}, \hat{x}-\hat{p}\right] \\ &= \tfrac{\imath}{\hbar}\left[\hat{p},\hat{x}\right] = 1 \ .\end{aligned} \tag{2.85}$$

Knowing $\hat{H}|\psi\rangle = E|\psi\rangle$ is it clear that $\hat{a}^\dagger\hat{a}$ is an observable with the eigenvalue $n \equiv \frac{E}{\hbar\omega} - \frac{1}{2}$,

$$\hat{a}^\dagger\hat{a}|\psi\rangle = \left(\tfrac{E}{\hbar\omega} - \tfrac{1}{2}\right)|\psi\rangle \equiv n|\psi\rangle \implies |\psi\rangle = |n\rangle \ . \tag{2.86}$$

Now, we show that the states $\hat{a}|\psi\rangle$ are eigenstates of the operator defined as $\hat{n} \equiv \hat{a}^\dagger\hat{a}$, since,

$$\begin{aligned}
\hat{a}^\dagger\hat{a}\hat{a}|\psi\rangle &= (\hat{a}\hat{a}^\dagger - [\hat{a},\hat{a}^\dagger])\hat{a}|\psi\rangle = (\hat{a}\hat{a}^\dagger\hat{a} - \hat{a})|\psi\rangle = \hat{a}(\hat{a}^\dagger\hat{a} - 1)|\psi\rangle = (n-1)\hat{a}|\psi\rangle \\
&\Longrightarrow \hat{a}|\psi\rangle \propto |n-1\rangle \equiv C|n-1\rangle \\
&\Longrightarrow n = \langle n|\hat{a}^\dagger\hat{a}|n\rangle = C^2\langle n-1|n-1\rangle \\
&\Longrightarrow C = \sqrt{n}\ .
\end{aligned} \tag{2.87}$$

We note that the quantum number of the new $|n-1\rangle$ is decreased by 1. Similarly, we show for the state $\hat{a}^\dagger|\psi\rangle$,

$$\begin{aligned}
\hat{a}^\dagger\hat{a}\hat{a}^\dagger|\psi\rangle &= \hat{a}^\dagger([\hat{a},\hat{a}^\dagger] + \hat{a}^\dagger\hat{a})|\psi\rangle = \hat{a}^\dagger(1 + \hat{a}^\dagger\hat{a})|\psi\rangle = (n+1)\hat{a}^\dagger|\psi\rangle \\
&\Longrightarrow \hat{a}^\dagger|\psi\rangle \propto |n+1\rangle \equiv C|n+1\rangle \\
&\Longrightarrow n+1 = \langle n|\hat{a}^\dagger\hat{a} + [\hat{a},\hat{a}^\dagger]|n\rangle = C^2\langle n+1|n+1\rangle \\
&\Longrightarrow C = \sqrt{n+1}\ .
\end{aligned} \tag{2.88}$$

Therefore, this new state is also an eigenvector $|n+1\rangle$, with a quantum number increased by one unit. $\hat{a}^\dagger$ and $\hat{a}$ are creation and annihilation operators of an energy packet,

$$\boxed{\hat{a}^\dagger|n\rangle = \sqrt{n+1}|n+1\rangle \qquad \text{and} \qquad \hat{a}|n\rangle = \sqrt{n}|n-1\rangle}\ . \tag{2.89}$$

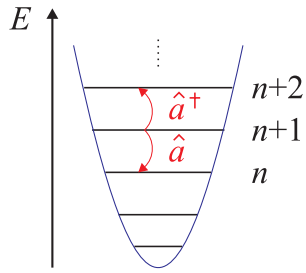

Figure 2.12: Equidistant ladder of vibrational levels showing the actions of the creation and the annihilation operator.

The matrix representation of the field operators is,

$$\hat{a}^\dagger = \sum_n \sqrt{n+1}|n+1\rangle\langle n| \qquad \text{and} \qquad \hat{a} = \sum_n \sqrt{n}|n-1\rangle\langle n|\ , \tag{2.90}$$

from which we deduce,

$$\hat{n} = \hat{a}^\dagger\hat{a} = \sum_n n|n\rangle\langle n| \qquad \text{and} \qquad \hat{H} = \hbar\omega\left(\hat{n} + \tfrac{1}{2}\right)\ . \tag{2.91}$$

Now it is clear, that $\hat{n}$ can be understood as a number operator [2]. The energy spectrum of the harmonic oscillator is equidistant,

$$\boxed{E_n = \hbar\omega\left(n + \tfrac{1}{2}\right)}\ . \tag{2.92}$$

[2]Also, we can define phase operators by $\widehat{\exp}(\mp\imath\phi) = \sum_n |n \mp 1\rangle\langle n|$.

The state with n quanta can be created from the vacuum,

$$|n\rangle = \frac{\hat{a}^\dagger}{\sqrt{n}}|n-1\rangle = \frac{\hat{a}^{\dagger n}}{\sqrt{n!}}|0\rangle \ . \tag{2.93}$$

The state $|n\rangle$ is called *number state* or *Fock state*.

2.5.1.1 Uncertainty in Fock states

We consider an OH of mass m and angular frequency ω prepared in the stationary state $|n\rangle$ which is an eigenstate of the Hamiltonian $\hat{H}$ with eigenvalue $(n+\frac{1}{2})\hbar\omega$. Defining the characteristic size of the OH, $a_{\rm ho} = \sqrt{\hbar/m\omega}$, the annihilation and creation operators can be written,

$$\hat{a} = \frac{1}{\sqrt{2}}\left(\frac{\hat{x}}{a_{\rm ho}} + \imath\frac{a_{\rm ho}}{\hbar}\hat{p}\right) \qquad \text{and} \qquad \hat{a}^\dagger = \frac{1}{\sqrt{2}}\left(\frac{\hat{x}}{a_{\rm ho}} - \imath\frac{a_{\rm ho}}{\hbar}\hat{p}\right) \ . \tag{2.94}$$

Therefore, the position and momentum operators are,

$$\sqrt{2}\frac{1}{a_{\rm ho}}\hat{x} = \hat{a} + \hat{a}^\dagger \qquad \text{and} \qquad \sqrt{2}\imath\frac{a_{\rm ho}}{\hbar}\hat{p} = \hat{a} - \hat{a}^\dagger \ . \tag{2.95}$$

The mean squared deviations of the position $\hat{x}$ and the momentum $\hat{p}$ are,

$$\begin{aligned}
\Delta x^2 &= \langle n|\hat{x}^2|n\rangle = \frac{a_{\rm ho}^2}{2}\langle n|\hat{a}\hat{a} + \hat{a}\hat{a}^\dagger + \hat{a}^\dagger\hat{a} + \hat{a}^\dagger\hat{a}^\dagger|n\rangle = \frac{a_{\rm ho}^2}{2}\langle n|2\hat{n}+1|n\rangle \\
&= \frac{a_{\rm ho}^2}{2}(2n+1) \qquad (2.96) \\
\Delta p^2 &= \langle n|\hat{p}^2|n\rangle = \frac{-\hbar^2}{2a_{\rm ho}^2}\langle n|\hat{a}\hat{a} - \hat{a}\hat{a}^\dagger - \hat{a}^\dagger\hat{a} + \hat{a}^\dagger\hat{a}^\dagger|n\rangle = \frac{-\hbar^2}{2a_{\rm ho}^2}\langle n|-2\hat{n}-1|n\rangle \\
&= \frac{\hbar^2}{2a_{\rm ho}^2}(2n+1) \ .
\end{aligned}$$

From the results of the previous item we obtain the uncertainty relation $\Delta x\Delta p$ for the OH in the state $|n\rangle$,

$$\Delta p\Delta x = \tfrac{\hbar}{2}(2n+1) \ . \tag{2.97}$$

Example 23 (*Localization energy*): The non-vanishing energy of the fundamental state of the harmonic oscillator, $E_0 = \hbar\omega/2$, is an immediate consequence of the Heisenberg principle $\Delta x\Delta p \geq \hbar$, because in analogy with example 19 we calculate,

$$\frac{\langle p^2\rangle}{2m} = \frac{\Delta p^2}{2m} > \frac{\hbar^2}{2m\Delta x^2} > \frac{\hbar^2}{2ma_{\rm ho}^2} = \frac{\hbar\omega}{2} \ .$$

In the case of an electromagnetic field this energy is called *vacuum fluctuation*.

2.5.2 Harmonic oscillator in spatial representation

To simplify the Schrödinger equation in spatial representation,

$$\left[-\frac{\hbar^2}{2m}\frac{d^2}{dx^2} + \frac{m}{2}\omega^2x^2\right]\psi(x) = \hbar\omega(n+\tfrac{1}{2})\psi(x) \ , \tag{2.98}$$

we use the scale $\tilde{x} \equiv x/a_{\rm ho}$, where $a_{\rm ho} = \sqrt{\hbar/m\omega}$ is the spatial extent of the ground state. Therefore,

$$\frac{2}{\hbar\omega}\left[-\frac{\hbar^2}{2m}\frac{d^2}{d(a_{\rm ho}\tilde{x})^2} + \frac{m}{2}\omega^2(a_{\rm ho}\tilde{x})^2\right]\tilde{\psi}(\tilde{x}) = \frac{2}{\hbar\omega}\left[-\frac{\hbar\omega}{2}\frac{d^2}{d\tilde{x}^2} + \frac{\hbar\omega}{2}\tilde{x}^2\right]\tilde{\psi}(\tilde{x})$$
$$= \left[-\frac{d^2}{d\tilde{x}^2} + \tilde{x}^2\right]\tilde{\psi}(\tilde{x}) = (2n+1)\tilde{\psi}(\tilde{x}) \ .$$

Now we start looking for asymptotic solutions. For $\tilde{x} \to \pm\infty$, that is, when the particle enters the classically forbidden region, we can neglect the total energy of the particle,

$$\left[-\frac{d^2}{d\tilde{x}^2} + \tilde{x}^2\right]\tilde{\psi}_\infty(\tilde{x}) \simeq 0 \ . \tag{2.99}$$

The solution of this equation is $\tilde{\psi}_\infty(\tilde{x}) = Ce^{-\tilde{x}^2/2}$, since

$$\left[-\frac{d^2}{d\tilde{x}^2} + \tilde{x}^2\right]e^{-\tilde{x}^2/2} = -\frac{d}{d\tilde{x}}(-\tilde{x})e^{-\tilde{x}^2/2} + \tilde{x}^2e^{-\tilde{x}^2/2} \tag{2.100}$$
$$= -\tilde{x}^2e^{-\tilde{x}^2/2} + e^{-\tilde{x}^2/2} + \tilde{x}^2e^{-\tilde{x}^2/2} = e^{-\tilde{x}^2/2} \simeq 0 \ .$$

This motivates the ansatz $\tilde{\psi}(\tilde{x}) \equiv e^{-\tilde{x}^2/2}H(\tilde{x})$ for the complete differential equation (2.98),

$$\left[-\frac{d^2}{d\tilde{x}^2} + \tilde{x}^2\right]e^{-\tilde{x}^2/2}H(\tilde{x}) = -e^{-\tilde{x}^2/2}\frac{d^2H(\tilde{x})}{d\tilde{x}^2} - 2\frac{de^{-\tilde{x}^2/2}}{d\tilde{x}}\frac{dH(\tilde{x})}{d\tilde{x}} - \frac{d^2e^{-\tilde{x}^2/2}}{d\tilde{x}^2}H(\tilde{x}) + \tilde{x}^2e^{-\tilde{x}^2/2}H(\tilde{x})$$
$$= -e^{-\tilde{x}^2/2}\frac{d^2H(\tilde{x})}{d\tilde{x}^2} - 2(-x)e^{-\tilde{x}^2/2}\frac{dH(\tilde{x})}{d\tilde{x}} + \left[-\tilde{x}^2e^{-\tilde{x}^2/2} + e^{-\tilde{x}^2/2}\right]H(\tilde{x}) + \tilde{x}^2e^{-\tilde{x}^2/2}H(\tilde{x})$$
$$\equiv (2n+1)e^{-\tilde{x}^2/2}H(\tilde{x}) \ . \tag{2.101}$$

Thus, the functions $H(\tilde{x})$ must satisfy the differential equation,

$$H''(\tilde{x}) = 2\tilde{x}H'(\tilde{x}) - 2nH(\tilde{x}) \ . \tag{2.102}$$

We can verify that the Hermite polynomials defined by,

$$H_n(\tilde{x}) = (-1)^n e^{\tilde{x}^2}\frac{d^n}{d\tilde{x}^n}e^{-\tilde{x}^2} \ , \tag{2.103}$$

transform the differential equation into a recursion formula,

$$H_{n+1}(\tilde{x}) = 2\tilde{x}H_n(\tilde{x}) - 2nH_{n-1}(\tilde{x}) \ , \tag{2.104}$$

which allows us to easily calculate the polynomials,

$$H_0(\tilde{x}) = 1 \quad , \quad H_1(\tilde{x}) = 2x \quad , \quad H_2(\tilde{x}) = 4x^2 - 2 \quad , \quad ... \tag{2.105}$$

In summary, the eigenfunction of a harmonic oscillator in the state of excitation n is,

$$\boxed{\langle x|n\rangle = \psi_n(x) = C_n e^{-x^2/2a_{\rm ho}^2}H_n(x/a_{\rm ho})} \ , \tag{2.106}$$

where the constant C_n is determined by the normalization condition (6.24), $\langle\psi_m|\psi_n\rangle = \delta_{m,n}$,

$$C_n = \frac{1}{\sqrt{a_{\rm ho}\sqrt{\pi}2^n n!}} \ . \tag{2.107}$$

The Hermite functions, H_n, are found in mathematical tables, see Sec. 6.3. The spatial and momentum wavefunctions for the vibrational ground state are,

$$\langle x|0\rangle = \frac{1}{\pi^{1/4}\sqrt{a_{\rm ho}}} e^{-x^2/2a_{\rm ho}^2} \quad \text{and} \quad \langle p|0\rangle = \frac{1}{\pi^{1/4}}\sqrt{\frac{a_{\rm ho}}{\hbar}} e^{-a_{\rm ho}^2 p^2/2\hbar^2} \ . \tag{2.108}$$

Here we will only show the graphical representation of $|\psi|^2$ in Fig. 2.13. The Exc. 2.5.6.1 asks to evaluate HO in a classically forbidden region and in Exc. 2.5.6.2 we will calculate the spectrum of a semi-harmonic HO.

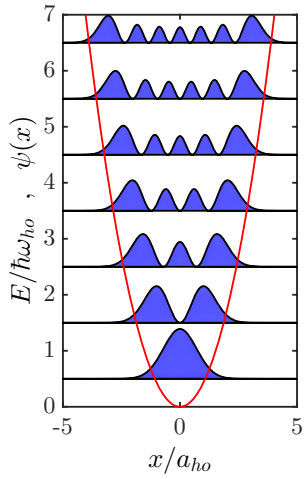

Figure 2.13: (code) Wavefunctions and energies for a harmonic potential.

2.5.3 Properties of the harmonic oscillator

We note that there are regions where $\psi(\tilde{x}) \neq 0$ even though $V(x) > E$. This effect is purely quantum. Classically, we can not find a particle in regions where its energy is below the potential.

We also note that for high quantum numbers, $n \to \infty$, we expect to recover the classical predictions, i.e.,

$$\lim_{n\to\infty} |\psi(x)|^2 = P_E(x) \ , \tag{2.109}$$

where P_E is the probability density of finding the oscillating particle at position x. The probability of finding the particle in a range dx close to the location x is easily calculated,

$$E = \frac{m}{2}v^2 + \frac{m}{2}\omega^2 x^2 \tag{2.110}$$

$$\Rightarrow \qquad P_E(x)dx = \frac{t(x+dx)-t(x)}{T} = \frac{dx}{vT} = \frac{dx}{T}\frac{1}{\sqrt{2E/m - \omega^2 x^2}} \ .$$

We see that for high energy values the wavefunction approaches the classical expectation.

We already mentioned that there exist solutions only for certain energies $E_n = \hbar\omega(2n+1)$. Consequently, the energy levels are equidistant, $E_{n+1} - E_n = \hbar\omega$, as if there were a box into which we add, one after the other, particles with the energy $\hbar\omega$ until we have accumulated n portions of energy. These particles are called *phonons* in the case of vibrations of massive particles, and *photons* in the case of a radiation field.

The fact that the energy distribution is the same as the one proposed by Planck for the black-body radiation suggests the use of the harmonic oscillator to describe the second quantization.

2.5.4 Time evolution of the unperturbed harmonic oscillator

Here we study the temporal evolution of a population distribution in a harmonic oscillator. The formal solution of the Schrödinger equation is,

$$|\psi(t)\rangle = e^{-\imath\hat{H}t/\hbar}|\psi(0)\rangle \ . \tag{2.111}$$

As the Hamiltonian is diagonal in the basis $|n\rangle$,

$$\hat{H} = \hbar\omega(\hat{n} + \tfrac{1}{2}) \ . \tag{2.112}$$

we can write,

$$e^{-\imath\hat{H}t/\hbar} = \sum_n |n\rangle e^{-\imath\omega t(n+1/2)}\langle n| \ . \tag{2.113}$$

If the initial state is $|\psi(0)\rangle = \sum_m c_m|m\rangle$, the final state and the eigenvalue of any observable will be,

$$|\psi(t)\rangle = \sum_n |n\rangle e^{-\imath\omega t(n+1/2)}\langle n|\psi(0)\rangle = \sum_n e^{-\imath\omega t(n+1/2)}c_n|n\rangle \tag{2.114}$$

$$\langle\psi(t)|\hat{A}|\psi(t)\rangle = \sum_m \langle m|e^{\imath\omega t(m+1/2)}c_m^*|\hat{A}|\sum_n e^{-\imath\omega t(n+1/2)}c_n|n\rangle = \sum_{m,n} c_m^* c_n e^{\imath\omega t(m-n)}\langle m|\hat{A}|n\rangle \ .$$

If the oscillator is initially in an eigenstate, $|\psi(0)\rangle = |k\rangle$, we obtain,

$$|\psi(t)\rangle = e^{-\imath\omega t(k+1/2)}|k\rangle \qquad \text{and} \qquad \langle\psi(t)|\hat{A}|\psi(t)\rangle = \langle k|\hat{A}|k\rangle \ , \tag{2.115}$$

that is, the *state remains stationary*. Motion needs non-diagonal elements of $\hat{A}$.

Another observation is that the populations do not change, even in the case of an initial superposition, since,

$$P_k(t) = |\langle k|\psi(t)\rangle|^2 = |e^{-\imath\omega t(k+1/2)}c_k|^2 = |c_k|^2 \ . \tag{2.116}$$

We conclude that

- movement of an observable $\hat{A}$ is possible, but only due to *variations of the phase factors*;

- to carry out transitions between the vibrational states is necessary to *perturb the oscillator*, e.g. by applying fields of electromagnetic radiation.

Example 24 (*Motion of a harmonic oscillator*): We now consider some specific examples. If the studied observable is the Hamiltonian and the initial state an arbitrary superposition, then

$$\langle\psi(t)|\hat{H}|\psi(t)\rangle = \hbar\omega \sum_{m,n} c_m^* c_n e^{\imath\omega t(m-n)} \langle m|\hat{n} + \tfrac{1}{2}|n\rangle = \hbar\omega \sum_n |c_n|^2 (n + \tfrac{1}{2}) \ .$$

That is, the total energy of the oscillator is the sum of the energies of the states weighted with the populations of those states. In the case of the position operator,

$$\begin{aligned}\langle\psi(t)|\hat{x}|\psi(t)\rangle &= \tfrac{a_{\rm ho}}{\sqrt{2}} \sum_{m,n} c_m^* c_n e^{\imath\omega t(m-n)} \langle m|\hat{a} + \hat{a}^\dagger|n\rangle \\ &= \tfrac{a_{\rm ho}}{\sqrt{2}} \sum_n \left(c_{n-1}^* c_n e^{-\imath\omega t}\sqrt{n} + c_{n+1}^* c_n e^{\imath\omega t}\sqrt{n+1}\right) \\ &\overset{m,n\to\infty}{\longrightarrow} a_{\rm ho}\sqrt{2} \sum_n \sqrt{n}|c_n|^2 \cos\omega t \ .\end{aligned}$$

That is, *the particle can only oscillate, if there are populations in consecutive states*. If this is not the case, $\langle\psi(t)|\hat{x}|\psi(t)\rangle = 0$. The oscillation frequency is always ω, independent of the energy of the particle. We will study this in Excs. 2.5.6.3, leaving the discussion of the temporal evolution of perturbed oscillators to later sections.

2.5.5 Multidimensional harmonic oscillator

The 3D harmonic potential is given by

$$V_{\rm ho}(\mathbf{r}) = \frac{m}{2}\omega_x^2 x^2 + \frac{m}{2}\omega_y^2 y^2 + \frac{m}{2}\omega_z^2 z^2 \ . \tag{2.117}$$

Making the ansatz

$$\psi(\mathbf{r}) = \psi_x(x)\psi_y(y)\psi_z(z) \ , \tag{2.118}$$

we can separate the spatial directions and obtain a one-dimensional equation for each coordinate, such that the coordinates can be considered separately. Each function $\psi_k(x_k)$ is of the form (2.106) and the energies are,

$$E_k = \hbar\omega_k(n_k + \tfrac{1}{2}) \ , \tag{2.119}$$

where $k = x, y, z$.

2.5.6 Exercises

2.5.6.1 Ex: Ground state of a harmonic oscillator

Equating the ground state energy of quantum HO to that of its classical analog, obtain the maximum elongation $x_{\rm m}$. Now, knowing that the ground state wavefunction is proportional to the Gaussian $\psi_0 \propto e^{-x^2/2x_{\rm m}^2}$, obtain the expression for the probability of finding the HO outside the classical limits and estimate its value.

2.5.6.2 Ex: Particle in a semi-harmonic well

Find the energy levels of a particle in a potential energy well of the form $V(x) = \infty$ for $x < 0$ and $V(x) = \frac{m\omega^2 x^2}{2}$ for $x > 0$. What is the parity of the allowed states?

2.5.6.3 Ex: Vibration of a harmonic oscillator

Consider a HO of mass m and angular frequency ω. At time $t = 0$ the oscillator's state is $|\psi(0)\rangle = \sum_n c_n |n\rangle$, where $|n\rangle$ are the stationary states of the HO with energy $(n + 1/2)\hbar\omega$.
a. What is the probability P for measuring, at an arbitrary time $t > 0$, an energy of the HO higher than $2\hbar\omega$? For the case when $P = 0$, what are the non-zero coefficients c_n?
b. From now on, we assume that only c_0 and c_1 are nonzero. Write down the normalization condition for $|\psi(0)\rangle$ and the mean value $\langle\hat{H}\rangle$ of energy in terms of c_0 and c_1. With the additional requirement $\langle\hat{H}\rangle = \hbar\omega$, calculate $|c_0|^2$ and $|c_1|^2$.
c. Given that the normalized state vector $|\psi(0)\rangle$ is defined to less than an overall phase factor, we determine this factor by choosing the real and positive coefficients c_0 and $c_1 = |c_1|e^{\imath\theta}$. Assuming $\langle\hat{H}\rangle = \hbar\omega$ and $\langle\hat{x}\rangle = \frac{1}{2}\sqrt{\hbar/m\omega}$, calculate θ.
d. With $|\psi(0)\rangle$ determined (according to the previous item), write down $|\psi(t)\rangle$ for $t > 0$ and calculate the value θ at this time t. Deduce the average value $\langle\hat{x}\rangle(t)$ of the position at time t.

2.6 Superposition states of a harmonic oscillator

As any other quantum system, a harmonic oscillator does not need to be in a particular vibrational eigenstate. In fact, it is much more common to encounter them in superpositions of many states. In a system in thermal equilibrium, the energetic distribution of occupied states reflects the temperature of the system.

2.6.1 Coherent states

The most common superposition for a harmonic oscillation is a Poissonian probability distribution of occupied vibrational (Fock) states. This state, called coherent or Glauber state, has particular features that we will discuss in the following sections.

2.6.1.1 Displacement operator

We now consider the so-called *displacement operator*,

$$\mathcal{D}(\alpha) \equiv e^{\alpha\hat{a}^\dagger - \alpha^*\hat{a}} \ , \tag{2.120}$$

which acts on the phase space of a harmonic oscillator spanned by the operators $\hat{a}$ and $\hat{a}^\dagger$, that is, $\hat{x} \propto \mathfrak{Re}\,\hat{a}$ and $\hat{p} \propto \mathfrak{Im}\,\hat{a}$, and try to discovers its features.

$\mathcal{D}(\alpha)$ is a unitary operator, since using Glauber's formula (1.313) we get,

$$\begin{aligned}\mathcal{D}^\dagger(\alpha)\mathcal{D}(\alpha) &= e^{\alpha^*\hat{a}-\alpha\hat{a}^\dagger}e^{\alpha\hat{a}^\dagger-\alpha^*\hat{a}} = e^{\alpha^*\hat{a}-\alpha\hat{a}^\dagger+\alpha\hat{a}^\dagger-\alpha^*\hat{a}+[\alpha^*\hat{a}-\alpha\hat{a}^\dagger,\alpha\hat{a}^\dagger-\alpha^*\hat{a}]/2} \\ &= e^{[\alpha^*\hat{a}-\alpha\hat{a}^\dagger,\alpha\hat{a}^\dagger-\alpha^*\hat{a}]/2} = e^{[\alpha^*\hat{a},\alpha\hat{a}^\dagger]/2+[-\alpha\hat{a}^\dagger,\alpha\hat{a}^\dagger]/2+[\alpha^*\hat{a},-\alpha^*\hat{a}]/2+[-\alpha\hat{a}^\dagger,-\alpha^*\hat{a}]/2} \\ &= e^{|\alpha|^2[\hat{a},\hat{a}^\dagger]/2+|\alpha|^2[\hat{a}^\dagger,\hat{a}]/2} = e^0 = \hat{1}\ .\end{aligned} \tag{2.121}$$

We can rewrite the displacement operator using Glauber's formula:

$$\begin{aligned}\mathcal{D}(\alpha) &= e^{\alpha\hat{a}^\dagger-\alpha^*\hat{a}} = e^{\alpha\hat{a}^\dagger}e^{-\alpha^*\hat{a}}e^{-[\alpha\hat{a}^\dagger,-\alpha^*\hat{a}]/2} = e^{\alpha\hat{a}^\dagger}e^{-\alpha^*\hat{a}}e^{|\alpha|^2[\hat{a}^\dagger,\hat{a}]/2} \\ &= e^{\alpha\hat{a}^\dagger}e^{-\alpha^*\hat{a}}e^{-|\alpha|^2/2}\ .\end{aligned} \tag{2.122}$$

The state resulting from the action of the operator $\mathcal{D}(\alpha)$ onto the ground state of the HO is,

$$\begin{aligned}|\alpha\rangle \equiv \mathcal{D}(\alpha)|0\rangle &= e^{-|\alpha|^2/2}e^{\alpha\hat{a}^\dagger}e^{-\alpha^*\hat{a}}|0\rangle = e^{-|\alpha|^2/2}\sum_{n=0}^{\infty}\frac{(\alpha\hat{a}^\dagger)^n}{n!}|0\rangle \\ &= e^{-|\alpha|^2/2}\left(1+\alpha\hat{a}^\dagger+\frac{(\alpha\hat{a}^\dagger)^2}{2!}+..\right)|0\rangle \\ &= e^{-|\alpha|^2/2}\left(|0\rangle+\frac{\alpha}{1!}\sqrt{1}|1\rangle+\frac{\alpha^2}{2!}\sqrt{2!}|2\rangle+..\right)\ ,\end{aligned} \tag{2.123}$$

that is, the state $|\alpha\rangle$ is a superposition distributed according to the *Poisson distribution*,

$$\boxed{|\alpha\rangle = e^{-|\alpha|^2/2}\sum_{n=0}^{\infty}\frac{\alpha^n}{\sqrt{n!}}|n\rangle}\ . \tag{2.124}$$

Applying the step-down operator $\hat{a}$ onto the state $|\alpha\rangle$, we find,

$$\begin{aligned}\hat{a}|\alpha\rangle &= e^{-|\alpha|^2/2}\sum_{n=0}^{\infty}\frac{\alpha^n}{\sqrt{n!}}\hat{a}|n\rangle = e^{-|\alpha|^2/2}\sum_{n=0}^{\infty}\frac{\alpha^n}{\sqrt{n!}}\sqrt{n}|n-1\rangle \\ &= e^{-|\alpha|^2/2}\sum_{n=0}^{\infty}\frac{\alpha^n}{\sqrt{(n-1)!}}|n-1\rangle\ ,\end{aligned} \tag{2.125}$$

that is,

$$\boxed{\hat{a}|\alpha\rangle = \alpha|\alpha\rangle}\ . \tag{2.126}$$

We can also write,

$$\langle\alpha|\hat{a}^\dagger = (\hat{a}|\alpha\rangle)^\dagger = (\alpha|\alpha\rangle)^\dagger = \langle\alpha|\alpha^*\ . \tag{2.127}$$

The state $|\alpha\rangle$ is called *coherent state* or *Glauber state* [3]. We note that, in spite of its appearance, the equation (2.126) is not an eigenvalue equation, since $\hat{a}$ is not observable.

Using the formula (1.280), we verify immediately,

[3] We can also define a *Bargmann state* as the eigenstate corresponding to the step-up operator using the notation $\hat{a}^\dagger||\alpha\rangle = \alpha||\alpha\rangle$.

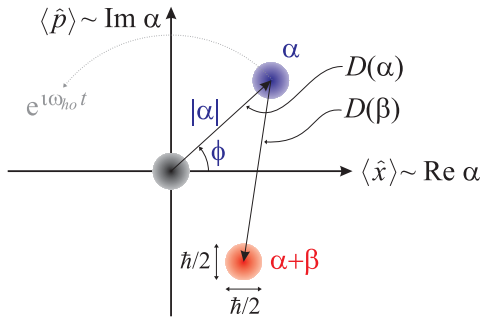

Figure 2.14: Illustration of the action of displacement operators $\mathcal{D}(\alpha)$ and $\mathcal{D}(\beta)$ on Glauber states in the phase space spanned by $\alpha = \mathfrak{Re}\,\alpha + \imath\ \mathfrak{Im}\,\alpha = |\alpha|e^{\imath\phi}$. The uncertainty of Glauber states Δx and Δp is represented by a finite distribution of the amplitude α in the phase space.

$$\mathcal{D}^\dagger(\alpha)\hat{a}\mathcal{D}(\alpha) = \hat{a} + \alpha\ . \tag{2.128}$$

Furthermore, the product of two displacement operators is, apart from a phase factor, another displacement operator satisfying,

$$\boxed{\mathcal{D}(\alpha)\mathcal{D}(\beta) = e^{(\alpha\beta^* - \alpha^*\beta)/2}\mathcal{D}(\alpha+\beta)}\ , \tag{2.129}$$

as will be verified in Exc. 2.6.6.1. When acting on an eigenket, the phase factor $e^{(\alpha\beta^* - \alpha^*\beta)/2}$ appears in each term of the resulting state, which makes it physically irrelevant.

2.6.1.2 Rotation operator

Another interesting operator is the *rotation operator* defined by,

$$\mathcal{R}(\varphi) \equiv e^{\imath\varphi\hat{a}^\dagger\hat{a}}\ . \tag{2.130}$$

Its properties are easily derived,

$$\mathcal{R}(\varphi)|n\rangle = e^{\imath\varphi n}|n\rangle \qquad \text{and} \qquad \mathcal{R}(\varphi)|\alpha\rangle = |e^{\imath\varphi}\alpha\rangle\ . \tag{2.131}$$

With the abbreviation $\hat{A} \equiv \imath\varphi\hat{a}^\dagger\hat{a}$, we can show,

$$\begin{aligned}\mathcal{R}^\dagger(\varphi)\hat{a}\mathcal{R}(\varphi) = e^{\hat{A}}\hat{a}e^{-\hat{A}} &= \hat{a} + [\hat{A},\hat{a}] + \tfrac{1}{2!}\left[\hat{A},[\hat{A},\hat{a}]\right] + \tfrac{1}{3!}\left[\hat{A},\left[\hat{A},[\hat{A},\hat{a}]\right]\right] + ... \\ &= \hat{a} + \imath\varphi\hat{a} + \tfrac{(\imath\varphi)^2}{2!}\hat{a} + \tfrac{(\imath\varphi)^3}{3!}\hat{a} + ... = e^{\imath\varphi}\hat{a}\ .\end{aligned} \tag{2.132}$$

In other words, the phase factor $e^{\imath\varphi}$ is the eigenvalue of the operator $\hat{a}\mathcal{R}(\varphi)$,

$$\mathcal{R}^\dagger(\varphi)\hat{a}\mathcal{R}(\varphi) = e^{\imath\varphi}\hat{a}\ . \tag{2.133}$$

Note also that,

$$\mathcal{R}(\varphi)\mathcal{D}(\alpha) \neq \mathcal{D}(\alpha)\mathcal{R}(\varphi)\ . \tag{2.134}$$

Do the Exc. 2.6.6.2.

Example 25 (*Operators acting on harmonic oscillators*): Other operators acting on single harmonic oscillator modes are the Kerr operator $\mathcal{K}$ studied in Exc. 14.3.5.15 and the squeezing operator $\mathcal{S}$ studied in Sec. 14.4.1. Tab. 2.1 lists the most common operators. Operators can also be designed to simultaneously manipulate different modes, thus establishing a coupling between them. Examples are the beam splitter $\mathcal{B}$ or the two-mode squeezer $\mathcal{S}_2$ studied in Sec. 14.5 or the Schrieffer-Wolff transform coupling a light mode and a collective atomic spin and studied in Exc. 23.2.4.12.

Table 2.1: List of basic transformation for harmonic oscillators.

unitary operation	action on field operators	action on field states
$\mathcal{D}(\beta)=e^{\beta\hat{a}^\dagger-\beta^*\hat{a}}$	$\mathcal{D}^\dagger\hat{a}\mathcal{D}=\hat{a}+\beta$	$\mathcal{D}\lvert n\rangle=\frac{1}{\sqrt{n!}}(\hat{a}^\dagger-\alpha^*)^n\lvert\alpha\rangle$ $\mathcal{D}\lvert\alpha\rangle=e^{(\alpha^*\beta-\alpha\beta^*)/2}\lvert\alpha+\beta\rangle$
$\mathcal{R}(\varphi)=e^{\imath\varphi\hat{a}^\dagger\hat{a}}$	$\mathcal{R}^\dagger\hat{a}\mathcal{R}=e^{\imath\varphi}\hat{a}$	$\mathcal{R}\lvert n\rangle=e^{\imath\varphi n}\lvert n\rangle$ $\mathcal{R}\lvert\alpha\rangle=e^{\imath\varphi\alpha}\lvert\alpha\rangle$
$\mathcal{S}(\xi)=e^{\xi^*\hat{a}^2/2-\xi\hat{a}^{\dagger 2}/2}$	$\mathcal{S}^\dagger\hat{a}\mathcal{S}=\hat{a}\cosh r-\hat{a}^\dagger e^{\imath\varphi}\sinh r$	$\mathcal{S}\hat{a}\mathcal{S}^\dagger\lvert\alpha,\xi\rangle=(\alpha\cosh r+\alpha^* e^{\imath\varphi}\sinh r)\lvert\alpha,\xi\rangle$
$\mathcal{K}(\tau)=e^{\imath\tau\hat{a}^{\dagger 2}\hat{a}^2/2}$	$\mathcal{K}^\dagger\hat{a}\mathcal{K}=e^{\imath\tau\hat{n}}\hat{a}$	$\mathcal{K}\lvert n\rangle=e^{(\imath\tau/2)n(n-1)}\lvert n\rangle$ $\mathcal{K}\lvert\alpha\rangle=e^{\imath(\tau/2)\alpha^2\hat{a}^{\dagger 2}}\lvert\alpha\rangle$
$\mathcal{B}(\theta)=e^{\theta(\hat{a}^\dagger\hat{b}-\hat{a}\hat{b}^\dagger)}$	$\mathcal{B}^\dagger\binom{\hat{a}}{\hat{b}}\mathcal{B}=\binom{\hat{a}}{\hat{b}}\cos\theta+\binom{\hat{b}}{-\hat{a}}\sin\theta$	
$\mathcal{S}_2(\theta)=e^{\xi^*\hat{a}\hat{b}/2-\hat{a}^\dagger\hat{b}^\dagger/2}$		

2.6.1.3 Uncertainty in Glauber states

Consider a HO prepared in a state $\lvert\alpha\rangle$. The eigenvalues of the observables $\hat{x}\equiv\frac{a_{\rm ho}}{\sqrt{2}}(\hat{a}^\dagger+\hat{a})$ and $\hat{p}\equiv\frac{\imath\hbar}{a_{\rm ho}\sqrt{2}}(\hat{a}^\dagger-\hat{a})$ are,

$$\begin{aligned}\tfrac{\sqrt{2}}{a_{\rm ho}}\langle\alpha|\hat{x}|\alpha\rangle&=\langle\alpha|\hat{a}+\hat{a}^\dagger|\alpha\rangle=\alpha+\alpha^*\\ \tfrac{\imath a_{\rm ho}\sqrt{2}}{\hbar}\langle\alpha|\hat{p}|\alpha\rangle&=\langle\alpha|\hat{a}-\hat{a}^\dagger|\alpha\rangle=\alpha-\alpha^*.\end{aligned}\tag{2.135}$$

With this the eigenvalues of the quadratures become,

$$\begin{aligned}\tfrac{2}{a_{\rm ho}^2}\langle\alpha|\hat{x}^2|\alpha\rangle&=\langle\alpha|(\hat{a}+\hat{a}^\dagger)^2|\alpha\rangle=\langle\alpha|\hat{a}\hat{a}+1+2\hat{a}^\dagger\hat{a}+\hat{a}^\dagger\hat{a}^\dagger|\alpha\rangle\\ &=\alpha^2+1+2|\alpha|^2+\alpha^{*2}=1+(\alpha+\alpha^*)^2=1+\tfrac{2}{a_{\rm ho}^2}\langle\alpha|\hat{x}|\alpha\rangle^2\\ \tfrac{-a_{\rm ho}^2 2}{\hbar^2}\langle\alpha|\hat{p}^2|\alpha\rangle&=\langle\alpha|(\hat{a}-\hat{a}^\dagger)^2|\alpha\rangle=\langle\alpha|\hat{a}\hat{a}-1-2\hat{a}^\dagger\hat{a}+\hat{a}^\dagger\hat{a}^\dagger|\alpha\rangle\\ &=\alpha^2-1-2|\alpha|^2+\alpha^{*2}=-1+(\alpha-\alpha^*)^2=-1-\tfrac{2a_{\rm ho}^2}{\hbar^2}\langle\alpha|\hat{p}|\alpha\rangle^2\ .\end{aligned}\tag{2.136}$$

The uncertainties defined in (1.178) become,

$$\begin{aligned}\Delta x^2&=\langle\alpha|\hat{x}^2|\alpha\rangle-\langle\alpha|\hat{x}|\alpha\rangle^2=\tfrac{a_{\rm ho}^2}{2}\\ \Delta p^2&=\langle\alpha|\hat{p}^2|\alpha\rangle-\langle\alpha|\hat{p}|\alpha\rangle^2=\tfrac{\hbar^2}{2a_{\rm ho}^2}\ .\end{aligned}\tag{2.137}$$

And finally, we find the Heisenberg relation,

$$\Delta p \Delta x = \tfrac{\hbar}{2} \ . \tag{2.138}$$

Comparing with the uncertainty relation (2.97) derived for Fock states, we conclude that the uncertainty is always *smallest* for Glauber states. In this sense, the Glauber states are the ones which are closest to classical states characterized by the absence of uncertainty.

Example 26 (*Quantum fluctuations*): We have seen that the displacement operator (2.120) can be used to generate any coherent state $\hat{a}$ from the vacuum state, which we will now call $\delta\hat{a}$,

$$\delta\hat{a} \equiv \mathcal{D}(\alpha)\hat{a}\mathcal{D}(\alpha)^\dagger = \hat{a} - \langle\hat{a}\rangle \ . \tag{2.139}$$

The uncertainty of the vacuum state is, obviously, the same,

$$\Delta(\delta\hat{a})^2 = \langle\delta\hat{a}^2\rangle - \langle\delta\hat{a}\rangle^2 = \langle(\hat{a}-\alpha)^2\rangle - \langle\hat{a}-\alpha\rangle^2 = \langle\hat{a}^2\rangle - \alpha^2 = \Delta\hat{a}^2 \ . \tag{2.140}$$

The procedure of separating quantum noise from an operator can be applied to other quantities than harmonic oscillators.

2.6.1.4 Orthogonality and completeness of Glauber states

Glauber are not orthogonal, since,

$$|\langle\alpha|\beta\rangle|^2 = e^{-|\alpha-\beta|^2} \ . \tag{2.141}$$

We leave the demonstration for Exc. 2.6.6.3, but we note here already that for $|\alpha-\beta| \gg 0$ the states are approximately orthogonal. The reason for this is, that the respective population distributions through the Fock states, $|\langle n|\alpha\rangle|^2$ and $|\langle n|\beta\rangle|^2$, do not overlap and hence do not interfere. Some more useful relationships are studied in Exc. 2.6.6.4. In Exc. 2.6.6.5 we show that the coherent state basis is not only complete,

$$\tfrac{1}{\pi}\int |\alpha\rangle\langle\alpha| d^2\alpha = \mathbb{I} \ , \tag{2.142}$$

but it is overcomplete. The state $|\alpha\rangle + |-\alpha\rangle$ is sometimes called *Schrödinger cat state*. In Exc. 2.6.6.6 we will show why such states are very difficult to detect.

2.6.2 Kicking a harmonic oscillator

Let us now study the dynamics of a harmonic oscillator subject to a *kick* or a dislocation or both in the same time. For this we need to remember the Galilei boost introduced in Sec. 1.7.3 and the unitary transformations corresponding to a spatial displacement (1.282) and to a kick (1.293),

$$\mathcal{U}_{\rm tr}(b) = e^{(-\imath/\hbar)b\hat{p}} \qquad \text{and} \qquad \mathcal{U}_{\rm kc}(k) = e^{\imath k\hat{x}} \ , \tag{2.143}$$

where we restrict to one dimension. The crucial point is that for a harmonic oscillator we know how to expand the operators $\hat{x}$ and $\hat{p}$ into linear combinations of the field operators $\hat{a}$ and $\hat{a}^\dagger$, which allows us to apply the whole formalism developed in the last sections to these transformation operators.

2.6.2.1 Transitions between vibrational states via momentum kick and dislocation

With the formalism developed in the last sections the displacement operator (2.123) can be decomposed in a combination of a spatial displacement and a kick operator (2.143). We can see this by simply substituting the field operators $\hat{a}$ and $\hat{a}^\dagger$ by linear combinations of position and momentum operators using (2.94),

$$\begin{aligned}\alpha\hat{a}^\dagger - \alpha^*\hat{a} &= \frac{\alpha}{\sqrt{2}}\left(\frac{\hat{x}}{a_{\rm ho}} - \imath\frac{a_{\rm ho}\hat{p}}{\hbar}\right) - \frac{\alpha^*}{\sqrt{2}}\left(\frac{\hat{x}}{a_{\rm ho}} + \imath\frac{a_{\rm ho}\hat{p}}{\hbar}\right) \\ &= -\imath\frac{\sqrt{2}a_{\rm ho}\mathfrak{Re}\,\alpha}{\hbar}\;\hat{p} + \imath\frac{\sqrt{2}\mathfrak{Im}\,\alpha}{a_{\rm ho}}\;\hat{x}\;.\end{aligned} \tag{2.144}$$

Using Glauber's rule,

$$\mathcal{D}(\alpha) = e^{\alpha\hat{a}^\dagger - \alpha^*\hat{a}} = e^{\imath\;\mathfrak{Re}\,\alpha\mathfrak{Im}\,\alpha}e^{(-\imath a_{\rm ho}\sqrt{2}/\hbar)\mathfrak{Re}\,\alpha\;\hat{p}}e^{(\imath\sqrt{2}/a_{\rm ho})\mathfrak{Im}\,\alpha\;\hat{x}}\;. \tag{2.145}$$

Hence, similarly to the Galilei boost in time and space, the displacement operator $D(\alpha)$ transforms the state of a harmonic oscillator, for example the ground state, $|\alpha\rangle = D(\alpha)|0\rangle$, by kicking its momentum by an amount,

$$\hbar k = \frac{\hbar\sqrt{2}}{a_{\rm ho}}\mathfrak{Im}\,\alpha\;, \tag{2.146}$$

and/or displacing its position suddenly by an amount,

$$b = \sqrt{2}a_{\rm ho}\mathfrak{Re}\,\alpha\;, \tag{2.147}$$

such that,

$$\alpha = \frac{b}{\sqrt{2}a_{\rm ho}} + \imath\frac{ka_{\rm ho}}{\sqrt{2}}\;. \tag{2.148}$$

The real and imaginary parts of α decide which contribution predominates, the kick or the dislocation,

$$\boxed{\mathcal{D}(\alpha) = e^{\imath\;\mathfrak{Re}\,\alpha\mathfrak{Im}\,\alpha}\;\mathcal{U}_{\rm tr}(\sqrt{2}a_{\rm ho}\mathfrak{Re}\,\alpha)\;\mathcal{U}_{\rm kc}(\tfrac{\hbar\sqrt{2}}{a_{\rm ho}}\mathfrak{Im}\,\alpha)}\;. \tag{2.149}$$

For example, if α is imaginary the operation describes a pure momentum kick by an amount $\hbar k$, which puts the harmonic oscillator into a coherent state with the mean occupation number,

$$n = |\alpha|^2 = |\mathfrak{Im}\,\alpha|^2 = \tfrac{1}{2}k^2a_{\rm ho}^2\;, \tag{2.150}$$

On the other hand, if α is real the operation describes a pure dislocation by an amount b, which puts the harmonic oscillator into a coherent state with the mean occupation number,

$$n = |\alpha|^2 = |\mathfrak{Re}\,\alpha|^2 = \frac{b^2}{2a_{\rm ho}^2}\;. \tag{2.151}$$

Now, let us focus on the kick operator and study how it acts on Fock states,

$$\begin{aligned}\langle n|e^{\imath k\hat{x}}|0\rangle = \langle n|\alpha\rangle &= \langle n|e^{-|\alpha|^2/2}\sum_{m=0}^{\infty}\frac{\alpha^m}{\sqrt{m!}}|m\rangle \\ &= e^{-|\alpha|^2/2}\frac{\alpha^n}{\sqrt{n!}} = e^{-|ka_{\rm ho}|^2/4}\frac{(\imath k a_{\rm ho})^n}{\sqrt{2^n n!}}\ ,\end{aligned} \tag{2.152}$$

using (2.148). This formula tells us that for small α, transitions may only occur to the vibrational states $|0\rangle$ and $|1\rangle$, since,

$$\langle n|e^{\imath k\hat{x}}|0\rangle \overset{ka_{\rm ho}\to 0}{\longrightarrow} \frac{\alpha^n}{\sqrt{n!}} \simeq \delta_{n,0} + \alpha\delta_{n,1}\ . \tag{2.153}$$

On the other hand for very large α, the exponential in (2.152) pulls the transition rate to a particular vibrational state $|n\rangle$ to zero, but this is simply due to the fact that the population is redistributed over many states, since,

$$\sum_n |\langle n|e^{\imath k\hat{x}}|0\rangle|^2 = e^{-(ka_{\rm ho})^2/2}\sum_{n=0}^{\infty}\frac{|\alpha|^{2n}}{n!} = e^{-(ka_{\rm ho})^2/2}e^{|\alpha|^2} = 1\ . \tag{2.154}$$

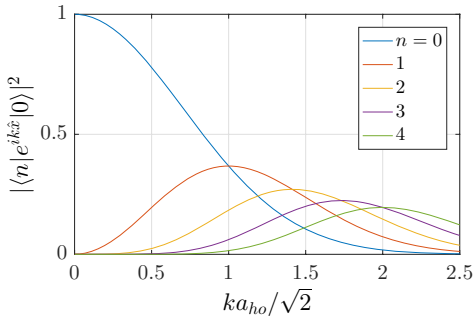

Figure 2.15: (code) Transition matrix element $|\langle n|e^{\imath k\hat{x}}|0\rangle|^2$ as a function of $ka_{\rm ho}$. The curves are Poisson distributions of photon numbers in coherent states.

For small momentum kicks we may approximate the transition matrix elements by,

$$\begin{aligned}\langle m|e^{\imath k\hat{x}}|n\rangle &\simeq \langle m|1 + \imath k\tfrac{a_{\rm ho}}{\sqrt{2}}(\hat{a}+\hat{a}^\dagger)|n\rangle \\ &= \delta_{m,n} + \tfrac{\imath k a_{\rm ho}}{\sqrt{2}}(\sqrt{n}\delta_{m,n-1} + \sqrt{n+1}\delta_{m,n+1})\ ,\end{aligned} \tag{2.155}$$

such that,

$$\sum_{m\neq n}|\langle m|e^{\imath k\hat{x}}|n\rangle|^2 \simeq k^2 a_{\rm ho}^2(n+\tfrac{1}{2})\ . \tag{2.156}$$

Formula (2.156) tell us that the probability for a transition between vibrational states depends on the parameter $ka_{\rm ho}$, which we will discuss in the next section. For small $ka_{\rm ho}$ it gets increasingly more difficult for the system to leave the original

vibrational state $|n\rangle$ and to form a coherent state. After a momentum kick, the population is coherently distributed over several vibrational states in a way to fulfill momentum and energy conservation. Let us consider, for simplicity, an initial state $|0\rangle$. If the kick is weak or the trap strong (i.e. if $|\alpha| < 1$), the atom will stay in $|0\rangle$ with a high probability amplitude and go to $|1\rangle$ only with a small probability amplitude. We will derive in Exc. 2.6.6.7 the general expression for the transition matrix element for arbitrary values of α [4],

$$\boxed{\langle m|e^{\imath k\hat{x}}|n\rangle = e^{|\alpha|^2/2}\sum_{k=0}^{n}\sqrt{\binom{n}{k}\binom{m}{k}}\langle n-k|\alpha\rangle\langle m-k|\alpha\rangle} \ . \tag{2.157}$$

The formula satisfies,

$$\sum_m |\langle m|e^{\imath k\hat{x}}|n\rangle|^2 = \sum_m \langle n|e^{\imath kx}|m\rangle\langle m|e^{-\imath kx}|n\rangle = \langle n|e^{\imath kx}e^{-\imath kx}|n\rangle = 1 \ . \tag{2.158}$$

Kicking a harmonic oscillator initially in state $|0\rangle$ we obtain for the expectation value of position and momentum,

$$\boxed{\begin{array}{lcl} \langle\alpha|\hat{p}|\alpha\rangle & = & \langle 0|D(\alpha)^\dagger \hat{p} D(\alpha)|0\rangle = \langle 0|e^{\imath k\hat{x}}\hat{p}e^{-\imath k\hat{x}}|0\rangle = \langle 0|\hat{p}|0\rangle + \hbar k \\ \langle\alpha|\hat{x}|\alpha\rangle & = & \langle 0|\hat{x}|0\rangle \end{array}} \ .$$

2.6.2.2 Lamb-Dicke regime

We already introduced $|\alpha|$ as the amplitude (2.151) of the coherent vibrational state created by kicking a harmonic oscillator. Defined as,

$$\boxed{\eta \equiv |\alpha| = \tfrac{1}{\sqrt{2}} k a_{\rm ho}} \qquad \text{with} \qquad a_{\rm ho} \equiv \sqrt{\frac{\hbar}{m\omega_{\rm ho}}} \ . \tag{2.159}$$

the so-called *Lamb-Dicke parameter* measures the *degree of confinement* of a particle in a harmonic trap with respect to the momentum kick. We say that we are in the *Lamb-Dicke regime*, when $\eta < 1$, that is when the particle is localized to a volume smaller than the wavelength, $2\pi x_0 \ll \lambda = 2\pi/k$, corresponding to the momentum change.

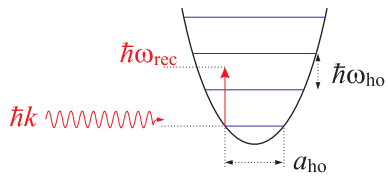

Figure 2.16: Illustration of the Lamb-Dicke parameter.

[4] See also 14.3.3.

We can also rewrite the Lamb-Dicke parameter in terms of the trap's secular frequency, $\omega_{\rm ho}$, and the recoil-shift,

$$\boxed{\eta = \sqrt{\frac{\omega_{\rm rec}}{\omega_{\rm ho}}}} \qquad \text{with} \qquad \omega_{\rm rec} \equiv \frac{\hbar k^2}{2m} \ , \tag{2.160}$$

where we understand the recoil-energy $\hbar\omega_{\rm rec}$ as the kinetic energy gained through the recoil acceleration. In this form the Lamb-Dicke parameter tells us that, in the Lamb-Dicke regime, the energy of the momentum kick is not sufficient to efficiently excite vibrational states,

$$(2n+1)\hbar k^2/m \ll \omega_{\rm ho} \ . \tag{2.161}$$

That is, cold particles in low vibrational states n can not accommodate the recoil shift within the vibrational spectrum of the trap. Consequently, the recoil cannot be transferred to the particle itself, but must be absorbed by the entire trap. This is the case of the *strong binding regime* in ion traps, which is analogous to the *Mößbauer effect* discussed later in Sec. 20.3.3.

Finally, the Lamb-Dicke parameter can be rewritten in terms of the *inverse Doppler modulation index*,

$$\boxed{\eta = \frac{k v_{\rm max}}{2\omega_{\rm ho}}} \qquad \text{with} \qquad \frac{m}{2} v_{\rm max}^2 = \hbar\omega_{\rm ho} \ . \tag{2.162}$$

Accelerated by the momentum kick, the atom will execute harmonic oscillations with frequency $\omega_{\rm ho}$ and with the maximum velocity-excursions $v_{\rm max}$. Hence, any quantity depending on the atomic velocity, e.g. the Doppler-shift of light scattered from the atom, will be modulated. We will see in Sec. 20.3.3 that the modulation generates a spectrum of frequency sidebands which, in case of small $\eta < 1$, are restricted to first-order sidebands located at $\pm\omega_{\rm ho}$ of the light frequency. Do the Exc. 2.6.6.8.

Example 27 (*Absorption of recoil by a molecular dimer*): To be able to discuss the validity of energy and momentum conservation in a kicked system, let us consider a molecule made of two atoms with masses m_1 and m_2 bound by a force obeying Hooke's law. Then we kick atom 1 via the momentum shift operator $e^{\imath k\hat{x}_1}$ (e.g. during a photon absorption process with the associated recoil) and analyze the motional dynamics of the whole system [5]. (We restrict ourselves to one dimension.)

The first step is to write down the Hamiltonian,

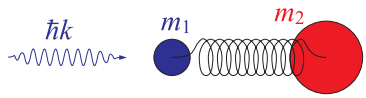

Figure 2.17: Illustration of a heteronuclear dimer kicked by photonic recoil.

$$\hat{H} = -\frac{\hbar^2}{2m_1}\frac{d^2}{dx_1^2} - \frac{\hbar^2}{2m_2}\frac{d^2}{dx_2^2} + \frac{\mu}{2}\omega_{\rm ho}^2(x_1 - x_2)^2 \ ,$$

[5] The selective kicking is realistic if we image both atoms being of different species with different transitions responding differently to incident radiation.

We transform in the center-of-mass system via,

$$M \equiv m_1 + m_2 \quad \text{and} \quad \frac{1}{\mu} \equiv \frac{1}{m_1} + \frac{1}{m_2}$$
$$R = \frac{m_1 x_1 + m_2 x_2}{M} \quad \text{and} \quad r = x_1 - x_2 \ .$$

Applying the separation ansatz $\psi(x_1, x_2) = \Theta(R)\phi(r)$ to the Schrödinger equation,

$$\left[-\frac{\hbar^2}{2m_1}\frac{d^2}{dx_1^2} - \frac{\hbar^2}{2m_2}\frac{d^2}{dx_2^2} + \frac{\mu}{2}\omega_{\rm ho}^2(\hat{x}_1 - \hat{x}_2)^2 \right] \psi(x_1, x_2) = E_{\rm tot}\psi(x_1, x_2) \ ,$$

we calculate for $i = 1, 2$,

$$\frac{d}{dx_i} = \frac{dR}{dx_i}\frac{d}{dR} + \frac{dr}{dx_i}\frac{d}{dr} = \frac{m_i}{M}\frac{d}{dR} \pm \frac{d}{dr}$$
$$\frac{d^2}{dx_i^2} = \frac{m_i^2}{M^2}\frac{d^2}{dR^2} \pm 2\frac{m_i}{M}\frac{d}{dR}\frac{d}{dr} + \frac{d^2}{dr^2}$$
$$-\frac{\hbar^2}{2m_1}\frac{d^2}{dx_1^2} - \frac{\hbar^2}{2m_2}\frac{d^2}{dx_2^2} = -\frac{\hbar^2}{2M}\frac{d^2}{dR^2} - \frac{\hbar^2}{2\mu}\frac{d^2}{dr^2} \ .$$

Hence, we get,

$$-\frac{\hbar^2}{2M}\frac{d^2}{dR^2}\Theta(R) = (E_{\rm tot} - E)\Theta(R) \quad , \quad \left[-\frac{\hbar^2}{2\mu}\frac{d^2}{dr^2} + \frac{\mu}{2}\omega_{\rm ho}^2\hat{r}^2 \right] \phi(r) = E\phi(r) \ ,$$

with the vibrational energy E and the energy of the center-of-mass motion $E_{\rm tot} - E$.

Now, we analyze the kick operator $e^{\imath k\hat{x}_1}$ with $\hat{x}_1 = \hat{R} - \frac{m_2}{M}\hat{r}$. We find that, because of $[\hat{R}, \hat{r}] = 0$,

$$e^{\imath k\hat{x}_1} = e^{\imath k\hat{R}} e^{-\imath k\frac{m_2}{M}\hat{r}} \ .$$

This means that the kick operator simultaneously acts on both: the center-of-mass receives a recoil accelerating it by an amount $p_{\rm cm} = \hbar k$, and the vibrational relative motion receives a kick of an amount $p_{\rm rel} = \hbar k m_2/M$ following the dynamics described in Sec. 2.6.2.

Obviously, the total system conserves momentum, which is imparted to the center-of-mass motion. Whether the kick also excites the relative motion depends on mass ratio. In the limit $m_1 \ll m_2$ we find $p_{\rm rel} = \hbar k$, while in the limit $m_1 \gg m_2$ we get $p_{\rm rel} \to 0$. In terms of the Lamb-Dicke parameter, we find,

$$\eta = \frac{p_{\rm rel} a_{\rm ho}}{\hbar\sqrt{2}} = \frac{k m_2}{M\sqrt{2}}\sqrt{\frac{\hbar}{\mu\omega_{\rm ho}}} = \frac{k m_2}{m_1 + m_2}\sqrt{\frac{\hbar}{2\omega_{\rm ho}}\left(\frac{1}{m_1} + \frac{1}{m_2}\right)} \ .$$

Hence, in the limit $m_1 \ll m_2$ we expect a much larger Lamb-Dicke parameter than for $m_1 \gg m_2$. In particular, considering the limit $m_2 \to \infty$, we recover the formula (2.160) holding for an atom confined in a harmonic potential,

$$\eta \overset{m_2\to\infty}{\longrightarrow} \sqrt{\frac{\hbar k^2}{\omega_{\rm ho} 2m_1}} = \sqrt{\frac{\omega_{\rm rec}}{\omega_{\rm ho}}} \ .$$

We find that the energy transferred to the relative motion quadratically decreases with the Lamb-Dicke parameter for $\eta < 1$ and quadratically increases for $\eta > 1$,

$$E_{\rm rel} = \frac{p_{\rm rel}^2}{2\mu} = \frac{1}{2\mu}\frac{2\hbar^2\eta^2}{a_{\rm ho}^2} = \hbar\omega_{\rm ho}\eta^2 \ .$$

2.6.3 Shaking a harmonic oscillator

As we mentioned below the formulae (1.294), the transformation in momentum space is not a realistic concept for a *kick*. In practice, a kick will always be the results of a collision, which is understood here as a scattering of a free (massive or massless) particle at our harmonically trapped particle. And the scattering process will take a finite amount of time, e.g. the duration of a radiative π-pulse required to excite an atomic transition.

More realistic is to expose the harmonic oscillator to periodic forcing,

$$\boxed{\hat{H}(t) = \hat{H}^{(0)} + \hat{H}^{(1)} = -\frac{\hbar^2}{2m}\frac{d^2}{dx^2} + \frac{m}{2}\omega_{\rm ho}^2\hat{x}^2 + \frac{\hbar\Omega}{2}(\hat{a}e^{\imath\nu t} + \hat{a}^\dagger e^{-\imath\nu t})} \ . \tag{2.163}$$

To study its time evolution we calculate,

$$|\psi(t)\rangle = e^{-(\imath/\hbar)\hat{H}t}\sum_n a_n|n\rangle \stackrel{a_n=\delta_{n,0}}{\longrightarrow} e^{-(\imath/\hbar)\hat{H}t}|0\rangle \ , \tag{2.164}$$

when the oscillator is initially in the state $|0\rangle$. We rewrite the time evolution propagator as,

$$e^{-(\imath/\hbar)\hat{H}t} = e^{-\imath\omega_{\rm ho}t(\hat{n}+1/2)-(\imath\Omega t/2)(\hat{a}e^{\imath\nu t}+\hat{a}^\dagger e^{-\imath\nu t})} \ . \tag{2.165}$$

To simplify the propagator, we first have a closer look at the terms $\hat{a}e^{\imath\omega_{\rm ho}t}$ and $\hat{a}^\dagger e^{-\imath\omega_{\rm ho}t}$, which we evaluate through their action on the complete system of unperturbed eigenfunctions,

$$\begin{aligned} e^{-(\imath/\hbar)\hat{H}^{(0)}t}\hat{a}e^{(\imath/\hbar)\hat{H}^{(0)}t}|n\rangle &= e^{-(\imath/\hbar)\hat{H}^{(0)}t}\hat{a}e^{(\imath/\hbar)E_n^{(0)}t}|n\rangle \\ &= e^{-(\imath/\hbar)E_{n-1}^{(0)}t}e^{(\imath/\hbar)E_n^{(0)}t}\hat{a}|n\rangle = e^{\imath\omega_{\rm ho}t}\hat{a}|n\rangle \ . \end{aligned} \tag{2.166}$$

Hence, defining the detuning $\Delta \equiv \nu - \omega_{\rm ho}$,

$$\begin{array}{rcccl} \hat{a}e^{\imath\nu t} & = & e^{\imath\omega_{\rm ho}t}\hat{a}e^{\imath\Delta t} & = & e^{-\imath\omega_{\rm ho}t(\hat{n}+1/2)}\hat{a}e^{\imath\Delta t}e^{\imath\omega_{\rm ho}t(\hat{n}+1/2)} \\ \hat{a}^\dagger e^{-\imath\nu t} & = & e^{-\imath\omega_{\rm ho}t}\hat{a}^\dagger e^{-\imath\Delta t} & = & e^{-\imath\omega_{\rm ho}t(\hat{n}+1/2)}\hat{a}^\dagger e^{-\imath\Delta t}e^{\imath\omega_{\rm ho}t(\hat{n}+1/2)} \\ \hat{n} & = & & & e^{-\imath\omega_{\rm ho}t(\hat{n}+1/2)}\hat{n}e^{\imath\omega_{\rm ho}t(\hat{n}+1/2)} \end{array} \ . \tag{2.167}$$

Substituting these expression into the propagator (2.165) we get,

$$e^{-(\imath/\hbar)\hat{H}t} = e^{e^{-\imath\omega_{\rm ho}t(\hat{n}+1/2)}\left[-\imath\omega_{\rm ho}t(\hat{n}+1/2)-(\imath\Omega t/2)\hat{a}e^{\imath\Delta t}-(\imath\Omega t/2)\hat{a}^\dagger e^{-\imath\Delta t}\right]e^{\imath\omega_{\rm ho}t(\hat{n}+1/2)}} \ . \tag{2.168}$$

Now, making use of the relationship,

$$e^{e^{-\hat{A}}\hat{B}e^{\hat{A}}} = \sum_n \frac{(e^{-\hat{A}}\hat{B}e^{\hat{A}})^n}{n!} = \sum_n \frac{e^{-\hat{A}}\hat{B}^n e^{\hat{A}}}{n!} = e^{-\hat{A}}e^{\hat{B}}e^{\hat{A}} \ , \tag{2.169}$$

which is easy to show by expansion of $e^{\hat{B}}$, we find [6],

$$e^{-(\imath/\hbar)\hat{H}t} = e^{-\imath\omega_{\rm ho}t(\hat{n}+1/2)}e^{-\imath\omega_{\rm ho}t(\hat{n}+1/2)-(\imath\Omega t/2)(\hat{a}e^{\imath\Delta t}+\hat{a}^\dagger e^{-\imath\Delta t})}e^{\imath\omega_{\rm ho}t(\hat{n}+1/2)} \ . \tag{2.170}$$

[6] Note, that this formula can not be simplified using Glauber's formula, because $[\hat{n},[\hat{n},\hat{a}]] \neq 0$. Note also, that the unitary transformation corresponds to a transformation into Dirac's interaction picture, which will be studied in the context of quantized radiation fields in Sec. 17.2.

In particular, for $\Delta = 0$,

$$\boxed{\langle n|e^{-(\imath/\hbar)\hat{H}t}|0\rangle = e^{-n\imath\omega_{\rm ho}t}\langle n|e^{-\imath\omega_{\rm ho}t(\hat{n}+1/2)-(\imath\Omega t/2)(\hat{a}+\hat{a}^\dagger)}|0\rangle} \ . \tag{2.171}$$

The dynamics is illustrated in Fig. 2.18. Again, we notice that the state generated

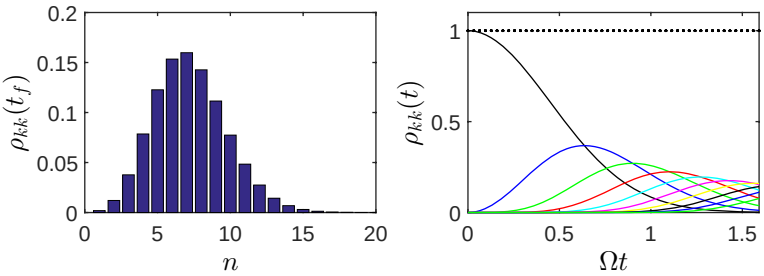

Figure 2.18: (code) (a) Populations of the vibrational states after a given interaction time. (b) Time evolution of the lowest populations.

is a coherent state. In Exc. 2.6.6.9 we will study how to generalize the problem to non-resonant excitation, $\Delta \neq 0$.

2.6.4 Forcing a harmonic oscillator

In Secs. 2.6.2 and 2.6.3 we studied two ways of exciting a harmonic oscillator. We found that the energy and momentum imparted to a harmonic oscillator upon excitation are determined by conservation laws. On the other hand, the excitation probability depends on the shape of the perturbation: While an abrupt kick *always* results in an excitation, a monochromatic excitation needs to satisfy a *resonance condition*. We will study this in more detail in Sec.5.4.2.

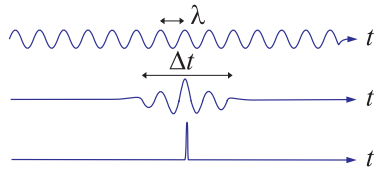

Figure 2.19: Illustration of possible shapes of an excitation field.

The transfer of momentum is the result of a (generally) constant force applied for a certain amount of time,

$$\hbar k = \int_{-\infty}^{\infty} mg\ \Theta_{[0,\Delta t]}(t)\ dt \ , \tag{2.172}$$

where g denotes the acceleration. That is, we expect that a harmonic oscillator,

$$\boxed{\hat{H}(t) = -\frac{\hbar^2}{2m}\frac{d^2}{dx^2} + \frac{m}{2}\omega_{\rm ho}^2\hat{x}^2 - mg\hat{x}\ \Theta_{[0,\Delta t]}(t)} \ , \tag{2.173}$$

forced for a period of time Δt should have suffered a kick.

2.6.4.1 Displaced harmonic oscillator

To begin with, we will derive the dynamics of a harmonic oscillator suddenly exposed to a homogeneous constant force $F(t) = mg\ \Theta_{[0,\infty]}(t)$. It is easy to see, that the above perturbed Hamiltonian can be cast into the form,

$$\hat{H}(t) = -\frac{\hbar^2}{2m}\frac{d^2}{dx^2} + \frac{m}{2}\omega_{\rm ho}^2\left(\hat{x} - \frac{g}{\omega_{\rm ho}^2}\right)^2 - \frac{mg^2}{2\omega_{\rm ho}^2}\ , \tag{2.174}$$

where the last constant term plays no role in the dynamics. That is, as we know from classical physics, the essential impact of a homogeneous force (e.g. gravity) on a harmonic oscillator consists in displacing its equilibrium position. Knowing the eigenvalues and -states of the unperturbed Hamiltonian, the obvious solution of the perturbed eigenvalue problem is,

$$\begin{aligned} &\hat{H}|\psi_n^{(1)}\rangle = E_n^{(1)}|\psi_n^{(1)}\rangle \qquad (2.175)\\ &\quad\text{with}\quad E_n^{(1)} = E_n - \frac{mg^2}{2\omega_{\rm ho}^2}\\ &\quad\text{and}\quad \langle x|\psi_n^{(1)}\rangle = \psi_n^{(1)}(x) = \psi_n(x - \tfrac{g}{\omega_{\rm ho}^2}) = \langle x - \tfrac{g}{\omega_{\rm ho}^2}|n\rangle\ . \end{aligned}$$

Using the properties (1.282) and (1.284) we may write,

$$\langle x - \tfrac{g}{\omega_{\rm ho}^2}|n\rangle = \langle x|U_{\rm tr}^\dagger(-\tfrac{g}{\omega_{\rm ho}^2})|n\rangle = \langle x|e^{-(\imath/\hbar)(g/\omega_{\rm ho}^2)\hat{p}}|n\rangle\ , \tag{2.176}$$

and using the representation (2.95) of the momentum operator by the field operators and introducing the abbreviation $\beta \equiv \frac{g}{\omega_{\rm ho}^2 a_{\rm ho}\sqrt{2}}$ we can rewrite,

$$\langle x - \tfrac{g}{\omega_{\rm ho}^2}|n\rangle = e^{-\beta(\hat{a}-\hat{a}^\dagger)}\langle x|n\rangle\ . \tag{2.177}$$

Note, that the transition from (2.173) to (2.175) can also be obtained by a redefinition of the field operators according to,

$$\hat{b} \equiv \hat{a} - \tfrac{mga_{\rm ho}}{\hbar\omega_{\rm ho}\sqrt{2}}\ , \tag{2.178}$$

since,

$$\hat{H} = \hbar\omega_{\rm ho}(\hat{a}^\dagger\hat{a} + \tfrac{1}{2}) - \tfrac{mga_{\rm ho}}{\sqrt{2}}(\hat{a} + \hat{a}^\dagger) = \hbar\omega_{\rm ho}(\hat{b}^\dagger\hat{b} + \tfrac{1}{2}) - \tfrac{mg^2}{2\omega_{\rm ho}^2} \tag{2.179}$$

and $\hat{a} - \hat{a}^\dagger = \hat{b} - \hat{b}^\dagger$.

The temporal evolution is given by the time-dependent Schrödinger equation. Since the jump is finite, the solution must be well behaved at time $t = 0$,

$$\begin{aligned} \langle x|\psi_n^{(1)}(t)\rangle &= \langle x|e^{-(\imath/\hbar)\hat{H}t}|\psi_n^{(1)}(0)\rangle \qquad (2.180)\\ &= \langle x|e^{-(\imath/\hbar)\hat{H}t}e^{-\beta(\hat{a}-\hat{a}^\dagger)}|n\rangle\\ &= \langle x|e^{-(\imath/\hbar)\hat{H}t}e^{-\beta(\hat{a}-\hat{a}^\dagger)}e^{(\imath/\hbar)\hat{H}t}e^{-(\imath/\hbar)\hat{H}t}|n\rangle\ . \end{aligned}$$

To simplify the first three exponential functions, we use the relationships (2.169) and (2.166) [7],

$$e^{-(\imath/\hbar)\hat{H}t}e^{-\beta(\hat{a}-\hat{a}^\dagger)}e^{(\imath/\hbar)\hat{H}t} = e^{-\beta e^{-(\imath/\hbar)\hat{H}t}(\hat{a}-\hat{a}^\dagger)e^{(\imath/\hbar)\hat{H}t}} = e^{-\beta\left(e^{\imath\omega_{\rm ho}t}\hat{a}-e^{-\imath\omega_{\rm ho}t}\hat{a}^\dagger\right)} , \tag{2.181}$$

and write the temporal solution,

$$\begin{aligned}\psi_n^{(1)}(x,t) &= e^{-\beta(\hat{a}e^{\imath\omega_{\rm ho}t}-\hat{a}^\dagger e^{-\imath\omega_{\rm ho}t})}e^{-(\imath/\hbar)\hat{H}t}\psi_n(x) \\ &= e^{-\beta(\hat{a}-\hat{a}^\dagger)\cos\omega_{\rm ho}t-\imath\beta(\hat{a}+\hat{a}^\dagger)\sin\omega_{\rm ho}t}e^{-(\imath/\hbar)E_n^{(0)}t}\psi_n(x) .\end{aligned} \tag{2.182}$$

Using Glauber's formula (1.313) we find,

$$\begin{aligned}&\psi_n^{(1)}(x,t) = e^{-\imath\beta(\hat{a}+\hat{a}^\dagger)\sin\omega_{\rm ho}t}e^{-\beta(\hat{a}-\hat{a}^\dagger)\cos\omega_{\rm ho}t}e^{\imath\beta^2\sin\omega_{\rm ho}t\cos\omega_{\rm ho}t}e^{-(\imath/\hbar)E_n^{(0)}t}\psi_n(x) \\ &= e^{-\imath(mg/\hbar\omega_{\rm ho})\hat{x}\sin\omega_{\rm ho}t}e^{-(\imath/\hbar)(g/\omega_{\rm ho}^2)\hat{p}\cos\omega_{\rm ho}t}e^{\imath\beta^2\sin\omega_{\rm ho}t\cos\omega_{\rm ho}t}e^{-(\imath/\hbar)E_n^{(0)}t}\psi_n(x) \\ &= e^{-\imath\beta(\hat{a}+\hat{a}^\dagger)\sin\omega_{\rm ho}t}e^{\imath\beta^2\sin\omega_{\rm ho}t\cos\omega_{\rm ho}t}e^{-(\imath/\hbar)E_n^{(0)}t}\psi_n(x-b\cos\omega_{\rm ho}t) .\end{aligned} \tag{2.183}$$

Finally,

$$\boxed{|\psi_n^{(1)}(x,t)|^2 = |\psi_n(x-\bar{x}(t))|^2 \qquad \text{where} \qquad \bar{x}(t) \equiv \tfrac{g}{\omega_{\rm ho}^2}\cos\omega_{\rm ho}t} . \tag{2.184}$$

This means that the spatial distribution of $\psi_n^{(1)}$ around $\bar{x}(t)$ is the same as of ψ_n around $\bar{x}=0$. The entire distribution oscillates without deformation. The momentum distribution follows from the Fourier transform,

$$\begin{aligned}\phi_n^{(1)}(p,t) &= \frac{1}{\sqrt{2\pi\hbar}}\int dx e^{-(\imath/\hbar)px}\psi_n^{(1)}(x,t) \\ &= \frac{1}{\sqrt{2\pi\hbar}}\int du\ e^{-(\imath/\hbar)pu}e^{-(\imath/\hbar)um\omega_{\rm ho}\frac{g}{\omega_{\rm ho}^2}\sin\omega_{\rm ho}t}e^{\imath\gamma(p,t)}\psi_n \\ &= e^{\imath\gamma(p,t)}\phi_n(p+m\omega_{\rm ho}\tfrac{g}{\omega_{\rm ho}^2}\sin\omega_{\rm ho}t) ,\end{aligned} \tag{2.185}$$

where the abbreviation $\gamma=\gamma^*$ contains all unitary transformations of (2.183), that do not depend on x. We obtain,

$$\boxed{|\phi_n^{(1)}(p,t)|^2 = |\phi_n(p-\bar{p}(t))|^2 \qquad \text{where} \qquad \bar{p}(t) \equiv -m\tfrac{g}{\omega_{\rm ho}}\sin\omega_{\rm ho}t} . \tag{2.186}$$

2.6.4.2 Discussion of the kick dynamics

For the acceleration of the harmonic oscillator to resemble a 'kick', the time during which the perturbation is active must be much smaller than a trap oscillation period, $\omega_{\rm ho}\Delta t \ll 1$. In this case, we may expand the oscillatory motion (2.184) and (2.186),

$$\bar{x} = \frac{g}{\omega_{\rm ho}^2} \qquad \text{and} \qquad \bar{p} = -mg\Delta t \equiv -\hbar k , \tag{2.187}$$

[7] We can use (2.166), because the shifted harmonic oscillator has, except from a constant offset the same eigenenergies.

which is consistent with the initial request (2.172). It is also clear that, for a given force mg, the maximum momentum that can be transmitted is limited, $\hbar k < mg/\omega_{\rm ho}$.

As long as the kick-approximation $\omega_{\rm ho}\Delta t \ll 1$ holds, we may simply describe the dynamics during the application of the force, via a time-dependent kick operator,

$$e^{\imath k(t)\hat{x}} = \mathcal{D}(\alpha(t)) \ , \tag{2.188}$$

where the acquired momentum increases linearly with time according to $k(t) = k\frac{\max(\min(t,\Delta t),0)}{\Delta t}$. I.e. the populations of the vibrational states evolve like (2.152) into a coherent state with increasing amplitude $|\alpha(t)|^2$. At the end of the kick, on a much slower time-scale $\omega_{\rm ho}^{-1}$, the wavefunctions will start to oscillate all in phase, according to (2.184).

The time-dependence of the states $|\alpha(t)\rangle$, as shown in Exc. 2.6.6.10 is given by,

$$\begin{aligned} |\alpha(t)\rangle &= e^{-(\imath/\hbar)\hat{H}t}|\alpha(0)\rangle = \sum_n e^{-(\imath/\hbar)E_n t}e^{-|\alpha(0)|^2/2}\frac{\alpha(0)^n}{\sqrt{n!}}|n\rangle \\ &= e^{-\imath\omega_{\rm ho}t/2}\sum_n e^{-|\alpha(0)|^2/2}\frac{(\alpha(0)e^{-\imath\omega_{\rm ho}t})^n}{\sqrt{n!}}|n\rangle = e^{-\imath\omega_{\rm ho}t/2}|\alpha(0)e^{-\imath\omega_{\rm ho}t}\rangle \ . \end{aligned} \tag{2.189}$$

With (2.166) we find,

$$\begin{aligned} \hat{x}(t) &= e^{-(\imath/\hbar)\hat{H}t}\hat{x}(0)e^{(\imath/\hbar)\hat{H}t} = \hat{x}(0)\cos\omega_{\rm ho}t + \tfrac{\hat{p}(0)}{m\omega_{\rm ho}}\sin\omega_{\rm ho}t \qquad \text{and} \\ \hat{p}(t) &= e^{-(\imath/\hbar)\hat{H}t}\hat{p}(0)e^{(\imath/\hbar)\hat{H}t} = m\omega_{\rm ho}\hat{x}(0)\sin\omega_{\rm ho}t + \hat{p}(0)\cos\omega_{\rm ho}t \ , \end{aligned} \tag{2.190}$$

or with (2.189),

$$\boxed{\begin{aligned} \langle\alpha(t)|\hat{x}|\alpha(t)\rangle &= \langle\alpha(0)|\hat{x}|\alpha(0)\rangle\cos\omega_{\rm ho}t + \tfrac{1}{m\omega_{\rm ho}}\langle\alpha(0)|\hat{p}|\alpha(0)\rangle\sin\omega_{\rm ho}t \\ \langle\alpha(t)|\hat{p}|\alpha(t)\rangle &= m\omega_{\rm ho}\langle\alpha(0)|\hat{x}|\alpha(0)\rangle\sin\omega_{\rm ho}t + \langle\alpha(0)|\hat{p}|\alpha(0)\rangle\cos\omega_{\rm ho}t \end{aligned}} \ . \tag{2.191}$$

We note, that the position and momentum wavefunctions $\langle x|n\rangle$ and $\langle p|n\rangle$ of the excited vibrational states are complicated Hermite polynomials, but we don't have to write them down explicitly to get to the last result. We will derive some further properties in Exc. 2.6.6.11.

2.6.4.3 Simulation of the displacement of a harmonic oscillator

The Hamiltonian of a harmonic oscillator subject to an external force can be cast into the form,

$$\begin{aligned} \hat{H}(t) &= -\frac{\hbar^2}{2m}\frac{d^2}{dx^2} + \frac{m}{2}\omega_{\rm ho}^2\hat{x}^2 + mg\hat{x} = \hbar\omega_{\rm ho}(\hat{a}^\dagger\hat{a} + \tfrac{1}{2}) + mg\tfrac{a_{\rm ho}}{\sqrt{2}}(\hat{a} + \hat{a}^\dagger) \\ &= \begin{pmatrix} \ddots & \ddots & & 0 \\ \ddots & (n+\frac{1}{2})\hbar\omega_{\rm ho} & mg\frac{a_{\rm ho}}{\sqrt{2}}\sqrt{n+1} & \\ & mg\frac{a_{\rm ho}}{\sqrt{2}}\sqrt{n+1} & (n+\frac{3}{2})\hbar\omega_{\rm ho} & \ddots \\ 0 & & \ddots & \ddots \end{pmatrix} \ . \end{aligned} \tag{2.192}$$

The temporal evolution of the state is given by,

$$|\psi(t)\rangle = e^{-(\imath/\hbar)\hat{H}t}|\psi(0)\rangle = e^{-(\imath/\hbar)\hat{H}t}\sum_n a_n|n\rangle \overset{a_n=\delta_{n,0}}{\longrightarrow} e^{-(\imath/\hbar)\hat{H}t}|0\rangle \ , \tag{2.193}$$

when the oscillator is initially in the state $|0\rangle$. Note that, without perturbation, $|\psi(t)\rangle = \sum_n e^{-\imath\omega_{\rm ho}(\hat{n}+1/2)t}a_n|n\rangle$.

Various quantities now are interesting to plot as a function of time. Firstly, we calculate the populations $|\langle n|\psi(t)\rangle|^2$ of the various states and the total energy from,

$$\boxed{\begin{array}{ll} \langle n|\psi(t)\rangle & = \langle n|e^{-(\imath/\hbar)\hat{H}t}\sum_m a_m|m\rangle \\ E_{\rm tot}(t) & = \sum_n \hbar\omega_{\rm ho}(n+\frac{1}{2})|\langle n|\psi(t)\rangle|^2 \end{array}} \ . \tag{2.194}$$

Secondly, we get for the temporal evolution of the spatial wavefunction,

$$\langle x|\psi(t)\rangle = \sum_n \langle x|n\rangle\langle n|\psi(t)\rangle = \sum_n \langle x|n\rangle\langle n|e^{-(\imath/\hbar)\hat{H}t}\sum_m a_m|m\rangle \ , \tag{2.195}$$

where $|\langle x|n\rangle\langle n|\psi(t)\rangle|^2$ is the spatial representation of the wavefunction of the n-th eigenstate derived in (2.106),

$$\langle x|n\rangle = \frac{e^{-x^2/2a_{\rm ho}^2}H_n(x/a_{\rm ho})}{\sqrt{a_{\rm ho}\sqrt{\pi}2^n n!}} \ , \tag{2.196}$$

weighed with instantaneous population (2.194) of this state. We thus obtain for the total wavefunction,

$$\boxed{\langle x|\psi(t)\rangle = \sum_n \frac{e^{-x^2/2a_{\rm ho}^2}H_n(x/a_{\rm ho})}{\sqrt{a_{\rm ho}\sqrt{\pi}2^n n!}}\langle n|e^{-(\imath/\hbar)\hat{H}t}|n\rangle} \ . \tag{2.197}$$

Furthermore, we may calculate the expectation values of the position and the momentum of the harmonic oscillator from the total wavefunction $\langle x|\psi(t)\rangle$,

$$\begin{aligned} \langle\psi(t)|\hat{x}|\psi(t)\rangle &= \int\langle\psi(t)|\hat{x}|x\rangle\langle x|\psi(t)\rangle dx = \int x|\psi(x,t)|^2dx \\ \langle\psi(t)|\hat{p}|\psi(t)\rangle &= \int\langle\psi(t)|\hat{p}|p\rangle\langle p|\psi(t)\rangle dp = \int p|\phi(p,t)|^2dp \ , \end{aligned} \tag{2.198}$$

where $\phi(p,t)$ is the Fourier transform of $\psi(x,t)$ according to (1.212). In practice, it is however easier to calculate them from the populations $\langle n|\psi(t)\rangle$,

$$\boxed{\begin{array}{ll} \langle\psi(t)|\hat{x}|\psi(t)\rangle & = \frac{a_{\rm ho}}{\sqrt{2}}\sum_n\langle\psi(t)|\hat{a}+\hat{a}^\dagger|n\rangle\langle n|\psi(t)\rangle \\ \langle\psi(t)|\hat{p}|\psi(t)\rangle & = \frac{\hbar}{\imath a_{\rm ho}\sqrt{2}}\sum_n\langle\psi(t)|\hat{a}-\hat{a}^\dagger|n\rangle\langle n|\psi(t)\rangle \end{array}} \ . \tag{2.199}$$

The temporal evolution of the forced harmonic oscillator defined by (2.193) can be numerically propagated. In cases where the force varies in time, the propagation can be done iteratively by subdividing time in intervals $t_k - t_{k-1}$ for $k \in \mathbb{N}$ sufficiently small that the force can be considered constant within them,

$$|\psi(t_k)\rangle = e^{-(\imath/\hbar)\hat{H}(t_k - t_{k-1})}|\psi(t_{k-1})\rangle \ . \tag{2.200}$$

The results of such a simulation are illustrated in Fig. 2.20.

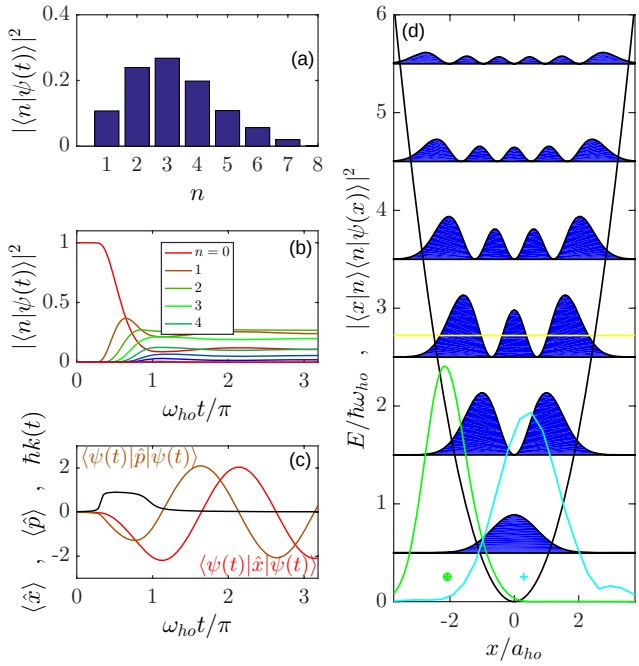

Figure 2.20: (code) Evolution of a harmonic oscillator subject to time-dependent forcing. (a) Histogram of the final population of the vibrational states. (b) Time evolution of the vibrational state populations. (c) Time evolution of the applied force (black) and of the expectation values of position (red) and momentum (brown). (d) Spatial wavefunctions $\langle n|\psi(x)\rangle|^2$ (Hermite polynomials) (blue) of the lowest vibrational states of the harmonic potential (black). The green Gaussian is the coherent sum of the spatial wavefunctions $|\sum_n \langle n|\psi(x)\rangle|^2$, and the cyan Gaussian the coherent sum of the momentum wavefunctions $|\sum_n \langle n|\psi(p)\rangle|^2$. The horizontal yellow line is the total energy of the system. You may also run a movie of the simulation clicking on (watch movie)! Furthermore, a presentation about the topic of recoil on trapped atoms is available at (watch talk)!

2.6.5 Quantization of the electromagnetic field

The quantization of light (also called *second quantization*) triggered by Max Planck's treatments of black-body radiation in 1905 resolved the problem of the ultraviolet

divergence and explained the photoelectric effect. Twenty years later the quantization of the atom by Niels Bohr (also called *first quantization*) explained the internal structure of the atom.

The operator for the electric field of a laser mode is given by,

$$\hat{\mathcal{E}} = \imath\mathcal{E}_1[\hat{a}e^{\imath\mathbf{k}\cdot\mathbf{r}-\imath\omega t} - \hat{a}^\dagger e^{-\imath\mathbf{k}\cdot\mathbf{r}+\imath\omega t}] \ , \tag{2.201}$$

where $\mathcal{E}_1 = \sqrt{\hbar\omega/2\varepsilon_0 V}$ is the electric field generated by a single photon in the mode volume V. Exc. 2.6.6.12 asks to calculate the eigenvalues $\langle\hat{\mathcal{E}}\rangle$ and $\Delta\hat{\mathcal{E}}$.

It is sometimes convenient to represent the light field by its quadratures. With the definition $\hat{a} \equiv \hat{x}_1 + \imath\hat{x}_2$, where $\hat{x}_{1,2}$ are non-commuting observables ($[\hat{x}_1, \hat{x}_2] = \imath/2$), we can write the field as,

$$\hat{\mathcal{E}} = -2\mathcal{E}_1[\hat{x}_1 \sin(\mathbf{k}\cdot\mathbf{r} - \omega t) + \hat{x}_2 \cos(\mathbf{k}\cdot\mathbf{r} - \omega t)] \ . \tag{2.202}$$

Heisenberg's uncertainty relations requires,

$$\Delta x_1 \Delta x_2 \geq \tfrac{1}{4} \ . \tag{2.203}$$

For coherent states, $\Delta x_1 = \Delta x_2 = \frac{1}{2}$.

2.6.6 Exercises

2.6.6.1 Ex: Sum of displacements operators

Prove formula (2.129). Find a geometric interpretation of the phase factor $(\alpha\beta^* - \alpha^*\beta)/2$ in the complex plane of Glauber states.

2.6.6.2 Ex: Rotation operator

Calculate $\mathcal{D}^\dagger(\alpha)\mathcal{R}(\varphi)\mathcal{D}(\alpha)$ and $\mathcal{R}^\dagger(\varphi)\mathcal{D}(\alpha)\mathcal{R}(\varphi)$ where $\mathcal{R}(\varphi) = e^{\imath\varphi\hat{a}^\dagger\hat{a}}$ and $\mathcal{D}(\alpha) = e^{\alpha\hat{a}^\dagger - \alpha^*\hat{a}}$.

2.6.6.3 Ex: Harmonic oscillator and coherent states

a. Verify whether the Glauber states of a harmonic oscillator are orthogonal.
b. Show that $\langle\alpha|\hat{n}|\alpha\rangle = |\alpha|^2$, $\langle\alpha|\hat{n}^2|\alpha\rangle = |\alpha|^4 + |\alpha|^2$, and $\Delta\hat{n} = |\alpha|$.
c. Now calculate the energy uncertainty $\Delta\hat{H}$ for a Glauber state.
d. What is the population of the state $|n\rangle$ of a harmonic oscillator in a Glauber state?

2.6.6.4 Ex: Annihilation operator acting on Fock and Glauber states

Show that the annihilation operator $\hat{a}$ does not reduce the photon number of a Glauber state in contrast to a Fock state.

2.6.6.5 Ex: Completeness of coherent states

a. Show,

$$\tfrac{1}{\pi}\int |\alpha\rangle\langle\alpha| d^2\alpha = \sum_{n=0}^{\infty} |n\rangle\langle n| = \mathbb{I}\ .$$

b. Show that coherent states can be expanded in terms of other coherent states and that, consequently, the coherent state basis is overcomplete.

2.6.6.6 Ex: Schrödinger cat state

Calculate the probability of finding n photons in Schrödinger's cat state $|\psi\rangle = 2^{-1/2}(|\alpha\rangle \pm |-\alpha\rangle)$.

2.6.6.7 Ex: Transition elements for arbitrary Lamb-Dicke parameters

Calculate the general expression for $\langle m|e^{\imath k\hat{x}}|n\rangle$ with the abbreviation $\alpha \equiv \imath k a_{\rm ho}/\sqrt{2}$ for arbitrary values of the Lamb-Dicke parameter using the following results of the discussion of the displacement operator $\mathcal{D}(\alpha) = e^{\alpha\hat{a}^\dagger - \alpha^*\hat{a}} = e^{-|\alpha|^2/2} e^{\alpha\hat{a}^\dagger} e^{-\alpha^*\hat{a}}$ for Glauber states. The relations

$$|n\rangle = \frac{(\hat{a}^\dagger)^n}{\sqrt{n!}}|0\rangle \qquad \text{and} \qquad \langle n|\alpha\rangle = e^{-|\alpha|^2/2}\frac{\alpha^n}{\sqrt{n!}}$$

describe the relation between Fock and Glauber states. Furthermore,

$$\mathcal{D}(-\alpha) = \mathcal{D}^\dagger(\alpha) \qquad \text{and} \qquad \mathcal{D}^\dagger(\alpha)\hat{a}^\dagger\mathcal{D}(\alpha) = \hat{a}^\dagger + \alpha^*\ .$$

2.6.6.8 Ex: Lamb-Dicke regime

A rubidium atom is trapped in an isotropic harmonic trap with secular frequency $\omega_{\rm ho} = (2\pi)\ 1\,\text{kHz}$. Determine whether, driven on its D_2 line, it is within the Lamb-Dicke regime.

2.6.6.9 Ex: Resonantly excited harmonic oscillator

Write down the Hamiltonian of a harmonic oscillator subject to an oscillating homogenous force, and numerically simulate the evolution of the vibrational states starting from the ground state.

2.6.6.10 Ex: Shifted harmonic oscillator

Consider a HO of mass m, angular frequency ω, and electric charge q immersed in a uniform electric field oriented parallel to the axis $\hat{\mathbf{e}}_x$ of the oscillator.
a. Get the energies of the stationary states of the HO and show how to get the corresponding eigenstates.
b. Calculate the expectation values $\langle x\rangle$ and $\langle p\rangle$ for the displaced oscillator now using Glauber states (or arbitrary superpositions of states) and taking advantage of the

formulas (2.95), (2.128), and (1.280).
c. Now, the electric field is suddenly turned off. Calculate the time evolution of the oscillator.

2.6.6.11 Ex: Spatial wavefunction of a particle in a coherent state

a. Derive the following relations for the harmonic oscillator having received a recoil momentum,

$$\langle\psi_n^{(1)}|\hat{x}|\psi_n^{(1)}\rangle = 0 \qquad \text{and} \qquad \langle\psi_n^{(1)}|\hat{p}|\psi_n^{(1)}\rangle = \hbar k \ .$$

b. Calculate the temporal evolution of the oscillator after having received the recoil via,

$$\langle x|e^{-\imath\hat{H}t/\hbar}e^{-\imath k\hat{x}}|n\rangle \ .$$

c. Calculate the spatial wavefunction of a particle in a coherent state,

$$\langle x|\alpha\rangle = \sum_n e^{-|\alpha|^2/2}\frac{\alpha^n}{\sqrt{n!}}\langle x|n\rangle \ .$$

2.6.6.12 Ex: Electric field amplitude and fluctuation

Calculate $\langle\hat{\mathcal{E}}\rangle$ and $\Delta\hat{\mathcal{E}}$ for a coherent state.

2.6.6.13 Ex: Beam splitting a Fock state

A beam splitter is a device dividing an input mode (e.g. a laser beam) into two output modes 1 and 2. Assuming that a beam splitter sends every single photon with equal probability to one of the two output modes and that the input mode be a Fock state, what would be the photon statistics in the output mode? **Help:** Create the total output state $|n_1, n_2\rangle$ from vacuum by successive application of the photon creation operator $\hat{a}_1^\dagger + \hat{a}_2^\dagger$.

2.6.6.14 Ex: Wavefunction of a harmonic oscillator in a Glauber state

Derive the wavefunction for a harmonic oscillator in a coherent state using the exponential generating function of Hermite polynomials,

$$e^{2xt-t^2} = \sum_{n=0}^{\infty}\frac{t^n}{n!}H_n(x) \ .$$

2.7 Further reading

A. Görlitz et al., *Observing the Position Spread of Atomic Wave Packets* [DOI]

2.7.1 on the Fourier grid method

R. Meyer, *Trigonometric Interpolation Method for One-Dimensional Quantum-Mechanical Problems* [DOI]

O. Dulieu, *Coupled channel bound states calculations for alkali dimers using the Fourier grid method* [DOI]

J. Stare et al., *Fourier Grid Hamiltonian Method for Solving the Vibrational Schroedinger Equation in Internal Coordinates Theory and Test Applications* [DOI]

C. Clay Marston et al., *The Fourier grid Hamiltonian method for bound state eigenvalues and eigenfunctions* [DOI]

2.7.2 on the harmonic oscillator

I. Bouchoule et al., *Neutral atoms prepared in Fock states of a one-dimensional harmonic potential* [DOI]

M.O. Scully and M.S. Zubairy, Cambridge University Press, *Quantum Optics* [ISBN]

Chapter 3

Rotations / Central potentials

Rotations are, on the same rights as translations, symmetry operations in space. They are of fundamental importance for the discussion of composite particles, such as atoms because they help us to formulate appropriate boundary conditions facilitating the solution of the three-dimensional Schrödinger equation.

3.1 Particle in a central potential

Many potentials do not have Cartesian symmetry, but fortunately, many problems have *some* kind of symmetry, cylindrical, spherical or periodic. Those with cylindrical or spherical symmetry can be solved by separating the curvilinear coordinates, as we will show in the following. Particularly important are spherical potentials caused by central forces, for example, the Coulomb force between the proton and the electron in the hydrogen atom.

3.1.1 Transformation to relative coordinates

The hydrogen atom represents a *two-body problem*. We consider the two masses $m_{1,2}$ of a proton and an electron separated by a distance $\mathbf{r}$ and interacting through a potential $V(\mathbf{r})$. The Hamiltonian is

$$\hat{H} = \frac{-\hbar^2}{2m_1}\nabla_{r1}^2 + \frac{-\hbar^2}{2m_2}\nabla_{r2}^2 + V(\mathbf{r}_1 - \mathbf{r}_2) \ , \tag{3.1}$$

where $\mathbf{r}_{1,2}$ are the positions of the proton and the electron. With the ansatz $\Xi(t, \mathbf{r}_1, \mathbf{r}_2) = \Xi(\mathbf{r}_1, \mathbf{r}_2)e^{-\imath E_{\rm tot}t/\hbar}$, the time-dependent Schrödinger equation

$$\hat{H}\Xi(t, \mathbf{r}_1, \mathbf{r}_2) = \imath\hbar\frac{d}{dt}\Xi(t, \mathbf{r}_1, \mathbf{r}_2) \ , \tag{3.2}$$

becomes stationary,

$$\left[\frac{-\hbar^2}{2m_1}\nabla_{r_1}^2 + \frac{-\hbar^2}{2m_2}\nabla_{r_2}^2 + V(\mathbf{r}_1 - \mathbf{r}_2)\right]\Xi(\mathbf{r}_1, \mathbf{r}_2) = E_{\rm tot}\Xi(\mathbf{r}_1, \mathbf{r}_2) \ . \tag{3.3}$$

Now we transform into the center-of-mass system making for the total wavefunction the ansatz $\Xi(\mathbf{r}_1, \mathbf{r}_2) = e^{-\imath\mathbf{P}\cdot\mathbf{R}/\hbar}\Psi(\mathbf{r})$ with $\mathbf{R} \equiv \frac{m_1}{M}\mathbf{r}_1 + \frac{m_2}{M}\mathbf{r}_2$ and $\mathbf{r} \equiv \mathbf{r}_1 - \mathbf{r}_2$ and introducing the abbreviation $M = m_1 + m_2$. This corresponds to a product of a plane

wave, describing the linear motion of the center of the masses, and a radial wave function, which describes the relative motion of the atom. The kinetic energy of one mass is:

$$\begin{aligned}
&\frac{-\hbar^2}{2m_1}\nabla_{r_1}^2 e^{-\imath\mathbf{P}\cdot\mathbf{R}/\hbar}\Psi(\mathbf{r}) \qquad (3.4)\\
&= \frac{-\hbar^2}{2m_1}\left[e^{-\imath\mathbf{P}\cdot\mathbf{R}/\hbar}\nabla_{r_1}^2\Psi(\mathbf{r}) + 2(-\tfrac{\imath m_1\mathbf{P}}{\hbar M})e^{-\imath\mathbf{P}\cdot\mathbf{R}/\hbar}\nabla_{r_1}\Psi(\mathbf{r}) + \Psi(\mathbf{r})(-\tfrac{\imath m_1}{\hbar^2 M}\mathbf{P})^2 e^{-\imath\mathbf{P}\cdot\mathbf{R}/\hbar}\right]\\
&= e^{-\imath\mathbf{P}\cdot\mathbf{R}/\hbar}\left[\frac{-\hbar^2}{2m_1}\nabla_{r_1}^2\Psi(\mathbf{r}) + \frac{\imath\hbar\mathbf{P}}{M}\nabla_{r_1}\Psi(\mathbf{r}) - \frac{m_1\mathbf{P}^2}{2M^2}\Psi(\mathbf{r})\right] .
\end{aligned}$$

Hence, for two atoms,

$$\begin{aligned}
&E_{\text{tot}}\Xi(\mathbf{r}_1,\mathbf{r}_2) - V(\mathbf{r})\Xi(\mathbf{r}_1,\mathbf{r}_2) \qquad (3.5)\\
&= e^{-\imath\mathbf{P}\cdot\mathbf{R}/\hbar}\left[\frac{-\hbar^2}{2m_1}\nabla_{r_1}^2\Psi(\mathbf{r}) + \frac{-\hbar^2}{2m_2}\nabla_{r_2}^2\Psi(\mathbf{r}) + \frac{\imath\hbar\mathbf{P}}{M}(\nabla_{r_1}+\nabla_{r_2})\Psi(\mathbf{r}) + \frac{\mathbf{P}^2}{2M}\Psi(\mathbf{r})\right] .
\end{aligned}$$

Using $\nabla_{r_1} = -\nabla_{r_2} = \nabla_r$, we see that the third term cancels, such that,

$$\frac{P^2}{2M}\Psi(\mathbf{r}) + \frac{-\hbar^2}{2m_1}\nabla_r^2\Psi(\mathbf{r}) + \frac{-\hbar^2}{2m_2}\nabla_r^2\Psi(\mathbf{r}) + V(\mathbf{r})\Psi(\mathbf{r}) = E_{\text{tot}}\Psi(\mathbf{r}) . \qquad (3.6)$$

Subtracting the energy of the center-of-mass motion with $E = E_{\text{tot}} - \frac{P^2}{2M}$ and introducing the abbreviation $m^{-1} = m_1^{-1} + m_2^{-1}$, we finally get,

$$\boxed{\left[\frac{-\hbar^2}{2m}\nabla_r^2 + V(\mathbf{r})\right]\Psi(\mathbf{r}) = E\Psi(\mathbf{r})} . \qquad (3.7)$$

3.1.2 Particle in a cylindrical potential

The equation (3.7) is three-dimensional because $\Psi(\mathbf{r})$ is a *scalar field* and the momentum operator in Cartesian coordinates is given by,

$$\nabla_r^2 = \frac{\partial^2}{\partial x^2} + \frac{\partial^2}{\partial y^2} + \frac{\partial^2}{\partial z^2} . \qquad (3.8)$$

However, in some situations, the symmetry of the system allows to reduce dimensionality similarly to the cases of the box potential and the three-dimensional harmonic oscillator. Let us now discuss the cases of cylindrical and spherical symmetry.

Electrons in magnetic fields are subject to the Lorentz force, which keeps them in a rotating motion. We can rewrite the momentum operator in cylindrical coordinates,

$$x = \rho\cos\varphi \quad , \quad y = \rho\sin\varphi \quad , \quad z = z , \qquad (3.9)$$

as

$$\nabla_r^2 = \frac{\partial^2}{\partial\rho^2} + \frac{1}{\rho}\frac{\partial}{\partial\rho} + \frac{1}{\rho^2}\frac{\partial^2}{\partial\varphi^2} + \frac{\partial^2}{\partial z^2} . \qquad (3.10)$$

Now, with the assumption that the potential only depends on ρ, $V(\mathbf{r}) = V(\rho)$, we can try the ansatz,

$$\Psi(\mathbf{r}) = R(\rho)\xi(\varphi)\zeta(z) , \qquad (3.11)$$

and obtain,

$$\frac{1}{R(\rho)}\left[-\frac{\hbar^2}{2m}\left(\frac{\partial^2}{\partial\rho^2}+\frac{1}{\rho}\frac{\partial}{\partial\rho}+V(\rho)\right)\right]R(\rho)-\frac{\hbar^2}{2m}\frac{1}{\zeta(z)}\frac{\partial^2}{\partial z^2}\zeta(z)-\frac{\hbar^2}{2m\rho^2}\frac{1}{\xi(\varphi)}\frac{\partial^2}{\partial\varphi^2}\xi(\varphi)=E\,. \tag{3.12}$$

First, we separate the axial motion,

$$-\frac{\zeta''}{\zeta}=const\equiv\frac{2mE_z}{\hbar^2}\equiv k_z^2\,, \tag{3.13}$$

the solution of this equation being a superposition of two plane waves counterpropagating along the axis z, $\zeta(z)=Ae^{\imath k_z z}+Be^{-\imath k_z z}$. Now, we separate the azimuthal motion,

$$\frac{\rho^2}{R(\rho)}\frac{\partial R^2(\rho)}{\partial\rho^2}+\frac{\rho}{R(\rho)}\frac{\partial R(\rho)}{\partial\rho}+\frac{2m\rho^2}{\hbar^2}[E-V(\rho)]-\rho^2k_z^2=-\frac{\xi''}{\xi}=const\equiv m_\varphi^2\,. \tag{3.14}$$

The solution of the right-hand part of the equation is $\xi(\varphi)=Ce^{\imath m_\varphi\varphi}+De^{-\imath m_\varphi\varphi}$. Finally, we have the radial equation,

$$\frac{1}{R(\rho)}\frac{\partial R(\rho)^2}{\partial\rho^2}+\frac{1}{\rho R(\rho)}\frac{\partial R(\rho)}{\partial\rho}-\frac{2m}{\hbar^2}[E-V(\rho)]-k_z^2-\frac{m_\varphi^2}{\rho^2}=0\,, \tag{3.15}$$

with the effective potential $V_{\text{eff}}=V(\rho)+\frac{\hbar^2m_\varphi^2}{2m\rho^2}$. For a homogeneous potential, $V(\rho)=V_0$, the solution will be a superposition of Bessel functions.

Example 28 (*Rigid rotor in cylindrical coordinates*): As an example, we disregard the potential, $V(\rho)=0$, and we consider for the particle an orbit with constant radius, $\rho=const$ such that $R(\rho)=\delta(\rho-\rho_0)$. In this case, we only need to treat the orbital motion described by the right part of Eq. (3.14). For the solution of this equation, $\xi(\varphi)=Ae^{\imath m_\varphi\varphi}$, to be well-defined, we need $\xi(\varphi)=\xi(\varphi+2\pi)$. This implies,

$$m_\varphi=0,\pm1,\pm2,..$$

and

$$E_\varphi=\frac{\hbar^2m_\varphi^2}{2m\rho^2}\,.$$

The allowed energies $E_{m_\varphi}=E_\varphi$ can be obtained by letting the Hamiltonian

$$\hat{H}=-\frac{\hbar^2}{2I}\frac{\partial^2}{\partial\varphi^2}\,,$$

with the moment of inertia $I=m\rho^2$ actuate on the azimuthal wavefunction $\xi(\varphi)$. We now define the operator,

$$\hat{l}_z=\frac{\hbar}{\imath}\frac{\partial}{\partial\varphi}\,.$$

This operator acts on the wavefunction ξ as follows,

$$\hat{l}_z\xi(\varphi)=\hbar m_\varphi\xi(\varphi)\,.$$

It is easy to show that wavefunctions with different values m_l are orthogonal. Note: 1. The state $m_\varphi=0$ has zero energy. That is, it has no zero-point energy, which is due to the absence of a confining potential. 2. The particle is delocalized within a ring of radius r: $\Delta l_z\Delta\sin\varphi\geq\frac{\hbar}{2}|\langle\cos\varphi\rangle|$.

3.1.3 Hamiltonian in spherical coordinates

We can rewrite the momentum operator in spherical coordinates,

$$x = r\sin\vartheta\cos\varphi \quad , \quad y = r\sin\vartheta\sin\varphi \quad , \quad z = r\cos\vartheta \ , \tag{3.16}$$

as [1],

$$\nabla_r^2 = \frac{1}{r^2}\frac{\partial}{\partial r}\left(r^2\frac{\partial}{\partial r}\right) + \frac{1}{r^2}\frac{\hat{\mathbf{L}}^2}{\hbar^2} \qquad \text{where} \qquad \frac{\hat{\mathbf{L}}^2}{\hbar^2} \equiv \frac{1}{\sin\vartheta}\frac{\partial}{\partial\vartheta}\left(\sin\vartheta\frac{\partial}{\partial\vartheta}\right) + \frac{1}{\sin^2\vartheta}\frac{\partial^2}{\partial\varphi^2} \ , \tag{3.17}$$

is an abbreviation called *Legendre operator*. For an isotropic potential, $V(\mathbf{r}) = V(r)$, we can try the ansatz,

$$\Psi(\mathbf{r}) = R(r)Y(\vartheta,\varphi) \tag{3.18}$$

to solve the Schrödinger equation (1.168),

$$\frac{r^2}{R(r)}\left[-\frac{\hbar^2}{2m}\frac{1}{r^2}\frac{\partial}{\partial r}\left(r^2\frac{\partial}{\partial r}\right) + V(r) - E\right]R(r) = \frac{-1}{2m}\frac{\hat{\mathbf{L}}^2 Y(\vartheta,\varphi)}{Y(\vartheta,\varphi)} = const \equiv -\frac{\hbar^2}{2m}\ell(\ell{+}1) \ , \tag{3.19}$$

where we choose a separation constant, $\ell(\ell+1)$, the significance of which we shall soon learn. Considering only the angular part,

$$\boxed{\hat{\mathbf{L}}^2 Y(\vartheta,\varphi) = \hbar^2\ell(\ell+1)Y(\vartheta,\varphi)} \ , \tag{3.20}$$

and making another separation ansatz,

$$Y(\vartheta,\varphi) = \Theta(\vartheta)\Phi(\varphi) \ , \tag{3.21}$$

we obtain,

$$\sin^2\vartheta\left(\frac{1}{\Theta(\vartheta)}\frac{1}{\sin\vartheta}\frac{\partial}{\partial\vartheta}\sin\vartheta\frac{\partial}{\partial\vartheta}\Theta(\vartheta) + \ell(\ell+1)\right) = -\frac{1}{\Phi(\varphi)}\frac{\partial^2}{\partial\varphi^2}\Phi(\varphi) = const \equiv m^2 \ , \tag{3.22}$$

where we choose a separation constant, m^2. Introducing another abbreviation,

$$\hat{L}_z \equiv \frac{\hbar}{\imath}\frac{\partial}{\partial\varphi} \ , \tag{3.23}$$

the azimuthal equation takes the form

$$\boxed{\hat{L}_z\Phi(\varphi) = \hbar m\Phi(\varphi)} \ . \tag{3.24}$$

As in the case of the cylindrical potential, the solution of the *azimuthal equation* is, using the normalization,

$$\Phi(\varphi) = \tfrac{1}{\sqrt{2\pi}}e^{\imath m\varphi} \ , \tag{3.25}$$

with the *magnetic quantum number* $m = 0, \pm1, \pm2, ...$

[1] We may also write: $\mathbf{p}^2 = (\hat{\mathbf{e}}_r\cdot\mathbf{p})^2 + (\hat{\mathbf{e}}_r\times\mathbf{p})^2 = p_r^2 + \frac{\mathbf{L}^2}{r^2}$, where p_r^2 is the radial part of the Laplace operator and $\frac{\mathbf{L}^2}{r^2}$ the angular part.

The *polar equation*,

$$\frac{1}{\Theta(\vartheta)}\frac{1}{\sin\vartheta}\frac{\partial}{\partial\vartheta}\sin\vartheta\frac{\partial}{\partial\vartheta}\Theta(\vartheta)+\ell(\ell+1)=\frac{m^2}{\sin^2\vartheta}\ , \tag{3.26}$$

is called Legendre's differential equation and can be solved by a power series in $\cos^k\vartheta$. For $m=0$, the solutions are the *Legendre polynomials*, $P_\ell(\cos\vartheta)$ with

$$P_\ell(z)=\frac{1}{2^\ell\ell!}\frac{d^\ell}{dz^\ell}[(z^2-1)^\ell]\ . \tag{3.27}$$

The first polynomials are,

$$P_0(z)=1\quad,\quad P_1(z)=z\quad,\quad P_2(z)=\tfrac{1}{2}(3z^2-1)\quad,\quad P_3(z)=\tfrac{1}{2}(5z^3-3z)\ . \tag{3.28}$$

For $m>0$, the solutions are the associated polynomials,

$$P_\ell^m(z)=(-1)^m(1-z^2)^{m/2}\frac{d^m}{dz^m}P_\ell(z)=\frac{(-1)^m}{2^\ell\ell!}(1-z^2)^{m/2}\frac{d^{\ell+m}}{dz^{\ell+m}}[(z^2-1)^\ell] \tag{3.29}$$

$$P_\ell^{-m}(z)=(-1)^m\frac{(\ell-m)!}{(\ell+m)!}P_\ell^m(z)\ .$$

The polar function must still be normalized,

$$\Theta_\ell^m(\vartheta)=P_\ell^m(\cos\vartheta)\sqrt{\frac{2\ell+1}{2}\frac{(\ell-m)!}{(\ell+m)!}}\ . \tag{3.30}$$

The functions $Y_{\ell m}(\vartheta,\varphi)$ are the *spherical harmonics*. They form an orthonormal system,

$$\int_0^\pi\int_0^{2\pi}Y^*_{\ell'm'}(\vartheta,\varphi)Y_{\ell m}(\vartheta,\varphi)\sin\vartheta d\vartheta d\varphi=\delta_{\ell'\ell}\delta_{m'm}\ . \tag{3.31}$$

Finite solutions only exist when the *angular momentum quantum number* is $\ell=0,1,..$ and for $|m|\le\ell$.

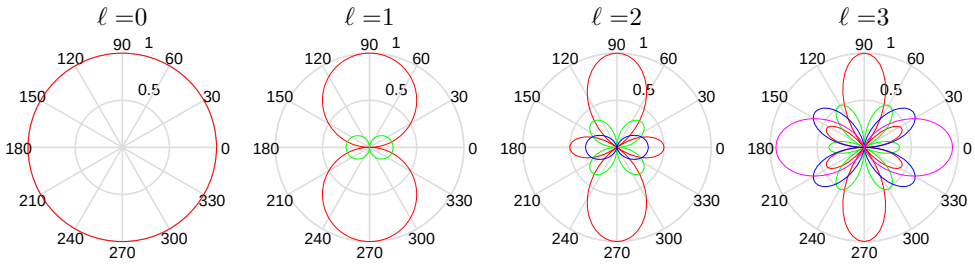

Figure 3.1: (code) Angular wavefunctions. Shown are the Legendre polynomials $P_\ell^m(\cos\vartheta)$ for $\ell=0,1,2,3$ and $m=0,..,\ell$. Red: $m=0$, green: $|m|=1$, blue: $|m|=2$, and magenta: $|m|=3$.

The solutions of the angular part of the Schrödinger equation for the hydrogen atom are finally,

$$\boxed{Y_{\ell m}(\vartheta,\varphi) = \frac{1}{\sqrt{2\pi}}\, P_\ell^m(\cos\vartheta)\sqrt{\frac{2\ell+1}{2}\frac{(\ell-m)!}{(\ell+m)!}}\, e^{\imath m\varphi}} \,. \tag{3.32}$$

The spherical harmonics are simultaneously eigenfunctions of the operators $\mathbf{L}^2$, as can be seen from Eq. (3.20), and of the operator L_z according to Eq. (3.24). The quantities represented by the quantum operators $\hat{H}, \hat{\mathbf{L}}^2, \hat{L}_z$ are conserved in the hydrogen system. The conservation of the angular momentum is due to the spherical symmetry of the Coulomb potential.

We will verify the parity of the spherical harmonics in Exc. 3.1.5.1.

3.1.4 Separation of radial motion

In Sec. 3.1.3 we derived, after having separated the motion of the center-of-mass (that is, of the heavy nucleus) and the angular coordinates, the radial equation (3.19) describing the radial component of the electronic motion,

$$\frac{1}{R(r)}\left[-\frac{\hbar^2}{2m}\frac{1}{r^2}\frac{\partial}{\partial r}\left(r^2\frac{\partial}{\partial r}\right) + V(r) - E\right] R(r) = -\frac{\hat{\mathbf{L}}^2}{2mr^2} \,, \tag{3.33}$$

Now, we make the substitution $R(r) = u(r)/r$ and the radial equation becomes,

$$\boxed{\left[-\frac{\hbar^2}{2m}\frac{\partial^2}{\partial r^2} + \frac{\hat{\mathbf{L}}^2}{2mr^2} + V(r)\right] u(r) = E u(r)} \,. \tag{3.34}$$

This equation is very similar to a one-dimensional Schrödinger equation, but there is an additional potential term called *centrifugal potential*,

$$V_\ell(r) \equiv \frac{\hat{\mathbf{L}}^2}{2mr^2} \,. \tag{3.35}$$

For example, for the potential of an electron orbiting a proton, we have,

$$\left[-\frac{\hbar^2}{2m}\frac{\partial^2}{\partial r^2} - \frac{Ze^2}{4\pi\varepsilon_0 r} + \frac{\hbar^2\ell(\ell+1)}{2mr^2} - E\right] u_{E\ell}(r) = 0 \,. \tag{3.36}$$

We will discuss this equation intensely in the context of the hydrogen atom.

In Exc. 3.1.5.2 we derive the radial Gross-Pitaevskii equation for a Bose-Einstein condensate trapped in a spherical potential. In the Exc. 3.1.5.3 we will study particles inside a central potential of zero depth, in the Excs. 3.1.5.4 and 3.1.5.5 we consider 3D spherical box potentials and in Exc. 3.1.5.6 a spherical harmonic potential.

> **Example 29 (*Rigid rotor in spherical coordinates*):** We continue the discussion of the rigid rotor, now in spherical coordinates. In the case that the orbit of the particle is fixed to a radius R, we can neglect the kinetic energy due

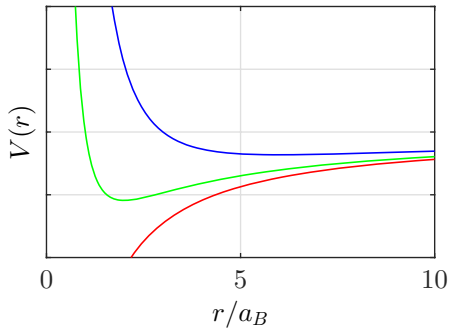

Figure 3.2: (code) Sum of a Coulomb potential and centrifugal potential for $\ell = 0$ (lower curve), $\ell = 1$ (center curve), and $\ell = 2$ (upper curve).

to the radial motion and the potential, both being constant. In this case the radial Schrödinger equation is,

$$\left[\frac{\hbar^2\ell(\ell+1)}{2mr^2}\right] u_{E\ell} = E_\ell u_{E\ell} \ .$$

The energies of the *rigid rotor* are

$$E_\ell = \frac{\hbar^2\ell(\ell+1)}{2I} \ ,$$

with the *momentum of inertia* $I = mR^2$.

3.1.5 Exercises

3.1.5.1 Ex: Parity of the spherical harmonic functions

We consider the parity transformation $\mathbf{P}$ with $(x, y, z) \xrightarrow{\mathbf{P}} (-x, -y, -z)$. Use spherical coordinates to show that $Y_{\ell m} \xrightarrow{\mathbf{P}} (-1)^\ell Y_{\ell m}$, and therefore that a spherical surface function has even parity when ℓ is even, and odd parity, when ℓ is odd.

3.1.5.2 Ex: Bose-Einstein condensate in an isotropic potential

The time-dependent Gross-Pitaevskii equation describing the wavefunction of a Bose-Einstein condensate reads,

$$\imath\hbar\frac{\partial\psi(\mathbf{r},t)}{\partial t} = \left(-\frac{\hbar^2}{2m}\nabla^2 + V_{\rm trp}(r) + g|\psi(\mathbf{r},t)|^2\right)\psi(\mathbf{r},t) \ ,$$

where the factor g depends on the force of the interatomic interaction and $V_{\rm trp}$ is the potential trapping the atoms. Derive the stationary Gross-Pitaevskii equation via the transform $\psi(\mathbf{r},t) = \psi(\mathbf{r})e^{-\imath\mu t/\hbar}$, where the constant μ is called the chemical potential. For $V(\mathbf{r}) = V(r)$ the wavefunction will have radial symmetry, $\psi(\mathbf{r}) = \frac{\phi(r)}{r}$. Rewrite the Gross-Pitaevskii equation for the function ϕ.

3.1.5.3 Ex: Motion of a free particle in spherical coordinates

Obtain the eigenfunctions of a free particle as the limiting case of its motion in a central force field with $V(r) \to 0$. Compare the derived eigenfunctions – associated with the complete set of observables $\hat{H}$, $\hat{L}^2$, and $\hat{L}_z$ – to those described by plane waves – associated with the motion characterized by the observables $\hat{p}_x$, $\hat{p}_y$, $\hat{p}_z$, and $\hat{H} = \hat{\mathbf{P}}^2/2m$ –, which also constitute a complete set of observables.

3.1.5.4 Ex: Particle in a spherical box

Find the energy levels and wavefunctions of a particle confined in a spherical box described by potential energy, $V(r) = 0$ for $r < a$ and $V(r) = \infty$ for $r \geq a$ considering the angular momentum $\ell = 0$.

3.1.5.5 Ex: Finite spherical 3D potential well

a. Derive the possible energy levels and associated wavefunctions for a particle trapped in a spherical 3D potential well of depth V_0 and radius a. Note that this problem is analogous to *Mie scattering* of scalar waves.
b. Discuss the case of a well surrounded by infinitely high walls.

3.1.5.6 Ex: Particle in a spherical harmonic potential

A quantum particle of mass m is subject to a potential

$$V = \tfrac{1}{2} m\omega^2 (x^2 + y^2 + z^2) \ .$$

a. Obtain the energy levels of this particle. That is, determine the eigenvalues of

$$-\frac{\hbar^2}{2m}\nabla^2\psi + V\psi = E\psi \ .$$

b. Consider the fundamental level and the first two excited levels. Set up a table showing for each of these three levels the energy value, the degeneracy, and the respective states in terms of the quantum numbers.
c. Using

$$\nabla^2\psi = \left[\frac{1}{r^2}\frac{\partial}{\partial r}\left(r^2\frac{\partial}{\partial r}\right) - \frac{L^2}{\hbar^2 r^2}\right]\psi$$

and remembering $\hat{\mathbf{L}}^2 Y_{\ell m}(\theta,\phi) = \hbar^2\ell(\ell+1)Y_{\ell m}$, write down the differential equation of item (a) for the radial part of the wavefunction (it is not necessary to solve it). Identify in this equation the effective potential $V_{\text{eff}}(r)$.
d. Solve the differential equation of the previous item for the case where $\ell = 0$ and determine the corresponding eigenvalue. To do this, allow for a solution of the type $e^{-\alpha r^2}$ and determine α.

3.2 Quantum treatment of hydrogen

According to Rutherford's and Bohr's planetary atomic model we may imagine an atom as a very heavy nucleus having a positive electric charge surrounded by a very

light negatively charged charge electronic cloud. Since the nucleus is very small compared to the electronic cloud, we treat it as an entity with mass M and charge Ze, where Z is the number of protons and corresponds to the order of the element in the periodic system.

The canonical procedure for calculating all properties of an atom is to establish its Hamiltonian, that is, to determine the kinetic energies of all components and all interaction energies between them, and to solve the Schrödinger equation. For each component we write the kinetic energy,

$$T_{\rm ncl} = \frac{P^2}{2M} \qquad \text{and} \qquad T_{ele} = \sum_{i=1}^{Z} \frac{p_i^2}{2m} \ . \tag{3.37}$$

Here, $(\mathbf{R}, \mathbf{P})$ are the nuclear coordinates and $(\mathbf{r}_i, \mathbf{p}_i)$ those of the electrons. The energies that corresponds to the interactions, that is, Coulombian attraction or repulsion, between the components of the atom are,

$$V_{\rm ncl:ele} = -\sum_{i=1}^{Z} \frac{Ze^2}{4\pi\varepsilon_0 |\mathbf{R} - \mathbf{r}_i|} \qquad \text{and} \qquad V_{\rm ele:ele} = \sum_{i\neq j=1}^{Z} \frac{e^2}{4\pi\varepsilon_0 |\mathbf{r}_i - \mathbf{r}_j|} \ . \tag{3.38}$$

There are also interactions due to the spin of the particles, which we will deal with later.

Obviously, the solution to this many-body problem is very complicated. For this reason, we will in this chapter, based on the Schrödinger equation, calculate the complete spectrum of the simplest possible atom, hydrogen. This atom consists of a proton and an electron, only.

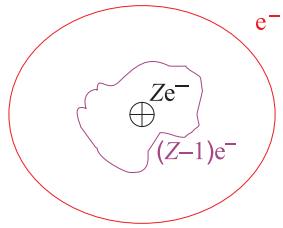

Figure 3.3: The hydrogen model applies to other atoms having a single valence electron occupying a sufficiently large space, that it sees the nucleus together with rest of the electrons shielding the nucleus as a single positive charge.

3.2.1 Bohr's model

Let us now turn our attention to the radial part of the Schrödinger equation describing a particle in a radial potential. We expect that the quantum solutions for the hydrogen atom are similar to the predictions of Bohr's model. Following this model, the orbit is stable when the attraction force is equal to the centrifugal force. But in addition, Bohr postulated, that only certain energies are allowed. For the hydrogen atom he found,

$$E_n = -\frac{1}{2}\frac{Ze^2}{4\pi\varepsilon_0}\frac{1}{r_n} = -\frac{Z^2\hbar^2}{2ma_{\rm B}^2}\frac{1}{n^2} = -\frac{Z^2e^2}{4\pi\varepsilon_0}\frac{1}{2a_{\rm B}n^2} = -\frac{Z^2}{n^2}\ 13.6\,{\rm eV} \ , \tag{3.39}$$

with the *Bohr radius*

$$a_{\rm B} \equiv 4\pi\varepsilon_0 \frac{\hbar^2}{me^2} \ . \tag{3.40}$$

With this equation he was able to explain the spectral observations. Electrons can only jump from one level to another, while emitting or absorbing a photon. The series observed in the hydrogen spectrum $(E_n - E_m)/\hbar$ are the Lyman ($m = 1$), the Balmer ($m = 2$), the Paschen ($m = 3$) an the Brackett series ($m = 4$).

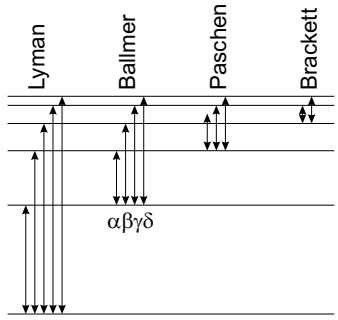

Figure 3.4: The hydrogen transitions.

The discussion of the hydrogen atom within quantum mechanics can start from the radial Schrödinger equation (3.36) with the Coulomb attraction potential,

$$\left[-\frac{\hbar^2}{2m}\frac{\partial^2}{\partial r^2} - \frac{Ze^2}{4\pi\varepsilon_0 r} + \frac{\hbar^2\ell(\ell+1)}{2mr^2} - E \right] u_{E\ell}(r) = 0 \ . \tag{3.41}$$

In order to facilitate comparison with Bohr's classical model, let us express the energy in terms of Bohr's energy, $E \equiv E_n = E_1/n^2$, and write the radius in units of $a_{\rm B}$, that is, $\tilde{r} \equiv Zr/a_{\rm B}$. This yields,

$$u''_{n\ell}(\tilde{r}) + \left(-\frac{\ell(\ell+1)}{\tilde{r}^2} + \frac{2}{\tilde{r}} - \frac{1}{n^2} \right) u_{n\ell}(\tilde{r}) = 0 \ . \tag{3.42}$$

To ensure that for large radii, $r \to \infty$, the solution is finite, we need an asymptotic behavior like $u_{n\ell}(\tilde{r} \to \infty) = e^{-\tilde{r}/n}$. To ensure that for small radii, $r \to 0$, the solution is finite, we need $u_{n\ell}(\tilde{r} \to 0) = \tilde{r}^{\ell+1}$. We derive the asymptotic solutions in Exc. 3.2.3.1. The resulting differential equation only has solutions for an integer and positive *main quantum number* n and when $\ell = 0, 1, .., n-1$. That is, in the relation $E = E_1/n^2$ the parameter n is integer and positive, such that energy levels remain degenerate in ℓ and m. This means that Bohr's postulate of discrete (i.e. quantized) energy levels is valid (uff!)

Substituting the ansatz,

$$u_{n\ell}(\tilde{r}) = D_{n\ell}\tilde{r}^{\ell+1}e^{-\tilde{r}/n}L(\tilde{r}) \ , \tag{3.43}$$

it's easy to show (see Exc. 3.2.3.2), that the differential equation (3.42) reduces to,

$$\tilde{r}L''(\tilde{r}) + 2\left[(\ell+1) - \tfrac{1}{n}\tilde{r}\right]L'(\tilde{r}) + 2\left[1 - \tfrac{1}{n}(\ell+1)\right]L(\tilde{r}) = 0 \ . \tag{3.44}$$

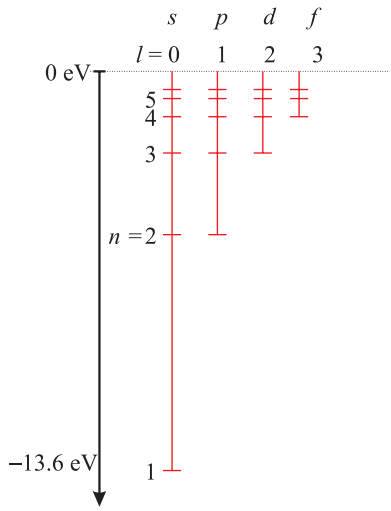

Figure 3.5: Level scheme.

Still with the abbreviation $\rho \equiv 2\tilde{r}/n = 2Zr/na_{\rm B}$ the ansatz

$$u_{n\ell}(\rho) = D_{n\ell}\rho^{\ell+1}e^{-\rho/2}L(\rho) \ , \tag{3.45}$$

leads to the differential equation [2]

$$\rho L''(\rho) + [2(\ell+1) - \rho]\, L'(\rho) + [n - \ell - 1]L(\rho) = 0 \ . \tag{3.46}$$

The solutions of this differential equation, $L^{(2\ell+1)}_{n-\ell-1}(\rho)$, are the *Laguerre polynomials*. These polynomials are listed in mathematical tables. Using the properties of these polynomials it is possible to show that the radial functions are orthogonal and can be normalized (see Exc. 3.2.3.3). Fig. 3.6 shows the curves for the lowest orbitals.

Finally, we can write the complete solutions of the Schrödinger equation $\hat{H}\psi = E\psi$,

$$\boxed{\psi_{n\ell m}(r,\theta,\phi) = \frac{u_{n\ell}(r)}{r}Y_{\ell m}(\theta,\phi) \qquad \text{and} \qquad E_n = -\frac{\hbar^2}{2ma_{\rm B}^2}\frac{Z^2}{n^2}} \ , \tag{3.47}$$

where $n = 1, 2, 3, ..$ and $\ell = 0, 1, .., n-1$ and $m = -\ell, -\ell+1, .., \ell$. Of course, each energy level n is,

$$\sum_{\ell=0}^{n-1}(2\ell+1) = n^2 \tag{3.48}$$

[2] *Laguerre's associated differential equation* is,

$$\rho\partial_\rho^2 L_\nu^{(\alpha)} + (\alpha + 1 - \rho)\partial_\rho L_\nu^{(\alpha)} + \nu L_\nu^{(\alpha)} = 0 \ .$$

The Laguerre polynomials are generated by

$$L_\nu^{(\alpha)}(\rho) = \frac{e^\rho \rho^{-\alpha}}{\alpha!}\frac{d^\nu}{d\rho^\nu}\left(e^{-\rho}\rho^{\nu+\alpha}\right) \ .$$

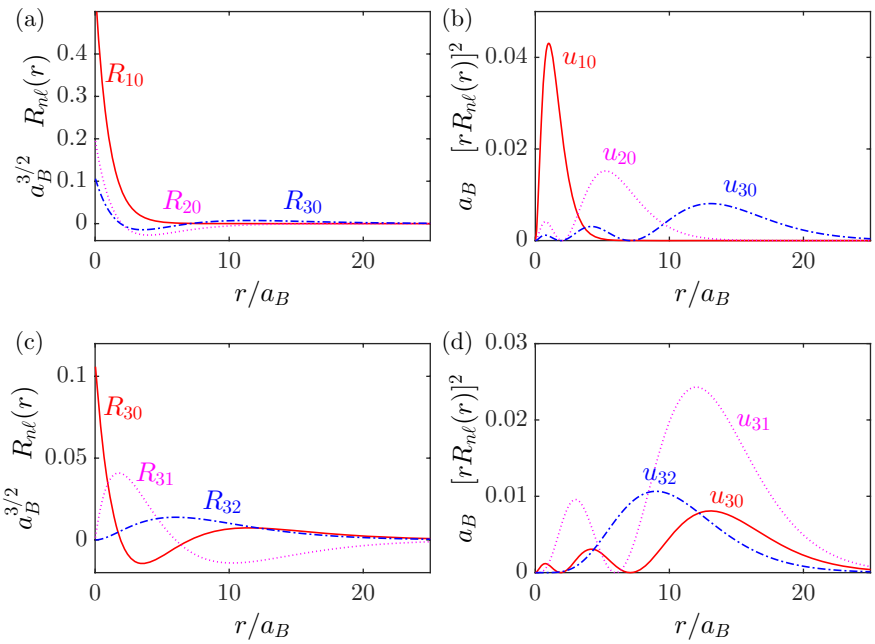

Figure 3.6: (code) (a,c) Radial wavefunctions $R_{n\ell}(r)$ and (b,d) square of the radial wavefunctions $u_{n\ell}(r)$ for various quantum numbers n and ℓ.

times degenerate.

From the normalization condition,

$$\begin{aligned} 1 &= \int_{\mathbb{R}^3} |\psi_{n\ell m}(r,\theta,\phi)|^2 d^3r \\ &= \int_0^\infty |u_{n\ell}(r)|^2 dr \int_{\mathbb{R}^2} |Y_{\ell m}(\theta,\phi)|^2 \sin\theta d\theta d\phi = \int_0^\infty |u_{n\ell}(r)|^2 dr \ , \end{aligned} \tag{3.49}$$

we obtain the constants,

$$D_{n\ell} = \sqrt{\left(\frac{2Z}{na_{\rm B}}\right)^3 \frac{(n-\ell-1)!}{2n(n+\ell)!}} \ , \tag{3.50}$$

and the radial wavefunctions finally read,

$$R_{n\ell}(r) = D_{n\ell} \left(\frac{2\tilde{r}}{n}\right)^\ell e^{-\tilde{r}/n} L_{n-\ell-1}^{(2\ell+1)}(\tfrac{2\tilde{r}}{n}) = D_{n\ell}\rho^\ell e^{-\rho/2} L_{n-\ell-1}^{(2\ell+1)}(\rho) \ , \tag{3.51}$$

using the previously introduced abbreviations.

Here is a list of the first wavefunctions of the hydrogen atom,

$$\begin{aligned}
\psi_{100} &= \tfrac{1}{\sqrt{\pi}} \left(\tfrac{Z}{a_{\mathrm{B}}}\right)^{3/2} e^{-\tilde{r}} \\
\psi_{200} &= \tfrac{1}{4\sqrt{2\pi}} \left(\tfrac{Z}{a_{\mathrm{B}}}\right)^{3/2} (2-\tilde{r}) e^{-\tilde{r}/2} \\
\psi_{210} &= \tfrac{1}{4\sqrt{2\pi}} \left(\tfrac{Z}{a_{\mathrm{B}}}\right)^{3/2} \tilde{r} e^{-\tilde{r}/2} \cos\theta \\
\psi_{21\pm1} &= \tfrac{1}{8\sqrt{\pi}} \left(\tfrac{Z}{a_{\mathrm{B}}}\right)^{3/2} \tilde{r} e^{-\tilde{r}/2} \sin\theta e^{\pm\imath\varphi} \\
\psi_{300} &= \tfrac{1}{81\sqrt{3\pi}} \left(\tfrac{Z}{a_{\mathrm{B}}}\right)^{3/2} (27 - 18\tilde{r} + 2\tilde{r}^2) e^{-\tilde{r}/3} \\
\psi_{31\pm1} &= \tfrac{\sqrt{2}}{81\sqrt{3\pi}} \left(\tfrac{Z}{a_{\mathrm{B}}}\right)^{3/2} (6-\tilde{r}) \tilde{r} e^{-\tilde{r}/3} \sin\theta e^{\pm\imath\varphi} \\
\psi_{320} &= \tfrac{1}{81\sqrt{6\pi}} \left(\tfrac{Z}{a_{\mathrm{B}}}\right)^{3/2} \tilde{r}^2 e^{-\tilde{r}/3} (3\cos^2\theta - 1) \ ,
\end{aligned} \tag{3.52}$$

where we use the abbreviation $\tilde{r} \equiv Zr/a_{\mathrm{B}}$. Using these wavefunctions we can now calculate important eigenvalues such as, for example,

$$\begin{aligned}
\langle 1 \rangle_{n\ell m} &= 1 \\
\langle \delta^{(3)}(\tilde{r}) \rangle_{n\ell m} &= \frac{\delta_{\ell,0}}{\pi n^3} \\
\langle \tilde{r} \rangle_{n\ell m} &= n^2 \left[1 + \frac{1}{2}\left(1 - \frac{\ell(\ell+1)}{n^2}\right)\right] \\
\langle \tilde{r}^2 \rangle_{n\ell m} &= n^4 \left[1 + \frac{3}{2}\left(1 - \frac{\ell(\ell+1) - \frac{1}{3}}{n^2}\right)\right] \\
\langle \tilde{r}^3 \rangle_{n\ell m} &= n^6 \left[\frac{35}{8} - \frac{35}{8n^2} - \frac{15}{4n^2}(\ell+2)(\ell-1) + \frac{3}{8n^4}(\ell+2)(\ell+1)\ell(\ell-1)\right] \\
\langle \tilde{r}^4 \rangle_{n\ell m} &= n^8 \left[\frac{63}{8} + \frac{35}{8n^2}(2\ell^2+2\ell-3) + \frac{5}{8n^4} 5\ell(\ell+1)(3\ell^2+3\ell-10) + \frac{12}{n^8}\right] \\
\left\langle \frac{1}{\tilde{r}} \right\rangle_{n\ell m} &= \frac{1}{n^2} \\
\left\langle \frac{1}{\tilde{r}^2} \right\rangle_{n\ell m} &= \frac{1}{n^3(\ell+\frac{1}{2})} \\
\left\langle \frac{1}{\tilde{r}^3} \right\rangle_{n\ell m} &= \frac{n}{n^4 \ell(\ell+\frac{1}{2})(\ell+1)} \\
\left\langle \frac{1}{\tilde{r}^4} \right\rangle_{n\ell m} &= \frac{\frac{3}{2}n^2 - \frac{1}{2}\ell(\ell+1)}{n^5(\ell+\frac{3}{2})(\ell+1)(\ell+\frac{1}{2})\ell(\ell-\frac{1}{2})} \ .
\end{aligned} \tag{3.53}$$

These results will become important later. In Exc. 3.2.3.4 we will calculate the eigenvalue $\langle r \rangle$ for several orbitals $|\psi_{n\ell m}\rangle$.

3.2.2 The virial theorem

Originally derived for classical mechanics, the *virial theorem* also holds for quantum mechanics, as shown for the first time by *Fock*. We evaluate the commutator between the Hamiltonian

$$\hat{H} = \hat{\mathbf{p}}^2/2m + V(\hat{\mathbf{r}}) \ , \tag{3.54}$$

and the product of the position operator $\hat{\mathbf{r}}$ with the momentum operator $\hat{\mathbf{p}} = -\imath\hbar\nabla$ of the particle:

$$[\hat{H}, \hat{\mathbf{r}} \cdot \hat{\mathbf{p}}] = [\hat{H}, \hat{\mathbf{r}}] \cdot \hat{\mathbf{p}} + \hat{\mathbf{r}} \cdot [\hat{H}, \hat{\mathbf{p}}] = -\imath\hbar \frac{\hat{\mathbf{p}}^2}{m} + \imath\hbar \hat{\mathbf{r}} \cdot \nabla V \ , \tag{3.55}$$

using the theorems of Ehrenfest. Therefore, we find for the operator $\hat{Q} = \hat{\mathbf{r}} \cdot \hat{\mathbf{p}}$ the commutator,

$$\frac{\imath}{\hbar}[\hat{H}, \hat{Q}] = 2E_{\text{kin}} - \hat{\mathbf{r}} \cdot \nabla V \ . \tag{3.56}$$

The left side of this equation is precisely $-d\hat{Q}/dt$, following the Heisenberg equation of motion. The eigenvalue $\langle d\hat{Q}/dt \rangle$ of the temporal derivative vanishes in steady state, therefore we obtain the virial theorem,

$$2\langle E_{\text{kin}} \rangle = \langle \hat{\mathbf{r}} \cdot \nabla V \rangle \ . \tag{3.57}$$

Example 30 (*Virial theorem applied to a central potential*): For example, for a central potential $V(r) \propto r^s$ we obtain,

$$2\langle E_{\text{kin}} \rangle = \langle \hat{\mathbf{r}} \cdot \hat{\mathbf{e}}_r \frac{\partial V}{\partial r} \rangle = \langle r \frac{\partial V}{\partial r} \rangle = s\langle V \rangle \ .$$

In Exc. 3.2.3.5 we calculate the eigenvalues $\langle r^{-1} \rangle$ and $\langle p^2 \rangle$ and we verify the virial theorem. Finally, in Exc. 3.2.3.6 we calculate transition matrix elements between different orbitals.

3.2.3 Exercises

3.2.3.1 Ex: Asymptotes of Laguerre's polynomials

Derive the asymptotic solutions of equation (3.42).

3.2.3.2 Ex: Laguerre equation

Show that the equation (3.42) transforms with the ansatz (3.43) into equation (3.44).

3.2.3.3 Ex: Laguerre functions

Using the orthogonality relation of associated Laguerre polynomials,

$$\int_0^\infty \rho^\alpha e^{-\rho} L_n^{(\alpha)}(\rho) L_m^{(\alpha)}(\rho) d\rho = \frac{\Gamma(n+\alpha+1)}{n!} \delta_{n,m}$$

$$\int_0^\infty \rho^{\alpha+1} e^{-\rho} L_n^{(\alpha)} \rho^2 d\rho = \frac{(n+\alpha)!}{n!}(2n+\alpha+1) \ ,$$

and the recursion formula,

$$nL_n^{(\alpha+1)}(\rho) = (n-\rho)L_{n-1}^{(\alpha+1)}(\rho r) + (n+\alpha)L_{n-1}^{(\alpha)}(\rho)$$
$$\rho L_n^{(\alpha+1)}(\rho) = (n+\alpha)L_{n-1}^{(\alpha)}(\rho) - (n-\rho)L_n^{(\alpha)}(\rho) \ ,$$

a. calculate the normalization constant $D_{n,l}$ for a hydrogen-like atom with atomic number Z;
b. calculate the mean value

$$\langle r\rangle_{nlm} = \frac{n^2 a_{\rm B}}{Z}\left[1+\frac{1}{2}\left(1-\frac{\ell(\ell+1)}{n^2}\right)\right] \ ;$$

c. calculate the mean value

$$\left\langle \frac{1}{r}\right\rangle_{n\ell m} = \frac{Z}{n^2 a_{\rm B}} \ .$$

3.2.3.4 Ex: Orbital radii in Bohr's model

Using the results of 3.2.3.3, obtain the expectation values $\langle r\rangle$ for the states ψ_{100}, ψ_{210} and ψ_{320} of the hydrogen atom. Compare the results with those of Bohr's model.

3.2.3.5 Ex: The virial theorem and Bohr's model

Calculate, for the state ψ_{320} of the hydrogen atom, the expectation values $\langle\frac{1}{r}\rangle$, $\langle\frac{\mathbf{L}^2}{r^2}\rangle$, and $\langle\mathbf{p}^2\rangle$.
From the results, obtain the expectation values for the kinetic and potential energies, $\langle T\rangle$ and $\langle V\rangle$, and show that, consistent with the virial theorem, $\langle T\rangle = -(1/2)\langle V\rangle$. Compare the results with Bohr's model.

3.2.3.6 Ex: Transition matrix elements

Using the following (non-normalized) wavefunctions of hydrogen, $\psi_{100}(\mathbf{r}) = e^{-\tilde{r}}$, $\psi_{210}(\mathbf{r}) = \tilde{r}e^{-\tilde{r}/2}\cos\theta$ and $\psi_{21\pm1}(\mathbf{r}) = \tilde{r}e^{-\tilde{r}/2}\sin\theta e^{\pm\imath\phi}$, calculate the matrix elements (a) $\langle\psi_{100}|\tilde{z}|\psi_{210}\rangle$, (b) $\langle\psi_{100}|\tilde{z}|\psi_{211}\rangle$, (c) $\langle\psi_{100}|\tilde{x}-\imath\tilde{y}|\psi_{210}\rangle$, and (d) $\langle\psi_{100}|\tilde{x}-\imath\tilde{y}|\psi_{211}\rangle$ using the formulae:

$$\int_0^\infty x^4 e^{-3x/2}dx = \tfrac{256}{81} \quad , \quad \int_0^\pi \sin^3 x dx = \tfrac{4}{3} \ ,$$
$$\int_0^\pi \cos x\sin^2 x dx = 0 \quad , \quad \int_0^\pi \cos^2 x\sin x dx = \tfrac{2}{3} \ .$$

Try to interpret the results.

3.3 Angular momentum

3.3.1 The orbital angular momentum operator

The definition of *orbital angular momentum* is adopted from classical mechanics:

$$\hat{\mathbf{L}} = \hat{\mathbf{r}} \times \hat{\mathbf{p}} = -\imath\hbar\hat{\mathbf{r}} \times \hat{\nabla} = -\imath\hbar \begin{vmatrix} \hat{\mathbf{e}}_x & \hat{\mathbf{e}}_y & \hat{\mathbf{e}}_z \\ x & y & z \\ \partial_x & \partial_y & \partial_z \end{vmatrix} . \tag{3.58}$$

To better understand the properties of the angular momentum operator in quantum mechanics we will derive in the Excs. 3.3.4.1 and 3.3.4.2 some of its properties.

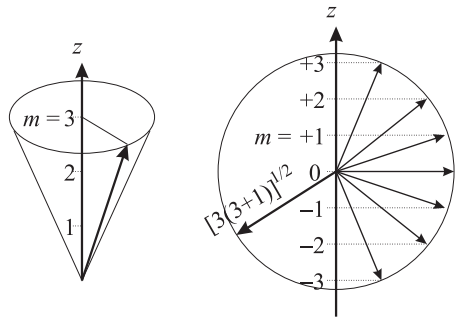

Figure 3.7: Illustration of angular momentum in quantum mechanics.

3.3.1.1 Constants of motion

The preceding chapter dealt with the resolution of the radial and angular equations for the case of a radial potential. The radial equation allowed to calculate the eigenenergies of the Hamiltonian $\hat{H}$,

$$\hat{H}|\psi\rangle = E_{n\ell}|\psi\rangle \ . \tag{3.59}$$

We also found the common eigenvalues and eigenfunctions of operators $\hat{\mathbf{L}}^2$ and $\hat{L}_z$ [see Eqs. (3.20) and (3.24)]. We now use the notation $|\ell, m\rangle \equiv Y_{\ell m}(\theta, \phi)$ for the eigenfunctions,

$$\hat{\mathbf{L}}^2|\ell, m\rangle = \hbar^2\ell(\ell+1)|\ell, m\rangle \qquad \text{and} \qquad \hat{L}_z|\ell, m\rangle = \hbar m|\ell, m\rangle \ . \tag{3.60}$$

With this we have,

$$\begin{aligned} &[\hat{H}, \hat{\mathbf{L}}^2]|\psi\rangle = \hat{H}\hbar^2\ell(\ell+1)|\psi\rangle - \hat{\mathbf{L}}^2 E|\psi\rangle = 0 \\ \text{and} \quad &[\hat{H}, \hat{L}_z]|\psi\rangle = \hat{H}\hbar m|\psi\rangle - \hat{L}_z E|\psi\rangle = 0 \ . \end{aligned} \tag{3.61}$$

Therefore, the operators $\hat{\mathbf{L}}^2$ and $\hat{L}_z$ are constants of motion,

$$[\hat{H}, \hat{L}_z] = 0 = [\hat{H}, \hat{\mathbf{L}}^2] \ . \tag{3.62}$$

Exc. 3.3.4.3 asks to show explicitly, at the example of an isotropic three-dimensional harmonic oscillator, that $\hat{\mathbf{L}}^2$ and $\hat{L}_z$ are constants of motion.

3.3.2 SU(2) algebra of angular momentum and spin

So far, we have solved the angular eigenvalue equation in the spatial representation for an orbital angular momentum, $\hat{\mathbf{L}} = \hat{\mathbf{r}} \times \hat{\mathbf{p}}$. But it is not clear, whether *every* angular momentum has this representation, which is derived from classical notions. Using the orbital angular momentum expression (3.58) it is easy to verify,

$$\hat{\mathbf{L}} \times \hat{\mathbf{L}} = \imath\hbar\hat{\mathbf{L}} \ . \tag{3.63}$$

However, it is not clear a priori, whether *any* quantity $\hat{\mathbf{J}}$ satisfying

$$\boxed{\hat{\mathbf{J}} \times \hat{\mathbf{J}} = \imath\hbar\hat{\mathbf{J}}} \qquad \text{or equivalently} \qquad [\hat{J}_m, \hat{J}_n] = \imath\hbar\epsilon_{kmn}\hat{J}_k \tag{3.64}$$

using the Levi-Civita symbol, can be represented like (3.58). In fact, we will see that the electron has an intrinsic spin with no orbiting charges, and cannot be represented as an orbital angular momentum. What needs to be done now is to show that (3.64) generates a consistent algebra even in cases beyond the representation (3.58).

Since $\hat{\mathbf{J}}^2$ and $\hat{J}_z$ commute (we show this from Eq. (3.64) in Exc. 3.3.4.4), they have common eigenfunctions $|j, m\rangle$. We can write the eigenvalues as,

$$\hat{\mathbf{J}}^2|j, m\rangle = \hbar^2 j(j+1)|j, m\rangle \qquad \text{and} \qquad \hat{J}_z|j, m\rangle = \hbar m|j, m\rangle \ , \tag{3.65}$$

where, for now, we only know that m is real and $j \geq 0$. But since $\langle j, m|\hat{\mathbf{J}}^2|j, m\rangle \geq \langle j, m|\hat{J}_z^2|j, m\rangle$, it is clear that $j(j+1) \geq m^2$.

3.3.2.1 Rising and lowering operator

Now we introduce the *rising operator* $\hat{J}_+$ and the *lowering operator* $\hat{J}_-$ via

$$\hat{J}_\pm \equiv \hat{J}_x \pm \imath\hat{J}_y \qquad \text{such that} \qquad \hat{J}_- = \hat{J}_+^\dagger \ . \tag{3.66}$$

It is easy to check the following relationships

$$[\hat{J}_z, \hat{J}_\pm] = \pm\hbar\hat{J}_\pm \qquad \text{and} \qquad [\hat{\mathbf{J}}^2, \hat{J}_\pm] = 0 \qquad \text{and} \qquad \hat{J}_\mp\hat{J}_\pm = \hat{\mathbf{J}}^2 - \hat{J}_z^2 \mp \hbar\hat{J}_z \ . \tag{3.67}$$

With this we find

$$\begin{aligned} &\hat{J}_z\hat{J}_\pm|j, m\rangle = ([\hat{J}_z, \hat{J}_\pm] + \hat{J}_\pm J_z)|j, m\rangle = \hbar(m \pm 1)\hat{J}_\pm|j, m\rangle \\ \text{and} \quad &\hat{\mathbf{J}}^2 J_\pm|j, m\rangle = \hat{J}_\pm\hat{\mathbf{J}}^2|j, m\rangle = \hbar^2 j(j+1)\hat{J}_\pm|j, m\rangle \ . \end{aligned} \tag{3.68}$$

That is, $\hat{J}_\pm|j, m\rangle$ is a eigenstate of $\hat{\mathbf{J}}^2$ and $\hat{J}_z$ with the eigenvalues j and $m \pm 1$, respectively, if $J_\pm|j, m\rangle \neq 0$. Hence,

$$\hat{J}_+|j, m\rangle \propto |j, m+1\rangle \ . \tag{3.69}$$

In order not to violate the condition $m^2 \leq j(j+1)$, we need to fix $\hat{J}_\pm|j, \pm j\rangle = 0$. Therefore, for a specified j, the m can have only one of the $2j+1$ possible values $m = -j, -j+1, .., j$. Since $2j+1$ is an integer, j can only have values $j = 0, \frac{1}{2}, 1, \frac{3}{2}, ...$ Thus, the eigenvalue equation of the observables $\hat{\mathbf{J}}^2$, $\hat{\mathbf{J}}$ is solved, since we could have chosen instead of $\hat{J}_z$ any one of the components of $\hat{\mathbf{J}}$, knowing that the others do not commute with the chosen one.

All spin components $\hat{J}_z$ and the scalar $\hat{\mathbf{J}}^2$ can only have discrete eigenvalues. The smallest unit is $\hbar/2$. With the normalization $\langle j,m|j',m'\rangle = \delta_{j,j'}\delta_{m,m'}$ we have,

$$\langle j,m|\hat{J}_\mp\hat{J}_\pm|j,m\rangle = \langle j,m|(\hat{\mathbf{J}}^2 - \hat{J}_z^2 \mp \hbar\hat{J}_z)|j,m\rangle = \hbar^2[j(j+1) - m(m\pm 1)] \ , \quad (3.70)$$

and

$$\boxed{\hat{J}_\pm|j,m\rangle = \hbar\sqrt{j(j+1)-m(m\pm 1)}|j,m\pm 1\rangle} \ . \quad (3.71)$$

In Exc. 3.3.4.5 we calculate the uncertainty of the angular momentum components, in Exc. 3.3.4.6 we write the operator $\hat{J}_x$ in a matrix form, and in Excs. 3.3.4.7 and 3.3.4.8 we calculate projections of the spin of the electron in different directions of the quantization axis.

3.3.3 The electron spin

Every angular momentum $\hat{\mathbf{J}}$ generates a *magnetic dipole moment* $\vec{\mu}_j \propto \hat{\mathbf{J}}$, which interacts with external magnetic fields, $V(\vec{\mathcal{B}}) = \vec{\mu}_j \cdot \vec{\mathcal{B}}$. *Inhomogeneous* magnetic fields exert forces on dipole moments, $\mathbf{F} = -\nabla(\vec{\mu}_j \cdot \vec{\mathcal{B}})$, which are detected by the *Stern-Gerlach experiment*. This experiment reveals not only the quantization of angular momentum, but also the presence of semi-integral values for the magnetic quantum number.

In 1925 Uhlenbeck and Goudsmit proposed that the electron could have an intrinsic angular momentum with the quantum number $s = 1/2$. This angular momentum, called *spin*, would not correspond to any orbiting mass or charge distribution within the classical radius of the electron of the type $\mathbf{L} = \mathbf{r} \times \mathbf{p}$. The spin is a purely quantum phenomenon because it disappears when $\hbar \to 0$. It is believed nowadays that the electron is actually point-like with no detectable deviation from Coulomb's law at any distance. The spin of the electron does not follow from the Schrödinger equation, but can be included, ad hoc. On the other hand, it is interesting that it is a necessary consequence of the stringent relativistic derivation of quantum mechanics by *Paul Dirac*.

To characterize the spin, we can use the whole SU(2) formalism of the quantum mechanics of angular momentum:

$$\hat{\mathbf{S}} \times \hat{\mathbf{S}} = \imath\hbar\hat{\mathbf{S}} \ , \quad (3.72)$$

and

$$\hat{\mathbf{S}}^2|\tfrac{1}{2},\pm\tfrac{1}{2}\rangle = \hbar^2\tfrac{3}{4}|\tfrac{1}{2},\pm\tfrac{1}{2}\rangle \quad , \quad \hat{S}_z|\tfrac{1}{2},\pm\tfrac{1}{2}\rangle = \pm\tfrac{\hbar}{2}|\tfrac{1}{2},\pm\tfrac{1}{2}\rangle \quad , \quad (3.73)$$
$$\hat{S}_\pm = \hbar\hat{\sigma}_\pm = \hbar|\tfrac{1}{2},\pm\tfrac{1}{2}\rangle\langle|\tfrac{1}{2},\mp\tfrac{1}{2}| \ .$$

The operators $\hat{\sigma}_\pm$ are the *Pauli spin matrices* defined in (1.154) for the basis chosen as,

$$|\tfrac{1}{2},+\tfrac{1}{2}\rangle = \begin{pmatrix}1\\0\end{pmatrix} \quad \text{and} \quad |\tfrac{1}{2},-\tfrac{1}{2}\rangle = \begin{pmatrix}0\\1\end{pmatrix} \ . \quad (3.74)$$

3.3.4 Exercises

3.3.4.1 Ex: Properties of the angular orbital momentum

Show that $\hat{\mathbf{L}} \times \hat{\mathbf{L}} = \imath\hbar\hat{\mathbf{L}}$ and $[\hat{L}_x, \hat{L}_y] = \imath\hbar\hat{L}_z$.

3.3.4.2 Ex: Levi-Civita tensor

a. Demonstrate $[\hat{L}_k, \hat{r}_m] = \imath\hbar\hat{r}_n\epsilon_{kmn}$ where the Levi-Civita tensor is defined by $\epsilon_{kmn} = 1$ when (kmn) is an even permutation of (123), $\epsilon_{kmn} = -1$ for an odd permutation, and $\epsilon_{kmn} = 0$ when two of the indices are equal.
b. Verify $\hat{J}_m\hat{J}_n = \frac{1}{4}\delta_{mn} + \frac{\imath}{2}\epsilon_{kmn}\hat{J}_k$.

3.3.4.3 Ex: Angular orbital momentum of a harmonic oscillator

Show for an isotropic three-dimensional harmonic oscillator: $[\hat{H}, \hat{\mathbf{L}}^2] = [\hat{H}, \hat{L}_z] = 0$. Make explicit calculations, that is, show

$$\left[\tfrac{\hat{p}^2}{2m}, \hat{L}_z\right] = 0 = \left[\frac{m}{2}\omega^2\hat{r}^2, \hat{L}_z\right] \qquad \text{and} \qquad \left[\tfrac{\hat{p}^2}{2m}, \hat{\mathbf{L}}^2\right] = 0 = \left[\frac{m}{2}\omega^2\hat{r}^2, \hat{\mathbf{L}}^2\right] \ .$$

3.3.4.4 Ex: Commutation of the absolute value and the components of the orbital angular momentum

Show $[\hat{\mathbf{J}}^2, \hat{\mathbf{J}}] = 0$.

3.3.4.5 Ex: Uncertainty of angular momentum components

Show that if $\hat{J}_z$ is precise, then $\hat{J}_x$ and $\hat{J}_y$ are imprecise.

3.3.4.6 Ex: Matrix representation of the components of the angular momentum

Calculate the matrix elements of $\hat{J}_x$ and $\hat{J}_x^2$ in the basis where $\hat{J}_z$ is observable. Give the general formula and examples for $j = \frac{1}{2}$ and $j = 1$.

3.3.4.7 Ex: Spin-1/2-particle in a magnetic field

Consider a spin-1/2-particle whose magnetic moment is $\vec{\mu} = \gamma\mathbf{S}$ (where γ is a constant). We can describe the quantum state of this particle in terms of the space generated by the eigenvectors $|+\rangle$ and $|-\rangle$ of the operator $\hat{S}_z$, which measures the spin projection in z-direction:

$$\hat{S}_z|+\rangle = \tfrac{\hbar}{2}|+\rangle \qquad , \qquad \hat{S}_z|-\rangle = -\tfrac{\hbar}{2}|-\rangle$$

Initially $(t = 0)$ the particle is in the state $\psi(t = 0)\rangle = |+\rangle$ and is subject to a uniform magnetic field $\vec{\mathcal{B}} = \mathcal{B}\hat{\mathbf{e}}_y$, so that:

$$\hat{H} = -\vec{\mu}\cdot\vec{\mathcal{B}} = -\gamma\mathcal{B}\hat{S}_y \ .$$

a. What are the possible measurements of the spin projection on the y-axis?
b. Find the eigenvectors of $\hat{S}_y$.
c. Get $|\psi(t)\rangle$ at $t > 0$ in terms of the eigenvectors $|+\rangle$ and $|-\rangle$ defined above.
d. Obtain the mean expectation values of the observables $\hat{S}_x$, $\hat{S}_y$ and $\hat{S}_z$ as a function of time.

3.3.4.8 Ex: Spin expectation value for a two-level system

Consider an arbitrary state of a two-level system $|\vartheta,\varphi\rangle = \cos\frac{\vartheta}{2}|+\rangle + e^{\imath\varphi}\sin\frac{\vartheta}{2}|-\rangle$ and calculate the expectation values of the ladder operators $\hat{S}_\pm$ and of the spin operator $\hat{\mathbf{S}}$. Also calculate the expectation values of $\hat{S}_\pm^2$, $\hat{S}_\pm\hat{S}_\mp$, $\hat{S}_\alpha^2$ with $\alpha = x,y,z$. Finally, calculate the uncertainties of $\hat{s}_\alpha$ and check the uncertainty relation.

3.4 Coupling of angular momenta

3.4.1 Singlet and triplet states with two electrons

In this section we first consider the spin states of two electrons, which can be combined into two groups with well-defined total spin. With this we can understand the energy spectrum of helium, which is very much dominated by Pauli's principle and quantum statistics. The introduced concepts can be extended to atoms with many electrons.

Angular momentum is an important quantum number in the treatment of the internal structure of atoms. The two electrons in the helium electronic shell each contribute a spin of $s = \frac{1}{2}$, which couple to a total angular momentum. Let us consider, for simplicity, two free electrons. The state of the two-particle system is an element of the product space of the two Hilbert spaces in which the individual electrons are described. We will now apply the formalism of Sec. 1.5.8 explicitly to a pair of electrons. The states that the two electrons can occupy are:

$$|\gamma_1\rangle = \begin{pmatrix}1\\0\end{pmatrix}\otimes\begin{pmatrix}1\\0\end{pmatrix} = \begin{pmatrix}1\\0\\0\\0\end{pmatrix} \equiv |\uparrow\uparrow\rangle \quad , \tag{3.75}$$

$$|\gamma_2\rangle = |\uparrow\downarrow\rangle \quad , \quad |\gamma_3\rangle = |\downarrow\uparrow\rangle \quad , \quad |\gamma_4\rangle = |\downarrow\downarrow\rangle \; .$$

The Pauli matrices act on the spin of the individual electrons. They can be extended to the product Hilbert space as follows,

$$\begin{aligned}
\tfrac{\hbar}{2}\hat{\sigma}_x\otimes\mathbb{I}_2 &= \tfrac{\hbar}{2}\begin{pmatrix}0 & \mathbb{I}_2\\ \mathbb{I}_2 & 0\end{pmatrix} \quad , \quad \tfrac{\hbar}{2}\mathbb{I}_2\otimes\hat{\sigma}_x = \tfrac{\hbar}{2}\begin{pmatrix}\hat{\sigma}_x & 0\\ 0 & \hat{\sigma}_x\end{pmatrix} \\
\tfrac{\hbar}{2}\hat{\sigma}_y\otimes\mathbb{I}_2 &= \tfrac{\hbar}{2}\begin{pmatrix}0 & \imath\mathbb{I}_2\\ -\imath\mathbb{I}_2 & 0\end{pmatrix} \quad , \quad \tfrac{\hbar}{2}\mathbb{I}_2\otimes\hat{\sigma}_y = \tfrac{\hbar}{2}\begin{pmatrix}\hat{\sigma}_y & 0\\ 0 & \hat{\sigma}_y\end{pmatrix} \\
\tfrac{\hbar}{2}\hat{\sigma}_z\otimes\mathbb{I}_2 &= \tfrac{\hbar}{2}\begin{pmatrix}-\mathbb{I}_2 & 0\\ 0 & \mathbb{I}_2\end{pmatrix} \quad , \quad \tfrac{\hbar}{2}\mathbb{I}_2\otimes\hat{\sigma}_z = \tfrac{\hbar}{2}\begin{pmatrix}\hat{\sigma}_z & 0\\ 0 & \hat{\sigma}_z\end{pmatrix} \; .
\end{aligned} \tag{3.76}$$

With these operators we can now build other operators. We first consider the three

components of the total angular momentum,

$$\hat{S}_k = \tfrac{\hbar}{2}(\hat{\sigma}_k \otimes \mathbb{I}_2 + \mathbb{I}_2 \otimes \hat{\sigma}_k) \qquad \text{such that} \tag{3.77}$$

$$\hat{S}_x = \tfrac{\hbar}{2}\begin{pmatrix} 0 & 1 & 1 & 0 \\ 1 & 0 & 0 & 1 \\ 1 & 0 & 0 & 1 \\ 0 & 1 & 1 & 0 \end{pmatrix} \quad , \quad \hat{S}_y = \tfrac{\imath\hbar}{2}\begin{pmatrix} 0 & 1 & 1 & 0 \\ -1 & 0 & 0 & 1 \\ -1 & 0 & 0 & 1 \\ 0 & -1 & -1 & 0 \end{pmatrix} \quad , \quad \hat{S}_z = \hbar\begin{pmatrix} -1 & 0 & 0 & 0 \\ 0 & 0 & 0 & 0 \\ 0 & 0 & 0 & 0 \\ 0 & 0 & 0 & 1 \end{pmatrix} .$$

The operator for the square of the absolute value of the total angular momentum is calculated as follows:

$$\hat{\mathbf{S}}^2 = \hat{S}_x^2 + \hat{S}_y^2 + \hat{S}_z^2 = \hbar^2\begin{pmatrix} 2 & 0 & 0 & 0 \\ 0 & 1 & 1 & 0 \\ 0 & 1 & 1 & 0 \\ 0 & 0 & 0 & 2 \end{pmatrix} . \tag{3.78}$$

Now, we look for the eigenvalues of the total angular momentum. The equation for the eigenvalues of $\hat{S}_z$,

$$\hat{S}_z|\gamma_k\rangle = M_S|\gamma_k\rangle \ , \tag{3.79}$$

is already diagonal in the introduced basis $\{\gamma_k\}$ with the eigenvalues,

$$M_S = -\hbar, 0, 0, \hbar \ . \tag{3.80}$$

For $\hat{\mathbf{S}}^2$ the situation is more interesting: The states $|\gamma_1\rangle$ and $|\gamma_4\rangle$ *are* eigenstates of $\mathbf{S}^2$ for the eigenvalue $2\hbar^2$, but the states $|\gamma_2\rangle$ and $|\gamma_3\rangle$ are *not* eigenstates. On the other hand, we know that the linear combination of two eigenstates with the same eigenvalue is also a eigenstate. Therefore, the states

$$|\tilde{\gamma}_1\rangle \equiv |\gamma_1\rangle \quad , \quad |\tilde{\gamma}_4\rangle \equiv |\gamma_4\rangle \quad , \quad |\tilde{\gamma}_a\rangle \equiv \tfrac{1}{\sqrt{2}}(|\gamma_2\rangle - |\gamma_3\rangle) \quad , \quad |\tilde{\gamma}_s\rangle \equiv \tfrac{1}{\sqrt{2}}(|\gamma_2\rangle + |\gamma_3\rangle) \, , \tag{3.81}$$

are *still* eigenstates of $\hat{S}_z$, but they *also* are eigenstates of $\hat{\mathbf{S}}^2$, since we can easily verify,

$$\hat{\mathbf{S}}^2|\gamma_s\rangle = 2\hbar^2|\gamma_s\rangle \qquad \text{and} \qquad \hat{\mathbf{S}}^2|\gamma_a\rangle = 0\hbar^2|\gamma_a\rangle \ , \tag{3.82}$$

using the matrices (3.77). In summary, for the eigenvalue $\langle\hat{\mathbf{S}}^2\rangle = 2\hbar^2$ there exist the following three states:

$$\left.\begin{array}{ll} |\gamma_1\rangle & M_s = 1 \\ |\gamma_4\rangle & M_s = -1 \\ |\gamma_s\rangle & M_s = 0 \end{array}\right\} \qquad \text{triplet} \ , \ S = 1 \tag{3.83}$$

For $\langle\mathbf{S}^2\rangle = 0$ there is only one state:

$$|\gamma_a\rangle \quad M_s = 0 \qquad \text{singlet} \ , \ S = 0 \ . \tag{3.84}$$

By exchanging the two electrons, the vectors $|\gamma_1\rangle$ and $|\gamma_4\rangle$ retain their shape, while the mixed vectors change their shape: $\gamma_2 \leftrightarrow \gamma_3$. Under particle exchange $|\gamma_a\rangle$ reverses

its sign, that is, it is antisymmetric, while $|\gamma_1\rangle$, $|\gamma_4\rangle$ and $|\gamma_c\rangle$ conserve their signs, that is, they are symmetrical.

In summary, the triplet states have the quantum number of the total angular momentum (with the expected value for $\hat{\mathbf{S}}^2$ of $\hbar^2 S(S+1) = 2\hbar^2$), and they are symmetrical about the exchange of particles. The singlet state has the quantum number of the total angular momentum $S = 0$, and it is antisymmetric about the exchange of particles. The transition from the original basis $\{|\gamma_1\rangle, |\gamma_2\rangle, |\gamma_3\rangle, |\gamma_4\rangle\}$ to the new basis $\{|\tilde{\gamma}_1\rangle, |\tilde{\gamma}_s\rangle, |\tilde{\gamma}_a\rangle, |\tilde{\gamma}_4\rangle\}$ described by Eqs. (3.81) is done by a unitary transformation,

$$|\tilde{\gamma}\rangle = \mathcal{U}_{\rm CGC}|\gamma\rangle \qquad \text{with} \qquad \mathcal{U}_{\rm CGC} = \begin{pmatrix} 1 & & & \\ & \frac{1}{\sqrt{2}} & \frac{1}{\sqrt{2}} & \\ & \frac{1}{\sqrt{2}} & -\frac{1}{\sqrt{2}} & \\ & & & 1 \end{pmatrix} , \tag{3.85}$$

whose components are known as Clebsch-Gordan coefficients. A similar treatment can be done with bosons, as will be discussed in Sec. 11.1.

3.4.2 Coupling two spins

We now consider a perturbation of the system which, for some reason, only affects the first spin. In the absence of the second atom we would have,

$$\hat{H}_1 = \begin{pmatrix} 0 & \Omega^* \\ \Omega & 0 \end{pmatrix} . \tag{3.86}$$

Including the second atom,

$$\hat{H} = \hat{H}_1 \otimes \mathbb{I} = \begin{pmatrix} & & \Omega^* & \\ & & & \Omega^* \\ \Omega & & & \\ & \Omega & & \end{pmatrix} . \tag{3.87}$$

In this case, the perturbation Hamiltonian does not commute with the total angular momentum,

$$[\hat{\mathbf{S}}^2, \hat{H}] \neq 0 . \tag{3.88}$$

Another type of perturbation affects both spin symmetrically (e.g., Dicke superradiance with two atoms in the same radiative mode or two counterpropagating modes in a ring cavity). The interaction Hamiltonian is now the sum of the individual perturbations,

$$\hat{H} = \hat{H}_1 \otimes \mathbb{I} + \mathbb{I} \otimes \hat{H}_1 = \begin{pmatrix} & \Omega^* & \Omega^* & \\ \Omega & & & \Omega^* \\ \Omega & & & \Omega^* \\ & \Omega & \Omega & \end{pmatrix} . \tag{3.89}$$

This Hamiltonian commutes with the total angular momentum,

$$[\hat{\mathbf{S}}^2, \hat{H}] = 0 . \tag{3.90}$$

S now is a good quantum number. Singlet states do not couple with triplets. This is the idea behind Dicke's superradiance. The absolute value of the total angular momentum is conserved. The quantum number S is called *Dicke cooperativity* [229].

Example 31 (*Two atoms interacting through their dipole moments*): As an example of a system exhibiting coupling of the type described in (3.89) we consider two two-level atoms $j = 1, 2$. As long as the atoms do not interact, the Hamiltonian will be,

$$\hat{H} = \hbar\omega_0 \hat{S}_z \ , \tag{3.91}$$

with $\hat{S}_z$ given by (3.77). Now, if the atoms interact via their dipole moments with an electromagnetic field assumed to be the same for both atoms,

$$\begin{aligned} \hat{H}_{int} = &- \tfrac{q}{m}\mathbf{A}(\mathbf{r}_1)\cdot(p_x\hat{\mathbf{e}}_x\hat{\sigma}_x\otimes\mathbb{I} + p_y\hat{\mathbf{e}}_y\hat{\sigma}_y\otimes\mathbb{I}) \\ &- \tfrac{q}{m}\mathbf{A}(\mathbf{r}_2)\cdot(p_x\hat{\mathbf{e}}_x\mathbb{I}\otimes\hat{\sigma}_x + p_y\hat{\mathbf{e}}_y\mathbb{I}\otimes\hat{\sigma}_y) \ , \end{aligned} \tag{3.92}$$

with $\mathbf{r}_1 \simeq \mathbf{r}_2$. By the rules (3.76) we find in matrix notation a Hamiltonian equivalent to (3.89). Using the abbreviations $\Omega_x \equiv \frac{q}{m}A_x p_x$, $\Omega_y \equiv \frac{q}{m}A_y p_y$, $\Omega_\pm \equiv \Omega_x \pm \imath\Omega_y$, and $\Omega \equiv \sqrt{\Omega_x^2 + \Omega_y^2}$,

$$\hat{H} = \begin{pmatrix} 0 & \Omega_- & \Omega_- & 0 \\ \Omega_+ & 0 & 0 & \Omega_- \\ \Omega_+ & 0 & 0 & \Omega_- \\ 0 & \Omega_+ & \Omega_+ & 0 \end{pmatrix} \ . \tag{3.93}$$

Using symbolic algebra software we find the eigenvector and eigenvalue matrices,

$$\mathcal{U} = \begin{pmatrix} \frac{\Omega_-}{\Omega_+} & -\frac{\Omega_-}{\Omega_+} & 0 & \frac{\Omega_-}{\Omega_+} \\ -\sqrt{\frac{\Omega_-}{\Omega_+}} & 0 & -1 & \sqrt{\frac{\Omega_-}{\Omega_+}} \\ -\sqrt{\frac{\Omega_-}{\Omega_+}} & 0 & 1 & \sqrt{\frac{\Omega_-}{\Omega_+}} \\ 1 & 1 & 0 & 1 \end{pmatrix} \quad \text{and} \quad \hat{E} = \begin{pmatrix} -2\Omega & 0 & 0 & 0 \\ 0 & 0 & 0 & 0 \\ 0 & 0 & 0 & 0 \\ 0 & 0 & 0 & 2\Omega \end{pmatrix} \ . \tag{3.94}$$

Now, we get for the evolution of the various states,

$$\mathcal{U}e^{\imath\hat{E}t}\mathcal{U}^{-1}\begin{pmatrix}0\\1\\1\\0\end{pmatrix} = \begin{pmatrix} -\sqrt{\frac{-\Omega_-}{\Omega_+}}\sin 2\Omega t \\ \cos 2\Omega t \\ \cos 2\Omega t \\ \sqrt{\frac{\Omega_+}{-\Omega_-}}\sin 2\Omega t \end{pmatrix} \quad \text{and} \quad \mathcal{U}e^{\imath\hat{E}t}\mathcal{U}^{-1}\begin{pmatrix}0\\1\\-1\\0\end{pmatrix} = \begin{pmatrix}0\\1\\-1\\0\end{pmatrix} \ . \tag{3.95}$$

That is, the Hamiltonian (3.92) does not mix antisymmetric singlet states and symmetric triplet states.

3.4.3 Decoupled and coupled bases

Electrically charged orbiting particles produce a magnetic field. This field can influence the motion of other particles. In the same way, the spin of an electron can influence its own orbital motion. That is, angular momenta can couple and interact in a complicated way. Even to describe the behavior of an atom as simple as hydrogen in an external field, we need to construct the eigenstates of the total angular momentum resulting from a coupling of the electron's intrinsic spin and its orbital motion.

On the other side, we have hitherto considered predominantly hydrogen and hydrogen-like atoms, that is, atoms with a nucleus and a single (valence) electron. But in fact atoms can have more than 100 electrons, which complicates the exact description. In atoms with many electrons, one of the most common coupling schemes is when the angular momenta of all electrons couple to a *total angular momentum*, $\hat{\mathbf{L}} = \sum_k \hat{\mathbf{l}}_k$, which then couples to the *total spin*, $\hat{\mathbf{S}} = \sum_k \hat{\mathbf{s}}_k$, to form the complete total angular momentum, $\hat{\mathbf{J}} = \hat{\mathbf{L}} + \hat{\mathbf{S}}$. We generally assign total momenta to capital letters.

Adopting an unbiased notation we study some properties of the total angular momentum, $\hat{\mathbf{J}} \equiv \hat{\mathbf{j}}_1 + \hat{\mathbf{j}}_2$. In Exc. 3.4.5.1 we find that the addition of angular momenta produces a quantity which is also an angular momentum, but not the subtraction.

The angular momenta of two particles or two angular momenta of different origins in a single particle represent independent degrees of freedom, $[\mathbf{j}_1, \mathbf{j}_2] = 0$. Without interaction between angular momenta the Hilbert spaces are orthogonal:

$$\mathcal{H}_1 \otimes \mathcal{H}_2 = \begin{pmatrix} \mathcal{H}_1 & 0 \\ 0 & \mathcal{H}_2 \end{pmatrix} . \tag{3.96}$$

The eigenfunctions act on a space of dimension, $\dim \mathcal{H}_1 \cdot \dim \mathcal{H}_2$:

$$|j_1, m_{j1}; j_2, m_{j2}\rangle . \tag{3.97}$$

That is, there is a complete set of commuting operators $\{\hat{\mathbf{j}}_1^2, \hat{j}_{1z}, \hat{\mathbf{j}}_2^2, \hat{j}_{2z}\}$. Therefore, we can specify quantum numbers j_1, j_2, m_{j1}, and m_{j2} simultaneously. On the other hand, the group $\{\hat{\mathbf{j}}_1^2, \hat{\mathbf{j}}_2^2, \hat{\mathbf{J}}^2, \hat{J}_z\}$ also represents a complete set of commuting operators, as shown in Exc. 3.4.5.2. It has the basis

$$|(j_1, j_2)J, M_J\rangle . \tag{3.98}$$

To describe the two angular momenta simultaneously, we must opt between the decoupled picture $|j_1, m_{j1}; j_2, m_{j1}\rangle$ and the coupled picture $|(j_1, j_2)J, M_J\rangle$. For now, the choice of the picture makes no difference, but we will see later that there may be an energy associated with the coupling [3]. In this case, as we will show, the choice of the coupled base is more natural, because generally the energy commutes like $[\hat{H}, \hat{\mathbf{J}}^2] = 0 = [\hat{H}, \hat{J}_z]$ and $[\hat{H}, \hat{\mathbf{j}}_1^2] = 0 = [\hat{H}, \hat{\mathbf{j}}_2^2]$, but $[\hat{H}, \hat{j}_{1z}] \neq 0 \neq [\hat{H}, \hat{j}_{2z}]$.

Example 32 (*Coupled basis*): For example, using the Hamiltonian (3.94) it is easy to see that,

$$[\hat{H}, (\hat{\sigma}_x \otimes \mathbb{I})^2 + (\hat{\sigma}_y \otimes \mathbb{I})^2 + (\hat{\sigma}_z \otimes \mathbb{I})^2] = 0 = [\hat{H}, (\mathbb{I} \otimes \hat{\sigma}_x)^2 + (\mathbb{I} \otimes \hat{\sigma}_y)^2 + (\mathbb{I} \otimes \hat{\sigma}_z)^2]$$
$$[\hat{H}, \hat{\sigma}_z \otimes \mathbb{I}] \neq 0 \neq [\hat{H}, \mathbb{I} \otimes \hat{\sigma}_z] .$$

[3] That is, the Hamiltonian of the system does not contain terms of type $\hat{\mathbf{j}}_\mathbf{1} \cdot \hat{\mathbf{j}}_\mathbf{2}$, but may have terms proportional to $\hat{\mathbf{j}}_\mathbf{1} + \hat{\mathbf{j}}_\mathbf{2}$.

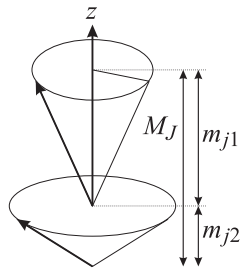

Figure 3.8: Illustration of the coupling of two angular momenta.

3.4.3.1 Allowed values of total angular momentum

As long as we do not specify an interaction energy between the spins or between spins and external fields, all states are energetically degenerate. In the decoupled image the degeneracy is easily calculated,

$$\# = \sum_{m_{j1}=-j_1}^{j_1} \sum_{m_{j2}=-j_2}^{j_2} 1 = (2j_1+1)(2j_2+1) \ . \tag{3.99}$$

Now, we want to find the possible values of J and M_J in the coupled picture. The values of M_J follow immediately from $\hat{\mathbf{j}}_1 + \hat{\mathbf{j}}_2 = \hat{\mathbf{J}}$,

$$M_J = m_{j1} + m_{j2} \ . \tag{3.100}$$

With $|m_{j1}| \leq j_1$ and $|m_{j2}| \leq j_2$ the values of M_J are limited to

$$|M_J| \leq j_1 + j_2 \ . \tag{3.101}$$

We often know the two angular momenta j_1 and j_2 and all their projections in the decoupled base,

$$|m_{j1}| \leq j_1 \qquad \text{and} \qquad |m_{j2}| \leq j_2 \ . \tag{3.102}$$

To find the quantum numbers in the coupled base, we arrange the states ordering them by their total magnetic quantum number M_J. We can, without loosing generality, concentrate on the situation $j_1 \geq j_2$. The following table reproduces the possible combinations. The x-symbols represent Clebsch-Gordan coefficients:

m_{j1} $+m_{j2}=$ M_J	J J	J $J-1$ $J-1$ $J-1$	J $J-1$ $J-2$ $J-2$ $J-2$ $J-2$		J $J-1$ $-J+1$ $-J+1$	J $-J$
j_1 j_2	x					
j_1 j_2-1 j_1-1 j_2		x x x x				
j_1 j_2-2 j_1-1 j_2-1 j_1-2 j_2			x x x x x x x x x			
				$\ddots$		
$-j_1+1$ $-j_2$ $-j_1$ j_2+1					x x x x	
$-j_1$ $-j_2$						x

The possible values for J are all those allowing for $J \geq |M_J| = |m_{j1} + m_{j2}|$, that is,

$$|j_1 - j_2| \leq J \leq j_1 + j_2 \ . \tag{3.103}$$

Each value of J has the degeneracy $2J+1$. Therefore, as will be verified in Exc. 3.4.5.3, the total degeneracy is,

$$\sum_{J=|j_1-j_2|}^{j_1+j_2} 2J+1 = (2j_1+1)(2j_2+1) \ . \tag{3.104}$$

Example 33 (*Spin states in the presence of* $\mathbf{L}\cdot\mathbf{S}$ *coupling*): As an example we consider two electrons occupying the $(5p)^2$ orbital. That is, both electrons have $s_i = \frac{1}{2}$ and $\ell_i = 1$. As illustrated in Fig. 3.9, the coupling first gives $S = s_1 + s_2 = 0, 1$ and $L = \ell_1 + \ell_2 = 0, 1, 2$. Then we determine the possible values of the total angular momentum $J = L + S = 0, 1, 2$ depending on the values of L and S.

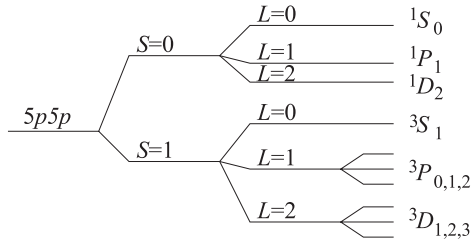

Figure 3.9: Possible spin states of two electrons occupying the $(5p)^2$ orbital. Spin-orbit coupling $\mathbf{L}\cdot\mathbf{S}$ leads to a splitting of the energy levels.

3.4.4 Clebsch-Gordan coefficients

Let us now describe how to add *two* angular momenta, $\hat{\mathbf{j}}_1$ and $\hat{\mathbf{j}}_2$. Since they act on different degrees of freedom,

$$[\vec{\alpha}_1 \cdot \hat{\mathbf{j}}_1, \vec{\alpha}_2 \cdot \hat{\mathbf{j}}_2] = 0 \tag{3.105}$$

for arbitrary vectors $\vec{\alpha}_1$ and $\vec{\alpha}_2$. We have a system of common eigenvectors, $|\eta, j_1, j_2, m_1, m_2\rangle$, where η are the eigenvalues of other observables commuting with $\hat{\mathbf{j}}_1$ and $\hat{\mathbf{j}}_2$. These eigenvectors give the values $\hbar^2 j_1(j_1+1)$ and $\hbar^2 j_2(j_2+1)$ for the observables $\hat{\mathbf{j}}_1^2$ and $\hat{\mathbf{j}}_2^2$, as well as $\hbar m_1$ and $\hbar m_2$ for the observables j_{z1} and j_{z2}. The number of states is $(2j_1+1)(2j_2+1)$. Now we want to construct the eigenstates of the total angular momentum $\hat{\mathbf{J}} = \hat{\mathbf{j}}_1 + \hat{\mathbf{j}}_2$. Since

$$[\hat{\mathbf{J}}, \hat{\mathbf{j}}_1^2] = 0 = [\hat{\mathbf{J}}, \hat{\mathbf{j}}_2^2] \ , \tag{3.106}$$

there exist common eigenstates $|j_1, j_2, J, M\rangle$ for the set of observables $\hat{\mathbf{j}}_1^2$, $\hat{\mathbf{j}}_2^2$, $\hat{\mathbf{M}}^2$ and $\hat{M}_z$. These eigenstates are linear combinations of the individual states,

$$\begin{aligned} |(j_1, j_2)J, M\rangle &= \sum_{m_1,m_2} |j_1, j_2, m_1, m_2\rangle\langle j_1, j_2, m_1, m_2|(j_1, j_2)J, M\rangle \\ &= \sum_{m_1,m_2} |j_1, j_2, m_1, m_2\rangle \begin{pmatrix} j_1 & j_2 \\ m_1 & m_2 \end{pmatrix} \begin{vmatrix} J \\ M \end{vmatrix} . \end{aligned} \tag{3.107}$$

The matrix coefficient is called *Clebsch-Gordan coefficient*. The Clebsch-Gordans disappear when the conditions [4]

$$|j_1 - j_2| \leq J \leq j_1 + j_2 \qquad \text{and} \qquad M = -j_1 - j_2, -j_1 - j_2 + 1, .., j_1 + j_2 \tag{3.108}$$

are not satisfied.

The unitary transformation matrices between decoupled and coupled bases,

$$|(j_1, j_2)J, M\rangle = \mathcal{U}_{\text{CGC}} |j_1, m_1; j_2, m_2\rangle \ , \tag{3.109}$$

are listed in tables of the Clebsch-Gordan coefficients.

Example 34 (*Clebsch-Gordans for the coupling of two spins* $\frac{1}{2}$): For example, for the system consisting of two $\frac{1}{2}$ spins we have,

$$\begin{pmatrix} |(\frac{1}{2},\frac{1}{2})1,+1\rangle \\ |(\frac{1}{2},\frac{1}{2})1,0\rangle \\ |(\frac{1}{2},\frac{1}{2})0,0\rangle \\ |(\frac{1}{2},\frac{1}{2})1,-1\rangle \end{pmatrix} = \begin{pmatrix} 1 & 0 & 0 & 0 \\ 0 & \sqrt{\frac{1}{2}} & \sqrt{\frac{1}{2}} & 0 \\ 0 & \sqrt{\frac{1}{2}} & -\sqrt{\frac{1}{2}} & 0 \\ 0 & 0 & 0 & 1 \end{pmatrix} \begin{pmatrix} |\frac{1}{2},+\frac{1}{2};\frac{1}{2},+\frac{1}{2}\rangle \\ |\frac{1}{2},-\frac{1}{2};\frac{1}{2},+\frac{1}{2}\rangle \\ |\frac{1}{2},+\frac{1}{2};\frac{1}{2},-\frac{1}{2}\rangle \\ |\frac{1}{2},-\frac{1}{2};\frac{1}{2},-\frac{1}{2}\rangle \end{pmatrix} .$$

In the Excs. 3.4.5.4 and 3.4.5.5 we write all possible states of two angular momenta in decoupled and coupled bases. In Excs. 3.4.5.6, 3.4.5.7, we derive the matrix representation of two spins in the decoupled and the coupled base. In 3.4.5.8, and 3.4.5.9 we practice the transformation between decoupled and coupled bases, and in Exc. 3.4.5.10 we verify a rule guaranteeing the unitarity of the Clebsch-Gordan transformation. Finally in 3.4.5.11, 3.4.5.12, and 3.4.5.13 we study $\mathbf{L} \cdot \mathbf{S}$-coupling.

3.4.4.1 Coupling of three angular moments

Three angular momenta can be coupled in three different configurations: First j_1 with j_2, then the total spin $(j_1, j_2)j_{12}$ with the third one j_3. We use the notation $|[(j_1, j_2)j_{12}, j_3]J\rangle$ or $|[(j_1, j_3)j_{13}, j_2]J\rangle$ or $|[(j_2, j_3)j_{23}, j_1]J\rangle$. The recoupling of three spins

$$\begin{array}{ccccc} \mathbf{j}_1 & + & \mathbf{j}_2 & = & \mathbf{j}_{12} \\ + & & & & + \\ \mathbf{j}_3 & & & & \mathbf{j}_3 \\ = & & & & = \\ \mathbf{j}_{13} & + & \mathbf{j}_2 & = & \mathbf{J} \end{array} \tag{3.110}$$

[4] The Clebsch-Gordans are related to the $(3j)$ de Wigner symbols.

is described by $\{6j\} = \begin{Bmatrix} j_1 & j_3 & j_{13} \\ J & j_{12} & j_2 \end{Bmatrix}$-symbols, for example,

$$|[(j_1, j_2)j_{12}, j_3]J\rangle = \sum_{j_{13}} \{6j\} |[(j_1, j_3)j_{13}, j_2]J\rangle \ . \tag{3.111}$$

3.4.4.2 Notation for atomic states with LS-coupling

In an atom, the spins of the electrons often couple to a total spin, $\mathbf{S} = \sum_k \mathbf{s}_k$, and separately the orbital angular momenta to a total orbital angular momentum, $\mathbf{L} = \sum_k \mathbf{l}_k$. These two total spins now couple to a total angular momentum, $\mathbf{J} = \mathbf{L}+\mathbf{S}$. When this **LS**-*coupling* happens, the following notation is used to characterize the electronic states in atoms:

$$^{2S+1}L_J \ . \tag{3.112}$$

For historical reasons the orbital angular momentum quantum number $L = 0, 1, 2, 3, ...$ is generally labeled by letters $L = S, P, D, F, ...$

3.4.4.3 jj-coupling

There is also the case that for each electron its spin couples to its own orbital angular momentum, $\mathbf{j}_k = \mathbf{l}_k + \mathbf{s}_k$, before coupling to the total angular momenta of other electrons, $\mathbf{J} = \sum_k \mathbf{j}_k$. This is called **jj**-*coupling*. In the case of two electrons the recoupling of the four involved spins

$$\begin{array}{ccccc} \mathbf{l}_1 & + & \mathbf{l}_2 & = & \mathbf{L} \\ + & & + & & + \\ \mathbf{s}_1 & + & \mathbf{s}_2 & = & \mathbf{S} \\ = & & = & & = \\ \mathbf{j}_1 & + & \mathbf{j}_2 & = & \mathbf{J} \end{array} \tag{3.113}$$

is described by $\{9j\} = \begin{Bmatrix} l_1 & l_2 & L \\ s_1 & s_2 & S \\ j_1 & j_2 & J \end{Bmatrix}$-symbols,

$$|[(l_1, s_1)j_1, (l_2, s_2)j_2]J\rangle = \sum_{L,S} \{9j\} |[(l_1, l_2)L, (s_1, s_2)S]J\rangle \ . \tag{3.114}$$

3.4.5 Exercises

3.4.5.1 Ex: Addition/subtraction of angular momenta

Show that $\hat{\mathbf{j}}_1 + \hat{\mathbf{j}}_2$ is an angular momentum, but not $\hat{\mathbf{j}}_1 - \hat{\mathbf{j}}_2$.

3.4.5.2 Ex: CSCO for coupled angular momenta

Be $\hat{\mathbf{J}} = \hat{\mathbf{j}}_1 + \hat{\mathbf{j}}_2$. Show that $\{\hat{\mathbf{j}}_1^2, \hat{\mathbf{j}}_2^2, \hat{\mathbf{J}}^2, \hat{J}_z\}$ is a CSCO; that is, show that
a. $\hat{\mathbf{J}}^2$ commutes with $\hat{\mathbf{j}}_1^2$ and $\hat{\mathbf{j}}_2^2$;
b. $\hat{\mathbf{J}}^2$ does not commute with $\hat{j}_{1z}$ or $\hat{j}_{2z}$ and that we can not specify m_{j1} or m_{j2} together with J.

3.4.5.3 Ex: Multiplicity of coupled angular momenta

Verify $\# = (2j_1 + 1)(2j_2 + 1)$ within the coupled representation.

3.4.5.4 Ex: Possible states of two (de-)coupled angular momenta

Find all possible states with the angular momenta $j_1 = 1$ and $j_2 = 1/2$ in decoupled and coupled pictures.

3.4.5.5 Ex: Fine and hyperfine structure of the rubidium atom ^{85}Rb

1. The rubidium atom ^{85}Rb has one valence electron. In the first excited state this electron has the orbital angular momentum, $L = 1$. What are the possible states?
2. In the fundamental state of this atom the total electronic angular momentum J couples with the spin of the nucleus, $I = 5/2$, to form the total angular momentum $\mathbf{F} = \mathbf{J} + \mathbf{I}$. Determine the possible values for the angular momentum F and the magnetic quantum number m_F.

3.4.5.6 Ex: Expansion of the hyperfine structure of the rubidium atom ^{87}Rb

Determine for the states $S_{1/2}$ and $P_{3/2}$ of an atom with nuclear spin $I = 3/2$ and hyperfine coupling $\hat{\mathbf{J}} \cdot \hat{\mathbf{I}}$ how the eigenstates of the coupled base expand into the decoupled base. Do not consider external magnetic fields.

3.4.5.7 Ex: Transition amplitudes between Zeeman sub-states

a. We consider the atom of ^{87}Rb having the nuclear angular momentum $I = 3/2$. What are the possible hyperfine states F resulting from a coupling of I with the total electronic state angular momentum of the ground state $^2S_{1/2}$? What are the possible Zeeman sub-states of F?
b. What are the possible hyperfine states F' resulting from a coupling of I with the total electronic angular momentum of the excited state $^2P_{3/2}$, $F' = 2$? What are the possible Zeeman sub-states of F'?
c. A transition between a ground hyperfine state and an excited hyperfine state can be described by a coupling of the total angular momentum F with the angular momentum of the photon κ forming the angular momentum of the excited state F'. To see this, we now consider the levels $F = 1$ and $F' = 2$. Expand the coupled angular momentum $|(F, \kappa)F', m_{F'}\rangle = |(1, 1)2, m_{F'}\rangle$ on a decoupled basis for every possible value $m_{F'}$. Use the table in Fig. 3.10 to determine the Clebsch-Gordan coefficients.
Note: The Clebsch-Gordans only compare the oscillator strengths of transitions between Zeeman sub-states of a given set (F, F'). In order to compare the oscillator strengths to other transitions (F, F') it is necessary to calculate $6j$-coefficients.

3.4.5.8 Ex: Gymnastics of angular momentum operators

Consider the problem of adding angular momenta $j_1 = 1$ and $j_2 = 1/2$:
a. What are the possible values of M and J, in which $\hat{J}^2|J, M\rangle = J(J + 1)\hbar^2|J, M\rangle$ and $J_z|j, m\rangle = M\hbar|J, M\rangle$?

b. What are the degeneracy $g_{j_1,j_2}(m)$?
c. Find the base states $\{|J,M\rangle\}$, which are common to the operators $\mathbf{j}_1^2$, $\mathbf{j}_2^2$, $\mathbf{J}$, J_z, expanded in the base $\{|j_1,m_1\rangle \otimes |j_2,m_2\rangle\}$ of the eigenstates of $\mathbf{j}_1^2$, $\mathbf{j}_2^2$, j_{1z}, j_{2z}.

3.4.5.9 Ex: (Un-)coupled bases of the spherical harmonics

Expand the triplet state ${}^3P_J$ of strontium in a decoupled basis and write down the transformation matrix between the bases.

3.4.5.10 Ex: Properties of Clebsch-Gordan coefficients

Given the momenta j_1 and j_2, and C_{m_1,m_2} denoting the Clebsch-Gordan coefficients, prove that $\sum_{m_1,m_2} |C_{m_1,m_2}|^2 = 1$.

3.4.5.11 Ex: Spin-orbit coupling

a. Show that the operator $\hat{\mathbf{L}} \cdot \hat{\mathbf{S}}$ associated with the spin-orbit coupling, satisfies the relation $\hat{\mathbf{L}} \cdot \hat{\mathbf{S}} = \hat{L}_z\hat{S}_z + (\hat{L}_+\hat{S}_- + \hat{L}_-\hat{S}_+)/2$.
Obtain the matrix representation of the operator $\mathbf{L} \cdot \mathbf{S}$, considering the bases:
b. $\{|m_L\rangle \otimes |m_S\rangle\}$ of the eigenstates which are common to the operators $\hat{\mathbf{L}}^2$, $\hat{\mathbf{S}}^2$, $\hat{L}_z$, $\hat{S}_z$;
c. $\{|J,M\rangle\}$, which is associated with the operators $\hat{\mathbf{L}}^2$, $\hat{\mathbf{S}}^2$, $\hat{\mathbf{J}}^2$, $\hat{J}_z$.
d. Give the explicit matrices for the case $L = 1$ and $S = \frac{1}{2}$ in the representations (b) and (c) and verify that the two representations yield the same eigenvalue spectrum.

3.4.5.12 Ex: Expansion of the spin-orbit coupling

Consider the problem of adding the orbital angular momentum ℓ and a spin 1/2. Obtain the $2\ell + 1$ states $|\ell + 1/2, m_j\rangle$, in addition to the 2ℓ states $|\ell - 1/2, m_j\rangle$ (which constitute a common basis for the operators $\mathbf{l}_1^2$, $\mathbf{s}_2^2$, $\mathbf{j}^2$, j_z), expanded in the base $|m_1, m_2\rangle$ of the eigenstates of the operators $\mathbf{l}^2$, $\mathbf{s}^2$, l_z, s_z. You can simplify the procedure by deriving two recurrence relationships from which the desired states follow [5].

3.4.5.13 Ex: External product of two spins

Derive the matrix representation of the spin-orbit coupling operator $\mathbf{L} \cdot \mathbf{S}$ for $L = 1$ and $S = 1/2$ from the definition of the outer product.

3.4.5.14 Ex: Coupling three spins

Express the states of three coupled $\frac{1}{2}$ spins in the uncoupled basis using the Clebsch-Gordan coefficients. Proceed by first coupling two spins and then coupling the result to the third spin. Compare the dimensions of the Hilbert spaces in both basis and discuss your findings.

[5] See Cohen-Tannoudji, Vol.2, Complement A_X.

3.5 Further reading

C. Cohen-Tannoudji, B. Diu, F. Laloe, Wiley Interscience, *Quantum mechanics, vol. 1,2* [ISBN]

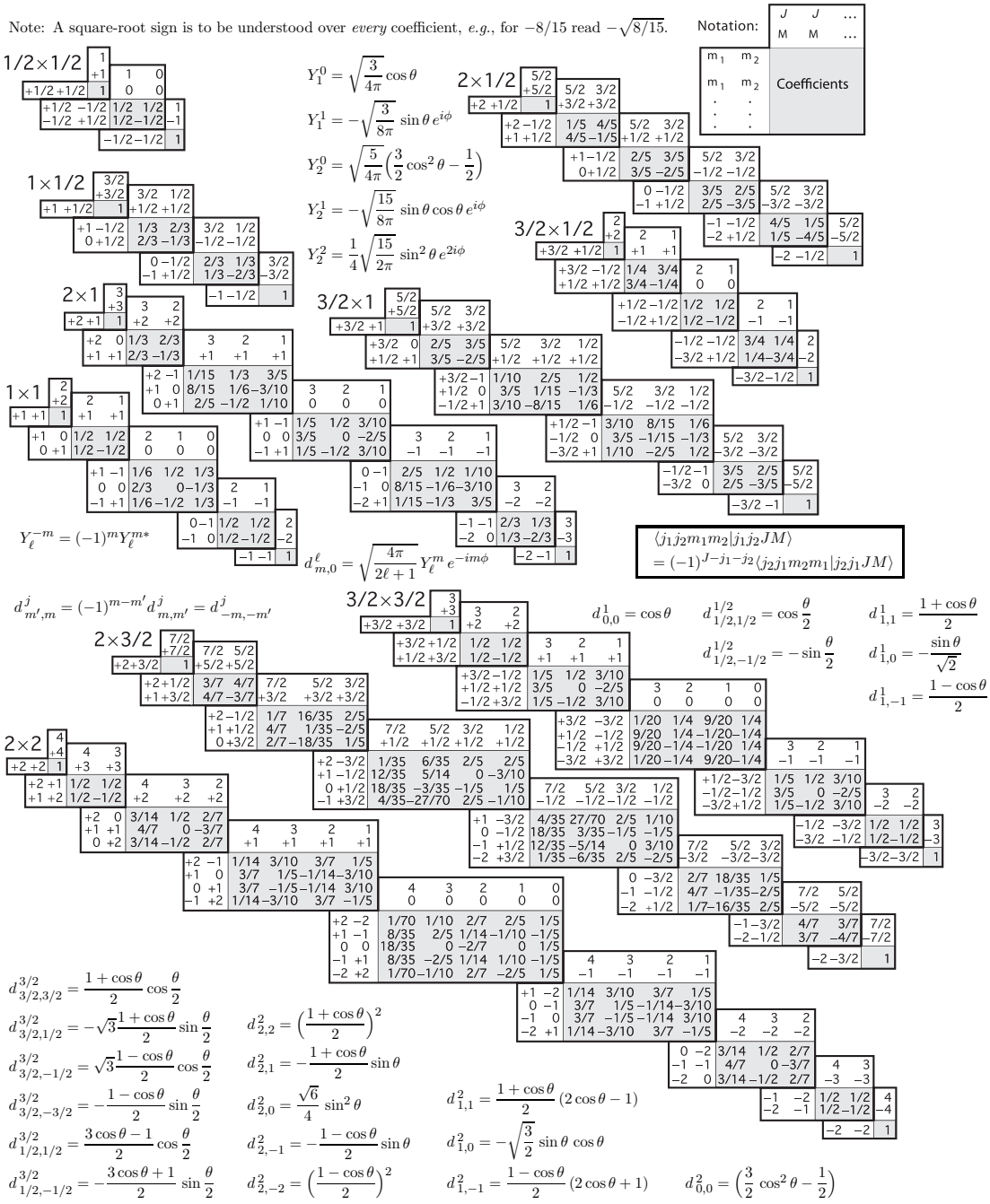

Figure 3.10: Clebsch-Gordan coefficients.

Chapter 4

Periodic systems

Many physical systems treat quantum particles in periodic potential. Examples are electrons in crystals or cold atoms in optical lattices. The periodicity gives rise to a wealth of new phenomena, such as Bragg scattering, the formation of energy bands, Mott insulators, or Bloch oscillations. Various theoretical approaches have been developed leading to a deep understanding of the features of crystals, metals, and optical lattices for atomic gases.

In the following sections we will mainly focus on the Bloch model, which is based on introducing periodic boundary conditions to the Schrödinger equation. In the Secs. 4.1 we will give a brief introduction into the Bloch model for electrons in solids, where the periodicity is imposed by the crystalline structure of the material. We will, however, not go into details leaving a comprehensive treatment to specialized textbooks [30, 469]. Then, in Sec. 4.2, we will dig deeper into the symmetries imposed by periodic potentials. In order to keep the formalism simple, we will concentrate on one-dimensional geometries and mostly on sinusoidal potentials. Such potentials are realized, for example, by optical lattices formed by counterpropagating laser beams, which under certain circumstances are capable of trapping atomic gases. The physical realization of these lattices, which can be realized with nearly perfect periodicity, have permitted the experimental observation of phenomena which had been elusive in solid state physics. For this situation we will develop a powerful formalism capable of computing energy spectra and quantum transport phenomena.

4.1 The Bloch model for electrons

The motion of an electron inside a crystal is ruled by a spatially periodic potential $V(\mathbf{r})$ originating from the positively charged crystal atoms and the mean field produced by the quasi-free electrons,

$$V(\mathbf{r}) = V(\mathbf{r} + \mathbf{R}) \ , \tag{4.1}$$

where $\mathbf{R}$ is a vector connecting two arbitrarily chosen atoms of the lattice. With the Hamiltonian

$$\hat{H} = -\frac{\hbar^2}{2m}\nabla^2 + V(\mathbf{r}) \tag{4.2}$$

we can write the Schrödinger equation,

$$\hat{H}\psi(\mathbf{r}) = E\psi(\mathbf{r}) \ . \tag{4.3}$$

Since V and ∇ are invariant under translations $U_{\rm tr}(\mathbf{R})\psi(\mathbf{r}) \equiv \psi(\mathbf{r}+\mathbf{R})$ by a fixed distance $\mathbf{R}$, where the translation operator has been defined in Eq. (1.282), we have,

$$\hat{H}U_{\rm tr}(\mathbf{R})\psi(\mathbf{r}) = EU_{\rm tr}(\mathbf{R})\psi(\mathbf{r}) \ . \tag{4.4}$$

That is, for a non-degenerate eigenvalue [1],

$$\psi(\mathbf{r}+\mathbf{R}) = f(\mathbf{R})\psi(\mathbf{r}) \ . \tag{4.5}$$

This relation holds for all vectors $\mathbf{R}$ of the lattice, such that,

$$f(\mathbf{R}_1+\mathbf{R}_2)\psi(\mathbf{r}) = \psi(\mathbf{r}+\mathbf{R}_1+\mathbf{R}_2) = f(\mathbf{R}_1)\psi(\mathbf{r}+\mathbf{R}_2) = f(\mathbf{R}_1)f(\mathbf{R}_2)\psi(\mathbf{r}) \ . \tag{4.6}$$

The relationship $f(\mathbf{R}_1+\mathbf{R}_2) = f(\mathbf{R}_1)f(\mathbf{R}_2)$ is satisfied by the ansatz $f(\mathbf{R}) \equiv e^{\imath\mathbf{k}\cdot\mathbf{R}}$, where $\mathbf{k}$ is an arbitrary vector of reciprocal space. We get the famous *Bloch theorem*,

$$\boxed{\psi_{\mathbf{k}}(\mathbf{r}+\mathbf{R}) = e^{\imath\mathbf{k}\cdot\mathbf{R}}\psi_{\mathbf{k}}(\mathbf{r})} \ , \tag{4.7}$$

which represents a necessary condition for any eigenfunction $\psi_{\mathbf{k}}$ of the Schrödinger equation with periodic potential. Bloch's theorem simply postulates that, apart from a phase factor, the wavefunction has the same periodicity as the potential.

The *Bloch function*,

$$\boxed{\psi_{\mathbf{k}}(\mathbf{r}) \equiv u_{\mathbf{k}}(\mathbf{r})e^{\imath\mathbf{k}\cdot\mathbf{r}} \qquad \text{with} \qquad u_{\mathbf{k}}(\mathbf{r}+\mathbf{R}) = u_{\mathbf{k}}(\mathbf{r})} \ , \tag{4.8}$$

automatically satisfies Bloch's theorem. That is, the wave function of the electron ψ is a plane wave $e^{\imath\mathbf{k}\cdot\mathbf{r}}$ modulated by a function $u_{\mathbf{k}}$ having the same periodicity as the lattice [478]. Although the vector of the electronic wave is arbitrary, it is possible (and useful) to restrict its value to the first *Brillouin zone* defined by $\mathbf{k} \in [-\pi/\mathbf{a}, \pi/\mathbf{a}]$, where $\mathbf{a}$ is an elementary vector of the lattice. The reason is that we can reduce a wavevector $\mathbf{k}$ in a wavefunction trespassing the first Brillouin zone by an appropriate vector $\mathbf{G}$ of the *reciprocal lattice*,

$$\mathbf{k}' = \mathbf{k} + \mathbf{G} \ , \tag{4.9}$$

yielding,

$$\psi_{\mathbf{k}}(\mathbf{r}) = u_{\mathbf{k}}(\mathbf{r})e^{\imath\mathbf{k}\cdot\mathbf{r}} = u_{\mathbf{k}}(\mathbf{r})e^{-\imath\mathbf{G}\cdot\mathbf{r}}e^{\imath\mathbf{k}'\cdot\mathbf{r}} \ . \tag{4.10}$$

We now define another function $u_{\mathbf{k}'}(\mathbf{r}) \equiv u_{\mathbf{k}}(\mathbf{r})e^{-\imath\mathbf{G}\cdot\mathbf{r}}$, which also satisfies the requirement (4.8), knowing that $\mathbf{G}\cdot\mathbf{R} = n2\pi$, we see,

$$u_{\mathbf{k}'}(\mathbf{r}+\mathbf{R}) = u_{\mathbf{k}}(\mathbf{r}+\mathbf{R})e^{-\imath\mathbf{G}\cdot(\mathbf{r}+\mathbf{R})} = u_{\mathbf{k}}(\mathbf{r})e^{-\imath\mathbf{G}\cdot\mathbf{r}} = u_{\mathbf{k}'}(\mathbf{r}) \ . \tag{4.11}$$

Hence,

$$\psi_{\mathbf{k}}(\mathbf{r}) = u_{\mathbf{k}'}(\mathbf{r})e^{\imath\mathbf{k}'\cdot\mathbf{r}} = \psi_{\mathbf{k}+\mathbf{G}}(\mathbf{r}) \ . \tag{4.12}$$

[1] This also holds true for degenerate eigenvalues if we choose suitable basis of eigenvectors.

4.1.1 Tight binding approximation for quasi-bound electrons

We now assume that the behavior of the electron near an atom is not influenced a lot by atoms further away, so that it is pretty much localized. It is then sensible to expand its wavefunction into states $w(\mathbf{r})$ localized near atoms,

$$\psi_{\mathbf{k}}(\mathbf{r}) = \sum_{j\in\text{lattice}} c_j(\mathbf{k}) w(\mathbf{r}-\mathbf{R}_j) \ . \tag{4.13}$$

In other words, the electron is exposed to a potential $V_{\text{at}}(\mathbf{r}-\mathbf{R}_j)$ in the vicinity of the atom itself located at the position $\mathbf{R}_j$, and it is described by the eigenfunction $w(\mathbf{r}-\mathbf{R}_j)$ with energy E_0,

$$\left[-\frac{\hbar^2}{2m}\nabla^2 + V_{\text{at}}(\mathbf{r}-\mathbf{R}_j)\right] w(\mathbf{r}-\mathbf{R}_j) = E_0 w(\mathbf{r}-\mathbf{R}_j) \ . \tag{4.14}$$

Even so, the function $\psi_{\mathbf{k}}(\mathbf{r})$ must satisfy Bloch's theorem. This is the case when $c_j(\mathbf{k}) = e^{\imath\mathbf{k}\cdot\mathbf{R}_j}$ and therefore,

$$\boxed{\psi_{\mathbf{k}}(\mathbf{r}) = \frac{1}{\sqrt{N}} \sum_{j\in\text{lattice}} e^{\imath\mathbf{k}\cdot\mathbf{R}_j} w(\mathbf{r}-\mathbf{R}_j)} \ . \tag{4.15}$$

The functions $w(\mathbf{r}-\mathbf{R}_j)$ are called *Wannier functions*. Only, if the spatial extend of $w(\mathbf{r})$ is smaller than the lattice spacing, the electron becomes completely bound to a particular atom.

Example 35 (*Ansatz for a quasi-bound electron wavefunction*): The ansatz (4.15) satisfies Bloch's theorem because,

$$\begin{aligned}\psi_{\mathbf{k}}(\mathbf{r}+\mathbf{R}_j) &= \sum_i e^{\imath\mathbf{k}\cdot\mathbf{R}_i} w(\mathbf{r}-(\mathbf{R}_i-\mathbf{R}_j)) \\ &= e^{\imath\mathbf{k}\cdot\mathbf{R}_j} \sum_i e^{\imath\mathbf{k}\cdot(\mathbf{R}_i-\mathbf{R}_j)} w(\mathbf{r}-(\mathbf{R}_i-\mathbf{R}_j)) = e^{\imath\mathbf{k}\cdot\mathbf{R}_j}\psi_{\mathbf{k}}(\mathbf{r}) \ .\end{aligned}$$

We now calculate the energy $E(\mathbf{k})$ of an electron with the wavevector $\mathbf{k}$ inserting the function $\psi_{\mathbf{k}}(\mathbf{r})$ of (4.15) in the Schrödinger equation (4.3) and obtain,

$$\left[-\frac{\hbar^2}{2m}\nabla^2 + V(\mathbf{r})\right] \sum_j e^{\imath\mathbf{k}\cdot\mathbf{R}_j} w(\mathbf{r}-\mathbf{R}_j) = E(\mathbf{k}) \sum_j e^{\imath\mathbf{k}\cdot\mathbf{R}_j} w(\mathbf{r}-\mathbf{R}_j) \ . \tag{4.16}$$

$V(\mathbf{r})$ is the potential energy of the electron illustrated in Fig. 4.1 together with the energy $V_{\text{at}}(\mathbf{r}-\mathbf{R}_j)$ of a free electron.

Substituting the kinetic energy term of (4.16) by the kinetic energy of (4.14), we calculate,

$$\sum_j e^{\imath\mathbf{k}\cdot\mathbf{R}_j} [-V_{\text{at}}(\mathbf{r}-\mathbf{R}_j) + E_0 + V(\mathbf{r}) - E(\mathbf{k})] w(\mathbf{r}-\mathbf{R}_j) = 0 \ . \tag{4.17}$$

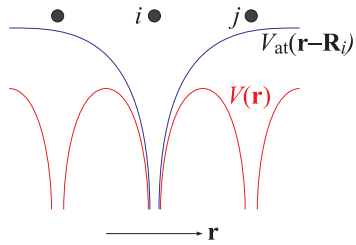

Figure 4.1: Potential energy $V(\mathbf{r})$ of a crystal electron (red) and potential energy $V_{\rm at}(\mathbf{r}-\mathbf{R}_j)$ of the electron of a free atom (blue).

Now, multiplying this equation with $\psi^*_{\mathbf{k}}(\mathbf{r}) = \sum_i e^{-\imath\mathbf{k}\cdot\mathbf{R}_i} w^*(\mathbf{r}-\mathbf{R}_i)$ and integrating over the volume of the crystal, we obtain,

$$[E(\mathbf{k}) - E_0] \sum_{i,j} e^{\imath\mathbf{k}\cdot(\mathbf{R}_j-\mathbf{R}_i)} \int w^*(\mathbf{r}-\mathbf{R}_i) w(\mathbf{r}-\mathbf{R}_j) d^3r \tag{4.18}$$
$$= \sum_{i,j} e^{\imath\mathbf{k}\cdot(\mathbf{R}_j-\mathbf{R}_i)} \int w^*(\mathbf{r}-\mathbf{R}_i)[V(\mathbf{r}) - V_{\rm at}(\mathbf{r}-\mathbf{R}_j)] w(\mathbf{r}-\mathbf{R}_j) d^3r \ .$$

The Wannier functions $w^*(\mathbf{r}-\mathbf{R}_i)$ and $w(\mathbf{r}-\mathbf{R}_j)$ overlap only a little, even for adjacent atoms. That is, they are nearly orthogonal, such that we can neglect the terms $i \neq j$ on the left side. The sum then corresponds to the number N of sites in the lattice. On the right side, we can not neglect the terms involving other sites, because even if the wavefunctions of adjacent sites overlap little, the contribution of the potential difference $|V(\mathbf{r}) - V_{\rm at}(\mathbf{r}-\mathbf{R}_j)|$ is much lower for $\mathbf{r} = \mathbf{R}_j$ than for $\mathbf{r} = \mathbf{R}_i$. On the other hand, as the wavefunctions $w(\mathbf{r}-\mathbf{R}_j)$ disappear quickly when $|\mathbf{r}-\mathbf{R}_j| > |\mathbf{R}_m - \mathbf{R}_j|$, we can focus on adjacent sites (called $\mathbf{R}_m$),

$$N[E(\mathbf{k}) - E_0] = N \int w^*(\mathbf{r}-\mathbf{R}_j)[V(\mathbf{r}) - V_{\rm at}(\mathbf{r}-\mathbf{R}_j)] w(\mathbf{r}-\mathbf{R}_j) d^3r \tag{4.19}$$
$$+ N \sum_{m=\text{adjacent}} e^{\imath\mathbf{k}\cdot(\mathbf{R}_j-\mathbf{R}_m)} \int w^*(\mathbf{r}-\mathbf{R}_m)[V(\mathbf{r}) - V_{\rm at}(\mathbf{r}-\mathbf{R}_j)] w(\mathbf{r}-\mathbf{R}_j) d^3r \ .$$

Example 36 (*Eigenenergies for s orbitals*): Now we further suppose that the eigenfunction $w(\mathbf{r})$ exhibits radial symmetry corresponding to an s orbital. We obtain for the eigenvalues from the Schrödinger equation,

$$E(\mathbf{k}) = E_0 - \alpha - \mathbf{G}amma \sum_{m \text{ adjacent of } j} e^{\imath\mathbf{k}\cdot(\mathbf{R}_j-\mathbf{R}_m)} \tag{4.20}$$
$$\text{with} \quad \alpha = \int w^*(\mathbf{r}-\mathbf{R}_j)[V_{\rm at}(\mathbf{r}-\mathbf{R}_j) - V(\mathbf{r})] w(\mathbf{r}-\mathbf{R}_j) d^3r$$
$$\text{and} \quad \mathbf{G}amma = \int w^*(\mathbf{r}-\mathbf{R}_m)[V_{\rm at}(\mathbf{r}-\mathbf{R}_j) - V(\mathbf{r})] w(\mathbf{r}-\mathbf{R}_j) d^3r \ .$$

The interpretation is as follows: The combination of the atoms in a lattice produces an energy displacement α. In addition, it generates a spitting into a continuous band of energies as a function of reduced wavevector $\mathbf{k}$.

4.1.1.1 Wannier functions

Wannier functions have been defined in (4.15) as a new basis of states localized near atoms in which the electronic wavefunction can be expanded. The transformation (4.15) can be inverted,

$$\boxed{w(\mathbf{r}-\mathbf{R}_j)=\frac{1}{\sqrt{N}}\sum_{\mathbf{k}} e^{-\imath\mathbf{k}\cdot\mathbf{R}_j}\psi_{\mathbf{k}}(\mathbf{r})}=\frac{V}{(2\pi)^d}\int_{BZ} e^{-\imath\mathbf{k}\cdot\mathbf{R}_j}\psi_{\mathbf{k}}(\mathbf{r})d^3k\ , \tag{4.21}$$

which can be checked quickly for one dimension ($R_j = ja$) by inserting the expression into one another,

$$\tfrac{1}{\sqrt{N}}\sum_j e^{\imath kja}w_j(z)=\tfrac{1}{N}\sum_{k'}\sum_j e^{\imath(k-k')ja}\psi_k(z)=\sum_{k'}\delta_{k,k'}\psi_k(z)=\psi_k(z)\ . \tag{4.22}$$

According to (4.21), Wannier functions of an isolated band are defined in terms of Bloch functions (4.8) of the same band. $\mathbf{R}_j$ are lattice points and V the volume of a unit cell. Wannier functions about different lattice points are orthonormal, as will be verified in Exc. 4.1.5.1.

Example 37 (*Wannier function in one dimension*): For example, in one dimension $\psi_k(z) = N^{-1/2}u_0(z)e^{\imath kz}$ for N atoms on a line of lattice constant a, so that $z_j = ja$,

$$w(z-z_n)=\frac{1}{\sqrt{N}}\sum_{k\in[-a/2,a/2]} e^{-\imath kz_j}\psi_k(z)=\frac{1}{N}\sum_k e^{\imath k(z-ja)}u_0(z)$$

$$\longrightarrow \frac{a}{2\pi}\int_{-\pi/a}^{\pi/a} e^{\imath k(z-ja)}u_0(z)dk\simeq\frac{a}{2\pi}u_0(z)\left.\frac{e^{\imath k(z-ja)}}{\imath(z-ja)}\right|_{-\pi/a}^{\pi/a}=u_0(z)\frac{\sin\frac{\pi}{a}(z-z_j)}{\frac{\pi}{a}(z-z_j)}\ .$$

4.1.2 Approximation for quasi-free electrons

Here we assume an essentially homogeneous potential acting on the free electrons and consider the impact of the periodic lattice as a small perturbation. The periodic potential can be decomposed into a Fourier series by the vectors $\mathbf{G}$ of the reciprocal lattice,

$$V(\mathbf{r})=\sum_{\mathbf{G}} U_{\mathbf{G}}e^{\imath\mathbf{G}\cdot\mathbf{r}}\ . \tag{4.23}$$

Consequently, we can make for Bloch functions (4.10) the following periodic ansatz,

$$\psi_{\mathbf{k}}(\mathbf{r})=u_{\mathbf{k}}(\mathbf{r})e^{\imath\mathbf{k}\cdot\mathbf{r}}\qquad\text{with}\qquad u_{\mathbf{k}}(\mathbf{r})=\tfrac{1}{\sqrt{V_c}}\sum_{\mathbf{G}} u_{\mathbf{G}}(\mathbf{k})e^{\imath\mathbf{G}\cdot\mathbf{r}}\ , \tag{4.24}$$

where V_c is the volume of the crystal.

Without periodic potential, the eigenfunctions would be those of a free particle,

$$\psi_{\mathbf{k}}(\mathbf{r})=\tfrac{1}{V_c}e^{\imath\mathbf{k}\cdot\mathbf{r}} \tag{4.25}$$

with the eigenenergies

$$E_0(\mathbf{k}) = V_0 + \frac{\hbar^2 k^2}{2m} \ . \tag{4.26}$$

Inserting the functions (4.23) and (4.24) in the Schrödinger equation, we obtain,

$$\left[-\tfrac{\hbar^2}{2m}\nabla^2 + \sum_{\mathbf{G}''} U_{\mathbf{G}''} e^{\imath \mathbf{G}''\cdot\mathbf{r}}\right] \tfrac{1}{\sqrt{V_c}} e^{\imath\mathbf{k}\cdot\mathbf{r}} \sum_{\mathbf{G}'} u_{\mathbf{G}'}(\mathbf{k}) e^{\imath\mathbf{G}'\cdot\mathbf{r}} = E(\mathbf{k}) \tfrac{1}{\sqrt{V_c}} e^{\imath\mathbf{k}\cdot\mathbf{r}} \sum_{\mathbf{G}} u_{\mathbf{G}'}(\mathbf{k}) e^{\imath\mathbf{G}'\cdot\mathbf{r}} \ , \tag{4.27}$$

that is,

$$\begin{aligned} &\tfrac{1}{\sqrt{V_c}} \sum_{\mathbf{G}'} \left[-\tfrac{\hbar^2}{2m}(\mathbf{k}+\mathbf{G}')^2 - E(\mathbf{k})\right] u_{\mathbf{G}'}(\mathbf{k}) e^{\imath(\mathbf{k}+\mathbf{G}')\cdot\mathbf{r}} \\ &\quad + \tfrac{1}{\sqrt{V_c}} \sum_{\mathbf{G}''} U_{\mathbf{G}''} e^{\imath\mathbf{G}''\cdot\mathbf{r}} \sum_{\mathbf{G}'} u_{\mathbf{G}'}(\mathbf{k}) e^{\imath(\mathbf{k}+\mathbf{G}')\cdot\mathbf{r}} = 0 \ . \end{aligned} \tag{4.28}$$

Now multiplying with $\frac{1}{\sqrt{V_c}} e^{\imath(\mathbf{k}+\mathbf{G})\cdot\mathbf{r}}$ and integrating over the volume of the crystal (knowing $\frac{1}{V_c}\int_{V_c} e^{\imath\mathbf{G}\cdot\mathbf{r}} dV = \delta_{\mathbf{G},0}$), we obtain,

$$\left[\tfrac{\hbar^2}{2m}(\mathbf{k}+\mathbf{G})^2 - E(\mathbf{k})\right] u_{\mathbf{G}}(\mathbf{k}) + \sum_{\mathbf{G}'} U_{\mathbf{G}-\mathbf{G}'} u_{\mathbf{G}'}(\mathbf{k}) = 0 \ , \tag{4.29}$$

for any value of $\mathbf{G}$.

To estimate the dependence of the Fourier components $u_{\mathbf{G}}(\mathbf{k})$ for $\mathbf{G} \neq 0$ we insert the unperturbed eigenenergies into the equation (4.29) only considering, in the sum over $\mathbf{G}'$, the terms of the first perturbative order, that is, those containing U_0 or $u_0(\mathbf{k})$,

$$\begin{aligned} &\frac{\hbar^2}{2m}[(\mathbf{k}+\mathbf{G})^2 - k^2] u_{\mathbf{G}}(\mathbf{k}) - U_0 u_{\mathbf{G}}(\mathbf{k}) + U_0 u_{\mathbf{G}}(\mathbf{k}) + U_{\mathbf{G}} u_0(\mathbf{k}) = 0 \\ &\implies \quad u_{\mathbf{G}}(\mathbf{k}) = \frac{U_{\mathbf{G}} u_0(\mathbf{k})}{\frac{\hbar^2}{2m}[k^2 - (\mathbf{k}+\mathbf{G})^2]} \ . \end{aligned} \tag{4.30}$$

Since the Fourier coefficients $U_{\mathbf{G}}$ have, for $\mathbf{G} \neq 0$, small values, the function $u_{\mathbf{G}}(\mathbf{k})$ is not negligible only for $k^2 \simeq (\mathbf{k}+\mathbf{G})^2$ that is,

$$-2\mathbf{k}\cdot\mathbf{G} \simeq |\mathbf{G}|^2 \ . \tag{4.31}$$

We now want to find out the meaning of this condition ...

For the coefficients $u_0(\mathbf{k})$ and $u_{\mathbf{G}}(\mathbf{k})$ we obtain,

$$\begin{aligned} \left[\tfrac{\hbar^2}{2m}k^2 - E(\mathbf{k})\right] u_0(\mathbf{k}) + U_0 u_0(\mathbf{k}) + U_{-\mathbf{G}}(\mathbf{k}) u_{\mathbf{G}}(\mathbf{k}) = 0 \\ \left[\tfrac{\hbar^2}{2m}k^2 - E(\mathbf{k})\right] u_{\mathbf{G}}(\mathbf{k}) + U_{\mathbf{G}} u_0(\mathbf{k}) + U_0(\mathbf{k}) u_{\mathbf{G}}(\mathbf{k}) = 0 \ . \end{aligned} \tag{4.32}$$

From this follows,

$$\left[\tfrac{\hbar^2}{2m}k^2 + U_0 - E(\mathbf{k})\right]^2 = U_{\mathbf{G}} U_{-\mathbf{G}} = 0 \ . \tag{4.33}$$

Since the potential $U(\mathbf{r})$ is real, $U_{-\mathbf{G}} = U_{\mathbf{G}}^*$. Therefore, introducing the eigenenergies $E_0(\mathbf{k})$ of free electrons (4.26),

$$E(\mathbf{k}) = E_0(\mathbf{k}) \pm |U_{\mathbf{G}}| \ . \tag{4.34}$$

Under the influence of the periodic perturbation potential we find at the surfaces of a Brillouin zone an energy splitting developing a forbidden gap in the spectrum. We can understand this observation as follows: In the crystal all electronic waves with wavevectors ending on a surface of a Brillouin zone are reflected by Bragg reflection. In the example of a one-dimensional lattice we understand that the superposition of an incident wave ($k = n\pi/a$) with the reflected one ($k = -n\pi/a$) produces a standing electronic probability density wave ρ being proportional to $\rho_1 \propto \cos^2 n\pi/a$ or $\rho_2 \propto \sin^2 n\pi/a$. The charge density ρ_1 is maximal at the location of the atom in this site, which corresponds to an increased interaction energy; the density ρ_2 is minimal at the location of the atom. This explains the splitting.

The Bloch model can explain many properties of metals, semiconductors and insulators.

4.1.3 The Kronig-Penney model

The *Kronig-Penney model* describes the band structure of a lattice. Let us assume a periodic potential of rectangular wells with valleys of widths a and peaks of widths b,

$$V(x) = U_0 \theta_{\mathrm{mod}(x,a+b)\in[a,a+b]} \ . \tag{4.35}$$

Inserting into the Schrödinger equation the plane wave ansatz $\psi = Ae^{\imath Kx} + Be^{-\imath Kx}$ for the wavefunction in the valley, $0 < x < a$, and $\psi = Ce^{Qx} + De^{-Qx}$ in the peak, $-b < x < 0$, we obtain $\varepsilon = \hbar^2 K^2/2m$ and $U_0 - \varepsilon = \hbar^2 Q^2/2m$. Choosing the constants A, B, C, D such that ψ and $\dot{\psi}$ are continuous in $x = 0, a$, we derive, using the periodicity of the Bloch wave $\psi(a < x < a + b) = \psi(-b < x < 0)e^{\imath k(a+b)}$,

$$\begin{pmatrix} 1 & 1 & -1 & -1 \\ \imath K & -\imath K & -Q & Q \\ e^{\imath Ka} & e^{-\imath Ka} & -e^{-Qb+\imath k(a+b)} & -e^{Qb+\imath k(a+b)} \\ \imath K e^{\imath Ka} & -\imath K e^{-\imath Ka} & -Qe^{-Qb+\imath k(a+b)} & Qe^{Qb+\imath k(a+b)} \end{pmatrix} \begin{pmatrix} A \\ B \\ C \\ D \end{pmatrix} = 0 \ . \tag{4.36}$$

The determinant of the matrix must be zero, or,

$$\frac{Q^2 - K^2}{2QK} \sinh Qb \sin Ka + \cosh Qb \cos Ka = \cos k(a + b) \ . \tag{4.37}$$

For δ-shaped peaks, we let $b = 0$ and $U_0 = \infty$ such that $Q^2 ba/2 = P$, this simplifies to,

$$\frac{P}{Ka} \sin Ka + \cos Ka = \cos ka \ . \tag{4.38}$$

The dispersion relation for light is different. According to [562],

$$-\frac{\sqrt{\varepsilon} + \sqrt{\varepsilon}^{-1}}{2} \sin(\sqrt{\varepsilon}\omega a/c) \sin(\omega a/c) + \cos(\sqrt{\varepsilon}\omega a/c) \cos(\omega a/c) = \cos ka \ . \tag{4.39}$$

For $\varepsilon = 1$ the equation simplifies to $ka = 2\omega a/c$.

4.1.3.1 Photonic density of states

The *photonic density of states* in free space in three dimensions is evaluated from [835],

$$dN = 2\left(\frac{L}{2\pi}\right)^3 \int d^3k = 2\left(\frac{L}{2\pi}\right)^3 k^2 dk \int d\phi d\cos\theta = \frac{L^3\omega^2}{\pi^2 c^3} d\omega \equiv D(\omega)d\omega \ . \quad (4.40)$$

In one dimension,

$$dN = 2\frac{L}{2\pi}dk = \frac{L}{\pi c}d\omega \ . \quad (4.41)$$

The density is normalized $\int_0^{\pi c/L} D(\omega)d\omega = 1$ and the total energy, if all states are populated, is $E \equiv \int_0^{\pi c/L} \omega D(\omega)d\omega = \pi c/L$. However, this applies only if $\omega = ck$. If the dispersion relation is more complicated, for example, inside a cavity or a forbidden photonic band, $\omega = \omega(k)$, we must generalize,

$$D(\omega) = \frac{L}{\pi}\frac{dk}{d\omega} \ . \quad (4.42)$$

Assuming that the dispersion relation is given by the Kronig-Penney model, we obtain gaps in the density-of-states for those values of ω which do not belong to any k.

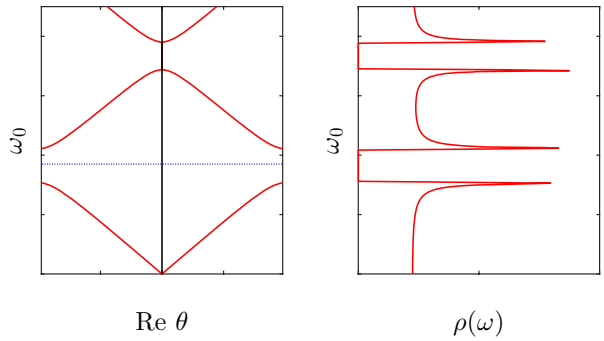

Figure 4.2: (code) Dispersion ratio and state density for a one-dimensional optical lattice.

4.1.4 Bloch oscillations

A *Bloch oscillation* is a phenomenon in solid state physics. It is the oscillation of a particle (e.g., an electron) confined to a periodic potential (e.g. a crystal), when a constant force (e.g., generated by a continuous electric field) acts on it. This phenomenon is very difficult to observe in solid crystals because, due to electron scattering by defects of the lattice [189, 645], the coherent evolution is limited to a small fraction of the Brillouin zone. However, Bloch oscillations were observed in semiconducting superlattices, in ultrathin *Josephson junctions*, and with cold atoms in optical lattices [369, 553].

Let us first show a simple treatment for electrons subject to a constant electric field $\mathcal{E}$. The one-dimensional equation of motion is,

$$\hbar \frac{dk}{dt} = -e\mathcal{E} \ , \tag{4.43}$$

with the solution,

$$k(t) = k(0) - \frac{e\mathcal{E}}{\hbar} t \ . \tag{4.44}$$

The velocity v of the electron is given by,

$$v(k) = \frac{1}{\hbar} \frac{d\mathcal{E}}{dk} \ , \tag{4.45}$$

where $\mathcal{E}(k)$ denotes the *dispersion relation* for a given energy band. We now assume that it has the following form (tight-binding limit),

$$\mathcal{E} = A \cos ak \ , \tag{4.46}$$

where a is the lattice parameter and A a constant. Then, $v(k)$ is given by,

$$v(k) = -\frac{Aa}{\hbar} \sin ak \ , \tag{4.47}$$

and the position of the electron by,

$$x(t) = \int v(k(t))dt = -\frac{A}{e\mathcal{E}} \cos\left(\frac{ae\mathcal{E}}{\hbar} t\right) \ . \tag{4.48}$$

This shows, that the electron is oscillating in real space. The oscillation frequency, called *Bloch frequency* is given by,

$$\omega_{\text{blo}} = \frac{ae|\mathcal{E}|}{\hbar} \ . \tag{4.49}$$

We will provide a deeper discussion in Sec. 4.2.2.

4.1.5 Exercises

4.1.5.1 Ex: Orthonomality of Wannier functions

Verify the orthonomality of Wannier functions.

4.1.5.2 Ex: Effective mass of particles in a lattice

The *effective mass* of particles in a lattice is defined as,

$$\frac{1}{m^*} = \frac{1}{\hbar^2} \frac{d^2 E(k)}{dk^2} \ .$$

Calculate the effective mass of a rubidium atom in a far-detuned optical standing wave.

4.2 One-dimensional optical lattices

In Chp. 2 we studied the motion of particles in free space and inside a potential and learned how to characterize it by states in position space $|z\rangle$, in momentum space $|k\rangle$, or by its energy $|E\rangle$. In free space the energy spectrum is *continuous*, while confined in a potential it is *discrete*, so that it can be labeled by integer numbers $|n\rangle$.

However, between the two opposite cases, totally free and totally confined, there exist more complex potential landscapes, e.g. double-well potentials or periodic potentials. The energy spectra of such potentials can be partially discrete and partially continuous. Generally, low-energy states are almost bound, while high-energy states are almost free. Periodic potentials are paradigmatic examples, as their symmetry allows us to introduce a powerful mathematical formalism based on the Bloch wave expansion [2]

Periodic potentials for quantum particles can be realized artificially. A prominent example are *optical lattices* formed by the interference patterns of intersecting laser beams. Tuned sufficiently far away from atomic resonances the periodically structured light field exerts optical forces on the atoms which can be derived from potentials being proportional to the local light intensity. As these forces are relatively weak, the kinetic energy of the atoms must be very low (typically μK) to allow for their impact to be relevant. In many cases, the depth of the optical lattice only allows for a small number of localized quantum states, so that the quantum nature of the atomic motion becomes highly relevant. Famous examples are the Bloch oscillations and the Mott insulating states.

We are not yet prepared to understand, how these potential arise from the light-atom interaction, as this topic will only be treated in the Secs. 20.2 and in Chp. 25.8.2. However, this is not necessary to understand many of the features of the atomic dynamics in optical lattices. We will thus simply impose a known periodic potential to a cold atomic cloud and study its energetic band structure and the atomic motion. Various three-dimensional crystalline geometries have been realized and studied [437, 352, 89]. In the following, we will mainly focus on one-dimensional lattices, leaving a discussion of phenomena specific to three-dimensional lattices to future sections.

In this section we will elaborate and deepen the formalism of the description of atomic motion in periodic potentials, first recalling the notions of unitary spatial translation, Bloch waves, and Wannier functions, and then applying them to understand the phenomena of localization, Bloch oscillation, and tunneling.

4.2.1 Translations and accelerations in periodic potentials

4.2.1.1 Free particles

In Sec. 1.7.1 we studied the behavior of systems under unitary transformation, in particular, translations and momentum kicks. Spatial translation by a distance a in one dimension along the z-axis was described by the operator $\mathcal{U}_{\mathrm{tr}}(a)$, which acts on

[2] This is somewhat similar to the way in which the second-quantization formalism turned the harmonic trap into an epitome for confining potentials.

position and momentum states,

$$\boxed{\mathcal{U}_{\rm tr}(a) \equiv e^{-\imath \hat{k} a} \quad , \quad \mathcal{U}_{\rm tr}(a)|z\rangle = |z+a\rangle \quad , \quad \mathcal{U}_{\rm tr}(a)|k\rangle = e^{-\imath k a}|k\rangle} \; . \tag{4.50}$$

Obviously, the free particle states $|k\rangle$ are the eigenstates of $\mathcal{U}_{\rm tr}(a)$. Due to the fact that the operator $U_{\rm tr}(a)$ commutes with the free particle Hamiltonian,

$$[\mathcal{U}_{\rm tr}, \hat{H}] = 0 \quad \text{with} \quad \hat{H} = \frac{\hbar^2 \hat{k}^2}{2m} \; , \tag{4.51}$$

the free particle states $|k\rangle$ are also eigenstates of the free particle Hamiltonian.

In Sec. 1.5.7 we showed, how the wavefunctions in position space $\psi(z) \equiv \langle z|\psi\rangle$ and in momentum space $\phi(k) \equiv \langle k|\psi\rangle$ are related via the Fourier theorem [3],

$$e^{\imath k z} = \tfrac{1}{\sqrt{2\pi}} \langle z|k\rangle \; , \tag{4.52}$$

yielding,

$$|z\rangle = \tfrac{1}{\sqrt{2\pi}} \int_{\mathbb{R}} |k\rangle e^{-\imath k z} dk \quad , \quad |k\rangle = \tfrac{1}{\sqrt{2\pi}} \int_{\mathbb{R}} |z\rangle e^{\imath k z} dz \; , \tag{4.53}$$

which allows us to expand any arbitrary state like,

$$|\psi\rangle = \int_{-\infty}^{\infty} |z\rangle \psi(z) dz = \int_{-\infty}^{\infty} |k\rangle \phi(k) dk \; . \tag{4.54}$$

The consistency of (4.53) can easily be checked using $\int_{\mathbb{R}} e^{\imath(k-k')z} dz = 2\pi\delta(k-k')$.

An acceleration g accumulating within a time interval Δt to a change in momentum of $\hbar\kappa = mg\Delta t$ along the z-axis was described in Sec. 1.7.1 by the kick operator $\mathcal{U}_{\rm kc}$, which acts on position and momentum states,

$$\boxed{\mathcal{U}_{\rm kc}(\kappa) \equiv e^{\imath \kappa \hat{z}} \quad , \quad \mathcal{U}_{\rm kc}(\kappa)|k\rangle = |k+\kappa\rangle \quad , \quad \mathcal{U}_{\rm kc}(\kappa)|z\rangle = e^{\imath \kappa z}|z\rangle} \; . \tag{4.55}$$

Obviously, the localized states $|z\rangle$ are the eigenstates of $\mathcal{U}_{\rm kc}(\kappa)$, and this holds even in the presence of a potential $V(z)$. However, the operator $\mathcal{U}_{\rm kc}(\kappa)$ does not commute with the Hamiltonian,

$$\mathcal{U}_{\rm kc}^\dagger(\kappa) \hat{H} \mathcal{U}_{\rm kc}(\kappa) = \mathcal{U}_{\rm kc}^\dagger(\kappa) \frac{\hbar^2 \hat{k}^2}{2m} \mathcal{U}_{\rm kc}(\kappa) = \frac{\hbar^2 (\hat{k}+\kappa)^2}{2m} \neq \hat{H} \; , \tag{4.56}$$

so that the eigenfunctions of the kick operator are NOT eigenfunctions of the Hamiltonian.

In the following, we will extend these thoughts to periodic potentials. In particular, we will see that Bloch and Wannier states represent a natural extension of momentum and position states $|k\rangle$ and $|z\rangle$, respectively. Also, we will use the kick operator extensively in Sec. 4.2.2 in the context of Bloch oscillations.

[3] Or $\langle \lambda^{-1}|z\rangle = e^{-2\pi\imath z/\lambda}$.

4.2.1.2 Periodic potentials

Let us now apply the translation operator (4.50) to particles subject to potentials,

$$\hat{H} = \frac{\hbar^2 \hat{k}^2}{2m} + V(\hat{z}) \ . \tag{4.57}$$

In this case,

$$\mathcal{U}_{\rm tr}^\dagger(a)\hat{H}U_{\rm tr}(a) = \frac{\hbar^2 \hat{k}^2}{2m} + V(\hat{z}+a) \neq \hat{H} \ . \tag{4.58}$$

We see that the translation operator only conserves energy if the potential is periodic, $V(\hat{z}) = V(\hat{z}+a_{\rm l})$ *and* if the distance of translation is $a = a_{\rm l}$. Indeed, in periodic systems,

$$\boxed{[\hat{H},\mathcal{U}_{\rm tr}(a_{\rm l})] = 0 \qquad \text{with} \qquad \mathcal{U}_{\rm tr}(a_{\rm l}) \equiv e^{-\imath \hat{k} a_{\rm l}}} \ . \tag{4.59}$$

If the translation operator commutes with the Hamiltonian, then any eigenstate of $\hat{H}$ is also an eigenstate of $\mathcal{U}_{\rm tr}(a_{\rm l})$, that is,

$$\hat{H}|\psi_k\rangle = E_k|\psi_k\rangle \quad \Longrightarrow \quad \mathcal{U}_{\rm tr}(a_{\rm l})|\psi_k\rangle = e^{-\imath k a_{\rm l}}|\psi_k\rangle \ , \tag{4.60}$$

and we can calculate,

$$\langle z - a_{\rm l}|\psi_k\rangle = \langle z|\mathcal{U}_{\rm tr}(a_{\rm l})|\psi_k\rangle = \langle z|e^{-\imath \hat{k} a_{\rm l}}|\psi_k\rangle = e^{-\imath k a_{\rm l}}\langle z|\psi_k\rangle \ , \tag{4.61}$$

or equivalently,

$$\boxed{\psi_k(z - a_{\rm l}) = e^{-\imath k a_{\rm l}}\psi_k(z)} \ . \tag{4.62}$$

4.2.1.3 Bloch waves

Let us study the kick operator (4.55) in a periodic potential. We define,

$$\hat{H}_{\rm u} \equiv \mathcal{U}_{\rm kc}^\dagger(k)\hat{H}\mathcal{U}_{\rm kc}(k) \qquad \text{and} \qquad |u_k\rangle \equiv \mathcal{U}_{\rm kc}^\dagger(k)|\psi_k\rangle \ , \tag{4.63}$$

so that, using the eigenvalue equation (4.60),

$$\hat{H}_{\rm u}|u_k\rangle = E_k|u_k\rangle \ . \tag{4.64}$$

I.e. the defined functions $|u_k\rangle$ are eigenfunctions of the Hamiltonian (4.63). Furthermore, using (4.62), we calculate,

$$\begin{aligned} u_k(z - a_{\rm l}) &= \mathcal{U}_{\rm kc}^\dagger(k)\psi_k(z - a_{\rm l}) = \mathcal{U}_{\rm kc}^\dagger(k)\mathcal{U}_{\rm tr}(a_{\rm l})\psi_k(z) \\ &= \mathcal{U}_{\rm kc}^\dagger(k)\mathcal{U}_{\rm tr}(a_{\rm l})\mathcal{U}_{\rm kc}(k)u_k(z) = e^{-\imath k(z-a_{\rm l})}e^{-\imath k a_{\rm l}}e^{\imath k z}u_k(z) = u_k(z) \ . \end{aligned} \tag{4.65}$$

This leads us to the Bloch theorem [30],

$$\boxed{\psi_k(z) = e^{\imath k z}u_k(z) \qquad \text{with} \qquad u_k(z) = u_k(z + a_{\rm l}) = u_k^*(z)} \ , \tag{4.66}$$

where we now label the wavefunction with the particle's momentum k. The amplitude $u_k(z)$, called *Bloch wave*, is periodic and can be chosen as real, since it doesn't depend on a phase factor any more. Do the Exc. 4.3.4.1.

In other words, the wavefunction of a particle moving in an infinite periodic potential is, apart from a phase factor $e^{\imath kz}$, periodic and has the amplitude,

$$u_k(z) \equiv |\psi_k(z)| \ . \tag{4.67}$$

Since the Bloch wave is periodic and real, it can be expanded into a Fourier series,

$$u_k(z) = \sum_{j \in \text{lattice}} c_j^k e^{2\imath j k_\text{l} z} \ . \tag{4.68}$$

The expansion coefficients c_j^k are obtained by solving an eigenvalue problem derived from the Schrödinger equation ruling the particle's motion, i.e. they depend on the depth and the shape of the periodic potential. We will see this in the next section.

4.2.2 Band structure in the Bloch state basis

As already pointed out, a sinusoidal periodic potential, $V(z) = V(z + a_\text{l})$, can be generated exploiting the dipolar force of two counterpropagating plane wave laser beams, $e^{\pm\imath k_\text{l} z}$, with wavevectors k_l and $-k_\text{l}$ and tuned to the red side of an atomic transition. In this situation the atoms are attracted to the maxima of the light intensity, the antinodes,

$$\boxed{V(z) = V_0 \cos^2 k_\text{l} z = \tfrac{V_0}{4} |e^{\imath k_\text{l} z} + e^{-\imath k_\text{l} z}|^2 = \tfrac{V_0}{2}[1 + \cos(2k_\text{l} z)]} \ , \tag{4.69}$$

with $V_0 < 0$. If the periodic potential is more complicated, it can be expanded into a Fourier series,

$$V(z) = \sum_{k_\text{l}} U_{k_\text{l}} e^{2\imath k_\text{l} z} \ , \tag{4.70}$$

but the procedure detailed in the following for the sinusoidal potential can be applied analogously. For the sinusoidal potential the Fourier coefficients are simply $U_0 = \frac{V_0}{2}$ and $U_{\pm k_\text{l}} = \frac{V_0}{4}$, so that,

$$V(z) = V_0(\tfrac{1}{2} + \tfrac{1}{4} e^{2\imath k_\text{l} z} + \tfrac{1}{4} e^{-2\imath k_\text{l} z}) \ , \tag{4.71}$$

where we suppressed the band index on the field operators for simplicity of notation, when discussing single-band problems. The goal is obviously to solve the Schrödinger equation,

$$\hat{H}|\psi\rangle = \left(-\frac{\hbar^2}{2m} \frac{\partial^2}{\partial z^2} + V(z) \right) |\psi\rangle = E|\psi\rangle \ . \tag{4.72}$$

4.2.2.1 Solving the Schrödinger equation

To solve the Schrödinger equation, we expand the wavefunction into plane waves,

$$\psi(z) = \sum_k c_k e^{\imath k z} \ , \tag{4.73}$$

and insert this expansion into Schrödinger's stationary equation (4.72),

$$\left(\frac{-\hbar^2}{2m} \frac{\partial^2}{\partial z^2} + V_0(\tfrac{1}{2} + \tfrac{1}{4} e^{2\imath k_\text{l} z} + \tfrac{1}{4} e^{-2\imath k_\text{l} z}) \right) \sum_k c_k e^{\imath k z} = E \sum_k c_k e^{\imath k z} \ . \tag{4.74}$$

taking the potential from (4.71). We get,

$$\left(\frac{\hbar^2 k^2}{2m} + \frac{V_0}{2}\right) c_k + \frac{V_0}{4} c_{k-2k_l} + \frac{V_0}{4} c_{k+2k_l} = E c_k \ . \tag{4.75}$$

We now define two new parameters, the *quasi-momentum* q and the *Bloch band* n such that,

$$\boxed{k = q + 2jk_l \quad \text{with} \quad q \in [-k_l, k_l] \quad \text{and} \quad j \in \mathbb{Z}} \ . \tag{4.76}$$

Also, we define an abbreviation called *recoil frequency* $\omega_{\rm rec}$ and use it to scale the energies [4],

$$\omega_{\rm rec} = \frac{\hbar {k_l}^2}{2m} \quad , \quad \tilde{V}_0 \equiv \frac{V_0}{\hbar\omega_{\rm rec}} \quad , \quad \tilde{E} \equiv \frac{E}{\hbar\omega_{\rm rec}} \quad , \quad \tilde{q} \equiv \frac{q}{k_l} \ . \tag{4.77}$$

With this, (4.75) reads,

$$[(2j+\tilde{q})^2 + \tfrac{1}{2}\tilde{V}_0] c_{2jk_l+q} + \tfrac{1}{4}\tilde{V}_0 c_{2jk_l+q-2k_l} + \tfrac{1}{4}\tilde{V}_0 c_{2jk_l+q+2k_l} = \tilde{E} c_{2jk_l+q} \ , \tag{4.78}$$

or in matrix notation,

$$\hat{H}\mathbf{c} = \hbar\omega_{\rm rec}\tilde{E}\mathbf{c} \ . \tag{4.79}$$

where the matrix is around $j = .., -1, 0, +1, ..$:

$$\boxed{\hat{H} = \hbar\omega_{\rm rec} \begin{pmatrix} \ddots & & & & \\ & (\tilde{q}-2)^2 + \frac{1}{2}\tilde{V}_0 & \frac{1}{4}\tilde{V}_0 & & \\ & \frac{1}{4}\tilde{V}_0 & \tilde{q}^2 + \frac{1}{2}\tilde{V}_0 & \frac{1}{4}V_0 & \\ & & \frac{1}{4}\tilde{V}_0 & (\tilde{q}+2)^2 + \frac{1}{2}\tilde{V}_0 & \\ & & & & \ddots \end{pmatrix} \quad , \quad \mathbf{c} = \begin{pmatrix} \vdots \\ c_{q-2k_l} \\ c_q \\ c_{q+2k_l} \\ \vdots \end{pmatrix}} \ . \tag{4.80}$$

The Hamiltonian in (4.80) is tridiagonal, i.e. it consists of only three diagonals, which is due to the sinusoidal shape of the optical potential. For non-sinusoidal potentials, whose Fourier expansion has more components, more side-diagonals will appear.

Solution of (4.80) yields a set of eigenenergies E and eigenvectors $\mathbf{c}$, whose number will be equal to the number of neighboring lattice sites j considered in the matrix of (4.80). Hence, for a given k, or equivalently (n, q),

$$\hat{H}|n, q\rangle = E_q^{(n)}|n, q\rangle \ , \tag{4.81}$$

[4] The reason for the terminology, which will become clear after a study of Sec. 20.2, is that the $\hbar\omega_{\rm rec}$ is the kinetic energy of an atom having received two units of photonic momenta.

and we can compute the particle's wavefunction from (4.73) [5,6],

$$\boxed{\langle z|n,q\rangle = \psi_q^{(n)}(z) = \frac{1}{\sqrt{2\pi}} \sum_{j\in\text{lattice}} c_{q+2jk_1}^{(n)} e^{\imath(q+2jk_1)z}} \ , \tag{4.82}$$

where from now on we will call the particle state $|\psi\rangle$ given in the Bloch basis a *Bloch state* $|n,q\rangle$. The eigenenergies $E_q^{(n)}$ are shown in Fig. 4.3(a) as a function of q for the lowest-lying Bloch bands, and Fig. 4.3(b) shows the spatial Bloch functions for the lowest bands. Eq. (4.82) allows us to expand a Bloch state in a position basis,

$$|n,q\rangle = \int_{\mathbb{R}} |z\rangle\langle z|n,q\rangle dz = \frac{1}{\sqrt{2\pi}} \sum_{j\in\mathbb{Z}} c_{q+2jk_1}^{(n)} \int_{\mathbb{R}} |z\rangle e^{\imath(q+2jk_1)z} dz \ . \tag{4.83}$$

Fig. 4.3 shows the energy spectrum of optical lattices for different lattice depths. Also shown in Fig. 4.3(a,c) is the level structure of a harmonic oscillator approximating a lattice site. Also shown in Fig. 4.3(b,d) as black dashed and dotted lines is the free particle dispersion relation corresponding to $V_0 = 0$.

4.2.2.2 Band structure of the energy spectrum

The energy spectrum calculated in Fig. 4.3 displays a hybrid structure consisting of partially bound and partially free states. The spectrum breaks down into energy intervals called *bands*, where a quasi-momentum q can be found so that the energy E_q is within this interval, and *band gaps* where no such quasi-momentum exists. At low energies ($\tilde{E} \ll 0$), the energy width of the bands converges toward a δ-function. At very low energies near the bottom ($E \simeq V_0$) where the standing wave potential resembles a harmonic oscillator, the energy levels are equidistant. On the other hand, closer to the threshold ($\tilde{E} \lesssim 0$), the bands become larger, and this is due to the possibility of tunneling between adjacent potential sites: the particles are not totally localized, but not totally free neither. At high energies ($\tilde{E}\mathbf{G}g0$), the bands join to a continuum, while the band gaps disappear. The dispersion relation then resembles that of a free particle.

The energy spectrum thus consists of a discrete sequence (labeled by an integer number $n \in \mathbb{N}$) of bands within which any energy state $E_q^{(n)}$ can be reached via a proper choice of the quasi-momentum q. It is not surprising that, unlike for states of totally free particles $|k\rangle$ and states of totally bound particles $|n\rangle$, two quantum numbers are necessary to label all possible states $|n,q\rangle$ [7,8].

[5] The requirement that $\psi(z)$ satisfies the Schrödinger equation is equivalent to the condition that $\mathbf{c}$ satisfies an eigenvalue equation. Let $\mathcal{U}$ be the matrix of the eigenvectors of $\hat{H}$ and $\hat{E}$ the diagonal matrix of eigenvalues: $\hat{H} = \mathcal{U}^{-1}\hat{E}\mathcal{U}$ gives $\hat{E}\mathcal{U}\mathbf{c} = E\mathcal{U}\mathbf{c}$, such that $\mathcal{U}\mathbf{c}$ can be understood as eigenvectors.

[6] Alternatively, we define $d_{2jk_1+k} \equiv c_{2jk_1+k+2k_1}/c_{2jk_1+k}$, in which case Eq. (4.79) becomes,

$$d_{2jk_1+k-2k_1} = \frac{V_0}{\frac{\hbar^2}{m}(2jk_1+k)^2 - 2\varepsilon - V_0(2+d_{2jk_1+k})} \ .$$

[7] This is intuitively clear, considering the fact that tunneling introduces a coupling between different potential sites.

[8] The necessity of two quantum numbers indicates that two commuting observables are required to form a complete set for description of the system.

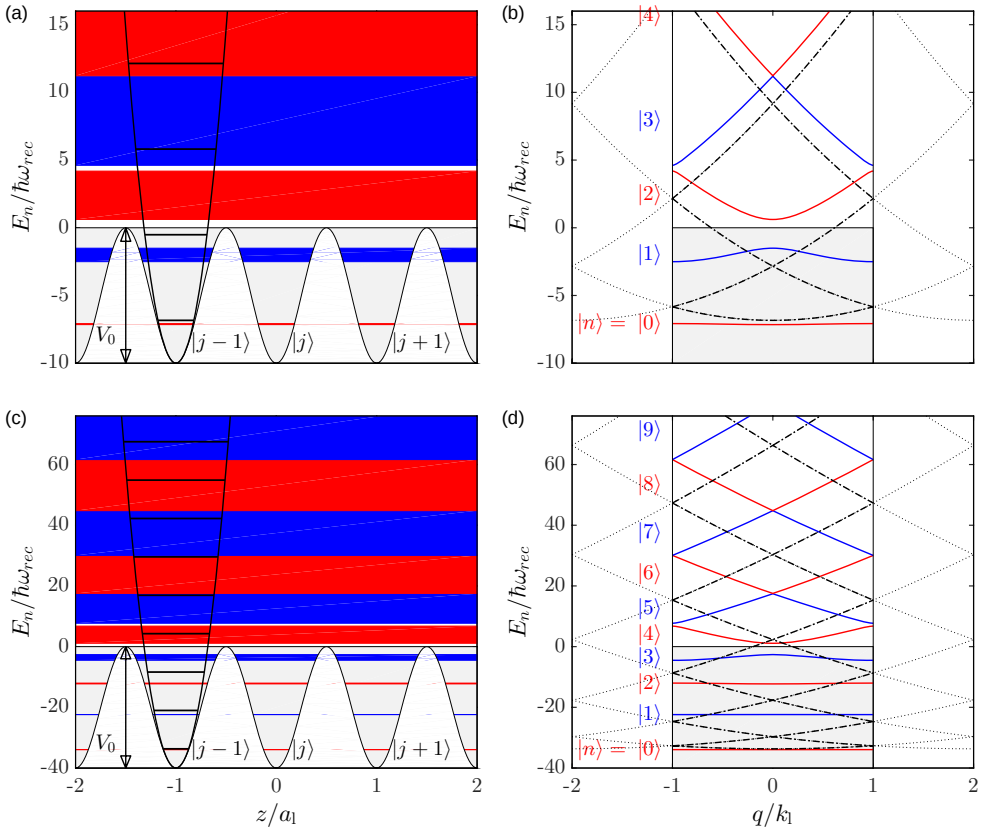

Figure 4.3: (code) (a,c) Lattice potential and band structure for $V_0/\hbar\omega_{\rm rec} = -10$ and -40, respectively. (b,d) Dispersion relation in momentum space and energy levels for the same potential depths as in (a,c). The colors of the solid lines correspond to the energy bands in (a,c).

To estimate the width of the forbidden band gap, we cut out a 2×2 matrix within the matrix $\hat{H}$ and neglect its coupling with the others submatrices,

$$\hat{H}_s = \hbar\omega_{\rm rec}\begin{pmatrix} (\tilde{q}-2)^2 + \frac{1}{2}\tilde{V}_0 & \frac{1}{4}\tilde{V}_0 \\ \frac{1}{4}\tilde{V}_0 & \tilde{q}^2 + \frac{1}{2}\tilde{V}_0 \end{pmatrix} . \tag{4.84}$$

At the edges of the Brillouin zone, $q = \pm k_l$, we get the eigenvalues,

$$E = \frac{2\hbar^2 {k_l}^2}{m} + V_0 \pm \tfrac{V_0}{2} = E_{\rm rec}\left(4 + \tilde{V}_0 + \tfrac{\tilde{V}_0}{2}\right) , \tag{4.85}$$

that is, the band gap is $\Delta E = V_0$.

Sufficiently large band gaps impede small forces to induce couplings to states with very different energies located in different bands. Exceptions are observed near band edges, where the bands approach each other and coupling may occur via Landau-Zener tunneling transitions.

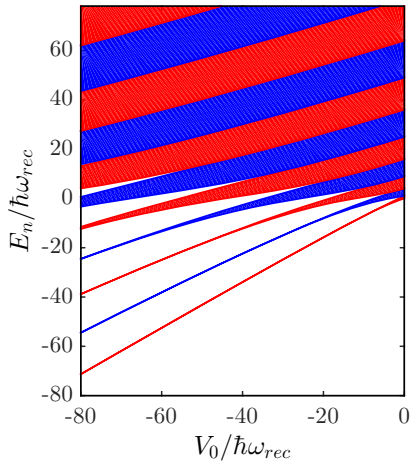

Figure 4.4: (code) Band structure as a function of potential depth. The colored areas are allowed energy bands.

Example 38 (*Very shallow and very deep potentials*): For very shallow potentials, $|V_0| \ll \hbar^2(2k_l)^2/2m$, we can neglect the coefficients V_0 in the Eq. (4.79) and we find,

$$E \simeq \frac{\hbar^2 q^2}{2m} = E_{\rm rec}\frac{q^2}{{k_l}^2} \ , \tag{4.86}$$

which corresponds to the dispersion relation for free particles.
On the other hand, looking *at the bottom* of very deep potentials, $V_0 \mathbf{G} g\hbar^2(2k_l)^2/2m$, we can harmonically approximate the cosine potential by $V(z) \approx 2V_0 + \frac{m}{2}\omega^2 z^2$ with $\omega = 2k_l\sqrt{V_0/m} = \hbar^{-1}\sqrt{2|V_0|E_{\rm rec}}$. For this case we expect,

$$E \simeq 2V_0 + \hbar\omega\left(n + \tfrac{1}{2}\right) \ . \tag{4.87}$$

4.2.2.3 Momentum representation of Bloch states

Instead of projecting the Bloch state onto position space, as done in (4.82), we may also project it on momentum space,

$$\begin{aligned}\langle k|n,q\rangle = \langle k|\int_{\mathbb{R}}|z\rangle\langle z|n,q\rangle dz &\overset{(4.52)}{=} \tfrac{1}{\sqrt{2\pi}}\int_{\mathbb{R}} e^{-\imath kz}\langle z|n,q\rangle(z)dz \\ &\overset{(4.82)}{=} \tfrac{1}{2\pi}\int_{\mathbb{R}} e^{-\imath kz}\sum_{j\in\mathbb{Z}} c^{(n)}_{q+2jk_l} e^{\imath(q+2jk_l)z}dz = \sum_{j\in\mathbb{Z}} c^{(n)}_{q+2jk_l}\delta(q+2jk_l-k) \ .\end{aligned} \tag{4.88}$$

Hence, we find, that,

$$\boxed{\langle k|n,q\rangle = c^{(n)}_k} \ , \tag{4.89}$$

which allows us to expand a Bloch state in a momentum basis,

$$|n,q\rangle = \int_{\mathbb{R}} |k\rangle\langle k|n,q\rangle dk = \int_{\mathbb{R}} |k\rangle c_k^{(n)} dk \tag{4.90}$$
$$= \int_{\mathbb{R}} |k\rangle \sum_{j\in\text{lattice}} c^{(n)}_{q+2jk_\text{l}} \delta(q+2jk_\text{l}-k)dk = \sum_j |q+2jk_\text{l}\rangle c^{(n)}_{q+2jk_\text{l}} \ .$$

Apparently, each Bloch state with a given quasi-momentum consists of a comb of real momenta, $k = q, q \pm 2k_\text{l}, q \pm 4k_\text{l}, ...$

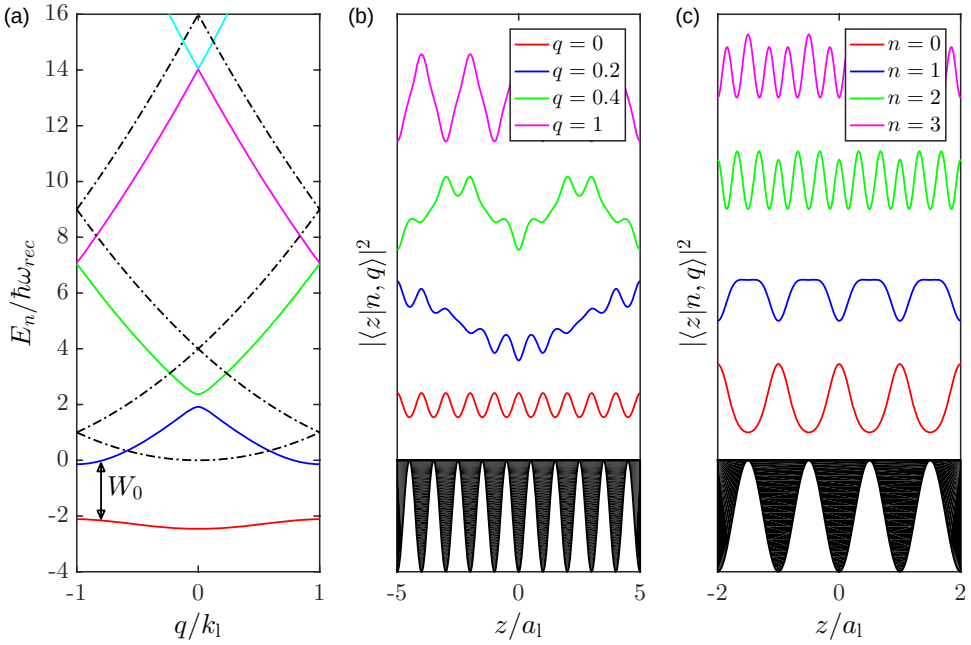

Figure 4.5: (code) (a) Bloch bands with a potential depth of $V_0 = -4\hbar\omega_\text{rec}$ and without potential, $V_0 = 0$ (black dash-dotted line). (b) Bloch waves for the same potential for the lowest Bloch band $n = 0$ at various quasi-momenta q. (c) Bloch waves for the four lowest Bloch bands at $q = 0.3k_\text{l}$.

Being eigenstates of a Hermitian operator, the Bloch states form an orthonormal basis,

$$\boxed{\langle n',q'|n,q\rangle = \int_{\mathbb{R}} \langle n',q'|z\rangle\langle z|n,q\rangle dz = \int_{\mathbb{R}} \langle n',q'|k\rangle\langle k|n,q\rangle dk = \delta_{n,n'}\delta(q-q')} \ , \tag{4.91}$$

and therefore behave much like momentum eigenstates.

4.2.3 Localization and tunneling in the Wannier state basis

In Sec. 4.2.2 we outlined the Bloch representation, which provides a basis *leaving the optical lattice Hamiltonian diagonal*,

$$\hat{H} = \sum_n \int_{-k_l}^{k_l} |n,q\rangle E_q^{(n)} \langle n,q| dq \ . \tag{4.92}$$

Thus, the Bloch basis is the basis of choice to calculate the energy spectra. For a given band, the Bloch states are (quasi-)momentum eigenstates q corresponding to plane waves in position space. Nevertheless, other auxiliary basis sets can be useful, e.g. for the description of transport phenomena. In the following, we will develop as an alternative the Wannier representation, which provides a basis of states localized in position space at lattice position sites j.

Table 4.1: Translation and kick acting on Bloch and Wannier states. Eigenvalue equations are emphasized in blue color.

	free space	lattice
Hamiltonian	$\hat{H} = \frac{\hbar^2 k^2}{2m}$	$\hat{H} = \frac{\hbar^2 k^2}{2m} + V_0 \cos^2 k_l z$
potential	$V(z) = 0$	$V(z) = V(z + a_l)$
translation	$\mathcal{U}_{\rm tr}(a) = e^{-\imath a \hat{k}}$	$\mathcal{U}_{\rm tr}(a_l) = e^{-\imath a_l \hat{k}}$
kick	$\mathcal{U}_{\rm kc}(\kappa) = e^{\imath \kappa \hat{z}}$	$\mathcal{U}_{\rm kc}(k_l) = e^{\imath k_l \hat{z}}$
symmetry	$\mathcal{U}_{\rm tr}^\dagger(a) \hat{H} \mathcal{U}_{\rm tr}(a) = \hat{H}$, $\forall a$	$\mathcal{U}_{\rm tr}^\dagger(j a_l) \hat{H} \hat{\mathcal{U}}_{\rm tr}(j a_l) = \hat{H}$, $\forall j$
	$\mathcal{U}_{\rm kc}^\dagger(a) \hat{H} \mathcal{U}_{\rm kc}(a) \neq \hat{H}$	$\mathcal{U}_{\rm kc}^\dagger(j a_l) \hat{H} \hat{\mathcal{U}}_{\rm kc}(j a_l) \neq \hat{H}$
eigenstates	$\lvert k\rangle \leftrightarrow \lvert z\rangle$	$\lvert n,q\rangle \leftrightarrow \lvert n,z_j\rangle$
Fourier	$\langle k \lvert z\rangle = \frac{1}{\sqrt{2\pi}} e^{-\imath k z}$	$\langle n,q \lvert n,z_j\rangle = \frac{1}{\sqrt{2\pi}} e^{-\imath \pi j \tilde{q}}$
translation	$\mathcal{U}_{\rm tr}(a) \lvert z\rangle = \lvert z + a\rangle$	$\mathcal{U}_{\rm tr}(a_l) \lvert n,z_j\rangle = \lvert n,z_{j+1}\rangle$
	$\mathcal{U}_{\rm tr}(a) \lvert k\rangle = e^{-\imath k a} \lvert k\rangle$	$\mathcal{U}_{\rm tr}(a_l) \lvert n,q\rangle = e^{-\imath q a_l} \lvert n,q\rangle$
kick	$\mathcal{U}_{\rm kc}(\kappa) \lvert z\rangle = e^{\imath \kappa z} \lvert z\rangle$	$\mathcal{U}_{\rm kc}(k_l) \lvert n,z_j\rangle = e^{\imath k_l z} \lvert n,z_j\rangle$
	$\mathcal{U}_{\rm kc}(\kappa) \lvert k\rangle = \lvert k + \kappa\rangle$	$\mathcal{U}_{\rm kc}(k_l) \lvert n,q\rangle = \lvert n+1,q\rangle$

Tab. 4.1 provides an overview comparing Bloch and Wannier states. We see that the Bloch states $|n,q\rangle$ are eigenstates of the translation operator $U_{\rm tr}(j a_l)$, and the eigenvalues are labeled by phase factors. Similarly, the Wannier states are eigenstates of the kick operator $U_{\rm kc}(k_l)$, and the eigenvalues are labeled by phase factors.

4.2.3.1 Localization

Let us for example consider a state perfectly localized at z_c in position space near a particular antinode of a standing wave, $|\psi_c\rangle \equiv |z_c\rangle$. According to (4.52), the wavefunctions of this in position and momentum space are,

$$\langle z|z_c\rangle = \delta(z - z_c) \qquad \text{and} \qquad \langle k|z_c\rangle = \tfrac{1}{\sqrt{2\pi}} e^{-\imath k z_c} \ , \tag{4.93}$$

which corresponds to a plane wave. Hence, we can expand the wavefunction in momentum space like,

$$|\psi_c\rangle = \tfrac{1}{\sqrt{2\pi}} \int_{-\infty}^{\infty} |k\rangle e^{-\imath k z_c} dk \equiv \tfrac{1}{\sqrt{2\pi}} \int_{-\infty}^{\infty} |k\rangle e^{\imath\varphi(k)} dk \ . \tag{4.94}$$

That is, to completely localize a particle, its momentum distribution must contain all components $k \in [-\infty, \infty]$ with equal amplitudes. For a particle in a single band of a 1D lattice, however, $q \in [-k_1, k_1]$ remembering $k_1 = 2\pi/\lambda_1 = \pi/a_1$, and the question is, which phase distribution $\varphi(q)$ can give optimal localization.

Example 39 (*Localization without potential*): The plane waves (4.93) are eigenstates of the particle's motion in the absence of a potential, $V_0 = 0$. Nevertheless, it is instructive to try localizing a particle within a single band,

$$|z_c\rangle = \int_{-k_1}^{k_1} |q\rangle e^{\imath\varphi(q)} dq \quad \Longrightarrow \quad \langle z|z_c\rangle = \frac{2\sin k_1(z - z_c)}{z - z_c} = 2k_1 \operatorname{sinc} \frac{z - z_c}{a_1} \ . \tag{4.95}$$

It is now remarkable, that states $|\psi_{z_c}\rangle$ localized at discrete values of the position coordinate, $z_c = j a_1$ with $j \in \mathbb{Z}$, are orthogonal. Indeed, we find,

$$\langle z_c'|z_c\rangle = \int_{-k_1}^{k_1}\int_{-k_1}^{k_1} \langle q'|q\rangle e^{\imath(q' z_c' - q z_c)} dq dq' = \frac{2\sin k_1(z_c' - z_c)}{z_c' - z_c} \tag{4.96}$$
$$\longrightarrow \frac{2\sin k_1(j' - j)a_1}{(j' - j)a_1} = 2k_1\delta_{j'j} \ .$$

4.2.3.2 Wannier functions for 1D optical lattices

In a (red-detuned) standing light wave generating a dipolar potential, we call 'lattice sites' the locations on the z-axis where the potential is minimized. For the cosine potential (4.69) with $V_0 < 0$ these locations are given by $z_j = j a_1$. We define the Wannier state localized near a lattice site as [9],

$$\boxed{|n, j\rangle \equiv \sqrt{a_1}|n, z_j\rangle = \sqrt{\tfrac{a_1}{2\pi}} \int_{-k_1}^{k_1} e^{-\imath q z_j} |n, q\rangle dq} \ , \tag{4.97}$$

[9] Remember that, with this definition, the Bloch states $|n, q\rangle$ have units of $\mathrm{cm}^{1/2}$, the Wannier states defined as $|n, z_j\rangle$ of $\mathrm{cm}^{-1/2}$, and the Wannier states defined as $|n, j\rangle \equiv \sqrt{a_1}|n, z_j\rangle$ are dimensionless. The normalization factor 2π appearing in the Fourier transform is symmetrically divided with the inverse Fourier transform.

where $|n,q\rangle$ is the Bloch state. Applying the discrete translation operator (4.56) to Bloch states,

$$\mathcal{U}_{\rm tr}(a_1)|n,q\rangle = e^{-\imath q a_1}|n,q\rangle \ , \tag{4.98}$$

we find that,

$$\mathcal{U}_{\rm tr}(a_1)|n,z_j\rangle = \mathcal{U}_{\rm tr}(a_1)\int_{-k_1}^{k_1}|n,q\rangle\tfrac{e^{-\imath q z_j}}{\sqrt{2\pi}}dq = \int_{-k_1}^{k_1}e^{-\imath q a_1}\tfrac{e^{-\imath q j a_1}}{\sqrt{2\pi}}|n,q\rangle dq = |n,z_{j+1}\rangle \ . \tag{4.99}$$

Because of this, we can reference all Wannier functions $|n,z_j\rangle$ to the $j=0$ one, so that each band has a unique Wannier function $|n,z_0\rangle$. We have,

$$|n,z_j\rangle = \mathcal{U}_{\rm tr}(z_j)|n,z_0\rangle = e^{-\imath q z_j}\int_{-k_1}^{k_1}\tfrac{1}{\sqrt{2\pi}}|n,q\rangle dq \ . \tag{4.100}$$

The inverse relationship to the definition (4.97) is easily derived,

$$|n,q\rangle = \int_{-k_1}^{k_1}\delta(q-q')|n,q'\rangle dq' = \tfrac{a_1}{2\pi}\int_{-k_1}^{k_1}\sum_j e^{\imath j(q-q')a_1}|n,q'\rangle dq' = \sum_j \tfrac{a_1}{\sqrt{2\pi}}e^{\imath q z_j}|n,z_j\rangle \ . \tag{4.101}$$

> **Example 40 (*Equivalence of Bloch and Wannier state basis*):** At first glance, the equivalence of the continuous basis of Bloch states labeled by their quasi-momentum q and the discrete basis of Wannier states labeled by their lattice sites may be surprising. The equivalence is, however, due to an approximation done by taking the continuum limit, $\sum_q \longrightarrow a_1\int dq/2\pi$. For finite lattices extending over M sites, the allowed quasi-momenta are $q=\pi j/Ma_1$ with $j=-M/2+1,...,M/2$.
>
> The mechanism at the origin of the formation of energy bands in periodic potentials is readily understood in a toy model. Fig. 4.6 shows numerically calculated wavefunctions of bound states in a double-well potential. We observe that the bound states split into a symmetric wavefunction with a large amplitude inside the barrier and an anti-symmetric wavefunction with a small amplitude. The energy distance decreases at larger barriers.

The **spatial representation** of a Wannier state is obtained by projecting onto position space,

$$\boxed{\langle z|n,z_j\rangle = \langle z|\int_{-k_1}^{k_1}\tfrac{e^{-\imath q z_j}}{\sqrt{2\pi}}|n,q\rangle dq = \int_{-k_1}^{k_1}\tfrac{e^{-\imath q z_j}}{\sqrt{2\pi}}\langle z|n,q\rangle dq} \ . \tag{4.102}$$

Again, because of $\langle z|n,z_j\rangle = \langle z-z_j|n,z_j\rangle$, there is a unique Wannier function for each band copied to each lattice site. Inserting the solution (4.82) for the Bloch states, we find,

$$\langle z|n,z_j\rangle = \tfrac{1}{2\pi}\int_{-k_1}^{k_1}e^{-\imath q z_j}\sum_{j\in\mathbb{Z}}c^{(n)}_{q+2jk_1}e^{\imath(q+2jk_1)z}dq \ . \tag{4.103}$$

Wannier function are real, definite parity, and decay exponentially fast at infinity,

$$\langle z|n,z_0\rangle = \langle z|n,z_0\rangle^* = \pm\langle -z|n,z_0\rangle \ . \tag{4.104}$$

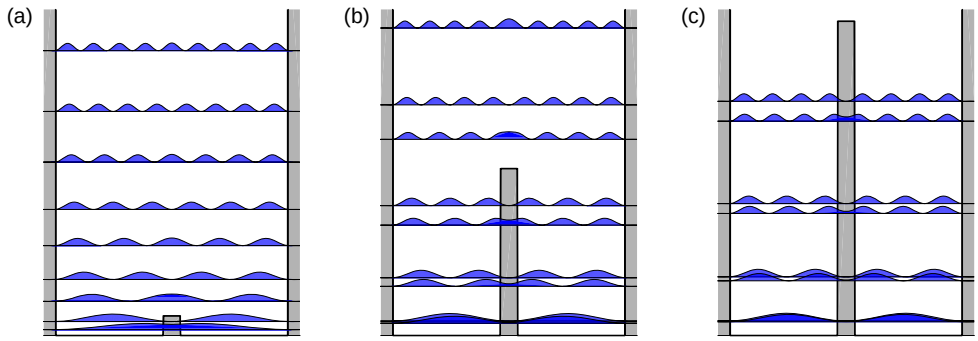

Figure 4.6: (code) Wavefunctions of bound states in a double-well potential calculated using the Fourier grid method (see Sec. 2.4.2).

Let us now calculate the **momentum representation** of Wannier states, which is obtained by projecting onto momentum space,

$$\boxed{\langle k|n,z_j\rangle = \langle k|\int_{-\infty}^{\infty}|z\rangle\langle z|n,z_j\rangle dz = \int_{-\infty}^{\infty}\frac{e^{-\imath kz}}{\sqrt{2\pi}}\langle z|n,z_j\rangle dz}\ . \tag{4.105}$$

The momentum representation of Wannier states is also related to the momentum representation of Bloch states,

$$\langle k|z_j\rangle = \langle k|\int_{-k_1}^{k_1}|n,q\rangle\langle n,q|n,z_j\rangle dq \overset{(4.89)}{=} \int_{-k_1}^{k_1}\frac{e^{-\imath qz_j}}{\sqrt{2\pi}}\langle k|n,q\rangle dk\ . \tag{4.106}$$

Hence we find that, in the same way as $|z\rangle$ and $|k\rangle$ in free space are Fourier transform pairs related by $\langle k|z\rangle = e^{-\imath kz}/\sqrt{2\pi}$, in a periodic potential $|n,q\rangle$ and $|n,z_j\rangle$ are Fourier transform pairs related by,

$$\langle n,q|n,z_j\rangle = \frac{e^{-\imath qz_j}}{\sqrt{2\pi}} = \frac{e^{-\imath\pi j\tilde{q}}}{\sqrt{2\pi}}\ . \tag{4.107}$$

Inserting the solution (4.82) for the Bloch states, we find,

$$\begin{aligned}\langle k|n,z_j\rangle &= \int_{-k_1}^{k_1}\frac{e^{-\imath qz_j}}{\sqrt{2\pi}}c_k^{(n)}dq \qquad (4.108)\\ &= \tfrac{1}{\sqrt{2\pi}}\sum_{j\in\mathbb{Z}}\int_{-k_1}^{k_1}e^{-\imath qz_j}c^{(n)}_{q+2jk_1}\delta(q+2jk_1-k)dq = \sum_{j\in\mathbb{Z}}\frac{e^{\imath(2jk_1-k)z_j}}{\sqrt{2\pi}}c_k^{(n)}\ .\end{aligned}$$

In other words, $\langle k|n,z_0\rangle$ is the continuous function that includes all the 'comb teeth' of

the Bloch functions. We can then rewrite any Bloch function in terms of $\langle k|n, z_0\rangle$ [10],

$$\langle k|n,q\rangle = \sum_{j\in\mathbb{Z}} \langle k|n,z_j\rangle\langle n,z_j|n,q\rangle = \sum_{j\in\mathbb{Z}} \frac{e^{\imath q z_j}}{\sqrt{2\pi}} \langle k|n,z_j\rangle \ . \tag{4.109}$$

Wannier states form an orthonormal basis just like Bloch states,

$$\boxed{\langle n', z_{j'}|n,z_j\rangle = \int \langle n', z_{j'}|z\rangle\langle z|n,z_j\rangle dz = \int \langle n', z_{j'}|k\rangle\langle k|n,z_j\rangle dk = \delta_{n,n'}\delta_{j,j'}} \ , \tag{4.110}$$

as we will show in Exc. 4.3.4.2.

In Exc. 4.3.4.3 we approximate Wannier functions for sinusoidal potentials.

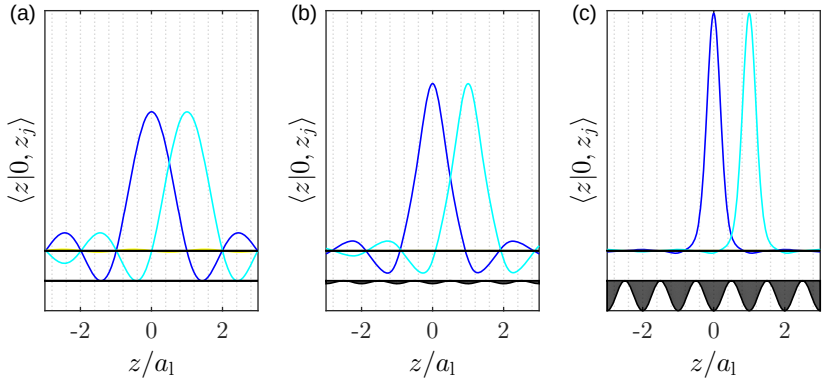

Figure 4.7: (code) Wannier functions for the lowest Bloch band $n = 0$ and different trap depths (a) $\tilde{E} = 0$, (b) $\tilde{E} = 1$, and (c) $\tilde{E} = 10$. The cyan curves are displaced with respect to the blue ones by one lattice site.

4.2.3.3 Tunneling between adjacent lattice sites

With *tunneling* we mean quantum transport between adjacent lattice sites. To develop the formalism for this phenomenon we use the second-quantized notation [817] in analogy to the procedure introduced for the harmonic oscillator in Sec. 2.5.1. The advantage of this formalism is that it not only allows to describe single atom dynamics, but can be extended to account for many interacting particles obeying certain exchange statistics, as we will see in Sec. 28.4.2.

From the single-atom eigenenergies of the Hamiltonian, that has already been

[10] Remembering Fourier transform and series,

$$\int_{\mathbb{R}} e^{\imath(k-k')x}dx = 2\pi\delta(k-k') \quad \Leftrightarrow \int_{\mathbb{R}} e^{\imath k(x-x')}dk = 2\pi\delta(x-x') \ , \quad \int_{\mathbb{R}} x e^{\imath k(x-x')}dx = 2\pi\delta(x-x')\imath\frac{d}{dk} \ ,$$
$$\sum_{j\in\mathbb{Z}} e^{\imath(k-k')ja} = \tfrac{2\pi}{a}\delta(k-k') \quad \Leftrightarrow \int_{-k_1}^{k_1} e^{\imath k(j-j')a}dk = \tfrac{2\pi}{a}\delta_{jj'} \ , \quad \sum_{j\in\mathbb{Z}} j e^{\imath(k-k')ja} = \tfrac{2\pi}{a}\delta(k-k')\tfrac{\imath}{a}\frac{d}{dk} \ .$$

Table 4.2: Summary of scalar products between states of the Bloch, Wannier, and Wannier-Stark basis in position and momentum representation. Red formulas are completeness relations. Green formulas establish links between the Bloch and Wannier pictures. Band indices are suppressed for clarity. The $\check{}$ on exponential functions simply indicates that the term should be divided by $\sqrt{2\pi}$.

	$\lvert z\rangle$	$\lvert k\rangle$	$\lvert n,q\rangle$	$\lvert n,z_j\rangle = \lvert n,j\rangle/\sqrt{a_1}$	$\lvert n,\ell\rangle$
$\langle z'\rvert$	$= \delta(z-z')$ $\mathbb{I} = \int_{\mathbb{R}} \lvert z\rangle\langle z\rvert dz$	$= \check{e}^{-\imath kz'}$	$= \sum_{j\in\mathbb{Z}} \check{e}^{\imath qz_j} \langle z'\rvert n,z_j\rangle$ $= \sum_{j\in\mathbb{Z}} c_{q+2jk_1} \check{e}^{\imath(q+2jk_1)z'}$ $= \int_{\mathbb{R}} \check{e}^{\imath kz'} \langle k\rvert n,q\rangle dk$	$= \int_{-k_1}^{k_1} \check{e}^{-\imath qz_j} \langle z'\rvert n,q\rangle dz'$ $= \int \sum_{j\in\mathbb{Z}} c_k \check{e}^{\imath kz'-\imath qz_j} dq$ $= \int_{\mathbb{R}} \check{e}^{\imath qz_j} \langle k\rvert n,z_j\rangle dk$	$= \sum_{j'\in\mathbb{Z}} J_{j'-\ell}(\nu) \langle z'\rvert n,j'\rangle$
$\langle k'\rvert$	$\check{e}^{\imath k'z}$	$= \delta(k-k')$ $\mathbb{I} = \int_{\mathbb{R}} \lvert k\rangle\langle k\rvert dk$	$= \int_{\mathbb{R}} \check{e}^{-\imath qz} \langle z\rvert n,q\rangle dz$ $\overset{(4.89)}{=} c_{k'}$ $= \sum_{j\in\mathbb{Z}} \check{e}^{\imath qz_j} \langle k\rvert w_j\rangle$	$= \int_{\mathbb{R}}^{k_1} \check{e}^{-\imath k'z} \langle z\rvert z_j\rangle dz$ $= \int_{-k_1}^{k_1} c_{k'} \check{e}^{-\imath qz_j} dq$ $= \int_{-k_1}^{k_1} \check{e}^{-\imath qz_j} \langle k\rvert n,q\rangle dq$	$= \sum_{j'\in\mathbb{Z}} J_{j'-\ell}(\nu) \langle k'\rvert n,j'\rangle$
$\langle n',q'\rvert$	$= \psi_{q'}^{(n')}(z)^*$		$= \delta(q-q')\delta_{n,n'}$ $\mathbb{I} = \sum_{n\in\mathbb{Z}} \int_{-k_1}^{k_1} \lvert n,q\rangle\langle n,q\rvert dq$	$= \check{e}^{-\imath q'z_j}$	$= \sqrt{a_1} \check{e}^{-\imath(q'z_\ell + \nu \sin a_1 q)}$
$\langle n',z_{j'}\rvert$			$= \check{e}^{\imath qz_{j'}}$	$= \frac{1}{a_1}\delta_{jj'}\delta_{n,n'}$ $\mathbb{I} = \sum_{n\in\mathbb{Z}} \sum_{j\in\mathbb{Z}} \lvert n,j\rangle\langle n,j\rvert$	$= J_{j'-\ell}(\nu)$
$\langle n',\ell'\rvert$					$= \delta_{\ell\ell'}\delta_{n,n'}$

diagonalized in (4.80), the total energy of the system is then obtained as the sum,

$$E = \sum_{n,q} E_q^{(n)} N_q^{(n)} \longrightarrow \sum_n \tfrac{a_1}{2\pi} \int_{-k_1}^{k_1} E_q^{(n)} N_q^{(n)} dq \ , \tag{4.111}$$

where $N_q^{(n)}$ is the number of atoms with quasi-momentum q in the n-th band and $E_q^{(n)}/2k_1$ is the spectral energy density. The transition to a continuous spectrum is valid in the limit of a large number of lattice sites. As usual, the 2nd quantization is done via the prescription,

$$N_q^{(n)} \quad \longrightarrow \quad \hat{N}_q^{(n)} \equiv \hat{\psi}_q^{(n)\dagger} \hat{\psi}_q^{(n)} \ , \tag{4.112}$$

where we defined a creation and an annihilation operator of a Bloch state, which satisfy a bosonic or fermionic commutation relation. In the tight binding limit, $\hat{H}$ breaks into bands, so that we can consider each band separately,

$$\hat{H} = \sum_n \hat{H}^{(n)} \qquad \text{with} \qquad \hat{H}^{(n)} = \tfrac{1}{2k_1} \int_{-k_1}^{k_1} E_q^{(n)} \hat{\psi}_q^\dagger \hat{\psi}_q dq \ , \tag{4.113}$$

where we suppressed the band index n at the field operators for simplicity of notation. This Hamiltonian coincides with the (4.92) provided we define the operator $\hat{\psi}_q^\dagger$ creating a Bloch state containing a single atom from vacuum as,

$$|n, q\rangle = \tfrac{1}{\sqrt{2k_1}} \hat{\psi}_q^\dagger |vac\rangle \ . \tag{4.114}$$

Correspondingly, the operator $\hat{w}_q^\dagger$ creates a Wannier state containing a single atom from vacuum,

$$|n, z_j\rangle \overset{(4.97)}{=} \int_{-k_1}^{k_1} \tfrac{e^{-\imath q z_j}}{\sqrt{2\pi}} |n, q\rangle dq = \tfrac{1}{\sqrt{2k_1}} \int_{-k_1}^{k_1} \tfrac{e^{-\imath q z_j}}{\sqrt{2\pi}} \hat{\psi}_q^\dagger |vac\rangle dq \equiv \tfrac{1}{\sqrt{a_1}} \hat{w}_j^\dagger |vac\rangle \ , \tag{4.115}$$

which satisfy the commutation relation $[\hat{w}_j, \hat{w}_j^\dagger] = 1$. From this follows,

$$\hat{w}_j^\dagger = \tfrac{1}{2k_1} \int_{-k_1}^{k_1} e^{-\imath q z_j} \hat{\psi}_q^\dagger dq \qquad \text{and} \qquad \hat{\psi}_q^\dagger = \sum_j e^{\imath q z_j} \hat{w}_j^\dagger \ . \tag{4.116}$$

Substituting the Bloch field operators, we can now rewrite the number operator and the Hamiltonian (4.113) in Wannier representation,

$$\begin{aligned} \hat{N}_j^{(n)} &= \hat{w}_j^\dagger \hat{w}_j \\ \hat{H}^{(n)} &= \tfrac{a_1}{2\pi} \sum_{j,j'} \int_{-a_1/\pi}^{a_1/\pi} E_q^{(n)} e^{\imath q (z_j - z_{j'})} \hat{w}_j^\dagger \hat{w}_{j'} dq \equiv - \sum_{j,j'} \mathfrak{J}(\Delta j) \hat{w}_j^\dagger \hat{w}_{j'} \ , \end{aligned} \tag{4.117}$$

where we defined as an the abbreviation the $\mathfrak{J}(\Delta j)$, called tunneling rate. *Notice, that the Hamiltonian is NOT diagonal in the Wannier basis, i.e. the Wannier states are NOT eigenstates of the optical lattice Hamiltonian, but of the kick operator, as stated in Sec. 4.2.3.* The expression $\hat{w}_j^\dagger \hat{w}_{j'}$ describes annihilation of an atom at lattice

site j' followed by its recreation at site j, that is, hopping from j' to j via quantum tunneling, if the lattice depth is deeper than the atom's energy. The tunneling rate is on one hand related to the matrix element, since,

$$\begin{aligned}\langle n, z_{j'}|\hat{H}^{(n)}|n, z_j\rangle &= -\langle n, z_{j'}|\sum_{i,i'}\mathfrak{J}(\Delta j)\hat{w}_{i'}^\dagger\hat{w}_i|n, z_j\rangle \\ &= -\langle vac|\sum_{i,i'}\mathfrak{J}(\Delta j)\delta_{i'j'}\delta_{ij}|vac\rangle = -\mathfrak{J}(\Delta j)\ .\end{aligned} \tag{4.118}$$

On the other hand,

$$\langle n, z_{j'}|\hat{H}^{(n)}|n, z_j\rangle = \int_{\mathbb{R}}\int_{\mathbb{R}}\langle n, z_{j'}|z'\rangle\langle z'|\left(\frac{\hat{p}_z^2}{2m} + V_0\cos^2 k_1\hat{z}\right)|z\rangle\langle z|n, z_j\rangle dz dz'\ . \tag{4.119}$$

With this we find,

$$\mathfrak{J}(\Delta j) = \mathfrak{J}(-\Delta j) = \mathfrak{J}^*(\Delta j)\ . \tag{4.120}$$

From the definition of $\mathfrak{J}(\Delta j)$ (4.117),

$$\boxed{-\mathfrak{J}(\Delta j) = \tfrac{a_1}{2\pi}\int_{-k_1}^{k_1} E_q^{(n)} e^{\imath q(z_{j'}-z_j)}dq = \int_{-1}^{1} E_q^{(n)}\cos(\pi\tilde{q}\Delta j)d\tilde{q}}\ , \tag{4.121}$$

where we exploited the fact $E_{-q}^{(n)} = E_q^{(n)}$. The expression (4.121) can be interpreted as Fourier coefficients of a Fourier expansion of the periodic function $E_q^{(n)}$,

$$E_q - \bar{E}_q = -2\sum_{\Delta j=1}^{\infty}\mathfrak{J}(\Delta j)\cos(a_1 q\Delta j)\ . \tag{4.122}$$

In other words, the dispersion relation $E_q^{(n)}$ allows evaluation of the tunneling rate between specific lattice sites j and j' via (4.121). The Hamiltonian in the Wannier state basis finally reads,

$$\boxed{\hat{H} = \sum_n\sum_{j,j'}\int_{-1}^{1} E_q^{(n)}\cos(\pi\tilde{q}\Delta j)d\tilde{q}\ \hat{w}_j^\dagger\hat{w}_{j'}\ .} \tag{4.123}$$

Example 41 (*Tight binding limit*): From Fig. 4.7 we see that for deep lattice, i.e. in the so-called *tight-binding regime* defined by $-V \gg \hbar\omega_{\rm rec}$ [369, 62, 193], the Wannier function decreases rapidly with the distance from the site. Then only nearest neighbor interactions are relevant, and the Hamiltonian simplifies to,

$$\begin{aligned}\hat{H} &= -\mathfrak{J}a_1\sum_{j,j'}|n, z_j\rangle\langle n, z_{j'}| \\ &\longrightarrow -\mathfrak{J}\sum_j|n, j+1\rangle\langle n, j| - \mathfrak{J}\sum_j|n, j-1\rangle\langle n, j| = -\mathfrak{J}[U_{\rm tr}(a_1) + U_{\rm tr}^\dagger(a_1)]\ ,\end{aligned} \tag{4.124}$$

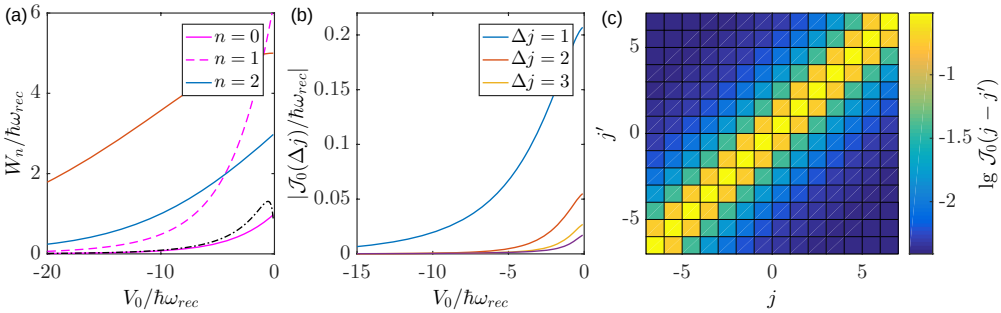

Figure 4.8: (code) (a) Width of allowed bands W_n as a function of potential depth V_0 for the lowest bands (see also Fig. 4.4). The dash-dotted line shows the tight-binding approximation (4.126). The magenta dashed line shows the width $W_0/\hbar\omega_{\rm blo}$ of the lowest band scaled to the Bloch oscillation frequency under the action of a force corresponding to $\omega_{\rm blo}/\omega_{\rm rec} = 0.158$, see Sec. 4.2.2. (b) Hopping rates between lattices sites distant by Δj as a function of V_0. (c) Two-dimensional representation of the hopping rates on a logarithmic false color scale $\lg W_0/\hbar\omega_{\rm rec}$.

and from (4.122),

$$E_q = -2\mathfrak{J}\cos(\pi\tilde{q}) \ . \tag{4.125}$$

As already illustrated in Fig. 4.4, with deepening potential $-V \longrightarrow \infty$ the allowed energy bands become thinner until they become discrete energy levels. This can be understood as an expression of a diminishing coupling between lattice sites, i.e. a diminishing tunneling rate. The band width can be shown to be approximated by [193],

$$\tilde{W}_1 \simeq \tfrac{16}{\sqrt{\pi}}\tilde{V}^{3/4}e^{-2\tilde{V}^{1/2}} \ , \tag{4.126}$$

in units of the recoil energy. The approximation is included in Fig. 4.8.

4.3 Bloch oscillations

Electrons moving in a crystal and exposed to electric fields undergo Bloch oscillations, as discussed in Sec. 4.1.4. An analogous phenomenon can be observed when neutral atoms in a vertical optical lattice are accelerated by gravity [189, 645]. To treat this case, we could simply replace the electric force $-e\vec{\mathcal{E}}$ in the expression (4.49) by the gravitational force mg and obtain the result,

$$\omega_{\rm blo} = \frac{mg\lambda_{\rm l}}{2\hbar} \ , \tag{4.127}$$

with the wavelength $\lambda_{\rm l} = 2a_{\rm l}$ of the counterpropagating lasers generating the standing wave. For didactic reasons, however, we will formulate the problem in the quantum optics language introduced in the previous section.

4.3.1 Bloch oscillations in shallow lattices in momentum space

4.3.1.1 Time-dependent Schrödinger equation

To reproduce the dynamics of a matter wave, we start from the time-dependent Schrödinger equation with the same periodic potential. We again expand the time-dependent wavefunction into plane waves via,

$$\psi(z,t) = \sum_{j=-\infty}^{\infty} c_j(t) e^{2\imath j k_1 z} \ , \tag{4.128}$$

and insert this ansatz into the Schrödinger equation,

$$\imath\hbar \frac{\partial \psi}{\partial t} = -\frac{\hbar^2}{2m}\frac{\partial^2 \psi}{\partial z^2} + \frac{V_0}{2}\cos(2k_1 z)\psi \ , \tag{4.129}$$

obtaining a set of equations of motion for the expansion coefficients c_n,

$$\boxed{\dot{c}_j = -4\imath\omega_{\rm rec} j^2 c_j + \frac{V_0}{2\imath\hbar}(c_{j+1} + c_{j-1})} \ . \tag{4.130}$$

The temporal evolution of the coefficients $c_j(t)$ can be simulated numerically.

Now we extend the Hamiltonian by the gravitational potential [11] (see also Exc. 1.7.6.2),

$$\hat{H} = -\frac{\hbar^2}{2m}\frac{\partial^2}{\partial z^2} + \frac{V_0}{2}\cos 2k_1\hat{z} + mg\hat{z} \ . \tag{4.131}$$

We define the transformation $\mathcal{U} \equiv e^{-\imath mg\hat{z}t/\hbar}$ and find with (1.267) and (1.316) the Hamiltonian in the accelerated frame,

$$\tilde{H} = \mathcal{U}^\dagger \hat{H}\mathcal{U} + \imath\hbar\dot{\mathcal{U}}^\dagger\mathcal{U} = \frac{\tilde{p}^2}{2m} + \frac{V_0}{4}\left(e^{2\imath k_1\hat{z}} + e^{-2\imath k_1\hat{z}}\right) \ . \tag{4.132}$$

with

$$\tilde{p} \equiv \hat{p} - mgt = \mathcal{U}^\dagger\hat{p}\mathcal{U} \ . \tag{4.133}$$

Now, we expand the operators using the rules (1.209) and (1.316) [12],

$$\begin{aligned} \tilde{p} &= \int p|p\rangle\langle p|dp \longrightarrow \sum_j (p + 2j\hbar k_1)|p + 2j\hbar k_1\rangle\langle p + 2j\hbar k_1| \\ e^{2\imath k_1\hat{z}} &= \int |p + 2\hbar k_1\rangle\langle p|dp \longrightarrow \sum_j |p + 2(j+1)\hbar k_1\rangle\langle p + 2j\hbar k_1| \ , \end{aligned} \tag{4.134}$$

based on the assumption that every atom can only exist in a superposition of discrete momentum states separated by $2\hbar k_1$, but can have an 'offset' momentum $p = mv$,

[11] For Bose-Einstein condensates, the procedure should be generalized taking into account the energy of the mean field due to interatomic collisions.

[12] See also (25.103) and (25.110).

e.g. due to thermal motion. Disregarding thermal motion, we may set in the accelerated frame $p = 0$. Then,

$$\tilde{p} = \sum_j 2j\hbar k_\mathrm{l} |2j\hbar k_\mathrm{l}\rangle\langle 2j\hbar k_\mathrm{l}| \qquad \text{and} \qquad e^{2\imath k_\mathrm{l}\hat{z}} = \sum_j |2j\hbar k_\mathrm{l} + 2\hbar k_\mathrm{l}\rangle\langle 2j\hbar k_\mathrm{l}| \ , \tag{4.135}$$

such that,

$$\tilde{H} = \sum_j 4j^2\hbar\omega_\mathrm{rec}|2j\hbar k_\mathrm{l}\rangle\langle 2j\hbar k_\mathrm{l}| + \tfrac{V_0}{4}\sum_j \left(|2j\hbar k_\mathrm{l} + 2\hbar k_\mathrm{l}\rangle\langle 2j\hbar k_\mathrm{l}| + |2j\hbar k_\mathrm{l}\rangle\langle 2j\hbar k_\mathrm{l} + 2\hbar k_\mathrm{l}|\right) \ . \tag{4.136}$$

With the expansion of the wavefunction $|\tilde{\psi}\rangle = \sum_j c_j|2j\hbar k_\mathrm{l}\rangle$ the Schrödinger equation becomes [721, 722],

$$\begin{aligned} \imath\hbar\frac{d}{dt}|\tilde{\psi}\rangle &= \imath\hbar\sum_j \dot{c}_j|2j\hbar k_\mathrm{l}\rangle \\ &= \sum_j \left(4j^2\hbar\omega_\mathrm{rec}c_j + \tfrac{V_0}{4}(c_{j-1} + c_{j+1})\right)|2j\hbar k_\mathrm{l}\rangle = \tilde{H}|\tilde{\psi}\rangle \ , \end{aligned} \tag{4.137}$$

that is,

$$\dot{c}_j = -4\imath j^2\omega_\mathrm{rec}c_j + \frac{V_0}{4\imath\hbar}(c_{j-1} + c_{j+1}) \ . \tag{4.138}$$

In the lab frame the wavefunction reads,

$$\begin{aligned} |\psi\rangle = \mathcal{U}|\tilde{\psi}\rangle &= e^{-\imath mg\hat{z}t/\hbar}\sum_j c_j|2j\hbar k_\mathrm{l}\rangle \\ &= \sum_j c_j|2n\hbar k_\mathrm{l} - mgt\rangle = \sum_j c_j|2\hbar k_\mathrm{l}(j - \nu_\mathrm{blo}t)\rangle \ , \end{aligned} \tag{4.139}$$

where we introduced the *Bloch frequency*,

$$\boxed{\nu_\mathrm{blo} = \frac{mg}{2\hbar k_\mathrm{l}}} \ . \tag{4.140}$$

Finally,

$$\boxed{\dot{c}_j = -4\imath(j - \nu_\mathrm{blo}t)^2\omega_\mathrm{rec}c_j + \frac{V_0}{4\imath\hbar}(c_{j-1} + c_{j+1})} \ . \tag{4.141}$$

The center-of-the mass momentum of the atomic matter wave is,

$$\frac{\langle p\rangle_{lab}}{\hbar k_\mathrm{l}} = \sum_j j|c_j(t)|^2 + \nu_\mathrm{blo}t \ . \tag{4.142}$$

4.3.1.2 Interpretation of Bloch oscillations as Bragg reflections

The Bloch oscillations can be understood in various pictures. The first one, illustrated in 4.9(a), is based on *Bragg reflection*: A resting atom has infinite de Broglie wavelength. Being constantly accelerated by gravity, the matter wave reduces its de

Broglie wavelength from ∞ to a value, where it becomes commensurate with the periodicity of the standing light wave potential. At this moment Bragg scattering comes into play, reflecting the atomic motion back into upward direction, and the process starts over again. The atoms evolve like jumping on a trampoline with a frequency given by ν_{blo}.

To understand the second picture, we need to address a question we have left aside so far, as this requires a notion of optical forces. It is the question in which way the matter wave interacts with the standing light wave. For the present discussion, it is sufficient to know that the atom must have an internal transition capable of scattering photons from the light beams. As any absorption and emission process transfers a recoil momentum of $\hbar k_{\mathrm{l}}$ to the atom, we can understand the Bragg scattering process as a so-called *Raman scattering* process: a photon of the laser beam generating the optical lattice coming from the left is absorbed and re-emitted to the left. This is best illustrated in the momentum domain sketched in Fig. 4.9(b). This Raman scattering transfers twice the photonic recoil to the atom. The requirement for commensurability of the Broglie wavelength and wavelength of the standing light wave is equivalent to saying that the matter wave momentum is equal to the recoil of a single photon. In other words, the matter wave always Bragg-reflected at the edge of a Brillouin zone.

Finally, in the *Bloch state picture*, the dispersion relation of a free particle is distorted due to the periodicity of the potential generated by the standing light wave such as to open a forbidden band. As a consequence, instead of being accelerated without limits, the atom enters the second Brillouin zone, which is to say that it is reflected to the other side of the first Brillouin zone.

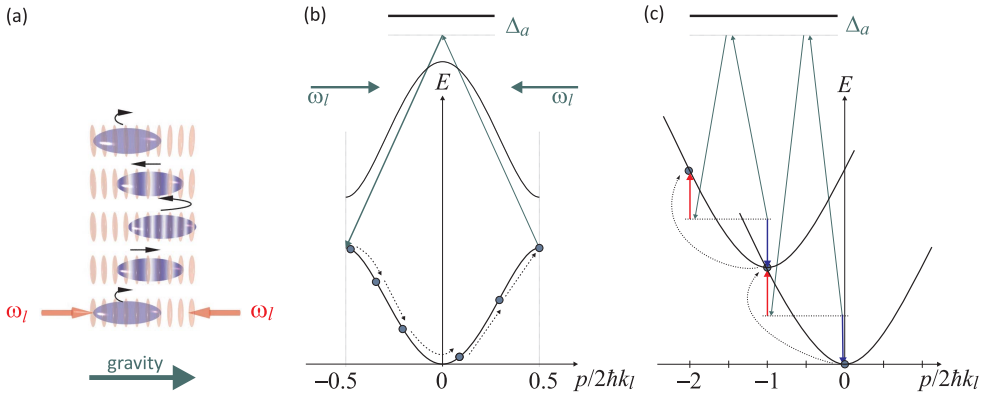

Figure 4.9: Illustration of Bloch oscillations (a) in real space, (b) in momentum space, and (c) in the moving frame. You may also run a movie of Bloch oscillations clicking on (watch movie)!

The additional term, which contains the frequency of the Bloch oscillation ν_{blo}, increases linearly over time. As time goes by, a resonance is crossed when $t = -j\tau_{\mathrm{blo}}$, and the crossing is periodically repeated at every $j = -1, -2, 0, \ldots$ Tracing the matter wave evolution in the laboratory system, we see that whenever the resonance is crossed, the momentum undergoes a change of sign corresponding to a reflection of its motion. We expand the population of the momentum states into plane (Bloch)

waves with $|c_j(t)|^2$.

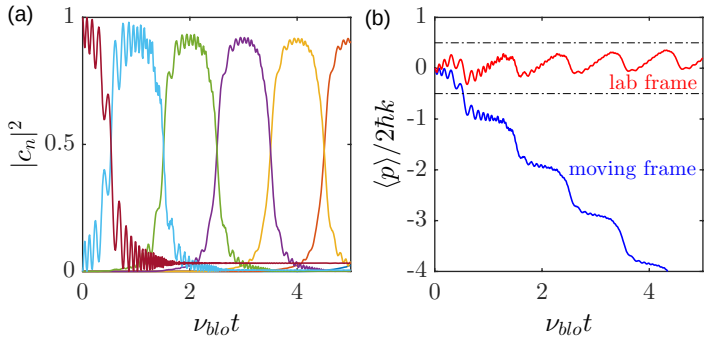

Figure 4.10: (code) Dynamics of Bloch's oscillations calculated from Eq. (4.130). (a) The colored curves show successively populated momentum states. (b) Center-of-mass motion of the wave packet in the lab frame (red) and in the moving frame (blue). The used parameters are $\omega_{\rm rec} = (2\pi)\ 4.8\,{\rm kHz}$, $2\pi\nu_{\rm blo} = 0.3\omega_{\rm rec}$, and $V_0 = -0.7\omega_{\rm rec}$.

Of course there are some conditions that need to be met to observe Bloch oscillations. The transfer of momentum is efficient only in the rapid adiabatic passage (ARP) regime characterized by the conditions $2(\nu_{\rm blo}/\omega_{\rm rec}) \ll (V_0/4\omega_{\rm rec})^2 \ll 16$. The first condition requires that the force that drives the atoms to perform the Bloch oscillations must be weak enough to avoid transitions between Bloch bands, which guarantees the adiabaticity of the process. The other condition requires that the optical lattice be weak enough so that the dynamics involves only two adjacent momentum states at the same time and the transfer between the two is successful. A talk on this subject can be watched at (watch talk). Do the Excs. 4.3.4.5 and 4.3.4.6.

We will come back to the topic of optical lattices holding matter waves in Sec. 28.4.2 in the context of Mott insulating states of Bose-Einstein condensates.

4.3.2 Bloch oscillations in the tight binding regime in position space

4.3.2.1 Wannier-Stark ladder

In the presence of an external force, the tight-binding Hamitonian (4.124) in the Wannier basis is generalized to,

$$\begin{aligned}\hat{H} &= -\mathfrak{J}\sum_{\pm}\sum_{j\in\mathbb{Z}}\hat{w}^\dagger_{j\pm1}\hat{w}_j + mga_{\rm l}\sum_{j\in\mathbb{Z}} j\hat{w}^\dagger_j\hat{w}_j \\ &= -\mathfrak{J}a_{\rm l}\sum_{\pm}\sum_{j\in\mathbb{Z}}|n,z_{j\pm1}\rangle\langle n,z_j| + mga_{\rm l}{}^2\sum_{j\in\mathbb{Z}} j|n,z_j\rangle\langle n,z_j|\ .\end{aligned} \tag{4.143}$$

Expanding the Wannier states in the Bloch basis via insertion of the completeness relation $\mathbb{I} = \int_{-k_{\rm l}}^{k_{\rm l}}|n,q\rangle\langle n,q|dq$, using $\langle n,z_j|n,q\rangle \overset{(4.107)}{=} \breve{e}^{ijqa_{\rm l}}$, and $\hat{w}^\dagger_j|vac\rangle \overset{(4.115)}{=} |n,j\rangle$,

we obtain,

$$\begin{aligned}\hat{H} &= -\mathfrak{J}a_1\frac{1}{2\pi}\sum_{\pm}\int_{-k_1}^{k_1}\int_{-k_1}^{k_1}|n,q\rangle e^{\mp\imath a_1 q}\sum_{j\in\mathbb{Z}}e^{\imath(q'-q)ja_1}\langle n,q'|dqdq' \\ &\qquad + mg{a_1}^2\frac{1}{2\pi}\int_{-k_1}^{k_1}\int_{-k_1}^{k_1}|n,q\rangle\sum_{j\in\mathbb{Z}}je^{\imath(q'-q)ja_1}\langle n,q'|dqdq' \\ &= -\mathfrak{J}a_1\frac{1}{2\pi}\sum_{\pm}\int_{-k_1}^{k_1}\int_{-k_1}^{k_1}|n,q\rangle e^{\mp\imath a_1 q}\frac{2\pi}{a_1}\delta(q'-q)\langle n,q'|dqdq' \\ &\qquad + mg{a_1}^2\frac{1}{2\pi}\int_{-k_1}^{k_1}\int_{-k_1}^{k_1}|n,q\rangle\frac{2\pi}{a_1}\delta(q'-q)\frac{\imath}{a_1}\frac{d}{dq}\langle n,q'|dqdq' \\ &= -\int_{-k_1}^{k_1}|n,q\rangle\left(2\mathfrak{J}\cos a_1 q - mg\,\imath\frac{d}{dq}\right)\langle n,q|dq \equiv \int_{-k_1}^{k_1}|n,q\rangle\hat{H}(q)\langle n,q|dq\ ,\end{aligned} \tag{4.144}$$

using the definition of the Bloch frequency (4.140), $mga_1 = \hbar\omega_{\rm blo}$. Obviously, the Hamiltonian (4.144) is diagonal in the quasi-momentum basis. The first term is the force-free dispersion relation, while the second one introduces an energy shift known as *Wannier-Stark ladder*. The eigenstates of the Hamiltonian

$$\hat{H}\langle n,q|\ell\rangle = \left(-2\mathfrak{J}\cos a_1 q + mg\,\imath\frac{d}{dq}\right)\langle n,q|\ell\rangle = E\langle n,q|\ell\rangle \tag{4.145}$$

are the Wannier-Stark states, whose **Bloch** or **quasi-momentum representation** is given by,

$$\langle n,q|n,\ell\rangle = \sqrt{\tfrac{a_1}{2\pi}}e^{-\imath[\ell q a_1 + 2\mathfrak{J}\sin(a_1 q)/(\hbar\omega_{\rm blo})]} = \sqrt{\tfrac{a_1}{2\pi}}e^{-\imath(jqa_1+\nu\sin a_1 q)}\ . \tag{4.146}$$

where we introduced the abbreviation,

$$\nu \equiv \frac{2\mathfrak{J}}{mga_1}\ . \tag{4.147}$$

With this normalization factor, these states obviously form an orthonormal basis,

$$\langle n,\ell'|n,\ell\rangle = \int_{-k_1}^{k_1}\langle n,\ell'|n,q\rangle\langle n,q|n,\ell\rangle dq = \delta_{\ell'\ell}\ . \tag{4.148}$$

Inserting them into the differential equation (4.145), we find,

$$\boxed{E_\ell = \ell\hbar\omega_{\rm blo} = \ell a_1 mg\ .} \tag{4.149}$$

4.3.2.2 Various representations of Wannier-Stark states

Apart from the Bloch representation (4.146), which projects the Wannier-Stark states $|n,\ell\rangle$ onto the Bloch basis $\langle n,q|$, we already got to know three other representations: The Wannier representation projecting onto the Wannier basis $\langle n,z_j|$, the position representation projecting onto $\langle z|$, and the momentum representation projecting onto $\langle k|$. Let us now derive the explicit wavefunctions of the various representations.

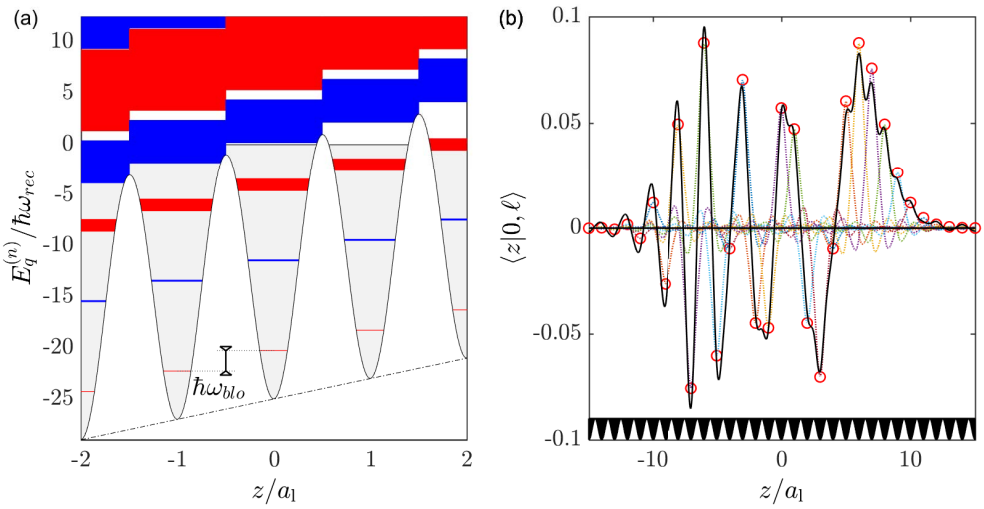

Figure 4.11: (code) (a) Wannier-Stark ladder for $V_0 = -25\hbar\omega_{\rm rec}$ and $\omega_{\rm blo} = 2\omega_{\rm rec}$. (b) Wannier representation (red circles) and position representation (black solid line) for $V_0 = -\hbar\omega_{\rm rec}$ and $\omega_{\rm blo} = 0.1\omega_{\rm rec}$ corresponding to $\nu = 7.7$ [369].

The **Wannier** or **lattice site representation** of the Wannier-Stark states is obtained from the Bloch representation (4.146) via Fourier transform, $\langle n, z_j|n, q\rangle = e^{\imath q z_j}/\sqrt{2\pi}$,

$$\begin{aligned}\langle n, z_j|n, \ell\rangle &= \int_{-k_l}^{k_l} \langle n, z_j|n, q\rangle\langle n, q|n, \ell\rangle dq \\ &= \int_{-k_l}^{k_l} \frac{e^{\imath q z_j}}{\sqrt{2\pi}} \sqrt{\frac{a_l}{2\pi}} e^{-\imath(\ell q a_l - \nu \sin a_l q)} dq \\ &= \frac{1}{2\pi\sqrt{a_l}} \int_{-\pi}^{\pi} e^{\imath(j-\ell)\tilde{q} - \imath\nu\sin\tilde{q}} d\tilde{q} = \frac{1}{\sqrt{a_l}} J_{j-\ell}(\nu)\ ,\end{aligned} \tag{4.150}$$

with the definition of the Bessel function [13]. Hence,

$$|n, \ell\rangle = a_l \sum_j |n, z_j\rangle\langle n, z_j|n, \ell\rangle = \sum_j J_{j-\ell}(\nu)|n, j\rangle\ . \tag{4.151}$$

The **position** and the **momentum representation** of the Wannier-Stark states are obtained from the position (respectively momentum) representations of the Wannier states,

$$\langle z|n, \ell\rangle = \sqrt{a_l}\sum_j J_{j-\ell}(\nu)\langle z|n, z_j\rangle \quad , \quad \langle k|n, \ell\rangle = \sqrt{a_l}\sum_j J_{j-\ell}(\nu)\langle k|n, z_j\rangle\ . \tag{4.152}$$

The position representation is visualized in Fig. 4.11(b). The momentum representa-

[13] $J_{m-n}(x) = \frac{1}{2\pi}\int_{-\pi}^{\pi} e^{\imath(m-n)u - \imath x\sin u} du$.

tion can alternatively be derived from (4.146),

$$\langle k|n,\ell\rangle = \langle k|\int_{-k_1}^{k_1}|n,q\rangle\langle n,q|dq|n,\ell\rangle = \int_{-k_1}^{k_1} c_k e^{-\imath(jqa_1-\nu\sin a_1 q)}dq\ . \tag{4.153}$$

From the properties of the Bessel functions we know that $J_{j-\ell}(\nu)$ is mainly localized in the interval $|j-\ell|<\nu$, i.e. the Wannier-Stark states extend over an interval ν. Outside this interval, the Bessel functions decay as $J_j(\nu)\propto\nu^j$. Furthermore, the Bessel functions strongly oscillate for negative values of the index because of the property $J_{-j}(\nu)=(-1)^jJ_j(\nu)$. We will see that the spatial extension of the Wannier-Stark state determines the boundaries of the Bloch oscillations [14]. The various representations of Wannier-Stark states are included in Tab. 4.2.

4.3.2.3 Bloch oscillations

Without external forcing the periodic potential is translation invariant, which entails complete delocalization of the spatial wavefunction in steady-state: If an atom can tunnel from site j to $j+1$, it also can tunnel from $j+1$ to $j+2$. The situation changes when an external force is applied because, according to Eq. (4.149), the energy bands are shifted between sites by an amount $h\nu_{\rm blo}$, see Fig. 4.11. This energy mismatch spoils the overlap between the Wannier functions at different sites and, as no energy is dissipated, energy conservation requires the states to remain localized: Tunneling violating energy conservation is only possible during a time period corresponding to the Heisenberg uncertainty relation, $\Delta t = h/\Delta E = \nu_{\rm blo}^{-1}$. That is, an atom trying to tunnel to other lattice site must return to its original position after a period $\nu_{\rm blo}^{-1}$. Let us now derive this quantitatively.

The evolution operator in the Bloch state basis [369] is obtained inserting the Wannier-Stark states (4.146) and the energy spectrum (4.149) into the propagator,

$$\begin{aligned}\mathcal{U}_{qq'}(t) &= \langle n,q'|e^{-\imath\hat{H}t}|n,q\rangle = \sum_j\langle n,q'|\ell\rangle e^{-\imath E_j t}\langle\ell|n,q\rangle \\ &= \tfrac{a_1}{2\pi}e^{-\imath\nu(\sin a_1 q-\sin a_1 q')}\sum_j e^{\imath j[(q-q')a_1-\hbar\omega_{\rm blo}t]} \\ &= e^{-\imath\nu(\sin a_1 q-\sin a_1 q')}\delta(q-q'-mgt)\ .\end{aligned} \tag{4.154}$$

The evolution operator in the Wannier state basis will be derived in Exc. 4.3.4.9,

$$\begin{aligned}\mathcal{U}_{jj'}(t) &= \langle n,j'|e^{-\imath\hat{H}t}|n,j\rangle = \sum_\ell\langle n,j'|\ell\rangle e^{-\imath E_\ell t}\langle\ell|n,j\rangle \\ &= e^{\imath(j-j')(\pi-\omega_{\rm blo}t)/2-\imath j'\omega_{\rm blo}t}J_{j-j'}(2\nu\sin\tfrac{\omega_{\rm blo}t}{2})\ .\end{aligned} \tag{4.155}$$

The propagators (4.154), respectively, (4.155) allow to calculate the time evolution of a wave packet. Fig. 4.12 visualizes the dynamics of a wave packet in a tilted periodic

[14] The Wannier-Stark states are orthonormalized. However, this breaks down in the presence of a cavity. After delocalization, only the overlap between the Wannier-Stark states and the cavity mode function couples to the cavity.

potential for different initial conditions, localized or spread over several lattice sites. We see that the Wannier states extend over a maximum number of populated sites,

$$|j| < \nu \left|\sin \tfrac{\nu_{\rm blo} t}{\pi}\right| \ , \tag{4.156}$$

The spreading of a wave packet is proportional to the width of an energy band, but depends inversely on $h\nu_{\rm blo}$, see Fig. 4.8(c). Hence, in order to maximize the spreading it is important to use a band n near the threshold $E^{(n)} \lesssim 0$.

Fig. 4.12 shows a simulation of,

$$\langle n, z_j | n, \ell(t)\rangle = \langle n, z_j | \mathcal{U}_{jj'}(t) | n, \ell(0)\rangle \tag{4.157}$$

with some initial distribution $\ell(0)\rangle = \sum_j c_j(0)|n, j\rangle$. The simulation reveals, that initial incoherent superpositions of many Wannier states localized in adjacent sites tend to wash out the oscillations.

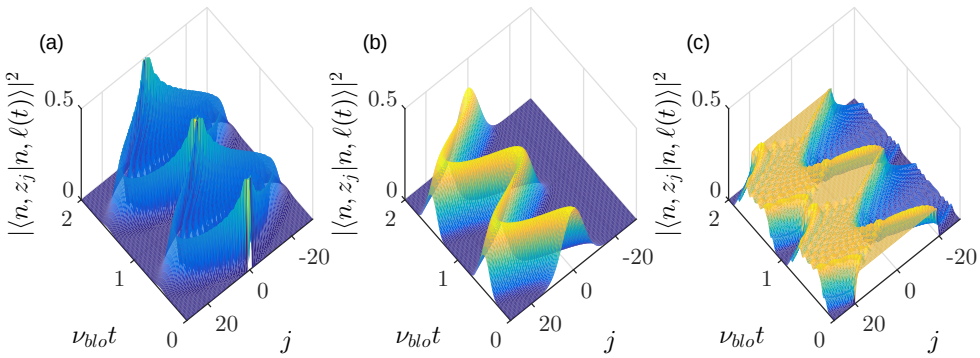

Figure 4.12: (code) Bloch oscillations in the tight-binding limit for $\nu = 25$. (a) The wave packet is assumed initially perfectly localized at a single lattice site, $|n, \ell(0)\rangle = \sum_j \delta_{0,j}|0, j\rangle$. (b) The wave packet is assumed initially spread over a $\sigma = 5$ lattice site large Gaussian distribution, $|n, \ell(0)\rangle = (\pi\sigma^2)^{-1/4} \sum_j e^{-j^2/2\sigma^2}|0, j\rangle$. (c) The wave packet is assumed initially spread equally over $j_{\rm max} = 25$ lattice sites, $|n, \ell(0)\rangle = (2j_{\rm max})^{-1/2} \sum_j \Theta(j_{\rm max} - |j|)|0, j\rangle$.

Example 42 (*Wavepacket propagation in the tight binding limit*): It is possible to impart a momentum to the wavepacket by multiplying the initial Wannier state distribution with a phase factor,

$$|n, \ell(0)\rangle = \sum_j e^{\imath j p} |n, j\rangle \ ,$$

as shown in Fig. 4.13(a).

Interestingly, the Bloch oscillations can be used to realize unidirectional quantum transport in a flipped *quantum ratchet* scheme. One just has to phase shift the standing wave potential after each Bloch oscillation period, as shown in Fig. 4.13(b) [369, 537, 705].

Example 43 (*Exciting and probing Bloch oscillations*): Bloch oscillations may excited by sudden quench or periodic modulation [902]. They may be probed by Raman spectroscopy [62], see Fig. 4.11(b).

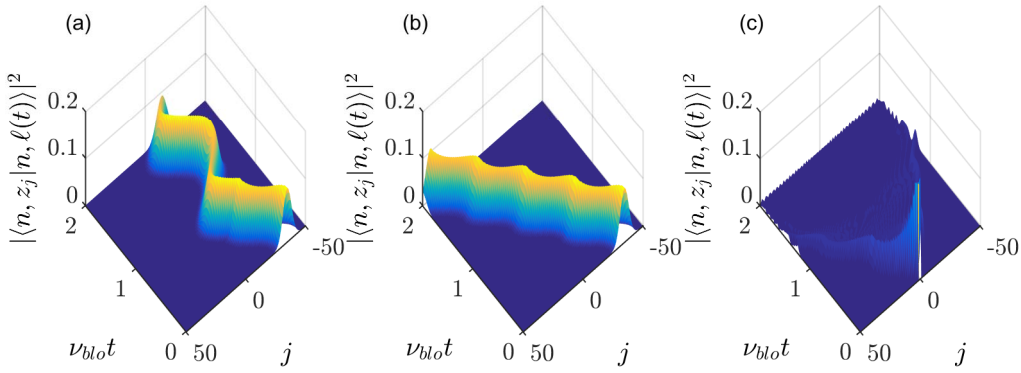

Figure 4.13: (code) (a) Propagation of a Gaussian wavepacket spread over a $\sigma = 5$ and initially localized around $z_j = -35a_1$. At time $t = \pi/2\omega_{\rm blo}$ a momentum kick $p = \pi$ is imparted to the wavepacket. (b) Propagation of the same Gaussian wavepacket when the phase of the periodic potential is shifted by π after each Bloch period. (c) Same as (b), but the particle is initially localized at a single lattice site $z_j = 0$.

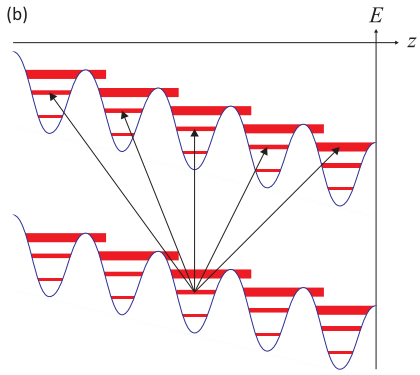

Figure 4.14: (b) Raman spectroscopy of the ladder states [62].

4.3.3 Extensions of the Bloch-Wannier model

4.3.3.1 Interacting atoms and three-dimensional lattices

As long as the particles in the lattice do not interact with each other the Bloch-Wannier model developed so far is sufficient to grasp all phenomena. Indeed, as long as the atoms evolve independently, the occupation probabilities of lattice sites are simply reinterpreted as populations. Nevertheless, an important advantage of Wannier basis is that it can be generalized to include interatomic interactions. The model, called the *Hubbard model*, will be investigated later in Sec. 28.4.2, where we will also extend it to three dimensions.

4.3.3.2 Interband transitions

The bands are separated by gaps. Hence, transitions can only occur due to time-dependent perturbations with Fourier frequencies sufficiently high to bridge the gap, see Sec. 5.4.3. The motion of an atom in the lattice potential represents such a perturbation, provided it is sufficiently fast. Such transitions are called *Landau-Zener transitions*. A rapid change of the lattice depth or energetic interatomic collisions represent other sources of interband transitions.

4.3.4 Exercises

4.3.4.1 Ex: Bloch theorem

Verify that,

$$\hat{H}|\psi_k\rangle = E_k|\psi_k\rangle \quad \Longrightarrow \quad \left(\frac{(\hat{k}+\kappa)^2}{2m} + V(z)\right)|u_k\rangle = E_k|u_k\rangle \ .$$

4.3.4.2 Ex: Spatial wavefunction of the Wannier state for the first band

Find the spatial wavefunction of the Wannier state for the first band, $w^{(1)}(z)$, in the case of $V = 0$. Plot the function, and give the location of its nodes.

4.3.4.3 Ex: Orthonormality of Wannier states

Show that, for the ground band, $|w_j\rangle$ and $|w_{j'}\rangle$ are orthogonal for $j \neq j'$.

4.3.4.4 Ex: Gaussian approximation for Wannier function

Consider a standing light wave producing a dipolar potential of the shape $V(x) = W_0 \sin^2 kx = \frac{W_0}{2} - \frac{W_0}{2}\cos 2kx$ with $W_0 \mathbf{G} g E_{\rm rec} = (\hbar k)^2/2m$.
a. Approximate the potential of a single lattice site around $x = 0$ by a harmonic potential. Calculate for which depth of the dipolar potential the approximated potential supports at least one bound state. What is the spacing of the levels and the characteristic size of the harmonic oscillator $a_{\rm ho}$. Write down the normalized ground state wavefunction of the harmonic oscillator.
b. Now, let us consider a 3D cubic lattice made of three identical orthogonal standing light waves. Approximate the ground state *Wannier function* of a lattice site by appropriately normalized ground state wavefunctions of a harmonic oscillator. Derive the formula $U^{\rm 3D} = \frac{8}{\pi} k a_d \left(\frac{W_0}{E_{\rm rec}}\right)^{3/4}$ starting from,

$$U^{\rm 3D} = g^{\rm 3D} \int \omega^4_{(0,0)}(x,y,z) d^3r$$

with $g^{\rm 3D} = \frac{4\pi\hbar a_d}{m}$.

4.3.4.5 Ex: Purification of Bloch oscillations

Simulations of Bloch oscillations of atoms in an optical lattice for $V_0 = 0.4\omega_{\rm rec}$ and $0.8\omega_{\rm rec}$ produce the dynamics exhibited in Fig. 4.15. Interpret the different behaviors.

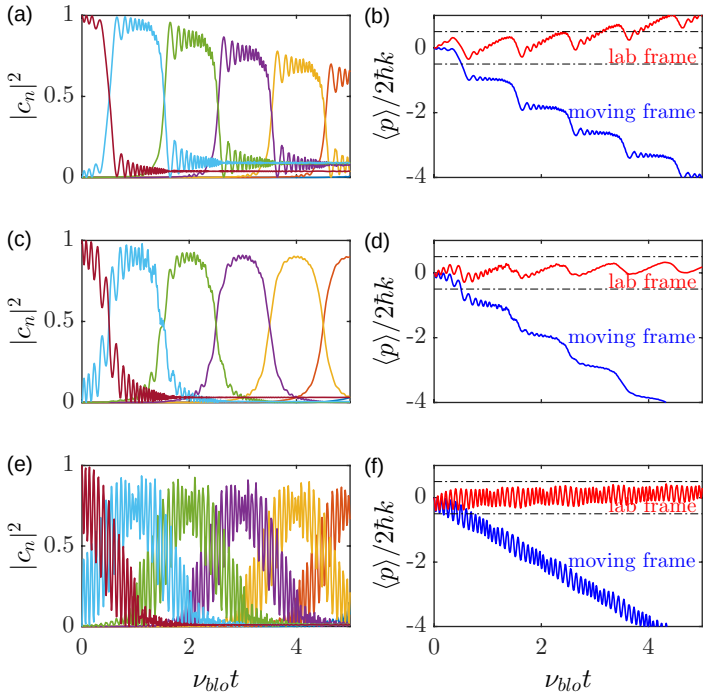

Figure 4.15: (code) Dynamics of Bloch oscillations (a-b) for $V_0 = 0.4\omega_{\rm rec}$, (c-d) for $V_0 = 0.8\omega_{\rm rec}$, and (e-f) for $V_0 = 1.6\omega_{\rm rec}$. Furthermore, $\omega_{\rm rec} = (2\pi)\ 4.8\,\text{kHz}$ and $\nu_{\rm blo} = 0.05\omega_{\rm rec}$.

4.3.4.6 Ex: Two-mode model for Bloch oscillations

Simplify the Bloch oscillation model assuming that at any time *at most* two momentum modes can be coupled via Bragg reflection.

4.3.4.7 Ex: Perturbative treatment of a weak lattice

A weak lattice potential with $V_0 < E_{\rm rec}$ can be treated in perturbation theory to motivate the resulting opening of a gap in the refolded energy parabola. The unperturbed Hamiltonian $\hat{H}_0 = p^2/2m$ contains only the kinetic energy and the perturbation is $V(z) = V\sin^2(kz) = \frac{1}{2}V - \frac{1}{4}V(e^{2\imath kz} + e^{-2\imath kz})$.

a. Calculate $\hat{V}(z)\phi_p(z)$ and show that $\langle\phi_{p\pm\hbar k}|\hat{V}|\phi_p\rangle$ are the only non-zero matrix elements of the perturbation $V(z)$ between the eigenstates of $\hat{H}_0$ (which are the orthonormal plane waves $\phi_p = e^{\imath pz/\hbar}$). Neglect the constant term of the potential, which only yields a global energy shift.

b. This coupling is relevant around those momenta p, where ϕ_p has the same energy $\phi_{p+\hbar k}$ or $\phi_{p-\hbar k}$. Show that these momenta are $p = \mp\hbar k$.
c. Consider the perturbed system restricted to the basis $\{|p = -\hbar k\rangle, |p = +\hbar k\rangle\}$ and give the Hamiltonian as 2×2 matrix.
d. Diagonalize the matrix and consider the difference of the eigenenergies. Use them to estimate the size of the gap, that the lattice opens between the two lowest bands.
e. Calculate the eigenstates and interpret them by comparing the probability density to the lattice potential.

4.3.4.8 Ex: Wannier-Stark ladder for strontium

For the strontium intercombination line the Bloch and the recoil frequencies are $\omega_{\text{blo}} = 2\pi\frac{mg}{2\hbar k} = (2\pi)\,786\,\text{Hz}$ and $\omega_{\text{rec}} = \frac{\hbar k^2}{2m} = (2\pi)\,4530\,\text{kHz}$, respectively. Calculate the Wannier-Stark ladder.

4.3.4.9 Ex: Propagator for Bloch oscillations in the Wannier basis

Derive the formula (4.155) for the time evolution in the Wannier basis.

4.4 Further reading

B. Pelle et al., *State-labeling Wannier-Stark atomic interferometers* [DOI]

Min-Kang Zhou et al., *Atomic multiwave interferometer in an optical lattice* [DOI]

T. Hartmann et al., *Dynamics of Bloch oscillations* [DOI]

N. Marzari et al., *Maximally localized Wannier functions: Theory and applications* [DOI]

L. Guidoni et al., *Optical Lattices: Cold Atoms Ordered by Light* [DOI]

N. Marzari et al., *Nonlinear Landau-Zener tunneling* [DOI]

E. Peik et al., *Bloch Oscillations of Atoms, Adiabatic Rapid Passage, and Monokinetic Atomic Beams* [DOI]

J. Zapata, *Gravity-induced Wannier-Stark ladder in an optical lattice* [DOI]

I. Bloch, *Ultracold quantum gases in optical lattices* [DOI]

J. Dalibard, *Optical traps and optical lattices* [http]

J.H. Thywissen, *Ultracold atoms in lattices* [http]

Chapter 5

Approximation methods

Virtually every problem going beyond the potential well, the harmonic oscillator, or the hydrogen atom without spin and external fields is impossible to solve analytically. In this chapter we will talk about techniques to solve approximately problems in more realistic situations. There are a number of methods of which we will discuss the only following: 1. The stationary or time-dependent perturbation method is useful for evaluating small perturbations of the system, for example, caused by external electric or magnetic fields; 2. the variational method, which serves to find and improve trial wavefunctions, the initial shapes of which are generally motivated by the symmetries of the system; 3. the semi-classical WKB method; 4. and finally the method of self-consistent fields, which is an iterative method of solving the Schrödinger equation.

5.1 Stationary perturbations

5.1.1 Time-independent perturbation theory

We first introduce *time-independent perturbation theory* (TIPT) for multilevel systems. We separate the Hamiltonian into an unperturbed part,

$$\hat{H}^{(0)}|\psi^{(0)}\rangle = E^{(0)}|\psi^{(0)}\rangle \ , \tag{5.1}$$

and perturbations, which are proportional to a small parameters λ,

$$\hat{H} = \hat{H}^{(0)} + \lambda\hat{H}^{(1)} + \lambda^2\hat{H}^{(2)} + .. \ . \tag{5.2}$$

The perturbed wavefunctions are,

$$|\psi\rangle = |\psi^{(0)}\rangle + \lambda|\psi^{(1)}\rangle + \lambda^2|\psi^{(2)}\rangle + .. \ , \tag{5.3}$$

and the energies

$$E = E^{(0)} + \lambda E^{(1)} + \lambda^2 E^{(2)} + .. \ . \tag{5.4}$$

The contributions $\propto \lambda^n$ are the *corrections* of order n. The equation we need to solve now is,

$$\hat{H}|\psi\rangle = E|\psi\rangle \ . \tag{5.5}$$

By inserting all the expansions above and segregating all orders of λ^k, we find the following system of equations,

$$\begin{aligned} \hat{H}^{(0)}|\psi^{(0)}\rangle &= E^{(0)}|\psi^{(0)}\rangle \\ (\hat{H}^{(0)} - E^{(0)})|\psi^{(1)}\rangle &= (E^{(1)} - \hat{H}^{(1)})|\psi^{(0)}\rangle \\ (\hat{H}^{(0)} - E^{(0)})|\psi^{(2)}\rangle &= (E^{(2)} - \hat{H}^{(2)})|\psi^{(0)}\rangle + (E^{(1)} - \hat{H}^{(1)})|\psi^{(1)}\rangle \\ &\dots \ . \end{aligned} \tag{5.6}$$

5.1.1.1 First order energy correction

We now consider eigenstates $|\psi_n^{(1)}\rangle$ of the perturbed system and expand the first-order correction of the wavefunction in a linear combination of unperturbed eigenvectors $|\psi_n^{(0)}\rangle \equiv |n\rangle$,

$$|\psi_n^{(1)}\rangle = \sum_m |m\rangle\langle m|\psi_n^{(1)}\rangle \ . \tag{5.7}$$

We insert this expansion into the second equation (5.6) and multiply with $\langle n|$,

$$\langle n|(\hat{H}^{(0)} - E_n^{(0)})\sum_m |m\rangle\langle m|\psi_n^{(1)}\rangle = 0 = \langle n|E_n^{(1)} - \hat{H}^{(1)}|n\rangle \ . \tag{5.8}$$

We obtain for the first order correction of the energy of unperturbed states,

$$\boxed{E_n^{(1)} = \langle n|\hat{H}^{(1)}|n\rangle} \ . \tag{5.9}$$

As a first example we will calculate in Exc. 5.1.3.1 the first order correction for the energy of a slightly deformed one-dimensional box potential.

5.1.1.2 First order correction for the wavefunction

Now let us have a look at the first-order correction for the wavefunction again considering the second equation (5.6),

$$\langle m|\hat{H}^{(0)} - E_n^{(0)}|\psi_n^{(1)}\rangle = \langle m|E_n^{(1)} - \hat{H}^{(1)}|n\rangle \ . \tag{5.10}$$

When $n = m$, the left side of this equation disappears. Therefore, $E_n^{(1)} - \langle n|\hat{H}^{(1)}|n\rangle = 0$, and we can restrict to the terms $n \neq m$ discarding the terms in $E_n^{(1)}$,

$$\langle m|\psi_n^{(1)}\rangle = \frac{E_n^{(1)}\delta_{mn} - \langle m|\hat{H}^{(1)}|n\rangle}{E_m^{(0)} - E_n^{(0)}} = \frac{\langle m|\hat{H}^{(1)}|n\rangle}{E_n^{(0)} - E_m^{(0)}} \ . \tag{5.11}$$

We obtain for the first-order correction for the energy of the states,

$$\boxed{|\psi_n^{(1)}\rangle = \sum_m |m\rangle\langle m|\psi_n^{(1)}\rangle = \sum_{m\neq n} |m\rangle \frac{\langle m|\hat{H}^{(1)}|n\rangle}{E_n^{(0)} - E_m^{(0)}}} \ . \tag{5.12}$$

This procedure simulates the distortion of the state by blending it with other states. The perturbation induces virtual transitions to other states. The perturbation is large when the blended levels are close.

See Exc. 5.1.3.2. In Exc. 5.1.3.3 we calculate the first order correction due to the finite extension of the hydrogen nucleus. In Exc. 5.1.3.4 we treat the coupling of the energy levels of a two-level system as a first order perturbation, and compare the result with the exact solution. The Stark effect for an electron confined in a box can be discussed (see Exc. 5.1.3.5) in first order TIPT.

5.1.1.3 Second order correction for the energy

To calculate the second order correction for the energy we expand the second order correction,

$$|\psi_n^{(2)}\rangle = \sum_m |m\rangle\langle m|\psi_n^{(2)}\rangle \ , \tag{5.13}$$

import it into the third equation (5.6) and multiply with $\langle n|$,

$$\langle n|(\hat{H}^{(0)}-E_n^{(0)})\sum_m |m\rangle\langle m|\psi_n^{(2)}\rangle = \langle n|(E_n^{(2)}-\hat{H}^{(2)})|n\rangle+\langle n|(E_n^{(1)}-\hat{H}^{(1)})\sum_m |m\rangle\langle m|\psi_n^{(1)}\rangle \ . \tag{5.14}$$

Now,

$$\sum_m \langle m|\psi_n^{(2)}\rangle(E_n^{(0)}-E_m^{(0)})\delta_{nm} = 0 = E_n^{(2)}-\langle n|\hat{H}^{(2)}|n\rangle+\sum_m \langle m|\psi_n^{(1)}\rangle\left(E_n^{(1)}\delta_{nm} - \langle n|\hat{H}^{(1)}|m\rangle\right) \ . \tag{5.15}$$

The left-hand side of this equation disappears. Also, on the right-hand side, for $n \neq m$, the term $E_n^{(1)}\delta_{nm}$ disappears, and for $n = m$ the whole parenthesis disappears. Therefore, we can discard the term $E_n^{(1)}$ and restrict the sum to terms with $n \neq m$. Inserting the coefficients $\langle m|\psi_n^{(1)}\rangle$ calculated in (5.11), we finally obtain,

$$\boxed{E_n^{(2)} = \langle n|\hat{H}^{(2)}|n\rangle + \sum_{m\neq n} \frac{\langle n|\hat{H}^{(1)}|m\rangle\langle m|\hat{H}^{(1)}|n\rangle}{E_n^{(0)} - E_m^{(0)}}} \ . \tag{5.16}$$

The first term is similar to the first order correction; the eigenvalue of the second order perturbation calculated in the base of the unperturbed states. The second term describes the shift of the energies through possible temporary transitions to other states.

In Exc. 5.1.3.6 we treat a system of three coupled levels up to the second perturbative order. The Stark effect discussed in Exc. 5.1.3.7 needs the TIPT calculation up to the second order.

5.1.2 TIPT with degenerate states

Exact calculations show that the effect of a perturbation is larger – but finite – for degenerate states. On the other hand, from the above expressions for the corrections of both energies and wavefunctions, we would infer that these corrections can become very large for small perturbations or even diverge.

Fortunately, the fact that every linear combination of degenerate wavefunctions is an eigenfunction of the Hamiltonian as well gives us the freedom to choose the combination, which is most similar to the final form of the perturbed wavefunctions.

For example, considering a perturbation by a magnetic field it may be advantageous to expand the spherical functions Y_{lm} on a basis of cylindrical coordinates [1]. We will see in the following that we can solve both problems, the selection of the initial combination and the prevention of divergent denominators at once, without explicitly specifying the expansion.

We consider eigenstates $|n,\nu\rangle$ with the energy $E_n^{(0)}$ being r times degenerate with respect to the quantum number ν, where $\nu = 1,..,r$. All states satisfy

$$\hat{H}^{(0)}|n,\nu\rangle = E_n^{(0)}|n,\nu\rangle \ . \tag{5.17}$$

We construct linear combinations that most resemble the perturbed states

$$|\psi_{n\mu}^{(0)}\rangle = \sum_{\nu=1}^{r} c_{\mu\nu}|n,\nu\rangle \ . \tag{5.18}$$

When the perturbation $\hat{H}^{(1)}$ is applied, we assume that the state $|\psi_{n\mu}^{(0)}\rangle$ is distorted towards the similar state $|\psi_{n\mu}\rangle$, and the energy changes from $E_n^{(0)}$ to $E_{n\mu}$. We now need the index μ to label the energy, since the degeneracy can be removed by the perturbation. As before, we write now,

$$\begin{aligned} \hat{H} &= \hat{H}^{(0)} + \lambda\hat{H}^{(1)} + .. \\ |\psi_{n\mu}\rangle &= |\psi_{n\mu}^{(0)}\rangle + \lambda|\psi_{n\mu}^{(1)}\rangle + .. \\ E_{n\mu} &= E_n^{(0)} + \lambda E_{n\mu}^{(1)} + .. \ . \end{aligned} \tag{5.19}$$

The replacement of these expansions in $\hat{H}|\psi_{n\mu}\rangle = E_{n\mu}|\psi_{n\mu}\rangle$, and a collection of the terms in λ up to first order gives,

$$\begin{aligned} \hat{H}^{(0)}|\psi_{n\mu}^{(0)}\rangle &= E_n^{(0)}|\psi_{n\mu}^{(0)}\rangle \\ (E_n^{(0)} - \hat{H}^{(0)})|\psi_{n\mu}^{(1)}\rangle &= (E_{n\mu}^{(1)} - \hat{H}^{(1)})|\psi_{n\mu}^{(0)}\rangle \ . \end{aligned} \tag{5.20}$$

As before, we try to express the first-order corrections for the wavefunctions through degenerate unperturbed wavefunctions $|\psi_{n\mu}^{(0)}\rangle$ and non-degenerate wavefunctions [2] $|\psi_m^{(0)}\rangle$:

$$|\psi_{n\mu}^{(1)}\rangle = \sum_{\nu} b_{\mu\nu}|\psi_{n\nu}^{(0)}\rangle + \sum_{m} a_{nm}|\psi_m^{(0)}\rangle \ . \tag{5.21}$$

Inserting this into the first-order equation (5.20), we obtain,

$$\sum_{\nu} b_{\mu\nu}(E_n^{(0)} - E_n^{(0)})|\psi_{n\nu}^{(0)}\rangle + \sum_{m} a_{nm}(E_m^{(0)} - E_n^{(0)})|\psi_m^{(0)}\rangle = (E_{n\mu}^{(1)} - \hat{H}^{(1)})|\psi_{n\mu}^{(0)}\rangle \ . \tag{5.22}$$

The first term disappears. Inserting the expansion (5.18),

$$\sum_{m} a_{nm}(E_m^{(0)} - E_n^{(0)})|\psi_m^{(0)}\rangle = (E_{n\mu}^{(1)} - \hat{H}^{(1)})\sum_{\nu} c_{\mu\nu}|n,\nu\rangle \ , \tag{5.23}$$

[1] Another example would be the preference for the coupled base $|(l,s)j,m_j\rangle$ in comparison to the decoupled base $|l,m_l,s,m_s\rangle$ knowing that the degeneracy in j is lifted, when there is an energy associated with interacting angular momenta and the degeneracy in m_j is lifted, when we apply a magnetic field.

[2] Note that we label all states *which are not degenerate with the state under investigation* $|\psi_{n\mu}^{(1)}\rangle$ with the index m, even if there are degeneracies between them.

and multiplying the two sides with $\langle n,\mu|$, we get zero on the left-hand side, since we can choose the non-degenerate states to be orthogonal $\langle n,\nu|m\rangle = \delta_{m,n}$. Hence,

$$\boxed{\sum_\nu c_{\mu\nu}\left[E^{(1)}_{n\mu}\langle n,\mu|n,\nu\rangle - \langle n,\mu|\hat{H}^{(1)}|n,\nu\rangle\right] = 0} \ . \tag{5.24}$$

This *secular equation* (one for each μ) represents, in fact, a set of r linear equations for the coefficients $c_{\mu\nu}$. The condition for having non-trivial solutions is,

$$\det\left(\langle n,\nu|\hat{H}^{(1)}|n,\mu\rangle - E^{(1)}_{n\mu}\delta_{\mu,\nu}\right)_{\mu,\nu} = 0 \ . \tag{5.25}$$

The solution of this *secular determinant* yields the solicited energies $E^{(1)}_\mu$. Now, the solution of the secular equation (5.24) *for each energy value* produces those coefficients, which represent the best linear combinations adapted to the perturbation. Unlike in previous calculations with degenerate states, here we consider linear combinations of vectors of the degenerate subspace prior to switching on the perturbation.

In practice, we apply perturbation theory only to the lowest relevant order. That is, we only calculate the second order correction if first order corrections vanish. One famous example is the *quadratic Stark effect* discussed in Sec. 10.3. In the case of eigenvalues, which are degenerate in the absence of perturbation, the first order will always produce a remarkable correction, as in the example of the *linear Stark effect*, also discussed in Sec. 10.3. For this reason, we need not discuss higher perturbation orders in the case of degenerate eigenvalues.

Example 44 (*Perturbation in a system with two degenerate states*): As an example, we consider the following Hamiltonian,

$$\hat{H} = \begin{pmatrix} \Delta & \Omega \\ \Omega & \Delta \end{pmatrix} \ .$$

The exact solution gives the eigenvalues and eigenvectors,

$$E_1 = \Delta+\Omega \quad , \quad E_2 = \Delta-\Omega \quad , \quad |\psi_1\rangle = \tfrac{1}{\sqrt{2}}\begin{pmatrix}1\\1\end{pmatrix} \quad , \quad |\psi_2\rangle = \tfrac{1}{\sqrt{2}}\begin{pmatrix}-1\\1\end{pmatrix} \ .$$

Now we divide the Hamiltonian into an unperturbed part and a perturbation,

$$\hat{H} \equiv \hat{H}^{(0)} + \hat{H}^{(1)} = \begin{pmatrix} \Delta & 0 \\ 0 & \Delta \end{pmatrix} + \begin{pmatrix} 0 & \Omega \\ \Omega & 0 \end{pmatrix} \ .$$

We get in zero order,

$$E^{(0)}_1 = \Delta = E^{(0)}_2 \quad , \quad |1\rangle = \begin{pmatrix}1\\0\end{pmatrix} \quad , \quad |2\rangle = \begin{pmatrix}0\\1\end{pmatrix} \ ,$$

The application of non-degenerate perturbation theory in first order would give,

$$\langle 1|\hat{H}^{(1)}|1\rangle = 0 = \langle 2|\hat{H}^{(1)}|2\rangle \quad , \quad |\psi^{(1)}_1\rangle = |1\rangle\frac{\langle 1|\hat{H}^{(1)}|2\rangle}{E^{(0)}_1 - E^{(0)}_2} \to \infty \leftarrow -|\psi^{(1)}_2\rangle \ .$$

That is, the correction of the energy vanishes in first order, while the correction of the wavefunction diverges. Obviously, the $|\nu\rangle$ obtained by the diagonalization of the matrix $\hat{H}^{(0)}$ is not adapted to the calculation of the matrix elements $\hat{H}^{(1)}$. Now, applying degenerate perturbation theory, we obtain by the secular determinant,

$$0 = \det\left[\langle\nu|\hat{H}^{(1)}|\mu\rangle - E_\mu^{(1)}\delta_{\mu,\nu}\right] = \det\begin{pmatrix} -E_\mu^{(1)} & \Omega \\ \Omega & -E_\mu^{(1)} \end{pmatrix} = (E_\mu^{(1)})^2 - \Omega^2 \ ,$$

eigenvalues are $E_1^{(1)} = \Omega$ and $E_2^{(1)} = -\Omega$ allowing the establishment of the secular equation,

$$\begin{aligned} c_{11}\left[E_1^{(1)} - \langle 1|\hat{H}^{(1)}|1\rangle\right] - c_{12}\langle 1|\hat{H}^{(1)}|2\rangle &= c_{11}[\Omega - 0] - c_{12}\Omega = 0 \\ -c_{21}\langle 2|\hat{H}^{(1)}|1\rangle + c_{22}\left[E_2^{(1)} - \langle 2|\hat{H}^{(1)}|2\rangle\right] &= -c_{21}\Omega + c_{22}[-\Omega - 0] = 0 \ . \end{aligned}$$

We obtain $c_{11} = c_{12}$ and $c_{21} = -c_{22}$ and with this,

$$|\psi_1^{(0)}\rangle = \sum_\nu c_{1\nu}|\nu\rangle = c_{11}|1\rangle + c_{12}|2\rangle = \tfrac{1}{\sqrt{2}}\begin{pmatrix}1\\1\end{pmatrix} \quad , \quad |\psi_2^{(0)}\rangle = c_{21}|1\rangle + c_{22}|2\rangle = \tfrac{1}{\sqrt{2}}\begin{pmatrix}-1\\1\end{pmatrix} \ .$$

Thus, we can verify that the corrections for the eigenenergies,

$$E_1 = E_1^{(0)} + \langle\psi_1^{(0)}|\hat{H}^{(1)}|\psi_1^{(0)}\rangle = \Delta + \Omega \quad , \quad E_2 = E_2^{(0)} + \langle\psi_2^{(0)}|\hat{H}^{(1)}|\psi_2^{(0)}\rangle = \Delta - \Omega \ ,$$

coincides with the exact calculation made at the beginning. The eigenfunctions $|\psi_1^{(0)}\rangle$ should be already corrected in zeroth order, which we verify by calculating,

$$|\psi_1^{(1)}\rangle = |\psi_1^{(0)}\rangle \frac{\langle\psi_1^{(0)}|\hat{H}^{(1)}|\psi_2^{(0)}\rangle}{E_1 - E_2} = 0 = |\psi_2^{(1)}\rangle \ .$$

In Exc. 5.1.3.8 we study a partially degenerate three-level system and the breakdown of the degeneracy due to a perturbation. And in Exc. 5.1.3.9 we will treat a perturbation in a box potential with degenerate energy levels.

5.1.3 Exercises

5.1.3.1 Ex: One-dimensional well with a deformation in the centre

Consider a one-dimensional potential well between $-L/2$ and $L/2$ with infinitely high walls. In the center of the well is a small deformation,

$$H^{(1)} = \begin{cases} \epsilon \text{ for } \frac{-a}{2} \le x \le \frac{a}{2} \\ 0 \text{ outside that region} \ . \end{cases}$$

Calculate the correction for the eigenenergies in first order and discuss the limits $a \ll L$ and $a \to L$.

5.1.3.2 Ex: Perturbation

Show that the scalar product $\langle\psi_n^{(0)}|\psi_n^{(1)}\rangle$ (from the first-order correction to the state of the 'perturbed' system with the n-th state of the free Hamiltonian), cancels out when we impose that the 'perturbed' state $|\psi(\lambda)\rangle$ be normalized and the the product $\langle\psi_n^{(0)}|\psi(\lambda)\rangle$ be real [3].

5.1.3.3 Ex: Extended nucleus

The expression $V(r) = -e^2/4\pi\varepsilon_0 r$ for the potential energy of an electron in the hydrogen atom implies that the nucleus (the proton) is treated as a point particle. Now suppose that, on the contrary, the charge of the proton $+e$ is evenly distributed over a sphere of radius $R = 10^{-13}$ cm.
a. Derive the modified potential $V_{\rm m}$, which corresponds to this distribution of the nuclear charge.
b. Assume that the wavefunction of the hydrogen atom does not change much due to the modified potential. Calculate in lowest order in $R/a_{\rm B}$ the average energetic displacement $\langle\Delta V\rangle$ for the state $(n = 1, \ell = 0, m = 0)$. How will the energy displacement be in comparison to the states $(n = 2, \ell = 0, m = 0)$ and $(n = 2, \ell = 1, m = 0)$?
c. Calculate in the same way $\langle\Delta V\rangle$ for muonic hydrogen in the ground state.

5.1.3.4 Ex: Perturbation of a two-level system

We consider a two-level system. Without perturbation the system would have the Hamiltonian $H^{(0)}$, the eigenenergies $E_{1,2}^{(0)}$ and the eigenfunctions $\psi_{1,2}^{(0)}$. Now we switch on a stationary perturbation of the form $H^{(1)} = \epsilon(|1\rangle\langle 2| + |2\rangle\langle 1|)$.
a. Calculate the eigenenergies directly solving the perturbed Schrödinger equation.
b. Calculate the perturbed energies using TIPT and compare to the exact calculation of the eigenenergies.
c. Calculate the eigenstates directly solving the perturbed Schrödinger equation.
d. Calculate the perturbed states using TPIT and compare to the exact calculation of the eigenfunctions.

5.1.3.5 Ex: Stark effect for an electron in a box

Consider an electron in a one-dimensional box, that is, in a well inside the interval $x \in [0, a]$ delimited by infinite walls. When a uniform electric field $\mathcal{E}$ is applied, also in x-direction, the electron experiences a force equal to $-e\mathcal{E}$, being $-e$ the electron charge, so that the potential energy inside the box becomes $e\mathcal{E}x$.
a. What is the energy of the ground state of the electron (in first order approximation)? We can assume that $e\mathcal{E}a$ is much smaller than the ground state energy the electron would have in the absence of electric fields.
b. Use first-order TIPT to get an approximation for the ground state wavefunction by calculating the first term of the correction.

[3] See [163], Cap XI, A-2.

5.1.3.6 Ex: Perturbed 3-level system until second order TIPT

Consider the following perturbed Hamiltonian:

$$H = H_0 + H_\lambda = \begin{pmatrix} E_1 & 0 & 0 \\ 0 & E_2 & 0 \\ 0 & 0 & E_3 \end{pmatrix} + \begin{pmatrix} 0 & \lambda & 0 \\ \lambda & 0 & \lambda \\ 0 & \lambda & 0 \end{pmatrix} .$$

a. Determine the perturbed eigenvalues and eigenfunctions in first order TIPT.
b. Determine the eigenvalues in second order TIPT.

5.1.3.7 Ex: Stark effect for a charge in a harmonic oscillator

Consider a charged harmonic oscillator, immersed in a uniform electric field $\mathcal{E}$, described by the Hamiltonian $\hat{H}^{(1)} = \hat{H} + e\mathcal{E}\hat{x}$, being $\hat{H} = \hat{p}^2/2m + m\omega^2\hat{x}^2/2$ the Hamiltonian of the free one-dimensional oscillator, and e the charge of the oscillator.
a. Obtain, through TIPT, the eigenenergies (first and second order corrections). Compare the results obtained by TIPT with the analytical ones [4].
b. Same thing for a perturbation of the form $\rho m\omega^2\hat{x}^2/2$.
c. Same thing for a perturbation $\sigma\hbar\omega\hat{x}^3$.

5.1.3.8 Ex: Three-level system with degeneracy

Consider the following Hamiltonian $\hat{H}^{(0)}$ and its perturbation $\hat{H}^{(1)}$

$$\hat{H}^{(0)} + \hat{H}^{(1)} = \begin{pmatrix} \Delta & 0 & 0 \\ 0 & \Delta & 0 \\ 0 & 0 & \Delta' \end{pmatrix} + \begin{pmatrix} 0 & \Omega & 0 \\ \Omega & 0 & \Omega \\ 0 & \Omega & 0 \end{pmatrix} .$$

Calculate the corrections for the eigenvalues and eigenfunctions up to first order.

5.1.3.9 Ex: Perturbation in a 3D well with degeneracy

Consider a particle confined to a three-dimensional, infinite cubic well described by the potential energy $V(x, y, z) = 0$ for $0 < x < a$, $0 < y < a$ and $0 < z < a$ and $V(x, y, z) = \infty$ outside this region. We know that the particle's stationary states are $\Psi^{(0)}_{n_x,n_y,n_z}(x, y, z) = \left(\frac{2}{a}\right)^{3/2} \sin\left(\frac{n_x\pi}{a}x\right) \sin\left(\frac{n_y\pi}{a}y\right) \sin\left(\frac{n_z\pi}{a}z\right)$, being n_x, n_y, n_z positive integers. The associated energies are $E^{(0)}_{n_x,n_y,n_z} = \frac{\pi^2\hbar^2}{2ma^2}(n_x^2 + n_y^2 + n_z^2)$. Note that the ground state is not degenerate while the first excited state is three times degenerate. Consider that the particle in this box is subject to a perturbation of the shape $H^{(1)} = V_0$ for $0 < x < a/2$ and $0 < y < a/2$ and $H^{(1)} = 0$ outside this region.
a. Obtain the first-order correction for the ground state energy.
b. Obtain the first-order correction for the (degenerate) energy of the first excited state, in addition to the *optimal base* (which follows from the linear combinations of degenerate states) which most closely approximates the perturbed states.

[4] See [163], Complement A_XI.

5.1.3.10 Ex: Vanishing perturbation orders

Show that it is impossible to design a perturbation Hamiltonian of the form,

$$\hat{H} = \hat{H}^{(0)} + \hat{H}^{(1)} = \begin{pmatrix} 0 & 0 & 0 \\ 0 & E_2 & 0 \\ 0 & 0 & E_3 \end{pmatrix} + \begin{pmatrix} 0 & \Omega_{12} & \Omega_{13} \\ \Omega_{12}^* & 0 & \Omega_{23} \\ \Omega_{13}^* & \Omega_{23}^* & 0 \end{pmatrix}$$

such that the first and second order corrections vanish.

5.2 Variational method

5.2.1 The Rayleigh fraction

Let us assume that we want to calculate the ground state energy E_g of a system described by a Hamiltonian $\hat{H}$, but we do not know the wavefunction, and we do not know how to solve the Schrödinger equation. If at least we had a good idea of the generic form of the solution (Gaussian, sinusoidal, ...), we could choose a trial function with a free parameter and optimize this parameter minimizing the energy, which ought to be minimal for the ground state. This is precisely the idea of the *variational method*. Note that the variational method only works for the ground state. Numerically it can be implemented by the method of steepest descent presented in Sec. 2.4.3.

For any function ψ we know that the *Rayleigh fraction* $\mathcal{E}$ satisfies,

$$E_\mathrm{g} \leq \frac{\langle\psi|\hat{H}|\psi\rangle}{\langle\psi|\psi\rangle} \equiv \mathcal{E} \ , \tag{5.26}$$

not only when ψ is the wavefunction of an excited state, but even when it represents a (imperfect) trial to the ground state. Assuming normalized wavefunctions we can discard the denominator $\langle\psi|\psi\rangle = 1$. To verify the theorem, we expand the function ψ into orthonormal (unknown) eigenfunctions, $|\psi\rangle = \sum_n c_n|\psi_n\rangle$. Since ψ is normalized,

$$1 = \langle\psi|\psi\rangle = \sum_{m,n}\langle\psi_m|c_m^* c_n|\psi_n\rangle = \sum_n |c_n|^2 \ . \tag{5.27}$$

In the same way,

$$\langle\psi|\hat{H}|\psi\rangle = \sum_{m,n}\langle\psi_m|c_m^* \hat{H} c_n|\psi_n\rangle = \sum_n E_n|c_n|^2 \ . \tag{5.28}$$

As the ground state is that of the lowest energy, $E_\mathrm{g} \leq E_n$, we have demonstrated the relationship (5.26)

$$E_\mathrm{g} = E_\mathrm{g}\sum_n |c_n|^2 \leq \sum_n E_n|c_n|^2 = \langle\hat{H}\rangle \ . \tag{5.29}$$

In practice, we arrange for the trial wavefunction to depend on a free parameter α. This ansatz ψ_α for the ground state wavefunction then allows us to calculate an

energy that must be minimized via

$$\boxed{\frac{\partial \langle\psi_\alpha|\hat{H}|\psi_\alpha\rangle}{\partial\alpha} = 0} \,. \tag{5.30}$$

In the Excs. 5.2.3.1 and 5.2.3.2 we will approach the fundamental state of a quartic potential and a harmonic oscillator, respectively, by trying several trial wavefunctions and optimizing their free parameters.

5.2.2 Rayleigh-Ritz method

A modification of the variational method is the *Rayleigh-Ritz method*. Here, instead of using a trial function, we use a linear combination of eigenfunctions with variable coefficients: $|\psi\rangle = \sum_k c_k|k\rangle$. These variables are then optimized to minimize the Rayleigh fraction,

$$E_\mathrm{g} \leq \frac{\sum_{k,m} c_k^* c_m \langle k|\hat{H}|m\rangle}{\sum_{k,m} c_k^* c_m \langle k|m\rangle} = \mathcal{E} \,, \tag{5.31}$$

where we assume real coefficients and eigenfunctions. For this, the derivatives with respect to all coefficients must vanish:

$$\begin{aligned} 0 \equiv \frac{\partial \mathcal{E}}{\partial c_q} &= \frac{\sum_{k,m} \frac{\partial}{\partial c_q} c_k^* c_m \langle k|\hat{H}|m\rangle}{\sum_{k,m} c_k^* c_m \langle k|m\rangle} - \frac{\sum_{k,m} c_k^* c_m \langle k|\hat{H}|m\rangle \sum_{k,m} \frac{\partial}{\partial c_q} c_k^* c_m \langle k|m\rangle}{\left(\sum_{k,m} c_k^* c_m \langle k|m\rangle\right)^2} \\ &= \frac{\sum_{k,m} c_k^* \delta_{qm} \langle k|\hat{H}|m\rangle}{\sum_{k,m} c_k^* c_m \delta_{km}} - \mathcal{E} \frac{\sum_{k,m} c_k^* \delta_{qm} \delta_{km}}{\sum_{k,m} c_k^* c_m \delta_{km}} = \sum_k c_k^* \langle k|\hat{H}|q\rangle - \mathcal{E} c_q^* \,, \end{aligned} \tag{5.32}$$

using the definition of $\mathcal{E}$ (5.31). For the expression $\partial\mathcal{E}/\partial c_q^*$ we get analogous results. Hence,

$$\boxed{0 = \sum_m c_m (\langle q|\hat{H}|m\rangle - \mathcal{E}\langle q|m\rangle)} \,. \tag{5.33}$$

The condition for the existence of solutions is that the secular determinant disappears,

$$0 = \det(\langle q|\hat{H}|m\rangle - \mathcal{E}\langle q|m\rangle) \,. \tag{5.34}$$

The solution of this equation leads to a set of values $\mathcal{E}$, and the lowest value, $\mathcal{E}_\mathrm{min}$, is the best approximation for the ground state energy. The coefficients of the wavefunction are obtained by solving the eigenvalue equation (5.33) with $\mathcal{E}_\mathrm{min}$.

In Exc. 5.2.3.3 we derive the regression formulas for a linear *least squares fit* from a Rayleigh-Ritz variational. In Exc. 5.2.3.4 we will use the Rayleigh-Ritz method to estimate the effect of a finite nuclear mass of the hydrogen atom on the energy levels. In Exc. 5.2.3.5 we will use the Rayleigh-Ritz method to find the maximum number of atoms allowing for a stable Bose-Einstein condensate made of atoms subject to an attractive interatomic force.

5.2.3 Exercises

5.2.3.1 Ex: Variational method applied to a quartic potential

Determine the ground state energy of the quartic potential $V(x) = bx^4$ making the variational ansatz $\psi_\alpha(x) = (\alpha/\pi)^{1/4} e^{-\alpha x^2/2}$. **Formulae**:

$$\int_{-\infty}^{\infty} e^{-x^2} dx = \sqrt{\pi} \quad , \quad \int_{-\infty}^{\infty} x^2 e^{-x^2} dx = \tfrac{1}{2}\sqrt{\pi} \quad , \quad \int_{-\infty}^{\infty} x^4 e^{-x^2} dx = \tfrac{3}{4}\sqrt{\pi}$$

5.2.3.2 Ex: Variational method applied to the harmonic oscillator

Obtain, through the variational method, the ground state energy of the one-dimensional harmonic oscillator described by the Hamiltonian $\hat{H} = -\frac{\hbar^2}{2m}\frac{d^2}{dx^2} + \frac{1}{2}m\omega^2 x^2$, and the corresponding wavefunction from the test functions
a. $\psi(x) = Ae^{-\alpha x^2}$ being α a constant;
b. $\psi(x) = A/(x^2 + \beta^2)$ being β a constant;
c. $\psi(x) = A\cos(\pi x/a)$ between the limits $\pm a/2$ being a a constant.

5.2.3.3 Ex: Linear least squares

Use the Raleigh-Ritz method to derive the regression coefficients for a linear fit $f(x_k) = ax_k + b$ to a set of data points (x_k, y_k).

5.2.3.4 Ex: Effect of finite nuclear mass on hydrogen via Rayleigh-Ritz

Use the Rayleigh-Ritz method to estimate the impact of the finite mass of the nucleus of the hydrogen atom. To do this, calculate the ground state energy using the exact Hamiltonian, but a basis of wavefunctions assuming an infinitely heavy nucleus. Only take into account the states ψ_{100} and ψ_{200}. **Help:** Express the exact Hamiltonian in terms of the infinite-mass Hamiltonian approximating for small corrections of the reduced mass: $m \equiv m_e/(1+\gamma) \simeq (1-\gamma)m_e$, where $\gamma \equiv m_e/m_p$.

5.2.3.5 Ex: Collapse of a condensate with attractive interactions

A Bose-Einstein condensate of ^{7}Li may become unstable due to attractive interatomic force, the scattering length being $a_s = -27.3a_\mathrm{B}$. Consider the radial Gross-Pitaevskii Hamiltonian derived in Exc. 3.1.5.2 with an external harmonic potential with the oscillation frequency $\omega_{trp}/(2\pi) = 50$ Hz. Using the variational method to determine the maximum number of atoms allowing for a stable condensate. (Note that the derived minimization condition must be evaluated numerically.)

5.3 WKB approximation

The *WKB approximation* (from Wentzel-Kramers-Brillouin) [119, 488, 863] is a method to find approximate solutions for linear differential equations with spatially variable coefficients. It is typically used for calculations in quantum mechanics where the wavefunction is reformulated as an exponential semi-classically expanded function,

and then the amplitude or phase is slowly changed. In the following, we present the WKB approximation applied to the Schrödinger equation and exemplify it in some canonical systems.

5.3.1 WKB approximation applied to the Schrödinger equation

Starting from the time-independent Schrödinger equation,

$$-\frac{\hbar^2}{2m}\frac{d^2}{dx^2}\psi(x) + V(x)\psi(x) = E\psi(x) \ , \tag{5.35}$$

and rewrite it as follows,

$$\frac{d^2\psi}{dx^2} = k(x)\psi(x) \ . \tag{5.36}$$

with $k(x) = \sqrt{2m[E - V(x)]/\hbar^2}$. For now, we will restrict ourselves to energies $E > V(x)$. In this scheme, the wavefunctions are usually complex functions, so that we can write them in polar coordinates, containing an amplitude $A(x)$ and a phase $\phi(x)$, which are both real numbers:

$$\psi(x) = A(x)e^{\imath\phi(x)} \ . \tag{5.37}$$

Substituting this function into the Schrödinger equation we obtain a system of coupled equations in terms of $A(x)$ and $\phi(x)$,

$$A'' = A\Big[(\phi')^2 - k^2\Big] \qquad \text{and} \qquad (A^2\phi')' = 0 \ . \tag{5.38}$$

The equations (5.39) and (5.37) are completely equivalent to the Schrödinger equation. The second Eq. (5.38) is easy to solve,

$$A = \frac{C}{\sqrt{\phi'}} \ , \tag{5.39}$$

being C a real constant. We can not say the same thing about the solution of the first Eq. (5.38). In order to solve it we are going to use the WKB approach, assuming that A varies slowly, so the term $A'' \to 0$. By doing this approximation we can rewrite Eq. (5.39) in this way:

$$(\phi')^2 = k^2 \ . \tag{5.40}$$

Solving this last expression we obtain two linearly independent solutions, $\phi' = \pm k$. So we get the expression for the phase:

$$\phi(x) = \pm \int k(x)dx \ . \tag{5.41}$$

We write this indefinite integral, because the constant term can be absorbed by the constant C. Finally, we obtain the expression for the wavefunction in the WKB approximation:

$$\boxed{\psi(x) = \frac{C}{\sqrt{|k(x)|}}e^{\pm\int|k(x)|dx}} \ . \tag{5.42}$$

Here, taking the absolute value of the wavevector, we have already generalized for the case that the energy E of the particle is lower than the potential $V(x)$ (classically forbidden region).

Example 45 (*WKB approximation*): The WKB approach is a semiclassical method for the solution of the Schrödinger equation that does not require the potential to be a perturbation of a soluble problem. Instead, it only assumes that certain classical quantities having the dimension of an action (energy per time) are much larger than Planck's constant. Inserting the ansatz

$$\psi(x) = Ae^{\imath S(x)/\hbar} ,$$

into the one-dimensional time-independent Schrödinger equation, we find,

$$-\tfrac{i\hbar}{2m}S''(x) + \tfrac{1}{2m}S'(x)^2 + V(x) - E = 0 .$$

Now we expand the exponent in orders of $\hbar$,

$$S(x) = S_0(x) + \hbar S_1(x) + \tfrac{\hbar^2}{2}S_2(x) + ... ,$$

and insert it in the above equation. Collecting the orders in $\hbar$, we find in the first orders,

$$\begin{aligned}\left[\tfrac{1}{2m}S_0'(x)^2 + V(x) - E\right]\hbar^0 &= 0\\ \left[-\tfrac{\imath\hbar}{2m}S_0''(x) + \tfrac{1}{m}S_0'(x)S_1'(x)\right]\hbar^1 &= 0\\ \left[\tfrac{1}{2m}S_1'(x)^2 - \tfrac{\imath}{2m}S_1''(x)\right]\hbar^2 &= 0 .\end{aligned}$$

The solution of the zeroth order equation, $S_0(x) = \pm\int^x \sqrt{2m[E-V(x')}dx'$, gives

$$\psi(x) = Ae^{\pm\frac{\imath}{\hbar}\int^x \sqrt{2m[E-V(x')}dx'} .$$

The WKB approximation can be used to describe continuous potentials (or barriers) by stepwise constant potentials. The transmission $|T|^2$ through these parts can be obtained by multiplying the individual tunneling probabilities,

$$\ln|T|^2 \simeq -2\int_{barrier}\kappa(x)dx ,$$

with $\kappa(x) = \frac{1}{\hbar}\sqrt{2m[V(x)-E]}$.

5.3.2 Connection formulas

Now let us derive the connection formulas that interconnect solutions with E above and below $V(x)$ at the turning points, precisely those regions where WKB fails. We will apply the derivation to a generic confining potential shown in Fig. 5.1.

Let us start with the right turning point Fig. 5.1(a)]. First, we shift the coordinate system so that the turning point coincides with zero, as shown in Fig. 5.1(b). As seen above, the WKB solutions will be given by the following equations:

$$\psi(x) \approx \begin{cases} \frac{1}{\sqrt{k(x)}}\left[Be^{\imath\int_x^0 k(x')dx'} + Ce^{-\imath\int_x^0 k(x')dx'}\right] & \text{if} \quad x \le 0\\ \frac{1}{\sqrt{k(x)}}De^{-\int_0^x |k(x')|dx'} & \text{if} \quad x \ge 0 \end{cases} . \qquad (5.43)$$

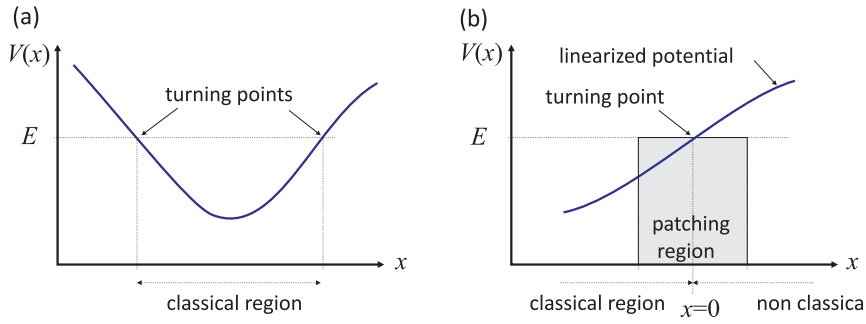

Figure 5.1: (a) Potential for which we want to obtain the connection formula. (b) Turning point.

In the vicinity of the turning point we approximate the potential by a straight line (Taylor series expansion up to first order) with the following functional dependence,

$$V(x) \approx E + V'(0)x \ . \tag{5.44}$$

The Schrödinger equation for this potential acquires the following format,

$$\frac{d^2\psi_{\rm t}}{dx^2} = \alpha^3 x \psi_{\rm t} \ , \tag{5.45}$$

with $\alpha = [\frac{2m}{\hbar^2}V'(0)]^{1/3}$. Through a change of variables, $z = \alpha x$, we fall back on Airy's equation,

$$\frac{d^2\psi_{\rm t}}{dz^2} = z\psi_{\rm t} \ , \tag{5.46}$$

having as solution a linear combination of the two solutions of the Airy equation,

$$\psi_{\rm t}(x) = a{\rm Ai}(\alpha x) + b{\rm Bi}(\alpha x) \ . \tag{5.47}$$

Now let's have a look at the WKB solutions in the two regions in the vicinity of the turning point. In the classically forbidden region we have $k(x) = \alpha^{3/2}\sqrt{-x}$, thus being $\int_0^x |k(x')|dx' = \frac{2}{3}(\alpha x)^{3/2}$. Thus, the WKB solution in the classically forbidden region near the turning point will be given by:

$$\psi(x) \approx \frac{D}{\sqrt{\hbar}\alpha^{3/4}x^{1/4}} e^{-\frac{2}{3}(\alpha x)^{3/2}} \ . \tag{5.48}$$

Using the asymptotic forms of Airy functions in the solution (5.47) we obtain the following expression for $\psi_t(x)$,

$$\psi_p(x) \approx \frac{a}{2\sqrt{\pi}(\alpha x)^{1/4}} e^{-\frac{2}{3}(\alpha x)^{3/2}} + \frac{b}{\sqrt{\pi}(\alpha x)^{1/4}} e^{\frac{2}{3}(\alpha x)^{3/2}} \ , \tag{5.49}$$

which when compared to equation (5.48) shows us that $a = \sqrt{\frac{4\pi}{\alpha\hbar}}D$ and $b = 0$. Repeating the previous steps in the negative region we see that the WKB solution in

the asymptotic forms of the Airy solutions for approximately linear potentials takes the following format (with $b = 0$):

$$\psi(x) \approx \frac{1}{\sqrt{\hbar}\alpha^{3/4}(-x)^{1/4}}\left[Be^{\imath\frac{2}{3}(-\alpha x)^{3/2}} + Ce^{-\imath\frac{2}{3}(-\alpha x)^{3/2}}\right], \tag{5.50}$$

and

$$\psi_p(x) \approx \frac{a}{\sqrt{\pi}(-\alpha x)^{1/4}}\frac{1}{2\imath}\left[e^{\imath\pi/4}e^{\imath\frac{2}{3}(-\alpha x)^{3/2}} - e^{-\imath\pi/4}e^{-\imath\frac{2}{3}(-\alpha x)^{3/2}}\right]. \tag{5.51}$$

When compared, $\frac{a}{2\imath\sqrt{\pi}}e^{\imath\pi/4} = \frac{B}{\sqrt{\hbar}\alpha}$ and $-\frac{a}{2\imath\sqrt{\pi}}e^{-\imath\pi/4} = \frac{C}{\sqrt{\hbar}\alpha}$. Having all this information we can rewrite the WKB solutions for all positions in the potential, including the turning points [5]:

$$\psi(x) \approx \begin{cases} \frac{2D}{\sqrt{k(x)}}\sin\left[\int_x^{x_2} k(x')dx' + \frac{\pi}{4}\right], & \text{if } x \le x_2 \\ \frac{D}{\sqrt{k(x)}}e^{-\int_{x_2}^{x}|k(x')|dx'}, & \text{if } x \ge x_2 \end{cases}. \tag{5.52}$$

Repeating the process for a decreasing turning point [left turning point of the potential of Fig. 5.1(a)], we obtain the following expression:

$$\psi(x) \approx \begin{cases} \frac{D'}{\sqrt{k(x)}}e^{-\int_{x}^{x_1}|k(x')|dx'}, & \text{if } x \le x_1 \\ \frac{2D'}{\sqrt{k(x)}}\sin\left[\int_{x_1}^{x} k(x')dx' + \frac{\pi}{4}\right], & \text{if } x \ge x_1 \end{cases}. \tag{5.53}$$

Example 46 (*Harmonic oscillator*): Now we apply the WKB method to a well-known system: the harmonic oscillator. We will calculate its energy levels and the respective eigenfunctions.
Eigenenergies: First, note that for a confining potential, and more specifically in the region where $E \ge V(x)$, we have the solutions obtained for the left and right turning point, these two solutions must match each other, that is,

$$\frac{2D}{\sqrt{k(x)}}\sin\left[\int_x^{x_2} k(x')dx' + \frac{\pi}{4}\right] \simeq \frac{2D'}{\sqrt{k(x)}}\sin\left[\int_{x_1}^{x} k(x')dx' + \frac{\pi}{4}\right],$$

and hence the zeros of these functions, so the arguments of those sines must be equal (except for a multiple of π),

$$\begin{aligned} \int_x^{x_2} kdx' + \frac{\pi}{4} &= -\int_{x_1}^{x_1} kdx' - \frac{\pi}{4} + n\pi \qquad (5.54) \\ \left(\int_{x_1}^{x} + \int_x^{x_2}\right)kdx' &= \left(n - \frac{1}{2}\right)\pi \\ \int_{x_1}^{x_2} kdx' &= \left(n - \frac{1}{2}\right)\pi, \end{aligned}$$

with $n = 1, 2...$ [6]. With this information we take a harmonic potential of the type $V(x) = \frac{1}{2}\kappa x^2$. In this case, the turning points for a given energy E will be at

[5] Note that we shifted the turning point to an arbitrary position x_2.
[6] Note that $n \neq 0$, because the integral (5.54) has to be greater than zero.

$-\sqrt{\frac{2E}{\kappa}}$ and $\sqrt{\frac{2E}{\kappa}}$. For this potential we will have that $k(x) = \sqrt{\frac{2m}{\hbar^2}(E - \frac{1}{2}\kappa x^2)}$. Calculating the integral of $k(x)$ between these two turning points we get,

$$\int_{x_1}^{x_2} k(x)dx = \frac{2m}{\hbar}\int_{-\sqrt{2E/k}}^{\sqrt{2E/k}} \sqrt{E - \frac{1}{2}\kappa x^2}dx = \pi E\frac{m}{\kappa} = \left(n - \frac{1}{2}\right)\pi\hbar \ ,$$

isolating E and taking $\omega = \sqrt{\kappa/m}$ we have,

$$E = (n - \tfrac{1}{2})\hbar\omega \ ,$$

with $n = 1, 2...$, the exact spectrum of the harmonic oscillator, but this is just a coincidence.

Eigenstates: Now we will calculate the eigenstates of the harmonic oscillator. The eigenfunctions were calculated on a computer. The first graph (Fig. 5.2) compares the first exact excited state with that obtained using the WKB method.

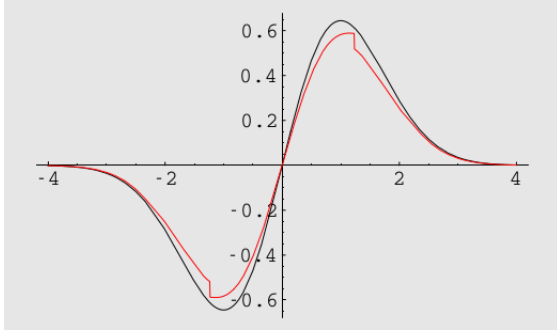

Figure 5.2: First excited state calculated accurately and through the WKB approximation.

Note that the WKB approach is very good when $x \to 0$ and $x \to \infty$, regions where the difference between the oscillator energy and the potential are large ($E \gg V(x \to 0)$ and $E \ll V(x \to \infty)$), because in these regions the wavelength $\lambda(x)$ acquires the lowest values, since it is proportional to $|1/\sqrt{E - V(x)}|$. Hence, the spatial region in which the potential needs to be practically constant is smaller, which explains why the approximation is closer to the exact solution. In the intermediate regions the difference between E and $V(x)$ begins to decrease, and the WKB approximation delivers its worst results.

As we increase the energy of the harmonic oscillator, the approximation becomes better (for the same reason as discussed in the previous paragraph). The following graph illustrates this effect for $n = 10$.

Example 47 (*Hydrogen atom*): Eigenenergies: For the hydrogen atom the effective potential is given by,

$$V(x) = -\frac{e^2}{4\pi\varepsilon_0}\frac{1}{r} + \frac{\hbar^2}{2m}\frac{l(l+1)}{r^2} \ .$$

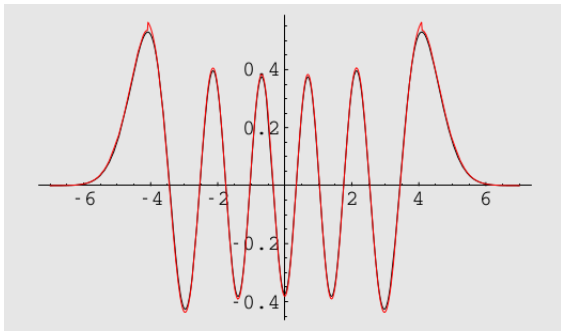

Figure 5.3: Wavefunction of the vibrational state $n = 10$ calculated exactly and using the WKB approximation.

Note that the WKB method for this case obeys the relation (5.54), hence we get,

$$\int_{r_1}^{r_2} p(r)dr = \sqrt{2m}\int_{r_1}^{r_2}\sqrt{E + \frac{e^2}{4\pi\varepsilon_0}\frac{1}{r} - \frac{\hbar^2}{2m}\frac{l(l+1)}{r^2}}dr$$
$$= \sqrt{-2mE}\int_{r_1}^{r_2}\frac{1}{r}\sqrt{-r^2 - \frac{e^2}{4\pi\varepsilon_0 E}r + \frac{\hbar^2}{2mE}l(l+1)}dr\ .$$

Notice that $E < 0$. Let us make the following substitution to facilitate algebraic manipulations,

$$B = -\frac{e^2}{4\pi\varepsilon_0 E} \qquad \text{and} \qquad C = -\frac{\hbar^2}{2mE}l(l+1)\ .$$

The turning points r_1 and r_2 are given by the following expressions,

$$r_1 = \frac{B - \sqrt{B^2 - 4C}}{2} \qquad \text{and} \qquad r_2 = \frac{B + \sqrt{B^2 - 4C}}{2}\ .$$

Thus, returning to the integral we will have the following:

$$\int_{r_1}^{r_2} p(r)dr = \sqrt{-2mE}\int_{r_1}^{r_2}\frac{1}{r}\sqrt{(r-r_1)(r_2-r)}dr = \sqrt{-2mE}\frac{\pi}{2}(\sqrt{r_2} - \sqrt{r_1})^2$$
$$= \sqrt{-2mE}\frac{\pi}{2}(r_1 + r_2 - 2r_1r_2) = \sqrt{-2mE}\frac{\pi}{2}(B - 2\sqrt{C})$$
$$= \frac{\pi}{2}\Big(-\frac{e^2\sqrt{2m}}{4\pi\varepsilon_0\sqrt{-E}} - 2\hbar\sqrt{l(l+1)}\Big) = \Big(n - \frac{1}{2}\Big)\pi\hbar\ .$$

Isolating E we obtain the energy spectrum of the hydrogen atom in the WKB approximation:

$$E = -\frac{m}{2\hbar}\Big(\frac{e^2}{4\pi\varepsilon_0}\Big)^2\frac{1}{\Big[n - 1/2 + l(l+1)\Big]^2} = -\frac{13.6}{\Big[n - 1/2 + l(l+1)\Big]^2}eV\ .$$

For high energies ($n \gg l$), we recover Bohr's expression.

5.3.3 Exercises

5.3.3.1 Ex: Energy levels of hydrogen via WKB

Use the WKB approach to calculate the energy levels of the hydrogen atom.

5.4 Time-dependent perturbations

Temporal perturbations typically occur when we suddenly switch on an external field that influences the motion or spin of the particles, or when the field varies over time, for example, an electromagnetic field. Let us first study a two-level system subject to a temporal perturbation.

5.4.1 Two-level systems

We write the perturbation as

$$\hat{H} = \hat{H}^{(0)} + \hat{H}^{(1)}(t) \ . \tag{5.55}$$

As in the case of a stationary perturbation, we write the eigenenergies and -functions of the unperturbed system as

$$\hat{H}^{(0)}|n\rangle = E_n|n\rangle \ . \tag{5.56}$$

Recalling that this stationary Schrödinger equation was obtained from the time-dependent Schrödinger equation via a separation ansatz (1.167), the temporal evolution of these eigenfunctions is given by,

$$|\psi_n^{(0)}(t)\rangle = |n\rangle e^{-\imath E_n t/\hbar} \ . \tag{5.57}$$

For small perturbations we can expect that the ansatz,

$$|\psi^{(1)}(t)\rangle = a_1(t)|\psi_1^{(0)}(t)\rangle + a_2(t)|\psi_2^{(0)}(t)\rangle \ , \tag{5.58}$$

be good. Note that not only do eigenfunctions oscillate, but the coefficients also depend on time, because the composition of the states can change. The instantaneous probability of finding the system in state n is $|a_n(t)|^2$. Importing the above linear combination into the Schrödinger equation,

$$\left[\hat{H}^{(0)} + \hat{H}^{(1)}(t)\right]|\psi^{(1)}(t)\rangle = \imath\hbar\frac{\partial}{\partial t}|\psi^{(1)}(t)\rangle \ , \tag{5.59}$$

we find,

$$\begin{aligned} &a_1\hat{H}^{(0)}|\psi_1^{(0)}\rangle + a_2\hat{H}^{(0)}|\psi_2^{(0)}\rangle + a_1\hat{H}^{(1)}|\psi_1^{(0)}\rangle + a_2\hat{H}^{(1)}|\psi_2^{(0)}\rangle \\ &\qquad = \imath\hbar\left[\frac{\partial a_1}{\partial t}|\psi_1^{(0)}\rangle + \frac{\partial a_2}{\partial t}|\psi_2^{(0)}\rangle + a_1\frac{\partial|\psi_1^{(0)}\rangle}{\partial t} + a_2\frac{\partial|\psi_2^{(0)}\rangle}{\partial t}\right] \\ \implies &a_1\hat{H}^{(1)}|\psi_1^{(0)}\rangle + a_2\hat{H}^{(1)}|\psi_2^{(0)}\rangle = \imath\hbar\dot{a}_1|\psi_1^{(0)}\rangle + \imath\hbar\dot{a}_2|\psi_2^{(0)}\rangle \ , \end{aligned} \tag{5.60}$$

because the other terms satisfy the Schrödinger equation of zero order. Replacing the stationary eigenfunctions,

$$a_1 e^{-\imath E_1 t/\hbar}\hat{H}^{(1)}|1\rangle + a_2 e^{-\imath E_2 t/\hbar}\hat{H}^{(1)}|2\rangle = \imath\hbar\dot{a}_1 e^{-\imath E_1 t/\hbar}|1\rangle + \imath\hbar\dot{a}_2 e^{-\imath E_2 t/\hbar}|2\rangle \ , \quad (5.61)$$

and multiplying this equation with $\langle 1|\times$ and $\langle 2|\times$, we find with the abbreviation $\hbar\omega_0 \equiv E_2 - E_1$,

$$\begin{aligned} \imath\hbar\dot{a}_1 &= a_1\langle 1|\hat{H}^{(1)}|1\rangle + a_2 e^{-\imath\omega_0 t}\langle 1|\hat{H}^{(1)}|2\rangle \quad (5.62)\\ \text{and} \qquad \imath\hbar\dot{a}_2 &= a_1 e^{\imath\omega_0 t}\langle 2|\hat{H}^{(1)}|1\rangle + a_2\langle 2|\hat{H}^{(1)}|2\rangle \ . \end{aligned}$$

Frequently, the perturbation induces only a coupling, but does not directly influence the energies very much, $\langle n|\hat{H}^{(1)}|n\rangle \simeq 0$,

$$\boxed{\dot{a}_1 = a_2\frac{e^{-\imath\omega_0 t}}{\imath\hbar}\langle 1|\hat{H}^{(1)}|2\rangle \qquad \text{and} \qquad \dot{a}_2 = a_1\frac{e^{\imath\omega_0 t}}{\imath\hbar}\langle 2|\hat{H}^{(1)}|1\rangle} \ . \quad (5.63)$$

Without perturbation, $\langle m|\hat{H}^{(1)}|n\rangle = 0$, no dynamics develops; the eigenfunctions evolve independently.

5.4.2 The time-dependent perturbation method

Now, let us turn our attention to systems with many levels.

In *time-dependent perturbation theory* (TDPT) we separate the Hamiltonian into a stationary part and a time-dependent part [7,8],

$$\hat{H}(t) = \hat{H}^{(0)} + \lambda\hat{H}^{(1)}(t) \ . \quad (5.64)$$

As usual, this Hamiltonian satisfies the Schrödinger equation,

$$\imath\hbar\frac{\partial}{\partial t}|\psi(t)\rangle = \hat{H}(t)|\psi(t)\rangle \ . \quad (5.65)$$

Now, we do a unitary transformation into the *interaction picture* with $S(t) = e^{-\imath\hat{H}^{(0)}t/\hbar}$ substituting $|\psi(t)\rangle \equiv S(t)|\psi_I(t)\rangle$ and $\hat{H}^{(1)}(t) \equiv S(t)\hat{W}(t)S^{-1}(t)$ in the Schrödinger equation. This procedure removes the stationary part, as shown in Sec. 1.6.4,

$$\imath\hbar\frac{\partial}{\partial t}|\psi_I(t)\rangle = \lambda\hat{W}(t)|\psi_I(t)\rangle \ . \quad (5.66)$$

If $\hat{W}(t)$ is also independent of time, the solution simply is $|\psi_I(t)\rangle = e^{-\imath\hat{W}t/\hbar}|\psi_I(0)\rangle$. Otherwise, we integrate the equation,

$$|\psi_I(t)\rangle = |\psi_I(0)\rangle + \frac{\lambda}{\imath\hbar}\int_0^t \hat{W}(\tau)|\psi_I(\tau)\rangle d\tau \ . \quad (5.67)$$

[7] See Becker-Sauter II, p.118ff and [813], p.104ff. An alternative treatment is found in [530], p.191ff or in Blochinzew, p.332ff.

[8] Note that by substituting $\hat{W}$ by $\hat{H}^{(1)}$, the equation (5.66), $\imath\hbar\partial_t|\psi_I(t)\rangle = \hat{H}^{(1)}(t)|\psi_I(t)\rangle$, corresponds to a first-order perturbative approximation, i.e., the perturbation eigenvalues $\hat{H}(1)$ are calculated with the eigenvectors of the unperturbed system. Thus, in first order TDPT we can substitute $\hat{W}$ for $\hat{H}^{(1)}$.

Substituting $|\psi_I(\tau)\rangle$ by $|\psi_I(t)\rangle$ we iterate this equation,

$$|\psi_I(t)\rangle = |\psi_I(0)\rangle + \frac{\lambda}{\imath\hbar}\int_0^t \hat{W}(\tau_1)\left(|\psi_I(0)\rangle + \frac{\lambda}{\imath\hbar}\int_0^{\tau_1}\hat{W}(\tau_2)|\psi_I(\tau_2)\rangle d\tau_2\right)d\tau_1 \tag{5.68}$$
$$= |\psi_I(0)\rangle + \frac{\lambda}{\imath\hbar}\int_0^t \hat{W}(\tau_1)d\tau_1|\psi_I(0)\rangle + \left(\frac{\lambda}{\imath\hbar}\right)^2\int_0^t\hat{W}(\tau_1)\int_0^{\tau_1}\hat{W}(\tau_2)|\psi_I(\tau_2)\rangle d\tau_2 d\tau_1\rangle$$
$$= \left[\sum\nolimits_{n=1}^{N}\left(\frac{\lambda}{\imath\hbar}\right)^n\int_0^t\hat{W}(\tau_1)\int_0^{\tau_1}\hat{W}(\tau_2)...\int_0^{\tau_{n-1}}\hat{W}(\tau_n)d\tau_1 d\tau_2...d\tau_n\right]|\psi_I(0)\rangle + o(\lambda^{N+1})\ .$$

This is called the *Dyson series*. For $N = 1$, we get the first order of the perturbation series [9],

$$|\psi_I(t)\rangle = \left(1 + \frac{\lambda}{\imath\hbar}\int_0^t\hat{W}(\tau)d\tau\right)|\psi_I(0)\rangle\ . \tag{5.69}$$

The stationary states of the unperturbed Hamiltonian are given by $\hat{H}^{(0)}|f\rangle = E_f|f\rangle$. Now, the perturbed states are expanded on this basis, $|\psi_I(t)\rangle = \sum_f |f\rangle a_f(t)$. The expansion coefficients are [10],

$$a_f(t) = \langle f|\psi_I(t)\rangle = \langle f|\psi_I(0)\rangle + \frac{\lambda}{\imath\hbar}\langle f|\int_0^t S^{-1}(\tau)\hat{H}^{(1)}(\tau)S(\tau)|\psi_I(0)\rangle d\tau\ . \tag{5.70}$$

Now, we assume that the system be initially in the eigenstate $|\psi_I(0)\rangle = |i\rangle$. The amplitudes then are,

$$a_{i\to f}(t) = \langle f|i\rangle + \frac{\lambda}{\imath\hbar}\int_0^t e^{\imath E_f\tau/\hbar}\langle f|\hat{H}^{(1)}(\tau)|i\rangle e^{-\imath E_i\tau/\hbar}d\tau \tag{5.71}$$
$$= \delta_{if} + \frac{\lambda}{\imath\hbar}\int_0^t\langle f|\hat{H}^{(1)}(\tau)|i\rangle e^{\imath\omega_{if}\tau}d\tau\ .$$

The time-varying potential generates a perturbation causing a variation of the system's state. As the energy is not conserved, $[\partial_t, \hat{H}(t)] \neq 0$, the time-dependence is not separable and the system exchanges energy with the potential. In first-order perturbation theory we only consider weak perturbations, i.e. the initial state is emptied only slowly, $a_{i\to i}(dt) \simeq a_{i\to i}(0) = 1$. On the other hand, for an initially empty state f the gain is obviously considerable. For $i \neq f$ we have,

$$\boxed{da_{i\to f}(t) = a_{i\to f}(t+dt) - a_{i\to f}(t) = \frac{\lambda}{\imath\hbar}\langle f|\hat{H}^{(1)}(t)|i\rangle e^{\imath\omega_{if}t}dt}\ . \tag{5.72}$$

This formula is nothing more than a generalization of the formula (5.63) obtained for a two-level system assuming that the initial state does not deplete considerably. In Exc. 5.4.5.1 we calculate the dynamics of a harmonic oscillator perturbed by a decaying force.

[9] For higher orders,

$$|\psi_I(t)\rangle \approx \left[\sum\nolimits_{n=1}^{N}\left(\frac{\lambda}{\imath\hbar}\right)^n\left(\int_0^t\hat{W}(\tau)d\tau\right)^n\right]|\psi_I(0)\rangle = T\left[\exp\left(\frac{\lambda}{\imath\hbar}\int_0^t\hat{W}(\tau)d\tau\right)\right]|\psi_I(0)\rangle\ .$$

[10] We could define the coefficients in Schrödinger's picture, $a_f \equiv \langle f|\psi\rangle$, but this would only introduce a phase factor, $a_{i\to f} \to a_{i\to f}e^{\imath(E_f-E_i)t/\hbar}$, which is unimportant for absolute values $|a_{i\to f}|^2$. This corresponds to a transformation to a rotating system, which will be discussed in Sec. 16.3.2.

5.4.3 Specific perturbations

5.4.3.1 Sudden switch-on of a constant perturbation

To begin with, we consider a constant perturbation $\hat{H}^{(1)}$ suddenly switched on at $t = 0$. In Schrödinger's picture we can rewrite Eq. (5.71),

$$a_{i\to f}(t) = \delta_{if} + \frac{\lambda}{\imath\hbar}\langle f|\hat{H}^{(1)}|i\rangle \int_0^t e^{\imath\omega_{if}\tau}d\tau = \delta_{if} + \frac{\lambda}{\imath\hbar}\langle f|\hat{H}^{(1)}|i\rangle \frac{-1+e^{\imath\omega_{if}t}}{\imath\omega_{if}} \ . \quad (5.73)$$

We obtain for $i \neq f$,

$$\boxed{|a_{i\to f}(t)|^2 = \frac{\lambda^2}{\hbar^2}|\langle f|\hat{H}^{(1)}|i\rangle|^2 \frac{\sin^2(\omega_{if}t/2)}{(\omega_{fi}/2)^2}} \ . \quad (5.74)$$

For long times we calculate the rate [11],

$$\frac{d}{dt}|a_{i\to f}(t)|^2 = \frac{\lambda^2}{\hbar^2}|\langle f|\hat{H}^{(1)}|i\rangle|^2 \frac{\sin\omega_{fi}t}{\omega_{fi}/2} \quad \overset{t\to\infty}{\longrightarrow} \quad \frac{2\pi\lambda^2}{\hbar^2}|\langle f|\hat{H}^{(1)}|i\rangle|^2\delta(\omega_f-\omega_i) \ , \quad (5.75)$$

where we use the representation of the Dirac function,

$$\delta(x) = \lim_{t\to\infty}\tfrac{1}{2\pi}\int_{-t}^{t} e^{\imath kx}dk = \lim_{t\to\infty}\tfrac{t}{\pi}\mathrm{sinc}\ xt \ . \quad (5.76)$$

The δ-function in (5.75) ensures that, for infinitely sharp steps, transitions are impossible, unless the energy of the final state is the same as the one of the initial state. This points to the fact that infinitely sharp steps are not a realistic physical concept.

In practice, the changes applied to a system are often slow and the observation times are long, because the frequencies of the transitions are high $\omega_{fi}/2\pi \simeq$ THz. Let us assume that the perturbation be switched on within a time constant γ^{-1}. In Exc. 5.4.5.2 we will study how the rapidity of a perturbation influences the transition rate. We will see via a temporal analysis of $|a_{i\to f}(t)|^2$, that for slow variations, $\gamma \ll \omega_{fi}$, the system adiabatically approaches the final situation. For $\gamma \simeq \omega_{fi}$, the system receives a shock and exhibits oscillating transients. For $\gamma > \omega_{fi}$, we observe violent oscillations with largest amplitudes.

5.4.3.2 Periodic perturbations

We now consider the case of an oscillatory perturbation, for example an electromagnetic field. In principle, knowledge of the system's response to periodic perturbations allows us to treat arbitrary perturbations, since we can expand them in Fourier series. We first treat transitions between discrete levels, before considering states embedded in continua,

$$\hat{H}^{(1)}(t) = \begin{cases} 0 \quad \text{for} \quad t < 0 \\ 2\hbar\hat{\Omega}_0\cos\omega t \quad \text{for} \quad t \geq 0 \end{cases} \ . \quad (5.77)$$

[11] We use the trigonometric rule $\sin x = 2\sin\frac{x}{2}\cos\frac{x}{2}$.

With the abbreviation $\Omega_{fi} \equiv \langle f|\hat{\Omega}_0|i\rangle$ the transition rate is,

$$a_{i\to f}(t) = -\imath\Omega_{fi}\int_0^t 2e^{\imath\omega_{fi}\tau}\cos\omega\tau d\tau \tag{5.78}$$
$$= -\imath\Omega_{fi}\left[\cancelto{0}{\frac{e^{\imath(\omega_{fi}+\omega)t}-1}{\imath(\omega_{fi}+\omega)}} + \frac{e^{\imath(\omega_{fi}-\omega)t}-1}{\imath(\omega_{fi}-\omega)}\right] .$$

The first term being small, we neglect it doing a so-called *rotating wave approximation* (RWA). We obtain,

$$|a_{i\to f}(t)|^2 = |\Omega_{fi}|^2\frac{\sin^2\frac{1}{2}(\omega_{fi}-\omega)t}{\frac{1}{4}(\omega_{fi}-\omega)^2} . \tag{5.79}$$

This result coincides with the formula (5.74), except that the energy difference between the states ω_{fi} is shifted by the frequency of the perturbation ω. The quantity $\Delta_{fi} \equiv \omega - \omega_{fi}$ is called a detuning. The transition probability is maximal, when we are at resonance, that is $\Delta_{fi} = 0$. In this case,

$$|a_{i\to f}(t)|^2 \longrightarrow |\Omega_{fi}|^2t^2 . \tag{5.80}$$

This can be seen by expanding the numerator in a Taylor series for small $(\omega_{fi}-\omega)t$.

Note, that the probability exceeds 1 for long times, which can not be. In fact, the restriction to the first order in the Taylor expansion used in the derivation of the last equation is no longer valid for long times, when $(\omega_{fi}-\omega)t > 1$, and we need to take into account higher orders.

Example 48 (*The Rabi formula*): Let us now come back to the two-level system studied in Sec. 5.4.1 and consider a periodic perturbation oscillating at frequency $\omega = \omega_0 + \Delta$, where Δ is called the *detuning* from the resonance whose frequency is ω_0,

$$H^{(1)} = -e\vec{\mathcal{E}}(\mathbf{r},t)\cdot\mathbf{r} = -e\mathcal{E}_0\hat{\varepsilon}\cos(kz-\omega t)\cdot\mathbf{r} . \tag{5.81}$$

Then,

$$\langle 2|H^{(1)}|1\rangle = -e\mathcal{E}_0\cos(kz-\omega t)\langle 2|r|1\rangle = \hbar\Omega\cos(kz-\omega t) , \tag{5.82}$$

where we call

$$\Omega \equiv \frac{-e\mathcal{E}_0\langle 2|r|1\rangle}{\hbar} \tag{5.83}$$

the *Rabi frequency*. With this abbreviation the Eqs. (5.63) become,

$$\dot{a}_1 = -\imath\Omega a_2e^{-\imath\omega_0t}\cos(kz-\omega t) \quad \text{and} \quad \dot{a}_2 = -\imath\Omega^*a_1e^{\imath\omega_0t}\cos(kz-\omega t) . \tag{5.84}$$

Neglecting fast-rotating terms doing the so-called *rotating wave approximation* (RWA) and choosing the position of the atom to be $z = 0$ we derive,

$$\dot{a}_1 \simeq -\frac{\imath\Omega}{2}a_2e^{\imath\Delta t} \quad \text{and} \quad \dot{a}_2 \simeq -\frac{\imath\Omega^*}{2}a_1e^{-\imath\Delta t} , \tag{5.85}$$

which coincides with the formulas derived in Sec. 5.4.1. With the equations of motion we can, starting from initial values for $a_1(0)$ and $a_2(0)$, calculate the temporal evolution.

We solve this system of differential equations by differentiating one and substituting the other,

$$\ddot{a}_2 = -\imath\dot{a}_1\frac{\Omega^*}{2}e^{-\imath\Delta t} - a_1\Delta\frac{\Omega^*}{2}e^{-\imath\Delta t} = -\frac{|\Omega|^2}{4}a_2 - \imath\Delta\dot{a}_2 \ . \tag{5.86}$$

We find solutions via the ansatz $a_2 = e^{-\imath\Delta t/2}(Ae^{\imath Gt/2}+Be^{-\imath Gt/2})$. The equation for a_2 yields,

$$\begin{aligned}(\tfrac{\imath}{2}G - \tfrac{\imath}{2}\Delta)^2 Ae^{\imath(G-\Delta)t/2} + (-\tfrac{\imath}{2}G - \tfrac{\imath}{2}\Delta)^2 Be^{\imath(-G-\Delta)t/2} \\ = -\tfrac{|\Omega|^2}{4}(Ae^{\imath(G-\Delta)t/2} + Be^{\imath(-G-\Delta)t/2} \\ - \imath\Delta\left[(\tfrac{\imath}{2}G - \tfrac{\imath}{2}\Delta)Ae^{\imath(G-\Delta)t/2} + (-\tfrac{\imath}{2}G - \tfrac{\imath}{2}\Delta)Be^{\imath(-G-\Delta)t/2}\right] \ .\end{aligned} \tag{5.87}$$

Separating the parts in A and in B we obtain two equations with the same result,

$$G^2 = |\Omega|^2 + \Delta^2 \ . \tag{5.88}$$

G is called the *generalized Rabi frequency*. Using the initial conditions, $a_1(0) = 1$ and $a_2(0) = 0$, we can fix one of the coefficients A and B, since $a_2(0) = A+B = 0$,

$$a_2 = 2\imath Ae^{-\imath\Delta t/2}\sin\tfrac{G}{2}t \ . \tag{5.89}$$

We now import this solution into the differential equation for a_1,

$$\dot{a}_1 = -\imath\frac{\Omega}{2}a_2e^{\imath\Delta t} = \Omega Ae^{\imath\Delta t/2}\sin\tfrac{G}{2}t \ . \tag{5.90}$$

The integral is,

$$a_1(t) = \int_0^t \Omega Ae^{\imath\Delta t'/2}\sin\tfrac{G}{2}t'dt' = -\frac{2A}{\Omega^*}e^{\imath\Delta t/2}\left(G\cos\tfrac{G}{2}t - \imath\Delta\sin\tfrac{G}{2}t\right) \ . \tag{5.91}$$

Using the normalization condition,

$$\begin{aligned}1 = |a_1|^2 + |a_2|^2 = \left|-\frac{2A}{\Omega^*}e^{\imath\Delta t/2}\left(G\cos Gt - \imath\Delta\sin\tfrac{G}{2}t\right)\right|^2 + \left|2\imath Ae^{-\imath\Delta t/2}\sin Gt\right|^2 \\ = \frac{4A^2}{|\Omega|^2}\left(G^2\cos^2\tfrac{G}{2}t + \Delta^2\sin^2\tfrac{G}{2}t\right) + 4A^2\sin^2\tfrac{G}{2}t = 4A^2\frac{G^2}{|\Omega|^2} \ .\end{aligned} \tag{5.92}$$

Hence, $A = |\Omega|/2G$. In general, we can choose Ω real, and the final solution is,

$$\boxed{a_1(t) = -e^{\imath\Delta t/2}\left(\cos\tfrac{G}{2}t + \tfrac{-\imath\Delta}{G}\sin\tfrac{G}{2}t\right) \qquad \text{and} \qquad a_2(t) = \tfrac{\imath\Omega}{G}e^{-\imath\Delta t/2}\sin\tfrac{G}{2}t} \ . \tag{5.93}$$

This results has already been obtained in Exc. 1.6.7.1 using an exact (i.e. not perturbative) calculus. When the energies E_n are degenerate, under the influence of the perturbation, the populations of the system oscillate with the Rabi frequency Ω. When the energies are different, the oscillation frequency G is higher, but the amplitude decreases as well. The initially empty state never reaches unitary population. In Exc. 5.4.5.3 we calculate the time required to allow the perturbation to invert the population of a two-level system, in Exc. 5.4.5.4 we study the maximum achievable inversion as a function of detuning, and in Exc. 5.4.5.5 we analyze the dynamics of a system subject to sequences of pulses.
In Exc. 5.4.5.6 we show a derivation using the Laplace transformation method.

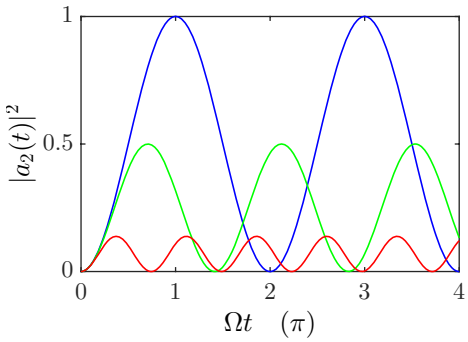

Figure 5.4: (code) Probability $|a_2(t)|^2$ for the atom to be in the excited state for $\Omega = \Gamma$ and $\Delta = 0$ (blue), $\Delta = \Gamma$ (green), and $\Delta = 2.5\Gamma$ (red). Time is in units of $1/\Gamma$.

5.4.3.3 Transitions to continuous levels

When there are several final states, $f \in F$, the formula (5.79) must be generalized. The total transition probability,

$$P_{i\to F}(t) = \sum_{f\in F} |a_{i\to f}(t)|^2 \ , \tag{5.94}$$

corresponds to the probability of the initial state $|i\rangle$ to be depleted. When the final state lies within a continuum, the sum in (5.94) must be replaced by an integral. With the *density of states* written in the form $\rho(E)$, where $\rho(E)dE$ is the number of states found in the energy range between E and $E + dE$, the transition probability is [12],

$$P_{i\to F}(t) = \int_{E_{\min}}^{E_{\max}} |a_{i\to f}(t)|^2 \rho(E_f) dE_f \ , \tag{5.95}$$

where $E \in [E_{\min}, E_{\max}]$ is the regime of energies within reach of the periodic perturbation. Now, plugging in the expression (5.79),

$$P_{i\to F}(t) = \int_{E_{\min}}^{E_{\max}} |\Omega_{fi}|^2 \frac{\sin^2 \frac{1}{2\hbar}(E_{fi}-E)t}{\frac{1}{4\hbar^2}(E_{fi}-E)^2} \rho(E_f) dE_f \ . \tag{5.96}$$

Again using the representation (5.76) of the Dirac function with the substitution $x \equiv (E_{fi} - E)/2\hbar$, we obtain after sufficiently long times [13],

$$P_{i\to F}(t) = \int_{E_{\min}}^{E_{\max}} |\Omega_{fi}|^2 t^2 \frac{\pi}{t} \delta(\tfrac{E_{fi}-E}{2\hbar}) \rho(E_f) dE_f = 2\pi\hbar t |\Omega_{fi}|^2 \rho(E_i + E) \ . \tag{5.97}$$

The transition rate is,

$$\frac{dP_{i\to F}(t)}{dt} = 2\pi\hbar |\Omega_{fi}|^2 \rho(E_i + E) \ . \tag{5.98}$$

[12] With $\rho(E) \equiv \sum_{f\in F} \delta(E_f - E)$ the integral is converted back into a sum.
[13] Remember $\delta(ax) = \frac{1}{a}\delta(x)$.

For a narrow distribution of final energies E centered around E_f we may substitute the density of states by a δ-distribution, $\rho(E) = \delta(E - E_f)$, so that,

$$\boxed{\frac{dP_{i\to F}}{dt} = \frac{2\pi}{\hbar}|\langle f|\hat{H}^{(1)}|i\rangle|^2\delta(E_{fi} - E)} \,, \tag{5.99}$$

where we went back to the definition of the perturbation Hamiltonian (5.77). This expression is called *Fermi's Golden rule*. In Exc. 5.4.5.7 we will calculate the *photo-electric effect*.

5.4.3.4 Continuous frequency distribution

To derive Eq. (5.79), we considered perturbations with fixed oscillation frequencies. To handle frequency distributions $\varrho(\omega)$, we must generalize this equation by calculating the integral,

$$\begin{aligned} |a_{i\to f}(t)|^2 &= |\Omega_{fi}|^2 \int \varrho(\omega)\frac{\sin^2\frac{1}{2}(\omega_{fi}-\omega)t}{\frac{1}{4}(\omega_{fi}-\omega)^2}d\omega \\ &\simeq |\Omega_{fi}|^2 t\varrho(\omega_{fi})\int_{-\infty}^{\infty}\mathrm{sinc}^2 x dx = 2\pi t|\Omega_{fi}|^2\varrho(\omega_{fi}-\omega) \,, \end{aligned} \tag{5.100}$$

again using the representation (5.76) of the Dirac function. The approximation $\varrho(\omega) = \varrho(\omega_{fi})$ can be used if the width of the sinc function is much narrower than the frequency distribution, which is the case for sufficiently long times, $t \gg \pi/2\Delta_{fi}$.

5.4.4 Transition rates for higher-order perturbations

The evolution from an initial state $|i\rangle$ that the system occupies at time t_0 to some final state $|\psi\rangle$, which may be a superposition, occupied at time t, is ruled by the solution of the Schrödinger equation,

$$|\psi\rangle = e^{-\imath\hat{H}(t-t_0)/\hbar}|i\rangle \,. \tag{5.101}$$

The probability to encounter $|\psi\rangle$ in a given state $|f\rangle$ is $|\langle f|\psi\rangle|^2$, and the *transition rate* is simply the derivative of this. The transition rate *out of the initial state* into any other final state is, consequently

$$\boxed{\frac{1}{\tau} = \sum_f \frac{d}{dt}|\langle f|e^{-\imath\hat{H}(t-t_0)/\hbar}|i\rangle|^2} \,. \tag{5.102}$$

From this formula we can already see, that at short times, when we can expand the exponential to first order, we will recover the results of (5.72).

Let us now consider a time-independent perturbation in the Schrödinger picture,

$$\hat{H}(t) = \hat{H}^{(0)} + \hat{H}^{(1)} \,, \tag{5.103}$$

where the time dependence is entirely left to the wavefunction. Now, we expand the propagator $e^{-\imath\hat{H}(t-t_0)}$ in a perturbative series [14]. Unfortunately, generally $[\hat{H}^{(0)}, \hat{H}^{(1)}] \neq$

[14] We drop the $\hbar = 1$ for the following calculation to simplify the notation.

0, so that we cannot simply assume $e^{-\imath\hat{H}t} \neq e^{-\imath\hat{H}^{(0)}t}e^{-\imath\hat{H}^{(1)}t}$. But we can calculate,

$$\imath\frac{d}{dt}e^{\imath\hat{H}^{(0)}t}e^{-\imath\hat{H}t} = -\hat{H}^{(0)}e^{\imath\hat{H}^{(0)}t}e^{-\imath\hat{H}t} + e^{\imath\hat{H}^{(0)}t}\hat{H}e^{-\imath\hat{H}t} = e^{\imath\hat{H}^{(0)}t}\hat{H}^{(1)}e^{-\imath\hat{H}t} \ . \quad (5.104)$$

Integrating both sides and resolving for $e^{-\imath\hat{H}t}$,

$$e^{-\imath\hat{H}t} = e^{-\imath\hat{H}^{(0)}t}\left\{e^{\imath\hat{H}^{(0)}t_0}e^{-\imath\hat{H}t_0} - \imath\int_{t_0}^{t} e^{\imath\hat{H}^{(0)}t_1}\hat{H}^{(1)}e^{-\imath\hat{H}t_1}dt_1\right\} \ . \quad (5.105)$$

We want to analyze a steady-state situation, that is, we assume that the interaction as gradually built up in an infinitely remote past. Hence, we can set $\hat{H} = \hat{H}^{(0)}$ for $t_0 \to -\infty$,

$$e^{-\imath\hat{H}t} = e^{-\imath\hat{H}^{(0)}t}\left\{1 - \imath\int_{-\infty}^{t} e^{\imath\hat{H}^{(0)}t_1}\hat{H}^{(1)}e^{\varepsilon t_1}e^{-\imath\hat{H}t_1}dt_1\right\} \ , \quad (5.106)$$

where the term $e^{\varepsilon t_1}$, with $\varepsilon \to 0$, is inserted to guarantee a smooth switch-on. We iterate,

$$\boxed{\begin{aligned} e^{-\imath\hat{H}t} &= e^{-\imath\hat{H}^{(0)}t}\left\{1 - \imath\int_{-\infty}^{t} e^{\imath\hat{H}^{(0)}t_1}\hat{H}^{(1)}e^{\varepsilon t_1}\times\right. \\ &\times \left. e^{-\imath\hat{H}^{(0)}t}\left[1 - \imath\int_{-\infty}^{t_1} e^{\imath\hat{H}^{(0)}t_2}\hat{H}^{(1)}e^{\varepsilon t_2}e^{-\imath\hat{H}t_2}dt_2\right]dt_1\right\} \end{aligned}} \ . \quad (5.107)$$

We calculate the matrix elements up to second order substituting $\hat{H}$ with $\hat{H}^{(0)}$ in the last integral,

$$\begin{aligned} &\langle f|e^{-\imath\hat{H}t}|i\rangle \quad (5.108)\\ &\simeq \langle f|e^{-\imath\hat{H}^{(0)}t}\left\{1 - \imath\int_{-\infty}^{t} e^{\imath\hat{H}^{(0)}t_1}\hat{H}^{(1)}e^{\varepsilon t_1}e^{-\imath\hat{H}^{(0)}t_1}\left[1 - \imath\int_{-\infty}^{t_1} e^{\imath\hat{H}^{(0)}t_2}\hat{H}^{(1)}e^{\varepsilon t_2}e^{-\imath\hat{H}^{(0)}t_2}dt_2\right]dt_1\right\}|i\rangle \\ &= e^{-\imath\omega_f i t}\langle f|i\rangle - \imath e^{-\imath\omega_f t}\int_{-\infty}^{t} e^{\imath\omega_f t_1}\langle f|\hat{H}^{(1)}|i\rangle e^{\varepsilon t_1}e^{-\imath\omega_i t_1}dt_1 \\ &\quad - e^{-\imath\omega_f t_1}\int_{-\infty}^{t} e^{\imath\omega_f t_1}\langle f|\hat{H}^{(1)}e^{\varepsilon t_1}e^{-\imath\omega_i t_1}\sum_m |m\rangle\langle m|\int_{-\infty}^{t_1} e^{\imath\hat{H}^{(0)}t_2}\hat{H}^{(1)}|i\rangle e^{\varepsilon t_2}e^{-\imath\omega_i t_2}dt_2 dt_1 \ . \end{aligned}$$

where we separated the perturbation orders and inserted $\sum_m |m\rangle\langle m| = \mathbb{I}$ using the

closure relation. Using the time-independence of $\hat{H}^{(1)}$,

$$\begin{aligned}
\langle f|e^{-\imath\hat{H}t}|i\rangle &\simeq e^{-\imath\omega_{fi}t}\delta_{fi} - \imath e^{-\imath\omega_f t}\langle f|\hat{H}^{(1)}|i\rangle \int_{-\infty}^{t} e^{(\imath\omega_f - \imath\omega_i+\varepsilon)t_1}dt_1 \\
&\quad - e^{-\imath\omega_f t}\sum_m \langle f|\hat{H}^{(1)}|m\rangle\langle m|\hat{H}^{(1)}|i\rangle \int_{-\infty}^{t} e^{(\imath\omega_f - \imath\omega_i+\varepsilon)t_1}\int_{-\infty}^{t_1} e^{(\imath\omega_m - \imath\omega_i+\varepsilon)t_2}dt_2dt_1 \\
&= e^{-\imath\omega_{fi}t}\delta_{fi} - \imath e^{-\imath\omega_f t}\langle f|\hat{H}^{(1)}|i\rangle \frac{e^{(\imath\omega_f - \imath\omega_i+\varepsilon)t}}{\imath(\omega_f-\omega_i)+\varepsilon} \\
&\quad - e^{-\imath\omega_f t}\sum_m \langle f|\hat{H}^{(1)}|m\rangle\langle m|\hat{H}^{(1)}|i\rangle \int_{-\infty}^{t} e^{(\imath\omega_f - \imath\omega_m+\varepsilon)t_1}\frac{e^{(\imath\omega_m - \imath\omega_i+\varepsilon)t_1}}{\imath(\omega_m-\omega_i)+\varepsilon}dt_1 \\
&= e^{-\imath\omega_{fi}t}\delta_{fi} - \imath\langle f|\hat{H}^{(1)}|i\rangle \frac{e^{(-\imath\omega_i+\varepsilon)t}}{\imath(\omega_f-\omega_i)+\varepsilon} \\
&\quad - e^{-\imath\omega_f t}\sum_m \frac{\langle f|\hat{H}^{(1)}|m\rangle\langle m|\hat{H}^{(1)}|i\rangle}{\imath(\omega_m-\omega_i)+\varepsilon}\int_{-\infty}^{t} e^{(\imath\omega_f - \imath\omega_i+2\varepsilon)t_1}dt_1 \\
&= e^{-\imath\omega_{fi}t}\delta_{fi} - \imath\langle f|\hat{H}^{(1)}|i\rangle \frac{e^{(-\imath\omega_i+\varepsilon)t}}{\imath(\omega_f-\omega_i)+\varepsilon} - \sum_m \frac{\langle f|\hat{H}^{(1)}|m\rangle\langle m|\hat{H}^{(1)}|i\rangle}{\imath(\omega_m-\omega_i)+\varepsilon}\frac{e^{(-\imath\omega_i+2\varepsilon)t}}{\imath(\omega_f-\omega_i)+2\varepsilon} .
\end{aligned} \tag{5.109}$$

These three terms represent the zeroth, first, and second perturbation orders of the propagation operator (5.101). They are also called *Feynman propagators*. Now, we can calculate the transition rate up to second order,

$$\begin{aligned}
\frac{1}{\tau} &= \frac{d}{dt}\sum_f \left|\langle f|e^{-\imath\hat{H}t}|i\rangle\right|^2 \\
&= \lim_{\varepsilon\to 0}\sum_f \left|\langle f|\hat{H}^{(1)}|i\rangle - \sum_m \frac{\langle f|\hat{H}^{(1)}|m\rangle\langle m|\hat{H}^{(1)}|i\rangle}{-\imath(\omega_m-\omega_i)-\imath\varepsilon}\right|^2 \frac{d}{dt}\left|\frac{e^{(-\imath\omega_i+\varepsilon)t}}{\imath(\omega_f-\omega_i)+\varepsilon}\right|^2 \\
&= \sum_f \left|\langle f|\hat{H}^{(1)}|i\rangle - \sum_m \frac{\langle f|\hat{H}^{(1)}|m\rangle\langle m|\hat{H}^{(1)}|i\rangle}{(\omega_m-\omega_i)}\right|^2 \lim_{\varepsilon\to 0}\frac{2\varepsilon e^{2\varepsilon t}}{(\omega_f-\omega_i)^2+\varepsilon^2} .
\end{aligned} \tag{5.110}$$

The last fraction is a representation of the δ-function. Reintroducing $\hbar$, we finally obtain,

$$\boxed{\frac{1}{\tau} = \frac{2\pi}{\hbar^2}\sum_f \left|\langle f|\hat{H}^{(1)}|i\rangle + \frac{1}{\hbar}\sum_m \frac{\langle f|\hat{H}^{(1)}|m\rangle\langle m|\hat{H}^{(1)}|i\rangle}{\omega_i-\omega_m}\right|^2 \delta(\omega_f-\omega_i)} . \tag{5.111}$$

The first term is *Fermi's Golden rule*, the second order corresponds to the *Kramers-Heisenberg formula*, which serves to describe Thomson, Rayleigh and Raman scattering. The generalization of this transition rate to all perturbation orders can be written,

$$\begin{aligned}
\frac{1}{\tau} = \frac{2\pi}{\hbar^2}\sum_f \Bigg|\langle f|\Bigg(\hat{H}^{(1)} + \frac{1}{\hbar}\sum_m \frac{\hat{H}^{(1)}|m\rangle\langle m|\hat{H}^{(1)}}{\omega_i-\omega_m} + \ \ldots \\
+ \frac{1}{\hbar^{n-1}}\sum_{m_1,\ldots,m_{n-1}} \frac{\hat{H}^{(1)}|m_1\rangle\langle m_1|\ldots|m_{n-1}\rangle\langle m_{n-1}|\hat{H}^{(1)}}{(\omega_i-\omega_{m_1})\ldots(\omega_i-\omega_{m_{n-1}})}\Bigg)|i\rangle\Bigg|^2 \delta(\omega_{fi}) .
\end{aligned} \tag{5.112}$$

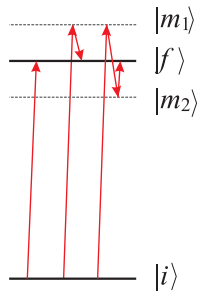

Figure 5.5: Graphical illustration of the various transitions orders. From left to right: absorption, Raman transition via an intermediate virtual state $|m_1\rangle$, three-photon process via two intermediate virtual states $|m_1\rangle$ and $|m_2\rangle$.

5.4.5 Exercises

5.4.5.1 Ex: Perturbed harmonic oscillator

Consider a one-dimensional harmonic oscillator (HO) initially prepared ($t = -\infty$) in the ground state $|0\rangle$ of the unperturbed Hamiltonian $H^{(0)} = \hbar\omega\hat{a}^\dagger\hat{a}$, such that $H^{(0)}|n\rangle = E_n|n\rangle$ with $E_n = n\hbar\omega$.
a. Through the expression, $a_f(t) \approx \frac{1}{i\hbar}\int_{t_i}^{t_f} W_{fi}e^{i\omega_{fi}t}dt$, and the perturbative Hamiltonian $W(t) = -e\mathcal{E}xe^{-t^2/\tau^2}$ (x is the position operator of the HO), applied between $t = -\infty$ and $t = +\infty$, calculate the probability of the system to be in the excited state $|n\rangle$, specifying n, at $t = +\infty$. Analyze the result.
b. Do the same for a shape-changing perturbation, $W(t) = \Lambda x^2 e^{-t^2/\tau^2}$.

5.4.5.2 Ex: Impact of the rapidity of a perturbation

Here we consider a slow variation,

$$\hat{W}(t) = \begin{cases} 0 & \text{for} \quad t < 0 \\ W_0(1 - e^{-\gamma t}) & \text{for} \quad t \geq 0 \end{cases},$$

with $\gamma \ll \omega_{fi}$.
a. Calculate the transition rate for long times, $t \gg \gamma^{-1}$.
b. Analyze the transition rate at a given time as a function of γ.

5.4.5.3 Ex: Rabi oscillation

The population of a degenerate two-level system be initially in state $|1\rangle$. What should be the duration of a perturbation to transfer the population to state $|2\rangle$?

5.4.5.4 Ex: Rabi method

Free atoms be illuminated by light pulses characterized by the Rabi frequency Ω, whose pulse area is (i) $\int_0^t \Omega\, dt = \pi$ and (ii) $= 2\pi$. For which frequency tuning $\Delta = \omega - \omega_0$ the excited state population is maximum? Draw the spectral profile of the population in the range $-5 < \Delta/\Omega < 5$.

5.4.5.5 Ex: Ramsey fringes

a. Consider a two-level atom illuminated by a $\frac{\pi}{2}$-pulse of nearly resonant light, $G \simeq \Omega$, and calculate the ground and excited state amplitudes.
b. How do the amplitudes evolve after the pulse if the detuning Δ is small but non-zero?
c. Derive the solution for $|a_2(t)|^2$ of the equations (5.63) for the resonant case ($\Delta = 0$) assuming the following initial conditions, $a_2(0) = \frac{e^{\imath\phi}}{\sqrt{2}}$ and $a_2(t = \frac{\pi}{2\Omega}) = 0$ if $\phi = 0$.
d. Discuss the case of two consecutive $\frac{\pi}{2}$-pulses separated by a time interval T.

5.4.5.6 Ex: Two-level atom via Laplace transformation

Solve the problem of a two-level atom interacting with a laser using the Laplace transformation method.

5.4.5.7 Ex: Photoelectric effect

A hydrogen atom ground state in the ground state $1s$ is placed in an electric field $\mathbf{E}(t) = \vec{\mathcal{E}}_0 \cos\omega t$, such that $W(t) = -e\mathbf{r}\cdot\vec{\mathcal{E}}(t) = W_0 e^{-\imath\omega t} + W_0^\dagger e^{\imath\omega t}$ with $W_0 = e\mathbf{r}\cdot\vec{\mathcal{E}}_0/2$. Find, via Fermi's Golden rule,

$$R = \frac{2\pi}{\hbar}|\langle f|W(t)|i\rangle|^2 \rho(E_f - E_i \mp \hbar\omega) \ ,$$

using the density of states $\rho(E_k)dE_k = V/(2\pi)^3 k^2 dk d\Omega$, the probability per unit of time for the atom to be ionized, by exciting from the ground state $\psi_{100}(\mathbf{r}) = e^{-r/a_B}/(\pi a_B^3)^{1/2}$ to the state described by the plane wave $\psi_{\mathbf{k}}(\mathbf{r}) = e^{-\imath\mathbf{k}\cdot\mathbf{r}}/V^{1/2}$. Simplify the calculation by assuming $\vec{\mathcal{E}}_0 = \mathcal{E}_0\hat{\mathbf{e}}_z$ and $\mathbf{k} = k\hat{\mathbf{e}}_z$.

5.4.5.8 Ex: Kicked harmonic oscillator in second order perturbation

Consider a one-dimensional harmonic oscillator initially in its ground state kicked via the $\hat{H}^{(1)}(t) = e^{\imath k\hat{x}}\Theta(t)$, as discussed in Sec. 2.6.2. Calculate the transition rate (5.102) to the final state $|f\rangle = |0\rangle$ in first and second order perturbation theory.

5.4.5.9 Ex: Dynamic Stark shift induced by blackbody radiation

Calculate the dynamic Stark shift induced by blackbody radiation at $T = 300\,\mathrm{K}$ on the 1 mHz large strontium intercombination line at 698 nm.

5.5 Further reading

C. Cohen-Tannoudji, B. Diu, F. Laloe, Wiley Interscience, *Quantum mechanics, vol. 1,2* [ISBN]

Chapter 6

Appendices to 'Quantum Mechanics'

This chapter compiles some fundamental functions and polynomials, which are relevant in quantum theory.

6.1 Quantities and formulas in quantum mechanics

6.1.1 Notations and conventions

quantity	notation	examples
scalars	italic letters	T
vectors	bold letters	$\mathbf{F}$
electromagnetic fields	calligraphic letters	$\vec{\mathcal{E}}$
Green function	calligraphic	$\mathcal{G}$
quantum observables	hat	$\hat{\mathbf{p}}$
(many-body) Hamiltonian		$\hat{H}$
single-particle Hamiltonian	gothic	$\mathfrak{H}$
Liouvillean	gothic	$\mathfrak{L}$
unitary transform	calligraphic	$\mathcal{U}$
displacement	calligraphic	$\mathcal{D}$
Laplace & Fourier transform	calligraphic	$\mathcal{L}$ & $\mathcal{F}$
number spaces		$\mathbb{N}, \mathbb{Z}, \mathbb{R}$
Hilbert space		$\mathbb{H}$

6.1.2 Atomic units

A commonly used system of units in atomic physics is the one of *atomic units*. This system is based on the system of Gaussian units (CGS) defined by setting,

$$e_{\rm cgs} \equiv \frac{e}{\sqrt{4\pi\varepsilon_0}} \qquad \text{and} \qquad \hbar \equiv 1 \ , \tag{6.1}$$

using $\alpha = e^2/4\pi\varepsilon_0\hbar c$ and $a_{\rm B} = 4\pi\varepsilon_0\hbar^2/m_e e^2$ and giving the energy in terms of $e^2_{\rm cgs}/a_{\rm B} = 1/\alpha^2 m_e c^2 \approx 4.36 \cdot 10^{-18}$ J, the wavevector in terms of $1/a_{\rm B}$, the distance in terms of $a_{\rm B}$ and the mass in terms of m_e we find,

$$\boxed{\begin{array}{rcl} \tilde{E} &=& E/(e^2_{\rm cgs}/a_{\rm B}) \\ \tilde{k} &=& k a_{\rm B} \\ \tilde{R} &=& R/a_{\rm B} \\ \tilde{\mu} &=& \mu/m_e \end{array}} \ . \tag{6.2}$$

This notation simplifies formulas in atomic physics. For example,

$$k = \sqrt{\tfrac{2\mu}{\hbar^2}(E-V)} \qquad \text{becomes} \qquad \tilde{k} = \sqrt{2\tilde{\mu}(\tilde{E}-\tilde{V})} \tag{6.3}$$

and the van der Waals potential

$$V = \frac{C_n}{R^n} \qquad \text{becomes} \qquad \tilde{V} = \frac{\tilde{C}_n}{\tilde{R}^n} \qquad \text{with} \qquad \tilde{C}_n \equiv \frac{C_n}{e^2_{\rm cgs} a_{\rm B}^{n-1}} \ . \tag{6.4}$$

Note that energies are sometimes given in wavenumbers,

$$V_{\rm wn} \equiv V/(100hc) \ . \tag{6.5}$$

6.2 Clebsch-Gordan and Wigner symbols

6.2.1 Clebsch-Gordan symbols

Clebsch-Gordan coefficients are used to describe spin coupling [1],

$$\langle j_1, m_1; j_2, m_2 | (j_1 j_2) j, m\rangle = \left(\begin{array}{cc|c} j_1 & j_2 & j \\ m_1 & m_2 & m \end{array} \right) = (-1)^{j_1 - j_2 + m} \sqrt{\Delta(j_1 j_2 j)} \times \tag{6.6}$$

$$\times \sqrt{(j_1+m_1)!(j_1-m_1)!(j_2+m_2)!(j_2-m_2)!(j+m)!(j-m)!}$$

$$\sum_t \frac{(-1)^t}{t!(-j_2+m_1+j+t)!(-j_1-m_2+j+t)!(j_1+j_2-j-t)!(j_1-m_1-t)!(j_2+m_2-t)!} \ .$$

[1] See [35], p.111 or [813], p.119.

6.2.2 $\{3j\}$-symbols

The Clebsch-Gordans are related to Wigner's $\{3j\}$-*symbols*,

$$\begin{pmatrix} j_1 & j_2 & j \\ m_1 & m_2 & m \end{pmatrix} = (-1)^{-j_1+j_2-m}\sqrt{2j+1}\begin{pmatrix} j_1 & j_2 & j \\ m_1 & m_2 & -m \end{pmatrix} , \tag{6.7}$$

with the abbreviation,

$$\Delta(j_1 j_2 j_3) \equiv \frac{(j_1+j_2-j_3)!(j_1-j_2+j_3)!(-j_1+j_2+j_3)!}{(j_1+j_2+j_3+1)!} . \tag{6.8}$$

Particular $\{3j\}$-symbols are,

$$\begin{pmatrix} j_1 & j_2 & j \\ 0 & 0 & 0 \end{pmatrix} = \frac{(-1)^{(j_1+j_2+j)/2}}{j_1/2+j_2/2+j/2+1}\frac{\sqrt{\Delta(j_1 j_2 j)}}{\Delta(\frac{j_1}{2}\,\frac{j_2}{2}\,\frac{j}{2})} , \tag{6.9}$$

and

$$\begin{pmatrix} 0 & j & j \\ 0 & 0 & 0 \end{pmatrix} = \frac{(-1)^j}{\sqrt{2j+1}} . \tag{6.10}$$

6.2.3 $\{6j\}$-symbols

$\{6j\}$-*symbols* describe the recoupling of two spins. They can be evaluated by,

$$\begin{Bmatrix} j_1 & j_2 & j_3 \\ J_1 & J_2 & J_3 \end{Bmatrix} = \sqrt{\Delta(j_1 j_2 j_3)\Delta(j_1 J_2 J_3)\Delta(J_1 j_2 J_3)\Delta(J_1 J_2 j_3)}\sum_t \frac{(-)^t(t+1)!}{f(t)} , \tag{6.11}$$

where,

$$\begin{aligned} f(t) = (t-j_1-j_2-j_3)!(t-j_1-J_2-J_3)!(t-J_1-j_2-J_3)!(t-J_1-J_2-j_3)! \\ (j_1+j_2+J_1+J_2-t)!(j_2+j_3+J_2+J_3-t)!(j_3+j_1+J_3+J_1-t)! . \end{aligned} \tag{6.12}$$

6.2.4 $\{9j\}$-symbols

$\{3j\}$-*symbols* describe the recoupling of three spins. They can be evaluated by,

$$\begin{Bmatrix} j_1 & j_2 & J_{12} \\ j_3 & j_4 & J_{34} \\ J_{13} & J_{24} & J \end{Bmatrix} = \sum_g (-)^{2g}(2g+1)\begin{Bmatrix} j_1 & j_2 & J_{12} \\ J_{34} & J & g \end{Bmatrix}\begin{Bmatrix} j_3 & j_4 & J_{34} \\ j_2 & g & J_{24} \end{Bmatrix}\begin{Bmatrix} J_{13} & J_{24} & J \\ g & j_1 & j_3 \end{Bmatrix} . \tag{6.13}$$

$\{9j\}$-symbols satisfy the following orthogonality relation,

$$\sum_{J_{12},J_{34}} \hat{J}_{12}\hat{J}_{34}\hat{H}_{13}\hat{H}_{24}\begin{Bmatrix} j_1 & j_2 & J_{12} \\ j_3 & j_4 & J_{34} \\ H_{13} & H_{24} & J \end{Bmatrix}\begin{Bmatrix} j_1 & j_2 & J_{12} \\ j_3 & j_4 & J_{34} \\ J_{13} & J_{24} & J \end{Bmatrix} = \delta_{J_{13}H_{13}}\delta_{J_{24}H_{24}} . \tag{6.14}$$

6.3 Functions and polynomials

6.3.1 The Gauss function

Indefinite integrals:

$$\int_{-\infty}^{\infty} e^{-ax^2}dx = \sqrt{\pi/a} \quad \text{and} \quad \int_0^{\infty} x^n e^{-ax^2}dx = \frac{\Gamma(\frac{n+1}{2})}{2a^{\frac{n+1}{2}}} \ . \tag{6.15}$$

Higher momenta:

$$\int_{x_0}^{x_1} e^{-ax^2}dx = xe^{-ax^2}\Big|_{x_0}^{x_1} + 2a\int_{x_0}^{x_1} x^2 e^{-ax^2}dx \ . \tag{6.16}$$

6.3.2 Bessel functions

The integral definition of the *Bessel function*, the *von Neumann function*, and the *Hankel function* of the first and second kind are:

$$\begin{aligned} J_k(x) &= \frac{1}{\pi}\int_0^{\pi} \cos(k\tau - x\sin\tau)d\tau = \frac{1}{2\pi}\int_{-\pi}^{\pi} e^{\imath(x\sin\tau - k\tau)}d\tau \\ N_k(x) &= ... \\ H_k^{(1,2)} &= J_k \pm \imath N_k \ . \end{aligned} \tag{6.17}$$

The derivative,

$$2\frac{dJ_k(x)}{dx} = J_{k-1}(x) - J_{k+1}(x) \ . \tag{6.18}$$

Sum rules (empirically found),

$$\sum_{k=-\infty}^{\infty} J_k(x) = \sum_{k=-\infty}^{\infty} J_k(x)^2 = 1 \neq \sum_{k=-\infty}^{\infty} |J_k(x)|^2 \ . \tag{6.19}$$

The *spherical Bessel function*, the *spherical von Neumann function*, and the *spherical Hankel function* of the first and second kind are defined by:

$$\begin{aligned} j_k(x) &= \sqrt{\frac{\pi}{2x}}J_{k+1/2}(x) \\ n_k(x) &= \sqrt{\frac{\pi}{2x}}N_{k+1/2}(x) = (-1)^{k+1}\sqrt{\frac{\pi}{2x}}J_{-k-1/2}(x) \\ h_k^{(1,2)} &= j_k \pm \imath n_k \ . \end{aligned} \tag{6.20}$$

The series,

$$j_k(x) = (-x)^k\left(\frac{1}{x}\frac{d}{dx}\right)^k \frac{\sin x}{x} \quad , \quad n_k(x) = -(-x)^k\left(\frac{1}{x}\frac{d}{dx}\right)^k \frac{\cos x}{x} \ . \tag{6.21}$$

The derivative,

$$j_k'(x) = \frac{k}{x}j_k(x) - j_{k+1}(x) \ . \tag{6.22}$$

6.3.3 Hermite polynomials

The definition of the *Hermite polynomials*:

$$H_n(x) = \left(2x - \frac{d}{dx}\right)^n \cdot 1 = (-1)^n e^{x^2} \frac{d^n}{dx^n} e^{-x^2} = \frac{2^n}{\sqrt{\pi}} \int_{-\infty}^{\infty} (x + \imath t)^n e^{-t^2} dt \quad (6.23)$$

$$He_n(x) \equiv 2^{-n/2} H_n(x) \ .$$

Orthogonality and normalization:

$$\int_{-\infty}^{\infty} e^{-x^2} H_m(x) H_n(x) dx = \sqrt{\pi} 2^n n! \delta_{mn} \ . \quad (6.24)$$

Recursion:

$$\frac{d}{dx} H_n(x) = 2H_{n-1}(x) \quad (6.25)$$

$$\frac{d}{dx} e^{-x^2} H_n(x) = e^{-x^2} H_{n+1}(x)$$

$$H_{n+1}(x) = 2xH_n(x) - 2nH_{n-1}(x) \ .$$

Particular values:

$$H_{2n+1}(0) = 0 \quad (6.26)$$

$$H_{2n+1}(0) = (-1)^n 2^n (2n-1)!!$$

Series:

$$H_{2n}(x) = \sum_{k=0}^{\infty} \frac{(2n)!}{(2k)!} \frac{(-1)^{n-k}}{(n-k)!} (2x)^{2k} \quad (6.27)$$

$$H_{2n-1}(x) = \sum_{k=0}^{\infty} \frac{(2n+1)!}{(2k+1)!} \frac{(-1)^{n-k}}{(n-k)!} (2x)^{2k+1}$$

$$H_n(x) = n! \sum_{k=0}^{\mathrm{int}(n/2)} \frac{1}{k!} \frac{(-1)^k}{(n-2k)!} (2x)^{n-2k} \ .$$

6.3.4 Laguerre polynomials

The definition of the *Laguerre polynomials* is:

$$L_n^{(m)}(x) \equiv \frac{e^x x^{-m}}{m!} \frac{d^n}{dx^n} (e^{-x} x^{n+m}) \quad (6.28)$$

$$L_n \equiv L_n^{(0)}(x) \ .$$

Series:

$$L_n^{(m)}(x) = \sum_{k=0}^{n} \binom{n+m}{n-k} \frac{(-x)^k}{k!} \ . \quad (6.29)$$

Recursion:

$$\frac{d}{dx} L_n^{(m)}(x) = -L_{n-1}^{(m+1)}(x) \ . \quad (6.30)$$

Related functions:

$$u_{mn}(\varepsilon) \equiv e^{-\varepsilon^2} \cdot (\imath\varepsilon)^{n-m} \cdot \sqrt{\tfrac{m!}{n!}} \cdot L_m^{n-m}(\varepsilon^2) \tag{6.31}$$
$$u_{mn}(0) \approx (\imath\varepsilon)^{n-m} \cdot \sqrt{\tfrac{n!}{m!(n-m)!^2}}$$
$$u_{n+1,n}(0) \approx \imath\varepsilon \cdot \sqrt{n+1}\ .$$

Fourier transforms:

$$\int_{-\infty}^{\infty} e^{-ax^2} x^{2k} \cos xp \cdot dx = \tfrac{(-1)^k\sqrt{\pi}}{2^k\sqrt{a^{2k+1}}} \cdot e^{p^2/4a} \cdot He_{2k}(p/\sqrt{2a}) \tag{6.32}$$
$$\int_{-\infty}^{\infty} e^{-x^2/2} x^{2m} L_n^{2m}(x^2) \cos xp \cdot dx = \tfrac{(-1)^m\sqrt{\pi}}{\sqrt{2}n!} \cdot e^{-p^2/2} \cdot He_n(p) He_{n+2m}(p)$$
$$\int_{-\infty}^{\infty} e^{-x^2/2} x^{2m+1} L_n^{2m+1}(x^2) \sin xp \cdot dx = \tfrac{(-1)^m\sqrt{\pi}}{\sqrt{2}n!} \cdot e^{-p^2/2} \cdot He_n(p) He_{n+2m+1}(p)$$
$$\int_{-\infty}^{\infty} e^{-ax-bp} f(|x-p|) \cdot dxdp = \tfrac{1}{a+b}\left[\int_{-\infty}^{\infty} e^{-ax} f(x)dx + \int_{-\infty}^{\infty} e^{-bp} f(p)dp\right]\ .$$

6.3.5 Legendre polynomials

The definition of *Legendre polynomials* is:

$$P_n(x) \equiv \frac{1}{2^n n!}\frac{d^n}{dx^n}(x^2-1)^n \tag{6.33}$$
$$P_n^{(-m)}(x) \equiv (1-x^2)^{m/2}\frac{d^m}{dx^m}P_l(x)\ .$$

Series:

$$P_n^{(m)}(x) = \frac{(-1)^m(n+m)!}{2^m m!(n-m)!}(1-x^2)^{m/2}\left[\begin{array}{c} 1 - \frac{(n-m)!(m+n+1)!}{1!(m+1)!}\frac{1-x}{2} + \\ + \frac{(n-m)!(n-m+1)!(m+n+1)!(m+n+2)!}{2!(m+1)!(m+2)!}\left(\frac{1-x}{2}\right)^2 - \ldots \end{array}\right]\ . \tag{6.34}$$

6.3.6 Spherical harmonics

The definition of *spherical harmonics* is [862]:

$$Y_{\ell m}(\vartheta,\varphi) \equiv \sqrt{\frac{2\ell+1}{4\pi}}\sqrt{\frac{(\ell-|m|)!}{(\ell+|m|)!}}P_\ell^{|m|}(\cos(\vartheta)e^{im\varphi}\ . \tag{6.35}$$

The lowest *spherical harmonics* are:

$$\begin{array}{lcllcl} Y_0^{(0)} & = & \frac{1}{2}\sqrt{\frac{1}{\pi}} & Y_0^{(1)} & = & \frac{1}{2}\sqrt{\frac{3}{\pi}}\cos\theta \\ Y_{\pm1}^{(1)} & = & \mp\frac{1}{2}\sqrt{\frac{3}{2\pi}}\sin\theta e^{\pm i\phi} & Y_0^{(2)} & = & \frac{1}{4}\sqrt{\frac{5}{\pi}}(3\cos^2\theta-1) \\ Y_{\pm1}^{(2)} & = & \mp\frac{1}{2}\sqrt{\frac{15}{2\pi}}\sin\theta\cos\theta e^{\pm i\phi} & Y_{\pm2}^{(2)} & = & \frac{1}{4}\sqrt{\frac{15}{2\pi}}\sin^2\theta e^{\pm 2i\phi} \end{array} \tag{6.36}$$

6.3.7 Vector spherical harmonics

The definition of *vector spherical harmonics* is [862]:

$$\mathbf{Y}_{j\ell m}(\mathbf{r}) \equiv (-1)^{1-\ell-m}\sqrt{2j+1}\sum_q \begin{pmatrix} \ell & 1 & j \\ m-q & q & -m \end{pmatrix} Y_{\ell\ m-q}(\vartheta,\varphi)\hat{\mathbf{e}}_q \ . \tag{6.37}$$

6.3.7.1 The Gamma function

The definition of the *Gamma function* is:

$$\Gamma(x+1) = x\Gamma(x) \quad , \quad \Gamma(1/2) = \sqrt{\pi} \ . \tag{6.38}$$

6.4 Rules of tensor algebra

Here are some rules for calculating with tensor products. Be $\hat{A}$, $\hat{B}$, ... operators, $\mathbf{u}$, $\mathbf{v}$, ... state vectors, and α, β, ... scalars [15],

$$\begin{aligned}
&\text{(i)} && (\hat{A}\otimes\hat{B})^\dagger = \hat{A}^\dagger\otimes\hat{B}^\dagger && (6.39)\\
&\text{(ii)} && (\hat{A}_1+\hat{A}_2)\otimes\hat{B} = \hat{A}_1\otimes\hat{B}+\hat{A}_2\otimes\hat{B}\\
&\text{(iii)} && (\hat{A}_1\otimes\hat{B}_1)(\hat{A}_2\otimes\hat{B}_2) = (\hat{A}_1\hat{A}_2)\otimes(\hat{B}_1\hat{B}_2)\\
&\text{(iv)} && [\hat{A}_1\otimes\hat{B}_1,\hat{A}_2\otimes\hat{B}_2] = \tfrac{1}{2}\Big([\hat{A}_1,\hat{A}_2]\otimes\{\hat{B}_1,\hat{B}_2\}+\{\hat{A}_1,\hat{A}_2\}\otimes[\hat{B}_1,\hat{B}_2]\Big)\\
&\text{(v)} && \{\hat{A}_1\otimes\hat{B}_1,\hat{A}_2\otimes\hat{B}_2\} = \tfrac{1}{2}\Big(\{\hat{A}_1,\hat{A}_2\}\otimes[\hat{B}_1,\hat{B}_2]+[\hat{A}_1,\hat{A}_2]\otimes\{\hat{B}_1,\hat{B}_2\}\Big)\\
&\text{(vi)} && \mathrm{Tr}\,(\hat{A}\otimes\hat{B}) = \mathrm{Tr}\,\hat{A}\,\mathrm{Tr}\,\hat{B}\\
&\text{(vii)} && (\hat{A}\otimes\hat{B})(\mathbf{u}\otimes\mathbf{v}) = \hat{A}\mathbf{u}\otimes\hat{B}\mathbf{v}\\
&\text{(viii)} && (\mathbf{u}_1+\mathbf{u}_2)\otimes\mathbf{v} = \mathbf{u}_1\otimes\mathbf{v}+\mathbf{u}_2\otimes\mathbf{v}\\
&\text{(ix)} && \mathbf{u}\otimes(\mathbf{v}_1+\mathbf{v}_2) = \mathbf{u}\otimes\mathbf{v}_1+\mathbf{u}\otimes\mathbf{v}_2\\
&\text{(x)} && \mathbf{u}\otimes(\mathbf{v}_1+\mathbf{v}_2) = \mathbf{u}\otimes\mathbf{v}_1+\mathbf{u}\otimes\mathbf{v}_2\\
&\text{(xi)} && \alpha\mathbf{u}\otimes\beta\mathbf{v} = \alpha\beta(\mathbf{u}\otimes\mathbf{v})\\
&\text{(xii)} && \begin{pmatrix}\hat{A}_1 & \hat{A}_2\\ \hat{A}_3 & \hat{A}_4\end{pmatrix}\otimes\hat{B} = \begin{pmatrix}\hat{A}_1\otimes\hat{B} & \hat{A}_2\otimes\hat{B}\\ \hat{A}_3\otimes\hat{B} & \hat{A}_4\otimes\hat{B}\end{pmatrix}\\
&\text{(xiii)} && \begin{pmatrix}a_1 & a_2\\ a_3 & a_4\end{pmatrix}\otimes\hat{B} = \begin{pmatrix}a_1\hat{B} & a_2\hat{B}\\ a_3\hat{B} & a_4\hat{B}\end{pmatrix}\\
&\text{(xiv)} && (\hat{A}\otimes\hat{B})^\dagger(\hat{A}\otimes\hat{B}) = \mathbb{I} \quad\Leftrightarrow\quad \hat{A}^\dagger\hat{A} = c_a\mathbb{I} \quad\text{and}\quad \hat{B}^\dagger\hat{B} = c_b\mathbb{I} \ .
\end{aligned}$$

6.5 Further reading

I.S. Gradshteyn and I.M. Ryzhik, *Table of integrals, series, and products* [ISBN]

Part II

Statistical Physics and Atomic Quantum Fields

Preface

All thermodynamic quantities studied in phenomenological thermodynamics (extensive or intensive) are quasi-continuous, i.e. macroscopic. The laws of thermodynamics found to rule the behavior of large systems were discovered empirically via experimental observations. The nature of the laws is thus phenomenological, i.e. not derived from first principles. Until now we totally neglected the fact that matter (gases, fluid, or solids) is composed of microscopic elementary particles (atoms or molecules). Instead, the properties of matter have been resumed in material parameters, such as heat capacity and compressibility. Nevertheless, it already became clear that the behavior of a system is somehow related to the properties of the particles that compose it. E.g. the degrees of freedom of a molecule that can be excited have an influence on the heat capacity of a gas composed of these molecules; the Joule-Thomson effect is due to intermolecular forces; and what we experience as heat, is actually an outward manifestation of molecular and atomic motion. Tracing back macroscopic properties and phenomena to microscopic models bears a formidable potential of deepening our level of understanding thermodynamic systems. It may even provide insight into the physical meaning of mysterious or elusive phenomenological concepts such as entropy production. Last not least, it may allow for a derivation of material parameters from first principles.

An atomistic description acknowledges the fact that matter is quantized into small portions called molecules [2]. Each molecule is understood as a (not necessarily rigid) body characterized by its center-of-mass coordinates, but also its rotations or internal vibrations. With typically 10^{23} atoms in just one liter of air the task of describing the *microstate* by all its coordinates is hopeless. The mathematical discipline that provides the tools capable of handling such big numbers is *statistics*, and the primary tool supplied for the purpose is the concept of the *distribution function*. The idea is to lump atoms having similar properties together to classes, e.g. energy levels. The distribution function then simply reports the number of particles in each class, which dramatically reduces the amount of information. The task of *statistical thermodynamics* is now the description of a thermodynamic state in terms of a distribution function called *macrostate*. The formulation of statistical thermodynamics by *Boltzmann* and *Gibbs* provided a solid microscopic foundation of phenomenological thermodynamics.

In chapter 7 we develop the foundations of statistical mechanics and establish the link to phenomenological thermodynamics with special attention to the role the quantum statistical nature of the particles under study.

[2] The 'quantization' of matter is not to be understood in the quantum mechanical sense. Nevertheless, the particles themselves are generally microscopic and, under certain circumstances, may behave following rules dictated by quantum mechanics. This can lead to macroscopically observable phenomena studied in the area of quantum statistics, as we will learn in Chp. 7.2.

Chapter 7

Statistical thermodynamics

We will begin this chapter with a calculation of the *Boltzmann distribution* of microstates over the macrostates in Sec. 7.1 and introduce the concept of *partition function*, from which all macroscopic state functions may be computed. As applications of this algorithm we will revisit the ideal gas and the Einstein model of a crystalline solid.

7.1 Microstates, macrostates, and entropy

7.1.1 Probabilities of microstates and the partition function

We consider a unary thermodynamic system composed of a very large number N of identical (albeit distinguishable) particles, each one sufficiently specified by a set of numbers (coordinates and internal quantum numbers). The list combining the sets of all particles completely describes the microstate of the system. It changes if a single number of just one particle is changed. The microstate also changes when we just exchange two particles, although the physics of the system cannot change if the particles are identical. Clearly, the macrostate of a system is invariant upon particle exchange.

On the other hand, the number of macrostates we attribute to a system depends on the information we want to gather. For example, we could split the volume occupied by a gas into two parts, V_1 and V_2, and call macrostate the situation when a specific number N_1 of particles is in volume V_1, no matter which particles. Or we could classify the particles by their velocities and prepare a histogram. Any distribution of the particles over the possible velocity classes leading to the exact same histogram would then belong to the same macrostate.

In general, the microstates outnumber the macrostates by many orders of magnitude such that, when a system evolves along a thermodynamic process, it moves through a large number of microstates. And since, a priori, all microstates have the same probability, the likeliness of a macrostate is just the number of microstates it encompasses. Let $1, 2, .., j, .., r$ denote the possible single-particle states that the system has to offer, n_j the number of particles being in the single-particle state j, and $\{n_1, n_2, .., n_j, .., n_r\}$ the actual macrostate. The number of microstates contributing

to the same macrostate is easily found by combinatorial analysis,

$$\boxed{W_{\{n_j\}} = \frac{N!}{n_1!n_2!...n_r!} = N! \prod_{j=1}^{r} \frac{1}{n_j!}} \,, \tag{7.1}$$

with the total number of particles $N = n_1 + n_2 + ... + n_r$. The total number of possible microstates is obviously r^N. Hence, the probability to encounter the system in a particular macrostate is [1],

$$\mathfrak{P}_{\{n_j\}} = \frac{W_{\{n_j\}}}{r^N} = N! \prod_{j=1}^{r} \frac{1}{n_j! r^{n_j}} \,. \tag{7.2}$$

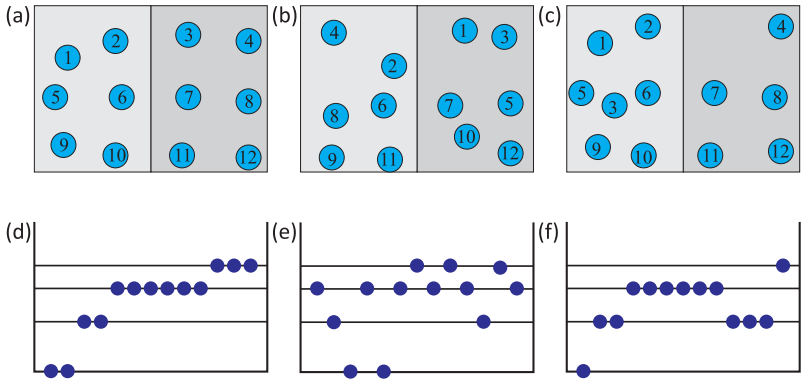

Figure 7.1: Illustration of micro- and macrostates with identical indistinguishable particles: (a-c) Distribution of 12 particles over 2 boxes. (d-f) Distribution of 13 particles over 4 energy levels. All schemes show different microstates, but only the schemes (a) and (b), respectively, (d) and (e) correspond to same macrostates.

Of all possible macrostates, there will be one containing the largest number of microstates, and the probability to encounter the system in this macrostate is highest. Examination of $\mathfrak{P}_{\{n_j\}}$ for a variety of macrostates $\{n_j\}$ reveals that the probability distribution is sharply peaked, and that macrostates deviating only slightly are already very unlikely. The most probable state is now interpreted as the *state of equilibrium*, and this hypothesis forms the basis for connecting phenomenological thermodynamics to an atomistic statistical description.

The equilibrium condition for highest probability in the statistical description is similar to the request for highest entropy in phenomenological thermodynamics, which suggests that both concepts are connected. But while the entropy is additive (the entropies of subsystems sum up to a global entropy), the number of macrostates is multiplicative. This led Boltzmann to his famous hypothesis,

$$\boxed{S = k_\mathrm{B} \ln W} \,. \tag{7.3}$$

Do the Excs. 7.1.7.1 to 7.1.7.7.

[1] For $r = 2$ we just obtain the binomial distribution, $\mathfrak{P}_{\{n_j\}} = \binom{N}{n_j} \left(\frac{1}{r}\right)^{n_j} \left(1 - \frac{1}{r}\right)^{N-n_j}$, obviously satisfying $\sum_{n_j=0}^{N} \mathfrak{P}_{\{n_j\}} = 1$.

7.1.2 Equilibrium in statistical thermodynamics

Evaluating Eq. (7.3) involves computation of large factorials, which is a challenging numerical task. Fortunately, large factorials can be very well approximated by *Stirling's formula*,

$$\ln n! \simeq n \ln n - n \ . \tag{7.4}$$

With this formula we can simplify Eq. (7.3),

$$S = k_{\rm B} \ln \frac{N!}{\prod_{j=1}^{r} n_j!} \simeq k_{\rm B}(N \ln N - N) - k_{\rm B} \sum_{j=1}^{r} (n_j \ln n_j - n_j) \tag{7.5}$$

$$= k_{\rm B} N \ln N - k_{\rm B} \sum_{j=1}^{r} n_j \ln n_j = -k_{\rm B} \sum_{j=1}^{r} n_j \ln \frac{n_j}{N} \ .$$

This expression allows to compute the entropy of any macrostate of the system.

To find the equilibrium macrostate $\{n_1, n_2, .., n_j, .., n_r\}_{\rm eq}$ in the atomistic description, we have to maximize the entropy (7.5). That is, we have to evaluate the total differential of entropy in the direction of changes $\{dn_1, dn_2, .., dn_j, .., dn_r\}$ of the macrostate under the constraint $N = \sum_{j=1}^{r} n_j$,

$$dS = \sum_{j=1}^{r} \left(\frac{\partial S}{\partial n_j} \right) dn_j + \left(\frac{\partial S}{\partial N} \right) dN = -k_{\rm B} \sum_{j=1}^{r} \left(1 + \ln \frac{n_j}{N} \right) dn_j + k_{\rm B} \sum_{j=1}^{r} \frac{n_j}{N} dN \ , \tag{7.6}$$

yielding,

$$\boxed{dS = -k_{\rm B} \sum_{j=1}^{r} \ln \frac{n_j}{N} \ dn_j} \ . \tag{7.7}$$

Application of the equilibrium criterion requires isolation from the environment, which sets constraints to the entropy evaluation in terms of particle and energy exchange,

$$N = \sum_{j=1}^{r} n_j \qquad \text{and} \qquad E = \sum_{j=1}^{r} \varepsilon_j n_j \ , \tag{7.8}$$

or equivalently [2],

$$dN = \sum_{j=1}^{r} dn_j = 0 \qquad \text{and} \qquad dE = \sum_{j=1}^{r} \varepsilon_j dn_j = 0 \ . \tag{7.9}$$

Here, ε_j is the energy of the single-particle state j occupied with n_j particles.

The maximum of the entropy function (7.5) under the constraints (7.9) can be found using the technique of Lagrange multipliers, which consists in solving the equation

$$0 = dS - \alpha k_{\rm B} \, dN - \beta k_{\rm B} \, dE = k_{\rm B} \sum_{j=1}^{r} \left(-\ln \frac{n_j}{N} - \alpha - \beta \varepsilon_j \right) dn_j \tag{7.10}$$

[2] Note that $d\varepsilon_j = 0$, if the energy levels do not vary along a thermodynamic process, only their population with particles.

for arbitrary factors α and β. This implies,

$$\frac{n_j}{N} = e^{-\alpha} e^{-\beta\varepsilon_j} \ , \tag{7.11}$$

for $j = 1, 2, ..., r$. The Lagrange multiplier α can readily be eliminated using the normalization constraint (7.8)(i),

$$1 = \sum_{j=1}^{r} \frac{n_j}{N} = e^{-\alpha} \sum_{j=1}^{r} e^{-\beta\varepsilon_j} \ , \tag{7.12}$$

leaving us with,

$$\frac{n_j}{N} = \frac{e^{-\beta\varepsilon_j}}{\sum_{j=1}^{r} e^{-\beta\varepsilon_j}} \ . \tag{7.13}$$

The denominator is called the canonical *partition function*,

$$\Xi_{\rm cn} \equiv \sum_{j=1}^{r} e^{-\beta\varepsilon_j} = e^{\alpha} \ . \tag{7.14}$$

To determine the Lagrange multiplier β, we compare the expressions obtained for the entropy variations in statistical and phenomenological thermodynamics. Solving (7.10) by dS and substituting α taken from (7.14) we get,

$$dS = -k_{\rm B} \sum_{j=1}^{r} \ln \frac{e^{-\beta\varepsilon_j}}{\Xi_{\rm cn}} \, dn_j = k_{\rm B} \sum_{j=1}^{r} (\beta\varepsilon_j + \ln \Xi_{\rm cn}) \, dn_j = k_{\rm B}\beta \ dE + k_{\rm B} \ln \Xi_{\rm cn} \ dN \ . \tag{7.15}$$

And from (??) we get,

$$dS = \frac{1}{T} dE + \frac{P}{T} dV - \frac{\mu}{T} dN \ , \tag{7.16}$$

where μ is the chemical potential per atom and $dV = 0$, since we assumed in this derivation, that every atom has access to the whole volume of the system. A comparison of the expressions (7.15) and (7.16) then yields,

$$\beta = \frac{1}{k_{\rm B} T} \qquad \text{and} \qquad \alpha = -\beta\mu = \ln \Xi_{\rm cn} \ . \tag{7.17}$$

Substitution into (7.13) and (7.14) finally yields,

$$\boxed{\frac{n_j}{N} = \frac{1}{\Xi_{\rm cn}} e^{-\varepsilon_j / k_{\rm B} T} \qquad \text{with} \qquad \Xi_{\rm cn} = \sum_{j=1}^{r} e^{-\varepsilon_j / k_{\rm B} T}} \ . \tag{7.18}$$

This expression is known as *Boltzmann distribution* [3,4,5].

7.1.3 Thermodynamic potentials in canonical ensembles

We wish now to express all state functions of the system in terms of the partition function (7.14). To this end we begin calculating the Helmholtz free energy using the expressions for the total energy (7.8)(ii) and the entropy (7.5),

$$F = E - TS = \sum_{j=1}^{r} n_j \varepsilon_j + k_{\mathrm{B}} T \sum_{j=1}^{r} n_j \ln \frac{e^{-\beta \varepsilon_j}}{\Xi_{\mathrm{cn}}} = -k_{\mathrm{B}} T \ln \Xi_{\mathrm{cn}} \ . \tag{7.19}$$

Hence, $\Xi_{\mathrm{cn}} = e^{-\beta F}$ and,

$$\frac{n_j}{N} = e^{\beta(F - \varepsilon_j)} \tag{7.20}$$

confirming the role of the free energy (??) for normalization of the canonical probability distribution.

The entropy function can now be expressed by the coefficient relation (??)(ii),

$$S = -\left(\frac{\partial F}{\partial T}\right)_V = k_{\mathrm{B}} \ln \Xi_{\mathrm{cn}} + k_{\mathrm{B}} T \left(\frac{\partial \ln \Xi_{\mathrm{cn}}}{\partial T}\right)_V \ , \tag{7.21}$$

the internal energy becomes,

$$E = F + TS = k_{\mathrm{B}} T^2 \left(\frac{\partial \ln \Xi_{\mathrm{cn}}}{\partial T}\right)_V \ , \tag{7.22}$$

and the heat capacity (??)(ii),

$$C_V = \left(\frac{\partial E}{\partial T}\right)_V = 2 k_{\mathrm{B}} T \left(\frac{\partial \ln \Xi_{\mathrm{cn}}}{\partial T}\right)_V + k_{\mathrm{B}} T^2 \left(\frac{\partial^2 \ln \Xi_{\mathrm{cn}}}{\partial T^2}\right)_V \ . \tag{7.23}$$

Note that for now we always consider fixed volumes, $dV = 0$. To compute the remaining thermodynamic potentials, V, H, G, and C_P, we would need to generalize

[3] We obtained the Boltzmann distribution from a microcanonical derivation, but since the Boltzmann distribution holds for any ensemble of classical particles, we can use it to derive the distribution function for canonical ensembles.

[4] A system of non-interacting particles can be separated into independent parts. If such a system is described by a canonical ensemble, then each part can be seen as a system unto itself and described by a canonical ensemble having the same temperature as the whole. In this way, the canonical ensemble provides exactly the Maxwell-Boltzmann statistics for systems of any number of particles. In comparison, the justification of the Boltzmann distribution from the microcanonical ensemble only applies for systems with a large number of particles, that is, in the thermodynamic limit. The Boltzmann distribution itself is one of the most important tools in applying statistical mechanics to real systems, as it dramatically simplifies the study of systems that can be separated into independent parts (e.g. particles in a gas, electromagnetic modes in a cavity, etc.).

[5] In a system of strongly interacting particles, it is usually not possible to find a way to separate the system into independent subsystems as done in the Boltzmann distribution. In these systems it is necessary to resort to using the full expression of the canonical ensemble in order to describe the thermodynamics of the system when it is thermostatted to a heat bath. The *Ising model*, which is a widely discussed toy model for the phenomena of ferromagnetism, is one of the simplest models showing a phase transition.

the partition function to include pressure dependence. We will show this in Sec. 7.1.6 at the example of an ideal gas.

In summary, the state of thermodynamic equilibrium is characterized by the fact the particles are distributed over the available energy levels according to the exponential function (7.11). Once the energy levels are known for a system, the partition function and all the thermodynamic potentials can be calculated. We will now study the algorithm at three examples.

7.1.4 Two-level systems

Let us consider a system consisting of only two allowed energy levels $\varepsilon_j = 0, \varepsilon$, that is, we set the energy of the ground state to zero. This system is relevant for atomic system in equilibrium with radiation fields driving electronic transitions between excitation levels. The Boltzmann partition function and the population (7.18) then become,

$$\Xi_{\rm cn} = \sum_{j=1}^{r} e^{-\beta\varepsilon_j} = 1 + e^{-\beta\varepsilon} \quad , \tag{7.24}$$

$$\frac{n_1}{N} = \frac{1}{\Xi_{\rm cn}} = \frac{1}{1+e^{-\beta\varepsilon}} \quad , \quad \frac{n_2}{N} = \frac{e^{-\beta\varepsilon}}{\Xi_{\rm cn}} = \frac{e^{-\beta\varepsilon}}{1+e^{-\beta\varepsilon}} \ . \tag{7.25}$$

In particular, the ratio between populations of consecutive levels is, $n_2/n_1 = e^{-\beta\varepsilon}$. At low temperature, $k_{\rm B}T \ll \varepsilon$, the excited state population is negligibly small, while at high temperature, $k_{\rm B}T \gg \varepsilon$, both energy levels have almost the same population. Do the Exc. 7.1.7.8.

With the partition function it is easy to evaluate the potentials,

$$F = -Nk_{\rm B}T \ln \Xi_{\rm cn} = -Nk_{\rm B}T \ln(1+e^{-\beta\varepsilon}) \tag{7.26}$$

$$S = Nk_{\rm B} \ln \Xi_{\rm cn} + Nk_{\rm B}T \left(\frac{\partial \ln \Xi_{\rm cn}}{\partial T}\right)_V = Nk_{\rm B} \ln(1+e^{-\beta\varepsilon}) + \frac{N\varepsilon}{T}\frac{e^{-\beta\varepsilon}}{1+e^{-\beta\varepsilon}}$$

$$E = Nk_{\rm B}T^2 \left(\frac{\partial \ln \Xi_{\rm cn}}{\partial T}\right)_V = N\varepsilon \frac{e^{-\beta\varepsilon}}{1+e^{-\beta\varepsilon}}$$

$$C_V = 2Nk_{\rm B}T \left(\frac{\partial \ln \Xi_{\rm cn}}{\partial T}\right)_V + Nk_{\rm B}T^2 \left(\frac{\partial^2 \ln \Xi_{\rm cn}}{\partial T^2}\right)_V = \frac{N\varepsilon^2}{k_{\rm B}T^2}\frac{e^{-\beta\varepsilon}}{(1+e^{-\beta\varepsilon})^2} \ .$$

7.1.5 Einstein-Debye model of solids

According to the equipartition theorem, every atom has three degrees of freedom due to its translational motion. Describing a solid simply as a conjunction of N atoms bound by a common potential, we expect the total energy and the specific heat following the *Dulong-Petit law*,

$$E = 3Nk_{\rm B}T \qquad \text{resp.} \qquad C_V = \left(\frac{\partial E}{\partial T}\right)_V = 3Nk_{\rm B} \ , \tag{7.27}$$

for all solids regardless of temperature.

It was observed, however, that the specific heat of solids decreases like $C_V \propto T^3$ as T approaches zero. Einstein proposed an alternative model treating the N atoms

as three-dimensional harmonic oscillators vibrating in a lattice. Indeed, many solids are crystalline, which means that they arrange in a periodic structure, in the simplest case a cubic lattice, where each atom has six neighbors arranged along Cartesian coordinates, as illustrated in Fig. 7.2. The interatomic bonds are described by springs storing energies like a quantized 3D harmonic oscillator,

$$\varepsilon_j = (j + \tfrac{3}{2})\hbar\omega \ . \tag{7.28}$$

The normal-mode frequency ω is related to the spring constant of the atomic bond and the atomic mass.

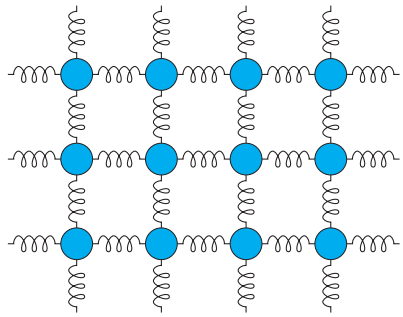

Figure 7.2: Einstein's model of a solid.

The energy spectrum (7.28) completely defines the model. The partition function is,

$$\Xi_{\rm cn} = \sum_{j=1}^{r} e^{-\beta\varepsilon_j} = e^{-3\beta\hbar\omega/2} \sum_{j=1}^{r} e^{-\beta\hbar\omega j} \simeq e^{-3\beta\hbar\omega/2} \sum_{j=0}^{\infty} e^{-\beta\hbar\omega j} = \frac{e^{-3\beta\hbar\omega/2}}{1 - e^{-\beta\hbar\omega}} \ . \tag{7.29}$$

The discrete energies $n\hbar\omega$ are identified with quasi-particles called *phonons*. The quantum nature of atoms does not matter, they just provide the medium supporting the phonons.

With the partition function it is easy to evaluate the potentials,

$$F = -Nk_{\rm B}T \ln \Xi_{\rm cn} = \frac{3N\hbar\omega}{2} + 3Nk_{\rm B}T \ln\left(1 - e^{-\beta\hbar\omega}\right) \tag{7.30}$$

$$S = Nk_{\rm B} \ln \Xi_{\rm cn} + Nk_{\rm B}T \left(\frac{\partial \ln \Xi_{\rm cn}}{\partial T}\right)_V = -3Nk_{\rm B} \ln\left(1 - e^{-\beta\hbar\omega}\right) + \frac{3N\hbar\omega}{T} \frac{1}{e^{\beta\hbar\omega} - 1}$$

$$E = Nk_{\rm B}T^2 \left(\frac{\partial \ln \Xi_{\rm cn}}{\partial T}\right)_V = \frac{3N\hbar\omega}{2} \frac{e^{\beta\hbar\omega} + 1}{e^{\beta\hbar\omega} - 1}$$

$$C_V = 2Nk_{\rm B}T \left(\frac{\partial \ln \Xi_{\rm cn}}{\partial T}\right)_V + Nk_{\rm B}T^2 \left(\frac{\partial^2 \ln \Xi_{\rm cn}}{\partial T^2}\right)_V = -3Nk_{\rm B} \left(\frac{\hbar\omega}{k_{\rm B}T}\right)^2 \frac{e^{\beta\hbar\omega}}{(e^{\beta\hbar\omega} - 1)^2} \ .$$

7.1.5.1 Debye model

In his model Einstein applied Planck's law on the distribution of energy in electromagnetic radiation, which treats radiation as a gas of *photons*, to the energy distribution

of atomic vibrations in a solid, treating them as a gas of *phonons* in a box (the box being the solid). Most of the steps of the calculation are identical, as both are examples of a massless bosonic gas with linear dispersion relation.

Following the Bose-Einstein statistics, we must replace in (7.27),

$$k_{\rm B}T \longrightarrow \frac{\hbar\omega}{e^{\hbar\omega/k_{\rm B}T}-1} \ , \tag{7.31}$$

yielding,

$$E = \frac{3N\hbar\omega}{e^{\beta\hbar\omega}-1} \qquad \text{resp.} \qquad C_V = 3Nk_{\rm B}\left(\frac{\hbar\omega}{k_{\rm B}T}\right)^2 \frac{e^{\hbar\omega/k_{\rm B}T}}{(e^{\hbar\omega/k_{\rm B}T}-1)^2} \ , \tag{7.32}$$

in accordance with (7.30).

Still, the disappearance of the specific heat at low temperatures,

$$C_V \simeq \frac{3N(\hbar\omega)^2}{k_{\rm B}T^2} e^{-\hbar\omega/(k_{\rm B}T)} \ , \tag{7.33}$$

which is related to the finite localization energy of harmonic oscillators, does not describe experimental observations very well, and the model had to be refined by Debye, later on.

While Einstein assumed monochromatic lattice vibrations, *Debye's* approach was to allow a *spectrum* of vibrational frequencies. With the density-of-states,

$$\rho(\nu)d\nu = \frac{4\pi V}{v^3}\nu^2 d\nu \ , \tag{7.34}$$

where v is the velocity of sound propagation and $\omega = 2\pi\nu$, the formula is totally equivalent to the density-of-states for photons in a cavity. Assuming that there is an upper bound ν_m for the vibrational frequencies, we normalize as $3N_0 = \int_0^{\nu_m}\rho(\nu)d\nu$. The energy now is [6],

$$E = \int_0^{\nu_m} \frac{\hbar\omega}{e^{\hbar\omega/k_{\rm B}T}-1}\frac{4\pi V}{v^3}\nu d\nu = 9Nk_{\rm B}\frac{T^4}{\theta^3}\int_0^{\theta/T}\frac{x^3dx}{e^x-1} \ . \tag{7.35}$$

The *Debye temperature* $\theta = h\nu_m/k_{\rm B}$ is characteristic for the metal. The derivative is then,

$$C_V = 9Nk_{\rm B}\left[4\left(\frac{T}{\theta}\right)^3\int_0^{\theta/T}\frac{x^3dx}{e^x-1} - \frac{\theta}{T}\frac{1}{e^{\theta/T}-1}\right] \ . \tag{7.36}$$

At low temperatures this formula reproduces the *Debye law*,

$$C_V \simeq 9Nk_{\rm B}\left[4\left(\frac{T}{\theta}\right)^3\int_0^{\infty}\frac{x^3dx}{e^x-1} - \frac{\theta}{Te^{\theta/T}}\right] = \frac{12\pi^4}{5}Nk_{\rm B}\left(T/\theta\right)^3 \ . \tag{7.37}$$

[6] The fact that the electron gas also has a heat capacity is neglected.

7.1.6 Maxwell-Boltzmann distribution of ideal gases

Here we consider a gas composed of identical monoatomic particles enclosed in a box of volume $V = \int_V d^3r$. The energy of every atom is just its kinetic energy associated with its flight through space,

$$\varepsilon = \frac{m}{2}v^2 = \frac{m}{2}v_x^2 + \frac{m}{2}v_y^2 + \frac{m}{2}v_z^2 \ . \tag{7.38}$$

Since the phase space of atomic motion is continuous, the partition function is now calculated as an integral,

$$\begin{aligned} \Xi_{\rm cn} &= \int_{\mathbb{R}^3}\int_{\mathbb{R}^3} e^{-\beta\varepsilon} d^3r d^3v \\ &= V\int_0^\infty 4\pi v^2 e^{-\beta m v^2/2} dv = V\left(\frac{2\pi k_{\rm B}T}{m}\right)^{3/2} \ . \end{aligned} \tag{7.39}$$

We will see later how to generalize the procedure in the presence of an inhomogeneous trapping potential $U(\mathbf{r})$. Insertion of the kinetic energy (7.38) generates the well-known *Maxwell-Boltzmann distribution*,

$$\boxed{\frac{n(\varepsilon)}{N} = \frac{1}{\Xi_{\rm cn}} e^{-\beta m v^2/2}} \ , \tag{7.40}$$

which will be studied in Excs. 7.1.7.9 to 7.1.7.16.

The potentials are easily calculated,

$$\begin{aligned} F &= -Nk_{\rm B}T \ln \Xi_{\rm cn} = -Nk_{\rm B}T\left(\ln V + \frac{3}{2}\ln\frac{2\pi k_{\rm B}T}{m}\right) \\ S &= Nk_{\rm B}\ln\Xi_{\rm cn} + Nk_{\rm B}T\left(\frac{\partial \ln \Xi_{\rm cn}}{\partial T}\right)_V = Nk_{\rm B}\left(\ln V + \frac{3}{2} + \frac{3}{2}\ln\frac{2\pi k_{\rm B}T}{m}\right) \\ E &= Nk_{\rm B}T^2\left(\frac{\partial \ln \Xi_{\rm cn}}{\partial T}\right)_V = \frac{3}{2}Nk_{\rm B}T \\ C_V &= 2Nk_{\rm B}T\left(\frac{\partial \ln \Xi_{\rm cn}}{\partial T}\right)_V + Nk_{\rm B}T^2\left(\frac{\partial^2 \ln \Xi_{\rm cn}}{\partial T^2}\right)_V = \frac{3}{2}Nk_{\rm B} \ . \end{aligned} \tag{7.41}$$

Furthermore,

$$P = -\left(\frac{\partial F}{\partial V}\right)_T = \frac{Nk_{\rm B}T}{V} \ . \tag{7.42}$$

7.1.6.1 Inclusion of vibrational and rotational degrees of freedom

If the gas under consideration is composed of molecules, energy may be stored in rotations of the molecules about some axis passing through their center of mass. The atoms composing the molecules may vibrate against each other. And finally, the motion of electrons within the molecules contribute to the internal energy of a gas. The development of models accounting for these energy contributions allows to compute heat capacities which, compared to experimental measurements, provide

insight in the molecular structure, as we have seen at the example of the Einstein-Debye model.

In the case of ideal molecular gases, the treatment of vibrational and rotational degrees of freedom is similar to that of the translational degrees of freedom as long as the corresponding energies can be brought into the form $\frac{b_\alpha}{2} v_\alpha^2$, where α labels the degree of freedom, v_α is the velocity of the respective motion, and b_α the mass or inertial moment. The partition function then needs to be calculated with the complete spectrum (see [212], p.155),

$$E = \sum_\alpha \frac{b_\alpha}{2} v_\alpha^2 \ . \tag{7.43}$$

7.1.7 Exercises

7.1.7.1 Ex: Probabilities

In a game, 5 ideal dices are rolled.
a. What is the probability that exactly two of these dices show the number one?
b. What is the probability that at least one dice shows the number one?

7.1.7.2 Ex: Probabilities

With what probability have out of
a. 1000 random numbers between 1 and 100 exactly five the value 50;
b. 100 two people on birthday January 1st.

7.1.7.3 Ex: Probabilities

What is the probability that you inhale at least one molecule that Julius Caesar exhaled during his last breath (Tu quoque, Brute, fili mi!)? Assume a breathing volume of 1 liter and an atmosphere height of approximately $h = 10\,\text{km}$. Assume the density of the atmosphere is approximately homogeneous.

7.1.7.4 Ex: Idiots roulette

A Bavarian, a Swabian and an East Frisian play Russian roulette together, each according to their own rules. The Bavarian inserts two cartridges into the drum of a six-shot revolver, sets the drum in a rapid rotation, aims at his own head and pulls the trigger once. The Swabian puts a cartridge in the revolver and pulls the trigger twice, the East Frisian puts a cartridge in the revolver, pulls the trigger once, turns the drum a second time and pulls the trigger again. What is the chance of survival of the three crazy people?

7.1.7.5 Ex: Students roulette

A student writes a multiple choice test in physics. It consists of 18 tasks. For each task, only one of the four proposed solutions is correct. Since he does not understand much about the topic, he trusts his luck and checks the possible solutions by chance. What is the probability that the student meets the minimum requirement of 8 correct answers?

7.1.7.6 Ex: Slot machine

A slot machine consists of three concentric rings. Each ring is evenly divided into 10 sections and the sections in each ring are labeled with letters from 'a' to 'j'. By pressing the start button, the three rings start to rotate independently. If the lock button is pressed, the rings brake independently of one another and three letters appear side by side in the viewing window. With three 'a' you win, with two 'a' there is a free spin.
a. Calculate the probability for one free spin per game.
b. What is the probability of getting exactly 3 free spins in 10 games?
c. What is the probability of winning at least once in 10 games?

7.1.7.7 Ex: Binomial distribution

Two drunks stagger on the x-axis. Starting from the origin, they take a step to the right or to the left with the same probability. The steps take place synchronously, and the steps of both people are the same and constant. Determine the probability that they will meet again after N steps.

7.1.7.8 Ex: Simple model for a solid

Consider a system of N atomic particles at a temperature T. The individual atoms can only be in one of two states. Either in state $|0\rangle$ at the energy $\varepsilon_0 = 0$ or in state $|1\rangle$ at energy $\varepsilon_1 = \varepsilon$. Apart from this energy ε_i the atoms have no kinetic or other energies.
a. Choosing the Boltzmann distribution, determine the population n_i, that is, the probability that a certain atom is in state $|i\rangle$. How should the normalization be chosen?
b. Determine the statistical mean $\bar{\varepsilon}$ for the energy of one atom. Which value results for $k_\mathrm{B}T = \varepsilon$? What is the expression for the total energy E of N atoms?
c. Calculate the population $n_1(T_j)$ to find a certain atom at the energy ε for four different temperatures: $k_\mathrm{B}T_j = 0.1 \times j\varepsilon$ for $j = 1, 2, 3, 4$. Also calculate the energy per atom $E(T_j)/N$ of the entire system at these temperatures.
d. Find an expression for the heat capacity C of this N-atom system. Note: For this system, the total energy is identical to the thermal energy.
e. Calculate the heat capacities C_j especially for the temperatures T_j from subtask (c). What does the result have to do with 'freezing degrees of freedom'?

7.1.7.9 Ex: Velocity distribution

The Maxwellian velocity distribution or Boltzmann distribution of a one-dimensional ideal gas of identical particles of mass m at temperature T is,

$$f(v)dv = \sqrt{\frac{m}{2\pi k_\mathrm{B}T}} e^{-mv^2/2k_\mathrm{B}T} dv \ .$$

This gives the average kinetic energy for each molecule of $\langle E_\mathrm{kin} \rangle = \frac{1}{2} k_\mathrm{B}T$. According to the equipartition theorem, Maxwell's velocity distribution of a three-dimensional gas is given by $f(v_x)dv_x\, f(v_y)dv_y\, f(v_z)dv_z$.

a. Write down the velocity distribution explicitly and determine the average kinetic energy of a molecule in the three-dimensional gas at temperature T.
Determine the average absolute velocity $\langle v\rangle = \langle|\mathbf{v}|\rangle$ and compare $\langle v\rangle^2$ with $\langle v^2\rangle$ for the three-dimensional case.
c. What is the number of particles $F(v)dv$ with an absolute velocity $v = |\mathbf{v}|$ in the range v and $v + dv$.
d. Consider a gas made of rubidium atoms ($m = 87u$) and sketch $F(v)$ for temperatures between 100 K and 300 K.
e. Consider the rubidium gas at room temperature ($T = 300\,\mathrm{K}$). What is the proportion of molecules whose average velocity $\langle v\rangle$ is greater than 1000 m/s?

7.1.7.10 Ex: Maxwell-Boltzmann distribution

Calculate the number of particles in an ideal homogeneous gas having velocities slower than $2v_{\mathrm{rms}}$.

7.1.7.11 Ex: Maxwell-Boltzmann distribution

Using the Maxwell-Boltzmann distribution $f(v)$ and the following formulas, calculate the velocities $\bar{v} \equiv \int_0^\infty v f(v) v^2 dv$ and $v_{\mathrm{rms}} \equiv \sqrt{\overline{v^2}}$:

$$\int_0^\infty x^n e^{-x^2} dx = \tfrac{1}{2}\Gamma(\tfrac{n+1}{2}) = \begin{cases} \frac{(2k-1)!!\sqrt{\pi}}{2^{k+1}} & \text{for} \quad n = 2k \\ \frac{k!}{2} & \text{for} \quad n = 2k+1 \end{cases} .$$

7.1.7.12 Ex: Mean velocity in a gas

The average velocity of the molecule in an ideal gas is 500 m/s. If the gas maintains the same temperature and the molecular masses are doubled, what will be the new average velocity?

7.1.7.13 Ex: Evaporation

a. A three-dimensional homogeneous gas consisting of $N = 10^8$ rubidium atoms (mass $m = 87u$) has the temperature $T = 100\,\mu\mathrm{K}$. How many atoms are faster on average than $v_1 = 10\,\mathrm{cm/s}$?
b. Now suppose that all atoms with a velocity $v > v_1$ were suddenly removed. After some time, a new thermal equilibrium is established due to collisions. What is the temperature of the gas now?

7.1.7.14 Ex: Trapped gases

The density distribution of a rubidium gas in a three-dimensional harmonic potential can be expressed by,

$$n(\mathbf{r})d^3r = n_0 e^{-U(\mathbf{r})/k_{\mathrm{B}}T} d^3r \ ,$$

where $U(\mathbf{r}) = \frac{m}{2}\omega^2 r^2$. Numerical values: $m = 87u$ and $\omega = 2\pi \cdot 50\,\mathrm{Hz}$.
a. Determine the size of the gas cloud ($1/\sqrt{e}$ full width of the distribution) at a given temperature $T = 100\,\mu\mathrm{K}$.

b. Determine the maximum density n_0 of the gas when $N = \int n(\mathbf{r})d^3r = 10^8$ is the total number of atoms.
c. The effective volume is defined by $V_{\text{eff}} = N/n_0$. How many atoms are in the effective volume?

7.1.7.15 Ex: Trapped gases

Calculate the internal energy and heat capacity of an ideal gas stored in a harmonic trap by explicit tracing over the density operator $\rho = e^{-\beta\varepsilon-\beta U}$, and compare the result with a free gas.

7.1.7.16 Ex: Trapped gases

An ultracold gas made of 10^8 rubidium atoms (mass number 87) is trapped in a three-dimensional potential of the form $U(r) = \frac{m}{2}\omega^2 r^2$ with the oscillation frequencies $\omega/2\pi = 100\,\text{Hz}$.
a. Assume the spatial distribution function for the atoms to be $n(\mathbf{r}) = n_0 e^{-U(r)/k_\text{B}T}$. What is its width at $1/\sqrt{e}$ of the maximum height? How does the width of the distribution function change when the number of atoms is doubled?
b. The trap potential is suddenly switched off. The atoms are robbed of their potential energy, while their kinetic energy leads to the ballistic expansion of the cloud. 20 ms after switching off the trapping potential, a $1/\sqrt{e}$ width of $\bar{r}_a = 0.2\,\text{mm}$ is experimentally measured for the distribution of the expanded atomic cloud. What was the temperature of the atomic cloud in the trap?
Help: Assume that the final size of the atomic cloud is much larger than the size of the trap. Neglect collisions between the atoms.

7.2 Quantum statistics

Considering a closed isolated system in a fixed volume (NVE-ensemble where $E, N, V = const$) we have derived in Sec. 7.1.1 the partition function for *microcanonical ensembles*, from which we obtained in Sec. 7.1.2 the *Boltzmann distribution* function.

The combinatorial derivation of the number of microstates contributing to the same macrostate (7.1) was based on the observation, that all particles constituting the system were identical, but distinguishable. The expression (7.1) is just the multinomial coefficient, i.e. the number of ways of arranging N items into r boxes, the j-th box holding n_j items, ignoring the permutation of items in each box. The problem, however, is that quantum mechanics postulates that identical particles are indistinguishable, and this has an impact on the numbers of states available upon permutation. Consequently, the partition function (7.1) needs to be corrected.

The problems ultimately results from the fact that *phase space* is quantized. If this weren't the case, the cells' size could be chosen so small that they admit at most one particle. Then quantum statistics would not apply, the system would be classical [7].

[7] The problem with undistinguishability is that it is not a classical concept and thus cannot be mapped immediately to classical computers, which will always need to know in which of its bits the information on what particle is stored. Bluring this information requires some trick, which is rather easy to implement in the symmetrization and more cumbersome in the case of (anti-)symmetrization. On the other hand, undistinguishability can be mapped to quantum computers.

7.2.1 Wavefunction symmetrization and detailed balance

We learn in quantum mechanics, that (anti-)symmetrization of the total wavefunction of a multiparticle system leads to Bose-enhancement (Pauli blocking). Consider a product state of two particles 1 and 2, $\Psi_{\rm o} = \psi_\alpha(1)\psi_\beta(2)$, and symmetrize it to

$$\Psi_{\rm s,a} = \tfrac{1}{\sqrt{2}}[\psi_\alpha(1)\psi_\beta(2) \pm \psi_\alpha(2)\psi_\beta(1)] \ . \tag{7.44}$$

Now assume that the single particle wavefunctions do completely overlap,

$$\alpha = \beta \qquad \Longrightarrow \qquad |\Psi_{\rm o,s,a}|^2 = (s+1)\ |\psi_\alpha(1)|^2|\psi_\beta(2)|^2 \ , \tag{7.45}$$

where $s = 0$ for Boltzmann particles (called *boltzons* here for simplicity), $s = 1$ for bosons, and $s = -1$ for fermions. Generalized to arbitrary numbers of particles we state: *If n bosons (fermions) are in state Ψ, the probability for another bosons (fermions) to joint this state is $1 + sn$ times the probability without (anti-) symmetrization.*

An intuitive derivation of the *quantum statistical* distribution function is based on the postulate of *detailed balance*. Let us consider the most fundamental process in physics, which is the collision between two particles initially in states 1 and 4 ending up in two other states 2 and 3 [see Fig. 7.3(a)]. All four states j are initially occupied with populations n_j. The detailed balance postulate claims that *equality of the rates $R_{14\to23}$ for two particles to change their states and the rate for the inverse process $R_{23\to14}$ is a sufficient condition for thermal equilibrium.* Using the bosonic enhancement (fermionic suppression) factor derived above, the postulate can be formulated,

$$\begin{aligned} R_{14\to23} &= |M_{14,23}|^2 n_1 n_4 (1+sn_2)(1+sn_3) = \\ R_{23\to14} &= |M_{14,23}|^2 n_2 n_3 (1+sn_1)(1+sn_4) \ , \end{aligned} \tag{7.46}$$

where $M_{14,23}$ is the matrix element of the collision process. Hence,

$$\frac{n_1}{1+sn_1}\frac{n_4}{1+sn_4} = \frac{n_2}{1+sn_2}\frac{n_3}{1+sn_3} \ . \tag{7.47}$$

Energy conservation requires,

$$\varepsilon_1 + \varepsilon_4 = \varepsilon_2 + \varepsilon_3 \ . \tag{7.48}$$

In a canonical ensemble in thermal equilibrium the population distribution among the levels must be a unique function of their energies,

$$n_j = f(\varepsilon_j) \ . \tag{7.49}$$

To satisfy Eqs. (7.47) and (7.48) f must have the functional form,

$$\boxed{f(\varepsilon_j) = \frac{1}{Ce^{\beta\varepsilon_j} - s}} \ , \tag{7.50}$$

where C is an arbitrary constant introduced to satisfy some normalization constraints. This can be verified easily by plugging the formula (7.50) into the Eq. (7.47).

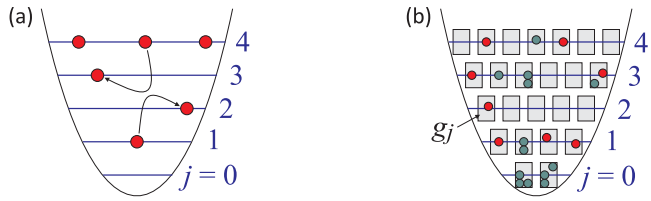

Figure 7.3: (a) Detailed balance entails thermal equilibrium. (b) Subdivision of energy levels j in subboxes g_j. Red circles are fermions and green particles bosons.

7.2.2 Microcanonical ensembles of indistinguishable particles

7.2.2.1 Boltzons

In order to hold for indistinguishable particles, the partition function (7.1) must be generalized allowing for the possibility that there is more than one way to put n_j particles into the box j. If the j-th box has a 'degeneracy', that is, it has g_j 'sub-boxes' with the same energy ε_j, such that any way of filling the j-th box where the number in the sub-boxes is changed is a distinct way of filling the box, then in order to get the right number of macrostates, the number of ways of filling the j-th box must be increased by the number of ways of distributing the n_j objects in the g_j sub-boxes. The number of ways of placing n_j distinguishable objects in g_j sub-boxes is $g_j^{n_j}$, since any particle can go into any of the g_j boxes. Thus the number of ways $W_{\{n_j\}}$ that a total of N particles can be classified into energy levels according to their energies, while each level j having g_j distinct states such that the j-th level accommodates n_j particles is,

$$\boxed{W_{\{n_j\}} = N! \prod_{j=1}^{r} \frac{g_j^{n_j}}{n_j!}} \,. \tag{7.51}$$

In analogy to the procedure outlined in Sec. 7.1.2 we derive the Boltzmann distribution by first taking the logarithm from (7.52) and then simplifying it using Stirling's formula (8.1),

$$\ln W = \ln N! + \sum_j [n_j \ln g_j - \ln n_j!] \simeq \ln N! + \sum_j [n_j \ln \frac{g_j}{n_j} + n_j] \,, \tag{7.52}$$

then calculating the differential,

$$d \ln W = \sum_j \left(\frac{\partial \ln W}{\partial n_j} \right) dn_j = \sum_j \ln \frac{g_j}{n_j} dn_j \,. \tag{7.53}$$

introducing Lagrange multipliers α and β and minimizing the functional,

$$f(\{n_j\}) \equiv \ln W + \alpha(N - \sum_j n_j) + \beta(E - \sum_j \varepsilon_j n_j) \,. \tag{7.54}$$

Relating the condition,

$$0 = df(n_j) = d \ln W - \alpha \sum_j dn_j - \beta \sum_j \varepsilon_j dn_j = \sum_j \left(\ln \frac{g_j}{n_j} - \alpha - \beta \varepsilon_j \right) dn_j \tag{7.55}$$

via the Boltzmann hypothesis (7.16) to entropy,

$$dS = \frac{1}{T}dE + \frac{P}{T}dV - \frac{\mu}{T}dN = k_{\mathrm{B}}\beta\, dE + k_{\mathrm{B}}\alpha\, dN = k_{\mathrm{B}}\, d\ln W \ , \tag{7.56}$$

we identify the Lagrange multipliers,

$$\beta = \frac{1}{k_{\mathrm{B}}T} \qquad \text{and} \qquad \alpha = -\frac{\mu}{k_{\mathrm{B}}T} \ , \tag{7.57}$$

and finally obtain the Boltzmann distribution by setting the parenthesis in (7.55) to zero,

$$\boxed{n_j = \frac{g_j}{e^{\beta(\varepsilon_j - \mu)}}} \ . \tag{7.58}$$

This is basically the same result as the Boltzmann distribution derived in (7.18) except for the appearance of the degeneracy factor g_j.

7.2.2.2 Bosons

Boltzmann's fundamental equation (7.3) relates the thermodynamic entropy S to the logarithm of the number of microstates $W_{\{n_j\}}$. It was pointed out by Gibbs however, that the above expression (7.51) does not yield an extensive entropy, and is therefore faulty [8]. This problem is known as the *Gibbs paradox*. The problem is that the particles considered by the above equation are *not indistinguishable*. In other words, for two particles (i and j) in two energy sublevels the population represented by $[i, j]$ is considered distinct from the population $[j, i]$, while for indistinguishable particles, they are not. Indeed, bosons have anti-symmetric wavefunctions, fermions have symmetric ones. Boltzons have all wavefunctions as eigenfunctions. In the limit of high temperatures all particles behave like boltzons.

Let us a system with a given one-particle energy spectrum ε_j. Now, every energy level labeled by j and containing n_j particles is discretized into a number of g_j subboxes degenerate with respect to energy (i.e. all having the same energy ε_j), but distinguished by some other quantum number [see Fig. 7.3(b)].

For bosons, each level g_j can hold arbitrarily many of the n_j particles. If we carry out the argument for indistinguishable particles, we are led to the expression for the

[8] This can be seen as follows: Consider two identical systems, $r' = r$ and $g'_{j'} = g_j$, with atom numbers $N = \sum_j n_j$ and $N' = \sum_j n'_j$. The partition function for boltzons is not multiplicative,

$$(N+N')! \prod_{j=1}^{r} \frac{g_j^{n_j}}{n_j!} \neq N! \prod_{j=1}^{r} \frac{g_j^{n_j}}{n_j!} \times N'! \prod_{j=1}^{r} \frac{g_j^{n'_j}}{n'_j!}$$

while for fermions it is. To see this we set $n'_{j'} \equiv n_{r+j}$ for $j' = r + j$ and $j = 1, ..., r$. Then,

$$\prod_{j=1}^{2r} \binom{g_j}{n_j} = \prod_{j=1}^{r} \binom{g_j}{n_j} \times \prod_{j=1}^{r} \binom{g_j}{n'_j} \ .$$

The same argument holds for bosons. A critical discussion of the above statements can be read in [435].

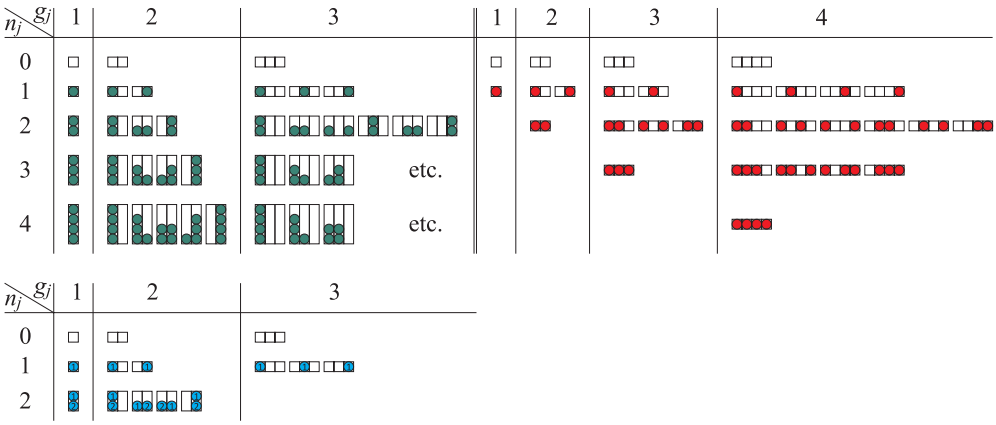

Figure 7.4: Distribution of n_j bosons (green), fermions (red), and boltzon (blue) over g_j boxes the number of possibilities being, respectively, $\binom{n_j+g_j-1}{n_j}$, $\binom{g_j}{n_j}$, and $\frac{N!g_j^{n_j}}{n_j!}$.

partition function for bosons [9],

$$\boxed{W_{\{n_j\}} = \prod_{j=1}^{r} \binom{n_j + g_j - 1}{n_j}} \,. \tag{7.59}$$

Analogously to (7.52) we calculate the logarithm using Stirling's formula,

$$\begin{aligned} \ln W &= \sum_j \left[\ln(n_j + g_j - 1)! - \ln n_j! - \ln(g_j - 1)!\right] \\ &\simeq \sum_j \left[n_j \ln \frac{g_j - 1 + n_j}{n_j} + (g_j - 1) \ln \frac{g_j - 1 + n_j}{g_j - 1} \right] \,, \end{aligned} \tag{7.60}$$

the differential,

$$d \ln W = \sum_j \left(\frac{\partial \ln W}{\partial n_j} \right) dn_j = \sum_j \ln \frac{n_j + g_j - 1}{n_j} dn_j \,, \tag{7.61}$$

and obtain the condition,

$$\begin{aligned} 0 = df(n_j) &= d \ln W - \alpha \sum_j dn_j - \beta \sum_j \varepsilon_j dn_j \\ &= \sum_j \left(\ln \frac{n_j + g_j - 1}{n_j} - \alpha \sum_j - \beta \sum_j \varepsilon_j \right) dn_j \end{aligned} \tag{7.62}$$

with the same Lagrange multipliers. This yields the Bose-Einstein distribution,

$$\boxed{n_j = \frac{g_j - 1}{e^{\beta(\varepsilon_j - \mu)} - 1}} \,. \tag{7.63}$$

[9] Note that this partition function converges toward the one for boltzons for $g_j \gg n_j \gg 1$, which can be seen by simplifying it using the Stirling formula.

The Boltzmann distribution follows from this Bose-Einstein distribution for temperatures well above absolute zero, implying that $g_j \gg 1$. The Boltzmann distribution also requires low density, implying that $g_j \gg n_j$. Under these conditions, we may use Stirling's approximation (8.1) for the factorial: $N! \approx N^N e^{-N}$.

7.2.2.3 Fermions

For fermions, each level g_j can hold at most one of the n_j particles, which implies that necessarily $g_j > n_j$ [see Fig. 7.3(b)]. Let us consider a single energy level j. The first of the n_j particles has the choice between g_j boxes. Since no box can be filled with more than one particle, the second particle has only $g_j - 1$ boxes at its disposal, and so on until all particles have been assigned. This corresponds to $g_j!/n_j!$ possible choices. However, we still need to respect the indistinguishability requirement. The overcounting can be removed by dividing by $(g_j - n_j)!$. The procedure is now repeated with all energy levels j, which leads to the partition function for fermions,

$$\boxed{W_{\{n_j\}} = \prod_{j=1}^{r} \binom{g_j}{n_j}} \,. \tag{7.64}$$

Again we calculate the logarithm using Stirling's formula,

$$\begin{aligned} \ln W &= \sum_j \left[\ln g_j! - \ln n_j! - \ln(g_j - n_j)!\right] \\ &\simeq \sum_j \left[n_j \ln \frac{g_j - n_j}{n_j} - g_j \ln \frac{g_j - n_j}{g_j}\right] \,, \end{aligned} \tag{7.65}$$

the differential,

$$d \ln W = \sum_j \left(\frac{\partial \ln W}{\partial n_j}\right) dn_j = \sum_j \ln \frac{g_j - n_j}{n_j} dn_j \,. \tag{7.66}$$

and obtain the condition,

$$\begin{aligned} 0 = df(n_j) &= d \ln W - \alpha \sum_j dn_j - \beta \sum_j \varepsilon_j dn_j \\ &= \sum_{j=1}^{r} \left(\ln \frac{g_j - n_j}{n_j} - \alpha - \beta \varepsilon_j\right) dn_j \,, \end{aligned} \tag{7.67}$$

with the same Lagrange multipliers. This yields the Fermi-Dirac distribution for $g_j \gg 1$,

$$\boxed{n_j = \frac{g_j}{e^{\beta(\varepsilon_j - \mu)} + 1}} \,. \tag{7.68}$$

Do the Exc. 7.2.6.1.

7.2.2.4 Thermodynamic potentials for bosons and fermions

Using the abbreviation $s = +1$ for bosons, $s = -1$ for fermions, and $s = 0$ for boltzons the distribution function can be expressed as,

$$\boxed{n_j = \frac{g_j}{e^{\beta(\varepsilon_j - \mu)} - s}} \,. \tag{7.69}$$

The chemical potential μ is fixed by the boundary conditions,

$$N = \sum_{j=1}^{r} n_j \qquad \text{and} \qquad E = \sum_{j=1}^{r} \varepsilon_j n_j \,, \tag{7.70}$$

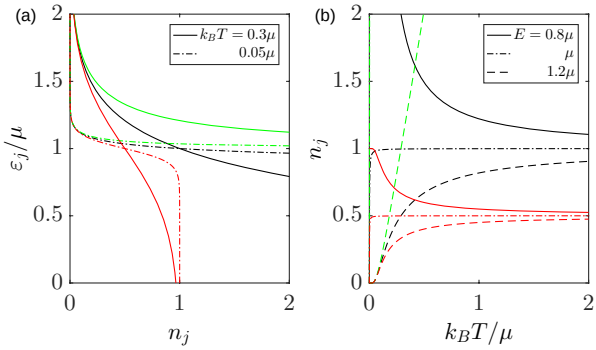

Figure 7.5: (code) Quantum statistical weight (7.50) for fermions (red dash-dotted line), bosons (green dashed line), and boltzons (black solid line). (a) Weight n_j as a function of level energy ε_j for two different temperatures (solid and dash-dotted lines). (b) Weight n_j as a function of temperature for various level energy ε_j (solid, dash-dotted, and dashed).

With this, knowing the energy spectrum ε_i and the distribution of states g_j of the system, we are able to calculate all thermodynamic potentials. E.g. the entropy reads,

$$\begin{aligned} S = k_\mathrm{B} \ln W_{\{n_j\}} &= k_\mathrm{B} \sum_j \left[n_j \ln\left(s + \frac{g_j}{n_j}\right) + s g_j \ln\left(1 + s\frac{n_j}{g_j}\right)\right] \\ &= k_\mathrm{B} \sum_j \left[\frac{s g_j \beta(\varepsilon_j - \mu)}{1 - s e^{-\beta(\varepsilon_j - \mu)}} + s g_j \ln\left(e^{\beta(\varepsilon_j - \mu)} - s\right)\right] \,. \end{aligned} \tag{7.71}$$

The Bose-Einstein and the Fermi-Dirac distribution both have many applications in quantum mechanics, e.g. for the explanation of the blackbody radiation, the heat capacity of metals, the laser, the Bose-Einstein condensation, and much more. In fact, these distributions must be used whenever quantum statistical effects are important. Prominent examples of systems where a quantum statistical treatment is crucial are electrons in metals and ultracold quantum gases. We will discuss the latter in Secs. 7.3 and 7.4.

7.2.3 Density-of-states in a trapping potential

An important boundary condition for the discussion of the quantum statistics of gases is that the atoms are often confined in trapping potentials. Suspended in space far from massive walls, they escape the perturbative influence of the environment. This however implies, that the system becomes inhomogeneous, which means that the number of states available to the atoms varies in space. In order to prepare subsequent evaluations of thermodynamic potentials, let us first characterize this spatial dependence by introducing the concept of the density-of-states.

In three dimensions the Hamiltonian of a trapped atoms is,

$$\hat{H} = -\frac{\hbar^2}{2m}\nabla^2 + U(\mathbf{r}) \ . \tag{7.72}$$

As the wavefunction is localized, the spectrum of possible energies organizes into discrete levels, and the atoms are allocated in populations of these levels. Such multidimensional systems are often degenerate, which means that the same total energy can be realized with different sets of quantum numbers [10]. The way an atomic cloud accommodates itself inside a trapping potential is governed by the density of available states. We now introduce the *density-of-states* $\eta(\epsilon)$ for an arbitrary potential via,

$$\boxed{\int \eta(\varepsilon)d\varepsilon \equiv \frac{1}{(2\pi)^3}\int d^3r d^3k = \frac{(2m)^{3/2}}{(2\pi)^2\hbar^3}\int d^3r \int d\varepsilon\sqrt{\varepsilon - U(\mathbf{r})}} \ , \tag{7.73}$$

with the substitution $k = \sqrt{\frac{2m}{\hbar^2}[\varepsilon - U(\mathbf{r})]}$.

As an example, let us consider a box potential of volume V. In this case, the expression (7.72) simply yields,

$$\boxed{\eta(\varepsilon) = \frac{(2m)^{3/2}}{(2\pi)^2\hbar^3}\int_V d^3r\sqrt{\varepsilon} = \frac{(2m)^{3/2}}{(2\pi)^2\hbar^3}V\sqrt{\varepsilon}} \quad \text{(box potential)} \ . \tag{7.74}$$

In the following we derive the density-of-states for the case of an harmonic oscillator potential. More general potentials are discussed in the Excs. 7.2.6.2 and 7.2.6.3.

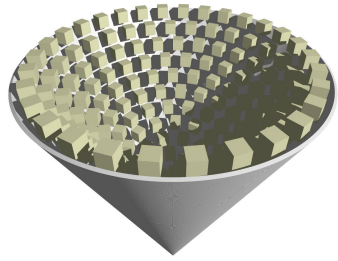

Figure 7.6: Artists's view of phase space cells in a trapping potential in two dimensions.

[10] This can be checked easily with separable potentials, such as the rectangular 3D box potential or the 3D harmonic oscillator, where the same energy $E = E_x + E_y + E_z$ can be reached with different combinations of E_x, E_y, and E_z.

Example 49 (*Density-of-states for a cylindrical harmonic oscillator potential*): Let us consider a cylindrical harmonic oscillator,

$$U(\mathbf{r}) = \frac{m}{2}\omega_r^2 r^2 + \frac{m}{2}\omega_z^2 z^2 \qquad \text{where} \qquad r^2 = x^2 + y^2 \ , \tag{7.75}$$

which can also be given in the form,

$$U(\mathbf{r}) = \frac{m}{2}\omega_r^2 \rho^2 \qquad \text{where} \qquad \rho^2 = x^2 + y^2 + \lambda^2 z^2 \qquad \text{with} \qquad \lambda = \frac{\omega_z}{\omega_r} \ . \tag{7.76}$$

We also define the mean oscillation frequency,

$$\bar{\omega} = (\omega_r^2 \omega_z)^{1/3} = \lambda^{1/3}\omega_r \ . \tag{7.77}$$

The single-particle levels of this Hamiltonian are,

$$\varepsilon_{n_x n_y n_z} = \hbar\omega_x n_x + \hbar\omega_y n_y + \hbar\omega_z n_z \ , \tag{7.78}$$

where the coefficients n_j with $j = x, y, z$ are integer numbers. For the cylindrical

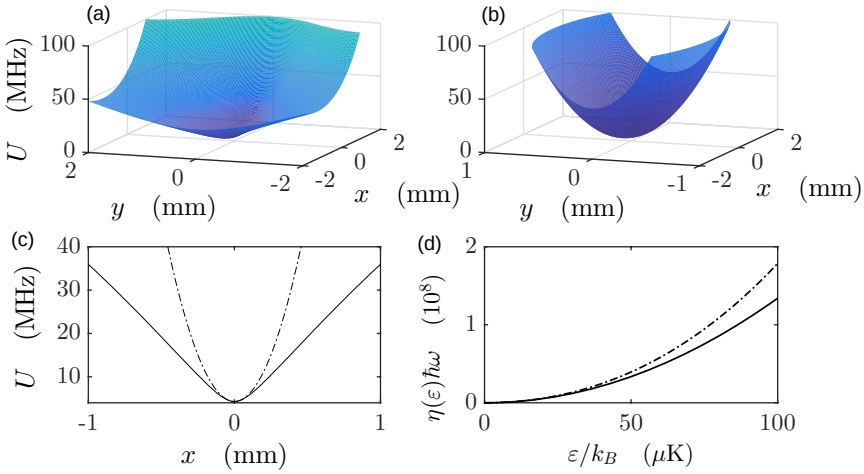

Figure 7.7: (code) (a) The figure shows two dimensions of a Ioffe-Pritchard type magnetic trapping potential (characterized by being approximately linear at large distances from the center and harmonic near the center). (b) Harmonic approximation (most experimentally feasible potentials are approximately harmonic near the center). (c) One-dimensional cut through the potential of (a,b). (d) Density-of-states for a harmonic (dotted line) and a Ioffe-Pritchard type potential (solid line).

harmonic trap defined in (7.74), we find with a little help from Dr. Bronstein [120],

$$\begin{aligned} \eta(\varepsilon) &= \frac{(2m)^{3/2}}{(2\pi)^2\hbar^3}\int d^3r \sqrt{\varepsilon - \frac{m}{2}\omega_r^2\rho^2} \\ &= \frac{1}{(2\pi)^2}\frac{8\varepsilon^2}{(\hbar\bar{\omega})^3}\int_{-1}^{1} d\tilde{x} \int_{-\sqrt{1-\tilde{x}^2}}^{\sqrt{1-\tilde{x}^2}} d\tilde{y} \int_{-\sqrt{1-\tilde{x}^2-\tilde{y}^2}}^{\sqrt{1-\tilde{x}^2-\tilde{y}^2}} d\tilde{z} \sqrt{1-\tilde{x}^2-\tilde{y}^2-\tilde{z}^2} \ . \end{aligned} \tag{7.79}$$

The resolution of the integral gives,

$$\boxed{\eta(\varepsilon) = \frac{\varepsilon^2}{2(\hbar\bar{\omega})^3}} \quad \text{(harmonic potential)} \; . \tag{7.80}$$

7.2.3.1 Application to the microcanonical partition function

Let us now come back to the distribution functions for ideal quantum gases introduced in Sec. 7.2.2. In the *thermodynamic limit*, $N \to \infty$, the distribution of states is assumed so dense, that it can be expressed by a continuous density,

$$\begin{array}{rcccl}
 & & \varepsilon_j & \longrightarrow & \varepsilon = \varepsilon_{\mathbf{r},\mathbf{p}} \\
 & & g_j & \longrightarrow & \eta(\varepsilon) \\
 & & \frac{1}{e^{\beta(\varepsilon_j-\mu)}-s} & \longrightarrow & \frac{1}{e^{\beta(\varepsilon-\mu)}-s} \equiv w_{T,\mu}(\varepsilon) \\
n_j & = & \frac{g_j}{e^{\beta(\varepsilon_j-\mu)}-s} & \longrightarrow & \eta(\varepsilon) w_{T,\mu}(\varepsilon) \\
 & & \sum_j g_j & \longrightarrow & \int \eta(\varepsilon) d\varepsilon = \frac{1}{(2\pi)^3} \int d^3r d^3k \\
N & = & \sum_j n_j & \longrightarrow & \int \eta(\varepsilon) w_{T,\mu}(\varepsilon) d\varepsilon \\
E & = & \sum_j \varepsilon_j n_j & \longrightarrow & \int \varepsilon \eta(\varepsilon) w_{T,\mu}(\varepsilon) d\varepsilon
\end{array} \tag{7.81}$$

where $s = 0$ stands for the 'Boltzmann', $s = -1$ for the 'Bose-Einstein', and $s = +1$ for the 'Fermi-Dirac' distributions derived in (7.58), (7.63), and (7.68). We also introduced the symbol $w_{T,\mu}$ to denote the statistical distribution function,

$$\boxed{w_{T,\mu}(\mathbf{r},\mathbf{p}) d^3r d^3p = \eta(\varepsilon) w_{T,\mu}(\varepsilon) d\varepsilon} \; . \tag{7.82}$$

In the following sections we will calculate all system variables based on the expressions (7.91) in the thermodynamic limit.

7.2.4 Grand canonical ensembles of ideal quantum gases

Let us now derive the statistics for physical conditions satisfied by a *grand canonical ensemble*, which is a good model for many systems in which the particle number is not conserved. A deeper discussion of the relation to the *canonical ensemble* and the role of the chemical potential will be provided in the last part of this section.

Supposing that the particles of a system do *not interact*, it is possible to compute a series of single-particle stationary states, each of which represents a separable part that can be included into the total quantum state of the system. Let us call these single-particle stationary states 'orbitals' in order to avoid confusion with the total many-body state. Every orbital represents a smallest possible cell in quantized phase space and has a distinct set of quantum numbers and may be occupied by several particles or be empty. In this sense, each orbital forms a separate grand canonical ensemble by itself, one so simple that its statistics can be immediately derived. Focusing on just one orbital labeled j, the total energy for a microstate of N particles in this orbital

will be $E = N\varepsilon_j$, where ε_j is the characteristic energy level of that orbital. The grand potential for the orbital is given by [11],

$$\Omega = -k_{\rm B}T \ln \Xi_{\rm gc} \qquad \text{with} \qquad \Xi_{\rm gc} = \sum_{\text{microstates}} e^{\beta(\mu N - E)} \ , \tag{7.83}$$

which is required for the microstates' probabilities to add up to 1, similarly to the procedure for canonical ensemble in (7.20).

In quantum mechanics the orbitals are understood as the eigenstates $|\psi_m\rangle$ of a single-particle Hamiltonian,

$$\hat{h}_m = \frac{\hat{\mathbf{p}}_m^2}{2m} + V_{\rm trap}(\hat{\mathbf{r}}_m) \ , \tag{7.84}$$

with $m = 1, \ldots, N$, whose spectrum is $\varepsilon_m = \langle \psi_m | \hat{h}_m | \psi_m \rangle$. That is, every single particle is completely characterized by the quantum number m [12]. A microstate $|\Psi_k\rangle$ is now identified as an eigenstate of the total many-particle Hamiltonian,

$$\hat{H} = \sum_{m=1}^{N} \hat{h}_m \qquad \text{with} \qquad |\Psi_k\rangle = \prod_{m=1}^{N} |\psi_m\rangle_k \ . \tag{7.85}$$

The request that the particles do not interact makes the system separable. The density operator and the grand canonical partition function are [185],

$$\boxed{\hat{\rho} = \frac{e^{-\beta(\hat{H} - \mu\hat{N})}}{\Xi_{\rm gc}} \qquad \text{and} \qquad \Xi_{\rm gc} = e^{-\beta\Omega} = \operatorname{Tr} e^{-\beta(\hat{H} - \mu\hat{N})}} \ , \tag{7.86}$$

obviously satisfying $\operatorname{Tr} \hat{\rho} = 1$. For the grand canonical ensemble the basis states of the total Hamiltonian $\hat{H}$ are all microstates composed of many particles, and the operators $\hat{N}$ and $\hat{\rho}$ can be expressed in the same basis.

We now migrate from the single-particle product state basis $\{|\Psi_k\rangle\}$ to a Fock state basis assigning a given number of particles n_j to every possible energy level ε_j, where $j = 1, \ldots, \infty$, as illustrated in Fig. 7.8,

$$|\Psi_k\rangle \longrightarrow |n_1, n_2, \ldots, n_j, \ldots\rangle \ . \tag{7.87}$$

I.e. we replace the distribution of microstates by a distribution of populations $\{n_j\}$ among the energy levels. Since the energy and particle numbers are separately conserved, the corresponding operators commute,

$$[\hat{H}, \hat{N}] = 0 \ , \tag{7.88}$$

and therefore it is possible to find a complete basis of simultaneous eigenstates,

$$\hat{H}|\ldots n_j \ldots\rangle = E|\ldots n_j \ldots\rangle \quad \text{with} \quad \hat{N}|\ldots n_j \ldots\rangle = N|\ldots n_j \ldots\rangle \tag{7.89}$$

[11] In case of multi-species ensembles, the potentials add up like $\mu_1 N_1 + \mu_2 N_2 + \ldots$.
[12] In practice, a set of several quantum numbers may be required.

with,

$$E = \sum_{j=0}^{\infty} \varepsilon_j n_j \qquad \text{and} \qquad N = \sum_{j=0}^{\infty} n_j \ . \tag{7.90}$$

This means that the number of particles is a conserved quantity and that $\hat{H}$ and $\hat{N}$ can be simultaneously diagonalized.

We can now evaluate the partition function (7.86),

$$\begin{aligned} \Xi_{\text{gc}} &= \sum_{k \in \{\text{microstates}\}} \langle \Psi_k | e^{-\beta(\hat{H}-\mu\hat{N})} | \Psi_k \rangle \\ &= \sum_{\{n_j\}} \langle \dots n_j \dots | e^{-\beta(\hat{H}-\mu\hat{N})} | \dots n_j \dots \rangle = \sum_{\{n_j\}} e^{-\beta(E-\mu N)} \ . \end{aligned} \tag{7.91}$$

The density operator in this new basis is,

$$\hat{\rho} = \sum_{\{n_j\}} \frac{|\dots n_j \dots\rangle e^{-\beta(E-\mu N)} \langle \dots n_j \dots|}{\sum_{\{n_j\}} e^{-\beta(E-\mu N)}} \ . \tag{7.92}$$

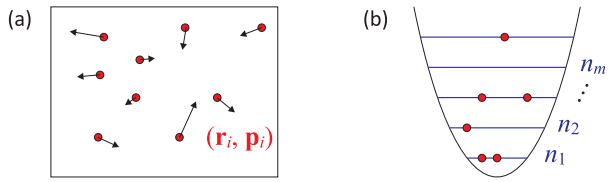

Figure 7.8: (a) Ensemble of N particles with different positions and velocities. (b) Distribution of the particles over the spectrum of allowed energies.

Using the conditions (7.90), the partition function becomes,

$$\begin{aligned} \Xi_{\text{gc}} &= \sum_{n_1, n_2, \dots} \langle \dots n_j \dots | e^{-\beta(\hat{H}-\mu\hat{N})} | \dots n_j \dots \rangle \\ &= \sum_{n_1} \langle n_1 | e^{-\beta(n_1 \hat{h}_1 - n_1 \mu)} | n_1 \rangle \sum_{n_2} \langle n_2 | e^{-\beta(n_2 \hat{h}_2 - n_2 \mu)} | n_2 \rangle \times \dots \equiv \prod_{j=1}^{\infty} \Xi_j \ , \end{aligned} \tag{7.93}$$

where in the last step we defined a *partial* partition sum,

$$\Xi_j \equiv \sum_{n_j} e^{-\beta(\varepsilon_j n_j - \mu n_j)} \ , \tag{7.94}$$

accounting for all possible populations of a particular energy level ε_j. Analogously, the density operator becomes,

$$\begin{aligned} \hat{\rho} &= \frac{e^{-\beta(\hat{H}-\mu\hat{N})}}{\Xi_{\text{gc}}} = \frac{1}{\Xi_{\text{gc}}} e^{-\beta\left(\sum_{\{n_j\}} (\varepsilon_j - \mu)\hat{n}_j\right)} \\ &= \frac{1}{\Xi_{\text{gc}}} e^{-\beta(\varepsilon_1-\mu)\hat{n}_1} e^{-\beta(\varepsilon_2-\mu)\hat{n}_2} \times \dots = \prod_{j=1}^{\infty} \hat{\rho}_j \ . \end{aligned} \tag{7.95}$$

Note, that breaking down the exponential of a sum of operators, $e^{-\sum \hat{n}_j}$, into a product of exponentials of that operators, $\prod e^{-\hat{n}_j}$, is only possible because the operators commute, $[\hat{n}_k, \hat{n}_j] = 0$, which is only the case for non-interacting particles. In the last step we defined,

$$\hat{\rho}_j \equiv \frac{e^{-\beta(\varepsilon_j-\mu)\hat{n}_j}}{\Xi_j} = |n_j\rangle \frac{e^{-\beta(\varepsilon_j-\mu)}}{\Xi_j} \langle n_j| \ . \tag{7.96}$$

The problem with this expression is, that the global wavefunction $|\Psi\rangle$ has not yet been (anti-)symmetrized according the particles' bosonic or fermionic nature. For bosons, n_j may be any non-negative integer and each value of n_j counts as one microstate due to the indistinguishability of particles. For fermions, the Pauli exclusion principle allows only two microstates for the orbital (occupation of 0 or 1), giving a two-term series [13], The partial partition sum (7.94) can thus be evaluated,

$$\Xi_j = \begin{cases} \sum_{n_j=0}^{\infty} e^{-\beta(n_j\varepsilon_j - n_j\mu)} = \frac{1}{1-e^{-\beta(\varepsilon_j-\mu)}} & \text{for bosons} \\ \sum_{n_j=0}^{1} e^{-\beta(n_j\varepsilon_j - n_j\mu)} = 1 + e^{-\beta(\varepsilon_j-\mu)} & \text{for fermions} \end{cases} \tag{7.97}$$

Hence,

$$\boxed{\Xi_{\text{gc}} = \prod_{j=1}^{\infty} (1 - s e^{-\beta(\varepsilon_j-\mu)})^{-s}} \ , \tag{7.98}$$

where $s = 1$ for bosons and $s = -1$ the lower for fermions.

The grand canonical potential per microstate becomes,

$$\Omega_j = -k_{\text{B}} T \ln \Xi_j = s k_{\text{B}} T \ln(1 - s e^{-\beta(\varepsilon_j-\mu)}) \ . \tag{7.99}$$

Considering again the entire system, the total Landau grand potential is found by adding up the Ω_j for all orbitals,

$$\Omega = \sum_{j=1}^{\infty} \Omega_j \ . \tag{7.100}$$

In any case the value [14]

$$\boxed{n_j = -\frac{\partial \Omega_j}{\partial \mu} = \frac{1}{e^{\beta(\varepsilon_j-\mu)} - s} \equiv w_{T,\mu}(\varepsilon_j)} \tag{7.101}$$

[13] Here, we introduce the statistics of indistinguishable particles *ad hoc*. The same result is obtained automatically introducing field operators satisfying bosonic or fermionic commutation rules. Indeed, we can rewrite the Hamiltonian and the number operator of any non-interacting system like [850],

$$\hat{H} = \sum_{\{n_j\}} \varepsilon_j \hat{a}_j^\dagger \hat{a}_j \qquad \text{and} \qquad \hat{N} = \sum_{\{n_j\}} \hat{a}_j^\dagger \hat{a}_j \ ,$$

where $\hat{a}_j^\dagger$ and $\hat{a}_j$ are the particle creation and annihilation operators introduced in the occupation number representation.

[14] Note the absence of the degeneracy factor g_j in comparison to the formula (7.69), which is simply due to the fact that here we only consider a potential with non-degenerate eigenstates. The degeneracy factor g_j can, however, simply added *ad hoc*.

gives the thermodynamic average number of particles on the orbital: the *Fermi-Dirac distribution* for fermions, and the *Bose-Einstein distribution* for bosons.

The problem is completely analogous to Planck's treatment of blackbody radiation, where the Bose-Einstein distribution function followed as a corollary from the Boltzmann statistics in thermal equilibrium and Planck's quantization hypothesis, $E = N\varepsilon_j$.

7.2.4.1 Grand potential and ensemble averages

Evaluating partial derivatives of the function $\Omega(\mu, V, T)$, looking up the relations (??), we find for the averages of numbers of particles, the Gibbs entropy, the average pressure, and the average energy,

$$\begin{aligned} 1 &= \mathrm{Tr}\,\hat{\rho} & & \\ N = \langle \hat{N} \rangle &= \mathrm{Tr}\,\hat{\rho}\hat{N} & &= -\left(\frac{\partial \Omega}{\partial \mu}\right)_{T,V} \\ S &= k_\mathrm{B}\mathrm{Tr}\,\hat{\rho}\ln\hat{\rho} & &= -\left(\frac{\partial \Omega}{\partial T}\right)_{\mu,V} \\ P & & &= -\left(\frac{\partial \Omega}{\partial V}\right)_{T,\mu} \\ E = \langle \hat{H} \rangle &= \mathrm{Tr}\,\hat{\rho}\hat{H} & &= TS + \mu N + \Omega \end{aligned} \quad . \tag{7.102}$$

We will derive Eq. (7.102)(iii) in Exc. 7.2.6.4.

Example 50 (*Calculation of ensemble averages*): Thermodynamic fluctuations can be calculated via the variances in energy and particle numbers. Starting from,

$$-\beta\Omega = \ln \Xi_\mathrm{gc} = \ln \mathrm{Tr}\, e^{-\beta(\hat{H}-\mu\hat{N})} \tag{7.103}$$

it is easy to show, that,

$$\frac{\partial \Xi_\mathrm{gc}}{\partial \mu} = \beta \mathrm{Tr}\,\hat{N} e^{-\beta(\hat{H}-\mu\hat{N})} = \beta \Xi_\mathrm{gc} \langle \hat{N} \rangle \tag{7.104}$$

$$-\beta\frac{\partial \Omega}{\partial \mu} = \frac{\mathrm{Tr}\,\hat{N} e^{-\beta(\hat{H}-\mu\hat{N})}}{\Xi_\mathrm{gc}} = \beta\langle \hat{N} \rangle$$

$$-\frac{\partial^2 \Omega}{\partial \mu^2} = \frac{\Xi_\mathrm{gc}\frac{\partial}{\partial\mu}\mathrm{Tr}\,\hat{N} e^{-\beta(\hat{H}-\mu\hat{N})} - \mathrm{Tr}\,\hat{N} e^{-\beta(\hat{H}-\mu\hat{N})}\frac{\partial}{\partial\mu}\Xi_\mathrm{gc}}{\Xi_\mathrm{gc}^2} = \beta(\langle \hat{N}^2 \rangle - \langle \hat{N} \rangle^2) \; .$$

Hence, the particle number fluctuations are,

$$\Delta\hat{N} = \langle \hat{N}^2 \rangle - \langle \hat{N} \rangle^2 = -\frac{1}{\beta}\frac{\partial^2 \Omega}{\partial \mu^2} = k_\mathrm{B}T\frac{\partial \langle \hat{N} \rangle}{\partial \mu} \; . \tag{7.105}$$

Similarly,

$$(\Delta\hat{H})^2 = \langle \hat{H}^2 \rangle - \langle \hat{H} \rangle^2 = k_\mathrm{B}T^2\frac{\partial \langle \hat{H} \rangle}{\partial T} + k_\mathrm{B}T\mu\frac{\partial \langle \hat{H} \rangle}{\partial \mu} \; , \tag{7.106}$$

as will be verified in Exc. 7.2.6.5.

If different species are present, it is interesting to calculate correlations in fluctuations [501]. The covariances of particle numbers and energy are then,

$$\langle N_1 N_2\rangle - \langle N_1\rangle\langle N_2\rangle = k_{\rm B}T\frac{\partial\langle\hat{N}_2\rangle}{\partial\mu_1} = k_{\rm B}T\frac{\partial\langle\hat{N}_1\rangle}{\partial\mu_2} \tag{7.107}$$
$$\langle\hat{N}_1\hat{H}\rangle - \langle\hat{N}_1\rangle\langle\hat{H}\rangle = k_{\rm B}T\frac{\partial\langle\hat{H}\rangle}{\partial\mu_1}\ .$$

From the above expressions, it can be seen that the function Ω has the *exact differential*,

$$d\Omega = -S\,dT - \langle\hat{N}\rangle d\mu - P\,dV\ . \tag{7.108}$$

Substituting the relationship (7.102)(v) for E into the exact differential of Ω, an equation similar to the *first law of thermodynamics* is found, except that some quantities only appear as averages,

$$d\langle\hat{H}\rangle = T\,dS + \mu\,d\langle\hat{N}\rangle - P\,dV\ . \tag{7.109}$$

7.2.4.2 Meaning of chemical potential

The key behind second quantization is to remove the restriction that the number of particles is fixed. Instead, the theory is built around the idea of Fock space, where the number of particles is not fixed. This is highly advantageous when dealing with many-body systems. This same idea, when extended to finite temperatures, is what we call the grand canonical ensemble. What we want is to consider some finite temperature density matrix $\hat{\rho}\sim e^{-\beta\hat{H}}$, where the number of particles is not fixed, but can fluctuate [501].

However, letting it fluctuate arbitrarily would make no physical sense. Instead, the basic idea of the grand canonical ensemble is to impose that the number of particles in the system is only fixed on average. That is, we impose that,

$$\langle\hat{N}\rangle = N\ . \tag{7.110}$$

In some systems, the number of particles does indeed fluctuate. This happens, for instance, in chemical solutions: if we look at a certain region of a liquid, the number of molecules there is constantly fluctuating due to molecules moving in and out from other regions. Of course, in many other systems, the number of particles is fixed. However, even in these cases, pretending it can fluctuate may still give good answers for large N (thermodynamic limit). The reason is that, as we have seen above, the variance of $\hat{N}$ scales as,

$$\Delta\hat{N}\propto\sqrt{N}\ , \tag{7.111}$$

which is small. Hence, when N is large, the grand canonical ensemble will give accurate answers, even if the number of particles is not actually allowed to fluctuate. This is the idea behind *ensemble equivalence*: we are allowed to use an ensemble where the number of particles fluctuates, even though it actually doesn't, because in the thermodynamic limit the fluctuations are small.

Because of $[\hat{H},\hat{N}]=0$ the eigenvalues of $\hat{N}$ are good quantum numbers alongside the eigenvalues of $\hat{H}$. We can now arrange the common eigenvectors of E and N in

such a way as to sort the eigenvalue sets (N, E) by total atom numbers, such that $\hat{H}$ is divided in sectors with well-defined N. In other words, $\hat{H}$ is block diagonal, and there are no terms connecting sectors with different N. The eigenvalues E are thus labeled by two indices $E(N, m)$, where m labels the quantum states within each sector,

$$\hat{H} = \left(\begin{array}{cc|cc|c} E(N_1,1) & & & & \\ & E(N_1,2) & & & \\ & & \ddots & & \\ \hline & & E(N_2,1) & & \\ & & & E(N_2,2) & \\ & & & & \ddots \end{array}\right) \quad . \tag{7.112}$$

Suppose now that the system is in thermal equilibrium with exactly N particles, which corresponds to a *canonical* ensemble. As resumed in Tab. **??**, the conditions for equilibrium are then obtained minimizing the Helmholtz free energy, $dF = 0$, and the corresponding *canonical* density operator and partition function are,

$$\hat{\rho}_{\rm cn} = \frac{e^{-\beta\hat{H}}}{\Xi_{\rm cn}(N)} \quad , \quad \Xi_{\rm cn}(N) = \sum_{m\in{\rm sector}} e^{-\beta E(N,m)} \quad , \quad F = -k_{\rm B}T\,\ln\Xi_{\rm cn}(N)\ . \tag{7.113}$$

This is a constrained sum, since we are only summing over that sector that has exactly N particles. This constraint makes it notoriously difficult to compute the sum in practice solving a Schrödinger equation with $\hat{H}$.

Instead, in the *grand canonical* ensemble we allow the number of particles to fluctuate but only fix them on average (7.110). To accomplish this we had to introduce a new parameter μ, called the chemical potential, so that the *grand canonical* equilibrium state is transformed to,

$$\rho_{\rm gc} = \frac{e^{-\beta(\hat{H}-\mu\hat{N})}}{\Xi_{\rm gc}} \quad , \quad \Xi_{\rm gc} = {\rm Tr}\, e^{-\beta(\hat{H}-\mu\hat{N})} \quad , \quad \Omega = -k_{\rm B}T\,\ln\Xi_{\rm gc}\ . \tag{7.114}$$

Apparently, the chemical potential enters by shifting the Hamiltonian,

$$\hat{H} \to \hat{H} - \mu\hat{N}\ . \tag{7.115}$$

As resumed in Tab. **??**, in grand canonical ensembles the conditions for equilibrium are obtained minimizing the Landau energy, $d\Omega = d(F - \mu N) = 0$. To obtain the energy spectrum in the case of fluctuating particle numbers, we need to solve a many-body Schrödinger equation (such as the Gross-Pitaevski equation) with the Hamiltonian substituted by $\hat{\Omega} = \hat{H} - \mu\hat{N}$ [238].

The logic behind μ is twofold. When the number of particles is allowed to fluctuate, the value of μ is fixed externally (like the temperature). As a consequence the number of particles $\langle\hat{N}\rangle = N(\mu, T)$ is interpreted as a function of μ and T. Conversely, if the

number of particles N is fixed, then $\mu = \mu(N, T)$ is to be interpreted as a function of N and T, which is to be determined as the solution of the implicit equation,

$$\langle \hat{N} \rangle = \frac{\mathrm{Tr}\, \hat{N} e^{-\beta(\hat{H}-\mu\hat{N})}}{\mathrm{Tr}\, e^{-\beta(\hat{H}-\mu\hat{N})}} = N \ . \tag{7.116}$$

Relevant cases in which the number of particles is not conserved are:

- Chemical reactions can convert one type of molecule to another; if reactions occur then the N_i must be defined such that they do not change during the chemical reaction.

- In high energy particle physics, ordinary particles can be spawned out of pure energy, if a corresponding antiparticle is created. Then, neither the number of particles nor antiparticles are conserved, only their difference.

- In a system composed of multiple compartments that share energy but do not share particles it is possible to set the chemical potentials separately for each compartment, for example, when a capacitor composed of two isolated conductors is charged by applying a difference in electron chemical potential.

- In some slow quasi-equilibrium situations it is possible to have distinct populations of the same kind of particle in the same location, which are each equilibrated internally but not with each other.

- The grand canonical ensemble is particularly useful for developing the *thermodynamics of large ideal trapped quantum gases*. While the phenomenon of BEC can be derived in any ensemble (in Sec. 7.2.2 we derived the bosonic partition function from the detailed balanced assumption using combinatorial arguments), when the dynamics of a condensate is the subject under study, it is often useful to consider it as a separate system being in thermal and chemical equilibrium with a reservoir. The role of a reservoir is played by the thermal cloud, which always coexists with the condensate and which exchanges particles and energy with it.

In order for a particle number to have an associated chemical potential, it must be conserved during the internal dynamics of the system, and only able to change when the system exchanges particles with an external reservoir. If the particles can be created out of energy during the dynamics of the system, then an associated μN term must not appear in the probability expression for the grand canonical ensemble, i.e. we require $\mu = 0$ for that kind of particle. Such is the case for *photons in a black cavity*, which can be annihilated or created due to absorption and emission on the cavity walls (see Exc. 7.2.6.6) [15].

[15] Note that photons in a highly reflective cavity can be conserved and caused to have a non-zero chemical potential μ.

7.2.4.3 Comparison of canonical and grand canonical ensembles

The *canonical ensemble* is used to represent the possible microstates of a mechanical system in thermal equilibrium with a heat bath at a fixed temperature. The system can exchange energy with the heat bath, so that the states of the system will differ in total energy. The principal thermodynamic variable of the canonical ensemble, determining the probability distribution of states, is the absolute temperature T. The ensemble typically also depends on mechanical variables, such as the number of particles N in the system and the system's volume V, each of which influence the nature of the system's internal states.

The canonical ensemble assigns a probability $\mathfrak{P}_{\rm cn}(E)$ to each distinct microstate given by the following exponential,

$$\boxed{\mathfrak{P}_{\rm cn}(E) = e^{\beta(F-E)} = \tfrac{1}{\Xi_{\rm cn}} e^{-E/(k_{\rm B}T)} \qquad \text{with} \qquad \Xi_{\rm cn} = e^{-F/(k_{\rm B}T)}} \,, \tag{7.117}$$

where E is the total energy of the microstate and $\Xi_{\rm cn}$ the canonical partition function.

In quantum mechanics the density operator and partition function are,

$$\boxed{\begin{array}{rcl} \hat{\rho}_{\rm cn} & = & e^{\beta(F-\hat{H})} = \frac{e^{-\beta\hat{H}}}{\Xi_{\rm cn}} = \frac{1}{\Xi_{\rm cn}} \sum_k |\psi_k\rangle e^{\beta(F-E_k)} \langle\psi_k| \\ \Xi_{\rm cn} & = & \mathrm{Tr}\, e^{-\beta\hat{H}} = e^{-\beta F} = \sum_k e^{-\beta E_k} \end{array}} \,. \tag{7.118}$$

The Helmholtz free energy F is constant for the ensemble. However, the probabilities and F will vary if different N, V, T are selected. The free energy F serves two roles: first, it provides a normalization factor for the probability distribution (the probabilities, over the complete set of microstates, must add up to one); second, many important ensemble averages can be directly calculated from the function $F(N, V, T)$.

The canonical ensemble is the ensemble that describes the possible states of a system that is in thermal equilibrium with a heat bath. It applies to systems of any size; while it is necessary to assume that the heat bath is very large (i.e. take a macroscopic limit), the system itself may be small or large.

The condition that the system is mechanically isolated is necessary in order to ensure it does not exchange energy with any external object besides the heat bath. In general, it is desirable to apply the canonical ensemble to systems that are in direct contact with the heat bath, since it is that contact that ensures the equilibrium. In practical situations, the use of the canonical ensemble is usually justified either (1) by assuming that the contact is mechanically weak, or (2) by incorporating a suitable part of the heat bath connection into the system under analysis, so that the connection's mechanical influence on the system is modeled within the system.

When the total energy is fixed but the internal state of the system is otherwise unknown, the appropriate description is not the canonical ensemble but the microcanonical ensemble. For systems where the particle number is variable (due to contact with a particle reservoir), the correct description is the grand canonical ensemble.

The *grand canonical ensemble* is used to represent the possible microstates of a system of particles that are in thermal and chemical equilibrium with a reservoir.

The system is said to be open in the sense that the system can exchange energy and particles with a reservoir, so that various possible states of the system can differ in both their total energy and total number of particles. The system's volume, shape, and other external coordinates are kept the same in all possible states of the system.

The thermodynamic variables of the grand canonical ensemble are chemical potential μ and absolute temperature T. The ensemble is also dependent on mechanical variables such as volume V which influence the nature of the system's internal states. As each of these is assumed to be constant in the grand canonical ensemble, it is sometimes called the μVT ensemble.

The grand canonical ensemble assigns a probability $\mathfrak{P}_{\mathrm{gc}}(E)$ to each distinct microstate given by the following exponential [16],

$$\boxed{\mathfrak{P}_{\mathrm{gc}} = e^{\beta(\Omega+\mu N-E)} = \tfrac{1}{\Xi_{\mathrm{gc}}} e^{\beta(\mu N-E)} \qquad \text{with} \qquad \Xi_{\mathrm{gc}} = e^{-\beta\Omega}} \,, \tag{7.119}$$

where N is the number of particles in the microstate and E is the total energy of the microstate.

The quantum mechanics the density operator and partition function are,

$$\boxed{\begin{aligned} \hat{\rho}_{\mathrm{gc}} &= e^{\beta(\Omega+\mu\hat{N}-\hat{H})} = \tfrac{e^{-\beta(\hat{H}-\mu\hat{N})}}{\Xi_{\mathrm{gc}}} = \tfrac{1}{\Xi_{\mathrm{gc}}} \textstyle\sum_k |\psi_k\rangle e^{\beta(\Omega+\mu n_k-E_k)} \langle\psi_k| \\ \Xi_{\mathrm{gc}} &= \mathrm{Tr}\, e^{-\beta(\hat{H}-\mu\hat{N})} = e^{-\beta\Omega} = \textstyle\sum_k e^{\beta(\mu n_k-E_k)} \end{aligned}} \,. \tag{7.120}$$

The grand potential Ω is constant for the ensemble. However, the probabilities and Ω will vary if different μ, V, T are selected. The grand potential Ω serves two roles: to provide a normalization factor for the probability distribution (the probabilities, over the complete set of microstates, must add up to one); second, many important ensemble averages can be directly calculated from the function $\Omega(\mu, V, T)$.

The grand canonical ensemble is the ensemble that describes the possible states of an isolated system that is in thermal and chemical equilibrium with a reservoir. The grand canonical ensemble applies to systems of any size, small or large; it is only necessary to assume that the reservoir with which it is in contact is much larger (i.e. to take the macroscopic limit).

The condition that the system is isolated is necessary in order to ensure it has well-defined thermodynamic quantities and evolution. In practice, however, it is desirable to apply the grand canonical ensemble to describe systems that are in direct contact with the reservoir, since it is that contact that ensures the equilibrium. The use of the grand canonical ensemble in these cases is usually justified either (1) by assuming that the contact is weak, or (2) by incorporating a part of the reservoir connection into the system under analysis, so that the connection's influence on the region of interest is correctly modeled. Alternatively, theoretical approaches can be used to model the influence of the connection, yielding an open statistical ensemble.

Another case in which the grand canonical ensemble appears is when considering a system that is large and thermodynamic (a system that is 'in equilibrium with

[16] In the case where more than one kind of particle is allowed to vary in number, the probability expression generalizes to $\mathfrak{P}_{\mathrm{gc}} = e^{\beta(\Omega+\mu_1 N_1+\mu_2 N_2+\cdots-E)}$, where μ_j is the chemical potential for the j-th kind of particles, N_j the number of that kind of particle in the microstate.

itself'). Even if the exact conditions of the system do not actually allow for variations in energy or particle number, the grand canonical ensemble can be used to simplify calculations of some thermodynamic properties. The reason for this is that various thermodynamic ensembles (microcanonical, canonical) become equivalent in some aspects to the grand canonical ensemble, once the system is very large. Of course, for small systems, the different ensembles are no longer equivalent even in the mean. As a result, the grand canonical ensemble can be highly inaccurate when applied to small systems of fixed particle number, such as atomic nuclei [17].

Grand ensembles are apt for use when describing systems such as electrons in a conductor or photons in a cavity, where the shape is fixed but the energy and number of particles can easily fluctuate due to contact with a reservoir (e.g. an electrical ground or a dark surface, in these cases). The grand canonical ensemble provides a natural setting for an exact derivation of the Fermi-Dirac statistics or Bose-Einstein statistics for a system of non-interacting quantum particles.

7.2.5 Thermodynamic limit and Riemann's zeta function

The partition functions (7.59) resp. (7.64) for microcanonical and (7.98) for grand canonical ensembles are evaluated over discrete distributions of microstates. Also, in Sec. 7.2.3 we argued that, in view of the huge number of microstates, it is desirable to introduce continuous distribution functions,

$$\sum_{\mathbf{r},\mathbf{p}} \ldots \longrightarrow h^{-3} \int d^3r d^3p \ldots \longrightarrow h^{-3} \int d\varepsilon \eta(\varepsilon) \ldots \ , \tag{7.121}$$

which, for confined ensembles, can even be simplified using the concept of density-of-states $\eta(\varepsilon)$. As long as we are deep in the thermodynamic limit, $N \to \infty$, we expect to obtain reliable results. Let us now do this exercise for an ideal quantum gas confined in a *box potential* of volume V, whose density-of-states is given by (7.74).

We begin with the request that the chemical potential satisfies the normalization condition,

$$N = \int w_{T,\mu}(\varepsilon)\eta(\varepsilon)d\varepsilon = \frac{V\sqrt{2m}}{(2\pi)^2\hbar^3} \int_0^\infty \frac{\sqrt{\varepsilon}d\varepsilon}{e^{\beta(\varepsilon-\mu)} \mp 1} \ . \tag{7.122}$$

Introducing the *thermal de Broglie wavelength*,

$$\boxed{\lambda_{\rm th} \equiv \sqrt{\frac{2\pi\hbar^2}{mk_{\rm B}T}}} \ , \tag{7.123}$$

and defining the *fugacity*,

$$\boxed{Z \equiv e^{\beta\mu}} \ , \tag{7.124}$$

and we may also write,

$$N = \frac{V}{\lambda_{\rm th}^3} \int_0^\infty \frac{\sqrt{x}dx}{Z^{-1}e^x \mp 1} \ . \tag{7.125}$$

[17] Note that even in the thermodynamic limit, in the presence of long range interactions, the ensembles may not be equivalent.

At this point, to simplify the notation, we introduce the *Bose function* and its integral representation,

$$g_\xi^+(Z) = \sum_{t=1}^{\infty} \frac{Z^t}{t^\xi} = \frac{1}{\Gamma(\xi)} \int_0^\infty \frac{x^{\xi-1} dx}{Z^{-1} e^x - 1} \equiv g_\xi(Z) \ , \tag{7.126}$$

where $\Gamma(\eta)$ denotes the Gamma function. Analogically, we can define the *Fermi function* via [18],

$$g_\xi^-(Z) = \sum_{t=1}^{\infty} -\frac{(-Z)^t}{t^\xi} = \frac{1}{\Gamma(\xi)} \int_0^\infty \frac{x^{\xi-1} dx}{Z^{-1} e^x + 1} \equiv f_\xi(Z) \ . \tag{7.127}$$

For classical particles,

$$g_\xi^0(Z) = \frac{1}{\Gamma(\xi)} \int_0^\infty \frac{x^{\xi-1} dx}{Z^{-1} e^x + 0} = Z \ , \tag{7.128}$$

because the integral just defined the Gamma function. That is, interestingly the classical function corresponding to the Bose or Fermi function is an *identity for all orders* of ξ. A particular value is the *Riemann zeta-function* defined as,

$$\zeta(\xi) = g_\xi^+(1) \ . \tag{7.129}$$

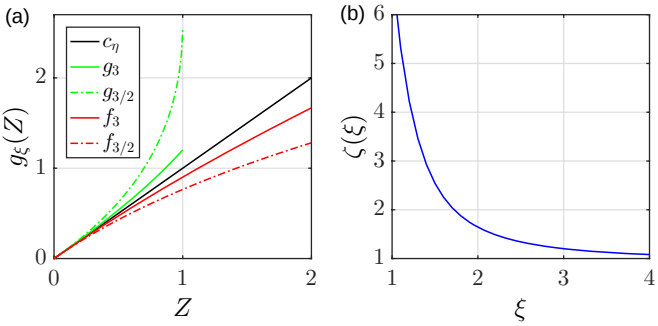

Figure 7.9: (code) (a) Bose and Fermi functions for box potentials ($g_{3/2}$ and $f_{3/2}$) and for harmonic potentials (g_3 and f_3). Note that the Bose function is only defined between $Z \in [0, 1]$. Also shown is the Boltzmann limit (7.128). (b) Riemann function.

Note that for $Z^{-1} e^x \gg 0$ all denominators in the expressions (7.126) or (7.128) converge to the classical limit, which is to say, that for highly excited atoms, $\varepsilon - \mu \gg k_B T$, all quantum statistical effects disappear.

With all these definitions we can now rewrite the expression (7.125),

$$\boxed{N = \frac{V}{\lambda_{\text{th}}^3} g_{3/2}^{(s)}(Z)} \ , \tag{7.130}$$

[18] When the context is clear, we will use the shorter notations g_ξ and f_ξ for Bose and Fermi functions, respectively.

where $s = +$ for bosons, $s = -$ for fermions, and $s = 0$ for boltzons. Apparently, we can identify the Bose/Fermi function as the thermal phase space density of an ideal gas,

$$\rho_{\rm th} \equiv \frac{N}{V}\lambda_{\rm th}^3 = g_{3/2}^{(s)}(Z) \ . \tag{7.131}$$

In a similar way we could now derive analytic expressions for all other thermodynamic potentials. We will, however, see in the next Sec. 7.3, that for ideal bosonic gases the result (7.130) must be corrected. The reason is rooted in a momentous quality of the Bose function, which is that it diverges for $Z > 1$, which limits the chemical potential to negative values.

7.2.6 Exercises

7.2.6.1 Ex: Quantum statistics

n particles are distributed over $g > n$ different cells with the same probability. Calculate the probabilities
a. that there is exactly one particle in each one of the first n cells;
b. that there is no cell with more than one particle.
Use the three different assumptions that:
i. the particles are boltzons, i.e. they are identifiable and arbitrarily many particles can be assigned to each cell;
ii. the particles are bosons, i.e. they are NOT identifiable and arbitrarily many particles can be assigned to each cell;
iii. the particles are fermions, i.e. they are NOT identifiable and only a single particle may be assigned to each cell.

7.2.6.2 Ex: Density-of-states for non-harmonic potentials

Calculate the density-of-states for non-harmonic potentials, $\hat{H} = \frac{\hbar^2 k^2}{2m} + \left|\frac{x}{2\bar{x}}\right|^p + \left|\frac{y}{2\bar{y}}\right|^l + \left|\frac{z}{2\bar{z}}\right|^q$ using Ref. [44]. Apply the result to a quadrupolar potential.

7.2.6.3 Ex: Electron gas model

A simple model for the behavior of electrons in a metal is the *Fermi gas model*. In this model the electrons move in a square well potential, a mean-field approach accounts globally for the periodic lattice of ions and the influence of all other electrons. The density-of-states and the electron density are the same as for blackbody radiation,

$$\rho(\varepsilon)d\varepsilon = \frac{V(2m^3)^{1/2}}{\pi^2\hbar^3}\sqrt{\varepsilon}d\varepsilon \ ,$$
$$n(\varepsilon)\rho(\varepsilon)d\varepsilon = \frac{1}{e^{(\varepsilon-\varepsilon_{\rm F})/k_{\rm B}T}+1}\rho(\varepsilon)d\varepsilon \ .$$

Calculate the maximum energy at $T = 0$.

7.2.6.4 Ex: Entropy in the grand canonical ensemble

Derive the relationship $S = k_{\rm B}{\rm Tr}\,\hat{\rho}\ln\hat{\rho}$.

7.2.6.5 Ex: Energy fluctuation in grand canonical ensembles

Derive the expression (7.106).

7.2.6.6 Ex: Black-body radiation

Derive the thermodynamics of the phenomenon of *black-body radiation*.
a. Which is the appropriate thermodynamic ensemble, and why?
b. For a single mode of a cavity, calculate the partition function, the density operator, the total energy, and the Helmholtz free energy.
c. Generalize the results for an arbitrary black-body.
d. Introducing the density-of-states, calculate the energy density in the cavity as a function of temperature.

7.3 Condensation of an ideal Bose gas

The clearest manifestation of quantum statistical effects is probably the phenomenon of Bose-Einstein condensation (BEC) predicted by Bose and Einstein in 1926 [107]. With the achievement of BEC in a dilute gas of atomic rubidium in 1995, Cornell *et al.* [172] confirmed the theory. Quantum degeneracy in Fermi gases was also observed a bit later [214, 628]. In this and the subsequent section, we will present a quantum statistical theory of *ideal* quantum gases for the cases of bosons, respectively, fermions. Clearly, the theory is unable to grasp many phenomena observed in BECs and linked to interatomic interactions, such as superfluidity. These will be discussed elsewhere [19].

7.3.1 Condensation of a gas confined in a box potential

At very low temperatures approaching $T = 0$, according to the Bose-Einstein distribution (7.101), we expect the atoms to pile up in the lowest energy state $\varepsilon_{j=0} = 0$ of the trap,

$$n_0 \overset{\varepsilon_0 \to 0}{\longrightarrow} w_{T,\mu}(0) = \frac{1}{e^{-\beta\mu} - 1} = \frac{1}{1/Z - 1} = N \ , \tag{7.132}$$

where we used the definition of the fugacity (7.124). In the thermodynamic limit,

$$Z = \frac{1}{1 + 1/N} \overset{N \to \infty}{\longrightarrow} 1 \ , \tag{7.133}$$

we find that the fugacity approaches unity. Thus, $Z = 1$ is the condition for a macroscopic ground state population.

Let us now calculate the ground state population at finite temperatures. For a free gas with energy spectrum, $\varepsilon = p^2/2m$, we derived the density-of-states $\eta(\varepsilon)$ in (7.74) [20]. Using the occupation number $w_{T,\mu}(\varepsilon)$ for the Bose-Einstein distribution (7.101) in the thermodynamic limit, we express the total number of atoms as we

[19] See script on *Quantum Mechanics applied to Atomic and Molecular Physics, Quantum and Atom Optics* (2025).

[20] We must, however, keep in mind that the state density approach is an approximation not valid for experiments with a limited number of atoms.

already did in Eq. (7.130),

$$N = \int_0^\infty w_{T,\mu}(\varepsilon)\eta(\varepsilon)d\varepsilon = \frac{V}{\lambda_{\rm th}^3} g_{3/2}(Z) \ . \tag{7.134}$$

The problem with the expression (7.134) now is, that the thermal de Broglie wavelength diverges for $T \to 0$, while the phase space density $g_{3/2}(Z)$ is bounded between $g_{3/2}(0) = 0$ and $g_{3/2}(1) \approx 2.612$, which we realize after a quick inspection of Fig. 7.9(a). Hence, according to this formula, even taking the largest possible value of the fugacity, $Z \stackrel{T\to 0}{\longrightarrow} 1$, the number of atoms in the lowest energy state tends to 0,

$$N = \frac{V}{\lambda_{\rm th}^3} g_{3/2}(Z) < \left(\frac{mk_{\rm B}T}{2\pi\hbar^2}\right)^{3/2} V g_{3/2}(1) \stackrel{T\to 0}{\longrightarrow} 0 \ . \tag{7.135}$$

This is obviously in contrast to the expectation of a large ground state population for $T \to 0$.

The reason is, that in the process of converting the sum to an integral (7.121), the density-of-states disappears as we approach the ground state, thus removing the ground state from the spectrum of energies that can be occupied. Einstein's idea to resolve the problem, was to explicitly maintain a discrete term accounting for the ground state population $N_{\rm c}$ and to add it to the expression (7.134),

$$\boxed{N = N_{\rm c} + \frac{V}{\lambda_{\rm th}^3} g_{3/2}(Z)} \ . \tag{7.136}$$

7.3.1.1 Critical temperature and condensed fraction

We can use Eq. (7.136) to calculate the critical temperature $T_{\rm c}$ for Bose-Einstein condensation. Above the phase transition, $T > T_{\rm c}$, the population is distributed over all states, each individual state being weakly populated; in particular, practically no atoms are condensed, $N_{\rm c} = 0$. The critical temperature $T_{\rm c}$ is the lowest temperature where there are still no condensed atoms.

Below the critical temperature, $T < T_{\rm c}$, the chemical potential is fixed by $\mu = 0$, and the fugacity reaches its maximum value, $Z = 1$. Above and at the critical temperature all atoms occupy excited states. Being a fixed parameter the total number of atoms N does not depend on temperature,

$$N = \frac{V}{\lambda_{\rm th}^3} g_{3/2}(Z) = \frac{V}{\lambda_{\rm c}^3} g_{3/2}(1) \qquad \text{for} \quad T \geq T_{\rm c} \ , \tag{7.137}$$

with $g_{3/2}(1) = 2.612$. The first part of Eq. (7.137) holds for $T \geq T_{\rm c}$ and provides a mean of determining Z from temperature and total atom number. The second part of Eq. (7.137) holds at $T = T_{\rm c}$. Resolving it by $T_{\rm c}$ we obtain,

$$k_{\rm B}T_{\rm c} = \frac{2\pi\hbar^2}{m}\left(\frac{N}{V g_{3/2}(1)}\right)^{2/3} \ . \tag{7.138}$$

Below the critical temperature we need to add an additional term $N_{\rm c}$. Resolving the full expression (7.136) by the fraction $N_{\rm c}/N$ of atoms condensed in the ground state

and substituting N from (7.137), we obtain,

$$\frac{N_\mathrm{c}}{N} = 1 - \frac{V}{N\lambda_\mathrm{th}^3} g_{3/2}(Z) = 1 - \frac{\lambda_\mathrm{c}^3}{\lambda_\mathrm{th}^3}\frac{g_{3/2}(Z)}{g_{3/2}(1)} = \begin{cases} 1 - \frac{\lambda_\mathrm{c}^3}{\lambda_\mathrm{th}^3} & \text{for } T \le T_\mathrm{c} \\ 0 & \text{for } T \ge T_\mathrm{c} \end{cases} \tag{7.139}$$

In summary we have,

$$\boxed{\frac{N_\mathrm{c}}{N} = 1 - \left(\frac{\min(T, T_\mathrm{c}^{(3/2)})}{T_\mathrm{c}^{(3/2)}}\right)^{3/2} \quad \text{with} \quad k_\mathrm{B} T_\mathrm{c}^{(3/2)} = \frac{2\pi\hbar^2}{m}\left(\frac{N}{V g_{3/2}(1)}\right)^{2/3}} \,. \tag{7.140}$$

The superscript (3/2) denotes the box potential shape of the trapping potential [21]. The abrupt occurrence of a finite occupation in a single quantum state at temperature below $T_\mathrm{c}^{(3/2)}$ indicates a spontaneous change in the system and a thermodynamic phase transition. Solve Exc. 7.3.4.1.

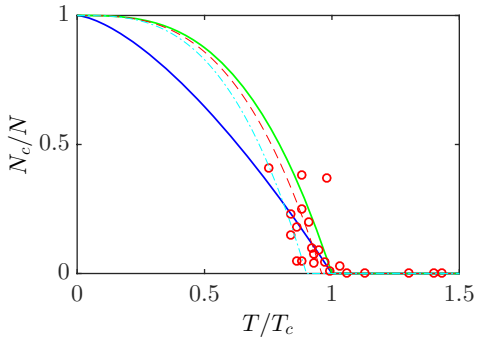

Figure 7.10: (code) Condensed fraction for an ideal Bose gas as a function of reduced temperature for a (blue) in a box potential and (green) in a harmonic trap. Red circles denote experimentally measured data points [367]. The red dashed line is a fit to the data. The cyan dash-dotted line is a theoretical curve taking into account finite size effects and interatomic interactions.

7.3.1.2 Thermodynamic potentials in a grand canonical ensemble

In order to calculate the density-of-states, state equation, mean values in the grand canonical ensemble, we start from the definitions of the partition sum Ξ_gc in Eq. (7.98) using the upper signs for bosons, the grand canonical potential Ω, the fugacity Z, the density operator $\hat{\rho}$, and the trace,

$$\Xi_\mathrm{gc} \equiv \prod_{j=1}^{\infty} (1 \mp Z e^{-\beta\varepsilon_j})^{\mp 1} \quad \text{and} \quad \Omega \equiv -k_\mathrm{B} T \ln \Xi_\mathrm{gc} \quad \text{and} \quad Z \equiv e^{\beta\mu}$$
$$\text{and} \quad \hat{\rho} \equiv \frac{e^{-\beta(\hat{H}_N - \mu\hat{N})}}{\Xi_\mathrm{gc}} \quad \text{and} \quad \mathrm{Tr}\ldots \equiv \sum_j \langle\psi_j|\ldots|\psi_j\rangle \,. \tag{7.141}$$

[21] See Exc. 7.3.4.3 for an explanation of the notation.

The parameters μ, V, T are held fixed. As we have seen, for large systems in the thermodynamic limit, the sum can be replaced by an integral, which, in turn, may be expressed by the Riemann zeta-function (see Secs. 7.2.5 and 8.1.2). The thermodynamic potentials and their expressions are summarized in the following table [22].

Table 7.1: Thermodynamic potentials for an ideal Bose gas (upper signs) or Fermi gas (lower signs) trapped in a box potential.

		$\mathrm{Tr}\,\hat{\rho}$	$\ln \Xi_{\mathrm{gc}}$	$\sum_{j=1}^{\infty}$	$\lim_{N\to\infty}$
Ω			$-\frac{1}{\beta}\ln \Xi_{\mathrm{gc}}$	$\sum_j \frac{\ln(1\mp Z e^{-\beta\varepsilon_j})}{\pm\beta}$	
μ				$\frac{1}{\beta}\ln Z$	
1		$\mathrm{Tr}\,\hat{\rho}$			
n_j	$-\left(\frac{\partial\Omega_j}{\partial\mu}\right)_{T,V}$	$w_{T,\mu}$	$-\frac{1}{\beta}\frac{\partial}{\partial\varepsilon_j}\ln \Xi_{\mathrm{gc}}$	$\frac{1}{e^{\beta\varepsilon_j}/Z\mp 1}$	
N	$-\left(\frac{\partial\Omega}{\partial\mu}\right)_{T,V}$	$\mathrm{Tr}\,\hat{N}\hat{\rho}$	$Z\frac{\partial}{\partial Z}\ln \Xi_{\mathrm{gc}}$	$\sum_j n_j$	$\frac{V}{\lambda_{\mathrm{th}}^3} g_{3/2}^{\pm} + \left\{\frac{1}{1/Z-1}\right\}$
S/k_{B}	$-\left(\frac{\partial\Omega}{k_{\mathrm{B}}\partial T}\right)_{\mu,V}$	$\mathrm{Tr}\,\hat{\rho}\ln\hat{\rho}$	$\ln \Xi_{\mathrm{gc}}$	$\pm\sum_j \ln\frac{n_j e^{\beta\varepsilon_j}}{Z}$	$\frac{5V}{2\lambda_{\mathrm{th}}^3} g_{5/2}^{\pm}$
P	$-\left(\frac{\partial\Omega}{\partial V}\right)_{T,\mu}$		$\frac{1}{\beta V}\ln \Xi_{\mathrm{gc}}$		$\frac{1}{\beta\lambda_{\mathrm{th}}^3} g_{5/2}^{\pm}$
E	$TS+\mu N+\Omega$	$\mathrm{Tr}\,\hat{H}\hat{\rho}$	$-\frac{\partial}{\partial\beta}\ln \Xi_{\mathrm{gc}}$	$\sum_j n_j\varepsilon_j$	$\frac{3k_{\mathrm{B}}TV}{2\lambda_{\mathrm{th}}^3} g_{5/2}^{\pm} \simeq \frac{3PV}{2}$
C_V	$\left(\frac{\partial E}{\partial T}\right)_{N,V}$				$\frac{15V}{4\lambda_{\mathrm{th}}^3} g_{5/2}^{\pm}$

With the particle number N we calibrate the chemical potential μ at a given temperature T via,

$$N = \frac{V}{\lambda_{\mathrm{th}}^3} g_{3/2}(Z) \Longrightarrow Z = g_{3/2}^{-1}\left(\lambda_{\mathrm{th}}^3 N/V\right) \ , \tag{7.142}$$

and knowing Z we can determine all thermodynamic potentials of the table 7.1. The internal energy with fixed volume is proportional to the pressure. Note that $\lim_{N\to\infty} S = 0$ and $\lim_{N\to\infty} C_V = 0$. Do the Exc. 7.3.4.2.

The Bose-Einstein phase transition occurs at some critical temperature T_{c}. At high temperature $T > T_{\mathrm{c}}$ the ground state population vanishes. At low temperature $T < T_{\mathrm{c}}$, we have to substitute in the above equations Z by 1. Since $g_{3/2}$ is limited for $Z = 0, .., 1$ the population balance must be equilibrated by an additional term describing the ground state population:

$$\begin{aligned} \frac{N}{V}\lambda_{\mathrm{th}}^3 &= \begin{cases} g_{3/2}^{+}(1) + \lambda_{\mathrm{th}}^3 \frac{N_{\mathrm{c}}}{V} & \text{for} \quad T \le T_{\mathrm{c}} \\ g_{3/2}^{+}(Z) & \text{for} \quad T \ge T_{\mathrm{c}} \end{cases} \\ \frac{P}{k_{\mathrm{B}}T}\lambda_{\mathrm{th}}^3 &= \begin{cases} g_{5/2}^{+}(1) & \text{for} \quad T \le T_{\mathrm{c}} \\ g_{5/2}^{+}(Z) & \text{for} \quad T \ge T_{\mathrm{c}} \end{cases} \end{aligned} \tag{7.143}$$

[22] The red terms in {} brackets only hold for bosons, because the integrals diverge otherwise.

In the thermal Bose-gas phase, $T \geq T_c$, we get from (7.143) the state equation,

$$\boxed{\frac{PV}{Nk_BT} = \frac{g^+_{5/2}(Z)}{g^+_{3/2}(Z)} \overset{T\to\infty}{\longrightarrow} 1} \,. \tag{7.144}$$

In the classical limit, obtained by noticing $g^0_\xi(Z) = Z$, follows the well-known classical ideal gas equation. In the Bose-condensate phase, $T \leq T_c$, using the definition of the critical temperature, we recover from (7.143) the *equation of state* (7.140).

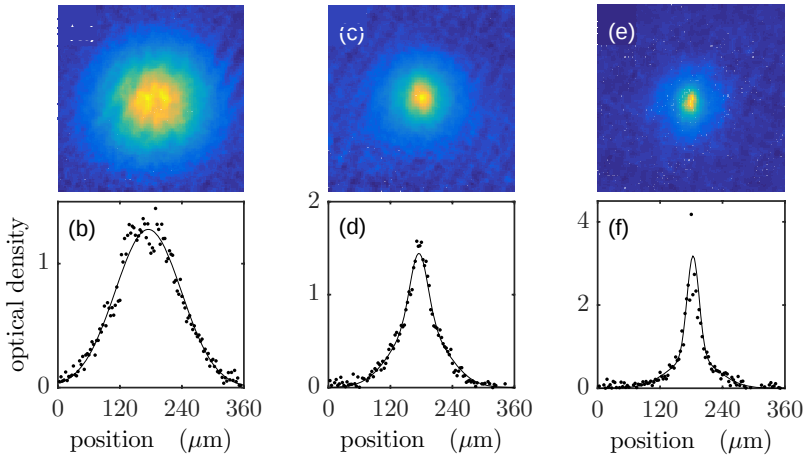

Figure 7.11: Ultracold ^{87}Rb gas at various temperatures (a,b) $T > T_c$, (c,d) $T \simeq T_c$, and (e,f) $T < T_c$ measured in experiment [367]. The figures (a,c,e) are two-dimensional false color images of the momentum distribution. The figures (b,d,f) are cuts through the images.

7.3.2 Condensation of a harmonically confined gas

The critical temperature T_c can be significantly altered, when the atoms are confined to a spatially inhomogeneous potential. The critical temperature depends on the general shape and the tightness of the potential. Let us consider N particles of an ideal Bose gas distributed over several quantum states of an arbitrary potential. The occupation number $w_{T,\mu}(\varepsilon)$ of particles at an energy level ε is still given by (7.101), the ground state energy is defined as zero. In the thermodynamic limit, the relation between the chemical potential and the total number of particles is still given by Eq. (7.142), with an adequate density-of-states $\eta(\varepsilon)$. The state density for an arbitrary confinement potential $U(\mathbf{r})$ can be found by generalizing the calculation of the free gas case. The phase space volume between the energy surfaces ε and $\varepsilon + d\varepsilon$ is proportional to the number of states in this energy range. However, the external potential limits the space available for the gas. For a harmonic potential (7.76) with the mean secular frequency $\bar{\omega}$ the density-of-states $\eta(\varepsilon)$ has already been calculated

in Eq. (7.80). With this, we can analogically to (7.142) and (7.140), calculate,

$$N = N_{\mathrm{c}} + \int_0^\infty w_{T,\mu}(\varepsilon)\eta(\varepsilon)d\varepsilon \tag{7.145}$$
$$= N_{\mathrm{c}} + \frac{1}{2(\hbar\bar{\omega})^3}\int_0^\infty \frac{\varepsilon^2 d\varepsilon}{e^{\beta(\varepsilon-\mu)}-1} = N_{\mathrm{c}} + \left(\frac{k_{\mathrm{B}}T}{\hbar\bar{\omega}}\right)^3 g_3(Z)\ .$$

In the same way as for a potential well we find for a harmonic potential,

$$N_{\mathrm{th}} = \left(\frac{k_{\mathrm{B}}T}{\hbar\bar{\omega}}\right)^3 g_3(1) = N\left(\frac{T}{T_{\mathrm{c}}^{(3)}}\right)^3\ , \tag{7.146}$$

with $g_3(1) = 1.202$. Since $N_{\mathrm{c}} + N_{\mathrm{th}} = N$, the number of particles in the ground state is,

$$\boxed{\frac{N_{\mathrm{c}}}{N} = 1 - \left(\frac{\min(T, T_{\mathrm{c}}^{(3)})}{T_{\mathrm{c}}^{(3)}}\right)^3 \qquad \text{with} \qquad k_{\mathrm{B}}T_{\mathrm{c}}^{(3)} = \hbar\bar{\omega}\left(\frac{N}{g_3(1)}\right)^{1/3}}\ . \tag{7.147}$$

The superscript (3) indicates the harmonic shape of the trap.

Fig. 7.10 traces the condensed fraction N_{c}/N measured as a function of the reduced temperature $T/T_{\mathrm{c}}^{(3)}$. Experiments [367, 267] confirm Bose's ideal gas theory in the thermodynamic limit. A particularity of inhomogeneous trapping potentials is, that the *condensed and the normal phase separate in position and in momentum space*, simply because the condensed atoms occupy only the ground state, whose spatial extend is small and where the atoms have low velocity, while thermal atoms are distributed over all energy levels. Fig. 7.11 shows a measurement of velocity distributions of a cloud of atoms close to the critical temperature.

We note that smaller trapping volumes (or tighter potentials) increase the critical temperature T_{c}, thus allowing for quantum degeneracy at higher temperatures, which can be advantageous in experimentation. Also, at a given temperature, a strongly confining potential reduces the total minimum number of atoms required to reach condensation.

7.3.2.1 Energy and heat capacity

When the number of atoms is limited, $N < \infty$, we expect a slightly reduced critical temperature [347]. In addition, the repulsive interatomic interaction reduces the critical temperature [44]. As the effects are small, they are difficult to observe in experiments. However, measurements of other thermodynamic quantities such as energy and heat capacity [214, 267] showed significant deviations from the ideal gas behavior due to interaction effects.

The *heat capacity* quantifies the system's ability to secure its energy. In conventional systems, the heat capacity is typically either specified at constant volume or at constant pressure. With this specification heat capacities are extensive state variables. When crossing a phase transition, the temperature-dependent heat capacity measures the degree of change in the system above and below the critical temperature and provides valuable information about the general type of phase transition.

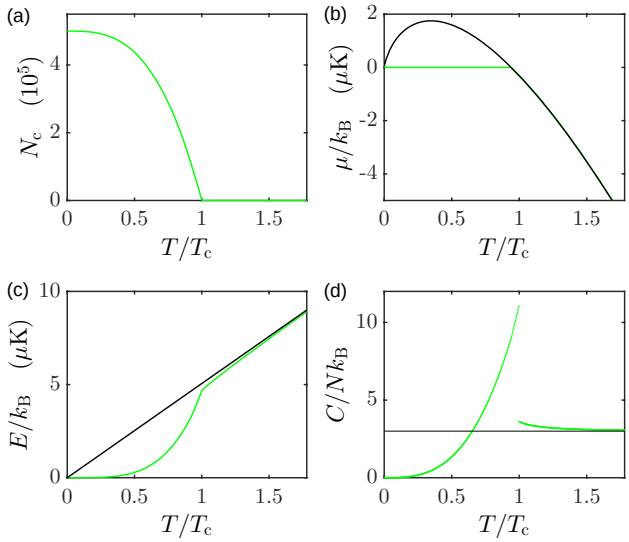

Figure 7.12: (code) Calculation of thermodynamic potentials as a function of temperature for a Bose gas (green lines) and a classical Boltzmann gas (black lines) of 500000 ^{88}Sr atoms trapped in a harmonic potential with secular frequency $\omega_{\rm ho}/2\pi = 416\,$Hz. (a) Chemical potential, (b) energy, (c) heat capacity per particle, and (d) total heat capacity. The critical temperature is $T_c = 1.7\,\mu$K.

Using (7.82) and (7.126), the total energy per particle is given by,

$$\frac{E}{N} = \frac{\int \varepsilon w_{T,\mu}(\mathbf{r},\mathbf{p}) d^3r d^3p}{\int w_{T,\mu}(\mathbf{r},\mathbf{p}) d^3r d^3p} = \frac{\int \varepsilon \eta(\varepsilon)(e^{\beta(\varepsilon-\mu)}-1)^{-1} d\varepsilon}{\int \eta(\varepsilon)(e^{\beta(\varepsilon-\mu)}-1)^{-1} d\varepsilon} = 3k_{\rm B}T \frac{g_4(Z)}{g_3(Z)} \ . \tag{7.148}$$

For a confined gas, volume and temperature are interdependent, and the concept of pressure is somewhat vague. In this case, we can not refer to the heat capacity at constant volume or pressure. However, one can define the heat capacity for a fixed number of particles,

$$C(T) = \left(\frac{\partial E(T)}{\partial T}\right)_N \ . \tag{7.149}$$

Fig. 7.12 shows the temperature dependence of some thermodynamic potentials for a harmonically trapped ultracold Bose gas. The discontinuity of the heat capacity at the critical temperature is known as *λ-point*. It interesting to note the rapid decrease of the heat capacity with temperature below T_c, which is absolutely not predicted by classical statistics. This obviously has important consequences for situations in which a Bose condensate of one species is to be used for sympathetic cooling of a gas of another species.

Calculating the second moments of the distributions obtained for the same density by time-of-flight of absorption images, we obtain the kinetic energy,

$$E_{\rm kin} = \int \frac{p^2}{2m} n(\mathbf{p}) d^3p \ . \tag{7.150}$$

For confined ideal gases, the virial theorem ensures $E_{\rm kin}+E_{\rm pot} = 2E_{\rm kin}$. For real gases, the repulsive energy of the mean field adds to this energy, $E = E_{\rm kin} + E_{\rm pot} + E_{\rm self}$. The sudden extinction of the trapping potential before time-of-flight takes away the potential energy $E_{\rm pot}$ non-adiabatically. The kinetic energy and the self-energy of the condensate are fully converted into kinetic energy during ballistic expansion. It is this energy, $p^2/2m = E_{\rm kin} + E_{\rm self}$, which is sometimes called *release energy*, which is measured after ballistic expansion [23]. Fig. 7.13(right) shows a measurement of the release energy. Solve the Exc. 7.3.4.3.

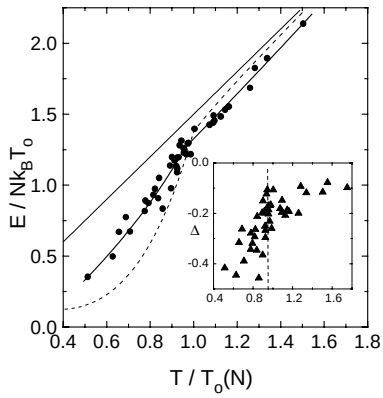

Figure 7.13: Measurement of the release energy [267].

7.3.2.2 Micro- and grand canonical Bose-condensates

The decision which thermodynamic ensemble to use for a theoretical model depends on the experimental situation. The question is particularly interesting in the context of Bose-Einstein condensation: Here it is related to the question which state better describes a BEC: A Fock state characterized by a fixed atom number or a Glauber state, where the atom number is fluctuating.

The condensates experimentally produced in alkali gases consist of relatively small atom numbers between 1000 to 10^7, so that the validity of the thermodynamic approximation and the use of the density-of-states approach has been questioned [347]. Also, the decision whether to use the grand canonical, the canonical or the microcanonical ensemble for calculating the thermodynamic quantities noticeably influences the results. Herzog and Olshanii [391] have shown that for small atom numbers on the order of 100 the canonical and grand canonical statistics lead to predictions on the condensed fraction that differ by up to 10% (see Fig. 7.10). On the other hand, they give the same results if the particle numbers are large. Which canonical statistics is more appropriate is not a trivial question and depends on the experimental setup and in particular on the time scale of the measurements. If we look at the sample

[23] It is interesting to measure the heat capacity of a partially condensed cloud near the critical point and analyze the discontinuity, because it contains important information about interatomic interactions and finite-size effects ([175], Sec. 3.4). In addition, the classification of Bose-Einstein condensation as a phase transition depends very much on the behavior of the thermodynamic potential near the critical point [499, 410].

for short times, the number of condensed atoms will be fixed, and we can assume a canonical ensemble. For longer times, however, the atom number may be an equilibrium parameter depending on the contact of the sample with a reservoir, and the grand canonical statistics is better suited.

7.3.3 Density and momentum distribution for a Bose gas

Bose-Einstein condensates consist of atoms sharing a single quantum state. In inhomogeneous potentials, the condensate and the thermal fraction form spatially separated clouds, concentrated around the center of the potential and therefore very dense. For this reason, interatomic interaction effects generally dominate the density and momentum distribution of the condensed fraction. However, the non-condensed (or normal, or thermal) fraction is also subject to modifications due to the bosonic nature of the atoms. Since the density of the normal fraction is generally much smaller, these modifications are weak. In this section, we will only discuss these effects briefly, but we note that the calculations are analogous to the calculations for fermionic gases presented in Sec. 7.4.4.

For an ideal Bose gas the density and momentum distributions are expressed by Bose functions $g_{3/2}(Z)$ [175]. For example, as will be derived in Exc. 7.3.4.4, the density and momentum distributions are,

$$\boxed{\begin{aligned} n(\mathbf{x}) &= \frac{1}{\lambda_{\rm th}^3}\, g_{3/2}(e^{-\beta[U(\mathbf{x})-\mu]}) \\ n(\mathbf{k}) &= \frac{a_{\rm ho}^6}{\lambda_{\rm th}^3}\, g_{3/2}(e^{\beta(\mu-\mathbf{p}^2/2m)}) \end{aligned}} \quad \text{(bosonic distribution functions)} \tag{7.151}$$

In the classical limit, we can calibrate the chemical potential by Eq. (7.142) for a box potential or by (7.145) for a harmonic potential,

$$g_{3/2}(e^{\beta\mu}) \to c_{3/2}(e^{\beta\mu}) = e^{\beta\mu} = \begin{cases} \frac{N}{V}\lambda_{\rm th}^3 & \text{(for a box potential)} \\ c_3(e^{\beta\mu}) = N\left(\frac{\hbar\bar{\omega}}{k_{\rm B}T}\right)^3 & \text{(for a harmonic potential)} \end{cases} \tag{7.152}$$

Hence, we obtain for the classical density distribution,

$$\begin{aligned} n(\mathbf{x}) &= \frac{1}{\lambda_{\rm th}^3} c_{3/2}(e^{-\beta[U(\mathbf{x})-\mu]}) = \frac{e^{\beta\mu}}{\lambda_{\rm th}^3} e^{-\beta U(\mathbf{x})} \\ &= \begin{cases} \frac{N}{V}\big|_{\mathbf{x}\in V} & \text{(for a box potential)} \\ N\sqrt{\frac{m\bar{\omega}^2}{2\pi k_{\rm B}T}}^3 e^{-\beta m\bar{\omega}^2 x^2/2} & \text{(for a harmonic potential)} \end{cases} \end{aligned} \tag{7.153}$$

Similarly, the momentum density distribution is given by,

$$\begin{aligned} n(\mathbf{k}) &= \frac{a_{\rm ho}^6}{\lambda_{\rm th}^3} c_{3/2}(e^{\beta(\mu-p^2/2m)}) = \frac{a_{\rm ho}^6 e^{\beta\mu}}{\lambda_{\rm th}^3} e^{-\beta p^2/2m} \\ &= \begin{cases} \frac{N}{V} a_{\rm ho}^6\big|_{\mathbf{x}\in V}\, e^{-\beta p^2/2m} & \text{(for a box potential)} \\ N\hbar^3\sqrt{\frac{1}{2\pi m k_{\rm B}T}}^3 e^{-\beta p^2/2m} & \text{(for a harmonic potential)} \end{cases} \end{aligned} \tag{7.154}$$

where we used the spatial extend of the ground state of the harmonic oscillator $a_{\rm ho} = \sqrt{\hbar/m\omega}$. We see that we recover the Maxwell-Boltzmann velocity distribution, as seen in Fig. 7.14,

$$n(\mathbf{v}) = n(\mathbf{k})\frac{m^3}{\hbar^3} = N\sqrt{\frac{m}{2\pi k_{\rm B}T}}^3 e^{-\beta m v^2/2} \ . \tag{7.155}$$

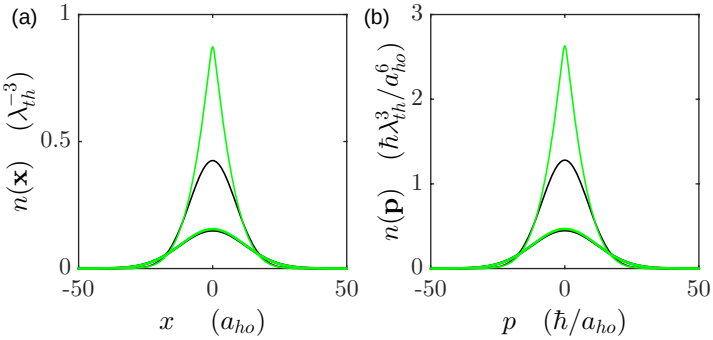

Figure 7.14: (code) (a) Density and (b) momentum distribution of a Bose gas (red) and a Boltzmann gas (green) at $T = 1.1T_{\rm c}$ (solid line) and at $T = 2T_{\rm c}$ (dotted line).

7.3.3.1 Ballistic expansion

To describe the density distribution of an ultracold Bose-gas after a time-of-flight we replace in the second Eq. (7.151): $\mathbf{k} = m\mathbf{r}/\hbar t_{\rm ToF}$. We obtain the density distribution,

$$\begin{aligned} n_{\rm ToF}(\mathbf{r}, t_{\rm ToF}) &= \left(\frac{m}{\hbar t_{\rm ToF}}\right)^3 n(\mathbf{k} = m\mathbf{r}/\hbar t_{\rm ToF}) = \left(\frac{m}{\hbar t_{\rm ToF}}\right)^3 \frac{a_{\rm ho}^6}{\lambda_{\rm th}^3} g_{3/2}(e^{(\mu - mr^2/2t_{\rm ToF}^2)/k_{\rm B}T}) \\ &\overset{T\to\infty}{\longrightarrow} \left(\frac{m}{\hbar t_{\rm ToF}}\right)^3 N\hbar^3\sqrt{\frac{1}{2\pi m k_{\rm B}T}}^3 e^{-mr^2/2t_{\rm ToF}^2 k_{\rm B}T} = \frac{N}{(2\pi)^{3/2} r_{\rm rms}^3} e^{-r^2/2r_{\rm rms}^2} \ , \end{aligned} \tag{7.156}$$

where we defined,

$$r_{\rm rms} \equiv \sqrt{\frac{k_{\rm B}T}{m}} t_{\rm ToF} \ . \tag{7.157}$$

This distribution does not directly depend on the potential $U(\mathbf{r})$, that is, the expansion is isotropic. In Exc. 7.3.4.4(b) we determine the time-of-flight density distribution of an ultracold Bose gas. For very long flight times (usually several 10 ms) the density resembles a Gaussian distribution [175]. Note however, that in interacting non-ideal gases the chemical potential does depend on the potential.

In a time-of-flight experiment, any deviation observed between the results (7.156) and (7.157) points towards an impact of quantum statistics. However, absorption images only record column densities, i.e. projections of the time-of-flight distribution on a plane, which tends to smear out the non-Gaussian features.

7.3.3.2 Adiabatic compression

Adiabaticity of a process means reversibility, while the atom number is unchanged $N = const$ and, hence, constant entropy $S = const$. According to Eq. (7.7) this implies an unchanged population distribution $n_j = const$ and, consequently, energy distribution $\beta\varepsilon_j/T = const$. Therefore we get $\beta\mu, \beta E = const$, and the phase space density keeps unchanged, e.g. for a box potential $\frac{N}{V}\lambda_{\rm th}^3 = const$. The process of adiabatically compressing a harmonic trap therefore changes the temperature like $T' = T\omega'/\omega$. This is valid above and below the transition point.

Example 51 (*Heat capacity measurement*): For an ideal Bose gas trapped in a harmonic potential the temperature dependence of the heat capacity at the threshold to condensation can easily be obtained as follows. The condensed fraction determines the chemical potential through,

$$N = N_0 + \left(\frac{k_{\rm B}T}{\hbar\omega}\right)^3 g_3(Z) \ , \tag{7.158}$$

where $Z(T) = e^{\mu/k_{\rm B}T}$ for a grand canonical ensemble. The condensed fraction vanishes above the critical temperature, the chemical potential vanishes below the critical temperature. $(k_{\rm B}T/\hbar\omega)^3 = 2\pi(a_{\rm ho}/\lambda_{\rm th})^3$ denotes the normalized volume of a phase space cell. Knowing $Z(T)$ from equation (7.158), we can calculate the total energy, the heat capacity and all the other thermodynamic potentials:

$$C_N = 12k_{\rm B}\left(\frac{k_{\rm B}T}{\hbar\omega}\right)^3 g_4(Z) - 9k_{\rm B}N\frac{g_3(Z)}{g_2(Z)} \ . \tag{7.159}$$

For an interacting Bose-gas we expect that the Eqs. (7.158) and (7.159) are not scrupulously obeyed. Indeed, the abrupt discontinuous change in the heat capacity at the phase transition to BEC, expected for ideal gases, is smeared out by atomic collisions [44].

For measuring the heat capacity of a gas we measure its temperature before and after a controlled experimental cycle including an adiabatic and a sudden variation, which transfers a quantifiable amount of energy to the system, as illustrated in Fig. 7.15. The measured heat capacity can then be compared to the theoretical model given by Eq. (7.159).

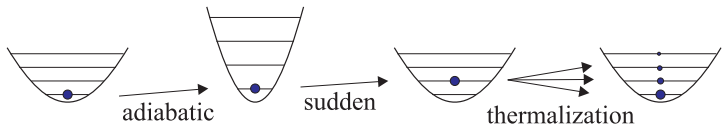

Figure 7.15: Population variation during a slow adiabatic compression followed by a sudden non-adiabatic decompression.

7.3.4 Exercises

7.3.4.1 Ex: Monoatomic gas as a canonical ensemble

Consider a classical monoatomic gas made up of N non-interacting atoms of mass m confined in a container of volume V, at temperature T. The Hamiltonian correspond-

ing to an atom is given by $\hat{H} = (\hat{p}_x^2 + \hat{p}_y^2 + \hat{p}_z^2)/2m$.
a. Show that the atomic canonical partition function is $\xi = V/\lambda_{\rm th}^3$, where $\lambda_{\rm th}$ is the thermal de Broglie wavelength defined in Eq. (7.123).
b. Using ξ of the previous item, obtain the system's partition function $\Xi_{\rm cn}$ and the Helmholtz free energy F. Also obtain the free energy per atom $f = F/N$ in the thermodynamic limit $N \longrightarrow \infty$, $V \longrightarrow \infty$, such that $v = N/V$ fixed.
c. Obtain internal energy E and the gas pressure p.
d. Calculate the chemical potential and entropy per atom in the thermodynamic limit, thus deriving the so-called *Sackur-Tetrode formula*.

7.3.4.2 Ex: Thermodynamic quantities for a Bose gas trapped in a box

Derive all expressions for the entropy and the pressure of Tab. 7.1.

7.3.4.3 Ex: Generalization for arbitrary potentials in reduced dimensions

The calculation of the thermodynamic potentials can be generalized to arbitrary trapping potentials and dimensions [107, 259, 205, 45, 890, 285, 46, 347, 391, 465, 458, 617, 499, 528, 267]. To do so, we consider a generic power law potential confining an ideal Bose gas in α dimensions,

$$U(\mathbf{r}) = \sum\nolimits_{i=1}^{\alpha} \left|\frac{x_i}{a_i}\right|^{t_i} ,$$

and define a parameter describing the confinement power of the potential,

$$\xi = \frac{\alpha}{2} + \sum\nolimits_{i=1}^{\alpha} \frac{1}{t_i} .$$

For example, for a three-dimensional potential, $\alpha = 3$. Now, for a 3D harmonic potential, $\xi = 3$, and for 3D box potential, $\xi = 3/2$.
a. Calculate the density-of-states η using the equation (7.72) employing Bose functions (7.126).
b. Prove the following expressions:

(bosonic potentials)

$$\begin{aligned}
\frac{N_{\rm c}}{N} &= 1 - \left(\frac{\min(T,T_{\rm c})}{T_{\rm c}}\right)^{\xi} \\
\frac{E}{Nk_{\rm B}T} &= \xi \frac{g_{\xi+1}(Z)}{g_{\xi}(Z)} \left(\frac{\min(T,T_{\rm c})}{T_{\rm c}}\right)^{\xi} \\
\frac{S}{Nk_{\rm B}} &= \xi \frac{g_{\xi+1}(Z)}{g_{\xi}(Z)} - \beta\mu \\
\frac{C}{Nk_{\rm B}} &= \xi(\xi+1)\frac{g_{\xi+1}(Z)}{g_{\xi}(Z)} \left(\frac{\min(T,T_{\rm c})}{T_{\rm c}}\right)^{\xi} - \xi^2 \frac{g_{\xi}(Z)}{g_{\eta-1}(Z)} \frac{\max(T-T_{\rm c},0)}{T-T_{\rm c}} \\
\frac{C_{T>T_{\rm c}}}{Nk_{\rm B}} &= \xi(\xi+1)\frac{g_{\xi+1}(Z)}{g_{\xi}(Z)} - \xi^2 \frac{g_{\xi}(Z)}{g_{\xi-1}(Z)} \quad , \quad \frac{C_{T<T_{\rm c}}}{Nk_{\rm B}} = \xi(\eta+1)\frac{g_{\xi+1}(1)}{g_{\xi}(1)} \\
\frac{\Delta C_{T_{\rm c}}}{Nk_{\rm B}} &= \frac{C_{T_{\rm c}^-} - C_{T_{\rm c}^+}}{Nk_{\rm B}} = \xi^2 \frac{g_{\xi}(1)}{g_{\xi-1}(1)}
\end{aligned} .$$

7.3.4.4 Ex: Time-of-flight distribution of a Bose-gas

a. Derive the formulae (7.151) describing the density and momentum distribution of an ultracold Bose-gas.
b. Calculate the time-of-flight distribution of a Bose-gas as a function of temperature (i) analytically for a harmonic potential and (ii) numerically for an arbitrary potential.

7.4 Quantum degeneracy of an ideal Fermi gas

Atoms are fermions or bosons, depending on whether their spin is integer or semi-integer. For example, ^{87}Rb atoms with their total integer spin of F are bosons, while ^{40}K atoms having a half-integer spin are fermions. At high phase space densities, atoms have to figure out how they will organize their coexistence. Bosons encourage each other to occupy the same phase space cell, in contrast to the reluctant fermions, which prefer to follow Pauli's exclusion principle. The different behavior is described by different quantum statistics that determine how the phase space (i.e., the available energy levels) has to be filled by the atoms. The Bose-Einstein distribution is valid for bosons, the distribution of Fermi-Dirac for fermions and both asymptotically approach the Boltzmann distribution at high temperatures. We have seen that bosons undergo a phase transition and condense in the ground state when the temperature is reduced below a critical threshold. On the other hand, the fermions organize their phase space, so that their energy levels are arranged like a ladder. The impact of fermionic quantum statistics on a cold cloud of atoms were observed experimentally by DeMarco and Jin [214, 628]. They cooled a two-components Fermi gas of 7×10^5 potassium atoms down to 300 nK, which corresponded to 60% of the atoms populating energy levels below the Fermi energy. The measured density distribution was found to deviate from the one expected for an ideal Boltzmann gas [24].

7.4.1 Chemical potential and Fermi radius for a harmonic trap

The phase space density for a *degenerate Fermi gas* in the thermodynamic limit has been derived in (7.127). We consider a cylindrically symmetric harmonic potential, as defined in (7.75), for which the density-of-states $\eta(\varepsilon)$ has been calculated in (7.80). In the same way as for a Bose gas, the chemical potential of the Fermi gas must satisfy the normalization condition,

$$N = \int w_{T,\mu}(\varepsilon)\eta(\varepsilon)d\varepsilon = \frac{1}{2(\hbar\bar{\omega})^3}\int_0^\infty \frac{\varepsilon^2 d\varepsilon}{e^{\beta(\varepsilon-\mu)}+1} = \left(\frac{k_{\rm B}T}{\hbar\bar{\omega}}\right)^3 f_3(Z)\ . \qquad (7.160)$$

For low temperatures, $\beta\mu \gg 1$, we can use the Sommerfeld expansion of the Fermi function, which in first order gives $f_\xi(e^x) \simeq x^\xi/\Gamma(\xi+1)$, where x is a placeholder for $\beta\mu$, Γ is the Γ-function, and $\xi = 3$ for a harmonic potential. From this we immediately obtain the chemical potential at zero temperature defined as the *Fermi energy*,

$$\boxed{E_{\rm F} \equiv \mu(T=0) = \hbar\bar{\omega}(6N)^{1/3}}\ , \qquad (7.161)$$

[24] We note that meanwhile ultracold two-components Fermi gas have been demonstrated to form bosonic Cooper-pairs, similarly to the phenomena known as superconductivity in some metals and as superfluidity of the fermionic ^{3}He.

and from that the momentum of free particles and the Fermi radius,

$$K_{\rm F} \equiv \sqrt{\frac{2mE_{\rm F}}{\hbar^2}} \quad \text{and} \quad r_{\rm F} \equiv \sqrt{\frac{2E_{\rm F}}{m\omega_r^2}} \quad , \quad z_{\rm F} = \sqrt{\frac{2E_{\rm F}}{m\omega_z^2}} \ . \tag{7.162}$$

At low but non-zero temperatures, $\varepsilon - \mu \ll k_{\rm B}T$, we use the second order of the Sommerfeld expansion,

$$f_\xi(e^x) \simeq \frac{x^\xi}{\Gamma(\xi+1)}\left(1 + \frac{\pi^2\xi(\xi-1)}{6x^2} + ...\right) \ , \tag{7.163}$$

and obtain for the chemical potential the equation, $0 = \mu^3 + (\pi k_{\rm B}T)^2\mu - E_{\rm F}^3$. The approximate solution of this equation, neglecting higher-order terms such as $4\pi^6 k_{\rm B}^6 T^6 \ll 27E_{\rm F}^6$, is

$$\mu = E_{\rm F}\left[1 - \frac{\pi^2}{3}\left(\frac{k_{\rm B}T}{E_{\rm F}}\right)^2\right] \ . \tag{7.164}$$

For highly excited atoms, $\varepsilon - \mu \gg k_{\rm B}T$, the Fermi function approaches the identity, $f_\xi(Z) \overset{Z\to 0}{\longrightarrow} Z$ (see Fig. 7.9), so that,

$$N = \left(\frac{k_{\rm B}T}{\hbar\bar{\omega}}\right)^3 e^{\beta\mu} = \left(\frac{k_{\rm B}T}{\hbar\bar{\omega}}\right)^3 (1 + \beta\mu + ...) \ , \tag{7.165}$$

$$\mu = k_{\rm B}T \ln Z \simeq k_{\rm B}T \ln N\left[\left(\frac{\hbar\bar{\omega}}{k_{\rm B}T}\right)^3\right] = k_{\rm B}T \ln\frac{1}{6}\left(\frac{E_{\rm F}}{k_{\rm B}T}\right)^3 \ ,$$

where in the last step we substituted the definition of the Fermi energy. This means that highly excited fermions behave like a *Boltzmann gas*, which satisfies an ideal gas equation similar to that of classical particles in a box potential,

$$N = \left(\frac{k_{\rm B}T}{\hbar\bar{\omega}}\right)^3 \ . \qquad \text{(Boltzmann)} \ . \tag{7.166}$$

Fig. 7.16(a) shows calculations of the chemical potential for an ideal Fermi gas along with the chemical potentials of a Boltzmann gas and a Bose gas.

7.4.2 Energy

Using (7.82), the total energy per particle, $E/N \equiv N^{-1}\int \varepsilon w_{T\mu} d^3x d^3k$, is given by,

$$\frac{E}{N} = \frac{\int \varepsilon w_{T,\mu}(\mathbf{x},\mathbf{k}) d^3x d^3k}{\int w_{T,\mu}(\mathbf{x},\mathbf{k}) d^3x d^3k} = \frac{\int \varepsilon\eta(\varepsilon)\left(e^{\beta(\varepsilon-\mu)}+1\right)^{-1} d\varepsilon}{\int \eta(\varepsilon)\left(e^{\beta(\varepsilon-\mu)}+1\right)^{-1} d\varepsilon} = 3k_{\rm B}T\frac{f_4(Z)}{f_3(Z)} \ , \tag{7.167}$$

in analogy to the expression (7.148) holding for a Bose gas. Again using the Sommerfeld approximation, we see that for low temperatures, $T \to 0$, the energy is limited by [see Fig. 7.16(b)],

$$E = \frac{3}{\beta(\beta\hbar\bar{\omega})^3} f_4(e^{\beta\mu}) = \frac{3\mu^4}{4E_{\rm F}^3}\left(1 + \frac{2\pi^2}{(\beta\mu)^2} + ...\right) \overset{T\to 0}{\longrightarrow} \frac{3}{4}E_{\rm F} \ . \qquad \text{(Fermi)} \tag{7.168}$$

Hence, the total energy per fermion does not vanish for $T \to 0$. The reason is that the atoms are forced to adopt states in the outermost regions of the harmonic trap.

For comparison, in the limit of high temperatures, $T \to \infty$, a classical gas has the energy per particle,

$$E = \frac{3}{\beta(\beta\hbar\bar{\omega})^3} f_4\left(f_3^{-1}\left(\tfrac{(\beta E_{\rm F})^3}{6}\right)\right) \simeq 3Nk_{\rm B}T \ . \qquad \text{(Boltzmann)} \qquad (7.169)$$

which is seen by taking the high temperature limit $f_\eta(Z) \overset{Z\to 0}{\longrightarrow} Z$ and extrapolating to all Z. This implies, $E_1/E_{\rm F} \overset{T\to\infty}{\longrightarrow} 3k_{\rm B}T/E_{\rm F}$.

And for bosons we have,

$$E = 3Nk_{\rm B}T\frac{g_4(Z)}{g_3(Z)}\left(\frac{\min(T,T_{\rm c})}{T_{\rm c}}\right)^3 \simeq 2.7Nk_{\rm B}T\left(\frac{T}{T_{\rm c}}\right)^3 \ . \qquad \text{(Bose)} \qquad (7.170)$$

Hence, the total energy per boson decreases very rapidly for $T \to 0$. The reason is that the atoms are bosonically encouraged to pile up in the inner region of the harmonic trap.

7.4.3 Entropy and heat capacity

The entropy per particle $S_1 = -\left(\frac{\partial\Omega}{\partial T}\right)_\mu$ can be calculated analogously to the Bose gas (see for example Excs. 7.3.4.2 and 7.3.4.3),

$$S_1 = 4k_{\rm B}\frac{f_4(Z)}{f_3(Z)} - \frac{\mu}{T} = \frac{4E_1}{3T} - \frac{\mu}{T} \ . \qquad (7.171)$$

The heat capacity per particle $C_1 = \left(\frac{\partial E_1}{\partial T}\right)_N$ is easily calculated using $Zf'_\eta(Z) = f_{\eta-1}(Z)$,

$$C_1 = 3k_{\rm B}\frac{f_4(Z)}{f_3(Z)} - \frac{3\mu}{T}\left(1 - \frac{f_4(Z)f_2(Z)}{f_3(Z)^2}\right) = \frac{E_1}{T} - \frac{3\mu}{T}\left(1 - \frac{f_4(Z)f_2(Z)}{f_3(Z)^2}\right) \ . \qquad (7.172)$$

For fermions well below the Fermi temperature, $T \to 0$, using the Sommerfeld approximation, we calculate,

$$C_1 \overset{T\to 0}{\longrightarrow} \frac{3\pi^2}{2}\frac{k_{\rm B}T}{T_{\rm F}} \ . \qquad \text{(Fermi)} \qquad (7.173)$$

For high temperature T

$$C_1 \approx 3k_{\rm B} \ . \qquad \text{(Boltzmann)} \qquad (7.174)$$

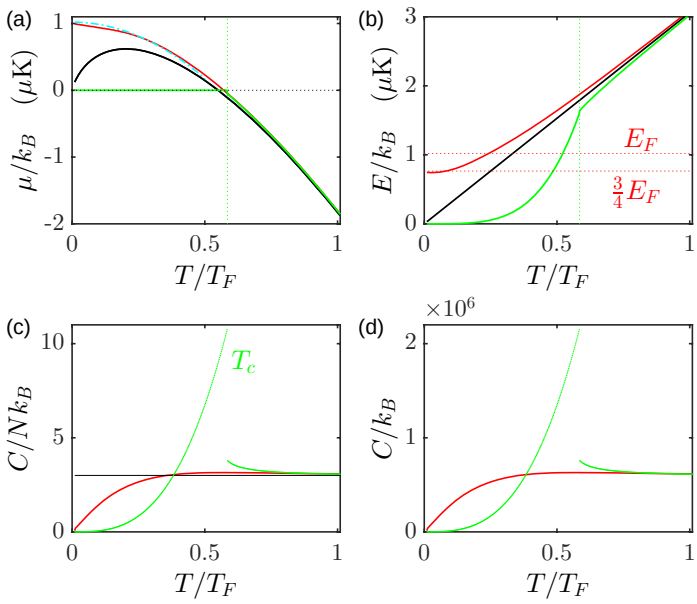

Figure 7.16: (code) Calculation of thermodynamic potentials for Bose (red), Fermi (green), and Boltzmann gases as a function of temperature for a given harmonic trapping potential. The gases are assumed to have same mass, same atom number $N = 200000$, and same trap frequencies $\omega_{\rm ho}/2\pi = 200\,{\rm Hz}$. (a) Chemical potential, (b) energy, (c) heat capacity per particle, and (d) total heat capacity. The dotted magenta line in (a) shows the chemical potential calculated from the Sommerfeld approximation.

7.4.4 Density and momentum distribution for a Fermi gas

7.4.4.1 Spatial distribution

The density distribution is,

$$n(\mathbf{x}) = \int w_{T,\mu}(\mathbf{x},\mathbf{k}) d^3k = \frac{1}{(2\pi)^2}\int \frac{2k^2 dk}{e^{\beta[\hbar^2k^2/2m + U(\mathbf{x}) - \mu]}+1} \tag{7.175}$$
$$= \frac{1}{(2\pi)^2}\left(\frac{2m}{\hbar^2}\right)^{3/2}\int \frac{\sqrt{\varepsilon}d\varepsilon}{e^{\beta[\varepsilon+U(\mathbf{x})-\mu]}+1} = \frac{1}{(2\pi)^2}\left(\frac{2m}{\beta\hbar^2}\right)^{3/2}\Gamma(3/2) f_{3/2}(e^{-\beta[U(\mathbf{x})-\mu]}) \ ,$$

such that,

$$\boxed{n(\mathbf{x}) = \lambda_{\rm th}^{-3} f_{3/2}(e^{-\beta[U(\mathbf{x})-\mu]})} \quad \text{(Fermi)} \ . \tag{7.176}$$

where $\lambda_{\rm th} = \sqrt{2\pi\hbar^2/mk_{\rm B}T}$.

At low temperatures, $T \to 0$, we can apply the Sommerfeld expansion [130], which

to first order gives $\mu \to E_{\rm F}$,

$$n(\mathbf{x}) \approx \frac{1}{(2\pi)^2}\frac{\Gamma(3/2)}{\Gamma(5/2)}\left(\frac{2m}{\hbar^2}\left[\mu - U(\mathbf{x})\right]\right)^{3/2} \tag{7.177}$$
$$= \frac{1}{(2\pi)^2}\frac{2}{3}\left(\frac{2m}{\hbar^2}\right)^{3/2}\left(E_{\rm F} - \frac{m}{2}\omega_r^2\rho^2\right)^{3/2} = \frac{8\lambda}{\pi^2}\frac{N}{R_{\rm F}^3}\left(1 - \frac{\rho^2}{R_{\rm F}^2}\right)^{3/2} .$$

At high temperatures, $T \to \infty$, we should recover the Boltzmann gas situation,

$$n(\mathbf{x}) = \lambda_{\rm th}^{-3} f_{3/2}(e^{-\beta[U(\mathbf{x})-\mu]}) \tag{7.178}$$
$$\approx \lambda_{\rm th}^{-3} N\left(\beta\hbar\bar{\omega}\right)^3 e^{-\beta U(\mathbf{x})} = \left(\frac{m\beta\bar{\omega}^2}{2\pi}\right)^{3/2} N e^{-\beta m(\omega_x^2 x^2 + \omega_y^2 y^2 + \omega_z^2 z^2)/2} .$$

It is easy to check that $\int n(\mathbf{x}) d^3\mathbf{x} = N$. Introducing the peak density n_0, we obtain,

$$\boxed{n(\mathbf{x}) = n_0 e^{-m\omega^2\rho^2/2k_{\rm B}T}} \quad \text{(Boltzmann)} . \tag{7.179}$$

The *rms*-radius of the distribution is $\sigma_j = \sqrt{k_{\rm B}T/m\omega_j^2}$, which seems contrary to the above results, $\frac{m}{2}\omega_j^2\left\langle x_j^2\right\rangle = k_{\rm B}T$.

7.4.4.2 Momentum distribution

The momentum distribution is,

$$\tilde{n}(\mathbf{k}) = \int w_{T,\mu}(\mathbf{x},\mathbf{k}) d^3x = \frac{1}{(2\pi)^2}\int \frac{rdrdz}{e^{\beta[\varepsilon(k)+m\omega_r^2\rho^2/2-\mu]}+1} \tag{7.180}$$
$$= \frac{1}{(2\pi)^3}\int \frac{4\pi\rho^2 d\rho}{e^{\beta[\varepsilon+m\omega_r^2\rho^2/2-\mu]}+1}$$
$$= \frac{1}{(2\pi)^2}\left(\frac{2}{\beta m\omega_r^2}\right)^{3/2}\int \frac{\sqrt{t}dt}{e^{\beta[\varepsilon+t-\mu]}+1} = \frac{1}{(2\pi)^2}\left(\frac{2}{\beta m\omega_r^2}\right)^{3/2}\Gamma(3/2) f_{3/2}(e^{\beta(\mu-\varepsilon)}) ,$$

such that,

$$\boxed{\tilde{n}(\mathbf{k}) = \lambda_{\rm th}^{-3} a_{\rm ho}^6 f_{3/2}(e^{\beta(\mu-\varepsilon)})} \quad \text{(Fermi)} . \tag{7.181}$$

where $a_{\rm ho} = \sqrt{\hbar/m\bar{\omega}}$.

At low temperatures, $T \to 0$,

$$\tilde{n}(\mathbf{k}) \approx \frac{1}{(2\pi)^2}\left(\frac{2}{\beta m\omega_r^2}\right)^{3/2}\frac{\Gamma(3/2)}{\Gamma(5/2)}(\beta\left[\mu-\varepsilon\right])^{3/2} \tag{7.182}$$
$$\approx \frac{1}{(2\pi)^2}\left(\frac{2}{m\omega_r^2}\right)^{3/2}\frac{2}{3}\left(E_{\rm F} - \frac{\hbar^2k^2}{2m}\right)^{3/2} = \frac{8}{\pi^2}\frac{N}{K_{\rm F}^3}\left(1 - \frac{k^2}{K_{\rm F}^2}\right)^{3/2} .$$

Do the Exc. 7.4.8.1.

At high temperatures, $T \to \infty$, we should recover the Boltzmann gas situation,

$$\boxed{\tilde{n}(\mathbf{k}) \approx \left(\frac{\hbar^2\bar{\omega}^2}{2\pi m\omega_r^2}\right)^{3/2} N e^{-\beta\varepsilon}} \quad \text{(Boltzmann)} . \tag{7.183}$$

Since ε is the kinetic energy, the *rms*-radius $\sqrt{k^2}$ of this distribution is $\beta\hbar^2\langle k^2\rangle = m$.

7.4.4.3 Time-of-flight distribution

To describe time-of-flight images we substitute $\mathbf{k} = m\mathbf{r}/\hbar t$. We obtain the density distribution from a convolution,

$$\begin{aligned} n_{\rm ToF}(\mathbf{x},t) &= \frac{1}{(2\pi)^3}\int d^3x_0 d^3k \frac{\delta^3(\mathbf{x}-\mathbf{x}_0-\mathbf{p}t/m)}{e^{\beta(\varepsilon(\mathbf{x}_0,\mathbf{p})-\mu)}+1} \qquad (7.184)\\ &= \frac{1}{(2\pi)^3}\int \frac{d^3k}{e^{\beta(\varepsilon(\mathbf{x}+\mathbf{p}t/m,\mathbf{p})-\mu)}+1} \\ &= \frac{1}{(2\pi)^3}\int \frac{dk_x dk_y dk_z}{e^{\beta\Sigma_j\left[\hbar^2k_j^2/2m+\frac{1}{2}m\omega_j^2(x_j+\hbar k_j t/m)^2\right]}/Z+1} \quad \text{where} \quad j=x,y,z\ldots \end{aligned}$$

We rewrite the exponent,

$$\begin{aligned} \hbar^2k_j^2/2m + \tfrac{1}{2}m\omega_j^2\left(x_j+\hbar k_j t/m\right)^2 &= \hbar^2k_j^2/2m(1+\omega_j^2t^2) + \omega_j^2 t x_j \hbar k_j + \tfrac{1}{2}m\omega_j^2x_j^2 \\ &= \left(\sqrt{\frac{\hbar^2k_j^2}{2m}(1+\omega_j^2t^2)} + \frac{\omega_j^2 t x_j\sqrt{2m}}{2\sqrt{1+\omega_j^2t^2}}\right)^2 + \frac{m\omega_j^2x_j^2}{2(1+\omega_j^2t^2)} \\ &= \xi_j + \frac{m}{2}\breve{\omega}_j^2x_j^2\ . \qquad (7.185) \end{aligned}$$

where we defined $\breve{\omega}_i \equiv \omega_i(1+\omega_i^2t^2)^{-1/2}$. With the substitution $d\xi_j = dk_j\sqrt{\frac{2\hbar^2}{m}\xi_j\left(1+\omega_j^2t^2\right)}$ we obtain

$$\begin{aligned} n_{\rm ToF}(\mathbf{x},t) &= \frac{1}{(2\pi)^3}\left(\frac{mk_{\rm B}T}{2\hbar^2}\right)^{3/2}\frac{1}{\prod_i\left(1+\omega_i^2t^2\right)}\int \frac{\beta^{3/2}\left(\xi_x\xi_y\xi_z\right)^{-1/2}d\xi_x d\xi_y d\xi_z}{e^{\beta\Sigma_j\left[\xi_j+\frac{m}{2}\breve{\omega}_j^2x_j^2\right]}/Z+1} \\ &= \frac{1}{2^3\pi^{3/2}}\frac{1}{\lambda_{\rm th}^3}\frac{\tilde{\omega}^3}{\bar{\omega}^3}\int \frac{\beta^{3/2}\xi^{-3/2}4\pi\xi^2 d\xi}{e^{\beta\Sigma_j\left[\xi+\frac{m}{2}\breve{\omega}_j^2x_j^2\right]}/Z+1}\ , \qquad (7.186) \end{aligned}$$

where $\bar{\omega} \equiv (\omega_x\omega_y\omega_z)^{1/3}$ and $\breve{\omega} \equiv (\breve{\omega}_x\breve{\omega}_y\breve{\omega}_z)^{1/3}$.

$$\boxed{n_{\rm ToF}(\mathbf{x},t) = \frac{1}{\lambda_{\rm th}^3}\frac{\breve{\omega}^3}{\bar{\omega}^3}f_{3/2}\left(e^{\beta\mu-\frac{1}{2}\beta m\Sigma_j\breve{\omega}_j^2x_j^2}\right)}\ . \qquad (7.187)$$

For long times-of-flight $t \gg \omega^{-1}$,

$$n_{\rm ToF}(\mathbf{x},t) = \frac{1}{\lambda_{\rm th}^3}\frac{1}{\bar{\omega}^2t^2}f_{3/2}\left(e^{\beta\left(\mu-m\mathbf{x}^2/2t^2\right)}\right) = \left(\frac{m}{\hbar t}\right)^3\tilde{n}(m\mathbf{x}/t)\ . \qquad (7.188)$$

At low temperatures,

$$\begin{aligned} n_{\rm ToF}(\mathbf{x},t) &= \left(\frac{m}{\hbar t}\right)^3\frac{N}{K_{\rm F}^3}\frac{8}{\pi^2}\left(1-\frac{(m\mathbf{x}/\hbar t)^2}{K_{\rm F}^2}\right)^{3/2} \qquad (7.189)\\ &= \left(\frac{m}{\hbar t}\right)^3\frac{R_{\rm F}^3}{6\pi^2\lambda}\left[1-\left(\frac{R_{\rm F}m\mathbf{x}/\hbar t}{(48N\lambda)^{1/3}}\right)^2\right]^{3/2} \end{aligned}$$

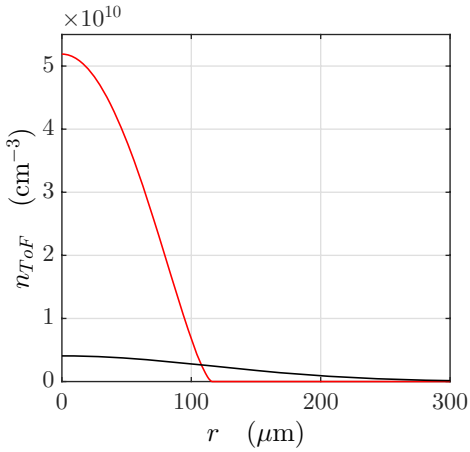

Figure 7.17: (code) Time-of-flight velocity distributions after $T_{\rm ToF} = 2\,$ms of (red) a Li Fermi gas at $T = 0$ with vanishing initial spatial distribution [130] and (black) a thermal gas at $T = T_{\rm F}$.

At high temperatures,

$$\begin{aligned} n_{\rm ToF}(\mathbf{x},t) &= \frac{1}{\lambda_{\rm th}^3}\frac{1}{\bar\omega^2 t^2} f_{3/2}(e^{\beta(\mu - m\mathbf{x}^2/2t^2)}) \qquad (7.190)\\ &\approx \frac{1}{\lambda_{\rm th}^3}\frac{1}{\bar\omega^2 t^2} e^{\beta(\mu - m\mathbf{x}^2/2t^2)} \\ &\approx \left(\frac{mk_{\rm B}T}{2\pi\hbar^2}\right)^{3/2}\frac{1}{\bar\omega^2 t^2} N\left(\frac{\hbar\bar\omega}{k_{\rm B}T}\right)^3 e^{-\beta m\mathbf{x}^2/2t^2} \approx N\frac{\bar\omega}{t^2}\left(\frac{m}{2\pi k_{\rm B}T}\right)^{3/2} e^{-\beta m\mathbf{x}^2/2t^2}\,. \end{aligned}$$

A *rms*-width is,

$$\begin{aligned} \langle r_{\rm ToF}^2\rangle &= \int r^2 n_{\rm ToF}(\mathbf{x},t) d^3\mathbf{x} \qquad (7.191)\\ &= \frac{1}{\lambda_{\rm th}^3}\frac{\breve\omega^3}{\bar\omega^3}\int r^2 f_{3/2}\left(e^{\beta\mu - \frac{1}{2}\beta m\Sigma_j \breve\omega_j^2 x_j^2}\right) d^3\mathbf{x} \\ &= \frac{2}{m\breve\omega_r^2 N}\int \frac{\varepsilon g(\varepsilon) d\varepsilon}{e^{\beta(\varepsilon-\mu)}+1} = \frac{k_{\rm B}T}{m\breve\omega_r^2}\frac{g_4(Z)}{g_3(Z)}\,. \end{aligned}$$

This shows that the width of the flight-of-time distribution can simply be obtained from the spatial distribution by substituting $\omega \to \omega/\sqrt{1+\omega^2 t^2}$. Of course this does not hold for condensed gases Bose.

Example 52 (*Equipartition theorem*): We find for harmonic traps,

$$\begin{aligned} E_{\rm pot,1} &= \frac{\int U(\mathbf{x}) w_{T,\mu}(\mathbf{x},\mathbf{k}) d^3\mathbf{x} d^3\mathbf{k}}{\int w_{T,\mu}(\mathbf{x},\mathbf{k}) d^3\mathbf{x} d^3\mathbf{k}} = \frac{1}{(2\pi)^3 N 2}\int \frac{m\omega^2 r^2 d^3\mathbf{x} d^3\mathbf{k}}{e^{\beta\left[\hbar^2k^2/2m + m\omega^2 r^2/2 - \mu\right]}+1} \\ &= \frac{16}{\pi N\beta^4(\hbar\omega)^3}\int \frac{u^4 v^2 du dv}{e^{u^2+v^2}/Z+1} \qquad (7.192)\\ &= \frac{1}{(2\pi)^3 N 2m}\int \frac{\hbar^2 k^2 d^3\mathbf{x} d^3\mathbf{k}}{e^{\beta\left[\hbar^2k^2/2m + m\omega^2 r^2/2 - \mu\right]}+1} = \frac{\int \hbar^2 k^2 w_{T,\mu}(\mathbf{x},\mathbf{k}) d^3\mathbf{x} d^3\mathbf{k}}{2m\int w_{T,\mu}(\mathbf{x},\mathbf{k}) d^3\mathbf{x} d^3\mathbf{k}} = E_{\rm kin,1}\,. \end{aligned}$$

This confirms the *equipartition theorem* for confined particles, which postulates,

$$E = E_{\rm kin} + E_{\rm pot} = 2E_{\rm kin} \ . \tag{7.193}$$

In flight time, however, $E_{\rm pot}$ suddenly vanishes.

7.4.4.4 Calibrating the number of atoms

Experimentally, to calibrate N, we can use either the measured value of $\langle k^2 \rangle$ at $T = 0$, which gives $\mu = E_{\rm F} = 4E/3$ and consequently,

$$N = \frac{32}{3} \left(\frac{\hbar^2 \langle k^2 \rangle}{6m\hbar\bar{\omega}} \right)^3 \ . \tag{7.194}$$

Or we determine the temperature $T_{\rm g}$ where the Boltzmann gas turns into a Fermi gas $3\mu/4 = 3k_{\rm B}T_{\rm g}$,

$$N = \frac{32}{3} \left(\frac{k_{\rm B}T_{\rm g}}{\hbar\bar{\omega}} \right)^3 \ . \tag{7.195}$$

7.4.5 Density and momentum distribution for anharmonic potentials

7.4.5.1 Width of momentum distribution for anharmonic potentials

If the potential is non-harmonic, the widths of Fermi distributions must in general be calculated numerically. I.e. first $\eta(\varepsilon)$ is determined by integrating for every value of ε the root $\sqrt{\varepsilon - U(\mathbf{x})}$ over the entire volume, where $U(\mathbf{x}) < \varepsilon$, i.e. in the case of cylindrical symmetry,

$$\eta(\varepsilon) = \frac{(2m)^{3/2}}{2\pi\hbar^3} \int \sqrt{\varepsilon - U(r,z)} r dr dz \ . \tag{7.196}$$

Second the chemical potential must also be calculated numerically from $N = \int \eta(\epsilon) \left(e^{\beta(\varepsilon-\mu)} + 1 \right)^{-1} d\varepsilon$ by minimizing the function,

$$o(Z) = \left| \beta N - \int \frac{\eta(x/\beta) dx}{e^x/Z + 1} \right| \ . \tag{7.197}$$

Finally, the *rms*-momentum width of a degenerate Fermi-gas is calculated from,

$$\frac{\langle k^2 \rangle}{k_{\rm F}^2} = \frac{E_1}{E_{\rm F}} = \frac{1}{NE_{\rm F}} \int \frac{\varepsilon\eta(\varepsilon) d\varepsilon}{e^{\beta(\varepsilon-\mu)} + 1} \ . \tag{7.198}$$

It is important to note that the temperature cannot be obtained from $\hbar^2 \langle k^2 \rangle / 2m = 3Nk_{\rm B}T$ any more. Rather for a given $\langle k^2 \rangle$ the parameter β in the integral (7.196) must be fitted to satisfy the equation.

Alternatively, we may assume a polynomial potential for which the density-of-states can be described by $\eta(\varepsilon) \propto \varepsilon^n$. Then,

$$\frac{\langle k^2 \rangle}{k_{\rm F}^2} = \frac{1}{E_{\rm F}} \frac{\int \varepsilon\eta(\varepsilon) \left(e^{\beta(\varepsilon-\mu)} + 1 \right)^{-1} d\varepsilon}{\int \eta(\varepsilon) \left(e^{\beta(\varepsilon-\mu)} + 1 \right)^{-1} d\varepsilon} = \frac{T}{T_{\rm F}} \frac{(n+1) f_{n+2}(Z)}{f_{n+1}(Z)} \ , \tag{7.199}$$

For a harmonic potential we recover the energy formula,

$$\frac{\langle k^2\rangle}{k_{\rm F}^2} = \frac{3T}{T_{\rm F}}\frac{f_4(Z)}{f_3(Z)} \ , \tag{7.200}$$

and for hot clouds the classical limit holds,

$$\frac{\langle k^2\rangle}{k_{\rm F}^2} = \frac{n+1}{\beta E_{\rm F}} \ . \tag{7.201}$$

Must for a single dimension the value be divided by three? $\hbar^2\langle k_j^2\rangle = 2mk_{\rm B}Tf_4(Z)/f_3(Z)$ setting $\varepsilon = \hbar^2k^2/m$.

For a harmonic potential $\eta(\varepsilon) \propto \varepsilon^2$ and for a linear potential $\eta(\varepsilon) \propto \varepsilon^{7/2}$. Intermediate values are possible for non isotropic traps, which are linear in some directions and harmonic in others, e.g. for a radially quadrupolar and axially harmonic trap, we expect $\eta(\varepsilon) \propto \varepsilon^3$ and thus $E = 4Nk_{\rm B}T$. In general, we may have more complicated situations, where the trap becomes non-harmonic beyond a certain distance from the origin. In those cases, the density-of-states may be approximated by series,

$$\eta(\varepsilon) \propto \varepsilon^2 + \varkappa\varepsilon^3 \ , \tag{7.202}$$

where η is a small parameter, so that,

$$\frac{\langle k^2\rangle}{k_{\rm F}^2} = \frac{1}{E_{\rm F}}\frac{\int(\varepsilon^3+\varkappa\varepsilon^4)(e^{\beta(\varepsilon-\mu)}+1)^{-1}d\varepsilon}{\int(\varepsilon^2+\varkappa\varepsilon^3)(e^{\beta(\varepsilon-\mu)}+1)^{-1}d\varepsilon} = \frac{T}{T_{\rm F}}\frac{3f_4(Z)+12\varkappa f_5(Z)}{f_3(Z)+3\varkappa f_4(Z)} \ , \tag{7.203}$$

which in the classical limit gives rise to energies $E = 3..4Nk_{\rm B}T$ depending on the value of $\varkappa$.

Such effects must be considered when the time-of-flight method is used for temperatures measurements. For example, if we underestimate $\eta(\varepsilon)$ by assuming a harmonic potential at all ε, although the potential is quadrupolar at large $\varepsilon \gg k_{\rm B}T$, we get a wrong estimate for the temperature $T_{\rm wrng} = E/3Nk_{\rm B}$ instead of $T_{\rm corr} = E/4Nk_{\rm B}$.

7.4.5.2 Width of the density distribution for anharmonic potentials

The result also permits to calculate the *rms* spatial width,

$$\sum\nolimits_{j=1}^{3}\frac{m}{2}\omega_j^2\langle x_j^2\rangle = 3k_{\rm B}T\frac{f_4(Z)}{f_3(Z)} \ . \tag{7.204}$$

Let us for simplicity assume $\omega_i = \omega_j$. So in the classical limit,

$$\frac{\langle x_j^2\rangle}{R_{\rm F}^2} = \frac{\langle \mathbf{x}^2\rangle}{3R_{\rm F}^2} = \frac{E_1}{3E_{\rm F}} = \frac{1..1.3T}{T_{\rm F}} \ . \tag{7.205}$$

If the potential is non-harmonic, the widths of Fermi distributions must in general be calculated numerically. We may use the same results for the density-of-states and the chemical potential as for the momentum width calculations. Then,

$$\frac{\langle x_j^2\rangle}{R_{\rm F}^2} = \frac{E_1}{3E_{\rm F}} = \frac{1}{3E_{\rm F}}\frac{\int\varepsilon\eta(\varepsilon)\left(e^{\beta(\varepsilon-\mu)}+1\right)^{-1}d\varepsilon}{\int\eta(\varepsilon)\left(e^{\beta(\varepsilon-\mu)}+1\right)^{-1}d\varepsilon} \ . \tag{7.206}$$

7.4.5.3 Momentum distribution for a classical gas

For high temperatures, $T \to \infty$, we should recover the ideal Boltzmann gas situation, $f_{3/2} \to id$,

$$\tilde{n}_{T\to\infty}(\mathbf{k}) = \frac{1}{(2\pi)^3}\int \frac{4\pi\rho^2 d\rho}{e^{\beta\left[\varepsilon+m\omega_{\rm ho}^2\rho^2/2-\mu\right]}} = \frac{1}{2\pi^2}e^{-\beta(\varepsilon-\mu)}\int e^{-\beta m\omega_{\rm ho}^2\rho^2/2}\rho^2 d\rho \quad (7.207)$$
$$= \left(\frac{1}{2\pi\beta m\omega_{\rm ho}^2}\right)^{3/2} e^{-\beta(\varepsilon-\mu)} = \lambda_{\rm th}^{-3}a_{\rm ho}^6\ e^{\beta(\mu-\varepsilon)}\ .$$

Since the chemical potential satisfies the normalization, $\int \tilde{n}_{T\to\infty}(\mathbf{k})d^3\mathbf{k} = 1$,

$$\tilde{n}_{T\to\infty}(\mathbf{k}) = \left(\frac{1}{2\pi\beta m\omega_{\rm ho}^2}\right)^{3/2} N\left(\frac{\hbar\omega_{\rm ho}}{k_{\rm B}T}\right)^3 e^{-\beta\varepsilon} = N\sqrt{\frac{\hbar^2}{2\pi mk_{\rm B}T}}^3\ e^{-\hbar^2k^2/2mk_{\rm B}T}\ . \quad (7.208)$$

This is easy to integrate by dimensions, so that,

$$\tilde{n}_{T\to\infty}(k_z) = \int_{-\infty}^{\infty}\int_{-\infty}^{\infty}\tilde{n}_{T\to\infty}(\mathbf{k})dk_x dk_y = N\sqrt{\frac{\hbar^2}{2\pi mk_{\rm B}T}}e^{-\hbar^2k_z^2/2mk_{\rm B}T}\ . \quad (7.209)$$

The rms-width of this distribution is,

$$\Delta k_z = \frac{\sqrt{mk_{\rm B}T}}{\hbar}\ . \quad (7.210)$$

7.4.6 Signatures for quantum degeneracy of a Fermi gas

Whether an atom is a *fermion* or a *boson* uniquely depends on its total spin. Halfinteger spin particles are fermions, integer spin particles are bosons. E.g. Rb atoms have in the ground state $J = 1/2, I = 7/2$, integer F, and are therefore bosons. Ca^+ ions have $J = 1/2$ and no hyperfine structure so that F is half-integer, and are therefore fermions. ^{6}Li has half-integer F and is a boson.

For a *composite particle* the quantum statistical nature may depend on the interaction strength of the partners. For weak interaction, e.g. Feshbach the total spins of the partners will couple to a total total spin, which determines the nature of the composite particle. A fermion pairing with a fermion or a boson pairing with a boson will be bosons. A fermion pairing with a boson will be a fermion. Composite trimers may be either bosonic or fermionic depending on the coupling scheme [684, 108, 323, 330, 397, 651].

7.4.6.1 Optical density of a Fermi gas

With the local density of a Fermi gas,

$$n_{\rm loc} = \frac{k_{\rm F}^3}{3\pi^2} \quad (7.211)$$

the *optical density* is at $T = 0$,

$$\int \sigma n dy = \frac{8\sigma}{\pi^2}\frac{N}{R_{\rm F}^3}\int_{-R_{\rm F}}^{R_{\rm F}}\left(1-\frac{x^2+y^2}{R_{\rm F}^2}-\frac{z^2}{Z_{\rm F}^2}\right)^{3/2}dy \tag{7.212}$$
$$= \frac{8\sigma}{\pi^2}\frac{N}{R_{\rm F}^3}\left(1-\frac{x^2}{R_{\rm F}^2}-\frac{z^2}{Z_{\rm F}^2}\right)^{3/2}\int_{-R_{\rm F}}^{R_{\rm F}}\left(1-\frac{y^2}{R_{\rm F}^2-x^2-R_{\rm F}^2z^2/Z_{\rm F}^2}\right)^{3/2}dy\ .$$

Writing $a = R_{\rm F}/\sqrt{R_{\rm F}^2 - x^2 - R_{\rm F}^2 z^2/Z_{\rm F}^2}$,

$$\int \sigma n dy = \frac{8\sigma}{\pi^2}\frac{N}{R_{\rm F}^2 a^4}\int_{-a}^{a}(1-\tilde{y}^2)^{3/2}d\tilde{y} \tag{7.213}$$
$$= \frac{2\sigma}{\pi^2}\frac{N}{R_{\rm F}^2 a^4}\left(9a\sqrt{1-a^2}-2a^3\sqrt{1-a^2}+3\arcsin a\right)\ .$$

In the center, $a = 1$,

$$\int \sigma n dy = \frac{3N\sigma}{\pi R_{\rm F}^2} = \frac{9m\omega_r^2 N}{k_{\rm L}^2 E_{\rm F}}\ , \tag{7.214}$$

such that for $E_{\rm F} \simeq 1\mu$K we expect $n_{\rm loc} \simeq 4\times10^{12}$ cm^{-3}.

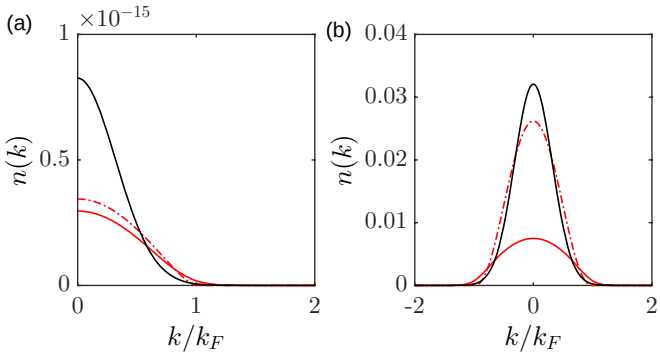

Figure 7.18: (code) (a) Radial momentum distribution and (b) distribution of momentum classes in the direction of k_z for a Fermi gas at $T/T_{\rm F} = 0.2\,\mu$K (red solid), a classical gas (black), and a Fermi gas at $T = 0$ (red dash-dotted).

7.4.6.2 'Pauli blocking' of sympathetic cooling

For a harmonic trap $U = \mu B = m\omega^2 r^2$ the *rms*-radius of a thermal cloud,

$$r_{\rm rms} = \sqrt{\frac{2k_{\rm B}T}{m\omega_r^2}} = \sqrt{\frac{k_{\rm B}T}{\mu\partial_r^2 B}}\ , \tag{7.215}$$

is independent on the atomic mass. This means that a Li and a Rb cloud in the same harmonic trap at the same temperature have the same radius. This ensures good overlap. E.g. at $T = 10\,\mu$K assuming the Rb secular frequencies $\omega_r \simeq 2\pi\times300$ Hz and $\omega_z \simeq 2\pi\times30$ Hz, we expect $r_{\rm rms} = 16\,\mu$m and $z_{\rm rms} = 160\,\mu$m. However below the

temperature $0.5T_F$, which is $T_F \simeq 1\,\mu K$ for $N_F = 10^4$, the quantum pressure stops the reduction of the fermion cloud while cooling. This evtl. reduces the overlap with the boson cloud, disconnects the two clouds and stops the evaporative cooling. On the other hand, the interaction energy of the boson cloud also increases its size, when the Rb cloud approaches the critical temperature $T_c \simeq 0.6\,\mu K$ for $N_B = 10^6$.

The *Pauli blocking* of sympathetic cooling is a signature for the advent of quantum statistics [215, 340, 629]. It is due to a reduced mobility (or better reduced available phase space upon collisions) of the atoms and not to be confused with the prohibition of s-wave collisions due to the *Pauli exlusion principle*. Furthermore, elastic collisions are suppressed [214], because atoms cannot be scattered into occupied trap levels [409, 829, 356, 358].

7.4.6.3 Superfluid suppression of sympathetic cooling

The fermions inside the bosonic cloud can be regarded as impurities. If they travel too slow, $v < c$, and if the condensed fraction is too large, the motion will be frictionless and thermalization stops. If they travel fast, quasiparticles are excited, which can be removed by evaporation. With the typical velocity of sound in the BEC $c = \hbar\sqrt{16\pi na}/2m_B \approx 2\,mm/s$, or $\frac{m}{2}c^2 \approx k_B \times 20\,nK$, we see that this is no real danger.

7.4.6.4 Component separation

If the interspecies interaction h is stronger than the inter-bosonic interaction, the components may separate [627]. Otherwise a small fermionic cloud stays inside the BEC.

7.4.6.5 Excess energy modifies 2^{nd} moment

Independent on any model, just look deviation from Gaussian (interaction energy plays no role for the fermions). Also calculate the 2^{nd} moment $E = \int E_{kin}(k)n(k)dk$, where $n(k)$ is measured in time-of-flight and $E_{kin} = \hbar^2k^2/2m$.

7.4.6.6 Modification of light scattering

The unavailability of final momentum states inhibits scattering in a similar way as the Lamb-Dicke effect. Forward scattering is suppressed, because all small momentum states are occupied. Furthermore, spontaneous emission is suppressed like in photonic band gaps. However, here it is rather an atomic momentum band gap. Could it be that because scattering is suppressed, in-situ images of fermions are hampered?

A condition for this effect to play a role is $k_{rec} \ll k_F$. For Li the temperature must be $k_BT_F = \hbar^2k_F^2/2m = \hbar\bar{\omega}(6N)^{1/3} \gg \hbar^2k_L^2/2m \approx k_B \times 3\,\mu K$. I.e. we need quite large Fermi gases.

7.4.6.7 Hole heating

Loss processes that remove particles from an atom trap leave holes behind in the single particle distribution if the trapped gas is a degenerate fermion system. The appearance of holes increases the temperature, because of an increase in the energy share per particle if cold particles are removed. Heating is significant if the initial

temperature is well below the Fermi temperature. Heating increases the temperature to $T > T_F/4$ after half of the systems lifetime, regardless of the initial temperature. The *hole heating* has important consequences for the prospect of observing Cooper pairing in atom traps.

7.4.7 Fermi gas in reduced dimensions

In n dimensions with the energy $\varepsilon = ap^s + br^t$ [517] we have to generalize the results of the last chapter,

$$N = g\frac{\Gamma\left(\frac{n}{s}+1\right)\Gamma\left(\frac{n}{t}+1\right)}{(2\hbar)^n a^{n/s} b^{n/t}\Gamma\left(\frac{n}{2}+1\right)^2}(k_B T)^{n/s+n/t} f_{n/s+n/t}(z)\ . \tag{7.216}$$

This gives for a harmonic trap where $\varepsilon = \frac{1}{2m}p^2 + \frac{m}{2}\omega^2 r^2$ and with the spin degeneracy factor $g = 1$,

$$N = \left(\frac{k_B T}{\hbar\omega}\right)^n f_n(z)\ . \tag{7.217}$$

The Fermi energy again follows from Sommerfeld's expansion,

$$E_F = (n!N)^{1/n}\hbar\omega\ . \tag{7.218}$$

We now assume a $1D$ potential $V = \frac{m}{2}\omega_z^2 r^2$ embedded in a $3D$ trap. A true $1D$ situation arises when the atoms occupy all low-lying axial levels with the lowest radial vibrational quantum number, i.e. $E_F \ll \hbar\omega_r$ which gives,

$$N \ll \frac{\omega_r}{\omega_z}\ . \tag{7.219}$$

Such quantum degenerate $1D$ fermion gases realize the so-called *Luttinger liquid*. One of the hallmarks of Luttinger liquids is *spin-charge separation*.

Example 53 (*Estimations for 1D*): Let us consider a Fermi gas in a very elongated microtrap: $\omega_r = \sqrt{\frac{87}{7}}2\pi \times 1.4\,\mathrm{kHz}$ and $\omega_z = \sqrt{\frac{87}{7}}2\pi \times 15\,\mathrm{Hz}$ for Rb. With $N_{Li} = 10^5$ the Fermi temperature is as high as $T_F \simeq 5\,\mu\mathrm{K}$. However we need $N \ll 100$ to see $1D$ features.
Assume $\varepsilon = \frac{1}{2m}p^2 + \frac{m^2}{4}b^4 r^4$,

$$N = \frac{1}{(\hbar b)^n}\frac{\Gamma\left(\frac{n}{4}+1\right)}{\Gamma\left(\frac{n}{2}+1\right)}(k_B T)^{3n/4} f_{3n/4}(z)$$

$$E_F \approx (\hbar b)^{4/3}\left(N\frac{\Gamma\left(\frac{n}{2}+1\right)\Gamma\left(\frac{3n}{4}+1\right)}{\Gamma\left(\frac{n}{4}+1\right)}\right)^{4/3n}\ .$$

In $1D$,

$$N = \frac{1.02}{\hbar b}(k_B T)^{3/4} f_{3/4}(z)$$

$$E_F \approx 0.87(N\hbar b)^{4/3}\ .$$

7.4.7.1 Fermi degeneracy

A completely analogous treatment to the Bose-gas yield for the case of fermion

$$E = \tfrac{3}{2} k_{\mathrm{B}} T N \left(1 + 2^{-5/2} n \lambda_{\mathrm{th}}^3\right) + \dots \,. \tag{7.220}$$

Bosonic ^{4}He has a very different behavior than fermionic ^{3}He. It stays gaseous at very low temperatures and becomes a Fermi gas before becoming fluid. Fermi gases have a higher pressure then classically predicted.

Electrons in a solid are characterized by a high density and a low mass. Hence, $n\lambda_{\mathrm{th}}^3 \approx 10^3$. The interelectronic repulsion is canceled by atomic attraction, so that they may be considered an ideal gas. For the density-of-states we get the same formula as for bosons in a box multiplied with the factor 2 to account for the spin degree of freedom. Thus, from

$$N = \int_0^{E_{\mathrm{F}}} \rho f_{\mathrm{FD}} d\varepsilon \;, \tag{7.221}$$

we derive the Fermi energy $E_{\mathrm{F}} = \frac{h^2}{8m}(3N/\pi V)^{2/3}$. The free electron gas is deep in the Fermi regime, the classical statistics may only be used at temperatures above $T > 10^5\,\mathrm{K}$. Hence the energy is temperature-independent and the heat capacity vanishes, *i.e.* the electron gas does not contribute to the heat capacity of a metal. It is only at very low temperatures of a few K, when the heat capacity of the atomic lattice drops due to the underlying bosonic statistics, that the electrons contribute.

Now, make the metallic box potential having a finite depth. An electron can then leave the metal, if it surmounts the *exit work* $W = -V_{\mathrm{min}} - E_{\mathrm{F}} \simeq 10\,\mathrm{eV}$, which is the difference between the potential depth and the Fermi energy. At high temperatures, the tail of the Fermi-Dirac distribution can leak into the unbound regime, which gives rise to *thermoionic emission*. This feature explains the existence of *contact potentials*: Metals with different W and E_{F} brought into contact exchange charges until their Fermi level is at same height.

7.4.8 Exercises

7.4.8.1 Ex: Integrated momentum distribution of a Fermi gas

Integrate the momentum distribution of a Fermi gas over two dimensions,

$$\tilde{n}_{T\to 0}(k_z) = \int_{-\infty}^{\infty}\int_{-\infty}^{\infty} \tilde{n}_{\mathrm{cl}}(\mathbf{k}) dk_x dk_y \;, \tag{7.222}$$

assuming (a) low temperatures and (b) for the general case.

7.4.8.2 Ex: Li Fermi gas

Programs on Li Fermi gases.

7.5 Further reading

7.5.1 on quantum statistics

R. DeHoff, *Thermodynamics in Material Science* [ISBN]

H.B. Callen, *Thermodynamics* [ISBN]

C. Kittel, *Introduction to Solid State Physics* [ISBN]

A.R. West, *Basic Solid State Chemistry* [ISBN]

D. Mc Quarry, *Statistical Thermodynamics* [ISBN]

J. Walraven, *Quantum gases* [http]

G.T. Landi, *Grand canonical ensemble* [http]

7.5.2 on ideal quantum gases

V.S. Bagnato et al., *Bose-Einstein Condensation in an External Potential* [DOI]

D.A. Butts et al., *Trapped Fermi gases* [DOI]

R.J. Dodd et al., *Two-gas description of dilute Bose-Einstein condensates at finite temperature* [DOI]

Chapter 8

Appendices to 'Statistical Physics'

8.1 Quantities and formulas in statistical physics

8.1.1 Statistical formulas

Stirling's formula is,

$$\boxed{\ln n! = n\ln n - n + O(\ln n)} \qquad \text{or} \qquad n! \simeq \sqrt{2\pi n} n^n e^{-n} \ . \tag{8.1}$$

Note that $O(\ln n) = \frac{\ln n + \ln 2\pi}{2\ln 2} + O(\frac{1}{n})$.

8.1.2 Polylogarithm

The polylogarithm (or Joncquière's function) is a function defined as,

$$Li_\eta(Z) \equiv \sum_{t=1}^{\infty} \frac{Z^t}{t^\eta} = \frac{1}{\Gamma(\eta)} \int_0^\infty \frac{x^{\eta-1}dx}{Z^{-1}e^x - 1} \ . \tag{8.2}$$

It serves to express the Bose and Fermi functions used in quantum statistics,

$$g_\eta^{(\pm)}(Z) = \pm Li_\eta(\pm Z) \ . \tag{8.3}$$

The upper sign holds for bosons, the lower for fermions.

8.1.2.1 Riemann zeta-function

The definition of the *Riemann zeta-function* is,

$$g_\xi(1) = \zeta(\xi) \ . \tag{8.4}$$

8.1.2.2 Bose/Fermi function

According to (8.3) the Bose-Fermi functions are given by,

$$g_\xi^\pm(Z) = \frac{1}{\Gamma(\xi)} \int_0^\infty \frac{x^{\xi-1}dx}{Z^{-1}e^x \mp 1} = \sum_{\ell=0}^{\infty} \frac{(\pm Z)^\ell}{\ell^\xi} \ , \tag{8.5}$$

where the second equation represents an expansion. The derivative satisfies a useful relationship,

$$\frac{\partial g_\xi^\pm(Z)}{\partial Z} = \sum_{\ell=0}^{\infty} \frac{\partial}{\partial Z} \frac{(\pm Z)^\ell}{\ell^\xi} = \sum_{\ell=1}^{\infty} \frac{\pm(\pm Z)^{\ell-1}}{\ell^{\xi-1}} = \frac{1}{Z} \sum_{\ell=1}^{\infty} \frac{(\pm Z)^\ell}{\ell^{\xi-1}} = \frac{g_{\xi-1}^\pm(Z)}{Z} \ . \tag{8.6}$$

The relationship can also be derive via partial integration exploiting,

$$\frac{d}{dx} \frac{-Z}{Z^{-1}e^x + 1} = \frac{e^x}{(e^x/Z \mp 1)^2} \ . \tag{8.7}$$

We calculate,

$$\frac{\partial g_\xi^\pm(Z)}{\partial Z} = \frac{1}{\Gamma(\xi)} \int_0^\infty \frac{-x^{\xi-1} \frac{\partial}{\partial Z}(Z^{-1}e^x \mp 1)}{(Z^{-1}e^x \mp 1)^2} dx = \frac{1}{Z^2\Gamma(\xi)} \int_0^\infty x^{\xi-1} \frac{e^x}{(Z^{-1}e^x \mp 1)^2} dx \tag{8.8}$$

$$= \frac{x^{\xi-1}e^x}{(e^x/Z \mp 1)^2}\Big|_0^\infty - \frac{1}{Z^2\Gamma(\xi)} \int_0^\infty (\xi-1)x^{\xi-2} \frac{-Z}{Z^{-1}e^x \mp 1} dx$$

$$= 0 + \frac{1}{Z\Gamma(\xi-1)} \int_0^\infty \frac{x^{\xi-2}}{Z^{-1}e^x \mp 1} dx = \frac{g_{\xi-1}^\pm(Z)}{Z} \ .$$

8.1.2.3 Sommerfeld expansion

Another useful relationship is the *Sommerfeld expansion*, which holds for Fermi functions,

$$\int_0^\infty \frac{\eta(x)dx}{e^{x-y}+1} = \int_0^y \eta(x)dx + \int_0^\infty \frac{\eta(y+x)^{\xi-1}dx}{e^x+1} - \int_0^x \frac{\eta(y-x)^{\xi-1}dx}{e^x+1} \tag{8.9}$$

$$\approx \int_0^y \eta(x)dx + \tfrac{\pi^2}{6}\eta'(x) + ...$$

holds for $z \gg 1$ and yields,

$$f_\xi(e^y) \approx \frac{x^\xi}{\Gamma(\xi+1)} \left(1 + \frac{\pi^2\xi(\xi-1)}{6x^2} + \frac{7\pi^4\xi(\xi-1)(\xi-2)(\xi-3)}{360x^4} + ...\right) \ . \tag{8.10}$$

For small z both functions converge towards,

$$c_\xi(z) = \frac{1}{\Gamma(\xi)} \int_0^\infty \frac{x^{\xi-1}dx}{z^{-1}e^x} = c_{\xi-1}(z) = z \ . \tag{8.11}$$

8.2 Special topic: Microcanonical ensembles

The *microcanonical ensemble* is used to represents the possible microstates of a mechanical system whose total energy E is exactly specified. The system is assumed to be isolated in the sense that it cannot exchange energy or particles with its environment, so that the energy of the system does not change with time. The primary

macroscopic variables of the microcanonical ensemble are the total number of particles N in the system, the system's volume V, as well as the total energy E in the system.

In the microcanonical ensemble an equal probability $\rho_{\rm mc}(E)$ is assigned to every microstate whose energy falls within a range centered at E. All other microstates are given a probability of zero. Since the probabilities must add up to 1, the probability is the inverse of the number of microstates W within the range of energy,

$$\boxed{\rho_{\rm mc} = W^{-1}} \ . \tag{8.12}$$

The range of energy ΔE is then reduced in width until it is infinitesimally narrow, still centered at E. The microcanonical ensemble is obtained in the limit of this process. For a given mechanical system (fixed N, V) and a given range of energy, the uniform distribution of probability $\rho_{\rm mc}$ over microstates maximizes the ensemble average $-\langle \ln \rho_{\rm mc} \rangle$.

8.2.1 Density of states

We consider an isolated system with N particles and energy E in a volume V. By definition, such a system exchanges neither particles nor energy with the surroundings. The assumption, that thermal equilibrium implies that the distribution function $\rho_{\rm mc}(q,p)$ of the system is a function of its energy [1],

$$\rho_{\rm mc}(r,p) = \rho(H(r,p)) \quad , \quad \frac{d}{dt}\rho_{\rm mc}(r,p) = \frac{\partial \rho}{\partial H}\dot{E} \equiv 0 \ , \tag{8.13}$$

leads to to a constant $\rho_{\rm mc}(r,p)$, which is manifestly consistent with the ergodic hypothesis and the postulate of a priori equal probabilities, i.e. a uniform distribution of microstates.

Now, we consider a small but finite energy shell $[E, E+\Delta E]$ close to the energy surface. The microcanonical ensemble is then defined by,

$$\rho_{\rm mc}(r,p) = \frac{1}{W(E,V,N)} f\left(\tfrac{H(r,p)-E}{\Delta E}\right) \quad \text{with} \quad f(x) = \theta(\tfrac{1}{2} - |x|) \ . \tag{8.14}$$

In this expression,

$$\begin{aligned} W(E,V,N) &= \int_{2|H(r,p)-E|<\Delta E} d^{3N}r d^{3N}p \\ &\overset{\Delta E \to 0}{\longrightarrow} \int \delta(E - H(r,p)) \Delta E d^{3N}r d^{3N}p \equiv \eta(E)\Delta E \end{aligned} \tag{8.15}$$

is the phase space volume occupied by the microcanonical ensemble, that is, the volume of the shell bounded by the two energy surfaces with energies E and $E+\Delta E$. The dependence on the spatial volume V comes from the limits of the integration over dr_i,

$$\eta(E) \equiv \int \delta(E - H(r,p)) d^{3N}r d^{3N}p \ . \tag{8.16}$$

[1] See e.g. Lecture by C. Gros.

8.2.2 Entropy

The expectation value of a classical observable $O(q,p)$ can be obtained by averaging over the probability density $\rho(q,p)$ of the microcanonical ensemble,

$$\langle O\rangle = \int \rho_{\rm mc}(r,p)O(r,p)d^{3N}rd^{3N}p = \frac{1}{W(E,V,N)}\int_{2|H(r,p)-E|<\Delta E} O(r,p)d^{3N}rd^{3N}p \ . \tag{8.17}$$

The entropy can, however, not be obtained as an average of a classical observable. It is instead a function of the overall number of available states.

The entropy is, according to ***Boltzmann's postulate***, proportional to the logarithm of the number of available states included in the phase space volume W,

$$S = k_{\rm B}\ln\frac{W(E,V,N)}{W_0(N)} \ . \tag{8.18}$$

Note that the normalization constant $W_0(N)$ introduced above cancels the dimensions of $W(E,V,N)$. Also, the number of particles N being one of the fundamental thermodynamic variables, the functional dependence of $W_0(N)$ on N is important. Let us now discuss the ramification of this postulate.

8.2.2.1 Incompleteness of classical statistics

Importantly, $W_0(N)$ *cannot correctly be derived within classical statistics.* In quantum statistics we will derive later,

$$W_0(N) = h^{3N}N! \ . \tag{8.19}$$

We consider this value also for classical statistics, noting that the factor h^{3N} defines the reference measure in phase space and that $N!$ is the counting factor for states obtained by permuting particles supposed to be indistinguishable. Even though one may be in a range of temperature and density where the motion of molecules can be treated to a very good approximation by classical mechanics, one cannot go so far as to disregard the essential indistinguishability of the molecules; one cannot observe and label individual atomic particles as though they were macroscopic billiard balls.

We will discuss later the Gibbs paradox, which arises when one regards the constituent particles as distinguishable. In this case there would be no factor $N!$ in $W_0(N)$.

8.2.2.2 Entropy as an expectation value

We rewrite the definition (8.18) of the entropy as,

$$S = -k_{\rm B}\int_{2|H(r,p)-E|<\Delta E} \rho_{\rm mc}(r,p)\ln[W_0(N)\rho_{\rm mc}(r,p)]d^{3N}rd^{3N}p \ , \tag{8.20}$$

where we have used that $\rho_{\rm mc}(q,p) = W(E,V,N)^{-1}$ within the energy shell and that

$$\int \rho_{\rm mc}(r,p)d^{3N}rd^{3N}p = \frac{1}{W(E,V,N)}\int_{2|H(r,p)-E|<\Delta E} d^{3N}rd^{3N}p = 1 \ . \tag{8.21}$$

We hence have [2],

$$S = -k_{\rm B} \ln\langle W_0(N)\rho(r,p)\rangle \ . \tag{8.22}$$

8.2.2.3 Thermodynamic consistency of the entropy definition

Since we have introduced the entropy definition in an ad-hoc way, we need to convince ourselves that it describes the thermodynamic entropy as a state function. The entropy must therefore fulfill the requirements of (1) additivity, (2) consistency with the definition of the temperature, (3) consistency with the second law of thermodynamics, and (4) adiabatic invariance.

(1) **Additivity, Gibbs' paradox.** The classical Hamiltonian $H(r,p) = H_{\rm kin}(p) + H_{\rm int}(r)$ is the sum of the kinetic energy and of the particle-particle interaction. The condition,

$$E < H_{\rm kin}(p) + H_{\rm int}(r) < E + \Delta E \tag{8.23}$$

limiting the available phase space volume $W(E,V,N)$ on the energy shell, as defined by (8.15) could then be fulfilled by a range of combinations of $H_{\rm kin}(p)$ and $H_{\rm int}(r)$.

The law of large numbers, which we will discuss in Sec. 8.2.5, implies however that both the kinetic and the interaction energies take well defined values for large particle numbers N.

The interaction between particles involves only pairs of particles, with the remaining $N-2 \simeq N$ particles moving freely within the available volume V. This consideration suggest together with an equivalent argument for the kinetic energy that the *phase space volume of the energy shell scales like*

$$\int_{E<H(r,p)<E+\Delta E} d^{3N}r d^{3N}p = W(E,V,N) \sim V^N w^N(E/N, V/N) \ . \tag{8.24}$$

We will verify this relation in Sec. 8.2.5 for the classical ideal gas. This assumption may not hold in the presence of long range interactions.

Using scaling relation (8.24) for the volume of the energy shell and the assumption that $W_0(N) = h^{3N}N!$ we then find that the entropy defined by (8.18) is extensive,

$$S = k_{\rm B} \ln \frac{V^N w^N(E,V,N)}{h^{3N}N!} = k_{\rm B} N \left(\ln \frac{V}{N}\frac{w}{h^3} + 1 \right) \equiv k_{\rm B} N \, s(E/N, V/N) \ , \tag{8.25}$$

where we have used the Stirling formula (8.1). The *extensivity of the entropy* result in (8.25) from the fact that $V^N/N! \simeq (V/N)^N$. Without the factor $N!$ in $W_0(N)$, which is however not justifiable within classical statistics, the entropy would not be extensive. This is the *Gibbs paradox*.

[2] The entropy coincides hence with Shannon's information-theoretical definition of the entropy, apart from the factors $k_{\rm B}$ and $W_0(N)$.

Two subsystems with particle numbers N_1 and N_2 have identical thermodynamic properties, if their intensive variables are the same, via temperature T, pressure P, particle density N/V, and energy density E/N [see illustration in Fig. 8.1(a)]. It then follows directly from (8.25) that,

$$S(E,V,N) = k_{\rm B}(N_1+N_2)s(E/N,V/N) = S(E_1,V_1,N_1)+S(E_2,V_2,N_2)\ . \tag{8.26}$$

That is, in the case of *identical thermodynamic states the entropy is additive.*

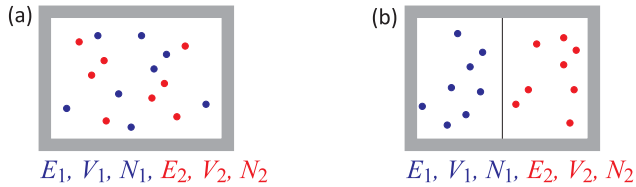

Figure 8.1: (a) Two subsystems sharing the same volume. (b) Two subsystems in thermal contact.

Two systems defined by E_1, V_1, N_1 and respectively E_2, V_2, N_2 in thermal contact may allow energy such that the total energy $E = E_1 + E_2$ is constant [see illustration in Fig. 8.1(b)]. For the argument of the entropy we have then,

$$\frac{W(E,V,N)}{W_0(N)} = \sum_{E_1} \frac{W(E_1,V_1,N_1)}{W_0(N_1)} \frac{W(E-E_1,V_2,N_2)}{W_0(N_2)}\ . \tag{8.27}$$

The law of large numbers tells us that the right-hand-side is sharply peaked at its maximum value $E_1 = E_{\rm max}$ and that the width of the peak has a width scaling with $\sqrt{E_{\rm max}}$. We hence have,

$$S(E_{\rm max}) < S(E,N,V) < k_{\rm B} \ln \sqrt{E_{\rm max}} + S(E_{\rm max})\ , \tag{8.28}$$

where the first inequality is due to the fact that a single term is smaller than the sum of positive terms. The second inequality in (8.28) results when when one replaces the sum on the r.h.s. of (8.27) by the product of the width $\sqrt{E_{\rm max}}$ of the peak and its height. We have defined in (8.28)

$$S(E_{\rm max}) = k_{\rm B} \ln \frac{W(E_{\rm max},V_1,N_1)}{W_0(N_1)} \frac{W(E-E_{\rm max},V_2,N_2)}{\Gamma_0(N_2)}\ , \tag{8.29}$$

from which follows that the *entropy for two systems in thermal contact is additive* $S(E,V,N) = S(E_1,V_1,N_1)+S(E_2,V_2,N_2)$. Note that the entropy $S(E_{\rm max})$ is extensive and that the term $\sim \ln(E_{\rm max})$ in (8.28) is hence negligible in the thermodynamic limit $N \to \infty$.

(2) **Consistency with the definition of the temperature.** Two systems with entropies $S_1 = S(E_1,V_1,N_1)$ and $S_2 = S(E_2,V_2,N_2)$ in thermal contact may exchange energy in the form of heat, with the total entropy,

$$0 = dS = \frac{\partial S_1}{\partial E_1} dE_1 + \frac{\partial S_2}{\partial E_2} dE_1 \quad , \quad dE_1 = -dE_2\ , \tag{8.30}$$

becoming stationary at equilibrium. Note that the total energy $E_1 + E_2$ is constant. The equilibrium condition (8.30) implies that there exists a quantity T, denoted temperature, such that

$$\frac{\partial S_1}{\partial E_1} = \frac{1}{T} = \frac{\partial S_2}{\partial E_2} \ . \tag{8.31}$$

The possibility to define the temperature, as above, is hence a direct consequence of the conservation of the total energy. From the microcanonical definition of the entropy one only needs that the entropy is a function only of the internal energy, via the volume $\Gamma(E, V, N)$ of the energy shell, and not of the underlying microscopic equation of motion.

(3) **Consistency with the second law of thermodynamics.** The statistical entropy defined by (8.18) need to satisfy the second law of thermodynamics saying that, '*if an isolated system undergoes a process between two states at equilibrium, the entropy of the final state cannot be smaller than that of the initial state.*'

Both the energy E and the number of particle N stay constant during a *free expansion*, defined by the absence of external heat transfer,

$$\delta Q = 0 \ . \tag{8.32}$$

According to (8.24), the phase space volume $W(E, V, N)$ of the energy shell increases when the volume increases from V_i to V_f. Since according to (8.18) the entropy increases with the phase space volume, while the normalization factor $W_0(N)$ remains constant, we have [3],

$$S(E, V_\mathrm{f}, N) > S(E, V_\mathrm{i}, N) \ . \tag{8.33}$$

(4) **Thickness of the energy shell.** The definition of the entropy (8.18) involves the volume in state space $W(E, V, N)$ of a shell of width ΔE centered around the energy E. It seems therefore that the entropy $S = S_{\Delta E}(E, V, N)$ depends on an unspecified parameter ΔE. The question then arises whether the entropy then not uniquely specified.

For small ΔE we may use the approximation

$$W(E, V, N) \simeq \eta(E)\Delta E \ , \tag{8.34}$$

where $\eta(E)$ is the density of states, as defined previously in (8.16). In order to decide whether a given ΔE is small or large, we compare it to some *reference energy* ΔE_0. One may take e.g. $\Delta E_0 \sim k_\mathrm{B}T$, which corresponds in order of magnitude to the thermal energy of an individual particle.

The entropy involves the logarithm of $W(E, V, N)$,

$$\ln \frac{W(E, V, N)}{W_0} = \ln \frac{\eta(E)\Delta E \Delta E_0}{W_0 \Delta E_0} = \underbrace{\ln \frac{\eta(E)\Delta E_0}{W_0}}_{\propto N} + \ln(\Delta E/\Delta E_0) \ , \tag{8.35}$$

[3] Dynamical constraints (viz bouncing from the wall) are mitigated when the volume is increased. The second law is *equivalent* to saying that the entropy rises when dynamical constraints are eliminated.

where we have taken care that the arguments of the logarithms are dimensionless. The key insight resulting from this representation is that the exact value of both ΔE and ΔE_0 is irrelevant in the *thermodynamic limit* $N \to \infty$ as long as [4],

$$|\ln(\Delta E/\Delta E_0)| \ll N \ . \tag{8.36}$$

We may also consider the limit of large ΔE to the extend that we may substitute the phase space volume $W(E, V, N)$ of the energy shell by the phase space volume of the sphere ,

$$\Phi(E) \equiv \sum_E W(E) = \int_0^E \eta(E) dE \ . \tag{8.37}$$

Now, the volume and surface of a phase space sphere with radius R of dimension $3N$ scale respectively like R^{3N} and R^{3N-1} (see Eq. (8.48) below). This scaling leads to,

$$\ln \Phi(E) \sim \ln R^{3N} = 3N \ln R \tag{8.38}$$

$$\ln W(E, V, N) \sim \ln R^{3N-1}\Delta = (3N-1)\ln R + \ln \Delta \sim 3N \ln R \sim 3N \ln R \ . \tag{8.39}$$

Hence,

$$\ln W(E, V, N) \simeq \ln \Phi(E) \ , \tag{8.40}$$

where we have disregarded the normalization factor W_0, did not perform here an analysis of the units involved, and neglected in particular the reference energy Δ_0.

8.2.3 Calculating with the microcanonical ensemble

In order to perform calculations in statistical physics one proceeds through the following steps:

1. Formulation of the Hamilton function $H(r, p) = H(r_1, ..., r_{3N}, p_1, ..., p_{3N}, z)$, where z is some external parameter, e.g. volume V. $H(r, p)$ specifies the microscopic interactions.

2. Determination of the phase space $W(E, V, N)$ and calculation of the density of states,

$$\rho(E, V, N) = \int d^{3N} r \int d^{3N} p \delta(E - H(r, p)) \ . \tag{8.41}$$

3. Calculation of the entropy from the volume $\Phi(E)$ of the energy sphere via

$$S(E, V, N) = k_{\mathrm{B}} \ln \frac{\Phi(E)}{W_0} \ . \tag{8.42}$$

[4] In quantum statistics this condition is ensured by energy quantization.

4. Calculation of P, T, and μ,

$$\frac{1}{T} = \left(\frac{\partial S}{\partial E}\right)_{V,N} \quad , \quad -\frac{\mu}{T} = \left(\frac{\partial S}{\partial N}\right)_{E,V} \quad , \quad \frac{P}{T} = \left(\frac{\partial S}{\partial V}\right)_{E,N} . \tag{8.43}$$

5. Calculation of the internal energy,

$$E = \langle H \rangle = E(S, V, N) . \tag{8.44}$$

6. Calculation of other thermodynamic potentials and their derivatives by application of the Legendre transformation,

$$\begin{aligned} F(T, V, N) &= E - TS \\ H(S, P, N) &= E + PVG(T, P, N) \qquad = E + PV - TS . \end{aligned} \tag{8.45}$$

7. One can calculate other quantities than the thermodynamic potentials, for instance, probability distribution functions of certain properties of the system, e.g., momenta/velocity distribution functions. If the phase space density of a system of N particles is given by,

$$\rho_{\rm mc}(r, p) = \rho_{\rm mc}(\mathbf{r}_1, ..., \mathbf{r}_N, \mathbf{p}_1, ..., \mathbf{p}_N) , \tag{8.46}$$

then the probability of finding particle i with momentum $\mathbf{p}$ is,

$$\begin{aligned} \rho_{i,{\rm mc}(\mathbf{p})} &= \langle \delta(\mathbf{p} - \mathbf{p}_i) \rangle \\ &= \int d^3q_1 ... d^3q_N d^3p_1 ... d^3p_N \rho_{\rm mc}(\mathbf{r}_1, ..., \mathbf{r}_N, \mathbf{p}_1, ..., \mathbf{p}_i, ..., \mathbf{p}_N) \delta(\mathbf{p} - \mathbf{p}_i) . \end{aligned} \tag{8.47}$$

Example 54 (*Hyperspheres*): Let us calculate for later purposes the volume,

$$\Omega_n(R) = \int_{\sum_{i=1}^n x_i^2 < R^2} d^n x = R^n \Omega_n(1) \tag{8.48}$$

of a hypersphere of n dimensions and radius R. We notice that the volume $\Omega_n(1)$ of the sphere with unity radius enters the determinant of the Jacobian when transforming *Euclidean to spherical coordinates* via,

$$d^n x = dx_1 ... dx_n = \Omega_n(1) n R^{n-1} dR . \tag{8.49}$$

This transformation is valid if the integrand depends exclusively on the radius R.
In order to evaluate (8.48) we make use of the fact that we can rewrite the *Gaussian integral*,

$$\int_{\mathbb{R}^3} e^{-(x_1^2 + ... + x_N^2)} dx_1 ... dx_n = \pi^{n/2} \tag{8.50}$$

as

$$\begin{aligned} \pi^{n/2} &= \int_0^\infty e^{-R^2} \Omega_n(1) n R^{n-1} dR \\ &= n\Omega_n(1) \int_0^\infty e^{-y} y^{(n-1)/2} \frac{dy}{2\sqrt{y}} = \tfrac{n}{2} \Omega_n(1) \int_0^\infty e^{-y} y^{n/2-1} dy , \end{aligned} \tag{8.51}$$

where we have used $\sum_i x_i^2 = R^2 \equiv y$ and $2RdR = dy$. With the definition,

$$\Gamma(z) = \int_0^\infty x^{z-1} e^{-x} dx \ , \tag{8.52}$$

of the Γ-function, comparing (8.50) and (8.50) we obtain,

$$\Omega_n(1) = \frac{\pi^{n/2}}{(n/2)\Gamma(n/2)} \ . \tag{8.53}$$

Note that we evaluated the volume of a hypersphere for formally dimensionless variables x_i.

8.2.4 Classical ideal gas

We consider now the steps given in the last section in order to analyze an ideal gas of N particles in a volume V, defined by the Hamilton function,

$$H(r,p) = \sum_{i=1}^{N} \frac{\mathbf{p}_i^2}{2m} \ , \tag{8.54}$$

where m is the mass of the particles.

We will make use of (8.40), namely that the volume $W(E,V,N)$ of the energy shell $E < H < E + \Delta E$ can be replaced by the volume of the energy sphere,

$$\Phi(E) = \iint\limits_{\sum_{i=1}^N p_i^2 \le 2mE} d^{3N}r d^{3N}p = V^N \int_{\sum_{i=1}^N p_i^2 \le 2mE} d^{3N}r = V^N W_{3N}(\sqrt{2mE}) \ , \tag{8.55}$$

when it comes to calculating the entropy in the thermodynamic limit. We have identified the last integral in (8.55) as the volume of a $3N$-dimensional sphere with radius $\sqrt{2mE}$. Using (8.48) and (8.51),

$$W_{3N}(\sqrt{2mE}) = \sqrt{2mE}^{3N} W_{3N}(1) \qquad \text{with} \qquad W_{3N}(1) = \frac{\pi^{3N/2}}{(3N/2)\Gamma(3N/2)} \ , \tag{8.56}$$

we obtain,

$$\Phi(E) = V^N W_{3N}(1) \sqrt{2mE}^{3N} \ . \tag{8.57}$$

8.2.4.1 Entropy

Using (8.57) we find,

$$S(E,V,N) = k_{\rm B} \ln \frac{\Phi(E)}{h^{3N} N!} = k_{\rm B} \ln \frac{V^N W_{3N}(1) \sqrt{2mE}^{3N}}{h^{3N} N!} \tag{8.58}$$

for the entropy of a classical gas. It is easy to check, that the argument of the logarithm is dimensionless as it should be.

For large $N \gg 1$, one may use the Stirling formula (8.1), to expand the Γ-function for integer argument as,

$$\ln \Gamma(N) = \ln(N-1)! \simeq (N-1)\ln(N-1) - (N-1) \simeq N \ln N - N \ , \tag{8.59}$$

in order to simplify the expression for $S(E,V,N)$. Using (8.19) we perform the following algebraic transformations to $W_{3N}(1)$,

$$\begin{aligned}\ln W_{3N}(1) &= \ln \frac{\pi^{3N/2}}{(3N/2)\Gamma(3N/2)} = \tfrac{3N}{2}\ln\pi - \left[\tfrac{3N}{2}\ln\tfrac{3N}{2} - \tfrac{3N}{2}\right] \\ &= N\left[\left(\tfrac{2\pi}{3N}\right)^{3/2} + \tfrac{3}{2} + O(\tfrac{\ln N}{N})\right] \ .\end{aligned} \tag{8.60}$$

We insert this expression in Eq. (8.58) and obtain,

$$S = k_{\rm B}N\left[\ln\frac{B(2mE)^{3/2}}{h^3} + \ln\left(\frac{2\pi}{3N}\right) + \frac{3}{2} - \underbrace{(\ln N - 1)}_{\ln N!/N}\right] \ . \tag{8.61}$$

Rewriting (8.61) as,

$$S = {\rm B}N\left\{\ln\left[\left(\frac{4\pi mE}{3h^2N}\frac{V}{N}\right)^{3/2}\right] + \frac{5}{2}\right\} \ , \tag{8.62}$$

we obtain the *Sackur-Tetrode equation*.

Now we can differentiate the Sackur-Tetrode equation to obtain the *caloric equation of state* (??) for the ideal gas,

$$\frac{1}{T} = \left(\frac{\partial S}{\partial E}\right)_{V,N} = Nk_{\rm B}\frac{3}{2}\frac{1}{E} \quad , \quad E = \tfrac{3}{2}Nk_{\rm B}T \ , \tag{8.63}$$

as well as the *thermal equation of state* for the ideal gas,

$$\frac{P}{T} = \left(\frac{\partial S}{\partial V}\right)_{E,T} = \frac{k_{\rm B}N}{V} \quad , \quad PV = Nk_{\rm B}T \ . \tag{8.64}$$

Example 55 (*'Classical' Sackur-Tetrode equation*): Note that, if we hadn't considered the factor $N!$ when working out the entropy, then one would obtain,

$$S_{\rm classical} = k_{\rm B}N\left\{\ln\left[\left(\frac{4\pi mE}{3h^2N}V\right)^{3/2}\right] + \frac{3}{2}\right\} \ , \tag{8.65}$$

With this definition, the entropy is non-additive, i.e.,

$$S(E,V,N) \neq Ns(\tfrac{E}{N},\tfrac{V}{N}) \ , \tag{8.66}$$

as mentioned previously. This was realized by *Gibbs paradox*, who introduced the factor $N!$ and attributed it to the fact that the particles are indistinguishable.

8.2.5 Quantum statistics

The quantum mechanics the microcanonical density operator and partition function are given by,

$$\boxed{\begin{array}{lcl}\hat\rho_{\rm mc} &=& \frac{1}{\Xi_{\rm mc}}\sum_k |\psi_k\rangle f(\frac{E-\varepsilon_k}{\Delta E})\langle\psi_k| \\ \Xi_{\rm mc} &=& \sum_k f(\frac{E-\varepsilon_k}{\Delta E}) \quad \text{with} \quad f(x) = \theta(\tfrac{1}{2} - |x|)\end{array}} \ . \tag{8.67}$$

8.2.5.1 Applicability

Because of its connection with the elementary assumptions of equilibrium statistical mechanics (particularly the postulate of a priori equal probabilities), the microcanonical ensemble is an important conceptual building block in the theory and is sometimes considered to be the fundamental distribution of equilibrium statistical mechanics. It is also useful in some numerical applications, such as molecular dynamics. On the other hand, most nontrivial systems are mathematically cumbersome to describe in the microcanonical ensemble, and there are also ambiguities regarding the definitions of entropy and temperature. For these reasons, other ensembles are often preferred for theoretical calculations.

The applicability of the microcanonical ensemble to real-world systems depends on the importance of energy fluctuations, which may result from interactions between the system and its environment as well as uncontrolled factors in preparing the system. Generally, fluctuations are negligible if a system is macroscopically large, or if it is manufactured with precisely known energy and thereafter maintained in near isolation from its environment. In such cases the microcanonical ensemble is applicable. Otherwise, different ensembles are more appropriate, such as the canonical ensemble (fluctuating energy) or the grand canonical ensemble (fluctuating energy and particle number).

8.2.5.2 Phase transitions and thermodynamic analogies

Under their strict definition, phase transitions correspond to non-analytic behavior in the thermodynamic potential or its derivatives. Using this definition, phase transitions in the microcanonical ensemble can occur in systems of any size. This contrasts with the canonical and grand canonical ensembles, for which phase transitions can occur only in the thermodynamic limit– i.e. in systems with infinitely many degrees of freedom. Roughly speaking, the reservoirs defining the canonical or grand canonical ensembles introduce fluctuations that 'smooth out' any non-analytic behavior in the free energy of finite systems. This smoothing effect is usually negligible in macroscopic systems, which are sufficiently large that the free energy can approximate non-analytic behavior exceedingly well. However, the technical difference in ensembles may be important in the theoretical analysis of small systems.

The volume entropy S_{vol} and associated temperature T_{vol} form a close analogy to thermodynamic entropy and temperature. It is possible to show exactly that,

$$dE = T_{\text{vol}} dS_{\text{vol}} - \langle P \rangle dV \ , \tag{8.68}$$

where $\langle P \rangle$ is the ensemble average pressure, as expected for the first law of thermodynamics. A similar equation can be found for the surface entropy and its associated temperature T_{sur}, however the 'pressure' in this equation is a complicated quantity unrelated to the average pressure.

The microcanonical T_{vol} and T_{sur} are not entirely satisfactory in their analogy to temperature. Outside of the thermodynamic limit, a number of artefacts occur.

- Nontrivial result of combining two systems: Two systems, each described by an independent microcanonical ensemble, can be brought into thermal contact

and be allowed to equilibriate into a combined system also described by a microcanonical ensemble. Unfortunately, the energy flow between the two systems cannot be predicted based on the initial T's. Even when the initial T's are equal, there may be energy transferred. Moreover, the T of the combination is different from the initial values. This contradicts the intuition that temperature should be an intensive quantity, and that two equal-temperature systems should be unaffected by being brought into thermal contact.

- Strange behavior for few-particle systems: Many results, such as the microcanonical equipartition theorem acquire a one- or two-degree of freedom offset when written in terms of T_{sur}. For a small systems this offset is significant, and so if we make S_{sur} the analogue of entropy, several exceptions need to be made for systems with only one or two degrees of freedom.

- Spurious negative temperatures: A negative T_{sur} occurs whenever the density of states decreases with energy. In some systems the density of states is not monotonic in energy, and so T_{sur} can change sign multiple times as the energy is increased. The preferred solution to these problems is to avoid using the microcanonical ensemble. In many realistic cases a system is thermostatted to a heat bath so that the energy is not precisely known. Then, a more accurate description is the canonical ensemble or grand canonical ensemble, both of which have complete correspondence to thermodynamics.

8.2.6 Exercises

8.2.6.1 Ex: Ideal gas in a uniform gravitational field in the microcanonical description

Calculate the microcanonical phase space volume, the velocity distribution, and the kinetic temperature explicitly for an ideal gas in a uniform gravitational field.

Part III

Atomic and Molecular Physics

Preface to the part *Atomic and Molecular Physics*

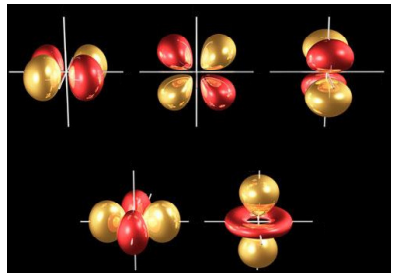

In quantum mechanics (see Chp. 3) we have learned how to handle rotationally symmetric systems and deduced Bohr's atom model for the case of Coulombian potentials. Real atoms are of course much more complicated and exhibit a complex energy level structure, which necessitates a deepening of the theory of atomic physics.

Important corrections arise from relativistic effects, such as the fact that electrons have a spin. These corrections will be presented in chapter 9. In Chp. 10 we will discuss the impact of external electric and magnetic fields on the atomic level structure. When several electrons are present in the shell, their mutual interaction and quantum statistical effects (already introduced in Chp. 7) must be accounted for, as will be shown in 11. Interactions between atoms may lead to the formation of molecules, rudimentarily discussed in Chp. 12 or collisions discussed in Chp. 13.

Chapter 9

Electron spin and the atomic fine structure

The energy structure of hydrogen calculated by Bohr's model from the non-relativistic Hamiltonian agrees very well with the experimental measurements. However, in high-resolution experiments, small deviations were observed as energy shifts and splittings of spectral lines. These deviations, called *fine structure*, were not predicted by theory, which suggests that there are weak additional effects that do not strongly affect the position of the spectral lines but remove the energy degeneracy of the orbital quantum number ℓ: $E = E_{n,\ell}$.

As a possible explanation we have the fact that the electrons present relativistic mass and momentum. In order to estimate the relevance of relativistic corrections let us estimate the electron velocity in the fundamental hydrogen states given by $E_1 = -\hbar^2/2m_e a_{\rm B}^2$. Using the definitions of the Bohr radius, $a_{\rm B} = 4\pi\varepsilon_0\hbar^2/(m_e e^2)$, and the *fine structure constant*

$$\alpha \equiv \frac{e^2}{4\pi\epsilon_0\hbar c} \simeq \frac{1}{137} \ , \tag{9.1}$$

we obtain,

$$v = \sqrt{\frac{2E_1}{m_e}} = \frac{\hbar}{m_e a_{\rm B}} = \frac{e^2}{4\pi\varepsilon_0\hbar} = \alpha c \ , \tag{9.2}$$

which shows that the electron velocity is very high and that relativistic effects may indeed be *non negligible*.

9.1 The Dirac equation

9.1.1 The Klein-Gordon equation for bosons

The Schrödinger equation for a free particle is based on the non-relativistic energy-momentum dispersion relation,

$$E = \frac{p^2}{2m_e} \ . \tag{9.3}$$

and the definitions of the quantum operators for energy and momentum,

$$\hat{E} = \imath\hbar\frac{\partial}{\partial t} \qquad \text{and} \qquad \hat{\mathbf{p}} = -\imath\hbar\nabla \ . \tag{9.4}$$

As already discussed in Sec. 1.3.2 we can, in order to find a relativistic wave equation, try the approach of inserting the quantum operators into the relativistic energy-momentum relation [1].

$$E^2 = c^2p^2 + m_e^2c^4 \ . \tag{9.5}$$

We obtain,

$$\boxed{\left[\frac{1}{c^2}\frac{\partial^2}{\partial t^2} - \nabla^2 + \left(\frac{m_e c}{\hbar}\right)^2\right]\psi = 0} \ . \tag{9.6}$$

This is the *Klein-Gordon equation*. The stationary solution of this equation is a spherical wave,

$$\psi = \psi_0 \frac{1}{r} e^{-2\pi r/\lambda_C} \ , \tag{9.7}$$

where $\lambda_C = h/m_e c$ is the *Compton wavelength*. We show this in Exc. 9.1.5.1. For example, in the case of heavy bosonic particles, such as a field of π-mesons, ψ is the *Yukawa potential*.

In the framework of the *standard model*, it is believed that matter is composed of two fundamental types of particles, bosons and fermions. Bosons are exchanged between fermions conveying the interaction between them. A typical example is the one of two electrons whose Coulomb interaction is mediated by the exchange of photons. Bosons obey the Klein-Gordon equation, fermions the Dirac equation derived in the following section.

9.1.2 The Dirac equation for fermions

In 1928 Paul Dirac, at the age of 26, developed an approach to a relativistic wave equation which differed from the Klein-Gordon equation. Motivated by the observation that the photon, being the relativistic particle *par excellence*, obeys a linear energy-momentum relation of the form $\omega = ck$, he attempted to derive a linear dispersion relation in E and p for heavy particles via the following ansatz:

$$E = \alpha_0 m_e c^2 + \alpha_1 c p_x + \alpha_2 c p_y + \alpha_3 c p_z \ . \tag{9.8}$$

Replacing energy and momentum with their respective operators [2],

$$\imath\hbar\frac{\partial}{\partial t}\phi = \alpha_0 m_e c^2 \phi - \imath c\hbar\left(\alpha_1\frac{\partial}{\partial x} + \alpha_2\frac{\partial}{\partial y} + \alpha_3\frac{\partial}{\partial z}\right)\phi \ . \tag{9.9}$$

We must now ensure that the relativistic energy-momentum condition (9.5) be satisfied.

Example 56 (*Derivation of the Dirac equation*): Taking the square on the right-hand side of the equation (9.9),

$$\begin{aligned}
&[\alpha_0 m_e c^2 - \imath c\hbar(\alpha_1\partial_x + \alpha_2\partial_y + \alpha_3\partial_z)][\alpha_0 m_e c^2 - \imath c\hbar(\alpha_1\partial_x + \alpha_2\partial_y + \alpha_3\partial_z)] \\
&= m_e^2c^4\alpha_0^2 - \imath c\hbar m_e c^2[(\alpha_0\alpha_1 + \alpha_1\alpha_0)\partial_x + (\alpha_0\alpha_2 + \alpha_2\alpha_0)\partial_y + (\alpha_0\alpha_3 + \alpha_3\alpha_0)\partial_z] \\
&\quad - c^2\hbar^2[\alpha_1^2\partial_x^2 + \alpha_2^2\partial_y^2 + \alpha_3^2\partial_z^2] \\
&\quad - c^2\hbar^2[(\alpha_1\alpha_2\partial_x\partial_y + \alpha_2\alpha_1\partial_y\partial_x) + (\alpha_2\alpha_3\partial_y\partial_z + \alpha_3\alpha_2\partial_z\partial_y) + (\alpha_3\alpha_1\partial_z\partial_x + \alpha_1\alpha_3\partial_x\partial_z)] \ .
\end{aligned}$$

[1] Using the covariant notation with $p_\mu \equiv (E/c, \mathbf{p})$: $p_\mu p^\mu = E^2/c^2 - p^2 = m_e^2c^2$ is a Lorentz invariant.

[2] We introduce the abbreviation $\partial_k \equiv \frac{\partial}{\partial x_k}$

For this expression to be identical to the relativistic energy-momentum condition (9.5),

$$m_e^2c^4 - c^2\hbar^2[\partial_x^2 + \partial_y^2 + \partial_z^2] \ ,$$

we need to postulate for all $i = 0, .., 3$, that $\alpha_i\alpha_j + \alpha_j\alpha_i = 2\delta_{ij}$.

Obviously, the condition

$$[\alpha_i, \alpha_j]_+ = 2\delta_{ij} \tag{9.10}$$

can not be satisfied if the α_i are numbers. The idea of Dirac was to interpret the variables α_i as matrices. These matrices act as operators on appropriate states, which are no longer scalar wavefunctions but vectors. Each component of the vector is a wavefunction in the usual sense. The Hilbert space is extended to be the product space of the usual spatial wavefunctions and a finite-dimensional vector space.

Example 57 (*Calculation with matrices of operator*): To give an idea of how the algebra works we consider a general situation. As the operator we choose the product,

$$\begin{pmatrix} 0 & 1 \\ 1 & 0 \end{pmatrix} \frac{\partial}{\partial x}$$

and as the wavefunction vector we choose,

$$\begin{pmatrix} e^{\imath k_1 x} \\ e^{\imath k_2 x} \end{pmatrix} .$$

Applying the operator on the state vector we get,

$$\begin{pmatrix} 0 & 1 \\ 1 & 0 \end{pmatrix} \frac{\partial}{\partial x} \begin{pmatrix} e^{\imath k_1 x} \\ e^{\imath k_2 x} \end{pmatrix} = \begin{pmatrix} 0 & \frac{\partial}{\partial x} \\ \frac{\partial}{\partial x} & 0 \end{pmatrix} \begin{pmatrix} e^{\imath k_1 x} \\ e^{\imath k_2 x} \end{pmatrix} = \begin{pmatrix} 0 + \frac{\partial}{\partial x} e^{\imath k_2 x} \\ \frac{\partial}{\partial x} e^{\imath k_1 x} + 0 \end{pmatrix} = \begin{pmatrix} \imath k_2 e^{\imath k_2 x} \\ \imath k_1 e^{\imath k_1 x} \end{pmatrix} .$$

The matrices α_i must satisfy the condition (9.10). It is possible to show that this requires at least four-dimensional matrices of the following form:

$$\alpha_0 = \begin{pmatrix} -\mathbb{I} & 0 \\ 0 & \mathbb{I} \end{pmatrix} \qquad \text{and} \qquad \alpha_j = \begin{pmatrix} 0 & \sigma_j \\ \sigma_j & 0 \end{pmatrix} \ , \tag{9.11}$$

where $j = x, y, z = 1, 2, 3$. In this notation the components of the matrices are themselves matrices, i.e. the *Pauli spin matrices* defined in (1.154). The state vector must also have four dimensions,

$$\vec{\vec{\Phi}}(\mathbf{r}, t) = \begin{pmatrix} \vec{\phi}(\mathbf{r}, t) \\ \vec{\chi}(\mathbf{r}, t) \end{pmatrix} \quad \text{with} \quad \vec{\phi}(\mathbf{r}, t) = \begin{pmatrix} \phi_1(\mathbf{r}, t) \\ \phi_2(\mathbf{r}, t) \end{pmatrix} \quad \text{and} \quad \vec{\chi}(\mathbf{r}, t) = \begin{pmatrix} \chi_1(\mathbf{r}, t) \\ \chi_2(\mathbf{r}, t) \end{pmatrix} . \tag{9.12}$$

ϕ_j are called *large components*, χ_j are called *small components*. This designation is explained later. Combining the matrices α_j to a three-dimensional vector $\vec{\alpha}$, we can now write the Dirac equation (9.9) like,

$$\boxed{\imath\hbar\partial_t \vec{\vec{\Phi}}(\mathbf{r}, t) = \left(m_e c^2 \alpha_0 + c\vec{\alpha} \cdot \hat{\mathbf{p}}\right) \vec{\vec{\Phi}}(\mathbf{r}, t)} \ . \tag{9.13}$$

Or, using the notation (9.11) and combining the Pauli matrices σ_j to a three-dimensional vector $\vec{\sigma}$, we can write the Dirac equation as:

$$\boxed{\imath\hbar\frac{\partial}{\partial t}\begin{pmatrix}\vec{\phi}\\ \vec{\chi}\end{pmatrix} = \left[m_e c^2\begin{pmatrix}-\mathbb{I} & 0\\ 0 & \mathbb{I}\end{pmatrix} + c\begin{pmatrix}0 & \vec{\sigma}\cdot\hat{\mathbf{p}}\\ \vec{\sigma}\cdot\hat{\mathbf{p}} & 0\end{pmatrix}\right]\begin{pmatrix}\vec{\phi}\\ \vec{\chi}\end{pmatrix}} \ . \tag{9.14}$$

The non-diagonal matrix,

$$\begin{pmatrix}0 & \vec{\sigma}\cdot\hat{\mathbf{p}}\\ \vec{\sigma}\cdot\hat{\mathbf{p}} & 0\end{pmatrix} \tag{9.15}$$

couples large and small components.

Example 58 (*Covariant and relativistically invariant form of Dirac's equation*): To demonstrate its relativistic invariance it is useful to rewrite the Dirac equation in a way in which time and space appear on equal footings. For this we introduce new matrices,

$$\gamma^0 \equiv \alpha_0 \qquad \text{and} \qquad \gamma^k = \gamma^0\alpha_k \ . \tag{9.16}$$

We obtain,

$$\gamma^0 = \begin{pmatrix}-\mathbb{I} & 0\\ 0 & \mathbb{I}\end{pmatrix} \qquad \text{and} \qquad \gamma^k = \begin{pmatrix}0 & \sigma_k\\ -\sigma_k & 0\end{pmatrix} \ . \tag{9.17}$$

We also define another important matrix by,

$$\gamma_5 \equiv \imath\gamma_0\gamma_1\gamma_2\gamma_3 = \begin{pmatrix}0 & \mathbb{I}\\ \mathbb{I} & 0\end{pmatrix} \ . \tag{9.18}$$

With this, using Einstein's notation [3], the Dirac equation (9.12) adopts the form,

$$\imath\hbar\gamma^\mu\partial_\mu\psi - m_e c\psi = 0 \ . \tag{9.19}$$

The complete system is summarized in the Minkowski metrics of time-space in the form,

$$[\gamma^\mu, \gamma^\nu]_+ = 2\eta^{\mu\nu} \ , \tag{9.20}$$

for $\mu, \nu = 0, .., 5$, that is, all matrices γ_k anticommute.
The Dirac equation can now be interpreted as an eigenvalue equation, where the rest mass is proportional to the eigenvalue of a momentum quadrivector, the proportionality constant being the speed of light:

$$\hat{p}_{\text{op}}\psi = m_e c\psi \ , \tag{9.21}$$

Using $\partial\!\!\!/$ in the Feynman slash notation, which includes the γ-matrices, as well as a summation over the components of the spinor in the derivative, the Dirac equation becomes:

$$\imath\hbar\partial\!\!\!/\psi - m_e c\psi = 0 \ . \tag{9.22}$$

A fundamental theorem states that, if two distinct sets of matrices are given, which both satisfy Clifford's relations, then they are connected to each other by a similarity transformation:

$$\gamma'^\mu = S^{-1}\gamma^\mu S \ . \tag{9.23}$$

[3] $\partial_0 \equiv \frac{1}{c}\partial_t$

If, in addition, the matrices are all unitary, as is the case of Dirac's set, then S is unitary,

$$\gamma'^{\mu} = \mathcal{U}^{\dagger}\gamma^{\mu}\mathcal{U} \ . \tag{9.24}$$

9.1.2.1 Anti-particles

Disregarding for a moment the non-diagonal matrix, the Dirac equation separates into two independent equations,

$$\imath\hbar\frac{\partial\vec{\phi}}{\partial t} = m_e c^2\vec{\phi} \quad \text{and} \quad \imath\hbar\frac{\partial\vec{\chi}}{\partial t} = -m_e c^2\vec{\chi} \ . \tag{9.25}$$

These are eigenenergy equations with the eigenvalues $m_e c^2$ and $-m_e c^2$. The state with negative energy is interpreted as *anti-particle*. Therefore, the non-diagonal matrix mixes particles and anti-particles. We will study in Exc. 9.1.5.2 the so-called *Zitterbewegung* as a solution of the Dirac equation.

9.1.2.2 Particles and anti-particles in the non-relativistic limit

To reduce the Dirac equation to the non-relativistic Schrödinger equation, we first need to get rid of the rest energy. To do so, we separate a fast oscillation, whose frequency corresponds to the rest mass of the electron via the following ansatz, where $\mathbf{u}$ and $\mathbf{v}$ vary slowly in time:

$$\vec{\vec{\Phi}}(\mathbf{r},t) = e^{-\imath\omega_0 t}\begin{pmatrix}\mathbf{u}(\mathbf{r},t)\\ \mathbf{v}(\mathbf{r},t)\end{pmatrix} \quad , \quad \hbar\omega_0 = m_e c^2 \ , \tag{9.26}$$

with the temporal derivative,

$$\imath\hbar\dot{\vec{\vec{\Phi}}} = \left[m_e c^2\begin{pmatrix}\mathbf{u}\\ \mathbf{v}\end{pmatrix} + \imath\hbar\begin{pmatrix}\dot{\mathbf{u}}\\ \dot{\mathbf{v}}\end{pmatrix}\right] e^{-\imath\omega_0 t} \ . \tag{9.27}$$

We insert this into the Dirac equation,

$$\left[m_e c^2\begin{pmatrix}\mathbf{u}\\ \mathbf{v}\end{pmatrix} + \imath\hbar\begin{pmatrix}\dot{\mathbf{u}}\\ \dot{\mathbf{v}}\end{pmatrix}\right] e^{-\imath\omega_0 t} = \left[m_e c^2\begin{pmatrix}\mathbf{u}\\ -\mathbf{v}\end{pmatrix} + c\vec{\sigma}\cdot\hat{\mathbf{p}}\begin{pmatrix}\mathbf{v}\\ \mathbf{u}\end{pmatrix}\right] e^{-\imath\omega_0 t} \tag{9.28}$$

finally obtaining,

$$\imath\hbar\dot{\mathbf{u}} = c(\vec{\sigma}\cdot\hat{\mathbf{p}})\mathbf{v} \quad , \quad \imath\hbar\dot{\mathbf{v}} = c(\vec{\sigma}\cdot\hat{\mathbf{p}})\mathbf{u} - 2m_e c^2\mathbf{v} \ . \tag{9.29}$$

Since $\mathbf{u}$ and $\mathbf{v}$ only vary slowly in time, the derivatives on the left-hand side are small quantities. However, the condition that both derivatives must vanish is too strong, because it leads to the trivial solution $\mathbf{u} = 0$ and $\mathbf{v} = 0$. We find the first non-trivial solution by the condition $\dot{\mathbf{v}} = 0$. The second equation then becomes,

$$\mathbf{v} = \frac{1}{2m_e c}(\vec{\sigma}\cdot\hat{\mathbf{p}})\mathbf{u} \ . \tag{9.30}$$

Inserted into the first equation,

$$\imath\hbar\dot{\mathbf{u}} = c\frac{(\vec{\sigma}\cdot\hat{\mathbf{p}})^2}{2m_e c}\mathbf{u}\ . \tag{9.31}$$

We need, therefore, to evaluate the expression $(\vec{\sigma}\cdot\hat{\mathbf{p}})^2$,

$$\vec{\sigma}\cdot\hat{\mathbf{p}} = \begin{pmatrix} -\hat{p}_z & \hat{p}_x + \imath\hat{p}_y \\ \hat{p}_x - \imath\hat{p}_y & \hat{p}_z \end{pmatrix} \qquad \text{and} \qquad (\vec{\sigma}\cdot\hat{\mathbf{p}})^2 = \hat{\mathbf{p}}^2\begin{pmatrix} 1 & 0 \\ 0 & 1 \end{pmatrix}\ . \tag{9.32}$$

Inserted into the differential equation (9.31) for $\mathbf{u}$ we obtain precisely the Schrödinger equation for a free particle,

$$\boxed{\imath\hbar\dot{\mathbf{u}} = \frac{\hat{\mathbf{p}}^2}{2m_e}\mathbf{u}}\ . \tag{9.33}$$

Let us return to the question, why we call $\mathbf{u}$ the *strong* component. We have from the equation (9.30),

$$\mathbf{v}^\dagger\mathbf{v} = \frac{1}{(2m_e c)^2}(\vec{\sigma}\cdot\hat{\mathbf{p}})^2\mathbf{u}^\dagger\mathbf{u} = \frac{1}{2m_e c^2}\frac{\hat{\mathbf{p}}^2}{2m_e}\mathbf{u}^\dagger\mathbf{u}\ , \tag{9.34}$$

and since $\frac{\hat{\mathbf{p}}^2}{2m_e} \ll m_e c^2$ follows immediately $\mathbf{v}^\dagger\mathbf{v} \ll \mathbf{u}^\dagger\mathbf{u}$.

In this non-relativistic approximation the components $\mathbf{u}$ are much larger than the components $\mathbf{v}$. The mixture between particles and antiparticles only matters when $\frac{\hat{\mathbf{p}}^2}{2m_e} \simeq m_e c^2$, resp., $\frac{1}{2}m_e v^2 \simeq m_e c^2$ or $|v| \simeq c$. The electron only receives small positronic contributions as it approaches the speed of light. In the ground state of the hydrogen atom the electron has a velocity of of $v = \alpha c \simeq c/137$. That is, the contribution of the weak components is small, but present.

Example 59 (*Vanishing rest mass*): Let us note that for the case of vanishing rest mass, $m_e = 0$, the Dirac equation (9.14) dramatically simplifies. Taking the time derivative of the upper equation (9.14) and inserting the lower equation (9.14), we find,

$$\frac{1}{c^2}\frac{\partial^2}{\partial t^2}\vec{\phi} = \frac{1}{c^2}\frac{c\vec{\sigma}\cdot\hat{\mathbf{p}}}{\imath\hbar}\frac{\partial}{\partial t}\vec{\chi} = -\frac{(\vec{\sigma}\cdot\hat{\mathbf{p}})^2}{\hbar^2}\vec{\phi} = -\frac{\hat{\mathbf{p}}^2}{\hbar^2}\vec{\phi} = \nabla^2\vec{\phi}\ . \tag{9.35}$$

I.e. we recover a Helmholtz type wave equation.

9.1.2.3 The spin

We consider the operator defined by [232, 233],

$$\hat{\mathbf{S}} \equiv \tfrac{\hbar}{2}\hat{\vec{\sigma}}\ , \tag{9.36}$$

and we calculate the commutation relations between its components. From the definitions of the Pauli matrices (1.154) we obtain the rule,

$$[\hat{S}_x, \hat{S}_y] = \tfrac{\hbar^2}{4}\begin{pmatrix} 0 & 1 \\ 1 & 0 \end{pmatrix}\begin{pmatrix} 0 & \imath \\ -\imath & 0 \end{pmatrix} - \tfrac{\hbar^2}{4}\begin{pmatrix} 0 & \imath \\ -\imath & 0 \end{pmatrix}\begin{pmatrix} 0 & 1 \\ 1 & 0 \end{pmatrix} = \frac{\hbar^2}{4}\begin{pmatrix} -2\imath & 0 \\ 0 & 2\imath \end{pmatrix} = \imath\hbar\hat{S}_z\ . \tag{9.37}$$

In general terms the following holds true: $[\hat{S}_i, \hat{S}_j] = \epsilon_{ijk}\imath\hbar\hat{S}_k$. It is interesting to compare this with the commutation relation for the orbital angular momentum $[\hat{L}_i, \hat{L}_j] = \epsilon_{ijk}\imath\hbar\hat{L}_k$. The coincidence suggests a generalization of the concept of angular momentum: We now call *angular momentum operator* every three-dimensional vector operator satisfying this commutation relation [4]. We consider the eigenvalue equation for $\hat{s}_z$, which is incorporated in the Dirac equation,

$$\hat{S}_z\vec{\phi} = \tfrac{\hbar}{2}\begin{pmatrix}-1 & 0\\ 0 & 1\end{pmatrix}\begin{pmatrix}\phi_1\\ \phi_2\end{pmatrix} = M_S\hbar\begin{pmatrix}\phi_1\\ \phi_2\end{pmatrix} \ . \tag{9.38}$$

The eigenvalues are obviously $M_S = \pm\frac{1}{2}$. The angular momentum related to the matrices $\hat{\mathbf{S}}$ is obviously half-integer. We are dealing here with a new type of angular momentum, which is not included in the usual definition of *orbital* angular momentum $\hat{\mathbf{L}} = \mathbf{r}\times\hat{\mathbf{p}}$. The new angular momentum is called *intrinsic* angular momentum or *spin* of the particle. The spin represents a new structure or dimension additional to space comparable to the polarization of light. The photons of a circularly polarized light beam also contribute to an intrinsic angular momentum, which however in this case is integer.

In Exc. 9.1.5.3 we will see that neither $\hat{L}_z$ nor $\hat{S}_z$ are constants of motion of the Hamiltonian (9.14), but the sum $\hat{J}_z \equiv \hat{L}_z + \hat{S}_z$,

$$[\hat{J}_z, \hat{H}] = 0 \ . \tag{9.39}$$

9.1.2.4 The stationary Dirac equation

By a similar treatment as in the Schrödinger equation one can deduce a stationary Dirac equation (9.13) via a separation of the time variable. Making for the time an exponential ansatz,

$$\vec{\phi}(\mathbf{r},t) = \vec{\phi}(\mathbf{r})e^{-\imath Et/\hbar} \quad \text{and} \quad \vec{\chi}(\mathbf{r},t) = \vec{\chi}(\mathbf{r})e^{-\imath Et/\hbar} \ , \tag{9.40}$$

we obtain coupled stationary equations for the large and small components,

$$(E - m_ec^2)\vec{\phi}(\mathbf{r}) = c\sigma\cdot\hat{\mathbf{p}}\vec{\chi}(\mathbf{r}) \quad \text{and} \quad (E + m_ec^2)\vec{\chi}(\mathbf{r}) = c\sigma\cdot\hat{\mathbf{p}}\vec{\phi}(\mathbf{r}) \ . \tag{9.41}$$

9.1.3 The relativistic electron in a central Coulomb field

9.1.3.1 Minimal coupling

In atomic physics we are mainly interested in electrons bound to a potential (e.g., generated by an atomic nucleus), that is, we must introduce electromagnetic forces into the Dirac equation. Therefore, we now consider the interaction of a charged particle with an electromagnetic field given by the vector potential $\mathbf{A}$ and by the electrostatic potential U, such that the electric and magnetic fields,

$$\vec{\mathcal{E}} = -\nabla U - \frac{\partial\mathbf{A}}{\partial t} \quad \text{and} \quad \vec{\mathcal{B}} = \nabla\times\mathbf{A} \ , \tag{9.42}$$

[4] This concept can be derived from the requirement of symmetry under rotation of space as discussed in Sec. 1.7.

allow to calculate the Coulomb-Lorentz force. In the Hamiltonian formulation of electrodynamics the interaction can be described simply by the transition [5],

$$\boxed{\hat{\mathbf{p}} \longrightarrow \hat{\mathbf{p}} - q\mathbf{A} \equiv \vec{\pi} \quad \text{and} \quad \hat{H} \longrightarrow \hat{H} + qU} \ . \tag{9.43}$$

called the *minimal coupling*. We briefly mentioned this already in Sec. 1.7.4, and the rules will be derived in Sec. 10.1. In addition to the substitution of the momentum, we must add the scalar potential qU, and we obtain the Dirac equation for a particle inside an applied electromagnetic field,

$$\imath\hbar\dot{\vec{\Phi}} = \left(m_e c^2\alpha_0 + c\vec{\alpha}\cdot\vec{\pi} + qU\right)\vec{\Phi} \ , \tag{9.44}$$

in generalization of Eq. (9.13).

9.1.3.2 Solving the stationary Dirac equation

Let us, for now, disregard external magnetic fields, $\mathbf{A} = 0$. Then, the stationary Dirac equation (9.41) becomes,

$$\begin{aligned} [E - qU(\mathbf{r}) - m_e c^2]\vec{\phi}(\mathbf{r}) &= c\sigma\cdot\hat{\mathbf{p}}\vec{\chi}(\mathbf{r}) \\ [E - qU(\mathbf{r}) + m_e c^2]\vec{\chi}(\mathbf{r}) &= c\sigma\cdot\hat{\mathbf{p}}\vec{\phi}(\mathbf{r}) \ . \end{aligned} \tag{9.45}$$

For the Coulomb potential,

$$qU(r) = -\frac{1}{4\pi\epsilon_0}\frac{e^2}{r} \tag{9.46}$$

the Dirac equation can be solved algebraically [234, 341, 346, 294] [6]. The calculation is more complicated than the resolution of the Schrödinger equation for hydrogen derived in Secs. 3.1.4 and 3.2.1 and will be sketched in the following.

> **Example 60 (*Dirac equation in spherical coordinates*):** The goal of the following calculation is to express the Dirac equation for an electron in a central Coulomb field in spherical coordinates, i.e. r and $\hat{p}_r = -\imath\hbar\partial_r$ instead of $\hat{\mathbf{p}}$. The starting point is the Dirac equation (9.14),
>
> $$\imath\hbar\partial_t\vec{\Phi}(\mathbf{r},t) = \hat{H}\vec{\Phi}(\mathbf{r},t) \ , \tag{9.47}$$
>
> with the Hamiltonian in the minimal coupling (9.43),
>
> $$\begin{aligned} \hat{H} &\equiv m_e c^2\alpha_0 + c\vec{\alpha}\cdot[\hat{\mathbf{p}} - q\mathbf{A}(\mathbf{r})] + qU(\mathbf{r}) \\ \text{with} \quad \mathbf{A} &= 0 \quad \text{and} \quad U(\mathbf{r}) = -\frac{e^2}{4\pi\varepsilon_0 r} \ . \end{aligned} \tag{9.48}$$
>
> We adopt the standard procedure from non-relativistic physics, which consists in rewriting the Hamiltonian in terms of observables, which commute with the Hamiltonian [7].

[5] In quadrivetorial notation: $\pi_\mu = p_\mu - qA_\mu$ with $p_\mu = \begin{pmatrix} E/c \\ \hat{\mathbf{p}} \end{pmatrix}$ and $A_\mu = \begin{pmatrix} U/c \\ \mathbf{A} \end{pmatrix}$.

[6] See also http://einstein.drexel.edu/~bob/Term_Reports/Whitehead_3.pdf

[7] Typical examples are the Hamiltonian of the harmonic oscillator (2.84) written in terms of $\hat{n} \equiv \hat{a}^\dagger\hat{a}$ or the Hamiltonian of the hydrogen atom (3.34) written in terms of $\mathbf{L}^2$.

The goal is to calculate the quantity $\vec{\alpha}\cdot\hat{\mathbf{p}}$ appearing in the above Hamiltonian. As a first steps we define the following quantities,

$$\boxed{\begin{array}{rcll} \hat{\mathbf{L}} & \equiv & \mathbf{r}\times\hat{\mathbf{p}} \quad \text{satisfying} & \hat{\mathbf{L}}\times\hat{\mathbf{L}} = \imath\hbar\hat{\mathbf{L}} \\ \hat{\mathbf{S}} & \equiv & \frac{\hbar}{2}\vec{\varsigma} \equiv \frac{\hbar}{2}\gamma_5\vec{\alpha} & \\ \hat{\mathbf{J}} & \equiv & \hat{\mathbf{L}}+\hat{\mathbf{S}} & \\ \hbar j' & \equiv & \alpha_0(\gamma_5\vec{\alpha}\cdot\hat{\mathbf{L}}+\hbar) & \\ r\varepsilon & \equiv & \vec{\alpha}\cdot\mathbf{r} & \end{array}} \ . \tag{9.49}$$

remembering that $\gamma_5 = -\imath\alpha_1\alpha_2\alpha_3 = \begin{pmatrix} 0 & \mathbb{I} \\ \mathbb{I} & 0 \end{pmatrix}$ is the transformation exchanging particles and anti-particles. The first important relationship we have to derive is,

$$(\vec{\alpha}\cdot\mathbf{B})(\vec{\alpha}\cdot\mathbf{C}) = (\mathbf{B}\cdot\mathbf{C}) + \imath\gamma_5\vec{\alpha}\cdot(\mathbf{B}\times\mathbf{C}) \ . \tag{9.50}$$

It holds for $[\vec{\alpha},\mathbf{B}] = 0 = [\vec{\alpha},\mathbf{C}]$ and will be proven in 9.1.5.4. Exploiting this relationship, we see that the scalar quantity ε satisfies,

$$\varepsilon^2 = \frac{1}{r^2}(\vec{\alpha}\cdot\mathbf{r})^2 = \frac{1}{r^2}[\mathbf{r}\cdot\mathbf{r} + \imath\vec{\alpha}\cdot(\mathbf{r}\times\mathbf{r})] = 1 \ . \tag{9.51}$$

Furthermore, with the definition of j' we show,

$$\begin{aligned} r\varepsilon\vec{\alpha}\cdot\hat{\mathbf{p}} = (\vec{\alpha}\cdot\mathbf{r})(\vec{\alpha}\cdot\hat{\mathbf{p}}) &= \mathbf{r}\cdot\hat{\mathbf{p}} + \imath\gamma_5\vec{\alpha}\cdot(\mathbf{r}\times\hat{\mathbf{p}}) \\ &= \mathbf{r}\cdot\hat{\mathbf{p}} + \imath\gamma_5\vec{\alpha}\cdot\mathbf{L} = r\hat{p}_r + \imath\alpha_0\hbar j' - \imath\hbar \ , \end{aligned} \tag{9.52}$$

where the relationship $\mathbf{r}\cdot\hat{\mathbf{p}} = r\hat{p}_r$ is verified in Exc. 9.1.5.5(c). Hence,

$$\vec{\alpha}\cdot\hat{\mathbf{p}} = \varepsilon\left(\hat{p}_r + \frac{\imath\hbar(\alpha_0 j' - 1)}{r}\right) \ , \tag{9.53}$$

The final radial Hamiltonian is,

$$\boxed{\hat{H} = m_e c^2\alpha_0 + c\varepsilon\left(p_r - \imath\frac{\hbar}{r}\right) + \frac{\imath c\varepsilon\alpha_0\hbar j'}{r} - \frac{e^2}{4\pi\varepsilon_0 r}} \ . \tag{9.54}$$

For now the choice of the quantities ε and j' must seem arbitrary, so we will have to discover their properties. We will see that j' is a non-zero integer related to the total angular momentum j. The following properties will be proven in Exc. 9.1.5.5(a) and (b),

$$\begin{aligned} (\hbar j')^2 &= \mathbf{J}^2 + \tfrac{\hbar^2}{4} \\ [\hbar j', \hat{H}]_- = [\varepsilon, \hat{H}]_- &= [\alpha_0, \hat{H}]_- = 0 \ . \end{aligned} \tag{9.55}$$

Hence, we got a collection of radial variables being constants of motion of the Dirac Hamiltonian.

Example 61 (*Resolving the spherical Dirac equation*): We will now search a solution to the spherical Dirac equation with the Hamiltonian (9.54). Noticing that the matrix α_0 is diagonal and the matrix ε counter-diagonal (just like the Dirac matrices $\vec{\alpha}$), we may break down the stationary radial Dirac equation

into 2 by 2 matrices. Using the fact that ε commutes with all other terms and anti-commutes with α_0 and that $\varepsilon^{-1} = \varepsilon^\dagger$ is a unitary transformation, we may go to a new basis via,

$$\begin{pmatrix} m_e c^2 - \frac{e^2}{4\pi\varepsilon_0 r} & -\imath c p_r - c\frac{\hbar}{r} - c\frac{\hbar j'}{r} \\ \imath c p_r + c\frac{\hbar}{r} - c\frac{\hbar j'}{r} & -m_e c^2 - \frac{e^2}{4\pi\varepsilon_0 r} \end{pmatrix} \begin{pmatrix} \vec{\phi} \\ \varepsilon\vec{\chi} \end{pmatrix} = E \begin{pmatrix} \vec{\phi} \\ \varepsilon\vec{\chi} \end{pmatrix} . \tag{9.56}$$

Substituting $\alpha = \frac{e^2}{4\pi\varepsilon_0\hbar c}$ and $a_\pm \equiv \frac{\hbar}{m_e c \mp E/c}$ (that is, $\pm m_e c^2 - E \equiv \pm\frac{\hbar c}{a_\pm}$), we find,

$$\begin{pmatrix} \frac{1}{a_+} - \frac{\alpha}{r} & -\frac{d}{dr} - \frac{j'+1}{r} \\ \frac{d}{dr} - \frac{j'-1}{r} & -\frac{1}{a_-} - \frac{\alpha}{r} \end{pmatrix} \begin{pmatrix} \vec{\phi} \\ \varepsilon\vec{\chi} \end{pmatrix} = 0 . \tag{9.57}$$

Assuming the existence of solutions of the form,

$$\begin{pmatrix} \vec{\phi} \\ \varepsilon\vec{\chi} \end{pmatrix} = \frac{e^{-r/a}}{r} \begin{pmatrix} \vec{f} \\ \vec{g} \end{pmatrix} , \tag{9.58}$$

where $a \equiv \sqrt{a_+ a_-} = \hbar\left(m_e^2 c^2 - \frac{E^2}{c^2}\right)^{-1}$ [that is, $\frac{d}{dr}\frac{e^{-r/a}}{r} = \frac{e^{-r/a}}{r}\left(-\frac{1}{a} - \frac{1}{r}\right)$], we find,

$$\begin{pmatrix} \frac{1}{a_+} - \frac{\alpha}{r} & -\frac{d}{dr} - \frac{1}{a} - \frac{j'}{r} \\ \frac{d}{dr} - \frac{1}{a} - \frac{j'}{r} & -\frac{1}{a_-} - \frac{\alpha}{r} \end{pmatrix} \begin{pmatrix} \vec{f} \\ \vec{g} \end{pmatrix} = 0 . \tag{9.59}$$

Next we expand the unknown function $\vec{f}$ and $\vec{g}$ as series,

$$\vec{f}(r) = \sum_{s=-\infty}^{\infty} f_s r^s \quad \text{and} \quad \vec{g}(r) = \sum_{s=-\infty}^{\infty} g_s r^s . \tag{9.60}$$

These are then substituted into our system of equations. In order for the equation to go to zero as required, each term in the resulting series must separately go to zero. The coefficient of the r_s terms are,

$$\begin{aligned} \frac{f_s}{a_+} - \alpha f_{s+1} - (s+1+j')g_{s+1} + \frac{g_s}{a} &= 0 \\ \frac{g_s}{a_-} - \alpha g_{s+1} - (s+1-j')f_{s+1} + \frac{f_s}{a} &= 0 . \end{aligned} \tag{9.61}$$

These can be combined by multiplying the first equation (9.61) by a and and the second by a_- and then subtracting the former from the latter. Exploiting $\frac{a}{a_+} = \frac{a_-}{a}$, this gives us an expression directly relating the f_s coefficients with the g_s coefficients,

$$[\alpha a - a_+(s-j')]f_s + [\alpha a_- + a(s+j')]g_s = 0 . \tag{9.62}$$

To obtain the values of the coefficients we consider the boundary conditions. The functions $\vec{f}(r)$ and $\vec{g}(r)$ must go to zero at $r = 0$, because the functions $\vec{\phi}$ and $\vec{\chi}$ would otherwise diverge there due to the r^{-1} term. This means that there is some smallest s below which the series does not continue. We call this s_0, and it has the property,

$$f_{s_0-1} = g_{s_0-1} = 0 . \tag{9.63}$$

Plugging this into the equations (9.61), we find,

$$\begin{aligned} \alpha f_{s_0} + (s_0 + j')g_{s_0} &= 0 \\ \alpha g_{s_0} - (s_0 - j')f_{s_0} &= 0 \ . \end{aligned} \tag{9.64}$$

Combining these equations we can write the value s_0 in a very simple form,

$$s_0 = \sqrt{j'^2 - \alpha^2} \ . \tag{9.65}$$

This places a lower bound on the series. Note that this bound becomes imaginary if $\alpha > j'$. This will be discussed in more detail shortly.
The upper bound of the series is also useful. It can be shown that the series must terminate if the energy eigenvalue is to be less than $m_e c^2$ [234]. The implication of this result is that if the series terminates at index s_1 such that,

$$f_{s_1+1} = g_{s_1+1} = 0 \ . \tag{9.66}$$

Then, using equations (9.61) and (9.62), we have,

$$\frac{s_1}{a} = \frac{1}{2}\left(\frac{1}{a_-} - \frac{1}{a_+}\right)\alpha = \frac{E}{\hbar c}\alpha \ , \tag{9.67}$$

where we have used the definitions of the coefficients $a_\pm$ to expand them. Squaring this expression and expanding a using its definition, we get,

$$s_1^2\left(m_e c^2 - \frac{E^2}{c^2}\right) = \alpha^2 \frac{E^2}{c^2} \ . \tag{9.68}$$

This can be solved for the energy eigenvalues,

$$E = \pm m_e c^2 \left(1 + \frac{\alpha^2}{s_1^2}\right)^{-1/2} \ . \tag{9.69}$$

Note that the 'negative energy' solution corresponds to positron energy levels. From here forward, we drop the negative root and look only at the electron solution.
The two end points of the series, the indices s_0 and s_1 are separated by an integer number of steps. Calling this integer n' we can write,

$$s_1 = n' + s_0 = n' + \sqrt{j'^2 - \alpha^2} \ . \tag{9.70}$$

Plugging this into (9.69) gives a result for the energy eigenvalues in terms of only the two quantum numbers n' and j',

$$E_{n',j'} = m_e c^2 \left[1 + \frac{\alpha^2}{\left(n' + \sqrt{j'^2 - \alpha^2}\right)^2}\right]^{-1/2} \ .$$

This is the final result quoted for the energy eigenvalues of the hydrogenic atom by Dirac [234]. It turns out that later developments in the field [341, 346] prefer to use an equivalent set of quantum numbers that maps more closely to the familiar ones. The number j' is closely related to the total angular momentum quantum number j. j' has the range 1, 2, 3, while j has the range $\frac{1}{2}$, $\frac{3}{2}$, $\frac{5}{2}$. It is natural, and in fact correct, to make the identifications,

$$j' = j + \tfrac{1}{2} \ , \tag{9.71}$$

and

$$n' = n - j' = n - j - \tfrac{1}{2} \ , \tag{9.72}$$

for the principal quantum number n [341]. Combining these two adjustments with equation (9.71), we get the *Sommerfeld fine-structure formula*,

$$\boxed{E_{n,j} = m_e c^2 \left[1 + \frac{\alpha^2}{\left(n - j - \frac{1}{2} + \sqrt{(j+\frac{1}{2})^2 - \alpha^2} \right)^2} \right]^{-1/2}} \ , \tag{9.73}$$

with $j = \left| \ell \pm \frac{1}{2} \right|$ and $\ell = 0, 1, ...$ The derivation of the form of the actual wave functions $\vec{\phi}(r)$ and $\vec{\chi}(r)$ is very tedious [341] and will not be reproduced here.

The energy predicted by the Sommerfeld fine-structure formula (9.73) depends on two quantum numbers. The degeneracy of the orbital angular momentum $\mathbf{j}$ is lifted, and the new quantum number besides the main quantum number n is that of the total angular momentum j. The intransparent expression can be expanded by α,

$$\boxed{E_{n,j} \simeq m_e c^2 \left[1 - \frac{\alpha^2}{2n^2} - \frac{\alpha^4}{2n^3} \left(\frac{1}{j+1/2} - \frac{3}{4n} \right) \right]} \ . \tag{9.74}$$

The second term reproduces the energy of Bohr's model, but there are correction terms proportional to α^4. We will show in Secs. 9.1.4, that the energy levels, called *fine structure*, result from several relativistic corrections of different origins.

In the expression (9.74) for the electron energy in the Coulomb potential, the last term is positive and proportional to $1/n^4$. It describes relaxation of the binding due to the contribution of weak components. The term containing the quantum number j is called the spin-orbit coupling. To better understand this contribution we must first analyze more deeply the matrices $\vec{\sigma}$.

9.1.3.3 Dirac's Hamiltonian in the sub-relativistic limit

Defining the energy $E' = E - m_e c^2$, the stationary Dirac equation (9.45) for an electron of charge $q = -e$ in an external electrostatic potential $U(\mathbf{r})$ can be written,

$$[E' - qU(\mathbf{r})]\vec{\phi} = c\vec{\sigma} \cdot \hat{\mathbf{p}}\vec{\chi} \qquad \text{and} \qquad [E' - qU(\mathbf{r}) + 2m_e c^2]\vec{\chi} = c\vec{\sigma} \cdot \hat{\mathbf{p}}\vec{\phi} \ . \tag{9.75}$$

resolving the second equation for the wavefunction $\vec{\chi}$ and substituting it into the first,

$$\boxed{E'\vec{\phi} = qU(\mathbf{r})\vec{\phi} + \vec{\sigma} \cdot \hat{\mathbf{p}} \frac{1}{2m_e} \left(1 + \frac{E' - qU(\mathbf{r})}{2m_e c^2} \right)^{-1} \vec{\sigma} \cdot \hat{\mathbf{p}}\vec{\phi}} \ . \tag{9.76}$$

In the non-relativistic limit,

$$E' - qU \simeq \frac{\hat{\mathbf{p}}^2}{2m_e} \ll m_e c^2 \ , \tag{9.77}$$

we get by Taylor expansion of the second term in the bracket,

$$E'\vec{\phi} \simeq qU(\mathbf{r})\vec{\phi} + \vec{\sigma} \cdot \hat{\mathbf{p}} \frac{1}{2m_e} \left(1 - \frac{E' - qU(\mathbf{r})}{2m_e c^2} \right) \vec{\sigma} \cdot \hat{\mathbf{p}}\vec{\phi} \ . \tag{9.78}$$

Now, $\vec{\sigma}\cdot\hat{\mathbf{p}}$ is an operator entity, which acts on the subsequent operators and wavefunctions. We thus have to apply the product rule, $(\vec{\sigma}\cdot\hat{\mathbf{p}})U(\mathbf{r})\psi = U(\mathbf{r})(\vec{\sigma}\cdot\hat{\mathbf{p}})\psi + [(\vec{\sigma}\cdot\hat{\mathbf{p}})U(\mathbf{r})]\psi$, in equation (9.78),

$$E'\vec{\phi} \simeq qU(\mathbf{r})\vec{\phi} + \tfrac{1}{2m_e}\left(1 - \tfrac{E'-qU(\mathbf{r})}{2m_ec^2}\right)(\vec{\sigma}\cdot\hat{\mathbf{p}})^2\,\vec{\phi} + \tfrac{q}{4m_e^2c^2}[(\vec{\sigma}\cdot\hat{\mathbf{p}})U(\mathbf{r})](\vec{\sigma}\cdot\hat{\mathbf{p}})\vec{\phi}\,. \quad (9.79)$$

In the following we will make use of a general relationship which is similar to (9.50),

$$(\vec{\sigma}\cdot\mathbf{B})(\vec{\sigma}\cdot\mathbf{C}) = (\mathbf{B}\cdot\mathbf{C}) + \imath\vec{\sigma}\cdot(\mathbf{B}\times\mathbf{C})\,. \quad (9.80)$$

It holds for $[\vec{\sigma},\mathbf{B}] = 0 = [\vec{\sigma},\mathbf{C}]$ and will be demonstrated in Exc. 9.1.5.4. The relationship yields,

$$(\vec{\sigma}\cdot\hat{\mathbf{p}})^2 = \hat{\mathbf{p}}^2 \qquad \text{and} \qquad [\vec{\sigma}\cdot\hat{\mathbf{p}}U(\mathbf{r})](\vec{\sigma}\cdot\hat{\mathbf{p}}) = \hat{\mathbf{p}}U(\mathbf{r})\cdot\hat{\mathbf{p}} + \imath\vec{\sigma}\cdot[\hat{\mathbf{p}}U(\mathbf{r})\times\hat{\mathbf{p}}]\,, \quad (9.81)$$

so that expressing the momentum operator by $\mathbf{p} = -\imath\hbar\nabla$ wherever it acts on the potential,

$$E'\vec{\phi} \simeq qU(\mathbf{r})\vec{\phi} + \tfrac{1}{2m_e}\left(1 - \tfrac{E'-qU(\mathbf{r})}{2m_ec^2}\right)\hat{\mathbf{p}}^2\vec{\phi} - \tfrac{\hbar^2q}{4m_e^2c^2}\nabla U(\mathbf{r})\cdot\nabla\vec{\phi} + \tfrac{\hbar}{4m_e^2c^2}\vec{\sigma}\cdot[\nabla U(\mathbf{r})\times\hat{\mathbf{p}}]\vec{\phi}\,. \quad (9.82)$$

Also, with $U(\mathbf{r}) = U(r)$,

$$\nabla U(r) = \frac{\partial U}{\partial r}\nabla r = \frac{\partial U}{\partial r}\frac{\mathbf{r}}{r} \qquad \text{and} \qquad \nabla U(r)\cdot\nabla = \frac{\partial U}{\partial r}\hat{\mathbf{e}}_r\cdot\nabla = \frac{\partial U}{\partial r}\frac{\partial}{\partial r}\,. \quad (9.83)$$

We get,

$$\begin{aligned} E'\vec{\phi} &= qU(\mathbf{r})\vec{\phi} + \frac{1}{2m_e}\left(1 - \frac{E'-qU(\mathbf{r})}{2m_ec^2}\right)\hat{\mathbf{p}}^2\vec{\phi} - \frac{\hbar^2}{4m_e^2c^2}\frac{\partial qU}{\partial r}\frac{\partial}{\partial r}\vec{\phi} + \frac{\hbar q}{4m_e^2c^2}\vec{\sigma}\cdot\left[\frac{1}{r}\frac{\partial U}{\partial r}\mathbf{r}\times\hat{\mathbf{p}}\vec{\phi}\right] \\ &\simeq \left(\frac{\hat{\mathbf{p}}^2}{2m_e} + qU(r) - \frac{\hat{\mathbf{p}}^4}{8m_e^3c^2} + \frac{q}{2m_e^2c^2}\frac{1}{r}\frac{\partial U}{\partial r}\mathbf{s}\cdot\mathbf{l} - \frac{\hbar^2q}{4m_e^2c^2}\frac{\partial U}{\partial r}\frac{\partial}{\partial r}\right)\vec{\phi}\,. \end{aligned} \quad (9.84)$$

where we again applied the non-relativistic approximation (9.77) in the second line and made use of the definitions $\hat{\mathbf{S}} = \frac{\hbar}{2}\vec{\sigma}$ and $\hat{\mathbf{L}} = \mathbf{r}\times\hat{\mathbf{p}}$. The term in the bracket can be used as the Hamiltonian allowing to calculate the fine structure as first-order perturbations to the non-relativistic energy levels obtained from non-relativistic theory,

$$\boxed{\hat{H} \simeq \frac{\hat{\mathbf{p}}^2}{2m_e} - \frac{1}{4\pi\varepsilon_0}\frac{e^2}{r} - \frac{\hat{\mathbf{p}}^4}{8m_e^3c^2} - \frac{e}{2m_e^2c^2}\frac{1}{r}\frac{\partial U}{\partial r}\hat{\mathbf{S}}\cdot\hat{\mathbf{L}} - \frac{\hbar^2e}{4m_e^2c^2}\frac{\partial U}{\partial r}\frac{\partial}{\partial r}}\,. \quad (9.85)$$

The first two terms are those arising from Bohr's atom model, the third one is a correction due to the relativistic velocity of the electron, the forth comes from the electron's spin-orbit coupling, and the fifth is called the Darwin term. All contributions represent perturbations to the non-relativistic Schrödinger theory of Bohr's atom and will be discussed extensively in Secs. 9.2. We will show in 9.1.5.6 that $\hat{\mathbf{L}}^2$, $\hat{\mathbf{S}}^2$, and $\hat{\mathbf{J}}^2$ are constants of motion of the above Hamiltonian.

9.1.4 The Pauli equation

When we calculated the electron's energy in the Coulomb potential (9.85), we only considered the electrostatic potential of the nucleus, letting the potential vector $\mathbf{A}$ be zero. As long as we do not apply an external magnetic field this is correct, because the internal magnetism of the atom is already completely enclosed in the Dirac equation. On the other hand, we know that the atom contains moving charges, that is, currents which generate magnetic fields [8]. Furthermore, the spins of the electron and of the proton produce magnetic moments, which ought to interact with the magnetic fields. Hence, the existence of magnetic effects in an atom is to be expected.

These magnetic effects can be discussed in a more transparent way applying a Schrödinger-like equation with minimal coupling to electromagnetic fields (9.43) to a two-component spinor $\vec{\phi}$. This Schrödinger-like equation can be obtained from Dirac's equation (9.75) via a stronger non-relativistic approximation, which consists in completely neglecting the weak component $[E' - qU(\mathbf{r})]\vec{\chi}$. On the other hand, we allow for the existence of magnetic fields via the substitution $\hat{\mathbf{p}} \to \vec{\pi}$. The equation for the strong component (9.76) then becomes,

$$\boxed{E'\vec{\phi} = qU(\mathbf{r})\vec{\phi} + \frac{(\vec{\sigma}\cdot\vec{\pi})^2}{2m_e}\vec{\phi}} \,. \tag{9.86}$$

We can again apply the formula (9.80) to calculate,

$$\begin{aligned}(\vec{\sigma}\cdot\vec{\pi})^2\psi &= \vec{\pi}^2\psi + \imath\vec{\sigma}\cdot(\vec{\pi}\times\vec{\pi})\psi = \vec{\pi}^2\psi + \imath q\vec{\sigma}\cdot[-\mathbf{p}\times\mathbf{A}(\mathbf{r}) - \mathbf{A}(\mathbf{r})\times\hat{\mathbf{p}}]\psi \\ &= \vec{\pi}^2\psi - \hbar q\vec{\sigma}\cdot\{\nabla\times[\mathbf{A}(\mathbf{r})\psi] + \mathbf{A}(\mathbf{r})\times\nabla\psi\} \\ &= \vec{\pi}^2\psi - \hbar q\vec{\sigma}\cdot[\nabla\times\mathbf{A}(\mathbf{r})]\psi = [\mathbf{p} - q\mathbf{A}(\mathbf{r})]^2\psi - \hbar q\vec{\sigma}\cdot\vec{\mathcal{B}}(\mathbf{r})\psi \,.\end{aligned} \tag{9.87}$$

In the case of an electron ($e = -q$) we obtain the so-called *Pauli equation*,

$$E'\vec{\phi} = \left[\frac{1}{2m_e}\left(-\imath\hbar\nabla + e\mathbf{A}\right)^2 + \frac{e\hbar}{2m_e}\vec{\sigma}\cdot\vec{\mathcal{B}} - eU(\mathbf{r})\right]\vec{\phi} \,, \tag{9.88}$$

which corresponds to a Schrödinger-like equation for a two-component spinor $\vec{\phi}$ with the Hamiltonian,

$$\boxed{\hat{H} \simeq \frac{\hat{\mathbf{p}}^2}{2m_e} - \frac{1}{4\pi\varepsilon_0}\frac{e^2}{r} - \frac{\imath\hbar e}{2m_e}(\nabla\cdot\mathbf{A} + \mathbf{A}\cdot\nabla) + \frac{e}{m_e}\mathbf{S}\cdot\vec{\mathcal{B}}} \,, \tag{9.89}$$

neglecting terms in $\mathbf{A}^2$. Note however, that the kinetic energy is calculated with the *momentum projected onto the spin*, $\vec{\sigma}\cdot\vec{\pi}$. The third term can be simplified within the Coulomb gauge $\nabla\cdot\mathbf{A} = 0$ yielding,

$$\hat{H}_{\text{int}} = \frac{e}{m_e}(\mathbf{A}\cdot\hat{\mathbf{p}}) \,. \tag{9.90}$$

The Pauli equation serves for a classical (non-relativistic) approach to the electron's spin-orbit coupling, as we will see below and in the discussion of the fine structure in Sec. 9.2.2.

[8] The spin of the electron does not generate a magnetic field, in contrast to the angular momentum caused by its *orbital motion*. It only interacts with the environment through the requirement of symmetrization for being a fermion.

9.1.4.1 Dipole moment of the orbital angular momentum

The rotational motion of a charge, $-e$, creates a current I, corresponding to a current density,

$$\mathbf{j}(\mathbf{r}') = I\hat{\mathbf{e}}_\phi \delta(r-r')\delta(z') = -e\frac{\mathbf{v}}{2\pi r}\delta(r-r')\delta(z') \ . \tag{9.91}$$

Hence, the dipole moment caused by the circular motion of an electron is,

$$\begin{aligned}\vec{\mu}_\ell &= \frac{1}{2}\int_V \mathbf{r}\times\mathbf{j}(\mathbf{r}')d^3r' \qquad (9.92)\\ &= \frac{1}{4\pi}\mathbf{r}\times\int_0^{2\pi}d\phi'\int_{-\infty}^{\infty}dz'\int_0^{\infty}r'dr'\frac{-e\mathbf{v}}{r}\delta(r-r')\delta(z') = \tfrac{-1}{2}e\mathbf{r}\times\mathbf{v} = \frac{-e}{2m_e}\mathbf{L}\ ,\end{aligned}$$

with the angular momentum $\mathbf{L} = \mathbf{r}\times m_e\mathbf{v}$. The quotient $\gamma_e \equiv -e/2m_e$ is called *gyromagnetic ratio* of the electron. We often use the *Bohr magneton*, $\mu_{\rm B} \equiv \hbar e/2m_e$, which represents the elementary unit of spin,

$$\boxed{\frac{\vec{\mu}_\ell}{\mu_{\rm B}} = -g_\ell\frac{\hat{\mathbf{L}}}{\hbar}} \ . \tag{9.93}$$

The *g-factor* of a system having any angular momentum $\hat{\mathbf{L}}$ is defined as a proportionality constant between the normalized dipole moment and the normalized angular momentum. $g_\ell \equiv \frac{\mu_\ell}{\ell\mu_{\rm B}} = 1$ takes into account possible corrections between our classical derivation and quantum mechanics.

9.1.4.2 Pauli's model of spin-orbit coupling

The aim of this section is to demonstrate the relationship between the spin-orbit coupling term in Dirac's Hamiltonian (9.85) and the spin-magnetic field coupling term in Pauli's Hamiltonian (9.89).

A comparison of Pauli's expression with the energy of a magnetic moment in the field $\vec{\mathcal{B}}$,

$$\hat{H}_{\ell s} = -\vec{\mu}_s\cdot\vec{\mathcal{B}} \ , \tag{9.94}$$

suggests the following connection between the spin and the magnetic moment:

$$-\vec{\mu}_s\cdot\vec{\mathcal{B}} = \frac{e\hbar}{2m_e}\vec{\sigma}\cdot\vec{\mathcal{B}} = \frac{e}{m_e}\hat{\mathbf{S}}\cdot\vec{\mathcal{B}} \ . \tag{9.95}$$

We conclude, that the electron carries, besides mass, charge and spin, also a magnetic dipole moment,

$$\boxed{\frac{\vec{\mu}_s}{\mu_{\rm B}} = -\frac{e}{m_e\mu_{\rm B}}\hat{\mathbf{S}} = -2\frac{\hat{\mathbf{S}}}{\hbar}} \ , \tag{9.96}$$

For the g-factor of the electron, we obtain $g_e = 2$ [9]. Neutron and proton are also fermions with spin $\frac{1}{2}$, but they do not obey the Dirac equation! Their g-factors are

[9] The exact value is $g_e \equiv \frac{\mu_s}{s\mu_{\rm B}} = 2.002319314...$ The deviation $g_e - 2 \simeq \frac{\alpha}{\pi} - 0.164\frac{\alpha^2}{\pi^2}$ is due to the coupling of the spin to the fluctuations of the electromagnetic vacuum. We need to use quantum electrodynamical methods to calculate the corrections.

$g_{proton} = 5.5858$ and $g_{neutron} = -3.8261$. The large deviation from $g = 2$ points to the existence of an internal structure.

The rapid motion of the electron within the electrostatic field $\vec{\mathcal{E}}$ of the nucleus produces, following the theory of relativity, in the electron's reference frame a magnetic field $\vec{\mathcal{B}}'$ with which the electronic spin can interact. As we will show in Exc. 9.1.5.7, the field seen by the electron can be approximated in first order in v/c by,

$$\vec{\mathcal{B}}' \simeq \frac{\mathbf{v}}{c^2} \times \vec{\mathcal{E}} \, . \tag{9.97}$$

With this the interaction energy (9.94) becomes,

$$\begin{aligned} \hat{H}_{\ell s} = -\vec{\mu}_s \cdot \vec{\mathcal{B}}' = \frac{e}{m_e c^2} \mathbf{s} \cdot (\mathbf{v} \times \vec{\mathcal{E}}) = -\frac{e}{m_e^2 c^2} \mathbf{s} \cdot (\hat{\mathbf{p}} \times \nabla U) \\ = -\frac{e}{m_e^2 c^2} \mathbf{s} \cdot \left(\hat{\mathbf{p}} \times \frac{\mathbf{r}}{r} \frac{\partial U}{\partial r} \right) = -\frac{1}{m_e^2 c^2 r} \hat{\mathbf{S}} \cdot \hat{\mathbf{L}} \frac{\partial V(r)}{\partial r} \, , \end{aligned} \tag{9.98}$$

with $V(r) = -eU(r)$.

The resulting interaction energy coincides, apart from a factor $\frac{1}{2}$ [814], with the one obtained in the from Dirac's equation (9.85). The deviation, called *Thomas factor*, is due to the necessity to transform back into the inertial system of the nucleus. This transformation, called *Thomas precession*, must be done by a Lorentz transformation, which is not trivial with electron continuously changing its propagation direction on its circular orbit. The transformation introduces the additional factor of $\frac{1}{2}$ [10].

9.1.5 Exercises

9.1.5.1 Ex: Yukawa potential

Show, that Yukawa's potential satisfies the Klein-Gordon equation.

9.1.5.2 Ex: Zitterbewegung

Zitterbewegung is a hypothetical rapid motion of elementary particles, in particular electrons, that obey the Dirac equation. The existence of such motion was first proposed by Erwin Schrödinger in 1930 as a result of his analysis of the wave packet solutions of the Dirac equation for relativistic electrons in free space, in which an interference between positive and negative energy states produces what appears to be a fluctuation (at the speed of light) of the position of an electron around the median, with a frequency of $2m_e c^2/\hbar$, or approximately $1.6 \cdot 10^{21}$ rad/s. For the hydrogen atom, the Zitterbewegung produces the Darwin term which plays the role in the fine structure as a small correction of the energy level of the s-orbitals.
Use the Heisenberg equation to derive, from Dirac's Hamiltonian, equations of motion for the position operator $\hat{\mathbf{r}}$ and the 'velocity operator' $\hat{\vec{\alpha}}$. Solve the equation of motion and identify the Zitterbewegung.
Zitterbewegung of a free relativistic particle has never been observed. However, it has been simulated in experiments engineered to obey equations similar to Dirac's. First,

[10] This is a kinematic effect in space-time: the Lorentz transformations for systems moving with non-collinear velocities can not simply be concatenated, but must be rotated, too [294, 425].

with a trapped ion, by putting it in an environment such that the non-relativistic Schrödinger equation for the ion has the same mathematical form as the Dirac equation (although the physical situation is different) [315]. Then, in 2013, it was simulated in a setup with Bose-Einstein condensates [505].

9.1.5.3 Ex: Constants of motion of Dirac's Hamiltonian 1

Show that $\hat{L}_z$ with $\hat{\mathbf{L}} \equiv \mathbf{r} \times \hat{\mathbf{p}}$ and $\hat{S}_z$ with $\hat{\mathbf{S}} \equiv \frac{\hbar}{2}\gamma_5\vec{\alpha}$ defining $\gamma_5 \equiv -\imath\alpha_1\alpha_2\alpha_3$ are not constants of motions, but $\hat{\mathbf{J}} = \hat{\mathbf{L}} + \hat{\mathbf{S}}$, that is,

$$[\hat{H}, \hat{J}_z] = [\hat{H}, \hat{L}_z + \hat{S}_z] = 0 \ . \tag{9.99}$$

9.1.5.4 Ex: Calculating with Dirac matrices

a. Prove that, if $[\mathbf{B}, \vec{\sigma}] = 0 = [\mathbf{C}, \vec{\sigma}]$ where $\vec{\sigma}$ are the Pauli matrices, then,

$$(\vec{\sigma} \cdot \mathbf{B})(\vec{\sigma} \cdot \mathbf{C}) = \mathbf{B} \cdot \mathbf{C} + \imath\vec{\sigma} \cdot (\mathbf{B} \times \mathbf{C}) \ . \tag{9.100}$$

b. Prove that, if $[\mathbf{B}, \vec{\alpha}] = 0 = [\mathbf{C}, \vec{\alpha}]$ where $\vec{\alpha}$ are the Dirac matrices, then,

$$(\vec{\alpha} \cdot \mathbf{B})(\vec{\alpha} \cdot \mathbf{C}) = \mathbf{B} \cdot \mathbf{C} + \imath\gamma_5\vec{\alpha} \cdot (\mathbf{B} \times \mathbf{C}) \ . \tag{9.101}$$

c. Show that the spin defined as,

$$\mathbf{S} = \tfrac{\hbar}{2}\vec{\varsigma} \qquad \text{where} \qquad \vec{\varsigma} \equiv \gamma_5\vec{\alpha} = \mathbb{I} \otimes \vec{\sigma} \tag{9.102}$$

obeys different commutation rules than the Dirac matrices.
d. Conclude that,

$$(\vec{\varsigma} \cdot \mathbf{B})(\vec{\varsigma} \cdot \mathbf{C}) = \mathbf{B} \cdot \mathbf{C} + \imath\vec{\varsigma} \cdot (\mathbf{B} \times \mathbf{C}) \ . \tag{9.103}$$

9.1.5.5 Ex: Constants of motion of Dirac's Hamiltonian 2

In this exercise we will prove the relationships (9.55):
a. Prove,

$$(\hbar j')^2 = \hat{\mathbf{J}}^2 + \tfrac{\hbar^2}{4} \ . \tag{9.104}$$

b. Prove,

$$[\hbar j', \hat{H}]_- = 0 \ . \tag{9.105}$$

c. Prove,

$$\mathbf{r} \cdot \hat{\mathbf{p}} = -\imath\hbar r \frac{\partial}{\partial r} \ . \tag{9.106}$$

d. Prove,

$$[\varepsilon, \hat{H}]_- = 0 \ . \tag{9.107}$$

9.1.5.6 Ex: Constants of motion in the $\hat{\mathbf{L}}\cdot\hat{\mathbf{S}}$-coupling

Consider a particle of mass μ described by the Hamiltonian $\hat{H} = -\frac{\hbar^2}{2\mu}\nabla^2 + V(r) + \xi(r)\hat{\mathbf{L}}\cdot\hat{\mathbf{S}}$, being $V(r)$ a central potential, $\hat{\mathbf{L}}$ and $\hat{\mathbf{S}}$ its orbital angular momentum and spin.
a. Obtain the commutation relations $[\hat{\mathbf{L}}, \hat{H}]$, $[\hat{\mathbf{S}}, \hat{H}]$ and $[\hat{\mathbf{L}}+\mathbf{S}, \hat{H}]$ for the cases without and with spin-orbit interaction $\xi(r)\hat{\mathbf{L}}\cdot\hat{\mathbf{S}}$ introduced by relativistic corrections.
b. Calculate $[\hat{\mathbf{L}}^2, \hat{H}]$, $[\hat{\mathbf{S}}^2, \hat{H}]$ and $[\hat{\mathbf{J}}^2, \hat{H}]$.

9.1.5.7 Ex: Magnetic field generated by the orbiting proton at the location of the electron

Calculate the magnetic field generated by the orbiting proton as it is perceived by the electron.

9.2 Fine structure of hydrogen-like atoms via TIPT

The wave equation that simultaneously satisfies the requirements of quantum mechanics and special relativity is the *Dirac equation*. In free space including electromagnetic interactions it describes all massive particles of semi-integer spin with parity as a symmetry, such as electrons and quarks. It was the first theory to fully explain special relativity in the context of quantum mechanics. The Dirac equation describes the fine structure of the hydrogen spectrum in a completely rigorous manner. The equation also implied the existence of a new form of matter, antimatter, previously unsuspected and unobserved. The equation also justifies a posteriori the introduction of spinors, that is, of the vector wavefunctions introduced by Pauli in a heuristic way. We have seen in the last section that, in the limit of high but non-relativistic velocities, the Dirac equation adopts the form of a Schrödinger equation with the modified Hamiltonian (9.85) [11],

$$\begin{aligned}\hat{H} &= \hat{H}_0 + \hat{H}_{\rm rel} + \hat{H}_{\ell s} + \hat{H}_{\rm dw} + \hat{H}_{\rm lamb} \\ &= \left(\frac{\hat{p}^2}{2m_e} - \frac{Ze^2}{4\pi\varepsilon_0 r}\right) - \frac{\hat{p}^4}{8m_e^3c^2} + \frac{1}{2m_e^2c^2}\frac{1}{r}\frac{dV}{dr}\hat{\mathbf{L}}\cdot\hat{\mathbf{S}} + \frac{\pi\hbar^2}{2m_e^2c^2}\frac{Ze^2}{4\pi\varepsilon_0}\delta^3(\mathbf{r}) + \hat{H}_{\rm lamb}\ .\end{aligned} \tag{9.108}$$

We will discuss the various terms in the following sections. Note that the expression for the Darwin term differs from that of (9.85). We will see in Exc. 9.2.6.1, that they are, in fact, equivalent.

9.2.1 Correction for relativistic velocities

The first correction in the expression, $\hat{H}_{\rm rel}$ in Eq. (9.108), comes from the expansion of the relativistic energy for small velocities up to second order,

$$E_{\rm kin} = \sqrt{p^2c^2 + m_e^2c^4} \simeq m_ec^2 + \frac{p^2}{2m_e} - \frac{p^4}{8m_e^3c^2} + \dots\ . \tag{9.109}$$

[11] From now in we will frequently drop the 'hat' on quantum operators, when their nature is clear in the context.

The correction is of the order of magnitude,

$$\frac{H_{\rm rel}}{H_0} = \frac{\frac{p^4}{8m_e^3c^2}}{\frac{p^2}{2m_e}} = \frac{v^2}{4c^2} \simeq \frac{\alpha^2}{4} \approx 0.01\% \ . \tag{9.110}$$

Due to the degeneracy of these states, it would be appropriate to use perturbation theory with degenerate states. However, as $\hat{H}_{\rm rel}$ only depends on spatial coordinates commuting with $\mathbf{l}$ and $\mathbf{s}$ (see Exc. 9.1.5.6), the degeneracy is not very important, since $\hat{H}_{\rm rel}$ is already diagonal in the base $|n,\ell,m\rangle$, that is, $\langle n,\ell,m|n',\ell',m'\rangle = \delta_{\ell\ell'}\delta_{mm'}$. Starting from,

$$\begin{aligned}\hat{H}_{\rm rel} &= -\frac{\hat{p}^4}{8m_e^3c^2} = -\frac{1}{2m_ec^2}\left(\frac{\hat{p}^2}{2m_e}\right)^2 = -\frac{1}{2m_ec^2}\left(\hat{H}_0 + \frac{Ze^2}{4\pi\varepsilon_0 r}\right)^2 \\ &= -\frac{1}{2m_ec^2}\left(\hat{H}_0 - \frac{2E_n n^2}{\tilde{r}}\right)^2 \ ,\end{aligned} \tag{9.111}$$

with $\tilde{r} \equiv \frac{Zr}{a_{\rm B}}$ and using as an abbreviation the energies of hydrogen following Bohr's model,

$$E_n = \langle n,\ell|\hat{H}_0|n,\ell\rangle = -\frac{Z^2e^2}{4\pi\varepsilon_0}\frac{1}{2a_{\rm B}n^2} = -\frac{m_ec^2}{2}\frac{Z^2\alpha^2}{n^2} \ . \tag{9.112}$$

We have

$$\begin{aligned}\Delta E_{\rm rel} &= \langle n,\ell|\hat{H}_{\rm rel}|n,\ell\rangle \\ &= -\frac{1}{2m_ec^2}\left[\langle n,\ell|\hat{H}_0^2|n,\ell\rangle - \langle n,\ell|\frac{4E_n n}{\tilde{r}}\hat{H}_0|n,\ell\rangle + \langle n,\ell|\left(\frac{2E_n n}{\tilde{r}}\right)^2|n,\ell\rangle\right] \\ &= \frac{Z^2\alpha^2}{4E_n n^2}\left[E_n^2 - 4E_n^2n^2\frac{1}{n^2} + 4E_n^2n^4\frac{1}{n^3(\ell+\frac{1}{2})}\right] \ ,\end{aligned} \tag{9.113}$$

using the eigenvalues calculated in (3.53). Finally, we obtain the following relativistic correction,

$$\boxed{\Delta E_{\rm rel} = E_n(Z\alpha)^2\left[\frac{1}{n(\ell+\frac{1}{2})} - \frac{3}{4n^2}\right]} \ . \tag{9.114}$$

Obviously, the degeneracy with respect to the angular momentum ℓ is lifted by this correction.

9.2.2 Correction due to spin-orbit coupling

The second correction, $\hat{H}_{\ell s}$ in the expression (9.108), called *spin-orbit interaction*, is a relativistic correction due to the fact that the electron moves rapidly within the electrostatic field $\vec{\mathcal{E}}$ generated by the nucleus. Considering the fundamental orbit and the fact that the angular momenta are of the order of $\hbar$ we can estimate the importance of this effect,

$$\frac{H_{\ell s}}{H_0} = \frac{\frac{1}{2m_e^2c^2}\frac{1}{r}\frac{e^2}{4\pi\varepsilon_0 r^2}\mathbf{l}\cdot\mathbf{s}}{\frac{p^2}{2m_e}} \simeq \frac{\frac{1}{2m_e^2c^2}\frac{e^2}{4\pi\varepsilon_0}\frac{1}{a_{\rm B}^3}\hbar^2}{\frac{e^2}{4\pi\varepsilon_0 a_{\rm B}}} = \frac{1}{2m_e^2c^2}\frac{\hbar^2}{a_{\rm B}^2} = \frac{\alpha^2}{2} \approx 0.01\% \ . \tag{9.115}$$

Example 62 (*Classical derivation of the spin-orbit interaction*): In the following, we will derive the expression (9.98) for the spin-orbit interaction energy from classical arguments borrowed from electrodynamic theory. Seen from the rest system of the electron being at position $\mathbf{x} = 0$, it is the proton that orbits around the electron. This orbit creates a current, $-\mathbf{j}(\mathbf{r}')$, which generates a magnetic field. Following the *Biot-Savart's law* the potential vector and the amplitude of the field are,

$$\mathbf{A}(\mathbf{x}) = \frac{\mu_0}{4\pi}\int_V \frac{-\mathbf{j}(\mathbf{r}')d^3r'}{|\mathbf{x}-\mathbf{r}'|} \ , \tag{9.116}$$

respectively,

$$\begin{aligned}\vec{\mathcal{B}}(\mathbf{x}) = \nabla_{\mathbf{x}}\times\mathbf{A}(\mathbf{x}) &= \frac{\mu_0}{4\pi}\int_V \frac{(\mathbf{x}-\mathbf{r}')\times\mathbf{j}(\mathbf{r}')}{|\mathbf{x}-\mathbf{r}'|^3}d^3r' \\ &= -\frac{\mu_0}{4\pi}\int_{-\infty}^{\infty}dz'\int_0^{\infty}r'dr'\int_0^{2\pi}d\phi\frac{(\mathbf{x}-\mathbf{r}')\times\mathbf{v}}{|\mathbf{x}-\mathbf{r}'|^3}\frac{Ze}{2\pi r}\delta(r-r')\delta(z') \\ &= \frac{Ze\mu_0}{4\pi}\frac{(\mathbf{x}-\mathbf{r})\times\mathbf{v}}{|\mathbf{x}-\mathbf{r}|^3} \ ,\end{aligned} \tag{9.117}$$

where we replaced the expression for the current density (9.91). With the expression for the *Coulomb potential* between the electron and the proton and its radial derivative,

$$V(r) = \frac{-Ze^2}{4\pi\varepsilon_0 r} \quad , \quad \frac{1}{r}\frac{dV(r)}{dr} = \frac{Ze^2}{4\pi\varepsilon_0 r^3} \ , \tag{9.118}$$

we have at the position of the electron,

$$\begin{aligned}\vec{\mathcal{B}}(\mathbf{0}) = \frac{Ze\mu_0}{4\pi}\frac{-\mathbf{r}\times\mathbf{v}}{r^3} &= -\frac{\varepsilon_0\mu_0}{e}\frac{\mathbf{r}\times\mathbf{v}}{r}\frac{dV(r)}{dr} \\ &= -\frac{1}{ec^2}\frac{\mathbf{r}\times\mathbf{v}}{r}\frac{dV(r)}{dr} = -\frac{1}{em_ec^2 r}\frac{dV(r)}{dr}\mathbf{L} \ .\end{aligned} \tag{9.119}$$

The advantage of maintaining the general potential V in the formula is, that this expression also holds for more complicated atoms with many electrons, where the potential may deviate considerably from the Coulombian potential. Note, that the magnetic field is very strong, $B \simeq \xi(a_{\mathrm{B}})\hbar/\mu_{\mathrm{B}} \approx 5\,\mathrm{T}$. Inserting the magnetic field into Pauli's expression (9.94) together with the magnetic moment of the spin (9.96) we arrive at,

$$\hat{H}_{\ell s} = -\vec{\mu}_s\cdot\vec{\mathcal{B}}(\mathbf{0}) = \frac{1}{m_e^2c^2}\mathbf{S}\cdot\mathbf{L}\frac{1}{r}\frac{dV(r)}{dr} \ . \tag{9.120}$$

where we still have to apply the corrective *Thomas factor* of $\frac{1}{2}$.

The interaction operator can be written,

$$\hat{H}_{\ell s} = \xi(r)\hat{\mathbf{L}}\cdot\hat{\mathbf{S}} \ , \tag{9.121}$$

with the abbreviation,

$$\xi(r) \equiv \frac{-1}{2m_e^2c^2r}\frac{dV}{dr} = -\frac{Ze^2}{8\pi\varepsilon_0 m_e^2c^2}\frac{1}{r^3} = \frac{E_nZ^2\alpha^2n^2}{\hbar^2}\frac{1}{\tilde{r}^3} \ , \tag{9.122}$$

with $\tilde{r} \equiv Zr/a_{\rm B}$ and using the formulas (3.53).

After the introduction of the spin, the Hilbert space of the particles' wavefunctions must be extended. The wavefunctions are now products of spatial wavefunctions and spin eigenvectors:

$$|n, \ell, m_\ell, m_s\rangle = R_{n\ell}(r) Y_{\ell m}(\theta, \phi) \begin{pmatrix} s_1 \\ s_2 \end{pmatrix} . \tag{9.123}$$

The new Hilbert space is the tensorial product of position space and spin space. The *radial* Hamiltonian for the hydrogen atom including the centrifugal term and the spin-orbit coupling now takes the form:

$$\hat{H} = \frac{p^2}{2m} + V(r) + \frac{\hat{\mathbf{L}}^2}{2m_e r^2} + \xi(r) \hat{\mathbf{L}} \cdot \hat{\mathbf{S}} . \tag{9.124}$$

We may again consider the energy term $V_{\ell s}$ as a small perturbation, and calculate it using unperturbed wavefunctions,

$$\begin{aligned} \Delta E_{\ell s} &= \langle n, \ell, s, m_\ell, m_s | V_{\ell s} | n, \ell, s, m_\ell, m_s \rangle \\ &= \langle n, \ell | \xi(r) | n, \ell \rangle \langle \ell, s, m_\ell, m_s | \hat{\mathbf{S}} \cdot \hat{\mathbf{L}} | \ell, s, m_\ell, m_s \rangle . \end{aligned} \tag{9.125}$$

Assuming a Coulombian potential, we first look at the radial part (9.122), which can easily be calculated using the formulae (3.53),

$$\langle n, \ell | \xi(r) | n, \ell \rangle = \frac{E_n Z^2 \alpha^2 n^2}{\hbar^2} \frac{1}{n^3 \ell (\ell + \frac{1}{2})(\ell + 1)} . \tag{9.126}$$

To diagonalize the angular part of the Hamiltonian, we need the common wavefunctions of $\hat{\mathbf{L}}^2$ and $\hat{\mathbf{L}} \cdot \hat{\mathbf{S}}$. We can rewrite the coupling term as:

$$\hat{\mathbf{L}} \cdot \hat{\mathbf{S}} = \tfrac{1}{2} (\hat{\mathbf{J}}^2 - \hat{\mathbf{L}}^2 - \hat{\mathbf{S}}^2) . \tag{9.127}$$

In the common eigensystem of $\hat{\mathbf{J}}^2$, $\hat{\mathbf{L}}^2$, and $\hat{\mathbf{S}}^2$ the Hamiltonian, therefore, is diagonal. We know the basis of this system from the theory of the addition of angular momenta. The states of the basis are linear combinations of the functions $|n, \ell, m_\ell, m_s\rangle$. Since the spins precess around each other, $\hat{L}_z$ and $\hat{S}_z$ are not good observables, the non-coupled basis is not appropriate. But $\hat{\mathbf{S}}^2$, $\hat{\mathbf{L}}^2$, and $\hat{\mathbf{J}}^2$ are good observables. In the coupled basis $\{n, (\ell, s) j, m_j\}$,

$$\langle n, (\ell, s) j, m_j | \hat{\mathbf{S}} \cdot \hat{\mathbf{L}} | n, (\ell, s) j, m_j \rangle = \tfrac{\hbar^2}{2} [j(j+1) - \ell(\ell+1) - s(s+1)] . \tag{9.128}$$

Since $j = \ell \pm 1/2$, we find that every level splits into two levels, one with the energy $E_{n\ell} + \ell \zeta_{n\ell}$ and the degeneracy $2\ell + 2$ and the other with the degeneracy $E_{n\ell} - (\ell+1)\zeta_{n\ell}$ with the degeneracy 2ℓ, where we introduced the abbreviation,

$$\zeta_{n\ell} \equiv \tfrac{\hbar^2}{2} \langle \xi(r) \rangle . \tag{9.129}$$

All in all, we get an energy correction due to the spin-orbit interaction of,

$$\boxed{\Delta E_{\ell s} = -E_n (Z\alpha)^2 \frac{j(j+1) - \ell(\ell+1) - \frac{3}{4}}{2n\ell(\ell + 1/2)(\ell + 1)}} . \tag{9.130}$$

Note, that the coupling $\hat{\mathbf{L}} \cdot \hat{\mathbf{S}}$ lifts the degeneracy with respect to $\hat{\mathbf{L}}$, but not with respect to $\hat{L}_z$ (see Fig. 9.1). As we have already seen in Exc. 9.1.5.6, in the presence of an energy associated with the $\mathbf{L} \cdot \mathbf{S}$ coupling, only the total angular momentum $\mathbf{L} + \mathbf{S}$ is a constant of motion.

9.2.3 Non-local electron-core interaction

Let us now discuss the third correction in the expression (9.108). The electron-nucleus interaction that we have considered so far is *local*, that is, the interaction at the point $\mathbf{r}$ sensed by the electron depends essentially on the field at that point in space. However, when relativistic theory is correctly applied, the electron-nucleus interaction becomes *non-local*, and the electron is then affected by all values of the nuclear field in a region around $\mathbf{r}$ [12]. The size of this region is of the order of the *Compton wavelength* of the electron, $\lambda_C/2\pi \equiv \hbar/m_e c$. This correction was introduced by *Sir Charles Galton Darwin* through a substitution in the Dirac equation that solved the problem of normalization of the wavefunction.

Imagine that instead of the potential $V(\mathbf{r})$, the potential of the electron is given by the integral,

$$\int f(r')V(\mathbf{r}+\mathbf{r}')d^3r' \ , \tag{9.131}$$

where $f(r')$ is a radially symmetric and normalized density-type function that takes significant values only in the vicinity of $\mathbf{r}$ within a volume $(\lambda_C/2\pi)^3$ centered at $\mathbf{r}' = 0$. Expanding the potential $V(\mathbf{r}+\mathbf{r}')$ near the origin,

$$V(\mathbf{r}+\mathbf{r}') = V(\mathbf{r}) + [\mathbf{r}' \cdot \nabla_r]V(\mathbf{r}) + \tfrac{1}{2!}[\mathbf{r}' \cdot \nabla_r]^2 V(\mathbf{r}) + \dots \ , \tag{9.132}$$

and inserting into the integral,

$$\begin{aligned} &\int f(r')V(\mathbf{r}+\mathbf{r}')d^3r' \\ &= V(\mathbf{r})\int f(r')d^3r' + \int \mathbf{r}' f(r')d^3r' \cdot \nabla_r V(\mathbf{r}) + \tfrac{1}{2!}\int r'^2 f(r')[\hat{\mathbf{e}}_{r'} \cdot \nabla_r]^2 d^3r' V(r) + \dots \\ &= V(\mathbf{r}) + 0 + \tfrac{1}{2!}\int r'^2 f(r')d^3r' \nabla^2 V(r) + \dots \ . \end{aligned} \tag{9.133}$$

The second term is null due to the parity of $f(r')$ and the third produces the Darwin correction using $V(\mathbf{r}) = V(r)$. Letting the function be constant within the volume, $f(\mathbf{r}) \simeq f_0$, and with the normalization,

$$1 = \int_{-\hbar/2m_e c}^{\hbar/2m_e c}\int_{-\hbar/2m_e c}^{\hbar/2m_e c}\int_{-\hbar/2m_e c}^{\hbar/2m_e c} f(r)dxdydz = f_0\left(\frac{\hbar}{m_e c}\right)^3 \ , \tag{9.134}$$

we get the integral

$$\int r^2 f(r)d^3r = \int_{-\hbar/2m_e c}^{\hbar/2m_e c}\int_{-\hbar/2m_e c}^{\hbar/2m_e c}\int_{-\hbar/2m_e c}^{\hbar/2m_e c} f(r)r^2 dxdydz = \left(\frac{\hbar}{2m_e c}\right)^2 \ . \tag{9.135}$$

[12] The smearing out of the electron's position is also known as *Zitterbewegung*. See Exc. 9.1.5.2.

Also,

$$\nabla^2 V(\mathbf{r}) = -e\nabla^2 \frac{Ze}{4\pi\varepsilon_0 r} = -e\frac{\varrho(\mathbf{r})}{\varepsilon_0} = -\frac{Ze^2\delta^3(\mathbf{r})}{\varepsilon_0} \ . \tag{9.136}$$

Hence,

$$\int f(r')V(\mathbf{r}+\mathbf{r}')d^3r' = -\frac{Ze^2}{4\pi\varepsilon_0 r} + \frac{\pi\hbar^2}{2m_e^2c^2}\frac{Ze^2}{4\pi\varepsilon_0}\delta^3(\mathbf{r}) + \dots \ , \tag{9.137}$$

which is precisely the electrostatic energy with the Darwin correction in the expressions (9.85) and (9.108).

To estimate the importance of this effect we inserting the wavefunctions (3.52) evaluated at the origin,

$$\begin{aligned}\langle \hat{H}_{\rm dw}\rangle &= \int d^3r \psi^*_{n\ell m}(\mathbf{r})\frac{\pi\hbar^2}{2m_e^2c^2}\frac{Ze^2}{4\pi\varepsilon_0}\delta^3(\mathbf{r})\psi_{n\ell m}(\mathbf{r}) \\ &= \frac{\pi\hbar^2}{2m_e^2c^2}\frac{Ze^2}{4\pi\varepsilon_0}|\psi_{n00}(0)|^2\delta_{\ell 0}\delta_{m0} = \frac{\pi\hbar^2}{2m_e^2c^2}\frac{Ze^2}{4\pi\varepsilon_0}\frac{Z^3}{\pi n^3 a_{\rm B}^3}\delta_{\ell 0} \ .\end{aligned} \tag{9.138}$$

We obtain,

$$\frac{H_{\rm dw}}{H_0} = \frac{\frac{\pi\hbar^2}{2m_e^2c^2}\frac{Ze^2}{4\pi\varepsilon_0}\frac{1}{\pi a_{\rm B}^3}}{\frac{e^2}{4\pi\varepsilon_0 a_{\rm B}}} = \frac{\hbar^2}{2m_e^2c^2}\frac{Z}{a_{\rm B}^2} = \frac{\alpha^2}{2} \approx 0.01\% \ . \tag{9.139}$$

Darwin's correction vanishes for angular momentum $\ell > 0$, such that,

$$\boxed{\Delta E_{\rm dw} = \langle \hat{H}_{\rm dw}\rangle = -E_n\frac{(Z\alpha)^2}{n}\delta_{\ell 0} \ .} \tag{9.140}$$

9.2.4 Summary of the corrections

Combining the $\mathbf{l}\cdot\mathbf{s}$ and relativistic corrections, we obtain,

$$\begin{aligned}\Delta E_{\rm fs} &= \Delta E_{\rm rel} + \Delta E_{\ell s} + \Delta E_{\rm dw} \\ &= E_n(Z\alpha)^2\left[\frac{1}{n(\ell+\frac{1}{2})} - \frac{3}{4n^2}\right] - E_n(Z\alpha)^2\frac{j(j+1)-\ell(\ell+1)-\frac{3}{4}}{2n\ell(\ell+\frac{1}{2})(\ell+1)} - E_n(Z\alpha)^2 \\ &= E_n(Z\alpha)^2\begin{cases}\frac{1}{nj} - \frac{3}{4n^2} - \frac{j(j+1)-(j-\frac{1}{2})(j+\frac{1}{2})-\frac{3}{4}}{2n(j-\frac{1}{2})j(j+\frac{1}{2})} - 1 & \text{para} \quad \ell = j-\frac{1}{2} \\ \frac{1}{n(j+1)} - \frac{3}{4n^2} - \frac{j(j+1)-(j+\frac{1}{2})(j+\frac{3}{2})-\frac{3}{4}}{2n(j+\frac{1}{2})(j+1)(j+\frac{3}{2})} - 1 & \text{para} \quad \ell = j+\frac{1}{2}\end{cases} \\ &= E_n(Z\alpha)^2\left[\frac{1}{n(j+\frac{1}{2})} - \frac{3}{4n^2} - 1\right] \ .\end{aligned} \tag{9.141}$$

That is, the levels are now degenerate in j (see Fig. 9.1) [13]. Obviously the levels which are most affected by relativistic corrections are those with low values of n and ℓ.

The levels are labeled by $n\ell_j$. For example, the state $3d_{5/2}$ has the main quantum number $n = 3$, the orbital angular momentum $\ell = 2$, and the total angular momentum

[13] It is interesting that the quantum treatment presented here, including relativistic corrections, coincidentally agrees with the corrections of *Arnold Johannes Wilhelm Sommerfeld*.

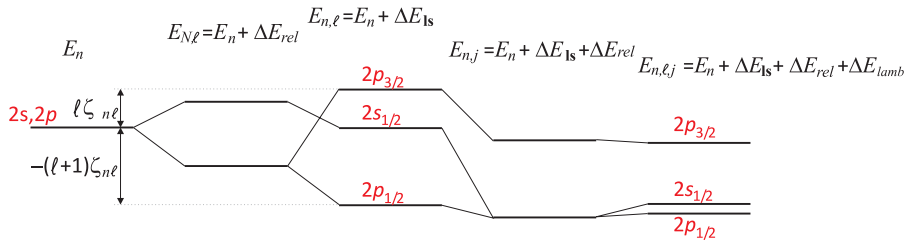

Figure 9.1: Hydrogen levels in the presence of various combinations of relativistic corrections.

$j = 5/2$. For large n or j the fine structure disappears. The new energy scheme is shown in Fig. 9.1. We note that, taking into account all relativistic corrections (but without the Lamb shift), we still have a partial degeneracy of the quantum number j. For example, the states $^2s_{1/2}$ and $^2p_{1/2}$ have the same energy. This is a particularity of the hydrogen atom.

9.2.5 Lamb shift

Only remains to discuss the fourth correction, $\hat{H}_{\text{lamb}}$ in the expression (9.6). The origin of the *Lamb shift* lies in quantum electrodynamics. Being due to the quantum nature of the electromagnetic field, this correction is not predicted within the Dirac equation.

We may imagine the Coulomb force between charged particles being mediated by a continuous exchange of virtual photons. But each isolated charge also continuously emits and reabsorbs virtual photons, with the result that the position of the electron is smeared over a region of 0.1 fm. This reduces the overlap between the electronic orbits and the nucleus. Hence, the Lamb shift causes corrections that are stronger for small n and small ℓ. For example in hydrogen, the $2p_{1/2}$ is $4.4 \cdot 10^{-6}$ eV $= 1$ GHz below the $2s_{1/2}$ (see Fig. 9.1).

9.2.6 Exercises

9.2.6.1 Ex: The Darwin term

Show that the expressions for the Darwin correction (9.85) and (9.108) are equivalent.

9.3 Hyperfine structure

Rutherford's measurements suggested a point-like and infinitely heavy atomic nucleus. In fact, the mass is finite and the nuclear charge is distributed over a finite volume and often in a non-isotropic manner, which leads to multipolar interactions with the electrons. In addition, many nuclei have a spin that can interact with the magnetic moment of the electrons. The energy corrections due to these effects are called *hyperfine structure* [14].

[14] See [163] p. 1229 and [837] p. 23 for further reading.

Because many of the following considerations will remain valid for many-electron systems to be discussed later, we will switch to a notation denoting by $\hat{\mathbf{L}}$ the total orbital angular momentum of the electronic shell, $\hat{\mathbf{S}}$ the total spin of the electronic shell, and $\hat{\mathbf{J}}$ the total angular momentum of the electronic shell, remembering that for hydrogen $\hat{\mathbf{S}} = \frac{\hbar}{2}\hat{\vec{\sigma}}$.

9.3.1 Coupling to the nuclear spin

9.3.1.1 Dipole moment of the nuclear spin

The nucleus may also have an angular momentum interacting with the angular momentum of the electrons. However, the momentum depends inversely on the masses. That is, the angular momentum of the nucleus is $\mu_{\rm N}/\mu_{\rm B} = m_e/m_p \simeq 10^{-3}$ times smaller, where $\mu_{\rm N} = \hbar e/2m_p$ is an abbreviation called *nuclear magneton*. Thus, we can assume that the interaction between the nucleus and the electron will not interfere with the $\mathbf{L}\cdot\mathbf{S}$-coupling between the orbital angular momentum and the spin of the electron. The spin of the nucleus will be oriented along the total momentum of the electrons $\hat{\mathbf{J}}$. However, this interaction will have the ability to lift the hydrogen degeneracy, even though the *splitting* will only be *hyperfine*. Indeed, the order of magnitude of *hyperfine splitting* is 10^{-6} eV.

Analogously to the expressions (9.93) and (9.96), we write the dipole moment of the nucleus,

$$\boxed{\frac{\vec{\mu}_I}{\mu_{\rm N}} = \frac{e}{2m_p\mu_{\rm N}} g_p \hat{\mathbf{I}} = g_p \frac{\hat{\mathbf{I}}}{\hbar}} \,, \tag{9.142}$$

where $g_p \equiv \mu_I/I$ is once again a factor taking into account possible corrections between the classical derivation and quantum mechanics [15].

9.3.1.2 Hyperfine splitting

In the derivation of the Pauli equation (9.89) from the Dirac equation (9.76) we discarded non-relativistic terms and reintroduced electronic spin-orbit coupling by hand allowing for $\mathbf{A}(\mathbf{r},t) \neq 0$. By an analogous calculation directly applied to the Dirac equation we may unravel the *hyperfine structure*. Instead of setting the vector potential to $\mathbf{A}(\mathbf{r},t) = 0$, as we did in (9.45), we now generalize the Dirac equation (9.76),

$$E'\vec{\phi} = qU(\mathbf{r})\vec{\phi} + \vec{\sigma}\cdot\vec{\pi}\frac{1}{2m_e}\left(1 + \frac{E'-U(\mathbf{r})}{2m_e c^2}\right)^{-1}\vec{\sigma}\cdot\vec{\pi}\vec{\phi}\,. \tag{9.143}$$

Assuming $\langle q\mathbf{A}\rangle \ll \langle \mathbf{p}\rangle$, we may only retain terms to the lowest order in $\mathbf{A}$ and neglect terms containing $q\mathbf{A}\frac{E'-U(\mathbf{r})}{2m_e c^2}$. Using the result of the calculation (9.87),

$$(\vec{\sigma}\cdot\vec{\pi})(\vec{\sigma}\cdot\vec{\pi}) = [\mathbf{p} - q\mathbf{A}]^2 - \hbar q\vec{\sigma}\cdot\vec{\mathcal{B}}\,, \tag{9.144}$$

[15] In fact, the proton factor g is anomalous, $g_p = 5.58$, which reduces the fraction μ_l/μ_I. For the neutron we have: $g_n = -3.83$

we find the generalization of the total energy (9.85),

$$\hat{H} \simeq \frac{[\hat{\mathbf{p}} - q\mathbf{A}(\mathbf{r})]^2}{2m_e} - \frac{1}{4\pi\varepsilon_0}\frac{e^2}{r} - \frac{\hat{\mathbf{p}}^4}{8m_e^3c^2} - \frac{e}{2m_e^2c^2}\frac{1}{r}\frac{\partial U}{\partial r}\hat{\mathbf{S}}\cdot\hat{\mathbf{L}} - \frac{\hbar^2 e}{4m_e^2c^2}\frac{\partial U}{\partial r}\frac{\partial}{\partial r} - \frac{\hbar q}{2m_e}\vec{\sigma}\cdot\vec{\mathcal{B}}(\mathbf{r}) \,, \tag{9.145}$$

and expanding the bracket

$$[\mathbf{p} - q\mathbf{A}]^2 \simeq \mathbf{p}^2 - q\mathbf{p}\cdot\mathbf{A} - q\mathbf{A}\cdot\mathbf{p} = \mathbf{p}^2 - 2q\mathbf{A}\cdot\mathbf{p} \tag{9.146}$$

in the Coulomb gauge, we see that two new terms are added to the energy called the hyperfine structure,

$$\boxed{\begin{array}{rcl} \hat{H} & = & \hat{H}_B + \hat{H}_{\rm fs} + \hat{H}_{\rm hfs} \\ \text{with} \quad \hat{H}_{\rm hfs} & = & \hat{H}_{LI} + \hat{H}_{SI} = \frac{e}{m_e}\mathbf{A}(\mathbf{r})\cdot\hat{\mathbf{p}} + \frac{2\mu_{\rm B}}{\hbar}\hat{\mathbf{S}}\cdot\vec{\mathcal{B}}(\mathbf{r}) \end{array}} \,, \tag{9.147}$$

with $\vec{\mu}_S = -\frac{e}{m_e}\hat{\mathbf{S}}$.

Up to now we did not say anything about the origin of the magnetic field. We only notice that any magnetic field will interact with the electron's orbit and with its spin. We now make use of our knowledge that the proton has a spin of its own which produces, at the position of the electrons, a magnetic vector potential,

$$\mathbf{A}(\mathbf{r}) = \frac{\mu_0}{4\pi}\frac{\vec{\mu}_I \times \mathbf{r}}{r^3} \,, \tag{9.148}$$

interacting with the angular momentum of the electron $\hat{\mathbf{L}}$ in the form,

$$\begin{aligned} \hat{H}_{LI} &= \frac{e}{m_e}\mathbf{A}\cdot\hat{\mathbf{p}} = \frac{e}{m_e}\frac{\mu_0}{4\pi r^3}(\vec{\mu}_I \times \mathbf{r})\cdot\hat{\mathbf{p}} \\ &= \frac{e}{m_e}\frac{\mu_0}{4\pi r^3}\frac{\mu_{\rm N}}{\hbar}g_p(\hat{\mathbf{I}}\times\mathbf{r})\cdot\hat{\mathbf{p}} = \frac{\mu_0}{2\pi r^3}\frac{\mu_{\rm B}}{\hbar}\frac{\mu_{\rm N}}{\hbar}g_p\hat{\mathbf{L}}\cdot\hat{\mathbf{I}} \,, \end{aligned} \tag{9.149}$$

using the definition of Bohr's magneton.

In addition, the potential vector (9.148) generated by the nuclear spin produces a magnetic field [425],

$$\vec{\mathcal{B}} = \nabla\times\mathbf{A} = \frac{\mu_0}{4\pi r^3}\left[3(\vec{\mu}_I\cdot\hat{\mathbf{e}}_r)\hat{\mathbf{e}}_r - \vec{\mu}_I\right] + \tfrac{2}{3}\mu_0\vec{\mu}_I\delta^3(\mathbf{r}) \,, \tag{9.150}$$

as will be shown in Exc. 9.3.3.1. This field interacts with the spin of the electron $\hat{\mathbf{S}}$ in the form,

$$\begin{aligned} \hat{H}_{SI} &= -\vec{\mu}_S\cdot\vec{\mathcal{B}} = -\frac{\mu_0}{4\pi r^3}\left[3(\vec{\mu}_I\cdot\hat{\mathbf{e}}_r)(\vec{\mu}_S\cdot\hat{\mathbf{e}}_r) - (\vec{\mu}_S\cdot\vec{\mu}_I)\right] - \tfrac{2}{3}\mu_0\vec{\mu}_S\cdot\vec{\mu}_I\delta^3(\mathbf{r}) \\ &= \frac{\mu_0}{4\pi r^3}\frac{\mu_{\rm B}}{\hbar}g_e\frac{\mu_{\rm N}}{\hbar}g_p\left[3(\hat{\mathbf{I}}\cdot\hat{\mathbf{e}}_r)(\hat{\mathbf{S}}\cdot\hat{\mathbf{e}}_r) - (\hat{\mathbf{S}}\cdot\hat{\mathbf{I}})\right] + \tfrac{2}{3}\mu_0 g_e\mu_{\rm B}\frac{\hat{\mathbf{S}}}{\hbar}\cdot g_p\mu_{\rm N}\frac{\hat{\mathbf{I}}}{\hbar}\delta^3(\mathbf{r}) \,, \end{aligned} \tag{9.151}$$

inserting the expressions (9.96) and (9.142). The first term gives the energy of the nuclear dipole in the field due to the electronic orbital angular momentum. The second term gives the energy of the 'finite distance' interaction of the nuclear dipole with the field due to the electron spin magnetic moments. The final term, often known as the *Fermi contact term* relates to the direct interaction of the nuclear dipole with the spin dipoles and is only non-zero for states with a finite electron spin density at the position of the nucleus (those with unpaired electrons in s-subshells).

We now discuss the two cases in which $\ell = 0$ or $\ell \neq 0$ separately in the following subsections [163, 715, 425].

9.3.1.3 Orbital angular momentum $\ell = 0$

For vanishing orbital angular momenta, $\ell = 0$, we only need to consider the contribution $\hat{H}_{SI}$. Furthermore, this contribution will be dominated by the Dirac term, because the s-orbitals have a high probability at the nuclear region, but fall off quickly at larger distances. Hence,

$$\hat{H}_{SI} \simeq \tfrac{2}{3}\mu_0 g_e \mu_B \frac{\hat{\mathbf{S}}}{\hbar} \cdot g_p \mu_N \frac{\hat{\mathbf{I}}}{\hbar} \delta^3(\mathbf{r}) \ . \tag{9.152}$$

Defining the complete total angular momentum of the atom,

$$\hat{\mathbf{F}} \equiv \hat{\mathbf{I}} + \hat{\mathbf{S}} \ , \tag{9.153}$$

we calculate from (9.151),

$$\begin{aligned} \Delta E_{\rm hfs}^{\ell=0} &= \langle (S,I)F, m_F | \hat{H}_{SI} | (S,I)F, m_F \rangle = \frac{2\mu_0 g_e g_p \mu_B \mu_N}{3\hbar^2} \langle \mathbf{S}\cdot\mathbf{I}\rangle \langle \delta^3(\mathbf{r})\rangle \qquad (9.154) \\ &= \tfrac{2}{3}\mu_0 g_e g_p \mu_B \mu_N [F(F+1) - I(I+1) - S(S+1)] \int \psi^*_{n00}(\mathbf{r}) \delta^3(\mathbf{r}) \psi_{n00}(\mathbf{r}) d^3r \\ &= \tfrac{2}{3}\mu_0 g_e g_p \mu_B \mu_N [F(F+1) - I(I+1) - S(S+1)] \left| \tfrac{1}{\sqrt{\pi}} \left(\frac{Z}{n a_B} \right)^{3/2} \right|^2 \ . \end{aligned}$$

As an example consider the hyperfine structure of the state $1s_{1/2}$ of the hydrogen atom. With $J = I = \frac{1}{2}$ and $Z = n = 1$ we obtain (see Exc. 9.3.3.2),

$$\begin{aligned} \Delta E_{\rm hfs}^{\ell=0}(F=1) - \Delta E_{\rm hfs}^{\ell=0}(F=0) &= \tfrac{2}{3}\mu_0 g_e \mu_B g_p \mu_N \ 2 \ \tfrac{1}{\pi} \left(\frac{Z}{n a_B} \right)^3 \qquad (9.155) \\ &= \frac{2 g_e g_p m_e^2 c^2}{3 m_p} \alpha^4 \approx (2\pi\hbar) \cdot 1.420\,\text{GHz} \ . \end{aligned}$$

The experimental value is 1.4204057518 GHz. This frequency corresponds to the spectral line used in radio astronomy, where the measurement of the angular distribution of this radiation allows the mapping of the spatial distribution of interstellar hydrogen.

9.3.1.4 Orbital angular momenta $\ell \neq 0$

In the case $\ell \neq 0$ both contributions, $\hat{H}_{SI}$ and $\hat{H}_{LI}$ have to be considered, however, we may neglect the Dirac term, because the orbitals with orbital angular momentum have vanishing probabilities at the nuclear region. Combining the two terms (9.149) and (9.151), we obtain,

$$\begin{aligned} \hat{H}_{JI} = \hat{H}_{LI} + \hat{H}_{SI} &= \frac{\mu_0}{4\pi r^3} \frac{\mu_B}{\hbar} g_e \frac{\mu_N}{\hbar} g_p \left[3(\hat{\mathbf{I}}\cdot\hat{\mathbf{e}}_r)(\mathbf{S}\cdot\hat{\mathbf{e}}_r) + \mathbf{L}\cdot\hat{\mathbf{I}} - \hat{\mathbf{S}}\cdot\hat{\mathbf{I}} \right] \qquad (9.156) \\ &= \frac{\mu_0}{4\pi r^3} \frac{\mu_B}{\hbar} g_e \frac{\mu_N}{\hbar} g_p \hat{\mathbf{N}}\cdot\hat{\mathbf{I}} \ , \end{aligned}$$

introducing $\hat{\mathbf{N}}$ as a quantity that only depends on the electronic shell:

$$\hat{\mathbf{N}} \equiv 3(\hat{\mathbf{S}}\cdot\hat{\mathbf{e}}_r)\hat{\mathbf{e}}_r + \hat{\mathbf{L}} - \hat{\mathbf{S}} \ . \tag{9.157}$$

Generalizing the complete total angular momentum of the atom (9.153),

$$\hat{\mathbf{F}} \equiv \hat{\mathbf{I}} + \hat{\mathbf{J}} \ , \tag{9.158}$$

is useful for calculating the coupling $\hat{\mathbf{I}} \cdot \hat{\mathbf{J}} = \frac{1}{2}(\hat{\mathbf{F}}^2 - \hat{\mathbf{I}}^2 - \hat{\mathbf{J}}^2)$. Now, as the $\mathbf{L} \cdot \mathbf{S}$-coupling is strong, we project the two angular momenta onto the total electronic angular momentum $\hat{\mathbf{J}}$,

$$\hat{\mathbf{N}} \longrightarrow \frac{\hat{\mathbf{N}} \cdot \hat{\mathbf{J}}}{|\mathbf{J}|} \frac{\hat{\mathbf{J}}}{|\mathbf{J}|} \quad , \quad \hat{\mathbf{I}} \longrightarrow \frac{\hat{\mathbf{I}} \cdot \hat{\mathbf{J}}}{|\mathbf{J}|} \frac{\mathbf{J}}{|\mathbf{J}|} \ . \tag{9.159}$$

We get for the coupling between the projected spins (9.159) of the electronic layer and the nucleus,

$$\hat{\mathbf{N}} \cdot \hat{\mathbf{I}} \longrightarrow \frac{(\hat{\mathbf{N}} \cdot \hat{\mathbf{J}})(\hat{\mathbf{I}} \cdot \hat{\mathbf{J}})}{|\mathbf{J}|^2} = \frac{(\hat{\mathbf{N}} \cdot \hat{\mathbf{J}})(\hat{\mathbf{F}}^2 - \hat{\mathbf{I}}^2 - \hat{\mathbf{J}}^2)}{2|\mathbf{J}|^2} \ . \tag{9.160}$$

We calculate

$$\begin{aligned} \Delta E_{\rm hfs}^{\ell \neq 0} &= \langle ((L,S)J,I)F, m_F | \hat{H}_{JI} | ((L,S)J,I)F, m_F \rangle \qquad (9.161) \\ &= \frac{\mu_0}{4\pi} \frac{\mu_{\rm B}}{\hbar} g_e \frac{\mu_{\rm N}}{\hbar} g_p \left\langle \frac{\hat{\mathbf{N}} \cdot \hat{\mathbf{I}}}{r^3} \right\rangle \\ &\longrightarrow \frac{\mu_0}{4\pi} \frac{\mu_{\rm B}}{\hbar} g_e \frac{\mu_{\rm N}}{\hbar} g_p \frac{\mathbf{N} \cdot \mathbf{J}[F(F+1) - I(I+1) - J(J+1)]}{2J(J+1)} \left(\frac{Z}{a_{\rm B}} \right)^3 \frac{n}{n^4 L(L+\frac{1}{2})(L+1)} \ . \end{aligned}$$

Introducing the *interval factor*,

$$A_J \equiv \frac{\mu_0}{4\pi} \frac{\mu_{\rm B}}{\hbar} g_e \frac{\mu_{\rm N}}{\hbar} g_p \left(\frac{Z}{a_{\rm B}} \right)^3 \frac{\mathbf{N} \cdot \mathbf{J}}{2J(J+1)} \frac{n}{n^4 L(L+\frac{1}{2})(L+1)} \ , \tag{9.162}$$

as a quantity that only depends on the electronic shell, we can write

$$\boxed{\Delta E_{\rm hfs}^{\ell \neq 0} = \tfrac{A_J}{2}[F(F+1) - J(J+1) - I(I+1)]} \ . \tag{9.163}$$

This formula includes the case $\ell = 0$ with the interval factor calculated from (9.154).

Note, that the $\mathbf{J} \cdot \mathbf{I}$-coupling breaks the degeneracy of $\hat{\mathbf{J}}$ in the hydrogen atom, but not of $\hat{J}_z$. We can derive the following *interval rule*,

$$\Delta E_{F+1} - \Delta E_F = A_J(F+1) \ . \tag{9.164}$$

Besides the magnetic interaction between the angular momenta of the nucleus and the electronic shell there is an interaction between the nucleus, when it is not spherically symmetric, and the shell. This interaction causes deviations from the interval rule and an additional splitting of the hyperfine states.

9.3.2 Electric quadrupole interaction

The fact that the nucleus is not perfectly spherical gives rise to new electron-nucleus corrections that are called *quadrupolar interaction*. The starting point is,

$$\hat{H}_{\text{quad}} = -\frac{1}{4\pi\varepsilon_0}\frac{e^2}{|\mathbf{r}_e - \mathbf{r}_N|} - \frac{1}{4\pi\varepsilon_0}\frac{e^2}{|\mathbf{r}_e|} \ , \tag{9.165}$$

where $\mathbf{r}_e$ is the electronic coordinate and $\mathbf{r}_N$ is the nuclear coordinate, both having their origin in the center mass of the nucleus. For $\mathbf{r}_e > \mathbf{r}_N$ this interaction can be obtained after several mathematical steps as [560],

$$\hat{H}_{\text{quad}} = B_J \frac{3(\hat{\mathbf{I}}\cdot\hat{\mathbf{J}})(2\hat{\mathbf{I}}\cdot\hat{\mathbf{J}}+1) - 2\hat{\mathbf{I}}^2\hat{\mathbf{J}}^2}{2I(I-1)2J(J-1)} \ , \tag{9.166}$$

where B_J is called the *constant of the quadrupolar electron-nucleus interaction*. With this expression we can calculate,

$$\Delta E_{\text{quad}} = \langle IJKm_K|\hat{H}_{\text{quad}}|IJKm_K\rangle = B_J \frac{\frac{3}{2}K(K+1) - 2I(I+1)J(J+1)}{2I(2I-1)2J(2J-1)} \ , \tag{9.167}$$

where $K \equiv 2\langle\hat{\mathbf{J}}\cdot\hat{\mathbf{I}}\rangle = F(F+1) - I(I+1) - J(J+1)$. It is important to remember that a nucleus with $I = 0$ or $I = \frac{1}{2}$ has no quadrupole moment, $B_J = 0$. Also for $J = \frac{1}{2}$ there will be no contribution.

Joining the contributions $\hat{\mathbf{J}}\cdot\hat{\mathbf{I}}$ of Eq. (9.163) and the quadrupolar contribution (9.167), the hyperfine structure can be described by,

$$\begin{aligned}\Delta E_{\text{hfs}} &= \Delta E_{JI} + \Delta E_{\text{quad}} \\ &= \frac{A_J}{2}K + \frac{B_J}{8IJ(2I-1)(2J-1)}[3K(K+1) - 4I(I+1)J(J+1)] \ ,\end{aligned} \tag{9.168}$$

where the constants A_J and B_J depend on the atom and the total electronic angular momentum.

Table 9.1: List of atomic data [786] showing the natural linewidth of the D_2 line, frequencies of the D_1 and D_2 lines, and the hyperfine splitting.

Element	$\gamma_{D2}/2\pi$	$D1$	$D2$	$\nu_{HFS}[S_{1/2}]$
	[MHz]	[cm^{-1}]	[cm^{-1}]	[MHz]
^{1}H	99.58	82264.000	82264.366	1420.4
^{2}H	99.58	82264.000	82264.366	–
^{6}Li	5.92	14901.000	14901.337	228.2
^{7}Li	5.92	14901.000	14901.337	803.5
^{23}Na	10.01	16956.000	16973.190	1771.6
^{39}K	6.09	12985.170	13042.876	461.7
^{40}K	6.09	12985.170	13042.876	−1285.8
^{41}K	6.09	12985.170	13042.876	254.0
^{85}Rb	5.98	12578.920	12816.469	3035.7
^{87}Rb	5.98	12578.920	12816.469	6834.7
^{133}Cs	5.18	11182.000	11737.000	9192.6
^{135}Cs	5.18	11182.000	11737.000	–

In Excs. 9.3.3.3 and 9.3.3.4 we determine the hyperfine structures of sodium and rubidium atoms.

9.3.3 Exercises

9.3.3.1 Ex: Field of a magnetic moment

a. Calculate the vector potential $\mathbf{A}(\mathbf{r})$ and the magnetic dipole moment $\vec{\mu}$ produced by an orbiting electron by Biot-Savart's law using the expansion of $|\mathbf{r}-\mathbf{r}'|^{-1}$ in Legendre polynomials.
b. Calculate the magnetic field $\vec{\mathcal{B}}(\mathbf{r})$.

9.3.3.2 Ex: Probability for finding the electron near the nucleus

Calculate the expectation value $\langle\delta^{(3)}(\mathbf{r})\rangle_{n\ell m}$ for encountering the electron of a hydrogen atom close to the nucleus.

9.3.3.3 Ex: Hyperfine structure of sodium

Determine the hyperfine structure of the ^2S and ^2P states of the sodium atom including energy shifts. See Tab. 16.1 for the hyperfine constants A_J and B_J.

Table 9.2: Hyperfine constants of some alkaline atoms.

atom	n	$A_J(n^2S_{1/2})$	$A_J(n^2P_{1/2})$	$A_J(n^2P_{3/2})$	$B_J(n^2P_{3/2})$
		[MHz·h]	[MHz·h]	[MHz·h]	[MHz·h]
^{1}H, $I = \frac{1}{2}$	1	1420	46.17	−3.07	−0.18
^{6}Li, $I = 1$	2	152.137	17.386	−1.155	−0.10
^{7}Li, $I = 3/2$	2	401.75	46.17	−3.07	−0.18
	3		13.5	−0.96	
^{23}Na, $I = \frac{3}{2}$	3	885.82	94.3	18.65	2.82
	4	202	28.85	6.00	0.86
^{85}Rb, $I = \frac{5}{2}$	5	1011.9	120.7	25.029	26.03
	6	239.3	39.11	8.25	8.16
^{87}Rb, $I = \frac{3}{2}$	5	3417.3	409.1	84.852	12.510
	6	809.1	132.5	27.70	3.947

9.3.3.4 Ex: Hyperfine structure of rubidium

Given the following energy distances $\nu_{F,F'}$ of the hyperfine levels of the rubidium isotopes ^{87}Rb and ^{85}Rb [59],

$$
\begin{aligned}
&^{87}\mathrm{Rb}, S_{1/2} \quad \text{splits into} \quad \nu_{1,2} = 6834.7\,\mathrm{MHz} \\
&^{87}\mathrm{Rb}, P_{3/2} \quad \text{splits into} \quad \nu_{0,1} = 72.3\,\mathrm{MHz}, \nu_{1,2} = 157.1\,\mathrm{MHz}, \nu_{2,3} = 267.2\,\mathrm{MHz} \\
&^{85}\mathrm{Rb}, S_{1/2} \quad \text{splits into} \quad \nu_{1,2} = 3035.7\,\mathrm{MHz} \\
&^{85}\mathrm{Rb}, P_{3/2} \quad \text{splits into} \quad \nu_{1,2} = 29.4\,\mathrm{MHz}, \nu_{2,3} = 63.4\,\mathrm{MHz}, \nu_{3,4} = 120.7\,\mathrm{MHz} \ ,
\end{aligned}
$$

calculate the positions of the barycenters.

9.3.3.5 Ex: Two particles

Consider a two-particle system of masses μ_1 and μ_2, exposed to a central potential $V(r)$ and an interaction potential $V(|\mathbf{r}_1 - \mathbf{r}_2|)$ which only depends on the distance between the particles. The Hamiltonian of the system in the interaction representation is $H = H_1 + H_2 + V(|\mathbf{r}_1 - \mathbf{r}_2|)$ with $H_\ell = -\frac{\hbar^2}{2\mu_\ell}\nabla_\ell^2 + V(r_\ell)$, $\ell = 1, 2, ...$ Show that the individual angular momenta $\mathbf{L}_\ell$ are not, in general, constants of the motion, unlike the *total* angular momentum $\mathbf{L} = \mathbf{L}_1 + \mathbf{L}_2$.

9.4 Exotic atoms

'Normal' atoms consist of a nucleus made of protons and neutrons and an electronic shell. But other two-particle systems are possible, e.g. where the nucleus or electron is replaced by another hadron or lepton (anti-proton, positron, muon, etc.). Such a system is called *exotic atom*. Atoms in Rydberg states also belong to this category.

9.4.1 Positronium and muonium

Positronium (e^+e^-) is a hydrogen-like system consisting of leptons, that is, an electron and a positron, which is the antiparticle of the electron. The muonium (μ^+e^-) is similar to positronium, except that here the positron is replaced by a muon whose mass is $m_{\mu^+} = 207m_e$. Leptons are, according to the present understanding, particles without internal structure. Both systems are unstable: the two particles annihilate each other producing γ-photons. The energy levels and orbits of the two particles are similar to that of the hydrogen atom. However, because of the reduced mass, the frequencies of the spectral lines are less than half of the corresponding hydrogen lines.

The fundamental state of positronium, like that of hydrogen, has two possible configurations depending on the relative orientation of the electron and positron spins. The singlet state with antiparallel spins ($S = 0$, $M_s = 0$) is known as para-positronium (p-Ps) and denoted by $^1S_0$. It has an average lifetime of

$$\tau = \frac{2\hbar}{m_e c^2 \alpha^5} = 124.4\,\text{ps} \tag{9.169}$$

and decays preferably in two gamma rays with energy of 511 keV each (in the center-of-mass). The triplet state with parallel spins ($S = 1, M_s = -1, 0, 1$) is known as ortho-positronium (o-Ps) and denoted as $^3S_1$. It has an average life of 138.6 ns, and the most common form of decay produces three photons. Other forms of decay are negligible. For example, the decay channel producing five photons is 10^{-6} times less likely. Measurements of these lifetimes and the positronium energy levels have been used in precision tests of quantum electrodynamics.

While the precise calculation of the positronium energy levels is based on the Bethe-Salpeter equation, the similarity between positronium and hydrogen allows for an approximate estimate. In this approach, the energy levels are suppodsed to be different from those of hydrogen because of the difference in the value of the reduced mass μ, used in the energy equation. Since $\mu = m_e/2$ for positronium, we have

$$E_n = -\frac{\mu q_e^4}{8h^2\varepsilon_0^2}\frac{1}{n^2} = -\frac{1}{2}\frac{m_e q_e^4}{8h^2\varepsilon_0^2}\frac{1}{n^2} = \frac{-6.8\,\text{eV}}{n^2}\ . \tag{9.170}$$

A di-positronium molecule, that is, a system of two bound positronium atoms, has already been observed. Positronium in high energy states has been conjectured to become the dominant form of atomic matter in the universe in the very distant future if the proton decay becomes tangible.

9.4.2 Hadronic atoms

In contrast to *leptons* (such as the electron e^-, the positron e^+ and the muons μ^+ and μ^-) that participate only in electromagnetic interactions and weak interactions, *hadrons* also participate in strong (nuclear type) interactions. There are two types of hadrons, *baryons* (such as the proton p and antiproton $\bar{p}$, the neutron n and antineutron $\bar{n}$, hyperons Σ, Ξ, ...) that have semi-integer spin and behave like fermions and *mesons* (like the π-meson, K-meson, ...) that have an integer spin. Every negatively charged hadron can be used to form a hydrogen-type *hadronic atom*. These systems contain a nucleus and negative hyperon and are known as hyperonic atoms. All of

these are unstable and due to the fact that they have a sufficiently long lifetime, some of their spectral lines have now been observed.

Since the hadrons interact strongly with the nucleus, the theory developed for hydrogen systems (in which only exist Coulomb interaction) can not be directly applied. In this way the values shown in Tab. 9.3 give only an estimate of the 'radius' and the ionization potential of the hadronic atoms $p\pi^-$, $p\kappa^-$, $p\bar{p}$ and $p\Sigma^-$.

Table 9.3: *Main features of some exotic atoms.*

system	reduced mass	radius a_μ	I_p
pe^-	$1836/1837 \approx 1$	$\approx a_\mathrm{B} = 1$	$e^2/2a_\mathrm{B} \approx 0.5$
e^+e^-	0.5	2	0.25
μ^+e^-	$207/208 \approx 1$	1	0.5
$p\mu^-$	≈ 186	$5.4 \cdot 10^{-3}$	93
$p\pi^-$	≈ 238	$4.2 \cdot 10^{-3}$	119
$p\kappa^-$	≈ 633	$1.6 \cdot 10^{-3}$	317
$p\bar{p}$	≈ 928	$1.1 \cdot 10^{-3}$	459
$p\Sigma^-$	≈ 1029	$9.7 \cdot 10^{-3}$	515

9.4.3 Muonic hydrogen

The muon mass is $m_\mu = 207 m_e$. When a muon is attached to a proton we have *muonic hydrogen*. Its size is smaller because of the reduced mass $a_\mu = a_\mathrm{B} \frac{1/m_e}{1/m_\mu + 1/m_p}$ and the binding energy and the energies of excitation are greater for the same reason. F.ex. while for $H = p^+e^-$ the transition $2S - 2P_{1/2}$ is at 10 eV $\triangleq$ 121 nm, for $p^+\mu^-$ it is at 1900 eV. Muonic atoms are interesting because they have amplified Lamb shifts, hyperfine interactions, and quantum electrodynamical corrections. Therefore, the displacement due to the finite distribution of charges in the proton $r_p = 0.8\,\mathrm{fm}$ should influence the spectrum. While in p^+e^- the $2S$ level is shifted upward by the Lamb shift by a value of 4.4×10^{-6} eV, in $p^+\mu^-$ it is shifted down by a value of 0.14 eV. In Exc. 9.4.5.2 we calculate the spectrum of the muonic hydrogen and in Exc. 5.1.3.3 we compare the energy corrections due to the finite extension of the nuclei for muonic and for standard hydrogen in first order TIPT.

9.4.4 Rydberg atoms

An atom excited to a state whose main quantum number is very high is called *Rydberg atom*. These atoms have a number of peculiar properties, including high sensitivity to electric and magnetic fields, long decay times, and wavefunctions that approximate classical electron orbits. The inner electrons protect the outer electron from the electric field of the nucleus such that, from a distance, the electric potential looks identical to that seen by the electron of a hydrogen atom.

Despite its flaws, Bohr's atom model is useful in explaining these properties. In Exc. 1.1.6.6 we derive Bohr's expression for the orbital radius in terms of the principal

quantum number n:

$$r = \frac{4\pi\varepsilon_0 n^2\hbar^2}{e^2 m} \ . \tag{9.171}$$

Thus, it is clear why Rydberg atoms have peculiar properties: the radius goes as n^2 (such that for example the state with $n = 137$ of hydrogen has a radius of $\sim 1\,\mathrm{mm}$) and the geometric cross section goes as n^4. Thus, Rydberg atoms are extremely large, with loosely bound valence electrons that are easily perturbed or ionized by collisions or external fields.

Since the binding energy of a Rydberg electron is proportional to $1/r$, and therefore falls as $1/n^2$, the spacing between energy levels falls as

$$\Delta E = E_1 \left(\frac{1}{(n+1)^2} - \frac{1}{n^2} \right) \overset{n\to\infty}{\longrightarrow} E_1 \left(-\frac{2}{n^3} + \frac{3}{n^4} + ... \right) \tag{9.172}$$

leading to less and less spaced levels. These Rydberg states form the *Rydberg series*.

9.4.4.1 Correspondence principle in Rydberg atoms

To calculate the oscillation frequency of an electron confined to a proton, we use the classical planetary model,

$$m\omega_n^2 = \frac{e^2}{4\pi\varepsilon_0 r} \qquad \text{and} \qquad m\omega r^2 = n\hbar \ . \tag{9.173}$$

Eliminating r,

$$\omega_n = \frac{me^4}{(4\pi\varepsilon_0)^2 n^3 \hbar^3} \ . \tag{9.174}$$

Radiation of this frequency will be emitted by an atomic antenna. On the other hand, the Bohr model predicts frequencies between orbitals,

$$\omega_n = \frac{E_{n+1} - E_n}{\hbar} = \frac{me^4}{2(4\pi\varepsilon_0)^2\hbar^2} \left(\frac{1}{(n+1)^2} - \frac{1}{n^2} \right) \overset{n\to\infty}{\longrightarrow} \frac{me^4}{2(4\pi\varepsilon_0)^2\hbar^2} \frac{2}{n^3} \ . \tag{9.175}$$

9.4.4.2 Production of Rydberg atoms

In the hydrogen atom only the ground state ($n = 1$) is actually stable. Other states must be excited by various techniques such as electron impact or charge exchange. In contrast to these methods, which produce a distribution of excited atoms at various levels, the optical excitation method allows to produce specific states, but only for alkali metals whose transitions fall into frequency regimes which are accessible to lasers.

9.4.4.3 Potential in a Rydberg atom

The valence electron in a Rydberg atom with Z protons in the nucleus and $Z - 1$ electrons in closed layers sees a spherically symmetric Coulomb potential:

$$U_\mathrm{C} = -\frac{e^2}{4\pi\varepsilon_0 r} \ . \tag{9.176}$$

The similarity of the effective potential 'seen' by the outer electron and the authentic hydrogen potential suggests a classical treatment within the planetary model. There are three notable exceptions:

- An atom can have two (or more) electrons in highly excited states with comparable orbital radii. In this case, the electron-electron interaction gives rise to a significant deviation from the hydrogen potential. For an atom in a multiple Rydberg state the additional term U_{ee} includes a sum over each pair of highly excited electrons:
$$U_{ee} = \frac{e^2}{4\pi\varepsilon_0} \sum_{i<j} \frac{1}{|\mathbf{r}_i - \mathbf{r}_j|} \ . \tag{9.177}$$

- If the valence electron has very low angular momentum (interpreted classically as an extremely eccentric elliptical orbit), it can pass close enough to the nucleus to polarize it, giving rise to an additional term,
$$U_{\text{pol}} = -\frac{e^2\alpha_d}{(4\pi\varepsilon_0)^2 r^4} \ . \tag{9.178}$$

- If the outer electron penetrates the inner electronic shells, it *sees* more of the charge of the nucleus and therefore feels a larger force. In general, the modification of the potential energy is not simple to calculate and should be based on some knowledge of the nucleus' geometry.

In hydrogen the binding energy is given by:
$$E_{\text{B}} = -\frac{E_1}{n^2} \ . \tag{9.179}$$
The binding energy is weak at high values of n, which explains the fragility of the Rydberg states that can easily be ionized, e.g. by collisions.

Additional terms modifying the potential energy of a Rydberg state require the introduction of a *quantum defect*, $\delta\ell$, in the expression for the binding energy:
$$E_{\text{B}} = -\frac{E_1}{(n-\delta_\ell)^2} \ . \tag{9.180}$$

The long lifetimes of Rydberg states with high orbital angular momentum can be explained in terms of overlapping wavefunctions. The wavefunction of an electron in a state with high ℓ (large angular momentum, 'circular orbit') has little overlap with the wavefunctions of the internal electrons and therefore stays relatively unperturbed. Also, the small energy difference between adjacent Rydberg states decreased the decay rate according to the result (16.40).

9.4.4.4 Rydberg atoms in external fields

The large distance between the electron and ionic nucleus in a Rydberg atom gives rise to an extremely large electric dipole moment d. There is an energy associated with the presence of an electric dipole in an electric field $\vec{\mathcal{E}}$, known as *Stark shift*,
$$E_{\text{S}} = -\mathbf{d} \cdot \vec{\mathcal{E}} \ . \tag{9.181}$$

Depending on the sign of the projection of the dipole moment onto the vector of the local electric field, the energy of a state increases or decreases with the intensity of the field. The narrow spacing between adjacent levels n in the Rydberg series means that the states can approach degeneracy even for relatively weak fields. Theoretically, the force of the field in which a level crossing would occur (assuming no coupling between the states) is given by the *Inglis-Teller limit*,

$$F_{\mathrm{IT}} = \frac{e}{12\pi\varepsilon_0 a_0^2 n^5} \,. \tag{9.182}$$

In hydrogen the pure Coulomb potential does not couple the Stark states of an n level, which results in a *real crossover*. In other elements, deviations from the ideal $1/r$-potential allow for *avoided crossings*.

9.4.5 Exercises

9.4.5.1 Ex: Positronium

Calculate and compare the fine and hyperfine structure of positronium.

9.4.5.2 Ex: Muonic hydrogen

Muonic hydrogen consists of a proton and a negatively charged muon. Calculate the binding energy of the ground state of muonic hydrogen in eV and write down the ground state's wavefunction.

9.5 Further reading

T. Mayer-Kuckuk, *Atomphysik, Teubner Studienbücher (1985)* [ISBN]

Ch.J. Foot, *Atomic Physics* [ISBN]

I.I. Sobelman, *Atomic Spectra and Radiative Transitions* [ISBN]

Chapter 10

Atoms with spin in external fields

The atomic fine structure was derived in the last chapter under the assumption that all electric and magnetic fields arise from the motion and spin of the electrons in the atomic shell and the nuclear spin. In this chapter, we will extend the treatment to include the reaction of the electrons to external electrostatic or electromagnetic fields. In this context, we will discuss the Zeeman and the Stark effect.

10.1 Charged particles in electromagnetic fields

10.1.1 Lagrangian and Hamiltonian of charged particles

A charge subject to an electromagnetic field feels the Lorentz force,

$$\mathbf{F} = q\vec{\mathcal{E}} + q\dot{\mathbf{r}} \times \vec{\mathcal{B}} \,, \tag{10.1}$$

where

$$\vec{\mathcal{E}} = -\nabla\Phi - \frac{\partial \mathbf{A}}{\partial t} \qquad \text{and} \qquad \vec{\mathcal{B}} = \nabla \times \mathbf{A} \,, \tag{10.2}$$

where Φ and $\mathbf{A}$ are called scalar and vector potential, respectively.

It is important to realize here, that the momentum $\mathbf{p}$ not only involves the momentum of the particle $m\mathbf{v}$, but the field also carries a momentum $q\mathbf{A}(\mathbf{r})$. As we learned in electrodynamics it is possible to derive the Lorentz force from a Lagrangian for the electronic motion,

$$\boxed{\mathcal{L}(r_i, \dot{r}_i) = \frac{m}{2}\dot{\mathbf{r}}^2 - q\Phi(\mathbf{r}) + q\dot{\mathbf{r}} \cdot \mathbf{A}(\mathbf{r})} \,. \tag{10.3}$$

With this aim we first determine the momentum by,

$$p_i = \frac{\partial \mathcal{L}}{\partial \dot{r}_i} = m\dot{r}_i + qA_i \,, \tag{10.4}$$

and the Hamiltonian by,

$$\mathcal{H} = \sum\nolimits_i p_i \dot{r}_i - \mathcal{L}(r_i, \dot{r}_i) = (m\mathbf{v} + q\mathbf{A}) \cdot \dot{\mathbf{r}} - \frac{m}{2}\dot{\mathbf{r}}^2 + q\Phi - q\dot{\mathbf{r}} \cdot \mathbf{A} = \frac{m}{2}\mathbf{v}^2 + q\Phi \,. \tag{10.5}$$

That is,

$$\boxed{\mathcal{H}(r_i, p_i) = \frac{1}{2m}(\mathbf{p} - q\mathbf{A})^2 + q\Phi} \ . \tag{10.6}$$

The following equations hold,

$$\dot{r}_i = \frac{\partial \mathcal{H}}{\partial p_i} \qquad \text{and} \qquad \dot{p}_i = -\frac{\partial \mathcal{H}}{\partial r_i} \ . \tag{10.7}$$

The first equation is easily verified by inserting the Hamiltonian (10.5). The second leads to the Lorentz force,

$$F_i = m\dot{v}_i = \dot{p}_i - q\dot{A}_i = -\frac{\partial \mathcal{H}}{\partial r_i} - q\dot{A}_i = q\mathcal{E}_i + q(\mathbf{v} \times \vec{\mathcal{B}})_i \ , \tag{10.8}$$

where the last step of the derivation will be shown in the Exc. 10.1.3.1 using the Coulomb gauge $\nabla \cdot \mathbf{A} = 0$.

10.1.2 Minimal coupling

Note that the same result (10.6) can be obtained by a canonical substitution,

$$m\mathbf{v} \longrightarrow \mathbf{p} - q\mathbf{A} \qquad \text{and} \qquad \mathcal{H} \longrightarrow \mathcal{H} + q\Phi \ . \tag{10.9}$$

This substitution rule, called *minimal coupling*, can be applied in quantum mechanics,

$$m\hat{\mathbf{v}} \longrightarrow -\imath\hbar\nabla - q\mathbf{A} \qquad \text{and} \qquad \hat{H} \longrightarrow \hat{H} + q\Phi \ . \tag{10.10}$$

In the case of the electron ($q = -e$) trapped in a central Coulomb potential $q\Phi = -\frac{Ze^2}{4\pi\varepsilon_0 r}$ and in the presence of any magnetic potential $\mathbf{A}$, we thus obtain,

$$\boxed{\hat{H} = \frac{m_e}{2}\hat{\mathbf{v}}^2 + q\Phi = \frac{-\hbar^2}{2m_e}\nabla^2 - \frac{\imath\hbar e}{2m_e}\mathbf{A}\cdot\nabla - \frac{\imath\hbar e}{2m_e}\nabla\cdot\mathbf{A} + \frac{e^2\mathbf{A}^2}{2m_e} + q\Phi} \ . \tag{10.11}$$

The fourth term called *diamagnetic term* is quadratic in $\mathbf{A}$ and usually so small that it can be neglected. The second and third terms describe the interaction of the electron through its momentum $\hat{\mathbf{p}}$ with the potential vector $\mathbf{A}$ produced by magnetic moments inside the atom or outer magnetic fields. Within the Coulomb gauge we have $(\nabla \cdot \mathbf{A})\psi = (\mathbf{A}\cdot\nabla)\psi + \psi(\nabla\cdot\mathbf{A}) = (\mathbf{A}\cdot\nabla)\psi$, such that,

$$\boxed{\hat{H}_{\text{int}} = \tfrac{e}{m_e}\mathbf{A}\cdot\hat{\mathbf{p}}} \ . \tag{10.12}$$

Example 63 (*Interaction Hamiltonian in dipolar approximation*): Note that the Hamiltonian (10.11) is not the only one correctly describing the system, since we may apply a unitary gauge transformation, as shown in (1.332). With the particular choice for the gauge field,

$$\chi(\mathbf{r}, t) \equiv -\mathbf{A}(\mathbf{r}, t)\cdot\mathbf{r} \ ,$$

assuming that the potential only weakly varies in space, such that,

$$\nabla\chi(\mathbf{r}, t) \simeq -\mathbf{A}(\mathbf{r}, t) \qquad \textit{and} \qquad \frac{\partial\chi(\mathbf{r}, t)}{\partial t} = -\mathbf{r}\cdot\frac{\partial\mathbf{A}(\mathbf{r}, t)}{\partial t} = -\mathbf{r}\cdot\vec{\mathcal{E}}(\mathbf{r}, t) \ ,$$

we get with $\mathbf{d} \equiv q\mathbf{r}$,

$$\hat{H} = \frac{1}{2m_e}(\hat{\mathbf{p}} - q\mathbf{A} + \nabla\chi)^2 + q\Phi + q\frac{\partial\chi(\mathbf{r},t)}{\partial t} \qquad (10.13)$$
$$\simeq \frac{\hat{\mathbf{p}}^2}{2m_e} + q\Phi - \mathbf{d}\cdot\vec{\mathcal{E}}(\mathbf{r},t) \ .$$

This is the interaction Hamiltonian in the dipolar approximation.

10.1.3 Exercises

10.1.3.1 Ex: Lagrangian of an electron in the electromagnetic field

a. Show that the Lagrangian (10.3) reproduces the Lorentz force (10.1).
b. Show that the Hamiltonian (10.5) reproduces the Lorentz force (10.1).

10.1.3.2 Ex: Atom-field coupling

We determine here the coupling Hamiltonian for an atom in a classical field under two equivalent forms (we have only considered the quantum case in the course). We consider the case of the simplest hydrogen atom, with a single electron (reduced mass m, charge $q = -e$) bound to a proton by the Coulomb potential Φ. This atom interacts also with a laser wave, whose potential and scalar vectors are $V(\mathbf{r},t)$ and $\mathbf{A}(\mathbf{r},t)$.
1. Derive the complete classical Hamiltonian of the atom from the standard form of the classical Lagrangian of a charge in a field: $\mathcal{L} = T - q(V+\Phi) + q\mathbf{v}\cdot\mathbf{A}$. What is the link between the electron's velocity and its momentum (conjugate with its position)?
2. Show that the quantum Hamiltonian is thus:

$$\hat{H} = \frac{1}{2m}(\mathbf{P} - q\mathbf{A}(\mathbf{R},t))^2 + q\Phi(\mathbf{R}) + qV(\mathbf{R}) \ .$$

3. Show that in the Coulomb gauge, $\nabla\cdot\mathbf{A} = 0$, V can be set to zero without loss of generality.
4. Show that in the Coulomb gauge, $\mathbf{A}\cdot\mathbf{P} = \mathbf{P}\cdot\mathbf{A}$. Develop accordingly the full Hamiltonian.
5. Under which hypotheses does $\hat{H}$ reduce to $\hat{H} = \hat{H}_0 - (q/m)\mathbf{P}\cdot\mathbf{A}(0,t)$, where $\hat{H}_0$ is the free atomic Hamiltonian?
We now transform the Hamiltonian under the more standard dipole form using the Göppert-Mayer transformation. We restart from the full Hamiltonian, with all terms including $V(\mathbf{r},t)$.
6. We neglect the terms quadratic in $\mathbf{A}$. The atom being small compared to the optical wavelength, give the Hamiltonian obtained by expanding $\mathbf{A}$ and $\mathbf{V}$ to the lowest relevant order. Use the notation $\mathbf{D} = q\mathbf{R}$.
7. Show that a proper gauge transformation cancels $\mathbf{A}(0,t)$.
8. Show that in this new gauge, the Hamiltonian reads $\hat{H} = \hat{H}_0 - \mathbf{D}\cdot\vec{\mathcal{E}}(0)$. Is this result gauge-dependent?

10.2 Interaction with magnetic fields

10.2.1 Normal Zeeman effect of the fine structure

The dipole moments of atoms can interact with external magnetic fields. The interaction leads to a shift of levels, which depends on the magnetic quantum number. Thus, the ultimate degeneracy in the energetic structure of the atom is lifted. This is called *Zeeman splitting*. We consider a uniform magnetic field $\vec{\mathcal{B}} = \mathcal{B}\hat{\mathbf{e}}_z$ with the potential vector,

$$\mathbf{A} = \tfrac{1}{2}\vec{\mathcal{B}} \times \mathbf{r} = -\tfrac{\mathcal{B}}{2}(-y\hat{\mathbf{e}}_x + x\hat{\mathbf{e}}_y) \ . \tag{10.14}$$

Thus the interaction energy between the electron and the field is given by the Hamiltonian (10.12),

$$\begin{aligned} \hat{V}_{\text{Zeem}}(\mathcal{B}) &= -\frac{\imath\hbar e}{m_e}\mathbf{A}\cdot\nabla = -\frac{\imath\hbar e}{2m_e}(\vec{\mathcal{B}}\times\mathbf{r})\cdot\nabla = -\frac{\imath\hbar e}{2m_e}\vec{\mathcal{B}}\cdot(\mathbf{r}\times\nabla) \\ &= -\frac{e}{2m_e}\vec{\mathcal{B}}\cdot\hat{\mathbf{L}} = -\frac{\mu_{\text{B}}}{\hbar}g_L\hat{\mathbf{L}}\cdot\vec{\mathcal{B}} = -\vec{\mu}_L\cdot\vec{\mathcal{B}} = -\frac{\mu_{\text{B}}}{\hbar}\hat{L}_z\mathcal{B} \ , \end{aligned} \tag{10.15}$$

with $g_L = 1$ using the relation (9.93), $\vec{\mu}_L = \frac{e}{2m_e}\mathbf{L}$, between the angular momentum of the electron and the resulting magnetic moment. This relationship holds for an atom without spin (two electrons can couple their spins to a singlet state) and no hyperfine structure (or an unresolved hyperfine structure). The energies are therefore,

$$\boxed{\Delta E_{\text{Zeem}}(\mathcal{B}) = -\frac{\mu_{\text{B}}}{\hbar}\mathcal{B}\langle n, L, m_L|\hat{L}_z|n, L, m_L\rangle = -\mu_{\text{B}}m_L\mathcal{B}} \ . \tag{10.16}$$

In the Excs. 10.2.7.1 and 10.2.7.2 we represent the interaction between an atomic angular momentum and a magnetic field in different bases characterized by different quantization axes.

10.2.2 Anomalous Zeeman effect

The anomalous Zeeman effect occurs when the ensemble of electrons has a spin. Using the already known expressions for the dipole moments of the orbital momentum and the spin of the electron, we obtain for the magnetic dipole moment,

$$\hat{\vec{\mu}}_J = \hat{\vec{\mu}}_L + \hat{\vec{\mu}}_S = \frac{\mu_{\text{B}}}{\hbar}g_L\hat{\mathbf{L}} + \frac{\mu_{\text{B}}}{\hbar}g_S\hat{\mathbf{S}} = \frac{\mu_{\text{B}}}{\hbar}(\hat{\mathbf{L}} + 2\hat{\mathbf{S}}) \ , \tag{10.17}$$

with $g_L = 1$ and $g_S = g_e = 2$. We can see that the dipole moment of the atom is not parallel to the total momentum, $\hat{\mathbf{J}} = \hat{\mathbf{L}} + \hat{\mathbf{S}}$.

When the magnetic field is weak, $\hat{V}_{\ell s} \gg \hat{V}_{\text{Zeem}}(\mathcal{B})$, the total momentum $\hat{\mathbf{J}}$ will be a good observable. Therefore, we must first project the momenta $\hat{\mathbf{L}}$ and $\hat{\mathbf{S}}$ onto $\hat{\mathbf{J}}$,

$$\hat{\mathbf{L}} \longrightarrow \left(\hat{\mathbf{L}}\cdot\tfrac{\hat{\mathbf{J}}}{|\mathbf{J}|}\right)\tfrac{\hat{\mathbf{J}}}{|\mathbf{J}|} \qquad \text{and} \qquad \hat{\mathbf{S}} \longrightarrow \left(\hat{\mathbf{S}}\cdot\tfrac{\hat{\mathbf{J}}}{|\mathbf{J}|}\right)\tfrac{\hat{\mathbf{J}}}{|\mathbf{J}|} \ , \tag{10.18}$$

before projecting the result onto the $\vec{\mathcal{B}}$-field. The potential is,

$$\begin{aligned}\hat{V}_{\rm Zeem}(\mathcal{B}) &= -\hat{\vec{\mu}}_J\cdot\vec{\mathcal{B}} = -\frac{\mu_{\rm B}}{\hbar}(\hat{\mathbf{L}}+2\hat{\mathbf{S}})\cdot\vec{\mathcal{B}} \longrightarrow -\frac{\mu_{\rm B}}{\hbar}\left[\left(\hat{\mathbf{L}}\cdot\tfrac{\hat{\mathbf{J}}}{|\hat{\mathbf{J}}|}\right)\tfrac{\hat{\mathbf{J}}}{|\hat{\mathbf{J}}|}\cdot\vec{\mathcal{B}}+2\left(\hat{\mathbf{S}}\cdot\tfrac{\hat{\mathbf{J}}}{|\hat{\mathbf{J}}|}\right)\tfrac{\hat{\mathbf{J}}}{|\hat{\mathbf{J}}|}\cdot\vec{\mathcal{B}}\right]\\ &= -\frac{\mu_{\rm B}}{\hbar|\mathbf{J}|^2}\left[\hat{\mathbf{L}}\cdot\hat{\mathbf{J}}+2\hat{\mathbf{S}}\cdot\hat{\mathbf{J}}\right]\hat{\mathbf{J}}\cdot\vec{\mathcal{B}} = -\frac{\mu_{\rm B}}{\hbar|\mathbf{J}|^2}\frac{1}{2}\left[\hat{\mathbf{J}}^2+\hat{\mathbf{L}}^2-\hat{\mathbf{S}}^2+2(\hat{\mathbf{J}}^2+\hat{\mathbf{S}}^2-\hat{\mathbf{L}}^2)\right]\hat{\mathbf{J}}\cdot\vec{\mathcal{B}}\\ &= -\frac{\mu_{\rm B}}{\hbar}\frac{1}{2}\frac{3\hat{\mathbf{J}}^2-\hat{\mathbf{L}}^2+\hat{\mathbf{S}}^2}{|\hat{\mathbf{J}}|^2}\hat{\mathbf{J}}\cdot\vec{\mathcal{B}}\,. \end{aligned} \tag{10.19}$$

And the energy is,

$$\Delta E_{\rm Zeem}(\mathcal{B}) = \left\langle\frac{\mu_{\rm B}}{\hbar}\left(1+\frac{J(J+1)-L(L+1)+S(S+1)}{2J(J+1)}\right)\hat{\mathbf{J}}\cdot\vec{\mathcal{B}}\right\rangle\,. \tag{10.20}$$

Introducing the *Landé factor*,

$$g_J \equiv 1+\frac{J(J+1)+S(S+1)-L(L+1)]}{2J(J+1)}\,, \tag{10.21}$$

we can write

$$\boxed{\Delta E_{\rm Zeem}(\mathcal{B}) = -\frac{\mu_{\rm B}}{\hbar}g_J\langle\hat{J}_z\rangle\mathcal{B} = -\mu_{\rm B}g_J m_J\mathcal{B}}\,. \tag{10.22}$$

This expression describes the *anomalous Zeeman effect*, for which $S\neq 0$. For the *normal Zeeman effect*, for which the spin is zero, we find again $g_J=1$.

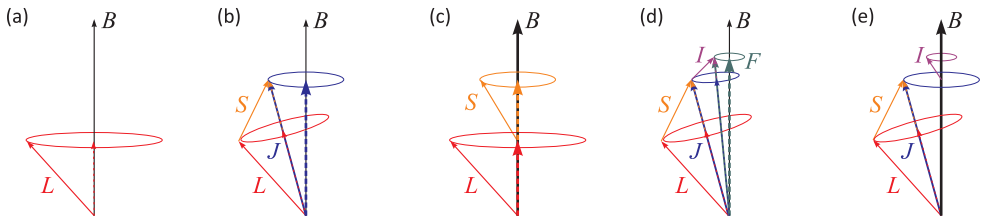

Figure 10.1: Coupling angular moments for the effect (a) Normal Zeeman effect, (b) anomalous Zeeman effect, (c) Paschen-Back effect, (d) Zeeman effect of the hyperfine structure, and (e) Paschen-Goudsmith effect.

10.2.3 Paschen-Back effect and intermediate magnetic fields

A very strong external magnetic field (>1 T), such that $\hat{V}_{\ell s}\ll\hat{V}_{\rm Zeem}(\mathcal{B})$, can break the $\hat{\mathbf{L}}\cdot\hat{\mathbf{S}}$-coupling. Both spins $\hat{\mathbf{L}}$ and $\hat{\mathbf{S}}$ now couple separately to the field,

$$\hat{\mathbf{L}}\longrightarrow\left(\hat{\mathbf{L}}\cdot\tfrac{\vec{\mathcal{B}}}{|\vec{\mathcal{B}}|}\right)\tfrac{\vec{\mathcal{B}}}{|\vec{\mathcal{B}}|}\qquad\text{and}\qquad\hat{\mathbf{S}}\longrightarrow\left(\hat{\mathbf{S}}\cdot\tfrac{\vec{\mathcal{B}}}{|\vec{\mathcal{B}}|}\right)\tfrac{\vec{\mathcal{B}}}{|\vec{\mathcal{B}}|}\,. \tag{10.23}$$

Therefore,

$$\hat{V}_{\rm PB}(\mathcal{B}) = -\frac{\mu_{\rm B}}{\hbar}(\hat{\mathbf{L}}+2\hat{\mathbf{S}})\cdot\vec{\mathcal{B}}\longrightarrow-\frac{\mu_{\rm B}}{\hbar}\left[\left(\hat{\mathbf{L}}\cdot\tfrac{\vec{\mathcal{B}}}{|\vec{\mathcal{B}}|}\right)\tfrac{\vec{\mathcal{B}}}{|\vec{\mathcal{B}}|}+2\left(\hat{\mathbf{S}}\cdot\tfrac{\vec{\mathcal{B}}}{|\vec{\mathcal{B}}|}\right)\tfrac{\vec{\mathcal{B}}}{|\vec{\mathcal{B}}|}\right]\cdot\vec{\mathcal{B}}\,, \tag{10.24}$$

such that

$$\boxed{\Delta E_{\rm PB}(\mathcal{B}) = -\mu_{\rm B}(m_L+2m_S)\mathcal{B}}\,. \tag{10.25}$$

This is the *Paschen-Back effect*.

10.2.3.1 Fine structure in the intermediate magnetic field regime

The derivations we have made so far have focused on simple situations well described by CSCOs in various coupling schemes. The projections on the different quantization axes [the total spin (10.18) in the Zeeman case or the applied magnetic field (10.23) in the Paschen-Back case] ensure that the Hamiltonians $\hat{V}_{\ell s}$ and $\hat{V}_{\mathrm{Zeem}}(\mathcal{B})$ in these CSCOs are described by diagonal matrices. However, in regimes *intermediate* between Zeeman and Paschen-Back, $\hat{V}_{\ell s} \simeq \hat{V}_{\mathrm{Zeem}}(\mathcal{B})$, it is generally not possible to find a diagonal representation.

In order to calculate the energy spectrum in intermediate regimes we must, therefore, determine all the components of the matrix,

$$\hat{V}_{\ell s} + \hat{V}_{\mathrm{Zeem}}(\mathcal{B}) = \xi(r)\hat{\mathbf{L}}\cdot\hat{\mathbf{S}} + \frac{\mu_{\mathrm{B}}}{\hbar}(\hat{\mathbf{L}} + 2\hat{\mathbf{S}}) \ . \tag{10.26}$$

Using $\hat{L}_{\pm} \equiv \hat{L}_x \pm \imath\hat{L}_y$ and $\hat{S}_{\pm} \equiv \hat{S}_x \pm \imath\hat{S}_y$, we can easily rewrite the energy in the following way,

$$\hat{V}_{\ell s} + \hat{V}_{\mathrm{Zeem}}(\mathcal{B}) = \xi(r)\left(\hat{L}_z\hat{S}_z + \tfrac{1}{2}\hat{L}_+\hat{S}_- + \tfrac{1}{2}\hat{L}_-\hat{S}_+\right) + \frac{\mu_{\mathrm{B}}}{\hbar}(\hat{\mathbf{L}} + 2\hat{\mathbf{S}})\cdot\vec{\mathcal{B}} \ . \tag{10.27}$$

This operator acts on the uncoupled states,

$$\begin{aligned}
&\Delta E_{\ell s} + \Delta E_{\mathrm{Zeem}}(\mathcal{B}) \qquad (10.28)\\
&= \langle L' m'_L; S' m'_S | \xi_{nl}(\hat{L}_z\hat{S}_z + \tfrac{1}{2}\hat{L}_+\hat{S}_- + \tfrac{1}{2}\hat{L}_-\hat{S}_+) + \mu_{\mathrm{B}}(\hat{L}_z + 2\hat{S}_z)\mathcal{B}| L m_L; S m_S\rangle\\
&= \hbar^2\xi_{nl}\left(m_L m_S \delta_{m_L,m'_L}\delta_{m_S,m'_S} + \tfrac{1}{2}L_+S_-\delta_{m_L,m'_L-1}\delta_{m_S-1,m'_S} + \tfrac{1}{2}L_-S_+\delta_{m_L-1,m'_L}\delta_{m_S,m'_S-1}\right)\\
&\quad + \hbar\mu_{\mathrm{B}}(m_L + 2m_S)\mathcal{B}\delta_{m_L,m'_L}\delta_{m_S,m'_S} \ ,
\end{aligned}$$

with the abbreviations $L_{\pm} \equiv \sqrt{L(L+1) - m_L(m_L \pm 1)}$. The energies are now the eigenvalues of this matrix. The factor ξ_{nl} is usually determined experimentally by letting $\mathcal{B} = 0$. In Exc. 10.2.7.3 we calculate the re-coupling of the spins of two electrons in an external magnetic field.

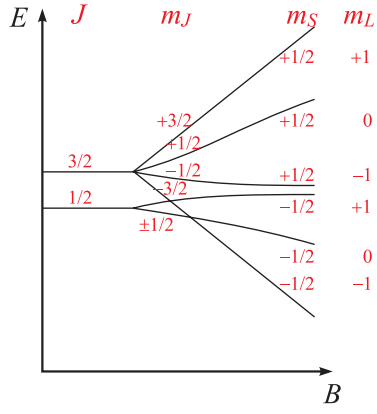

Figure 10.2: Transition between the Zeeman regime and the Paschen-Back regime for the case $L = 1$ and $S = 1/2$.

10.2.4 Zeeman effect of the hyperfine structure

When the energy of the interaction with the magnetic field is comparable to the hyperfine interactions, but much weaker than that of the fine interactions, the fields do not disturb the coupling between the total electronic momentum $\hat{\mathbf{J}}$ and the spin of the nucleus $\hat{\mathbf{I}}$. Hence, J, I, F, and m_F are good quantum numbers. Therefore, to calculate the interaction energy,

$$\hat{V}_{\rm hfs} + \hat{V}_{\rm Zeem}(\mathcal{B}) = \hat{V}_{\rm hfs} - \hat{\vec{\mu}}_F \cdot \vec{\mathcal{B}} \,, \tag{10.29}$$

where $\hat{\vec{\mu}}_F$ is the total magnetic momentum,

$$\hat{\vec{\mu}}_F = \hat{\vec{\mu}}_J + \hat{\vec{\mu}}_I = -\frac{\mu_{\rm B}}{\hbar} g_J \hat{\mathbf{J}} + \frac{\mu_{\rm N}}{\hbar} g_p \hat{\mathbf{I}} \,. \tag{10.30}$$

we project the nuclear spin and the total electronic momentum separately in the direction of $\hat{\mathbf{F}}$,

$$\hat{\mathbf{J}} \longrightarrow \left(\hat{\mathbf{J}} \cdot \tfrac{\hat{\mathbf{F}}}{|\mathbf{F}|}\right) \tfrac{\hat{\mathbf{F}}}{|\mathbf{F}|} \qquad \text{and} \qquad \hat{\mathbf{I}} \longrightarrow \left(\hat{\mathbf{I}} \cdot \tfrac{\hat{\mathbf{F}}}{|\mathbf{F}|}\right) \tfrac{\hat{\mathbf{F}}}{|\mathbf{F}|} \,. \tag{10.31}$$

Note the negative sign in (10.30) due to the negative charge of the electron. The Landé factor g_J [see (10.21)] is the one caused by the coupling of the orbital angular momentum $\hat{\mathbf{L}}$ and the electron spin $\hat{\mathbf{S}}$ and depends on the state under consideration. Thereby,

$$\begin{aligned} \hat{V}_{\rm Zeem}(\mathcal{B}) &= \left[-\frac{\mu_{\rm B}}{\hbar} g_J \left(\hat{\mathbf{J}} \cdot \tfrac{\hat{\mathbf{F}}}{|\mathbf{F}|}\right) \tfrac{\hat{\mathbf{F}}}{|\mathbf{F}|} + \frac{\mu_{\rm N}}{\hbar} g_p \left(\hat{\mathbf{I}} \cdot \tfrac{\hat{\mathbf{F}}}{|\mathbf{F}|}\right) \tfrac{\hat{\mathbf{F}}}{|\mathbf{F}|}\right] \vec{\mathcal{B}} \\ &= \left(-\frac{\mu_{\rm B}}{\hbar |\hat{\mathbf{F}}|^2} g_J \hat{\mathbf{J}} \cdot \hat{\mathbf{F}} + \frac{\mu_{\rm N}}{\hbar |\hat{\mathbf{F}}|^2} g_p \hat{\mathbf{I}} \cdot \hat{\mathbf{F}}\right) (\mathcal{B} \cdot \hat{F}_z) \,. \end{aligned} \tag{10.32}$$

Using $\hat{\mathbf{J}} \cdot \hat{\mathbf{F}} = \frac{1}{2}(\hat{\mathbf{F}}^2 + \hat{\mathbf{J}}^2 - \hat{\mathbf{I}}^2)$ and $\hat{\mathbf{I}} \cdot \hat{\mathbf{F}} = \frac{1}{2}(\hat{\mathbf{F}}^2 - \hat{\mathbf{J}}^2 + \hat{\mathbf{I}}^2)$ we write,

$$\hat{V}_{\rm Zeem}(\mathcal{B}) = -\frac{\mu_{\rm B}}{\hbar} g_J \frac{\hat{\mathbf{F}}^2 + \hat{\mathbf{J}}^2 - \hat{\mathbf{I}}^2}{2|\mathbf{F}|^2} \, \mathcal{B}\hat{F}_z + g_p \frac{\mu_{\rm N}}{\hbar} \frac{\hat{\mathbf{F}}^2 - \hat{\mathbf{J}}^2 + \hat{\mathbf{I}}^2}{2|\hat{\mathbf{F}}|^2} \, \mathcal{B}\hat{F}_z \,, \tag{10.33}$$

such that

$$\boxed{\Delta E_{\rm hfs} + \Delta E_{\rm Zeem}(\mathcal{B}) \simeq \Delta E_{\rm hfs} + \mu_{\rm B} g_F m_F \mathcal{B}} \,, \tag{10.34}$$

using the *Landé factor* g_F for the state F,

$$g_F \simeq g_J \frac{F(F+1) + J(J+1) - I(I+1)}{2F(F+1)} - g_p \frac{\mu_{\rm N}}{\mu_{\rm B}} \frac{F(F+1) - J(J+1) + I(I+1)}{2F(F+1)} \,, \tag{10.35}$$

where the second term can be neglected.

The splitting of electronic states with the momentum $\hat{\mathbf{F}}$ into $2F+1$ sublevels $m_F = -F, .., F$ is called *Zeeman effect of the hyperfine structure*. The result (10.32) only applies to weak magnetic fields. For strong fields the Zeeman splitting becomes a Paschen-Back splitting of the hyperfine structure.

10.2.5 Paschen-Back effect of the hyperfine structure

When the interaction with the magnetic field exceeds the hyperfine interaction, the nuclear spin $\hat{\mathbf{I}}$ decouples from the total momentum $\hat{\mathbf{J}}$, and both couple separately to the external magnetic field,

$$\hat{\mathbf{J}} \longrightarrow \left(\hat{\mathbf{J}} \cdot \frac{\vec{\mathcal{B}}}{|\vec{\mathcal{B}}|}\right) \frac{\vec{\mathcal{B}}}{|\vec{\mathcal{B}}|} \qquad \text{and} \qquad \hat{\mathbf{I}} \longrightarrow \left(\hat{\mathbf{I}} \cdot \frac{\vec{\mathcal{B}}}{|\vec{\mathcal{B}}|}\right) \frac{\vec{\mathcal{B}}}{|\vec{\mathcal{B}}|} \ . \tag{10.36}$$

The Zeeman effect of the hyperfine structure becomes a hyperfine structure of the Zeeman effect, also called *Paschen-Back effect of the hyperfine structure* or *Paschen-Goudsmith effect*. We can diagonalize the potential on a basis, where I, m_I, J, and m_J are good quantum numbers. Using the expression (9.168) but disregarding the quadrupolar contribution to the hyperfine interaction, $B_J \simeq 0$, we obtain,

$$\begin{aligned} \hat{V}_{\rm hfs} + \hat{V}_{\rm Zeem}(\mathcal{B}) &= \hat{V}_{\rm hfs} - (\hat{\vec{\mu}}_J + \hat{\vec{\mu}}_I^{\,\simeq 0}) \cdot \vec{\mathcal{B}} \simeq \frac{A_J}{\hbar^2} \hat{\mathbf{J}} \cdot \hat{\mathbf{I}} - \hat{\vec{\mu}}_J \cdot \vec{\mathcal{B}} \\ &\longrightarrow \frac{A_J}{\hbar^2} \left(\hat{\mathbf{J}} \cdot \frac{\vec{\mathcal{B}}}{\mathcal{B}}\right) \frac{\vec{\mathcal{B}}}{\mathcal{B}} \cdot \left(\hat{\mathbf{I}} \cdot \frac{\vec{\mathcal{B}}}{\mathcal{B}}\right) \frac{\vec{\mathcal{B}}}{\mathcal{B}} - \mu_{J_z} \mathcal{B} = \frac{A_J}{\hbar^2} \hat{J}_z \hat{I}_z + \frac{\mu_{\rm B}}{\hbar} g_J \hat{J}_z \mathcal{B} \ , \end{aligned} \tag{10.37}$$

where we neglect the interaction of the dipole moment of the nucleus with the external magnetic field, $\vec{\mu}_I \simeq 0$. We obtain for strong magnetic fields,

$$\boxed{\Delta E_{\rm hfs} + \Delta E_{\rm Zeem}(\mathcal{B}) \simeq A_J m_J m_I + \mu_{\rm B} g_J m_J \mathcal{B}} \ . \tag{10.38}$$

The re-coupling of the state $|F m_F\rangle$ to $|m_I m_J\rangle$ in strong magnetic fields is described by Clebsch-Gordan coefficients,

$$|F m_F\rangle = \sum\nolimits_{m_I + m_J = m_F} |m_I m_J\rangle \langle m_I m_J | F m_F\rangle \ . \tag{10.39}$$

Example 64 (*Nuclear magnetic resonance*): In Eq. (10.37) we have neglected the nuclear dipole moment for being small in comparison to the electronic one. Taking it into account, we get an additional term $\hat{V}_{\rm nmr}$,

$$\hat{V}_{\rm hfs} + \hat{V}_{\rm Zeem} + \hat{V}_{\rm nmr} = \frac{A_J}{\hbar^2} \hat{\mathbf{J}} \cdot \hat{\mathbf{I}} + \hat{\vec{\mu}}_J \cdot \vec{\mathcal{B}} + \hat{\vec{\mu}}_I \cdot \vec{\mathcal{B}} = \frac{A_J}{\hbar^2} \hat{J}_z \hat{I}_z + \mu_{J_z} \mathcal{B} + \mu_{I_z} \mathcal{B} \ . \tag{10.40}$$

Considering a hydrogen atom ^{1}H in a $\vec{\mathcal{B}} = 10\,\mathrm{T}$ strong magnetic field, we have the following hierarchy of energies:

$$\begin{aligned} \Delta E_{\rm Zeem}(\mathcal{B}) &= \mu_{\rm B} g_e m_J \simeq h \cdot 140\,\mathrm{GHz} \\ \Delta E_{\rm hfs}(\mathcal{B}) &\simeq h \cdot 1.4\,\mathrm{GHz} \\ \Delta E_{\rm nmr}(\mathcal{B}) &= \mu_{\rm N} g_p m_I \simeq h \cdot 213\,\mathrm{MHz} \ , \end{aligned} \tag{10.41}$$

where $g_e = 2.002..$ is the g-factor of the electron and $g_p = 5.586..$ of the proton. Now, in large molecules the most electrons are paired, such that $\hat{\mathbf{J}} = 0$. In that case, we are left with the interaction between the nuclear spin and the applied magnetic field,

$$\Delta E_{\rm nmr}(\mathcal{B}) = \mu_{\rm N} g_I m_I \mathcal{B} \ , \tag{10.42}$$

where the g-factor of the nucleus g_I must be looked up in data tables. This is the regime where *nuclear magnetic resonances* (NMR) can be excited with a large variety of applications in spectroscopy and imaging.

10.2.5.1 Hyperfine structure in the intermediate field regime

Knowing the dipolar magnetic A_J and quadrupolar B_J interval factors, it is possible to calculate the Zeeman shift of the hyperfine structure in magnetic fields intermediate between the Zeeman and Paschen-Back regimes. For this, we must determine all the components of the matrix $\hat{V}_{\rm hfs}+\hat{V}_{\rm Zeem}(\mathcal{B})$ and calculate the eigenvalues. The relevant terms of the Eqs. (9.168) and the Eq. (10.36) are,

$$\hat{V}_{\rm hfs}+\hat{V}_{\rm Zeem}(\mathcal{B})=\frac{A_J}{\hbar^2}\hat{\mathbf{I}}\cdot\hat{\mathbf{J}}+\frac{B_J}{\hbar^2}\frac{6(\hat{\mathbf{I}}\cdot\hat{\mathbf{J}})^2+3\hat{\mathbf{I}}\cdot\hat{\mathbf{J}}-2\hat{\mathbf{J}}^2\hat{\mathbf{I}}^2}{2I(2I-1)2J(2J-1)}+g_J\mu_{\rm B}\vec{\mathcal{B}}\cdot\hat{\mathbf{J}}-g_I\mu_{\rm N}\vec{\mathcal{B}}\cdot\hat{\mathbf{I}}\ . \tag{10.43}$$

We develop the complete matrix representation of this Hamiltonian within the uncoupled base, where m_J, m_I are good quantum numbers, introducing the abbreviations

$$I_\pm\equiv\sqrt{I(I+1)-m_I(m_I\pm1)}\qquad\text{and}\qquad I_{\pm\pm}\equiv\sqrt{I(I+1)-(m_I\pm1)(m_I\pm2)}\ . \tag{10.44}$$

The SU(2) algebra provides useful expressions, $\hat{\mathbf{I}}\cdot\hat{\mathbf{J}}=\hat{I}_z\hat{J}_z+\frac{1}{2}(\hat{I}_+\hat{J}_-+\hat{I}_-\hat{J}_+)$. The elements of the matrix are,

$$\begin{aligned}
&\langle m_I'm_J'|H_{\rm hfs}+H_B|m_Im_J\rangle=\left[A_J+\tfrac{3B_J}{2I(2I-1)2J(2J-1)}\right]\times \\
&\times\left\{m_Im_J\delta_{m_I'\ m_I}\delta_{m_J'\ m_J}+\tfrac{1}{2}I_+J_-\delta_{m_I'\ m_I+1}\delta_{m_J'\ m_J-1}+\tfrac{1}{2}I_-J_+\delta_{m_I'\ m_I-1}\delta_{m_J'\ m_J+1}\right\} \\
&+\tfrac{6B_J}{2I(2I-1)2J(2J-1)}\langle m_I'm_J'|\left(\tfrac{\mathbf{I}\cdot\mathbf{J}}{\hbar}\right)^2|m_Im_J\rangle \\
&+\left[-\tfrac{B_J2I(I+1)J(J+1)}{2I(2I-1)2J(2J-1)}+(g_Jm_J-g_I\mu_{\rm N}m_I)\mu_{\rm B}\mathcal{B}\right]\delta_{m_I'\ m_I}\delta_{m_I'\ m_I}
\end{aligned} \tag{10.45}$$

where

$$\begin{aligned}
\langle m_I'm_J'|\left(\tfrac{\hat{\mathbf{I}}\cdot\hat{\mathbf{J}}}{\hbar}\right)^2|m_Im_J\rangle=&\left[(m_Im_J)^2+\tfrac{1}{4}I_-^2J_+^2+\tfrac{1}{4}I_+^2J_-^2\right]\delta_{m_I'\ m_I}\delta_{m_J'\ m_J}+ \\
&+\tfrac{1}{2}\left(m_I'm_J'+m_Im_J\right)I_+J_-\delta_{m_I'\ m_I+1}\delta_{m_J'\ m_J-1}+ \\
&+\tfrac{1}{2}\left(m_I'm_J'+m_Im_J\right)I_-J_+\delta_{m_I'\ m_I-1}\delta_{m_J'\ m_J+1}+ \\
&+\tfrac{1}{4}I_+J_-I_{++}J_{--}\delta_{m_I'\ m_I+2}\delta_{m_J'\ m_J-2}+ \\
&+\tfrac{1}{4}I_-J_+I_{--}J_{++}\delta_{m_I'\ m_I-2}\delta_{m_J'\ m_J+2}\ .
\end{aligned} \tag{10.46}$$

The matrix $\langle m_I'm_J'|H_{\rm hfs}+H_B|m_Im_J\rangle$ is divided into $2F+1$ diagonal blocks, each labeled m_F. The total number of levels is,

$$\sum_{F=|I-J|,..,I+J}2F{+}1=(2I{+}1)(2J{+}1)=\sum_{m_F=|-F,..,F|}\left(\sum_{m_I=|-I,..,I|,\ m_J=|-J,..,J|,\ m_I+m_J=m_F}1\right)\ .$$

In this form the matrix can be programmed, e.g. using computational software such as MATLAB, and all eigenvalues of the Hamiltonian for any state $^{2S+1}X_J$ and nuclear spin I can be calculated numerically. Obviously, the eigenvalues follow from a diagonalization of the matrix and do not depend on the chosen base. Fig. 10.3 shows the result obtained for ^{6}Li ($I=1$) in the states $2s\ ^2S_{1/2}$ and $2s\ ^2P_{3/2}$ (see Tab. 16.1).

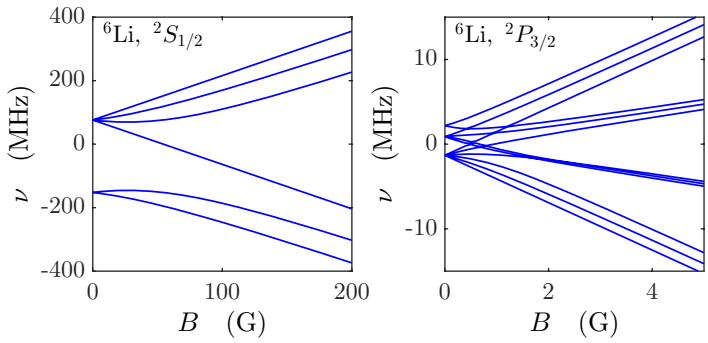

Figure 10.3: (code) Hyperfine and Zeeman structure of the states $2s\ ^2S_{1/2}$ and $2s\ ^2P_{3/2}$ of ^{6}Li, which has the nuclear spin $I = 1$.

Example 65 (*Fully stretched states*): It is interesting to analyze the so-called *fully stretched Zeeman states* defined by $F = I + J$ and $|m_F| = F$. For these states, the spin K defined in (9.167) becomes,

$$\begin{aligned} K \equiv 2\langle \hat{\mathbf{J}} \cdot \hat{\mathbf{I}} \rangle &= F(F+1) - I(I+1) - J(J+1) \\ &= (I+J)(I+J+1) - I(I+1) - J(J+1) = 2JI \ , \end{aligned}$$

and the hyperfine structure (9.168) becomes,

$$\Delta E_{\rm hfs} = \frac{A_J}{2} K + \frac{B_J}{8I(2I-1)J(2J-1)}[3K(K+1) - 4I(I+1)J(J+1)] = A_J IJ + \tfrac{B_J}{4} \ .$$

That is, the hyperfine structure does not depend on the F quantum number at any $\mathcal{B}$-field amplitude, which means that the m_J, m_I, and m_F will be good quantum numbers at arbitrary $\mathcal{B}$-field strengths. So see this, we calculate the Landé-factor (10.35),

$$g_F = g_J \frac{J}{F} - g_J \frac{\mu_{\rm N}}{\mu_{\rm B}} \frac{I}{F} \ ,$$

and consider the particular Zeeman state $m_F = F$, $m_J = J$, and $m_I = I$,

$$\begin{aligned} \hat{V}_{\rm hfs} + \hat{V}_{\rm Zeem}(\mathcal{B}) &= A_J IJ + \tfrac{B_J}{4} + g_J \mu_{\rm B} \vec{\mathcal{B}} \cdot \hat{\mathbf{J}} - g_I \mu_{\rm N} \vec{\mathcal{B}} \cdot \hat{\mathbf{I}} \\ &= A_J IJ + \tfrac{B_J}{4} + \mu_{\rm B} g_F m_F \mathcal{B} = A_J IJ + \tfrac{B_J}{4} + (\mu_{\rm B} g_J J - \mu_{\rm N} g_J I)\mathcal{B} \ . \end{aligned}$$

The energy displacement of the fully stretched states is always linear in the magnetic field. We can also look at the matrix elements $I_+ = 0$ and $I_- = \sqrt{2I}$ and note that all non-diagonal terms vanish.

When one of the spins, J or I, is equal to $1/2$ only two possible hyperfine states exist: $F = I \pm J$. For this case there is an approximate analytic formula called the *Breit-Rabi formula* [49], which will be derived in Exc. 10.2.7.4,

$$\begin{aligned} \Delta E_{\rm hfs} + \Delta E_{\rm Zeem}(\mathcal{B}) &= \langle \tfrac{A_J}{\hbar^2} \hat{\mathbf{I}} \cdot \hat{\mathbf{J}} + g_J \mu_{\rm B} \vec{\mathcal{B}} \cdot \hat{\mathbf{J}} - g_I \mu_{\rm N} \vec{\mathcal{B}} \cdot \hat{\mathbf{I}} \rangle \\ &= -\frac{A_J}{4} + \mu_{\rm N} g_N m_F \mathcal{B} \pm \frac{A_J(I+\frac{1}{2})}{2} \sqrt{1 + \frac{4m_F}{2I+1} x + x^2} \ , \end{aligned} \tag{10.47}$$

with the abbreviation $x \equiv \frac{2(\mu_B g_J - \mu_N g_I)\mathcal{B}}{A_J}$. Resolve also Exc. 10.2.7.5.

Atoms with paired electrons have no spin and therefore no magnetic dipole moment. For example, helium or strontium in their ground state $^1S_0$. These systems are diamagnetic due to the Hamiltonian term (10.11) being quadratic in $\vec{\mathcal{B}}$, as we shall see in Exc. 10.2.7.6.

10.2.6 Landau levels in two-dimensional systems subject to magnetic fields

Magnetic field can also have interesting effects in *artificial atoms*, e.g. quantum dots. An important example is the formation of *Landau levels*. We consider a two-dimensional system of non-interacting particles with charge q and spin S confined to an area $A = L_x L_y$ in the xy plane. We apply a uniform magnetic field,

$$\vec{\mathcal{B}} = \mathcal{B}\hat{\mathbf{e}}_z \tag{10.48}$$

along the z axis. The Hamiltonian of this system is,

$$\hat{H} = \tfrac{1}{2m}(\hat{\mathbf{p}} - q\hat{\mathbf{A}})^2 \ , \tag{10.49}$$

where $\hat{\mathbf{p}}$ is the operator of the canonical momentum and $\hat{\mathbf{A}}$ is the potential vector, related to the magnetic field by $\vec{\mathcal{B}} = \nabla \times \hat{\mathbf{A}}$. The vector potential,

$$\mathbf{A} = \tfrac{1}{2}\begin{pmatrix} -\mathcal{B}y \\ \mathcal{B}x \\ 0 \end{pmatrix} \tag{10.50}$$

reproduces the field (10.48). However, we have the freedom of choosing the potential vector, given by the gauge transformation, to add the gradient of a scalar field, for example,

$$\chi \equiv \tfrac{1}{2}\mathcal{B}xy \quad \Longrightarrow \quad \nabla\chi = \tfrac{1}{2}\begin{pmatrix} \mathcal{B}y \\ \mathcal{B}x \\ 0 \end{pmatrix} \quad \Longrightarrow \quad \mathbf{A}' \equiv \mathbf{A} + \nabla\chi = \mathcal{B}x\hat{\mathbf{e}}_y \ . \tag{10.51}$$

The potential vector $\mathbf{A}'$ gives the same magnetic field and only changes the general phase of the wavefunction, but the physical properties do not change. In this gauge, which is called *Landau gauge*, the Hamiltonian is,

$$\hat{H} = \frac{\hat{p}_x^2}{2m} + \frac{1}{2m}\left(\hat{p}_y - \frac{q\mathcal{B}}{c}\hat{x}\right)^2 \ . \tag{10.52}$$

The operator $\hat{p}_y$ commutes with this Hamiltonian, since the $\hat{y}$ operator is absent due to the choice of the gauge. Thus, the operator $\hat{p}_y$ can be replaced by its eigenvalue $\hbar k_y$. Hence, by introducing the *cyclotron frequency*,

$$\omega_c \equiv \frac{q\mathcal{B}}{mc} \ , \tag{10.53}$$

we obtain,

$$\boxed{\hat{H} = \frac{\hat{p}_x^2}{2m} + \frac{m\omega_c^2}{2}\left(\hat{x} - \frac{\hbar k_y}{m\omega_c}\right)^2} \,. \tag{10.54}$$

This is exactly the Hamiltonian of the quantum harmonic oscillator, except that the minimum of the potential is displaced in position space by the value,

$$x_0 \equiv \frac{\hbar k_y}{m\omega_c} \,. \tag{10.55}$$

To find the energies, we note that the translation of the potential of the harmonic oscillator does not affect the energies. The energies of this system are therefore identical to those of the standard quantum harmonic oscillator,

$$E_n = \hbar\omega_c \left(n + \tfrac{1}{2}\right) \,, \tag{10.56}$$

for $n \geq 0$. Since the energy does not depend on the quantum number k_y, we will have degeneracy. To derive the wavefunctions, we remember that $\hat{p}_y$ commutes with the Hamiltonian. Then the wavefunction splits into a product of eigenstates of the momentum in y-direction and eigenstates of the harmonic oscillator $|\phi_n\rangle$ shifted by a value x_0 in x-direction:

$$\Psi(x, y) = e^{\imath k_y y}\phi_n(x - x_0) \,. \tag{10.57}$$

That is, the state of the electron is characterized by two quantum numbers, n and k_y.

Each set of wavefunctions with the same n is called *Landau level*. Effects due to Landau levels are only observed, when the average thermal energy is lower than the separation of the energy levels, which means that low temperatures and strong magnetic fields are required. Each Landau level is degenerate, because of the second quantum number k_y which, for being confined in the xy plane, can adopt the values,

$$k_y = \frac{2\pi N}{L_y} \,, \tag{10.58}$$

with $N \in \mathbb{N}$. The allowed values of N are further restricted by the condition that the center of mass of the oscillator, x_0, must be physically inside the system, $0 \leq x_0 < L_x$. Using (10.55) this gives the following range for N,

$$0 \leq N < \frac{m\omega_c L_x L_y}{2\pi\hbar} \,. \tag{10.59}$$

For particles with charge $q = Ze$, the upper limit in N can simply be written as a ratio of fluxes,

$$Z\frac{\Phi}{\Phi_0} = \frac{Z\mathcal{B}L_x L_y}{(hc/e)} = N_{\max} \,, \tag{10.60}$$

where $\Phi_0 = h/2e$ is the fundamental *flux quantum* and $\Phi = \mathcal{B}A$ the flux through the system (with area $A = L_x L_y$). Thus, for particles with spin S, the maximum number of particles per Landau level is,

$$N_{\max} = Z(2S + 1)\frac{\Phi}{\Phi_0} \,. \tag{10.61}$$

10.2.6.1 Integer and fractional quantum Hall effect

In general, Landau levels are observed in electronic systems with $Z = 1$ and $S = 1/2$. As the magnetic field increases, more and more electrons can fit a certain Landau level. The occupation of the highest Landau level ranges from entirely full to entirely empty, leading to oscillations in various electronic properties (see *de Haas-van Alphen effect*, *Shubnikov-de Haas effect* and *quantum Hall effect*. The most direct observation

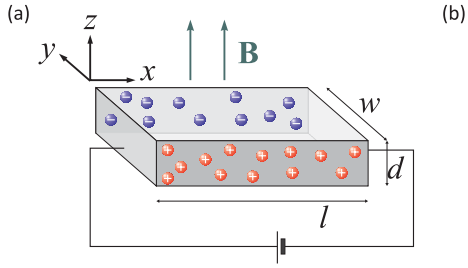

Figure 10.4: Scheme of the Quantum Hall effect.

of the Landau levels is done via the quantum Hall effect. To discuss this effect let us briefly recapitulate the Hall effect. In the scheme of Fig. 10.4, charges are deviated by the Lorentz force exerted by an applied magnetic field $\vec{\mathcal{B}}$ from a driven current density j_x into a current density j_y until a sufficient amount of surface charge density has accumulated to generate an electric field exerting a Coulomb force on the charges which neutralizes the Lorentz force, $\mathbf{F} = q(\vec{\mathcal{E}} + \mathbf{v} \times \vec{\mathcal{B}}) = 0$. Resolving this condition by $\mathbf{v}$, we obtain for the current density,

$$\mathbf{j} = \varrho q \mathbf{v} = \varrho q \frac{\mathcal{E}}{\mathcal{B}} \hat{\mathbf{e}}_x = \varsigma \vec{\mathcal{E}} \,, \tag{10.62}$$

where the last equation is Ohm's law and

$$\varsigma = \begin{pmatrix} \varsigma_{xx} & \varsigma_{xy} \\ -\varsigma_{xy} & \varsigma_{yy} \end{pmatrix} \qquad \text{and} \qquad \varrho = \varsigma^{-1} = \frac{1}{\varsigma_{xx}^2 + \varsigma_{yy}^2} \begin{pmatrix} \varsigma_{xx} & -\varsigma_{xy} \\ \varsigma_{xy} & \varsigma_{yy} \end{pmatrix} \tag{10.63}$$

the conductivity and the resistivity, respectively. The Hall resistivity does therefore depend linearly on the magnetic field,

$$\varrho_{xy} = \frac{\mathcal{E}}{j} = \frac{\mathcal{B}}{\varrho q} \,. \tag{10.64}$$

In two-dimensional systems this is, however, not observed. Instead, plateaus emerge whenever the magnetic field is ramped across a value where a new Landau level is possible binding one more electron,

$$\varrho_{xy} = \frac{2\pi\hbar}{e^2} \frac{1}{\nu} \qquad \text{with} \qquad \nu \in \mathbb{Z} \,. \tag{10.65}$$

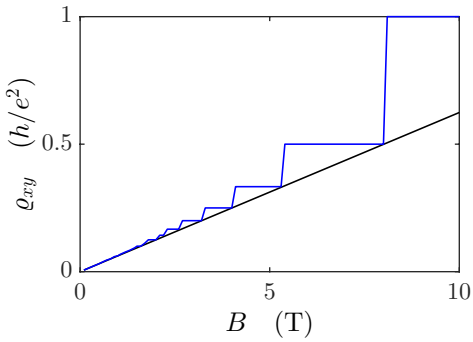

Figure 10.5: (code) Scheme of the quantum Hall effect.

10.2.7 Exercises

10.2.7.1 Ex: Zeeman effect with different quantization axes

The Zeeman effect can be described in several ways depending on the choice of the quantization axis. Consider a magnetic field $\vec{\mathcal{B}} = \mathcal{B}_x \hat{\mathbf{e}}_x$ and calculate the interaction Hamiltonian $V(\mathcal{B}) = -\vec{\mu}_J \cdot \vec{\mathcal{B}}$
a. choosing the quantization axis $\hat{\mathbf{e}}_x$ in the direction of the magnetic field,
b. choosing the quantization axis $\hat{\mathbf{e}}_z$ perpendicular to the direction of the magnetic field.

10.2.7.2 Ex: Zeeman shift and quantization axes

Choosing the fixed quantization axis $\hat{\mathbf{e}}_z$ and a magnetic field $\vec{\mathcal{B}}(\mathbf{r})$ in an arbitrary direction, calculate the Hamiltonian of the Zeeman interaction with an angular momentum $J = 1$ and show that the energy shift depends only on absolute value $|\vec{\mathcal{B}}(\mathbf{r})|$.

10.2.7.3 Ex: Coupling of two electrons

Consider a two-electron system.
a. Show that the operator $(\hbar A/\hbar^2)\hat{\mathbf{s}}_1 \cdot \hat{\mathbf{s}}_2$ distinguishes the triplet from the singlet states.
b. Consider now, that the electrons are exposed to a magnetic field $\mathcal{B}$ applied in the direction $\hat{\mathbf{e}}_z$, so that they acquire the interaction energy with the field $(\mu_B \mathcal{B}/\hbar)(g_1 \hat{s}_{1z} + g_2 \hat{s}_{2z})$. Obtain the matrix associated with the total Hamiltonian and demonstrate that in the regime $\hbar A \gg \mu_B \mathcal{B}$, the representation that favors the total momentum is more adequate.
c. Show that in the regime $\hbar A \ll \mu_B \mathcal{B}$, it is convenient to use the representation that privileges the *individual* spins of the total momentum.
d. Analyze the intermediate regime $\hbar A \simeq \mu_B \mathcal{B}$.

10.2.7.4 Ex: Breit-Rabi formula

Derive the analytical Breit-Rabi formula for the hyperfine structure (10.47) supposing $J = \frac{1}{2}$.

10.2.7.5 Ex: Reciprocal pollution of the Paschen-Back and Zeeman regimes

a. Determine the interaction matrix $\langle \tilde{m}_J \tilde{m}_I | \hat{V}_{\text{hfs}} + \hat{V}_{\text{Zeem}}(\mathcal{B}) | m_J m_I \rangle$ of an atom with electron spin **J** and nuclear spin **J** in the decoupled base without considering the quadrupolar terms.
b. Determine the interaction matrix explicitly for the case of ^{6}Li ($I = 1$) in its ground state $^2S_{1/2}$ ($A_J = h \cdot 152.137\,\text{MHz}$) for a magnetic field of $\mathcal{B} = 100$ G.
c. For the system defined in (b) determine the eigenvalues $E(\mathcal{B})$ of the interaction matrix and the eigenvectors $|\alpha(\mathcal{B})\rangle$ on the decoupled base $|m_J m_I\rangle$.
d. For the system defined in (c) determine the eigenvectors $|\alpha(\mathcal{B})\rangle$ in the coupled base $|F m_F\rangle$.
e. How good are the selection rules for transitions $S_{1/2} - P_{3/2}$ in the intermediate regime between Zeeman and Paschen-Back? We start by calculating the Zeeman shifts for both levels (s denotes the structure $S_{1/2}$, p the structure $P_{3/2}$)

$$
\begin{aligned}
{}_B\langle m_J^s m_I^s | H_{\text{hfs}} + H_B | m_J^s m_I^s \rangle_B &= E^s(\mathcal{B}) \\
{}_B\langle m_J^p m_I^p | H_{\text{hfs}} + H_B | m_J^p m_I^p \rangle_B &= E^p(\mathcal{B}) \ .
\end{aligned}
$$

For the level $P_{3/2}$ the interval factor is less. In particular for ^{6}Li it is so small that we are immediately in the Paschen-Back scheme. This means that the matrix $\overline{{}_\infty\langle \tilde{m}_J^p \tilde{m}_I^p | m_J^p m_I^p \rangle_B} = \delta_{m_J^p, \tilde{m}_J^p} \delta_{m_I^p, \tilde{m}_I^p}$ is diagonal. The element of the transition matrix is then,

$$
\begin{aligned}
&{}_B\langle m_J^p m_I^p | T_q^{(E\kappa)} | m_J^s m_I^s \rangle_B \\
&\quad = \sum_{\tilde{m}_J^s \tilde{m}_I^s} \sum_{\tilde{m}_J^p \tilde{m}_I^p} \overline{{}_\infty\langle \tilde{m}_J^p \tilde{m}_I^p | m_J^p m_I^p \rangle_B}\ {}_\infty\langle \tilde{m}_J^s \tilde{m}_I^s | m_J^s m_I^s \rangle_B\ {}_\infty\langle \tilde{m}_J^p \tilde{m}_I^p | T_q^{(E\kappa)} | \tilde{m}_J^s \tilde{m}_I^s \rangle_\infty \\
&\quad = \sum_{\tilde{m}_J^s \tilde{m}_I^s} {}_\infty\langle \tilde{m}_J^s \tilde{m}_I^s | m_J^s m_I^s \rangle_B\ {}_\infty\langle m_J^p m_I^p | T_q^{(E\kappa)} | \tilde{m}_J^s \tilde{m}_I^s \rangle_\infty \ .
\end{aligned}
$$

The matrix elements in the pure Zeeman regime can be expressed by [Deh07, unpublished],

$$
\begin{aligned}
&\langle F^p m_F^p | T_q^{(E\kappa)} | F^s m_F^s \rangle =_0 \langle m_J^p m_I^p |\, T_q^{(E\kappa)}\, | m_J^s m_I^s \rangle_0 \\
&\quad = \begin{pmatrix} J^s & \kappa & J^p \\ m_J^s & \text{sign}(m^p - m^s) & -m_J^p \end{pmatrix}^2 \begin{Bmatrix} J^p & J^s & \kappa \\ F^s & F^p & I \end{Bmatrix}^2 \frac{(2F^s+1)(2J^p+1)(2\kappa+1)}{2I+1} \ .
\end{aligned}
$$

Discuss the pure Paschen-Back regime via ${}_\infty\langle m_J^p m_I^p | T_q^{(E\kappa)} | m_J^s m_I^s \rangle_\infty$.

10.2.7.6 Ex: Diamagnetism of the ground states of H atoms

Calculate the quadratic Zeeman effect for the ground state of the hydrogen atom caused by the (usually neglected) diamagnetic term of the Hamiltonian in first order TPIT. Write down the energy shift as $\Delta E = -\frac{\chi}{2}\mathcal{B}^2$ assuming a constant magnetic field in order to obtain the diamagnetic susceptibility χ.

10.3 Interaction with electric fields

10.3.1 Stark Effect

Electric fields interact with the electrons of the atom. Describing the atom by its dipole moment, according to (10.13), the interaction energy is,

$$\hat{V}_{\text{Stark}} = -\hat{\mathbf{d}} \cdot \vec{\mathcal{E}} \ . \tag{10.66}$$

This is the *Stark effect*. This effect is usually weak, and its observation requires strong fields or high spectral resolution. Stationary perturbation theory TIPT gives,

$$E_n^{(1)} = \langle \psi_n^{(0)} | - \hat{\mathbf{d}} \cdot \mathcal{E} | \psi_n^{(0)} \rangle = e\mathcal{E}_z \int_{\mathbb{R}^3} z |\psi_n^{(0)}|^2 d^3r = 0 \ , \tag{10.67}$$

with $\mathbf{d} = -e\mathbf{r}$ and $\vec{\mathcal{E}}_z = \mathcal{E}_z \hat{\mathbf{e}}_z$. This only applies when the states have well-defined parity and are NOT degenerate in ℓ. When they ARE degenerate in ℓ, which is the case of hydrogen, the states have no defined parity $(-1)^\ell$. For example, the states s and p contributing to the same state $|\psi_{n,j}\rangle$ have different parities. In this case, the condition (10.67) is not automatically satisfied, and the first perturbation order yields a value. This is the case of the *linear Stark effect*. In the Excs. 10.3.2.1 and 10.3.2.2 we explicitly calculate the Stark energy shift for a hydrogen atom subject to an electric field.

Other atoms do not have this degeneracy, and we must calculate the *quadratic Stark effect* in second order TIPT,

$$|\psi_n^{(1)}\rangle = e\mathcal{E}_z \sum_{n' \neq n} |\psi_{n'}^{(0)}\rangle \frac{\langle \psi_{n'}^{(0)} | \hat{z} | \psi_n^{(0)} \rangle}{E_n - E_{n'}} \ . \tag{10.68}$$

and

$$E_n^{(2)} = e^2 \mathcal{E}_z^2 \sum_{n' \neq n} \frac{|\langle \psi_{n'}^{(0)} | \hat{z} | \psi_n^{(0)} \rangle|^2}{E_n - E_{n'}} \ . \tag{10.69}$$

To simplify the matrix elements, we separate the radial part from the angular part,

$$\langle \psi_{n'}^{(0)} | \hat{z} | \psi_n^{(0)} \rangle = \langle n' J' m'_J | \hat{z} | n J m_J \rangle = \int_0^\infty r^3 R_{n'J'} R_{nJ} dr \int Y^*_{J'm'_J} \tfrac{z}{r} Y_{Jm_J} d\Omega \ . \tag{10.70}$$

The radial part, written as

$$\langle n'_J J' || \hat{z} || n_J J \rangle \equiv \int_0^\infty r^3 R_{n'_J J'} R_{n_J J} dr \ , \tag{10.71}$$

and called the *irreducible matrix element*, no longer depends on the magnetic quantum number. On the other hand, the angular part may be expressed by Clebsch-Gordan coefficients, as will be discussed more extensively in Sec. 16.2.3. The result is called *Wigner-Eckart theorem*,

$$\boxed{\frac{\langle n'_J J' m'_J | \hat{z} | n_J J m_J \rangle}{\langle n'_J J' || \hat{z} || n_J J \rangle} = \int Y^*_{J'm'_J} \tfrac{z}{r} Y_{Jm_J} d\Omega = \frac{1}{2J'+1} \begin{pmatrix} J & 1 & J' \\ m_J & 0 & -m'_J \end{pmatrix}} \ . \tag{10.72}$$

With $[\hat{z}, \hat{L}_z] = 0$, which was shown in Exc. 3.3.4.2, and obviously $[\hat{z}, \hat{S}_z] = 0$ we find,

$$0 = \langle J' m'_J | [\hat{z}, \hat{J}_z] | J m_J \rangle = (m_J - m'_J) \langle J' m'_J | \hat{z} | J m_J \rangle \ . \tag{10.73}$$

This means that for $m_J \neq m'_J$, the matrix elements $\langle J' m'_J | \hat{z} | J m_J \rangle$ should disappear. Therefore, the matrix is diagonal in m_J. We consider dipole transitions with $|J - J'| \leq 1$ [1],

$$\begin{aligned}
\begin{pmatrix} J & 1 & J+1 \\ m_J & 0 & -m_J \end{pmatrix} &= \frac{(J+1)^2 - m_J^2}{(2J+1)(J+1)}, \\
\begin{pmatrix} J & 1 & J \\ m_J & 0 & -m_J \end{pmatrix} &= \frac{m_J^2}{J(J+1)} \ , \\
\begin{pmatrix} J & 1 & J-1 \\ m_J & 0 & -m_J \end{pmatrix} &= \frac{J^2 - m_J^2}{J(2J+1)} \ .
\end{aligned} \tag{10.74}$$

States with the same $|m_J|$ lead to the same quadratic Stark effect,

$$\Delta E \sim A + B |m_J|^2 \ . \tag{10.75}$$

The factors A and B depend on the main quantum number n and also on L, S, J. Moreover, they depend on the energy distance of all contributing levels, because of the denominator in the perturbation equation (10.68). Only levels with different parity $(-1)^L$ contribute. The formulae (10.74) will be derived explicitly in Exc. 10.3.2.3.

10.3.2 Exercises

10.3.2.1 Ex: Stark effect in hydrogen

Consider the hydrogen atom immersed in a uniform electric field $\vec{\mathcal{E}}$ applied along the $\hat{\mathbf{e}}_z$-direction. The term corresponding to this interaction in the total Hamiltonian is $\hat{H}^{(1)} = -e\vec{\mathcal{E}}\hat{z}$. For typical electric fields produced in laboratory, the condition $\hat{H}^{(1)} \ll \hat{H}_0$, which allows the use of TIPT, is satisfied. The effect of the perturbation $\hat{H}^{(1)}$, called Stark effect, is the removal of the degeneracy of some of the hydrogen atom states. Calculate the Stark effect for the state $n = 2$.

10.3.2.2 Ex: Stark effect in the $1s$ hydrogen level

Calculate the Stark shift of the hydrogen ground state by taking into account the contributions of the excited states $n = 2, 3, ...$

10.3.2.3 Ex: Stark effect

Derive the Eqs. (10.74) from the formula (6.7).

[1] For it is possible to show that $\langle n'_J J' || \hat{z} || n_J J \rangle = 0$ for $|J - J'| > 1$.

10.4 Further reading

T. Mayer-Kuckuk, *Atomphysik, Teubner Studienbücher (1985)* [ISBN]

Ch.J. Foot, *Atomic Physics* [ISBN]

I.I. Sobelman, *Atomic Spectra and Radiative Transitions* [ISBN]

Chapter 11

Atoms with many electrons

The electronic shell of an atom consists of many electrons occupying different quantum states and interacting with each other. Being fermions forced into the lowest energy states of a tight potential imposed by their attraction to the Coulomb potential of a nucleus, the electronic wavefunction must obey quantum statistical symmetrization rules. The rules have been derived in Sec. ??, so that we can restrict here to a brief recapitulation focusing to the case of an electronic shell. This will be done in Sec. 11.1. In Sec. 11.2 we will discuss consequences of the symmetrization requirement at the simplest possible case, which is the helium atom. In Sec. 11.3 we extend the discussion to many-electron systems, which leads us finally to the explanation of the periodic system of elements presented in Sec. 11.4.

11.1 Symmetrization of bosons and fermions

Quantum mechanics must be formulated in a way to avoid any possibility of distinguishing identical particles. However, the language of mathematics (based on 'classical' letters and symbols) automatically assigns a particle to a wavefunction; for example, $\psi_a(x_1)$ is the wavefunction a of particle 1 and $\psi_b(x_2)$ the wavefunction b of particle 2. In the absence of interactions, the total wavefunction, $\Psi = \psi_a(x_1)\psi_b(x_2)$, solves the Schrödinger equation of two particles. Now, by changing the coordinates of the particles we get a different state $\Psi' = \psi_a(x_2)\psi_b(x_1)$ [1]. This erroneously suggests that the wavefunction of a particle plays the role of a *label* (or 'soul') characterizing the particle beyond its set of quantum numbers. Why this is a problem, we will see in the following example [2].

[1] We note that the states are orthogonal, because

$$\int \Psi^{*(1,2)}\Psi^{(2,1)}dx_1dx_2 = \int \psi_a^*(x_1)\psi_b^*(x_2)\psi_a(x_2)\psi_b(x_1)dx_1dx_2$$
$$= \int \psi_a^*(x_1)\psi_b(x_1)dx_1 \int \psi_b^*(x_2)\psi_a(x_2)dx_2 = \delta_{n_a,n_b} \ .$$

[2] Ultimately, all this is simply a consequence of the uncertainty principle, which forbids us to specify a wavefunction as a function of two non-commuting coordinates: We have to choose one coordinate on which the wavefunction depends and treat the other as a quantum number, for example, $\psi_{\mathbf{k}}(\mathbf{r}) = e^{\imath\mathbf{k}\cdot\mathbf{r}}$ or $\psi_n(x) = \cos\frac{n\pi x}{L}$. When we now exchange the coordinates of two particles without changing their quantum numbers, we get obviously different states. In classical physics, the wavefunction of a particle would be written $\psi(x,p)$. If two classical particles are not distinct by any other mean, an exchange of *all* their coordinates would reproduce exactly the same state.

Example 66 (*Indistinguishability of particles*): We consider a system of two non-interacting spinless particles in an infinite potential well. The total wavefunction is,

$$\Psi^{(1,2)} \equiv \psi_a(x_1)\psi_b(x_2) = C \cos\frac{n_a\pi x_1}{L}\cos\frac{n_b\pi x_2}{L} \tag{11.1}$$

with the energy,

$$E_{a,b} = \frac{\pi^2 n_a^2}{2mL^2} + \frac{\pi^2 n_b^2}{2mL^2} \ .$$

For observable quantities, such as $|\Psi^{(1,2)}|^2$, we must ensure, $|\Psi^{(1,2)}|^2 = |\Psi^{(2,1)}|^2$, that is,

$$C^2\cos^2\tfrac{n_a\pi x_1}{L}\cos^2\tfrac{n_b\pi x_2}{L} = C^2\cos^2\tfrac{n_a\pi x_2}{L}\cos^2\tfrac{n_b\pi x_1}{L} \ ,$$

but this is not valid for $n_a \neq n_b$. Only if $n_a = n_b$, we have $\psi_a = \psi_b$. In this case, the particles stay in the same state, and we do not need to worry about indistinguishability:

$$\Psi^{(2,1)} = \psi_a(x_2)\psi_b(x_1) = \Psi^{(1,2)} \qquad \text{and} \qquad E_{a,b} = E_{b,a} \ .$$

However, the fact that this state is never observed with two electrons shows, that theory must be corrected to allow for a true description of reality. Will deepen this argument in Exc. 11.1.3.1.

We need to construct the total wavefunction in another way. Let us consider linear combinations of $\Psi^{(1,2)}$,

$$\Psi^{\mathrm{S,A}} \equiv \tfrac{1}{\sqrt{2}}(\Psi^{(1,2)} \pm \Psi^{(2,1)}) = \tfrac{1}{\sqrt{2}}\left[\psi_a(x_1)\psi_b(x_2) \pm \psi_a(x_2)\psi_b(x_1)\right] \ . \tag{11.2}$$

This *(anti-)symmetrized* represents a trick to eradicate the *label* sticking to the particles. For, under position exchange described by the operator $\mathcal{P}_x\psi_a(x_1)\psi_b(x_2) \equiv \psi_a(x_2)\psi_b(x_1)$, the (anti-)symmetrized functions behave like [3],

$$\mathcal{P}_x\Psi^{\mathrm{S,A}} = \pm\Psi^{\mathrm{S,A}} \qquad \text{while} \qquad \mathcal{P}_x\Psi^{(1,2)} = \Psi^{(2,1)} \neq \mp\Psi^{(1,2)} \ . \tag{11.3}$$

The (anti-)symmetrized function solves the Schrödinger equation, as well. As $[\hat{H}, \mathcal{P}_x] = 0$, we can say that the system exhibits an *exchange symmetry* or *exchange degeneracy* upon particle exchange. Observables such as $\Psi^{*S,A}\Psi^{\mathrm{S,A}}$ stay conserved, for example, the probability

$$\begin{aligned} |\Psi^{\mathrm{S,A}}|^2 &= \tfrac{1}{2}\left[|\psi_a(x_1)\psi_b(x_2)|^2 + |\psi_a(x_2)\psi_b(x_1)|^2\right] \\ &\pm \tfrac{1}{2}\left[\psi_a^*(x_1)\psi_b^*(x_2)\psi_a(x_2)\psi_b(x_1) + \psi_a^*(x_2)\psi_b^*(x_1)\psi_a(x_1)\psi_b(x_2)\right] = \mathcal{P}_x|\Psi^{\mathrm{S,A}}|^2 \end{aligned} \tag{11.4}$$

does not change, when we exchange x_1 for x_2. For $x_1 = x_2$, we observe,

$$|\Psi^{\mathrm{S,A}}|^2 = |\psi_a(x)\psi_b(x)|^2 \pm |\psi_a(x)\psi_b(x)|^2 \ . \tag{11.5}$$

That is, for a symmetric system, the probability of finding two particles at the same location is doubled, whereas for an antisymmetric system, this probability is zero.

[3] To guarantee $|\mathcal{P}_x\Psi^{\mathrm{S,A}}|^2 = |\Psi^{\mathrm{S,A}}|^2$, we have $\mathcal{P}_x\Psi^{\mathrm{S,A}} = e^{\imath\phi}\Psi^{\mathrm{S,A}}$. From this, $\mathcal{P}_x\mathcal{P}_x\Psi^{\mathrm{S,A}} = e^{2\imath\phi}\Psi^{\mathrm{S,A}} = \Psi^{\mathrm{S,A}}$. Hence, $\mathcal{P}_x\Psi^{\mathrm{S,A}} = \pm\Psi^{\mathrm{S,A}}$.

Wolfgang Pauli showed that the (anti-)symmetric character is related to the spin of the particles. Particles with *integer spin* called *bosons* must be symmetric. Particles with *semi-integer spin* called *fermions* must be antisymmetric. Electrons are fermions. Therefore, in an atom, they can not be in the same state (location), but must be distributed over a complicated shell of orbitals. We note, that this applies not only to elementary particles, but also to composed particles such as, for example, atoms. We will determine in Exc. 11.1.3.2 the bosonic or fermionic character of several atomic species.

11.1.1 Pauli's Principle

Two electrons with anti-parallel spins can be separated by inhomogeneous magnetic fields, even if they are initially in the same place. Therefore, they are distinguishable and the wavefunction need not be antisymmetric. But if we exchange the spin along with the position, the particles must be indistinguishable. This must be taken into account in the wavefunction by assigning a spin coordinate, $\psi_a(x_1, s_1)$. The exchange operator should now be generalized,

$$\mathcal{P}_{x,s}\Psi^{(1,2)} \equiv \mathcal{P}_{x,s}\psi_a(x_1, s_1)\psi_b(x_2, s_2) = \psi_a(x_2, s_2)\psi_b(x_1, s_1) = \Psi^{(2,1)} \ . \tag{11.6}$$

We now assume that the electrons not only do *not* interact with each other, but there is also *no interaction* between the position and the spin of each electron. That is, for a while we will discard $\mathbf{L}\cdot\mathbf{S}$-coupling [4]. We can then write the total wavefunction of an electron as the *product* of a spatial function, $\psi(x)$, and a spin function, $\chi(s) = \alpha\uparrow + \beta\downarrow$, where α and β are probability amplitudes of finding the electron in the respective spin state, such that,

$$\psi(x, s) = \psi(x)\chi(s) \ . \tag{11.7}$$

For two particles, the total spin function is,

$$X^{(1,2)} = \chi_a(s_1)\chi_b(s_2) \ . \tag{11.8}$$

The (anti-)symmetrized version is

$$X^{\mathrm{S,A}} = \tfrac{1}{\sqrt{2}}(X^{(1,2)} \pm X^{(2,1)}) = \tfrac{1}{\sqrt{2}}[\chi_a(s_1)\chi_b(s_2) \pm \chi_a(s_2)\chi_b(s_1)] \ , \tag{11.9}$$

as we have already seen in Sec. 3.4.1. Since there are only two spin directions, there are four possibilities to attribute the spins $\uparrow$ and $\downarrow$ to the functions $\chi_m(s_n)$,

$$X^{\mathrm{S}} = \begin{cases} \uparrow\uparrow & = \chi_{1,1} \\ \frac{1}{\sqrt{2}}(\uparrow\downarrow + \downarrow\uparrow) & = \chi_{1,0} \\ \downarrow\downarrow & = \chi_{1,-1} \end{cases} \qquad \text{and} \qquad X^{\mathrm{A}} = \tfrac{1}{\sqrt{2}}(\uparrow\downarrow - \downarrow\uparrow) = \chi_{0,0} \tag{11.10}$$

For the total wavefunction, which must be antisymmetric for electrons, there are two

[4] In the case of $\mathbf{L}\cdot\mathbf{S}$-coupling, the total wavefunction can not be written as a product of spatial and spin functions, but it must be antisymmetric anyway.

possibilities,

$$\Theta^{\rm A} = \begin{cases} \Psi^{\rm S} X^{\rm A} = \frac{1}{2}(\Psi^{(1,2)} + \Psi^{(2,1)})(X^{(1,2)} - X^{(2,1)}) = \frac{1}{\sqrt{2}}[\psi_a(x_1)\psi_b(x_2) + \psi_a(x_2)\psi_b(x_1)]\chi_{0,0} \\ \Psi^{\rm A} X^{\rm S} = \frac{1}{2}(\Psi^{(1,2)} - \Psi^{(2,1)})(X^{(1,2)} + X^{(2,1)}) = \frac{1}{\sqrt{2}}[\psi_a(x_1)\psi_b(x_2) - \psi_a(x_2)\psi_b(x_1)] \begin{cases} \chi_{1,1} \\ \chi_{1,0} \\ \chi_{1,-1} \end{cases} \end{cases} . \tag{11.11}$$

That is, the two electrons may be in a *triplet* state with the antisymmetric spatial wavefunction, or in a *singlet* state with the symmetric spatial wavefunction [5].

How to generalize these considerations to N particles? The symmetric wavefunctions contain all permutations of the label a_k, where we understand by a_k the set of quantum numbers unambiguously specifying the state of the particle k,

$$\Theta^{\rm S} = \mathcal{N} \sum_{\mathcal{P}_{x,s} a_k} \psi_{a_1}(x_1)...\psi_{a_N}(x_N) \ , \tag{11.12}$$

with a normalization factor $\mathcal{N}$ [6]. The (anti-)symmetrized wavefunction is obtained from the *Slater determinant*,

$$\Theta^{\rm A} = \frac{1}{N!} \det \psi_{a_k}(x_n) = \frac{1}{N!} \begin{vmatrix} \psi_{a_1}(x_1) & \cdots & \psi_{a_1}(x_N) \\ \vdots & \ddots & \vdots \\ \psi_{a_N}(x_1) & \cdots & \psi_{a_N}(x_N) \end{vmatrix} . \tag{11.13}$$

This function satisfies

$$\mathcal{P}_{x,s} \Theta^{A,(1,..,i,j,..,N)} = \Theta^{A,(1,..,j,i,..,N)} = -\Theta^{A,(1,..,i,j,..,N)} \ . \tag{11.14}$$

The Slater determinant is zero, when two sets of quantum numbers are identical, $a_i = a_j$. For example, for two electrons in an electronic shell, $|n_i, l_i, m_i, s_i\rangle = |n_j, l_j, m_j, s_j\rangle$. This is *Pauli's strong exclusion principle*:

> *The total wavefunction must be antisymmetric with respect to the exchange of any pair of identical fermions and symmetrical with respect to exchange of any pair of identical bosons.*

Pauli's weak exclusion principle (usually sufficient for qualitative considerations) says that two fermions in identical states can not occupy the same region in space. That is, their Broglie waves interfere destructively, as if Pauli's principle exerted a repulsive interaction on the particles. This 'force' has a great impact on the phenomenology of the bonds between atoms, as we will discuss in the following sections.

11.1.2 Consequences for quantum statistics

The indistinguishability of quantum particles has interesting consequences on the statistical behavior of bosons and fermions. This becomes obvious when we consider

[5] In the coupled image, the total spin $\mathbf{S} = \mathbf{s}_1 + \mathbf{s}_2$ can have the following values $S = |s_1 - s_2|, .., s_1 + s_2 = 0, 1$. In the case $S = 0$ the magnetic quantum number can only have one value (singlet), $m_S = 0$. In the case $S = 1$ it can have three values $m_S = -1.0, +1$ (triplet) (see Exc. 10.2.7.3).

[6] It is possible to show $\mathcal{N} = \sqrt{\frac{\Pi_{k=1}^{m} n_k!}{N!}}$, where n_k is the population of state ψ_{a_k}, that is, the number of particles with the same set of quantum numbers a_k.

two particles 1 and 2 being able to adopt two different states a and b. Distinguishable particles can be in one of the following four states,

$$\Psi = \{\psi_a(x_1)\psi_a(x_2), \psi_a(x_1)\psi_b(x_2), \psi_b(x_1)\psi_a(x_2), \psi_b(x_1)\psi_b(x_2)\} \tag{11.15}$$

with the same probability of $p = 1/4$. When the quantum particles approach each other, $x_1 \simeq x_2$, they must become indistinguishable. Bosonic indistinguishable particles can stay in one of the following three states,

$$\Psi = \{\psi_a(x_1)\psi_a(x_2), \tfrac{1}{\sqrt{2}}[\psi_a(x_1)\psi_b(x_2) + \psi_b(x_1)\psi_a(x_2)], \psi_b(x_1)\psi_b(x_2)\} \tag{11.16}$$

with the same probability of $p = 1/3$. Finally, fermionic indistinguishable particles can only be in one state,

$$\Psi = \{\tfrac{1}{\sqrt{2}}[\psi_a(x_1)\psi_b(x_2) - \psi_b(x_1)\psi_a(x_2)]\} \tag{11.17}$$

with the probability of $p = 1$. We see that a simple two-particle system already exhibits qualitative modifications of its statistical behavior. These differences generate different physics as we deal with systems of large numbers of particles, as we can see in the cases of the free electron gas and the Bose-Einstein condensate.

We finally note a result of the standard model of particle physics assigning a fermionic character to all fundamental constituent particles of matter while the mediators of fundamental forces are always bosons.

11.1.3 Exercises

11.1.3.1 Ex: Indistinguishability of particles

Consider the observable quantity $\int_0^{L/2}\int_0^{L/4}|\Psi(x_1,x_2)|^2dx_1dx_2$ for the case of the wavefunction defined in (11.1) and show, that it *does* depend on particle exchange.

11.1.3.2 Ex: Bosonic and fermionic isotopes

Consulting an isotope table determine the bosonic or fermionic character of the following atomic species: ^{87}Sr, ^{86}Sr, ^{87}Rb, ^{39}K, and ^{40}K.

11.1.3.3 Ex: Interference of bosons and fermions

a. Consider two clouds of ultracold bosonic atoms (BECs at temperature $T = 0$) moving into opposite direction with velocities $v_\pm = \pm v$, respectively. Describe the matter wave interference pattern.
b. Repeat the consideration for the case of (i) fermionic clouds and (ii) only two counterpropagating atoms. Is matter wave interference possible at all for fermions?

11.2 Helium

The simplest atom to discuss Pauli's principle is helium. The helium atom has a charged nucleus $Z = +2e$ and mass $m_{\mathrm{He}} \approx 4m_{\mathrm{H}}$.

11.2.1 The ground state

The ground state of the *helium* atom brings together the two electrons, that is, $(1s)^2$. To treat the helium atom, we can, as a first trial, describe the atom by the Bohr model, assuming independent electrons. Neglecting the electronic repulsion term (which depends on $r_{12} = |\mathbf{r}_1 - \mathbf{r}_2|$), we can separate the total wavefunction:

$$\Psi(\mathbf{r}_1, \mathbf{r}_2) = \Psi_1(\mathbf{r}_1)\Psi_2(\mathbf{r}_2) \ , \tag{11.18}$$

and we get two Schrödinger equations, the Hamiltonian being equal to the one of hydrogen-like atoms:

$$\left[-\frac{\hbar^2}{2\mu}\nabla_i^2 - \frac{e^2}{4\pi\varepsilon_0}\frac{Z}{r_i}\right]\Psi_i(\mathbf{r}_i) = E_n^{(i)}\Psi_i(\mathbf{r}_i) \ , \tag{11.19}$$

with $i = 1, 2$. For hydrogen-like atoms we have,

$$E = E_n^{(1)} + E_n^{(2)} = E_\mathrm{B} Z^2 \left(\frac{1}{n_1^2} + \frac{1}{n_2^2}\right) \ , \tag{11.20}$$

with $E_\mathrm{B} = -13.6\,\mathrm{eV}$. With this, we get the energy for the ground state:

$$E_\mathrm{He}(1s) = -2Z^2 E_\mathrm{B} = -108.8\,\mathrm{eV} \ . \tag{11.21}$$

The value predicted by Bohr's model is far from experimental reality: The ionization energy measured for the first electron is 24.6 eV, for the second 54.4 eV, totalizing a binding energy for two electrons of $-78.983\,\mathrm{eV}$. This corresponds to an error of about 38%. The lower energy of the first electron is due to the shielding of the nucleus by the second.

11.2.1.1 First-order perturbation of the energy

Treating the repulsion term between the electrons as a perturbation [35] and using the eigenfunctions of hydrogen atoms $|n, \ell, m_\ell\rangle$, the total wavefunction is $|n_1, \ell_1, m_{\ell_1}; n_2, \ell_2, m_{\ell_2}\rangle$, we obtain as first order TIPT correction for the energy:

$$\Delta E = \langle n_1, \ell_1, m_{\ell_1}; n_2, \ell_2, m_{\ell_2}|\frac{e^2}{4\pi\varepsilon_0 r_{12}}|n_1, \ell_1, m_{\ell_1}; n_2, \ell_2, m_{\ell_2}\rangle \ . \tag{11.22}$$

This correction is called the *Coulomb integral* and has the value:

$$\Delta E = \frac{e^2}{4\pi\varepsilon_0}\int |\Psi_{n_1,\ell_1,m_{\ell_1}}(\mathbf{r}_1)|^2 \left(\frac{1}{r_{12}}\right) |\Psi_{n_2,\ell_2,m_{\ell_2}}(\mathbf{r}_2)|^2 dV_1 dV_2 \ . \tag{11.23}$$

This integral is always positive. The term $|\Psi_{n_1,\ell_1,m_{\ell_1}}(\mathbf{r}_1)|^2 dV_1$ is the probability of finding the electron inside the volume element dV_1 and, when multiplied by $-e$, gives the charge associated with that region. Thus, the integral represents the Coulombian interaction energy of the confined charges within the two volume elements dV_1 and dV_2. ΔE is the total contribution to the potential energy. Calculating the Coulomb integral for the ground state, which will be done in Exc. 11.2.3.1, we obtain,

$$\Delta E = \frac{5Z}{4}\left(\frac{e^2}{4\pi\varepsilon_0 2a_\mathrm{B}}\right) = \frac{5Z}{4}E_\mathrm{B} \ , \tag{11.24}$$

with $a_{\rm B}$ the Bohr radius. ΔE corresponds to 34 eV. Thus, the ground state energy is $E_{\rm He}(1s) = -108.8\,{\rm eV} + 34\,{\rm eV} = -74.8\,{\rm eV}$. Comparing with the experimental value of $-78.983\,{\rm eV}$ we still have an error around 5.3%.

11.2.1.2 Shielding of the nuclear charge

We can make the approximation in which we consider that each electron moves in a Coulombian potential, with respect to the nucleus, shielded by the charge distribution of the other electron [219]. The resulting potential will be generated by an effective charge $\zeta e \equiv (Z - B)e$. The quantity $B \in [0, 1]$ is called the shielding constant.

The first electron feels a total nuclear charge Ze, while the second feels an effective nuclear charge ζe. We exchange Z for ζ in the energy term for hydrogen-like atoms,

$$E_n = -\zeta \frac{E_{\rm B}}{n^2} \ , \tag{11.25}$$

and the energy for the ground state becomes, assuming total shielding, $B = 1$,

$$E = E_1 + E_2 = -Z^2 E_{\rm B} - \zeta^2 E_{\rm B} = -4E_{\rm B} - E_{\rm B} = -5E_{\rm B} = -67.5\,{\rm eV} \ . \tag{11.26}$$

Comparing with the experimental value of $-78.983\,{\rm eV}$ we have an error around 15%. For a shielding constant of around $B = 0.656$ the experimental value is reproduced. This means that the effective nuclear charge felt by the second electron is only *partly* shielded by the former. The TPIT method (11.22) and the shielding concept (11.25) can be combined in a variational calculation, where the effective charge ζ is the variational parameter. In Exc. 11.2.3.2 we study the reciprocal shielding of the electrons at the example of the helium-type ion H^-.

11.2.2 Excited states

Let us now investigate the excited states of helium, in particular those, where *only one electron* is excited, the other one being in the ground state, $(1s)^1(2s)^1$ and $(1s)^1(2p)^1$. All energies are considerably higher (weaker binding) than predicted by Bohr's model with $Z = 2$, because of the interaction with the other electron. Also, the $(2s)$ and $(2p)$ levels are no longer degenerate, because the electrostatic potential is no longer Coulombian (see Fig. 11.1).

As we have seen in the discussion of the fine structure of hydrogen, the energy of the $\mathbf{L} \cdot \mathbf{S}$-coupling given by (9.130) is $\propto E_n(Z\alpha)^2 \propto Z^4$. For helium which still has a small Z, the energy of the coupling is weak ($\sim 10^{-4}\,{\rm eV}$), so that we can count on a direct coupling of the spins of the two electrons. If in an excited state the orbits of the electrons are different, we can construct combinations of symmetric **or** antisymmetric spatial wavefunctions $\Psi^{\rm S,A}$, and therefore combinations $X^{A,S}$ of antiparallel or parallel spins. When the spins are parallel ($S = 1$), the spatial wavefunction is antisymmetric, when they are antiparallel ($S = 0$), it is symmetric. From the symmetry of the wavefunction depends the energy of the Coulombian interelectronic interaction, because in the symmetric state the average distance of the electrons is much smaller than in the antisymmetric state, where *the total spatial function disappears for zero distance*. Consequently, the configuration $(1s)^1(2s)^1$ has two states with $S = 0$ and $S = 1$, with energy $E_{S=0} > E_{S=1}$. Likewise, all configurations are

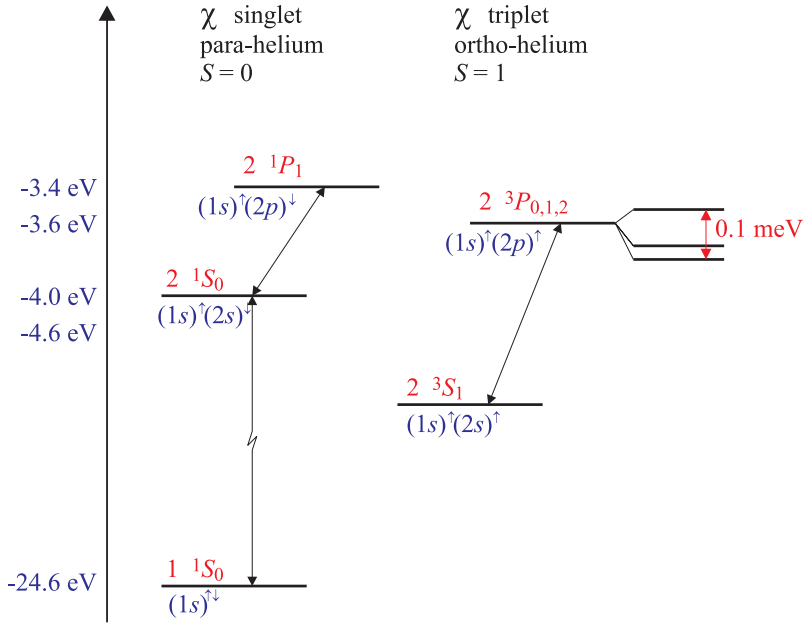

Figure 11.1: Helium levels for the excitation of the first electron and allowed singlet and triplet transitions. Note that the state $(1s)^{\uparrow\uparrow} \equiv (1s)^{\uparrow}(1s)^{\uparrow}$ does not exist, because it would be totally symmetric.

split, as shown in Fig. 11.1. The energy difference ($\sim 0.6\,\mathrm{eV}$) is considerable and larger than the energy of fine structure interaction. This explains why the two spins first couple to a total spin, $\mathbf{s}_1 + \mathbf{s}_2 = \mathbf{S}$, before this spin couples to the total orbital angular momentum, $\mathbf{S} + \mathbf{L} = \mathbf{J}$. This is the $\mathbf{L} \cdot \mathbf{S}$-coupling.

11.2.2.1 Exchange energy

The energy difference between the two states $S = 0$ and $S = 1$ is called *exchange energy*. It comes out of a first-order perturbation calculation perfomed with symmetrized states. For example, for the two possible states $(1s)^1(2s)^1$, we write the total antisymmetric wavefunctions,

$$\Theta^{\mathrm{A}}_{\pm} = \tfrac{1}{\sqrt{2}} \left[\psi_{100}(\mathbf{r}_1)\psi_{200}(\mathbf{r}_2) \pm \psi_{100}(\mathbf{r}_2)\psi_{200}(\mathbf{r}_1)\right] \cdot \chi^{A,S} \ , \tag{11.27}$$

where the (+) sign holds for $\chi^{\rm A}$ ($S=0$) and the (−) sign for $\chi^{\rm S}$ ($S=1$). The energies are,

$$\begin{aligned}\Delta E^{\rm S,A} &= \tfrac{1}{2}\int dr_1^3\int dr_2^3\Theta_\pm^{*A}\frac{e^2}{4\pi\varepsilon_0|\mathbf{r}_1-\mathbf{r}_2|}\Theta_\pm^{\rm A} \qquad (11.28)\\ &= \tfrac{1}{2}\int dr_1^3\int dr_2^3\frac{e^2}{4\pi\varepsilon_0|\mathbf{r}_1-\mathbf{r}_2|}[|\psi_{100}(\mathbf{r}_1)|^2|\psi_{200}(\mathbf{r}_2)|^2+|\psi_{100}(\mathbf{r}_2)|^2|\psi_{200}(\mathbf{r}_1)|^2]\\ &\quad\pm\tfrac{1}{2}\int dr_1^3\int dr_2^3\frac{e^2}{4\pi\varepsilon_0|\mathbf{r}_1-\mathbf{r}_2|}2\psi_{100}^*(\mathbf{r}_1)\psi_{200}^*(\mathbf{r}_2)\psi_{100}(\mathbf{r}_2)\psi_{200}(\mathbf{r}_1)\\ &\equiv \Delta E_{\rm Coulomb}\pm\Delta E_{\rm exchange}\ .\end{aligned}$$

The first integral,

$$\Delta E_{\rm Coulomb}=\int dr_1^3\int dr_2^3\frac{e^2}{4\pi\varepsilon_0|\mathbf{r}_1-\mathbf{r}_2|}|\psi_{100}(\mathbf{r}_1)|^2|\psi_{200}(\mathbf{r}_2)|^2\ , \qquad (11.29)$$

is the Coulomb energy (11.23) between the electronic orbitals. We note that this part can be calculated from the Hamiltonian using *non-symmetrized* orbitals. The second integral,

$$\Delta E_{\rm exchange}=\int dr_1^3\int dr_2^3\frac{e^2}{4\pi\varepsilon_0|\mathbf{r}_1-\mathbf{r}_2|}\psi_{100}^*(\mathbf{r}_1)\psi_{200}^*(\mathbf{r}_2)\psi_{100}(\mathbf{r}_2)\psi_{200}(\mathbf{r}_1)\ , \qquad (11.30)$$

called *exchange energy* corresponds to the interference terms of the symmetrization and must be added or subtracted according to their symmetry character. It is interesting to note that up to this point the spin does not enter directly into the helium Hamiltonian,

$$\hat{H}^{\rm S,A}=\frac{p_1^2}{2m}+\frac{p_2^2}{2m}+V(r_1)+V(r_2)+V(|\mathbf{r}_1-\mathbf{r}_2|)\pm\Delta E_{\rm exchange}\ , \qquad (11.31)$$

but only through the symmetry character of the spatial wavefunction. On the other hand, on a much smaller energy scale, the spin enters through the $\mathbf{L}\cdot\mathbf{S}$-interaction.

The potential is not spherically symmetric, the term r_{12} depends on the angle between $\mathbf{r}_1$ and $\mathbf{r}_2$. Thus, the total wavefunction $\Psi(\mathbf{r}_1,\mathbf{r}_2)$ is not separable into a radial and an angular part. By consequence, unlike for hydrogen, the Schrödinger equation with the Hamiltonian (11.21) has no analytical solution.

Example 67 (*TIPT for excited helium states*): We consider the two electrons of a helium atom occupying different orbits described by wavefunctions denoted by $\psi_a(1)\equiv\psi_{n_1,\ell_1,m_{\ell_1}}(\mathbf{r}_1)$ and $\psi_b(2)\equiv\psi_{n_2,\ell_2,m_{\ell_2}}(\mathbf{r}_2)$. Applying the Hamiltonian without the interelectronic interaction term, the total states $\Theta=\psi_a(1)\psi_b(2)$ and $\psi_a(2)\psi_b(1)$ have the same energy E_a+E_b. To calculate the energy correction, we use TIPT for degenerate states. We have to calculate the secular determinant $\det(\langle n,\nu|H^{(1)}|n,\mu\rangle-E_{n,\mu}^{(1)}\delta_{\mu,\nu})$. The terms of the perturbation matrix $H^{(1)}$ are:

$$\begin{aligned}H_{11}^{(1)}&=\langle\psi_a(1)\psi_b(2)|\frac{e^2}{4\pi\varepsilon_0 r_{12}}|\psi_a(1)\psi_b(2)\rangle\\ H_{22}^{(1)}&=\langle\psi_a(2)\psi_b(1)|\frac{e^2}{4\pi\varepsilon_0 r_{12}}|\psi_a(2)\psi_b(1)\rangle\\ H_{12}^{(1)}&=\langle\psi_a(1)\psi_b(2)|\frac{e^2}{4\pi\varepsilon_0 r_{12}}|\psi_a(2)\psi_b(1)\rangle=H_{21}^{(1)}\ .\end{aligned}$$

The terms $J \equiv H_{11}^{(1)} = H_{22}^{(1)}$ are Coulomb integrals. The term $K \equiv H_{12}^{(1)}$ is called *exchange integral*:

$$K = \frac{e^2}{4\pi\varepsilon_0}\langle\psi_a(1)\psi_b(2)|\frac{1}{r_{12}}|\psi_a(2)\psi_b(1)\rangle \ .$$

Hence, as J and K are positive, the determinant is:

$$\begin{vmatrix} J-E & K \\ K & J-E \end{vmatrix} = 0 \ ,$$

yielding,

$$E^{(1)} = J \pm K \ .$$

That is, the states that were previously degenerate with energy $E = E_a + E_b$ are now split into two states with energies $E = E_a + E_b + J \pm K$. And the corresponding eigenfunctions are:

$$\Psi^{\mathrm{S,A}}(1,2) = \frac{1}{\sqrt{2}}[\psi_a(1)\psi_b(2) \pm \psi_b(1)\psi_a(2)] \ .$$

This result shows that the repulsion between the two electrons breaks the degeneracy (of separable functions written in product form) into states with an energy difference $2K$. Note that the eigenfunctions are symmetric, which is discussed in the next section.

11.2.2.2 The spectrum of helium

So far we have seen that, if the electrons are in the same orbital, we have an energy term $E = 2E_a + J$ and, when they are in *different orbitals*, we have $E = E_a + E_b + J \pm K$, with a separation between levels of $2K$.

In practice, we consider only the excitation of *one* electron, because the energy to excite the two electrons exceeds the ionization energy of the helium atom. To find the selection rules for transitions between symmetric and antisymmetric states, we calculate the dipole moment of the transition. For a two-electron system the dipole moment is $\hat{\mathbf{d}} = -e\mathbf{r}_1 - e\mathbf{r}_2$, which is symmetric with respect to a permutation of the two electrons. The matrix element for the dipolar transition is:

$$\langle\Psi^{\mathrm{A}}|\hat{\mathbf{d}}|\Psi^{\mathrm{S}}\rangle = -e\int \Psi^{*A}(\mathbf{r}_1,\mathbf{r}_2)(\mathbf{r}_1+\mathbf{r}_2)\Psi^{\mathrm{S}}(\mathbf{r}_1,\mathbf{r}_2)dV_1dV_2 \ . \tag{11.32}$$

If we exchange the electrons, the above integral changes sign, because $\Psi^{\mathrm{A}}(\mathbf{r}_1,\mathbf{r}_2)$ changes sign. But the integral can not depend on the nomenclature of the integration variables, so *it must be zero*. The transition between a symmetric and an antisymmetric state can not occur. Looking at the spin wavefunction in $\Theta = \Psi^{\mathrm{S}}\chi^{\mathrm{A}}$ or $\Psi^{\mathrm{A}}\chi^{\mathrm{S}}$, we find that transitions are only allowed between singlet states or between triplet states. That is, there is a *selection rule* for the spin postulating $\Delta S = 0$ [7,8].

[7] Moreover, transitions between the states $^1S_0$ and $^3S_1$ are impossible, because they violate the selection rule for the angular momentum, $\Delta L = \pm 1$.

[8] We can understand the selection rules as follows: As long as the wavefunction can be written as a product, $\Theta = \Psi(x)\chi(s)$, the symmetry character is preserved for the two functions separately. The eigenvalues of the operators $\mathcal{P}_x$ and $\mathcal{P}_s$ are then good quantum numbers. But this only holds for

Because of the differences observed in the singlet and the triplet spectrum of helium, illustrated in Fig. 11.1, it was first believed that they belong to different atomic species, called *para-helium* and *ortho-helium*. A chemical analysis showed later that it was the same element.

11.2.3 Exercises

11.2.3.1 Ex: Helium atom

Compare the measured binding energy with the prediction of Bohr's model considering the inter-electronic interaction up to first order TIPT.

11.2.3.2 Ex: Shielding in helium

The helium atom (or helium-like atoms such as H^-) has two interacting electrons in its composition, which means that these systems have no exact solution. To circumvent this problem we have to come up with a series of approximate methods for calculating their eigenstates and their respective eigenenergies. Among these methods, a widely used one, due mainly to its ease and practicality, is the variational method, in which we calculate the fundamental state of a given problem through a test function that is not a solution of the original problem. This method, when applied to a helium atom, uses as test function the solution of the problem without coulombian interaction between the electrons, which only feel the interaction with the original charge of the nucleus. However, this method could be further improved if we considered an effective nuclear charge, due to its interaction with the electrons themselves, and then obtaining the test function. Apply this correction to the case of helium. Interpret the result. **Help:**

$$\int \frac{\sin\theta_2}{\sqrt{r_1^2+r_2^2-2r_1^2r_2^2\cos\theta_2}}d\theta_2 = \frac{\sqrt{r_1^2+r_2^2-2r_1^2r_2^2\cos\theta_2}}{r_1r_2} \quad \text{and} \quad \left\langle\frac{1}{r}\right\rangle = \frac{Z}{a_B}\ .$$

11.3 Electronic shell structure

The interelectronic interaction and the need to antissimetrize the wavefunction of the electrons both contribute to excessively increase the complexity of multielectronic atoms. The Hamiltonian describing a multielectronic atom of atomic number Z,

$$\hat{H} = E_{\text{kin}} + V_{\text{ncl:ele}} + V_{\text{ele:ele}} = \sum_{i=1}^{Z}\frac{p_i^2}{2m} - \sum_{i=1}^{Z}\frac{Ze^2}{4\pi\varepsilon_0|\mathbf{r}_i|} + \sum_{i<j=1}^{Z}\frac{e^2}{4\pi\varepsilon_0|\mathbf{r}_i-\mathbf{r}_j|}\ , \quad (11.33)$$

is extremely complicated to solve, even for the simplest case ($Z = 2$) we must use approximation methods.

weak $\mathbf{L}\cdot\mathbf{S}$-coupling. The electric dipole operator for the transition does not act on the spin (which prevents the recoupling $S = 1 \leftrightarrow S = 0$ via $E1$-radiation) and also does not act on the symmetry character of the orbitals (which prevents transitions $\Psi^{\text{S}} \leftrightarrow \Psi^{\text{A}}$).
In principle, this holds for any species of atoms with two valence electrons. In reality however, the influence of the $\mathbf{L}\cdot\mathbf{S}$-coupling grows with Z, which weakens the interdiction of the intercombination transition. In this case, only the operator $\mathcal{P}_{x,s}$ yields good eigenvalues.

11.3.1 TIPT method

Note that, if we assume independent electrons ($V_{\text{ele:ele}} = 0$), that is, each electron moves independently of the others within the electrostatic potential generated by the nucleus and the other $Z-1$ electrons, the problem would be solvable: We could solve the Schrödinger equation for a product state of all the electronic wavefunctions, and we would know the eigenfunctions and individual eigenenergies of each electron (as for the hydrogen atom). In principle, we should use antisymmetric wavefunctions, but as a first approach we can choose to only respect Pauli's weak principle, that is, assign an *individual and unique* set of quantum numbers to each electron. The total energy would be the sum of the energy of every electron, and the associated physical eigenstates would be obtained by means of an antisymmetrization of the tensor product of the multielectronic state.

Thus, as a first approximation, we use the states of individual electrons (orbital approximation) and consider $V_{\text{ele:ele}}(|\mathbf{r}_i - \mathbf{r}_j|)$ as a perturbation making use of *time-independent perturbation theory*. However, this term is not small enough to justify this procedure, since approximating

$$V_{\text{ncl:ele}} \simeq \frac{Z^2 e^2}{a_{\text{B}}} \quad \text{and} \quad V_{\text{ele:ele}} \simeq \frac{Z(Z-1)e^2}{2a_{\text{B}}} \,, \tag{11.34}$$

we realize that $V_{\text{ele:ele}}/V_{\text{ncl:ele}}$ varies between $\frac{1}{4}$ for $Z = 2$ and $\frac{1}{2}$ for $Z \gg 1/2$. For this reason the use of alternative methods to describe multielectronic atoms is necessary. Nevertheless, the set of quantum numbers derived from Bohr's atomic model are still the same as those used for many-electron atoms, and the orbitals are used as starting points for more sophisticated methods.

To calculate most of the atomic properties we need reasonably realistic potentials. The most important terms of the Hamiltonian are the Coulombian potential between the nucleus and the electrons, V_{ne}, being naturally spherical, and the interaction potentials between the electrons, V_{ee}, which we will try to approximate by a spherical potential and treat the deviations caused by the approximation afterward. Knowing the effect of the shielding of the nucleus by electronic charges, we already know the asymptotes (see Fig. 11.2),

$$V_{\text{eff}} = -\frac{Ze^2}{4\pi\varepsilon_0 r} \quad \text{for} \quad r \to 0 \quad \text{and} \quad V_{\text{eff}} = -\frac{e^2}{4\pi\varepsilon_0 r} \quad \text{for} \quad r \to \infty. \tag{11.35}$$

11.3.2 Thomas-Fermi model for an electron gas

A first approach to getting a reasonable *effective potential* V_{eff} is provided by the *Thomas-Fermi model*. This is a semi-classical model that aims to roughly describe the total energy of the electrons as a *density functional* of atomic/molecular electrons. It serves as a basis for more sophisticated methods aiming at determining the electronic structure, such as *density functional theory* (DFT), and the wavefunctions determined by this method often serve as a starting point for the Hartree method discussed below. One of the important predictions of the *Thomas-Fermi model* is that the average radius of an atom depends on the nuclear charge as $\bar{R} \propto Z^{-1/3}$.

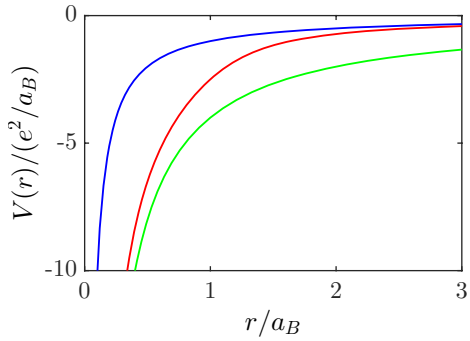

Figure 11.2: (code) External potential (shielded Coulombian) $V_{\rm C} \propto \frac{e^2}{r}$ (blue, upper curve), interior potential (non-shielded Coulombian for $Z = 4$) $V_{\rm nsh} \propto \frac{Ze^2}{r}$ (green, lower curve), and effective potential (red, middle curve).

The Thomas-Fermi model allows us to understand the electronic configuration of the fundamental states and provides the basis for the periodic system of elements. In this model, the electrons are treated as independent particles, on one side forming an effective radial electric potential, on the other side being subjected to this potential. Instead of requiring anti-symmetry of the wavefunction, it is only necessary to ensure that all electrons are distinguished by at least one quantum number. The orbitals of complex atoms are similar to the wavefunctions of hydrogen. So, we can use these quantum numbers n, ℓ, m_ℓ, and m_s for every electron.

However, the effective radial potential depends very much on the species and is quite different from the Coulomb potential. So, the degeneracy in ℓ is lifted. In general, electrons with small ℓ are more strongly bound, because they have a higher probability of being near the nucleus, where the potential is deeper (see Fig. 11.2). The same argument explains why electrons with small n are more strongly bound. We will discuss these effects in more depth in Sec. 11.4.1 by comparing the excitation levels of the valence electron in different alkalis.

11.3.2.1 Density of states in the Fermi gas model

Even though the real potential sensed by the electrons bound to a nucleus is very different from the three-dimensional well, we can roughly imagine that the atom is subdivided into small volumes, understood as box potentials, all filled with electrons. From this we can calculate the distribution of the electronic charge, such that the average local energy is homogeneous and the electronic cloud in equilibrium. The distribution, in turn, serves to determine the shape of the electrostatic potential which, when subdivided into small volumes filled with electrons, produces the same charge distribution. This principle is called *self-consistency*.

According to the Fermi gas model, we consider an infinite potential well, that we gradually fill up with electrons. The Pauli principle allows us to place at most two electrons in each orbital,

$$\Psi = \psi_{1,\uparrow}(x_1)\psi_{1,\downarrow}(x_2)\psi_{2,\uparrow}(x_3)\psi_{2,\downarrow}(x_4)\cdot \ldots . \tag{11.36}$$

This total wavefunction satisfies the weak Pauli principle, but is obviously not antisymmetric. The approximation is good, when the interaction between the electrons is negligible. Otherwise, we need to consider the exchange energy terms. This model, called *Fermi gas model*, is often used to describe the behavior of electrons that can freely move within the conductance band of a metal.

We divide the atom into small volumes (cells) containing uniformly distributed non-interacting electrons, whose total number is N, and we analyze each cell individually. The whole volume can be modeled by a box potential: $V(\mathbf{r}) = 0$ for $0 \leq x, y, x \leq L$ and $V(\mathbf{r}) = \infty$ in all other places. In this case we find the possible states $\{|n_x, n_y, n_z\rangle\}$ with $n_x, n_y, n_z = 1, 2, 3$ and the single electron energies,

$$E_{n_x,n_y,n_z} = \frac{\pi^2\hbar^2}{2m_eL^2}(n_x^2 + n_y^2 + n_z^2) = \frac{\hbar^2}{2m_e}\mathbf{k}^2_{n_x,n_y,n_z} \ , \tag{11.37}$$

where $\mathbf{k}^2_{n_x,n_y,n_z} = k_x^2 + k_y^2 + k_z^2 = (\frac{n_x\pi}{L})^2 + (\frac{n_y\pi}{L})^2 + (\frac{n_z\pi}{L})^2$. Each set of values $\mathbf{k} = (k_x, k_y, k_z)$ corresponds to an accessible state of the system, and each state is associated with a volume element $(\pi/L)^3$ in k-space. Defining the density of states $\eta(E)$, we can express the total number of states below a particular energy E by,

$$\begin{aligned} n(E) &= \int_0^E \eta(E')dE' \equiv \frac{1}{(2\pi)^3}\int d^3r d^3k = \frac{L^3}{(2\pi)^3}4\pi\int k^2dk \\ &= \frac{L^3}{(2\pi)^3}4\pi\left(\frac{2m_e}{\hbar^3}\right)^{3/2}\int_0^E \sqrt{E'}dE' = \frac{L^3}{3\pi^2}\left(\frac{2m_eE}{\hbar^3}\right)^{3/2} \ . \end{aligned} \tag{11.38}$$

$\eta(E)dE$ is the number of states with energies between E and $E + dE$.

At temperature $T = 0$ K all N electrons are in their energetically lowest available state, obeying the Pauli exclusion principle and considering the spin. The energy of the N-th electron (the most energetic one) is then called the *Fermi energy* E_F. That is, below E_F all states are occupied, and all states above E_F are unoccupied. The total energy is given by the sum of the energies of the N less energetic states, and the final physical state is given by the antisymmetrization of the corresponding wavefunction. With the formula (11.38), we can express the Fermi energy via $n(E_\mathrm{F}) \equiv N$, such that,

$$E_\mathrm{F} = \frac{\hbar^2}{2m_eL^2}(3\pi^2N)^{2/3} \ , \tag{11.39}$$

so that the density of states can be expressed as,

$$\boxed{\eta(E) = \frac{dn(E)}{dE} = \frac{L^3}{2\pi^2}\left(\frac{2m_e}{\hbar^2}\right)^{3/2}E^{1/2} = \frac{3N}{2}\frac{E^{1/2}}{E_\mathrm{F}^{3/2}}} \ . \tag{11.40}$$

11.3.2.2 Thomas-Fermi energy

Fermi's box potential trick allowed us to model the impact of Pauli's principle on the spatial distribution of fermions in a restricted volume, but we did not take into account yet the fact that electrons are charged and will interact. Hence, the energy calculated so far is purely kinetic and will have to be complemented by potential energy.

The total kinetic energy of the electrons with the system in its ground state is,

$$E_{\rm tot} = \int_0^{E_{\rm F}} E\eta(E)dE = \frac{L^3}{2\pi^2}\left(\frac{2m_e}{\hbar^2}\right)^{3/2}\int_0^{E_{\rm F}} E^{3/2}dE \tag{11.41}$$
$$= \frac{L^3}{5\pi^2}\left(\frac{2m_e}{\hbar^2}\right)^{3/2} E_{\rm F}^{5/2} = \frac{\hbar^2 3^{5/3}\pi^{4/3}}{10m_e}L^3\left(\frac{N}{L^3}\right)^{5/3} = CL^3\rho^{5/3} \ ,$$

where $\rho \equiv N/L^3$ is the density of electrons per unit volume and C just a proportionality constant. Now understanding ρ as a quantity depending on position in space, we calculate the total number of electrons as,

$$N = \int_{\mathbb{R}^3} \rho(\mathbf{r})d^3r \ , \tag{11.42}$$

and the kinetic energy density by,

$$u_{\rm kin}(\mathbf{r}) = C\rho^{5/3}(\mathbf{r}) \ , \tag{11.43}$$

such that the total kinetic energy of the electrons in the electronic shell is,

$$T[\rho] = C\int \rho^{5/3}(\mathbf{r})d^3r \ . \tag{11.44}$$

The potential associated with the electron-nucleus interaction is,

$$V_{ep}[\rho] = -\frac{Ze^2}{4\pi\varepsilon_0}\int \frac{\rho(\mathbf{r}')}{r'}d^3r' = \int V_p(\mathbf{r}')\rho(\mathbf{r}')d^3r' \ , \tag{11.45}$$

with the electrical potential generated by the nucleus,

$$\Phi_p(\mathbf{r}) = \frac{V_p(\mathbf{r})}{-e} = \frac{Ze}{4\pi\varepsilon_0}\frac{1}{r} \tag{11.46}$$

The potential associated with the electron-electron interaction is,

$$V_{ee}[\rho] = \frac{1}{2}\frac{e^2}{4\pi\varepsilon_0}\int \frac{\rho(\mathbf{r})\rho(\mathbf{r}')}{|\mathbf{r}-\mathbf{r}'|}d^3rd^3r' = \int V_e(\mathbf{r}')\rho(\mathbf{r}')d^3r' \ , \tag{11.47}$$

with the electrical potential generated by the electron cloud,

$$\Phi_e(\mathbf{r}) = \frac{V_e(\mathbf{r})}{-e} = -\frac{1}{2}\frac{e}{4\pi\varepsilon_0}\int \frac{\rho(\mathbf{r}')}{|\mathbf{r}-\mathbf{r}'|}d^3r' \tag{11.48}$$

Thus, the total energy (*Thomas-Fermi energy*) can be written as a functional of the electronic density of the atom,

$$\boxed{H_{\rm TF}[\rho] = T[\rho] + V_{ep}[\rho] + V_{ee}[\rho]} \ . \tag{11.49}$$

11.3.2.3 Electronic density and the Thomas-Fermi equation

Exploiting the variational principle, we are interested in the electronic density $\rho(\mathbf{r})$ which minimizes the Thomas-Fermi energy. We can perform this process via Lagrange multipliers under the constraint, that the number of electrons remains constant in the atom. Thus,

$$0 = \delta \left\{ H_{\mathrm{TF}}[\rho] - \mu \left(\int \rho(\mathbf{r}) d^3r - N \right) \right\} \ . \tag{11.50}$$

Inserting the Thomas-Fermi energy (11.49) we calculate,

$$\mu = \frac{\delta}{\delta\rho(\mathbf{r})} \left\{ C\rho^{5/3}(\mathbf{r}) + V_p(\mathbf{r})\rho(\mathbf{r}) + V_e(\mathbf{r})\rho(\mathbf{r}) \right\} = \tfrac{5}{3} C\rho^{2/3}(\mathbf{r}) + V_p(\mathbf{r}) + V_e(\mathbf{r}) \ . \tag{11.51}$$

Resolving for the electronic density,

$$\rho(\mathbf{r}) = \left(\frac{3}{5C} \right)^{3/2} [\mu - V_p(\mathbf{r}) - V_e(\mathbf{r})]^{3/2} \ . \tag{11.52}$$

The above expression is called the *Thomas-Fermi equation* and describes the electron density of the atom in its ground state. The expression (11.48) can be rewritten as a Poisson equation,

$$\nabla^2 V_e(\mathbf{r}) = \frac{e^2}{2\varepsilon_0} \rho(\mathbf{r}) \ , \tag{11.53}$$

so that,

$$\nabla^2 V_e(\mathbf{r}) = \frac{e^2}{2\varepsilon_0} \left(\frac{3}{5C} \right)^{3/2} [\mu - V_p(\mathbf{r}) - V_e(\mathbf{r})]^{3/2} \ . \tag{11.54}$$

For the effective potential introduced via $V_{\mathrm{eff}} = V_p + V_e$, we find,

$$\begin{aligned} \nabla^2 V_{\mathrm{eff}}(\mathbf{r}) &= \nabla^2 \left(-\frac{Ze^2}{4\pi\varepsilon_0} \frac{1}{r} \right) + \nabla^2 V_e(\mathbf{r}) \\ &= -\frac{Ze^2}{\varepsilon_0} \delta^3(\mathbf{r}) + \frac{e^2}{2\varepsilon_0} \left(\frac{3}{5C} \right)^{3/2} [\mu - V_{\mathrm{eff}}(\mathbf{r})]^{3/2} \ . \end{aligned} \tag{11.55}$$

We note that, with (11.50), we can identify the Lagrange multiplier μ as a *chemical potential*. In particular, for non-interacting neutral atoms, we have $\mu = 0$. In addition, since for an atom both the potential and the electronic density must have spherical symmetry, we can write for $r \neq 0$,

$$\frac{1}{r} \frac{\partial^2}{\partial r^2} [r V_{\mathrm{eff}}(r)] = \frac{e^2}{2\varepsilon_0} \left(\frac{3}{5C} \right)^{3/2} [-V_{\mathrm{eff}}(\mathbf{r})]^{3/2} \ . \tag{11.56}$$

We now make the ansatz,

$$V_{\mathrm{eff}}(r) \equiv -\frac{Z}{r} \chi(\alpha r) \qquad \text{setting} \qquad \alpha \equiv \frac{3e^{4/3}}{5C\varepsilon_0^{2/3}} Z^{1/3} \ . \tag{11.57}$$

This transforms the expression (11.56) into,

$$\frac{\partial^2}{\partial r^2} \chi(\alpha r) = -\frac{e^2}{Z\varepsilon_0} \left(\frac{3Z}{5C} \right)^{3/2} \frac{\chi^{3/2}(\alpha r)}{r^{1/2}} \ , \tag{11.58}$$

or, substituting $x \equiv \alpha r$,

$$\frac{d^2\chi}{dx^2} = -\frac{\chi^{3/2}}{x^{1/2}} \ . \tag{11.59}$$

It is important to note the last equation does not depend on the parameter Z, thus being a general result for any neutral atom. The function $\chi(x)$ is determined numerically, but we can analyze its asymptotic values given the expected behavior of the effective potential $V_{\text{eff}}(r)$: for $r \to 0$ we expect that $V_{\text{eff}}(r) = V_p(r)$, hence $\chi(0) = 1$. On the other hand, for $r \to \infty$, we expect $V_{\text{eff}}(r) = 0$, hence $\chi(\infty) = 0$. Do the Exc. 11.3.5.1.

With $\chi(x)$ known, we obtain the charge density $\rho(x)$, and hence we are able to calculate the total energy of the atom under investigation. Thus, it is possible to show that [35],

$$H_{\text{TF}}[\rho] = -0.7687 \frac{e^2}{4\pi\varepsilon_0 a_{\text{B}}} Z^{7/3} \ . \tag{11.60}$$

It is important to highlight some points:

1. The result holds for neutral atoms.
2. There is no electronic shell structure assumed; apart from the fact that the kinetic energy was derived in a way as to respect Pauli's principle, the whole calculation was done within the laws of classical electromagnetism; no quantum mechanics was involved and, hence, no set of quantum numbers has been found.
3. Apart from the Pauli principle used to calculate the density of states (11.40), quantum statistical effects of identical particles (such as wavefunction anti-symmetrization) are not taken into account.

A more refined model which deals with third criticism and, in addition, is closer to density functional theory (DFT) is the Thomas-Fermi-Dirac model.

11.3.3 Hartree method

The effective potential obtained from the Thomas-Fermi model can serve as a starting point for quantum treatments. Assuming that all electrons are subject to the same effective potential V_{eff}, we numerically solve the Schrödinger equation for each electron independently,

$$\hat{H}_i = \left(-\frac{\hbar^2}{2m}\nabla_i^2 + V_{\text{eff}} \right) \psi_i(\mathbf{r}_i) = e_i \psi_i(\mathbf{r}_i) \ . \tag{11.61}$$

With this we calculate all energies and eigenfunctions (only the radial parts are of interest) minimizing the total energy and respecting the weak Pauli principle, that is, we classify the states in the order of increasing energies e_i and fill them successively with electrons. For the total wavefunction we obtain,

$$\left(\sum_{i=1}^{N} \hat{H}_i \right) \Psi_N = E_n \Psi_N \quad \text{with} \quad \Psi_N = \psi_1 \cdot .. \cdot \psi_N \quad \text{and} \quad E_n = \sum_{i=1}^{N} e_i \ . \tag{11.62}$$

With the eigenfunctions we calculate the charge densities $e|\psi_j(\mathbf{r}_j)|^2$. We integrate the interaction energy between these charge densities and the potentials exerted by the

nucleus and all other electrons $j \neq i$ to obtain an effective potential that represents an improved estimation for the electronic mean field,

$$V_{\text{eff}} \longleftarrow -\frac{Ze^2}{4\pi\varepsilon_0 r_i} + \sum_{j\neq i} \int d^3r_j \frac{e^2}{4\pi\varepsilon_0 |\mathbf{r}_i - \mathbf{r}_j|} |\psi_j(\mathbf{r}_j)|^2 \ . \tag{11.63}$$

We replace that potential in the Schrödinger equation, and repeat the whole process from the beginning, until the total energy $\sum_i e_i$ does not get any lower. This self-consistent method is called *Hartree method*. Fock improved these calculations using antisymmetric wavefunctions for the valence electrons. This method is called *Hartree-Fock method*.

11.3.4 Hartree-Fock method

The Hartree-Fock method used to treat atomic or molecular many-body systems aims at obtaining the electronic wavefunction of the system. Dealing with anti-symmetrized wavefunctions, it represents a refinement of the Hartree method. The method is based on the variational principle and on the assumption that we can write the global wavefunction as a Slater determinant, with each electron occupying a specific orbital state (spin-orbital) and interacting with an effective potential stemming from the electrons which occupy other orbitals. Instead of solving the Schrödinger equation, we must now solve a set of equations called Hartree-Fock equations of the type $\hat{F}\psi_k(1) = \epsilon_k\psi_k(1)$. The method is performed iteratively until convergence of the atomic orbitals and their respective energies is reached. The procedure is then called *self-consistent*: Starting from an initial trial global wavefunction we calculate the effective potential in each orbital and a new set of wavefunctions which, in turn, generate a new effective potential. This new potential is then used in a new set of Hartree-Fock equations.

11.3.4.1 Hartree-Fock equations

To start with, we write the Hamiltonian (11.33) of a multi-electronic atom as [35],

$$\hat{H} = \sum_{i=1}^{Z} \hat{h}_i + \tfrac{1}{2} \sum_{i\neq j} \hat{V}_{ij} \ , \tag{11.64}$$

where $\hat{h}_i$ is the Hamiltonian only of the electron i, and $\hat{V}_{ij}$ is the interaction term between the electrons i and j. To implement the method we must suppose that the multi-electronic state can be written as the product of the individual states of each electron:

$$\Psi'(1, ..., Z) = \psi_1(1)\psi_2(2)...\psi_Z(Z) \ , \tag{11.65}$$

where $\psi_i(1) = \phi_i(r_1)\chi(\alpha) = \psi_i^\alpha(r_1)$ represents the spin-orbital state of electron 1, that is, the spatial wavefunction of the electron in the state i and with spin α. However, due to the symmetrization postulate, the physical state of the system must be expressed by a Slater determinant,

$$\Psi(1, ..., Z) = \frac{1}{\sqrt{Z!}} \det\ [\psi_1(1)\psi_2(2)...\psi_Z(Z)] \ . \tag{11.66}$$

Now, we use the variational principle to minimize the expectation value of the ground state energy by varying the functions $\psi_k(n)$. In this way, the correct orbitals are those that minimize the energy. The expectation value is written as,

$$E = \langle\Psi|\hat{H}|\Psi\rangle = \langle\Psi|\sum_{i=1}^{Z}\hat{h}_i|\Psi\rangle + \langle\Psi|\tfrac{1}{2}\sum_{i\neq j}\hat{V}_{ij}|\Psi\rangle \ . \tag{11.67}$$

It is possible to show that,

$$\langle\Psi|\sum_{i=1}^{Z}\hat{h}_i|\Psi\rangle = \sum_{i=1}^{Z}\langle\psi_i|\hat{h}_i|\psi_i\rangle \qquad \text{and} \tag{11.68}$$

$$\langle\Psi|\tfrac{1}{2}\sum_{i\neq j}\hat{V}_{ij}|\Psi\rangle = \tfrac{1}{2}\sum_{i,j}^{Z}[\langle\psi_i\psi_j|\hat{V}_{ij}|\psi_i\psi_j\rangle - \langle\psi_j\psi_i|\hat{V}_{ij}|\psi_j\psi_i\rangle] \ .$$

Hence,

$$E = \sum_{i=1}^{Z}\langle\psi_i|\hat{h}_i|\psi_i\rangle + \tfrac{1}{2}\sum_{i,j}^{Z}[\langle\psi_i\psi_j|\hat{V}_{ij}|\psi_i\psi_j\rangle - \langle\psi_j\psi_i|\hat{V}_{ij}|\psi_j\psi_i\rangle] \ . \tag{11.69}$$

The above expression can be minimized via Lagrange multipliers under the constraint that the states are orthogonal $\langle\psi_i|\psi_j\rangle = \delta_{ij}$,

$$\delta\left\{\langle\Psi|\hat{H}|\Psi\rangle - \sum_{i,j}\epsilon_{ij}[\langle\psi_i\psi_j|\hat{V}_{ij}|\psi_i\psi_j\rangle - \langle\psi_j\psi_i|\hat{V}_{ij}|\psi_j\psi_i\rangle]\right\} \tag{11.70}$$

Thus, we obtain the following set of *Hartree-Fock equations*:

$$\hat{F}\psi_k(1) = \epsilon_k\psi_k(1) \qquad \text{where} \qquad \hat{F} = \hat{h}_1 + \sum_i(2\hat{J}_i - \hat{K}_i) \tag{11.71}$$

is the Fock operator and ϵ_k is the energy associated with the spin-orbital ψ_k. The operator $\hat{J}_i$, called *Coulomb operator*, represents the mean potential sensed by electron 1 in the orbital k due to the presence of electron 2 in the orbital i:

$$\hat{J}_i\psi_k(1) = \left\{\int \psi_i^*(2)V_{12}\psi_i(2)dr_2\right\}\psi_k(1) \ . \tag{11.72}$$

The operator $\hat{K}_i$, denominated *exchange operator*, is a consequence of the symmetrization process and therefore a purely quantum effect, that is, without classical analogue:

$$\hat{K}_i\psi_k(1) = \left\{\int \psi_i^*(2)V_{12}\psi_k(2)dr_2\right\}\psi_k(1) \ . \tag{11.73}$$

Once we know all wavefunctions, the energies of the orbitals can be obtained in the following way:

$$\int dr_1\psi_k^*(1)\left\{\hat{h}_1 + \sum_i(2\hat{J}_i - \hat{K}_i)\right\}\psi_k^*(1) = \epsilon_k\int dr_1\psi_k^*(1)\psi_k(1) = \epsilon_k \ , \tag{11.74}$$

that is,

$$\epsilon_k = \int dr_1 \psi_k^*(1)\hat{h}_1\psi_k^*(1) + \sum_i (2\hat{J}_{ki} - \hat{K}_{ki}) \ , \tag{11.75}$$

where,

$$\hat{J}_{ki} = \int dr_1 \psi_k^*(1)\hat{J}_i\psi_k(1) \qquad \text{is the Coulomb integral} \tag{11.76}$$

$$\hat{K}_{ki} = \int dr_1 \psi_k^*(1)\hat{K}_i\psi_k(1) \qquad \text{is the exchange integral .}$$

The total atomic energy can be calculated by,

$$E = 2\sum_k \epsilon_k - \sum_{k,i} (2\hat{J}_{ki} - \hat{K}_{ki}) \ . \tag{11.77}$$

Furthermore, if assuming that, taking an electron away from the orbital ψ_k the electronic distribution remains unchanged, it is possible to associate the energy ϵ_k with the ionization energy of the electron in this orbital, $I_k \simeq \epsilon_k$. This equality is known as *Koopman's theorem*.

11.3.5 Exercises

11.3.5.1 Ex: Effective potential in the Thomas-Fermi model

Calculate numerically and plot the effective potential in the Thomas-Fermi model from the differential equation (11.59) for $Z = 40$ [900].

11.4 The periodic system of elements

Completely filled principal layers n, ℓ are isotropic, $\Psi_N(\mathbf{r}) = \Psi(r)$, as we will show in Exc. 11.4.4.1. It is important to distinguish three different energetic sequences: 1. Tab. 11.5 shows, for a given atom, the excited orbitals of the *last electron*. 2. The energy sequence shown in Tab. 11.6 tells us in which orbital the next electron will be placed, when we go to the *next atom* in the periodic table 11.8 which has one more proton in the nucleus. 3. The inner electrons are subject to different potentials and, hence, follow a different sequence energetic sequence: While for the inner electrons we find,

$$E_{n,\ell} < E_{n,\ell+1} \ll E_{n+1,\ell} \ , \tag{11.78}$$

the sequence is partially inverted for the outermost electron. Note that it is the outermost electrons that determine the chemical reactivity of the atom. The sequence is illustrated in Fig. 11.4.

Noble gases have small radii, high excitation energies and high ionization energies. The outermost electrons in a noble gas atom must overcome a large energy gap to any higher quantum numbers. Halogens have strong electro-affinities, since the outer electron layer (n_{max}) is incomplete and therefore malleable, such that an electron approaching the halogen perceives the nuclear charge through a partially transparent shield. Alkalis are similar to hydrogen and have excitation energies in the optical

regime. Their fundamental state $^2S_{1/2}$ is determined by a single valence electron in the $\ell = 0$ orbital. Unlike hydrogen, excitation energies are highly dependent on ℓ, since orbits with small ℓ correspond to eccentric ellipses and have higher probabilities to be in the unshielded region $-Z^2e^2/r$ than orbits with large ℓ, who spend more time in the shielded region $-e^2/r$. For the same reason, energies corresponding to larger n resemble more those of the hydrogen spectrum.

11.4.0.1 Inner shell electrons

The interior shell structure of the atoms can be analyzed by X-ray scattering. Electrons decelerated by atoms emit a continuous spectrum called *Bremsstrahlung*, but they can also expel electrons from the inner layers leaving a hole behind. When a hole is filled by cascades of electrons falling down from higher layers, the atom emits a specific X-ray spectrum ($\approx 10^4$ eV). The selection rules $\Delta\ell = \pm 1$ and $\Delta j = \pm 1$ split the lines in two components. X-ray spectra of neighboring elements in the periodic table are very similar, because the inner layers not being shielded, they see a potential close to $\propto Z^2/r$ dominating the interaction with electrons from the outer layers. Therefore, the Z-dependency of inner energy levels along a horizontal rows in the periodic table is more or less $\omega \propto Z^2$, as predicted by Bohr's atomic model.

11.4.1 Electronic shell model

In the Fermi gas model, each of the energy levels contains several states, and each of these states can be occupied by a single electron, according to the Pauli principle. In this way, we obtain the electronic configuration for the atoms of the periodic system. In this picture, the energies of the ground states of the elements, normalized by $1/Z^2$, can be arranged in the scheme of Fig. 11.3.

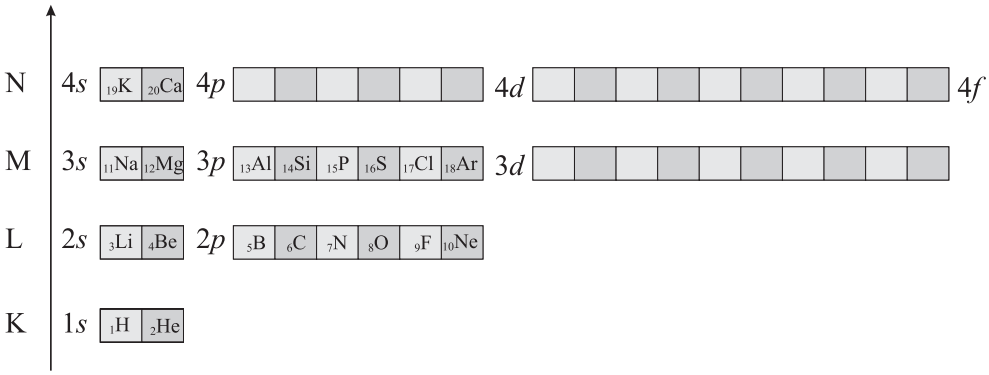

Figure 11.3: Periodic order.

This only works for atoms with up to 18 electrons. When the layer $3p$ is completely filled, the next to be occupied is not $3d$ but the $4s$. The new scheme is illustrated in Fig. 11.4. The anomalies beginning at $Z = 18$ arise due to electron-electron interaction. The real potential evolves from one to the other Coulombian potential, as distance from the nucleus is increased, as illustrated in Fig. 11.2. Near the nucleus,

the electrons shield the positive charge less than for large distances r. Thus, those states that have a high probability near the nucleus are energetically lowered. That is,

$$E_{2s} < E_{2p} \quad \text{and} \quad E_{6s} < E_{6p} < E_{6d} \ . \tag{11.79}$$

The degeneracy of the orbital angular momentum in the Schrödinger model is thus lifted. The shielding is, as can be seen in the example of the excited states of lithium, a large effect in the range of some eV.

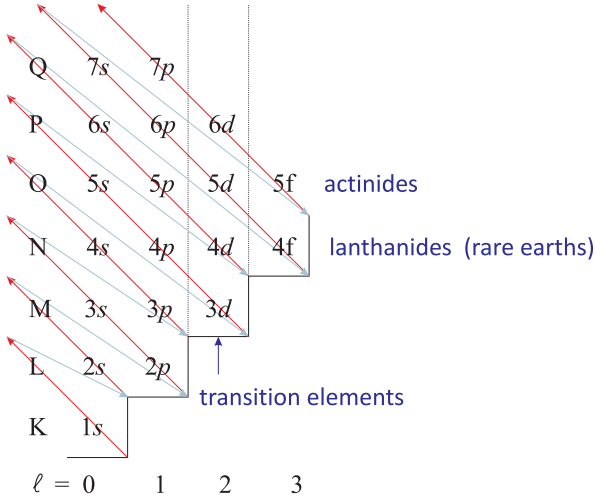

Figure 11.4: Illustration of the sequence of filling the orbitals with electrons.

The shielding also accounts for the anomalies in the periodic system, such as in K or Ca. Since $E_{4s} < E_{3d}$, the $4s$ state is filled before the $3d$. Similar anomalies also occur in Rb ($5s$), Cs ($6s$), and Fr ($7s$). In rare earths the shielding effect is even more pronounced. Here, the energy of the state $6s$ is even below the energy of the $4f$, which means that the shells $6s$, $5s$, $5p$, and $5d$ protect the $4f$ shell very well [9]. Resolve Exc. 11.4.4.2.

11.4.1.1 Alkalines

The electronic shell structure of alkalines consists of a completed noble gas shell and an additional valence electron. Their spectrum is therefore very similar to hydrogen. An empirical approach can be stressed to describe this feature,

$$E_{n,\ell} = -\frac{\mu_{\mathrm{EG}} c^2}{2} \frac{Z^2 \alpha^2}{(n - \Delta_{n,\ell})^2} \ , \tag{11.80}$$

where μ_{EG} is the reduced mass relative to the noble gas shell and $\Delta_{n,\ell}$ is called *quantum defect*. The quantum defect is tabulated for most alkaline states and is

[9] An example of this is Nd:YAG (Neodymium in Yttrium Aluminum Garnet). In this crystal, optical transitions can be excited within the $4f$ shell of the Nd. However, these transitions are only allowed due to perturbations of the crystalline field. The very strong shielding ensures a long life of the excited state. For this reason this crystal is an excellent laser material.

particularly important for low energy states. For sodium, for example, the values are:

ℓ	$n=3$	$n=4$	$n=5$	$n=6$
s	1.37	1.36	1.35	1.34
p	0.88	0.87	0.86	0.86
d	0.10	0.11	0.13	0.11
f	-	0.00	-0.01	0.008

For states with a large angular momentum, the quantum defect disappears. In these states, the electron is far from the nucleus and the potential is similar to that of hydrogen. Alkalines are currently widely studied in quantum optics laboratories, for being comparatively simple, but having a sufficiently rich structure to be interesting. The fundamental electronic transitions typically lie in the visible and near-infrared spectral range and can be excited with comparatively simple laser sources. The lifetime of excited states is typically longer than 20 ns, which corresponds natural linewidths of approximately (2π) 10 MHz.

11.4.1.2 Excited states

The experimentally easiest and most precise approach to determining orbital energies consists in measuring excitation spectra of valence electrons. The diagram of Fig. 11.5 compares such excitation spectra for various alkaline atoms. Although this is not to be confused with the binding energies of valence electrons of different atoms, it gives us a qualitative idea of the impact of shielding and indicates, which orbital will be occupied by the additional valence electron of the next species in the periodic table.

11.4.2 LS and jj-coupling

Following Hund's rule, the $\mathbf{L}\cdot\mathbf{S}$-coupling is energetically favorable compared to the $\mathbf{j}\cdot\mathbf{j}$-coupling, which means that the spins of the outermost electrons, that is, the electrons outside of filled subshells (n,ℓ), prefer to orient their spins in parallel in order to anti-symmetrize the spatial wavefunctions and thus maximize the distance between the electrons. Every sub-layer of the series shown in Fig. 11.4 must be filled in the listed order before placing new electrons in the next layer.

In the case of helium, we have seen that the Pauli principle first determines the relative orientation of the electron spins. The spins $\mathbf{s}_i$ of the individual electrons therefore add up to a total angular momentum $\mathbf{S}$. The *orbital* angular momenta $\mathbf{l}_i$ also adopt a relative orientation. It is determined by a residual spherically non-symmetric Coulomb interaction: A certain combination $\mathbf{L}$ of orbital angular momenta leads to a certain spatial distribution of the electrons and thus to a certain electrostatic energy distribution.

The total spin $\mathbf{S}$ and the total orbital angular momentum $\mathbf{L}$ subsequently couple to a total angular momentum $\mathbf{J}$ very similar to the $\mathbf{l}\cdot\mathbf{s}$ spin-orbit coupling in single electron systems. States with different $\mathbf{J}$ then have the respective energies that the

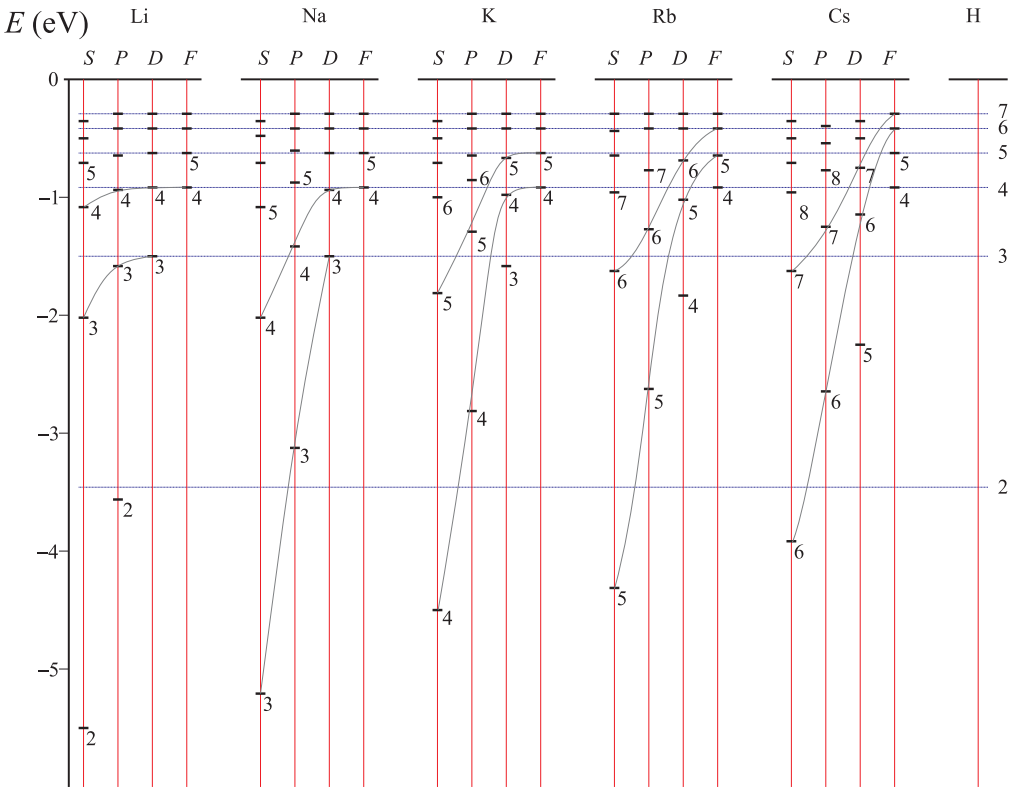

Figure 11.5: Comparison of the excitation energies of the *valence electron* for several alkaline atoms. Grey line are meant to guide the eye.

total spin $\mathbf{S}$ adopts in the field generated by the total orbital angular momentum $\mathbf{L}$ [10].

The above coupling scheme is called *Russel-Saunders coupling* or *LS-coupling*. It works well when the spin-orbit coupling of individual electrons is small. In this case, intercombination is forbidden, which means that there can be no electromagnetic transition between states with different spins (see the case of metastable helium in Sec. 11.2.2).

Since $E_{\ell s} \simeq (Z\alpha)^4 \simeq Z^4$, as shown in (9.130), for heavy atoms, the coupling of an electronic spin to its own orbital momentum grows strongly with Z, as well as the symmetrization and the exchange energy, which mutually orient the spins, and the residual Coulomb interaction, which mutually couples the angular orbital momenta. In this case, the orientation of $\mathbf{L}_i$ relative to $\mathbf{S}_i$ delivers more energy than the exchange energy and the residual energy cost. Hence, the spin and the orbital angular momentum of an individual electron couple first,

$$\mathbf{j}_i = \mathbf{l}_i + \mathbf{s}_i \ . \tag{11.81}$$

[10] In addition, there are the small contributions due to $\mathbf{l}_i \cdot \mathbf{l}_j$-coupling and to $\mathbf{s}_i \cdot \mathbf{s}_j$-coupling, where $i \neq j$.

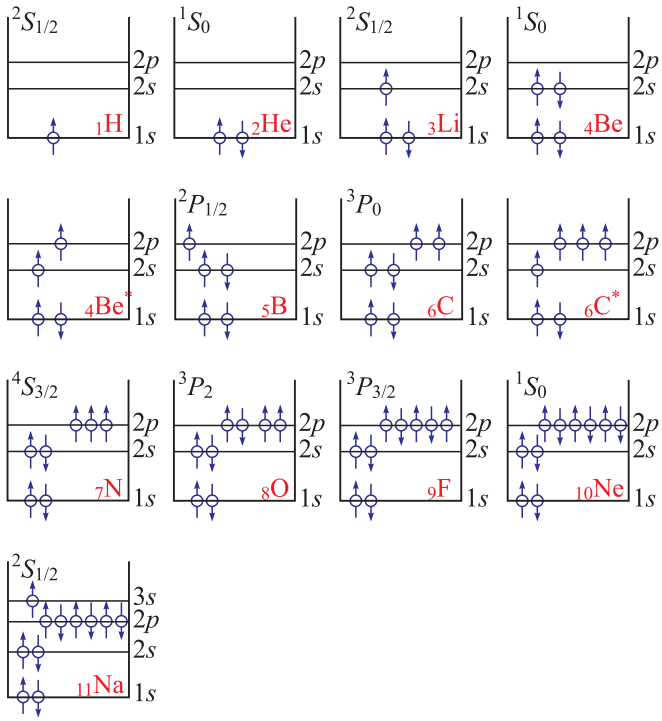

Figure 11.6: Illustration of Hund's rule.

We obtain a new Hamiltonian of fine structure of the form,

$$H_{\rm fs} \propto \mathbf{j}_i \cdot \mathbf{j}_j \ . \tag{11.82}$$

Pure jj-coupling only exists for very heavy nuclei. Normally, we have a so-called *intermediate coupling*, which is a mixture of LS and jj-coupling. This can considerable relax the intercombination prohibition. When the coupling is pure, we have the following dipolar selection rules:

LS-coupling: $\Delta S = 0$, $\Delta L = \pm 1$, $\Delta \ell = \pm 1$

jj-coupling: $\Delta j = 0, \pm 1$ for one e^-, $\Delta j = 0$ for all others

In addition we have for the two couplings: $\Delta J = 0, \pm 1$, but $J, J' = 0$ is forbidden, $\Delta m_J = 0, \pm 1$ when $\Delta J = 0$ but $m_J, m_{J'} = 0$ is forbidden.

11.4.3 Summary of contributions to the atomic energy levels

The total Hamiltonian of a single atom is composed of the kinetic energy of the nucleus and the electrons, of various interaction potentials between the nucleus and the electrons, and of interactions with various types of external electromagnetic fields.

$$\hat{H} = -\frac{\hbar^2}{2m}\nabla_R^2 + \sum_{i=1}^{N}\left(-\frac{\hbar^2}{2m}\nabla_{r_i}^2\right) + V(\mathbf{r}_1, \mathbf{s}_1, .., \mathbf{r}_N, \mathbf{s}_N) + V_{\rm ext} \ . \tag{11.83}$$

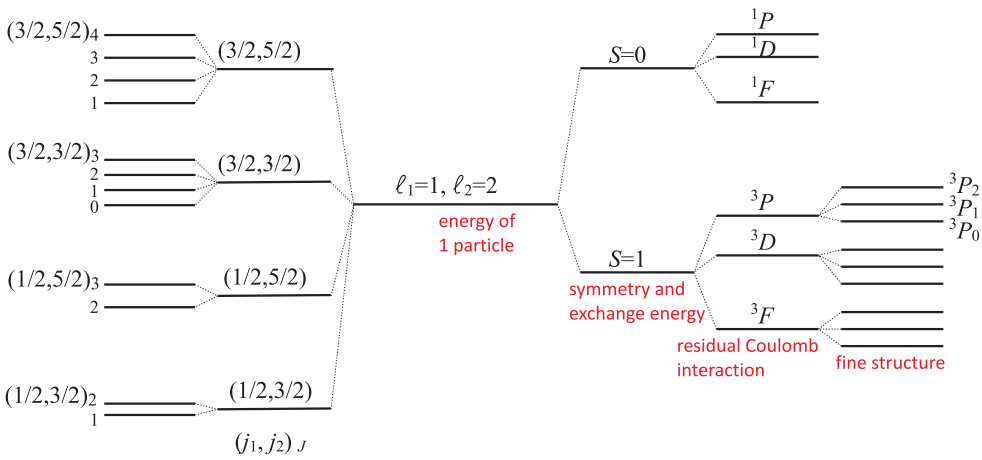

Figure 11.7: Hierarchy of coupling energies at the example of two electrons out of closed shells, $(2p)(3d)$, under the presumption of perfect jj-coupling (left) or LS-coupling (right).

Of course, with the presence of other atoms, other interactions may generate other relevant contributions to the Hamiltonian.

The following interactions contribute to the potential V: The Coulomb interactions,

$$V_{\text{ncl:ele}} = -\sum_{i=1}^{Z} \frac{Ze^2}{4\pi\varepsilon_0|\mathbf{r}-\mathbf{r}_i|} \quad \text{and} \quad V_{\text{ele:ele}} = \sum_{i<j=1}^{Z} \frac{e^2}{4\pi\varepsilon_0|\mathbf{r}_i-\mathbf{r}_j|} \ , \tag{11.84}$$

the antisymmetry of the wavefunction, that is, exchange integrals,

$$V_{\text{sym}} \ , \tag{11.85}$$

the energies of spin-orbit couplings,

$$V_{\ell s} = -\sum_{i=1}^{Z} \frac{1}{e2m^2c^2} \frac{1}{|\mathbf{r}-\mathbf{r}_i|} \frac{dV_{\text{C}}}{dr_i} (\mathbf{l}_i \cdot \mathbf{s}_i) \ , \tag{11.86}$$

the energies of spin-spin couplings,

$$V_{ss} = \sum_{i\neq j=1}^{Z} \frac{e^2}{m^2} \left[\frac{\sigma_\mathbf{i} \cdot \sigma_\mathbf{j}}{|r_i - r_j|^3} - 3\frac{[\sigma_\mathbf{i} \cdot (\mathbf{r}_i - \mathbf{r}_j)][\sigma_\mathbf{j} \cdot (\mathbf{r}_i - \mathbf{r}_j)]}{(\mathbf{r}_i - \mathbf{r}_j)^5} \right] \ , \tag{11.87}$$

the energies of orbit-orbit couplings,

$$V_{ll} = \sum_{i\neq j=1}^{Z} c_{ij} (\mathbf{l}_i \cdot \mathbf{l}_j) \ , \tag{11.88}$$

interactions between the spin of the electrons and the nuclear spin and between the orbital angular momentum of the electrons and the nuclear spin,

$$V_{\text{hfs}} = \frac{A}{\hbar^2} \mathbf{J} \cdot \mathbf{I} \ , \tag{11.89}$$

and relativistic corrections.

$$V_{\rm rel} \ , \tag{11.90}$$

In addition, static external fields may displace energy levels and can influence the internal coupling of angular momenta and spins,

$$V_{\rm ext} = -\mathbf{d}\cdot\vec{\mathcal{E}} \ , \ \ -\vec{\mu}\cdot\vec{\mathcal{B}} \ . \tag{11.91}$$

What quantum numbers are good depends on the relative amplitudes of intra-atomic interactions:
Case 1: fine structure with $\mathbf{L}\cdot\mathbf{S}$-coupling plus Zeeman splitting of hyperfine structure: $V_{\rm ncl:ele}, V^r_{\rm ele:ele} \gg V^a_{\rm ele:ele}, V_{\rm sym} \gg V_{\ell s} \gg V_{\rm hfs} \gg V_B$ the quantum number are $|n_i, \ell_i, \mathbf{L}, \mathbf{S}, \mathbf{J}, \mathbf{F}, m_F\rangle$.
Case 2: fine structure with $\mathbf{j}\cdot\mathbf{j}$-coupling plus Zeeman splitting of hyperfine structure: $V_{\rm ncl:ele}, V^r_{\rm ele:ele} \gg V_{\ell s} \gg V^a_{\rm ele:ele}, V_{\rm sym} \gg V_{\rm hfs} \gg V_B$ the quantum number are $|n_i, \ell_i, j_i, \mathbf{J}, \mathbf{F}, m_F\rangle$.
Case 3: fine structure with $\mathbf{L}\cdot\mathbf{S}$-coupling plus hyperfine structure of Zeeman splitting: $V_{\rm ncl:ele}, V^r_{\rm ele:ele} \gg V^a_{\rm ele:ele}, V_{\rm sym} \gg V_{\ell s} \gg V_B \gg V_{\rm hfs}$ the quantum number are $|n_i, \ell_i, \mathbf{L}, \mathbf{S}, \mathbf{J}, m_J, m_I\rangle$.
Case 4: fine structure with $\mathbf{L}\cdot\mathbf{S}$-coupling plus Paschen-Back splitting of fine structure: $V_{\rm ncl:ele}, V^r_{\rm ele:ele} \gg V^a_{\rm ele:ele}, V_{\rm sym} \gg V_B \gg V_{\ell s} \gg V_{\rm hfs}$ the quantum number are $|n_i, \ell_i, \mathbf{L}, \mathbf{S}, m_L, m_S, m_I\rangle$.

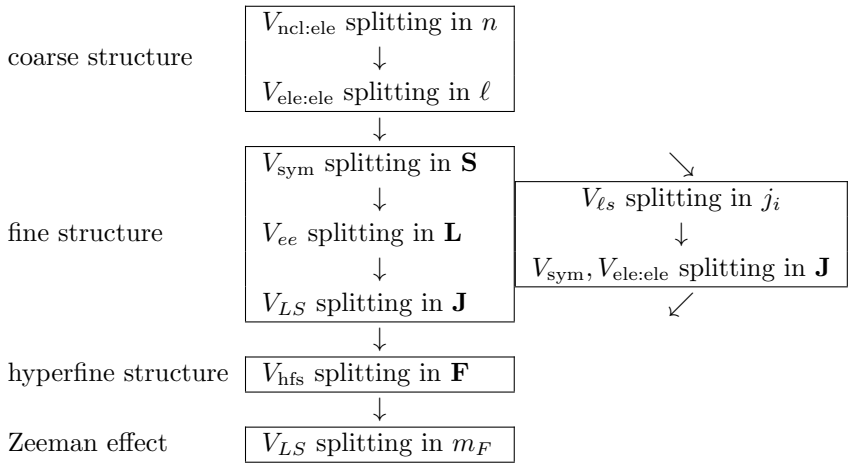

11.4.4 Exercises

11.4.4.1 Ex: Filled electronic shells

Show at the example of hydrogen that completely filled electronic layer are isotropic.

11.4.4.2 Ex: Electronic excitation levels of alkaline

Explain why
a. state [Li] $(2s)^2 S_{1/2}$ has lower energy than [H] $(2s)^2 S_{1/2}$;

b. state [Li] $(2s)^2 S_{1/2}$ has lower energy than [Li] $(2p)^2 P_J$;
c. state [Na] $(4s)^2 S_{1/2}$ has lower energy than [Na] $(3d)^2 D_J$.

11.5 Further reading

P.W. Atkins and R.S. Friedman, (3^{rd} ed. Oxford University (2001), *Molecular Quantum Mechanics* [ISBN]

I.N. Levine, Allyn and Bacon, 7^{th} ed. Pearson (1983), *Quantum Chemistry* [ISBN]

J.I. Steinfeld, The MIT Press, Cambridge (2005), *Molecules and Radiation* [ISBN]

B.H. Bransden, C.J. Joachain, John Wiley & Sons (1983), *Physics of Atoms and Molecules* [ISBN]

p-table, *Periodic Table* [http]

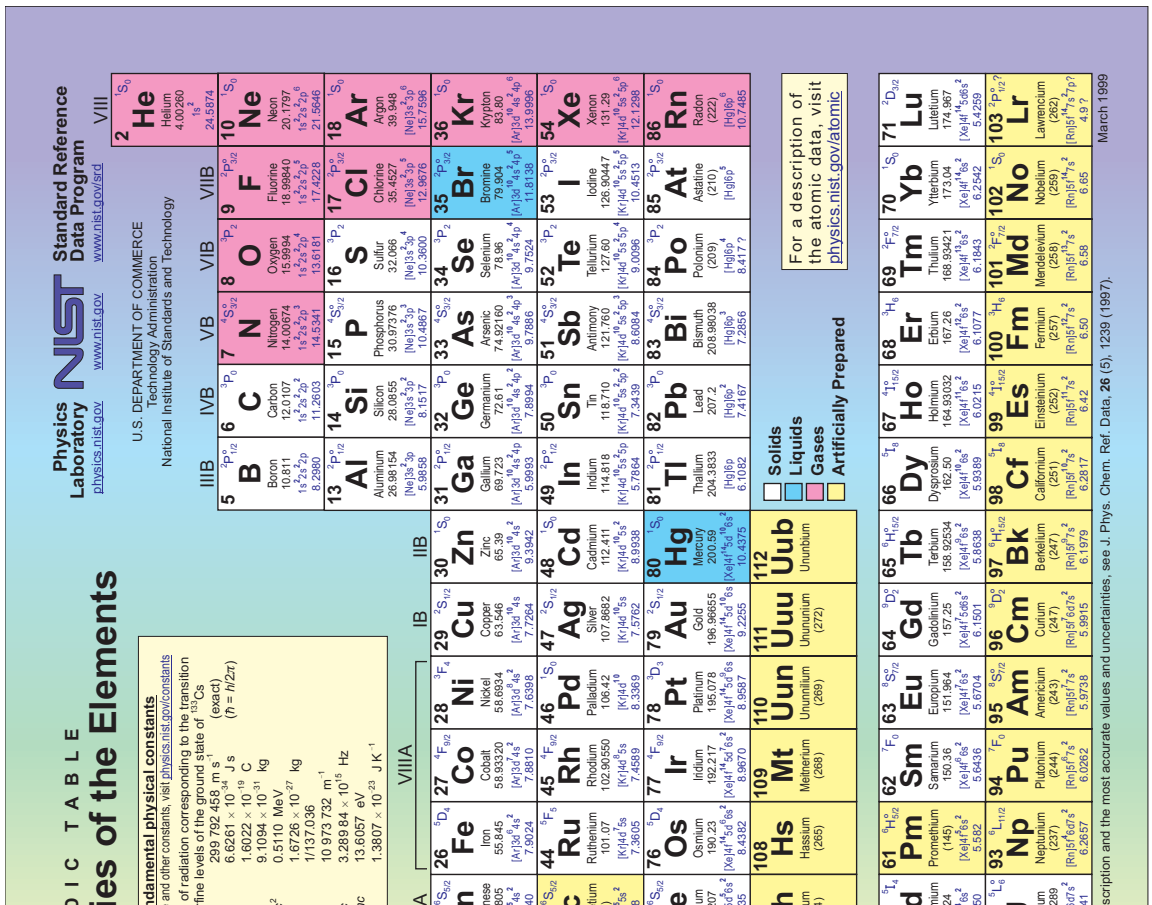

Figure 11.8: Periodic table.

Chapter 12

Molecular dimers

In systems of many particles (gases, fluids, or solids) interatomic interactions must be considered. These interactions usually have electrostatic origins, but generally can not be given in the form of closed expressions. For example, the collision of two atoms i and j can occur in a multitude of channels, that is, interaction potentials $V(\mathbf{r}_i - \mathbf{r}_j)$. Interatomic forces do not only govern collisions, but can sustain molecular bound states. This introduces new degrees of freedom in the systems of many particles through possible excitations of vibration or rotation movements.

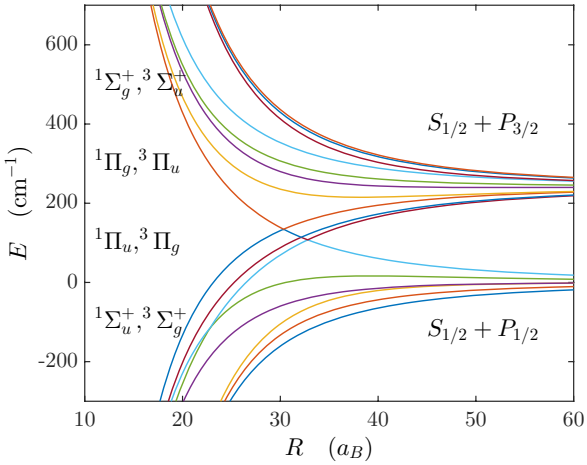

Figure 12.1: (code) Example of an interatomic potential spaghetti: The lowest states of the molecule $^{85}Rb_2$.

In this course, we will not go beyond homo- or heteronuclear dimers, that is, molecules consisting of two identical or different atoms.

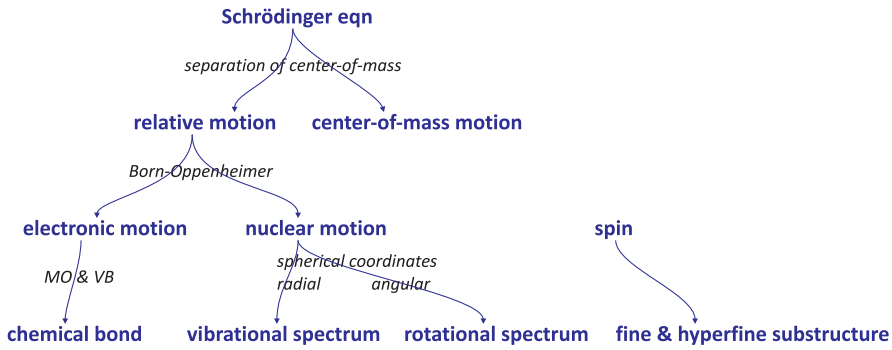

Figure 12.2: Approximations made in the molecular physics.

12.1 Molecular binding

12.1.1 Ionic and covalent binding

There are two fundamental ways of binding two atoms together, the ionic bond and the covalent bond [1]. The *ionic bond* is ruled by the quantities *electroaffinity* (EA), *electronegativity* (EN), and *ionization energy* (IE):

- **Ionization energy:** This energy is needed for the release of an electron by a neutral atom, e.g. $\mathrm{Na} + 5.1\,\mathrm{eV} \rightarrow \mathrm{Na}^+ + e^-$.
- **Electroaffinity**: This energy is released by the capture of an electron by a neutral atom, e.g. $\mathrm{Cl} + e^- \rightarrow \mathrm{Cl}^- + 3.8\,\mathrm{eV}$.
- **Electronegativity**: This quantity measures the stability of a valence orbital, e.g. that of fluorine (3.98) is more stable than that of cesium (0.79), such that fluorine holds its electrons tighter than cesium.

At short distances, the exchange of an electron between atoms can decrease energy. The so-called *ionic bond* is then sustained by the Coulombian attraction between two ions, and the binding energy can be estimated through electrostatic interaction.

Example 68 (*Ionic binding in NaCl*): For example, a sodium and a chlorine atom gain energy by forming a molecule,

$$\begin{aligned} \mathrm{Na} + 5.1\,\mathrm{eV} &\rightarrow \mathrm{Na}^+ + e^- \\ \mathrm{Cl} + e^- &\rightarrow \mathrm{Cl}^- + 3.8\,\mathrm{eV} \\ \mathrm{Na}^+ + \mathrm{Cl}^- &\rightarrow \mathrm{NaCl} + 4.9\,\mathrm{eV} \\ \hline \mathrm{Na} + \mathrm{Cl} &\rightarrow \mathrm{NaCl} + (-5.1 + 3.8 + 4.9)\,\mathrm{eV} \ . \end{aligned} \tag{12.1}$$

[1] We are not considering metallic bonds nor hydrogen bridge bonds, here.

The molecules are polar and, therefore, have a permanent electric dipole moment. The bond has no preferential direction, since each atom is perfectly isotropic. Therefore, this type is well suited for the construction of crystalline lattices.

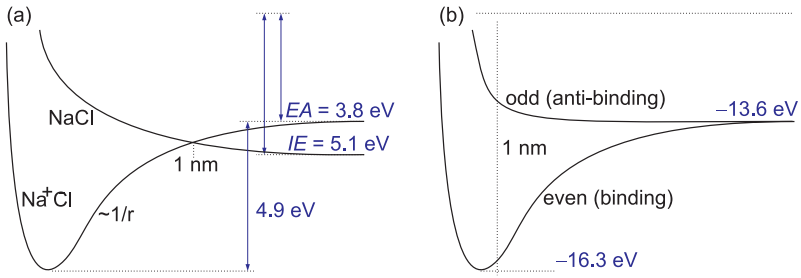

Figure 12.3: Scheme for (a) ionic binding of NaCl and (b) covalent binding of H_2.

To understand *covalent bond*, we consider the example $H_2{}^+$ and estimate the interaction energy for each distance R between the nuclei. In this case, in contrast to atoms, the spherical symmetry is broken, and therefore the energy degeneracy with respect to parity is abolished, that is, for wavefunctions $\psi(-x) = \pm\psi(x)$ the energies vary differently with R. The even wavefunction, which has an increased probability of the electron of being between the nuclei, is binding, which means that the interaction potential exhibits a minimum at a certain distance. The odd wavefunction, which disappears between the nuclei, is anti-binding, which means that the interaction potential is repulsive at all distances. In fact, an electron located at the center between two positive charges can overcome the Coulomb repulsion between the nuclei, whose mutual distance is twice. Obviously, the energy can not fall below that of the fundamental state of He^+, being approximately $-4 \times 13.6\,\text{eV}$. With two electrons, as in the case of the neutral molecule H_2, the anti-parallel orientation of the spins, $\uparrow\downarrow$, allows us to place the two electrons in the same orbital, while for parallel orientation, $\uparrow\uparrow$, we expect anti-binding. Each electron without a partner in an orbital can form a covalent bond, for example, phosphorus [P]=[Ne]$3s^2 3p^{\uparrow\uparrow\uparrow}$ has three available orbitals corresponding to different magnetic quantum numbers. The covalent bond is directional (sp^1, sp^2, or sp^3 hybridization), which is essential for the molecular structure such as in CH_4. Do the Exc. 12.1.6.1.

12.1.2 Born-Oppenheimer approximation and the $H_2{}^+$ molecule

The *Born-Oppenheimer approximation* in molecular physics consists in considering, at first, the positions of the nuclei as being fixed in space. This allows us to study the stationary states of the electrons subject to the potential created by the nuclei for a given internuclear distance R. Varying R, the electronic energies (computed for a fixed R) remain the same, because the electronic wavefunctions adjust instantaneously due to their mass being much lower than that of the nuclei. The non-varying electronic energies play the role of interaction potential energies between the nuclei [35].

12.1.2.1 Separation of the center-of-mass

Let us consider two heavy masses, $M_{a,b} = M$ separated by a distance R and interacting through a potential $V_{nn}(R)$. Furthermore, there is a light-weighted mass m_e interacting with the other masses through $V_{ne}(r)$. The Hamiltonian is,

$$\hat{H} = \frac{-\hbar^2}{2M}\nabla_a^2 + \frac{-\hbar^2}{2M}\nabla_b^2 + \frac{-\hbar^2}{2m_e}\nabla_e^2 + V_{nn}(|\mathbf{R}_a - \mathbf{R}_b|) + V_{ne}(|\mathbf{R}_a - \mathbf{R}_e|) + V_{ne}(|\mathbf{R}_b - \mathbf{R}_e|) \ . \tag{12.2}$$

We transform to the center-of-mass system of the two heavy masses anchored at

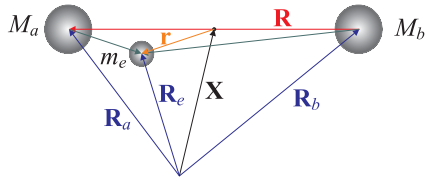

Figure 12.4: System with two heavy and one light mass.

$\mathbf{X} \equiv \frac{M_a\mathbf{R}_a + M_b\mathbf{R}_b}{M} = \frac{1}{2}(\mathbf{R}_a + \mathbf{R}_b)$. The distance of the *heavies* is $\mathbf{R} \equiv \mathbf{R}_a - \mathbf{R}_b$, and the coordinate of the light mass counting from the center-of-mass is $\mathbf{r} = \mathbf{R}_a - \frac{1}{2}\mathbf{R} - \mathbf{R}_e$. Introducing the reduced mass of the *heavies* $M_r = \frac{M}{2}$,

$$\left[\frac{-\hbar^2}{2M}\nabla_X^2 + \frac{-\hbar^2}{2M_r}\nabla_R^2 + V_{nn}(R) + \frac{-\hbar^2}{2m_e}\nabla_r^2 + V_{ne}(|\mathbf{r} + \tfrac{\mathbf{R}}{2}|) + V_{ne}(|\mathbf{r} - \tfrac{\mathbf{R}}{2}|)\right]\Theta(\mathbf{X})\Psi(\mathbf{R}, \mathbf{R}_e)$$
$$= E_{tot}\Theta(\mathbf{X})\Psi(\mathbf{R}, \mathbf{R}_e) \ , \tag{12.3}$$

Here, we made the ansatz for the total wavefunction $\Psi = \Theta(\mathbf{X})\Psi(\mathbf{R}, \mathbf{R}_e)$, assuming that the center-of-mass is only determined by the heavy masses,

$$\frac{-\hbar^2}{2M}\nabla_X^2\Theta(\mathbf{X}) = E_{cm}\Theta(\mathbf{X}) \tag{12.4}$$
$$\left[\frac{-\hbar^2}{2M_r}\nabla_R^2 + V_{nn}(R) + \frac{-\hbar^2}{2m_e}\nabla_r^2 + V_{ne}(|\mathbf{r} + \tfrac{1}{2}\mathbf{R}|) + V_{ne}(|\mathbf{r} - \tfrac{1}{2}\mathbf{R}|)\right]\Psi(\mathbf{R}, \mathbf{R}_e) = E\Psi(\mathbf{R}, \mathbf{R}_e) \ ,$$

where $E_{tot} = E_{cm} + E$.

12.1.2.2 Adiabatic approximation

The Born-Oppenheimer approximation now consists in assuming that the movement of the *heavies* is independent of the position of m_e, which allows us to separate the corresponding wavefunction ϕ via the ansatz $\Psi(\mathbf{R}, \mathbf{R}_e) = \psi(\mathbf{R}, \mathbf{r})\phi(\mathbf{R})$. On the other hand, the orbital ψ of the light mass m_e does not change much, when we vary the distance of the *heavies*, $\nabla_R\psi(\mathbf{R}, \mathbf{r}) \simeq 0$. This is only valid, as long as the *heavies* are inert on the time scale of the movement of m_e. Therefore, we can approximate the second derivative,

$$\nabla_R^2[\psi(\mathbf{R}, \mathbf{r})\phi(\mathbf{R})] = \phi(\mathbf{R})\nabla_R^2\psi(\mathbf{R}, \mathbf{r}) + 2[\nabla_R\phi(\mathbf{R})] \cdot [\nabla_R\psi(\mathbf{R}, \mathbf{r})] + \psi(\mathbf{R}, \mathbf{r})\nabla_R^2\phi(\mathbf{R})$$
$$\simeq \psi(\mathbf{R}, \mathbf{r})\nabla_R^2\phi(\mathbf{R}) \ , \tag{12.5}$$

postulating that the first two terms are negligible compared to the third. We can now separate the second equation (12.4) in two parts, the first being,

$$\boxed{\left[\frac{-\hbar^2}{2m_e}\nabla_r^2 + V_{ne}(|\mathbf{r}+\tfrac{1}{2}\mathbf{R}|) + V_{ne}(|\mathbf{r}-\tfrac{1}{2}\mathbf{R}|)\right]\psi(\mathbf{r},\mathbf{R}) = \varepsilon(R)\psi(\mathbf{r},\mathbf{R})}\,. \tag{12.6}$$

We solve this equation for the electronic degree of freedom $\mathbf{r}$ by choosing a fixed internuclear distance $\mathbf{R}$, and we substitute in the second expression (12.4), which gives,

$$\boxed{\left[\frac{-\hbar^2}{2M_r}\nabla_R^2 + V_{nn}(R) + \varepsilon(R)\right]\phi(\mathbf{R}) = E\phi(\mathbf{R})}\,. \tag{12.7}$$

Treating the interatomic distance R as a fixed parameter, the solution of Eq. (12.6) provides the electronic orbitals and their energies $\varepsilon(R)$. The *Born-Oppenheimer potential* is composed of the electrostatic repulsive potential of the nuclei and the kinetic energy of the electron, $V_{nn}(R) + \varepsilon(R)$. In other words, the presence of the electrons generates an additional interaction energy between the nuclei. By inserting this complete interatomic potential into Eq. (12.7), we can determine its vibrational structure $\phi_{\text{vib}}(\mathbf{R})$.

Fig. 12.5 shows an example of binary effective nuclear potentials, as a function of the distance R between the two nuclei. Each curve corresponds to a different solution of the electronic equation, that is, to a different electronic state. In many cases, such nuclear potentials have a stable equilibrium region. The bound states located in these regions are *molecular* bound states of two atoms.

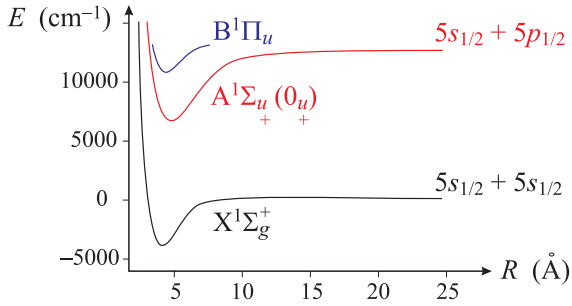

Figure 12.5: Effective nuclear potentials for the interaction between two rubidium atoms (Rb_2).

In practice, the calculation of adiabatic Born-Oppenheimer potentials is difficult and makes it the subject of sophisticated theories, such as the *molecular orbital model* or the *valence bond model* [2]. We study in Exc. 12.1.6.2 a generalization of the Born-Oppenheimer approximation.

[2] Note that the Born-Oppenheimer approximation is no longer good in the presence of relativistic or spin-orbit coupling effects.

12.1.3 Linear combination of orbitals and the H_2 molecule

In the following we will discuss the electronic structure of the simplest neutral molecule: H_2. For the low electron states of this molecule, the Born-Oppenheimer approximation is totally satisfactory, that is, we want to solve a Schrödinger type equation (12.6), but with two electrons. We are, therefore, interested in the electronic Hamiltonian,

$$\boxed{\hat{H} = -\frac{\hbar^2}{2m_e}(\nabla_1^2 + \nabla_2^2) + \frac{e^2}{4\pi\varepsilon_0}\left(\frac{1}{R_{ab}} - \frac{1}{|\mathbf{r}_1-\mathbf{R}_a|} - \frac{1}{|\mathbf{r}_1-\mathbf{R}_b|} - \frac{1}{|\mathbf{r}_2-\mathbf{R}_a|} - \frac{1}{|\mathbf{r}_2-\mathbf{R}_b|} + \frac{1}{r_{12}}\right)}\,, \tag{12.8}$$

where '1' and '2' denote the two electrons and 'a' and 'b' the nuclei.

This problem can not be solved analytically. The standard procedure begins with choosing a suitable basis, i.e. a very compact basis which does not depend on the configuration of the molecule. That is, we want the basis to be composed of functions that do not depend on the distance between the two nuclei, R_{ab}, to avoid calculations for different bond lengths.

The most natural basis functions are the available atomic orbitals of the individual hydrogen atoms. When the bond length is too large, the system approaches the limit of two non-interacting hydrogen atoms. In this case, the electron wavefunction can be approximated by the product of *atomic orbitals* (AO) of atom 'a' and atom 'b'. Therefore, the smallest basis that gives us a realistic picture of the fundamental state of the H_2 molecule must comprise two functions: $|1s_a\rangle$ and $|1s_b\rangle$. For finite bond lengths, it is advisable to allow the AOs to polarize and deform in response to the presence of the other electron (and the other nucleus). However, the $|1s_a\rangle$ and $|1s_b\rangle$ functions do not have to be exactly the hydrogenic eigenfunctions. It is sufficient to require them to be similar to the $1s$ orbitals and be centered on them. Since the actual shape of the orbitals is not yet fixed, we will give all the expressions in abstract matrix form, leaving the spatial integration for once the shape of the orbitals has been specified. This is the method of *linear combination of atomic orbitals* (LCAO).

12.1.4 Molecular orbital theory

We are now in a position to discuss the basic principles of the *molecular orbital method* (MO), which is the basis of the theory of the electronic structure of real molecules. The first step in any MO approach is to separate the Hamiltonian into two parts, one part describing the electrons '1' and '2' separately and one part counting for the interaction between them:

$$\hat{H} = \hat{h}(1) + \hat{h}(2) + \hat{V}_{12} + \frac{e^2}{4\pi\varepsilon_0}\frac{1}{R_{ab}} \qquad \text{with} \tag{12.9}$$

$$\hat{h}(i) = -\frac{\hbar^2\nabla_i}{2m_e} - \frac{e^2}{4\pi\varepsilon_0}\left(\frac{1}{|\mathbf{r}_i - \mathbf{R}_a|} + \frac{1}{|\mathbf{r}_i - \mathbf{R}_b|}\right) \qquad \text{and} \qquad \hat{V}_{12} = \frac{e^2}{4\pi\varepsilon_0}\frac{1}{r_{12}}\,,$$

where $i = 1, 2$. We must remember that, within the BO approximation, R_{ab} is just a number. We choose the Hamiltonian $h(i)$ as the one-electron part of the complete Hamiltonian in matrix representation on the minimum basis:

$$\begin{pmatrix} \langle 1s_a|\hat{h}|1s_a\rangle & \langle 1s_a|\hat{h}|1s_b\rangle \\ \langle 1s_b|\hat{h}|1s_a\rangle & \langle 1s_b|\hat{h}|1s_b\rangle \end{pmatrix} \equiv \begin{pmatrix} \epsilon & h_{ab} \\ h_{ab} & \epsilon \end{pmatrix}\,, \tag{12.10}$$

defining the average one-electron energy $\epsilon \equiv \langle 1s_a|\hat{h}|1s_a\rangle$ and the non-diagonal coupling (often called *resonance integral*) $h_{ab} \equiv \langle 1s_a|\hat{h}|1s_b\rangle = \langle 1s_a|\hat{h}|1s_b\rangle$. We can immediately diagonalize this matrix, the eigenvalues and the eigenvalues being:

$$\epsilon_\pm = \epsilon \pm h_{ab} \qquad \text{and} \qquad |\phi_\pm\rangle \propto \tfrac{1}{2}(|1s_a\rangle \pm |1s_b\rangle) \ . \tag{12.11}$$

The one-electron effective Hamiltonian eigenstates are called *molecular orbital* (MO). They are one-electron wavefunctions delocalized over the spatial regions of the molecule.

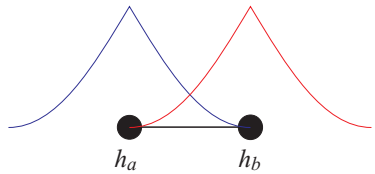

Figure 12.6: Illustration of the atomic orbitals.

We need to first normalize the MOs, which is more complicated than it might seem, because the AOs are not orthogonal. For example, when the atoms approach each other, their AOs may have the shape shown in Fig. 12.6. However, by defining the overlap integral by $S \equiv \langle 1s_a|1s_b\rangle$, we can normalize as follows:

$$|\phi_\pm\rangle = \tfrac{1}{\sqrt{2(1\pm S)}}(|1s_a\rangle \pm |1s_b\rangle) \ , \tag{12.12}$$

since,

$$\langle\phi_\pm|\phi_\pm\rangle = \tfrac{1}{2(1\pm S)}(\langle 1s_a|1s_a\rangle \pm \langle 1s_a|1s_b\rangle \pm \langle 1s_b|1s_a\rangle + \langle 1s_b|1s_b\rangle) = 1 \ . \tag{12.13}$$

These eigenfunctions merely show the symmetry of the molecule. The two hydrogen atoms are equivalent and, therefore, the eigenorbital must give equal weight to each $1s$ orbital. Thus, our choice of the one-electron Hamiltonian does not really matter that much, because every one-electron Hamiltonian exhibiting the symmetry of the molecule would give the same molecular orbitals. For historical reasons, $|\phi_+\rangle$ is denoted by $|\sigma\rangle$ and $|\phi_-\rangle$ by $|\sigma^*\rangle$.

The second step in MO theory consists of constructing the determinant from the MOs corresponding to the wanted states. For illustration we will look at the lowest singlet state constructed from molecular orbitals. We note that $h_{ab} < 0$, such that $|\sigma\rangle$ has an energy inferior to $|\sigma^*\rangle$. Neglecting the interaction, the lowest singlet state,

$$|\Phi_{\rm MO}\rangle = |\sigma\rangle|\sigma^*\rangle \ , \tag{12.14}$$

is the molecular ground state of H_2. To estimate the validity of the approximation, we calculate the expectation value of the energy, $\left|\langle\sigma|\langle\sigma^*|\hat{H}|\sigma\rangle|\sigma^*\rangle\right|$, decomposing the wavefunction into spin and spatial parts, noting that the spin part is normalized:

$$\begin{aligned}\left|\langle\sigma|\langle\sigma^*|\hat{H}|\sigma\rangle|\sigma^*\rangle\right| &= \langle\sigma(1)|\langle\sigma(2)|\hat{H}|\sigma(1)\rangle|\sigma(2)\rangle\langle\Phi_{\rm spin}|\Phi_{\rm spin}\rangle \\ &= \langle\sigma(1)|\langle\sigma(2)|\hat{H}|\sigma(1)\rangle|\sigma(2)\rangle \ .\end{aligned} \tag{12.15}$$

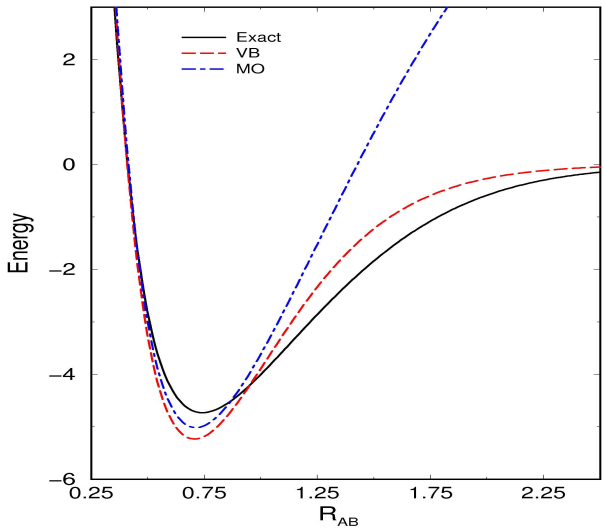

Figure 12.7: Total energy as a function of interatomic distance.

Hence, with (12.10) we get,

$$\begin{aligned}
\langle\sigma(1)|\langle\sigma(2)|\hat{h}(2)|\sigma(1)\rangle|\sigma(2)\rangle &= \langle\sigma(1)|\sigma(1)\rangle\langle\sigma(2)|h(2)|\sigma(2)\rangle = \langle\sigma(2)|h(2)|\sigma(2)\rangle \equiv \epsilon_\sigma \\
\langle\sigma(1)|\langle\sigma(2)|\hat{h}(1)|\sigma(1)\rangle|\sigma(2)\rangle &= \langle\sigma(1)|h(1)|\sigma(1)\rangle\langle\sigma(2)|\sigma(2)\rangle = \langle\sigma(1)|h(1)|\sigma(1)\rangle \equiv \epsilon_\sigma \\
\langle\sigma(1)|\langle\sigma(2)|\hat{V}_{12}|\sigma(1)\rangle|\sigma(2)\rangle &\equiv J_{\sigma\sigma} \ . \qquad (12.16)
\end{aligned}$$

Putting these facts together, we can write,

$$\begin{aligned}
\langle\Phi_{\rm MO}|\hat{H}|\Phi_{\rm MO}\rangle &= \langle\Phi_{\rm MO}|\hat{h}_1|\Phi_{\rm MO}\rangle + \langle\Phi_{\rm MO}|\hat{h}_2|\Phi_{\rm MO}\rangle + \langle\Phi_{\rm MO}|\hat{V}_{12}|\Phi_{\rm MO}\rangle + \frac{e^2}{4\pi\varepsilon_0 R_{ab}} \\
&= 2\epsilon_\sigma + J_{\sigma\sigma} + \frac{e^2}{4\pi\varepsilon_0 R_{ab}} \ . \qquad (12.17)
\end{aligned}$$

Each of the first two terms represents the energy of a single electron (either 1 or 2) in the field produced by both the nuclei ($\hat{h}$), while the third is the average repulsion between the two electrons. Note that the first and second term are both positive, such that the bond must come from the one-electron part. This is the MO energy for the ground state of the H_2. We can try a more reasonable ansatz for the $1s$-type basis functions [3] by determining the unknown quantities from above (ϵ_σ and $J_{\sigma\sigma}$) numerically and plot the total energy as a function of R_{ab} (blue dotted curve in Fig. 12.7). The exact adiabatic energy function determined from experimental data (solid black curve) agrees well at low energies. Summarizing the results with some key numbers, we note that MO theory predicts a bond distance of 0.072 nm in reasonable agreement with the exact value of 0.074 nm. We can also compare the

[3] It turns out that it is more convenient to adjust the exponential decomposition of the hydrogenic orbitals to a sum of Gaussians.

binding energies,

$$D_e = E_{H_2}(R_{\text{equil}}) - 2E_H \ . \tag{12.18}$$

MOs theory predicts a binding energy of 5.0 eV compared to the experimental value of 4.75 eV. In view of the simplicity of the wavefunction and the absence of adjustable parameters the agreement is not so bad. Unfortunately, far away from the equilibrium distance, we have an unpleasant surprise: the molecule does not dissociate into two hydrogen atoms!

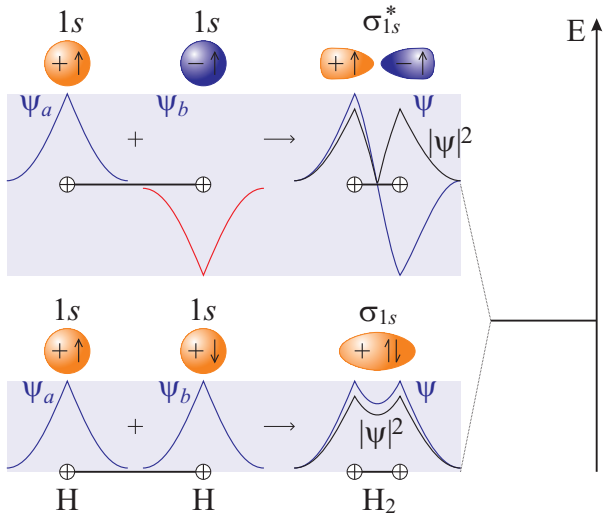

Figure 12.8: Illustration of MO theory for a dimer of two equal atoms, each one with a valence electron in the atomic 1*s* orbital: When the atoms approach, the atomic orbitals form new molecular binding and anti-biding orbitals.

To get an idea of what is happening near dissociation, we expand the fundamental MO state in terms of AO configurations:

$$\begin{aligned} |\Phi_{\text{MO}}\rangle &\propto |\sigma(1)\rangle|\sigma(2)\rangle|\Phi_{\text{spin}}\rangle \\ &= \tfrac{1}{2(1+S)}(|1s_a(1)\rangle + |1s_b(1)\rangle)(|1s_a(2)\rangle + |1s_b(2)\rangle)|\Phi_{\text{spin}}\rangle \\ &= \tfrac{1}{2(1+S)}(|1s_a(1)\rangle|1s_a(2)\rangle + |1s_a(1)\rangle|1s_b(2)\rangle + |1s_b(1)\rangle|1s_a(2)\rangle + |1s_b(1)\rangle|1s_b(2)\rangle)|\Phi_{\text{spin}}\rangle \ . \end{aligned} \tag{12.19}$$

The two terms in the middle of the last line, called *covalent configurations*, are exactly what we expect near dissociation: one electron in each hydrogen atom. However, the first and last term (which are called *ionic configurations*) correspond to having two electrons in one atom and none in the other, which gives us H^+ and H^- at dissociation! Since the weight of these terms is fixed, it is obvious that we got the wrong wavefunction (and therefore the wrong energy) when dissociating the molecule. Near the equilibrium point, the ionic terms contribute significantly to the true wavefunction, such that the MO theory is good at this point. But it is always terrible at dissociation.

12.1.5 Valence binding

An alternative to MO theory represents the *valence bond* theory (VB). Here, we use significantly more physical intuition and discard the ionic configurations from the MO wavefunction. Thus, the VB ground state wavefunction is:

$$\begin{aligned}|\Psi\rangle &\propto \frac{|1s_a(1)\rangle|1s_a(2)\rangle + |1s_b(1)\rangle|1s_a(2)\rangle}{\sqrt{2}} \frac{|\uparrow(1)\rangle|\downarrow(2)\rangle + |\downarrow(1)\rangle|\uparrow(2)\rangle}{\sqrt{2}} \\ &\equiv |\Psi_{\rm space}\rangle|\Psi_{\rm spin}\rangle \ . \end{aligned} \tag{12.20}$$

VB theory assumes that this wavefunction is a good approximation to the true wavefunction at *all* binding distances and not only at large distances R_{ab}. To verify this approximation, we can calculate the average energy for this VB state. First, we normalize the VB wavefunction,

$$\begin{aligned}\langle\Psi|\Psi\rangle &= \langle\Psi_{\rm space}|\langle\Psi_{\rm spin}|\Psi_{\rm space}\rangle|\Psi_{\rm spin}\rangle = \langle\Psi_{\rm space}|\Psi_{\rm space}\rangle \\ &= \tfrac{1}{2}\left(\langle 1s_a(1)|\langle 1s_b(2)| + \langle 1s_b(1)\langle 1s_a(2)|\right)\left(|1s_a(1)\rangle|1s_a(2)\rangle + |1s_b(1)\rangle|1s_a(2)\rangle\right) \\ &= \tfrac{1}{2}\left(\langle 1s_a(1)|1s_b(2)|1s_a(1)\rangle|1s_b(2)\rangle + \langle 1s_a(1)|1s_b(2)|1s_b(1)\rangle|1s_a(2)\rangle\right. \\ &\quad \left.+\langle 1s_b(1)|1s_a(2)|1s_a(1)\rangle|1s_b(2)\rangle + \langle 1s_b(1)|1s_a(2)|1s_b(1)\rangle|1s_a(2)\rangle\right) \\ &= \tfrac{1}{2}(1+S^2+S^2+1) = 1+S^2 \ . \end{aligned} \tag{12.21}$$

Therefore, the correctly normalized VB wavefunction is:

$$|\Psi_{\rm VB}\rangle = \frac{1}{2\sqrt{1+S^2}}\left(|1s_a(1)\rangle|1s_a(2)\rangle + |1s_b(1)\rangle|1s_a(2)\rangle\right)\left(|\uparrow(1)\rangle|\downarrow(2)\rangle - |\downarrow(1)\rangle|\uparrow(2)\rangle\right) \ . \tag{12.22}$$

Now we want to calculate $\langle\hat{H}_{el}\rangle$ for this state. We note that the spin part does not matter, since the Hamiltonian is independent of spin:

$$\begin{aligned}\langle\Psi_{\rm VB}|\hat{H}|\Psi_{\rm VB}\rangle &= \langle\Psi_{\rm spin}|\langle\Psi_{\rm space}|\hat{H}|\Psi_{\rm space}\rangle|\Psi_{\rm spin}\rangle \\ &= \langle\Psi_{\rm space}|\hat{H}|\Psi_{\rm space}\rangle\langle\Psi_{\rm spin}|\Psi_{\rm spin}\rangle = \langle\Psi_{\rm space}|\hat{H}|\Psi_{\rm space}\rangle \ . \end{aligned} \tag{12.23}$$

The only remnant of the spin state is the fact that the spatial wavefunction is symmetric, which is only possible when the spin part is antisymmetric. Treating each term in $\langle\hat{H}\rangle$ separately,

$$\begin{aligned}\langle\Psi|\hat{h}_1|\Psi\rangle &= \tfrac{1}{2}\left(\langle 1s_a(1)|\langle 1s_b(2)| + \langle 1s_b(1)|1s_a(2)|\right)\hat{h}_1\left(|1s_a(1)\rangle|1s_a(2)\rangle + |1s_b(1)\rangle|1s_a(2)\rangle\right) \\ &= \tfrac{1}{2}\Big(\langle 1s_a(1)|1s_b(2)|\hat{h}_1|1s_a(1)\rangle|1s_b(2)\rangle + \langle 1s_a(1)|1s_b(2)|\hat{h}_1|1s_b(1)\rangle|1s_a(2)\rangle \\ &\quad +\langle 1s_b(1)|1s_a(2)|\hat{h}_1|1s_a(1)\rangle|1s_b(2)\rangle + \langle 1s_b(1)|1s_a(2)|\hat{h}_1|1s_b(1)\rangle|1s_a(2)\rangle\Big) \\ &= \tfrac{1}{2}(\epsilon + Sh_{ab} + \epsilon + Sh_{ab}) \ , \end{aligned} \tag{12.24}$$

or,

$$\boxed{\langle\Psi_{\rm VB}|\hat{h}_1|\Psi_{\rm VB}\rangle = \frac{\epsilon + Sh_{ab}}{1+S^2}} \ . \tag{12.25}$$

Since the two electrons are identical, the elements of the $\hat{h}_2$ are the same as those of $\hat{h}_1$. The only remaining term is the average value of the interaction:

$$\langle\Psi|\hat{V}_{12}|\Psi\rangle = \tfrac{1}{2}\left(\langle 1s_a(1)|\langle 1s_b(2)| + \langle 1s_b(1)|1s_a(2)|\right)\hat{V}_{12}\left(|1s_a(1)\rangle|1s_a(2)\rangle + |1s_b(1)\rangle|1s_a(2)\rangle\right) \tag{12.26}$$

$$= \tfrac{1}{2}\Big(\langle 1s_a(1)|1s_b(2)|\hat{V}_{12}|1s_a(1)\rangle|1s_b(2)\rangle + \langle 1s_a(1)|1s_b(2)|\hat{V}_{12}|1s_b(1)\rangle|1s_a(2)\rangle + \langle 1s_b(1)|1s_a(2)|\hat{V}_{12}|1s_a(1)\rangle|1s_b(2)\rangle + \langle 1s_b(1)|1s_a(2)|\hat{V}_{12}|1s_b(1)\rangle|1s_a(2)\rangle\Big) \ .$$

The second and third terms are the same. They are called *exchange integrals*, because the 'bra' orbitals have switched order as compared to the 'kets':

$$K = \langle 1s_a(1)|1s_b(2)|\hat{V}_{12}|1s_b(1)\rangle|1s_a(2)\rangle = \langle 1s_b(1)|1s_a(2)|\hat{V}_{12}|1s_a(1)\rangle|1s_b(2)\rangle \ . \tag{12.27}$$

The first and forth terms are also the same. They are called *Coulomb integrals*, because they seem to be due to the Coulomb interaction between two charge densities:

$$J = \langle 1s_b(1)|1s_a(2)|\hat{V}_{12}|1s_a(1)\rangle|1s_b(2)\rangle = \langle 1s_a(1)|1s_b(2)|\hat{V}_{12}|1s_b(1)\rangle|1s_a(2)\rangle \ . \tag{12.28}$$

Therefore, we have the result,

$$\boxed{\langle\Psi_{\rm VB}|\hat{V}_{12}|\Psi_{\rm VB}\rangle = \frac{J+K}{1+S^2}} \ . \tag{12.29}$$

Adding all terms, we get:

$$\langle\Psi_{\rm VB}|\hat{H}|\Psi_{\rm VB}\rangle = \langle\Psi_{\rm VB}|\hat{h}_1|\Psi_{\rm VB}\rangle + \langle\Psi_{\rm VB}|\hat{h}_2|\Psi_{\rm VB}\rangle + \langle\Psi_{\rm VB}|\hat{V}_{12}|\Psi_{\rm VB}\rangle + \frac{1}{R_{ab}}$$

$$= 2\frac{\epsilon + Sh_{ab}}{1+S^2} + \frac{J+K}{1+S^2} + \frac{1}{R_{ab}} \ . \tag{12.30}$$

The Coulomb and exchange terms are positive. Nuclear repulsion is clearly positive. Thus, the only terms that lead to binding in this picture are the average energy of an electron ϵ and the resonance integral h_{ab}. If the first term is dominant, the bond is due to *electronic delocalization*, since an electron located near one of the atoms would only contribute the atomic value to ϵ, which does not imply a bound state. If h_{ab} is large, the bond involves some resonance character, which can be related to the familiar concept of resonance between different Lewis point structures.

A numerical evaluation of all integrals gives the potential curve presented in Fig. 12.7 for VB theory. As expected, this simple VB wavefunction gives the correct dissociation threshold, where MO theory fails. In addition, the accuracy of the simple VB result is surprisingly good even near the equilibrium distance: The VB predicts a bond distance of 0.071 nm (compared to the correct value of 0.074 nm) and $D_e = 5.2$ eV (compared to 4.75 eV). Thus, the VB wavefunction also gives a good agreement without adjustable parameters. But more importantly, it indicates a way of improving the wavefunction whenever we encounter an obvious error: in this case, we saw that the description of the dissociation was weak, and we constructed a VB ansatz curing the problem. This approach to VB is often generalized as follows

when dealing with polyatomic molecules. We write the wavefunction as a product of a spatial part and a spin:

$$|\Psi\rangle = |\Psi_{\text{space}}\rangle|\Psi_{\text{spin}}\rangle \ . \tag{12.31}$$

The main assumption in VB theory is that the spatial part can be well represented by a product of atomic-like functions. For example, for water, we would immediately write a spatial part as:

$$|\Psi_{\text{space}}\rangle \simeq |1s_{H_a}\rangle|1s_{H_b}\rangle|1s_O\rangle|1s_O\rangle|2s_O\rangle|2s_O\rangle|2p_{xO}\rangle|2p_{xO}\rangle|2p_{yO}\rangle|2p_{yO}\rangle \ . \tag{12.32}$$

However, there are two things wrong with this wavefunction. First, we know that atomic orbitals hybridize in a molecule. Therefore, we need to make appropriate linear combinations of AOs (in this case sp^3 hybrids) to obtain the hybridized AOs. In this case, the four sp^3 hybrids can be written symbolically as:

$$|sp^3\rangle = c_{s,i}|2s\rangle + c_{x,i}|2p_x\rangle + c_{y,i}|2p_y\rangle + c_{z,i}|2p_z\rangle \ . \tag{12.33}$$

and therefore, a more appropriate spatial configuration is:

$$|\Psi_{\text{space}}\rangle \simeq |1s_{H_a}\rangle|1s_{H_b}\rangle|1s_O\rangle|1s_O\rangle|sp^3_{1O}\rangle|sp^3_{1O}\rangle|sp^3_{2O}\rangle|sp^3_{2O}\rangle|sp^3_{3O}\rangle|sp^3_{4O}\rangle \ . \tag{12.34}$$

The other problem with this state is that it lacks the adequate symmetry to describe fermions; the general state must be antisymmetric. In the case of two electrons this concept is easy to apply - singlets have symmetric space parts and triplets antisymmetric ones. However, in the case of many electrons, the rules are not so simple; in fact, the time of numerical computation grows exponentially with the number of electrons.

Formally, we will leave the derivation at this point to defining an operator $\mathcal{A}$ which 'antisymmetrizes' the wavefunction. In this case,

$$|\Psi_{\text{space}}\rangle \simeq \mathcal{A}\left[|1s_{H_a}\rangle|1s_{H_b}\rangle|1s_O\rangle|1s_O\rangle|sp^3_{1O}\rangle|sp^3_{1O}\rangle|sp^3_{2O}\rangle|sp^3_{2O}\rangle|sp^3_{3O}\rangle|sp^3_{4O}\rangle\right] \ . \tag{12.35}$$

In general, the results of VB theory are very accurate for small systems, where it can be applied. The predicted bond lengths are rather short, and the binding energies tend to be too small, but the results are nevertheless qualitatively excellent. In addition, the correct hybridized atomic orbitals fall directly off the calculation, giving a good qualitative insight. Also, note that the atomic configurations should not change (or very little) when the geometry of the molecule changes (since the orbitals depend on the atom and not on the molecular structure). Therefore, these VB wavefunctions have a strong connection to the diabatic states discussed above. However, the exponential amount of time that one must invest to perform these calculations makes them impractical for most molecules of interest.

12.1.6 Exercises

12.1.6.1 Ex: Classical model of the covalent binding

Consider the molecule H_2^+ with the two nuclei separated by 1 nm and an electron located in the middle between the nuclei. Calculate the electrostatic force acting on the nuclei.

12.1.6.2 Ex: Beyond the Born-Oppenheimer approximation for molecules

For molecules, the Born-Oppenheimer approximation may fail in some situations. Therefore, it is common to use another approach known as Born-Huang. To illustrate this approach, we consider a diatomic molecule in the laboratory frame.
a. Write down the many-body Hamiltonian of the molecule in atomic units.
b. If we change the coordinate system to the position of the center-of-mass of the nuclei of the molecule, we eliminate the dependency on the global translation of the molecule. The Hamiltonian is now given by,

$$-\frac{\nabla_R^2}{2\mu_{AB}} - \sum_{i,j}\frac{1}{2M}\nabla_i\nabla_j - \sum_i \frac{\nabla_i^2}{2} + V$$

where that the Coulombian interactions are included in the fifth term. Write down the time-independent Schrödinger equation for this molecule.
c. The Born-Huang approximation consists in assuming that the total wavefunction can be expanded on a basis of wavefunctions of the nuclei and the electrons, that is,

$$\Psi(\mathbf{r},\mathbf{R}) = \sum_k |\chi_k(\mathbf{R})\rangle|\phi_k(\mathbf{r},\mathbf{R})\rangle \ ,$$

where χ and ϕ are the wavefunctions of the nuclei and the electrons, respectively. For the Schrödinger equation calculated in the previous item, use the Born-Huang approximation and obtain the set of coupled equations

$$\left\{\sum_k\left[-\frac{1}{2\mu_{AB}}\left(\nabla_R^2 + \langle\phi_k|\nabla_R^2|\phi_k\rangle + 2\langle\phi_k|\nabla_R|\phi_k\rangle.\nabla_R|\right)\right] - \right.$$
$$\left.\sum_k\left[\frac{1}{2M}\left(\sum_{i,j}\langle\phi_i|\nabla_i.\nabla_j|\phi_k\rangle\right) + \frac{1}{2}\sum_i\langle\phi_i|\nabla_i^2|\phi_k\rangle - \langle\phi_i|V|\phi_k\rangle|\right]\right\}|\chi_k\rangle = E\sum_k|\chi_k\rangle$$

which includes, although approximately, the kinetic energy of nuclei and electrons. **Help:** Use $\nabla^2(\alpha\beta) = \alpha\nabla^2\beta + \beta\nabla^2\alpha + 2\nabla\alpha\cdot\nabla\beta$.
d. Make a brief comparison between the Born-Huang approximation (and the coupled equations obtained in the previous equation) and the Born-Oppenheimer approximation.

12.1.6.3 Ex: Classical model of the covalent bond

Calculate the energies of the ground state and the last bound state of the potential $V_n = -\frac{C}{r^n}$ for any n.

12.1.6.4 Ex: Homonuclear collision

We consider the example of homonuclear collisions of ^{85}Rb atoms. For ground state collisions in the channel $^3\Sigma_+$, $|f=2, m_f=-2\rangle$, the long-range part of the potential is fixed by $C_6 = 4550$, $C_8 = 550600$, and $C_{10} = 7.67\times10^7$ [178, 700], where $R_m = 9.8a_B$, $D_m = 0.13$, and $B_m = 1/2.5a_B$. The potentials can be merged at a given distance $R_t = 27.6a_B$. Prepare a plot of potential.

12.2 Rovibrational structure of molecular potentials

The separation of the motion of the nuclei from the electronic dynamics made in the Born-Oppenheimer approximation led to equations (12.6) and (12.7). In a preceding section we analyzed in detail the equation (12.6) with the objective of understanding the phenomenon of molecular binding.

In the following section we will analyze the equation (12.7), which determines the motion of the nuclei. By separating the radii and angular parts of the motion, we will discover vibrational and rotational states.

12.2.1 The radial and angular equations

The interaction between two identical atoms is described by the following Hamiltonian, where $M_r = (M_a^{-1} + M_b^{-1})^{-1} = M/2$ is the *reduced mass* of the nuclei,

$$\hat{H} = \frac{\mathbf{P}^2}{2M_r} + V_{\rm mol}(R) \qquad \text{with} \qquad V_{\rm mol}(R) = \frac{e^2}{4\pi\epsilon_0 R} + V_{BO}(R)\ . \tag{12.36}$$

The interaction potential $V_{\rm mol}$ is composed of a repulsive internuclear Coulomb force and a Born-Oppenheimer adiabatic potential due to the interaction of the electrons with each other and with the two nuclei [4]. The kinetic energy is that of the relative motion (the center-of-mass motion has already been separated in Sec. 12.1.2, such that this inertial system is free of translational kinetic energy). In spherical coordinates,

$$\frac{\mathbf{P}^2}{2M_r}\phi(\mathbf{R}) = -\frac{\hbar^2}{2M_r}\left[\frac{1}{R}\frac{\partial^2}{\partial R^2}[R\phi(\mathbf{R})] + \frac{1}{R^2}\frac{\hat{\mathbf{L}}^2}{\hbar^2}\phi(\mathbf{R})\right]\ . \tag{12.37}$$

The wavefunction can be separated into an angular part and a radial part, $\phi(\mathbf{R}) = \mathcal{R}_v(R)Y_{\ell m}(\theta,\phi)$. The angular part, which was discussed in Sec. 3.1.3, describes a *rigid rotation* of the homonuclear atoms around their center-of-mass with the rotation energy,

$$\boxed{V_\ell(R) = \frac{\mathbf{L}^2}{2M_r R^2} = \frac{\hbar^2\ell(\ell+1)}{2M_r R^2}}\ , \tag{12.38}$$

also called *centrifugal barrier*. The radial part is ruled by,

$$\boxed{\left[-\frac{\hbar^2}{2M_r}\frac{\partial^2}{\partial R^2} + V_\ell(R) + V_{BO}(R)\right]u_v(R) = E u_v(R)}\ , \tag{12.39}$$

where $u_v(R) = r\mathcal{R}_v(R)$ is the radial wavefunction of nuclear motion. The interatomic potential causes a motion of *vibration*. The vibrational states of the adiabatic potential are quantized and characterized by a well-defined vibrational energy. We will discuss the ro-vibrational structure in the following sections.

[4] We note here that at great distances other forces called *van der Waals forces* dominate the interatomic interaction. These will be discussed in Sec. 12.3.

12.2.1.1 Rotational and vibrational bands

Molecules have much more degrees of freedom than atoms. For example, the atoms of a molecular dimer may vibrate inside the mutual interaction potential. In the center-of-mass system we can imagine these vibrations as oscillations of an atom with reduced mass and quantized energy. The molecule can rotate and have a momentum of inertia. These degrees of freedom contribute energies to the molecule's Hamiltonian, either directly or through interactions with other degrees of freedom. Therefore, molecular spectra are characterized by a much greater complexity.

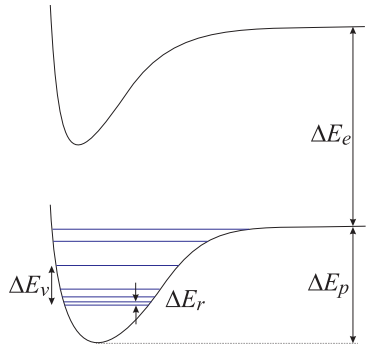

Figure 12.9: Molecular energy scales.

However, the energy regimes of the strongest excitations are quite different. A typical range for binding energies (depth of the interatomic potential) is $\Delta E_p \simeq$ 20..200 THz (0.1..1 eV) [5]. Electronic excitations occur in the regime $\Delta E_e \simeq 100..1000$ THz (1..10 eV). The spacing between vibrational excitations typically is $E_{v+1} - E_v \simeq$ THz (0.01 eV). Finally, the rotational excitations are on the scale of $E_{\ell+1} - E_\ell \simeq 100$ MHz (10^{-6} eV). Since at room temperature (a gas of molecules in thermal equilibrium at $T = 300$ K) the energy is on a scale of 2.5×10^{-2} eV, the degree of freedom of the electronic excitation is frozen, while a wide distribution of vibrational and rotational states can be excited (e.g. by intermolecular collisions). The large difference of scales facilitates their separation and, therefore, the identification of the origin of the observed states in experimental measurements.

12.2.2 Vibrational molecular states

The potential energy of a molecule grows when the nuclei are displaced from their equilibrium positions. When the displacement, $x \equiv R - R_e$ is small, we can expand the potential energy,

$$V_{\rm mol}(x) = V_{\rm mol}(0) + \frac{dV_{\rm mol}(0)}{dx} x + \frac{1}{2} \frac{d^2 V_{\rm mol}(0)}{dx^2} x^2 + .. \,. \tag{12.40}$$

[5] Electronically excited states (that is, one of the valence electrons moves to an excited orbital) are more weakly bound, because the electrons are not in the most binding orbital.

The equilibrium energy is not of interest here, and the first derivative disappears in equilibrium. Therefore,

$$V_{\rm mol}(x) \simeq \tfrac{1}{2}k^2x^2 \qquad \text{with} \qquad k \equiv \frac{d^2V_{\rm mol}(0)}{dx^2} \ . \tag{12.41}$$

Using the effective mass we can write the Hamiltonian,

$$\hat{H}_{\rm mol} = -\frac{\hbar^2}{2m_1}\frac{d^2}{dx_1^2} - \frac{\hbar^2}{2m_2}\frac{d^2}{dx_2^2} + \frac{1}{2}kx^2 = -\frac{\hbar^2}{2M_r}\frac{d^2}{dx^2} + \frac{1}{2}kx^2 \ . \tag{12.42}$$

The energy spectrum of this degree of freedom, therefore, is

$$\boxed{E_v = \hbar\omega(v+\tfrac{1}{2})} \ . \tag{12.43}$$

with $\omega = \sqrt{k/M_r}$. That is, at the bottom of deep potentials, the energy levels are equidistant.

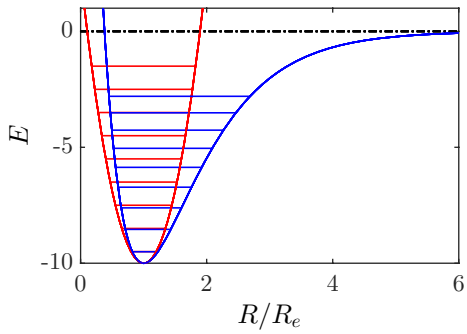

Figure 12.10: (code) Many potentials are approximately harmonic at the center such as, for instance, the Morse potential (blue). The red curve shows the approximate harmonic potential.

12.2.2.1 Anharmonic vibrations in the Morse potential

For larger displacements we can no longer despise the anharmonic terms in the Taylor expansion. A better approximation is the *Morse potential*. This potential (blue in Fig. 12.10), unlike the harmonic potential (red in Fig. 12.10), is characterized by an asymptote for large interatomic distances. Therefore, it is often used as an analytical approximation to molecular potentials,

$$\boxed{V_{\rm Morse} = D_e(1-e^{-a(R-R_e)})^2} \ , \tag{12.44}$$

where r is the interatomic distance, r_e the equilibrium bond distance, D_e the depth of the potential measuring from the *dissociation limit*, and a a parameter controlling the range of the potential. At the bottom of the potential we can make the harmonic

approximation, $V_{\rm Morse}(R) \simeq \frac{k}{2}(R-R_e)^2$ with $k = 2a^2 D_e$. Rewriting the potential in the form,

$$\tilde{V}(R) \equiv V(R) - D_e = D_e(e^{-2a(R-R_e)} - 2e^{-a(R-R_e)}) \ , \tag{12.45}$$

we see, that it is a combination of a short-range repulsive potential and long-range attractive potential (similar to the Lennard-Jones's potential).

The calculation of the energy spectrum of this potential is more difficult [190],

$$E_v = \hbar\omega(v+1/2) - \hbar\omega\chi_e(v+1/2)^2 - D_e, \tag{12.46}$$

with $\omega\chi_e \equiv \frac{\hbar a^2}{2M_r}$ and $\omega \equiv \sqrt{k/M_r}$, but the availability of an analytical expression is interesting for the calibration of numerical methods. The second term of the expression (12.46), which is proportional to the anharmonicity constant χ_e, becomes dominant at high excitations. The potential is finite with a dissociation energy of,

$$D_0 = D_e - E_0 \ . \tag{12.47}$$

The number of vibrational states is limited $v = 0, 1, .., v_{\rm max}$. With $E < 0$, we find,

$$v_{\rm max} < \tfrac{1}{x_e} - \tfrac{1}{2} \ . \tag{12.48}$$

Example 69 (*Morse potential*): To solve the Schrödinger equation

$$\left(-\frac{\hbar^2}{2m}\frac{\partial^2}{\partial R^2} + V(R)\right)\Psi(v) = E_v\Psi(v) \ ,$$

it is convenient to introduce new variables,

$$x \equiv aR \quad , \quad \lambda \equiv \frac{\sqrt{2mD_e}}{a\hbar} \quad , \quad \varepsilon_v \equiv \frac{2m}{a^2\hbar^2}E_v \ ,$$

such that,

$$\left(-\frac{\partial^2}{\partial x^2} + V(x)\right)\Psi_n(x) = \varepsilon_n\Psi_n(x) \quad \text{with} \quad V(x) = \lambda^2\left(e^{-2(x-x_e)} - 2e^{-(x-x_e)}\right) \ .$$

The eigenvalues and eigenfunctions are [190]:

$$\varepsilon_n = 1 - \tfrac{1}{\lambda^2}\left(\lambda - n - \tfrac{1}{2}\right)^2 = \tfrac{2}{\lambda}(n+\tfrac{1}{2})^2 - \tfrac{1}{\lambda^2}(n+\tfrac{1}{2})^2 \quad \text{and} \quad \Psi_n(z) = N_n z^{\lambda-n-\frac{1}{2}}e^{-\frac{1}{2}z}L_n^{(2\lambda-2n-1)}(z) \ ,$$

where $z = 2\lambda e^{-(x-x_e)}$ and $N_n = \left[\frac{n!(2\lambda-2n-1)}{\Gamma(2\lambda-n)}\right]^{\frac{1}{2}}$ and,

$$L_n^{(\alpha)}(z) = \frac{z^{-\alpha}e^z}{n!}\frac{d^n}{dz^n}\left(z^{n+\alpha}e^{-z}\right) = \frac{\Gamma(\alpha+n+1)/\Gamma(\alpha+1)}{\Gamma(n+1)}\ {}_1F_1(-n, \alpha+1, z) \ ,$$

is the generalized Laguerre polynomial. The matrix elements of the spatial operator $\hat{x}$ are (assuming $m > n$ and $N = \lambda - \frac{1}{2}$),

$$\langle\Psi_m|x|\Psi_n\rangle = \frac{2(-1)^{m-n+1}}{(m-n)(2N-n-m)}\sqrt{\frac{(N-n)(N-m)\Gamma(2N-m+1)m!}{\Gamma(2N-n+1)n!}} \ .$$

In the original variables the eigenenergies are:

$$E_v = \hbar\omega(v+1/2) - \frac{[\hbar\omega(v+1/2)]^2}{4D_e} \ ,$$

where v is the vibrational quantum number and $\omega = a\sqrt{\frac{2D_e}{m}}$. The energy difference between adjacent levels decreases with v,

$$E_{v+1} - E_v = \hbar\omega - (\hbar\omega)^2 \frac{v+1}{2D_e} \ .$$

This fact describes well the vibrational structure of non-rotating molecules. However, the equation fails above some value of $v > v_{\max}$, where $E_{v_{\max}+1} - E_{v_{\max}}$ is zero or negative,

$$v_{\max} = \frac{2D_e - \hbar\omega}{\hbar\omega} \ .$$

This failure is due to the finite number $v_{\max}$ of bound states in the Morse potential. For energies above $v_{\max}$ all energies are possible, and the equation for E_v is no longer valid.

12.2.2.2 Vibrational selection rules

Electromagnetic fields of the type $E1$, e.g., black body radiation, can induce transitions between vibrational states and redistribute their populations such as to establish a thermal equilibrium. However, as the stronger transitions are induced by dipole migrations of charges, we need to analyze in more detail the selection rules imposed on the dipole moment $\langle f|\mathbf{d}|i\rangle$.

The states which are relevant for vibrational transitions are specified by $|\epsilon, v\rangle$, where ϵ denotes the electronic state of the molecule, since the vibrational spectrum depends on the electronic structure. The *Born-Oppenheimer approximation* allows us to consider the slow vibrations separately from the dynamics of the electrons. The time scale for electronic transitions is $1/\Delta E_e = 10^{-16}\,\mathrm{s}^{-1}$, and for a nuclear vibration it is $1/\Delta E_v = 10^{-13}\,\mathrm{s}^{-1}$. For each internuclear distance the electrons form an adapted stationary state, minimizing their energy for that distance. This is equivalent to the formation of an adiabatic interaction potential between the nuclei on which the nuclei can vibrate. To find out which vibrational transitions are possible, we need to calculate the matrix,

$$\langle \epsilon', v'|\hat{\mathbf{d}}|\epsilon, v\rangle = \langle v'|\hat{\mathbf{d}}_\epsilon|v\rangle \ . \tag{12.49}$$

The dipole moment, $\mathbf{d}_\epsilon = \langle\epsilon|\hat{\mathbf{d}}|\epsilon\rangle$, of the molecule depends on the distance of the nuclei, since the electronic orbitals $|\epsilon\rangle$ depend on distance. Therefore, we can expand,

$$\hat{\mathbf{d}} = \hat{\mathbf{d}}_0 + \frac{d\hat{\mathbf{d}}_0}{dx}\hat{x} + \frac{1}{2}\frac{d^2\hat{\mathbf{d}}_0}{dx^2}\hat{x}^2 + .. \ . \tag{12.50}$$

Therefore, the transition matrix is,

$$\langle \epsilon', v'|\hat{\mathbf{d}}|\epsilon, v\rangle = \hat{\mathbf{d}}_0\delta_{v,v'} + \frac{d\hat{\mathbf{d}}_0}{dx}\langle v'|\hat{x}|v\rangle + \frac{d^2\hat{\mathbf{d}}_0}{dx^2}\langle v'|\hat{x}^2|v\rangle + .. \ . \tag{12.51}$$

The first term disappears, that is, transitions can only occur, when the dipole moment varies with the distance. Therefore, *homonuclear dimers do not undergo vibrational transitions.*

For heteronuclear molecules with electronic charges that do not depend on the interatomic distance, the dipole moment varies linearly with small displacements. In this case, we only need the second term of the expansion. Within the harmonic

approximation, the position operator can be expressed by, $\hat{x} \propto \hat{a} + \hat{a}^\dagger$. Therefore, only transitions $\Delta v = \pm 1$ are possible. However, due to anharmonicities, higher order terms, $\hat{x}^n \propto (\hat{a} + \hat{a}^\dagger)^n$ become influential, and transitions with $\Delta v = \pm 2, \pm 3, ..$ become possible.

Thus, in anharmonic potentials, the vibrational selection rules are replaced by the concept the overlapping wavefunctions called *Franck-Condon factor*.

Raman spectroscopy is a very useful tool to analyze ro-vibrational spectra. In this method, inelastic Raman scattering gives rise to Stokes and anti-Stokes lines in the spectrum at frequencies corresponding to $\Delta v = \pm 1, \pm 2$. The ground state spectrum is asymmetric, because of the absence of the lower state. In homonuclear dimers, the nuclear spins have a major impact on the Raman spectra. Parity considerations show that there can only be odd or even lines.

12.2.3 The Franck-Condon principle

The intensity of molecular transitions are, qualitatively, described by the *Franck-Condon principle*, whose *classical* formulation goes as follows:

> *The jump of an electron in a molecular transition occurs during a very small time compared to the time scale of the nuclear motion, so that immediately after the jump, the nuclei remain practically at the same positions and at the same velocities as before the jump* [390].

For this reason, the transitions are drawn vertically in the scheme of potentials shown in Fig. 12.11(right). To yield considerable rates, transitions must occur when the nuclear velocities in the two coupled states are similar, which is the case at the classical turning points. At these points, the wavefunctions are maximal [6].

With this Franck-Condon principle, we can determine which are the strongest transitions between vibrational levels of a molecule, as represented in Fig. 12.11(left). In particular, we are interested in transitions between vibrational levels of different electronic states.

The exact transition probabilities are calculated via the square module of the *transition dipole moment* (TDM). The TDM is an out-of-diagonal matrix element of the electric dipole operator $\mathbf{M}$, given by:

$$\mathbf{M}_{AB} = \langle \Psi^{(A)} | \hat{\mathbf{M}} | \Psi^{(B)} \rangle \ , \tag{12.52}$$

being $|\Psi^{(A)}\rangle$ and $|\Psi^{(B)}\rangle$ two molecular states.

Still within the Born-Oppenheimer approximation, we can split the dipole moment operator into two terms, a nuclear and an electronic term, according to:

$$\hat{\mathbf{M}}(\mathbf{r}, \mathbf{R}) = \hat{\mathbf{M}}_e(\mathbf{r}, \mathbf{R}) + \hat{\mathbf{M}}_n(\mathbf{R}) \ . \tag{12.53}$$

Thus, the TDM is:

$$\begin{aligned} \mathbf{M}_{AB} &= \int \Psi^{(A)*} \hat{\mathbf{M}} \Psi^{(B)} dR dr \qquad (12.54) \\ &= \int \hat{\mathbf{M}}_e \psi_e^{(A)*} \ \psi_e^{(B)} \ \psi_n^{(A)*} \ \psi_n^{(B)} dR dr + \int \hat{\mathbf{M}}_n \psi_n^{(A)*} \ \psi_n^{(B)} \int \psi_e^{(A)*} \ \psi_e^{(B)} dr dR \ . \end{aligned}$$

[6] Note that the presence of a hyperfine structure can modify the selection rules.

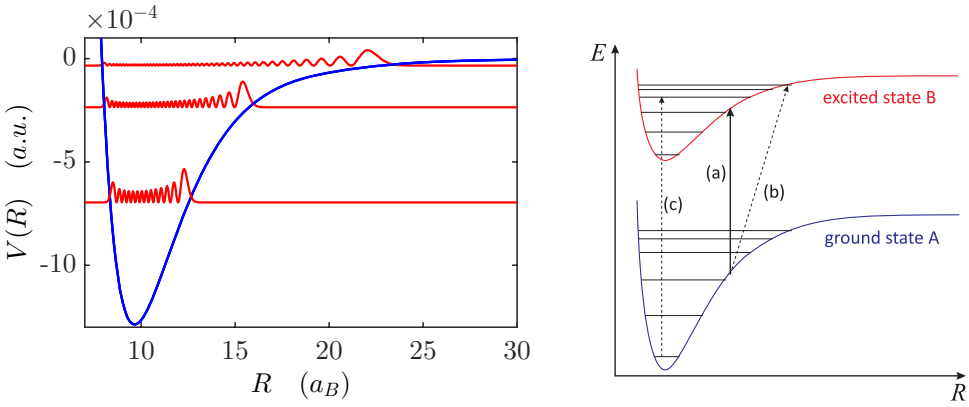

Figure 12.11: (Left, code) Molecular wavefunctions in a potential for three different vibrational states. (Right) Pictorial representation of the classical statement of the Franck-Condon principle. Transition (a) has high intensity (or probability), because here both, the position and the relative velocity of the nuclei do not change. Transitions (b) and (c) are unlikely, because they necessitate either a change in the position of the nuclei (case b) or in velocity (case c).

Since the electronic wavefunctions of different states are orthogonal, it follows that $\int \psi_e^{(A)*}\psi_e^{(B)}dr = 0$, canceling the second term.

Looking at the first term, we note that the electronic dipole moment $\hat{\mathbf{M}}_e(\mathbf{r},\mathbf{R})$ also depends on the nuclear coordinates as a parameter. The quantum formulation of the Franck-Condon principle consists in stating that, in a *molecular state, the electronic dipole moment varies little with the nuclear coordinates.* Thus, along with the condition of the Born-Oppenheimer approximation, we can split the first TDM term into electronic and nuclear integrals:

$$\mathbf{M}_{AB} = \int \hat{\mathbf{M}}_e \psi_e^{(A)*}\ \psi_e^{(B)}\ dr\ \int \psi_n^{(A)*}\ \psi_n^{(B)} dR\ . \tag{12.55}$$

Thus, we have a comparative expression for the transition probability given by:

$$P_{AB} \propto |\mathbf{M}_{AB}|^2 = \left|\int \hat{\mathbf{M}}_e \psi_e^{(A)*}\ \psi_e^{(B)}\ dr\right|^2 \left|\int \psi_n^{(A)*}\ \psi_n^{(B)} dR\right|^2 . \tag{12.56}$$

The second factor in equation (12.56) is called *Franck-Condon factor*. When we study the transitions between two electronic states, this factor compares the intensities of the transitions between distinct pairs of vibrational levels.

Example 70 (*Ultracold molecules*): Ultracold molecules have been proposed for a variety of applications, such as ultra high resolution spectroscopy [564], test of fundamental laws of physics [217, 736], quantum computation [216] and others[141]. Most of these applications, however, require that the molecular sample be in a single quantum state. This is an experimental challenge, since molecules have more degrees of freedom than atoms, such as rotation and vibration.

To create a sample of molecules trapped in the ground state of vibration, a possible method is to first produce the molecules from ultracold atoms using a process called *photoassociation*, and then pump these molecules to the vibrational ground state.

Photoassociation consists in the excitation of a pair of free atoms to the bound state of an excited electronic potential by the absorption of a photon. The pair then decays by spontaneous emission either back to the state of two free atoms (which is not desirable), or to a bound state of the fundamental electronic potential. For Rb_2 molecules, photoassociation is efficient at certain frequencies [569], with the $A^1\Sigma_u^+$ potential as the excited state (see Fig. 12.12).

Soon after being formed, the molecules are usually in levels of high vibrational energy (around $\nu \approx 80$), because these levels connect best (high Franck-Condon overlap) to the excited state. The transfer of population to the fundamental state of vibration is done by 'optical pumping'.

Vibrational cooling via optical pumping can be done by irradiating a broad frequency band of light that excites transitions to vibrational levels of the excited nuclear potential. These excited states are chosen such that their Franck-Condon overlap with the ground states of lower vibrational energy is larger. As a consequence, a molecule sent to an excited state returns with higher probability to a level of lower vibrational energy. The absorption and emission cycles are repeated, until the molecules reach the fundamental vibrational state.

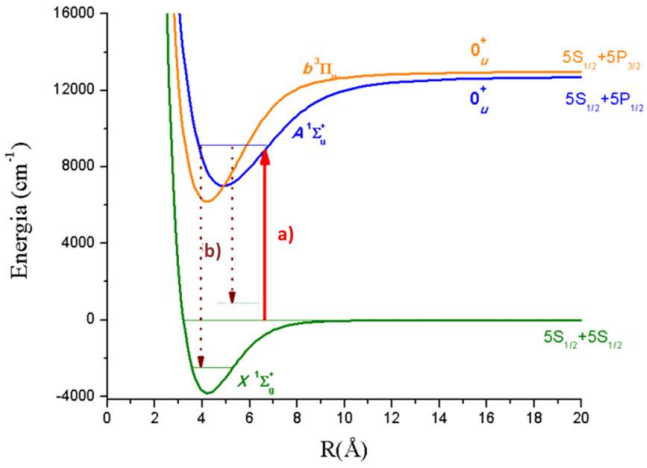

Figure 12.12: Photoassociation scheme to form Rb_2 molecules. In process (a), a pair of free atoms absorbs a photon of the incident radiation, forming a bound state in the excited potential. Then, in (b), the newly formed molecule decays by spontaneous emission to a bound state of the fundamental potential, or it can return to a state of two free atoms.

12.2.4 Rotational progression

Until now we neglected the centrifugal energy (12.38),

$$V_\ell(R) = \frac{\mathbf{L}^2}{2M_r R^2} = \frac{\hbar^2 \ell(\ell+1)}{2M_r R^2} \ . \tag{12.57}$$

As we shall now see, this energy creates a substructure of the vibrational levels.

The moments of inertia in the three axes of space are,

$$I_{qq} = \sum_i m_i r_i^2(q) \ . \tag{12.58}$$

The kinetic energy of the rotation is,

$$E_{\rm rot} = \tfrac{1}{2} \sum_{q=1,2,3} m_q \mathbf{v}_q^2 = \tfrac{1}{2} \sum_{q=1,2,3} I_{qq}\omega_q^2 = \frac{L_x^2}{2I_{xx}} + \frac{L_y^2}{2I_{yy}} + \frac{L_z^2}{2I_{zz}} \ , \tag{12.59}$$

with the angular momentum $L_q = I_{qq}\omega_q$.

Many molecules have a symmetry axis, such that there are two different moments of inertia, $I_\perp \equiv I_{xx} = I_{yy}$ and $I_\parallel \equiv I_{zz}$. Interpreting angular momenta as quantum operators,

$$\hat{H} = \frac{\hat{\mathbf{L}}^2}{2I_\perp} + \left(\frac{1}{2I_\parallel} - \frac{1}{2I_\perp}\right) \hat{L}_z^2 \ . \tag{12.60}$$

We must first consider the rotation of the molecule relative to the symmetry axis of the molecule. Forgetting external fields we calculate the energy of the molecule associated with the observables $\hat{\mathbf{L}}^2$ with the quantum number ℓ and $\hat{\mathbf{L}}_z$ with the quantum number K. We find the eigenvalues,

$$E(\ell, K, M_\ell) = \frac{\hbar^2 \ell(\ell+1)}{2I_\perp} + \left(\frac{1}{2I_\parallel} - \frac{1}{2I_\perp}\right) \hbar^2 K^2 = B\ell(\ell+1) + (A-B)K^2 \ , \tag{12.61}$$

with $\ell = 0, 1, .., \ K = -\ell, .., \ell$, and $M_\ell = -\ell, .., \ell$ and introducing the *rotational constants*, $A \equiv \hbar^2/2I_\parallel$ and $B \equiv \hbar^2/2I_\perp$. We then analyze this equation in the context of applying an external field that defines both, the direction $\hat{\mathbf{e}}'_z$ in the laboratory as well as the projection of the angular motion $\hat{\mathbf{L}}^2$ on this direction, m_ℓ. That is, we have two axes, the internuclear axis $\hat{\mathbf{e}}_z$ and the rotation axis of the molecule $\hat{\mathbf{e}}'_z$.

Each level $|\ell, m_\ell\rangle$ is $2(2\ell+1)$ times degenerate, because $K = -\ell, .., \ell$ and K can be positive or negative. Each level ℓ contains $2\ell+1$ states. Note that for spherical molecules, $A = B$, and the degree of freedom K disappears. In Exc. 12.2.6.2 we calculate the rotational spectrum of a homonuclear diatomic molecule.

The rotational constant can be approximated by,

$$E_{\rm rot} = \frac{\hbar^2 \ell(\ell+1)}{2M_r \langle R^2 \rangle} \ , \tag{12.62}$$

where $\sqrt{\langle R^2 \rangle}$ is the expectation value for the outer turning point of the vibrational level. As an example, the rotational constant for the vibrational state of $^{87}Rb_2$ which is 5.9 cm^{-1} below the dissociation limit is $B_v = \nu_{\rm rot}^{\ell=1} - \nu_{\rm rot}^{\ell=0} = 81$ MHz. To be more precise, we would need to calculate $\langle R^2 \rangle_v = \langle \psi_v | R^2 | \psi_v \rangle$.

Transitions between vibrational levels occur together with rotational transitions $\Delta\ell = \pm 1$. Therefore, the frequencies of transitions depend on the rotational constant B_v, which depends on the vibrational state. The energies of the molecule are,

$$E_{v,\ell} = \hbar\omega(v+1/2) - \hbar\omega x_e(v+1/2)^2 + .. + hcB_v\ell(\ell+1) - hcD_v\ell^2(\ell+1)^2 + .. \ . \quad (12.63)$$

Under the influence of a rapid rotation, the atoms of the molecule are subjected to centrifugal force and, hence, are further away from each other [7].

Since at ambient temperatures many rotational levels are populated, we experimentally observe many lines known as P-branch, when $\Delta\ell = -1$, as Q-branch, when $\Delta\ell = 0$, and as R-branch, when $\Delta\ell = 1$. See Exc. 12.2.6.3.

12.2.4.1 Rotational selection rules

For transitions between electronic states, the selection rules are $\Delta r = 0, \pm 1$. Rotational transitions can occur between levels $\Delta r = \pm 1$. $\Delta r = 0$ is not allowed, because it violates the conservation of parity. Note also that the nuclear isotope influences the ro-vibrational levels via the reduced mass.

We consider a linear molecule in the state $|\epsilon, \ell, M_\ell\rangle$, where ϵ denotes the electronic and vibrational state of the molecule. To find out which transitions are possible, we need to calculate the matrix,

$$\langle \epsilon', \ell', M'_\ell | \mathbf{d} | \epsilon, \ell, M_\ell \rangle = \langle \ell', M'_\ell | \mathbf{d}_\epsilon | \ell, M_\ell \rangle \ , \quad (12.64)$$

with $\mathbf{d}_\epsilon = \langle \epsilon | \mathbf{d} | \epsilon \rangle$. Here, we apply the *Born-Oppenheimer approximation*, which allows us to separate the dynamics of the electrons and also the vibrations of the molecule, because these movements are so fast, that they are always in a steady state, adiabatically following the slow movement of the rotation.

The selection rules can now be derived from the *Wigner-Eckart theorem*,

$$\frac{\langle \ell', M'_\ell | \mathbf{d}_\epsilon | \ell, M_\ell \rangle|^2}{|\langle \ell' \parallel \mathbf{d}_\epsilon \parallel \ell, M_\ell \rangle|^2} = \frac{1}{2\ell'+1} \begin{pmatrix} \ell & 1 & \ell' \\ m_\ell & \kappa & -m'_\ell \end{pmatrix} \ . \quad (12.65)$$

We find $\Delta\ell = 1$ e $\Delta M_\ell = 0, \pm 1$. See Exc. 12.2.6.4.

12.2.5 Computation of vibrational states

12.2.5.1 Estimation of the localization energy

One consequence of Heisenberg's uncertainty relation is that a certain *localization energy* is always required to localize a particle. The zero-point energy of the harmonic oscillator is an example: If the potential is shallower than this energy, it will not be capable of localizing a particle.

As another example, let us consider the attractive potential,

$$V = -\frac{C_n}{R^n} \ . \quad (12.66)$$

[7] See [35], p.326

The space available for the particle is limited between the classical turning point, which for a given energy is $R_t = (C_n/|E|)^{1/n}$. The momentum corresponding to this energy is $k_t = (2m_{\rm red}|E|/\hbar^2)^{1/2}$. Heisenberg's uncertainty relation requires,

$$k_t R_t > \pi \ , \tag{12.67}$$

that is, at least half of the wavelength must fit within the potential (between 0 and R_t) at the height of the bound state. Therefore,

$$\boxed{|E| > E_{\rm loc} \equiv \left(\frac{\pi\hbar^2}{2m_{\rm red}}\right)^{1/(1-2/n)} C_n^{1/(1-n/2)}} \ . \tag{12.68}$$

For a Coulomb potential, with $n = 1$ and $C_1 = e^2/4\pi\varepsilon_0$, we obtain the energy of the ground state of the hydrogen atom,

$$E > E_1 = -\frac{e^2}{4\pi\varepsilon_0 2a_B}\frac{4}{\pi^2} \ , \tag{12.69}$$

apart from a numerical factor. Note that the condition $k_t R_t > 2n$ yields the correct Bohr energies, $E = E_1/m^2$.

For $n = 2$, we do not get a condition for the energy. For the Casimir-Polder potential, $n = 3$ and $C_3 = 3\hbar\Gamma/2k^3$, we obtain,

$$E < -\frac{\pi^6\hbar^6}{8m_{\rm red}^3 C_3^2} = \frac{(\pi\hbar k)^6}{2m_{\rm red}^3(3\hbar\Gamma)^2} \ . \tag{12.70}$$

This means that for $n \geq 3$, in contrast to the Coulomb potential, to minimize the momentum-position uncertainty, the *binding energy* must be *lower* than a certain limit.

We find that for a Coulomb potential the state with the smallest momentum-position uncertainty is the ground state. No other state can have a lower energy, but there is an infinite number of states just below the threshold. In contrast, for a $1/R^3$ potential the state with the smallest momentum-position uncertainty is the least bound state. No other state can have a higher energy, but there is an infinite number of states at the bottom of the potential. In other words, $1/R$ *potentials do not have a lid and* $1/R^3$ *potentials do not have a bottom.*

12.2.5.2 The LeRoy-Bernstein method

The *LeRoy-Bernstein method* allows us to estimate the highest bound levels. It only applies near the dissociation limit, where the semi-classical formula of quantization is valid,

$$v + \tfrac{1}{2} = \sqrt{\frac{8m_{\rm red}}{\hbar^2}} \int_0^{R_t} dR\sqrt{E(v) - V(R)} \ . \tag{12.71}$$

Inserting the potential

$$V(R) = D_e - \frac{C_n}{R^n} \ , \tag{12.72}$$

we get

$$\boxed{E(v^*) = D_e - E_{\rm loc}\left(\frac{(n-2)\Gamma\left(1+\frac{1}{n}\right)}{\sqrt{\pi}\,\Gamma\left(\frac{1}{2}+\frac{1}{n}\right)}\,v^*\right)^{2n/(n-2)}}\,, \tag{12.73}$$

where $v^* = v_D - v$ is a number counting the vibrational levels from the top to the bottom starting at the dissociation limit and $E_{\rm loc}$ is the localization energy calculated in (12.68).

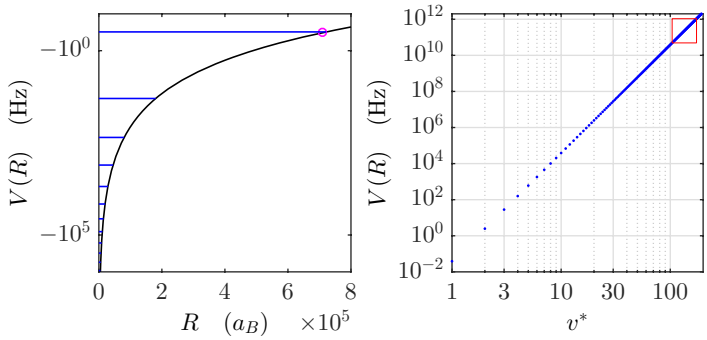

Figure 12.13: (code) (a) Highest vibrational states of the $(2)\Sigma_u^+$ potential of Yb_2 dimers obtained by the LeRoy-Bernstein method. The magenta circle corresponds to the localization energy calculated in (12.74). (b) Energies of the highest vibrational states as a function of the vibrational quantum number v^*. The states inside the red box have been measured [809].

Again, for the Casimir-Polder potential we get [809],

$$E(v^*) = D_e - X_0(v_D - v)^6 \qquad \text{with} \qquad X_0 = \frac{h^6}{m_{\rm red}^3 C_3^2}\left(\frac{\Gamma(4/3)}{2\sqrt{2\pi}\Gamma(5/6)}\right)^6 . \tag{12.74}$$

Do the Exc. 12.2.6.5.

12.2.5.3 Open channels

For a given interatomic potential $V(R)$, neglecting the spin structure [445], the relative wavefunction of a two-atom system satisfies the Schrödinger equation,

$$\left[-\tfrac{1}{2\mu}\Delta + V(R)\right]\psi(\mathbf{R}) = E\psi(\mathbf{R})\ . \tag{12.75}$$

Separating the radial and angular contributions, $\psi(\mathbf{R}) \equiv Y(\vartheta,\varphi)f(R)/R$, we obtain,

$$\left[-\frac{1}{2\mu}\frac{\partial^2}{\partial R^2} + V(R) + \frac{l(l+1)}{2\mu R^2}\right] f(R) = E f(R)\ . \tag{12.76}$$

Now, we introduce the local wavevector, $k(R) = \sqrt{2\mu[E - V(R)] - l(l+1)/R^2}$ and write,

$$f'' = -k^2 f\ . \tag{12.77}$$

This differential equation can be solved numerically [see Fig. 12.14(a)].

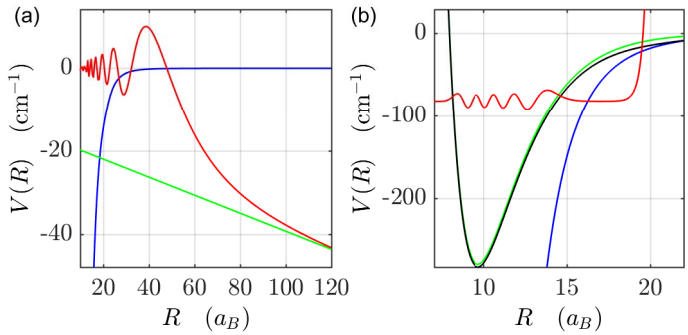

Figure 12.14: (code) (a) Numerical computation of the relative wavefunction for a low energy collision, $E \gtrsim 0$ and $\ell = 0$. The blue curve shows the interatomic Li-Rb potential (a)$^3\Sigma$, the red curve illustrates the relative Broglie wavefunction of the molecule. The asymptote of this extrapolated wavefunction (green curve) cuts the abscissa at $a_s = -120a_B$, which is just the scattering length for collisions in this channel. (b) Numerical computation of the wavefunction for a vibrational state. The potential is an interpolation (black) between a short-range Morse potential (green), and a long range potential (blue). The red curve illustrates the relative wavefunction for the ninth vibrational state (counting from ground state).

12.2.5.4 Milne equation

The Schrödinger equation,

$$\left[\frac{d^2}{dR^2} + k(R)^2\right]\Psi(R) = 0 \qquad \text{with} \qquad k(R) = \sqrt{\tfrac{2m_{\rm red}}{\hbar^2}(E-V)} \tag{12.78}$$

can be transformed using the following ansatz,

$$\Psi(R) \equiv \sqrt{\frac{2m_{\rm red}}{\pi\hbar^2}}\alpha(R)\sin\beta(R)\ . \tag{12.79}$$

Insertion yields,

$$\left(\alpha'' + k^2\alpha - \alpha\beta'^2\right)\sin\beta + (2\alpha'\beta' + \alpha\beta'')\cos\beta = 0\ . \tag{12.80}$$

Setting the oscillatory terms separately to zero, we obtain,

$$\frac{\beta''}{\beta'} = -\frac{2\alpha'}{\alpha} \qquad \text{and} \qquad \alpha'' + k^2\alpha - \alpha\beta'^2 = 0\ . \tag{12.81}$$

The first differential equation is solved by,

$$\beta' = \frac{1}{\alpha^2} \qquad \text{that is} \qquad \beta(R) = \int \frac{dR}{\alpha(R)^2}\ . \tag{12.82}$$

Insertion into the second one yields the so-called *Milne equation* ,

$$\alpha'' + k^2\alpha - \frac{1}{\alpha^3} = 0\ . \tag{12.83}$$

Example 71 (*Milne equation for van der Waals potentials*): Here, we analyze the solution of the Milne equation for a C_6-potential at very long range, $R \to \infty$, and vanishing temperature, $E \to 0$. Semi-classically, the amplitude $\alpha_{WKB}(R) \simeq 1/\sqrt{k(R)}$ diverges asymptotically, so that,

$$\left(\frac{d^2}{dR^2} - \frac{2m_{\rm red}C_6}{\hbar^2 R^6}\right)\alpha \simeq 0$$

with the solution for $R \gg R_B$,

$$\alpha(R) = \alpha_\infty\left(1 - (R/R_B)^4\right) \qquad \text{with} \qquad R_B \equiv \left(\frac{2m_{\rm red}C_6}{20\hbar^2}\right)^{1/4} .$$

Substituting this into the phase equation,

$$\begin{aligned}\beta(R) &= k_\infty(R_\infty - a_s) + \int_{R_\infty}^{R}\frac{dR}{\alpha(R)^2} \\ &\simeq k_\infty(R_\infty - a_s) - \tfrac{1}{\alpha_\infty^2}\int_R^{R_\infty}\left(1 + 2\left(\tfrac{R}{R_B}\right)^4\right)^2 dR = k_\infty\left(R - a_s - \frac{2}{3}\left(\tfrac{R_B}{R}\right)^4 R\right)\end{aligned}$$

with $\beta_\infty = k_\infty(R_\infty - a_s)$ and a_s is the s-wave scattering length.

12.2.5.5 Bound states

For bound states, we must simultaneously satisfy the eigenvalue problem. We can, for example, guess an eigenvalue E, calculate the associated wavefunction $f(R)$, check whether it diverges for $R \to \infty$, and vary E until $f(R)$ no longer diverges. Fig. 12.14(b) shows the wavefunction of a vibrational state obtained by solving the Schrödinger equation and adjusting the energy until the function stops diverging in the classically forbidden range.

12.2.5.6 The Fourier grid method

Another, extremely rapid, numerical method for determining the spectrum of vibrational states of a potential, is the *Fourier grid method*. It is based on the discretization of the Hamiltonian along the interatomic potential. We write the Hamiltonian as,

$$H\psi(R) = [T(R) + V(R)]\psi(R) = E\psi(R) \ , \tag{12.84}$$

and put it in a matrix form using the set of functions of the basis $\phi_i(R_j) = \delta(R_i - R_j)$ with $i = 1, .., N$, where $R_i = R_0 + i(R_N - R_0)/N$. This problem has N eigenvalues E_i. The Fourier grid method now evaluates the kinetic energy at each point in the grid. We insert the local terms $H_{ii} = H(R_i)$ and the non-local terms $H_{ij} = H(R_i, R_j)$ into the Hamiltonian, as well as the potential energies $V_{ij} = V(R_i)\delta_{ij}$. The kinetic energy is the inverse Fourier transform from momentum space of $T_{rs} = T(k_r)\delta_{rs} = (k_r^2/2\mu)\delta_{rs}$ and becomes [575, 550, 250],

$$H_{ij} = \frac{\pi^2}{4\mu(R_N - R_1)^2}(-1)^{i-j}\left(\frac{1}{\sin^2\frac{\pi(i-j)}{2N}} - \frac{1}{\sin^2\frac{\pi(i+j)}{2N}}\right) \qquad \text{for} \qquad i \neq j \tag{12.85}$$

$$H_{ij} = \frac{\pi^2}{4\mu(R_N - R_1)^2}\left(\frac{2N^2+1}{3} - \frac{1}{\sin^2\frac{\pi i}{2N}}\right) + V(R_i) \qquad \text{for} \qquad i = j \ .$$

To improve the wavefunction, we can interpolate,

$$\psi(q) = \sum\nolimits_{j=1}^{n} \psi(q_j)\ \mathrm{sinc}\frac{\pi(q-q_j)}{\Delta q}\ . \tag{12.86}$$

The method can be extended to coupled channels $\sigma = A, B$ via,

$$H_{\{i\sigma\}\{j\tau\}} = T_{ij}\delta_{\sigma\tau} + V_{\sigma\tau}(R_i)\delta_{ij}\ . \tag{12.87}$$

The Hamiltonian has the general form,

$$H = \begin{pmatrix} T & 0 \\ 0 & T \end{pmatrix} + \begin{pmatrix} V_A & 0 \\ 0 & V_B \end{pmatrix} + \begin{pmatrix} W_{AA} & W_{AB} \\ W_{AB} & W_{BB} \end{pmatrix}\ , \tag{12.88}$$

where all matrices V_k and W_k are diagonal [8].

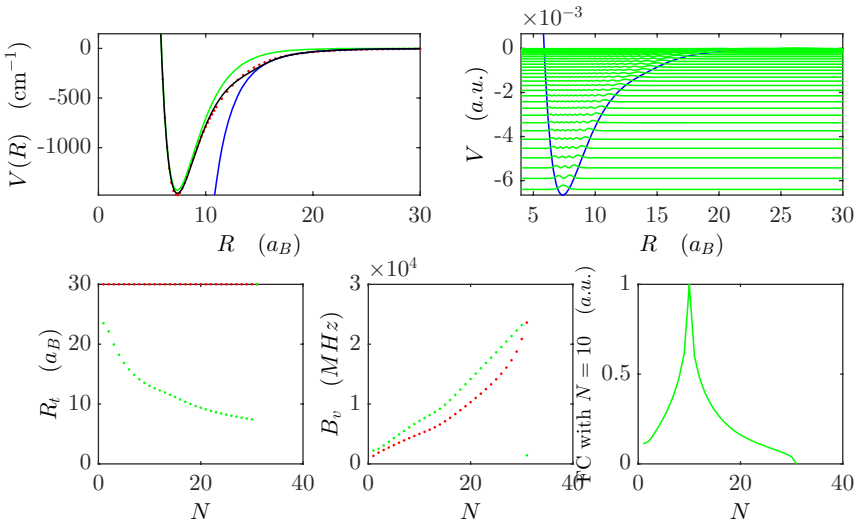

Figure 12.15: (code) Numerical computation of the wavefunction using the Fourier grid method at example of the interatomic potential Li-Rb (1)$^1\Pi$. (a) Short range Morse potential (green), long range (blue), interpolation (black) and [480]. (b) Vibrational wavefunctions, (c) external turning point (red) and center of mass (green), (d) rotational progression, and (e) Franck-Condon overlap with the tenth vibrational state.

12.2.6 Exercises

12.2.6.1 Ex: Transitions between vibrational states

Calculate the dipole moment between two arbitrary vibrational states of (a) a harmonic potential and (b) a Morse potential.

[8] Note that the Fourier grid method can be improved by using a grid with spacings adjusted to the potential gradient [477, 820, 521].

12.2.6.2 Ex: Rotational spectrum of diatomic molecules

Calculate the rotational spectrum for a diatomic molecule from the result (12.59).

12.2.6.3 Ex: Ro-vibrational spectrum

Determine the frequency spectra of ro-vibrational transitions for the branches P, Q, and R.

12.2.6.4 Ex: Rotational spectrum

Determine the rules and the spectrum of rotational transitions for a spherical molecule.

12.2.6.5 Ex: Momentum-position uncertainty for various potentials

a. Calculate the momentum-position uncertainty in Fock states of a 1D harmonic oscillator.
b. Calculate the radial momentum-position uncertainty of the Bohr levels ($\ell = 0$) in a hydrogen atom.
c. Calculate the radial momentum-position uncertainty of the vibrational states of two bound atoms numerically.
d. Interpret the results.

12.3 Van der Waals forces and spin coupling

The individual atoms have a complex substructure due to the angular momenta of the electronic motion, its spins and the nuclear spin. All of these angular momenta can interact, couple and generate new energy terms, which need to be taken into account when calculating the various potentials of interatomic interaction,

$$\hat{H} = \frac{\mathbf{P}^2}{2M_r} + V_{\text{Coulomb}}(R) + \sum_{k=1,2} \left(V_{\text{hfs}}^{(k)} + V_{\text{Zeem}}^{(k)} \right) + V_{\text{dipole,spin:spin}}(R) + V_{\text{dipole,spin:orbit}}(R) \,, \tag{12.89}$$

where k labels the two atoms. The Coulomb interaction for interacting alkaline gases can be expressed as:

$$V_{\text{Coulomb}}(R) = V_{\text{Coulomb}}^{S=0} \mathcal{P}_{S=0} + V_{\text{Coulomb}}^{S=1} \mathcal{P}_{S=1} \,. \tag{12.90}$$

The projectors $\mathcal{P}_{S=0,1}$ will be required to expand the Hilbert space for the degrees of freedom of the spins.

The *van der Waals forces* include all intermolecular forces. These are long-range forces that occur between mutually induced atomic dipoles [9].

[9] They also occur, in a pure form, in optical resonators such as in the *Casimir effect*. Since the lowest frequency in a cavity is $\omega = \sqrt{2}\pi c/L$, the zero point energies inside and outside the cavity are different. This causes an attractive force between the cavity mirrors $\sim 1/r^3, 1/r^4$.

12.3.1 Analytical models for short and long-range potentials

In general, the potentials are estimated by ab initio Hartree-Fock calculations. A short-range potential, or *Morse potential*, can be approximated by,

$$\boxed{V_{\text{Morse}} = D_m \left(\left[1 - e^{-B_m (R - R_m)} \right]^2 - 1 \right)} \, . \tag{12.91}$$

Here, B_m is the width of the minimum, R_m the position of the minimum, D_m the length. A long-range potential can be written,

$$\boxed{V_{\text{vdW}}(R) = D_e - \frac{C_6}{R^6} - \frac{C_8}{R^8} - \frac{C_{10}}{R^{10}}} \, . \tag{12.92}$$

D_e is the energy of dissociation. The *van der Waals coefficients* C_k, which determine the potential shape at large distances, can be calculated using other methods with higher precision. To obtain a closed formula, the short and long range parts can be joined by,

$$V = V_{\text{Morse}} F + V_{\text{vdW}} (1 - F) \, , \tag{12.93}$$

where $F \equiv e^{-(R/R_t)^{10}}$.

The situation is different for collisions of identical atoms, one in the ground and the other in an excited state. In this case, an additional *Movre-Pichler potential* dominated by a coefficient C_3 arises,

$$\boxed{V^e_{\text{vdW}} = -\frac{C_3}{R^3}} \, . \tag{12.94}$$

The interaction is interpreted as an exchange of excitation between resonances of two neighboring atoms and can be derive from the vectorial Green tensor for the interaction between two classical dipoles [10]. In the limit of small distances as compare to an optical wavelength, $kR \ll 1$, we find,

$$V^e_{\text{vdW}}(R) = -\frac{3}{2} \lambda \Gamma^{(0)} \hat{\mathbf{e}}^*_d \mathfrak{Re}\, \mathcal{G}_b(\mathbf{r}, \mathbf{r}', \omega) \hat{\mathbf{e}}_d = -\frac{3}{2} \lambda \Gamma^{(0)} \frac{2}{k^3 R^3} \frac{k}{4\pi} \equiv \frac{C_3}{R^3} \, . \tag{12.95}$$

Hence, the potential depends mainly on the decay rate Γ,

$$C_3 = \frac{3\hbar\Gamma}{2k^3} \, , \tag{12.96}$$

and as it comes into play at larger distances, orbital characteristics will only cause minor deviations of the C_3 coefficient from the value (12.96).

In contrast, excited state collisions of different species are non-resonant, and hence $C_3 = 0$.

[10] See script on *Electrodynamics: Electricity, Magnetism and Radiation* (2025), Sec. 7.3.1.3.

12.3.2 Spin coupling in dimers, molecular quantum numbers

We consider two interacting alkaline atoms, each being described by a set of quantum numbers of internal angular momenta, they couple their spins:

$$\begin{aligned}
\mathbf{l}_i & \quad \text{angular momentum of the individual atom} \\
\mathbf{s}_i & \quad \text{electronic spin} \\
\mathbf{i}_i & \quad \text{nuclear spin} \\
\mathbf{l}_i + \mathbf{s}_i = \mathbf{j}_i & \quad \text{total electronic angular momentum} \\
\mathbf{j}_i + \mathbf{i}_i = \mathbf{f}_i & \quad \text{total angular momentum .}
\end{aligned} \tag{12.97}$$

When the atoms approach each other, at intermediate distances, they couple their spins:

$$\begin{aligned}
\ell \perp \hat{\mathbf{e}}_z & \quad \text{molecular rotation} \\
\mathbf{\Lambda} \equiv |M_L| \hat{\mathbf{e}}_z & \quad \text{projection of } \mathbf{L} \text{ onto the interatomic } \hat{\mathbf{e}}_z \\
\mathbf{\Sigma} \equiv M_S \hat{\mathbf{e}}_z & \quad \text{projection of } \mathbf{S} \text{ onto the interatomic } \hat{\mathbf{e}}_z \\
\mathbf{\Omega} \equiv \mathbf{\Lambda} + \mathbf{\Sigma} & \quad \text{projection of } \mathbf{L} + \mathbf{S} \text{ onto the interatomic } \hat{\mathbf{e}}_z \ .
\end{aligned} \tag{12.98}$$

At short distances, they form a molecular dimer described by the quantum numbers:

$$\begin{aligned}
\mathbf{L} = \mathbf{l}_1 + \mathbf{l}_2 & \quad \text{total electronic angular momentum} \\
\mathbf{S} = \mathbf{s}_1 + \mathbf{s}_2 & \quad \text{electronic spin} \\
\mathbf{I} = \mathbf{i}_1 + \mathbf{i}_2 & \quad \text{nuclear spin} \\
\mathbf{f} = \mathbf{f}_1 + \mathbf{f}_2 & \quad \text{total angular momentum or } (\mathbf{L}, \mathbf{S})\mathbf{k} + \mathbf{I} \\
\mathbf{J} = \mathbf{\Omega} + \ell & \\
\mathbf{F} = \mathbf{f} + \ell & \quad .
\end{aligned} \tag{12.99}$$

The quantum numbers couple like,

$$\begin{array}{ccccccccccccc}
\mathbf{l}_1 & + & \mathbf{l}_2 & = & \mathbf{L} & \xrightarrow{\hat{\mathbf{e}}_z} & \mathbf{\Lambda} & & & & & & \\
+ & & + & & + & & + & & & & & & \\
\mathbf{s}_1 & + & \mathbf{s}_2 & = & \mathbf{S} & \xrightarrow{\hat{\mathbf{e}}_z} & \mathbf{\Sigma} & & & & & & \\
= & & = & & = & & = & & & & & & \\
\mathbf{j}_1 & + & \mathbf{j}_2 & = & \mathbf{j} & \xrightarrow{\hat{\mathbf{e}}_z} & \mathbf{\Omega} & + & \ell & = & \mathbf{J} & & \\
+ & & + & & + & & & & & & + & & \\
\mathbf{i}_1 & + & \mathbf{i}_2 & = & \mathbf{I} & & & & & & \mathbf{I} & & \\
= & & = & & = & & & & & & = & & \\
\mathbf{f}_1 & + & \mathbf{f}_2 & = & \mathbf{f} & & & + & \ell & = & \mathbf{F} & &
\end{array} \tag{12.100}$$

Obviously, the atomic angular momentum is no longer a conserved quantity, but its projection onto the interatomic molecular axis is. The various possibilities how $\mathbf{L}$, $\mathbf{S}$, and $\mathbf{j}$ are projected onto the internuclear axis or directly couple to the rotational angular momentum ℓ are handled by Hund's cases (a) to (e). The spin coupling is described by $\{9j\}$-symbols, as discussed below.

12.3.3 Hund's coupling cases

The coupling force between atomic spins depends on the distance between the atoms. Due to the variety of spins appearing in atoms, there are many possibilities how they can couple. These were classified by Hund into five cases.

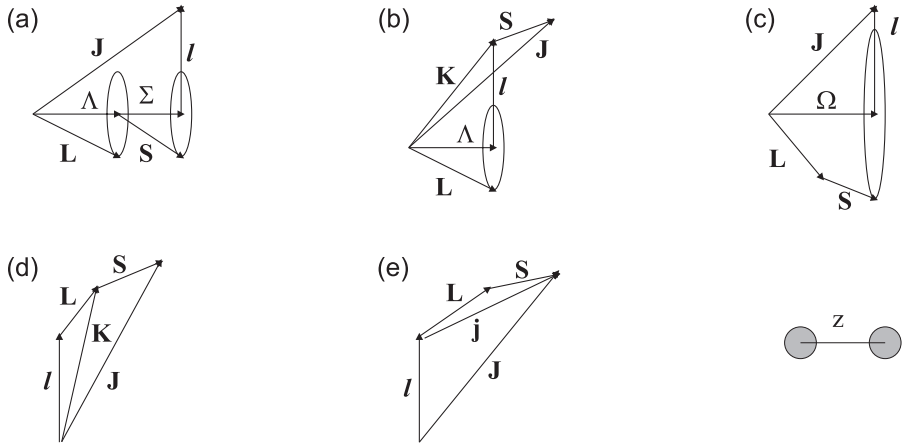

Figure 12.16: Hund's coupling cases.

12.3.3.1 Hund's case (a)

The molecular interaction is so strong that $\mathbf{L}$ and $\mathbf{S}$ couple to the z-axis instead of coupling to each other. This case is analogous to the Paschen-Back effect,

$$\begin{aligned} &\mathbf{L} \to \mathbf{\Lambda} \qquad \text{and} \qquad \mathbf{S} \to \mathbf{\Sigma} \\ &((\mathbf{\Lambda}, \mathbf{\Sigma})\mathbf{\Omega}, \ell)\mathbf{J} \ . \end{aligned} \tag{12.101}$$

A common notation is to label the states $\mathbf{\Lambda} = \mathbf{\Sigma}, \mathbf{\Pi}, \mathbf{\Delta}, ...$ That is, in the symbol $X(^{2S+1}\Lambda_\Omega)^\pm_\sigma$, where $\sigma = g, u$ is the inversion symmetry, $X, A, B, ..$ and $a, b, ..$ are the singlet and triplet series starting from the lowest energy levels. An alternative notation is to assign labels ordered by energy $X = (1), (2), ...$ Finally, $\pm$ is the symmetry upon reflection. For example, $X^1\Sigma^+_g$.

12.3.3.2 Hund's case (b)

$\mathbf{L}$ is projected onto the z-axis before coupling to ℓ. The resulting angular momentum afterward directly couples to $\mathbf{S}$.

$$\begin{aligned} &\mathbf{L} \to \mathbf{\Lambda} \\ &((\mathbf{L}, \ell)\mathbf{k}, \mathbf{S})\mathbf{J} \ . \end{aligned} \tag{12.102}$$

12.3.3.3 Hund's case (c)

L and **S** couple together instead of projecting themselves onto the z-axis. This case is analogous to the Zeeman effect,

$$\begin{aligned}(\mathbf{L},\mathbf{S})\mathbf{j} &\to \mathbf{\Omega} \\ (\mathbf{\Omega},\ell)\mathbf{J}\ .\end{aligned} \tag{12.103}$$

A common notation is to label the states by $\mathbf{\Omega} = 0, 1, 2, ...$ That is, in the symbol $X(\Omega)^{\pm}_{s}$, the letter $X = 1, 2, ..$ is a label ordered by energy. For example $2(0^{-}_{g})$.

12.3.3.4 Hund's case (d)

L is not projected on the z- axis, but directly couples to the rotational angular momentum. The resulting angular momentum afterward only couples to the **S**

$$((\mathbf{L},\ell)\mathbf{k},)\mathbf{J}\ . \tag{12.104}$$

12.3.3.5 Hund's case (e)

L and **S** mutually couple as in the case (c), but are not projected on the z-axis, but couple directly with ℓ, which is quantized,

$$((\mathbf{L},\mathbf{S})\mathbf{j},\ell)\mathbf{J}\ . \tag{12.105}$$

12.3.4 Molecular hyperfine structure

The scattering length in specific channels can be expressed via singlet and triplet scattering lengths,

$$a_{|f_1,m_{f1}\rangle+|f_2,m_{f2}\rangle} = P_{S=0}a_s + P_{S=1}a_t\ . \tag{12.106}$$

The projectors are $P_S = |\langle S|(f_1 f_2)f\rangle|$. According to [125, 577] the recoupling from the uncoupled hyperfine representation into the short range representation is given by,

$$\langle Sm_S\ Im_I\ \ell' m_{\ell'}|f_1 m_{f1}\ f_2 m_{f2}\ \ell m_\ell\rangle = \delta_{\ell\ell'}\delta_{m_\ell m'_\ell}\sum_{f,m_f}\langle Sm_S\ Im_I|fm_f\rangle\langle f_1 m_{f1}\ f_2 m_{f2}|fm_f\rangle\times$$
$$\times\begin{Bmatrix} s_1 & s_2 & S \\ i_1 & i_2 & I \\ f_1 & f_2 & f\end{Bmatrix}\sqrt{\hat{S}\hat{I}\hat{f}_1\hat{f}_2}\left(\frac{1-(1-\delta_{f_1 f_2})(-1)^{S+I+\ell}}{\sqrt{2-\delta_{f_1 f_2}}}\right)\ . \tag{12.107}$$

The last bracket is dropped for unsymmetrized recoupling. We will study examples of spin recoupling in the ground state channels in Exc. 12.3.5.1, 12.3.5.2, and 12.3.5.3.

12.3.5 Exercises

12.3.5.1 Ex: Spin recoupling of identical ^{87}Rb ground state channels

a. Unravel the molecular hyperfine structure of identical ^{87}Rb ground state channels.
b. Project the collisional channels $|f_1 m_{f1}\ f_2 m_{f2}\rangle = |1\ -1\ 1\ -1\rangle$ and $|22\ 22\rangle$ on the singlet and triplet potentials, $S = 0, 1$.

12.3.5.2 Ex: Spin recoupling of ^{6}Li^{87}Rb ground state channels

a. Unravel the molecular hyperfine structure of ^{6}Li^{87}Rb ground state channels.
b. Project the collisional channels on short range potentials.

12.3.5.3 Ex: Hyperfine structure of ^{6}Li^{23}Na and ^{6}Li^{87}Rb

a. Unravel the molecular hyperfine structure of ^{6}Li^{23}Na and ^{6}Li^{87}Rb bound state.
b. How about the open channels?

12.4 Further reading

et al., [DOI]

Chapter 13

Collisions

Until now, we mostly restricted our studies to individual atoms or molecules. In practice, however, we investigate atomic or molecular gases by spectroscopic methods. The constituents of thermal gases are constantly in motion. They are subject to Doppler-shifts of their spectral lines and they collide with each other. Colliding atoms often get so close, that the electronic orbitals affect each other, which leads to distortions of the interaction potentials, spectral lineshifts and modifications of the interatomic forces. These are the topics to be addressed in the present chapter.

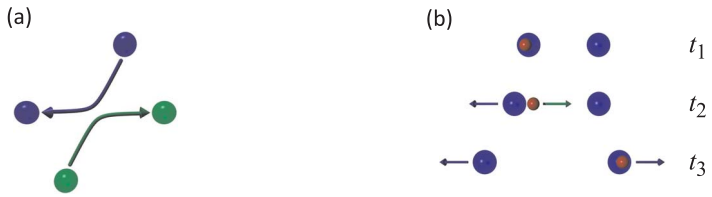

Figure 13.1: Atoms may interact via exchange of (a) virtual photons or (b) real photons.

13.1 Motion of interacting neutral atoms

The following sections, devoted to the relative motion of two neutral atoms, are adapted from J. Walraven's excellent lectures on *Quantum Gases* available at [850]. The atoms are presumed to move slowly, typically at large separation, and to interact pair wise through a potential of the Van der Waals type. The term slowly refers to,

$$k_{\rm therm} r_0 \ll 1 \qquad \text{where} \qquad \lambda_{\rm therm} = \frac{2\pi}{k_{\rm therm}} = \sqrt{\frac{2\pi\hbar^2}{m k_{\rm B} T}} \tag{13.1}$$

is the *thermal de Broglie wavelength* and r_0 the range of the interaction potential. As the Van der Waals interaction gives rise to elastic collisions, the total energy of the relative motion is conserved in time. As the potential energy vanishes at large interatomic separation the total energy is usually expressed in the form $E = \hbar^2 k^2/2m_r$. This implies that also the wavenumbers for the relative motion before and after the collision must be the same and shows that, far from the potential center, the collision can only affect the phase of the wavefunction - not its wavelength. Apparently, the appearance of a shift in phase relative to the free atomic motion

provides the key to the quantum mechanical description of elastic collisions. This being said, we postpone the discussion of the actual collisional behavior to Sec. 13.2. First we prepare ourselves for this discussion by analyzing the stationary states for the motion in the presence of an interaction potential.

An important simplifying factor in the description of ultracold collisions is the emergence of universal behavior in the relative motion of the atoms. The latter applies to low-energy collisional states as well as to weakly bound states. Universal means in this context that, asymptotically (for $r \gg r_0$), the wavefunctions become independent of the details of the interaction potential but can be characterized in terms of a few parameters, each representing some characteristic length scale of the collisional system. In other words, very different short-range physics can give rise to the same scattering behavior. From a theory point of view this universality has the enormous advantage that the essential features of ultracold collisions can be described with the aid of simple model potentials for which analytical solutions can be obtained.

In our analysis of the collisional motion three characteristic length scales will appear, the interaction range r_0 the scattering length a and the effective range r_e, each expressing a different aspect of the interaction. The range r_0 is the distance beyond which the interaction may be neglected even for $k \to 0$. The second characteristic length, the s-wave scattering length a, acts as an effective hard-sphere diameter. It is a measure for the interaction strength and determines the collision cross section in the limit $k \to 0$ as will be elaborated on in Sec. 13.2. The third characteristic length, the effective range re expresses how the potential affects the energy dependence of the cross section and determines when the $k \to 0$ limit is reached.

The s-wave scattering length is the central parameter for the theoretical description of bosonic quantum gases. It determines both the thermodynamic and the collisional properties of these gases. In single-component fermionic gases the s-wave scattering length plays no role because the wavefunction for the relative motion of the atoms has to be antisymmetric. In two-component fermionic gases this restriction is absent for collisions between atoms of different components. As a consequence, in these systems the inter-component s-wave scattering length determines the collision related properties - for instance the thermalization rate.

In Sec. 13.1.1 we show how the phase shift appears as a result of interatomic interaction in the wavefunction for the relative motion of two atoms. For free particles the phase shift is zero. An integral expression for the phase shift is derived. In Sec. 13.1.2 and beyond we specialize to the case of low-energy collisions ($kr_0 \ll 1$). The basic phenomenology is introduced and analyzed for simple model potentials like the hard-sphere (Sec. 13.1.2) and the spherical well (Sec. 13.1.3), where the existence of a short range is manifest. For the discussion of arbitrarily shaped potentials, we refer to the script [850].

13.1.1 The collisional phase shift

13.1.1.1 Schrödinger equation

The starting point for the description of the relative motion of two atoms at energy E is the Schrödinger equation (3.33),

$$\left[\frac{1}{2m_r}\left(p_r^2+\frac{\mathbf{L}^2}{r^2}\right)+V(r)\right]\psi(r,\vartheta,\varphi)=E\psi(r,\vartheta,\varphi)\ . \tag{13.2}$$

Here m_r is the reduced mass of the atom pair and $V(r)$ the interaction potential. As discussed in Sec. 3.1.3 the eigenfunctions $\psi(r,\vartheta,\varphi)$ can be separated in a radial and a angular part, $\psi = R_\ell(r)Y_{\ell m}(\vartheta,\varphi)$, where the functions $Y_{\ell m}$ are spherical harmonics and the functions $R_\ell(r)$ satisfy the radial wave equation,

$$\left[\frac{\hbar^2}{2m_r}\left(-\frac{d^2}{dr^2}-\frac{2}{r}\frac{d}{dr}+\frac{\ell(\ell+1)}{r^2}\right)+V(r)\right]R_\ell(r)=ER_\ell(r)\ . \tag{13.3}$$

By the separation procedure the angular momentum term is replaced by a repulsive effective potential,

$$V_{\rm rot}(r)=\frac{\hbar^2\ell(\ell+1)}{2m_r r^2}\ , \tag{13.4}$$

representing the rotational energy of the atom pair at a given distance and for a given rotational quantum number ℓ. In combination with an attractive interaction it gives rise to a centrifugal barrier for the radial motion of the atoms. This is illustrated in Fig. 13.2 for the example of hydrogen.

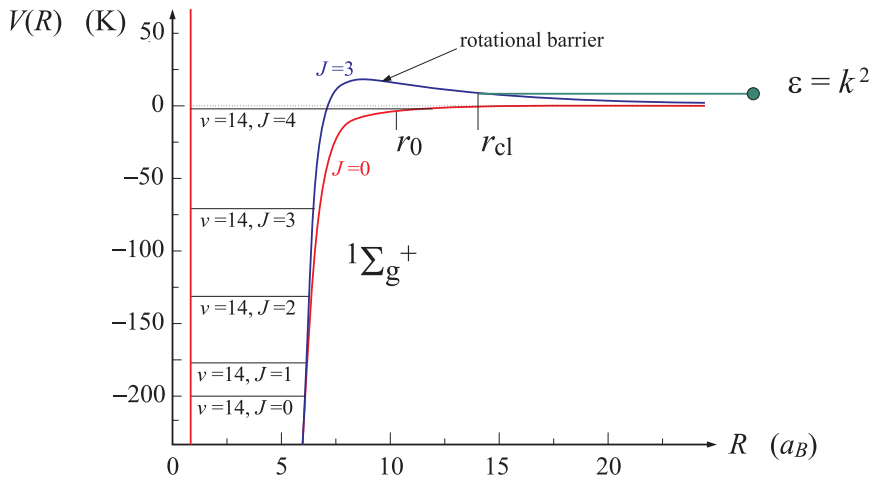

Figure 13.2: Example showing the high-lying bound states near the continuum of the singlet potential $^1\Sigma_g^+$ (the bonding potential) of the hydrogen molecule; v and J are the vibrational and rotational quantum numbers, respectively. The dashed line shows the effect of the $J = 3$ centrifugal barrier. The presence of a rotational barrier gives rise to an exponential suppression of the radial wavefunction for $r < r_{tp}$ and is negligible at distances where the interaction becomes noticeable $r \ll r_0$.

To analyze the radial wave equation we introduce reduced energies,

$$\varepsilon = \frac{2m_r E}{\hbar^2} = \begin{cases} k^2 & \text{for } k > 0 \\ -\kappa^2 & \text{for } k < 0 \end{cases} \quad \text{and} \quad \tilde{V}(r) = \frac{2m_r V(r)}{\hbar^2} \ , \tag{13.5}$$

choosing k and κ as real positive number. This puts Eq. (13.3) in the form,

$$\boxed{R_\ell'' + \frac{2}{r} R_\ell' + \left[\varepsilon - \tilde{V}(r) - \frac{\ell(\ell+1)}{r^2}\right] R_\ell = 0} \ . \tag{13.6}$$

With the substitution $u_\ell(r) = r R_\ell(r)$ it reduces to a 1D Schrödinger equation,

$$\boxed{u_\ell'' + \left[\varepsilon - \tilde{V}(r) - \frac{\ell(\ell+1)}{r^2}\right] u_\ell = 0} \ . \tag{13.7}$$

13.1.1.2 Low-energy limit: the s-wave regime

For two atoms with relative angular momentum $\ell > 0$ there exists a distance r_{tp}, called the classical turning point, below which the rotational energy exceeds the total energy E,

$$k^2 = \frac{\ell(\ell+1)}{r_{tp}^2} \ . \tag{13.8}$$

This is illustrated in Fig. 13.2. In the classically inaccessible region of space ($r < r_{tp}$) the radial wavefunction is exponentially suppressed [1]. Combining Eq. (13.8) with the condition (13.1) we obtain the inequality,

$$k r_0 = \sqrt{\ell(\ell+1)} \frac{r_0}{r_{tp}} \ll 1 \ , \tag{13.9}$$

which implies that, for $\ell \neq 0$, the classical turning point is found at a distance much larger than the range r_0 of the interaction. As the range r_0 defines the distance beyond which the potential can be neglected, this inequality shows that the radial motion is not affected by the presence of the potential $V(r)$ in the radial wave equation. The notable exception is the case $\ell = 0$, where the barrier is absent and the potential gives rise to a substantial distortion of the radial waves. In other words, for $kr_0 \ll 1$ phase shifts (i.e. scattering) can *only arise from collisions with zero angular momentum.* The range of collision energies where the inequalities (13.9) are valid is called the s-wave regime.

13.1.1.3 Free particle motion

We first have a look at the case of free particles or particles in a homogeneous potential, $V(r) = V_0$. By introducing the dimensionless variable $\varrho = kr$, where $k \equiv \sqrt{2m(E - V_0)/\hbar^2}$, the radial wave equation (13.6) can be rewritten in the form of the spherical Bessel differential equation,

$$R_\ell'' + \frac{2}{\varrho} R_\ell' + \left[1 - \frac{\ell(\ell+1)}{\varrho^2}\right] R_\ell = 0 \ . \tag{13.10}$$

[1] At this point we exclude tunneling through the barrier and the occurrence of shape resonances.

Here, the derivatives are with respect to the new variable.

The general solution of Eq. (13.10) for angular momentum ℓ is a linear combination of two particular solutions, one regular with amplitude A_ℓ, the spherical Bessel function $j_\ell(\varrho)$, and one irregular with amplitude B_ℓ, the spherical Neumann function $n_\ell(\varrho)$:

$$\boxed{R_\ell(\varrho) = A_\ell j_\ell(\varrho) + B_\ell n_\ell(\varrho) = c_\ell[\cos\eta_\ell \; j_\ell(\varrho) + \sin\eta_\ell \; n_\ell(\varrho)]} \; , \tag{13.11}$$

where the new parameters c_ℓ and η_ℓ, defined by

$$A_\ell \equiv c_\ell \cos\eta_\ell \qquad \text{and} \qquad B_\ell \equiv c_\ell \sin\eta_\ell \; , \tag{13.12}$$

represent the amplitude c_ℓ and the asymptotic phase η_ℓ of the wavefunction. Note that this equation is singular in the origin except for the case of vanishing phase shifts. Therefore, in the case of free particles we require $\eta_\ell = 0$ for all angular momentum values ℓ. This implies that the general solution reduces to the regular one,

$$R_\ell(\varrho) = c_\ell \cos\eta_\ell \; j_\ell(\varrho) \; . \tag{13.13}$$

13.1.1.4 Significance of the phase shifts

To investigate the effect of a short-range interaction potential $V(r)$ we return to the radial wave equation (13.6). As the potential is of short range it may be neglected for $r \gg r_0$ and the general solutions coincide with those of the spherical Bessel equation,

$$R_\ell(k,r) \underset{r\gg r_0}{\longrightarrow} c_\ell[\cos\eta_\ell \; j_\ell(kr) + \sin\eta_\ell \; n_\ell(kr)] \; . \tag{13.14}$$

For $r \gg 1/k$ the spherical Bessel and Neumann functions assume their asymptotic form and we find,

$$\begin{aligned} R_\ell(k,r) &\underset{kr\to\infty}{\longrightarrow} \frac{c_\ell}{kr}[\cos\eta_\ell \sin(kr - \tfrac{1}{2}\ell\pi) + \sin\eta_\ell \cos(kr - \tfrac{1}{2}\ell\pi)] \\ &= \frac{c_\ell}{kr}\sin(kr + \eta_\ell - \tfrac{1}{2}\ell\pi) \; . \end{aligned} \tag{13.15}$$

where we introduced a the constant η_ℓ representing the asymptotic phase shift. For a given value of k this phase shift fixes the general solution of the radial wavefunction $R_\ell(k,r)$ up to an ℓ dependent normalization constant c_ℓ. Note that in view of the k dependence of the phase shift, R_ℓ is a function of k and r rather than a function of the product kr. Whereas in the case of free particles the phase shifts must all vanish, in the presence of the interaction they provide the proper asymptotic form of the distorted waves. The non-zero asymptotic phase shift is the signature of the interaction at short distance; the motion becomes free-particle like (undistorted) only at large distance from the scattering center. In elastic scattering the relative energy $\hbar^2k^2/2m$ is conserved; hence, asymptotically also k and the de Broglie wavelength. This leaves only the asymptotic phase of the wave to be affected.

Example 72 (*Scattering matrix*): Rewriting Eq. (13.15) in complex notation,

$$R_\ell(k,r) \underset{r\to\infty}{\simeq} \frac{c_\ell}{2k}\imath\left[e^{-\imath\eta_\ell}\frac{e^{-\imath(kr-\frac{1}{2}\ell\pi)}}{r} - e^{i\eta_\ell}\frac{e^{\imath(kr-\frac{1}{2}\ell\pi)}}{r}\right] \; , \tag{13.16}$$

we see that for $r \to \infty$ the stationary solution $R_\ell(k,r)$ can be regarded as an 'incoming' spherical wave interfering with an 'outgoing' spherical wave. It is convention to choose the phase of the normalization constant such that the phase of the incoming wave is zero,

$$R_\ell(k,r) \underset{r\to\infty}{\simeq} \frac{c'_\ell}{2k}\imath \left[\frac{e^{-\imath kr}}{r} - e^{-\imath\ell\pi}e^{2\imath\eta_\ell}\frac{e^{\imath kr}}{r}\right] , \tag{13.17}$$

Apart from the sign, the ratio of the phase factors of the outgoing over the incoming wave is,

$$\mathcal{S}_\ell = e^{2\imath\eta_\ell} . \tag{13.18}$$

This quantity is called the scattering matrix ($\mathcal{S}$ matrix) or, better, the l-wave contribution to the $\mathcal{S}$ matrix. Being unitary it does not suffer from the divergences of the ratio $B_\ell/A_\ell = \tan\eta_\ell$. In the present context the name scattering matrix is a bit heavy because we only have a single matrix element (1×1 matrix). The term matrix finds its origin in the description of scattering of particles with an internal degree of freedom (like spin), for which the phase factor is replaced by a unitary matrix.

13.1.2 Hard-sphere potentials

We now turn to analytical solutions for model potentials in the limit of low energy. We first consider the case of two hard spheres of equal size. These can approach each other to a minimum distance equal to their diameter a. For $r \le a$ the radial wave function vanishes, $R_\ell(r) = 0$: Outside the hard sphere we have free atoms, $V(r) = 0$, with relative wave number $k = [2m_r E/\hbar^2]^{1/2}$. Thus, for $r \le a$ the general solution for the radial wave functions of angular momentum ℓ is given by the free atom expression (13.11), which asymptotically this takes the form (13.15) of a phase-shifted spherical Bessel function,

$$R_\ell(k,r) = c_\ell[\cos\eta_\ell\ j_\ell(kr) + \sin\eta_\ell\ n_\ell(kr)] \underset{r\to0}{\simeq} \frac{c_\ell}{kr}\sin(kr + \eta_\ell - \tfrac{1}{2}\ell\pi) . \tag{13.19}$$

To determine the phase shift we require as a boundary condition that $R_\ell(k,r)$ vanishes at the surface of the hard sphere (see Fig. 13.3),

$$\cos\eta_\ell\ j_\ell(ka) + \sin\eta_\ell\ n_\ell(ka) = 0 . \tag{13.20}$$

Hence, the phase shift follows from the expression,

$$\tan\eta_\ell = \frac{j_\ell(ka)}{n_\ell(ka)} . \tag{13.21}$$

This expression allows to derive asymptotic expressions (for $ka \ll 1$ and for $ka \gg 1$) for the radial wave function (13.19), as will be shown in Exc. 13.1.5.1.

13.1.2.1 s-wave phase shifts for hard spheres

For the case $\ell = 0$, inserting the analytical expressions for the Bessel and von Neumann function, (13.19) becomes without approximation,

$$R_0(k,r) = \frac{c_0}{kr}(\cos\eta_0\sin kr + \sin\eta_0\cos kr) = \frac{c_0}{kr}\sin(kr+\eta_0) . \tag{13.22}$$

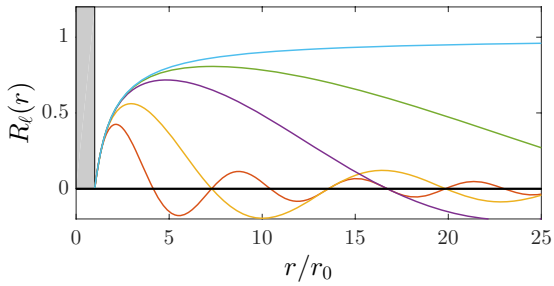

Figure 13.3: (code) Radial wavefunctions ($\ell = 0$) for various values of k (down to the $k \to 0$ limit) in the case of a hard sphere potential. The boundary condition is fixed by the requirement that the wavefunction vanishes at the edge of the hard sphere, $R_0(ka) = 0$.

The phase shift follows from the boundary condition $R_0(k, a) = 0$, which can be written in the form,

$$\cos \eta_0 \sin ka + \sin \eta_0 \cos ka = 0 \ . \tag{13.23}$$

Hence, the phase shift is

$$\eta_0 = -ka \ . \tag{13.24}$$

With this expression Eq. (13.22) reduces to

$$R_0(k, r) = \frac{c_0}{kr} \sin[k(r - a)] \ . \tag{13.25}$$

This expression is exact for any value of k, as announced above. The linear k dependence of η_0 simply expresses its definition in which the shift of the wave (by a) is compared to the de Broglie wavelength λ_{dB}, $\eta_0 = -2\pi a/\lambda_{dB}$. As a consequence the phase shift vanishes for $k \to 0$,

$$\lim_{k\to 0} \eta_0(k) = 0 \ . \tag{13.26}$$

This result is obvious when comparing the finite shift a to the diverging wavelength $\lambda_{\rm therm}$. Interestingly, in the limit $k \to 0$ the expression (13.25) becomes k independent,

$$R_0(r) \underset{k\to 0}{\sim} 1 - \frac{a}{r} \qquad \text{for} \qquad a \le r \ll 1/k \ . \tag{13.27}$$

This important result is illustrated in Fig. 13.3. In the limit $k \to 0$ the wavefunction is essentially constant throughout space (up to a distance $1/k \to \infty$ at which it starts to oscillate), except for a small region of radius a around the potential center.

13.1.3 Spherical wells with a flat bottom

The second model potential to consider is the spherical well of range r_0 sketched in Fig. 13.4,

$$\tilde{V}(r) = \begin{cases} 2m_r V_0/\hbar^2 = \tilde{V}_0 = -\kappa_0^2 & \text{for } r \le r_0 \\ 0 & \text{for } r > r_0 \end{cases} \ . \tag{13.28}$$

Here $|U_0| = \kappa_0^2$ is called the well depth (κ_0 is chosen to be real and positive, $\kappa_0 > 0$). The energy of the continuum states is given by $\varepsilon = k^2$. In analogy, the energy of the bound states is written as,

$$\varepsilon_b = -\kappa^2 \ . \tag{13.29}$$

We now have to solve the radial wave equation (13.6) with the spherical well potential (13.28). Since the potential is constant inside the well ($r \leq r_0$) the wavefunction has to be free-particle like with the wave number given by,

$$K_+ = \sqrt{2m_r(E - V_0)/\hbar^2} = \sqrt{\kappa_0^2 + k^2} \ . \tag{13.30}$$

As the wavefunction has to be regular in the origin, inside the well it is given by,

$$R_\ell(r) = C_\ell j_\ell(K_+ r) \quad \text{for } r \leq r_0 \ , \tag{13.31}$$

where C_ℓ is a normalization constant. This expression holds for $E > V_0$ (both $E > 0$ and $E \leq 0$).

Outside the well ($r > r_0$) we have for $E > 0$ free atoms, $\tilde{V}(r) = 0$, with relative wavevector $k = [2m_r E/\hbar^2]^{1/2}$. Thus, for $r > r_0$ the general solution for the radial wave functions of angular momentum ℓ is given by the free atom expression (13.11),

$$R_\ell(k, r) = c_\ell[\cos\eta_\ell \ j_\ell(kr) + \sin\eta_\ell \ n_\ell(kr)] \quad \text{for } r > r_0 \ . \tag{13.32}$$

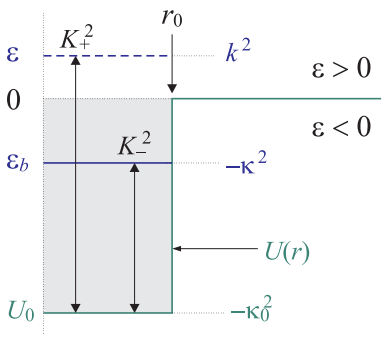

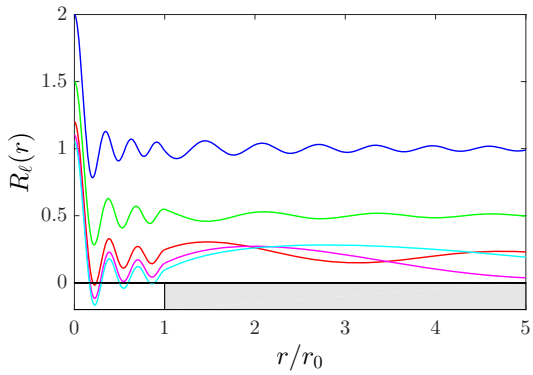

Figure 13.4: (code) (Left) Scheme of the flat bottom potential. (Right) (a) Radial wavefunctions for square wells: (a) continuum state ($\varepsilon = k^2 > 0$); (b) Zero energy state ($\varepsilon = k^2 = 0$) in the presence of an asymptotically bound level ($\varepsilon = -\kappa^2 = 0$); (c) bound state ($\varepsilon = -\kappa^2 < 0$). Note the continuity of $R_0(r)$ and $R_0'(r)$ at $r = r_0$. The wavefunctions are not normalized and are shifted relative to each other only for reasons of visibility.

The full solution [see Fig. 13.4(a)] is obtained by the continuity conditions for $R_\ell(r)$ and $R_\ell'(r)$ at the boundary $r = r_0$. These imply continuity of the logarithmic derivative with respect to r,

$$K_+ \frac{j_\ell'(\varrho_i)}{j_\ell(\varrho_i)} = \frac{R_\ell'(r)}{R_\ell(r)}\bigg|_{r=r_0} = k \frac{\cos\eta_\ell \ j_\ell'(\varrho_e) + \sin\eta_\ell \ n_\ell'(\varrho_e)}{\cos\eta_\ell \ j_\ell(\varrho_e) + \sin\eta_\ell \ n_\ell(\varrho_e)} \ , \tag{13.33}$$

where we defined the abbreviations $\varrho_i \equiv K_+ r_0$ and $\varrho_e \equiv k r_0$. This ratio suffices to determine η_ℓ independently of the normalization constants C_ℓ and c_ℓ. Once the phase shift is known, the relation between C_ℓ and c_ℓ follows from the continuity condition for $R_\ell(r)$. Furthermore, it shows that the asymptotic phase shift η_ℓ can take any (real) value depending on the depth of the well. In view of the importance of the $\mathcal{S}$ matrix in scattering theory Sec. 13.2, it is advantageous to determine $e^{2\imath\eta_\ell}$ rather than η_ℓ itself. Expressing $\sin\eta_\ell$ and $\cos\eta_\ell$ in terms of $e^{\imath\eta_\ell}$ and $e^{-\imath\eta_\ell}$ Eq. (13.33) becomes,

$$K_+ \partial_\varrho \ln j_\ell(\varrho_i) = k \frac{e^{2\imath\eta_\ell} h_\ell^{(2)\prime}(\varrho_e) + h_\ell^{(1)\prime}(\varrho_e)}{e^{2\imath\eta_\ell} h_\ell^{(2)}(\varrho_e) + h_\ell^{(1)}(\varrho_e)} \ , \tag{13.34}$$

with the definition of the Hankel functions of the first and second kind: $h_\ell^{(1,2)} \equiv j_\ell \pm \imath n_\ell$. Solving for $e^{2i\eta_\ell}$ this leads to the following expression for the ℓ-wave contribution to the $\mathcal{S}$ matrix,

$$\boxed{e^{2i\eta_\ell} = -\frac{h_\ell^{(1)}(\varrho_e)}{h_\ell^{(2)}(\varrho_e)} \frac{K_+ \partial_\varrho \ln j_\ell(\varrho_i) - k \partial_\varrho \ln h_\ell^{(1)}(\varrho_e)}{K_+ \partial_\varrho \ln j_\ell(\varrho_i) - k \partial_\varrho \ln h_\ell^{(2)}(\varrho_e)}} \ , \tag{13.35}$$

where the expression $\partial_\varrho \ln$ stands for the logarithmic derivative. This expression may look a bit heavy, but is valuable as it represents the exact result for arbitrary ℓ. In Exc. 13.1.5.2 we simplify this formula for $\ell = 0$. As the formula (13.35) lacks transparency from the physical point of view, we analyze in the coming sections the case $\ell = 0$ directly discussing the radial wavefunctions u_ℓ.

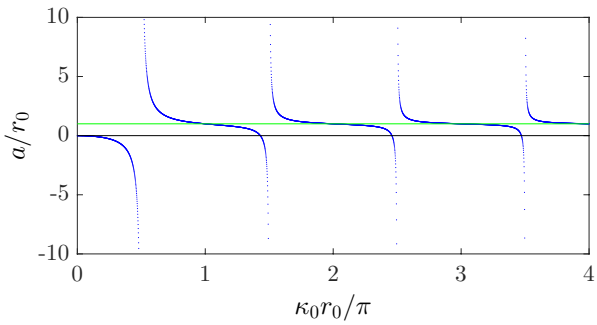

Figure 13.5: (code) The s-wave scattering length a normalized on r_0 as a function of the depth of a spherical square potential well (blue curve). Note that, typically, $a \simeq r_0$ (green line), except near the resonances at $\kappa_0 r_0 = (n + \frac{1}{2})\pi$ being an integer.

13.1.3.1 s-wave scattering ($E > 0$)

The analysis of spherical well potentials becomes particularly simple for the case $\ell = 0$. Let us first consider the case $E > 0$, for which the radial wave equation can be written as a 1D-Schrödinger equation (13.7) of the form,

$$u_0'' + [k^2 - \tilde{V}(r)] u_0 = 0 \ . \tag{13.36}$$

The solution is,

$$u_0(kr) = \begin{cases} C_0 \sin(K_+ r) & \text{for } r \le r_0 \\ c_0 \sin(kr + \eta_0) & \text{for } r > r_0 \end{cases} . \tag{13.37}$$

To determine $\eta_0(k)$ it is sufficient to apply the boundary condition for continuity of the logarithmic derivative at the edge of the well,

$$\left.\frac{u_0'}{u_0}\right|_{r=r_0} = K_+ \cot K_+ r_0 = k \cot(kr_0 + \eta_0) . \tag{13.38}$$

Note that this expression coincides with the general result given by Eq. (13.33) for the case $\ell = 0$; i.e. the boundary condition of continuity for u_0'/u_0 coincides with that for R_0'/R_0, as we know from a calculation left to Exc. 13.1.5.3. Furthermore, for a vanishing potential ($\kappa_0 \to 0$) we have $K_+ \to k$ and the boundary condition properly yields a zero phase shift ($\eta_0 = 0$).

At this point we introduce the effective hard-sphere diameter $a(k)$ to describe, in analogy with Eq. (13.24), the behavior of the phase shift,

$$\eta_0(k) \equiv -ka(k) . \tag{13.39}$$

By this procedure we extract the linear k dependence as well as the negative sign from the phase shift. This is a good idea because the linear k-dependence does not arise from the potential but simply from the definition of the phase in which, as discussed earlier, the shift of the wave is compared to the de Broglie wavelength. In the limit $k \to 0$, we have $K_+ r_0 \to \kappa_0 r_0$ and with the definition,

$$a \equiv \lim_{k\to 0} a(k) = -\lim_{k\to 0} \eta(k)/k \tag{13.40}$$

the boundary condition (13.38) becomes,

$$\left.\frac{u_0'}{u_0}\right|_{r=r_0} = \kappa_0 \cot \kappa r_0 = \frac{1}{r_0 - a} . \tag{13.41}$$

Solving for a we find,

$$a = r_0 \left(1 - \frac{\tan\gamma}{\gamma}\right) , \tag{13.42}$$

where the dimensionless positive quantity,

$$\gamma \equiv \kappa_0 r_0 \tag{13.43}$$

is called the well parameter. As shown in Fig. 13.5, the value of a can be positive, negative or zero depending on the value of γ. Therefore, rather than using the pictorial term effective hard-sphere diameter the name scattering length is used for a. Next to the range, the scattering length represents the second characteristic length that can be associated with the interaction potential. As the name suggest, it is a measure for the scattering behavior of atoms, and we elaborate on this in Sec. 13.2. Also, in Sec. ?? we will show that a is also a measure for the effective strength of the interaction.

Fig. 13.5 and Eq. (13.42) show that a is typically a quantity of the size of r_0, although for $\gamma = \tan\gamma$ it is zero and for $\gamma = (\nu + \frac{1}{2})\pi$, with ν being an integer,

it diverges. The latter condition points to a resonance phenomenon occurring when (with increasing γ) a new bound level enters the potential well. For the square well potential the scattering length is mostly positive; it is negative in the regions with $\gamma < \tan\gamma$, which become narrower for increasing γ. This unlikely occurrence of negative a is atypical for the general case; e.g. for Van der Waals potentials the probability to find a negative scattering length is 25% .

For $r \geq r_0$ the radial wavefunction corresponding to Eq. (13.37) is of the form,

$$R_0(k,r) = \frac{c_0}{kr}\sin[kr - ka(k)] \ . \tag{13.44}$$

Recalling the definitions (13.39) and (13.40) we find that for $k \to 0$ this radial wavefunction becomes k-independent,

$$R_0(r) \underset{k\to 0}{\sim} 1 - \frac{a}{r} \qquad \text{for} \qquad r_0 < r \ll \frac{1}{k} \ . \tag{13.45}$$

The latter two expressions for the radial wavefunction have the same formal appearance as the hard sphere results (13.25) and (13.27). However, whereas the diameter of the hard-sphere has a fixed value, the scattering length for the well depends on γ. As shown in Fig. 13.6, for positive scattering length the s-wave has a characteristic node at $r = a$; for negative scattering length this becomes a virtual node.

Importantly, because Eq. (13.45) reaches the asymptotic value 1 only for distances $r \gg a$, the use of this equation in the modeling of dilute gases is only justified if a is much smaller than the interparticle spacing,

$$na^3 \ll 1 \ . \tag{13.46}$$

Otherwise, the interaction with neighboring atoms will distort the relative motion of the colliding pair. This violates the binary scattering approximation on which Eq. (13.45) is based. The dimensionless quantity na^3 is called the gas parameter. When its value is small, the gas is called nearly ideal or weakly interacting [2].

13.1.3.2 Bound s-levels ($E \leq 0$)

Let us turn to the case $E \leq 0$. We shall show that the divergences of the scattering length obtained by analyzing the continuum states ($E > 0$) result from the appearance of the next bound s-level when increasing the well parameter. The 1D Schrödinger equation takes the form,

$$u_0'' + [-\kappa^2 - \tilde{V}(r)]u_0(r) = 0 \ . \tag{13.47}$$

where $\varepsilon = -\kappa^2$ is the discrete energy eigenvalue of a bound state with $\ell = 0$. The solutions are of the type (see Fig. 13.29),

$$u_0(k,r) = \begin{cases} C_0 \sin K_- r & \text{for } r \leq r_0 \\ c_0 e^{-\kappa r} & \text{for } r \leq r_0 \end{cases} \tag{13.48}$$

[2] Note that weakly interacting does not mean that that the potential is 'shallow'. Any gas can be made weakly interacting by making the density sufficiently small.

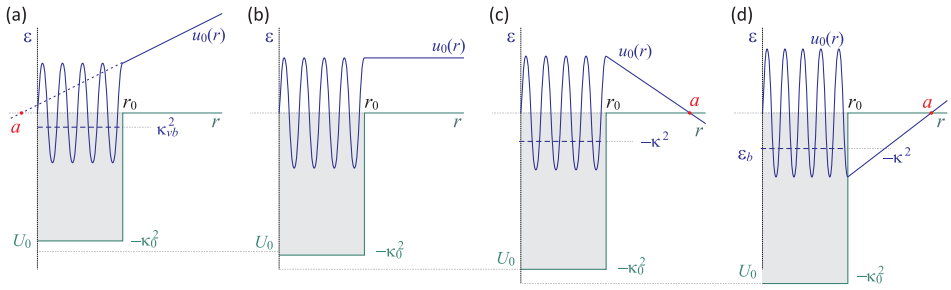

Figure 13.6: Reduced radial wavefunctions $u_0(r)$ for continuum states ($\varepsilon > 0$) in the $k \to 0$ limit for increasing well depth near the threshold value $\kappa_0 r_0 = (n + \frac{1}{2})\pi$: (a) presence of an almost bound state ($a < 0$); (b) presence of zero-energy resonance ($\kappa_{vb} = 0$, $a \to \pm\infty$); (c) presence of a weakly bound state ($a > 0$); (d) deeper binding of the least bound state. For $r > r_0$ the wavefunction is given by $u_0(r) = c_0(r - a)$; hence, the value of a is given by the intercept with the horizontal axis. This gives rise to a characteristic node at $r = a$, which is *real* for $a > 0$ (just as for hard spheres of diameter a), but *virtual* for $a < 0$. The wavefunctions are not normalized.

where $\kappa > 0$ because the bound state wavefunction has to be normalized. The bound state energy is obtained by requiring the continuity of the logarithmic derivative when connecting the inner part of the wavefunction to the outer part,

$$\left.\frac{u_0'(r)}{u_0(r)}\right|_{r=r_0} = K_- \cot K_- r_0 = -\kappa \ , \tag{13.49}$$

where $\kappa > 0$ and

$$K_- = [2m_r(E - V_0)/\hbar^2]^{1/2} = (\kappa_0^2 - \kappa^2)^{1/2} \ . \tag{13.50}$$

With decreasing γ, the least bound level disappears in the limit $\kappa \to 0$, $K_- \to \kappa_0$. In this limit Eq. (13.49) reduces to,

$$\left.\frac{u_0'(r)}{u_0(r)}\right|_{r=r_0} = \kappa_0 \cot \kappa_0 r_0 \underset{\kappa\to 0}{=} 0 \ , \tag{13.51}$$

Increasing from zero the vibrational levels appear sequentially for

$$\gamma = (v + \tfrac{1}{2})\pi \ , \tag{13.52}$$

where $v = 0, 1, .., r_{max}$ is the vibrational quantum number. This shows that a minimum well parameter ($\gamma = \pi/2$) is required to bind the first state [3]. For the least-bound level, v_{max}, we have,

$$(v_{max} + \tfrac{1}{2})\pi = \text{Int } (\tfrac{\gamma}{\pi} - \tfrac{1}{2}) \tag{13.53}$$

and the total number of bound s levels follows with,

$$N_b = v_{max} + 1 = \text{Int } (\tfrac{\gamma}{\pi} + \tfrac{1}{2}) \ . \tag{13.54}$$

[3] This conclusion cannot be extended to lower dimensions; in two dimensions bound states appear for arbitrarily shallow potentials.

The relation between κ and v for a given vibrational level depends on the ratio κ/K_- and is given by

$$\cot K_- r_0 = -\frac{\kappa}{K_-} \ . \tag{13.55}$$

Note that this relation corresponds to $K_- r_0 \simeq (v_{max} + \frac{1}{2})\pi$ for the least-bound state

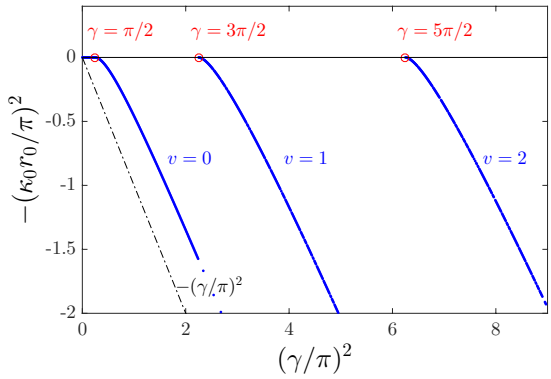

Figure 13.7: (code) Appearance and increase of binding of the first three bound levels for increasing well depth. The quadratic dependence near threshold is universal (i.e. independent of the well shape). The full crossover curve is obtained by numerical solution of Eq. (13.49) and corresponds to a $\pi/2$ phase shift of $K_+ r_0$ near threshold. The dashed line shows the increase in well depth.

$(\kappa/K- \ll 1)$ and to $K_- r_0 \simeq (v_{max} + 1)\pi$ for deeply bound levels $(K_-/\kappa \ll 1)$, as is illustrated in Fig. 13.8(a).

13.1.3.3 Weakly bound s-level: halo states

For weakly bound s levels $(0 < \kappa r_0 \ll 1)$ we have $K_- \to \kappa_0$ and Eq. (13.49) may be approximated by

$$\left.\frac{u_0'(r)}{u_0(r)}\right|_{r=r_0} = \kappa_0 \cot \kappa_0 r_0 = -\kappa \ , \tag{13.56}$$

Furthermore, we recall that in the presence of a weakly bound s-level the scattering length is large and positive, $a \gg r_0$. From Eq. (13.41) we recall that for $k \to 0$ the logarithmic derivative also satisfies the relation

$$\left.\frac{u_0'(r)}{u_0(r)}\right|_{r=r_0} = \kappa_0 \cot \kappa_0 r_0 = \frac{1}{r_0 - a} \simeq -\frac{1}{a} \ , \tag{13.57}$$

Interestingly, for $a \gg r_0$ the logarithmic derivative of the continuum states becomes independent of r_0 and κ_0; i.e. it becomes independent of the shape of the potential well. As we shall see it only depends on the well parameter γ and not on the well shape. This points to a universal limiting shape of the wavefunction for large scattering length. As is sketched in Fig. 13.8(b), for decreasing κ the least-bound state turns into a halo state; i.e. for $\kappa r_0 \ll 1$ most of the probability of the bound state is found in the classically inaccessible region outside the potential well, thus surrounding the

potential center like a halo. This behavior holds for arbitrary short-range potentials.

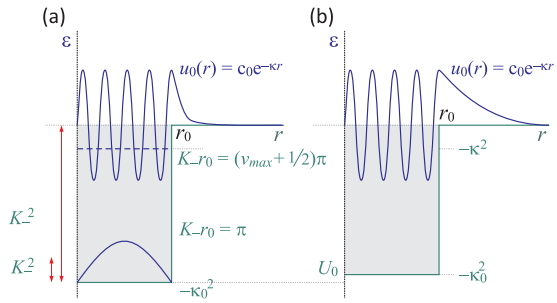

Figure 13.8: Bound states oscillate inside the well and decay exponentially outside the well: (a) the boundary condition depends on the ratio κ/K_-; (b) a slight reduction of the well depth can turn the least bound state into a halo state.

With Eqs. (13.56) and (13.57) we have obtained two expressions for $\kappa_0 \cot \kappa_0 r_0$ and arrive at the conclusion that in the presence of a weakly bound state the scattering length is given by,

$$a \underset{\kappa \to 0}{\simeq} 1/\kappa \ . \tag{13.58}$$

This expression reveals the tight relation between the binding energy of the least-bound state, given by Eq. (13.29), and the scattering length,

$$\boxed{E_b = -\frac{\hbar^2 \kappa^2}{2m_r} \underset{\kappa \to 0}{\longrightarrow} -\frac{\hbar^2}{2m_r a^2}} \ . \tag{13.59}$$

13.1.3.4 *s*-wave resonances in the continuum: The Breit-Wigner formula

To obtain the k-dependence of the phase shift for large but otherwise arbitrary well parameter ($\gamma \gg 1$) we rewrite the boundary condition (13.38) in the form,

$$\eta_0(k) = -kr_0 + \arctan \frac{kr_0}{K_+ r_0 \cot K_+ r_0} \equiv \eta_{bg} + \eta_{\rm res} \ . \tag{13.60}$$

The first term of (13.60) is called the *background contribution* to the phase shift and the second term the *s*-wave *resonance contribution*. Note that the background contribution shows the same phase development as we found in Sec. 13.1.2 for hard spheres. The phase development of the resonance contribution is shown in Fig. 13.9(a) for the case of a large well parameter slightly detuned from the threshold value (at $\gamma = 31.5\pi \approx 98.960169$) such that the scattering length is negative ($\Delta_\gamma = -0.5$). For potentials with $\gamma \gg 1$ the argument of the arctangent is predominantly small, $kr_0/|K_+ r_0 \cot K_+ r_0| \ll 1$, because

$$K_+ r_0 = \kappa_0 r_0 (1 + k^2/\kappa_0^2)^{1/2} > \gamma \gg 1 \ . \tag{13.61}$$

However, the argument of the arctangent diverges when $\cot K_+ r_0$ passes through zero; i.e. for

$$K_+ r_0 = (\tilde{v} + \tfrac{1}{2})\pi \ , \tag{13.62}$$

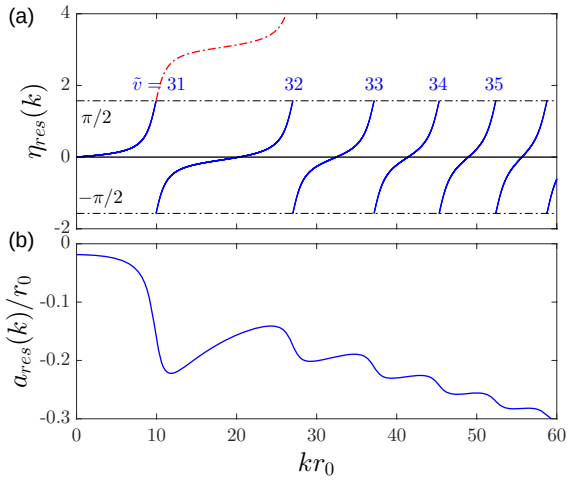

Figure 13.9: (code) (a) Resonance contribution to the s-wave phase shift $\eta_0(k)$ for a large well parameter slightly detuned from the threshold value (at $\gamma = 31.5\pi$), such that the scattering length is negative ($\Delta\gamma = -0.5$): The linear shift of the background contribution is not included in the plot. Note that the π phase jumps arise from the modulo-π representation of the arctangent and do not represent an observable phenomenon; the physical phase increases monotonically and equals $\eta_{\rm res} = \frac{1}{2}$ (modulo π) at the center of the resonances; (b) contribution of the resonances to the effective hard sphere diameter $a(k) = -\eta_0(k)/k$. As (in this example) the lowest resonance is not close to threshold the resonant enhancement is small, $|a_{\rm res}(k)| = r_0 \ll 1$.

where $\tilde{v}$ is an integer called the resonance index. This divergence is observed as a small resonant enhancement of $a(k)$, as shown in Fig. 13.9(b). The physical phase is a continuous function of k, which changes by π when sweeping across the resonance. Because the arctangent remains finite for $\cot K_+ r_0 = 0$ also the resonant phase shift remains finite, having the value $\eta_{\rm res}(k) = \frac{1}{2}\pi$ (modulo π) at the center of each resonance.

In the remainder of this section we shall analyze the width and separation of the s-wave resonances for the case $\gamma \gg 1$. Since $K_+ \geq \kappa_0 \geq K_-$, we have,

$$\tilde{v} \geq \tfrac{\gamma}{\pi} - \tfrac{1}{2} \geq v_{max} \ , \tag{13.63}$$

which shows that for $\gamma \gg 1$ the value of $\tilde{v}$ is large ($\tilde{v}_{min} \geq \tilde{v}_{max} \gg 1$). Hence, the resonance numbering starts where the numbering of bound states ends. To discuss the resonances we denote the wavevectors k and K_+ at resonance by $k_{\rm res}$ and $K_{\rm res} \equiv \sqrt{\kappa_0^2 + k_{\rm res}^2}$, respectively. The resonance energies $\varepsilon_{\rm res} = k_{\rm res}^2$ satisfy the condition,

$$\varepsilon_{\rm res} = K_{\rm res}^2 - \kappa_0^2 = (\tilde{v} + \tfrac{1}{2})\pi(\tfrac{\pi}{r_0})^2 - \kappa_0^2 \geq 0 \ . \tag{13.64}$$

The exceptional case for which the equal sign applies ($\tilde{v} = v_{max}$) corresponds to a resonant bound state ($\kappa = 0$) and the resonance is called a resonance at threshold or zero-energy resonance ($k_{\rm res} = 0$).

Let us first analyze s-wave resonances for large well parameters ($\tilde{v} = v_{max}$) and far from threshold, ($\kappa = 0$). The energy spacing between two subsequent resonances

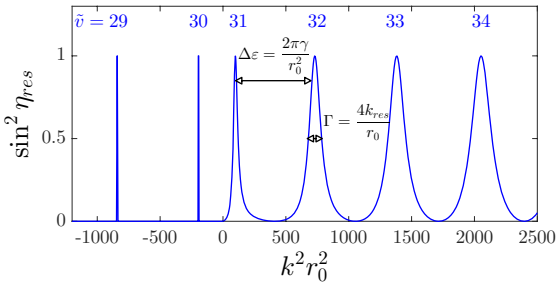

Figure 13.10: (code) (a) Transition from bound states to Breit-Wigner s-wave resonances plotted for $\Delta\gamma = -0.5$ with respect to the threshold at $\gamma = 31.5\pi$ (same conditions as Fig. 13.9). The bound states are indicated as zero-width spikes at energies $\varepsilon = -\kappa^2$, with κ following from Eq. (13.49). For $\varepsilon > 0$ the plot is based on Eqs. (13.60). The width of the resonances increases with the square root of the energy. Note that the band of energies typical for the quantum gases ($kr_0 \ll 1$) corresponds to a narrow zone, unresolved on the energy scale of the plot.

is,

$$\Delta\varepsilon_{\rm res} = \varepsilon_{\rm res}^{(\tilde{v}+1)} - \varepsilon_{\rm res}^{(\tilde{v})} = 2(\tilde{v}+1)\tfrac{\pi^2}{r_0^2} \simeq \tfrac{2\pi\gamma}{r_0^2} \ . \tag{13.65}$$

To analyze a given resonance we expand $K_+ \cot K_+ r_0$ about the point of zero crossing. For this purpose we introduce the notation,

$$K_+ = \sqrt{\kappa_0^2 + (k_{\rm res}+\delta k)^2} = K_{\rm res} + \frac{\delta k\ k_{\rm res}}{K_{\rm res}} \ , \tag{13.66}$$

where $\delta k = k - k_{\rm res}$ is called the detuning from resonance. Thus, restricting ourselves to the low-energy (but not zero energy) s-wave resonances ($1 < k_{\rm res}r_0 \ll K_{\rm res}r_0 \simeq \gamma$), we may approximate $K_+ \cot K_+ r_0 \simeq K_{\rm res} \cot K_+ r_0$. Expanding $\cot K_+ r_0$ about the zero crossing at $K_+ r_0 = (\tilde{v}+1/2)\pi$ and retaining only the linear term we obtain (see Problem 3.4),

$$K_{\rm res} \cot K_+ r_0 = -\delta k\ k_{\rm res} r_0 \ . \tag{13.67}$$

Hence, the diverging argument of the arctangent becomes,

$$\tan\eta_{\rm res} = \frac{k}{K_+ \cot K_+ r_0} \simeq -\frac{1}{\delta k\ r_0} = \frac{-(k+k_{\rm res})}{(k^2-k_{\rm res}^2)r_0} \simeq \frac{-2k_{\rm res}/r_0}{\varepsilon-\varepsilon_0} \ . \tag{13.68}$$

The expansion (13.66) is valid over the full range of the resonant change in phase provided the following condition holds,

$$\delta k\ r_0 \ll \frac{K_{\rm res}}{k_{\rm res}} \simeq \tfrac{\gamma}{k_{\rm res}r_0} \ , \tag{13.69}$$

which is satisfied for the lowest resonances as long as the well parameter is sufficiently large ($\gamma \gg k_{\rm res}r_0$). As long as $\delta k \ll k_{\rm res}$ we may further approximate $k \simeq k_{\rm res}$. With these approximations and after restoring the dimensions, Eq. (13.68) can be written as a function of the energy $E = \hbar^2 2k^2/2m_r$,

$$\tan\eta_{\rm res} = \frac{k}{K_+ \cot K_+ r_0} \simeq \frac{-\Gamma^2}{\varepsilon-\varepsilon_{\rm res}} \ , \tag{13.70}$$

where

$$\Gamma/2 = 2k_{\rm res}/r_0 \tag{13.71}$$

is called the spectral width of the resonance. Comparing the expressions for Γ and $\Delta E_{\rm res}$ we find that for given r_0 the width Γ is independent of γ, whereas the resonance spacing is proportional to γ . Thus, only for sufficiently large well parameters ($\gamma \gg 1$) the spectral width becomes smaller than the resonance spacing,

$$\Gamma \ll \Delta\varepsilon_{\rm res} \Longleftrightarrow k_{\rm res} r_0 \ll \pi\gamma \ . \tag{13.72}$$

Knowing the tangent of $\eta_{\rm res}$, we readily obtain the sine and Eq. (13.70) is replaced by the *Breit-Wigner formula*,

$$\sin^2 \eta_{\rm res} = \frac{(\Gamma/2)^2}{(\varepsilon - \varepsilon_0)^2 + (\Gamma/2)^2} \ . \tag{13.73}$$

For optical resonances this energy dependence is known as the Lorentz lineshape. Note that Γ corresponds to the full-width-at-half-maximum (FWHM) of this line shape. The lowest energy resonances are plotted in Fig. 13.10 along with the highest-energy bound states.

The resonance near threshold (almost bound level) deserves special attention, as this type of resonance is the only one that can play an important role within the band of energies relevant for the quantum gases ($kr_0 \ll 1$). Fig. 13.10 shows that near the threshold (at $\gamma = 31.5\pi$) the resonance narrows down and becomes asymmetric, which means that the Breit-Wigner lineshape is lost. Using Eq. (13.54) we calculate $\tilde{v} = 31$. The narrow line is reminiscent of a bound level but the scattering length is negative (see Fig. 13.10). Under these conditions the wavefunction has a virtual node at $r = -|a|$ (see Fig. 13.29). Accordingly, the level is called a virtual level and the wavefunction is said to represent a virtual bound state. In analogy with the bound states its energy is written as $\varepsilon = \kappa_{\rm res}^2$, where κ is to be defined later.

13.1.4 Other types of potentials

13.1.4.1 Zero-range potentials

An important model potential is obtained by considering a spherical well in the zero-range limit $r_0 \to 0$. As illustrated in Fig.13.11, it is possible to construct a zero-range well in such a way that the long-range properties of the wavefunction are unaffected; i.e. the scattering length a and the binding energy $\varepsilon = -\kappa^2$ of the least-bound state remain unchanged.

For $E < 0$ this can be demonstrated with the aid of the boundary condition (13.49),

$$-\kappa = K_- \cot K_- r_0 \ . \tag{13.74}$$

Reducing the radius r_0 the value of the binding energy $\varepsilon = -\kappa^2$, can be conserved by increasing κ_0. In the limit $r_0 \to 0$ the well depth should diverge in accordance with,

$$-\frac{\kappa}{K_-} = \cot K_- r_0 \to 0 \ . \tag{13.75}$$

This condition is satisfied for $K_- r_0 \simeq \pi/2$. To elucidate this point we consider the least-bound level with vibrational quantum number $v = v_{max}$, for which $K_- r_0 =$

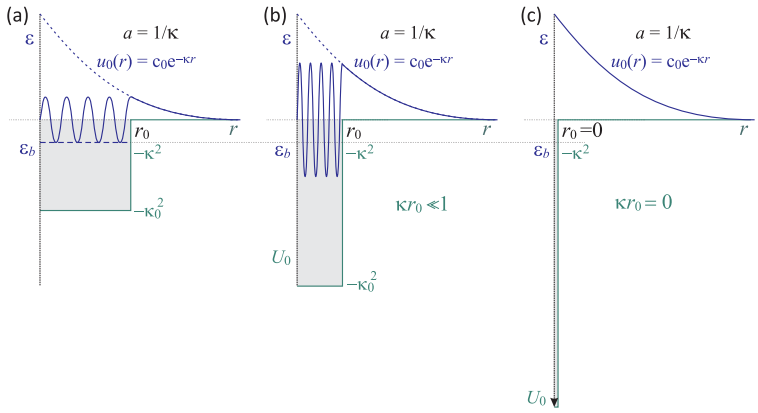

Figure 13.11: Wavefunctions corresponding to the same binding energy ($\varepsilon = -\kappa^2$) plotted for three different values of r_0. Outside r_0 the wavefunctions fall off exponentially, always with the same decay exponent κ; this is the essence of the Bethe-Peierls boundary condition. The dashed lines show the extrapolation for $r \to 0$. (a) reference case; (b) for $\kappa r_0 \ll 1$ most of the probability density of a bound state is found outside the well (halo state); (c) for zero-range potentials ($\kappa r_0 = 0$) the oscillating part of the wavefunction is compressed into a delta function and only the decaying exponent remains (universal limit). Note that these wavefunctions do not share the same normalization.

$(v_{max} + 1/2)\pi$. Reducing r_0 by a factor of 2 the wavenumber K_- has to be doubled to conserve the number of nodes in the wavefunction (i.e. to conserve v_{max}). This means that the kinetic energy inside the well has to increases by a factor 4. Since for the least-bound level we have $K_- r_0 \simeq \gamma$, it means that in this case the binding energy can be conserved at effectively constant well parameter. Obviously, the freedom to conserve (for decreasing r_0) the binding energy of one of the levels can only be used once. It does not hold for the other levels because the level separation diverges with κ_0. In the zero range limit the potential only supports a single bound state and the wavefunction of that state is given by,

$$R_0(r) = c_0 \frac{e^{-\kappa r}}{r} \qquad \text{for} \qquad r > 0 \ , \tag{13.76}$$

and with $\kappa > 0$. Unit normalization, $\int r^2 R_0^2(r) dr = 1$, is obtained for $c_0 = \sqrt{2\kappa}$. For $E > 0$ we can arrive at the same conclusion. The boundary condition for $k \to 0$ and given value of r_0 is given by Eq. (13.41), which we write in the form,

$$\frac{1}{r_0 - a} = \kappa_0 \cot \kappa_0 r_0 \ . \tag{13.77}$$

Reducing the radius r_0, the scattering length a can be conserved by increasing κ_0. In the limit $r_0 \to 0$ the well depth should diverge in accordance with,

$$-\frac{1}{\kappa_0 a} = \cot \kappa_0 r_0 \to 0 \ . \tag{13.78}$$

This is again satisfied for $\kappa_0 r_0 \simeq \pi/2$. In the zero-range limit the radial wavefunction

for $k \to 0$ is given by,

$$R_0(k,r) = \frac{1}{kr}\sin[k(r-a)] \qquad \text{for} \qquad r > 0 \ , \tag{13.79}$$

which implies $R_0(k,r) \simeq 1 - a/r$ for $0 < r \ll 1/k$.

13.1.4.2 Bethe-Peierls boundary condition

Note that Eq. (13.76) is the solution for $E < 0$ of the 1D-Schrödinger equation in the zero-range approximation,

$$u_0'' - \kappa^2 u_0 \qquad \text{for} \qquad r > 0 \ , \tag{13.80}$$

under the boundary condition,

$$\left.\frac{u_0'}{u_0}\right|_{r\to 0} = -\kappa \ . \tag{13.81}$$

The latter relation is called the *Bethe-Peierls boundary condition* and was first used to describe the deuteron, the weakly bound state of a proton with a neutron [**?**]. It shows that for weakly bound states the wavefunction has the universal form of a halo state, which only depends on the binding energy, $\varepsilon_0 = -\kappa^2$ (see Fig. 13.11).

For $E > 0$ the 1D-Schrödinger equation in the zero-range approximation is given by,

$$u_0' + k^2 u_0 = 0 \qquad \text{for} \qquad r > 0 \ . \tag{13.82}$$

The general solution is $u_0(k,r) = c_0 \sin[kr + \eta_0]$. Using the Bethe-Peierls boundary condition we obtain,

$$k \cot \eta_0(k) = -\kappa \ , \tag{13.83}$$

which yields after substituting $\eta_0(k \to 0) \simeq -ka$ the universal relation between the scattering length and the binding energy in the presence of a weakly bound s-level, $\varepsilon_0 = -\kappa^2 = -1/a^2$.

13.1.4.3 Power-law potentials

The general results obtained in the previous sections presumed the existence of a finite range of interaction, r_0. Thus far this presumption was based only on the heuristic argument presented in Sec. **??**. To derive a proper criterion for the existence of a finite range and to determine its value r_0 we have to analyze the asymptotic behavior of the interatomic interaction [605]. For this purpose we consider potentials of the power-law type,

$$V(r) = -\frac{C_s}{r^s} \ , \tag{13.84}$$

where $C_s = V_0 r_c^s$ is the power-law coefficient, with $V_0 \equiv |V(r_c)| \equiv \hbar^2\kappa_c^2/2m_r$ the well depth. These power-law potentials are important from the general physics point of view, because they capture major features of interparticle interactions.

For power-law potentials, the radial wave equation (13.6) takes the form,

$$R_\ell'' + \frac{2}{r}R_\ell' + \left[k^2 + \frac{\kappa_c^2 r_c^s}{r^s} - \frac{\ell(\ell+1)}{r^2}\right] = 0 \ . \tag{13.85}$$

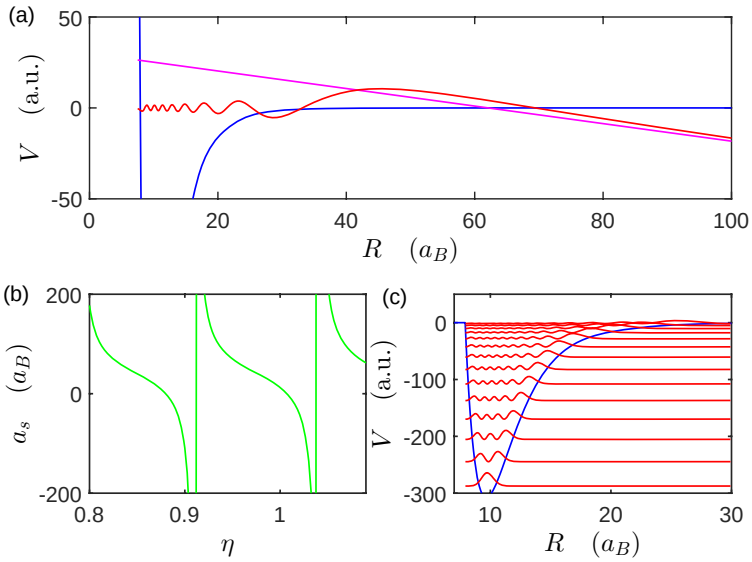

Figure 13.12: (code) Dependence of the scattering length on the potential depth.

Because this equation can be solved analytically in the limit $k \to 0$ it is ideally suited to analyze the conditions under which the potential $V(r)$ may be neglected and thus to determine r_0. To solve Eq. (13.85) we look for a clever substitution of the variable r and the function $R_\ell(r)$ to optimally exploit the known r dependence of the potential in order to bring the differential equation in a well-known form. To leave exibility in the transformation we search for functions of the type,

$$G_\ell(x) = r^{-\nu} R_\ell(r) \ , \tag{13.86}$$

where the power ν is to be selected in a later stage.

13.1.4.4 Computation of the scattering length

The scattering length depends on the *binding energy* E_v of weakly bound states. If a is positive and much greater than the range of the potential, then [342, 290] (13.59),

$$E_v = -\frac{\hbar^2}{2m_r a^2} \ . \tag{13.87}$$

More precisely, for a potential behaving at long range as,

$$V = -\frac{C_6}{R^6} \ , \tag{13.88}$$

we get,

$$E_v = -[(v_D - v)H(m_r, C_6)]^{-1/3} \ , \tag{13.89}$$

where v_D is the vibrational quantum number at the dissociation limit and H a constant. Also,

$$a = \frac{\Gamma(3/4)}{2\sqrt{2}\Gamma(5/4)} \left(\frac{2\mu C_6}{\hbar^2}\right)^{1/4} \left[1 - \tan \pi(v_D + \tfrac{1}{2})\right] \ . \tag{13.90}$$

13.1.4.5 Second method

It yields for $\gamma = \alpha, \beta$,

$$\tfrac{d^2}{dR^2}\varepsilon_\gamma(R) = 2m_r V(R)\varepsilon_\gamma(R) \ . \tag{13.91}$$

Successive approaches start with $\varepsilon_\alpha^{(0)} = R$ and $\varepsilon_\beta^{(0)} = 1$ and get superior orders via,

$$\tfrac{d^2}{dR^2}\varepsilon_\gamma^{(k+1)}(R) = 2m_r V(R)\varepsilon_\gamma^{(k)}(R) \ . \tag{13.92}$$

We define $\delta_\gamma^{(k)} \equiv \varepsilon_\gamma^{(k)} - \varepsilon_\gamma^{(k-1)}$ starting with $\delta_\gamma^{(0)} = \varepsilon_\gamma^{(0)}$, such that,

$$\tfrac{d^2}{dR^2}\delta_\gamma^{(k+1)}(R) = 2m_r V(R)\delta_\gamma^{(k)}(R) \ . \tag{13.93}$$

$\delta_\alpha(R \to \infty) = \delta_\beta(R \to \infty) = 0$. Since $\varepsilon_\alpha = \lim_{k\to\infty} \varepsilon_\alpha^{(k)}$, the wavefunction is thus obtained from,

$$U(R) = \alpha(1 + \delta_\alpha^{(1)} + \delta_\alpha^{(2)} + ..) + \beta(R + \delta_\beta^{(1)} + \delta_\beta^{(2)} + ..) \ . \tag{13.94}$$

This long-range expression must match the short-range value at a certain point R_0:

$$\begin{aligned} U(R_0) &= \alpha\varepsilon_\alpha(R_0) + \beta\varepsilon_\beta(R_0) \ . \\ U'(R_0) &= \alpha\tfrac{d}{dR}\varepsilon_\alpha(R_0) + \beta\tfrac{d}{dR}\varepsilon_\beta(R_0) \end{aligned} \tag{13.95}$$

and

$$a = -\frac{\beta}{\alpha} = \frac{U(R_0)\frac{d}{dR}\varepsilon_\alpha(R_0) - U'(R)\varepsilon_\alpha(R_0)}{U(R_0)\frac{d}{dR}\varepsilon_\beta(R_0) - U'(R)\varepsilon_\beta(R_0)} = \frac{\frac{d}{dR}\frac{\varepsilon_\alpha(R_0)}{U(R_0)}}{\frac{d}{dR}\frac{\varepsilon_\beta(R_0)}{U(R_0)}} \ . \tag{13.96}$$

Let us consider a specific potential,

$$\begin{aligned} V(R) &= \frac{1}{2}BR^{m_r}e^{-\eta R} - \left(\frac{C_6}{R^6} + \frac{C_8}{R^8} + \frac{C_{10}}{R^{10}}\right) f_c(R) \\ f_c(R) &= \theta(R_c - R)e^{-(R_c/R-1)^2} + \theta(R - R_c) \ . \end{aligned} \tag{13.97}$$

At very long range we have $V(R) \simeq -\frac{C_6}{R^6}$, such that,

$$\begin{aligned} \delta_\gamma^{(k+1)} &= \int_0^R 2m_r V\delta_\gamma^{(k+1)}dR = \delta_\gamma^{(k)}(\infty) - \int_R^\infty -\frac{2m_r C_6}{R^6}\delta_\gamma^{(k)}dR \\ &= 2m_r C_6 \int_R^\infty \frac{\delta_\gamma^{(k)}}{R^6}dR \ . \end{aligned} \tag{13.98}$$

In particular,

$$\begin{aligned} \delta_\alpha^{(1)} &= 2m_r C_6 \frac{-1}{4R^4} \quad , \quad \delta_\alpha^{(2)} = (2m_r C_6)^2 \frac{-1}{4\cdot 9R^9} \\ \delta_\beta^{(1)} &= 2m_r C_6 \frac{1}{5R^5} \quad , \quad \delta_\beta^{(2)} = (2m_r C_6)^2 \frac{1}{5\cdot 10R^{10}} \ . \end{aligned} \tag{13.99}$$

13.1.4.6 Third method

To estimate the scattering length for a particular interaction consult [549, **?**, 638]. Following [549] we write the Schrödinger equation in atomic units as,

$$\frac{d^2U}{dR^2} = 2m_r V(R)U(R) \ . \tag{13.100}$$

The ansatz $U(R) = \alpha\varepsilon_\alpha(R) + \beta\varepsilon_\beta(R)$ with $\varepsilon_\alpha(R \to \infty) = R$ and $\varepsilon_\beta(R \to \infty) = 1$ shows that $a = -\beta/\alpha$ is the desired scattering length.

13.1.4.7 Fourth method

The equation for the accumulated phase follows from the Schrödinger equation,

$$\begin{aligned} \phi(r_0) &\equiv \int_\infty^{r_0} k(r)dr \\ k^2(r) &= \frac{2m_r}{\hbar^2}\sqrt{E - V(r) - \frac{\hbar^2 l(l+1)}{2m_r r^2}} \ . \end{aligned} \tag{13.101}$$

According to [638] we start resolving,

$$\frac{d}{dR}\delta_{k,0}(R) = -k^{-1}V(R)\sin^2[kR + \delta_{k,0}(R)] \ . \tag{13.102}$$

13.1.4.8 Pseudo potentials

As in the low-energy limit ($k \to 0$) the scattering properties only depend on the asymptotic phase shift it is a good idea to search for the simplest mathematical form that generates this asymptotic behavior. The situation is similar to the case of electrostatics, where a spherically symmetric charge distribution generates the same far field as a properly chosen point charge in its center. Not surprisingly, the suitable mathematical form is a point interaction. It is known as the pseudo potential and serves as an important theoretical Ansatz at the two-body level for the description of interacting many-body systems [276, 410]. The existence of such pseudo potentials is not surprising in view of the zero-range square well solutions discussed in Sec. 13.6.2.

As the pseudo potential cannot be obtained at the level of the radial wave equation, we return to the full 3D Schrödinger equation for a pair of free atoms,

$$(\nabla^2 + k^2)\psi_k(r) = 0 \ , \tag{13.103}$$

where $k = \sqrt{2m_r E/\hbar^2}$ is the wavenumber for the relative motion. Restricting ourselves to s-wave collisions we derived earlier the solution of this equation as being given by $\psi_k(r) = \frac{c_0}{kr}\sin kr$. However, we are now looking a solution of the type (13.37), which includes a phase shift η_0,

$$\psi_k(r) = \frac{c_0}{kr}\sin(kr + \eta_0) \ . \tag{13.104}$$

Inserting this expression into the wave equation (13.103) we encounter the problem that the solution is irregular in the origin when $\eta_0 \neq 0$. Apparently, we need to complement the wave equation by a (pseudo-)potential to remove this problem.

Our claim is now that the operator,

$$-\frac{4\pi}{k\cot\eta_0}\delta^3(\mathbf{r})\frac{\partial}{\partial r}r \tag{13.105}$$

is the wanted s-wave *pseudo potential* $\tilde{V}(r)$. That is, the wave equation,

$$\boxed{\left(\nabla^2+k^2+\frac{4\pi}{k\cot\eta_0}\delta^3(\mathbf{r})\frac{\partial}{\partial r}r\right)\psi_k(r)=0} \tag{13.106}$$

lets the phase-shifted wavefunction (13.104) be regular at the origin.

The presence of the delta function makes the pseudo-potential act as a boundary condition at $r=0$,

$$\begin{aligned}\frac{4\pi\delta^3(\mathbf{r})}{k\cot\eta_0}\left[\frac{\partial}{\partial r}r\psi_k(r)\right]_{r=r_0} &= 4\pi\delta^3(\mathbf{r})\frac{c_0}{k}\sin\eta_0 \\ &= -4\pi\delta^3(\mathbf{r})\frac{c_0}{k}\sin(ka) \underset{k\to0}{\simeq} -4\pi a c_0\delta^3(\mathbf{r}) \ ,\end{aligned} \tag{13.107}$$

where we used the expression for the s-wave phase shift, $\eta_0=-ka$. This is the alternative boundary condition we were looking for. Substituting this into Eq. (13.106) we obtain the inhomogeneous equation

$$(\nabla^2+k^2)\psi_k(r) \underset{k\to0}{\simeq} -4\pi a c_0\delta^3(\mathbf{r}) \ . \tag{13.108}$$

This inhomogeneous equation has the solution (13.104), as demonstrated in Exc. 13.1.5.4.

For functions $f(\mathbf{r})$ with regular behavior in the origin we have [4],

$$\left[\frac{\partial}{\partial r}rf(\mathbf{r})\right]_{r=0} = f(\mathbf{0})+r\left[\frac{\partial}{\partial r}f(\mathbf{r})\right]_{r=0} = f(\mathbf{0}) \ , \tag{13.109}$$

and the pseudo potential takes the form of a delta function potential [5],

$$\tilde{V}(r) = -\frac{4\pi}{k\cot\eta_0}\delta^3(\mathbf{r}) \underset{k\to0}{\simeq} 4\pi a\delta^3(\mathbf{r}) \ , \tag{13.110}$$

or, equivalently, restoring the dimensions,

$$\boxed{V(r)=\frac{g}{2}\delta^3(\mathbf{r}) \qquad \text{with} \qquad g=\frac{4\pi\hbar^2}{m_r}} \ . \tag{13.111}$$

[4] Note that the wavefunction ψ_k is irregular,

$$\delta^3(\mathbf{r})\frac{\partial}{\partial r}[r\psi_k(r)] = \delta^3(\mathbf{r})\frac{\partial}{\partial r}\left(r\frac{c_0\sin(kr+\eta_0)}{kr}\right) = \delta^3(\mathbf{r})c_0\cos[k(r-a)] \underset{k\to0}{=} c_0\delta^3(\mathbf{r}) \ .$$

On the other hand,

$$\delta^3(\mathbf{r})\frac{\partial}{\partial r}[r\psi_k(r)] = \delta^3(\mathbf{r})\frac{c_0\sin(kr+\eta_0)}{kr} = \delta^3(\mathbf{r})\frac{c_0\sin[k(r-a)]}{kr} \underset{k\to0}{=} c_0\delta^{(3)}(\mathbf{r})[1-\tfrac{a}{r}] \ .$$

[5] Note that the dependence on the relative position vector $\mathbf{r}$ rather than its modulus r is purely formal as the delta function restricts the integration to only zero-length vectors. This notation is used to indicate that normalization involves a 3-dimensional integration, $\int\delta^3(\mathbf{r})d^3r$. Pseudo potentials do not carry physical significance but are mathematical constructions that can chosen such that they provide wavefunctions with the proper phase shift.

This expression, for $na^3 \ll 1$ valid in the zero energy limit, is convenient for calculating the interaction energy, as will be shown in Sec. ??.

13.1.4.9 Coupling of potentials

When molecular potentials cross and couple via collisions, via radiative coupling, or via a Feshbach resonance (cf. Sec. 13.4.2), new adiabatic potentials are formed. These are obtained as the r-dependent eigenvalues of the coupling Hamiltonian,

$$\hat{H}_{cpl} = \begin{pmatrix} V_1(R) & \Omega \\ \Omega & V_2(R) \end{pmatrix} . \tag{13.112}$$

Such calculations are known as *coupled channels* calculations.

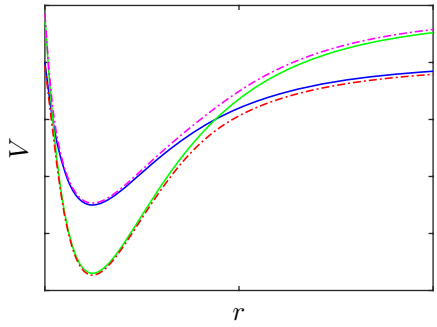

Figure 13.13: (code) The coupling of molecular potentials (solid lines) generates new adiabatic potentials (dash-dotted lines).

13.1.5 Exercises

13.1.5.1 Ex: Asymptotic radial function for hard-sphere potentials

Using asymptotic expressions for the Bessel and von Neumann functions derive the radial function $R_\ell(k, r)$ for the two limiting cases $ka \ll 1$ and $ka \gg 1$.

13.1.5.2 Ex: s-wave collision on flat bottom potentials

Simplify the scattering matrix (13.35) for the collisional flat bottom potential for the case of s-wave collisions.

13.1.5.3 Ex: Equivalence of boundary conditions

Show that the radial wavefunction R_ℓ and u_ℓ satisfy equivalent boundary conditions at the surface of the spherical box potential.

13.1.5.4 Ex: Derivation of a linear expansion

Derive the linear expansion (13.67).

13.1.5.5 Ex: Pseudo-potential for s-wave scattering

Verify the equation $(\nabla^2 + k^2)\psi_k(r) = 4\pi\delta^3(\mathbf{r})\frac{1}{k}\sin\eta_0$ by direct substitution of the solution (13.104) setting $c_0 = 1$.

13.2 Scattering theory

In this chapter we discuss scattering by time independent potentials satisfying $rV(r \to \infty) \to 0$, that is short-range potentials. Such a potential may have attractive regions supporting bound states with energy $E < 0$. Here, however, we only consider states $E > 0$. Since the potential is supposed independent of time, $\partial_t \hat{H} = 0$, we will focus on time-independent problems,

$$\hat{H}\psi_{\mathbf{k}}(\mathbf{r}) = E_k\psi_{\mathbf{k}}(\mathbf{r}) \ , \tag{13.113}$$

with $\hat{H} = p^2/2m + V(\mathbf{r})$ and $E_{\mathbf{k}} = \hbar^2k^2/2m$. The boundary conditions are given by the scattering geometry in such a way that at long distances the wavefunction behaves as (see Fig. 13.14),

$$\psi_{\mathbf{k}}(\mathbf{r}) \sim e^{\imath\mathbf{k}\cdot\mathbf{r}} + f_k(\Omega)\frac{e^{\imath k_s r}}{r} \ . \tag{13.114}$$

For elastic scattering processes we have $k_s = k$. The *scattering amplitude* $f_k(\Omega)$ depends on the energy E_k and on the scattering solid angle. Experimentally, we scatter individual particles described by wave packets. Since the scattering theory is linear, we can describe the packets by superpositions of stationary solutions $\psi_{\mathbf{k}}$ [6].

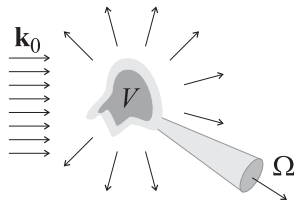

Figure 13.14: Scattering of incident light (wavevector $\mathbf{k}_0$) by a potential V.

13.2.1 Lippmann-Schwinger equation

In order to consider the example of two particles involved in a collision we may go into the center-of-mass system (using reduced masses), fix the origin of the coordinate system on one of the particles, and analyze the trajectory of the second particle inside the interaction potential.

The scattering theory is based on *Green's method*, which we already know from electrostatics. So, let us start of a brief reminder of the use of the *Green's function* as a method to solve electrostatic problems.

[6] Note that $\mathbf{k}$ is not a quantum number, since $\psi_{\mathbf{k}}$ contains momentum components $\neq \mathbf{k}$.

Example 73 (*Green's method in electrostatics*): From Maxwell's third equation we obtain,

$$\nabla^2\phi(\mathbf{r}) = -\varepsilon_0^{-1}\rho(\mathbf{r}) \ .$$

Being defined by,

$$\nabla^2 G(\mathbf{r}) = \delta^3(\mathbf{r}) \ ,$$

the Green function is,

$$G(\mathbf{r}) = \frac{-1}{4\pi}\frac{1}{|\mathbf{r}|} \ .$$

With this, we find the solution of the Maxwell equation,

$$\phi(\mathbf{r}) = \left(-G \star \varepsilon_0^{-1}\rho(\mathbf{r})\right)(\mathbf{r}) = -\frac{1}{\varepsilon_0}\int_V \rho(\mathbf{r}_0)G(\mathbf{r}-\mathbf{r}_0)d^3\mathbf{r}_0 = \frac{1}{4\pi\varepsilon_0}\int_V \frac{\rho(\mathbf{x})}{|\mathbf{r}-\mathbf{x}|}d^3\mathbf{x} \ ,$$

known as *Poisson's law*.

13.2.1.1 Green's method in quantum mechanics

Green's method can be used to solve Schrödinger's equation with the boundary condition (13.114). We start from the reduced stationary Schrödinger equation (13.113) [813],

$$(\Delta + k^2)\psi_{\mathbf{k}}(\mathbf{r}) = \tfrac{2m}{\hbar^2}V(\mathbf{r})\psi_{\mathbf{k}}(\mathbf{r}) \ . \tag{13.115}$$

This equation is not a common eigenvalue problem, since any energy E_k generates a solution. The equation (13.115) is a partial inhomogeneous differential equation with the left side describing free propagation and the right side describing a source that depends on the solution. Such differential equations are usually solved using Green's functions. We choose a point source and we solve,

$$(\Delta + k^2)G(\mathbf{r}, k) = \delta^3(\mathbf{r}) \ , \tag{13.116}$$

along with the boundary conditions. The solution takes the form [88],

$$G(\mathbf{r}, k) = -\frac{1}{4\pi}\frac{e^{\imath k|\mathbf{r}|}}{|\mathbf{r}|} \ , \tag{13.117}$$

such that,

$$\boxed{\psi_{\mathbf{k}}(\mathbf{r}) = e^{\imath\mathbf{k}\cdot\mathbf{r}} + \left(G \star \tfrac{2m}{\hbar^2}V\psi_{\mathbf{k}}\right)(\mathbf{r}) = e^{\imath\mathbf{k}\cdot\mathbf{r}} + \tfrac{2m}{\hbar^2}\int_V d^3r' G(\mathbf{r}-\mathbf{r}', k)V(\mathbf{r}')\psi_{\mathbf{k}}(\mathbf{r}')} \ . \tag{13.118}$$

The equation (13.118) is called *Lippmann-Schwinger equation*. Of course, this equation does not solve, but only reformulate the problem taking into account the boundary conditions. It is more appropriate for an implementation of approximations. See Exc. 13.2.7.1 and 13.2.7.2.

Now let us consider the far field, $r \to \infty$, to verify the asymptotic behavior and find an expression for $f_k(\Omega)$ as a function of $V(\mathbf{r})$. For $r \to \infty$ we can approximate

$$k|\mathbf{r}-\mathbf{r}'| = kr\sqrt{(\hat{\mathbf{e}}_r - \mathbf{r}'/r)^2} = kr\sqrt{1 - 2\hat{\mathbf{e}}_r\cdot\mathbf{r}'/r + (r'/r)^2} \simeq kr - \mathbf{k}'\cdot\mathbf{r}' \simeq kr \ , \tag{13.119}$$

with $\mathbf{k}' \equiv k\hat{\mathbf{e}}_r$. With this the Lippmann-Schwinger equation (13.118) becomes,

$$\begin{aligned}\psi(\mathbf{r}) &\to e^{\imath\mathbf{k}\cdot\mathbf{r}} - \frac{2m}{\hbar^2}\int_V \frac{1}{4\pi}\frac{e^{\imath k|\mathbf{r}-\mathbf{r}'|}}{|\mathbf{r}-\mathbf{r}'|}V(\mathbf{r}')\psi(\mathbf{r}')d^3r' \\ &= e^{\imath\mathbf{k}\cdot\mathbf{r}} - \frac{2m}{4\pi\hbar^2}\frac{e^{\imath kr}}{kr}\int_V e^{-\imath\mathbf{k}'\cdot\mathbf{r}'}V(\mathbf{r}')\psi(\mathbf{r}')d^3r' \equiv \psi_{\text{in}} + f_k(\Omega)\frac{e^{\imath kr}}{r}\ ,\end{aligned} \tag{13.120}$$

giving, in comparison with the expression (13.114), the *scattering amplitude*,

$$f_k(\Omega) = \frac{2m}{4\pi\hbar^2}\int_V e^{-\imath\mathbf{k}'\cdot\mathbf{r}'}V(\mathbf{r}')\psi(\mathbf{r}')d^3r'\ . \tag{13.121}$$

Starting from the wavefunctions $\psi_{\text{in}} \equiv e^{\imath\mathbf{k}\cdot\mathbf{r}}$ and $\psi_s \equiv f_k(\Omega)e^{\imath kr}/r$ we can calculate the current densities,

$$\begin{aligned}\mathbf{J}_{\text{in}} &= \frac{\hbar}{2m\imath}(\psi_{\text{in}}^\dagger\nabla\psi_{\text{in}} - c.c.) = \frac{\hbar\mathbf{k}}{m} \\ \mathbf{J}_s &= \frac{\hbar}{2m\imath}(\psi_s^\dagger\partial_r\psi_s - c.c.)\hat{\mathbf{e}}_r = \frac{\hbar\mathbf{k}'}{m}\frac{1}{r^2}|f_k(\Omega)|^2 + \mathcal{O}(r^{-3})\ .\end{aligned} \tag{13.122}$$

The number $dI(\Omega)$ of particles scattered per second into the solid angle $d\Omega$ is simply $dI(\Omega) = |\mathbf{J}_s|r^2d\Omega$. With this we can calculate the *differential effective cross section* defined by the ratio between $dI(\Omega)$ and the number $|\mathbf{J}_{\text{in}}|$ of incident particles per second,

$$\boxed{\frac{d\sigma}{d\Omega} \equiv \frac{dI(\Omega)}{|\mathbf{J}_{\text{in}}|d\Omega} = |f_k(\Omega)|^2}\ . \tag{13.123}$$

Finally we define the *total effective cross section*,

$$\sigma = \int d\Omega|f_k(\Omega)|^2\ . \tag{13.124}$$

13.2.2 Wave packets

We now let a *wave packet* defined at a time $t = t_0$,

$$\psi(\mathbf{r}, t_0) = \int \frac{d^3k}{(2\pi)^3}a_{\mathbf{k}}e^{\imath\mathbf{k}\cdot\mathbf{r}}\ , \tag{13.125}$$

impinge on a scattering potential. The amplitude $a_{\mathbf{k}}$ be concentrated around $\mathbf{k}_0$, such that the wave packet approaches the scatterer with the velocity $\mathbf{v}_0 = \hbar\mathbf{k}_0/m$. The time evolution of the wavefunction $\psi(\mathbf{r}, t)$ determines the signal measured by a detector at a later time $t = t_0$. Our task is to determine $\psi(\mathbf{r}, t > t_0)$. The scattered states $\psi_{\mathbf{k}}$ solving the Schrödinger equation (13.113) are complete in the space of the extended wavefunctions, and we can write the temporal evolution as,

$$\psi(\mathbf{r}, t) = \int \frac{d^3k}{(2\pi)^3}A_{\mathbf{k}}\psi_{\mathbf{k}}(\mathbf{r})e^{-\imath E_k(t-t_0)/\hbar}\ . \tag{13.126}$$

At time t_0 the results (13.125) and (13.126) must match. To verify this, we write (13.125) replacing the plane wave $e^{\imath \mathbf{k}\cdot\mathbf{r}}$ using the Lippmann-Schwinger equation (13.118) with Green's function (13.117), and then we compare the coefficients,

$$\psi(\mathbf{r},t_0) = \int \frac{d^3k}{(2\pi)^3} a_{\mathbf{k}} \left[\psi_{\mathbf{k}}(\mathbf{r}) + \frac{m}{2\pi\hbar^2} \int d^3r' \frac{e^{\imath k|\mathbf{r}-\mathbf{r}'|}}{|\mathbf{r}-\mathbf{r}'|} V(\mathbf{r}')\psi_{\mathbf{k}}(\mathbf{r}') \right] . \tag{13.127}$$

The scattering process is illustrated in Fig. 13.15. To simplify the calculation of the

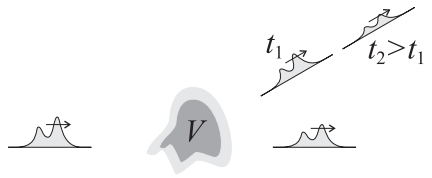

Figure 13.15: Scattering of wave packet at a potential.

second term in this equation, we assume that $\psi_{\mathbf{k}}$ is smooth, that is, there are no resonances, such that we can approximate, $\psi_{\mathbf{k}} \simeq \psi_{\mathbf{k}_0}$. With $k \simeq \mathbf{k}\cdot\hat{\mathbf{e}}_{k_0}$ we obtain,

$$\begin{aligned} \int \frac{d^3k}{(2\pi)^3} a_{\mathbf{k}} e^{\imath k|\mathbf{r}-\mathbf{r}'|} \psi_{\mathbf{k}}(\mathbf{r}') &= \int \frac{d^3k}{(2\pi)^3} a_{\mathbf{k}} e^{\imath \mathbf{k}\cdot(\hat{\mathbf{e}}_{k_0}|\mathbf{r}-\mathbf{r}'|)} \psi_{\mathbf{k}_0}(\mathbf{r}') \\ &\overset{(13.125)}{=} \psi(\hat{\mathbf{e}}_{k_0}|\mathbf{r}-\mathbf{r}'|,t_0)\psi_{\mathbf{k}_0}(\mathbf{r}') . \end{aligned} \tag{13.128}$$

Here, $\psi(\hat{\mathbf{e}}_{k_0}|\mathbf{r}-\mathbf{r}'|,t_0)$ is the incident wave package evaluated to the right, where by definition it is $\simeq 0$. The expression (13.127) therefore has the form,

$$\psi(\mathbf{r},t_0) = \int \frac{d^3k}{(2\pi)^3} a_{\mathbf{k}} \psi_{\mathbf{k}}(\mathbf{r}) , \tag{13.129}$$

and a comparison of the coefficients with (13.126) gives, $A_{\mathbf{k}} = a_{\mathbf{k}}$. Finally, we evaluate $\psi(\mathbf{r},t)$ at the time of detection $t > t_0$ to understand, that the above stationary analysis is actually physically correct. According to (13.126) we have,

$$\begin{aligned} \psi(\mathbf{r},t) &= \int \frac{d^3k}{(2\pi)^3} A_{\mathbf{k}} \psi_{\mathbf{k}}(\mathbf{r}) e^{-\imath E_k(t-t_0)/\hbar} \\ &\overset{(13.120)(13.125)}{\simeq} \psi_0(\mathbf{r},t) + \int \frac{d^3k}{(2\pi)^3} a_{\mathbf{k}} \frac{e^{\imath kr}}{r} f_k(\Omega) e^{-\imath E_k(t-t_0)/\hbar} . \end{aligned} \tag{13.130}$$

Hence, $\psi_0(\mathbf{r},t)$ describes the evolution of the wave packet without scatterer,

$$\psi_0(\mathbf{r},t) = \underbrace{\int \frac{d^3k}{(2\pi)^3} a_{\mathbf{k}} e^{\imath \mathbf{k}\cdot\mathbf{r}}}_{\psi(\mathbf{r},t_0)} e^{-\imath E_k(t-t_0)/\hbar} . \tag{13.131}$$

If f_k it's smooth around $\mathbf{k} = \mathbf{k}_0$, which allows us to place this amplitude ($f_k \simeq f_{k_0}$) in front of the integral, and with $k \simeq \mathbf{k}\cdot\hat{\mathbf{k}}_0$ we obtain,

$$\psi(\mathbf{r},t) \overset{t \text{ large}}{\Longrightarrow} \underbrace{\psi_0(\mathbf{r},t)}_{\text{packet not scattered}} + \underbrace{\frac{f_{k_0}(\Omega)}{r} \psi_0(\hat{k}_0 r,t)}_{\text{packet scattered}} . \tag{13.132}$$

The scattering process is illustrated in Fig. 13.15: According to the last equation the scattering process involves the superposition of the non-scattered packet and a packet scattered in the direction Ω. The latter involves the amplitude $\Psi_0(\hat{k}_0 r, t)$ of a packet propagating in forward direction, which only needs to be evaluated at the right time and distance. This packet will then be multiplied with the amplitude describing the angular dependency f_{k_0}; the angle, therefore, only appears through this amplitude and not in the wavefunction ψ_0. In two situations the above analysis can not be applied :

- when V is long-ranged, f.ex., $V = 1/r$,
- when the incident energy E_k is resonant.

13.2.3 Born approximation

The Lippmann-Schwinger equation suggests the following perturbative iteration called *Born series* [88],

$$\begin{aligned}\psi(\mathbf{r}) &= \psi_{\rm in}(\mathbf{r}) + \left(G \star \tfrac{2m}{\hbar^2} V\psi\right)(\mathbf{r}) \\ &= \psi_{\rm in}(\mathbf{r}) + \tfrac{2m}{\hbar^2}(G \star V\psi_{\rm in})(\mathbf{r}) + \left(\tfrac{2m}{\hbar^2}\right)^2 [G \star V(G \star V\psi_{\rm in})](\mathbf{r}) \\ &= \psi_{\rm in}(\mathbf{r}) + \tfrac{2m}{\hbar^2}\int_V G(\mathbf{r}-\mathbf{r}')V(\mathbf{r}')\psi_{\rm in}(\mathbf{r}')d^3\mathbf{r}' \\ &\quad + \left(\tfrac{2m}{\hbar^2}\right)^2 \int_V G(\mathbf{r}-\mathbf{r}')V(\mathbf{r}')G(\mathbf{r}-\mathbf{r}'')V(\mathbf{r}'')\psi_{\rm in}(\mathbf{r}'')d^3r'd^3r'' \ .\end{aligned} \tag{13.133}$$

In the so-called *Born approximation* we consider only the first perturbation order, and inserting a plane wave, $\psi_{\rm in}(\mathbf{r}) = e^{\imath kz}/(2\pi)^{3/2}$, we obtain,

$$\psi(\mathbf{r}) = \frac{e^{\imath kz}}{(2\pi)^{3/2}} - \frac{m}{(2\pi)^{3/2}2\pi\hbar^2}\int_V \frac{e^{\imath k|\mathbf{r}-\mathbf{r}'|}}{|\mathbf{r}-\mathbf{r}'|}V(\mathbf{r}')e^{\imath kz'}d^3r' \ . \tag{13.134}$$

The asymptotic behavior $r \gg r'$, it follows with (13.119) using $z' = \mathbf{r}'\cdot\hat{\mathbf{e}}_z$ and defining $\mathbf{k}_s = k\hat{\mathbf{e}}_r$ and $\mathbf{k}_i = k\hat{\mathbf{e}}_z$,

$$\begin{aligned}\psi(\mathbf{r}) &\simeq \frac{e^{\imath kz}}{(2\pi)^{3/2}} - \frac{m}{(2\pi)^{3/2}2\pi\hbar^2}\int_V \frac{e^{\imath k(r-\mathbf{r}\cdot\mathbf{r}'/r)}}{r}V(\mathbf{r}')e^{\imath\mathbf{k}\cdot\mathbf{r}'}d^3r' \\ &= \frac{e^{\imath kz}}{(2\pi)^{3/2}} + \frac{m}{(2\pi)^{3/2}2\pi\hbar^2}\frac{e^{\imath kr}}{r}\int_V V(\mathbf{r}')e^{\imath(\mathbf{k}_i-\mathbf{k}_s)\cdot\mathbf{r}'}d^3r' \\ &\equiv \frac{1}{(2\pi)^{3/2}}\left(e^{\imath kz} + \frac{e^{\imath kr}}{r}f(k_i,k_s)\right) \ ,\end{aligned} \tag{13.135}$$

with

$$\boxed{f(k_i,k_s) \equiv \frac{m}{2\pi\hbar^2}\int_V V(\mathbf{r}')e^{\imath(\mathbf{k}_i-\mathbf{k}_s)\cdot\mathbf{r}'}d^3r' = -\frac{m}{2\pi\hbar^2}\langle k_s|\tilde{V}|k_i\rangle} \ .$$

13.2.4 Spherical potentials

For spherically symmetric scattering potentials, $V(\mathbf{r}) = V(r)$, the Hamiltonian $\hat{H} = p^2/2m + V(r)$ commutes with the rotation operators $U_{\vec{\omega}} = e^{-\imath\vec{\omega}\cdot\mathbf{L}/\hbar}$ around any axis $\hat{\mathbf{e}}_{\vec{\omega}}$. Therefore, we can separate the angular problem and decompose the scattering problem following the irreducible representations of the rotation group. This *partial wave* decomposition can be written,

$$\psi_{\mathbf{k}}(\mathbf{r}) = \sum_{\ell=0}^{\infty}(2\ell+1)\imath^{\ell}P_{\ell}(\cos\theta)R_{l}(r)\ , \tag{13.136}$$

where the factor $(2\ell+1)i^{\ell}$ is a convention facilitating the calculation later on. By inserting this separation ansatz for the radial and angular variables into the stationary Schrödinger equation (13.113), we obtain the radial Schrödinger equation,

$$\left[\frac{\partial^2}{\partial r^2} - \frac{\ell(\ell+1)}{r^2} + k^2\right] rR_{\ell}(r) = \frac{2m}{\hbar^2}V(r)rR_{\ell}(r)\ , \tag{13.137}$$

where $\psi_{\mathbf{k}}$ must satisfy the boundary conditions (13.114). Fortunately, we can also expand the incident wave by partial waves [7],

$$e^{\imath kz} = e^{\imath r\cos\theta} = \sum_{\ell=0}^{\infty}(2\ell+1)\imath^{\ell}j_{\ell}(kr)P_{\ell}(\cos\theta)\ . \tag{13.138}$$

We now use the result (13.138) to find the boundary conditions for the radial waves R_ℓ. In the infinity we have $rV(r) \overset{r\to\infty}{\longrightarrow} 0$. For this reason,

$$R_{\ell}(r) \overset{r\to\infty}{\longrightarrow} \alpha_{\ell}[h_{\ell}^{(2)}(kr) + s_{\ell}h_{\ell}^{(1)}(kr)]\ , \tag{13.139}$$

where the Hankel functions $h_{\ell}^{(1,2)}(kr) \sim e^{\pm\imath(\rho-(\ell+1)\pi/2)}$ describe, respectively, incident $(h_{\ell}^{(2)})$ and outgoing $(h_{\ell}^{(1)})$ spherical waves.

To determine the coefficients α_ℓ and s_ℓ we note first that, without potential, $V(r) = 0$, the solution of the radial equation (13.137) is known,

$$R_{\ell}(r) = j_{\ell}(kr) = \tfrac{1}{2}[h_{\ell}^{(2)}(kr) + h_{\ell}^{(1)}(kr)]\ , \tag{13.140}$$

such that $\alpha_\ell = \frac{1}{2}$ and $s_\ell = 1$. For $V(r) \neq 0$ the incident wave $h_\ell^{(2)}$ is the same, but not the incident $h_\ell^{(1)}$, which results in $s_\ell \neq 1$. However, particle number conservation requires that the number of particles entering the potential is equal to the number of particles coming out. That is, the total radial flow must be,

$$0 = j_r^{\ell}(r) = \frac{\hbar}{2\imath m}[R_{\ell}^{*}\partial_r R_{\ell} - R_{\ell}\partial_r R_{\ell}^{*}] = \frac{\hbar}{4mkr^2}[|s_{\ell}|^2 - 1]\ , \tag{13.141}$$

[7] For the more general case of arbitrary vectors $\mathbf{k}$ e $\mathbf{r}$, we use the addition theorem for $Y_{\ell m}$ and express $P_\ell(\cos\theta)$ by spherical functions,

$$e^{\imath\mathbf{k}\cdot\mathbf{r}} = 4\pi\sum_{\ell=0}^{\infty}\sum_{m=-\ell}^{\ell}\imath^{\ell}j_{\ell}(kr)Y_{\ell m}^{*}(\Omega_{\mathbf{k}})Y_{\ell m}(\Omega_{\mathbf{r}})\ .$$

approximating $2R_\ell \simeq \frac{e^{-\imath(kr+w_\ell)}}{kr} + s_\ell \frac{e^{\imath(kr+w_\ell)}}{kr}$. Hence, $|s_\ell| = 1$, that is,

$$s_\ell = e^{2\imath\delta_\ell(k)} \ , \tag{13.142}$$

where $\delta_\ell(k)$ is the *scattering phase*. The scattering phase determines the solution of the scattering problem, because it fixes the scattering amplitude: Evaluating the solution (13.136) in the asymptotic limit by the formula (13.138),

$$\begin{aligned}\psi_{\mathbf{k}}(\mathbf{r}) &\sim \tfrac{1}{2}\sum_{\ell=0}^{\infty}(2\ell+1)\imath^\ell P_\ell(\cos\theta)[h_\ell^{(2)}(kr) + e^{2i\delta_\ell}h_\ell^{(1)}(kr)] \qquad (13.143)\\ &= e^{\imath\mathbf{k}\cdot\mathbf{r}} + \tfrac{1}{2}\sum_{\ell=0}^{\infty}(2\ell+1)\imath^\ell P_\ell(\cos\theta)[e^{2\imath\delta_\ell}-1]h_\ell^{(1)}(kr) = e^{\imath\mathbf{k}\cdot\mathbf{r}} + f_k(\theta)\frac{e^{\imath kr}}{r} \ ,\end{aligned}$$

we obtain the scattering amplitude in the form [8]

$$\boxed{f_k(\theta) = \tfrac{1}{k}\sum_\ell (2\ell+1)P_\ell(\cos\theta)e^{\imath\delta_\ell}\sin\delta_\ell} \ . \tag{13.144}$$

We call

$$\frac{e^{2\imath\delta_\ell}-1}{2ik} = \frac{e^{\imath\delta_\ell}\sin\delta_\ell}{k} \equiv f_\ell \tag{13.145}$$

the *amplitude of the partial wave* [858, 111].

13.2.5 Scattering phase and length

In summary, we can, within the Born approximation, express the collisional state of any type of particles by isotropic potentials,

$$\psi(\mathbf{r}) \sim e^{\imath\mathbf{k}\cdot\mathbf{r}} + \frac{e^{\imath kr}}{r} f_k(\Omega) \ . \tag{13.146}$$

The scattering cross section can be written,

$$\begin{aligned}\sigma &= \int d\Omega |f_{\mathbf{k}}(\Omega)|^2 = \tfrac{1}{k^2}\int d\Omega |\sum_\ell (2\ell+1)P_\ell(\cos\theta)\sin\delta_\ell|^2 \qquad (13.147)\\ &= \frac{4\pi}{k^2}\sum_\ell (2\ell+1)\sin^2\delta_\ell = 4\pi\sum_\ell (2\ell+1)|f_\ell|^2 \ .\end{aligned}$$

The quantity

$$\boxed{\sigma_\ell = \frac{4\pi}{k^2}(2\ell+1)\sin^2\delta_\ell = \frac{4\pi}{k^2}(2\ell+1)|f_\ell|^2} \tag{13.148}$$

is called *effective partial cross section*. Obviously, $\sigma_\ell \le \frac{4\pi}{k^2}(2\ell+1)$ holds. The phase shift $e^{2i\delta_\ell}$ has a simple physical interpretation: We consider the function,

$$\begin{aligned}e^{\imath\delta_\ell} j_\ell(kr+\delta_\ell) &= \tfrac{e^{\imath\delta_\ell}}{2}[h_\ell^{(2)}(kr+\delta_\ell) + h_\ell^{(1)}(kr+\delta_\ell)] \qquad (13.149)\\ &\sim \frac{e^{\imath\delta_\ell}}{2}\left[\frac{(-\imath)^\ell e^{i(kr+\delta_\ell)}}{kr+\delta_\ell} + \frac{(+\imath)^\ell e^{-\imath(kr+\delta_\ell)}}{kr+\delta_\ell}\right] \overset{kr\gg\delta_\ell}{\longrightarrow} \tfrac{1}{2}[h_\ell^{(2)} + e^{2\imath\delta_\ell}h_\ell^{(1)}] \sim R_\ell \ .\end{aligned}$$

[8] With $h_\ell^{(1)} \sim (-\imath)^{\ell+1}\frac{e^{\imath kr}}{kr}$.

Now comparing the case $V = 0$ giving $R_\ell(r) = j_\ell(kr)$ with the case $V \neq 0$ giving $R_\ell(r) \sim e^{\imath\delta_\ell} j_\ell(kr + \delta_\ell)$, we notice that a positive displacement, $\delta_\ell > 0$, pulls the wavefunction into the potential, while a negative displacement, $\delta_\ell < 0$, pushes the wavefunction out, as illustrated in Fig. 13.16.

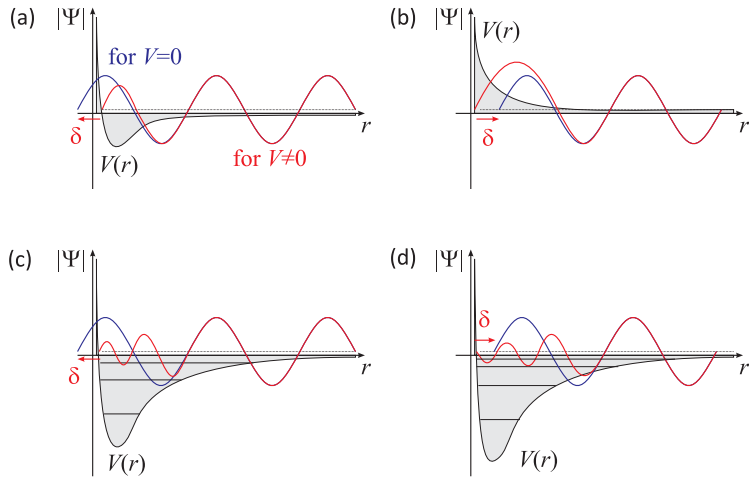

Figure 13.16: Phase shift $\delta_\ell(k)$ of the scattered wavefunction. (a) An attractive potential increases the kinetic energy and the wavefunction oscillates faster, which causes a positive phase shift and a negative scattering length. (b) A repulsive potential slows down the wavefunction oscillation and produces a positive scattering length. (c,d) In an attractive potential deep enough to support vibrational states, the wavefunction performs several oscillations. The sign of the scattering length then depends on the distance of the last bound state to the continuum.

13.2.6 Optical theorem

Consider the amplitude for forward scattering $f(0)$ by writing its imaginary part as,

$$\text{Im } f(0) = \tfrac{1}{k} \sum_k (2\ell+1) P_\ell(\cos\theta) \sin^2\delta_\ell\big|_{\theta=0} = \tfrac{1}{k} \sum_k (2\ell+1) \sin^2\delta_\ell \equiv \frac{k}{4\pi}\sigma \ . \quad (13.150)$$

With this we obtain the *optical theorem*,

$$\boxed{\sigma = \tfrac{4\pi}{k} \text{Im } f(0)} \ . \quad (13.151)$$

The deeper meaning of the optical theorem is the conservation of particle number: The flux of scattered particles, $(\hbar k/m)\sigma = I_{sct}$, must be extracted from the incident flux I_0 by scattering, and therefore, is missing in the forward direction. It is the interference of the scattered wave with the incident wave, which diminishes the non-scattered wave and therefore creates a shadow of the scatterer in the forward direction. The particles missing in the shadow of the scatterer are precisely those that have been scattered. This is the message of the optical theorem, which is always valid in the absence of possible (inelastic) processes leading to trapping or a transformation of the particles.

Table 13.1: List of scattering length for various alkaline species.

Element	a_s^{mixed}	$a_s^{triplet}$	$a_p^{triplet}$	$B_{FB,s-wave}$	$B_{FB,p-wave}$
	$[a_B]$	$[a_B]$	$[a_B]$	[G]	[G]
^{1}H		1.23			
^{2}H		−6.8			
^{6}Li			−35		160, 186, 215
^{7}Li	10	−27.3			
^{23}Na	52	85			
^{39}K	118	81.1			
^{40}K	158	1.7	−100	200	200
^{41}K	225	286			
^{85}Rb	−450	−363		156	
^{87}Rb	105	109.3		685.43, 911.74, 1007.34	
^{133}Cs	−240	−350			
^{135}Cs	163	138			

13.2.6.1 Born approximation for the scattering phase

The scattering problem can be considered as solved when we know the scattering amplitude $f_k(\theta)$, since this quantity gives us the flux measured by the detector. Now, $f_k(\theta)$ is known, when we know the scattering phases $\delta_{\ell,k}$. These are, in general, determined by integrating the radial equation (13.137). Here, we expect that only angular momenta $\ell < kR_0$ (R_0 is the range of potential) produce significant phase shifts. Particles with larger angular momenta have collision parameters $b \sim \ell/k$ out of the potential reach. We notice that partial s-waves are always scattered, whereas partial p-waves (or higher) are only weakly scattered when the energy is weak, $E < \hbar^2/2mR_0^2$. In these cases an approximate calculation of δ_ℓ is sufficient: We insert (13.136) and $e^{\imath kz} = \sum_\ell \frac{1}{2}\sqrt{4\pi(2\ell+1)}\int_{-1}^{1} dz P_\ell(z) e^{ikz}$ into (13.121) and integration over Ω' yields,

$$\begin{aligned} f_k(\theta) &= \frac{2m}{4\pi\hbar^2}\int_V e^{-\imath \mathbf{k}'\cdot\mathbf{r}'} V(\mathbf{r}')\psi(\mathbf{r}')d^3\mathbf{r}' \\ &= -\tfrac{2m}{\hbar^2}\sum_{\ell=0}^{\infty}(2\ell+1)P_\ell(\cos\theta)\int_0^\infty dr\ r^2 V(r) j_\ell(kr) R_\ell(r)\ . \end{aligned} \tag{13.152}$$

Comparing this formula with (13.144) we find,

$$e^{\imath\delta_\ell}\sin\delta_\ell = -\tfrac{2mk}{\hbar^2}\int_0^\infty dr\ r^2 V(r) j_\ell(kr) R_\ell(r) \overset{R_\ell \simeq j_\ell}{\simeq} -\tfrac{2mk}{\hbar^2}\int_0^\infty dr\ r^2 V(r) j_\ell^2(kr)\ . \tag{13.153}$$

The result (13.153) is the Born approximation for the scattering phase $\delta_\ell(k)$. Note that $R_\ell \simeq j_\ell$ is not a good approximation, in ranges where V is large and R_ℓ strongly suppressed (f.ex., inside hard cores). For ℓ large we have $j_\ell \sim r^\ell$, and $\delta\ell$ is small for a limited potential $V(r)$.

13.2.6.2 Analyticity of $s_\ell(E)$

We consider a short-range potential that disappears at $r > R_0$. The radial solution out of the reach of the potential will then be given by,

$$R_\ell(r) = \tfrac{1}{2}[h_\ell^{(2)}(kr) + s_\ell h_\ell^{(1)}(kr)] \ , \tag{13.154}$$

while for $r < R_0$ the solution R_ℓ must be found by integrating the radial equation (13.137). The scattering phase s_ℓ must be chosen in a way that R_ℓ and $\partial_r R_\ell$ be continuous at R_0. The normalization factor vanishes in the logarithmic derivative, such that,

$$\gamma_\ell \equiv \partial_r \ln R_\ell|_{R_0^-} = \left.\frac{1}{R_\ell}\frac{\partial R_\ell}{\partial r}\right|_{R_0^-} = \left.\frac{\partial_r h_\ell^{(2)} + s_\ell \partial_r h_\ell^{(1)}}{h_\ell^{(2)} + s_\ell h_\ell^{(1)}}\right|_{R_0^+} . \tag{13.155}$$

Now [9]

$$s_\ell - 1 = \left.\frac{2(\partial_r - \gamma_\ell) j_\ell}{(\gamma_\ell - \partial_r) h_\ell^{(1)}}\right|_{R_0} \tag{13.156}$$

or with $s_\ell - 1 = \frac{2\imath}{\cot\delta_\ell - \imath}$ expressing δ_ℓ by γ_ℓ,

$$\cot\delta_\ell = \left.\frac{(\partial_r - \gamma_\ell) n_\ell}{(\partial_r - \gamma_\ell) j_\ell}\right|_{R_0} . \tag{13.157}$$

The partial effective cross section is,

$$\sigma_\ell = \frac{4\pi}{k^2}(2\ell+1)\sin^2\delta_\ell = \frac{4\pi}{k^2}\frac{2\ell+1}{1+\cot^2\delta_\ell} . \tag{13.158}$$

Analyzing the expressions for $s_\ell(\cot\delta_\ell)$ and $\sigma_\ell(\cot\delta_\ell)$ we find that

- for $\cos\delta_\ell = \imath$ the scattering phase s_ℓ has a pole and $\sigma_\ell \to \infty$;
- for $\cos\delta_\ell = 0$ the scattering phase is $s_\ell - 1$ and $\sigma_\ell = 4\pi(2\ell+1)/k^2$ is maximal.

The poles of s_ℓ are just the bound states: A bound state asymptotically satisfies $R_\ell(r) \sim h_\ell^{(1)}(\imath\kappa r) \propto e^{-\kappa r}$ with the binding energy $E_B = -\hbar^2\kappa^2/2m$. The condition of continuity is given by,

$$\gamma_\ell = \left.\frac{\partial_r h_\ell^{(1)}}{h_\ell^{(1)}}\right|_{R_0} , \tag{13.159}$$

and the insertion into the general continuity condition (13.157) gives,

$$\cot\delta_\ell = \frac{h_\ell^{(1)}\partial_r n_\ell - n_\ell \partial_r h_\ell^{(1)}}{h_\ell^{(1)}\partial_r j_\ell - j_\ell \partial_r h_\ell^{(1)}} = \imath . \tag{13.160}$$

[9] We have for the spherical Hankel functions: $h_\ell^{(1,2)}(x) = j_\ell(x) \pm \imath y_\ell(x)$.

In the same way the zero crossings of $\cot\delta_\ell$ correspond precisely to the scattering resonances. To see this, we expand around a resonance,

$$\cot\delta_\ell(E) \simeq \cot\delta_\ell(E_r) - \frac{1}{\sin^2\delta_\ell}\left.\frac{d\delta_\ell}{dE}\right|_{E_r}(E-E_r) = -\left.\frac{d\delta_\ell}{dE}\right|_{E_r}(E-E_r) \equiv -\frac{2}{\Gamma_r}(E-E_r)\,, \tag{13.161}$$

defining the width $\Gamma_r = \left.\frac{2}{\partial_E\delta_\ell}\right|_{E_r}$ of the resonance peak in the effective section σ_ℓ in the form,

$$\sigma_\ell = \frac{4\pi}{k^2}(2\ell+1)\frac{(\Gamma_r/2)^2}{(E-E_r)^2+(\Gamma_r/2)^2}\ . \tag{13.162}$$

See Fig. 13.17,

$$s_\ell - 1 = \frac{-\imath\Gamma_r}{E-(E_r-\imath\gamma_r/2)}\ . \tag{13.163}$$

The scattering phase δ_ℓ increases by π. The value $\delta_\ell(E=0)$ gives the number of bound states, $\delta_\ell(0) = n^\ell_{\rm bound}\pi$.

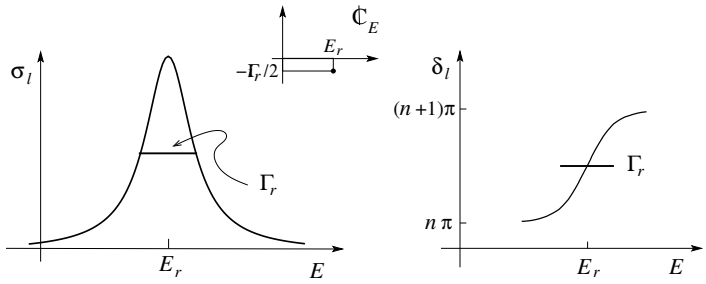

Figure 13.17: Peak of the resonance of width Γ_r: (Left) effective cross section $\sigma_\ell(E)$, (right) scattering phase $\delta_\ell(E)$, and (center) scheme of the position of the pole in the complex energy plane E.

13.2.7 Exercises

13.2.7.1 Ex: Green's method

Show that, knowing the solution of (13.116), that is, knowing the Green function, we can write the solution of the scattering problem (13.115) as,

$$\psi_{\mathbf{k}}(\mathbf{r}) = e^{\imath\mathbf{k}\cdot\mathbf{r}} + \tfrac{2m}{\hbar^2}\int d^3\mathbf{r}'\mathcal{G}(\mathbf{r}-\mathbf{r}',k)V(\mathbf{r}')\psi_{\mathbf{k}}(\mathbf{r})\ .$$

13.2.7.2 Ex: Green's function

Calculate the Green function of the equation (13.116).

13.2.7.3 Ex: Rutherford scattering

Consider the scattering of a particle of charge Q by a static charge distribution $\rho(\mathbf{r}) = \rho_0 e^{-\alpha r}$ totaling the charge Q'. Derive from (13.136) the formula (1.10) describing the Rutherford scattering.

13.2.7.4 Ex: Scattering length for hard-core potentials

Calculate the scattering length for a spherical box barrier and a spherical box potential as a function of potential depth (see also Excs. 3.1.5.4 and 3.1.5.5 and [849]).

13.3 Cold atomic collisions

Modern techniques developed in the area of atomic optics allow to cool atomic gases to temperatures well below 1 μK. We use the expansions $j_\ell \sim x^\ell/(2\ell+1)!!$ and $n_\ell \sim (2\ell-1)!!/x^{\ell+1}$ in the equation (13.157), and obtain for $kR_0 \ll 1$,

$$\cos\delta_\ell \simeq \frac{2\ell+1)!!(2\ell-1)!!}{(kR_0)^{2\ell+1}} \frac{\ell+1+R_0\alpha_\ell(E)}{\ell-R_0\alpha_\ell(E)} \ . \tag{13.164}$$

A coarse approximation leads to

$$\cos\delta_\ell = \frac{\cos\delta_\ell}{\sin\delta_\ell} \overset{\delta_\ell \ll 1}{\simeq} \frac{1}{\sin\delta_\ell} \simeq \frac{1}{(R_0k)^{2\ell+1}} \ , \tag{13.165}$$

that is,

$$\sin\delta_\ell \simeq (R_0k)^{2\ell+1} \ . \tag{13.166}$$

In other words, the scattering phases decrease rapidly, in the regime of cold collisions, with increasing ℓ, and $\ell = 0$ type collisions dominate,

$$k\cot\delta_0 \overset{\alpha_\ell(E)\simeq\alpha_\ell(0)}{\simeq} -\frac{1+R_0\alpha_0(0)}{R_0^2\alpha_\ell(E)} \ . \tag{13.167}$$

The s-wave *scattering length* defined by,

$$a_s \equiv \frac{R_0^2\alpha_\ell(E)}{1+R_0\alpha_0(0)} = \frac{\sin\delta_0}{k} \tag{13.168}$$

then it is the only relevant parameter of the collision. For $R_0\alpha_0 \gg 1$ we find $a \simeq R_0$. For example, for a hard sphere we have $R_\ell(R_0) = 0$, $\alpha_\ell = \infty$, $a = R_0 > 0$ and $\cot\delta_0 = -1/kR_0$. For small kR_0 we obtain $\delta_0 \simeq -kR_0 < 0$, which corresponds to a negative phase shift for the repulsive potential, as expected. The effective cross section is,

$$\boxed{\sigma_0 = \frac{4\pi}{k^2}\frac{1}{1+\cot^2\delta_0} \simeq \frac{4\pi}{k^2+1/a_s^2}} \ . \tag{13.169}$$

In comparison to the effective cross section for higher angular momenta, $\sigma_\ell \propto \frac{\sin^2\delta_\ell}{k^2}$ behaves like,

$$\sigma_\ell \propto R_0^2(R_0k)^{4\ell} \to 0 \ . \tag{13.170}$$

In contrast, we find that the scattering at low energies has an s-wave character, σ being dominated by σ_0,

$$\sigma(E=0) = 4\pi a_s^2 \ . \tag{13.171}$$

For a hard sphere ($a = R_0$) we find an effective cross section *four times larger* than classically expected ($\sigma_{cl} = \pi R_0^2$).

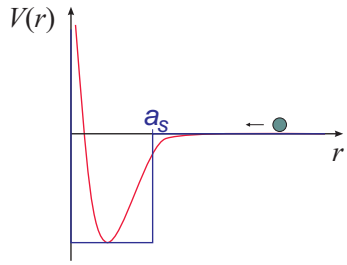

Figure 13.18: The cold collision can be described by a hard core potential.

In summary, for kinetic energies below the centrifugal barrier, only s-wave collisions are significant. The higher-order partial waves are *frozen* behind the centrifugal barrier. That is, the energy of cold collisions is not enough to excite a rotational motion, not even the one with the lowest rotational energy allowed by quantum mechanics. Such a collision is called *cold collision* or *s-wave collision*.

The relative wavefunction tends asymptotically to $\psi(R) \overset{R\to\infty}{\longrightarrow} k_{dB}^{-1} \sin\left[k_{dB}(R-a)\right] \overset{T\to 0}{\longrightarrow} R - a$. This means that for temperatures so low that the length of the Broglie wave of the relative motion is much longer than the potential range $k_{dB}^{-1} \gg R_{turning}$, the scattering becomes independent of temperature, and the scattering length a becomes well defined [10]

Generally, a repulsive interaction potential corresponds to a positive scattering length and an attractive potential to a negative one. However, if the attractive potential supports bound states, the value of the scattering length depends on the energy of the last bound state with respect to the dissociation threshold [849, 850].

13.3.1 Collision cross section, unitarity regime

Note that the scattering length a may have a value quite different from r_e, especially in the presence of a Feshbach resonance. The meaning of *universality*, $|a| \gg r_e$, is that short-range properties play no role in the dynamics.

At low temperatures, $kr_e \to 0$, we have the equation (13.169). In contrast, in the *unitarity limit*, $k \to \infty$, but $r_e \to 0$, we have,

$$\sigma = \frac{8\pi}{k^2} \ , \tag{13.172}$$

and the cross section becomes independent of atomic particularities. What the equation (13.169) says is, that the maximum attainable cross-section is limited to the

[10] At temperatures at which the trajectory of atoms is described by de Broglie waves the only difference between an atom before and after an elastic collision is the phase shift δ_0 of this wave.

smallest of the values $8\pi a$ and $8\pi/k$. Even though $a(B)$ can be increased to divergent values near a Feshbach resonance, for finite collision energies it will never exceed an effective value $a_{eff} = 1/\sqrt{a^2 + 1/k^2}$. For a thermal gas, $k = \hbar^{-1}\sqrt{2\pi m k_B T}$, while for a pure condensate $k = 2\pi/L$, where L is the size of the condensate. Therefore, the effective scattering length can not exceed the size of the condensate. Unitarity also means that the kinetic energy exceeds the binding energy, $k_B T \equiv \frac{\hbar^2 k^2}{2m} \leq \frac{\hbar^2}{2ma^2}$.

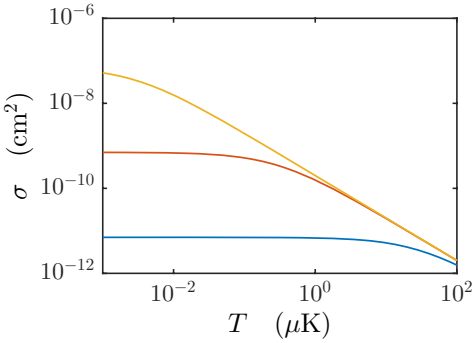

Figure 13.19: (code) Temperature dependence of the collision cross section for various scattering lengths. For higher scattering lengths, the unitarity limit is reached at lower temperatures.

The collision rate depends on the density, temperature and collisional cross section [458],

$$\gamma_{coll.peak} = \sqrt{2}\sigma_{elast}\bar{v}n_0 \ , \qquad (13.173)$$
$$\gamma_{coll.aver} = \gamma_{coll.peak}/2\sqrt{2} \ .$$

Note that at the unitary limit, as $\bar{v} \propto \sqrt{T}$, we have that $\sigma_{elas} \propto T$ and $n_0 \propto \bar{r}^{-3} \propto T^{-3/2}$, such that the collision rate is independent of temperature.

At low temperatures, $k \to 0$, the delocalization of the colliding particles is greater than its short-range structure. This is the *Wigner threshold law* [865, 858]. For elastic collisions of neutral ground state atoms, the cross section (13.169) becomes temperature-independent. Thus, the rate coefficient decreases as $\langle\sigma\bar{v}\rangle \propto \sqrt{T}$, while the collision rate increases as $\langle\sigma\bar{v}n_0\rangle \propto T^{-1}$.

For inelastic collisions, $\sigma \propto T^{-1}$. For three-body collisions see [271].

13.3.2 Collisions between identical particles

We consider collisions of two identical particles. Separating the center-of-mass coordinates, $\mathbf{R} = \mathbf{r}_1 + \mathbf{r}_2$, from the relative ones, $\mathbf{r} = \mathbf{r}_1 - \mathbf{r}_2$, we see that $\mathbf{R}$ is symmetric and $\mathbf{r}$ antisymmetric in $\mathbf{r}_1$ and $\mathbf{r}_2$. We separate the wavefunction into orbital and spin parts,

$$\Psi(x_1, x_2) = e^{\imath \mathbf{P}\cdot\mathbf{R}}\psi(\mathbf{r})\chi(s_1, s_2) \ . \qquad (13.174)$$

For indistinguishable particles the result of the scattering has the asymptotic form,

$$\psi(\mathbf{r}) \sim e^{\imath \mathbf{k}\cdot\mathbf{r}} + f(\theta)\frac{e^{\imath kr}}{r} \ . \qquad (13.175)$$

13.3.2.1 Spin 0 bosons

For bosons with spin 0 we have $\chi = 1$ and, because of the symmetry of Ψ, holds $\psi(\mathbf{r}) = \psi(-\mathbf{r})$. Consequently, we must symmetrize the result of the scattering. We make use of the fact that the exchange of particles via $\mathbf{r} \to -\mathbf{r}$ in polar coordinates corresponds to the transformation $\theta \to \pi - \theta$, $r \to r$,

$$\psi \sim (e^{\imath \mathbf{k}\cdot\mathbf{r}} + e^{-\imath \mathbf{k}\cdot\mathbf{r}}) + [f(\theta) + f(\pi - \theta)]\frac{e^{\imath kr}}{r} \ . \tag{13.176}$$

For the effective differential cross section we obtain,

$$\frac{d\sigma}{d\Omega} = |f(\theta) + f(\pi - \theta)|^2 = |f(\theta)|^2 + |f(\pi - \theta)|^2 + 2\mathfrak{Re}\,[f^*(\theta) f(\pi - \theta)] \ . \tag{13.177}$$

The first two terms are classical. The third (interference) term appears because of quantum statistics. The angles showing up in (13.177) are illustrated in Fig. 13.20. For bosons, the interference terms double the cross section as compared to the classical case, when $\theta = \pi/2$,

$$\boxed{\frac{d\sigma}{d\Omega} = 4|f(\tfrac{\pi}{2})|^2} \ . \tag{13.178}$$

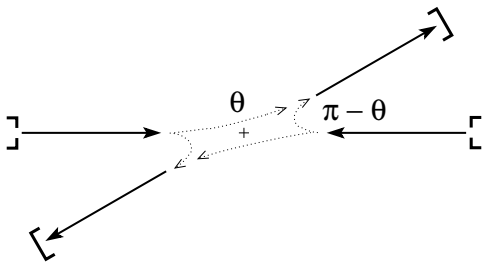

Figure 13.20: The symmetrization of the collision wavefunction produces two paths with angles θ and $\pi - \theta$, which must be added coherently.

For the isotropic potential $V(r)$ we use the partial wave representation,

$$f(\theta) = \sum_\ell \imath^\ell f_\ell P_\ell(\cos\theta) \ . \tag{13.179}$$

With $P_\ell(\cos\theta) = (-1)^\ell P_\ell(\pi - \cos\theta)$ we get,

$$f(\theta) - f(\pi - \cos\theta) = 2\sum_{\ell_{\rm par}} \imath^\ell f_\ell P_\ell(\cos\theta) \ , \tag{13.180}$$

and we find that only *even angular momenta* appear [11]

[11] For ℓ odd the Legendre polynomial changes sign, and the contributions vanish.

13.3.2.2 Spin 1/2 fermions

In the case of fermions with spin $\frac{1}{2}$ two situations are possible [12]:

1. The singlet spin state $\chi_s = \frac{1}{\sqrt{2}}[(|\uparrow\downarrow\rangle - |\downarrow\uparrow\rangle]$ is antisymmetric and, consequently, the orbital part,
$$\psi(\mathbf{r}) = \psi(-\mathbf{r}) \tag{13.181}$$
must be symmetric. The cross section is the same as for spin 0 bosons,
$$\left.\frac{d\sigma}{d\Omega}\right|_s = |f(\theta) + f(\pi - \theta)|^2 \ . \tag{13.182}$$

2. The triplet spin states,
$$\chi_s = \begin{cases} |\uparrow\uparrow\rangle \\ \frac{1}{\sqrt{2}}(|\uparrow\downarrow\rangle + |\downarrow\uparrow\rangle) \\ |\downarrow\downarrow\rangle \end{cases} \tag{13.183}$$
require an antisymmetric orbital wavefunction, $\psi(\mathbf{r}) = -\psi(-\mathbf{r})$, and we obtain a scattering amplitude, $f(\theta) \to f(\theta) - f(\pi - \theta)$, which only contains *odd angular momenta* ℓ. With this, the cross section becomes,
$$\left.\frac{d\sigma}{\Omega}\right|_t = |f(\theta) - f(\pi - \theta)|^2 \overset{\theta=\pi/2}{=} 0 \ , \tag{13.184}$$
Note that polarized fermions only scatter in channels of odd angular momenta: cold bosonic atoms show a *contact potential* due to s-wave collisions (13.180)), polarized fermionic atoms only interact weakly in the p-channel. In the case of a statistically mixed ensemble of non-polarized fermions we have a the weighted average,
$$\frac{d\sigma}{d\Omega} = \frac{3}{4}\left.\frac{d\sigma}{\Omega}\right|_t + \frac{1}{4}\left.\frac{d\sigma}{\Omega}\right|_s = |f(\theta)|^2 + |f(\pi - \theta)|^2 - \mathfrak{Re}\left[f^*(\theta) f(\pi - \theta)\right] \ . \tag{13.185}$$

13.3.2.3 Molecular spectra

Here we consider rotational spectra of low energies $E_{\rm rot} = \hbar^2\ell(\ell+1)/2\Theta \ll E_{eletronico} \sim eV$. In slow time scales we can consider the electronic shell to be rigid. We look at two examples of molecules with bosonic and fermionic nuclei:

- Molecules $(C^{12})_2$: the nuclei are 0-spin bosons, so only collisions with even ℓ are allowed.
- Molecules H_2: the nuclei are spin-$\frac{1}{2}$ fermions, so we have for a spin wavefunction,
$$\chi = \chi_s : \ell = \text{even, para-hydrogen}, \chi = \chi_t : \ell = \text{odd, ortho-hydrogen.} \tag{13.186}$$
The transformation of ortho-hydrogen into para-hydrogen is difficult (the nuclei being well shielded), such that we observe two types of gases with,
$$E_{rot,para} = 0, \frac{3}{\Theta}, \frac{10}{\Theta}, \frac{21}{\Theta}, ... E_{rot,orto} = \frac{1}{\Theta}, \frac{6}{\Theta}, \frac{15}{\Theta}, ... \ . \tag{13.187}$$

[12] This is analogous to the case of helium, where the spatial function of the state $2s^2\uparrow\uparrow$ is always antisymmetric, but for the $2s\uparrow 2p\uparrow$ exist symmetric spatial orbitals.

13.3.3 Collisions between hot atoms

Angular moments with $\ell \leq kR_0$ should contribute a lot to σ, since the collision parameter is inside R_0. For a hard sphere we have $\alpha_\ell = \infty$ and $\cot\delta_\ell = n_\ell(kR_0)/j_\ell(kR_0)$. With the asymptotic expressions of j_ℓ and n_ℓ we obtain $\cot\delta_\ell \sim -\cot(kR_0 - \ell\pi/2)$, that is, $\delta_\sim - kR_0 + \ell\pi/2$ $(+\pi)$. With these scattering phases we can calculate the scattering cross section,

$$\sigma \simeq \tfrac{4\pi}{k^2}\sum_{\ell=0}^{kR_0}(2\ell+1)\sin^2\delta_\ell \tag{13.188}$$

$$\simeq \tfrac{4\pi}{k^2}\sum_{\ell=0}^{kR_0}(\ell+1)\cos^2[kR_0-(\ell+1)\pi/2] + \ell\sin^2(kR_0-\ell\pi/2)$$

$$= \tfrac{4\pi}{k^2}\sum_{\ell=0}^{kR_0}\ell(\cos^2+\sin^2) = \tfrac{4\pi}{k^2}\frac{kR_0(kR_0+1)}{2} = 2\pi R_0^2\ , \tag{13.189}$$

which is the double of the classical value.

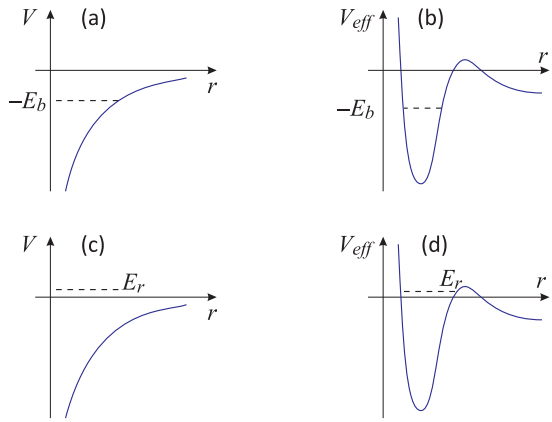

Figure 13.21: (a) Bound state for $\ell = 0$. (b) Bound state for $\ell > 0$ in a potential including the centrifugal barrier $\hbar^2\ell(\ell+1)/2mr^2$. (c) Resonances for $\ell = 0$ are broad and possibly not defined with $\Gamma_r > E_r$. A defined resonance with $\Gamma_r < E_r$ requires that $|\partial_E\alpha_0|$ be large. (d) For $\ell > 0$ we obtain narrow resonances called *shape resonances*, because the decay of the state is suppressed by the centrifugal barrier.

13.3.4 Ground state collisions

13.3.5 Hyperfine structure

We consider the scheme (12.100), we set $\mathbf{l}_j = 0$, and concentrate on s-waves, $\ell = 0$,

$$\begin{array}{ccccccc} \mathbf{s}_1 & + & \mathbf{s}_2 & = & \mathbf{S} & \xrightarrow{\hat{z}} & \mathbf{\Omega} \\ + & & + & & + & & \\ \mathbf{i}_1 & + & \mathbf{i}_2 & = & \mathbf{I} & & \\ = & & = & & = & & \\ \mathbf{f}_1 & + & \mathbf{f}_2 & = & \mathbf{f} & & \end{array} \tag{13.190}$$

At short distances the coupling $((S, I)f_1, f_2)f$ breaks up and a $((s_1, s_2)S, I)f$ coupling emerges. This does not hold for fully stretched spin states $f_1 + f_2 = f$, because f is a good quantum number at all distances (and small enough magnetic fields). In contrast m_f is a good quantum number at all distances and at all fields.

In order to obtain the potentials coupled by hyperfine interaction, we first calculate for a *single vibrational level* the relative wavefunctions $|\psi_{(f_1,f_2)f}(R)\rangle$ from the known perturbed but uncoupled potentials $V(R) + V_{hf}$, where,

$$V_{hf} = h a_{hf,1} \mathbf{s}_1 \cdot \mathbf{i}_1 + h a_{hf,2} \mathbf{s}_2 \cdot \mathbf{i}_2 \ . \tag{13.191}$$

The antisymmetric part is negligible [840], so that $V_{hf} \simeq \frac{1}{2} h a_{hf,1} \mathbf{S} \cdot \mathbf{i}_1 + \frac{1}{2} h a_{hf,2} \mathbf{S} \cdot \mathbf{i}_2$. Then couple the channels via,

$$|\psi_{(S,I)f}(R)\rangle = A \sum_{f_1,f_2} \sqrt{\hat{S}\hat{I}\hat{f}_1\hat{f}_2} \begin{Bmatrix} s_1 & s_2 & S \\ i_1 & i_2 & I \\ f_1 & f_2 & f \end{Bmatrix} |\psi_{(f_1,f_2)f}(R)\rangle \tag{13.192}$$

$$|\psi_{(f_1,f_2)f}(R)\rangle = A^{-1} \sum_{S,I} \sqrt{\hat{S}\hat{I}\hat{f}_1\hat{f}_2} \begin{Bmatrix} s_1 & s_2 & S \\ i_1 & i_2 & I \\ f_1 & f_2 & f \end{Bmatrix} |\psi_{(S,I)f}(R)\rangle \ .$$

which satisfies the orthogonality relation (see Tables in 6.2).

13.3.6 Scattering length in specific channels

The scattering length in specific channels can be expressed via singlet and triplet scattering length,

$$a_{|f_1,m_{f1}\rangle+|f_2,m_{f2}\rangle} = P_{S=0} a_s + P_{S=1} a_t \ . \tag{13.193}$$

The projectors are $P_S = |\langle S|(f_1 f_2)f\rangle|$. According to [125] or [577] the recoupling from the uncoupled hyperfine representation into the short range representation is given by,

$$\langle S m_S \ I m_I \ \ell' m_{\ell'} | f_1 m_{f1} \ f_2 m_{f2} \ \ell m_\ell \rangle = \delta_{\ell\ell'} \delta_{m_\ell m'_\ell} \sum_{f,m_f} \langle S m_S \ I m_I | f m_f \rangle \langle f_1 m_{f1} \ f_2 m_{f2} | f m_f \rangle \times \tag{13.194}$$

$$\times \begin{Bmatrix} s_1 & s_2 & S \\ i_1 & i_2 & I \\ f_1 & f_2 & f \end{Bmatrix} \sqrt{\hat{S}\hat{I}\hat{f}_1\hat{f}_2} \left(\frac{1 - (1 - \delta_{f_1 f_2})(-1)^{S+I+\ell}}{\sqrt{2 - \delta_{f_1 f_2}}} \right) \ .$$

The last bracket is dropped for unsymmetrized recoupling. Calculations have been done for ^{87}Rb collisions and for ^{6}Li^{87}Rb collisions. It turns out that the fully stretched states have pure triplet character.

Note that in strong magnetic fields the coupling $(i_1, i_2)I$ easily breaks up, and the recoupling to be considered is rather $\langle Sm_S\ m_{i1}\ m_{i2}\ \ell' m_{\ell'} | f_1 m_{f1}\ f_2 m_{f2}\ \ell m_\ell \rangle$.

13.3.7 Hyperfine coupling in magnetic fields

13.3.7.1 Zeeman splitting of bound states

The splitting of the bound state is described by [840],

$$\begin{aligned} H_{int}^{+} &= V_{hf}^{+} + V_{Zeeman} \\ &= E_B + \frac{1}{2} h a_{hf,1} \mathbf{S}\cdot\mathbf{i}_1 + \frac{1}{2} h a_{hf,2} \mathbf{S}\cdot\mathbf{i}_2 + \mu_B \mathbf{B}(g_S \mathbf{S} + g_1 \mathbf{i}_1 + g_2 \mathbf{i}_2)\ , \end{aligned} \tag{13.195}$$

such that,

$$\begin{aligned} &\langle m'_{i1} m'_{i2} m'_S | H_{hfs} + H_B | m_S m_{i2} m_{i1} \rangle \\ &= E_B + (g_S m_S + g_{i1} m_{i1} + g_{i2} m_{i2}) \mu_B B \delta_{m'_{i1}\ m_{i1}} \delta_{m'_{i2}\ m_{i2}} \delta_{m'_S\ m_S} \\ &+ \tfrac{1}{2} h (a_{hf,1} m_{i1} m_S + a_{hf,2} m_{i2} m_S) \delta_{m'_{i1}\ m_{i1}} \delta_{m'_{i2}\ m_{i2}} \delta_{m'_S\ m_S} \\ &+ \tfrac{1}{4} h a_{hf,1} (i_{1,+} S_- \delta_{m'_S\ m_S+1} \delta_{m'_{i1}\ m_{i1}-1} + i_{1,-} S_+ \delta_{m'_{i1}\ m_{i1}-1} \delta_{m'_S\ m_S+1}) \delta_{m'_{i2}\ m_{i2}} \\ &+ \tfrac{1}{4} h a_{hf,2} (i_{2,+} S_- \delta_{m'_S\ m_S+1} \delta_{m2\ m_{i2}-1} + i_{2,-} S_+ \delta_{m'_{i2}\ m_{i2}-1} \delta_{m'_S\ m_S+1}) \delta_{m'_{i1}\ m_{i1}}\ . \end{aligned} \tag{13.196}$$

For an example on how to evaluate the matrix at various magnetic fields and obtain the hyperfine structure of a bound state in the Zeeman and the Paschen-Back regime, we propose the systems ^{6}Li^{23}Na and ^{6}Li^{87}Rb.

13.3.7.2 Magnetic dipole interaction

Reads,

$$V_{dd} = \frac{\mu_0}{4\pi R^3} \left[\mu_1 \cdot \mu_1 - 3(\mu_2 \cdot \mathbf{R})(\mu_2 \cdot \mathbf{R}) \right] \tag{13.197}$$

neglecting nuclear spin.

13.3.7.3 Second-order spin-orbit interaction

First-order spin-orbit interaction disappears for ground state collisions. But second-order spin-orbit interaction may occur. These lead to inelastic losses (see next section).

13.3.7.4 Selection rules

The selection rules for bosonic homonuclear collisions are,

$$\begin{aligned} S &= 0, .., s_1 + s_2 \\ I &= 0, .., i_1 + i_2 \\ f_j &= |i_j - s_j|, .., i_j + s_j \\ |I - S| \leq F &\leq I + S \\ |f_1 - f_2| \leq F &\leq f_1 + f_2 \\ (-1)^I &= (-1)^S \quad \text{for all } F \\ (-1)^{f_1} &= -(-1)^{f_2} \quad \text{for all odd } F \ . \end{aligned} \tag{13.198}$$

What does they look like for fermions? What does they look like for heteronuclear collisions?

13.3.8 Inelastic collisions

13.3.8.1 Spin changing collisions

These have their origin in *spin exchange* and spin dipole-dipole processes. Spin exchange occurs when the colliding electronic clouds overlap. At short distances the $((S, I)f_1, f_2)f$ breaks up and a $((s_1, s_2)S, I)f$ coupling remixes, as shown in Exc. 12.3.5.1. Hence, collisions between atoms $|f_1, m_{f1}\rangle|f_2, m_{f2}\rangle$ are subject to spin exchange induced by coupling of the spin states via the exchange interaction, e.g. $|2, 1\rangle|2, 1\rangle \rightarrow |2, 2\rangle|2, 0\rangle$. Typical exchange rates are on the order of $10^{-10}\,\mathrm{cm}^3/\mathrm{s}$.

Since f is a good quantum number at all distances (for $B = 0$), spin exchange processes conserve ℓ and f. Hence, the fully stretched spin states $f_1 + f_2 = f$ cannot decay into other states, except by higher-order processes, such as dipolar relaxation. Consequently, the relaxation rates for $|2, 2\rangle + |2, 2\rangle$ or $|1, -1\rangle + |1, -1\rangle$ states are only on the order of $10^{-15}\,\mathrm{cm}^3/\mathrm{s}$.

The cross section for inelastic spin exchange collisions is [861, 174],

$$\sigma = M_{if}\pi(a_t - a_s)^2 \ , \tag{13.199}$$

where,

$$\begin{aligned} M_{if} &= \left[\sum_{m_S, I, m_I} (C_{S=0} C'_{S=0} - C_{S=1} C'_{S=1}) \right]^2 \\ C &= \langle S, m_S; I, m_I | F_1 m_1; F_2 m_2 \rangle \ . \end{aligned} \tag{13.200}$$

See also [759]. The reason for the above dependence can be understood as follows. a_s and a_t determine the energy of the last bounds states of the singlet and triplet potentials. The more those energies are different, the stronger the coupling $\propto |E_t - E_s|^{-1}$. An alternative, physical picture is given in [126].

13.3.8.2 Dipolar relaxation

The fully stretched spin states, such as ^{87}Rb $|f = 2, m_f = 2\rangle$ are expected to be quite stable. However, relativistic effects (retardation?) (and 2^{nd} order spin-orbit coupling) break the degeneracy of the molecule-fixed projection $|\Omega| = 0, 1$ of the $^3\Sigma$ potential [577]. When the atoms approach their spins recouple, i.e. from $[(s_1, i_1)f_1\ ,\ (s_2, i_2)f_2]f$ towards $[(s_1, s_2)s\ ,\ (i_1, i_2)i]f$ as described by the $9j$ coefficients Eq. (13.190). Due to the symmetry of the problem, f and its projection m_f are good quantum numbers at all distances. However, if there is a higher-order admixture of the orbit l_j, the symmetry is broken, and the quantum number depends on the coupling schemes. Consequently, transitions between different m_f become possible, i.e. dipolar relaxation may change f, m_f or $\ell = 0$, e.g. a collision can be s-wave in the entrance and d-wave in the exit channel.

13.3.8.3 Three-body collisions

The trapped low-field seeking alkali gases are metastable versus 3-body recombination. 3-body recombination is the combination of two colliding atoms to a dimer in presence of a third atom receiving the excess energy as kinetic energy and results in trap loss of the molecule and of the atom. They are suppressed as the gas gets more and more dilute since the rate goes like n^3. There might be interesting 3-body resonance phenomena like the *Efimov state* predicted for Helium droplets [257], [519] and recently seen in experiment [487, 796, 111, 538].

3-body recombination is in contrast to the more controlled way of creating molecules via photoassociation or coherent free-bound coupling.

Ultracold collisions are crucial for BEC. They provide the thermalizing elastic collisions necessary for evaporative cooling, they are the cause for the condensate self-energy and give rise to nonlinearities in the condensate dynamics. But they are also interesting by themselves. The spectrum of two-body collisions exhibits interesting features like shape- and Feshbach resonances [178, 415]. Their analysis facilitates detailed conclusions on the nature of the interaction potentials. Three body collisions are important to investigate, because they constitute a decay mechanism of the intrinsically metastable system that represents a trapped Bose-gas.

Three body collisions are not a quantum statistical effect and don't require the presence of a BEC, but they occur only at very high densities comparable to those necessary for BEC. It should be possible to detect them in *photoassociation* (PA) spectra. Photoassociation provides a tool to explore the level structure of excited states by shining in a laser with frequency ν tuned between the colliding channel and a vibrational bound level of the excited state potential. Since the excited state preferentially decays into the continuum, where the atoms have high kinetic energy, the transition rate may be monitored via trap losses. Or we can shine in an additional laser that further excites the excited atoms into the ionized continuum where they can be registered by an ion detector.

Three-body photoassociation processes should reveal themselves by additional lines in the two-body photoassociation spectra. Those lines should only appear at very high densities and their strength should scale as the density cubed,

$$Rb + Rb + Rb + h\nu \rightarrow Rb_3^* \ . \tag{13.201}$$

13.3.8.4 Other processes

Majorana spin flips and collisions involving higher partial waves ℓ can eventually lead to spin relaxation. In Eq. (12.100) we see that f is not necessarily a good quantum number in contrast to F, $|2,2\rangle|2,2\rangle \to |2,1\rangle|2,0\rangle + E_{\rm rot}$. However, the particles must tunnel across the centrifugal barrier, which sets temperature constraints.

13.3.8.5 Collisions between fermions

Very cold three-body collisions are suppressed for fermions, because two of them necessarily must have the same quantum state, which violates the Pauli exclusion principle. This is useful for employing Feshbach resonances to form molecular BECs made of fermions.

13.3.9 Excited states collisions

13.3.9.1 Adiabatic potentials

We consider the scheme (12.100), we set $\mathbf{I} = 0$, and we concentrate on s-waves, $\ell = 0$,

$$\begin{array}{ccccccc} \mathbf{l}_1 & + & \mathbf{l}_2 & = & \mathbf{L} & \xrightarrow{\hat{z}} & \mathbf{\Lambda} \\ + & & + & & + & & + \\ \mathbf{s}_1 & + & \mathbf{s}_2 & = & \mathbf{S} & \xrightarrow{\hat{z}} & \mathbf{\Sigma} \\ = & & = & & = & & = \\ \mathbf{j}_1 & + & \mathbf{j}_2 & = & \mathbf{j} & \xrightarrow{\hat{z}} & \mathbf{\Omega} \end{array} \tag{13.202}$$

The *spin-orbit interaction* splits the potential curves. The recoupling is described by,

$$|\psi_{(L,S)j}(R)\rangle \sim \sum_{j_1,j_2} \sqrt{\hat{L}\hat{S}j_1j_2} \begin{Bmatrix} l_1 & l_2 & L \\ s_1 & s_2 & S \\ j_1 & j_2 & j \end{Bmatrix} |\psi_{(j_1,j_2)j}(R)\rangle \ . \tag{13.203}$$

13.3.9.2 Homonuclear collisions

Let us consider the example of the fine structure in homonuclear ^{87}Rb collisions. Without hyperfine, rotational and Zeeman splitting the recoupling goes like illustrated in Fig. 13.22.

From Fig. 13.22 we see that the molecular states are remixed at long range: Every state $0_g^-, 0_u^-, 0_g^+, 0_u^+, 1_g, 1_u, 2_g, 2_u$ has several molecular states to which it connects, e.g. 0_g^- connects within the fine structure to $(2)^3\Sigma_g^+$ and $(2)^3\Pi_g$. Those multiplets form a closed interacting subspace. According to Movre and Pichler [606, 821] we get

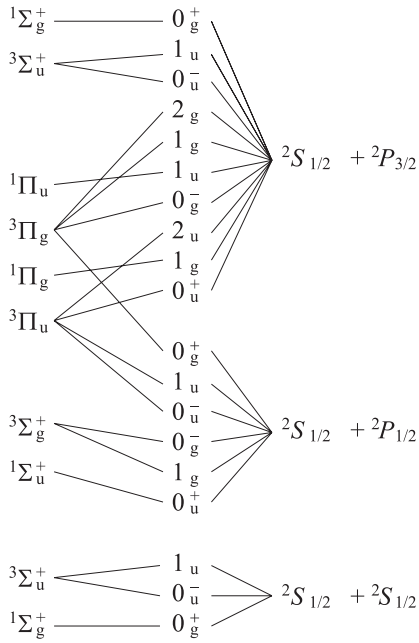

Figure 13.22: Movre coupling scheme.

with $\Delta = E(^2P_{3/2}) - E(^2P_{1/2}) = \frac{3}{2}A_{so}$,

$$0_\sigma^- = \begin{pmatrix} E(^3\Pi_\sigma) - \frac{1}{3}\Delta & \frac{\sqrt{2}}{3}\Delta \\ -\frac{\sqrt{2}}{3}\Delta & E(^3\Sigma_\sigma^+) \end{pmatrix} \quad , \quad 0_\sigma^+ = \begin{pmatrix} E(^3\Pi_\sigma) - \frac{1}{3}\Delta & -\frac{\sqrt{2}}{3}\Delta \\ -\frac{\sqrt{2}}{3}\Delta & E(^1\Sigma_\sigma^+) \end{pmatrix} \tag{13.204}$$

$$1_\sigma = \begin{pmatrix} E(^3\Pi_\sigma) & \frac{1}{3}\Delta & -\frac{1}{3}\Delta \\ \frac{1}{3}\Delta & E(^1\Pi_\sigma) & -\frac{1}{3}\Delta \\ -\frac{1}{3}\Delta & -\frac{1}{3}\Delta & E(^3\Sigma_\sigma^+) \end{pmatrix} \quad , \quad 2_\sigma = \left(^3\Pi_\sigma\right) \ .$$

At short range the potentials approximately go like,

$$\begin{aligned} E(^1\Sigma_g^+), E(^3\Sigma_u^+) &\propto 2C_3/R^3 \\ E(^1\Pi_u), E(^3\Pi_g) &\propto C_3/R^3 \\ E(^1\Pi_g), E(^3\Pi_u) &\propto -C_3/R^3 \\ E(^1\Sigma_u^+), E(^3\Sigma_g^+) &\propto -2C_3/R^3 \ . \end{aligned} \tag{13.205}$$

Inserting the short range potentials and defining $X = \sigma C_3/3\Delta R^3$, $Y = E/\Delta$ and

$\sigma = +$ for g and $-$ for u,

$$0^-_\sigma = \begin{pmatrix} 3X+\frac{1}{3} & \frac{\sqrt{2}}{3} \\ \frac{\sqrt{2}}{3} & -6X+\frac{2}{3} \end{pmatrix} \quad , \quad 0^+_\sigma = \begin{pmatrix} 3X+\frac{1}{3} & \frac{\sqrt{2}}{3} \\ \frac{\sqrt{2}}{3} & 6X+\frac{2}{3} \end{pmatrix} \tag{13.206}$$

$$1_\sigma = \begin{pmatrix} 3X+\frac{1}{3} & \frac{1}{3} & -\frac{1}{3} \\ \frac{1}{3} & -3X+\frac{1}{3} & -\frac{1}{3} \\ -\frac{1}{3} & -\frac{1}{3} & -6X+\frac{2}{3} \end{pmatrix} \quad , \quad 2_\sigma = (3X+1) \; .$$

Note that the structure looks very much like the transition from the Zeeman to the Paschen-Back regime, where X plays the role of the magnetic field and Y the level shift. The characteristic equations are,

$$\begin{aligned} Y^2 - (1-3X)Y - 18X^2 = 0 \quad & \text{for} \quad 0^-_\sigma \\ Y^2 - (1+9X)Y + (4X+18X^2) = 0 \quad & \text{for} \quad 0^+_\sigma \\ Y^3 + (-2+6X)Y^2 + (1-8X-9X^2)Y + (2X+6X^2-54X^3) = 0 \quad & \text{for} \quad 1_\sigma \\ Y - (1+3X) = 0 \quad & \text{for} \quad 2_\sigma \end{aligned} \tag{13.207}$$

13.3.10 Heteronuclear collisions

For a collision in the channel ^{6}Li P ^{87}Rb S we get the $\{9j\}$-symbol,

$$\begin{Bmatrix} l_6 & l_{87} & L \\ s_6 & s_{87} & S \\ j_6 & j_{87} & j \end{Bmatrix} = \begin{Bmatrix} 0 & 1 & 1 \\ \frac{1}{2} & \frac{1}{2} & S \\ \frac{1}{2} & j_{87} & j \to \Omega \end{Bmatrix} \; . \tag{13.208}$$

We thus expect a fine structure $j_{87} = \frac{1}{2}, \frac{3}{2}$ at long range and exchange interactions $S = 0, 1$ at short range. For the projection onto the internuclear axis $|L - S| \leq \Omega \leq L + S$.

Let $V_k(R)$ be the uncoupled potentials and,

$$\Delta_{kl}(R) = D_{kl} + A_{kl}\left([1 - e^{-B_{kl}(R-R_{kl})}]^2 - 1\right) \tag{13.209}$$

the spin-orbit functions modeled as Morse potentials, where D_{kl} is related to the fine-structure splitting, $D_{kl} = \frac{1}{3}(E_k - E_l)$, for diagonal and, $D_{kl} = \frac{\sqrt{2}}{3}(E_k - E_l)$, for off-diagonal elements. For heteronuclear molecules like ^{6}Li^{87}Rb we have matrices like [74, 73],

H	$\vert^3\Sigma^+\rangle$	$\vert^3\Pi\rangle$	$\vert^1\Sigma^+\rangle$	$\vert^3\Pi\rangle$	$\vert^3\Sigma^+\rangle$	$\vert^1\Pi\rangle$	$\vert^3\Pi\rangle$	$\vert^3\Pi\rangle$
$\langle^3\Sigma^+_{\Omega=0^-}\vert$	$V(^3\Sigma)$	$\Delta_{cb}\sqrt{2}$						
$\langle^3\Pi_{\Omega=0^-}\vert$	$\Delta_{cb}\sqrt{2}$	$V(^3\Pi) - \Delta_{bb}$						
$\langle^1\Sigma^+_{\Omega=0^+}\vert$			$V(^1\Sigma)(-2\Delta_{bb})$	$-\Delta_{bb}$				
$\langle^3\Pi_{\Omega=0^+}\vert$			$-\Delta_{bb}$	$V(^3\Pi)\,(+\Delta_{bb})$				
$\langle^3\Sigma^+_{\Omega=1}\vert$					$V(^3\Sigma)$	Δ_{cB}	Δ_{cb}	
$\langle^1\Pi_{\Omega=1}\vert$					Δ_{cB}	$V(^1\Pi)$	$-\Delta_{bB}$	
$\langle^3\Pi_{\Omega=1}\vert$					Δ_{cb}	$-\Delta_{bB}$	$V(^3\Pi)$	
$\langle^3\Pi_{\Omega=2}\vert$								$V(^3\Pi) + \Delta_{bb}$

(13.210)

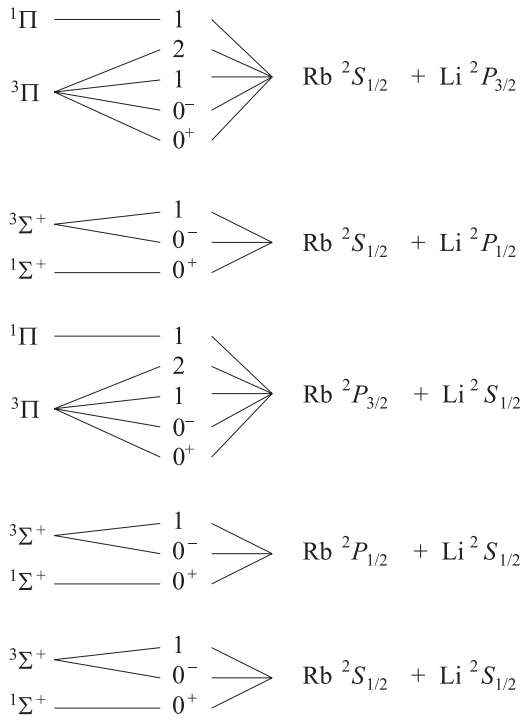

Figure 13.23: Movre type spin-orbit recoupling scheme for heteronuclear molecules.

for every fine structure. For example, there is a matrix for the two ^{6}Li $S_{1/2}$ ^{87}Rb$P_{1,3/2}$ asymptotes and another one for the ^{6}Li $P_{1/2,3/2}$ ^{87}Rb S_1 asymptotes. Additional terms enter via rotational effects [74].

Concretely,

$$\begin{aligned}
\Delta_{bb}(R \to \infty) &= \frac{1}{3}(E_{3/2} - E_{1/2}) \\
\Delta_{cB}(R \to \infty) &= \frac{1}{3}(E_{3/2} - E_{1/2}) \\
\Delta_{bB}(R \to \infty) &= \frac{1}{3}(E_{3/2} - E_{1/2}) \\
\Delta_{cb}(R \to \infty) &= \frac{1}{3}(E_{3/2} - E_{1/2}) \ .
\end{aligned} \tag{13.211}$$

13.3.10.1 Inelastic trap losses

Between ground and excited states *fine changing collisions* and *radiative escape* are possible. Between two ground states only *hyperfine changing collisions* may occur.

The nature of the collision process, whether it is a one- [13], two-, or three-body collision, reveals itself via the temporal behavior of trap losses. Using the abbrevia-

[13] By one-body collision we mean collisions with atoms of the background gas.

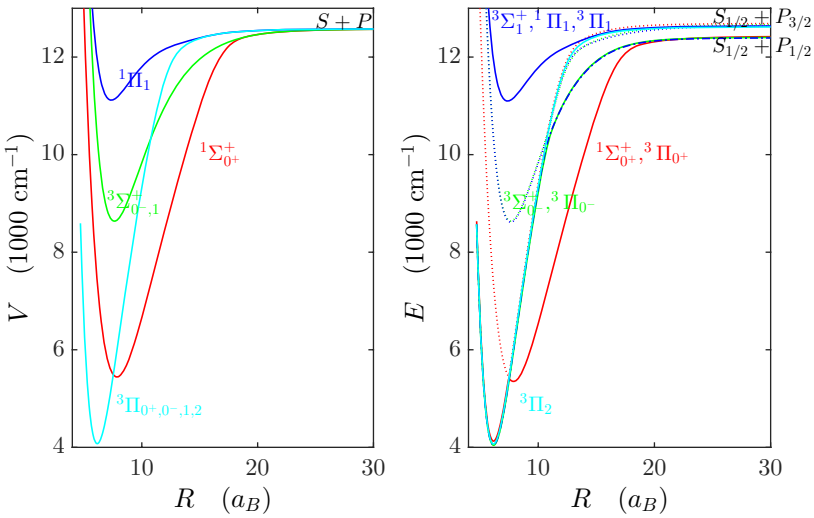

Figure 13.24: (code) Adiabatic potentials.

tion,

$$\langle \eta \rangle \equiv \frac{1}{N} \int \eta(\mathbf{r}) n(\mathbf{r}) d^3 r \ , \tag{13.212}$$

we can write the loss rates due to inelastic one-, two-, and three-body collisions,

$$B\langle 1 \rangle N \quad , \quad K\langle n \rangle N \quad , \quad L\langle n^2 \rangle N \ . \tag{13.213}$$

the prefactors depend on the collision velocity (that is, the temperature of the sample) and atomic parameters (for example, the collision cross section for two-body collisions, which may itself depend on temperature). Hence, the total number of trapped atoms evolves according to,

$$\boxed{\dot{N} = -B\langle 1 \rangle N - K\langle n \rangle N - L\langle n^2 \rangle N} \ . \tag{13.214}$$

Assuming a gaussian density distribution,

$$n(\mathbf{r}) = \frac{N}{(2\pi)^{3/2}\bar{r}^3} e^{-r^2/2\bar{r}^2} \ , \tag{13.215}$$

we calculate,

$$\dot{N} = -BN - \frac{K}{(4\pi)^{3/2}\bar{r}^3} N^2 - \frac{L}{3^{3/2}(2\pi)^3\bar{r}^6} N^3 \ . \tag{13.216}$$

Fig. 13.25 shows a simulation of Eq. (13.216).

For condensates in the Thomas-Fermi limit [771] found the following differential equations for two- and three-body collisions,

$$\frac{\dot{N}}{N} = -Gc_2 N^{2/5} - \frac{1}{\tau} \quad \text{and} \quad \frac{\dot{N}}{N} = -Lc_3 N^{4/5} - \frac{1}{\tau} \ . \tag{13.217}$$

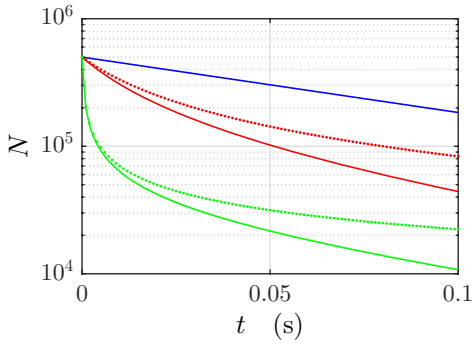

Figure 13.25: (code) One-, two-, and three-body losses.

13.3.11 Heteronuclear electric dipole moment

The *electric dipole moment* of a dimer is highest for big mass difference, as in the case of LiRb and for low vibrational quantum number [481, 37]. The electric dipole moment determines the rate for spontaneous and *black-body radiation*, $\bar{n} = (e^{-\beta\hbar\omega} - 1)^{-1}$, induced transitions between rovibrational states [482], $\Gamma^{tot}_{vlm} = \Gamma^{spnt}_{vlm} + \Gamma^{bb}_{vlm}$. With the transition rate between individual levels,

$$\Gamma^{\alpha}_{vlm\to v'l'm'} = \frac{8\pi}{3}\frac{\omega^3}{hc^3}|\langle|d|\rangle|^2 \ , \tag{13.218}$$

we can estimate the rates for spontaneous emission,

$$\Gamma^{spnt}_{vlm} = \sum\nolimits_{v'l'm'} \Gamma^{em}_{vlm\to v'l'm'} \ , \tag{13.219}$$

and for black-body radiation,

$$\Gamma^{bb}_{vlm} = \sum_{v'l'm'} \bar{n}\Gamma^{em}_{vlm\to v'l'm'} + \sum_{v''l''m''} \bar{n}\Gamma^{abs}_{vlm\to v''l''m''} \ . \tag{13.220}$$

Note that selection rules require $|l - l'| \leq 1$ and $|m - m'| \leq 1$, rotational transitions are inhibited by small ω^3, spontaneous emission is high for intermediate levels for which on one hand ω^3 is large enough and enough final states are available.

From calculations of the R-dependence of the electric dipole moments [37] the dipole moment of a specific vibrational state is easily estimated from,

$$d = \frac{\int \psi(R) R \psi(R) dR}{\int \psi(R)\psi(R) dR} \ . \tag{13.221}$$

In electric fields the dipole moments will lead to Stark shifts. For $|d| = 1$ Debye in a field of 1 V/m we expect a Stark shift of $H_{Stark} \approx 500$ kHz. It may be possible to measure this by photoassociation spectroscopy. Note also that since homonuclear dimers do not have a permanent electric dipole moment, transitions between vibrational ground states are forbidden.

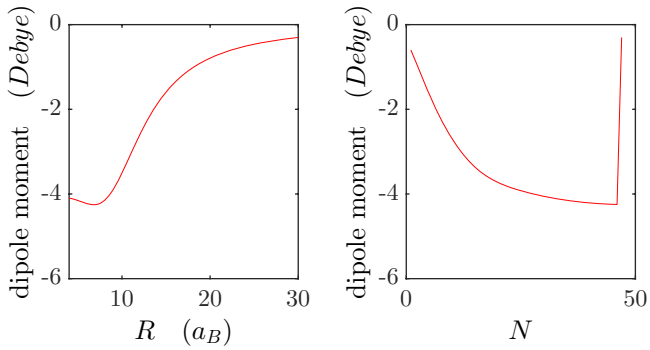

Figure 13.26: (code) (a) Dipole moment at the example of LiRb as a function of interatomic distance. (b) Dipole moment at the example of LiRb as a function of vibrational quantum number.

13.3.12 Exercises

13.3.12.1 Ex: Vibrational structure of LiRb

Calculations of the vibrational structures of several ground states of the heteronuclear molecule LiRb.

13.4 Resonances in cold collisions

13.4.1 Shape resonances

The 'centrifugal' term can give rise to repulsive walls for attractive potentials. Behind these walls, quasi-bound states can develop and give rise to collision resonances. That is, resonances emerge in the collision cross section as a function of the collision temperature called *shape resonance*s.

13.4.2 Feshbach resonances

The so-called *Feshbach resonance* is due to an energetic match between a collision channel and a bound molecular state [277, 816, 818, 589, 274, 590, 841]. They allow to vary the scattering length a_s almost arbitrarily from zero, where the atomic cloud turns into an ideal gas, up to values exceeding the total size of the cloud.

The impact of a Feshbach resonance can be understood as a perturbation of the collisional channel leading to a modification of the depth of the scattering potential. When this leads to the promotion of one more vibrational state into (or from) the continuum, this obviously leads to a dramatic modification of the scattering length a_s [14]

Let us consider two very cold atoms colliding on an attractive interatomic potential $V(R)$ (see Fig. 13.28,right). At long distances the relative wavefunction is a sine

[14] Note that the divergence of the scattering length is an artifact of the hard core approximation, that is, the regularization of the interaction potential, since the matrix $\mathcal{T}$ by itself does not diverge.

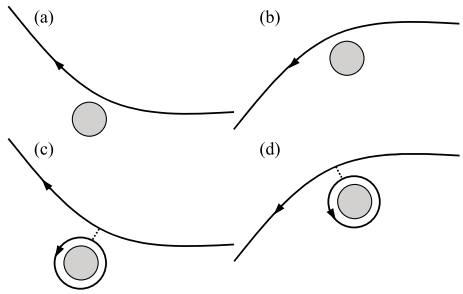

Figure 13.27: Classical illustration of a scattering resonance.

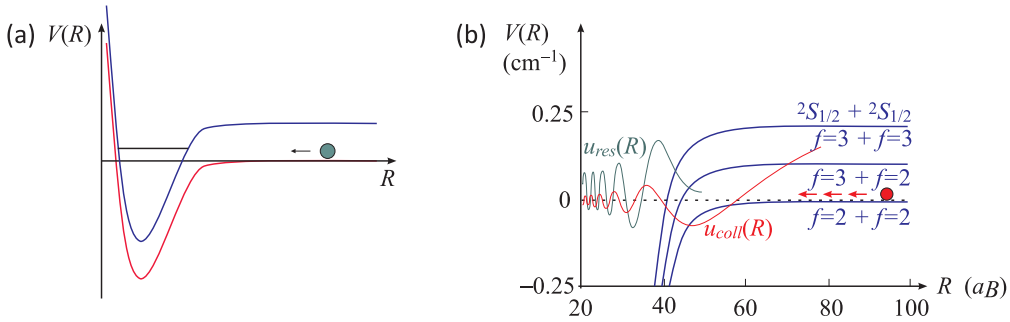

Figure 13.28: (a) The Feshbach resonance is due to a coincidence of collisional and bound channels. (b) Feshbach resonance in ^{85}Rb. The atoms collide in the hyperfine state $F = 2$, and the resonant bound state is in the $F = 3$ multiplet (courtesy [178]).

characterized by the Broglie wave vector k_{dB}. As the atoms approach each other, they mutually accelerate, and the Broglie wave performs some small and rapid oscillations within the potential. The number of nodes of the wavefunction within the potential corresponds to the number of bound vibrational levels that the potential with a given depth can support. The scattering length a_s is defined as the phase slip, which the Broglie wave would acquire during the collision at the boundary $k_{dB} \to \infty$.

With the possibility of gradually decreasing the depth of the molecular potential, at some point the last state below the ionization threshold goes to the continuum of unbound states, the wavefunction decreases the number of nodes by one unit, while the scattering cross section crosses a singularity. In fact, the potential $V(R)$ *can be manipulated* with the help of radiation fields [274, 94, 590] or, near a collisional *Feshbach resonance*, by magnetic fields [818, 819]. Feshbach resonances were predicted in nuclear systems [277]. Its recent revival in the context of cold atomic collisions is due to the prospect of its use for manipulating the scattering length and thus controlling the mean-field energy of a Bose-Einstein condensate [15]

[15] It is even possible to invert the sign of the scattering length. This was a prerequisite for condensation of the atomic species of ^{85}Rb [701]. In addition, Feshbach resonances are interesting because they can install a coherent free-bound coupling between an *open-channel* of colliding atoms and a bound molecular state of the same atoms, as shown in Fig. 13.28. This coupling can lead to the creation of molecular condensates.

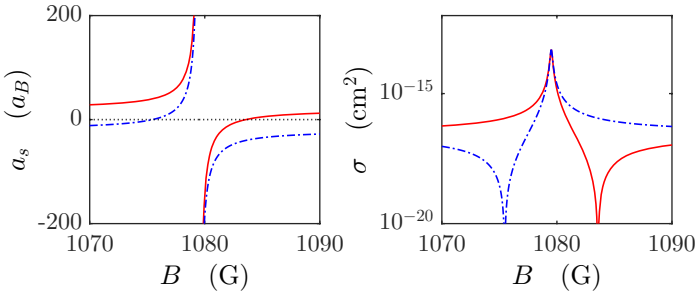

Figure 13.29: (code) (a) Scattering length and (b) collision cross section upon crossing a Feshbach resonance. The scattering length can be positive (solid red line) or negative (dashed blue line). A movie on a simulation of a Feshbach resonance can be watched here (watch movie).

The collisional *Feshbach resonance* arises when the energy of the state of two colliding atoms coincides with the energy of a vibrational molecular level belonging to a higher energy asymptote (see Fig. 13.28,right). This coincidence can strongly perturb the collisional channel, because the resonance shifts the phase of the relative de Broglie wavefunction and allows the atoms to tunnel into the molecular state for a short period of time, the duration of which is determined by the Heisenberg uncertainty relation. If the sum of the magnetic dipole moments of the atoms is different from the dipole moment of the molecule, the resonance can be tuned via external magnetic fields exploring the Zeeman effect. When a Feshbach resonance is crossed, the scattering length crosses a singularity, as shown in Fig. 13.29(left) [16].

13.4.3 Exercises

13.5 Light-assisted collisions

13.5.1 Optical shielding

The adiabatic potential for ground state collisions can be manipulated using light to admix an another potential. The laser light can either be blue-detuned to the continuum of states of a repulsive excited state potential or red-detuned to vibrational resonances of an attractive excited state potential [444, 274, 845, 858]. We can also admix another ground state potential with two-photon Raman transitions.

At cold collisions, the atom undergoes *Landau-Zener transitions* between the mixed states with the probability

$$P_{\mathrm{LZ}} = 1 - \exp\left(-\frac{2\pi\hbar\Omega^2}{D_C v}\right) , \tag{13.222}$$

where

$$D_C = \left|\frac{d}{dR}[V_e(R) - V_g(R)]\right|_{R=R_C} \tag{13.223}$$

16

is the slope of the difference potential evaluated at the Condon point. In the dressed states picture the dressed potentials display an avoided crossing. This modification of the collisional potential modifies the dynamics of the collision and the scattering length.

An example is the phenomenon of *optical suppression* or *shielding*. Here, two colliding atoms are inhibited to approach farther than a certain distance defined by the resonance condition set by a laser which is blue-detuned to a repulsive excited potential. The inhibition is probed by a photoassociation laser tuned to a resonance condition at smaller interatomic distances. The optical shielding scheme can be extended in the following way. Two lasers, one tuned to a repulsive another to an attractive excited state potential resonant at different interatomic distances.

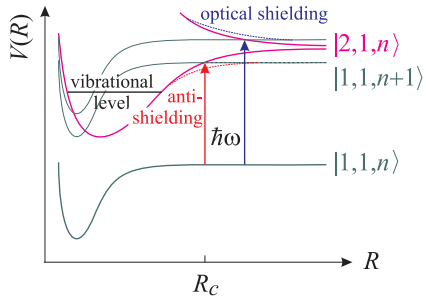

Figure 13.30: Molecular states (green and pink) resonantly coupled by a light field at the Condon point form an avoided intersection in the dressed states basis. For red detuning vibrational states can be populated, for blue detuning we get optical shielding.

13.5.2 Photoassociation during cold collisions

Ultra-cold collisions provide an interesting playground for studies on how light can be used to control the result of inelastic or reactive collisions. Here we discuss as a specific example *photoassociation*. The upper panel of Fig. 13.30 shows schematic curves of (bare) potentials relevant to our discussion. Two atoms in the ground state form a relatively shallow vibrational molecular ground state characterized by electrostatic dispersion

$$V_g(r) = -\frac{C_6}{R^6} \ . \tag{13.224}$$

or long-range *van der Waals potential*. Two other vibrational states arise from the interaction of an excited atom with the ground state atom. The predominant term of the interaction is the potential of resonant dipole-dipole interactions,

$$V_e(r) = D \pm \frac{C_3}{R^3} \ . \tag{13.225}$$

which gives rise to an attractive and a repulsive potential. The R^{-3} dependence of the resonant dipole interaction means that the associated potentials greatly modify the asymptotic level even at internuclear distances, where the ground state van der Waals potential is still relatively shallow. The photoassociation process involves a

slow approach of two identical ground state atoms. A mono-modal optical field, tuned to the red of the atomic resonance, is applied. When the two atoms reach an internuclear distance R such that the energy of the applied field $\hbar\omega$ exactly coincides with the potential difference $V_e(R) - V_g(R)$, the probability of transferring population from a fundamental molecular state to an excited molecular state is maximal. If now the potential $V_g(R)$ supports a vibrational state at the energy $E_C = V_g(R_C)$, the resonance condition is fulfilled,

$$V_e(R_C) - V_g(R_C) = \hbar\omega_C \ , \tag{13.226}$$

and a transition can occur. The distance R_C is called *Condon point*, and it corresponds to the classical outer turning point of the molecular potential [858]. In a quantum picture the turning point corresponds to a maximum of the delocalized wavefunction describing the vibration of the bound atoms.

Within quantum mechanics, the proper conventional way of calculating this probability follows the procedure elaborated in Sec. 16.1.1 for a two-level atom:

1. solve the time-independent molecular Schrödinger equation to obtain the vibrational wavefunctions;

2. write down the coupled differential equations by describing the time dependence of the expansion coefficients of the relevant vibrational wavefunctions;

3. solve for the coefficients and calculate the square of their absolute values;

4. integrate the transition probability inside a region ΔR around the Condon point, where the transition probability is not negligible.

The dressed states picture illustrated in Fig. 13.30 allows to reduce this rather laborious program, essentially, to a problem of a curve crossing of two levels. The basis states are now product states made up of the field and the molecular levels. Furthermore, we approximate the molecular states themselves as products of atomic states. This approximation is justified by the long range, weakly perturbative influence of the van der Waals and resonant dipoles interactions. Calling the ground and excited states $|1\rangle$ and $|2\rangle$, respectively, the dressed state molecular curves $|2, 1, n\rangle$ and $|1, 1, n+1\rangle$ intersect at the Condon point and optically couple to the applied field. This optical coupling produces an *avoided crossing* near R_C and mixes the states of the molecule-field basis. The probability of traversing from one adiabatic molecular state to another is expressed by the Landau-Zener formula as a function of the interaction strength, the relative velocity of the collision partners, and the relative slopes of the two curves. Resolve Exc. 13.5.4.1.

13.5.2.1 Blue detuning

The S-matrix element describing the coupling of a ground state wavefunction by $\Psi_g(R, E) = \langle R|\Psi_g(E)\rangle$ via a light field of frequency ω_a to an excited state wavefunction $\langle R|\Psi_e(E + \omega_a)\rangle$ is,

$$S_{eg}(E, \Delta_a) = -2\pi\imath\hbar\langle\Psi_e(E + \hbar\omega_a)|\Omega_{eg}(R)|\Psi_g(E)\rangle \ , \tag{13.227}$$

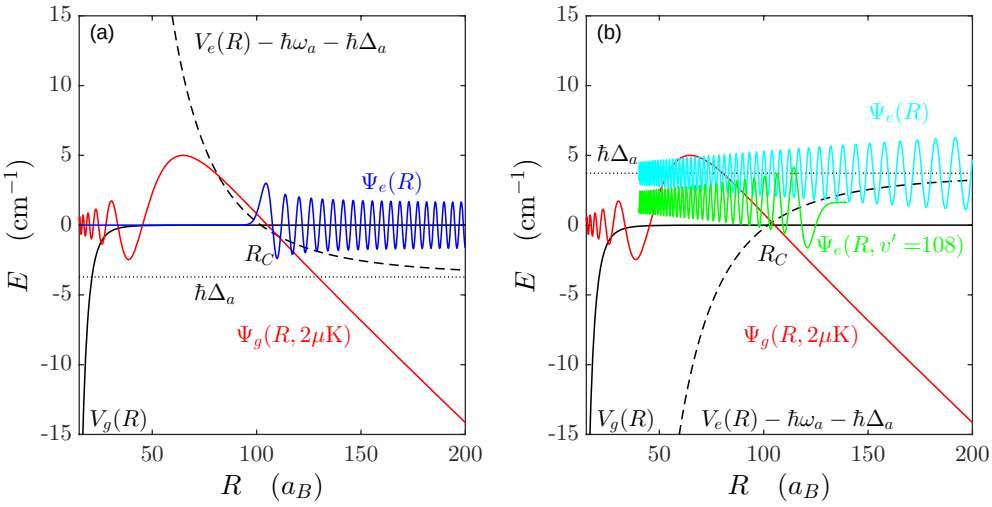

Figure 13.31: (code) Collisional and vibrational wavefunctions in C_6 ground state and C_3 excited state potentials [444] in the presence of (a) blue and (b) red-detuned light ($C_6 = 1500\,\mathrm{a.u.}$, $C_3 = 18\,\mathrm{a.u.}$, $\Delta_a = (2\pi)\ 700\,\mathrm{GHz}$). The colored curves denote (red) the wavefunction of two atoms colliding on their ground state with a velocity corresponding to $2\,\mu\mathrm{K}$, (blue) a wavefunction repelled from the excited state potential, (cyan) an unbound wavefunction of the excited state potential, and (green) a vibrational wavefunction of the excited state potential.

where the molecular Rabi frequency $\Omega_{eg}(R)$ may differ from the atomic Rabi frequency Ω_a. Now, with the probability

$$P_e(E, \Delta_a) = |S_{eg}(E, \Delta_a)|^2 \tag{13.228}$$

for the event by which two ground state atoms collide in a light field and produce one excited and one ground state atom, both of which have enough kinetic energy to escape any weak trapping potential, the event rate coefficient, averaged over ground state velocities $v_g = \hbar k_g / m_{\mathrm{red}}$, is

$$K_e(\Delta_a) = \left\langle \frac{\pi v_g}{k_g^2} P_e(E, \Delta_a) \right\rangle \ . \tag{13.229}$$

Assuming that the Rabi frequency does not depart much from its value near the Condon point, $\Omega_{eg}(R) \simeq \Omega_{eg}(R_C) \equiv \Omega_C$. Then,

$$P_e(E, \Delta_a) = 4\pi^2 \Omega_C^2 F_{eg}(E, \Delta_a) \ . \tag{13.230}$$

where we defined the Franck-Condon overlap,

$$\boxed{F_{eg}(E, \Delta_a) = |\langle \Psi_e(R, E + \hbar\omega_a) | \Psi_g(R, E) \rangle|^2} \ . \tag{13.231}$$

It is now possible to show [444], that within the reflection approximation,

$$F_{eg}(E, \Delta_a) \simeq \frac{|\Psi_g(R_C, E)|^2}{D_C} \ . \tag{13.232}$$

I.e. the Franck-Condon factor is directly proportional to the square of the ground state wavefunction. It only depends on the excited state through the slope term DC.

13.5.2.2 Red detuning

Bound states,

$$|S_{eg}(E,\Delta_a)|^2 = \frac{\gamma_p\gamma_s(E,v,\Delta_a)}{(E-\Delta_a)^2/\hbar^2+(\gamma_p+\gamma_s(E,v,\Delta_a)+\gamma_0)^2/4} \ . \tag{13.233}$$

with

$$\gamma_s(E,v,\Delta_a) = \tfrac{2\pi}{\hbar}|\langle\Psi_e(v)|\Omega_C|\Psi_g(E)\rangle|^2 \simeq \tfrac{2\pi}{\hbar}\Omega_C^2 F_{eg}(E,v,\Delta_a) \tag{13.234}$$

vibrational spacing,

$$\frac{\partial E_v}{\partial v} = \hbar\omega_{vib} \simeq \frac{E_{v+1}-E_v}{2} \ . \tag{13.235}$$

In analogy to (13.232) we now get the Franck-Condon factor,

$$F_{eg}(E,v,\Delta_a) = \frac{\partial E_v}{\partial v}\frac{|\psi_g(R_C,E)|^2}{D_C} \ . \tag{13.236}$$

Example 74 (*Dimers*): For a C_6 ground state potential and a C_3 excited state potential at a given detuning Δ_a the Condon point R_C is given by,

$$\Delta_a = V_e(R_C) - V_g(R_C) = -\frac{C_3}{R_C^3} + \frac{C_6}{R_C^6} = -\frac{C_3}{R_C^3} \tag{13.237}$$

and the differential slope is,

$$\begin{aligned} D_C = \left|\frac{d}{dR}(V_e(R)-V_g(R))\right|_{R=R_C} &= \frac{d}{dR}\left(-\frac{C_3}{R^3}+\frac{C_6}{R^6}\right)\Big|_{R=R_C} \\ &= \frac{3C_3}{R_C^4} - \frac{6C_6}{R_C^7} \simeq \frac{3C_3}{R_C^4} = \frac{3|\Delta_a|}{R_C} \ . \end{aligned} \tag{13.238}$$

Hence, for red-detuning,

$$F_{eg}(E,\Delta_a) \simeq R_C^4\frac{|\Psi_g(R_C,E)|^2}{3C_3} = (C_3/\Delta_a)^{1/3}\frac{|\Psi_g((C_3/\Delta_a)^{1/3},E)|^2}{3|\Delta_a|} \ . \tag{13.239}$$

13.5.2.3 Photoassociation spectroscopy

Photoassociation is based on binary collisions. Transitions to excited states are followed by spontaneous decay and can be monitored in trap loss experiments. An alternative way, which suits especially well for sodium is photoassociative ionization. The trap loss rate can be expressed as,

$$\dot{n} = -2K_{\rm pa}n^2 \ . \tag{13.240}$$

The event rate for photoassociation in a thermal cloud with Boltzmann velocity distribution is:

$$K_{\rm pa}(T,\Delta_1,I_1) = \left\langle \frac{\pi v}{k^2}\sum_\ell (2\ell+1)|S(E,\ell,\Delta_1,I_1)|^2 \right\rangle \ , \tag{13.241}$$
$$= \frac{2\pi\hbar}{m_{\rm red}k}\sum_\ell (2\ell+1)\int_0^\infty |S(E,\ell,\Delta_1,I_1)|^2 e^{-\beta E} d(\beta E) \ ,$$

where the *S-matrix* is given by (13.233), γ_1 is the spontaneous linewidth and $\gamma_s(E,\ell,I_1)/2\pi \approx \Omega_1^2|\langle b_1|E,\ell\rangle|^2$ is the Franck-Condon overlap between the colliding channel and the excited state bound level. For cold ultra-cold collisions, we may only consider s-wave collisions, $\ell = 0$. In the regime of Bose-Einstein condensation $T \lesssim 1\,\mu$K and $n \gtrsim 10^{14}\,$cm^{-3}, we can replace $e^{-\beta E} \to \delta(E)$ and $E \to 0$. The photoassociation rate then simplifies to [127],

$$K_{\rm pa}(\Delta_1,I_1) \approx \frac{2\pi\hbar}{m_{\rm red}k}\frac{\gamma_1\gamma_s}{\Delta^2 + \frac{1}{4}(\gamma_1+\gamma_s)^2} \ . \tag{13.242}$$

Thus the S-matrix is maximized in resonance and saturation, i.e. $\Delta_1 = E$ and $\gamma_s = \gamma_1$ so that $|S|^2 = 1$, which case is called the *unitarity limit*. Note that increasing the laser power beyond saturation, $\gamma_s > \gamma_1$, decreases the photoassociation efficiency again because of *Autler-Townes splitting* [738].

13.5.3 Two-color photoassociation

We can also shine in a second laser frequency tuned between the excited potential bound state and a ground potential bound state. This second laser power broadens the resonance and spoils the transition rate for the first laser. Following [94]:

$$K_{\rm pa}(T,\Delta_1,\Delta_2,I_1,I_2) = \left\langle \frac{\pi v}{k^2}\sum_\ell (2\ell+1)|S(E,\ell,\Delta_1,\Delta_2,I_1,I_2)|^2 \right\rangle \ , \tag{13.243}$$

where,

$$|S|^2 = \frac{(E-\Delta_2)^2\gamma_1\gamma_s}{(E-\Delta_+)^2(E-\Delta_-)^2 + \frac{1}{4}(\gamma_1+\gamma_s)^2(E-\Delta_2)^2} \ , \tag{13.244}$$

where,

$$\Delta_\pm = \tfrac{1}{2}(\Delta_1+\Delta_2) \pm \tfrac{1}{2}\sqrt{(\Delta_1-\Delta_2)^2 + 4\Omega_{12}^2} \ . \tag{13.245}$$

Note that $\gamma_s(E,\ell,I_1)/2\pi \approx \Omega_1^2\,|\langle b_1|E,\ell\rangle|^2$ and $\Omega_{12} = \Omega_2\langle b_1|b_2\rangle$. The one-color signal follows with $\Omega_{12} \to 0$. Assuming the unitarity limit for the free-bound transition, $\Delta_1 = E$ and $\gamma_s = \gamma_1$ the two-color signal reads:

$$|S|^2 = \frac{1}{1+\Omega_{12}^4/(\Delta_1-\Delta_2)^2\gamma_1^2} \ . \tag{13.246}$$

The width of the two-color spectral lines is mainly limited by the Boltzmann distribution of kinetic energies in the atomic cloud. At very low temperatures, we may .... and the two-color resonance dip may be interpreted as a true dark resonance.

Two-color PA lines have been observed for ^{85}Rb in a FORT [305]. In order to measure this for very low temperatures and even for condensates, one has to switch to ^{87}Rb in a dark MOT. A technical requirement is, of course, that the two lasers involved in the Raman process be very stable, at least with respect to each other. This is easiest achieved by using AOMs, which limits the range of levels to be studied to a few GHz binding energy.

Another important aspect is the requirement of a reasonable Raman transition probability, i.e. large Franck-Condon overlap between the collisional and the bound excited state and between the two bound states. Note also that selection rules hold.

13.5.4 Exercises

13.5.4.1 Ex: Photoassociation

Consider a laser focused into a cold, confined cloud of Na atoms at a temperature of 450 µK. For a detuning of 600 MHz, calculate the laser intensity (in W/cm^2) required to produce a 25% probability of photoassociation. The transition moment (a.u.) of Na is 2.55.

13.6 Further reading

13.6.1 on cold collisions

P.S. Julienne, *Literature on cold binary collisions in a light field* [DOI]

J.M. Vogels et al., *Coupled Singlet-Triplet Analysis of Two-Color Cold-Atom Photoassociation Spectra* [DOI]

H. Ouerdane et al., *Scattering Parameters for Cold LiRb and NaRb Collisions Derived from Variable Phase Theory* [DOI]

M. Marinescu et al., *Long-Range Potentials for Two-Species Alkali-Metal Atoms* [DOI]

S.B. Weiss et al., *Calculation of the Interspecies S-Wave Scattering Length in an Ultracold Na-Rb Vapor* [DOI]

13.6.2 on Feshbach resonances

Ph.W. Courteille et al., *Observation of a Feshbach resonance in Cold Atom Scattering* [DOI]

S. Inouye et al., *Observation of Feshbach resonances in a Bose-Einstein condensate* [DOI]

C. Chin et al., *Feshbach Resonances in Ultracold Gases* [DOI]

Part IV

Quantum Optics

Preface to the part *Quantum Optics*

Quantum optics is the field of physics which studies quantum characteristics of light fields. We have seen in Sec. 2.6 how to describe light in quantum mechanics as a quantum harmonic oscillator and introduced photon number states and coherent superposition states. In Chp. 14 the lecture these concepts will be deepened and extended to arbitrary photonic superposition states and to the coupling of different light modes. In Chp. 15 we will discuss the dynamics of light fields in optical cavities, their characterization, and their impact on the density-of-modes,

Chapter 14

Quantized radiation fields

We begin this chapter with the quantization of the light field in Sec. 14.1 and then present various ways of characterizing classical and quantum light fields in Secs. 14.2 and 14.3. In Sec. 14.4 we deepen the discussion for a particular type of quantum correlations known as *squeezed states of light* and in Sec. 14.5 we turn our attention to the coupling of different light modes via beam splitters.

14.1 Quantization of the electromagnetic field

We have already seen that the energy of a monochromatic light field with frequency ω is quantized in small equal portions, such that the total energy is $N\hbar\omega$, where N is an integer number. The energy spectrum is the same as the one of the harmonic oscillator. Therefore, we can identify a light mode with an oscillator and adopt the entire formalism developed for the harmonic oscillator. The formalism will be assumed as known in the following. We will, for simplicity use the term *photon* (respectively *phonon*) for excitations of a harmonic oscillator mode. It is however important to be aware that a photon is not a particle, as it simply *disappears when performing the transition from quantum to classical mechanics* [497].

14.1.1 Field operators

The basic idea behind field quantization is the replacement of the classical harmonic oscillators discussed in Sec. 2.5 by quantum oscillators. The simplest approach to perform this quantization is to introduce the scalar potential Φ and the potential vector $\mathbf{A}$ as done in electrodynamic theory [1]. In free space, without charges nor currents, and within the *Coulomb gauge* we have the solution of the wave equation (16.5) generalized to a distribution of wavevectors $\mathbf{k}$ [2],

$$\mathbf{A}(\mathbf{r},t) = \sum_{\mathbf{k}} \vec{\epsilon}_{\mathbf{k}} [A^{+}_{0\mathbf{k}} e^{-\imath(\mathbf{k}\cdot\mathbf{r}-\omega_{\mathbf{k}}t)} + A^{-}_{0\mathbf{k}} e^{\imath(\mathbf{k}\cdot\mathbf{r}-\omega_{\mathbf{k}}t)}] \,, \tag{14.1}$$

where we already isolated the vectorial character due to the polarization $\vec{\epsilon}_{\mathbf{k}}$ of the light mode $\mathbf{k}$. Obviously, $A^{-}_{0\mathbf{k}} = (A^{+}_{0\mathbf{k}})^{*}$. As each amplitude and polarization of the wave

[1] See script on *Electrodynamics: Electricity, Magnetism and Radiation* (2025).

[2] The atom-light interaction may depend on the polarization of the light with respect to the quantization axis of the atom, as defined e.g. by a magnetic field. In these cases we need to extend the index $\mathbf{k}$ to include the polarization state $(\mathbf{k}, \lambda)$.

given by the vector potential $\mathbf{A}_\mathbf{k}$ and $\mathbf{A}^*_\mathbf{k}$ must satisfy the wave equation separately, we arrive at the dispersion relation,

$$\omega_\mathbf{k} = ck \ . \tag{14.2}$$

With the results (16.7) and (16.8) we know that the energy in each radiative mode containing $n_\mathbf{k}$ photons is,

$$E_\mathbf{k} = \hbar\omega_\mathbf{k} n_\mathbf{k} = u_\mathbf{k} V = 2\varepsilon_0 V \omega_\mathbf{k}^2 \overline{\mathbf{A}_{0\mathbf{k}}^2} = 2\varepsilon_0 V \omega_\mathbf{k}^2 (A_{0\mathbf{k}}^- A_{0\mathbf{k}}^+ + A_{0\mathbf{k}}^+ A_{0\mathbf{k}}^-) \ , \tag{14.3}$$

where the bar denotes cycle-averaging. The second quantization now consists in interpreting the mode as a *quantum harmonic oscillator*, that is, we understand the observables as *operators* satisfying commutation rules, such as $[\hat{A}_{0\mathbf{k}}^-, \hat{A}_{0\mathbf{k}'}^+] \propto \delta_{\mathbf{k},\mathbf{k}'}$, and hence being affected by quantum fluctuations:

$$\hat{H}_\mathbf{k} = \hbar\omega_\mathbf{k}(\hat{n}_\mathbf{k} + \tfrac{1}{2}) = 2\varepsilon_0 V \omega_\mathbf{k}^2 (\hat{A}_{0\mathbf{k}}^- \hat{A}_{0\mathbf{k}}^+ + \hat{A}_{0\mathbf{k}}^+ \hat{A}_{0\mathbf{k}}^-) \ . \tag{14.4}$$

We introduce normalized field operators following the commutation rule (2.85) via,

$$\hat{a}_\mathbf{k} \sqrt{\tfrac{\hbar}{4\varepsilon_0 V \omega_\mathbf{k}}} \equiv \hat{A}_{0\mathbf{k}}^+ \qquad \text{and} \qquad \hat{a}_\mathbf{k}^\dagger \sqrt{\tfrac{\hbar}{4\varepsilon_0 V \omega_\mathbf{k}}} \equiv \hat{A}_{0\mathbf{k}}^- \ , \tag{14.5}$$

such that,

$$\hat{H}_\mathbf{k} = \hbar\omega_\mathbf{k}(\hat{a}_\mathbf{k}^\dagger \hat{a}_\mathbf{k} + \tfrac{1}{2}) \ . \tag{14.6}$$

The analogy allows us to interpret them as *creation operator* and *annihilation operator* of photons. Finally, we can rewrite (14.1) as,

$$\boxed{\hat{\mathbf{A}}_\mathbf{k}(\mathbf{r}, t) = \sqrt{\tfrac{\hbar}{4\varepsilon_0 V \omega_\mathbf{k}}} \vec{\epsilon}_\mathbf{k} \left[\hat{a}_\mathbf{k} e^{-\imath(\mathbf{k}\cdot\mathbf{r} - \omega_\mathbf{k} t)} + \hat{a}_\mathbf{k}^\dagger e^{\imath(\mathbf{k}\cdot\mathbf{r} - \omega_\mathbf{k} t)} \right]} \ . \tag{14.7}$$

We already know such combinations of operators and their complex conjugates from the quantum harmonic oscillator (2.95).

In the Coulomb gauge, the electric and magnetic field operators for the cavity modes can be constructed from,

$$\boxed{\begin{aligned} \hat{\vec{\mathcal{E}}}_\mathbf{k} &= -\frac{\partial \hat{\mathbf{A}}_\mathbf{k}}{\partial t} = \imath \sqrt{\tfrac{\hbar\omega_\mathbf{k}}{2\varepsilon_0 V}} \left(\hat{a}_\mathbf{k} e^{-\imath(\mathbf{k}\cdot\mathbf{r} - \omega_\mathbf{k} t)} - \hat{a}_\mathbf{k}^\dagger e^{\imath(\mathbf{k}\cdot\mathbf{r} - \omega_\mathbf{k} t)} \right) \vec{\epsilon}_k \\ \hat{\vec{\mathcal{B}}}_\mathbf{k} &= \nabla \times \mathbf{A}_\mathbf{k} = \imath \sqrt{\tfrac{\hbar\omega_\mathbf{k}}{2\varepsilon_0 V}} \left(\hat{a}_\mathbf{k} e^{-\imath(\mathbf{k}\cdot\mathbf{r} - \omega_\mathbf{k} t)} - \hat{a}_\mathbf{k}^\dagger e^{\imath(\mathbf{k}\cdot\mathbf{r} - \omega_\mathbf{k} t)} \right) \mathbf{k} \times \vec{\epsilon}_k \end{aligned}} \ . \tag{14.8}$$

We can calculate the cycle-averaged energy of the $\mathbf{k}$-th cavity mode from a quantum version of Eq. (14.3),

$$\bar{E}_\mathbf{k} = \tfrac{\varepsilon_0}{2} \int \langle n_\mathbf{k} | \hat{\vec{\mathcal{E}}}_\mathbf{k} \cdot \hat{\vec{\mathcal{E}}}_\mathbf{k} | n_\mathbf{k} \rangle dV \ . \tag{14.9}$$

The result (14.6) is exactly Planck's quantum hypothesis (although strictly speaking, he rather suggested a quantization of oscillators in the conducting walls of the cavity, not of the field) on the distribution of the spectral intensity radiated by a black body. We now can see that it follows naturally from the quantization of the cavity field modes. With the results of the previous section the complete field Hamiltonian reads,

$$\hat{H}_\text{field} = \sum_\mathbf{k} \hbar\omega_\mathbf{k}(\hat{a}_\mathbf{k}^\dagger \hat{a}_\mathbf{k} + \tfrac{1}{2}) \ . \tag{14.10}$$

Solve Excs. 14.1.2.1 and 14.1.2.2.

14.1.2 Exercises

14.1.2.1 Ex: Photon statistics

An optical resonator contains on average 10 photons in the mode TEM_{00q}. What is the probability of finding, at any time, 1 photon resp. 10 photons, when the light is (a) thermal, (b) coherent? For case (a), what is the temperature of the light for $\lambda = 633\,\mathrm{nm}$?

14.1.2.2 Ex: Photon wavefunction

a. Show that for the *photonic wavefunction* $\mathbf{\Psi}$ and the current density $\mathbf{J}$ [717],

$$\mathbf{\Psi} = \mathbf{\Psi}^+ + \mathbf{\Psi}^- \quad \text{with} \quad \mathbf{\Psi}^\pm = \sqrt{\tfrac{\varepsilon_0}{2}}\vec{\mathcal{E}}_\pm \pm \imath\sqrt{\tfrac{1}{2\mu_0}}\vec{\mathcal{B}}_\pm \quad \text{and} \quad \hat{\sigma}\mathbf{\Psi}^\pm = \pm\mathbf{\Psi}^\pm$$

$$\mathbf{J} = \mathbf{J}_f + \nabla\times\vec{\mathcal{M}} + \frac{\partial\vec{\mathcal{P}}}{\partial t}\ ,$$

where $\vec{\mathcal{E}} \equiv \vec{\mathcal{E}}_+ + \vec{\mathcal{E}}_-$ and $\vec{\mathcal{B}} \equiv \vec{\mathcal{B}}_+ + \vec{\mathcal{B}}_-$ are the real electric and magnetic fields of the photon and $\hat{\sigma}$ is the helicity, the Bialynicki-Birula-Sipe wave equation

$$\boxed{\imath\hbar\frac{\partial\mathbf{\Psi}}{\partial t} = \hbar c\hat{\sigma}\nabla\times\mathbf{\Psi} - \tfrac{\imath\hbar}{\sqrt{2\varepsilon_0}}\mathbf{J} \quad \text{and} \quad \nabla\cdot\mathbf{\Psi} = 0}$$

is equivalent to the Maxwell equations.
b. Use the plane wavefunction

$$\mathbf{\Psi} \equiv \sum_s \int d^3k \sqrt{\tfrac{\hbar\omega}{(2\pi)^3}} e^{\imath(\mathbf{k}\cdot\mathbf{r}-\omega t)}\hat{a}_{\mathbf{k}s}\hat{\mathbf{e}}_{\mathbf{k}s}$$

to calculate the total energy $\hat{H} = \frac{1}{2}\int d^3r[\mathbf{\Psi}^\dagger(\mathbf{r},t), \mathbf{\Psi}(\mathbf{r},t)]_+$.

14.2 Density matrix

As long as we are only interested in coherent reversible processes the Schrödinger equation suffices to describe the evolution of a system. A problem arises when we want to describe dissipative processes, such as spontaneous emission or transmission of photons through a cavity mirror. Dissipation is due to coupling of the degree of freedom under investigation to other degrees of freedom imposed by the environment. While the impact of dissipation on the state of the system can be important, the impact of the system on the environment is generally negligible or not interesting. Therefore, we would like to remove it from the equations of motion, while maintaining its influence on the system. The disregarding of the environment represents a loss of information on the state of the whole system plus reservoir, which transform an initially pure state into a statistical distribution. This situation can not be described by a single wavefunction, but only by a distribution of wavefunctions, and we can only expect to calculate the probability of finding the system within this distribution. The Schrödinger equation, therefore, no longer applies, and we need to trace the time evolution of a system characterized by a density operator describing a statistical

mixture of quantum states. The equations which describe the time evolution of the matrix elements of this density operator are called master equations, and we must use them instead of the Schrödinger equation. We begin by reviewing the rudiments of the density matrix theory.

14.2.1 The density operator

We define the *statistical operator* or *density operator* [3],

$$\boxed{\hat{\rho} \equiv \sum_k p_k \hat{P}_k \qquad \text{where} \qquad \hat{P}_k \equiv |\psi_k\rangle\langle\psi_k|} \ , \tag{14.11}$$

where $\{|\psi_k\rangle\}$ is a complete set of orthonormal states of the system under study. We consider a statistical distribution of these states with p_j being the probability of finding $|\psi_j\rangle$ in the set. Obviously, $\sum_k p_k = 1$. That is, the density operator acts on a member of the set $\{|\psi_k\rangle\}$ in a way to extract the probability of finding the system in $|\psi_j\rangle$,

$$\hat{\rho}|\psi_j\rangle = \sum_k p_k |\psi_k\rangle\langle\psi_k|\psi_j\rangle = p_j|\psi_j\rangle \ . \tag{14.12}$$

If all members of the set are in the same state, for example $|\psi_k\rangle$, the density operator reduces to,

$$\hat{\rho} = |\psi_k\rangle\langle\psi_k| \ , \tag{14.13}$$

and the system is in a *pure state* with $p_k = \delta_{1k}$. Each time a quantum state can be expressed by a single wave function, it is a pure state, but it does not have to be an eigenstate. Starting from the equation (14.12) we find,

$$\langle\psi_k|\hat{\rho}|\psi_j\rangle = p_j\delta_{kj} \ . \tag{14.14}$$

The diagonal elements of the density matrix are the probabilities of finding the system in $|\psi_j\rangle$, and assuming that all $|\psi_k\rangle$ are orthonormal, the non-diagonal elements of the incoherent sum (14.11) are necessarily zero [4], Besides that,

$$\sum_k \langle\psi_k|\hat{\rho}|\psi_k\rangle = 1 \ , \tag{14.15}$$

so that $\hat{\rho}$ contains all *available* information about the system, that is, our *knowledge* about its state. When the state of the system is unknown, $\hat{\rho}$ describes the probability

[3] In the presence of degeneracy or a continuous spectrum we can generalize the definition:

$$\hat{\rho} \equiv \sum_k p_k \hat{P}_k + \int p_\lambda \hat{P}_\lambda d\lambda \quad \text{where} \quad \hat{P}_k \equiv \sum_m |km\rangle\langle km| \quad \text{and} \quad \hat{P}_\lambda \equiv \int |\lambda\mu\rangle\langle\lambda\mu| d\mu \ .$$

Here, m and μ are degenerate quantum numbers, m, n are discrete, and λ, μ are continuous quantum numbers. The set of quantum numbers is complete, when

$$\sum\nolimits_{k,m} |km\rangle\langle km| = \mathbb{I} = \int |\lambda\mu\rangle\langle\lambda\mu| d\lambda d\mu \ .$$

The degree of degeneracy of a state $|k\rangle$ is $\mathrm{Tr}\,\hat{P}_k = \sum_m 1$. The probability of finding the system in the state $|k\rangle$ is $\langle\hat{P}_k\rangle = p_n \sum_m 1$.

[4] This is simply because we constructed the density operator to be diagonal in the basis $\{|\psi_k\rangle\}$. It does not mean, that the density operator cannot have non-diagonal elements in another basis.

of finding the system in each state. When the state is fully known, $\hat{\rho}$ describes a pure state, that is, a vector in the Hilbert space, which is unequivocally determined by a complete set of observables with their respective quantum numbers.

The properties of the density operator are,

$$\boxed{\begin{array}{rcll} \hat{\rho} & = & \hat{\rho}^\dagger & \\ \langle\hat{\rho}\rangle & \geq & 0 & \\ \mathrm{Tr}\,\hat{\rho} & = & 1 & \\ \mathrm{Tr}\,\hat{\rho}^2 & \leq & 1 & \\ \det\hat{\rho} & = & 0 & \\ \hat{\rho} & = & \hat{\rho}^2 & \text{for a pure state} \end{array}} \quad . \tag{14.16}$$

Example 75 (*Inhomogeneous atomic clouds*): For example, a thermal atomic cloud of N two-level atoms needs in general to be described by a density operator, because the state of every atom is independent of the state of the other atoms. If we knew that all atoms behave exactly in the same way, for instance, when exposed to a radiation field, we could restrict to calculating the evolution of a single atom and extrapolate to N atoms. However, atomic motion and interatomic interactions often influence the dynamics in a way that the atoms behave differently.

14.2.2 Matrix formalism

The next step is to develop matrix representations of the density operator by expanding the state vectors $|\psi_k\rangle$ in a complete orthonormal basis,

$$|\psi_k\rangle = \sum_n c_{nk}|n\rangle = \sum_n |n\rangle\langle n|\psi_k\rangle \ , \tag{14.17}$$

using the *completeness relation* (1.183), that is, $\sum_n |n\rangle\langle n| = \mathbb{I}$, and defining,

$$c_{nk} \equiv \langle n|\psi_k\rangle \tag{14.18}$$

as the projection of the state vector $|\psi_k\rangle$ on the basis vector $|n\rangle$. Now, we can write the density operator matrix representation within the basis $\{|n\rangle\}$ using the definition of $\hat{\rho}$ in Eq. (14.11) and replacing $|\psi_k\rangle$ and $\langle\psi_k|$ by their expansions (14.17):

$$\hat{\rho} = \sum_k p_k|\psi_k\rangle\langle\psi_k| = \sum_k p_k \sum_{m,n} |n\rangle\langle n|\psi_k\rangle\langle\psi_k|m\rangle\langle m| = \sum_k p_k \sum_{m,n} c_{nk}c^*_{mk}|n\rangle\langle m| \ . \tag{14.19}$$

The matrix elements of $\hat{\rho}$ in this representation are

$$\rho_{nm} \equiv \langle n|\hat{\rho}|m\rangle = \sum_k p_k c_{nk}c^*_{mk} \tag{14.20}$$

with the diagonal elements $\langle n|\hat{\rho}|n\rangle = \sum_k p_k|c_{nk}|^2$ and,

$$\rho^*_{nm} = \langle n|\hat{\rho}|m\rangle^* = \sum_k p_k c^*_{nk}c_{mk} = \sum_k p_k\langle m|\psi_k\rangle\langle\psi_k|n\rangle = \langle m|\rho|n\rangle = \rho_{mn} \ , \tag{14.21}$$

which means that the operator $\hat{\rho}$ is Hermitian.

Example 76 (*Density operator for a single atom*): For a very simple system such as a single atom with several levels, that without spontaneous emission can be described by a single wavefunction $|\psi_1\rangle$, we can let $p_k = \delta_{1k}$. That is, the equations (14.19) and (14.21) reduce to,

$$\hat{\rho} = \sum_{m,n} c_{n1} c^*_{m1} |n\rangle\langle m| \qquad \text{and} \qquad \langle n|\rho|m\rangle = c_{n1} c^*_{m1} \ . \tag{14.22}$$

14.2.3 Measurement and trace

The sum of the diagonal elements of a matrix representing an operator is called the *trace*. This quantity represents a fundamental property of the density operator, since it is invariant with respect to any unitary transformation:

$$\mathrm{Tr}\,\hat{\rho} \equiv \sum_n \langle n|\hat{\rho}|n\rangle \ . \tag{14.23}$$

With the definition of the density operator (14.11) we can write the Eq. (14.23) as,

$$\mathrm{Tr}\,\hat{\rho} \equiv \sum_{n,k} p_k \langle n|\psi_k\rangle\langle\psi_k|n\rangle \ . \tag{14.24}$$

Now, using the completeness relation,

$$\mathrm{Tr}\,\hat{\rho} \equiv \sum_{n,k} p_k \langle\psi_k|n\rangle\langle n|\psi_k\rangle = \sum_k p_k \langle\psi_k|\psi_k\rangle = 1 \ , \tag{14.25}$$

which shows that the trace of the density operator representation is always 1 regardless of the basis of the matrix representation.

Example 77 (*Density operator for a statistical mixture*): Let us imagine an experiment with a single three-level atom coupling a state $|1\rangle$ to two other possible states $|2\rangle$ and $|3\rangle$ via a $\frac{\pi}{2}$-pulse, such that one of the two states,

$$|\psi_1\rangle = \tfrac{1}{\sqrt{2}}(|1\rangle + |2\rangle) \qquad \text{or} \qquad |\psi_2\rangle = \tfrac{1}{\sqrt{2}}(|1\rangle + |3\rangle)$$

be generated with equal probability. We also suppose that the performed experiment doesn't tell us which one of the two states was generated, so that we have to describe the system by a density operator,

$$\hat{\rho} = \sum_{k=1,2} \tfrac{1}{2} |\psi_k\rangle\langle\psi_k| = \tfrac{1}{2}\left[\frac{|1\rangle + |2\rangle}{\sqrt{2}}\,\frac{\langle 1| + \langle 2|}{\sqrt{2}}\right] + \tfrac{1}{2}\left[\frac{|1\rangle + |3\rangle}{\sqrt{2}}\,\frac{\langle 1| + \langle 3|}{\sqrt{2}}\right] \ .$$

Choosing an obvious basis, we can represent the density operator by a matrix,

$$\hat{\rho} = \begin{pmatrix} \frac{1}{2} & \frac{1}{4} & \frac{1}{4} \\ \frac{1}{4} & \frac{1}{4} & 0 \\ \frac{1}{4} & 0 & \frac{1}{4} \end{pmatrix} \ ,$$

for which we verify,

$$\hat{\rho} = \hat{\rho}^\dagger \qquad \text{and} \qquad \mathrm{Tr}\,\hat{\rho} = 1 \ ,$$

but,

$$\hat{\rho}^2 \neq \hat{\rho} \qquad \text{and} \qquad \mathrm{Tr}\,\hat{\rho}^2 = \tfrac{5}{8} \leq 1 \ .$$

Hence the state is not pure.

Expectation values of observables are expressed by,

$$\langle \hat{A} \rangle = \sum_k p_k \langle \psi_k | \hat{A} | \psi_k \rangle \ . \tag{14.26}$$

On the other hand,

$$\hat{\rho}\hat{A} = \sum_k p_k |\psi_k\rangle\langle\psi_k|\hat{A} \ , \tag{14.27}$$

and in the basis $\{|n\rangle\}$,

$$\langle n|\hat{\rho}\hat{A}|m\rangle = \langle n| \sum_k p_k |\psi_k\rangle\langle\psi_k|\hat{A}|m\rangle = \sum_k p_k \langle n|\psi_k\rangle\langle\psi_k|\hat{A}|m\rangle = \sum_k p_k \langle\psi_k|\hat{A}|m\rangle\langle n|\psi_k\rangle \ . \tag{14.28}$$

Now, along the diagonal, we have,

$$\langle n|\hat{\rho}\hat{A}|n\rangle = \sum_k p_k \langle\psi_k|n\rangle\langle n|\hat{A}|\psi_k\rangle \ . \tag{14.29}$$

With the closure relation in the basis $\{|n\rangle\}$, we now have [5],

$$\boxed{\mathrm{Tr}\,\hat{\rho}\hat{A} = \sum_k p_k \langle\psi_k|\hat{A}|\psi_k\rangle = \langle\hat{A}\rangle} \ . \tag{14.30}$$

The Eq. (14.30) says that the ensemble average of any dynamic observable $\hat{A}$ can be calculated from the diagonal elements of the operator matrix $\hat{\rho}\hat{A}$: Since the trace is independent of the basis (this will be shown in Exc. 14.2.4.1), each unitary transformation taking the matrix representation from a basis $\{|n\rangle\}$ to another one $\{|t\rangle\}$ leaves the trace invariant. Using the definition of a unitary transformation we can easily show that the trace of a cyclic permutation of a product is invariant. For example,

$$\mathrm{Tr}\,[\hat{A}\hat{B}\hat{C}] = \mathrm{Tr}\,[\hat{C}\hat{A}\hat{B}] = \mathrm{Tr}\,[\hat{B}\hat{A}\hat{C}] \ , \tag{14.31}$$

and in particular

$$\mathrm{Tr}\,[\hat{\rho}\hat{A}] = \mathrm{Tr}\,[\hat{A}\hat{\rho}] = \langle\hat{A}\rangle \ . \tag{14.32}$$

In the Excs. 14.2.4.2 and 14.2.4.3 we apply the density operator to pure and mixed states of a two-level system. In Excs. 14.2.4.4 and 14.2.4.5 we study thermal mixtures and Exc. 14.2.4.6 Glauber states.

14.2.3.1 Measurement process

If an observable $\hat{A}$ has a spectral representation $\hat{A} = \sum_n a_n |a_n\rangle\langle a_n| = \sum_n a_n \hat{P}_n$, with $\hat{P}_n = |a_n\rangle\langle a_n|$, the measurement process will transform the density operator to,

$$\hat{\rho}' = \sum_n \hat{P}_n \hat{\rho} \hat{P}_n \ . \tag{14.33}$$

[5] In the presence of degeneracy or a continuous part of the spectrum we can generalize the definition of the expectation,

$$\langle\hat{X}\rangle \equiv \mathrm{Tr}\,\hat{\rho}\hat{X} = \sum_{k,m} \langle km|\hat{\rho}\hat{X}|km\rangle \ .$$

That is, after the *measurement*, the density operator becomes diagonal on the basis of the eigenvalues of $\hat{A}$ [6], as explained in Sec. 1.4.7. The expression can be thought of as the mathematical formulation of von Neumann's state reduction postulate.

We note that the density operator (14.33) describes the whole ensemble after the measurement. The sub-ensemble corresponding to a particular result a_n of the measurement is described by a different density operator,

$$\hat{\rho}'_n = \frac{\hat{P}_n \hat{\rho} \hat{P}_n}{\mathrm{Tr}\,[\hat{\rho}\hat{P}_n]} \ . \tag{14.34}$$

This is true, when $|a_n\rangle$ is the only eigenvector with the eigenvalue a_n. If not, $\hat{P}_n$ in the expression (14.34) should be replaced by the projection operator onto the sub-space of a_n [7]. In Exc. 14.2.4.7 we study the projection of Glauber states and in Exc. 14.2.4.8 of entangled states.

14.2.3.2 Entropy

In a very general sense, the *entropy* determines in what direction a reversible process will take place. It is related to the size of the available phase space on both sides of the reaction. For example, the coupling of discrete and continuous modes is governed by entropy considerations.

Entropy measures of the lack of information about a system from which we only know $\langle \hat{H} \rangle$,

$$S \equiv -k_{\mathrm{B}} \langle \ln \hat{\rho} \rangle = -k_{\mathrm{B}}\ \mathrm{Tr}\,(\hat{\rho} \ln \hat{\rho}) \ . \tag{14.35}$$

The *information entropy* (or *von Neumann entropy*) of statistically independent systems $\hat{\rho} \equiv \hat{\rho}_1 \otimes \hat{\rho}_2$ is additive $S = S_1 + S_2$. We can also define absolute temperatures by $T^{-1} \equiv \partial S / \partial \langle \hat{H} \rangle$. The entropy of a pure state is 0. Hamiltonian processes conserve entropy, for they correspond to non-dissipative unitary transformations. On the other side, relaxation increases the entropy and the phase space volume. Another common definition is the so-called *purity* or *Renyi entropy*,

$$S_R \equiv \langle 1 - \hat{\rho} \rangle = 1 - \mathrm{Tr}\,(\hat{\rho}^2) \ . \tag{14.36}$$

Quantum states can exhibit coherences. For example, if we express a state $|\psi\rangle$ on a basis of eigenstates $|1\rangle$ and $|2\rangle$:

$$\hat{\rho} = |\psi\rangle\langle\psi| = \begin{pmatrix} |\langle\psi|1\rangle|^2 & \langle 1|\psi\rangle\langle\psi|2\rangle \\ \langle 2|\psi\rangle\langle\psi|1\rangle & |\langle\psi|2\rangle|^2 \end{pmatrix} \ . \tag{14.37}$$

[6] A projective measure always increases entropy. The entropy of a pure state is zero, while that of a mixture is always greater than zero. Therefore, a pure state can be converted into a mixture by a measurement, but the reverse can not happen. Thus, the action of measuring induces an irreversible change in the density matrix reminiscent of the collapse of the wavefunction. Strangely, the measurement *reduces* the amount of information by quenching the quantum interference of the compound system in a process called quantum decoherence. A subsystem can be taken from a mixed state to a pure state only at the price of increasing the von Neumann entropy elsewhere in the global system.

[7] In general, assuming that f is a function associating each observable $\hat{A}$ with a number $f(\hat{A})$ (which we may imagine as the expectation value), we can state the following: If f satisfies some natural properties (such as the one to produce positive values for positive operators), then there exists a unique density matrix $\hat{\rho}$, such that $f(\hat{A}) = \mathrm{Tr}\,(\hat{\rho}\hat{A})$ for all $\hat{A}$. That is, every reasonable 'family' of expectation values' can be represented by a density matrix, which suggests that the density matrix provides the most general description of a quantum state.

The evolution of such a state is described by the von Neumann equation,

$$i\hbar\partial_t\hat{\rho}(t) = [\hat{H}, \hat{\rho}(t)] \ . \tag{14.38}$$

The measurement process is not described by this equation. A pure state will always remain pure. If the eigenstates do not interact, the density operator will remain diagonal. The von Neumann equation conserves the properties of hermiticity, $\hat{\rho} = \hat{\rho}^\dagger$, completeness, $\mathrm{Tr}\,\hat{\rho} = 1$, and purity $\det\hat{\rho} = 0$.

The density operator for a *statistical mixture* in a canonical ensemble (where S is maximum, U is variable, and N is fixed) follows from a variational problem with the Lagrange parameters $\delta(S - k_\mathrm{B}\alpha\langle\mathbb{I}\rangle - k_\mathrm{B}\beta\langle\hat{H}\rangle) = 0$, since $\mathrm{Tr}\,\hat{\rho}$ and $\langle\hat{H}\rangle$ are fixed by boundary conditions. We find,

$$\boxed{\hat{\rho} = \frac{1}{Z}e^{-\hat{H}/k_\mathrm{B}T} \qquad \text{with} \qquad Z \equiv \mathrm{Tr}\,e^{-\hat{H}/k_\mathrm{B}T}} \ . \tag{14.39}$$

We also have the expectation values, $\langle H\rangle = -\partial \ln Z/\partial\beta$ and $(\Delta H)^2 = -\partial\langle\hat{H}\rangle/\partial\beta$ with the abbreviation $\beta \equiv (k_\mathrm{B}T)^{-1}$. All quantities are fixed, except the kinetic energy, which balances the interaction with a heat bath. T is the only equilibrium parameter. The density operator satisfies a Boltzmann distribution [8],

$$U = \langle\hat{H}\rangle = \frac{p^2}{2m} = -\frac{\partial}{\partial(1/k_\mathrm{B}T)}\ln\int e^{-p^2/2mk_\mathrm{B}T}dp = \frac{k_\mathrm{B}}{2}T \ . \tag{14.40}$$

14.2.3.3 Systems and subsystems

Density operators are very useful for playing with systems and subsystems. Let us, for instance, assume that we have two quantum systems defined on the Hilbert spaces $\mathcal{H}_1$ and $\mathcal{H}_2$. The composite system is then the tensor product $\mathcal{H}_1 \otimes \mathcal{H}_2$. We now suppose that the compound system is in a pure state, $|\psi\rangle \in \mathcal{H}_1 \otimes \mathcal{H}_2$. If the state can be written in the form $|\psi\rangle = |\psi_1\rangle \otimes |\psi_2\rangle$, this means that the state of the first subsystem is $|\psi_1\rangle$. However, in general, $|\psi\rangle$ does not decompose like this. Of course, every vector in $\mathcal{H}_1 \otimes \mathcal{H}_2$ is a linear combination of tensorial products of $\mathcal{H}_1$ and $\mathcal{H}_2$. If $|\psi\rangle$ can not be decomposed as a tensor product, we say that the two systems are *entangled*. In this case, there is no reasonable way of associating a pure state $|\psi_1\rangle \in \mathcal{H}_1$ to the state $\psi \in \mathcal{H}_1 \otimes \mathcal{H}_2$. If, for example, in the case of a two particle wavefunction $\Psi(x_1, x_2)$ there is no way to construct a wavefunction (i.e. a pure state) $\psi_1(x_1)$ describing the state of the first particle, then $\Psi(x_1, x_2) \neq \psi_1(x_1)\psi_2(x_2)$.

The point of the discussion is that, even if the total system is in a pure state, the various subsystems that compose it will normally be in mixed states. On the other hand, regardless of whether the composite system is in a pure or mixed state, we can perfectly construct a density matrix that describes the state. Therefore, the use of density matrices is inevitable. Let $\hat{\rho}$ be the density matrix of the system composed of two subsystems. Then the state in $\mathcal{H}_2$ is described by a reduced density operator given by the partial trace of $\hat{\rho}$ over $\mathcal{H}_2$. In the particular case, where the state the

[8] The von Neumann entropy S of a mixture can be expressed in terms of the eigenvalues or in terms of the trace and the logarithm of the density operator $\hat{\rho}$. Since $\hat{\rho}$ is a semi-definite positive operator, its spectrum λ_i, given by $\rho = \sum_i \lambda_i|\varphi_i\rangle\langle\varphi_i|$ where $\{|\varphi_i\rangle\}$ is an orthonormal basis, satisfies $\lambda_i > 0$ and $\sum\lambda_i = 1$. Then the entropy becomes $S = -\sum_i \lambda_i \ln\lambda_i = -\mathrm{Tr}\,(\rho\ln\rho)$.

density matrix has the form $\hat{\rho} = \hat{\rho}_1 \otimes \hat{\rho}_2$, where $\hat{\rho}_1$ and $\hat{\rho}_2$ are the density matrices in $\mathcal{H}_1$ and $\mathcal{H}_2$, then the partial trace is simply, $\mathrm{Tr}_{\mathcal{H}_2} \hat{\rho}\hat{\rho}_1$.

14.2.4 Exercises

14.2.4.1 Ex: Trace of an operator

The trace of an operator $\hat{A}$ is defined by $\mathrm{Tr}\,\hat{A} = \sum_n \langle n|\hat{A}|n\rangle$.
a. Show that the trace is independent of the chosen basis!
b. Show that $\mathrm{Tr}\,\hat{A}\hat{B} = \mathrm{Tr}\,\hat{B}\hat{A}$!

14.2.4.2 Ex: Pure states and mixtures

Consider a system of two levels coupled by a light mode. The Hamiltonian can be written ($\hbar \equiv 1$),

$$\hat{H} = \begin{pmatrix} 0 & \frac{1}{2}\Omega \\ \frac{1}{2}\Omega & \omega_0 \end{pmatrix} .$$

Calculate $\hat{\rho}$, $\hat{\rho}^2$ and $\langle \hat{H} \rangle$ for the following two cases:
a. The atom is in a superposition state, $|\psi\rangle = \alpha|1\rangle + \beta|2\rangle$ and
b. the atom is a statistical mixture of eigenstates, $\hat{\rho} = \mu|1\rangle\langle 1| + \nu|2\rangle\langle 2|$.

14.2.4.3 Ex: Mixture of states

A two-level atom is initially in a superposition of two states $|\psi\rangle = \frac{1}{\sqrt{2}}|1\rangle + \frac{1}{\sqrt{2}}|2\rangle$. An apparatus measures the populations of the states, but the experimenter forgot to read the indicated result.
a. Describe the state the atom by the density operator.
b. Now the experimenter returns to the device. Calculate with which probability he reads the state $|1\rangle$.

14.2.4.4 Ex: Thermal mixture

We consider a thermal non-interacting atomic gas in one dimension. Instead of describing the state of the atomic ensemble, we can consider a single atom with a distributed probability of having a given velocity v. The density operator of the continuous degree of freedom can be written,

$$\hat{\rho} = \int dv \sqrt{\frac{m}{2\pi k_\mathrm{B} T}} e^{-mv^2/2k_\mathrm{B}T} |v\rangle\langle v| ,$$

and the trace of an arbitrary observable $\hat{A}$,

$$\langle \hat{A} \rangle = \mathrm{Tr}\,\hat{\rho}A = \int du \langle u|\hat{\rho}\hat{A}|u\rangle .$$

Now imagine a device capable of measuring the speed of a single atom randomly chosen within the cloud.
a. Express the probability of measuring a specific velocity v' for this atom using the density operator.
b. Express the expectation value of the average velocity by the density operator.

14.2.4.5 Ex: Thermal population of a harmonic oscillator

In thermal equilibrium the energy states of a system are populated following Boltzmann's law,

$$P_n = \frac{e^{-n\beta\hbar\omega}}{\sum_m e^{-m\beta\hbar\omega}} \qquad \text{with} \qquad \beta \equiv \frac{1}{k_B T} \ .$$

a. Consider a one-dimensional harmonic oscillator characterized by the secular frequency ω and, using the density operator, calculate the mean quantum number of the population and the mean energy.
b. For an energy spacing of $\omega/2\pi = 10\,\text{MHz}$, how many levels of the harmonic oscillator are necessary at room temperature to accumulate a population of at least 50%. How many for an energy spacing of $\omega/2\pi = 10\,\text{GHz}$. Repeat the calculation for a $1\,\mu\text{K}$ cold atomic cloud.

14.2.4.6 Ex: Density operator of a Glauber state

a. Write down the density operator of a Glauber state and calculate its purity.
b. How does the density operator look after a measurement of its vibrational level before acknowledging the result? Is it pure?
c. How does it look having acknowledged the result? Is it pure?

14.2.4.7 Ex: Reduced density operator of a Glauber state

Project the density operator of a Glauber state onto its two lowest Fock states using the formula (14.34). Show that the resulting density operator is pure.

14.2.4.8 Ex: Partial measurements

Consider the density operator describing the quantum state of two spins, $|\Psi\rangle = |\psi_a\rangle \otimes |\psi_b\rangle$, with $|\psi_a\rangle = a_1|\uparrow\rangle + a_2|\downarrow\rangle$ and $|\psi_b\rangle = b_1|\rightarrow\rangle + b_2|\leftarrow\rangle$.
a. Write down the density operator for the complete system in terms of the expansion coefficients $c_{ij} = a_i b_j$.
b. Assume that the spin $|\psi_b\rangle$ is measured and verify whether the new density operator describing our knowledge of the system is pure.
c. Now consider the entangled state $|\Psi_e\rangle = c_{11}|\uparrow\rangle|\rightarrow\rangle + c_{22}|\downarrow\rangle|\leftarrow\rangle$. Write down again the density operator for the complete system, measure the spin $|\psi_b\rangle$, and verify whether the new density operator describing our knowledge of the system is pure.

14.3 (Quasi-)probability distribution functions of the coherent state basis

In the previous section we have seen that a light mode can be identified with a harmonic oscillator, which enabled us to harness the whole powerful formalism developed in Secs. 2.5 and 2.6 for the characterization of the quantum states of light. As we have seen in those sections, quantum observables are intrinsically affected by quantum noise, which leads to a spreading of their representation in phase space. For the case of Glauber states of a harmonic oscillator we illustrated in Fig. 2.14 the uncertainty of

conjugate variables by circles around their expectation values whose areas are determined by the Heisenberg uncertainty relation. These circular areas represent phase space probability distribution functions. These are distribution functions measuring the probability to encounter the observables at specific points in phase space.

States other than Glauber states are possible, for instance Fock or cat states. Some of these states may exhibit quantum correlations, which we would like to identify in probability distributions. Quantum correlations in systems with small Hilbert spaces, such as the two-level atom, are conveniently represented by a density operator or by the Bloch vector introduced in Eq. (1.154). Large or infinite Hilbert spaces require different approaches. We have seen in Sec. 2.6.1 how to expand the state of a harmonic oscillator on a Fock state basis. On the other hand, we have seen that Glauber states are more 'natural' states for a harmonic oscillator, so that we would like to visualize expansions of arbitrary states into a coherent state basis.

The following sections are devoted to introducing various such distribution functions [749, 737] and to calculating them for a selection of particular states, such as the Fock and the Glauber state, the thermal state, and the Schrödinger cat state. We will mostly restrict the discussion to pure states, postponing a discussion of the representation of statistical mixtures to Sec. 17.2, where we will also extend the discussion to quantum correlations in light fields resulting from a Jaynes-Cummings type interaction of an atom with a light mode.

14.3.1 The density operator and distribution functions

14.3.1.1 The density operator

We define the *density operator* for a pure state as,

$$\hat{\rho} \equiv |\psi\rangle\langle\psi| \ . \tag{14.41}$$

A detailed discussion of the density operator for non pure states, that is, statistical mixtures has been given in Sec. 14.2. The definition (14.41) is independent from a chosen basis, but a proper representation can be found by simply expanding the state $|\psi\rangle$ on a proper basis. The expansion we had in mind in Sec. 14.2.2 was on eigenstates of atomic excitations, which are typically discrete and limited in number. The expansion of the density operator in the infinite but discrete spectrum of Fock states is essentially the same as for atomic excitations and thus straightforward,

$$\begin{aligned} \hat{\rho} &= \sum_n \hat{\rho}|n\rangle\langle n| \equiv \sum_n p_n |n\rangle\langle n| \\ \Longrightarrow p_m = \langle m|\hat{\rho}|m\rangle &= \sum_n p_n |\langle m|n\rangle|^2 \\ &= \sum_n p_n \delta_{mn} = p_m \ , \end{aligned} \tag{14.42}$$

where the first line can be read as a definition of the photon number distribution function p_n. An analogous expansion in the continuous Glauber basis is, however,

more complicated, because the coherent states are not orthogonal,

$$\hat{\rho} = \tfrac{1}{\pi}\int \hat{\rho}|\alpha\rangle\langle\alpha| d^2\alpha \equiv \int P(\alpha,\alpha^*)|\alpha\rangle\langle\alpha| d^2\alpha \qquad (14.43)$$
$$\Longrightarrow \pi Q(\beta,\beta^*) \equiv \langle\beta|\hat{\rho}|\beta\rangle = \int P(\alpha,\alpha^*)|\langle\beta|\alpha\rangle|^2 d^2\alpha$$
$$= \int P(\alpha,\alpha^*) e^{-|\alpha-\beta|^2} d^2\alpha \neq P(\beta,\beta^*)\ .$$

That is, we end up with two distribution functions, the so-called *P-function* $P(\alpha,\alpha^*)$ (or *Glauber-Sudarshan representation*) and the *Q-function* $Q(\alpha,\alpha^*)$ (or *Husimi representation*) which, according to (14.43) they are not equal. Before we deepen the discussion in the upcoming sections let us already state here, that the reason for the complication is rooted in the non-commutativity of the field operators $[\hat{a},\hat{a}^\dagger] = 1$. Indeed, expressing the density operator of a system as a function of field operators we have (at least) two choices called the *normal-ordered* arrangement (label N) and the *antinormal-ordered* arrangement (label A) [9],

$$\hat{\rho}_{\rm N}(\hat{a},\hat{a}^\dagger) = \sum_{m,n} c_{m,n}\hat{a}^{\dagger m}\hat{a}^n \qquad \text{and} \qquad \hat{\rho}_{\rm A}(\hat{a},\hat{a}^\dagger) = \sum_{m,n} c'_{m,n}\hat{a}^m\hat{a}^{\dagger n}\ . \qquad (14.44)$$

Although both expressions can be converted into each other, the functional form of the density operator depends on the arrangement. We will show in Exc. 14.3.5.1 that the $P(\alpha,\alpha^*)$-function defined by the first line of (14.43) is more natural for the antinormal-ordered density operator $\hat{\rho}_{\rm A}$, while the $Q(\alpha,\alpha^*)$-function defined by the second line of (14.43) is more natural for the normal-ordered density operator $\hat{\rho}_{\rm N}$:

$$\rho_{\rm N}(\alpha,\alpha^*) = \tfrac{1}{\pi}Q(\alpha,\alpha^*) \qquad \text{and} \qquad \rho_{\rm A}(\alpha,\alpha^*) = \pi P(\alpha,\alpha^*)\ . \qquad (14.45)$$

We will discuss the distribution functions more deeply in the upcoming sections.

To prepare the subsequent derivations, let us define the two-dimensional complex Fourier transform by,

$$(\mathcal{F}\chi)(\beta,\beta^*) = \tfrac{1}{\pi}\int \chi(\alpha,\alpha^*) e^{\beta\alpha^* - \beta^*\alpha} d^2\alpha\ , \qquad (14.46)$$

with $d^2\lambda = d\mathfrak{Re}\,\lambda\ d\mathfrak{Im}\,\lambda = dr_\lambda dp_\lambda$. Twofold application of the Fourier transform reproduces the original function,

$$(\mathcal{F}\mathcal{F}\chi)(\gamma,\gamma^*) = \tfrac{1}{\pi}\int (\mathcal{F}\chi)(\beta,\beta^*) e^{\gamma\beta^* - \gamma^*\beta} d^2\beta \qquad (14.47)$$
$$= \tfrac{1}{\pi^2}\int \chi(\alpha,\alpha^*) \int e^{\beta^*(\gamma-\alpha) - \beta(\gamma^*-\alpha^*)} d^2\beta d^2\alpha$$
$$= \tfrac{1}{\pi^2}\int \chi(\alpha,\alpha^*)\pi^2\delta^{(2)}(\gamma-\alpha) d^2\alpha = \chi(\gamma,\gamma^*)\ ,$$

[9] Normal ordering is often denoted by double colons $: \ldots :$. For example, $: \hat{a}\hat{a}^\dagger : = \hat{a}^\dagger\hat{a} = \hat{a}\hat{a}^\dagger - 1$, and for an arbitrary density operator $\hat{\rho}(\hat{a},\hat{a}^\dagger)$ the normal-ordered counterpart is, $\hat{\rho}_{\rm N}(\hat{a},\hat{a}^\dagger) = : \hat{\rho}(\hat{a},\hat{a}^\dagger) :$.

where we used,

$$\delta^{(2)}(\alpha) = \tfrac{1}{\pi^2} \int e^{\lambda^*\alpha - \lambda\alpha^*} d^2\lambda \ . \tag{14.48}$$

The formula (14.48) can be extended to include field operators [749],

$$\delta(\alpha^* - \hat{a}^\dagger)\delta(\alpha - \hat{a}) = \tfrac{1}{\pi^2} \int e^{-\lambda(\alpha^* - \hat{a}^\dagger)} e^{\lambda^*(\alpha - \hat{a})} d^2\lambda \tag{14.49}$$

$$\delta(\alpha - \hat{a})\delta(\alpha^* - \hat{a}^\dagger) = \tfrac{1}{\pi^2} \int e^{\lambda^*(\alpha - \hat{a})} e^{-\lambda(\alpha^* - \hat{a}^\dagger)} d^2\lambda \ ,$$

which will be useful in the following.

14.3.1.2 The Glauber-Sudarshan P-distribution

The Glauber-Sudarshan P-function can be formally defined by [749],

$$\boxed{P(\alpha, \alpha^*) \equiv \mathrm{Tr}\ \hat{\rho}\delta(\alpha^* - \hat{a}^\dagger)\delta(\alpha - \hat{a})} \ . \tag{14.50}$$

The definition (14.43) of the P-function, that is,

$$\boxed{\hat{\rho} \equiv \int P(\alpha, \alpha^*)|\alpha\rangle\langle\alpha| d^2\alpha} \ , \tag{14.51}$$

is equivalent to the definition (14.50), as will be verified in Exc. 14.3.5.2. From (14.51) we see, that the Glauber-Sudarshan P-function is just the distribution that leaves the density matrix diagonal in the coherent state basis. Since $\hat{\rho}$ is Hermitian, $P(\alpha, \alpha^*)$ is real, and since $\mathrm{Tr}\ \hat{\rho} = 1$, it is normalized, $\int P(\alpha, \alpha^*) d^2\alpha = 1$. Hence, the P-distribution functions can be interpreted as the probability of finding the coherent state $|\alpha\rangle$ within the statistical mixture given by (14.51).

In order to unravel its properties let us consider an arbitrary operator $\hat{O}$ being a function of the field operators $\hat{a}$ and $\hat{a}^\dagger$. Using the commutation rule $[\hat{a}, \hat{a}^\dagger] = 1$ the operator can always be brought in normal-ordered form,

$$\hat{O}_{\mathrm{N}}(\hat{a}, \hat{a}^\dagger) = \sum_{m,n} o_{m,n} \hat{a}^{\dagger m} \hat{a}^n \ . \tag{14.52}$$

The expectation value of this operator is,

$$\langle \hat{O}_{\mathrm{N}}(\hat{a}, \hat{a}^\dagger) \rangle = \mathrm{Tr}\ \hat{\rho}\hat{O}_{\mathrm{N}}(\hat{a}, \hat{a}^\dagger) = \int P(\alpha, \alpha^*) O_{\mathrm{N}}(\alpha, \alpha^*) d^2\alpha \ , \tag{14.53}$$

as we will show in Exc. 14.3.5.3.

14.3.1.3 The Husimi Q-distribution

The Husimi Q-function is formally defined by [749],

$$\boxed{Q(\alpha, \alpha^*) \equiv \mathrm{Tr}\ \hat{\rho}\delta(\alpha - \hat{a})\delta(\alpha^* - \hat{a}^\dagger)} \ . \tag{14.54}$$

The definition (14.43) of the Q-function, that is,

$$\boxed{\langle\alpha|\hat{\rho}|\alpha\rangle = \pi Q(\alpha,\alpha^*)}\ , \tag{14.55}$$

is equivalent to the definition (14.50), as will be verified in Exc. 14.3.5.2. From (14.55) we see, that the Q-distribution function can be interpreted as the expectation value of the density operator (14.41).

The expression resembles Eq. (14.50) except for the order of the δ-functions. We now consider the same arbitrary operator $\hat{O}$ as in (14.52), but now expressed in antinormal ordered form of the field operators $\hat{a}$ and $\hat{a}^\dagger$,

$$\hat{O}_{\rm A}(\hat{a},\hat{a}^\dagger) = \sum_{m,n} o_{m,n}\hat{a}^m\hat{a}^{\dagger n}\ . \tag{14.56}$$

As we will show in Exc. 14.3.5.3, the expectation value of this operator is,

$$\langle\hat{O}_{\rm A}(\hat{a},\hat{a}^\dagger)\rangle = {\rm Tr}\ \hat{\rho}\hat{O}_{\rm A}(\hat{a},\hat{a}^\dagger) = \int Q(\alpha,\alpha^*)O_{\rm A}(\alpha,\alpha^*)d^2\alpha\ . \tag{14.57}$$

14.3.1.4 The Wigner-Weyl distribution

The *Wigner function* represents something like the spectrum of two-dimensional phase-space correlation function. For a pure state and a one-dimensional system it is defined by,

$$W(x,p) \equiv \tfrac{1}{\pi}\int_{-\infty}^{\infty}\langle\psi|x+y\rangle\langle x-y|\psi\rangle e^{2\imath py/\hbar}dy\ . \tag{14.58}$$

Example 78 (*Wigner function of a free particle in 3D*): For example, for a free particle described by the wavefunction in three-dimensional space,

$$\langle\mathbf{r}|\psi\rangle = \tfrac{1}{\sqrt{V}}e^{\imath\mathbf{k}\cdot\mathbf{r}}\ ,$$

the Wigner function is,

$$\begin{aligned} W(\mathbf{r},\mathbf{p}) &= \frac{1}{\pi^3}\int_{-\infty}^{\infty}\tfrac{1}{\sqrt{V}}e^{-\imath\mathbf{k}\cdot(\mathbf{r}+\mathbf{x})}\tfrac{1}{\sqrt{V}}e^{\imath\mathbf{k}\cdot(\mathbf{r}-\mathbf{x})}e^{(2\imath/\hbar)\mathbf{p}\cdot\mathbf{x}}d^3x \\ &= \frac{1}{\pi^3 V}\int_{-\infty}^{\infty}e^{-2\imath(\mathbf{k}-\mathbf{p}/\hbar)\cdot\mathbf{x}}d^3x = \tfrac{1}{V}\delta^3(\mathbf{p}-\hbar\mathbf{k})\ . \end{aligned}$$

For a harmonic oscillator, we would like to embed the Wigner function into the formalism of the coherent states distribution functions, such that it can be used to evaluate expectation values,

$$\langle\hat{O}_{\rm S}(\hat{a},\hat{a}^\dagger)\rangle = {\rm Tr}\ \hat{\rho}\hat{O}_{\rm S}(\hat{a},\hat{a}^\dagger) = \int W(\alpha,\alpha^*)O_{\rm S}(\alpha,\alpha^*)d^2\alpha\ , \tag{14.59}$$

where the index S denotes *symmetric order*. How this can be done will be detailed in the next section and in Exc. 14.3.5.3.

Example 79 (*Symmetric order*): Simple examples for Wigner-Weyl ordering are,

$$\begin{aligned}
\hat{a}\hat{a}^\dagger &= \tfrac{1}{2}(\hat{a}\hat{a}^\dagger + \hat{a}^\dagger\hat{a}) - \tfrac{1}{2} \\
\hat{a}^\dagger\hat{a} &= \tfrac{1}{2}(\hat{a}\hat{a}^\dagger + \hat{a}^\dagger\hat{a}) + \tfrac{1}{2} \\
\hat{a}^2\hat{a}^\dagger &= \tfrac{1}{2}(\hat{a}^2\hat{a}^\dagger + \hat{a}^\dagger\hat{a}^2) + \hat{a} \\
\hat{a}\hat{a}^\dagger\hat{a} &= \tfrac{1}{2}(\hat{a}^2\hat{a}^\dagger + \hat{a}^\dagger\hat{a}^2) \\
\hat{a}^\dagger\hat{a}^2 &= \tfrac{1}{2}(\hat{a}^2\hat{a}^\dagger + \hat{a}^\dagger\hat{a}^2) - \hat{a}\ .
\end{aligned}$$

14.3.2 Relation between the P, Q, and Wigner distributions

All three distribution function studied here, the P, the Q, and the Wigner distributions can be brought into a common generic shape writing the density operator as [749],

$$\boxed{\begin{aligned}
\hat{\rho} \;&=\; \pi \int F_X(\alpha,\alpha^*)\Delta_X(\alpha-\hat{a},\alpha^*-\hat{a}^\dagger)d^2\alpha \\
\text{with}\qquad &\Delta_{\rm N}(\alpha-\hat{a},\alpha^*-\hat{a}^\dagger) = \tfrac{1}{\pi^2}\int e^{-\lambda(\alpha^*-\hat{a}^\dagger)+\lambda^*(\alpha-\hat{a})}e^{-|\lambda|^2/2}d^2\lambda \\
&\Delta_{\rm S}(\alpha-\hat{a},\alpha^*-\hat{a}^\dagger) = \tfrac{1}{\pi^2}\int e^{-\lambda(\alpha^*-\hat{a}^\dagger)+\lambda^*(\alpha-\hat{a})}d^2\lambda \\
&\Delta_{\rm A}(\alpha-\hat{a},\alpha^*-\hat{a}^\dagger) = \tfrac{1}{\pi^2}\int e^{-\lambda(\alpha^*-\hat{a}^\dagger)+\lambda^*(\alpha-\hat{a})}e^{|\lambda|^2/2}d^2\lambda
\end{aligned}}\ , \tag{14.60}$$

with the indices $X = N, S, A$ and the respective distribution functions $F_{\rm N} = P$, $F_{\rm S} = W$, and $F_{\rm A} = Q$. A useful formula helping us to break down the exponential functions is obtained from Glauber's formula (1.313) applied to the displacement operator $D(\alpha) = e^{\lambda\hat{a}^\dagger - \lambda^*\hat{a}}$ defined in (2.130),

$$e^{\lambda\hat{a}^\dagger-\lambda^*\hat{a}} = e^{-\lambda^*\hat{a}}e^{\lambda\hat{a}^\dagger}e^{|\lambda|^2/2} = e^{\lambda\hat{a}^\dagger}e^{-\lambda^*\hat{a}}e^{-|\lambda|^2/2}\ . \tag{14.61}$$

as it allows us to rewrite the formulas (14.60) as,

$$\begin{aligned}
\Delta_{\rm N}(\alpha-\hat{a},\alpha^*-\hat{a}^\dagger) &= \mathcal{F}[e^{-\lambda^*\hat{a}}e^{\lambda\hat{a}^\dagger}] \\
\Delta_{\rm S}(\alpha-\hat{a},\alpha^*-\hat{a}^\dagger) &= \mathcal{F}[e^{\lambda\hat{a}^\dagger-\lambda^*\hat{a}}] \\
\Delta_{\rm A}(\alpha-\hat{a},\alpha^*-\hat{a}^\dagger) &= \mathcal{F}[e^{\lambda\hat{a}^\dagger}e^{-\lambda^*\hat{a}}]\ .
\end{aligned} \tag{14.62}$$

Inserting the density operator (14.60) into definition (14.50) of the Glauber-Sudarshan P-function we calculate,

$$\begin{aligned}
P(\alpha,\alpha^*) &= \mathrm{Tr}\ \hat{\rho}\delta(\alpha^*-\hat{a}^\dagger)(\alpha-\hat{a}) \\
&= \tfrac{1}{\pi^2}\int e^{\lambda^*\alpha-\lambda\alpha^*}\,\mathrm{Tr}\ \hat{\rho}e^{\lambda\hat{a}^\dagger}e^{-\lambda^*\hat{a}}d^2\lambda = \mathcal{F}[\chi_{\rm N}(\lambda,\lambda^*)]\ ,
\end{aligned} \tag{14.63}$$

where we defined the so-called normal-ordered *characteristic function* $\chi_{\rm N} \equiv {\rm Tr}\ \hat{\rho} e^{\lambda \hat{a}^\dagger} e^{-\lambda^* \hat{a}}$. Similarly, inserting the density operator (14.60) into definition (14.54) of the Husimi Q-function we calculate,

$$\begin{aligned} Q(\alpha, \alpha^*) &= {\rm Tr}\ \hat{\rho} \delta(\alpha - \hat{a})(\alpha^* - \hat{a}^\dagger) \\ &= \tfrac{1}{\pi^2} \int e^{\lambda^* \alpha - \lambda \alpha^*} {\rm Tr}\ \hat{\rho} e^{-\lambda^* \hat{a}} e^{\lambda \hat{a}^\dagger} d^2\lambda = \mathcal{F}[\chi_{\rm A}(\lambda, \lambda^*)] \ , \end{aligned} \tag{14.64}$$

where we defined the antinormal-ordered characteristic function $\chi_{\rm A} \equiv {\rm Tr}\ \hat{\rho} e^{-\lambda^* \hat{a}} e^{\lambda \hat{a}^\dagger}$. By analogy we find for the Wigner distribution,

$$W(\alpha, \alpha^*) = \mathcal{F}[\chi_{\rm A}(\lambda, \lambda^*)] = \tfrac{1}{\pi^2} \int e^{\lambda^* \alpha - \lambda \alpha^*} {\rm Tr}\ \hat{\rho} e^{\lambda \hat{a}^\dagger - \lambda^* \hat{a}} d^2\lambda \ . \tag{14.65}$$

In summary, the three coherent distribution functions are expressed by inverse Fourier transforms of the following characteristic functions [10],

$$\boxed{\begin{array}{rclcrcl} \chi_{\rm N}(\lambda, \lambda^*) & = & {\rm Tr}\ \hat{\rho} e^{\lambda \hat{a}^\dagger} e^{-\lambda^* \hat{a}} & , & P & = & \mathcal{F}\chi_{\rm N} \\ \chi_{\rm S}(\lambda, \lambda^*) & = & {\rm Tr}\ \hat{\rho} e^{\lambda \hat{a}^\dagger - \lambda^* \hat{a}} & , & W & = & \mathcal{F}\chi_{\rm S} \\ \chi_{\rm A}(\lambda, \lambda^*) & = & {\rm Tr}\ \hat{\rho} e^{-\lambda^* \hat{a}} e^{\lambda \hat{a}^\dagger} & , & Q & = & \mathcal{F}\chi_{\rm A} \end{array}} \ . \tag{14.66}$$

We see that the distribution functions $\chi_{N,S,A}$ are related to each other via (14.61). We derive in Exc. 14.3.5.4 the so-called disentangling theorem [316],

$$e^{-|\lambda|^2/2} \chi_{\rm N}(\lambda) = \chi_{\rm S}(\lambda) = e^{|\lambda|^2/2} \chi_{\rm A}(\lambda) \ . \tag{14.67}$$

Thus, Q-function corresponds to a smoothed Wigner function, which in turn corresponds to a smoothed P-function. The inverse complex Fourier transformation converts the products in (14.67) into convolutions. Exploiting the useful integral formula,

$$\tfrac{1}{\pi} \int e^{-a|\lambda|^2 + b\lambda + c\lambda^*} d^2\lambda = \tfrac{1}{a} e^{bc/a} \ , \tag{14.68}$$

we find,

$$W = P \star \frac{2}{\pi} e^{-2|\lambda|^2} \qquad \text{and} \qquad Q = W \star \frac{2}{\pi} e^{-2|\lambda|^2} = P \star \frac{1}{\pi} e^{-|\lambda|^2} \ . \tag{14.69}$$

What still needs to be proven is, that the generic definition of the distribution function (14.63), (14.64), and (14.65) coincides with the earlier definitions (14.50), (14.54), and (14.58). This will be done in Exc. 14.3.5.5. Also solve the Excs. 14.3.5.6 to 14.3.5.7.

Example 80 (*Generalized phase space representations*): The fact that the probability distributions Q, W, and P are intrinsically connected suggests setting up a generalized formalism based on the displacement operator

[10] For pure states, the definition of the characteristic functions is simplified to,

$$\chi_X(\lambda, \lambda^*) = \langle \psi | ... | \psi \rangle \ .$$

$\mathcal{D}(\alpha)|0\rangle = e^{\lambda\hat{a}^\dagger - \lambda^*\hat{a}}|0\rangle = |\alpha\rangle$ introduced in (2.130) and the parity operator Π_s [472]. Defining the s-parametrized probability distribution,

$$X_\rho(\alpha, s) = \mathrm{Tr}\ \hat{\rho}\mathcal{D}(\alpha)\Pi_s\mathcal{D}^\dagger(\alpha) \longrightarrow \langle\psi|\mathcal{D}(\alpha)\Pi_s\mathcal{D}^\dagger(\alpha)|\psi\rangle\ , \tag{14.70}$$

where the second expression holds for pure states, we recover the probability distributions Q, W, and P from,

$$Q_\rho(\alpha) \equiv X_\rho(\alpha, -1) \qquad \text{with} \qquad \Pi_{-1} = \sum_{m,n}\delta_{n0}\delta_{mn}|m\rangle\langle n| \tag{14.71}$$

$$W_\rho(\alpha) \equiv X_\rho(\alpha, 0) \qquad \text{with} \qquad \Pi_0 = \sum_{m,n} 2e^{\imath\pi n}\delta_{mn}|m\rangle\langle n|$$

$$\text{so that} \qquad \Pi_0|\alpha\rangle = \sum_n 2e^{\imath\pi n}|n\rangle\langle n|\alpha\rangle = \sum_n 2e^{-|\alpha|^2/2}\frac{(-\alpha)^n}{\sqrt{n!}}|n\rangle = 2|-\alpha\rangle$$

$$P_\rho(\alpha) \equiv X_\rho(\alpha, 1) \qquad \text{with} \qquad \Pi_1 = \sum_{m,n}\infty\delta_{mn}|m\rangle\langle n|\ .$$

In particular, for the vacuum state we calculate,

$$Q_{|0\rangle}(\alpha) = \sum_n \langle 0|\mathcal{D}(\alpha)\delta_{n0}|n\rangle\langle n|\mathcal{D}^\dagger(\alpha)|0\rangle = |\langle 0|-\alpha\rangle|^2 = e^{-|\alpha|^2} \tag{14.72}$$

$$W_{|0\rangle}(\alpha) = \sum_n \langle 0|\mathcal{D}(\alpha)2e^{\imath\pi n}|n\rangle\langle n|\mathcal{D}^\dagger(\alpha)|0\rangle = 2\sum_n e^{\imath\pi n}|\langle n|-\alpha\rangle|^2 = 2e^{-2|\alpha|^2}$$

$$P_{|0\rangle}(\alpha) = ... = \delta^{(2)}(\alpha)\ .$$

The convolution of distribution functions yields,

$$[Y \star X](\alpha) = \int [\mathcal{D}^{-1}(\alpha)Y(\alpha')]X(\alpha')d\alpha' = \int Y(\alpha'-\alpha)X(\alpha')d\alpha'$$

$$X_{|0\rangle}(\alpha, s') \star X_\rho(\alpha, s) = X_\rho(\alpha, s+s'-1)\ . \tag{14.73}$$

For example,

$$P_{|0\rangle}(\alpha) \star X_\rho(\alpha, s) = X_{|0\rangle}(\alpha, 1) \star X_\rho(\alpha, s) = X_\rho(\alpha, s)\ . \tag{14.74}$$

identifying the Glauber-Sudarshan distribution as the identity operator, and

$$W_{|0\rangle}(\alpha) \star W_\rho(\alpha) = X_{|0\rangle}(\alpha, 0) \star X_\rho(\alpha, 0) = X_\rho(\alpha, -1) = Q_\rho(\alpha)\ . \tag{14.75}$$

14.3.3 Characteristic functions for arbitrary HO states in the Fock basis

The various states that a light field can adopt can now be expressed either by photon number distribution in a Fock state basis, or by two-dimensional weighting functions P, Q, W in a coherent state basis. Here, are some examples for these representations.

If a state of a harmonic oscillator can be expanded into Fock states,

$$|\psi\rangle = \sum_n c_n|n\rangle\ , \tag{14.76}$$

the normal-ordered characteristic function (14.66) will be composed of terms like $\langle m|e^{\lambda\hat{a}^\dagger}e^{-\lambda^*\hat{a}}|n\rangle$. To evaluate these terms, we begin calculating [11],

$$\hat{a}^k|n\rangle = \sqrt{\frac{n!}{(n-k)!}}|n-k\rangle \quad \text{for} \quad k \leq n \qquad \text{and} \qquad \hat{a}^k|n\rangle = 0 \quad \text{for} \quad k \geq n \ , \tag{14.77}$$

and,

$$e^{-\lambda^*\hat{a}}|n\rangle = \sum_{k=0}^{\infty}\frac{(-\lambda^*\hat{a})^k}{k!}|n\rangle = \sum_{k=0}^{n}\frac{(-\lambda^*)^k}{\sqrt{k!}}\sqrt{\binom{n}{k}}|n-k\rangle \ . \tag{14.78}$$

Hence, assuming $m \geq n$,

$$\begin{aligned}\langle m|e^{\lambda\hat{a}^\dagger}e^{-\lambda^*\hat{a}}|n\rangle &= \sum_{k=0}^{n}\frac{(-\lambda^*)^k\lambda^{m-n+k}}{\sqrt{k!(m-n+k)!}}\sqrt{\binom{n}{k}\binom{m}{m-n+k}} \\ &= \sqrt{\frac{n!}{m!}}\lambda^{m-n}\sum_{k=0}^{n}\binom{m}{k+m-n}\frac{(-|\lambda|^2)^k}{k!} = \sqrt{\frac{n!}{m!}}\lambda^{m-n}L_n^{m-n}(|\lambda|^2) \ ,\end{aligned} \tag{14.79}$$

where L_n^{m-n} are Laguerre polynomials. Now, exploiting the fact that

$$\begin{aligned}\langle m|e^{\lambda\hat{a}^\dagger}e^{-\lambda^*\hat{a}}|n\rangle &= (\langle n|e^{-\lambda\hat{a}^\dagger}e^{\lambda^*\hat{a}}|m\rangle)^\dagger = \overline{\langle n|e^{-\lambda\hat{a}^\dagger}e^{\lambda^*\hat{a}}|m\rangle} \\ &= \sqrt{\frac{m!}{n!}}(-\lambda^*)^{n-m}L_n^{n-m}(|\lambda|^2) \ ,\end{aligned} \tag{14.80}$$

and with the expansion (14.76) we obtain for the normally-ordered characteristic function,

$$\begin{aligned}\chi_{\rm N}(\lambda) &= \sum_{m,n}c_m^*c_n\langle m|e^{\lambda\hat{a}^\dagger}e^{-\lambda^*\hat{a}}|n\rangle \\ &= \sum_{m\geq n}(1-\tfrac{1}{2}\delta_{m,n})\left(c_m^*c_n\langle m|e^{\lambda\hat{a}^\dagger}e^{-\lambda^*\hat{a}}|n\rangle + \overline{c_m^*c_n\langle m|e^{-\lambda\hat{a}^\dagger}e^{\lambda^*\hat{a}}|n\rangle}\right) \ .\end{aligned} \tag{14.81}$$

finally yielding,

$$\boxed{\chi_{\rm N}(\lambda) = \sum_{m\geq n}(1-\tfrac{1}{2}\delta_{m,n})\left[c_m^*c_n\lambda^{m-n} + c_mc_n^*(-\lambda^*)^{m-n}\right]\sqrt{\tfrac{n!}{m!}}L_n^{m-n}(|\lambda|^2)} \ . \tag{14.82}$$

Remembering that the symmetrically ordered function is given by $\chi_{\rm S}(\lambda) = e^{-|\lambda|^2}\chi_{\rm N}(\lambda)$ we may obtain the Wigner function by a numerical two-dimensional FFT,

$$W(\alpha) = \tfrac{1}{\pi^2}\int e^{-|\lambda|^2}\chi_{\rm N}(\lambda)e^{\lambda^*\alpha-\lambda\alpha^*}d^2\lambda \ . \tag{14.83}$$

We will use this result in Sec. 17.2.3 to characterize correlations in an optical mode emanating from a Jaynes-Cummings type coupling to an atom. In Exc. 14.3.5.8 we will try to find an analytic solution for this integral.

[11] See also 2.6.6.7.

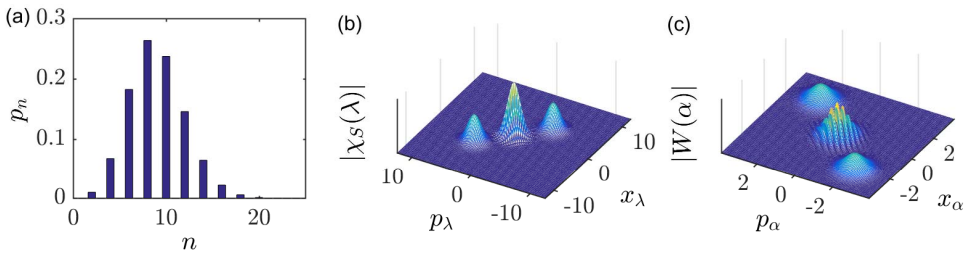

Figure 14.1: (code) Starting from a cat-state photon distribution, as shown in (a), we calculate the symmetrically ordered characteristic function (b) from the expression (14.81), and the Wigner function (c) by an FFT.

14.3.4 Representation of particular states in the Fock and Glauber basis

14.3.4.1 Representations of Glauber states

We have seen earlier that coherent states $|\beta\rangle$ can be expanded on a Fock state basis $|n\rangle$. For the state function, the density operator, and the photon number distribution we have,

Glauber states in the Fock basis

$$\begin{aligned} |\beta\rangle &= e^{-|\beta|/2}\sum_n \frac{\beta^n}{\sqrt{n!}}|n\rangle \\ \hat{\rho} &= |\beta\rangle\langle\beta| = e^{-|\beta|^2}\sum_{m,n}\frac{\beta^n\beta^{*m}}{\sqrt{m!n!}}|n\rangle\langle m| \\ P_n &= |\langle n|\beta\rangle|^2 = e^{-|\beta|^2}\frac{|\beta|^{2n}}{n!} \end{aligned} \tag{14.84}$$

Expanding a coherent state on a basis of Glauber states, we will derive in Exc. 14.3.5.9 the P-function, the density matrix, the Q-function, and the Wigner function,

Glauber states in the Glauber basis

$$\begin{aligned} |\beta\rangle &= \mathcal{D}(\beta)|0\rangle \\ \hat{\rho} &= |\beta\rangle\langle\beta| = \int \delta^{(2)}(\alpha-\beta)|\alpha\rangle\langle\alpha|d^2\alpha \\ P_{|\beta\rangle}(\alpha) &= \delta^{(2)}(\alpha-\beta) \\ Q_{|\beta\rangle}(\alpha) &= \tfrac{1}{\pi}e^{-|\alpha-\beta|^2} \\ W_{|\beta\rangle}(\alpha) &= \tfrac{2}{\pi}e^{-2|\alpha-\beta|^2} \end{aligned} \tag{14.85}$$

Example 81 (*State of a laser*): Following [873, 716], the correct *state of a*

laser beam is not simply a coherent state, but rather,

$$\hat{\rho} = \int |\alpha e^{\imath\varphi}\rangle\langle\alpha e^{\imath\varphi}| \frac{d\varphi}{2\pi} \ . \tag{14.86}$$

After averaging, this state can be written as a superposition of Fock states [187],

$$\hat{\rho} = \sum_n P_n |n\rangle\langle n| \qquad \text{with} \qquad P_n = \frac{e^{-|\alpha|^2}|\alpha|^2 n}{n!} \ , \tag{14.87}$$

but without a specific phase,

$$\hat{\rho} \neq \sum_{m,n} c_m^* c_n |m\rangle\langle n| \ . \tag{14.88}$$

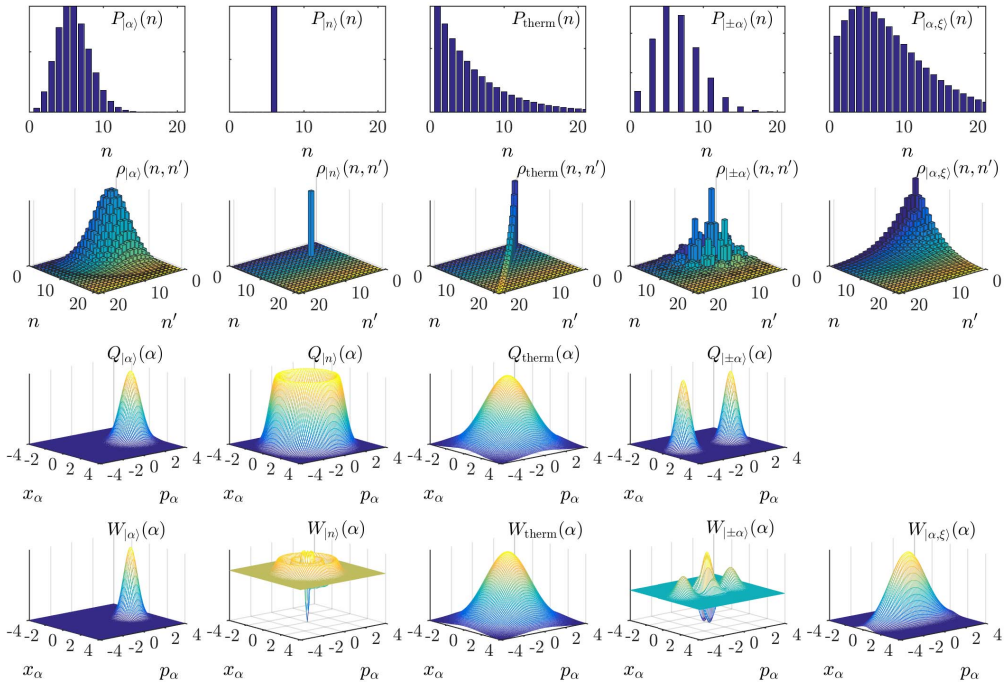

Figure 14.2: (code) (upper row) Photon number distributions $P(n)$, (second row) density matrices ρ, (third row) Q functions, and (lower row) Wigner functions of (first column) a Glauber state, (second column) a Fock state, (third column) a thermal state, (forth column) a Schrödinger cat state, and (last column) a squeezed state.

14.3.4.2 Representations of Schrödinger cat states

Schrödinger cat states are correlated states of many particles (or quasi-particles). The expansion of the *Schrödinger cat state* $|\beta_0\rangle \pm |\beta_1\rangle$ on a Fock state basis yields, as we have seen in Exc. 2.6.6.6,

Schrödinger cat states in the Fock basis

$$\begin{aligned} |\psi_\pm\rangle &= \sum_n \frac{e^{-|\beta_0|^2/2}\beta_0^n \pm e^{-|\beta_1|^2/2}\beta_1^n}{\sqrt{2n!}}|n\rangle \\ \hat{\rho} &= |\psi_\pm\rangle\langle\psi_\pm| \\ P_n &= |\langle n|\psi_\pm\rangle|^2 \longrightarrow e^{-|\beta_0|^2}\frac{|\beta_0|^{2n}}{n!}\frac{|1\pm(-1)^n|^2}{2} \qquad \text{for} \quad \beta_0 = -\beta_1 \end{aligned} \tag{14.89}$$

Expanding a Schrödinger cat state on a basis of Glauber states, we will derive in Exc. 14.3.5.10 the P-function, the density matrix, the Q-function, and the Wigner function,

Schrödinger cat states in the Glauber basis

$$\begin{aligned} |\psi_\pm\rangle &= \tfrac{1}{C}(|\beta_0\rangle \pm |\beta_1\rangle) \qquad \text{with} \qquad C = \sqrt{2 \pm 2e^{-|\beta_0-\beta_1|^2}} \\ \hat{\rho} &= |\psi_\pm\rangle\langle\psi_\pm| \\ P_{|\beta_0\rangle|\beta_1\rangle}(\alpha) &= \delta^{(2)}(\alpha-\beta_0) + \delta^{(2)}(\alpha-\beta_1) \\ Q_{|\beta_0\rangle|\beta_1\rangle}(\alpha) &= \tfrac{1}{\pi}e^{-|\alpha-\beta_0|^2} + \tfrac{1}{\pi}e^{-|\alpha-\beta_1|^2} \\ W_{|\beta_0\rangle|\beta_1\rangle}(\alpha) &= \tfrac{2}{C^2\pi}\Big(e^{-2|\alpha-\beta_0|^2} + e^{-2|\alpha-\beta_1|^2} \\ &\pm 2e^{-|\beta_0|^2/2-|\beta_1|^2/2}\mathfrak{Re}\, e^{-2(\beta_1-\alpha)(\beta_0^*-\alpha^*)+\beta_0^*\beta_1}\Big) \end{aligned} \tag{14.90}$$

We know from microscopic systems, for instance a two-level atom, that they can live in superposition states $|1\rangle + |2\rangle$. In contrast, the Schrödinger cat states discussed above occur in continuous Schrödinger fields involving many particles. Macroscopic quantum interferences (i.e. interferences that are detectable with macroscopic apparatuses, for example in heterodyne schemes) are named *fuzzy Schrödinger cats*, if the interfering states are conspicuously separated in phase space.

At this point, we have to emphasize the fundamental difference between Schrödinger cats and superpositions of modes,

$$\begin{aligned} |\psi\rangle &= |\alpha\rangle + |\beta\rangle &&\neq |\alpha\rangle|\beta\rangle \\ \hat{\rho} &= |\alpha\rangle\langle\alpha| + |\beta\rangle\langle\beta| + |\alpha\rangle\langle\beta| + |\beta\rangle\langle\alpha| &&\neq |\alpha\beta\rangle\langle\alpha\beta| \end{aligned} \quad . \tag{14.91}$$

Schrödinger cats exhibit interferences in phase space, whereas for mode superpositions, interferences only appear when a parameter is varied (e.g., the length of an interferometer arm).

Schrödinger cat states are very sensitive to dissipation and easily converted into statistical mixtures. For example, $|\alpha\rangle \pm |-\alpha\rangle$ contains only odd (even) photon numbers in the distribution function P_n. After some time $\sim \tau_{cav}/N$, the distribution is converted into a Poisson distribution. The higher the particle number N, the faster the decoherence will be. Consequently, *truely macroscopic* cat states have never been observed.

14.3.4.3 Representations of Fock states

On the Fock state basis $|n\rangle$, a number state is characterized by,

Fock states in the Fock basis

$$\begin{aligned} |n\rangle &= \tfrac{(\hat{a}^\dagger)^n}{\sqrt{n!}}|0\rangle \\ \hat{\rho} &= |n\rangle\langle n| = \tfrac{1}{n!}(\hat{a}^\dagger)^n|0\rangle\langle 0|\hat{a}^n \\ P_k &= \delta_{nk} \end{aligned} \tag{14.92}$$

This state can be expanded into Glauber states $|\alpha\rangle$ by following procedure. For large n we first calculate the P-distribution function,

$$P_{|n\rangle}(\alpha) = \delta^{(1)}(|\alpha| - \sqrt{n}) \ , \tag{14.93}$$

because it allows us to derive the density matrix via the formula (14.51),

$$\begin{aligned} \hat{\rho}_{|n\rangle} &= \int \delta^{(1)}(|\alpha| - \sqrt{n})|\alpha\rangle\langle\alpha| d^2\alpha \\ &= \int_0^\infty \int_0^{2\pi} \delta^{(1)}(|\alpha| - \sqrt{n})|\alpha\rangle\langle\alpha| \ |\alpha| d|\alpha| d\varphi_\alpha = \sqrt{n}\int_0^{2\pi} |\alpha\rangle\langle\alpha| d\varphi_\alpha \ . \end{aligned} \tag{14.94}$$

The Q-distribution function becomes, inserting the density operator obtained in (14.94),

$$\begin{aligned} Q_{|n\rangle}(\alpha) &= \tfrac{1}{\pi}\langle\alpha|\hat{\rho}_{|n\rangle}|\alpha\rangle \\ &= \tfrac{1}{\pi} n \int_0^{2\pi} |\langle\alpha|\beta\rangle|^2 d\varphi_\beta = \frac{1}{\pi} n \int_0^{2\pi} e^{-|\alpha - |\beta| e^{\imath\varphi_\beta}|^2} d\varphi_\beta \triangleq \frac{|\alpha|^{2n}}{\pi n!} e^{-|\alpha|^2} \ , \end{aligned} \tag{14.95}$$

and finally the Wigner function is,

$$W_{|n\rangle}(\alpha) = \frac{2}{\pi} e^{-2|\alpha|^2} (-1)^n \sum_{m=0}^{n} \binom{n}{m} \frac{(-4|\alpha|^2)^m}{m!} = \frac{2}{\pi} e^{-2|\alpha|^2} (-1)^n L_n(4|\alpha|^2) \ , \tag{14.96}$$

where $L_m(4|\alpha|^2)$ are Laguerre polynomials. In Excs. 14.3.5.11 and 14.3.5.12 we will learn how to derive the above distribution functions directly from the characteristic functions. In summary, we have [429],

Fock states in the Glauber basis

$$\begin{aligned} |n\rangle &= \frac{\sqrt{n!}}{2\pi r^n} e^{r^2/2} \int_0^{2\pi} e^{-\imath n\varphi_\alpha} |\alpha\rangle d\varphi_\alpha \\ \hat{\rho} &= \sqrt{n} \int_0^{2\pi} |\alpha\rangle\langle\alpha| d\varphi_\alpha \\ P_{|n\rangle}(\alpha) &= \delta^{(1)}(|\alpha| - \sqrt{n}) \\ Q_{|n\rangle}(\alpha) &= \frac{|\alpha|^{2n}}{\pi n!} e^{-|\alpha|^2} \\ W_{|n\rangle}(\alpha) &= \tfrac{2}{\pi} e^{-2|\alpha|^2} (-1)^n L_n(4|\alpha|^2) \end{aligned} \tag{14.97}$$

14.3.4.4 Representations of thermal states

A light mode in a *thermal mixture can not be represented by a pure state*, but requires a density matrix description beyond (14.41). The concept of statistical mixtures has been introduced in Sec. 14.2. The following formulas will be derived in Exc. 14.3.5.13 [749],

thermal states in the Fock basis

$$\begin{aligned} \hat{\rho} &= \sum_n \frac{\bar{n}^n}{(1+\bar{n})^{1+n}} |n\rangle\langle n| \\ P_n &= \tfrac{\bar{n}^n}{(1+\bar{n})^{1+n}} \end{aligned} \tag{14.98}$$

The density matrix does not show coherences, only populations following the Boltzmann distribution [see Eq. (1.59)].

The coherent distribution P-function is,

thermal states in the Glauber basis

$$\begin{aligned} \hat{\rho} &= \frac{1}{\pi\bar{n}} \int e^{-|\alpha|^2/\bar{n}} |\alpha\rangle\langle\alpha| d^2\alpha \\ P_{\text{therm}}(\alpha) &= \tfrac{1}{\pi\bar{n}} e^{-|\alpha|^2/\bar{n}} \\ Q_{\text{therm}}(\alpha) &= \tfrac{1}{\pi(\bar{n}+1)} e^{-|\alpha|^2/(\bar{n}+1)} \\ W_{\text{therm}}(\alpha) &= \tfrac{1}{\pi(\bar{n}+1/2)} e^{-|\alpha|^2/(\bar{n}+1/2)} \end{aligned} \tag{14.99}$$

Resolve the Excs. 14.3.5.14 and 14.3.5.15.

14.3.5 Exercises

14.3.5.1 Ex: Glauber-Sudarshan and Husimi distribution

a. Show that $\rho_{\rm A}(\alpha,\alpha^*) = \pi P(\alpha,\alpha^*)$ for an anti-normally ordered density operator $\hat{\rho}_{\rm A}(\hat{a},\hat{a}^\dagger)$.
b. Show that $\rho_{\rm N}(\alpha,\alpha^*) = \frac{1}{\pi}Q(\alpha,\alpha^*)$ for a normally ordered density operator $\hat{\rho}_{\rm N}(\hat{a},\hat{a}^\dagger)$.

14.3.5.2 Ex: Glauber-Sudarshan and Husimi distribution

a. Show that the definitions of the Glauber-Sudarshan distribution given by (14.60) and (14.51) are equivalent.
b. Show that the definitions of the Husimi distribution given by (14.60) and (14.55) are equivalent.

14.3.5.3 Ex: Moments of Glauber states

a. Prove Eq. (14.53).
b. Prove Eq. (14.57).
c. Prove $\frac{1}{2}\langle \hat{a}\hat{a}^\dagger + \hat{a}^\dagger\hat{a}\rangle = \int W(\alpha,\alpha^*)\alpha\alpha^* d^2\alpha$.
d. Prove $\langle\{\hat{a}_j^{\dagger m}\hat{a}_k^n\}_{\rm S}\rangle = \int W(\alpha)\alpha_j^m\alpha_k^{*n}\, d\alpha$, where the index S denotes *symmetric ordering*. Symmetric or *Weyl ordering* means that all products $\hat{r}\hat{p}$ must be replaced by the symmetric expressions, such as $(\hat{r}\hat{p}+\hat{p}\hat{r})/2$.
e. Then prove Eq. (14.59).

14.3.5.4 Ex: Relationship between the characteristic functions

Derive the disentangling theorem (14.67) between the characteristic functions of the Glauber state basis.

14.3.5.5 Ex: General form of the distribution functions

Show that from the definition (14.60) the common definition of the distribution functions (14.51) and (14.55) are recovered.

14.3.5.6 Ex: Characteristic functions

a. Evaluate the expression $\left.\frac{\partial^{m+n}\chi_X(\lambda)}{\partial\lambda^{*m}\partial(-\lambda)^n}\right|_{\lambda=0}$ for $X = N, S, A$.
b. Consider the particular case of a coherent state.

14.3.5.7 Ex: Calculating with Wirtinger derivatives

Prove the following identities called *Wirtinger derivatives* [316],

$$\hat{a}^\dagger - \alpha^* = \frac{\partial}{\partial \underrightarrow{\alpha}} \qquad \text{and} \qquad \hat{a}^\dagger - \alpha = \frac{\partial}{\partial \underleftarrow{\alpha}^*} \ .$$

Note, that with the bosonic operators we can construct the observables,

$$\hat{x} + \imath\hat{p} = \sqrt{2}\hat{a} \quad , \quad \partial_x - \imath\partial_p = 2\underrightarrow{\partial_\alpha} \quad , \quad \partial_x + \imath\partial_p = 2\underleftarrow{\partial_{\alpha^*}} \ .$$

In two dimensions [280], $d^2\alpha = d(\mathfrak{Re}\,\alpha)d(\mathfrak{Im}\,\alpha) = dxdp$.

14.3.5.8 Ex: Wigner function for arbitrary HO states in the Fock basis

Search an analytic solution for the integral (14.82).

14.3.5.9 Ex: P-, Q-, and Wigner distribution functions for Glauber states

Starting from the characteristic functions $\chi_{A,S,N}(\lambda)$ derive for a coherent state $|\beta\rangle$ (a) the Husimi representation, (b) the Glauber-Sudarshan representation, and (c) the Wigner representation.

14.3.5.10 Ex: P-, Q-, and Wigner distribution functions for cat states

Starting from the characteristic functions $\chi_{A,S,N}(\lambda)$ derive for a normalized cat state $C^{-1}(|\beta_0\rangle + |\beta_1\rangle)$ (a) the Husimi representation, (b) the Glauber-Sudarshan representation, and (c) the Wigner representation.

14.3.5.11 Ex: P-, Q-, and Wigner distribution functions for Fock states

Starting from the characteristic functions $\chi_{A,S,N}(\lambda)$ derive for a number state $|n\rangle$ (a) the Husimi representation, (b) the Glauber-Sudarshan representation, and (c) the Wigner representation.

14.3.5.12 Ex: Wigner distribution function of a Fock state

Calculate the Wigner function for a harmonic oscillator in a Fock state from its wavefunction $\langle x|n\rangle$.

14.3.5.13 Ex: Thermal state

a. Show that $\langle -\beta|\hat{\rho}|\beta\rangle e^{|\beta|^2}$ and $P(\alpha,\alpha^*)e^{-|\alpha|^2}$ are related by Fourier transform.
b. Using the relationship of (a), derive the density operator and the distribution function of the Fock and the Glauber basis for a thermal state.

14.3.5.14 Ex: Phase space distributions

1. Compute the three characteristic functions for the coherent state $\alpha\rangle$.
2. Show that $Q_{[\rho]}(\alpha) = \frac{1}{\pi}\langle 0|\mathcal{D}(-\alpha)\rho\mathcal{D}(\alpha)|0\rangle = \frac{1}{\pi}\mathrm{Tr}[|0\rangle\langle 0|\mathcal{D}(-\alpha)\rho\mathcal{D}(\alpha)|0\rangle]$. **Hint:** use linearity of the trace, the closure relations of coherent states.
3. Compute the Q function of a coherent state and of a Fock state.
4. **Difficult:** Show that $W(x,p) = \frac{1}{\pi}\int du\langle\frac{u}{2}|\mathcal{D}(-\alpha)\rho\mathcal{D}(\alpha)\mathcal{P}|\frac{u}{2}\rangle = \frac{2}{\pi}\mathrm{Tr}\,[\mathcal{D}(-\alpha)\rho\mathcal{D}(\alpha)\mathcal{P}]$.

14.3.5.15 Ex: Kerr states

Here, we study the so called optical *Kerr state* generated by the unitary operator

$$\mathcal{U}_{\rm Kerr}(\tau) = e^{\imath(\tau/2)\hat{a}^{\dagger 2}\hat{a}^2}\ . \tag{14.100}$$

a. Show that the Fock states are eigenstates of this operator and determine the eigenvalues.
b. How does the operator act on Glauber states?
c. Verify the transformation rule,

$$U_{\text{Kerr}}^{\dagger}\hat{a}U_{\text{Kerr}} = e^{\imath\tau\hat{n}}\hat{a} \ . \tag{14.101}$$

14.4 Squeezed states of the harmonic oscillator

14.4.1 The squeezing operator

Let us consider a Hamiltonian of the following form,

$$\boxed{\hat{H}_{\text{sqz}} = \hbar\omega\hat{a}^{\dagger}\hat{a} + \tfrac{\imath}{2}\hbar\xi\hat{a}^{\dagger 2} - \tfrac{\imath}{2}\hbar\xi^{*}\hat{a}^{2}} \ . \tag{14.102}$$

leading to the equation of motion,

$$\dot{\hat{a}} = -\imath\omega\hat{a} + 2g\hat{a}^{\dagger} \ . \tag{14.103}$$

The non-linear, i.e. quadratic, appearance of the field operators suggests that the interaction should include correlated pair production, as is the case for parametric processes or four-wave mixing. We will see later that cavities are good for generating squeezing. However, the unused ports of a cavity let uncorrelated vacuum fluctuations enter, which partially overrule squeezing.

For now, we study, in analogy with the displacement operator (2.130), the propagator $e^{-\imath\hat{H}_{\text{sqz}}t/\hbar}$, i.e the operator given by,

$$\mathcal{S}(\xi) \equiv e^{\xi^{*}\hat{a}^{2}/2 - \xi\hat{a}^{\dagger 2}/2} \ , \tag{14.104}$$

which we will call the *squeezing operator* because, applied to the vacuum state, $|\xi\rangle = S(\xi)|0\rangle$, this operator will compress the uncertainty of one quadrature component, as we will see shortly. It is easy to see that [316],

$$\mathcal{S}^{\dagger}(\xi) = \mathcal{S}(-\xi) = \mathcal{S}^{-1}(\xi) \ . \tag{14.105}$$

In analogy with the calculation (2.131), using the commutation rules, it is possible to verify the unitarity of this operator [531] (see Exc. 14.4.4.1). In particular, using the relationship (1.280) and the abbreviation $\hat{A} \equiv -\frac{\xi^{*}}{2}\hat{a}^{2} + \frac{\xi}{2}\hat{a}^{\dagger 2}$, we can show [795] (see Exc. 14.4.4.2),

$$\begin{aligned}\mathcal{S}^{\dagger}(\xi)\hat{a}\mathcal{S}(\xi) = e^{\hat{A}}\hat{a}e^{-\hat{A}} &= \hat{a} + [\hat{A},\hat{a}] + \tfrac{1}{2!}[\hat{A},[\hat{A},\hat{a}]] + \tfrac{1}{3!}\left[\hat{A},[\hat{A},[\hat{A},\hat{a}]]\right] + \ldots \\ &= \hat{a} - \xi\hat{a}^{\dagger} + \tfrac{1}{2!}\xi\xi^{*}\hat{a} - \tfrac{1}{3!}\xi\xi^{*}\xi\hat{a}^{\dagger} + \ldots = \hat{a}\cosh|\xi| - \tfrac{|\xi|}{\xi^{*}}\hat{a}^{\dagger}\sinh|\xi| \ ,\end{aligned} \tag{14.106}$$

and similarly for $\hat{a}^{\dagger}$, such that with $\xi \equiv re^{\imath\varphi}$,

$$\mathcal{S}^\dagger(\xi)\hat{a}\mathcal{S}(\xi) = \hat{a}\cosh r - \hat{a}^\dagger e^{\imath\varphi}\sinh r \ . \tag{14.107}$$

The formulas (14.107) describe a *Bogolubov transform*, as they can be cast into the form,

$$\boxed{\hat{b} \equiv u\hat{a} + v\hat{a}^\dagger \qquad , \qquad \hat{b}^\dagger \equiv u^*\hat{a}^\dagger + v^*\hat{a}} \ , \tag{14.108}$$

for complex numbers u and v. By postulating the same commutation relation for new operators, $[\hat{b}, \hat{b}^\dagger] = 1$, we immediately get the condition,

$$|u|^2 - |v|^2 = 1 \ . \tag{14.109}$$

Comparing with the hyperbolic identity $\cosh^2 r - \sinh^2 r = 1$, we can parametrize the constants as,

$$u = \cosh r \qquad \text{and} \qquad v = e^{\imath\varphi}\sinh r \ . \tag{14.110}$$

This is interpreted as a linear simplectic transformation in phase space between pairs of annihilation and creation operators satisfying the same commutation relation $[\hat{a}, \hat{a}^\dagger] = 1$.

14.4.1.1 Relation between squeezing and displacement operator

The squeezing operator *does not commute* with the displacement operator. However, in Exc. 14.4.4.3 we derive the following simple relation,

$$\mathcal{S}(\xi)\mathcal{D}(\alpha) \neq \mathcal{D}(\alpha)\mathcal{S}(\xi) = \mathcal{S}(\xi)\mathcal{D}(\alpha\cosh r + \alpha^* e^{\imath\varphi}\sinh r) \ . \tag{14.111}$$

Squeezed coherent states are generated by coherent displacement of a *squeezed vacuum*,

$$\boxed{|\alpha, \xi\rangle = \mathcal{D}(\alpha)|0, \xi\rangle = \mathcal{D}(\alpha)\mathcal{S}(\xi)|0\rangle} \ . \tag{14.112}$$

On the other hand, from (14.111),

$$\begin{aligned} \mathcal{D}(\alpha)\mathcal{S}(\xi)|0\rangle &= \mathcal{S}(\xi)\mathcal{D}(\alpha\cosh r + \alpha^* e^{\imath\varphi}\sinh r)|0\rangle \\ &= \mathcal{S}(\xi)|\alpha\cosh r + \alpha^* e^{\imath\varphi}\sinh r\rangle \ . \end{aligned} \tag{14.113}$$

In Exc. 14.4.4.4 we show that the coherent squeezed state $|\alpha, \xi\rangle$ is an eigenstate of the operator $\hat{a}\cosh r + \hat{a}^\dagger e^{\imath\varphi}\sinh r$. That is,

$$\begin{aligned} \mathcal{S}(\xi)\hat{a}\mathcal{S}^\dagger(\xi)|\alpha, \xi\rangle &= (\hat{a}\cosh r + \hat{a}^\dagger e^{\imath\varphi}\sinh r)|\alpha, \xi\rangle \\ &= (\alpha\cosh r + \alpha^* e^{\imath\varphi}\sinh r)|\alpha, \xi\rangle \ . \end{aligned} \tag{14.114}$$

The squeezed states form a complete basis with the closure relation,

$$\tfrac{1}{\pi}\int |\alpha, \xi\rangle\langle\alpha, \xi| d^2\alpha = \mathbb{I} \ . \tag{14.115}$$

14.4.1.2 Squeezing of the uncertainty relation

Let us consider a squeezed mode $\hat{b}$ generated by application of the transformation (14.107). The real and imaginary parts defined by $\hat{b} = \hat{x}_b + \imath\hat{p}_b$, are Hermitian and satisfy the Heisenberg uncertainty relation (1.201),

$$[\hat{x}_b, \hat{p}_b] = \tfrac{\imath}{2} \qquad \text{and} \qquad \Delta\hat{x}_b \Delta\hat{p}_b \geq \tfrac{1}{2\imath}\langle[\hat{x}_b, \hat{p}_b]\rangle = \tfrac{1}{4} \ . \tag{14.116}$$

However, let us take a look at the uncertainties separately. They relate to the Glauber mode via,

$$\begin{aligned}
\hat{x}_b &= \tfrac{1}{2}(\hat{b} + \hat{b}^\dagger) = \tfrac{1}{2}(\hat{a}\cosh r - \hat{a}^\dagger e^{\imath\varphi}\sinh r) + \tfrac{1}{2}(\hat{a}^\dagger \cosh r - \hat{a}e^{-\imath\varphi}\sinh r) \qquad (14.117)\\
&= \hat{x}_a \cosh r - \tfrac{1}{2}\sinh r(\hat{a}^\dagger e^{\imath\varphi} + \hat{a}e^{-\imath\varphi}) \overset{\varphi=0}{\longrightarrow} \hat{x}_a e^r \\
\hat{p}_b &= \tfrac{1}{2\imath}(\hat{b} - \hat{b}^\dagger) = \tfrac{1}{2\imath}(\hat{a}\cosh r - \hat{a}^\dagger e^{\imath\varphi}\sinh r) - \tfrac{1}{2\imath}(\hat{a}^\dagger \cosh r - \hat{a}e^{-\imath\varphi}\sinh r) \\
&= \hat{p}_a \cosh r - \tfrac{1}{2\imath}\sinh r(\hat{a}^\dagger e^{\imath\varphi} - \hat{a}e^{-\imath\varphi}) \overset{\varphi=0}{\longrightarrow} \hat{p}_a e^{-r} \ .
\end{aligned}$$

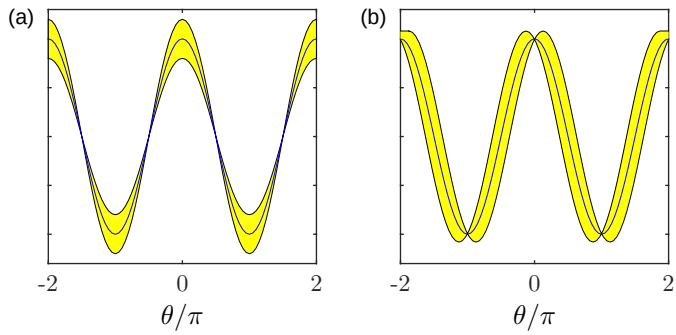

Figure 14.3: (code) Illustration of (a) amplitude squeezing and (b) phase squeezing.

The individual fluctuations are (assuming $\varphi = 0$),

$$\begin{aligned}
\Delta\hat{x}_b^2 &= \langle\hat{x}_b^2\rangle - \langle\hat{x}_b\rangle^2 = e^{2r}\left(\langle\hat{x}_a^2\rangle - \langle\hat{x}_a\rangle^2\right) \qquad (14.118)\\
&= \tfrac{1}{4}e^{2r}\left(1 + \langle\hat{a}^2\rangle + \langle\hat{a}^\dagger\rangle^2 + 2\langle\hat{a}^\dagger\hat{a}\rangle - \langle\hat{a}\rangle^2 - \langle\hat{a}^\dagger\rangle^2 - 2\langle\hat{a}^\dagger\rangle\langle\hat{a}\rangle\right) \ .
\end{aligned}$$

Considering coherent vacuum, $|\alpha\rangle = |0\rangle$ so that $\hat{a}|\alpha\rangle = 0$,

$$\begin{aligned}
\Delta\hat{x}_b^2 &= e^{2r}\left(\tfrac{1}{2}\mathfrak{Re}\,\langle\hat{a}^2\rangle + \tfrac{1}{4} + \tfrac{1}{2}\langle\hat{a}^\dagger\hat{a}\rangle\right) \qquad (14.119)\\
\Delta\hat{p}_b^2 &= e^{-2r}\left(-\tfrac{1}{2}\mathfrak{Re}\,\langle\hat{a}^2\rangle + \tfrac{1}{4} + \tfrac{1}{2}\langle\hat{a}^\dagger\hat{a}\rangle\right) \ .
\end{aligned}$$

hence,

$$\Delta\hat{x}_b = \tfrac{1}{2}e^r \qquad \text{and} \qquad \Delta\hat{p}_b = \tfrac{1}{2}e^{-r} \ , \tag{14.120}$$

and the squeezed state is at the uncertainty minimum.

Example 82 (*Detection of squeezing*): One method of detecting squeezing in a light mode is via balanced homodyne detection (see Sec. 32.4.2). The idea consists in mixing the squeezed light mode with a strong local oscillator at a 50% beam splitter, as will be discussed in Sec. 14.5.3.

14.4.2 Squeezed state in the Fock basis

The number of photons in the squeezed state is [531],

$$\langle n|\alpha,\xi\rangle = \frac{(\zeta/2)^{n/2}}{\sqrt{n!\cosh r}} e^{-\frac{1}{2}(|\alpha|^2+\alpha^*\zeta)} H_n\left(\frac{\alpha+\alpha^*\zeta}{\sqrt{2\zeta}}\right) , \tag{14.121}$$

with the abbreviation $\zeta \equiv e^{i\theta}\tanh r$. For squeezed vacuum $\alpha = 0$, noting that $H_n(0) = (-2)^{n/2}(n-1)!!$ for even n and $H_n(0) = 0$ for odd n, we find,

$$\langle n|0,\xi\rangle = \frac{(-\zeta)^{n/2}(n-1)!!}{\sqrt{n!\cosh r}} \tag{14.122}$$

for even photon number. Odd photon numbers are excluded. Hence,

squeezed states in the Fock basis

$$\begin{aligned} |\alpha,\xi\rangle &= \sum_n |n\rangle\langle n|\alpha,\xi\rangle \\ \hat\rho &= |\alpha,\xi\rangle\langle\alpha,\xi| \\ P_n &= |\langle n|\alpha,\xi\rangle|^2 \end{aligned} \quad . \tag{14.123}$$

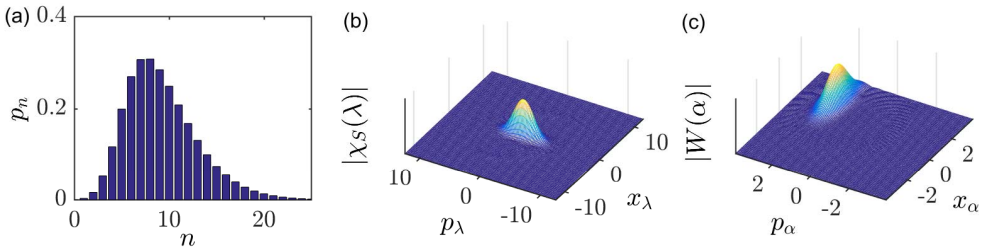

Figure 14.4: (code) Starting from a squeezed state photon distribution with $r = 0.5$, as shown in (a), we calculate the symmetrically ordered characteristic function (b) from the expression (14.82), and the Wigner function (c) by an FFT.

In the photon representation, as shown in Exc. 14.4.4.2, the squeezed vacuum is (unlike the coherent and the Fock vacuum) not empty,

$$\begin{aligned} \langle\alpha,\xi|\hat n|\alpha,\xi\rangle &= |\alpha|^2 + \sinh^2|\xi| &&\stackrel{\alpha\to 0}{\longrightarrow} \sinh^2|\xi| \\ \Delta_{\alpha,\xi}\hat n &= |\alpha| + 2\cosh^2|\xi|\sinh^2|\xi| &&\stackrel{\alpha\to 0}{\longrightarrow} 2\cosh^2|\xi|\sinh^2|\xi| \end{aligned} \quad . \tag{14.124}$$

Squeezed vacuum contains contributions from many $|n\rangle$.

For the squeezed vacuum state the photon number distribution displays odd-even-oscillations. This can be explained by the mathematical form of the squeezing operator, that resembles the operator for two-photon generation and annihilation processes. Photons in a squeezed vacuum state are more likely to appear in pairs.

14.4.3 Squeezed state in the Glauber basis

The *squeezed state* contains non-classical quantum correlations, as we will show in Exc. 14.4.4.5 by calculating $g^{(2)}$ for squeezed states,

$$g^{(2)}(\tau) = \frac{\langle \hat{b}^\dagger \hat{b}^\dagger(\tau)\hat{b}(\tau)\hat{b}\rangle}{\langle \hat{b}^\dagger\rangle^2\langle \hat{b}\rangle^2} \xrightarrow{\tau\to 0} 3 + \frac{1}{\sinh^2 r} \ . \tag{14.125}$$

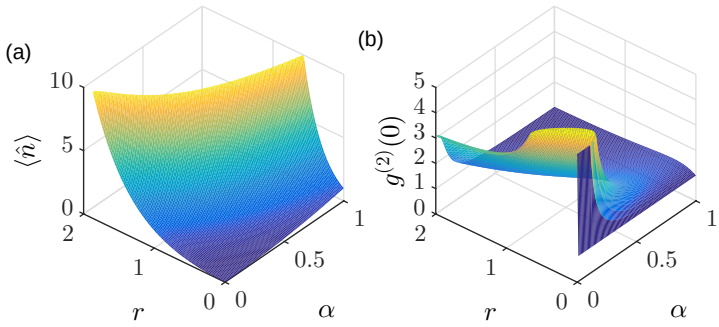

Figure 14.5: (code) (a) Photon number and (b) correlation function $g^{(2)}$ as a function of amplitude and squeezing parameter.

The distribution functions in the coherent representation are,

squeezed states in the Glauber basis

$$\begin{aligned}
|\psi\rangle &= |\beta,\xi\rangle \\
\hat{\rho} &= |\beta,\xi\rangle\langle\beta,\xi| \\
P_{|\beta\rangle}(\alpha) &= \\
Q_{|\beta\rangle}(\alpha) &= \tfrac{\operatorname{sech} r}{\pi}\, e^{-(|\alpha|^2+|\beta|^2)+2\mathfrak{Re}\,(\alpha^*\beta)\operatorname{sech} r - \frac{1}{2}\left[e^{\imath\theta}(\alpha^{*2}-\beta^{*2})+e^{-\imath\theta}(\alpha^2-\beta^2)\right]\tanh r} \\
W_{|\beta\rangle}(\alpha) &= \tfrac{1}{2\pi}\exp(-\tfrac{(\alpha+\alpha^*)^2}{2e^{-2r}} + \tfrac{(\alpha-\alpha^*)^2}{2e^{2r}})
\end{aligned} \tag{14.126}$$

14.4.4 Exercises

14.4.4.1 Ex: Unitarity of the squeezing operator

Verify the unitarity of the squeezing operator.

14.4.4.2 Ex: Transformation by the squeezing operator

a. Demonstrate the relationships (14.106).
b. Using them, calculate $\langle\alpha,\xi|\hat{n}|\alpha,\xi\rangle$ and show with $\alpha \to 0$, that the squeezed vacuum is not empty.

14.4.4.3 Ex: Studying the squeezing operator

Using the Baker-Campbell-Hausdorff braiding identity,

$$e^{\hat{x}}e^{\hat{y}}e^{-\hat{x}} = e^{\hat{y}+[\hat{x},\hat{y}]+\frac{1}{2!}[\hat{x},[\hat{x},\hat{y}]]+\ldots}$$

a. demonstrate the relationship (14.111) and
b. evaluate the expression $e^{\hat{a}^{\dagger 2}/2}e^{\hat{a}^2/2}e^{-\hat{a}^{\dagger 2}/2}$.

14.4.4.4 Ex: Squeezed states

a. Verify that the squeezed coherent states $|\alpha,\xi\rangle$ are eigenstates of the operator $\hat{a}\cosh r + e^{\imath\varphi}\hat{a}^\dagger \sinh r$.
b. Show that the squeezed vacuum state

$$|0,\xi\rangle = |0,re^{\imath\varphi}\rangle = \frac{1}{\sqrt{\cosh r}}\sum_{n=0}^{\infty}(-1)^n\frac{\sqrt{(2n)!}}{2^n n!}e^{\imath n\varphi}\tanh^n r|2n\rangle$$

is an eigenstate of the operator

$$\hat{a}\cosh r + \hat{a}^\dagger e^{\imath\varphi}\sinh r$$

with eigenvalue 0.

14.4.4.5 Ex: Correlation function of squeezed states

a. Calculate the photon number $\langle\hat{n}\rangle$, its variance $\delta\hat{n}$, and the correlation function $g^{(2)}(0)$ of coherent states $|\beta\rangle$.
b. Calculate the same quantities for of squeezed vacuum states $|0,\xi\rangle$.
c. Generalize the calculation for squeezed coherent states $|\alpha,\xi\rangle$.

14.5 Beam splitting, quantum amplification, and nonlinear mode coupling

The beam splitter is one of the most important devices not only in practical optical setups, but also for its conceptual role in quantum mechanics. It thus deserves a dedicated section.

A classical beam splitter divides a beam of light into two branches, which are distinct by their orientation in space or by other degrees of freedom. On the other hand, a photonic picture obviously requires a quantum description. For one reason, the photon numbers scattered into the two branches are quantum mechanically entangled. Furthermore, the very concept of the beam splitter necessitates a second entrance port which, even if empty, unavoidably introduces quantum noise. Finally, in quantum mechanics, as we already learned for the case of measurement devices, the beam splitting device needs to be included in a full description of the beam splitting dynamics, which has important concequences. In fact, quantum mechanically the beam splitting resembles more a scattering problem, where the light beam represents one entrance and output channel and the physical beam splitter the other one (see Fig. 14.6).

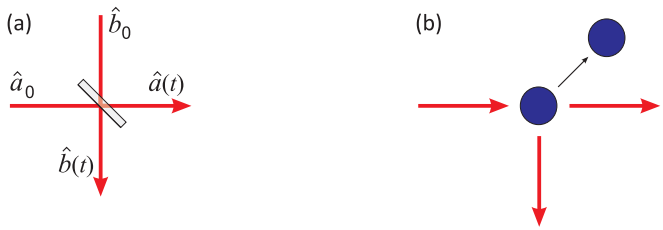

Figure 14.6: (a) Classical beam splitting. (b) Scattering of two modes.

This section is organized as follows. In Secs. 14.5.1 and 14.5.2 we discuss beam splitting at a macroscopic splitting device, i.e. we neglect backaction of the beam splitting event on the splitting device (e.g. recoil or transitions between electronic levels). Backaction on the splitting device is then treated in 14.5.6.

14.5.1 The beam splitter in various representations

We have learned in Sec. 17.2 how a two-level quantum systems couples to a harmonic oscillator via terms in the Hamiltonian containing expressions such as $\hat{\sigma}_+\hat{a}$. We will now see how two quantum harmonic oscillators couple together via terms such as $\hat{a}^\dagger\hat{b}$, where $\hat{a}$ and $\hat{b}$ are the field operators of two oscillator modes. A device providing such a coupling is called *beam splitter*. It *mixes two modes* according to the Hamiltonian,

$$\boxed{\hat{H} = \tfrac{\hbar}{2}\Omega(\hat{a}\hat{b}^\dagger + \hat{a}^\dagger\hat{b})} \,. \tag{14.127}$$

The beam splitter can be described in the Schrödinger or the Heisenberg picture exploiting the formalism introduced in Sec. 2.5.

14.5.1.1 Schrödinger picture

In the Schrödinger picture, if $|\psi_0\rangle = |\alpha_0\rangle|\beta_0\rangle$ is the state of the modes before the beam splitter, the Schrödinger equation, $\imath\hbar\partial_t|\psi(t)\rangle = \hat{H}|\psi(t)\rangle$, gives us the state after the splitter via its solution,

$$\boxed{|\psi(t)\rangle = e^{\imath\Omega t/2(\hat{a}\hat{b}^\dagger + \hat{a}^\dagger\hat{b})}|\psi_0\rangle} \,. \tag{14.128}$$

A 50% beam splitter corresponds to a $\Omega t = \pi/2$ pulse.

14.5.1.2 Heisenberg picture

We can also describe the beam splitter in the Heisenberg picture. With the commutation rules,

$$[\hat{a}, \hat{a}^\dagger] = 1 = [\hat{b}, \hat{b}^\dagger] \qquad , \qquad [\hat{a}, \hat{b}] = 0 = [\hat{a}, \hat{b}^\dagger] \,, \tag{14.129}$$

and the Heisenberg equations,

$$\begin{aligned} \dot{\hat{a}} &= \tfrac{\imath}{\hbar}[\hat{H}, \hat{a}] = \tfrac{\imath}{2}\Omega[(\hat{a}\hat{b}^\dagger + \hat{a}^\dagger\hat{b}), \hat{a}] = -\tfrac{\imath}{2}\Omega\hat{b} \\ \dot{\hat{b}} &= \tfrac{\imath}{\hbar}[\hat{H}, \hat{b}] = \tfrac{\imath}{2}\Omega[(\hat{a}\hat{b}^\dagger + \hat{a}^\dagger\hat{b}), \hat{b}] = -\tfrac{\imath}{2}\Omega\hat{a} \,, \end{aligned} \tag{14.130}$$

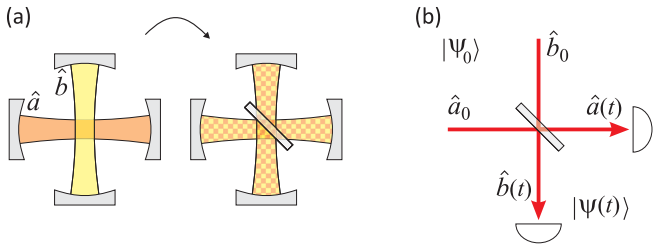

Figure 14.7: (a) Coupling of two cavity modes by insertion of a beam splitter. (b) Beam splitter mixing two propagating modes.

we calculate,

$$\ddot{\hat{a}} = -\tfrac{1}{4}\Omega^2\hat{a} \qquad \text{and} \qquad \ddot{\hat{b}} = -\tfrac{1}{4}\Omega^2\hat{b}\ , \tag{14.131}$$

the solution of which is,

$$\begin{pmatrix}\hat{a}(t)\\ \hat{b}(t)\end{pmatrix} = \begin{pmatrix}\cos\frac{1}{2}\Omega t & -\imath\sin\frac{1}{2}\Omega t\\ -\imath\sin\frac{1}{2}\Omega t & \cos\frac{1}{2}\Omega t\end{pmatrix}\begin{pmatrix}\hat{a}_0\\ \hat{b}_0\end{pmatrix}\ . \tag{14.132}$$

The matrix in (14.132) represents a unitary transformation, and it is easy to verify $[\hat{a}(t),\hat{b}(t)] = [\hat{a}_0,\hat{b}_0]$.

Introducing the abbreviation $\eta \equiv \cos^2(\Omega t/2)$, we can describe the evolution as,

$$\boxed{\begin{pmatrix}\hat{a}(t)\\ \hat{b}(t)\end{pmatrix} = \begin{pmatrix}\sqrt{\eta} & -\imath\sqrt{1-\eta}\\ -\imath\sqrt{1-\eta} & \sqrt{\eta}\end{pmatrix}\begin{pmatrix}\hat{a}_0\\ \hat{b}_0\end{pmatrix}}\ . \tag{14.133}$$

For a $\Omega t = \pi/2$ pulse, we get,

$$\begin{pmatrix}\hat{a}(t)\\ \hat{b}(t)\end{pmatrix} = \sqrt{\tfrac{1}{2}}\begin{pmatrix}1 & -\imath\\ -\imath & 1\end{pmatrix}\begin{pmatrix}\hat{a}_0\\ \hat{b}_0\end{pmatrix}\ . \tag{14.134}$$

that each the reflected beam suffers a phase shift of $\pi/2$ [12]. Resolve the Excs. 14.5.8.1 to 14.5.8.3.

14.5.1.3 Glauber representation

In the Heisenberg picture, the wavefunctions of the quantum states (and hence the density operator and the Wigner function) remain unchanged during the evolution, i.e.,

$$\begin{aligned}|\psi\rangle \equiv |\alpha\rangle|\beta\rangle = |\alpha_0\rangle|\beta_0\rangle \equiv |\psi_0\rangle\ ,\\ \rho_{|\psi\rangle} = \rho_{|\psi_0\rangle}\ ,\\ W_{|\psi\rangle}(\gamma) = W_{|\psi_0\rangle}(\gamma)\ ,\\ P_{|\psi\rangle}(\gamma) = P_{|\psi_0\rangle}(\gamma)\ ,\\ Q_{|\psi\rangle}(\gamma) = Q_{|\psi_0\rangle}(\gamma)\ ,\end{aligned} \tag{14.135}$$

[12] This fact is a consequence of *time-reversal invariance* at the beam splitter. We will see later that, in fact, only the beam reflected at the surface of an optically denser medium suffers a phase-shift of π, while the beam reflected at an optically thinner medium does not suffer any phase shift.

where the $|\psi\rangle$ are arbitrary quantum states and the $|\gamma\rangle$ are Glauber's states. This means that two field modes mixed at a beam splitter do not interfere with phase space, i.e. do not develop quantum correlations. Of course, that would be too easy, indeed; we will soon see in Sec. 14.4, that we need to work a little harder to produce quantum correlations.

Setting $\theta \equiv \Omega t/2$ and $\hat{b} \curvearrowright -\imath\hat{b}$ in the propagator of Eq. (14.128), we may define a beam splitting operator in analogy to the displacement operator (2.130),

$$\mathcal{B}(\theta) \equiv e^{\theta(\hat{a}^\dagger \hat{b} - \hat{a}\hat{b}^\dagger)} \ , \tag{14.136}$$

which is an equivalent beam splitter description. We find,

$$\begin{aligned} \mathcal{B}(\theta)^\dagger \hat{a} \mathcal{B}(\theta) &= \hat{a}\cos\theta + \hat{b}\sin\theta \\ \mathcal{B}(\theta)^\dagger \hat{b} \mathcal{B}(\theta) &= -\hat{a}\sin\theta + \hat{b}\cos\theta \end{aligned} \ , \tag{14.137}$$

as will be shown in Exc. 14.5.8.4 [13].

14.5.1.4 Fock representation

Alternatively, we can describe the beam splitter in the Fock representation [14]. The Hamiltonian of the beam splitter couples two modes of harmonic oscillators. Expanding on a two-dimensional Fock basis via $|\psi\rangle \equiv (...|0\rangle|n_a\rangle....|n_b\rangle|0\rangle...)$ we can gain more insight:

$$\begin{aligned} \hat{H} &= \tfrac{\hbar}{2}\Omega(\hat{a}\hat{b}^\dagger + \hat{a}^\dagger\hat{b}) \\ &= \tfrac{\hbar}{2}\Omega \sum_{n_a,n_b} \sqrt{n_a(n_b+1)}|n_a-1,n_b+1\rangle\langle n_a,n_b| + \sqrt{(n_a+1)n_b}|n_a+1,n_b-1\rangle\langle n_a,n_b| \\ &= \sum_{n_a+n_b} \hat{H}_{a+b} \ , \end{aligned} \tag{14.138}$$

where,

$$\hat{H}_{a+b} = \tfrac{\hbar}{2}\Omega \begin{pmatrix} 0 & \sqrt{1n_b} & & & \\ \sqrt{1n_b} & 0 & \sqrt{2(n_b-1)} & & \\ & \sqrt{2(n_b-1)} & \ddots & & \\ & & & \ddots & \sqrt{n_a 1} \\ & & & \sqrt{n_a 1} & 0 \end{pmatrix} . \tag{14.139}$$

The sub-spaces with n_a+n_b+1 photons are completely degenerate, since $\det(\lambda\mathbb{I}_{a+b} - \hat{H}_{a+b}) = \lambda^{n_a+n_b+1} = 0$. The degeneracy is removed, when we introduce loss mechanisms into one of the modes. Thus, the Hamiltonian can be understood as a Dicke system with the multiplicity $\frac{1}{2}\widehat{(n_a+n_b)} = n_a+n_b+1$. See also Exc. 14.5.8.2.

[13] Compare to the formulas (2.128), (2.133), and (14.107).
[14] A more in-depth discussion is found in Ref. [510].

Example 83 (*Beam splitter with 0 or 1 photons*): As an example, we consider $n_a, n_b = 0, 1$. Then, in the basis $\begin{pmatrix} |0,0\rangle & |0,1\rangle & |1,0\rangle & |0,2\rangle & |1,1\rangle & |2,0\rangle & \cdots \end{pmatrix}^t$ the matrix of the Hamiltonian becomes,

$$\hat{H} = \tfrac{1}{2}\Omega \begin{pmatrix} 0 & & & & & & \\ & 0 & 1 & & & & \\ & 1 & 0 & & & & \\ & & & 0 & \sqrt{2} & 0 & \\ & & & \sqrt{2} & 0 & \sqrt{2} & \\ & & & 0 & \sqrt{2} & 0 & \end{pmatrix} .$$

It is easily verified that the matrix of eigenvectors and the matrix of eigenvalues,

$$U = \begin{pmatrix} 1 & 0 & 0 & 0 & 0 & 0 \\ 0 & -1 & 1 & 0 & 0 & 0 \\ 0 & 1 & 1 & 0 & 0 & 0 \\ 0 & 0 & 0 & -\frac{1}{2}\sqrt{2} & -1 & \frac{1}{2}\sqrt{2} \\ 0 & 0 & 0 & 1 & 0 & 1 \\ 0 & 0 & 0 & -\frac{1}{2}\sqrt{2} & 1 & \frac{1}{2}\sqrt{2} \end{pmatrix} \quad \text{respectively} \quad E = \tfrac{\hbar}{2}\Omega \begin{pmatrix} 0 & 0 & 0 & 0 & 0 & 0 \\ 0 & -1 & 0 & 0 & 0 & 0 \\ 0 & 0 & 1 & 0 & 0 & 0 \\ 0 & 0 & 0 & -2 & 0 & 0 \\ 0 & 0 & 0 & 0 & 0 & 0 \\ 0 & 0 & 0 & 0 & 0 & 2 \end{pmatrix}$$

satisfy $U^{-1}HU = E$. Hence,

$$|\psi\rangle = U^{-1}e^{\imath Et}U|\psi_0\rangle \ ,$$

and we find, that the state $|1,1\rangle = \begin{pmatrix} 0 & 0 & 0 & 0 & 1 & 0 \end{pmatrix}^T$ is transformed into a superposition,

$$\begin{pmatrix} 0 & 0 & 0 & \frac{1}{\sqrt{2}}\imath\sin\Omega t & \cos\Omega t & \frac{1}{\sqrt{2}}\imath\sin\Omega t \end{pmatrix}^T \overset{\Omega t=\pi/2}{\longrightarrow} \frac{\imath}{\sqrt{2}}(|0,2\rangle + |2,0\rangle) \ .$$

Similarly, we find that the superposition state $\frac{1}{\sqrt{2}}(|1,0\rangle + |0,1\rangle) = \begin{pmatrix} 0 & 1 & -1 & 0 & 0 & 0 \end{pmatrix}^T$ is transformed into,

$$e^{-\frac{1}{2}\imath\Omega t}\begin{pmatrix} 0 & 1 & -1 & 0 & 0 & 0 \end{pmatrix}^T \overset{\Omega t=\pi/2}{\longrightarrow} e^{-\imath\pi/4}\frac{1}{\sqrt{2}}(|1,0\rangle + |0,1\rangle) \ .$$

14.5.2 Fock and Glauber states at a beam splitter

A beam splitter divides a Fock state containing N photons into two Glauber states,

$$\begin{aligned} |\psi\rangle &= \frac{1}{2^{N/2}\sqrt{N!}}(\hat{a}_1^\dagger + \hat{a}_2^\dagger)^N|0,0\rangle = \frac{1}{2^{N/2}\sqrt{N!}}\sum_{n=0}^{N}\binom{N}{n}(\hat{a}_1^\dagger)^n(\hat{a}_2^\dagger)^{N-n}|0,0\rangle \quad (14.140) \\ &= \frac{1}{2^{N/2}}\sum_{n=0}^{N}\sqrt{\binom{N}{n}}|n,N-n\rangle = \sum_{n=0}^{N}\sqrt{\binom{N}{n}0.5^n 0.5^{N-n}}|n,N-n\rangle \\ &\simeq \sum_{n=0}^{N}\sqrt{\frac{(N/2)^n}{n!}e^{-N/2}}|n,N-n\rangle = e^{-|\alpha|/2}\sum_{n=0}^{N}\frac{\alpha^n}{\sqrt{n!}}|n,N-n\rangle \ , \end{aligned}$$

approximating the binomial distribution by the Poisson distribution,

$$\binom{N}{n}p^n(1-p)^{N-n} \overset{N\to\infty}{\longrightarrow} \frac{(pN)^n}{n!}e^{-pN} \ . \tag{14.141}$$

and defining $\alpha \equiv N/2$. The normalization is $\langle\psi|\psi\rangle = 1$. The population in an individual mode is,

$$\begin{aligned}\langle\hat{n}_1\rangle = \langle\psi|\hat{a}_1^\dagger\hat{a}_1|\psi\rangle &= \frac{1}{2^N}\langle m, N-m| \sum_{n,m=0}^{N}\sqrt{\binom{N}{m}}\hat{a}_1^\dagger\hat{a}_1\sqrt{\binom{N}{n}}|n, N-n\rangle \\ &= \frac{1}{2^N}\sum_{n=0}^{N}\binom{N}{n}n = \frac{N}{2} \ .\end{aligned} \tag{14.142}$$

The result (14.140) shows that, ignoring (tracing over) one of the modes, the other mode automatically becomes a Glauber state [15].

Besides that,

$$\begin{aligned}\langle\hat{n}_1^2\rangle &= \frac{1}{2^n}\sum_{n=0}^{n}\binom{N}{n}n^2 = \frac{N}{2^n}\sum_{n=0}^{N-1}\binom{N}{n}(n+1) = \frac{N(N+1)}{4} \\ \langle\hat{n}_1\hat{n}_2\rangle &= \frac{1}{2^n}\sum_{n=0}^{n}\sqrt{\binom{N}{n}}n(N-n) = N\langle\hat{n}_1\rangle - \langle\hat{n}_1^2\rangle = \frac{N(N-1)}{4}\end{aligned} \tag{14.143}$$

The squeezing parameter is,

$$\xi_{12} = \frac{\sigma^2(\hat{n}_1-\hat{n}_2)}{\langle\hat{n}_1\rangle+\langle\hat{n}_2\rangle} = \frac{\langle\hat{n}_1^2-2\hat{n}_1\hat{n}_2+\hat{n}_2^2\rangle}{N} = \frac{2\langle\hat{n}_1^2\rangle-2\langle\hat{n}_1\hat{n}_2\rangle}{N} = 1 \ . \tag{14.144}$$

The correlation functions at equal times are,

$$\begin{aligned}g_{11} &= \frac{\left\langle\hat{a}_1^\dagger\hat{a}_1^\dagger\hat{a}_1\hat{a}_1\right\rangle}{\langle\hat{n}_1\rangle^2} = \frac{1}{\langle\hat{n}_1\rangle^2}\frac{1}{2^n}\sum_{n=2}^{n}\binom{N}{n}n(n-1) = \frac{\langle\hat{n}_1^2\rangle-\langle\hat{n}_1\rangle}{\langle\hat{n}_1\rangle^2} = 1 \\ g_{12} &= \frac{\left\langle\hat{a}_1^\dagger\hat{a}_2^\dagger\hat{a}_2\hat{a}_1\right\rangle}{\langle\hat{n}_1\rangle\langle\hat{n}_2\rangle} = \frac{1}{\langle\hat{n}_1\rangle^2}\frac{1}{2^n}\sum_{n=0}^{N}\binom{N}{n}n(N-n) = \frac{N\langle\hat{n}_1\rangle-\langle\hat{n}_1^2\rangle}{\langle\hat{n}_1\rangle^2} = \frac{N-1}{N}\end{aligned} \tag{14.145}$$

The Cauchy-Schwarz inequality and the quantum inequality are both met,

$$\begin{aligned}g_{12} &\le \sqrt{g_{11}g_{22}} \\ g_{12} &\le \sqrt{\left(g_{11}+\frac{1}{\langle\hat{n}_1\rangle}\right)\left(g_{22}+\frac{1}{\langle\hat{n}_2\rangle}\right)}\end{aligned} \tag{14.146}$$

[15] This does not mean that the output modes are uncorrelated. For instance, if we measure n photons in one mode, we know that the other must contain exactly $N-n$ photons. However, the correlations are so dense in phase space that they are not resolvable or decohere rapidly. In fact, it can be shown that coherent states are the only pure states that produce uncorrelated outputs when mixed by a passive linear-optics device [10, 9].

In comparison, a Glauber state is normally divided,

$$|\psi\rangle = |\alpha_1\rangle|\alpha_2\rangle = e^{-|\alpha_1|^2/2}\sum_n \frac{\alpha_1^n}{\sqrt{n!}}|n\rangle e^{-|\alpha_2|^2/2}\sum_m \frac{\alpha_2^m}{\sqrt{m!}}|m\rangle \tag{14.147}$$
$$= e^{-|\alpha_1|^2/2-|\alpha_2|^2/2}\sum_{n,m}\frac{\alpha_1^n\alpha_2^m}{\sqrt{n!}\sqrt{m!}}|n\rangle|m\rangle \ .$$

14.5.2.1 Density matrix representation

The density matrix for a pure state is,

$$\hat{\rho} = |\psi\rangle\langle\psi| = \begin{pmatrix} |\langle\psi|1\rangle|^2 & \langle 1|\psi\rangle\langle\psi|2\rangle \\ \langle 2|\psi\rangle\langle\psi|1\rangle & |\langle\psi|2\rangle|^2 \end{pmatrix} \ . \tag{14.148}$$

The evolution of such a state is described by the von Neumann equation:

$$\imath\hbar\partial_t\hat{\rho}(t) = [\hat{H},\hat{\rho}(t)] \ . \tag{14.149}$$

For the beam splitter we obtain,

$$\hat{\rho} = |\psi\rangle\langle\psi| = \begin{pmatrix} |\langle\psi|0,0\rangle|^2 & \langle 0,0|\psi\rangle\langle\psi|0,1\rangle & \langle 0,0|\psi\rangle\langle\psi|1,0\rangle & \\ \langle 0,1|\psi\rangle\langle\psi|0,0\rangle & |\langle\psi|0,1\rangle|^2 & \langle 0,1|\psi\rangle\langle\psi|1,0\rangle & \\ \langle 1,0|\psi\rangle\langle\psi|0,0\rangle & \langle 1,0|\psi\rangle\langle\psi|0,1\rangle & |\langle\psi|1,0\rangle|^2 & \\ & & & \ddots \end{pmatrix} \ . \tag{14.150}$$

Example 84 (*Density matrix for the beam splitter with 0 or 1 photons*): For the case of the superposition states, $|\psi\rangle = \frac{1}{\sqrt{2}}(|0,1\rangle \pm |1,0\rangle)$,

$$\hat{\rho} = \begin{pmatrix} 0 & 0 & 0 & \\ 0 & \frac{1}{2} & \pm\frac{1}{2} & \\ 0 & \pm\frac{1}{2} & \frac{1}{2} & \\ & & & \ddots \end{pmatrix} \ .$$

Obviously, $\hat{\rho} = \hat{\rho}^2$. For the above superposition state, $\partial_t\hat{\rho}(t) = 0$.

14.5.3 Ordinary and balanced homodyne detection

In Secs. 2.5.1 and 2.6.1 we have calculated the quantum noise of a harmonic oscillator in the Fock and the Glauber basis. We will now discuss a method to measure this noise called *homodyne detection* or *phase-sensitive detection*. The signal is obtained by superposing the field mode of interest with a local oscillator with a relative phase θ at a 50% beam splitter and a subtraction of the photo currents in the two ports of the interferometer.

To begin with, let us describe both the field mode $\hat{a}$ and the local oscillator $\hat{b}$ on equal footings as quantized modes [see Fig. 14.8(a)]. The *ordinary homodyne signal* is obtained by superposing the field mode of interest with a local oscillator with a

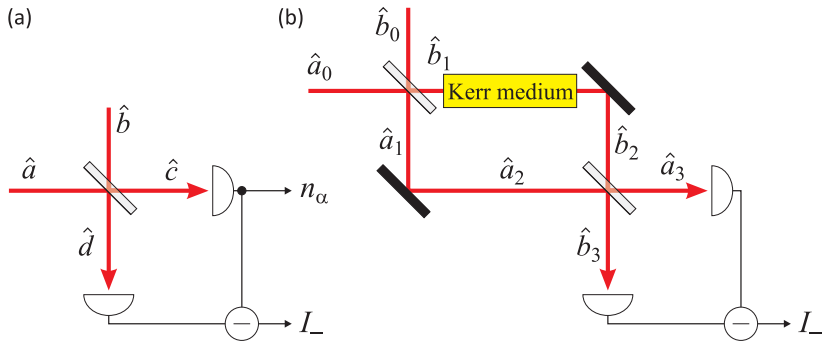

Figure 14.8: (a) Homodyne detection scheme. Output n_α delivers the *ordinary homodyne signal*, and output I_- the *balanced homodyne signal*. (b) Homodyne detection of squeezing in a Mach-Zehnder interferometer.

relative phase θ at a beam splitter and measuring the photo currents in the two ports $\hat{c}$ and $\hat{d}$ of the interferometer. From Eq. (14.134) we obtain for a 50% beam splitter,

$$\hat{c} = \tfrac{1}{\sqrt{2}}(\hat{a} - \imath\hat{b}) \quad , \quad \hat{d} = \tfrac{1}{\sqrt{2}}(-\imath\hat{a} + \hat{b}) \tag{14.151}$$

and

$$\begin{aligned} \hat{I}_c &= \hat{c}^\dagger\hat{c} = \tfrac{1}{2}(\hat{a}^\dagger\hat{a} + \hat{b}^\dagger\hat{b} - \imath\hat{a}^\dagger\hat{b} + \imath\hat{b}^\dagger\hat{a}) \\ \hat{I}_d &= \hat{d}^\dagger\hat{d} = \tfrac{1}{2}(\hat{a}^\dagger\hat{a} + \hat{b}^\dagger\hat{b} + \imath\hat{a}^\dagger\hat{b} - \imath\hat{b}^\dagger\hat{a}) \ . \end{aligned} \tag{14.152}$$

To obtain the *balanced homodyne signal* we add or subtract both photo currents,

$$\begin{aligned} \hat{I}_+ &= \hat{I}_c + \hat{I}_d = \hat{a}^\dagger\hat{a} + \hat{b}^\dagger\hat{b} \\ \hat{I}_- &= \hat{I}_c - \hat{I}_d = \imath(\hat{b}^\dagger\hat{a} - \hat{a}^\dagger\hat{b}) \ . \end{aligned} \tag{14.153}$$

In order to quantify the intensity noise, we also need to calculate the square values [284],

$$\begin{aligned} \hat{I}_+^2 &= \ (\hat{a}^\dagger\hat{a} + \hat{b}^\dagger\hat{b})^2 = (\hat{n}_a + \hat{n}_b)^2 \\ \hat{I}_-^2 &= -(\hat{b}^\dagger\hat{a} - \hat{a}^\dagger\hat{b})^2 = -\hat{a}^2\hat{b}^{\dagger 2} - \hat{a}^{\dagger 2}\hat{b}^2 + \hat{a}\hat{a}^\dagger\hat{b}^\dagger\hat{b} + \hat{a}^\dagger\hat{a}\hat{b}\hat{b}^\dagger \ , \end{aligned} \tag{14.154}$$

yielding,

$$\begin{aligned} \Delta I_+^2 &= \langle\hat{I}_+^2\rangle - \langle\hat{I}_+\rangle^2 = \Delta\hat{n}_a^2 + \Delta\hat{n}_b^2 \\ \Delta I_-^2 &= \langle\hat{I}_-^2\rangle - \langle\hat{I}_-\rangle^2 \\ &= -\Delta\hat{a}^2\langle\hat{b}^{\dagger 2}\rangle - \Delta\hat{a}^{\dagger 2}\langle\hat{b}\rangle^2 + \langle\hat{a}\hat{a}^\dagger\rangle\langle\hat{b}^\dagger\hat{b}\rangle + \langle\hat{a}^\dagger\hat{a}\rangle\langle\hat{b}\hat{b}^\dagger\rangle - 2\langle\hat{a}^\dagger\rangle\langle\hat{a}\rangle\langle\hat{b}^\dagger\rangle\langle\hat{b}\rangle \ . \end{aligned} \tag{14.155}$$

Assuming the local oscillator in a coherent state, $|\beta\rangle = ||\beta|e^{\imath(\pi/2-\theta)}\rangle$, we obtain,

$$\boxed{\begin{aligned} \Delta I_+^2 &\xrightarrow{|\beta\rangle} \Delta\hat{n}_a^2 + |\beta|^2 \\ \Delta I_-^2 &\xrightarrow{|\beta\rangle} |\beta|^2 e^{\imath 2\theta}\Delta\hat{a}^2 + |\beta|^2 e^{-\imath 2\theta}\Delta\hat{a}^{\dagger 2} + 2|\beta|^2(\langle\hat{n}_a\rangle - \langle\hat{a}^\dagger\rangle\langle\hat{a}\rangle) + \langle\hat{n}_a\rangle + |\beta|^2 \end{aligned}} \ . \tag{14.156}$$

To determine the shot noise, we simply block the local oscillator $\hat{b}$ and obtain,

$$\Delta I_+^2 \overset{\beta=0}{\longrightarrow} \Delta n_a^2 \qquad \text{and} \qquad \Delta I_-^2 \overset{\beta=0}{\longrightarrow} \langle \hat{n}_a \rangle \ . \tag{14.157}$$

Hence, Δn_a^2 is the intensity noise of mode $\hat{a}$, and $\langle \hat{n}_a \rangle$ is the shot noise, which is present even though the intensities I_c and I_d are perfectly balanced and should cancel out in subtraction (see the Exc. 14.5.8.5).

14.5.3.1 Phase-dependent noise for specific probe light fields

Now, let us consider specific light fields. For a coherent probe, $|\psi\rangle \equiv |\alpha\rangle$,

$$\Delta \hat{I}_+^2 \overset{|\psi\rangle\equiv|\alpha\rangle}{\longrightarrow} |\alpha|^2 + |\beta|^2 \overset{|\psi\rangle\equiv|\alpha\rangle}{\longleftarrow} \Delta \hat{I}_-^2 \ . \tag{14.158}$$

That is, as illustrated in Fig. 14.9, the noise of neither the sum nor difference intensities vary with the phase of the local oscillator. Note that here, the coherent light modes of neither the probe nor the local oscillator are treated as classical; otherwise the noise should disappear.

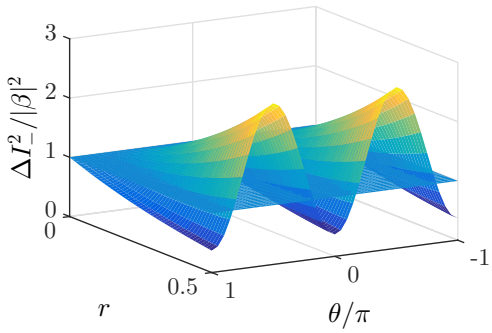

Figure 14.9: (code) Noise in the subtracted intensities ΔI_-^2 as a function of squeezing parameter r and homodyning phase θ. The plane at $\Delta I_-^2/|\beta|^2 = 1$ corresponds to coherent vacuum, the modulated curve to squeezed vacuum.

Now, for squeezed vacuum, $|\psi\rangle \equiv |0,\xi\rangle = \mathcal{S}(\xi)|0\rangle$, using the results of Exc. 14.4.4.5, namely,

$$\begin{aligned} \langle \hat{a} \rangle &= 0 = \langle \hat{a}^\dagger \rangle \qquad (14.159) \\ \langle \hat{n}_a \rangle &= \sinh^2 r \\ \langle 0,\xi|\hat{a}^2|0,\xi\rangle &= \langle 0|\mathcal{S}^\dagger(\xi)\hat{a}\mathcal{S}(\xi)\mathcal{S}^\dagger(\xi)\hat{a}\mathcal{S}(\xi)|0\rangle \\ &= \langle 0|(\hat{a}\cosh r - \hat{a}^\dagger e^{\imath\varphi}\sinh r)^2|0\rangle = -e^{\imath\varphi}\sinh r\cosh r \\ \langle 0,\xi|\hat{a}^{\dagger 2}|0,\xi\rangle &= -e^{-\imath\varphi}\sinh r\cosh r \ , \qquad (14.160) \end{aligned}$$

we get,

$$\begin{aligned} \Delta \hat{I}_+^2 &\overset{|\psi\rangle\equiv|0,\xi\rangle}{\longrightarrow} 2\sinh^2 r\cosh^2 r \qquad (14.161) \\ \Delta \hat{I}_-^2 &\overset{|\psi\rangle\equiv|0,\xi\rangle}{\longrightarrow} -2|\beta|^2\cos(2\theta+\varphi)\sinh r\cosh r + 2|\beta|^2\sinh^2 r + \sinh^2 r + |\beta|^2 \ . \end{aligned}$$

We see that $\Delta\hat{I}_-^2$ depends on the phase of the local oscillator and, as illustrated in Fig. 14.9 can have values below that expected for coherent vacuum.

The generalization to squeezed coherent light, $|\psi\rangle \equiv |\alpha,\xi\rangle = \mathcal{D}(\alpha)|0,\xi\rangle = \mathcal{D}(\alpha)\mathcal{S}(\xi)|0\rangle$ is simple. We just need to separate the probe mode into a classical and a quantum part, $\hat{a} = \alpha + \delta\hat{a}$. Obviously, $\langle\delta\hat{a}\rangle = 0$ and $\Delta\hat{a}^2 = \Delta(\delta\hat{a})^2$, so that the only modification expected for $\Delta\hat{I}_-^2$ is an additional term $|\alpha|^2$, which however is negligible if the local oscillator $|\beta|^2$ is much stronger.

14.5.3.2 Shot noise

Like any quantized degree of freedom, a light mode is subject to intrinsic quantum noise imposed by the Heisenberg uncertainty relation, as we have seen for the harmonic oscillator (2.138). In the case of a light mode the quantum noise originates in the fact, that any power measurement based on photon counting involves *projection* onto a discrete number of photons. Often the light mode will be in a 'classical' coherent state, which is not an eigenstate of the photon number measurement operator. The projection onto Fock states introduces unavoidable *quantum projection noise* in this case is called *shot noise* and introduces the Heisenberg limit in the quadrature phases of the light intensity.

14.5.3.3 Inverse Radon transform

The expectation value of $\Delta\hat{I}_-$ is afflicted with the Heisenberg uncertainty and can be expressed as the first moment of the Wigner function $W(\alpha)$:

$$\begin{aligned}\langle\psi|\hat{I}_-|\psi\rangle &= \int W_{|\psi\rangle}(\alpha)\hat{I}_- d^2\alpha \\ &= \sqrt{2}|\beta_{\rm LO}|\int W_{|\psi\rangle}(x_\theta,p_\theta)x_\theta dx_\theta dp_\theta = \sqrt{2}|\beta_{\rm LO}|\int_{-\infty}^{\infty} w_\theta(x_\theta)x_\theta dx_\theta \ .\end{aligned} \tag{14.162}$$

Here, the distribution function integrated over a rotated quadrature component p_θ is given by,

$$w_\theta(x_\theta) \equiv \int_{-\infty}^{\infty} W_\theta(x_\theta,p_\theta)dp_\theta \ . \tag{14.163}$$

This is called the *radon transform*. The distribution function $w_\theta(p_\theta)$ as well as the Wigner function are normalized to 1. Multiple measurements of the expectation value $x_\theta = \langle\psi|\hat{x}_\theta|\psi\rangle$ now yields a histogram $H_{|\psi\rangle}(x_\theta)$ reflecting, if normalized, $w_{|\psi\rangle}(x_\theta) = H_{|\psi\rangle}(x_\theta)/\int H_{|\psi\rangle}(x_\theta)$ exactly the distribution function.

Considering the finite detector efficiency [510] $w_\theta(x_\theta)$ must be generalized to a convolution with an apparatus function $\zeta(x)$:

$$w_\theta^{\rm real}(\sqrt{\eta}x_\theta) = (w_\theta^{\rm ideal} \star \zeta) \qquad \text{where} \qquad \zeta(x) = \frac{1}{\sqrt{\pi(1-\eta)}}e^{-\eta\alpha^2/(1-\eta)} \ . \tag{14.164}$$

A finite detector efficiency degrades the contrast of the quantum interference structures.

With the procedure of optical *homodyne tomography* or *quantum state endoscopy* the Wigner function for e.g. a Schrödinger cat state can be reconstructed from a set

of distribution functions $w_\theta(x_\theta) = \int W(\alpha e^{\imath\theta}) dp_\theta$ measured for various phases θ [510]. To do this the data set is exposed to an inverse *radon transform*:

$$W(\alpha) = \frac{1}{4\pi^2} \int_{-\infty}^{\infty} \int_0^{\pi} \int_{-\infty}^{\infty} w_\theta(x_\theta) |\zeta| e^{\imath\zeta\left[\mathfrak{Re}\,(2^{-1/2}\alpha e^{-\imath\theta}) - x_\theta\right]} dx d\theta d\zeta \ . \tag{14.165}$$

In contrast to the conventional homodyne detection, where the phase dependency of amplitude noise is recorded, the homodyne tomography allows the complete reconstruction of a quantum state through measurement of the distribution of the amplitude noise power,

$$P_s = \frac{\omega_s}{2\pi} \int_0^{\omega_s/2\pi} dt |\langle I(t) \rangle|^2 \tag{14.166}$$

for various phases.

Alternatively, to the homodyne method, one may reconstruct the photon distribution in field modes from their temporal evolution [847]. Another method could be to use atoms as sensors for the quantum state of a light field in a Jaynes-Cummings type dynamics.

14.5.4 Quantum amplifier

We will call in the following as *quantum signals* degrees of freedom subject to quantum noise. Typically a quantum signal will be a mode of an electric field, represented by an annihilation operator $\hat{a}$. Such a mode can be enhanced by *quantum amplifier*, which is a device amplifying quantum signals according to the rules of quantum mechanics. Examples include the active elements of lasers and optical parametric amplifiers. A quantum amplifier is characterized by its gain and its own intrinsic quantum noise, which are interdependent parameters; the higher the gain, the larger the uncertainty noise. In the case of lasers, the uncertainty corresponds to the amplified spontaneous emission of the active medium.

Quantum amplification is a unitary transformation $\hat{U}$, acting in an initial state $|\text{in}\rangle$ and producing (in the Schrödinger figure) the amplified state,

$$|\text{out}\rangle = \hat{U}|\text{in}\rangle \ . \tag{14.167}$$

The amplification depends on the mean value $\langle \hat{a} \rangle$ of the annihilation operator and its dispersion $\langle \hat{a}^\dagger \hat{a} \rangle - \langle \hat{a}^\dagger \rangle \langle \hat{a} \rangle$. A coherent state is a state with minimal uncertainty; when the state is transformed, the uncertainty may increase. This increase can be interpreted as noise in the amplifier. The gain G can be defined as follows:

$$G = \frac{\langle \hat{a} \rangle_{\text{out}}}{\langle \hat{a} \rangle_{\text{in}}} \ . \tag{14.168}$$

The quantum amplifier can also be described in the Heisenberg picture; the changes are attributed to the amplification of the field operator. Thus, the evolution of the operator $\hat{a}_{\text{out}}$ is given by

$$\hat{a}_{\text{out}} = \hat{U}^\dagger \hat{a} \hat{U} \ , \tag{14.169}$$

while the state vector remains unchanged. The gain is then given by,

$$G = \frac{\langle \hat{a}_{\rm out} \rangle_{\rm in}}{\langle \hat{a} \rangle_{\rm in}} \ . \tag{14.170}$$

In general, the gain G may be complex, and it may depend on the initial state. For laser applications, the amplification of coherent states is important. Therefore, it is usually assumed that the initial state is a coherent state characterized by a complex-valued initial parameter α, such that $|{\rm in}\rangle = |\alpha\rangle$. Even with such a restriction, the gain may depend on the amplitude or phase of the initial field.

In the following, the Heisenberg representation is used; all brackets are assumed to be evaluated with respect to the initial coherent state,

$$\text{noise} = \langle \hat{a}^\dagger_{\rm out} \hat{a}_{\rm out} \rangle - \langle \hat{a}^\dagger_{\rm out} \rangle \langle \hat{a}_{\rm out} \rangle - (\langle \hat{a}^\dagger \hat{a} \rangle - \langle \hat{a}^\dagger \rangle \langle \hat{a} \rangle) \ . \tag{14.171}$$

The expectation values are assumed to be evaluated with respect to the initial coherent state. This quantity characterizes the increase of the uncertainty of the field due to amplification. As the uncertainty of the field operator does not depend on its parameter, the quantity above shows how much output field differs from a coherent state.

14.5.4.1 Linear phase-invariant amplifier

Linear phase-invariant amplifiers may be described as follows. Assume that the unitary operator U amplifies in such a way that the input $\hat{a}$ and the output $\hat{a}_{\rm out} = \hat{U}^\dagger \hat{a} \hat{U}$, are related by a linear equation,

$$\hat{a}_{\rm out} = c\hat{a} + s\hat{b}^\dagger \ , \tag{14.172}$$

where c and s are c-numbers and $\hat{b}^\dagger$ is a creation operator characterizing the amplifier. Without loss of generality, it may be assumed that c and s are real. The commutator of the field operators is invariant under unitary transformation U:

$$[\hat{a}_{\rm out}, \hat{a}^\dagger_{\rm out}] = 1 = [\hat{a}, \hat{a}^\dagger] \quad , \quad [\hat{a}_{\rm in}, \hat{a}^\dagger_{\rm out}] = 0 = [\hat{a}_{\rm out}, \hat{a}^\dagger_{\rm in}] \ . \tag{14.173}$$

From the unitarity of U, it follows that $\hat{b}$ satisfies the same commutation relations. The c-numbers are then $c^2 - s^2 = 1$. Hence, the phase-invariant amplifier acts by introducing an additional mode to the field, with a large amount of stored energy, behaving as a boson. Calculating the gain and the noise of this amplifier, one finds $G = c$, and

$$\text{noise} = \mathrm{c}^2 - 1 \ . \tag{14.174}$$

The coefficient $g = |G|^2$ is sometimes called the intensity amplification coefficient. The noise of the linear phase-invariant amplifier is given by $g - 1$. The gain can be dropped by splitting the beam; the estimate above gives the minimal possible noise of the linear phase-invariant amplifier. The linear amplifier has an advantage over the multi-mode amplifier: if several modes of a linear amplifier are amplified by the same factor, the noise in each mode is determined independently; that is, modes in a linear quantum amplifier are independent.

To obtain a large amplification coefficient with minimal noise, one may use homodyne detection, constructing a field state with known amplitude and phase, corresponding to the linear phase-invariant amplifier. The uncertainty principle sets the lower bound of quantum noise in an amplifier. In particular, the output of a laser system and the output of an optical generator are not coherent states.

The multiplicative amplifier $\mathcal{D}$ also adds additive noise F. We have $\mathcal{D}\mathcal{D}^\dagger = 1$,

$$\begin{pmatrix} \hat{a}^\dagger_{\rm out} \\ \hat{a}_{\rm out} \end{pmatrix} = \mathcal{D} \begin{pmatrix} \hat{a}^\dagger_{\rm in} \\ \hat{a}_{\rm in} \end{pmatrix} + \begin{pmatrix} F_1 \\ F_2 \end{pmatrix} \ . \tag{14.175}$$

14.5.5 Coupled quantum oscillators with/out counter-rotating terms

The Hamiltonian of a beam splitter resembles the one of a system of two *coupled oscillators* with identical eigenfrequencies. Here, we are interested in calculating the time evolution of such a system. We rewrite the Hamiltonian in terms of the *normal modes*. We start from the Hamiltonian with counter-rotating terms [273],

$$\boxed{\hat{H} = \hbar\omega(\hat{a}^\dagger\hat{a} + \tfrac{1}{2}) + \hbar\omega(\hat{b}^\dagger\hat{b} + \tfrac{1}{2}) + \tfrac{\hbar\Omega}{2}(\hat{a} + \hat{a}^\dagger)(\hat{b} + \hat{b}^\dagger)} \ , \tag{14.176}$$

which we rewrite in terms of the quadrature components given by,

$$\begin{pmatrix} \hat{x}_a \\ \hat{p}_a \\ \hat{x}_b \\ \hat{p}_b \end{pmatrix} = \mathcal{T}_{ab} \begin{pmatrix} \hat{a} \\ \hat{a}^\dagger \\ \hat{b} \\ \hat{b}^\dagger \end{pmatrix} \qquad \text{with} \qquad \mathcal{T}_{ab} \equiv \sqrt{\frac{\hbar\omega}{2}} \begin{pmatrix} \omega^{-1} & \omega^{-1} & 0 & 0 \\ \imath & -\imath & 0 & 0 \\ 0 & 0 & \omega^{-1} & \omega^{-1} \\ 0 & 0 & \imath & -\imath \end{pmatrix} \ , \tag{14.177}$$

as

$$\hat{H} = \tfrac{1}{2}(\hat{p}_a^2 + \omega^2\hat{x}_a^2) + \tfrac{1}{2}(\hat{p}_b^2 + \omega^2\hat{x}_b^2) + \Omega\omega\hat{x}_a\hat{x}_b \ . \tag{14.178}$$

Setting $\omega_\pm = \sqrt{\omega^2 \pm \Omega\omega}$ allows us to rewrite the Hamiltonian as,

$$\hat{H} = \tfrac{1}{4}(\hat{p}_a + \hat{p}_b)^2 + \tfrac{1}{4}\omega_+^2(\hat{x}_a + \hat{x}_b)^2 + \tfrac{1}{4}(\hat{p}_a - \hat{p}_b)^2 + \tfrac{1}{4}\omega_-^2(\hat{x}_a - \hat{x}_b)^2 \ . \tag{14.179}$$

Now, we apply the transform,

$$\begin{pmatrix} \hat{x}_A \\ \hat{p}_A \\ \hat{x}_B \\ \hat{p}_B \end{pmatrix} = \mathcal{M} \begin{pmatrix} \hat{x}_a \\ \hat{p}_a \\ \hat{x}_b \\ \hat{p}_b \end{pmatrix} \qquad \text{with} \qquad \mathcal{M} \equiv \sqrt{\frac{1}{2}} \begin{pmatrix} 1 & 0 & 1 & 0 \\ 0 & 1 & 0 & 1 \\ 1 & 0 & -1 & 0 \\ 0 & 1 & 0 & -1 \end{pmatrix} = M^{-1} \ , \tag{14.180}$$

and rewrite the Hamiltonian again as,

$$\hat{H} = \tfrac{1}{2}(\hat{p}_A^2 + \omega_+^2\hat{x}_A^2) + \tfrac{1}{2}(\hat{p}_B^2 + \omega_-^2\hat{x}_B^2) \ . \tag{14.181}$$

We go back from the quadrature components to the field mode operators via,

$$\begin{pmatrix} \hat{x}_A \\ \hat{p}_A \\ \hat{x}_B \\ \hat{p}_B \end{pmatrix} = \mathcal{T}_{AB} \begin{pmatrix} \hat{A} \\ \hat{A}^\dagger \\ \hat{B} \\ \hat{B}^\dagger \end{pmatrix} \qquad \text{with} \qquad \mathcal{T}_{AB} \equiv \sqrt{\frac{\hbar}{2}} \begin{pmatrix} 1/\sqrt{\omega_+} & 1/\sqrt{\omega_+} & 0 & 0 \\ \imath\sqrt{\omega_+} & -\imath\sqrt{\omega_+} & 0 & 0 \\ 0 & 0 & 1/\sqrt{\omega_-} & 1/\sqrt{\omega_+} \\ 0 & 0 & \imath\sqrt{\omega_-} & -\imath\sqrt{\omega_+} \end{pmatrix} \ , \tag{14.182}$$

and finally obtain,

$$\boxed{\hat{H} = \hbar\omega_+(\hat{A}^\dagger\hat{A} + \tfrac{1}{2}) + \hbar\omega_-(\hat{B}^\dagger\hat{B} + \tfrac{1}{2})}\,. \tag{14.183}$$

The Heisenberg equations of motion for the oscillator modes,

$$\frac{d}{dt}\begin{pmatrix}\hat{a}\\ \hat{a}^\dagger\\ \hat{b}\\ \hat{b}^\dagger\end{pmatrix} = -\tfrac{\imath}{\hbar}\left[\begin{pmatrix}\hat{a}\\ \hat{a}^\dagger\\ \hat{b}\\ \hat{b}^\dagger\end{pmatrix}, \hat{H}\right] = \mathcal{X}\begin{pmatrix}\hat{a}\\ \hat{a}^\dagger\\ \hat{b}\\ \hat{b}^\dagger\end{pmatrix} \qquad \text{with} \qquad \mathcal{X} \equiv \begin{pmatrix} -\imath\omega & 0 & -\frac{\imath\Omega}{2} & -\frac{\imath\Omega}{2} \\ 0 & \imath\omega & \frac{\imath\Omega}{2} & \frac{\imath\Omega}{2} \\ -\frac{\imath\Omega}{2} & -\frac{\imath\Omega}{2} & -\imath\omega & 0 \\ \frac{\imath\Omega}{2} & \frac{\imath\Omega}{2} & 0 & \imath\omega \end{pmatrix}, \tag{14.184}$$

are difficult to integrate. In contrast, the Heisenberg equations for the normal modes,

$$\frac{d}{dt}\begin{pmatrix}\hat{A}\\ \hat{A}^\dagger\\ \hat{B}\\ \hat{B}^\dagger\end{pmatrix} = -\tfrac{\imath}{\hbar}\left[\begin{pmatrix}\hat{A}\\ \hat{A}^\dagger\\ \hat{B}\\ \hat{B}^\dagger\end{pmatrix}, \hat{H}\right] = E_{\mathcal{X}}\begin{pmatrix}\hat{A}\\ \hat{A}^\dagger\\ \hat{B}\\ \hat{B}^\dagger\end{pmatrix} \tag{14.185}$$

$$\text{with} \qquad E_{\mathcal{X}} = U_{\mathcal{X}}^{-1}\mathcal{X}U_{\mathcal{X}} = \begin{pmatrix} -\imath\omega_+ & 0 & 0 & 0 \\ 0 & \imath\omega_+ & 0 & 0 \\ 0 & 0 & -\imath\omega_- & 0 \\ 0 & 0 & 0 & \imath\omega_- \end{pmatrix}$$

$$\text{and} \qquad U_{\mathcal{X}} = \begin{pmatrix} -1-\frac{2}{\Omega}(\omega+\omega_+) & -1-\frac{2}{\Omega}(\omega-\omega_+) & 1-\frac{2}{\Omega}(\omega+\omega_-) & 1-\frac{2}{\Omega}(\omega-\omega_-) \\ 1 & 1 & -1 & -1 \\ -1-\frac{2}{\Omega}(\omega+\omega_+) & -1-\frac{2}{\Omega}(\omega-\omega_+) & -1+\frac{2}{\Omega}(\omega+\omega_-) & -1+\frac{2}{\Omega}(\omega-\omega_-) \\ 1 & 1 & 1 & 1 \end{pmatrix},$$

are easily solved by,

$$\begin{pmatrix}\hat{A}(t)\\ \hat{A}^\dagger(t)\\ \hat{B}(t)\\ \hat{B}^\dagger(t)\end{pmatrix} = e^{E_{\mathcal{X}}t}\begin{pmatrix}\hat{A}(0)\\ \hat{A}^\dagger(0)\\ \hat{B}(0)\\ \hat{B}^\dagger(0)\end{pmatrix} \qquad \text{with} \qquad e^{E_{\mathcal{X}}t} \equiv \begin{pmatrix} e^{-\imath\omega_+ t} & 0 & 0 & 0 \\ 0 & e^{\imath\omega_+ t} & 0 & 0 \\ 0 & 0 & e^{-\imath\omega_- t} & 0 \\ 0 & 0 & 0 & e^{\imath\omega_- t} \end{pmatrix}. \tag{14.186}$$

Hence, the oscillator modes evolve as,

$$\begin{pmatrix}\hat{a}(t)\\ \hat{a}^\dagger(t)\\ \hat{b}(t)\\ \hat{b}^\dagger(t)\end{pmatrix} = e^{\mathcal{X}t}\begin{pmatrix}\hat{a}(0)\\ \hat{a}^\dagger(0)\\ \hat{b}(0)\\ \hat{b}^\dagger(0)\end{pmatrix} \qquad \text{with} \qquad e^{\mathcal{X}t} = \mathcal{T}_{ab}^{-1}\mathcal{M}^{-1}\mathcal{T}_{AB}e^{E_{\mathcal{X}}t}\mathcal{T}_{AB}^{-1}\mathcal{M}\mathcal{T}_{ab} = U_{\mathcal{X}}e^{E_{\mathcal{X}}t}U_{\mathcal{X}}^{-1}\,. \tag{14.187}$$

14.5.5.1 Rotating-wave approximation

The rotating-wave approximation is performed via $\omega_\pm \simeq \omega \pm \frac{1}{2}\Omega$. It leads to the Hamiltonian,

$$\boxed{\hat{H} = \hbar\omega(\hat{a}^\dagger\hat{a} + \tfrac{1}{2}) + \hbar\omega(\hat{b}^\dagger\hat{b} + \tfrac{1}{2}) + \tfrac{\hbar\Omega}{2}(\hat{a}\hat{b}^\dagger + \hat{a}^\dagger\hat{b})}\,. \tag{14.188}$$

In this approximation, we find $\mathcal{T}_{AB}^{-1}\mathcal{M}\mathcal{T}_{ab} \simeq \mathcal{M}$ and the transformation defined in (14.180),

$$\begin{pmatrix} \hat{A} \\ \hat{A}^\dagger \\ \hat{B} \\ \hat{B}^\dagger \end{pmatrix} = \mathcal{M} \begin{pmatrix} \hat{a} \\ \hat{a}^\dagger \\ \hat{b} \\ \hat{b}^\dagger \end{pmatrix} , \tag{14.189}$$

takes us directly from the Hamiltonian (14.188) to [16],

$$\boxed{\hat{H} = (\hbar\omega + \tfrac{\hbar\Omega}{2})(\hat{A}^\dagger\hat{A} + \tfrac{1}{2}) + (\hbar\omega - \tfrac{\hbar\Omega}{2})(\hat{B}^\dagger\hat{B} + \tfrac{1}{2})} . \tag{14.190}$$

Do the Excs. 14.5.8.6 and 14.5.8.7.

Note, that two coupled oscillator model becomes *criticality*, when the atom-field coupling strength exceeds the frequencies of the mode and the atomic two-level system.

14.5.6 Backaction on the splitting device

In all above considerations we treated the beam splitter as a classical device splitting or combining modes, which can be quantized. This is, of course, an idealization, because the action of splitting and combination requires interaction between the modes and the beam splitter. That is, the beam splitter itself must be considered as a (potentially quantized) degree of freedom and included into a global description. In a complete quantum picture beam splitting invloves at least an interaction between two degrees of freedom: the mode suffering the splitting (which we already treated quantum mechanically in the preceding sections), and the splitting device (which we will treat as an ancilla in the following, similarly as we did for a quantum measurement). In classical beam splitters, the dynamics of the ancilla is neglected, but in quantum beam splitters the ancilla serves as a witness of a splitting event. In practice, it can be a recoiling atom, a phase shift of an internal atomic state, or something else.

A complete generic model should allow to describe quantum mechanically (i) strong measurement directly on the system or (ii) weak measurements via an ancilla. For simplicity, we will assume the beam splitting device to be a two-level atom including its internal and external degrees of freedom. The light mode may then interact with the atom (or not) and be scattered into different directions of space. In order to emulate a beam splitter we need to ensure the existence of only two scattered exit modes. This can be done by putting the atom in a ring cavity, where the only modes available are the forward and the backward scattered mode. It is fair to say that this model represents the simplest possible beam splitter description including backaction. In the same time, the system exhibits a dynamics known as collective atomic recoil lasing (CARL), which is extensively discussed in Chp. 25.

[16] Note the different behavior of a beam splitter under this transformation,

$$\begin{aligned} \hat{H} &= \hbar\omega(\hat{a}^\dagger\hat{a} + \tfrac{1}{2}) + \hbar\omega(\hat{b}^\dagger\hat{b} + \tfrac{1}{2}) + \tfrac{\hbar\Omega}{2}\left(\hat{a}\hat{b}^\dagger - \hat{a}^\dagger\hat{b}\right) \\ &= \hbar\omega(\hat{A}^\dagger\hat{A} + \tfrac{1}{2}) + \hbar\omega(\hat{B}^\dagger\hat{B} + \tfrac{1}{2}) + \tfrac{\hbar\Omega}{2}(-\hat{A}\hat{B}^\dagger + \hat{A}^\dagger\hat{B}) . \end{aligned}$$

14.5.6.1 Interaction-free measurement

Beam splitters and coupled cavities have been proposed for the realization of *interaction-free measurements* 14.5.8.8 and 14.5.8.9 [262, 834, 495, 479]. Resolve also the Excs. 14.5.8.11 to 14.5.8.12.

14.5.7 Multimode squeezing

We have seen earlier that a beam splitting operator (14.136) can be defined, which mixes two modes in a linear fashion. By analogy we may define a squeezing operator mixing two modes in a non-linear way.

We define,

$$\hat{b} = \mu\hat{a} + \nu\hat{c}^\dagger \ . \tag{14.191}$$

Again using $\mu^2 - \nu^2 = 1$, the standard commutation rules for $\hat{a}$ and $\hat{c}$ give,

$$\begin{aligned} [\hat{b}, \hat{b}^\dagger] &= 1 \\ [\hat{b}_r, \hat{b}_p] &= \tfrac{\imath}{2} \ . \end{aligned} \tag{14.192}$$

The individual variances read,

$$\begin{aligned} \Delta\hat{b}_r^2 &= \langle \hat{b}_r^2 \rangle - \langle \hat{b}_r \rangle^2 \\ &= \tfrac{1}{4}\langle (\hat{b} + \hat{b}^\dagger)^2 \rangle - \tfrac{1}{4}\langle \hat{b} + \hat{b}^\dagger \rangle^2 \\ &= \tfrac{1}{4}\langle (\mu\hat{a} + \mu\hat{a}^\dagger + \nu\hat{c} + \nu\hat{c}^\dagger)^2 \rangle \\ &= \tfrac{1}{4}\mu^2 + \tfrac{1}{4}\nu^2 + \tfrac{1}{2}\mu^2\langle \hat{a}^\dagger\hat{a} \rangle + \tfrac{1}{2}\nu^2\langle \hat{c}^\dagger\hat{c} \rangle + \tfrac{1}{2}\mu\nu \left(\langle \hat{a}\hat{c} \rangle + \langle \hat{a}^\dagger\hat{c}^\dagger \rangle \right) \ . \end{aligned} \tag{14.193}$$

using $\langle \hat{a} \rangle = \langle \hat{c} \rangle = \langle \hat{a}^\dagger\hat{c} \rangle = 0$.

Two-mode squeezing can exist even if the individual modes are not squeezed,

$$|r, \phi\rangle = \cosh^{-1} r \sum\nolimits_n \tanh^n r e^{\imath n\phi} |r, \phi\rangle_a |r, \phi\rangle_b \ . \tag{14.194}$$

A *two-mode squeezed vacuum state* can be generated by the squeezing operator,

$$\mathcal{S}(\xi) \equiv e^{\xi^* \hat{a}\hat{b}/2 - \xi\hat{a}^\dagger\hat{b}^\dagger/2} \ . \tag{14.195}$$

Remember that the single-mode squeezing is obtained if $\hat{a} = \hat{b}$. In a number state base,

$$|r, \phi\rangle = \frac{1}{\cosh r} \sum\nolimits_n (\tanh r)^n e^{\imath n\phi} |n\rangle_a |n\rangle_b \ . \tag{14.196}$$

Two-mode relative number squeezing parameter

$$\xi_{i,j} = \frac{\sigma^2(n_i - \langle n_j \rangle)}{\langle n_i \rangle + \langle n_j \rangle} \ . \tag{14.197}$$

14.5.8 Exercises

14.5.8.1 Ex: Conservation law at a beam splitter 1

Show that the beam-splitting transformation

$$\begin{pmatrix} \hat{c} \\ \hat{d} \end{pmatrix} = \begin{pmatrix} t & -r \\ r & t \end{pmatrix} \begin{pmatrix} \hat{a} \\ \hat{b} \end{pmatrix}$$

preserves the commutations relations and the photon number. More generally,

$$\begin{pmatrix} \hat{c} \\ \hat{d} \end{pmatrix} = \mathcal{U} \begin{pmatrix} \hat{a} \\ \hat{b} \end{pmatrix} \qquad \Longrightarrow \qquad [\hat{c}, \hat{d}] = [\hat{a}, \hat{b}] \det U \ .$$

14.5.8.2 Ex: Conservation law at a beam splitter 2

Derive from the Hamiltonian (14.127) that $\hat{a}^\dagger \hat{a} + \hat{b}^\dagger \hat{b} = const.$

14.5.8.3 Ex: Beam splitter

Show that $\hat{B}|1,0\rangle = \cos\theta|1,0\rangle - \sin\theta|0,1\rangle$ and $\hat{B}|0,n\rangle = \sum_{k=0}^{\infty} \sqrt{\binom{n}{k}} \cos^k\theta \sin^{n-k}\theta |n-k,k\rangle$.

14.5.8.4 Ex: Beam splitter

Show that for $\hat{B} \equiv e^{\theta(\hat{a}\hat{b}^\dagger - \hat{a}^\dagger \hat{b})}$ holds,

$$\hat{B}\hat{a}\hat{B}^\dagger = \hat{a}\cos\theta + \hat{b}\sin\theta \qquad \text{and} \qquad \hat{B}\hat{b}\hat{B}^\dagger = -\hat{a}\sin\theta + \hat{b}\cos\theta \ .$$

14.5.8.5 Ex: Homodyne detection of squeezing

Consider the beam bath shown in Fig. 14.8(b), where the Kerr medium is assumed to generate squeezing in the mode $\hat{a}_1$. Calculate the balanced homodyne signal $\hat{a}_3^\dagger \hat{a}_3 - \hat{b}_3^\dagger \hat{b}_3$.

14.5.8.6 Ex: Coupled harmonic oscillators with different eigenfrequencies and damping

Here, we generalize the calculation of Sec. 14.5.5 for coupling of oscillators with different eigenfrequencies.
a. From,

$$\hat{H} = \hbar\omega_a(\hat{a}^\dagger\hat{a} + \tfrac{1}{2}) + \hbar\omega_b(\hat{b}^\dagger\hat{b} + \tfrac{1}{2}) + \tfrac{\hbar\Omega}{2}(\hat{a}\hat{b}^\dagger + \hat{a}^\dagger\hat{b}) + \tfrac{\hbar\Omega'}{2}(\hat{a}\hat{b} + \hat{a}^\dagger\hat{b}^\dagger)$$

derive the Hamiltonian in terms of the quadrature components $\hat{x}_{a,b}$ and $\hat{p}_{a,b}$.
b. Set up the Heisenberg equations for the field operators $\hat{a}$, $\hat{a}^\dagger$, $\hat{b}$, and $\hat{b}^\dagger$ and determine the eigenvalues of the matrix $\mathcal{X}$ defined by,

$$\frac{d}{dt}\begin{pmatrix}\hat{a}\\ \hat{a}^\dagger\\ \hat{b}\\ \hat{b}^\dagger\end{pmatrix} = X\begin{pmatrix}\hat{a}\\ \hat{a}^\dagger\\ \hat{b}\\ \hat{b}^\dagger\end{pmatrix} \quad .$$

c. Extend the Heisenberg equations by including loss terms for the cavity modes κ_a and κ_b and determine the corresponding matrix $\mathcal{X}_\kappa$, as well as its eigenvalues for the simplifying case $\Omega' \equiv \Omega$.

14.5.8.7 Ex: Equivalence of beam splitter and coupled oscillator models

Show that the beam splitter and the coupled oscillators model for degenerate frequencies are equivalent.

14.5.8.8 Ex: Elitzur and Vaidman bomb tester

a. Write down the beam splitter Hamiltonian in the Fock representation for a the case of a single photon, diagonalize it, and determine the propagator $e^{\imath\hat{H}t/\hbar}$ for a 50/50 beam splitter.
b. Based on the propagator derived in (a) draw an analogy between a Mach-Zehnder interferometer and a resonantly driven two-level system. Interpreting the interferometer as a qubit explain the *Elitzur and Vaidman bomb testing problem*. What is the probability?
c. Reformulate the interaction-free bomb tester in a quantum computing language.

14.5.8.9 Ex: Multiple beam splitters for improved bomb testing

In the original Elitzur and Vaidman bomb tester photons are sent through a single interferometer. Now, let the photons be sent repeatedly through the same beam splitter. Assume the photon wavepacket to be shorter than the length of the interferometer arms so that it *does not interfere with itself*. How many times must the photons be sent to the beam splitter to be totally transferred?

14.5.8.10 Ex: Hamiltonian approach to coupled cavities for improved bomb testing

a. Consider two identical weakly coupled cavities. Solving the Heisenberg equations with the Hamiltonian for two coupled oscillators calculate how the photon numbers evolve in each cavity (see Exc. 14.5.8.6). How do the field amplitudes change after one cavity round trip?
b. How does the photon number in cavity 'b' evolve if an absorber is inserted into the cavity 'a' [495]? How does the field amplitudes change in this case after one cavity round trip?
c. Now, we model the absorber by a two-level atom being in resonance with the light

field and subject to spontaneous emission. Set up the Hamiltonian, derive the equations of motion, and solve them numerically. Interpret the results.
Comments: The multiple path model leading to the Airy formulas describes a physical process involving beam propagation and reflection and transmission at a real object like an atom or a beam splitter. The complete dynamics is only partially grasped by a Hamiltonian and a master equation treating the cavity as a closed system and being restricted to describing energy fluxes into and out of the system.
One manifestation of it is the necessity of approximating the Airy function close to resonance by a Lorentzian in order to link the cavity transmission to a decay rate.
Another manifestation is the discrepancy in the coupled cavity description via multiple paths and via Hamiltonian for coupled oscillators: The models only coincide of $r = \sqrt{R} \stackrel{!}{=} 1$.

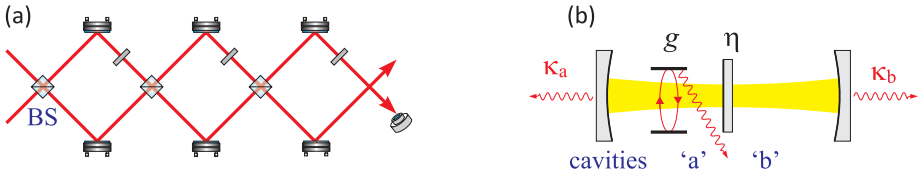

Figure 14.10: (a) Illustration of the multiple paths model and (b) the coupled cavities model for improved bomb testing.

14.5.8.11 Ex: Simulation of the quantum Zeno effect with qubit gates

Design a quantum circuit simulating the quantum Zeno effect ruling the bomb tester and its extension to multiple paths.

14.5.8.12 Ex: Link between entanglement and squeezing

Prove that, if $\hat{a}_1$ and $\hat{a}_2$ are EPR-entangled beams with respect to quadrature components, then beams $\hat{b}_{1,2} = \frac{1}{\sqrt{2}}(\hat{a}_1 \pm \hat{a}_2)$ are squeezed with respect to two orthogonal quadrature components and vice versa [687, 688, 533].

14.6 Further reading

Ch.C. Gerry and P.L. Knight, Cambridge University Press (2005), *Introductory Quantum Optics* [ISBN]

P. Meystre and M. Sargent III, Springer-Verlag, Berlin (1990), *Elements of Quantum Optics* [ISBN]

M.O. Scully and M.S. Zubairy, Cambridge University Press (1997), *Quantum Optics* [ISBN]

W. Schleich, Wiley VCH (2001), *Quantum Optics in Phase Space* [ISBN]

E.T. Jaynes et al., *Comparison of quantum and semiclassical radiation theories with application to the beam maser* [DOI]

F. Albarelli et al., *Nonlinearity as a resource for nonclassicality in anharmonic systems* [DOI]

J.P. Bartolotta et al., *Entropy transfer from a quantum particle to a classical coherent light field* [DOI]

K.E. Cahill et al., *Density Operators and Quasiprobability Distributions* [DOI]

C.M. Caves et al., *Quantum-mechanical noise in an interferometer* [DOI]

C.M. Caves, *Quantum limits on noise inlinear amplifiers* [DOI]

J. Dalibard et al., *Wave-Function Approach to Dissipative Processes in Quantum Optics* [DOI]

R.G. DeVoe et al., *Observation and Superradiant and Subradiant Spontaneous Emission of Two Trapped Ions* [DOI]

R. Dum et al., *Monte Carlo simulation of master equations in quantum optics for vacuum, thermal, and squeezed reservoirs* [DOI]

J. Eschner et al., *Light interference from single atoms and their mirror images* [DOI]

Z. Ficek et al., *Effect of interatomic interactions on resonance fluorescence of two atoms coherently driven by strong resonant laser field* [DOI]

J.C. García-Melgarejo et al., *A Numerical Perspective on the Jaynes-Cummings Model Wigner Function* [DOI]

K. Nakayama et al., *Precise intensity correlation measurement for atomic resonance fluorescence from optical molasses* [DOI]

U. Leonhardt et al., *Measuring the quantum state of light* [DOI]

P. Longo et al., *Far-Field Signatures of a Two-Body Bound State in Collective Emission from Interacting Two-Level Atoms on a Lattice* [DOI]

R. Loudon et al., *Squeezed light* [DOI]

L.A. Lugiato et al., *Quantum imaging* [DOI]

B.R. Mollow et al., *Power spectrum of light scattered by two-level systems* [DOI]

K. Mølmer et al., *Monte Carlo wave-function method in quantum optics* [DOI]

F.A. de Oliveira et al., *Properties of displaced number states* [DOI]

M.D. Reid, *Quantum Correlations of Phase in Nondegenerate Parametric Oscillation* [DOI]

M.D. Reid, *Demonstration of the Einstein-Podolsky-Rosen paradox using nondegenerate parametric amplification* [DOI]

D. Stoler, *Equivalence Classes of Minimum Uncertainty Packets* [DOI]

M. Uria et al., *Deterministic Generation of Large Fock States* [DOI]

H.P. Yuen et al., *Two-photon coherent states of the radiation field* [DOI]

M. Schubert et al., *Photon antibunching and non-Poissonian fluorescence of a single three-level ion* [DOI]

Y. Stalgies et al., *The Spectrum of Single-Atom Resonance Fluorescence* [DOI]

Y. Gutiérrez et al., *Mollow triplet in cold atoms* [DOI]

G.S. Agarwal et al., *Inhibition of Decoherence due to Decay in a Continuum* [DOI]

Ho Trung Dung et al., *Electromagnetic-field quantization and spontaneous decay in left-handed media* [DOI]

14.6.1 on second quantization

W.E.Jr. Lamb, *Anti-Photon* [DOI]

14.6.2 on beam splitters

L.E. Estes et al., *Quantum-Mechanical Description of Two Coupled Harmonic Oscillators* [DOI]

U. Leonhardt, *Quantum physics of simple optical instruments* [DOI]

Chapter 15

Optical cavities

So far we have considered the coherent dynamics between atoms and radiation fields in free space, and we extended the theory to take into account the dissipative coupling to the electromagnetic vacuum by spontaneous emission and atomic motion. The vacuum represents a homogeneous and isotropic reservoir characterized by a continuous white energy spectrum. The situation changes completely when we place the atom inside an optical cavity which breaks the translational and rotational symmetries and imprints a resonance structure into the density of photonic states. Obviously, the cavity will profoundly change the atomic coupling to the electromagnetic vacuum, and hence the way in which the atom reacts to incident light, as much with respect to light scattering as with respect to optical forces.

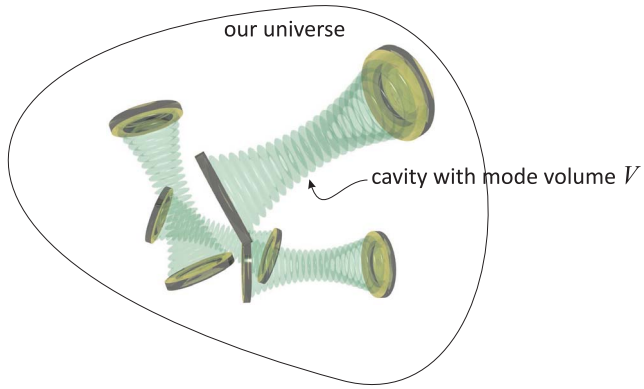

Figure 15.1: Illustration of the mode structure of empty space.

In this chapter we analyze the coupled dynamics of atoms interacting with the optical field modes of a cavity pumped by incident laser beams. We first concentrate in Sec. 15.2 on empty cavities. Later, in Chp. 22 we turn our attention to the impact of atoms on the cavity dynamics, in particular its transmission spectrum. Cooperative and collective effects that may be induced by cavities will be discussed in Chps. 24 and 25.

15.1 Open systems and the master equation

Let us now derive the master equation for an open quantum system. We assume that the environment (also called *bath* or *reservoir*) and the system under consideration are quantum systems in the sense that (1) the relevant degrees of freedom are completely characterized by state vectors (or density matrices), and (2) the temporal evolution of the total system is unitary $\mathcal{U}(t) = e^{-\imath\hat{H}t}$. The total Hamiltonian, $\hat{H} = \hat{H}_{\rm sys} + \hat{H}_{\rm res} + V$ is assumed to be independent of time and consists of three parts, namely the Hamiltonian of the system $\hat{H}_{\rm sys}$, the Hamiltonian of the bath $\hat{H}_{\rm res}$, and the interaction V between the system and the bath. The purpose of the master equation is to find the dynamics of the system by tracing over all degrees of freedom of the bath. This is not always possible, and we will assume that the interaction V is sufficiently weak, so that perturbation theory is applicable [500].

15.1.1 Temporal evolution of the density operator

As shown in Secs. 1.6.2 to 1.6.4, the equations governing the temporal evolution of a quantum system depend on the choice of the picture, i.e. Schrödinger's (1.242), Heisenberg's (1.248), or the interaction picture (1.255). This, of course, also applies to a system represented by a density matrix.

Returning to the density operator definition (14.11), we can express its temporal dependence in terms of time-dependent quantum states and of the time evolution operator (1.245),

$$\hat{\rho}(t) = \sum_k p_k |\psi_k(t)\rangle\langle\psi_k(t)| = \sum_k p_k \mathcal{U}(t,t_0)|\psi_k(t_0)\rangle\langle\psi_k(t_0)|\mathcal{U}^\dagger(t,t_0) \ . \tag{15.1}$$

Writing,

$$\hat{\rho}(t_0) = \sum_k p_k |\psi_k(t_0)\rangle\langle\psi_k(t_0)| \ , \tag{15.2}$$

we see immediately,

$$\hat{\rho}(t) = \mathcal{U}(t,t_0)\hat{\rho}(t_0)\mathcal{U}^\dagger(t,t_0) \ , \tag{15.3}$$

where, for the common case of a time-independent Hamiltonian,

$$\mathcal{U}(t,t_0) = e^{-\imath\hat{H}(t-t_0)/\hbar} \ . \tag{15.4}$$

Now we find the time derivative of the density operator differentiating the two sides of (15.3) and substituting the Eqs.

$$\frac{d\mathcal{U}}{dt} = \frac{1}{\imath\hbar}\hat{H}\mathcal{U} \qquad \text{and} \qquad \frac{d\mathcal{U}^\dagger}{dt} = -\frac{1}{\imath\hbar}\mathcal{U}^\dagger\hat{H} \tag{15.5}$$

for the time derivatives $\mathcal{U}$ and $\mathcal{U}^\dagger$. The result is

$$\boxed{\frac{d\hat{\rho}(t)}{dt} = \frac{\imath}{\hbar}[\hat{\rho}(t),\hat{H}]} \ . \tag{15.6}$$

The commutator itself can be considered as a *superoperator* acting, not any more on states but on operators, that is, we can write,

$$\mathfrak{L}\hat{\rho}(t) \equiv \frac{\imath}{\hbar}[\hat{\rho}(t), \hat{H}] \ , \tag{15.7}$$

where $\mathfrak{L}$ is called *Liouville operator*. The equation (15.6) is called *Liouville equation* or *von Neumann equation*. The Liouville equation describes the *time evolution of the density operator* which, in turn, describes the distribution of an ensemble of quantum states. Even though the form of the Liouville equation resembles a Heisenberg equation, Eq. (15.1) shows that $\hat{\rho}(t)$ is in the *Schrödinger picture* [1].

In the interaction representation the evolution of the total density matrix $\hat{\rho}_{\rm tot}$ becomes,

$$\boxed{\imath\hbar\frac{d\tilde{\rho}_{\rm tot}}{dt} = [\tilde{V}(t), \tilde{\rho}_{\rm tot}]} \ . \tag{15.8}$$

where $\tilde{\rho}_{\rm tot}(t) \equiv U_0^\dagger \rho_{\rm tot} U_0$ and $\tilde{V}(t) \equiv U_0^\dagger V U_0$ and $U_0 = e^{-\imath(\hat{H}_{\rm sys}+\hat{H}_{\rm res})t/\hbar}$. This evolution is, for the time being, very general, and the solution can be formally written,

$$\tilde{\rho}_{\rm tot}(t) = \tilde{\rho}_{\rm tot}(0) + \frac{1}{\imath\hbar}\int_0^t dt_1[\tilde{V}(t_1), \tilde{\rho}_{\rm tot}(t_1)] \ . \tag{15.9}$$

Iterating once again:

$$\tilde{\rho}_{\rm tot}(t) = \tilde{\rho}_{\rm tot}(0) + \frac{1}{\imath\hbar}\int_0^t dt_1[\tilde{V}(t_1), \tilde{\rho}_{\rm tot}(0)] + \frac{1}{(\imath\hbar)^2}\int_0^t dt_1 \int_0^{t_1} dt_2 \left[\tilde{V}(t_1), [\tilde{V}(t_2), \tilde{\rho}_{\rm tot}(t_2)\right] \ . \tag{15.10}$$

In the following, we will call several approximations to simplify the calculations, in particular, the Born approximation, the assumption that the initial state is a product state and, later-on, the Markov approximation.

15.1.2 Born approximation for weak coupling

We will now assume the interaction $\tilde{V}$ to be weak. We can then expect that, repeating the iterative process, the series will converge and write the general solution as,

$$\tilde{\rho}_{\rm tot}(t) = \tilde{\rho}_{\rm tot}(0) + \sum_{n\geq 1}\frac{1}{(\imath\hbar)^n}\int_0^t dt_1 ... \int_0^{t_{n-1}} dt_n \left[\tilde{V}(t_1), ..., [\tilde{V}(t_n), \tilde{\rho}_{\rm tot}(0)]\right] \ . \tag{15.11}$$

This way of terminating an iterative equation by $\rho_{\rm tot}(0)$ is generally known as the *Born approximation*. Here, we will just go to second order in $\tilde{V}$. Tracing over the bath,

$$\tilde{\rho}_{\rm sys}(t) = {\rm Tr}_{\rm res}\ \tilde{\rho}_{\rm tot}(t) \ , \tag{15.12}$$

we extract the density matrix for only the system,

$$\tilde{\rho}_{\rm sys}(t) = \tilde{\rho}_{\rm sys}(0) + \frac{1}{\imath\hbar}\int_0^t dt_1 {\rm Tr}_{\rm res}[\tilde{V}(t_1), \tilde{\rho}_{\rm tot}(0)] + \frac{1}{(\imath\hbar)^2}\int_0^t dt_1 \int_0^{t_1} dt_2 {\rm Tr}_{\rm res}\left[\tilde{V}(t_1), [\tilde{V}(t_2), \tilde{\rho}_{\rm tot}(0)]\right] \ . \tag{15.13}$$

[1] The Heisenberg equation for the density operator in the Schrödinger picture or the master equation in the Heisenberg picture are $d\hat{\rho}_H/dt = 0$.

15.1.3 Assumption of an initial product state

Next, we need to make the quite important assumption, that the initial state between the system and the environment are not correlated, or mathematically speaking, they can be written as product states,

$$\tilde{\rho}_{\rm tot}(0) = \tilde{\rho}_{\rm sys}(0) \otimes \rho_{\rm res}(0) \ . \tag{15.14}$$

Another assumption, which is not essential but often valid, is that $\mathrm{Tr}_{\rm res}[\tilde{V}(t_1), \tilde{\rho}_{\rm tot}(0)] = 0$. If this is the case, then the first-order term will vanish. In second order, we can write,

$$\begin{aligned} &\tilde{\rho}_{\rm sys}(t) = e^{\mathcal{M}(t)} \tilde{\rho}_{\rm sys}(0) \qquad (15.15)\\ &\text{where} \quad \mathcal{M}(t)\chi \equiv \frac{1}{(i\hbar)^2} \int_0^t dt_1 \int_0^{t_1} dt_2 \mathrm{Tr}_{\rm res} \left[\tilde{V}(t_1), [\tilde{V}(t_2), \chi \otimes \rho_{\rm res}]\right] \ , \end{aligned}$$

is a *superoperator* acting on the operator density of the system. Taking the temporal derivative, we have the explicit master equation,

$$\boxed{\begin{array}{rcl} \frac{d\tilde{\rho}_{\rm sys}(t)}{dt} = \mathfrak{L}\rho_{\rm sys}(t) & = & \frac{d}{dt}\left(\mathcal{M}(t)\tilde{\rho}_{\rm sys}(t)\right) \\ & = & \frac{1}{(i\hbar)^2}\int_0^t d\tau \ \mathrm{Tr}_{\rm res}\left[\tilde{V}(t), [\tilde{V}(\tau), \tilde{\rho}_{\rm sys}(t) \otimes \rho_{\rm res}]\right] \end{array}} \ . \tag{15.16}$$

The superoperator $\mathfrak{L}$ is called *Lindblad operator*.

15.1.4 Markov approximation for short memory

Here, we have to evaluate the terms involving the average with respect to the thermal bath, which is assumed to have a short memory, in the sense that the correlation time is very short. Mathematically,

$$\begin{aligned} \int_0^t d\tau \ \mathrm{Tr}_{\rm res}\left(\tilde{V}(t)\tilde{V}(\tau)\rho_{\rm res}\right) &= \int_0^t d\tau \ \mathrm{Tr}_{\rm res}\left(\tilde{V}(t-\tau)\tilde{V}(0)\rho_{\rm res}\right) \qquad (15.17)\\ &\simeq \int_0^\infty d\tau \ \mathrm{Tr}_{\rm res}\left(\tilde{V}(t-\tau)\tilde{V}(0)\rho_{\rm res}\right) \ . \end{aligned}$$

In other words, the two-point correlation function is significant only, when $t \simeq \tau$, and it is valid to extend the upper bound to infinity. This is the *Markov approximation*.

15.1.5 Example: Damped harmonic quantum oscillator

As an example, we let us consider the master equation for the *Brownian motion of a quantum harmonic oscillator*. It can be written,

$$\frac{d\tilde{\rho}_{\rm sys}}{dt} = \frac{1}{(i\hbar)^2}\int_0^t d\tau \ \mathrm{Tr}_{\rm res}\left\{ \begin{array}{c} \tilde{V}(t)\tilde{V}(\tau)\tilde{\rho}(t) \otimes \rho_{\rm res} - \tilde{V}(t)\tilde{\rho}_{\rm sys}(t) \otimes \rho_{\rm res}\tilde{V}(\tau) \\ -\tilde{V}(\tau)\tilde{\rho}_{\rm sys}(t) \otimes \rho_{\rm res}\tilde{V}(t) + \tilde{\rho}_{\rm sys}(t) \otimes \rho_{\rm res}\tilde{V}(\tau)\tilde{V}(t) \end{array} \right\} \ . \tag{15.18}$$

The coupling of the system to the bath is assumed to be of the form,

$$\tilde{V} = \hbar \left(\hat{a}^\dagger \hat{\Gamma}(t) e^{\imath\Omega t} + \hat{a} \hat{\Gamma}^\dagger(t) e^{-\imath\Omega t} \right) \ , \tag{15.19}$$

where $\hat{\Gamma}(t) = \sum_k g_k \hat{b}_k e^{-\imath\omega_k t}$, the bosonic operators $\hat{a}$ and $\hat{b}_k$ act, respectively, on the system (with the frequency Ω) and the bath (with the frequency ω_k). Here, g_k characterizes the coupling force between the oscillators of the system and the bath. Hence,

$$\frac{d\tilde{\rho}_{\rm sys}}{dt} = -\int_0^t d\tau \, {\rm Tr}_{\rm res} \left\{ \begin{array}{l} \left(\hat{a}^\dagger \hat{\Gamma}(t) e^{\imath\Omega t} + \hat{a} \hat{\Gamma}^\dagger(t) e^{-\imath\Omega t} \right) \left(\hat{a}^\dagger \hat{\Gamma}(\tau) e^{\imath\Omega\tau} + \hat{a} \hat{\Gamma}^\dagger(\tau) e^{-\imath\Omega\tau} \right) \tilde{\rho}(t) \otimes \rho_{\rm res} \\ - \left(\hat{a}^\dagger \hat{\Gamma}(t) e^{\imath\Omega t} + \hat{a} \hat{\Gamma}^\dagger(t) e^{-\imath\Omega t} \right) \tilde{\rho}(t) \otimes \rho_{\rm res} \left(\hat{a}^\dagger \hat{\Gamma}(\tau) e^{\imath\Omega\tau} + \hat{a} \hat{\Gamma}^\dagger(\tau) e^{-\imath\Omega\tau} \right) \\ - \left(\hat{a}^\dagger \hat{\Gamma}(\tau) e^{\imath\Omega\tau} + a \hat{\Gamma}^\dagger(\tau) e^{-\imath\Omega\tau} \right) \tilde{\rho}(t) \otimes \rho_{\rm res} \left(\hat{a}^\dagger \hat{\Gamma}(t) e^{\imath\Omega t} + a \hat{\Gamma}^\dagger(t) e^{-\imath\Omega t} \right) \\ + \tilde{\rho}(t) \otimes \rho_{\rm res} \left(\hat{a}^\dagger \hat{\Gamma}(\tau) e^{\imath\Omega\tau} + \hat{a} \hat{\Gamma}^\dagger(\tau) e^{-\imath\Omega\tau} \right) \left(\hat{a}^\dagger \hat{\Gamma}(t) e^{\imath\Omega t} + \hat{a} \hat{\Gamma}^\dagger(t) e^{-\imath\Omega t} \right) \end{array} \right\} . \tag{15.20}$$

Let's take a closer look at one of the terms,

$$\begin{aligned} \hat{T} &\equiv -\int_0^t d\tau {\rm Tr}_{\rm res} \left\{ \hat{a}^\dagger \hat{\Gamma}(t) e^{\imath\Omega t} \hat{a} \hat{\Gamma}^\dagger(\tau) e^{-\imath\Omega\tau} \tilde{\rho}(t) \otimes \rho_{\rm res} \right\} \\ &= -\hat{a}^\dagger \hat{a} \tilde{\rho}(t) \int_0^t d\tau \langle \hat{\Gamma}(t) \hat{\Gamma}^\dagger(\tau) \rangle_{\rm res} e^{\imath\Omega t} e^{-\imath\Omega\tau} \ . \end{aligned} \tag{15.21}$$

We will have to evaluate quantities such as

$${\rm Tr}_{\rm res} \left(V(t) V(s) \rho_{\rm res} \right) = \hbar^2 \hat{a}^\dagger \hat{a} \langle \hat{\Gamma}(t) \hat{\Gamma}^\dagger(t) \rangle_{\rm res} e^{\imath\Omega(t-s)} + \hbar^2 \hat{a} \hat{a}^\dagger \langle \hat{\Gamma}^\dagger(t) \hat{\Gamma}(t) \rangle_{\rm res} e^{-\imath\Omega(t-s)} \ , \tag{15.22}$$

where $\langle \hat{\Gamma}(t) \hat{\Gamma}^\dagger(t) \rangle_{\rm res} \equiv {\rm Tr}_{\rm res}[\hat{\Gamma}(t) \hat{\Gamma}^\dagger(t) \rho_{\rm res}]$, and for the thermal bath, $\langle \hat{b}_j^\dagger \hat{b}_k \rangle = \delta_{jk} n_k$ and $\langle \hat{b}_j \hat{b}_k^\dagger \rangle = \delta_{jk}(1 + n_k)$ and $n_k = (e^{\beta\hbar\omega_k} - 1)^{-1}$. Hence,

$$\begin{aligned} \hat{T} &= -\hat{a}^\dagger \hat{a} \tilde{\rho}(t) \sum_{j,k} g_j g_k \langle b_j b_k^\dagger \rangle_{\rm res} \int_0^t d\tau e^{\imath(\omega_j t - \omega_k \tau)} e^{\imath\Omega(t-\tau)} \\ &\simeq -\hat{a}^\dagger \hat{a} \tilde{\rho}(t) \sum_k g_k^2 n_k \int_0^\infty d\tau e^{\imath(\omega_k - \Omega)(t-\tau)} \ . \end{aligned} \tag{15.23}$$

Then we will have to use the relationship,

$$\int_0^\infty d\tau e^{\pm\imath\varepsilon\tau} = \pi\delta(\varepsilon) \pm \imath PV \ , \tag{15.24}$$

where PV denotes Cauchy part of the principal value. These correspond to a 'Lamb shift' and a 'Stark shift' of the frequency, which are considered to be small in comparison to Ω and should be neglected here,

$$\begin{aligned} \hat{T} &= -\hat{a}^\dagger \hat{a} \tilde{\rho}(t) \sum_k g_k^2 \left(e^{\beta\hbar\omega_k} - 1 \right)^{-1} \int_0^\infty d\tau e^{\imath(\omega_k - \Omega)(t-\tau)} \\ &= -\hat{a}^\dagger \hat{a} \tilde{\rho}(t) \sum_k g_k^2 \left(e^{\beta\hbar\omega_k} - 1 \right)^{-1} \pi\delta(\omega_k - \Omega) \\ &= -\hat{a}^\dagger \hat{a} \tilde{\rho}(t) \sum_k g_k^2 \left(e^{\beta\hbar\Omega} - 1 \right)^{-1} \pi = -\pi \bar{n} \hat{a}^\dagger \hat{a} \tilde{\rho}(t) \sum_k g_k^2 \delta(\omega_k - \Omega) = \bar{n} \hat{a} \hat{a}^\dagger \tilde{\rho}(t) \pi \frac{\gamma}{2} \ . \end{aligned} \tag{15.25}$$

where $\bar{n} \equiv \left(e^{\beta\hbar\Omega} - 1\right)^{-1}$. We define $\frac{\gamma}{2} \equiv \sum_k g_k^2 \delta(\omega_k - \Omega)$. The procedure can be repeated for all terms in the master equation. We then obtain the master equation for a damped harmonic oscillator,

$$\frac{d\tilde{\rho}}{dt} = \tfrac{\gamma}{2}(\bar{n}+1)\left(2\hat{a}\tilde{\rho}\hat{a}^\dagger - \hat{a}^\dagger\hat{a}\tilde{\rho} - \tilde{\rho}\hat{a}^\dagger\hat{a}\right) - \tfrac{\gamma}{2}\bar{n}\left(2\hat{a}^\dagger\tilde{\rho}\hat{a} - \hat{a}\hat{a}^\dagger\tilde{\rho} - \tilde{\rho}\hat{a}\hat{a}^\dagger\right) \ . \tag{15.26}$$

See Excs. 15.1.7.1 and 15.1.7.2.

15.1.6 Deriving the Heisenberg-Langevin from the master equation

The Heisenberg-Langevin equation for the operators $\hat{A}$ of a system subject to dissipation with rates γ_k via the degrees of freedom $\hat{L}_k$ and the *master equation* for the density operator $\hat{\rho}$ are equivalent descriptions for the time-evolution of a system [500],

$$\boxed{\begin{array}{rcccl} \frac{d\hat{\rho}}{dt} & = & \mathfrak{L}\hat{\rho} & = & -\frac{\imath}{\hbar}[\hat{H},\hat{\rho}] + \sum_k \gamma_k \left(\hat{L}_k\hat{\rho}\hat{L}_k^\dagger - \frac{1}{2}\hat{L}_k^\dagger\hat{L}_k\hat{\rho} - \frac{1}{2}\hat{\rho}\hat{L}_k^\dagger\hat{L}_k\right) \\ \frac{d\hat{A}}{dt} & = & \mathfrak{L}^\dagger\hat{A} & = & \frac{\imath}{\hbar}[\hat{H},\hat{A}] + \sum_k \gamma_k \left(\hat{L}_k^\dagger\hat{A}\hat{L}_k - \frac{1}{2}\hat{L}_k^\dagger\hat{L}_k\hat{A} - \frac{1}{2}\hat{A}\hat{L}_k^\dagger\hat{L}_k\right) \end{array}} \ , \tag{15.27}$$

as we will show in Exc. 15.1.7.3. The former stresses the Schrödinger picture and the latter the Heisenberg picture. In particular, the dissipative *Lindblad terms* are equivalent. That is, open systems are sufficiently characterized by the system Hamiltonian $\hat{H}$ and a set of the so-called *jump operators* $\hat{L}_k$ with their corresponding rates γ_k. Note that, while the master equation preserves the trace, the Heisenberg equation is unital, i.e. it preserves the identity operator $\mathbb{I}$.

15.1.7 Exercises

15.1.7.1 Ex: Master equation for cavities

Consider a cavity laser-pumped at a rate η, subject to losses by transmission through the mirrors at a rate κ, and incoherently pumped by thermal photons at a rate $\kappa\bar{n}$, where $\bar{n}$ is the number of thermal photons.
a. Write down the Hamiltonian and the Heisenberg-Liouville equation for an arbitrary operator $\hat{a}$ of the system.
b. Derive the equation of motion for the field annihilation operator $\hat{a}$ and for the photon number operator $\hat{n}$.
c. Solve the equation of motion for the photon number operator for the case of no coherent pumping, $\eta = 0$.
d. Write down the master equation of the system.
e. Derive the equation of motion for the components of the density operator $\rho_{m,n}$.
f. Calculate the photon number evolution from (e).

15.1.7.2 Ex: Photon number distribution in a driven cavity

Simulate the evolution of a light field in a cavity pumped at a rate η and subject to decay κ being initially in a Fock state toward steady-state. Illustrate via representations of the density matrix, the photon number distribution, and the Husimi distribution for the light field

15.1.7.3 Ex: Deriving the Heisenberg-Langevin from the master equation

Derive the Heisenberg-Langevin from the master equation including the dissipative Lindblad terms.

15.2 Dynamics of light fields in empty cavities

The quantization of the electromagnetic field has been introduced in Chp. 17. Nevertheless, we will consider the degree of freedom to be studied in this chapter, that is, the electric field amplitude of a light field developing in a mode of an optical cavity, as a classical entity. Therefore, there is no need to stress quantum mechanics to derive the fundamental equations of motion, and a classical derivation is shown in Sec. 22.1.5. Nevertheless, for reasons of consistency with later discussions, where quantization is required, we will reproduce here the standard procedure, which consists in constructing the Hamiltonian for the relevant degrees of freedom. The degree of freedom under study being a mode of a cavity, we will label it by the field operator $\hat{a}$ normalized to the electric field strength $\vec{\mathcal{E}}_1$ generated by a single photon, such that $|\langle\hat{a}\rangle|^2 = n$ represents the number of photons in the cavity.

In this first section of this chapter we will only consider a bare cavity not containing any matter which could interact with light. The mode of a linear cavity or the two counterpropagating modes of a ring cavity are pumped by incident laser light. We will first set up the equations of motion for the cavity fields and then discuss the main quantities characterizing a cavity, such as free spectral range, mode volume, decay rate, and single-photon field strength. Finally, we will calculate the density of states of cavities.

15.2.1 Master equation

The Hamiltonian of a laser-pumped linear cavity mode $\hat{a}$ coupled to the continuum of a heat bath represented by operators $\hat{a}_\omega$ is ($\hbar = 1$) (see Sec. 15.1.5 and Exc. 15.1.7.1),

$$\begin{aligned}
\hat{H} &= \hat{H}_{\text{cavity}} + \hat{H}_{\text{bath}} + \hat{H}_{\text{cavity:bath}} + \hat{H}_{\text{laser:cavity}} \\
\hat{H}_{\text{cavity}} &= \omega_0 \hat{a}^\dagger \hat{a} \\
\hat{H}_{\text{bath}} &= \sum_\omega \omega \hat{a}^\dagger_\omega \hat{a}_\omega \\
\hat{H}_{\text{cavity:bath}} &= \sum_\omega g_{\text{cavity:bath}} \hat{a}^\dagger_\omega \hat{a} + h.c. \\
\hat{H}_{\text{laser:cavity}} &= \imath\eta \hat{a}^\dagger + h.c.
\end{aligned} \quad , \tag{15.28}$$

with $[\hat{a}_\omega, \hat{a}^\dagger_{\omega'}] = \delta_{\omega,\omega'}$. The part of the Hamiltonian $\hat{H}_{\text{laser:cavity}}$ describes pumping of the cavity with an external light field matched to the cavity mode. The standard procedure consists in setting up the quantum Liouville equation for the total density operator $\hat{\rho}_{\text{total}} = \hat{\rho}_{\text{cavity}} \otimes \hat{\rho}_{\text{bath}}$ and tracing the over the bath's degrees of freedom [304, 169]. From this procedure, as shown in Sec. 15.1.5, we derive a master equation for the reduced density operator $\hat{\rho}_{\text{cavity}}$.

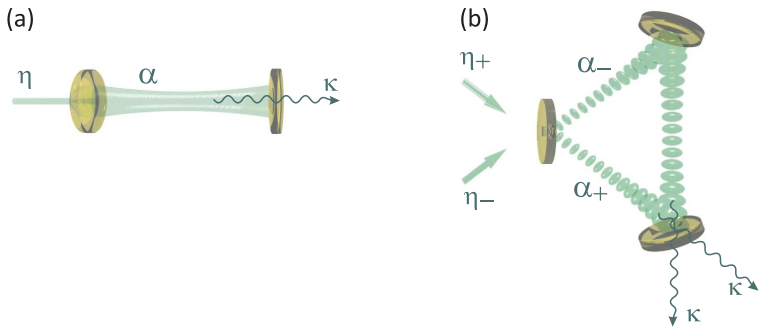

Figure 15.2: Scheme of (a) a linear cavity and (b) a ring cavity with optical modes $\alpha_\pm$ pumped by incident light fields $\eta_\pm$ and decaying into the void with rate κ.

The inevitable coupling of the cavity to the environment, described by $\hat{H}_{\text{cavity:bath}}$, leads to irreversible losses. These losses can be described as spontaneous decay to the continuous vacuum heat bath. The irreversibility of the process is readily understood in terms of the phase space offered by the vacuum being much larger. In fact, whenever discrete states are coupled to a continuum, the equilibrium is very much on the side of the continuum, that is, *discrete states decay*. Since an optical cavity can be considered a *temperature reservoir* T, where,

$$\bar{n} = \frac{1}{1 - e^{-\hbar\omega/k_B T)}} \ , \tag{15.29}$$

is the mean thermal photon number, the *Lindblad operator* is,

$$\begin{aligned} \mathfrak{L}_{\text{bath}}\hat{\rho} = {} & \tfrac{\kappa}{2}(\bar{n}+1)(2\hat{a}\hat{\rho}\hat{a}^\dagger - \hat{a}^\dagger\hat{a}\hat{\rho} - \hat{\rho}\hat{a}^\dagger\hat{a}) + \tfrac{\kappa}{2}\bar{n}(2\hat{a}^\dagger\hat{\rho}\hat{a} - \hat{a}\hat{a}^\dagger\hat{\rho} - \hat{\rho}\hat{a}\hat{a}^\dagger) \\ & + \beta(2\bar{n}+1)(2\hat{a}^\dagger\hat{a}\hat{\rho}\hat{a}^\dagger\hat{a} - (\hat{a}^\dagger\hat{a})^2\hat{\rho} - \hat{\rho}(\hat{a}^\dagger\hat{a})^2) \ . \end{aligned} \tag{15.30}$$

We have shown this in Exc. 15.1.7.1. The constants are the *cavity decay rate* κ and the phase decay β. Note that at room temperature in the microwave regime, $\bar{n}$ may be as large as a few hundred photons, whereas in the optical regime we may neglect the thermal excitation,

$$\begin{aligned} \dot{\hat{\rho}} &= -\tfrac{\imath}{\hbar}[\hat{H}, \hat{\rho}] + \mathfrak{L}_{\text{bath}}\hat{\rho} \\ \mathfrak{L}_{\text{bath}}\hat{\rho}(t) &= \kappa[2\hat{a}\hat{\rho}(t)\hat{a}^\dagger - \hat{a}^\dagger\hat{a}\hat{\rho}(t) - \hat{\rho}(t)\hat{a}^\dagger\hat{a}] \end{aligned} \ . \tag{15.31}$$

15.2.1.1 Expectation values via master equation

The master equation (15.31) permits to calculate the time evolution of pure or mixed quantum states *in the Schrödinger picture*, where the operators are assumed as time independent [see Eq. (1.275) versus (1.276)]. The general procedure consists in using a master equation (see Exc. 15.1.7.3),

$$\frac{d\hat{\rho}}{dt} = -\imath[\hat{H}, \hat{\rho}] + \mathfrak{L}_{\kappa,\hat{L}}\hat{\rho} = -\imath\langle[\hat{H}, \hat{\rho}]\rangle + \kappa(2\hat{L}\hat{\rho}\hat{L}^\dagger - \hat{L}\hat{L}^\dagger\hat{\rho} - \hat{\rho}\hat{L}\hat{L}^\dagger) \tag{15.32}$$

to calculate the expectation values,

$$\begin{aligned}\frac{d\langle\hat{A}\rangle}{dt} &= \mathrm{Tr}\,\hat{A}\frac{d\hat{\rho}}{dt} = -\mathrm{Tr}\,\hat{A}\imath[\hat{H},\hat{\rho}] + \kappa\mathrm{Tr}\,\hat{A}(2\hat{L}\hat{\rho}\hat{L}^\dagger - \hat{L}\hat{L}^\dagger\hat{\rho} - \hat{\rho}\hat{L}\hat{L}^\dagger) \\ &= -\mathrm{Tr}\,\imath\hat{\rho}(\hat{A}\hat{H} - \hat{H}\hat{A}) + \kappa\mathrm{Tr}\,\hat{\rho}(2\hat{L}^\dagger\hat{A}\hat{L} - \hat{A}\hat{L}\hat{L}^\dagger - \hat{L}\hat{L}^\dagger\hat{A}) \\ &= \imath\langle[\hat{H},\hat{A}]\rangle + \langle\mathfrak{L}^\dagger_{\kappa,\hat{L}}\hat{A}\rangle\ .\end{aligned} \tag{15.33}$$

Coming back to our cavity Hamiltonian

$$\hat{H} = \hat{H}_{\text{cavity}} + \hat{H}_{\text{laser:cavity}} = -\Delta_{\text{c}}\hat{a}^\dagger\hat{a} + \eta(\hat{a} + \hat{a}^\dagger)\ , \tag{15.34}$$

we get,

$$\frac{d\langle\hat{A}\rangle}{dt} = \imath\langle[\hat{H},\hat{A}]\rangle + \kappa\langle 2\hat{a}^\dagger\hat{A}\hat{a} - \hat{A}\hat{a}^\dagger\hat{a} - \hat{a}^\dagger\hat{a}\hat{A}\rangle \qquad \text{where} \qquad \langle\hat{A}\rangle(t) = \mathrm{Tr}\,\hat{A}\hat{\rho}(t)\ . \tag{15.35}$$

Since $\hat{a} = \hat{a}(0)$ is stationary, we may choose $\hat{a} \equiv \hat{a}$ and, using the pump Hamiltonian $\hat{H} = \eta(\hat{a} + \hat{a}^\dagger)$, evaluate the terms, yielding for example,

$$\begin{aligned}\frac{d\langle\hat{a}\rangle}{dt} &= \mathrm{Tr}\,\hat{a}\frac{d\hat{\rho}}{dt} = -\imath\eta - \kappa\langle\hat{a}\rangle \\ \frac{d\langle\hat{a}^\dagger\hat{a}\rangle}{dt} &= \mathrm{Tr}\,\hat{a}^\dagger\hat{a}\frac{d\hat{\rho}}{dt} = \imath\eta(\langle\hat{a}\rangle - \langle\hat{a}^\dagger\rangle) - 2\kappa\langle\hat{a}^\dagger\hat{a}\rangle\ .\end{aligned} \tag{15.36}$$

These equations are also termed quantum Langevin equations.

15.2.2 Mean field dynamics of laser-pumped cavities

The expectation values are given by a *quantum Langevin equation* [169], which in the mean field approximation (neglecting quantum noise) reduces to,

$$\boxed{\dot{\alpha} = \langle\dot{\hat{a}}\rangle = \frac{\imath}{\hbar}\langle[\hat{H},\hat{a}]\rangle - \kappa\langle\hat{a}\rangle = (-\kappa - \imath\Delta_{\text{c}})\alpha + \eta}\ , \tag{15.37}$$

whose solution is easy to derive,

$$\boxed{\alpha(t) = \left(\alpha(0) - \frac{\eta}{\kappa + \imath\Delta_{\text{c}}}\right)e^{(-\kappa-\imath\Delta_{\text{c}})t} + \frac{\eta}{\kappa + \imath\Delta_{\text{c}}}}\ , \tag{15.38}$$

or, using the electric field normalized to the amplitude of the field generated by a single photon, $\vec{\mathcal{E}}^+_{\text{cav}} = \vec{\mathcal{E}}_1\alpha$,

$$\begin{aligned}\vec{\mathcal{E}}_{\text{cav}}(z,t) &= \mathfrak{Re}\left[\vec{\mathcal{E}}_1 e^{\imath(kz-\omega t)}\alpha(t) + \vec{\mathcal{E}}_1 e^{\imath(-kz-\omega t)}\alpha(t)\right] \\ &= 2\vec{\mathcal{E}}_1\cos kz\mathfrak{Re}\left[e^{-\imath\omega t}\alpha(t)\right] \\ &= 2\vec{\mathcal{E}}_1\cos kz\mathfrak{Re}\left[\left(\alpha(0) - \frac{\eta}{\kappa + \imath\Delta_{\text{c}}}\right)e^{(-\kappa-\imath\omega_c)t} + \frac{\eta}{\kappa + \imath\Delta_{\text{c}}}e^{-\imath\omega t}\right]\ .\end{aligned} \tag{15.39}$$

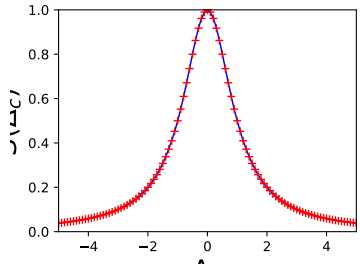

Figure 15.3: (code) Transmission spectrum of a cavity via numerical solution of the master equation (15.38) (solid line) and via the stationary solution (15.40) (crosses).

The stationary solution is simply a Lorentzian,

$$|\alpha(\infty)|^2 = \frac{|\eta|^2}{\kappa^2 + \Delta_c^2} \ , \tag{15.40}$$

which represents an approximation of the Airy function.

The result (15.39) shows that, letting $\eta = 0$, we see that the cavity field decays with the time constant κ from the stationary situation. κ also corresponds to the HWHM of the *field intensity*, $|\alpha(|\Delta_c| = \kappa)|^2 = \frac{1}{2}|\alpha(0)|^2$. Note, that the intensity decays as 2κ, and the HWHM of the *field amplitude* is $\left|\alpha(|\Delta_c| = \sqrt{3}\kappa)\right| = \frac{1}{2}|\alpha(0)|$.

Example 85 (*Evolution of the modes of a linear cavity*): (15.39) also shows that a cavity initially filled with a strong resonant light field $|\alpha(0)| \gg \eta/\kappa$ begins to oscillate at its own frequency ω_c, before the pump dominates and imposes its own frequency ω. This is illustrated in Fig. 15.4. .

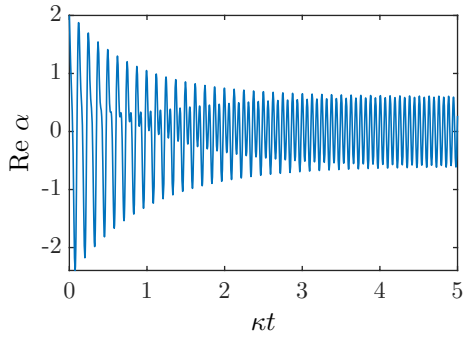

Figure 15.4: (code) Transient oscillations in a cavity pumped out of resonance.

Frequently, we are interested in the light reflected from a cavity. The reflective response of the cavity to an incident pump beam $\vec{\mathcal{E}}_{\rm in}$ is,

$$\vec{\mathcal{E}}^+_{\rm refl} = r_{\rm in}\vec{\mathcal{E}}^+_{\rm in} + t_{\rm in}\vec{\mathcal{E}}^+_{\rm cav} \ . \tag{15.41}$$

Also we may want to consider a temporal variation of the input field, for example of its detuning, $\Delta_c(t)$. In such cases, the equation (15.37) can not be integrated easily, and we need to resort to numerical methods. The simplest (and least convergent) method in a Newtonian iteration like,

$$\vec{\mathcal{E}}^{+}_{\rm refl}(t+dt) = \vec{\mathcal{E}}^{+}_{\rm refl}(t) + dt\ t_{\rm in}\left[(-\kappa - \imath\Delta_c(t))\vec{\mathcal{E}}^{+}_{\rm cav}(t) + \eta\vec{\mathcal{E}}^{+}_{\rm in}(t)\right] \ . \tag{15.42}$$

We will study in Exc. 15.2.5.1 how a sudden change of the pump laser detuning may lead to *ringing* with a fixed frequency Δ_c. In Excs. 15.2.5.2 and 15.2.5.3 we will show, how it is possible to empty an optical cavity in times shorter than $1/\kappa$.

15.2.2.1 Mean field dynamics of laser-pumped ring cavities

Linear cavities are characterized by the fact that they sustain standing light waves. That is, at every point of the mode volume, there are field components pointing into two counterpropagating orientations. In case of a ring cavity, we have two counter-propagating modes $\alpha_\pm$, which may be independently pumped by laser beams $\eta\pm$. Hence, the quantum Langevin equation (15.37) must be generalized to,

$$\boxed{\dot{\alpha}_\pm(t) = (-\kappa - \imath\Delta_c)\alpha_\pm + \eta_\pm} \ , \tag{15.43}$$

and the general solution (15.38) to,

$$\boxed{\alpha_\pm(t) = \left(\alpha_\pm(0) - \frac{\eta_\pm}{\kappa + \imath\Delta_c}\right) e^{(-\kappa-\imath\Delta_c)t} + \frac{\eta_\pm}{\kappa+\imath\Delta_c}} \ . \tag{15.44}$$

The two counterpropagating field modes will, provided they have the same polarization, interfere and form a standing light wave. In contrast to linear cavities, the phase of this standing wave is represents a degree of freedom, as it depends on the phases of the two field modes $\alpha_\pm$, which in turn can be controlled by the incident laser fields $\eta_\pm$. To better understand the behavior of the phase as a function of the pump beams, we analyze the interference of the two modes, which is described by,

$$\begin{aligned}\alpha_+\alpha_-^* = &\left(\alpha_+(0)\alpha_-^*(0) - \frac{\eta_-^*\alpha_+(0)}{\kappa-\imath\Delta_c} - \frac{\eta_+\alpha_-^*(0)}{\kappa+\imath\Delta_c} + \frac{\eta_+\eta_-^*}{\kappa^2+\Delta_c^2}\right) e^{-2\kappa t} + \frac{\eta_+\eta_-^*}{\kappa^2+\Delta_c^2} + \\ &+ \left(\alpha_+(0)\frac{\eta_-^*}{\kappa-\imath\Delta_c} - \frac{\eta_+\eta_-^*}{\kappa^2+\Delta_c^2}\right) e^{(-\kappa-\imath\Delta_c)t} + \left(\alpha_-^*(0)\frac{\eta_+}{\kappa+\imath\Delta_c} - \frac{\eta_+\eta_-^*}{\kappa^2+\Delta_c^2}\right) e^{(-\kappa+\imath\Delta_c)t} \ .\end{aligned} \tag{15.45}$$

To simplify this expression, we assume a symmetric pump, $\eta_\pm = \eta e^{\pm\imath\phi}$. We are interested in the reaction of the field's phase to a sudden change of ϕ. Now, we define the initial stationary conditions for $\phi = 0$ to be $\alpha_\pm(0) = \frac{\eta}{\kappa+\imath\Delta_c}$ and obtain,

$$\boxed{\alpha_+\alpha_-^* = \frac{\eta^2}{\kappa^2+\Delta_c^2}\left[(1-e^{\imath\phi})^2 e^{-2\kappa t} + e^{2\imath\phi} + 2e^{\imath\phi}(1-e^{\imath\phi})e^{-\kappa t}\cos\Delta_c t\right]} \ . \tag{15.46}$$

In resonance, $\Delta_c = 0$, the expression (15.46) simplifies to,

$$\alpha_+\alpha_-^* = \frac{\eta^2}{\kappa^2}\left[(1-e^{-\kappa t})e^{\imath\phi} + e^{-\kappa t}\right]^2 \ . \tag{15.47}$$

This results shows that the cavity phase adjusts itself to the pump field in exponential time κ^{-1}:

$$\tan\theta = \frac{\mathfrak{Im}\,\alpha_+\alpha_-^*}{\mathfrak{Re}\,\alpha_+\alpha_-^*} = \frac{(1-e^{-\kappa t})^2\sin 2\phi + 2(1-e^{-\kappa t})e^{-\kappa t}\sin\phi}{(1-e^{-\kappa t})^2\cos 2\phi + 2(1-e^{-\kappa t})e^{-\kappa t}\cos\phi + e^{-2\kappa t}} \ . \quad (15.48)$$

For small phase slips $\phi \ll \pi$, this reduces to,

$$\theta = 2\phi(1-e^{-\kappa t}) \quad , \quad \dot\theta \simeq \kappa(2\phi-\theta) \quad , \quad \ddot\theta \simeq -\kappa\dot\theta \ . \quad (15.49)$$

Hence, the pump represents a friction force for the phase.

Out of resonance but with negligible decay, $\kappa \simeq 0$, the expression (15.46) simplifies to,

$$\alpha_+\alpha_-^* = \frac{\eta^2}{\Delta_c^2}\left[1 + 2(e^{2\imath\phi} - e^{\imath\phi})(1-\cos\Delta_c t)\right] + \ , \quad (15.50)$$

such that,

$$\tan\theta = \frac{2(\sin 2\phi - \sin\phi)(1-\cos\Delta_c t)}{1 + 2(\cos 2\phi - \cos\phi)(1-\cos\Delta_c t)} \ , \quad (15.51)$$

which, for very small angles ϕ, reduces to,

$$\theta \simeq 4\phi\sin^2\frac{1}{2}\Delta_c t \ . \quad (15.52)$$

15.2.2.2 Transfer function of a ring cavity

Cavities have a finite response time to frequency or amplitude fluctuations of the pump light. To study this, we assume the light pumping a ring cavity to be subject to a phase modulation with frequency Ω and amplitude ϕ_0, that is, the quantum Langevin equation (15.37) is,

$$\boxed{(\partial_t + \kappa + \imath\Delta_c)\alpha_\pm = \eta e^{\pm\imath\phi_0\sin\Omega t}} \ , \quad (15.53)$$

and has the solution,

$$\alpha_\pm(t) = e^{(-\kappa-\imath\Delta_c)t}\left(\alpha_\pm(0) + \eta\int_0^T e^{(\kappa+\imath\Delta_c)\tau \pm \imath\phi_0\sin\Omega\tau}d\tau\right) \ . \quad (15.54)$$

For small amplitude oscillations, we can expand the pump term into a Fourier series of Bessel functions,

$$\begin{aligned}
\alpha_\pm(t) &= e^{(-\kappa-\imath\Delta_c)t}\left(\alpha_\pm(0) + \eta\int_0^T \left(e^{(\kappa+\imath\Delta_c)\tau} \pm \tfrac{\phi_0}{2}e^{(\kappa+\imath\Delta_c)\tau+\imath\Omega\tau} \mp \tfrac{\phi_0}{2}e^{(\kappa+\imath\Delta_c)\tau-\imath\Omega\tau}\right)d\tau\right) \\
&= e^{(-\kappa-\imath\Delta_c)t}\alpha_\pm(0) + \eta\frac{1-e^{(-\kappa-\imath\Delta_c)t}}{\kappa+\imath\Delta_c} \pm \tfrac{\phi_0}{2}\frac{e^{\imath\Omega t}-e^{(-\kappa-\imath\Delta_c)t}}{\kappa+\imath\Delta_c+\imath\Omega} \mp \tfrac{\phi_0}{2}\frac{e^{-\imath\Omega t}-e^{(-\kappa-\imath\Delta_c)t}}{\kappa+\imath\Delta_c-\imath\Omega} \\
&= \frac{\eta}{\kappa+\imath\Delta_c} \pm \tfrac{\phi_0\eta}{2}\frac{e^{\imath\Omega t}-e^{(-\kappa-\imath\Delta_c)t}}{\kappa+\imath\Delta_c+\imath\Omega} \mp \tfrac{\phi_0\eta}{2}\frac{e^{-\imath\Omega t}-e^{(-\kappa-\imath\Delta_c)t}}{\kappa+\imath\Delta_c-\imath\Omega} \\
&= \frac{\eta}{\kappa} \pm \imath\phi_0\eta\frac{\kappa\sin\Omega t - \Omega\cos\Omega t + \Omega e^{-\kappa t}}{\kappa^2+\Omega^2} \ .
\end{aligned} \quad (15.55)$$

In the last two steps, we defined for simplicity, $\alpha_\pm(0) = \frac{\eta}{\kappa + \imath\Delta_c}$ and set $\Delta_c = 0$. After some initial transients, when $t \gg \kappa^{-1}$, we can write,

$$\alpha_\pm \alpha_\pm^* = \frac{\eta^2}{\kappa^2} + \phi_0^2 \eta^2 \left(\frac{\kappa \sin \Omega t - \Omega \cos \Omega t}{\kappa^2 + \Omega^2} \right)^2 \tag{15.56}$$
$$\alpha_\pm \alpha_\mp^* = \left(\frac{\eta}{\kappa} \pm \imath \phi_0 \eta \frac{\kappa \sin \Omega t - \Omega \cos \Omega t}{\kappa^2 + \Omega^2} \right)^2 ,$$

giving in analogy to (15.48),

$$\theta = \arctan \frac{2\phi_0(\kappa^2 + \Omega^2)\left(\kappa^2 \sin \Omega t - \kappa\Omega \cos \Omega t\right)}{(\kappa^2 + \Omega^2)^2 - \phi_0^2 \left(\kappa^2 \sin \Omega t - \kappa\Omega \cos \Omega t\right)^2} \simeq 2\phi_0 \frac{\kappa^2 \sin \Omega t - \kappa\Omega \cos \Omega t}{\kappa^2 + \Omega^2} .$$

At low frequencies, $\Omega \ll \kappa$, the phase of the cavity field goes as, $\theta(\phi_0) \simeq 2\phi_0 \sin \Omega t$, and for high frequencies, $\Omega \gg \kappa$, as, $\theta(\phi_0) \simeq -2\phi_0 \frac{\kappa}{\Omega} \cos \Omega t$. Thus, we observe a low-pass behavior of the phase excursions of the cavity field with a cut-off frequency, κ^{-1}:

$$\boxed{\theta_m \simeq \frac{2\phi_0}{1 + \Omega/\kappa}} . \tag{15.57}$$

15.2.3 Beyond mean field dynamics via master equation

Up to this point we concentrated on the dynamics of expectation values of the field operators, which is obtained in the mean field approximation via the substitution $\hat{a} \to \langle \hat{a} \rangle$. This approximation disregards possible correlations, $\langle \hat{a}^\dagger \hat{a} \rangle \simeq \langle \hat{a}^\dagger \rangle \langle \hat{a} \rangle$ found in the Hamiltonian (15.28) and in the Lindbladian (15.31). As long as the light field can be assumed as classical, the mean field approximation is very good. However, when non-classical light fields (such as Fock states or squeezed states of light) are investigated, the approximation fails. In this section we will seek general solutions of the master equation for a bosonic channel.

15.2.3.1 Time dependent formal solution for decaying cavities

The master equation for a non-driven cavity (15.31),

$$\frac{d\hat{\rho}}{dt} = \mathfrak{L}_{\kappa,\hat{a}} \hat{\rho} = \kappa(2\hat{a}\hat{\rho}\hat{a}^\dagger - \hat{a}^\dagger \hat{a}\hat{\rho} - \hat{\rho}\hat{a}^\dagger \hat{a}) , \tag{15.58}$$

can be solved formally.

In order to derive the time-dependent solution, we apply the substitution $\tan^2 \phi = e^{\kappa t} - 1$, with $\phi \in [0, \frac{\pi}{2}]$. This transforms the master equation into,

$$\frac{d\hat{\rho}}{d\phi} = \frac{\tan \phi}{\kappa} \mathfrak{L}_{\kappa,\hat{a}} \hat{\rho} , \tag{15.59}$$

which is easy to check. The general solution of this equation [5],

$$\boxed{\hat{\rho}(\phi) = \sum_{n=0}^{\infty} \frac{\sin^{2n} \phi}{n!} \cos^{\hat{a}^\dagger \hat{a}} \phi \, \hat{a}^n \hat{\rho}_0 \hat{a}^{\dagger n} \cos^{\hat{a}^\dagger \hat{a}} \phi} , \tag{15.60}$$

as will be shown in Exc. 15.2.5.4.

The solution (15.60) permits to calculate time evolutions of classical or non-classical states of light. For example, we check in Exc. 15.2.5.4 that for Glauber states,

$$\mathrm{Tr}\,\hat{\rho}_{|\alpha\rangle}(t) = 1 = \mathrm{Tr}\,\hat{\rho}^2_{|\alpha\rangle}(t) \quad \text{and} \quad \langle\hat{n}(t)\rangle = \mathrm{Tr}\,\hat{n}\hat{\rho}_{|\alpha\rangle}(t) = |\alpha|^2 e^{-\kappa t} \ . \tag{15.61}$$

That is, Glauber states remain pure during cavity decay. In contrast, for Fock states,

$$\mathrm{Tr}\,\hat{\rho}_{|n_0\rangle}(t) = 1 > \mathrm{Tr}\,\hat{\rho}^2_{|n_0\rangle}(t) \quad \text{and} \quad \langle\hat{n}(t)\rangle = \mathrm{Tr}\,\hat{n}\hat{\rho}_{|n_0\rangle}(t) = n_0 e^{-\kappa t} \ . \tag{15.62}$$

That is, Fock states evolve into mixtures.

The solution (15.60) can easily be numerically simulated in the Fock basis using,

$$\hat{a} = \sum_{n=0}^{\infty} \sqrt{n} n|n\rangle\langle n+1| \ , \tag{15.63}$$

and

$$\cos^{\hat{a}^\dagger \hat{a}}\,\phi = e^{\hat{n}\ln\cos\phi} = \sum_{n=0}^{\infty} \cos^n\phi |n\rangle\langle n| \ . \tag{15.64}$$

Fig. 15.5(a) shows the density matrix after some evolution time. It is interesting to note, that *cavity decay does not transform an initial Fock state into a Glauber state* as, differently from Glauber states, the density matrix in the Fock basis only contains diagonal elements (similarly to thermal states, except for the fact that the population of thermal states follow a Boltzmann distribution). Rather, the *decay transforms an initial Fock state into an incoherent mixture of Fock states*. Panel (b) shows the time evolution of the normalization, the purity, and the photon number in the cavity. Similar results are obtained for squeezed states.

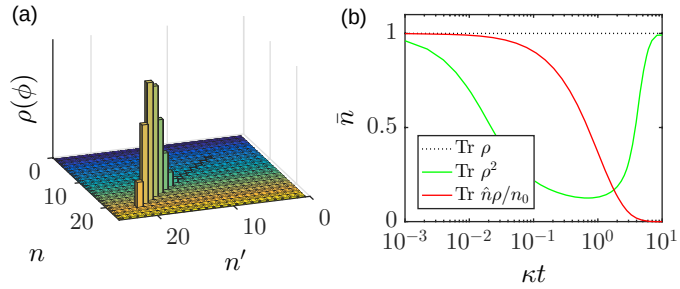

Figure 15.5: (code) (a) Density matrix of an evolved Fock state in a decaying cavity with no pumping. (b) Time evolution of the normalization, the purity, and the photon number in the cavity.

15.2.3.2 Steady state solution for resonantly driven cavities

The master equation can also be formally solved for the case that the cavity is resonantly driven, $\Delta_c = 0$. Describing the drive by the Hamiltonian,

$$\hat{H} = \eta(\hat{a} + \hat{a}^\dagger) \ , \tag{15.65}$$

the master equation can be transformed by the substitution,

$$\tilde{a} \equiv \hat{a} + \tfrac{\imath\eta}{\kappa}\mathbb{I} \quad \text{and} \quad \tilde{a}^\dagger \equiv \hat{a}^\dagger - \tfrac{\imath\eta}{\kappa}\mathbb{I}\,, \tag{15.66}$$

into,

$$\begin{aligned}\frac{d\hat{\rho}}{dt} &= \imath[\hat{\rho}, \hat{H}] + \mathfrak{L}_{\kappa,\hat{a}}\hat{\rho} \\ &= \imath\eta\left(\hat{\rho}\hat{a} + \hat{\rho}\hat{a}^\dagger - \hat{a}\hat{\rho} - \hat{a}^\dagger\hat{\rho}\right) + \kappa(2\hat{a}\hat{\rho}\hat{a}^\dagger - \hat{a}^\dagger\hat{a}\hat{\rho} - \hat{\rho}\hat{a}^\dagger\hat{a}) \\ &= \kappa\left(2\tilde{a}\hat{\rho}\tilde{a}^\dagger - \tilde{a}^\dagger\tilde{a}\hat{\rho} - \hat{\rho}\tilde{a}^\dagger\tilde{a}\right)\ .\end{aligned} \tag{15.67}$$

The steady state solution is,

$$\boxed{\hat{\rho}(\infty) = C^{-1}\tilde{a}^{-1}\tilde{a}^{\dagger-1} = C^{-1}(\hat{a} + \tfrac{\imath\eta}{\kappa}\mathbb{I})^{-1}(\hat{a}^\dagger - \tfrac{\imath\eta}{\kappa}\mathbb{I})^{-1}}\,, \tag{15.68}$$

where C is a normalization constant obtained from the condition $\mathrm{Tr}\,\rho(\infty) = 1$, (see Exc. 15.2.5.5).

Fig. 15.6(a) shows the steady state photon number calculated from,

$$\langle\hat{n}\rangle = \mathrm{Tr}\,\hat{n}\hat{\rho}(\infty) = C^{-1}\mathrm{Tr}\,\hat{n}\tilde{a}^{-1}\tilde{a}^{\dagger-1} = \frac{\mathrm{Tr}\,\hat{a}^\dagger\hat{a}\,\tilde{a}^{-1}\tilde{a}^{\dagger-1}}{\mathrm{Tr}\,\tilde{a}^{-1}\tilde{a}^{\dagger-1}}\ . \tag{15.69}$$

We see that, for large enough cut-off photon numbers used in the simulation, the intracavity photon number tends toward $\langle\hat{n}\rangle \to (\eta/\kappa)^2$, as expected. Fig. 15.6(b) shows the photon number uncertainty calculated from,

$$\langle\Delta\hat{n}^2\rangle = \mathrm{Tr}\,\hat{n}^2\hat{\rho}(\infty) - [\mathrm{Tr}\,\hat{n}\hat{\rho}(\infty)]^2\ . \tag{15.70}$$

We see that it tends toward $\langle\Delta\hat{n}^2\rangle \to \langle\hat{n}\rangle$, as expected for a Glauber state, but not for a Fock state, for which we know $\langle\Delta\hat{n}^2\rangle \to 0$ or for a squeezed state (see Exc. 14.4.4.5).

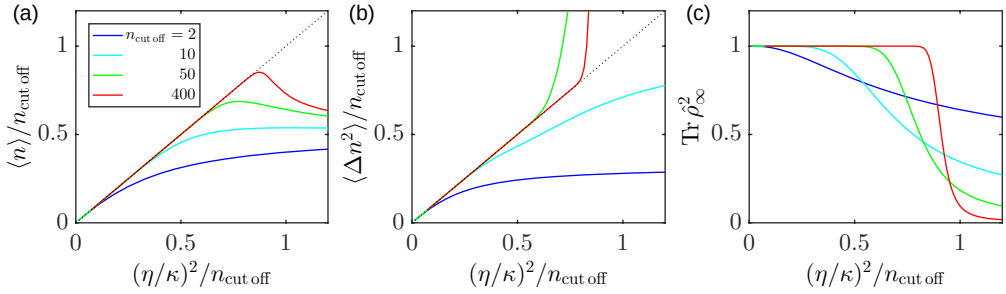

Figure 15.6: (code) Steady state photon number in a driven cavity for various cut-off photon numbers.

15.2.3.3 Time dependent solution for driven cavities

Since $[\tilde{a}, \tilde{a}^\dagger] = 1$ and $\tilde{a}^\dagger\tilde{a}$ is diagonal, the result (15.60) obtained for the purely dissipative cavity hold as well for the driven-dissipative cavity with the substitutions (15.66). That is, the time dependent solution is,

$$\hat{\rho}(\phi) = \sum_{n=0}^{\infty} \frac{\sin^{2n}\phi}{n!} \cos^{\tilde{a}^\dagger\tilde{a}}\phi \; \tilde{a}^n \hat{\rho}_0 \tilde{a}^{\dagger n} \cos^{\tilde{a}^\dagger\tilde{a}}\phi \; , \tag{15.71}$$

or with $\cos^{\hat{a}^\dagger\hat{a}}\phi = (e^{-\kappa t/2})^{\hat{a}^\dagger\hat{a}}$ and $\sin^2\phi = 1 - e^{-\kappa t}$,

$$\boxed{\hat{\rho}(t) = \sum_{n=0}^{\infty} \frac{(1-e^{-\kappa t})^n}{n!} e^{-\kappa t\tilde{a}^\dagger\tilde{a}/2} \; \tilde{a}^n \hat{\rho}_0 \tilde{a}^{\dagger n} e^{-\kappa t\tilde{a}^\dagger\tilde{a}/2}} \; . \tag{15.72}$$

The simulation shown in Fig. 15.7 reveals that the *driving transforms any initial state, be it a Glauber, Fock, or squeezed state, into a pure Glauber state* after some time. The mean photon number evolves toward $\tilde{\eta}^2$, where $\tilde{\eta} \equiv \eta/\kappa$. The photon number uncertainty evolves toward $\tilde{\eta}$.

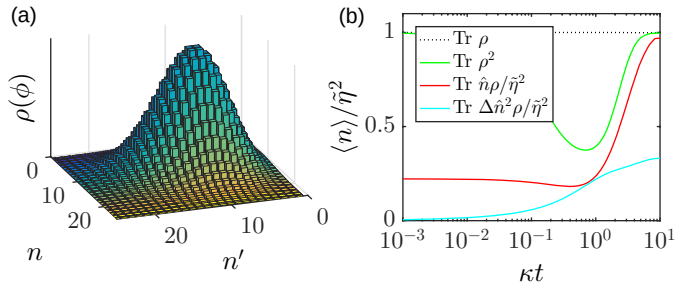

Figure 15.7: (code) (a) Density matrix calculated from Eq. (15.72) for an evolved Fock state in a driven cavity with $\eta^2/\kappa^2 = 3$. (b) Time evolution of the normalization, the purity, the photon number and its variance in the cavity starting from an initial photon number of $\langle\hat{n}_0\rangle = 2 \approx 0.22\tilde{\eta}^2$.

Note that the master equation can also be propagated numerically via,

$$\hat{\rho}(t+dt) = \hat{\rho}(t) + dt\,\imath[\hat{\rho}(t), \hat{H}] + dt\,\kappa\left[2\hat{a}^\dagger\hat{\rho}(t)\hat{a} - \hat{a}^\dagger\hat{a}\hat{\rho}(t) - \hat{\rho}(t)\hat{a}^\dagger\hat{a}\right] \; . \tag{15.73}$$

15.2.4 Beyond mean field dynamics via Heisenberg equation

Instead of the master equation (15.31), we solve the driven-dissipative cavity system by a set of Heisenberg equations of all degrees of freedom (here only the field operator $\hat{a}$). Then, with the Hamiltonian (15.65) and the Hermitian conjugate of the Lindbladian (15.58), we write,

$$\hat{H} = \eta(\hat{a} + \hat{a}^\dagger) \quad , \quad \mathfrak{L}^\dagger_{\kappa,\hat{a}}\hat{A} = \kappa\left(2\hat{a}^\dagger\hat{A}\hat{a} - \hat{a}^\dagger\hat{a}\hat{A} - \hat{A}\hat{a}^\dagger\hat{a}\right) \; . \tag{15.74}$$

Applying the same substitution (15.66) as for the master equation,

$$\begin{aligned}\frac{d\hat{A}}{dt} &= \imath[\hat{H},\hat{A}] + \mathfrak{L}^{\dagger}_{\kappa,\hat{a}}\hat{A} \\ &= \imath\eta(\hat{a}\hat{A} + \hat{a}^{\dagger}\hat{A} - \hat{A}\hat{a} - \hat{A}\hat{a}^{\dagger}) + \kappa(2\hat{a}^{\dagger}\hat{A}\hat{a} - \hat{a}^{\dagger}\hat{a}\hat{A} - \hat{A}\hat{a}^{\dagger}\hat{a}) \\ &= \kappa(2\tilde{a}^{\dagger}\hat{A}\tilde{a} - \tilde{a}^{\dagger}\tilde{a}\hat{A} - \hat{A}\tilde{a}^{\dagger}\tilde{a}) \ .\end{aligned} \tag{15.75}$$

In Exc. 15.2.5.6 we show that the operator

$$\hat{A}(\infty) = \hat{a}^{-1}\hat{a}^{\dagger -1} = \hat{\rho}(\infty) \tag{15.76}$$

is also the steady state solution of the Heisenberg equation.

Numerical comparison between expectation values obtained from the master and the Heisenberg equation yields,

$$\mathrm{Tr}\,\hat{A}(0)\hat{\rho}(t) = \langle\hat{A}(t)\rangle = \mathrm{Tr}\,\hat{A}(t)\hat{\rho}(0) \ . \tag{15.77}$$

This is shown for $\hat{A}(t) \equiv \hat{n}(t)$ in Fig. 15.8, which also shows the mean field solution (15.38). We notice that the master and the Heisenberg approach yield identical results. To calculate the photon number evolution in the mean field approximation, we plug the solution of the first equation (15.36),

$$\langle\hat{a}(t)\rangle = [\langle\hat{a}(0)\rangle + \tfrac{\imath\eta}{\kappa}]e^{-\kappa t} - \tfrac{\imath\eta}{\kappa} \tag{15.78}$$

into the second, yielding,

$$\langle\dot{n}(t)\rangle = \imath\eta[\langle\hat{a}(0)\rangle - \langle\hat{a}^{\dagger}(0)\rangle]e^{-\kappa t} + \tfrac{2\eta^2}{\kappa}(1 - e^{-\kappa t}) - 2\kappa\langle\hat{a}^{\dagger}\hat{a}\rangle \ , \tag{15.79}$$

which is then solved numerically. For comparison, Fig. 15.8 also shows the evolution $\langle\hat{a}^{\dagger}(t)\rangle\langle\hat{a}(t)\rangle$.

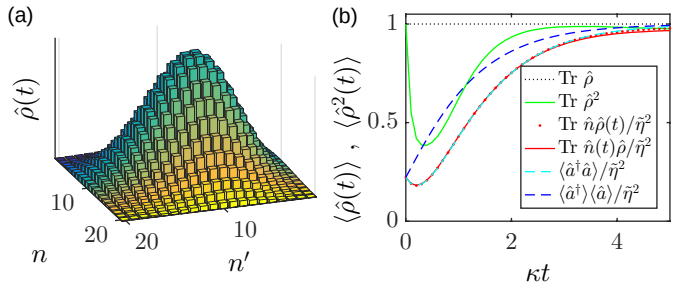

Figure 15.8: (code) (a) Density matrix simulated from Eq. (15.73) for an evolved Fock state in a driven cavity with $\eta^2/\kappa^2 = 3$. (b) Time evolution of the normalization, the purity, and the photon number in the cavity starting from an initial photon number of $\langle\hat{n}_0\rangle = 2 \approx 0.22\tilde{\eta}^2$. The dashed lines are analytical solutions according to Eqs. (15.78) and (15.79).

It is tempting to use commutation relations between the evolution operator $\hat{A}(t)$, which is time dependent in the Heisenberg picture, and the jump operator $\hat{a} = \hat{a}(0)$, which is stationary. However, even for the choice $\hat{A}(t) \equiv \hat{a}(t)$ we must accept, $[\hat{a}(0), \hat{a}^{\dagger}(t)] \neq 1$ and $[\hat{a}(0), \hat{a}(t)] \neq 0$. Otherwise, we draw false conclusions, as shown in Exc. 15.2.5.7.

15.2.5 Exercises

15.2.5.1 Ex: Ringing of an optical cavity

Consider a linear cavity with resonant frequency ω_c and the decay rate κ pumped by a laser beam whose frequency is swept linearly over a range $\omega \in [-10\kappa, 10\kappa]$. Prepare a numerical simulation varying the time Δt of the sweep.

15.2.5.2 Ex: Quick ullage of an optical cavity

Consider a linear cavity resonantly pumped by a laser beam until a stationary state is reached. Suddenly, the phase of the incident light is changed by 180°. Based on equation (15.38), analyze the evolution of the light field inside the cavity [703].

15.2.5.3 Ex: Photon number distribution in a driven cavity

In Exc. 16.4.4.15 we have seen that atoms can be deexcited faster than Γ using an adequate driving laser switch-off time and in Exc. 15.2.5.1 that optical cavities can be emptied faster than κ by injecting light having an inverted phase. Study and discuss the possibility of reducing the ullage rate by just adapting the driving laser switch-off time.

15.2.5.4 Ex: Formal solution of the master equation

a. Check that the expression (15.60) solved the master equation (15.59).
b. Evaluate the expression (15.60) for an initial Fock state, $\hat{\rho}_0 \equiv |n_0\rangle\langle n_0|$.
c. Evaluate the expression (15.60) for an initial Glauber state, $\hat{\rho} = |\alpha\rangle\langle\alpha|$. For (b) and (c) check normalization and purity during evolution.

15.2.5.5 Ex: Steady state photon number in a driven cavity

a. Expand the steady state solution (15.68) in power series of $\hat{a}$ respectively $\hat{a}^{\dagger -1}$, and determine the normalization constant when the Fock basis is truncated at a photon number of N.
b. Calculate the steady state photon number and its variance.

15.2.5.6 Ex: Steady state of the Heisenberg equation

Verify whether $\hat{A}(\infty) = \hat{a}^{-1}\hat{a}^{\dagger -1} = \hat{\rho}(\infty)$ is also the steady state solution of the Heisenberg equation for the dissipative cavity.

15.2.5.7 Ex: Wrong use of Heisenberg equations

Solve the Heisenberg equation for the photon annihilation operator $\hat{a}(t)$ in a driven-dissipative cavity under the (false) assumption that it satisfies with the jump operator $\hat{a}(0)$ the commutation rule $[\hat{a}(t), \hat{a}^{\dagger}(0)] = 1$. Show that the result cannot be correct.

15.2.5.8 Ex: Emission spectrum of a decaying cavity

Calculate the emission spectrum of a decaying cavity initially filled with a field $\hat{a}(0)$.

15.3 Mode structure and density-of-states of cavities

15.3.1 Characterization of the bare cavity

We first consider a linear cavity of length L pumped by a laser without any scatterer located inside the cavity. The cavity spectrum is an equidistant comb of eigenfrequencies separated by,

$$\delta_{\rm fsr} \equiv \tau_{\rm rt}^{-1} = \frac{c}{2L} \ . \tag{15.80}$$

The *free spectral range* $\delta_{\rm fsr}$ is given in units of a real frequency. $\tau_{\rm rt}^{-1}$ is the time for a photon to make a round trip in the cavity. The amplitude *decay rate of the cavity*,

$$\boxed{\kappa = \tau_\kappa^{-1} = \frac{\pi \delta_{\rm fsr}}{F}} \ . \tag{15.81}$$

The intensity decay rate of the cavity, measured by 'cavity ring-down' is $\kappa_{\rm int} = 2\kappa$. Note, that $\kappa_{\rm int}$ is also the FWHM width of the intensity transmission spectrum [2], such that the finesse

$$F = \frac{\delta_{\rm fsr}}{\kappa_{\rm int}/2\pi} \tag{15.82}$$

is simply the ratio between the free spectral range and the FWHM of the cavity intensity transmission curve, both measured in Hertz.

> **Example 86 (*Finesse of a cavity*):** For example, for a cavity of length $L = 10\,\text{cm}$ an intensity decay time of $\tau_{\rm int} = 20\,\mu\text{s}$ is measured, and we want to evaluate the finesse. We begin calculating the free spectral range $\delta_{\rm fsr} = c/2L \approx 1.5\,\text{GHz}$. Since the cavity field decays like $\mathcal{E}(t) = \mathcal{E}_0 e^{-\kappa t}$ and the intensity like $I(t) = \mathcal{E}_0^2 e^{-2\kappa t}$, we get $\kappa = 1/\tau_\kappa = 1/2\tau_{\rm int} \approx (2\pi)\ 4\,\text{kHz}$. Finally, the finesse is $F = \pi\delta_{\rm fsr}/\kappa \approx 189000$.

For a cavity with a given geometry filled with a Gaussian mode of light with power P, the intensity is determined by Gaussian optics (see) [3],

$$I(\mathbf{r}) = \frac{2P}{\pi w^2(z)} e^{-2\rho^2/w^2(z)} \qquad \text{and} \qquad w(z) = w_0\sqrt{1+\left(\frac{\lambda z}{\pi w_0^2}\right)^2} \ . \tag{15.83}$$

Defining the *mode volume* via $I(0)V_{\rm m} \equiv \int I(\mathbf{r})dV$ and evaluating the spatial integral over the Gaussian mode along the cavity, we obtain,

$$\boxed{V_{\rm m} = \frac{1}{I(0)}\int_0^L \int_0^\infty \int_0^{2\pi} \frac{2P}{\pi w^2(z)} e^{-2\rho^2/w^2(z)} d\phi\rho d\rho dz = \tfrac{\pi}{2} L w_0^2} \ . \tag{15.84}$$

[2] See script on *Electrodynamics: Electricity, Magnetism and Radiation* (2025), Sec. 7.3.5 and Exc. 7.3.6.17.

[3] See script on *Electrodynamics: Electricity, Magnetism and Radiation* (2025), Sec. 7.4.1 and Exc. 7.3.7.18.

Defining the amplitude of the electric field generated by a *single photon* via,

$$I(\mathbf{r}) = n\varepsilon_0 c\mathcal{E}_1^2(\mathbf{r}) \ , \tag{15.85}$$

where n is the number of photons in the cavity, we calculate for the energy stored in the cavity,

$$\frac{\hbar\omega}{2} = \int u_1(\mathbf{r})dV = \frac{1}{c}\int I_1(\mathbf{r})dV = \frac{1}{c}I_1(0)V_\mathrm{m} \ . \tag{15.86}$$

Hence,

$$\boxed{|\vec{\mathcal{E}}_1(0)| = \sqrt{\frac{I_1(0)}{\varepsilon_0 c}} = \sqrt{\frac{\hbar\omega}{2\varepsilon_0 V_\mathrm{m}}}} \ . \tag{15.87}$$

The light power in the linear cavity can now be expressed using its free spectral range (15.80),

$$P = \frac{\pi w_0^2}{2}I(0) = \frac{2V_\mathrm{m}}{L}n\varepsilon_0 c|\vec{\mathcal{E}}_1^2(0)| = 2V_\mathrm{m}\delta_\mathrm{fsr}n\varepsilon_0\frac{\hbar\omega}{2\varepsilon_0 V_\mathrm{m}} = \delta_\mathrm{fsr}n\hbar\omega \ . \tag{15.88}$$

We assume that the cavity is pumped by a laser beam. To estimate the pump rate, we assume that the power P_input be measured in transmission. The coefficient η for resonant pumping is related to the number n of photons inside the cavity,

$$n = |\alpha|^2 = \frac{\eta^2}{\kappa^2} \ . \tag{15.89}$$

The intracavity field is resonantly amplified by the finesse,

$$\boxed{\alpha = \sqrt{\frac{F}{\pi}}\alpha_\mathrm{input} = \sqrt{\frac{\delta_\mathrm{fsr}}{\kappa}}\alpha_\mathrm{input}} \ . \tag{15.90}$$

This gives,

$$\eta = \kappa\alpha = \kappa\sqrt{\frac{I}{c\hbar\omega}V_\mathrm{m}} = \sqrt{\kappa\delta_\mathrm{fsr}}\alpha_\mathrm{input} = \sqrt{\kappa\delta_\mathrm{fsr}}\sqrt{\frac{I_\mathrm{input}}{c\hbar\omega}V_\mathrm{m}} \ . \tag{15.91}$$

In practice, the pump rate will depend on the quality of the phase matching of the Gaussian beams and the impedance matching (in case of partially absorbing mirrors).

We will pursue the characterization of ring cavities including their interaction with scattering atoms in Sec. 22.1.2.

15.3.1.1 The Schawlow-Townes limit

The *Schawlow-Townes limit* results from phase fluctuation of the standing light wave in the cavity demand $\Delta\phi = \frac{1}{n}$. Using the relationships (15.88) and (15.90), we find [873],

$$\Delta\omega_\mathrm{laser} = \frac{\kappa}{|\alpha|^2} = \kappa\frac{\delta_\mathrm{fsr}\hbar\omega_\mathrm{laser}}{P_\mathrm{cav}} = \kappa\frac{\delta_\mathrm{fsr}\hbar\omega_\mathrm{laser}}{\frac{\delta_\mathrm{fsr}}{\kappa}P_\mathrm{out}} = \kappa^2\frac{\hbar\omega_\mathrm{laser}}{P_\mathrm{out}} \ . \tag{15.92}$$

Example 87 (*Schawlow-Townes limit of a HeNe laser*): For a typical HeNe laser, $F = 100$, $P_\mathrm{out} = 1\,\mathrm{mW}$, $L = 20\,\mathrm{cm}$, we estimate,

$$\Delta\omega_\mathrm{laser} = \left(\frac{\pi\delta_\mathrm{fsr}}{F}\right)^2\frac{h\nu_\mathrm{laser}}{P_\mathrm{out}} = \left(\frac{\pi c}{2LF}\right)^2\frac{h\nu_\mathrm{laser}}{P_\mathrm{out}} \approx (2\pi)30\,\mathrm{mHz} \ .$$

15.3.2 Calculation of the density of states

The density of states $\rho(\omega, \mathbf{k})$ of an optical cavity is defined by,

$$\int_{\mathcal{R}} \rho(\omega, \mathbf{k}) d\omega d\Omega = \frac{1}{(2\pi)^3} \int d^3x d^3k \ , \tag{15.93}$$

where $\mathcal{R}$ denotes the boundary imposed by the cavity. For free space photons we calculate (see Eq. (16.22)),

$$4\pi \int \rho_{\text{free}}(\omega, \mathbf{k}) d\omega = \frac{V}{(2\pi)^3} \int k^2 \sin\theta d\theta d\phi dk = \frac{Vk^3}{6\pi^2} = \frac{V\omega^3}{6\pi^2 c^3} \ , \tag{15.94}$$

such that,

$$\rho_{\text{free}}(\omega, \mathbf{k}) = \rho_{\text{free}}(\omega) = \frac{V\omega^2}{(2\pi c)^3} \ , \tag{15.95}$$

is isotropic.

For light in a cavity, the density of states is modified with respect to free space, because it becomes frequency-dependent and anisotropic. The frequency dependence is expressed by the Airy formula,

$$\mathfrak{L}(\omega) \equiv \frac{I_{\text{cav}}}{I_{\text{in}}} = \frac{\sqrt{1 + (2F/\pi)^2}}{1 + (2F/\pi)^2 \sin^2 kL} \ , \tag{15.96}$$

which will be derived in Excs. 15.3.4.1, 15.3.4.2, and 15.3.4.3, and the anisotropy by,

$$\mathcal{R}(\hat{\mathbf{e}}_k) = 1 \qquad \forall \qquad \hat{\mathbf{e}}_k \in \Omega_{\text{cav}} \ , \tag{15.97}$$

where Ω_{cav} is the solid angle covered by the cavity mode. The formula,

$$\boxed{\rho_{\text{cav}}(\omega, \mathbf{k}) = \rho_{\text{free}}(\omega)[1 - \mathcal{R}(\hat{\mathbf{e}}_k)] + \rho_{\text{free}}(\omega)\mathfrak{L}(\omega)\mathcal{R}(\hat{\mathbf{e}}_k)} \tag{15.98}$$

expresses that the density of states is nothing more than the *structure factor* of the cavity.

15.3.2.1 Confocal cavities

For a confocal cavity the solid angle is easy to calculate [376, 377]. Denoting by b is the clear aperture of the cavity mirrors, we get,

$$\Omega_{\text{cav,con}} = 2 \int_0^{2\pi} \int_0^{\arcsin(2b/L)} \sin\theta d\theta d\phi = 4\pi \left(1 - \sqrt{1 - 4\frac{b^2}{L^2}} \right) \ . \tag{15.99}$$

Expanding the root for small $b \ll L$, we get,

$$\boxed{\Omega_{\text{cav,con}} \simeq \frac{8\pi b^2}{L^2}} \ . \tag{15.100}$$

For non-degenerate geometries the functions $\mathfrak{L}$ and $\mathcal{R}$ depend on the order mn of the transverse Gaussian modes:

$$\mathfrak{L}_{mn}(\omega) = \frac{\sqrt{1 + (2F/\pi)^2}}{1 + (2F/\pi)^2 \sin^2(kL + \varphi_{mn})} \qquad \text{and} \qquad \mathcal{R}_{mn}(\hat{\mathbf{e}}_k) = 1 \quad \forall \quad \hat{\mathbf{e}}_k \in \Omega_{mn} \ ,$$

where φ_{mn} is the frequency shift of the transverse modes.

15.3.2.2 Expansion into Hermite-Gaussian modes

More correctly, $\hat{\mathbf{e}}_k \in \Omega_{mn}$ means that we must weigh the density of states by the structure factor of the mode volume, which is nothing more than the Fourier transform of the cavity mode function,

$$\boxed{\mathcal{R}_{mn}(\hat{\mathbf{e}}_k) = \int_{\hat{\mathbf{e}}_k \in \Omega_{mn}} d^2k = \int_{\mathbb{R}^2} \mathcal{F}\left[\frac{u_{mn}(\mathbf{r})}{\hbar\omega}\right] d^2k} \,. \tag{15.101}$$

For a Hermite-Gaussian mode with waist $w(z)$,

$$u_{mn}(\mathbf{r}) = \hbar\omega \frac{w_0}{w} e^{-2(x^2+y^2)/w^2} H_m(\sqrt{2}x/w)^2 H_n(\sqrt{2}y/w)^2 \,. \tag{15.102}$$

The Hermite polynomials are the eigenfunctions of the Fourier transform,

$$\mathcal{F}[e^{-x^2/2} H_n(x)] = (-\imath)^n e^{-k^2/2} H_n(k) \,. \tag{15.103}$$

Hence,

$$\begin{aligned}
\mathcal{F}\left[\tfrac{1}{\hbar\omega} u_{mn}(\mathbf{r})\right] &= \frac{1}{\hbar\omega}\frac{w_0}{w} \mathcal{F}\left[e^{-2(x^2+y^2)/w^2} H_m(\sqrt{2}x/w)^2 H_n(\sqrt{2}y/w)^2\right] \qquad (15.104)\\
&= \frac{1}{\hbar\omega}\frac{w_0}{w} \mathcal{F}\left[e^{-2x^2/w^2} H_m(\sqrt{2}x/w)^2\right] \mathcal{F}\left[e^{-2y^2/w^2} H_n(\sqrt{2}y/w)^2\right] \\
&= \frac{1}{\hbar\omega}\frac{w_0}{w} e^{-2k_x^2 w^2} H_m(\sqrt{2}k_x w)^2 e^{-2k_y^2 w^2} H_n(\sqrt{2}k_y w)^2 \overset{m,n=0}{\longrightarrow} \frac{1}{\hbar\omega}\frac{w_0}{w} e^{-2\left(k_x^2+k_y^2\right)w^2} \,.
\end{aligned}$$

Finally,

$$\begin{aligned}
\mathcal{R}_{mn}(\hat{\mathbf{e}}_k) &= \int \mathcal{F}\left[\frac{u_{mn}(\mathbf{r})}{\hbar\omega}\right] d\left(\tfrac{k_x}{k}\right) d\left(\tfrac{k_y}{k}\right) \qquad (15.105)\\
&= \frac{1}{\hbar\omega}\frac{w_0}{w} \int e^{-2k_x^2 w^2} H_m(\sqrt{2}k_x w)^2 d\left(\tfrac{k_x}{k}\right) \int e^{-2k_y^2 w^2} H_n(\sqrt{2}k_y w)^2 d\left(\tfrac{k_y}{k}\right) \,.
\end{aligned}$$

For the TEM_{00} mode, we get,

$$\mathcal{R}_{00}(\hat{\mathbf{e}}_k) = \frac{\pi}{2k^2 w^2} \,, \tag{15.106}$$

using $P = \int I_{mn}(\mathbf{r}) dxdy = \frac{1}{2}\pi w^2 I_0$. This coincides with the intuition, that for the TEM_{00}, the aperture is simply the divergence angle of the Gaussian mode.

The solid angle of a Gaussian mode in a non-degenerate cavity is calculated via,

$$\Omega_{\mathrm{cav}} = 2 \cdot \frac{\pi w(z)^2}{z^2} = 2 \cdot \frac{\pi w_0^2}{z^2}\left(1 + \left(\frac{\lambda z}{\pi w_0^2}\right)^2\right) \,. \tag{15.107}$$

In the far field, we get,

$$\boxed{\Omega_{\mathrm{cav}} \overset{z\to\infty}{\longrightarrow} \frac{8\pi}{k^2 w_0^2}} \,. \tag{15.108}$$

Example 88 (*Solid angle for Hermite-Gaussian modes in a confocal cavity*): For confocal cavities, we must add $\sum_{mn} \mathcal{F}\left[\frac{1}{\hbar\omega} u_{mn}(\mathbf{r})\right]$ up to a limit, where the maximum $H_m(\sqrt{2}kw)$ is cut by the finite aperture of the mirrors of the cavity. Empirically, we find that $H_n(\xi)^2 e^{-\xi^2}$ has its maximum at $\xi_{\max} = 13.7 \cdot n^{1/2}$. From the condition $u_{mn}(x, y, L) = 0$ for $xy > a^2$, we obtain,

$$x_{\max} y_{\max} < a^2$$
$$\left(13.7 \cdot n^{1/2}\right)^2 = \frac{\sqrt{2}x_{\max}}{w(L)} \frac{\sqrt{2}y_{\max}}{w(L)} < \frac{2a^2}{w(L)^2} \to \frac{a^2 k^2 w_0^2}{2L^2} ,$$

using $w(L) = w_0\sqrt{1 + \left(\frac{\lambda L}{\pi w_0^2}\right)^2} \to \frac{\lambda L}{\pi w_0}$. Finally,

$$\sum_{mn} \mathcal{F}\left[\frac{1}{\hbar\omega} u_{mn}(\mathbf{r})\right] = \frac{\pi}{2k^2w^2} \sum_{13.7^2 m,n < a^2k^2w_0^2/2L^2} = \frac{\pi}{2k^2w^2} \frac{1}{13.7^2} \frac{a^2k^2w_0^2}{2L^2} = \frac{1}{13.7^2} \frac{\pi a^2}{4L^2} .$$

15.3.3 Cumulant expansion of correlation functions and power spectra

15.3.3.1 Correlation functions

The evolution of the two-time correlation function of two operators $\hat{A}$ and $\hat{B}$ given by,

$$R(t, \tau) \equiv \langle \hat{A}(t + \tau)\hat{B}(t)\rangle \quad , \quad R(\tau) = \lim_{t\to\infty} \langle \hat{A}(t + \tau)\hat{B}(t)\rangle , \tag{15.109}$$

with respect to the time delay τ is determined by,

$$\frac{d}{d\tau} R(t, \tau) = \langle [\partial_\tau \hat{A}(t + \tau)]\hat{B}(t)\rangle . \tag{15.110}$$

Hence, the set of equations required to compute the correlation function can be derived from the equation of motion for the operator $\hat{A}$. The cumulant expansion of the correlation function then follows the same procedure as for a standard time evolution: the set of equations is expanded to a certain order and completed. Solve Exc. 15.3.4.4.

15.3.3.2 Steady state

If the original system is evolved up to a time t such that it is in steady state, i.e. expectation values no longer change after that time, the set of equations determining the correlation function has a special property. specifically, after the cumulant expansion has been performed, there can only be a single term in each product on the right-hand-side of the set of equations that depends on τ. All other terms depend on t alone, meaning that they are constant since they no longer change after the time t. Therefore, the system of equations from which the correlation function is computed is linear, in the sense that it can be written as,

$$\frac{d}{d\tau} \mathbf{y}(\tau) = \mathbf{M}\mathbf{y}(\tau) + \mathbf{d} , \tag{15.111}$$

where $\mathbf{y}(\tau)$ is the vector of τ-dependent variables. The elements of the matrix $\mathbf{M}$ as well as the vector $\mathbf{d}$ are given by steady-state expectation values and parameters, i.e. they are independent of τ.

15.3.3.3 Power spectra

According to the Wiener-Khinchin theorem. the spectral density associated with a correlation function is given by its Fourier transform,

$$S(t,\omega) = 2\mathfrak{Re} \int e^{-\imath\omega\tau} R(t,\tau) d\tau \ . \tag{15.112}$$

In order to compute this, we can solve the system of equations determining $R(t,\tau)$, subsequently taking the Fourier transform. However, if we are not interested in the temporal behavior of the correlation function, and if the system of which we want to compute the spectrum is in steady state, we can directly compute the spectrum from Eq. (15.111). To this end, we define

$$\mathbf{x}(s) = \mathfrak{L}[y(\tau)] \ , \tag{15.113}$$

where $\mathfrak{L}$ denotes the Laplace transform with respect to τ. Taking the Laplace transform of Eq. (15.111), we have,

$$(s\mathbb{I} - \mathbf{M})\mathbf{x}(s) = \mathbf{y}(0) + \frac{\mathbf{d}}{s} \ . \tag{15.114}$$

Note that the Laplace transform is equivalent to the Fourier transform at the point where $s = \imath\omega$, i.e. $S(\omega) = 2\mathfrak{Re}\,\mathbf{x}_1(\imath\omega)\}$. Hence, instead of computing the time evolution of the correlation function we can directly compute the spectrum by solving the linear equation,

$$\mathbf{x} = (\imath\omega\mathbb{I} - \mathbf{M})^{-1}[\mathbf{y}(0) + \tfrac{1}{\imath\omega}\mathbf{d}] \ . \tag{15.115}$$

For larger systems, the method using a Laplace transform is usually faster than integrating a system of equations of the same size. Additionally, it avoids numerical errors of the integration and the subsequent discrete Fourier transform.

15.3.4 Exercises

15.3.4.1 Ex: Derivation of the Airy formula

Derive the Airy formula (15.96).

15.3.4.2 Ex: Airy formula for ring cavities

Derive the Airy formulas for a ring cavity laser-pumped through an incoupling mirror with reflectivity $r_{\rm ic}$ and comprising two more high-reflecting mirrors with reflectivity $r_{\rm hr}$. Calculate (a) the intracavity intensity, (b) the intensity of the light reflected from the incoupler, and (c) the intensity of the light transmitted through the first encountered high reflector. For each for intensity study the cases that (i) the ring cavity is resonant and (ii) off-resonance. Also study the limit $r_{\rm hr} \to 1$. Disregard absorption losses.

15.3.4.3 Ex: Filling rate for long cavities

Using the solution (15.38) try to calculate the transmission of a 15 km long cavity of finesse $F = 1000$ as a function of time, when it is pumped by a suddenly switched on laser. Analyze the results in the light of local causality.

15.3.4.4 Ex: Fluorescence spectrum of an empty cavity

a. Calculate the fluorescence spectrum of an empty cavity pumped at a rate η classically via the autocorrelation function $\langle \alpha^*(t+\tau)\alpha(t)\rangle$.
b. Calculate the time evolution of the cumulants $\langle \hat{a}\rangle$, $\langle \hat{a}^\dagger \hat{a}\rangle$, $\langle \hat{a}^\dagger \hat{a}^\dagger \hat{a}\rangle$, $\langle \hat{a}\hat{a}^\dagger \hat{a}\rangle$, and $\langle \hat{a}^\dagger \hat{a}\hat{a}^\dagger \hat{a}\rangle$ expanding up to forth order.
c. Based on the results obtained in (b) and applying the quantum regression theorem derive a set of linear differential equations for the autocorrelation functions $\langle \hat{a}(\tau)\rangle$, $\langle \hat{a}^\dagger(t+\tau)\hat{a}(t)\rangle$, $\langle \hat{a}^\dagger(t+\tau)\hat{a}^\dagger(t)\hat{a}(t)\rangle$, $\langle \hat{a}(t+\tau)\hat{a}^\dagger(t)\hat{a}(t)\rangle$, and $\langle \hat{a}^\dagger(t+\tau)\hat{a}(t+\tau)\hat{a}^\dagger(t)\hat{a}(t)\rangle$. Express them in matrix notation.
d. Calculate $g^{(1)}(\tau)$, the fluorescence spectrum, and $g^{(2)}(\tau)$ for the case $\eta = 0$.
e. Repeat the calculations in (c) to the case $\eta \neq 0$.

15.4 Further reading

A.N. Poddubny et al., *Microscopic model of Purcell enhancement in hyperbolic metamaterials* [DOI]

Wenlong Gao et al., *Topological Photonic Phase in Chiral Hyperbolic Metamaterials* [DOI]

Haibin Wu et al., *Observation of Intracavity Electromagnetically InducedTransparency and Polariton Resonances in a Doppler-Broadened Medium* [DOI]

Xiaodong Zeng et al., *Spontaneous emission interference enhancement with a μ-negative metamaterial slab* [DOI]

Xiaodong Zeng et al., *Enhancement of the vacuum Rabi oscillation via surface plasma modes in single-negative metamaterials* [DOI]

F. Dubin et al., *Photon Correlation versus Interference of Single-Atom Fluorescence in a Half-Cavity* [DOI]

U. Dorner et al., *Laser-driven atoms in half-cavities* [DOI]

P. Lambropoulos et al., *Fundamental quantum optics in structured reservoirs* [DOI]

15.4.1 on cavities

B. Yurke et al., *Quantum network theory* [DOI]

C.W. Gardiner et al., *A multimode quantum theory of a degenerate parametric amplifier in a cavity* [DOI]

D.J. Heinzen et al., *Enhanced and Inhibited Visible Spontaneous Emission by Atoms in a Confocal Resonator* [DOI]

D.J. Heinzen et al., *Vacuum Radiative Level Shift and Spontaneous-Emission Linewidth of an Atom in an Optical Resonator* [DOI]

Part V

Light-Matter Interaction

Preface to the part *Light-Matter Interaction*

We have seen in previous lectures, how to describe light in quantum mechanics and how to unravel the atomic structure. The topic of this part of the lecture is the description of how both interact with special emphasis on non-classical features.

Chapter 16

Semiclassical theory of light-atom interaction

In Part III of this script we solved the problem of a *stationary* atom using the formalism of quantum mechanics developed in Part I. We now come back to Bohr's original idea that *transitions* between atomic states be induced by absorption and emission of electromagnetic radiation and develop a semi-classical theory of light-atom interaction. That is, the atom will be treated as a quantum object, while the radiation is assumed to obey the rules of classical electrodynamics. The main objective of this chapter will be to derive an equation describing the temporal evolution of atoms interacting with a radiation field.

We begin with a perturbative approach to the excitation of atomic transitions in Sec. 16.1. In quantum mechanics we learned (see in Sec. 5.4) how time-dependent perturbations, such as suddenly applied force fields or periodic oscillations, can induce transitions between eigenstates. We will not repeat the concepts here. Rather we will focus on the calculation of transitions rates employing Fermi's Golden rule derived in Eq. (5.111). In Secs. 1.2 we introduced the Einstein coefficients A and B, which we associated with Planck's spectral distribution of black-body radiation. This procedure allowed us to connect the coefficients for spontaneous and stimulated transitions, but did not provide any method to calculate them from the intrinsic properties of the atoms. The purpose of Sec. 16.2 is to find expressions for the matrix elements coupling different atomic states using quantum mechanics and relate them to the Einstein coefficients in order to calculate the rates of absorption and emission of atomic radiation. In particular, we will dedicate some space to the dipolar approximation and to the derivation of selection rules allowing to quantify transition probabilities as a function of the quantum numbers characterizing the atomic states coupled by radiation.

Perturbation theory can describe the light-atom dynamics only at interaction times short enough, that the initially occupied atomic states is not noticeably depleted. An exception is the two-level atom, for which perturbation theory reproduces the exact results obtained by solving the time-dependent Schrödinger equation. This, however, only holds as long as spontaneous processes can be neglected. To portray systems that contain excitation and relaxation processes occurring simultaneously, a theory based on Schrödinger's equation is no longer sufficient, because it is only capable of explaining stimulated processes, such as the absorption of a monochromatic wave. Dissipative processes, such as spontaneous emission, require a more general approach to describe the evolution of a system. A single wavefunction is, in general, not enough

to represent such a system nor to quantify the probabilities associated with each of its states, but we rather need an ensemble of wavefunctions, which requires the description of the atom in terms of a density operator. This has been done in Sec. 14.2.

The equations of motion ruling the time evolution of the density operator are the so-called Bloch equations. They will be derived and studied in Sec. 16.3, and in Sec. 16.4 we will phenomenologically include spontaneous emission. In Sec. 16.5 we will discuss line broadening mechanisms and in Sec. 16.6 generalize the Bloch equation formalism to multilevel systems.

16.1 Perturbative approach to atomic excitation

In a model of an isolated atom, the atomic energy levels are eigenstates of the Hamiltonian and describe the system completely, i.e. they do not undergo any evolution. Transitions between atomic energy levels may, however, be induced by oscillatory perturbations, such as electromagnetic radiation accelerating bound electrons.

16.1.1 Time-dependent perturbation by a plane wave

Looking at the Hamiltonian (10.11) describing the interaction of a charged particle with an electromagnetic field, we find that the term $\mathbf{A}\cdot\nabla \propto e^{\imath\omega t}$ oscillates with frequency ω, while the term $\mathbf{A}^2 \propto e^{2\imath\omega t}$ oscillates with twice that frequency. We will only consider the interaction term (10.12), which is linear in $\mathbf{A}$, and we will treat this term as first-order perturbation by *time-dependent perturbation theory* (TPDT).

With this scope we separate the Hamiltonian in a stationary part and a time-dependent part [1],

$$\hat{H}(t) = \hat{H}^{(0)} + \hat{H}_{\text{int}}(t) \qquad \text{with} \qquad \hat{H}_{\text{int}} = \tfrac{e}{m}\mathbf{A}(\mathbf{r},t)\cdot\hat{\mathbf{p}}\ , \tag{16.1}$$

where $\hat{H}^{(0)}$ contains the kinetic energy and the Colombian potential of Eq. (10.11). In Sec. 5.4.4, inserting the expansion,

$$|\psi\rangle = \sum_k a_k(t)|k\rangle e^{-\imath E_k t/\hbar}\ , \tag{16.2}$$

along with the Hamiltonian (16.1) in the Schrödinger equation, we obtained the first order perturbative approximation (5.72). Setting the initial condition to $c_k(t\le 0) = \delta_{ki}$ and supposing that the probability of finding the atom initially in the ground state $|i\rangle$ for short times is 1, we got,

$$\boxed{a_f^{(1)}(t) \simeq \frac{1}{\imath\hbar}\int_0^t \langle f|\hat{H}_{\text{int}}|i\rangle e^{\imath\omega_{fi}t'}\,dt'}\ . \tag{16.3}$$

We now consider a perturbation by an electromagnetic plane wave within the Coulomb gauge,

$$\Phi = 0 \qquad \text{and} \qquad \nabla\cdot\mathbf{A} = 0\ . \tag{16.4}$$

[1] The energy of the light field is not considered in the Hamiltonian, because it is treated as classical, that is, its energy commutes with the other observables of the system.

The solution of the wave equation can be written,

$$\mathbf{A}(\mathbf{r},t) = \mathbf{A}_0^*(\mathbf{r})e^{\imath\omega t} + \mathbf{A}_0(\mathbf{r})e^{-\imath\omega t} \ . \tag{16.5}$$

For plane waves,

$$\mathbf{A}_0(\mathbf{r}) = \mathbf{A}_0 e^{\imath\mathbf{k}\cdot\mathbf{r}} \tag{16.6}$$

and $k = \omega/c$ and $\mathbf{k}\cdot\mathbf{A}_0 = 0$. With this, it is possible to show (see Exc. 16.1.4.1), that the energy density is,

$$u(\omega) = \tfrac{\varepsilon_0}{2}\vec{\mathcal{E}}^2 + \tfrac{1}{2\mu_0}\vec{\mathcal{B}}^2 = 2\varepsilon_0\omega^2 A_0^2 \ . \tag{16.7}$$

On the other hand, the energy density is proportional to the number of photons $N(\omega)$ inside the volume V,

$$u(\omega) = \frac{N(\omega)\hbar\omega}{V} \ . \tag{16.8}$$

The intensity corresponds to a flow of energy,

$$I(\omega) = u(\omega)c \ . \tag{16.9}$$

Separating the polarization $\hat{\epsilon}$ from the amplitude A_0,

$$\mathbf{A} = \hat{\epsilon}A_0 e^{\imath\mathbf{k}\cdot\mathbf{r}}e^{-\imath\omega t} + c.c. \ , \tag{16.10}$$

and inserting the perturbation (16.1) into the approximation (16.3),

$$\begin{aligned} a_f^{(1)}(t) &= -\tfrac{e}{m}\int_0^t dt'\langle f|\mathbf{A}\cdot\nabla|i\rangle e^{\imath\omega_{fi}t'}dt' \qquad (16.11)\\ &= -\tfrac{eA_0}{m}\langle f|e^{\imath\mathbf{k}\cdot\mathbf{r}}\hat{\epsilon}\cdot\nabla|i\rangle\int_0^t dt' e^{\imath(\omega_{fi}-\omega)t'}dt' - \tfrac{eA_0}{m}\langle f|e^{-\imath\mathbf{k}\cdot\mathbf{r}}\hat{\epsilon}\cdot\nabla|i\rangle\int_0^t dt' e^{\imath(\omega_{fi}+\omega)t'}dt' \ . \end{aligned}$$

Which one of the two processes described by Eq. (16.11) takes place, depends on the initial and final energies. For $E_f = E_i + \hbar\omega$ the first term describing the process of *absorption* will dominate, for $E_f = E_i - \hbar\omega$ the second term describing *emission* prevails.

16.1.2 Absorption and stimulated emission

16.1.2.1 Absorption

We define the *matrix element*,

$$M_{fi} \equiv \langle f|e^{\imath\mathbf{k}\cdot\mathbf{r}}\hat{\epsilon}\cdot\nabla|i\rangle \ , \tag{16.12}$$

and concentrate on the absorption process. Defining the detuning by $\Delta \equiv \omega - \omega_{fi}$ and evaluating the integral,

$$\left|\int_0^t e^{-\imath\Delta t'}dt'\right|^2 = \left|\frac{e^{-\imath\Delta t}-1}{-\imath\Delta}\right|^2 = 4\frac{\sin^2\frac{\Delta t}{2}}{\Delta^2} \simeq 2\pi t\delta(\Delta) \ , \tag{16.13}$$

at short times (see the formula (5.76)), the absorption probability becomes,

$$|a_f^{(1)}(t)|^2 = \frac{e^2}{m^2} A_0(\omega)^2 |M_{fi}|^2 \left| \int_0^t dt' e^{\imath(\omega_{fi}-\omega)t'} dt' \right|^2 = \frac{e^2}{m^2} A_0(\omega)^2 |M_{fi}|^2 2\pi t \delta(\Delta) \ . \tag{16.14}$$

The $\delta(\Delta = 0)$ function simply represents conservation of energy. Of course this is only an approximation not taking into account the finite width of the transition line.

Expressing the field by the intensity (16.10), we obtain the transition rate for absorption,

$$\boxed{W_{fi}^{(\mathrm{ab})} = \frac{d}{dt}|a_f^{(1)}(t)|^2 = 2\pi \left(\frac{eA_0}{m}\right)^2 |M_{fi}|^2 \delta(\omega - \omega_{fi}) = \frac{\pi e^2}{\varepsilon_0 m^2 c} \frac{I(\omega)}{\omega^2} |M_{fi}|^2 \delta(\omega - \omega_{fi})} \ . \tag{16.15}$$

We note that the absorption rate is proportional to the intensity of the radiation, which characterizes a typically linear effect.

If we want to express the rate of absorption by atoms in terms of energy, we simply multiply W_{fi} by $\hbar\omega$ and, hence, we can define the cross section for the absorption of radiative energy as,

$$\sigma_{i\to f} \equiv \frac{\text{absorption rate}}{\text{incident intensity}} = \frac{\hbar\omega W_{fi}}{I(\omega)} = \frac{\pi e^2}{\varepsilon_0 m^2 c} \frac{\hbar}{\omega} |M_{fi}(\omega_{fi})|^2 \delta(\omega - \omega_{fi}) \ . \tag{16.16}$$

16.1.2.2 Stimulated emission

For $E_f = E_i - \hbar\omega$ the equation describes the process of *stimulated emission*. Analogously to the calculation of the absorption, we obtain,

$$\boxed{W_{if}^{(\mathrm{st})} = \frac{\pi e^2}{\varepsilon_0 m^2 c} \frac{I(\omega)}{\omega^2} |M_{if}^*|^2 \delta(\omega + \omega_{fi})} \ , \tag{16.17}$$

with $M_{fi}^* = \langle f | e^{-\imath \mathbf{k}\cdot\mathbf{r}} \hat{\epsilon} \cdot \nabla | i \rangle$. Of course,

$$W_{if}^{(\mathrm{st})} = W_{fi}^{(\mathrm{ab})} \ . \tag{16.18}$$

The fact that, in a coupled atom-radiation system in equilibrium, the radiation field excites the same number of transitions in absorption $i \to f$ as in stimulated emission $f \to i$ is called the principle of *detailed balance*.

Obviously, the situation is different, if instead of two states we have several states that can be excited by radiation or decay.

16.1.3 Spontaneous emission

Absorption and stimulated emission are due to the interaction of an atom with a radiation field. However, even in the absence of radiation the atom couples to the field of the electromagnetic vacuum, and an accurate description of the atom must account for this fact. The total system has different eigenstates and their projection on the unperturbed eigenstates changes over time, as any excited atomic state has a constant probability, depending on the coupling to the electromagnetic field, to decay

to another state. The probability of measuring a specific lifetime thus follows a Poisson distribution. The decay process caused by atomic interaction with fluctuations of the electromagnetic vacuum is called *spontaneous emission*. It is understood in the framework of *quantum electrodynamics*, and a thorough discussion is postponed to Sec. 17.4. Here, we will adopt a preliminary heuristic treatment.

Replacing in Eq. (16.17) the intensity by the number of photons (16.8), we obtain,

$$W_{if}^{(\mathrm{st})} = \frac{\pi\hbar e^2 N(\omega)}{\varepsilon_0 m^2 \omega V} |M_{fi}|^2 \delta(\omega - \omega_{fi}) \ . \tag{16.19}$$

In fact, the introduction of the concept of photons already implies the quantization of the electromagnetic field. Adding to the number of photons a photon representing the vacuum fluctuations, $N(\omega) \longrightarrow N(\omega) + 1$, we are able to include spontaneous emission,

$$\boxed{W_{if}^{(\mathrm{st})} + W_{if}^{(\mathrm{sp})} = \frac{\pi\hbar e^2 [N(\omega) + 1]}{\varepsilon_0 m^2 \omega V} |M_{fi}|^2 \delta(\omega + \omega_{fi})} \ . \tag{16.20}$$

This means that even in the absence of a classical radiation field, $N(\omega) = 0$, there is an emission probability. We note that $W_{if}^{(\mathrm{sp})}$ depends on the volume confining the atom, that is, the cavity, since it describes the transfer of energy to this volume. Here, it is clear that an argument is still missing, because the transfer rate must depend in some way on the number of states available to accommodate the emitted photon, that is, on the *density of states* within the cavity. The calculation of this density of states should allow us to evaluate the quantization volume V.

16.1.3.1 Density of states

In Sec. 1.2.2 we calculated the isotropic spectral *density of modes* per volume (1.53),

$$\varrho(\omega) = \frac{\omega^2}{\pi^2 c^3} \ . \tag{16.21}$$

The density of modes in a specific direction of free space (i.e. no boundary conditions imposed e.g. by dielectric surfaces) regardless of the mode volume is then given by [2],

$$\int_{4\pi} \rho_{free}(\omega) d\Omega = V \varrho(\omega) \ , \tag{16.22}$$

that is,

$$\rho_{free}(\omega) = \frac{V}{(2\pi)^3} \frac{\omega^2}{c^3} \ . \tag{16.23}$$

Thus, the spontaneous emission rate of photons into the solid angle $d\Omega$ is,

$$\begin{aligned} \mathcal{W}_{if}^{(\mathrm{sp})} \ d\Omega &= \left(\int_\omega W_{if}^{(\mathrm{sp})} \rho_{free}(\omega) d\omega \right) \ d\Omega \qquad (16.24) \\ &= \int_\omega \frac{\pi\hbar e^2}{\varepsilon_0 m^2 \omega V} |M_{fi}|^2 \delta(\omega + \omega_{fi}) \frac{V}{(2\pi)^3} \frac{\omega^2}{c^3} d\omega \ d\Omega = \frac{\hbar e^2}{8\pi^2 \varepsilon_0 m^2 c^3} |M_{fi}|^2 \omega_{fi} \ d\Omega \ , \end{aligned}$$

[2] See also (15.94) and (22.10) in Sec. 22.1.1.

This simplified treatment with only two atomic states considers light as a scalar field. In fact, light is a vector field and can have two independent orthogonal polarizations. The transition matrix may depend on polarization, such that,

$$\mathcal{W}_{if}^{(\mathrm{sp})} = \frac{\hbar e^2}{8\pi^2 \varepsilon_0 m^2 c^3} \int \sum_{\lambda=1,2} |M_{fi}^{\lambda}|^2 \omega_{fi}\, d\Omega \ . \tag{16.25}$$

Example 89 (*Natural linewidth of a transition*): Be $\Gamma \equiv \sum_f W_{if}^{(\mathrm{sp})}$ the spontaneous decay rate of a state $|i\rangle$. This means that its population is decreasing,

$$\dot{N}_i = -\Gamma N_i \ . \tag{16.26}$$

Since $N_i = \langle\psi_i|\psi_i\rangle$, we have $|\psi_i(t)\rangle = |\psi_i(0)\rangle e^{\imath\omega_{if}t - \Gamma t/2}$. The Fourier transform is,

$$\begin{aligned} |\xi(\omega)\rangle &= \frac{1}{\sqrt{2\pi}} \int_0^\infty |\psi_i(t)\rangle e^{-\imath\omega t} dt = \frac{1}{\sqrt{2\pi}} \int_0^\infty e^{\imath\omega_{if}t - \imath\omega t - \Gamma t/2} dt |\psi_i(0)\rangle \quad (16.27) \\ &= \frac{1}{\sqrt{2\pi}} \lim_{t\to\infty} \frac{e^{\imath(\omega_{if}-\omega)t - \Gamma t/2} - 1}{\imath(\omega_{if} - \omega) - \Gamma/2} |\psi_i(0)\rangle = \frac{1}{\sqrt{2\pi}} \frac{1}{\imath(\omega - \omega_{if}) + \Gamma/2} |\psi_i(0)\rangle \ . \end{aligned}$$

The spectrum,

$$|\xi(\omega)|^2 = \frac{1}{2\pi} \frac{1}{(\omega - \omega_{if})^2 + \Gamma^2/4} \ , \tag{16.28}$$

is a *Lorentz distribution*. Note, that the natural linewidth can be blurred by line broadening effects, such as the Doppler broadening or collisions between atoms. These effects will be discussed in the Sec. 16.5.

Excited states can sometimes decay into various states of lower energy. In this case the linewidth is simply given by the sum of the partial decay rates, since the convolution of Lorentz distributions $\mathfrak{L}_{\Gamma_k}$ with widths Γ_k is again a Lorentzian with the total width $\Gamma = \sum_k \Gamma_k$.

16.1.4 Exercises

16.1.4.1 Ex: Energy density of plane waves

Derive the result (16.7) for the temporal averages of the squares of the fields $\overline{\vec{\mathcal{E}}(\mathbf{r},t)^2} = \overline{[-\partial_t \mathbf{A}(\mathbf{r},t)]^2}$ and $\overline{\vec{\mathcal{B}}(\mathbf{r},t)^2} = \overline{[\nabla \times \mathbf{A}(\mathbf{r},t)]^2}$.

16.2 The dipolar approximation and beyond

16.2.1 Dipolar transitions

So far, we have used the matrix element $M_{fi}^{\lambda}(\omega_{fi})$ without saying how it can be calculated, nor when it is significant. In many cases of interest the calculation of this matrix element is considerably simplified by an expansion of the term $e^{-\imath\mathbf{k}\cdot\mathbf{r}}$, which is part of the matrix element (16.12) [3],

$$e^{-\imath\mathbf{k}\cdot\mathbf{r}} = 1 - \imath\mathbf{k}\cdot\mathbf{r} - \tfrac{1}{2!}(\mathbf{k}\cdot\mathbf{r})^2 + \ldots \ . \tag{16.29}$$

[3] Note however, that doing the dipole approximation via $e^{\imath\mathbf{k}\cdot\hat{\mathbf{r}}} \simeq 1$ also deactivates the operator function of the recoil operator dipole, $e^{\imath\mathbf{k}\cdot\hat{\mathbf{r}}} = |\mathbf{p} + \hbar\mathbf{k}\rangle\langle\mathbf{k}|$. For discussions of photonic recoil the operator character must be maintained even in the dipole approximation, which can be done by reinserting the recoil operator in the Hamiltonian after the dipole approximation has been applied.

This expansion is justified by the fact that the wavelength ($\sim 600\,\text{nm}$ in the visible spectrum) is much larger than the size of the scattering atom, $ka_\text{B} \ll 1$. The *dipolar approximation* supposes,

$$e^{-\imath \mathbf{k}\cdot\mathbf{r}} \simeq 1 \ , \tag{16.30}$$

such that we can remove the spatial dependence. In this approximation there is only an interaction of the *electric field* of the radiation with the atom via an electric dipole term $\mathbf{d}\cdot\vec{\mathcal{E}}$. Thus,

$$M^\lambda_{fi}(\omega_{fi}) = \langle f|e^{-\imath\mathbf{k}\cdot\mathbf{r}}\hat{\epsilon}\cdot\nabla|i\rangle \simeq \hat{\epsilon}\tfrac{\imath}{\hbar}\langle f|\hat{\mathbf{p}}|i\rangle = \hat{\epsilon}\tfrac{\imath m}{\hbar}\langle f|\dot{\hat{\mathbf{r}}}|i\rangle \ . \tag{16.31}$$

We can calculate the expectation value of the velocity of the moving charge by the Heisenberg equation using the unperturbed Hamiltonian,

$$M^\lambda_{fi}(\omega_{fi}) \simeq \hat{\epsilon}\tfrac{\imath m}{\hbar}\langle f|\tfrac{1}{\imath\hbar}[\hat{\mathbf{r}},\hat{H}_0|i\rangle = \hat{\epsilon}\tfrac{m}{\hbar^2}\langle f|\hat{\mathbf{r}}\hat{H}_0 - \hat{H}_0\hat{\mathbf{r}}|i\rangle = \hat{\epsilon}\tfrac{m}{\hbar^2}(E_i - E_f)\langle f|\hat{\mathbf{r}}|i\rangle \ . \tag{16.32}$$

The interpretation of the last equation is, that the states $|i\rangle$ and $|f\rangle$ are connected through a displacement of the electronic cloud which, therefore, represents the induction of an electric dipole during the electronic transition. It is convenient to introduce the *electric dipole moment* [4].

$$\mathbf{d}_{fi} \equiv -e\langle f|\hat{\mathbf{r}}|i\rangle \ . \tag{16.33}$$

As a result, the matrix element becomes,

$$\boxed{M^\lambda_{fi}(\omega_{fi}) \simeq \tfrac{m\omega_{fi}}{e\hbar}\hat{\epsilon}\cdot\mathbf{d}_{fi}} \tag{16.34}$$

and the absorption rate (16.15) is then, in the dipolar approximation,

$$\begin{aligned} W^{(\text{dp})}_{fi} &= \frac{\pi e^2}{\varepsilon_0 m^2 c}\frac{I(\omega_{fi})}{\omega^2_{fi}}|M_{fi}|^2\delta(\omega-\omega_{fi}) \\ &= \frac{\pi}{\varepsilon_0\hbar^2 c}I(\omega_{fi})|\hat{\epsilon}\cdot\mathbf{d}_{fi}|^2\delta(\omega-\omega_{fi}) = \frac{4\pi^2\alpha}{\hbar}I(\omega_{fi})|\hat{\epsilon}\cdot\mathbf{r}_{fi}|^2\delta(\omega-\omega_{fi}) \ . \end{aligned} \tag{16.35}$$

using the definition of the fine structure constant $\alpha = e^2/4\pi\varepsilon_0\hbar c$.

16.2.1.1 Polarization dependence

Following Eq. (16.34) the absorption rate depends on the orientation of the dipole moment with respect to the polarization of light, which therefore plays an important role in this transition. When $\mathbf{d}_{fi}$ between two states is zero, the transition via electric dipole radiation is prohibited. This is not to say that there is no transition, since other terms of the expansion (16.29) are not necessarily zero, and there may be transitions of higher multipolar orders. Even the matrix element $M^\lambda_{fi}(\omega_{fi})$ being zero for transitions involving one photon, there is still the possibility of two-photon transitions.

Setting θ as the angle between $\hat{\epsilon}$ and $\mathbf{d}_{fi}$ we obtain,

$$W^{(\text{dp})}_{fi} = \frac{\pi}{\varepsilon_0\hbar^2 c}I(\omega_{fi})|\mathbf{d}_{fi}|^2\cos^2\theta\ \delta(\omega-\omega_{fi}) \ . \tag{16.36}$$

[4] In the presence of several atoms $\mathbf{d} = -e\sum_j \mathbf{r}_j$, where the $\mathbf{r}_j$ are the radii of the orbits of the various electrons of the atom.

In case of unpolarized (or randomly polarized) radiation we can replace the angular distribution $\cos^2\theta$ by its average value,

$$\overline{\cos^2\theta} = \frac{1}{4\pi}\int_0^{2\pi}\int_0^{\pi}\cos^2\theta\sin\theta d\theta d\phi = \tfrac{1}{3}\ , \tag{16.37}$$

such that,

$$\boxed{W_{fi}^{(\mathrm{dp,no\text{-}pol})} = \frac{\pi}{3\varepsilon_0\hbar^2 c}I(\omega_{fi})|\mathbf{d}_{fi}|^2\delta(\omega-\omega_{fi})}\ . \tag{16.38}$$

This expression also represents the stimulated emission rate in the electric dipole approximation.

The total spontaneous emission rate can be obtained from Eq. (16.25) integrating over all possible orientations,

$$\begin{aligned}\mathcal{W}_{fi}^{(\mathrm{sp})} &= \frac{\hbar e^2}{8\pi^2\varepsilon_0 m^2c^3}\int\sum_{\lambda=1,2}|M_{fi}^{\lambda}|^2\omega_{fi}d\Omega \\ &= 2\frac{\hbar e^2}{8\pi^2\varepsilon_0 m^2c^3}\int_0^{2\pi}\int_0^{\pi}\left|\frac{m\omega_{fi}}{e\hbar}\hat{\epsilon}\cdot\mathbf{d}_{fi}\right|^2\omega_{fi}\sin\theta d\theta d\phi \\ &= \frac{e^2}{4\pi^2\varepsilon_0\hbar c^3}\omega_{fi}^3|\mathbf{r}_{fi}|^2\int_0^{2\pi}\int_0^{\pi}\cos^2\theta\sin\theta d\theta d\phi = \frac{e^2}{3\pi\varepsilon_0\hbar c^3}\omega_{fi}^3|\mathbf{r}_{fi}|^2\ ,\end{aligned} \tag{16.39}$$

such that, for non-polarized light,

$$\boxed{\mathcal{W}_{fi}^{(\mathrm{sp})} = \frac{4\alpha}{3c^2}\omega_{fi}^3|\mathbf{r}_{fi}|^2 = \frac{4\alpha}{3c^2}\omega_{fi}^3|\mathbf{r}_{fi}|^2 = \Gamma}\ . \tag{16.40}$$

This is the rate of spontaneous decay of an excited atomic state. It can be measured experimentally which, in turn, allows the calculation of the *induced dipole moment*,

$$d_{fi} = \sqrt{\frac{3\pi\varepsilon_0\hbar\Gamma}{k^3}}\ . \tag{16.41}$$

In Exc. 16.2.6.1 we calculate the Rabi frequency from the dipole moment of an atomic transition and the electric field of a radiation field.

16.2.2 Einstein transition rates

Considering the problem of the transfer of energy between the electromagnetic field and a sample of atoms in thermal equilibrium, Einstein realized that the processes of absorption and stimulated emission are not sufficient to understand the radiative coupling between two energy levels, that is, the coupling is not correctly described by Fermi's Golden rule, and we need to introduce the notion of spontaneous emission. Differently from the derivation of the preceding section, Einstein considered atoms whose populations of energy states are in thermal equilibrium with the electromagnetic field of a *black-body*. With this picture he came to the same result for the spontaneous emission rate (16.38), as we will show in the following.

The famous *Einstein coefficients* A_{fi} and B_{fi} are given by (1.70),

$$A_{fi}N_f = W_{fi}^{(\mathrm{sp})} \qquad \text{and} \qquad \frac{A_{fi}}{B_{fi}} = \frac{\hbar\omega_{fi}^3}{\pi^2 c^3} \ , \tag{16.42}$$

where N_f is the population of the excited state. This shows that, in fact, spontaneous emission is a necessary consequence of the interaction of an atom with a *thermal bath* (also called *reservoir*).

We now consider the problem of energy transfer between an electromagnetic field and a sample of atoms. The rate of *absorption* of a light field is,

$$R_{i\to f} \equiv \tfrac{1}{3}\dot{P}_{i\to f} = \frac{\pi}{6\hbar^2}\mathcal{E}_0^2|d_{fi}|^2\varrho(\omega_{fi}) \ , \tag{16.43}$$

with $W_0 = \mathcal{E}_0 d_{fi}$ and d_{fi} being the transition matrix element between atomic states. The factor $\frac{1}{3}$ comes from the fact that the vector $\vec{\mathcal{E}}$ of the electric field can have any polarization, but only polarizations along the direction of the oscillation of the dipole moment contribute.

For a single atom, the result (16.43) is symmetric with respect to an exchange of the initial and final states, that is, the rates for absorption and *induced emission* of light are the same. For a sample of atoms being in *thermal equilibrium*, the populations N_i of the ground state and N_f of the excited state are unequal according to Boltzmann's law. Therefore, as we have shown in Sec. 1.2.5,

$$N_f R_{f\to i} \neq N_i R_{i\to f} \ . \tag{16.44}$$

Thus, Einstein came to the conclusion that Fermi's golden rule correctly describes absorption, but does not contain all contributions of emission. The rates being related to the Einstein coefficients by the equation (1.65), we find,

$$R_{f\to i} = B_{fi}N_f u(\omega_{fi}) \tag{16.45}$$

and

$$\mathcal{S}_{f\to i} = A_{fi}N_f = \frac{\hbar\omega_{fi}^3}{\pi^2 c^3}B_{if}N_f = \frac{\hbar\omega_{fi}^3}{\pi^2 c^3}\frac{R_{i\to f}}{u(\omega_{fi})} = \frac{\omega_{fi}^3}{3\pi\epsilon_0\hbar c^3}|d_{fi}|^2 \ , \tag{16.46}$$

exploiting the relation (1.70).

Example 90 (*Line and oscillator strength*): Several disciplines such as spectrometry, spectroscopy and astrophysics have developed their own terminologies to describe absorption and emission of light by matter. We will explain how the most frequently used parameters are interrelated by placing particular emphasis on the simplest system, which is the two-level atom with no degeneracy and no spin.
In addition to the Einstein coefficients A_{21}, B_{21}, and B_{12}, the amplitude of the transition dipole moments d_{12} and the absorption cross-section $\sigma_{0a}(\omega)$, three other quantities are sometimes used to characterize atomic transitions: the oscillator strength f, the line strength S, and the spectral absorption cross section σ_ω. In the following sections, we will connect these different concepts.

The line strength S is defined as the square of the transition dipole moment summed over all degeneracies of the ground and excited states,

$$S_{12} = S_{21} = \sum_{m_1,m_2} |\langle\psi_{1,m_1}|d|\psi_{2,m_2}\rangle|^2 \ . \tag{16.47}$$

The notion of the line strength becomes significant when working with real atoms characterized by degenerate ground and excited states. In such cases we need to extend the meaning of d_{12} and consider transitions between each of the degenerate sublevels. For a non-degenerate two-level atom, the quantities d_{12} and A_{21} are simply related by,

$$A_{21} = \frac{\omega_0^3}{3\pi\epsilon_0\hbar c^3} d_{12}^2 \ . \tag{16.48}$$

If the lower level would be degenerate, the spontaneous emission rate coefficient would be given by the sum of all possible deexcitation rates. In this case, d_{12}^2 is defined as the sum of the elements of the transition matrix coupling the excited and the lower states,

$$d_{12}^2 = \sum_{m_1} |\langle\psi_{1,m_1}|d|\psi_2\rangle|^2 \ . \tag{16.49}$$

Now, it can be shown that the spontaneous emission rate from any sublevel of a degenerate excited state toward a lower level (that is, the sum over all lower sublevels) is the same for all excited sublevels [5] This statement reflects the intuitively plausible idea that spontaneous emission must be isotropic and unpolarized, if the sublevels of an excited state are uniformly populated. Therefore, the insertion of Eq. (16.49) into (16.48) should produce correct results, even when the excited state is degenerate. Comparing the sum over all upper and lower degeneracies with the line strength S,

$$S_{12} = \sum_{m_1,m_2} |\langle\psi_{1,m_1}|d|\psi_{2,m_2}\rangle|^2 = g_2 d_{12}^2 \ . \tag{16.50}$$

Therefore, the insertion of Eq. (16.50) into (16.48) must be accompanied by a factor of $1/g_2$ to correct for the fact that all excited sub-levels radiate at the same rate. Therefore, using the S_{12} of Eq. (16.50) the correct expression relating the transition dipole between degenerate levels to the spontaneous emission rate is,

$$S_{12} = g_2 \frac{3\pi\epsilon_0\hbar c^3}{\omega_0^3} A_{21} \ , \tag{16.51}$$

meaning that the line strength is proportional to the sum of the spontaneous emission rates A_{21} from each one of the g_2 excited levels toward all fundamental levels.

For an atom with two levels separated by an energy $\hbar\omega_0$ the *oscillator strength for emission* is defined as a measure for the radiative decay rate A_{21} as compared to the radiative decay rate γ_e of a classical electronic oscillator with frequency ω_0:

$$f_{21} = -\frac{1}{3}\frac{A_{21}}{\gamma_e} \ . \tag{16.52}$$

[5] This applies to Zeeman sublevels (summing up $(3j)$-coefficients). Check for other degeneracy (also summing up $\{6j\}$-coefficients)!

In case of degeneracy the *oscillator strength for absorption* is consequently defined by,

$$f_{12} = -\frac{g_2}{g_1} f_{21} = \frac{g_2}{3g_1} \frac{A_{21}}{\gamma_e} \ . \tag{16.53}$$

The transitions $S \leftrightarrow P$ in real atoms behave roughly as classical oscillators, that is, $A_{21} \simeq \gamma_e$. The factor $\frac{1}{3}$ in the definition compensates for the triple degeneracy of the P levels. So, a transition $S \leftrightarrow P$ which behaves exactly as a classical oscillator would be characterized by an oscillator strength for emission of $f_{21} = -\frac{1}{3}$ and an oscillator strength for absorption of $f_{12} = 1$. The classical expression for γ_e derived from the *Lorentz model* is [345],

$$\gamma_e = \frac{e^2 \omega_0^2}{6\pi\epsilon_0 m_e c^3} \ . \tag{16.54}$$

Therefore, in terms of the A_{21} coefficient and of fundamental constants, the oscillator strength for absorption is given by,

$$f_{12} = A_{21} \frac{2\pi\epsilon_0 m_e c^3}{e^2 \omega_0^2} \ . \tag{16.55}$$

Oscillator strengths obey certain sum rules that are useful for analyzing the relative intensities of atomic spectral lines. For example, atoms with single valence electrons (which are closer to the classical situation) obey the following sum rule,

$$\sum_k f_{ik} = 1 \ , \tag{16.56}$$

where the sum goes over all the excited states reached from the ground state. Alkaline atoms are approximately one-electron systems, and the oscillator strength of the first transition $S \longrightarrow P$ is typically of the order of $f_{12} = 0.7 - 0.95$. The sum rule tells us that most of the total transition probability for the excitation of the valence electron is concentrated in the first transition $S \rightarrow P$, and that transitions to higher states will be comparatively weaker. Another sum rule exists for the excitation and spontaneous emission from excited intermediate states j:

$$\sum_{i<j} f_{ji} + \sum_{k>j} f_{jk} = Z \ , \tag{16.57}$$

which is called the *Thomas-Reiche-Kuhn sum rule*. In the form of many electrons [Eq. (16.57)] this rule is very useful, when Z is the number of equivalent electrons, that is, electrons with the same quantum numbers n, l. Note also, that the numbers are intrinsically negative. Oscillator strengths are often used in astrophysics and plasma spectroscopy [6]. They are sometimes tabulated as $\log gf$, where,

$$g_1 f_{12} = -g_2 f_{21} \equiv gf \ . \tag{16.58}$$

16.2.3 Selection rules and electronic transitions

The selection rules that determine which transitions between two sets of quantum numbers $i \rightarrow f$ are allowed, reflect the symmetry properties of the system, e.g. the

[6] To find information about the atomic transition lines see 'http://www.nist.gov/pml/data/asd.cfm'.

conservation of angular momentum (including the spin of the photon) or the change of parity, which can be understood by the fact that the emission of a photon in a particular direction must in some way alter the spatial isotropy of the atom. Note that radially symmetric oscillations of the shape of the charge distribution *do not radiate*.

Since the electronic transitions via electric dipole radiation are described by $|\hat{\epsilon}\cdot\mathbf{r}_{fi}|$, we expect a strong dependence of the transition rate on the orientation of the polarization state of the light with respect to the electronic displacement $\mathbf{r}_{fi}$. Let us express $\hat{\epsilon}$ and $\mathbf{r}_{fi}$ in spherical coordinates, which are more adapted to the problem [7]. For an arbitrary vector $\mathbf{r}$ we have,

$$x=\mathbf{r}\cdot\hat{\mathbf{e}}_x=r\sin\vartheta\cos\varphi \quad , \quad y=\mathbf{r}\cdot\hat{\mathbf{e}}_y=r\sin\vartheta\sin\varphi \quad , \quad z=\mathbf{r}\cdot\hat{\mathbf{e}}_z=r\cos\vartheta \ . \tag{16.59}$$

Defining,

$$\hat{\mathbf{e}}_{\pm1}\equiv\tfrac{1}{\sqrt{2}}(\mp\hat{\mathbf{e}}_x-\imath\hat{\mathbf{e}}_y) \qquad , \qquad \hat{\mathbf{e}}_0\equiv\hat{\mathbf{e}}_z \ . \tag{16.60}$$

we obtain

$$\begin{aligned} r_{\pm1}&\equiv\mathbf{r}\cdot\hat{\mathbf{e}}_\pm=\mathbf{r}\cdot\tfrac{1}{\sqrt{2}}(\mp\hat{\mathbf{e}}_x-\imath\hat{\mathbf{e}}_y)=\tfrac{1}{\sqrt{2}}(\mp x-\imath y)=\mp\tfrac{1}{\sqrt{2}}r\sin\vartheta e^{\pm\imath\varphi}=r\sqrt{\tfrac{4\pi}{3}}Y_{1,\pm1}(\vartheta,\varphi)\\ r_0&\equiv\mathbf{r}\cdot\hat{\mathbf{e}}_0=\mathbf{r}\cdot\hat{\mathbf{e}}_z=z=r\cos\vartheta=r\sqrt{\tfrac{4\pi}{3}}Y_{1,0}(\vartheta,\varphi) \ . \end{aligned} \tag{16.61}$$

Now, applying the expansion into spherical coordinates to the polarization, we get,

$$\epsilon_{\pm1}\equiv\hat{\epsilon}\cdot\hat{\mathbf{e}}_\pm \qquad , \qquad \epsilon_0\equiv\hat{\epsilon}\cdot\hat{\mathbf{e}}_0 \ . \tag{16.62}$$

and applying the expansion to the matrix element $\mathbf{r}_{fi}=\langle f|\mathbf{r}|i\rangle$ with $\hat{\mathbf{e}}_q\cdot\hat{\mathbf{e}}_{q'}=\delta_{qq'}$, it is easy to check,

$$\hat{\epsilon}\cdot\mathbf{r}_{fi}=\sum_{q=0,\pm1}(\hat{\epsilon}\cdot\hat{\mathbf{e}}_q)\hat{\mathbf{e}}_q\cdot\sum_{q=0,\pm1}(\mathbf{r}_{fi}\cdot\hat{\mathbf{e}}_q)\hat{\mathbf{e}}_q=\sum_{q=0,\pm1}\epsilon_q\langle f|r_q|i\rangle=\sqrt{\tfrac{4\pi}{3}}\sum_{q=0,\pm1}\epsilon_q\langle f|rY_{1,q}|i\rangle \ . \tag{16.63}$$

The matrix elements are evaluated inserting the ansatz (3.18) separating the radial from the angular part of the wavefunction, where the angular part is solved by (3.32),

$$\begin{aligned} \langle f|r_q|i\rangle&=\sqrt{\tfrac{4\pi}{3}}\langle n_f\ell_fm_f|rY_{1,q}|n_i\ell_im_i\rangle\\ &=\int_0^\infty r^3R_{n_f,\ell_f}R_{n_i,\ell_i}dr\ \sqrt{\tfrac{4\pi}{3}}\int Y^*_{\ell_f,m_f}Y_{1,q}Y_{\ell_i,m_i}d\Omega \ . \end{aligned} \tag{16.64}$$

The angular integral,

$$\int Y^*_{\ell_f,m_f}Y_{\kappa,q}Y_{\ell_i,m_i}d\Omega=\sqrt{\tfrac{(2\ell_i+1)(2\ell_f+1)}{4\pi(2\kappa+1)}}\left(\begin{array}{cc|c}\ell_i&\kappa&\ell_f\\0&0&0\end{array}\right)\left(\begin{array}{cc|c}\ell_i&\kappa&\ell_f\\m_i&q&m_f\end{array}\right) \ , \tag{16.65}$$

[7] In the presence of a magnetic field it is often useful to choose the quantization axis along the field direction, because this simplifies the interpretation of π and $\sigma_\pm$ transitions in terms of light polarizations (see also Secs. 16.6.4 and 16.7.2).

here with $\kappa = 1$, is only non-zero, if the values of ℓ_i, m_i, ℓ_f, m_f and q satisfy certain conditions called *selection rules* [8].

The radial integral, together with the coefficients of (16.65) which do not depend on the magnetic quantum numbers, is called *reduced matrix element* or *irreducible matrix element* with the notation,

$$\langle n_f \ell_f || r || n_i \ell_i \rangle \equiv \int_0^\infty r^3 R_{n_f,\ell_f} R_{n_i,\ell_i} dr \, \sqrt{\tfrac{(2\ell_i+1)(2\ell_f+1)}{3(2\kappa+1)}} \begin{pmatrix} \ell_i & \kappa & \ell_f \\ 0 & 0 & 0 \end{pmatrix} . \tag{16.66}$$

Defining the electric dipole tensor operator,

$$Q_1^q(\mathbf{r}) = e r_q(\mathbf{r}) = \sqrt{\tfrac{4\pi}{3}} Y_{1,q}(\vartheta, \varphi) e r \ , \tag{16.67}$$

we can finally write,

$$\boxed{\langle n_f \ell_f m_f | Q_1^q(\mathbf{r}) | n_i \ell_i m_i \rangle = \langle n_f \ell_f || e r || n_i \ell_i \rangle \begin{pmatrix} \ell_i & 1 & \ell_f \\ m_i & q & m_f \end{pmatrix}} . \tag{16.68}$$

This is the *Wigner-Eckart theorem*. The electric dipole operator is a simpler example of a tensor operator $Q_\kappa^q(\mathbf{r})$ characterizing the transition between atomic states. In Excs. 16.2.6.2 and 16.2.6.3 we explicitly calculate, for a hydrogen atom subjected to a magnetic field, components of the electric dipole operator. Resolve Exc. 16.2.6.4.

Selection rules may be violated in higher orders, e.g. by multipolar radiation, as in the cases of *magnetic dipole transitions* or *electric quadrupole transitions*. This also is the case of the phenomenon of *phosphorescence*, which is a type of fluorescence emitted by metastable states.

16.2.3.1 Parity

The *parity* of a state has been defined as,

$$\mathcal{P} \psi_{n\ell m}(\mathbf{r}) = \psi_{n\ell m}(-\mathbf{r}) = (-1)^\ell \psi_{n\ell m}(\mathbf{r}) \ , \tag{16.69}$$

as shown above. That is, states with ℓ pair (impair) have even (odd) parity. Now the integral (16.67) only does not vanish, when $\ell_i + \ell_f + 1 = even$. Therefore, *dipole transitions must change the parity of the states*. F.ex. transitions $S \to P$ would be possible, while $S \to S$ would be prohibited.

16.2.3.2 Angular momentum

The irreducible matrix element (16.66) with $\kappa = 1$ is only non-zero, when $|\ell_f - \ell_i| \leq 1 \leq \ell_f + \ell_i$. That is, *dipole transitions can not change the angular momentum by more than one unit.*

[8] Frequently used are the $(3j)$-symbols connected to the Clebsch-Gordan coefficients by,

$$\langle j_i m_i, j_f m_f | J, M \rangle = (-1)^{j_i - j_f + M} \sqrt{2J+1} \begin{pmatrix} j_i & j_f & J \\ m_i & m_f & -M \end{pmatrix} .$$

16.2.3.3 Magnetic quantum number

In the decomposition (16.68) the Clebsch-Gordan coefficient is only non-zero, when $|q| \leq 1$. That is, *dipole transitions can not change the magnetic quantum number by more than one unit.* This can also be seen from,

$$\int Y^*_{\ell_f,m_f} Y_{\kappa,q} Y_{\ell_i,m_i} d\Omega \propto \int e^{\imath(m_i+q-m_f)} d\Omega \propto \delta_{m_i+q,m_f} \ . \tag{16.70}$$

16.2.3.4 Selection rules for emission in certain directions

As shown in Eq. (16.63), the excitation rate induced by a light field depends on the relative orientation of the laser polarization $\hat{\epsilon}$ and the atomic quantization axis (which may be set by the orientation of an applied magnetic field $\vec{\mathcal{B}}$). To take this dependence into account, we decompose the polarization vector (which can be linear or elliptical) on a coordinate basis, as shown in Eq. (16.62). Thus, the relative amplitude of the transitions $\Delta m_J = 0$ is proportional to the projection of the polarization vector onto the quantization axis, $\epsilon_0 \equiv \hat{\epsilon} \cdot \hat{\mathbf{e}}_0$. To estimate the amplitude of the transitions $\Delta m_J = \pm 1$, we must project onto the coordinates $\epsilon_{\pm 1} \equiv \hat{\epsilon} \cdot \hat{\mathbf{e}}_\pm$. Note that the direction of incidence of the beam, given by the wavevector $\mathbf{k}$, does not influence the transition probability directly (after all, the spatial dependence $e^{\imath \mathbf{k}\cdot\mathbf{r}}$ was removed by the dipolar approximation (16.29)); only through the fact, that the polarization is perpendicular to the propagation vector, $\hat{\epsilon} \perp \mathbf{k}$.

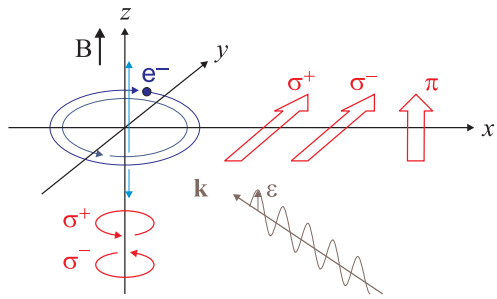

Figure 16.1: Selection rules due to polarization $\hat{\epsilon}$ of the incident light. The projection of this vector onto the axes $\pi = \hat{\epsilon} \cdot \hat{\mathbf{e}}_0$ and $\sigma_\pm = \hat{\epsilon} \cdot \hat{\mathbf{e}}_\pm$ is proportional to the excitation probability (and, obviously, also to the emission probability).

16.2.4 Reduction of the fine and hyperfine structure

In Sec. 16.2.3 we developed the Wigner-Eckart theorem for arbitrary angular momenta ℓ_i and ℓ_f. We will now be more specific identifying them with orbital angular momenta, $(\ell_i, \ell_f) = (\mathbf{L}, \mathbf{L}')$, total angular momenta of the electron shell, $(\ell_i, \ell_f) = (\mathbf{J}, \mathbf{J}')$, or total angular momenta including hyperfine structure, $(\ell_i, \ell_f) = (\mathbf{F}, \mathbf{F}')$.

16.2.4.1 Summary of selection rules including fine structure

The fine structure is due to a coupling of the type $\mathbf{L}+\mathbf{S}=\mathbf{J}$. The reduced matrix element (16.66) can then be recoupled as follows,

$$\boxed{\begin{array}{rcl}\langle J', m'_J|\hat{\mathbf{d}}|J, m_J\rangle &=& \langle J'||\hat{\mathbf{d}}||J\rangle \left(\begin{array}{cc|c} J & \kappa & J' \\ m_J & q & m'_J \end{array}\right) \quad \text{with} \\ \langle (L', S')J'||\hat{\mathbf{d}}||(L, S)J\rangle &=& (-1)^{J+L'+1+S}\sqrt{(2J+1)(2L'+1)} \left\{\begin{array}{ccc} L' & L & 1 \\ J & J' & S \end{array}\right\} \langle L'||\hat{\mathbf{d}}||L\rangle \end{array}} \,, \tag{16.71}$$

where the matrix in the second line represents a so-called *{6j}-symbol*, and the first line rewrites the Wigner-Eckart theorem (16.68) for total angular momenta. In this case,

$$\begin{aligned}\langle (L, S)Jm_J|er|(L', S')J'm'_J\rangle &= (-1)^{J+L'+1+S}\sqrt{2J+1}\sqrt{2L'+1} \times \\ &\times \delta_{S'S} \left\{\begin{array}{ccc} L & L' & 1 \\ J' & J & S \end{array}\right\} \left(\begin{array}{ccc} J' & 1 & J \\ m'_J & q & -m_J \end{array}\right) \langle n'L'||er||nL\rangle \\ &\propto \delta_{S'S} \left\{\begin{array}{ccc} L & L' & 1 \\ J' & J & S \end{array}\right\} \left(\begin{array}{ccc} J' & 1 & J \\ m'_J & q & -m_J \end{array}\right) \left(\begin{array}{ccc} L' & 1 & L \\ 0 & 0 & 0 \end{array}\right) \,, \end{aligned} \tag{16.72}$$

Electric dipolar transitions are excited by Stark-like perturbations,

$$\hat{V}_{\text{Stark}} = -e\mathbf{d}\cdot\mathcal{E} \,, \tag{16.73}$$

where $\mathcal{E}=\mathcal{E}_0\cos(\mathbf{k}\cdot\mathbf{r}-\omega t)$ is the electric field of an electromagnetic oscillating wave with polarization $\mathcal{E}_0$. With $\mathbf{d}=ez\hat{\mathbf{e}}_z$, in order to determine which dipole transitions are possible, we must look at the matrix $\langle J'm'_J|\hat{z}|Jm_J\rangle$. Applying the Wigner-Eckart theorem (10.72), it is already possible to determine, between which magnetic quantum numbers m_J and m'_J transitions may occur.

We can compare the amplitudes of the various transitions between states $|m_J\rangle$ and $|m'_J\rangle$ via the Clebsch-Gordan coefficients (see Exc. 10.3.2.1). Again, transitions are only possible between states for which the corresponding Clebsch-Gordan coefficient does not zero. Looking at the equations (10.74), we find for dipolar transitions the following selection rules,

$$\begin{aligned} &\Delta J = 0, \pm 1 \quad \text{but} \quad (J=0) \to (J'=0) \quad \text{is prohibited} \\ &\Delta m_J = 0, \pm 1 \quad \text{but} \quad (m_J=0) \to (m'_J=0) \quad \text{is prohibited when} \quad \Delta J = 0 \,. \end{aligned} \tag{16.74}$$

In addition, we have for the $\mathbf{L}\cdot\mathbf{S}$ coupling,

$$\Delta S = 0, \Delta L = \pm 1 \quad \text{and for the electron undergoing the transition} \quad \Delta\ell = \pm 1 \,. \tag{16.75}$$

In the presence of a strong magnetic field (Paschen-Back regime) breaking up the $\mathbf{L}\cdot\mathbf{S}$-coupling the selection rules are,

$$\Delta m_S = 0, \Delta m_L = 0, \pm 1 \,. \tag{16.76}$$

For $\mathbf{j}\cdot\mathbf{j}$-coupling,

$$\Delta j = 0, \pm 1 \quad \text{for one electron and} \quad \Delta j = 0 \quad \text{for all others} \,. \tag{16.77}$$

For all dipole transitions the parity must change between even and odd.

Table 16.1: Allowed transitions: (1-3) rigorous rules, (4-5) LS-coupling, and (6) intermediate coupling (https://en.wikipedia.org/wiki/Selection_rule).

	(E1)	(M1)	(E2)	(M2)	(E3)	(M3)
(1)	$\Delta J = 0, \pm 1$ ($\Delta J = 0 \nleftrightarrow 0$)		$\Delta J = 0, \pm 1, \pm 2$ ($\Delta J = 0 \nleftrightarrow 0, 1; \frac{1}{2} \nleftrightarrow \frac{1}{2}$)		$\Delta J = 0, \pm 1, \pm 2, \pm 3$ ($0 \nleftrightarrow 0, 1, 2; \frac{1}{2} \nleftrightarrow \frac{1}{2}, \frac{3}{2}; 1 \nleftrightarrow 1$)	
(2)	$\Delta M_J = 0, \pm 1$		$\Delta M_J = 0, \pm 1, \pm 2$		$\Delta M_J = 0, \pm 1, \pm 2, \pm 3$	
(3)	$\mathcal{P}_f = -\mathcal{P}_i$	$\mathcal{P}_f = \mathcal{P}_i$		$\mathcal{P}_f = -\mathcal{P}_i$		$\mathcal{P}_f = \mathcal{P}_i$
(4)	one e^- jump $\Delta L = \pm 1$	no e^- jump $\Delta L = 0; \Delta n \neq 0$	none or one e^- jump $\Delta L = 0, \pm 2$	one e^- jump $\Delta L = \pm 1$	one e^- jump $\Delta L = \pm 1, \pm 3$	one e^- jump $\Delta L = 0, \pm 2$
(5)	if $\Delta S = 0$ $\Delta L = 0, \pm 1$ ($L = 0 \nleftrightarrow 0$)	if $\Delta S = 0$ $\Delta L = 0$	if $\Delta S = 0$ $\Delta L = 0, \pm 1, \pm 2$ ($L = 0 \nleftrightarrow 0, 1$)		if $\Delta S = 0$ $\Delta L = 0, \pm 1, \pm 2, \pm 3$ ($L = 0 \nleftrightarrow 0, 1, 2; 1 \nleftrightarrow 1$)	
(6)	if $\Delta S = \pm 1$ $\Delta L = 0, \pm 1, \pm 2$		if $\Delta S = \pm 1$ $\Delta L = 0, \pm 1, \pm 2, \pm 3$ ($L = 0 \nleftrightarrow 0$)	if $\Delta S = \pm 1$ $\Delta L = 0, \pm 1$ ($L = 0 \nleftrightarrow 0$)	if $\Delta S = \pm 1$ $\Delta L = 0, \pm 1, \pm 2, \pm 3, \pm 4$ ($L = 0 \nleftrightarrow 0, 1$)	if $\Delta S = \pm 1$ $\Delta L = 0, \pm 1, \pm 2$ ($L = 0 \nleftrightarrow 0$)

Example 91 (*Transitions allowed and prohibited in the dipolar approximation*): Examples of allowed transitions are ${}^2S_{1/2} \leftrightarrow {}^2P_{1/2}$, ${}^1S_0 \leftrightarrow {}^1P_0$. Prohibited transitions are ${}^1S_0 \nleftrightarrow {}^3P_1$, ${}^2S_{1/2} \nleftrightarrow {}^2D_{3/2}$, $(5s)^2\,{}^3P_0 \nleftrightarrow (5s6s)\,{}^3P_0$.

16.2.4.2 Summary of selection rules including hyperfine structure

The fine structure is due to a coupling of the type $\mathbf{J} + \mathbf{I} = \mathbf{F}$. The reduced matrix element (16.66) can then be recoupled in a similar way as for the fine structure. Applying the Wigner-Eckart theorem (3.107) to the *hyperfine structure* [862],

$$\begin{aligned}
\langle F', m'_F|\hat{\mathbf{d}}|F, m_F\rangle &= \langle F'||\hat{\mathbf{d}}||F\rangle \begin{pmatrix} F & \kappa & F' \\ m_F & q & m'_F \end{pmatrix} \quad \text{with} \\
\langle (J', I')F'||\hat{\mathbf{d}}||(J, I)F\rangle &= (-1)^{F+J'+1+I}\sqrt{(2F+1)(2J'+1)} \begin{Bmatrix} J' & J & 1 \\ F & F' & I \end{Bmatrix} \langle J'||\hat{\mathbf{d}}||J\rangle \\
\langle (L', S')J'||\hat{\mathbf{d}}||(L, S)J\rangle &= (-1)^{J+L'+1+S}\sqrt{(2J+1)(2L'+1)} \begin{Bmatrix} L' & L & 1 \\ J & J' & S \end{Bmatrix} \langle L'||\hat{\mathbf{d}}||L\rangle
\end{aligned} \quad . \tag{16.78}$$

16.2.5 Irreducible tensor operators

Irreducible tensor operators are defined by their commutation relation with the angular momentum $\mathbf{J}$,

$$[\mathbf{J}, \mathbb{T}^{(k)}_q] = \sum_{q'} \langle kq|\mathbf{J}|kq'\rangle T^{(k)}_{q'} \ . \tag{16.79}$$

Using the spherical unit vectors $\hat{\mathbf{e}}_{\pm 1} = \frac{1}{\sqrt{2}}(\mp\hat{\mathbf{e}}_x - \imath\hat{\mathbf{e}}_y)$ and $\hat{\mathbf{e}}_0 = \hat{\mathbf{e}}_z$, we can reduce Cartesian vector operators to first-order tensor operators:

$$\vec{T} = \sum_q T^{(1)}_q \hat{\mathbf{e}}_q \qquad \text{resp.} \qquad T^{(1)}_q = \vec{T} \cdot \hat{\mathbf{e}}_q \ . \tag{16.80}$$

Examples for tensor operators are $\mathbb{I}_0^{(0)}$, $\hat{\mathbf{e}}_q^{(1)}$, $\mathbf{J}_q^{(1)}$, and $Y_q^{(k)}$. The most general tensor product is defined by:

$$(\mathbb{T}^{(k)} \times \mathbb{U}^{(k')})_m^{(j)} \equiv \sum_{q,q'} \begin{pmatrix} k & k' & j \\ q & q' & -m \end{pmatrix} \mathbb{T}_q^{(k)} \mathbb{U}_{q'}^{(k')} \ . \tag{16.81}$$

With this product it is possible to represent scalar, vector or tensor products of higher ranks,

$$\begin{aligned}
(\mathbb{T}^{(1)} \times \mathbb{U}^{(1)})_0^{(0)} &= \tfrac{1}{\sqrt{3}} \vec{\mathbb{T}} \cdot \vec{\mathbb{U}} \\
(\mathbb{T}^{(1)} \times \mathbb{U}^{(1)})_m^{(1)} &= \tfrac{1}{\sqrt{2}} (\vec{\mathbb{T}} \times \vec{\mathbb{U}}) \cdot \hat{\mathbf{e}}_m \\
(\mathbb{T}^{(1)} \times \mathbb{U}^{(1)})_0^{(2)} &= -\tfrac{1}{\sqrt{6}} (3\mathbb{T}_z \mathbb{U}_z - \vec{\mathbb{T}} \cdot \vec{\mathbb{U}}) \\
(\mathbb{T}^{(1)} \times \mathbb{U}^{(1)})_{\pm 1}^{(2)} &= \pm \tfrac{1}{2} [(\mathbb{T}_x \mathbb{U}_z + \mathbb{T}_z \mathbb{U}_x) \pm \imath (\mathbb{T}_y \mathbb{U}_z + \mathbb{T}_z \mathbb{U}_y)] \\
(\mathbb{T}^{(1)} \times \mathbb{U}^{(1)})_{\pm 2}^{(2)} &= -\tfrac{1}{2} [(\mathbb{T}_x \mathbb{U}_x - \mathbb{T}_y \mathbb{U}_y) \pm \imath (\mathbb{T}_x \mathbb{U}_y + \mathbb{T}_y \mathbb{U}_x)] \ .
\end{aligned} \tag{16.82}$$

16.2.5.1 The Wigner-Eckart theorem

Be $\mathbb{T}_q^{(k)}$ an irreducible tensor of rank k. Then, there exists then an irreducible matrix element $\langle j||\mathbb{T}^{(k)}||j'\rangle$, which does not depend on the Zeeman sublevels:

$$\langle jm|\mathbb{T}_q^{(k)}|j'm'\rangle = \begin{pmatrix} j' & k & j \\ m' & q & -m \end{pmatrix} \frac{1}{\sqrt{2j+1}} \langle j||\mathbb{T}^{(k)}||j'\rangle \ . \tag{16.83}$$

From the possible values for the Clebsch-Gordan coefficients follow directly the selection rules for multipolar radiation:

$$\begin{aligned}
\langle jm|\mathbb{T}_q^{(k)}|j'm'\rangle = 0 \qquad \text{else} \qquad & E' - E = \hbar\omega \\
& |j' - j| \le k \le j' + j \\
& m' - m = q \\
& \tau' \tau = T \ .
\end{aligned} \tag{16.84}$$

For tensor products the reduced matrix element can be reduced:

$$\langle j||(\mathbb{T}^{(k)} \times \mathbb{U}^{(k')})^{(l)}||j'\rangle = (-)^{j+\ell+j'} \sqrt{2\ell+1} \sum_q \begin{Bmatrix} k & k' & \ell \\ j' & j & q \end{Bmatrix} \langle j||\mathbb{T}^{(k)}||q\rangle \langle q||\mathbb{U}^{(k')}||\mathbb{j}'\rangle \ . \tag{16.85}$$

In particular, it is possible to show,

$$\begin{aligned}
\langle j||\mathbb{I}^{(0)}||j'\rangle &= \sqrt{2j+1}\delta_{jj'} \\
\langle j||\mathbb{J}^{(1)}||j'\rangle &= \sqrt{2j+1}\sqrt{j(j+1)}\delta_{jj'} \\
\langle j||\mathbb{Y}^{(k)}||j'\rangle &= \imath^{j+k+j'} \frac{\sqrt{2j+1}\sqrt{2k+1}\sqrt{2j'+1}}{4\pi} \begin{pmatrix} j & k & j' \\ 0 & 0 & 0 \end{pmatrix} \ .
\end{aligned} \tag{16.86}$$

16.2.5.2 Matrix element for angular momentum coupling

We consider states $|(l,s)j\rangle$. If the factors $\mathbb{T}$ and $\mathbb{U}$ of the tensor product act on different angular momenta, it can be reduced as follows:

$$\langle (l,s)j||(\mathbb{T}^{(k)}\times\mathbb{U}^{(k')})^{(l)}||(l',s')j'\rangle = \sqrt{2l+1}\sqrt{2j+1}\sqrt{2j'+1}\begin{Bmatrix} l' & s' & j' \\ k & k' & l \\ l & s & j \end{Bmatrix}\langle l||\mathbb{T}^{(k)}||l'\rangle\langle s||\mathbb{U}^{(k')}||s'\rangle\,. \tag{16.87}$$

Assuming, in particular, $\mathbb{U}^{(k')} \equiv \mathbb{I}^{(0)}$, we get, with $\mathbb{T}^{(k)} = \left(\mathbb{T}^{(k)}\times\mathbb{I}^{(0)}\right)^{(k)}$,

$$\langle (l,s)j||\mathbb{T}^{(k)}||(l',s')j'\rangle = (-)^{l+s+j'+k}\delta_{ss'}\sqrt{2j+1}\sqrt{2j'+1}\begin{Bmatrix} l & l' & k \\ j' & j & s \end{Bmatrix}\langle l||\mathbb{T}^{(k)}||l'\rangle\,. \tag{16.88}$$

The last equation therefore applies when $\mathbb{T}^{(k)}$ only acts on the angular momentum component ℓ. If on the other hand, $\mathbb{T}^{(k)}$ only acts on j, then we obviously have,

$$\langle (l,s)j||\mathbb{T}^{(k)}||(l',s')j'\rangle = \langle j||\mathbb{T}^{(k)}||j'\rangle\,. \tag{16.89}$$

16.2.6 Exercises

16.2.6.1 Ex: Rabi frequency

From the expression for the dipole moment d and the relationship between the intensity I and the electric field derive the Rabi frequency Ω produced by a laser beam of intensity I by exciting an atomic dipole transition with the wavelength λ and decay width Γ.

16.2.6.2 Ex: Non-stationary state

Construct a non-stationary hydrogen wavefunction with equal contributions of $(n = 1, \ell = 0, m = 0)$ and $(n = 2, \ell = 1, m = 1)$. Calculate the expectation values $\langle|\mathbf{r}|\rangle$ and $\langle\mathbf{r}\rangle$ as a function of time.

16.2.6.3 Ex: Transitions between Zeeman substates

Consider a hydrogen atom immersed in a uniform magnetic field, described by the Hamiltonian $\hat{H} = \hat{H}^{(0)} + \hat{H}^{(1)}$, being $\hat{H}^{(0)} = \hat{\mathbf{p}}^2/2m + V(r)$ and $H^{(1)} = -(\mu_B/\hbar)\hat{\mathbf{L}}\cdot\vec{\mathcal{B}}$ despising the spin [9].

a. Given the initial function, $|\psi_m(0)\rangle = \cos\alpha|\phi_{000}\rangle + \sin\alpha|\phi_{21m}\rangle$, determine its shape at time t.

b. Calculate the mean value $\langle\mathbf{d}\rangle_m(t) = \langle\psi_m(t)|\mathbf{d}|\psi_m(t)\rangle$ of the electric dipole operator of the atom $\mathbf{d} = q\mathbf{R}$.

c. Analyze the frequencies and polarizations of the emitted radiation by the transition of the excited states $|\phi_{21m}\rangle$ to the ground state.

[9] See Cohen-Tannoudji, Complemento D_VII

16.2.6.4 Ex: Derivation of selection rules

a. Prove $[L_k, r_m] = \imath\hbar r_n \epsilon_{kmn}$ for an *orbital angular momentum.*
b. Using the commutator derived in (a) derive the selection rules for transitions $\langle \alpha' L' m' | \vec{\varepsilon} \cdot \hat{\mathbf{r}} | \alpha L m \rangle$, where $\vec{\varepsilon}$ is the polarization vector of the radiation field chosen to be $\hat{\mathbf{e}}_0$ or $\hat{\mathbf{e}}_\pm$.
c. Prove $[\hat{L}^2, [\hat{L}^2, \hat{\mathbf{r}}]] = 2\hbar^2(\hat{\mathbf{r}}\hat{L}^2 + \hat{L}^2\hat{\mathbf{r}})$ for an orbital angular momentum $\hat{\mathbf{L}}$.
d. Using the commutator derived in (b) derive the selection rule for $\hat{L}^2$.

16.3 Bloch equations for two-level atoms

In this section we will begin to apply the ideas and tools developed in the previous sections. Let us first make use of the density matrix to describe a two-level atom coupled to a single-mode light field without spontaneous emission. We will then introduce the atomic Bloch vector as a convenient and suggestive method to describe the time evolution of a coupled two-level atom.

The internal structure of atoms is analyzed in atomic physics, where we find that the energy levels are discrete (Bohr's axiom). The center of mass motion of the atoms and collisions with other atoms are ignored, and concerning the interaction of the atoms with light, we are only interested in the aspect, that the interaction can induce transitions between internal states via absorption or emission of photons. It is the duty of atomic physics to calculate the frequencies and strengths of transitions (by Hartree-Fock or similar methods), as well as their behavior in external electric and magnetic fields. The results of these calculations are visualized in energy level schemes called *Grotrian diagrams*. In quantum optics we do not care, how the energies of the levels were calculated, but accept them as given. That is, we assume the Hamiltonian of the unperturbed atom to be diagonalized, so that its internal structure can be written as,

$$\hat{H}_{\text{atom}} = \sum_j \hbar\omega_j |j\rangle\langle j| \ . \tag{16.90}$$

16.3.1 Liouville equation

As long as we are only interested in stimulated processes, such as the absorption of a monochromatic wave, the Schrödinger equation suffices to describe the light-atom interaction. A problem arises when we want to describe relaxation processes at the same time as excitation processes. Spontaneous emission (and any other dissipative process) must therefore be included in the physical description of the temporal evolution of our light-atom system. In this case, however, our system is no longer restricted to a single mode of the light field and the two atomic states of excitation. Spontaneous emission populates a statistical distribution of states of the light field and leaves the atom in a superposition of many momentum states. This situation can not be described by a single wavefunction, but only by a distribution of wavefunctions, and we can only expect to calculate the probability of finding the system within this distribution. The Schrödinger equation, therefore, no longer applies, and we need to trace the time evolution of a system characterized by a density operator describing a statistical mixture of quantum states. The equations which describe the

time evolution of the matrix elements of this density operator are the optical Bloch equations, and we must use them instead of the Schrödinger equation. In order to appreciate the origin and the physical content of the optical Bloch equations we begin by reviewing the rudiments of the density matrix theory.

16.3.1.1 Transformation to the interaction picture

For a two-level system perturbatively interacting with a light field, the Hamiltonian can be decomposed as in (1.252) into a stationary part and a time-dependent part,

$$\hat{H} = \hat{H}_{\text{atom}} + \hat{H}_{\text{atom:field}}(t) \ , \tag{16.91}$$

where $\hat{H}_{\text{atom}}$ is the part of the Hamiltonian describing the atomic structure and $\hat{H}_{\text{atom:field}}(t)$ the interaction of the dipole transition with the classical oscillating electric field. The interaction picture is the natural choice for this type of problem. In this case, we can transform the density operator into the interaction picture defined by (1.253),

$$\tilde{\rho}(t) = e^{\imath \hat{H}_{\text{atom}}(t-t_0)/\hbar} \hat{\rho}(t_0) e^{-\imath \hat{H}_{\text{atom}}(t-t_0)/\hbar} \ , \tag{16.92}$$

where the 'tilde' decoration (replacing the 'hat') emphasizes, that we are now in the *interaction picture*. We look for the time evolution rate of $\tilde{\rho}(t)$ analogously to the Liouville equation. Calculating the time derivatives on both sides of (16.92) and substituting Eq. (15.6) for $\frac{d\hat{\rho}}{dt}$ results in,

$$\boxed{\frac{d\tilde{\rho}(t)}{dt} = \frac{\imath}{\hbar}[\tilde{\rho}(t), \hat{H}_{\text{atom:field}}(t)]} \ . \tag{16.93}$$

This equation shows that the time evolution of the density operator in the interaction picture depends only on the time-dependent part of the total Hamiltonian.

In the following we will derive a ready-to-use form of the Hamiltonian governing the interaction of a weak single-mode light field with a two-level atom in the dipolar approximation.

16.3.1.2 Semi-classical two-level atom in the dipolar approximation

According to (16.91) the semi-classical light-atom interaction Hamiltonian comprises two terms which, in the dipolar approximation, can be written,

$$\hat{H} = \begin{pmatrix} 0 & 0 \\ 0 & \hbar\omega_0 \end{pmatrix} - \hat{\mathbf{d}} \cdot \vec{\mathcal{E}}(\mathbf{r}, t) \quad \text{where} \quad \hat{\mathbf{d}} = -e\hat{\mathbf{r}} = \begin{pmatrix} 0 & \langle 1|\mathbf{d}|2\rangle \\ \langle 2|\mathbf{d}|1\rangle & 0 \end{pmatrix} \tag{16.94}$$

is the dipole operator and

$$\vec{\mathcal{E}}(\mathbf{r}, t) = \frac{\vec{\epsilon}}{2}\left[\mathcal{E}_0(\mathbf{r}) e^{\imath(\mathbf{k}\cdot\mathbf{r}-\omega t)} + \mathcal{E}_0^*(\mathbf{r}) e^{-\imath(\mathbf{k}\cdot\mathbf{r}-\omega t)}\right] \tag{16.95}$$

the electric field. Note that via $\mathcal{E}_0(\mathbf{r}) \to \imath\sqrt{\frac{\hbar\omega}{2\varepsilon_0 V}}\hat{a}$, we can quantize the radiation mode, as will be shown in Sec. 17.1.1. Introducing the Rabi frequencies

$$\hbar\Omega(\mathbf{r}) \equiv -\mathcal{E}_0(\mathbf{r})\vec{\epsilon}\cdot\langle 2|\mathbf{d}|1\rangle \qquad \text{and} \qquad \hbar\Theta(\mathbf{r}) \equiv -\mathcal{E}_0(\mathbf{r})\vec{\epsilon}\cdot\langle 1|\mathbf{d}|2\rangle \tag{16.96}$$

as an abbreviation, we can write the Hamiltonian,

$$\hat{H} = \hbar \begin{pmatrix} 0 & \frac{\Theta(\mathbf{r})}{2} e^{\imath(\mathbf{k}\cdot\mathbf{r}-\omega t)} + \frac{\Omega^*(\mathbf{r})}{2} e^{-\imath(\mathbf{k}\cdot\mathbf{r}-\omega t)} \\ \frac{\Omega(\mathbf{r})}{2} e^{\imath(\mathbf{k}\cdot\mathbf{r}-\omega t)} + \frac{\Theta^*(\mathbf{r})}{2} e^{-\imath(\mathbf{k}\cdot\mathbf{r}-\omega t)} & \hbar\omega_0 \end{pmatrix} . \tag{16.97}$$

As shown in Sec. 1.6.5 the transformation from the Schrödinger to Dirac's interaction picture, is done via,

$$\hat{H}_{\text{atom:field}} \equiv \mathcal{U}^\dagger \hat{H} \mathcal{U} + \hbar \dot{\mathcal{U}}^\dagger \mathcal{U} \qquad \text{with} \qquad \mathcal{U} = e^{-\imath \hat{H}_{\text{atom}} t/\hbar} . \tag{16.98}$$

Introducing the abbreviation $\Delta = \omega - \omega_0$ we obtain,

$$\begin{aligned} \hat{H}_{\text{atom:field}} &= \begin{pmatrix} 0 & \frac{\hbar}{2}\Omega^*(\mathbf{r}) e^{-\imath(\mathbf{k}\cdot\mathbf{r}-\Delta t)} \\ \frac{\hbar}{2}\Omega(\mathbf{r}) e^{\imath(\mathbf{k}\cdot\mathbf{r}-\Delta t)} & 0 \end{pmatrix} \\ &+ \begin{pmatrix} 0 & \frac{\hbar}{2}\Theta(\mathbf{r}) e^{\imath(\mathbf{k}\cdot\mathbf{r}-\omega t-\omega_0 t)} \\ \frac{\hbar}{2}\Theta^*(\mathbf{r}) e^{-\imath(\mathbf{k}\cdot\mathbf{r}-\omega t-\omega_0 t)} & 0 \end{pmatrix} \equiv \hat{H}^{(\text{slow})}_{\text{atom:field}} + \hat{H}^{(\text{fast})}_{\text{atom:field}} . \end{aligned} \tag{16.99}$$

16.3.1.3 The rotating wave approximation

The transition amplitude in first-order time-dependent perturbation theory is according to (5.71),

$$\begin{aligned} a_{i\to f}(t) &= \frac{1}{\imath\hbar} \int_0^t \langle 2|\hat{H}_{\text{atom:field}}(\tau)|1\rangle d\tau = \frac{\hbar}{2}\frac{1}{\imath\hbar} \int_0^t \left[\Omega(\mathbf{r}) e^{\imath(\mathbf{k}\cdot\mathbf{r}-\Delta t)} + \Theta^*(\mathbf{r}) e^{-\imath(\mathbf{k}\cdot\mathbf{r}-\omega t-\omega_0 t)}\right] d\tau \\ &= \frac{\Omega(\mathbf{r}) e^{\imath\mathbf{k}\cdot\mathbf{r}}}{2\Delta}(e^{-\imath\Delta t} - 1) + \frac{\Theta^*(\mathbf{r}) e^{-\imath\mathbf{k}\cdot\mathbf{r}}}{2(\omega+\omega_0)}\left(e^{-\imath(\omega+\omega_0)\Delta t} - 1\right) \\ &\simeq \frac{\Omega(\mathbf{r}) e^{\imath\mathbf{k}\cdot\mathbf{r}}}{2\Delta}(e^{-\imath\Delta t} - 1) , \end{aligned} \tag{16.100}$$

where the last step corresponds to the *rotating wave approximation*. This allows us to neglect $\hat{H}^{(\text{fast})}_{\text{atom:field}}$.

16.3.1.4 Transformation into the rotating frame

Now, we further transform into rotating frame using,

$$\tilde{H}_{\text{atom:field}} = \mathcal{U}^\dagger \hat{H}_{\text{atom:field}} \mathcal{U} + \imath\hbar \dot{\mathcal{U}}^\dagger \mathcal{U} \qquad \text{with} \qquad \mathcal{U} = \begin{pmatrix} 1 & 0 \\ 0 & e^{-\imath\Delta t} \end{pmatrix} . \tag{16.101}$$

This yields,

$$\tilde{H}_{\text{atom:field}} = \begin{pmatrix} 0 & \frac{\hbar}{2}\Omega^*(\mathbf{r}) e^{-\imath\mathbf{k}\cdot\mathbf{r}} \\ \frac{\hbar}{2}\Omega(\mathbf{r}) e^{\imath\mathbf{k}\cdot\mathbf{r}} & -\hbar\Delta \end{pmatrix} . \tag{16.102}$$

We always can write the Rabi frequency as $\Omega = |\Omega| e^{\imath\phi}$ and attribute the phase to the atomic position if necessary. Locating the atom in the center of the coordinate system, we finally get,

$$\tilde{H}_{\text{atom:field}} = \begin{pmatrix} 0 & \frac{\hbar}{2}\Omega^* \\ \frac{\hbar}{2}\Omega & -\hbar\Delta \end{pmatrix} , \tag{16.103}$$

yielding the new Liouville equation,

$$\boxed{\frac{d\rho(t)}{dt} = \frac{\imath}{\hbar}[\rho(t), \tilde{H}_{\text{atom:field}}]} \ . \tag{16.104}$$

The matrix representation of the Hamiltonian given in this section are given in the basis of the unperturbed states, but we still need to derive the matrix form of the Liouville equations (15.6), (16.93), and (16.93) in the various pictures. This will be the topic of the next section.

16.3.2 The matrix elements of the density operator

Since the optical Bloch equations are coupled differential equations relating the elements of the density operator matrix, we must examine the temporal dependence of these matrix elements, based on our knowledge of the operator's properties. This can be done in the Schrödinger picture using Eq. (15.6), in the interaction picture using Eq. (16.93), or directly in the co-rotating frame using Eq. (16.102). For didactic reason we will begin with the Schrödinger picture and then derive the interaction picture once again.

So, let us begin with the Liouville equation (15.6) and evaluate the elements of the matrix,

$$\begin{aligned}\langle m|\frac{d\hat{\rho}(t)}{dt}|n\rangle &= \tfrac{\imath}{\hbar}\langle m|[\hat{\rho}(t), \hat{H}]|n\rangle = \tfrac{\imath}{\hbar}\langle m|[\hat{\rho}(t), \hat{H}_{\text{atom}} + \hat{H}_{\text{atom:field}}(t)]|n\rangle \\ &= \tfrac{\imath}{\hbar}(E_n - E_m)\langle m|\hat{\rho}(t)|n\rangle + \tfrac{\imath}{\hbar}\langle m|[\hat{\rho}(t), \hat{H}_{\text{atom:field}}(t)]|n\rangle \ ,\end{aligned} \tag{16.105}$$

where $|m\rangle$ and $|n\rangle$ are members of a complete set of vectors of a basis $\{|k\rangle\}$ which are also eigen-kets of $\hat{H}_{\text{atom}}$ and span the space of $\hat{H}$. Now, we insert the closing expression $\sum_k |k\rangle\langle k| = \mathbb{I}$ in the commutator on the right-hand side of Eq. (16.105):

$$\begin{aligned}&\langle m|[\hat{\rho}(t), \hat{H}_{\text{atom:field}}(t)]|n\rangle \\ &= \sum_k [\langle m|\hat{\rho}(t)|k\rangle\langle k|\hat{H}_{\text{atom:field}}|n\rangle - \langle m|\hat{H}_{\text{atom:field}}|k\rangle\langle k|\hat{\rho}(t)|n\rangle] \ .\end{aligned} \tag{16.106}$$

For our two-level atom the complete set only includes two states: $|1(t)\rangle = |1\rangle$ and $|2(t)\rangle = e^{-\imath\omega_0 t}|2\rangle$. In addition, the matrix elements of the dipole coupling operator $\hat{H}_{\text{atom:field}}$ are only non-diagonal,

$$V \equiv \langle 1|\hat{H}_{\text{atom:field}}|2\rangle = \overline{\langle 2|\hat{H}_{\text{atom:field}}|1\rangle} = V^* \ . \tag{16.107}$$

Hence, Eq. (16.105) adopts the form,

$$\boxed{\begin{aligned}\frac{d\hat{\rho}_{11}}{dt} &= \tfrac{\imath}{\hbar}[\hat{\rho}_{12}V^* - \hat{\rho}_{21}V] \\ \frac{d\hat{\rho}_{22}}{dt} &= \tfrac{\imath}{\hbar}[\hat{\rho}_{21}V - \hat{\rho}_{12}V^*] = -\frac{d\hat{\rho}_{11}}{dt} \\ \frac{d\hat{\rho}_{12}}{dt} &= \imath\omega_0\hat{\rho}_{12} + \tfrac{\imath}{\hbar}[V(\hat{\rho}_{11} - \hat{\rho}_{22})] \\ \frac{d\hat{\rho}_{21}}{dt} &= -\imath\omega_0\hat{\rho}_{21} + \tfrac{\imath}{\hbar}[V^*(\hat{\rho}_{22} - \hat{\rho}_{11})] = \frac{d\hat{\rho}^*_{12}}{dt}\end{aligned}} \ , \tag{16.108}$$

remembering that the dash of the diagonal terms, called *populations*, must be unitary, and that the non-diagonal terms, called *coherences*, must be complex,

$$\hat{\rho}_{11} + \hat{\rho}_{22} = 1 \quad , \quad \hat{\rho}_{21} = \hat{\rho}_{12}^* \; . \tag{16.109}$$

The above set of equations constitutes the *optical Bloch equations* in the *Schrödinger picture*. We transform the Bloch equations to the *interaction picture* by replacing the Liouville equation (15.6) by (16.93), and calculating the matrix elements. We obtain,

$$\frac{d\tilde{\rho}_{22}}{dt} = \frac{\imath}{\hbar}(V\tilde{\rho}_{21} - V^*\tilde{\rho}_{12}) \quad \text{and} \quad \frac{d\tilde{\rho}_{12}}{dt} = \frac{\imath}{\hbar}V(\tilde{\rho}_{11} - \tilde{\rho}_{22}) \; . \tag{16.110}$$

We would also have obtained this expression via the substitution $\hat{\rho}_{12} = \tilde{\rho}_{12}e^{\imath\omega_0 t}$ in the equations (16.108). The interaction picture simplifies the expressions for the temporal dependence of the coherences by eliminating the first term on the right-hand side. Transforming to the interaction picture removes the temporal dependence of the basis vectors spanning the Hilbert space of the two-level atom.

We have derived the optical Bloch equations from the Liouville equation, which is the fundamental equation of motion of the density operator, and we have seen how a unitary transformation can be used to *represent* these equations in the Schrödinger, Heisenberg or interaction picture. So far, the Bloch equations do not include the possibility of spontaneous emission. We will learn later, how to include this phenomenon.

16.3.2.1 Rotating wave approximation

In the following, we will only consider exponentials rotating with the frequency $\Delta \equiv \omega - \omega_0$, and we will neglect terms rotating like $\Delta \equiv \omega + \omega_0$ in the time dependence of the coupling operator,

$$V(t) = \hbar\Omega \cos\omega t \to \tfrac{\hbar}{2}\Omega e^{-\imath\omega t} \; , \tag{16.111}$$

neglecting the part $\frac{1}{2}\hbar\Omega e^{\imath\omega t}$. The amplitude Ω is called *Rabi frequency*. This approximation, called *rotating wave approximation* (RWA) is good, when the Rabi frequency is sufficiently small, $\Omega \ll \omega$. Otherwise, we observe an energy correction of the levels called *Bloch-Siegert shift*.

Once the RWA made, we can transform to the rotating system by the prescription,

$$\rho_{12} \equiv \hat{\rho}_{12}e^{-\imath\omega t} \quad , \quad \rho_{22} \equiv \hat{\rho}_{22} \; , \tag{16.112}$$

which, applied to the Bloch equations in the *Schrödinger picture* Eq. (16.108), yields,

$$\frac{d\rho_{22}}{dt} = \frac{\imath\Omega}{2}\rho_{21} - \frac{\imath\Omega^*}{2}\rho_{12} \quad , \quad \frac{d\rho_{12}}{dt} = -\imath\Delta\rho_{12} + \frac{\imath\Omega}{2}(\rho_{11} - \rho_{22}) \; . \tag{16.113}$$

In Exc. 16.3.7.1 we derive the Bloch equations from the equations of motion for the population amplitudes a_1 and a_2.

16.3.3 Solution of the optical Bloch equations

For arbitrary starting conditions, the solution of these equations is not simple. To solve the problem we write the equations in a matrix form,

$$\boxed{\vec{\rho} \equiv \begin{pmatrix} \rho_{11} \\ \rho_{22} \\ \rho_{12} \\ \rho_{21} \end{pmatrix} \quad , \quad \mathcal{M} \equiv \begin{pmatrix} 0 & 0 & \frac{\imath}{2}\Omega^* & -\frac{\imath}{2}\Omega \\ 0 & 0 & -\frac{\imath}{2}\Omega^* & \frac{\imath}{2}\Omega \\ \frac{\imath}{2}\Omega & -\frac{\imath}{2}\Omega & -\imath\Delta & 0 \\ -\frac{\imath}{2}\Omega^* & \frac{\imath}{2}\Omega^* & 0 & \imath\Delta \end{pmatrix} \quad , \quad \dot{\vec{\rho}} = \mathcal{M}\vec{\rho} \; .} \tag{16.114}$$

To solve this system of differential equations, we calculate the eigenvalues of the matrix,

$$\begin{aligned} \det(\mathcal{M} - \lambda \mathbb{I}_4) = \lambda^2(\Delta^2 + |\Omega|^2) + \lambda^4 = 0 \\ \lambda = 0, \pm\imath G \; , \end{aligned} \tag{16.115}$$

with the so-called *generalized Rabi frequency* $G \equiv \sqrt{\Delta^2 + |\Omega|^2}$. Therefore, the general solution is,

$$\begin{aligned} \rho_{22}(t) &= \rho_{22}^{(1)} + \rho_{22}^{(2)} e^{\imath G t} + \rho_{22}^{(3)} e^{-\imath G t} \\ \rho_{12}(t) &= \rho_{12}^{(1)} + \rho_{12}^{(2)} e^{\imath G t} + \rho_{12}^{(3)} e^{-\imath G t} \; . \end{aligned} \tag{16.116}$$

The coefficients follow from the Bloch equations with particular starting conditions. With a little algebra we get

$$\begin{aligned} \rho_{22}^{(1)} &= \rho_{22}(0) + \tfrac{1}{2G^2}\left[|\Omega|^2\left(1 - 2\rho_{22}(0)\right) - \Delta\left(\Omega\rho_{12}^*(0) + \Omega^*\rho_{12}(0)\right)\right] \\ \rho_{22}^{(2)} &= \tfrac{1}{4G^2}\left[-|\Omega|^2(1 - 2\rho_{22}(0)) + (\Delta + G)\Omega\rho_{12}^*(0) + (\Delta - G)\Omega^*\rho_{12}(0)\right] \\ \rho_{22}^{(3)} &= \tfrac{1}{4G^2}\left[-|\Omega|^2(1 - 2\rho_{22}(0)) + (\Delta - G)\Omega\rho_{12}^*(0) + (\Delta + G)\Omega^*\rho_{12}(0)\right] \\ \rho_{12}^{(1)} &= \tfrac{1}{2G^2}\left[\Delta\Omega(1 - 2\rho_{22}(0)) + \Omega\left(\Omega\rho_{12}^*(0) + \Omega^*\rho_{12}(0)\right)\right] \\ \rho_{12}^{(2)} &= \tfrac{\Delta - G}{4G^2}\left[-\Omega(1 - 2\rho_{22}(0)) + (\Delta + G)\tfrac{\Omega}{\Omega^*}\rho_{12}^*(0) + (\Delta - G)\rho_{12}(0)\right] \\ \rho_{12}^{(3)} &= \tfrac{\Delta + G}{4G^2}\left[-\Omega(1 - 2\rho_{22}(0)) + (\Delta - G)\tfrac{\Omega}{\Omega^*}\rho_{12}^*(0) + (\Delta + G)\rho_{12}(0)\right] \; . \end{aligned} \tag{16.117}$$

We derive this solution in Exc. 16.3.7.2.

To begin the discussion of this solution, let us consider a sample of atoms initially in the ground state when the light field is switched on at time $t = 0$,

$$\rho_{11}(0) = 1 = 1 - \rho_{22}(0) \quad , \quad \rho_{12}(0) = 0 = \rho_{21}(0) \; . \tag{16.118}$$

In this case, the conditions (16.117) simplify to,

$$\begin{aligned} \rho_{22}^{(1)} &= \tfrac{|\Omega|^2}{2G^2} \quad , \quad \rho_{12}^{(1)} = \tfrac{1}{2G^2}\Delta\Omega \\ \rho_{22}^{(2)} &= \tfrac{-|\Omega|^2}{4G^2} \quad , \quad \rho_{12}^{(2)} = \tfrac{G - \Delta}{4G^2}\Omega \\ \rho_{22}^{(3)} &= \tfrac{-|\Omega|^2}{4G^2} \quad , \quad \rho_{12}^{(3)} = \tfrac{-G - \Delta}{4G^2}\Omega \; , \end{aligned} \tag{16.119}$$

such that,

$$\rho_{22} = \rho_{22}^{(1)} + \rho_{22}^{(2)} e^{\imath Gt} + \rho_{22}^{(3)} e^{-\imath Gt} = \frac{|\Omega|^2}{4G^2}(2 - e^{\imath Gt} - e^{-\imath Gt}) \tag{16.120}$$

$$\rho_{12} = \rho_{12}^{(1)} + \rho_{12}^{(2)} e^{\imath Gt} + \rho_{12}^{(3)} e^{-\imath Gt} = \frac{\Delta\Omega}{2G^2} - \frac{\Delta - G}{4G^2}\Omega e^{\imath Gt} - \frac{\Delta + G}{4G^2}\Omega e^{-\imath Gt}$$

$$= \frac{2\Omega}{4G^2}(\Delta - \Delta\cos Gt + \imath G \sin Gt) \ .$$

Using $\cos x = 1 - 2\sin^2\frac{x}{2}$ and $\sin x = 2\sin\frac{x}{2}\cos\frac{x}{2}$, we finally obtain,

$$\boxed{\rho_{22} = \frac{|\Omega|^2}{G^2}\sin^2\frac{Gt}{2} \quad , \quad \rho_{12} = \frac{\Omega}{G^2}\sin\frac{Gt}{2}\left(\Delta\sin\frac{Gt}{2} + \imath G\cos\frac{Gt}{2}\right)} \ . \tag{16.121}$$

And comparing with the solutions of the Schrödinger equation for a coupled two-level atom obtained in Exc. 1.6.7.1 and (5.93), we verify,

$$\rho_{22} = \left|\tfrac{\imath\Omega}{G} e^{-\imath t\Delta/2}\sin\tfrac{Gt}{2}\right|^2 = |a_2|^2 \tag{16.122}$$

$$\rho_{12} = -e^{-\imath t\Delta/2}\left[\cos\tfrac{Gt}{2} - \imath\tfrac{\Delta}{G}\sin\tfrac{Gt}{2}\right] \ \tfrac{-\imath\Omega}{G} e^{\imath t\Delta/2}\sin\tfrac{Gt}{2} = a_1^* a_2 \ .$$

16.3.4 Pauli matrices and the atomic Bloch vector

Let us come back to the unperturbed atomic Hamiltonian (16.90). The electronic states are orthonormal $\langle i|j\rangle = \delta_{ij}$, and we define the transition operators by

$$\hat\sigma_{ij}|k\rangle = \delta_{jk}|i\rangle \ , \tag{16.123}$$

and $\hat\sigma_{ij}^\dagger = \hat\sigma_{ji}$ satisfying the commutation relation,

$$[\hat\sigma_{ij}, \hat\sigma_{lk}] = \delta_{jl}\hat\sigma_{ik} - \delta_{ik}\hat\sigma_{lj} \ . \tag{16.124}$$

Many times we will restrict ourselves to atoms of two or three levels. For a two-level system we obtain the *Pauli spin matrix* defined in (1.152). Every 2×2 matrix can be expanded on a Pauli matrix basis (see Exc. 16.3.7.3),

$$\begin{pmatrix}\rho_{11} & \rho_{12}\\ \rho_{21} & \rho_{22}\end{pmatrix} = |1\rangle\rho_{11}\langle 1| + |1\rangle\rho_{12}\langle 2| + |2\rangle\rho_{21}\langle 1| + |2\rangle\rho_{22}\langle 2| \tag{16.125}$$

$$= \rho_{11}(\tfrac{1}{2} + \tfrac{1}{2}\hat\sigma_z) + \rho_{12}\hat\sigma^- + \rho_{21}\hat\sigma^+ + \rho_{22}(\tfrac{1}{2} - \tfrac{1}{2}\hat\sigma_z)$$

$$= \rho_{11}\hat\sigma^-\hat\sigma^+ + \rho_{12}\hat\sigma^- + \rho_{21}\hat\sigma^+ + \rho_{22}\hat\sigma^+\hat\sigma^- = \begin{pmatrix}\langle\hat\sigma^-\hat\sigma^+\rangle & \langle\hat\sigma^-\rangle\\ \langle\hat\sigma^+\rangle & \langle\hat\sigma^+\hat\sigma^-\rangle\end{pmatrix} \ .$$

For the two-level case it is useful to introduce an alternative notation based on the *Bloch vector* defined in (1.159),

$$\vec\varrho \equiv \langle\hat{\vec\sigma}\rangle \equiv \begin{pmatrix}2\,\mathfrak{Re}\,\rho_{12}\\ 2\,\mathfrak{Im}\,\rho_{12}\\ \rho_{22} - \rho_{11}\end{pmatrix} = \begin{pmatrix}\langle\hat\sigma^+\rangle + \langle\hat\sigma^-\rangle\\ \imath(\langle\hat\sigma^+\rangle - \langle\hat\sigma^-\rangle)\\ \langle\hat\sigma^+\hat\sigma^-\rangle - \langle\hat\sigma^-\hat\sigma^+\rangle\end{pmatrix} = \begin{pmatrix}\langle\hat\sigma_x\rangle\\ \langle\hat\sigma_y\rangle\\ \langle\hat\sigma_z\rangle\end{pmatrix} \ . \tag{16.126}$$

We also define the torque vector,

$$\boxed{\mathbf{G} \equiv \begin{pmatrix} \mathfrak{Re}\,\Omega \\ \mathfrak{Im}\,\Omega \\ -\Delta \end{pmatrix} \qquad \text{with} \qquad \|\mathbf{G}\| = G = \sqrt{|\Omega|^2 + \Delta^2}} \ , \tag{16.127}$$

the length of which is simply the generalized Rabi frequency. Note that here we allow for the possibility of complex Rabi frequency.

Now, using $\hat{\sigma}_z = [\hat{\sigma}^+, \hat{\sigma}^-]$, we may write the Hamiltonian of an unperturbed two-level system,

$$\hat{H}_0 = -\hbar\Delta\hat{\sigma}^+\hat{\sigma}^- = -\tfrac{\hbar}{2}\Delta(\hat{\sigma}_z + \mathbb{I}_2) = -\tfrac{\hbar}{2}\Delta\hat{\sigma}_z + \text{offset} \ . \tag{16.128}$$

For the perturbed system,

$$\hat{H} = \hat{\mathbf{s}} \cdot \mathbf{G} = \tfrac{\hbar}{2}\mathbf{G} \cdot \hat{\vec{\sigma}} = -\tfrac{\hbar}{2}\hat{\sigma}_z\Delta + \tfrac{\hbar}{2}\hat{\sigma}_x\mathfrak{Re}\,\Omega + \tfrac{\hbar}{2}\hat{\sigma}_y\mathfrak{Im}\,\Omega = \begin{pmatrix} \frac{\hbar}{2}\Delta & \frac{\hbar}{2}\Omega^* \\ \frac{\hbar}{2}\Omega & -\frac{\hbar}{2}\Delta \end{pmatrix} \ . \tag{16.129}$$

The Bloch equations (16.128) then follow as the Heisenberg equation with the Hamiltonian (16.130) using $[\hat{\sigma}_k, \hat{\sigma}_m] = 2\imath\epsilon_{klm}\hat{\sigma}_m$,

$$\begin{aligned} \frac{d\hat{\vec{\sigma}}}{dt} &= \tfrac{\imath}{\hbar}[\hat{H}, \hat{\vec{\sigma}}] = \tfrac{\imath}{2}[\mathbf{G} \cdot \hat{\vec{\sigma}}, \hat{\vec{\sigma}}] \qquad (16.130) \\ &= \tfrac{\imath G_x}{2}[\hat{\sigma}_x, \hat{\vec{\sigma}}] + \tfrac{\imath G_y}{2}[\hat{\sigma}_y, \hat{\vec{\sigma}}] + \tfrac{\imath G_z}{2}[\hat{\sigma}_z, \hat{\vec{\sigma}}] = \begin{pmatrix} G_y\hat{\sigma}_z - G_z\hat{\sigma}_y \\ G_z\hat{\sigma}_x - G_x\hat{\sigma}_z \\ G_x\hat{\sigma}_y - G_y\hat{\sigma}_x \end{pmatrix} = \mathbf{G} \times \hat{\vec{\sigma}} \ . \end{aligned}$$

The expectation values yield,

$$\boxed{\frac{d\vec{\varrho}}{dt} = \mathbf{G} \times \vec{\varrho}} \ . \tag{16.131}$$

As will be shown in Exc. 16.3.7.4, these equations are identical to the Liouville equations (16.114). ρ_{12} describes the polarization and $\rho_{22} - \rho_{11}$ the *population inversion* of the atom. The equation is analogous to the equation of motion for a *rigid rotor* or *spinning top* (for example, a dipole in a homogeneous field). It displays phenomena such as *precession* and *nutation*. The physical content and usefulness of the Bloch vector will become clearer when we use the formalism to analyze electric and magnetic couplings. In Exc. 16.3.7.5 we verify that the Bloch vector is normalized (as long as spontaneous emission is not considered).

16.3.5 State manipulations by sequences of radiation pulses

The temporal dependence of the three components of the atomic Bloch vector provides a useful illustration of the atom-field interaction. Resonant coupling, $\Delta = 0$ and $G = \Omega$, puts the solutions (16.121) into the form,

$$\rho_{22}(t) = \tfrac{1}{2}(1 - \cos\Omega t) \qquad , \qquad \rho_{12}(t) = \tfrac{\imath}{2}\sin\Omega t \ , \tag{16.132}$$

that is,

$$\vec{\varrho}(t) = \begin{pmatrix} 0 \\ \sin \Omega t \\ -\cos \Omega t \end{pmatrix} . \tag{16.133}$$

That is, a resonant pulse rotates a Bloch vector initially pointing in the direction $-z$ within the plane z-y, until it arrives, at time $t = \frac{\pi}{2\Omega}$, at the $+y$ direction and at time $t = \frac{\pi}{\Omega}$ at the $+z$ direction. This means that the entire population has been transferred to the excited state. The Bloch vector continues to rotate (the movement is called *nutation*) around the torque vector $\mathbf{G}$ which, as can be seen from Eq. (16.128), points at the $+x$ direction when $\Delta = 0$. The nutation frequency is proportional to the force Ω of the atom-field interaction. With the Eq. (16.121) we see that the population oscillates between the ground and excited state with the frequency Ω. This means that the energy $\hbar\omega$ is periodically exchanged between the atom and the field. A pulse of resonant light of duration such that $\tau = \pi/2\Omega$ is called a $\pi/2$-pulse. The nutation is illustrated in Fig. 16.2(a).

Once the coherence has been excited by a detuned radiation, $\Delta \neq 0$, the Bloch vector does not stand still, even after the radiation has been switched off. To see this, we consider again the general solution (16.117) now entering $\Omega = 0$. If the Bloch vector is initially at a point in the unitary circle of the plane z-y, it will rotate according to the formula,

$$\rho_{22}(t) = \rho_{22}(0) \quad , \quad \rho_{12}(t) = \rho_{12}(0) e^{-\imath \Delta t} , \tag{16.134}$$

that is,

$$\vec{\varrho}(t) = \begin{pmatrix} \rho_{12}(0) \sin \Delta t \\ \rho_{12}(0) \cos \Delta t \\ 2\rho_{22}(0) - 1 \end{pmatrix} . \tag{16.135}$$

That is, the Bloch vector performs a motion of *precession* around the symmetry axis. The precession is illustrated in Fig. 16.2(b).

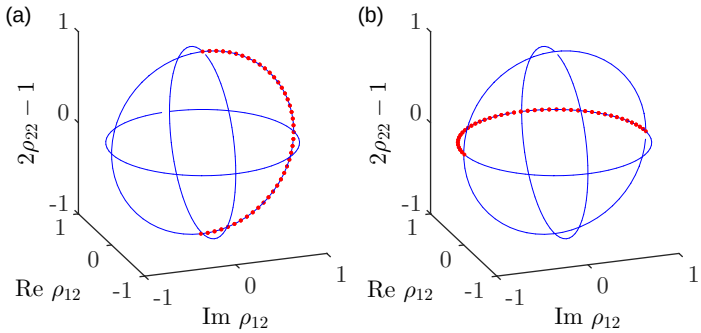

Figure 16.2: (code) (a) Nutation of the Bloch vector. The red circles show the evolution of the Bloch vector on the Bloch sphere for a resonant π-pulse. (b) Precession of the Bloch vector.

The evolution of the Bloch vector on the surface of the Bloch sphere under the influence of radiation fields can be considered a coherent trajectory of the wavefunction

of the atomic state, which is therefore subject to interference phenomena [411]. Interferometers can be realized by sequences of consecutive pulses splitting populations, exciting coherences, and remixing populations.

Sensors based on interferometry of atomic excitation are nowadays among the most accurate and most sensitive. We will discuss the method of radiation pulse sequences in several exercises: In the Excs. 16.3.7.6, 16.3.7.7, and 16.3.7.8 the *Ramsey method*.

16.3.5.1 Atomic ensembles

While it is technically challenging to observe the dynamics of single atoms, it is relatively easy monitor the dynamics of ensembles of atoms, provided that they react synchronously to incident radiation. The concentration of a sufficient number of atoms in a small volume can, however, introduce additional (desirable or undesirable) effects. Collisions, for instance, induce (irreversible) decoherence. On the other hand, if the ensemble is sufficiently dense that the mean distance between atoms is less than a resonant wavelength, then the transition dipoles of the individual atoms will couple to produce a collective dipole moment and generate effects known as superradiance.

Thermal motion of the atoms is another undesired effect, because every atom will interact with the radiation on a different Doppler-shifted frequency. This leads to diffusion of the individual atomic Bloch vectors in the x-y-plane, which in turn limits the resolution of interferometric applications. We will discuss in Exc. 16.3.7.9 the *photon echo method*, which allows to circumvent this problem.

16.3.6 Nuclear magnetic resonance

Nuclear magnetic resonance (NMR) is a physical phenomenon in which nuclei in a strong constant magnetic field (up to 20 T) are perturbed by a weak oscillating magnetic field (in the near field) and respond by producing an electromagnetic signal with a frequency characteristic of the magnetic field at the nucleus. This process occurs near resonance, when the oscillation frequency (typically 60..1000 MHz) matches the intrinsic frequency of the nuclei, which depends on the strength of the static magnetic field, the chemical environment, and the magnetic properties of the isotope involved. NMR spectroscopy is widely used to determine the structure of organic molecules in solution and in advanced medical imaging techniques, such as in magnetic resonance imaging (MRI). The most commonly used nuclei are ^{1}H and ^{13}C.

NMR transitions can be excited, when the electron spins do not participate in the interaction, e.g. because they are paired (see Eq. (10.41)), and when the nucleus has an intrinsic nuclear magnetic moment $\hat{\vec{\mu}}_I$ and hence an angular momentum $\hat{\mathbf{I}}$. This is the case for an odd number of protons and/or neutrons. Nuclides with even numbers of both have a total spin of zero and are therefore NMR-inactive.

The principle of NMR usually involves three sequential steps: (i) The alignment of the magnetic nuclear spins in an applied, constant magnetic field $\vec{\mathcal{B}}_0$. (ii) The perturbation of this alignment of the nuclear spins by a weak oscillating magnetic field $\vec{\mathcal{B}}_1(t)$ called rf-pulse. (iii) The detection of the NMR signal during or after the rf-pulse via the voltage induced in a detection coil due to the precession of the nuclear spins around $\vec{\mathcal{B}}_0$. After an rf-pulse, the nuclear dipole moment precesses at

the nuclei's intrinsic Larmor frequency without involving transitions between spin states. Choosing the two magnetic fields perpendicular to each other, one maximizes the NMR signal strength,

$$\vec{\mathcal{B}}(t) = \mathcal{B}_{\rm rf}(t)\hat{\mathbf{e}}_x + \mathcal{B}_0\hat{\mathbf{e}}_z \ , \tag{16.136}$$

where, because of $|\mathcal{B}_{\rm rf}(t)| \ll \mathcal{B}_0$, we choose the z-axis as the quantization axis and the rf-field as a perturbation along the x-axis.

The energy of a nuclear magnetic dipole moment placed in a magnetic field is [231],

$$\boxed{\hat{H} = -\hat{\vec{\mu}} \cdot \vec{\mathcal{B}} = -\gamma_I \hat{\mathbf{I}} \cdot \vec{\mathcal{B}}} \ , \tag{16.137}$$

where γ_I is the *gyromagnetic ratio* of the specific nucleus and $\hat{\mathbf{I}}$ the nuclear spin satisfying the usual commutation relation $[\hat{I}_m, \hat{I}_n] = \imath\hbar\epsilon_{kmn}\hat{I}_k$. Hence, as shown in Exc. 16.3.7.10, we can derive from the Heisenberg equation,

$$\imath\hbar \frac{d\hat{\vec{\mu}}}{dt} = [\hat{\vec{\mu}}, \hat{H}] \ , \tag{16.138}$$

the Bloch equations,

$$\boxed{\frac{d\hat{\vec{\mu}}}{dt} = \gamma_I \hat{\vec{\mu}} \times \vec{\mathcal{B}}} \ . \tag{16.139}$$

Now, let us restrict to a two-level system, $I = \frac{1}{2}$ such that $\hat{I}_z = \frac{\hbar}{2}\hat{\sigma}_z$. In thermal equilibrium, without time-dependent perturbation,

$$\hat{H}_0 = -\hat{\vec{\mu}} \cdot \vec{\mathcal{B}}_0 = -\hat{\mu}_z \mathcal{B}_0 = -\gamma_I \hat{I}_z \mathcal{B}_0 \equiv -\omega_{\rm L} \hat{I}_z \ . \tag{16.140}$$

where we introduced the *Larmor frequency* $\omega_{\rm L}$. We expect energy levels,

$$E = -\hbar\gamma_I m \mathcal{B}_0 \ , \tag{16.141}$$

with $m = \pm\frac{1}{2}$. The energy difference between the two states, $\Delta E = \gamma_I \hbar \mathcal{B}_0$, results in a small population bias favoring the lower energy state in thermal equilibrium and, hence, in a net spin magnetization $\vec{\mathcal{M}} = \frac{1}{V}\sum_i \langle \vec{\mu}_i \rangle$ along the magnetic field $\vec{\mathcal{B}}_0$. For a thermal statistical mixture, as shown in (14.39), we write the density operator [10],

$$\boxed{\hat{\rho} = \frac{e^{-\hat{H}_0/k_{\rm B}T}}{Z} = \frac{e^{-\frac{1}{2}\beta\hbar\omega_{\rm L}\hat{\sigma}_z}}{Z} = \sum_{m=\pm 1/2} |I,m\rangle \frac{e^{-\beta\hbar\omega_{\rm L} m}}{Z} \langle I,m|} \ , \tag{16.142}$$

with the partition function,

$$Z \equiv {\rm Tr}\, e^{-\hat{H}_0/k_{\rm B}T} = \sum_{m=\pm 1/2} e^{-\beta\hbar\omega_{\rm L} m} \ . \tag{16.143}$$

[10] Note that at high temperatures we get, $Z \simeq 1$ and may approximate,

$$\hat{\rho} - 1 \simeq \beta\hbar\omega_{\rm L}\hat{I}_z \ .$$

Now, as shown in (16.92), we can express the time-evolution of the density operator as,

$$\hat{\rho}(t) = e^{-\imath\hat{H}_0 t}\hat{\rho}(0)e^{\imath\hat{H}_0 t} = e^{-\imath\beta\hbar\omega_{\rm L}\hat{I}_z t}\hat{\rho}(0)e^{\imath\beta\hbar\omega_{\rm L}\hat{I}_z t} \ . \tag{16.144}$$

Then, as shown in Exc. 16.3.7.11,

$$\langle\hat{\mathbf{I}}(t)\rangle = \begin{pmatrix} \cos\omega_{\rm L}t & -\sin\omega_{\rm L}t & 0 \\ \sin\omega_{\rm L}t & \cos\omega_{\rm L}t & 0 \\ 0 & 0 & 1 \end{pmatrix} \langle\hat{\mathbf{I}}(0)\rangle \ , \tag{16.145}$$

which corroborates the result (16.139). Apparently, the nuclear magnetic dipole moment (and hence the spin magnetization) precesses around the magnetic field with the Larmor frequency leaving the populations of the energy levels unaffected.

A perturbation of nuclear spin orientations from equilibrium will occur when an oscillating magnetic field is applied whose frequency $\omega_{\rm rf}$ sufficiently closely matches the Larmor precession frequency $\omega_{\rm L}$. The populations of the spin-up and -down energy levels then undergo Rabi oscillations. The stronger the oscillating field, the faster the Rabi oscillations or the precession around the effective field in the rotating frame. After a certain time (typically on the order of 2..1000 µs), a resonant rf-$\pi/2$-pulse flips the spin magnetization to the transverse plane, while after a twice longer time, the initial magnetization is inverted (π-pulse). It is the transverse magnetization generated by a resonant oscillating field which is usually detected in NMR.

The most important perturbation of the NMR frequency for applications of NMR is the 'shielding' effect of the surrounding shells of electrons. Electrons, similar to the nucleus, are also charged and rotate with a spin to produce a magnetic field opposite to the applied magnetic field. In general, this electronic shielding reduces the magnetic field at the nucleus. The corresponding shift in the NMR frequency due to the electronic molecular orbital coupling to the external magnetic field is called chemical shift, and it explains why NMR is able to probe the chemical structure of molecules, which depends on the electron density distribution in the corresponding molecular orbitals.

After perturbation the nuclear spins return to thermodynamic equilibrium due to relaxation processes. These are phenomenological included in the Bloch equations via decay time constants T_i,

$$\frac{d\hat{\vec{\mu}}}{dt} = \gamma_I\hat{\vec{\mu}} \times \vec{\mathcal{B}} - \frac{\hat{\mu}_z}{T_1}\hat{\mathbf{e}}_z - \frac{\hat{\mu}_x}{T_2}\hat{\mathbf{e}}_x \ . \tag{16.146}$$

$T_1 = \Gamma^{-1}$ is the time constant for 'longitudinal magnetic' relaxation and refers to the mean time for an individual nucleus to return to its thermal equilibrium state of the spins. The precessing nuclei can also fall out of alignment with each other and gradually stop producing a signal. This is called T_2 or transverse relaxation, where $T_2 = 2\gamma^{-1}$. Because of the difference in the actual relaxation mechanisms involved (for example, intermolecular versus intramolecular magnetic dipole-dipole interactions), T_1 is usually longer than T_2, which, in practice, also depends on significant static magnetic field inhomogeneities.

16.3.7 Exercises

16.3.7.1 Ex: Derivation of Bloch equations

Derive the Bloch equations explicitly based on the temporal evolutions of the coefficients $a_{1,2}$ (5.63) knowing that $\rho_{ij} = a_i^* a_j$.

16.3.7.2 Ex: General solution of Bloch equations

Derive the solution (16.117) of the Bloch equations (16.114).

16.3.7.3 Ex: Expansion in Pauli matrices

Show explicitly $\mathrm{Tr}\,\hat{\rho}\hat{\sigma}^-\hat{\sigma}^+ = \rho_{11}$.

16.3.7.4 Ex: Bloch vector and Bloch equations

Show that Eq. (16.131) is equivalent to the Bloch equations (16.114).

16.3.7.5 Ex: Normalization of the Bloch vector

Verify $\|\vec{\rho}\| = 1$.

16.3.7.6 Ex: Sequence of Ramsey pulses

Many atomic clocks work according to the Ramsey spectroscopy method: The two-level atom is resonantly excited by a microwave $\pi/2$-pulse. Then, the phase of atomic coherence precesses freely over a period of time T accumulating an angle ϕ. Finally, a second $\pi/2$-pulse is applied and the population of the upper-level is measured. Calculate this population as a function of the angle ϕ. Neglect spontaneous emission.

16.3.7.7 Ex: Analytical treatment of the Ramsey experiment

Derive the analytic formula for the final population ρ_{22} for the Rabi and Ramsey experiments. Derive and compare the line widths of the 'interference fringes' in these two experiments.

16.3.7.8 Ex: Atomic clocks by the Ramsey method with spontaneous emission

In this exercise we study the Ramsey method used in atomic clocks. For this, we will consider a two-level system $|1\rangle$ and $|2\rangle$ excited by a microwave radiation field characterized by the Rabi frequency Ω_{12}, and we will compare two cases: without and with spontaneous emission:
a. Write down the Hamiltonian of the system, propose a sequence of pulses allowing the observation of the Ramsey fringes, do a numerical simulation of the Schrödinger equation (based on the prescription (16.246)), and prepare a graph of the type Fig. 16.2 illustrating the temporal evolution of the Bloch vector during the sequence.

b. Calculate numerically from the Schrödinger equation the population ρ_{22} immediately after the pulse sequence as a function of the detuning Δ_{12} of the radiation field, and prepare a graph of the spectrum. Also, assuming a decay rate of $\Gamma_{12} = 0.1\Omega_{12}$, calculate the population ρ_{22} as a function of detuning Δ_{12} from the Bloch equations (making sequences of type (16.246)), prepare a new graph, and compare it with the previous graph obtained by the Schrödinger equation.
c. What happens to the width of the fringes, when the free precession time τ between the Ramsey pulses is increased? Prepare a graph of the inversion $2\rho_{22}-1$ as a function of Δ_{12} and τ and interprete the results.

16.3.7.9 Ex: Photon echo

'Photon echo' is a powerful spectroscopic technique that allows circumvention of certain dephasing processes, for example, the Doppler shift due to the atomic motion in a thermal sample of atoms. The technique resembles the Ramsey method with the difference, that between the two Ramsey $\pi/2$-pulses, that is, during the free precession time, we apply an additional π-pulse, which inverts the imaginary part of the coherence. We will study this method by numerical simulation of the Schrödinger equation and the Bloch equations for a two-level system with and without spontaneous emission:
a. Write down the Hamiltonian of the system and do a numerical simulation of the Schrödinger equation (concatenating the pulses as explained in Eq. (16.246)) for the following temporal pulse sequence:
(i) resonant $\pi/2$-pulse ($\Delta_{12} = 0$) choosing $\Omega_{12} = 2$,
(ii) evolution for a time T without radiation ($\Omega_{12} = 0$),
(ii) resonant π-pulse using the same parameters as in (i),
(iv) evolution for a time T without radiation, and
(v) resonant $\pi/2$-pulse identical to the first pulse.
Prepare a graph of type Fig. 16.2 illustrating the temporal evolution of the Bloch vector during the sequence. Now, repeat the sequence taking into account a possible Doppler shift leading to $\Delta_{12} \neq 0$.
b. Repeat the calculation of (a), now numerically solving the Bloch equations, which allow the occurrence of spontaneous emission ($\Gamma_{12} = 0.03\Omega_{12}$). Interpret the results.

16.3.7.10 Ex: Time-evolution of NMR spin components

Derive the coherent part of the Bloch equations (16.138) from the Heisenberg equation (16.137).

16.3.7.11 Ex: Precession of the nuclear spin in a magnetic field

Show for $\hat{H}_0 = -\frac{\hbar\omega_L}{2}\hat{\sigma}_z$ that,

$$\langle\hat{\vec{\sigma}}(t)\rangle = \begin{pmatrix} \cos\omega_L t & -\sin\omega_L t & 0 \\ \sin\omega_L t & \cos\omega_L t & 0 \\ 0 & 0 & 1 \end{pmatrix} \langle\hat{\vec{\sigma}}(0)\rangle \ .$$

16.4 Bloch equations with spontaneous emission

In this section we will introduce spontaneous emission and the important concepts of polarization and susceptibility emanating from an excited sample of oscillating dipoles. Optical Bloch equations including spontaneous emission will be given and their stationary solutions will be discussed. Dissipative processes always broaden transition lines, and thus we will discuss various broadening mechanisms.

16.4.1 Phenomenological inclusion of spontaneous emission

To find the Bloch equations including spontaneous emission, we proceed similarly for Eq. (16.26) and insert the phenomenological decay term $-\imath\gamma a_2$ into the Eqs. (5.63),

$$\Omega^* \cos\omega t e^{\imath\omega_0 t} a_1 - \imath\gamma a_2 = \imath \frac{da_2}{dt} \ , \tag{16.147}$$

that is, the equations of motion can be corrected by simply replacing,

$$\frac{da_2}{dt} \curvearrowright \left(\frac{d}{dt} + \gamma\right) a_2 \ . \tag{16.148}$$

Knowing $\rho_{mn} = a_m^* a_n$, it is easy to check,

$$\frac{d\rho_{22}}{dt} \curvearrowright \left(\frac{d}{dt} + \Gamma\right) \rho_{22} \qquad \text{and} \qquad \frac{d\rho_{12}}{dt} \curvearrowright \left(\frac{d}{dt} + \gamma\right) \rho_{12} \ , \tag{16.149}$$

with $\gamma = \Gamma/2$, such that the Bloch equations become,

$$\boxed{\frac{d}{dt}\begin{pmatrix}\rho_{11}\\ \rho_{22}\\ \rho_{12}\\ \rho_{21}\end{pmatrix} = \begin{pmatrix} 0 & \Gamma & \frac{\imath}{2}\Omega & -\frac{\imath}{2}\Omega \\ 0 & -\Gamma & -\frac{\imath}{2}\Omega & \frac{\imath}{2}\Omega \\ \frac{\imath}{2}\Omega & -\frac{\imath}{2}\Omega & -\imath\Delta - \gamma & 0 \\ -\frac{\imath}{2}\Omega & \frac{\imath}{2}\Omega & 0 & \imath\Delta - \gamma \end{pmatrix}\begin{pmatrix}\rho_{11}\\ \rho_{22}\\ \rho_{12}\\ \rho_{21}\end{pmatrix}} \ . \tag{16.150}$$

Example 92 (*Langevin equation*): The *Heisenberg equation* for the evolution of the internal degrees of freedom, including the phenomenologically introduced decay, is also called *Langevin equation*. It can be written as,

$$\imath \frac{d\hat{\sigma}^-}{dt} = \tfrac{1}{\hbar}[\hat{\sigma}^-, \hat{H}] - \tfrac{\imath}{2}\Gamma\hat{\sigma}^- \ ,$$

and analogously for $\hat{\sigma}_z$. With the Hamiltonian $\hat{H} = \hbar\Delta\hat{\sigma}^+\hat{\sigma}^- + \frac{1}{2}\hbar\Omega(e^{\imath\omega t}\hat{\sigma}^- + h.c.)$ we obtain, using the Pauli spin matrices, exactly the Bloch equations,

$$\imath\dot{\hat{\sigma}}^- = \Delta[\hat{\sigma}^-, \hat{\sigma}^+\hat{\sigma}^-] + \tfrac{1}{2}\Omega e^{-\imath\omega t}[\hat{\sigma}^-, \hat{\sigma}^+] - \tfrac{\imath}{2}\Gamma\hat{\sigma}^- = \Delta\hat{\sigma}^- - \tfrac{1}{2}\Omega e^{-\imath\omega t}\hat{\sigma}_z - \tfrac{\imath}{2}\Gamma\hat{\sigma}^-$$
$$\imath\dot{\hat{\sigma}}_z = \Delta[\hat{\sigma}_z, \hat{\sigma}^+\hat{\sigma}^-] + \tfrac{1}{2}\Omega e^{-\imath\omega t}[\hat{\sigma}_z, \hat{\sigma}^+] + \tfrac{1}{2}\Omega e^{\imath\omega t}[\hat{\sigma}_z, \hat{\sigma}^-] - \tfrac{\imath}{2}\Gamma\hat{\sigma}_z = \Omega(\hat{\sigma}^- - \hat{\sigma}^+) - \tfrac{\imath}{2}\Gamma\hat{\sigma}_z \ .$$

16.4.1.1 Stationary solution of the Bloch equations

The dissipation introduced by the spontaneous emission allows the system to reach a steady state. Letting the time derivatives be 0, we obtain the stationary solutions,

$$\boxed{\rho_{22}(\infty) = \frac{\frac{1}{4}|\Omega|^2}{\Delta^2 + \frac{1}{2}|\Omega|^2 + \frac{1}{4}\Gamma^2} \qquad \text{and} \qquad \rho_{12}(\infty) = e^{\imath\Delta t}\frac{\frac{1}{2}\Omega(\Delta - \frac{\imath}{2}\Gamma)}{\Delta^2 + \frac{1}{2}|\Omega|^2 + \frac{1}{4}\Gamma^2}} \; . \tag{16.151}$$

This will be shown in Exc. 16.4.4.1. We see that the populations and coherences both have a Lorentzian frequency dependence, which is similar to the one of the absorption cross section σ derived in (1.72). However, the denominators have an extra term $\frac{1}{2}\Omega^2$ contributing to an *effective* widths of ρ_{22} and ρ_{12},

$$\Gamma_{\text{eff}} = \sqrt{2|\Omega|^2 + \Gamma^2} \; . \tag{16.152}$$

This effect, called *power broadening* or *saturation broadening*, has already been discussed in (1.102). The phase factor $e^{\imath\Delta t}$ describes the optical precession of the Bloch vector.

By introducing the *saturation parameter*,

$$s \equiv \frac{2|\Omega|^2}{4\Delta^2 + \Gamma^2} \; , \tag{16.153}$$

we can rewrite the stationary dipole moment and the excited state population (16.151) as,

$$\boxed{\rho_{22}(\infty) = \frac{s/2}{1+s} \qquad , \qquad \rho_{12}(\infty) = e^{\imath\Delta t}\frac{\Delta - \imath\Gamma/2}{\Omega}\frac{s}{1+s} \; .} \tag{16.154}$$

and

$$|\rho_{12}(\infty)|^2 = \frac{s/2}{(1+s)^2} \; . \tag{16.155}$$

Fig. 16.3(a) shows the Rabi oscillations damped by spontaneous emission. For long times the population of the excited state ρ_{22} converges to the asymptote (16.154). Fig. 16.3(b) shows the temporal evolution of the Bloch vector subject to spontaneous emission. In Exc. 16.4.4.2 we the behavior of the phase of the dipole moment ρ_{12} with respect to the driving field. In Exc. 16.4.4.3 and 16.4.4.4 we calculate the impact of the spontaneous emission on the determinant of the density operator. Solve the Excs. 16.4.4.5, 16.4.4.6, 16.4.4.7, and 16.4.4.8.

> **Example 93 (*Resonant excitation and weak excitation*):** A case where the Bloch equations can be analytically treated is under resonant excitation, $\Delta = 0$. In this case, for the initial conditions, $\rho_{12}(0) = \rho_{22}(0) = 0$, the solution including decay is,
>
> $$\rho_{22}(t) = \frac{\Omega^2}{2|\Omega|^2 + \Gamma^2}\left[1 - e^{-3\Gamma t/4}\left(\cos\lambda t + \frac{3\Gamma}{4\lambda}\sin\lambda t\right)\right] \qquad \text{and} \qquad \rho_{12}(t) = 0 \; , \tag{16.156}$$
>
> where $\lambda \equiv \sqrt{\Omega^2 - \Gamma^2}$. This solution (which will be derived in Exc. 16.4.4.9), describes the optical nutation of the Bloch vector along the ρ_z axis. We note here that, due to spontaneous emission, the norm of the Bloch vector is NOT

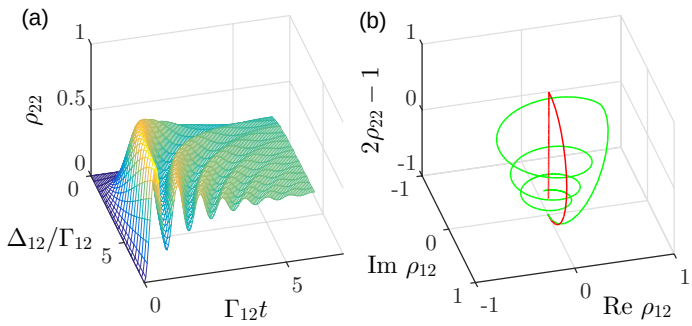

Figure 16.3: (code) (a) Rabi oscillations damped by spontaneous emission for Rabi frequencies between $\Omega/\Gamma = 0.2, .., 5$. (b) Evolution of the Bloch vector subject to spontaneous emission ($\Gamma_{12} = 0.05\Omega_{12}$) after application of a resonant π-pulse (red) and after a π-pulse with detuning $\Delta_{12} = \Omega_{12}/2$ (green).

conserved, i.e. the Bloch vector evolves to the interior of the Bloch sphere. Another case that can be solved analytically is the weakly excited atom, $|\Omega| \ll \Gamma$,

$$\rho_{22} \simeq \frac{\Omega^2}{4G^2}\left(1 + e^{-2\Gamma t} - 2\cos\Delta t\right) \tag{16.157}$$

$$\text{and} \qquad \rho_{12}(t) \simeq \frac{-\imath\Omega}{2\imath\Delta + 2\Gamma}\left(e^{-(\imath\Delta+\Gamma)t} - 1\right) + \rho_{12}(0)e^{-(\imath\Delta+\Gamma)t} \ .$$

16.4.1.2 Nonlinearity of the Bloch equations

Because the Bloch equation go beyond perturbation theory they contain nonlinear optics. We can see this by the simple fact that strong radiation field can saturate atomic transitions. For example, expanding the population and coherence (16.151) by the incident electric field amplitude $\mathcal{E} \propto \Omega$,

$$\rho_{22}(\infty) \simeq \frac{1}{4\Delta^2 + \Gamma^2}\Omega^2 - \frac{2}{(4\Delta^2 + \Gamma^2)^2}\Omega^4 + ... \tag{16.158}$$

$$\rho_{12}(\infty) \simeq e^{\imath\Delta t}\frac{2\Delta - \imath\Gamma}{4\Delta^2 + \Gamma^2}\Omega - 2e^{\imath\Delta t}\frac{2\Delta - \imath\Gamma}{(4\Delta^2 + \Gamma^2)^2}\Omega^3 + ... \ .$$

The theory of nonlinear optics will be developed in Sec. 17.5.2 and Chp. 19.

Example 94 (*Complex susceptibility and absorption coefficient*): The objective of this section is to obtain an expression for the susceptibility in the presence of spontaneous emission. For the present discussion we are only concerned with the temporal dependence of the actual light wave, which we write as,

$$\vec{\mathcal{E}}(t) = \vec{\mathcal{E}}_0 \cos\omega t = \tfrac{1}{2}[e^{\imath\omega t} + e^{-\imath\omega t}] \ . \tag{16.159}$$

Then we consider how to write the polarization in terms of a susceptibility when the field contains two conjugate frequencies, $\pm\omega$. Substituting into the polarization , we get,

$$\vec{\mathcal{P}}(t) = \varepsilon_0\chi_e\vec{\mathcal{E}} = \tfrac{1}{2}\varepsilon_0\vec{\mathcal{E}}_0[\chi_e(\omega)e^{\imath\omega t} + \chi_e(-\omega)e^{-\imath\omega t}] \ . \tag{16.160}$$

The polarization can also be expressed in terms of the density of the transition dipoles in a gas of two-level atoms,

$$\vec{\mathcal{P}}(t) = \frac{N}{V}\mathbf{d}_{12}(t) \longrightarrow \frac{N}{V}\langle \mathbf{d}_{12}(t)\rangle \ . \tag{16.161}$$

where $\mathbf{d}$ is the transition dipole of only one atom, N/V is the atomic density, and the quantum expectation value for the transition dipole moment is,

$$\langle \mathbf{d}_{12}\rangle = -e \int \Psi \sum_j \mathbf{r}_j \Psi d^3 r \ . \tag{16.162}$$

Now, from Eq. (5.58),

$$\langle \mathbf{d}_{12}\rangle = -e \left[a_1^* a_2 \langle \psi_1| \sum_j \mathbf{r}_j |\psi_2\rangle e^{-\imath\omega_0 t} + a_1 a_2^* \langle \psi_2| \sum_j \mathbf{r}_j |\psi_1\rangle e^{\imath\omega_0 t} \right] \ . \tag{16.163}$$

To simplify the notation we define $\langle \mathbf{r}_{mn}\rangle \equiv \langle \psi_m| \sum_j \mathbf{r}_j |\psi_n\rangle$ and obtain,

$$\langle \mathbf{d}_{12}\rangle = -e[a_1^* a_2 \langle \mathbf{r}_{12}\rangle e^{-\imath\omega_0 t} + a_1 a_2^* \langle \mathbf{r}_{21}\rangle e^{\imath\omega_0 t}] \ . \tag{16.164}$$

Now, we only need to replace the solutions of the coupled equations by relating a_1 and a_2 of the Eqs. (5.63) in (16.164) which, in turn, can be inserted into the equation (16.160). Thus we obtain an expression for the polarization in terms of properties of the atoms and the incident field.
The crucial point now is, that the solution for a_2, Eq. (5.79), does not consider spontaneous emission. Therefore, as already done in Sec. 16.4.1, we will introduce an ad hoc modification of Eq. (5.63) by including a radiative loss constant γ,

$$\Omega^* \cos\omega t e^{\imath\omega_0 t} a_1 - \imath\gamma a_2 = \imath \frac{da_2}{dt} \ . \tag{16.165}$$

This term does NOT EXPLAIN spontaneous emission. It simply takes into account the existence of the effect and characterizes its amplitude through γ: If the incident field is turned off ($\Omega^* = 0$)

$$-\imath\gamma a_2 = \imath \frac{da_2}{dt} \tag{16.166}$$

and

$$a_2(t) = a_2(0) e^{-\gamma t} \ . \tag{16.167}$$

Then, the probability of finding an atom in the excited state (or the fraction of excited atoms in an ensemble) is,

$$N_2/N = |a_2(t)|^2 = |a_2(0)|^2 e^{-2\gamma t} \ . \tag{16.168}$$

Comparing this behavior with the result obtained from the Einstein rate equation, we see immediately,

$$A_{21} = 2\gamma \equiv \Gamma \ . \tag{16.169}$$

Now, the solution for our improved $a_2(t)$ coefficient is,

$$a_2(t) = -\tfrac{1}{2}\Omega^* \left[\frac{e^{\imath(\omega_0+\omega)t}}{\omega_0 + \omega - \imath\gamma} + \frac{e^{\imath(\omega_0-\omega)t}}{\omega_0 - \omega - \imath\gamma} \right] \ , \tag{16.170}$$

which solves the differential equation (16.165) in the weak field limit, $a_1(t) \simeq 1$, as will be verified in Exc. 16.4.4.10.

Making the weak field approach, replacing the values obtained for $a_{1,2}$ in the transition dipole (16.164) and replacing the average of the orientations, $|\langle r_{12}\rangle|^2 \longrightarrow \frac{1}{3}|\langle r_{12}\rangle|^2$, in the polarization (16.161), we obtain,

$$\begin{aligned}\vec{\tilde{\mathcal{P}}}(t) &= \varepsilon_0 \tilde{\chi}_e \vec{\mathcal{E}} \qquad (16.171)\\ &= \frac{N}{V}\frac{e^2|\langle r_{12}\rangle^2 \vec{\mathcal{E}}_0}{6\hbar}\left[\frac{e^{\imath\omega t}}{\omega_0+\omega-\imath\gamma}+\frac{e^{\imath\omega t}}{\omega_0-\omega+\imath\gamma}+\frac{e^{-\imath\omega t}}{\omega_0-\omega-\imath\gamma}+\frac{e^{-\imath\omega t}}{\omega_0+\omega+\imath\gamma}\right] .\end{aligned}$$

Apparently, the presence of spontaneous emission turns the susceptibility into a complex number .
Comparing this result with Eq. (16.160) and identifying the susceptibility $\tilde{\chi}_e(\omega)$ in terms of the atomic properties and the frequency of the incident field, we find,

$$\begin{aligned}\tilde{\chi}_e(\omega) &= \frac{Ne^2|\langle r_{12}\rangle|^2}{3\epsilon_0\hbar V}\left[\frac{1}{\omega_0-\omega-\imath\gamma}+\frac{1}{\omega_0+\omega-\imath\gamma}\right] \qquad (16.172)\\ &= \frac{Ne^2|\langle r_{12}\rangle^2}{3\epsilon_0\hbar V}\left[\frac{\omega_0-\omega}{(\omega_0-\omega)^2+\gamma^2}+\frac{\omega_0+\omega}{(\omega_0+\omega)^2+\gamma^2}\right.\\ &\quad \left.+\imath\gamma\left(\frac{1}{(\omega_0-\omega)^2+\gamma^2}+\frac{1}{(\omega_0+\omega)^2+\gamma^2}\right)\right] .\end{aligned}$$

In most practical situations in the laboratory ω will not be tuned more than some 100 GHz away from ω_0, hence $|\omega_0-\omega| \lesssim 10^{11}$ Hz. With optical frequencies $\omega \simeq 10^{15}$ Hz, it is clear that the second term on the right hand side of Eq. (16.172) will be negligible compared to the first one. Therefore, we can discard the second term and write the susceptibility as,

$$\begin{aligned}\chi_e(\omega) &\simeq \frac{Ne^2|\langle r_{12}\rangle|^2}{3\epsilon_0\hbar V}\frac{1}{\omega_0-\omega-\imath\gamma} \qquad (16.173)\\ &= \frac{Nd_{12}^2}{3\epsilon_0\hbar V}\frac{-\Delta+\imath\Gamma/2}{\Delta^2+(\Gamma/2)^2} = \frac{n\hbar\Omega^2}{3\epsilon_0 E_0^2}\frac{-\Delta+\imath\Gamma/2}{\Delta^2+(\Gamma/2)^2} .\end{aligned}$$

We identify the real and imaginary parts, $\tilde{\chi}_e = \chi_e' + \imath\chi_e''$, and express the absorption coefficient as ,

$$K = \frac{\omega}{c\eta}\chi_e''(\omega) = \frac{\pi N d_{12}^2\omega_0}{3\epsilon_0\hbar c V}\frac{\Gamma/2\pi}{\Delta^2+(\Gamma/2)^2} = \frac{\pi N d_{12}^2\omega_0}{3\epsilon_0\hbar c V}\mathfrak{L}(\omega-\omega_0) . \qquad (16.174)$$

The Lorentzian profile term governs the frequency dependence of the absorption coefficient. We see that K exhibits a peak at the resonance frequency ω_0 and a width of Γ. The factor of π inserted in the numerator and denominator of the right term of Eq. (16.174) allows to normalize the profile. We have also assumed in Eq. (16.174) that the gas is sufficiently dilute for $n \simeq 1$ to hold, and that the line is sufficiently narrow to be able to replace ω with ω_0, such that,

$$\frac{\omega}{c\eta} \longrightarrow \frac{\omega_0}{c} . \qquad (16.175)$$

The absorption cross section has the same lineshape, since from Eqs. (1.72) and (16.174) we have,

$$\sigma_{0a} = \frac{\pi d_{12}^2\omega_0}{3\epsilon_0\hbar c V}\mathfrak{L}(\omega-\omega_0) , \qquad (16.176)$$

consistent with our previous expression for the frequency dependence of the absorption cross-section. We can also write the imaginary component of the susceptibility in terms of the cross section using the Eqs. (1.72) and (16.174)

$$\chi_e'' = \frac{cN}{\omega_0 V}\sigma_{0a} \ . \tag{16.177}$$

The frequency-dependent linear *susceptibility* completely describes the linear propagation of an electromagnetic wave within a medium. It is related to the index of refraction and the absorption coefficient. Nonlinear processes should be described by higher order susceptibilities. Electric fields $\vec{\mathcal{E}} = \vec{\mathcal{E}}_0 e^{\imath\omega t} + c.c.$ induce in media characterized by a given susceptibility $\tilde{\chi}_e$ the polarization $\vec{\mathcal{P}} = \varepsilon_0 \tilde{\chi}_e \vec{\mathcal{E}}$. The polarization is the sum of the dipole moments of the individual atoms, $\vec{\mathcal{P}} = n\langle \mathbf{d} \rangle$, where $n = N/V$ is the atomic density. The susceptibility can therefore be expressed by the Hamiltonian interaction $\hat{H} = -\mathbf{d} \cdot \vec{\mathcal{E}}$,

$$\chi_e = -\frac{n}{|\vec{\mathcal{E}}|^2} \ \langle \hat{H} \rangle \ . \tag{16.178}$$

Using the two-level Hamiltonian (16.172) we obtain,

$$\chi_e = -n \ \frac{\hbar\Omega}{2|\vec{\mathcal{E}}|^2} \ \rho_{12} e^{\imath\Delta t} + c.c. \tag{16.179}$$

for the polarization,

$$\vec{\mathcal{P}} = n \ \mathbf{d}\rho_{12} + c.c. \tag{16.180}$$

and for the susceptibility,

$$\chi_e(\omega) = \frac{2nd^2}{3\varepsilon_0\hbar} \frac{\Delta + \imath\Gamma}{4\Delta^2 + 2|\Omega|^2 + \Gamma^2} \qquad \text{with} \qquad d = \sqrt{\frac{3\pi\varepsilon_0\hbar\Gamma}{k^3}} \ . \tag{16.181}$$

We can insert the new expression (16.151) for ρ_{12} into our previous expression for $\langle d_{12} \rangle$ (16.164) and get new expressions for the polarization $\vec{\mathcal{P}}(t)$, (16.161) and (16.171), and the susceptibility χ (16.173). The modified expression for the susceptibility is,

$$\chi_e = \frac{Nd_{12}^2}{3\epsilon_0\hbar V} \frac{-\Delta + \frac{1}{2}\Gamma}{\Delta^2 + \frac{1}{2}|\Omega|^2 + \frac{1}{4}\Gamma^2} \ . \tag{16.182}$$

In the imaginary component we obtain the new absorption coefficient,

$$K = \frac{\omega}{cn}\chi_e''(\omega) = \frac{\pi N e^2 |\langle \mathbf{r}_{12} \rangle|^2 \omega_0}{3\epsilon_0\hbar c V} \frac{\Gamma/2\pi}{\Delta^2 + \frac{1}{2}\Omega^2 + \frac{1}{4}\Gamma^2} \ , \tag{16.183}$$

and the *optical cross-section* for absorption,

$$\sigma_{0a} = \frac{\pi e^2 |\langle \mathbf{r}_{12} \rangle|^2 \omega_0}{3\epsilon_0\hbar c} \frac{\Gamma/2\pi}{\Delta^2 + \frac{1}{2}\Omega^2 + \frac{1}{4}\Gamma^2} \ . \tag{16.184}$$

The important new property is the effective width Γ_{eff}, which appears in χ_e, K, and σ_{0a}.

16.4.2 Liouville equation for two levels

In the previous section we chose to include spontaneous emission in the Bloch equations by phenomenological arguments. However, as we will show more ahead, dissipation can be treated from general principles. This treatment, named after *Weisskopf-Wigner*, derives from a Liouville type equation (15.6), but which holds for a total density operator $\rho_{atom:field}$ describing the atom and the electromagnetic modes, an equation for the density operator of only the atom. The price to pay for this simplification is an additional term appearing in the equation now called *master equation*,

$$\boxed{\begin{array}{rcl} \dot{\hat{\rho}}(t) & = & (\mathfrak{L}_0 + \mathfrak{L}_{\rm sp})\hat{\rho}(t) \qquad \text{with} \\ \mathfrak{L}_0\hat{\rho}(t) & \equiv & \frac{\imath}{\hbar}[\hat{\rho}(t), \hat{H}] \qquad \text{and} \qquad \mathfrak{L}_{\rm sp} = \frac{\Gamma}{2}(2\hat{\sigma}^-\hat{\rho}\hat{\sigma}^+ - \hat{\sigma}^+\hat{\sigma}^-\hat{\rho} - \hat{\rho}\hat{\sigma}^+\hat{\sigma}^-) \end{array}} \ , \tag{16.185}$$

where $\hat{\sigma}^\pm$ are the Pauli matrices. We show in Exc. 16.4.4.11, that the known Bloch equations can be derived from the master equation.

16.4.3 The effective Hamiltonian approach

In Sec. 16.4.1 we have shown that spontaneous emission can be phenomenologically be included by substituting $\frac{d}{dt} \curvearrowright \frac{d}{dt} + \frac{\Gamma}{2}$ in the Schrödinger equation,

$$\imath\left(\tfrac{d}{dt} + \tfrac{\Gamma}{2}|2\rangle\langle 2|\right)|\psi\rangle = \hat{H}|\psi\rangle \ . \tag{16.186}$$

Rewriting the Schrödinger equation as,

$$\imath\tfrac{d}{dt}|\psi\rangle = (\hat{H} - \imath\tfrac{\Gamma}{2}|2\rangle\langle 2|)|\psi\rangle \equiv \hat{H}_{\rm eff}|\psi\rangle \ , \tag{16.187}$$

it is tempting to study how far we can go [66, 67] with the emulation of dissipative processes by the Schrödinger equation using a non-Hermitian *effective Hamiltonian*.

More generally let us define,

$$\hat{H}_{\rm eff} \equiv \hat{H} - \imath\hat{D} \ . \tag{16.188}$$

Rederiving the master equation from Schrödinger equation with this Hamiltonian, we get,

$$\begin{aligned} \dot{\hat{\rho}} &= |\psi\rangle\frac{d\langle\psi|}{dt} + \frac{d|\psi\rangle}{dt}\langle\psi| = \imath\hat{\rho}\hat{H}^*_{\rm eff} - \imath\hat{H}_{\rm eff}\hat{\rho} \\ &= \imath[\hat{\rho}, \hat{H}] - \{\hat{\rho}, \hat{D}\} \ . \end{aligned} \tag{16.189}$$

And for the Heisenberg equation,

$$\begin{aligned} \tfrac{d}{dt}\langle\hat{A}\rangle &= \langle\dot{\psi}|\hat{A}|\psi\rangle + \langle\psi|\hat{A}|\dot{\psi}\rangle = \imath\langle\psi|\hat{H}^*_{\rm eff}\hat{A}|\psi\rangle - \imath\langle\psi|\hat{A}\hat{H}_{\rm eff}|\psi\rangle \\ &= \imath\langle\psi|[\hat{H}, \hat{A}]|\psi\rangle - \langle\psi|\{\hat{D}, \hat{A}\}|\psi\rangle \ . \end{aligned} \tag{16.190}$$

Apparently, the dissipation term adds an anti-commutator to the evolution equations. It is now interesting to compare the dissipative terms of the expressions (16.185) and (16.189).

16.4.3.1 Saturation effects by the effective Hamiltonian

The eigenvalues of the *effective Hamiltonian* of a two-level system excited by radiation,

$$\hat{H}_{\text{eff}} = \begin{pmatrix} 0 & \frac{1}{2}\Omega \\ \frac{1}{2}\Omega & \Delta - \frac{i}{2}\Gamma \end{pmatrix} , \tag{16.191}$$

describe possible effects of line broadening and/or displacement due to coupling,

$$\boxed{E_{\pm} = \tfrac{1}{2}\left(\Delta - \tfrac{i}{2}\Gamma\right) \pm \tfrac{1}{2}\sqrt{\left(\Delta - \tfrac{i}{2}\Gamma\right)^2 + \Omega^2}} . \tag{16.192}$$

The real parts of the eigenvalues $\mathfrak{Re}\, E$ describe shifts and/or splittings of the transition line. The imaginary parts $\mathfrak{Im}\, E$ describe broadening effects of the lines.

In the simplest case, $\Delta = 0$ and $\Gamma > 4\Omega$, we find the *saturation broadening* already discussed in (16.152), and we will deepen it in Exc. 16.7.3.2. For the case $\Gamma < 4\Omega$, we observe a splitting of the line called *Autler-Townes splitting*, which will be studied in Exc. 16.7.3.1. If $\Omega \neq 0$, the spectrum becomes asymmetrical. In the case of weak excitation, $\Gamma \gg 4\Omega$, we observe a shift of the transition line with dispersive dependence (near the resonance) on the frequency of the incident radiation. This is the *dynamic Stark shift* (or *light shift*). In the case of strong excitation, $\Gamma \ll 4\Omega$, we observe again at the split spectrum, but now the two lines exhibit an *avoided crossing*-type dependence on the radiation frequency. We study these effects in Excs. 16.4.4.12 and Exc. 16.4.4.13.

Obviously, these effects can be studied by the Bloch equation formalism containing the terms of spontaneous relaxation.

16.4.4 Exercises

16.4.4.1 Ex: Stationary solution of the Bloch equations

Derive the stationary solution of the Bloch equations including spontaneous emission. How does the spectrum $\rho_{22}(\Delta)$ change in the presence of phase noise, $\gamma = \frac{\Gamma}{2} + \beta$, in particular if $\beta \gg \frac{\Gamma}{2}$?

16.4.4.2 Ex: Detuning-dependent phase-shift of the dipole moment

Calculate the phase-shift of the dipole moment with respect to the driving field across resonance.

16.4.4.3 Ex: Determinant of the Bloch matrix

In Sec. 14.2.1 we already saw that $\det \hat{\rho} = 0$ for conservative systems. Now, show explicitly for the Bloch matrix of a two-level system, that $\det \hat{\rho} = 0$ only holds in the absence of spontaneous emission.

16.4.4.4 Ex: Density operator with dissipation

Discuss the phenomenon of dissipation at the example of
a. a thermal sample of two-level systems $|i\rangle = |1\rangle, |2\rangle$ characterized by the density

operator $\hat{\rho} = |i\rangle\langle i| \otimes |v\rangle\langle v|$, where $|v\rangle$ is the velocity state of the atom and
b. a two-level atom coupled to a radiation field, $\hat{\rho} = |i\rangle\langle i| \otimes |n\rangle\langle n|$, where $|n\rangle$ is the number of photons inside the mode.

16.4.4.5 Ex: Bloch vector

A two-level atom with decay rate $\Gamma = 2\pi \times 6\,\mathrm{MHz}$ be excited by a light field detuned by $\Delta = 2\Gamma$ and whose intensity is a quarter of the saturation intensity. Write down the Bloch vector for $t \to \infty$.

16.4.4.6 Ex: Purity of two-level atoms with spontaneous emission

Calculate for a driven two-level atom in the stationary limit Tr $\hat{\rho}$ and Tr $\hat{\rho}^2$.

16.4.4.7 Ex: Bloch sphere

Check the temporal evolution of the norm of the Bloch vector defined by $\vec{\rho} \equiv (2\ \mathfrak{Re}\,\sigma_+\ ,\ 2\ \mathfrak{Im}\,\sigma_-\ ,\ \sigma_z)$, where the σ_k are the Pauli matrices, for a resonantly excited two-level system with and without spontaneous emission.

16.4.4.8 Ex: Atomic beam

An atomic beam is illuminated perpendicular to its propagation direction by (quasi-)monochromatic, collimated laser pulses having the intensity $I = 1\,\mathrm{W/cm^2}$, the wavelength $\lambda = 780\,\mathrm{nm}$, and the duration 200 ns. The laser is tuned to the center of an atomic resonance line ($\Gamma/2\pi = 6\,\mathrm{MHz}$).
a. How does the population of the upper atomic state develop?
b. How does the dynamics change, when the light is detuned by 100 MHz?

16.4.4.9 Ex: Solution of the Bloch equations for resonant excitation

Derive the solution (16.156) of the Bloch equations with spontaneous emission for resonant excitation.

16.4.4.10 Ex: Solution for the susceptibility

Show that the solution of Eq. (16.165) is given by the result (16.170).

16.4.4.11 Ex: General form of the master equation

Show that the general form of the master equation: $\dot{\hat{\rho}} = -\frac{\imath}{\hbar}[\hat{H}, \hat{\rho}] - \frac{\Gamma}{2}(2\hat{\sigma}\hat{\rho}\hat{\sigma}^+ - \hat{\sigma}^+\hat{\sigma}\hat{\rho} - \hat{\rho}\hat{\sigma}^+\hat{\sigma})$, reproduces the Bloch equations including spontaneous emission.

16.4.4.12 Ex: Light-shift

Calculate the light-shift in a driven two-level system from the *effective Hamiltonian*,

$$\hat{H}_{\mathrm{eff}} = \begin{pmatrix} 0 & \frac{1}{2}\Omega \\ \frac{1}{2}\Omega & \Delta - \frac{\imath}{2}\Gamma \end{pmatrix} .$$

Prepare spectra of the eigenvalues for $\Gamma/\Omega = 0$, 0.5, and 2.

16.4.4.13 Ex: Light-shift

In this exercise we study the effect of the dynamic Stark shift (or light shift) of the energy levels of a two-level system $|1\rangle$ and $|2\rangle$ excited by a laser with the Rabi frequency Ω_{12} and the detuning Δ_{12}:
a. From the eigenvalues $E_{1,2}$ of the effective Hamiltonian (16.191) system, find approximations for weak coupling ($\Omega_{12} \ll \Gamma_{12}$) and strong coupling ($\Omega_{12} \gg \Gamma_{12}$). Prepare a graph showing the eigenvalue spectrum (separating the parts $\mathfrak{Re}\, E_{1,2}$ and $\mathfrak{Im}\, E_{1,2}$) as a function of detuning Δ_{12} for various values of Ω_{12}. Also search for approximations valid for large detunings $\Delta_{12} \gg \Gamma_{12}, \Omega_{12}$ and add them to the graph.
The light shift can be experimentally measured in a three-level system in Λ-configuration, as illustrated in Fig. 16.7(a). To reproduce the experiment by numerical simulations of the Bloch equations (16.238),
b. write the Liouville matrix $\mathcal{M}_{\text{red}}$ reduced by the condition to the trace (16.243) and calculate the stationary Bloch vector from equation (16.245) varying the detunings of the two lasers Δ_{12} and Δ_{23}. Choosing the parameters $\Gamma_{23} = \Gamma_{12}$, $\Gamma_{13} = 0.01\Gamma_{12}$, $\Omega_{12} = 2\Gamma_{12}$, and $\Omega_{23} = 0.2\Gamma_{12}$, prepare a 3D curve [similar to Fig. 16.3(a)] of the stationary population $\rho_{22}(\infty)$. Interpret the results.

16.4.4.14 Ex: Line broadening by phase noise and optical repumping

a. For a two-level system calculate ρ_{22} as a function of detuning Δ and a phase noise rate β added to the coherence decay rate $\Gamma/2$, such that $\gamma = \Gamma/2 + \beta$.
b. Check that incoherent optical pumping from the ground into the excited state introduces a transverse decay rate R leading to line broadening, and plot ρ_{22} as a function of detuning Δ and the pump rate R.

16.4.4.15 Ex: Superradiant decay upon fast switch-off

We consider a laser-driven two-level system having reached steady-state and want to study the population decay as a function of the switch-off time of the driving laser light. In certain parameter regimes (low saturation and large detuning) the population decay is found to be faster than Γ, when the switch-off time is chosen on the order of Γ^{-1} [34]. Simulate the evolution of the population as a function of switch-off time and interpret the observations.

16.5 Line broadening mechanisms

The resolution of atomic spectroscopy is generally limited by several perturbative effects, many of them originating in the atomic motion. They manifest themselves as broadening and/or shifts of atomic resonances. Free atoms, as well as atoms confined in potentials, have kinetic energy and evolve on extended phase space trajectories. If the spatial localization is less than the effective cross section of the exciting laser beam, then the interaction time is limited and the resonance lines are broadened by the Fourier effect in a process called *transit time broadening*, and the efficiency of fluorescence collection is reduced. The same happens with the *Doppler effect*: Only those atoms that have a specific velocity along the optical axis defined by the laser

beam can interact. Free as well as confined atoms can only scatter when they are in specific cells of the phase space.

There are two different fundamental types of broadening. The so-called *homogeneous broadening* affects all atoms in the same way regardless of their positions or velocities. It usually gives rise to Lorentzian line profiles and can be incorporated into the Bloch equations by a simple modification of relaxation rates. Examples are the natural linewidth, saturation broadening, collision broadening, or phase noise induced by laser fluctuations.

The so-called *inhomogeneous broadening* is due to a displacement of atomic levels, which may be different for each atom. Averaging over a large sample of atoms, the displacements generate an *effective* broadening usually with a Gaussian line profile. It *can not* be included in the single-atom Bloch equations, but only as an average over all trajectories of all atoms. It does not correspond to an accelerated relaxation. Inhomogeneous broadening is often due to external perturbations, e.g., Doppler broadening and broadening due to temporal fluctuations or spatial inhomogeneities of external electric or magnetic fields. In Exc. 16.5.6.1 we calculate the optical density of atomic clouds. In Exc. 16.5.6.2 we present a spectroscopic technique bypassing the Doppler broadening called *Doppler-free spectroscopy* and calculate the *Lamb-dip* profile. Finally, in Exc. 16.5.6.3, we discuss a cooling technique allowing for the reduction of Doppler broadening, called *Zeeman slower*.

16.5.1 Saturation broadening

Eq. (16.152) shows that when the power of the incident light increases, the population of the excited state saturates at a limit value of $\rho_{22} = \frac{1}{2}$. The *saturation parameter* defined in (16.153) measures the degree of saturation. When the narrowband light source is tuned to resonance, the saturation parameter is basically a measure for the ratio between the stimulated population transfer rate Ω and the spontaneous decay rate A_{21}. We can rewrite the stationary population of the excited level as in (16.154). In resonance and with the saturation parameter $s = 1$, we obtain

$$\Omega = \tfrac{1}{\sqrt{2}}\Gamma \ . \tag{16.193}$$

We can use equation (16.193) to define the *saturation intensity* $I_{\rm sat}$ for an atom with the transition dipole d_{12}. From Eq. (1.41) we have,

$$\mathcal{E}_0 = \sqrt{\frac{2\bar{I}}{\varepsilon_0 c}} \ . \tag{16.194}$$

Therefore, using the definition of the Rabi frequency, $\hbar\Omega = d_{12}\mathcal{E}_0$, and the relationship between d_{12} and Γ given by Eq. (16.41), we have [11],

$$\boxed{I_{\rm sat} = \frac{g_1}{g_2}\frac{2\pi^2 c\hbar}{3\lambda_0^3}\Gamma} \ , \tag{16.195}$$

taking into account the degeneracies g_j of the levels. In Excs. 16.5.6.4 and 16.5.6.5 we calculate the *saturation intensity* of popular atomic transitions.

[11] Some authors define the saturation for $s = 2$, as happens when $\Omega = \Gamma$.

16.5.2 Collision broadening

The theory of atomic collisions covers a large area of research, including elastic and inelastic, reactive and ionizing processes. In low-pressure gases at room temperature or hotter we need only consider the simpler processes: long-range van der Waals interactions that result in *elastic collisions*. The 'low pressure' criterion requires that the average free path between collisions be greater than any linear dimension of the gas volume. Under these conditions, collisions can be modeled with straight trajectories, along which the interaction time is short and the time between collisions is long in comparison with the radiative lifetime of the excited atomic state. Then, the impact of a collision on the emission of a radiating atom causes a loss of coherence due to a phase interruption of the excited state atomic wavefunction. The term 'elastic' means that the collision does not disturb the populations of the internal states, so we only need to consider the off-diagonal elements of the density matrix,

$$\frac{d\rho_{12}}{dt} = \imath\frac{\Omega_0}{2}e^{\imath(\omega-\omega_0)t}(\rho_{11}-\rho_{22}) - \gamma'\rho_{12} \ , \tag{16.196}$$

where γ' is the sum of the spontaneous emission γ and the collision rate $\gamma_{\rm col}$,

$$\boxed{\gamma' = \gamma + \gamma_{\rm col}} \ . \tag{16.197}$$

The inverse of the collision rate is simply the time between phase interruptions or the time between collisions. Now, for collisions between hard cores of atoms of mass m (with reduced mass $m_{\rm red} = m/2$) and with radius ρ in a gas with density n consisting of a single species, a standard analysis based on the kinetic theory of dilute gases shows that the time between collisions is given by the *collision rate*,

$$\gamma_{\rm col} = \tau_{\rm col}^{-1} = \sigma n\bar{v} \ , \tag{16.198}$$

where $\bar{v} = \sqrt{\frac{8k_{\rm B}T}{\pi m_{\rm red}}}$ is the average collision velocity in a homogeneous gas at the temperature T and $\sigma = \sqrt{8}\pi\rho^2$ the collision cross section. Thereby,

$$\boxed{\gamma_{\rm col} = \frac{8\rho^2 n}{\sqrt{m_{\rm red}/\pi k_{\rm B}T}}} \ . \tag{16.199}$$

We can now relate this simple result of gas kinetics to the phase interruption rate by reinterpreting the meaning of the *collision radius*. When an excited atom propagating through space suffers a collision, the long-range interaction will produce a time-dependent perturbation of the energy levels of the radiating atom and a phase shift in the radiation,

$$\eta = \int_{-\infty}^{\infty}[\omega(t)-\omega_0]dt = \int_{-\infty}^{\infty}\Delta\omega(t)dt \ . \tag{16.200}$$

The long-range van der Waals interaction is expressed by,

$$\Delta E = \hbar\omega = \frac{C_n}{[b^2+(vt)^2]^{n/2}} \ , \tag{16.201}$$

where b is the impact parameter of the collision trajectory and v the collision velocity. The phase shift is then

$$\eta = \frac{1}{\hbar}\int_{-\infty}^{\infty} \frac{C_n}{[b^2+(vt)^2]^{n/2}} dt \ . \tag{16.202}$$

The integral is easily assessed for the two most frequent cases: non-resonant van der Waals interactions $n = 6$ and resonant van der Waals interactions $n = 3$. The phase shifts are,

$$\eta_6(b) = \frac{2\pi}{3\hbar}\frac{C_6}{b_6^5 v} \qquad \text{and} \qquad \eta_3(b) = \frac{4\pi}{3\sqrt{3}\hbar}\frac{C_3}{b_3^2 v} \ . \tag{16.203}$$

Now, if instead of using the *hard core approximation*, we define a collision as an encounter causing a phase shift of at least 1 radians, we have a new condition for the collision radius,

$$b_6 = \left(\frac{2\pi}{3\hbar}\frac{C_6}{v}\right)^{1/5} \qquad \text{and} \qquad b_3 = \left(\frac{4\pi}{3\sqrt{3}\hbar}\frac{C_3}{v}\right)^{1/2} \ . \tag{16.204}$$

Replacing these collision radiuses for the radius ρ in Eq. (16.199) and inserting the average collision velocity, we find the collision rate,

$$\gamma_{c6} = 4n\left(\frac{\sqrt{2}\pi^2 C_6}{3\hbar}\right)^{2/5}\left(\frac{4\pi k_{\rm B}T}{\mu}\right) \qquad \text{and} \qquad \gamma_{c3} = 4n\left(\frac{2}{3}\right)^{3/2}\left(\frac{\pi^2 C_3}{\hbar}\right)^{3/10} \ . \tag{16.205}$$

Substituting the generalized γ' of (16.197) for γ in the Bloch equations (16.151), we find the stationary solutions,

$$\rho_{22} = \frac{\frac{1}{4}\frac{\gamma'}{\gamma}|\Omega|^2}{\Delta^2 + \frac{1}{2}\frac{\gamma'}{\gamma}|\Omega|^2 + \gamma'^2} \qquad \text{and} \qquad \rho_{12} = e^{\imath(\omega-\omega_0)t}\frac{\frac{1}{2}\Omega(\Delta - \imath\gamma')}{\Delta^2 + \frac{1}{2}\frac{\gamma'}{\gamma}|\Omega|^2 + \gamma'^2} \ . \tag{16.206}$$

The effective linewidth (radiative and collisions) is,

$$\Gamma'_{\rm eff} = 2\sqrt{\gamma'^2 + \tfrac{1}{2}\tfrac{\gamma'}{\gamma}|\Omega|^2} \ . \tag{16.207}$$

When the excitation is sufficiently weak, so that power broadening can be neglected in comparison to collision broadening, the second term can be discarded,

$$\Gamma'_{\rm eff} = 2(\gamma + \gamma_{\rm col}) \ . \tag{16.208}$$

The equations (16.152) and (16.208) express the linewidths in the limits of dominating power and collision broadening, respectively. Note that the susceptibility, absorption coefficient, and absorption cross-section retain their Lorentzian profile, but with a larger width due to collisions. Since each atom is subject to the same broadening mechanism, the broadening is homogeneous. Solve Excs. 16.5.6.6.

16.5.3 Doppler broadening

The *Doppler broadening* is simply the apparent frequency distribution of a sample of radiating atoms at temperature T. The contribution of each atom to the radiation

appears detuned by the *Doppler shift* because of its velocity. The frequency shift for a non-relativistically moving particle is $\omega = \omega_0/(1 - \frac{v}{c})$, such that,

$$\Delta \equiv \omega - \omega_0 \simeq \omega_0 \frac{v}{c} = \mathbf{k} \cdot \mathbf{v} = k v_z \ , \tag{16.209}$$

where $\mathbf{k}$ is the wavevector of the light and $\mathbf{v}$ is the velocity of the atom. This distribution of Doppler shifts of a gaseous sample in thermal equilibrium follows the probability distribution of velocities,

$$P(v_z)dv_z \propto e^{-mv_z^2/2k_\mathrm{B}T} dv_z = e^{-mc^2\Delta^2/2\omega_0^2 k_\mathrm{B}T} \frac{c}{\omega_0} d\omega \ . \tag{16.210}$$

This frequency distribution is a Gaussian centered at $\omega = \omega_0$ and with the width,

$$\mathrm{FWHM} = 2\omega_0 \left(\frac{2k_\mathrm{B}T \ln 2}{mc^2} \right)^2 \ . \tag{16.211}$$

A measure of the width is also the *standard deviation*,

$$2\sigma = \frac{2\omega_0}{c} \sqrt{\frac{k_\mathrm{B}T}{m}} = \frac{\mathrm{FWHM}}{1.177} \ . \tag{16.212}$$

From Eq. (16.210) we can see that the line profile is,

$$\mathcal{D}(\omega - \omega_0) \equiv \frac{1}{\sqrt{2\pi}} \frac{m}{k_\mathrm{B}T} e^{-(\omega-\omega_0)^2/2\sigma^2} d\omega \ . \tag{16.213}$$

The profile compares with the Lorentzian profile Eq. (1.73) associated with natural, power, or collision broadening. Doppler broadening is a property of the atomic ensemble, each atom suffering a unique but different displacement than the other atoms. Hence, it is called *inhomogeneous broadening*.

The Liouville equation (16.104) used to derive the Bloch equations assumes immobile atoms. However, we can easily apply the Galilei transformation to a system, where the atoms move with the given velocity $\mathbf{v}$,

$$(\partial_t + \mathbf{v} \cdot \nabla)\hat{\rho}(\mathbf{r}, t) = -\tfrac{\imath}{\hbar}[\hat{H}, \hat{\rho}(\mathbf{r}, t)] \ . \tag{16.214}$$

Since the light fields propagate as $e^{\imath(\omega t - \mathbf{k}\cdot\mathbf{r})}$, the solution of the above equation simply follows from the immobile solution with the substitution $\Delta \to \Delta - \mathbf{k} \cdot \mathbf{v}$. For a cloud obeying Maxwell's velocity distribution, $P(v) \sim e^{-mv^2/k_\mathrm{B}T}$,

$$\bar{\rho}(\Delta) = \frac{1}{\sqrt{2\pi}\sigma} \int_{\mathbb{R}} e^{-(\mathbf{k}\cdot\mathbf{v})^2/2\delta^2} \hat{\rho}(\Delta - \mathbf{k} \cdot \mathbf{v}) d(\mathbf{k} \cdot \mathbf{v}) \ . \tag{16.215}$$

The average of the density operator over all velocities, $\bar{\rho}$, therefore follows as the convolution of the density operator ρ (obtained as the solution of the Bloch equation) and the Gaussian function $G(\Delta) = (2\pi\sigma^2)^{-1/2} e^{-\Delta^2/2\sigma^2}$,

$$\boxed{\bar{\rho}(\Delta) = (G \star \hat{\rho})(\Delta)} \ . \tag{16.216}$$

16.5.4 Voigt profile

It is clear that in many practical circumstances homogeneous and inhomogeneous processes simultaneously contribute to the broadening of lines. In these cases, we can consider that the radiation of each atom, homogeneously broadened by phase-interruption processes (such as spontaneous emission or collisions), is displaced by the Doppler effect within the Maxwell-Boltzmann distribution corresponding to the temperature T. The profile of the gaseous sample, therefore, is a convolution of homogeneous and inhomogeneous profiles. The resulting profile is called *Voigt profile*:

$$V(\omega-\omega_0) = \int_{-\infty}^{\infty} \mathfrak{L}(\omega-\omega_0-\omega')\mathcal{D}(\omega-\omega_0)d\omega' \tag{16.217}$$
$$= \frac{\gamma}{2\sigma\sqrt{2\pi}}\int_{-\infty}^{\infty}\frac{e^{-(\omega-\omega_0)^2/2\sigma^2}}{(\omega-\omega_0-\omega')^2+(\gamma/2)^2}d\omega' \ .$$

This integral has no analytical solution, but it is easy to solve numerically. Resolve Excs. 16.5.6.7, 16.5.6.8, and 16.5.6.9.

16.5.5 Bloch equations with phase modulation

In some situations, the atom vibrates thus producing an oscillating Doppler shift. Also, external magnetic fields or oscillating laser frequencies can produce this effect. We incorporate this temporal modulation (frequency Ω_a) of the light frequency shifts, induced by the Doppler effect, into the optical Bloch equations via the substitution [742],

$$\Delta_{ij} \to \Delta_{ij} + \mathbf{k}_{ij}\cdot\mathbf{v}\ \cos\Omega_a t \ . \tag{16.218}$$

The Bloch equations can then be brought into the form,

$$\dot{\hat{\rho}} = (\mathbf{L} + 2\mathbf{X}\ \cos\Omega_a t)\hat{\rho} + \mathbf{b} \ , \tag{16.219}$$

where the matrix $\mathbf{X}$ contains the modulation index of the atomic motion $\mathbf{k}_{ij}\mathbf{v}$. The stationary solution of the differential equation, averaged over the time of an oscillation period, can be expressed as an infinite continuous fraction:

$$\hat{\rho}(\infty) = -(\mathbf{L}+\mathbf{S}^+ + \mathbf{S}^-)^{-1}\mathbf{b} \tag{16.220}$$
$$\text{where}\quad \mathbf{S}^{\pm} = -\mathbf{X}\cfrac{1}{\mathbf{L}\pm\imath\Omega_a\mathbf{1}-\mathbf{X}\cfrac{1}{\mathbf{L}\pm\imath\Omega_a\mathbf{1}-\mathbf{X}\frac{1}{\ddots}\mathbf{X}}\mathbf{X}} \ .$$

This solution replicates the correct excitation spectra even for a multilevel system.

Let us be more specific for a two-level system. In this case the Hamiltonian is given by $\hat{H}_{\text{int}} = \frac{1}{2}\hbar\Omega e^{-\imath[\omega t - \mathbf{k}\cdot\mathbf{v}/\Omega_a\ \sin\Omega_a t]}$, such that the Bloch equation is,

$$\begin{pmatrix}\dot{\rho}_{22}\\ \dot{\rho}_{12}\\ \dot{\rho}_{21}\end{pmatrix} = \left[\begin{pmatrix}-\Gamma & -\frac{\imath}{2}\Omega & \frac{\imath}{2}\Omega\\ -\frac{\imath}{2}\Omega & -\Lambda & 0\\ \frac{\imath}{2}\Omega & 0 & -\Lambda^*\end{pmatrix} + 2\cos\Omega_a t\begin{pmatrix}0&0&0\\0&-\frac{\imath}{2}kv&0\\0&0&\frac{\imath}{2}kv\end{pmatrix}\right]\begin{pmatrix}\rho_{22}\\ \rho_{12}\\ \rho_{21}\end{pmatrix} + \begin{pmatrix}0\\ \frac{\imath}{2}\Omega\\ -\frac{\imath}{2}\Omega\end{pmatrix} \ . \tag{16.221}$$

We look for the stationary solution by expanding $\hat{\rho} = \sum_{n=-\infty}^{\infty}\hat{\rho}_n e^{-\imath n\Omega_a t}$, letting $\dot{\hat{\rho}}_n = 0$, and projecting on $e^{-\imath n\Omega_a t}$ via,

$$(\mathbf{L}+\imath n\Omega_a\mathbf{1})\hat{\rho}_n + \mathbf{X}(\hat{\rho}_{n+1}+\hat{\rho}_{n-1}) + \mathbf{b}\delta_{n0} = 0 \ . \tag{16.222}$$

Now we define $\hat{\rho}_{n\pm1} = \mathbf{S}^{\pm}\hat{\rho}_n$ for $n \gtrless 0$. Then, equation (16.222) becomes,

$$\begin{aligned} \hat{\rho}_0 &= -[\mathbf{L} + \mathbf{X}(\mathbf{S}_0^+ + \mathbf{S}_0^-)]^{-1}\mathbf{b} \qquad \text{for} \qquad n = 0, \\ \mathbf{S}_{n\mp1}^{\pm} &= -[\mathbf{L} + \imath n\Omega_a \mathbf{1} + \mathbf{X}\mathbf{S}_n^{\pm}]^{-1}\mathbf{b} \qquad \text{for} \qquad n \gtrless 0 \ . \end{aligned} \tag{16.223}$$

Substituting the equation below into the equation above,

$$\hat{\rho}_0 = -\left[\mathbf{L} + \left(\frac{-\mathbf{X}|}{|\mathbf{L} + \imath\Omega_a} + \frac{-\mathbf{X}|}{|\mathbf{L} + 2\imath\Omega_a} + \ldots\right) + \left(\frac{-\mathbf{X}|}{|\mathbf{L} + \imath\Omega_a} + \frac{-\mathbf{X}|}{|\mathbf{L} + 2\imath\Omega_a} + \ldots\right)\right]^{-1}\mathbf{b} \ . \tag{16.224}$$

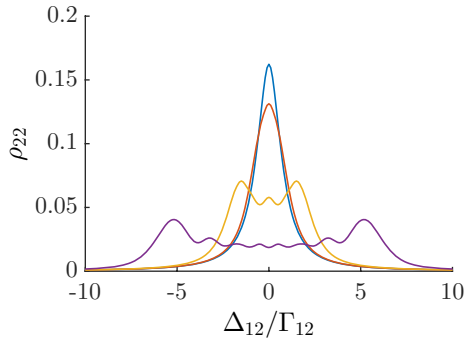

Figure 16.4: (code) Spectral broadening due to the periodic movement of the atom.

16.5.6 Exercises

16.5.6.1 Ex: Optical density of a cold cloud

The cross section of an atom with the resonant frequency ω_0 moving with velocity v and irradiated by a laser beam of frequency ω is,

$$\sigma(v) = \frac{6\pi}{k^2}\frac{\Gamma^2}{4(\omega - \omega_0 - kv)^2 + \Gamma^2} \ .$$

The normalized one-dimensional Maxwell distribution,

$$\rho(v)dv = \sqrt{\frac{m}{2\pi k_{\mathrm{B}}T}}e^{-mv^2/2k_{\mathrm{B}}T}dv \ .$$

a. Calculate the absorption profile of the resonance line at 461 nm ($\Gamma_{461} = (2\pi)\ 30.5$ MHz) of a strontium gas cooled to the Doppler limit ($k_{\mathrm{B}}T_D = \hbar\Gamma$) of this transition.
b. Calculate the absorption profile of the resonance line at 689 nm ($\Gamma_{689} = (2\pi)\ 7.6$ kHz) of a strontium gas cooled to the Doppler limit of the transition at 461 nm.
c. Compare the optical densities in case of resonance.
Help: To evaluate the convolution integral approximate the narrower distribution by a δ-function maintaining the integral over the distribution normalized.

16.5.6.2 Ex: Saturated absorption spectroscopy

Saturated absorption spectroscopy is a technique to avoid Doppler broadening. The setup, shown in Fig. 16.5, consists of a cell filled with a rubidium gas (resonance frequency $\omega_0 = ck = 2\pi c/780\,\text{nm}$, decay rate $\Gamma = (2\pi)\ 6\,\text{MHz}$) and two laser beams with the same frequency ω but counterpropagating, one called saturation and another called probe. The one-dimensional and normalized Maxwell velocity distribution is,

$$\rho(v)dv = \sqrt{\frac{m}{2\pi k_B T}} e^{-mv^2/2k_B T} dv \ .$$

The gas is at $T = 300\,\text{K}$, where the partial pressure of rubidium is around $P = 10^{-1}\,\text{mbar}$. The length of the cell is $L = 10\,\text{cm}$. The probe laser has an intensity below the saturation limit, such that the cross section of an atom moving at velocity v is,

$$\sigma(v) = \frac{6\pi}{k^2} \frac{\Gamma^2}{4(\omega - \omega_0 - kv)^2 + \Gamma^2} \ .$$

The saturation laser has high intensity. We suppose here, $\Omega \equiv 10\Gamma$, where Ω is the frequency of Rabi caused by the saturation beam. In this way it creates a population N_e of atoms in the excited state. As this population lacks in the ground state, $N_g = N - N_e$, the absorption of the probe beam is decreased by the factor,

$$\frac{N_e}{N} = \frac{\Omega^2}{4(\omega - \omega_0 + kv)^2 + 2\Omega^2 + \Gamma^2} \ .$$

To obtain the laser probe transmission spectrum, first calculate the optical density, $OD(\omega) = Ln \int_{-\infty}^{\infty} \frac{N_g - N_e}{N} \sigma(v)\rho(v)dv$ where n is the gas density, and then the intensity of light transmitted through the cell using the Lambert-Beer law $\frac{I}{I_0} = e^{-OD}$.

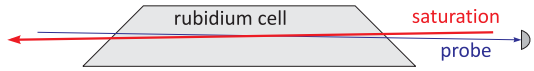

Figure 16.5: Scheme of saturation spectroscopy.

16.5.6.3 Ex: The Zeeman slower

Consider a tube through which passes a collimated beam of atoms, all having the same initial velocity $v = v_0$. In the opposite direction to the atomic motion travels a collimated and monochromatic light beam with frequency $\omega = kc$. The absorption rate for photons by an atom has a Lorentzian profile, which can be written as:

$$W(v) = \frac{W_0}{2\pi} \frac{\Gamma^2}{(\omega - \omega_0 + kv)^2 + (\Gamma/2)^2} \ ,$$

where Γ is the natural width of the spectral line at ω_0, and W_0 is a constant. The frequency of the light is tuned in order to compensate for the Doppler effect at the beginning of the tube, $\delta = \omega - \omega_0 = -kv_0$ (the light is tuned to the red of the resonance). As the atoms are decelerated, they cease to be resonant with the light

beam and fail to absorb photons. This can be avoided by employing the so-called Zeeman-slowing technique, which compensates for the effect using the Zeeman-shift induced by magnetic fields. In this exercise, we will study what happens if this technique is not used.

a. For an atom with velocity v, write an expression for the mean travel distance

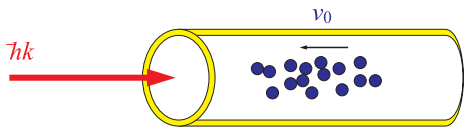

Figure 16.6: Zeeman slower scheme.

$\Delta s(v)$ before it absorbs a photon as a function of the parameters Γ, v_0, k, and W_0. (The mean time it takes to absorb a photon is $W(v)^{-1}$).

b. The velocity of the atom as a function of the number of absorbed photons is $v_n = v_0 - n\frac{\hbar k}{m}$, the second term being the recoil due to the absorption of a single photon. The average total distance traveled by an atom after absorbing N photons is estimated by:

$$S = \sum_{n=0}^{N} \Delta s(v_n) \simeq \int_0^N \Delta s(v_n) dn \ .$$

Calculate the average distance required for the atoms to be slowed down to $v = 0$ (ignoring the Doppler limit). Write the expression as a function of Γ, v_0, k, and W_0. **Help:** Do the following change of variables to simplify the evaluation of the integral: $n \to v$.

c. Typically, the detuning of the light, $|\delta| = kv_0$, is much larger than the natural width Γ of the transition. What happens to S in the limit when $kv_0 \gg \Gamma$? Interpret this result, justifying the need for the Zeeman-slowing technique.

16.5.6.4 Ex: Saturation intensity

Calculate the saturation intensity for the sodium transition $3s\ ^2S_{1/2}, F = 2 \longleftrightarrow 3p\ ^2P_{3/2}, F' = 3$. The natural width of the transition is $\Gamma/2\pi = 9.89\,\text{MHz}$ and the wavelength $\lambda = 590\,\text{nm}$.

16.5.6.5 Ex: Saturation intensity of an octupole transition

Calculate the saturation intensity for the $^2S_{1/2}$-$^2F_{7/2}$ transition in Yb^+-ions (neglecting the Zeeman substructure) at $\lambda = 467\,\text{nm}$ (decay time $\tau = 8\,\text{a}$) and the Rabi frequency, when the transition is resonantly driven by a laser beam of $P = 10\,\text{mW}$ power focused into a $w_0 = 20\,\mu\text{m}$ waist.

16.5.6.6 Ex: Pressure broadening

At what pressure the collision broadening [given by the expression (16.199)] between sodium atoms in the ground state dominates the width of the D2-transition at ambient temperature. The natural width of the D2-line is $\Gamma/2\pi = 6\,\text{MHz}$.

16.5.6.7 Ex: Optical density of a hot cloud

Calculate and draw the effective Lorentz profile, Gauss profile and Voigt profile for the resonance line at 461 nm ($\Gamma = (2\pi)\ 32\,\text{MHz}$) of a strontium gas heated to the temperature 400 C and the pressure $P = 10^{-4}$ mbar inside a 15 cm long cell.

16.5.6.8 Ex: Rate equations as a limiting case of Bloch equations

We show in this exercise that, in the limit $\Gamma \gg \Omega$, we can derive, from the Bloch equations, the Einstein rate equations. Proceed as follows:
a. Apply the condition $\dot{\rho}_{12} = 0$ to the Bloch equations for a two-level system (16.151), determine $\rho_{12}(\infty)$, and replace this stationary value in the equations for the populations $\rho_{kk}(t)$ using, as an abbreviation, the transition rate $R \equiv \gamma s$, where s is the saturation parameter (16.153).
b. Integrate the rate equations over the entire spectrum, i.e. $\Delta \in [-\infty, \infty]$, and derive Einstein's equations using the relations (16.7), (16.41), and (16.42).

16.5.6.9 Ex: Blackbody radiation-induced transitions

Blackbody radiation induces incoherent transitions (see Exc. 16.5.6.8). Show that the Lindbladian of the master equation,

$$\dot{\hat{\rho}} = \mathfrak{L}_{bb}\hat{\rho} = -\tfrac{R}{2}\left([\hat{\rho}\hat{\sigma}, \hat{\sigma}^\dagger] + [\hat{\sigma}, \hat{\sigma}^\dagger\hat{\rho}]\right) - \tfrac{R+\Gamma}{2}\left([\hat{\rho}\hat{\sigma}^\dagger, \hat{\sigma}] + [\hat{\sigma}^\dagger, \hat{\sigma}\hat{\rho}]\right)$$

reproduces the Einstein rate equation for $\Gamma = 2A_{12}$ and $R = B_{12}u(\omega)$.

16.5.6.10 Ex: Lorentzian versus Gaussian line profile

Beyond what detuning is a Doppler-broadened transition dominated by the Lorentzian profile of the transition?

16.6 Bloch equations for multi-level systems

The two-level system represents an idealization of the real atom, since at least one of the levels is usually degenerate. Many important phenomena in quantum optics are not found in this system, but conditioned to the existence of a third level. Examples are optical pumping (essential for laser operation), quantum jumps or dark resonances [which are at the basis of the phenomenon of electromagnetically induced transparency (EIT)].

To derive the Bloch equations for atoms with several levels excited by several lasers and coupled to free space (i.e. without external cavity), we can use the same master equation (16.185), but with a generalized Hamiltonian in the semiclassical

approximation [12] and a Lindblad operator,

$$\boxed{\begin{aligned}
\hat{H}_{\rm atom} &= \textstyle\sum_i \hbar\omega_i \hat{\sigma}_{ji}\hat{\sigma}_{ij} = \sum_i |i\rangle\hbar\omega_i\langle i| \\
\hat{H}_{\rm atom:field} &= \tfrac{\hbar}{2}\Omega_{ij}\left(e^{-\imath\omega_{ij}t}\hat{\sigma}_{ij} + e^{\imath\omega_{ij}t}\hat{\sigma}_{ji}\right) = \textstyle\sum_{i<j}|i\rangle\tfrac{\hbar}{2}\Omega_{ij}\langle j|e^{\imath\omega_{ij}t} + c.c. \\
\mathfrak{L}_{\rm decay}\hat{\rho} &= \mathfrak{L}_\gamma + \mathfrak{L}_R + \mathfrak{L}_\beta \\
\mathfrak{L}_\gamma &= \textstyle\sum_{i,j}\gamma_{ij}\left([\hat{\sigma}_{ij},\hat{\rho}\hat{\sigma}^\dagger_{ij}] + [\hat{\sigma}_{ij}\hat{\rho},\hat{\sigma}^\dagger_{ij}]\right) \\
\mathfrak{L}_R &= \textstyle\sum_{i,j}R_{ij}\left([\hat{\sigma}^\dagger_{ij},\hat{\rho}\hat{\sigma}_{ij}] + [\hat{\sigma}^\dagger_{ij}\hat{\rho},\hat{\sigma}_{ij}]\right) \\
\mathfrak{L}_\beta &= \textstyle\sum_{i,j}2\beta_{ij}\left([\hat{\sigma}_{ij}\hat{\sigma}^\dagger_{ij},\hat{\rho}\hat{\sigma}_{ij}\hat{\sigma}^\dagger_{ij}] + [\hat{\sigma}_{ij}\hat{\sigma}^\dagger_{ij}\hat{\rho},\hat{\sigma}_{ij}\hat{\sigma}^\dagger_{ij}]\right)
\end{aligned}} \quad . \tag{16.225}$$

Here, $\hat{\sigma}_{ij} \equiv |i\rangle\langle j| = \hat{\sigma}^\dagger_{ji}$. The constants R_{ij} are eventual incoherent pump rates due to optical pumping, β_{ij} take account of homogeneous broadening, e.g. due to finite laser linewidths. The levels have the energy $\hbar\omega_i$ above the ground level. The Rabi frequency Ω_{ij} is a measure for the force at which the levels $|i\rangle$ and $|j\rangle$ are coupled by the resonantly irradiated light field. The master equation can be simplified by applying the rotating wave approximation and transforming to the coordinate system which rotates with the light frequencies ω_{ij}:

$$\rho_{ij} \to \hat{\rho}_{ij}e^{\imath\omega_{ij}t} \quad , \quad \hat{H}_{\rm atom:field} \to e^{-\imath\hat{H}t/\hbar}\hat{H}_{\rm atom:field}e^{\imath\hat{H}t/\hbar} \ . \tag{16.226}$$

16.6.1 Liouville equation for many levels

The indices for the atomic levels are joined to a single index, such that the master equation takes a simpler form after having introduced a *Liouville operator*:

$$\begin{aligned}
\hat{\rho} &= (...\rho_k...) \equiv \sum\nolimits_{i,j}|i\rangle\rho_{ij}\langle j| \ , \\
\dot{\hat{\rho}} &= \mathfrak{L}\hat{\rho}, \\
\hat{\rho} &= e^{\mathfrak{L}_{\rm atom}t}\hat{\rho}_0 \ .
\end{aligned} \tag{16.227}$$

The relation with the *von Neumann equation* with $\hat{H} = \sum_{i,j}|i\rangle H_{ij}\langle j|$ and $\hat{\rho} = \sum_{k,l}|k\rangle\rho_{kl}\langle l|$ and $\hat{\sigma}_{ij} = |i\rangle\langle j|$ is:

$$\mathfrak{L}_{\rm atom}\hat{\rho} = -\tfrac{\imath}{\hbar}[\hat{H},\hat{\rho}] = -\imath\sum\nolimits_{k,l,j}H_{kl}\rho_{lj}|k\rangle\langle j| + \imath\sum\nolimits_{k,l,j}H_{lj}\rho_{kl}|k\rangle\langle j| \ . \tag{16.228}$$

For example, for the two-level system with the definition of the external product (1.226):

$$\mathfrak{L}_{\rm atom}\hat{\rho} = -\imath\hat{H}\otimes\mathbb{I}\hat{\rho} + \imath\mathbb{I}\otimes\hat{H}\hat{\rho} \ . \tag{16.229}$$

The relaxation terms for spontaneous decay obtained from (16.225) are,

$$\mathfrak{L}_{\rm decay}\hat{\rho} = \sum\nolimits_{i,j,k}\left(2\gamma_{ji}\delta_{kj}\rho_{ii} - \gamma_{ij}\rho_{kj} - \gamma_{ik}\rho_{kj}\right)|k\rangle\langle j| \ . \tag{16.230}$$

[12] That is, the atom is quantized and consists of several levels $|i\rangle$ with energies $\hbar\omega_i$, while the light fields are described by factors $e^{\imath\omega_{ij}t}$, with frequencies ω_{ij} tuned near the transitions $|i\rangle - |j\rangle$.

Example 95 (*Liouville equation for two levels*): For example, for the two-level system,

$$\mathfrak{L}_{\text{atom}} = \begin{pmatrix} 2\gamma_{11} & 0 & 0 & 2\gamma_{21} \\ 0 & 0 & 0 & 0 \\ 0 & 0 & 0 & 0 \\ 2\gamma_{12} & 0 & 0 & 2\gamma_{22} \end{pmatrix} - \begin{pmatrix} 2(\gamma_{11}+\gamma_{12}) & 0 & 0 & 0 \\ 0 & \sum_{(kj)}\gamma_{(kj)} & 0 & 0 \\ 0 & 0 & \sum_{(kj)}\gamma_{(kj)} & 0 \\ 0 & 0 & 0 & 2(\gamma_{22}+\gamma_{21}) \end{pmatrix} .$$

Here, we consider $(kj) = (11\ 12\ 21\ 22)$ as a single index.

16.6.1.1 Derivation of the multilevel Bloch equation

Now, inserting the Hamiltonian in the RWA,

$$\hat{H} = \hat{H}_{\text{atom}} + \hat{H}_{\text{atom:field}} = \sum_i \hbar\omega_i |i\rangle\langle i| + \tfrac{\hbar}{2}\sum_{i<j} \Omega_{ij}\hat{\sigma}_{ij} + h.c. \ , \tag{16.231}$$

into the von Neumann equation together with the dissipative Lindbladian (16.230) and $\rho_{jk} \equiv \langle j|\hat{\rho}|k\rangle$, we derive the multilevel master equation,

$$\dot{\rho}_{jk} = \frac{\imath}{\hbar}\langle j|[\hat{\rho}, \hat{H}]|k\rangle + \langle j|\mathfrak{L}_{\text{decay}}\hat{\rho}|k\rangle \ . \tag{16.232}$$

First we calculate the unperturbed Hamiltonian part,

$$\begin{aligned} \langle k|[\hat{\rho}, \hat{H}_{\text{atom}}]|m\rangle &= \hbar\langle k|\hat{\rho}\sum_a |a\rangle\langle a|\sum_i \omega_i|i\rangle\langle i|m\rangle - \hbar\langle k|\sum_i \omega_i|i\rangle\langle i|\sum_a |a\rangle\langle a|\hat{\rho}|m\rangle \\ &= \hbar(\omega_m - \omega_k)\rho_{km} \ . \end{aligned} \tag{16.233}$$

For the interaction part we get,

$$\begin{aligned} &\langle k|[\hat{\rho}, \hat{H}_{\text{atom:field}}]|m\rangle \\ &= \tfrac{\hbar}{2}\sum_a\sum_{i<j}\left[\langle k|\hat{\rho}|a\rangle\langle a|\left(\Omega_{ij}|i\rangle\langle j| + \Omega_{ij}^*|j\rangle\langle i|\right)|m\rangle - \langle k|\left(\Omega_{ij}|i\rangle\langle j| + \Omega_{ij}^*|j\rangle\langle i|\right)|a\rangle\langle a|\hat{\rho}|m\rangle\right] \\ &= \tfrac{\hbar}{2}\sum_{i<j}\left(\Omega_{ij}\rho_{ki}\delta_{jm} + \Omega_{ij}^*\rho_{kj}\delta_{im} - \Omega_{ij}\rho_{jm}\delta_{ki} - \Omega_{ij}^*\rho_{im}\delta_{kj}\right) \ , \end{aligned} \tag{16.234}$$

and for the dissipative part,

$$\begin{aligned} \langle k|\mathfrak{L}_{\text{decay}}\hat{\rho}|m\rangle &= \langle k|\sum_{i,j}\gamma_{ij}(2|i\rangle\langle j|\hat{\rho}|j\rangle\langle i| - |j\rangle\langle i|i\rangle\langle j|\hat{\rho} - \hat{\rho}|j\rangle\langle i|i\rangle\langle j|)|m\rangle \\ &= \sum_j 2\gamma_{mj}\delta_{km}\rho_{jj} - \sum_i(\gamma_{ik}+\gamma_{im})\rho_{km} \ . \end{aligned} \tag{16.235}$$

So all in all,

$$\boxed{\begin{aligned} \dot{\rho}_{km} &= 2\sum_j \gamma_{mj}\rho_{jj}\delta_{km} - \left[\sum_i(\gamma_{ik}+\gamma_{im}) + \imath(\omega_k - \omega_m)\right]\rho_{km} \\ &+ \tfrac{\imath}{2}\sum_{i<j}\left(\Omega_{ij}\rho_{ki}\delta_{jm} + \Omega_{ij}^*\rho_{kj}\delta_{im} - \Omega_{ij}\rho_{jm}\delta_{ki} - \Omega_{ij}^*\rho_{im}\delta_{kj}\right) \end{aligned}} \ , \tag{16.236}$$

where the index j runs over all levels $|j\rangle$ into which a population ρ_{kk} can decay and the index i runs over all levels $|i\rangle$ into which the levels $|k\rangle$ and $|m\rangle$ of a dipole moment ρ_{km} can decay. In Exc. 16.6.5.1 we will apply this formula to three-level systems.

Finally, the master equation can be reformulated by introducing a *generalized Bloch vector* $\vec{\rho}$, and the matrix representation of the Liouville superoperator $\mathfrak{L}$ as a linear system of n^2 coupled differential equations,

$$\frac{d}{dt}\vec{\rho} = \mathcal{M}\vec{\rho} \quad , \quad \vec{\rho} = (\rho_{11} \ \ldots \ \rho_{nn} \ \rho_{12} \ \rho_{21} \ \ldots \ \rho_{n-1\ n} \ \rho_{n\ n-1}) \ , \tag{16.237}$$

where the Bloch matrix $\mathcal{M}$ is obtained from the Liouvillean $\mathfrak{L}$ simply by rearranging the matrix elements.

Alternatively to the complex formulation, the differential equations can be written for the real and imaginary part of the Bloch vector. The components ρ_{ii} correspond to the population probabilities of the levels $|i\rangle$, the non-diagonal elements ρ_{ij} describe the coherences between $|i\rangle$ and $|j\rangle$. Now, we must insert the Hamiltonian (16.225) and the density operator ρ_{ij} into the Liouville equation (15.6) in order to derive the generalized Bloch equations. In practice, these calculations are simple but heavy. Therefore, we describe in Sec. 16.6.4 a simplified recipe for compiling Bloch equations for arbitrary level systems for real atoms.

16.6.2 Bloch equations for three levels

In principle, three-level system can exist in there possible configurations, shown in Fig. 16.7. Note that it is not possible to describe a three-level system with all levels pairwise coupled by three lasers within the formalism of Bloch's equations [13].

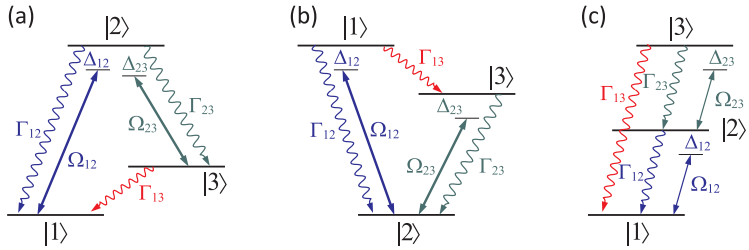

Figure 16.7: Three level system (a) in Λ-configuration, (b) in V-configuration, and (c) in cascade configuration.

Defining the Bloch vector by $\vec{\rho}$, the Bloch equation matrix for three levels in Raman configuration (that is, in Λ-configuration) using the labeling of Fig. 16.7(a),

[13] For the same reason that the three-body problem has no general analytic solution.

is,

$$\dot{\vec{\rho}} = \mathcal{M}\vec{\rho} = \tag{16.238}$$

$$\left(\begin{array}{ccc|ccccccc}
0 & \Gamma_{12} & \Gamma_{13} & \frac{\imath}{2}\Omega_{12} & -\frac{\imath}{2}\Omega_{12} & 0 & 0 & 0 & 0 \\
0 & -\Gamma_{12}-\Gamma_{23} & 0 & -\frac{\imath}{2}\Omega_{12} & \frac{\imath}{2}\Omega_{12} & 0 & 0 & \frac{\imath}{2}\Omega_{23} & -\frac{\imath}{2}\Omega_{23} \\
0 & \Gamma_{23} & -\Gamma_{13} & 0 & 0 & 0 & 0 & -\frac{\imath}{2}\Omega_{23} & \frac{\imath}{2}\Omega_{23} \\
\hline
\frac{\imath}{2}\Omega_{12} & -\frac{\imath}{2}\Omega_{12} & 0 & -\Lambda_{12} & 0 & \frac{\imath}{2}\Omega_{23} & 0 & 0 & 0 \\
-\frac{\imath}{2}\Omega_{12} & \frac{\imath}{2}\Omega_{12} & 0 & 0 & -\Lambda_{12}^* & 0 & -\frac{\imath}{2}\Omega_{23} & 0 & 0 \\
0 & 0 & 0 & \frac{\imath}{2}\Omega_{23} & 0 & -\Lambda_{13} & 0 & -\frac{\imath}{2}\Omega_{12} & 0 \\
0 & 0 & 0 & 0 & -\frac{\imath}{2}\Omega_{23} & 0 & -\Lambda_{13}^* & 0 & \frac{\imath}{2}\Omega_{12} \\
0 & \frac{\imath}{2}\Omega_{23} & -\frac{\imath}{2}\Omega_{23} & 0 & 0 & -\frac{\imath}{2}\Omega_{12} & 0 & -\Lambda_{23} & 0 \\
0 & -\frac{\imath}{2}\Omega_{23} & \frac{\imath}{2}\Omega_{23} & 0 & 0 & 0 & \frac{\imath}{2}\Omega_{12} & 0 & -\Lambda_{23}^*
\end{array}\right)
\left(\begin{array}{c}
\rho_{11} \\ \rho_{22} \\ \rho_{33} \\ \rho_{12} \\ \rho_{21} \\ \rho_{13} \\ \rho_{31} \\ \rho_{23} \\ \rho_{32}
\end{array}\right)$$

with $\Lambda_{mn} = \imath\Delta_{mn} + \gamma_{mn}$ and,

$$\begin{aligned}
&\Delta_{13} = \Delta_{12} - \Delta_{23} \qquad\qquad (16.239)\\
&\gamma_{12} = \tfrac{1}{2}(\Gamma_{12}+\Gamma_{23}) \quad , \quad \gamma_{23} = \tfrac{1}{2}(\Gamma_{12}+\Gamma_{23}+\Gamma_{13}) \quad , \quad \gamma_{13} = \tfrac{1}{2}\Gamma_{13}\ .
\end{aligned}$$

In Exc. 16.6.5.2 we will derive the matrix (16.238).

The coherent terms of the same matrix can be used for the V- and the cascade configurations shown in Figs. 16.7(b,c). Obviously, the incoherent terms, that is, the submatrix 3×3 separated in the matrix (16.238) containing the population decay rates must be adjusted, as well as the decay rates of the coherences on the diagonal. Finally, the definition of the Raman detuning Δ_{13} must be adjusted. For the system in V-configuration we have,

$$\begin{aligned}
&\mathcal{M}_{\text{incoh}} = \begin{pmatrix} -\Gamma_{12}-\Gamma_{13} & 0 & 0 \\ \Gamma_{12} & 0 & \Gamma_{23} \\ \Gamma_{13} & 0 & -\Gamma_{23} \end{pmatrix} \quad , \quad \Delta_{13} = \Delta_{12} - \Delta_{23} \qquad (16.240)\\
&\gamma_{12} = \tfrac{1}{2}(\Gamma_{12}+\Gamma_{13}) \quad , \quad \gamma_{23} = \tfrac{1}{2}\Gamma_{23} \quad , \quad \gamma_{13} = \tfrac{1}{2}(\Gamma_{12}+\Gamma_{13}+\Gamma_{23})\ .
\end{aligned}$$

For the cascade system we have,

$$\begin{aligned}
&\mathcal{M}_{\text{incoh}} = \begin{pmatrix} 0 & \Gamma_{12} & \Gamma_{13} \\ 0 & -\Gamma_{12} & \Gamma_{23} \\ 0 & 0 & -\Gamma_{13}-\Gamma_{23} \end{pmatrix} \quad , \quad \Delta_{13} = \Delta_{12} - \Delta_{23} \qquad (16.241)\\
&\gamma_{12} = \tfrac{1}{2}\Gamma_{12} \quad , \quad \gamma_{23} = \tfrac{1}{2}(\Gamma_{12}+\Gamma_{23}+\Gamma_{13}) \quad , \quad \gamma_{13} = \tfrac{1}{2}(\Gamma_{13}+\Gamma_{23})\ .
\end{aligned}$$

These matrices serve to describe quantitatively a wealth of phenomena, some of them to be discussed in Sec. 16.7.

16.6.3 Numerical treatment of Bloch equations

Since the differential Bloch equations are linear, they can be easily solved. For example, the prescription

$$\boxed{\vec{\rho}(t) = e^{\mathcal{M}t}\vec{\rho}(0)} \tag{16.242}$$

propagates the Bloch vector to later times.

The matrix $\mathcal{M}$ is not invertible, but by applying the condition $\mathrm{Tr}\,\rho = 1$, a component of the density matrix can be eliminated, for example by letting,

$$\rho_{11} = 1 - \sum_k \rho_{kk} \ . \tag{16.243}$$

The resulting state vector, $\vec{\rho}_{\rm red}$, has the length $n^2 - 1$, and from $\mathcal{M}$ we obtain the (trace-)reduced, now invertible matrix $\mathcal{M}_{\rm red}$ and the inhomogeneity vector $\mathbf{b}$. The differential equation is now,

$$\frac{d}{dt}\vec{\rho}_{\rm red} = \mathcal{M}_{\rm red}\vec{\rho}_{\rm red} + \mathbf{b} \ , \tag{16.244}$$

with the stationary and time-dependent solutions,

$$\boxed{\vec{\rho}_{\rm red}(\infty) = -\mathcal{M}_{\rm red}^{-1}\mathbf{b} \quad , \quad \vec{\rho}_{\rm red}(t) = e^{\mathcal{M}_{\rm red}t}\vec{\rho}_{\rm red}(0) + (1 - e^{\mathcal{M}_{\rm red}t})\vec{\rho}_{\rm red}(\infty)} \ . \tag{16.245}$$

Once the matrix $\mathcal{M}$ or the matrix $\mathcal{M}_{\rm red}$ and the inhomogeneity vector $\mathbf{b}$ are determined for a system, the state of the atom can be calculated at any time, as well as the populations and coherences. The system's free parameters are the natural transition linewidths and the detunings, as well as the intensities and emission bandwidths of the incident light fields.

16.6.3.1 Simulation of the Schrödinger and Bloch equation

Once we have written the solution of the Schrödinger equation in the form (1.244) with a time-independent Hamiltonian $\hat{H}$, or of the Bloch equations in the form (16.242) or (16.245) with a time-independent Liouvillian $\mathcal{M}$, we can easily simulate temporal evolutions of quantum systems. If the Hamiltonian or Liouvillian depend on time, for example, when the Rabi frequencies are pulsed or the detunings are ramped, we must solve the equations iteratively. That is, we chose time intervals Δt sufficiently short, so that the Hamiltonian (or the Liouvillian) can be considered constant during this interval, and we propagate the wavefunction (or the Bloch vector) to later times via:

$$|\psi(t + \Delta t)\rangle = e^{\imath\hat{H}(t)\Delta t}|\psi(t)\rangle \qquad \text{or} \qquad \vec{\rho}(t + \Delta t) = e^{\mathcal{M}(t)\Delta t}\vec{\rho}(t) \ , \tag{16.246}$$

and insert the solution obtained again into equations (16.246) with the Hamiltonian $\hat{H}(t + \Delta t)$ (or the Liouvillian $\mathcal{M}(t + \Delta t)$) adjusted to the new time.

16.6.4 General rules for setting up multilevel Bloch equations

The canonical way of deriving multi-level Bloch equations starts from a von Neumann equation for the total density operator for the atom embedded in the electromagnetic mode structure of the environment including incident laser beams. After tracing over the degrees of freedom of the electromagnetic vacuum and using the Markov and the Born approximations [303], one arrives at a master equation of the form (16.225). Simple but tedious algebraic transformations of the master equation lead, in the rotating wave approximation, to a set of linear first-order differential equations in the populations of the atomic excitation levels and the coherences between them. The equations are called the optical Bloch equations.

Alternatively, the Bloch equations may be found by breaking down the multi-level scheme into a set of three-level systems. Respecting a few symmetry considerations, the multi-level Bloch equations can then be reassembled from the three-level Bloch equations corresponding to every possible combination of three levels. Based on such considerations, we provide in the following a simple recipe for setting up Bloch matrices for arbitrary level schemes. A movie showing a simulation of multi-level Bloch equations for Li atoms can be watched under the following link: (watch movie).

Let us regard a N-level atom. Its internal state is fully described by the populations ρ_{kk} and the (complex) coherences ρ_{kl}, with $k, l = 1, .., N$. In this work we describe the coherences by their real and imaginary parts. The labeling is such that the levels are sorted according to their excitation energy, $E_k < E_l$ for $k < l$. We define the Bloch vector,

$$\vec{\varrho} \equiv (\rho_{11} \cdots \rho_{NN} \ \rho_{12} \ \rho_{21} \ \rho_{13} \ \rho_{31} \cdots \rho_{1N} \ \rho_{N1} \ \rho_{23} \ \rho_{32} \cdots \rho_{N-1,N} \ \rho_{N,N-1}) \ . \tag{16.247}$$

The Bloch equations then formally read,

$$\dot{\vec{\varrho}} = \mathcal{M} \vec{\varrho} \ , \tag{16.248}$$

where in the given Bloch vector basis the matrix $\mathcal{M}$ has the following structure,

$$\mathcal{M} = \begin{pmatrix} (A) & (B) \\ (-B^\dagger) & \begin{pmatrix} (C) & (D) \\ (D) & (C) \end{pmatrix} \end{pmatrix} \ . \tag{16.249}$$

The different blocks of the matrix have the following significations. Block A handles the transfer of populations by spontaneous decay. Its rank corresponds to the number of levels N. The diagonal elements of this block are the decay rates Γ of the excited states. The off-diagonal elements Γ_{kl} denote the gain of level k from a decaying level l. Conservation of energy thus requires that the sum of the transition rates cancels for every column of matrix A, $\Gamma = \sum_k \Gamma_{kl}$, as it is the case for the two-level Bloch matrix. If the levels are sublevels of a Zeeman and/or hyperfine split multiplet, the rates have to be weighted with Wigner's $(3j)$ and $\{6j\}$ symbols, $\Gamma_{kl} = \Gamma S_{kl}$. The relative oscillator strengths S_{kl} are given in Sec. 16.6.4.2.

The blocks B treat the interdependence of the populations and the coherences. B describes how the coherence between any pair of states driven by a light field generating a Rabi frequency Ω_{kl} influences the populations. The block consists of convoluted 2×2 matrices of the form,

$$\begin{pmatrix} \dot{\rho}_{kk} \\ \dot{\rho}_{ll} \end{pmatrix} \sim \begin{pmatrix} \frac{i}{2}\Omega_{kl} & -\frac{i}{2}\Omega_{kl} \\ -\frac{i}{2}\Omega_{kl} & \frac{i}{2}\Omega_{kl} \end{pmatrix} \begin{pmatrix} \rho_{kl} \\ \rho_{lk} \end{pmatrix} \ . \tag{16.250}$$

B_2 describes how the populations in turn influence the coherences,

$$\begin{pmatrix} \dot{\rho}_{kl} \\ \dot{\rho}_{lk} \end{pmatrix} \sim \begin{pmatrix} \frac{i}{2}\Omega_{kl} & -\frac{i}{2}\Omega_{kl} \\ -\frac{i}{2}\Omega_{kl} & \frac{i}{2}\Omega_{kl} \end{pmatrix} \begin{pmatrix} \rho_{kk} \\ \rho_{ll} \end{pmatrix} \ . \tag{16.251}$$

The Rabi frequencies have to be weighted not only with the relative oscillator strength S_{kl}, but also with the projection H_{kl} of the laser polarization onto the orientation

of the magnetic field and the laser polarization, $\Omega_{kl} = \Omega_x S_{kl} H_{kl}$. Here Ω_x is the Rabi frequency generated by a laser on a transition, whose oscillator strength is 1. The projection is calculated in Sec. 16.6.4.3 for the three possible laser polarizations, i.e. for $\sigma^{\pm}$ and for π light.

The matrix C rules the influence of the decays of the coherences, of the detunings $\Delta_{kl} = \omega_x - \omega_{\rm atom}$, and the laser linewidths β_{kl}. Note that the detuning of the laser frequency ω_x is negative for red-detuned light. In the chosen basis it breaks down into an array 2×2 matrices aligned along the diagonal of $\mathcal{M}$. Their shape is,

$$\begin{pmatrix} \dot\rho_{kl} \\ \dot\rho_{lk} \end{pmatrix} \sim \begin{pmatrix} -\frac{\gamma_{kl}}{2} - \imath\Delta_{kl} & 0 \\ 0 & -\frac{\gamma_{kl}}{2} + \imath\Delta_{kl} \end{pmatrix} \begin{pmatrix} \rho_{kl} \\ \rho_{lk} \end{pmatrix} \ . \tag{16.252}$$

where $\gamma_{kl} = \sum_{m,E_m<E_k,E_l} (\Gamma_{km} + \Gamma_{lm}) + 2\beta_{kl}$. Often the levels are sublevels of a Zeeman and/or hyperfine split multiplets. In this case the frequency shift Z_{kl} of the level is added to the detuning Δ_{kl}. The shift is calculated in Sec. 16.6.4.4 for the example of the ^{6}Li D_2 line.

The block D governs the interdependences of all laser-driven coherences of the atom. The block contains 2×2 submatrices at any place of the matrix $\mathcal{M}$, where the row index pair (mn) and the column index pair (kl) have one index in common provided the two different indices correspond to the Rabi frequency of an incident laser,

$$\begin{pmatrix} \dot\rho_{mn} \\ \dot\rho_{mn} \end{pmatrix} \sim \begin{pmatrix} \pm\frac{\imath}{2}\Omega_{kl} & \\ 0 & \pm\frac{\imath}{2}\Omega_{kl} \end{pmatrix} \begin{pmatrix} \rho_{pq} \\ \rho_{pq} \end{pmatrix} \ . \tag{16.253}$$

The submatrix elements indexed by column (pq) and row (mn) are non-zero if one of the indices p or q is equal to one of the indices m or n and the unequal indices correspond to a laser-driven transition. In order to find the correct signs of the submatrix elements, we distinguish four cases:

1. For $m = p$, $n = k$, and $q = l$ the signs are: $(^{-}\ _{+})$;
2. for $n = q$, $m = k$, and $p = l$ the signs are: $(^{+}\ _{-})$;
3. for $m = q$, $n = k$, and $p = l$ the signs are: $(^{+}\ _{+})$; and
4. for $n = p$, $m = k$, and $q = l$ the signs are: $(^{-}\ _{-})$.

A proper parametrization is proposed in the next section.

16.6.4.1 Recipe for D transitions in alkalines

In order to give a simple algorithm we parametrize the particular choice of sorting the components of the vector, we define a new index μ running from 1 to N^2 by setting $(\varrho_\mu) \equiv (\rho_{kl})$, where,

$$\mu(k,l) = k\delta_{kl} + (2Nk - N - k^2 - k + 2l - 1)\delta_{k<l} + (2Nk - N - k^2 - k + 2l)\delta_{k>l} \ , \tag{16.254}$$

so that,

$$\varrho_{\mu(k,k)} = \rho_{kk} \quad , \quad \varrho_{\mu(k,l)} = \rho_{kl} \quad , \quad \varrho_{\mu(k,l)+1} = \rho_{lk} \ . \tag{16.255}$$

The Bloch equations then formally read,

$$\boxed{\dot{\varrho}_\mu = \mathcal{M}_{\mu\nu}\varrho_\nu} \ . \tag{16.256}$$

Let us now study the case of a multiplet G of ground states coupled by various light fields to a multiplet E of excited states.

> **Example 96 (*Lithium D_2 line*):** To illustrate the procedure we may have in mind the case of the ^{6}Li D_2 line with 6 ground states $k \in G \equiv \{1, ..., 6\}$ belonging to the $^2S_{1/2}$ hyperfine levels $F = \frac{1}{2}, \frac{3}{2}$ and 12 excited states $k \in E \equiv \{7, ..., 18\}$ belonging to the $^2P_{3/2}$ hyperfine levels $F = \frac{1}{2}, \frac{3}{2}, \frac{5}{2}$.

According to the parametrization (16.248) block A of the matrix $\mathcal{M}$ is filled with the following components,

$$\mathcal{M}_{\mu(k,k),\mu(k,k)} = \Gamma S_{kl}\delta_{k\in G}\delta_{l\in E} - \Gamma\delta_{kl}\delta_{k\in E} \ , \tag{16.257}$$

where the relative oscillator strengths S_{kl} will be given by Eq. (16.262).

Block B of the matrix $\mathcal{M}$ is filled with the components,

$$\begin{aligned} \mathcal{M}_{\mu(k,k),\nu(k,l)} &= -\mathcal{M}_{\mu(l,l),\nu(k,l)} \\ &= -2\mathcal{M}_{\mu(k,l),\nu(k,k)} = 2\mathcal{M}_{\mu(k,l),\nu(l,l)} \\ &= -\Omega_{kl}S_{kl}H_{kl} \ , \end{aligned} \tag{16.258}$$

for $k \in G$ and $l \in E$. The projection onto the quantization axis $H_{kl} = H_{kl}\left(\frac{\hat{\epsilon}_{kl}}{|\hat{\epsilon}_{kl}|}, \vec{\mathcal{B}}, m_l - m_k\right)$ is given by Eq. (16.265).

Block C contains the components,

$$\begin{aligned} \mathcal{M}_{\mu(k,l)\mu(k,l)} &= \mathcal{M}^*_{\mu(l,k)\mu(l,k)} \\ &= -\sum_{m\in G}\tfrac{\Gamma S_{ml}}{2}\delta_{k\in G}\delta_{l\in E} \\ &\quad -\beta_{\rm pb}\delta_{2<k<7} - \beta_{\rm rp}\delta_{k\leq 2} \\ &\quad -\imath\Delta_{\rm pb}\delta_{k>2} - \imath\Delta_{\rm rp}\delta_{k<3} + \imath Z_{kl}(\mathcal{B}) \end{aligned} \tag{16.259}$$

for $k \in G \cup E$ and $l \in E$. $\beta_{\rm pb}$ and $\beta_{\rm rp}$ are the laser linewidths of probe and pump lasers. $\Delta_{\rm pb}$ and $\Delta_{\rm rp}$ are the detunings of the probe and pump lasers from their respective transitions in the absence of Zeeman splitting. The Zeeman shift Z_{kl} is given by Eq. (16.266).

Finally, the block D is filled with the components,

$$\begin{aligned} \mathcal{M}_{\mu(k,f),\mu(f,l)+1} &= (\delta_{f<k} - \tfrac{1}{2})\Omega_{kl}S_{kl}H_{kl} \\ \mathcal{M}_{\mu(k,f)+1,\mu(f,l)} &= (\delta_{l<f} - \tfrac{1}{2})\Omega_{kl}S_{kl}H_{kl} \\ \mathcal{M}_{\mu(l,f),\mu(f,k)+1} &= (\delta_{l<f} - \tfrac{1}{2})\Omega_{kl}S_{kl}H_{kl} \\ \mathcal{M}_{\mu(l,f)+1,\mu(f,k)} &= (\delta_{f<k} - \tfrac{1}{2})\Omega_{kl}S_{kl}H_{kl} \ , \end{aligned} \tag{16.260}$$

where,

$$\begin{aligned}\Omega_{kl} &\equiv (\Omega_{\rm rp}\delta_{k\leq 2} + \Omega_{\rm pb}\delta_{k\geq 3})\delta_{l\geq 7} \\ \hat{\epsilon}_{kl} &\equiv (\hat{\epsilon}_{\rm rp}\delta_{k\leq 2} + \hat{\epsilon}_{\rm pb}\delta_{k\geq 3})\delta_{l\geq 7}\ .\end{aligned} \tag{16.261}$$

for $k \in G \cup E$ and $l \in E$ and $f \in G \cup E$ but $f \neq k, l$. The projection onto the quantization axis $H_{kl} = H_{kl}\left(\frac{\hat{\epsilon}_{kl}}{|\hat{\epsilon}_{kl}|}, \vec{\mathcal{B}}, m_l - m_k\right)$ is given by Eq. (16.265).

The Eqs. (16.257)-(16.260) form together an algorithm to generate the matrix allowing one to numerically solve the Bloch equations (16.256), as has been done in the main text.

16.6.4.2 Relative forces of oscillators

Spontaneous transitions between hyperfine- and Zeeman split levels have to be weighted according to the Wigner-Eckardt theorem using Clebsch-Gordan $(3j)$ and Wigner $\{6j\}$ symbols. Consider the transition $|(J_k, I)F_k, m_k\rangle \leftrightarrow |(J_l, I)F_l, m_l\rangle$. The relative oscillator strength is,

$$S_{kl} = \begin{pmatrix} F_k & \kappa & F_l \\ m_k & \text{sign}\,(m_l - m_k) & -m_l \end{pmatrix}^2 \begin{Bmatrix} J_l & J_k & \kappa \\ F_k & F_l & I \end{Bmatrix}^2 \frac{(2F_k+1)(2J_l+1)(2\kappa+1)}{2I+1}\ . \tag{16.262}$$

16.6.4.3 Elliptical laser polarization

The transition rates additionally depend on the relative orientation of the laser polarizations and the magnetic field direction. This dependence is accounted for by decomposing the polarization vector into the,

$$\hat{\mathbf{e}}_3 = \frac{\vec{\mathcal{B}}}{B} \quad , \quad \hat{\mathbf{e}}_2 = \frac{\hat{\mathbf{e}}_3 \times \hat{\mathbf{g}}}{|\hat{\mathbf{e}}_3 \times \hat{\mathbf{g}}|} \quad , \quad \hat{\mathbf{e}}_1 = \frac{\hat{\mathbf{e}}_2 \times \hat{\mathbf{e}}_3}{|\hat{\mathbf{e}}_2 \times \hat{\mathbf{e}}_3|}\ , \tag{16.263}$$

where $\hat{\mathbf{g}}$ is an arbitrarily chosen direction, e.g. gravity. The relative amplitude of the transitions $\Delta m_J = 0$ is proportional to the projection of the polarization vector on the magnetic field axis $\zeta_0 = (\hat{\varepsilon} \cdot \hat{\mathbf{e}}_3)^2$ for π-polarized light. To estimate the amplitude of the transitions $\Delta m_J = \pm 1$, we must project onto the coordinates,

$$\hat{\mathbf{e}}_\pm = \tfrac{1}{\sqrt{2}}(\mp\hat{\mathbf{e}}_1 - \imath\hat{\mathbf{e}}_2)\ , \tag{16.264}$$

and we obtain $\zeta_{\pm 1} = (\hat{\varepsilon} \cdot \hat{\mathbf{e}}_\pm)^2$ for $\sigma^\pm$-polarized light. Hence,

$$H_{kl} = \zeta_{\Delta m_J} = \zeta_{m_l - m_k}\ . \tag{16.265}$$

With this generalization the Bloch equations can e.g. be employed to calculate Hanle resonances quantum mechanically. The Hanle effect occurs when a magnetic and an optical field compete for the quantization axis.

16.6.4.4 Hyperfine and Zeeman splitting

The nuclear spin of the ^{6}Li atom is $I = 1$, its electron spin is $S = \frac{1}{2}$. The excitation states are characterized by quantum numbers J_k, F_k, m_k. The electron angular orbital momentum is $L_k = \delta_{k\geq 7}$, and the electron angular orbital momentum is $J_k = \frac{1}{2}\delta_{k\leq 6} + \frac{3}{2}\delta_{k\geq 7}$. The hyperfine structure of the excited state $^2P_{3/2}$ can be written as $\nu_{hf1} = -2.8\,\mathrm{MHz}$, $\nu_{hf2} = 0\,\mathrm{MHz}$, and $\nu_{hf3} = 1.7\,\mathrm{MHz}$. Hence, the hyperfine splitting is inferior to the natural decay rate $\Gamma = (2\pi)\,6\,\mathrm{MHz}$,

$$Z_{kl} = \tfrac{\mu_B|\vec{\mathcal{B}}|}{2\pi\hbar}(g_{F_k}m_k - g_{F_l}m_l) + \nu_{\mathrm{hf1}}\delta_{7\leq l\leq 8} + \nu_{\mathrm{hf2}}\delta_{8\leq l\leq 13} + \nu_{\mathrm{hf3}}\delta_{13\leq l\leq 16}\ , \quad (16.266)$$

where g_{F_k} is the Landé factor of hyperfine level F_k.

16.6.5 Exercises

16.6.5.1 Ex: Derivation of three-level Bloch equations

Derive from the general formula (16.236) the three-level Bloch equations for the system $|1\rangle \overset{\Omega_{12}}{\longleftrightarrow} |2\rangle \overset{\Omega_{23}}{\longleftrightarrow} |3\rangle$.

16.6.5.2 Ex: Bloch equations for three levels

An excited Λ-shaped atom consists of two ground states $|1\rangle$ and $|3\rangle$, which are coupled by two lasers with Rabi frequencies and detunings Ω_{12} and Δ_{12} respectively Ω_{23} and Δ_{23} through an excited level $|2\rangle$. Derive the Bloch equations from this system from the general master equation.

16.6.5.3 Ex: Adiabatic elimination

Derive the effective two-level Bloch equations for a Λ-type three-level system adiabatically eliminating the excited state under the Raman condition. **Help**: Start from the Liouvillean (16.238), set $\rho_{22} = 0$, assume $\Gamma_{13} \ll \Gamma_{12}, \Gamma_{23} \ll |\Delta_{12}|, |\Delta_{23}|$, and $\Delta_{12} = -\Delta_{23}$.

16.7 Multi-level phenomena

The multi-level Bloch equations, and in particular the three-level Bloch equations (16.238), allow for the theoretical description of many phenomena beyond the two-level approximation. Among them are the phenomena of *light shift* treated in Excs. 16.4.4.12 and 16.4.4.13, the *Autler-Townes splitting* treated in Exc. 16.7.3.1, the *dark resonances* treated in Excs. 16.7.3.3 to 16.7.3.6, the *STIRAP* method treated in Exc. 16.7.3.7, *adiabatic sweeps* treated in Exc. 16.7.3.8, the dispersive interaction between atoms and light treated in Exc. 16.7.3.9, *Fano resonance*-type line profiles of dark resonances treated in Exc. 16.7.3.10, and the *quantum jumps*, which will be studied in later chapters. In Excs. 16.7.3.11 and 16.7.3.12 we will show, that an atomic gas may have *negative permittivity* and *negative permeability* and, consequently, properties usually only found in artificial metamaterials, as for example, a *negative refractive index*.

16.7.1 Electromagnetically induced transparency

In some special cases, the three-level Bloch equations can be solved analytically. The system in Λ-configuration schematized in Fig. 16.7(a), where the two lasers satisfy the condition $\Delta_{12} = \Delta_{23}$ can exhibit a *dark resonance* leading to the phenomena of *electromagnetically induced transparency* (*EIT*) and *electromagnetically induced absorption*. In these resonances a dramatic change of the refractive index is observed despite the fact that the atom becomes transparent, $\mathfrak{Re}\,\chi \gg 0$ and $|\mathfrak{Im}\,\chi| \ll \mathfrak{Re}\,\chi$:

$$\mathfrak{Re}\, n = \sqrt{1 + \mathfrak{Re}\,\chi} \gg 1 \ , \tag{16.267}$$

resulting in a high group velocity,

$$v_g = \frac{c}{n + \omega \frac{dn}{d\omega}} \ . \tag{16.268}$$

EIT is usually studied in Λ-type systems, but similar phenomena can be found in cascade-type systems [898, 883], which will be studied here. Disregarding the decay rate Γ_{13}, the Bloch equations (16.238) and (16.241) give the coherences,

$$\begin{aligned}
\dot\rho_{12} &= -\Lambda_{12}\rho_{12} + \tfrac{\imath\Omega_{12}}{2}(\rho_{11} - \rho_{22}) - \tfrac{\imath\Omega_{23}}{2}\rho_{13} \\
\dot\rho_{13} &= -\Lambda^*_{13}\rho_{13} - \tfrac{\imath\Omega_{12}}{2}\rho_{23} - \tfrac{\imath\Omega_{23}}{2}\rho_{12} \\
\dot\rho_{23} &= -\Lambda_{23}\rho_{23} + \tfrac{\imath\Omega_{23}}{2}(\rho_{22} - \rho_{33}) - \tfrac{\imath\Omega_{12}}{2}\rho_{13} \ .
\end{aligned} \tag{16.269}$$

Assuming stationarity and negligible depletion of the ground state, $\rho_{11} = 1$,

$$\begin{aligned}
0 &= -\Lambda_{12}\rho_{12} + \tfrac{\imath\Omega_{12}}{2} - \tfrac{\imath\Omega_{23}}{2}\rho_{13} \\
0 &= -\Lambda^*_{13}\rho_{13} - \tfrac{\imath\Omega_{12}}{2}\rho_{23} - \tfrac{\imath\Omega_{23}}{2}\rho_{12} \\
0 &= -\Lambda_{23}\rho_{23} - \tfrac{\imath\Omega_{12}}{2}\rho_{13} \ .
\end{aligned} \tag{16.270}$$

Substituting the third into the first equation,

$$\begin{aligned}
0 &= -\Lambda_{12}\rho_{12} + \tfrac{\imath\Omega_{12}}{2} - \tfrac{\imath\Omega_{23}}{2}\rho_{13} \\
0 &= -\Lambda^*_{13}\rho_{13} - \tfrac{\Omega_{12}^2}{4\Lambda_{23}}\rho_{13} - \tfrac{\imath\Omega_{23}}{2}\rho_{12} \ .
\end{aligned} \tag{16.271}$$

and finally,

$$\boxed{\rho_{12} = \frac{\imath\Omega_{12}}{2}\frac{4\Lambda^*_{13}\Lambda_{23} + \Omega_{12}^2}{\Lambda_{12}\,(4\Lambda^*_{13}\Lambda_{23} + \Omega_{12}^2) + \Omega_{23}^2\Lambda_{23}}} \ . \tag{16.272}$$

The macroscopic polarization is now $\mathcal{P} = \frac{N}{V} d_{12}\rho_{21}$, with the number of atoms N. In the limit of weak probes, the *dressed* susceptibility follows from $\mathcal{P} = \varepsilon_0\chi\mathcal{E}_{12} = \frac{N}{V} d_{12}\rho_{21}$,

$$\chi = \frac{N d_{12}}{V\varepsilon_0\mathcal{E}_{12}}\rho_{21} = \frac{N|d_{12}|^2}{V\varepsilon_0\hbar\Omega_{12}}\rho_{21} \ . \tag{16.273}$$

For a resonant probe laser, $\Delta_{23} = 0$ and with $\Gamma_{13} \simeq 0$, we have $\Lambda_{13} = \frac{1}{2}\Gamma_{23} + \imath\Delta_{12}$ and $\Lambda_{23} = \frac{1}{2}(\Gamma_{23} + \Gamma_{12})$. The susceptibility in the probe transition is now, using

$\Theta \equiv \Gamma_{23} + \frac{\Omega_{12}^2}{2\Lambda_{23}}$,

$$\chi = \frac{N|d_{12}|^2}{V\varepsilon_0\hbar\Omega_{12}}\imath\Omega_{12}\frac{\Gamma_{23}+\frac{\Omega_{12}^2}{2\Lambda_{23}}-2\imath\Delta_{12}}{\left(\Gamma_{23}+\frac{\Omega_{12}^2}{2\Lambda_{23}}-2\imath\Delta_{12}\right)(\Gamma_{12}+2\imath\Delta_{12})+\Omega_{23}^2} \tag{16.274}$$
$$= \frac{N|d_{12}|^2}{V\varepsilon_0\hbar\Omega_{12}}\imath\Omega_{12}\frac{\Theta-2\imath\Delta_{12}}{(\Theta-2\imath\Delta_{12})(\Gamma_{12}+2\imath\Delta_{12})+\Omega_{23}^2} = \chi' + \imath\chi'' \ .$$

Example 97 (*EIT in a cascade system*): We consider, for example, the intercombination line of atomic strontium ${}^1S_0$-${}^3P_1$ ($\lambda_{12} = 689\,\text{nm}$ and $\Gamma_{12} = (2\pi)\ 7.6\,\text{kHz}$) be the 'dressing' transition ${}^3P_1$-(5s4d)${}^3D_1$ ($\lambda_{23} = 2700\,\text{nm}$ and $\Gamma_{23} = (2\pi)\ 90.3\,\text{kHz}$), be the 'dressing' transition ${}^3P_1$-(5s5d)${}^3D_1$ ($\lambda_{23} = 497\,\text{nm}$ and $\Gamma_{23} = (2\pi)\ 2.3\,\text{MHz}$), both characterized by $\Gamma_{23} \gg \Omega_{12}, \Gamma_{12}, |\Delta_{12}|$, such that $\Theta \simeq \Gamma_{23}$. Hence,

$$\chi' + \imath\chi'' = \frac{N|d_{12}|^2}{V\varepsilon_0\hbar}\frac{2\Delta_{12}+\imath\Gamma_{23}}{\Omega_{23}} \ .$$

The refraction index follows with,

$$n = \sqrt{1+\chi} \simeq 1 + \tfrac{1}{2}\chi \ .$$

Its imaginary part originates from the decay term of the atom: it is here responsible for the absorbing nature of the cloud. EIT is characterized by a pronounced dispersion and a small concomitant absorption.

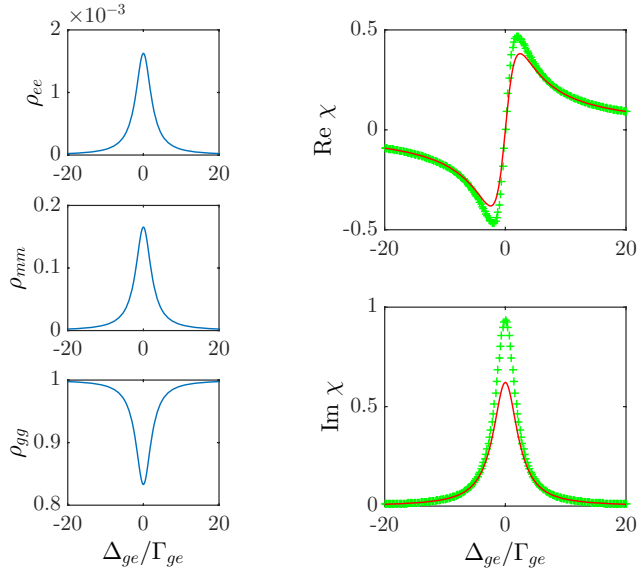

Figure 16.8: (code) EIT signal for the cascade system of strontium with the transitions at 689 nm and 497 nm with $\Omega_{12} = \Gamma_{12}$, $\Omega_{23} = \Gamma_{23}$ and $\Delta_{23} = 0$. The red lines are calculated by numerical integration of the Bloch equations. The dotted lines are obtained from analytical formulas based on the assumptions of weak ground state depletion (which is not really correct in the chosen parameter regime).

16.7.2 Polarization, alignment, and orientation

16.7.2.1 Polarization and helicity

Photons may have the angular momenta $\hat{\mathbf{L}}$, $\hat{\mathbf{S}}$, and $\hat{\mathbf{J}}$, but due to the fact that photons have zero mass, only $\hat{\mathbf{J}}$ is of importance. The *helicity* is defined as,

$$\hat{\mathbf{J}} \cdot \mathbf{k} = (\hat{\mathbf{L}} + \hat{\mathbf{S}}) \cdot \mathbf{k} = \hat{\mathbf{S}} \cdot \mathbf{k} = m_s = \pm 1 \ , \tag{16.275}$$

in beam direction and the *polarization* is,

$$\hat{\mathbf{J}} \cdot \hat{\mathbf{e}}_z = m_j = -j, ...j \ . \tag{16.276}$$

Polarizers prepare the photon in its eigenstate. The angular momentum with respect to $\hat{\mathbf{J}}$ in a basis $\hat{\mathbf{e}}_z$ orthogonal to $\mathbf{k}$ is,

$$\hat{\mathbf{J}} \cdot \mathbf{k} |m\rangle_y = a_m |1\rangle_z + b_m |-1\rangle_z \ . \tag{16.277}$$

The state $|0\rangle_z$ does not exist. For example,

$$\hat{\mathbf{J}} \cdot \mathbf{k} |1\rangle_y = \hat{J}_z \left(\tfrac{1}{2} |1\rangle_z + \imath |0\rangle_z - \tfrac{1}{2} |-1\rangle_z \right) = \tfrac{1}{2} (|1\rangle_z + |-1\rangle_z) \ . \tag{16.278}$$

16.7.2.2 Orientation and alignment

A level $|j\rangle$ with Zeeman degeneracy $|jm\rangle$ can be irreducibly described by Cartesian polarization tensors. Those are the *orientation* and the *alignment* [463, 810],

$$\boxed{\begin{array}{rcl} O_i & \equiv & \langle \hat{J}_i \rangle \\ A_{ij} & \equiv & \frac{3}{2} \langle [\hat{J}_i, \hat{J}_j]_+ \rangle - \langle \hat{\mathbf{J}}^2 \rangle \delta_{ij} \end{array}} \ , \tag{16.279}$$

with $i, j = x, y, z$. The expectation value is calculated as usual, $\langle ... \rangle = \mathrm{Tr}\, \hat{\rho} ... = \sum_m \langle jm | \hat{\rho} ... | jm \rangle$. If $O_i \neq 0$ then the system is said *oriented*, if $A_{ij} \neq 0$ the system is said *aligned* and if either $O_i \neq 0$ or $A_{ij} \neq 0$ then the system is said *polarized*.

The orientation and the alignment depend on the choice of the quantization axis and on the Zeeman splitting of level $|j\rangle$. Choosing z as quantization axis and disregarding Zeeman coherences $\langle m | \hat{\rho} | m' \rangle \sim \delta_{mm'}$, we get the orientation,

$$\mathbf{O} = \hbar \hat{\mathbf{e}}_z \sum_m m \rho_{mm} \tag{16.280}$$

and the alignment,

$$(A_{ij}) = -\hbar^2 j(j+1) - \begin{pmatrix} -\frac{3}{2} & 0 & 0 \\ 0 & -\frac{3}{2} & 0 \\ 0 & 0 & 3 \end{pmatrix} \sum_m \hbar^2 m^2 \rho_{mm} \ , \tag{16.281}$$

if the atom is with certainty in level $|j\rangle$ so that $\mathrm{Tr}\, \hat{\rho} = 1$. These results will be derived in Exc. 16.7.3.14.

16.7.2.3 Hanle effect

The *Hanle effect* occurs when a magnetic and an optical field compete for the quantization axis. Imagine an atom irradiated by a laser from direction $\mathbf{k} = k\hat{\mathbf{e}}_x$, linearly polarized $\varepsilon = \hat{\mathbf{e}}_y$ and subject to a magnetic field $\vec{\mathcal{B}} = \mathcal{B}\hat{\mathbf{e}}_z$. The fluorescence is detected in direction $\hat{\mathbf{e}}_y$ through a linear polarizer [218]. If $\mathcal{B} = 0$, no light is emitted into the detector since the dipole radiation pattern is a torus with symmetry axis $\hat{\mathbf{e}}_y$. If $\mathcal{B}$ is now increased, the quantization axis is tilted and the torus slowly precesses about the $\hat{\mathbf{e}}_x$ axis. Plotting the time-averaged fluorescence as a function of the magnetic field $\mathcal{B}$, we observe a *dark resonance*. These arguments are rather classical.

Quantum mechanically, Hanle resonances are easily calculated. The transition rates additionally depend on the relative orientation of the laser polarization and the magnetic field direction. This dependence is accounted for by decomposing the polarization vector into the coordinates defined by,

$$\hat{\mathbf{e}}_3 = \frac{\vec{\mathcal{B}}}{\mathcal{B}} \quad , \quad \hat{\mathbf{e}}_2 = \frac{\hat{\mathbf{e}}_3 \times \hat{\mathbf{g}}}{|\hat{\mathbf{e}}_3 \times \hat{\mathbf{g}}|} \quad , \quad \hat{\mathbf{e}}_1 = \frac{\hat{\mathbf{e}}_2 \times \hat{\mathbf{e}}_3}{|\hat{\mathbf{e}}_2 \times \hat{\mathbf{e}}_3|} \ , \tag{16.282}$$

where $\hat{\mathbf{g}}$ is an arbitrarily chosen direction, e.g. gravity. The relative amplitude of the transitions $\Delta m_J = 0$ is proportional to the projection of the polarization vector on the magnetic field axis $\zeta_\pi = (\hat{\varepsilon} \cdot \hat{\mathbf{e}}_3)^2$. To estimate the amplitude of the transitions $\Delta m = \pm 1$, we must project onto the coordinates,

$$\hat{\mathbf{e}}_\pm = \tfrac{1}{\sqrt{2}}(\mp\hat{\mathbf{e}}_1 - \imath\hat{\mathbf{e}}_2) \ , \tag{16.283}$$

and we obtain $\zeta_{\sigma^\pm} = (\hat{\varepsilon} \cdot \hat{\mathbf{e}}_\pm)^2$.

Example 98 (*Hanle effect with rate equations*): As long as the Zeeman splitting is inferior to the atomic decay width, the Hanle effect can be described without coherences, i.e. using only rate equations. Fig. 16.9 shows such a simulation for the case of three ground Zeeman states $|1\rangle = |g, m = +1\rangle$, $|2\rangle = |g, m = 0\rangle$, and $|3\rangle = |g, m = -1\rangle$, and one excited state $|4\rangle = |e, m = 0\rangle$. The rate equations are,

$$\dot{\rho}_{kk} = \mathcal{M}\rho_{kk} \tag{16.284}$$

$$\text{with} \quad \mathcal{M} = \begin{pmatrix} -\Omega_{14} & 0 & 0 & \Omega_{14} + \frac{1}{3}\Gamma \\ 0 & -\Omega_{24} & 0 & \Omega_{24} + \frac{1}{3}\Gamma \\ 0 & 0 & -\Omega_{34} & \Omega_{34} + \frac{1}{3}\Gamma \\ \Omega_{14} & \Omega_{24} & \Omega_{34} & -\Omega_{14} - \Omega_{24} - \Omega_{34} - \Gamma \end{pmatrix}$$

$$\text{and} \quad \Omega_{14} = \Omega_{34} = \zeta_{\sigma^\pm}\Omega \quad \text{and} \quad \Omega_{24} = \zeta_\pi\Omega \ .$$

In Exc. 16.7.3.15 we study the Hanle effect at the Ca^+ Zeeman degenerate level system.

16.7.3 Exercises

16.7.3.1 Ex: Autler-Townes splitting

In this exercise we study the Autler-Townes effect in a two-level system $|1\rangle$ and $|2\rangle$ resonantly excited ($\Delta_{12} = 0$) by a laser with the Rabi frequency Ω_{12}:

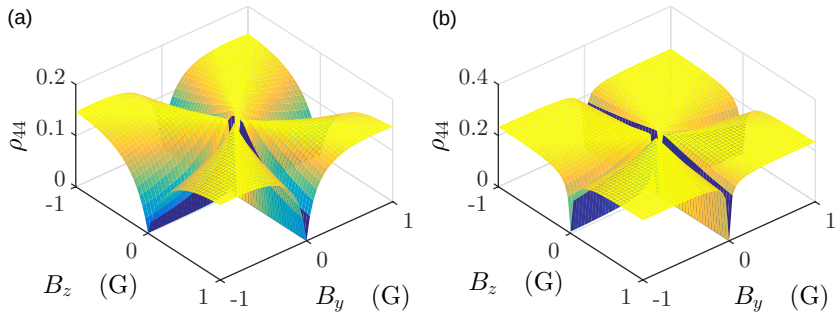

Figure 16.9: (code) Hanle effect in a four-level system with three ground and one excited state with $\hat{\varepsilon} = \hat{\mathbf{e}}_y$ and (a) $\Omega = 0.5\Gamma$ and (b) $\Omega = 5\Gamma$.

a. From the eigenvalues $E_{1,2}$ of the effective Hamiltonian (16.191) of the system, describe the behavior of the real part (energy shift) and the imaginary part (linewidth) as a function of the Rabi frequency. Prepare diagrams Ω_{12} versus $\mathfrak{Re}\, E_{1,2}$ and versus $\mathfrak{Im}\, E_{1,2}$ and discuss the limits $\Omega_{12} > \frac{1}{2}\Gamma_{12}$ and $\Omega_{12} < \frac{1}{2}\Gamma_{12}$.
The Autler-Townes effect can be measured experimentally by probing the population of level $|2\rangle$ via excitation of a third (higher) level by a second laser with the Rabi frequency Ω_{23}. Thus, we obtain a three-level system in cascade configuration, as shown in Fig. 16.7(c). In order to reproduce the experiment by numerical simulations of the Bloch equations (16.238),
b. write down the Liouville matrix $\mathcal{M}_{\text{red}}$ reduced by the trace condition (16.243) and
c. compute the stationary Bloch vector from equation (16.245) varying the detuning of the probe laser Δ_{23} and the Rabi frequency Ω_{12} of the system under study ($|1\rangle$ and $|2\rangle$). Choosing the parameters $\Gamma_{23} = 0.5\Gamma_{12}$, $\Gamma_{13} = 0.01\Gamma_{12}$, $\Omega_{23} = 0.1\Gamma_{12}$, prepare a 3D curve [similar to Fig. 16.3(a)] of the stationary population $\rho_{22}(\infty)$. Interpret the results.

16.7.3.2 Ex: Quantum Zeno effect and saturation broadening

In this exercise we study saturation broadening effect in a three-level system $|1\rangle$, $|2\rangle$, and $|3\rangle$ in V-configuration, as shown in Fig. 16.7(b), excited by two resonant lasers with the Rabi frequencies Ω_{12} and Ω_{23}.
a. From the eigenvalues $E_{1,2}$ of the effective Hamiltonian (16.191) of the system, describe the behavior of the real part (energy shift) and the imaginary part (linewidth) as a function of the Rabi frequency. Prepare diagrams Ω_{12} versus $\mathfrak{Re}\, E_{1,2}$ and versus $\mathfrak{Im}\, E_{1,2}$ and discuss the limits $\Omega_{12} > \frac{1}{2}\Gamma_{12}$ and $\Omega_{12} < \frac{1}{2}\Gamma_{12}$.
Saturation broadening can be measured experimentally in a three-level system in V-configuration. To reproduce the experiment by numerical simulations of the Bloch equations (16.238),
b. write down the Liouville matrix $\mathfrak{L}$ of the system and calculate the time evolution of the Bloch vector via equation (16.242) varying the Rabi frequency Ω_{12}. Choosing the parameters $\Gamma_{23} = 0.01\Gamma_{12}$, $\Gamma_{13} = 0.0001\Gamma_{12}$, $\Omega_{23} = 400\Gamma_{23}$, and $\Delta_{12} = 0 = \Delta_{23}$, prepare a 3D curve [similar to Fig. 16.3(a)] of the population $\rho_{33}(t)$ as a function of time and the Rabi frequency Ω_{12}.

c. Interpret the results in terms of broadening by saturation. The broadening can also be understood in terms of the quantum Zeno effect, where the transition $|1\rangle$-$|2\rangle$ plays the role of the 'observed system' and the transition $|2\rangle$-$|3\rangle$ the role of the measuring device or 'meter' (for example, we can observe the light scattered on the 'meter transition' to infer the evolution of the 'system transition').

16.7.3.3 Ex: EIT and dark resonances

In this exercise we study so-called *dark resonances*, which are responsible for the phenomenon of *electromagnetically induced transparency* (EIT). Such resonances are observed in three-level systems $|1\rangle$-$|2\rangle$-$|3\rangle$ in Λ-configuration, as shown in Fig. 16.7(a), when the laser detunings are chosen so as to satisfy $\Delta_{12} = \Delta_{23}$.
a. From the Bloch equations (16.238) show analytically that, in a stationary situation, the population of the excited state is $\rho_{22}(\infty) = 0$ in the center of the dark resonance. Dark resonances can be observed experimentally. To reproduce the experiment by numerical simulations of the Bloch equations (16.238), write down the Liouville matrix $\mathcal{M}_{\text{red}}$ reduced by the trace condition (16.242) and calculate the stationary Bloch vector from equation (16.243) varying the detunings of the two lasers Δ_{12} and Δ_{23}. Choosing the parameters such that $\Gamma_{23} = \Gamma_{12}$, $\Gamma_{13} = 0.01\Gamma_{12}$, $\Omega_{12} = 2\Gamma_{12}$, and $\Omega_{23} = 0.2\Gamma_{12}$, prepare a 3D curve [similar to Fig. 16.3(a)] of the population $\rho_{22}(\infty)$. Interpret the results.

16.7.3.4 Ex: Coherent trapping and dark states

Consider a three-level system $|1\rangle$, $|2\rangle$, and $|3\rangle$ in Λ-configuration interacting with two electromagnetic fields with frequencies ω_a and ω_b. The two states $|1\rangle$ and $|3\rangle$ of lower energies $\hbar\omega_1$ and $\hbar\omega_3$ are coupled to a state $|2\rangle$ of higher energy $\hbar\omega_2$, as illustrated in Fig. 16.7(a). Assume that the transition $|1\rangle \leftrightarrow |3\rangle$ is forbidden and that the Hamiltonian of the system has the form $\hat{H} = \hat{H}_0 + \hat{H}_{\text{int}}$ where,

$$\hat{H}_0 = E_1|1\rangle\langle 1| + E_2|2\rangle\langle 2| + E_3|3\rangle\langle 3|$$
$$\hat{H}_{\text{int}} = -\tfrac{\hbar}{2}(\Omega_{12}e^{-\imath\omega_a t}|2\rangle\langle 1| + \Omega_{12}^{*}e^{\imath\omega_a t}|1\rangle\langle 2|) - \tfrac{\hbar}{2}(\Omega_{23}e^{-\imath\omega_b t}|2\rangle\langle 3| + \Omega_{23}^{*}e^{\imath\omega_b t}|3\rangle\langle 2|)\ .$$

a. Assuming that the system's state is described by $|\psi\rangle = c_1|1\rangle + c_2|2\rangle + c_3|3\rangle$ find the system of equations that describe the dynamics of probability amplitudes c_i with $(i = 1, 2, 3)$.
b. Rewrite the equations for the case where the frequencies of the applied fields are resonant (that is, $\omega_a = \omega_2 - \omega_1$ and $\omega_b = \omega_2 - \omega_3$). Simplify the system by writing in terms of the variables $u_i = c_i e^{\imath\omega_i t}$.
c. Assuming the initial condition $|\psi(0)\rangle = (|1\rangle + |3\rangle)/\sqrt{2}$, solve the system of equations for the resonant case and interpret the result.

16.7.3.5 Ex: Cascade EIT scheme in strontium

Consider the Bloch equations for the ^{88}Sr 7-level system consisting of the following levels: $|1\rangle \equiv (5s^2)\ ^1S_0$, $|2-4\rangle \equiv (5s5p)\ ^3P_1$, and $|5-7\rangle \equiv (5s5d)\ ^3D_1$, and check under which circumstances it is possible to observed dark resonances. The Sr level scheme can be consulted under (Sr level scheme). The Liouvillean can be consulted at (Sr Liouvillean).

16.7.3.6 Ex: Dark resonances with Zeeman splitting

Calculate the dark resonance spectrum for the Ca^+ three-level system with Zeeman sub-structure consisting of the levels $|1\rangle \equiv {}^2S_{1/2}$, $|2\rangle \equiv {}^2P_{1/2}$, and $|3\rangle \equiv {}^2D_{3/2}$ using optical Bloch equations. **Help:** The decay rates are $\Gamma_{12}/2\pi = 23\,\mathrm{MHz}$, $\Gamma_{23}/2\pi = 1.6\,\mathrm{MHz}$, and $\Gamma_{13}/2\pi = 1\,\mathrm{Hz}$. Assume that both incident lasers saturate the transitions, $\Omega_{12} = \Gamma_{12}$ and $\Omega_{23} = \Gamma_{23}$.

16.7.3.7 Ex: STIRAP

In experiments with cold atoms it is often necessary to transfer populations between ground states, for example, between specific levels of a hyperfine structure. One possible procedure is the method of optical pumping, from the initial ground state to an excited state, which subsequently decays to the final state by spontaneous emission. The problem with this incoherent procedure is, that one can control into which ground state level the atom will decay, and that it heats atoms due to the photonic recoil associated with the scattering of light. In this exercise we studied an alternative method, called *Stimulated Raman Adiabatic Passage* (STIRAP), which allows the coherent transfer of population between two states by counter-intuitive pulse sequences:
a. Consider a three-level system in Λ-configuration, as shown in Fig. 16.7(a), initially being in the state $|1\rangle$. Write the system's Hamiltonian in the interaction picture. Now, choose $\Delta_{12} = 0 = \Delta_{23}$, and a temporal variation of the Rabi frequencies described by $\Omega_{12}(t) = \Gamma_{12}(\frac{1}{2} + \frac{1}{\pi}\arctan\Gamma_{12}t)$ and $\Omega_{23}(t) = \Gamma_{12}(\frac{1}{2} - \frac{1}{\pi}\arctan\Gamma_{12}t)$. With this, solve the Schrödinger equation (16.246) iteratively within the time interval $t \in [-40/\Gamma_{12}, 40/\Gamma_{12}]$, while continuously adjusting the Rabi frequencies.
b. The dynamics can also be calculated via a numerical simulations of the Bloch equations (16.238). Write down the Liouville matrix and prepare a simulation using the same parameters as in (b) and additionally $\Gamma_{23} = \Gamma_{12}/2$, $\Gamma_{13} = \Gamma_{12}/500$.
c. Interpret the results.

16.7.3.8 Ex: Adiabatic sweeps

In experiments with cold atoms it is often necessary to transfer populations between ground states, for example, between specific levels of a Zeeman structure. One possible procedure is the method of optical pumping, from the initial ground state to an excited state, which subsequently decays to the final state by spontaneous emission. The problem with this incoherent procedure is, that one can control into which ground state level the atom will decay, and that it heats atoms due to the photonic recoil associated with the scattering of light. In this exercise we study an alternative method, called *adiabatic sweep*, which allows the coherent transfer of population between the two outer states of a degenerate multiplet, as shown in Fig. 16.10, via an adiabatic ramp of the frequency of the incident radiation:
a. Write down the Hamiltonian of the system in the interaction picture. Now, choose $\Omega/2\pi = 8\,\mathrm{kHz}$ and apply a linear ramp of the radiation detuning between $-50\,\mathrm{kHz} < \Delta(t)/2\pi < 50\,\mathrm{kHz}$ during a time interval of 2 ms. With this, solve the Schrödinger equation (16.238) iteratively varying the detuning.
b. Write down the Liouville matrix of the system and do a numerical simulation

of the Bloch equations (16.238) using the same parameters as in (a). Interpret the results. What you observe when you introduce a decay rate between adjacent levels of $\Gamma/2\pi = 200\,\text{Hz}$?

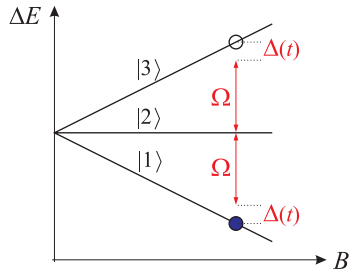

Figure 16.10: Energy levels of an atom in the ground state with Zeeman structure (for example, $|J = 1, m_J = -1, 0, +1\rangle$) as a function of the applied magnetic field.

16.7.3.9 Ex: Dispersive interaction between an atom and light

Radiation which is tuned far from a resonance can change the phase of an atomic dipole moment without changing the populations [14]. We study this effect in a three-level system in cascade configuration excited by two radiation fields, as illustrated in Fig. 16.7(c), simulating the Schrödinger equation and the Bloch equations.
a. Write down the Hamiltonian $\hat{H}$ for this system letting $\Delta_{12} = 0$.
b. Now, consider the subsystem $|2\rangle$-$|3\rangle$, write down its Hamiltonian $\hat{H}_{23}$, determine the eigenvalues, and assume that this transition be excited very far-off resonance. That is, for $\Delta_{23} \gg \Omega_{23}, \Gamma_{23}$ expand the eigenvalues of $\hat{H}_{23}$ up to second order in Ω_{23}. Finally, replace the submatrix $\hat{H}_{23}$ in the complete Hamiltonian $\hat{H}$ by the matrix of the expanded eigenvalues. This procedure corresponds to treating the transition $|2\rangle$-$|3\rangle$ as a perturbation of the transition $|1\rangle$-$|2\rangle$ until second order.
c. Assume that the atom is initially in the ground state and compute the time evolution of the state via the Schrödinger equation (16.246) using (a) the perturbed Hamiltonian and (b) the exact Hamiltonian for the following *sequence of pulses*:
(i) a $\pi/2$-pulse on the transition $|1\rangle$-$|2\rangle$,
(ii) a pulse with a variable duration between 0 and $\Delta t = \Omega_{23}^2/4\pi\Delta_{23}$ applied to the transition $|2\rangle$-$|3\rangle$,
(iii) a $\pi/2$-pulse on the transition $|1\rangle$-$|2\rangle$. What you observe?
d. Establish the Liouville matrix $\mathfrak{L}$ for the same system and calculate the time evolution of the Bloch vector during the sequence by the Bloch equations (16.246) choosing the same parameters as in (c) and additionally $\Gamma_{23} = 1$, $\Gamma_{13} = \Gamma_{23}$, $\Gamma_{12} = 0.01\Gamma_{23}$, and $\Omega_{12} \ggg \Delta_{23}, \Gamma_{23}$. Prepare a 3D curve [similar to Fig. 16.3(b)] of the population $\rho_{22}(t)$. Interpret the results.

16.7.3.10 Ex: Fano profile of a dark resonance

The dark resonance studied in Exc. 16.7.3.3 may in some circumstances adopt an asymmetric profile. Calculate, for a three-level system in Λ-configuration, as shown

[14] This type of interaction is used in the implementation of quantum gates in quantum computing.

in Fig. 16.7(a), starting from the Bloch equations (16.238) with the Liouville matrix $\mathcal{M}_{\rm red}$ reduced by the trace condition (16.242), the spectrum $\rho_{22}(\Delta_{23})$ for the following set of parameters: $\Gamma_{12} = 2$, $\Gamma_{23} = \Gamma_{12}/2$, $\Gamma_{23} = 0.1\Gamma_{12}$, $\Omega_{12} = 10\Gamma_{12}$, $\Omega_{23} = 5\Gamma_{23}$, $\Delta_{12} = -5\Gamma_{12}$ and $\Delta_{23} = [-1 : .01 : 1]\Gamma_{23}$. Interpret the spectrum in terms of a Fano resonance.

16.7.3.11 Ex: Gas with negative permittivity

Study EIT on the strontium cascade system consisting of the transitions 689 nm and 497 nm and draw a spectrum of the permittivity. Compare with the permittivity of the 689 nm two-level system. What densities are necessary to get a negative permittivity?

16.7.3.12 Ex: Gas with negative permeability

Theoretically, under certain conditions, gases may exhibit *negative* permittivity and permeability, and therefore refraction [753, 751, 752, 630, 496]. To study this phenomenon we consider a three-level system in Λ-configuration with an electric dipole transition and another magnetic dipole transition. The objective is to balance the electrical dipole moment excited by a probe laser and the magnetic dipole moment excited via a Raman transition by both, the probe laser and a control laser. The Raman transition simulates an effective magnetic field. Since the magnetic moment is smaller by a factor of α^2, the electric moment must be reduced by detuning the probe laser, as shown in Fig. 16.11.

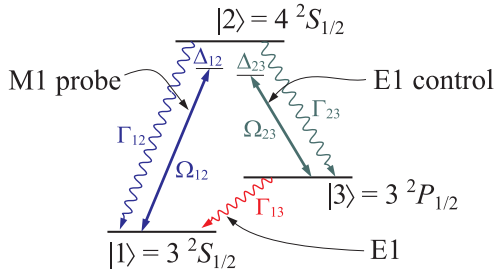

Figure 16.11:

a. Consider a three-level system in Λ-configuration. The transitions $|1\rangle$-$|2\rangle$ and $|2\rangle$-$|3\rangle$ are assumed to be electric dipoles and $|1\rangle$-$|3\rangle$ a magnetic dipole, such that, $\Gamma_{12}, \Gamma_{23} \gg \Gamma_{13}$. Extract from the Bloch equation (16.238) the equations for the coherences ρ_{12}, ρ_{13}, and ρ_{23}.
b. Suppose, that the excitation on the probe transition be so weak, $\Omega_{12} \ll \Gamma_{12}$, that it does not succeed to empty the ground state. In this approximation eliminate the dynamics of ρ_{23} and deduce the stationary solution for ρ_{12} and ρ_{13}.
c. Calculate the magnetic susceptibility χ_m [752] with the following parameters $\Gamma_{12} = 7 \cdot 10^7\,\mathrm{s}^{-1}$, $\Gamma_{23} = 3 \cdot 10^7\,\mathrm{s}^{-1}$, $\Gamma_{13} = 2 \cdot 10^7\,\mathrm{s}^{-1}$, $\Omega_{12} = 0.1\Gamma_{12}$, $\Omega_{23} = 2 \cdot 10^8\,\mathrm{s}^{-1}$, $\Delta_{23} = 0$ in the regime $\Delta_{12} = [-15\Gamma_{23}, 15\Gamma_{23}]$.
d. Simulate the Bloch equations (16.238) and compare with the numerical solution.

16.7.3.13 Ex: Magnetic dipole transitions in strontium

Magnetic dipole transitions are characterized by the selection rules $\Delta J = 0, \pm 1$, $\Delta S = 0$, $\Delta L = 0$, and $\Delta n = 0$. There are several transitions starting from the $5s5p\ ^3P_J$ metastable states going to the $5p^2\ 3P_J$ states with strong linewidths:

- $5s5p\ ^3P_1^o \leftrightarrow 5p^2\ ^3P_2$ at 472.2278 nm with $\Gamma = (2\pi)\ 5.7$ MHz
- $5s5p\ ^3P_1^o \leftrightarrow 5p^2\ ^3P_1$ at 478.4320 nm with $\Gamma = (2\pi)\ 4.8$ MHz

Check whether it is possible to reach negative permeability in a cold strontium gas.

16.7.3.14 Ex: Orientation and alignment

Derive the formulas (16.280) and (16.281).

16.7.3.15 Ex: Hanle effect in Ca

Simulate the Hanle effect for the Ca^+ three-level system of Exc. 16.7.3.6 using optical Bloch equations.

16.7.3.16 Ex: Control of saturation via quenching

In this exercise we study the possibility of '*quenching*' a narrow transition, i.e. homogeneously broadening its transversal decay width without affecting the longitudinal one, with the goal of obtaining control over the saturation parameter on the narrow transition by coupling it via a strong transition to a third level.

a. Set up the Bloch equations for the three-level cascade system sketched in Fig. 16.12.

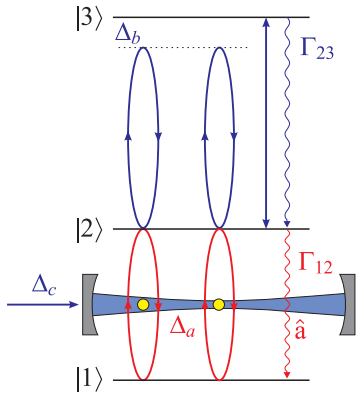

Figure 16.12: Strontium level scheme with $|1\rangle \equiv (5s^2)^1S_0$, $|2\rangle \equiv (5s5p)^3P_1$, and $|3\rangle \equiv (5s6s)^3S_1$.

b. Based on the assumptions $\Gamma_{23} \gg \Gamma_{12} \gg \Gamma_{13} = 0$ and tuning the control laser to resonance, $\Delta_{23} = 0$, calculate the diagonal elements Λ_{ij} of the Liouvillean $\mathcal{M}$ of the Bloch equations.

c. Now, assume that the control laser be sufficiently weak not to deplete the state $|2\rangle$.

Neglecting $\rho_{33} = 0 = \rho_{23}$ derive the reduced Bloch equations for the system ρ_{22}, ρ_{12}, and ρ_{13} and solve it by ρ_{22}.
d. Calculate the 'generalized saturation parameter'.
e. Recover the two-level saturation parameter in the limit $\Omega_{23}^2 \ll \Gamma_{12}\Gamma_{13}$. Plot the population ρ_{22} as a function of the saturation parameters s_{12} and s_{23}.

16.8 Further reading

J. Weiner and P-T. Ho, Springer-Verlag, Berlin (2003), *Light-Matter Interaction: Fundamentals and Applications* [ISBN]

R. Loudon, Oxford Science Publications, Oxford (1982), *The quantum theory of light* [ISBN]

M.O. Scully, *From lasers and masers to phaseonium and phasers* [DOI]

I.I. Sobelman, Springer Verlag, Berlin (1972), *Introduction to the Theory of Atomic Spectra* [ISBN]

M. Weissbluth, (Academic Press, Boston, 1989), *Photon-Atom Interactions* [ISBN]

M. Weissbluth, *Atoms and Molecules* [ISBN]

A. Corney, Clarendon Press, Oxford (1977), *Atomic and Laser Spectroscopy* [ISBN]

M. Tanifuji, World Scientific (2018), *Polarization Phenomena in Physics* [ISBN]

C.M. Tokarsky Dieguez et al., *Os fundamentos quânticos da Ressonância Magnética Nuclear* [DOI]

Y. Stalgies et al., *Light shift and Fano resonances in a single cold ion* [DOI]

M. Fleischhauer et al., *Electromagnetically induced transparency, Optics in coherent media* [DOI]

L.V. Hau et al., *Light Speed Reduction to 17 Metres per Second in an Ultracold Atomic Gas* [DOI]

16.8.1 on negative refraction

A. Poddubny et al., *Hyperbolic metamaterials* [DOI]

Jian-Qi Shen et al., *How to realize a negative refractive index material at the atomic level in an optical frequency range* [DOI]

Jian-Qi Shen et al., *Negatively refracting atomic vapour* [DOI]

Jian-Qi Shen et al., *Negative permeability in a Λ-type three-level atomic vapor* [DOI]

F. Bello, *Negative index of refraction in a four-level system with magnetoelectric cross coupling and local field corrections* [DOI]

Yi S. Ding et al., *Possible realization of negative refraction in Bose-Einstein condensates* [DOI]

A. Alù et al., *Pairing an Epsilon-Negative Slab With a Mu-Negative Slab Resonance, Tunneling and Transparency* [DOI]

M.Ö. Oktel et al., *Electromagnetically induced left-handedness in a dense gas of three-level atoms* [DOI]

P.P. Orth et al., *Negative refraction with tunable absorption in an active dense gas of atoms* [DOI]

D.E. Sikes et al., *Negative refraction using Raman transitions and chirality* [DOI]

P. Shekhar et al., *Strong Coupling in Hyperbolic Metamaterials* [DOI]

Chapter 17

Atoms in quantized radiation fields

So far we have treated the light-atom interaction always assuming the light field as a stationary or propagating classical wave, while our two-level atom has been regarded as an entity obedient to the laws of quantum mechanics and subject to an induced perturbation by an oscillatory electromagnetic field. This procedure naturally leads to oscillations of the atomic states' populations and the coherences between them. However, in strong fields, when atomic energy spectrum is significantly modified, a non-perturbative, time-independent approach can be fruitful. Time-independent solutions for the Schrödinger equation for atoms coupled to fields is called *dressed states*. They were used for the first time to interpret the *splitting* of rotational molecular spectra in the presence of intense classical radiofrequency fields. While the semi-classical treatment is suitable for a wide variety of phenomena and has the virtue of mathematical simplicity and familiarity, it is sometimes worth considering the field as a quantum entity as well. In the dressed states picture, the atom-field interaction corresponds to an exchange of energy quanta between the field (photons) and the atom. This approach allows us to express photonic *number states*, also called *Fock states*, on equal footings with the discrete states of atom excitation and to write the state functions of the coupled atom-field system in a basis of photonic and atomic product states. Diagonalization of the dipole coupling terms in the system's Hamiltonian generates time-independent solutions of dressed states in a completely quantum Schrödinger equation.

We begin this chapter expressing the atom-field interaction in a fully quantized form. We will examine some examples illustrating how the dressed states picture can provide useful information on the light-matter interactions.

17.1 Interaction of quantized fields with atoms

17.1.1 Hamiltonian for interaction of quantized fields with atoms

With the results of the previous section the complete field Hamiltonian reads,

$$\hat{H}_{\text{field}} = \sum_{\mathbf{k}} \hbar\omega_{\mathbf{k}} (\hat{a}^{\dagger}_{\mathbf{k}} \hat{a}_{\mathbf{k}} + \tfrac{1}{2}) \ . \tag{17.1}$$

Now, that we have a clear picture of the quantized field with the energies in the modes given by Eq. (14.9) and the photon number states given by the eigenstates $|n\rangle$ of the quantized harmonic oscillator, we are in a position to consider our two-level atom interacting with this quantized radiation field. If for the moment, we exclude spontaneous emission and stimulated processes, the Hamiltonian of the combined atom-field system is,

$$\hat{H} = \hat{H}_{\text{atom}} + \hat{H}_{\text{field}} + \hat{H}_{\text{atom:field}} \ . \tag{17.2}$$

We describe the atom by a two-level system,

$$\hat{H}_{\text{atom}} = \hbar\omega_g|g\rangle\langle g| + \hbar\omega_e|e\rangle\langle e| = \hbar\omega_g|g\rangle\langle g| + \hbar(\omega_g+\omega_0)|e\rangle\langle e| \ , \tag{17.3}$$

where $\hat{H}_{\text{field}}$ is the Hamiltonian of the quantized field, expressed by Eq. (14.6), and $\hat{H}_{\text{atom:field}}$ the atom-field interaction. For the Hamiltonian without interaction, $\hat{H} = \hat{H}_{\text{atom}} + \hat{H}_{\text{field}}$, the eigenstates are simply product states of the atomic states and the photon number states,

$$|g,n\rangle = |g\rangle|n\rangle \qquad \text{and} \qquad |e,n\rangle = |e\rangle|n\rangle \ . \tag{17.4}$$

The left side of Fig. 17.1 shows, how the eigenenergies of the product states consist of two ladders, being displaced by the energy difference $\hbar\Delta$, which corresponds to the detuning. We write the Hamiltonian of the atom Eq. (17.3) as the sum of projectors on unperturbed eigenstates using the completeness relation and the orthogonality of eigenstates. With the same idea we can rewrite the dipole operator defined in Eq. (16.33),

$$\begin{aligned}\hat{\mathbf{d}} &= \sum_i |\psi_i\rangle\langle\psi_i|\hat{\mathbf{d}}|\sum_j |\psi_j\rangle\langle\psi_j| = \sum_{i,j} |i\rangle\langle i|e^{\imath(\omega_i-\omega_j)t}\hat{\mathbf{d}}|j\rangle\langle j| \\ &= \sum_{i,j} e^{\imath(\omega_i-\omega_j)t}\mathbf{d}_{ij}|i\rangle\langle j| = \sum_{i<j} e^{\imath(\omega_i-\omega_j)t}\mathbf{d}_{ij}|i\rangle\langle j| + e^{-\imath(\omega_i-\omega_j)t}\mathbf{d}_{ij}|j\rangle\langle i| \equiv \hat{\mathbf{d}}^{(+)} + \hat{\mathbf{d}}^{(-)} \ .\end{aligned} \tag{17.5}$$

using $|\psi_n(t)\rangle = e^{-\imath\omega_n t}|n\rangle$. Note that $\hat{\mathbf{d}}$ only has non-diagonal elements.

Now, let us use the electric field of Eqs. (14.8) to describe the atom-field interaction through the Hamiltonian $\hat{H}_{\text{atom:field}} = -\hat{\mathbf{d}}\cdot\hat{\vec{\mathcal{E}}}$,

$$\hat{H}_{\text{atom:field}} = \imath\sum_{\mathbf{k}}\sum_{i,j}\sqrt{\tfrac{\hbar\omega_{\mathbf{k}}}{2\varepsilon_0 V}}\mathbf{d}_{ij}e^{\imath(\omega_j-\omega_i)t}|i\rangle\langle j|\cdot\vec{\epsilon}_{\mathbf{k}}\left[\hat{a}_{\mathbf{k}}e^{-\imath(\mathbf{k}\cdot\mathbf{r}-\omega_{\mathbf{k}}t)} - \hat{a}^\dagger_{\mathbf{k}}e^{\imath(\mathbf{k}\cdot\mathbf{r}-\omega_{\mathbf{k}}t)}\right] \ . \tag{17.6}$$

For our two-level atom interacting with a single mode radiation field, we only have,

$$\begin{aligned}\hat{H}_{\text{atom:field}} = \imath\sqrt{\tfrac{\hbar\omega_{\mathbf{k}}}{2\varepsilon_0 V}}\mathbf{d}_{ge}\left[e^{\imath(\omega_e-\omega_g)t}|g\rangle\langle e| + e^{\imath(\omega_g-\omega_e)t}|e\rangle\langle g|\right]\cdot \\ \cdot\vec{\epsilon}_{\mathbf{k}}\left[\hat{a}_{\mathbf{k}}e^{-\imath(\mathbf{k}\cdot\mathbf{r}-\omega_{\mathbf{k}}t)} - \hat{a}^\dagger_{\mathbf{k}}e^{\imath(\mathbf{k}\cdot\mathbf{r}-\omega_{\mathbf{k}}t)}\right] \ .\end{aligned} \tag{17.7}$$

17.1.1.1 Rotating wave approximation for dressed states

We can simplify the notation by identifying $\hat{\sigma}^+ = |e\rangle\langle g|$ and $\hat{\sigma}^- = |g\rangle\langle e|$ of the Eqs. (16.124) and introducing as an abbreviation the *Rabi frequency*,

$$\tfrac{1}{2}\hbar\Omega_1(\mathbf{r}) \equiv \sqrt{\tfrac{\hbar\omega_{\mathbf{k}}}{2\varepsilon_0 V}}\mathbf{d}_{ge}\cdot\vec{\epsilon}_{\mathbf{k}}e^{\imath\mathbf{k}\cdot\mathbf{r}} \ . \tag{17.8}$$

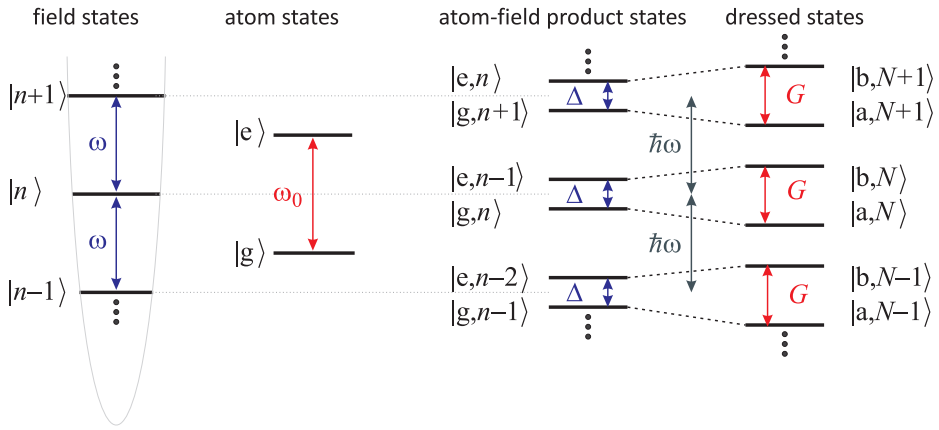

Figure 17.1: (Left) Photons number states and the two stationary states of the two-levels atom. (Center) Double ladder showing the basis of products states of photon number and atomic states. (Right) Dressed states constructed by diagonalization of the full Hamiltonian in the basis of the product states.

The interaction Hamiltonian then becomes,

$$\begin{aligned}\hat{H}_{\text{atom:field}} = &\tfrac{\imath}{2}\hbar\Omega_1(\mathbf{r})e^{\imath(\omega_{\mathbf{k}}-\omega_0)t}\hat{\sigma}^+\hat{a}_{\mathbf{k}} + \tfrac{\imath}{2}\hbar\Omega_1(\mathbf{r})e^{\imath(\omega_{\mathbf{k}}+\omega_0)t}\hat{\sigma}^-\hat{a}_{\mathbf{k}} \\ &- \tfrac{\imath}{2}\hbar\Omega_1^*(\mathbf{r})e^{-\imath(\omega_{\mathbf{k}}+\omega_0)t}\hat{\sigma}^+\hat{a}_{\mathbf{k}}^\dagger - \tfrac{\imath}{2}\hbar\Omega_1^*(\mathbf{r})e^{-\imath(\omega_{\mathbf{k}}-\omega_0)t}\hat{\sigma}^-\hat{a}_{\mathbf{k}}^\dagger\ .\end{aligned} \tag{17.9}$$

This Hamiltonian contains four terms describing the following processes [1],

$|g,n\rangle \longrightarrow |e,n-1\rangle$ the atom is excited by the absorption of a photon;

$|e,n\rangle \longrightarrow |g,n-1\rangle$ the atom is deexcited by the absorption of a photon;

$|g,n\rangle \longrightarrow |e,n+1\rangle$ the atom is excited by the emission of a photon;

$|e,n\rangle \longrightarrow |g,n+1\rangle$ the atom is deexcited by the emission of a photon.

Obviously, only the first and forth terms respect energy conservation (in first-order processes) and can serve as initial and final states in real physical processes. Fig. 17.3 shows schemes of these four terms. We see, that neglecting the second and third process (i.e., terms $\propto \hat{\sigma}^\pm\hat{a}^\pm$ of the Hamiltonian) is equivalent to making the rotating wave approximation (RWA), where we despise the terms rotating with the frequency $\pm(\omega_{\mathbf{k}}+\omega_0)$, and that we really only need to consider the coupling between the two dressed states $|g,n\rangle$ and $|e,n-1\rangle$.

Finally, within the RWA the Hamiltonian reads,

$$\boxed{\hat{H}_{\text{atom:field}} = \tfrac{\imath}{2}\hbar\Omega_1(\mathbf{r})e^{-\imath\Delta_{\mathbf{k}}t}\hat{\sigma}^+\hat{a}_k - \tfrac{\imath}{2}\hbar\Omega_1^*(\mathbf{r})e^{\imath\Delta_{\mathbf{k}}t}\hat{\sigma}^-\hat{a}_k^\dagger}\ , \tag{17.10}$$

where we introduced the detuning $\Delta_{\mathbf{k}} \equiv \omega_{\mathbf{k}} - \omega_0$ as short hand notation.

[1] Remember that the four processes contained in the Hamiltonian are all coherent (absorption and stimulated emission), and that spontaneous emission must be treated separately see next Sec. 17.4.

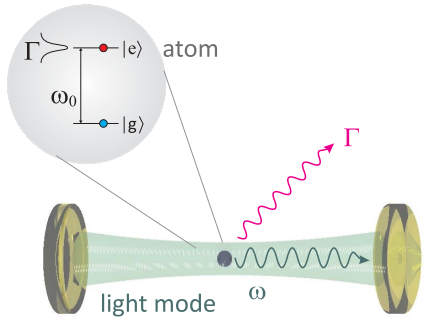

Figure 17.2: Two-level atom interacting with a cavity mode.

It is important to note that the first and fourth term can be important in higher order processes, such as multiphotonic absorption or Raman scattering processes, where the excited state would be a virtual level. In fact, when the Rabi frequency is very large, $\Omega_1 \simeq \omega$, the excitation and deexcitation processes follow each other so rapidly, that energy conservation can be violated for short times. The energy shift caused by terms neglected in the RWA are called *Bloch-Siegert shift* [2].

17.1.2 Dressed states

Within the new dressed states basis, the atom-light coupling problem is reduced to diagonalizing the Hamiltonian of a quasi-degenerate two-level atom ($|\Delta| \ll \omega_0$), in which the non-diagonal elements are given by $\frac{1}{2}\hbar\Omega_1$. The eigenenergies of the complete Hamiltonian $\hat{H}$ are,

$$E_\pm = \tfrac{\hbar}{2}(\omega_{g,n} + \omega_{e,n-1}) \pm \tfrac{\hbar}{2} G_n \ . \tag{17.11}$$

where $\hbar\omega_{g,n}$ and $\hbar\omega_{e,n-1}$ are the energies of the product states $\hbar\omega_g + n\hbar\omega_{\mathbf{k}}$ and $\hbar\omega_e + (n-1)\hbar\omega_{\mathbf{k}}$. The separation between constituents of the same dressed state is $G_n = \sqrt{n\Omega_1^2 + \Delta^2}$. Fig. 17.4 illustrates how the coupling between a field mode and a two-level atom leads to an avoided crossing.

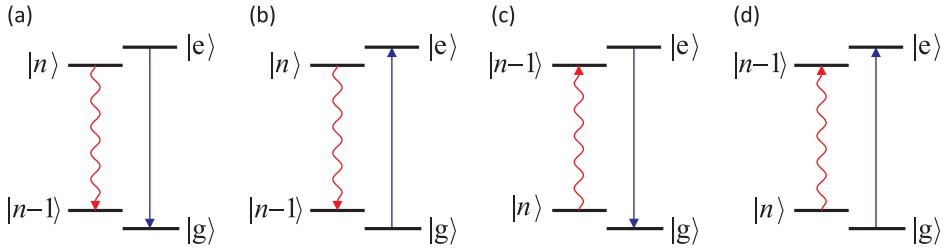

Figure 17.3: Illustration of the four processes in the atom-field interaction. Terms (b) and (c) conserve energy in first-order processes, while (a) and (d) do not conserve.

The atom-field product states offer a natural basis for the Hamiltonian of Eq. (17.2).

[2] The shift is not observed, when the non-rotating terms $\sigma^\pm a^\pm$ are forbidden by other conservation or selection rules. For example, when a resonance is excited by $\sigma^\pm$ light, the RWA is accurate.

The states resulting from the diagonalization of the Hamiltonian on this basis are called *dressed states*. As indicated in Fig. 17.1, the neighboring doublets the double ladder 'repel' each other under the influence of the interaction $\hat{H}_{\text{atom:field}}$ in Eq. (17.2). The mixed coefficients form the familiar problem of two levels, now called $|a\rangle$ and $|b\rangle$. Note that the semiclassical product state picture and the dressed states picture follow from each other via unitary transformation,

$$\boxed{\begin{pmatrix} |a,N\rangle \\ |b,N\rangle \end{pmatrix} = \mathcal{U} \begin{pmatrix} |g,n\rangle \\ |e,n-1\rangle \end{pmatrix}}\,, \tag{17.12}$$

and, hence, are equivalent descriptions of the same reality. But while in the product state picture the system Hamiltonian is diagonal in the *absence* of atom-light interaction, in the dressed states picture the Hamiltonian is diagonal in the *presence* of interaction. The numbers n denote the amount of photons in the laser beam, the numbers N denote the amount of energy packets within the system, that is, the photons *plus* the possible excitation of the atom. The expression of the unitary transformation matrix will be derived in Sec. 17.2.1.

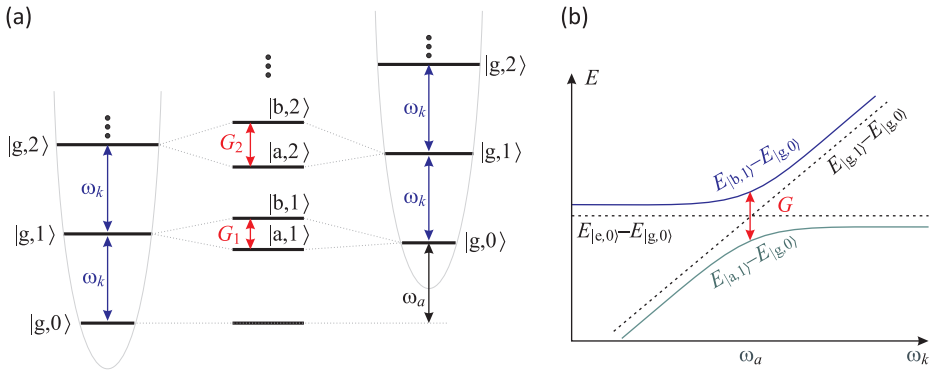

Figure 17.4: (a) Rabi splitting of the lowest dressed states. (b) Avoided crossing of dressed states.

17.1.3 Dipole moments for vector transitions

Until now, we restricted to transitions between two levels without accounting for their possible substructure, which interacts with the vectorial nature of the driving light fields. Resuming the discussion of Sec. 16.2.3, we generalize the treatment of the preceding section considering a two-level atom with an arbitrary hyperfine level substructure $|g,(I,J)F,m\rangle \leftrightarrow |e,(I,J')F',m'\rangle$. The Hamiltonian is,

$$\hat{H} = \sum_{\alpha,\beta} \hbar\omega_{g\alpha}|g_\alpha\rangle\langle g_\alpha| + \hbar\omega_{e\beta}|g_\beta\rangle\langle g_\beta|\,. \tag{17.13}$$

Generalizing the expression (17.5) to vectorial transitions, the electric dipole operator reads,

$$\begin{aligned}\hat{\mathbf{d}} &= \sum_{i,j} |i\rangle\langle i|e^{\imath(\omega_i-\omega_j)t}\hat{\mathbf{d}}|j\rangle\langle j| \qquad (17.14)\\ &= \sum_{\alpha,\beta} |g_\alpha\rangle\langle g_\alpha|e^{\imath(\omega_{g\alpha}-\omega_{e\beta})t}\hat{\mathbf{d}}|e_\beta\rangle\langle e_\beta| + |e_\beta\rangle\langle e_\beta|e^{-\imath(\omega_{g\alpha}-\omega_{e_\beta})t}\hat{\mathbf{d}}|g_\alpha\rangle\langle g_\alpha| \ .\end{aligned}$$

Example 99 (*Vector transition in strontium*): The simplest possible vectorial level scheme consists of one ground and three excited Zeeman states, such as realized, for instance, in the strontium $^1S_0$-$^1P_1$ transition,

$$\hat{H}_{strontium} = \sum_\beta \hbar\omega_{e\beta}|g_\beta\rangle\langle g_\beta| \ , \qquad (17.15)$$

setting $\omega_{ga} \equiv 0$. For strontium, we may introduce the vectorial lowering operator [228],

$$\hat{\vec{\sigma}} = \hat{\sigma}_x\hat{\mathbf{e}}_x + \hat{\sigma}_y\hat{\mathbf{e}}_y + \hat{\sigma}_z\hat{\mathbf{e}}_z \quad \text{with} \quad \hat{\sigma}_\beta = |g\rangle\langle e_\beta| \quad \text{with} \quad \beta = x, y, z \ . \ (17.16)$$

In this case, the electric dipole operator reads,

$$\begin{aligned}\hat{\mathbf{d}}_{strontium} &= \sum_\beta |g\rangle\langle g|e^{-\imath\omega_{e\beta}t}\hat{\mathbf{d}}|e_\beta\rangle\langle e_\beta| + |e_\beta\rangle\langle e_\beta|e^{\imath\omega_{e\beta}t}\hat{\mathbf{d}}|g\rangle\langle g| \qquad (17.17)\\ &= d\sum_\beta e^{-\imath\omega_{e\beta}t}|g\rangle\langle e_\beta|\hat{\mathbf{e}}_\beta + c.c. = de^{-\imath\omega_e t}\hat{\vec{\sigma}} + c.c. \ ,\end{aligned}$$

with $\langle g|\hat{\mathbf{d}}|e_\beta\rangle = d\hat{\mathbf{e}}_\beta$ and $\omega_{e\beta} = \omega_e$.

17.1.4 Exercises

17.1.4.1 Ex: Converting a pure state into a mixture by incomplete measurement

Consider a dressed two-level atom with the atomic states $|1\rangle$ and $|2\rangle$ and the photon number state $|n\rangle$.
a. Write down the general normalized dressed state and the density operator.
b. Now, perform a measurement of the atomic state tracing over the atomic degree of freedom and verify whether the resulting density operator represents a pure state.
c. Now, perform a measurement of the photon number and verify whether the resulting density operator represents a pure state.

17.2 The Jaynes-Cummings model

The *Jaynes-Cummings model* describes the dynamics of a single dressed two-level atom in a single monochromatic laser mode in the absence of spontaneous emission processes. The model, illustrated in Fig. 17.2 has become a paradigm of quantum mechanics with applications in quantum information, where it applies to the formulation of entanglement protocols of atomic states and the implementation of quantum gates. In the following, we will first study the interaction of an atom with an optical mode

neglecting dissipation effects and leave the discussion on the impact of dissipation processes to later sections.

The dynamic evolution of pure states is then obtained from the Schrödinger equation. The Hamiltonian of this system is given by (17.10). Letting $\hbar = 1$ and assuming that the atom is located at the origin [such that $\Omega_1(\mathbf{r})e^{\imath\mathbf{k}\cdot\mathbf{r}} = \Omega_1(\mathbf{0})$], we can write the time-dependent Hamiltonian in the *interaction picture* as,

$$\boxed{\begin{aligned}\hat{H}_{\text{atom:field}} &= \tfrac{\imath}{2}\Omega_1 e^{-\imath\Delta t}\hat{\sigma}^+\hat{a} - \tfrac{\imath}{2}\Omega_1 e^{\imath\Delta t}\hat{\sigma}^-\hat{a}^\dagger \\ &= \begin{pmatrix} 0 & \frac{\imath}{2}\Omega_1 e^{-\imath\Delta t}\hat{a} \\ -\frac{\imath}{2}\Omega_1 e^{\imath\Delta t}\hat{a}^\dagger & 0 \end{pmatrix}\end{aligned}} \ . \tag{17.18}$$

where ω is the frequency of the radiation, ω_0 the frequency of the atomic transition, $\Delta \equiv \omega - \omega_0$ the detuning, and Ω_1 the Rabi frequency generated by a single photon. The atomic operators $\sigma^\pm$ are related to the *Pauli spin matrices* (1.154), and we use the conventions $\hat{\sigma}^z = [\hat{\sigma}^+, \hat{\sigma}^-] = |2\rangle\langle 2| - |1\rangle\langle 1| = 2\hat{\sigma}^+\hat{\sigma}^- - \mathbb{I}$ and $\omega_0 \equiv \omega_2 - \omega_1 > 0$.

Starting from this Hamiltonian the Jaynes-Cummings model is translated into the *Schrödinger picture* via the unitary transform,

$$\mathcal{U} = e^{-\imath(\hat{n}+1/2)\omega t}e^{\imath\hat{\sigma}^z\omega_0 t/2} \ , \tag{17.19}$$

for which we find the relationships,

$$\begin{aligned} -\imath\mathcal{U}\dot{\mathcal{U}}^\dagger &= \omega(\hat{n}+\tfrac{1}{2}) - \tfrac{1}{2}\omega_0\hat{\sigma}^z \\ \mathcal{U}\hat{a}\mathcal{U}^\dagger &= \Sigma_{n'}|n'\rangle e^{-\imath n'\omega t}\langle n'|\hat{a}\Sigma_n|n\rangle e^{\imath n\omega t}\langle n| = e^{\imath\omega t}\hat{a} \\ \mathcal{U}\hat{\sigma}^-\mathcal{U}^\dagger &= e^{\imath\omega_0 t}\hat{\sigma}^- \ . \end{aligned} \tag{17.20}$$

Obviously, the dynamics of the states is now given by $|\psi(t)\rangle = \mathcal{U}|\psi_I(t)\rangle$, and the new Hamiltonian in the Schrödinger picture reads,

$$\boxed{\begin{aligned}\tilde{H}_{\text{atom:field}} &= \mathcal{U}\hat{H}_{\text{atom:field}}\mathcal{U}^\dagger - \imath\mathcal{U}\dot{\mathcal{U}}^\dagger \\ &= \omega(\hat{n}+\tfrac{1}{2}) - \tfrac{1}{2}\omega_0\hat{\sigma}^z + \tfrac{1}{2}\Omega_1(\hat{a}\hat{\sigma}^+ + \hat{a}^\dagger\hat{\sigma}^-) \\ &= \begin{pmatrix} (\hat{n}+\frac{1}{2})\omega - \frac{1}{2}\omega_0 & \frac{1}{2}\Omega_1\hat{a}^\dagger \\ \frac{1}{2}\Omega_1\hat{a} & (\hat{n}+\frac{1}{2})\omega + \frac{1}{2}\omega_0 \end{pmatrix}\end{aligned}} \ . \tag{17.21}$$

We choose the Fock representation (2.90) for the radiation mode, we represent the atomic transitions by the Pauli matrices (1.152), and we span the product space $\hat{\rho}_{\text{field}} \otimes \hat{\rho}_{\text{atom}}$ generalizing the operators $\hat{a}^\pm \curvearrowright \hat{a}^\pm \otimes \mathbb{I}$ and $\hat{\sigma}^\pm \curvearrowright \mathbb{I} \otimes \hat{\sigma}^\pm$. Explicitly we get,

$$\begin{aligned} \hat{a}^\dagger &= \sum_n \sqrt{n+1}|n+1\rangle \begin{pmatrix} 1 & 0 \\ 0 & 1 \end{pmatrix}\langle n| \quad \text{and} \quad \hat{\sigma}^+ = \sum_n |n\rangle \begin{pmatrix} 0 & 0 \\ 1 & 0 \end{pmatrix}\langle n| \\ \hat{a} &= \sum_n \sqrt{n}|n-1\rangle \begin{pmatrix} 1 & 0 \\ 0 & 1 \end{pmatrix}\langle n| \quad \text{and} \quad \hat{\sigma}^- = \sum_n |n\rangle \begin{pmatrix} 0 & 1 \\ 0 & 0 \end{pmatrix}\langle n| \ . \end{aligned} \tag{17.22}$$

17.2.1 Dressed states representation

The basis

$$|1,n\rangle = \begin{pmatrix}1\\0\end{pmatrix}|n\rangle \quad , \quad |2,n-1\rangle = \begin{pmatrix}0\\1\end{pmatrix}|n-1\rangle \tag{17.23}$$

spans a sub-space of two energetically nearly degenerate states with n photons in the system one out of which can have been absorbed by the atom. The density operator for the subspace is,

$$\hat{\rho}_n = \begin{pmatrix} |n\rangle|1\rangle\langle 1|\langle n| & |n\rangle|1\rangle\langle 2|\langle n-1| \\ |n-1\rangle|2\rangle\langle 1|\langle n| & |n-1\rangle|2\rangle\langle 2|\langle n-1| \end{pmatrix} . \tag{17.24}$$

We project the Hamiltonian onto that basis via the projectors $\hat{P} = |1,n\rangle\langle 1,n| + |2,n-1\rangle\langle 2,n-1|$,

$$\boxed{\hat{H}_n = \hat{P}\tilde{H}_{\text{atom:field}}\hat{P} = \begin{pmatrix} n\omega + \frac{\Delta}{2} & \frac{1}{2}\Omega_1\sqrt{n} \\ \frac{1}{2}\Omega_1\sqrt{n} & n\omega - \frac{\Delta}{2}\end{pmatrix}} . \tag{17.25}$$

That is, the Hamiltonian can be decomposed into sub-hyperspaces which are all orthogonal, because the Hamiltonian $\tilde{H}_{\text{atom:field}}$ only contains terms conserving the total number of photons + excitations.

Example 100 (*Orthogonality of submatrices with same numbers of excitations*): This can be seen by expanding the Hamiltonian matrix:

$$\tilde{H}_{\text{atom:field}} = \bigoplus_n \hat{H}_n \tag{17.26}$$

$$= \sum_n \left[|n\rangle \begin{pmatrix} n\omega + \frac{\Delta}{2} & 0 \\ 0 & n\omega - \frac{\Delta}{2}\end{pmatrix} + |n-1\rangle \begin{pmatrix} 0 & 0 \\ \frac{\Omega_1}{2}\sqrt{n} & 0\end{pmatrix} + |n+1\rangle \begin{pmatrix} 0 & \frac{\Omega_1}{2}\sqrt{n+1} \\ 0 & 0\end{pmatrix}\right]\langle n|$$

$$= \begin{pmatrix} \frac{\Delta}{2} & & & & & \\ & \omega + \frac{\Delta}{2} & \frac{\Omega_1}{2} & & & \\ & \frac{\Omega_1}{2} & \omega - \frac{\Delta}{2} & & & \\ & & & 2\omega + \frac{\Delta}{2} & \frac{\Omega_1}{2}\sqrt{2} & \\ & & & \frac{\Omega_1}{2}\sqrt{2} & 2\omega - \frac{\Delta}{2} & \\ & & & & & 3\omega + \frac{\Delta}{2} & \cdots \\ & & & & & \vdots & \ddots \end{pmatrix} .$$

The eigenvalues can be easily calculated by [3],

$$\det \sum_n \hat{H}_n = \sum_n \det \hat{H}_n \ , \tag{17.27}$$

[3] The following rules apply to determinants,

$$\det(AB) = \det A \det B \quad \text{and} \quad (\det A)^{-1} = \det A^{-1} .$$

defining the generalized n-photon Rabi frequency, $\varpi_n \equiv \sqrt{\Delta^2 + n\Omega_1^2} = |\varpi_n| e^{\imath \mathbf{k}\cdot\mathbf{R}}$, which contains the spatial mode function of the radiation field. Using the standard procedure outlined in Sec. 1.5.4 we find the diagonal matrix of eigenvalues,

$$\hat{E}_n = \begin{pmatrix} n\omega + \frac{\varpi_n}{2} & 0 \\ 0 & n\omega - \frac{\varpi_n}{2} \end{pmatrix} . \tag{17.28}$$

From the transformation $\hat{H}_n \mathcal{U}_n = \mathcal{U}_n \hat{E}_n$, under the condition that $\mathcal{U}_n$ is unitary and Hermitian, $\mathcal{U}_n^\dagger \mathcal{U}_n$, and using the abbreviation $\tan 2\phi_n \equiv \sqrt{n}\Omega_1/\Delta$, we obtain:

$$\mathcal{U}_n = \begin{pmatrix} \cos\phi_n & \sin\phi_n \\ -\sin\phi_n & \cos\phi_n \end{pmatrix} . \tag{17.29}$$

The unitary matrix $\mathcal{U}_n$ describes the transform from the product state basis (17.23) to the dressed state basis (17.12), as illustrated in Fig. 17.4.

The temporal evolution of the Jaynes-Cummings state, $|\psi(t)\rangle = e^{-\imath \tilde{H}_{\text{atom:field}} t} |\psi(0)\rangle$, is described by the transformation,

$$\boxed{\begin{aligned} & e^{-\imath \hat{H}_n t} = \mathcal{U}_n e^{-\imath \hat{E}_n t} \mathcal{U}_n^\dagger = e^{-\imath n\omega t} \times \\ & \times \begin{pmatrix} \cos^2\phi_n e^{-\imath\varpi_n t/2} + \sin^2\phi_n e^{\imath\varpi_n t/2} & \cos\phi_n \sin\phi_n (e^{\imath\varpi_n t/2} - e^{-\imath\varpi_n t/2}) \\ \cos\phi_n \sin\phi_n (e^{\imath\varpi_n t/2} - e^{-\imath\varpi_n t/2}) & \sin^2\phi_n e^{-\imath\varpi_n t/2} + \cos^2\phi_n e^{\imath\varpi_n t/2} \end{pmatrix} , \end{aligned}} \tag{17.30}$$

which is essentially the same formula as for the time evolution of a two-level atom driven by a classical light field derived in Exc. 1.6.7.1. The transition probability between dressed states is,

$$|\langle 2, n-1 | e^{-\imath \hat{H}_n t} | 1, n \rangle|^2 = \frac{n\Omega_1^2}{\varpi_n^2} \sin^2 \frac{\varpi_n t}{2} . \tag{17.31}$$

The temporal evolution follows with [436],

$$\hat{\rho}(t) = e^{-\imath \hat{H}_n t} \hat{\rho}(0) e^{\imath \hat{H}_n t} \equiv \mathcal{L}(t) \hat{\rho}(0) . \tag{17.32}$$

Alternatively to the master equation (17.32) we could describe the time evolution of the system by Heisenberg equations, as done in Exc. 17.2.5.1.

17.2.2 Classical and quantum limits

17.2.2.1 The limit of high laser intensities and resonant interaction

The classical limit is recovered for $n \to \infty$, where a single photon makes no difference, that is, we can treat the states $|n\rangle$ and $|n+1\rangle$ as equivalent. Then, we can approximate the Hamiltonian of the system (17.21) by the trace of this same Hamiltonian taken over the number of photons,

$$\hat{H}_{\text{atom:field}} \simeq \hat{H}_{\text{semi}} = \lim_{n\to\infty} \text{Tr}_{\text{field}} \hat{\rho} \tilde{H}_{\text{atom:field}} = \sum_m \langle m | \hat{\rho} \tilde{H}_{\text{atom:field}} | m \rangle . \tag{17.33}$$

This situation, as illustrated in Fig. 17.5, describes well the state of a laser as a coherent state, $|\alpha\rangle = \sum_n \frac{\alpha^n}{\sqrt{n!}}|n\rangle e^{-|\alpha|^2/2}$. For $n \to \infty$, the uncertainty of the Poisson distribution is small, $\Delta n/\bar{n} = 1/\sqrt{n} \to 0$, such that the light mode is characterized by the average number of photons, and fluctuations are negligible. This allows us to replace the Poisson distribution, $P_n = |\langle n|\alpha\rangle|^2 = \delta_{n\bar{n}}$. The Hamiltonian (17.25) then becomes,

$$\hat{H}_{\rm semi} = \hat{H}_{\rm field} + \hat{H}_{\rm atom} + \hat{H}_{\rm atom:field} = \sum_m \langle m|\alpha\rangle\langle\alpha|\hat{H}|m\rangle = \langle\alpha|\hat{H}|\alpha\rangle \simeq \langle\bar{n}|\hat{H}|\bar{n}\rangle$$
$$= \hat{H}_{\bar{n}} = \begin{pmatrix} \bar{n}\omega & 0 \\ 0 & (\bar{n}-1)\omega \end{pmatrix} + \begin{pmatrix} -\frac{\omega_0}{2} & 0 \\ 0 & \frac{\omega_0}{2} \end{pmatrix} + \begin{pmatrix} 0 & \frac{\varpi_{\bar{n}}}{2} \\ \frac{\varpi^*_{\bar{n}}}{2} & 0 \end{pmatrix} . \tag{17.34}$$

Now, in the case of a resonant interaction, $\Delta = 0$, the Jaynes-Cummings evolution is,

$$\boxed{e^{-\imath\hat{H}_{\bar{n}}t} = \frac{1}{\sqrt{2}} e^{-\imath(\bar{n}-1/2)\omega t} \begin{pmatrix} \cos\frac{1}{2}\varpi_{\bar{n}}t & \imath\sin\frac{1}{2}\varpi_{\bar{n}}t \\ \imath\sin\frac{1}{2}\varpi_{\bar{n}}t & \cos\frac{1}{2}\varpi_{\bar{n}}t \end{pmatrix}} , \tag{17.35}$$

which is a result already obtained in Exc. 1.6.7.1.

Example 101 (*Resonant* $\pi/2$*-pulse*): In this example, we consider resonant $\pi/2$-pulses, that is, $\sqrt{\bar{n}}\Omega_1 t = \frac{1}{2}\pi$. The Jaynes-Cummings evolution now simplifies to,

$$e^{-\imath\hat{H}_{\bar{n}}t} = \frac{1}{2} e^{-\imath(\bar{n}-1/2)\omega t} \begin{pmatrix} 1 & \imath \\ \imath & 1 \end{pmatrix} . \tag{17.36}$$

For large $\bar{n}$, a resonant $\pi/2$-pulse does (ignoring irrelevant dynamical phases),

$$\begin{pmatrix} |1\rangle|\bar{n}\rangle \\ |2\rangle|\bar{n}-1\rangle \end{pmatrix} \overset{\pi/2}{\curvearrowright} \begin{pmatrix} (\imath|2\rangle|\bar{n}-1\rangle + |1\rangle|\bar{n}\rangle) \\ (|2\rangle|\bar{n}-1\rangle + \imath|1\rangle|\bar{n}\rangle) \end{pmatrix} , \tag{17.37}$$

that is, for a coherent field,

$$\begin{pmatrix} |1\rangle|\alpha\rangle \\ |2\rangle|\alpha\rangle \end{pmatrix} \overset{\pi/2}{\curvearrowright} \begin{pmatrix} (\imath|2\rangle + |1\rangle)|\alpha\rangle \\ (|2\rangle + \imath|1\rangle)|\alpha\rangle \end{pmatrix} . \tag{17.38}$$

Obviously, the structure of the field $|\alpha\rangle$ is not affected, and we recover the dynamics of a two-level atom excited by a resonant classical *radiation* as described by the Bloch equations (16.114). In the language of quantum computation the operation (17.36) corresponds to a Hadamard gate.

17.2.2.2 Dispersive interaction, the limit of large detunings

The dispersive Jaynes-Cummings dynamics can be implemented by irradiating a light field, which is sufficiently detuned to avoid Rayleigh scattering processes, as shown in Fig. 17.5. This interaction results in a phase shift of the atomic levels. For $|\Delta| \gg \sqrt{n}\Omega_1$ we consider the radiative coupling as a small perturbation,

$$\hat{H}_n = \hat{H}_n^{(0)} + \hat{H}_n^{(1)} = \begin{pmatrix} n\omega - \frac{\Delta}{2} & 0 \\ 0 & n\omega + \frac{\Delta}{2} \end{pmatrix} + \begin{pmatrix} 0 & \frac{\Omega_1}{2}\sqrt{n} \\ \frac{\Omega_1}{2}\sqrt{n} & 0 \end{pmatrix} . \tag{17.39}$$

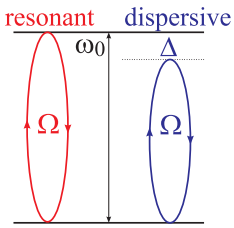

Figure 17.5: Atomic level scheme for the implementation of resonant interactions with classical radiation fields (on the lower transition) and dispersive interactions with quantum fields (on the upper transition).

In the unperturbed case we have, $\hat{H}_n^{(0)}|\psi_{j,n}\rangle = E_{j,n}|\psi_{j,n}\rangle$, where the n-photon subspace is spanned by the basis $|j\rangle = (1\ 0)$ and $(0\ 1)$. In second perturbation order,

$$\langle\psi_{j,n}|\hat{H}_n^{(1)}|\psi_{j,n}\rangle \simeq \cancelto{0}{\langle j|\hat{H}_n^{(1)} + \hat{H}_n^{(2)}|j\rangle} + \sum_{j\neq i} \frac{\langle j|\hat{H}_n^{(1)}|i\rangle\langle i|\hat{H}_n^{(1)}|j\rangle}{E_{j,n}^{(0)} - E_{i,n}^{(0)}} = \mp\frac{n\Omega_1^2}{4\Delta} \ , \quad (17.40)$$

where the upper sign holds for $|j\rangle = (1\ 0)$. This result was already obtained in the Excs. 5.1.3.4 and 16.4.4.13. In matrix notation [4],

$$\hat{H}_n^{(1)} \simeq \begin{pmatrix} n\Omega_1^2/4\Delta & 0 \\ 0 & -n\Omega_1^2/4\Delta \end{pmatrix} . \quad (17.41)$$

The temporal propagation operator (17.30) then simplifies to,

$$\boxed{e^{-\imath\hat{H}_n^{(1)}t} = \begin{pmatrix} e^{\imath n\Omega_1^2 t/4\Delta} & 0 \\ 0 & e^{-\imath n\Omega_1^2 t/4\Delta} \end{pmatrix}} . \quad (17.42)$$

The fact that the ground and excited atomic states evolve with different phase factors is important, as we will show in the following example.

Example 102 (*Dispersive π-pulse*): As in the previous case, we consider a two-level atom subject to a coherent field, but now tuned out of resonance. Introducing the abbreviation $\varphi \equiv \Omega_1^2 t/4\Delta$, the Jaynes-Cummings evolution is,

$$e^{-\imath\hat{H}_n^{(1)}t} = \begin{pmatrix} e^{\imath n\varphi} & 0 \\ 0 & e^{-\imath n\varphi} \end{pmatrix} . \quad (17.43)$$

The fact that the phase shift $n\varphi$ depends on the number of photons, and that it goes in opposite directions for the ground and excited states, is crucial. We

[4] Note, that the same perturbation expansion applied to the complete Hamiltonian in the interaction picture yields,

$$\tilde{H}_I^{(1)} = \begin{pmatrix} 0 & \frac{1}{2}\Omega_1\hat{a}^\dagger \\ \frac{1}{2}\Omega_1\hat{a} & 0 \end{pmatrix} = \tfrac{1}{2}\Omega_1\hat{a}\hat{\sigma}^+ + \tfrac{1}{2}\Omega_1\hat{a}^\dagger\hat{\sigma}^-$$
$$\simeq \frac{\tilde{H}_I^{(1)}|2\rangle\langle 2|\tilde{H}_I^{(1)}}{\omega_2-\omega_1} + \frac{\tilde{H}_I^{(1)}|1\rangle\langle 1|\tilde{H}_I^{(1)}}{\omega_1-\omega_2} = \tfrac{\Omega_1^2}{4\Delta}(\hat{\sigma}^-\hat{\sigma}^+\hat{a}^\dagger\hat{a} - \hat{\sigma}^+\hat{\sigma}^-\hat{a}\hat{a}^\dagger) = \tfrac{\Omega_1^2}{4\Delta}\begin{pmatrix} -\hat{a}^\dagger\hat{a} & 0 \\ 0 & \hat{a}\hat{a}^\dagger \end{pmatrix} .$$

have already studied in Exc. 16.7.3.9, that the dispersive interaction of the atom with a radiation field can phase-shift the Bloch vector. Now, we observe that in addition, it causes a phase shift of the probability amplitude of having n photons in the radiation field by a value proportional to n, i.e. (ignoring irrelevant dynamical phases),

$$\begin{pmatrix} |1\rangle|n\rangle \\ |2\rangle|n-1\rangle \end{pmatrix} \overset{n\varphi}{\curvearrowright} \begin{pmatrix} e^{-\imath n\varphi}|1\rangle|n\rangle \\ e^{\imath n\varphi}|2\rangle|n-1\rangle \end{pmatrix} . \tag{17.44}$$

Applying this result to Glauber states,

$$\begin{pmatrix} |1\rangle|\alpha\rangle \\ |2\rangle|\alpha\rangle \end{pmatrix} \overset{n\varphi}{\curvearrowright} \begin{pmatrix} |1\rangle \sum_n \frac{\alpha^n}{\sqrt{n!}} e^{-\imath n\varphi}|n\rangle \\ |2\rangle \sum_n \frac{\alpha^n}{\sqrt{n!}} e^{\imath n\varphi}|n\rangle \end{pmatrix} = \begin{pmatrix} |1\rangle|\alpha e^{-\imath\varphi}\rangle \\ |2\rangle|\alpha e^{\imath\varphi}\rangle \end{pmatrix} . \tag{17.45}$$

Apparently, the phase of the radiation field is shifted by a value φ, which depends on the state of the atom.

We note here, that the dynamics studied in the last example provides a method of *transferring coherence from an atomic superposition to a quantum correlation of a radiation field*. All we have to do, is to bring the atom into a superposition of states $|1\rangle + |2\rangle$, and the field will automatically evolve toward a Schrödinger cat state $|\alpha e^{\imath\varphi}\rangle + |\alpha e^{-\imath\varphi}\rangle$. The transfer of quantum correlations between coupled degrees of freedom can induce a temporal complete disappearance of any signatures of quantum coherence in the light field. This phenomenon termed *quantum collapse and revival* is genuine of the Jaynes-Cummings model and will be studied in Excs. 17.2.5.2 and 17.2.5.3. Another phenomenon is *vacuum Rabi splitting*, which will be studied in 17.2.5.4.

17.2.3 Observables and correlations of the Jaynes-Cummings dynamics

In the limit of low laser intensities we must consider photonic distributions that are not necessarily coherent. The stationary solution of the Schrödinger equation consists of the dressed states $|1, n\rangle$ and $|2, n-1\rangle$. If we now expand a general Jaynes-Cummings state in amplitudes $c_{jn}(t)$,

$$|\psi\rangle = \sum_n (c_{1,n}|1, n\rangle + c_{2,n-1}|2, n-1\rangle) , \tag{17.46}$$

they will follow the Schrödinger equation,

$$\imath\hbar \frac{d}{dt} \begin{pmatrix} c_{1,n} \\ c_{2,n-1} \end{pmatrix} = \hat{H}_n \begin{pmatrix} c_{1,n} \\ c_{2,n-1} \end{pmatrix} . \tag{17.47}$$

The evolution of the coefficients c_{jn} completely describes the Jaynes-Cummings dynamics of the system through the formula (17.30). Obviously, the Jaynes-Cummings state is normalized because,

$$\langle\psi|\psi\rangle = \mathrm{Tr}_{\mathrm{field}}\ |\psi\rangle\langle\psi| = \sum_{n=0}^{\infty} (|c_{1,n}|^2 + |c_{2,n}|^2) = 1 . \tag{17.48}$$

As dissipation processes are neglected, we get a pure state described by,

$$\hat{\rho} = |\psi\rangle\langle\psi| \ . \tag{17.49}$$

The Jaynes-Cummings dynamics involves two coupled degrees of freedom characterized by with their respective observables. If we are interested in them, we can do two things: (a) We ignore the degrees of freedom NOT under study by NOT DOING a measurement of the other degrees. That is, we simply remove the non-interesting degrees of freedom from the state. For example, if our focus is on the optical mode, we ignore the atomic state,

$$|\gamma\rangle \equiv \sum_{j=1,2} \langle j|\psi\rangle = \sum_n c_{1,n}|n\rangle + c_{2,n-1}|n-1\rangle \ . \tag{17.50}$$

Our new density operator remains pure, that is,

$$\hat{\rho}_{\rm field}^{\rm (pure)} = \sum_{i,j=1,2} \langle j|\hat{\rho}|i\rangle = \sum_{i,j=1,2} \langle j|\psi\rangle\langle\psi|i\rangle = |\gamma\rangle\langle\gamma| \ . \tag{17.51}$$

On the other hand, ignoring the optical mode via,

$$|\gamma\rangle \equiv \sum_n \langle n|\psi\rangle = \sum_n c_{1,n}|1\rangle + c_{2,n-1}|2\rangle \ . \tag{17.52}$$

Again, our new density operator remains pure, that is,

$$\hat{\rho}_{\rm atom}^{\rm (pure)} = \sum_{m,n} \langle m|\hat{\rho}|n\rangle = \sum_{m,n} \langle m|\psi\rangle\langle\psi|n\rangle = |\gamma\rangle\langle\gamma| \ . \tag{17.53}$$

(b) We trace over the degrees of freedom NOT under study by DOING a measurement. For example, if again our focus is on the optical mode, we trace over the atomic states,

$$\begin{aligned} \hat{\rho}_{\rm field}^{\rm (mix)} = {\rm Tr}_{\rm atom}\ \hat{\rho} &= \sum_{j=1,2} \langle j|\hat{\rho}|j\rangle = \sum_{j=1,2} \langle j|\psi\rangle\langle\psi|j\rangle \\ &= \sum_{n,m} c_{1,m}^* c_{1,n}|n\rangle\langle m| + c_{2,m-1}^* c_{2,n-1}|n-1\rangle\langle m-1| \neq \hat{\rho}_{\rm field}^{\rm (pure)} \ . \end{aligned} \tag{17.54}$$

It is clear, that this incomplete measurement converts the reduced density operator into a statistical mixture, which is free of inneratomic correlations of the type $c_{2,m}^* c_{1,n}$, but this means that we also loose possible field correlations. On the other hand, tracing over the field mode,

$$\begin{aligned} \hat{\rho}_{\rm atom}^{\rm (mix)} = {\rm Tr}_{\rm field}\ \hat{\rho} &= \sum_{n=0}^{\infty} \langle n|\hat{\rho}|n\rangle = \sum_{n=0}^{\infty} \langle n|\psi\rangle\langle\psi|n\rangle \\ &= \sum_n \left(c_{1,n}|1\rangle + c_{2,n}|2\rangle\right)\left(c_{1,n}^*\langle 1| + c_{2,n}^*\langle 2|\right) \neq \hat{\rho}_{\rm atom}^{\rm (pure)} \ . \end{aligned} \tag{17.55}$$

After these preliminary remarks let us have a look a some interesting observables.

17.2.3.1 Temporal evolution of the Bloch vector

The expectation value for field observables $\hat{A}|n\rangle = A_n|n\rangle$ is,

$$\langle\psi|\hat{A}|\psi\rangle = \text{Tr}\ \hat{\rho}\hat{A}\sum_{i,n}\langle i|\langle n|\psi\rangle\langle\psi|\hat{A}|n\rangle|i\rangle = \sum_n A_n(|c_{1,n}|^2 + |c_{2,n}|^2)\ . \tag{17.56}$$

An example for a field observable is the photon number operator $\hat{n}$. And for the annihilation operator $\hat{a}|n\rangle = \sqrt{n}|n\rangle$ we have,

$$\langle\psi|\hat{a}|\psi\rangle = \sum_n \sqrt{n}(c^*_{1,n-1}c_{1,n} + c^*_{2,n-1}c_{2,n})\ . \tag{17.57}$$

To determine the internal state of the atom, we must trace over the light field. The populations and coherences are, therefore,

$$\boxed{\rho_{ij} = \langle i|\text{Tr}_{\text{field}}\ \hat{\rho}|j\rangle = \langle i|\sum_n\langle n|\psi\rangle\langle\psi|n\rangle|j\rangle = \sum_n c_{i,n}c^*_{j,n}}\ . \tag{17.58}$$

The projection onto the atomic state is done by,

$$\frac{|j\rangle\langle j|\psi\rangle}{\langle\psi|j\rangle\langle j|\psi\rangle} = \frac{\sum_m c_{j,n}|j,n\rangle}{\sum_m |c_{j,m}|^2}\ . \tag{17.59}$$

With (17.58), we can calculate the atomic Bloch vector (16.126), whose norm is interestingly NOT preserved, since,

$$\begin{aligned}|\vec{\rho}| = \left\|\begin{pmatrix} 2\ \mathfrak{Re}\,\rho_{12} \\ 2\ \mathfrak{Im}\,\rho_{12} \\ \rho_{22}-\rho_{11}\end{pmatrix}\right\| &= 2|\rho_{12}|^2 - 2\rho_{11}\rho_{22} = -2\det\hat{\rho} \\ &= 2\sum_n c_{1,n}c^*_{2,n}\sum_n c^*_{1,n}c_{2,n} - 2\sum_n|c_{2,n}|^2\sum_n|c_{1,n}|^2 \neq 1\ .\end{aligned} \tag{17.60}$$

17.2.3.2 The photon number distribution

To determine the state of the light field, we must trace over the atomic state. For example, the probability amplitude of encountering the state $|\psi\rangle$ in $|n\rangle$ is,

$$\langle n|\psi\rangle = c_{1,n}|1\rangle + c_{2,n}|2\rangle\ , \tag{17.61}$$

such that,

$$\boxed{p_n = \langle n|\text{Tr}_{\text{atom}}\ \hat{\rho}|n\rangle = \langle n|\sum_{i=1,2}\langle i|\psi\rangle\langle\psi|i\rangle|n\rangle = |\langle n|\psi\rangle|^2 = |c_{1,n}|^2 + |c_{2,n}|^2}\ . \tag{17.62}$$

17.2.3.3 The Glauber-Sudarshan Q-function

To characterize the optical field separately from the atomic state, we can try, by a calculation similar to (17.56), to project the Jaynes-Cummings state onto a basis of

coherent states. Thus, the probability amplitude of encountering the state $|\psi\rangle$ in $|\alpha\rangle$ is,

$$\langle\alpha|\psi\rangle = e^{-|\alpha|^2/2}\sum_n \frac{\alpha^{*n}}{\sqrt{n!}}(c_{1,n}|1\rangle + c_{2,n}|2\rangle) \tag{17.63}$$

$$|\langle\alpha|\psi\rangle|^2 = e^{-|\alpha|^2}\sum_n \frac{\alpha^{*n}\alpha^m}{\sqrt{n!}\sqrt{m!}}(c^*_{1,m}c_{1,n} + c^*_{2,m}c_{2,n}) \ ,$$

such that,

$$\boxed{\pi Q(\alpha) \equiv \langle\alpha|\mathrm{Tr}_{\mathrm{atom}}\ \hat{\rho}|\alpha\rangle = e^{-|\alpha|^2}\left(\left|\sum_n c_{1,n}\frac{\alpha^n}{\sqrt{n!}}\right|^2 + \left|\sum_n c_{2,n}\frac{\alpha^n}{\sqrt{n!}}\right|^2\right)} \ . \tag{17.64}$$

We will derive this result in Exc. 17.2.5.5. This quantity, called *Q-function*, allows the illustration of the state in a coordinate system spanned by $\mathfrak{Re}\,\alpha$ and $\mathfrak{Im}\,\alpha$ [93]. It is generally easy to calculate, but does not exhibit much information, e.g., on interference phenomena caused by quantum correlations. In the following section, we will calculate the Wigner function, which can also be evaluated from the Jaynes-Cummings coefficients [261].

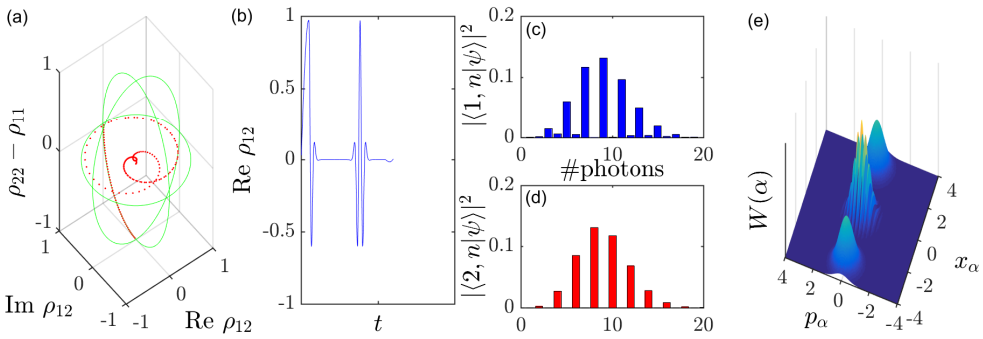

Figure 17.6: (code) Evolution of the state during a Jaynes-Cummings type interaction: (a) Bloch vector, (b,c) photon distribution after projection on the ground and excited atomic state, (d) time evolution of the coherence ρ_{12} showing the phenomenon of collapse and revival, and (e) $W(\alpha)$ function.

The Jaynes-Cummings dynamics illustrated in Fig. 17.6 demonstrates the transfer of coherence between an atom and a light field. In Exc. 17.2.5.6 we study how to create, via a sequence of Ramsey pulses, a Schrödinger cat state in a light field.

17.2.3.4 The Wigner function in the Glauber picture

We found in (17.42) that a dispersive phase shift of the atomic state $|2\rangle$ leads to a time-dependent phase shift of the Glauber field,

$$|\psi\rangle = \sum_{\mathrm{N}}(c_{1,n}|1,n\rangle + c_{2,n-1}|2,n-1\rangle) = |1,\beta\rangle + e^{i\varphi(t)}|2,\beta\rangle \quad \text{or} \quad \hat{\rho} = |\psi\rangle\langle\psi| \ , \tag{17.65}$$

with

$$c_{1,n} = e^{-|\beta|^2/2}\frac{\beta^n}{\sqrt{n!}} \qquad \text{and} \qquad c_{2,n} = e^{-|\beta|^2/2}\frac{(e^{\imath\varphi(t)}\beta)^n}{\sqrt{n!}} \ . \tag{17.66}$$

We will now concentrate on the field state by explicitly IGNORING the atomic states $|j\rangle$,

$$|\gamma\rangle = \sum_{j=1,2}\langle j|\psi\rangle = |\beta\rangle + |e^{\imath\varphi}\beta\rangle \qquad \text{or} \qquad \hat{\rho}^{(\text{pure})}_{\text{field}} = \sum_{i,j=1,2}\langle j|\psi\rangle\langle\psi|i\rangle = |\gamma\rangle\langle\gamma| \ . \tag{17.67}$$

From the optical cat pure state wavefunction (17.67), we can easily calculate the Wigner function in the Glauber picture, as done in (14.90) and Exc. 14.3.5.10,

$$\boxed{W(\alpha) = \frac{2}{C^2\pi}\left(e^{-2|\alpha-\beta|^2} + e^{-2|\alpha-\beta e^{\imath\varphi}|^2} \pm 2e^{-|\beta|^2}\mathfrak{Re}\, e^{-2(\beta e^{\imath\varphi}-\alpha)(\beta^*-\alpha^*)+|\beta|^2 e^{\imath\varphi}}\right)} \ . \tag{17.68}$$

Now, what happens if we MEASURE the atomic state before we analyze the field state? The incomplete measurement corresponds to tracing over the atomic degrees of freedom, which transforms our initially pure state (17.65) into a statistical mixture. With $|\psi\rangle$ given by (17.65),

$$\hat{\rho}^{(\text{mix})}_{\text{field}} = \text{Tr}_{\text{atom}}\hat{\rho} = \sum_{j=1,2}\langle j|\psi\rangle\langle\psi|j\rangle = |\beta\rangle\langle\beta| + |e^{\imath\varphi}\beta\rangle\langle e^{\imath\varphi}\beta| \neq |\gamma\rangle\langle\gamma| \ . \tag{17.69}$$

Calculating the Wigner function from this density operator consequently must yield a different result, because any correlations are lost. A movie of the dynamics can be watched here (watch movie) [136, 206, 10, 833].

17.2.3.5 The Wigner function in the Fock picture

Let us now calculate the Wigner function in the Fock state picture. This will allow us to consider more general states later on. We start from the expansion,

$$|\psi\rangle = \sum_n c_{1,n}|1,n\rangle + c_{2,n-1}|2,n-1\rangle \ . \tag{17.70}$$

As before, we can now choose to DO or NOT DO a measurement of the atomic state. If we do a measurement tracing over the atomic states, we calculate the normally ordered characteristic function using the density operator (17.54),

$$\begin{aligned}\chi_{\text{N}}(\lambda) &= \text{Tr}\ \hat{\rho}^{(\text{mix})}_{\text{field}} e^{\lambda\hat{a}^\dagger} e^{-\lambda^*\hat{a}} = \sum_{n'}\langle n'|\hat{\rho}^{(\text{mix})}_{\text{field}} e^{\lambda\hat{a}^\dagger} e^{-\lambda^*\hat{a}}|n'\rangle \\ &= \sum_{n,m} c^*_{1,m}c_{1,n}\langle m|e^{\lambda\hat{a}^\dagger} e^{-\lambda^*\hat{a}}|n\rangle + c^*_{2,m-1}c_{2,n-1}\langle m-1|e^{\lambda\hat{a}^\dagger} e^{-\lambda^*\hat{a}}|n-1\rangle \ .\end{aligned} \tag{17.71}$$

Obviously, this formula does not contain inneratomic correlations and, since nonclassical field correlation would be entangled with atomic superposition states, we expect no interesting field correlations, neither.

If on the other hand we decide to ignore the atomic state, we calculate the normally ordered characteristic function using the density operator (17.51),

$$\begin{aligned}\chi_{\rm N}(\lambda) &= \mathrm{Tr}\ \hat\rho_{\rm field}^{(\rm pure)} e^{\lambda\hat a^\dagger} e^{-\lambda^*\hat a} = \langle\gamma|e^{\lambda\hat a^\dagger}e^{-\lambda^*\hat a}|\gamma\rangle \qquad (17.72)\\ &= \sum_{n,m}\Big(c^*_{1,m}c_{1,n}\langle m|e^{\lambda\hat a^\dagger}e^{-\lambda^*\hat a}|n\rangle + c^*_{2,m-1}c_{2,n-1}\langle m-1|e^{\lambda\hat a^\dagger}e^{-\lambda^*\hat a}|n-1\rangle\\ &\qquad + c^*_{1,m}c_{2,n-1}\langle m|e^{-\lambda\hat a^\dagger}e^{\lambda^*\hat a}|n-1\rangle + c^*_{2,m-1}c_{1,n}\langle m-1|e^{\lambda\hat a^\dagger}e^{-\lambda^*\hat a}|n\rangle\Big)\ ,\end{aligned}$$

which now contains field correlations. Inserting the results derived in (14.81) we can express the characteristic functions by Laguerre polynomials and obtain the Wigner function as the two-dimensional FFT according to Eq. (17.68). This will be done in Exc. 17.2.5.8.

17.2.4 Jaynes-Cummings model with dissipation

Applying the numerical method of *quantum Monte Carlo wavefunction simulation* to the Jaynes-Cummings model, we write the effective Hamiltonian of the light field as [307],

$$\hat H_{\rm eff} = \omega\hat a^\dagger\hat a + \omega_0\left(\hat\sigma^+\hat\sigma - \tfrac12\right) + \tfrac{\Omega_1}{2}\left(\hat a\hat\sigma^+ + \hat a^\dagger\hat\sigma^-\right) + \tfrac{\imath\Gamma}{2}\hat\sigma^+\hat\sigma^-\ . \qquad (17.73)$$

Or in matrix notation,

$$H_{\rm eff} = \begin{pmatrix} -\frac12\omega_0 & 0 & & & & & & \\ 0 & \omega-\frac12\omega_0 & \frac12\Omega_1 & & & & & \\ & \frac12\Omega_1 & \frac12\omega_0-\frac{\imath}{2}\Gamma & 0 & & & & \\ & & 0 & 2\omega-\frac12\omega_0 & \sqrt2\frac12\Omega_1 & & & \\ & & & \sqrt2\frac12\Omega_1 & \omega+\frac12\omega_0-\frac{\imath}{2}\Gamma & 0 & & \\ & & & & 0 & 3\omega-\frac12\omega_0 & & \\ & & & & & & \ddots & \end{pmatrix}. \qquad (17.74)$$

The simulation flowchart is,

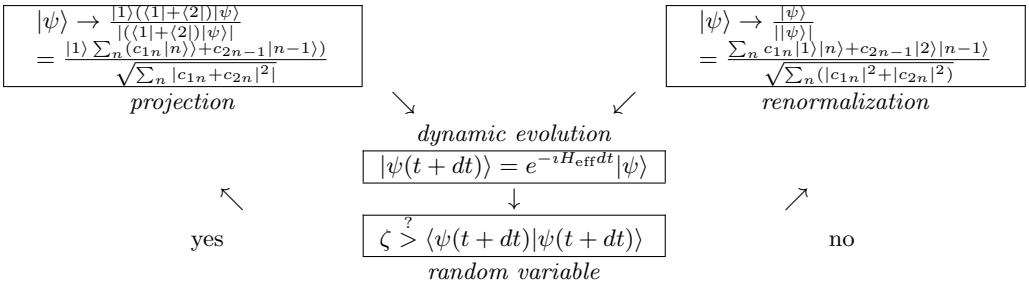

Absorption or scattering of light causes the optical field to decay as $\alpha(t) \propto e^{-\kappa t/2}$. The projection (in component notation) is implemented by,

$$c'_{jn} \equiv \frac{1}{\sqrt{\sum_n(|c_{1n}|^2+|c_{2n}|^2)}}c_{jn}\ , \qquad (17.75)$$

and the dynamical evolution by $c'_{jn} \equiv e^{-\kappa n t/2} c_{jn}$. Note, that the dissipation due to cavity losses can also be taken into account by a *master equation*.

17.2.5 Exercises

17.2.5.1 Ex: Time-evolution in the Jaynes-Cummings model

Derive the equations of motion for $\hat{\sigma}^-$, $\hat{\sigma}_z$, and $\hat{a}$ in the Jaynes-Cummings model. Show that the number of photons is not a constant of motion, but the total number of excitations.

17.2.5.2 Ex: The Jaynes-Cummings model

Consider the Jaynes-Cummings Hamiltonian.
a. Determine from the Schrödinger equation the system of differential equations for the temporal evolution of the coefficients $c_{2,n}(t)$ and $c_{1,n+1}(t)$ in the interaction picture within the rotating wave approximation (RWA).
b. Calculate the time evolution for the start condition $c_{2,n}(0) = 1$ and $c_{1,n+1}(0) = 0$ for the particular case $\omega = \omega_0$.
c. Generalize the result of item (a) for a multimode field, for which initially (i) all modes of field $\mathbf{k}$ are empty $|0\rangle$ and (ii) the atom is in the excited state $|a\rangle$. Use the ansatz,

$$|\psi(t)\rangle = c_2(t) e^{-\imath E_2 t/\hbar} |2, 0\rangle + \sum_{\mathbf{k}} c_{1,\mathbf{k}}(t) e^{-\imath [E_1/\hbar + \omega_{\mathbf{k}}] t} |1, 1_{\mathbf{k}}\rangle \ ,$$

and determine the equations of motion for the amplitudes c_2 and $c_{1,\mathbf{k}}$.

17.2.5.3 Ex: Quantum collapse and revival in the Jaynes-Cummings model

Consider the Jaynes-Cummings Hamiltonian and show that the quantum coherence between the two atomic levels can disappear altogether for long periods and reappear later. Explain how this is possible.

17.2.5.4 Ex: Vacuum Rabi splitting

Calculate the Autler-Townes splitting for an excited atom interacting with an empty cavity.

17.2.5.5 Ex: The Q-function in a Jaynes-Cummings state

Calculate the Q-function for a Jaynes-Cummings state from its definition (17.64).

17.2.5.6 Ex: Creation of quantum correlations in an optical mode

a. We will show in this exercise how, via coherent operations in a three-level system, we can create Schrödinger-type quantum-type correlations in an optical mode. In the system shown in Fig. 17.7 we imagine the lower transition excited by $\pi/2$-pulses of a classical resonant microwave radiation (as described by the operation (17.35)). The upper transition is excited by quantum laser pulses tuned very far out of resonance,

thus creating a dispersive dynamics (as described by the operation (17.35)). At time $t = 0$ the atom is in state $|1\rangle$. Now, we apply the following pulse sequence: (i) a microwave pulse with $\sqrt{\bar{n}}\Omega_{12}t = \pi/2$, (ii) an optical pulse with $\Omega_{23}^2 t/4\Delta_{23} = \pi$, (iii) another microwave $\pi/2$-pulse, and finally (iv) an optical pulse of light which is resonant with the transition $|2\rangle$-$|3\rangle$ and projects the population of the atom into one of the states of the microwave transition. Describe the evolution of the state of the system during the sequence and determine the final state of the optical mode.
b. Calculate the number of photons for the two cases that, after a measurement, the atom is found in (i) the lower state and (ii) the upper state. Interprete the results.

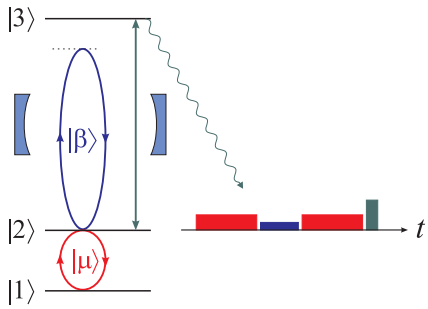

Figure 17.7: (a) Level scheme and (b) pulse sequence.

17.2.5.7 Ex: Master equation derived from JC model Hamiltonian for two-level systems

Write down the Liouvillean for a JC system in matrix form for a density operator defined like,

$$\left(\cdots \quad \rho_{11}^{n-1} \quad \rho_{22}^{n} \quad \rho_{12}^{n} \quad \rho_{21}^{n} \quad \rho_{11}^{n} \quad \rho_{22}^{n+1} \quad \cdots\right) .$$

17.2.5.8 Ex: Laguerre polynomials

Calculate the Wigner function for the field generated by a Jaynes-Cummings dynamics in the photon picture.

17.3 Correlation functions

In the preceding sections and in Sec. 14.3 we have learned, how to characterize quantum fields by (quasi-)probability distribution functions, and how to represent correlations in the Fock or the Glauber basis. But we did not propose experimental schemes allowing to detect them. Experimental devices, such as interferometers or photon correlators, necessarily involve space or time coordinates. Hence, we need to devise quantities for the characterization of correlations, that are compatible with experimental devices. The *correlation functions* are such quantities, and in the next section we will focus our attention them.

In order to be able to distinguish classical from genuinely quantum correlations, we will first a classical description, before introducing a quantum description of the light field [530].

17.3.1 Classical first and second order coherence

The coherence properties of a light field (or a matter wave) are measured by n^{th} space time order correlation functions. In quantum mechanics, these are defined by,

$$g^{(n)}(\mathbf{r}_1,t_1,..,\mathbf{r}_{2n},t_{2n}) \equiv \frac{\langle \hat{\mathcal{E}}^-(\mathbf{r}_1,t_1)..\hat{\mathcal{E}}^-(\mathbf{r}_n,t_n)\hat{\mathcal{E}}^+(\mathbf{r}_{n+1},t_{n+1})..\hat{\mathcal{E}}^+(\mathbf{r}_{2n},t_{2n})\rangle}{\sqrt{\langle \hat{\mathcal{E}}^-(\mathbf{r}_1,t_1)\hat{\mathcal{E}}^+(\mathbf{r}_1,t_1)\rangle..\langle \hat{\mathcal{E}}^-(\mathbf{r}_{2n},t_{2n})\hat{\mathcal{E}}^+(\mathbf{r}_{2n},t_{2n})\rangle}} \ . \tag{17.76}$$

In the following, we will only consider temporal coherences, e.g. one or more collinear light beams, $\mathbf{k}_m \parallel \mathbf{k}_n$, impinging on a photodetector, $(t_m - \frac{z_m}{c}) - (t_n - \frac{z_n}{c}) = \tau$, since $\hat{\mathcal{E}}(\mathbf{r},t) = \hat{\mathcal{E}}(\omega t - \mathbf{k}\cdot\mathbf{r})$, we can define the the 1^{st} and 2^{nd} order correlation functions $g^{(1)}$ and $g^{(2)}$, which are particularly important,

$$\boxed{g^{(1)}(\tau) \equiv \frac{\langle \hat{\mathcal{E}}^-(t)\hat{\mathcal{E}}^+(t+\tau)\rangle}{\langle \hat{\mathcal{E}}^-(t)\hat{\mathcal{E}}^+(t)\rangle} \quad \text{and} \quad g^{(2)}(\tau) \equiv \frac{\langle \hat{\mathcal{E}}^-(t)\hat{\mathcal{E}}^-(t+\tau)\hat{\mathcal{E}}^+(t+\tau)\hat{\mathcal{E}}^+(t)\rangle}{\langle \hat{\mathcal{E}}^-(t)\hat{\mathcal{E}}^+(t)\rangle^2}} \ . \tag{17.77}$$

Ignoring the quantized nature of light, we may substitute the field operators by complex numbers, $\hat{\mathcal{E}}^+ \to \mathcal{E}$ and $\hat{\mathcal{E}}^- \to \mathcal{E}^*$ and interprete the brackets as pure time averages,

$$\langle \cdots \rangle_t = \lim_{t\to\infty} \frac{1}{t} \int_0^t \cdots dt' \ . \tag{17.78}$$

Defining the intensity as $I = 2\varepsilon_0 c \mathcal{E}^* \mathcal{E}$, the coherences become,

$$g^{(1)}(\tau) \equiv \tfrac{2\varepsilon_0 c}{I}\langle \mathcal{E}^*(t)\mathcal{E}(t+\tau)\rangle \quad \text{and} \quad g^{(2)}(\tau) \equiv \left(\tfrac{2\varepsilon_0 c}{I}\right)^2 \langle I(t)I(t+\tau)\rangle \ . \tag{17.79}$$

The correlation functions must be calculated from the field operators simultaneously respecting *time order* and *normal order*. These functions are useful quantities to describe phenomena such as photon *bunching* or to understand the fluorescence spectra or the scattering of light from correlated atoms. $g^{(1)}$ measures the *coherence* of a light field (how much it resembles a sine wave). $g^{(2)}$ measures, for a given degree of coherence, the deviation of the light field from the quantum state that most closely approximates a classical light (how much it resembles a laser).

The correlation functions $g^{(1)}$ and $g^{(2)}$ are experimentally measured in *Young's experiment* and in the *Hanbury Brown-Twiss experiment*. The experimental schemes are explained in Figs. 17.8.

Coherence and chaos are contrary properties of light. They leave their imprint in the spectrum of the light or in the autocorrelation functions. The emission spectrum of a light source generally emerges as a combination of various physical effects: The active medium gives rise resonances and broadenings, a resonator containing the active medium imprints a modal structure, and the coupling to a thermal bath gives rise to a thermal distribution of the radiation energy according to $P_n = e^{-\hbar\omega(n+1/2)/k_BT} / \sum_n e^{-\hbar\omega(n+1/2)/k_BT}$.

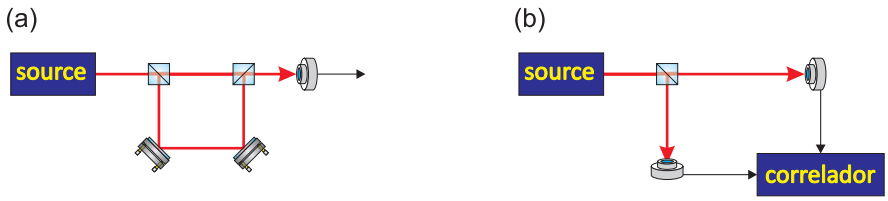

Figure 17.8: (a) Scheme of Young's experiment. (b) Scheme of the experiment of Hanbury, Brown, and Twiss. Young's experiment reveals the coherence of a field, that is, its ability to interfere. In contrast, the Hanbury-Brown-Twist experiment reveals correlations between the (quasi-)particles constituting the field, that is, effects due to quantum statistics or interactions.

17.3.2 The Wiener-Khintchine theorem

When the time dependence of a wave is given by $\mathcal{E}(t)$, we call

$$R_{\mathcal{E}}(\tau) = \langle \mathcal{E}^*(t)\mathcal{E}(t+\tau)\rangle_t \tag{17.80}$$

the autocorrelation function and the power density

$$S_{\mathcal{E}}(\omega) = (\mathcal{F}R_{\mathcal{E}})(\omega) = |(\mathcal{F}\mathcal{E})(\omega)|^2 \tag{17.81}$$

the *spectrum*. This relation is called the *Wiener-Khintchine theorem*. We may also consider the normalized quantities, dividing (17.80) and (17.81) by $R_{\mathcal{E}}(0) = \langle \hat{\mathcal{E}}^*(t)\hat{\mathcal{E}}(t)\rangle_t = \int_{-\infty}^{\infty} |(\mathcal{F}\mathcal{E})(\omega)|^2 d\omega = \int_{-\infty}^{\infty} S_{\mathcal{E}}(\omega)d\omega$. We obtain,

$$g^{(1)}(\tau) = \frac{R_{\mathcal{E}}(\tau)}{R_{\mathcal{E}}(0)} \ , \tag{17.82}$$

and,

$$\boxed{F_{\mathcal{E}}(\omega) \equiv (\mathcal{F}g^{(1)})(\omega) = \frac{S_{\mathcal{E}}(\omega)}{R_{\mathcal{E}}(0)} = \frac{1}{2\pi}\int_{-\infty}^{\infty} g^{(1)}(\tau)e^{\imath\omega\tau}d\tau} \ . \tag{17.83}$$

The quantity $F_{\mathcal{E}}(\omega)$ is called line profile or *spectrum*. Note that, since,

$$g^{(1)}(-\tau) = g^{(1)}(\tau)^* \ , \tag{17.84}$$

we may also write,

$$F_{\mathcal{E}}(\omega) = \mathfrak{Re}\,\frac{1}{\pi}\int_0^{\infty} g^{(1)}(\tau)e^{\imath\omega\tau}d\tau \ . \tag{17.85}$$

Furthermore,

$$g^{(2)}(-\tau) = g^{(2)}(\tau) \ . \tag{17.86}$$

17.3.3 Coherent and chaotic light

The temporal and spectral properties of a light field are largely determined by the processes leading to its generation in the light source, that is, whether the light is

generated by stimulated or spontaneous emission, by a laser or by blackbody radiation, by a single atom or by atomic gases subject to collisional and Doppler-broadening. As we have seen above, these properties can be characterized by correlation functions, which can be calculated from models describing the temporal behavior of the electric field $\vec{\mathcal{E}}(t)$.

Before we do this for some examples, let us anticipate some important results. Zero delay correlation functions are easy to calculate for states whose density operator is known. For some systems we derived them previously:

Table 17.1: Zero delay correlation functions for various types of light fields.

correlation function	first order	second order
coherent	$g^{(1)}(0) = 1$	$g^{(2)}(0) = 1$
2nd order coherent	$g^{(1)}(0) = 1$	$g^{(2)}(0) \geq 1$
thermal	$g^{(1)}(0) = 1$	$g^{(2)}(0) = 2$
squeezed	$g^{(1)}(0) = 1$	$g^{(2)}(0) = 3 + \frac{1}{\sinh^2 r}$
bunched	$g^{(1)}(0) = 1$	$g^{(2)}(0) > 1$
anti-bunched	$g^{(1)}(0) = 1$	$g^{(2)}(0) < 1$

The temporal behavior of the correlation functions is more tricky and requires some modeling of the light emission processes: Let us now look at some specific

Table 17.2: Time dependent correlation functions for various types of light fields.

correlation function	first order	second order
perfectly coherent monochrom.	$\lvert g^{(1)}(\tau)\rvert = 1$	$\begin{cases} 0 \leq g^{(2)}(\tau) \leq \infty \\ g^{(2)}(0) \geq g^{(2)}(\tau) \overset{\tau \gg \tau_c}{\longrightarrow} 1 \end{cases}$
perfectly chaotic (incoherent)	$\lvert g^{(1)}(\tau)\rvert = \delta(0)$	$g^{(2)}(\tau) = 1 + \lvert g^{(1)}(\tau)\rvert^2$
partially coherent	$\lvert g^{(1)}(\tau)\rvert < \infty$	
bichromatic or modulated	Excs. 17.3.6.1 to 17.3.6.3	

cases, for which the correlation functions and spectra can be calculated.

17.3.3.1 Correlation functions for laser light

With the definitions (17.77) it is easy to calculate the autocorrelation functions and the spectrum of a *laser* light field,

laser

$$\begin{aligned} \mathcal{E}(t) &= e^{\imath\omega_0 t} \\ \Longrightarrow \quad g^{(1)}(\tau) &= \frac{t^{-1}\int e^{-\imath\omega_0\tau}dt}{t^{-1}\int dt} = e^{-\imath\omega_0\tau} \\ \Longrightarrow \quad \mathcal{F}\left[g^{(1)}(\tau)\right] &= \frac{1}{2\pi}\int_{-\infty}^{\infty} e^{\imath(\omega-\omega_0)\tau}d\tau = \delta(\Delta) \\ g^{(2)}(\tau) &= 1 \end{aligned} \quad . \tag{17.87}$$

We see that the absolute values of the first and second-order coherences are constant, and that the spectrum is narrow like a δ-function.

17.3.3.2 Correlation functions for chaotic light

For a totally emission *chaotic light*,

chaotic light

$$\begin{aligned} g^{(1)}(\tau) &= \delta(0) \\ \mathcal{F}[g^{(1)}(\tau)] &= 1 \\ g^{(2)}(\tau) &= 1 + |g^{(1)}(\tau)| \end{aligned} \quad . \tag{17.88}$$

The last expression is known as *Siegert relation*. Mono-mode chaotic light can be seen as incoherent multi-mode light, where all modes except a single mode are filtered by a Fabry-Pérot etalon. This light is characterized by $|g^{(1)}(\tau)| = 1$ and $g^{(2)}(\tau) = 2$, despite the coherence length being $\tau \to \infty$. Do the Excs. 17.3.6.1 to 17.3.6.3.

17.3.3.3 Correlation functions for laser light subject to white noise

For a laser subject to *white phase noise* (ζ be a normally distributed random number) we have ,

noisy laser

$$\begin{aligned} \mathcal{E}(t) &= e^{\imath[\omega_0 t+\zeta(t)]} \\ \Longrightarrow \quad g^{(1)}(\tau) &= \frac{\int e^{-\imath[\omega_0\tau+\zeta(t+\tau)-\zeta(t)]}dt}{\int dt} = e^{\imath\omega_0\tau-\gamma|\tau|} \\ \Longrightarrow \quad \mathcal{F}[g^{(1)}(\tau)] &= \frac{\gamma/\pi}{\Delta^2+\gamma^2} \\ g^{(2)}(\tau) &= 1 \end{aligned} \quad . \tag{17.89}$$

We see, that the first-order coherence decays exponentially, $|g^{(1)}(\tau)| = e^{-\gamma|\tau|}$ [5], such that the spectrum has a *Lorentzian profile*. For this reason light having this characteristic is also called *Lorentzian chaotic light*. This result has already been

[5] Note that, in order to satisfy (17.84), we must take the absolute value of the delay $|\tau|$.

derived in Eq. (16.28) for the natural linewidth of a transition subject to spontaneous emission. We understand the connection by interpreting spontaneous emission as being induced by *vacuum fluctuations, which do have a white noise spectrum*, indeed.

Example 103 (*Laser broadening due to spontaneous emission*): Laser light is generated by stimulated emission on a transition between two quantized levels. The alternance of absorption and stimulated emission induces coherent Rabi oscillations ensuring the coherence of the emitted light. But we have seen earlier that spontaneous emission leads to randomly occurring interruptions of the coherent Rabi oscillations. The probability of finding a coherent interval decreases exponentially with the evolution time,

$$p(\tau)d\tau = \gamma e^{-\gamma\tau}d\tau \ ,$$

where γ is the spontaneous decay rate of the dipole moment. From $\mathcal{E}(t) = e^{\imath\omega_0 t+\imath\zeta(t)}$ we calculate,

$$R_{\mathcal{E}}(\tau) = \langle e^{\imath\omega_0 t+\imath\zeta(t)}e^{-\imath\omega_0(t+\tau)-\imath\zeta(t+\tau)}\rangle = e^{-\imath\omega_0\tau}\lim_{t\to\infty}\frac{1}{t}\int_0^t e^{\imath[\zeta(t)-\zeta(t+\tau)]}dt$$
$$= e^{-\imath\omega_0\tau}\int_\tau^\infty p(\tau')d\tau' = e^{-\imath\omega_0\tau}e^{-\gamma|\tau|} \ ,$$

and,

$$F_{\mathcal{E}}(\omega) = \frac{1}{2\pi}\int_{-\infty}^{\infty}\frac{R_{\mathcal{E}}(\tau)}{R_{\mathcal{E}}(0)}e^{\imath\omega\tau}d\tau = \frac{1}{2\pi}\int_{-\infty}^{\infty}e^{-\imath\omega_0\tau}e^{-\gamma|\tau|}e^{\imath(\omega-\omega_0)\tau}d\tau = \frac{\gamma/\pi}{\Delta^2+\gamma^2} \ .$$

An alternative derivation from Bloch or rate equations is shown in Excs. 17.4.4.3 and 17.4.4.4.

17.3.3.4 Correlation functions for light emitted from pressure-broadened atomic clouds

In Sec. 16.5.2 we have already seen, that collision or *pressure broadening* can be treated by assuming that the light is emitted as a superposition of coherent waves all having the same frequency, but being randomly interrupted by phase jumps,

$$\mathcal{E}(t) = \sum_n \mathcal{E}_n(t) \qquad \text{with} \qquad \mathcal{E}_n(t) = e^{\imath\omega_0 t+\imath\phi_n(t)} \ . \tag{17.90}$$

The autocorrelation function is then,

$$\langle\mathcal{E}^*(t)\mathcal{E}(t+\tau)\rangle = \frac{1}{t}\int\sum_n e^{-\imath\omega_0 t-\imath\phi_n(t)}\sum_m e^{\imath\omega_0 t+\imath\omega_0\tau+\imath\phi_m(t+\tau)}dt \tag{17.91}$$
$$= e^{\imath\omega_0\tau}\sum_{n,m}\frac{1}{t}\int e^{\imath\phi_m(t+\tau)-\imath\phi_n(t)}dt = N\langle\mathcal{E}_n^*(t)\mathcal{E}_m(t+\tau)\rangle\delta_{nm} \ .$$

The crossed terms $n \neq m$ of this expressions vanish. The pressure broadening is homogeneous, but the fact that the wavepackets are scattered by different atoms results in a modified first-order coherence,

$$\langle\mathcal{E}_n^*(t)\mathcal{E}_n(t+\tau)\rangle = e^{\imath\omega_0\tau}\sum_n\int e^{\imath\phi_n(t+\tau)-\imath\phi_n(t)}dt = e^{\imath\omega_0\tau}\int_\tau^\infty p(\tau)d\tau \ . \tag{17.92}$$

The probability density of finding a coherent interval of duration τ is $p(\tau)d\tau = \gamma_c e^{-\gamma_c \tau} d\tau$, which finally gives,

$$\langle \mathcal{E}^*(t)\mathcal{E}(t+\tau)\rangle = N e^{\imath\omega_0\tau - \gamma_c|\tau|} \ . \tag{17.93}$$

The calculation for the 2^{nd} order correlation function (17.79) is analogous,

$$\begin{aligned}
&\langle \mathcal{E}^*(t)\mathcal{E}^*(t+\tau)\mathcal{E}(t+\tau)\mathcal{E}(t)\rangle = \sum_{n,m,n',m'} \langle \mathcal{E}^*_m(t)\mathcal{E}_n(t)\mathcal{E}^*_{m'}(t+\tau)\mathcal{E}_{n'}(t+\tau)\rangle \qquad (17.94)\\
&= \sum_n \langle \mathcal{E}^*_n(t)\mathcal{E}_n(t)\mathcal{E}^*_n(t+\tau)\mathcal{E}_n(t+\tau)\rangle \\
&+ \left(\sum_{n\neq m} \langle \mathcal{E}^*_n(t)\mathcal{E}_n(t)\mathcal{E}^*_m(t+\tau)\mathcal{E}_m(t+\tau)\rangle + \langle \mathcal{E}^*_m(t)\mathcal{E}_n(t)\mathcal{E}^*_n(t+\tau)\mathcal{E}_m(t+\tau)\rangle \right) \ ,
\end{aligned}$$

neglecting all terms which do not satisfy either $\mathcal{E}^*_n(t)\mathcal{E}_n(t)$ or $\mathcal{E}^*_n(t)\mathcal{E}_n(t+\tau)$. Now, assuming a large amount of identical atoms,

$$\begin{aligned}
&\langle \mathcal{E}^*(t)\mathcal{E}^*(t+\tau)\mathcal{E}(t+\tau)\mathcal{E}(t)\rangle \qquad (17.95)\\
&= N\langle \mathcal{E}^*_n(t)\mathcal{E}_n(t)\mathcal{E}^*_n(t+\tau)\mathcal{E}_n(t+\tau)\rangle + N(N-1)\left(\langle \mathcal{E}^*_n(t)\mathcal{E}_n(t)\rangle^2 + |\langle \mathcal{E}_n(t)\mathcal{E}^*_n(t+\tau)\rangle|^2\right) \\
&\simeq N^2\left(\langle \mathcal{E}^*_n(t)\mathcal{E}_n(t)\rangle^2 + |\langle \mathcal{E}_n(t)\mathcal{E}^*_n(t+\tau)\rangle|^2\right) \ .
\end{aligned}$$

Finally, exploiting the result (17.91) and the definitions of the 1^{st} and 2^{nd} order correlations functions,

$$g^{(2)}(\tau) = \frac{\langle \mathcal{E}^*_n(t)\mathcal{E}_n(t)\rangle^2 + |\langle \mathcal{E}_n(t)\mathcal{E}^*_n(t+\tau)\rangle|^2}{\langle \mathcal{E}^*_n(t)\mathcal{E}_n(t)\rangle^2} = 1 + |g^{(1)}(\tau)|^2 \ . \tag{17.96}$$

In summary,

light emitted from pressure-broadened atomic clouds

$$\begin{aligned}
\mathcal{E}(t) &= \textstyle\sum_n e^{\imath\omega_0 t + \imath\phi_n(t)} \\
\Longrightarrow \quad g^{(1)}(\tau) &= e^{\imath\omega_0\tau - \gamma_c|\tau|} \\
\Longrightarrow \quad \mathcal{F}\left[g^{(1)}(\tau)\right] &= \frac{\gamma/\pi}{\Delta^2 + \gamma_c^2} \\
g^{(2)}(\tau) &= 1 + e^{-\gamma_c|\tau|}
\end{aligned} \ . \tag{17.97}$$

The spectrum is a Lorentzian with the full linewidth $\gamma' = \gamma + \gamma_c$.

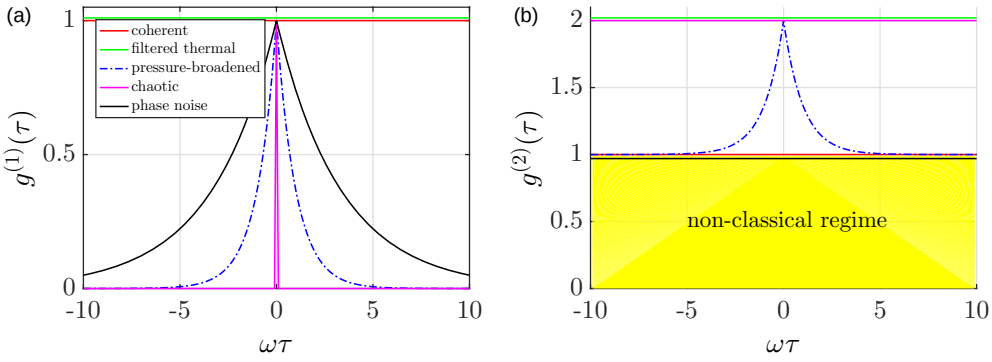

Figure 17.9: (code) First and second-order correlation functions for (red) a laser, (cyan) a laser subject to phase noise, (blue) a laser subject to collision broadening, (magenta) chaotic light, and (green) spectrally filtered thermal light.

17.3.3.5 Correlation functions for light emitted from Doppler-broadened atomic clouds

For light emitted by an ensemble of non-colliding atoms in thermal motion, we must allow for different frequencies, $\mathcal{E}_n(t) = e^{\imath\omega_n t+\imath\phi_n}$, but time-independent phases,

$$\begin{aligned}\langle\mathcal{E}^*(t)\mathcal{E}(t+\tau)\rangle &= \int \sum_n e^{-\imath\omega_n t-\imath\phi_n} \sum_m e^{\imath\omega_m t+\imath\omega_m\tau+\imath\phi_m} dt \\ &= \sum_{n,m} \int e^{-\imath\omega_n t-\imath\phi_n+\imath\omega_m t+\imath\omega_m\tau+\imath\phi_m} dt = \sum_n e^{\imath\omega_n\tau} \ .\end{aligned} \tag{17.98}$$

The crossed terms $n \neq m$ of this expressions vanish. *Doppler broadening* is inhomogeneous. Hence, the probability density for frequencies emitted by thermal atoms is a Gaussian, $p(\omega)d\omega = (2\pi\delta)^{-1/2}e^{-(\omega_n-\omega_0)^2/2\delta^2}d\omega$. For this reason light having this characteristic is also called *Gaussian chaotic light*. With the definitions (17.77) it is easy to calculate the autocorrelation functions and the spectrum of a laser light field,

light emitted from Doppler-broadened atomic clouds

$$\begin{aligned}\langle\mathcal{E}^*(t)\mathcal{E}(t+\tau)\rangle &= \frac{N}{\sqrt{2\pi\delta}} \int e^{\imath\omega_n\tau} e^{-(\omega_n-\omega_0)^2/2\delta^2} d\omega_n \\ \Longrightarrow \quad g^{(1)}(\tau) &= e^{\imath\omega\tau-\delta^2\tau^2/2} \\ \Longrightarrow \quad \mathcal{F}[g^{(1)}(\tau)] &= \sqrt{\frac{\ln 2}{\pi\delta^2}} e^{-\ln 2\cdot\omega^2/\delta^2} \\ g^{(2)}(\tau) &= 1 + e^{-\delta^2\tau^2/2}\end{aligned} \quad . \tag{17.99}$$

In Exc. 17.3.6.5 we calculate the correlation functions at zero delay.

17.3.4 Quantum signatures in first and second order coherence

All calculations of correlation functions made up to this point assumed classical light fields, except for the anti-bunched $g^{(2)}(0)$ listed in Tab. 17.1. We will see in the following that a quantum calculation yields some features of the second order coherence that cannot be explained by assuming classical fields. But this does not mean that we can always decide whether a beam is quantum just by looking at $g^{(2)}(0)$: A light beam may have quantum correlations that do not violate the classical rules exhibited in Tabs. 17.1 and 17.2. This is the case, e.g. for squeezed light.

17.3.5 Photon counting statistics

The physical quantities measured in practice are intensities of light fields, i.e. energies propagating through finite areas of space during finite integration times. Very sensitive detectors may sense the arrival of single photons during finite times (called dead times) needed to process the information. In semiclassical theory we ignore the existence of photons, nevertheless the photoeffect signal is delivered by single electrons, amplified to avalanches of electrons that we will call 'photocount', and that sum up to currents for long enough integration times.

17.3.5.1 Quantum correlations

Defining the intensity as $\hat{I} = 2\varepsilon_0 c\hat{\mathcal{E}}^+\hat{\mathcal{E}}^-$, the coherences become,

$$g^{(1)}(\tau) \equiv \tfrac{2\varepsilon_0 c}{I}\langle \mathcal{TN}\hat{\mathcal{E}}^-(t)\hat{\mathcal{E}}^+(t+\tau)\rangle \qquad \text{and} \qquad g^{(2)}(\tau) \equiv \left(\tfrac{2\varepsilon_0 c}{I}\right)^2 \langle \mathcal{TN}\hat{I}(t)\hat{I}(t+\tau)\rangle \ . \tag{17.100}$$

The correlation functions must be calculated from the field operators simultaneously respecting *time order* and *normal order*.

One rule is easy to derive,

$$g^{(2)}(0) = \frac{\langle \hat{a}^\dagger\hat{a}^\dagger\hat{a}\hat{a}\rangle}{\langle \hat{a}^\dagger\hat{a}\rangle^2} = \frac{\langle \hat{n}^2\rangle - \langle \hat{n}\rangle}{\langle \hat{n}\rangle^2} = 1 - \frac{1}{\langle \hat{n}\rangle} + \frac{(\Delta\hat{n})^2}{\langle \hat{n}\rangle^2} \geq 1 - \frac{1}{\langle \hat{n}\rangle} \geq 0 \ , \tag{17.101}$$

for $\langle \hat{n}\rangle \geq 1$. For $\langle \hat{n}\rangle < 1$ we have $g^{(2)}(0) = 0$.

17.3.5.2 Applications of correlated photons

Correlated photons have many applications in modern *quantum sensing*. Correlations can be encoded in space, colors, polarization, or time giving rise to phenomena such as ghost imaging, spooky spectra, time-correlated spectroscopy, two-photon absorption with femtosecond time resolution, and virtual state spectroscopy among others.

17.3.6 Exercises

17.3.6.1 Ex: Correlation functions for two light modes

a. Calculate $|g^{(1)}(\tau)|$, $F_{\mathcal{E}}(\omega)$, and $|g^{(2)}(\tau)|$ for two interfering and non-interfering modes neglecting fluctuations.
b. What changes when one mode is broadened by random noise, e.g. induced by spontaneous emission?

17.3.6.2 Ex: Correlation functions and spectra of phase- and amplitude-modulated light

a. Calculate $g^{(1)}(\tau)$, $S_{\mathcal{E}}(\omega)$, and $g^{(2)}(\tau)$ for amplitude-modulated light: $\mathcal{E}_{am}(t) = e^{\imath\omega_0 t}(1 + M\cos\Omega t)$.
b. Calculate $g^{(1)}(\tau)$, $S_{\mathcal{E}}(\omega)$, and $g^{(2)}(\tau)$ for phase-modulated light: $\mathcal{E}_{pm}(t) = e^{\imath\omega_0 t + \imath M\cos\Omega t}$.
c. Repeat the calculation (a) for exponentially decaying amplitude-modulated light: $\mathcal{E}_{dam}(t) = e^{-\gamma t}e^{\imath\omega_0 t}(1 + M\cos\Omega t)$.

17.3.6.3 Ex: Phase modulation

a. Show that it is not possible to construct a periodic phase modulation function such that the signal has only two sidebands.
b. From $1 = |e^{\imath M\sin\Omega t}|^2$ derive a sum rule for the Bessel functions.
c. Discuss the difference of the spectra $\sum_{k=-\infty}^{\infty} J_k(M)e^{\imath k\Omega t}$ and $\sum_{k=-\infty}^{\infty} |J_k(M)|e^{\imath k\Omega t}$.

17.3.6.4 Ex: Non-classicality of antibunched states

Quantized radiation fields can exhibit the feature of antibunching, which is incompatible with the classical concept of radiation. Show that $g^{(2)}(0) < 1$ entails the possibility of negative values for the Glauber-Sudarshan P-function, that is, $P(\alpha) < 0$ at least for some α.

17.3.6.5 Ex: Zero delay correlation functions

Calculate the zero delay correlation functions for (a) Fock states and (b) thermal light.

17.4 Spontaneous emission and light scattering

17.4.1 Interaction of atoms with vacuum modes

The Jaynes-Cummings Hamiltonian (17.2), discussed in Sec. 17.2, describes the purely coherent dynamics of a single immobile two-level atom interacting with a single cavity mode. The model is simple enough to allow for analytical solutions. However, it does not include processes of spontaneous emission, which can be understood as the interaction of the atom with the light modes of the vacuum. That is, we must extend the Hamiltonian,

$$\hat{H} = \hat{H}_{\text{atom}} + \hat{H}_{\text{field}} + \hat{H}_{\text{atom:field}} + \hat{H}_{\text{vacuum}} + \hat{H}_{\text{atom:vacuum}} \,. \tag{17.102}$$

The evolution of the system represented by the Hamiltonian (17.102) is described by a total density operator, $\hat{\rho}_{\text{total}}(t)$, obeying the *von Neumann equation*,

$$\boxed{\frac{d\hat{\rho}_{\text{total}}}{dt} = -\frac{\imath}{\hbar}[\hat{H}, \hat{\rho}_{\text{total}}]} \,, \tag{17.103}$$

which has the solution,

$$\hat{\rho}_{\text{total}}(t) = e^{-\imath\hat{H}t/\hbar}\hat{\rho}_{\text{total}}(0)e^{\imath\hat{H}t/\hbar} \equiv e^{-\imath\mathcal{L}t}\hat{\rho}_{\text{total}}(0) \ . \tag{17.104}$$

Often, we are only interested in *either* the evolution of the light field, *or* the internal state of the atom. In these cases, we calculate the trace over all those degrees of freedom, which are we are NOT interested in,

$$\hat{\rho}_{\text{atom}} = \text{Tr}_{\text{vacuum}}\ \hat{\rho}_{\text{total}} \ . \tag{17.105}$$

The procedure is the following. We begin choosing the initial state of the electromagnetic vacuum as the photonic vacuum $\hat{\rho}_{\text{vacuum}} = |\{0\}\rangle\langle\{0\}|$ and defining a projection operator onto this state, $\hat{P}... \equiv \hat{\rho}_{\text{vacuum}}(0)\text{Tr}_{\text{vacuum}}\ ... = \hat{P}^2....$ Then we apply to the von Neumann equation the rotating wave, the Markov and the Born approximations. Finally, tracing over the vacuum field variables, we obtain after some calculations the *Bloch-Lindbladt equation* or *master equation* [677] for the atom interacting with the driving field. For a discussion of the validity of the Born-Markov approximation [608]. For the relation between the Markov approximation and the Fermi's Golden Rule [11].

We emphasize that the Hamiltonian (17.102) describes the interaction of light with a *single immobile atom* at the most fundamental level. However, it excludes many-body effects introduced by quantum statistics or interatomic interactions (to be discussed in Chp. 27), as well as the center-of-mass motion of the atom and the impact of photonic recoil (to be discussed in Chp. 20).

In the following section we give a simplified derivation concentrating us on the situation of a single motionless atom, excited by a laser and emitting photons into the electromagnetic vacuum.

17.4.1.1 Spontaneous emission

Spontaneous emission can be understood as an energy diffusion process from a system with a restricted number of degrees of freedom into a large thermal bath. For example, although a two-dimensional Hilbert space is sufficient to describe a laser-driven two-level atom, this atom couples to a huge phase-space by spontaneously emitting photons into arbitrary directions. We account for his fact by including in the Hamiltonian not only the interaction of the atom with the incident laser (wavevector $\mathbf{k}_0$, frequency $\omega_{\mathbf{k}_0}$), but also with the modes of the electromagnetic vacuum (wavevector $\mathbf{k}$, frequency $\omega_{\mathbf{k}}$). We will see, that with this Hamiltonian, we can derive, in a calculation is known as *Weisskopf-Wigner theory*, the Schrödinger equation for the amplitudes of the atomic levels (16.147) including spontaneous emission.

Denoting the frequency of the atomic resonance by ω_a, the interaction part of the Hamiltonian is,

$$\begin{aligned}\hat{H} &= \hbar g_{\mathbf{k}_0}\left(\hat{\sigma}^- e^{-\imath\omega_a t} + \hat{\sigma}^+ e^{\imath\omega_a t}\right)\left(\hat{a}^\dagger_{\mathbf{k}_0} e^{\imath\omega_0 t - \imath\mathbf{k}_0\cdot\mathbf{r}} + \hat{a}_{\mathbf{k}_0} e^{-\imath\omega_0 t + \imath\mathbf{k}_0\cdot\mathbf{r}}\right) \\ &+ \sum_{\mathbf{k}} \hbar g_{\mathbf{k}}\left(\hat{\sigma}^- e^{-\imath\omega_a t} + \hat{\sigma}^+ e^{\imath\omega_a t}\right)\left(\hat{a}^\dagger_{\mathbf{k}} e^{\imath\omega_{\mathbf{k}} t - \imath\mathbf{k}\cdot\mathbf{r}} + \hat{a}_{\mathbf{k}} e^{-\imath\omega_{\mathbf{k}} t + \imath\mathbf{k}\cdot\mathbf{r}}\right)\end{aligned} \ . \tag{17.106}$$

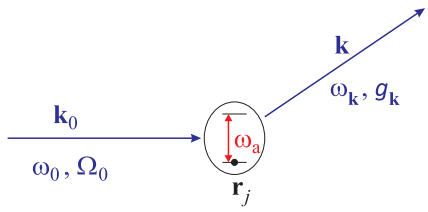

Figure 17.10: Scattering of a laser beam by an atom.

$g_{\mathbf{k}_0}$ is the coupling strength of the interaction between the atom and the pump mode, $\hat{\sigma}^-$ is the atomic deexcitation operator, $\hat{a}_{\mathbf{k}}$ is the annihilation operator of a photon, and $g_{\mathbf{k}} = d\sqrt{\omega/(\hbar\varepsilon_0 V)}$ describes the coupling between the atom and a vacuum mode whose volume is V. The atom has two states, the ground state $|g\rangle$ and excited state $|e\rangle$. Since we are considering only one atom fixed in space [6], we can as well locate it at the origin $\mathbf{r} = 0$. In addition, considering a high power incident laser,

$$\hat{a}_{\mathbf{k}_0}|n_0\rangle_{\mathbf{k}_0} = \sqrt{n_0}|n_0 - 1\rangle_{\mathbf{k}_0} \simeq \sqrt{n_0}|n_0\rangle_{\mathbf{k}_0} \ , \tag{17.107}$$

$\hat{a}_{\mathbf{k}_0}$ is approximately an observable proportional to the root of the intensity. As $[\hat{a}_{\mathbf{k}_0}, \hat{a}^\dagger_{\mathbf{k}_0}] \simeq 0$, we can disregard the quantum nature of the incident field and replace, $\Omega_0 \equiv 2\sqrt{n_0} g_{\mathbf{k}_0}$. Within the rotating wave approximation (RWA), the Hamiltonian becomes,

$$\hat{H} = \tfrac{\hbar}{2}\Omega_0 \left[\hat{\sigma}^- e^{\imath\Delta_0 t} + h.c.\right] + \hbar \sum_{\mathbf{k}} \left[g_{\mathbf{k}} \hat{\sigma} \hat{a}^\dagger_{\mathbf{k}} e^{\imath\Delta_{\mathbf{k}} t} + h.c.\right] \ , \tag{17.108}$$

where we introduced the abbreviations,

$$\Delta_0 \equiv \omega_0 - \omega_a \qquad \text{and} \qquad \Delta_{\mathbf{k}} \equiv \omega_{\mathbf{k}} - \omega_a \ . \tag{17.109}$$

The general state of the system is given by,

$$|\Psi(t)\rangle = \alpha(t)|g\rangle_a|0\rangle_{\mathbf{k}} + \beta(t)|e\rangle_a|0\rangle_{\mathbf{k}} + \sum_{\mathbf{k}} \gamma_{\mathbf{k}}(t)|g\rangle_a|1\rangle_{\mathbf{k}} \ , \tag{17.110}$$

where $|j\rangle_a$ denotes the atomic state and $|n\rangle_{\mathbf{k}}$ the number of photons in the scattering mode.

The temporal evolution of the amplitudes is obtained by inserting the Hamiltonian (17.108) and the ansatz (17.110) into the Schrödinger equation,

$$\frac{\partial}{\partial t}|\Psi(t)\rangle = -\frac{\imath}{\hbar}\hat{H}|\Psi(t)\rangle \ . \tag{17.111}$$

As verified in Exc. 17.4.4.1, we obtain,

$$\begin{aligned} \dot{\alpha}(t) &= -\imath\tfrac{\Omega_0}{2} e^{\imath\Delta_0 t}\beta(t) \\ \dot{\beta}(t) &= -\imath\tfrac{\Omega_0}{2}\alpha(t)e^{-\imath\Delta_0 t} - \sum\nolimits_{\mathbf{k}} \imath g_{\mathbf{k}}\gamma_{\mathbf{k}}(t)e^{-\imath\Delta_{\mathbf{k}} t} \\ \dot{\gamma}_{\mathbf{k}}(t) &= -\imath g_{\mathbf{k}} e^{\imath\Delta_{\mathbf{k}} t}\beta(t) \ . \end{aligned} \tag{17.112}$$

[6] We do not let the atom be accelerated by photonic recoil.

Now, we chose the initial conditions,

$$\alpha(0) = 1 \qquad \text{and} \qquad \beta(0) = 0 \qquad \text{and} \qquad \gamma_{\mathbf{k}}(0) = 0 \ , \tag{17.113}$$

we integrate the third equation,

$$\gamma_{\mathbf{k}}(t) = -\imath g_{\mathbf{k}} \int_0^t e^{\imath \Delta_{\mathbf{k}} t'} \beta(t') dt' \ , \tag{17.114}$$

and we substitute it in the second equation,

$$\dot{\beta}(t) = -\imath \tfrac{\Omega_0}{2} \alpha(t) e^{-\imath \Delta_0 t} - \sum_{\mathbf{k}} g_{\mathbf{k}}^2 \int_0^t e^{\imath \Delta_{\mathbf{k}} (t'-t)} \beta(t') dt' \ . \tag{17.115}$$

17.4.1.2 The Markov approximation

For small systems (which certainly is the case of a single atom), we can apply the *Markov approximation* [7] claiming that the temporal variation of the amplitudes $\beta(t')$ is slower than the evolution of the system given by $e^{\imath(\omega_{\mathbf{k}} - \omega_a)t}$ in the integro-differential equation, which is equivalent to an arbitrarily high-order equation. Hence, substituting $\beta(t') \to \beta(t)$ into the integro-differential equation, we reduce it to a simple first-order differential equation.

In practice, we redefine the integration variable, $t'' \equiv t - t'$, to obtain,

$$\begin{aligned} \frac{d}{dt}\beta(t) &= -\imath \tfrac{\Omega_0}{2} \alpha(t) - \sum_{\mathbf{k}} g_k^2 \int_0^t e^{\imath(\omega_{\mathbf{k}} - \omega_a)(t'-t)} \beta(t') dt' \\ &= -\imath \tfrac{\Omega_0}{2} \alpha(t) - \sum_{\mathbf{k}} g_k^2 \int_0^t e^{-\imath(\omega_{\mathbf{k}} - \omega_a)t''} \beta(t - t'') dt'' \ , \end{aligned} \tag{17.116}$$

and implement the Markov approximation by setting $\beta(t - t'') \simeq \beta(t)$, and with $\lim_{t\to\infty} \int_0^t e^{-\imath(\omega_{\mathbf{k}} - \omega_a)t'} dt' = \pi\delta(\omega_{\mathbf{k}} - \omega_a)$, and replacing $\sum_{\mathbf{k}} \longrightarrow \frac{V}{(2\pi)^3} \int d^3\mathbf{k}$, we arrive at,

$$\begin{aligned} \frac{d}{dt}\beta(t) &\simeq -\imath \tfrac{\Omega_0}{2} \alpha(t) - \sum_{\mathbf{k}} g_{\mathbf{k}}^2 \beta(t) \pi\delta(\omega_{\mathbf{k}} - \omega_a) \\ &= -\imath \tfrac{\Omega_0}{2} \alpha(t) - \tfrac{V}{(2\pi)^3} \beta(t) \int g_{\mathbf{k}}^2 \pi\delta(\omega_{\mathbf{k}} - \omega_a) d^3\mathbf{k} \\ &= -\imath \tfrac{\Omega_0}{2} \alpha(t) - \tfrac{V}{(2\pi)^3} \beta(t) 4\pi g_{\mathbf{k}_a}^2 \pi k_a^2 \tfrac{1}{c} = -\imath \tfrac{\Omega_0}{2} \alpha(t) - \tfrac{\Gamma}{2} \beta(t) \ . \end{aligned} \tag{17.117}$$

In the last step we introduced, as an abbreviation, the spontaneous emission rate,

$$\Gamma \equiv \sum_{\mathbf{k}} 2 g_{\mathbf{k}}^2 \pi\delta(\omega_{\mathbf{k}} - \omega_a) = \tfrac{V}{\pi c} k_a^2 g_{\mathbf{k}_a}^2 \ , \tag{17.118}$$

Finally,

$$\boxed{\frac{d}{dt}\alpha(t) = -\imath \frac{\Omega_0}{2} \beta(t) \qquad \text{and} \qquad \frac{d}{dt}\beta(t) = -\imath \frac{\Omega_0}{2} \alpha(t) - \frac{\Gamma}{2} \beta(t)} \ . \tag{17.119}$$

[7] The approximation does not necessarily hold for large clouds of atoms.

These are exactly the equations for the probability amplitudes (16.147) derived from the Schrödinger equation, only that now, the spontaneous emission term has been derived explicitly. Solve the Exc. 17.4.4.2.

Example 104 (*Emission stimulated by vacuum fluctuations*): Spontaneous emission can be regarded as an emission stimulated by vacuum fluctuations. To see this, we write down the resonant optical cross section ($\omega_0 = \omega_a$) of a driven two-level atom without degeneracies, $\sigma_0 = \lambda^2/2\pi$, and the intensity of an incident laser field, $\bar{I} = cN\hbar\omega_0/V$, generating the Rabi frequency (see (1.107)),

$$\Omega_0^2 = \sigma_0 \frac{\bar{I}}{\hbar\omega_a}\Gamma = \frac{2\pi c}{k_a^2}\frac{N}{V}\Gamma \ . \tag{17.120}$$

Now, we assume that the field is, in fact, a vacuum mode containing only half a photon, $N = 1/2$, which corresponds to vacuum fluctuations in the mode k_0. Then,

$$\Omega_{1/2}^2 = \frac{\pi c}{k_a^2 V}\Gamma = g^2 \ . \tag{17.121}$$

17.4.2 Resonance fluorescence and (in-)coherent light scattering

The typical situation for a spectroscopy experiment is illustrated in Fig. 17.11: When a beam of light, understood as a plane wave, strikes an atom (or a cloud of many atoms), a part of the light is absorbed and reemitted into a direction indicated by a solid angle $d\Omega$. Light scattering is, of course, a second order process involving two atomic transitions, one absorption and one emission.

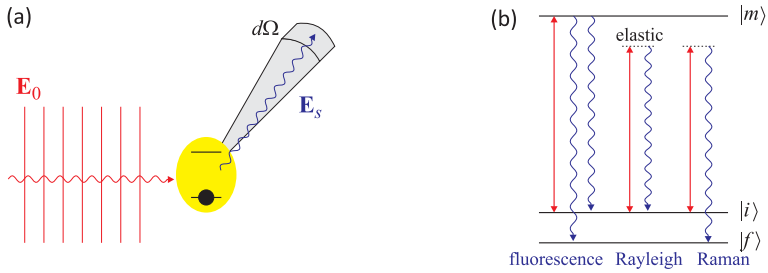

Figure 17.11: (a) Geometry of a scattering experiment. (b) Spectral contributions of light scattered elastically and inelastically by a three-level atom.

Radiation can be absorbed or scattered by an atom in different ways, depending on whether the interaction is an *elastic scattering* or an *inelastic scattering* process, a coherent or incoherent, a spontaneous or (bosonically) stimulated process. These properties characterize many processes, in particular, resonance fluorescence (i.e. absorption and reemission), *Rayleigh scattering*, or *Raman scattering*. In the following, we will clarify this classification.

Every scattering process is either spontaneous or stimulated [8]. Rayleigh scattering is elastic, that is, the kinetic energy of the scattering atom is the same, before and

[8] Classical theories of light scattering through the excitation of an electronic motion based on the

after the scattering process. In contrast, Raman scattering is inelastic. Spontaneous emission is due to the decay of population from an excited state, and spontaneous Rayleigh scattering is due to the decay of an induced dipole moment. Both spontaneous processes can be regarded as being stimulated by vacuum fluctuations.

17.4.2.1 Deriving the source field expression

We will now calculate the electric field due to spontaneous emission by an atom from the interaction Hamiltonian for atom-vacuum coupling (17.106) in the RWA,

$$\hat{H} = \sum_{\mathbf{k}} \hbar g_{\mathbf{k}} \hat{\sigma}^- \hat{a}^\dagger_{\mathbf{k}} e^{\imath\omega_{\mathbf{k}} t - \imath\omega_a t - \imath\mathbf{k}\cdot\mathbf{R}} + h.c. \ . \tag{17.122}$$

Now, we assume isotropic coupling, $g_{\mathbf{k}} = g_k$, and $\omega_{\mathbf{k}} = \omega_k$, and for simplicity we position the atom in the origin, $\mathbf{R} = 0$. We use the Heisenberg equation with the commutation rule $[\hat{a}_{\mathbf{k}}, \hat{a}^\dagger_{\mathbf{k}'}] = \delta_{\mathbf{k},\mathbf{k}'}$ to derive the temporal evolution of the field operators,

$$\frac{d\hat{a}_{\mathbf{k}}}{dt} = \tfrac{1}{\imath\hbar}[\hat{a}_{\mathbf{k}}, \hat{H}] = -\imath\hat{\sigma}^- g_k e^{\imath(\omega_k - \omega_a)t} \ . \tag{17.123}$$

Neglecting for simplicity polarization, the electric field is given by,

$$\hat{\mathcal{E}}^+_{sct}(\mathbf{r}, t) = \sum_{\mathbf{k}} \mathcal{E}_1 \hat{a}_{\mathbf{k}}(t) e^{\imath(\mathbf{k}\cdot\mathbf{r} - \omega_k t)} \ , \tag{17.124}$$

where $\mathbf{r}$ is now the observation point of the electric field. We restrict to the far-field and substitute the annihilation operator with the integral of Eq. (17.123) using the initial condition $\hat{a}_{\mathbf{k}}(0) = 0$,

$$\hat{\mathcal{E}}^+_{sct}(\mathbf{r}, t) = \sum_{\mathbf{k}} \mathcal{E}_1 g_k \int_0^t \hat{\sigma}^-(t') e^{\imath(\omega_k - \omega_a)t'} dt' e^{\imath(\mathbf{k}\cdot\mathbf{r} - \omega_k t)} \ . \tag{17.125}$$

Now, we substitute the sum over $\mathbf{k}$ by an integral, as done in (17.117),

$$\hat{\mathcal{E}}^+_{sct}(\mathbf{r}, t) = -\imath \frac{V}{(2\pi)^3} \int_{\mathbb{R}^3} \mathcal{E}_1 g_k \int_0^t \hat{\sigma}^-(t') e^{\imath(\omega_k - \omega_a)t'} dt' e^{\imath(\mathbf{k}\cdot\mathbf{r} - \omega_k t)} d^3k \ . \tag{17.126}$$

Using the relationships,

$$g_k = \frac{d_{12}\mathcal{E}_1}{\hbar} \qquad \text{and} \qquad \mathcal{E}_1 = \sqrt{\frac{\hbar\omega_k}{2\varepsilon_0 V}} \ , \tag{17.127}$$

the final result of the integration yields [530],

$$\hat{\mathcal{E}}^+_{sct}(\mathbf{r}, t) \simeq -\imath \frac{d_{12} k_a^2}{4\pi\varepsilon_0 r} \hat{\sigma}^-(t - \tfrac{r}{c}) \ . \tag{17.128}$$

models of Lorentz or Drude can be found in the script Electrodynamics. Although being classical, these model are useful for a deeper understanding of many aspects of *Compton scattering*, *Thomson scattering*, and *Rayleigh scattering*.

17.4.2.2 Resonance fluorescence

When we introduced the second quantization (14.8) we learned that the field of light emitted by a radiator in the radiation zone ($\lambda \ll r$) is, taking into account retardation [9], given by,

$$\langle \hat{\vec{\mathcal{E}}}_{\rm s}^{+}(\mathbf{r},t)\rangle \propto \langle \hat{\sigma}^{-}\rangle \propto \tilde{\rho}_{21} \qquad \text{and} \qquad \langle \hat{\vec{\mathcal{E}}}_{\rm s}^{-}(\mathbf{r},t)\hat{\vec{\mathcal{E}}}_{\rm s}^{+}(\mathbf{r},t)\rangle \propto \langle \hat{\sigma}^{+}\hat{\sigma}^{-}\rangle \propto \rho_{22}\ . \tag{17.129}$$

Therefore, the electric field emitted by an atom and the intensity of scattered light are given by,

$$\boxed{\begin{aligned} \langle \hat{\vec{\mathcal{E}}}_{\rm s}^{+}(\mathbf{r},t)\rangle &= -\frac{e\omega_a^2 \hat{\epsilon}\cdot\mathbf{r}_{12}}{4\pi\varepsilon_0 c^2 r}\tilde{\rho}_{21}(t-\tfrac{r}{c})e^{-\imath\omega(t-r/c)} \\ \bar{I}_{\rm s} = c\varepsilon_0\langle \hat{\vec{\mathcal{E}}}_{\rm s}^{-}(\mathbf{r},t)\hat{\vec{\mathcal{E}}}_{\rm s}^{+}(\mathbf{r},t)\rangle &= \frac{\alpha\hbar\omega_a^4|\hat{\epsilon}\cdot\mathbf{r}_{12}|^2}{4\pi c^2 r^2}\rho_{22}(t-\tfrac{r}{c}) \end{aligned}}\ , \tag{17.130}$$

with the definition of the Sommerfeld constant $\alpha = e^2/4\pi\varepsilon_0\hbar c$. We calculate the total flux of emitted photons,

$$\begin{aligned} W_{fi}^{(sp)} &= \int \frac{\bar{I}_{\rm s} r^2}{\hbar\omega_a} d\Omega = \frac{1}{\hbar\omega_a}\int \frac{\alpha\hbar\omega_a^4|\mathbf{r}_{12}|^2\cos^2\theta}{4\pi c^2}\rho_{22}(t-\tfrac{r}{c})\sin\theta d\theta d\phi \\ &= \frac{8\pi}{3\hbar\omega_a}\frac{\alpha\hbar\omega_a^4|\mathbf{r}_{12}|^2}{4\pi c^2}\rho_{22}(t-\tfrac{r}{c}) = \frac{2\alpha}{3c^2}\omega_a^3|\mathbf{r}_{12}|^2\rho_{22}(t-\tfrac{r}{c})\ . \end{aligned} \tag{17.131}$$

The result *coincides with the spontaneous emission rate* Γ calculated in (16.40).

A *differential scattering cross section* can be defined by,

$$\frac{d\sigma}{d\Omega} \equiv \frac{\omega \bar{I}_{\rm s} r^2}{\omega_s \bar{I}_0}\ . \tag{17.132}$$

17.4.2.3 Coherently scattered light and saturation

The total intensity of the scattered light being $\bar{I}_{\rm s}$, the fraction of the coherently scattered light is,

$$\frac{\bar{I}_{\rm s}^{\rm coh}}{\bar{I}_{\rm s}} = \frac{\langle \hat{\vec{\mathcal{E}}}_{\rm s}^{-}(\mathbf{r},t)\rangle\langle \hat{\vec{\mathcal{E}}}_{\rm s}^{+}(\mathbf{r},t)\rangle}{\langle \hat{\vec{\mathcal{E}}}_{\rm s}^{-}(\mathbf{r},t)\hat{\vec{\mathcal{E}}}_{\rm s}^{+}(\mathbf{r},t)\rangle}\ . \tag{17.133}$$

Inserting the expressions (17.130) and the stationary solution of the Bloch equations (16.151) with the saturation parameter defined in (16.153),

$$\frac{\bar{I}_{\rm s}^{\rm coh}}{\bar{I}_{\rm s}} = \frac{|\tilde{\rho}_{21}(\infty)|^2}{\rho_{22}(\infty)} = \frac{1}{1+s} = 1 - \frac{\bar{I}_{\rm s}^{\rm incoh}}{\bar{I}_{\rm s}}\ . \tag{17.134}$$

That is, since the resonance fluorescence is proportional to the excited state population, we may define a quantity $S_{tot} \equiv \rho_{22}(\infty)$, so that the coherent and incoherent

[9] The classical version of this formula can be found in the script Electrodynamics, Sec. 9.1.3, Eq. (8.41).

parts of the fluorescence are,

$$\boxed{S_{\rm coh} = |\rho_{21}(\infty)|^2 = \frac{s/2}{(1+s)^2} \qquad \text{and} \qquad S_{\rm incoh} = \rho_{22}(\infty) - |\rho_{21}(\infty)|^2 = \frac{s^2/2}{(1+s)^2}} \ . \tag{17.135}$$

Hence, $S_{\rm incoh} = sS_{\rm coh}$.

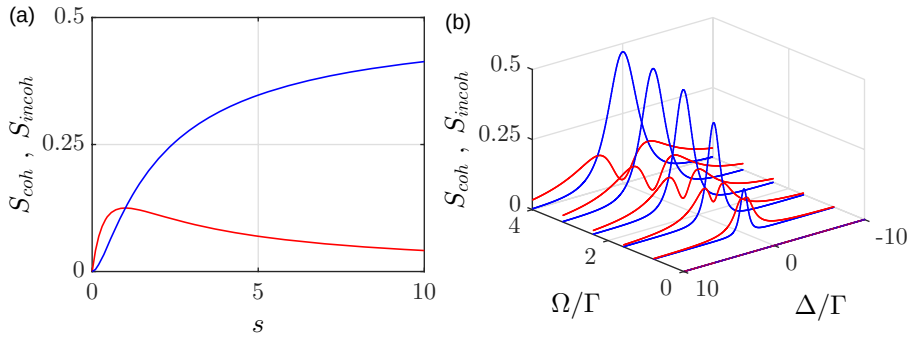

Figure 17.12: (code) Elastic (red) versus inelastic scattering (blue) as a function of the saturation parameter (a) at resonance and (b) for various detunings.

The result (17.135), illustrated in Fig. 17.12(a), means that *below saturation* scattering is dominated by elastic scattering. Incident light excites the atomic dipole moment ρ_{12}, that is, charge oscillations which, in turn, emit electromagnetic radiation like a classical antenna. *Above saturation* the excited atomic state accumulates an considerable amount of population ρ_{22} giving rise to spontaneous emission, which is interpreted as inelastic scattering. This intrinsically quantum feature is a consequence of the quantized nature of the atomic energy levels and has no classical counterpart. Another interesting feature seen in Fig. 17.12(b) is that, when the incident light is tuned sufficiently far from resonance, elastic scattering will dominate at any saturation parameter.

17.4.3 The spectrum of resonance fluorescence

The *correlation functions* defined in (17.77) represent an interesting concept for describing resonance fluorescence and for phenomena such as *antibunching* observed in resonance fluorescence.

17.4.3.1 The quantum regression theorem

From (17.83) we see that, to compute the spectra of *resonance fluorescence*, we only need to compute the correlation function $g^{(1)}$, i.e. the amplitudes of the field $\hat{\mathcal{E}}(t)$, which in turn are related to the field operators (14.8). The field operators follow the solutions of the Bloch equation, which, being linear, have the following generic form,

$$\rho_{ij}(t+\tau) = \sum_{k,l} \alpha_{ijkl}(\tau)\rho_{ij}(t) + \beta_{ij}(\tau) \ . \tag{17.136}$$

The trace condition is satisfied, when $(i,j),(k,l) \neq (1,1)$.

To be able to explore the above relationship to calculate correlation functions, we have to invoke the so-called *quantum regression theorem*,

$$\boxed{\langle \hat{A}(t+\tau)\rangle = \sum_i \xi_i(\tau)\langle \hat{A}_i(t)\rangle \quad \Longrightarrow \quad \langle \hat{B}(t)\hat{A}(t+\tau)\hat{C}(t)\rangle = \sum_i \xi_i(\tau)\langle \hat{B}(t)\hat{A}_i(t)\hat{C}(t)\rangle}\,. \tag{17.137}$$

Example 105 (*Quantum regression applied to the Langevin equation*): We have,

$$\begin{aligned} \dot{A}_\mu &= D_\mu(t) + F_\mu(t) \\ \langle F_\mu(t)F_\nu(t)\rangle &= 2\langle D_{\mu\nu}\rangle\delta(t-t')\ . \end{aligned} \tag{17.138}$$

We know,

$$\langle A_\mu(t)F_\nu(t)\rangle = \langle D_{\mu\nu}\rangle \qquad \text{and} \qquad \langle F_\mu(t)A_\nu(t)\rangle = \langle D_{\mu\nu}\rangle \tag{17.139}$$

and the quantum regression theorem gives,

$$\frac{d}{dt}\langle A_\mu(t)A_\nu(t')\rangle = \langle D_\mu(t)A_\nu(t')\rangle\ , \tag{17.140}$$

because if $t' < t$, the term $\langle F_\mu(t)A_\nu(t')\rangle$ vanishes for a *Markovian process*.

17.4.3.2 Bloch equation for a two-level system

The Fourier transform of the first-order coherence, $g^{(1)}(\tau) = e^{-\imath\omega\tau}G(\tau)$, gives,

$$F(\nu) = (\mathcal{F}g^{(1)})(\nu) = \mathcal{F}[e^{-\imath\omega\tau}] \star \mathcal{F}[G(\tau)] = \delta(\nu-\omega)\star\mathcal{F}[G(\tau)] = (\mathcal{F}G)(\nu-\omega)\ . \tag{17.141}$$

Therefore, we can look at the unshifted spectrum, $(\mathcal{F}G)(\nu)$. Since the fluorescence spectrum is determined by the first-order coherence, which depends on the field operators, which in turn depend on the atomic populations and coherences, we have to solve the Bloch equation.

For a two-level atom the Bloch equations, having been reduced by the normalization condition (16.243) are,

$$\dot{\vec{\rho}}_{\text{red}} = \mathcal{M}\vec{\rho}_{\text{red}} + \mathbf{b} = \begin{pmatrix} -\Gamma & -\frac{\imath}{2}\Omega & \frac{\imath}{2}\Omega \\ -\imath\Omega & -\frac{1}{2}\Gamma - \imath\Delta & 0 \\ \imath\Omega & 0 & -\frac{1}{2}\Gamma + \imath\Delta \end{pmatrix}\begin{pmatrix}\rho_{22}\\ \rho_{12}\\ \rho_{21}\end{pmatrix} + \begin{pmatrix} 0 \\ \frac{\imath}{2}\Omega \\ -\frac{\imath}{2}\Omega\end{pmatrix} \tag{17.142}$$

with the solution (16.245), that is, $\vec{\rho}(t+\tau) = e^{\mathcal{M}\tau}\vec{\rho}(t) + (1-e^{\mathcal{M}\tau})\vec{\rho}(\infty)$ with $\rho(\infty) = -\mathcal{M}^{-1}b$. This solution can be cast in the following form,

$$\rho_{kl}(t+\tau) = \sum_{(mn)} \alpha_{(kl)(mn)}(\tau)\rho_{mn}(t) + \beta_{(kl)}(\tau)\ , \tag{17.143}$$

where $(mn),(kl) = (22),(12),(21)$ identifying,

$$\alpha_{(kl)(mn)}(\tau) = \begin{pmatrix} \alpha_{22,22} & \alpha_{12,22} & \alpha_{21,22} \\ \alpha_{22,12} & \alpha_{12,12} & \alpha_{21,12} \\ \alpha_{22,21} & \alpha_{12,21} & \alpha_{21,21} \end{pmatrix} \equiv \begin{pmatrix} (e^{\mathcal{M}\tau})_{11} & . & . \\ . & . & . \\ . & . & . \end{pmatrix} = e^{\mathcal{M}\tau} \tag{17.144}$$

$$\beta_{(kl)}(\tau) = \begin{pmatrix} \beta_{22} \\ \beta_{12} \\ \beta_{21} \end{pmatrix} \equiv \begin{pmatrix} -[(1-e^{\mathcal{M}\tau})\mathcal{M}^{-1}\mathbf{b}]_1 \\ . \\ . \end{pmatrix} = -(1-e^{\mathcal{M}\tau})\mathcal{M}^{-1}\mathbf{b} \ .$$

Using quantum operators in the interaction image, $|k\rangle\langle l| = \hat{\sigma}_{kl}$, we have,

$$\langle\hat{\sigma}_{12}(t)\rangle = \langle\hat{\sigma}_{21}^{\dagger}(t)\rangle = \rho_{12}(t)e^{\imath\omega_0 t} \qquad \text{and} \qquad \langle\hat{\sigma}_{22}(t)\rangle = \langle\hat{\sigma}_{12}(t)\hat{\sigma}_{21}(t)\rangle = \rho_{22}(t) \ . \tag{17.145}$$

yielding,

$$\langle e^{(k-l)\imath\omega_0(t+\tau)}\hat{\sigma}_{kl}(t+\tau)\rangle = \sum_{(mn)} \alpha_{(kl)(mn)}(\tau)\langle e^{(m-n)\imath\omega_0 t}\hat{\sigma}_{mn}(t)\rangle + \beta_{(mn)}(\tau)\langle 1\rangle \ , \tag{17.146}$$

or,

$$\begin{aligned} &\langle\hat{\sigma}_{kl}(t+\tau)\rangle \\ &= \sum_{(mn)} e^{(l-k)\imath\omega_0\tau}\alpha_{(kl)(mn)}(\tau)\langle e^{(l-k+m-n)\imath\omega_0 t}\hat{\sigma}_{mn}(t)\rangle + e^{(l-k)\imath\omega_0\tau}\beta_{(mn)}(\tau)\langle e^{(l-k)\imath\omega_0 t}\rangle \ . \end{aligned} \tag{17.147}$$

Applying the quantum regression theorem to the Bloch equations, we get for an arbitrary time-dependent operator $\hat{B}(t)$,

$$\boxed{\begin{aligned} \langle\hat{B}(t)\hat{\sigma}_{kl}(t+\tau)\rangle \quad = \quad & \sum_{(mn)} e^{(l-k)\imath\omega_0\tau}\alpha_{(kl)(mn)}(\tau)\langle e^{(l-k+m-n)\imath\omega_0 t}\hat{B}(t)\hat{\sigma}_{mn}(t)\rangle \\ & + e^{(l-k)\imath\omega_0\tau}\beta_{(mn)}(\tau)\langle e^{(l-k)\imath\omega_0 t}\hat{B}(t)\rangle \end{aligned}} \ . \tag{17.148}$$

17.4.3.3 Correlation functions

We now look at the radiation field, which is related to the dipole moment operator via,

$$\hat{\mathcal{E}}^{-} = \gamma\hat{\sigma}_{21} \ , \tag{17.149}$$

where γ is simply a constant. Substituting this relation in the correlation functions (17.77) we obtain,

$$\begin{aligned} g^{(1)}(\tau) &= \frac{\langle\hat{\sigma}_{21}(t)\hat{\sigma}_{12}(t+\tau)\rangle}{\langle\hat{\sigma}_{21}(t)\hat{\sigma}_{12}(t)\rangle} = \frac{\langle\hat{\sigma}_{21}(t)\hat{\sigma}_{12}(t+\tau)\rangle}{\langle\hat{\sigma}_{22}(t)\rangle} \\ g^{(2)}(\tau) &= \frac{\langle\hat{\sigma}_{21}(t)\hat{\sigma}_{21}(t+\tau)\hat{\sigma}_{12}(t+\tau)\hat{\sigma}_{12}(t)\rangle}{\langle\hat{\sigma}_{21}(t)\hat{\sigma}_{12}(t)\rangle^2} = \frac{\langle\hat{\sigma}_{22}(t)\hat{\sigma}_{22}(t+\tau)\rangle}{\langle\hat{\sigma}_{22}(t)\rangle^2} \ . \end{aligned} \tag{17.150}$$

Now we can calculate, letting $\xi_i(\tau) \equiv \alpha_{(12)(mn)}$, $\hat{C}(t) \equiv 1$, and $\hat{B}(t) \equiv \hat{\sigma}_{21}(t)$,

$$g^{(1)}(\tau) = \frac{\sum_{(mn)} e^{\imath\omega_0(t+\tau)} e^{(m-n)\imath\omega_0 t} \alpha_{(12)(mn)}(\tau) \langle \hat{\sigma}_{21}(t)\hat{\sigma}_{mn}(t)\rangle + e^{\imath\omega_0(t+\tau)}\beta_{(12)}(\tau)\langle\hat{\sigma}_{21}(t)\rangle}{\langle\hat{\sigma}_{22}(t)\rangle} \tag{17.151}$$

$$g^{(2)}(\tau) = \frac{\sum_{(mn)} e^{(m-n)\imath\omega_0 t} \alpha_{(22)(mn)}(\tau) \langle \hat{\sigma}_{22}(t)\hat{\sigma}_{mn}(t)\rangle + \beta_{(22)}(\tau)\langle\hat{\sigma}_{22}(t)\rangle}{\langle\hat{\sigma}_{22}(t)\rangle^2} \,.$$

Using $\hat{\sigma}_{21}\hat{\sigma}_{mn} = \hat{\sigma}_{2n}\delta_{m1}$,

$$g^{(1)}(\tau) = e^{\imath\omega_0\tau} \frac{\alpha_{(12)(12)}(\tau)\langle\hat{\sigma}_{21}(t)\hat{\sigma}_{12}(t)\rangle + \beta_{(12)}(\tau)\langle e^{\imath\omega_0 t}\hat{\sigma}_{21}(t)\rangle}{\langle\hat{\sigma}_{22}(t)\rangle} \tag{17.152}$$

$$g^{(2)}(\tau) = \frac{\alpha_{(22)(21)}(\tau)\langle e^{\imath\omega_0 t}\hat{\sigma}_{22}(t)\hat{\sigma}_{21}(t)\rangle + \alpha_{(22)(22)}(\tau)\langle\hat{\sigma}_{22}(t)\hat{\sigma}_{22}(t)\rangle + \beta_{(22)}(\tau)\langle\hat{\sigma}_{22}(t)\rangle}{\langle\hat{\sigma}_{22}(t)\rangle^2} \,.$$

Returning to the density operator and letting $t \to \infty$,

$$g^{(1)}(\tau) = e^{\imath\omega_0\tau}\left[\alpha_{(12)(12)}(\tau) + \beta_{(12)}(\tau)\frac{\rho_{21}(\infty)}{\rho_{22}(\infty)}\right] \qquad \text{and} \qquad g^{(2)}(\tau) = e^{\imath\omega_0\tau}\frac{\beta_{(22)}(\tau)}{\rho_{22}(\infty)} \,, \tag{17.153}$$

that is,

$$\boxed{\begin{aligned} g^{(1)}(\tau) &= e^{\imath\omega_0\tau}\left[\left[e^{\mathcal{M}\tau}\right]_{(12)(12)} - \left[(\mathbb{I}-e^{\mathcal{M}\tau})\mathcal{M}^{-1}\mathbf{b}\right]_{(12)}\frac{\left[\mathcal{M}^{-1}\mathbf{b}\right]_{(21)}}{\left[\mathcal{M}^{-1}\mathbf{b}\right]_{(22)}}\right] \\ g^{(2)}(\tau) &= e^{\imath\omega_0\tau}\frac{\left[(\mathbb{I}-e^{\mathcal{M}\tau})\mathcal{M}^{-1}\mathbf{b}\right]_{(22)}}{\left[\mathcal{M}^{-1}\mathbf{b}\right]_{(22)}} \end{aligned}} \,. \tag{17.154}$$

These correlation functions can easily be calculated via a numerical resolution of the Bloch equations (17.142). Fig. 17.13 shows the correlation functions and the fluorescence spectrum derived by Fourier transform of the first-order correlation function (17.82). Assuming resonant excitation, $\Delta = 0$, analytic formulas can be derived, as will be exercised in Excs. 17.4.4.3 and Exc. 17.4.4.4.

The spectrum 17.13(d) exhibits three lines known as the *Mollow triplet*. Note that the spontaneous emission triplet is only observed in the presence of a driving laser, because it is the laser excitation which causes the splitting. Indeed, the splitting and the position of the lines are easily understood in the dressed states picture visualized in Fig. 17.1: The coupling of the two-level atom to a light field splits up the levels $|n\rangle$ and $|n+1\rangle$ by an amount corresponding to the Rabi frequency Ω. Now, the transition from the two excited state $|n+1\rangle$ levels to the ground state $|n\rangle$ levels can occur on three different frequencies. In Exc. 17.4.4.5 we calculate the Mollow spectrum for a transition between one ground and three excited Zeeman states. Fig. 17.14 illustrates the various methods to analyze scattered light, but not all of them yield information on the Mollow triplet.

17.4.3.4 Mollow spectrum from effective Hamiltonian

The Mollow triplet is easily understood in the dressed states picture. On the other hand, we know that (for classical light) the semi-classical picture is totally equivalent

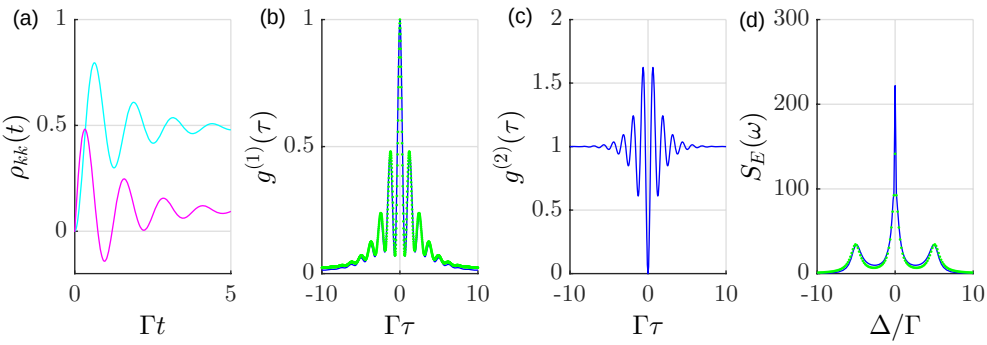

Figure 17.13: (code) (a) Temporal evolution of the excited state population $\rho_{22}(t)$ (cyan) and coherence $\rho_{12}(t)$ (magenta) of a laser-driven two-level atom with $\Omega = 5\Gamma$. (b) Correlation function $g^{(1)}(\tau)$ and (c) $g^{(2)}(\tau)$. The blue curves in (b-c) are obtained by numerical simulations of the Bloch equations and subsequent application of the quantum regression theorem (17.154). The green dots are obtained from an analytic solution derived in Exc. 17.4.4.3. (d) Mollow spectrum obtained by numerical FFT of $g^{(1)}(\tau)$.

(its just a unitary transform of the dressed states picture). Developing a physical picture the Mollow triplet in the semi-classical framework may give us a deeper insight. Generally, the Mollow spectrum is anyhow calculated using the semi-classical Bloch equations, via the correlation function $g^{(1)}(\tau)$ and the Wiener-Khintchine theorem, but the on the way the physical intuition is lost.

For example, looking at the stationary solution of the Bloch equations (16.151), we see that $\vec{\rho}(\infty)$ is time-independent, so that we might be *surprised to see correlations in time domain* (and consequently a structured spectrum) at all. This surprise results from a common misconception that may arise considering the damping of $\vec{\rho}(t)$ predicted by the Bloch model, as illustrated e.g. in Fig. 16.3: It seems that the atoms eventually cease oscillating between the ground and excited states. In most experiments, measurement are made on a large number of atoms and indeed the oscillations are damped.

In fact, however, every individual atom undergoes a complicated unpredictable trajectory alternating times of coherent evolution with spontaneous emission events (called quantum jumps). The damped behavior only results as an average over many such quantum trajectories. In this light, the reason for $g^{(1)}$-type correlations is a subtle interplay between coherently and incoherently scattered light: *The spontaneous emission probability is amplitude-modulated with the Rabi frequency.*

An alternative way to calculate the Mollow spectrum consists in solving the Schrödinger equation with the effective Hamiltonian, as done in Exc. 17.4.4.2 and 17.4.4.6. The results are shown in Fig. 17.15. While providing an intuitive picture of the origin of of the Mollow triplet a quantitatively correct treatment requires a Monte-Carlo wavefunction simulation [594] (see Sec. 18.1.2).

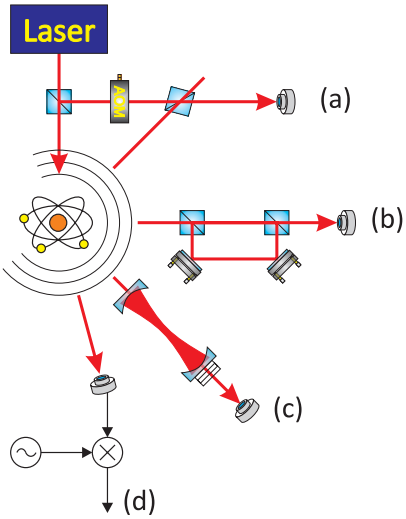

Figure 17.14: Schemes for analyzing resonance fluorescence: (a) Heterodyning [634], (b) temporal correlation, (c) spectrum [778, 635], (d) demodulation. Only the schemes (b) and (c) yield information on the Mollow triplet.

17.4.3.5 Weak excitation and the role of collisions

For the case of a weakly excited two-level atom, $|\Omega| \ll \Gamma$, we have analytic solutions (16.157) of the Bloch equation. We can then take the coefficients α_{ijkl} and β_{ij} and insert them into the correlation functions,

$$\begin{aligned} g^{(1)}(\tau) &= e^{-\imath\omega\tau} \ , \\ g^{(2)}(\tau) &= 1 + e^{-2\gamma\tau} - 2\cos\Delta\tau \ , \\ F(\omega_s) &= (\mathcal{F}g^{(1)})(\omega_s) = \delta(\omega_s - \omega) \ . \end{aligned} \tag{17.155}$$

These functions show that the spectrum is essentially composed of *Rayleigh scattering* at the frequency of the incident light. The δ-shaped fluorescence spectrum shows, that the contribution of elastically scattered light dominates below saturation, which confirms the results (17.135) illustrated in Fig. 17.12. The light is 'antibunched' and, at higher τ exhibits a damped oscillation around the value 1.

If pressure broadening is taken into account, the two-level Bloch equations are given by (16.151), where $\gamma' = \gamma + \gamma_{coll}$ is the width of the collision-broadened line. Within this model and in the limit $\Omega \ll \Gamma$, the resonance fluorescence spectrum is given by [530],

$$F(\omega_s) = \frac{\gamma' - \Gamma}{\gamma'} \frac{\gamma'/\pi}{(\omega_0 - \omega_s)^2 + \gamma'^2} + \frac{\Gamma}{\gamma'}\delta(\omega_s - \omega) \ . \tag{17.156}$$

So, we find that, even at low intensities, a continuous spectrum due to *inelastic scattering* appears around the resonance frequency ω_0 additionally to the elastic Rayleigh peak.

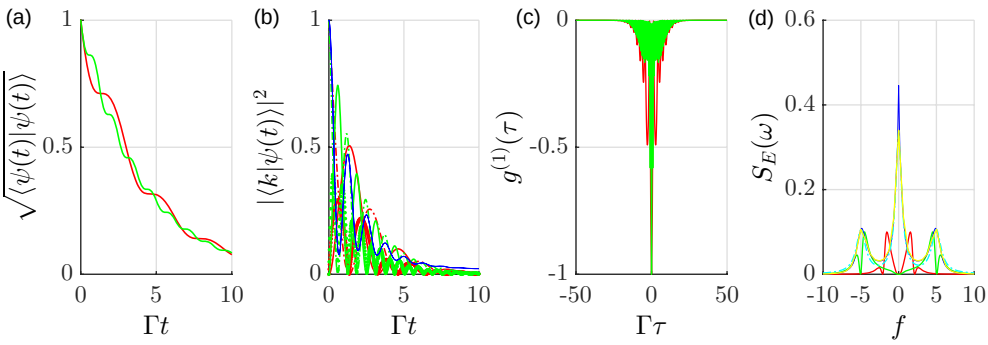

Figure 17.15: (code) (a) Time evolution of the norm of a decaying driven two-level atom. (b) Time evolution of the ground and excited state amplitudes. (c) First-order autocorrelation function, and (d) spectrum.

17.4.4 Exercises

17.4.4.1 Ex: Derivation of the rate equations for two-level atoms

Inserting the ansatz (17.110) into the Schrödinger equation, derive the equations of motion (17.112) for the wavefunction amplitudes.

17.4.4.2 Ex: Non-Hermitian time evolution

Study the time evolution $|\psi(t)\rangle = e^{-\imath\hat{H}_{\rm eff}t/\hbar}|\psi(0)\rangle$ with the effective Hamiltonian,

$$\hat{H}_{\rm eff} = \begin{pmatrix} 0 & \frac{\hbar}{2}\Omega \\ \frac{\hbar}{2}\Omega & -\frac{\imath\hbar}{2}\Gamma \end{pmatrix}$$

starting from the initial condition $\langle 2|\psi(0)\rangle = 1$. Calculate the evolution of $|\psi(t)\rangle$ and the norm $\langle\psi(t)|\psi(t)\rangle$. Plot the time evolution of the norm for various ratios Ω/Γ and interpret the curves. **Alternative solution:**
We set $\hbar = 1$ and calculate the eigenvalues $E_\pm$ and the unitary transformation matrix $\mathcal{U}$, where $\mathcal{U}\hat{H}_{\rm eff} = \hat{E}\mathcal{U}$ and

$$\hat{E} \equiv \begin{pmatrix} E_+ & 0 \\ 0 & E_- \end{pmatrix} .$$

The eigenvalues are,

$$E_\pm = -\tfrac{\imath\Gamma}{4} \pm \tfrac{1}{4}\sqrt{4\Omega^2 - \Gamma^2} \overset{\Omega\to 0}{\longrightarrow} 0, -\tfrac{\imath}{2}\Gamma .$$

The unitary transformation matrix is nothing else than the eigenvector matrix,

$$\mathcal{U} = \begin{pmatrix} \frac{2E_+ + \imath\Gamma}{\Omega} & \frac{2E_- + \imath\Gamma}{\Omega} \\ 1 & 1 \end{pmatrix} = \begin{pmatrix} \frac{\imath\Gamma}{2\Omega} + \sqrt{1 - \frac{\Gamma^2}{4\Omega^2}} & \frac{\imath\Gamma}{2\Omega} - \sqrt{1 - \frac{\Gamma^2}{4\Omega^2}} \\ 1 & 1 \end{pmatrix} .$$

We get for the evolution,

$$
\begin{aligned}
e^{-\imath\hat{H}_{\text{eff}}t}\begin{pmatrix}0\\1\end{pmatrix} &= \mathcal{U}e^{-\imath\hat{E}t}\mathcal{U}^{-1}\begin{pmatrix}0\\1\end{pmatrix} \\
&= \begin{pmatrix}\frac{2E_+ +\imath\Gamma}{\Omega} & \frac{2E_- +\imath\Gamma}{\Omega}\\ 1 & 1\end{pmatrix}\begin{pmatrix}e^{-\imath E_+ t} & 0\\ 0 & e^{-\imath E_- t}\end{pmatrix}\begin{pmatrix}\frac{2E_+ +\imath\Gamma}{\Omega} & \frac{2E_- +\imath\Gamma}{\Omega}\\ 1 & 1\end{pmatrix}^{-1}\begin{pmatrix}0\\1\end{pmatrix} \\
&= \begin{pmatrix}-\frac{(2E_+ +\imath\Gamma)(2E_- +\imath\Gamma)}{2\Omega(E_+ - E_-)}(e^{-\imath E_+ t} - e^{-\imath E_- t}) \\ -\frac{(2E_- +\imath\Gamma)}{2(E_+ - E_-)}e^{-\imath E_+ t} + \frac{(2E_+ +\imath\Gamma)}{2(E_+ - E_-)}e^{-\imath E_- t}\end{pmatrix} \\
&= \begin{pmatrix}\frac{\Omega}{\sqrt{4\Omega^2-\Gamma^2}}(e^{-\imath E_+ t} - e^{-\imath E_- t}) \\ \frac{1}{2}\left(1 - \frac{\imath\Gamma}{\sqrt{4\Omega^2-\Gamma^2}}\right)e^{-\imath E_+ t} + \frac{1}{2}\left(1 + \frac{\imath\Gamma}{\sqrt{4\Omega^2-\Gamma^2}}\right)e^{-\imath E_- t}\end{pmatrix} \\
&= e^{-\Gamma t/4}\begin{pmatrix}\frac{-2\imath\Omega}{\sqrt{4\Omega^2-\Gamma^2}}\sin\frac{t\sqrt{4\Omega^2-\Gamma^2}}{4} \\ \cos\frac{t\sqrt{4\Omega^2-\Gamma^2}}{4} - \frac{\Gamma}{\sqrt{4\Omega^2-\Gamma^2}}\sin\frac{t\sqrt{4\Omega^2-\Gamma^2}}{4}\end{pmatrix} .
\end{aligned}
$$

The result is identical to the one previously derived.

17.4.4.3 Ex: Resonance fluorescence and antibunching via Bloch equations

a. Derive the analytic solution of the Bloch equations for a resonantly driven two-level atom.
b. Calculate the 1^{st}-order correlation function $g^{(1)}(\tau)$ from the formula (17.154).
c. Derive the spectrum of resonance fluorescence [593].
d. Derive the 2^{nd}-order correlation function $g^{(2)}(\tau)$ from the formula (17.154).

17.4.4.4 Ex: Resonance fluorescence via rate equations

Repeat Exc. 17.4.4.3 neglecting coherences, i.e. replacing the Bloch equations by rate equations,

$$
\dot{\vec{\rho}} = \begin{pmatrix}-R & R+\Gamma & 0 & 0\\ R & -R-\Gamma & 0 & 0\\ 0 & 0 & -\gamma & 0\\ 0 & 0 & 0 & -\gamma\end{pmatrix}\vec{\rho} ,
$$

where $R = \Omega^2/2\gamma$ is the pump rate.

17.4.4.5 Ex: Fluorescence spectrum of a four-level system

A more realistic transition, allowing for a vectorial nature of the radiation field, involves one ground and three excited Zeeman states (e.g. the strontium ${}^1S_0$-${}^1P_1$ transition). In this case, the emitted light is,

$$
\hat{\mathcal{E}}^-(t) = \hat{\mathcal{E}}^-_{\sigma^-}(t) + \hat{\mathcal{E}}^-_{\pi}(t) + \hat{\mathcal{E}}^-_{\sigma^+}(t) .
$$

Calculate the first-order correlation function and the fluorescence spectrum of this transition.

17.4.4.6 Ex: Semi-classical picture of the Mollow triplet

Calculate the first-order correlation function from the solution of the Schrödinger equation with the effective Hamiltonian derived in Exc. 17.4.4.2.

17.4.4.7 Ex: Monte-Carlo simulation of the Mollow triplet

Implement a Monte-Carlo simulation of the Mollow triplet for a driven two-level atom according to [194, 594].

17.5 Light scattering from multi-level atoms

17.5.1 Quantum beats

The phenomenon of *quantum beats* is another simple example of effects beyond semi-classical theory, requiring a full second-quantized calculation. In semi-classical theory (SCT), there is an interference or beat note term for both V-type and Λ-type atoms, while in quantum electrodynamics (QED) only V-type atoms exhibits a beat term.

In the semi-classical picture, the state vector of electrons is [749],

$$\psi(t)\rangle = c_1 e^{-\imath\omega_1 t}|1\rangle + c_2 e^{-\imath\omega_2 t}|2\rangle + c_3 e^{-\imath\omega_3 t}|3\rangle \ . \tag{17.157}$$

Writing the non-vanishing dipole matrix elements as $d_{12} = e\langle 1|r|2\rangle$, $d_{23} = e\langle 2|r|3\rangle$ a three-level atom has two microscopic oscillating dipoles,

$$\mathcal{P}(t) = d_{12}(c_1^* c_2)e^{\imath\omega_{12}t} + d_{23}(c_2^* c_3)e^{\imath\omega_{23}t} + c.c. \ . \tag{17.158}$$

In the semi-classical picture, the radiated field will be a sum of these two terms,

$$\mathcal{E}^+ = \mathcal{E}_1 e^{-\imath\omega_{12}t} + \mathcal{E}_2 e^{-\imath\omega_{23}t} \ . \tag{17.159}$$

This leads to an interference or beat note term in a square-law detector,

$$|\mathcal{E}^+|^2 = |\mathcal{E}_{12}|^2 + |\mathcal{E}_{23}|^2 + \mathcal{E}_{12}^* \mathcal{E}_{23} e^{[\imath(\omega_{12}-\omega_{23})t]} + c.c. \ , \tag{17.160}$$

regardless of whether state $|2\rangle$ decays simultaneously to $|1\rangle$ and $|3\rangle$ or vice versa.

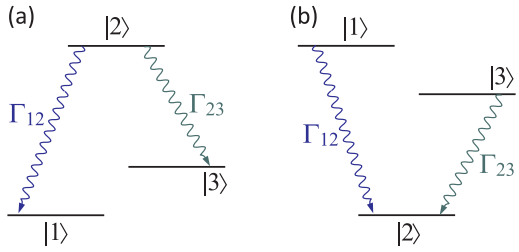

Figure 17.16: Level configuration of a Λ-system (left) and a V-system (right).

17.5.1.1 Quantum electrodynamics calculation

For the quantum electrodynamical calculation, we use the creation and annihilation operators from second quantization of quantum mechanics. Let $\hat{\mathcal{E}}_n^+ = \hat{a}_n e^{-\imath\omega_n t}$ be the annihilation operator and $\hat{\mathcal{E}}_n^- = \hat{a}_n^\dagger e^{\imath\omega_n t}$ be the creation operator with $n = (12)$ or $n = (23)$. Then the beat note becomes,

$$\langle\psi_V(t)|\hat{\mathcal{E}}_{12}^-(t)\hat{\mathcal{E}}_{23}^+(t)|\psi_V(t)\rangle \quad \text{and} \quad \langle\psi_\Lambda(t)|\hat{\mathcal{E}}_{12}^-(t)\hat{\mathcal{E}}_{23}^+(t)|\psi_\Lambda(t)\rangle \tag{17.161}$$

for the Λ and the V-system, respectively. The state vector for each type of system is,

$$|\psi_V(t)\rangle = \sum_{i=1,2,3} c_i|i,0\rangle + c_1|c,1_{12}\rangle + c_2|c,1_{23}\rangle \tag{17.162}$$

and,

$$|\psi_\Lambda(t)\rangle = \sum_{i=1,2,3} c_i'|i,0\rangle + c_1'|b,1_{12}\rangle + c_2'|c,1_{23}\rangle \ . \tag{17.163}$$

The beat note term becomes,

$$\begin{aligned}\langle\psi_V(t)|\hat{\mathcal{E}}_1^-(t)\hat{\mathcal{E}}_2^+(t)|\psi_V(t)\rangle &= \kappa\langle 1_{12}0_{23}|a_1^\dagger a_2|0_{12}1_{23}\rangle e^{[\imath(\omega_{12}-\omega_{23})t]}\langle 3|3\rangle \\ &= \kappa e^{[\imath(\omega_{12}-\omega_{23})t]}\langle 3|3\rangle\end{aligned} \tag{17.164}$$

for the V-system and

$$\begin{aligned}\langle\psi_\Lambda(t)|\hat{\mathcal{E}}_1^-(t)\hat{\mathcal{E}}_2^+(t)|\psi_\Lambda(t)\rangle &= \kappa'\langle 1_{12}0_{23}|a_1^\dagger a_2|0_{12}1_{23}\rangle e^{[\imath(\omega_{12}-\omega_{23})t]}\langle 2|3\rangle \\ &= \kappa' e^{[\imath(\omega_{12}-\omega_{23})t]}\langle 2|3\rangle\end{aligned} \tag{17.165}$$

for the Λ-system. However, orthogonality of the eigenstates requires $\langle 3|3\rangle = 1$ and $\langle 2|3\rangle = 0$. Therefore, there is a quantum beat note term for V-type atoms, but not for Λ-type atoms.

This difference originates in quantum mechanical uncertainty. A V-type atom decays to state $|3\rangle$ via the emission with ω_{12} and ω_{23}. Since both transitions decayed to the same state, one cannot determine along which path each decayed, similar to Young's double-slit experiment. However, Λ-type atoms decay to two different states. Therefore, in this case we can identify the path by the end product.

Quantum beat spectroscopy is a technique which allows for Doppler-free resolution provided the separation of the adjacent levels is less than the Doppler width. It consists in generating a coherently distributed population of two upper states, e.g. via a short laser pulse, and detecting the beat frequency.

17.5.2 Two-photon transitions

We will now apply the *Kramers-Heisenberg formula* (5.111) to photon scattering processes $\omega \to \omega_s$. The states are then product states of atomic excitations and photonic modes $|m,n,n_s\rangle$. In particular, the final state must take into account the mode into

which light is scattered,

$$\frac{1}{\tau} = \frac{2\pi}{\hbar^2}\sum_f\sum_{\mathbf{k}_s}\left|\langle f,n-1,1|\hat{H}^{(2)}|i,n,0\rangle\right. \tag{17.166}$$
$$\left. +\frac{1}{\hbar}\sum_m \frac{\langle f,n-1,1|\hat{H}^{(1)}|m\rangle\langle m|\hat{H}^{(1)}|i,n,0\rangle}{\omega_i-\omega_m}\right|^2 \delta(\omega_f-\omega_i)\ .$$

The initial energy is $\omega_i \to n\omega$, the final energy $\omega_f \to (n-1)\omega+\omega_s+\omega_f$, two intermediate states are possible, $|m\rangle \to |m,n-1,0\rangle$ and $|m\rangle \to |m,n,1\rangle$ over which we must sum, that is $\omega_m \to \omega_m+(n-1)\omega$ and $\omega_m \to \omega_m+n\omega+\omega_s$. They are illustrated by the Feyman diagrams in Fig. xx. Hence, and neglecting the non-linear contribution $\hat{H}^{(2)}$,

$$\frac{1}{\tau} = \frac{2\pi}{\hbar^3}\sum_f\sum_{\mathbf{k}_s}\left|\sum_m \frac{\langle f,n-1,1|\hat{H}^{(1)}|m,n,0\rangle\langle m,n,0|\hat{H}^{(1)}|i,n,0\rangle}{\omega-\omega_m}\right. \tag{17.167}$$
$$\left. +\frac{\langle f,n-1,1|\hat{H}^{(1)}|m,n-1,1\rangle\langle m,n-1,1|\hat{H}^{(1)}|i,n,0\rangle}{-\omega_m-\omega_s}\right|^2 \delta(\omega_f-\omega+\omega_s)\ .$$

Evaluated far from resonance, $\omega \gg \omega_m$, this result leads to Thomson and Compton scattering. Close to resonance the second term of the sum may neglected.

The matrix elements can be evaluated by the electric dipole Hamiltonian in second quantization,

$$\frac{1}{\tau} = \frac{2\pi}{\hbar}\sum_{\mathbf{k}_s}\left|\sum_m \frac{\Omega_{fm}\Omega_{mi}}{\omega-\omega_m}\right|^2 \delta(\omega_f-\omega+\omega_s)\ . \tag{17.168}$$

We convert the transition rate into a cross section via,

$$\sum_{\mathbf{k}_s} \to \frac{V}{(2\pi)^3}\int\int k_s^2 dk_s d\Omega = \frac{V}{(2\pi c)^3}\int\int \omega_s^2 d\omega_s d\Omega\ . \tag{17.169}$$

17.5.2.1 Transition rates for n-photon processes

It is adequate to move to a continuum of final states of the field. The sum over the final states includes a sum over the modes $\mathbf{k}$ and the polarizations λ,

$$\sum_f = \sum_{\mathbf{k}}\sum_\lambda \longrightarrow \frac{1}{h^3}\int_{\mathbb{R}^6} d^3p d^3r \sum_\lambda = \frac{V}{(2\pi c)^3}\int_\Omega d\Omega\ d\omega\ \omega^2 \sum_\lambda\ . \tag{17.170}$$

We now insert for the matrix element (first term in ()) the cartesian multipole expansion () and obtain,

$$\frac{1}{\tau} = \frac{2\pi}{\hbar^2}\sum_f\left|\langle f| - \imath e\sqrt{\frac{\hbar\omega}{2\varepsilon_0 V}}[\hat{\varepsilon}\cdot\mathbf{d}_E+...]|i\rangle\right|^2 \delta(\omega-\omega_f)\sum_\lambda \tag{17.171}$$
$$\longrightarrow \frac{2\pi}{\hbar^2}\frac{V}{(2\pi c)^3}\frac{e^2\hbar\omega}{2\varepsilon_0 V}\omega^2\sum_\lambda\int|\hat{\varepsilon}\cdot\langle g|\mathbf{d}_E|e\rangle + \imath\hat{\varepsilon}\cdot\langle g|\mathbf{q}_E|e\rangle\cdot\mathbf{k}...] - ...|^2\, d\Omega\ .$$

Finally, letting $\sum_\lambda = 2$,

$$\frac{1}{\tau} = \frac{\alpha\omega^3}{\pi c^2} \int |\hat{\varepsilon} \cdot \langle g|\text{multipole-tensor}|e\rangle \text{wavenumber-tensor}|^2 \, d\Omega \ . \tag{17.172}$$

For example, for dipole radiation, letting $\hat{\varepsilon} = \hat{\mathbf{e}}_z$,

$$\begin{aligned} \frac{1}{\tau} &= \frac{\alpha\omega^3}{\pi c^2} \int |\hat{\varepsilon} \cdot \langle g|\mathbf{d}_E|e\rangle|^2 \, d\cos\theta d\phi \\ &= \frac{\alpha\omega^3}{\pi c^2} |\langle g|\mathbf{d}_E|e\rangle|^2 \int |\cos\theta|^2 d\cos\theta d\phi = \frac{4\alpha\omega^3}{3c^2} |\langle g|\mathbf{d}_E|e\rangle|^2 \ . \end{aligned} \tag{17.173}$$

17.5.2.2 Absorption

In first order perturbation theory we have Fermi's Golden rule,

$$\frac{1}{\tau} = \frac{2\pi}{\hbar^2} \sum_f |\langle f|\hat{H}_{\rm int}|i\rangle|^2 \delta(\omega_f - \omega_i) \ . \tag{17.174}$$

In the dipolar approximation, $\hat{H}_{\rm int} = -\mathbf{d} \cdot \vec{\mathcal{E}}$, and separating the field and atomic degrees of freedom, $|f\rangle = |N_f\rangle|A_f\rangle$, we get for absorption processes,

$$\frac{1}{\tau} = \frac{2\pi e^2}{\hbar^2} \sum_{N_f} \left| \langle N_f|\hat{\mathcal{E}}^-|N_i\rangle \cdot \langle A_f|\hat{\varepsilon} \cdot \hat{\mathbf{d}}|A_i\rangle \right|^2 \delta(\omega_f - \omega_i) \ . \tag{17.175}$$

Generalizing to a statistical mixture of Fock states via $\sum_{N_f,N_i} \langle N_i|\hat{E}^+|N_f\rangle p_i \langle N_f|\hat{E}^-|N_i\rangle = \text{Tr}\ (\hat{\rho}\hat{\mathcal{E}}^+\hat{\mathcal{E}}^-)$, we may also write,

$$\frac{1}{\tau} = \frac{2\pi e^2}{\hbar^2} |M_{\rm abs}|^2 \delta(\omega_f - \omega_i) \text{Tr}\ (\hat{\rho}\hat{\mathcal{E}}^+\hat{\mathcal{E}}^-) \ , \tag{17.176}$$

where

$$|M_{\rm abs}|^2 \equiv \langle A_f|\hat{\varepsilon} \cdot \hat{\mathbf{d}}|A_i\rangle \ . \tag{17.177}$$

For an incoming photon ω, we get $\omega_f = E_f$ and $\omega_i = E_i + \omega$. See Fig. 17.17(a).

17.5.2.3 Spontaneous and stimulated emission

In complete analogy to the absorption process, but now using the scattered field, $\hat{H}_{\rm int} = -\mathbf{d} \cdot \hat{\vec{\mathcal{E}}}_{\rm s}$, we get for emission processes,

$$\frac{1}{\tau} = \frac{2\pi e^2}{\hbar^2} |M_{\rm em}|^2 \delta(\omega_f - \omega_i) \text{Tr}\ (\hat{\rho}\hat{\mathcal{E}}_{\rm s}^+\hat{\mathcal{E}}_{\rm s}^-) \ , \tag{17.178}$$

where

$$|M_{\rm em}|^2 \equiv \langle A_f|\hat{\varepsilon}_s \cdot \hat{\mathbf{d}}|A_i\rangle \ . \tag{17.179}$$

For an outgoing photon ω_s, we get $\omega_f = E_f + \omega_s$ and $\omega_i = E_i$.

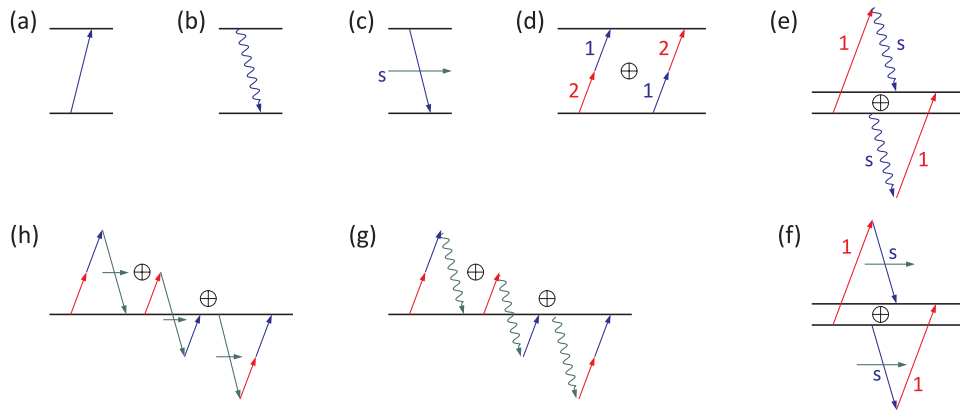

Figure 17.17: Feynman graphs for (a) absorption, (b) spontaneous emission, (c) stimulated emission, (d) two-photon absorption, (e) spontaneous Raman, (f) stimulated Raman, (g) spontaneous second harmonic generation, (h) and stimulated second harmonic generation.

17.5.2.4 Two-photon absorption

In second order perturbation theory we have the Kramers-Heisenberg rule,

$$\frac{1}{\tau} = \frac{2\pi}{\hbar^2} \sum_f \left| \sum_m \frac{\langle f|\hat{H}_{\rm int}|m\rangle\langle m|\hat{H}_{\rm int}|i\rangle}{\omega - \omega_m} \right|^2 \delta(\omega_f - \omega_i) \ . \tag{17.180}$$

In the dipolar approximation, $\hat{H}_{\rm int} = -\mathbf{d}\cdot\hat{\vec{\mathcal{E}}}_1 - \mathbf{d}\cdot\hat{\vec{\mathcal{E}}}_2$, and separating the field and atomic degrees of freedom, $|f\rangle = |N_f\rangle|A_f\rangle$, we get for two-photon absorption processes,

$$\frac{1}{\tau} = \frac{2\pi e^4}{\hbar^4} \sum_{N_f} \left| \sum_{N_m, A_m} \frac{\langle N_f|\mathcal{E}_2^-|N_m\rangle\langle N_m|\mathcal{E}_1^-|N_i\rangle\langle A_f|\hat{\varepsilon}_2\cdot\hat{\mathbf{d}}|A_m\rangle\langle A_m|\hat{\varepsilon}_1\cdot\hat{\mathbf{d}}|A_i\rangle}{\omega_1 - \omega_m} \right. \tag{17.181}$$

$$\left. + \frac{\langle N_f|\mathcal{E}_1^-|N_m\rangle\langle N_m|\mathcal{E}_2^-|N_i\rangle\langle A_f|\hat{\varepsilon}_1\cdot\hat{\mathbf{d}}|A_m\rangle\langle A_m|\hat{\varepsilon}_2\cdot\hat{\mathbf{d}}|A_i\rangle}{\omega_2 - \omega_m} \right|^2 \delta(\omega_f - \omega_1 - \omega_2) \ .$$

Generalizing to a statistical mixture of Fock states via $\sum_{N_f,N_i} p_i |\langle N_f|\hat{\mathcal{E}}_2^-\hat{\mathcal{E}}_1^-|N_i\rangle = {\rm Tr}\,(\hat{\rho}\hat{\mathcal{E}}_1^+\hat{\mathcal{E}}_2^+\hat{\mathcal{E}}_2^-\hat{\mathcal{E}}_1^-)$, we may also write,

$$\frac{1}{\tau} = \frac{2\pi e^4}{\hbar^4} |M_{tpa}|^2 \delta(\omega_f - \omega_i) {\rm Tr}\,(\hat{\rho}\hat{\mathcal{E}}_1^+\hat{\mathcal{E}}_2^+\hat{\mathcal{E}}_2^-\hat{\mathcal{E}}_1^-) \ , \tag{17.182}$$

where

$$M_{tpa} \equiv \langle A_f|\hat{\varepsilon}_2\cdot\hat{\mathbf{d}}G(E_i+\omega_1)\hat{\varepsilon}_1\cdot\hat{\mathbf{d}}|A_i\rangle + \langle A_f|\hat{\varepsilon}_1\cdot\hat{\mathbf{d}}G(E_i+\omega_2)\hat{\varepsilon}_2\cdot\hat{\mathbf{d}}|A_i\rangle \ . \tag{17.183}$$

For two incoming photons ω, we get $\omega_f = E_f$ and $\omega_i = E_i + \omega_1 + \omega_2$. Here, G denotes the *photon propagator*,

$$G(\omega) = \sum_m \frac{|A_m\rangle\langle A_m|}{\omega - E_m} \ . \tag{17.184}$$

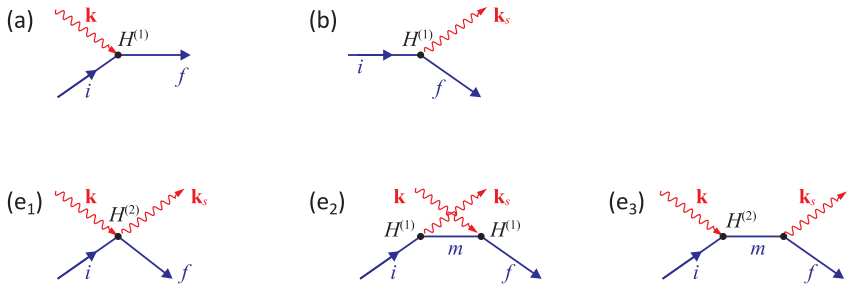

Figure 17.18: Feynman graphs for (a) absorption, (b) spontaneous emission, (c) stimulated emission, (e)(i-iii) spontaneous Raman.

17.5.2.5 Spontaneous and stimulated Raman process

In complete analogy to the two-photon absorption process, but now using the incident and the scattered fields, $\hat{H}_{\rm int} = -\mathbf{d}\cdot\vec{\mathcal{E}}_1 - \mathbf{d}\cdot\vec{\mathcal{E}}_{\rm s}$, we get for spontaneous and stimulated Raman processes,

$$\frac{1}{\tau} = \frac{2\pi e^4}{\hbar^4}|M_{ram}|^2\delta(\omega_f-\omega_i){\rm Tr}\left(\hat{\rho}\hat{\mathcal{E}}_1^+\hat{\mathcal{E}}_{\rm s}^-\hat{\mathcal{E}}_{\rm s}^+\hat{\mathcal{E}}_1^-\right) , \tag{17.185}$$

where

$$M_{ram} \equiv \langle A_f|\hat{\varepsilon}_s\cdot\hat{\mathbf{d}}G(E_i+\omega_1)\hat{\varepsilon}_1\cdot\hat{\mathbf{d}}|A_i\rangle + \langle A_f|\hat{\varepsilon}_1\cdot\hat{\mathbf{d}}G(E_i-\omega_s)\hat{\varepsilon}_s\cdot\hat{\mathbf{d}}|A_i\rangle \ . \tag{17.186}$$

For an incoming photon ω_1 and a scattered photon ω_s, we get $\omega_f = E_f+\omega_s$ and $\omega_i = E_i+\omega_1$.

17.5.2.6 General n-photon processes

The transition probability in n-th order perturbation theory can be formulated in a general way as,

$$\frac{1}{\tau} = \frac{2\pi e^2}{\hbar^{2n}}|M_{fi}^{(n)}|^2\delta(\omega_f-\omega_i){\rm Tr}\left(\hat{\rho}\hat{\mathcal{E}}_1^{\pm}\hat{\mathcal{E}}_2^{\pm}...\hat{\mathcal{E}}_2^{\mp}\hat{\mathcal{E}}_1^{\mp}\right) , \tag{17.187}$$

where

$$\begin{aligned} M_{fi}(\omega_n,...,\omega_1) \equiv \mathcal{S}_p\langle A_f|\hat{\varepsilon}_n\hat{\mathbf{d}}G(E_i\pm\omega_1\pm...\pm\omega_{n-2}\pm\omega_{n-1})\ ... \\ ...\ \hat{\varepsilon}_{n-1}\hat{\mathbf{d}}G(E_i\pm\omega_1\pm...\pm\omega_{n-2})\ ... \\ ...\ \hat{\varepsilon}_1\cdot\hat{\mathbf{d}}G(E_i\pm\omega_1)|A_i\rangle \ . \end{aligned} \tag{17.188}$$

The upper signs hold for absorbed photons (up to n), the lower for emitted photons, $\omega_f = E_f+\omega_1+...+\omega_n$ and $\omega_i = E_i+\omega_1+...+\omega_n$.

For n-photon processes, there are theoretically up to $n+1$ different types, each one with $n!$ possible temporal sequences, which can be illustrated in Feynman graphs.

Additionally, for every emitted photon can be either spontaneous or stimulated. The number of possible time sequences is reduced, if some absorbed or emitted photons have the same frequency by $m!$ (if m is the number og identical photons).

For example there are (3+1) different types of three-photon processes: 3 photons in, 2 photons in 1 out, 1 photon in 2 out, 3 photons out.

For example second harmonic generation: 3! possible time sequences, 2 processes, 2 equivalent photons = $\frac{3!2}{2!}$ possible Feynman graphs.

17.5.3 Exercises

17.5.3.1 Ex: Two-photon transitions in rubidium

Considering the following transitions of rubidium, $5S_{1/2} - 5P_{1/2}$ at 795 nm with $\Gamma_{795} = (2\pi)$ 6 MHz linewidth $5S_{1/2} - 5P_{3/2}$ at 780 nm with $\Gamma_{780} = (2\pi)$ 6MHz, and $5P_{3/2} - 5D_{5/2}$ at 776 nm with $\Gamma_{776} = (2\pi)$ 700 kHz linewidth. Calculate the rate for resonant two-photon transitions from the ground state to the $5D_{5/2}$ level without bothering about hyperfine splitting induced by a laser intensity of $I = 1$ mW/cm^2.

17.5.3.2 Ex: Spin relaxation in a dipole trap

Consider a transition in a hypothetical atomic species without nuclear spin between two levels $^2S_{1/2}$ and $^2P_{1/2}$ driven far-off resonance. Calculate the spin relaxation rate as a function of the detuning.

17.5.3.3 Ex: Rayleigh scattering and spin relaxation

Derive the rates for Rayleigh scattering and spin relaxation for ^{87}Rb driven far-off resonance. **Help**: Determine the hyperfine structure of the D1 and D2 lines and calculate the transition rates between sublevels from the Kramers-Heisenberg formula.

17.6 Further reading

Ch.C. Gerry and P.L. Knight, Cambridge University Press (2005), *Introductory Quantum Optics* [ISBN]

P. Meystre and M. Sargent III, Springer-Verlag, Berlin (1990), *Elements of Quantum Optics* [ISBN]

M.O. Scully and M.S. Zubairy, Cambridge University Press (1997), *Quantum Optics* [ISBN]

W. Schleich, Wiley VCH (2001), *Quantum Optics in Phase Space* [ISBN]

E.T. Jaynes et al., *Comparison of quantum and semiclassical radiation theories with application to the beam maser* [DOI]

F. Albarelli et al., *Nonlinearity as a resource for nonclassicality in anharmonic systems* [DOI]

J.P. Bartolotta et al., *Entropy transfer from a quantum particle to a classical coherent light field* [DOI]

K.E. Cahill et al., *Density Operators and Quasiprobability Distributions* [DOI]

C.M. Caves et al., *Quantum-mechanical noise in an interferometer* [DOI]

C.M. Caves, *Quantum limits on noise inlinear amplifiers* [DOI]

J. Dalibard et al., *Wave-Function Approach to Dissipative Processes in Quantum Optics* [DOI]

R.G. DeVoe et al., *Observation and Superradiant and Subradiant Spontaneous Emission of Two Trapped Ions* [DOI]

R. Dum et al., *Monte Carlo simulation of master equations in quantum optics for vacuum, thermal, and squeezed reservoirs* [DOI]

J. Eschner et al., *Light interference from single atoms and their mirror images* [DOI]

Z. Ficek et al., *Effect of interatomic interactions on resonance fluorescence of two atoms coherently driven by strong resonant laser field* [DOI]

J.C. García-Melgarejo et al., *A Numerical Perspective on the Jaynes-Cummings Model Wigner Function* [DOI]

K. Nakayama et al., *Precise intensity correlation measurement for atomic resonance fluorescence from optical molasses* [DOI]

U. Leonhardt et al., *Measuring the quantum state of light* [DOI]

P. Longo et al., *Far-Field Signatures of a Two-Body Bound State in Collective Emission from Interacting Two-Level Atoms on a Lattice* [DOI]

R. Loudon et al., *Squeezed light* [DOI]

L.A. Lugiato et al., *Quantum imaging* [DOI]

B.R. Mollow et al., *Power spectrum of light scattered by two-level systems* [DOI]

K. Mølmer et al., *Monte Carlo wave-function method in quantum optics* [DOI]

F.A. de Oliveira et al., *Properties of displaced number states* [DOI]

M.D. Reid, *Quantum Correlations of Phase in Nondegenerate Parametric Oscillation* [DOI]

M.D. Reid, *Demonstration of the Einstein-Podolsky-Rosen paradox using nondegenerate parametric amplification* [DOI]

D. Stoler, *Equivalence Classes of Minimum Uncertainty Packets* [DOI]

M. Uria et al., *Deterministic Generation of Large Fock States* [DOI]

H.P. Yuen et al., *Two-photon coherent states of the radiation field* [DOI]

M. Schubert et al., *Photon antibunching and non-Poissonian fluorescence of a single three-level ion* [DOI]

Y. Stalgies et al., *The Spectrum of Single-Atom Resonance Fluorescence* [DOI]

Y. Gutiérrez et al., *Mollow triplet in cold atoms* [DOI]

G.S. Agarwal et al., *Inhibition of Decoherence due to Decay in a Continuum* [DOI]

Ho Trung Dung et al., *Electromagnetic-field quantization and spontaneous decay in left-handed media* [DOI]

17.6.1 on the Jaynes-Cummings model

J. Eiselt et al., *Quasiprobability distributions for the Jaynes-Cummings model with cavity damping* [DOI]

M. Brune et al., *Manipulation of photons in a cavity by dispersive atom-field coupling: Quantum-nondemolition measurement and generation of "Schrödinger cat" states* [DOI]

K. Gietka et al., *Quantum-enhanced interferometry with cavity QED-generated non-classical light* [DOI]

M. Mohammad et al., *Cavity quantum electrodynamics with atom-like mirrors* [DOI]

Chapter 18

Quantum measurement

Since its foundation, the theory of quantum mechanics was driven by the urge to clarify the relationship between the world and what we can learn about it, that is, between reality and the observer. Scientists such as Bohr, Heisenberg, Schrödinger, and Einstein defended controversial positions and struggled for the correct interpretation of quantum mechanics. The *measurement* process is supposed to provide information about the world out there, but it is not clear whether this information can be complete and accurate, or whether there are limitations or hidden variables. Also, it was unclear, to what extend a measurement can be non-invasive or whether it would always perturb the phenomenon under investigation. The most important step in this question was the *Copenhagen interpretation* formulated by Bohr, Heisenberg and Born in 1927 and elaborated later by von Neumann and Dirac. Although contested many times in the past, it's essence still remains valid today.

In this chapter we will study the measurement process from the viewpoint quantum mechanics and discuss some seemingly paradoxical effects, that will allow us to deepen our understanding. Among them are the quantum jump, Schrödinger's cat, the quantum Zeno effect, and the Einstein-Podolski-Rosen paradox.

18.1 The reality and the observer

According to the Copenhagen interpretation, theoretical predictions have a probabilistic character. However, this is not an expression of the imperfection of the theory, but of the intrinsically indeterministic character of quantum processes [1]. Moreover, the Copenhagen interpretation desists to attribute to objects of the quantum formalism, such as wavefunctions and operators, an immediate reality. Instead, the objects of the formalism only represent vehicles for a probabilistic prediction of the results of measurements. These results are *only truly real* elements of quantum theory. It is obvious, that the quantum theory and its interpretations are of fundamental importance to the scientific view of the world and our concept of nature.

18.1.1 Schrödinger's cat

In the microscopic world, the relationship between the sample and the observer is very delicate. And this delicacy is at the origin of quantum effects that seem paradoxical

[1] Note that it is problematic to identify unpredictability and indeterminism. We may be unable to predict specific events, without having to assume that these events occur in a random manner.

through our classical concept of the world. It is, thus, not surprising that one of the most fascinating areas of investigations is the *interface* between the classical and the quantum, the macroscopic and the microscopic worlds. For the pioneers of quantum mechanics the most important questions were of the type: 'How is it possible that a microscopic particle flies simultaneously through two slits?' Nowadays, we are accustomed to such paradoxes, and we simply accept the fact that we have to consider a particle as a wave. Nevertheless, we still do not understand very well, why the classical and the quantum world behave so differently. 'Why does quantum mechanics allow for quantum superpositions states, which are absolutely forbidden in classical physics?', 'Why are the fundamental laws of the quantum world invariant to the arrow of time, while the macroscopic world always evolves from the past to the future?, 'How can it be that quantum mechanics allows for effects having no cause, like spontaneous emission, while the everyday world seems to be deterministic?'

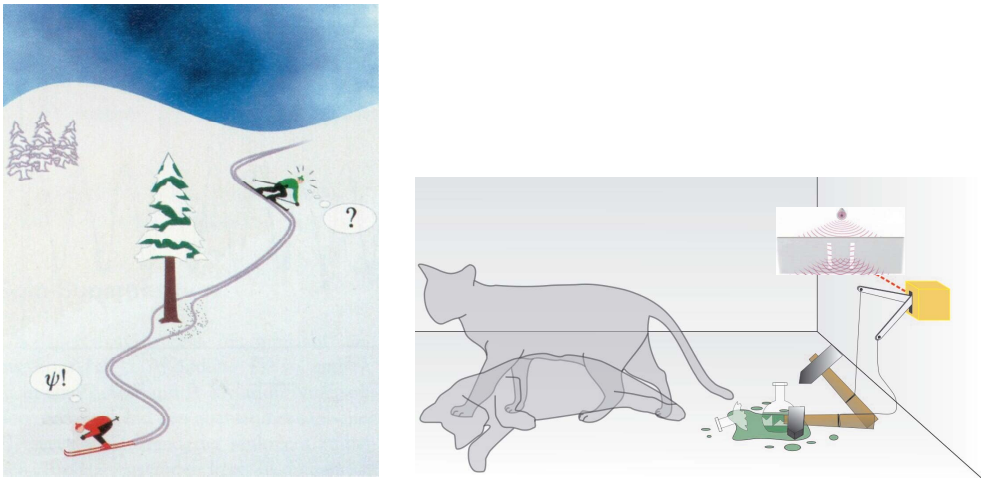

Figure 18.1: Double slit and Schrödinger's cat.

Quantum mechanics must, in some limit, clearly encompass classical physics. But in spite of *Ehrenfest's correspondence principle*, this fact is far from being trivial. Some predictions of classical and quantum physics are fundamentally different and, in some cases, even contradictory. The famous *Schrödinger cat* states are the epitome of this fact: In one version of this paradox, a particle crosses a double slit. Behind one of the slits is a detector which, as soon as it registers a particle, actuates a device killing a cat. We know that in quantum reality the particle crosses both slits in a superposition state, so that the cat should be in a superposition state as well. Hence, quantum cats can be in a superposition of 'dead' and 'alive'.

We believe nowadays that the answers to the above questions are somehow buried in processes that destroy the quantum superposition of Schrödinger cats during the transition from the microscopic to the macroscopic world. However, the details of these quantum coherence destruction processes, called *decoherence*, are very complicated and the subject of serious efforts in contemporary research. It is one of the motivations for trying to create in laboratories the largest possible (quasi-macroscopic) quantum systems, bring them in Schrödinger cat-like superposition states and study

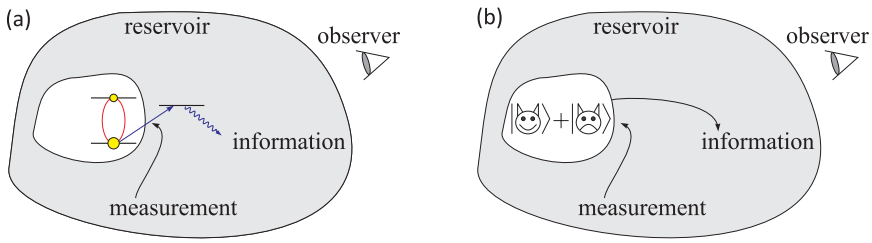

Figure 18.2: The measurement of a quantum system presupposes the interaction of the system with a reservoir, which disturbs its dynamics.

their decoherence [2].

18.1.1.1 Quantum measurement

Every unperturbed system follows the Schrödinger equation. Once its Hamiltonian has been determined, the formal solution,

$$|\psi\rangle = e^{-\imath\hat{H}t/\hbar}|\psi_0\rangle \ , \tag{18.1}$$

allows to calculate the time evolution, that is, the trajectory of the wavefunction. The evolution is *coherent and reversible* in time.

Now, the process of measuring a pure quantum state includes –according the Copenhagen interpretation and as discussed in Sec. 1.4.7– two consecutive steps: In the *first step*, the interaction of the quantum sample with the measuring device (which from now on we will call *meter*) destroys all coherences and projects the pure state into a statistical mixture of eigenstates of the meter. Following von Neumann, the impact of the meter on the quantum system is so strong, that its coherent evolution is interrupted and it is projected onto the degree of freedom that the apparatus wants to measure, e.g. its position or its momentum, but not both in the same time. The projection transforms a pure quantum state $|\psi\rangle$ into a statistical mixture ρ of eigenstates,

$$\hat{\rho}_{\rm sample} = |\psi(t)\rangle\langle\psi(t)| \curvearrowright \hat{\rho}_{\rm proj} = \sum\nolimits_k |\langle\psi|k\rangle|^2 |k\rangle\langle k| \ . \tag{18.2}$$

This process is irreversible, that is, it separates the past from the future. The projection is *not* described by the Schrödinger equation. Instead, the sudden reduction of the state must be postulated, as done by von Neumann's famous axiom.

In a *second step*, the observer looks at the measuring device and confirms one of the possible results. Thus, he transforms the state into a eigenstate of the device [3]:

$$\hat{\rho}_{\rm proj} \curvearrowright \hat{\rho}_{\rm meter} = |k\rangle\langle k| \ . \tag{18.3}$$

From this moment, we can again leave the quantum system alone until the next measure.

[2] There are attempts to introduce the concept of the time arrow also in the microscopic world: 'In an isolated system, spontaneous processes occur in the direction of increasing entropy.' [582, 312].

[3] We note that, only if *all* commuting observables of the system are measured *and* acknowledged, $\hat{\rho}_{\rm meter}$ becomes a pure state. Otherwise $\rho_{\rm meter}$ remains a partial mixture.

From the viewpoint of the quantum system, the evolution of the measurement process appears *discontinuous*, because it destroys all possible coherences between its states. In fact, the problem comes from the non-ideal behavior of the measuring device (symbolized by $|\uparrow\rangle$ before the measurement). An ideal non-invasive measurement [4] would leave the quantum state $|\psi\rangle$ unchanged:

$$|\psi\rangle|\uparrow\rangle \xrightarrow{H} |\psi\rangle|\nearrow\rangle \ , \tag{18.4}$$

while the measuring device changes to a state ($|\nearrow\rangle$ after the measurement) indicating the current state of the system. However, this is normally impossible without previously established correlation between $|\psi\rangle$ and $|\uparrow\rangle$. In a real meter device, the coupling between $|\psi\rangle$ and $|\uparrow\rangle$ requires that the meter and the system to be non-orthogonal.

18.1.1.2 Measurement-induced decoherence

A more modern view of the quantum measurement is the following: When the outer world (called reservoir, observer or meter) *reads* a quantum system, it causes, due to this transfer of information, an irreversible demolition of coherence. Consequently, the density operator condenses to its diagonal. On the other hand, the system as a whole (including the sample and the reservoir) always evolves coherently according to the von Neumann equation with the Hamiltonian of everything $\hat{H}_{\text{all}}$:

$$\dot{\hat{\rho}} = \frac{\imath}{\hbar}[\hat{\rho}, \hat{H}_{\text{all}}] \ . \tag{18.5}$$

If $\hat{H}_{\text{sample}}$ is the small quantum system under investigation, a complete description of the measurement process requires the inclusion of the observer, that is, the total Hamiltonian is,

$$\hat{H} = \hat{H}_{\text{sample}} \otimes \hat{H}_{\text{meter}} = \begin{pmatrix} \text{sample} & 0 \\ 0 & \text{meter} \end{pmatrix} \ . \tag{18.6}$$

Ideally, the system evolves independently without being disturbed by the meter. Unfortunately, this also means that the meter evolves independently, that is, it is not influenced by the system and thus does not provide information about the system. To allow a transfer of information, we need to couple the respective spaces by an interaction Ω, such that,

$$\hat{H} = \begin{pmatrix} \text{sample} & \Omega \\ \Omega & \text{meter} \end{pmatrix} \ . \tag{18.7}$$

Tracing over all degrees of freedom of the universe *except* those of the quantum system, the von Neumann equation (18.5) turns into a master equation,

$$\dot{\hat{\rho}}_{\text{sample}} = \frac{\imath}{\hbar}[\hat{\rho}, \hat{H}_{\text{sample}}] + \mathcal{L}_{\text{reserv}}\rho \ . \tag{18.8}$$

[4] See the discussion of the *quantum non-demolition measurement*.

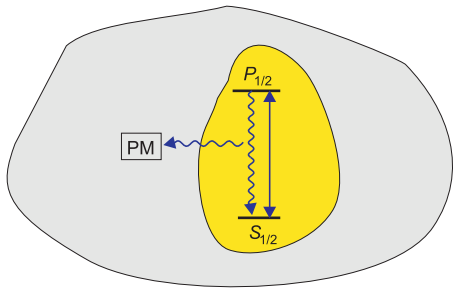

Figure 18.3: Spontaneous emission can be seen as a coupling of the system under investigation to an external meter, because it delivers information to the meter, even if only to tell us: 'The system was in an excited state, but now it's in a ground state.'

Example 106 (*Quantum measurement in a two-qubit system*): To discuss this at an example, we consider the simplest imaginable system: Two two-level atoms, the first one representing the quantum system under investigation and the second the meter. We introduce the following basis:

$$|1\rangle \equiv |\downarrow\rangle|\downarrow\rangle = \begin{pmatrix}1\\0\\0\\0\end{pmatrix} , \; |2\rangle \equiv |\uparrow\rangle|\downarrow\rangle = \begin{pmatrix}0\\1\\0\\0\end{pmatrix} , \; |3\rangle \equiv |\downarrow\rangle|\uparrow\rangle = \begin{pmatrix}0\\0\\1\\0\end{pmatrix} , \; |4\rangle \equiv |\uparrow\rangle|\uparrow\rangle = \begin{pmatrix}0\\0\\0\\1\end{pmatrix} .$$

The Hamiltonian of independent atoms is,

$$\hat{H} = |\downarrow\rangle\langle\downarrow| \otimes |\uparrow\rangle\langle\uparrow| .$$

The discussion about the correct interpretation of the measurement process is still ongoing. Modern theories describe the state reduction in terms of *quantum decoherence* due to interactions of the system with the environment. Other interpretations involve *decoherent histories* or assume *multiple worlds* [643]. On the practical side, the current interest in quantum decoherence is motivated by the fact that this phenomenon may turn out to be the fundamental factor limiting the useful operation of quantum computers. Another interesting area where quantum mechanics meets classical physics is the phenomenon of quantum chaos.

18.1.2 The quantum jump

Obviously, the whole quantum measurement process, including the discontinuity of the state projection, could be fully understood within a grand model of the complete system, which would include the measuring device. In practice, this is illusory, because of the excessive number of degrees of freedom of the classical measuring device (e.g. a Schrödinger cat).

On the other hand, many characteristics of quantum measurement can be illustrated in a simple *three-level atom* with a weak transition representing the quantum sample and a strong transition representing the meter. The assertion defended in

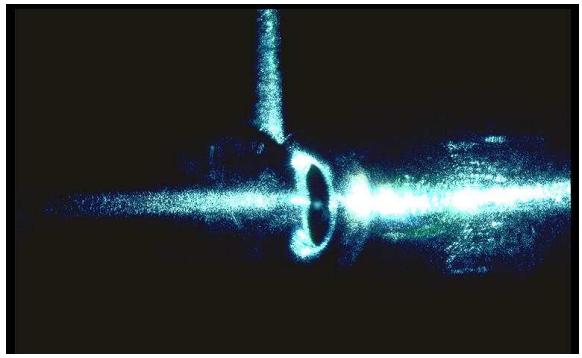

Figure 18.4: One of the first pictures of a single Ba^+ ion.

the following is, that this three-level system, called *quantum amplifier*, gives a deep insight into what happens during the process of state reduction and, therefore, can be considered as paradigmatic for theories on quantum measurement.

To be able to discuss the dynamics of this system on a firmer ground, we will first introduce the quantum Monte Carlo wavefunction simulation method (MCWF).

18.1.2.1 Quantum Monte-Carlo wavefunction simulation of a two-level system

The possible occurrence of spontaneous emission produces a dynamics called *quantum trajectory*, which can be described by a non-hermitian *effective Hamiltonian*,

$$\hat{H}_{\text{eff}} = \hbar\Delta\sigma_z + \hbar\Omega\sigma^+ + c.c. - \frac{\imath}{2}\Gamma\sigma_z = \begin{pmatrix} 0 & \Omega \\ \Omega & \Delta - \imath\frac{\Gamma}{2} \end{pmatrix} , \tag{18.9}$$

aiming at including energy dissipation processes. The problem with this Hamiltonian is that, for being non-hermitian, $[\hat{H}_{\text{eff}}, \hat{H}^\dagger_{\text{eff}}] \neq 0$, it also generates a non-unitary dynamics, $e^{-\imath\hat{H}_{\text{eff}}t} \neq e^{\imath\hat{H}^\dagger_{\text{eff}}t}$. This means that the mere *possibility* of spontaneous emission prevents the reversibility of the dynamics. We observe a temporal decrease of the norm $\langle\psi(t)|\psi(t)\rangle$ indicating a loss of energy,

$$\langle\psi|\psi\rangle = \langle\psi_0|e^{-\imath\hat{H}_{\text{eff}}t}e^{\imath\hat{H}_{\text{eff}}t}|\psi_0\rangle \longrightarrow e^{-\Gamma t} . \tag{18.10}$$

The loss of normalization during the evolution, until the next quantum jump occurs, is due to the dissipation of energy toward the reservoir,

$$\text{Tr } \rho_{\text{sample}} \to 0 \qquad \text{while} \qquad \text{Tr} \begin{pmatrix} \rho_{\text{sample}} & 0 \\ 0 & \rho_{\text{reserv}} \end{pmatrix} = 1 , \tag{18.11}$$

and represents a measure of the probability that an irreversible process has occurred during the evolution time.

Dissipative processes can be simulated by playing dices with random numbers ζ. We divide time into small intervals dt and propagate the wavefunction from $\psi(t)$ to $\psi(t + dt)$. After each interval we evaluate the probability $p = 1 - \langle\psi(t)|\psi(t)\rangle$

accumulated during the time period $[0, t + dt]$ that a dissipative process (such as spontaneous emission) has occurred. Now, we generate a random number ζ, uniformly distributed between 0 and 1, which we compare to probability the probability p. In case, $\zeta > 1 - \langle\psi(t)|\psi(t)\rangle$, we conclude that there was no dissipative process, and we let the system proceed in peace, only renormalizing the wavefunction to compensate for the losses [580, 194]. Otherwise, if $\zeta < 1 - \langle\psi(t)|\psi(t)\rangle$, we conclude that there was a dissipative process, and the system is projected into the eigenstate ψ_0. This projection is abrupt and called *quantum jump*. Now, the evolution restarts from zero, ruled by the effective Hamiltonian. The simulation implemented via,

$$|\psi(t)\rangle \curvearrowright |\psi(t+dt)\rangle \equiv \begin{pmatrix} \frac{(1-\imath\hat{H}dt)|\psi(t+dt)\rangle}{\sqrt{\langle\psi(t)|\psi(t)\rangle}} & \text{if} \quad \zeta > 1 - \langle\psi(t)|\psi(t)\rangle \\ |\psi_0\rangle \quad \text{if} \quad \zeta < 1 - \langle\psi(t)|\psi(t)\rangle \end{pmatrix} . \tag{18.12}$$

This is the method called *quantum Monte Carlo wavefunction simulation*.

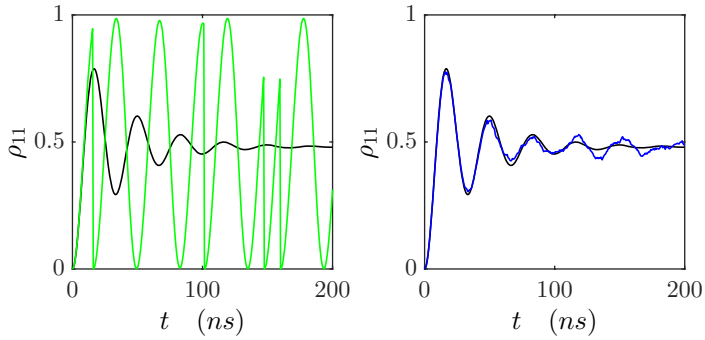

Figure 18.5: (code) a) Quantum Monte Carlo wavefunction simulation. It is important to be aware, that a trajectory generated by a MCWF simulation (18.12) only represents *one* of many possible trajectories of the system. (b) The evolution of the density matrix $\rho(t) = |\psi(t)\rangle\langle\psi(t)|$ (blue curve) is nothing else, than the average (black curve) over all possible MCWF trajectories for the system. A movie of this simulation can be watched here (watch movie).

The effective two-level Hamiltonian (18.9) dissipates via spontaneous emission, which is included in the dynamics through the *possibility* for the system to suffer a *state reduction*. The modification of $|\psi(t)\rangle$ by *non-observation* of spontaneous emission, reduces the population of the state excited by $1 - \frac{1}{2}\Gamma dt$, while the ground state population remains unchanged. Every quantum jump projecting the system into the ground state constitutes a measurement, because it corresponds to a detected fluorescence photon.

18.1.2.2 Three-level systems: The epitome of quantum measurement

Let us now return to the mysterious interaction between the sample and the meter, which we want to unravel by comparing two possible procedures: 1. treating the sample and the meter separately and explain the extraction of information following the von Neumann postulate; 2. treating the sample and the meter by a global theory.

As said above, the inclusion of the meter in a global theory is, in general, difficult. For this reason, to perform the comparison, we choose the simplest imaginable system: the *three-level system* with two transitions connecting to a common ground state and excited by radiation fields. As shown in Fig. 18.6(a) this three-level system can be an atom with a strong transition and a weak transition, for example, the dipolar transition $S_{1/2} - P_{1/2}$ and the forbidden quadrupolar transition $S_{1/2} - D_{5/2}$ in a single Ba^+ ion. We will now name the 'strong transition' as *meter* and the 'weak transition' as *sample* and show that this system allows to study the von Neumann measurement process including the direct observation of quantum jumps [5]. At the same time, the system is simple enough for a complete theoretical description. In this sense, the three-level system becomes the *epitome of a quantum measurement device*.

We turn our attention to the three-level atom: Obviously, the atom will preferentially scatters photons on its strong dipolar transition. However, at times when the valence electron is 'shelved' in the metastable state excited by the quadrupole transition, no fluorescence can be observed on the strong transition.

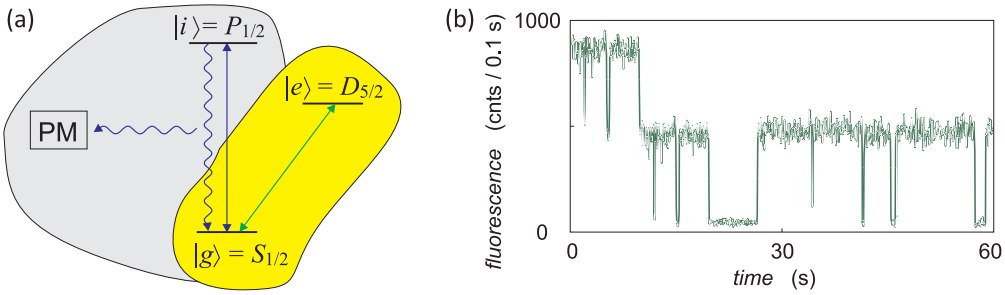

Figure 18.6: (a) Quantum measurement at the example of a three-level atom incorporating a weak (sample) transition and a strong (meter) transition. (b) *Random Telegraph signal* in the resonance fluorescence due to quantum jumps.

Quantum jumps were experimentally observed in single trapped ions, whose lowest energies form a three-level systems [616, 727, 728, 75].

18.1.2.3 Quantum Monte-Carlo wavefunction simulation of the quantum amplifier

When both lasers driving the weak and the strong transition are irradiated simultaneously, the coherence on the weak transition is easily perturbed by the dynamics of the strong transition. To resolve this problem *Dehmelt* invented what he called the *quantum amplifier*. The idea consists in alternately irradiating the *sample* laser (at stage $S - D$ in Fig. 18.7) and the *meter* laser (at stage $S - P$ in Fig. 18.7) [6].

[5] The observability of quantum jumps as manifestations of sudden state reductions has been the object of long-standing debates: 'If we have to go on with these damned quantum jumps, then I'm sorry that I ever got involved with quantum mechanics.' [741].

[6] The absence of the 'meter' laser during the 'sample' stage avoids saturation broadening and light-shifts of the ground state. Since the ground state is shared by both transitions, its broadening would reduce the spectral overlap between the 'sample' transition and the driving laser and therefore the probability to excite the metastable level. This inhibition of the coherent dynamic by too strong or too frequent measurements is known as *quantum Zeno effect*: The more an observer tries to

The alternating irradiation of the lasers $S-D$ and $S-P$ can also be treated by the Monte Carlo quantum wavefunction simulation method (18.12) using the effective Hamiltonian,

$$\hat{H}_{\text{eff}} = \begin{pmatrix} 0 & \frac{1}{2}\Omega_{sp} & \frac{1}{2}\Omega_{sd} \\ \frac{1}{2}\Omega_{sp} & -\Delta_{sp} - \frac{\imath}{2}\Gamma_{sp} & 0 \\ \frac{1}{2}\Omega_{sd} & 0 & -\Delta_{sd} \end{pmatrix} , \tag{18.13}$$

where the Rabi frequencies Ω_{sd} and Ω_{sd} are switched on alternately.

In the simulation 18.7 the quantum jumps to the shelved metastable state $D_{5/2}$ appear as long periods without population in the $P_{1/2}$ level (first period $S-P$, where the population of $S_{1/2}$, illustrated by the red curve, gradually tends to 0 for long times). The reduction of the system to the shelved state actually occurs by *non-observation* of fluorescence on the strong transition. The projection needs a finite time, simply because we can not be sure whether the non-observation is actually due to shelving or the incidental absence of scattering events on the $S-P$ transition: After all, it is not predictable, when the next photon will be spontaneously emitted, even though the lifetime of the excited state is short. But for longer observation times it becomes increasingly unlikely that the absence of photons is *not* due to shelving. It is this unlikeliness, which lets the population rapidly converge towards the metastable state. In the second $S-P$ period, Fig. 18.7 shows fast transitions to the $P_{1/2}$ followed by sudden decays to the ground state. These processes correspond to photon absorption and spontaneous reemission by the strong transition. The succession of the photon scattering events is so fast, that the signal recorded by photodetectors appears as a continuous fluorescence. The sudden transitions between bright and dark periods shown in Fig. 18.6(b), which occur totally randomly, are interpreted as quantum jumps.

18.1.2.4 Comparison with Bloch equations and interpretation of quantum jumps

We already mentioned in Fig. 18.5, that a trajectory generated by a MCWF simulation (18.12) represents *one* possible evolution of the system. In Chp. 16 we got to know an alternative way of predicting the evolution of a system, based on density operator obeying a *master equation*, which in the context of atomic excitation levels is called Bloch equation. Comparing MCWF trajectories (red curves in Fig. 18.7) with Bloch vector evolutions (green curves) it becomes apparent, that the Bloch vector evolution does not produce quantum jumps, but is always smooth and continuous.

In most cases, our knowledge about the actual state of an atom comes from the collection of spontaneously emitted photons. The observation of a photon projects the atomic state into the ground state. However, this concept is not included in the Bloch equations, as we just saw in Fig. 18.7. So, as it seems, we have to take back our statement, that the three-level Bloch equation describe the complete system, although they somehow contain spontaneous emission.

Let us go one step back and ask, where the Bloch equations came from. In fact, as we learned in Sec. 17.4 and will deepen in Sec. 15.1, they are derived from a von Neumann equation for the three-level system *plus* the degrees of freedom of the

extract information from a system, the more he inhibits its evolution. We will discuss this effect in more detail in Sec. 35.3.2.2.

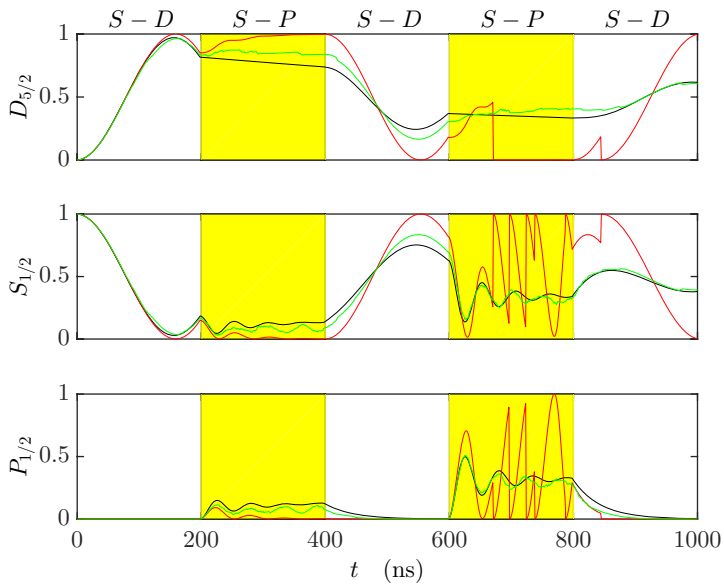

Figure 18.7: (code) Quantum amplifier comparing Monte-Carlo quantum simulations (red lines) and Bloch equations (black lines), which coincide well with the averages over 100 Monte-Carlo trajectories (green lines). The periods $S-D$ (white background) represent the free evolution of the quantum system, the periods $S-P$ (yellow background) represent the measurement periods.

vacuum modes receiving the spontaneously emitted photons by *tracing over the latter ones*.

We will not be able to handle all degrees of freedom. However, we can generalize the Bloch equations in the following way [593, 907]. We project the total density operator ρ_{AFR} of the atom plus the driving field plus the reservoir of vacuum modes into the subspace of the atom and the driving field consisting of exactly n photons,

$$\rho^{(n)} = \mathrm{Tr}_R \left(P^{(n)} \rho_{\mathrm{AFR}} \right) , \tag{18.14}$$

and derive, from the von Neumann equation, the master equation for the atomic state $\rho^{(n)}$ under the constraint of a fixed number of photons n in the field. The master equation differs only in one term from the usual Bloch equations: The expression $\Gamma_{12}\rho_{22}^{(n)}$, which describes the spontaneous decay of the population of the excited state of the meter transition, is replaced by the expression $\Gamma_{12}\rho_{22}^{(n-1)}$:

$$\frac{d}{dt}\rho^{(n)} = (\mathcal{L}|1\rangle\Gamma_{12}\langle 2|)\rho_{(n)} + |1\rangle\Gamma_{12}\langle 2|\rho^{(n-1)} , \tag{18.15}$$

The substate with of n photons violates the trace condition, $\sum_j \rho_{jj}^{(n)} \neq 1$. The physical explanation for this is the following: While induced emission and absorption maintain the number of photons in the combined light-atom system (like in the Jaynes-Cummings model), spontaneous emission decreases the number of photons, leading to an irreversible loss of energy. The quantum jump observed in MCWF model

corresponds, in the modified equations (18.15), to a collapse of the subspace described by $\rho^{(n)}$ with the time constant Γ_{12} and a birth of another subspace $\rho^{(n-1)}$, whose evolution is guided by another (analogous) Bloch equation, now for $n-1$ photons. Each fluorescence detection at time $t=0$ determines the initial condition for the future development of the system: $\rho^{(n)}(0)=0$ and $\rho^{(n-1)}(0)=|1\rangle\langle 1|$. The probability density $c(t)$ for a new observation of spontaneous emission at time t with detection efficiency η, or in other words, the histogram of the durations of dark periods in the fluorescence signal is related to the solution $\rho^{(n)}$ of the homogeneous part of the equation (18.14) via,

$$c(t)=\eta\Gamma_{12}\tilde{\rho}_{22}^{(n)}(t)=\eta\sum_{j=1}^{4}\frac{d}{dt}\tilde{\rho}_{jj}^{(n)}(t)\ , \tag{18.16}$$

The second step immediately follows from the homogeneous part of equation (18.15).

18.1.2.5 Final remarks

The explanations of the last sections show that Bohr's and Schrödinger's views can be reconcealed. They simply depend on whether the measuring transition is excluded or included in the description of the dynamics. *The quantum jump is an* ***artifact*** *arising from the separation of the quantum system under study (object) from the meter (observer) assumed to strongly interact with the system!* In any case (strong or weak interaction), this separation is not compulsory once a more complete model including the meter is at hand. However, as the dynamics of the meter and the object evolve on different time scales, a separation of the dynamics leading to apparently discontinuous trajectories is *only meaningful for strong meter interactions.*

As soon as this has been understood, that is since the 1980-th, the apparent paradox is simply not on the agenda any more. Recent claims of having unraveled the mystery [586] are just not timely and only show that the author did not understand the full meaning of a 'quantum jump' or, at most, did not read the pertinent literature.

18.1.2.6 Kraus operator for position measurement

As a canonical example of a Kraus operator [53, 143] we take $\hat{H}=\hat{x}\otimes\hat{p}$, where the position and the momentum satisfy the commutation relation, $[\hat{x},\hat{p}]=\imath$. The initial state of the ancilla be a Gaussian distribution,

$$|\phi\rangle=\frac{1}{(2\pi\sigma^2)^{1/4}}\int dq' e^{-q'^2/4\sigma^2}|q'\rangle\ . \tag{18.17}$$

The position wavefunction of the ancilla is,

$$\phi(q)=\langle q|\phi\rangle=\frac{1}{(2\pi\sigma^2)^{1/4}}e^{-q^2/4\sigma^2}\ . \tag{18.18}$$

The Kraus operators are (compared to the previous discussion, we now let $\lambda=1$),

$$M(q)=\langle q|e^{-\imath\hat{x}\otimes\hat{p}}|\phi\rangle=\frac{1}{(2\pi\sigma^2)^{1/4}}e^{-(q-x)^2/4\sigma^2}\ , \tag{18.19}$$

since the operator $e^{-\imath\hat{x}\otimes\hat{p}}$ makes a spatial translation when applied to the degree of freedom of the position. The corresponding POVM elements are,

$$E(q) = M_q^\dagger M_q = \frac{1}{\sqrt{2\pi\sigma^2}} e^{-(q-x)^2/2\sigma^2} \ , \tag{18.20}$$

which obey $\int dq E(q) = \mathbb{I}$.

Calculate $\langle\psi_q|\psi_q\rangle = \langle\psi'|M(q)^\dagger M(q)|\psi'\rangle$.

Note that $\lim_{\sigma\to 0} E(q) = |x = q\rangle\langle x = q|$. That is, in a particular limit, these operators converge to a strong measurement of position. For $\sigma \to \infty$, we speak of weak measurement.

Another example would be the three-level atom of Dehmelt's quantum amplifier.

18.1.3 *Welcher Weg* information

18.1.3.1 The Elitzur and Vaidman bomb testing problem

Mixing the concepts of particles and waves we sometimes arrive at seemingly paradoxical conclusions. One example is Elitzur and Vaidman's *bomb testing problem*. They imagined a Mach-Zehnder interferometer with the particularity that the reflecting mirror of one of the arms be connected to a device measuring the photonic recoil. That is, when a photon passes through this arm, the mirror undergoes a small acceleration, which is sufficient to activate an explosive bomb.

Now, we distinguish two cases: 1. The recoil detector *does not work*, i.e. the bomb is not armed. 2. The bomb is *armed*. We now adjust the interferometer in a way to produce destructive interference in one of the two interferometer output ports. If, having sent many photons through the interferometer, we never saw any photons in the 'dark' port, we can be almost sure that the bomb is *not operational*.

In case the bomb is operational, the observation of a photonic recoil destroys the interference pattern at the interferometer outputs. It *has* to do so, because the exploding bomb informs us, in which arm the photon has passed. However, with an operational bomb the interference pattern is *also* destroyed, when the photon passes through the other arm, since the fact that the bomb didn't explode tells us, that the photon went the other way.

The funny conclusion is now, that it may happen, that a photon traverses the interferometer in the arm that does *not* contain the bomb and exits through the 'dark port'. The probability of this happening is only 25%, but nevertheless the observation of a photon in the 'dark port' informs to us that the pump is operative without ever having interacted with it [7].

18.1.4 Exercises

18.1.4.1 Ex: Schwartzeneggers cat

Explain why we will never observe a real cat in a dead-alive superposition.

[7] See https://www.thorlabs.com/newgrouppage9.cfm?objectgroup_id=6635

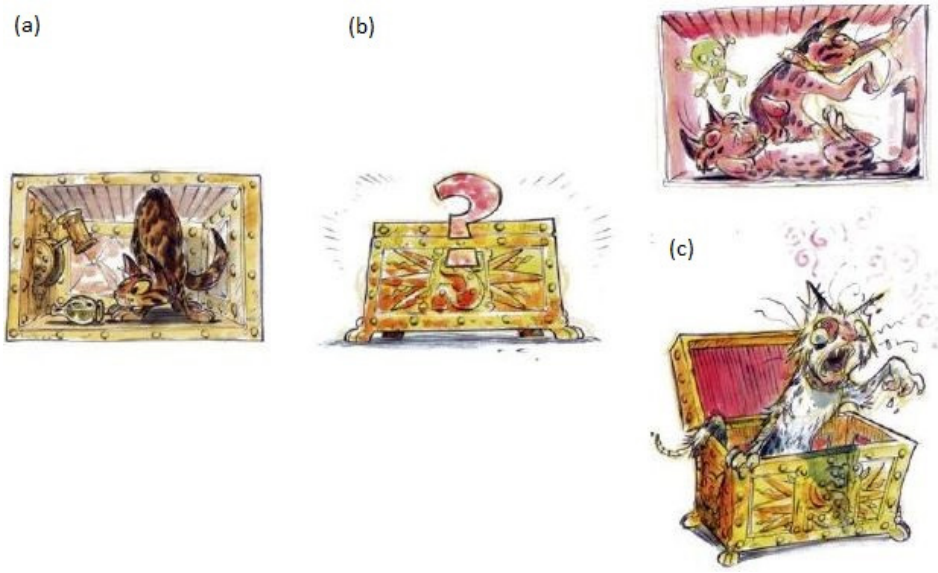

Figure 18.8: Schrödinger's cat according to *Ekhö, Le monde miroir* by Arleston and Barbucco: Quantum superposition or zombie cat?

18.1.4.2 Ex: Dispersive quantum jumps

Consider a three-level system in V-configuration, as depicted in Fig. 16.7(b), with an unstable state $|1\rangle$, a ground state $2\rangle$, and a metastable state $|3\rangle$. Discuss whether the atom shelved in state $|3\rangle$ is sensitive to light-shift and power broadened induced by a laser resonant to the $|1\rangle - |2\rangle$ transition. E.g. will power-broadening only effect the transition rate $|1\rangle \longrightarrow |3\rangle$ or also $|3\rangle \longrightarrow |1\rangle$?

18.2 Repeated measurements

18.2.1 The quantum Zeno effect

A famous problem raised by the Greek philosopher (490-430 AC) *Zeno* goes like this: Achilles and a turtle organize a race. The arrogant Achilles leaves a 100-meter lead to the turtle. The race begins. Achilles soon covers the 100 meters, only to find out that meanwhile the turtle has advanced by 10 meters. He continues running to cover the 10 meters, only to find out that meanwhile the turtle has advanced by 1 meter, and so on [8]. A presentation on the subject is available at (watch talk).

Interestingly, Zeno's problem has a counterpart in quantum mechanics. Let us do the following Gedankenexperiment: A laser beam passes through a dense series of n

[8] In another version of his paradox, Zeno questions the possibility of motion at the example of a flying arrow: At any instant of time it occupies a space equal to its size. That is, at any particular moment of its flight, it is at rest, in a space that does not move. That is, any kind of motion is impossible. Nowadays, we know that this paradox is false, because time and motion are not discrete. But this can only be understood on the basis of infinitesimal calculus [587].

polarizers, each one being rotated by an angle $\frac{\pi}{2n}$ with respect to the preceding one. Each polarizer performs a local measurement of beam polarization. The result of this arrangement is that, in the limit of an infinitely dense series, the continuous measurement of the system completely governs its evolution and rotates the polarization by an angle of $\pi/2$ [9].

In every version of the *Zeno effect*, the system is inhibited from evolving freely, because of too frequent measurements of its current state. Achilles would surely be able to overtake the turtle, if he did not always check on her to assess the remaining distance [420] [10].

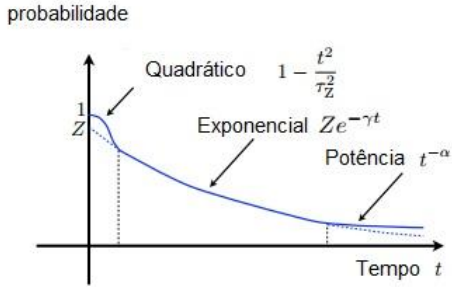

Figure 18.9: Quadratic time dependence of an excited state population.

The temporal evolution of the wavefunction of a system described by the Hamiltonian $\hat{H}$ is $|\psi(t)\rangle = e^{-\imath\hat{H}t/\hbar}|\psi_0\rangle$. We can then calculate the amplitude and probability for the system to stay in the initial state,

$$\langle\psi_0|\psi(t)\rangle = \langle\psi_0|e^{-\imath\hat{H}t/\hbar}|\psi_0\rangle \qquad \text{and} \qquad P(t) = |\langle\psi_0|\psi(t)\rangle|^2 \ . \tag{18.21}$$

For short times we can expand,

$$\langle\psi_0|\psi(\delta t)\rangle = |\psi_0\rangle - \frac{\imath}{\hbar}\hat{H}\delta t/\hbar|\psi_0\rangle - \frac{1}{2\hbar^2}\hat{H}^2\delta t^2|\psi_0\rangle + ... = |\psi_0\rangle + |\delta\psi\rangle \ , \tag{18.22}$$

such that,

$$\langle\psi_0|\psi(\delta t)\rangle \simeq 1-\frac{\imath}{\hbar}\hat{H}\delta t-\frac{1}{2\hbar^2}\hat{H}^2\delta t^2 \quad \text{and} \quad P(\delta t) \simeq 1-\frac{1}{\hbar^2}(\langle\hat{H}^2\rangle_0-\langle\hat{H}\rangle_0^2)\delta t^2 \ . \tag{18.23}$$

In this way we can extract the Zeno time from the above equations, $\tau_Z = \hbar^2/\sqrt{\langle\hat{H}^2\rangle_0 - \langle\hat{H}\rangle_0^2}$. We now make N successive von Neumann measurements within a time t, which leads to a measurement frequency of τ^{-1}. The measurements are conceived as to verify, whether the system is still in its initial state, but each measurement projects our

[9] An analogous experiment can be imagined by a series of Stern-Gerlach measurements of the spin of an atom.

[10] The quantum Zeno effect was often used to justify the physical relevance of the state reduction postulate. It was shown, however, that this postulate is not essential for understanding the quantum Zeno effect [63]. The effect already follows directly from the Schrödinger equation and therefore has a purely dynamical nature. This shows that the projection is a purely mathematical construct without physical reality (see Sec. 18.1.2).

system back to its initial state, from where it has to start the transition process from scratch. Under these conditions, the population of the initial state will evolve like,

$$P^{(N)}(\tau) = P^{(N)}(t/N)^N \ . \tag{18.24}$$

Fig. 18.10 shows the evolution for five measurements separated by time intervals τ. In comparison with the evolution, when no measurements are taken (dashed line), the evolution with measurements inhibits the depletion of the initial state. Extrapolating the number of measurements to infinity, the probability (18.24) converges to 1,

$$\left[1 - \left(\frac{t}{N\tau_Z}\right)^2\right]^N \overset{N\ large}{\longrightarrow} e^{-t^2/N\tau_Z^2} \overset{N\to\infty}{\longrightarrow} 1 \ . \tag{18.25}$$

See Excs. 18.2.4.1 and 18.2.4.2.

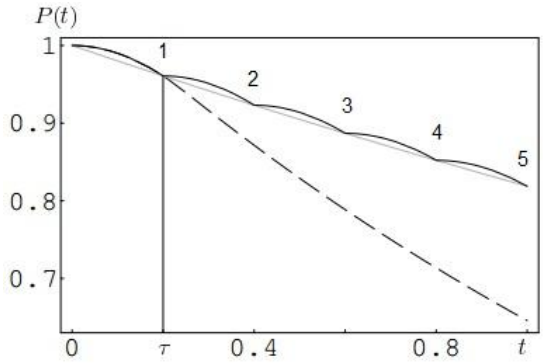

Figure 18.10: Inhibition of the decay of a state by repeated measurements (here $N = 5$). The dashed (solid) line represents the survival probability with (without) measurements. The gray line represents an exponential interpolation function.

Suppression of the evolution of a quantum system due to the quantum Zeno effect was observed experimentally [420] using beryllium ions. Nevertheless, the discussion about the correct interpretation of this effect and its relationship to trivial power broadening is not closed. Some works have even proposed the possibility of an anti-Zeno effect [16, 844], where observation would accelerate the evolution of the system. Currently the quantum Zeno effect is also studied for possible applications in metrology, computation, and quantum information [464].

When the quantum Zeno effect was proposed for the first time, it was considered a paradox: How could an unstable particle never decay, just by being continually observed? And what would happen to Schrödinger's cat, whose live depends on state of the particle? Could we save it from its cruel fate just by observing it?

Another interesting question concerns the quantum nature of the quantum Zeno effect. Is it really non-classical? On one hand, the quantum Zeno effect supposes the complete reduction of the system to an eigenstate. However, we can imagine classical measurements that also reduce the state (such as the above-mentioned measurement of the polarization of a beam of light).

18.2.2 Quantum projection noise

The intrinsic indeterminism of quantum mechanics has serious consequences for metrology. To show this, we consider the example of a system of two levels $|+\rangle$ and $|-\rangle$. This system can be in a superposition state $|\psi\rangle$. The probability [11] to find the system in one of the two states $|\pm\rangle$ is,

$$p_\pm = \langle \hat{P}_\pm \rangle = |\langle \psi | \pm \rangle|^2 = 1 - p_\mp \ , \tag{18.26}$$

where $\hat{P}_\pm$ is the projection operator. The result of a measurement of the population is afflicted by an inherent uncertainty expressed by the variance,

$$(\Delta p_\pm)^2 = \langle \hat{P}_\pm^2 \rangle - \langle \hat{P}_\pm \rangle^2 = \langle \pm|\psi\rangle\langle\psi|\psi\rangle\langle\psi|\pm\rangle - (\langle \pm|\psi\rangle\langle\psi|\pm\rangle)^2 = p_\pm(1-p_\pm) \ . \tag{18.27}$$

In other words, the random projection of the system on the eigenstate basis induces a noise called *quantum projection noise* [12]. This noise inhibits the determination of the probabilities $p_\pm$ in a single measurement. On the other hand, by measuring populations on a sample of N atoms or by repeating the measurement N times with a single atom under identical conditions, we can reduce the uncertainty. The probability of finding an atom r times in the state $|+\rangle$ is [419],

$$\boxed{P_{N,r,+} = \binom{N}{r} p_+^r (1-p_+)^{N-r}} \ . \tag{18.28}$$

The expectation value and variance of this binomial distribution are [419],

$$\bar{r} = \sum_{r=0}^{N} r P_{N,r,+} = N p_+ \quad , \quad (\Delta r)^2 = \sum_{r=0}^{N} (r - N p_+)^2 P_{N,r,+} = N p_+ (1-p_+) \ . \tag{18.29}$$

Thus, the standard deviation decreases with the number of atoms or measurements,

$$\sigma = \frac{\Delta r}{\bar{r}} \sim \frac{1}{\sqrt{N}} \ . \tag{18.30}$$

The increase of knowledge on the population of a two-level system by repeated measurements can be illustrated by a simple simulation exhibited in Fig. 18.11(a). Experiments are performed by comparing p_2 with a random number η. Two outcomes are possible $r = 0, 1$. The histograms narrow as the number of experiments increases. In practice, a measurement is performed using the quantum amplifier method illustrated in Fig. 18.6 [411].

In a sense, the coin behaves as quantum, which is not surprising. It is more surprising that an atom behaves in a quantum way as well, which is the message of Bohr's quantization postulate. However, the atoms have a crucial advantage over coins: they can be entangled with other atoms. Entanglement comes down to a violation of the statistical independence assumption underlying the binomial distribution and all results and consequences derived from it, e.g. the standard quantum limit.

[11] We adopt here the viewpoint of the Copenhagen interpretation of the quantum state reduction, but we note that a discussion based on statistical mixtures described by density matrices gives the same results.

[12] Projection noise can be interpreted as *shot noise*. However, the optical shot noise in photodetectors is generated by the repartition of the field energy into discrete photons, the projection noise is the consequence of the discretization of the electronic excitation levels.

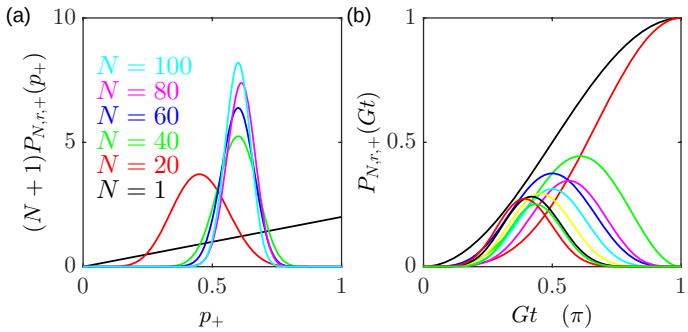

Figure 18.11: (code) (a) Simulation of the increase of knowledge on the population of a two-level system by repeated measurement, $P_{N,r,+}(p_+)/\int_0^1 P_{N,r,+}(p_+)dp_+$. The population of the state $|+\rangle$ was set to $p_+ = 0.2$. (b) Determination of the most likely Rabi pulse length $Gt = 2\arcsin(r/N)^{1/2}$.

Example 107 (*Quantumness and discreteness*): Quantum mechanics is generally associated with phenomena like (i) a wave-like propagation of matter and the ensuing possibility of superposition states, (ii) a discretization of eigenvalue spectra resulting from localization, and (iii) the possibility of entanglement. Criteria (i) and (ii) are, however, not exactly unique to quantum mechanics.
(i)
(ii) We may define discrete states in classical physics, as well. In this sense, quantum projection noise and the quantum Zeno effect are not intrinsically quantum effects. They result from a *discretization* of states, but are not conditioned to the Schrödinger equation. For example, projection noise can be observed when tossing a coin, and the 'quantum' Zeno effect can be observed by repeatedly projecting a laser beam onto one of two polarization axes.

Example 108 (*Spontaneous emission and saturation*): Another more subtle example is the saturation of strongly driven two-level systems. Only 'quantum' emitters are saturable, but their quantumness really only comes from their discrete level structure, so that one might be tempted to consider classical saturable emitters with discrete levels. The problem which arises here is, however, that transitions between orthogonal states are classically forbidden.
What do we mean when we say that the phenomenon of saturation is an intrinsic 'quantum' feature! ? (See example 111.)
An atomic two-level system is 'quantum' in the sense that is has discrete states. On the other hand, a coin also does.
An atom weakly driven by radiation can be described in the linear optics regime like a classical antenna.
Strongly driven, the atom can evolve into a superposition of those two states. The evolution is grasped by Bloch equations. But the evolution of a classical spinning top subject to torque (or a classical electric dipole inside an electric field) is described by the same equations.
We observe Ramsey fringes with a spinning top! So, interference fringes are not

necessarily associated with a wave-like nature of some degree of freedom, light wave or matter wave! However, we need something oscillating (like a wave). In the case of an excited spinning top it is the precessional motion.
In this sense, atomic clocks operate in a classical regime?!? How to recognize quantumness 1.0? In which regime does any classical description fails? Can a spinning top be saturated? Is it really impossible to simulate a classical system exhibiting saturation?
Saturability is not essential, because clock transitions are saturable and yet behave classical. More relevant is spontaneous emission. At weak saturation spontaneous emission can be neglected because the excited state is not populated, which justifies classical description by linear optics. At strong saturation spontaneous emission can be neglected because stimulated emission is overwhelming, which also justifies classical description.

18.2.2.1 Rabi experiments

The method of repeated measurements can be extended to map time-dependent dynamics of the two-level system. Under the influence of a radiation field, the population of the two-level system (which we assume free of spontaneous emission) performs Rabi oscillations, $\rho_{++}(t) = \frac{\Omega^2}{G^2}\sin^2\frac{Gt}{2}$, where $G = \sqrt{\Delta^2+\Omega^2}$. The probability of finding the system in state $|2\rangle$, therefore, varies in time, $p_+(t) = \rho_{++}(t)$, and the binomial distribution (18.28) becomes,

$$P_{N,r,+}(t) = \binom{N}{r}\left(\tfrac{\Omega}{G}\right)^{2N}\sin^{2r}\tfrac{Gt}{2}\cos^{2N-2r}\tfrac{Gt}{2}\ . \tag{18.31}$$

When we increase the number of measurements, $N\to\infty$, this function condenses around a narrow peak at the position $Gt = 2\arcsin\sqrt{r/N}$. The width of the peak evolves like $2\arccos(2^{-1/2N})$. Fig. 18.11(b) shows a simulation demonstrating how repeated measurements gradually pin down the pulse area Ωt.

In summary, even for perfectly efficient population measurements (e.g. using the microwave-optical double resonance method) it is impossible to measure the probability p_+ with a single atom in a single experiment. As such an observation only admits two possible results, 'fluorescence observed' or 'fluorescence not observed', i.e. $\rho_{++}=1$ or $\rho_{++}=0$, a whole range of possible populations between 0 and 1 is excluded. Therefore, a single observation only provides 'partial' information, which can be gradually improved with each consecutive observation.

A presentation on this topic is available here (watch talk).

18.2.2.2 Ramsey experiments

The Ramsey experiment is basically equivalent to the Rabi experiment described above except for an additional rotation in configuration space allowing for the measurement of the phase precession of the coherence between the Ramsey pulses via population spectroscopy. The Ramsey fringes are approximated by $p_+ = 0.5(1+\cos[(\omega-\omega_0)T])$. The interesting magnitude is the frequency uncertainty,

$$\frac{\Delta r}{(\partial r/\partial\omega)|_{(\omega-\omega_0)T=\pi/2}} = \frac{\sqrt{Np_+(1-p_+)}}{N(\partial p_+/\partial\omega)} = \frac{1}{T\sqrt{N}}\ . \tag{18.32}$$

18.2.2.3 Spin squeezing and the Heisenberg limit

The above considerations apply to *independent measurements*. When the atoms are maximally correlated they occupy EPR-like states, $|\psi\rangle = p_+|+++..\rangle + p_-|---..\rangle$, such that it is sufficient to measure a single atom to know the state of all others. This means that the ratio $\Delta r/\bar{r}$ is just the one of a single measurement, but the signal strength and hence the signal-to-noise ratio increase by the factor N. Thus the standard deviation scales with $1/N$ rather than with $1/\sqrt{N}$. This is the so-called *Heisenberg limit*. For Ramsey interferometers we get [869, 97, 110, 576],

$$\frac{\Delta r}{(\partial r/\partial\omega)|_{(\omega-\omega_0)T=\pi/2}} = \frac{1}{TN} \ . \tag{18.33}$$

Example 109 (*Interferometry with condensates*): It is an interesting question, whether condensates can improve metrology and enhance the precision of atomic clocks. The answer is *no*, if we only replace the thermal atomic cloud by a condensate! To see this, we consider an interferometer in configuration space measuring a phase (and therefore a frequency shift) by the method of Ramsey spectroscopy. The states are coupled by a radiation adjusted for $\pi/2$ pulses. The condensate *Fock state* factorizes the Schrödinger equation with the Hamiltonian $\hat{H} = \sum_{i=1}^{N}(H^{(i)} + V_{12}^{(i)})$ into N identical equations for every single atom. The dynamic evolution of this state will be the same as the one for a thermal state. However, this is not true for two Fock state condensates in both entrance channels of the interferometer.
The first radiative beamsplitter divides N_1. This division produces an atom number uncertainty in each state, which come together with a well-defined phase relationship between the two states. By providing at the second port of the interferometer another Fock state N_2, one increases the atom number uncertainty and therefore (because entropy must be conserved in coherent processes) the phase precision. It's a bit like a massive parallel computing for every possible repartition of the populations of both states. Of course the two Fock states cannot be obtained by dividing a single condensate in two in a coherent manner, except if the repartition is measured afterward.
The Fock state is a maximally *spin-squeezed state* (sub-Poissonian statistics). The beam-splitters (which only perform unitary rotations) create starting from the Fock state a quantum entanglement, which is the deeper reason for the improvement of the resolution of the interferometer up the the Heisenberg limit by reducing the *quantum projection noise* [110].

Quantum correlations and spin-squeezed states are the same phenomena seen in different bases. Often the term of *quantum entanglement* is used in an energy bases, while spin squeezing is described in a Dicke state bases.

We may also consider real space interferometers. This allows us to use for creating the Fock states the recently discovered method of transforming BECs into *Mott insulator* states. Of course it is important to use condensates. First of all, we need Fock states, i.e. states with strong on-site quantum correlations with well-defined phase relations between every pair of atoms from the same site. Furthermore, Mott insulators have thus far only been seen with CBEs.

18.2.3 Quantum non-demolition measurements

18.2.4 Exercises

18.2.4.1 Ex: The quantum Zeno effect

Discuss the quantum Zeno effect at the example of a laser beam passing through a birefringent medium. Compare the situations without polarizers and with an infinite number of vertical polarizers.

18.2.4.2 Ex: The quantum Zeno effect

A two-level atom resonantly driven by a laser can be described by the Hamiltonian:

$$H = \begin{pmatrix} 0 & \frac{1}{2}\Omega \\ \frac{1}{2}\Omega & 0 \end{pmatrix} .$$

The solution of the Schrödinger equation gives,

$$|\psi(t)\rangle = e^{-\imath t\hat{H}/\hbar}|\psi_0\rangle = \begin{pmatrix} \cos\frac{1}{2}\Omega t & \imath\sin\frac{1}{2}\Omega t \\ \imath\sin\frac{1}{2}\Omega t & \cos\frac{1}{2}\Omega t \end{pmatrix}\begin{pmatrix} 1 \\ 0 \end{pmatrix}$$

provided the atom is initially in the ground state $\langle\psi_0| = \begin{pmatrix} 1 & 0 \end{pmatrix}$. A measurement of the ground state population can only be done by a projection of the wavefunction, that is, the measurement yields the result $\||1\rangle\langle 1|\psi(t)\rangle\|^2$. What is the final state of the atom,
a. when the ground state population is measured once after an evolution time of $t = \pi/\Omega$;
b. when the ground state population is measured once after n time intervals $t_n = \pi/n\Omega$;
c. when the ground state population is measured n times after evolution times of $t_n = \pi/n\Omega$;
d. when $n \to \infty$.

18.2.4.3 Ex: The quantum Zeno effect

Consider a system described by a time-independent Hamiltonian $\hat{H}$.
a. Calculate the probability $P(t)$ of the system to remain in its initial state $|\Psi_0\rangle$ in the short time approximation, that is, considering until the second-order expression expansion term for the probability. Use the simplification:

$$\tau_z = \frac{\hbar}{\sqrt{\langle\hat{H}^2\rangle - \langle\hat{H}\rangle^2}} ,$$

where the term τ_z is called the Zeno time.
b. If N measurements are performed during a time t, we have the time interval $T = t/N$ between measurements. When a measurement is performed, the system is projected on the initial state and the temporal evolution must start from zero. Thus, after N measurements, the probability of the system remaining in the initial state is given by $[P(T)]^N$. Show that for an infinite number of measurements, $N \to \infty$, the

system remains in the initial state without loss of probability: $[P(T)]^N = 1$. Interpret the result.
c. One of the simplest imaginable systems, a laser-driven two-level system executing Rabi oscillation, is described by the Hamiltonian:

$$\hat{H} = \begin{pmatrix} 0 & \Omega \\ \Omega & 0 \end{pmatrix} .$$

Find the expression for τ_z as a function of the Rabi frequency Ω for the initial state $(1 \;\; 0)^\dagger$.
d. Choosing the evolution time $t = 0.01\tau_z \ll \tau_z$ and performing $N = 5$ measurements during this time interval, how likely is the system to remain in the initial state?
e. Let us now include a decay channel for the state $(0 \;\; 1)^\dagger$ with $\Gamma = 4\gamma$, such as to simulate a system with continuous measurement. The system is initially prepared in the state $(1 \;\; 0)^\dagger$. If we now observe emission by decay, it means that the system *left* the initial state. We now have the effective Hamiltonian:

$$\hat{H} = \begin{pmatrix} 0 & \Omega \\ \Omega & -2\imath\gamma \end{pmatrix} .$$

For this system, the probability amplitude for the initial state is:

$$\langle \Psi_0 | \Psi(t) \rangle = \frac{1}{2}\left(1 + \frac{\gamma}{\Delta}\right) e^{-(\gamma-\Delta)t/\hbar} + \frac{1}{2}\left(1 - \frac{\gamma}{\Delta}\right) e^{-(\gamma+\Delta)t/\hbar} ,$$

with $\Delta = \sqrt{\gamma^2 - \Omega^2}$. For a decay rate $\gamma \ll \Omega$, calculate the probability that the system remains in the initial state. Interpret the result.
Formulas:

$$e^x = 1 + x + \tfrac{x^2}{2} + \mathcal{O}(x^3) \quad , \quad (1-x)^N = 1 - Nx + \mathcal{O}(x^2)$$

$$\cos^2(x) = 1 - x^2 + \mathcal{O}(x^3) \quad , \quad \hat{H} = \begin{pmatrix} 0 & \Omega \\ \Omega & 0 \end{pmatrix} \to e^{-i\hat{H}t/\hbar} = \begin{pmatrix} \cos\frac{\Omega t}{\hbar} & -\imath \sin\frac{\Omega t}{\hbar} \\ -\imath \sin\frac{\Omega t}{\hbar} & \cos\frac{\Omega t}{\hbar} \end{pmatrix} .$$

18.3 Geometric and topological phases

We consider a Hamiltonian $\hat{H}(\mathbf{R}(t))$, which only depends implicitly on time, that is, via some time-dependent parameter $\mathbf{R}(t)$. Then the Hamiltonian evolves by developing a *non-measurable* dynamic phase and additionally accumulates a *geometric phase* (also called *topological phase* or *Berry phase*. This geometric phase, which *depends on the trajectory*, is adiabatically followed in parameter space. Let us consider the time-evolution of a state $|\psi(t)\rangle$ [77],

$$\hat{H}|\psi(t)\rangle = \imath\hbar\partial_t|\psi(t)\rangle \; , \tag{18.34}$$

assuming that at any instant of time the system stays in a eigenstate $|n(\mathbf{R})\rangle$,

$$\hat{H}|n(\mathbf{R})\rangle = E_n(\mathbf{R})|n(\mathbf{R})\rangle \; . \tag{18.35}$$

When $\hat{H}$ moves along a trajectory $C : t \to \mathbf{R}(t)$, then we see from,

$$\boxed{|\psi(t)\rangle = \exp\left[-\tfrac{\imath}{\hbar}\int_0^t E_n(\mathbf{R}(t'))dt'\right]\exp(\imath\gamma_n(C))|n(\mathbf{R}(t))\rangle} \ , \tag{18.36}$$

that, while the first exponential describes the standard dynamical phase, the phase $\gamma_n : C \to \gamma_n(C)$ is not integrable, i.e. γ_n cannot be expressed as a function of $\mathbf{R}(t)$ and is not single-valued meaning that from $\mathbf{R}(T) = \mathbf{R}(0)$ we cannot infer $\gamma_n(T) = \gamma_n(0)$. Substituting (18.36) in (18.34), we find,

$$\hat{H}(\mathbf{R}(t))|\psi(t)\rangle = \imath\hbar|\dot{\psi}(t)\rangle = \left(E_n + \imath\hbar\dot{\gamma}_n(t) + \imath\hbar\dot{\mathbf{R}}(t)\cdot\nabla_{\mathbf{R}}\right)|\psi(t)\rangle \ . \tag{18.37}$$

Since for a particular eigenstate,

$$\hat{H}(\mathbf{R}(t))|n(\mathbf{R}(t))\rangle = E_n|n(\mathbf{R}(t))\rangle \ , \tag{18.38}$$

we infer,

$$\dot{\gamma}_n(t) = \imath\dot{\mathbf{R}}(t)\cdot\langle n(\mathbf{R}(t))|\nabla_{\mathbf{R}}|n(\mathbf{R}(t))\rangle \ . \tag{18.39}$$

The integrated phase change upon evolution of the state from $|\psi(0)\rangle$ to $|\psi(T)\rangle$ around a closed loop is then,

$$\boxed{\gamma_n(C) = \imath\oint_C \langle n(\mathbf{R})|\nabla_{\mathbf{R}}|n(\mathbf{R})\rangle\cdot d\mathbf{R} \equiv \oint_C \vec{\mathcal{A}}(\mathbf{R})\cdot d\mathbf{R}} \ , \tag{18.40}$$

where $\vec{\mathcal{A}}$ is known as *Berry connection*.

The condition of adiabaticity is essential for emergence of geometric phases. The system always remains in an eigenstate (fixed quantum numbers) when we vary parameters of the environment more slowly than all characteristic constants of the system, even when the Hamiltonian is time-dependent (variable eigenvalues).

18.3.1 Properties of the Berry phase

18.3.1.1 Gauge invariance

We have seen in 1.7.4 that the gauge transformation (1.326), $U_{cl}(\xi) = e^{-\imath\xi(\mathbf{R})}$, leaves the Schrödinger equation invariant. Applied to an eigenstate,

$$|\tilde{n}(\mathbf{R})\rangle = e^{-\imath\xi(\mathbf{R})}|n(\mathbf{R})\rangle \ , \tag{18.41}$$

the Berry connection becomes,

$$\tilde{\vec{\mathcal{A}}}(\mathbf{R}) = \imath\langle e^{\imath\xi(\mathbf{R})}n(\mathbf{R})|\nabla_{\mathbf{R}}|e^{-\imath\xi(\mathbf{R})}n(\mathbf{R})\rangle = \vec{\mathcal{A}}(\mathbf{R}) + \nabla_{\mathbf{R}}\xi(\mathbf{R}) \ . \tag{18.42}$$

It is apparently gauge-dependent, so that the local Berry connection $\vec{\mathcal{A}}_n(\mathbf{R})$ can never be physically observable. On the other hand, the Berry phase is,

$$\tilde{\gamma}_n(C) = \gamma_n(C) + \int_C \nabla_{\mathbf{R}}\xi\cdot d\mathbf{R} = \gamma_n(C) + \xi(t) - \xi(0) \ . \tag{18.43}$$

For a *closed loop*, continuity of the gauge field requires $\xi(T) - \xi(0) = 2\pi m$. Hence, up to an integer multiple of 2π, *closed loop Berry phases remain gauge-invariant* under arbitrary gauge transformation and may be related to physical observables.

18.3.1.2 Berry curvature

It is often advantageous to convert the path integral (18.40) into a surface integral using Stokes' theorem. Defining the Berry curvature as,

$$\vec{\mathcal{V}}_n(\mathbf{R}) \equiv \nabla_{\mathbf{R}} \times \mathbf{A}_n(\mathbf{R}) \ , \tag{18.44}$$

we obtain,

$$\gamma_n(C) = \iint_S \vec{\mathcal{V}}_n(\mathbf{r}) \cdot d\mathbf{S} \ . \tag{18.45}$$

The Berry curvature can be expressed as [77],

$$\mathbf{V}_n(\mathbf{r}) = \mathrm{Im} \sum_{m \neq n} \frac{\langle n(\mathbf{r})|\nabla_{\mathbf{r}} \hat{H}(\mathbf{r})|m(\mathbf{r})\rangle \cdot \langle m(\mathbf{r})|\nabla_{\mathbf{r}} \hat{H}(\mathbf{r})|n(\mathbf{r})\rangle}{(E_m(\mathbf{r}) - E_n(\mathbf{r}))^2} \ . \tag{18.46}$$

This will be shown in Exc. 18.3.3.1.

Example 110 (*Geometric phase in a two-level system*): We consider the following state [686],

$$n_\pm(\mathbf{r}) = \cos\theta|g\rangle \pm e^{\pm \imath\phi} \sin\theta|e\rangle \ .$$

Now, we want to calculate the geometric phase,

$$\gamma_\pm = \oint_C \imath\langle n_\pm(\mathbf{r})|\nabla_{\mathbf{r}}|n_\pm(\mathbf{r})\rangle d\mathbf{r} \ .$$

Applying the gradient in spherical coordinates,

$$\nabla_{\mathbf{r}} = \hat{\mathbf{e}}_\theta \frac{1}{r}\frac{\partial}{\partial\theta} + \hat{\mathbf{e}}_\phi \frac{1}{\mathbf{r}\sin\theta}\frac{\partial}{\partial\phi} + \hat{\mathbf{e}}_r \frac{\partial}{\partial r}$$

to the function $|n_+\rangle$, we find,

$$\nabla_{\mathbf{r}}|n_+(\mathbf{r})\rangle = -\hat{\mathbf{e}}_\theta \frac{\sin\theta}{r}|g\rangle + \hat{\mathbf{e}}_\theta \frac{e^{\pm\imath\phi}\cos\theta}{\mathbf{r}}|e\rangle + \hat{\mathbf{e}}_\phi \frac{\imath e^{\imath\phi}}{r}|e\rangle \ ,$$

and,

$$\imath\langle n_\pm(\mathbf{r})|\nabla_{\mathbf{r}}|n_\pm(\mathbf{r})\rangle = \imath\hat{\mathbf{e}}_\phi \frac{\imath\sin\theta}{r} \ .$$

Finally,

$$\gamma_+ = \oint_C \frac{-\sin\theta}{r}\hat{\mathbf{e}}_\phi d\mathbf{R} = \oint_C \frac{-\sin\theta}{r} r\sin\theta d\phi = \oint_C \sin^2\theta\dot{\phi}dt \ .$$

Example 111 (*Berry phase on the Bloch sphere*): We consider the example of a two-level system without decay described by the Bloch vector $\vec{\varrho}$ defined in (16.126) and whose evolution is govern by the Hamiltonian (16.129),

$$\hat{H} = \tfrac{1}{2}\mathbf{G}\cdot\sigma \equiv \begin{pmatrix} \mathfrak{Re}\,\Omega \\ \mathfrak{Im}\,\Omega \\ \Delta/2 \end{pmatrix} \begin{pmatrix} \sigma_x \\ \sigma_y \\ \sigma_z \end{pmatrix} \ .$$

Now, we change the parameters regrouped in $\mathbf{G}$ adiabatically. It is easy to see that,

$$E_\pm = \pm R/2 \qquad \text{and} \qquad \nabla_{\mathbf{G}} \hat{H} = \vec{\sigma}/2 \ ,$$

such that,

$$\mathbf{V}_n(\mathbf{r}) = \mathrm{Im} \frac{\langle n_\pm(\mathbf{G}) | \nabla_{\mathbf{G}} \hat{H}(\mathbf{G}) | n_\mp(\mathbf{G}) \rangle \cdot \langle n_\mp(\mathbf{G}) | \nabla_{\mathbf{G}} \hat{H}(\mathbf{G}) | n_\pm(\mathbf{G}) \rangle}{(E_+(\mathbf{G}) - E_-(\mathbf{G})^2} = \pm \frac{\mathbf{G}}{2G^3} \ .$$

The geometric phase accumulated on a closed loop $C = \partial S$ surrounding an area $S = 4\pi\Omega_S$ on the surface of the Bloch sphere is,

$$\gamma_n(C) = \mp \oint_C \frac{dS}{2G^2} = 4\pi \mp \oint_C dR = \mp \frac{\Omega_S(C)}{2}$$

and thus equal to half the enclosed solid angle Ω_S. The Berry phase can be measured in Ramsey experiments, as discussed in Exc. 18.3.3.2.

18.3.1.3 Generalization of the Berry phase according to Aharonov

We will now drop the conditions imposed to the Hamiltonian with regard to its adiabatic behavior and request that the state must be a eigenstate [161]:

$$\hat{H}|\psi(t)\rangle = \imath\hbar|\dot{\psi}(t)\rangle \ . \tag{18.47}$$

A process is cyclic, when there is a τ, such that,

$$|\psi(\tau\rangle = e^{\imath[f(\tau)-f(0)]}|\psi(0)\rangle \ . \tag{18.48}$$

Defining the space of radii by $|\tilde{\psi}(t)\rangle = e^{-\imath f(t)}|\psi(t)\rangle$, we obtain,

$$|\tilde{\psi}(\tau)\rangle = |\tilde{\psi}(0)\rangle \ , \tag{18.49}$$

and from the Schrödinger equation we obtain,

$$f(t) - f(0) = -\tfrac{1}{\hbar} \int_0^t \langle \psi(t)|\hat{H}(t)|\psi(t)\rangle dt + \int_0^t \langle \tilde{\psi}(t)|\imath \tfrac{d}{dt}|\tilde{\psi}(t)\rangle \equiv \delta + \beta \ . \tag{18.50}$$

Therefore, in the space of radii we have a closed curve:

$$\begin{array}{c} C : [0,\tau] \longrightarrow \psi(t) \in \mathcal{H} \\ \downarrow e^{-\imath f(t)} \\ C' : [0,\tau] \longrightarrow \tilde{\psi}(t) \in \mathcal{P} \ . \end{array} \tag{18.51}$$

The dynamic phase δ can be zeroed by an appropriate choice of $\hat{H}(t)$, but not the topological phase β. β does not depend on $\hat{H}(t)$, but is a geometric property of the curve, which projects $\mathcal{H}$ onto $\mathcal{P}$. In contrast to $e^{\imath\beta}$, the phase β is only determined modulo $2\pi n$.

18.3.2 Aharonov-Bohm effect

A particular case for topological phases is the *Aharonov-Bohm effect*, which we will discuss in the following. The only observables of electromagnetism are the forces of Coulomb and Lorentz which, in the theory of electrodynamics, are described by electric and magnetic fields. Electromagnetic potentials can be introduced to simplify calculations, but they are not observables with a physical reality. In contrast, in quantum mechanics, electromagnetic potentials are more fundamental than electromagnetic fields. This is demonstrated by the Aharonov-Bohm effect.

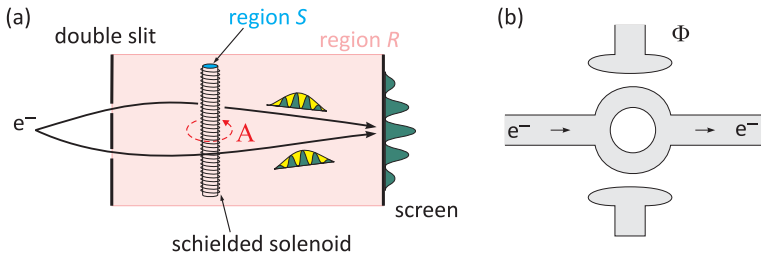

Figure 18.12: (a) Scheme for measuring the Aharonov-Bohm effect. The electrons propagate as wavepackets whose centers-of-mass are not subject to forces, but whose de Broglie waves are phase-shifted by the vector potential. (b) Aharonov-Casher effect: the electrodes Φ do not produce electric fields inside the conductors; even so, one observes constructive or destructive interference at the output of the interferometer, depending on the applied potential.

The idea of this effect is schematized in Fig. 18.12. An electron beam is coherently divided into two arms (e.g. by a double slit) passing both sides of an infinitely extended and perfectly shielded solenoid. In this way the magnetic field $\vec{\mathcal{B}}$ vanishes in the region outside the solenoid, but there must exist nonetheless a potential vector $\mathbf{A}$, because we observe on the screen an interference pattern of the two arms of the electronic interferometer. When pass a current through the solenoid, we observe a displacement of the interference pattern.

18.3.2.1 Aharonov-Bohm effect and gauge transformation

Let R and S be two disconnected spatial regions. Suppose that the electric and magnetic fields are kept zero in region R. Then, it is *classically impossible* to measure some change in the dynamics of a body confined to the region R resulting from a change of the magnetic field confined to the region S. The Aharonov-Bohm effect shows that the *opposite* is true: Electrons in the magnetic field-free region R do sense magnetic field fluxes in a region S, despite the regions R and S having no intersection!

In the classical theory of electromagnetism, in a region of empty space (except for electric charges and electric currents), the electric $\vec{\mathcal{E}}(\mathbf{r},t)$ and magnetic fields $\vec{\mathcal{B}}(\mathbf{r},t)$ are related to the electric charge $\rho(\mathbf{r},t)$ and current densities $\mathbf{j}(\mathbf{r},t)$ according to the *Maxwell equations*. When we know for a spatial region the sources ρ and $\mathbf{j}$ and the

boundary conditions that the fields $\vec{\mathcal{E}}$ and $\vec{\mathcal{B}}$ must fulfill, we can determine the fields as solutions of Maxwell's system of partial differential equations.

In classical electrodynamics, observed from some inertial frame, the electromagnetic force $\mathbf{F}_{\text{em}}$ acting on a point-like body with charge q, at position $\mathbf{r}$, and with velocity $\mathbf{v}$, is given by the Lorentz force:

$$\mathbf{F}_{\text{em}}(\mathbf{r}(t),t) = q\vec{\mathcal{E}}(\mathbf{r}(t),t) + q\mathbf{v}(t)\times\vec{\mathcal{B}}(\mathbf{r}(t),t)\ . \tag{18.52}$$

Electrodynamic theory affirms the existence of two functions $\Phi(\mathbf{r},t)$ and $\mathbf{A}(\mathbf{r},t)$, such that,

$$\vec{\mathcal{B}}(\mathbf{r},t) = \nabla\times\mathbf{A}(\mathbf{r},t) \qquad \text{and} \qquad \vec{\mathcal{E}}(\mathbf{r},t) = -\nabla\Phi(\mathbf{r},t) - \frac{\partial\mathbf{A}(\mathbf{r},t)}{\partial t}\ . \tag{18.53}$$

Thus, we can use the equations (18.53) to rewrite the Maxwell equations.

The so-defined potentials Φ and $\mathbf{A}$ are not unique, but any Φ and $\mathbf{A}$ leading to the same fields $\vec{\mathcal{E}}$ and $\vec{\mathcal{B}}$, and thus to the same physics, are equivalent. We will, however, fix Φ and $\mathbf{A}$ adopting an additional condition that must be obeyed, i.e. we will adopt a particular gauge. For the discussion of the Aharonov-Bohm effect, we will adopt the *Lorentz gauge* defined by,

$$\nabla\cdot\mathbf{A}(\mathbf{r},t) + \frac{1}{c^2}\frac{\partial\Phi(\mathbf{r},t)}{\partial t} = 0\ , \tag{18.54}$$

where c is the propagation velocity of light in vacuum.

18.3.2.2 Equation for quantum particle exposed to a vector potential A

Assume a particle (without spin) of mass m and charge q, whose wavefunction is confined to a region R (connected by paths). We demand $\Phi = 0$ and $\vec{\mathcal{E}} = 0 = \vec{\mathcal{B}}$, but we let $\mathbf{A} \neq 0$, that is, $\nabla\times\mathbf{A}(\mathbf{r},t) = 0$. Note that along with (18.53) this forces $\mathbf{A}$ to be stationary. According to quantum mechanics the wavefunction Ψ of the particle must obey the following Schrödinger equation:

$$\frac{1}{2m}\left(\frac{\hbar}{\imath}\nabla - q\mathbf{A}(\mathbf{r})\right)^2\Psi(\mathbf{r},t) + V(\mathbf{r})\Psi(\mathbf{r},t) = \imath\hbar\frac{\partial\Psi(\mathbf{r},t)}{\partial t}\ . \tag{18.55}$$

In (18.55) the potential vector $\mathbf{A}$ is present, even if ϕ, $\vec{\mathcal{E}}$, and $\vec{\mathcal{B}}$ are kept zero throughout the region R.

Since the rotation $\mathbf{A}$ vanishes in R, considering that the integral can be calculated for any path contained in R that is deformable to a (arbitrarily chosen) point $O \in R$, we can define the following scalar field:

$$g(\mathbf{r}) \equiv \frac{q}{\hbar}\int_0^{\mathbf{r}}\mathbf{A}(\mathbf{x})\cdot d\mathbf{x}\ . \tag{18.56}$$

From (18.56) we have:

$$\nabla g(\mathbf{r}) = \frac{q}{\hbar}\mathbf{A}(\mathbf{r})\ . \tag{18.57}$$

Now, we have already shown in Sec. 1.7.4, that the wavefunction

$$\psi(\mathbf{r},t) \equiv e^{-\imath g(\mathbf{r})}\Psi(\mathbf{r},t) \tag{18.58}$$

corresponds to the gauge transform (1.326) and, given the condition (1.325), satisfies the same Schrödinger equation as $\Psi(\mathbf{r},t)$. We showed this explicitly in Exc. 18.3.3.3. Thus, the presence of a potential vector in the region R, even in the absence of fields, causes a phase shift $e^{ig(\mathbf{r})}$ of the wavefunction. An interesting issue studied in Exc. 18.3.3.4 is, whether this implies that the freedom of choice of the gauge field is lost.

Example 112 (*Observation of the Aharonov-Bohm effect*): Imagine an electron beam passing through a double-slit, as shown in Fig. 18.12(a). The electronic wavefunction diffracts through both slits, which produces an interference pattern on a subsequent screen. Now, just after the double-slit, in the shade of the region separating the two slits, we place an ideal infinitely long solenoid traversed on its axis by a constant, however, adjustable flux of magnetic field. The magnetic (and also the electric) field of the solenoid is confined to a region S, and the confinement can be guaranteed, e.g. with layers of shielding materials, including superconductors. On the other hand, the wavefunctions of the electrons are manifestly zero in this S region. In the R region, where the electronic wavefunction may be non-zero, the fields are kept zero. R and S have no overlap, both R and S are *separately* connected by paths.
We will show that the flux of the magnetic field in S can be measured through the electronic dynamics in the region R, although the electron is *never* in the region S, but confined to the field-free region R. This is the Aharonov-Bohm (magnetic) effect.
The field $\vec{\mathcal{B}}$ in the inner region of the solenoid is given by (I is the electric current in the wire, N is the density of windings),

$$\vec{\mathcal{B}}(\mathbf{r},t) = \mu_0 I N \hat{\mathbf{e}}_z \ .$$

Outside the solenoid, that is, for $\rho > a$, we have,

$$\mathbf{A}(\mathbf{r},t) = \frac{\Phi_B}{2\pi\rho}\hat{\mathbf{e}}_\phi \ ,$$

where $\Phi_B = \pi a^2 B(0,t)$ is the magnetic field flux $\vec{\mathcal{B}}$ through the cross section of the solenoid.
At a point $\mathbf{r}_{sim}$ of the screen, located in the plane of symmetry of the system, we calculate $g(\mathbf{r}_{sim})$ from Eq. (18.56) for two different paths: both starting at the source and ending at the screen, but one going through the left slit, the other through the right slit:

$$g(\mathbf{r}_{sim}) = \frac{q}{\hbar}\int_0^{\mathbf{r}_{sim}} \mathbf{A}(\mathbf{x})\cdot d\mathbf{x} = \frac{q\Phi_B}{2\pi\hbar}\int \left(\frac{1}{\rho}\hat{\phi}\right)\cdot(\rho\hat{\phi}d\phi) = \pm\frac{q\Phi_B}{2\hbar} \ .$$

The + sign means, that the integration was done in the sense parallel to $\mathbf{A}$, and thus in the sense of I in the solenoid. The sign - holds for the other integration path. The phase difference, at point $\mathbf{r}_{sim}$, between these two paths will be:

$$\delta = \frac{q\Phi_B}{\hbar} \ .$$

That is, the phase difference (experimentally observable via a shift of the interference pattern) is directly proportional to the magnetic field flux $\vec{\mathcal{B}}$, even though the wavefunction is zero in the region S, where the $\vec{\mathcal{B}}$ field is confined.
Let us also imagine another situation: Instead of an electron source producing

a beam, let us confine an electronic wavefunction on a closed path circling the solenoid at a distance b, but inside the region of R. That is, the electron follows a field line $BA \propto \hat{\mathbf{e}}_\phi$. Then it can be shown, that the flow Φ_B removes the degeneracy of the energy levels of the electron:

$$E_n = \frac{\hbar^2}{2mb}\left(n - \frac{q\Phi_B}{2\pi\hbar}\right)^2 ,$$

with integer, that is, $n = 0, \pm 1, \pm 2, ...$ [344].

The *Aharonov-Bohm phase is a (topological) Berry-phase* [77]. This is shown explicitly in Exc. 18.3.3.5.

18.3.2.3 Generalizations of the Aharonov-Bohm effect

The Aharonov-Bohm effect can be generalized to the internal degrees of freedom of a single atom, that is, from real space to configuration space. Let us imagine a Mach-Zehnder interferometer, where one of the arms crosses a constant homogeneous field region. The corresponding Lorentz force $\mathbf{F} = \int d^3r\ \rho(\mathbf{r})\vec{\mathcal{E}}(\mathbf{r}) + \mathbf{j}(\mathbf{r}) \times \vec{\mathcal{B}}(\mathbf{r})$ vanishes, but the de Broglie wave undergoes a phase shift $\chi = \int \hat{H}_{\text{int}} dt$:

scalar potentials		
$\chi = -\int e\phi dt$	$\nabla\phi = 0$	for e^-
$-\int \mathbf{d} \cdot \vec{\mathcal{E}} dt$	$\nabla \times \vec{\mathcal{E}} = \nabla \cdot \vec{\mathcal{E}} = 0$	Mg, Yb^+
$-\int \vec{\mu} \cdot \vec{\mathcal{B}} dt$	$\nabla \times \vec{\mathcal{B}} = \nabla \cdot \vec{\mathcal{B}} = 0$	n, Yb^+
vector potentials		
$-\oint e\mathbf{A} d\mathbf{r}$	$\nabla \times \mathbf{A} = 0$	e^-, (ABE)
$-\oint d \times \vec{\mathcal{B}} d\mathbf{r}$		?
$-\oint \mu \times \vec{\mathcal{E}} d\mathbf{r}$		n, Ca, (ACE)

Example 113 (*Topological phase in configuration space*): We consider a temporal Ramsey experiment with a single trapped ion by exciting a hyperfine transition. Between the pulses we apply a magnetic field for a time t. The accumulated phase will be $\phi = (\vec{\mu} \cdot \vec{\mathcal{B}}/\hbar)t$. This phase corresponds to the precession of the dipole moment excited by the first Ramsey pulse. The phase can be interpreted in analogy to Aharonov-Bohm effect, considering that 1. the magnetic field is homogeneous, and 2. despite this fact still acts on the spin, not exerting a force, but causing a phase shift.

18.3.3 Exercises

18.3.3.1 Ex: Derivation of the Berry curvature

Derive the expression (18.46) for the Berry curvature.

18.3.3.2 Ex: Measurement of the Berry phase in a two-level system

Discuss how the Berry phase in a two-level system can be measured via a Ramsey experiment.

18.3.3.3 Ex: The Aharonov-Bohm effect as a gauge transform

Show explicitly that the wavefunction transformed by a gauge transformation (18.58) satisfies the Schrödinger equation.

18.3.3.4 Ex: Aharonov-Bohm effect and gauge transformation

The phase of the interference pattern in the Aharonov-Bohm effect is fixed by the magnetic flux through the solenoid. Does that mean, that we lose the freedom of choosing an arbitrary gauge potential?

18.3.3.5 Ex: Aharonov-Bohm effect as a geometric phase

Show that the Aharonov-Bohm effect represents a particular case of a geometric phase.

18.4 Further reading

P.L. Saldanha et al., *Inconsistency of a realistic interpretation of quantum measurements a simple example* [DOI]

B. Hacker et al., *Deterministic creation of entangled atom-light Schrödinger-cat states* [DOI]

18.4.1 on quantum jumps

A. Schenzle et al., *Macroscopic quantum jump in a single atom* [DOI]

A. Schenzle et al., *Possibility of quantum jumps* [DOI]

W. Nagourney et al., *Shelved Optical Electron Amplifier: Observation of Quantum Jumps* [DOI]

P. Zoller et al., *Quantum jumps in atomic systems* [DOI]

T. Erber et al., *Resonance Fluorescence and Quantum Jumps in Single Atoms, Testing the Randomness of Quantum Mechanics* [DOI]

J. Dalibard et al., *Wave-Function Approach to Dissipative Processes in Quantum Optics* [DOI]

K. Mølmer et al., *Monte-Carlo Wave-Function Method in Quantum Optics* [DOI]

Z. K. Minev et al., *To catch and reverse a quantum jump mid-flight* [DOI]

18.4.2 on projection noise

R.H. Dicke, *Coherence in Spontaneous Radiation Processes* [DOI]

M. Kitagawa et al., *Spin-squeezed states* [DOI]

W.M. Itano et al., *Quantum projection noise: Population fluctuations in two-level systems* [DOI]

D.J. Wineland et al., *Squeezed atomic states and projection noise in spectroscopy* [DOI]

Ph. Bouyer et al., *Heisenberg-Limited Spectroscopy with Degenerate Bose-Einstein Gases* [DOI]

R. Huesmann et al., *Single-Atom Interferometry* [DOI]

L. Salvi et al., *Squeezing on Momentum States for Atom Interferometry* [DOI]

18.4.3 on geometric phases

M.V. Berry, *Quantal Phase Factors Accompanying Adiabatic Changes* [DOI]

Y. Aharonov et al., *Significance of Electromagnetic Potentials in the Quantum Theory* [DOI]

E. Cohen et al., *Geometric phase from Aharonov-Bohm to Pancharatnam-Berry and beyond* [DOI]

Chapter 19

Nonlinear optics

The discipline of *nonlinear optics* studies phenomena that occur as a consequence of modifications of the optical properties of materials by the presence of light. Such modifications are appreciable only, when the interacting light is sufficiently intense, i.e. of the order of the interatomic electric field,

$$\mathcal{E}_{\rm at} = \frac{e^2}{4\pi\varepsilon_0 a_B^2} \simeq 5.14 \cdot 10^{11}\,{\rm V/m}\ , \tag{19.1}$$

which explains that nonlinear effects could only be studied properly after the advent of the laser.

In general, light-matter interaction is expressed through the relationship between the polarization induced in the medium, $\mathcal{P}(\omega)$, with the optical light field, $\mathcal{E}(\omega)$. In linear optics this relation can be expressed as,

$$\tilde{\mathcal{P}}(\omega) = \varepsilon_0 \chi(\omega)\tilde{\mathcal{E}}(\omega)\ . \tag{19.2}$$

But in the perturbative regime of non-linear optics this expression must be generalized to a series of powers of the electric field,

$$\tilde{\mathcal{P}}(\omega) = \varepsilon_0[\chi^{(1)}(\omega)\tilde{\mathcal{E}}(\omega) + \chi^{(2)}(\omega)\tilde{\mathcal{E}}^2(\omega) + \chi^{(3)}(\omega)\tilde{\mathcal{E}}^3(\omega) + ...]\ , \tag{19.3}$$

so that higher order polarization terms, $\mathcal{P}^{(n)}(\omega) = \varepsilon_0\chi^{(n)}\mathcal{E}^N(\omega)$, are considered. Therefore, the phenomena are non-linear in the sense that they depend non-linearly on the optical field applied to the material. In a more complete treatment, in terms of the optical properties of materials, $\tilde{\mathcal{P}}$ and $\tilde{\mathcal{E}}$ are vector fields and the electric susceptibility is a tensor. However, to simplify the treatment, we consider the fields as scalars and $\chi^{(n)}$ as constants independent of the frequency ω.

Examples of non-linear optical phenomena are: parametric processes of sum and difference frequency generation, as shown in Fig. 19.1, optical parametric oscillation, and the dependence of the refractive index with the optical intensity. Examples of non-parametric processes are: multi-photonic absorption, stimulated Raman scattering, and saturated absorption. In the latter example, the absorption coefficient of the material decreases with increasing light intensity:

$$\alpha = \frac{\alpha_0}{1 + I/I_s}\ . \tag{19.4}$$

Saturated absorption is an example where a perturbative approach is not capable of providing good results, and its most reliable description is given by the approximation of a two-level quantum system.

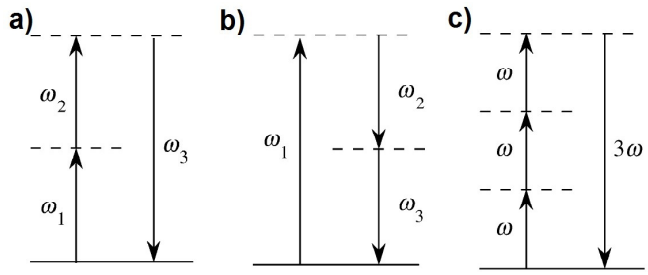

Figure 19.1: Parametric (a) sum and (b) difference frequency generation. (c) Third harmonic generation.

It is also important to emphasize that parametric processes are those, in which the initial and final quantum states of a system are identical. Consequently, the population of an initial state can only be moved to a virtual state, different in energy by ΔE, for a short time lapse limited by Heisenberg's uncertainty principle ($\hbar/\Delta E$). Nonparametric processes are those involving population transfer between real energy levels, eigenstates of the system's Hamiltonian. In terms of the electrical susceptibility of the medium, $\chi^{(n)}$ is a real quantity for parametric and an imaginary one for non-parametric processes.

19.1 The nonlinear optical susceptibility

The description of nonlinear optical phenomena can be approached from a variety of perspectives, most of which are semi-classical in the sense that the matter is treated quantum mechanically, while the electromagnetic radiation is treated classically. One possible description explores the wave nature of the radiation, using Maxwell's equations to describe the generation of new spectral components by the nonlinear terms of the polarization. More generally, this description explains how different frequencies can be coupled through their nonlinear interaction with the material. It can be shown that the electromagnetic wave equation in the nonlinear regime is,

$$\nabla\tilde{\mathcal{E}} - \frac{n^2}{c^2}\frac{\partial^2}{\partial t^2}\tilde{\mathcal{E}} = \frac{1}{\varepsilon_0 c^2}\frac{\partial^2}{\partial t^2}\tilde{\mathcal{P}} \ , \tag{19.5}$$

such that $\tilde{\mathcal{P}} = \tilde{\mathcal{P}}^{(1)} + \tilde{\mathcal{P}}^{(\mathrm{nl})}$. In this view, $\tilde{\mathcal{P}}^{(\mathrm{nl})}$ acts as a source of frequencies, several of that are incident.

Although electromagnetic theory is capable of explaining several aspects of nonlinear optics, it is the quantum description that provides explicit expressions for nonlinear optical susceptibility. There are three main motivations for obtaining quantum expressions:

- They reveal a functional form of the nonlinear optical susceptibility and show how they depend on microscopic parameters of the material, such as transition dipole moments and atomic energy levels.
- They exhibit the intrinsic symmetries of nonlinear susceptibility.

- They can be used to calculate numerically the values of nonlinear susceptibilities.

The numerical predictions of quantum theory for nonlinear optical susceptibilities are particularly accurate in the case of atomic vapors, because the atomic parameters of these are known with sufficient precision for the theory to provide reliable results.

Two quantum mechanical formalisms can be used for the calculation of nonlinear optical susceptibilities. Perturbation theory is used to make predictions on non-resonant systems, i.e. situations where the photon energy is much smaller than the energy separation between two eigenstates of the material. On the other hand, when the interactions are close to resonance, such that it becomes necessary to include relaxation processes, the state-density matrix formalism is used. Although this approach is more complex, it provides better results.

19.1.1 Exercises

19.2 Quantum interference

We have seen earlier that a *dark resonance* in Λ-shaped three-level systems create superposition states between the two stable ground states which allow the adiabatic elimination of the excited state. Dark resonances may be understood as destructively interfering excitation paths at Raman-coherences between inneratomic transitions. Quantum interference is at the origin of various other phenomena which are discussed in the following sections.

19.2.1 Lasing without inversion

The question of the necessity of population inversion to construct a laser has been the subject of debates. Indeed, even an ordinary two-level system may exhibit gain with a small frequency interval [592] known as *Mollow gain*. Lasing without population inversion may also result from a splitting of emission and absorption spectra caused by atomic recoil as in the example of CARL [101].

Various schemes of a *laser without inversion* (LWI) have been proposed. Here is one of them [619]. We will discuss an example in Exc. 19.2.3.1.

19.2.2 Brillouin scattering

Stimulated scattering of phonons is called *stimulated Brillouin scattering* (SBS). Like *Raman-scattering* (SRS) Brillouin-scattering is a limiting factor for the transmission efficiency in optical fibers. It is used in acousto-optic modulators (AOM). While SBS is based on the exchange of phonons between atoms bound in crystals, SRS is based on the exchange of phonons between atoms bound in molecules.

Raman-scattering (in a restricted historical sense) is very common technique of molecular spectroscopy. The process is Rayleigh-scattering at an electronic transition, but towards a different vibrational substate. Brillouin-scattering also involves the motional state of the scatterer, but its center-of-mass motion rather than some internal degree of freedom. It is also related to *polariton scattering* in solids, which produces optical phonons, rather than acoustic phonons.

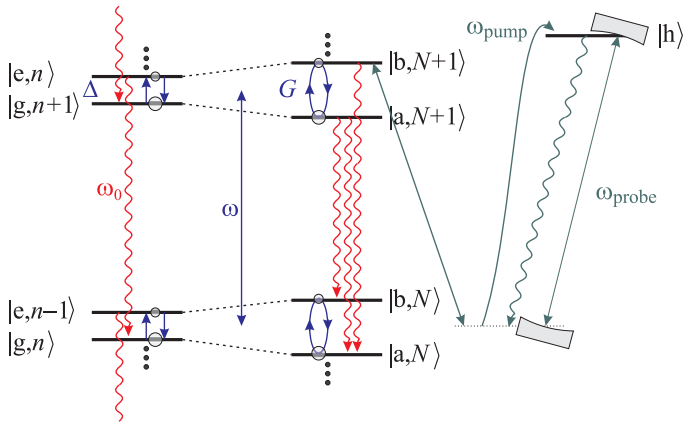

Figure 19.2: Dressed states level scheme for LWI. Quantum interference between two possible Raman transitions (green) leads to a cancellation of the ground state population. When the upper level $|h\rangle$ is incoherently pumped, gain can be reached for a weak probe field. Inserting the atoms in a cavity one can reach lasing [408].

If a strong electromagnetic field (pump laser) is irradiated into a medium (typically a crystal or a fluid) it produces a time-varying *electrostrictive strain*, which can be understood as the reaction force of particles dislocated from their equilibrium position. The strain is quantized into *phonons* and may drive a sound wave. This wave modulates the optical dielectric constant ε and thus create a periodic polarization $\vec{\mathcal{P}}$. This polarization may now interact with the incident electric field (pump laser $\omega_2, \mathbf{k}_2, \vec{\mathcal{E}}_2$). The resulting energy exchange can, under suitable circumstances, lead to simultaneous amplification of a probe wave $(\omega_2, \mathbf{k}_2, \vec{\mathcal{E}}_2)$ and a sound wave $(\omega_s, \mathbf{k}_s, u_s)$.

Let us consider a $1D$ geometry, $\mathbf{k}_j = k_j \hat{\mathbf{e}}_z$ and $\vec{\mathcal{E}}_j = \mathcal{E}_j \hat{\mathbf{e}}_x$. (More general geometries can be considered [892]). The pump field $\mathcal{E}_2(t,z)$ causes a strain $\partial u_s/\partial z$ via longitudinal displacements $u_s(z,t)$ of test volumes. This strain produces a modulation of ε by $\delta\varepsilon = -\gamma \partial u_s/\partial z$, where γ is the strain coefficient (or coupling strength). The modulation of the dielectric constant $\delta\varepsilon$ now modulates the interaction energy $\delta U = -\frac{1}{2}\delta\varepsilon \mathcal{E}_2$, which exerts work $p\partial u_s/\partial z = \delta U$ against the pressure p. The pressure modulation creates a force $F = -\partial p/\partial z = \frac{1}{2}\gamma \partial \mathcal{E}_2^2/\partial z$. We can now set up a Fokker-Planck type force equation,

$$\rho \frac{\partial^2 u_s}{\partial t^2} = \frac{\gamma}{2}\frac{\partial \mathcal{E}_2^2}{\partial z} - \eta \frac{\partial u_s}{\partial t} + T \frac{\partial^2 u_s}{\partial z^2} \ , \tag{19.6}$$

where ρ is the mass density, T the elastic constant and η acoustic dissipation. $v_s \equiv \omega_s/k_s = \sqrt{T/\rho}$ is the free propagation velocity of sound. Simultaneously we know that the light wave propagates like,

$$\frac{\partial^2 \mathcal{E}_j}{\partial z^2} + \mu\varepsilon \frac{\partial^2 \mathcal{E}_j}{\partial t^2} + \mu \frac{\partial^2 \mathcal{P}_{NL,j}}{\partial t^2} \ . \tag{19.7}$$

We insert the ansatz $\mathcal{E}_j(t,z) = \frac{1}{2}\mathcal{E}_{0j}(z) e^{\imath(\omega_j t - k_j z)} + c.c.$ and $u_s(t,z) = \frac{1}{2} u_{0s}(z) e^{\imath(\omega_s t - k_s z)} + c.c.$ first into the above equations. We use the approximations $k_s^2 u_s \gg d^2 u_s/dz^2 \ll$

$k_s du_s/dz$ and $|\partial(\mathcal{E}_2\mathcal{E}_1^*)/\partial z| \ll |k_s\mathcal{E}_2\mathcal{E}_1^*|$ and focus on the real parts. Assuming that the pump field $\mathcal{E}_2$ is undepleted, stimulated Brillouin-scattering is described by the following set of equations,

$$\begin{aligned}\frac{d\mathcal{E}_1^*}{dz} &= -\frac{\alpha}{2}\mathcal{E}_1^* - \frac{\gamma k_1 k_s}{4\varepsilon_1}\mathcal{E}_2^* u_s \\ \frac{du_s}{dz} &= -\frac{\eta}{2\rho v_s}u_s - \frac{\gamma}{8\rho v_s^2}\mathcal{E}_2\mathcal{E}_1^* \ .\end{aligned} \tag{19.8}$$

Here ρ is the mass density, optical losses are described by α, and η is the dissipation constant for phonons. $\varepsilon_1 \approx \varepsilon_0$. The scattering satisfies the *Bragg condition* $\mathbf{k}_2 - \mathbf{k}_1 = \mathbf{k}_s$. The above equations describe *exponential gain* and *threshold behavior* for $\mathcal{E}_1$ and u_s. For backscattering $\mathbf{k}_1\mathbf{k}_2 = -k_1k_2$ the rate of growth for the probe $\mathcal{E}_1$ is influenced by the values of $\mathcal{E}_1$ lying ahead in the direction $\mathbf{k}_1$. This is by virtue of the sound beam propagating in opposite direction to E_1 and provides the positive feedback being at the origin of exponential gain.

The equations are reminiscent to the CARL equations. The difference is the nature of the mediating force field: The CARL force is mediated by photons. The mediation is thus instantaneous. Photons do not require a medium in order to propagate. In contrast, the Brillouin-gain is mediated by phonons. Phonons propagate through a gas by collisions. Sound needs a medium to propagate. In dilute gases where CARL is observed, collisions are totally neglegible. Brillouin-scattering may lead to bunching, which propagates along $\mathbf{k}_s$. But similar to water waves, which do not transport the water molecules, the bunching does not lead to a net transport of atoms.

Just like CARL and the superradiant Rayleigh scattering in BECs SBS can be understood as being mediated by dipole-dipole interactions (i.e. the exchange of real or virtual photons between atoms). In a BECs SBS can be interpreted as phonon-like excitations (smaller momentum transfer) due to dipole-dipole interactions [324], while CARL are particle-like excitations due to dipole-dipole interactions (the nature of scattered particles changes from recoiling atoms to phonons). Note that while ultralow temperatures are necessary, these effects are not base on superfluidity, i.e. binary collisions. Thus the speed of sound is not the Bogolubov sound. The question is whether quantum degeneracy plays a role.

19.2.3 Exercises

19.2.3.1 Ex: Lasing without inversion

Explain the phenomenon of lasing without inversion in the dressed states picture for a V-type three-level system.

19.3 Further reading

G. Kurizki et al., *Free-electron lasing without inversion by interference of momentum states* [DOI]

D. Bloch et al., *Atom-wall interaction* [DOI]

G. Nienhuis, *Nonlinear selective reflection from an atomic vapor at arbitrary incidence angle* [DOI]

E. Pleghaar, *Quantitative investigation of the effect of resonant absorbers on the Goos-Hänchen shift* [DOI]

Chapter 20

Atomic motion in force fields

So far –and especially in Sec. 2.7.2– we analyzed the motion of quantum particles in potential landscapes without specifying the physical origin of the potentials. We know the *gravitational force*, which can be derived from the Earth's homogeneous attraction,

$$\mathbf{F} = -\nabla V_{\text{grav}} = -\nabla(mgz) = -gm\hat{\mathbf{e}}_z \ . \tag{20.1}$$

Another fundamental force comes from electromagnetism. We have already studied –mainly in Sec. 10.4– the reaction of the electronic shell in atoms subjected to applied electromagnetic fields.

In contrast, the present chapter is devoted to the motion of the *atomic center-of-mass* subject to forces resulting from interactions with *electromagnetic fields*. We will begin, in the first section, with electromagnetic forces of the Coulomb-Lorentz type acting on charges (e.g. ions), permanent electric dipoles (e.g. polar molecules), or permanent magnetic dipoles (e.g. paramagnetic atoms). Also, more complex situations will be discussed, such as the scattering of light by confined atoms, atoms interacting with optical cavities, and adiabatic potentials.

The second section will entirely be devoted to the forces exerted by light beams, in particular the *radiation pressure* and the *optical dipole force*, which are nowadays widely used in atomic cooling and trapping experiments. We will leave the issue of the application of these forces to Chp. 26 and concentrate here on the (semiclassical or quantum) derivation and the interpretation of the forces. In fact, to understand optical forces acting on atoms, we need to consider their internal degrees of freedom.

Apart from the degrees of freedom related to their center-of-mass motion (kinetic or potential energy), many quantum objects are endowed with internal degrees of freedom, for example, the motion of electrons inside atoms or molecules. In the simplest case, the Hamiltonian of such a system is composed of an outer part, comprising the kinetic and the potential energy, and an inner part counting for the excitation energy $\hbar\omega_0$ of an internal state $|e\rangle$,

$$\hat{H}_{\text{atom}} = \frac{\mathbf{p}^2}{2m} + V(\mathbf{r}) + \hbar\omega_0 |e\rangle\langle e| \ . \tag{20.2}$$

The time scale of the electronic motion is usually very rapid compared to the motion of the nucleus, where (almost) the entire mass of the atom is concentrated. Therefore, the external (nuclear) dynamics decouples from the internal (electronic) one, which allows the separation of the total wavefunction in two parts,

$$|\psi\rangle = |\psi\rangle_{\text{ext}} |\psi\rangle_{\text{ele}} \ , \tag{20.3}$$

where for a simple two-level atom, $|\psi(t)\rangle_{\rm ele} = c_g(t)|g\rangle + c_e(t)|e\rangle$, with the atomic ground state $|g\rangle$ and the excited state $|e\rangle$. The external states are eigenstates of the momentum in the case of a free particle, $|\psi\rangle_{\rm ext} = |\mathbf{p}\rangle$. For particles confined in a potential the external states are the vibrational eigenstates, $|\psi\rangle_{\rm ext} = |n\rangle$. The temporal evolutions of the internal and external degrees of freedom are governed by independent Schrödinger equations. For cold atomic clouds the kinetic energy is much smaller than the excitation energy, which allows the separation of the energy scales. That is, the internal degrees of freedom are frozen in the ground state. Many phenomena, for example, Bose-Einstein condensation and the dynamics of condensates are described in this regime.

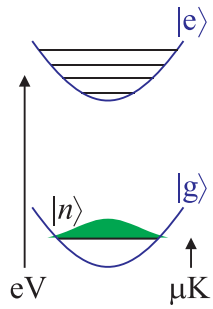

Figure 20.1: The internal degrees of freedom of cold atoms are thermally frozen.

Nevertheless, the fact that it is thermally frozen does not prevent the intentional excitation of the internal degree of freedom by irradiating electromagnetic fields tuned close to resonances and coupling electronic energy levels. In the case of coupling, the external and internal degrees of freedom must both be considered.

20.1 Electromagnetic forces

Obviously, in order to allow for forces acting on the atomic center-of-mass, the atomic Hamiltonian must contain terms depending on the center-of-mass coordinates:

$$\mathbf{F} = -\langle \nabla \hat{H}_{\rm atom:field} \rangle \ . \tag{20.4}$$

We will see shortly that some of the terms may be dissipative, other conservative.

The impact of electromagnetic fields on the internal dynamics of atoms has already been studied in the Chp. 10. Here, we will focus on the force on the center-of-mass exerted by the gradient of *electromagnetic potentials*, where the Hamiltonian in Eq. (20.4) of a charge interacting with electromagnetic fields is obtained in minimum coupling (10.11) by,

$$\boxed{\hat{H}_{\rm atom:field} = \frac{1}{2m}(-\imath\hbar\nabla - q\mathbf{A})^2 + q\Phi \simeq \frac{-\hbar^2}{2m}\nabla^2 + \frac{\imath\hbar q}{m}\mathbf{A}\cdot\nabla + q\Phi} \ . \tag{20.5}$$

From this formula we can, in principle, calculate all electromagnetic forces.

The coupling of external and internal degrees of freedom is mediated by the photonic recoil transferred to the atom during absorption and emission processes. That

is, the feature that the interaction with light simultaneously *excites* the atom and exerts a *force* couples the degrees of freedom. This fact manifests itself in the Hamiltonian of the atom interacting with a light field (17.8) by the appearance of terms joining operators acting on different degrees of freedom,

$$\hat{H} = \hbar\omega\hat{a}^\dagger\hat{a} + \hat{H}_{\text{atom:field}} + \hat{H}_{\text{atom}} \qquad (20.6)$$
$$\text{where} \qquad \hat{H}_{\text{atom:field}} = \hbar g(\hat{\mathbf{r}}) e^{\imath\mathbf{k}\cdot\hat{\mathbf{r}}}\hat{a}^\dagger\hat{\sigma} + c.c. \ ,$$

where $\hat{\sigma} \equiv |g\rangle\langle e|$ and $\hat{a} \equiv \sum_n \sqrt{n}|n\rangle\langle n+1|$ and $\hbar g(\hat{\mathbf{r}}) \equiv \mathbf{d}_{12}\cdot\vec{\mathcal{E}}_1(\hat{\mathbf{r}})$ is the coupling constant or one-photon *Rabi frequency*. The Hamiltonian is that of the Jaynes-Cummings model, except that in addition to the field operators $\hat{a}$ and the atom transition operators $\hat{\sigma}$, appears an operator for the position of the atom $\hat{\mathbf{r}}$, whose quantum features we have not taken very seriously so far. It appears in the Rabi frequency and also in the term $e^{\imath\mathbf{k}\cdot\hat{\mathbf{r}}}$. Now, we must remember, that

$$\mathcal{U}_{\text{rec}} = e^{-\imath\mathbf{k}\cdot\hat{\mathbf{r}}} = |\mathbf{p} + \hbar\mathbf{k}\rangle\langle\mathbf{p}| \qquad (20.7)$$

is the unitary operator of the photonic recoil in the absorption process introduced in Sec. 1.7.3 and extensively discussed in Sec. 2.6.2. We shall shortly see, that it is precisely this term in the Hamiltonian that gives rise to all phenomena related to light forces on atoms.

The presence of the position operator in the Jaynes-Cummings Hamiltonian introduces a new degree of freedom. With no external potential (that is, the system is invariant to spatial translations), this degree of freedom is simply the atomic center-of-mass momentum, such that the new set of quantum numbers is $|j, n, \mathbf{p}\rangle$. Strictly speaking we have to span the whole Hilbert space by an external product, $\hat{H}_{\text{ele}} \otimes \hat{H}_{\text{field}} \otimes \hat{H}_{\text{ext}}$.

Often a *semi-classical* description treating the light field a classically is sufficient, $\hat{a} \simeq \sqrt{n}$ with n the number of photons. Then the Hamiltonian (20.6) simplifies to,

$$\hat{H}_{\text{atom:field}} = \tfrac{\hbar}{2}\Omega(\hat{\mathbf{r}}) e^{\imath\mathbf{k}\cdot\hat{\mathbf{r}}}\hat{\sigma} + c.c. \ , \qquad (20.8)$$

with the Rabi frequency $\Omega(\mathbf{r}) = \sqrt{n}2g(\mathbf{r})$.

20.1.1 Forces on charges and electric dipole moments

As shown in Eq. (10.8), the equations (20.4) and (20.5) (obviously) lead to Coulomb-Lorentz forces on charges and currents.

In atomic optics, the Coulomb-Lorentz force is used, for example, to accelerate or trap ions (see Sec. 26.5) and other electrically charged particles.

Atoms naturally do not exhibit *permanent electric dipole moments*, when they are not subject to external electric fields. In contrast, polar molecules (such as heteronuclear dimers), which have permanent electric dipole moments can have their motion be influenced by inhomogeneous electric fields (see Sec. 26.5.3).

20.1.2 Forces on magnetic dipole moments

Neutral atoms are insensitive to electric fields. But as we have already seen in Chp. 10, the orbital motion of the electrons corresponds to a circular current generating a permanent magnetic dipole moment $\vec{\mu}$, which can interact with external magnetic fields. We have already shown in the calculation (10.15) and (10.19) that the interaction energy (20.5) can be written as,

$$\hat{H}_{\rm magn} = -\vec{\mu}_J \cdot \vec{\mathcal{B}} = -\frac{g_J \mu_{\rm B}}{\hbar} \mathbf{J} \cdot \vec{\mathcal{B}} \longrightarrow -\frac{g_J \mu_{\rm B}}{\hbar} |\mathbf{J}|\, |\vec{\mathcal{B}}| = -g_J \mu_{\rm B} m_J \mathcal{B} \ , \tag{20.9}$$

where the *Landé factor* is given by the formula (10.21),

$$g_J = 1 + \frac{J(J+1) + S(S+1) - L(L+1)}{2J(J+1)} \ . \tag{20.10}$$

Here, $\mathbf{J} = \mathbf{L} + \mathbf{S}$ is the total angular momentum resulting from the coupling of the total angular orbital momentum and the total spin of all electrons. If the atom has a nuclear spin I other than zero, then $\mathbf{F} = \mathbf{J} + \mathbf{I}$ replaces $\mathbf{J}$ in Eq. (20.9), and the g-factor generalizes to (10.35) [1],

$$g_F \simeq g_J \frac{F(F+1) + J(J+1) - I(I+1)}{2F(F+1)} \ . \tag{20.11}$$

In Sec. 10.2 we used the formula (20.9) to calculate the Zeeman shift of internal energy levels. But, according to the formula (20.4), the interaction also generates a force acting on the center-of-mass of atom,

$$\boxed{\mathbf{f} = -g_F \mu_{\rm B} m_F \nabla \mathcal{B}} \ . \tag{20.12}$$

In case of absence of hyperfine structure we simply replace F by J.

Obviously, force is conditioned by the existence of a gradient of the absolute value of the magnetic field. It was first used in the famous *Stern-Gerlach experiment*, which led to the discovery of the electron (see Sec. 3.3.3). In atomic optics (see Sec. 26.4), this force is widely used to create *magnetic traps* for cold atoms. Resolve the Excs. 10.2.7.2, 20.1.4.1, and 20.1.4.2.

20.1.3 Adiabatic potentials

Adiabatic potentials can be used to realize more complicated trapping geometries [177]. To study adiabatic potentials we consider the two-level system $|\frac{1}{2}, \frac{1}{2}\rangle \leftrightarrow |\frac{1}{2}, -\frac{1}{2}\rangle$ coupled by an incident radiation (e.g. a radiofrequency). A generalization to multilevel systems $F > \frac{1}{2}$ is simple. The dressed states Hamiltonian of our two-level system is a 2×2 matrix,

$$\hat{H}_{\rm adiab}(z) = \begin{pmatrix} \frac{1}{2}\mu_{\rm B} g_F \mathcal{B}(z) - \frac{1}{2}\hbar\omega & \frac{1}{2}\hbar\Omega \\ \frac{1}{2}\hbar\Omega & -\frac{1}{2}\mu_{\rm B} g_F \mathcal{B}(z) + \frac{1}{2}\hbar\omega \end{pmatrix} \ . \tag{20.13}$$

[1] Note that the formula only applies to weak fields. For strong fields the Zeeman unfolding changes to the Paschen-Back unfolding of the hyperfine structure.

For simplicity, we assume a one-dimensional geometry, $\mathcal{B} = \mathcal{B}(z)$, but we can easily generalize to three dimensions. The eigenvalues of $\hat{H}$ are,

$$E_{\pm}(z) = \pm\tfrac{1}{2}\sqrt{\hbar^2\Omega^2 + [\mu_{\rm B} g_F \mathcal{B}(z) - \hbar\omega]^2}\ . \tag{20.14}$$

Sufficiently far from resonance, $\hbar\Omega \ll |\mu_{\rm B} g_F \mathcal{B}(z) - \hbar\omega|$, we obtain,

$$E_{\pm}(z) \simeq \pm\tfrac{1}{2}[\mu_{\rm B} g_F \mathcal{B}(z) - \hbar\omega] \pm \frac{\hbar^2\Omega^2}{4[\mu_{\rm B} g_F \mathcal{B}(z) - \hbar\omega]}\ , \tag{20.15}$$

where the second term can be interpreted as the dynamic Stark shift of the energy levels.

To illustrate the influence of the radiofrequency, we calculate the potential energy and the dressed states assuming a linear $1D$ magnetic field gradient $\mathcal{B}(z) \equiv zb$. Fig. 20.2(a) illustrates the radiofrequency coupling and Fig. 20.2(b) the dressed states for two magnetic substates coupled by a radiofrequency. The minimum emerging in

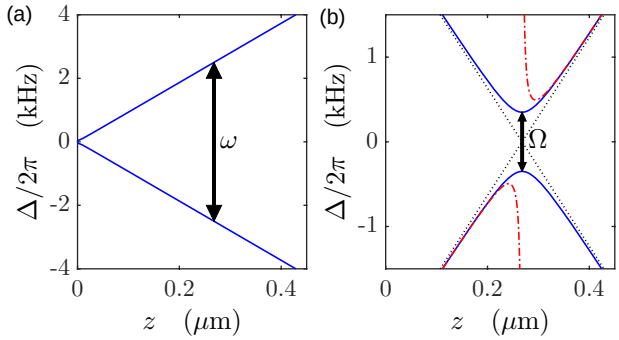

Figure 20.2: (code) (a) Potential energies for a hyperfine structure $F = \frac{1}{2}$ with a g-fator of $g = -\frac{2}{3}$ (as e.g. in the ground state $^2S_{1/2}$ of ^{6}Li). A radiofrequency (arrow) couples the substates $m_F = \pm\frac{1}{2}$. Here, $b = 200\,\mathrm{G/cm}$ and $\omega = 2\pi \times 5\,\mathrm{kHz}$. (b) Uncoupled dressed states (dotted line), coupled dressed states (solid line), and dynamic Stark shifts (dash-dotted) approximated far away from resonance. The Rabi frequency is $\Omega = 2\pi \times 700\,\mathrm{Hz}$.

the upper curve of Fig. 20.2(a) may serve as a confinement potential. Using an rf-radiation composed by several frequencies, potential minima can be realized at several distances z. In Exc. 20.1.4.3 we calculate an example.

In the dressed states basis with the Hamiltonian (20.13), the force is calculated from,

$$\mathbf{F}(\mathbf{r}) = \langle\hat{\mathbf{F}}(\mathbf{r})\rangle = -\mathrm{Tr}_{\rm atom:laser}\ \hat{\rho}\nabla_{\mathbf{r}}\hat{H}_{\rm adiab} = -\sum_{n,j}\langle n,j|\hat{\rho}\nabla_{\mathbf{r}}\hat{H}_{\rm adiab}|j,n\rangle\ . \tag{20.16}$$

We consider only one dimension and disregard the degrees of freedom of the radiation field,

$$F(z) = -\mathrm{Tr}_{\rm atom:laser}\ \hat{\rho}\partial_z\hat{H}_{\rm adiab} \tag{20.17}$$
$$= -\sum_j \langle j|\hat{\rho}\partial_z\left(\tfrac{\mu_{\rm B} g_F \mathcal{B}}{2}|1\rangle\langle 1| - \tfrac{\hbar\omega}{2}|1\rangle\langle 1| - \tfrac{\mu_{\rm B} g_F \mathcal{B}}{2}|2\rangle\langle 2| + \tfrac{\hbar\omega}{2}|2\rangle\langle 2| + \tfrac{\hbar\Omega}{2}e^{\imath kz}\hat{\sigma}^+ + c.c.\right)|j\rangle\ .$$

Here we neglect any possible position dependence of Ω,

$$F(z) = -\tfrac{1}{2}\mu_{\rm B} g_F \partial_z \mathcal{B} \sum_j \langle j|\hat{\rho}(|1\rangle\langle 1| - |2\rangle\langle 2|)|j\rangle = -\tfrac{1}{2}\mu_{\rm B} g_F \partial_z \mathcal{B}(\rho_{11} - \rho_{22}) \ . \quad (20.18)$$

If the atoms enter the coupling area adiabatically, the populations of the adiabatic potentials will only depend on z. This is analogous to the *adiabatic transfer* via adiabatic sweeps or STIRAP pulse sequences. If the atoms are too fast, the populations also depend on history (i.e. the recent trajectory of the atoms), which can result in Landau-Zener transitions to other (possibly untrapped) states.

20.1.4 Exercises

20.1.4.1 Ex: The Stern-Gerlach effect

Consider initially motionless ^{87}Rb atoms trapped in a superposition of two the trappable Zeeman states $|F, m_F\rangle = |2, +2\rangle$ and $|1, -1\rangle$. Suddenly a magnetic gradient of $\partial_z \mathcal{B} = 100\,\mathrm{G/cm}$ is applied for 2 ms. Calculate the spatial separation of the atoms being in either one of the two states after 10 ms of ballistic expansion.

20.1.4.2 Ex: Potential for magnetic trapping

Invent a potential for magnetic confinement.

20.1.4.3 Ex: Adiabatic potentials

An *adiabatic potential* can be used to create more complicated trapping potentials [177]. To study these potentials we consider a system of two Zeeman states $m = \frac{1}{2}$ coupled by a radiofrequency radiation $\hbar\omega$. The dressed states Hamiltonian of our two-level system is a 2×2 matrix,

$$\hat{H} = \begin{pmatrix} \frac{1}{2}\mu_{\rm B}\mathcal{B} - \frac{1}{2}\hbar\omega & \frac{1}{2}\hbar\Omega \\ \frac{1}{2}\hbar\Omega & -\frac{1}{2}\mu_{\rm B}\mathcal{B} + \frac{1}{2}\hbar\omega \end{pmatrix} ,$$

defining the energetic zero in the middle between the states. Now, assume that the magnetic field grows linearly along the axis z, $\mathcal{B}(z) = z\partial_z\mathcal{B}$, where $\partial_z\mathcal{B}$ is the gradient. Also assume that the radiofrequency is tuned in resonance with the difference of the energies of the Zeeman states at some distance z_0 such that, $\hbar\omega = \mu_{\rm B} z_0 \partial_z \mathcal{B}$.
a. Calculate the eigenenergies of the coupled system as a function of z.
b. Expands eigenenergies around the position z_0.
c. What would be the oscillation frequency of the trapped atoms inside the adiabatic potential?
d. Expands the eigenenergies in $\hbar\Omega$ for locations away from resonance.

20.2 Optical forces

Light carries momentum, and the scattering of light by an object produces a force on that object. Although these properties of light are direct consequences of Maxwell's classical theory of electromagnetism, they were only verified in 1933 by *Frisch*, who

observed a very small transverse deviation ($3 \cdot 10^{-5}$ rad) of an atomic sodium beam exposed to the light of a lamp. With the invention of the laser, it became easier to observe the light's mechanical effects, because the more intense and highly directional laser light exerts much larger forces. Although these results sparked the interest in using light forces to control the motion of neutral atoms, the fundamental bases for understanding the physics of light forces were not developed before the late 1970s. Unequivocal experimental demonstrations of cooling and trapping of atoms were not performed before the mid-1980s. In this section we will discuss some fundamental aspects of light forces. Practical schemes used to cool and trap neutral atoms will be presented in Secs. 26.2 and 26.3.

The light force acting on an atom can be of two types: a spontaneous dissipative force and a conservative dipole force. The spontaneous force arises from the recoil experienced by an atom when it absorbs or emits a quantum of light. As we saw in Sec. 1.2.6, when an atom scatters light, the resonant scattering cross section can be written as in Eq. (1.72), $\sigma_{0a} = \frac{g_2}{g_1}\frac{\lambda_0^2}{2\pi}$, where λ_0 is the resonant wavelength. In the optical region of the electromagnetic spectrum the wavelengths of light are of the order of several hundred nanometers, and the resonant cross sections for scattering become very large, ($\sim 10^{-9}\,\mathrm{cm}^2$). Each absorbed photon transfers a quantum of momentum $\hbar k$ to the atom in the direction of propagation. Spontaneous emission following an absorption process occurs in random directions and, hence, averaged over many absorption-emission cycles, it cancels to zero. Consequently, the total spontaneous force acts on the atom in the propagation direction of the light, as shown schematically in the diagram of Fig. 20.3. The saturated photon scattering rate via spontaneous emission (the reciprocal value of the excited state's lifetime) sets the upper limit for the magnitude of the force. This force is called *radiation pressure* force.

The *dipolar gradient force* can be easily understood by considering light as a classical wave. It is simply the time-averaged force resulting from the interaction of the transition dipole –induced by the oscillating electric field of the light– with the gradient of the electric field amplitude. The strength of this gradient can be controlled, e.g. by focusing the light beam. By tuning the optical frequency below or above an atomic transition, we can control the sign of the force acting on the atom: Tuning the light below resonance attracts the atom to the center of the light beam, tuning it above resonance repels it. The dipole force is a stimulated process without energy exchange between the field and the atom. Photons are absorbed in one light mode and reappear by stimulated emission in another one. However, conservation of momentum requires that the change in the propagation direction of the scattered photons from an initial mode to a final mode leaves the atom with a recoil. Contrary to spontaneous force, there is, in principle, no upper limit for the magnitude of the dipole force, since it is a function of the field gradient only and the detuning.

Within the theory of electromagnetism we calculate radiative forces on charges via *Maxwell's stress tensor* [2]. The interaction of radiation with atoms having internal degrees of freedom exhibiting resonances can be treated qualitatively by the *Lorentz*

[2] See script on *Electrodynamics: Electricity, Magnetism and Radiation* (2025), Sec. 6.2.3.

model [3].

In the following, we will show quantitative semi-classical and quantum calculations: The force of a light beam on an atom can be calculated in many different ways, each emphasizing a slightly different aspect: From the classical Lorentz force exerted on an atom by electromagnetic fields we can derive a semi-classical Fokker-Planck equation [793]. In Sec. 20.2.1 we will derive the two contributions (dipole force and radiative pressure) within a semi-classical theory [328]. Wineland *et al.* [871] chose as starting point the cross section for an elementary scattering process (Sec. 20.2.3). Dalibard *et al.* [195] developed a quantum theory using the dressed states representation (Sec. 20.2.2). And Cirac *et al.* [155] showed an approach based on the master equation (Sec. 20.2.3).

20.2.1 The dipolar gradient force and the radiation pressure force

To compute the forces of light on an atom, we describe the atom as a two-level system: A fundamental level $|1\rangle$ and an excited level $|2\rangle$ decaying to the fundamental level with the rate Γ. The energy difference between the levels is $\omega_0 \equiv E_2 - E_1$. The light with frequency ω is derived from a laser beam, which can be detuned from the atomic transition, $\Delta \equiv \omega - \omega_0$. To describe the interaction, we consider the part (20.8) of the total Hamiltonian describing the interaction [195]. Using the semi-classical density operator $\hat{\rho}$ [4], we can calculate the force that the light field exerts on the atom,

$$\begin{aligned}
\mathbf{F}(\mathbf{r}) = \langle \hat{\mathbf{F}}(\mathbf{r}) \rangle &= -\mathrm{Trat}\ \hat{\rho} \nabla_{\mathbf{r}} \hat{H}_{\text{atom:field}} \\
&= -\tfrac{1}{2}\hbar \sum\nolimits_j \langle j|\hat{\rho}|\nabla_{\mathbf{r}} \left(\Omega(\mathbf{r}) e^{\imath \mathbf{k}\cdot\mathbf{r} - \imath\Delta t} |2\rangle\langle 1| + \Omega(\mathbf{r}) e^{-\imath \mathbf{k}\mathbf{r} + \imath\Delta t} |1\rangle\langle 2| \right) |j\rangle \\
&= -\tfrac{1}{2}\hbar \nabla_{\mathbf{r}} \Omega(\mathbf{r}) \left(\langle 1|\hat{\rho} e^{\imath \mathbf{k}\cdot\mathbf{r} - \imath\Delta t}|2\rangle + \langle 2|\hat{\rho} e^{-\imath \mathbf{k}\cdot\mathbf{r} + \imath\Delta t}|1\rangle \right) \\
&\quad - \tfrac{\imath}{2}\hbar \mathbf{k} \Omega(\mathbf{r}) \left(\langle 1|\hat{\rho} e^{\imath \mathbf{k}\cdot\mathbf{r} - \imath\Delta t}|2\rangle - \langle 2|\hat{\rho} e^{-\imath \mathbf{k}\cdot\mathbf{r} + \imath\Delta t}|1\rangle \right) .
\end{aligned} \tag{20.19}$$

Now, we let the atom be at the position $\mathbf{r} = 0$,

$$\mathbf{F}(\mathbf{0}) = -\tfrac{1}{2}\hbar \nabla_{\mathbf{r}} \Omega(\mathbf{0}) (\rho_{12} e^{-\imath\Delta t} + \rho_{21} e^{\imath\Delta t}) - \tfrac{\imath}{2}\hbar \mathbf{k} \Omega(\mathbf{0}) (\rho_{12} e^{-\imath\Delta t} - \rho_{21} e^{\imath\Delta t}) . \tag{20.20}$$

The quantities $\rho_{12} \equiv \langle 1|\hat{\rho}|2\rangle = \rho_{21}^*$ are the coherences, which develop in a two-level system excited by a laser beam. Inserting the stationary solutions of the Bloch equations (16.151),

$$\rho_{22} = \frac{\Omega^2}{4\Delta^2 + 2\Omega^2 + \Gamma^2} \qquad \text{and} \qquad \rho_{12} = \frac{(2\Delta - \imath\Gamma)\Omega}{4\Delta^2 + 2\Omega^2 + \Gamma^2} e^{-\imath\Delta t} , \tag{20.21}$$

we obtain

$$\mathbf{F}(\mathbf{0}) = -\tfrac{1}{2}\hbar \frac{4\Delta\Omega}{4\Delta^2 + 2\Omega^2 + \Gamma^2} \nabla_{\mathbf{r}} \Omega + \hbar \mathbf{k} \frac{\Gamma\Omega^2}{4\Delta^2 + 2\Omega^2 + \Gamma^2} . \tag{20.22}$$

[3] See script on *Electrodynamics: Electricity, Magnetism and Radiation* (2025), Sec. 7.2.4.

[4] Treating the motional and the optical degrees of freedom as classical the density operator only contains the atomic excitation.

With the definition of the cross section, $\sigma_a(\Delta) = \sigma_{a0}\frac{\Gamma^2}{4\Delta^2+2\Omega^2+\Gamma^2}$,

$$\mathbf{F}(\mathbf{0}) = -\tfrac{1}{2}\hbar\Delta\nabla_{\mathbf{r}}\ln\left(1+\frac{2\Omega^2}{4\Delta^2+\Gamma^2}\right) + \hbar\mathbf{k}\frac{\Omega^2}{\Gamma}\frac{\sigma_a(\Delta)}{\sigma_{a0}} \ . \tag{20.23}$$

The resonant cross section for a 'classical' transition is $\sigma_{a0} = 3\lambda^2/2\pi$.

Apparently, the force comprises two contributions. The *dipolar gradient force* can be derived from a potential. It is proportional to the intensity gradient and can be interpreted as resulting from absorption processes immediately followed by self-stimulated emission. Near resonance it is dispersive. Far from resonance it can be approximated by,

$$\boxed{\mathbf{F}_{\rm dp} = \nabla_{\mathbf{r}}\frac{-\hbar\Delta\Omega^2}{4\Delta^2+\Gamma^2} \overset{|\Delta|\gg\Gamma}{\longrightarrow} -\nabla_{\mathbf{r}}\frac{\hbar\Omega^2}{4\Delta}} \ . \tag{20.24}$$

The *radiation pressure* force is dissipative. Close to resonance it is absorbing. It is proportional to the phase gradient and the only force exerted by plane waves. It can be interpreted as resulting from absorption processes followed by spontaneous emission. With $\Omega^2 = \sigma_{a0}\Gamma I/\hbar\omega$ we get a formula,

$$\boxed{\mathbf{F}_{\rm rp} = \hbar\mathbf{k}\frac{I}{\hbar\omega}\sigma_a(\Delta) = \hbar\mathbf{k}\gamma_{\rm sct}} \ , \tag{20.25}$$

which describes the force as a product of the number of photons in the incident beam, $I/\hbar\omega$, the absorption cross section, $\sigma_a(\Delta)$, and the recoil momentum per photon, $\hbar k$. $\gamma_{\rm sct}$ is the scattering rate. Fig. 20.3(a) illustrates the radiation pressure force.

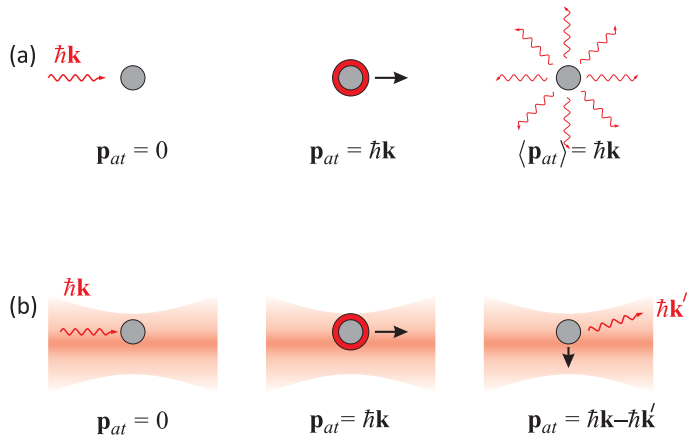

Figure 20.3: (a) Upon absorption of a photon an initially resting atom receives a recoil momentum kick $\hbar k$. As the re-emission is isotropic, averaged over many absorption-emission cycles, the net force is only given by the absorption process. (b) The dipole force may be interpreted as a coherent redistribution of photons between spatial modes of a focused light beam.

The dipole gradient force (and the associated potential) is often used to spatially confine atoms, and the radiation pressure force is often used to cool them down. Note

that we still need to correct Eqs. (20.24) and (20.25) to take into account the square of the average over the possible spatial orientations of the transition matrix element $d_{12}/3$. As illustrated in Fig. 20.3(b), the dipole force may be interpreted as being due to coherent redistribution of photons between partial spatial modes of a non-uniform (e.g. focused) light beam. The orientation of the force depends on the sign of the detuning and can be understood in terms of the Lorentz model treating the atom as classical radiator [5].

The saturation parameter,

$$s = \frac{\frac{1}{2}\Omega^2}{\Delta^2 + \frac{1}{4}\Gamma^2} \ , \tag{20.26}$$

allows to write the dipolar gradient force and the radiative pressure force as,

$$\mathbf{F}_{\rm dp} = -\frac{\hbar\Delta}{6}\frac{1}{1+s}\nabla s = \frac{\hbar\Delta}{6}\nabla \ln[1+s] \qquad \text{and} \qquad \mathbf{F}_{\rm rp} = \frac{\hbar\mathbf{k}\Gamma}{6}\frac{s}{1+s} \ . \tag{20.27}$$

Eq. (20.27) shows that the radiation pressure force 'saturates' as s increases, and is therefore limited by the spontaneous emission rate. The saturation parameter essentially describes the relative importance of terms appearing in the denominator of the line profile function for the light forces. The spontaneous emission rate is an intrinsic property of the atom, proportional to the square of the atomic transition dipole moment, whereas the square of the Rabi frequency is a function of the incident laser intensity. If $s \ll 1$, the spontaneous emission is fast compared to any stimulated process, and the light field is said to be weak. If $s \gg 1$, the Rabi oscillation is fast compared to spontaneous emission and the field is considered as strong. The line profile factor indicates a 'power broadening' by saturation of a factor of $\sqrt{2}$. Note that the dipolar gradient force and potential, Eqs. (20.27), do not saturate when the intensity of the light field is increased. Usually $\mathbf{F}_{\rm dp}$ and $U_{\rm dp}$ are used to manipulate and trap atoms in a laser beam tuned far away from resonance in order to avoid absorption.

Often, the transition moment can be oriented using circularly polarized light. In this case, all previous expressions for $\mathbf{F}_{\rm dp}$, $\mathbf{F}_{\rm rp}$, and $U_{\rm dp}$ should be multiplied by 3. From now on we will abandon the average over the orientations and only use d_{12}^2 for the square of the transition dipole moment. Solve Excs. 20.2.5.1 and 20.2.5.2.

20.2.2 Semiclassical calculation of dipole force and radiative pressure

In quantum mechanics we calculate the force from the Heisenberg equation [328],

$$\hat{\mathbf{F}} = \frac{d}{dt}\hat{\mathbf{p}} = \frac{\imath}{\hbar}[\hat{H}, \hat{\mathbf{p}}] = -\nabla_{\mathbf{r}}\hat{H}_{\text{atom:field}} \ . \tag{20.28}$$

Thus, the force is given by the gradient of the interaction energy between the atom and the light field. Within the dipole approximation the interaction energy is given

[5] See script on *Electrodynamics: Electricity, Magnetism and Radiation* (2025), Sec. 7.2.4.

by $\mathbf{d}\cdot\vec{\mathcal{E}}(\mathbf{r})$. The force is now,

$$\mathbf{F}(\mathbf{r}) = \langle\hat{\mathbf{F}}(\mathbf{r})\rangle = \langle\nabla_{\mathbf{r}}[\mathbf{d}\cdot\vec{\mathcal{E}}(\mathbf{r})]\rangle = \langle(\mathbf{d}\cdot\nabla_{\mathbf{r}})\vec{\mathcal{E}}(\mathbf{r})\rangle - \langle\mathbf{d}\times(\nabla_{\mathbf{r}}\times\vec{\mathcal{E}}(\mathbf{r}))\rangle \equiv \mathbf{F}_{\rm C}(\mathbf{r}) + \mathbf{F}_{\rm L}(\mathbf{r}) \ . \tag{20.29}$$

The first contribution can be interpreted as the Coulomb force acting on the electron performing rapid oscillations at the position $\mathbf{r}(t) = \mathbf{r}_0 + e^{-1}\vec{\mathcal{P}}(\mathbf{r}_0,t)$. The second term is the time-averaged Lorentz force acting on the oscillating electric dipolar moment [381, 384, 382],

$$\mathbf{F}_{\rm C} = e\langle\vec{\mathcal{E}}\rangle \qquad \text{and} \qquad \mathbf{F}_{\rm L} = -\langle\mathbf{d}\times\partial_t\vec{\mathcal{B}}\rangle = \langle\partial_t\mathbf{d}\times\vec{\mathcal{B}}\rangle \ . \tag{20.30}$$

The relation between the light-induced electric dipole moment and the polarizability, $\mathbf{d} = \alpha(\vec{\mathcal{E}})\vec{\mathcal{E}}$, where $\alpha_{\nu\nu} \equiv \alpha_\nu + \imath\beta_\nu$ and $\mathcal{E}_\nu \equiv \sqrt{I_\nu}e^{\imath\psi_\nu}$, becomes,

$$\mathbf{F} = \sum_{\nu=1}^{3}\alpha_\nu\nabla I_\nu + 2\sum_{\nu=1}^{3}\beta_\nu I_\nu\nabla\psi_\nu \ . \tag{20.31}$$

20.2.3 Force exerted by a quantized radiation field

Photons carry one unit of momentum $\mathbf{p} = \hbar\mathbf{k}$, which they transfer to the atom during an absorption or emission process. That is, the light exerts a recoil on the atoms. Spontaneous emission couples to all radiative modes of the electromagnetic vacuum, $\hat{H}_{\text{cm:vacuum}} = \sum_j \hat{H}_{\text{cm:laser}}(\mathbf{k}_j)$. We can trace over these variables and only keep those of the atom and the laser. Following Cirac *et al.* [871, 155], the randomness of the recoil by spontaneous emission is accounted for by,

$$\hat{\rho} \to \int_{4\pi\mathbb{R}^2} S(\mathbf{r})e^{\imath\mathbf{k}\cdot\mathbf{r}}\hat{\rho}e^{-\imath\mathbf{k}\cdot\mathbf{r}}d\Omega \ , \tag{20.32}$$

such that the *Lindblad operator* becomes,

$$\mathcal{L}_{\rm atom}\hat{\rho} = -\Gamma\{\hat{\sigma}^\dagger\hat{\sigma}\hat{\rho}(t) - \tfrac{3}{4\pi}\int S(\mathbf{r})e^{\imath\mathbf{k}\cdot\mathbf{r}}\hat{\sigma}\hat{\rho}(t)\hat{\sigma}^\dagger e^{-\imath\mathbf{k}\cdot\mathbf{r}}d\Omega + \hat{\rho}(t)\hat{\sigma}^\dagger\hat{\sigma}\} \tag{20.33}$$

$$\mathcal{L}_{\rm cavity}\hat{\rho} = -\kappa\{\hat{a}^\dagger\hat{a}\hat{\rho}(t) - 2\hat{a}\rho(t)\hat{a}^\dagger + \hat{\rho}(t)\hat{a}^\dagger\hat{a}\} \ ,$$

where $e^{\pm\imath\mathbf{k}\cdot\mathbf{r}} = \sum_{\mathbf{p}}|\mathbf{p}\mp\imath\mathbf{k}\cdot\mathbf{r}\rangle\langle\mathbf{p}|$ and $S(\mathbf{r}) = \frac{1}{2}\left(1 + (\frac{\mathbf{k}\cdot\mathbf{r}}{kr})^2\right)$ and $d\Omega = d\varphi d\cos\vartheta$. From this they calculate the force and establish a *Fokker-Planck equation* for the *Wigner function*.

20.2.4 Refraction of atoms by light and of light by atoms

Non-resonant light acts on the external degrees of freedom of atoms by a *phase shift of the Broglie wave*, $\exp\left[\imath\hbar^{-1}\int U(\mathbf{r},t)dt\right]$, and simultaneously on the internal degrees of freedom by a *dynamic Stark shift* or *light shift* of the energy levels by the value of $U(\mathbf{r})$. The Bloch vector defined by,

$$\rho \equiv \begin{pmatrix} \frac{1}{\sqrt{2}}c_g c_e^* \\ \frac{1}{\sqrt{2}}c_g^* c_e \\ |c_e|^2 - |c_g|^2 \end{pmatrix} \tag{20.34}$$

describes, under the influence of the dispersive interaction, a precession around the polar axis. This was discussed in Exc. 16.7.3.9. The Stark shift causes a rotation of $\hbar^{-1}U(\mathbf{r})t$. Simultaneously, the atom is subjected to a force, which corresponds to the gradient of the potential $-\nabla U(\mathbf{r})$, as illustrated in Fig. 20.4(a). We see that the phase shifts of the Broglie wave and the Bloch vector are equal. Finally, the light mode phase is also shifted by the same amount in an effect called *refraction*. That is, the internal, external, and optical degrees of freedom are entangled.

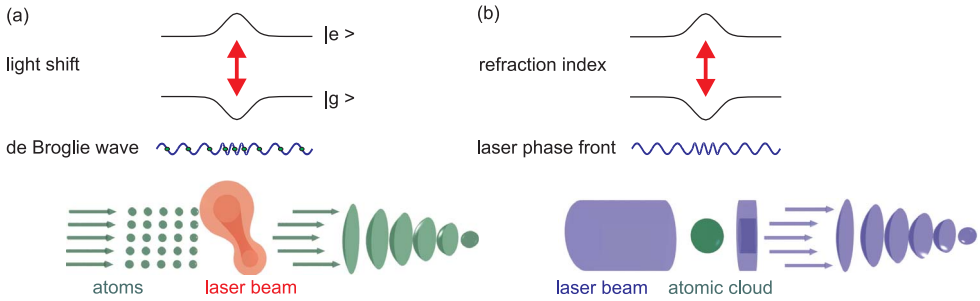

Figure 20.4: Diagram (a) shows product states and dressed states for blue detuning. Note that the population is in the upper level and that the atom is subject to a repulsive weak field seeking force when it enters the laser beam. Diagram (b) is similar, but for red detuning. The population is in the lower level and the atom is subject to an attractive high field seeking force.

This fact has a practical use in atomic interferometers, because it is often easier to detect an interference of internal excitation states rather than of Broglie waves. Because of the entanglement, it is sufficient to measure *one* interference pattern to know the *other one*.

By local variations of the potential $U(\mathbf{r})$, e.g. induced by a focused laser beam, it is possible to manipulate a Broglie wavefront in the same way that, in classical optics, we manipulate the wavefront of a light beam by lenses or other objects, such as for instance, the refractive index represented by an atomic cloud near resonance, as illustrated in Fig. 20.4(b).

The orientation of the force depends on the light frequency as compared to the resonant frequency. The dipolar force attracts the atom to regions where the light field is strong, when the frequency is tuned below ω_0, and it attracts the atom to regions of weak fields, when tuned above ω_0. Integration over the relevant spatial coordinates results in an effective potential or barrier to the atom. The qualitative behavior of the dipolar potential and its effect on the motion of atoms is easily visualized in the dressed states picture. Fig. 20.5 shows what happens when an atom enters a well defined region of an optical field, for example a focused laser beam.

Outside the atom-dipole coupling zone the expression $\hbar\Omega$ is despicable and the 'dressed states' are just the atom-field product states. When the atom enters the field, this expression becomes nonzero and the atom-field states combine to produce a set of dressed states. The energy levels of the product states 'repel' each other and approach the dressed states levels. Assuming that the laser is sufficiently detuned to maintain the absorption rate negligible, the population remains in the ground state.

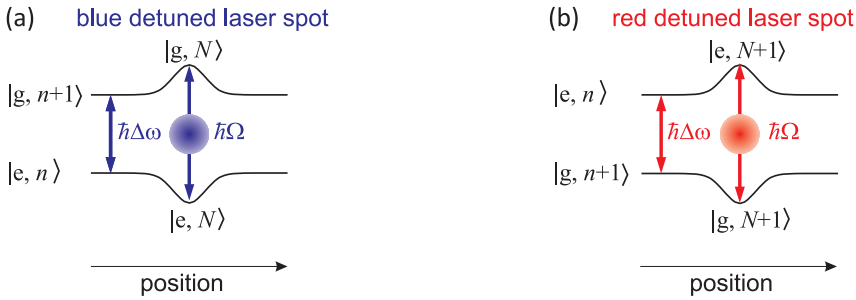

Figure 20.5: Analogy between light optics and atomic optics.

We see that blue (red) detuning leads to a repulsive (attractive) potential for atoms remaining in the grounded state. In addition, since $\hbar\Omega$ is directly proportional to the root of the laser intensity, an increase in that intensity (optical power per unit area) obviously amplifies the force on the atom ($\mathbf{F} \simeq \nabla_R \Omega$).

20.2.5 Exercises

20.2.5.1 Ex: Dipole force for large detunings

Verify that in the limit of large detunings the dipole potential Eq. (20.23) tends to $\longrightarrow \frac{\Omega^2}{4\Delta}$.

20.2.5.2 Ex: Radiation pressure

Calculate the radiation pressure force exerted on a strontium atom by a laser beam in plane wave geometry ($I = 100\,\mathrm{mW/cm^2}$) tuned (i) at resonance and (ii) $\Delta/2\pi = -50\,\mathrm{MHz}$ below the resonance at 461 nm ($\Gamma/2\pi = 30.5\,\mathrm{MHz}$).

20.2.5.3 Ex: lin-lin standing wave

Calculate the electric field of two counter-propagating linearly polarized laser beams of equal intensities,

$$\vec{\mathcal{E}}_{\mathrm{lat}}(\mathbf{r}, t) = \tfrac{1}{2} \sum_{\mathbf{k}=\pm k\hat{\mathbf{e}}_z} \mathcal{E}_0 \vec{\varepsilon}_{\mathbf{k}} e^{\imath(\mathbf{k}\cdot\mathbf{r} - \omega_{\mathbf{k}} t + \phi_{\mathbf{k}})} + c.c.\ ,$$

but different polarizations in the spherical basis.

20.2.5.4 Ex: Sub-lattices

Consider two laser standing wave laser beams crossing each other under an angle of 90°,

$$\vec{\mathcal{E}}_1 = \vec{\varepsilon}_1 e^{\imath(kx - \omega t)} \qquad \text{and} \qquad \vec{\mathcal{E}}_2 = \vec{\varepsilon}_2 e^{\imath(ky - \omega t)}\ ,$$

with arbitrary elliptical polarizations $\vec{\varepsilon}_i$ and study the scalar light-shift potential,

$$U_s = -\frac{\alpha_s}{4} |\vec{\mathcal{E}}|^2\ ,$$

as well as the vector light-shift potential,

$$U_v = \vec{\mathcal{B}}_{eff} \cdot \mathbf{F} \qquad \text{where} \qquad \vec{\mathcal{B}}_{eff} = \imath\alpha_v \vec{\varepsilon}^* \times \vec{\varepsilon}$$

in the xy-plane. α_v is the vector part of the atomic polarizability and $\vec{\mathcal{B}}_{eff}$ an effective magnetic field [225, 508, 17].

20.3 Photonic recoil on free and confined atoms

A trap confining the atomic motion can dramatically modify the way in which they interact with light [6]. For instance, a trapping potential may alter the scattering rate, the scattering angle, and the transfer of photonic recoil. However, *potentials do not exist* in microscopic reality, not more than friction forces do. What exists, as we learn in electrodynamics, are *electromagnetic fields* exerting Coulomb and Lorentz forces. When we write down the Hamiltonian $\hat{H} = \mathbf{p}^2/2m + V(\mathbf{r})$ in quantum mechanics, we already make an important approximation, because the potential $V(\mathbf{r})$ is an artifact obtained by tracing over all those degrees of freedom, which are necessary to generate a force field that can be approximated by a conservative potential.

In the great majority of situations, the approximation is very good. Problems may however arise, when the momentum conservation comes into play, which is the case e.g. of light scattering from ultracold atoms being accelerated by the photonic recoil and shifting the scattered light via the Doppler effect. We then have to address the issue of photonic recoil conserving (or not) the momentum.

Let us begin with a recapitulation of the classical picture of the scattering process applying the rules of energy and momentum conservation to the elastic collision between a free atom and a photon. This process is known as *Compton scattering*.

20.3.1 Recoil- and Doppler-shift in classical mechanics

In classical mechanics we speak of *elastic scattering* when no energy is transferred to internal degrees of freedom of the collision partners, so that *kinetic* energy and momentum stay conserved. This concept can be transferred to quantum particles (e.g. atoms) and photons. In elastic Compton scattering, if the atoms keep their initial internal excitation, the law of momentum conservation requires the transfer of photonic momentum to the scattering atom which, consequently, changes its kinetic energy. To compensate for this kinetic energy change, the frequency of the scattered light must change in order to preserve the total energy, as illustrated in Fig. 20.6(b).

We will calculate in the following the frequency distribution of the light scattered by an atom as a function of its initial velocity $\mathbf{p}_1$, of the frequency ω_1 of the incident light and of the scattering angle, that is, the angle between the modes $\mathbf{k}_1$ and $\mathbf{k}_2$. We begin by writing the laws of conservation of energy and momentum,

$$\begin{aligned} \hbar\mathbf{k}_1 + \mathbf{p}_1 &= \hbar\mathbf{k}_2 + \mathbf{p}_2 \\ \hbar\omega_1 + \frac{p_1^2}{2m} &= \hbar\omega_2 + \frac{p_2^2}{2m} \ . \end{aligned} \tag{20.35}$$

[6] The interaction also depends on other parameters, such as the geometry of the confinement potential and on cooperative effects (bosonic stimulation), but this will be discussed later.

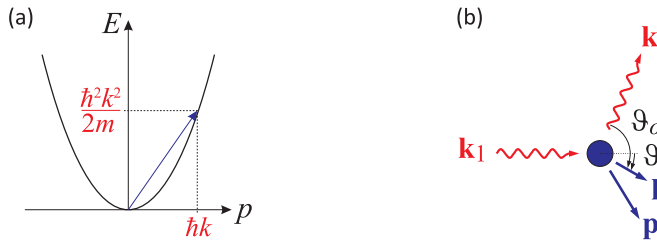

Figure 20.6: (a) Kicking an atom along its dispersion relation. (b) Scheme of the Compton-scattering of light.

Eliminating $\mathbf{p}_2$ from the second equations, we obtain,

$$\hbar\omega_1 - \frac{\hbar^2 k_1^2}{2m} - \frac{\hbar \mathbf{k}_1 \cdot \mathbf{p}_1}{m} = \hbar\omega_2 + \frac{\hbar^2 k_2^2}{2m} - \frac{(\hbar \mathbf{k}_1 + \mathbf{p}_1) \cdot \hbar \mathbf{k}_2}{m} \ . \tag{20.36}$$

The photonic recoils of the incident and of the scattered light are almost equal,

$$\omega_{\rm rec} \equiv \frac{\hbar k_1^2}{2m} \simeq \frac{\hbar k_2^2}{2m} \ , \tag{20.37}$$

such we can approximate,

$$\omega_2 = \omega_1 \frac{1 - \frac{\hbar\omega_1}{mc^2} - \frac{p_1}{mc}\cos\sphericalangle(k_1, p_1)}{1 - \frac{\hbar\omega_1}{mc^2}\cos\sphericalangle(k_1, k_2) - \frac{p_1}{mc}\cos\sphericalangle(p_1, k_2)} \ , \tag{20.38}$$

using $\omega_1 = ck_1$, or also,

$$\omega_2 - \omega_1 = \omega_1 \frac{\frac{\hbar\omega_1}{mc^2}\left[-1 + \cos(\vartheta_{in} - \vartheta_{out})\right] + \frac{p_1}{mc}(\cos\vartheta_{out} + \cos\vartheta_{in})}{1 - \frac{\hbar\omega_1}{mc^2}\cos(\vartheta_{in} - \vartheta_{out}) - \frac{p_1}{mc}\cos\vartheta_{out}} \ , \tag{20.39}$$

where we call the angles $\vartheta_{in} = \sphericalangle(k_1, p_1)$, $\vartheta_{out} = \sphericalangle(k_2, p_1)$, and $\vartheta = \vartheta_{in} - \vartheta_{out} = \sphericalangle(k_1, k_2)$. For non-relativistic velocities, the denominator is approximately 1:

$$\boxed{\omega_2 - \omega_1 = 2\omega_{\rm rec}(-1 + \cos\vartheta) + k_1 v_1(\cos\vartheta_{out} + \cos\vartheta_{in})} \ , \tag{20.40}$$

with $\mathbf{p}_1 = m\mathbf{v}_1$. The first term describes the recoil shift and the second term the Doppler shift.

The second term vanishes for initially at resting atoms, $\mathbf{p}_1 = 0$, and Eq. (20.40) simplifies to,

$$\omega_2 - \omega_1 = 2\omega_{\rm rec}(-1 + \cos\vartheta) \ . \tag{20.41}$$

It also vanishes for atoms which have no velocity component in the scattering plane spanned by the wavevectors $\mathbf{k}_1$ and $\mathbf{k}_2$, that is $\vartheta_{out} = 180° - \vartheta_{in}$ [7], for which case we get the maximum recoil shift,

$$\omega_2 - \omega_1 = -4\omega_{\rm rec} \ . \tag{20.42}$$

[7] This situation is often realized in Bragg scattering from optical lattices [766, 768, 767].

The recoil shift is a consequence of momentum conservation.

The recoil shift is typically on the order of $\omega_2 - \omega_1 \approx (2\pi)$ 10 kHz, which in many situations is negligible (e.g. when we deal with thermal atomic clouds), such that we can consider the scattering as elastic., i.e. the first term can be disregarded. Considering, for simplicity, only backscattering, $\cos\vartheta_{out} = \cos\vartheta_{in} = 1$, then Eq. (20.40) simplifies to,

$$\omega_2 - \omega_1 = 2k_1 v_1 \ . \tag{20.43}$$

Obviously, the frequency shift depends on the initial velocity through the Doppler shift $k_1 v_1$. In a thermal gas, the velocities are distributed according to the Maxwell-Boltzmann distribution. Therefore, Rayleigh scattering of light off a cloud of free thermal atoms is subject to Doppler broadening [8].

20.3.2 Kicking a free atom

A conceptual difficulty arises from the incompatibility of scattering picture (generally described in homogeneous space with momentum conservation) and the trapping picture (when it is described in inhomogeneous space without momentum conservation). The difficulty can be avoided by separating the processes into a 'kick' followed by a harmonic oscillation, for which we have to calculate the time-dependence of the states and the observables. We will leave the discussion of such a scattering process to 20.3.3 and for the time being just focus on the time evolution of a harmonic oscillator that just received a kick.

By a 'kicking' an atom we denote a change of momentum within an arbitrarily short amount of time. The shorter the kick-time the larger is, according to Heisenberg's uncertainty relation, the spectrum of possible kinetic energies that can be reached by the kick (see Sec. 5.4.3). However, the spectrum is restricted by the free-particle dispersion relation, as illustrated in Fig. 20.6(a).

The kick is not a realistic physical concept, as it corresponds to an infinitely strong and infinitely short force [9]. In a microscopic scattering process it assumes an infinitely heavy collision partner, while we are more interested in photon scattering. Consequently, in this case the spectrum of reachable energies is determined by the frequency of the photon *and* the free-particle dispersion relation. We will now turn our attention to the (Compton-)scattering of light by free atoms.

20.3.3 (In-)elastic light scattering from a single weakly or strongly confined atom

We mentioned in the last subsection that a scattering process is elastic when none of the collision partners changes its internal excitation energy. The situation becomes, however, more complex when one of the collision partners is confined in a potential, as we will show in the following.

[8] This Doppler broadening is explored e.g. in RIR spectroscopy, where the momentum distribution in p_1 reveals as a frequency distribution $\Delta\omega = \omega_2 - \omega_1$ of Bragg-scattered light, which can be measured by beating with an irradiated idler mode, which can be chosen as being identical to $\mathbf{k}_2$.

[9] which is what allows us to write down a potential

20.3.3.1 Cooperativity in light scattering

In light scattering *cooperativity* means *breaking of the isotropic symmetry* for the angular distribution of scattered modes. In this sense, the anisotropic scattering from an atom confined in an anisotropic trap is cooperative. But there are other cooperative scattering effects messing with isotropy and shaping the density-of-states, like the Purcell effect in the presence of an optical cavity or a photonic band gap concentrating optical modes in a specific solid angles [376]. Another cooperative effect, which is observed in the presence of other atoms, has to do with bosonic stimulation by the optical output mode (as in Bragg scattering [766, 768, 767]) or the momentum sidemode (as in stimulated matter wave 4WM). These effects, which all need to be considered in calculations of the static structure factor ruling the scattering of light, are often strong enough to hide the role of an anisotropic trapping potential. In the following subsections we will disregard all these effects and concentrate on a *single trapped atom*.

The simple picture of Compton scattering presented in Sec. 20.3.1 holds for *free atoms*, whose dynamics is totally understood in terms of their internal electronic excitation ($\hat{H}_{\rm ele}$), the kinetic energy of their center-of-mass ($\hat{H}_{\rm cm} = \frac{\mathbf{p}^2}{2m}$), the radiation field ($\hat{H}_{\rm rad}$) (which may be treated classically under the circumstances discussed here), and the coupling ($\hat{H}_{\rm int}$) of all three degrees of freedom,

$$\hat{H}_{free} = \hat{H}_{\rm ele} + \hat{H}_{\rm cm} + \hat{H}_{\rm rad} + \hat{H}_{\rm int} \ . \tag{20.44}$$

Transition probabilities are readily calculated using Fermi's Golden rule, because the density-of-states distributions for the final radiation modes receiving the scattered photons (photonic density-of-states) and the recoil modes receiving the scattered atoms (phononic density-of-states) are white, that is, without resonances, and isotropic.

In the presence of an imposed trapping potential, an additional term appears in the Hamiltonian, which has the capacity of dramatically changing the scattering features,

$$\hat{H}_{\rm cm} = \frac{\mathbf{p}^2}{2m} + \hat{V}_{\rm trp}(\mathbf{r}) \ . \tag{20.45}$$

The confining potential may or may not depend on the internal state of the atom. For ions in a Paul trap it does not depend, but for atoms in magnetic traps it usually depends,

$$\begin{aligned} \hat{H}_{\rm atom} &= |g\rangle \hat{H}_{{\rm cm},g} \langle g| + |e\rangle (\hat{H}_{{\rm cm},e} + \hbar\omega_0) \langle e| \\ \hat{H}_{{\rm cm},j} &= \frac{\hat{p}^2}{2m} + V_j(\mathbf{r}) \ , \end{aligned} \tag{20.46}$$

where ω_0 is the frequency of the atomic transition. In the following, however, we will treat potentials that are independent of the internal atomic state.

20.3.3.2 Resolved sideband regime

As discussed in Sec. 16.5.5, incident light is absorbed by an atom harmonically oscillating in a trap with frequency $\omega_{\rm trp}$ on a spectrum of discrete sidebands separated

by $\omega_{\rm trp}$ with amplitudes given by $J_n(kv_0/\omega_{\rm trp})$. The modulation index $kv_0/\omega_{\rm trp} = kx_0 = 2\pi x_0/\lambda$ corresponds to the Lamb-Dicke parameter. When the modulation amplitude is within the so-called *Lamb-Dicke regime*, $kv_0 \ll \omega_{\rm trp}$, the first sidebands become smaller than the carrier, $J_1(kv_0/\omega_{\rm trp}) < J_0(kv_0/\omega_{\rm trp})$ and, therefore, do not contribute to the Doppler width of the frequency distribution. That is, the linear Doppler effect vanishes.

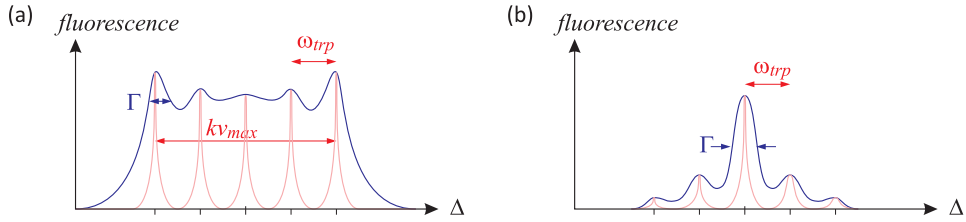

Figure 20.7: Absorption profile in the regimes of (a) weak binding ($\eta > 1$) for the cases of and unresolved sidebands (blue curve) and resolved sidebands (red curve), and (b) strong binding (Lamb-Dicke regime $\eta < 1$) for the same cases as in (a).

The relative size of the characteristic frequencies $\omega_{\rm rec}$, $\omega_{\rm trp}$, and Γ define characteristic regimes, as illustrated in the table.

confinement		sidebands	
weak	$\eta > 1$	unresolved	$\frac{\omega_{\rm trp}}{\Gamma} < 1$
strong	$\eta < 1$	resolved	$\frac{\omega_{\rm trp}}{\Gamma} > 1$

20.3.3.3 The Mößbauer effect

The role of photonic recoil in the scattering of light by confined atoms has been unraveled by *Mößbauer*, who performed scattering experiments of γ-photons on a ^{57}Fe crystal on a narrow transition of this isotope at 14 keV (0.086 nm). The linewidth of this transition, $\Gamma \approx (2\pi)\ 1\,{\rm MHz}$, is much narrower than the recoil-shift, $\omega_{\rm rec} \approx (2\pi)\ 500\,{\rm MHz} \gg \Gamma$, so that we should expect the scattered light to be considerably recoil-shifted and Doppler-broadened. In fact, the recoil-shift should be so large, that scattered photons cannot be reabsorbed by other atoms on this transition being at rest. This is *not* what Mößbauer observed in his experiments. He found that scattered photons can be reused for subsequent scattering, which means that the scattering must be elastic.

The explanation for this unexpected observation is that, if the nucleus is embedded in a crystal, the vibrational frequencies, which are even higher than the photonic recoil frequency, $\omega_{\rm trp} \approx 2\pi \cdot 3\,{\rm THz}$, are unreachable. That is to say, we are in the *resolved sidebands Lamb-Dicke regime*, $\omega_{\rm trp} \gg \omega_{\rm rec} \gg \Gamma$. Here, the phonons corresponding to the vibrations cannot be excited, so that the recoil momentum must be absorbed by the whole lattice, whose entire mass is so large, that the photon frequency is not recoil-shifted by the scattering process. Hence, the first-order *Doppler effect* is avoided and the measured width of the transition is just the natural linewidth. Furthermore,

the atom remains in the same vibrational state of their localizing potential. This is the *Mößbauer effect*.

	γ for ^{57}Fe	optical for $^{172}Yb^{+}$
photon energy	$\approx 14\,\mathrm{keV}$ $\approx 4\times10^{18}\,\mathrm{Hz}$	$\approx 3\,\mathrm{eV}$ $\approx 640\,\mathrm{THz}$
recoil	$\approx 2\,\mathrm{meV}$ $\approx 500\,\mathrm{MHz}$ $\approx 10^{-10}$	$\approx 20\,\mathrm{peV}$ $\approx 5\,\mathrm{kHz}$ $\approx 10^{-11}$
linewidth	$\approx 5\,\mathrm{neV}$ $\approx 1\,\mathrm{MHz}$ $\approx 2\times10^{-13}$	$\approx 5\,\mathrm{feV}$ $\approx 1\,\mathrm{Hz}$ $\approx 2\times10^{-15}$
lattice vibrations	$\approx 10\,\mathrm{meV}$ $\approx 3\,\mathrm{THz}$	$\approx 3\,\mathrm{neV}$ $\approx 1\,\mathrm{MHz}$

Table 20.1: Comparison of γ-radiation and the optical regime.

A similar effect can be observed with trapped atoms driven on very narrow transitions, as we will discuss in the following.

20.3.3.4 Coupling of internal and external motion by photonic recoil, tracing over the internal excitation

When discussing the transfer of momentum to a harmonic oscillator in 2.6.2, we did not say how the momentum shift could be realized in practice. As we have seen in the example of the Mößbauer effect, a possible way is via the photonic recoil received on a light scattering process. The coupling of the relevant degrees of freedom of the system induced by the absorption of a photon by an atom is accounted for by an additional interaction term $\hat{H}_{\rm int}$ in the Hamiltonian. The relevant degrees of freedom are the electronic orbital $|i\rangle$, the vibrational state $|n\rangle$, and the number of photons $|N\rangle$ in the light mode, assumed to be a plane wave $\vec{\mathcal{E}}(\mathbf{r},t) = E_0\hat{\mathbf{e}}_y e^{\imath k_z z-\imath\omega t}$. Neglecting the quantum nature of the light, we will disregard this degree of freedom in the following. Assuming that the trapping potential is the same for all electronic orbitals, as in (20.46), the total state can be expressed as a product state, $|n,i\rangle \equiv |i\rangle\otimes|n\rangle$. The interaction Hamiltonian,

$$\hat{H}_{\rm int} = \frac{\hbar\Omega}{2}(e^{\imath k\hat{z}}\hat{a}|e\rangle\langle g| + e^{-\imath k\hat{z}}\hat{a}^\dagger|g\rangle\langle e|) - |e\rangle\hbar\omega\langle e| \ , \tag{20.47}$$

couples the dynamics on the internal transition, given by the Rabi frequency $\hbar\Omega \equiv \langle e|d_y|g\rangle\mathcal{E}_0$, with the absorption (or stimulated emission) of a photon $\hat{a}$, and the transfer of a recoil momentum. The last term comes from the transformation into the interaction picture [10]. With this our total Hamiltonian (20.46) becomes,

$$\boxed{\hat{H} = \hbar\omega_{\rm trp}(\hat{b}^\dagger\hat{b}+\tfrac{1}{2}) + |e\rangle\hbar(\omega_0-\omega)\langle e| + \tfrac{\hbar\Omega}{2}(e^{\imath k\hat{z}}|e\rangle\langle g| + e^{-\imath k\hat{z}}|g\rangle\langle e|)} \ . \tag{20.48}$$

So, vibrational states are only coupled via electronic transitions,

$$\langle n,g|\hat{H}_{\rm int}|0,g\rangle = 0 \qquad \text{and} \qquad \langle n,e|\hat{H}_{\rm int}|0,g\rangle = \tfrac{1}{2}\hbar\Omega\langle n,e|e^{\imath k\hat{z}}|0,g\rangle \ . \tag{20.49}$$

[10] Note, that this Hamiltonian cannot be used to describe spontaneous emission. To do so, we need to allow for 3D systems and decay modes,

$$\hat{H} = \hbar\omega_{\rm trp}(|\mathbf{n}\rangle\langle\mathbf{n}|+\tfrac{1}{2}) + \hbar(\omega_0-\omega)|e\rangle\langle e| + \tfrac{\hbar\Omega}{2}(e^{-\imath\mathbf{k}_i\cdot\hat{\mathbf{r}}}\hat{\sigma}^\dagger\hat{a}_{\mathbf{k}_i} + c.c.) + \hbar g\sum_{\mathbf{k}_f}(e^{\imath\mathbf{k}_f\cdot\hat{\mathbf{r}}}\hat{\sigma}\hat{a}^\dagger_{\mathbf{k}_f} + c.c.) \ .$$

Hence, we have to span the complete Hilbert space of all operators like $\hat{\sigma}^\dagger = \sum_n |n\rangle\langle n| \otimes |e\rangle\langle g|$.

We can expand the system's state into,

$$|\psi(t)\rangle = \sum_{n=0}^{\infty} (c_{n,g}|n,g\rangle + c_{n,e}|n,e\rangle \ , \tag{20.50}$$

and insert it together with the Hamiltonian (20.48) into the Schrödinger equation. Projecting onto the states $\langle n,g|$ and $\langle n,e|$, we easily derive the following equations of motion,

$$\boxed{\begin{aligned} \frac{dc_{n,g}}{dt} &= -\imath\omega_{\rm trp}(n+\tfrac{1}{2})c_{n,g} - \frac{\imath\Omega}{2}\sum_{m=0}^{\infty} c_{m,e}\langle n|e^{-\imath k\hat{z}}|m\rangle \\ \frac{dc_{n,e}}{dt} &= -\imath\omega_{\rm trp}(n+\tfrac{1}{2})c_{n,e} - \imath(\omega_0-\omega)c_{n,e} - \frac{\imath\Omega}{2}\sum_{m=0}^{\infty} c_{m,g}\langle n|e^{\imath k\hat{z}}|m\rangle \end{aligned}} \ . \tag{20.51}$$

The fact that only terms proportional to $\langle n|e^{ik\hat{z}}|m\rangle$ contribute can be understood in terms of the *Franck-Condon overlap* between the vibrational states to be coupled. And the fact that the energy of the harmonic oscillator, and thus the effective detuning $\Delta_n \equiv \omega - \omega_0 - \omega_{\rm trp}(n+\frac{1}{2})$, depend on the vibrational state couples the internal and the external dynamics.

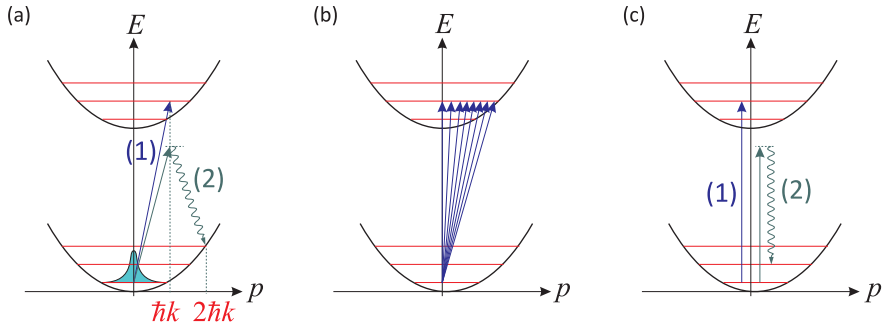

Figure 20.8: (a) Absorption (1) and Rayleigh scattering (2) in a weakly confining trap, where the momentum must stay conserved. (b) Illustration of the regime $\omega_{\rm rec} > \Gamma$, where the atom moves during the absorption process. (c) Absorption and Rayleigh scattering in a strongly confining trap.

Nevertheless, the off-diagonal coupling elements only contain the degrees of freedom of the harmonic oscillator.

20.3.3.5 Momentum kick by photonic recoil

We said earlier that a momentum kick can drive an atom from the vibrational ground state $|0\rangle$ into a coherent superposition of states $|\alpha\rangle$, except when the Lamb-Dicke parameter is very small. When the kick is realized via photonic recoil, e.g. when an

electronically excited atom decays to the ground state, the frequency of the emitted photon depends on the final vibrational state of the atom. That is we expect a coherent superposition of light frequencies, which in the limit $\eta > 1$ generates a *Doppler broadening* and in the limit $\eta < 1$ stays unshifted as for *elastic scattering*.

Let us now consider a single confined atom and address the question of the absorption probability. In first-order perturbation, using the Hamiltonian (20.48), the transition rate for absorption of a photon incident in z-direction is given by Fermi's Golden Rule,

$$\begin{aligned}\frac{1}{\tau} &= \frac{d}{dt}|\langle n,e|e^{\imath\hat{H}t/\hbar}|0,g\rangle|^2 \simeq \frac{2\pi}{\hbar^2}|\langle n,e|\hat{H}|0,g\rangle|^2 \\ &= \frac{2\pi}{\hbar^2}|\langle n,e|\tfrac{\hbar\Omega}{2}(e^{\imath k\hat{z}}\hat{\sigma}^\dagger + e^{-\imath k\hat{z}}\hat{\sigma})|0,g\rangle|^2 = \frac{\pi\Omega^2}{2}|\langle n,e|e^{\imath k\hat{z}}|0,e\rangle|^2 \ .\end{aligned} \tag{20.52}$$

Obviously, it is thus sufficient to calculate $\langle n|e^{ik\hat{z}}|0\rangle$, i.e. we can trace over the internal degrees of freedom. Using our previous results (2.152), we find with $\alpha = -ika_{\rm trp}/\sqrt{2}$,

$$\boxed{\frac{1}{\tau} = \frac{\pi\Omega^2}{2}|\langle n|\alpha\rangle|^2 = \frac{\pi\Omega^2}{2}e^{-|\alpha|^2}\frac{|\alpha^n|^2}{n!}} \ . \tag{20.53}$$

The interpretation of this result is that the absorption of a photon by an atom in state $|0,g\rangle$ transfers recoil by *leaving the vibrational state of the atom in a coherent superposition state*. Inversely, for the emission process from state $|0,e\rangle$ within the Lamb-Dicke regime, most of the time we will encounter the emitted photon at the resonance frequency ω_0, and rarely at $\omega_0 - \omega_{\rm trp}$. In any case, energy conservation is satisfied, since,

$$\begin{aligned}&\sum_n n\hbar\omega_{\rm trp}\langle n|\alpha\rangle\langle\alpha|n\rangle = \sum_n n\hbar\omega_{\rm trp}e^{-|\alpha|^2}\frac{|\alpha|^{2n}}{n!} \quad = \hbar\omega_{\rm trp}|\alpha|^2\sum_n ne^{-|\alpha|^2}\frac{|\alpha|^{2n-2}}{(n-1)!} \\ &= \frac{\hbar^2k^2}{2m}\langle\alpha|\alpha\rangle = \hbar\omega_{\rm rec} \ .\end{aligned} \tag{20.54}$$

Thus energy and momentum conservation are automatically satisfied by the way the kick is implemented.

20.3.3.6 A single anisotropically trapped atom in first-order perturbation

Let us now consider a single atom (e.g. a trapped ion) confined in an 3-dimensional anisotropic trap (e.g. strong confinement in one and weak confinement in the other direction) and address the question, whether the scattering will be anisotropic, as well. We generalize the problem to three dimensions by allowing for quantized vibrational states in three dimensions, $\hat{\sigma}^\dagger = \sum_{\mathbf{n}}|\mathbf{n}\rangle\langle\mathbf{n}|\otimes|e\rangle\langle g|$ with $|\mathbf{n}\rangle = |n_x,n_y,n_z\rangle$.

In first-order perturbation, using the Hamiltonian (20.48), the transition rate for absorption or emission is given by Fermi's Golden Rule,

$$\begin{aligned}\frac{1}{\tau} &= \frac{d}{dt}|\langle\mathbf{n},e|e^{\imath\hat{H}t/\hbar}|\mathbf{0},g\rangle|^2 \simeq \frac{2\pi}{\hbar^2}|\langle\mathbf{n},e|\tfrac{\hbar\Omega}{2}(e^{\imath\mathbf{k}\cdot\hat{\mathbf{r}}}\hat{\sigma}^\dagger + e^{-\imath\mathbf{k}\cdot\hat{\mathbf{r}}}\hat{\sigma})|\mathbf{0},g\rangle|^2 \\ &= \frac{\pi\Omega^2}{2}|\langle n_x,e|e^{\imath k\hat{x}}|0,e\rangle\langle n_y,e|e^{\imath k\hat{y}}|0,e\rangle\langle n_z,e|e^{\imath k\hat{z}}|0,e\rangle|^2 \ .\end{aligned} \tag{20.55}$$

Obviously, it is thus sufficient to calculate $\langle n_j|e^{\imath k\hat{z}}|0\rangle$, i.e. we can trace over the internal degrees of freedom. Using our previous results (2.152), we find with $\alpha_j = -\imath k_j a_{\mathrm{trp,j}}/\sqrt{2}$,

$$\boxed{\frac{1}{\tau} = \frac{\pi\Omega^2}{2}|\langle n_x|\alpha_x\rangle\langle n_y|\alpha_y\rangle\langle n_z|\alpha_z\rangle|^2 = \frac{\pi\Omega^2}{2}e^{-|\alpha_x|^2-|\alpha_y|^2-|\alpha_z|^2}\frac{|\alpha_x^{n_x}\alpha_y^{n_y}\alpha_z^{n_z}|^2}{n_x!n_y!n_z!}}\,.$$

In Exc. 20.3.4.1 we calculate and illustrate the transition matrix elements $\langle\mathbf{0}|e^{\imath k\hat{z}}|0\rangle$ and $\langle\mathbf{n}|e^{\imath k\hat{z}}|0\rangle$.

20.3.3.7 A single anisotropically trapped atom in second-order perturbation

To understand Rayleigh scattering, we need to go to second perturbation order summing over all intermediate vibrational states according to the Kramers-Heisenberg formula,

$$\begin{aligned}
\frac{d\sigma}{d\Omega} &= \frac{d}{dt}|\langle\mathbf{n},g,\mathbf{k}_f|e^{\imath\hat{H}t/\hbar}|\mathbf{0},g,\mathbf{k}_i\rangle|^2 \simeq \frac{2\pi}{\hbar^2}|\langle\mathbf{n},g,\mathbf{k}_f|\sum_{\mathbf{m}}\frac{\hat{H}^{(1)}|\mathbf{m},e\rangle\langle\mathbf{m},e|\hat{H}^{(1)}}{\omega_i-\omega_m}|\mathbf{0},g,\mathbf{k}_i\rangle|^2 \\
&= \frac{\pi\hbar^2\Omega^4}{8}\left|\sum_{\mathbf{m}}\frac{\langle\mathbf{n},\mathbf{k}_f|e^{-\imath\mathbf{q}\cdot\hat{\mathbf{r}}}|\mathbf{m}\rangle\langle\mathbf{m}|e^{\imath\mathbf{q}\cdot\hat{\mathbf{r}}}|\mathbf{0},\mathbf{k}_i\rangle}{E_i/\hbar+(0\omega_x+0\omega_y+0\omega_z+\frac{3}{2})-E_m/\hbar-(m_x\omega_x+m_y\omega_y+m_z\omega_z+\frac{3}{2})}\right|^2 \\
&= \frac{\pi\hbar^2\Omega^4}{8}\left|\sum_{m_x,m_y,m_z}\frac{\langle n_x,n_y,n_z|e^{-i\mathbf{k}_f\cdot\hat{\mathbf{r}}}|m_x,m_y,m_z\rangle\langle m_x,m_y,m_z|e^{\imath\mathbf{k}_i\cdot\hat{\mathbf{r}}}|0,0,0\rangle}{(E_i-E_m)/\hbar-m_x\omega_x-m_y\omega_y-m_z\omega_z}\right|^2 \\
&= \frac{\pi\hbar^2\Omega^4}{8}\left|\sum_{m_x,m_y,m_z}\prod_{j=x,y,z}\frac{\langle n_j|e^{-ik_{jf}r_j}|m_j\rangle\langle m_j|e^{ik_{ji}\mathbf{r}_j}|0\rangle}{(E_i-E_m)/\hbar-m_x\omega_{mx}-m_y\omega_{my}-m_z\omega_{mz}}\right|^2 .
\end{aligned} \tag{20.56}$$

The transition matrix elements can be calculated via (2.157). This expression represents (in the same time) the *dynamic structure factor* of the single trapped atom.

Example 114 (*Axial incidence*): Let us consider the particular case of Rayleigh scattering from the ground state of light incident in the direction $\mathbf{k}_i \equiv k_{iz}\hat{\mathbf{e}}_z$. We can then simplify,

$$\begin{aligned}
\frac{d\sigma}{d\Omega} &= \frac{\pi\hbar^2\Omega^4}{8}\left|\sum_{m_z}\frac{\langle 0|e^{-\imath k_{xf}\hat{x}}|0\rangle\langle 0|e^{-\imath k_{yf}\hat{y}}|0\rangle\langle 0|e^{-\imath k_{zf}\hat{z}}|m_z\rangle\langle m_z|e^{\imath k_{zi}\hat{z}}|0\rangle}{-m_z\omega_{\mathrm{trp}}}\right|^2 \\
&= \frac{\pi\hbar^2\Omega^4}{8}e^{-|\alpha_{fx}|^2-|\alpha_{fy}|^2-|\alpha_{fz}|^2-|\alpha_{iz}|^2}\left|\sum_{m_z}\frac{1}{(E_m-E_i)/\hbar-m_z\omega_{\mathrm{trp,z}}}\frac{\alpha_{fz}^{m_z}\alpha_{iz}^{m_z}}{m_z!}\right|^2 \\
&= \frac{\pi\hbar^2\Omega^4}{8}e^{-(\mathbf{k}_f\cdot\mathbf{a}_{\mathrm{trp}})^2/2-(\mathbf{k}_i\cdot\mathbf{a}_{\mathrm{trp}})^2/2}\left|\sum_{m_z}\frac{1}{(E_m-E_i)/\hbar-m_z\omega_{\mathrm{trp,z}}}\frac{(-\frac{1}{2}k_{fz}k_{iz}a_{\mathrm{trp,z}}^2)^{m_z}}{m_z!}\right|^2 ,
\end{aligned}$$

where $\mathbf{a}_{\mathrm{trp}} \equiv (a_{\mathrm{trp,x}}\ a_{\mathrm{trp,y}}\ a_{\mathrm{trp,z}})$. Looking into scattering into transverse direction, $\mathbf{k}_{f,z} = 0$, we get,

$$\left(\frac{d\sigma}{d\Omega}\right)_{\perp} = \frac{\pi\hbar^4\Omega^4}{8|E_m-E_i|^2}e^{-\mathbf{k}_{fx}^2a_{\mathrm{trp,x}}^2/2-\mathbf{k}_{fy}^2a_{\mathrm{trp,y}}^2/2-\mathbf{k}_{iz}^2a_{\mathrm{trp,z}}^2/2}\,.$$

Looking into backscattering, $\mathbf{k}_{f,z} = -\mathbf{k}_{i,z}$,

$$\left(\frac{d\sigma}{d\Omega}\right)_{\parallel} = \frac{\pi\hbar^2\Omega^4}{8} e^{-\mathbf{k}_i a_{\mathrm{trp,z}})^2} \left| \sum_{m_z} \frac{1}{(E_m - E_i)/\hbar - m_z\omega_{\mathrm{trp,z}}} \frac{(-\frac{1}{2}k_{iz}^2 a_{\mathrm{trp,z}}^2)^{m_z}}{m_z!} \right|^2 .$$

we expect a spectrum with vibrational resonances.

20.3.4 Exercises

20.3.4.1 Ex: Transition elements in anisotropic harmonic traps

a. Calculate and illustrate $\langle \mathbf{0}|e^{-\imath\mathbf{k}\cdot\hat{\mathbf{r}}}|\mathbf{0}\rangle$ for an anisotropic trap with cylindrical symmetry.
b. Calculate $\langle \mathbf{n}|e^{-\imath\mathbf{k}\cdot\hat{\mathbf{r}}}|\mathbf{0}\rangle$ and $\sum_{n_x,n_y,n_z}\langle \mathbf{n}|e^{-\imath\mathbf{k}\cdot\hat{\mathbf{r}}}|\mathbf{0}\rangle$.

20.3.4.2 Ex: Periodicity of a lattice

Calculate $e^{\imath a\hat{p}} e^{2\imath k\hat{z}} e^{-\imath a\hat{p}}$.

20.3.4.3 Ex: Energy commutators

Calculate the commutator between the kinetic and the potential energy for (a) a harmonic oscillator and (b) a standing wave dipolar potential.

20.4 Further reading

H.J. Metcalf, P. van der Straten, Graduate Texts in Contemporary Physics, Springer (1999), *Laser Cooling and Trapping* [http]

Ch.J. Foot, *Atomic Physics* [ISBN]

G. Vandegrift, *The Moessbauer effect explained* [DOI]

20.4.1 on optical forces

T.W. Hänsch et al., *Cooling of Gases by Laser Radiation* [DOI]

D.J. Wineland et al, *Laser Cooling of Atoms* [DOI]

A. Ashkin, *Trapping of atoms by resonance radiation pressure* [DOI]

E.L. Raab et al., *Trapping of Neutral Sodium Atoms with Radiation Pressure* [DOI]

Ph.W. Courteille et al., *Highly Versatile Atomic Micro Traps Generated by Multi-frequency Magnetic Field Modulation* [DOI]

Part VI

Collective Scattering of Light and Correlations

Preface to the part *Collective Scattering of Light and Correlations*

In Chp. 16 we discussed the interaction of light with individual atoms. In the practice of spectroscopy, however, we often work with ensembles of scatterers. Depending on their *spatial distribution* (e.g. disordered, quasi-continuous, periodic), their *motion* (hot gas or cold cloud), the possible existence of *correlations* between them, the presence of *boundary conditions* (e.g., free space, cavities, or photon bands), and finally, in case of degenerate quantum gases, of a possible *bosonic stimulation* of the scattering process, we expect new collective effects.

In chapter 22 we will discuss several examples, in particular, localization effects induced by disorder, super- and subradiance, Bragg scattering, and the formation of forbidden photonic bands in periodic lattices. Chp. 22 is devoted to the impact of optical cavities on scattering. In Chp. 23 we discuss effects resulting from correlations between many atoms. In Chp. 24 we turn our attention to quantum information. Finally, phenomena leading to self-organization, such as the collective atomic recoil laser, will be discussed in Chp. 25.

Chapter 21

Cooperativity in light scattering

This chapter starts with introducing as the main theoretical tools the *structure factor* and the *coupled dipoles model*. In Sec. 21.1 we will derive the formalism and learn, how to employ it to calculate, e.g. the spatial distribution of light scattered by an atomic cloud and the radiation pressure force on the atoms focusing on situations, where interatomic interactions induced by the incident light can be neglected. In Sec. 21.3 we will, disregarding the atomic's cloud graininess and disorder, introduce the *smooth density approximation* and compare it to macroscopic Mie scattering. In Sec. 21.4 we will focus on cooperative effects inducing collective lineshifts and broadenings, such as the Lorentz-Lorenz and the Lamb shift. We will also discuss disorder-induced localization effects, super- and subradiance. In Sec. 21.3 we investigate Bragg scattering, i.e. scattering from periodically ordered atoms, and finally in Sec. 22.1 we study scattering from correlated atoms.

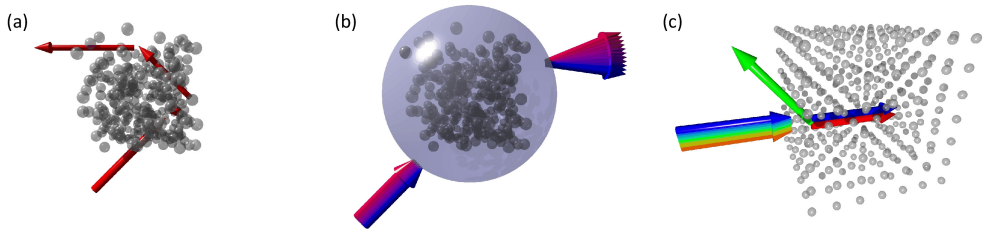

Figure 21.1: (a) Artist's view of multiple scattering of a photon through a dilute cloud. (b) Atomic cloud as a bulk object characterized by a refraction index $n(\mathbf{r})$. (c) Illustration of a photonic band in an optical lattice.

21.1 Theoretical tools and models

As mentioned above, the process of light scattering by an atomic cloud depends on several factors, many of which can be summarized by a quantity called the *structure factor*. This structure factor, obtained in perturbation theory, describes the probability for the light to be scattered into a particular direction as a function of the

properties of the atomic cloud (spatial distribution, motion, etc.). The quantity is well suited for dealing with stationary situations.

On the other hand we have at our disposal a microscopic theory called the *coupled dipole model*. In this model we treat every individual atom as a dipole, which interacts with all other atoms by rescattering the incident light. The resolution of the Schrödinger equation allows, several approximations having been made, to calculate the dynamics of the system.

21.1.1 The structure factor and definition of cooperativity

One way of characterizing the scattering process is by structure factor. The *static structure factor* is the normalized response of a system to a perturbation with the wave vector $\mathbf{q}$. It can be understood as the final density of states for the atom after the scattering process. In contrast, the *dynamic structure factor* also considers the final density of states for the emitted or scattered photon. That is, on one hand, the frequency and momentum of the photon must satisfy the Bragg condition. On the other hand, the density of available states can also be structured, for example, when the scattering process takes place inside a cavity.

In lowest-order perturbation theory (Fermi's Golden Rule) we get the general expressions [460],

$$\boxed{\frac{d\sigma}{d\Omega_s d\omega} = \left(\frac{d\sigma}{d\Omega_s}\right)_1 S(\mathbf{q},\omega)}\,, \tag{21.1}$$

that is, the effective scattering cross section is reduced to the effective Rayleigh scattering cross section by an isolated atom times a geometric term called *dynamic structure factor*,

$$\boxed{S(\mathbf{q},\omega) \equiv \tfrac{1}{2\pi}\int dt e^{\imath\omega t}\langle\hat{\rho}(\mathbf{q},t)\hat{\rho}^\dagger(\mathbf{q},0)\rangle}\,, \tag{21.2}$$

where,

$$\hat{\rho}(\mathbf{q},t) = \int_V \hat{n}(\mathbf{r},t)e^{\imath\mathbf{q}\cdot\mathbf{r}}d^3r \tag{21.3}$$

is Fourier transform of the atomic density. Thus, $S(\mathbf{q},\omega)$ is the Fourier transform of the density-density correlation function. On the other hand, $\int e^{\imath\omega t}d\omega = 2\pi\delta(t)$, and we calculate the *static structure factor*,

$$\boxed{S(\mathbf{q}) \equiv \int S(\mathbf{q},\omega)d\omega = \langle\hat{\rho}(\mathbf{q},0)\hat{\rho}^\dagger(\mathbf{q},0)\rangle}\,. \tag{21.4}$$

In the equations (21.2) and (21.3) we have written the quantities $\hat{\rho}(\mathbf{q},t)$ and $\hat{n}(\mathbf{r},t)$ as operators, in order to allow for the possibility, that the atomic ensemble is a quantum gas, i.e. a Bose-Einstein condensate characterized by a single wavefunction $\hat{\psi}(\mathbf{r},t)$ normalized to the density distribution, $\hat{\rho}(\mathbf{r},t) = \hat{\psi}^\dagger(\mathbf{r},t)\hat{\psi}(\mathbf{r},t)$. We shall return to this subject in Sec. 29.1.1. In the following, we will restrict ourselves to atoms localized in space with well-defined velocities and calculate the structure factor (i) for disordered clouds of atoms excited by the passage of a photon in Sec. 21.1.6 and (ii) for Bragg scattering by optical lattices in Sec. 21.5. In these cases, we find in the

literature often another definition of the structure factor as the expectation value of the Fourier transform of the atomic density,

$$\mathcal{S}(\mathbf{q}) = \langle \hat{\rho}(\mathbf{q}) \rangle \ , \tag{21.5}$$

Thus, it describes the amplitude of the electric field of the scattered radiation. In order to avoid confusion we will call this quantity *structure coefficient* and denote it by a calligraphic $\mathcal{S}$. We study the structure factor for various atomic density distributions in Excs. 21.1.8.1 to 21.1.8.3.

Example 115 (*Structure factor of a discrete cloud*): In case of discrete clouds, $n(\mathbf{r},t) = \sum_j \delta^{(3)}(\mathbf{r}-\mathbf{r}_j)$, we can disregard the quantum nature of the operators. The relationship (21.3) immediately gives,

$$\rho(\mathbf{q},t) = \sum_j e^{\imath \mathbf{q}\cdot\mathbf{r}_j(t)} \tag{21.6}$$

and the relationship (21.2),

$$S(\mathbf{q},\omega) = \tfrac{1}{2\pi}\int dt e^{\imath\omega t}\rho(\mathbf{q},t)\rho^*(\mathbf{q},0) = \tfrac{1}{2\pi}\int dt e^{\imath\omega t}\sum_{j,k} e^{\imath\mathbf{q}\cdot[\mathbf{r}_j(t)-\mathbf{r}_k(0)]} \ . \tag{21.7}$$

Assuming atoms fixed in space, $\mathbf{r}_j(t) = \mathbf{r}_j$,

$$S(\mathbf{q},\omega) = \sum_{j,k} e^{\imath\mathbf{q}\cdot(\mathbf{r}_j-\mathbf{r}_k)}\delta(\omega) \ . \tag{21.8}$$

That is, without recoil the light must be scattered elastically.

The notion of *cooperativity* is fundamental for any problem involving scattering of radiation and, depending on the specific area of physics, is called by many different names, such as Purcell factor, cavity-to-free-space scattering ratio, or phase matching condition. Here, we will regard cooperativity as any ***deviation of the structure factor from isotropy***. For example, Bragg scattering and optical cavities are highly cooperative, because they favor scattering in particular directions [1].

21.1.2 The scalar coupled dipoles model

In the following, we develop the coupled dipoles model, within which we define the structure factor for light scattering by a cloud of scatterers making the following assumptions:

- The light is (mostly) treated as a scalar field. That is, we disregard effects due to the polarization of light and assume two-level atoms. Generalizations are shown in Sec. 21.6.4 [763, 559].
- Atoms are supposed to be fixed in space. That is, we disregard the Doppler shift of moving atoms and the photonic recoil. Therefore, it will suffice to consider the static structure factor.

[1] Note that cooperativity does not request the atoms to interact and exists in the single scattering regime. In the multiple scattering regime other forms of collective phenomena, such as collective Lamb shifts emerge, as we will see later on.

- Atoms are initially uncorrelated and not degenerate. That means that we neglect effects such as bosonic stimulation or Fermi blocking [2].

Be ω_0 the frequency of the incident light, $\omega_{\rm a}$ the frequency of the atomic resonance, and ω the frequency of the scattered light. The Hamiltonian is nothing more than the generalization of (17.106) to several assumed atoms located at the positions r_j,

$$\boxed{\begin{aligned}\hat{H} &= \sum_{j=1}^{N}\hbar g_{\mathbf{k}_0}(\hat{\sigma}_j e^{-\imath\omega_{\rm a}t}+\hat{\sigma}_j^\dagger e^{\imath\omega_{\rm a}t})(\hat{a}_{\mathbf{k}_0}^\dagger e^{\imath\omega_0 t-\imath\mathbf{k}_0\cdot\mathbf{r}_j}+\hat{a}_{\mathbf{k}_0}e^{-\imath\omega_0 t+\imath\mathbf{k}_0\cdot\mathbf{r}_j})\\ &+ \sum_{\mathbf{k}}\sum_{j=1}^{N}\hbar g_{\mathbf{k}}(\hat{\sigma}_j e^{-\imath\omega_{\rm a}t}+\hat{\sigma}_j^\dagger e^{\imath\omega_{\rm a}t})(\hat{a}_{\mathbf{k}}^\dagger e^{\imath\omega_k t-\imath\mathbf{k}\cdot\mathbf{r}_j}+\hat{a}_{\mathbf{k}}e^{-\imath\omega_k t+\imath\mathbf{k}\cdot\mathbf{r}_j})\end{aligned}} \quad . \tag{21.9}$$

Here, $\Omega_0 = 2g_{k_0}\sqrt{n_0}$ is the Rabi frequency of the interaction between an atom and the incident light (which is treated as a classical field with n_0 photons), $\hat{\sigma}_j$ is the deexcitation operator for the j-th atom, $\hat{a}_{\mathbf{k}}$ is the photon annihilation operator, and $g_k = d\sqrt{\omega/(\hbar\varepsilon_0 V_{\rm ph})}$ describes the coupling between the atom and the vacuum modes the volume of which is $V_{\rm ph}$. The j-th atom has its lower and upper states denoted by $|g_j\rangle$ and $|e_j\rangle$, respectively. That is, we treat the atoms as simple two-level systems. We also assume that all atoms are excited by the same unperturbed incident laser beam, thus neglecting their dephasing along the laser path or induced by near-field effects (which could arise for large spatial densities).

Within the *rotating wave approximation* RWA the Hamiltonian simplifies to,

$$\begin{aligned}\hat{H} &= \hbar\sum_{j=1}^{N}[g_{k_0}\hat{\sigma}_j\hat{a}_{\mathbf{k}_0}^\dagger e^{\imath(\omega_0-\omega_{\rm a})t-\imath\mathbf{k}_0\cdot\mathbf{r}_j}+h.c.] \\ &+\hbar\sum_{j=1}^{N}\sum_{\mathbf{k}}[g_k\hat{\sigma}_j\hat{a}_{\mathbf{k}}^\dagger e^{\imath(\omega_k-\omega_{\rm a})t-\imath\mathbf{k}\cdot\mathbf{r}_j}+h.c.]\ .\end{aligned} \tag{21.10}$$

The RWA only considers energy-conserving terms in single-photon processes. But this is an artifact from the field quantization. Energy conservation can be warranted by considering multi-photon virtual processes, which as a whole, conserve energy. These terms appear in the full Hamiltonian, but are neglected in the RWA. While the RWA often is a good assumption in single atom quantum optics, this is frequently not the case for collective scattering. Here, we adopt the RWA to a simplify the subsequent solution of the Schrödinger equation, but we will need to generalize the results obtained a posteriori, as shown in the discussion of Sec. 21.1.4.

We call $|0\rangle_{\rm a} = |g_1,..,g_N\rangle$ the atomic ground state, $|j\rangle_{\rm a} = |g_1,..,e_j,..,g_N\rangle$ the state where only the atom j is excited, and we assume that the system is in a the

[2] Spontaneous emission by an atom in a Fermi gas of temperature $T = 0$ can not occur if the photon wave vector is inside the Fermi lake, $q < k_F$.

superposition of states described by [3],

$$|\Psi(t)\rangle = \alpha(t)|0\rangle_{\rm a}|n_0\rangle_{\mathbf{k}_0}|0\rangle_{\mathbf{k}} + \sum_{j=1}^{N}\beta_j(t)|j\rangle_{\rm a}|n_0-1\rangle_{\mathbf{k}_0}|0\rangle_{\mathbf{k}} + \sum_{\mathbf{k}}\gamma_{\mathbf{k}}(t)|0\rangle_{\rm a}|n_0-1\rangle_{\mathbf{k}_0}|1\rangle_{\mathbf{k}} \ . \tag{21.11}$$

With this ansatz we imply that at every instant of time, there can be at most only one excitation in the atomic cloud. The temporal evolution of the amplitudes is obtained by inserting the Hamiltonian and the ansatz into the Schrödinger equation, $\imath\hbar\partial_t|\Psi(t)\rangle = \hat{H}|\Psi(t)\rangle$. Once the evolution of the amplitudes is calculated, we can determine the observables of the system, such as the radiative pressure force or the amplitudes of the scattered radiation fields or the fields inside the cloud.

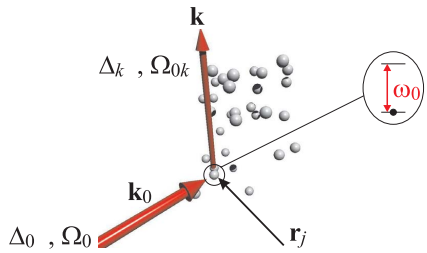

Figure 21.2: Scheme of the interaction of a light beam with a sample of atoms.

Example 116 (*Interaction Hamiltonian in the rotating frame*): The Hamiltonian in the rotating wave approximation is,

$$\hat{H} = \hbar g\left(\hat{\sigma}e^{-\imath\omega_{\rm a}t} + \hat{\sigma}^\dagger e^{\imath\omega_{\rm a}t}\right)\left(\hat{a}^\dagger e^{\imath\omega_0 t} + \hat{a}e^{-\imath\omega_0 t}\right) \simeq \hbar g\left(\hat{\sigma}\hat{a}^\dagger e^{\imath\Delta_0 t} + \hat{\sigma}^\dagger\hat{a}e^{-\imath\Delta_0 t}\right) \ .$$

For the Pauli matrices we have the following rules,

$$[\hat{\sigma}_z,\hat{\sigma}] = -\hat{\sigma} \qquad \text{and} \qquad [\hat{\sigma}_z,\hat{\sigma}^\dagger] = \hat{\sigma}^\dagger \ ,$$

such that,

$$\begin{aligned}
[\hat{\sigma}_z,\hat{H}] &= \hbar g\left(-e^{\imath\Delta_0 t}\hat{a}^\dagger\hat{\sigma} + e^{-\imath\Delta_0 t}\hat{a}\hat{\sigma}^\dagger\right)\\
[\hat{\sigma}_z,[\hat{\sigma}_z,\hat{H}]] &= \hbar g\left(e^{\imath\Delta_0 t}\hat{a}^\dagger\hat{\sigma} + e^{-\imath\Delta_0 t}\hat{a}\hat{\sigma}^\dagger\right) = \hat{H}\\
[\hat{\sigma}_z,[...[\hat{\sigma}_z,\hat{H}]]...] &= \hbar g\left[(-1)^n e^{\imath\Delta_0 t}\hat{a}^\dagger\hat{\sigma} + e^{-\imath\Delta_0 t}\hat{a}\hat{\sigma}^\dagger\right] \ .
\end{aligned}$$

[3] This ansatz is well adapted to situations where the RWA holds. Otherwise, additional counter-rotating terms must be included [286].

Using the Baker-Haussdorff formula,

$$\begin{aligned} e^{\imath\omega_0 t\hat{\sigma}_z}\hat{H}e^{-\imath\omega_0 t\hat{\sigma}_z} &= \hat{H} + [\imath\omega_0 t\hat{\sigma}_z, \hat{H}] + \tfrac{1}{2!}[\imath\omega_0 t\hat{\sigma}_z, [\imath\omega_0 t\hat{\sigma}_z, \hat{H}]] + ... \\ &= \hbar g \sum_{n=0}^{\infty} \tfrac{(\imath\omega_0 t)^n}{n!} \left[(-1)^n e^{\imath\Delta_0 t}\hat{a}^\dagger\hat{\sigma} + e^{-\imath\Delta_0 t}\hat{a}\hat{\sigma}^\dagger\right] \\ &= \hbar g e^{\imath\Delta_0 t}\hat{a}^\dagger\hat{\sigma}\sum_{n=0}^{\infty}\tfrac{(-\imath\omega_0 t)^n}{n!} + \hbar g e^{-\imath\Delta_0 t}\hat{a}\hat{\sigma}^\dagger\sum_{n=0}^{\infty}\tfrac{(\imath\omega_0 t)^n}{n!} \\ &= \hbar g\left(e^{-\imath\omega_a t}\hat{a}^\dagger\hat{\sigma} + e^{\imath\omega_a t}\hat{a}\hat{\sigma}^\dagger\right) . \end{aligned}$$

21.1.2.1 Temporal evolution of the amplitudes

The time evolution of the amplitudes is obtained by inserting the Hamiltonian $\hat{H}$ and the ansatz $|\Psi(t)\rangle$ into the Schrödinger equation,

$$\frac{\partial}{\partial t}|\Psi(t)\rangle = -\frac{\imath}{\hbar}\hat{H}|\Psi(t)\rangle \ . \tag{21.12}$$

one obtains with $\Omega_0 = 2g_{k_0}\sqrt{n_0}$,

$$\begin{aligned} \dot{\alpha}(t) &= -\imath\tfrac{\Omega_0}{2}e^{\imath\Delta_0 t}\sum_{j=1}^{N}\beta_j(t)e^{-\imath\mathbf{k}_0\cdot\mathbf{r}_j} \\ \dot{\beta}_j(t) &= -\imath\tfrac{\Omega_0}{2}\alpha(t)e^{-\imath\Delta_0 t+\imath\mathbf{k}_0\cdot\mathbf{r}_j} - \sum_{\mathbf{k}}\imath g_k\gamma_{\mathbf{k}}(t)e^{-\imath\Delta_k t+\imath\mathbf{k}\cdot\mathbf{r}_j} \\ \dot{\gamma}_{\mathbf{k}}(t) &= -\imath g_k e^{\imath\Delta_k t}\sum_{j=1}^{N}\beta_j(t)e^{-\imath\mathbf{k}\cdot\mathbf{r}_j} \ . \end{aligned} \tag{21.13}$$

We set the initial conditions,

$$\alpha(0) = 1 \quad , \quad \beta_j(t) = 0 \quad , \quad \gamma_{\mathbf{k}}(t) = 0 \ . \tag{21.14}$$

For low excitation rate, we can set $\alpha(t) \simeq 1$. Integrating the third equation,

$$\gamma_{\mathbf{k}}(t) = -\imath g_k\sum_{j=1}^{N}e^{-\imath\mathbf{k}\cdot\mathbf{r}_j}\int_0^t e^{\imath\Delta_k t'}\beta_j(t')dt' \ , \tag{21.15}$$

and substituting it into the second equation,

$$\dot{\beta}_j(t) = -\imath\tfrac{\Omega_0}{2}\alpha(t)e^{-\imath\Delta_0 t+\imath\mathbf{k}_0\cdot\mathbf{r}_j} - \sum_{\mathbf{k}}g_k^2\sum_{m=1}^{N}e^{\imath\mathbf{k}\cdot(\mathbf{r}_j-\mathbf{r}_m)}\int_0^t e^{\imath\Delta_k(t'-t)}\beta_m(t')dt' \ . \tag{21.16}$$

21.1.3 The Markov approximation

For small systems, $R < \lambda$, we can make use of the Markov approximation, which holds when the collective decay time $t_{decay} < R/c$. Larger systems persist memory effects, which may lead to (Rabi) *collective Rabi oscillations*. In the Markov approximation given by $\beta_j(t') \simeq \beta_j(t)$ the integro-differential equation (which is equivalent to a differential equation of arbitrarily high order) reduces to a simple first order differential equation. Defining [4],

$$\beta_j \equiv \tilde{\beta}_j e^{-\imath\Delta_0 t + \imath \mathbf{k}_0\cdot\mathbf{r}_j} \ , \tag{21.17}$$

we obtain,

$$\frac{d}{dt}\alpha(t) = -\imath\frac{\Omega_0}{2}\sum_{j=1}^{N}\tilde{\beta}_j(t) \tag{21.18}$$

$$\frac{d}{dt}\tilde{\beta}_j(t) = \imath\Delta_0\tilde{\beta}_j(t) - \frac{\Omega_0^2}{4}\sum_{m=1}^{N}\int_0^t \tilde{\beta}_m(t')dt' - \sum_{\mathbf{k}} g_k^2 \sum_{m=1}^{N} e^{\imath(\mathbf{k}-\mathbf{k}_0)\cdot(\mathbf{r}_j-\mathbf{r}_m)}\int_0^t e^{-\imath(\omega_k-\omega_0)t''}\tilde{\beta}_m(t-t'')dt'' \ ,$$

where we substituted $t'' \equiv t - t'$ in the last integral. Now, using the Markov approximation $\tilde{\beta}_m(t-t'') \simeq \tilde{\beta}_m(t)$, with $\lim_{t\to\infty}\int_0^t e^{-\imath(\omega_k-\omega_0)t'}dt' = \pi\delta(\omega_k-\omega_0)$, and with the rate of spontaneous emission,

$$\boxed{\Gamma \equiv \frac{V_{\rm ph}}{\pi c}k_0^2 g_{k_0}^2} \ , \tag{21.19}$$

the third term becomes for the case $m = j$,

$$\sum_{\mathbf{k}} g_k^2\int_0^t e^{-\imath(\omega_k-\omega_0)t''}\tilde{\beta}_j(t-t'')dt'' \simeq \sum_{\mathbf{k}} g_k^2\tilde{\beta}_j(t)\pi\delta(\omega_k-\omega_0) \tag{21.20}$$
$$= \frac{V_{\rm ph}}{(2\pi)^3}\tilde{\beta}_j(t)\int g_k^2\pi\delta(\omega_k-\omega_0)d^3k = \frac{V_{\rm ph}}{(2\pi)^3}\tilde{\beta}_j(t)4\pi g_{k_0}^2\pi k_0^2\frac{1}{c} = \frac{\Gamma}{2}\tilde{\beta}_j(t) \ .$$

The third term becomes for the case $m \neq j$, evaluating the sum over the wavevectors by $\sum_{\mathbf{k}} \to \frac{V_{\rm ph}}{(2\pi)^3}\int d^3k$,

$$\sum_{\mathbf{k}} g_k^2\sum_{m\neq j}^{N} e^{\imath(\mathbf{k}-\mathbf{k}_0)\cdot(\mathbf{r}_j-\mathbf{r}_m)}\int_0^t e^{-\imath(\omega_k-\omega_0)t''}\tilde{\beta}_m(t-t'')dt'' \tag{21.21}$$
$$\simeq \sum_{\mathbf{k}} g_k^2\sum_{m\neq j}^{N} e^{\imath(\mathbf{k}-\mathbf{k}_0)\cdot(\mathbf{r}_j-\mathbf{r}_m)}\tilde{\beta}_m(t)\pi\delta(\omega_k-\omega_0)$$
$$= \frac{V_{\rm ph}}{(2\pi)^3}\sum_{m\neq j}^{N}\tilde{\beta}_m(t)\int g_k^2 e^{\imath(\mathbf{k}-\mathbf{k}_0)\cdot(\mathbf{r}_j-\mathbf{r}_m)}\pi\delta(\omega_k-\omega_0)d^3k = \frac{\Gamma}{2}\sum_{m\neq j}^{N}\gamma_{jm}\tilde{\beta}_m(t) \ ,$$

[4] Later on we will be particularly interested in so-called *timed Dicke states* characterized by $\tilde{\beta}_j = \tilde{\beta}$ independent on j.

with

$$\gamma_{jm} \equiv \frac{2}{\Gamma}\frac{V_{\rm ph}}{(2\pi)^3}\int_0^\infty\int_0^\pi\int_0^{2\pi} g_k^2 e^{\imath(\mathbf{k}-\mathbf{k}_0)\cdot(\mathbf{r}_j-\mathbf{r}_m)}\frac{\pi}{c}\delta(k-k_0)k^2\sin\theta dk d\theta d\phi \ . \quad (21.22)$$

Finally,

$$\frac{d}{dt}\tilde{\beta}_j(t) = \imath\Delta_0\tilde{\beta}_j(t) - \frac{\Omega_0^2}{4}\sum_{m=1}^N\int_0^t\tilde{\beta}_m(t')dt' - \frac{\Gamma}{2}\sum_{m=1}^N\gamma_{jm}\tilde{\beta}_m(t) \ , \quad (21.23)$$

or

$$\frac{d}{dt}\alpha(t) = -\imath\frac{\Omega_0}{2}\sum_{j=1}^N\tilde{\beta}_j(t) \quad (21.24)$$

$$\frac{d}{dt}\tilde{\beta}_j(t) = \imath\Delta_0\tilde{\beta}_j(t) - \imath\frac{\Omega_0}{2}\alpha(t) - \frac{\Gamma}{2}\sum_{m=1}^N\gamma_{jm}\tilde{\beta}_m(t) \ .$$

This means that the problem is reduced to finding the γ_{jm}. Continuing the evaluation of Eq. (21.22),

$$\begin{aligned}\gamma_{jm} &= \frac{1}{\Gamma}g_k^2\frac{V_{\rm ph}}{4\pi^2 c}e^{-\imath\mathbf{k}_0\cdot(\mathbf{r}_j-\mathbf{r}_m)}\int_0^\infty\int_0^{2\pi}\int_{-1}^1 e^{\imath k|\mathbf{r}_j-\mathbf{r}_m|\cos\theta}d\cos\theta d\phi\delta(k-k_0)k^2dk \\ &= \frac{1}{\Gamma}g_k^2\frac{V_{\rm ph}}{\pi c}e^{-\imath\mathbf{k}_0\cdot(\mathbf{r}_j-\mathbf{r}_m)}\int_0^\infty\frac{\sin k|\mathbf{r}_j-\mathbf{r}_m|}{k|\mathbf{r}_j-\mathbf{r}_m|}\delta(k-k_0)k^2dk \\ &= e^{-\imath\mathbf{k}_0\cdot(\mathbf{r}_j-\mathbf{r}_m)}\frac{\sin k_0|\mathbf{r}_j-\mathbf{r}_m|}{k_0|\mathbf{r}_j-\mathbf{r}_m|} \ . \end{aligned} \quad (21.25)$$

Isolating the self-decaying term and assuming low saturation, $\alpha(t) = 1$, we get,

$$\boxed{\dot{\tilde{\beta}}_j = \left(\imath\Delta_0 - \frac{\Gamma}{2}\right)\tilde{\beta}_j - \frac{\imath\Omega_0}{2} - \frac{\Gamma}{2}\sum_{m\neq j}\gamma_{jm}\tilde{\beta}_m} \ . \quad (21.26)$$

In Exc. 21.1.8.4 we will analyze the validity of the Markov approximation for typical cold atoms experiments.

21.1.4 General solution with exponential kernel, validity of the RWA

The RWA is valid for $\max(\Omega, \Gamma_n) \ll \omega$,

$$\int_0^t dt\cdot e^{-\imath(\omega_k-\omega_0)t} \simeq \mathcal{P}\left(\frac{1}{\omega_k+\omega_0}\right) - \imath\mathcal{P}\left(\frac{1}{\omega_k-\omega_0}\right) + \pi\delta(\omega_k-\omega_0) \ . \quad (21.27)$$

The whole expression leads to the exponential kernel, the first two terms are the cosine part, the third term is the sine part. The rotating wave approximation consists in neglecting the first term, i.e. it only concerns the cosine part of the kernel.

Within the RWA we got [5,6],

$$\gamma_{jm} = e^{-\imath \mathbf{k}_0 \cdot (\mathbf{r}_j - \mathbf{r}_m)} \frac{\imath \sin(k_0 |\mathbf{r}_j - \mathbf{r}_m|)}{\imath k_0 |\mathbf{r}_j - \mathbf{r}_m|} \ . \tag{21.28}$$

Without the RWA we would have found [750, 745, 746, 805],

$$\gamma_{jm} = e^{-\imath \mathbf{k}_0 \cdot (\mathbf{r}_j - \mathbf{r}_m)} \frac{e^{\imath k_0 |\mathbf{r}_j - \mathbf{r}_m|}}{\imath k_0 |\mathbf{r}_j - \mathbf{r}_m|} \ . \tag{21.29}$$

An alternative derivation from a Green function approach to the master equation is presented in Sec. 23.3.2 (see Eq. (23.133)).

There has been a controversy between Friedberg and Scully about the role of virtual photons (or *collective Lamb-shift*) [292, 804, 293, 747]. These terms result from counterrotating terms in the rotating wave approximation. Scully assumes timed Dicke states in *infinitely large* clouds and finds the contributions weak. Friedberg does a mode expansion of the cloud and finds that different modes decay at different velocities. This yields time-dependent radiation patterns, which can be temporarily larger in backward direction.

Normally, the RWA is a good approximation, when $\Omega \ll \omega$. Deviations from this approximations lead e.g. to the Bloch-Siegert shift and important corrections for very far-detuned (quasi-electrostatic) optical trapping. The above requirement is not well satisfied for our experiment, since $\Omega_N = \sqrt{N}\Omega \simeq 1..10\,\mathrm{THz}$.

Be $|b_1 b_2 ... a_j ... b_N\rangle$ the state with all atoms in the ground state except atom j being in the excited state. Hence, the cloud's state is simply expressed by the wavefunction,

$$\Psi_{atom}(t) = \sum_{j=1}^{N} \beta_j(t) |b_1 b_2 ... a_j ... b_N\rangle \ . \tag{21.30}$$

For large σ the radiation pressure is independent on the choice of the kernel. In fact we may even set the kernel to 0. For small σ there appears a considerable deviation. Interestingly, the imaginary part of the kernel gets important for higher densities, even when the optical density is maintained, e.g. by compressing the cloud in z-direction. This means that the collective Lamb shift becomes more apparent is small compressed clouds. But we postpone a more thorough discussion to Sec. 21.4.

The analytic expansion into eigenmodes assumes the RWA. Hence, the numerics deviate from the analytics for small σ and large N. Is it possible to generalize the expansion to the exponential kernel (see [805])? The authors also suggest that the scattered radiation be frequency-shifted due to the imaginary part of the kernel. This might be an interesting observable for experiments.

21.1.4.1 Low collective saturation

Note that for low *saturation*, $\alpha(t) = 1$, the first term simply becomes $-\frac{\imath}{2}\Omega_0$. Even though the single atom excitation rate may be small in case of large detuning, the

[5] Note that dipole-dipole interactions are mediated by the exchange of virtual photons. Hence, they are included in the Hamiltonian when the RWA is NOT applied.

[6] Note that Maxwell's equations contain non-RWA terms.

collective Rabi frequency $\sqrt{N}\Omega$ can be large. The presence of many excitations in the cloud means, that higher Dicke states are populated. Then we may expect a complicated many-body dynamics, if decay into other states than the timed Dicke state is possible.

Even though the single atom excitation rate may be small in case of large detuning, the *collective* Rabi frequency $\sqrt{N}\Omega$ can be large. The presence of many excitations in the cloud means, that higher Dicke states are populated. Then we may expect a complicated many-body dynamics, if decay into other states than the timed Dicke state is possible.

The model we use (ground state + first excited state in the times Dicke basis) does not allow more than 1 photon for N atoms. For such a model, neglecting saturation means 'much' less than 1 atom in the excited state, i.e. the probability of having the any atom in the excited state is less than 1. But having N atoms, this means that each atoms should have a excited state population of much less than $1/N$. Including the saturation in the naive way, means that when this term $N\Omega_0^2$ is not negligible, than we will have less atoms in the first excited state of the timed Dicke basis, than if when we would neglect saturation. This is precisely why we call this saturation, we cannot take more atoms away from the ground state, because the system cannot absorb more than one photon. But when this term is not longer negligible, then in a cloud of N atoms, this does not prevent us from taking atoms away from the ground state (we have N atoms which each can take one photon). Either the term is negligible (and we could drop it) or we will try to keep its contribution (even at first order in $N\Omega_0^2$), but then we cannot neglect the possibility of having 2 atoms excited.

21.1.4.2 Steady-state solution

In steady-state the equations of the coupled dipoles model can be solved numerically for an arbitrary (ordered or disordered) cloud of immobile atoms located at positions $\mathbf{r}_j$ illuminated by an electric field.

Assuming scalar light and the validity of the Markov approximation, and furthermore defining $\bar{\beta}_j \equiv \tilde{\beta}_j e^{\imath \mathbf{k}_0 \cdot \mathbf{r}_j}$ and $\bar{\Omega}_0(\mathbf{r}_j) \equiv \Omega_0(\mathbf{r}_j) e^{\imath \mathbf{k}_0 \cdot \mathbf{r}_j}$, and using the exponential kernel,

$$\bar{\gamma}_{jm} = \frac{e^{\imath k_0 |\mathbf{r}_j - \mathbf{r}_m|}}{\imath k_0 |\mathbf{r}_j - \mathbf{r}_m|} \ , \tag{21.31}$$

the Eq. (21.26) for the atomic states reads,

$$\frac{d}{dt}\bar{\beta}_j = \left(\imath\Delta_0 - \frac{\Gamma}{2}\right)\bar{\beta}_j - \frac{\imath\bar{\Omega}_0(\mathbf{r}_j)}{2} - \frac{\Gamma}{2}\sum_{m\neq j}\bar{\gamma}_{jm}\bar{\beta}_m \ . \tag{21.32}$$

Defining the matrix,

$$M_{jm} \equiv (\imath\Delta_0 - \tfrac{\Gamma}{2})\delta_{jm} - \tfrac{\Gamma}{2}(1-\delta_{jm})\bar{\gamma}_{jm} = \begin{pmatrix} \imath\Delta_0 - \frac{\Gamma}{2} & \imath\gamma_{12}\frac{\Gamma}{2} & \cdots \\ \imath\gamma_{21}\frac{\Gamma}{2} & \imath\Delta_0 - \frac{\Gamma}{2} & \\ \vdots & & \ddots \end{pmatrix} \ , \tag{21.33}$$

we can rewrite Eq. (21.34) as,

$$\boxed{\frac{d}{dt}\bar{\beta}_j = \sum_m M_{jm}\bar{\beta}_m - \frac{\imath}{2}\bar{\Omega}_0(\mathbf{r}_j)} \; . \tag{21.34}$$

The steady-state solution of is simply obtained by $\dot{\bar{\beta}}_j = 0$ [176, 134],

$$M_{jm}\bar{\beta}_m(\infty) = \tfrac{\imath}{2}\bar{\Omega}_0(\mathbf{r}_j) \; . \tag{21.35}$$

This equation can now be solved by the dipole moment amplitudes,

$$\boxed{\bar{\beta}_m(\infty) = (M_{jm})^{-1} \; \tfrac{\imath}{2}\bar{\Omega}_0(\mathbf{r}_j)} \; , \tag{21.36}$$

where we use the exponential kernel,

$$\gamma_{jm} = \frac{e^{\imath k_0(|\mathbf{r}_j - \mathbf{r}_m| + \delta_{jm})}}{\imath k_0(|\mathbf{r}_j - \mathbf{r}_m| + \delta_{jm})} \; , \tag{21.37}$$

where the trick with the δ_{jm}-symbol helps to remove divergences for equal atom positions.

In this form the solution is immediately suitable for numerical implementation of the coupled dipoles model, although in practice the number of atoms is limited to $N < 10000$ for ordinary PCs.

21.1.4.3 Limit of dilute clouds

Dilute clouds are characterized by a large interatomic distance $k_0|\mathbf{r}_j - \mathbf{r}_m| \gg 1$. In this case, the non-diagonal elements of the kernel (21.33) quickly vanish, and the equations of motion (21.34) decouple to,

$$\frac{d}{dt}\bar{\beta}_j = \left(\imath\Delta_0 - \frac{\Gamma}{2}\right)\bar{\beta}_j - \frac{\imath}{2}\bar{\Omega}_0(\mathbf{r}_j) \; . \tag{21.38}$$

21.1.4.4 Characterization of the atomic cloud in steady-state

Plot the spacial dependence of the phases of the atomic dipoles, $\phi(\mathbf{r}_j) = \mathfrak{Im}\,(\ln\tilde{\beta}_j)$.

21.1.4.5 Time-dependence

In order to calculate the time-dependence, we reconsider the equation (21.34) for the excitation amplitudes. Its solution is formally given by the sum of the general solution of the homogeneous equation and a particular (e.g. the asymptotic) solution of the inhomogeneous equation,

$$\bar{\beta}_j(t) = e^{M_{jm}t}\bar{\beta}_m(0) + (\mathbb{I} - e^{M_{jm}t})\bar{\beta}_m(\infty) \; . \tag{21.39}$$

Inserting the steady-state solution we finally get,

$$\boxed{\bar{\beta}_j(t) = e^{M_{jm}t}\bar{\beta}_m(0) + (\mathbb{I} - e^{M_{jn}t})M^{-1}_{mn} \; \tfrac{\imath}{2}\bar{\Omega}_0(\mathbf{r}_m)} \; . \tag{21.40}$$

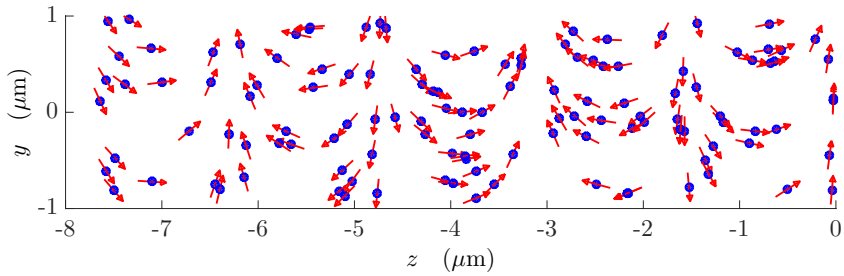

Figure 21.3: Phase delay in the excitation of the atomic dipoles (a) without rescattering ($\gamma_{jm} = 0$) and (b) with rescattering.

21.1.5 Calculation of light scattering in steady-state

To calculate the distribution of scattered light, we start from the Heisenberg equation for the field operator [286],

$$\frac{d\hat{a}_{\mathbf{k}}}{dt} = \frac{1}{\imath\hbar}[\hat{a}_{\mathbf{k}}, \hat{H}] = -\imath g_{\mathbf{k}} e^{\imath(\omega_{\mathbf{k}}-\omega_{\rm a})t} \sum_{j=1}^{N} \hat{\sigma}_j e^{-\imath\mathbf{k}\cdot\mathbf{r}_j} \ . \tag{21.41}$$

where the fast oscillating term proportional to $e^{\imath(\omega_{\mathbf{k}}+\omega_{\rm a})t}$ has been neglected. Now,

$$\hat{\mathcal{E}}_{\rm sct}(\mathbf{r}, t) = \sum_{\mathbf{k}} \mathcal{E}_k \hat{a}_{\mathbf{k}}(t) e^{\imath(\mathbf{k}\cdot\mathbf{r}-\omega_k t)} \ , \tag{21.42}$$

where $\mathcal{E}_k = \sqrt{\hbar\omega_k/2\varepsilon_0 V_{\rm ph}}$. Integrating Eq. (21.41) with $\hat{a}_{\mathbf{k}}(0) = 0$, inserting it in Eq. (21.42), and approximating the sum over the modes $\mathbf{k}$ by an integral, we obtain,

$$\hat{\mathcal{E}}_{\rm sct}(\mathbf{r}, t) = -\imath \frac{V_{\rm ph}}{8\pi^3} \sum_{j=1}^{N} \int_0^t dt' \hat{\sigma}_j(t-t') e^{\imath\omega_{\rm a} t} \int d^3k \ \mathcal{E}_k g_k e^{\imath\mathbf{k}\cdot(\mathbf{r}-\mathbf{r}_j)-\imath ckt'} \ . \tag{21.43}$$

Introducing spherical coordinates, $d^3k = dkk^2 d\phi d\theta \sin\theta$, and integrating the angular part Eq. (21.43) becomes,

$$\begin{aligned} \hat{\mathcal{E}}_{\rm sct}(\mathbf{r}, t) = -\imath \frac{V_{\rm ph}}{4\pi^2} \sum_{j=1}^{N} \frac{1}{|\mathbf{r}-\mathbf{r}_j|} \int_0^t dt' \hat{\sigma}_j(t-t') e^{\imath\omega_{\rm a} t'} \times \\ \times \int dk k \mathcal{E}_k g_k [e^{-\imath ck(t'-|\mathbf{r}'-\mathbf{r}_j|/c)} - e^{-\imath ck(t'+|\mathbf{r}'-\mathbf{r}_j|/c)}] \ . \end{aligned} \tag{21.44}$$

Assuming the radiation spectrum centered around $k \simeq k_0$, we approximate $k\mathcal{E}_k g_k \simeq k_0 \mathcal{E}_{k_0} g_{k_0}$. Then, extending the lower limit of integration of k to $-\infty$, we obtain for $t < |\mathbf{r}-\mathbf{r}_j|/c$ [666, 530],

$$\hat{\mathcal{E}}_{\rm sct}(\mathbf{r}, t) \simeq -\frac{dk_0^2}{4\pi\varepsilon_0} \sum_{j=1}^{N} \frac{e^{\imath k_0|\mathbf{r}-\mathbf{r}_j|}}{|\mathbf{r}-\mathbf{r}_j|} \hat{\sigma}_j(t-|\mathbf{r}-\mathbf{r}_j|/c) \ . \tag{21.45}$$

where we may neglect the radiation retardation in the limit $t \gg \sigma_R/c$. Using (21.19) and expressing the coupling strength,

$$\hbar g_k = d\mathcal{E}_k \qquad \text{with} \qquad \mathcal{E}_k = \sqrt{\frac{\hbar\omega_k}{2\varepsilon_0 V_{\rm ph}}} \ , \tag{21.46}$$

we get,

$$\hat{\mathcal{E}}_{\rm sct}(\mathbf{r},t) \simeq -\frac{\imath\hbar\Gamma}{2d}\sum_{j=1}^{N}\gamma_{oj}(\mathbf{r})\hat{\sigma}_j(t) \ , \tag{21.47}$$

where we defined the abbreviation,

$$\gamma_{oj}(\mathbf{r}) \equiv \frac{e^{\imath k_0|\mathbf{r}-\mathbf{r}_j|}}{\imath k_0|\mathbf{r}-\mathbf{r}_j|} \ . \tag{21.48}$$

When applied on the state of Eq. (21.11), neglecting virtual transitions, it yields $\hat{\mathcal{E}}_{\rm sct}|\Psi\rangle = \mathcal{E}_{\rm sct}|g_1,...,g_N\rangle$, where $\mathcal{E}_{\rm sct}$ is the electric field radiated by the excited atoms. Once the excitation amplitudes $\beta_j(\infty)$ are known, the scattered light field and the total field can easily be calculated via [720],

$$\boxed{\mathcal{E}_{\rm sct}(\mathbf{r}) = \langle\hat{\mathcal{E}}_{\rm sct}(\mathbf{r})\rangle = -\frac{\imath\hbar\Gamma}{2d}\sum_{j=1}^{N}\gamma_{oj}(\mathbf{r})\beta_j(\infty) \qquad \text{and} \qquad \mathcal{E}_{tot} = \mathcal{E}_{las} + \mathcal{E}_{\rm sct}} \ , \tag{21.49}$$

Example 117 (*Light scattering from a Gaussian beam*): Fig. 21.4 shows an example of light scattering from an incident light field parametrized as a Gaussian beam,

$$\mathcal{E}_{las}(\mathbf{r}) = \hat{\epsilon}\mathcal{E}_0\frac{w_0}{w(z)}e^{-r^2/w(z)^2+\imath kz+z\imath kr^2/2R(z)-\imath\varphi(z)} = \hat{\epsilon}\frac{\hbar}{|\mathbf{d}|}\Omega_0(\mathbf{r})e^{\imath\mathbf{k}_0\cdot\mathbf{r}} \ . \tag{21.50}$$

Note that, for the chosen parameters, the result does not depend on the interaction terms. I.e. we can as well set the kernel to 0.

Note, that the phase factor $e^{\imath\mathbf{k}_0\cdot\mathbf{r}}$ can either be attributed to the atomic dipole moments or to the field. Here, $N = 125$ atoms are periodically arranged in a three-dimensional cubic lattice.

21.1.6 Calculation of the steady-state radiation pressure force

Let us now calculate the radiative pressure force exerted by an incident beam of light $\mathbf{k}_0$ on an atom j located at position $\mathbf{r}_j$ inside an atomic cloud, as illustrated in Fig. 21.2,

$$\frac{d\hat{\mathbf{p}}_j}{dt} = \hat{\mathbf{F}}_j = -\nabla_{\mathbf{r}_j}\hat{H} \ . \tag{21.51}$$

Inserting the Hamiltonian in the RWA (21.10),

$$\begin{aligned}\hat{\mathbf{F}}_j = {} & \imath\hbar\mathbf{k}_0 g_{k_0}\left[\hat{\sigma}_j\hat{a}^\dagger_{\mathbf{k}_0}e^{\imath(\omega_0-\omega_{\rm a})t-\imath\mathbf{k}_0\cdot\mathbf{r}_j} - h.c.\right] \\ & + \sum_{\mathbf{k}}\imath\hbar\mathbf{k}g_k\left[\hat{\sigma}_j\hat{a}^\dagger_{\mathbf{k}}e^{\imath(\omega_k-\omega_{\rm a})t-\imath\mathbf{k}\cdot\mathbf{r}_j} - h.c.\right] \ .\end{aligned} \tag{21.52}$$

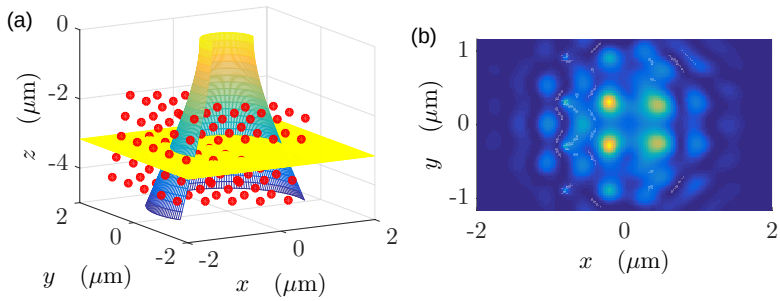

Figure 21.4: (code) (a) Geometry of light scattering from a cubic lattice with lattice constant $d = 100\,\mathrm{nm}$. The light is irradiated from below and is partially reflected. (b) Intensity distribution of scattered light along the yellow plane.

Introducing $\Delta_0 = \omega_0 - \omega_\mathrm{a}$, the expectation value of the force separates in two contribution,

$$\begin{aligned}\langle\hat{\mathbf{F}}_j\rangle \equiv \mathbf{F}_{aj} + \mathbf{F}_{ej} &= \imath\hbar\mathbf{k}_0 g_{k_0}\left[\alpha^*(t)\beta_j(t)e^{\imath\Delta_0 t - \imath\mathbf{k}_0\cdot\mathbf{r}_j} - c.c.\right] \\ &\quad + \sum_{\mathbf{k}} \imath\hbar\mathbf{k} g_k \left[\beta_j(t)\gamma^*_{\mathbf{k}}(t)e^{\imath(\omega_k-\omega_\mathrm{a})t - \imath\mathbf{k}\cdot\mathbf{r}_j} - c.c.\right] \\ &= \imath\hbar\mathbf{k}_0 g_{k_0}[\alpha^*(t)\tilde{\beta}_j(t) - c.c.] \\ &\quad + \sum_{\mathbf{k}} \imath\hbar\mathbf{k} g_k \left[\tilde{\beta}_j(t)e^{-\imath(\omega_0-\omega_k)t + \imath(\mathbf{k}_0-\mathbf{k})\cdot\mathbf{r}_j}\gamma^*_{\mathbf{k}}(t) - c.c.\right] ,\end{aligned} \tag{21.53}$$

where we reintroduced the abbreviation (21.17). In particular, the term $m = j$ in the sum of $\mathbf{F}_{ej}$ vanishes since $\sum_{\mathbf{k}} \mathbf{k} = 0$. Substituting $\gamma_{\mathbf{k}}$ with equation (21.16),

$$\begin{aligned}\mathbf{F}_{aj} + \mathbf{F}_{ej} &= \imath\hbar\mathbf{k}_0 g_{k_0}[\alpha^*(t)\tilde{\beta}_j(t) - c.c.] \\ &\quad - \sum_{\mathbf{k}} \hbar\mathbf{k} g_k^2 \left[\tilde{\beta}_j(t)e^{-\imath(\omega_0-\omega_k)t + \imath(\mathbf{k}_0-\mathbf{k})\cdot\mathbf{r}_j}\sum_{m=1}^{N} e^{\imath\mathbf{k}\cdot\mathbf{r}_m}\int_0^t e^{-\imath(\omega_k-\omega_\mathrm{a})t'}\tilde{\beta}^*_m(t')dt' - c.c.\right] \\ &= -2\hbar\mathbf{k}_0 g_{k_0}\mathfrak{Im}\left[\alpha^*(t)\tilde{\beta}_j(t)\right] \\ &\quad - \sum_{\mathbf{k}} \hbar\mathbf{k} g_k^2 \sum_{m=1}^{N}\left[\tilde{\beta}_j(t)e^{\imath(\mathbf{k}_0-\mathbf{k})\cdot(\mathbf{r}_j-\mathbf{r}_m)}\int_0^t e^{\imath(\omega_0-\omega_k)(t'-t)}\tilde{\beta}^*_m(t')dt' - c.c.\right] ,\end{aligned} \tag{21.54}$$

and applying the Markov approximation (21.20),

$$\begin{aligned}\mathbf{F}_{aj} + \mathbf{F}_{ej} &= -2\hbar\mathbf{k}_0 g_{k_0}\mathfrak{Im}\left[\alpha^*(t)\tilde{\beta}_j(t)\right] \\ &\quad - \sum_{\mathbf{k}} \hbar\mathbf{k} g_k^2 \sum_{m=1}^{N}\left[e^{\imath(\mathbf{k}_0-\mathbf{k})\cdot(\mathbf{r}_j-\mathbf{r}_m)}\frac{\pi}{c}\delta(k-k_0)\tilde{\beta}_j(t)\tilde{\beta}^*_m(t) - c.c.\right] .\end{aligned} \tag{21.55}$$

This is the expression for the force acting on an atom at the position $\mathbf{r}_j$. Knowing the stationary excitation amplitudes $\beta_j(\infty)$ and assuming $\alpha(\infty) \simeq 1$, the radiation pressure force can numerically be calculated. Remembering $\Omega_0 = 2g_{k_0}$ we get for the

absorption force acting on atom j,

$$\mathbf{F}_{aj} = -2\hbar\mathbf{k}_0 g_{k_0}\,\mathfrak{Im}\,\tilde{\beta}_j(\infty)\ . \tag{21.56}$$

To evaluate the emission force acting on atom j, for every atom m of the sum, we need to average over all possible scattering angles. To do so, we choose a reference frame in which the z-component of $\mathbf{k}$ is directed along $\hat{\mathbf{r}}_{jm} = \frac{\mathbf{r}_j - \mathbf{r}_m}{|\mathbf{r}_j - \mathbf{r}_m|}$, that is,

$$\mathbf{k} = \hat{\mathbf{e}}_{x,jm} k \sin\theta_{jm}\cos\phi_{jm} + \hat{\mathbf{e}}_{y,jm} k \sin\theta_{jm}\sin\phi_{jm} + \hat{\mathbf{r}}_{jm} k\cos\theta_{jm}\ , \tag{21.57}$$

and evaluate the sum over the wavevectors by $\sum_{\mathbf{k}} \to \frac{V_{\rm ph}}{(2\pi)^3}\int d^3k$,

$$\begin{aligned}
\mathbf{F}_{ej} &= -\sum_{m=1}^{N} \tilde{\beta}_j(\infty)\tilde{\beta}_m^*(\infty)\frac{V_{\rm ph}}{(2\pi)^3}\frac{\pi}{c}\int_{\mathbb{R}^3} d\theta_{jm}d\phi_{jm}dk\ \hbar k \begin{pmatrix}\sin\theta_{jm}\cos\phi_{jm}\\ \sin\theta_{jm}\sin\phi_{jm}\\ \cos\theta_{jm}\end{pmatrix}\times \\
&\quad \times g_k^2[e^{\imath(\mathbf{k}_0-\mathbf{k})\cdot(\mathbf{r}_j-\mathbf{r}_m)}\delta(k-k_0)k^2\sin\theta_{jm} - c.c. \\
&= -\hbar k_0\frac{\Gamma}{8\pi}\sum_{m=1}^{N} e^{\imath\mathbf{k}_0\cdot(\mathbf{r}_j-\mathbf{r}_m)}\tilde{\beta}_j(\infty)\tilde{\beta}_m^*(\infty)\int_0^{\pi}\int_0^{2\pi} d\theta_{jm}d\phi_{jm}\begin{pmatrix}\sin\theta_{jm}\cos\phi_{jm}\\ \sin\theta_{jm}\sin\phi_{jm}\\ \cos\theta_{jm}\end{pmatrix}\times \\
&\quad \times e^{-\imath k\cdot|\mathbf{r}_j-\mathbf{r}_m|\cos\theta_{jm}}\sin\theta_{jm} - c.c.\ .
\end{aligned} \tag{21.58}$$

remembering $\Gamma = \frac{V_{\rm ph}}{\pi c}k_0^2 g_{k_0}^2$ from Eq. (21.19). The integrals over ϕ_{jm} vanishes whereas the integral over θ_{jm} becomes, using,

$$\int_0^{\pi} d\theta\sin\theta\cos\theta e^{-\imath\alpha\cos\theta} = 2\imath\frac{\alpha\cos\alpha - \sin\alpha}{\alpha^2} = -2\imath j_1(\alpha)\ , \tag{21.59}$$

we find,

$$\begin{aligned}
\mathbf{F}_{ej} &= -\hbar k_0\frac{\Gamma}{4}\sum_{m=1}^{N} e^{\imath\mathbf{k}_0\cdot(\mathbf{r}_j-\mathbf{r}_m)}\tilde{\beta}_j(\infty)\tilde{\beta}_m^*(\infty)\hat{\mathbf{r}}_{jm}\times \\
&\quad \times\int_0^{\pi}\cos\theta_{jm}\sin\theta_{jm}e^{-\imath k|\mathbf{r}_j-\mathbf{r}_m|\cos\theta_{jm}}d\theta_{jm} - c.c. \\
&= \imath\hbar k_0\frac{\Gamma}{2}\sum_{m=1}^{N} e^{\imath\mathbf{k}_0\cdot(\mathbf{r}_j-\mathbf{r}_m)}\tilde{\beta}_j(\infty)\tilde{\beta}_m^*(\infty)\hat{\mathbf{r}}_{jm}j_1(k|\mathbf{r}_j-\mathbf{r}_m|) - c.c. \\
&= -\imath\hbar k_0\frac{\Gamma}{2}\sum_{m=1}^{N}\mathbf{f}_{jm}\tilde{\beta}_j(\infty)\tilde{\beta}_m^*(\infty) - c.c.\ ,
\end{aligned} \tag{21.60}$$

where we defined [7],

$$\mathbf{f}_{jm} = -j_1(k|\mathbf{r}_j-\mathbf{r}_m|)e^{\imath\mathbf{k}_0\cdot(\mathbf{r}_j-\mathbf{r}_m)}\hat{\mathbf{r}}_{jm}\ . \tag{21.61}$$

[7] For exploitation in MATLAB we may express the spherical Bessel function by a Bessel function of the first kind: $j_n(x) = \sqrt{\pi/2x}J_{n+1/2}(x)$.

In summary we got,

$$\boxed{\begin{aligned}\mathbf{F}_{aj} &= -\imath\hbar k_0\Omega_0\Im\mathfrak{m}\,\tilde{\beta}_j(\infty)\\ \mathbf{F}_{ej} &= -\imath\hbar k_0\Gamma\sum_{m=1}^{N}\mathbf{f}_{jm}\Im\mathfrak{m}\,[\tilde{\beta}_j(\infty)\tilde{\beta}^*_m(\infty)]\end{aligned}}\ . \tag{21.62}$$

The steady state absorption and the emission part of the radiation pressure force on the *center of mass* of the atomic cloud follow from,

$$\mathbf{F}_{\rm a} = \frac{1}{N}\sum_j\langle\hat{\mathbf{F}}_{aj}\rangle \qquad \text{and} \qquad \mathbf{F}_e = \frac{1}{N}\sum_j\langle\hat{\mathbf{F}}_{ej}\rangle\ . \tag{21.63}$$

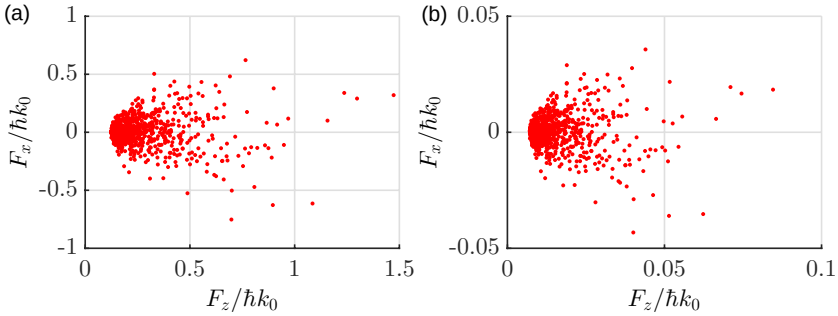

Figure 21.5: (code) Force distribution upon scattering of a photon by an atom of an spherical Gaussian cloud (a) without and (b) with rescattering according to Eqs. (21.63).

As long as the RWA and the Markov approximation are valid and only the lowest Dicke state is considered (no collective saturation), this simulation is supposed to be exact and contains all the physics including, e.g. multiple scattering. Fig. 21.5 shows a comparison of the cases when the off-diagonal components of the kernel (21.37) are present or not. Apparently, the presence of rescattering dramatically spoils the radiation pressure force, a phenomenon that we will extensively study in Secs. 21.1.7 and 21.3 [286, 39, 40, 657, 79, 41].

21.1.7 The structure coefficient of the 'timed' Dicke state

When a beam of light passes through an atomic cloud, its phase fronts will excite the atomic dipole moments as it traverses the cloud. That is, understanding the beam as a plane wave $e^{\imath(\mathbf{k}_0\cdot\mathbf{r}-\omega t)}$, the dipoles start to oscillate with relative phase delays $e^{\imath\mathbf{k}_0\cdot(\mathbf{r}_j-\mathbf{r}_m)}$ depending on their position along the optical axis $\mathbf{k}_0$. The resulting collective state has been termed *timed Dicke state* [748]. Assuming that this phase delay is the only parameter distinguishing two atoms, we may write with Eq. (21.17),

$$\tilde{\beta}_j(t) = \beta_j(t)e^{\imath(\Delta_0 t-\mathbf{k}_0\cdot\mathbf{r}_j)} \equiv \frac{1}{\sqrt{N}}\beta(t)\ , \tag{21.64}$$

where β is the macroscopic dipole moment. Note, that the fact that $\beta(t)$ does not depend on the atomic position does not imply a continuous density distribution. The atoms are still sitting at their positions $\mathbf{r}_j$; only are their dipole moments synchronized to the incident light wave.

The assumption of a timed Dicke state for the atomic cloud is, nevertheless, an approximation which is not always good [286]. For example, it neglects dispersive phase shifts of the excitation of the atomic dipole moments by the pump laser beam being delayed on its propagation due to its interaction with the atoms. If such phase shifts (and absorption as well) are radially inhomogeneous, this can lead to deformation of the pump laser beam's phase front and thus to lensing. We will discuss this in Exc. 21.1.8.5 and in Sec. 21.3.

21.1.7.1 Structure coefficient for 'timed' Dicke states

We start again with the Eqs. (21.24) inserting the ansatz of *timed Dicke* states,

$$\begin{aligned}\dot{\beta}(t) &= \frac{1}{N}\sum_{j=1}^{N}\dot{\beta}(t) = \frac{1}{\sqrt{N}}\sum_{j=1}^{N}\frac{d}{dt}\tilde{\beta}_j(t) \\ &= \frac{1}{\sqrt{N}}\sum_{j=1}^{N}\left(\imath\Delta_0\tilde{\beta}_j(t) - \imath\frac{\Omega_0}{2}\alpha(t) - \frac{\Gamma}{2}\sum_{m=1}^{N}\gamma_{jm}\tilde{\beta}_m(t)\right) \\ &= \left(\imath\Delta_0 - \frac{\Gamma}{2}Ns_N\right)\beta(t) - \imath\frac{\sqrt{N}\Omega_0}{2}\alpha(t)\ ,\end{aligned} \tag{21.65}$$

where we introduced the abbreviation,

$$s_N \equiv \frac{1}{N}\frac{1}{N}\sum_{j,m=1}^{N}\gamma_{jm}\ . \tag{21.66}$$

Taking the kernel from (21.25), we get,

$$\begin{aligned}s_N &= \frac{1}{N}\frac{2}{\Gamma}\frac{V_{\rm ph}}{(2\pi)^3}\int_{\mathbb{R}^3} g_k^2\frac{1}{N}\sum_{j,m=1}^{N} e^{\imath(\mathbf{k}-\mathbf{k}_0)\cdot(\mathbf{r}_j-\mathbf{r}_m)}\frac{\pi}{c}\delta(k-k_0)k^2\sin\theta dk d\theta d\phi \\ &= \frac{1}{N}\frac{2}{\Gamma}\frac{V_{\rm ph}}{(2\pi)^3}\int_0^\infty\int_0^\pi\int_0^{2\pi} g_k^2 N|S_N(k,\theta,\phi)|^2\frac{\pi}{c}\delta(k-k_0)k^2\sin\theta dk d\theta d\phi \\ &= \frac{1}{4\pi}\int_0^\pi\int_0^{2\pi}|S_N(k_0,\theta,\phi)|^2\sin\theta d\theta d\phi\ ,\end{aligned} \tag{21.67}$$

introducing the normalized *structure coefficient*,

$$\boxed{\mathcal{S}_N(\mathbf{k}) \equiv \rho(\mathbf{q}) = \frac{1}{N}\sum_{j=1}^{N} e^{\imath(\mathbf{k}-\mathbf{k}_0)\cdot\mathbf{r}_j}}\ , \tag{21.68}$$

where $\mathbf{q} = \mathbf{k} - \mathbf{k}_0$ and $\rho(\mathbf{q})$ is the structure coefficient defined in (21.3).

In steady state, $\dot{\beta}(t) = 0$, and disregarding saturation, $\alpha(t) \simeq 1$, the solution of (21.65) reads,

$$\boxed{\beta(\infty) = \frac{\sqrt{N}\Omega_0}{2\Delta_0 + \imath\Gamma N s_N}}\,, \tag{21.69}$$

such that,

$$\begin{aligned} |\beta(\infty)|^2 &= \frac{N\Omega_0^2}{4\Delta_0^2 + N^2\Gamma^2 s_N^2} \\ \mathfrak{Im}\left[\alpha(\infty)\beta^*(\infty)\right] &= \frac{N^{3/2}\Gamma\Omega_0 s_N}{4\Delta_0^2 + N^2\Gamma^2 s_N^2}\,. \end{aligned} \tag{21.70}$$

The time-dependent solution is easily obtained as,

$$\beta(t) = \beta(0)e^{(\imath\Delta_0 - \Gamma N s_n/2)t} + \beta(\infty)\,. \tag{21.71}$$

The evolution of the cloud very much depends on the initial conditions, e.g. $\beta_j(0) = 1$ for the uniformly excited *symmetric state* $\beta_j(0) = e^{\imath\mathbf{k}_0\cdot\mathbf{r}_j}$ for timed Dicke states.

In cylindrical coordinates the structure coefficient can be written,

$$\mathcal{S}(k,\theta,\phi) = \frac{1}{N}\sum_{j=1}^{N} e^{\imath(kx_j\sin\theta\cos\phi + ky_j\sin\theta\cos\phi + (k\cos\theta - k_0)z_j)}\,. \tag{21.72}$$

It basically tells the angular distribution of the scattered light. Fig. 21.6 shows numerical calculations and analytical approximations of the structure factor for various shapes and sizes of the atomic cloud. Obviously, the radiation pattern very much depends on the size of the spherical cloud. For $R < \lambda$ it is isotropic, for $R > \lambda$ scattering mainly occurs in forward direction. Furthermore, if the cloud is ellipsoidal the radiation pattern is shifted into forward direction.

21.1.7.2 Time evolution of radiation modes

We are interested in the power emitted into the solid angle $\Omega_{\mathbf{k}}$, $P(t) \propto |\gamma_{\mathbf{k}}(t)|^2$. For timed Dicke state (21.64) we get immediately from the equations of motion,

$$\begin{aligned} \dot{\gamma}_{\mathbf{k}}(t) &= -\imath g_k e^{\imath\Delta_k t}\sum_{j=1}^{N}\beta_j(t)e^{-\imath\mathbf{k}\cdot\mathbf{r}_j} \\ &= -\imath g_k e^{\imath(\Delta_k - \Delta_0)t}\frac{1}{\sqrt{N}}\beta(t)\sum_{j=1}^{N} e^{\imath(\mathbf{k}_0 - \mathbf{k})\cdot\mathbf{r}_j} = -\imath g_k e^{\imath(\Delta_k - \Delta_0)t}\sqrt{N}\mathcal{S}_N(\mathbf{k})\,. \end{aligned} \tag{21.73}$$

We see that the time-dependence factorizes from the structure factor, which is the only component containing an angular dependence. The same holds for *symmetric Dicke states* defined by $|\beta_j| = |\beta_m|$.

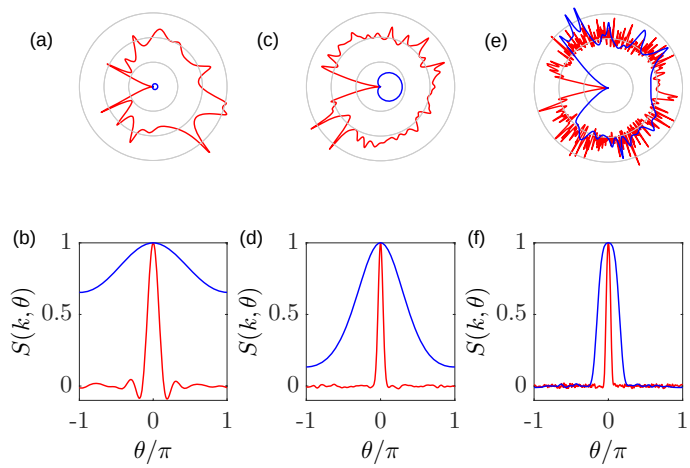

Figure 21.6: (code) Numerical calculation of $\mathcal{S}(k,\theta)$ according to (21.68) for 10^4 atomic positions r_j chosen by a random number generator. For the graphs (a-b) the cloud is *homogeneous and spherical* and has the sizes $R = \lambda$ (red) and $R = 10\lambda$ (blue). For the graphs (c-d) the cloud is *Gaussian and spherical* and has the same sizes as (a-b). For the graphs (d-e) the cloud is *homogeneous and ellipsoidal with aspect ratio* $R_z/R_\rho = 3$ and has the same radial sizes as in (a-b).

21.1.7.3 Light scattering in the 'timed Dicke state'

The scalar electric field scattered by an arbitrary distribution of atoms has been calculated in (21.49). Substituting the stationary timed Dicke state (21.69), we get,

$$\mathcal{E}_{\rm sct}(\mathbf{r}) = -\frac{\imath\hbar\Gamma}{2d}\frac{\sqrt{N}\Omega_0}{2\Delta_0 + \imath\Gamma N s_N}\sum_{j=1}^{N}\frac{e^{\imath k_0|\mathbf{r}-\mathbf{r}_j|}}{\imath k_0|\mathbf{r}-\mathbf{r}_j|}\ . \tag{21.74}$$

Note that the 'timed Dicke' state starts from the assumption of an infinitely extended plane wave incident light field. This excludes situations where the incident beam size is smaller than the cloud's size.

21.1.7.4 Force in the 'timed Dicke state' on a particular atom in a cloud

The time-dependent expressions (21.56) for the forces in the coupled dipoles model can be further evaluated for timed Dicke states (21.64),

$$\begin{aligned}
&\mathbf{F}_{aj} + \mathbf{F}_{ej} \qquad\qquad (21.75)\\
&= -\frac{2\hbar\mathbf{k}_0 g_{k_0}}{\sqrt{N}}\Im\mathrm{m}\,\beta(t) - \sum_{\mathbf{k}}\frac{\hbar\mathbf{k}g_k^2}{N}\sum_{m=1}^{N}\left[e^{\imath(\mathbf{k}_0-\mathbf{k})\cdot(\mathbf{r}_j-\mathbf{r}_m)}\frac{\pi}{c}\delta(k-k_0)|\beta(t)|^2 - c.c.\right]\\
&= -\frac{2\hbar\mathbf{k}_0 g_{k_0}}{\sqrt{N}}\Im\mathrm{m}\,\beta(t) - \sum_{\mathbf{k}}\hbar\mathbf{k}g_k^2\left[\mathcal{S}_N(\mathbf{k})e^{-\imath(\mathbf{k}-\mathbf{k}_0)\cdot\mathbf{r}_j}\frac{\pi}{c}\delta(k-k_0)|\beta(t)|^2 - c.c.\right]\ .
\end{aligned}$$

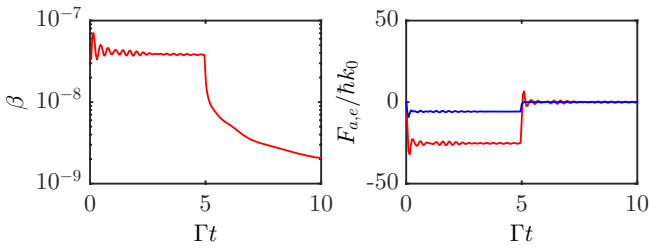

Figure 21.7: (code) Time-dependent of (a) the dipole amplitudes and (b) the forces for $\sigma = 1$, $\Delta_0 = 20\Gamma$, $\Omega_0 = 0.01\Gamma$, and $\eta = 1$.

Evaluating the sum over the wavevectors by $\sum_{\mathbf{k}} \to \frac{V_{\rm ph}}{(2\pi)^3}\int d^3k$,

$$\mathbf{F}_{aj} + \mathbf{F}_{ej} = \frac{-2\hbar\mathbf{k_0} g_{k_0}}{\sqrt{N}} \Im\mathfrak{m}\,\beta(t) \tag{21.76}$$
$$- |\beta(t)|^2 \frac{V_{\rm ph}}{(2\pi)^3}\int_0^\infty\int_0^\pi\int_0^{2\pi} \hbar\mathbf{k} g_k^2 \left[\mathcal{S}_N(k,\theta,\phi)e^{-i(\mathbf{k}-\mathbf{k}_0)\cdot\mathbf{r}_j}\frac{\pi}{c}\delta(k-k_0) - c.c.\right] k^2\sin\theta d\theta d\phi dk \ .$$

Let us consider an atom sitting on axis, $\mathbf{r}_j = 0$, and use cylindrical coordinates, $\mathbf{k}_0 = k_0\hat{\mathbf{e}}_z$ and $\mathbf{k} = \hat{\mathbf{e}}_x k\sin\theta\cos\phi + \hat{\mathbf{e}}_y k\sin\theta\sin\phi + \hat{\mathbf{e}}_z k\cos\theta$, and using the definition (21.19) of Γ,

$$\mathbf{F}_{aj} + \mathbf{F}_{ej} = \frac{-2\hbar k_0 g_{k_0}}{\sqrt{N}} \hat{\mathbf{e}}_z \Im\mathfrak{m}\,\beta(t) \tag{21.77}$$
$$- |\beta(t)|^2 \frac{\Gamma}{8\pi}\hbar k_0 \int_0^\pi\int_0^{2\pi} (\hat{\mathbf{e}}_x\sin\theta\cos\phi + \hat{\mathbf{e}}_y\sin\theta\sin\phi + \hat{\mathbf{e}}_z\cos\theta)\left[\mathcal{S}_N(k,\theta,\phi) - c.c.\right]\sin\theta d\theta d\phi \ .$$

Using the abbreviation,

$$\tilde{f}_N \equiv \frac{1}{4\pi}\int_0^\pi\int_0^{2\pi} \mathfrak{Re}\,\mathcal{S}_N(k_0,\theta,\phi)\sin\theta\cos\theta d\theta d\phi \ , \tag{21.78}$$

the z-component becomes,

$$F_{zaj} + F_{zej} = -\frac{2\hbar k_0 g_{k_0}}{\sqrt{N}}\Im\mathfrak{m}\,\beta(t) - |\beta(t)|^2\Gamma\hbar k_0\tilde{f}_N \ . \tag{21.79}$$

In steady state and normalizing to the standard radiation pressure,

$$F_{z1j} = \Gamma\hbar k_0\frac{\Omega_0^2}{4\Delta_0^2+\Gamma^2} = \hbar k_0\sigma(\Delta)\frac{I}{\hbar\omega} \ , \tag{21.80}$$

where $\sigma(\Delta_0)$ is the optical cross section and I the intensity of the incident light, we can write,

$$\frac{F_{zaj}+F_{zej}}{F_{z1j}} = \left(-\frac{2\hbar k_0 g_{k_0}}{\sqrt{N}}\Im\mathfrak{m}\,\beta(\infty) - |\beta(\infty)|^2\Gamma\hbar k_0\tilde{f}_N\right)\frac{4\Delta_0^2+\Gamma^2}{\Gamma\hbar k_0\Omega_0^2} \ . \tag{21.81}$$

Finally, inserting the the expression (21.69) for the dipole moment, we obtain for the timed Dicke state,

$$\boxed{\frac{F_{zaj}+F_{zej}}{F_{z1j}} = \frac{(2\Delta_0/\Gamma)^2+1}{(2\Delta_0/\Gamma)^2+N^2 s_N^2}N(s_N-\tilde{f}_N)} \ , \tag{21.82}$$

using $\Omega_0 = 2g_{k_0}$.

The factors s_N and f_N can be calculated exactly, as will be done in Exc. 21.1.8.6,

$$s_N = \frac{1}{N^2}\sum_{j,m=1}^{N}\frac{\sin(k_0|\mathbf{r}_j-\mathbf{r}_m|)}{k_0|\mathbf{r}_j-\mathbf{r}_m|}\cos[k_0(z_j-z_m)] \tag{21.83}$$

$$f_N = \sqrt{\frac{\pi}{2}}\frac{1}{N^2}\sum_{j,m=1}^{N}\frac{J_{3/2}(k_0|\mathbf{r}_j-\mathbf{r}_m|)}{(k_0|\mathbf{r}_j-\mathbf{r}_m|)^{3/2}}k_0(z_j-z_m)\sin[k_0(z_j-z_m)]\ .$$

However, this is only practicable for atom numbers small enough for numerical simulations. For larger atom number we may use the analytic expressions including the disorder term [80].

21.1.7.5 Force on the center of mass of the cloud

The force acting on the center of mass of the atomic cloud is given by the average of the forces (21.76) sensed by particular atoms,

$$\begin{aligned}\mathbf{F}_{\rm a}+\mathbf{F}_e &= \frac{1}{N}\sum_{j=1}^{N}(\mathbf{F}_{aj}+\mathbf{F}_{ej}) \qquad (21.84)\\ &= -\frac{2\hbar\mathbf{k_0}g_{k_0}}{\sqrt{N}}\mathfrak{Im}\,\beta(t)\\ &\quad -|\beta(t)|^2\frac{V_{\rm ph}}{(2\pi)^3}\int_{\mathbb{R}^3}\hbar\mathbf{k}g_k^2\left[\mathcal{S}_N(k,\theta,\phi)\frac{1}{N}\sum_{j=1}^{N}e^{-\imath(\mathbf{k}-\mathbf{k}_0)\cdot\mathbf{r}_j}\frac{\pi}{c}\delta(k-k_0)-c.c.\right]k^2\sin\theta d\theta d\phi dk\\ &= \frac{-2\hbar\mathbf{k_0}}{\sqrt{N}}g_{k_0}\mathfrak{Im}\,\beta(t)-|\beta(t)|^2\frac{V_{\rm ph}}{(2\pi)^3}\int_{\mathbb{R}^3}\hbar\mathbf{k}g_k^2 2|\mathcal{S}_N(k,\theta,\phi)|^2\frac{\pi}{c}\delta(k-k_0)k^2\sin\theta d\theta d\phi dk\ .\end{aligned}$$

Using cylindrical coordinates, $\mathbf{k}_0 = k_0\hat{\mathbf{e}}_z$ and $\mathbf{k} = \hat{\mathbf{e}}_x k\sin\theta\cos\phi + \hat{\mathbf{e}}_y k\sin\theta\sin\phi + \hat{\mathbf{e}}_z k\cos\theta$, and the definition of Γ,

$$\begin{aligned}\mathbf{F}_{\rm a}+\mathbf{F}_e &= \frac{-2\hbar k_0}{\sqrt{N}}\hat{\mathbf{e}}_z g_{k_0}\mathfrak{Im}\,\beta(t) \qquad (21.85)\\ &\quad -|\beta(t)|^2\frac{\Gamma}{8\pi}\hbar k_0\int_0^{\pi}\int_0^{2\pi}(\hat{\mathbf{e}}_x\sin\theta\cos\phi+\hat{\mathbf{e}}_y\sin\theta\sin\phi+\hat{\mathbf{e}}_z\cos\theta)\,2|\mathcal{S}_N(k,\theta,\phi)|^2\sin\theta d\theta d\phi\ .\end{aligned}$$

Using the abbreviation,

$$f_N \equiv \frac{1}{4\pi}\int_0^{\pi}\int_0^{2\pi}|\mathcal{S}_N(k_0,\theta,\phi)|^2\sin\theta\cos\theta d\theta d\phi\ , \tag{21.86}$$

we get for the z-component an analogous formula to (21.79),

$$\begin{aligned}F_{za}+F_{ze} &= \frac{-2\hbar k_0 g_{k_0}}{\sqrt{N}}\mathfrak{Im}\,\beta(t)-|\beta(t)|^2\frac{\Gamma}{8\pi}\hbar k_0\int_0^{\pi}\int_0^{2\pi}2|\mathcal{S}_N(k,\theta,\phi)|^2\sin\theta\cos\theta d\theta d\phi\\ &= -\frac{2\hbar k_0 g_{k_0}}{\sqrt{N}}\mathfrak{Im}\,\beta(t)-|\beta(t)|^2\Gamma\hbar k_0 f_N\ . \qquad (21.87)\end{aligned}$$

In steady state and normalizing again to the standard radiation pressure (21.80),

$$\frac{F_{za}+F_{ze}}{F_{z1}} = \left(-\frac{2\hbar k_0 g_{k_0}}{\sqrt{N}}\mathfrak{Im}\,\beta(\infty)-|\beta(\infty)|^2\Gamma\hbar k_0 f_N\right)\frac{4\Delta_0^2+\Gamma^2}{\Gamma\hbar k_0\Omega_0^2}\ . \tag{21.88}$$

Finally, inserting the the expression (21.69) for the dipole moment, we obtain for the timed Dicke state,

$$\boxed{\frac{F_{za}+F_{ze}}{F_{z1}} = \frac{(2\Delta_0/\Gamma)^2+1}{(2\Delta_0/\Gamma)^2+N^2 s_N^2} N(s_N - f_N)} \,, \tag{21.89}$$

using $\Omega_0 = 2g_{k_0}$. Inserting the expressions (21.67) for s_N and (21.86) for f_N, we may also write,

$$\frac{F_{0a}+F_{0e}}{F_{z1}} = \frac{(2\Delta_0/\Gamma)^2+1}{(2\Delta_0/\Gamma)^2+N^2 s_N^2} N \frac{1}{4\pi} \int_0^\pi \int_0^{2\pi} |\mathcal{S}_N(k,\theta,\phi)|^2 (1-\cos\theta)\sin\theta d\theta d\theta d\phi \,. \tag{21.90}$$

Let us assume in the following that the scattering of every single photon can be treated independently [746]. In particular, the density distribution may change between two scattering events. The force is something like the first moment of the structure factor. This makes it so adapted to measure fluctuation-induced deviations from the structure coefficient [8].

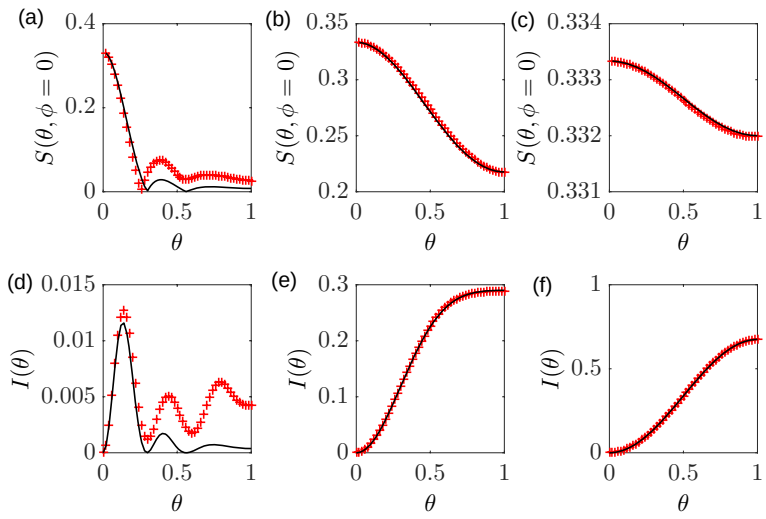

Figure 21.8: (code) (a-c) Calculation of the structure coefficient $|\mathcal{S}(k=k_0,\theta,\phi=0)|^2$ for an isotropic homogeneous density distribution. (d-f) Calculation of the force $I(\theta) = \int_0^{2\pi} |\mathcal{S}(k = k_0,\theta,\phi)|^2(1-\cos\theta)d\phi$. The red curves show numerical calculations based on (21.68), the green curves show analytical calculations according to (21.119). (a,d) $k_0 R = 1$ and $N = 100$. (b,e) $k_0 R = 5$ and $N = 100$. (c,f) $k_0 R = 5$ and $N = 1000$.

We want to compare this force to the force acting on a cloud of N uncorrelated scatterers, i.e. atoms receiving recoil from the pump photons but reemitting isotrop-

[8] Insert a clarifying discussion of what we said in the EPDJ and what we did not: We said there is a collective effect coming from the structure factor of the cloud. We did NOT say that interatomic interactions are essential...!

ically,

$$\langle F_{\mathrm{unc,z}}\rangle = \frac{V_{\mathrm{ph}}}{(2\pi)^3}\sigma(\Delta)\frac{I}{\hbar\omega}\hbar k_0 \int_0^\infty \int_0^\pi \int_0^{2\pi} |\mathcal{S}_N(k,\theta,\phi)|^2 k^2 \sin\theta d\theta d\phi dk \ . \tag{21.91}$$

For such a cloud the structure coefficient is $\mathcal{S}_N = N^{-1/2}$. Note that this is unlike N atoms in the Dicke limit, where $\mathcal{S}_N = 1$.

A dense homogeneous cloud with $\mathcal{S}_N(\mathbf{k}) \propto \delta^3(\mathbf{k}_0 - \mathbf{k})$ does not scatter light and experiences no force, $\langle F_{\mathrm{hom}}\rangle = 0$. This is however not true any more in the limit of small extended clouds, where fluctuations introduce disorder. This can be shown by simulating a random atomic distribution $\mathbf{r}_j$ and integrating the resulting force over all possible $\mathbf{k}$. For simplicity we assume a very sharp momentum distribution, $|\mathbf{k}| = |\mathbf{k}_0|$ or $\frac{V_{\mathrm{ph}}}{2\pi^2}\int_0^\infty k^2 dk = 1$,

$$\langle F_z\rangle = \sigma(\Delta)\frac{I}{\hbar\omega}k_0(s_N - f_N) \ . \tag{21.92}$$

Finally to compare with experiment we evaluate the ratio,

$$\frac{\langle F_z\rangle}{\langle F_{\mathrm{unc,z}}\rangle} = 1 - \frac{f_N}{s_N} \ . \tag{21.93}$$

We describe the cloud as being made of two fractions: An isotropically scattering fraction of $N_0 = \sqrt{N}$ disordered atoms, whose structure factor is $\mathcal{S}_{\mathrm{iso}}(\mathbf{k}) = 1$, and a forward scattering homogeneous cloud with structure factor $\mathcal{S}_{\mathrm{hom}}(\mathbf{k}) = \delta_{\mathbf{k}_0,\mathbf{k}}$. The surface integration of the total structure factor,

$$\mathcal{S}_N(\mathbf{k}) = \frac{N_0}{N}\mathcal{S}_{\mathrm{iso}}(\mathbf{k}) + \frac{N-N_0}{N}\mathcal{S}_{\mathrm{hom}}(\mathbf{k}) = \frac{N_0}{N} + \frac{N-N_0}{N}\delta_{\mathbf{k}_0,\mathbf{k}} \simeq \frac{N_0}{N} \tag{21.94}$$

yields the same N-dependence of the force,

$$\frac{\langle F_z\rangle}{\langle F_{\mathrm{iso,z}}\rangle} = \frac{1}{4\pi N^2}\int_0^\pi \int_0^{2\pi} |\sqrt{N}|^2(1-\cos\theta)\sin\theta d\theta d\phi = \frac{1}{N} \ . \tag{21.95}$$

The interpretation is the following. In the experimentally realized situation, we are very far in the large cloud limit completely dominated by forward scattering, which means that *if the cloud were homogeneous no radiation pressure force should be expected* at all. However diffuse scattering from disordered atoms (or fluctuations) disturbs the forward scattering. It is this scattering which gives rise to radiation pressure.

There is an interesting analogy: Diffuse scattering not only inhibits forward scattering in homogeneous clouds, but also coherent backscattering from ordered structures. E.g. in optical lattices [767] it disturbs the detection of photonic band gaps. In an optical lattice the atoms are in the Dicke limit and do not absorb photonic recoil. Hence, no displacement due to radiation pressure is expected. However, diffuse scattering is observed as absorptive features in the spectra [82, 767].

The Bragg scattering is expressed by a periodic structure factor. A widely used approach to describe the impact of disordered atoms in lattices is to divide the cloud into a perfectly ordered part with density nf_{DW} and isotropically scattering part with density $n(1-f_{DW})$ [767]. The factor f_{DW} is known as Debye-Waller factor. In Exc. 21.1.8.7 we try an alternative traetment of radiation pressure based on a Monte-Carlo simulation.

21.1.7.6 Cooperative scattering and single photon superradiance

A non-isotropic structure factor scattering light into a specific direction of space (e.g. the Bragg angle) at a rate scaling like N^α with $\alpha > 1$ needs several 'cooperating' particles. In this sense cooperation only means, that the particles be arranged in space in a particular way, i.e. in a lattice or in a particular bulk shape like a homogeneous sphere or a Gaussian cigar-shaped density distribution. It also immediately becomes clear that disorder ought to play a major role. However, cooperation goes further, since cooperative scattering can be observed in spontaneous emission of an atomic cloud being excited by just a single photon. Single-photon superradiance is the topic of the following sections.

For now let us state that a non-isotropic structure factor results in collective scattering. The density distribution (which is the Fourier transform of the structure factor) can adopt two extremes: A periodic lattice results in backscattering into specific directions, a homogeneous clouds shows nothing but forward scattering. Both situations are never perfectly realized, but are subject to density fluctuations (Debye-Waller factor in a lattice, radiation pressure in a homogeneous cloud).

A single photon on its trip through an atomic cloud successively excites the atomic dipole moment thus establishing a phase relation between potential radiators [254, 806, 747, 807]. One could think that the scattering process localizes atom and photon, i.e. only one atom scatters. However, we don't know which atom scatters, and this introduces a correlation of the dipole moments along the propagation direction of the light beam.

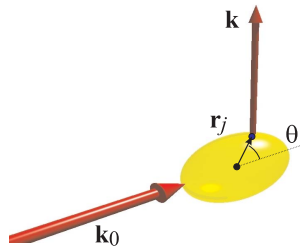

Figure 21.9: Scattering of a photon by an atom of an ellipsoidal cloud.

While normally the radiation rate of a dilute cloud is $\propto N$, in the presence of coherent interactions it scales as $\propto N^2$. Coherent interactions are not conditioned to overlapping space functions of the atoms, i.e. it is not compulsory that the density be $n^{-1/3} > \lambda$. For example, scattering from ordered structures also scales as $\propto N^2$ [446]. However, the scattering will be dramatically different if $n^{-1/3} < \lambda$.

Spontaneous emission radiation pattern from uncorrelated scatterers only depend on the relative orientation of $\hat{\sigma}$ and $\vec{\mathcal{B}}$, but not on the $\mathbf{k}$-vector of the incident light. This also holds for Dicke superradiance in the small cloud limit, but not for large clouds. Here forward scattering dominates.

We have seen in this section that, despite its simplicity, the coupled dipoles model has a large range of applications. It allows for a deeper understanding of known classical phenomena and, as we will study in Excs. 23.2.4.9 to 23.2.4.2 and in forthcoming sections, it allows to unravel new effects.

21.1.8 Exercises

21.1.8.1 Ex: Structure coefficient of a linear array

a. Based on the definition (21.1) compute the structure factor of a linear array of point-like scatterers.
b. Based on the definition (21.2) compute the structure factor of a linear array of 10 Gaussian density distributions.

21.1.8.2 Ex: Structure factor of a cloud

a. Based on the definition (21.1) compute the structure coefficient of (i) a slit, (ii) a pinhole, and (iii) a homogeneous spherical cloud.
b. Based on the definition (21.3) compute the structure coefficient of a homogeneous spherical cloud.

21.1.8.3 Ex: Structure coefficient and Snell's law

Calculate the structure coefficient for a light beam passing through a plane interface between two dielectrics.

21.1.8.4 Ex: Validity of Markov approximation

a. Calculate the single-atom scattering rate for a rubidium cloud of $N = 10^6$ atoms driven with $P = 100\,\mathrm{mW}$ laser power focused into a waist of $w_0 = 100\,\mu\mathrm{m}$ and detuned by $\Delta = (2\pi)\,100\,\mathrm{GHz}$ from the D_2-line at 780 nm [134].
b. Assume for the cloud a homogeneous spherical density distribution with radius $R = 250/k_0$. Based on Ref. [806] estimate whether the Markov approximation is valid.

21.1.8.5 Ex: Lensing by a dense atomic cloud with the coupled dipoles model

Simulate the pump laser phase shift and lensing by a small dense cloud by the coupled dipoles model for red and blue detuning. Discuss the influence of rescattering by removing artificially the off-diagonal terms from the scattering kernel. Discuss whether lensing is observed within the timed Dicke approximation.

21.1.8.6 Ex: Exact calculation of projected structure coefficients

Calculated the integrals (21.66), (21.78), and (21.86).

21.1.8.7 Ex: Monte-Carlo simulation of cooperative radiation pressure

In a regime of negligible interatomic interaction single photons are scattered by individual atoms, which thereby receive the entire photonic recoil. That is, the acceleration occurs in quantized steps, which can be easily resolved in experiments [416, 765] with Bose-Einstein condensates. In the absence of collective effects, we generally observe halo-shaped momentum distributions. Because of the recoil received upon absorption, the halos are centered at $\hbar k$, and since the emission is generally isotropic,

they have a radius of $\hbar k$. On the other hand, as we have seen earlier, cooperative effects can suppression radiation pressure. In the following we try a different approach based on a Monte-Carlo simulation with a Langevin force.
This approach starts from the idea that it is possible to simulate the radiation pressure without explicit calculation of the force by treating the scattering process as a Langevin force. The simulation describes the scattering of single photons by individual atoms. Cooperativity is included 1. in the scattering rate, which is *influenced by collective effects*, 2. by weighing the probability for the direction (θ, ϕ) into which the photons are scattered with the structure factor. The enhancement of the collective scattering rate corresponds to the rate of absorption part of the radiation pressure, [9,10]

$$\gamma_c = \gamma_R \frac{F_{\mathrm{c,abs}}}{F_{\mathrm{1,abs}}} = \sigma_{\mathrm{opt}}(\Delta_0)\frac{I}{\hbar\omega} \cdot \frac{4\Delta_0^2 + \Gamma^2}{4\Delta_0^2 + N^2\Gamma^2 s_N^2} N \ ,$$

where $s_N = N^{-1} + (2\sigma)^{-2}$. The structure factor is numerically calculated for a randomly distributed cloud.

21.1.8.8 Ex: Super- and subradiance with two atoms

Super- and subradiance have been observed in two ion crystals [665, 227]. In this exercise, we study this system in the framework of the coupled dipoles model.
a. Calculate the structure coefficient of this system.
b. Write down the equations of motion (21.26) and solve them in steady-state.

21.1.8.9 Ex: Signatures of subradiance

Super- and subradiance are contained in the coupled dipoles model. Try to identify the presence of subradiant states via a reduced decay rate of $\beta(t)$ starting from the timed Dicke state.

21.1.8.10 Ex: Other applications of the coupled dipoles model

Discuss whether the coupled dipoles model can be extended to provide a microscopic description of gaseous metamaterials (negative refractive index) and the Goos-Hänchen, Imbert-Fedorov, Spin-Hall, and *Ewald-Oseen effects*, and interference with a LO. Is it possible to check Ewald-Oseen's theorem in media with negative refractive index?

[9] Note that in reality the scattering of a photon converts the scattering atom into a coherent superposition of directions into which the atom might have scattered. This is of course not described by the simulation.

[10] Although the atomic motion is frozen, it is not correct to say that the external degree of freedom is not involved in the collective dynamics, since the spatial atomic distribution shapes the structure factor.

21.2 Coupled dipoles model with real atoms

21.2.1 Limitations of the classical vectorial Green function

The vectorial Green function (ED) correctly describes the interaction between point-like classical oscillating dipoles at all inter-dipolar distances R [153]. It contains terms oscillating with kR, where k is the wavenumber of the radiation, and scaling with the distances as $1/R$, $1/R^2$, and $1/R^3$. Although the Green function ignores any internal structure of the dipoles, it has been successfully used within the coupled dipoles model (CDM) to describe the coupling between atoms interacting with each other by exchanging radiation near an atomic transition.

In reality, however, the internal atomic structure consists of electronic orbitals which react to the presence of other atoms via van der Waals forces and by forming adiabatic molecular potentials causing frequency shifts of the atomic resonances at small interatomic distances. Moreover, the molecular potentials resulting from interatomic forces develop a rich ro-vibrational structure, which contributes to the complexity of the collision process in the presence of light. The ro-vibrational spectra may even reach into the molecular decay widths. That is, there are bound states at energies below the dissociation limits smaller than Γ. At sufficiently high densities the vibrational levels of excited state potentials may add a resonance structure causing red-blue asymmetries e.g. in transmission spectra.

The calculation of molecular potentials is a difficult task [858]. At long range the molecular potentials have terms proportional to $1/R^6$, $1/R^8$, and $1/R^{10}$. However, the vibrational level structure also depends on the shape of the potential at short range. In the case of cold collisions the atoms do not penetrate deeply into the adiabatic potentials, which then may be modeled by a generic shape whose few parameters are adjusted for coincidence between the vibrational level structure and experimental data. Experimentally, the ro-vibrational structure is revealed by photoassociation spectroscopy [858]. For introductory literature on cold binary collisions in a light field see f.ex. [858, 444].

Even in the absence of radiation, colliding atoms exert forces on each other. However, if the primary focus is the transport of light through the atomic cloud, we may at first neglect the force induced by the molecular potentials and concentrate on level shifts.

At long range resonant dipole interaction scaling as R^{-3} will dominate the atomic collision dynamics in the presence of light. It mainly depends on the radiative decay width and only weakly on short range features of the molecular potentials. Thus, as a first step in understanding how the existence of atomic degrees of freedom can be incorporated into the CDM, we may concentrate on this interaction.

Here, we want to study all this for dense ^{88}Sr (and ^{172}Yb) clouds. In Sec. 21.2.2 we recapitulate the molecular level structure, and in Sec. 21.2.4 we look more closely at the vectorial Green tensor.

21.2.1.1 Delocalized atoms

If one wants to understand the interaction of light with dense clouds of atoms, the assumption of classical motionless atoms is somewhat paradox: If the atoms stand still, they have an infinite de Broglie wavelength; that is, they 'sense' the presence of all

other atoms. Even if Sr atoms are as hot as 1 μK the thermal de Broglie wavelength is about $\lambda_{therm} = 200\,\mathrm{nm}$, which corresponds to a density of $\lambda_{therm}^{-3} = 10^{14}\,\mathrm{cm}^{-3}$. Atomic clouds with this temperature and density approach unit phase space density.

Even if we disregard wavefunction symmetrization issues and quantum statistics, by the fact that the atoms are delocalized, their interaction with light is modulated with the Frank-Condon overlap of their wavefunctions.

21.2.2 Molecular level structure

The low-lying adiabatic potentials of Sr_2 dimers have been determined through ab initio calculations [109] and photoassociation measurements [808, 614]. We find to find reliable data on the strontium-88 ground state potential $X^1\Sigma_g^+$ connecting to the $^1S_0{+}^1S_0$ collisional channel and the excited state potentials $A^1\Pi_g$, $A^1\Pi_u$, and $A^1\Sigma_g^+$ connecting to the $^1S_0{+}^1P_1$ collisional channel.

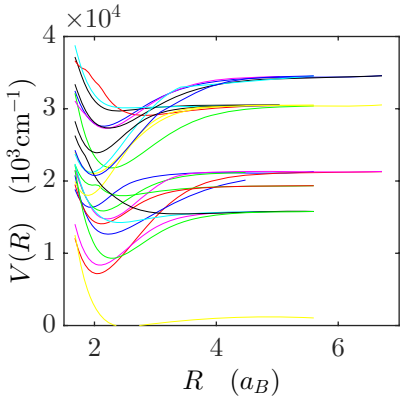

Figure 21.10: Sr_2 potentials connecting to $^1S_0{+}^1S_0$ and $^1S_0{+}^1P_1$.

Fig. 21.10 shows the excited state potential spaghetti found in [808]. The potentials which are relevant for our Sr1 experiment need to be identified. The ground state potential is given in [788, 204].

21.2.2.1 $^{88}Sr_2$ ground state potential $X^1\Sigma_g^+$

The $X^1\Sigma_g^+$ potential has been determined via two-color photoassociation spectrocopy [788],

$$V_{X^1\Sigma_g^+}(R) = \begin{cases} A + \frac{B}{R^n} & \text{for} \quad R < R_i \\ T_m + \sum_i a_i x^i & \\ -\frac{C_6}{R^6} - \frac{C_8}{R^8} - \frac{C_{10}}{R^{10}} & \text{for} \quad R > R_o \end{cases} \tag{21.96}$$

where $x \equiv (R - R_m)/(R + bR_m)$ and $v_{last} = 62, J = 0$ and $R_{rot} = 100 a_B$.

21.2.2.2 $^{88}Sr_2$ excited state potential $(2)^1\Sigma_u^+$

The $(2)^1\Sigma_u^+$ long-range potential at large internuclear distances,

$$V_{^1\Sigma_u^+}(R) = D - \frac{C_3}{R^3} + \frac{\hbar^2[J(J+1)+2]}{2\mu R^2} \tag{21.97}$$

with the reduced mass $\mu = m_{Sr}/2$, the transition wavelength $\lambda = 460.73\,\text{nm}$, the decay width $\Gamma = (2\pi)\ 30.5\,\text{MHz}$, and the resonant dipole interaction coefficient

$$C_3 \simeq \frac{3\hbar\Gamma}{2k^3} = 18.5013\,\text{a. u.}\ , \tag{21.98}$$

which can be obtained from the Green function in the limit of small distances, $kR \ll 1$.

$X^1\Sigma_g^+$	$hc \times \text{cm}^{-1}\ \mathbf{r}A^{\ n}$	a.u. [788]	a.u. [204]
C_6	1.4955×10^7	3103.5	3103
C_8	5.1175×10^8	3.7926×10^5	3.792×10^5
C_{10}	2.495×10^{10}	6.6034×10^7	4.215×10^7
$(2)^1\Sigma_u^+$			
C_3	5.9712×10^5	18.3609	
C_6	-5.1541×10^7	-10696	
C_8	8.9977×10^8	6.6682×10^5	

Table 21.1: For the transformation between SI units and a.u. see Sec. 6.1.2.

Example 118 (*Ytterbium potentials*): The $^{174}Yb_2$ potentials are characterized by $\Gamma = (2\pi)\ 29.128\,\text{MHz}$ and $\lambda = 399\,\text{nm}$ [809, 824, 266, 467].

21.2.2.3 Vibrational levels and wavefunctions

Once the relevant potentials are known, we need to calculate their vibrational structure. To this end we probably need to fit the potentials with analytic functions, calculate the vibrational levels using the Fourier grid method [550, 250, 785], and check that the results coincides with photoassociation spetra such as the ones obtained in [614, 663, 895, 788, 204]. An example of a Fourier grid calculation is shown in Fig. 21.11(a).

The Fourier grid calculations also deliver the vibrational radial wavefuntions. Collisional wavefunctions can be obtained by solving the radial Schrödinger equation, see red curve in Fig. 21.11.

Note, that in Fig. 21.11 the Fourier grid method yields good results for the $X^1\Sigma_g^+$ ground state potential, which is relatively shallow and short ranged, yielding 63 bound states. This is not the case for the $(2)^1\Sigma_u^+$ excited state potentials, which extends to huge range and supports hundreds of bound states. Here, an adapted Fourier grid method must be employed [477].

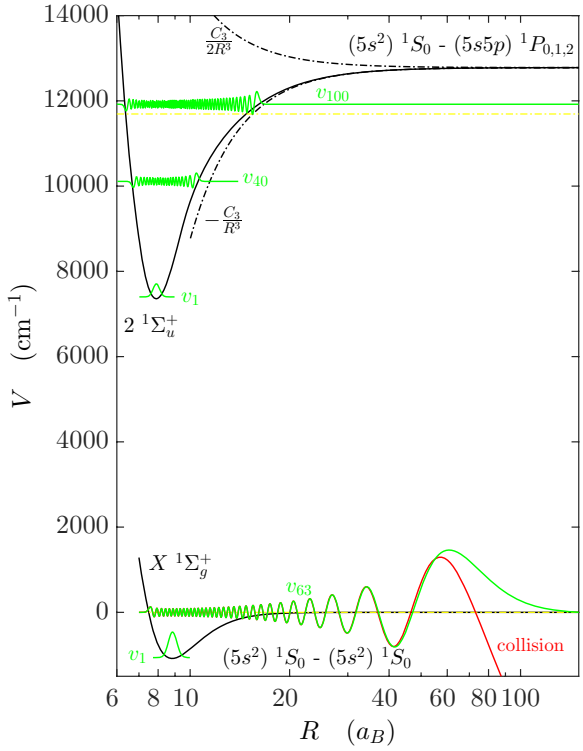

Figure 21.11: Fourier grid calculation for the states $X^1\Sigma_g^+$ and $(2)^1\Sigma_u^+$. Potentials (black) and vibrational structure. The dash-dotted potential only accounts for the C_3 long range force. The red wavefunction is the collisional channel at $T = 0$. The green wavefunctions are vibrational states, the depth in the potential corresponds to the eigenenergies, the indicated vibrational quantum number v' is counted from the dissociation limit.

21.2.3 Photoassociation

To calculate the interaction strength, as we will show below, we must evaluate the Franck-Condon overlap between the collisional ground state wavefunction and resonant repulsive or near-resonant vibrational excited state wavefunctions. In the context of the CDM we are predominantly interested in small light detunings. In this case, only very long range wavefunction play a role, which are dominated by long range van der Waals forces. We may therefore neglect the short range potential and set,

$$V_g(R) = -\frac{C_6}{R^6} \qquad \text{and} \qquad \pm\frac{C_3}{R^3}\ , \tag{21.99}$$

and only consider the highest bound states.

21.2.3.1 The LeRoy-Bernstein method

The LeRoy-Bernstein method allows us to estimate the highest bound levels. It only applies near the dissociation limit, where the semi-classical formula of quantization is

valid,

$$v + \tfrac{1}{2} = \sqrt{\frac{8m_{\rm red}}{\hbar^2}} \int_0^{R_t} dR \sqrt{E(v) - V(R)} \ . \tag{21.100}$$

Inserting the potential (21.112) we get,

$$E(v^*) = -E_{loc} \left(\sqrt{2\pi} \frac{(n-2)\Gamma\left(1+\frac{1}{n}\right)}{2\Gamma\left(\frac{1}{2}+\frac{1}{n}\right)} v^* \right)^{2n/(n-2)} \ , \tag{21.101}$$

where $v^* = v_D - v$ is a number counting the vibrational levels from the top to the bottom starting at the dissociation limit and E_{loc} is the localization energy calculated in (21.114),

$$E_{loc} = -\frac{8\hbar^6}{m^3 C_3^2} \ . \tag{21.102}$$

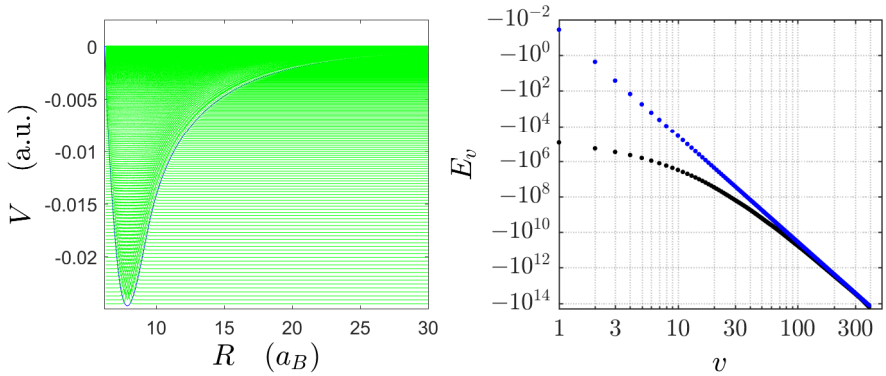

Figure 21.12: (a) Vibrational states of the $(2)\Sigma_u^+$ potential of Yb_2 dimers obtained by the mapped Fourier grid method [477]. (b) Energies of the highest vibrational states as a function of the vibrational quantum number v^* obtained by the LeRoy-Bernstein method. The states inside the red box have been measured [809].

Fig. 21.13 shows a comparison of the vibrational states bound via the Fourier grid method (green dots) and the LeRoy-Bernstein formula (blue dots). Although the coincidence should be good at low v' the contrary is observed. The reason is a failure of the Fourier grid method at extremely long range.

21.2.3.2 Long range wavefunctions

21.2.3.3 Optical cross sections

Calculate optical cross sections at all relative velocities.

21.2.3.4 PA spectra

Calculate PA spectra as a function of temperature.

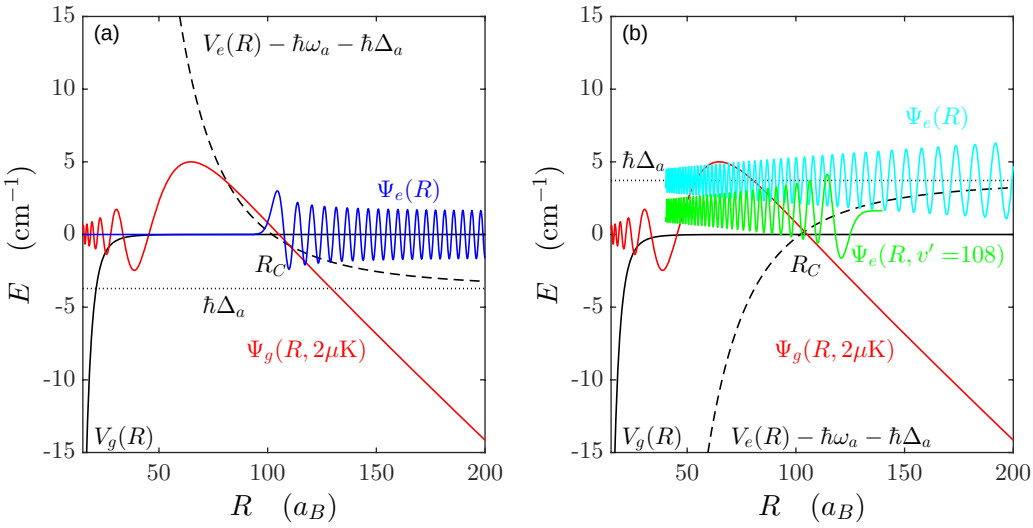

Figure 21.13: Collisional and vibrational wavefunctions in C_6 ground state and C_3 excited state potentials [444] in the presence of (a) blue and (b) red-detuned light ($C_6 = 1500\,\mathrm{a.u.}$, $C_3 = 18\,\mathrm{a.u.}$, $\Delta_\mathrm{a} = (2\pi)\ 700\,\mathrm{GHz}$). The colored curves denote (red) the wavefunction of two atoms colliding on their ground state with a velocity corresponding to 2 µK, (blue) a wavefunction repelled from the excited state potential, (cyan) an unbound wavefunction of the excited state potential, and (green) a vibrational wavefunction of the excited state potential.

21.2.4 Generalization of the CDM

Discuss whether this can be treated in a generalized Green function or in a generalized CDM.

Discuss similarities with Rydberg dressing/blockade?

21.2.4.1 Hamiltonian for the CDM

The many-body Hamiltonian and the Lindbladian read,

$$\hat{H} = \tfrac{1}{2}\sum_j \left[\Omega(\mathbf{r}_j)\hat{\sigma}_j^+ + h.c.\right] - \sum_{i,j}\Delta_{ji}\hat{\sigma}_j^+\hat{\sigma}_i^- \tag{21.103}$$

$$\mathcal{L}^\dagger[\hat{A}] = \tfrac{1}{2}\sum_{i,j}\Gamma_{ij}(2\hat{\sigma}_i^+\hat{A}\hat{\sigma}_j^- - \hat{\sigma}_i^+\hat{\sigma}_j^-\hat{A} - \hat{A}\hat{\sigma}_i^+\hat{\sigma}_j^-)\ .$$

How to include van der Waals forces [631]?

21.2.4.2 Exclusion volume

At short distances the CDM is wrong, because the inner degrees of freedom come into play. In the past the problem has been avoided by introducing an 'exclusion volume', i.e. a volume determined by an interatomic distance which are simply discarded from the analysis. The radius was typically set to $r_{min} = n^{-1/3}/\pi \approx 73\,\mathrm{nm} = 1400 a_B$.

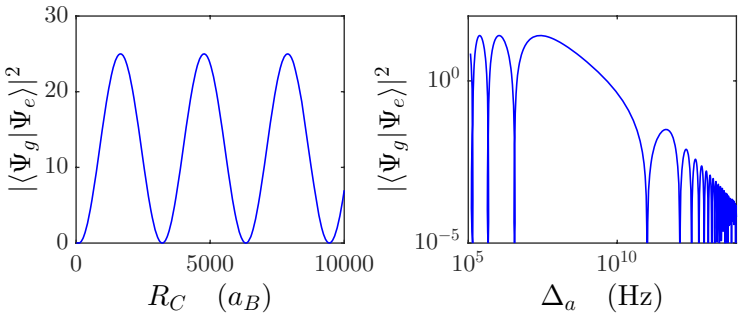

Figure 21.14: [444].

21.2.5 Green tensor for parallel classical dipoles

The Purcell factor allows us to calculate the modification of the decay rate in the presence of a Green tensor. Assuming that the interacting dipoles are parallel, $\hat{\mathbf{e}}_d = \hat{\mathbf{e}}'_d$, we have,

$$\begin{aligned}\Gamma_{ij} &= 3\lambda\Gamma^{(0)}\hat{\mathbf{e}}_d^*\,\mathfrak{Im}\,\mathcal{G}(\mathbf{r}_i,\mathbf{r}_j,\omega)\,\hat{\mathbf{e}}_d \\ &= \tfrac{3}{2}\Gamma^{(0)}\left[(1-(\hat{\mathbf{e}}_d\cdot\hat{\mathbf{e}}_R)^2)\frac{\sin kR}{kR}\right. \\ &\quad \left.+(1-3(\hat{\mathbf{e}}_d\cdot\hat{\mathbf{e}}_R)^2)\left(\frac{\cos kR}{k^2R^2}-\frac{\sin kR}{k^3R^3}\right)\right]\ ,\end{aligned} \tag{21.104}$$

where $\mathbf{R}\equiv\mathbf{r}_i-\mathbf{r}_j$.

Similarly, the Lamb shift can be calculated,

$$\begin{aligned}\Delta_{ij} &= -\tfrac{3}{2}\lambda\Gamma^{(0)}\hat{\mathbf{e}}_d^*\,\mathfrak{Re}\,\mathcal{G}(\mathbf{r}_i,\mathbf{r}_j,\omega)\,\hat{\mathbf{e}}_d \\ &= \tfrac{3}{4}\Gamma^{(0)}\left[(1-(\hat{\mathbf{e}}_d\cdot\hat{\mathbf{e}}_R)^2)\frac{\cos kR}{kR}\right. \\ &\quad \left.-(1-3(\hat{\mathbf{e}}_d\cdot\hat{\mathbf{e}}_R)^2)\left(\frac{\sin kR}{k^2R^2}+\frac{\cos kR}{k^3R^3}\right)\right]\ .\end{aligned} \tag{21.105}$$

At long distances, $kR>1$, the results (21.104) and (21.105) simplify to,

$$\begin{aligned}\Delta_{ij} &\simeq -\tfrac{3}{4}\Gamma^{(0)}[1-(\hat{\mathbf{e}}_d\cdot\hat{\mathbf{e}}_R)^2]\frac{\cos kR}{kR} \\ \Gamma_{ij}^{(b)} &\simeq \tfrac{3}{2}\Gamma^{(0)}[1-(\hat{\mathbf{e}}_d\cdot\hat{\mathbf{e}}_R)^2]\frac{\sin kR}{kR}\ .\end{aligned} \tag{21.106}$$

And since the radiatively induced dipoles are perpendicular to their distance, $\hat{\mathbf{e}}_d\cdot\hat{\mathbf{e}}_R$,

$$\begin{aligned}\Delta_{ij} &\simeq -\tfrac{3}{4}\Gamma^{(0)}\frac{\cos kR}{kR} \\ \Gamma_{ij}^{(b)} &\simeq \tfrac{3}{2}\Gamma^{(0)}\frac{\sin kR}{kR}\ ,\end{aligned} \tag{21.107}$$

we recover the scalar model. Obviously, at very long distances, $kR \gg 1$, $\Delta_{ij} \to 0 \leftarrow \Gamma_{ij}$.

At small distances, $kR \ll 1$, the results (21.104) and (21.105) simplify to,

$$\begin{aligned} \Delta_{ij} &= -\tfrac{3}{4}\Gamma^{(0)} \frac{3(\hat{\mathbf{e}}_d \cdot \hat{\mathbf{e}}_R)^2 - 1}{k^3 R^3} \\ \Gamma_{ij} &= \tfrac{3}{2}\Gamma^{(0)} \frac{1 - (\hat{\mathbf{e}}_d \cdot \hat{\mathbf{e}}_R)^2}{kR} \ . \end{aligned} \tag{21.108}$$

and assuming interaction between induced dipoles the same formula becomes,

$$\Delta_{ij} \simeq \frac{C_3}{R^3} \begin{cases} -1 & \text{for} \quad \hat{\mathbf{e}}_d = \hat{\mathbf{e}}_R \\ \frac{1}{2} & \text{for} \quad \hat{\mathbf{e}}_d \perp \hat{\mathbf{e}}_R \end{cases} \tag{21.109}$$

with the abbreviation,

$$C_3 = \frac{3\Gamma}{2k^3} \ . \tag{21.110}$$

21.2.5.1 Van der Waals C_3 coefficient

Hence, the C_3 coefficient of van der Waals resonant dipole interaction is obtained directly from the vectorial Green tensor. This indicates that the corresponding long range potential,

$$V_{lr}(R) = -\frac{C_3}{R^3} \tag{21.111}$$

results from a reorientation of the atomic dipoles due to molecular forces [152] p. 56. This effect is (probably) accounted for in the CDM at short distances, $kR < 100 a_B \approx 5 \cdot 10^{-9}$.

21.2.5.2 Estimation of the localization energy

One consequence of Heisenberg's uncertainty relation is that a certain localization energy is always required to localize a particle. The zero-point energy of the harmonic oscillator is an example: If the potential is shallower than this energy, it will not be capable of localizing a particle.

As another example, let us consider the attractive potential,

$$V = -\frac{C_n}{R^n} \ . \tag{21.112}$$

The space available for the particle is limited between the classical turning point, which for a given energy is $R_t = (C_n/|E|)^{1/n}$. The momentum corresponding to this energy is $k_t = (2m_{\rm red}|E|/\hbar^2)^{1/2}$. Heisenberg's uncertainty relation requires,

$$k_t R_t > \pi \ , \tag{21.113}$$

that is, at least half of the wavelength must fit within the potential (between 0 and R_t) at the height of the bound state. Therefore,

$$\boxed{|E| > E_{loc} \equiv \left(\frac{\pi\hbar^2}{2m_{\rm red}}\right)^{1/(1-2/n)} C_n^{1/(1-n/2)}} \ . \tag{21.114}$$

For a Coulomb potential, with $n = 1$ and $C_1 = e^2/4\pi\varepsilon_0$, we obtain the energy of the ground state of the hydrogen atom,

$$E > E_1 = -\frac{e^2}{4\pi\varepsilon_0 2a_B}\frac{4}{\pi^2} \ , \tag{21.115}$$

apart from a numerical factor. Note that the condition $k_t R_t > 2n$ yields the correct Bohr energies, $E = E_1/m^2$.

For $n = 2$, we do not get a condition for the energy. For the Casimir-Polder potential, $n = 3$ and $C_3 = 3\hbar\Gamma/2k^3$, we obtain,

$$E < -\frac{\pi^6\hbar^6}{8m_{\rm red}^3 C_3^2} = \frac{(\pi\hbar k)^6}{2m_{\rm red}^3(3\hbar\Gamma)^2} \ . \tag{21.116}$$

This means that, in contrast to the Coulomb potential, in order to minimize the momentum-position uncertainty, the binding energy must be *lower* than a certain limit.

21.2.6 Exercises

21.3 Continuous density distributions and Mie scattering

In the last sections we developed the coupled dipoles model describing light scattering from ensembles of individual microscopic particles by a set of equations of motion, in the simplest case, one for every atomic dipole. This limits the number of atoms that can be considered in numerical simulations to a few 1000. On the other hand, most cold atom experiments nowadays are performed with 10^5 to 10^9 atoms. The following section are devoted to introducing concepts and approximations allowing us to understand light scattering from large atomic clouds.

The main step will consist in an approximation called smooth or *continuous density approximation*, where the discrete distribution of point-like scatterers is replaced by an inhomogeneous but smooth continuous density distribution characterized by a refraction index field $n_{\rm rfr}(\mathbf{r})$. The interaction of this density distribution with light is then treated in the framework of Maxwell's equations, i.e. inhomogeneities are treated as macroscopic boundary conditions to the electromagnetic fields. In the following we will term this regime as *Mie scattering*.

At first sight Rayleigh scattering from point-like particles and Mie scattering from extended objects are quite different phenomena. Rayleigh scattering exhibits resonances due to the internal structure of the particles, e.g. an atom. Mie scattering shows resonances induced by the boundary conditions the scattering objects impose to the field. On the other hand, from a microscopic viewpoint, any extended object (e.g. a dielectric sphere) is nothing but an assembly of microscopic scattering particles. The question we need to study is then whether a description of the diffraction from this object as the sum of the radiation patterns scattered from the individual constituent particles is correct; or in how far the graininess of the cloud's density distribution and cooperative effects arising from the interaction *between* the individual particles play a role [134].

Interesting phenomena are expected in the transition regime between the limits of a dense bunch of individual scatterers and macroscopic dielectric objects. One of them is a strong modification of the radiation pressure force [176], which can conveniently be studied with atomic ensembles. The reason is that, in the smooth density approximation, the cloud can be understood as a macroscopic object characterized by a refraction index, which can be tuned over huge ranges by changing the cloud's density and volume, or by tuning the frequency of the incident light exploiting the existence of atomic resonances. We will see in the following that it is possible to study radiation pressure with cold atoms in the Rayleigh-Debye-Gans limit of small phase-shifts, as well as in the Mie limit of large phase shifts [39]. Despite the absence of sharp boundaries for the atomic cloud, we predict the occurrence of Mie resonances, which could be detected experimentally [40].

21.3.1 Continuous density approximation

In light scattering experiments, disorder (or granularity) plays a role when the number of atoms projected onto a cross section perpendicular to the incident beam is small enough so that a light mode focused down to the diffraction limit (that is $\sim \lambda^2$) would be able to resolve and count the atoms. In other words, the stochastic fluctuations induced by the random positions of the atoms can be neglected when the total number of atoms N is larger than the number of modes $\sim \sigma^2$ that fit into the cloud's cross section, i.e. when the optical density is $b_0 = 3N/\sigma^2 \gg 1$. Under this hypothesis, the differential equation (21.26) for $\tilde{\beta}_j$ can be simplified by replacing the discrete sum over atom positions by an integral over a density distribution $\rho(\mathbf{r})$,

$$\boxed{\sum_{j=1}^{N} \to \int \rho(\mathbf{r}')d^3r' \qquad \text{and} \qquad \tilde{\beta}_j(t) \to \tilde{\beta}(\mathbf{r}',t)} \,. \tag{21.117}$$

For example, the smoothed structure coefficient reads,

$$\mathcal{S}(\mathbf{k}) = \frac{1}{N}\sum_{j=1}^{N} e^{\imath(\mathbf{k}-\mathbf{k}_0)\mathbf{r}_j} = \frac{1}{N}\int d^3r' \; \rho(\mathbf{r}')e^{\imath(\mathbf{k}-\mathbf{k}_0)\mathbf{r}'} \,. \tag{21.118}$$

In the Exc. 21.3.5.1 we calculate the structure coefficients for a homogeneous spherical cloud of radius R and for a Gaussian ellipsoidal cloud with the *rms*-width $\sigma_{\rho,z}$:

$$\begin{aligned} \mathcal{S}_{\text{homog.sphere}}(\mathbf{k}) &= \tfrac{3}{q^3R^3}(\sin qR - qR\cos qR) \\ \mathcal{S}_{\text{gauss.ellipse}}(\mathbf{k}) &= e^{-\frac{1}{2}k^2\sigma_\rho^2\sin^2\theta - \frac{1}{2}\sigma_z^2(k\cos\theta - k_0)^2} \,. \end{aligned} \tag{21.119}$$

The simulated structure factor (red curve in Figs. 21.15) agrees well with the analytical expression (green curve). Since small clouds have a larger fluctuations, the fact that the total force is a sum of intensities rather than amplitudes leads to a finite value at large scattering angles θ.

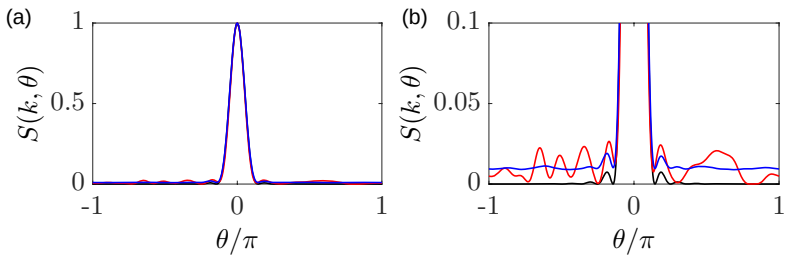

Figure 21.15: (code) (a) The red curve shows a calculation of the structure factor: $|\mathcal{S}(k = k_0, \theta, \phi = 0)|^2$ for 200 atoms randomly distributed in a homogeneous spherical cloud of size $R = 10/k_0$. The blue curve shows an average over 500 realizations of such a cloud according to $\sum_{m=1}^{200} |\mathcal{S}(k, \theta, \phi = 0)|^2$. The black curve is an analytical calculation according to Eq. (21.119) [806]. (b) Same curves as in (a) but with a stretched y-axis.

In the continuous limit defined by (21.117) for the equations of motion (21.32) [11],

$$\dot{\tilde{\beta}}(\mathbf{r},t) = \imath\left(\Delta_0 + \imath\frac{\Gamma}{2}\right)\tilde{\beta}(\mathbf{r},t) - \frac{\imath}{2}\Omega_0 - \frac{\Gamma}{2}\int d^3r'\rho(\mathbf{r}')\frac{\sin(k_0|\mathbf{r}-\mathbf{r}'|)}{k_0|\mathbf{r}-\mathbf{r}'|}\tilde{\beta}(\mathbf{r}',t)e^{-\imath\mathbf{k}_0\cdot(\mathbf{r}-\mathbf{r}')} . \tag{21.120}$$

Transforming back to $\beta_j \equiv \tilde{\beta}e^{\imath\mathbf{k}_0\cdot\mathbf{r}}$, we obtain the fundamental equation for the dipolar excitation field,

$$\boxed{\dot{\beta}(\mathbf{r},t) = \imath\left(\Delta_0 + \imath\frac{\Gamma}{2}\right)\beta(\mathbf{r},t) - \frac{\imath\Omega_0}{2}e^{\imath\mathbf{k}_0\cdot\mathbf{r}} - \frac{\Gamma}{2}\int d^3r'\rho(\mathbf{r}')\frac{\sin(k_0|\mathbf{r}-\mathbf{r}'|)}{k_0|\mathbf{r}-\mathbf{r}'|}\beta(\mathbf{r}',t)} . \tag{21.121}$$

Example 119 (*Connection between coupled dipoles model and Helmholtz equation*): The steady-state solution of (21.121) can also be obtained from the *Helmholtz equation* of Maxwell's theory [286, 39, 40], as shown in [12],

$$\boxed{[\nabla^2 + k_0^2 n_{\rm rfr}^2(\mathbf{r})]\beta(\mathbf{r}) = 0 \qquad \text{defining} \qquad n_{\rm rfr}^2(\mathbf{r}) \equiv 1 - \frac{4\pi\rho(\mathbf{r})}{k_0^3(2\Delta_0/\Gamma + \imath)}} . \tag{21.122}$$

21.3.2 Simulations of the time evolution

We start from the second equation (21.18),

$$\dot{\tilde{\beta}}_j(t) = \imath\Delta_0\tilde{\beta}_j(t) - \frac{\Omega_0^2}{4}\sum_{m=1}^{N}\int_0^t \tilde{\beta}_m(t')dt' \tag{21.123}$$
$$- \sum_{\mathbf{k}} g_k^2 \sum_{m=1}^{N} e^{\imath(\mathbf{k}-\mathbf{k}_0)(\mathbf{r}_j-\mathbf{r}_m)}\int_0^t e^{-\imath(\omega_k-\omega_0)(t-t')}\tilde{\beta}_m(t')dt' .$$

[11] Note that the 'timed Dicke' assumption (21.64) has not been used here.
[12] See script on *Electrodynamics: Electricity, Magnetism and Radiation* (2025)Sec. 21.3.2.

Substituting the timed Dicke state (21.64),

$$\dot{\beta}(t) = \frac{1}{N}\sum_{j=1}^{N}\dot{\beta}(t) = \frac{1}{\sqrt{N}}\sum_{j=1}^{N}\dot{\tilde{\beta}}_j(t) \tag{21.124}$$
$$= \imath\Delta_0\beta(t) - \frac{N\Omega_0^2}{4}\int_0^t \beta(t')dt' - \frac{V_{\rm ph}}{(2\pi)^3}\int d^3k\; g_k^2 N^2 |\mathcal{S}(\mathbf{k})|^2 \int_0^t e^{-\imath(\omega_k-\omega_0)(t-t')}\frac{\tilde{\beta}_m(t')}{\sqrt{N}}dt' \;,$$

where we used $\sum_{m=1}^{N} e^{\imath(\mathbf{k}-\mathbf{k}_0)(\mathbf{r}_j-\mathbf{r}_m)} = N^2|\mathcal{S}(\mathbf{k})|^2$ from Eq. (21.67). Finally, at resonance and low saturation we may neglect the first two terms,

$$\dot{\beta}(t) = -N\frac{V_{\rm ph}}{(2\pi)^3}\int_{\mathbb{R}} d^3k \int_0^t dt'\; g_k^2\beta(t')e^{\imath(\nu_k-\omega)(t-t')}|\mathcal{S}(\mathbf{k})|^2 \tag{21.125}$$
$$= -N\frac{V_{\rm ph}}{(2\pi)^3}\int_0^t dt'\;\beta(t')\int_0^\infty\int_0^\pi g_k^2 e^{\imath(\nu_k-\omega)(t-t')}|\mathcal{S}(k,\theta)|^2 2\pi k^2\sin\theta d\theta dk$$
$$= -N\frac{V_{\rm ph}}{(2\pi)^3}g_k^2\int_0^t dt'\;\beta(t')\int_0^\infty e^{\imath(\nu_k-\omega)(t-t')}k^2 I(k)dk = -\Omega_N^2\int_0^t dt'\;\beta(t')G(t-t') \;,$$

with the collective Rabi frequency $\Omega_N = \sqrt{N}g_k$ and the surface integrated structure factor,

$$I(k) = \int_0^{2\pi}\int_0^\pi |\mathcal{S}(k,\theta,\phi)|^2\sin\theta d\theta d\phi \;, \tag{21.126}$$

and

$$G(\tau) = \frac{V_{\rm ph}}{(2\pi)^3}e^{-\imath\omega\tau}\int_0^\infty e^{\imath ck\tau}k^2 I(k)dk \;, \tag{21.127}$$

with $\omega = ck_0$ and $\nu_k = ck$. The integral $I(k)$ has been solved by Nicola for an ellipsoidal Gaussian density distribution. It is quite close to,

$$I(k) \simeq I(k_0) \simeq \sqrt{\frac{\pi}{2}}\frac{1}{k\sigma_z}e^{F^2/2}[1-\mathrm{erf}\,(F/\sqrt{2})] \;, \tag{21.128}$$

with the Fresnel number $F = k\sigma_r^2/\sigma_z$.

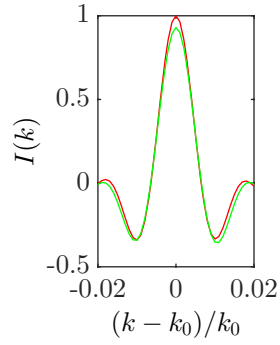

Figure 21.16: (code) Averaging of the structure factor over the whole k-space.

21.3.2.1 Analytical method

To evaluate the above integro-differential equation, we use the rule for differentiating integrals with variable boundaries,

$$\frac{\partial}{\partial t}\int_{\phi(t)}^{\psi(t)} f(x,t)dx = \int_{\phi(t)}^{\psi(t)} \frac{\partial f(x,t)}{\partial t}dx + f(\psi(t),t)\psi'(t) - f(\phi(t),t)\phi'(t) \ , \quad (21.129)$$

it is easy to show,

$$\frac{\partial}{\partial t}\int_0^t f(t')G(t-t')dt' = f(t)G(0) + \int_0^t f(t')\dot{G}(t-t')dt' \quad (21.130)$$

and to thusly evaluate the integral until $\frac{\partial^n}{\partial t^n}G(t-t')$ gets smooth enough to be neglected.

21.3.2.2 Numerical method

We can directly solve the integro-differential equation numerically using,

$$G(\tau) = \left[1 + \frac{3c}{4R}\tau - \frac{c^3}{16R^3}\tau^3\right]\Theta(3R - c\tau) \ , \quad (21.131)$$

for a homogeneous spherical cloud and,

$$G(\tau) = \frac{k\sigma_r^2}{k\sigma_r^2 + ic\tau}e^{-(c\tau/\sigma_z)^2/2} \ , \quad (21.132)$$

for an ellipsoidal Gaussian cloud. The iteration is done via,

$$\beta(t+dt) = \beta(t) - dt\ \Omega_N^2\int_0^t \beta(t')G(t-t')dt' \ . \quad (21.133)$$

The discretization is done via,

$$t_{m+1} = t_m + dt \quad (21.134)$$
$$\beta_{m+1} = \beta_m - dt\ Ng_k^2\sum_{m'=1}^{m}\beta_{m'}G(t_m - t_{m'})dt \ .$$

With the solution of the integro-differential equation $\beta(t)$, we can calculate the probability that atoms are excited [806] [13],

$$P(t) = |\beta(t)|^2 = \sum_j |\beta_j(t)|^2 = \int d^3r|\beta(t,\mathbf{r})|^2 \ . \quad (21.135)$$

[13] Compare to Jaynes-Cummings model in a CQED environment: A single photon is coherently exchanged between the cavity and the atomic excitation, we get Rabi oscillations. Here, the atomic cloud is the cavity.
We know that the Mollow triplet in the dressed states picture gives rive to an oscillating decay curve resembling that of Fig. 21.17. Does this curve also have an interpretation in terms of collective dressed states?

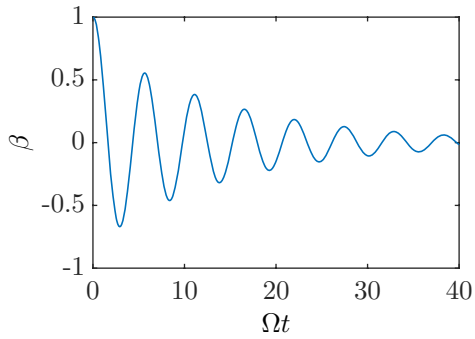

Figure 21.17: (code) Calculation of the time evolution of β for a homogeneous spherical cloud. The parameters are $\lambda \simeq 780\,\text{nm}$ and $c/\Omega \simeq 30\,\text{cm}$ with $\Omega = \sqrt{N} g_k$ for typically $g_k \simeq 1\,\text{MHz}$ and $N \simeq 10^6$.

Example 120 (*Solutions for a homogeneous spherical cloud*): For a homogeneous spherical cloud, we find three regimes characterized by the size of the cloud compared to the two length scales λ and c/Ω:

$$\beta(t) = \beta(0) \begin{cases} e^{-N\Gamma t} & \text{for} \quad R < \lambda \ll c/\Omega \\ e^{-27N\Gamma t/8(k_0 R)^2} & \text{for} \quad \lambda < R \ll c/\Omega \\ \cos\Omega t e^{-3ct/8R} & \text{for} \quad \lambda \ll c/\Omega < R \end{cases} .$$

21.3.2.3 Complete numerical simulation

In order to be independent from initial conditions, we generate a random distribution $\mathbf{r}_{j'}$ and solve the differential equation,

$$\dot{\beta}_j(t) = -N g_k^2 \int_0^t dt' \, \frac{V_{\text{ph}}}{(2\pi)^3} \int d^3k \, \frac{1}{N} \sum_{j'=1}^{N} \beta_{j'}(t') e^{\imath(\nu_k - \omega)(t-t') + \imath \mathbf{k}(\mathbf{r}_j - \mathbf{r}_{j'})} \, . \quad (21.136)$$

We propagate the amplitudes in time via,

$$\beta_j(t+dt) = \beta_j(t) - dt g_k^2 \frac{V_{\text{ph}}}{(2\pi)^3} \int_0^t dt' \, \sum_{j'=1}^{N} \beta_{j'}(t') \int_0^\infty k^2 e^{\imath(ck-\omega)(t-t')} I_{jj'}(k) dk \, , \quad (21.137)$$

where $I_{jj'}(k) \equiv \int_0^\pi \int_0^{2\pi} e^{\imath k \left[(x_j - x_{j'}) \sin\theta\cos\phi + (y_j - y_{j'}) \sin\theta \sin\phi + (z_j - z_{j'})\cos\theta\right]} \sin\theta d\theta d\phi$, and discretize via,

$$t_{m+1} = t_m + dt \quad (21.138)$$

$$\beta_j(t_{m+1}) = \beta_j(t_m) - dt^2 g_k^2 \sum_{m'=1}^{m} \sum_{j'=1}^{N} \beta_{j'}(t_{m'}) G_{jj'}(t_m - t_{m'}) \, ,$$

with $G_{jj'}(t_m - t_{m'}) = \frac{V_{\text{ph}}}{(2\pi)^3} \int_0^\infty k^2 e^{\imath(ck-\omega)(t_m - t_{m'})} I_{jj'}(k) dk$.

21.3.3 Radiation pressure force in macro- and microscopic scattering

As mentioned at the beginning of this section, scattering of light by an extended object such as an atomic ensemble or a dielectric sphere is fundamentally different from scattering at a point-like scatterer such as a single atom. On one hand, the finite size of the object leads to Mie scattering. On the other hand, the spatial distribution of the scatterers rules the degree of cooperativity. Homogeneous and periodic distributions tend to scatter cooperatively, whereas disorder suppresses cooperativity. In an atomic cloud, the amount of disorder can be tuned via the optical density seen by the incident light, and its role can be studied via the radiation pressure exerted by the light on the atomic cloud. We present an analytic expression for the radiation pressure valid for any numbers of atoms and arbitrary density distributions, which interpolates between the regimes of dominating disorder and dominating cooperativity. Furthermore, we present first experimental signatures of radiation pressure reduction due to cooperative scattering.

The radiation pressure exerted by a plane wave laser beam with frequency ω_0 and wave vector $\mathbf{k}_0 = k_0\hat{\mathbf{e}}_z$ on a single two-level atom with resonance frequency $\omega_\mathrm{a} = \omega_0 - \Delta_0$ is correctly described by the standard formula (21.80). Generalization to scattering by atomic ensembles and extended objects is only possible, if a number of effects is explicitly taken into account. The most important ones are named in the following. a. *Cooperativity* and b. *disorder*: Cooperativity is the tendency of atoms located in the same area of space, forming regular structures or being forced by the mode structure of the environment (e.g. optical cavities) to scatter light synchronously into the same direction, as in the case of Dicke superradiance. While homogeneously or periodically distributed atoms concentrate the scattered light in specific solid angles by forward or Bragg scattering, randomly distributed atoms do not cooperate and scatter light isotropically. In this respect, cooperativity and disorder are antagonists. c. *Mie scattering and refraction*: The finite volume and the shape of the cloud represent an inhomogeneity at which light is scattered in a global way. As long as the optical density is low, the pump mode depletion is mainly due to the fact, that the atomic cloud distorts the phase front of the incident light. For high optical density, scattering is predominantly absorptive. d. *Multiple scattering* and e. *resonance fluorescence*: Near resonance, multiple scattering leads to radiation trapping. Even off-resonance, inelastic scattering pumps resonant photons into the atomic cloud, which have a high probability to be reabsorbed. Taking account of all these effects, the real radiation pressure can differ by orders of magnitude from the naive prediction of the above formula.

For smooth density distributions F_c is only limited by Mie scattering at the inhomogeneity represented by the *finite extend* of the atomic cloud [176]. The radiation pressure depends on the number of atoms N in the volume, and the scaling $F_c(N)$ depends on the pump laser detuning and the radial cross section of the cloud. But small scale inhomogeneity *within the cloud*, i.e. disorder, can play an eminent role for collective scattering. This is the case, when the number of atoms is beyond a critical value, which mainly depends on the volume and shape of the cloud. In the following we will derive an analytic expression for the radiation pressure as a function of atom number, which interpolates between the regimes of dominating disorder (single-atom

Rayleigh scattering) and dominating cooperativity (pure Mie scattering).

On the other hand, we point out, that we do not consider multiple scattering in our treatment. This is a good assumption far from resonance, where the scattering is predominantly Rayleigh scattering and inelastic scattering can safely be disregarded. In contrast, our extensions of single to multi-atom scattering are not valid near resonance.

The radiation pressure provides sensitive signatures for the impact of cooperativity and disorder. We describe an experiment measuring the displacement of cold atoms confined in a far-off resonance dipole trap and interpret our observations in terms of collective scattering.

21.3.3.1 Radiation pressure for timed Dicke states

As a first approach we will calculate the radiation pressure for a timed Dicke state from Eq. (21.89) by explicit analytical integration of the surface-integrated structure factors s_∞ and f_∞ in the smooth density limit (21.117) for an ellipsoidal Gaussian smooth density distribution, as shown in Exc. 21.3.5.2. In the spherical case,

$$\rho(\mathbf{r}) = \rho_0 e^{-r^2/2\bar{r}^2} \qquad \text{with} \qquad \rho_0 = \frac{N}{(2\pi)^{3/2}\bar{r}^3} \ , \tag{21.139}$$

and introducing $\sigma \equiv k\bar{r}$, we get,

$$\begin{aligned} s_\infty &= \frac{1-e^{-4\sigma^2}}{4\sigma^2} \overset{\sigma\gg1}{\longrightarrow} \frac{1}{4\sigma^2} \\ f_\infty &= \frac{1}{4\sigma^2}\left[1 - \frac{1}{2\sigma^2} + \left(1+\frac{1}{2\sigma^2}\right)e^{-4\sigma^2}\right] \overset{\sigma\gg1}{\longrightarrow} s_\infty - 2s_\infty^2 \ . \end{aligned} \tag{21.140}$$

Hence,

$$\boxed{\frac{F_{za}+F_{ze}}{F_{z1}} = \frac{(2\Delta_0/\Gamma)^2+1}{(2\Delta_0/\Gamma)^2+N^2 s_\infty^2} N(s_\infty - f_\infty)} \ . \tag{21.141}$$

Note that the radiation pressure calculated from Eq. (21.141) also holds for elongated ellipsoidal Gaussian clouds characterized by an aspect ratio $\eta > 1$, even though the expressions for the surface-integrated structure factors become more complicated.

It is revealing to compare the smooth density expressions (21.141) with numerical simulations based on randomly generated atomic distributions from which the structure factor is directly from the sum (21.68). Interestingly, we find in certain parameter regimes (in particular at low atom numbers) considerable deviations between s_N, f_N and s_∞, f_∞ and consequently between the numerical simulations and the analytic calculations of the radiation pressure. We attribute these deviations to disorder in the atomic cloud, which is not seen in the smooth density limit, but naturally incorporated in the numerical approach.

By comparison to numerical simulations [black solid lines and blue circles in Figs. 21.18(a)] we found that the surface-integrated structure factors in the presence of disorder are well described by [80],

$$s_N = \frac{1}{N} + s_\infty \qquad \text{and} \qquad f_N = f_\infty \ . \tag{21.142}$$

21.3.3.2 Cooperativity versus disorder

We expect disorder to play a dominant role, when the coarse graininess, which is related to the average distance between two atoms, $|\mathbf{r}_i - \mathbf{r}_j|$, can be resolved by the incident light. For the *absorption process*, this means that disorder gets important, when the number of spatial modes supported by the pump laser in a radial cross section of the atomic cloud,

$$N_{ca} = s_\infty^{-1} \simeq 4\sigma^2 \ , \tag{21.143}$$

(for voluminous clouds) surpasses the number of atoms, $N < N_{ca}$. This is just the case, when the mean resonant optical density (for a ray passing through the center of the cloud $x = y = 0$) is larger than 1,

$$b_0 = \int_{-\infty}^{\infty} dz \ \rho(z)\sigma_{\rm opt} = \frac{3N}{\sigma^2} = \frac{12N}{N_{ca}} > 1 \ , \tag{21.144}$$

where $\sigma_{\rm opt} = \frac{3\lambda^2}{2\pi}$ is the resonant optical cross section and $\rho(\mathbf{r})$ the spherical Gaussian density distribution (21.139). For the *scattering process*, the number of modes available for the reemitted light also counts. Hence, the critical number of atoms that can be resolved by light scattering is larger than N_{ca}:

$$N_{ce} = (s_\infty - f_\infty)^{-1} \simeq \tfrac{1}{2}(2\sigma)^4 = \tfrac{1}{2} N_{ca} \cdot \sigma^2 \ . \tag{21.145}$$

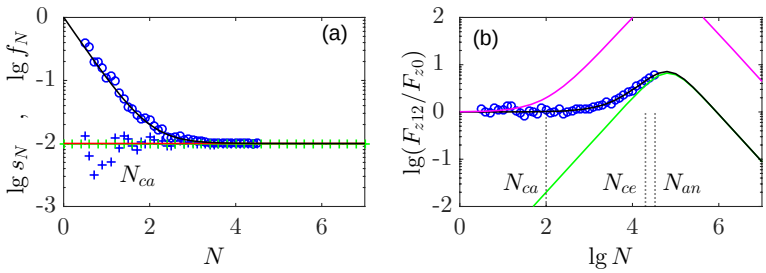

Figure 21.18: (code) (a) Numerical evaluation of s_N (blue circles) and f_N (blue crosses) [134]. Analytical calculation of s_N (black solid line) according to Eq. (21.142). Smooth density limit of s_∞ (red solid line) and f_∞ (green crosses). The cloud is assumed spherical, $\eta = 1$, and Gaussian with size $\sigma = 5$. (b) Numerical evaluation (blue circles) of the corresponding force ratio as a function of atom number N for $\Delta_0 = (2\pi)\ 2\,\mathrm{GHz}$ and small collective saturation, $\sqrt{N}\Omega_0 \ll \Delta_0$. Analytical calculation in the smooth density limit (green solid line) and according to Eq. (21.147) (black solid line). The magenta line traces the radiation pressure force resulting from pump photon absorption only.

In order to simplify the discussion, we neglect saturation, $\Omega_0 \to 0$. Using $\Delta_0 \gg \Gamma$ and defining a third characteristic atom number,

$$N_{cr} = \frac{2\Delta_0}{\Gamma s_\infty} \ , \tag{21.146}$$

Eq. (21.141) can be written,

$$\frac{F_c}{F_1} \simeq \frac{1 + N/N_{ce}}{1 + (N/N_{cr})^2} \,. \tag{21.147}$$

In the limit of very large detunings, $\Delta_0/\Gamma \gg \sigma^2 \gg 1$, the three introduced characteristic atom numbers introduced in Eqs. (21.143), (21.145) and (21.146) satisfy $N_{ca} < N_{ce} < N_{cr}$, and we obtain the N-dependence of the radiation pressure depicted in Fig. 21.18.

In the regime $N < N_{ca}$, radiation pressure is dominated by the absorption process, $s_N \gg f_N$, because the emission is isotropic. The absorption radiation pressure exerted on a hypothetical smooth density distribution occupying the same volume as the atomic cloud [green line in Fig. 21.18] is dramatically reduced with respect to the single-atom radiation pressure (cyan dash-dotted line). However, disorder suppresses cooperativity and increases the radiation pressure up to the single-atom value. The novelty as compared to Ref. [746] is the fact that cooperativity and disorder not only influence the collective emission of a photon by an atomic cloud, but also the collective *absorption* of a photon from a pump laser beam.

Neglecting the photon reemission at higher atom numbers would result in an increase of radiation pressure in the regime $N_{ca} < N < N_{ce}$ (magenta line). However, in this regime, the emission process becomes increasingly important, $s_N \simeq f_N$, because the emission changes its radiation pattern from isotropic to forward scattering. Consequently, the radiation pressure is reduced with respect to its purely absorptive component. This regime is still ruled by disorder, so that the critical atom number for the impact of disorder on the absorption process, N_{ca}, has no impact. It does not even show up in the formula (21.147).

In the regime $N_{ce} < N < N_{cr}$, disorder steps back and cooperativity wins, so that the radiation pressure approaches the smooth density limit. Since in this regime, the smooth density radiation pressure depends on atom number like $\propto N$, as already shown in Ref. [176], we observe an increase of the radiation pressure beyond the single-atom value. This is only possible, because the collective enhancement of absorption (magenta line) rises as fast with N, as the collective enhancement of emission.

For even higher atom numbers, $N_{cr} < N$, the radiation pressure dramatically alters its N-dependency from $\propto N$ to $\propto N^{-1}$. This change of behavior is *not* caused by the interplay of cooperativity and disorder, but can be understood within the framework of Mie scattering, as discussed in the next section.

21.3.3.3 Rayleigh-Debye-Gans versus Mie scattering

Radiation pressure is observed in many experiments, as it is the basis for optical cooling techniques (like magneto-optical traps) and limits the efficiency of resonant absorption imaging of cold atoms, because their acceleration leads to considerable Doppler-shifts. However, as stated before, the impact of disorder on radiation pressure can only be seen for large optical densities, $b \gg 1$, which may partially explain, why this effect has not been observed until two experiments explicitly searched for it [80, 68] (see Fig. 21.19).

Depending on the parameter regime chosen, the measurements exhibited in Fig. 21.19 present data for reduced or enhanced radiation pressure for larger N. As explained

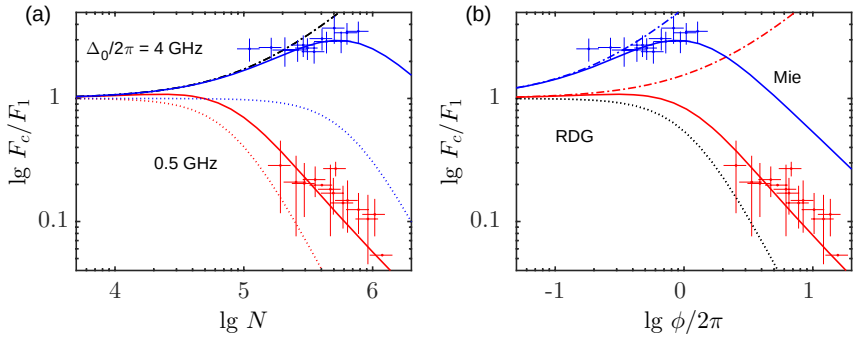

Figure 21.19: (code) (a) Double-logarithmic plot of the measured (symbols) and calculated (lines) N dependence of the radiation pressure force. The red symbols and lines correspond to the detuning $\Delta_0 = (2\pi)\,0.5\,\mathrm{GHz}$ and the intensity $I_0 = 95\,\mathrm{mW/cm^2}$. For the blue symbols and lines, $\Delta_0 = (2\pi)4\,\mathrm{GHz}$ and $I_0 = 730\,\mathrm{mW/cm^2}$. The red (bottom) and blue (top) solid lines show calculations based on the full expression (21.141) without adjustable parameters. The red (bottom) and blue (top) dotted lines represent just the fraction of expression (21.141). The dash-dotted lines representing just the parentheses coincide for both values of Δ_0. (b) Same data as (a), but plotted as a function of the push beam phase shift φ. In this diagram the dotted lines representing the fraction coincide for both values of Δ_0 [68].

above, the reduction is understood as microscopic Rayleigh scattering at disordered atoms together with superradiant acceleration of the decay, while the enhancement is observed when the bulk cloud becomes so small and dense that it turns into an inhomogeneous dielectric sphere refracting and lensing incident light by macroscopic Mie scattering.

The question then remains why the radiation pressure, with increasing N, after an initial rise the drops again. To answer this question we must have a look at the phase shift induced in the pumjp light by the cloud's refraction index.. From calculations done in Secs. 1.2.7 and 26.6.1 we know that (below saturation) the optical density b and the phase shift φ are linked to the refraction index $n_{\rm rfr}$ and the optical scattering cross section $\sigma_{\rm opt}$ via,

$$\frac{\imath b}{2} + \varphi = \frac{\omega}{c}\int_{-\infty}^{\infty}[n_{\rm rfr}(\mathbf{r})-1]dz = \left(\imath - \frac{2\Delta_0}{\Gamma}\right)\sigma_{\rm opt}(\Delta_0)\int_{-\infty}^{\infty}\rho(\mathbf{r})dz \qquad (21.148)$$

$$\text{where}\quad \sigma_{\rm opt}(\Delta_0) = \frac{2\pi}{k^2}\frac{\Gamma^2}{4\Delta_0^2+\Gamma^2} \qquad \text{and} \qquad n_{\rm rfr}(\mathbf{r}) - 1 = -\frac{4\pi\rho(\mathbf{r})}{k_0^3(2\Delta_0/\Gamma+\imath)}\ ,$$

such that,

$$\boxed{b = -\sigma_{\rm opt}(\Delta_0)\int_{-\infty}^{\infty}\rho(\mathbf{r})dz = b_0\frac{\Gamma^2}{4\Delta_0^2+\Gamma^2} \qquad \text{and} \qquad \varphi = \frac{2\Delta_0}{\Gamma}b}\ . \qquad (21.149)$$

Estimating coarsely $k\int_{-\infty}^{\infty}[n_{\rm rfr}(\mathbf{r})-1]dz \simeq \sigma[n_{\rm rfr}(\mathbf{r})-1]$, where $\sigma \equiv k\bar{r}$, we may simplify,

$$\frac{\imath b}{2} + \varphi = \sigma[n_{\rm rfr}(\mathbf{r})-1]\ . \qquad (21.150)$$

At high atom numbers (i.e. in the smooth density limit), the dependency of the radiation pressure on atom number (21.147) exhibits a maximum at N_{cr}. For an atomic cloud with density n and the resonant optical density b_0, the characteristic atom number can be expressed in terms of the phase shift φ experienced by the pump laser beam on its path across the cloud. Absorption losses for the pump beam (e.g. resonance fluorescence, whose differential cross section contributes σ_{opt} to the total scattering cross section [530]) is completely negligible at large detunings. Only elastic Rayleigh scattering occurs, which in the smooth density limit of Mie scattering becomes pure *diffraction* (real part of the refraction index). We can than understand the atomic cloud as a non-absorbing dielectric sphere with a Gaussian index of refraction.

Rewriting Eq. (21.147) in terms of the refraction index,

$$\frac{F_c}{F_1} \simeq \frac{N}{1+(2\varphi)^2}\frac{2}{(2\sigma)^4} \ , \tag{21.151}$$

we see that, as long as $\varphi < \frac{1}{2}$, the force increases linearly like $\propto N$. The proportionality comes from the perfect (in the sense of not spoiled by disorder) cooperative enhancement of the scattering rate in the smooth density limit. The enhancement is only limited by the finite size σ of the cloud, which is accounted for in the second fraction. This regime, characterized by [14],

$$\sigma[n_{\text{rfr}}(\mathbf{r})-1] \ll 1 \tag{21.152}$$

is termed the *Rayleigh-Debye-Gans regime*.

For larger phase shifts, $\varphi > \frac{1}{2}$, refraction more and more distorts the wavefront of the pump beam, which spoils the pump mode depletion and hence reduces radiation pressure. Consequently, the radiation pressure decreases again like N^{-1}. This is the *Mie regime* of scattering. The maximum is thus a pure diffraction effect, a so-called Mie resonance. It corresponds to the n_{rfr}, where the Rayleigh-Debye-Gans scattering approximation looses its validity according to (21.152). In Excs. 21.3.5.3 and 21.3.5.4 we study Mie and Rayleigh-Debye-Gans scattering, and in 21.3.5.5 we discuss the question is whether recoil is imparted to individual atoms or to the center-of-mass of the whole cloud.

In the limit of the approximations made, our formula correctly describes the radiation pressure force on extended objects. These objects can either be ensembles of scatterers like homogeneous, ordered or disordered atomic clouds of arbitrary shapes and volumes, or macroscopic objects like dielectric spheres. The formula thus represents a bridge between microscopic Rayleigh scattering and macroscopic Mie scattering. At very low atom numbers, the atomic cloud basically represents a randomly distributed bunch of scatterers, whose intrinsic disorder spoils cooperativity. The radiation pressure is then well described by the single-atom value. At large atom numbers, the atomic cloud forms a smooth density distribution characterized by an almost perfect a cooperativity, which is only limited by Mie scattering.

[14] Note the necessity of another condition $[n_{\text{rfr}}(\mathbf{r})-1] \ll 1$ termed Born approximation, which demands that the incident wave be not appreciably reflected.

21.3.3.4 Light scattering in the continuous density approximation

The scalar electric field scattered by an arbitrary distribution of atoms has been calculated in (21.49). In the continuous density approximation (21.117), we get,

$$\vec{\mathcal{E}}_{\rm sct}(\mathbf{r}) = -\frac{\imath\hbar\Gamma}{2d}\sum_{j=1}^{N}\frac{e^{\imath k_0|\mathbf{r}-\mathbf{r}_j|}}{\imath k_0|\mathbf{r}-\mathbf{r}_j|}\beta_j(\infty) \to -\frac{\imath\hbar\Gamma}{2d}\int d^3r'\rho(\mathbf{r}')\frac{e^{\imath k_0|\mathbf{r}-\mathbf{r}'|}}{\imath k_0|\mathbf{r}-\mathbf{r}'|}\beta(\mathbf{r}',\infty)\ . \tag{21.153}$$

In particular, for a timed Dicke state,

$$\begin{aligned}\vec{\mathcal{E}}_{\rm sct}(\mathbf{r}) &= -\frac{\imath\hbar\Gamma}{2d}\frac{\sqrt{N}\Omega_0}{2\Delta_0+\imath\Gamma N s_N}\sum_{j=1}^{N}\frac{e^{\imath k_0|\mathbf{r}-\mathbf{r}_j|}}{\imath k_0|\mathbf{r}-\mathbf{r}_j|} \\ &\to -\frac{\imath\hbar\Gamma}{2d}\frac{\sqrt{N}\Omega_0}{2\Delta_0+\imath\Gamma(1+N s_\infty)}\int d^3r'\rho(\mathbf{r}')\frac{e^{\imath k_0|\mathbf{r}-\mathbf{r}'|}}{\imath k_0|\mathbf{r}-\mathbf{r}'|}\ .\end{aligned} \tag{21.154}$$

21.3.4 Spherical harmonics expansion and generalized timed Dicke state

The results derived in (21.141) assumed the cloud to be in a timed Dicke state. As we have seen in Exc. 21.1.8.5, timed Dicke states do not account for pump laser phase shifts induced by the cloud's refraction index. The timed Dicke states might work well for homogeneous cylinders, but not for ellipsoidal clouds, which we assume in our analytical treatments. Therefore, a better approach consists in expanding the cloud into spherical harmonics. Under the assumption that the cloud is radially symmetric, $\rho(\mathbf{r}) = \rho(r)$, we get [286],

$$\beta(r,\theta,t) = \sum_{n=0}^{\infty}\sqrt{\frac{2n+1}{4\pi}}\alpha_n(t)j_n(k_0 r)P_n(\cos\theta)e^{-\imath k_0 r\cos\theta}\ , \tag{21.155}$$

where the coefficients α_n are the solutions of,

$$\dot{\alpha}_n = \left[\imath\Delta_0 - \frac{\Gamma}{2}(1+\lambda_n)\right]\left[\alpha_n - \alpha_n(\infty)\right]\ , \tag{21.156}$$

In steady state,

$$\alpha_n(\infty) = \frac{2\imath^n\sqrt{\pi(2n+1)}\Omega_0}{2\Delta_0+\imath\Gamma(1+\lambda_n)}\ , \tag{21.157}$$

where,

$$\lambda_n \equiv 4\pi\int_0^\infty dr\rho(r)j_n^2(k_0 r) \tag{21.158}$$

is the decay rate of eigenmode n.

Inserting this into the steady-state solution (21.121) and integrating over the volume,

$$\begin{aligned}\langle\beta_\infty\rangle &\equiv \frac{2\pi}{N}\int_0^{2\pi}d\theta\sin\theta\int_0^\infty dr^2\rho(r)\beta(r,\theta) = \frac{\Omega_0}{N}\sum_{n=0}^{\infty}\frac{(2n+1)\lambda_n}{2\Delta_0+\imath\Gamma(1+\lambda_n)} \\ \langle|\beta_\infty|^2\rangle &\equiv \frac{2\pi}{N}\int_0^{2\pi}d\theta\sin\theta\int_0^\infty dr^2\rho(r)|\beta(r,\theta)|^2 = \frac{\Omega_0^2}{N}\sum_{n=0}^{\infty}\frac{(2n+1)\lambda_n}{4\Delta_0^2+\Gamma^2(1+\lambda_n)^2}\ .\end{aligned} \tag{21.159}$$

Example 121 (*Spherical harmonics expansion for a Gaussian density distribution*): The density distribution determines the coefficients λ_n. For a Gaussian distribution $n(r) = N/[(2\pi)^{3/2}\sigma_R^3]e^{-r^2/2\sigma_R^2}$ using the sine kernel,

$$\lambda_n = N\sqrt{\frac{\pi}{2}}\frac{e^{-\sigma^2}}{\sigma}I_{n+1/2}(\sigma^2) \ .$$

For a homogeneous sphere, $n(r) = n_0$, of radius $\sigma = k_0 R$, using the sine kernel [[805], Eq. (18)],

$$\lambda_n = \frac{3N}{2}[j_n^2(\sigma) - j_{n-1}(\sigma)j_{n+1}(\sigma)] \ .$$

21.3.4.1 Expansion of the radiation pressure forces

This allows us to calculate the forces,

$$F_a = -\hbar k_0 \Omega_0 \Gamma \Im\mathfrak{m}\,\langle\beta_\infty\rangle \tag{21.160}$$

$$F_e = -\hbar k_0 \Omega_0^2 \Gamma \sum_{n=0}^{\infty} \frac{2(n+1)\lambda_n\lambda_{n+1}[4\Delta_0^2 + \Gamma^2(1+\lambda_n)(1+\lambda_{n+1})]}{[4\Delta_0^2 + \Gamma^2(1+\lambda_n)(1+\lambda_{n+1})]^2 + 4\Delta^2\Gamma^2(\lambda_{n+1}-\lambda_n)^2} \ .$$

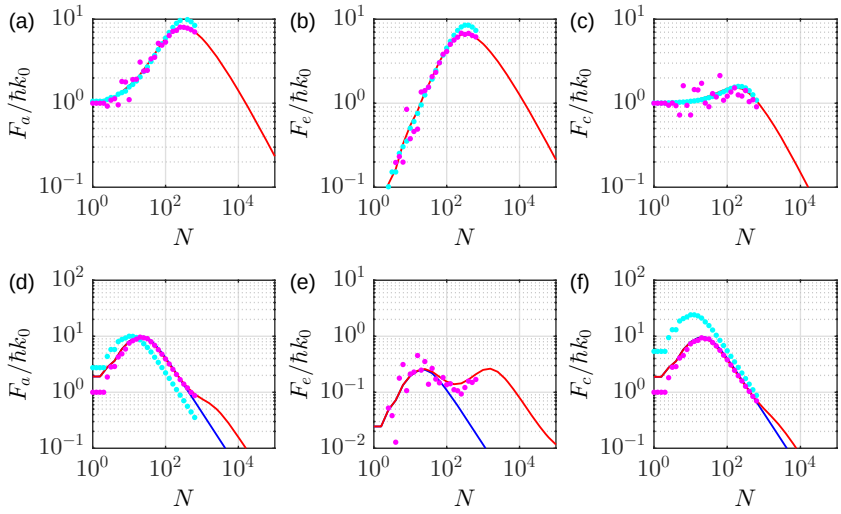

Figure 21.20: (code) (a) Absorption, (b) emission, and (c) total force for a Gaussian cloud with the following parameters: $\sigma = 2$, $\Delta_0 = 10\Gamma$, $\Omega_0 = 0.001\Gamma$, and $\eta = 1$. The magenta dots show a fully numerical calculation for a randomly generated cloud according to formula (21.63). The red lines show a calculation according to the complete formula (21.160). The cyan dots show a calculation assuming timed Dicke states according to (21.82) via numerical calculation of the structure factor according to (21.83) for the same randomly generated cloud as for the full simulation. The blue lines are obtained within the timed Dicke state approximation with structure factors estimated from formula (21.141). (d-f) Same as (a-c) but with $\sigma = 0.2$.

As seen in Fig. 21.20, the results obtained via the complete analytical formula (21.160) coincide with the fully numerical simulations according to formula (21.63). But both disagree with analytical and numerical results obtained within the timed Dicke state approximation.

It is possible to approximate the Bessel function $I_{n+1/2}(\sigma^2)$ and to obtain analytical solutions. The new formula works for $\sigma \gg 1$ and $\eta = 1$ [286],

$$F_{\rm a} = \frac{\Omega_0^2}{\Gamma}\frac{\sigma^2}{N}\ln\left(1+\frac{N^2\Gamma^2 s_N}{\sigma^2(4\Delta_0^2+\Gamma^2)}\right) = \frac{\Omega_0^2}{4N\Gamma s_\infty}\ln\left(1+\frac{4N^2\Gamma^2 s_\infty s_N}{4\Delta_0^2+\Gamma^2}\right) \tag{21.161}$$

$$F_e = -F_{\rm a} + \frac{\Omega_0^2}{\Delta_0}\frac{\sigma^2}{N}\arctan\frac{\Delta\Gamma N}{\sigma^2\left(4\Delta_0^2+\Gamma^2+\frac{\Gamma^2 N}{2\sigma^2}\right)} = \frac{\Omega_0^2}{4N\Delta_0 s_\infty}\arctan\frac{4\Delta_0\Gamma N s_\infty}{4\Delta_0^2+\Gamma^2+2\Gamma^2 N s_\infty}$$

$$b_0 = \frac{3N}{\sigma^2}$$

$$s_N = \frac{1}{N} + s_\infty = \frac{1}{N} + \frac{1}{(2\sigma)^2}\ .$$

21.3.4.2 Expansion of the scattered radiation intensity

The incident electric field is ...

The radiated electric field $\hat{\vec{\mathcal{E}}}^{(+)}(\mathbf{r},t)|\psi\rangle$ where $\hat{\vec{\mathcal{E}}}^{(+)}(\mathbf{r},t) = \sum_{\mathbf{k}} \varepsilon_{\mathbf{k}}\hat{a}_{\mathbf{k}} e^{\imath\mathbf{k}\cdot\mathbf{r}-\imath\omega_k t}$,

$$\begin{aligned}\hat{\vec{\mathcal{E}}}^{(+)}(\mathbf{r},t)|\psi\rangle &= \sum_{\mathbf{k}} \varepsilon_{\mathbf{k}}\gamma_{\mathbf{k}}(t) e^{\imath\mathbf{k}\cdot\mathbf{r}-\imath\omega_k t}|0\rangle|1\rangle_{\mathbf{k}} \\ &= -\imath\frac{V_{\rm ph} g_{k_0}\varepsilon_{k_0}k_0}{4\pi c\sqrt{N}} e^{-\imath\omega_0 t}\sum_{j=1}^{N}\beta_j(t)e^{\imath\mathbf{k}_0\cdot\mathbf{r}_j}\frac{e^{\imath k_0|\mathbf{r}-\mathbf{r}_j|}-e^{-\imath k_0|\mathbf{r}-\mathbf{r}_j|}}{|\mathbf{r}-\mathbf{r}_j|}\ .\end{aligned} \tag{21.162}$$

We neglect the second term, which describes an incoming wave and go to smooth densities. We expand into spherical harmonics and obtain,

$$\hat{\vec{\mathcal{E}}}^{(+)}(\mathbf{r},t)|\psi\rangle = e^{-\imath\omega_0 t}\sum_{n=0}^{\infty}\frac{V_{\rm ph} g_{k_0}\varepsilon_{k_0}}{c\sqrt{N}}\frac{\lambda_n}{2\Delta_0+\imath\Gamma(1+\lambda_n)}\Omega_0(2n+1)\imath^n h_n^{(1)}(k_0 r)P_n(\cos\theta)\ . \tag{21.163}$$

21.3.4.3 Mie resonances

It is an interesting question whether the maxima found in the curves of Fig. 21.20 can be associated with Mie resonances [96, 775, 71]. To show this we need to apply the formalism of Mie scattering to atomic clouds with the smooth density approximation, where it is described by a continuous refraction index, as studied in Ref. [39]. The Mie formalism had been developed for homogeneous spheres, which can be dielectric or absorptive. For more general refractive index distribution the formalism gets quickly cumbersome [15]. Also Mie resonances are generally though of being conditioned to the existence of sharp boundaries.

The results of Ref. [39] surprisingly show that Mie resonances are expected for parabolic distributions of atoms, as is the case for example for Bose-Einstein condensates in the Thomas-Fermi limit. However, the spectra of Mie resonances exhibit

[15] There is a treatment for parabolic radial variations [455].

much less structure. This is understood by the fact that 'whispering galery' Mie resonances may live on the surface of a sphere whose refraction index drops quadratically to zero, while cavity type Mie resonances may not.

21.3.5 Exercises

21.3.5.1 Ex: Structure coefficient of a homogeneous spherical and of a Gaussian ellipsoidal cloud

a. Calculate the structure coefficient of a homogeneous spherical cloud of radius R, and discuss the limits $qR < 1$ and $qR < 1$. Plot the structure coefficient as a function of θ for various radii R.
b. Calculate the structure coefficient of an ellipsoidal Gaussian cloud having the *rms*-widths σ_z and σ_r, and discuss the limits $qR < 1$ and $qR < 1$. Plot the structure coefficient as a function of θ for various aspect ratios σ_z/σ_ρ.

21.3.5.2 Ex: Force coefficients of a homogeneous spherical and of a Gaussian ellipsoidal cloud

a. Calculate the force coefficients s_N, $\tilde{f}_N$, and f_N from the Eqs. (21.66), Eqs. (21.78), and Eqs. (21.86), respectively, for a homogeneous spherical cloud of radius R.
b. Repeat the calculation of (a) for an ellipsoidal Gaussian cloud having the *rms*-widths σ_z and σ_r.

21.3.5.3 Ex: RDG and Mie

Estimate whether it is possible to distinguish Rayleigh-Debye-Gans scattering from Mie scattering in strontium spectra.

21.3.5.4 Ex: Mie scattering from absorbing spheres

Calculate the force on a homogeneous dielectric sphere as a function of the absorptive and dispersive part of the refraction index [455].

21.3.5.5 Ex: Momentum halos and heating, is the recoil cooperative?

Discuss the question is whether recoil is imparted to individual atoms or to the center-of-mass of the whole cloud.

21.4 Scattering from disordered and dense clouds

21.4.0.1 Vectorial light

The procedure can be generalized to the vectorial case [764, 763, 559], where we get a similar steady-state solution as in (21.37),

$$\boxed{\vec{\beta}_j = (M_{jm})^{-1}\ \hat{\epsilon}\ \tfrac{\imath}{2}\Omega_0(\mathbf{r}_m)}\,, \tag{21.164}$$

only that the dipole moment amplitudes and the incident light field are now considered as vectors. The expression for the matrix M_{jm} is the same as in (21.36). However, the vectorial kernel must be calculated in a different way. Using the abbreviations,

$$\mathbf{r}_{jm} = \mathbf{r}_j - \mathbf{r}_m \quad , \quad r_{jm} = |\mathbf{r}_j - \mathbf{r}_m| + \delta_{jm} \quad , \quad c_{jm} = \frac{\imath}{k_0 r_{jm}} - \frac{1}{(k_0 r_{jm})^2} \ , \tag{21.165}$$

the new vectorial kernel can be written,

$$\gamma^{(3)}_{jm} = \frac{3\gamma_{jm}}{2} \ \frac{(1+c_{jm}) r_{jm}^2 \delta_{mn} - (1+3c_{jm}) \mathbf{r}_{jm} \mathbf{r}_{jm}^{\mathsf{T}}}{r_{jm}^2} \ . \tag{21.166}$$

The steady-state scattered light field and the total field are now,

$$\vec{\mathcal{E}}_{\rm sct}(\mathbf{r}) = -\frac{\imath\Gamma}{2} \sum_{j=1}^{N} \frac{3\gamma_{oj}(\mathbf{r})}{2} \ \frac{(1+c_{oj}(\mathbf{r})) k_0^2 |\mathbf{r}-\mathbf{r}_j|^2 \vec{\beta}_j - (1+3c_{oj}(\mathbf{r}))[(\mathbf{r}-\mathbf{r}_j)\cdot\vec{\beta}_j](\mathbf{r}-\mathbf{r}_j)}{|\mathbf{r}-\mathbf{r}_j|^2} \ . \tag{21.167}$$

A movie can be assisted at (watch movie).

21.4.0.2 Coherent backscattering

Shining coherent light on a homogeneous cloud, we expect no coherent scattering (exception made of multiple-atom scattering in backward direction, CBS and of fluctuations like speckle patterns). Like radiation trapping, *coherent backscattering* (CBS) is a manifestation of interference in multiple scattering. Just like photon echoes it is *not* due to interatomic correlations. While in radiation trapping this leads to an energy storage inside the atomic cloud connected to destructive interference of the radiation emitted to the cloud's outside, when the coherent beam is reflected at a diffuse scattered, one observes *speckle patterns*. This holds as well for laser light reflection as for atomic wave reflections at a rough surface. See also (watch talk).

The coherent backscattering is an effect of constructive interference between two light scattering paths having the exact time-reversed single scattering sequence,

$$I = \left| \sum_j \vec{\mathcal{E}}_j e^{\imath\varphi_j} \right|^2 = \sum_j \left| \vec{\mathcal{E}}_j \right|^2 + \sum_{j\neq k} \vec{\mathcal{E}}_j \vec{\mathcal{E}}_k^{*} e^{\imath(\varphi_j - \varphi_k)} \ . \tag{21.168}$$

Only the second term makes speckles. However, the atomic motion smoothes out the speckle pattern in all directions. Only in the presence of correlations in the atomic positions they do not. E.g. in crystals or in the backscattering directions. Therefore, the constructive interference depends strongly on the backscattering angle ϑ. Fast atomic motion internal excitations can dynamically break the time-reversal symmetry of the scattering path, esp. when the laser is close to resonance and the phase delay per scattering process is long. Coherent backscattering is a weak form of *Anderson localization* (also strong localization) of light.

21.4.1 Exercises

21.4.1.1 Ex: The green flash

Discuss whether the '*green flash*' at sunset could be due to *superradiant extinction*. It can last seconds because refraction sweeps the ray through the spectrum (see the

movie *Le rayon vert* by Éric Rohmer).

21.4.1.2 Ex: Faraday effect with vectorial kernel in the coupled dipoles model

Try to simulate the pump laser phase shift and lensing by a small dense cloud by the coupled dipoles model for red and blue detuning. Discuss the influence of rescattering.

21.5 Scattering from periodic structures and photonic bands

Long-range spatial ordering can have a dramatic influence on the propagation of light and the cooperativity of scattering, as we have already pointed out in the introduction of the structure factor in Sec. 21.1.1. This is true for the scattering of electronic waves in crystals. But atomic gases can also be arranged in periodic luminous potentials generated by dipolar forces (introduced in Sec. 20.2.2) exerted by counterpropagating laser beams. Such potentials, called *optical lattices*, can be realized with various geometries in 1, 2 or 3 dimensions.

Periodic structures are usually probed by Bragg scattering. This procedure can be applied to atoms ordered in optical lattices [82, 856, 766, 768]: A test beam with wavevector $\mathbf{k}_{\mathrm{brg}}$ and intensity I_{brg} is irradiated into the atomic cloud, and the power P_s of the first-order reflected beam by Bragg is detected under a solid angle Ω_{s}. Bragg diffraction is an interference effect of radiation patterns emitted by Rayleigh scattering from periodically aligned point-like antennas, the interference being constructive in only specified directions.

For optically dilute lattices, where multiple reflections can be neglected, the imaginary part of the atomic response is sufficient to describe Bragg reflection. For optically dense lattices, multiple reflections between consecutive atomic layers lead to interference phenomena between reflected and transmitted light fields and cause the emergence of frequency bands, inside which the propagation of light waves through the cloud is prohibited. These bands are known as *forbidden photonic bands*.

Photonic bands in optical lattices are interesting for several reasons:

1. They may facilitate the study of the phenomenon of Anderson localization. In fact, Anderson location of light in atomic gases requires very high densities or very large optical cross sections. Now, it is expected that, if the disorder is realized within periodic structures near the Bragg condition, the high density requirement is dramatically relaxed.

2. They modify the local density of states in a way to suppress spontaneous emission.

3. In optical lattices, unlike other systems, the scattering is very weak except when the light is tuned close to atomic resonances. Consequently, the expected forbidden bands are very narrow. This bears the advantage that we can adjust the optical density and tune the photon energy and the Bragg angle (i.e. the

quasi-momentum) independently, which facilitates the mapping of the dispersion relation.

4. Crystals are always hampered by defects in the periodicity [473]. In latest-generation photonic crystals, the typical distance over which coherent light turns diffuse is limited to less than 20 μm. This limitation plays no role in optical lattices, where the delocalized photons rigorously guarantee perfect long-range order, even though the Debye-Waller factor may introduce local disorder.

Spectra of photonic bands in atomic clouds were detected experimentally [735] in one-dimensional structures. Most of the above mentioned effects require omnidirectional photonic bands, but this is technically very difficult, mainly because of the narrow linewidth of the atomic transitions. We will develop this point in the course of this section. We also mention the prediction of forbidden photon bands in Bose condensates [554].

A presentation on this subject is available here (watch talk).

21.5.1 Bragg scattering

21.5.1.1 The reciprocal lattice

Let us consider a periodic *direct lattice* in real three-dimensional space whose elementary cells are located at positions,

$$\mathbf{R_n} = n_1\mathbf{a}_1 + n_2\mathbf{a}_2 + n_3\mathbf{a}_3 \ , \tag{21.169}$$

where $\mathbf{n} = (n_1, n_2, n_3)$ with $n_j \in \mathbb{Z}$ and $\mathbf{a}_j$ are linearly independent vectors describing the distance of two adjacent elementary cells [182]. Functions extended over the lattice, e.g. density distributions, are then supposed to be periodic,

$$n(\mathbf{r}) = n(\mathbf{r} + \mathbf{R_n}) \ , \tag{21.170}$$

such that they can be expanded in Fourier series similarly as we did for the introduction of the Bloch waves in Sec. 4.1,

$$n(\mathbf{r}) = \tfrac{1}{V}\sum_{\mathbf{m}} \rho_{\mathbf{m}} e^{\imath \mathbf{G_m}\cdot\mathbf{r}} \ , \tag{21.171}$$

where $\mathbf{m} = (m_1, m_2, m_3)$ with $m_j \in \mathbb{Z}$. The Fourier coefficients are [16],

$$\rho_{\mathbf{m}} = \int_0^{a_1}\int_0^{a_2}\int_0^{a_3} n(\mathbf{r}) e^{-2\pi\imath(m_1 x/a_1 + m_2 y/a_2 + m_3 z/a_3)} dxdydz = \int_0^1 n(\tilde{\mathbf{r}}) e^{2\pi\imath \mathbf{m}\cdot\tilde{\mathbf{r}}} d^3\tilde{r} \ . \tag{21.172}$$

The condition (21.170) then yields,

$$n(\mathbf{r}) = \tfrac{1}{V}\sum_{\mathbf{m}} \rho_{\mathbf{m}} e^{\imath \mathbf{G_m}\cdot\mathbf{r}} = \tfrac{1}{V}\sum_{\mathbf{m}} \rho_{\mathbf{m}} e^{\imath \mathbf{G_m}\cdot\mathbf{r}} e^{\imath \mathbf{G_m}\cdot\mathbf{R_n}} = n(\mathbf{r} + \mathbf{R_n}) \ , \tag{21.173}$$

from which we conclude that the vectors $\mathbf{G_n}$ of the reciprocal lattice must satisfy,

$$\tfrac{1}{2\pi}\mathbf{G_m}\cdot\mathbf{R_n} \in \mathbb{Z} \ . \tag{21.174}$$

[16] In crystallography $\rho_{\mathbf{m}}$ is called *structure factor*, but it is not to be confused with the structure factor defined in (21.5).

Example 122 (*The reciprocal lattice in crystallography*): In three dimensions the reciprocal lattice can be constructed by,

$$\mathbf{G_m} = m_1\mathbf{b}_1 + m_2\mathbf{b}_2 + m_3\mathbf{b}_3 \tag{21.175}$$
$$\text{with} \quad \mathbf{b}_1 \equiv \frac{\mathbf{a}_2 \times \mathbf{a}_3}{V} \quad , \quad \mathbf{b}_2 \equiv \frac{\mathbf{a}_3 \times \mathbf{a}}{V} \quad , \quad \mathbf{b}_3 \equiv \frac{\mathbf{a}_1 \times \mathbf{a}_2}{V}$$
$$\text{and} \quad V \equiv \mathbf{a}_1 \cdot (\mathbf{a}_2 \times \mathbf{a}_3) \ .$$

Knowing the density $n_1(\mathbf{r})$ within a single cell, which is often the case when the overlap between the density distributions of adjacent cells is negligible, we can write the global density distribution as,

$$\boxed{n(\mathbf{r}) = n_1(\mathbf{r}) \star \sum_{\mathbf{m}} \delta^{(3)}(\mathbf{r} - \mathbf{R_m})} \ . \tag{21.176}$$

Example 123 (*Elementary cell with Gaussian distribution*): With the ansatz $n_1(\mathbf{r}) = n_0 e^{-r^2/2\bar{r}^2}$, such that $\int n_1(\mathbf{r}) d^3r = n_0(2\pi)^{3/2}\bar{r}^3 = N_1$,

$$\begin{aligned}\rho(\Delta\mathbf{k}) &= \sum_m e^{\imath m \Delta\mathbf{k}\cdot\mathbf{R}} \int_V n_1(\mathbf{r}) e^{\imath\Delta\mathbf{k}\cdot\mathbf{r}} d^3\mathbf{r} \qquad (21.177)\\ &= \frac{1 - e^{\imath N_s \Delta k R}}{1 - e^{\imath \Delta k R}} \times n_0 \int_V e^{-x^2/2\bar{r}^2} e^{-y^2/2\bar{r}^2} e^{-z^2/2\bar{r}^2} e^{\imath\Delta\mathbf{k}\cdot\mathbf{r}} d^3\mathbf{r}\\ &\approx N_s \delta(\Delta k - 2\pi/R) n_0 (2\pi)^{3/2}\bar{r}^3 e^{-6\Delta k^2\bar{r}^2} = N\delta(\Delta k - 2\pi/R) e^{-6\Delta k_x^2\bar{r}^2} \ .\end{aligned}$$

21.5.1.2 Impact of disorder in one-dimensional lattices

A wave be incident on a lattice in the direction $\mathbf{k}_0$ and scattered into the direction $\mathbf{k}_s \equiv \mathbf{k}_0 + \Delta\mathbf{k}$. The *structure coefficient* $\rho_{\mathbf{m}}$ describes the amplitude of radiation field scattered by the lattice,

$$\rho_{\mathbf{m}} = \int_V \rho(\mathbf{r}) e^{\imath\Delta\mathbf{k}\cdot\mathbf{r}} d^3\mathbf{r} \ . \tag{21.178}$$

Let the density distribution be,

$$n(\mathbf{r}) = \sum_j \rho_j(\mathbf{r}) \star \delta^{(3)}(\mathbf{r} - \mathbf{r}_j) = n_1(\mathbf{r}) \star \sum_j \delta(\mathbf{r} - j\hat{\mathbf{e}}_z \tfrac{\lambda_{\rm dip}}{2}) \ , \tag{21.179}$$

that is, for perfect periodicity, introducing the density distribution of a unit cell and a $1D$ lattice.

The *Debye-Waller factor* describes the diffusion of the density over the sites of the lattice due to the thermal motion,

$$\begin{aligned}\overline{\rho_{\mathbf{m}}} &= \int_V n_1(\mathbf{r}) e^{\imath\Delta\mathbf{k}\cdot\mathbf{r}} d^3r \sum_j \overline{e^{\imath(j\hat{\mathbf{e}}_z\lambda_{\rm dip}/2 + \mathbf{u})\Delta\mathbf{k}}} \qquad (21.180)\\ &= f_i \sum_j \overline{e^{\imath(j\hat{\mathbf{e}}_z\lambda_{\rm dip}/2 + \mathbf{u})\Delta\mathbf{k}}} = \rho_{\mathbf{m}} \overline{e^{\imath\mathbf{u}\Delta\mathbf{k}}} \ ,\end{aligned}$$

with

$$\overline{e^{\imath \mathbf{u}\Delta\mathbf{k}}} \approx e^{-|\mathbf{G}|^2\overline{u^2}/6} \ . \tag{21.181}$$

Example 124 (*Optical lattice*): The exponential distribution $e^{-6\Delta k_x^2 \bar{r}^2}$ is called Debye-Waller factor and describes the smearing out of the population over the lattice due to the thermal motion of the atoms. The δ-function sets the wavevector of emitted light. That is, the power of light is only emitted in particular directions given by the Bragg condition. Here, the solid angle $\Delta\Omega_s$ does not depend on the thermal distribution (as long as the atoms are within the Lamb-Dicke regime), but on the lattice size, which determines the goodness of the approximation of the Airy function (the sum in the above equation) by a Dirac δ-function. The width of the Airy function for a lattice of size w_0 is approximately $\Delta k = 2\sqrt{3}/w_0$. With this the solid angle is,

$$\Delta\Omega_s = \frac{12}{k^2 w_0^2} \ . \tag{21.182}$$

We can also estimate the solid angle from the diameter d of the Gaussian beam at a distance x away from a scattering medium of size w_0,

$$d = w_0\sqrt{1+\left(\frac{\lambda x}{\pi w_0^2}\right)^2} \tag{21.183}$$

$$\Delta\Omega_s = \frac{\pi d^2}{x^2} = \frac{\lambda^2}{\pi w_0^2} = \frac{4\pi}{k^2 w_0^2} \ .$$

The power scattered into this solid angle is,

$$P_s = |A_s|^2 F^2 \Delta\Omega_s = |A_s|^2 e^{-2W} N^2 \Delta\Omega_s \ . \tag{21.184}$$

It depends quadratically on the number of atoms. Strictly speaking, the derivation only applies to perfectly ordered lattices, i.e. all the lattice sites are equally occupied. Defects lead to diffuse scattering, i.e. a background of isotropically distributed power at the expense of Bragg scattering. The sharpness of the Bragg radiation distribution remains intact.

We parametrize the density in an optical $1D$ lattice as follows:

$$n_l(\mathbf{r}) = n_0 e^{(-x^2-y^2)/2\sigma_r^2} e^{-z^2/2\sigma_z^2} \tag{21.185}$$

$$n_{\mathrm{a}}(\mathbf{r}) = \sum_{m=1}^{N_s} \delta(\mathbf{r} - md\hat{\mathbf{e}}_z) \star n_l(\mathbf{r}) = \sum_{m=1}^{N_s} n_l(\mathbf{r} - md\hat{\mathbf{e}}_z) \ .$$

We will show in Exc. 21.5.5.1, that the structure factor is then,

$$\boxed{\mathcal{S}_{\mathbf{k}_0}(\mathbf{k}) = \frac{n_0}{N}\frac{1-e^{\imath N_s dq_z}}{e^{-\imath dq_z}-1} e^{-q_x^2\sigma_r^2/2} e^{-q_y^2\sigma_r^2/2} e^{-q_z^2\sigma_z^2/2}} \ . \tag{21.186}$$

In Exc. 21.5.5.2 we derive the structure factor in spherical coordinates.

Some comments are needed:

1. The structure factor treatment assumes low optical density, which is not necessarily guaranteed when the laser is tuned close to a resonance [766].

2. As the structure factor is independent of the laser detuning, it will not reveal any spectral structure, such as a band-gap or dip due to diffuse scattering. Also, absorption is not incorporated into the model.

21.5.1.3 The structure factor and the Bragg condition

The reciprocal space, obtained by Fourier transformation of the periodic density distribution, also adopts the shape of a periodic lattice. The Bragg condition requires that the difference between the incident and emitted wavevectors, $\Delta\mathbf{k} \equiv \mathbf{k}_s - \mathbf{k}_i$, matches a vector of the reciprocal lattice, $\mathbf{r}_j = j\mathbf{G}$. The Bragg condition is thus automatically incorporated into the structure factor (21.191).

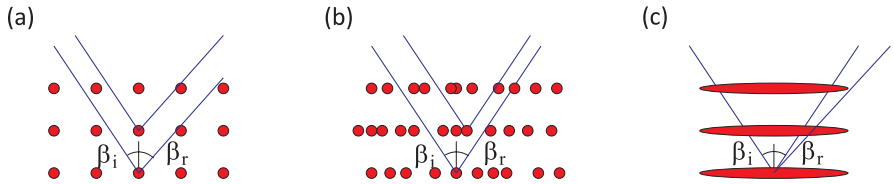

Figure 21.21: Several Bragg lattices.

With the lattice constant $d = \frac{1}{2}\lambda_{\rm dip}$ the interference is constructive when the difference of the paths of two beams reflected by different layers is a multiple of the wavelength,

$$\tfrac{1}{2}\lambda_{\rm dip}\cos\beta_i + \tfrac{1}{2}\lambda_{\rm dip}\cos\beta_s = \lambda \ . \tag{21.187}$$

This is illustrated in Fig. 21.21(a). If the transverse distribution can be considered as homogeneous, as shown in Fig. 21.21(b), we have as second condition,

$$\beta_i = -\beta_s \ . \tag{21.188}$$

That is, the angles of incidence and reflection must be the same, as if we were dealing with a dielectric mirror. In contrast, if the transverse extent of the atomic layers gets smaller (until converging to the limit of a one-dimensional chain of point-scatterers, $\mathbf{G} \equiv 2k_{\rm dip}\hat{\mathbf{e}}_z$), we return to the condition (21.187). In intermediate situations, illustrated in Fig. 21.21(c), and for $\lambda_{\rm dip}\cos\beta_i \neq \lambda$ the reflection angle does not follow any of the relations (21.187) and (21.188).

21.5.1.4 Incoherent background

A finite size or defects in the periodic ordering of the atoms may lead to an isotropic background of Rayleigh-scattered light,

$$\frac{dP_s}{d\Omega_{\rm s}} = |A_s|^2\left[e^{-2W}|F|^2 + N_1N(1-e^{-2W})\right] \ . \tag{21.189}$$

The amount of photons scattered into the *same solid angle* as the one of Bragg scattering is typically for $1D$ lattices,

$$\frac{(1-e^{-2W})N_1N}{e^{-2W}|F|^2} = (e^{2W}-1)\frac{N_1}{N} \approx 0.002 \ . \tag{21.190}$$

However, if we compare the total amount of coherently Bragg-scattered light, we obtain,

$$\frac{(1-e^{-2W})N_1N}{e^{-2W}|F|^2}\,\frac{4\pi}{d\Omega_{\rm s}} \approx 2500 \ . \tag{21.191}$$

21.5.2 Scattering and transfer matrices

For one-dimensional optical lattices, that is, when the atoms are trapped in a potential dipole generated by a stationary light wave, we may consider applying the transfer matrix formalism developed in Secs. 2.3. The premisses of this model are the homogeneity and the infinite extent of the cloud in a direction transverse to the optical axis.

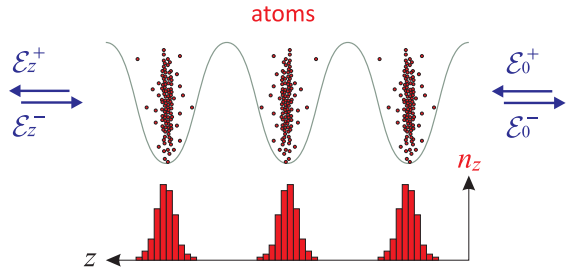

Figure 21.22: Scheme for transfer matrices calculations on $1D$-lattices.

With the notation introduced in Fig. 21.22 we find the equations relating the incident electric fields with the transmitted and reflected ones. If the $\mathcal{T}$-matrix and the $\mathcal{S}$-matrix are defined by [226],

$$\boxed{\begin{pmatrix}\mathcal{E}_z^+\\ \mathcal{E}_0^-\end{pmatrix} = \mathcal{S}\begin{pmatrix}\mathcal{E}_0^+\\ \mathcal{E}_z^-\end{pmatrix} \qquad \text{and} \qquad \begin{pmatrix}\mathcal{E}_z^+\\ \mathcal{E}_z^-\end{pmatrix} = \mathcal{T}\begin{pmatrix}\mathcal{E}_0^+\\ \mathcal{E}_0^-\end{pmatrix}}\,, \tag{21.192}$$

they are connected by,

$$\mathcal{S} = \begin{pmatrix}S_{11} & S_{12}\\ S_{21} & S_{22}\end{pmatrix} = \begin{pmatrix}T_{11} - \frac{T_{12}T_{21}}{T_{22}} & \frac{T_{12}}{T_{22}}\\ -\frac{T_{21}}{T_{22}} & \frac{1}{T_{22}}\end{pmatrix} \tag{21.193}$$

$$\text{and} \qquad \mathcal{T} = \begin{pmatrix}T_{11} & T_{12}\\ T_{21} & T_{22}\end{pmatrix} = \begin{pmatrix}S_{11} - \frac{S_{12}S_{21}}{S_{22}} & \frac{S_{12}}{S_{22}}\\ -\frac{S_{21}}{S_{22}} & \frac{1}{S_{22}}\end{pmatrix}\,.$$

Depending on the boundary conditions the $\mathcal{S}$ and $\mathcal{T}$-matrices can have very different shapes. For example, for classical beam splitters we require *energy conservation*, while for atomic scatterers we require *reciprocity*, meaning that the $\mathcal{S}$ shall not depend on the direction of incidence. On the other hand, energy does not need to be conserved, since it may be dissipated via spontaneous emission.

21.5.2.1 Transfer matrices for propagation in free space

Propagation in free space along the optical axis by a distance d is described by the matrices,

$$\boxed{\mathcal{S}_d = \begin{pmatrix}e^{\imath kd} & 0\\ 0 & e^{\imath kd}\end{pmatrix} \quad , \quad \mathcal{T}_d = \begin{pmatrix}e^{\imath kd} & 0\\ 0 & e^{-\imath kd}\end{pmatrix}}\,. \tag{21.194}$$

The determinants are,

$$\det \mathcal{S}_d = e^{2\imath kd} \neq 1 = \det \mathcal{T}_d\,, \tag{21.195}$$

which shows that only the $\mathcal{T}$-matrix is unitary.

If the incident beam hits the cloud under an angle, $\mathbf{k}\cdot\mathbf{d} = kd\cos\theta = k_z d$, the $\mathcal{T}$-matrix must be generalized [17],

$$\mathcal{T}_d = \begin{pmatrix} e^{\imath\mathbf{k}\cdot\mathbf{d}} & 0 \\ 0 & e^{-\imath\mathbf{k}\cdot\mathbf{d}} \end{pmatrix} . \tag{21.197}$$

21.5.2.2 Transfer matrices for beam splitters

Beam splitters are described by the matrices,

$$\boxed{\mathcal{S}_{\rm bs} = \begin{pmatrix} t_{\rm bs} & -r_{\rm bs} \\ r_{\rm bs} & t_{\rm bs} \end{pmatrix} \quad , \quad \mathcal{T}_{\rm bs} = \begin{pmatrix} t_{\rm bs} + \frac{r_{\rm bs}^2}{t_{\rm bs}} & -\frac{r_{\rm bs}}{t_{\rm bs}} \\ -\frac{r_{\rm bs}}{t_{\rm bs}} & \frac{1}{t_{\rm bs}} \end{pmatrix} = \begin{pmatrix} 1 & -\frac{r_{\rm bs}}{t_{\rm bs}} \\ -\frac{r_{\rm bs}}{t_{\rm bs}} & \frac{1}{t_{\rm bs}} \end{pmatrix}} , \tag{21.198}$$

where the beam splitter transmissity $t_{\rm bs}$ and reflectivity $r_{\rm bs}$ are real numbers. These matrices satisfy the energy conservation condition,

$$\begin{aligned} 1 &= |S_{11}|^2 + |S_{21}|^2 = |t_{\rm bs}|^2 + |r_{\rm bs}|^2 = |S_{12}|^2 + |S_{22}|^2 \\ 0 &= S_{11}S_{12}^* + S_{21}S_{22}^* \ . \end{aligned} \tag{21.199}$$

Also,

$$\det \mathcal{S}_{\rm bs} = t_{\rm bs}^2 + r_{\rm bs}^2 = 1 = \det \mathcal{T}_{\rm bs} \ . \tag{21.200}$$

21.5.2.3 Transfer matrices for atomic scatterers

Atomic scatterers are described by the matrices,

$$\boxed{\mathcal{S}_{\rm at} = \begin{pmatrix} t_{\rm at} & r_{\rm at} \\ r_{\rm at} & t_{\rm at} \end{pmatrix} \quad , \quad \mathcal{T}_{\rm at} = \begin{pmatrix} t_{\rm at} - \frac{r_{\rm at}^2}{t_{\rm at}} & \frac{r_{\rm at}}{t_{\rm at}} \\ -\frac{r_{\rm at}}{t_{\rm at}} & \frac{1}{t_{\rm at}} \end{pmatrix}} . \tag{21.201}$$

Note, that t and r may be complex numbers.

For the $\mathcal{S}$-matrix we find,

$$\mathbb{I} = \mathcal{S}_{\rm at}^\dagger \mathcal{S}_{\rm at} = \begin{pmatrix} |t_{\rm at}|^2 + |r_{\rm at}|^2 & t_{\rm at}^* r_{\rm at} + r_{\rm at}^* t_{\rm at} \\ t_{\rm at}^* r_{\rm at} + r_{\rm at}^* t_{\rm at} & |t_{\rm at}|^2 + |r_{\rm at}|^2 \end{pmatrix} . \tag{21.202}$$

Apparently, the $\mathcal{S}$-matrix does not describe a unitary transform unlike the $\mathcal{T}$-matrix, for which we find that by construction,

$$\det \mathcal{S}_{\rm at} = t_{\rm at}^2 - r_{\rm at}^2 \neq 1 = \det \mathcal{T}_{\rm at} \ . \tag{21.203}$$

To evaluate the components of the scattering matrices, we calculate the reflection coefficient β of a classical polarizable sample from the microscopic polarizability and

[17] Furthermore, as shown in [226] Eq. (A10), the single-atom reflection coefficient must be generalized by replacing,

$$\beta \to \frac{\beta}{2}(\cos^{-1}\theta + \cos\theta) \ . \tag{21.196}$$

However, for $\theta < 60^\circ$ the correction is small.

the optical density (depth) of a thin layer, $n\,\delta z\,\sigma_0$, where σ_0 is the resonant optical cross section,

$$\beta = n\frac{k_{\rm brg}\,\delta z}{2}\frac{\alpha_{\rm pol}}{\varepsilon_0} = \frac{n\,\delta z}{2}\frac{6\pi}{k_{\rm brg}^2}\frac{-1}{\imath + 2\Delta_{\rm brg}/\Gamma} = \frac{n\,\delta z\,\sigma_0}{2}\frac{-1}{\imath + 2\Delta_{\rm brg}/\Gamma}\ . \tag{21.204}$$

We remember that the polarizability is linked to the macroscopic susceptibility $\chi_e = n\alpha_{\rm pol}/\varepsilon_0$ [18]. The reflection and transmission coefficients are now,

$$\boxed{r_{\rm at} = \frac{\imath\beta}{1-\imath\beta} \qquad \text{and} \qquad t_{\rm at} = \frac{1}{1-\imath\beta}}\ . \tag{21.205}$$

Example 125 (*Absorption and spontaneous emission*): The real part of both coefficients is associated to amplitude and the imaginary part to phase,

$$\Re\mathfrak{e}\,t_{\rm at} = \frac{1}{1+\beta^2} = 1 + \Re\mathfrak{e}\,r_{\rm at} \qquad , \qquad \Im\mathfrak{m}\,r_{\rm at} = \frac{\beta}{1+\beta^2} = \Im\mathfrak{m}\,t_{\rm at}\ . \tag{21.206}$$

Let us also recalculate the quantities (21.202),

$$|\det \mathcal{S}_{\rm at}| = |t_{\rm at}^2 - r_{\rm at}^2| = \left|\frac{1+\imath\beta}{1-\imath\beta}\right| \stackrel{?}{=} 1 \tag{21.207}$$

$$|t_{\rm at}|^2 + |r_{\rm at}|^2 = \frac{1+\beta\beta^*}{1-\imath\beta+\imath\beta^*+\beta\beta^*} \stackrel{?}{=} 1$$

$$r_{\rm at}t_{\rm at}^* + r_{\rm at}^* t_{\rm at} = \frac{\imath\beta-\imath\beta^*}{1-\imath\beta+\imath\beta^*+\beta\beta^*} \stackrel{?}{=} 0\ .$$

This means that the $\mathcal{S}$-matrix is not unitary, unless the imaginary part of the β-coefficient vanishes. A look at the expression (21.204) tells us, that this comes down to neglecting spontaneous emission, which only is a good assumption far away from resonance,

$$\beta \stackrel{\Delta_{\rm brg}\gg\Gamma}{\longrightarrow} \frac{n\,\delta z\,\sigma_0}{2}\frac{2\Delta_{\rm brg}/\Gamma}{1+4\Delta_{\rm brg}^2/\Gamma^2} \simeq \frac{n\,\delta z\,\sigma_0\Gamma}{4\Delta_{\rm brg}}\ . \tag{21.208}$$

On the other hand, the fact that the $\mathcal{T}$-matrix is always unitary makes a good choice for theoretical calculations.

With the substitution (21.205) we get for the scattering and the transfer matrices,

$$\boxed{\mathcal{S}_\beta = \frac{1}{1-\imath\beta}\begin{pmatrix}1 & \imath\beta\\ \imath\beta & 1\end{pmatrix} \qquad \text{and} \qquad \mathcal{T}_\beta = \begin{pmatrix}1+\imath\beta & \imath\beta\\ -\imath\beta & 1-\imath\beta\end{pmatrix}}\ . \tag{21.209}$$

We note that the employed model is classical, since we describe the gas by a sequence of layers, each characterized by a refractive index. Applying the transfer matrix model, we calculate how the incident and reflected light fields transform from one layer to another. The intrinsically 1D model allows to calculate the reflection, transmission, and absorption by the atomic lattice as a function of the incident laser frequency.

[18] Note the analogy to the calculation (22.34) made for the reflection coefficient of an atom in a cavity in Sec. 22.1.2,

$$\beta = \frac{k}{\pi w^2}\frac{\alpha_{\rm pol}}{\varepsilon_0} = \frac{6}{k^2w^2}\frac{-1}{2\Delta/\Gamma+\imath} = \frac{\sigma_0}{\pi w^2}\frac{-1}{2\Delta/\Gamma+\imath}\ .$$

21.5.2.4 Concatenating transfer matrices

Transfer matrices for propagation through a structure, such as the passage through an interface between media with different reflective indices or absorption by a homogeneous atomic gas, are obtained by concatenating the matrices. For example, the propagation of the incident beam through the layer, such that the transfer matrix for passing the beam through an atomic layer is,

$$\mathcal{T} = \mathcal{T}_\beta \, \mathcal{T}_d \ . \tag{21.210}$$

For a periodic structure with N_s identical layers we must obviously concatenate the matrices like $\mathcal{T}^{N_s}$.

The reflection coefficient is obtained from the $\mathcal{S}$-matrix,

$$\begin{pmatrix} \mathcal{E}_z^+ \\ \mathcal{E}_0^- \end{pmatrix} = \mathcal{S} \begin{pmatrix} \mathcal{E}_0^+ \\ \mathcal{E}_z^- \end{pmatrix} = \begin{pmatrix} T_{11} - \frac{T_{12}T_{21}}{T_{22}} & \frac{T_{12}}{T_{22}} \\ -\frac{T_{21}}{T_{22}} & \frac{1}{T_{22}} \end{pmatrix} \begin{pmatrix} \mathcal{E}_0^+ \\ \mathcal{E}_z^- \end{pmatrix} \ . \tag{21.211}$$

If no beam enters the structure form the reverse side, $\mathcal{E}_z^- = 0$,

$$\begin{pmatrix} \mathcal{E}_z^+ \\ \mathcal{E}_0^- \end{pmatrix} \longrightarrow \begin{pmatrix} \left(T_{11} - \frac{T_{12}T_{21}}{T_{22}}\right) \mathcal{E}_0^+ \\ -\frac{T_{21}}{T_{22}} \mathcal{E}_0^+ \end{pmatrix} \ . \tag{21.212}$$

Hence, the total reflectivity and transmissivity of the structure are,

$$\boxed{t \equiv \frac{\mathcal{E}_z^+}{\mathcal{E}_0^+} = T_{11} - \frac{T_{12}T_{21}}{T_{22}}} \quad , \quad r \equiv \frac{\mathcal{E}_0^-}{\mathcal{E}_0^+} = -\frac{T_{21}}{T_{22}} \ . \tag{21.213}$$

and can be evaluated numerically or analytically [226].

21.5.2.5 Intensity distribution and within a structure

The transfer matrix formalism outlined in Sec. 21.5.2 not only allows to calculate the overall reflectivity of a structure, but also the local intensity $I \propto |\mathcal{E}_\mathrm{a}^+ + \mathcal{E}_\mathrm{a}^-|^2$ at a point $z = a$ inside a structure assumed to extend between an input at $z = 0$ and an output at $z = b$ of the optical axis [767]. To calculate this intensity, we first derive the scattering matrix for the total structure,

$$\begin{pmatrix} \mathcal{E}_b^+ \\ \mathcal{E}_b^- \end{pmatrix} = \mathcal{T} \begin{pmatrix} \mathcal{E}_0^+ \\ \mathcal{E}_0^- \end{pmatrix} \qquad \Longleftrightarrow \qquad \begin{pmatrix} \mathcal{E}_b^+ \\ \mathcal{E}_0^- \end{pmatrix} = \mathcal{S} \begin{pmatrix} \mathcal{E}_0^+ \\ \mathcal{E}_b^- \end{pmatrix} \ , \tag{21.214}$$

and then set up the transfer matrix $\mathcal{T}^{(a)}$ from $z = 0$ to $z = a$ with $0 < a < b$ and obtain the intensity as,

$$\begin{pmatrix} \mathcal{E}_\mathrm{a}^+ \\ \mathcal{E}_\mathrm{a}^- \end{pmatrix} = \mathcal{T}^{(a)} \begin{pmatrix} \mathcal{E}_0^+ \\ \mathcal{E}_0^- \end{pmatrix} = \mathcal{T}^{(a)} \begin{pmatrix} \mathcal{E}_0^+ \\ 0 \end{pmatrix} + \mathcal{T}^{(a)} \begin{pmatrix} 0 \\ \mathcal{E}_0^- \end{pmatrix} = \mathcal{X}^{(a)} \begin{pmatrix} \mathcal{E}_0^+ \\ \mathcal{E}_b^- \end{pmatrix} \ , \tag{21.215}$$

defining

$$\mathcal{X}^{(a)} \equiv \mathcal{T}^{(a)} \left[\begin{pmatrix} 1 & 0 \\ 0 & 0 \end{pmatrix} + \begin{pmatrix} 0 & 0 \\ 0 & 1 \end{pmatrix} \mathcal{S} \right] \ . \tag{21.216}$$

In the last step we used (21.211) and exploited the boundary condition that, $\mathcal{E}_0^+$ being preset, there is no reflection of light behind the structure. Explicitly,

$$\begin{pmatrix} \mathcal{E}_\mathrm{a}^+ \\ \mathcal{E}_\mathrm{a}^- \end{pmatrix} = \mathcal{T}^{(a)} \begin{pmatrix} 1 \\ -\mathcal{T}_{21}/\mathcal{T}_{22} \end{pmatrix} \mathcal{E}_0^+ \ . \tag{21.217}$$

The sum gives,

$$\boxed{\mathcal{E}_\mathrm{a}^+ + \mathcal{E}_\mathrm{a}^- = \left(\mathcal{T}_{11}^{(a)} + \mathcal{T}_{21}^{(a)} - \frac{\mathcal{T}_{21}}{\mathcal{T}_{22}} (\mathcal{T}_{12}^{(a)} + \mathcal{T}_{22}^{(a)}) \right) \mathcal{E}_0^+} \ . \tag{21.218}$$

Fig. 21.23 shows as an example the intensity distribution inside an optical lattice.

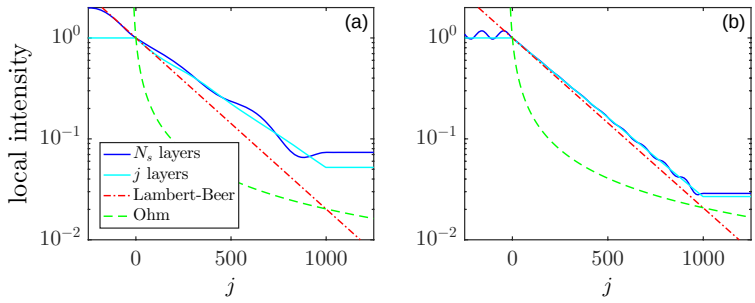

Figure 21.23: (code) The intensity decreases exponentially over a infinite lattice. For a finite lattice (here $N_s = 1000$), the intensity approaches a constant value at the end of the lattice. The graphs show in solid blue the intensity evaluated at each lattice site, in dash-dotted red the exponential decay due to absorption in a homogeneous cloud (Lambert-Beer law), in dashed green the hyperbolic decay following Ohm's law (calibrated to Lambert Beer's law), in cyan the transmission at the end of a lattice of j layers. The parameters are $\Delta_\mathrm{a} = \Gamma/2$, average density $n = 10^{11}\,\mathrm{cm}^{-3}$, and for panel (a) $\Delta_\mathrm{lat} = 5 \cdot 10^8 \Gamma$ while for panel (b) $\Delta_\mathrm{lat} = 5 \cdot 10^8 \Gamma$.

21.5.2.6 Transfer matrices for optical cavities

The transfer matrix formalism can be applied to obtain the transmission and reflection spectra of optical cavities. It can be extended to ring cavities and, in the presence of (non-saturated) atoms interacting with the cavity, it correctly describes normal mode splitting [180].

21.5.3 Transfer matrices for optical lattices

A particularly interesting application if the transfer matrix formalism are optical lattices, which we will treat in the following.

21.5.3.1 Limit of optically dilute clouds

For optically dilute clouds, $r \ll 1$, we expect standard Bragg scattering. The atomic transfer matrix (21.209) can be approximated by,

$$\mathcal{T}_\beta = \begin{pmatrix} 1 & \imath\beta \\ -\imath\beta & 1 \end{pmatrix} , \tag{21.219}$$

so that we find for the single-layer and transfer matrix,

$$\boxed{\mathcal{T} = \mathcal{T}_\beta \mathcal{T}_d \simeq \begin{pmatrix} e^{\imath k_z d} & \imath\beta e^{-\imath k_z d} \\ -\imath\beta e^{\imath k_z d} & e^{-\imath k_z d} \end{pmatrix}} . \tag{21.220}$$

Near the Bragg angle we have $\cos\theta \simeq \cos\theta_{\rm brg} = \lambda_{\rm sp}/\lambda_{\rm dip}$ and near resonance we have $2\pi/k = \lambda \simeq \lambda_{\rm sp}$, so that, with $d = \lambda_{\rm dip}/2$, we obtain $k_z d \simeq \pi$ and,

$$\mathcal{T}^{N_s} \simeq \begin{pmatrix} e^{\imath\pi} & \imath\beta e^{-\imath\pi} \\ -\imath\beta e^{\imath\pi} & e^{-\imath\pi} \end{pmatrix}^{N_s} = \begin{pmatrix} -1 & -\imath\beta \\ \imath\beta & -1 \end{pmatrix}^{N_s} = (-1)^{N_s} \begin{pmatrix} 1 & N_s\imath\beta \\ -N_s\imath\beta & 1 \end{pmatrix} , \tag{21.221}$$

which we will verify in Exc. 21.5.5.3. The total reflectivity being $r_{N_s} \simeq N_s\imath\beta$, we get the reflection,

$$|r_{N_s}|^2 \simeq \frac{N_s^2\beta_{\rm sp}^2\Gamma_{\rm sp}^2}{4\Delta^2 + \Gamma_{\rm sp}^2} . \tag{21.222}$$

Thus, the profile of the reflection curve is Lorentzian.

> **Example 126 (*Estimation of the reflectivity in the dilute cloud limit*):** In resonance we estimate for typical experimental values $N_s = 1000$, $n = 10^{17}\,{\rm cm}^3$, $\lambda_{\rm dip} = 797\,{\rm nm}$, and $\Lambda_{\rm brg} = 422\,{\rm nm}$,
>
> $$|r_{N_s}| = N_s \frac{nd\sigma_{\rm sp}}{2} = N_s n \lambda_{\rm dip} \frac{3\lambda_{\rm sp}^2}{8\pi} \approx 1.7 .$$
>
> The high reflectivity is not physical, which shows that the assumption of optically diluted clouds is not necessarily satisfied in experimentally achievable parameter regimes. On the contrary we can expect to reach regimes, where the clouds are optically so dense, that photonic bands can be expected. That is, if the goal is to detect a band gap, it helps to have (1) many layers filled with atoms, (2) high atomic densities per layer.

21.5.3.2 Limit of optically dense clouds

In order to obtain analytical expressions in the regime of dense clouds, we write the transfer matrix for a single layer, using the expressions (21.209) and (21.211), as follows [226],

$$\boxed{\mathcal{T} = \mathcal{T}_\beta \mathcal{T}_d = \begin{pmatrix} (1+\imath\beta)e^{\imath\mathbf{k}\cdot\mathbf{d}} & \imath\beta e^{-\imath\mathbf{k}\cdot\mathbf{d}} \\ -\imath\beta e^{\imath\mathbf{k}\cdot\mathbf{d}} & (1-\imath\beta)e^{-\imath\mathbf{k}\cdot\mathbf{d}} \end{pmatrix}} . \tag{21.223}$$

Given that $\det\mathcal{T} = 1$, the matrix represents a unitary transformation and the eigenvalues can be cast into the form $e^{\pm\imath\phi}$. Letting,

$$\cos\Theta \equiv \tfrac{1}{2}{\rm Tr}\ \mathcal{T} = \cos k_z d - \beta \sin k_z d , \tag{21.224}$$

we can write the matrix,

$$\mathcal{T} = \mathbb{I}\cos\Theta + \imath A \sin\Theta = e^{\imath\Theta A} \tag{21.225}$$

with

$$A = \frac{1}{\sin\Theta}\begin{pmatrix} \beta\cos k_z d + \sin k_z d & \beta e^{-\imath k_z d} \\ -\beta e^{\imath k_z d} & -\beta\cos k_z d - \sin k_z d \end{pmatrix} \tag{21.226}$$

The eigenvectors of $\mathcal{T}$, and therefore of each power of $\mathcal{T}$, are *Bloch states of the periodic lattice*. We verify in Exc. 21.5.5.4, that the following relationships are satisfied,

$$\text{Tr } A = 0 \quad , \quad A^2 = 1 \quad , \quad \det A = 1 \ . \tag{21.227}$$

The eigenvalues of $A\sin\Theta$ are $\lambda_A \pm 1$. The eigenvalues of the transfer matrix are,

$$\begin{aligned} \lambda &= \cos k_z d - \beta \sin k_z d \pm \imath\sqrt{1-(\cos k_z d - \beta\sin k_z d)^2} = \cos\Theta \pm \imath\sin\Theta \\ &= e^{\pm\imath \arccos(\cos k_z d - \beta \sin k_z d)} = e^{\pm\imath\Theta} \ . \end{aligned} \tag{21.228}$$

This decomposition allows us to calculate the transfer matrix for a succession of N_s layers. We get,

$$\begin{aligned} \mathcal{T}^{N_s} &= e^{\imath N_s \Theta A} = \mathbb{I}\cos(N_s\Theta) + \imath A \sin(N_s\Theta) \\ &= \mathbb{I}\cos\left[N_s \arccos(\cos k_z d - \zeta \sin k_z d)\right] + \imath A \sin\left[N_s \arccos(\cos k_z d - \zeta \sin k_z d)\right] \ , \end{aligned} \tag{21.229}$$

which gives us the reflection coefficient,

$$\begin{aligned} r_\mu &= \frac{(\mathcal{T}^{N_s})_{12}}{(\mathcal{T}^{N_s})_{22}} = \frac{\imath\sin(\mu\Theta)\mathcal{T}_{12}}{\cos(N_s\Theta) + \imath\sin(\mu\Theta)\mathcal{T}_{22}} \\ &= \frac{-\imath\beta e^{\imath k_z d}}{\sin\Theta\cot(N_s\Theta) - \imath\sin k_z d - \imath\beta\cos k_z d} \ . \end{aligned} \tag{21.230}$$

This is the final result. Near the Bragg angle, $\cos\Theta \simeq 1$, we have,

$$\begin{aligned} r_{N_s} &= \frac{\imath\beta}{\sin\Theta\cot(N_s\Theta) - \imath\beta} \simeq \frac{\imath N_s\zeta}{1 - \imath N_s\beta} \\ |r_{N_s}|^2 &\simeq \frac{N_s^2\beta_{\rm sp}^2\Gamma_{\rm sp}^2}{4\Delta^2 + (1+n\beta_{\rm sp}^2)\Gamma_{\rm sp}^2} \ . \end{aligned} \tag{21.231}$$

The intensity reflection profile, therefore, is a Lorentzian also in the limit of thick clouds. The additional condition for the occurrence of prohibited photonic bands is a large number of atomic layers, $N_s \gg 1$. We note that the model is an extension of the *Kronig-Penney model* introduced in Sec. 4.1.3.

21.5.3.3 Application of transfer matrices to real $1D$ optical lattices

The analytical treatment shown in the previous sections does not take account of possible lattice imperfections, since the atomic layers are assumed to be identical, infinitely thin, immobile and located at fixed periodic distances. Realistic optical lattices are different for several reasons:

1. Atomic clouds are not perfectly localized in ultra-thin layers, but distributed in a Gaussian way as a function of the cloud's temperature. The Debye-Waller factor (21.180) describes the impact of this distribution on the Bragg model.

2. The atoms are in thermal motion causing an inhomogeneous Doppler shift and are affected by the photonic recoil received in each scattering process. This causes a broadening of the reflection profiles and decreases the interference capability.

3. The number of atoms per layer may vary. Also, the global extent of the cloud is not infinite, that is, we have N_s layers filled with atoms with a gradual decrease at the confines of the cloud.

4. The atoms trapped in the optical potential are subjected to a dynamic Stark shift [19] causing an inhomogeneous broadening of the atomic transition as well.

5. The periodicity of the lattice is slightly modified because the refractive index experienced by the laser beams creating the dipole potential locally depends on the atomic density concentrated in the lattice's anti-nodes. The consequence is a local decrease of the lattice constant d [20].

All of the aforementioned imperfections may be included in a numerical treatment of the transfer matrices. For this we subdivide the atomic cloud into sufficiently thin sublayers, as shown in Fig. 21.22. Each sublayer, being characterized by its own 2D atomic density and its own shift from resonance, is described by an individual transfer matrix. The matrices are concatenated, and the reflection profile is computed, as shown in the expression (21.213) [767]. Fig. 21.24 shows a numerical calculation of a photonic band in a rubidium optical lattice. The experimental variables are the incidence angle θ of the probe laser and its tuning Δ from a transition $\lambda_{\rm sp}$. Δ determines σ and β via the polarizability (21.193) [21] and thus governs the propagation of light inside the layers. θ determines $k_z d$ and thus probes the periodicity *between* the layers.

Depending on the atomic density we can identify different behaviors [22]:

1. At the limit of thin lattices, we do not expect multiple scattering. The absorptive (imaginary) part of polarizability dominates, $\beta \approx \mathfrak{Im}\,\beta$. Thus, the reflection coefficient is almost real, $re^{\imath\phi} \approx |r|$, the phase shifts are negligible, the profile of the reflection spectrum is symmetric. In this scheme, the interference of the radiation patterns of individual atoms is destructive in all directions, except

[19] Or 'light-shift', see Exc. 16.4.4.13.

[20] More correctly: If between $\lambda_{\rm dip}$ and λ_{D1} a photonic band were created for the laser beams that produce the optical lattice [226, 855], these beams would be reflected without being able to penetrate the lattice. In fact, the periodicity changes in such a way, that the frequency of the beams is at the edge of the band gap. Deutsch *et al.* [226] showed that a self-consistent solution gives the modified lattice constant,

$$d' = \frac{\lambda_{\rm dip}}{2}\left[1 + \frac{\phi_{\rm dip}}{\pi}(1 - {\rm sign}\Delta_{\rm dip})\right] ,$$

where $\phi_{\rm dip} = \arctan\left(-\frac{\Delta_{\rm dip}}{\Gamma} n d\, \sigma_{D1}(\Delta_{\rm dip})\right)$.

[21] Δ also enters $k_z d$, but so weakly, that we can despise this dependence.

[22] The densities are assumed to be sufficiently low to eliminate collective effects such as, for example, superradiance.

under the Bragg angle. There are losses caused by scattering in non-paraxial modes. They are also due to elastic Rayleigh scattering but, because of the finite Debye-Waller factor, the radiation becomes diffuse and incoherent.

2. At the limit of thick lattices, we have multiple scattering. The (real) dispersive part of the polarizability is $\beta \approx \mathfrak{Re}\,\beta$. Thus, absorption is suppressed, we observe large phase shifts and the reflection spectrum profile is asymmetric. Multiple beam interference gives rise to global scattering.

Physically, the set parameters consistent of the quasi-momentum and the energy of the Bloch wave, (Θ, Δ), is more relevant because it allows analyzing the *dispersion relation* [23]. We observe the existence of energies Δ, where the real part of the quasi-momentum vanishes (modulo π). The 3D representation in Fig. 21.24(e) illustrates the occurrence of an *avoided crossing* due to the band gap at the edge of the Brillouin zone.

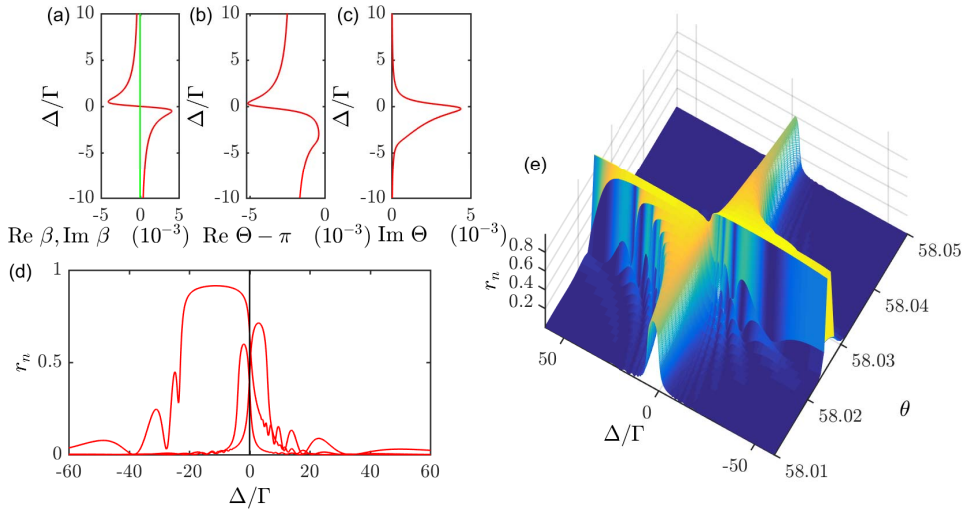

Figure 21.24: (code) Numerical calculation of a photonic band in a 1D optical lattice (wavelength $\Lambda_{\rm dip} = 797$ nm) far-tuned from the rubidium D1 transition ($\lambda_{D1} = 795\,$nm). The probe laser exciting the Bragg resonance is tuned close to the rubidium resonance at $\lambda_{\rm sp} = 422$ nm. We assume atomic densities of $n = 4 \cdot 10^{11}\,{\rm cm}^{-3}$ and $N_s = 40000$ atomic layers. (a) Real and imaginary parts of the reflection index ($\propto$ polarizability) as a function of detuning Δ. (b,c) Real and imaginary parts of the quasi-momentum (x-axis) as a function of the detuning Δ. (d,e) 2D and 3D representation of the reflection coefficient.

In fact, Bragg resonances can be understood in reciprocal space as reflections at the edges of the Brillouin zone. Through the angle of incidence of the injected light beam, we adjust the quasi-momentum. The frequency of the light beam determines the energy. The forbidden photonic bands are caused by the formation of an energetic gap in the dispersion relation induced by the interaction of the atoms with the optical lattice.

[23] We note, that Θ via the relation (21.224) of the angle of incidence θ, but only weakly of the energy Δ.

21.5.3.4 LDOS and the suppression of spontaneous emission in forbidden photonic bands

The *local density of states* (LDOS) in a photonic band can be evaluated from [835, 317],

$$N(\omega) = 2\omega \sum_{\mathbf{k}} \delta(\omega^2 - \omega_{\mathbf{k}}^2) \ . \tag{21.232}$$

William found out:

$$k_{\text{eff}} = \frac{d\phi}{dz} \ , \tag{21.233}$$

with $\phi = \arctan(\mathfrak{Im}\,\mathcal{E}/\mathfrak{Re}\,\mathcal{E})$. The $\mathcal{E}$-field between two layers can be calculated using transfer matrices. The density of the states is given as the derivative of the inverse function of the dispersion relation:

$$N(\omega) = \frac{dk_{\text{eff}}(\omega)}{d\omega} \ . \tag{21.234}$$

The decrease in the LDOS is equivalent to the suppression of spontaneous emission [24], that is, an excited atom located inside the lattice will not be able to emit its photon. This is the condition for a forbidden photonic band to be *omnidirectional*. Omnidirectional bands need three-dimensional lattices. Nevertheless, the reduction of the spontaneous emission rate has already been observed in [376, 875], which can be interpreted as $1D$ photonic crystals.

21.5.3.5 Impurities

The formalism allows for the calculation of the impact of localized defects in numerical simulations. For example, it is instructive to look at the intensity profile along the structure in the presence of a localized lattice defect. In Fig. 21.25(c) we observe an intensity peak located at the 100-th atomic layer, exactly where the defect was introduced. This peak corresponds to a localized evanescent wave. Photons can not propagate freely through the lattice: they prefer to tunnel between lattice defects the rather than propagate by radiation.

The curves (a-b) of Fig. 21.25 illustrate how an empty photonic band fills up with localized states with well-defined energies when noise is added to the periodicity of the lattice. This situation is similar to that in semi-conductors doped by donor and acceptor states.

21.5.4 Photonic bands in the Bloch and the coupled dipoles models

The transfer matrix model is limited in several respects:

1. Firstly, being intrinsically 1D, the model does not apply to 2D or 3D lattices.
2. Also, it does not incorporate the possibility of transverse disorder or effects linked to the finite transverse extension of the atomic layers, for example, the limitation of the number of layers participating in multiple reflection ('walk-off') [768] or the impact of an imperfect mode matching [766].

[24] For the same reason, resonant dipole-dipole interactions are suppressed [493].

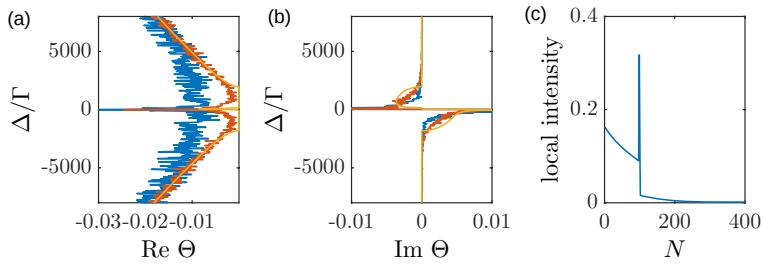

Figure 21.25: (code) (a,b) Dispersion relation as in Fig. 21.24, but in the presence of randomly distributed defects. (c) Intensity profile along the lattice with a defect located in the 100^{esima} atomic layer.

In contrast, the coupled dipoles model offers several advantages. An optical lattice is, after all, nothing more than a periodically ordered diluted sample of atoms. Hence, we can apply the coupled dipoles model introduced in Sec. 21.1.2 [721, 720]. The advantages of this model are its applicability to 3D systems and finite and disordered lattices. It also allows the inclusion of all kinds of inhomogeneities such as, for example, the spatial intensity distribution of a focused incident laser, or the deviation of the laser beam penetrating an atomic cloud due to refraction. On the other hand, the model only lends itself to heavy numerical simulations, limiting it to some 10000 atoms.

21.5.4.1 The Bloch model and forbidden electronic bands

The *Bloch model* is another model to describe 3D periodic systems [25]. It was introduced in Chp. 4 for 1D optical lattices. Its disadvantages are that it supposes infinite lattices and the absence of defects.

The Bloch model is commonly used to describe the scattering of electron waves in a solid, where the band gap originates from the Coulomb interaction of the electron with the atoms of the solid crystal. In contrast, in photonic crystals, the modes with high (low) frequency ω concentrate their energy in spatial regions with low (high) dielectric index ϵ. Close to geometric (Mie) resonances this causes a repulsion in the density distribution of photonic states, and the opening of a gap separating high frequency bands (air bands) from low frequency bands.

In optical lattices the photons interact with the atomic resonances. Photons and electrons are distinguished by their different dispersion relations and by the fact that electronic waves are scalar and photonic waves are vectorial. The electrons of a crystal are bound to an energy surface and follow the lines of the dispersion relation without leaving the metal. In contrast, photons are usually injected into the structure, which gives an additional degree of freedom. Therefore, any point in the phase diagram can be reached and the dispersion relation only informs, where at which point the transmission is stronger.

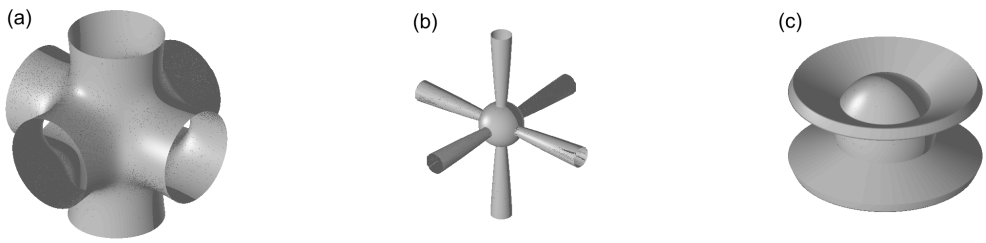

Figure 21.26: Attempt of an artistic illustration of the isoenergetic surfaces for electrons in a metal (left), photons in a 3D optical lattice (center), and photons in a 1D optical lattice (right). The interaction of atoms with the lattice is much weaker than the interaction of electrons with the metal, except close to resonances. Therefore, photonic bands are much narrower than electronic bands.

Table 21.2: Comparison between band gaps photonic crystals and metals.

	photonic crystal	metal
lattice structure	atoms in a stationary wave	atoms in a crystal
particles	photons	electrons in a metal
equations of motion	Maxwell	Schrödinger
dispersion relation	$\hbar k/c$	$\hbar k^2/2m$
tune	Bragg angle and frequency	voltage
band gap origin	$\mathfrak{Im}\,\alpha$ absorption by atoms	e^- interacting with the atomic nuclei
band gap width	$< \omega_0 - \omega_{\rm dip}$	interaction energy

21.5.5 Exercises

21.5.5.1 Ex: Structure coefficient of a 1D lattice

Calculate the structure coefficient of the density distribution (21.185) and the square $|S_{\mathbf{k}_0}(\mathbf{k})|^2$.

21.5.5.2 Ex: Structure coefficient in spherical coordinates

Write the structure coefficient (21.185) in spherical coordinates.

21.5.5.3 Ex: Reflection in the dilute cloud limit

Verify the calculation (21.229).

21.5.5.4 Ex: Reflection in the dense cloud limit

Verify the representation (21.225).

21.5.5.5 Ex: Photonic band spectra

Plot the 1D-photonic band gap spectrum in a standing wave as a function of Δ_{pr} and n.

21.5.5.6 Ex: Intensity drop inside photonic bands

Plot the intensity of the probe on its passage through the 1D optical lattice.

21.5.5.7 Ex: Intensity drop inside photonic bands in the presence of disorder

Simulate the intensity of the probe on its passage through the 1D optical lattice inthe presence of disorder.

21.5.5.8 Ex: Photonic bands with sidebands

Plot the intensity of the probe on its passage through the 1D optical lattice as a function of detuning in the presence of modulation sidebands.

21.5.5.9 Ex: Photonic bands versus absorption

Compare the signatures of band gaps with absorption.

21.5.5.10 Ex: Structure of a diamond lattice

A geometric configuration of point-like scatterers that can exhibit a broad omnidirectional photonic bandgap is the one of a diamond lattice [160, 726, 25]. In this exercise we will study such a diamond-shaped lattice.
a. Produce a geometric representation of the primitive cell and a Wigner-Seitz cell.
b. Study the optical lattice generated by the following configuration of incident lasers,

$$\mathbf{k}_0 = \tfrac{\pi}{a}(0,-2,-1) \quad , \quad \mathbf{k}_1 = \tfrac{\pi}{a}(2,0,1) \quad , \quad \mathbf{k}_2 = \tfrac{\pi}{a}(0,2,-1) \quad , \quad \mathbf{k}_3 = \tfrac{\pi}{a}(-2,0,1)$$

with $k_{laser} = \omega_{laser}/c = \sqrt{5}\pi/a$.
c. Calculate the forbidden band according to [160, 726, 25].

21.6 Further reading

21.6.1 on the coupled dipoles model

E. Akkermans et al., *Photon Localization and Dicke Superradiance in Atomic Gases* [DOI]

R. Bachelard et al., *Cooperative scattering and radiation pressure force in dense atomic clouds* [DOI]

R. Bachelard et al., *Resonances in Mie scattering by an inhomogeneous atomic cloud* [DOI]

R. Bachelard et al., *Collective effects in the radiation pressure force* [DOI]

H. Bender et al., *Observation of cooperative Mie scattering from an ultracold atomic cloud* [DOI]

T. Bienaimé et al., *Observation of cooperative radiation pressure in presence of disorder* [DOI]

T. Bienaimé et al., *Atom and photon measurement in cooperative scattering by cold atoms* [DOI]

T. Bienaimé et al., *Controlled Dicke Subradiance from a Large Cloud of Two-Level Systems* [DOI]

R. Kaiser et al., *Quantum Multiple Scattering* [DOI]

R. Friedberg et al., *Frequency shifts in emission and absorption by resonant systems ot two-level atoms* [DOI]

R. Friedberg et al., *Effects of including the counterrotating term and virtual photons on the eigenfunctions and eigenvalues of a scalar photon collective emission theory* [DOI]

R. Friedberg et al., *Reply to: Comment on: Effects of including the counterrotating term and virtual photons on the eigenfunctions and eigenvalues of a scalar photon collective emission theory; Phys. Lett. A 372 (2008) 2514; Phys. Lett. A 372 (2008) 5732* [DOI]

R. Friedberg et al., *The dynamical Cooperative Lamb Shift in a system of two-level atoms* [DOI]

R. Friedberg et al., *Cooperative Lamb shift in an ellipsoid* [DOI]

M.O. Scully et al., *Directed Spontaneous Emission from an Extended Ensemble of N Atoms: Timing Is Everything* [DOI]

M.O. Scully et al., *The effects of the N atom collective Lamb shift on single photon superradiance* [DOI]

M.O. Scully et al., *The super of superradiance* [DOI]

M.O. Scully et al., *Collective Lamb Shift in Single Photon Dicke Superradiance* [DOI]

M.O. Scully et al., *The Lamb Shift-Yesterday, Today, and Tomorrow* [DOI]

A.A. Svidzinsky et al., *Dynamical Evolution of Correlated Spontaneous Emission of a from a Uniformly Excited Cloud of Atoms* [DOI]

A.A. Svidzinsky et al., *Cooperative spontaneous emission as a many-body eigenvalue problem* [DOI]

A.A. Svidzinsky et al., *Evolution of collective N atom states in single photon superradiance: Effect of virtual Lamb shift processes* [DOI]

A.A. Svidzinsky et al., *Cooperative spontaneous emission of N atoms: Many-body eigenstates, the effect of virtual Lamb shift processes, and analogy with radiation of N classical oscillators* [DOI]

J. Ruostekoski et al., *Lorentz-Lorenz shift in a Bose-Einstein condensate* [DOI]

R. Röhlsberger et al., *The collective Lamb shift in nuclear c-ray superradiance* [DOI]

R. Röhlsberger et al., *Collective Lamb Shift in Single-Photon Superradiance* [DOI]

S.E. Skipetrov et al., *Absence of Anderson Localization of Light in a Random Ensemble of Point Scatterers* [DOI]

S.E. Skipetrov et al., *Red light for Anderson localization* [DOI]

D. Pavolini et al., *Experimental evidence for subradiance* [DOI]

C.E. Máximo et al., *Spatial and temporal localization of light in two dimensions* [DOI]

Ph.W. Courteille et al., *Modification of radiation pressure due to cooperative scattering of light* [DOI]

R.T. Sutherland et al., *Collective dipole-dipole interactions in an atomic array* [DOI]

W.R. Garrett et al., *Large Multiple Collective Line Shifts Observed in Three-Photon Excitations of Xe* [DOI]

C.C. Kwong et al., *Cooperative Emission of a Coherent Superflash of Light* [DOI]

J. Keaveney et al., *Cooperative Lamb Shift in an Atomic Vapor Layer of Nanometer Thickness* [DOI]

E. Shahmoon et al., *Cooperative Resonances in Light Scattering from Two-Dimensional Atomic Arrays* [DOI]

Ch. Weitenberg et al., *Coherent Light Scattering from a Two-Dimensional Mott Insulator* [DOI]

21.6.2 on Bragg scattering

G. Birkl et al., *Bragg scattering from atoms in optical lattices* [DOI]

M. Weidemüller et al., *Bragg diffraction in an atomic lattice bound by light* [DOI]

M. Weidemüller et al., *Local and global properties of light-bound atomic lattices investigated by Bragg diffraction* [DOI]

S. Slama et al., *Dimensional crossover in Bragg scattering from an optical lattice* [DOI]

S. Slama et al., *Multiple reflections and diffuse scattering in Bragg scattering at optical lattices* [DOI]

21.6.3 on photonic bands

M. Woldeyohannes et al., *Coherent control of spontaneous emission near a photonic band edge* [DOI]

O. Toader et al., *Photonic band gap architectures for holographic lithography* [DOI]

G. Vandegrift et al., *The Moessbauer effect explained* [DOI]

D. Mogilevtsev et al., *Light propagation and Anderson localization in disordered superlattices containing dispersive metamaterials Effects of correlated disorder* [DOI]

M. Antezza et al., *Fano-Hopfield model and photonic band gaps for an arbitrary atomic lattice* [DOI]

M. Antezza et al., *Spectrum of Light in a Quantum Fluctuating Periodic Structure* [DOI]

M. Antezza et al., *Photonic band gap in an imperfect atomic diamond lattice: Penetration depth and effects of finite size and vacancies* [DOI]

Deshui Yu, *Photonic band structure of the three-dimensional ^{88}Sr atomic lattice* [DOI]

D.V. van Coevorden et al., *Photonic band structure of atomic lattices* [DOI]

N.V. Cohan et al., *Band structure of diamond* [DOI]

W. Saslow et al., *Band structure and optical properties of diamond* [DOI]

K. M. Ho et al., *Existence of a photonic gap in periodic dielectric structures* [DOI]

K.I. Petsas et al., *Crystallography of optical lattices* [DOI]

I.H. Deutsch et al., *Photonic Band Gaps in Optical Lattices* [DOI]

M. Artoni et al., *Resonantly absorbing one-dimensional photonic crystals* [DOI]

G. Boedecker et al., *All-frequency effective medium theory of a photonic crystal* [DOI]

M. Artoni et al., *Optically tunable photonic stop bands in homogeneous absorbing media* [DOI]

A. Schilke et al., *Photonic Band Gaps in One-Dimensionally Ordered Cold Atomic Vapors* [DOI]

A. Schilke et al., *Optical parametric oscillation with distributed feedback in cold atoms* [DOI]

A. André et al., *Manipulating light pulses via dynamically controlled photonic band gap* [DOI]

J.M. Bendickson et al., *Analytic expressions for the electromagnetic mode density in finite, one-dimensional, photonic band-gap structures* [DOI]

D. Petrosyan, *Tunable photonic band gaps with coherently driven atoms in optical lattices* [DOI]

Jin-Hui Wu et al., *Controlling the photonic band structure of optically driven cold atoms* [DOI]

K. Ishizaki et al., *Realization of three-dimensional guiding of photons in photonic crystals* [DOI]

D. Petrosyan, *Tunable photonic band gaps with coherently driven atoms in optical lattices* [DOI]

21.6.4 on noise analysis of Bragg scattering

M.O. Scully et al., *The Super of Superradiance* [DOI]

J. Chabé et al., *Experimental Observation of the Anderson Metal-Insulator Transition with Atomic Matter Waves* [DOI]

I.B. Mekhov et al., *Cavity-Enhanced Light Scattering in Optical Lattices to Probe Atomic Quantum Statistics* [DOI]

I.B. Mekhov et al., *Light scattering from ultracold atoms in optical lattices as an optical probe of atomic statistics* [DOI]

I.B. Mekhov et al., *Quantum Nondemolition Measurements and State Preparation in Quantum Gases by Light Detection* [DOI]

Ph.T. Ernst et al., *Probing superfluids in optical lattices by momentum-resolved Bragg spectroscopy* [DOI]

Chapter 22

Individual atoms in optical cavities

So far we have considered the coherent dynamics between atoms and radiation fields in free space, and we extended the theory to take into account the dissipative coupling to the electromagnetic vacuum by spontaneous emission and atomic motion. The vacuum represents a homogeneous and isotropic reservoir characterized by a continuous white energy spectrum. The situation changes completely when we place the atom inside an optical cavity which breaks the translational and rotational symmetries and imprints a resonance structure into the density of photonic states. Obviously, the cavity will profoundly change the atomic coupling to the electromagnetic vacuum, and hence the way in which the atom reacts to incident light, as much with respect to light scattering as with respect to optical forces.

In this chapter we analyze the coupled dynamics of atoms interacting with the optical field modes of a cavity pumped by incident laser beams. We first concentrate in Sec. 15.2 on empty cavities. Then in Sec. 22.1 we turn our attention to the impact of atoms on the cavity dynamics, in particular its transmission spectrum. Cooperative and collective effects that may be induced by cavities will be discussed in Chps. 24 and 25.

22.1 Interaction of a cavity with one atom

In Sec. 17.1 we have shown how to describe the dynamics of a *single two-level atom* driven by a quantized electromagnetic field and embedded in an electromagnetic vacuum under the assumption that the driving field be a plane wave and the vacuum be isotropic. In the following, we want to relax these conditions. We generalize Eq. (14.7) replacing the plane wave $e^{i\mathbf{k}\cdot\mathbf{r}}$ by a mode function $u_{\mathbf{k}}(\mathbf{r})$ and allowing the coupling constant (17.8) $g_{\mathbf{k}}$ to depend on $\mathbf{k}$. Such a situation corresponds to placing the atom inside an optical cavity whose macroscopic boundary conditions create a cooperative environment for the atom. We note that the role of the cavity can be understood as generating mirror images with which the atom interacts. Furthermore, both the atomic excitation and the radiation fields may decay. On the other hand, we restrict to non-interacting atoms, that is, free atoms or atoms trapped in external potentials that only interact with each other via re-scattering of an incident radiation field, i.e. no collisions and no properties requiring symmetrization of their wavefunctions.

In Sec. 22.1.1 we study a single atom in a cooperative environment (e.g. a cavity).

In particular, we will find that spontaneous emission is affected by the presence of a cavity. A wider discussion of scattering from correlated atoms and of how cavities can generate correlations is postponed to Sec. 23.1. Then, in Sec. 22.1.2 we will introduce some parameters characterizing the interaction between atoms and cavities. In particular, we will relate the important notions of the *cooperativity* of several atoms and the structure factor for light scattering introduced in 21.1.1 with the cavity-to-free space scattering ratio, the finesse and the density-of-states of a cavity, simply by pointing out that a cavity multiplies the number of atoms interacting with a light mode by the number of its mirror images. In Secs. 22.1.3, 22.1.4, and 22.1.6 we study the Hamiltonian governing the dynamics of a cavity mode interacting with a single immobile atom emphasizing the phenomenon of normal mode splitting. In Sec. 22.1.5 we simplify the equations of motion by adiabatically eliminating the internal atomic degree of freedom. Finally, in Secs. 22.1.7 and 22.1.8 we study the impact of the atomic center-of-mass degree of freedom (position and velocity) on the dynamics of the cavity fields. The discussion of backaction of the cavity fields on the atomic motion is postponed to Chp. 25.

22.1.1 Spontaneous emission in a cooperative environment

22.1.1.1 Atoms in a cooperative environment

The quantization of the electromagnetic field has been presented in Sec. 14.1.1 for the case of plane wave radiation modes. In the following, we want to generalize the treatment to arbitrary field modes characterized by mode functions $\mathbf{u}_{\mathbf{k}\lambda}(\mathbf{r})$ labeled by a wavevector and a polarization. These are classical vector functions satisfying the vector Helmholtz equation and the transversality condition,

$$[\nabla^2 + k_\lambda^2]\mathbf{u}_{\mathbf{k}\lambda}(\mathbf{r}) = 0 \qquad \text{and} \qquad \nabla \cdot \mathbf{u}_{\mathbf{k}\lambda}(\mathbf{r}) = 0 \ , \tag{22.1}$$

with $k_\lambda = \omega_{\mathbf{k}\lambda}/c$ [583]. These classical functions are chosen to form an orthonormal set,

$$\int_V \mathbf{u}^*_{\mathbf{k}\lambda}(\mathbf{r}) \cdot \mathbf{u}_{\mathbf{k}'\lambda'}(\mathbf{r}) d^3r = \delta_{\mathbf{k}\mathbf{k}'}\delta_{\lambda,\lambda'} \ . \tag{22.2}$$

In free space, the plane wave approximation is generally good,

$$\mathbf{u}^{\text{free}}_{\mathbf{k}\lambda}(\mathbf{r}) = \frac{\vec{\epsilon}_\lambda}{\sqrt{V}} e^{\imath \mathbf{k}\cdot\mathbf{r}} \ , \tag{22.3}$$

where $\vec{\epsilon}_{\mathbf{k}\lambda}$ is a polarization vector such that $\mathbf{k}\cdot\vec{\epsilon}_{\mathbf{k}\lambda} = 0$ and V is the photon quantization volume.

Let us now rewrite the quantized transverse vector potential of the radiation field (14.7) as,

$$\boxed{\hat{\mathbf{A}}(\mathbf{r},t) = \sum_{\mathbf{k}\lambda} \sqrt{\tfrac{\hbar}{2\omega_{\mathbf{k}\lambda}\varepsilon_0}} [\mathbf{u}_{\mathbf{k}\lambda}(\mathbf{r})\hat{a}_{\mathbf{k}\lambda}(t) + \mathbf{u}^*_{\mathbf{k}\lambda}(\mathbf{r})\hat{a}^\dagger_{\mathbf{k}\lambda}(t)]} \ . \tag{22.4}$$

The quantum properties of the electric and magnetic field operators are determined by the bosonic annihilation and creation operators, $\hat{a}_{\mathbf{k}\lambda}(t)$ and $\hat{a}^\dagger_{\mathbf{k}\lambda}(t)$, respectively, with usual commutation relations: $[\hat{a}_{\mathbf{k}\lambda}(t), \hat{a}_{\mathbf{k}'\lambda'}(t)] = 0$ and $[\hat{a}_{\mathbf{k}\lambda}(t), \hat{a}^\dagger_{\mathbf{k}'\lambda'}(t)] = \delta_{\mathbf{k}\mathbf{k}'}\delta_{\lambda\lambda'}$.

For weak-coupling between the atoms and the field, one has the contributions to the Hamiltonian,

$$\boxed{\begin{aligned} \hat{H}_{atom} &= \hbar\omega_0\hat{\sigma}^z \\ \hat{H}_{field} &= \sum_{\mathbf{k}} \hbar\omega_{\mathbf{k}}[\hat{a}^\dagger_{\mathbf{k}\lambda}(t)\hat{a}_{\mathbf{k}\lambda}(t) + \tfrac{1}{2}] \\ \hat{H}_{atom:field} &= -\imath\hbar\sum_{\mathbf{k},\lambda}(\hat{\sigma}^+ + \hat{\sigma}^-)[g_{\mathbf{k}\lambda}(\mathbf{r})\hat{a}_{\mathbf{k}\lambda} - g^*_{\mathbf{k}\lambda}(\mathbf{r})\hat{a}^\dagger_{\mathbf{k}\lambda}] \end{aligned}} \quad , \tag{22.5}$$

and,

$$g_{\mathbf{k}\lambda}(\mathbf{r}) \equiv \sqrt{\frac{\omega_{\mathbf{k}}}{2\varepsilon_0\hbar}}\mathbf{d}\cdot\mathbf{u}_{\mathbf{k}\lambda}(\mathbf{r}) \tag{22.6}$$

is a complex function associated with the coupling strength between the atom and the field.

By solving the Heisenberg equations of motion for the atomic and field operators within the Born and Markov approximations (or using the procedure leading to the expression (17.118)), one obtains the spontaneous emission rate on a transition $|e\rangle \to |g\rangle$ of frequency ω_0:

$$\Gamma(\mathbf{r}) = 2\pi\sum_{\mathbf{k},\lambda}|g_{\mathbf{k}\lambda}(\mathbf{r})|^2\delta(\omega_{\mathbf{k}} - \omega_0) \ . \tag{22.7}$$

which is the same result obtained by the Weisskopf-Wigner theory [583]. To evaluate the sum we need go to a continuous k-space via,

$$\sum_{\mathbf{k},\lambda} \longrightarrow \lim_{V\to\infty}\sum_{\lambda}\frac{V}{8\pi^3}\int d^3k \ . \tag{22.8}$$

Hence, in free space, inserting the mode function (22.3),

$$\begin{aligned} \Gamma(\mathbf{r}) &= \frac{\pi\omega_0}{\varepsilon_0\hbar}\sum_{\mathbf{k},\lambda}|\mathbf{d}\cdot\mathbf{u}_{\mathbf{k}\lambda}(\mathbf{r})|^2\delta(\omega_{\mathbf{k}} - \omega_0) \\ &= \frac{\hbar\omega_0}{8\pi^2\varepsilon_0\hbar^2}\lim_{V\to\infty}\sum_{\lambda}\int d^3k \ |\mathbf{d}\cdot\vec{\epsilon}_{\mathbf{k}\lambda}|^2\delta(\omega_{\mathbf{k}} - \omega_0) \\ &= \lim_{V\to\infty}\sum_{\lambda}\int\frac{|\mathbf{d}\cdot\vec{\epsilon}_{\mathbf{k}\lambda}|^2\vec{\mathcal{E}}^2_{\mathbf{k}}}{\hbar^2}2\pi\delta(\omega_{\mathbf{k}} - \omega_0)\frac{V}{8\pi^3c}k^2d\Omega_{\mathbf{k}}d\omega_{\mathbf{k}} \ . \end{aligned} \tag{22.9}$$

Obviously, in free space the decay rate does not depend on position. Plugging in the density of states for free space (1.53) and (16.23), we finally get,

$$\Gamma = \sum_{\lambda}\int\frac{|\mathbf{d}\cdot\vec{\epsilon}_{\mathbf{k}\lambda}|^2\vec{\mathcal{E}}^2_{\mathbf{k}}}{\hbar^2}2\pi\delta(\omega_{\mathbf{k}} - \omega_0)\rho(\omega_{\mathbf{k}},\mathbf{k})d\Omega_{\mathbf{k}}d\omega_{\mathbf{k}} \ , \tag{22.10}$$

where the density of states can now be arbitrarily shaped by the presence of boundary conditions, such as optical cavities or dielectric or metallic surfaces.

22.1.1.2 Modification of the natural linewidth by cavities

The *cooperativity parameter* of a cavity is defined as the rate at which an atom emits into the volume of a cavity mode normalized to the rate at which it would scatter into free space,

$$\boxed{\Upsilon \equiv \frac{\Gamma_{\rm cav}}{\Gamma_{\rm free}}} \ . \tag{22.11}$$

In a cavity, spontaneous emission is strongly modified [376, 377, 378]. An atom interacting with a cavity will spontaneously emit into the cavity mode at an increased (reduced) rate, depending on whether the cavity is resonant or out of resonance. The natural width due to spontaneous decay and the line shift are calculated by integration over the coupling force between the atom and every available field mode [see (22.9)],

$$\boxed{\begin{aligned} \Gamma &= \iint \frac{|\mathbf{d}_{eg}\cdot\vec{\epsilon}_{\mathbf{k}}|^2|\vec{\mathcal{E}}_{\mathbf{k}}|^2}{\hbar^2} 2\pi\delta(\omega_0-\omega_{\mathbf{k}})\rho(\omega_{\mathbf{k}},\mathbf{k})d\Omega_{\mathbf{k}}d\omega_{\mathbf{k}} \\ \Delta\omega &= \sum_i \iint \frac{|\mathbf{d}_{ei}\cdot\vec{\epsilon}_{\mathbf{k}}|^2|\vec{\mathcal{E}}_{\mathbf{k}}|^2}{\hbar^2} \frac{1}{\omega_{ei}-\omega_{\mathbf{k}}} \rho(\omega_{\mathbf{k}},\mathbf{k})d\Omega_{\mathbf{k}}d\omega_{\mathbf{k}} \end{aligned}} \ , \tag{22.12}$$

with the field amplitude per photon, $|\vec{\mathcal{E}}_{\mathbf{k}}| = \sqrt{\hbar\omega_{\mathbf{k}}/2\varepsilon_0 V}$, derived in (15.87), and the index i running over all internal atomic states. These formulas are simply applications of second-order perturbation theory (5.16) and of Fermi's golden rule (5.111) for transition probabilities both weighed with dynamic structure factor of the cavity.

We use the number of modes per unit of frequency range and per unit of solid angle in free space derived in (15.95) (ρ/V is the density of states),

$$\rho_{\rm free}(\omega_{\mathbf{k}}) = \frac{V\omega_{\mathbf{k}}^2}{(2\pi)^3 c^3} \ . \tag{22.13}$$

Setting $\theta_{\mathbf{k}}$ as the angle between the atomic dipole moment and the cavity axis (which is not in place, yet, as we are still in free space), $\mathbf{d}\cdot\hat{\epsilon}_{\mathbf{k}} = d\cos\alpha_{\mathbf{k}} = d\cos(90^\circ-\theta_{\mathbf{k}}) = d\sin\theta_{\mathbf{k}}$,

$$\begin{aligned} \Gamma_{\rm free} &= \int \frac{d^2\sin^2\theta_{\mathbf{k}}}{\hbar^2}\frac{\hbar\omega_0}{2\varepsilon_0 V} 2\pi \frac{V\omega_0^2}{(2\pi)^3c^3}\sin\theta d\theta d\phi \\ &= \frac{d^2k^3}{4\pi\varepsilon_0\hbar}\int_0^\pi \sin^3\theta d\theta = \frac{d^2k^3}{3\pi\varepsilon_0\hbar} \ . \end{aligned} \tag{22.14}$$

Since the integration covers the whole solid angle of space 4π and the free space is isotropic, there is no preferred orientation, and we can perform the integration setting $\theta \equiv \theta_{\mathbf{k}}$. The result coincides with earlier calculations (16.46).

Now, we put the cavity in place, but tune it off resonance, such that no photons can be emitted into the solid angle covered by the cavity. That is, in the presence of the cavity, the solid angle of free space into which photons can be emitted is restricted. We repeat the calculation (22.14), but now we are not free to choose the axis of the coordinate system arbitrarily. Instead, we we assume that $\theta_{\mathbf{k}}(\theta,\phi) \simeq const$ over the

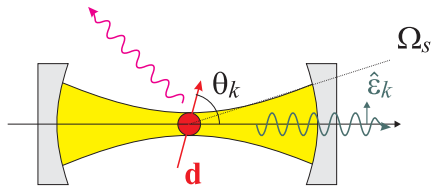

Figure 22.1: Illustration of cooperativity in a cavity. An excited atom can decay by emitting light into a cavity mode or into free space. Note that the cavity is not pumped directly by an incident laser beam.

small solid angle covered by the cavity, $\theta, \phi \in \Omega_{\rm cav}$,

$$\begin{aligned}\Gamma_{{\rm free}\notin{\rm cav}} &= \int_{\hat{\mathbf{e}}_k\notin{\rm cav}} \frac{d^2\sin^2\theta_k}{\hbar^2}\frac{\hbar\omega_0}{2\varepsilon_0 V}2\pi\frac{V\omega_0^2}{(2\pi)^3c^3}\sin\theta d\theta d\phi \\ &\simeq \Gamma_{\rm free} - \frac{d^2k^3\sin^2\theta_{\mathbf{k}}}{8\pi^2\varepsilon_0\hbar}\int_{\hat{\mathbf{e}}_k\in{\rm cav}}\sin\theta d\theta d\phi = \Gamma_{\rm free}\left(1-\frac{3}{8\pi}\Omega_{\rm cav}\sin^2\theta_{\mathbf{k}}\right) .\end{aligned} \tag{22.15}$$

Finally, we study the situation, when the cavity is in place but now tuned on resonance. Then the density of states in the photon emission directions $\mathbf{k} \in$ cavity is modulated by the Airy function (15.96),

$$\rho_{\rm cav}(\omega_{\mathbf{k}},\mathbf{k}) = \rho_{\rm free}(\omega_{\mathbf{k}})\mathfrak{L}(\omega_{\mathbf{k}}) . \tag{22.16}$$

That is, photons can be emitted into the cavity mode with increased probability. Once again we repeat the calculation (22.14), but now inserting the density of states of the cavity,

$$\begin{aligned}\Gamma_{\rm cav} &= \int_{\hat{\mathbf{e}}_k\in{\rm cav}} \frac{d^2\sin^2\theta_{\mathbf{k}}}{\hbar^2}\frac{\hbar\omega_0}{2\varepsilon_0 V}2\pi\mathfrak{L}(\omega_0)\frac{V\omega_0^2}{(2\pi)^3c^3}\sin\theta d\theta d\phi \\ &\simeq \frac{d^2k^3\sin^2\theta_{\mathbf{k}}}{8\pi^2\varepsilon_0\hbar}\mathfrak{L}(\omega_0)\int_{\hat{\mathbf{e}}_k\in{\rm cav}}\sin\theta d\theta d\phi = \Gamma_{\rm free}\mathfrak{L}(\omega_0)\frac{3}{8\pi}\Omega_{\rm cav}\sin^2\theta_{\mathbf{k}} ,\end{aligned} \tag{22.17}$$

where, in the last step, we substituted the free space decay rate (22.14). An analogous calculation for the *cooperative Lamb shift* $\Delta\omega_{\rm cav}$ is left to the Exc. 22.1.11.1:

$$\boxed{\begin{aligned}\Gamma_{\rm cav} &= \Gamma_{\rm free}\tfrac{3}{8\pi}\Omega_{\rm cav}\sin^2\theta_{\mathbf{k}}\mathfrak{L}(\omega_0) \\ \Delta\omega_{\rm cav} &= \Gamma_{\rm free}\tfrac{3}{32\pi}\Omega_{\rm cav}\sin^2\theta_{\mathbf{k}}\tfrac{\mathfrak{L}'(\omega_0)}{\mathfrak{L}(\omega_0)}2\delta_{\rm fsr}\end{aligned}} . \tag{22.18}$$

The quantities $\Gamma_{\rm cav}$ and $\Gamma_{free\in cav}$ are scattering rates into complementary solid angles. Now, the total spontaneous emission rate, which determines the lifetime of the radiating excited state and the spectral width of the transition is simply the sum of the partial scattering rates,

$$\begin{aligned}\Gamma &= \Gamma_{free\notin cav} + \Gamma_{\rm cav} \\ &= \Gamma_{\rm free}\left(1-\tfrac{3}{8\pi}\Omega_{\rm cav}\right)\sin^2\theta_{\mathbf{k}} + \Gamma_{\rm free}\mathfrak{L}(\omega_0)\tfrac{3}{8\pi}\Omega_{\rm cav}\sin^2\theta_{\mathbf{k}} \\ &= \Gamma_{\rm free}\left[1+(\mathfrak{L}(\omega_0)-1)\tfrac{3}{8\pi}\Omega_{\rm cav}\right]\sin^2\theta_{\mathbf{k}} .\end{aligned} \tag{22.19}$$

Assuming for simplicity, $\theta_{\mathbf{k}} = \pi/2$, we find the extremes of the spontaneous emission rate, Γ_{enh} and Γ_{inh}, when the cavity is on or off resonance. With a resonant high finesse cavity the emission is obtained via $kL \to 0$,

$$\Gamma_{enh} = \Gamma_{\rm free}\left[1+\left(\sqrt{1+\left(\tfrac{2F}{\pi}\right)^2}-1\right)\tfrac{3}{8\pi}\Omega_{\rm cav}\right] \simeq \Gamma_{\rm free}\left(1+\tfrac{3}{4\pi^2}F\Omega_{\rm cav}\right) \ . \tag{22.20}$$

assuming high finesse, $F \gg 1$. With a non-resonant cavity, the emission is obtained via $kL \to \pi/2$,

$$\Gamma_{inh} = \Gamma_{\rm free}\left[1+\left(\frac{1}{\sqrt{1+\left(\tfrac{2F}{\pi}\right)^2}}-1\right)\tfrac{3}{8\pi}\Omega_{\rm cav}\right] \simeq \Gamma_{\rm free}\left(1-\tfrac{3}{8\pi}\Omega_{\rm cav}\right) \ . \tag{22.21}$$

For a small solid angle, we can expect a big increase of the scattering into the cavity, but without noticeable inhibition of the total decay, $\Gamma_{inh} \simeq \Gamma_{\rm free}$.

If the atoms are saturated by an incident laser, they scatter light into the cavity at a rate (apart from a factor $\frac{1}{2}$),

$$\Gamma_{\rm cav} = \Gamma_{\rm free}\mathfrak{L}(\omega_0)\tfrac{3}{8\pi}\Omega_{\rm cav} \ . \tag{22.22}$$

Without cavity the emission into the same solid angle is obtained via $F \to 0$,

$$\Gamma_{free\in cav} = \Gamma_{\rm free}\tfrac{3}{8\pi}\Omega_{\rm cav} \ . \tag{22.23}$$

The scattering will fill the cavity with photons, until the leakage equalizes the pumping. When the balance is reached, $\Gamma_{\rm cav}$ will also be the rate at which photons are emitted by the cavity mode. We calculate an example in Exc. 22.1.11.2.

22.1.1.3 Purcell factor for confocal and concentric cavities

Using the solid angle of a confocal cavity (15.102), the cooperativity parameter is,

$$\Upsilon \simeq \frac{3F}{4\pi^2}\Omega_{\rm cav} = \frac{3F}{4\pi^2}\frac{8\pi b^2}{L^2} \ , \tag{22.24}$$

where b is the clear aperture of the cavity mirrors. That is,

$$\boxed{\Upsilon = \frac{F}{\pi}\frac{6b^2}{L^2} \ .} \tag{22.25}$$

22.1.1.4 Purcell factor for the TEM$_{00}$ cavity mode

With the solid angle (15.108) calculated for a this TEM$_{00}$ cavity mode we calculate the *cooperativity parameter*,

$$\begin{aligned}\Upsilon \equiv \frac{\Gamma_{\rm cav}}{\Gamma_{\rm free}} &= \mathfrak{L}(\omega_0)\tfrac{3}{8\pi}\Omega_{\rm cav} = \sqrt{1+\left(\frac{2F}{\pi}\right)^2}\,\frac{3}{8\pi}\Omega_{\rm cav} \\ &\simeq \frac{3F}{4\pi^2}\Omega_{\rm cav} = \frac{\Gamma_{enh}}{\Gamma_{\rm free}} - 1 = \frac{3F}{4\pi^2}\frac{8\pi}{k^2w_0^2} \ ,\end{aligned} \tag{22.26}$$

that is,

$$\boxed{\Upsilon = \frac{F}{\pi}\frac{6}{k^2 w_0^2}} \,, \tag{22.27}$$

which is also called *Purcell factor*.

Now, exploiting the relationships (15.108), (22.27), and (15.81),

$$\Omega_{\rm cav} = \frac{8\pi}{k^2 w_0^2} \quad , \quad \Upsilon = \frac{F}{\pi}\frac{6}{k^2 w_0^2} \quad , \quad \frac{F}{\pi} = \frac{\delta_{\rm fsr}}{\kappa} \,, \tag{22.28}$$

and defining a new quantity,

$$g^2 = \tfrac{1}{4}\Upsilon\kappa\Gamma_{\rm free} \,, \tag{22.29}$$

which we will call the atom-field coupling strength, we may rewrite the prefactor $\Gamma_{\rm free}\frac{3}{8\pi}\Omega_{\rm cav}$ for the case of Gaussian cavity modes,

$$\Gamma_{\rm free}\frac{3}{8\pi}\Omega_{\rm cav} = \frac{g^2}{2\delta_{\rm fsr}} \,. \tag{22.30}$$

Close to a cavity resonance, $kL = \omega/2\delta_{\rm fsr} = (\omega_c + \Delta_c)/2\delta_{\rm fsr} = 2\pi N + \Delta_c/2\delta_{\rm fsr}$, the sine appearing in the Airy function (15.96) may be expanded $\sin kL = \sin \Delta_c/2\delta_{\rm fsr} \simeq \Delta_c/2\delta_{\rm fsr}$. Furthermore, assuming a high finesse, $F \gg 1$, the Airy function simplifies to,

$$\mathfrak{L}(\omega_0) = \frac{\sqrt{1+(2F/\pi)^2}}{1+(2F/\pi)^2\sin^2\frac{\omega}{2\delta_{\rm fsr}}} \simeq \frac{2F/\pi}{1+\Delta_{\rm a}^2/\kappa^2} \,. \tag{22.31}$$

Inserting this into the formulae (22.18), where we set $\theta_{\mathbf{k}} = \frac{\pi}{2}$,

$$\boxed{\begin{array}{rcl} \Gamma_{\rm cav} & \simeq & \frac{g^2\kappa}{\Delta_{\rm c}^2+\kappa^2} \\ \Delta\omega_{\rm cav} & \simeq & \frac{-2g^2\Delta_{\rm c}}{\Delta_{\rm c}^2+\kappa^2} \end{array}} \,. \tag{22.32}$$

Obviously, the atom-field coupling strength g plays a central role in the modification of the emission spectra of atoms interaction with cavities. Therefore, we will have to study this quantity more deeply in the next sections.

Example 127 (*Cooperativity of non-degenerate and confocal cavities*): For example, for a non-degenerate linear cavity with finesse $F = 110000$ and waist $w_0 = 50\,\mu\text{m}$ at 689 nm, the cooperativity is relatively weak, $\Upsilon \simeq 1$. Still, at this cooperativity, half of the spontaneously emitted photons go into a tiny solid angle represented by the cavity. Confocal or concentric cavities may present more favorable geometries [376, 377, 378]. With $N_0 = 10^4$ saturated strontium atoms, the light power scattered into the cavity is $P_j = 20\,\text{fW}$. Estimation the cavity transmission by $T \simeq \pi/F$, we expect that a number of $T\frac{P_{\rm cav}}{\hbar\omega} = 10^7\,\text{s}^{-1}$ photons can be detected by a photodetector recording the photon number leaking out of the cavity.

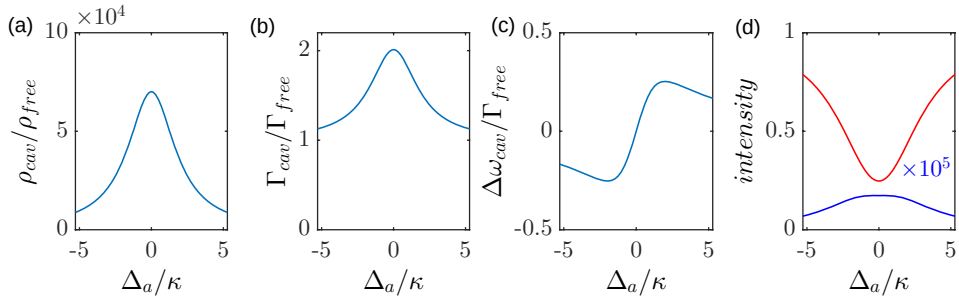

Figure 22.2: (code) Spontaneous emission on the strontium atom cooling transition ($\lambda = 689\,\mathrm{nm}$, $\Gamma = (2\pi)\ 7.6\,\mathrm{kHz}$) in a $L = 3.6\,\mathrm{cm}$ long cavity with $F = 110000$ and $w_0 = 50\,\mu\mathrm{m}$. (a) Cooperativity $\mathfrak{L}(\omega)$ from Eq. (15.96) as a function of the detuning of the cavity. (b) Linewidth Γ_{cav} from (22.18)(ii) and (c) frequency shift of the strontium transition from Eq. (22.18)(ii). (d) Spontaneous emission into the cavity (blue) and into the open space (red).

22.1.2 Characterization of the atom-field coupling

In Sec. 15.3.1 we started introducing a number of quantities characterizing empty cavities. We will now pursue this task including their interaction with atoms. In particular, we will introduce three important quantities allowing us to measure the degree of quantization of the system: the cooperativity Υ, the saturation parameter s, and the cavity resolution r.

22.1.2.1 The atomic dipole moment

As usual, the interaction strength of an atom with a light field is measured by the atom-field coupling constant, which is precisely HALF the single photon Rabi frequency. Using relationships derived in Sec. 15.3.1 and the expression (16.41) for the atomic dipole moment d, we find,

$$g \equiv \frac{d\mathcal{E}_1(0)}{\hbar} = \sqrt{\frac{3\pi\Gamma\omega}{2k^3 V_{\mathrm{m}}}} = \sqrt{\frac{6\Gamma\delta_{\mathrm{fsr}}}{k^2 w^2}}\ , \tag{22.33}$$

where $\mathcal{E}_1(0)$ the electric field produced by a single photon inside the cavity mode volume $V_{\mathrm{m}} = \frac{\pi}{2} L w_0^2$ calculated in (15.84), δ_{fsr} the free spectral range calculated in (15.80), and Γ is the spontaneous decay rate. See also (watch talk).

22.1.2.2 Single atom reflection coefficient

Based on the complex atomic polarizability ,

$$\frac{\alpha_{\mathrm{pol}}}{\varepsilon_0} \simeq \frac{6\pi}{k^3}\frac{-1}{\imath + 2\Delta/\Gamma}\ , \tag{22.34}$$

the *single atom reflection coefficient* is defined as,

$$\beta_\Delta = \frac{k}{\pi w^2}\frac{\alpha_{\mathrm{pol}}}{\varepsilon_0} = \frac{6}{k^2 w^2}\frac{-1}{\imath + 2\Delta/\Gamma}\ , \tag{22.35}$$

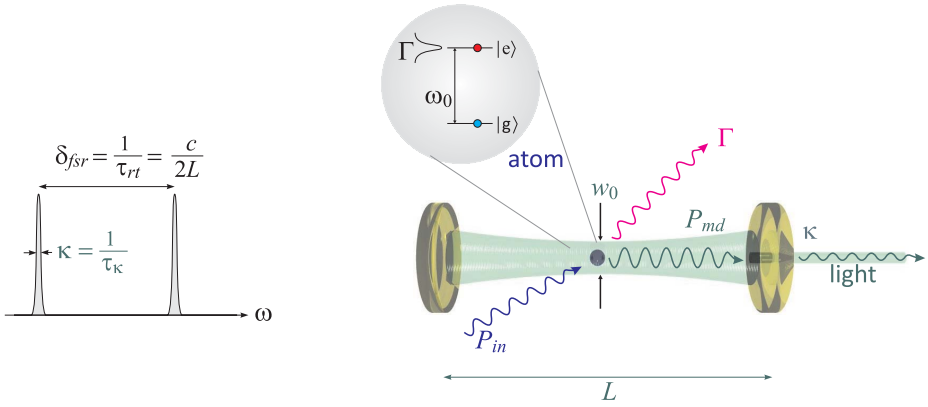

Figure 22.3: Relevant parameters for an atom interacting with a cavity.

where $\Delta_a = \omega - \omega_0$. The resonant reflection coefficient can be interpreted in terms of a phase shift that depends on the matching between the resonant optical cross-section of the atom, $\sigma_0 = 3\lambda^2/2\pi$, and the cross section of the optical mode,

$$-\imath\beta_0 = \frac{\sigma_0}{\pi w^2} = \frac{6}{k^2 w^2} = \frac{2g^2}{\delta_{\rm fsr}\Gamma} \ . \tag{22.36}$$

The total reflection coefficient multiplied with the free spectral range of the cavity,

$$\delta_{\rm fsr}\beta_\Delta = \frac{6\delta_{\rm fsr}}{k^2 w^2}\frac{-1}{\imath + 2\Delta/\Gamma} = g^2\frac{\Delta - \imath\Gamma/2}{\Delta^2 + \Gamma^2/4} = U_0 - \imath\gamma_0 = U_\gamma \ , \tag{22.37}$$

is just the *single-photon light-shift* combined with the single-photon Rayleigh scattering rate.

Using the dipole moment $d = \sqrt{3\pi\varepsilon_0\hbar\Gamma/k^3}$ and defining the electric field amplitude per photon $\mathcal{E}_1$ by the photon number n, the power P, and the intensity $I = \varepsilon_0 c n_{\rm ph}\mathcal{E}_1^2 = 2P/\pi w^2$, we calculate for the single-photon Rabi frequency (or atom-field coupling strength),

$$g = \frac{d\mathcal{E}_1}{\hbar} = \sqrt{\frac{1}{\hbar^2}\frac{3\pi\varepsilon_0\hbar\Gamma}{k^3}\frac{I}{\varepsilon_0 c n_{\rm ph}}} = \sqrt{\frac{1}{\hbar^2}\frac{3\pi\varepsilon_0\hbar\Gamma}{k^3}\frac{1}{\varepsilon_0 c n_{\rm ph}}\frac{2P}{\pi w^2}} = \sqrt{\frac{6}{k^2 w^2}\Gamma\frac{P}{n_{\rm ph}\hbar\omega}} \ . \tag{22.38}$$

Far from resonance, the single-photon light shift (or atom-atom coupling strength) is,

$$U_0 = \frac{g^2}{|\Delta_{\rm a}|} = \frac{6}{k^2 w^2}\frac{\Gamma}{|\Delta_{\rm a}|}\frac{P}{n_{\rm ph}\hbar\omega} = \beta_\Delta\frac{P}{n_{\rm ph}\hbar\omega} \ , \tag{22.39}$$

and the single-photon Rayleigh scattering rate,

$$\gamma_0 = \frac{g^2\Gamma}{\Delta_{\rm a}^2} = \frac{6}{k^2 w^2}\frac{\Gamma^2}{\Delta_{\rm a}^2}\frac{P}{n_{\rm ph}\hbar\omega} \ . \tag{22.40}$$

In a cavity the flux $\delta_{\rm fsr} = P/n_{\rm ph}\hbar\omega$ is just the photon round trip rate (or free spectral range). $1/\delta_{\rm fsr}$ is the time a photon interacts with an atom. In free space,

this does not make sense to me, because I don't know how define the mode volume. I can however consider the interaction of a photon with an extended sample of length L. In this case, a photon interacts with the sample for the time L/c, so that,

$$U_0 = \frac{g^2}{|\Delta_\mathrm{a}|} = \frac{6}{k^2 w^2}\frac{\Gamma}{|\Delta_\mathrm{a}|}\frac{c}{L} = \beta_\Delta \frac{c}{L} \ , \tag{22.41}$$

and

$$\gamma_0 = \frac{g^2\Gamma}{\Delta_\mathrm{a}^2} = \frac{6}{k^2 w^2}\frac{\Gamma^2}{\Delta_\mathrm{a}^2}\frac{c}{L} \ . \tag{22.42}$$

This means, we can use the CARL equations derived for a ring cavity also in free space by just substituting $\kappa = \delta_\mathrm{fsr} = c/L$, where L is now not the cavity but the sample length.

22.1.2.3 Collective cooperativity

The frequency shift accumulated during a round trip in the cavity, $\delta_\mathrm{fsr}\beta_0$, becomes noticeable, when it exceeds the linewidth of the cavity κ. From this condition, we obtain the optical depth for a single passage through the atomic sample multiplied by the finesse of the cavity, which is precisely the *cooperativity parameter*,

$$\boxed{\Upsilon \equiv \frac{\delta_\mathrm{fsr}\beta_0}{\kappa} = \frac{F}{\pi}\frac{6}{k^2 w^2} = \frac{4g^2}{\kappa\Gamma}} \ . \tag{22.43}$$

The sensitivity to the atom number can be measured in terms of a *critical atom number* N_crt, which the system can resolve,

$$N_\mathrm{crt} = \frac{4\pi}{F\beta_0} = \frac{1}{\Upsilon} \ . \tag{22.44}$$

While the strong coupling regime of the CQED requires $\Upsilon > 1$ with a single atom, collective cooperativity is reached with N atoms if $N\Upsilon > 1$ [117, 170]. In this case, the atomic ensemble couples to the mode like a single 'super-atom', the coupling force being magnified to $g_N = g_1\sqrt{N}$. We have already obtained this result within the Jaynes-Cummings model for two indistinguishable atoms coupling to the same light mode and forming a *Dicke state* (see Sec. 23.1.1).

22.1.2.4 Optical density

Lambert-Beer's law relates the amplitude of the field transmitted to the incident [see also Eq. (26.133)],

$$\frac{\mathcal{E}_\mathrm{t}}{\mathcal{E}_0} = \exp\left[\imath\sigma(\Delta_\mathrm{a})\left(\frac{\imath}{2} - \frac{\Delta_\mathrm{a}}{\Gamma}\right)\int_{-\infty}^{\infty} n(\mathbf{r})dz\right] = e^{-b/2}e^{\imath\varphi} \ . \tag{22.45}$$

I.e. the field is shifted by an amount φ and absorbed by an amount b. The exponent (called optical density) can be rewritten, if we assume a number of N atoms homogeneously distributed over a cylinder with length L and radius $\bar{r} = w_0$. Using with

(1.72),

$$b = OD(\Delta_{\rm a}) = -2\imath\sigma(\Delta_{\rm a})\left(\frac{\imath}{2} - \frac{\Delta_{\rm a}}{\Gamma}\right)\int_{-\infty}^{\infty} n(\mathbf{r})dz \tag{22.46}$$
$$= -\imath\frac{g_2}{g_1}\frac{\lambda^2}{2\pi}\frac{\frac{1}{2}\Gamma^2}{\Delta_{\rm a}^2 + \frac{1}{4}\Gamma^2}\left(\frac{\imath}{2} - \frac{\Delta_a}{\Gamma}\right)\int_{-\infty}^{\infty}\frac{N}{\frac{\pi}{2}w_0^2 L}dz = \frac{12N}{\pi k^2 w_0^2}\frac{1}{1 - 2\imath\Delta_{\rm a}/\Gamma}\ .$$

Hence, the optical density is nothing else than the collective cooperativity divided by the finesse,

$$\boxed{OD(0) = \frac{12N}{\pi k^2 w_0^2} = \frac{4g_N^2}{\pi\delta_{\rm fsr}\Gamma} = \frac{\kappa\Upsilon_N}{\pi\delta_{\rm fsr}} = \frac{\Upsilon_N}{F}}\ . \tag{22.47}$$

22.1.2.5 Saturation parameter in cavities

The *saturation parameter* for a single photon is given by,

$$\boxed{s = \frac{2\Omega_1^2}{\Gamma^2} = \frac{8g^2}{\Gamma^2}}\ , \tag{22.48}$$

where Ω_1 is the single photon Rabi frequency. Therefore, the number of photons needed to saturate an atomic transition is,

$$n_{\rm sat} = \frac{1}{s}\ . \tag{22.49}$$

We see, that there is a *symmetry* between Υ and s, that is, between $N_{\rm crt}$ and $n_{\rm sat}$. The regime $N\Upsilon > 1$ denotes the collective behavior of N atoms in the same way as $n_{\rm sat} > 1$ indicates saturation. While Υ depends only on the phase matching between the atomic antenna and the cavity, s also depends on the cavity mode volume and the natural decay rate.

22.1.2.6 Cavity resolution parameter

Comparing the photonic recoil, which is given by,

$$\omega_{\rm rec} = \frac{\hbar k^2}{2m}\ , \tag{22.50}$$

with the resolution power of a cavity κ, we can define the *resolution parameter*,

$$\boxed{r \equiv \frac{\omega_{\rm rec}}{\kappa}}\ . \tag{22.51}$$

With the three parameters defined in Eqs. (22.43), (22.48), and (22.51) we are able to measure the degree of quantization of the degrees of freedom involved in the matter-light interaction in a cavity. The cooperativity Υ measures the resolvability of single atoms in the atomic cloud, which depends on the phase matching between the atomic antenna (i.e. its optical cross section) and the focus of the optical mode. The saturation parameter s measures the resolvability of single photons in the cavity.

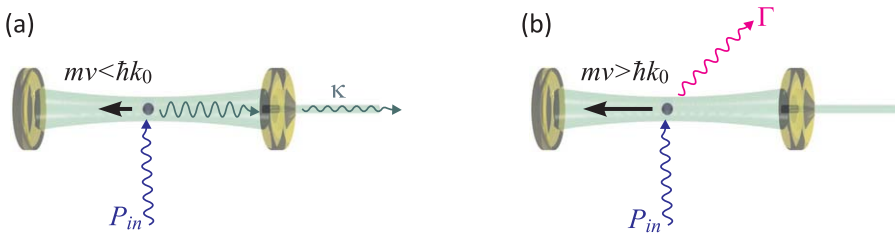

Figure 22.4: (a) If the recoil-induced Doppler shift of the atom moving along the cavity axis is smaller than the cavity linewidth, the light is preferentially scattered into the cavity mode. (b) Else it is scattered outside the mode.

And the cavity resolution parameter r measures the resolvability of the Doppler-shift due to the atomic center-of-mass motion caused by the absorption of a single photon. If one wants to operate in an environment, where all degrees of freedom involved in the atom-light interactions are fully quantized, the atoms need to be placed into a cavity whose characteristic quantities are all large, $\Upsilon, s, r \gg 1$.

In Exc. 22.1.11.3 we compare the coupling force and other characteristic parameters for various combinations of atomic species and optical cavities. In Exc. 22.1.11.4 we calculate the number of photons in a cavity pumped in or out of resonance.

22.1.3 Jaynes-Cummings model for one or two radiation modes

To study the dynamics of the coupled atom-cavity system, we consider the Jaynes-Cummings Hamiltonian (17.18) (or (22.5)), for a more concrete situation. That is, we allow for optical pumping and decay of internal states with the rates R and Γ, respectively, and we allow for inhomogeneous (however, mostly one-dimensional) mode functions $g(z) = ge^{\imath kz}$. On the other hand, we stick to a single atom (or N uncorrelated atoms), we disregard polarization and multi-mode excitation, and we will explicitly consider and compare two well distinct cases, linear and ring cavities.

22.1.3.1 Linear and ring cavities

From the Heisenberg equations with the Hamiltonian (22.5),

$$\boxed{\begin{aligned} \hat{H}_{\rm atom} &= -\Delta_{\rm a}\hat{\sigma}^{+}\hat{\sigma}^{-} \\ \hat{H}_{\rm cav} &= -\Delta_{\rm c}\hat{a}^{\dagger}\hat{a} \\ \hat{H}_{\rm atom:cav} &= g(z)\hat{a}^{\dagger}\hat{\sigma}^{-} + h.c. \\ \hat{H}_{\rm laser:cav} &= -\imath\eta(\hat{a} - \hat{a}^{\dagger}) \end{aligned}} \,. \tag{22.52}$$

The Hamiltonian for a single motionless atom interacting with two cavity modes $|+\rangle$ and $|-\rangle$ (we may, for instance, consider the counterpropagating modes of a ring

cavity) reads,

$$\boxed{\begin{array}{rcl} \hat{H}_{\rm atom} &=& -\Delta_{\rm a}\hat{\sigma}^+\hat{\sigma}^- \\ \hat{H}_{\rm cav} &=& -\Delta_+\hat{a}_+^\dagger\hat{a}_+ - \Delta_-\hat{a}_-^\dagger\hat{a}_- \\ \hat{H}_{\rm atom:cav} &=& g(z)\hat{a}_+^\dagger\hat{\sigma}^- + h.c. + g(z)\hat{a}_-^\dagger\hat{\sigma}^- + h.c. \\ \hat{H}_{\rm laser:cav} &=& -\imath\eta_+(\hat{a}_+ - \hat{a}_+^\dagger) - \imath\eta_-(\hat{a}_- - \hat{a}_-^\dagger) \end{array}} \ . \tag{22.53}$$

22.1.3.2 Time-evolution of an atom in a ring cavity

The coupling of the atom to the cavities $g(z)$ will, in general, depend on the atomic position. For simplicity let us, however, consider uniform and identical coupling, $g_+(z) = g_-(z) = g$, and furthermore assume that both cavities be on resonance, $\Delta_+ = \Delta_- = 0$. Finally, neglecting spontaneous emission and pumping, the total number of photons is conserved. With $\Delta_{\rm a} = \omega - \omega_{\rm a}$ we get,

$$\hat{H} = \omega\hat{a}_+^\dagger\hat{a}_+ + \omega\hat{a}_-^\dagger\hat{a}_- + \omega_0(\hat{\sigma}^+\hat{\sigma} - \tfrac{1}{2}) + g\hat{a}_+^\dagger\hat{\sigma}^- + g\hat{a}_-^\dagger\hat{\sigma}^- + h.c. \ . \tag{22.54}$$

Expanding the operators $\hat{a}_\pm = \sum_{n_\pm} |n_\pm - 1\rangle\langle n_\pm|$ and $\hat{\sigma}^- = |1\rangle\langle 2|$ we can, expand the state of the system like,

$$|\psi(t)\rangle = \sum_{k=0}^{n} c_{j,n_+,n_-}|j, n_+, n_-\rangle \ . \tag{22.55}$$

Alternatively, in analogy with Sec. 17.2.2, we may organize the Hilbert space in orthogonal subspaces, $\hat{H} = \bigoplus_n \hat{H}_n$, each one having $N \equiv j + n_+ + n_-$ energy units distributed over the atomic excitation state $j = 0, 1$ and the numbers of photons $n_\pm$ in each mode. Hence, every subspace is of dimension $2N + 1$. In this dressed states picture, introducing the photon imbalance $D \equiv n_+ - n_- = -N, ..., N$, we may expand the coupled state like,

$$\boxed{|\psi(t)\rangle = \sum_{N=0}^{\infty}\sum_{D=-N}^{N} \tilde{c}_{N,D}|N, D\rangle} \ . \tag{22.56}$$

Obviously, the set of three quantum numbers $\{j, n_+, n_-\}$ is equivalent to the set of two quantum numbers $\{N, D\}$ and can be recovered by,

$$j = 1 + (-1)^{N+D-1} \quad , \quad n_\pm = \tfrac{1}{2}(N \pm D - j) \ . \tag{22.57}$$

Hence, states with odd $N+D$ are excited atomic states, and states with even $N+D$ are ground states. We may now write down the Hamiltonian,

$$\hat{H}_N = (N-\tfrac{1}{2})\omega\mathbb{I}_{2N+1} + \tag{22.58}$$
$$+\frac{1}{2}\begin{pmatrix} \Delta & g_+\sqrt{N} & & & & & & \\ g_+\sqrt{N} & -\Delta & g_-\sqrt{1} & & & & & \\ & g_-\sqrt{1} & \Delta & g_+\sqrt{N-1} & & & & \\ & & g_+\sqrt{N-1} & \ddots & g_-\sqrt{N-1} & & & \\ & & & g_-\sqrt{N-1} & \Delta & g_+\sqrt{1} & & \\ & & & & g_+\sqrt{1} & -\Delta & g_-\sqrt{N} & \\ & & & & & g_-\sqrt{N} & \Delta & \end{pmatrix}.$$

The subscripts of the coupling constants $g_+ = g_-$ are there only to clarify to which mode the photon belongs. Very far from resonance, where the interaction is dispersive, we may treat the light field perturbatively, as shown in (17.40),

$$\hat{H}_N = (N-\tfrac{1}{2})\omega\mathbb{I}_{2N+1} + \tag{22.59}$$
$$+\begin{pmatrix} \frac{\Delta}{2}+\frac{Ng_+^2+0g_-^2}{4\Delta} & & & & \\ & -\frac{\Delta}{2}-\frac{Ng_+^2+1g_-^2}{4\Delta} & & & \\ & & \frac{\Delta}{2}+\frac{(N-1)g_+^2+1g_-^2}{4\Delta} & & \\ & & & -\frac{\Delta}{2}-\frac{(N-1)g_+^2+2g_-^2}{4\Delta} & \\ & & & & \ddots \end{pmatrix},$$

or with $g_+ = g_-$,

$$(\hat{H}_N)_{DD'} = \left[\left(N+\frac{1}{2}\right)\omega - \frac{1}{2}\frac{g^2}{4\Delta} + (-1)^{N+D}\left(\frac{\Delta}{2}+\left(N+\frac{1}{2}\right)\frac{g^2}{4\Delta}\right)\right]\delta_{DD'}\,. \tag{22.60}$$

If only the upper level of the atom interacts with both light fields, all terms with negative light shift disappear,

$$(\hat{H}_N)_{DD'} = \left[\left(N+\frac{1}{2}\right)\omega + \frac{1}{2}\frac{Ng^2}{4\Delta} + (-1)^{N+D}\left(\frac{\Delta}{2}+\frac{N}{2}\frac{g^2}{4\Delta}\right)\right]\delta_{DD'}\,. \tag{22.61}$$

As shown in Sec. 17.2.2, we propagate the evolution of the coupled state via $|\psi(t)\rangle = e^{-\imath\hat{H}t}|\psi(0)\rangle$. As the initial condition we may choose the atom to be in its ground state and the two field modes in uncorrelated Glauber states,

$$c_{j,n_+,n_-} = \langle j,n_+,n_-|\psi\rangle = e^{-|\alpha_+|^2/2-|\alpha_-|^2/2}\frac{\alpha_+^{n_+}\alpha_-^{n_-}}{\sqrt{n_+!n_-!}}\delta_{j,0} \tag{22.62}$$
$$= \tilde{c}_{N,\delta} = e^{-|\alpha_+|^2/2-|\alpha_-|^2/2}\frac{\alpha_+^{(N+\delta-j)/2}\alpha_-^{(N-\delta-j)/2}}{\sqrt{(\frac{N+\delta-j}{2})!(\frac{N-\delta-j}{2})!}}\delta_{1+(-1)^{N+\delta-1},0}\,.$$

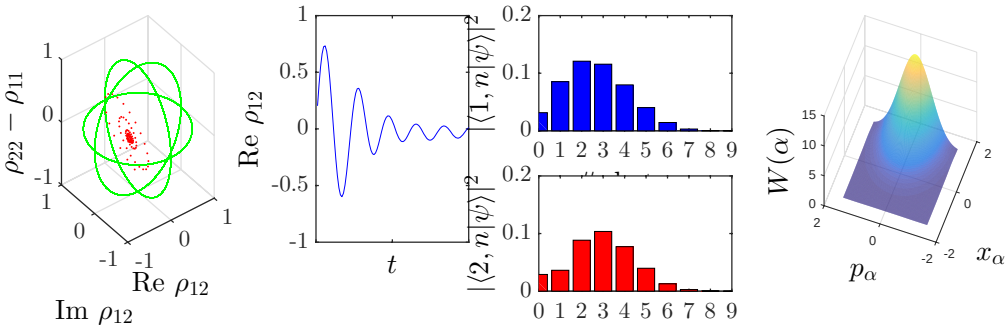

Figure 22.5: (code) Evolution of the coupled atom-ring cavity system. (a) Bloch vector, (b) photon distributions, and (c) Husimi function.

The observables of interest are the atomic Bloch vector (16.126), whose components are obtained from,

$$\rho_{ij} = \langle i|\mathrm{Tr}_{n_+,n_-}\hat{\rho}|j\rangle = \sum_{n_+,n_-}\langle i,n_+,n_-|\psi\rangle\langle\psi|j,n_+,n_-\rangle \tag{22.63}$$
$$= \sum_{n_+,n_-} c^*_{i,n_+,n_-}c_{j,n_+,n_-} = \sum_{n_+,n_-}\tilde{c}^*_{n_++n_-+i,n_+-n_-}\tilde{c}_{n_++n_-+j,n_+-n_-} \ ,$$

the photon statistics in each mode,

$$p_{n_+} = \langle n_+|\mathrm{Tr}_{i,n_-}\hat{\rho}|n_+\rangle = \sum_{j,n_-}\langle j,n_+,n_-|\psi\rangle\langle\psi|j,n_+,n_-\rangle \tag{22.64}$$
$$= \sum_{j,n_-}|c_{j,n_+,n_-}|^2 = \sum_{j,n_-}|\tilde{c}_{n_++n_-+j,n_+-n_-}|^2 \ ,$$

and analogously for p_{n_-}, and the field distribution functions, such as the Husimi function,

$$\pi Q_+(\alpha) \equiv \langle\alpha_+|\mathrm{Tr}_{\ i,n-}\hat{\rho}|\alpha_+\rangle \tag{22.65}$$
$$= e^{-|\alpha_+|^2}\sum_{n_-}\left(\left|\sum_{n_+}c_{1,n_+,n_-}\frac{\alpha^n}{\sqrt{n!}}\right|^2 + \left|\sum_{n_+}c_{2,n_+,n_-}\frac{\alpha^n}{\sqrt{n!}}\right|^2\right) \ ,$$

and analogously for $Q_-(\alpha)$, or the Wigner functions $W_\pm(\alpha)$ from the coefficients $\tilde{c}_{j,n_+,n_-}$, respectively, $\tilde{c}_{N,\delta}$, as shown in Secs. 14.3.2 and 17.2.3.

22.1.4 Normal-mode splitting in linear and ring cavities

The Jaynes-Cummings model introduced in Sec. 17.2 represents an idealized model of the interaction of a single cavity mode with a single atom. In this section we reconsider this model taking into account the facts that the coupling strength may vary in space (via the introduction of mode functions) and that the cavity may interact with a reservoir (via the introduction of couplings to pump fields and losses.

We will also study the phenomenon of *normal mode splitting*, which is one of the most direct witnesses of an ongoing atom-cavity interaction (see the vacuum Rabi splitting discussed in Exc. 17.2.5.4).

22.1.4.1 Linear cavities

The starting point is the full Jaynes-Cummings Hamiltonian within the RWA (22.52) for an atom interacting with one mode of a linear optical cavity,

$$\boxed{\hat{H}_{\rm JC} = -\Delta_{\rm a}\hat{\sigma}^+\hat{\sigma}^- - \Delta_{\rm c}\hat{a}^\dagger\hat{a} + g\sin kz(\hat{a}^\dagger\hat{\sigma}^- + \hat{a}\hat{\sigma}^+) - \imath\eta(\hat{a} - \hat{a}^\dagger)} \,. \tag{22.66}$$

For linear cavities normal mode splitting is derived in Exc. 22.1.11.5, where we compare the solution obtained by full numerical integration of the Jaynes-Cummings Hamiltonian (22.52) with an analytical approximation obtained in the weak excitation limit $g|\alpha|^2 \ll \Gamma, \Delta_{\rm a}$ [1],

$$\alpha \simeq \frac{\eta}{\kappa - \imath\Delta_{\rm c} + \frac{Ng^2}{\Gamma - \imath\Delta_{\rm a}}} = \frac{\eta}{\kappa + N\gamma_0 + \imath(NU_0 - \Delta_{\rm c})} \,. \tag{22.67}$$

The solution coincides with one obtained for a system, where the atomic degree of freedom is adiabatically eliminated atom (see Sec. 22.1.5).

22.1.4.2 Ring cavities

The starting point is the full Jaynes-Cummings Hamiltonian within the RWA (22.53) for an atom interacting with two modes of an optical cavity. For two counter-propagating modes of a ring cavity it reads,

$$\boxed{\hat{H}_{\rm JC} = -\Delta_{\rm a}\hat{\sigma}^+\hat{\sigma}^- - \sum_{\pm} \Delta_{\rm c}\hat{a}_\pm^\dagger\hat{a}_\pm + g(\hat{a}_\pm^\dagger\hat{\sigma}^- e^{\mp\imath kz} + \hat{a}_\pm\hat{\sigma}^+ e^{\pm\imath kz}) - \imath\eta_\pm(\hat{a}_\pm - \hat{a}_\pm^\dagger)} \,. \tag{22.68}$$

Note, that here, we do not treat the recoil $e^{\mp\imath kz}$ as a degree of freedom, but just as a parameter depending on the location of the atom. (We will come back to this in Chp. 25.) Decay processes can be considered in a master or in Heisenberg equations via jump operators $\hat{L}_k = \hat{\sigma}^-,\ \hat{\sigma}^+,\ \hat{a}_+, \hat{a}_-$ describing decay processes occurring, respectively, at rates $\gamma_k = 2\Gamma,\ 2R,\ 2\kappa,\ 2\kappa$.

22.1.4.3 (Anti-)Symmetric modes

Let us now introduce symmetric and anti-symmetric modes by,

$$\hat{b}_{\rm s} = \tfrac{1}{\sqrt{2}}(\hat{a}_+ e^{\imath kz} + \hat{a}_- e^{-\imath kz}) \qquad \text{and} \qquad \hat{b}_{\rm a} = \tfrac{1}{\sqrt{2}}(\hat{a}_+ e^{\imath kz} - \hat{a}_- e^{-\imath kz}) \,, \tag{22.69}$$

[1] Note that for N uncorrelated atoms, defining a bunching parameter via $b \equiv \frac{1}{N}\sum_j \sin kz_j$ and introducing the abbreviations $U_\gamma \equiv U_0 - \imath\gamma_0$ and $\Delta_\kappa \equiv \Delta_{\rm c} + \imath\kappa$, the result (22.67) can be generalized to,

$$\alpha \simeq \frac{-\imath\eta}{NbU_\gamma - \Delta_\kappa} \,.$$

that is,

$$\hat{a}_+ = \frac{\hat{b}_\mathrm{s} + \hat{b}_\mathrm{a}}{\sqrt{2}e^{\imath kz}} \qquad \text{and} \qquad \hat{a}_- = \frac{\hat{b}_\mathrm{s} - \hat{b}_\mathrm{a}}{\sqrt{2}e^{-\imath kz}} \ , \tag{22.70}$$

which satisfy the commutations rules $[\hat{b}_\mathrm{s}, \hat{b}_\mathrm{s}^\dagger] = 1 = [\hat{b}_\mathrm{a}, \hat{b}_\mathrm{a}^\dagger]$. We can then rewrite the Hamiltonian,

$$\begin{aligned}\hat{H}_\mathrm{JC} &= -\Delta_\mathrm{a}\hat{\sigma}^+\hat{\sigma}^- + \sqrt{2}g(\hat{b}_\mathrm{s}^\dagger\hat{\sigma}^- + \hat{b}_\mathrm{s}\hat{\sigma}^+) - \sum_\pm \Delta_\mathrm{c}\hat{a}_\pm^\dagger\hat{a}_\pm - \imath\eta_\pm(\hat{a}_\pm - \hat{a}_\pm^\dagger) \qquad (22.71)\\ &= \hat{H}_\mathrm{atom} + \hat{H}_\mathrm{atom:cav} + \hat{H}_\mathrm{cav} + \hat{H}_\mathrm{laser:cav} \ .\end{aligned}$$

We see that only the symmetric mode couples to the atom. On the other hand, both modes contribute to the field energy,

$$\hat{H}_\mathrm{cav} = \Delta_\mathrm{c}(\hat{a}_+^\dagger\hat{a}_+ + \hat{a}_-^\dagger\hat{a}) = \Delta_\mathrm{c}(\hat{b}_\mathrm{s}^\dagger\hat{b}_\mathrm{s} + \hat{b}_\mathrm{a}^\dagger\hat{b}_\mathrm{a}) \ . \tag{22.72}$$

Now, let us check the pump terms,

$$\begin{aligned}\hat{H}_\mathrm{laser:cav} &= \imath\eta_+(\hat{a}_+ - \hat{a}_+^\dagger) + \imath\eta_-(\hat{a}_- - \hat{a}_-^\dagger) \qquad (22.73)\\ &= \tfrac{\imath}{\sqrt{2}}\Big[(\eta_+e^{-\imath kz} + \eta_-e^{\imath kz})\hat{b}_\mathrm{s} - (\eta_+e^{\imath kz} + \eta_-e^{-\imath kz})\hat{b}_\mathrm{s}^\dagger\\ &\qquad +(\eta_+e^{-\imath kz} - \eta_-e^{\imath kz})\hat{b}_\mathrm{a} - (\eta_+e^{\imath kz} - \eta_-e^{-\imath kz})\hat{b}_\mathrm{a}^\dagger\Big] \ .\end{aligned}$$

For $\eta_+ = \eta_- = \eta$ we get,

$$\hat{H}_\mathrm{laser:cav} = \eta\sqrt{2}\Big[\imath(\hat{b}_\mathrm{s} - \hat{b}_\mathrm{s}^\dagger)\cos kz + (\hat{b}_\mathrm{a} + \hat{b}_\mathrm{a}^\dagger)\sin kz\Big] \ . \tag{22.74}$$

Hence, for $kz = 0$ only the symmetric mode is pumped (no central peak). On the other hand, for $kz = \frac{\pi}{2}$ only the anti-symmetric mode is pumped, so that no normal-mode splitting is expected.

For $\eta_- = 0$ we get,

$$\hat{H}_{laser:cav} = \tfrac{\imath\eta_+}{\sqrt{2}}\Big[e^{-\imath kz}(\hat{b}_\mathrm{s} + \hat{b}_\mathrm{a}) - e^{\imath kz}(\hat{b}_\mathrm{s}^\dagger + \hat{b}_\mathrm{a}^\dagger)\Big] \ . \tag{22.75}$$

Hence, both modes are pumped and we observe three peaks. The normal-mode splitting can be observed in transmission spectra, as we will demonstrate in the following.

22.1.4.4 Normal modes of a ring cavity

We start from the Hamiltonian (22.68) and derive the Heisenberg equations,

$$\begin{aligned}\dot{\hat{\sigma}}^- &= (\imath\Delta_\mathrm{a} - \tfrac{\Gamma}{2})\hat{\sigma}^- - \imath g(e^{\imath kz}\hat{a}_+ + e^{-\imath kz}\hat{a}_-)\hat{\sigma}^z \qquad (22.76)\\ \dot{\hat{\sigma}}^z &= 2\imath g(e^{\imath kz}\hat{a}_+ + e^{-\imath kz}\hat{a}_-)\hat{\sigma}^+ - 2\imath g\hat{\sigma}^-(e^{-\imath kz}\hat{a}_+^\dagger + e^{\imath kz}\hat{a}_-^\dagger) - \Gamma(\mathbb{I}_2 + \hat{\sigma}^z)\\ \dot{\hat{a}}_\pm &= (\imath\Delta_\mathrm{c} - \kappa)\hat{a}_\pm - \imath g\hat{\sigma}^- e^{\mp\imath kz} + \eta_\pm \ .\end{aligned}$$

The stationary solution follows from the expectation values of these equations,

$$\begin{aligned}0 &= (\imath\Delta_\mathrm{a} - \tfrac{\Gamma}{2})\langle\hat{\sigma}^-\rangle + \imath g(e^{\imath kz}\langle\hat{a}_+\hat{\sigma}^z\rangle + e^{-\imath kz}\langle\hat{a}_-\hat{\sigma}^z\rangle) \qquad (22.77)\\ 0 &= 2\imath g(e^{\imath kz}\langle\hat{a}_+\hat{\sigma}^+\rangle + e^{-\imath kz}\langle\hat{a}_-\hat{\sigma}^+\rangle) - 2\imath g(e^{-\imath kz}\langle\hat{a}_+^\dagger\hat{\sigma}^-\rangle + e^{\imath kz}\langle\hat{a}_-^\dagger\hat{\sigma}^-\rangle) - \Gamma(1 + \langle\hat{\sigma}^z\rangle)\\ 0 &= (\imath\Delta_\mathrm{c} - \kappa)\langle\hat{a}_\pm\rangle - \imath g\langle\hat{\sigma}^-\rangle e^{\mp\imath kz} + \eta_\pm \ .\end{aligned}$$

Neglecting all correlations, we derive from (22.77)(i),

$$\langle\hat{\sigma}^-\rangle = \frac{-\imath g}{\frac{\Gamma}{2}-\imath\Delta_\mathrm{a}}(e^{\imath kz}\alpha_+ + e^{-\imath kz}\alpha_-)\langle\hat{\sigma}^z\rangle \ . \tag{22.78}$$

Substituting $\langle\hat{\sigma}^\pm\rangle$ in (22.77)(ii),

$$\left(1+\frac{2g^2}{\frac{\Gamma^2}{4}+\Delta_\mathrm{a}^2}(|\alpha_+|^2+|\alpha_-|^2+e^{2\imath kz}\alpha_-^*\alpha_+ + e^{-2\imath kz}\alpha_+^*\alpha_-)\right)\langle\hat{\sigma}^z\rangle = -1 \ , \tag{22.79}$$

and in (22.77)(iii),

$$(\kappa-\imath\Delta_\mathrm{c})\alpha_\pm - \frac{g^2}{\frac{\Gamma}{2}-\imath\Delta_\mathrm{a}}(e^{\imath kz\mp\imath kz}\alpha_+ + e^{-\imath kz\mp\imath kz}\alpha_-)\langle\hat{\sigma}^z\rangle = \eta_\pm \ . \tag{22.80}$$

Substituting $\langle\hat{\sigma}^z\rangle$ from (22.77) in (22.77),

$$(\kappa-\imath\Delta_\mathrm{c})\alpha_\pm - \frac{g^2(\frac{\Gamma}{2}+\imath\Delta_\mathrm{a})(\alpha_\pm+e^{\mp 2\imath kz}\alpha_\mp)}{\frac{\Gamma^2}{4}+\Delta_\mathrm{a}^2+2g^2(|\alpha_+|^2+|\alpha_-|^2+e^{2\imath kz}\alpha_-^*\alpha_+ + e^{-2\imath kz}\alpha_+^*\alpha_-)} = \eta_\pm \ . \tag{22.81}$$

Assuming weak excitation, $g|\alpha_\pm|^2 \ll \Gamma, \Delta_\mathrm{a}$, this last expression simplifies to,

$$\left(\kappa-\imath\Delta_\mathrm{c}-\frac{g^2}{\frac{\Gamma}{2}-\imath\Delta_\mathrm{a}}\right)\alpha_\pm - \frac{g^2}{\frac{\Gamma}{2}-\imath\Delta_\mathrm{a}}e^{\mp 2\imath kz}\alpha_\mp \simeq \eta_\pm \ , \tag{22.82}$$

or, using the abbreviations,

$$U_\gamma \equiv U_0 - \imath\gamma_0 \equiv \frac{g^2}{\Delta_\mathrm{a}+\imath\Gamma} = \frac{g^2(\Delta_\mathrm{a}-\imath\frac{\Gamma}{2})}{\frac{\Gamma^2}{4}+\Delta_\mathrm{a}^2} \ , \tag{22.83}$$

we write,

$$[\kappa+\imath(U_\gamma-\Delta_\mathrm{c})]\alpha_\pm + \imath U_\gamma e^{\mp 2\imath kz}\alpha_\mp \simeq \eta_\pm \ . \tag{22.84}$$

Resolving for $\alpha_\pm$,

$$\boxed{\alpha_\pm \simeq \frac{\eta_\pm\left[\kappa+\gamma_0+\imath(U_0-\Delta_\mathrm{c})\right]-\eta_\mp(\gamma_0+\imath U_0)e^{\mp 2\imath kz}}{\left[\kappa+\gamma_0+\imath(U_0-\Delta_\mathrm{c})\right]^2-(\gamma_0+\imath U_0)^2}} \ , \tag{22.85}$$

from which we can determine the transmission,

$$T_\pm = \left|\frac{\kappa\alpha_\pm}{\eta_\pm}\right|^2 \ . \tag{22.86}$$

This is illustrated in Fig. 22.6.

Example 128 (*Generalization for many atoms*): For N uncorrelated atoms, defining a bunching parameter via $b \equiv \frac{1}{N}\sum_j e^{2\imath kz_j}$ and introducing the abbreviations $U_\gamma \equiv U_0 - \imath\gamma_0$ and $\Delta_\kappa \equiv \Delta_\mathrm{c} + \imath\kappa$, the result (22.67) can be generalized to,

$$\alpha_\pm \simeq -\imath\frac{\eta_\pm(NU_\gamma-\Delta_\kappa)-\eta_\mp NbU_\gamma}{(NU_\gamma-\Delta_\kappa)^2-(N|b|^2U_\gamma)^2} \ . \tag{22.87}$$

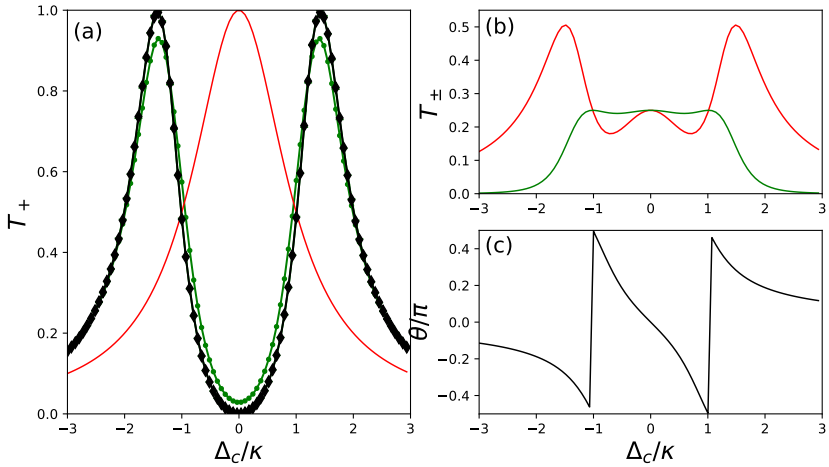

Figure 22.6: (code) Normal-mode splitting in a ring cavity observed in transmission spectra T_+ calculated from (22.86) with $g = \kappa$, $\eta_+ = 0.1\kappa$, and $\Gamma = R = 0$. (a) The blue curve is obtained for one-sided pumping ($\eta_- = 0$), the green curve for symmetric pumping ($\eta_- = \eta_+$ and $kz = 0$), and the red curve for anti-symmetric pumping ($\eta_- = \eta_+$ and $kz = \pi/2$). The green dots are obtained for symmetric pumping via numerical integration of the Hamiltonian (22.68). (b) Transmission spectra T_+ (green) and T_- (red) for one-sided pumping. (c) Phase of the standing wave formed by backscattering of probe light into the mode α_-.

Example 129 (*Level splitting for some limiting cases*): The first limiting case consists in setting $\eta_\pm = 0$ and assuming the light field to be classical. Then we obtain the Rabi Hamiltonian studied in previous sections,

$$\hat{H}_{\rm Rabi} = -\Delta_{\rm a}\hat{\sigma}^+\hat{\sigma}^- + \tfrac{1}{2}\Omega(\hat{\sigma}^+ + \hat{\sigma}^-) = \begin{pmatrix} 0 & \frac{1}{2}\Omega \\ \frac{1}{2}\Omega & -\Delta_{\rm a} \end{pmatrix} .$$

Its eigenvalues: $E_{1,2} = -\frac{1}{2}\Delta_{\rm a} \pm \sqrt{\Delta_{\rm a}^2 + \Omega^2}$ exhibit the famous Autler-Townes splitting.
The second limiting case consists adiabatically eliminating the atomic states. This is valid if $|\Delta_{\rm a}| \gg \Gamma$. Then we obtain the cavity Hamiltonian,

$$\hat{H}_{\rm cav} = U_0(e^{-2\imath kz}\hat{a}_+^\dagger\hat{a}_- + e^{2\imath kz}\hat{a}_+\hat{a}_-^\dagger) + \sum_\pm (U_0 - \Delta_{\rm c})\hat{a}_\pm^\dagger\hat{a}_\pm - \imath\eta_\pm(\hat{a}_\pm - \hat{a}_\pm^\dagger) ,$$

with $L_k = \hat{a}_+, \hat{a}_-$ and $\gamma_k = 2\kappa, 2\kappa$, again for the case $z = \eta_\pm = 0$. The spectrum is asymmetric because $\Delta_{\rm a} \neq 0$ [2,3]

[2]We note that, setting $z = \eta_\pm = 0$, the cavity Hamiltonian $\hat{H}_{\rm cav} = U_0(\hat{a}_+^\dagger\hat{a}_- + \hat{a}_+\hat{a}_-^\dagger) - (\Delta_{\rm c} - U_0)\sum_\pm \hat{a}_\pm^\dagger\hat{a}_\pm$ has the same structure as the Rabi Hamiltonian, which we can write, introducing annihilation and creation operators $\hat{\psi}_{g,e}$ and $\hat{\psi}_{g,e}^\dagger$ for atoms in ground and excited states, $\hat{H}_{\rm Rabi} = \frac{1}{2}\Omega(\hat{\psi}_e^\dagger\hat{\psi}_g + \hat{\psi}_g^\dagger\hat{\psi}_e) - \Delta_{\rm a}\sum_{j=g,e}\hat{\psi}_j^\dagger\hat{\psi}_j$. This emphasizes the analogy between Autler-Townes and normal-mode splitting.

[3]As the atomic degrees of freedom have been eliminated, spontaneous emission must be reintroduced by hand when required.

22.1.5 Adiabatic elimination of internal states

The equations of motion (15.43) describe the evolution of the light fields in counterpropagating modes of a ring cavity. Without scatterer located in the mode volume, the modes evolve independently. In contrast, a scatterer (e.g. an atom or a beam splitter) may redistribute photons between the modes, whose dynamics thereby becomes coupled.

We will in the following assume the scatterer as immobile, except for Sec. 22.1.8, where we consider a vibrating scatterer. Immobile scatterers can, for example, be heavy masses, such as imperfections on the surfaces of the mirrors of the cavity (scratches, dust particles, etc.), which can scatter light both, out of the cavity and into the reverse cavity mode. In *laser gyroscopes* this backscattering may induce a locking of counterpropagating modes and hamper their proper operation.

22.1.5.1 Classical derivation of coupled atom-ring cavity equations

The equations of motion (15.43) describe the light fields classically. Hence, it is not surprising that they can be derived with entirely classical arguments. Here, we will show this for a ring cavity in the presence of an atom sitting at a fixed position z on the cavity's optical axis. We understand the atom as a beamsplitter located within the mode volume of the resonator and partially reflecting and transmitting incident light with reflection and transmission coefficients $(r_\beta, t_\beta) = (\imath\beta, 1+\imath\beta)$ such that $r_\beta^2 + t_\beta^2 = 1$. Transmitted (forward scattered) photons may be phase-shifted, while reflected photons are backscattered into the counterpropagating mode of the resonator.

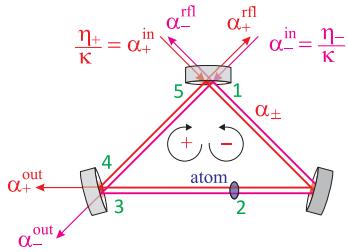

Figure 22.7: Scheme of a ring cavity containing an atom.

Similarly, we treat the incoupling mirror as a beam splitter with coefficients $(r_{\rm in}, t_{\rm in})$. The incident field $\alpha_{\rm in}$ produces, in the cavity, field amplitudes of $\alpha_\pm$ for the co- and counterpropagating waves. As in (15.39), we normalize the amplitudes by the numbers of photons $n_\pm \equiv |\alpha_\pm|^2$. After a round-trip time $\tau = \delta_{\rm fsr}^{-1}$ through the mode volume we have in the position of the incoupling mirror (marked as (1) in Fig. 22.7) the field,

$$\begin{aligned}
\alpha_+(t+\tau) &= -r_{\rm in}(1+\imath\beta)e^{\imath kL}\alpha_+(t) + \imath\beta r_{\rm in}^2 e^{2\imath kL - 2\imath kz}\alpha_-(t) + t_{\rm in}\alpha_+^{in}(t) \qquad (22.88)\\
\alpha_-(t+\tau) &= -r_{\rm in}(1+\imath\beta)e^{\imath kL}\alpha_-(t) + \imath\beta e^{2\imath kz}\alpha_+(t) + t_{\rm in}(1+\imath\beta)e^{\imath kL}\alpha_-^{in}(t)\ .
\end{aligned}$$

L is the total length of the ring cavity. For the three mirror ring cavity depicted in

Fig. 22.7 we have after one round trip $\tau\dot{\alpha}_\pm = \alpha_\pm(t+\tau) + \alpha_\pm(t)$ [4]. Thus, we obtain,

$$\begin{aligned}\tau\dot{\alpha}_+ &= -\left[1 + r_{\rm in}(1+\imath\beta)e^{\imath kL}\right]\alpha_+ + \imath\beta r_{\rm in}^2 e^{2\imath kL - 2\imath kz}\alpha_- + t_{\rm in}\alpha_+^{in} \\ \tau\dot{\alpha}_- &= -\left[1 + r_{\rm in}(1+\imath\beta)e^{\imath kL}\right]\alpha_- + \imath\beta e^{2\imath kz}\alpha_+ + t_{\rm in}(1+\imath\beta)e^{2\imath kL}\alpha_-^{\rm in} \ .\end{aligned} \tag{22.89}$$

Obviously, we have $kL = \omega/\delta_{\rm fsr}$. In the vicinity of a resonance we have, $\Delta_{\rm c} \ll \delta_{\rm fsr}$, and the quantity $\omega/\delta_{\rm fsr}$ is almost integer, $\omega = 2\pi N\delta_{\rm fsr} - \Delta_{\rm c}$, such that we can expand the exponential, $e^{\imath kL} \simeq 1 - \imath\Delta_{\rm c}/\delta_{\rm fsr}$. Neglecting the exponential $e^{\imath kL}$ in all terms except the first ones of both equations and also using $\tau = \delta_{\rm fsr}^{-1}$, we get,

$$\begin{aligned}\dot{\alpha}_+ &= -\delta_{\rm fsr}\left[1 - r_{\rm in}(1+\imath\beta)\left(1 - \imath\Delta_{\rm c}/\delta_{\rm fsr}\right)\right]\alpha_+(t) + \delta_{\rm fsr}\imath\beta r_{\rm in}^2 e^{-2\imath kz}\alpha_-(t) + \delta_{\rm fsr}t_{\rm in}\alpha_+^{\rm in}(t) \\ \dot{\alpha}_- &= -\delta_{\rm fsr}\left[1 - r_{\rm in}(1+\imath\beta)\left(1 - \imath\Delta_{\rm c}/\delta_{\rm fsr}\right)\right]\alpha_-(t) + \delta_{\rm fsr}\imath\beta e^{2\imath kz}\alpha_+(t) + \delta_{\rm fsr}t_{\rm in}(1+\imath\beta)\alpha_-^{\rm in}(t) \ .\end{aligned} \tag{22.90}$$

We now connect the transmission of the coupling mirror $t_{\rm in}$ with the decay constant κ assuming that the light can only leave the cavity through this mirror. We identify,

$$\kappa_{\rm int} = \kappa = \frac{T_{\rm in}}{\tau} = \frac{t_{\rm in}^2}{\tau} \tag{22.91}$$

as the part of the light *intensity* lost during one round trip. Thus, $t_{\rm in} = \sqrt{\kappa/\delta_{\rm fsr}}$. Now, we simplify the prefactor of the first term in Eqs. (22.90) neglecting β and replacing $r_{\rm in} = \sqrt{1 - t_{\rm in}^2} \simeq 1 - \frac{t_{\rm in}^2}{2} = 1 - \frac{2\kappa\tau}{2}$,

$$\delta_{\rm fsr}\left[1 - r_{\rm in}(1+\imath\beta)\left(1 - \tfrac{\imath\Delta_{\rm c}}{\delta_{\rm fsr}}\right)\right] \simeq \delta_{\rm fsr}\left[1 - \left(1 - \tfrac{t_{\rm in}^2}{2}\right)\left(1 - \tfrac{\imath\Delta_{\rm c}}{\delta_{\rm fsr}}\right)\right] = \kappa + \imath\Delta_{\rm c} \ . \tag{22.92}$$

It gives the cavity losses for the two modes during one round trip. We assume here that losses can only occur via the coupling mirror. However, all losses can be included in a single appropriate κ. There are usually other losses due to scattering on the surface of the mirrors or absorption by the atoms. Finally, we obtain for weak atomic reflection and in resonance, that is, for $\beta \ll \kappa$ and $\Delta_{\rm c} = 0$ the system of equations,

$$\begin{aligned}\dot{\alpha}_+ &= -(\kappa + \imath\Delta_{\rm c})\alpha_+ + \imath\delta_{\rm fsr}\beta e^{-2\imath kz}\alpha_- + \sqrt{\kappa\delta_{\rm fsr}}\alpha_+^{\rm in} \\ \dot{\alpha}_- &= -(\kappa + \imath\Delta_{\rm c})\alpha_- + \imath\delta_{\rm fsr}\beta e^{2\imath kz}\alpha_+ + \sqrt{\kappa\delta_{\rm fsr}}\alpha_-^{\rm in}\end{aligned} \tag{22.93}$$

To calculate the value of β, we need the reflection coefficient of a single atom. It depends on the polarizability,

$$r_\beta = \frac{k}{\pi w^2}\frac{\alpha_{\rm pol}}{\varepsilon_0} \ \left(= \frac{\sigma_0}{\pi w^2}\frac{\Gamma}{2\Delta_{\rm a}}\right) \ . \tag{22.94}$$

The optical potential to which the atom is exposed is,

$$\phi = \frac{I}{2c}\frac{\alpha_{\rm pol}}{\varepsilon_0} \ , \tag{22.95}$$

[4] For a four mirror ring cavity we would have $\tau\dot{\alpha}_\pm(t+\tau) = \alpha_\pm(t+\tau) - \alpha_\pm(t)$, and the sign of the first term in (22.88) would have to be inverted, because any reflection of the intracavity field at a cavity mirror introduces a phase shift of π.

where we write the intensity of light as,

$$I = 2\varepsilon_0 c\mathcal{E}_1^2|\alpha_+ e^{\imath kZ} + \alpha_- e^{-\imath kZ}| \ . \tag{22.96}$$

We normalize once more to the field generated by a single photon, $\mathcal{E}_1 = \sqrt{\hbar\omega/2\varepsilon_0 V_{\rm m}}$ with the mode volume, $V_{\rm m} = \frac{\pi}{2}Lw^2$. On the other hand, the potential can be determined directly through the Rabi frequency,

$$\phi(\mathbf{r}) = \frac{\hbar\Omega(\mathbf{r})^2}{4\Delta_{\rm a}} \ , \tag{22.97}$$

The Rabi frequency $\Omega(\mathbf{r})^2 = 4g^2|\alpha_+ e^{\imath kZ} + \alpha_- e^{-\imath kZ}|^2$ is normalized to the frequency of Rabi generated by a photon g. Using the frequency shift (light-shift) by photon (22.37), $U_0 = \frac{g^2}{\Delta_{\rm a}}$, we can also write,

$$\phi(\mathbf{r}) = \hbar U_0|\alpha_+ e^{\imath kZ} + \alpha_- e^{-\imath kZ}|^2 \ . \tag{22.98}$$

A comparison of the above equations gives,

$$r_\beta = \frac{\imath U_0}{\delta_{\rm fsr}} \ . \tag{22.99}$$

With an atom in the resonator, we have,

$$\beta = \frac{\imath U_0}{\delta_{\rm fsr}} \ . \tag{22.100}$$

We define for convenience, $\eta_\pm = \sqrt{\kappa\delta_{\rm fsr}}\alpha_\pm^{in}$ and we suppose, that $t_{\rm in} \ll 1$, $r_\beta \ll 1$ and $\beta \ll 1$. This ultimately leads to the result,

$$\dot{\alpha}_\pm = -\kappa\alpha_\pm - \imath U_0 e^{\mp 2\imath kz}\alpha_\mp + \eta_\pm \ . \tag{22.101}$$

Example 130 (*Classical CARL equations*): If we were to treat the atomic position z as a degree of freedom, we could calculate the classical potential of the stationary light wave, and therefore the dipole force,

$$F = -\nabla\phi = -\hbar U_0 \nabla_{Z=z}|\alpha_+ e^{\imath kZ} + \alpha_- e^{-\imath kZ}|^2 \ , \tag{22.102}$$

and, consequently, derive the dynamics of the scatterer via,

$$m\ddot{z} = -2\imath\hbar k U_0(\alpha_+\alpha_-^* e^{2\imath kz} - \alpha_+^*\alpha_- e^{-2\imath kz}) \ . \tag{22.103}$$

This will be studied in Chp. 25. In the remaining sections of this chapter we will assume the atom to be located at a fixed position.

In the above derivation we assumed, for simplicity, the pump laser on resonance with the cavity, $\Delta_{\rm c} = 0$. Relaxing this condition, an analogous derivation yields [5],

$$\dot{\alpha}_\pm = (-\kappa + \imath\Delta_{\rm c} - \imath U_0)\alpha_\pm - \imath U_0 e^{\mp 2\imath kz}\alpha_\mp + \eta_\pm \ . \tag{22.104}$$

[5] Note, that we have not allowed for spontaneous emission by the atomic scatterer out of the cavity mode. This approximation is only good far from resonance, $\Delta_{\rm a} \gg \Gamma$. We will see in Sec. 25.1.3, how to generalize the equations of motion for near resonance cases.

22.1.5.2 Adiabatically simplified Hamiltonian

In a ring cavity, the simplified Hamiltonian,

$$\boxed{\hat{H} = (U_0 - \Delta_c)\sum_{\pm} \hat{a}_{\pm}^{\dagger}\hat{a}_{\pm} - \imath\eta_{\pm}(\hat{a}_{\pm} - \hat{a}_{\pm}^{\dagger}) + U_0(\hat{a}_{+}\hat{a}_{-}^{\dagger}e^{2\imath kz} + \hat{a}_{+}^{\dagger}\hat{a}_{-}e^{-2\imath kz})} \ , \tag{22.105}$$

which can be obtained from the full Hamiltonian via adiabatic elimination of the excited atomic state, already exhibits this phenomenon. With the above Hamiltonian we derive from the Heisenberg equation,

$$\dot{\hat{a}}_{\pm} = -\imath[\hat{a}_{\pm}, \hat{a}] - \kappa\hat{a}_{\pm} = (-\kappa + \imath\Delta_c - \imath U_0)\hat{a}_{\pm} - \imath U_0 e^{\mp 2\imath kz}\hat{a}_{\mp} + \eta_{\pm} \ , \tag{22.106}$$

which, after taking the expectation values and disregarding correlations, reproduces the equations of motion (22.104). Of course, as we eliminated the internal atomic degree of freedom, spontaneous emission is not accounted for. We may, however, include it phenomenologically via the substitution $U_0 \to U_\gamma \equiv U_0 - \imath\gamma_0$. The stationary solution of Eq. (22.106) is *exactly the same* as the one derived for the full Jaynes-Cummings model (22.85) under the assumption of weak excitation, $g|\alpha_{\pm}| \ll \Gamma, \Delta_a$,

$$\boxed{\alpha_{\pm} = -\imath\frac{\eta_{\pm}(U_\gamma - \Delta_\kappa) - U_\gamma e^{\mp 2\imath kz}\eta_{\mp}}{(U_\gamma - \Delta_\kappa)^2 - U_\gamma^2}} \tag{22.107}$$

with the abbreviations,

$$U_\gamma \equiv U_0 - \imath\gamma_0 \quad , \quad \Delta_\kappa \equiv \Delta_c + \imath\kappa \ . \tag{22.108}$$

Solve the Exc. 22.1.11.6.

22.1.6 Normal mode splitting induced by beam splitting

The fact that (in the weak excitation limit) normal mode splitting is fully described by the classical field equations (22.104) shows that the phenomenon clearly is *not a quantum effect*: a classical beam splitter inserted into the cavity does the same job. We will now discuss the normal mode splitting in detail based on the adiabatically simplified equations (22.108).

The equation (22.104) can be written as follows,

$$\imath\dot{\vec{\alpha}} = W\vec{\alpha} + \imath\vec{\eta} \ , \tag{22.109}$$

where $\vec{\alpha}$ and $\vec{\eta}$ regroup the amplitudes $\alpha_{\pm}$ and $\eta_{\pm}$. This equation takes the form of a Schrödinger equation, where,

$$W \equiv \begin{pmatrix} U_0 - \Delta_c - \imath\kappa & U_0 e^{-2\imath kz} \\ U_0 e^{2\imath kz} & U_0 - \Delta_c - \imath\kappa \end{pmatrix} \tag{22.110}$$

would be the Hamiltonian describing the coupling between counterpropagating modes. The eigenvalues of this matrix are,

$$W^{(1,2)} = 2U_0 - \Delta_c - \imath\kappa \quad , \quad -\Delta_c - \imath\kappa \ . \tag{22.111}$$

This *normal mode splitting* [6] of the cavity results from the coupling of the two cavity modes $\hat{a}_+^\dagger \hat{a}_-$. Obviously, the energies and widths of the eigenvalues do not depend neither on the pump intensities $\eta_\pm$ nor the z-position of the atom. On the other hand, the spectral behavior of $\alpha_\pm$, and hence the observable quantities, such as the transmission

$$T_\pm \equiv \left| \frac{\kappa \alpha_\pm}{\eta_\pm} \right|^2 \tag{22.112}$$

depend on these parameters. In the following, we will study normal mode splitting in a ring cavity by a discussion of the expression (22.85) for the cases of (i) anti-symmetric pumping, (ii) symmetric pumping, and (iii) uni-directional pumping.

(i) Assuming $\gamma_0 = 0$ and anti-symmetric pumping, $\eta_- = \eta_+$ and $kz = \pi/2$, the expression (22.85) becomes,

$$\begin{aligned} \alpha_+ &= \eta_+ \frac{\kappa - \imath(\Delta_c - 2U_0)}{[\kappa - \imath(\Delta_c - U_0)]^2 + U_0^2} \\ \Rightarrow \quad \left| \frac{\alpha_+}{\eta_+} \right|^2 &= \frac{1}{\kappa^2 + \Delta_c^2} \ . \end{aligned} \tag{22.113}$$

That is, the transmission profile is a Lorentzian.

(ii) For symmetric pumping, $\eta_- = \eta_+$ and $kz = 0$,

$$\begin{aligned} \alpha_+ &= \eta_+ \frac{\kappa - \imath\Delta_c}{[\kappa - \imath(\Delta_c - U_0)]^2 + U_0^2} \\ \Rightarrow \quad \left| \frac{\alpha_+}{\eta_+} \right|^2 &= \frac{1}{\kappa^2 + (\Delta_c - 2U_0)^2} \ . \end{aligned} \tag{22.114}$$

Setting $\Delta_c = \Delta_a$ we find from $0 \equiv \frac{d}{d\Delta_c} \left| \frac{\alpha_+}{\eta_+} \right|^2$ a minimum at $\Delta_c = 0$ and two maxima at $\Delta_c = 2U_0 = \sqrt{2}g$. This is the usual normal mode splitting for a ring cavity.

(iii) For uni-directional pumping, $\eta_- = 0$,

$$\begin{aligned} \alpha_+ &= \eta_+ \frac{\kappa - \imath(\Delta_c - U_0)}{[\kappa - \imath(\Delta_c - U_0)]^2 + U_0^2} \\ \Rightarrow \quad \left| \frac{\alpha_+}{\eta_+} \right|^2 &= \frac{\kappa^2 + (\Delta_c - U_0)^2}{[\kappa^2 - \Delta_c(\Delta_c - 2U_0)]^2 + 4\kappa^2(\Delta_c - U_0)^2} \ . \end{aligned} \tag{22.115}$$

That is, the transmission profile is a more complicated and may exhibit up to three peaks.

22.1.6.1 Unidirectional pumping

For unilateral pumping, $\eta_- = 0$, and approximating $\gamma_0 = 0$, the solution (22.85) simplifies to,

$$\alpha_+(\infty) = \eta_+ \frac{\chi}{\chi^2 + U_0^2} \qquad \text{and} \qquad \alpha_-(\infty) = \eta_+ \frac{\imath U_0 e^{2\imath kz}}{\chi^2 + U_0^2} \ . \tag{22.116}$$

[6] The splitting is not exactly the *vacuum Rabi splitting*, which occurs when the excitation can not be eliminated adiabatically. The vacuum Rabi splitting results from the Jaynes-Cummings [815, 186] and is caused by the coupling of internal and external states $\hat{a}^\dagger \hat{\sigma}$.

These formulas show that, for weak coupling, $U_0 \ll \kappa$, the counterpropagating mode receives little light. On the other side, for strong coupling (or very high finesse) and $\Delta_c = 0$, the intensity is equally distributed, $|\alpha_+|^2 = |\alpha_-|^2 = \frac{\eta_\pm}{2\kappa}$ [7]. We calculate the splitting of normal modes in Exc. 22.1.11.7.

The counterpropagating modes form, by interference, a standing light wave giving rise to a dipole potential in the form of a one-dimensional optical lattice. Defining the phase $\theta = \theta_1 - \theta_2$ through,

$$\alpha_+ \equiv |\alpha_+| e^{-\imath\theta_1} \qquad \text{and} \qquad \alpha_- \equiv |\alpha_-| e^{-\imath\theta_2} \ , \tag{22.117}$$

we verify by the equation (15.39),

$$\mathcal{E}^+(\zeta,t) = \mathcal{E}_1 |\alpha_+(t)| e^{\imath k\zeta} + \mathcal{E}_1 |\alpha_-(t)| e^{-\imath\theta(t)} e^{-\imath k\zeta} \ , \tag{22.118}$$

and,

$$\begin{aligned} \tfrac{1}{2\varepsilon_0 c \mathcal{E}_1^2} I(\zeta,t) &= \tfrac{1}{\mathcal{E}_1^2} \mathcal{E}^+(\zeta,t)\mathcal{E}^-(\zeta,t) \\ &= |\alpha_+(t)|^2 + |\alpha_-(t)|^2 + 2|\alpha_+(t)||\alpha_-(t)| \cos(2k\zeta + \theta) \ . \end{aligned} \tag{22.119}$$

That is, the phase indicates the positions of the potential maxima. Inserting the stationary solution for unilateral pumping (22.116), we derive the expression,

$$\tan\theta = \frac{\mathfrak{Im}\, \alpha_+(\infty)\alpha_-^*(\infty)}{\mathfrak{Re}\, \alpha_+(\infty)\alpha_-^*(\infty)} = \frac{\mathfrak{Im}\, \chi\imath e^{-2\imath kz}}{\mathfrak{Re}\, \chi\imath e^{-2\imath kz}} = \frac{\kappa\cos 2kz + (U_0 - \Delta_c)\sin 2kz}{\kappa \sin 2kz - (U_0 - \Delta_c)\cos 2kz} \ . \tag{22.120}$$

Or in other words, the phase of light determines the equilibrium position of the atom (or vice versa). Two cases are interesting: (i) For $\Delta_c = 0$ and $U_0 \gg \kappa$ the condition (22.124) turns into $\tan\theta = -\tan 2kz$. In this case, the phase of the backscattered field adjusts in such a way, that the atom stays at the valleys of the anti-nodes. (ii) For $\Delta_c = U_0$ (or alternatively, when $\kappa \gg U_0, \Delta_c$) the condition (22.124) turns into $\tan\theta = -\tan(2kx + \frac{\pi}{2})$, such that the atom is at half height of the potential slope, exactly at the position, where it is able to backscatter the maximum of photons from the pumped mode α_+ to the mode α_-.

22.1.6.2 (Anti-)Symmetric pumping

Let us assume equal intensities for the pumps, but variable phases, $\eta_\pm = \eta e^{\pm\imath\phi}$, such that $\xi = e^{-2\imath kz - \imath\phi}$. Then, equation (22.85) simplifies to,

$$\alpha_\pm(\infty) = \eta_\pm \frac{\chi - \imath U_\gamma \xi^\pm}{\chi^2 + U_\gamma^2} = \eta \frac{\chi - \imath U_\gamma e^{\mp 2\imath kz \mp \imath\phi}}{\chi^2 + U_\gamma^2} \ . \tag{22.121}$$

The potential is calculated in the same way as in (22.119). The coherences are,

$$\begin{aligned} \alpha_\pm(\infty)\alpha_\pm^*(\infty) &= \eta^2 \tfrac{(\kappa - \imath\Delta_c \mp 2U_0 e^{\mp\imath kz}\sin kz)(\kappa + \imath\Delta_c \mp 2U_0 e^{\pm\imath kz}\sin kz)}{(\kappa^2 + 2U_0\Delta_c - \Delta_c^2)^2 + 4\kappa^2(U_0 - \Delta_c)^2} \\ \alpha_\pm(\infty)\alpha_\mp^*(\infty) &= \eta^2 \tfrac{\kappa^2 + (\Delta_c \mp 2\imath U_0 e^{\mp\imath kz}\sin kz)^2}{(\kappa^2 + 2U_0\Delta_c - \Delta_c^2)^2 + 4\kappa^2(U_0 - \Delta_c)^2} \\ e^{\pm 2\imath kz} &= \tfrac{\alpha_\mp \alpha_\pm^*}{|\alpha_- \alpha_+^*|} \end{aligned} \ , \tag{22.122}$$

[7] This observation explains why perturbing effects such as backscattering from mirrors imperfections are dramatically magnified when the finesse is high.

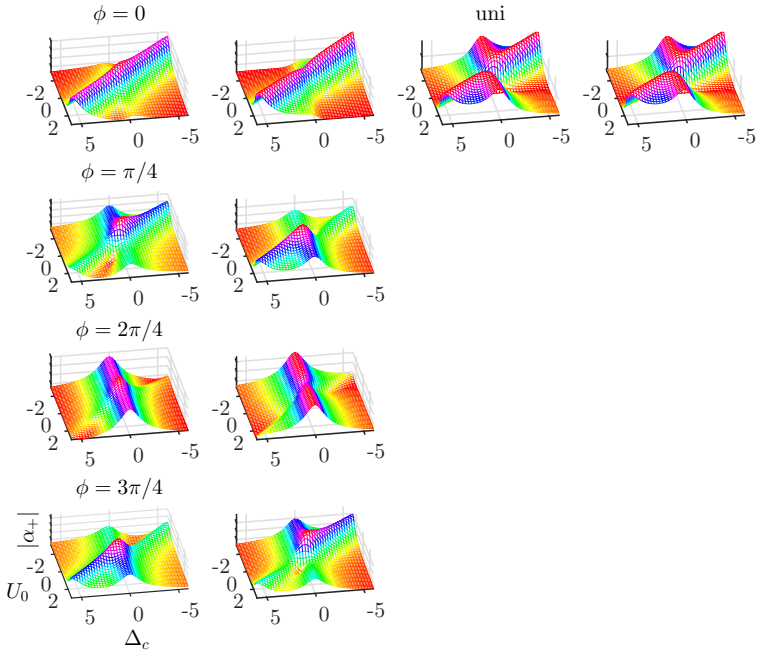

Figure 22.8: (code) (columns 1 and 2) Steady state field values according to (22.109) for bidirectional pumping with a single scatterer located at ϕ. (columns 3 and 4) Same for unidirectional pumping. Here the location of the scatterer does not matter.

such that the relative phase of the counter-propagating waves adjusts itself to,

$$\tan\theta = \frac{\mathfrak{Im}\,\alpha_+(\infty)\alpha_-^*(\infty)}{\mathfrak{Re}\,\alpha_+(\infty)\alpha_-^*(\infty)} = \frac{\kappa^2\sin 2\phi + 4U_0^2\sin^2(kz+\phi)\sin 2kz}{\kappa^2\cos 2\phi - 4U_0^2\sin^2(kz+\phi)\cos 2kz}\ . \tag{22.123}$$

The quantity η^2/κ^2 denotes the number of intracavity photons. According to the formula (22.123), for a weak atom-field coupling, $U_0 \ll \kappa$, the phase adjusts itself to the external pumps, $\theta \to 2\phi$, while for strong coupling, it adjusts to the position of the atom, $\theta \to 2kz$.

Example 131 (*'Pulling' of the optical mode by the atom*): We study the case $U_0 \simeq \kappa$ considering $\gamma_0 = 0 = \Delta_c$ and a particular external phase [301], $\phi = \pi/2$,

$$\alpha_\pm(\infty) = \pm\imath\eta\frac{\kappa + \imath U_0 \pm U_0 e^{\mp 2\imath kz}}{\kappa^2 + 2\imath\kappa U_0} \tag{22.124}$$
$$\theta(\infty) = \arctan\frac{-4U_0^2\cos^2 kz\sin 2kz}{\kappa^2 + 4U_0^2\cos^2 kz\cos 2kz} \simeq \arctan\frac{-8U_0^2}{\kappa^2+4U_0^2}kz\ ,$$

expanding the last formula around $kz = 0$. Fig. 22.9 shows how, with the increase in the coupling force between the field and the atoms, U_0, the phase tends to lock to the atomic position. However, the phase imposed by the external pump competes for this privilege. Curiously, this is independent of laser power, but depends only on the ratio between U_0 and κ.

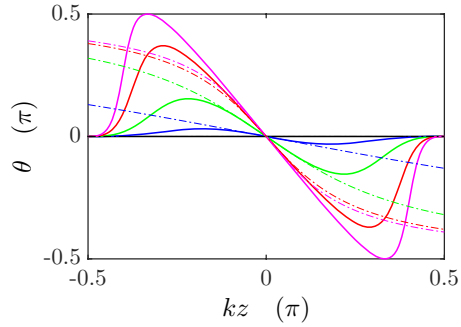

Figure 22.9: (code) 'Pulling' of the phase by the atoms for $U_0/\kappa = 0$, 0.2, 0.5, 1 and $\sqrt{2}$. The solid curves show the exact phase, the 'dash-dotted' curves the linear approximation (22.128).

Example 132 (*Resonant case*): Assuming that the cavity is in resonance, $\Delta_c = 0$, and pumped in a single direction, $\eta_- = 0$, neglecting spontaneous emission, $\gamma_0 = 0$, and assuming low backscattering rates, $U_s \ll \kappa$,

$$\alpha_+(\infty) \simeq \frac{\eta_+}{\kappa} \quad \text{and} \quad |\alpha_-(\infty)| = \frac{U_s}{\kappa}|\alpha_+(\infty)| \ .$$

Looking at short times, we find that the dynamics of the unpumped mode is delayed, since,

$$\dot\alpha_+(0) \simeq \eta_+ \quad \text{and} \quad \dot\alpha_-(0) \simeq -\imath U_s \alpha_+ e^{-2\imath k r_s} \ ,$$

giving,

$$\alpha_+(0) \simeq \eta_+ t \quad \text{and} \quad \alpha_-(0) \simeq -\imath U_s \eta_+ \frac{t^2}{2} e^{-2\imath k r_s} \ .$$

The complete solution of the equations (22.112) with unidirectional pumping, $\eta_- = 0$, will be derived in Exc. 22.1.11.8.

22.1.7 Time-dependent solutions

22.1.7.1 Time-dependent solution without pump

To calculate the homogeneous time-dependent solution of the equation of motion of the ring cavity with $\eta_\pm = 0$, we solve the Schrödinger equation (22.109) the way we learned in quantum mechanics. We start by diagonalizing the matrix (22.110),

$$W = \begin{pmatrix} U_0 - \imath\kappa & U_0 e^{-2\imath kz} \\ U_0 e^{2\imath kz} & U_0 - \imath\kappa \end{pmatrix} \tag{22.125}$$
$$= \begin{pmatrix} e^{-2\imath kz} & -e^{-2\imath kz} \\ 1 & 1 \end{pmatrix} \begin{pmatrix} 2U_0 - \imath\kappa & 0 \\ 0 & -\imath\kappa \end{pmatrix} \begin{pmatrix} e^{-2\imath kz} & -e^{-2\imath kz} \\ 1 & 1 \end{pmatrix}^{-1} = U E_W U^{-1} \ ,$$

where E_W is the matrix of eigenvalues and U a unitary transformation. So,

$$\vec\alpha = e^{-\imath W t}\vec\alpha_0 = U e^{-iE_W t} U^{-1}\vec\alpha_0 \tag{22.126}$$
$$= e^{-\kappa t - \imath U_0 t} \begin{pmatrix} \cos U_0 t & -\imath e^{-2\imath kz} \sin U_0 t \\ -\imath e^{2\imath kz} \sin U_0 t & \cos U_0 t \end{pmatrix} \vec\alpha_0 \ .$$

In Exc. 22.1.11.6 we study the equation of motion numerically. We'll see an alternative calculation in Exc. 22.1.11.10. We calculate the coherence by,

$$\alpha_+(t)\alpha_-^*(t) = e^{-2\kappa t}\left[\alpha_{0+}\alpha_{0-}(\cos^2 U_0 t + e^{-4\imath kz}\sin^2 U_0 t) + \tfrac{1}{2}(\alpha_{0+}^2 - \alpha_{0-}^2)\imath e^{-2\imath kz}\sin 2U_0 t\right]$$
$$\stackrel{z\to 0}{\longrightarrow} e^{-2\kappa t}\left[\alpha_{0+}\alpha_{0-} + \tfrac{1}{2}(\alpha_{0+}^2 - \alpha_{0-}^2)\imath \sin 2U_0 t\right] \ , \tag{22.127}$$

making the transition to the Lamb-Dicke regime by $z \to 0$. The phase of the standing wave is,

$$\tan\theta = \frac{\mathfrak{Im}\,\alpha_+(t)\alpha_-^*(t)}{\mathfrak{Re}\,\alpha_+(t)\alpha_-^*(t)} \stackrel{z\to 0}{\longrightarrow} \frac{\alpha_{0+}^2 - \alpha_{0-}^2}{2\alpha_{0+}\alpha_{0-}}\sin 2U_0 t \ . \tag{22.128}$$

We see that, in resonance and without pumping, the field adjusts its phase to the atom and also decays with the rate κ, while the atom redistributes the photons between modes with the (Rabi-)frequency $2U_0$. The formula (22.128) does not show any damping of the phase dynamics in the Lamb-Dicke regime. Thus, in the absence of pumping, the cavity dissipation reduces only the field amplitudes, but does not damp the adjustment of the phase to the atomic position.

22.1.7.2 Time-dependent solution with fixed pump

To find the complete solution of the inhomogeneous Schrödinger equation (22.109), we first calculate the stationary solution,

$$\vec{\alpha}(\infty) = -\imath W^{-1}\vec{\eta} \ . \tag{22.129}$$

This particular solution of the inhomogeneous equation, added to the general solution of the homogeneous equation, gives the general solution of the inhomogeneous Schrödinger equation,

$$\vec{\alpha}(t) = e^{-\imath Wt}\vec{\alpha}(0) + (1 - e^{-\imath Wt})\vec{\alpha}(\infty) \ . \tag{22.130}$$

We derive and analyze this solution in the Exc. 22.1.11.11.

Analytical solutions only exist in particular cases. However, they allow a better understanding of the dynamics. So let's consider some limiting cases. In Exc. 22.1.11.12 we determine the steady state of an atom interacting with the modes of a unidirectionally pumped annular cavity and calculate the stationary position of the atom in a unidirectionally pumped ring cavity. In Exc. 22.1.11.13 we derive motion equations for the 'intensities' $\alpha_\pm\alpha_\pm^*$ and 'coherences' $\alpha_\pm\alpha_\mp^*$.

22.1.8 Forced atomic vibration in a ring cavity

We now assume, that the atom is forced to vibrate by an external force. The vibration is described by,

$$kz = kz_0 \sin\omega t \ . \tag{22.131}$$

We consider small modulation excursions, $1 \gtrsim kz_0 = \frac{kv}{\omega} = \frac{2\omega_{\rm rec}}{\omega}$, which is equivalent to saying that the oscillation frequency should exceed to recoil shift. In this (Lamb-Dicke) regime the Bessel-expansion yields,

$$e^{\pm 2\imath kz_0 \sin\omega t} = \sum_n J_n(\pm 2kz_0)e^{\imath n\omega t} \simeq J_0(2kz_0) \pm 2\imath J_1(2kz_0)\sin\omega t \simeq 1 \pm 2\imath kz_0 \sin\omega t \ . \tag{22.132}$$

The differential equations for the two counterpropagating ring cavity-field (22.104) can then be written:

$$\boxed{\dot{\alpha}_\pm = (\mathbf{L} - 2\imath\mathbf{X}\sin\omega t)\alpha_\pm + \eta_\pm}\,, \tag{22.133}$$

where,

$$\mathbf{L} = \begin{pmatrix} -\kappa - \imath U_0 & -\imath U_0 J_0 \\ -\imath U_0 J_0 & -\kappa - \imath U_0 \end{pmatrix} \quad \text{and} \quad \mathbf{X} = \begin{pmatrix} 0 & -\imath U_0 J_1 \\ \imath U_0 J_1 & 0 \end{pmatrix}. \tag{22.134}$$

We insert the ansatz $\alpha_\pm = \sum_n \alpha_\pm^{(n)} e^{\imath n\omega t}$, where $\dot{\alpha}_\pm^{(n)} = 0$, into the equations and project onto the basis $e^{\imath n\omega t}$:

$$\begin{aligned} &\imath n\omega_x \sum_n \alpha_\pm^{(n)} e^{\imath n\omega t} = \left(\mathbf{L} - \mathbf{X}(e^{\imath\omega t} - e^{-\imath\omega t})\right) \sum_n \alpha_\pm^{(n)} e^{\imath n\omega t} + \eta_\pm \\ &\Longrightarrow (\mathbf{L} - \imath n\omega)\alpha_\pm^{(n)} + \mathbf{X}(\alpha_\pm^{(n+1)} - \alpha_\pm^{(n-1)}) = -\eta_\pm \delta_{n0}\,. \end{aligned} \tag{22.135}$$

We define operators $\mathbf{S}_n^{\uparrow\downarrow}$ by $\alpha_\pm^{(n+1)} = \mathbf{S}_n^\uparrow \alpha_\pm^{(n)}$ for $n \geq 0$ and $\alpha_\pm^{(n-1)} = \mathbf{S}_n^\downarrow \alpha_\pm^{(n)}$ for $n \leq 0$ and obtain,

$$\left[\mathbf{L} - \imath n\omega + \mathbf{X}(\mathbf{S}_n^\uparrow - \mathbf{S}_n^\downarrow)\right] \alpha_\pm^{(n)} = -\eta_\pm \delta_{n0}\,. \tag{22.136}$$

For $n = 0$, we get,

$$\alpha_\pm(\infty) = \alpha_\pm^{(0)} = -\left[\mathbf{L} + \mathbf{X}(\mathbf{S}_0^\uparrow - \mathbf{S}_0^\downarrow)\right]^{-1} \eta_\pm\,. \tag{22.137}$$

If we substitute in equation (22.135) $\alpha_\pm^{(n)} = \mathbf{S}_{n-1}^\uparrow \alpha_\pm^{(n-1)} = \mathbf{S}_{n+1}^\downarrow \alpha_\pm^{(n+1)}$, we get for $n \gtrless 0$,

$$\mathbf{S}_{n-1}^\uparrow = \left[\mathbf{L} - \imath n\omega + \mathbf{X}\mathbf{S}_n^\uparrow\right]^{-1} \mathbf{X} \quad \text{and} \quad \mathbf{S}_{n+1}^\downarrow = \left[\mathbf{L} - \imath n\omega - \mathbf{X}\mathbf{S}_n^\downarrow\right]^{-1} \mathbf{X}\,. \tag{22.138}$$

By recursive substitution of the lower into the upper equation, the stationary solution can now be written by means of continued fractions,

$$\mathbf{S}_0^{\uparrow\downarrow} \equiv \frac{1}{\mathbf{L} - \imath\omega \pm \mathbf{X}\frac{1}{\mathbf{L} - 2\imath\omega \pm \mathbf{X}\frac{1}{\cdots}}\mathbf{X}}\mathbf{X}\,. \tag{22.139}$$

$\alpha_\pm(\infty)$ in Eq. (22.137) gives us the stationary solution of the differential equation, time-averaged over an oscillation period.

If we are deep in the Lamb-Dicke regime, we need only consider the first order of the continued fractions. We set $\mathbf{S}_1^{\uparrow\downarrow} = \mathbf{1}$ and obtain the simplified equations,

$$\begin{aligned} &\mathbf{S}_0^\uparrow = \left[\mathbf{L} - \imath\omega + \mathbf{X}\right]^{-1}\mathbf{X} \quad \text{and} \quad \mathbf{S}_0^\downarrow = \left[\mathbf{L} - \imath\omega - \mathbf{X}\right]^{-1}\mathbf{X} \\ &\alpha_\pm^{(0)} = -\left[\mathbf{L} + \mathbf{X}\left(\mathbf{S}_0^\uparrow - \mathbf{S}_0^\downarrow\right)\right]^{-1} \eta_\pm \\ &\alpha_\pm^{(1)} = \mathbf{S}_0^\uparrow \alpha_\pm^{(0)} \quad \text{and} \quad \alpha_\pm^{(-1)} = \mathbf{S}_0^\downarrow \alpha_\pm^{(0)}\,. \end{aligned} \tag{22.140}$$

Explicitly,

$$\mathbf{S}_0^{\uparrow\downarrow} = \frac{U_0 k z_0}{(\kappa + \imath U_0 + \imath\omega)^2 + U_0^2(1-k^2x_0^2)} \begin{pmatrix} -U_0(1 \pm k z_0) & \imath(\kappa + \imath U_0 + \imath\omega) \\ -\imath(\kappa + \imath U_0 + \imath\omega) & -U_0(-1 \pm k z_0) \end{pmatrix}$$

$$\mathbf{S}_0^{\uparrow} - \mathbf{S}_0^{\downarrow} = \frac{-2U_0^2 k^2 x_0^2}{(\kappa + \imath U_0 + \imath\omega)^2 + U_0^2(1-k^2x_0^2)} \mathbb{I}_2$$

$$\alpha_\pm = \alpha_\pm^{(0)} + \alpha_\pm^{(1)} e^{\imath\omega t} + \alpha_\pm^{(-1)} e^{-\imath\omega t} \ . \tag{22.141}$$

Finally,

$$\boxed{\alpha_\pm = -[1 + \mathbf{S}_0^{\uparrow} e^{\imath\omega t} + \mathbf{S}_0^{\downarrow} e^{-\imath\omega t}][\mathbf{L} + \mathbf{X}(\mathbf{S}_0^{\uparrow} - \mathbf{S}_0^{\downarrow})]^{-1}\eta_\pm} \ . \tag{22.142}$$

The Fig. 22.10 shows how the phase of the ring cavity behaves in time for various atom-field coupling constants.

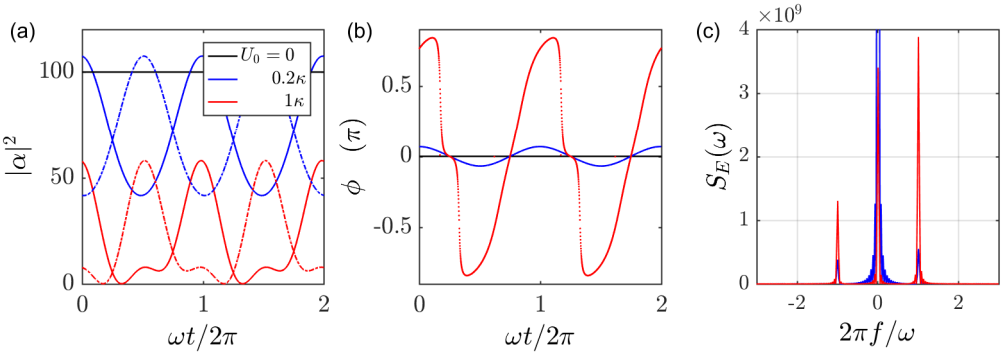

Figure 22.10: (code) (a) Photon number and (b) phase shift of the cavity in response to a modulated atomic position. The parameters are $kz_0 = 1$, $\kappa = (2\pi)\ 20\,\mathrm{kHz}$, $\omega = 2.5\kappa$, and $\eta_\pm = 10\kappa$. (c) Spectrum recorded behind a cavity mirror with the transmittivity $t_{\rm hr}$. The spectrum is obtained as the Fourier transform of the $g^{(1)}(\tau)$ correlation function of the transmitted field $\mathcal{E}_{\rm out} = t_{\rm hr} e^{\imath k a} \mathcal{E}_{\rm cav}$, where $e^{\imath k a}$ is a fixed phase factor depending on the mirror position a (see Sec. 17.3.2).

It is interesting to study the oscillatory response of the cavity-field to a forced atomic vibration, because it yields information about the cavity backaction. In fact, as shown above, the vibrating atom imprints sidebands to the intracavity refractive index [724, 7]. The sidebands appear in the cavity transmission spectrum. A more sophisticated method to detect the backaction could be to watch the response in the beat signal to a periodic modulation of the incoupled fields with a vibrating atom,

$$\dot\alpha_\pm = (-\kappa - \imath U_0)\alpha_\pm - \imath U_0 e^{\mp 2\imath k z_0 \sin\omega t}\alpha_\mp + \eta e^{\pm\imath\phi_0 \sin\omega_\phi t} \ . \tag{22.143}$$

We would expect a clear signature for resonance, $\omega_\phi = \omega$. The sidebands of the modulated pump would be coupled in, if they coincide. Instead of monitoring the cavity field, we could search the signature of the backaction in the atomic response. We will come back to this, when we discuss collective effects and the frequency shift of the center-of-mass motion. Do the Exc. 22.1.11.14.

22.1.9 Input-output theory for a single-ended linear cavity

Until now, we treated the in- and output fields of a cavity as classical variables (see Secs. 15.2.1), which is not helpful if we wish to detect quantum correlations outside the cavity. On the other hand, we treated the coupling of a cavity to free space as beam splitters in steady-state in Sec. 14.5.1. A generalization to time-dependent systems is provided by the so-called *input-output theory* [169, 304, 395, 498].

We consider a Hamiltonian containing the cavity and the input field as independent variables subject to noise,

$$\begin{aligned}\hat{H} &= \hat{H}_{\rm atm} + \hat{H}_{\rm cav} + \hat{H}_{\rm int} \\ &= \hat{H}_{\rm atm} - \hbar\Delta_{\rm c}\hat{a}^\dagger\hat{a} + \hbar g(\hat{a}\hat{S}_+ + \hat{S}_-\hat{a}^\dagger) - \hbar\imath\sqrt{\kappa\delta_{\rm fsr}}(\hat{a}\hat{a}_{\rm in}^\dagger - \hat{a}^\dagger\hat{a}_{\rm in})\end{aligned} \tag{22.144}$$

with

$$\hat{\mathbf{S}} = \sum_{j=1}^{N}\hat{\mathbf{s}}_j \qquad \text{and} \qquad \eta \to \sqrt{\kappa\delta_{\rm fsr}}\hat{a}_{\rm in}^\dagger\ . \tag{22.145}$$

With this Hamiltonian the Heisenberg equations of motion can be derived for every dynamic variable $\hat{a}$, $\hat{S}_+$, $\hat{S}_z$, and $\hat{a}_{\rm in}$.

22.1.10 Emission spectra of cavities interacting with atoms

The spectral features of light emitted from cavities reveal important information on the physical processes underlying the atom-cavity interaction. For example, when atoms interacting with a 'bad cavity' are incoherently pumped rather than the cavity mode itself, in certain parameter regimes the emission spectra reveals extremely narrow bandwidths [565, 135] known as superradiant lasing. When in contrast the cavity is pumped, at sufficiently high collective cooperativity we expect normal-mode splitting of the emission spectrum.

Below saturation, the atomic states can be adiabatically eliminated, i.e. we end up with equations of motion only depending on $\hat{a}$ and $\hat{a}^\dagger$. An interesting question is whether this may facilitate the calculations of $\langle\hat{a}^\dagger(t+\tau)\hat{a}(t)\rangle \longrightarrow \langle\alpha^*(t+\tau)\alpha(t)\rangle$. It is not obvious and certainly wrong for the saturated regime. In Exc. 22.1.11.15 we study the spectrum of resonance fluorescence emitted by a ring cavity incorporating a beam splitter.

Numerically, the spectra can easily be calculated using the 'QuantumOptics.jl' or the 'QuantumCumulants.jl' frameworks for the Julia programming language [135, 661]. Fig. ?? shows an example calculated for a single atom and a cavity mode expanded into a Fock basis assuming various photon cut-off numbers.

The spectra exhibited in Fig. 22.11 are understood within the Jaynes-Cummings model as transitions between the lowest-lying levels, whose energies E_n in the resonant case $\Delta_{\rm c} = 0 = \Delta_{\rm a}$ are given by $E_0 = 0$, $E_1 = \omega \pm g$, $E_1 = 2\omega, 2\omega \pm g\sqrt{2}$ and $E_2 = 3\omega \pm (\sqrt{3}-\sqrt{2}), 3\omega \pm g(\sqrt{3}+\sqrt{2})$.

The approach used in Fig. 22.11 is limited to modest cut-off photon numbers and thus relatively low saturation parameters, $ns_1 \approx 11.7\eta_+^2/\kappa^2$. An alternative approach is the cumulant expansion method [661]. In Exc. 22.1.11.16 we study the spectrum of resonance fluorescence emitted by a linear cavity interacting with a single atom.

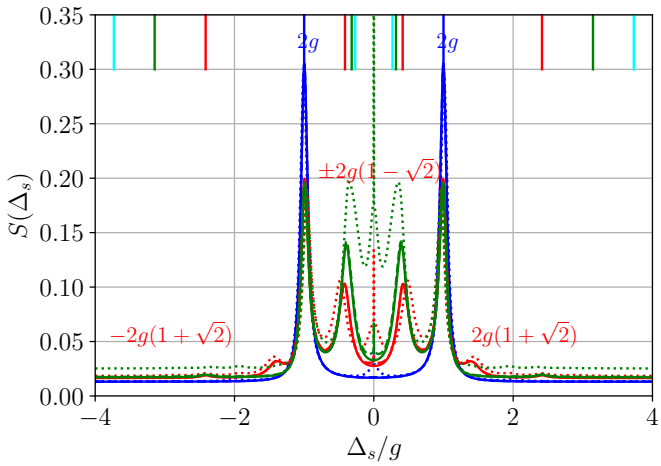

Figure 22.11: (code) Emission spectra of a linear cavity interacting with $N = 1$ atom and $\Gamma = 0.0022\kappa$, $g = 6\kappa$, and $\eta_- = 0$. The lines colors denote pump rates of (blue) $\eta_+ = 0.1$, (red) $\eta_+ = 0.5\kappa$, and (green) $\eta_+ = 1\kappa$. The line styles denote photon cut-off numbers of (solid) $n_{\text{cutoff}} = 1$, (dashed) $n_{\text{cutoff}} = 2$, and $n_{\text{cutoff}} = 5$.

22.1.11 Exercises

22.1.11.1 Ex: Cooperative Lamb shift in a cavity

Calculate the cooperative Lamb shift in a cavity from the second formula (22.12) and plot the result as a function of the cavity detuning.

22.1.11.2 Ex: Cooperative amplification for a rubidium gas in a cavity

Consider an non-degenerate cavity characterized by $\delta_{\text{fsr}} = 2\,\text{GHz}$, $F = 80$, and $w_0 = 6\,\mu\text{m}$. In order to benefit from the cooperativity of the cavity, the atoms must be within a volume axially delimited by the Rayleigh length and radially by the diameter of the mode near its waist.
a. Calculate the Rayleigh length for a wavelength of 780 nm and the mode volume.
b. For a given partial pressure of rubidium at room temperature of $p \approx 10^{-5}\,\text{Pa}$, calculate the average number of atoms within the mode volume.
c. Of these atoms only those with an axial Doppler shift below $kv_z < \kappa$ emit resonantly into the cavity. Calculate the number of these atoms from the Maxwell-Boltzmann distribution.
d. Calculate the cooperative amplification of the emission rate into the cavity.

22.1.11.3 Ex: Characteristic parameters for various atom-cavity systems

Complete the following table calculating κ, $V_{\rm m}$, ω_r, g_1, Υ, s, and r,

	rubidium	strontium
Γ	6 MHz	6.8 kHz
$\mathcal{F}$	250000	250000
L	100 μm	3 cm
w_0	20 μm	70 μm

22.1.11.4 Ex: Number of photons in a cavity

a. How many photons are in the mode of a cavity with finesse $F = 80000$ (i) in resonance and (ii) out of resonance resonantly pumped with a laser power of $P_{\rm in} = 100\,\mu$W?
b. What power must be injected to produce 1 photon inside the cavity?
c. Resonant backscattering by the cavity mirrors can scatter photons into the reverse mode. Typically, $P_-/P_+ \simeq 0.005$. Hence, $n^{on}_{-,cav} = 1.5\times10^7$ and $n^{off}_{-,cav} = 0.01$. Using advanced techniques it is possible to reduce the number of backscattered photons by factor of > 20. Assuming that the losses due to backscattering are $S = 1$ ppm. Can the resonant backscattering by the mirrors destroy a BEC?
d. What is the amplitude of the output signal in terms of photons?

22.1.11.5 Ex: Saturation-induced bistability in a linear cavity

a. Derive the equations of motion for N immobile atoms located at positions z_j along the optical axis of and interacting with a linear cavity.
b. Assuming steady-state and doing the mean-field approximation isolate an equation for the cavity field $\alpha \equiv \langle \hat{a} \rangle$.
c. Simplify the equation for α for the case of perfect bunching $z_j = z$ and solve it analytically. Identify the instability.
d. Discuss the weak excitation limit.
e. Derive the transmission spectrum in the weak excitation limit.
f. Write down the equation for $n = |\alpha|^2$ for the resonant case, $\Delta_{\rm c} = 0 = \Delta_{\rm a}$, in terms of the single-atom cooperativity parameter $\Upsilon \equiv 4g^2/\gamma\Gamma$ and the single-photon saturation parameter $s_1 \equiv 8g^2/\Gamma^2$.

22.1.11.6 Ex: PDH-probing atoms in a ring cavity

Calculate the steady-state reflection of a phase-modulated laser beam from a ring cavity neglecting backscattering from the atoms. Demodulate the reflection signal with the modulation frequency.

22.1.11.7 Ex: Normal mode splitting of a ring cavity

Consider the stationary fields (22.87) developing in a ring cavity containing a homogeneous cloud of atoms and pumped in one direction, $\eta_- = 0$. For this system.
a. Calculate the transmission of the cavity in the direction of mode α_+ as a function of the detunings $\Delta_{\rm a}$ and $\Delta_{\rm c}$ and the number of atoms.

Transmission spectra can be recorded under various boundary conditions. Calculate the transmission
b. keeping the laser at a fixed frequency ω and varying the cavity length ω_c;
c. tuning a cavity resonance to the atomic transition, $\omega_c = \omega_a$, and varying the laser frequency ω;
d. same as (d), but now calculate the detunings Δ_{ch} where the transmission drops to 1/2;
e. keeping the cavity constant at an *arbitrary* frequency ω_c and varying the laser frequency ω;
f. keeping the laser locked to the cavity, $\omega = \omega_c + NU_0$, and now ramping the cavity across the atomic resonance.

22.1.11.8 Ex: Time-dependent solution for a ring cavity pumped from one side below saturation

Derive the complete solution of the adiabatic field equations (22.104).

22.1.11.9 Ex: Filling and drainage of a ring cavity with one fixed atom

Calculate by simulation of the classical cavity equations, how a laser-pumped ring cavity fills and looses photons in the presence of a single immobile atom.

22.1.11.10 Ex: Position of the phase without pumping of the cavity

Solve the Schrödinger equation (22.110) by inserting ansatz,

$$\vec{\alpha} = \vec{\alpha}_1 e^{-\lambda_1 t} + \vec{\alpha}_2 e^{-\lambda_2 t} \ ,$$

where $\lambda_1 = \kappa + 2\imath U_0$ and $-\lambda_2 = \kappa$ are the eigenvalues of the matrix (22.110).

22.1.11.11 Ex: Dynamics of a standing wave in a symmetrically pumped ring cavity

Solve and discuss the equation (22.130).

22.1.11.12 Ex: Stationary position of the atom in a unidirectionally pumped ring cavity

What is the steady state position of an atom interacting with the modes of a unidirectionally pumped ring cavity?

22.1.11.13 Ex: Equations of motion for intensities and coherences in a ring cavity

Derive from the equations (22.104) the equations of motion for intermodal coherences $\alpha_+\alpha_+^*$, $\alpha_-\alpha_-^*$, $\alpha_+\alpha_-^*$, and $\alpha_-\alpha_+^*$.

22.1.11.14 Ex: Backaction of atomic vibration on the modes of a symmetrically pumped ring cavity

a. Calculate the Lamb-Dicke parameter for gravitation-induced Bloch oscillations in a strontium gravimeter, as well as the modulation index. Is the continued fractions method applicable?
b. Study the dynamics of the counterpropagating light modes of a ring cavity in the presence of an atom whose position is periodically modulated with a given frequency by numerical integration of the equations of motion (22.104). Compare with the results obtained by the method of continued fractions proposed in Sec. 22.1.8.

22.1.11.15 Ex: Fluorescent emission of a ring cavity for one-sided pumping in the adiabatic approximation

Based on the solution of the adiabatic field equations derived in Exc. 22.1.11.8 calculate the emission spectrum of the ring cavity driven below saturation (where the adiabatic approximation is good) from one side ($\eta_- = 0$) for both counter-propagating directions ($\alpha_\pm$). Compare with numerical solutions.

22.1.11.16 Ex: Emission spectrum of atoms in a linear cavity below saturation

a. Derive the mean-field evolution equation for the intracavity field $\alpha(t) = \langle \hat{a}(t) \rangle$ for a linear cavity driven below saturation.
b. Is it possible to calculate the autocorrelation spectrum and the emission spectrum of the cavity from $\langle \alpha^*(t+\tau)\alpha(t) \rangle$ [135, 661]?
c. Calculate numerically the emission spectrum of a linear cavity interacting with many atoms using for the cavity mode a Fock state expansion up to a cut-off photon number of $n_{\text{cutoff}} = 10$. Assume $(\eta, \Gamma, N, g_1, \Delta) = (0.1\kappa, 0.002\kappa, 100000, 0.002\kappa, 0)$. Interpret the result [621, 309].

22.2 Interaction of atoms with surfaces

22.2.1 Local density of states for atoms near surfaces

In the following sections we consider two-level atoms interacting with meta-materials. An atom consists of a discrete set of levels between which electric or magnetic transitions characterized by dipole moments $\mathbf{d}$ can be excited via vectorial laser light. The meta-material medium is defined by its spatially and frequency dependent relative permittivity, $\varepsilon(\mathbf{r};\omega)$ and relative permeability, $\mu(\mathbf{r};\omega)$ [8].

The way how the atom and the medium interact can be understood introducing the notion of the photonic local density of states (LDOS). The medium shapes, via ε and μ, the LDOS for any radiation field the medium can sustain, assuming that the atom itself does not modify the LDOS. To calculate the density of states one must solve Maxwell equations and obtain the Green function $\mathcal{G}(\mathbf{r}, \mathbf{r}';\omega)$, which completely describes the material. The density of states is proportional to the imaginary part

[8] Note that the assumption of Drude type function is often a good one.

of Green function. Furthermore, the Green function permits to calculate easily the propagation of an incident light field through the medium [9], and hence the local radiation intensity $\vec{\mathcal{E}}(\mathbf{r};\omega)$.

After this, one has to set up the Hamiltonian for the atom located at position $\mathbf{r}_a$ near the dielectric and solve, with a suitable ansatz, the Schrödinger equation. This yields the time evolution of the atomic state excitation probabilities [442, **?**].

22.2.1.1 Density of states from Maxwell's equations

The density of states (DOS), the group velocity, and the distribution function are necessary for calculating various macroscopic quantities like specific heat, thermal conductivity, energy density, and radiation intensity. The local density of states (LDOS) is a generalization of the DOS and, unlike the DOS, a position dependent quantity. Like the DOS, the LDOS depends on the type of carrier - electron, phonon, or photon. It is generally related to the Green's function of the appropriate governing equation (Schrödinger equation for electrons, wave equation for long wavelength phonons, and Maxwell's equation for photons) and boundary conditions. Here, we are concerned with the photonic or electromagnetic LDOS [618].

The electromagnetic LDOS is related to the dyadic Green's function (DGF) of the vector Helmholtz equation. In free space the electric field and the magnetic field contributions are equal in the absence of scatterers. In other circumstances, however, there is a contribution to the LDOS from the magnetic field energy, and it is related to the magnetic DGF. Since the pioneering work of *Purcell* it is well known that the spontaneous emission rate of molecules is strongly affected by their vicinity to macroscopic objects. The LDOS (both electric and magnetic) also plays an important role in *Casimir* forces between objects. The Maxwell stress tensor in vacuum at thermal equilibrium can be expressed compactly in terms of the electric and magnetic DGF.

22.2.1.2 Local density of states (LDOS) and the decay rate

The concepts of density of states (DOS) and local density of states (LDOS) can be introduced starting from the situation of a non-absorbing and non-dispersive medium, $\varepsilon(\mathbf{r};\omega) = \varepsilon(\mathbf{r}) \in R^{>0}$, embedded in a closed cavity with volume $V = L^3$ assuming that $L \ll \lambda$, λ being the wavelength in vacuum). Then, a discrete set of eigenmodes of the vector Helmholtz equation can be obtained solving the eigenvalue equation [140],

$$\nabla \times \nabla \times \mathbf{e}_n(\mathbf{r}) = \varepsilon(\mathbf{r}) \frac{\omega_n^2}{c^2} \mathbf{e}_n(\mathbf{r}) \ , \tag{22.146}$$

yielding the eigenvalues ω_n/c as well as the eigenfunctions $\mathbf{e}_n(\mathbf{r})$. Since the differential operator is Hermitian, the eigenfunctions are orthogonal,

$$\int \varepsilon(\mathbf{r}) \mathbf{e}_m^*(\mathbf{r}) \cdot \mathbf{e}_n(\mathbf{r}) d^3r = \delta_{mn} \ . \tag{22.147}$$

[9] Note that even without incident radiation the medium influences the atomic dynamics via the LDOS.

The DOS $\rho(\omega)$ at a frequency ω counts the number of eigenmodes in an infinitely small frequency range and is defined as,

$$\rho(\omega) = \tfrac{1}{V} \sum_n \delta(\omega - \omega_n) \ . \tag{22.148}$$

This DOS is a global quantity that characterizes the spectral density of eigenmodes of the medium as a whole. A local quantity $\rho(\mathbf{r}, \omega)$ (LDOS) can be introduced through a summation weighted by the amplitude of the eigenmodes at point $\mathbf{r}$,

$$\boxed{\rho(\mathbf{r}, \omega) = \sum_n |\hat{\mathbf{e}}_n(\mathbf{r})|^2 \delta(\omega - \omega_n)} \ . \tag{22.149}$$

This relation defines the LDOS in the particular case of a medium for which a discrete set of eigenmodes can be introduced.

The (electric) LDOS (22.149) can be reformulated in terms of the electric Green function $\mathcal{G}(\mathbf{r}, \mathbf{r}', \omega)$ being the solution of the vector Helmholtz equation derived in electrodynamics,

$$\left[\nabla \times \nabla \times - \varepsilon_r(\mathbf{r}, \omega) \frac{\omega^2}{c^2} \right] \mathcal{G}(\mathbf{r}, \mathbf{r}' \omega) = \delta^{(3)}(\mathbf{r} - \mathbf{r}') \mathbb{I} \ . \tag{22.150}$$

The solution can be cast into the shape,

$$\boxed{\mathcal{G}(\mathbf{r}, \mathbf{r}', \omega) = c^2 \sum_n \hat{\mathbf{e}}_n^*(\mathbf{r}') \otimes \hat{\mathbf{e}}_n(\mathbf{r}) \left[\mathcal{PV} \left(\frac{1}{\omega_n^2 - \omega^2} \right) + \frac{\imath \pi}{2\omega_n} \delta(\omega - \omega_n) \right]} \ . \tag{22.151}$$

With this result, the LDOS can be written,

$$\begin{aligned} \rho(\mathbf{r}, \omega) &= \frac{2\omega}{\pi c^2} \mathfrak{Im} \, \mathrm{Tr} \ \mathcal{G}(\mathbf{r}, \mathbf{r}, \omega) \qquad (22.152) \\ &= \frac{2\omega}{\pi c^2} \mathrm{Tr} \ c^2 \sum_n \mathbf{e}_n^*(\mathbf{r}) \otimes \mathbf{e}_n(\mathbf{r}) \frac{\pi}{2\omega_n} \delta(\omega - \omega_n) = \sum_n \mathbf{e}_n^*(\mathbf{r}) \cdot \mathbf{e}_n(\mathbf{r}) \delta(\omega - \omega_n) \ . \end{aligned}$$

This result shows that shows that the correct counting of eigenmodes is implicit in the Green function, although the latter can be computed by solving the Helmholtz equation without referring to any set of eigenmodes. In particular, the expression (22.152) even holds for lossy media, when a basis of eigenmodes cannot be defined [140].

22.2.1.3 Power radiated by a classical dipole

The Green tensor defined by (22.150) permits the calculation of the electric field generated by a current density according to,

$$\vec{\mathcal{E}}(\mathbf{r}, \omega) = \imath \omega \mu_0 \int_V d^3 r' \mathcal{G}(\mathbf{r}, \mathbf{r}', \omega) \cdot \mathbf{j}(\mathbf{r}', \omega) \ . \tag{22.153}$$

For a classical point-dipole the solution can be given explicitly. The radiated power is simply,

$$P = -\tfrac{1}{2} \mathfrak{Re} \int \mathbf{j}^*(\mathbf{r}) \cdot \vec{\mathcal{E}}(\mathbf{r}) d^3 r \ . \tag{22.154}$$

With the current density parametrized as $\mathbf{j}(\mathbf{r}) = \dot{\mathbf{d}}_{eg}\delta(\mathbf{r}-\mathbf{r}_s) = -\imath\omega\mathbf{d}_{eg}\delta(\mathbf{r}-\mathbf{r}_s)$ we get,

$$P = \frac{\omega}{2}\mathfrak{Im}\left[\mathbf{d}_{eg}^* \cdot \vec{\mathcal{E}}(\mathbf{r}_s)\right] . \tag{22.155}$$

From (22.154) we obtain,

$$P = \frac{\mu_0\omega^3}{2}|\mathbf{d}_{eg}|^2\mathfrak{Im}\left[\hat{\mathbf{e}}_d\ \mathcal{G}(\mathbf{r},\mathbf{r}',\omega)\ \hat{\mathbf{e}}_d\right] , \tag{22.156}$$

where $\hat{\mathbf{e}}_d$ is the unit vector along the dipole. In this expression we assume that the source point $\mathbf{r}_s$ is located in vacuum, but the Green function $\mathcal{G}(\mathbf{r},\mathbf{r}_s,\omega)$ can describe an arbitrary environment surrounding the emitter. In particular, the emitted power calculated in this way accounts both for far-field radiation and absorption in the environment.

In the case of a dipole with a fixed orientation $\hat{\mathbf{e}}_d$, we can define a projected LDOS (sometimes called partial LDOS),

$$\rho_{\mathbf{d}}(\mathbf{r}_s,\omega) = \frac{2\omega}{\pi c^2}\mathfrak{Im}\left[\hat{\mathbf{e}}_d\ \mathcal{G}(\mathbf{r}_s,\mathbf{r}_s,\omega)\ \hat{\mathbf{e}}_d\right] \tag{22.157}$$

so that the full LDOS is,

$$\rho(\mathbf{r}_s,\omega) = \sum_{\hat{\mathbf{e}}_{dx},\hat{\mathbf{e}}_{dy},\hat{\mathbf{e}}_{dz}} \rho_{\mathbf{d}}(\mathbf{r}_s,\omega) = \frac{2\omega}{\pi c^2}\mathfrak{Im}\,\mathrm{Tr}\ \mathcal{G}(\mathbf{r}_s,\mathbf{r}_s,\omega) . \tag{22.158}$$

The projected LDOS accounts for radiation by an electric dipole with a given orientation,

$$\boxed{P = \frac{\pi\omega^2}{4\varepsilon_0}|\mathbf{d}_{eg}|^2\rho_{\mathbf{d}}(\mathbf{r}_s,\omega)} . \tag{22.159}$$

Example 133 (*LDOS in free space*): In the particular case of a dipole placed in 3D free space, the power transferred to the environment equals the power radiated to far-field radiation. It can be obtained from the free-space dyadic Green function $\mathcal{G}_0(\mathbf{r},\mathbf{r}_s,\omega)$, whose imaginary part at $\mathbf{r}=\mathbf{r}_s$ is obtained from the Green tensor calculated for a bulk medium by setting $\mathbf{r}=\mathbf{r}'=\mathbf{r}_s$,

$$\mathfrak{Im}\,\mathcal{G}^{(0)}(\mathbf{r}_s,\mathbf{r}_s,\omega) = \frac{k_0}{6\pi}\mathbb{I} . \tag{22.160}$$

With this, the projected LDOS (22.157) along $\hat{\mathbf{e}}_d$ becomes,

$$\rho_{\mathbf{d}}^{(0)}(\mathbf{r}_s,\omega) = \frac{\omega^2}{3\pi^2c^3} , \tag{22.161}$$

and the full LDOS (22.158),

$$\rho^{(0)}(\mathbf{r}_s,\omega) = \frac{\omega^2}{\pi^2c^3} . \tag{22.162}$$

The emitted power becomes,

$$P^{(0)} = \frac{\omega^4}{12\pi\varepsilon_0c^3}|\mathbf{d}_{eg}|^2 . \tag{22.163}$$

22.2.1.4 Spontaneous emission by a quantum emitter in the weak coupling regime

The spontaneous emission rate can be evaluated in perturbation theory from Fermi's golden rule,

$$\frac{P}{\hbar\omega} \longrightarrow \frac{\pi\omega^2}{4\varepsilon_0}|\mathbf{d}|^2\rho_{\mathbf{d}}(\mathbf{r}_s,\omega) = \frac{\pi\omega_{eg}}{\hbar\varepsilon_0}|\hat{\mathbf{d}}_{eg}|^2\rho_{\mathbf{d}}(\mathbf{r}_s,\omega_{eg}) = \Gamma \ . \tag{22.164}$$

The correction factor comes from the fact that in quantum mechanics, unlike in in classical mechanics, positive and negative frequency components are treated separately as absorption resp. stimulated emission.

In free space, with the formula (22.161) we calculate for the relationship between spontaneous emission rate and the induced dipole moment,

$$\boxed{\Gamma^{(0)} = \frac{\omega_{eg}^3}{3\pi\hbar\varepsilon_0 c^3}|\mathbf{d}_{eg}|^2} \ , \tag{22.165}$$

which coincides with the expression (16.41).

22.2.1.5 Purcell factor and Lamb shift

The Purcell factor is defined as the ratio between the decay rates in the presence and in the absence of boundary conditions. It can this be evaluated from the expression (22.164) as,

$$\frac{\Gamma}{\Gamma^{(0)}} = \frac{\rho_{\mathbf{d}}(\mathbf{r}_s,\omega)}{\rho_{\mathbf{d}}^{(0)}(\mathbf{r}_s,\omega)} = \frac{6\pi c}{\omega_{eg}}\mathfrak{Im}\,\hat{\mathbf{e}}_d\ \mathcal{G}(\mathbf{r}_s,\mathbf{r}_s,\omega)\ \hat{\mathbf{e}}_d \ . \tag{22.166}$$

22.2.2 Interaction between atomic dipoles

Until now we concentrated on simple dipole in the environment of dielectric boundaries. We will now extend the formalism to interacting dipoles located at positions $\mathbf{r}_i$ and $\mathbf{r}_j$.

Intermolecular energy transfer can occur through two mechanisms, namely, radiationless short-range transfer, also called *Förster transfer*, and radiative long-range transfer [252, 731]. In the former the distance R between donor and acceptor is small compared with the electronic-energy-transfer wavelength $R \ll \lambda_A$. The free-space transfer rate behaves as R^{-6}, which can be explained by the instantaneous (longitudinal) Coulomb interaction between the two molecules. In the latter the intermolecular distance substantially exceeds the transition wavelength, $R \gg \lambda_A$. The observed R^{-2} dependence of the transfer rate can be regarded as being the result of emission and reabsorption of real (transverse) photons, see Sec. 22.1.1.

The Purcell factor (22.166) allows us to calculate the modification of the decay rate in the presence of a Green tensor. In the absence of boundaries we use the bulk

medium Green tensor,

$$\begin{aligned}\Gamma^{(b)} &= 3\lambda\Gamma^{(0)}\hat{\mathbf{e}}_d^*\ \mathfrak{Im}\,\mathcal{G}_b(\mathbf{r},\mathbf{r}',\omega)\ \hat{\mathbf{e}}_d \\ &= \tfrac{3}{2}\Gamma^{(0)}\left[\left(j_0(kR)-\frac{j_1(kR)}{kR}\right)\mathbb{I}+j_2(kR)(\hat{\mathbf{e}}_d\cdot\hat{\mathbf{e}}_R)^2\right] \\ &= \tfrac{3}{2}\Gamma^{(0)}\left[(1-(\hat{\mathbf{e}}_d\cdot\hat{\mathbf{e}}_R)^2)\frac{\sin kR}{kR}+(1-3(\hat{\mathbf{e}}_d\cdot\hat{\mathbf{e}}_R)^2)\left(\frac{\cos kR}{k^2R^2}-\frac{\sin kR}{k^3R^3}\right)\right]\ ,\end{aligned} \tag{22.167}$$

where $k^2=(\omega/c)^2\varepsilon\mu$ and $\mathbf{R}\equiv\mathbf{r}-\mathbf{r}'$ and j_n are the spherical Bessel functions of the first kind.

Similarly, the Lamb shift can be calculated,

$$\begin{aligned}\Delta^{(b)} &= -\tfrac{3}{2}\lambda\Gamma^{(0)}\hat{\mathbf{e}}_d^*\ \mathfrak{Re}\,\mathcal{G}_b(\mathbf{r},\mathbf{r}',\omega)\ \hat{\mathbf{e}}_d \\ &= \tfrac{3}{4}\Gamma^{(0)}\left[\left(y_0(kR)-\frac{y_1(kR)}{kR}\right)\mathbb{I}+y_2(kR)(\hat{\mathbf{e}}_d\cdot\hat{\mathbf{e}}_R)^2\right] \\ &= \tfrac{3}{4}\Gamma^{(0)}\left[(1-(\hat{\mathbf{e}}_d\cdot\hat{\mathbf{e}}_R)^2)\frac{\cos kR}{kR}-(1-3(\hat{\mathbf{e}}_d\cdot\hat{\mathbf{e}}_R)^2)\left(\frac{\sin kR}{k^2R^2}+\frac{\cos kR}{k^3R^3}\right)\right]\ ,\end{aligned} \tag{22.168}$$

where y_n are the spherical Bessel functions of the second kind. Again, the second line is obtained for free space.

At long distances, $kR>1$, the results (22.167) and (22.168) simplify to,

$$\boxed{\begin{array}{rcl}\Delta^{(b)} &\simeq& \tfrac{3}{4}\Gamma^{(0)}[1-(\hat{\mathbf{e}}_d\cdot\hat{\mathbf{e}}_R)^2]\frac{\cos kR}{kR}\\ \Gamma^{(b)} &\simeq& \tfrac{3}{2}\Gamma^{(0)}[1-(\hat{\mathbf{e}}_d\cdot\hat{\mathbf{e}}_R)^2]\frac{\sin kR}{kR}\end{array}}\ , \tag{22.169}$$

and at very long distances, $kR\gg1$, $\Delta^{(b)}\to0\leftarrow\Gamma^{(b)}$. This atomic dipole-dipole interaction will play a role in the generation of interatomic correlations studied in Sec. 23.3.2. Do the Exc. 22.2.3.1.

At short distances, $kR\ll1$, and assuming, $\hat{\mathbf{e}}_d=\hat{\mathbf{e}}_R$, the same formula becomes,

$$\boxed{\begin{array}{rcl}\Delta^{(b)} &\simeq& -\tfrac{3}{2}\lambda\Gamma^{(0)}\hat{\mathbf{e}}_d^*\mathfrak{Re}\,\mathcal{G}_b(\mathbf{r},\mathbf{r}',\omega)\hat{\mathbf{e}}_d\to-\frac{C_3}{R^3}\\ \Gamma^{(b)} &\simeq& 3\lambda\Gamma^{(0)}\hat{\mathbf{e}}_d^*\mathfrak{Im}\,\mathcal{G}_b(\mathbf{r},\mathbf{r}',\omega)\hat{\mathbf{e}}_d\to0\end{array}} \tag{22.170}$$

with $C_3=\frac{3\Gamma^{(0)}}{2k^3}$.

22.2.2.1 Derivation of the Hamiltonian

First for one atom interacting with a dielectric then for two atoms,

$$\hat{H}=\int d^3r\int_0^\infty d\omega\hbar\omega\hat{\mathbf{f}}^\dagger(\mathbf{r},\omega)\hat{\mathbf{f}}(\mathbf{r},\omega)+\sum_{i=0}^{N}\hbar\omega_i\hat{\sigma}_i^+\hat{\sigma}_i-\sum_{i=0}^{N}\int_0^\infty d\omega\left[\hat{\mathbf{d}}_i\cdot\vec{\mathcal{E}}(\mathbf{r}_i,\omega)+H.c.\right]\ . \tag{22.171}$$

Here, $\hat{\mathbf{f}}(\mathbf{r},\omega)$ are polaritonic bosonic operators associated with the annihilation of the corresponding matter-light elementary excitations. The field operator is [297, 762],

$$\vec{\mathcal{E}}(\mathbf{r},\omega)=\imath\vec{\epsilon}\sqrt{\frac{\hbar}{\pi\varepsilon_0}}\frac{\omega^2}{c^2}\int\sqrt{\mathfrak{Im}\,\varepsilon_r(\mathbf{r}',\omega)}\mathcal{G}(\mathbf{r},\mathbf{r}',\omega)\hat{\mathbf{f}}(\mathbf{r}',\omega)d^3r'\ . \tag{22.172}$$

22.2.3 Exercises

22.2.3.1 Ex: Coupled dipoles model near dielectrics

Develop the vectorial coupled dipoles model in the vicinity of a dielectric using the Green tensor formalism.

22.2.3.2 Ex: Scattering Green tensor above a dielectric surface

In this exercise we calculate the Green tensor for two atomic dipoles above a homogeneous dielectric filling the $z < 0$ half space.
a. Formulate the problem.
b. Simplify the scattering Green tensor obtained by [442] for that situation.
c. Simplify the Green tensor by assuming all atoms aligned along the y-axis at equal height from the dielectric.
d. Assume the atomic dipole moment to be aligned along the z-axis.
e. Derive the Green tensor for a single atom above the dielectric.

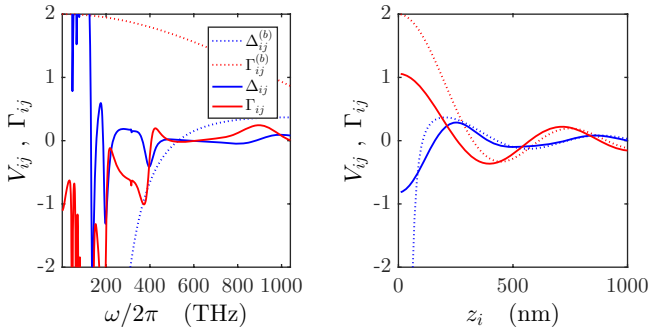

Figure 22.12: Scattering Green tensor for region-wise homogeneous dielectrics.

22.3 Further reading

A.N. Poddubny et al., *Microscopic model of Purcell enhancement in hyperbolic metamaterials* [DOI]

Wenlong Gao et al., *Topological Photonic Phase in Chiral Hyperbolic Metamaterials* [DOI]

Haibin Wu et al., *Observation of Intracavity Electromagnetically InducedTransparency and Polariton Resonances in a Doppler-Broadened Medium* [DOI]

Xiaodong Zeng et al., *Spontaneous emission interference enhancement with a μ-negative metamaterial slab* [DOI]

Xiaodong Zeng et al., *Enhancement of the vacuum Rabi oscillation via surface plasma modes in single-negative metamaterials* [DOI]

F. Dubin et al., *Photon Correlation versus Interference of Single-Atom Fluorescence in a Half-Cavity* [DOI]

U. Dorner et al., *Laser-driven atoms in half-cavities* [DOI]

P. Lambropoulos et al., *Fundamental quantum optics in structured reservoirs* [DOI]

Chapter 23

Dicke model and spin squeezing

In Chps. 16 to 20 we concentrated on understanding the interaction of *single* atoms with light fields. In particular, we introduced the Rabi and the Jaynes-Cummings model. In Chp. 21 we introduced the coupled dipoles model for the interaction of many atoms with a single photon. In the following chapters, we will extend these models to several and many atoms and many photons.

It does not come as a surprise that totally new phenomena arise from the collective interaction of several atoms with a single light mode. For instance, the atomic cloud can evolve toward a spin-squeezed or an entangled state, or it can emit light in a super- and subradiant way. The interplay between collective processes and processes favoring an individualization of the atom-light interaction is subtle, and the different models used to understand the processes only grasp partial aspects. The difficulty arises from the complexity of the task of describing the dynamics of N evolving in a Hilbert space of dimension 2^N. Approximations used to reduce the complexity of the Hilbert space come at the price of eventually loosing some interesting features. On the other hand, they may also help to crystallize fundamental symmetries, which allow us to deepen our intuition on the collective behavior of the many-body system.

Famous models used in the description of collective scattering are (among others) the Dicke model and the Tavis-Cummings model (see table above). The Dicke model (presented in Sec. 23.1) assumes a total indistinguishability of the atoms, the Tavis-Cummings (discussed in Sec. 23.2 and used for the purpose of quantum computation) makes use of the rotating-wave approximation. Both models are based on the assumption of non-interacting atoms, neither by ground state collisions nor via radiation exchange, which certainly is a good assumption in the case of dilute atomic samples. On the other hand, we saw in the discussion of the coupled dipoles model in Chp. 21 that already the presence of a single photon in an atomic cloud leads noticeable interatomic interaction effects. In Sec. 23.3 we will extend the Dicke model to interacting atoms.

Finally, new phenomena arise from the presence of optical cavities shaping the spatial and spectral distribution of electromagnetic vacuum modes (see Chp. 22) and from the consideration of photonic recoil (see Chp. 25).

23.1 The Dicke model of collective spin states

As we have seen in Sec. 1.5.8, the Hilbert space increases exponentially with the numbers of particles considered, the dimension of the Hilbert space of N particles being 2^N. This obviously presents a problem for numerical simulations, and simplifying models are needed. One of them is the *Dicke model*, where the N atoms are described as spin-$\frac{1}{2}$ particles and their collective interaction with a *single mode* light field via a single collective spin $\mathbf{S}$ with $S = N/2$. In this model, the dimension of the Hilbert space only scales polynomially as $2S + 1$.

In the next sections, we will introduce this model detailing its advantages and limitations and emphasizing its relations to super- and subradiance, spin squeezing and entanglement. In particular we will show that, when the coupling between the light and matter crosses a critical value, the Dicke model shows a mean-field phase transition to a superradiant phase.

23.1.1 Dicke states

The Hilbert space of the Dicke model [229, 387] is given by (the tensor product of) the states of the cavity and of the two-level atoms [1]. The Hilbert space of the cavity can be spanned by Fock states $|n\rangle$. Choosing the basis $|+\rangle \equiv \binom{0}{1}$ and $|-\rangle \equiv \binom{1}{0}$, the states of each two-level atom $j = 1, 2, .., N$ are defined through the spin operators $\hat{\mathbf{s}}_j = (\hat{s}_j^x, \hat{s}_j^y, \hat{s}_j^z)$ acting only an individual atom [2],

$$\begin{aligned} \hat{s}_j^x|... \pm ...\rangle &= \tfrac{1}{2}|... \mp ...\rangle \\ \hat{s}_j^y|... \pm ...\rangle &= \pm\imath\tfrac{1}{2}|... \mp ...\rangle \\ \hat{s}_j^z|... \pm ...\rangle &= \pm\tfrac{1}{2}|... \pm ...\rangle \ , \end{aligned} \tag{23.1}$$

and satisfying the spin algebra,

$$[\hat{s}_j^x, \hat{s}_k^y] = \imath\hat{s}_j^z\delta_{j,k} \ , \tag{23.2}$$

and related to the *Pauli spin matrices* (1.154) via,

$$\hat{\mathbf{s}} = \tfrac{1}{2}\vec{\hat{\sigma}} \quad , \quad \hat{s}^{\pm} = \hat{s}^x \pm \imath\hat{s}^y = \tfrac{1}{2}(\hat{\sigma}_x \pm \imath\hat{\sigma}_y) = \hat{\sigma}^{\pm} \ . \tag{23.3}$$

The Hamiltonian of the Dicke model is,

$$\hat{H} = -\Delta_c\hat{a}^\dagger\hat{a} + \sum_{j=1}^{N}\left(-\Delta_a\hat{s}_j^z + 2g(\hat{a} + \hat{a}^\dagger)\hat{s}_j^x + 2\imath g(\hat{a} - \hat{a}^\dagger)\hat{s}_j^y\right) \ . \tag{23.4}$$

Sometimes in literature the single-atom coupling strength (or half the single-atom single-photon Rabi frequency) is normalized to the atom number, $g \equiv \lambda/\sqrt{N}$. The coupling can be written as the sum of two terms: a co-rotating term that conserves the number of excitations and is proportional to $\hat{a}\hat{\sigma}^+ + \hat{a}^\dagger\hat{\sigma}^-$ and a counter-rotating term proportional to $\hat{a}\hat{\sigma}^- + \hat{a}^\dagger\hat{\sigma}^+$.

[1] Dicke states can also be introduced in the context of the Jaynes-Cummings model (see Sec. 23.1.1).

[2] Note, that here and in the following we set $\hbar \equiv 0$ for simplicity.

The above Hamiltonian assumes that all the spins are identical, i.e. they have the same transition frequency, they do not interact with each other, and they equally couple to the radiation field (e.g. a cavity mode). For the simple system of only two not mutually interacting spins, $\mathbf{s}_1$ and $\mathbf{s}_2$, simultaneously coupling to the same radiation field, the Dicke model has been introduced in Sec. 3.4.2. There, we have shown that the spin operators can be added, $\hat{\mathbf{S}} = \hat{\mathbf{s}}_1 + \hat{\mathbf{s}}_2$, and the total system be represented in a coupled basis, where $[\hat{s}_1 \cdot \hat{s}_2, \hat{\mathbf{S}}^2] = 0 = [\hat{s}_1 \cdot \hat{s}_2, \hat{S}_z^2]$. This concept can be generalized to an arbitrary number of spins, that is, under the above assumption, one can define macroscopic collective spin operators,

$$\hat{S}_\alpha \equiv \sum_{j=1}^{N} \hat{s}_j^\alpha \qquad \text{with} \qquad [\hat{S}_x, \hat{S}_y] = \imath \hat{S}_z \ , \tag{23.5}$$

and $\alpha = x, y, z$. Using these operators, one can rewrite the above Hamiltonian as

$$\hat{H} = -\Delta_\mathrm{c} \hat{a}^\dagger \hat{a} - \Delta_\mathrm{a} \hat{S}_z + 2g \hat{a}_\mathrm{r} \hat{S}_x - 2g \hat{a}_\mathrm{i} \hat{S}_y \tag{23.6}$$

with $\hat{a} = \hat{a}_\mathrm{r} + \imath \hat{a}_\mathrm{i}$, and it is easy to see that,

$$[\hat{H}, \hat{\mathbf{S}}^2] = 0 \neq [\hat{H}, \hat{S}_z] \ . \tag{23.7}$$

That is, the Dicke Hamiltonian preserves the spin $\langle \hat{\mathbf{S}}^2 \rangle$, but interaction with a light field can change the projection $\langle \hat{S}_z \rangle$. We will see in the following that this fact as important consequences for interaction dynamics of atomic ensembles coupled to a single light mode.

> **Example 134 (*Conservation of total spin under coherent interaction*):** More generally, a coherent interaction described by a Hamiltonian that only depends on collective spin components, $H = H(\hat{S}_x, \hat{S}_y, \hat{S}_z)$, cannot change the total spin $|\mathbf{S}|$. This is easy to see by doing a Taylor expansion of the Hamiltonian in the spin components and using $[\hat{\mathbf{S}}, \hat{\mathbf{S}}^2] = 0$. As a consequence a coherent (superradiant) spin state will stay coherent forever, unless individual atom-light interactions or decay processes occur.

23.1.1.1 Degeneracies of Dicke states

Let us now look at states having the same number N of energy packets counting free photons n and atomic excitations $N-n$. For example with $N = 2$, the following states are possible. The normalization factors are simply the Clebsch-Gordan coefficients. See Exc. 23.1.9.1.

$\lvert S, M\rangle$ $\lvert n\rangle$	$\lvert \frac{N}{2}, M\rangle$ $\# = 1$	$\lvert \frac{N}{2}-1, M\rangle$ $\# = 1$
0	$\lvert 1,1\rangle = \lvert ++\rangle$	
1	$\lvert 1,0\rangle = \frac{1}{\sqrt{2}}(\lvert +-\rangle + \lvert -+\rangle)$	$\lvert 0,0\rangle = \frac{1}{\sqrt{2}}(\lvert +-\rangle - \lvert -+\rangle)$
2	$\lvert 1,-1\rangle = \lvert --\rangle$	

The right column of the above table contains a singlet state, which decouples from the triplet states (center column). The fact that it decouples from the deexcited triplet

state makes the singlet state stable or *subradiant* [3]. See also Fig. 23.10.

For example with $N = 3$ (see also Exc. 3.4.5.14),

$\|S, M\rangle$ n	$\|\frac{N}{2}, M\rangle$ $\# = 1$	$\|\frac{N}{2}-1, M\rangle$ $\# = 2$
0	$\|\frac{3}{2}, \frac{3}{2}\rangle = \|+++\rangle$	
1	$\|\frac{3}{2}, \frac{1}{2}\rangle \sim \|++-\rangle + \|+-+\rangle + \|-++\rangle$	$\|\frac{1}{2}, \frac{1}{2}\rangle$
2	$\|\frac{3}{2}, -\frac{1}{2}\rangle \sim \|+--\rangle + \|-+-\rangle + \|--+\rangle$	$\|\frac{1}{2}, -\frac{1}{2}\rangle$
3	$\|\frac{3}{2}, -\frac{3}{2}\rangle = \|---\rangle$	

Example with N arbitrary,

$\|S, M\rangle$ $\|n\rangle$	$\|\frac{N}{2}, M\rangle$ $\# = 1$	$\|\frac{N}{2}-1, M\rangle$ $\# = N-1$	$\|\frac{N}{2}-2, M\rangle$ $\# = \frac{N(N-3)}{2}$
0	$\|\frac{N}{2}, \frac{N}{2}\rangle = \|++++...\rangle$		
1	$\|\frac{N}{2}, \frac{N}{2}-1\rangle \sim \sum_{\text{perm.}} \|-+++...\rangle$	$\|\frac{N}{2}-1, \frac{N}{2}-1\rangle$	
2	$\|\frac{N}{2}, \frac{N}{2}-2\rangle \sim \sum_{\text{perm.}} \|--++...\rangle$	$\|\frac{N}{2}-1, \frac{N}{2}-2\rangle$	$\|\frac{N}{2}-2, \frac{N}{2}-1\rangle$
$\vdots$	$\vdots$	$\vdots$	
N	$\|\frac{N}{2}, -\frac{N}{2}\rangle = \|----..\rangle$		

We see that the Dicke states are not made to unambiguously label degenerate states. States $|S, M\rangle$ with $S < |M|$ are largely degenerate. The degeneracy of a Dicke state with $S \leq \frac{N}{2}$, that is, the number of states $|+\rangle^{N_+}|-\rangle^{N_-}$ composing a single Dicke state labeled by $|S, M\rangle$ is [306],

$$\# = \frac{(2S+1)N!}{(\frac{N}{2}+S+1)!(\frac{N}{2}-S)!} \ . \tag{23.8}$$

Transitions between energetically degenerate states $|S, M\rangle$ and $|S, M'\rangle$ with $M = M'$ but $S \neq S'$ are prohibited.

23.1.1.2 Mean-field approximation and light field elimination

The *mean-field approximation* consists in replacing the photonic operators by their expectation values, i.e. assuming classical light. This allows us to remove the light energy term from the Hamiltonian and replace the coupling strength by the n-photon Rabi frequency, $\Omega = 2g\sqrt{n}$. The Hamiltonian then becomes just a generalization of the semiclassical one-atom Hamiltonian (16.129) to large spins,

$$\hat{H} = \hat{\mathbf{S}} \cdot \mathbf{G} = -\Delta_{\mathrm{a}} \ \hat{S}_z + \mathfrak{Re}\,\Omega \ \hat{S}_x + \mathfrak{Im}\,\Omega \ \hat{S}_y \ , \tag{23.9}$$

allowing for complex Rabi frequencies. We will see in Sec. 23.4.1 how this simplified Hamiltonian can be derived from (23.6) for the case that the light field is a single mode in a 'bad cavity'.

In the absence of spontaneous emission, any pure *single-atom* state is given by,

$$|\psi\rangle = |\vartheta, \varphi\rangle = \cos\tfrac{\vartheta}{2}|+\rangle + e^{\imath\varphi}\sin\tfrac{\vartheta}{2}|-\rangle \ , \tag{23.10}$$

[3] Note that, while superradiance as well as subradiance can be explained by classical radiator models, such as the coupled dipoles model.

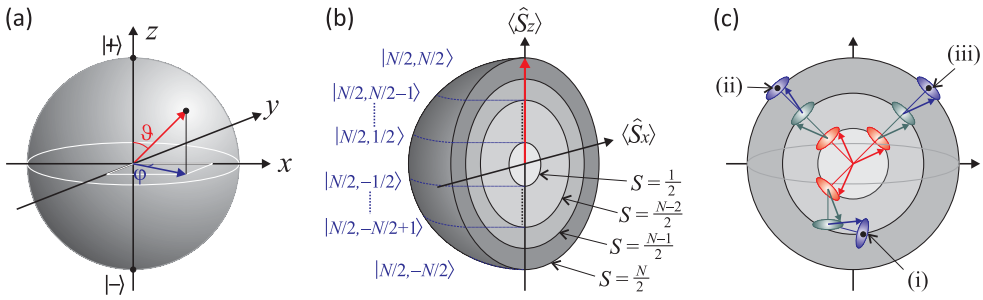

Figure 23.1: (a) Illustration of the Bloch sphere. (b) Bloch spheres of the various super/-subradiant states with $N = 5$ atoms. (c) Illustration of (i) a subradiant state, (ii) a fully stretched coherent spin state, and (iii) a spin-correlated state for $N = 3$ atoms.

where the angles ϑ and φ point to a location on the Bloch sphere characterizing the state of the atom. For example, a single initially deexcited atom having been subject to a $\frac{\pi}{2}$-pulse ends up in the state $|\frac{\pi}{2}, 0\rangle$. The expectation value of the spin operator in this state is simply obtained from,

$$\begin{aligned}\langle\vartheta,\varphi|\hat{S}_z|\vartheta,\varphi\rangle &= \cos^2\tfrac{\vartheta}{2}\langle+|\hat{S}_z|+\rangle + \sin^2\tfrac{\vartheta}{2}\langle-|\hat{S}_z|-\rangle = \tfrac{1}{2}\cos\vartheta \\ \langle\vartheta,\varphi|\hat{S}_+|\vartheta,\varphi\rangle &= e^{\imath\varphi}\sin\tfrac{\vartheta}{2}\cos\tfrac{\vartheta}{2}\langle+|\hat{S}_+|-\rangle = \tfrac{1}{2}e^{\imath\varphi}\sin\vartheta\ ,\end{aligned} \tag{23.11}$$

yielding,

$$\langle\vartheta,\varphi|\hat{\mathbf{S}}|\vartheta,\varphi\rangle = \tfrac{1}{2}\begin{pmatrix}\cos\varphi\sin\vartheta\\ \sin\varphi\sin\vartheta\\ \cos\vartheta\end{pmatrix}\ . \tag{23.12}$$

We will also denote the probability of finding the system in state $|\pm\rangle$ by,

$$p_+ = \langle\hat{P}_\pm\rangle = |\langle+|\psi\rangle|^2 = \cos^2\tfrac{\vartheta}{2} = 1 - p_-\ . \tag{23.13}$$

23.1.1.3 Collective spin states

Let us now study the system obeying the Hamiltonian (23.9) in detail. The spin operators $\hat{\mathbf{S}}$ satisfy a SU(2) algebra explained in Sec. 3.3.2, i.e. $\hat{\mathbf{S}} \times \hat{\mathbf{S}} = \imath\hat{\mathbf{S}}$. The common eigenstates of $\hat{\mathbf{S}}^2$ and $\hat{S}_z$ are denoted by $|S, M\rangle$,

$$\begin{aligned}\hat{S}_z &= \hat{S}_+\hat{S}_- - \hat{S}_-\hat{S}_+ \qquad \text{with} \qquad \hat{S}_z|S,M\rangle = M|S,M\rangle \\ \hat{N}_\pm &\equiv \tfrac{1}{2}(N\mathbb{I} \pm \hat{S}_z) \qquad \text{with} \qquad \hat{N}_\pm|S,M\rangle = \tfrac{1}{2}(N \pm M)|S,M\rangle\ .\end{aligned} \tag{23.14}$$

From this we conclude that $S = N/2$ is half the number of atoms and M the inversion.

We consider an ensemble of $N = N_+ + N_-$ two-level atoms excited by a definite number of M photons, such that,

$$N = N_+ + N_- \qquad \text{and} \qquad 2M = N_+ - N_-\ . \tag{23.15}$$

Hence, $N_\pm = \frac{N}{2} \pm M$ is the number of atoms in each of the two states. The N atoms can occupy 2^N different collective states. However, when the atoms are identical and

couple uniformly to the same light mode, all states where the same number of atoms is excited are energetically degenerate, and the total energy available to the system is,

$$E = M\omega_c \ . \tag{23.16}$$

The degeneracy of each many-body state with a given inversion M is given by the binomial coefficient,

$$\# = \binom{N}{\frac{N}{2}+M} = \binom{N}{N_+} = \binom{N}{N_-} \qquad \text{such that} \qquad \sum_{N_+=0}^{N} \binom{N}{N_+} = 2^N \ . \tag{23.17}$$

Therefore, we may set,

$$\boxed{|S,M\rangle \equiv |+\rangle^{N_+}|-\rangle^{N_-}} \ . \tag{23.18}$$

These states are called *Dicke states* [4].

For the special case $N = 2$ the transformation from the basis $|+\rangle^{N_+}|-\rangle^{N_-}$, used in the *Tavis-Cummings model*, to the basis $|S,M\rangle$, used in the Dicke model, is a unitary transformation. It has been extensively discussed in Sec. 3.4 at the example of two spins, whose complete Hilbert space can be expanded in the uncoupled or in the coupled basis. For $N > 2$ the situation is more complicated, since the degeneracies of both models are different. It is important to be aware that S is not simply half the atom number, but runs over $S = \frac{N}{2}, \frac{N}{2}-1, ...$, depending on how the individual spins couple together. The degeneracy of an angular momentum state $|S,M\rangle$ with a specific inversion M but undefined orbital momentum S is determined by the condition $0 \leq S \leq M$, and given by,

$$\# = \tfrac{N}{2} - |M| + 1 \ . \tag{23.19}$$

For example, for $N = 2$ the possible spin states are given by $|s_1 - s_2| \leq S \leq s_1 + s_2$, that is, $S = 0, 1$. And for $N = 5$, $M = \frac{3}{2}$ is supported by $S = \frac{3}{2}$ and $\frac{5}{2}$. Obviously, the degeneracy (23.19) is lower than (23.17) except for $N = 2$. Dicke states may be represented as vectors pointing to the surface of a so-called Bloch sphere of radius,

$$\|\langle N,S,M|\hat{\mathbf{S}}^2|N,S,M\rangle\| = S(S+1) \ , \tag{23.20}$$

as illustrated in Fig. 23.1(b).

Example 135 (*Schwinger bosonization*): The two levels $|+\rangle$ and $|-\rangle$ may be interpreted as bosonic modes $\hat{a}$ and $\hat{b}$ populated with $S+M$ respectively $S-M$ atoms,

$$\hat{S}_+ = \hat{a}^\dagger\hat{b} \quad , \quad \hat{S}_- = \hat{a}\hat{b}^\dagger \quad , \quad \hat{N} = \hat{a}^\dagger\hat{a} + \hat{b}^\dagger\hat{b} \ . \tag{23.21}$$

Consequently,

$$\hat{S}_x = \tfrac{1}{2}(\hat{a}^\dagger\hat{b} + \hat{b}^\dagger\hat{a}) \quad , \quad \hat{S}_y = \tfrac{1}{2i}(\hat{a}^\dagger\hat{b} - \hat{b}^\dagger\hat{a}) \quad , \quad \hat{S}_z = \tfrac{1}{2}(\hat{a}^\dagger\hat{a} - \hat{b}^\dagger\hat{b}) \ . \tag{23.22}$$

This is the so-called *Schwinger bosonization*.

[4] In Sec. 3.4.3 we used for the coupling of two spins the notation $|(s_1,s_2)s,m\rangle$. For coupling N spins, we should write in analogy,

$$|(\overbrace{\tfrac{1}{2},..,\tfrac{1}{2}}^{N}),S,M\rangle \equiv |N,S,M\rangle \ .$$

Mostly, we will however drop the (constant) number N.

23.1.1.4 Dicke Hamiltonian for 2 atoms from the Tavis-Cummings model

We start from the collective Dicke Hamiltonian (23.4) for two atoms assuming $\omega_{a1} = \omega_{a2}$ and $g_1 = g_2$, that is, both atoms are identical and inside the mode volume of the field to which they couple with equal strength, and apply the rotating wave approximation. The Hamiltonian then factorizes into a diagonal matrix of 4 by 4 blocks characterized by a given number of total excitations,

$$\hat{H}_n = \begin{pmatrix} (n+1)\omega_c - \omega_a & g\sqrt{n} & g\sqrt{n} & 0 \\ g\sqrt{n} & n\omega_c & 0 & g\sqrt{n} \\ g\sqrt{n} & 0 & n\omega_c & g\sqrt{n} \\ 0 & g\sqrt{n} & g\sqrt{n} & (n-1)\omega_c + \omega_a \end{pmatrix} . \tag{23.23}$$

Each block has two degenerate non-shifted eigenvalues and two non-degenerate shifted eigenvalues,

$$E = n\omega_c \quad \text{and} \quad E = n\omega_c \pm \varpi_n \quad \text{with} \quad \varpi_n \equiv \sqrt{(\omega_c + \omega_a)^2 - 4g^2 n} \, . \tag{23.24}$$

The description of the dynamics can be simplified by reducing the order of the matrix by calculating the average of the lines 2 and 3,

$$\hat{H}_D = \begin{pmatrix} (n+1)\omega_c - \omega_a & g\sqrt{2n} & 0 \\ g\sqrt{2n} & n\omega_c & g\sqrt{2n} \\ 0 & g\sqrt{2n} & (n-1)\omega_c + \omega_a \end{pmatrix} , \tag{23.25}$$

and opting for a new base defined by,

$$|\psi\rangle = \sum_n \begin{pmatrix} c_{22\ n-1} \\ c_{12\ n} \\ c_{11\ n+1} \end{pmatrix} |n\rangle \, , \tag{23.26}$$

with $c_{12\ n} = c_{21\ n}$. The new Hamiltonian (23.25) has exactly the same eigenvalues as the complete one (23.25), $\lambda = n\omega_c, n\omega_c \pm \varpi_n$, but without degeneracies. If we assume furthermore that the excitation is resonant, $\omega_c = \omega_a$, with high intensity, $n = |\alpha|^2$ for all n, defining the Rabi frequency $\Omega \equiv 2g\sqrt{n}$ our matrix becomes,

$$\hat{H}_D \simeq \begin{pmatrix} |\alpha|\omega & \frac{\Omega}{\sqrt{2}} & 0 \\ \frac{\Omega}{\sqrt{2}} & |\alpha|\omega & \frac{\Omega}{\sqrt{2}} \\ 0 & \frac{\Omega}{\sqrt{2}} & |\alpha|\omega \end{pmatrix} , \tag{23.27}$$

with the eigenvalue matrix,

$$E_n = \mathcal{U}_n^\dagger \hat{H}_D \mathcal{U}_n \simeq \begin{pmatrix} |\alpha|\omega - \Omega & & \\ & |\alpha|\omega & \\ & & |\alpha|\omega + \Omega \end{pmatrix} , \tag{23.28}$$

and the eigenvector matrix,

$$\mathcal{U}_n \simeq \tfrac{1}{2} \begin{pmatrix} -1 & \sqrt{2} & 1 \\ \sqrt{2} & 0 & -\sqrt{2} \\ 1 & -\sqrt{2} & -1 \end{pmatrix} . \tag{23.29}$$

With this we can derive the propagator,

$$e^{-\imath\hat{H}_n t} = \tfrac{1}{2} e^{-\imath\alpha^2\omega\mathbf{t}} \begin{pmatrix} 1+\cos\alpha\Omega t & -\sqrt{2}\imath\sin\alpha\Omega t & -1+\cos\alpha\Omega t \\ -\sqrt{2}\imath\sin\alpha\Omega t & 2\cos\alpha\Omega t & -\sqrt{2}\imath\sin\alpha\Omega t \\ -1+\cos\alpha\Omega t & -\sqrt{2}\imath\sin\alpha\Omega t & 1+\cos\alpha\Omega t \end{pmatrix}$$
$$\overset{\alpha\Omega t=\pi/2}{\longrightarrow} \tfrac{1}{2} e^{-\imath\pi/2\cdot\alpha\omega/\Omega} \begin{pmatrix} 1 & -\sqrt{2}\imath & -1 \\ -\sqrt{2}\imath & 0 & -\sqrt{2}\imath \\ -1 & -\sqrt{2}\imath & 1 \end{pmatrix} .$$

The generalization to three atoms or N atoms is straightforward and will be left to Exc. 23.1.9.2.

23.1.2 Coherent spin states

By the fact that the individual spins are additive and the Hamiltonian linear in the spin operators, $\hat{H} \propto \hat{S}_z$, we know that the Schrödinger equation will be satisfied by *product states*,

$$|\Psi_N\rangle = \prod_{k=1}^{N} |\vartheta_k, \varphi_k\rangle_k \ , \tag{23.30}$$

where $|\vartheta_k, \varphi_k\rangle_k$ is the state of the k-the atom given by (23.10).

Coherent spin states now consist of N atoms, all being in the same state. In Exc. 23.1.9.3 we present another equivalent definition. Since the atoms are indistinguishable by the radiation field, we may as well drop the labeling index k,

$$\begin{aligned} |\Psi_N\rangle = |S, \vartheta, \varphi\rangle = |\vartheta, \varphi\rangle^N &= \left(\cos\tfrac{\vartheta}{2}|+\rangle + e^{\imath\varphi}\sin\tfrac{\vartheta}{2}|-\rangle\right)^N \\ &= \sum_{k=0}^{N} \sqrt{\binom{N}{k}} \cos^{N-k}\tfrac{\vartheta}{2}|+\rangle^{N-k}\ e^{\imath k\varphi}\sin^k\tfrac{\vartheta}{2}|-\rangle^k \ , \end{aligned} \tag{23.31}$$

in agreement with (18.30), or equivalently, using the Dicke state notation (23.18),

$$\boxed{|\vartheta, \varphi\rangle^N = \sum_{k=0}^{2S} \sqrt{\binom{2S}{k}} \cos^{2S-k}\tfrac{\vartheta}{2}\ e^{\imath k\varphi}\sin^k\tfrac{\vartheta}{2}|S, S-k\rangle} \ . \tag{23.32}$$

Hence, similarly to the coherent state of a harmonic oscillator, which consists of a Poissonian distribution of number states, the coherent spin state consists of a binomial distribution of N_+ atoms in one state and $N - N_+$ in the other. Note also, that by construction, the coherent spin states are **stretched**, $S = N/2$. That is, they can be represented by a vector of length N equal to the radius of the (generalized) Bloch sphere [5]. In other words, S is a conserved quantum number as already shown in (23.7), and this feature does not change under the influence of the Hamiltonian (23.9). These states are called superradiant. Nevertheless, other states $|S, M\rangle$ are possible with $S \leq \frac{N}{2}$. These are squeezed, subradiant, or entangled states.

[5] An illustration of the generalized Bloch sphere is attempted in Fig. 24.10.

In the following we will study some of the properties of the coherent spin states. For instance, in Exc. 23.1.9.5(a) we calculate the expectation values of coherent spin states,

$$\langle\vartheta,\varphi|^N\hat{\mathbf{S}}|\vartheta,\varphi\rangle^N = S\begin{pmatrix}\cos\varphi\sin\vartheta\\ \sin\varphi\sin\vartheta\\ \cos\vartheta\end{pmatrix} . \tag{23.33}$$

Hence, the spin evolves on the surface of a Bloch sphere with radius,

$$\|\langle\vartheta,\varphi|^N\hat{\mathbf{S}}|\vartheta,\varphi\rangle^N\| = S \qquad \text{while still} \qquad \|\langle\vartheta,\varphi|^N\hat{\mathbf{S}}^2|\vartheta,\varphi\rangle^N\| = S(S+1) . \tag{23.34}$$

For the number of atoms in each state we expect,

$$\langle\hat{N}_+\rangle = \tfrac{N}{2} + \tfrac{1}{2}\langle\hat{S}_z\rangle = N\cos^2\tfrac{\vartheta}{2} = Np_+ = N(1-p_-) = N - \langle N_-\rangle . \tag{23.35}$$

23.1.3 Rotations, spin excitation and precession

We learn in quantum mechanics how to use Pauli matrices to describe rotations in the Bloch vector space (see Exc. 1.5.9.5). We will now extend this formalism to our collective spin space. A useful rule for the subsequent calculations, proved in Exc. 23.1.9.6, is the following,

$$e^{\imath F(\hat{S}_z)}\hat{S}_+e^{-\imath F(\hat{S}_z)} = \hat{S}_+e^{\imath[F(\hat{S}_z+\mathbb{I})-F(\hat{S}_z)]} , \tag{23.36}$$

where F is an arbitrary function. For $F(\hat{S}_z)\equiv\phi\hat{S}_z$ the unitary transform $e^{\imath F(\hat{S}_z)}$ denotes a rotation about the z-axis, which we will study in the example below. For $F(\hat{S}_z)\equiv\zeta\hat{S}_z^2$ it generates squeezing along the z-axis, which we will study in the next section. Furthermore, we define the rotation matrices about the Cartesian axis (for clockwise rotation about the respective axis),

$$R_x(\gamma)\equiv\begin{pmatrix}1&0&0\\0&\cos\gamma&-\sin\gamma\\0&\sin\gamma&\cos\gamma\end{pmatrix} , \qquad R_y(\gamma)\equiv\begin{pmatrix}\cos\gamma&0&\sin\gamma\\0&1&0\\-\sin\gamma&0&\cos\gamma\end{pmatrix} ,$$
$$R_z(\gamma)\equiv\begin{pmatrix}\cos\gamma&-\sin\gamma&0\\\sin\gamma&\cos\gamma&0\\0&0&1\end{pmatrix} , \tag{23.37}$$

for which it is possible to show (with $\alpha = x,y,z$),

$$\boxed{R_\alpha(\gamma)\hat{\mathbf{S}} = e^{\imath\gamma\hat{S}_\alpha}\hat{\mathbf{S}}e^{-\imath\gamma\hat{S}_\alpha}} . \tag{23.38}$$

Example 136 (*Rotation about* $\hat{S}_z$): Defining $F(\hat{S}_z)\equiv\phi\hat{S}_z$ the relationship (23.36) tells us,

$$e^{\imath\phi\hat{S}_z}\hat{S}_+e^{-\imath\phi\hat{S}_z} = \hat{S}_+e^{\imath\phi} ,$$

and consequently,

$$e^{\imath\phi\hat{S}_z}\hat{\mathbf{S}}e^{-\imath\phi\hat{S}_z} = \begin{pmatrix}\frac{1}{2}(e^{\imath\phi}\hat{S}_+ + e^{-\imath\phi}\hat{S}_-)\\ \frac{1}{2\imath}(e^{\imath\phi}\hat{S}_+ - e^{-\imath\phi}\hat{S}_-)\\ \hat{S}_z\end{pmatrix} = \begin{pmatrix}\cos\phi&-\sin\phi&0\\\sin\phi&\cos\phi&0\\0&0&1\end{pmatrix}\hat{\mathbf{S}} \equiv R_z(\phi)\hat{\mathbf{S}} .$$

Furthermore,

$$e^{-\imath\phi\hat{S}_z}|\vartheta,\varphi\rangle^N = \sum_{k=0}^{2S}\sqrt{\binom{2S}{k}}\cos^{N-k}\tfrac{\vartheta}{2}e^{\imath k\varphi}\sin^k\tfrac{\vartheta}{2}e^{-\imath\phi(S-k)}|S,S-k\rangle$$
$$= e^{-\imath\phi S}\left(e^{-\imath\phi}\cos\tfrac{\vartheta}{2}|+\rangle + e^{\imath(\varphi+\phi)}\sin\tfrac{\vartheta}{2}|-\rangle\right)^N = e^{-\imath\phi S}|\vartheta,\varphi+\phi\rangle^N \ .$$

We also find,

$$\langle\vartheta,\varphi|^N R_z(\phi)\hat{\mathbf{S}}|\vartheta,\varphi\rangle^N = \tfrac{N}{2}\begin{pmatrix}\cos(\varphi+\phi)\sin\vartheta\\ \sin(\varphi+\phi)\sin\vartheta\\ \cos\vartheta\end{pmatrix} = \langle\vartheta,\varphi+\phi|^N\hat{\mathbf{S}}|\vartheta,\varphi+\phi\rangle^N \ .$$

To vary the polar angle ϑ of a coherent spin state $|\vartheta,\varphi\rangle$, we first rotate the coordinate system about the z-axis until $\varphi=0$, then rotate about the y-axis by the desired angle θ, and finally rotate back about the z-axis to reach the initial azimuth φ,

$$\langle\vartheta,\varphi|^N R_z(\varphi)R_y^{-1}(\theta)R_z^{-1}(\varphi)\hat{\mathbf{S}}|\vartheta,\varphi\rangle^N = \tfrac{N}{2}\begin{pmatrix}\cos\varphi\sin(\theta+\vartheta)\\ \sin\varphi\sin(\theta+\vartheta)\\ \cos(\theta+\vartheta)\end{pmatrix} = \langle\vartheta+\theta,\varphi|^N\hat{\mathbf{S}}|\vartheta+\theta,\varphi\rangle^N \ .$$

The rotation about the x-axis is derived in Exc. 23.1.9.7, and in Exc. 23.1.9.8 we write down the explicit rotation matrix for two atoms.

Rotations such as the ones described by $R_\alpha(\gamma)$ are generated by the Dicke Hamiltonian (23.9), since the solution of the Schrödinger equation is,

$$\boxed{|\Psi(t)\rangle = e^{-\imath\hat{H}t}|\Psi(0)\rangle = e^{-\imath t\hat{S}_x\mathfrak{Re}\,\Omega_x - \imath t\hat{S}_y\mathfrak{Im}\,\Omega_y - \imath t\hat{S}_z\Delta}|\Psi(0)\rangle} \ . \tag{23.39}$$

That is, the Dicke Hamiltonian generates rotations $R_x(\mathfrak{Re}\,\Omega_x t)$, $R_y(\mathfrak{Im}\,\Omega_y t)$, and $R_z(\Delta t)$. This confirms that rotations do only transform coherent states into each other. Nevertheless, there are other unitary operations that transform coherent states into states that cannot be represented by coherent states. One example for this is squeezing.

23.1.3.1 Rotation algebra

The example 136 shows that rotations from an initial towards an arbitrary coherent spin states can be parametrized by a pair of Euler angles. Using (1.303) [200],

$$\mathcal{U}_{\rm rt}(\vartheta,\varphi) = e^{\imath\varphi\hat{S}_z}e^{\imath\vartheta\hat{S}_y} = e^{-\imath\vartheta\hat{\mathbf{e}}_\varphi\cdot\hat{\mathbf{S}}} = e^{-\imath\vartheta(-\hat{S}_x\sin\varphi+\hat{S}_y\cos\varphi)} = e^{-\frac{\vartheta}{2}(\hat{S}_+e^{-\imath\varphi}-\hat{S}_-e^{\imath\varphi})} = e^{-\imath\vartheta\hat{S}_\varphi}$$
$$R(\vartheta,\varphi)\hat{\mathbf{S}} \equiv \mathcal{U}_{\rm rt}^\dagger(\vartheta,\varphi)\hat{\mathbf{S}}\mathcal{U}_{\rm rt}(\vartheta,\varphi) \tag{23.40}$$

with $\hat{\mathbf{e}}_\varphi = -\hat{\mathbf{e}}_x\sin\varphi + \hat{\mathbf{e}}_y\cos\varphi$. With this we find,

$$|\vartheta,\varphi\rangle^N = \mathcal{U}_{\rm rt}(\vartheta,\varphi)|S,S\rangle \ . \tag{23.41}$$

23.1.4 Uncertainties and quantum projection noise

Measuring the population of a coherently excited two-level system by projecting it onto an energy eigenstate introduces *quantum projection noise*. Although this inherent noise spoils the determination of the resonance frequency, it can to some extent be surpassed by *spin squeezing* [869]. The projection noise limit has been observed with ions [419, 411] and with atomic clouds [725]. The reduction of the noise by spin squeezing has been observed with ions [714], micromasers [683], and atomic clouds [361, 494]. Also, a weakly entangled state of two modes was observed for continuous spin variables [443]. Very strong squeezing spin can be obtained in a *Mott insulator* state, as demonstrated by [337].

First, we want to show that the Heisenberg uncertainty of a coherent spin state is nothing else than the quantum projection noise studied in Sec. 18.2.2. On one hand, we have,

$$\begin{aligned}\langle\vartheta,\varphi|^N(\Delta\hat{S}_z)^2|\vartheta,\varphi\rangle^N &= \langle\vartheta,\varphi|^N\hat{S}_z^2|\vartheta,\varphi\rangle^N - (\langle\vartheta,\varphi|^N\hat{S}_z|\vartheta,\varphi\rangle^N)^2 \\ &= \sum_{k=0}^{N}\binom{N}{k}(\tfrac{N}{2}-k)^2p_+^{N-k}p_-^k - \left(\sum_{k=0}^{N}\binom{N}{k}(\tfrac{N}{2}-k)p_+^{N-k}p_-^k\right)^2 \\ &= \left(\tfrac{N^2}{4} - N^2p_+p_- + Np_+p_-\right) - \left(\tfrac{N}{2}(p_+-p_-)\right)^2 = Np_+p_- \ .\end{aligned} \tag{23.42}$$

On the other hand, we have seen in (18.29) that this results corresponds to the variance of quantum projection noise,

$$\begin{aligned}(\Delta r)^2 &= \sum_{r=0}^{N}(r-Np_\pm)^2P_{N,r,\pm} \\ &= \sum_{k=0}^{N}(\tfrac{N}{2}-k+\tfrac{N}{2}(p_+-p_-))^2\binom{N}{k}p_+^{N-k}p_-^k = Np_+p_- \ .\end{aligned} \tag{23.43}$$

The Heisenberg uncertainty relation (1.201) applied to angular momentum operator satisfying $[\hat{S}_x,\hat{S}_y]=\imath\hat{S}_z$ states,

$$\langle\Delta\hat{S}_x\rangle\langle\Delta\hat{S}_y\rangle \geq \tfrac{1}{2}|\langle\hat{S}_z\rangle| \ . \tag{23.44}$$

Since there are no quantum correlations between the particles, the uncertainty of coherent spin states is additive (see Exc. 3.3.4.5),

$$(\Delta\hat{S}_\alpha)^2 = \sum_{k=0}^{N}(\Delta\hat{s}_k^\alpha)^2 \ . \tag{23.45}$$

For a coherent spin state we can calculate explicitly [see Exc. 23.1.9.5(b)],

$$\langle\vartheta,\varphi|^N\begin{pmatrix}\Delta\hat{S}_x^2\\ \Delta\hat{S}_y^2\\ \Delta\hat{S}_z^2\end{pmatrix}|\vartheta,\varphi\rangle^N = \tfrac{N}{4}\begin{pmatrix}1-\sin^2\vartheta\cos^2\varphi\\ 1-\sin^2\vartheta\sin^2\varphi\\ \sin^2\vartheta\end{pmatrix} \ . \tag{23.46}$$

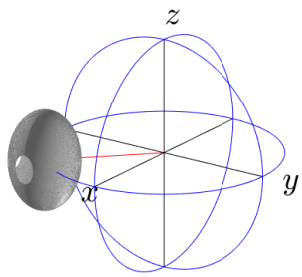

Figure 23.2: Illustration of the uncertainty of the spin components of a coherent spin state.

Example 137 (*Uncertainty of a coherent spin state after a $\frac{\pi}{2}$-pulse*): A $\frac{\pi}{2}$-pulse applied to a cloud in the collective ground state generates the state $|\vartheta,\varphi\rangle = |\frac{\pi}{2},0\rangle$. This is somewhat analogous to the beam splitting of a photonic Fock state discussed in Sec. 14.5. Interestingly, a Fock state seems more natural for an atomic cloud, while the Glauber state is more natural for a photonic mode. For example, for the particular state $|\frac{\pi}{2},0\rangle$ we find from (23.46),

$$(\Delta\hat{S}_x)^2 = 0 \qquad \text{and} \qquad (\Delta\hat{S}_y)^2 = (\Delta\hat{S}_z)^2 = \tfrac{S}{2}\ .$$

Note, that spin squeezing along the z-axis could be obtained by quantum non-demolition measurement of the inversion, that is, by measuring $\hat{S}_z$ without influencing the populations of the ground and excited state.

23.1.4.1 Projection onto the generalized Bloch sphere

The eigenstates of any convex combination $\mathbf{n}\cdot\hat{\mathbf{S}}$ form a basis with respect to the axis $\mathbf{n}$, denoted $\{|S,M;\mathbf{n}\rangle\}$. These basis vectors are called Dicke states and the whole basis is called a Dicke basis, where the projection eigenvalue M runs from $-S$ to S in integer steps. In spherical coordinates, the vector,

$$\mathbf{n} = \begin{pmatrix} \sin\vartheta\cos\varphi \\ \sin\vartheta\sin\varphi \\ \cos\vartheta \end{pmatrix} = \frac{\langle\hat{\mathbf{S}}\rangle}{S} \tag{23.47}$$

points to (ϑ,φ) on the sphere S^2; this is the phase space generated by SU(2) symmetry [200]. It is common to work entirely in the n_z Dicke basis, denoted $\{|S,M\rangle\}$. What really matters for spin squeezing is not the uncertainty ellipse, but its projection onto the generalized Bloch sphere. We calculate it via transformation into a local coordinate frame using spherical coordinates (23.33) ,

$$\boxed{\begin{pmatrix} \hat{S}_r \\ \hat{S}_\vartheta \\ \hat{S}_\varphi \end{pmatrix} = R_{\rm rt}(\vartheta,\varphi)\begin{pmatrix} \hat{S}_x \\ \hat{S}_y \\ \hat{S}_z \end{pmatrix} \quad \text{with} \quad R_{\rm rt}(\vartheta,\varphi) = \begin{pmatrix} \sin\vartheta\cos\varphi & \sin\vartheta\sin\varphi & \cos\vartheta \\ \cos\vartheta\cos\varphi & \cos\vartheta\sin\varphi & -\sin\vartheta \\ -\sin\varphi & \cos\varphi & 0 \end{pmatrix}.} \tag{23.48}$$

It is easy to verify,

$$[\hat{S}_\vartheta, \hat{S}_\varphi] = \imath \hat{S}_r \ . \tag{23.49}$$

For any collective spin satisfying the SU_2 algebra we know,

$$\langle \hat{\mathbf{S}}^2 \rangle = \langle \hat{S}_x^2 \rangle + \langle \hat{S}_y^2 \rangle + \langle \hat{S}_z^2 \rangle = S(S+1) \ . \tag{23.50}$$

However,

$$(\langle \vartheta, \varphi |^N \hat{S}_x | \vartheta, \varphi \rangle^N)^2 + (\langle \vartheta, \varphi |^N \hat{S}_y | \vartheta, \varphi \rangle^N)^2 + (\langle \vartheta, \varphi |^N \hat{S}_z | \vartheta, \varphi \rangle^N)^2 = S^2 \tag{23.51}$$

only holds for superradiant states, such as coherent spin states, but not generally, e.g. not for subradiant states. Let us define other radii via,

$$\begin{aligned} S_r^2 &\equiv \langle \hat{S}_x \rangle^2 + \langle \hat{S}_y \rangle^2 + \langle \hat{S}_z \rangle^2 &< S^2 \\ S_\varrho^2 &\equiv \langle \hat{S}_x \rangle^2 + \langle \hat{S}_y \rangle^2 &< S_r^2 \end{aligned} \tag{23.52}$$

allowing us to rewrite the rotation matrix (23.48) as,

$$R_{\mathrm{rt}}(\vartheta, \varphi) = \tfrac{1}{S_r} \begin{pmatrix} \langle \hat{S}_x \rangle & \langle \hat{S}_y \rangle & \langle \hat{S}_z \rangle \\ \langle \hat{S}_x \rangle \langle \hat{S}_z \rangle / S_\varrho & \langle \hat{S}_y \rangle \langle \hat{S}_z \rangle / S_\varrho & -S_\varrho \\ -\langle \hat{S}_y \rangle S_r / S_\varrho & \langle \hat{S}_x \rangle S_r / S_\varrho & 0 \end{pmatrix} \ . \tag{23.53}$$

Using this transformation it is easy to verify,

$$\begin{aligned} \langle \hat{S}_r \rangle^2 + \langle \hat{S}_\vartheta \rangle^2 + \langle \hat{S}_\varphi \rangle^2 &= \langle \hat{S}_x \rangle^2 + \langle \hat{S}_y \rangle^2 + \langle \hat{S}_z \rangle^2 &= S_r^2 \\ \langle \hat{S}_r^2 \rangle + \langle \hat{S}_\vartheta^2 \rangle + \langle \hat{S}_\varphi^2 \rangle &= \langle \hat{S}_x^2 \rangle + \langle \hat{S}_y^2 \rangle + \langle \hat{S}_z^2 \rangle &= S(S+1) \end{aligned} \tag{23.54}$$

Example 138 (*Rotations about the x- and y-axis*): For particular azimuthal angles we find,

$$\begin{aligned} R_{\mathrm{rt}}(\vartheta, 0) &= \begin{pmatrix} \sin\vartheta & 0 & \cos\vartheta \\ \cos\vartheta & 0 & -\sin\vartheta \\ 0 & 1 & 0 \end{pmatrix} = \tfrac{1}{S_r} \begin{pmatrix} \langle \hat{S}_x \rangle & 0 & \langle \hat{S}_z \rangle \\ \langle \hat{S}_z \rangle & 0 & -\hat{S}_x \\ 0 & S_r & 0 \end{pmatrix} \\ R_{\mathrm{rt}}(\vartheta, \tfrac{\pi}{2}) &= \begin{pmatrix} 0 & \sin\vartheta & \cos\vartheta \\ 0 & \cos\vartheta & -\sin\vartheta \\ -1 & 0 & 0 \end{pmatrix} = \tfrac{1}{S_r} \begin{pmatrix} 0 & \langle \hat{S}_y \rangle & \langle \hat{S}_z \rangle \\ 0 & \langle \hat{S}_z \rangle & -\langle \hat{S}_y \rangle \\ -S_r & 0 & 0 \end{pmatrix} \ . \end{aligned} \tag{23.55}$$

Knowing the collective spin state may can now calculate the uncertainty projection onto the generalized Bloch sphere. For a state represented by an arbitrary density matrix we get,

$$\boxed{\langle \Delta S_\alpha^2 \rangle = \mathrm{Tr}\, \hat{\rho} \hat{S}_\alpha^2 - (\mathrm{Tr}\, \hat{\rho} \hat{S}_\alpha)^2 \qquad , \qquad \alpha = r, \vartheta, \varphi} \ . \tag{23.56}$$

Example 139 (*Uncertainty projections for coherent spin states*): Using the unitary transform (23.40),

$$|\vartheta, \varphi\rangle^N = \mathcal{U}_{\mathrm{rt}} |S, S\rangle \qquad \text{where} \qquad \mathcal{U}_{\mathrm{rt}} = e^{-\frac{\vartheta}{2}(\hat{S}_+ e^{-\imath\varphi} - \hat{S}_- e^{\imath\varphi})} = e^{-\imath\vartheta \hat{S}_\varphi} \ , \tag{23.57}$$

where the angles are given by,

$$\sin\vartheta = \frac{S_\varrho}{S_r} \quad , \quad \sin\varphi = \frac{\langle \hat{S}_y\rangle}{S_\rho} \ , \tag{23.58}$$

the same transformation into the local coordinate frame can be achieved via,

$$\boxed{\begin{aligned} \hat{S}_\vartheta &= \mathcal{U}_{\rm rt}\hat{S}_x\mathcal{U}_{\rm rt}^\dagger \\ \hat{S}_\varphi &= \mathcal{U}_{\rm rt}\hat{S}_y\mathcal{U}_{\rm rt}^\dagger \\ \hat{S}_r &= \mathcal{U}_{\rm rt}\hat{S}_z\mathcal{U}_{\rm rt}^\dagger \end{aligned}} \tag{23.59}$$

We can now calculate the uncertainties in the local coordinate frame,

$$\begin{aligned} \langle\vartheta,\varphi|^N\Delta\hat{S}_r^2|\vartheta,\varphi\rangle^N &= \langle\vartheta,\varphi|^N\hat{S}_r^2|\vartheta,\varphi\rangle^N - (\langle\vartheta,\varphi|^N\hat{S}_r|\vartheta,\varphi\rangle^N)^2 \\ &= \langle\vartheta,\varphi|^N\mathcal{U}_{\rm rt}\hat{S}_z\mathcal{U}_{\rm rt}^\dagger\mathcal{U}_{\rm rt}\hat{S}_z\mathcal{U}_{\rm rt}^\dagger|\vartheta,\varphi\rangle^N - (\langle\vartheta,\varphi|^N\mathcal{U}_{\rm rt}\hat{S}_z\mathcal{U}_{\rm rt}^\dagger|\vartheta,\varphi\rangle^N)^2 \\ &= \langle S,S|\hat{S}_z^2|S,S\rangle - \langle S,S|\hat{S}_z|S,S\rangle^2 = \langle S,S|\Delta\hat{S}_z^2|S,S\rangle \end{aligned} \tag{23.60}$$

and analogously for the other spin components. Hence, for a coherent spin state,

$$\begin{aligned} &\langle\vartheta,\varphi|^N\Delta\hat{S}_r^2|\vartheta,\varphi\rangle^N = 0 \\ &\langle\vartheta,\varphi|^N\Delta\hat{S}_\varphi^2|\vartheta,\varphi\rangle^N = \tfrac{S}{2} = \langle\vartheta,\varphi|^N\Delta\hat{S}_\varphi^2|\vartheta,\varphi\rangle^N \ . \end{aligned} \tag{23.61}$$

Hence, the local basis the Heisenberg uncertainty is satisfied with two spin components,

$$\langle\Delta S_\vartheta^2\rangle\langle\Delta S_\varphi^2\rangle > \tfrac{S^2}{4} \quad , \quad \langle[\hat{S}_\vartheta,\hat{S}_\varphi]\rangle = \imath S_r \ . \tag{23.62}$$

The panels (a-d) in Fig. 23.3 show the uncertainties of the coherent spin state in the Dicke basis, $\Delta\hat{S}_{x,y,z}$, as a function of the Euler angles ϑ and φ.
The panels (e-h) in Fig. 23.3 show the uncertainties of the coherent spin state in the local basis. Noticeably, the uncertainties projected on the superradiant Bloch sphere are flat. Hence, the Heisenberg relation does not hold [see panel (j)]. Do the Exc. 23.1.9.9.

Since $\langle\vartheta,\varphi|^N\Delta\hat{S}_r^2|\vartheta,\varphi\rangle^N = 0$ for all angles, we may as well disregard the radial component and concentrate on the *projection onto the surface of the Bloch sphere.*

23.1.4.2 Projection onto the equatorial plane

For future reference it is interesting to define operators only acting in the equatorial plane,

$$\boxed{\begin{pmatrix}\hat{S}_\varrho\\ \hat{S}_\varphi\end{pmatrix} = \begin{pmatrix}\cos\varphi & \sin\varphi\\ -\sin\varphi & \cos\varphi\end{pmatrix}\begin{pmatrix}\hat{S}_x\\ \hat{S}_y\end{pmatrix}}\ . \tag{23.63}$$

It is easy to verify,

$$[\hat{S}_\varphi,\hat{S}_\varrho] = \tfrac{1}{2\imath}[\hat{S}_-,\hat{S}_+] = \imath\hat{S}_z \ . \tag{23.64}$$

We see that this is consistent with the previous definition $S_\varrho = \langle\hat{S}_\varrho\rangle$ and (23.48), such that,

$$\begin{pmatrix}\hat{S}_\varrho\\ \hat{S}_\varphi\end{pmatrix} = \begin{pmatrix}\langle\hat{S}_x\rangle/S_\varrho & \langle\hat{S}_y\rangle/S_\varrho\\ -\langle\hat{S}_y\rangle/S_\varrho & \langle\hat{S}_x\rangle/S_\varrho\end{pmatrix}\begin{pmatrix}\hat{S}_x\\ \hat{S}_y\end{pmatrix} \ . \tag{23.65}$$

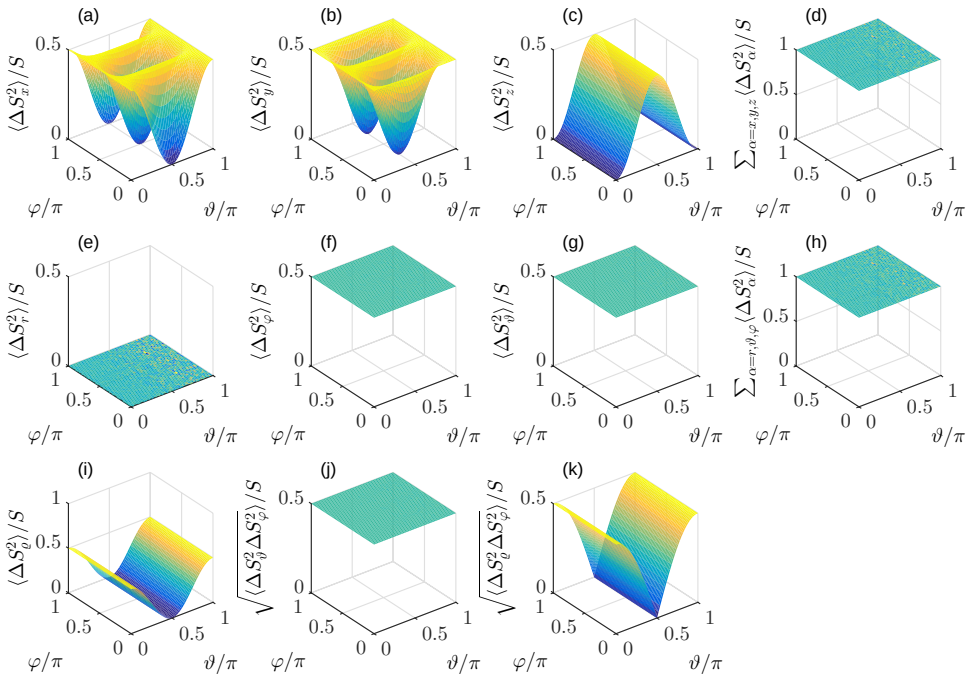

Figure 23.3: (code) Uncertainty of the spin components of a coherent spin state.

Using this transformation it is easy to see,

$$\begin{aligned} \langle \hat{S}_\varrho \rangle^2 + \langle \hat{S}_\varphi \rangle^2 &= \langle \hat{S}_x \rangle^2 + \langle \hat{S}_y \rangle^2 = S_\varrho^2 \\ \langle \hat{S}_\varrho^2 \rangle + \langle \hat{S}_\varphi^2 \rangle &= \langle \hat{S}_x^2 \rangle + \langle \hat{S}_y^2 \rangle \end{aligned} \tag{23.66}$$

such that,

$$\langle \hat{S}_\varphi \rangle = 0 \quad \text{and} \quad \langle \hat{S}_\varrho \rangle = S_\varrho \ . \tag{23.67}$$

Example 140 (*Uncertainty projections for coherent spin states*): Let us now calculate for a coherent spin state,

$$\langle \vartheta, \varphi |^N \Delta \hat{S}_\alpha^2 | \vartheta, \varphi \rangle^N = \langle \vartheta, \varphi |^N \hat{S}_\alpha^2 | \vartheta, \varphi \rangle^N - (\langle \vartheta, \varphi |^N \hat{S}_\alpha | \vartheta, \varphi \rangle^N)^2 \tag{23.68}$$

for $\alpha = \varrho, \varphi$. The panels (f,j,k) in Fig. 23.3 show the uncertainties of the coherent spin state projected onto the equatorial plane. Noticeably, the uncertainty projected on the equatorial plane [panel(i)] is not flat. Hence, the Heisenberg relation does not hold [see panel (k)]. Do the Exc. 23.1.9.10.

23.1.5 Hamiltonian spin squeezing by one-axis twisting

We have seen in the last section, that rotations influence the distribution of the uncertainty among the Cartesian coordinates in a specific way. It is, however, possible to manipulate the uncertainty distribution without rotating the collective spin state. An example with great practical importance is the concept of spin squeezing. It

consists in establishing appropriate quantum correlations are between the individual spins, such as to partly cancel out fluctuations in one direction augmenting them in the other direction.

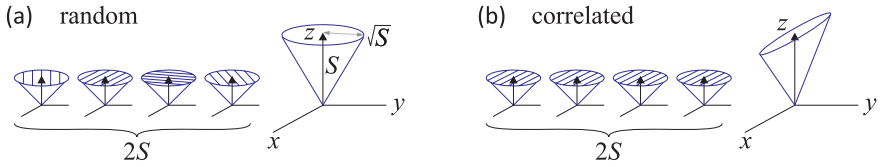

Figure 23.4: Illustration of the uncertainty in (a) a coherent state and (b) a spin-squeezed state.

Squeezing of spin is not as straightforward as squeezing of bosons, since the uncertainty relations are essentially different [468]. To study spin-squeezing along the z-axis let as analyze the unitary transformation,

$$\boxed{\mathcal{Q}_z(\zeta)\hat{\mathbf{S}} \equiv e^{\imath\zeta\hat{S}_z^2}\hat{\mathbf{S}}e^{-\imath\zeta\hat{S}_z^2}} \ . \tag{23.69}$$

Specifying the rule (23.36) for the particular case $F(\hat{S}_z) \equiv \zeta\hat{S}_z^2$, we get,

$$e^{\imath\zeta\hat{S}_z^2}\hat{S}_+e^{-\imath\zeta\hat{S}_z^2} = \hat{S}_+e^{2\imath\zeta(\hat{S}_z+1/2)} \ , \tag{23.70}$$

and hence,

$$\mathcal{Q}_z(\zeta)\hat{\mathbf{S}} = e^{\imath\zeta\hat{S}_z^2}\hat{\mathbf{S}}e^{-\imath\zeta\hat{S}_z^2} = \begin{pmatrix} \frac{1}{2}(\hat{S}_+e^{2\imath\zeta(\hat{S}_z+1/2)} + e^{-2\imath\zeta(\hat{S}_z+1/2)}\hat{S}_-) \\ \frac{1}{2\imath}(\hat{S}_+e^{2\imath\zeta(\hat{S}_z+1/2)} - e^{-2\imath\zeta(\hat{S}_z+1/2)}\hat{S}_-) \\ \hat{S}_z \end{pmatrix} \ . \tag{23.71}$$

Let us now apply the *squeezing operator* to the state $|\frac{\pi}{2},0\rangle$. In Exc. 23.1.9.11 we show that,

$$\langle\tfrac{\pi}{2},0|^N e^{\imath\zeta\hat{S}_z^2}\hat{\mathbf{S}}e^{-\imath\zeta\hat{S}_z^2}|\tfrac{\pi}{2},0\rangle^N = \begin{pmatrix} 1 \\ 0 \\ 0 \end{pmatrix} \tfrac{N}{2}\cos^{N-1}\zeta \tag{23.72}$$

$$\langle\tfrac{\pi}{2},0|^N e^{\imath\zeta\hat{S}_z^2}\begin{pmatrix} \hat{S}_x^2 \\ \hat{S}_y^2 \\ \hat{S}_z^2 \end{pmatrix} e^{-\imath\zeta\hat{S}_z^2}|\tfrac{\pi}{2},0\rangle^N = \begin{pmatrix} N+1 \\ N+1 \\ 2 \end{pmatrix} \tfrac{N}{8} + \begin{pmatrix} 1 \\ -1 \\ 0 \end{pmatrix} \tfrac{N(N-1)}{8}\cos^{N-2}2\zeta \ .$$

The dependencies of the uncertainties as a function of the squeezing parameter are plotted in Fig. 23.5. We see that the uncertainties never get smaller than the unsqueezed value. The reason is that, since the unitary transform $e^{\imath\zeta\hat{S}_z^2}$ commutes with $\hat{S}_z$, the prescription (23.69) does not immediately lead to squeezing along the z-axis.

Nevertheless, the prescription does generate quantum correlations in $\hat{S}_x$ and $\hat{S}_y$, which can be transformed to squeezing by subsequently rotating the collective spin

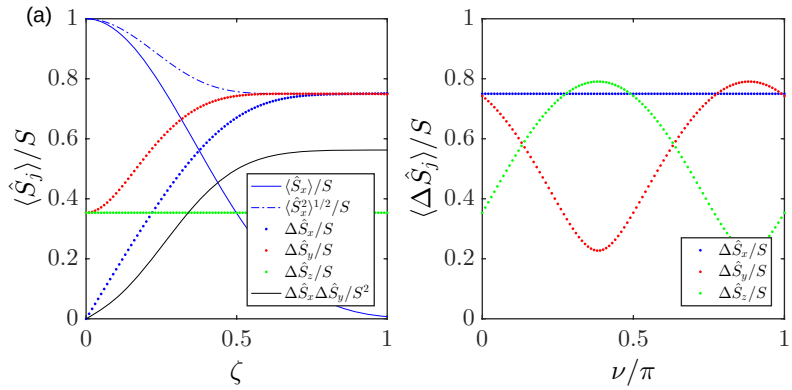

Figure 23.5: (code) (a) Uncertainties calculated in (23.72) as a function of the squeezing parameter. (b) Uncertainties after application of squeezing operator as a function of the rotation angle ν about the x-axis.

about the x-axis [468]. As shown in Exc. 23.1.9.12, a rotation by an angle ν does not modify the x-component,

$$\begin{aligned}\langle\tfrac{\pi}{2},0|^N e^{\imath\nu\hat{S}_x}e^{\imath\zeta\hat{S}_z^2}\Delta\hat{S}_x^2 e^{-\imath\zeta\hat{S}_z^2}e^{-\imath\nu\hat{S}_x}|\tfrac{\pi}{2},0\rangle^N \\ = \tfrac{N(N+1)}{8}+\tfrac{N(N-1)}{8}\cos^{N-2}2\zeta-\tfrac{N^2}{4}\cos^{2N-2}\zeta\ ,\end{aligned} \tag{23.73}$$

but it modifies the other ones,

$$\begin{aligned}\langle\tfrac{\pi}{2},0|^N e^{\imath\nu\hat{S}_x}e^{\imath\zeta\hat{S}_z^2}\Delta\hat{S}_{y,z}^2 e^{-\imath\zeta\hat{S}_z^2}e^{-\imath\nu\hat{S}_x}|\tfrac{\pi}{2},0\rangle^N \\ = \tfrac{N}{4}\{1+\tfrac{N-1}{4}[A\pm\sqrt{A^2+B^2}\cos(2\nu+\arctan\tfrac{B}{A})]\}\ ,\end{aligned} \tag{23.74}$$

with $A\equiv 1-\cos^{N-2}2\zeta$ and $B\equiv 4\sin\zeta\cos^{N-2}\zeta$. We study spin squeezing in Exc. 23.1.9.13 to 23.1.9.16. In Exc. 23.1.9.17 we investigate, whether double Fock states can lead to Heisenberg-limited interferometry, and in Exc. 23.1.9.18 we study entanglement witnesses with coherent spin states.

Obviously, since squeezed states are obtained from coherent states by unitary transform, they are still normalized,

$$\langle\vartheta,\varphi|^N e^{-\imath\zeta\hat{S}_z^2}e^{\imath\zeta\hat{S}_z^2}|\vartheta,\varphi\rangle^N=1\ . \tag{23.75}$$

Example 141 (*Conditional spin-squeezing by non-demolition measurement*): Technically, spin-squeezed states can be generated in experiments by quantum non-demolition measurements [95, 183, 718]. Another idea would be to arrange for totally uniform spin-spin coupling, since this generates terms like,

$$\hat{H}_{\rm ss}=\sum_{i,j\neq i}^{N}\kappa_{ij}\hat{s}_i^z\hat{s}_j^z\simeq\kappa\sum_{i,j\neq i}^{N}\hat{s}_i^z\hat{s}_j^z=\kappa\hat{S}_z^2\ . \tag{23.76}$$

In a cloud this latter idea is not realizable, because the interatomic coupling strength depends on the distance between the atoms, but if the atoms are coupled via their interaction with a common mode of an optical cavity it should be feasible.

23.1.6 Bosonic modes: Harmonic oscillators and collective spin states

Owing to the equidistant spectrum of their excitation levels, harmonic oscillator modes and collective spin states share many particularities, which will allow us to transfer various notions from the well-known harmonic oscillator studied in Sec. 2.6 to the spin ensembles. Respectively expanded on Fock states and Dicke states, the oscillator operators and the spin operators are approximately linked by the Holstein-Primakoff prescription, which will be worked out below. Also, we appreciated in Sec. 14.3 the utility of quasi-probability distributions for the estimation of quantum correlations in light modes, which we will apply to spin systems below. Light fields and spin systems are examples of what is called a *bosonic mode*.

23.1.6.1 Construction of coherent states spin

The goal of this example is to demonstrate, in analogy to the construction of optical coherent states from vacuum using photon creation operators, that the coherent spin states can be constructed from the ground/inverted state using rising/lowering operators.

First we calculate the impact of the rising/lowering operator on the ground/inverted state,

$$\begin{aligned}\hat{S}_{\pm}^{k}|S,\mp S\rangle &= \prod_{m=0}^{k-1}\sqrt{S(S+1)-(\mp S\pm m)(\mp S+1\pm m)}|S,\mp S\pm k\rangle \\ &= k!\sqrt{\binom{N}{k}}|S,\mp S\pm k\rangle\ ,\end{aligned} \tag{23.77}$$

where we made use of the formulas $k! = \Gamma(k+1)$ and $(-1)^k\Gamma(k-N)\Gamma(N-k+1) = \Gamma(-N)\Gamma(1+N)$. Let us now study the impact of the rotation operator $e^{\mu\hat{S}_{\pm}}$,

$$e^{\mu\hat{S}_{\pm}}|S,\mp S\rangle = \sum_{k=0}^{n}\frac{\mu^k}{k!}\hat{S}_{\pm}^{k}|S,\mp S\rangle = \sum_{k=0}^{n}\sqrt{\binom{N}{k}}\mu^k|S,\mp S\pm k\rangle\ . \tag{23.78}$$

Setting $\mu \equiv e^{\imath\varphi}\tan\frac{\vartheta}{2}$ we find [676],

$$\begin{aligned}\frac{1}{(1+|\mu|^2)^S}e^{\mu\hat{S}_{-}}|S,S\rangle &= \cos^{2S}\tfrac{\vartheta}{2}\sum_{k=0}^{n}\sqrt{\binom{N}{k}}e^{\imath k\varphi}\tan^k\tfrac{\vartheta}{2}|S,S-k\rangle \\ &= \sum_{k=0}^{n}\sqrt{\binom{N}{k}}\cos^{N-k}\tfrac{\vartheta}{2}e^{\imath k\varphi}\sin^k\tfrac{\vartheta}{2}|S,S-k\rangle\ ,\end{aligned} \tag{23.79}$$

and analogically for $\hat{S}_{+}$. The result is identical to the definition of a coherent spin state (23.32). Thus, coherent spin states can be constructed from the ground/inverted state using rising/lowering operator,

$$|\mu\rangle \equiv |\vartheta,\varphi\rangle^n = \frac{1}{(1+|\mu^{\mp 1}|^2)^S}e^{\mu^{\mp 1}\hat{S}_{\pm}}|S,\mp S\rangle\ . \tag{23.80}$$

They are not orthogonal, since $\langle\mu|\mu\rangle = \langle\vartheta,\varphi|^n\vartheta,\varphi\rangle^n = 1$, but

$$\begin{aligned}\langle\lambda|\mu\rangle &= \left(\frac{(1+\lambda^*\mu)^2}{(1+|\lambda|^2)(1+|\mu|^2)}\right)^S \\ &= \left(\cos\tfrac{\theta}{2}\cos\tfrac{\vartheta}{2} + e^{\imath(\varphi-\phi)}\sin\tfrac{\theta}{2}\sin\tfrac{\vartheta}{2}\right)^{2S} = \langle\theta,\phi|^n\vartheta,\varphi\rangle^n \ .\end{aligned} \tag{23.81}$$

However, they are complete in the sense,

$$\frac{2S+1}{\pi}\int\frac{|\mu\rangle\langle\mu|}{(1+|\mu|^2)^2}d^2\mu = \frac{2S+1}{\pi}\int\cos^4\tfrac{\vartheta}{2}|\mu\rangle\langle\mu|d^2\mu = \mathbb{I}\ . \tag{23.82}$$

Also,

$$\begin{aligned}\langle\lambda|\hat{S}_+|\mu\rangle &= \langle\theta,\phi|^n S e^{\imath\varphi}\sin\vartheta|\vartheta,\varphi\rangle^n = \frac{2S}{e^{-\imath\varphi}\cot\frac{\vartheta}{2}+e^{-\imath\phi}\tan\frac{\theta}{2}}\langle\lambda|\mu\rangle \\ &= \frac{2Se^{\imath\varphi}\tan\frac{\vartheta}{2}}{1+e^{-\imath\phi}\tan\frac{\theta}{2}e^{\imath\varphi}\tan\frac{\vartheta}{2}}\langle\lambda|\mu\rangle = \frac{2S\mu}{1+\lambda^*\mu}\langle\lambda|\mu\rangle\end{aligned}$$

and analogously,

$$\langle\lambda|\hat{S}_-|\mu\rangle = ... = \frac{2S\lambda^*}{1+\lambda^*\mu}\langle\lambda|\mu\rangle\ . \tag{23.83}$$

In particular

$$\langle\mu|\hat{S}_+|\mu\rangle = \langle\mu|\hat{S}_-|\mu\rangle^* = \frac{2S\mu}{1+|\mu|^2} = Se^{\imath\varphi}\sin\vartheta = \langle\vartheta,\varphi|^n\hat{S}_+|\vartheta,\varphi\rangle^n\ . \tag{23.84}$$

23.1.6.2 Mapping Fock and Dicke states

The operators $\hat{a},\hat{a}^\dagger$ contain all information on a light mode. Similarly, $\hat{S}_+,\hat{S}_-,\hat{S}_z$ contain all information on a collective spin state. In the Heisenberg picture their unitary evolution under some operation (displacement, rotation, squeezing, etc.) is obtained from,

$$\hat{a}^\pm(t) = \mathcal{U}(t)\hat{a}^\pm(0)\mathcal{U}^\dagger(t) \qquad \text{versus} \qquad \hat{\mathbf{S}}(t) = \mathcal{U}(t)\hat{\mathbf{S}}(0)\mathcal{U}^\dagger(t)\ . \tag{23.85}$$

While the state of a light mode is given by an expectation value corresponding to a point in an infinite two-dimensional quadrature phase space, the state of a spin ensemble is represented as a vector in a generalized Bloch sphere,

$$\alpha(t) = \langle\psi(0)|\hat{a}^\pm(t)|\psi(0)\rangle \qquad \text{versus} \qquad \mathbf{S}(t) = \langle\Psi_N(0)|\hat{\mathbf{S}}(t)|\Psi_N(0)\rangle\ . \tag{23.86}$$

By the fact that the light mode is represented by a 2D complex plane, the commutation rule involves two field operators, while for the Bloch sphere, which is embedded in 3D space, with respect to a fixed coordinate system the commutation rule involves three field operators,

$$[\hat{a},\hat{a}^\dagger] = 1 \qquad \text{versus} \qquad [\hat{S}_+,\hat{S}_-] = 2\hat{S}_z\ . \tag{23.87}$$

This has consequences for the uncertainty relations,

$$[\hat{x}, \hat{p}^\dagger] \geq \tfrac{1}{2} \qquad \text{versus} \qquad [\hat{S}_x, \hat{S}_y] \geq \tfrac{1}{2}|\langle S_z \rangle| \ . \tag{23.88}$$

On the other hand, as long as we are only interested in coherent evolutions, as shown in the example 134, the total angular momentum is a constant of motion. This means that an initially fully stretched collective spin state is restricted to evolve on the outer (superradiant) shell of the generalized Bloch sphere, which is a two-dimensional surface,

$$|\alpha\rangle = |\mathfrak{Re}\,\alpha, \mathfrak{Im}\,\alpha\rangle \qquad \text{versus} \qquad |\Psi_N\rangle = |\vartheta, \varphi\rangle^N \ . \tag{23.89}$$

As shown in Sec. 23.1.3, rotations do not influence any spin correlations. Therefore, we may as well introduce a local Cartesian coordinate system, rotated such that $\hat{S}_z$ is diagonal on this basis, and calculate its expectation value $\langle S_z \rangle = M$. We immediately see that the commutation rules (23.87) then become equivalent,

$$[\hat{a}, \hat{a}^\dagger] = 1 \qquad \text{versus} \qquad [\hat{S}_+, \hat{S}_-] = 2M \ , \tag{23.90}$$

as well as the corresponding uncertainty relations. In this basis the correlations can be expanded on a 2D phase space parametrized by the angles ϑ and φ.

23.1.7 The Holstein-Primakoff prescription

In the limit of large atom numbers the Dicke Hamiltonian can be approximated by a system of two coupled quantum oscillators. The mapping is done via the so-called *Holstein-Primakoff transformation*. The transformation is a mapping of the spin operators to boson creation and annihilation operators, effectively truncating their infinite-dimensional Fock space to finite-dimensional subspaces. Let us consider a spin operator $\hat{\mathbf{S}}$ defined by its commutation behavior $[\hat{S}_x, \hat{S}_y] = \imath \hat{S}_z$ and characterized by its eigenvectors $|S, M\rangle$,

$$\hat{\mathbf{S}}^2 |S, M\rangle = S(S+1)|S, M\rangle \qquad , \qquad \hat{S}_z |S, M\rangle = M|S, M\rangle \ , \tag{23.91}$$

with the projection quantum number $M = -S, -S+1, \ldots, S-1, S$. We consider a single particle of spin S and take the state $|S, M = +S\rangle$ as a vacuum for a set of boson operators, and each subsequent state with lower projection quantum number as a boson excitation of the previous one,

$$|S, S-n\rangle \mapsto \frac{1}{\sqrt{n!}} (\hat{b}^\dagger)^n |0\rangle \ . \tag{23.92}$$

Each additional boson then corresponds to a decrease of M in the spin projection. Thus, the spin raising and lowering operators $\hat{S}_\pm = \hat{S}_x \pm \imath \hat{S}_y$ satisfying so that $[\hat{S}_+, \hat{S}_-] = 2\hat{S}_z$ correspond to bosonic annihilation and creation operators, respectively. The precise relations between the operators must be chosen to ensure the correct commutation relations for the spin operators. The resulting Holstein-Primakoff transformation can be written as,

$$\boxed{\hat{S}_+ = \sqrt{2S}\sqrt{1 - \tfrac{\hat{b}^\dagger \hat{b}}{2S}}\ \hat{b} \quad , \quad \hat{S}_- = \sqrt{2S}\ \hat{b}^\dagger \sqrt{1 - \tfrac{\hat{b}^\dagger \hat{b}}{2S}} \quad , \quad \hat{S}_z = S - \hat{b}^\dagger \hat{b}} \ . \tag{23.93}$$

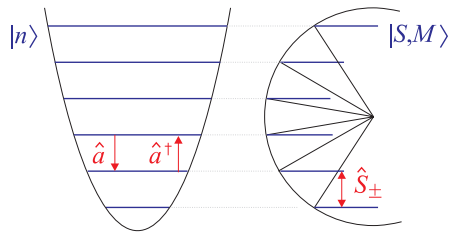

Figure 23.6: Illustration of the Holstein-Primakoff transformation.

The transformation is particularly useful in the case where S is large, when the square roots can be expanded as Taylor series, to give an expansion in decreasing powers of S [803, 81]. We will verify the commutation relations in Exc. 23.1.9.19. The Holstein-Primakoff approximation allows us to rewrite the Hamiltonian (23.6) as,

$$\begin{aligned}\hat{H}_{\mathrm{HoPr}} &= -\Delta_{\mathrm{c}}\hat{a}^\dagger\hat{a} - \Delta_{\mathrm{a}}\hat{S}_z + 2g(\hat{a}+\hat{a}^\dagger)\hat{S}_x \\ &= -\Delta_{\mathrm{c}}\hat{a}^\dagger\hat{a} - \Delta_{\mathrm{a}}(S-\hat{b}^\dagger\hat{b}) + 2g(\hat{a}+\hat{a}^\dagger)\sqrt{2S}\left(\sqrt{1-\tfrac{\hat{b}^\dagger\hat{b}}{2S}}\;\hat{b} + \hat{b}^\dagger\sqrt{1-\tfrac{\hat{b}^\dagger\hat{b}}{2S}}\right) \\ &\simeq -\Delta_{\mathrm{c}}\hat{a}^\dagger\hat{a} - \tfrac{1}{2}\Delta_{\mathrm{a}}\hat{b}^\dagger\hat{b} + 2g_N(\hat{a}+\hat{a}^\dagger)(\hat{b}+\hat{b}^\dagger)\ ,\end{aligned} \tag{23.94}$$

with the collective coupling strength $g_N \equiv g\sqrt{N}$. The Hamiltonian (23.94) describes two coupled quantum oscillators without rotating-wave approximation [273] [6], a system which has already been discussed in Sec. 14.5.5 in the context of beam splitters.

Example 142 (*Eigenvalue spectrum in the Holstein-Primakoff approximation*): We can rewrite the Dicke Hamiltonian (Eq. (11) in [694]), simplifying for a linear cavity, neglecting the pumping term, and assuming perfect bunching as,

$$\hat{H} = -\Delta_{\mathrm{c}}\hat{a}^\dagger\hat{a} - \Delta_{\mathrm{a}}\hat{S}_+\hat{S}_- + g(\hat{a}\hat{S}_+ + \hat{a}^\dagger\hat{S}_-)\ . \tag{23.95}$$

For large atom numbers we apply the Holstein-Primakoff prescription (23.93) [1, 306], yielding,

$$\hat{H} = -\Delta_{\mathrm{c}}\hat{a}^\dagger\hat{a} - \Delta_{\mathrm{a}}\hat{b}^\dagger\hat{b} + g\sqrt{N}(\hat{a}\hat{b}^\dagger + \hat{a}^\dagger\hat{b})\ . \tag{23.96}$$

For $\Delta_{\mathrm{c}} = \Delta_{\mathrm{a}} \equiv \Delta$ the Hamiltonian (23.96) describes two resonant coupled harmonic oscillators. It can easily be transformed into a normal-mode basis via,

$$\begin{pmatrix}\hat{A}\\ \hat{A}^\dagger\\ \hat{B}\\ \hat{B}^\dagger\end{pmatrix} = \tfrac{1}{\sqrt{2}}\begin{pmatrix}1&0&1&0\\0&1&0&1\\1&0&-1&0\\0&1&0&-1\end{pmatrix}\begin{pmatrix}\hat{a}\\ \hat{a}^\dagger\\ \hat{b}\\ \hat{b}^\dagger\end{pmatrix}\ , \tag{23.97}$$

yielding,

$$\hat{H} = -(\Delta - g\sqrt{N})\hat{A}^\dagger\hat{A} - (\Delta + g\sqrt{N})\hat{B}^\dagger\hat{B}\ . \tag{23.98}$$

[6] The Jaynes-Cummings model describes coupling of an atom to a harmonic oscillator mode [273]. In contrast ().

With the Holstein-Primakoff bosons satisfying $[\hat{b}, \hat{b}^\dagger] = 1$, the quadratures defined as

$$\hat{x} \equiv \tfrac{1}{\sqrt{2}}(\hat{b} + \hat{b}^\dagger) \qquad \text{and} \qquad \hat{p} \equiv \tfrac{1}{\imath\sqrt{2}}(\hat{b} - \hat{b}^\dagger) \tag{23.99}$$

obviously satisfy $[\hat{x}, \hat{p}] = \imath$. This allows us to extend the Holstein-Primakoff prescription to Cartesian coordinates. Using the expansion,

$$\sqrt{1 - \tfrac{\hat{b}^\dagger \hat{b}}{2S}} \simeq 1 - \tfrac{\hat{b}^\dagger \hat{b}}{4S} \ , \tag{23.100}$$

which holds for large atom numbers, we find the length of the collective spin,

$$\boxed{\begin{array}{llll} \hat{S}_x & = \frac{1}{2}(\hat{S}_- + \hat{S}_+) & \simeq \hat{x}\sqrt{S} - \frac{\hat{b}^\dagger \hat{x} \hat{b}}{4\sqrt{S}} & = \hat{x}\sqrt{S} - O(S^{-1/2}) \\ \hat{S}_y & = \frac{1}{2\imath}(\hat{S}_- - \hat{S}_+) & \simeq -\hat{p}\sqrt{S} + \frac{\hat{b}^\dagger \hat{p} \hat{b}}{4\sqrt{S}} & = -\hat{p}\sqrt{S} + O(S^{-1/2}) \\ \hat{S}_z & = \frac{1}{2}[\hat{S}_+, \hat{S}_-] & \simeq S - \frac{3}{4}\hat{b}^\dagger \hat{b} + \frac{4}{S}\hat{b}^\dagger \hat{b}^\dagger \hat{b} \hat{b} & = S + O(S^0) \end{array}} \ . \tag{23.101}$$

23.1.7.1 The Holstein-Primakoff prescription on a local coordinate system

In the limit of large particle numbers, we may regard the outer shell of the generalized Bloch as being locally flat. This allows us to map the harmonic oscillator formalism on a tangent plane touching the Bloch sphere at point $\hat{\mathbf{S}}$. Concentrating on the meridian $\varphi = 0$ and defining a local coordinate system [see (23.48)], as illustrated in Fig. 23.7,

$$\begin{pmatrix} \hat{S}_\vartheta \\ \hat{S}_y \\ \hat{S}_\rho \end{pmatrix} = \begin{pmatrix} \cos\vartheta & 0 & -\sin\vartheta \\ 0 & 1 & 0 \\ \sin\vartheta & 0 & \cos\vartheta \end{pmatrix} \begin{pmatrix} \hat{S}_x \\ \hat{S}_y \\ \hat{S}_z \end{pmatrix} \simeq \begin{pmatrix} \hat{x}\sqrt{S} \\ -\hat{p}\sqrt{S} \\ S \end{pmatrix} \ , \tag{23.102}$$

or resolving by the Cartesian spin,

$$\begin{pmatrix} \hat{S}_x \\ \hat{S}_y \\ \hat{S}_z \end{pmatrix} = \begin{pmatrix} \cos\vartheta & 0 & \sin\vartheta \\ 0 & 1 & 0 \\ -\sin\vartheta & 0 & \cos\vartheta \end{pmatrix} \begin{pmatrix} \hat{S}_\vartheta \\ \hat{S}_y \\ \hat{S}_\rho \end{pmatrix} \ . \tag{23.103}$$

We verify easily,

$$[\hat{S}_\vartheta, \hat{S}_y] = \imath \hat{S}_\rho \simeq \imath S = [\hat{x}\sqrt{S}, \hat{p}\sqrt{S}] \ . \tag{23.104}$$

Solve Excs. 23.1.9.20 and 23.1.9.21. We will use this description in Sec. 23.5.2.

23.1.8 Quasi-probability distributions on the Bloch sphere

The operators contain all information on possible quantum correlations, and it is now interesting to quantify and illustrate the formation of such correlations under some manipulation. This is the purpose of the quasi-probability distributions.

The evolution of collective states and operators of a harmonic oscillator (resp. spin system) under the influence of a Hamiltonian is conveniently calculated by expanding

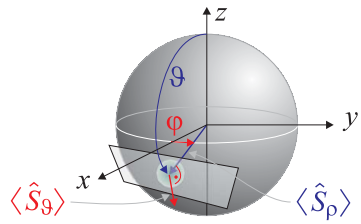

Figure 23.7: Scheme of a local coordinate system.

them on a Fock (resp. Dicke) basis and evaluating propagators via unitary transformations, as in Eq. (23.85). On the other hand, quantum correlations become more visible on a Glauber (resp. coherent spin state) basis.

Now, the close analogy between harmonic oscillators and spin systems allows us to apply concepts elaborated for the harmonic oscillator to collective spin states. One example is the notion of quasi-probability distributions introduced in Sec. 14.3 for Glauber states, which we will apply to collective spin states below. In quantum optics a frequently used distribution function is the Wigner function $W_\rho(\alpha, \alpha^*)$ characterizing a light mode via an expansion into a coherent states basis $|\alpha\rangle$ spanning the complex quadrature plane. The purpose of this section is to derive an analogous function for collective spin states $W_\rho(\vartheta, \varphi)$.

We proceed by expanding an arbitrary state of a light mode on the Fock basis (2.93), which is similar to expanding coherent spin states on the Dicke basis (23.32),

$$|\psi\rangle = \sum_{n=0}^{\infty} c_n |n\rangle \qquad \text{versus} \qquad |\Psi_N\rangle = \sum_{M=+S,..,-S} c_{S,M} |S, M\rangle \tag{23.105}$$

with

$$c_n(t) = \langle n | e^{-\imath \hat{H} t} \psi(0) \rangle \qquad \text{versus} \qquad c_{S,M}(t) = \langle n | e^{-\imath \hat{H} t} \Psi_N(0) \rangle \ . \tag{23.106}$$

In particular for coherent states (resp. spin states),

$$|\alpha\rangle = \sum_{n=0}^{\infty} \frac{e^{-|\alpha|^2/2} \alpha^n}{\sqrt{n!}} |n\rangle \tag{23.107}$$

$$\text{versus} \qquad |\vartheta, \varphi\rangle^N = \sum_{M=+S,..,-S} \sqrt{\binom{N}{S+M}} \cos^{S-M} \tfrac{\vartheta}{2} e^{\imath (S+M)\varphi} \sin^{S+M} \tfrac{\vartheta}{2} |S, M\rangle \ .$$

We note that both Fock and Dicke states have no phase in phase space. Phases are generated by summing Fock (resp. Dicke) states with different dynamical phase factors corresponding to their energies.

For numerical simulations we also expand operators on the Fock (resp. Dicke)

basis,

$$\hat{a} = \sum_{n,n'=0}^{\infty} \delta_{n',n-1}\sqrt{n}|n'\rangle\langle n| \quad , \quad \hat{a}^\dagger = \sum_{n,n'=0}^{\infty} \delta_{n',n+1}\sqrt{n+1}|n'\rangle\langle n|$$

$$\text{versus} \quad \hat{S}_\pm = \sum_{M,M'=+S,..,-S} \delta_{M',M\pm1}\sqrt{S(S+1)-M(M\pm1)}|S,M'\rangle\langle S,M|$$

$$\hat{S}_z = \sum_{M,M'=+S,..,-S} \delta_{M',M} M|S,M'\rangle\langle S,M| \; . \tag{23.108}$$

In the case of light modes, any point in phase space is reached via a displacement operator (see Eq. (2.130)). Similarly, any point on the Bloch sphere is reached via rotations about two axes [472, 200] (see Eq. (23.40)),

$$\begin{aligned} |\alpha\rangle &= D(\alpha)|0\rangle \qquad \text{versus} \quad |\vartheta,\varphi\rangle^N &= U_{\rm rt}(\vartheta,\varphi)|S,-S\rangle \\ &= e^{\alpha\hat{a}^\dagger-\alpha^*\hat{a}}|0\rangle &= e^{-(\vartheta/2)e^{-\imath\varphi}\hat{S}_+ + (\vartheta/2)e^{\imath\varphi}\hat{S}_-}|S,-S\rangle \; . \end{aligned} \tag{23.109}$$

The Fock (resp. Dicke) basis may not the best one to reveal the existence of quantum correlations. The purpose of quasi-probability distributions defined on a basis of Glauber (resp. coherent spin) states is to provide a better characterization, in particular, on non-Gaussian collective states.

23.1.8.1 Distributions for Gaussian spin states (coherent and squeezed)

Let us now define proper quasi-probability distributions in analogy to those introduced for Glauber space in Sec. 14.3 [7]. In analogy to the example 80 we may, based on the rotation operator $R(\vartheta,\varphi)|S,S\rangle = e^{\imath\vartheta(\hat{S}_x\sin\varphi-\hat{S}_y\cos\varphi)}|S,S\rangle \equiv |\vartheta,\varphi\rangle^N$ introduced in (23.40) and the parity operator for rotations given by [653, 472],

$$M_s = \frac{1}{R}\sum_{\ell=0}^{2S}\sqrt{\frac{2\ell+1}{4\pi}}(\gamma_\ell)^{-s}\mathbf{T}_{\ell 0} \qquad \text{with} \qquad \gamma_\ell = \frac{R\sqrt{4\pi}(2S)!}{\sqrt{(2S+\ell+1)!}\sqrt{(2S-\ell)!}} \tag{23.110}$$

$$\text{and} \qquad \mathbf{T}_{\ell m} = \sqrt{\frac{2\ell+1}{2S+1}}\sum_{M,M'=-S}^{S}\begin{pmatrix} S & \ell & S \\ M' & m & M\end{pmatrix}|S,M'\rangle\langle S,M|$$

with $R=\sqrt{S/2\pi}$ define a generalized probability distribution,

$$X_\rho(\vartheta,\varphi,s) = \text{Tr}\;\hat{\rho}\mathcal{U}_{\rm rt}(\vartheta,\varphi)M_s\mathcal{U}_{\rm rt}^\dagger(\vartheta,\varphi) \longrightarrow \langle\Psi_N|\mathcal{U}_{\rm rt}(\vartheta,\varphi)M_s\mathcal{U}_{\rm rt}^\dagger(\vartheta,\varphi)|\Psi_N\rangle \; , \tag{23.111}$$

where the second expression holds for pure states. The displacement operator from (14.70) is here replaced by a rotation parametrized by two Euler angles. From (23.111) the usual probability distributions follow as,

$$Q_\rho(\vartheta,\varphi) \equiv X_\rho(\vartheta,\varphi,-1) \quad , \quad W_\rho(\vartheta,\varphi) \equiv X_\rho(\vartheta,\varphi,0) \quad , \quad P_\rho(\vartheta,\varphi) \equiv X_\rho(\vartheta,\varphi,1) \tag{23.112}$$

[7] Compare (14.79) to (2.158).

The parity operator is expanded on the Dicke basis according to the recipe (23.110). To visualize a distribution function, we evaluate (23.111) for every point (ϑ, φ) of the Bloch sphere.

With increasing spin number S, the parity operators M_s converge to the infinite-dimensional operators Π_s of (14.71), while rotations transform into translations along the tangent of a sphere. For pure states the Wigner function is thus given by a rotation of the parity operator.

23.1.8.2 Expansion of non-Gaussian spin states

As long as a collective spin state can be expanded on a collective Dicke basis of superradiant states or reached by coherent evolution from such a state, it remains pure and can be represented by a probability distribution using the procedure outlined in (23.112). But non-Gaussian spin states can be represented as well. The Dicke state $|S,0\rangle$, the cat state $|\text{cat}\rangle$, the coherent state $|\vartheta,\varphi\rangle^N$, and a squeezed state are illustrated in Fig. 23.8,

$$\begin{aligned}
|\text{W}\rangle &= |S, S-1\rangle \qquad (23.113)\\
|\text{GHZ}\rangle &= \tfrac{1}{\sqrt{2}}(|\uparrow\rangle^{2S}|\downarrow\rangle^0 + |\uparrow\rangle^0|\downarrow\rangle^{2S}) = \tfrac{1}{\sqrt{2}}(|S,S\rangle + |S,-S\rangle)\\
|\text{N00N}\rangle &= \tfrac{1}{\sqrt{2}}(|\uparrow\rangle^{2S}|\downarrow\rangle^0 + e^{\imath N\vartheta}|\uparrow\rangle^0|\downarrow\rangle^{2S}) = \tfrac{1}{\sqrt{2}}(|S,S\rangle + e^{\imath 2S\vartheta}|S,-S\rangle)\\
|\text{cat}\rangle &= \cos\tfrac{\vartheta}{2}|S,S\rangle + e^{\imath\varphi}\sin\tfrac{\vartheta}{2}|S,-S\rangle\\
|\text{squeezed}\rangle &= e^{\imath\zeta\hat{S}_y^2/2}|\pi/2,\pi/2\rangle^N \ .
\end{aligned}$$

Note that the Dicke state labeled as $|S,0\rangle$ in Fig. 23.8 corresponds to a twin Fock state [653], as it corresponds to exactly half the atoms in the lower and in the upper state. Rotating this state about the x or the y-axis, we obtain a state with a perfectly defined phase but completely undefined population.

For pure states the density matrix is readily obtained in the Dicke basis via,

$$\hat{\rho}_{|\psi\rangle} = |\psi\rangle\langle\psi| \ . \qquad (23.114)$$

For some states it is illustrated in Fig. 23.9

23.1.9 Exercises

23.1.9.1 Ex: Dicke states and Clebsch-Gordan coefficients

Discuss the relationship between coherent Dicke states and Clebsch-Gordan coefficients at the example of two coupled spins.

23.1.9.2 Ex: Dicke Hamiltonian for 3 atoms

Generalize the Dicke Hamiltonian (23.25) to 3 atoms.

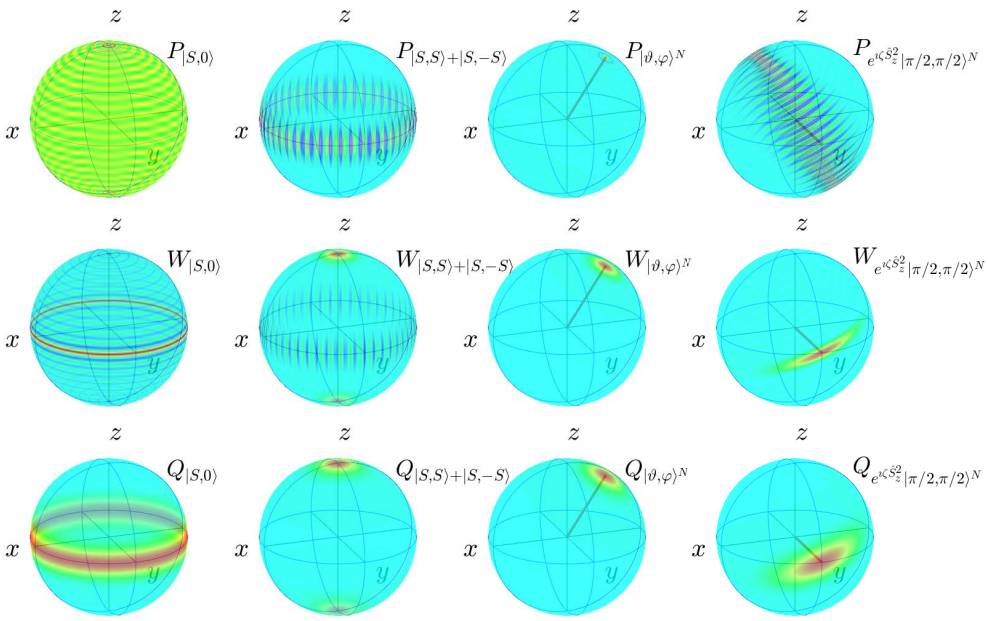

Figure 23.8: (code) P, W, and Q-distributions on the Bloch sphere for various states with $N = 50$.

23.1.9.3 Ex: Coherent spin states

Show that the coherent spin state is an eigenstate of the operator $\hat{S}_{\vartheta,\varphi} \equiv \hat{S}_x \sin\vartheta\cos\varphi + \hat{S}_y \sin\vartheta\sin\varphi + \hat{S}_z\cos\vartheta$.

23.1.9.4 Ex: Orthogonality and completeness of CSS

Check the orthogonality and completeness of CSS in analogy the Glauber states studied in Excs. 2.6.6.3 and 2.6.6.5.

23.1.9.5 Ex: Collective spin of a coherent spin state

a. Calculate the expectation values for all spin components of the collective spin $\hat{\mathbf{S}}$ in a coherent spin state see also Exc. 3.3.4.8.
b. Calculate the uncertainties for all spin components of the collective spin $\hat{\mathbf{S}}$ in a coherent spin state and check the uncertainty relation.

23.1.9.6 Ex: Unitary spin transformations

Prove the relationship $e^{\imath F(\hat{S}_z)}\hat{S}_+ e^{-\imath F(\hat{S}_z)} = \hat{S}_+ e^{\imath[F(\hat{S}_z+\mathbb{I})-F(\hat{S}_z)]}$.

23.1.9.7 Ex: Rotation about the x-axis

How does the collective spin transform under rotation about the x-axis?

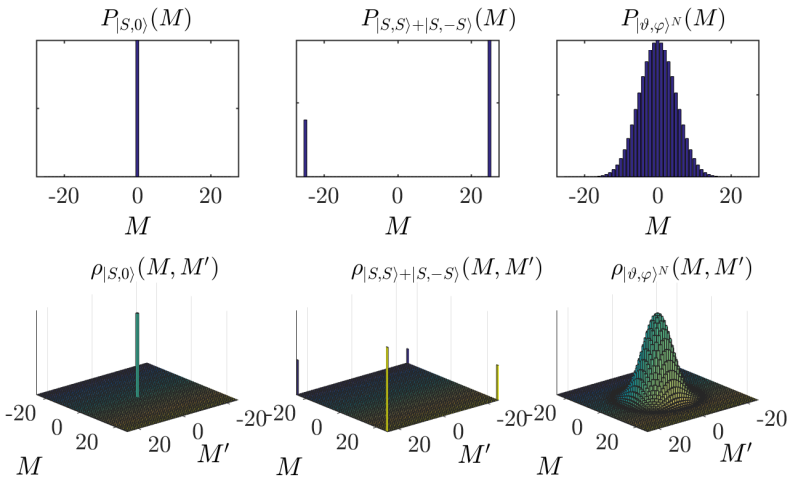

Figure 23.9: (code) Density matrix of several states in the Dicke basis.

23.1.9.8 Ex: Spin operators for two atoms

Calculate explicitly for the case of two atoms the rotation matrices $e^{\imath\gamma\hat{S}_\alpha}$ for $\alpha = x, y, z$. Check the relationship $e^{\imath\gamma\hat{S}_\alpha}\hat{\mathbf{S}}e^{-\imath\gamma\hat{S}_\alpha} = R_\alpha(\gamma)\hat{\mathbf{S}}$ by explicit calculation.

23.1.9.9 Ex: Projection of spin operators onto the superradiant Bloch sphere surface

a.

23.1.9.10 Ex: Projection of spin operators onto the equatorial plane

a. Evaluate $\Delta\hat{S}_x^2+\Delta\hat{S}_y^2+\Delta\hat{S}_z^2$ for coherent collective spin states. Simplify $\Delta\hat{S}_+^2\pm\Delta\hat{S}_-^2$ for arbitrary spin states.
b. Calculate for arbitrary collective spin states $\hat{S}_\rho \mp \imath\hat{S}_\varphi$ and $[\hat{S}_\varphi, \hat{S}_\rho]$ and their expectation values, where $\hat{S}_\rho = \frac{1}{2}(\hat{S}_- e^{\imath\varphi} + \hat{S}_+ e^{-\imath\varphi})$ and $\hat{S}_\varphi = \frac{1}{2\imath}(\hat{S}_- e^{\imath\varphi} - \hat{S}_+ e^{-\imath\varphi})$.
c. Evaluate $\Delta\hat{S}_\rho^2 + \Delta\hat{S}_\varphi^2 + \Delta\hat{S}_z^2$ for arbitrary collective spin states.

23.1.9.11 Ex: Spin squeezing

a. Calculate $\langle\frac{\pi}{2},0|^N e^{\imath\zeta\hat{S}_z^2}\hat{\mathbf{S}}e^{-\imath\zeta\hat{S}_z^2}|\frac{\pi}{2},0\rangle^N$.
b. Calculate $\langle\frac{\pi}{2},0|^N e^{\imath\zeta\hat{S}_z^2}\Delta\hat{S}_{x,y,z}^2 e^{-\imath\zeta\hat{S}_z^2}|\frac{\pi}{2},0\rangle^N$.

23.1.9.12 Ex: Rotation of spin squeezed states

Calculate $\langle\frac{\pi}{2},0|^N e^{\imath\nu\hat{S}_x}e^{\imath\zeta\hat{S}_z^2}\Delta\hat{S}_{x,y,z}^2 e^{-\imath\zeta\hat{S}_z^2}e^{-\imath\nu\hat{S}_x}|\frac{\pi}{2},0\rangle^N$.

23.1.9.13 Ex: Spin squeezing with two atoms

a. For a system of two atoms, write down the coherent state $|\vartheta,\varphi\rangle^2 = |\frac{\pi}{2},0\rangle^2$ in the Tavis-Cummings basis and in the Dicke state basis.
b. Derive the matrix representation for the squeezing operator along the z-axis and apply this operator to the above coherent spin state.
c. Compare spin squeezing with entanglement.

23.1.9.14 Ex: Mølmer-Sørensen gate

Derive the matrix representation for the two-qubit Mølmer-Sørensen gate $e^{\imath\zeta\hat{S}_x^2}$.

23.1.9.15 Ex: Spin-squeezing via one-axis twisting

For a Dicke state with $N = 8$ atoms, program the matrix representations of the operators $\hat{S}_\pm$, $\hat{\mathbf{S}}$, $R_\alpha(\theta)$, and $\mathcal{Q}_\alpha(\zeta)$ for $\alpha = x, y, z$ defined in the script, as well as the vector representation of the state $|\vartheta,\varphi\rangle$.
a. Starting from the ground state $|\vartheta,\varphi\rangle = |0,0\rangle$, simulate the following time evolution: (i) $\frac{\pi}{2}$-pulse with the Hamiltonian $\hat{H} = \Omega\hat{S}_x$, where Ω is the Rabi frequency, (ii) interaction-free precession with the Hamiltonian $\hat{H} = \Delta\hat{S}_z$ where Δ is the detuning during a time T, (iii) $\frac{\pi}{2}$-pulse with the Hamiltonian $\hat{H} = \Omega\hat{S}_x$, (iv) projection of the energy axis. Plot the time evolution of the expectation values $\langle\hat{S}_\alpha\rangle$ and $\Delta\hat{S}_\alpha$.
b. Starting from the ground state $|\vartheta,\varphi\rangle = |0,0\rangle$, simulate the following time evolution: (i) $\frac{\pi}{2}$-pulse with the Hamiltonian $\hat{H} = \Omega\hat{S}_y$, where Ω is the Rabi frequency, (ii) squeezing pulse along the z-axis with the squeezing parameter $\zeta = 0.6$, (iii) $\frac{\pi}{2}$-pulse with the Hamiltonian $\hat{H} = \Omega\hat{S}_x$. Plot the time evolution of the expectation values $\langle\hat{S}_\alpha\rangle$ and $\Delta\hat{S}_\alpha$. Movies can be seen at (watch movie).

23.1.9.16 Ex: Two-axis countertwisting

Study the Hamiltonian,

$$\hat{H} = \zeta(\hat{S}^2_{\pi/2,\pi/4} - \hat{S}^2_{\pi/2,-\pi/4}) = \tfrac{\zeta}{2\imath}(\hat{S}_+^2 - \hat{S}_-^2)$$

with $\hat{S}_{\vartheta,\varphi}$ defined in Exc. 23.1.9.3 in view of its squeezing features of an initial coherent spin state $|0,\varphi\rangle$ [468].

23.1.9.17 Ex: Interferometry with double Fock states

Discuss numerically whether, assuming as the initial state a double spin Fock state of the form $|+\rangle^{N_1}|-\rangle^{N_2}$, Heisenberg limited interferometry can be done within the Dicke model [110, 516].

23.1.9.18 Ex: Entanglement criteria

A sufficient entanglement criterion for an N-qubit state is, that it violates one of the following inequalities [826, 827],

$$\begin{aligned}
\frac{\langle\Delta\hat{S}_z^2\rangle}{\langle\hat{S}_x\rangle^2+\langle\hat{S}_y\rangle^2} &\geq \frac{1}{N} \\
\langle\hat{S}_x^2\rangle+\langle\hat{S}_y^2\rangle+\langle\hat{S}_z^2\rangle &\leq \tfrac{N(N+2)}{4} \\
\langle\Delta\hat{S}_x^2\rangle+\langle\Delta\hat{S}_y^2\rangle+\langle\Delta\hat{S}_z^2\rangle &\geq \tfrac{N}{2} \\
\langle\hat{S}_k^2\rangle+\langle\hat{S}_m^2\rangle-\tfrac{N}{2} &\leq (N-1)\langle\Delta\hat{S}_n^2\rangle \\
(N-1)[\langle\Delta\hat{S}_k^2\rangle+\langle\Delta\hat{S}_m^2\rangle] &\geq \langle\hat{S}_k^2\rangle+\tfrac{N(N-2)}{4} \ ,
\end{aligned}$$

for $(kmn)=(123)$. Verify that, according to these criteria, coherent Dicke states are not entangled.

23.1.9.19 Ex: Consistency of the Holstein-Primakoff transform

Verify that the relations (23.93) satisfy $[\hat{S}_+,\hat{S}_-]\simeq 2\hat{S}_z$ and $[\hat{S}_x,\hat{S}_y]\simeq \frac{\imath}{2}\hat{S}_z$.

23.1.9.20 Ex: Holstein-Primakoff expansion on the Bloch sphere for coherent spin states

Calculate the uncertainties for coherent spin states $|\vartheta_N\rangle\equiv|\vartheta,0\rangle^{\otimes N}$ in the local basis.

23.1.9.21 Ex: Uncertainty relation in different bases

In Exc. 23.1.9.5 the principal axes of the uncertainty ellipsoid of a coherent spin state have been derived for a fixed Cartesian coordinate system. Now, express the uncertainty ellipsoid in a local Cartesian basis anchored to spherical coordinates by $\hat{\mathbf{e}}'_x=\hat{\mathbf{e}}_r$, $\hat{\mathbf{e}}'_y=\hat{\mathbf{e}}_\theta$, and $\hat{\mathbf{e}}'_z=\hat{\mathbf{e}}_\phi$. Why is the radial projection onto the surface of the generalized Bloch sphere invariant upon rotation? Interpret the projection of the uncertainty ellipsoid onto the radial axis and its dependency on rotation.

23.1.9.22 Ex: Dicke model of Bloch oscillations in the two-mode approximation

In the limit where Bloch oscillations can be modeled by a two-level system [722] we may try a representation within the Dicke model and illustrate the dynamics on a Bloch sphere [718]. The gravitational acceleration corresponds to a modification of kinetic energy without modification of the momentum state populations and without excitation of quantum coherences between them. That is, at any time the system remains in an eigenstate of the momentum operator. Since the kinetic energy is represented by the vertical axis of the Bloch sphere, we may visualize acceleration via a rotation of the Bloch sphere, e.g. about the y-axis. The interpretation of the rotated Bloch sphere remains the same: the xy-plane shows the coherences and the z-axis the populations. Once this works, we can treat the thermal atomic cloud as

a coherent spin state, e.g. squeeze it [468] or simulate trajectory of individual atoms inhomogeneously [211] [8,9]. A movie can be seen at (watch movie).

23.1.9.23 Ex: Error estimation in Rabi and Ramsey experiments

The precision of the estimation of a parameter ϑ from a measurement of an observable $\hat{A}$ which depends on that parameter is obtained from error propagation (see Secs. 24.4.3) [825],

$$(\Delta\vartheta)^2 = \frac{\langle\Delta\hat{A}\rangle^2}{|\partial_\vartheta\langle\hat{A}\rangle|^2} = \frac{\langle\hat{A}^2\rangle - \langle\hat{A}\rangle^2}{|\partial_\vartheta\langle\hat{A}\rangle|^2} \ .$$

a. Estimate for a coherent collective spin state the uncertainty in determining the angle ϑ from a measurements of one of the spin components, that is, $\hat{A} \equiv \hat{S}_{x,y,z}$.
b. Consider a Ramsey experiment where the collective spin state has been rotated into the equatorial plane by a first $\pi/2$ nutation pulse, such that the state becomes an eigenstate of $\hat{S}_x$. Now, the spin starts precessing about the z-axis according to $\mathcal{U} = e^{\imath\hat{H}t}$ due to an interaction $\hat{H} = \varphi\hat{S}_z$. Estimate for a coherent collective spin state the uncertainty in determining the angle φ from a measurement of $\hat{S}_y$.

23.2 Super- and subradiance in open systems

The abstract spin formalism developed in the last sections revealed propagators allowing us to rotate and squeeze coherent spin states, but it did not tell us how to implement them physically. For this, we need to solve equations of motion derived from Hamiltonians realizable in the laboratory. In the following sections, we will set up the fundamental equations of motion (master or Heisenberg-Liouville) for open systems of N atoms subject to spontaneous emission collectively interacting with a single light mode subject to cavity decay and pumped by an external source.

We will discuss constants of motion of the Dicke and of the Tavis-Cummings model and phase transitions to superradiant states in the mean-field and in the Holstein-Primakoff approximation. Finally, we will present recent experimental realizations of Dicke phase transitions, namely superradiant self-ordering and superradiant lasing.

23.2.1 Models for open systems and phase transitions

We have already seen, that the spin quantum number S is preserved under the effect of the Dicke Hamiltonian (23.6). The spherical harmonics $|S, M\rangle$ are orthonormal and the spin operators $\hat{S}_\pm$ and $\hat{S}_{x,y,z}$ or their combinations do not allow for transitions between states with different S,

$$[\hat{H}, \hat{\mathbf{S}}^2] = 0 \qquad \text{with} \qquad \hat{\mathbf{S}}^2 = \tfrac{1}{2}(\hat{S}_+\hat{S}_- + \hat{S}_-\hat{S}_+) + \hat{S}_z^2 \tag{23.115}$$
$$\text{but} \qquad [\hat{H}, \hat{S}_z] = \imath(\mathfrak{Im}\,\Omega\ \hat{S}_x - \mathfrak{Re}\,\Omega\ \hat{S}_y) \neq 0 \ .$$

Hence, under the effect of the Dicke Hamiltonian an initial state $|N, S, M\rangle$ can only change its magnetic quantum number $|N, S, M\rangle \longrightarrow |N, S, M'\rangle$, and the manifolds

[8] Note that, in order to simulate a series of Bloch oscillations, we must change the basis by hand after each Bragg reflection.
[9] An interesting question is, whether the Dicke picture can be extended to CARL (see Sec. 25.3.4).

with a given S form closed sub-spaces (see Exc. 23.2.4.2). In other words, once we start in a superradiant state $|N, S, M\rangle = |N, \frac{N}{2}, +\frac{N}{2}\rangle$, spin conservation excludes subradiant states, which allowed us to restrict to the superradiant Dicke subspace. Transitions between Dicke subspaces are only possible via physical processes that act on individual atoms, e.g. decay or phase fluctuation processes, as we will see later [310, 903].

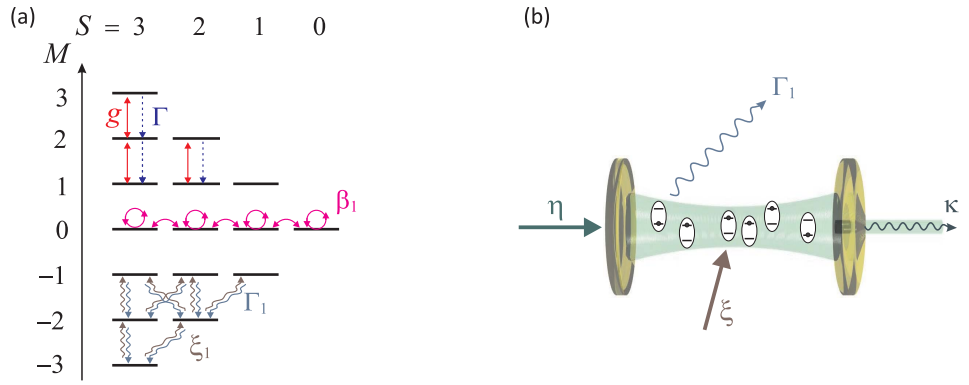

Figure 23.10: (a) Illustration of the Dicke states for $N = 6$. Hamiltonian interactions are in depicted in red. Superradiant decay occurs through a cascade from state $M = S$ to state $M = -S$. Spontaneous emission and phase noise leads to transitions along the blue arrows. The lowest states in each S subspace are dark and can only decay through a (subradiant) dark states cascade. (b) Scheme of the Dicke model.

23.2.1.1 The generalized open Dicke model

In the presence of spontaneous decay or dephasing, superradiant spin conservation is no longer guaranteed. Let us have a look at the master equation for a set of N atoms coupled with the strength g to the mode of a cavity and additionally pumped by a classical laser field η [78, 466] (see (15.27)). After transformation into the rotating frame we have,

$$\dot{\hat{\rho}} = \imath[\hat{\rho}, \hat{H}_{gD}] + \sum_\gamma \mathfrak{L}_{\gamma,\hat{L}}\hat{\rho} \quad \text{or} \quad \dot{\hat{A}} = \mathfrak{L}_{\text{tot}}\hat{A} = -\imath[\hat{A}, \hat{H}_{gD}] + \sum_\gamma \mathfrak{L}^\dagger_{\gamma,\hat{L}}\hat{A}$$

$$\hat{H}_{gD} = -\Delta_c\hat{a}^\dagger\hat{a} - \Delta_a\hat{S}_z + g(\hat{a}\hat{S}_+ + \hat{S}_-\hat{a}^\dagger) + g'(\hat{a}\hat{S}_- + \hat{S}_+\hat{a}^\dagger) - \imath\eta(\hat{a} - \hat{a}^\dagger)$$

$$\text{and} \quad \mathfrak{L}_{\gamma,\hat{L}}\hat{\rho} \equiv \gamma(2\hat{L}\hat{\rho}\hat{L}^\dagger - \hat{L}^\dagger\hat{L}\hat{\rho} - \hat{\rho}\hat{L}^\dagger\hat{L})$$

$$\text{and} \quad \mathfrak{L}^\dagger_{\gamma,\hat{L}}\hat{A} \equiv \gamma(2\hat{L}^\dagger\hat{A}\hat{L} - \hat{L}^\dagger\hat{L}\hat{A} - \hat{A}\hat{L}^\dagger\hat{L}) \tag{23.116}$$

The different coupling strengths g and g' allow us to isolate the counter-rotating terms, in order to discuss their relevance. The usual *open Dicke model* is obtained from the generalized Dicke Hamiltonian $\hat{H}_{gD}$ by setting $g' \equiv g$, while the rotating wave approximation is done by setting $g' \equiv 0$. The rates γ describe possible decay

processes to which the degrees of freedom $\hat{L}$ are subject. The most relevant decay processes are listed in the following table:

decay rate γ	dissipative operator $\hat{L}$	physical process
κ	$\hat{a}$	cavity decay
ϕ	$\hat{a}^\dagger\hat{a}$	cavity phase jitter
$\gamma = \Gamma/2$	$\hat{S}_- = \sum_j \hat{s}_j^-$	collective (superradiant) atomic decay
$\gamma_1 = \Gamma_1/2$	$\hat{s}_j^-$	(transverse) single-atom decay
ξ_1	$\hat{s}_j^+$	single-atom optical pumping
β_1	$\hat{s}_j^z$	single-atom dephasing

$\Gamma = 2\gamma$ is the collective longitudinal atomic decay, κ and ϕ describe collective decay respectively collective phase noise of the cavity, while $\Gamma_1 = 2\gamma_1$, ξ_1, and β_1 stand for spontaneous emission, optical pumping via higher-lying levels, and phase fluctuation of individual atoms. The latter decay processes are described by sums of Lindbladians over all atoms. In Exc. 23.2.4.4 we derive the Heisenberg equations for the relevant degrees of freedom,

$$
\begin{aligned}
\langle\dot{\hat{A}}\rangle &= \langle\mathfrak{L}_{\rm tot}\hat{A}\rangle \qquad \text{with} \\
\mathfrak{L}_{\rm tot}\hat{a} &= (\imath\Delta_{\rm c} - \kappa - \phi)\hat{a} - \imath(g\hat{S}_- + g'\hat{S}_+) + \eta \\
\mathfrak{L}_{\rm tot}\hat{S}_- &= (\imath\Delta_{\rm a} - \gamma_1 - \xi_1 - \beta_1 + \Gamma\hat{S}_z)\hat{S}_- + 2\imath\hat{S}_z(g\hat{a} + g'\hat{a}^\dagger) \\
\mathfrak{L}_{\rm tot}\hat{S}_z &= -\imath\hat{S}_+(g\hat{a} + g'\hat{a}^\dagger) + \imath(g\hat{a}^\dagger + g'\hat{a})\hat{S}_- - \Gamma\hat{S}_+\hat{S}_- - N(\gamma_1 - \xi_1)\mathbb{I} - 2(\gamma_1 + \xi_1)\hat{S}_z \\
\mathfrak{L}_{\rm tot}\hat{s}_j^- &= (\imath\Delta_{\rm a} - \gamma_1 - \xi_1 - \beta_1)\hat{s}_j^- + 2\imath(g\hat{a} + g'\hat{a}^\dagger)\hat{s}_j^z \\
\mathfrak{L}_{\rm tot}\hat{s}_j^z &= -\imath(g\hat{a} + g'\hat{a}^\dagger)\hat{s}_j^+ + \imath(g\hat{a}^\dagger + g'\hat{a})\hat{s}_j^- - \gamma_1(\mathbb{I} - 2\hat{s}_j^z) + \xi_1(\mathbb{I} + 2\hat{s}_j^z)\ .
\end{aligned}
\tag{23.117}
$$

In the derivation we make extensive use of commutation relations between operators $\hat{A}$ representing the degrees of freedom and operators $\hat{L}$ representing dissipation processes. However, we have to remember that these commutation relations only hold for stationary operators $\hat{A} = \hat{A}(0)$. This forces us to describe the time evolution of pure or mixed states in the Schrödinger picture [see Eq. (1.275) versus (1.276)] and to write down the final equations of motion only for expectation values.

In Exc. 23.2.4.5 we verify that these equations of motion do not change the spin $\hat{\mathbf{S}}$. Neglecting all dissipation processes but Γ, the Eqs. (23.117) can be rewritten in terms of observables as,

$$
\mathfrak{L}_{\rm tot}\hat{\mathbf{S}} = \begin{pmatrix} (g+g')(\hat{a}+\hat{a}^\dagger) \\ \imath(g-g')(\hat{a}-\hat{a}^\dagger) \\ -\Delta_{\rm a} \end{pmatrix} \times \hat{\mathbf{S}} + \tfrac{\Gamma}{2}\begin{pmatrix} -\hat{S}_x + \{\hat{S}_x, \hat{S}_z\} \\ -\hat{S}_y + \{\hat{S}_y, \hat{S}_z\} \\ -2\hat{S}_z - 2\hat{S}_x^2 - 2\hat{S}_y^2 \end{pmatrix}\ . \tag{23.118}
$$

Only the terms $\mathfrak{L}_{\gamma_1}$, $\mathfrak{L}_{\xi_1}$, and $\mathfrak{L}_{\beta_1}$ can change $\hat{\mathbf{S}}^2$. The $\hat{\mathbf{S}}^2$ and $\hat{S}_z$ eigenvalues determine the coupling strength of the many-atom (Dicke) state to the cavity mode and the coherent, external drive. This coupling determines the rate of cavity photon generation as well as the pumping strength. The magnitude of the coupling strength distinguishes between superradiance and subradiance. For superradiant states the coupling strength scales superlinear in N, while for subradiant states the scaling is

sublinear in N, and some subradiant states are dark. Dark means that the collective coupling to the cavity and the coherent, external drive of these states vanishes, meaning these states cannot decay via collective interactions e.g. by creating a cavity photon. However these states still decay into other states via the decay and dephasing processes $\mathfrak{L}_{\gamma_1}$ and $\mathfrak{L}_{\beta_1}$ acting individually on the emitters, see Fig. 23.10. Hence, spontaneous decay is an individualization process [310]. Generally, the spin preserving contributions in the master equation (23.120) generate quantum correlations leading to collective behavior (both super- and subradiance are collective effects) and the non-preserving terms destroy correlations leading to individualization (all properties scale exactly linear in N). However only the spin non-preserving contributions introduce coupling between superradiant and subradiant states, thus in order to prepare subradiant states an interplay of collectivity and individualization is necessary. Based on these considerations, we may distinguish between collective versus individual behavior and superradiant versus subradiant behavior. The latter are special cases of collective behavior. This twofold distinction seems crucial when investigating super- and subradiance in the presence of dephasing and individual decay. In Exc. 23.2.4.6 we study superradiant decay.

23.2.1.2 Symmetries of the Dicke model with/out rotating wave approximation

The total number of excitations,

$$\hat{N}_{\text{ex}} \equiv \hat{a}^\dagger \hat{a} + \hat{S}_z \tag{23.119}$$

is a constant of motion only for the Tavis-Cummings Hamiltonian, i.e. the Dicke Hamiltonian with RWA, $g' = 0$, and in the absence of pumping, $\eta = 0$, commutes with the excitation number,

$$[\hat{H}_{\text{gD}}, \hat{N}_{\text{ex}}] = \eta(\hat{a} - \hat{a}^\dagger) + 2g'(\hat{S}_- \hat{a} - \hat{S}_+ \hat{a}^\dagger) \xrightarrow{\eta=0} 0 \ . \tag{23.120}$$

That is, the Dicke Hamiltonian preserves the excitation number, except for the counter-rotating terms, which can only change the excitation number by ± 2.

The Dicke model without RWA, $g' = g$, has one global symmetry [10],

$$(\hat{a}, \hat{\sigma}^\pm) \xrightarrow{\mathcal{P}} (-\hat{a}, -\hat{\sigma}^\pm) \ , \tag{23.121}$$

where the parity operator is,

$$\mathcal{P} = e^{\imath\pi \hat{N}} \quad , \quad [\hat{H}_{\text{gD}}, \mathcal{P}] = 0 \ , \tag{23.122}$$

as shown in Exc. 23.2.4.1. Because $\mathcal{P}$ squares to unity, it has two eigenvalues, 1 and -1. This symmetry is associated with a conserved quantity: the parity of the total number of excitations, $\mathcal{P} = (-1)^{N_{\text{ex}}}$. This parity conservation is a consequence of the preserved excitation number. A state of the Dicke model is said to be normal when this symmetry is preserved, and superradiant when this symmetry is spontaneously broken.

[10] For a Dicke picture of CARL see Exc. 25.5.7.1.

Note that, at low coupling strength the two subspaces belonging to different parities are degenerate, but in the thermodynamic limit $N \to \infty$ at high enough coupling strength they may split upon a Dicke quantum phase transition [11].

model	RWA	symmetry	atom #	photon #	section
Rabi	no	$\mathcal{P}$	1	n	16.3
Jaynes-Cummings	yes	$U(1)$	1	n	17.2
Dicke	no	$\mathcal{P}$	> 1	n	23.1
Tavis-Cummings	yes	$U(1)$	> 1	n	23.2.2, 23.4

23.2.2 Superradiant Dicke phase transition

The interesting feature of the set of equations (23.117) is, that the degrees of freedom are macroscopically populated, yet, they follow the rules of quantum mechanics. For instance, we may expect them to behave as order parameters for macroscopic phase transitions. We will study one such example in the following.

23.2.2.1 Equilibrium Dicke phase transition

The Dicke model predicts a phase transition to a superradiant state, when the coupling strength g exceeds a certain critical value. To see this we simplify the Hamiltonian (23.6) by the mean-field approximation,

$$\Delta_{\rm c}\hat{a}^\dagger\hat{a} = \Delta_{\rm c}\alpha^2 \ , \tag{23.123}$$

where the field amplitude α is a real number, and calculate the free energy as a function of α,

$$\begin{aligned} F(\alpha) \equiv -\tfrac{1}{\beta}\ln\Xi(\alpha) \qquad \text{with} \qquad & \Xi(\alpha) = \mathrm{Tr}\, e^{-\beta\hat{H}} \\ \text{and} \qquad & \hat{H} = -\Delta_{\rm c}\alpha^2 + \sum\nolimits_j \hat{h}_j \\ \text{and} \qquad & \hat{h}_j = -\Delta_{\rm a}\hat{s}_j^z + 4g\alpha\hat{s}_j^x \ . \end{aligned} \tag{23.124}$$

$\Xi(\alpha)$ is the partition function, $\hat{h}_j$ the single-atom Hamiltonian, and $\beta \equiv 1/k_{\rm B}T$. Carried out in Exc. 23.2.4.7, the calculation results in,

$$\begin{aligned} F(\alpha) &= \Delta_{\rm c}\alpha^2 - \tfrac{N}{\beta}\ln(2\cosh\beta E) \\ \text{where} \qquad \pm E &\equiv \langle\hat{h}_j\rangle = \pm\sqrt{\left(\tfrac{\Delta_{\rm a}}{2}\right)^2 + (g\alpha)^2} \end{aligned} \tag{23.125}$$

are the single-atom energy eigenvalues. The minimum of the free energy as a function of the field amplitude, $F'(\alpha) = 0$, yields a critical coupling strength $g_{\rm c}$,

$$g_{\rm c}\sqrt{N} = \tfrac{1}{2}\sqrt{\Delta_{\rm c}\Delta_{\rm a}\coth\tfrac{\beta\Delta_{\rm a}}{2}} \ , \tag{23.126}$$

Below $g_{\rm c}$ the free energy minimizes for $\alpha = 0$, and beyond $g_{\rm c}$ it minimizes for $\alpha > 0$, as seen in Fig. 23.11.

[11] Other models, such as the Ising model, the Heisenberg model, or the Bose-Hubbard model are not treated here.
$\mathcal{P}$ is the parity operator defined in Eq. (23.121). The unitary group $U(1)$ corresponds to the circle group consisting of all complex numbers with absolute value 1 under multiplication.

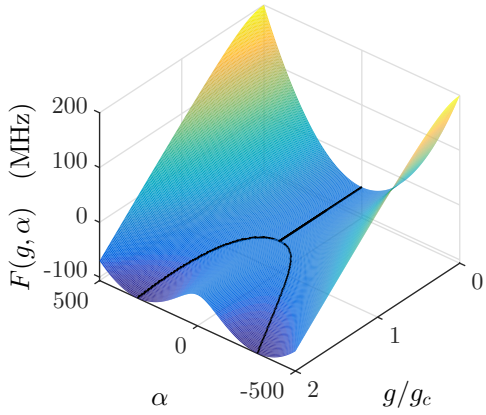

Figure 23.11: (code) Free energy as a function of coupling strength and photon number. Beyond the critical coupling strength g_c the minimum of the free energy splits opening the way for two possible equilibrium states of the mean-field phase.

Note that the critical coupling smoothly evolves down to zero temperature ($\beta \to 0$), where one obtains $g_c = \sqrt{\Delta_c \Delta_a / 2N}$ [12].

23.2.3 Beyond mean-field

We already applied the mean-field approximation in the derivation of the semiclassical Dicke Hamiltonian (23.9) and the Dicke phase transition (23.123). Some effects, however, are intrinsically to the existence of interatomic correlations, as for example, superradiant lasing [13]

23.2.3.1 Cumulant expansion

Often we are interested in quantum correlations rather than in the mean-field behavior of an operator. The *cumulant expansion* allows to study higher-order correlations by gradually removing lower-order ones. We introduce the correlation or cumulant expectation value between operators $\hat{A}$ and $\hat{B}$ [491, 723],

$$\begin{aligned} \langle \hat{A} \rangle &\equiv \langle \hat{A} \rangle_c \\ \langle \hat{A}\hat{B} \rangle &\equiv \langle \hat{A} \rangle \langle \hat{B} \rangle + \langle \hat{A}\hat{B} \rangle_c \\ \langle \hat{A}\hat{B}\hat{C} \rangle &\equiv \langle \hat{A} \rangle \langle \hat{B} \rangle \langle \hat{C} \rangle + \langle \hat{A} \rangle \langle \hat{B}\hat{C} \rangle_c + \langle \hat{B} \rangle \langle \hat{A}\hat{C} \rangle_c + \langle \hat{C} \rangle \langle \hat{A}\hat{B} \rangle_c + \langle \hat{A}\hat{B}\hat{C} \rangle_c \ . \end{aligned} \tag{23.127}$$

The lowest order mean-field approximation consists in neglecting $\langle \hat{A}\hat{B} \rangle_c \simeq 0$.

[12] Note, that in the thermodynamic limit, $N \to \infty$, the operators can be replaced by [466]:

$$\hat{S}_x \overset{N\to\infty}{\longrightarrow} \tfrac{1}{2}\hat{N}\cos\hat{\varphi} \qquad \text{and} \qquad \hat{S}_y \overset{N\to\infty}{\longrightarrow} \tfrac{1}{2}\hat{N}\sin\hat{\varphi} \ .$$

In this case, the operators commute $[\hat{S}_x, \hat{S}_y] \to 0$.

[13] Interestingly, spin-squeezing, which is also based on interatomic correlations, can be described within the mean-field approximation.

Example 143 (*Superradiant lasing*): In a conventional laser amplification and optical phase coherence are established by stimulated photon emission from a population-inverted medium. This results in the Schawlow-Townes spectral linewidth, proportional to the square of the cavity decay width and inversely proportional to the photon number in the cavity. As Dicke showed, the coherence can also be stored in the emitters that constitute the gain medium provided they interact collectively with common radiation field modes [207]. If the spontaneous decay rate is much smaller than the cavity decay rate very narrow emission bandwidths far below the cavity decay width can be achieved. In Exc. 23.2.4.8 we study *superradiant lasing* in the Dicke model [565]. Cavity-mediated superradiance can also be described within the *Tavis-Cummings model* [135]. It represents an extension of the Jaynes-Cummings model for several atoms. We will discuss such systems in Sec. 24.2.

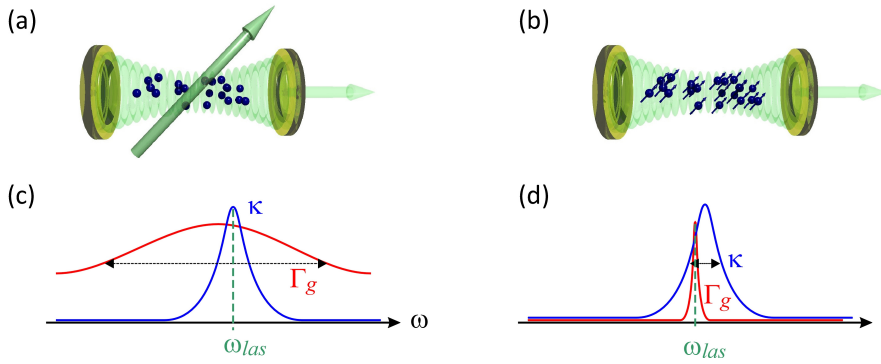

Figure 23.12: (a) Principle scheme of standard lasing. Here, the coherence is stored in the cavity field. The gain profile is much larger than the cavity width (good-cavity limit, $\kappa \ll \frac{1}{2}\Gamma_{\rm g}$), as shown in (c). The laser frequency follows any (technical) cavity fluctuation: $\omega_{\rm las} = \omega_{\rm cav} + \omega_{\rm g}\frac{2\kappa}{\Gamma_{\rm g}}$. (b) *Superradiant lasing*. Here, the coherence is stored in the gain. We are in the bad-cavity limit, $\kappa \gg \Gamma_{\rm g}$, as shown in (d). The laser frequency is robust to cavity fluctuations: $\omega_{\rm las} = \omega_{\rm g} + \omega_{\rm cav}\frac{\Gamma_{\rm g}}{2\kappa}$.

23.2.3.2 Superradiant lasing in the Holstein-Primakoff approximation

The superradiant phase transition was originally predicted by the Dicke model [229, 387]. It occurs when the strength of the interaction between the atoms and the field is greater than the energy of the non-interacting part of the system [14]. The collective Lamb shift, relating to the system of atoms interacting with the vacuum fluctuations, becomes comparable to the energies of atoms alone, and the vacuum fluctuations cause the spontaneous self-excitation of matter.

The transition can be readily understood by the use of the Holstein-Primakoff transformation applied to an ensemble of two-level atoms, as shown in Sec. 23.1.6, as a result of which the atoms become harmonic oscillators with frequencies equal to

[14] This is similar to the case of superconductivity in ferromagnetism, which leads to the dynamic interaction between ferromagnetic atoms and the spontaneous ordering of excitations below the critical temperature.

the difference between the energy levels. If the interaction between the atomic and the field oscillator is so strong that the system collapses in a ferroelectric-like phase transition. In Exc. 23.2.4.10 we will derive the Heisenberg equations for the open Dicke model in the Holstein-Primakoff approximation.

Example 144 (*Finding instabilities via retarded Green's functions*): Let us consider a set of linear Heisenberg equations,

$$\dot{v}_i(t) = M_{ij} v_j(t) \qquad \text{and} \qquad \dot{v}_i^\dagger(t) = M_{ij}^\dagger v_j^\dagger(t) \ .$$

The retarded *Green's function* is defined by,

$$G_{ij}(t) \equiv -\imath \langle [v_i(t), v_j^\dagger(0)] \rangle \theta(t) \ .$$

Its time derivative is,

$$\dot{G}_{ij}(t) \equiv -\imath \langle [v_i(t), v_j^\dagger(0)] \rangle \delta(t) - \imath \langle \dot{v}_i(t) v_j^\dagger(t) \rangle \theta(t) + \imath \langle v_j^\dagger(t) \dot{v}_i(t) \rangle \theta(t) \ .$$

Defining the equal-time correlation function by,

$$S_{ij} \equiv \langle [v_i(0), v_j^\dagger(0)] \rangle \ ,$$

we get,

$$\begin{aligned} \dot{G}_{ij}(t) &= -\imath S_{ij} \delta(t) - \imath M_{ik} \langle v_k(t) v_j^\dagger(t) \rangle \theta(t) + \imath M_{ik} \langle v_j^\dagger(t) v_k(t) \rangle \theta(t) \\ &= -\imath S_{ij} \delta(t) - \imath M_{ik} \langle [v_k(t), v_j^\dagger(t)] \rangle \theta(t) = -\imath S_{ij} \delta(t) + M_{ik} G_{kj}(t) \ . \end{aligned}$$

With the Fourier transform $f(\omega) = \int_{-\infty}^{\infty} dt e^{\imath \omega t} f(t)$ we finally get,

$$G(\omega) = (M + \imath \omega \mathbb{I})^{-1} \imath S \ .$$

For example, we may consider the system of two coupled oscillators studied in Sec. 14.5.5. In this case,

$$\mathbf{v} \equiv \begin{pmatrix} \hat{a} \\ \hat{a}^\dagger \\ \hat{b} \\ \hat{b}^\dagger \end{pmatrix} \qquad \text{such that} \qquad S = \text{diag}\ (1, -1, 1, -1) \ .$$

In Exc. 14.5.8.8 we have shown that (setting $\Omega' \equiv \Omega$),

$$M = \begin{pmatrix} -\imath\omega - \kappa_{\rm a} & 0 & -\frac{\imath\Omega}{2} & -\frac{\imath\Omega}{2} \\ 0 & \imath\omega - \kappa_{\rm a} & \frac{\imath\Omega}{2} & \frac{\imath\Omega}{2} \\ -\frac{\imath\Omega}{2} & -\frac{\imath\Omega}{2} & -\imath\omega - \kappa_{\rm b} & 0 \\ \frac{\imath\Omega}{2} & \frac{\imath\Omega}{2} & 0 & \imath\omega - \kappa_{\rm b} \end{pmatrix} \ .$$

Thus,

$$G^{\rm R}(\omega)^{-1} = S^{-1}(\omega \mathbb{I} - \imath M) = \begin{pmatrix} \omega - \omega_{\rm a} + \imath\kappa_{\rm a} & 0 & -\frac{\Omega}{2} & -\frac{\Omega}{2} \\ 0 & -\omega - \omega_{\rm a} - \imath\kappa_{\rm a} & -\frac{\Omega}{2} & -\frac{\Omega}{2} \\ -\frac{\Omega}{2} & -\frac{\Omega}{2} & \omega - \omega_{\rm b} + \imath\kappa_{\rm b} & 0 \\ -\frac{\Omega}{2} & -\frac{\Omega}{2} & 0 & -\omega - \omega_{\rm b} - \imath\kappa_{\rm b} \end{pmatrix} \ .$$

The superradiant transition corresponds to the requirement that one of the eigenvalues of M goes to zero [207, 466], or equivalently,

$$0 = \det G^{\rm R}(\omega)^{-1} = \omega_{\rm a}^2\omega_{\rm b}^2 + \omega_{\rm a}^2\kappa_{\rm b}^2 - \omega_{\rm a}\Omega^2\omega_{\rm b} + \kappa_{\rm a}^2\omega_{\rm b}^2 + \kappa_{\rm a}^2\kappa_{\rm b}^2 \ ,$$

yielding,

$$\Omega = \sqrt{\frac{(\omega_{\rm a}^2+\kappa_{\rm a}^2)(\omega_{\rm b}^2+\kappa_{\rm b}^2)}{\omega_{\rm a}\omega_{\rm b}}} \ .$$

Example 145 (*Dicke phase transition with a superfluid gas in an optical cavity*): [60].

23.2.3.3 Zeeman splitting in the Holstein-Primakoff approximation

The Dicke Hamiltonian in the Holstein-Primakoff approximation has been derived in Eq. (23.94). We now generalize it for the presence of three collective atomic modes $\hat{b}_{0\pm}$ accounting for Zeeman splitting [868],

$$\begin{aligned}\hat{H} \simeq & -\Delta_{\rm c}\hat{a}^\dagger\hat{a} \\ & - \tfrac{1}{2}(\Delta_{\rm a}+\Delta_{\rm zeem})\hat{b}_-^\dagger\hat{b}_- - \tfrac{1}{2}\Delta_{\rm a}\hat{b}_0^\dagger\hat{b}_0 - \tfrac{1}{2}(\Delta_{\rm a}-\Delta_{\rm zeem})\hat{b}_+^\dagger\hat{b}_+ \\ & + 2g_N(\hat{b}_-^\dagger\hat{a}+\hat{a}^\dagger\hat{b}_-) + 2g_N(\hat{b}_0^\dagger\hat{a}+\hat{a}^\dagger\hat{b}_0) + 2g_N(\hat{b}_+^\dagger\hat{a}+\hat{a}^\dagger\hat{b}_+) + \eta(\hat{a}-\hat{a}^\dagger) \ .\end{aligned} \tag{23.128}$$

From this we derive the equations of motion,

$$\begin{aligned}\dot{\hat{a}} &= (\imath\Delta_{\rm c}-\kappa)\hat{a} - 2\imath g_N\hat{b}_- - 2\imath g_N\hat{b}_0 - 2\imath g_N\hat{b}_+ + \imath\eta \\ \dot{\hat{b}}_\mu &= \tfrac{1}{2}(\imath\Delta_{\rm a} - \mu\imath\Delta_{\rm zeem} - \Gamma)\hat{b}_\mu - 2\imath g_N\hat{a} \ ,\end{aligned} \tag{23.129}$$

with $\mu = 0, \pm 1$. Their solution is shown in Fig. 23.13.

23.2.4 Exercises

23.2.4.1 Ex: Parity considerations

a. Show that the excitation number $\hat{N} = \hat{a}^\dagger\hat{a} + \hat{S}_z + S$ is conserved by the Hamiltonian within rotating wave approximation,

$$\hat{H}_{\rm rw} = -\Delta_{\rm a}\hat{S}_z - \Delta_{\rm c}\hat{a}^\dagger\hat{a} + g(\hat{a}^\dagger\hat{S}_- + \hat{a}\hat{S}_+) \ .$$

b. Show that the parity operator defined by $\mathcal{P} = e^{\imath\pi\hat{N}}$ is conserved by the Hamiltonian without rotating wave approximation [265],

$$\hat{H} = -\Delta_{\rm a}\hat{S}_z - \Delta_{\rm c}\hat{a}^\dagger\hat{a} + g(\hat{a}^\dagger + \hat{a})(\hat{S}_+ + \hat{S}_-) \ .$$

23.2.4.2 Ex: Coupling super- and subradiant modes

a. Discuss whether super- and subradiant states can be transformed into each other via unitary transformations.

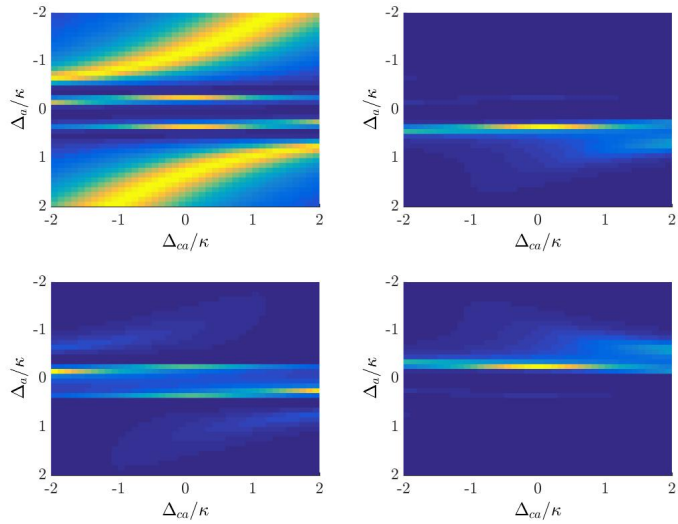

Figure 23.13: (left) inversion $(\hat{\sigma}^z + 1)/2$, (right) light transmission $\kappa^2|\alpha|^2/\eta^2$ through the cavity.

23.2.4.3 Ex: Relationship between super- and subradiance and cooperativity

Seek an interpretation of super- and subradiance as a modification of the structure factor by cooperativity.

23.2.4.4 Ex: Heisenberg equation for the open Dicke model

Derive the Heisenberg equation for the open Dicke model.

23.2.4.5 Ex: Spin conservation in the open Dicke model

a. Show that the Dicke Hamiltonian (23.116) with $g' = g$ preserves the spin $\hat{\mathbf{S}}^2$.
b. Show that the Dicke Hamiltonian (23.116) with $g' = 0$ preserves the spin $\hat{\mathbf{S}}^2$.
c. Verify whether the dissipative terms of the open Dicke model preserve the spin $\hat{\mathbf{S}}^2$.

23.2.4.6 Ex: Superradiant enhancement

For the open Dicke model consider the Heisenberg equations (23.117) without coherent mean-field, $\hat{a} = 0$, and disregarding single-atom decoherence, $\gamma_1 = \xi_1 = \beta_1 = 0$. Solve the equation of motion for the collective spin projection $\hat{S}_z$ for an arbitrary coherent spin state $|S, M\rangle$ and discuss the collective decay rate as a function of the collective inversion $\langle \hat{S}_z \rangle$.

23.2.4.7 Ex: Equilibrium phase transition

a. Calculate the free energy of the Hamiltonian (23.6) in the mean-field approximation.
b. Minimize the free energy as a function of the field amplitude α for various coupling strengths g. **Help:** Expand the expression for $F'(\alpha)$ for small values of α. Derive the expression for the critical coupling strength.

23.2.4.8 Ex: Superradiant lasing

a. Consider the generalized open Dicke model Hamiltonian (23.116) neglecting counter-rotating terms, $g' \equiv 0$, as well as pumping and phase fluctuations of the cavity modes, $\eta = \phi \equiv 0$. Derive the Heisenberg equations for the operators $\hat{a}$, $\hat{s}_j^-$, $\hat{s}_j^z$, $\hat{a}^\dagger \hat{s}_j^-$, $\hat{s}_i^+ \hat{s}_j^-$, and $\hat{a}^\dagger \hat{a}$.
b. Calculate the expectation values of the equations of motion for all degrees of freedom and for the products specified in (a) assuming that all atoms are equal. Now, assume that the phase-invariance is not broken, $\langle \hat{a} \rangle = \langle \hat{a}^\dagger \rangle = \langle \hat{s}_1^\pm \rangle = 0$, and apply a cumulant expansion up to second order.
c. Assuming the system to be in steady state solve the system of equations for the operators and products specified in (a) analytically. Assume $\gamma_1 \ll g \ll \kappa$ and plot $\hat{a}^\dagger \hat{a}$ as a function of the atom number N and the optical pumping rate ξ_1.
d. In which parameter regimes do you observe superradiant lasing?
e. Express $\langle \hat{\mathbf{S}}^2 \rangle$ and $\langle S_z \rangle$ in terms of single particle spin operators.
f. Evaluating $\langle \mathbf{S}^2 \rangle$ and $\langle S_z \rangle$ via the solution of the equations of motion, we find the steady-state quantum numbers always around $M \simeq \pm S$ [207]. Explain how this fact can induce squeezing, once $\langle S_z \rangle > 0$.

23.2.4.9 Ex: Superradiant lasing and the Schawlow-Townes limit

Discuss whether superradiant lasing beats the Schawlow-Townes limit.

23.2.4.10 Ex: Heisenberg equation for the open Dicke model in the Holstein-Primakoff approximation

Derive the Heisenberg equations for the open Dicke model in the Holstein-Primakoff approximation.

23.2.4.11 Ex: Critical exponent of the phase transitions

Calculate the critial exponent of the superradiant phase transition.

23.2.4.12 Ex: Schrieffer-Wolff transform of the Dicke Hamiltonian

a. Calculate the operator $\hat{H}_{\rm SW} = \mathcal{U} \hat{H} \mathcal{U}^\dagger$, where $\mathcal{U} \equiv e^{\imath\eta(\hat{a}^\dagger + \hat{a})\hat{S}_y}$ is the called the *Schrieffer-Wolff transform* [318].
b. Show that the states,

$$\mathcal{S}(\xi)\rangle|n\rangle \otimes |S, -S\rangle \quad \text{with} \quad \mathcal{S}(\xi) \equiv e^{(\xi/2)\hat{a}^{\dagger 2} - (\xi^*/2)\hat{a}^2} \quad \text{and} \quad \xi = -\tfrac{1}{4}\ln[1-(g/g_{\rm c})^2]$$

where $g_{\rm c} \equiv \sqrt{\Delta_{\rm c}\Delta_{\rm a}}$ are eigenstates of the Dicke-Schrieffer-Wolff Hamiltonian provided $g < g_{\rm c}$.

23.3 Atoms interacting in free space

When two atoms excited to an internal level of energy hc/λ are so close together that the range of their dipole moments overlap without forming a molecular bonding, $a_B \ll R \ll \lambda$, they may exhibit cooperative relaxation. The atoms are coupled via the radiation that they are susceptible to emit into the same continuum. The coupled atomic dipoles oscillate and decay in phase. The decays is accelerated one leads to an intense burst of coherent and spatially directional radiation. This phenomenon is termed *superradiance* [229, 685]. We may view superradiance as destructive interference of the dipolar radiation patterns of all atoms in all but one direction of space triggered by the first spontaneous decay. The superradiant enhancement is largest when half of the atoms are deexcited. The correlated atoms can be in a Dicke state (then the total dipole moment is always zero) or in a product state (then the net dipole moment is non-zero at half-deexcitation). In the second case, we also talk about *superfluorescence*. In this case, an excited initially incoherent sample develops correlations due to the emission process. One can also imagine the case that the emission patterns pairwise cancel, and the decay is thus inhibited. This is called *subradiance*. Superradiance has been used in the microwave domain as a spectroscopic method in the observation of photon echoes.

Correlated quantum jumps are, in a sense, the few-atoms precursors of superradiance. Accelerated spontaneous decay has been predicted for atoms whose distance is shorter than the wavelength of the decaying transition [743, 515]. Super- and subradiance has been observed in a system of two ion trapped in a Paul trap [227].

23.3.1 Rydberg blockade

Rydberg atoms (i.e. atoms in excited Rydberg states) exhibit huge polarizabilities inducing large interaction energies even at relatively modest densities. These can be so strong, that the presence of a single Rydberg-excited atom can drive out of resonance the frequencies of transitions connected to the Rydberg state for several neighboring atoms once the exciting laser is sufficiently narrow-band. This effect called *Rydberg blockade* can be described by the following interaction Hamiltonian [702, 784],

$$\hat{H}_{\rm Rydberg} = \sum_{i>j} \kappa_{ij} \tfrac{1}{2}(\hat{\sigma}_i^z - 1)\tfrac{1}{2}(\hat{\sigma}_j^z - 1) \qquad \text{with} \qquad \kappa_{ij}/2\pi = \frac{C_6}{r_{ij}^6} \,, \tag{23.130}$$

where $\frac{1}{2}(\hat{\sigma}_i^z - 1) = |e\rangle_i\langle e|$ is the probability of finding the i-th atom in an excited state and C_6 interatomic van der Waals interaction coefficient of the transition.

Example 146 (*Two interacting Rydberg atoms*): In this example we study Rydberg blockade for two interacting Rydberg atoms. In this case, the Hamiltonian can be cast into the matrix form,

$$\hat{H} = -\Delta_{\rm a}\hat{S}_z + \Omega\hat{S}_+ + \Omega^*\hat{S}_- + \hat{H}_{\rm Rydberg} = \begin{pmatrix} \Delta_{\rm a} & \frac{1}{2}\Omega & \frac{1}{2}\Omega^* & 0 \\ \frac{1}{2}\Omega^* & 0 & 0 & \frac{1}{2}\Omega^* \\ \frac{1}{2}\Omega & 0 & 0 & \frac{1}{2}\Omega \\ 0 & \frac{1}{2}\Omega & \frac{1}{2}\Omega^* & -\Delta_{\rm a} + \kappa_{12} \end{pmatrix} .$$

The master equation can be numerically solved using the procedure outlined in example 144. The result of such a simulation is shown in Fig. 23.14. Comparing

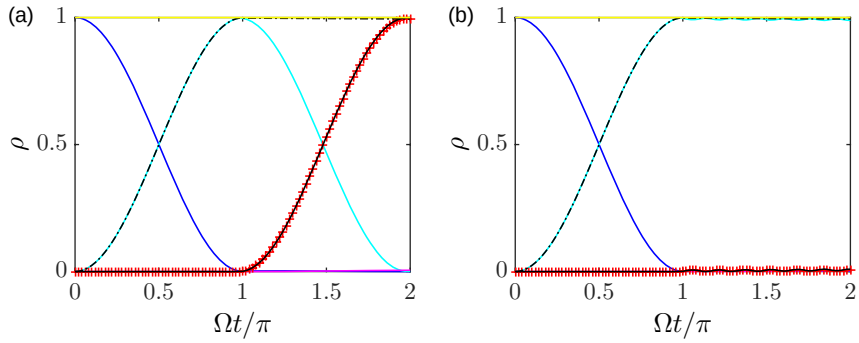

Figure 23.14: (code) Populations in a system of two two-level atoms interaction via van der Waals forces. Initially ($\Omega t < \pi$) only one atom is driven, after that only the other. We assume $\Omega \gg \Gamma$ and $C_6 = 4 \cdot 10^7$. The interatomic distance is (a) $kr_{12} = 0.5$, respectively, (a) $kr_{12} = 5$. (blue) $\rho_{11,11}$, (cyan) $\rho_{12,12}$, (magenta) $\rho_{21,21}$, (red) $\rho_{22,22}$, (black dotted) $\rho_{22}^{(1)}$, and (black) $\rho_{22}^{(2)}$.

the evolutions calculated in Fig. 23.14 for large and small interatomic distances, we see that the excitation of the first atom impedes the excitation of the second one when the interaction is strong.

Note, that an interesting situation occurs when the coupling is completely uniform (e.g. mediated by a cavity), $\kappa_{ij} \simeq \kappa$,

$$\hat{H}_{\text{Rydberg}} \simeq \tfrac{1}{8}\kappa(\hat{S}_z^2 - 2\hat{S}_z + 1) \ , \tag{23.131}$$

as pointed out in Eq. (23.76). Such Hamiltonians may be interesting for the generation of spin-squeezing.

23.3.2 Dipole-dipole interactions in the non-linear optics regime

The mean-field Dicke model totally neglects interactions between the atoms due to the exchange of real or virtual photons, i.e. neither resonant dipole-dipole interactions nor van der Waals interactions are considered [28, 78, 242, 265, 693, 702, 754]. That is, interaction terms such as [15],

$$\hat{H}_{\text{Ising}} = -\sum_{i,j\neq i}^{N} \Delta_{ij}\hat{\sigma}_j^+\hat{\sigma}_i^- \tag{23.132}$$

are absent from the Hamiltonian. Spin-spin interactions are studied in the so-called *Ising model*, which is interesting in the context of (anti-)*ferromagnetism* [298, 299, 311,

[15] It is impossible to write write the Ising Hamiltonian for a free cloud as a product of collective spin operators, because of inhomogeneities induced by dipole-dipole interactions Δ_{ji}. Hence, the total spin $\hat{\mathbf{S}}^2$ is *not* conserved.

466, 905]. The negligence of interaction was, of course, the reason for the simplicity of the Dicke model and its manageability for large atom numbers. On the other hand, in Sec. 21.1.2 we have studied dipole-dipole interactions in the linear optics regime allowing for at most a single photon to interact with the cloud.

In this section, we will consider dipole-dipole interactions in very small dilute clouds interacting with an arbitrary number of photons. The possibility for the cloud of storing as many photons as there are atoms is common to the Dicke model. Here, we will call it the *non-linear optics* regime, as several photons may team up to excite higher Dicke excitations states. In particular, we will study two interacting atoms as done by the milestone experiment of DeVoe and Brewer [227]. Do the Exc. 23.3.4.1.

The starting point is the collective many-atoms Hamiltonian (21.9) of the scalar coupled dipoles model. After tracing over the vacuum modes, one obtains the master equation [16] [691],

$$\begin{aligned}
\hat{H} &= \tfrac{1}{2}\sum_j \left[\Omega(\mathbf{r}_j)\hat{\sigma}_j^+ + h.c.\right] - \sum_{i,j}\Delta_{ji}\hat{\sigma}_j^+\hat{\sigma}_i^- \\
\mathfrak{L}[\hat{\rho}] &= \tfrac{1}{2}\textstyle\sum_{i,j}\Gamma_{ij}\left(2\hat{\sigma}_j^-\hat{\rho}\hat{\sigma}_i^+ - \hat{\sigma}_i^+\hat{\sigma}_j^-\hat{\rho} - \hat{\rho}\hat{\sigma}_i^+\hat{\sigma}_j^-\right) \\
\mathfrak{L}^\dagger[\hat{A}] &= \tfrac{1}{2}\textstyle\sum_{i,j}\Gamma_{ij}\left(2\hat{\sigma}_i^+\hat{A}\hat{\sigma}_j^- - \hat{\sigma}_i^+\hat{\sigma}_j^-\hat{A} - \hat{A}\hat{\sigma}_i^+\hat{\sigma}_j^-\right) \\
\Delta_{i\neq j} &\equiv -\tfrac{3\lambda\Gamma}{2}\,\hat{\mathbf{e}}_d^*\,\mathfrak{Re}\,\mathcal{G}(\mathbf{r}_i,\mathbf{r}_j,\omega_0)\,\hat{\mathbf{e}}_d \quad \text{and} \quad \Delta_{jj}\equiv\Delta_\mathrm{a} \\
\Gamma_{i\neq j} &\equiv 3\lambda\Gamma\,\hat{\mathbf{e}}_d^*\,\mathfrak{Im}\,\mathcal{G}(\mathbf{r}_i,\mathbf{r}_j,\omega_0)\,\hat{\mathbf{e}}_d \quad \text{and} \quad \Gamma_{jj}\equiv\Gamma
\end{aligned} \tag{23.133}$$

The expression for the line shifts Δ_{ij} and the decay rates Γ_{ij} have been derived in Sec. 22.2.1 from the bulk Green's tensor in free space. Assuming $\Delta_{ji} = 0 = \Gamma_{ji}$ and $\Omega(\mathbf{r}_j) = \Omega$ we recover the mean-field Dicke model, where interaction terms are completely neglected,

$$\hat{H} = \tfrac{1}{2}\Omega\sum_j(\hat{\sigma}_j^+ + h.c.) - \Delta_\mathrm{a}\sum_j\hat{\sigma}_j^+\hat{\sigma}_j^- \ . \tag{23.134}$$

With (23.130) we set up either the master or the Heisenberg-Liouville equations,

$$\begin{aligned}
\dot{\hat{\rho}} &= -\imath[\hat{H},\hat{\rho}] + \mathfrak{L}[\hat{\rho}] \\
\dot{\hat{A}} &= -\imath[\hat{A},\hat{H}] + \mathfrak{L}^\dagger[\hat{A}] \ .
\end{aligned} \tag{23.135}$$

Note that in principle, the collective many-atom system (23.130) can be mapped to a single-atom multilevel system,

$$\frac{d}{dt}\hat{\vec{\varrho}} = \mathcal{M}\vec{\varrho}\ , \tag{23.136}$$

which is more amenable to numeric simulation using the methods presented in Sec. 16.6. However, analytically this is only simple to do in the case of two atoms, which can be mapped to a four-level system. This will be shown in Exc. 23.3.4.2.

[16] In return, the equations of motion (21.26) for the excitation amplitude should follow as the Heisenberg equation with the above Hamiltonian.

Example 147 (*Diagonalizing collective decay*): The Lindbladian describing collective decay in (23.133) can be recast into a standard form by diagonalizing the real matrix $\mathbf{\Gamma} \equiv (\Gamma_{ij})$ [691], that is, we define a unitary transformation $\mathcal{T} = (\mathcal{T}^\intercal)^{-1} \equiv (T_{jk})$,

$$D = \mathcal{T}^\intercal \mathbf{\Gamma} \mathcal{T} \Longrightarrow \tilde{\Gamma}_k \delta_{kj} = \sum_j T^\intercal_{ik} \Gamma_{ij} T_{jk}$$
$$\text{or} \qquad \mathbf{\Gamma} = \mathcal{T} D \mathcal{T}^\intercal \Longrightarrow \Gamma_{ij} = \sum_k T_{jk} \tilde{\Gamma}_k \delta_{kj} T^\intercal_{jk} \ .$$

Note that all coefficients not ornamented by a 'hat' can be moved around freely. Now, substituting the Γ_{ij},

$$\mathfrak{L}[\hat{\rho}] = \tfrac{1}{2} \sum_{k,i,j} \left[2\hat{\sigma}_i^- T_{ik} \tilde{\Gamma}_k \delta_{ki} T^\intercal_{jk} \hat{\rho} \hat{\sigma}_j^+ - \hat{\sigma}_i^+ T_{ik} \tilde{\Gamma}_k \delta_{ki} T^\intercal_{jk} \hat{\sigma}_j^- \hat{\rho} - \hat{\rho} \hat{\sigma}_i^+ T_{ik} \tilde{\Gamma}_k \delta_{ki} T^\intercal_{jk} \hat{\sigma}_j^- \right] .$$

Now, defining new composite decay channels,

$$\hat{\Pi}_k^- = \sum_j T_{kj} \hat{\sigma}_j^- \qquad , \qquad \hat{\Pi}_k^+ = \sum_j \hat{\sigma}_j^+ T^\intercal_{kj} \ ,$$

we find,

$$\mathfrak{L}[\hat{\rho}] = \tfrac{1}{2} \sum_k \tilde{\Gamma}_k [2\hat{\Pi}_k^+ \hat{\rho} \hat{\Pi}_k^- - \hat{\Pi}_k^+ \hat{\Pi}_k^- \hat{\rho} - \hat{\rho} \hat{\Pi}_k^+ \hat{\Pi}_k^-] \ .$$

Single-atom spontaneous emission simply follows from the assumption that $\Gamma_{ij} = \Gamma_1 \delta_{ij}$,

$$\mathfrak{L}[\rho] = \tfrac{1}{2} \sum_j \Gamma [2\hat{\sigma}_j^- \hat{\rho} \hat{\sigma}_j^+ - \hat{\sigma}_j^+ \hat{\sigma}_j^- \hat{\rho} - \hat{\rho} \hat{\sigma}_j^+ \hat{\sigma}_j^-] \ .$$

On the other hand, Dicke superradiance follows from the assumption that $\Gamma_{ij} = \Gamma$. Introducing the collective spin operator, $\hat{S}^\pm \equiv \sum_j \hat{\sigma}_j^\pm$,

$$\begin{aligned} \mathfrak{L}[\rho] &= \tfrac{1}{2} \sum_{i,j} \Gamma [2\hat{\sigma}_i^- \hat{\rho} \hat{\sigma}_j^+ - \hat{\sigma}_i^+ \hat{\sigma}_j^- \hat{\rho} - \hat{\rho} \hat{\sigma}_i^+ \hat{\sigma}_j^-] \\ &= \tfrac{1}{2} \Gamma [2\hat{S}^- \hat{\rho} \hat{S}^+ - \hat{S}^+ \hat{S}^- \hat{\rho} - \hat{\rho} \hat{S}^+ \hat{S}^-] \ . \end{aligned}$$

The uniform all-to-all coupling required for Dicke superradiance can be realized, when the atoms are localized in an area of space smaller than λ^3 or in a cavity.

23.3.2.1 Equations of motion in the presence of dipole-dipole coupling

We start from the Hamiltonian and jump operators (23.130) and derive the Heisenberg-Liouville equation (23.135),

$$\begin{aligned} \dot{\hat{\sigma}}_k^- &= -\imath [\hat{\sigma}_k^-, \hat{H}] + \mathfrak{L}^\dagger [\hat{\sigma}_k^-] \qquad (23.137) \\ &= \tfrac{\imath}{2} \Omega(\mathbf{r}_k) \hat{\sigma}_k^z - \imath \Delta_{\mathrm{a}} \hat{\sigma}_k^z \hat{\sigma}_k^- - \imath \sum_{j \neq k}^N \Delta_{kj} \hat{\sigma}_k^z \hat{\sigma}_j^- + \tfrac{\Gamma}{2} \hat{\sigma}_k^z \hat{\sigma}_k^- + \sum_{j \neq k}^N \tfrac{\Gamma_{kj}}{2} \hat{\sigma}_k^z \hat{\sigma}_j^- \ . \end{aligned}$$

Now, we assume low atomic excitation, $\langle\hat{\sigma}_k^z\rangle \simeq -1$, that is, most atoms are in the ground state. Then we may neglect correlations and find [17],

$$\dot{\hat{\sigma}}_k^- \simeq \left(\imath\Delta_{\rm a} - \tfrac{\Gamma}{2}\right)\hat{\sigma}_k^- - \tfrac{\imath}{2}\Omega(\mathbf{r}_k) + \sum_{j\neq k}^{N}\left(\imath\Delta_{kj} - \tfrac{\Gamma_{kj}}{2}\right)\hat{\sigma}_j^- \tag{23.138}$$

or taking the expectation values,

$$\dot{\beta}_k \simeq \left(\imath\Delta_{\rm a} - \tfrac{\Gamma}{2}\right)\beta_k - \tfrac{\imath}{2}\Omega(\mathbf{r}_k) + \sum_{j\neq k}^{N}\left(\imath\Delta_{kj} - \tfrac{\Gamma_{kj}}{2}\right)\beta_j \ . \tag{23.139}$$

These are just the equations of motion of the coupled dipoles model derived in Sec. 21.1.2. Evaluation of the coeffficients (23.130)(iv-v) yields the exponential kernel postulated in (21.29).

In Exc. 23.3.4.3 we derive them from the linear optics scalar coupled dipoles model,

$$\Delta_{j\neq i} \equiv -\frac{\Gamma\cos kr_{ji}}{kr_{ji}} \qquad \text{and} \qquad \Gamma_{j\neq i} \equiv \frac{\Gamma\sin kr_{ji}}{kr_{ji}} \tag{23.140}$$

with $r_{ji} = |\mathbf{r}_j - \mathbf{r}_i|$. These terms arise from the so-called scalar approximation of (22.169), where we neglect $1/R^2$ and $1/R^3$ terms and set $(\hat{\mathbf{e}}_d\cdot\hat{\mathbf{e}}_R) = 0$.

Example 148 (*Two atoms with dipole-dipole interactions*): For the case of only two atoms located at $\mathbf{r}_j$, using the basis defined in (3.75), we find the Hamiltonian [154],

$$\hat{H} = \begin{pmatrix} 0 & \frac{1}{2}\Omega^*(\mathbf{r}_2) & \frac{1}{2}\Omega^*(\mathbf{r}_1) & 0 \\ \frac{1}{2}\Omega(\mathbf{r}_2) & -\Delta_{\rm a} & \frac{1}{2}\Delta_{21} & \frac{1}{2}\Omega^*(\mathbf{r}_1) \\ \frac{1}{2}\Omega(\mathbf{r}_1) & \frac{1}{2}\Delta_{12} & -\Delta_{\rm a} & \frac{1}{2}\Omega^*(\mathbf{r}_2) \\ 0 & \frac{1}{2}\Omega(\mathbf{r}_1) & \frac{1}{2}\Omega(\mathbf{r}_2) & -2\Delta_{\rm a} \end{pmatrix} , \tag{23.141}$$

with $\Omega(\mathbf{r}) = \Omega_0 e^{\imath\mathbf{k}\cdot\mathbf{r}_j}$. For two atoms the master equations (23.130) can easily be solved numerically by setting [18],

$$\hat{\sigma}_1^{\pm} = \hat{\sigma}^{\pm}\otimes\mathbb{I} \qquad \text{and} \qquad \hat{\sigma}_2^{\pm} = \mathbb{I}\otimes\hat{\sigma}^{\pm} \ , \tag{23.142}$$

as usual and,

$$\langle i,j|\hat{\rho}|m,n\rangle = \rho_{ij,mn} \ , \tag{23.143}$$

where the indices $i,m = 1,2$ refer to the first atom and the indices $j,n = 1,2$ to the second. The populations of the Dicke states $|11\rangle$, $|12\rangle$, $|21\rangle$, and $|22\rangle$

[17] Note that the same result is obtained from $\dot{\hat{\sigma}}_k^- = -\imath[\hat{\sigma}_k^-, \hat{H}_{eff}]$ using the effective Hamiltonian $\hat{H}_{eff} \equiv \hat{H}_{\rm coh} - \imath\hat{H}_{diss}$ with,

$$\hat{H}_{\rm coh} = -\Delta_{\rm a}\sum_j \hat{\sigma}_j^+\hat{\sigma}_j^- + \tfrac{\Omega_0}{2}\sum_j(\hat{\sigma}_j^- e^{-\imath\mathbf{k}_0\cdot\mathbf{r}} + \hat{\sigma}_j^+ e^{\imath\mathbf{k}_0\cdot\mathbf{r}})$$

$$\hat{H}_{diss} = \tfrac{\Gamma}{2}\sum_j \hat{\sigma}_j^+\hat{\sigma}_j^- + \tfrac{1}{2}\sum_{j\neq i}(\Gamma_{ji} + \imath\Delta_{ji})\hat{\sigma}_j^+\hat{\sigma}_i^-$$

[18] Remember, that the formal solution of coherent part of the master equation can be written as $\hat{\rho}(t) = \mathfrak{L}(t)\hat{\rho}(0) = e^{-\imath\hat{H}t}\hat{\rho}(0)e^{\imath\hat{H}t}$.

are then given by $\rho_{ij,ij}$, and the populations of the (anti-)symmetric states $|\psi\rangle^{(s,a)} = \frac{1}{\sqrt{2}}(|1,2\rangle \pm |2,1\rangle)$ are calculated via,

$$\langle\psi|^{(s,a)}\hat{\rho}|\psi\rangle^{(s,a)} = \tfrac{1}{2}(\rho_{12,12} \pm \rho_{12,21} \pm \rho_{21,12} + \rho_{21,21}) \; . \tag{23.144}$$

The temporal evolution of the populations in one and two atom systems, initially driven by a laser field which is then suddenly switched off, is shown in Fig. 23.15. Note that super and subradiance do occur for $\Delta_{12} = 0 = \Delta_a$ but necessitate $\Gamma_{ij} \neq 0$.

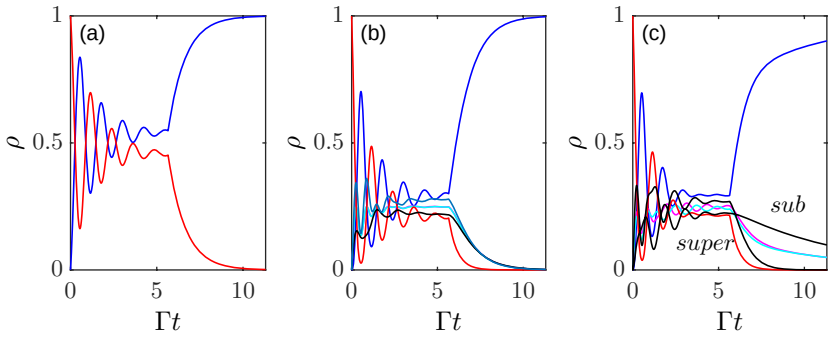

Figure 23.15: (code) (a) Response of a single two-level atom driven by a laser light with $\Omega = 5\Gamma$, $\Delta = -\Gamma$. The curves show (blue) the ground state and (red) the excited state populations. The light is switched off at $\Gamma t = 0.5$. (b) Response of two atoms $j = 1, 2$ located at $kz_j = \pm 5$ driven by the same laser light as in (a). (cyan and magenta) populations of the states $|eg\rangle$ and $|ge\rangle$. The two black lines show the populations of the (anti-)symmetric states $\frac{1}{\sqrt{2}}(|eg\rangle \pm |ge\rangle)$. (c) Same as (b) but with $kz_j = \pm 0.5$.

In Excs. 23.3.4.4 to 23.3.4.6 we study the impact of dipole-dipole interactions on super- and subradiance. In Exc. 23.3.4.7 we study three interacting two-level atoms. In Exc. 23.3.4.8 we compare Rydberg blockade and dipole-dipole interaction.

Example 149 (*Blackbody radiation-induced superradiance*): In Exc. 16.5.6.9 we studied blackbody radiation-induced transitions in a single atom. The procedure can be generalized to several atoms [854]. For two atoms the Liouvillean reads,

$$\begin{aligned}\dot{\hat{\rho}} &= \mathfrak{L}_{bb}\hat{\rho} \\ &= -\tfrac{1}{2}\sum_{i,j=1,2}\Gamma_{ij}\left([\hat{\rho}\hat{\sigma}_i, \hat{\sigma}_j^\dagger] + [\hat{\sigma}_i, \hat{\sigma}_j^\dagger\hat{\rho}]\right) - \tfrac{1}{2}\sum_{i,j=1,2}(\Gamma_{ij} + \gamma\delta_{ij})\left([\hat{\rho}\hat{\sigma}_j^\dagger, \hat{\sigma}_i] + [\hat{\sigma}_j^\dagger, \hat{\sigma}_i\hat{\rho}]\right) \; ,\end{aligned}$$

with $\Gamma_{ij}\delta(t-t') \propto \langle\hat{E}_i(t)\hat{E}_j(t')\rangle$ containing both the real and the virtual photon exchange.

23.3.2.2 Van der Waals interactions

The scalar kernel (23.140) for dipole-dipole interactions represents a good approximation at low densities. At higher density the vectorial kernel must be used. However, then other interatomic forces come into play, in particular van der Waals interactions.

23.3.3 Interacting atoms in a cooperative environment

The interactions studied so far in this section were described by Hamiltonians only containing direct interaction terms [see Eqs. (23.141) and (23.141)]. Doing so we conceal the fact that these interactions are necessarily mediated by electromagnetic forces. That is, the full Hamiltonian contains terms such as,

$$\hat{a}_{\mathbf{k}\lambda}\hat{\sigma}_j^+ + \hat{\sigma}_j^- \hat{a}_{\mathbf{k}\lambda}^\dagger \ , \tag{23.145}$$

which describe the exchange of photons through a local common field mode ($\mathbf{k}\lambda$). As these modes rapidly decay, they may be *adiabatically eliminated*, leaving behind terms like $\hat{\sigma}_j^+\hat{\sigma}_i^-$ [19].

Let us now consider several excited atoms labeled by j, located at $\mathbf{r}_j$, and described by two of their eigenstates, $\{|g_j\rangle, |e_j\rangle\}$. As usual, $|g_j\rangle$ is the eigenstate with lowest energy ($E_{g_j} = -\frac{1}{2}\hbar\omega_j$) and longer lifetime, i.e. the ground state, whereas $|e_j\rangle$ is the eigenstate with highest energy ($E_{e_j} = +\frac{1}{2}\hbar\omega_j$). In presence of an external electromagnetic field, the Hamiltonian of the two atom-field system in the electric dipolar approximation is,

$$\begin{aligned} \hat{H} &= \sum_{j=1,2} [\hat{H}^{(j)}_{\text{atom}} + \hat{H}^{(j)}_{\text{atom:field}}] + \hat{H}_{\text{field}} \\ \text{where} \quad \hat{H}^{(j)}_{\text{atom}} &\equiv \tfrac{1}{2}\omega_j\hat{\sigma}_j^z \quad , \quad \hat{H}^{(j)}_{\text{atom:field}} \equiv -\hat{\mathbf{d}}_j \cdot \hat{\vec{\mathcal{E}}}(\mathbf{r}_j) \ . \end{aligned} \tag{23.146}$$

The electric dipole moment operator satisfies $\langle e_j|\hat{\mathbf{d}}_j|e_j\rangle = \mathbf{0} = \langle g_j|\hat{\mathbf{d}}_j|g_j\rangle$ and has non-vanishing off-diagonal elements, i.e. the eigenstates have no permanent dipole moment. We define the dipole-moment matrix element as $\mathbf{d}_j \equiv \langle e_j|\hat{\mathbf{d}}_j|g_j\rangle$. The description of the field is identical to the case of one atom (22.3).

For weak-coupling between the atoms and the field, the interaction Hamiltonian becomes [772, 512],

$$\hat{H}_{\text{atom:field}} = -\imath \sum_{\mathbf{k},\lambda}\sum_j (\hat{\sigma}_j^+ + \hat{\sigma}_j^-)[g_{\mathbf{k}\lambda}(\mathbf{r}_j)\hat{a}_{\mathbf{k}\lambda} - g^*_{\mathbf{k}\lambda}(\mathbf{r}_j)\hat{a}^\dagger_{\mathbf{k}\lambda}] \ . \tag{23.147}$$

By solving the Heisenberg equations of motion for the atomic and field operators within the Born and Markov approximations, one obtains the spontaneous emission rate on a transition $|e_j\rangle \to |g_j\rangle$ of frequency ω_j, as done in Sec. 22.1.1,

$$\Gamma_j = 2\pi \sum_{\mathbf{k},\lambda} |g_{\mathbf{k}\lambda}(\mathbf{r}_j)|^2 \delta(\omega_{\mathbf{k}} - \omega_j) = \frac{\pi\omega_j}{\varepsilon_0\hbar} \sum_{\mathbf{k},\lambda} |\mathbf{d}_j \cdot \mathbf{u}_{\mathbf{k}\lambda}(\mathbf{r}_j)|^2 \delta(\omega_{\mathbf{k}} - \omega_j) \ , \tag{23.148}$$

which is the same result obtained by the Weisskopf-Wigner theory [583]. In addition, due to the coupling between the atoms through the vacuum field, one also has the cross-damping spontaneous emission rate:

$$\Gamma_q(\mathbf{r}_i, \mathbf{r}_j) = \Gamma_q(\mathbf{r}_j, \mathbf{r}_i) = \frac{\pi\omega_0}{\varepsilon_0\hbar} \sum_{\mathbf{k},\lambda} \mathfrak{Re}\left[\mathbf{d}_i \cdot \mathbf{u}_{\mathbf{k}\lambda}(\mathbf{r}_i)\mathbf{u}^*_{\mathbf{k}\lambda}(\mathbf{r}_j) \cdot \mathbf{d}_j^*\right] \delta(\omega_{\mathbf{k}} - \omega_j) \ , \tag{23.149}$$

which shows explicitly the cooperative effect of the dipole-dipole interaction in the spontaneous emission rate.

[19] The adiabatic elimination procedure for the case of cavity modes will be studied in Sec. 23.4.1

23.3.4 Exercises

23.3.4.1 Ex: Calculating with collective operators

The collective spin operators for an ensemble of J atoms with M internal levels are defined as,

$$\hat{S} = \sum_{j=1}^{J} \hat{\sigma}_j = \hat{\sigma} \otimes \mathbb{I}_M \otimes \mathbb{I}_M \otimes ... + \mathbb{I}_M \otimes \hat{\sigma} \otimes \mathbb{I}_M \otimes + ... \ ,$$

or more explicitly,

$$\hat{S}_{kl} = \sum_{j=1}^{J} \hat{\sigma}_j^{kl} = |k\rangle\langle l| \otimes \mathbb{I}_M \otimes \mathbb{I}_M \otimes ... + \mathbb{I}_M \otimes |k\rangle\langle l| \otimes \mathbb{I}_M \otimes + ... \ ,$$

with the spin matrices satisfying,

$$\begin{aligned} \hat{\sigma}_j^{kl}\hat{\sigma}_j^{mn} &= \delta_{lm}\hat{\sigma}_j^{kn} \qquad \text{and} \qquad [\hat{\sigma}_i^{kl}, \hat{\sigma}_j^{mn}] = \delta_{ij}(\delta_{lm}\hat{\sigma}_j^{kn} - \delta_{kn}\hat{\sigma}_j^{ml}) \\ \textstyle\sum_{m=1}^{M} \hat{\sigma}_j^{mm} &= \mathbb{I}_M \qquad \text{and} \qquad \textstyle\sum_{j=1}^{J}\sum_{m=1}^{M} \hat{\sigma}_j^{mm} = N\mathbb{I}_M \ . \end{aligned}$$

Verify that for the case of atoms subject to spin-spin interaction,

$$\hat{H} \neq \sum_{j,m} \hat{\sigma}_j^{mm} \hat{H} \hat{\sigma}_j^{mm} \ .$$

23.3.4.2 Ex: Liouvillean for two dipole-coupled atoms

a. From the master equation (23.130) set up the Liouvillean $\mathcal{M}$ for a system of two atoms coupled via dipolar radiation allowing to write the master equation as $\dot{\vec{\varrho}} = \mathcal{M}\vec{\varrho}$.
b. Discuss the Lindblad term in the limit, $kr_{12} \to 0$.
c. We have seen in Exc. 16.5.6.9, how to write down the master equation for a two-level atom whose levels are coupled by blackbody radiation. Extend the procedure to two dipole-coupled two-level atoms whose levels are only coupled by blackbody radiation.

23.3.4.3 Ex: Super- and subradiant linewidth and decay rates from the coupled dipoles model

Calculate super- and subradiance linewidth and lineshifts for two atoms interacting via dipole-dipole interaction using the linear optics scalar coupled dipoles model culminating in Eq. (21.26) using the exponential kernel (21.29).

23.3.4.4 Ex: Super- and subradiance in a two atom system

Calculate the temporal behavior of the (anti-)symmetric states $\rho_{S,A} = \frac{1}{2}(\rho_{12,12} + \rho_{21,21} \pm \rho_{12,21} \pm \rho_{21,12})$ from the master equation (23.135)(i) or the Liouville equation (23.135)(ii). Consider in particular the case of absent driving, $\Omega = 0$.

23.3.4.5 Ex: Two-atom toy model for super- and subradiance

Calculate the eigenvalues and eigenvectors of the Hamiltonian (23.141) for two two-level atoms located at $\mathbf{r}_j = \pm\frac{r_{12}}{2}\hat{\mathbf{e}}_z$ with $r_{ji} = |\mathbf{r}_j - \mathbf{r}_i| \ll \lambda$ [227]. Consider the limits (a) absent coupling, $\Delta_{12} = 0$, (b) resonant driving, $\Delta_\mathrm{a} = 0$, and (c) absent driving, $\Omega = 0$. (d) Analyze the full Hamiltonian.

23.3.4.6 Ex: Impact of dipole-dipole interactions on super- and subradiance

Here, we use the two-atom toy model studied in Fig. 23.15 to demonstrate the emergence of subradiant modes as a consequence of dipole-dipole interaction [227, 154]. Calculate numerically the anti-symmetric state population $\hat{\rho}_\mathrm{a}$ given in Eq. (23.144) at very long times as a function of the saturation parameter s and the interatomic distance kr_{ij}. Interpret the results. Note that subradiant modes may saturate at lower intensities than single atoms.

23.3.4.7 Ex: Three interacting atoms

Numerically integrate the master equation (23.130) for three atoms.

23.3.4.8 Ex: Rydberg blockade versus spin-spin interaction

a. Direct interactions (e.g. dipole-dipole coupling or van der Waals interaction) generate collective energy shifts Δ_{ij} and collective decay Γ_{ij} (see Sec. 23.3.2 or examples 144 and 145). Discuss why these terms are not observed in Hamiltonians describing Rydberg blockade.
b. Verify whether the operators $\hat{S}_z\hat{S}_z$ or $\hat{S}_+\hat{S}_-$ generate anti-diagonal terms in the Hamiltonian [623].

23.4 Cavity-mediated spin-exchange interactions

In the preceding sections we got to know two fundamentally different types of interatomic interactions, that is, Rydberg and dipole-dipole type interactions. Both are generally nearest neighbor interactions and thus inhomogeneous. Let us nevertheless make the assumption of uniform coupling to simplify the discussion. Then the Rydberg blockade term (23.141) reads,

$$\hat{H} = \tfrac{1}{2}\sum_{i\neq j}\kappa_{ij}\hat{\sigma}_j^z\hat{\sigma}_i^z \simeq \kappa\hat{S}_z^2 \ , \tag{23.150}$$

and the Ising interaction term (23.132) becomes,

$$\hat{H}_\mathrm{Ising} = -\sum_{i\neq j}\Delta_{ij}\hat{\sigma}_j^+\hat{\sigma}_i^- \simeq -\Delta_\mathrm{Ising}\hat{S}_+\hat{S}_- \ . \tag{23.151}$$

A way of achieving uniform coupling consists in coupling all atoms with the same strength to the same cavity mode. This is what we will discuss in the next subsection.

In the full open system Dicke model κ and, Γ_1 describe physical processes, namely cavity decay and atomic spontaneous emission, while Γ is introduced as a mere collective decay rate, not rooted in a physical process. In reality, collective decay processes may be caused by interatomic contact interactions, but as we will see in the following, they can also be induced by coupling of the atoms to a common light mode.

Indeed, in the bad cavity limit, upon adiabatic elimination of the light mode, the cavity parameters Δ_c and κ are replaced by U_c and κ_c, which take over the role of a collective shift and decay process. This is seen in the Hamiltonian and the Lindbladian, after adiabatic elimination of the light mode, by the fact that the terms depending on κ_c have exactly the same structure as those for which collective decay at a rate Γ had been postulated in the full open Dicke model.

The systems do not differ in concept, but only in details: uniform coupling versus nearest neighbors, inhomogeneities of the light field versus disordered clouds, etc..

23.4.1 Adiabatic elimination of the modes of a bad high-finesse cavity

The collective Jaynes-Cummings Hamiltonian (23.116) for a linear cavity (see Exc. 22.1.11.5),

$$\hat{H}_{\rm JC} = -\Delta_c \hat{a}^\dagger \hat{a} - \imath\eta(\hat{a} - \hat{a}^\dagger) + \sum_{i=1}^{N} \left[-\tfrac{\Delta_a}{2}(\mathbb{I}_2 + \hat{\sigma}_i^z) + g \sin kz_i (\hat{\sigma}_i^+ \hat{a} + \hat{a}^\dagger \hat{\sigma}_i^-) \right] , \quad (23.152)$$

becomes in the case of perfect bunching, $z_i = z$, using the abbreviation $g \to g \sin kz$,

$$\hat{H}_{\rm JC} = -\Delta_c \hat{a}^\dagger \hat{a} - \imath\eta(\hat{a} - \hat{a}^\dagger) - \Delta_a(\tfrac{N}{2}\mathbb{I} + \hat{S}_z) + g(\hat{S}_+ \hat{a} + \hat{a}^\dagger \hat{S}_-) , \quad (23.153)$$

where we introduced collective operators, $\hat{S}_\alpha \equiv \frac{1}{2}\sum_{i=1}^{N} \hat{\sigma}_i^\alpha$ for $\alpha = x, y, z$. The Heisenberg equations are those derived in (23.117), but now we consider the rotating wave approximation, $g' = 0$, and disregard optical pumping, $\xi_1 = 0$, and phase fluctuations, $\beta_1 = 0$,

$$\boxed{\begin{aligned} \langle \dot{\hat{a}} \rangle &= \langle (\imath\Delta_c - \kappa)\hat{a} - \imath g \hat{S}_- + \eta \rangle \\ \langle \dot{\hat{S}}_- \rangle &= \langle (\imath\Delta_a - \tfrac{\Gamma_1}{2} + \Gamma \hat{S}_z)\hat{S}_- + 2\imath g \hat{S}_z \hat{a} \rangle \\ \langle \dot{\hat{S}}_z \rangle &= \langle -(\Gamma_1 \tfrac{N}{2}\mathbb{I} + \Gamma_1 \hat{S}_z + \Gamma \hat{S}_+ \hat{S}_-) - \imath g(\hat{S}_+ \hat{a} - \hat{a}^\dagger \hat{S}_-) \rangle \end{aligned}} . \quad (23.154)$$

Γ stands for collective decay and Γ_1 for single-atom decay. Using $\eta \equiv \eta_r + \imath\eta_i$ we can reshape (23.154) in a real notation,

$$\begin{aligned} \langle \dot{\hat{a}}_r \rangle &= \langle \tfrac{1}{2}(\dot{\hat{a}} + \dot{\hat{a}}^\dagger) \rangle &&= \langle -\kappa \hat{a}_r - \Delta_c \hat{a}_i - g\hat{S}_y + \eta_r \rangle \\ \langle \dot{\hat{a}}_i \rangle &= \langle \tfrac{1}{2\imath}(\dot{\hat{a}} - \dot{\hat{a}}^\dagger) \rangle &&= \langle -\kappa \hat{a}_i + \Delta_c \hat{a}_r - g\hat{S}_x + \eta_i \rangle \\ \langle \dot{\hat{S}}_x \rangle &= \langle \tfrac{1}{2}(\dot{\hat{S}}_- + \dot{\hat{S}}_+) \rangle &&= \langle -(\tfrac{\Gamma_1}{2} + \tfrac{\Gamma}{2})\hat{S}_x + \Delta_a \hat{S}_y - g\{\hat{a}_i, \hat{S}_z\} - \imath g[\hat{a}_r, \hat{S}_z] + \tfrac{\Gamma}{2}\{\hat{S}_x, \hat{S}_z\} \rangle \\ \langle \dot{\hat{S}}_y \rangle &= \langle \tfrac{\imath}{2}(\dot{\hat{S}}_- - \dot{\hat{S}}_+) \rangle &&= \langle -(\tfrac{\Gamma_1}{2} + \tfrac{\Gamma}{2})\hat{S}_y - \Delta_a \hat{S}_x - g\{\hat{a}_r, \hat{S}_z\} + \imath g[\hat{a}_i, \hat{S}_z] + \tfrac{\Gamma}{2}\{\hat{S}_y, \hat{S}_z\} \rangle \\ \langle \dot{\hat{S}}_z \rangle &= \langle \partial_t \tfrac{1}{2}[\hat{S}_+, \hat{S}_-] \rangle &&= \langle -(\Gamma_1 + \Gamma)\hat{S}_z + g(\{\hat{a}_i, \hat{S}_x\} + \{\hat{a}_r, \hat{S}_y\} + \imath[\hat{a}_r, \hat{S}_x] - \imath[\hat{a}_i, \hat{S}_y]) \\ & & & \quad - \tfrac{N}{2}\Gamma_1 \mathbb{I} - \Gamma(\hat{S}_x^2 + \hat{S}_y^2) \rangle \end{aligned} \quad (23.155)$$

The equations are equivalent to those derived by [523].

Example 150 (*Simplification for uncorrelated $\hat{a}$ and $\hat{\mathbf{S}}$*): As long as $\hat{a}$ and $\hat{\mathbf{S}}$ are uncorrelated, we may simply set $\{\hat{a}, \hat{\mathbf{S}}\} = 2\hat{a}\hat{\mathbf{S}}$ and $[\hat{a}, \hat{\mathbf{S}}] = 0$. Assuming furthermore that $[\hat{S}_k, \hat{S}_l] \simeq 0$ the equations simplify even more. The equations (23.155) can then be written in compact matrix notation,

$$\dot{\hat{\mathbf{S}}} = -\imath[\hat{\mathbf{S}}, \hat{H}] + \mathfrak{L}_{\Gamma_1/2}\hat{\mathbf{S}} \quad \Longrightarrow \tag{23.156}$$

$$\langle\dot{\hat{\mathbf{S}}}\rangle = \langle \begin{pmatrix} -\frac{1}{2}(\Gamma_1+\Gamma) & \Delta_{\rm a} & -2g\hat{a}_{\rm i} \\ -\Delta_{\rm a} & -\frac{1}{2}(\Gamma_1+\Gamma) & -2g\hat{a}_{\rm r} \\ 2g\hat{a}_{\rm i} & 2g\hat{a}_{\rm r} & -(\Gamma_1+\Gamma) \end{pmatrix} \begin{pmatrix} \hat{S}_x \\ \hat{S}_y \\ \hat{S}_z \end{pmatrix} - \Gamma_1 \begin{pmatrix} 0 \\ 0 \\ \frac{N}{2}\mathbb{I} \end{pmatrix} - \Gamma \begin{pmatrix} -\hat{S}_x\hat{S}_z \\ -\hat{S}_y\hat{S}_z \\ \hat{S}_x^2+\hat{S}_y^2 \end{pmatrix} \rangle$$

$$= \langle \begin{pmatrix} 2g\hat{a}_{\rm r} \\ -2g\hat{a}_{\rm i} \\ -\Delta_{\rm a} \end{pmatrix} \times \begin{pmatrix} \hat{S}_x \\ \hat{S}_y \\ \hat{S}_z \end{pmatrix} - \Gamma_1 \begin{pmatrix} \frac{1}{2}\hat{S}_x \\ \frac{1}{2}\hat{S}_y \\ \frac{N}{2}\mathbb{I}+\hat{S}_z \end{pmatrix} \rangle \ .$$

The equations (23.155) are just the Heisenberg-Liouville equations (23.118) derived from the open Dicke model and the open Tavis-Cummings model Hamiltonian, restricting to many immobile atoms and a single cavity mode. In the bad cavity limit, $\kappa \gg g$, the cavity field is effectively slaved to the internal atomic dynamics. Hence, we may assume $\dot{\hat{a}} \equiv 0$ and adiabatically eliminate the field. Setting $\dot{\hat{a}}_{\rm r} = 0 = \dot{\hat{a}}_{\rm i}$ in Eq. (23.155)(i-ii) we calculate,

$$\begin{aligned} \hat{\Omega}_{\rm r} &\equiv 2g\hat{a}_{\rm r} = 2U_{\rm c}(\hat{S}_x - \eta_{\rm i}/g) - 2\kappa_{\rm c}(\hat{S}_y - \eta_{\rm r}/g) \\ \hat{\Omega}_{\rm i} &\equiv 2g\hat{a}_{\rm i} = -2\kappa_{\rm c}(\hat{S}_x - \eta_{\rm i}/g) - 2U_{\rm c}(\hat{S}_y - \eta_{\rm r}/g) \ , \end{aligned} \tag{23.157}$$

where we introduced the abbreviations,

$$U_\kappa \equiv U_{\rm c} - \imath\kappa_{\rm c} \qquad \text{with} \qquad U_{\rm c} \equiv \frac{g^2\Delta_{\rm c}}{\Delta_{\rm c}^2+\kappa^2} \qquad \text{and} \qquad \kappa_{\rm c} \equiv \frac{g^2\kappa}{\Delta_{\rm c}^2+\kappa^2} \ . \tag{23.158}$$

$U_{\rm c}$ is the cooperative cavity Lamb-shift and $\kappa_{\rm c}$ is the Purcell-enhanced cavity decay rate. Substituting (23.157) in the Eqs. (23.155)(iii-v) leads to [20,21],

$$\boxed{\begin{aligned} \langle\dot{\hat{S}}_x\rangle &= \langle -(\tfrac{\Gamma_1}{2}+\tfrac{\Gamma_{\rm c}}{2})\hat{S}_x + (\Delta_{\rm a}-U_{\rm c})\hat{S}_y - 2(U_{\rm c}\bar{\eta}_{\rm r} + \kappa_{\rm c}\bar{\eta}_{\rm i})\hat{S}_z + U_{\rm c}\{\hat{S}_y, \hat{S}_z\} + \tfrac{\Gamma_{\rm c}}{2}\{\hat{S}_x, \hat{S}_z\}\rangle \\ \langle\dot{\hat{S}}_y\rangle &= \langle -(\tfrac{\Gamma_1}{2}+\tfrac{\Gamma_{\rm c}}{2})\hat{S}_y - (\Delta_{\rm a}-U_{\rm c})\hat{S}_x + 2(U_{\rm c}\bar{\eta}_{\rm i} - \kappa_{\rm c}\bar{\eta}_{\rm r})\hat{S}_z - U_{\rm c}\{\hat{S}_x, \hat{S}_z\} + \tfrac{\Gamma_{\rm c}}{2}\{\hat{S}_y, \hat{S}_z\}\rangle \\ \langle\dot{\hat{S}}_z\rangle &= \langle -(\Gamma_1+\Gamma_{\rm c})\hat{S}_z - \tfrac{N}{2}\Gamma_1\mathbb{I} + 2(U_{\rm c}\bar{\eta}_{\rm r} + \kappa_{\rm c}\bar{\eta}_{\rm i})\hat{S}_x - 2(U_{\rm c}\bar{\eta}_{\rm i} - \kappa_{\rm c}\bar{\eta}_{\rm r})\hat{S}_y - \Gamma_{\rm c}(\hat{S}_x^2+\hat{S}_y^2)\rangle \end{aligned}} \ , \tag{23.159}$$

with the definitions,

$$\bar{\eta} \equiv \eta/g \qquad \text{and} \qquad \Gamma_{\rm c} \equiv \Gamma + 2\kappa_{\rm c} \qquad \text{and} \qquad \Gamma_{\rm tot} \equiv \Gamma_1 + \Gamma_{\rm c} \ . \tag{23.160}$$

[20] Equivalently, in complex notation,

$$\begin{aligned} \Delta_\kappa\hat{a} &= g\hat{S}_- + \imath\eta \\ (\partial_t + \tfrac{\Gamma_1}{2})\hat{S}_- &= \imath\Delta_{\rm a}\hat{S}_- + 2U_\kappa(\imath\hat{S}_- - \tfrac{1}{g}\eta)\hat{S}_z \\ (\partial_t + \Gamma_1)\hat{S}_z &= -\Gamma_1\tfrac{N}{2}\mathbb{I} - \kappa_{\rm c}\{\hat{S}_+, \hat{S}_-\} + \tfrac{1}{g}\eta U_\kappa\hat{S}_+ + \tfrac{1}{g}\eta^* U_\kappa^*\hat{S}_- \ . \end{aligned}$$

[21] According to [773] the adiabatic elimination does only hold for $g\sqrt{N} \ll \kappa$. The question is then, why do our bistability curves agree so well?

The colored terms correspond to those in Eqs. (23.155). It is interesting to note that, after adiabatic elimination of the cavity, the cavity decay rate κ_c appears in the equations of motion at the same locations as the collective decay rate Γ introduced *ad hoc* in the open Dicke model (23.116) via a Liouvillean $\mathfrak{L}^\dagger_{\Gamma_c/2,\hat{S}_-}$.

The number of intracavity photons is found via,

$$\hat{n} = \tfrac{1}{2g}(\hat{\Omega}_r^2 + \hat{\Omega}_i^2) = 2|U_\kappa/g|^2[(g\hat{S}_x - \eta_i)^2 + (g\hat{S}_y - \eta_r)^2] \; . \tag{23.161}$$

It is always interesting to consider special cases. In Exc. 23.4.4.1 we show that in for strong driving the cavity feedback disappears such that we recover the linear collective Dicke model. And in Exc. 23.4.4.2 we show that for weak driving the detuning-dependence of $\langle\hat{n}\rangle$ exhibits standard normal mode splitting.

23.4.1.1 Hamiltonian for the Tavis-Cummings model after adiabatic elimination of the modes

Alternatively, we can try to derive a simplified Hamiltonian from which the Heisenberg-Liouville equations under adiabatic elimination of the cavity mode can be derived directly.

We have seen in Sec. 16.4.3, using the effective Hamiltonian approach, that the Heisenberg equation decomposes in a commutator and an anti-commutator. The complete Heisenberg-Liouville equation reads,

$$\begin{aligned} \dot{\hat{\mathbf{S}}} &= -\imath[\hat{\mathbf{S}}, \hat{H}] + \mathfrak{L}^\dagger_{\kappa_c,\hat{S}_-}\hat{\mathbf{S}} + \mathfrak{L}^\dagger_{\Gamma/2,\hat{S}_-}\hat{\mathbf{S}} + \sum_j \mathfrak{L}^\dagger_{\Gamma_1/2,\hat{s}_j^-}\hat{\mathbf{S}} \\ \hat{H}_{\rm ad} &= -2\Im\mathfrak{m}\,(\bar{\eta}U_\kappa)\hat{S}_x - 2\Re\mathfrak{e}\,(\bar{\eta}U_\kappa)\hat{S}_y - \Delta_a\hat{S}_z + U_c\hat{S}_+\hat{S}_- \end{aligned} \; . \tag{23.162}$$

As shown in Exc. 23.4.4.4, we recover exactly the equations of motion (23.159). The complete absence of the field from the equations of motion shows that, in the bad cavity limit, any coherence of the coupled atom-cavity system is entirely contained in the atomic cloud.

Comparing this model to the one of the open system Dicke model (23.116), we notice that the cavity decay plays an important role not only in collective decay, but also in the coherent evolution of the system. We can calculate the intracavity field from (23.157),

$$\hat{a} = \hat{a}_r + \imath\hat{a}_i = \tfrac{U_\kappa}{g}\left(\hat{S}_x - \imath\hat{S}_y + \tfrac{\imath\eta}{g}\right) = \tfrac{U_\kappa}{g}\left(\hat{S}_- + \imath\tfrac{\eta}{g}\right) \; . \tag{23.163}$$

Example 151 (*Alternative notations*): The Hamiltonian (23.162) can also be expressed in complex notation [512],

$$\hat{H}_{\rm ad} = \tfrac{\Omega}{2}\hat{S}_+ + \tfrac{\Omega^*}{2}\hat{S}_- - \Delta_a\hat{S}_z + U_c\hat{S}_+\hat{S}_- \; , \tag{23.164}$$

with the abbreviation $\Omega \equiv 2\imath\bar{\eta}U_\kappa$. Particularly interesting is the non-linear term, which contributes to the equations of motion as,

$$\begin{aligned} \hat{H}_{\rm ad} = U_c\hat{S}_+\hat{S}_- \quad\Longrightarrow\quad -\imath[\hat{\mathbf{S}}, \hat{H}_{\rm ad}] &= -\imath U_c[\hat{\mathbf{S}}, \hat{S}_+\hat{S}_-] \\ \mathfrak{L}_{\kappa_c,\hat{S}_-}\hat{\mathbf{S}} &= \kappa_c(2\hat{S}_+\hat{\mathbf{S}}\hat{S}_- - \hat{\mathbf{S}}\hat{S}_+\hat{S}_- - \hat{S}_+\hat{S}_-\hat{\mathbf{S}}) \end{aligned} \tag{23.165}$$

or using an effective Hamiltonian with $U_\kappa = U_c - \imath\kappa_c$,

$$\hat{H}_{\rm eff} = U_\kappa \hat{S}_+\hat{S}_- \quad \Longrightarrow \quad -\imath[\hat{\mathbf{S}}\hat{H}_{\rm eff} - \hat{H}_{\rm eff}^\dagger\hat{\mathbf{S}}] = -\imath U_c[\hat{\mathbf{S}},\hat{S}_+\hat{S}_-] - \kappa_c(\hat{\mathbf{S}}\hat{S}_+\hat{S}_- + \hat{S}_+\hat{S}_-\hat{\mathbf{S}})$$
$$\mathfrak{L}^{\rm eff}_{\kappa_c,\hat{S}_-}\hat{\mathbf{S}} = 2\kappa_c\hat{S}_+\hat{\mathbf{S}}\hat{S}_- \ . \qquad (23.166)$$

That is, two terms of the Liouvillean can be attributed to an effective Hamiltonian.

23.4.1.2 Constants of motion

Let us now address the question, under which conditions the equations of motions (23.159) preserve the total spin. The Heisenberg equation for $\hat{\mathbf{S}}^2$ is,

$$\frac{d}{dt}\hat{\mathbf{S}}^2 = -\imath[\hat{\mathbf{S}}^2,\hat{H}_{\rm ad}] + \mathfrak{L}_{\kappa_c\hat{S}_-}\hat{\mathbf{S}}^2 + \tfrac{\Gamma_1}{2}\sum\nolimits_j \mathfrak{L}_{\Gamma_1/2,\hat{s}_j^-}\hat{\mathbf{S}}^2 \qquad (23.167)$$
$$= -\imath[\hat{\mathbf{S}}^2,\hat{H}_{\rm ad}] + \kappa_c(\hat{S}_+[\hat{\mathbf{S}}^2,\hat{S}_-] + [\hat{S}_+,\hat{\mathbf{S}}^2]\hat{S}_-) + \tfrac{\Gamma_1}{2}\sum_j(\hat{s}_j^+[\hat{\mathbf{S}}^2,\hat{s}_j^-] + [\hat{s}_j^+,\hat{\mathbf{S}}^2]\hat{s}_j^-) \ .$$

Plugging in the Hamiltonian (23.162), because of $[\mathbf{S}^2,\hat{S}_\alpha] = 0$ we immediately see that all commutators involving only collective spins vanish. The spontaneous emission terms do not vanish, because $\mathbf{S}^2$ does not commute with individual spin components, as shown in Exc. 3.4.5.2,

$$\frac{d}{dt}\langle\hat{\mathbf{S}}^2\rangle = \sum_j \mathfrak{L}_{\Gamma_1/2,\hat{s}_j^-}\hat{\mathbf{S}}^2 \neq 0 \ . \qquad (23.168)$$

This result confirms a calculation made for the complete Hamiltonian before adiabatic elimination done in Exc. 23.2.4.5. Thus, the collective character of the fully stretched spin expressed by $\langle\hat{\mathbf{S}}^2\rangle$ remains upon collective decay κ_c and only decays via spontaneous emission Γ_1 toward subradiant states.

On the other hand, it is interesting to verify the conservation of the length of the collective spin vector $\langle\hat{\mathbf{S}}^2\rangle$. We find readily,

$$\frac{d}{dt}\langle\hat{\mathbf{S}}\rangle^2 = 2\langle\hat{\mathbf{S}}\rangle\langle\dot{\hat{\mathbf{S}}}\rangle = 2\langle\hat{\mathbf{S}}\rangle\left\langle -\imath[\hat{\mathbf{S}},\hat{H}_{\rm ad}] + \mathfrak{L}_{\kappa_c\hat{S}_-}\hat{\mathbf{S}} + \tfrac{\Gamma_1}{2}\sum\nolimits_j \mathfrak{L}_{\Gamma_1/2,\hat{s}_j^-}\hat{\mathbf{S}}\right\rangle \qquad (23.169)$$
$$= -2\imath\langle\hat{\mathbf{S}}\rangle\langle[\hat{\mathbf{S}},\hat{H}]\rangle + 2\kappa_c\langle\hat{\mathbf{S}}\rangle\left\langle\hat{S}_+[\hat{\mathbf{S}},\hat{S}_-] + [\hat{S}_+,\hat{\mathbf{S}}]\hat{S}_-\right\rangle$$
$$+ \Gamma_1\sum\nolimits_j\langle\hat{\mathbf{S}}\rangle\left\langle\hat{s}_j^+[\hat{\mathbf{S}},\hat{s}_j^-] + [\hat{s}_j^+,\hat{\mathbf{S}}]\hat{s}_j^-\right\rangle \ .$$

The Hamiltonian term again vanishes. For the collective decay term we find,

$$\langle\hat{\mathbf{S}}\rangle\langle\mathfrak{L}_{\kappa_c\hat{S}_-}\hat{\mathbf{S}}\rangle/\kappa_c \qquad (23.170)$$
$$= -\langle\hat{S}_x\rangle^2 - \langle\hat{S}_y\rangle^2 - 2\langle\hat{S}_z\rangle^2 + \langle\hat{S}_x\rangle\langle\{\hat{S}_x,\hat{S}_z\}\rangle + \langle\hat{S}_y\rangle\langle\{\hat{S}_y,\hat{S}_z\}\rangle - 2\langle\hat{S}_z\rangle\langle\hat{S}_x^2 + \hat{S}_y^2\rangle \ .$$

In the mean field approximation, we neglect quantum correlations, which implies that the anti-commutators in (23.159) can be replaced by simple products, $\langle\hat{S}_\alpha\hat{S}_\beta\rangle = \langle\hat{S}_\alpha\rangle\langle\hat{S}_\beta\rangle$, we find,

$$\langle\hat{\mathbf{S}}\rangle\langle\mathfrak{L}_{\kappa_c\hat{S}_-}\hat{\mathbf{S}}\rangle/\kappa_c \simeq -S_x^2 - S_y^2 - 2S_z^2 \ . \qquad (23.171)$$

Thus, in contrast to $\langle\hat{\mathbf{S}}^2\rangle$, all terms in (23.159) depending on Γ_1 or κ_c reduce the length of the collective spin (see Exc. 23.4.4.3).

23.4.1.3 Stationary mean field equations and saturation-induced nonlinearity

It is interesting to study the stationary behavior of Eqs. (23.154) and (23.159) by setting $\dot{\hat{a}} = 0 = \dot{\hat{\mathbf{S}}}$. We must, however, be aware that by this assumption we *miss some important physics*, as discussed in Sec. 23.5.

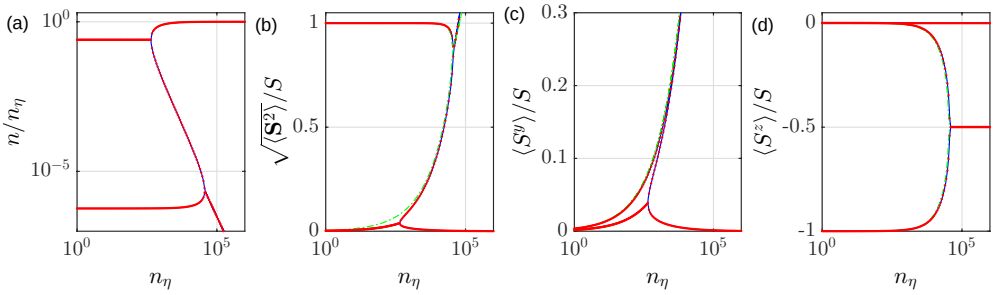

Figure 23.16: (code) Pump power dependence of (a) the intracavity photon number, (b) the stationary value of the mean field total atomic spin, and (c,d) its projection onto the y- and z-axis. The red dotted lines are numerical solutions of the full equations Eqs. (23.155), the blue solid lines are analytical solutions of the adiabatically simplified Eqs. (23.159) under the assumption of resonance, $\Delta_\mathrm{c} = \Delta_\mathrm{a} = \bar{\eta}_\mathrm{i} = 0$, and the green dash-dotted lines are analytical approximations (see Exc. 23.4.4.3 and Ref. [512]). The other parameters are taken from [694].

23.4.2 Spin squeezing in the XX-Heisenberg model

Without pumping and neglecting spontaneous emission, $\eta = \Gamma_1 = 0$, we obtain the simplified Hamiltonian of the Tavis-Cummings model (23.118) with RWA, $g' = 0$,

$$\hat{H}_\mathrm{XX} = -\Delta_\mathrm{a}\hat{S}_z + U_\mathrm{c}\hat{S}_+\hat{S}_- \ , \tag{23.172}$$

also known as the effective Hamiltonian of the *XX-Heisenberg model*. For large $N \gg 1$ the second term can safely be approximated by $\frac{1}{2}U_\mathrm{c}\{\hat{S}_+, \hat{S}_-\}$ [623], because $[\hat{S}_+, \hat{S}_-] = 2\hat{S}_z$ is small compared to terms scaling with $\hat{S}_z^2$. The Heisenberg-Liouville equations can then be written,

$$\langle \dot{\hat{\mathbf{S}}} \rangle = \left\langle \begin{pmatrix} 2U_\mathrm{c}\hat{S}_x - 2\kappa_\mathrm{c}\hat{S}_y \\ 2U_\mathrm{c}\hat{S}_y + 2\kappa_\mathrm{c}\hat{S}_x \\ -\Delta_\mathrm{a} \end{pmatrix} \times \hat{\mathbf{S}} \right\rangle = \left\langle \begin{pmatrix} \hat{\Omega}_\mathrm{r} \\ -\hat{\Omega}_\mathrm{i} \\ -\Delta_\mathrm{a} \end{pmatrix} \times \hat{\mathbf{S}} \right\rangle \ . \tag{23.173}$$

Analogously, for the Dicke model (23.118) without RWA, $g' = g$, we obtain,

$$\langle \dot{\hat{\mathbf{S}}} \rangle = \left\langle \begin{pmatrix} 4U_\mathrm{c}\hat{S}_x - 4\kappa_\mathrm{c}\hat{S}_y \\ 0 \\ -\Delta_\mathrm{a} \end{pmatrix} \times \hat{\mathbf{S}} \right\rangle \ . \tag{23.174}$$

The intracavity field (23.157) takes for $\eta = 0$ a particularly simple form,

$$\hat{a} = \tfrac{U_\kappa}{g}\hat{S}_- \ . \tag{23.175}$$

Example 152 (*One-axis twisting in the XX-Heisenberg model*): The coupling strength $\sqrt{N_+N_-} \leq \frac{N}{2}$ between the cavity mode and the atoms depends on the inversion. Hence, this leads to an inversion-dependent frequency shift known as *one-axis twisting* [22]. In the mean field treatment we simply replace the operators by their expectation values. Setting $\Delta_a = 0$ in the Heisenberg-Liouville equations (23.173) and neglecting terms $\dot{\hat{S}}_z \propto \hat{S}_z$, we get,

$$\langle \dot{\hat{\mathbf{S}}} \rangle \simeq \langle \begin{pmatrix} 2(\kappa_c \hat{S}_x + U_c \hat{S}_y)\hat{S}_z \\ 2(\kappa_c \hat{S}_y - U_c \hat{S}_x)\hat{S}_z \\ -2\kappa_c(\hat{S}_x^2 + \hat{S}_y^2) \end{pmatrix} \rangle \ .$$

Starting from the initial condition, $\langle \hat{\mathbf{S}} \rangle = (0, 0, N/2)$, we see that the instantaneous collective dipole moment $\hat{S}_x^2 + \hat{S}_y^2$ determines the decay of the inversion, while the inversion $\hat{S}_z$ twists the dipole moment [565, 543, 625, 624, 623]. Collective decay occurs at a rate $\hat{S}_- \sqrt{\kappa_c/2}$. It is easy to see that $\partial_t \hat{\mathbf{S}}^2 = \hat{\mathbf{S}}\cdot\dot{\hat{\mathbf{S}}} + \dot{\hat{\mathbf{S}}}\cdot\hat{\mathbf{S}} = 0$. In the equator plane, where $\langle \hat{S}_z \rangle \simeq 0$, the equations of motion simplify to,

$$\dot{\hat{\mathbf{S}}} \simeq \begin{pmatrix} 0 \\ 0 \\ -2\kappa_c S^2 \end{pmatrix} \ .$$

Near the poles, where $\langle \hat{S}_z \rangle \simeq \pm\frac{N}{2}$,

$$\langle \dot{\hat{\mathbf{S}}} \rangle \simeq \langle \pm N \begin{pmatrix} \kappa_c \hat{S}_x + U_c \hat{S}_y \\ \kappa_c \hat{S}_y - U_c \hat{S}_x \\ 0 \end{pmatrix} \rangle \quad \Longrightarrow \quad \langle \dot{\hat{S}}_\pm \simeq \pm N(\kappa_c \pm \imath U_c)\hat{S}_\pm \rangle \ .$$

Hence, near the poles the cavity field will oscillate at a frequency of about $\pm\imath 2NU_c$ and decay at a rate κ_c.

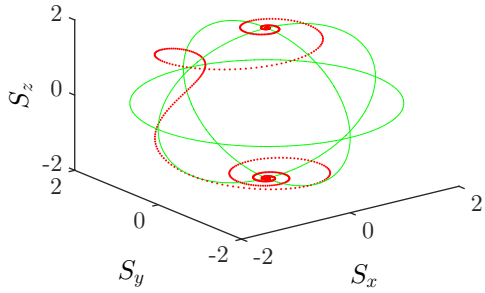

Figure 23.17: (code) One-axis twisting.

Example 153 (*Experimental observation of one-axis twisting*): In the experiment [623] the main inhomogeneity arises because they trap the atoms in a standing wave at 813 nm which is incommensurate with 698 nm (where of course they cannot trap). They first drive the transition by pumping the cavity,

[22] This is somewhat analogous to the photon number-dependent phase shift observed in dispersive interaction in the Jaynes-Cummings model.

then switch off the cavity and measure the field subsequently emitted from the cavity by heterodyne beating. In this way they extract the frequency shift and superradiant decay rate of the cavity,

$$S(\omega) = \mathcal{F}\langle \hat{a}^\dagger(t+\tau)\hat{a}(t)\rangle$$
$$\text{with} \quad \langle \hat{a}^\dagger(t+\tau)\hat{a}(t)\rangle = \langle \hat{S}_+(t+\tau)\hat{S}_-(t)\rangle \simeq \langle \hat{S}_+(t+\tau)\rangle\langle \hat{S}_-(t)\rangle \ ,$$

in the mean-field approximation.

23.4.2.1 Repumping on a narrow transition

Saturation-induced bistability has been observed in the bad cavity limit [694]. Here, we want to analyze, how incoherent optical pumping at a rate R will affect the normal mode spectra. The ultimate goal is to prepare studies of superradiant lasing [624, 523].

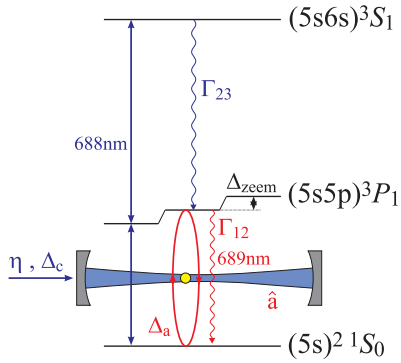

Figure 23.18: (code) Scheme for optical pumping of a metastable excited state, here for the case of atomic strontium [694], in order to generate inversion. The cavity drives the narrow transition.

We consider the situation sketched in Fig. 23.18 and start from the Hamiltonian (11) of [694] for the interaction between strontium atoms and the modes of a ring cavity. We simply add a jump operator for incoherent transfer from the ground to the excited state. With the definition of $\hat{\mathcal{L}}^\dagger_{\gamma,\hat{L}}\hat{A}$ given in (23.116) the relevant jump operators are,

$$\begin{aligned}
\hat{\mathcal{L}}^\dagger_{\kappa,\hat{a}}\hat{a} &= -\kappa\hat{a} \\
\hat{\mathcal{L}}^\dagger_{\Gamma/2,\hat{\sigma}_i^-}\hat{\sigma}_j^- &= -\delta_{ij}\tfrac{\Gamma}{2}\hat{\sigma}_i^- \quad , \quad \hat{\mathcal{L}}^\dagger_{R/2,\hat{\sigma}_i^+}\hat{\sigma}_j^- = -\delta_{ij}\tfrac{R}{2}\hat{\sigma}_i^- \quad . \\
\hat{\mathcal{L}}^\dagger_{\Gamma/2,\hat{\sigma}_i^-}\hat{\sigma}_j^z &= -\delta_{ij}\Gamma(\mathbb{I}+\hat{\sigma}_i^z) \quad , \quad \hat{\mathcal{L}}^\dagger_{R/2,\hat{\sigma}_i^+}\hat{\sigma}_j^z = \delta_{ij}R(\mathbb{I}-\hat{\sigma}_i^z)
\end{aligned} \tag{23.176}$$

Therefore, the generalized Heisenberg-Liouville equations read,

$$\begin{aligned}
\dot{\hat{\sigma}}_i^- &= (\imath\Delta_{\rm a} - \tfrac{\Gamma}{2} - \tfrac{R}{2})\hat{\sigma}_i^- + \imath g(e^{\imath kz_i}\hat{a}_+ + e^{-\imath kz_i}\hat{a}_-)\hat{\sigma}_i^z \\
\dot{\hat{\sigma}}_i^z &= -2\imath g(e^{\imath kz_i}\hat{a}_+ + e^{-\imath kz_i}\hat{a}_-)\hat{\sigma}_i^+ + 2\imath g(e^{-\imath kz_i}\hat{a}_+^\dagger + e^{\imath kz_i}\hat{a}_-^\dagger)\hat{\sigma}_i^- - (\Gamma - R)\mathbb{I} - (\Gamma + R)\hat{\sigma}_i^z \\
\dot{\hat{a}}_\pm &= (\imath\Delta_{\rm c} - \kappa)\hat{a}_\pm - \imath g\sum_j \hat{\sigma}_j^- e^{\mp\imath kz_j} + \eta_\pm \ .
\end{aligned} \tag{23.177}$$

With this and the abbreviations,

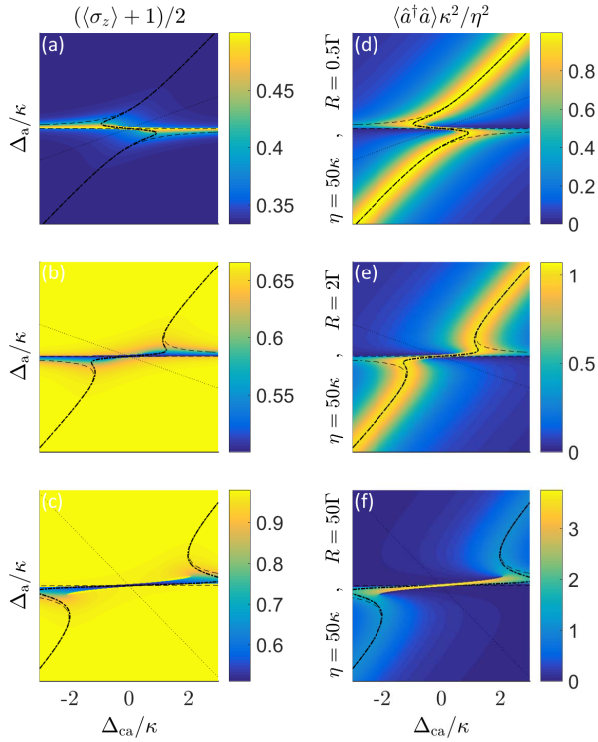

Figure 23.19: (left) inversion $(\hat{\sigma}^z+1)/2$, (right) light transmission $\kappa^2|\alpha|^2/\eta^2$ through the cavity. The repumping rate is set to $R=0.5\Gamma$ (upper row), $R=2\Gamma$ (center row), and $R=50\Gamma$ (lower row). The other parameters are taken from [694].

$$\Gamma_\pm \equiv \Gamma \pm R \qquad \text{and} \qquad \tilde{U}_\gamma \equiv \frac{g^2(\Delta_a - \imath\frac{\Gamma_+}{2})}{\Delta_a^2 + \frac{\Gamma_+^2}{4}} \;, \tag{23.178}$$

the calculation of [694] is straightforward to generalize, yielding,

$$\sum_j \frac{-\frac{\Gamma_-}{\Gamma_+}\tilde{U}_\gamma(\alpha_+ + e^{\mp 2\imath kz_j}\alpha_-)}{1+2|\tilde{U}_\gamma/g|^2|e^{\imath kz_j}\alpha_+ + e^{-\imath kz_j}\alpha_-|^2} = \imath\eta_\pm - \Delta_\kappa\alpha_\pm \;. \tag{23.179}$$

That is, all results obtained for $R=0$ remain valid, one just has to redefine $\tilde{U}_\gamma$ and rescale η and Δ_κ. For one-sided probing and a homogeneous cloud and with this and the abbreviations $\bar{\eta}_\pm \equiv \frac{\Gamma_+}{\Gamma_-}\eta_\pm$ and $\tilde{\Delta}_\kappa \equiv \frac{\Gamma_+}{\Gamma_-}\Delta_\kappa$ we recover the same Eq. (3) of [694],

$$\boxed{\alpha_+ = \frac{\imath\bar{\eta}_\pm}{\tilde{\Delta}_\kappa - \frac{N\tilde{U}_\gamma}{1+2|\tilde{U}_\gamma/g|^2|\alpha_+|^2}}} \tag{23.180}$$

and

$$\boxed{\langle\hat\sigma_i^z\rangle = \frac{-\Gamma_-/\Gamma_+}{1+2|\tilde U_\gamma/g|^2|\alpha_+|^2}} \ . \tag{23.181}$$

The graphs in Fig. 23.19 were obtained for the experimental parameters of [694] and additional repumping. We find inversion once $R > \Gamma$. Close to resonance $\Delta_{\rm a} = 0$ but $\Delta_{\rm ca} \simeq \kappa$ the transmission becomes slightly > 1. The ridges are obtained in the same way as in [694] by setting $\mathfrak{Im}\,\alpha_+ \equiv 0$, yielding,

$$\Delta_{\rm ca} = \Delta_{\rm a} - \frac{\Gamma_-}{\Gamma_+}\frac{Ng^2\Delta_{\rm a}}{\Delta_{\rm a}^2 + \frac{\Gamma_+^2}{4} + 2g^2n} \ . \tag{23.182}$$

23.4.3 Cumulant expansion of the open Dicke model

In the Heisenberg-Liouville equations applied to the Dicke Hamiltonian for a laser-pumped linear cavity are,

$$\begin{aligned}
[\partial_t - \imath\Delta_{\rm c} + \kappa]\hat a &= -\imath g\textstyle\sum_j \hat\sigma_j^- \sin kz_j + \eta \\
[\partial_t - \imath\Delta_{\rm a} + \tfrac{\Gamma}{2}]\hat\sigma_i^- &= -\imath g\hat a\hat\sigma_i^z \sin kz_i \\
[\partial_t - \Gamma]\hat\sigma_i^z &= 2\imath g\sin kz_i(\hat a\hat\sigma_i^+ - \hat a^\dagger\hat\sigma_i^-) - \Gamma\hat\sigma_i^z \ .
\end{aligned} \tag{23.183}$$

Note that the presence of pumping represents a serious complication with respect to superradiant lasing models [565, 135, 661], since phase-dependent terms such as $\langle\hat a\rangle$ and $\langle\hat\sigma^-\rangle$ only vanish if $\eta \neq 0$. Products of operators are differentiated like,

$$\frac{d}{dt}(\hat A\hat B) = \hat A\frac{d\hat B}{dt} + \frac{d\hat A}{dt}\hat B \ . \tag{23.184}$$

Hence,

$$\begin{aligned}
[\partial_t + 2\kappa]\hat a^\dagger\hat a &= \imath g\textstyle\sum_j\left(\hat a\hat\sigma_j^+ - \hat a^\dagger\hat\sigma_j^-\right)\sin kz_j + \eta(\hat a^\dagger + \hat a) \\
[\partial_t - \imath\Delta_{\rm a} + \imath\Delta_{\rm c} + \tfrac{\Gamma}{2} + \kappa]\hat a^\dagger\hat\sigma_i^- &= -\imath g\hat a^\dagger\hat a\hat\sigma_i^z\sin kz_i + \imath g\textstyle\sum_j\hat\sigma_j^+\hat\sigma_i^-\sin kz_j + \eta\hat\sigma_i^- \\
[\partial_t + \imath\Delta_{\rm c} + \kappa - \Gamma]\hat a^\dagger\hat\sigma_i^z &= 2\imath g\sin kz_i(\hat a^\dagger\hat a\hat\sigma_i^+ - \hat a^\dagger\hat a^\dagger\hat\sigma_i^-) + \Gamma\hat a^\dagger + \imath g\textstyle\sum_j\hat\sigma_j^+\hat\sigma_i^z\sin kz_j + \eta\hat\sigma_i^z \\
[\partial_t + \Gamma]\hat\sigma_i^+\hat\sigma_j^- &= \imath g(\hat a^\dagger\hat\sigma_i^z\hat\sigma_j^-\sin kz_i - \hat a\hat\sigma_i^+\hat\sigma_j^z\sin kz_j) \ .
\end{aligned} \tag{23.185}$$

For perfect bunching, $\sum_j g\sin kz \longrightarrow Ng$, and using $\hat\sigma^\pm\hat\sigma^z = \pm\hat\sigma^\pm$ and $\hat\sigma^z\hat\sigma^\pm = \mp\hat\sigma^\pm$,

$$\begin{aligned}
[\partial_t - \imath\Delta_{\rm c} + \kappa]\hat a &= -\imath Ng\hat\sigma_j^- + \eta \\
[\partial_t - \imath\Delta_{\rm a} + \tfrac{\Gamma}{2})]\hat\sigma_i^- &= -\imath g\hat a\hat\sigma_i^z \\
[\partial_t - \Gamma]\hat\sigma_i^z &= 2\imath g(\hat a\hat\sigma_i^+ - \hat a^\dagger\hat\sigma_i^-) - \Gamma\hat\sigma_i^z \\
[\partial_t + 2\kappa]\hat a^\dagger\hat a &= \imath Ng(\hat a\hat\sigma_j^+ - \hat a^\dagger\hat\sigma_j^-) + \eta(\hat a^\dagger + \hat a) \\
[\partial_t - \imath\Delta_{\rm a} + \imath\Delta_{\rm c} + \tfrac{\Gamma}{2} + \kappa]\hat a^\dagger\hat\sigma_i^- &= -\imath g\hat a^\dagger\hat a\hat\sigma_i^z + \imath g[\hat\sigma_i^+\hat\sigma_i^- + (N-1)\hat\sigma_{j\neq i}^+\hat\sigma_i^-] + \eta\hat\sigma_i^- \\
[\partial_t + \imath\Delta_{\rm c} + \kappa - \Gamma]\hat a^\dagger\hat\sigma_i^z &= 2\imath g(\hat a^\dagger\hat a\hat\sigma_i^+ - \hat a^\dagger\hat a^\dagger\hat\sigma_i^-) + \Gamma\hat a^\dagger + \imath g[\hat\sigma_i^+ + (N-1)\hat\sigma_{j\neq i}^+\hat\sigma_i^z] + \eta\hat\sigma_i^z \\
[\partial_t + \Gamma]\hat\sigma_i^+\hat\sigma_j^- &= \imath g(\hat a^\dagger\hat\sigma_i^z\hat\sigma_j^- - \hat a\hat\sigma_i^+\hat\sigma_j^z) \ .
\end{aligned} \tag{23.186}$$

For a single atom,

$$
\begin{aligned}
[\partial_t - \imath\Delta_\mathrm{c} + \kappa]\hat{a} &= -\imath N g\hat{\sigma}^- + \eta \\
[\partial_t - \imath\Delta_\mathrm{a} + \tfrac{\Gamma}{2})]\hat{\sigma}^- &= -\imath g\hat{a}\hat{\sigma}^z \\
[\partial_t - \Gamma]\hat{\sigma}^z &= 2\imath g(\hat{a}\hat{\sigma}^+ - \hat{a}^\dagger\hat{\sigma}^-) - \Gamma\hat{\sigma}^z \\
[\partial_t + 2\kappa]\hat{a}^\dagger\hat{a} &= \imath N g(\hat{a}\hat{\sigma}^+ - \hat{a}^\dagger\hat{\sigma}^-) + \eta(\hat{a}^\dagger + \hat{a}) \\
[\partial_t - \imath\Delta_\mathrm{a} + \imath\Delta_\mathrm{c} + \tfrac{\Gamma}{2} + \kappa]\hat{a}^\dagger\hat{\sigma}_i^- &= -\imath g\hat{a}^\dagger\hat{a}\hat{\sigma}_i^z + \imath g\hat{\sigma}_j^+\hat{\sigma}_i^- + \eta\hat{\sigma}_i^- \\
[\partial_t\hat{a}^\dagger\hat{\sigma}_i^z) &= 2\imath g(\hat{a}^\dagger\hat{a}\hat{\sigma}^+ - \hat{a}^\dagger\hat{a}^\dagger\hat{\sigma}^-) + \Gamma\hat{a}^\dagger + \imath N g\hat{\sigma}^+ + \eta\hat{\sigma}^z \\
[\partial_t\hat{\sigma}_i^+\hat{\sigma}_j^-) &= \imath g(\hat{a}^\dagger\hat{\sigma}^- - \hat{a}\hat{\sigma}^+) \; .
\end{aligned}
\tag{23.187}
$$

We now take the expectation values of these equations performing the cumulant expansion,

$$
\langle\hat{A}\hat{B}\hat{C}\rangle = \langle\hat{A}\hat{B}\rangle\langle\hat{C}\rangle + \langle\hat{A}\hat{C}\rangle\langle\hat{B}\rangle + \langle\hat{B}\hat{C}\rangle\langle\hat{A}\rangle - 2\langle\hat{A}\rangle\langle\hat{B}\rangle\langle\hat{C}\rangle \; . \tag{23.188}
$$

Assuming steady-state for $\langle\hat{a}\rangle$ and $\langle\hat{\sigma}^-\rangle$, $\langle\hat{\sigma}^z\rangle$, we obtain a linear set of differential equations,

$$
\frac{d}{dt}\begin{pmatrix}
\langle\hat{a}\rangle \\ \langle\hat{a}^\dagger\rangle \\ \langle\hat{\sigma}_i^-\rangle \\ \langle\hat{\sigma}_i^+\rangle\langle\hat{\sigma}_i^z\rangle \\ \langle\hat{a}^\dagger\hat{a}\rangle \\ \langle\hat{a}\hat{\sigma}_i^+\rangle \\ \langle\hat{a}^\dagger\hat{\sigma}_i^-\rangle \\ \langle\hat{a}\hat{\sigma}_i^z\rangle \\ \langle\hat{a}^\dagger\hat{\sigma}_i^z\rangle \\ \langle\hat{\sigma}_i^+\hat{\sigma}_i^-\rangle
\end{pmatrix} = \mathcal{M}\begin{pmatrix}
\langle\hat{a}\rangle \\ \langle\hat{a}^\dagger\rangle \\ \langle\hat{\sigma}_i^-\rangle \\ \langle\hat{\sigma}_i^+\rangle \\ \langle\hat{\sigma}_i^z\rangle \\ \langle\hat{a}^\dagger\hat{a}\rangle \\ \langle\hat{a}\hat{\sigma}_i^+\rangle \\ \langle\hat{a}^\dagger\hat{\sigma}_i^-\rangle \\ \langle\hat{a}\hat{\sigma}_i^z\rangle \\ \langle\hat{a}^\dagger\hat{\sigma}_i^z\rangle \\ \langle\hat{\sigma}_i^+\hat{\sigma}_i^-\rangle
\end{pmatrix} + \begin{pmatrix}
\eta \\ \eta \\ 0 \\ 0 \\ \Gamma \\ 0 \\ 0 \\ 0 \\ 0 \\ 0 \\ \langle\hat{a}_\infty^\dagger\rangle\langle\hat{a}_\infty\rangle\langle\hat{\sigma}_\infty^z\rangle
\end{pmatrix} \; . \tag{23.189}
$$

with

$$
\mathcal{M} = \tag{23.190}
$$

$$
\begin{pmatrix}
\imath\Delta_\mathrm{c} - \kappa & 0 & -\imath N g & 0 & 0 & 0 & 0 & 0 & 0 & 0 & 0 \\
0 & -\imath\Delta_\mathrm{c} - \kappa & 0 & \imath N g & 0 & 0 & 0 & 0 & 0 & 0 & 0 \\
0 & 0 & \imath\Delta_\mathrm{a} - \frac{\Gamma}{2} & 0 & 0 & 0 & 0 & 0 & -\imath g & 0 & 0 \\
0 & 0 & 0 & -\imath\Delta_\mathrm{a} - \frac{\Gamma}{2} & 0 & 0 & 0 & 0 & 0 & \imath g & 0 \\
0 & 0 & 0 & 0 & \Gamma & 0 & 2\imath g & -2\imath g & 0 & 0 & 0 \\
\eta & \eta & 0 & 0 & 0 & -2\kappa & \imath N g & -\imath N g & 0 & 0 & 0 \\
0 & 0 & 0 & \eta & 0 & \imath N g\langle\hat{\sigma}_\infty^z\rangle & 0 & 0 & 0 & 0 & \imath N g \\
0 & 0 & \eta & 0 & 0 & -\imath N g\langle\hat{\sigma}_\infty^z\rangle & 0 & 0 & 0 & 0 & \imath N g \\
\Gamma & 0 & -\imath N g & \eta & \langle\hat{\sigma}^-\rangle & 0 & 0 & 0 & 0 & 0 & 0 \\
0 & \Gamma & 0 & \imath N g & \eta & \langle\hat{\sigma}^+\rangle & 0 & 0 & 0 & 0 & 0 \\
0 & 0 & 0 & 0 & 0 & 0 & -\imath g & \imath g & 0 & 0 & 0
\end{pmatrix}
$$

23.4.3.1 Correlation functions

Often it is interesting to analyze two-times *correlation functions* of the types $g^{(1)}(\tau) = \langle\hat{A}^\dagger(t+\tau)\hat{A}(t)\rangle$ or $g^{(2)}(\tau) = \langle\hat{A}^\dagger(t)\hat{A}^\dagger(t+\tau)\hat{A}(t+\tau)\hat{A}(t)\rangle$. As long as we are able to solve the Heisenberg-Liouville equation for the whole operator,

$$
\frac{d}{dt}\hat{A} = \mathfrak{L}[\hat{A},\hat{B},\hat{C}] \quad \Longrightarrow \quad \hat{A}(t+\tau) = \hat{A}(t) + \tau\;\mathfrak{L}[\hat{A},\hat{B},\hat{C}] \tag{23.191}
$$

this task is easy. In particular, for the case of unitary evolutions,

$$\hat{A}(t+\tau) = e^{-\imath\hat{H}\tau}\hat{A}(t)e^{\imath\hat{H}\tau} \quad \Longrightarrow \quad \langle\hat{A}^\dagger(t+\tau)\hat{A}(t)\rangle = \langle e^{-\imath\hat{H}\tau}\hat{A}(t)e^{\imath\hat{H}\tau}\hat{A}(t)\rangle \ . \tag{23.192}$$

Often, however, we just know the expectation values of equal time correlations, because they follow from a cumulant expansion of the Heisenberg-Liouville equations for all possible combinations, e.g. $\langle\hat{A}(t)\hat{B}(t)\rangle$. This is when we can use the *quantum regression theorem*,

$$\begin{aligned} &\langle\hat{A}(t+\tau)\rangle = \alpha(\tau)\langle\hat{A}(t)\rangle + \beta(\tau)\langle\hat{B}(t)\rangle \\ &\Longrightarrow \quad \langle\hat{A}(t+\tau)\hat{X}(t)\rangle = \alpha(\tau)\langle\hat{A}(t)\hat{X}(t)\rangle + \beta(\tau)\langle B(t)\hat{X}(t)\rangle \ . \end{aligned} \tag{23.193}$$

Applied to the Heisenberg-Liouville equations,

$$\begin{aligned} &\hat{A}(t+\tau) = \hat{A}(t) + \tau\ \mathfrak{L}[\hat{A},\hat{B},\hat{C}] \\ &\Longrightarrow \quad \langle\hat{A}^\dagger(t+\tau)\hat{A}(t)\rangle = \langle\hat{A}(t)^\dagger\hat{A}(t)\rangle + \tau\ \langle\mathfrak{L}[\hat{A},\hat{B},\hat{C}]^\dagger\hat{A}(t)\rangle \ , \end{aligned} \tag{23.194}$$

which only holds for very short times τ.

23.4.4 Exercises

23.4.4.1 Ex: No feedback in the strong driving limit

For strong driving, $\hat{S}_{x,y} \ll \eta$, the evolution of coupled atom-cavity system is externally controlled by the pump, which impedes a self-determined dynamics, i.e. a dynamics ruled by cavity feedback. Show that in this limit, which is obtained from (23.156) via decorrelation of the atomic spins, we recover the linear collective Dicke model.

23.4.4.2 Ex: Linearization for weak driving

For weak driving we may assume $\hat{S}_z \simeq -\frac{N}{2}\mathbb{I}$. This approximation underlies the *coupled dipoles model* and leads to a linearization of the equations of motion also known as *linear optics regime*.
a. Derive the stationary solution.
b. Setting $\Delta_\mathrm{a} = \Delta_\mathrm{c}$, show that $\langle\hat{n}\rangle$ exhibits the standard normal mode spectrum.

23.4.4.3 Ex: Solution of the mean field equations after adiabatic elimination of the cavity

a. Do the mean field approximation of the adiabatically simplified Eqs. (23.159) and assume $\Delta_\mathrm{c} = \Delta_\mathrm{a} = \bar{\eta}_\mathrm{r} = 0$.
b. Show that the total spin $\mathbf{S}^2$ is NOT a constant of motion, unless $\Gamma_1 = 0 = \Gamma_\mathrm{tot}$ with $\Gamma_\mathrm{tot} = \Gamma_1 + 2\kappa_\mathrm{c}$ even though $\kappa_\mathrm{c} \neq 0$ [512]. Interpret the result.
c. Derive the steady state solution of the equations obtained in (a).
d. Approximate the cubic equation by a quadratic one assuming $2\kappa_\mathrm{c} \ll \Gamma_1 \ll 2\kappa_\mathrm{c}S_z$.
e. Compare with the stationary solution of (23.154) assuming $\Delta_\mathrm{a} = \Delta_\mathrm{c} = \Gamma = 0$.
f. Perform a stability analysis of the equations derived under (a).

23.4.4.4 Ex: Adiabatic elimination of the cavity mode, general case

Derive the equations of motion (23.159) for a system consisting of many atoms interacting with a single cavity mode after adiabatic elimination of the cavity mode.

23.4.4.5 Ex: Comparison of collective Hamiltonians

Compile a list of all collective Hamiltonians studied so far, compare and discuss them.

23.5 Driven-dissipative Dicke model

Until now we mostly considered stationary or coherently evolving systems. We will now study driven-dissipative atom-cavity systems that may or may not reach equilibrium and exhibit phenomena such as *cooperative resonance fluorescence* (CRF) [248, 139]. The bistable behavior of the atom-cavity system in Sec. 23.4.1 and Exc. 23.4.4.3 was calculated in the mean field approximation and assuming complete stationarity, $\dot{\hat{a}} = 0 = \hat{\mathbf{S}}$. The bistability curves of Fig. 23.16 then represent the full mathematically exact solution. We show them again in Fig. 23.20 with a different scaling. Panel (b) emphasizes the eminent role played by the collective cooperativity in the bistability,

$$\Upsilon_N = \frac{4Ng^2}{\Gamma_1\kappa} = \frac{4N\kappa_c}{\Gamma_1} \ . \tag{23.195}$$

Apparently, it rules the relation between collective and individual decay processes.

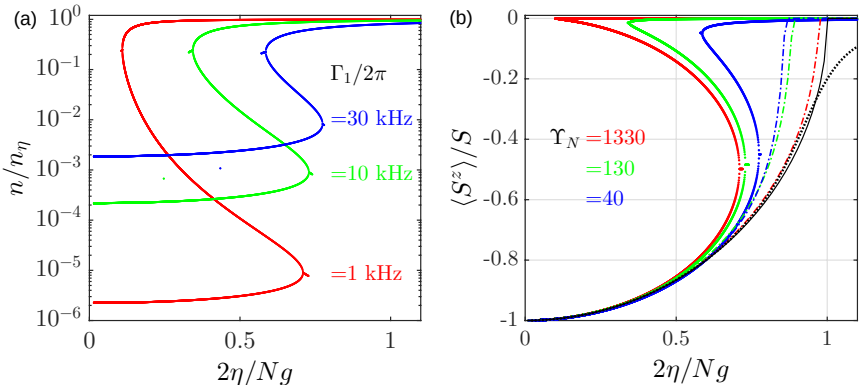

Figure 23.20: (code) The solid lines indicate bistability curves calculated under steady state conditions for various collective cooperativities using full or adiabatically simplified Heisenberg equations. (a) Intracavity photon number. (b) Collective atomic inversion. The dash-dotted lines indicate mean field values of the collective atomic inversion evaluated after long evolution times without steady state assumption. The black dotted line is an analytical solution [Eq. (23.210)] without mean field approximation but also without spontaneous emission for 30 atoms.

The stationarity assumption is, however, not always realistic. Let us think, for example, of the case of a single driven two-level atom whose dynamics is described by Bloch equations (see Sec. 16.4.1). Subject to strong driving the atom will undergo Rabi oscillations, and reach a steady state only after the oscillations are damped out due to spontaneous emission. If we want to observe such behavior in the collective Dicke model, we need to give up the stationarity condition [694].

Indeed, the equations of motion can have other solutions, which may not necessarily be stationary. In the following, we will study how the interplay between driving force (at a rate η), collective decay (at a rate κ_c), and individual decay (at a rate Γ_1) rules the collective dynamics in the bistable region [512, 773].

23.5.1 Cooperative resonance fluorescence in mean field approximation

The major problem is however that, near phase transitions *quantum fluctuations may overwhelm decay terms*. In that case, we do not expect the mean field approximation to be good. In order to still get meaningful approximate results, and we shall rather neglect decay term at the profit of correlation terms.

23.5.1.1 Critical Rabi frequency

For the following we use the definition of the Rabi frequency proposed in Eqs. (23.157),

$$\hat{\Omega} = \hat{\Omega}_r + \imath\hat{\Omega}_i = 2U_c(\hat{S}_x - \tfrac{\eta_i}{g}) - 2\kappa_c(\hat{S}_y - \tfrac{\eta_r}{g}) = U_\kappa^*(\hat{S}_- + \imath\tfrac{\eta}{g}) + U_\kappa(\hat{S}_+ - \imath\tfrac{\eta^*}{g}) \ . \quad (23.196)$$

We evaluate this definition on resonance,

$$\hat{\Omega} \overset{\Delta_c=0}{\longrightarrow} 2\kappa_c(\hat{S}_y + \tfrac{\eta_r}{g}) = \imath\kappa_c\hat{S}_- - \imath\kappa_c\hat{S}_+ + 2\kappa_c\tfrac{\eta_r}{g} \equiv \tfrac{1}{2}(\hat{\Omega}_- + \hat{\Omega}_+) + \Omega_\eta \ . \quad (23.197)$$

In the last expression we defined superradiant Rabi frequency operators

$$\hat{\Omega}_\mp \equiv \pm 2\imath\kappa_c\hat{S}_\mp \quad (23.198)$$

and a pump Rabi frequency [that is, the maximum Rabi frequency in a resonant empty cavity,

$$\Omega_\eta \equiv 2\imath\tfrac{\eta}{g}U_\kappa = 2g\frac{\eta}{\kappa} = 2\kappa_c\frac{\eta}{g} \ . \quad (23.199)$$

Now, the superradiant Rabi frequency is maximum at the equator, since

$$\langle\hat{S}_-\rangle \simeq \sqrt{S(S+1) - M(M\pm 1)} \lesssim \tfrac{N}{2} \ . \quad (23.200)$$

We call the upper limit the *critical Rabi frequency*,

$$\Omega_c \equiv N\kappa_c \geq 2\kappa_c\langle\hat{S}_-\rangle = -\imath\langle\hat{\Omega}_-\rangle \ . \quad (23.201)$$

It can be used to normalize the pump Rabi frequency,

$$\tilde{\Omega}_\eta \equiv \frac{\Omega_\eta}{\Omega_c} = \frac{2\eta}{Ng} \ . \quad (23.202)$$

We will see in the following, that for $\Omega_\eta < \Omega_c$, drive and dissipative superradiance counter-balance until the system reaches a steady-state. For $\Omega_\eta > \Omega_c$, the drive enforces Rabi flopping and no steady-state is reached (see Fig. 23.21).

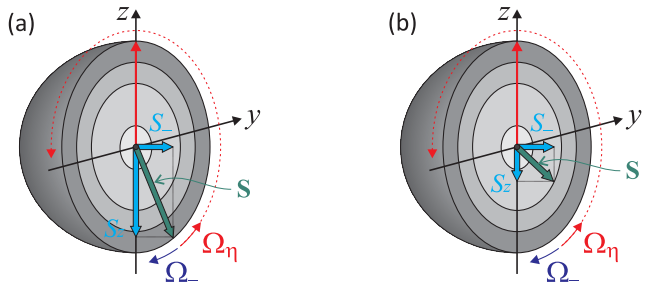

Figure 23.21: Illustration of the equilibrium between drive and superradiance. (a) In the absence of spontaneous emission the collective spin vector (green arrow) remains on the outer shell with its position determined by an equilibrium between superradiant decay Ω_- and the drive assumed to be weak, $\Omega_\eta < \Omega_c$ (blue and red solid arrows). If $\Omega_\eta > \Omega_c$, the overwhelming drive induced Rabi oscillations (dotted arrow). (b) In the presence of spontaneous emission the collective spin vector evolves into inner shells.

23.5.1.2 Time-dependent mean field solution of the Heisenberg equations *without* adiabatic elimination

We start from the full equations (23.154) evaluated on resonance and neglecting collective decay Γ (other than the one induced by the cavity),

$$\begin{aligned}\dot{\hat{a}} &= -\kappa\hat{a} - \imath g\hat{S}_- + \eta \\ \dot{\hat{S}}_- &= -\tfrac{\Gamma_1}{2}\hat{S}_- + 2\imath g\hat{S}_z\hat{a} \\ \dot{\hat{S}}_z &= -\Gamma_1(\tfrac{N}{2} + \hat{S}_z) - \imath g(\hat{S}_+\hat{a} - \hat{a}^\dagger\hat{S}_-)\ .\end{aligned} \tag{23.203}$$

Disregarding for a while spontaneous decay Γ_1 and exploiting the above definitions,

$$\begin{aligned}\dot{\hat{a}} &= -\kappa\hat{a} + \tfrac{\kappa}{2g}(\Omega_\eta - \hat{\Omega}_-) \\ \dot{\hat{S}}_- &= 2\imath g\hat{S}_z\hat{a} \\ \dot{\hat{S}}_z &= -\imath g(\hat{S}_+\hat{a} - \hat{a}^\dagger\hat{S}_-)\ .\end{aligned} \tag{23.204}$$

From the second equation we see that steady-state requires $\hat{a} = 0$. Hence,

$$\imath\hat{S}_- = \tfrac{\eta}{g} \qquad \text{i.e.} \qquad \hat{\Omega}_- = \Omega_\eta\ . \tag{23.205}$$

That is, the superradiant Rabi frequency self-adjusts until it compensates the pump field. This, however, is only possible until the superradiant Rabi frequency reaches its maximum allowed value, that we will call the critical Rabi frequency [773].

Figs. 23.22 show the mean field behavior of the cavity field and the collective spin simulated from Eqs. (23.204). We see that, below the critical pumping strength $\Omega_\eta < \Omega_c$ (red curves), the cavity field quickly vanishes and the collective spin tends toward a stationary value. Above the critical pumping strength $\Omega_\eta > \Omega_c$ (blue curves) the cavity field and the collective spin both start to oscillate, such that no steady state is reached, unless we allow for single atom spontaneous decay. Then, a mean field

simulation of Eqs. (23.204) (dashed curves) shows relaxation toward finite stationary values for the cavity field the collective spin.

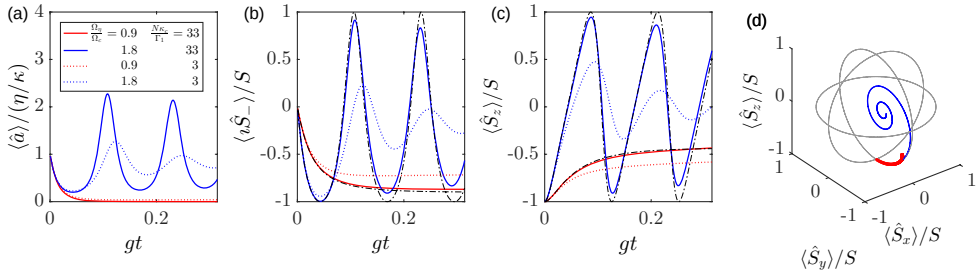

Figure 23.22: (code) Mean field values of cavity field and collective spin calculated from Eqs. (23.203) for various strength η of the drive and two different values of $\Gamma_1 = (2\pi)\,10\,\mathrm{kHz}$ (solid lines) and $100\,\mathrm{kHz}$ (dashed lines). The other parameters are $\kappa = (2\pi)\,3\,\mathrm{MHz}$, $g = (2\pi)\,10\,\mathrm{kHz}$, and $N = 10000$. Note that simulations of the adiabatically simplified Eqs.(23.215) yield exactly the same curves. The dash-dotted black lines are obtained from an analytical solution derived in example 156.

Example 154 (*Continuous superradiant transition*): In the mean field approximation,

$$\begin{aligned}\dot{\alpha} &= -\kappa\alpha - \imath g\langle\hat{S}_-\rangle + \eta \\ \langle\dot{S}_-\rangle &= -\tfrac{\Gamma_1}{2}\langle\hat{S}_-\rangle + 2\imath g\alpha\langle\hat{S}_z\rangle \\ \langle\dot{S}_z\rangle &= -\Gamma_1(\tfrac{N}{2} + \langle\hat{S}_z\rangle) - \imath g(\langle\hat{S}_+\rangle\alpha - \alpha^*\langle\hat{S}_-\rangle)\ .\end{aligned} \tag{23.206}$$

For $\Gamma_1 = 0$ assuming $\varphi = 0$, we expect,

$$\langle\hat{S}_-\rangle = \tfrac{N}{2}\sin\vartheta \qquad \text{and} \qquad \langle\hat{S}_z\rangle = \tfrac{N}{2}\cos\vartheta\ , \tag{23.207}$$

so that,

$$\begin{aligned}\dot{\alpha} &= -\kappa\alpha - \imath g\tfrac{N}{2}\sin\vartheta + \eta \\ \dot{\vartheta} &= 2\imath g\alpha = \imath g(\alpha - \alpha^*)\ .\end{aligned} \tag{23.208}$$

For steady state $\dot{\alpha} = 0 = \dot{\vartheta}$ we get,

$$\sin\vartheta = -\frac{2\imath\eta}{Ng}\ , \tag{23.209}$$

and consequently,

$$\langle\hat{S}_z\rangle = \frac{N}{2}\cos\vartheta = \frac{N}{2}\sqrt{1 - \left(\frac{2\imath\eta}{Ng}\right)^2}\ . \tag{23.210}$$

The solution is shown as black solid line in Fig. 23.20. It describes a continuous second-order phase transition, in contrast to the colored solid lines in this figure, which describe an abrupt first-order phase transition. Analytical solutions for this phase transition were derived in Exc. 23.4.4.3.

23.5.1.3 Time-dependent mean field solution of the Heisenberg equations *after* adiabatic elimination of the cavity field

Let us now repeat the calculation using the adiabatically simplified Heisenberg-Liouville equations (23.159) for the resonant case, $\Delta_a = 0 = \Delta_c$, imaginary pump corresponding to a rotation about the y-axis, $\bar{\eta}_r = 0$, and no collective decay apart from the cavity, $\Gamma = 0$,

$$\dot{\hat{\mathbf{S}}} = -\imath[\hat{\mathbf{S}}, \hat{H}] + \mathfrak{L}^{\dagger}_{\kappa_c,\hat{S}_-}\hat{\mathbf{S}} + \sum_j \mathfrak{L}^{\dagger}_{\Gamma_1/2,\hat{s}_j^-}\hat{\mathbf{S}} \qquad \text{with} \qquad \hat{H} = 2\bar{\eta}_i\kappa_c\hat{S}_y \ , \tag{23.211}$$

or in the effective Hamiltonian notation,

$$\begin{aligned}\dot{\mathbf{S}} &= -\imath[\hat{\mathbf{S}}, \hat{H}_{\rm eff}] + 2\kappa_c\hat{S}_+\hat{\mathbf{S}}\hat{S}_- + \Gamma_1\sum_j(2\hat{s}_j^+\hat{\mathbf{S}}\hat{s}_j^- - \hat{s}_j^+\hat{s}_j^-\hat{\mathbf{S}} - \hat{\mathbf{S}}\hat{s}_j^+\hat{s}_j^-) \\ \hat{H}_{\rm eff} &= 2\bar{\eta}_i\kappa_c\hat{S}_y - \imath\kappa_c\hat{S}_+\hat{S}_-\end{aligned} \tag{23.212}$$

We see that after adiabatic elimination of a bad cavity, one part of the cavity decay κ_c enters the Hamiltonian, another the Lindbladian. The corresponding equations of motion are,

$$\begin{aligned}\dot{\hat{S}}_x &= -\kappa_c(\hat{S}_x - \{\hat{S}_x, \hat{S}_z\}) - 2\bar{\eta}_i\kappa_c\hat{S}_z - \tfrac{\Gamma_1}{2}\textstyle\sum_j(\hat{s}_j^x - \{\hat{s}_j^x, \hat{s}_j^z\}) \\ \dot{\hat{S}}_y &= -\kappa_c(\hat{S}_y - \{\hat{S}_y, \hat{S}_z\}) - \tfrac{\Gamma_1}{2}\textstyle\sum_j(\hat{s}_j^y - \{\hat{s}_j^y, \hat{s}_j^z\}) \\ \dot{\hat{S}}_z &= -2\kappa_c(\hat{S}_z + \hat{S}_x^2 + \hat{S}_y^2) + 2\bar{\eta}_i\kappa_c\hat{S}_x - \Gamma_1\textstyle\sum_j(\hat{s}_j^z + \hat{s}_j^{x2} + \hat{s}_j^{y2})\end{aligned} \ . \tag{23.213}$$

Example 155 (*Evaluation of individual spins*): For the products of individual and collective spins we find [139],

$$\sum_j \hat{s}_j^\alpha\hat{s}_j^\beta = \hat{S}_\alpha\hat{S}_\beta - \sum_j \hat{s}_j^\alpha\sum_{i\neq j}\hat{s}_i^\beta = \hat{S}_\alpha\hat{S}_\beta - N(N-1)\hat{s}_1^\alpha\hat{s}_1^\beta \ . \tag{23.214}$$

With this the Eqs. (23.213) can be rewritten as [512],

$$\begin{aligned}\dot{\hat{S}}_x &= -(\kappa_c + \tfrac{\Gamma_1}{2})(\hat{S}_x - \{\hat{S}_x, \hat{S}_z\}) - 2\bar{\eta}_i\kappa_c\hat{S}_z + \tfrac{\Gamma_1}{2}N(N-1)\{\hat{s}_1^x, \hat{s}_1^z\} \\ \dot{\hat{S}}_y &= -(\kappa_c + \tfrac{\Gamma_1}{2})(\hat{S}_y - \{\hat{S}_y, \hat{S}_z\}) + \tfrac{\Gamma_1}{2}N(N-1)\{\hat{s}_1^y, \hat{s}_1^z\} \\ \dot{\hat{S}}_z &= -(2\kappa_c + \Gamma_1)(\hat{S}_z + \hat{S}_x^2 + \hat{S}_y^2) + 2\bar{\eta}_i\kappa_c\hat{S}_x - \Gamma_1 N(N-1)(\hat{s}_1^{x2} + \hat{s}_1^{y2}) \ .\end{aligned} \tag{23.215}$$

Neglecting the quadratic terms of individual spins,

$$\begin{aligned}\dot{\hat{S}}_x &= -\kappa_c(\hat{S}_x - 2\hat{S}_x\hat{S}_z + 2\bar{\eta}_i\hat{S}_z) - \tfrac{\Gamma_1}{2}\hat{S}_x \\ \dot{\hat{S}}_y &= -\kappa_c(\hat{S}_y - 2\hat{S}_y\hat{S}_z) - \tfrac{\Gamma_1}{2}\hat{S}_y \\ \dot{\hat{S}}_z &= -2\kappa_c(\hat{S}_z + \hat{S}_x^2 + \hat{S}_y^2 - \bar{\eta}_i\hat{S}_x) - \Gamma_1(\tfrac{N}{2} + \hat{S}_z) \ .\end{aligned} \tag{23.216}$$

The mean field solution of these equations yield exactly the same curves as shown in Fig. 23.22.

Example 156 (*Continuous superradiant transition*): We start from (23.216) doing the mean field approximation, $S_\alpha = \langle \hat{S}_\alpha \rangle$, and setting $\Gamma_1 = 0$ and $\kappa_c = 0$ *only in linear terms*,

$$\begin{aligned} \dot{S}_x &= 2\kappa_c S_x S_z - 2\kappa_c \bar{\eta}_i \hat{S}_z \\ \dot{S}_y &= 2\kappa_c S_y S_z \\ \dot{S}_z &= -2\kappa_c (S_x^2 + S_y^2) + 2\kappa_c \bar{\eta}_i \hat{S}_x \ . \end{aligned} \tag{23.217}$$

Under such circumstances and doing the mean field approximation, as shown in Exc. 23.4.4.3, the total spin $\mathbf{S}^2 = \frac{N^2}{4}$ is conserved. Hence, we may set,

$$S_x = \tfrac{N}{2} \sin\vartheta \qquad \text{and} \qquad S_z = \tfrac{N}{2} \cos\vartheta \ , \tag{23.218}$$

and find from either the first or third equation,

$$\sin\vartheta = \frac{2\bar{\eta}_i}{N} \tag{23.219}$$

and consequently,

$$S_z = \frac{N}{2} \sqrt{1 - \left(\frac{2\eta_i}{Ng} \right)^2} \ . \tag{23.220}$$

The differential equations can be analytically solved for the initial condition $\mathbf{S} = \left(0, 0, -\frac{N}{2}\right)$. We find,

$$\begin{aligned} \dot{S}_x &= 2\kappa_c S_x S_z - 2\kappa_c \bar{\eta}_i S_z \\ \dot{S}_z &= -2\kappa_c S_x^2 + 2\kappa_c \bar{\eta}_i S_x \ . \end{aligned} \tag{23.221}$$

Substituting (23.218), the initial condition becomes $\vartheta = \pi$ and the differential equations simplify to,

$$\dot{\vartheta} = \kappa_c (N \sin\vartheta - 2\bar{\eta}_i) \ . \tag{23.222}$$

Let us have a look at the red curves in Figs. 23.22, which are obtained for low driving ($\Omega_\eta < \Omega_c$), and at the dash-dotted lines in Fig. 23.20. We see that higher spontaneous emission rate *increases* $\langle \hat{S}_z \rangle$. This is because (slow) individual decay spoils (fast) superradiant decay. This is illustrated in Fig. 23.21.

23.5.2 Driven-dissipative spin squeezing beyond mean field

In Sec. 23.4.2 we have seen that the XX-Heisenberg model predicts spin squeezing when the cavity is *detuned from the resonance*, $U_c \neq 0$, which is immediately clear by the presence of a non-linear term (such as S_z^2) in the Hamiltonian (23.162), $\hat{H} \sim U_c \hat{S}_+ \hat{S}_-$. As in the XX-Heisenberg model no equilibrium is reached, specific Gaussian spin states (coherent or squeezed) must be generated by pulsed application of a (linear or non-linear) Hamiltonian interaction, which rotates or squeezes an initial ground state into any point of the superradiant Bloch sphere, where it stays forever as long as no dissipation nor driving occurs.

On resonance, $U_c = 0$, and the above non-linear term vanishes. However, the non-linearity survives in the dissipative part of the effective Hamiltonian (23.212),

$\hat{H}_{\rm eff} \sim -\imath\kappa_{\rm c}\hat{S}_+\hat{S}_-$. In the following we will show that, *induced by dissipation*, spin squeezing may also occur on resonance and that, *pumped on the mean field*, squeezed states even represent the steady state of the system in certain parameter regimes.

A necessary condition for spin squeezing is however, as we have seen in the previous section, that (i) the drive is weak enough not to overrule the self-determined dynamics resulting from an *equilibrium between drive and superradiance* and (ii) that this equilibrium is *not spoiled by spontaneous emission*. In the following we will concentrate on studying this equilibrium neglecting single atom decay.

In order to obtain bistability indicating a first order phase transition, we previously had to accept the mean field approximation and the steady-state assumption. In the following we will see that these assumptions are wrong and that, at least on resonance, there is no phase transition. Indeed, solving the stationary master equation neglecting for a while spontaneous emission, but seeking an exact solution, we find that the bistability totally disappears. On the other hand, we see spin squeezing, which was beyond the mean field model. We conclude that *collective effects spoil bistability*.

Now, reincluding single-atom spontaneous emission, we find that this spoils collective effects and thus (partially) reintroduces bistability. This is somewhat surprising, as we didn't need spontaneous emission to observe bistability in the mean field approximation.

23.5.2.1 Steady-state solution of the master equation *without* adiabatic elimination of the cavity field

Setting $\Delta_{\rm c} = \Delta_{\rm a} = \Gamma_1 = 0$, the full master equation (23.116) for the atom-cavity system becomes,

$$\begin{aligned}\dot{\hat{\rho}} &= \imath[\hat{\rho}, \hat{H}] + \mathfrak{L}_{\kappa,\hat{a}}\hat{\rho} \\ &= \imath g[\hat{\rho}, \hat{S}_+\hat{a} + \hat{a}^\dagger\hat{S}_-] + \eta[\hat{\rho}, \hat{a} - \hat{a}^\dagger] + \kappa(2\hat{a}\hat{\rho}\hat{a}^\dagger - \hat{a}^\dagger\hat{a}\hat{\rho} - \hat{\rho}\hat{a}^\dagger\hat{a}) \ .\end{aligned} \tag{23.223}$$

We now express the spin operators in a local reference frame anchored to the mean field spin vector on the meridian at $\varphi = 0$, as shown in Eq. (23.102),

$$\hat{S}_- = \hat{S}_x - \imath\hat{S}_y = \hat{S}_\vartheta\cos\vartheta + \hat{S}_\rho\sin\vartheta - \imath\hat{S}_y \simeq \sqrt{S}(\hat{x}\cos\vartheta + \imath\hat{p}) + S\sin\vartheta \ . \tag{23.224}$$

In the last step, we approximated the local spin operators by Holstein-Primakoff bosons, which holds for large enough atom numbers $N \to \infty$. With this we obtain for the first term,

$$\begin{aligned}&\imath g[\hat{\rho}, \hat{S}_+\hat{a} + \hat{a}^\dagger\hat{S}_-] \\ &\simeq \imath g\sqrt{S}\left([\hat{\rho}, (\hat{x}\cos\vartheta - \imath\hat{p} + \sqrt{S}\sin\vartheta)\hat{a}] + [\hat{\rho}, \hat{a}^\dagger(\hat{x}\cos\vartheta + \imath\hat{p} + \sqrt{S}\sin\vartheta)]\right) \\ &\simeq \imath g\sqrt{S}\left([\hat{\rho}, (\hat{x}\cos\vartheta - \imath\hat{p})\hat{a}] + [\hat{\rho}, \hat{a}^\dagger(\hat{x}\cos\vartheta + \imath\hat{p})]\right) \ .\end{aligned} \tag{23.225}$$

In steady state $\dot{\hat{\rho}} = 0$, *below the critical pump rate*, the system evolves towards a pure

state that we will call $\hat{\rho} = |S,\alpha\rangle\langle S,\alpha|$,

$$\begin{aligned} 0 = {} & \imath g\sqrt{S}|S,\alpha\rangle\langle S,\alpha|(\hat{x}\cos\vartheta - \imath\hat{p})\hat{a} - \imath g\sqrt{S}(\hat{x}\cos\vartheta - \imath\hat{p})\hat{a}|S,\alpha\rangle\langle S,\alpha| \\ & + |S,\alpha\rangle\langle S,\alpha|\hat{a}^\dagger(\hat{x}\cos\vartheta + \imath\hat{p}) - |S,\alpha\rangle\langle S,\alpha|\hat{a}^\dagger(\hat{x}\cos\vartheta + \imath\hat{p}) \\ & + 2\kappa\hat{a}|S,\alpha\rangle\langle S,\alpha|\hat{a}^\dagger - \kappa\hat{a}^\dagger\hat{a}|S,\alpha\rangle\langle S,\alpha| - \kappa|S,\alpha\rangle\langle S,\alpha|\hat{a}^\dagger\hat{a} \ . \end{aligned} \tag{23.226}$$

provided that

$$\boxed{\hat{a}|S,\alpha\rangle = (\hat{x}\cos\vartheta + \imath\hat{p})|S,\alpha\rangle = 0} \ . \tag{23.227}$$

This means, that the light field is then a vacuum state. With this, we obtain from Eq. (23.224),

$$\boxed{\hat{S}_-|S,\alpha\rangle = S\sin\vartheta|S,\alpha\rangle} \ , \tag{23.228}$$

which means that the states $|S,\alpha\rangle$ are *eigenstates of the spin-down operator* $\hat{S}_-$.

Furthermore, from the calculation

$$\begin{aligned} 0 &= \langle S,\alpha|(\hat{x}\cos\vartheta - \imath\hat{p})(\hat{x}\cos\vartheta + \imath\hat{p})|S,\alpha\rangle \\ &= \langle S,\alpha|\hat{x}^2\cos^2\vartheta + \hat{p}^2 + \imath[\hat{x},\hat{p}]\cos\vartheta|S,\alpha\rangle = \langle S,\alpha|2\hat{p}^2 - \cos\vartheta|S,\alpha\rangle \ , \end{aligned} \tag{23.229}$$

we derive,

$$\langle S,\alpha|\hat{S}_y^2|S,\alpha\rangle \simeq S\hat{p}^2 = \tfrac{S}{2}\cos\vartheta \ , \tag{23.230}$$

which means that the collective spin state is squeezed as compared to the coherent spin state (CSS) for which we derived in Excs. 23.1.9.5 and 23.1.9.20,

$$\langle\vartheta,0|^N\hat{S}_y^2|\vartheta,0\rangle^N = \tfrac{S}{2} \ . \tag{23.231}$$

23.5.2.2 Steady-state solution of the master equation *after* adiabatic elimination of the cavity field

Let us again repeat the calculation of the previous section using the adiabatically simplified master equation based on the Hamiltonian (23.164), neglecting single atom spontaneous emission, $\mathfrak{L}_{\Gamma_1/2,\hat{s}_j^-} \to 0$, and only retaining collective decay, $\mathfrak{L}_{\kappa_c,\hat{S}_-}$. Defining,

$$\tilde{S}_\pm \equiv \hat{S}_\pm \mp \frac{\imath\Omega}{4\kappa_c}\mathbb{I} = \hat{S}_\pm \mp \frac{\imath\eta}{2g}\mathbb{I} \tag{23.232}$$

and using the Hamiltonian (23.162) the master equation can be rewritten as,

$$\begin{aligned} \dot{\hat{\rho}} &= \imath[\hat{\rho},\hat{H}_{\rm ad}] + \mathfrak{L}_{\kappa_c,\hat{S}_-}\hat{\rho} \qquad \text{where} \qquad \hat{H}_{\rm ad} = \tfrac{\eta\kappa_c}{g}\hat{S}_x \\ &= \imath\tfrac{\Omega}{2}[\hat{\rho},\hat{S}_+ + \hat{S}_-] + \kappa_c(2\hat{S}_-\hat{\rho}\hat{S}_+ - \hat{S}_+\hat{S}_-\hat{\rho} - \hat{\rho}\hat{S}_+\hat{S}_-) \\ &= \kappa_c(2\tilde{S}_-\hat{\rho}\tilde{S}_+ - \tilde{S}_+\tilde{S}_-\hat{\rho} - \hat{\rho}\tilde{S}_+\tilde{S}_-) \ . \end{aligned} \tag{23.233}$$

The steady state solution is simply,

$$\boxed{\hat{\rho}_{\rm ds} = C^{-1}\tilde{S}_-^{-1}\tilde{S}_+^{-1}} \ , \tag{23.234}$$

where C is a constant chosen to satisfy the normalization condition $\mathrm{Tr}\,\hat{\rho}_{\rm ds} = 1$. From now on the subscript 'ds' will denote the steady state of the driven dissipative spin system. Scaling the collective spin as,

$$\hat{S}_\pm \equiv \frac{\eta}{2g}\bar{S}_\pm \ , \tag{23.235}$$

the steady state solution can also be written,

$$\hat{\rho}_{\rm ds} = C^{-1}\bar{S}_-^{-1}\bar{S}_+^{-1} = \frac{(\bar{S}_- + \imath\mathbb{I})^{-1}(\bar{S}_+ - \imath\mathbb{I})^{-1}}{\mathrm{Tr}\,(\bar{S}_- + \imath\mathbb{I})^{-1}(\bar{S}_+ - \imath\mathbb{I})^{-1}} \ . \tag{23.236}$$

We see that all results obtained within this model only depend on two experimental parameters: the ratio $\eta/2g$ determining the scaling of $\hat{S}_\pm$ and the total spin S determining the dimension of the matrices $\hat{S}_\pm$, which can be expanded on the Dicke basis as,

$$\hat{S}_- = \sum_{M=-S}^{S} \sqrt{S(S+1) - M(M-1)}|S,M\rangle\langle S,M+1| \ . \tag{23.237}$$

Note that the steady state does not depend on the cavity decay rate κ, which only rules how long it takes to reach the steady state.

Example 157 (*Analytical steady state solution*): The steady state solution (23.232) can be solved numerically with current software. On the other hand, it is enlightening to derive analytical solutions. To do so, we expand [676, 139]

$$\tilde{S}_\pm^{-1} = \sum_{n=0}^{N}\left(\mp\frac{\imath\Omega}{4\kappa_{\rm c}}\right)^{N-n}\hat{S}_\pm^n \ . \tag{23.238}$$

The normalization condition $\mathrm{Tr}\,\hat{\rho} = 1$ requests,

$$C = \sum_{n=0}^{N}\sum_{m=0}^{N}\frac{(N-n+m)!n!}{(n-m)!(N-n)!}\left(\frac{\Omega}{4\kappa_{\rm c}}\right)^{2(N-m)} \ , \tag{23.239}$$

so that we can write the steady state solution as,

$$\hat{\rho}_{\rm ds} = \tfrac{1}{C}\sum_{n,m=0}^{N}\imath^{n-m}\left(\frac{\Omega}{4\kappa_{\rm c}}\right)^{2N-n-m}\hat{S}_-^n\hat{S}_+^m \ . \tag{23.240}$$

With this the steady state collective spin can be derived from,

$$\begin{aligned}\langle\hat{\mathbf{S}}(\infty)\rangle &= \mathrm{Tr}\,\hat{\rho}_{\rm ds}\hat{S}_z = \sum_{M=-S}^{S}\langle S,M|\hat{\rho}_{\rm ds}\hat{\mathbf{S}}|S,M\rangle \qquad (23.241)\\ &= \tfrac{1}{C}\sum_{M=-S}^{S}\sum_{n,m=0}^{N}(-\imath)^{n-m}\left(\frac{\Omega}{4\kappa_{\rm c}}\right)^{2N-n-m}\langle S,M|\hat{S}_-^n\hat{S}_+^m\hat{\mathbf{S}}|S,M\rangle \ .\end{aligned}$$

In particular we find,

$$\begin{aligned}\langle\hat{S}_z^n(\infty)\rangle &= \mathrm{Tr}\,\hat{S}_z^n(\infty)\hat{\rho}_{\rm ds} \qquad (23.242)\\ &= \frac{1}{C}\sum_{p=0}^{2S}\sum_{k=0}^{p}(S-m)^n\frac{(2S-p+k)!p!}{(2S-p)!(p-k)!}\left(\frac{\Omega}{4\kappa_{\rm c}}\right)^{2(2S-k)} \ .\end{aligned}$$

Substituting $\hat{S}_\pm \to \langle \hat{S}_\pm \rangle = S e^{\imath\varphi} \cos\vartheta$ we find,

$$\hat{\rho}_{\rm ds} \to \frac{1}{\left| S e^{\imath\varphi} \sin\vartheta + \frac{\imath\Omega}{4\kappa_c} \right|^2} \,. \tag{23.243}$$

A direct comparison between analytical and numerical solutions in Fig. 23.25 yields identical results.

Comparison to coherent spin states.– In Sec. 15.2.3 we showed that a laser-pumped cavity evolves toward a coherent state. Let us now study what happens when we introduce some non-linearity into the cavity, e.g. saturable atoms. We note that earlier studies [121] have shown that Kerr type non-linearities can induce non-classical correlations in cavities.

Figs. 23.23(a-d) show the absolute value of the density matrix $\hat{\rho}_{\rm ds}$ at different pump rates. Below threshold it is close to that of a coherent state. Above threshold it converges toward that of an incoherent mixture containing only diagonal elements. Figs. 23.23(e-h) show the density matrix $\hat{\rho}_{\rm cs}$ of a coherent spin state rotated from the ground Dicke state $|S,-S\rangle$ to the same Euler angles as the steady state density matrix,

$$\hat{\rho}_{\rm coh} = \mathcal{U}_{\rm rt}^\dagger \, |S,-S\rangle\langle S,-S| \, \mathcal{U}_{\rm rt} \qquad \text{with} \qquad \mathcal{U}_{\rm rt} = e^{-\frac{1}{2}\vartheta(\hat{S}_+ e^{\imath\varphi} - \hat{S}_- e^{-\imath\varphi})} \,. \tag{23.244}$$

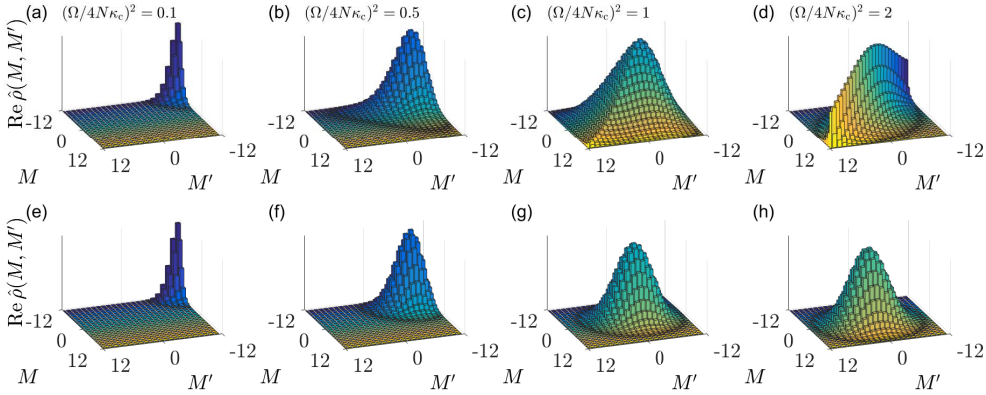

Figure 23.23: (code) (a-d) Absolute value of the steady state density matrix $\hat{\rho}_{\rm ds}$ at different pump rates. (e-h) Density matrix $\hat{\rho}_{\rm cs}$ of a corresponding coherent spin state.

Does $\mathrm{Tr}\,\rho_{\rm ds}^2 < 1$ above threshold imply a loss of coherence allowing us to go into the mean field approximation?

Comparison to coherent spin states.– The time evolution can be followed by numerical simulations,

$$\hat{\rho}(t+dt) = \hat{\rho}(t) + \imath[\hat{\rho}, \hat{H}] + \mathfrak{L}_{\kappa,\hat{a}}\hat{\rho} \,. \tag{23.245}$$

Fig. 23.24 shows such a simulation.

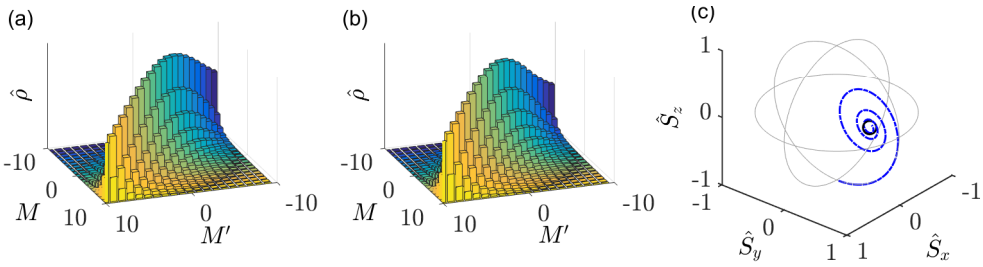

Figure 23.24: (code) (a) Steady state density matrix. (b) Density matrix after a long time evolution. (c) Expectation values of the spin components.

23.5.2.3 Expectation values and uncertainties of the spin components

The steady state density matrix can be used to numerically evaluate steady state values of the spin operator,

$$\langle \hat{\mathbf{S}}(\infty)\rangle_{\rm ds} = \mathrm{Tr}\,\hat{\rho}_{\rm ds}\hat{\mathbf{S}} = \sum_{M=-S}^{S} \langle S,M|\hat{\rho}_{\rm ds}\hat{\mathbf{S}}|S,M\rangle \ , \tag{23.246}$$

as well as of its uncertainties,

$$\langle \Delta\hat{S}^2_{x,y,z}\rangle_{\rm ds} = \mathrm{Tr}\,\hat{\rho}_{\rm ds}\hat{S}^2_{x,y,z} - (\mathrm{Tr}\,\hat{\rho}_{\rm ds}\hat{S}_{x,y,z})^2 \ . \tag{23.247}$$

The expectation values and uncertainties of the spin components are plotted in Figs. 23.25(b,c). Panel (b) of Fig. 23.25 shows the expectation values of the collective spin for various atom numbers. Below the critical pump rate the inversion depends quadratically on the collective excitation rate. Panel (c) shows the collective spin represented on the generalized Bloch sphere. The color coding is the same as for panel (b), except for the black solid line following the meridian given by $\langle \hat{S}_y\rangle = 0$, which is obtained by artificially converting the collective state into a coherent spin state, $\hat{\rho}_{\rm ds} \to \hat{\rho}_{\rm cs}$, as explained above. Panel (e) shows the uncertainty of collective spin component $\langle \hat{S}_z\rangle$. Same color coding as for panels (b-d), the solid lines now being calculated with the steady state density matrix and the dash-dotted lines with the coherent spin state density matrix $\rho_{\rm cs}$.

Reduced length of Bloch vector.– In the absence of spontaneous emission the spheres with different S are orthogonal. That is, if we start with a fully stretched state, $S = N/2$, we stick to it forever. In Exc. 23.5.3.1(a) we show that $\frac{d}{dt}\langle \hat{\mathbf{S}}^2\rangle = 0$, and in Fig. 23.25(d) we numerically verify that for arbitrary spin states $\langle \hat{\mathbf{S}}^2\rangle = S(S+1)$ at all pump rates η.

On the other hand, the spin $\langle \hat{\mathbf{S}}\rangle^2$ only sticks to the outer shell when the evolution is coherent, as we will verify in Exc. 23.5.3.1(b). In the presence of collective decay it moves to the interior of the Bloch sphere (analogous to the single atom Bloch vector upon spontaneous emission). In Fig. 23.25(d) we numerically verify that $\langle \hat{\mathbf{S}}\rangle^2 < S^2$ at sufficiently high pump rates η.

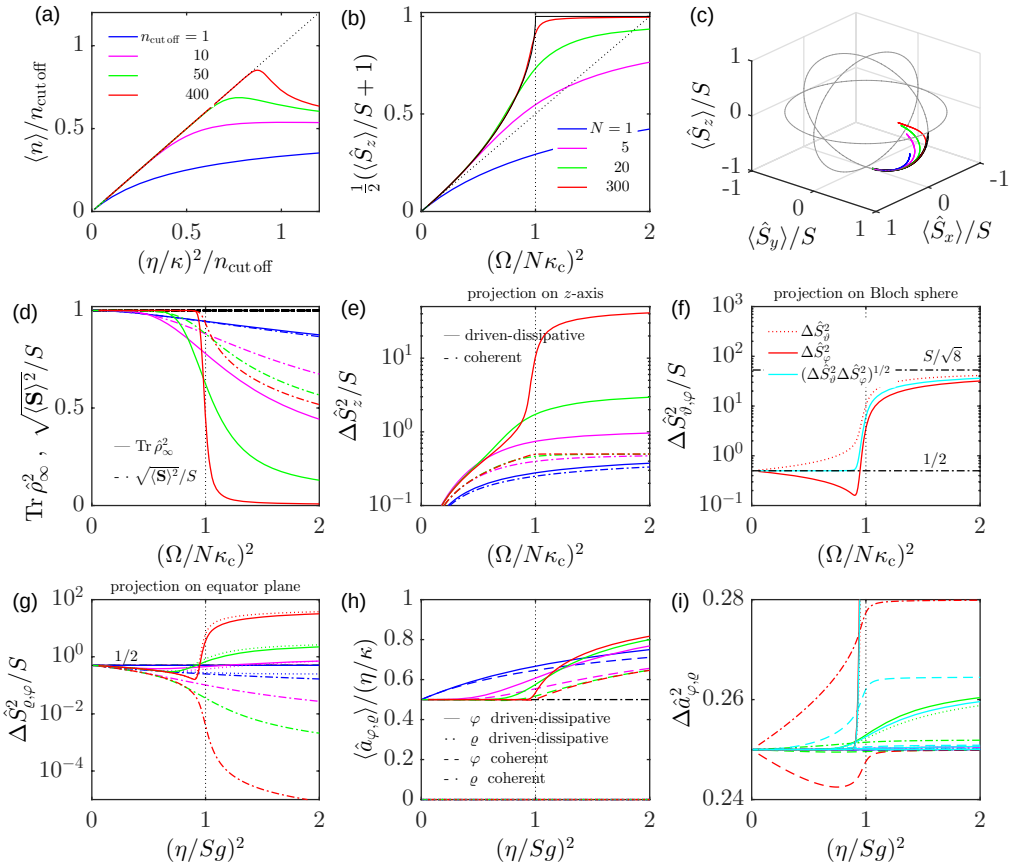

Figure 23.25: (code) See text for explanation.

Decoupling of subradiant states.– Above the critical pump rate, the steady state collective spin turns into a mixture. The atomic spins seem to dephase, so that their sum is not coherent any more and averages to zero. The reason might be that, above the critical pump rate, the steady state will be reached only after a number of collective Rabi oscillations during which the atoms have time to dephase (see Fig.23.22). In other words, the stationarity assumption underlying the solution is becoming increasingly distant.

The collective spin master equation holds for any super- and subradiant Bloch sphere with $0 < S < N/2$. It is, however, important to emphasize that, as long as no spontaneous emission is considered, there is no individualization, meaning that the collective spin description does not break down! I.e. the collectively reduced Bloch vector does not couple to a subradiant Bloch vector of the same length.

Spontaneous emission and saturation.– Spontaneous emission couples all subradiant spaces. In the absence of spontaneous emission individual atoms are *always*

saturated. Saturation of the collective spin may be defined analogously,

$$s \equiv \frac{8g^2}{\Gamma^2} \qquad \text{versus} \qquad s_{\text{coll}} \equiv \frac{\Omega^2}{N^2\kappa_{\text{c}}^2} = \frac{\eta^2}{S^2 g^2} \ . \tag{23.248}$$

Example 158 (*Comparison to bosonic field results*): The master equation (15.67) describing a light mode in a cavity as a harmonic oscillator and the master equation (23.233) describing a collective spin system are formally identical. The master equation for the light mode has been solved in Sec. 15.2.3, one of the findings being that, over time, any non-classical state evolves toward a Glauber state. Furthermore, the Holstein-Primakoff prescription allows to approximate the collective spin system as a harmonic oscillator [512]. The question thus arises, whether non-coherent collective spin states possible at all.
Fig. 23.25 presents a comparison of the steady state behavior of both systems. Panel (a) shows the mean photon number in a decaying cavity as a function of the pump strength for various cut-off photon numbers. Panel (b) shows the collective spin inversion calculated for various atom numbers $N = 2S$ with the steady state density matrix obtained from the exact formulas (23.232) or (23.241) without mean field approximation, but also without spontaneous emission. The black solid line is obtained from $\hat{S}_z = S - \sqrt{N^2 - (\frac{\Omega}{\kappa_{\text{c}}})^2}$.
We see that, indeed, the systems behave quite similar (for comparison see also Fig. 15.6). At weak driving both, the mean photon number and the spin inversion tend toward the pump rate,

$$\langle \hat{n} \rangle \overset{\eta \ll \kappa}{\to} \frac{\eta^2}{\kappa^2} \qquad \text{while} \qquad \langle \hat{S}_z/N \rangle + \tfrac{1}{2} \overset{\Omega \ll \kappa_{\text{c}}}{\to} \frac{\Omega^2}{N^2\kappa_{\text{c}}^2} \ . \tag{23.249}$$

At strong driving both, the mean photon number and the spin inversion saturate; the intracavity photon number to the cut-off and the spin system to $\langle \hat{S}_z \rangle = 0$. At intermediate driving both systems seem to feature a phase transition, which however, for the photon system is not real because the cut-off photon is artificial, while the total spin is limited by the available number of atoms.
Comparing the real photon number dependence [dotted black line in panel (a)] with the spin system, we notice very different behaviors: The spin system reveals much richer features, than the bosonic mode, which implies that the Holstein-Primakoff approximation fails at intermediate or strong driving. Apparently, the different commutation relations holding for photonic operators and for collective spin operators induce different solutions for identical master equations.

23.5.2.4 Expectation values and uncertainties in the local coordinate frame

In the example 138 we argued that the uncertainties are better characterized in the local coordinate frame. To do so, we calculate the local spin operators from their definition (23.48) of (23.53), and subsequently the uncertainties via,

$$\Delta S_\alpha^2 = \text{Tr}\, \hat{\rho} \hat{S}_\alpha^2 - (\text{Tr}\, \hat{\rho} \hat{S}_\alpha)^2 \qquad , \qquad \alpha = r, \vartheta, \varphi \ . \tag{23.250}$$

Panel (f) of Fig. 23.25 shows the uncertainties of the collective spin components projected onto the superradiant Bloch sphere. In all plots we compare driven-dissipative steady spin states (DSS) with coherent spin states (CSS).

Fig. 23.25 reveals a number of other interesting results, which we will discuss in the following.

Reduction of coherence by collective decay.– Approaching saturation the DSS collective spin ceases to be superradiant, that is, the length of the collective spin vector $S_r^2 = \langle\hat{S}_x\rangle_{\rm ds}^2 + \langle\hat{S}_y\rangle_{\rm ds}^2 + \langle\hat{S}_z\rangle_{\rm ds}^2 < S^2$ shrinks, which is obviously not the case for the CSS. For any state $\langle\hat{\mathbf{S}}^2\rangle = \langle\hat{S}_x^2\rangle + \langle\hat{S}_y^2\rangle + \langle\hat{S}_z^2\rangle = S(S+1)$ must obviously always be satisfied.

Loss of purity.– Panel (d) of Fig. 23.25 shows the purity of a DSS as a function of the driving strength with the same color coding as for panel (c). Approaching collective saturation the purity of the collective spin state gets spoiled. Above threshold it tends to 0. This indicates that, at low saturation the collective state is nearly coherent, and at higher saturation turns more and more into a mixture. In contrast the purity of CSSs is always 1.

Spin squeezing below threshold.– Below collective saturation the projection of the uncertainties of the DSS onto the superradiant Bloch sphere exhibits squeezing. The uncertainty $\Delta_{\rm ds}\hat{S}_\varphi^2$ is reduced, while $\Delta_{\rm ds}\hat{S}_\vartheta^2$ is increased. The uncertainty product respects the Heisenberg limit,

$$\sqrt{\Delta_{\rm ds}\hat{S}_\varphi^2\Delta_{\rm ds}\hat{S}_\vartheta^2} \simeq \tfrac{S}{2} \ . \tag{23.251}$$

In comparison, in uncertainty projection of a CSS shows no squeezing (compare to Exc. 23.1.9.5) but is bounded by the standard quantum limit,

$$\Delta_{\rm cs}\hat{S}_{\vartheta,\varphi}^2 = \tfrac{S}{2} \ . \tag{23.252}$$

The Heisenberg limit is expected at,

$$\Delta_{\rm cs}\hat{S}_{\vartheta,\varphi}^2 = \tfrac{1}{4S} \ . \tag{23.253}$$

Decorrelation of Dicke states above threshold.– Above saturation the uncertainties of both quadratures explode and converge toward,

$$\Delta_{\rm ds}\hat{S}_{\vartheta,\varphi}^2 \overset{\Omega\gg\kappa_{\rm c}}{\to} \frac{S^2}{\sqrt{8}} \gg 1 \ . \tag{23.254}$$

The explosion of noise above threshold may have to do with decorrelation.

Unlike spontaneous emission collective decay cannot cause 'individualization' of atoms. Rather Fig. 23.23(d) suggests that one gets an incoherent superposition of (highly non-classical) Dicke states. Indeed, if everyone of the N collective Dicke states $|S,N\rangle$ evolves at its own pace, this may lead to decorrelation.

23.5.2.5 Expectation values and uncertainties of the cavity light field

For the adiabatic elimination of the cavity field we set in (23.154) $\dot{\hat{a}} = 0$, yielding,

$$\hat{a} = \hat{c} - \imath\frac{g}{\kappa}\hat{S}_- \qquad \text{with} \qquad \hat{c} = \frac{\eta}{\kappa}\mathbb{I} \ . \tag{23.255}$$

Hence, we may calculate $\hat{a}$ from the known spin operator $\hat{S}_-$. Using the definitions and the results of (a), we get,

$$\begin{aligned}\hat{a}_\varphi &\equiv \tfrac{\imath}{2}(\hat{a}e^{\imath\varphi} - \hat{a}^\dagger e^{-\imath\varphi}) = \tfrac{\imath}{2}(\hat{c}e^{\imath\varphi} - \hat{c}^\dagger e^{-\imath\varphi}) + \tfrac{g}{2\kappa}(\hat{S}_- e^{\imath\varphi} + \hat{S}_+ e^{-\imath\varphi}) = \hat{c}_\varphi + \tfrac{g}{\kappa}\hat{S}_\varrho \\ \hat{a}_\varrho &\equiv \tfrac{1}{2}(\hat{a}e^{\imath\varphi} + \hat{a}^\dagger e^{-\imath\varphi}) = \tfrac{1}{2}(\hat{c}e^{\imath\varphi} + \hat{c}^\dagger e^{-\imath\varphi}) + \tfrac{g}{2\imath\kappa}(\hat{S}_- e^{\imath\varphi} - \hat{S}_+ e^{-\imath\varphi}) = \hat{c}_\varrho + \tfrac{g}{\kappa}\hat{S}_\varphi \ .\end{aligned} \tag{23.256}$$

Inserting the results of (a), we calculate the uncertainties,

$$\begin{aligned}\Delta\hat{a}_\varphi^2 &= \langle\hat{a}_\varphi^2\rangle - \langle\hat{a}_\varphi\rangle^2 = \langle(\hat{c}_\varphi + \tfrac{g}{\kappa}\hat{S}_\varrho)^2\rangle - \langle\hat{c}_\varphi + \tfrac{g}{\kappa}\hat{S}_\varrho\rangle^2 \\ &= \Delta\hat{c}_\varphi^2 + \tfrac{g^2}{\kappa^2}\Delta\hat{S}_\varrho^2 + \tfrac{g}{\kappa}\langle\hat{c}_\varphi\hat{S}_\varrho + \hat{S}_\varrho\hat{c}_\varphi\rangle - \tfrac{2g}{\kappa}\langle\hat{c}_\varphi\rangle\langle\hat{S}_\varrho\rangle \\ \Delta\hat{a}_\varrho^2 &= \langle\hat{a}_\varrho^2\rangle - \langle\hat{a}_\varrho\rangle^2 = \langle(\hat{c}_\varrho + \tfrac{g}{\kappa}\hat{S}_\varphi)^2\rangle - \langle\hat{c}_\varrho + \tfrac{g}{\kappa}\hat{S}_\varphi\rangle^2 \\ &= \Delta\hat{c}_\varrho^2 + \tfrac{g^2}{\kappa^2}\Delta\hat{S}_\varphi^2 + \tfrac{g}{\kappa}\langle\hat{c}_\varrho\hat{S}_\varphi + \hat{S}_\varphi\hat{c}_\varrho\rangle - \tfrac{2g}{\kappa}\langle\hat{c}_\varrho\rangle\langle\hat{S}_\varphi\rangle \ .\end{aligned} \tag{23.257}$$

Assuming the cavity field $|\alpha\rangle$ as coherent and uncorrelated it is easy to see,

$$\begin{aligned}\Delta\hat{c}_\varrho^2 \quad &= \langle\alpha|\hat{c}_\varrho^2|\alpha\rangle - \langle\alpha|\hat{c}_\varrho|\alpha\rangle^2 \quad &&= \tfrac{1}{4} \qquad &&= \Delta\hat{c}_\varphi^2 \\ \Delta(\hat{c}_\varphi\hat{S}_\varrho) \quad &= \langle\hat{c}_\varphi\hat{S}_\varrho\rangle - \langle\hat{c}_\varphi\rangle\langle\hat{S}_\varrho\rangle \quad &&= \tfrac{g}{4\kappa}\langle\hat{S}_z\rangle \quad &&= \Delta(\hat{c}_\varrho\hat{S}_\varphi)\end{aligned} \ . \tag{23.258}$$

We finally get,

$$\begin{aligned}\Delta\hat{a}_\varphi^2 - \tfrac{1}{4} &= \tfrac{g^2}{\kappa^2}(\Delta\hat{S}_\varrho^2 + \tfrac{1}{2}\langle\hat{S}_z\rangle) \\ \Delta\hat{a}_\varrho^2 - \tfrac{1}{4} &= \tfrac{g^2}{\kappa^2}(\Delta\hat{S}_\varphi^2 + \tfrac{1}{2}\langle\hat{S}_z\rangle) \ .\end{aligned} \tag{23.259}$$

In Fig. 23.25(g) we plot the projected uncertainties $\Delta\hat{S}_x^2$ and $\Delta\hat{S}_y^2$, in panel (h) the observables $\hat{a}_\rho$ and $\hat{a}_\varphi$, and in panel (i) their uncertainties. Radial DSS components are denoted by dotted lines, azimuthal components by solid lines, radial CSS components by dash-dotted lines, and azimuthal components by dashed lines. A number of interesting observations are exposed in the following.

Spin projection on equatorial plane.– For CSS, $\Delta_{\rm cs}\hat{S}_\varphi^2 = 1/2 \gg \Delta_{\rm cs}\hat{S}_\varrho^2$ at all pump rates. For DSS, $\Delta_{\rm ds}\hat{S}_\varphi^2 \simeq 1/2 \gg \Delta_{\rm cs}\hat{S}_\varrho^2$, meaning that the projection onto the equator plane is spherical, like for a Glauber state. At low pump rates, $\Delta_{\rm ds}\hat{S}_{\varphi,\varrho} \lesssim 1/2$, while at high pump rates, $\Delta_{\rm ds}\hat{S}_{\varphi,\varrho}^2 \gg 1/2$, that is, above the phase transition the spin uncertainty explodes toward $\sqrt{N}$.

Impact of normal mode splitting and saturation.– The radial quadrature component of the cavity field vanishes for CSS at well as for DSS at all pump rates, $\langle\hat{a}_\varrho\rangle_{\rm css,dss} = 0$. The azimuthal component tends at low pump rates to $\langle\hat{a}_\varphi\rangle_{\rm css,dss} \overset{\eta\to 0}{\longrightarrow} 1/2$, particularly for large atom numbers. At large pump rates $\langle\hat{a}_\varphi\rangle_{\rm css,dss} \overset{\eta\to\infty}{\longrightarrow} 1$, but for DSS the convergence is much faster.

The dependence on atom number reveals the role of normal mode splitting and (collective) saturation. We observe that in the presence of large atom numbers higher pump rates are required to inject light into the cavity. This can be explained by normal

mode splitting scaling with $\sqrt{N}$. The normal mode splitting is only overruled by saturation which becomes more and more collective as the atom number is increased. It is also interesting to note that collective saturation is twice as fast for DSS as for CSS [23].

Spin squeezing of CSS.– The uncertainties of the are very different for CSS and DSS states. Below threshold for DSS states the uncertainties are coherent state-like, $\Delta_{\rm ds}\hat{a}^2_{\varphi,\varrho} = 1/4$, while for CSS we observe squeezing, $\Delta_{\rm cs}\hat{a}^2_{\varphi} > 1/4 > \Delta_{\rm cs}\hat{a}^2_{\varrho}$. Above threshold the squeezing of CSS states is lost and we have even excess noise in the radial component [24]. For DSS states both, the radial and the azimuthal components, exhibit huge noise.

Bistability in the presence of correlations.– In the mean field approximation we find bistability [694]. Correlations beyond the mean field approximation spoil bistability. On the other hand, spontaneous emission spoils correlations, so that we may expect to partially recover bistability.

23.5.2.6 Solution using effective Hamiltonian

For an arbitrary Hamiltonian and Lindbladian we write the master equation,

$$\begin{aligned}\dot{\hat{\rho}} &= \imath[\hat{\rho},\hat{H}_{\rm ad}] + \mathfrak{L}_{\kappa_{\rm c},\hat{S}_-}\hat{\rho} \\ &= \imath[\hat{\rho},\hat{H}_{\rm ad}] + \kappa_{\rm c}(2\hat{S}_-\hat{\rho}\hat{S}_+ - \hat{S}_+\hat{S}_-\hat{\rho} - \hat{\rho}\hat{S}_+\hat{S}_-) \\ &= \imath(\hat{\rho}\hat{H}^\dagger_{\rm eff} - \hat{H}_{\rm eff}\hat{\rho}) + 2\kappa_{\rm c}\hat{S}_-\hat{\rho}\hat{S}_+ \\ &= \imath(|S,\alpha\rangle\langle S,\alpha|\hat{H}^\dagger_{\rm eff} - \hat{H}_{\rm eff}|S,\alpha\rangle\langle S,\alpha|) + 2\kappa_{\rm c}\hat{S}_-|S,\alpha\rangle\langle S,\alpha|\hat{S}_+ \ .\end{aligned} \tag{23.260}$$

where we introduced the effective Hamiltonian $\hat{H}_{\rm eff} \equiv \hat{H}_{\rm ad} - \imath\kappa_{\rm c}\hat{S}_+\hat{S}_-$ and expressed the density operator as a pure state $\hat{\rho} \equiv |S,\alpha\rangle\langle S,\alpha|$. Now, if and only if $\hat{S}_-$ and $\hat{H}_{\rm eff}$ have common eigenstates such that,

$$\hat{S}_-|S,\alpha\rangle = \alpha|S,\alpha\rangle \qquad \text{and} \qquad \hat{H}_{\rm eff}|S,\alpha\rangle = h_{\rm eff}|S,\alpha\rangle \tag{23.261}$$

with $h_{\rm eff} = \langle H_{\rm ad}\rangle - \imath\kappa_{\rm c}|\alpha|^2$, the density operator remains steady in a pure state [889],

$$\dot{\hat{\rho}} = [\imath(h^*_{\rm eff} - h_{\rm eff}) + 2\kappa_{\rm c}|\alpha|^2]\hat{\rho} = 0 \ . \tag{23.262}$$

For the spin operator we then find,

$$\begin{aligned}\langle S,\alpha|\hat{S}_x|S,\alpha\rangle &= \tfrac{1}{2}(\alpha+\alpha^*) \\ \langle S,\alpha|\hat{S}_y|S,\alpha\rangle &= \tfrac{\imath}{2}(\alpha-\alpha^*) \\ \langle S,\alpha|\hat{S}_z|S,\alpha\rangle &= 0 \\ \langle S,\alpha|\hat{S}_+\hat{S}_-|S,\alpha\rangle &= |\alpha|^2 \ .\end{aligned} \tag{23.263}$$

[23] It is essential to be aware that spontaneous emission is disregarded; hence, there is no absorption, no amplification, but reflection. At low pump rates normal mode splitting impedes photons to enter the cavity $\longrightarrow$ reduced transmission ($\alpha_{\rm out} < \frac{\eta}{\kappa}$).

[24] Note that, according to [853], the photon uncertainty should be reduced (see Sec. 24.4.5).

Hence, the uncertainty of the spin-down operator in the state $|S,\alpha\rangle$ is,

$$\langle S,\alpha|\Delta\hat{S}_-^2|S,\alpha\rangle = 0 \ , \tag{23.264}$$

while for a *coherent spin state* (CSS) we calculated in Exc. 23.1.9.5 [25],

$$\langle\vartheta,\varphi|^N\Delta\hat{S}_\pm^2|\vartheta,\varphi\rangle^N = -\tfrac{N}{4}e^{\pm 2\imath\varphi}\sin^2\vartheta \ . \tag{23.265}$$

Collective radiation $\hat{S}_-$ is stimulated by the cavity, unlike spontaneous emission $\hat{s}_j^-$. In the presence of spontaneous emission the theorem (23.261) looses its validity, which means that the state generated will not be the perfect CRSS any more [512].

Let us now consider the Hamiltonian (23.162) which with the abbreviation (23.199) delivers the effective Hamiltonian,

$$\begin{aligned}\hat{H}_{\rm eff} = \hat{H}_{\rm ad} - \imath\kappa_{\rm c}\hat{S}_+\hat{S}_- &= -2\mathfrak{Im}\,(\bar{\eta}U_\kappa)\hat{S}_x - 2\mathfrak{Re}\,(\bar{\eta}U_\kappa)\hat{S}_y - \Delta_{\rm a}\hat{S}_z + U_\kappa\hat{S}_+\hat{S}_- \\ &= \tfrac{\Omega}{2}\hat{S}_+ + \tfrac{\Omega^*}{2}\hat{S}_- - \Delta_{\rm a}\hat{S}_z + U_\kappa\hat{S}_+\hat{S}_- \ ,\end{aligned} \tag{23.266}$$

Its expectation value becomes,

$$\begin{aligned}h_{\rm eff} = \langle S,\alpha|\hat{H}_{\rm eff}|S,\alpha\rangle &= -\mathfrak{Im}\,(\bar{\eta}U_\kappa)(\alpha+\alpha^*) - \mathfrak{Re}\,(\bar{\eta}U_\kappa)\imath(\alpha-\alpha^*) + U_\kappa|\alpha|^2 \\ &= \tfrac{\Omega}{2}\alpha^* + \tfrac{\Omega^*}{2}\alpha + U_\kappa|\alpha|^2 \ .\end{aligned} \tag{23.267}$$

Since $\hat{S}_-$ is a constant of motion of the effective Hamiltonian $\hat{H}_{\rm eff}$,

$$\begin{aligned}0 = [\hat{S}_-,\hat{H}_{\rm eff}] &= \tfrac{\Omega}{2}[\hat{S}_-,\hat{S}_+] - \Delta_{\rm a}[\hat{S}_-,\hat{S}_z] + U_\kappa[\hat{S}_-,\hat{S}_+]\hat{S}_- \\ &= -\Omega\hat{S}_z - \Delta_{\rm a}\hat{S}_- - 2U_\kappa\hat{S}_z\hat{S}_- \ .\end{aligned} \tag{23.268}$$

On resonance, $\Delta_{\rm a}=0$, we find,

$$\alpha = \langle S,\alpha|\hat{S}_-|S,\alpha\rangle = -\frac{\Omega}{2U_\kappa} = \imath\bar{\eta} \ . \tag{23.269}$$

We thus found a new class of spin states apparently sharing features with Glauber states of light, as they can be represented in a two-dimensional plane. We will call them *coherently radiating spin states* (CRSS) [853, 772, 512]. The analogy between spin states and the harmonic oscillator has been worked out in Sec. 23.1.8. In particular, the action of the lowering operator on a number state is given by,

$$\hat{a}|n\rangle = \sqrt{n}|n-1\rangle \qquad \text{versus} \qquad \hat{S}_\pm|S,M\rangle = \sqrt{S(S+1)-M(M\pm1)}|S,M-1\rangle \ . \tag{23.270}$$

The states $|n\rangle$ are highly non-classical, similarly to $|S,M\rangle$. Furthermore,

$$\hat{a}|\alpha\rangle = \alpha|\alpha\rangle \qquad \text{versus} \qquad \hat{S}_\pm|S,\vartheta,\varphi\rangle = Se^{\pm\imath\varphi}\sin\vartheta|S,\vartheta,\varphi\rangle \ . \tag{23.271}$$

These are not really eigenvalue equations, since α, respectively, $e^{\pm\imath\varphi}\sin\vartheta$ are complex numbers.

[25] Note that $\langle S,\alpha|\hat{S}_-|S,\alpha\rangle = \alpha$ does not necessarily imply $\hat{S}_-|S,\alpha\rangle = \alpha|S,\alpha\rangle$, since the error made on writing down this latter equation can be compensated by the projection on $\langle S,\alpha|$.

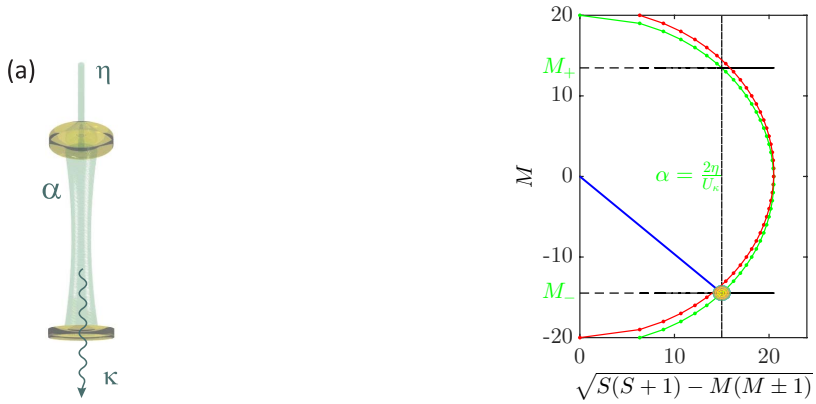

Figure 23.26: (code) (a) Driven-dissipative cavity. (b) Construction of a CRSS state with $N = 40$ atoms.

23.5.2.7 Construction of coherently radiating spin states

The problem with CRSSs is, however, more profound and related to the finiteness of the system. While Glauber states can be expanded into Poissonian distributions of Fock states to perfect approximation, there is no exact analytical expression for CRSSs.

> **Example 159 (*Eigenvalue of spin-down operator*):** To see this, let us first have a quick look at Glauber states, $|\alpha\rangle = e^{-|\alpha|^2/2}\sum_{k=0}^{\infty}\frac{\alpha^n}{\sqrt{n!}}|n\rangle$, for which the expression $\hat{a}|\alpha\rangle = \alpha|\alpha\rangle$ is a very good approximation to an eigenvalue equation, but this is only because ∞ is big,
>
> $$\hat{a}|\alpha\rangle \simeq \alpha|\alpha\rangle \quad \Longrightarrow \quad \sum_{n=0}^{\infty-1}\frac{\alpha^{n+1}}{\sqrt{n!}}|n\rangle \simeq \sum_{n=0}^{\infty}\frac{\alpha^{n+1}}{\sqrt{n!}}|n\rangle \ . \tag{23.272}$$
>
> We may expect a similar behavior for spin states, provided the atom number N is large enough.

Let us suppose there is a state $|S,\alpha\rangle$ satisfying the eigenvalue equations (23.261) and expand it onto the Dicke state basis

$$|S,\alpha\rangle = \sum_{M=-S}^{S} a_M|S,M\rangle \ , \tag{23.273}$$

yielding,

$$\hat{S}_-|S,\alpha\rangle \simeq \alpha|S,\alpha\rangle \tag{23.274}$$
$$\Longrightarrow \sum_{M=-S}^{S-1} a_{M+1}\sqrt{S(S+1)-M(M+1)}|S,M\rangle \simeq \sum_{M=-S}^{S}\alpha a_M|S,M\rangle \ .$$

This formula is analogous to (23.272) with the difference that $S < \infty$. Consequently, we may expect the eigenvalue equation to be a good approximation only if the atom number is very large.

From (23.274) we obtain the recursion formula [772],

$$\begin{aligned} \alpha a_M &= 0 && \text{for} \quad M = S \\ \alpha a_M &= a_{M+1}\sqrt{S(S+1) - M(M+1)} && \text{for} \quad M = -S, ..., S-1 \end{aligned} \tag{23.275}$$

Hence, if $\alpha > 0$, then $a_S = 0$ and all other coefficients are $a_M = 0$ as well. In the non-trivial case $a_M \neq 0$ the operators $\hat{S}_\pm$ have only one eigenstate with eigenvalue $\alpha = 0$. The state obtained is a coherent spin ground state.

Now, let us *postulate* the existence of an *approximate* eigenstate $|S, \alpha\rangle$ of the operator $\hat{S}_-$ with eigenvalue $\alpha > 0$. One approach is the following. Guided by the observation that the highest and lowest states on the Dicke ladder are eigenstates, $\hat{S}_\pm|S, \pm S\rangle = 0$, we write approximately,

$$\begin{aligned} \hat{S}_-|S, M_+ + 1\rangle &= \sqrt{S(S+1) - M_+(M_+ + 1)}|S, M_+\rangle \\ &\simeq \sqrt{S(S+1) - M_+(M_+ + 1)}|S, M_+ + 1\rangle = \alpha|S, M_+ + 1\rangle \ , \end{aligned} \tag{23.276}$$

yielding,

$$\begin{aligned} M_\pm &= \pm\sqrt{S(S+1) - \alpha^2 + \tfrac{1}{4}} - \tfrac{1}{2} && \text{for} \quad M = S \\ \alpha a_M &= a_{M+1}\sqrt{S(S+1) - M(M+1)} && \text{for} \quad M = -S, ..., S-1 \end{aligned} \tag{23.277}$$

The other states follow from the same recursion formula as in (23.274)(ii). Thus, the CRSS state obeys,

$$\boxed{|S, \alpha\rangle = \sum_{M=-S}^{M_+} a_M |S, M\rangle} \ . \tag{23.278}$$

An intuitive justification for the truncation of the Dicke state expansion (23.278) might be that, differently from *rotations*, decay processes break the symmetry between $\hat{S}_\pm$, because only energetically lower states can be reached via superradiant emission. In Exc. 23.5.3.2 we will derive from the recursion formula (23.277) an approximate analytical expression for the coefficients a_M [772].

23.5.2.8 Characterization of coherently radiating spin states

The truncated Dicke state expansion (23.278) together with the recursion formulas (23.277) and the normalization condition allows us to discover some properties of CRSSs.

In Fig. 23.27(left) we plot the amplitudes a_M of the Dicke states for CSSs and CRSSs as well as their approximations by Gaussian formulas. Figs. 23.27(center and right) show the quasi-probability distributions P, W, and Q calculated for the same states. Clearly visible in Wigner distribution (middle row) is spin squeezing for the CRSS state $|S, \alpha\rangle$, but not for the CSS state $|\vartheta, \varphi\rangle^N$. For the projection onto the equatorial plane it is just the opposite: The projection of the CSS is squeezed, but not of the CRSS [26].

[26] The projection of the observable $\hat{S}_x = \frac{1}{2}(\hat{S}_- + \hat{S}_+)$ onto a non-compatible basis represented by the operator $\hat{S}_-$ necessarily introduces projection noise, which overrules spin squeezing.

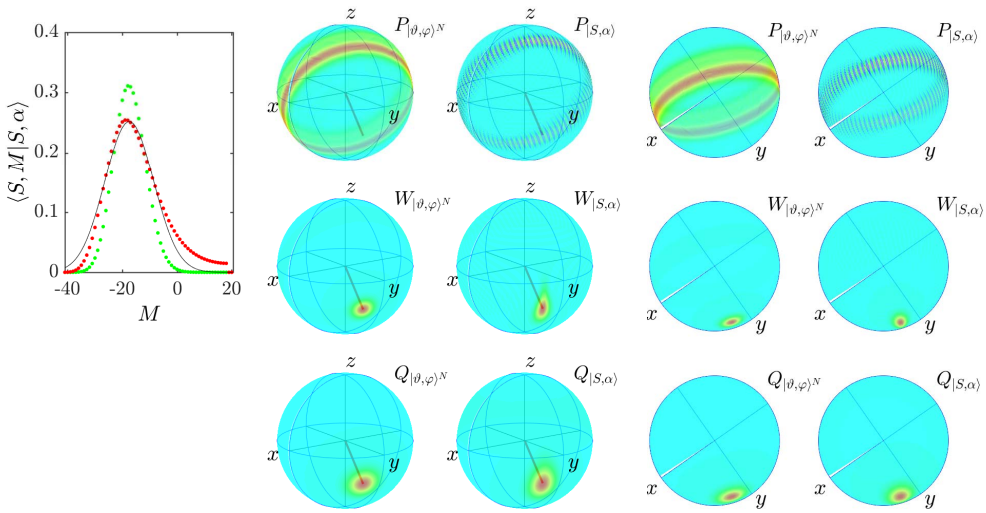

Figure 23.27: (code) (left) Excitation amplitudes for a CSS (green dots), for a CRSS (red dots), and for CRSS in the Gaussian approximation. (center) Quasi-probability distributions for a CSS and for a CRSS on the Bloch sphere. (right) Projections of the distributions onto the equator plane.

To calculate the squeezing parameter we just need to evaluate the definition,

$$\boxed{\xi^2 \equiv \frac{2S}{|\langle\hat{\mathbf{S}}\rangle|^2}\min_\varphi \Delta\hat{S}_\perp^2(\varphi)}\,, \tag{23.279}$$

where

$$\Delta\hat{S}_\perp^2(\varphi) = \langle S,\alpha|\hat{S}_\perp(\varphi)^2|S,\alpha\rangle - \langle S,\alpha|\hat{S}_\perp(\varphi)|S,\alpha\rangle^2 \qquad \hat{S}_\perp(\varphi) = \tfrac{1}{2}(e^{\imath\varphi}\hat{S}_- + e^{-\imath\varphi}\hat{S}_+)$$
$$\langle\hat{\mathbf{S}}\rangle = \sqrt{\langle\hat{S}_x\rangle^2 + \langle\hat{S}_y\rangle^2 + \langle\hat{S}_z\rangle^2}\,.$$

Fig. 23.28 demonstrates how spin-squeezing increases parameter with $r = S\sin\vartheta$ [772].

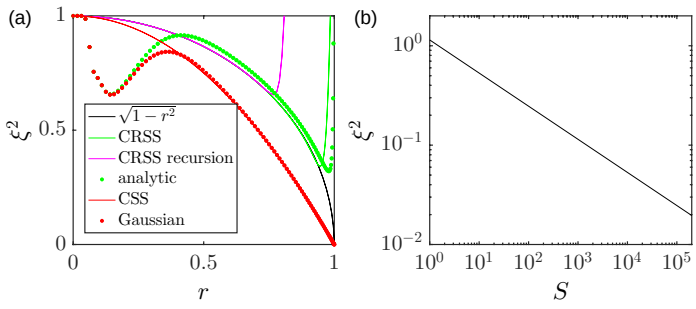

Figure 23.28: (code) Squeezing parameter as a function of (a) r and (b) S.

23.5.2.9 Light as spin squeezing witness

The cloud-cavity interaction is ruled by terms like $\hat{H} = g(\hat{a}^\dagger \hat{S}_- + \hat{S}_+ \hat{a})$. The field emitted $\hat{a}(t) = \hat{a}_0(t) + G\hat{S}_-(t)$ is continuously measured, i.e. we constantly force it into an eigenstate. We may thus assume that the system is pumped into $|S, \alpha\rangle$ with [772],

$$\hat{S}_-(0)|S, \alpha(t)\rangle = \alpha(t)|S, \alpha(t)\rangle \ . \tag{23.280}$$

The evolution $e^{-\imath \hat{H} t}$ is the displacement operator of the field, generating a coherent light state out of an initial vacuum state,

$$\mathcal{U}(t) = e^{-\imath \hat{H} t} = e^{-\imath g(\hat{S}_+ \hat{a} + \hat{a}^\dagger \hat{S}_-)t} = e^{-\imath g(\alpha^* \hat{a} + \alpha \hat{a}^\dagger)t} \ , \tag{23.281}$$

so that

$$\hat{a}(t) = \mathcal{U}^\dagger(t)\hat{a}(0)\mathcal{U}(t) = \hat{a}(0) - \imath g \alpha t \ , \tag{23.282}$$

This coherent light state is an eigenstate of the operator $\hat{S}_-$ represented in the Glauber xy-plane,

$$\hat{a}_-|S, \alpha\rangle = \alpha|S, \alpha\rangle \qquad \text{with} \qquad \alpha = Sre^{-\imath\varphi} \qquad \text{where} \qquad r < 1 \ , \tag{23.283}$$

which by construction is a coherent state of light if $\hat{a}(0)|\psi(0)\rangle = 0$ is initially the vacuum state [27]. See also Exc. 23.5.3.3.

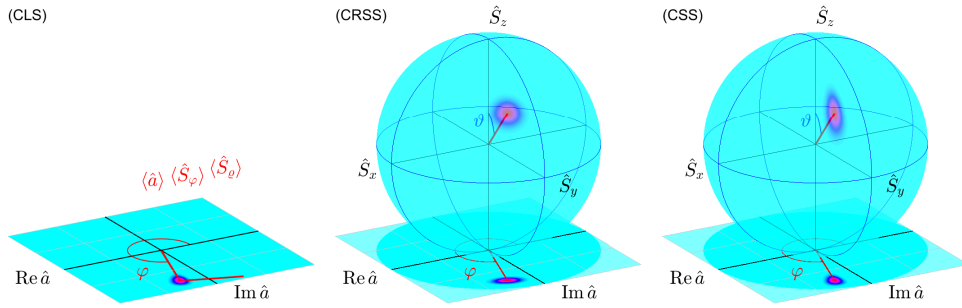

Figure 23.29: Illustration of the quadratures of a coherent state of light (CLS), and of a CRSS and a CSS on the generalized Bloch sphere.

Interesting signal are delivered by the photon emission rate [275],

$$\gamma(t) = \langle \hat{S}_+ \hat{S}_- \rangle = \mathrm{Tr}\,[\hat{S}_+ \hat{S}_- \hat{\rho}(t)] \tag{23.284}$$

and the correlation function,

$$g_N^{(2)}(t, t) = \frac{\langle \hat{S}_+ \hat{S}_+ \hat{S}_- \hat{S}_- \rangle_t}{\langle \hat{S}_+ \hat{S}_- \rangle_t^2} = \frac{\mathrm{Tr}\,[\hat{S}_+ \hat{S}_+ \hat{S}_- \hat{S}_- \hat{\rho}(t)]}{\mathrm{Tr}\,[\hat{S}_+ \hat{S}_- \hat{\rho}(t)]^2} \ . \tag{23.285}$$

[27] Even if one manages to generate intracavity squeezed light, it is necessary to verify that the light transmitted through a cavity mirror is still squeezed and not spoiled by vacuum fluctuations. Then one might try to homodyne it with a local oscillator [534, 535, 567, 706].

Example 160 (*Equal-time correlation for CSS and CRSS*): Let us first calculate the correlation functions for a CRSS (see (23.263)),

$$\langle S,\alpha|\hat{S}_+\hat{S}_-|S,\alpha\rangle \simeq |\alpha|^2 = S^2\sin^2\vartheta \tag{23.286}$$
$$\langle S,\alpha|\hat{S}_+\hat{S}_+\hat{S}_-\hat{S}_-|S,\alpha\rangle \simeq |\alpha|^4 \ .$$

Hence, $g^{(1)}=1=g^{(2)}$.
For the CSS, we found in Exc. 23.1.9.5,

$$\langle\vartheta,\varphi|^N\hat{S}_+\hat{S}_-|\vartheta,\varphi\rangle^N = Np_+^2 + N^2p_+p_- \tag{23.287}$$
$$= N\cos^4\tfrac{\vartheta}{2} + N^2\sin^2\tfrac{\vartheta}{2}\cos^2\tfrac{\vartheta}{2} = \tfrac{N}{4}(\cos\vartheta+1)^2 + \tfrac{N^2}{4}\sin^2\vartheta \ .$$

Also,

$$\langle\vartheta,\varphi|^N\hat{S}_+\hat{S}_+\hat{S}_-\hat{S}_-|\vartheta,\varphi\rangle^N \tag{23.288}$$
$$= N^4p_+^2p_-^2 + 2N^3p_+^2(3p_+-1)p_- + N^2p_+^2(11p_+^2-10p_++1) - 2Np_+^3(3p_+-2) \ .$$

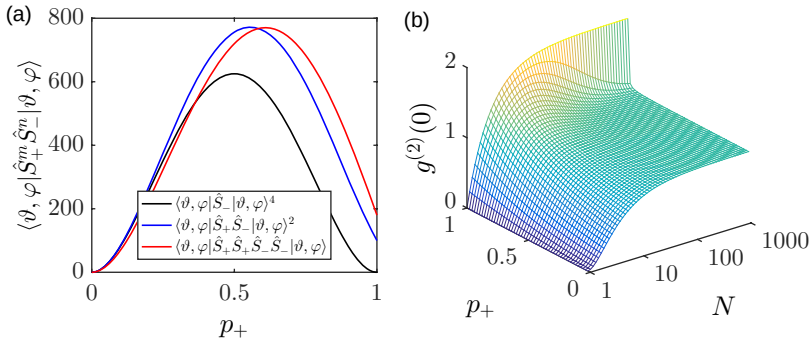

Figure 23.30: (code) (a) Correlation functions as a function of $p_+ = Sr = S\sin\theta$ for $N=10$ atoms. (b) Second order coherence $g^{(2)}(0)$.

The time-dependent correlation functions can be evaluated using the quantum regression theorem exposed in (23.194).

Example 161 (*Equal-time correlation for the cavity field*): From (23.154) at resonance,

$$\dot{\hat{a}} = -\kappa\hat{a} - \imath g\hat{S}_- + \eta \ .$$

In steady state,

$$\hat{S}_- = \imath\tilde{\eta} + \imath\frac{\kappa}{g}\hat{a} \ .$$

Hence, the second order-correlation depends on

$$\langle\hat{S}_+\hat{S}_+\hat{S}_-\hat{S}_-\rangle$$
$$= \tfrac{1}{g^4}\left(\kappa^4\langle\hat{a}^\dagger\hat{a}^\dagger\hat{a}\hat{a}\rangle - 2\imath\eta\kappa^3\langle\hat{a}^\dagger\hat{a}\hat{a} - \hat{a}^\dagger\hat{a}^\dagger\hat{a}\rangle - \eta^2\kappa^2\langle\hat{a}^\dagger\hat{a}^\dagger - 4\hat{a}^\dagger\hat{a} + \hat{a}\hat{a}\rangle + 2\imath\eta^3\kappa\langle\hat{a}^\dagger - \hat{a}\rangle + \eta^4\right)$$
$$= \tfrac{1}{g^4}\left(\eta^2 + 2\eta\kappa\mathfrak{Im}\,\alpha + \kappa^2|\alpha|^2\right)^2 \ .$$

We will see in the following, how the interplay between coherent pumping η and collective decay κ_c leads to spin squeezing [512]. In Exc. 23.4.4.3 we study the mean field approximation of the equations (23.213) and derive analytical formulas for the steady state. The solutions, which will be discussed in the following, are exhibited in Figs. 23.20.

The stable branches are those with positive slope, leaving two accessible branches a lower and an upper one. The lower branch corresponds to weak intracavity power and hence small inversion. Here, the normal mode splitting is so large that it inhibits the penetration of pump light into the cavity. The upper branch is characterized by high intracavity power and hence strong saturation generating an inversion approaching 50%. According to [512] states located in the upper branch of the bistable regime are CRSSs, states located in the lower branch are CSSs. This can be understood in the light of Fig. 23.26: The state close to 50% inversion is exposed to strong superradiant decay, in contrast to the state close to 0% inversion dominated by spontaneous emission.

23.5.3 Exercises

23.5.3.1 Ex: Norm of Bloch vector under coherent and dissipative evolution

Verify that for any Hamiltonian being a function of collective spin components, $\hat{H} = \hat{H}(\hat{S}_\alpha)$,
a. in the absence of spontaneous emission $\frac{d}{dt}\langle \mathbf{S}^2 \rangle = 0$;
b. in the absence of any dissipation $\frac{d}{dt}\langle \mathbf{S} \rangle^2 = 0$.
See also Eq. (??) and Excs. 23.2.4.5 and 23.4.4.3!

23.5.3.2 Ex: Coherently radiating spin states (CRSS)

a. Search for general states satisfying,

$$\hat{S}_-|S,\alpha\rangle = \alpha|S,\alpha\rangle \qquad \text{with} \qquad \alpha \equiv Se^{-\imath\varphi}\sin\vartheta \ .$$

Proceed by inserting the ansatz

$$|S,\alpha\rangle_{\text{ans}} = \sum_{M=-S}^{M_+} a_M|S,M\rangle \ .$$

b. Compare with the CSS obtained by letting $M_+ \to S$.
c. Calculate the uncertainties for a CSS.
d. Calculate the uncertainties for a CRSS.

23.5.3.3 Ex: Light and spin squeezing in the CSS and the CRSS

a. Derive the Heisenberg uncertainty relations for the electric field operators $\hat{c}_\varphi$ and $\hat{c}_\varrho = \hat{c}_{\varphi-\pi/2}$ defined in Eq. (2.201) and for the collective spin operators $\hat{S}_\varphi$ and $\hat{S}_\varrho = \hat{S}_{\varphi-\pi/2}$ defined in Eq. (23.40).
b. Upon adiabatic elimination of the cavity field we end up with the expression,

$\hat{a} = \hat{c} - \imath\frac{g}{\kappa}\hat{S}_-$, where $\hat{c} = \frac{\eta}{\kappa}\mathbb{I}$ is the cavity field generated by direct pumping of the cavity. Based on this connection between field and collective spin operators, derive the condition for $\langle \hat{S}_z \rangle$ to obtain light squeezing.

23.6 Three-level atoms in a cavity

Inclusion of a third atomic level considerably enriches the possibilities of controlling the collective interaction of atoms and cavities, in particular, when the collective synchronization of atomic dipole moments is done on a different transition as the clock/interferometry transition. In this section, we study a collection of three-level atoms $|1\rangle$-$|2\rangle$-$|3\rangle$ in cascade configuration, as illustrated in Fig. 23.31(a). The atoms interact with a linear cavity tuned quasi-resonant to the upper $|2\rangle$-$|3\rangle$ transition. In certain regimes controlled by parameters of the upper transitions, we observe excitation blockade on the lower transition, similar to what is observed in dense clouds of Rydberg atoms. With respect to Rydberg blockade systems this has the advantage of generating uniform coupling between all atoms located in the mode volume of the cavity [887, 319, 591, 774, 407]. In other parameter regimes the dispersive interaction of the cavity field with the $|2\rangle$-$|3\rangle$ transition can induce quantum correlations such as spin-squeezing on the $|1\rangle$-$|2\rangle$ transition.

Based on the open Tavis-Cummings model for N three-level atoms, we set up in Sec. 23.6.1 the full master equation expanding the transition operators on the product state basis $|\psi\rangle = \bigotimes_{j=1}^{N} (a_j|1\rangle_j + b_j|2\rangle_j + c_j|3\rangle_j)$. In particular, we will numerically study a simple toy model with two atoms interacting via a cavity field, which predicts cavity-mediated blockade effects. Then we gradually simplify the model in order to obtain numerically tractable formulas. In Sec. 23.6.2 we adiabatically eliminate the excited state $|3\rangle$ and rewrite the equations of motion in a two-level spin notation. At the hand of the toy model, we will compare numerical simulations within the simplified and the full model. In Sec. 23.6.3, supposing uniform coupling of the atoms to the light, we once more rewrite the equations of motion in a collective spin formalism suited for representing the coupled atom-cavity system expanding the spin operators on the Dicke state basis, $|\psi\rangle = |S, M\rangle$, which suits well for larger ensembles of up to 50 atoms. In particular, within the Dicke model we will discuss the occurrence of spin-squeezing. In Sec. 23.6.4 we adiabatically eliminate the cavity field and linearize the Heisenberg equations for small collective coupling. Finally, in Sec. 23.6.5 we neglect higher-order correlations for the case of many atoms to study one-axis twisting and the emergence of phases and instabilities using the mean-field approximation and calculating second-order moments [565, 207].

23.6.1 Open Tavis-Cummings model for the three-level system

The basic idea consists in a sequence of pulse radiation fields to the three-level system exhibited in Fig. 23.31(a) [28]. The lower transition $|1\rangle$-$|2\rangle$, assumed to be forbidden, is driven by $\pi/2$ classical light pulses. The upper transition $|2\rangle$-$|3\rangle$ is driven far from resonance by the light field stored in a laser-pumped optical cavity operated in the

[28] Alternatively, we may consider a V-shaped level configuration with two narrow transitions and $|2\rangle \equiv {}^1S_0$, $|1\rangle \equiv (5s5p)^3P_0$, and $|3\rangle \equiv (5s5p)^3P_1$. Since $\Gamma_{12} \simeq 0$ the energetic order of levels $|1\rangle$ and $|2\rangle$ doesn't matter.

bad-cavity limit. As illustrated in Fig. 23.31(b), the pump laser frequency is tuned to the edge of the cavity's transmission profile. Now, only atoms which are excited from the ground state the state $|2\rangle$ will interact with the cavity, thus modifying its resonance frequency, and changing the effective pump rate. This in turn modifies the light shift of level $|2\rangle$ induced by the intra-cavity light and the effective Rabi frequency at which other atoms can be excited from the ground state. See Exc. 23.6.6.1.

In the following, we will show how this cavity-mediated feedback may lead to non-linear dynamics reminiscent to Rydberg blockade and to spin-squeezing.

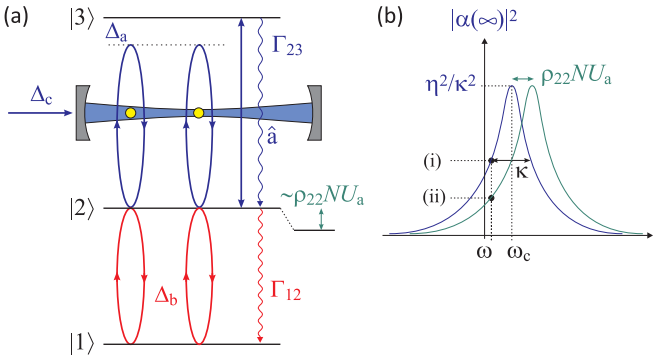

Figure 23.31: (a) Level scheme and driven transitions. For the sake of concreteness, one might consider the strontium level scheme $|1\rangle \equiv {}^1S_0$, $|2\rangle \equiv (5s5p)^3P_1$, and $|3\rangle \equiv (5s6s)^3S_1$ with the respective transition wavelength $\lambda_{12} = 689\,\text{nm}$ and $\lambda_{23} = 688\,\text{nm}$ and the decay widths $\Gamma_{12}/2\pi = 7.6\,\text{kHz}$ and $\Gamma_{23}/2\pi = 4\,\text{MHz}$. (b) Stationary cavity field intensity as a function of the population $\sum_j \text{Tr}\,\hat{\rho}\sigma_j^{22}$ of level $|2\rangle$.

The light field driving the lower transition is treated classically, i.e. $[\hat{a}, \hat{\rho}] = 0$, while the cavity mode $\hat{a}$ is treated *either as classical or quantum*. The atoms are denoted by lower indices, their internal excitations by upper indices,

$$\begin{aligned} \hat{\sigma}_1^{mn} &\equiv |m\rangle\langle n| \otimes \mathbb{I}_3 \otimes \mathbb{I}_3 \otimes \dots\,, \\ \hat{\sigma}_2^{mn} &\equiv \mathbb{I}_3 \otimes |m\rangle\langle n| \otimes \mathbb{I}_3 \otimes \dots\,, \end{aligned} \tag{23.289}$$

etc.. Assuming a sufficiently dilute sample we may disregard dipole-dipole interactions. The Hamiltonian is then ($\hbar = 1$),

$$\begin{aligned} \hat{H} &= \hat{H}_{\text{cav}} + \textstyle\sum_{j=1}^N \hat{H}_j \qquad \text{with} \\ \hat{H}_{\text{cav}} &= -\imath\eta(\hat{a} - \hat{a}^\dagger) - \Delta_c \hat{a}^\dagger \hat{a} \\ \hat{H}_j &= -\Delta_b \hat{\sigma}_j^{22} + \tfrac{\Omega_b}{2}(\hat{\sigma}_j^{12} + \hat{\sigma}_j^{21}) + g(z_j)(\hat{a}^\dagger \hat{\sigma}_j^{23} + \hat{\sigma}_j^{32}\hat{a}) - \Delta_a \hat{\sigma}_j^{33} \end{aligned} \tag{23.290}$$

where Ω_b is the Rabi frequency on the lower transition $|1\rangle$-$|2\rangle$ and Δ_b the detuning from resonance of the laser driving this transition, Δ_a is the detuning of the laser driving the upper transition $|2\rangle$-$|3\rangle$, Δ_c the detuning of the latter laser from the resonance frequency of the cavity, η the pump rate of the cavity, and $g(\mathbf{r}_j) = g\cos kz_j$ (assuming for one-dimensionality for simplicity) the atom-cavity coupling strength or

single-photon Rabi frequency generated on the upper transition, which depends on the atomic positions.

As indicated in (23.116), the time evolution is governed by a master equation for the density operator $\hat{\rho}$, or by Heisenberg equations for particular degrees of freedom $\hat{A}$, or by combinations of both. Incoherent processes are described by jump operators $\hat{L}$ and their corresponding rates γ. In our simulations we consider spontaneous emission occurring via the processes $\hat{L} = \hat{\sigma}_{12}$ and $\hat{L} = \hat{\sigma}_{23}$ with the respective decay rates $\gamma = \frac{1}{2}\Gamma_{12}$ and $\gamma = \frac{1}{2}\Gamma_{23}$. Assuming $\Gamma_{23} \gg \Gamma_{12} \gg \Gamma_{13} \simeq 0$, we may disregard the decay rate Γ_{13}. Incoherent optical pumping from lower to higher levels, for instance the one described by $\hat{L} = \hat{\sigma}_{31}$ occurring at a rate $\gamma = \xi_{31}$, may also be included. Finally, the cavity field decays as $\hat{L} = \hat{a}$ at a rate $\gamma = \kappa$. On the other hand, we disregard phase fluctuations of the cavity field and of the atomic dipole moments.

The dynamics ruled by the Hamiltonian (23.290) and the decay terms compiled using the expressions (23.116) is conveniently simulated using the QuantumOptics.jl framework for the JULIA language. To do so, we construct the density operator for the atoms only using the tensor products (23.289), which evolves according to a master equation, and derive a separate Heisenberg equation for the light field [466],

$$\boxed{\begin{aligned} \frac{d}{dt}\hat{a} &= \imath[\hat{H},\hat{a}] + \mathfrak{L}_{\kappa}^{\dagger}\hat{a} = (\imath\Delta_{\rm c} - \kappa)\hat{a} + \eta - \imath\sum_{j=1}^{N} g(z_j)\hat{\sigma}_j^{23} \\ \frac{d}{dt}\hat{\rho} &= \imath[\hat{\rho},\hat{H}] + \mathfrak{L}_{\Gamma_{12}/2}\hat{\rho} + \mathfrak{L}_{\Gamma_{23}/2}\hat{\rho} + \mathfrak{L}_{\xi_{12}}\hat{\rho} + \mathfrak{L}_{\xi_{23}}\hat{\rho} \end{aligned}} \,. \tag{23.291}$$

$\hat{\rho}$ is the density operator for the internal atomic states and represented by a $3N \times 3N$ matrix,

$$\hat{\rho} = \sum_{m,n} |m\rangle\langle n| \otimes \sum_{m,n} |m\rangle\langle n| = \sum_{m,n} \hat{\sigma}_1^{mn} \sum_{m,n} \hat{\sigma}_2^{mn} \,. \tag{23.292}$$

23.6.1.1 Mean-field approximation

To simplify the code for the three-level equations of motion (23.291) when using the MATLAB software, we treat the light field as classical. That is, we take the expectation value of Eq. (23.291)(i),

$$\frac{d}{dt}\alpha = (\imath\Delta_{\rm c} - \kappa)\alpha + \eta - \imath\sum_{j=1}^{N} g(z_j)\mathrm{Tr}\,\hat{\rho}\hat{\sigma}_j^{23} \tag{23.293}$$

$$\begin{aligned} \frac{d}{dt}\hat{\rho} = &\sum_{j=1}^{N} \imath\Delta_{\rm b}[\hat{\sigma}_j^{22},\hat{\rho}] - \tfrac{\imath}{2}\Omega_{\rm b}[\hat{\sigma}_j^{12} + \hat{\sigma}_j^{21},\hat{\rho}] + \imath\Delta_{\rm a}[\hat{\sigma}_j^{33},\hat{\rho}] - \imath g(z_j)[\alpha^*\hat{\sigma}_j^{23} + \alpha\hat{\sigma}_j^{32},\hat{\rho}] \\ &+ \mathfrak{L}_{\Gamma_{12}/2}\hat{\rho} + \mathfrak{L}_{\Gamma_{23}/2}\hat{\rho} \,, \end{aligned}$$

where we now disregard optical pumping terms $\mathfrak{L}_{\xi_{12}}\hat{\rho}$ and $\mathfrak{L}_{\xi_{23}}\hat{\rho}$. Initially, we may assume that both atoms are in their ground states, i.e.,

$$\hat{\rho}(0) = |1\rangle\langle 1| \otimes |1\rangle\langle 1| = \begin{pmatrix} 1 & 0 \\ 0 & 0 \end{pmatrix} \otimes \begin{pmatrix} 1 & 0 \\ 0 & 0 \end{pmatrix} \,, \tag{23.294}$$

and that the cavity field is that of a resonantly pumped empty cavity,

$$\alpha(0) = \frac{\eta}{\kappa} \ . \tag{23.295}$$

The populations of the atomic excitation states are extracted from $\hat{\rho}(t)$ via,

$$\rho_j^{nn}(t) = \mathrm{Tr}\ \hat{\rho}(t)\hat{\sigma}_j^{nn} \ , \tag{23.296}$$

using the operators defined in (23.289).

23.6.2 Adiabatic elimination of excited state

As already mentioned, we assume that the upper transition is driven far from resonance. This allows us to adiabatically eliminate the excited state from the description, which considerably simplifies the model,

$$|\Delta_\mathrm{a}| \gg \Gamma_{23}, |\alpha|g \ . \tag{23.297}$$

We also disregard optical pumping, $\xi_{mn} = 0$. Then, $\rho_{33} \simeq 0$, and we may adiabatically eliminate state $|3\rangle$. To this end, we derive the Heisenberg equation for $\hat{\sigma}_j^{23}$ from the Hamiltonian (23.290) and set,

$$\begin{aligned} 0 \simeq \frac{d}{dt}\hat{\sigma}_j^{23} &= \imath[\hat{H}, \hat{\sigma}_j^{23}] + \mathfrak{L}_{\Gamma_{23}/2,\hat{\sigma}_j^{23}}\hat{\sigma}_j^{23} \\ &= (\imath\Delta_\mathrm{a} - \imath\Delta_\mathrm{b} - \tfrac{\Gamma_{23}}{2})\hat{\sigma}_j^{23} + \tfrac{\imath\Omega_\mathrm{b}}{2}\hat{\sigma}_j^{13} + \imath g(\hat{\sigma}_j^{33} - \hat{\sigma}_j^{22})\hat{a} \\ &\simeq (\imath\Delta_\mathrm{a} - \imath\Delta_\mathrm{b} - \tfrac{\Gamma_{23}}{2})\hat{\sigma}_j^{23} - \imath g\hat{\sigma}_j^{22}\hat{a} \ , \end{aligned} \tag{23.298}$$

where in the last step we neglected $\hat{\sigma}_j^{13} = 0 = \hat{\sigma}_j^{33}$. Hence,

$$\hat{\sigma}_j^{23} = \hat{\sigma}_j^{22}\frac{g\hat{a}}{\Delta_\mathrm{a} - \Delta_\mathrm{b} + \frac{\imath}{2}\Gamma_{23}} \ . \tag{23.299}$$

Inserting this in the Hamiltonian (23.290) we get,

$$\hat{H} = \hat{H}_\mathrm{cav} + \sum_{j=1}^{N}[\tfrac{\Omega_\mathrm{b}}{2}(\hat{\sigma}_j^{12} + \hat{\sigma}_j^{21}) + 2U_\mathrm{a}\hat{a}^\dagger\hat{\sigma}_j^{22}\hat{a} - \Delta_\mathrm{b}\hat{\sigma}_j^{22}] \tag{23.300}$$

with the abbreviation,

$$U_\mathrm{a} \equiv \frac{g^2(\Delta_\mathrm{a} - \Delta_\mathrm{b})}{(\Delta_\mathrm{a} - \Delta_\mathrm{b})^2 + \frac{1}{4}\Gamma_{23}^2} \simeq \frac{g^2}{\Delta_\mathrm{a}} \ , \tag{23.301}$$

where we assume $|\Delta_\mathrm{a}| \gg |\Delta_\mathrm{b}|$. As the excited state $|3\rangle$ does not appear in the Hamiltonian any more, we may as well use the spin notation,

$$\hat{H} = \hat{H}_\mathrm{cav} + \sum_{j=1}^{N}\left[\tfrac{\Omega_\mathrm{b}}{2}(\hat{s}_j^- + \hat{s}_j^+) + 2U_\mathrm{a}(z_j)\hat{a}^\dagger(\hat{s}_j^z + \tfrac{1}{2}\mathbb{I})\hat{a} - \Delta_\mathrm{b}(\hat{s}_j^z + \tfrac{1}{2}\mathbb{I})\right] \ . \tag{23.302}$$

From this Hamiltonian we can derive new approximate equations of motion for an effective two-level system,

$$\boxed{\begin{aligned}\frac{d}{dt}\hat{a} &= \imath[\hat{H},\hat{a}] - \kappa\hat{a} = (\imath\Delta_{\rm c} - \kappa)\hat{a} + \eta - 2\imath\sum_{j=1}^{N} U_{\rm a}(z_j)(\hat{s}_j^z + \tfrac{1}{2}\mathbb{I})\hat{a} \\ \frac{d}{dt}\hat{\rho} &= \imath[\hat{\rho},\hat{H}] + \mathfrak{L}_{\Gamma_{12}/2}\hat{\rho}\end{aligned}} \quad . \tag{23.303}$$

The density operator $\hat{\rho}$ for the internal atomic states is now represented by a $2N \times 2N$ matrix.

23.6.2.1 Mean-field approximation

In analogy to the three-level case, to simplify the code for the two-level equations of motion (23.303) when using the MATLAB software, we treat the light field as classical. That is, we take the expectation value of Eq. (23.303)(i), and obtain,

$$\frac{d}{dt}\alpha = (\imath\Delta_{\rm c} - \kappa)\alpha + \eta - 2\imath\sum_{j=1}^{N} U_{\rm a}(z_j)\alpha(\mathrm{Tr}\,\hat{\rho}\hat{s}_j^z + \tfrac{1}{2}) \tag{23.304}$$

$$\frac{d}{dt}\hat{\rho} = \sum_{j=1}^{N} -\tfrac{\imath}{2}\Omega_{\rm b}[\hat{s}_j^- + \hat{s}_j^+, \hat{\rho}][\imath\Delta_{\rm b} - 2\imath|\alpha|^2 U_{\rm a}(z_j)][\hat{s}_j^z, \hat{\rho}] + \mathfrak{L}_{\Gamma_{12}/2}\hat{\rho}\ .$$

Again, the populations of the atomic excitation states are extracted from $\hat{\rho}(t)$ as shown in Eq. (23.296).

23.6.2.2 Cavity at steady-state

The elimination of the dynamic variable $\hat{a}$ allows to convert the master equation (23.304)(ii) into a Liouville equation, which is much easier to solve. If κ dominates all time scales, $\dot{\alpha} \simeq 0$ and,

$$\alpha = \frac{\eta}{\imath\Delta_{\rm c} - \kappa + \eta - 2\imath\sum_{j=1}^{N} U_{\rm a}(z_j)\alpha(\mathrm{Tr}\,\hat{\rho}\hat{s}_j^z + \frac{1}{2})} \ . \tag{23.305}$$

Example 162 (*Two-atoms toy model, cavity blockade and anti-blockade*): We consider a toy model consisting of only two three-level atoms coupled to a single classical light mode, $\hat{a} \to \alpha$. We perform numerical simulations with the QuantumOptics.jl framework for the JULIA language or with the MATLAB software for (i) the full model (23.293) an compare the results with approximations consisting in (ii) the adiabatic elimination of the excited state [see (23.304)], and (iii) the adiabatic elimination of the cavity field [see (23.305)].
We choose a good parameter regime according to the following criteria. For the system illustrated in Fig. 23.31,

1. we choose $\Omega_{\rm b} \gg \Gamma_{12}$, in order not to be affected by spontaneous emission on the $|1\rangle$-$|2\rangle$ transition;
2. the cavity should adiabatically follow the internal dynamics, $\kappa \gg \Omega_{\rm b}$;

3. we avoid population of level $|3\rangle$ by choosing large detuning $|\Delta_\mathrm{a}| \gg \Gamma_{12}, \Gamma_{23}, \Omega_\mathrm{b}$;

4. to reach small signal behavior, we set the laser driving the cavity to the halfwidth of the cavity resonance $\Delta_\mathrm{c} = \pm\kappa$;

5. we aim at a reasonably but not too strong light shift due to the presence of a single atom, i.e.,

$$\frac{|\alpha|\,|U_\mathrm{a}|}{\kappa} = |\alpha|^2 \frac{g^2}{|\Delta_\mathrm{a}|\kappa} \lesssim 1 \ ,$$

which, together with the condition (2) implies, $g \gg \kappa$; and

6. in order to satisfy the last condition, we then need,

$$|\alpha|^2 \lesssim \frac{|\Delta_\mathrm{a}|\kappa}{g^2} \ ,$$

which we can achieve with $\eta = \kappa$;

7. the only free parameter left is the detuning of the laser on the lower transition, which we want to set to resonance to the Stark-shifted transition, such that the Rabi oscillations reach maximum amplitude, but without the light shift from the cavity,

$$\Delta_\mathrm{b} = \frac{\eta^2 U_\mathrm{a}}{2\kappa^2} = \frac{\eta^2 g^2}{2\kappa^2 |\Delta_\mathrm{a}|} = \frac{25\kappa}{72} \ .$$

With these settings, we compare time evolutions simulated via (i) the set of equations (23.307) based on the full three-level Hamiltonian (23.290), (ii) the reduced Hamiltonian (23.301), and (iii) the Hamiltonian (23.311) where the cavity field has been eliminated. The operators appearing in the respective equations are generated by the prescriptions (23.289). For the chosen parameters all simulations are in perfect agreement, as seen in Fig. 23.32. Fig. 23.32 shows an interesting behavior. Apparently, the excitation of a first atom to level $|2\rangle$ is able to influence the subsequent excitation of a second one, since the maximum inversion reached for the second atom is lower than 1. This behavior is reminiscent to the phenomenon of spin-blockade mostly studied in ensembles of Rydberg atoms. For much larger coupling strengths g the blockade becomes dramatic, as demonstrated in Fig. 23.32. However, the approximations start to fail, so that in Fig. 23.32 we only show a simulation based on the full equations (23.307).
Interestingly, a blockade may be observed even in the limit that the light field

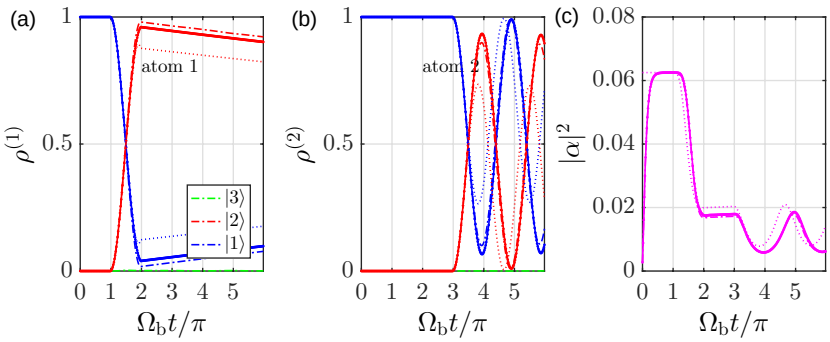

Figure 23.32: (code) Cavity blockade in a two-atom toy model. Panel (a) shows the populations of the first atom, panel (b) of the second atom and panel (c) of the cavity mode. Blue curves denote the population of level $|1\rangle$, red curves of level $|2\rangle$, and green curves of level $|3\rangle$. At time $\Omega_b t = \pi$ atom 1 is excited to level $|2\rangle$ via a π-pulse, and from time $\Omega_b t = 3\pi$ on, atom 2 is continuously excited. The parameters are scaled to Γ_{12} and $\zeta = 0.5$. Dash-dotted lines denote simulations based on Eqs. (23.293). Solid lines are obtained using Eqs. (23.304). Dashed lines are obtained using Eqs. (23.304), but with the cavity field assumed in steady-state according to Eq. (23.305). Dotted lines are obtained using Heisenberg equation derived from the Hamiltonian for (23.302) for α and $\rho_{mn} = \langle \hat{\sigma}^{mn} \rangle$.

is treated as classical [29].

$$
\begin{aligned}
\Gamma_{12} &= (2\pi)\ 7.5\,\mathrm{kHz} & U_a &= g^2/\Delta_a = 1.7\kappa \\
\Gamma_{23} &= 50\Gamma_{12} & \Omega_a &= 22.5\Gamma_{23} \\
\kappa &= 750\Gamma_{12} & \zeta_0 &= 2\eta^2 U_a/\kappa^2 = 0.21\kappa \\
\eta &= 0.25\kappa & \zeta_1 &= 4\eta^2 U_a^3/\kappa^3 = 0.72\kappa \\
\Delta_c &= 0 & \Upsilon &= 4g^2/\kappa\Gamma_{12} \\
\Delta_b &= U_a\eta^2/\kappa^2 = 1.7\kappa & & \\
\Delta_a &= 15\kappa & & \\
g &= 5\kappa & & \\
\Omega_b &= 200\Gamma_{12} & &
\end{aligned}
\quad .
$$

23.6.3 Open Dicke model for the two-level system

For very few atoms the equations of motion derived for the open Tavis-Cummings model [811] Eqs. (23.291) or (23.303) can be solved numerically. However, for the simulation of more (several tens of) atoms, the model becomes increasingly impracticable, as the dimension of the Hilbert space scales with 3^N for a three-level system and 2^N for a two-level system. In this case, the Dicke model is useful as the Hilbert space only scales as $N+1$. The expression in terms of collective operators $\hat{S}_{mn}$ allows

[29] Note that the parameters are not realistic, since,

$$g = \sqrt{\frac{6\Gamma_{23}\delta_{fsr}}{k^2 w^2}} = 5\kappa \Longrightarrow \delta_{fsr} = 825\,\mathrm{THz}\ .$$

On the other hand, with 10^5 atoms, $\delta_{fsr} = 8.25\,\mathrm{GHz}$.

us to use the usual Dicke state formalism [229]. We just need to represent them in a Dicke basis. The downside of the Dicke model is, that the atoms *loose their individuality* with respect to the driving light field, i.e. they cannot be addressed one by one any more.

Neglecting $\hat{\sigma}_j^{33} = 0$ and assuming uniform coupling, $g(z_j) = g$, we may introduce collective spin operators,

$$\begin{aligned} \hat{S}_{m\neq n} = \sum_j \hat{\sigma}_j^{m\neq n} \quad , \quad \hat{S}_{nn} = \tfrac{1}{2}\sum_j \hat{\sigma}_j^{nn} \\ \hat{S}_z \equiv \hat{S}_{22} - \hat{S}_{11} \quad , \quad \tfrac{N}{2} = \hat{S}_{22} + \hat{S}_{11} \quad , \quad \hat{S}_- = \hat{S}_{12} \ , \end{aligned} \tag{23.306}$$

helping us to simplify the Hamiltonian (23.302),

$$\hat{H} = \hat{H}_{\rm cav} + \Omega_{\rm b}\hat{S}_x + 2U_{\rm a}\hat{a}^\dagger(\hat{S}_z + \tfrac{N}{2}\mathbb{I})\hat{a} - \Delta_{\rm b}(\hat{S}_z + \tfrac{N}{2}\mathbb{I}) \ . \tag{23.307}$$

From this Hamiltonian we can derive Heisenberg equations [466],

$$\frac{d}{dt}\hat{A} = -\imath[\hat{A}, \hat{H}] + \mathfrak{L}^\dagger_{\kappa,\hat{a}}\hat{A} + \mathfrak{L}^\dagger_{\Gamma_{12}/2,\hat{\sigma}_j^{12}}\hat{A} + \mathfrak{L}^\dagger_{\Gamma_{23}/2,\hat{\sigma}_j^{23}}\hat{A} \ , \tag{23.308}$$

for all observables $\hat{A} \equiv \hat{a}$ and $\hat{S}_{x,y,z}$,

$$\boxed{\begin{aligned} \left(\frac{d}{dt} + \kappa\right)\hat{a} &= \imath(\Delta_{\rm c} - 2U_{\rm a}\hat{S}_z - NU_{\rm a})\hat{a} + \eta \\ \left(\frac{d}{dt} + \tfrac{1}{2}\Gamma_{12}\right)\hat{S}_x &= \Delta_{\rm b}\hat{S}_y - 2U_{\rm a}\hat{a}^\dagger\hat{S}_y\hat{a} \\ \left(\frac{d}{dt} + \tfrac{1}{2}\Gamma_{12}\right)\hat{S}_y &= -\Delta_{\rm b}\hat{S}_x + 2U_{\rm a}\hat{a}^\dagger\hat{S}_x\hat{a} - \Omega_{\rm b}\hat{S}_z \\ \tfrac{N}{2}\Gamma_{12} + \left(\frac{d}{dt} + \Gamma_{12}\right)\hat{S}_z &= \Omega_{\rm b}\hat{S}_y \end{aligned}} \ . \tag{23.309}$$

The quantity $(N + 2\hat{S}_z)U_{\rm a}$ represents the frequency shift of the cavity resonance due to the refractive index change generated by presence in the mode volume of atoms in their internal state $|2\rangle$.

23.6.4 Cavity at steady-state and small signal approximation

Now, assuming that the cavity field quickly adjusts to the atomic dynamics we may eliminate the cavity field from the equations of motion. Assuming the cavity in steady-state $\dot{\hat{a}} = 0$, we get from (23.309)(i),

$$\boxed{\hat{a} = (\kappa - \imath\Delta_{\rm c} + \imath NU_{\rm a} + 2\imath U_{\rm a}\hat{S}_z)^{-1}\eta} \ . \tag{23.310}$$

The equations (23.309)(i,iii) include non-linear terms $\hat{a}^\dagger \hat{S}_{x,y} \hat{a}$. Now, let us assume $\langle \hat{S}_z \rangle \simeq 0$ and expand the field operator (23.310) for *small deviations*,

$$\hat{a} \simeq \frac{1}{\kappa + \imath N U_\mathrm{a} - \imath \Delta_\mathrm{c}} + \frac{2U_\mathrm{a}}{(\kappa + \imath N U_\mathrm{a} - \imath \Delta_\mathrm{c})^2} \hat{S}_z + ... = \alpha + \delta\hat{a} \ . \tag{23.311}$$

With this we find up to first order,

$$\begin{aligned} \hat{a}^\dagger \hat{S}_{x,y} \hat{a} &= \eta^2 \left(\kappa - \imath N U_\mathrm{a} + \imath \Delta_\mathrm{c} - 2\imath U_\mathrm{a} \hat{S}_z \right)^{-1} \hat{S}_{x,y} \left(\kappa + \imath N U_\mathrm{a} - \imath \Delta_\mathrm{c} + 2\imath U_\mathrm{a} \hat{S}_z \right)^{-1} \\ &\simeq \frac{\eta^2 \hat{S}_{x,y}}{\kappa^2 + (N U_\mathrm{a} - \Delta_\mathrm{c})^2} + \frac{2\eta^2 U_\mathrm{a}}{\kappa^2 + (N U_\mathrm{a} - \Delta_\mathrm{c})^2} \left(\frac{\hat{S}_z \hat{S}_{x,y}}{\kappa - \imath N U_\mathrm{a} + \imath \Delta_\mathrm{c}} + \frac{\hat{S}_{x,y} \hat{S}_z}{\kappa + \imath N U_\mathrm{a} - \imath \Delta_\mathrm{c}} \right) . \end{aligned} \tag{23.312}$$

Setting the cavity on the light-shifted resonance, $\Delta_\mathrm{c} = N U_\mathrm{a}$, we find,

$$2U_\mathrm{a} \hat{a}^\dagger \hat{S}_{x,y} \hat{a} \simeq \zeta_0 \hat{S}_{x,y} + \zeta_1 \{ \hat{S}_{x,y}, \hat{S}_z \} \ , \tag{23.313}$$

defining

$$\zeta_0 \equiv \frac{2\eta^2 U_\mathrm{a}}{\kappa^2} \qquad \text{and} \qquad \zeta_1 = \frac{4\eta^2 U_\mathrm{a}^2}{\kappa^3} \ , \tag{23.314}$$

where ζ_1 is called the squeezing parameter. Terms like (23.313) can be derived from a Hamiltonian, $\hat{H}_\zeta = \zeta_0 \hat{S}_z + \zeta_1 \hat{S}_z^2$. That is, the Hamiltonian where the cavity field is adiabatically eliminated is approximated by,

$$\hat{H} = \Omega_\mathrm{b} \hat{S}_x + (\zeta_0 - \Delta_\mathrm{b}) \hat{S}_z + \zeta_1 \hat{S}_z^2 \qquad \text{for} \qquad \Delta_\mathrm{c} = N U_\mathrm{a} \ . \tag{23.315}$$

with the corresponding equations of motion,

$$\boxed{\begin{aligned} \left(\frac{d}{dt} + \frac{\Gamma_{12}}{2} \right) \hat{S}_x &= (\Delta_\mathrm{b} - \zeta_0) \hat{S}_y - \zeta_1 \{ \hat{S}_y, \hat{S}_z \} \\ \left(\frac{d}{dt} + \frac{\Gamma_{12}}{2} \right) \hat{S}_y &= -(\Delta_\mathrm{b} - \zeta_0) \hat{S}_x + \zeta_1 \{ \hat{S}_x, \hat{S}_z \} - \Omega_\mathrm{b} \hat{S}_z \\ \tfrac{N}{2} \Gamma_{12} + \left(\frac{d}{dt} + \Gamma_{12} \right) \hat{S}_z &= \Omega_\mathrm{b} \hat{S}_y \end{aligned}} \ . \tag{23.316}$$

The quadratic term in the Hamiltonian (23.315) has been shown in Sec. 23.1.5 and Exc. 23.1.9.15 to induce one-axis twisting and spin-squeezing. It is also reminiscent to the Rydberg interaction Hamiltonian (23.150) [702, 784]. We may hence expect similar phenomena, such as the emergence of an excitation blockade.

Another interesting regime might be $\Delta_\mathrm{c} - N U_\mathrm{a} = \pm\kappa$. We derive the corresponding Hamiltonian in Exc. 23.6.6.2.

23.6.4.1 Mean-field approximation

Note, that if the light field were classical, the non-linear term $|\alpha|^2 \hat{S}_{x,y}$ would not lead to quantum correlations, because the equations of motion could then be derived from

a Hamiltonian, which is linear in the collective spin components. From (23.307) we get,

$$\sum_j \hat{H}_j = \Omega_\mathrm{b}\hat{S}_x + (2U_\mathrm{a}|\alpha|^2 - \Delta_\mathrm{b})(\hat{S}_z + \tfrac{N}{2}) \ . \tag{23.317}$$

In analogy,

$$\begin{aligned}
\frac{d}{dt}\alpha &= (\imath\Delta_\mathrm{c} - \kappa)\alpha + \eta - \imath N U_\mathrm{a} - 2\imath U_\mathrm{a}\alpha \,\mathrm{Tr}\,\hat{\rho}\hat{S}_z \\
\frac{d}{dt}\hat{S}_x &= (\Delta_\mathrm{b} - 2\imath|\alpha|^2 U_\mathrm{a})\hat{S}_y - \tfrac{\Gamma_{12}}{2}\hat{S}_x \\
\frac{d}{dt}\hat{S}_y &= -(\Delta_\mathrm{b} - 2\imath|\alpha|^2 U_\mathrm{a})\hat{S}_x - \Omega_\mathrm{b}\hat{S}_z - \tfrac{\Gamma_{12}}{2}\hat{S}_y \\
\frac{d}{dt}\hat{S}_z &= \Omega_\mathrm{b}\hat{S}_y - \Gamma_{12}\hat{S}_z - \tfrac{N}{2}\Gamma_{12}\hat{S}_z \ .
\end{aligned} \tag{23.318}$$

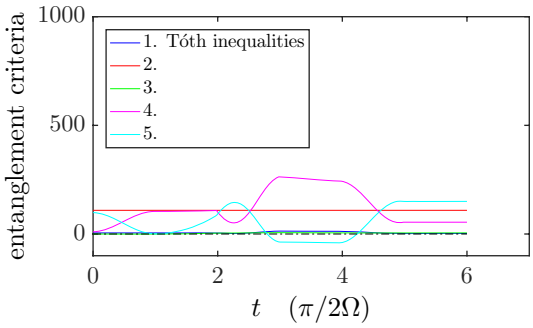

Figure 23.33: (code) Time evolution of the Tóth inequalities calculated from Heisenberg equations directly derived from the Hamiltonian Eq.(23.315).

Hence, for the adiabatically approximated two-level system, treating the light classically, we may set $\dot{\alpha} = 0$ in Eq. (23.309)(i) and obtain,

$$\alpha = \frac{\eta}{\kappa - \imath\Delta_\mathrm{c} + \imath N U_\mathrm{a} + 2\imath U_\mathrm{a}\mathrm{Tr}\,\hat{\rho}\hat{S}_z} \ . \tag{23.319}$$

This expression can replace Eq. (23.318)(i) in numerical simulations. For small deviations around $\Delta_\mathrm{c} = \pm\kappa$, we may linearize the steady-state solution by expanding $|\alpha|^2$ in $U_\mathrm{a}\mathrm{Tr}\,\hat{\rho}\hat{S}_{22}$,

$$|\alpha|^2 = \frac{\eta^2}{\kappa^2 + (\Delta_\mathrm{c} - U_\mathrm{a}\mathrm{Tr}\,\hat{\rho}\hat{S}_{22})^2} \simeq \frac{\eta^2}{\kappa^2 + \Delta_\mathrm{c}^2} + \frac{2\eta^2\Delta_\mathrm{c}}{(\kappa^2 + \Delta_\mathrm{c}^2)^2} U_\mathrm{a}\mathrm{Tr}\,\hat{\rho}\hat{S}_{22} \ , \tag{23.320}$$

and on resonance,

$$|\alpha|^2 = \frac{\eta^2}{2\kappa^2} \pm \frac{\eta^2}{2\kappa^3} U_\mathrm{a}\mathrm{Tr}\,\hat{\rho}\hat{S}_{22} = \frac{\eta_0}{4} \pm \frac{\eta_1}{8} U_\mathrm{a}\mathrm{Tr}\,\hat{\rho}\hat{S}_{22} \ . \tag{23.321}$$

With this the Hamiltonian (23.317) reads,

$$\sum_j \hat{H}_j = \Omega_\mathrm{b}\hat{S}_x + \left(\tfrac{\eta^2 U_\mathrm{a}}{2\kappa^2} - \Delta_\mathrm{b}\right)\hat{S}_{22} \pm \tfrac{\eta}{2}\hat{S}_{22}\mathrm{Tr}\,\hat{\rho}\hat{S}_{22} \ . \tag{23.322}$$

23.6.5 Cumulant expansion for many atoms, the role of cooperativity

To handle the case of many atoms (we have in mind $N = 10000$) under the premises of uniform coupling $[g(z_j) = g]$ we derive the equations of motion for the light field and all populations and coherences of the three-level system and treat them as c-numbers, which obviously discards the possibility of individual manipulations of the atoms. From the collective Hamiltonian for three levels,

$$\begin{aligned}\hat{H} &= \imath\eta(\hat{a} - \hat{a}^\dagger) - \Delta_{\rm c}\hat{a}^\dagger\hat{a} + \tfrac{\Omega_{\rm b}}{2}(\hat{S}_{12} + \hat{S}_{21}) - \Delta_{\rm b}\hat{S}_{22} \\ &\quad + g(\hat{a}^\dagger\hat{S}_{23} + \hat{S}_{32}\hat{a}) - \Delta_{\rm a}\hat{S}_{33}\end{aligned} \quad , \tag{23.323}$$

as shown in Exc. 23.6.6.3, we derive the equations of motion from the Heisenberg equation,

$$\boxed{\begin{aligned}\frac{d}{dt}\hat{a} &= \imath[\hat{H}, \hat{a}] + \mathfrak{L}_\kappa^\dagger\hat{a} \\ \frac{d}{dt}\hat{S}_{mn} &= \imath[\hat{H}, \hat{S}_{mn}] + \mathfrak{L}_\Gamma^\dagger\hat{S}_{mn} + \mathfrak{L}_\gamma^\dagger\hat{\sigma}_j^{mn}\end{aligned}} \; . \tag{23.324}$$

The collective decay terms, if they existed would be given by,

$$\mathfrak{L}_\Gamma^\dagger\hat{S}_{mn} = \sum_\Gamma \Gamma\left(\hat{L}_\Gamma^\dagger[\hat{S}_{mn}, \hat{L}_\Gamma] + [\hat{L}_\Gamma^\dagger, \hat{S}_{mn}]\hat{L}_\Gamma\right) \; , \tag{23.325}$$

where Γ are possible collective decay channels and $\hat{L}_\Gamma$ the operators describing the decay. For example, the operator $\hat{L}_{\Gamma_{12}} \equiv \hat{S}_{12}$ describes collective spontaneous emission from $|2\rangle$ to $|1\rangle$. However, in the absence interatomic interaction, we do not expect collective spontaneous emission, so that we may set $\Gamma_{mn} = 0$. On the other hand, spontaneous emission leads to decay of individual atoms, here denoted by γ_{mn}. That is, we assume the decay rates are the same for all atoms and there is no interatomic correlation (that is, no super- or subradiance). The Lindblad expression for the decay terms is,

$$\mathfrak{L}_\gamma^\dagger\hat{\sigma}_j^{mn} = \sum_\gamma \gamma\left(\hat{L}_\gamma^\dagger[\hat{\sigma}_j^{mn}, \hat{L}_\gamma] + [\hat{L}_\gamma^\dagger, \hat{\sigma}_j^{mn}]\hat{L}_\gamma\right) \; . \tag{23.326}$$

23.6.5.1 Mean-field approximation

In lowest order we neglect all correlations and obtain for the expectation values,

$$\begin{aligned}\frac{d}{dt}\alpha &= (\imath\Delta_{\rm c} - \kappa)\alpha - \imath g\,{\rm Tr}\,\hat{\rho}\hat{S}_{23} - \eta \\ \frac{d}{dt}\vec{\rho} &= \mathcal{M}\vec{\rho}\,,\end{aligned} \tag{23.327}$$

where $\vec{\rho}$ is Bloch vector of the three-level system and $\mathcal{M}$ the Liouvillean explicitly derived in Exc. 23.6.6.3.

Fig. 23.34 illustrates the spin blockade effect. When the atom number in linearly increased, under the influence of a constant excitation of the lower transition, the

fraction of excited atoms first increases linearly, as well. But beyond a critical population of the level $|22\rangle$, the excitation remains constant. (Well, this is what I hoped to see, but it seems not that simple.)

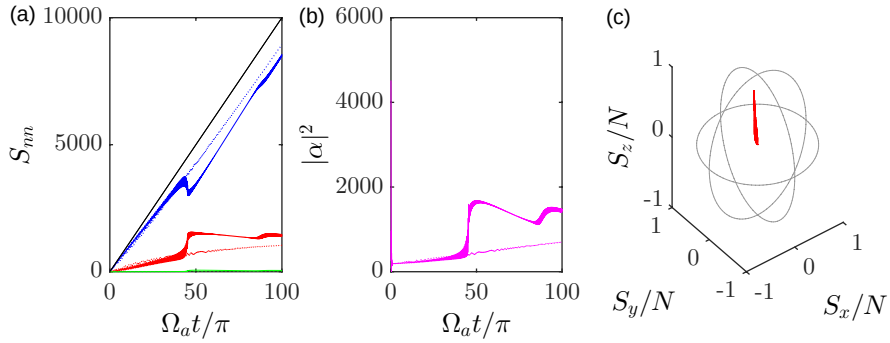

Figure 23.34: (code) Spin blockade in a large ensemble of three-level atoms. To illustrate the effect, the atom number is linearly increased from $N = 0$ to 10000. Panel (a) shows the time evolution of the populations $\langle S_{11}\rangle$ (blue), $\langle S_{22}\rangle$ (red) , and $\langle S_{33}\rangle$ (green) and panel (b) of the cavity field $|\alpha|^2$. Panel (c) visualizes the Bloch vector of the lower transition, $\left(\mathfrak{Re}\,\hat{S}_{12}\ ,\ \mathfrak{Im}\,\hat{S}_{12}\ ,\ \hat{S}_{22}-\hat{S}_{11}\right)$, in configuration space. Solid lines refer to full simulation of Eqs. (23.325), for the dotted lines the light field was assumed in steady state. Same parameters as in Fig. 23.32 except for $\Omega_b/2\pi = 1\,\mathrm{MHz}$, $g = 0.5\kappa$, $\eta = 70\kappa$, and $\Delta_c = 5\kappa$.

23.6.5.2 One-axis twisting

Far from resonance, $|\Delta_a| \gg U_a$, the spin-spin interaction strength of (23.311) is approximated by,

$$\frac{\zeta}{\kappa} = \frac{\eta^2}{\kappa^4}\frac{g^4\Delta_a^2}{(\Delta_a^2+\gamma_{23}^2)^2} \simeq \frac{\eta^2}{\kappa^4}\frac{g^4\Delta_a^2}{(\Delta_a^2+\gamma_{23}^2)^2} < \frac{\eta^2}{\kappa^4}\frac{g^4}{4\gamma_{23}^2} = \frac{|\alpha_\infty|^2}{4}\Upsilon^2 \ . \tag{23.328}$$

Requesting that the cooperative cavity Lamb shift,

$$U_c \equiv \frac{g^2\Delta_c}{\Delta_c^2+\kappa^2} \ , \tag{23.329}$$

be larger than the decay rate γ_{23} of the driven atomic transition implies,

$$1 < \frac{NU_c}{\gamma_{23}} = \frac{1}{\gamma_{23}}\frac{Ng^2\Delta_c}{\Delta_c^2+\kappa^2} < \frac{Ng^2}{2\kappa\gamma_{23}} = \frac{N\Upsilon}{2} \ . \tag{23.330}$$

That is, for this condition to be fulfilled is is sufficient to have strong 'collective' cooperativity,

$$\Upsilon_N \equiv N\Upsilon \ . \tag{23.331}$$

Let us now consider $N = 10^4$, which is the number of atoms we typically load into our ring cavity [694]. We call,

$$\gamma_c \equiv \frac{g^2\kappa}{\Delta_c^2 + \kappa^2} \tag{23.332}$$

the Purcell-enhanced atomic decay rate [376, 378].

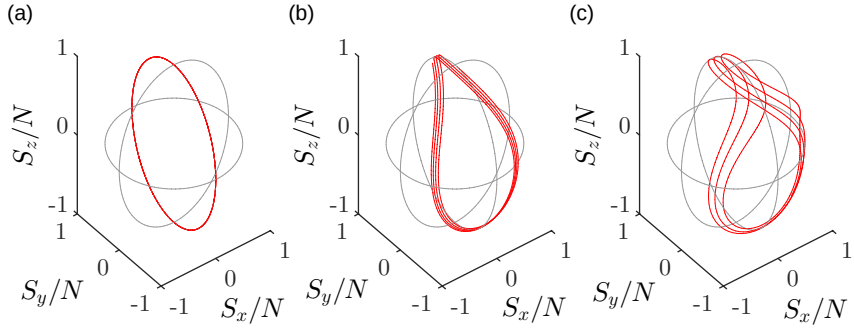

Figure 23.35: (code) One-axis twisting (inversion-dependent frequency shift) according to Eq. (??) with $N = 10000$ atoms and $\Omega_b/2\pi = 1\,\mathrm{MHz}$ and $\Delta_b = 0$. The squeezing parameter is (a) $N\zeta = 0$, (b) $N\zeta = 2\Omega_b$, and (c) $N\zeta = 4\Omega_b$.

23.6.6 Exercises

23.6.6.1 Ex: Two non-interacting three-level atoms in free space

Extend the two two-level atoms toy model of example 145 to two non-interacting three level atoms $|1\rangle$-$|2\rangle$-$|3\rangle$ in cascade configuration.
a. Write down the total Hamiltonian and its matrix representation chosing an appropriate basis.
b. Write down the Lindbladian and numerically solve the master equation.

23.6.6.2 Ex: Spin-squeezing Hamiltonian

Simplifying the expression (23.312) for $\Delta_c - NU_a = \pm\kappa$ derive the Hamiltonian and, if necessary the Lindbladian, generating the equations of motion (23.309).

23.6.6.3 Ex: Collective spin description for three levels

Derive a collective spin description for the three-level system interacting with a cavity.

23.7 Further reading

23.7.1 on collective spin states

R.H. Dicke, *Coherence in Spontaneous Radiation Processes* [DOI]

D. Gottesman et al., *Encoding a qubit in an oscillator* [DOI]

K. Baumann et al., *Dicke quantum phase transition with a superfluid gas in an optical cavity* [DOI]

B.M. Garraway, *The Dicke model in quantum optics: Dicke model revisited* [DOI]

W. Guerin, *Subradiance in a Large Cloud of Cold Atoms* [DOI]

M. Gegg et al., *Superradiant to subradiant phase transition in the open system Dicke model: dark state cascades* [DOI]

P. Kirton et al., *Introduction to the Dicke Model: From Equilibrium to Nonequilibrium, and Vice Versa* [DOI]

M. Reitz et al., *Cooperative Quantum Phenomena in Light-Matter Platforms* [DOI]

B. Koczor et al., *Continuous phase-space representations for finite-dimensional quantum states and their tomography* [DOI]

J. Davis et al., *Wigner negativity in spin-j systems* [DOI]

S. Omanakuttan et al., *Spin-squeezed Gottesman-Kitaev-Preskill codes for quantum error correction in atomic ensembles* [DOI]

23.7.2 on spin squeezing

M. Kitagawa et al., *Spin-squeezed states* [DOI]

D.J. Wineland et al., *Squeezed atomic states and projection noise in spectroscopy* [DOI]

Ph. Bouyer et al., *Heisenberg-Limited Spectroscopy with Degenerate Bose-Einstein Gases* [DOI]

G. Co et la., *Analytical and numerical analysis of the complete Lipkin-Meshkov-Glick Hamiltonian* [DOI]

I.D. Leroux et al., *Implementation of Cavity Squeezing of a Collective Atomic Spin* [DOI]

M. Schleier-Smith et al., *Squeezing the collective spin of a dilute atomic ensemble by cavity feedback* [DOI]

L. Salvi et al., *Squeezing on Momentum States for Atom Interferometry* [DOI]

Zilong Chen et al., *Conditional Spin Squeezing of a Large Ensemble via the Vacuum Rabi Splitting* [DOI]

J.G. Bohnet et al., *A steady-state superradiant laser with less than one intracavity photon* [DOI]

J.G. Bohnet et al., *Reduced spin measurement back-action for a phase sensitivity ten times beyond the standard quantum limit* [DOI]

K. Cox et al., *Deterministic Squeezed States with Collective Measurements and Feedback* [DOI]

L. Pezze et al., *Quantum metrology with nonclassical states of atomic ensembles* [DOI]

B. Braverman et al., *Near-Unitary Spin Squeezing in 171Yb* [DOI]

E. Pedrozo-Penafiel et al., *Spinsqueezing on an optical atomic-clock transition* [DOI]

S. Colombo et al., *Time-reversal-based quantum metrology with many-body entangled states* [DOI]

S. Colombo et al., *Spinsqueezing-Enhanced Optical Atomic Clocks* [DOI]

G. Bornet et al., *Scalable spin squeezing in a dipolar Rydberg atom array* [DOI]

R.J. Lewis-Swan et al., *Robust Spin Squeezing via Photon-Mediated Interactions on an Optical Clock Transition* [DOI]

Zeyang Li et al., *Collective Spin-Light and Light-Mediated Spin-Spin Interactions in an Optical Cavity* [DOI]

23.7.3 on superradiant lasing

M. Tavis et al., *Exact solution for an N-molecule-radiation-field Hamiltonian* [DOI]

J. Krause et al., *Quantum theory of the micromaser: Symmetry breaking via off-diagonal atomic injection* [DOI]

C. Emary et al., *Chaos and the quantum phase transition in the Dicke model* [DOI]

A.F. Huss et al., *Phase Correlation of Laser Waves with Arbitrary Frequency Spacing* [DOI]

B.M. Peden et al., *Nondestructive cavity QED probe of Bloch oscillations in a gas of ultracold atoms* [DOI]

D. Meiser et al., *Prospects for a Millihertz-Linewidth Laser* [DOI]

Th. Maier et al., *A superradiant clock laser on a magic wavelength optical lattice* [DOI]

M.A. Norcia et al., *Strong coupling on a forbidden transition in strontium and non-destructive atom counting* [DOI]

M.A. Norcia et al., *Superradiance on the millihertz linewidth strontium clock transition* [DOI]

M.A. Norcia et al., *Cold-Strontium Laser in the Superradiant Crossover Regime* [DOI]

M.A. Norcia et al., *Cavity-mediated collective spin-exchange interactions in a strontium superradiant laser* [DOI]

Zhang Yuan et al., *Monte-Carlo simulations of superradiant lasing* [DOI]

K. Debnath et al., *Lasing in the superradiant crossover regime* [DOI]

A. Bychek et al., *Superradiant lasing in inhomogeneously broadened ensembles with spatially varying coupling* [DOI]

M. Reitz et al., *Cooperative Quantum Phenomena in Light-Matter Platforms* [DOI]

23.7.4 on driven-dissipative spin squeezing

P.D. Drummond et al., *Volterra cycle and the cooperative fluorescence critical point* [DOI]

R.R. Puri et al., *Exact steady-state density operator for a collective atomic system in an external field* [DOI]

H.J. Carmichael, *Analytical and numerical results for the steady state in cooperative resonance fluorescence* [DOI]

N. Yamamoto, *Parametrization of the feedback Hamiltonian realizing a pure steady state* [DOI]

T.-L. Wang et al., *Quantum Fisher information as a signature of the superradiant quantum phase transition* [DOI]

O. Somech et al., *Heisenberg-Langevin approach to driven superradiance* [DOI]

O. Somech et al., *Quantum entangled states of a classically radiating macroscopic spin* [DOI]

N. Leppenen et al., *Quantum bistability at the interplay between collective and individual decay* [DOI]

Chapter 24

Quantum information science

24.1 Quantum correlations and entanglement

The concept of *entanglement* arose in quantum mechanics by Einstein, Podolski and Rosen's famous Gedankenexperiment, today called the *EPR paradox* [260]. In his Gedankenexperiment, Einstein tried to prove the necessity of hidden variables for quantum mechanics to be a complete theory. Consequently, we begin this chapter by introducing the notion of entangled particles and recapitulating the discussion of the EPR paradox.

Since Feynman discovered the utility of entangled states for quantum computation [646, 158], this area of research exploded with thousands of theoretical researchers, but few experiments, due to the enormous technical difficulties of creating and controlling these states. On the other side, states of entangled photons already play an important role in *quantum cryptography* [69]. And in the context of metrology, *spin-squeezed* correlated quantum states offer the possibility of quantum noise reduction in frequency standards [869].

Among the various systems proposed for the realization of entangled states and quantum computing gates we will only discuss one idea, which is based on the mutual coupling of atoms through a Jaynes-Cummings-like interaction mediated by an optical mode.

24.1.1 The EPR paradox and GHZ states

Let us imagine two maximally correlated particles produced by a suitable source, which fly freely without interaction in opposite directions along the y-axis toward two detectors a and b. The particles have an internal degree of freedom (spin) $|\pm\rangle_{a,b}$, which can be measured in various directions, for example, z or x by operators $\hat{\sigma}_z^{a,b}$ or $\hat{\sigma}_x^{a,b}$. Since the particles are completely entangled, the result of a measurement on the first particle $\hat{\sigma}_z^a$ allows the prediction of the result of another measurement $\hat{\sigma}_z^b$ performed on the second particle, and similarly for $\hat{\sigma}_x^a$ and $\hat{\sigma}_x^b$. Why is that?

The theory of *hidden variables* proposed by Einstein, Podolsky and Rosen [260] postulates, that the total state describing the two particles contains all information about the way, how the particles should behave at the detectors. The information was imprinted on each one of the two particle's when they were created in the source,

i.e. the total state must be of the type,

$$|\psi\rangle = \begin{pmatrix} \pm_z^a & \pm_z^b \\ \pm_x^a & \pm_x^b \end{pmatrix} , \tag{24.1}$$

where the notation should be read as a decision table.

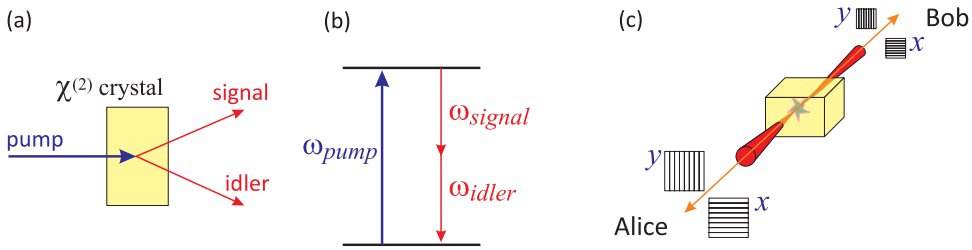

Figure 24.1: (a) Generation of entangled photon via parametric down-conversion. (b) Energy conservation upon parametric down-conversion. (c) Illustration of the EPR paradox.

On the other hand, quantum mechanics postulates that the reduction of the wavepacket describing the particle at detector a decides *spontaneously* on the result of the measurement at detector b. This decision *has no physical cause*. If the particles move with the speed of light, this decision is not restricted by *local causality* [379]. The state, also called *Bell state*, can be given in the form,

$$|\psi\rangle = |+_a \ +_b\rangle + |-_a \ -_b\rangle \ . \tag{24.2}$$

In Exc. 24.1.3.1 we check that this state cannot be expressed as a product state. Let us have a closer look at the EPR state (24.2) and imagine that particle 'a' (the one that will later be analyzed by detector a) is embarked with Alice on a starship, while particle 'b' flies with Bob in opposite direction.

We introduce a basis choosing z as the quantization axis, that is, the basis vectors

$$|+\rangle_z = \begin{pmatrix} 1 \\ 0 \end{pmatrix} \quad , \quad |-\rangle_z = \begin{pmatrix} 0 \\ 1 \end{pmatrix} \tag{24.3}$$

are eigenvectors of the Pauli matrix $\hat{\sigma}_z$. On the other hand,

$$|+\rangle_x = \tfrac{1}{\sqrt{2}} \begin{pmatrix} 1 \\ 1 \end{pmatrix} \quad , \quad |-\rangle_x = \tfrac{1}{\sqrt{2}} \begin{pmatrix} 1 \\ -1 \end{pmatrix} \tag{24.4}$$

are eigenvectors of the Pauli matrix $\hat{\sigma}_x$. Quantum mechanics now tells us that, before any measurement, the wavefunction is in a superposition of states $|+\rangle$ and $|-\rangle$. That is, in the z-basis, using the tensor notation, we may write the entangled state (24.2) as,

$$\boxed{|\psi\rangle = \tfrac{1}{\sqrt{2}} \left(|+\rangle_z \otimes |+\rangle_z + |-\rangle_z \otimes |-\rangle_z \right)} \ . \tag{24.5}$$

But we can also express it in the x-basis,

$$
\begin{aligned}
|\psi\rangle &= \tfrac{1}{\sqrt{2}}\left(\tfrac{|+\rangle_x+|-\rangle_x}{\sqrt{2}}\otimes\tfrac{|+\rangle_x+|-\rangle_x}{\sqrt{2}}+\tfrac{|+\rangle_x-|-\rangle_x}{\sqrt{2}}\otimes\tfrac{|+\rangle_x-|-\rangle_x}{\sqrt{2}}\right) \\
&= \tfrac{1}{2\sqrt{2}}\begin{pmatrix} |+\rangle_x\otimes|+\rangle_x+|+\rangle_x\otimes|-\rangle_x+|-\rangle_x\otimes|+\rangle_x+|-\rangle_x\otimes|-\rangle_x \\ +|+\rangle_x\otimes|+\rangle_x-|+\rangle_x\otimes|-\rangle_x-|-\rangle_x\otimes|+\rangle_x+|-\rangle_x\otimes|-\rangle_x \end{pmatrix} \\
&= \tfrac{1}{\sqrt{2}}\left(|+\rangle_x\otimes|+\rangle_x+|-\rangle_x\otimes|-\rangle_x\right) \ .
\end{aligned}
\tag{24.6}
$$

A generalization of this calculation to arbitrary rotations of the detector will be studied in Exc. 24.1.3.2.

After some time, Alice measures her spin in z-direction, i.e. performs a measurement of $\hat{\sigma}_z$. Her measurement not only collapses the wavefunction of Alice's spin a in either one of the states $|\pm\rangle_z$, but it instantaneously also collapses the wavefunction of Bob's spin along the z-direction,

$$
|\psi\rangle \curvearrowright \begin{cases} |+\rangle_z\otimes|+\rangle_z = |+\rangle_z\otimes\frac{|+\rangle_x+|-\rangle_x}{\sqrt{2}} \\ |-\rangle_z\otimes|-\rangle_z = |+\rangle_z\otimes\frac{|+\rangle_x-|-\rangle_x}{\sqrt{2}} \end{cases}
\tag{24.7}
$$

Hence, if Bob measures along the z-axis, his measurement will be predefined by Alice's measurement. On the other hand, if tries to measure along the x-axis, he will find a random result with a probability of $\frac{1}{2}$ for each outcome [1]. That is, the direction of measurement in Alice's experiment fixes the quantization axis for Bob's experiment.

Two hypotheses have been put forward: The first one is that Alice's experiment sends information to Bob's experiment. Alice's particle told Bob's particle which spin state he should be in. But this hypothesis violates the locality requirement of special relativity claiming that information cannot travel faster than light. Einstein called it 'spooky action at a distance'. The second hypothesis is to assume that quantum mechanics does not violate locality, but that the particles carry with them 'local hidden variables' [2] (like a proper DNA) whose values would be set right from the moment of the separation of the particles and which would determine the outcomes of any future spin measurement. Then, quantum mechanics would not be a complete theory, because it has nothing to say about these hidden variables.

24.1.1.1 Bell's inequality

In 1964 John S. Bell suggested an experimental test for the EPR paradox [65]. He proposed a theorem formulated as an inequality, the famous *Bell's inequality*, stating that *if the local hidden variables hypothesis proposed by Einstein is correct, then the inequality must be satisfied by experiment.*

There are many versions of Bell's inequality, all of them are equivalent. Let us follow Bell's argumentation and assume Alice and Bob to use Stern-Gerlach magnets

[1] Due to Bob's measurement along the x-axis Alice's wavefunction should collapse along the x-axis, as well. But according to quantum mechanics, Alice should be unable to know the spin value in x-direction, since she already knows the spin the z-direction, which is not allowed by the commutation rules,

$$
[\hat{\sigma}_z^a, \hat{\sigma}_x^a] = \imath\hbar\hat{\sigma}_y^a \qquad , \qquad [\hat{\sigma}_z^b, \hat{\sigma}_x^b] = \imath\hbar\hat{\sigma}_y^b \ .
$$

[2] Note the difference to *non-local hidden variables* assumed by de Broglie and David Bohm in their formulation of quantum mechanics.

oriented in arbitrary directions $\mathbf{a} \equiv \hat{\mathbf{e}}_{\vartheta,\varphi}$, respectively, $\mathbf{b} \equiv \hat{\mathbf{e}}_{\vartheta',\varphi'}$ to measure the expectation values,

$$\langle\psi|\hat{\vec{\sigma}}\cdot\mathbf{a}\otimes\mathbb{I}|\psi\rangle \qquad \text{and} \qquad \langle\psi|\mathbb{I}\otimes\hat{\vec{\sigma}}\cdot\mathbf{b}|\psi\rangle \tag{24.8}$$

respectively, on an anti-symmetric entangled two-spin state [3],

$$\boxed{|\psi\rangle = \tfrac{1}{\sqrt{2}}(|+\rangle_z\otimes|-\rangle_z - |+\rangle_z\otimes|-\rangle_z)} \ . \tag{24.9}$$

Let us first do the quantum calculation. Using the rules for Pauli matrices and the anti-symmetry of the entangled state,

$$\hat{\sigma}_x|\pm\rangle_z = |\mp\rangle_z \quad , \quad \hat{\sigma}_y|\pm\rangle_z = \pm\imath|\mp\rangle_z \quad , \quad \hat{\sigma}_z|\pm\rangle_z = \pm|\pm\rangle_z \ , \tag{24.10}$$

we derive in Excs. 24.1.3.3 and 24.1.3.4 the general relationship,

$$\langle\psi|\hat{\vec{\sigma}}\cdot\mathbf{a}\otimes\hat{\vec{\sigma}}\cdot\mathbf{b}|\psi\rangle = -\mathbf{a}\cdot\mathbf{b} \ , \tag{24.11}$$

which is the quantum mechanical correlation function for a joined measurement of Alice and Bob.

On the other hand, if local hidden variables exist, Alice's measurement is determined by the orientation $\mathbf{a}$ of her magnets and a (set of) hidden variable(s) λ, which are also available to Bob, whose measurement is determined by the orientation $\mathbf{b}$ of his magnets,

$$A(\mathbf{a},\lambda) \equiv \langle\psi|\hat{\vec{\sigma}}\cdot\mathbf{a}\otimes\mathbb{I}|\psi\rangle = \pm 1 \qquad \text{and} \qquad B(\mathbf{b},\lambda) \equiv \langle\psi|\mathbb{I}\otimes\hat{\vec{\sigma}}\cdot\mathbf{b}|\psi\rangle = \pm 1 \ , \tag{24.12}$$

with the crucial assumption that A does not depend on $\mathbf{b}$ and B not $\mathbf{a}$. Let us assume a probability distribution $\rho(\lambda)$ for the hidden variable satisfying $\int\rho(\lambda)d\lambda = 1$. Then the joint probability distribution $P(\mathbf{a},\mathbf{b})$ should coincide with the quantum mechanical correlation function,

$$P(\mathbf{a},\mathbf{b}) = \int A(\mathbf{a},\lambda)B(\mathbf{b},\lambda)\rho(\lambda)d\lambda = \langle\psi|\hat{\vec{\sigma}}\cdot\mathbf{a}\otimes\hat{\vec{\sigma}}\cdot\mathbf{b}|\psi\rangle \geq -1 \ . \tag{24.13}$$

For example, let the hidden variable now be unit vector $\vec{\lambda}$ with uniform probability distribution over all directions, such that,

$$A(\mathbf{a},\lambda) = \text{sign}(\mathbf{a}\cdot\vec{\lambda}) \qquad \text{and} \qquad B(\mathbf{b},\lambda) = -\text{sign}(\mathbf{b}\cdot\vec{\lambda}) \ . \tag{24.14}$$

Then,

$$\begin{aligned} P(\mathbf{a},\mathbf{b}) &= -\int \text{sign}(\cos\vartheta_{a\lambda})\text{sign}(\cos\vartheta_{b\lambda})\rho(\vartheta_\lambda)d\vartheta_\lambda \\ &= -\int_{\vartheta_a}^{\vartheta_b}\text{sign}(\cos\vartheta_\lambda)d\vartheta_\lambda = -1 + \tfrac{2}{\pi}\angle(\mathbf{a},\mathbf{b}) \ . \end{aligned} \tag{24.15}$$

This probability distribution clearly deviates from the quantum prediction, in particular at angles $\angle(\mathbf{a},\mathbf{b}) = \frac{\pi}{2}$, as seen in Fig. 24.2(a).

[3] The anti-symmetric state is chosen here for symmetry reasons facilitating the quantum calculation, but the arguments hold for any entangled state.

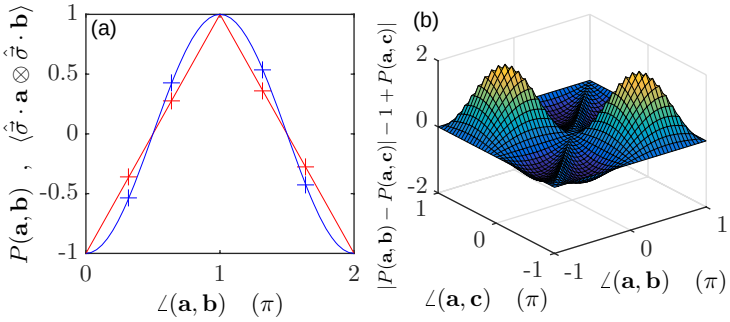

Figure 24.2: (code) (a) Joint probability distribution $P(\mathbf{a},\mathbf{b})$ in local hidden variables theory (red) and correlation function $\langle\psi|\vec{\sigma}\cdot\mathbf{a}\otimes\vec{\sigma}\cdot\mathbf{b}|\psi\rangle$ in quantum mechanics (blue). (b) Verification of Bell's inequality.

Let us finally derive Bell's inequality. Because of (24.12) for the anti-symmetric state we have the relation $B(\mathbf{b},\lambda)=-A(\mathbf{b},\lambda)$ and $A(\mathbf{a},\lambda)=A(\mathbf{a},\lambda)^{-1}$ allowing us to derive,

$$\begin{aligned} P(\mathbf{a},\mathbf{b})-P(\mathbf{a},\mathbf{c}) &= -\int\left[A(\mathbf{a},\lambda)A(\mathbf{b},\lambda)-A(\mathbf{a},\lambda)A(\mathbf{c},\lambda)\right]\rho(\lambda)d\lambda \\ &= \int A(\mathbf{a},\lambda)A(\mathbf{b},\lambda)\left[A(\mathbf{b},\lambda)A(\mathbf{c},\lambda)-1\right]\rho(\lambda)d\lambda\ , \end{aligned} \tag{24.16}$$

and

$$\begin{aligned} |P(\mathbf{a},\mathbf{b})-P(\mathbf{a},\mathbf{c})| &\le \int|A(\mathbf{a},\lambda)A(\mathbf{b},\lambda)\left[A(\mathbf{b},\lambda)A(\mathbf{c},\lambda)-1\right]|\rho(\lambda)d\lambda \\ &\le \int[1-A(\mathbf{b},\lambda)A(\mathbf{c},\lambda)]\rho(\lambda)d\lambda \\ &= \int\rho(\lambda)d\lambda+\int A(\mathbf{b},\lambda)B(\mathbf{c},\lambda)\rho(\lambda)d\lambda=1+P(\mathbf{b},\mathbf{c})\ . \end{aligned} \tag{24.17}$$

This inequality derived from the local hidden variables assumption is violated by quantum mechanics, since,

$$\begin{aligned} |\langle\hat{\vec{\sigma}}\cdot\mathbf{a}\otimes\hat{\vec{\sigma}}\cdot\mathbf{b}\rangle-\langle\hat{\vec{\sigma}}\cdot\mathbf{a}\otimes\hat{\vec{\sigma}}\cdot\mathbf{c}\rangle| &= |-\mathbf{a}\cdot\mathbf{b}+\mathbf{a}\cdot\mathbf{c}| \\ &\le 1-\mathbf{b}\cdot\mathbf{c}=1+\langle\hat{\vec{\sigma}}\cdot\mathbf{b}\otimes\hat{\vec{\sigma}}\cdot c\rangle \end{aligned} \tag{24.18}$$

is not satisfied for arbitrary choices of $\mathbf{a}$, $\mathbf{b}$, and $\mathbf{c}$. To see this we plot in Fig. 24.2(b),

$$1-\cos\angle(\mathbf{b},\mathbf{c})-|\cos\angle(\mathbf{a},\mathbf{b})-\cos\angle(\mathbf{a},\mathbf{c})|\ , \tag{24.19}$$

finding that this quantity becomes negative for some choices of the projection vectors.

Example 163 (*EPR paradox using GHZ states*): Here, we show a modified version of the EPR experiment proposed by Greenberger, Horne and Zeilinger (GHZ) based on the *GHZ state* [336]. They imagined a source creating three correlated non-interacting spin $\frac{1}{2}$ particles labeled a, b, and c flying toward

three Stern-Gerlach type magnetic detectors, which measure the spins in x or in y-direction. The correct state is either quantum,

$$|\psi\rangle = |+_a \ +_b \ +_c\rangle_z - |-_a \ -_b \ -_c\rangle_z \ , \tag{24.20}$$

or

$$\boxed{|\psi\rangle = |+\rangle_z \otimes |+\rangle_z \otimes |+\rangle_z - |-\rangle_z \otimes |-\rangle_z \otimes |-\rangle_z} \ , \tag{24.21}$$

in tensor notation, or it contains hidden variables, that is, instructions telling the detectors which measurement result to exhibit upon arrival of a particle,

$$|\psi\rangle = \begin{pmatrix} \pm_x^a \ \pm_x^b \ \pm_x^c \\ \pm_y^a \ \pm_y^b \ \pm_y^c \end{pmatrix} . \tag{24.22}$$

Now, using the quantum mechanical rules (24.10), we obtain,

$$\hat\sigma_x \otimes \hat\sigma_x \otimes \hat\sigma_x |\psi\rangle \equiv \hat\sigma_x^a \hat\sigma_x^b \hat\sigma_x^c |\psi\rangle = -|\psi\rangle \ , \tag{24.23}$$

but also,

$$\hat\sigma_x^a \hat\sigma_y^b \hat\sigma_y^c |\psi\rangle = \hat\sigma_y^a \hat\sigma_x^b \hat\sigma_y^c |\psi\rangle = \hat\sigma_y^a \hat\sigma_y^b \hat\sigma_x^c |\psi\rangle = |\psi\rangle \ . \tag{24.24}$$

Hidden variables in a state $|\psi\rangle$ that *is not a coherent superposition* should at

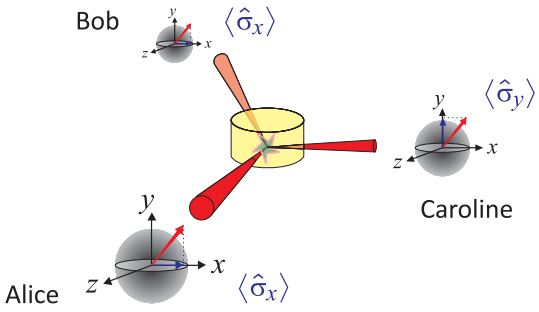

Figure 24.3: Scheme of the EPR experiment proposed by Greenberger, Horne and Zeilinger.

least be able to predict how each particle will behave in its respective detector, when we measure each one of the two spin components. From all possible combination only eight combinations can satisfy the requirement (24.24) written as,

$$\langle\hat\sigma_x^a\rangle\langle\hat\sigma_y^b\rangle\langle\hat\sigma_y^c\rangle = \langle\hat\sigma_y^a\rangle\langle\hat\sigma_x^b\rangle\langle\hat\sigma_y^c\rangle = \langle\hat\sigma_y^a\rangle\langle\hat\sigma_y^b\rangle\langle\hat\sigma_x^c\rangle = 1 \ . \tag{24.25}$$

These are,

$$\begin{pmatrix} \langle\sigma_x^a\rangle & \langle\sigma_x^b\rangle & \langle\sigma_x^c\rangle \\ \langle\sigma_y^a\rangle & \langle\sigma_y^b\rangle & \langle\sigma_y^c\rangle \end{pmatrix} = \tag{24.26}$$

$$\begin{pmatrix} +\,+\,+ \\ +\,+\,+ \end{pmatrix} \begin{pmatrix} +\,-\,- \\ +\,-\,- \end{pmatrix} \begin{pmatrix} -\,+\,- \\ -\,+\,- \end{pmatrix} \begin{pmatrix} -\,-\,+ \\ -\,-\,+ \end{pmatrix} \begin{pmatrix} +\,+\,+ \\ -\,-\,- \end{pmatrix} \begin{pmatrix} +\,-\,- \\ -\,+\,+ \end{pmatrix} \begin{pmatrix} -\,+\,- \\ +\,-\,+ \end{pmatrix}$$

but none of them satisfies (24.23) written as,

$$\langle\hat\sigma_x^a\rangle\langle\hat\sigma_x^b\rangle\langle\hat\sigma_x^c\rangle = -1 \ . \tag{24.27}$$

Therefore, the local hidden variables assumption is incompatible with quantum mechanics, and the EPR critique of quantum mechanics regarding its incompleteness must be refuted [4].

Which one of the two pictures is correct, the local hidden variables assumption or quantum mechanics, can actually be tested by Wheeler's *delayed choice* experiment. It consists of using pairs of correlated photons emitted in different directions, where they are expected by photodetectors. Polarizers located in front of the detectors fix the quantization axis to $\hat{\mathbf{e}}_x$ or $\hat{\mathbf{e}}_y$, but the choice of the axis is made only after the photons were created by the source, in order to avoid possible backactions of the polarizers on the source [5]. Bell's inequality condition [65] predicts a statistics for the results of repeated measurements where the orientation of the polarizers is randomly varied. The experiment run by Aspect [32, 31] showed that the assumption of local hidden variables violates *local realism* and thus confirmed quantum mechanics as being a complete theory.

24.1.2 Information entropy

According to von Neumann, we can define the *von Neumann entropy*, also called quantum *information entropy* as,

$$\boxed{S \equiv -\langle \log_2 \hat{\rho} \rangle = \mathrm{Tr}\,(\hat{\rho} \log_2 \hat{\rho}) = -\sum_n \hat{\rho}_n \log_2 \hat{\rho}_n} \,, \tag{24.28}$$

where $\rho_n \equiv \langle n|\hat{\rho}|n\rangle$. For statistically independent systems the density operator is $\hat{\rho} = \hat{\rho}_1 \otimes \hat{\rho}_2$ and the entropy is additive $S = S_1 + S_2$. The entropy is observable, that is, independent of the basis and invariant with respect to unitary transformations. Therefore, $\hat{\rho}$ can be diagonalized and can be assumed diagonal in the following examples. For N independent qubits the density operator $\hat{\rho}^{(N)}$ and the entropy $S^{(N)}$ are:

$$\begin{aligned}
&\hat{\rho}^{(0)} = |+\rangle\langle +| && , \quad S^{(0)} = 0 \text{ bit} \\
&\hat{\rho}^{(1)} = \tfrac{1}{2}(|+\rangle\langle +| + |-\rangle\langle -|) && , \quad S^{(1)} = 1 \text{ bits} \\
&\hat{\rho}^{(2)} = \tfrac{1}{4}(|++\rangle\langle ++| + |+-\rangle\langle +-| + |-+\rangle\langle -+| + |--\rangle\langle --|) && , \quad S^{(2)} = 2 \text{ bits} \\
&\hat{\rho}^{(N)} = \tfrac{1}{2^N}(|++...\rangle\langle ++...| + ...) && , \quad S^{(N)} = N \text{ bits} \,.
\end{aligned} \tag{24.29}$$

The set is canonical and the entropy maximal. On the other hand, if the states are entangled, the entropy is always less than $S^{(N)} = N$ bits. For the state of maximally entangled spins, we have,

$$\rho^{(N)}_{\mathrm{corr}} = \tfrac{1}{2^N}(|++...+\rangle\langle ++...+| + |--...-\rangle\langle --...-|) \quad , \quad S^{(N)}_{\mathrm{corr}} = 1 \text{ bit} \,. \tag{24.30}$$

[4] Note that the coupling of different degrees of freedom *is not* an entanglement, but it is the *condition* for being able to generate entanglement.

[5] We note that first attempts to demonstrate wave-particle duality with single photons in dilute laser beams are not really conclusive, because the attenuation of a coherent state does NOT result in a single photon states (non-classical Fock state). Even if on average only less than one photon is in the interferometer, this may still be a Glauber state. Nonetheless, real single photon experiments involving the deexcitation of individual atoms by emission of two photons, produced the same result.

Entropy is a measure for the degree of entanglement of a system. For a Dicke state $|J, M\rangle$ the entropy is,

$$S_{JM} = -\log_2 \binom{2J}{J+M} . \tag{24.31}$$

For beam splitters, the information entropy is calculated as follows: A Fock state $|N\rangle = |+\rangle^N$ divided by a beam splitter is described by,

$$\begin{aligned} 2^{-N/2}(|+\rangle + |-\rangle)^N &= \tfrac{1}{2^{N/2}} \sum_{n=0}^{N} \binom{N}{n} |+\rangle^{N-n} |-\rangle^n \qquad (24.32) \\ \rho_{\text{split}}^{(N)} &= \tfrac{1}{2^N} \sum_{n,m=0}^{N} \binom{N}{n}\binom{N}{m} |+\rangle^{N-n} |-\rangle^n \langle+|^{N-m} \langle-|^m \\ \rho_{\text{split}}^{(N)} &= \tfrac{1}{2^N} \sum_{n=0}^{N} \binom{N}{n}\binom{N}{n} |+\rangle^{N-n} |-\rangle^n \langle+|^{N-n} \langle-|^n . \end{aligned}$$

For the information entropy, we obtain,

$$S_{\text{split}}^{(N)} = N + \tfrac{1}{2^N} \sum_{n=0}^{N} \binom{N}{n} \log_2 \binom{N}{n} . \tag{24.33}$$

The division of a beam is an incoherent process in the sense that it increases the entropy. The process is *irreversible*. The divided beams can not be recombined by a coherent process. For example, an interferometer always has two output ports. However, the phase is preserved.

The *quantum information content* is defined by the deviation from maximum entropy,

$$Q = S_{\text{mx}} - S_{\text{actual}} . \tag{24.34}$$

If the system is in a mixed state, the entropy measures deviations from a pure state behavior [57].

24.1.2.1 Separability and entanglement

Separable states are defined by,

$$\hat{\rho}_{\text{sep}} = \sum_m \hat{\rho}_m^{(1)} \otimes ... \otimes \hat{\rho}_m^{(N)} , \tag{24.35}$$

where $\hat{\rho}_m^{(n)}$ are single-particle pure states. Separable states are essentially states that can be created without an inter-particle interaction, just by mixing product states [825]. States that are not separable are called *entangled*.

24.1.3 Exercises

24.1.3.1 Ex: Bell states

Show that the Bell states cannot be written as products of two states.

24.1.3.2 Ex: Behavior of entanglement upon rotation of the quantization axis

Show that the anti-symmetric entangle Bell state remains entangled upon rotation of the quantization axis, that is,

$$|+\rangle_{\vartheta,\varphi}\otimes|-\rangle_{\vartheta,\varphi}-|-\rangle_{\vartheta,\varphi}\otimes|+\rangle_{\vartheta,\varphi}\ \propto\ |+\rangle_z\otimes|-\rangle_z-|-\rangle_z\otimes|+\rangle_z\ ,$$

where $|\pm\rangle_{\vartheta,\varphi}$ are the eigenstates of the Pauli spin operator $\hat{\vec{\sigma}}$.

24.1.3.3 Ex: Rotations with Pauli matrices

a. Verify,

$$e^{-\imath(\pi/4)\hat{\sigma}_k}\hat{\sigma}_m e^{\imath(\pi/4)\hat{\sigma}_k}=\epsilon_{kmn}\hat{\sigma}_n+\delta_{km}\hat{\sigma}_k\qquad\text{with}\qquad(kmn)=(xyz)\ .$$

b. Prove,

$$|\vartheta,\varphi\rangle=e^{-\imath\varphi(\hat{\sigma}_z-I)/2}e^{-\imath\vartheta\hat{\sigma}_y/2}|0,0\rangle=e^{\imath\varphi/2}e^{-\imath\varphi\hat{\sigma}_z/2}e^{-\imath\vartheta\hat{\sigma}_y/2}|+\rangle\ .$$

c. Solve the eigenvalue equations,

$$\hat{\vec{\sigma}}\cdot\hat{\mathbf{e}}_z|\vartheta,\varphi\rangle=m|\vartheta,\varphi\rangle\qquad\text{and}\qquad\hat{\vec{\sigma}}\cdot\hat{\mathbf{e}}_\rho|\vartheta,\varphi\rangle=m|\vartheta,\varphi\rangle\ ,$$

with $\hat{\mathbf{e}}_\rho\equiv\hat{\mathbf{e}}_x\cos\phi+\hat{\mathbf{e}}_y\sin\phi$.

24.1.3.4 Ex: Projections of single-atom spins and their correlations

a. Calculate explicitly $\langle\vartheta,\varphi|\hat{\vec{\sigma}}|\vartheta,\varphi\rangle$ and $\langle\vartheta',\varphi'|\hat{\vec{\sigma}}\cdot\hat{\mathbf{e}}_{\vartheta,\varphi}|\vartheta',\varphi'\rangle$, where $|\vartheta,\varphi\rangle$ are the states defined in (23.10), using the basis ${}_z\langle+|=(1\ 0)$ and ${}_z\langle-|=(0\ 1)$.
b. For the anti-symmetric entangled two-atom spin state defined in (24.9) calculate the spin projection correlations $\langle\psi|\hat{\vec{\sigma}}\cdot\hat{\mathbf{e}}_{\vartheta,\varphi}\otimes\hat{\vec{\sigma}}\cdot\hat{\mathbf{e}}'_{\vartheta,\varphi}|\psi\rangle$.

24.1.3.5 Ex: No cloning theorem

Based upon the superposition principle of quantum mechanics, prove the *no-cloning theorem* which states that a quantum state $|\psi\rangle$ cannot evolve into two separable (non-entangled) copies described by the tensor product state $|\psi\rangle|\psi\rangle$.

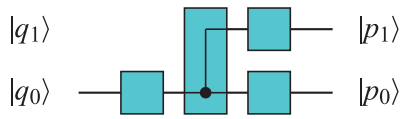

Figure 24.4: Illustration of the 'no-cloning theorem'. The transformation must be reversible, but from the state $|q_1,q_0\rangle$ we cannot infer the state $|p_1,p_0\rangle$.

24.1.3.6 Ex: Entanglement

Upon detecting the polarization of one photon in an entangled photon pair the polarization of the other photon gets determined. Does this lead to a faster than light communication? Justify your answer. How would you demonstrate the *no-cloning theorem* from the assumption that relativistic causality should prevail.

24.1.3.7 Ex: Entanglement

Three photon are prepared in the GHZ state defined as,

$$|\psi\rangle = \frac{1}{\sqrt{3}}\left(|h\rangle_1|h\rangle_2|h\rangle_3 + |v\rangle_1|v\rangle_2|v\rangle_3\right) \ .$$

Show that, when the components of polarization are measured along the axes that have an angle of 45° with respect to the original axes, corresponding to the states,

$$|h'\rangle = \frac{1}{\sqrt{2}}(|h\rangle + |v\rangle) \qquad \text{and} \qquad |v'\rangle = \frac{1}{\sqrt{2}}(|h\rangle - |v\rangle) \ ,$$

one gets necessarily an even number of photons with vertical polarization v'.

24.1.3.8 Ex: NOON state

A *NOON state* is a quantum-mechanical many-body entangled state:

$$|\psi_{\text{NOON}}\rangle = \frac{|N\rangle_a|0\rangle_b + e^{\imath N\theta}|0\rangle_a|N\rangle_b}{\sqrt{2}} \ , \tag{24.36}$$

which represents a superposition of N particles in mode a with zero particles in mode b, and vice versa. Usually, the particles are photons, but in principle any bosonic field can support NOON states.
Two-photon NOON states, where $N = 2$, can be created deterministically from two identical photons and a 50:50 beam splitter. This is called the *Hong-Ou-Mandel effect* in quantum optics. Three- and four-photon NOON states cannot be created deterministically from single-photon states, but they have been created probabilistically via post-selection using spontaneous parametric down-conversion.

24.2 Creating quantum correlations

Since the experimental verification of *Bell's inequality* [33] numerous ideas were proposed for the creation and application of correlated states in distant particles. Realistic proposals on how to create such states are often based on a Jaynes-Cummings type coupling between states of atomic excitation and the degrees of freedom of a harmonic oscillator. The Jaynes-Cummings dynamics has been extensively studied in micromasers, where the non-resonant interaction of an atomic transition with the TEM_{00} mode of a stored radiation field generates quantum coherences. In very high finesse cavities, light field states with sub-Poissonian photon statistics can be generated and stored for macroscopic times, and schemes for the creation of Fock states and Schrödinger cat states were proposed and tested. Furthermore, the electronic excitation states of atoms successively traversing a micromaser can be correlated under suitable conditions. The availability of fundamental techniques motivated proposals for the investigation of phenomena such as EPR correlations, quantum teleportation, and quantum switching [241]. On the other hand, quantum coherences are very fragile to dissipation and rapidly decay when exposed to perturbations.

Jaynes-Cummings type dynamics can also be realized with a single ion stored in a Paul trap, where the interaction of its mechanical motion with an electronic transition [93] can induce very stable quantum coherences in the vibrational degrees of freedom.

Schrödinger cat states have already been demonstrated in this system [563], as well as fundamental parts of a quantum computer, the quantum *controlled not gate* [563] and the quantum *phase gate* [832]. In Sec. 24.2.1 we present a possible extension of these ideas to several atoms in a collective Jaynes-Cummings type interaction (also called Tavis-Cummings model) with a single harmonic oscillator mode.

In order to correlate particles, they must be able to exchange information, that is, they must interact in some way. One method uses ions trapped in a linear Paul trap, where they form a straight chain, individually driven by laser beams and coupled to each other via their vibrational degrees of freedom mediated through Coulomb repulsion [158]. We present this idea in Sec. 24.2.2. Such scenarios have been implemented to create the first quantum computers. Another way consists in trapping neutral atoms in a dual optical lattice and let them undergo *controlled collisions* [426], as will be discussed in Sec. 24.2.3.

Alternative approaches to realizing quantum gates use dipole-dipole interactions [118], conditional Raman adiabatic passages by laser-induced excitation of interatomic dipole-dipole interactions [536], or interactions between permanent dipoles of atoms in Rydberg states [427] [6]

24.2.1 Correlating atoms in the Jaynes-Cummings model

In Sec. 17.2 we showed already that the Jaynes-Cummings model is able to perform coherent operations on a two-level system –which from now on we will call *qubit*–, such as the *population inversion* (NOT-gate) and the controlled dephasing of an excited dipole moment (phase gate). These operations are fundamental for applications in quantum information, however, we still lack essential ingredients allowing us to entangle states of two, three or more qubits in order to perform a *quantum register* of *qubits*. Once these register are realized, we must define coherent quantum operations called *quantum gates*.

24.2.1.1 Tavis-Cummings model for 2 atoms

In Sec. 17.2 we showed, how a Jaynes-Cummings interaction between an atom and a radiation field can exchange quantum correlations. It is reasonable to expect that, when we have two (or more) atoms interacting with the same radiation field, we can exchange correlations between atoms via the field. This would allow the implementation of entanglement protocols and quantum gates. We will disregard spontaneous processes, such that all couplings are then coherent and the processes reversible.

In Sec. 1.5.8 we learned, how to span a Hilbert space of various particles. We will now apply these notions in the scope of generalizing the Jaynes-Cummings model to *two atoms interacting with the same optical mode*, without spontaneous decay processes considered. The system is often referred to as the *Tavis-Cummings model*. The Hamiltonian of the system, which consists of two non-interacting atoms, both coupled in the same optical mode, is,

$$\boxed{\hat{H} = \omega \hat{a}^\dagger \hat{a} + \sum_{i=1,2} \omega_{ai} (\hat{\sigma}_i^+ \hat{\sigma}_i^- - \tfrac{1}{2}) + \sum_{i=1,2} \tfrac{1}{2} g_i(t) (\hat{a} \hat{\sigma}_i^+ + \hat{a}^+ \hat{\sigma}_i^-)} \,. \tag{24.37}$$

[6] A system to create quantum correlations is the *optical parametric oscillator* (OPO).

The suffix denotes the individual atoms. Note that the coupling constant $g_i(t)$ can be considered as time dependent, which may be useful for modeling radiation pulse envelopes. In matrix representation the Hamiltonian acting on the subspace of n photons is,

$$|\psi\rangle = \sum_n \begin{pmatrix} c_{11\ n+1} \\ c_{12\ n} \\ c_{21\ n} \\ c_{22\ n-1} \end{pmatrix} |n\rangle \qquad \text{where} \qquad c_{ij} \equiv_1 {}_2\langle j|{}_1\langle i|n\rangle|\psi\rangle \tag{24.38}$$

for example, $\langle n| \otimes \langle 1| \otimes \langle 1| = \langle n|(1\ 0\ 0\ 0)$, $\langle n| \otimes \langle 2| \otimes \langle 1| = \langle n|(0\ 1\ 0\ 0)$, and so on. The atomic transition operators are generalized to,

$$\hat{\sigma}_1^- = \sum_n |n\rangle\hat{\sigma}^- \otimes \mathbb{I}\langle n| = \sum_n |n\rangle \begin{pmatrix} & & 1 & \\ & & & 1 \\ 0 & & & \\ & 0 & & \end{pmatrix} \langle n| \tag{24.39}$$

$$\hat{\sigma}_2^- = \sum_n |n\rangle\mathbb{I} \otimes \hat{\sigma}^-\langle n| = \sum_n |n\rangle \begin{pmatrix} & 1 & & \\ 0 & & & \\ & & & 1 \\ & & 0 & \end{pmatrix} \langle n| \quad \text{, etc. .}$$

The Hamiltonian is, on this basis,

$$\hat{H} = \sum_n |n\rangle \begin{pmatrix} n\omega - \frac{\omega_{a1}}{2} - \frac{\omega_{a2}}{2} & & & \\ & n\omega - \frac{\omega_{a1}}{2} + \frac{\omega_{a2}}{2} & & \\ & & n\omega + \frac{\omega_{a1}}{2} - \frac{\omega_{a2}}{2} & \\ & & & n\omega + \frac{\omega_{a1}}{2} + \frac{\omega_{a2}}{2} \end{pmatrix} \langle n| + \sum_n |n-1\rangle\sqrt{n} \begin{pmatrix} 0 & & & \\ g_2 & & & \\ g_1 & & & \\ 0 & g_1 & g_2 & 0 \end{pmatrix} \langle n| + \sum_n |n+1\rangle\sqrt{n+1} \begin{pmatrix} 0 & g_2 & g_1 & 0 \\ & & & g_1 \\ & & & g_2 \\ & & & 0 \end{pmatrix} \langle n| \ . \tag{24.40}$$

Now, we can rearrange the subspaces and finally get,

$$\hat{H} = \sum_n |n\rangle \begin{pmatrix} (n+1)\omega - \frac{\omega_{a1}}{2} - \frac{\omega_{a2}}{2} & g_1\sqrt{n} & g_2\sqrt{n} & \\ g_1\sqrt{n} & n\omega + \frac{\omega_{a1}}{2} - \frac{\omega_{a2}}{2} & & g_2\sqrt{n+1} \\ g_2\sqrt{n} & & n\omega - \frac{\omega_{a1}}{2} + \frac{\omega_{a2}}{2} & g_1\sqrt{n+1} \\ & g_2\sqrt{n+1} & g_1\sqrt{n+1} & (n-1)\omega + \frac{\omega_{a1}}{2} + \frac{\omega_{a2}}{2} \end{pmatrix} \langle n| \ . \tag{24.41}$$

The density operator for the subspace is,

$$\hat{\rho} = \begin{pmatrix} |n+1\rangle|1\rangle_1|1\rangle_2\ {}_1\langle 1|{}_2\langle 1|\langle n+1| & |n+1\rangle|1\rangle_1|1\rangle_2\ {}_1\langle 1|{}_2\langle 2|\langle n| & \ldots \\ |n\rangle|1\rangle_2|1\rangle_2\ {}_1\langle 1|{}_2\langle 1|\langle n+1| & \ldots & \\ |n\rangle|2\rangle_1|2\rangle_2\ {}_1\langle 1|{}_2\langle 1|\langle n+1| & \ldots & \\ |n-1\rangle|2\rangle_1|2\rangle_2\ {}_1\langle 1|{}_2\langle 1|\langle n+1| & \ldots & \end{pmatrix} , \tag{24.42}$$

if the basis is again defined by equation (24.39).

24.2.1.2 Resonant excitation

To discuss the case of resonant excitation, $\Delta_1 = \Delta_2 = 0$, let us assume identical atoms, $\omega_{a1} = \omega_{a2} \equiv \omega_0$, and equal Rabi frequencies, $g_1 = g_2 \equiv g$. Assuming dipolarly forbidden strongly saturated transition, $n = \alpha^2$ for all n, the Hamiltonian simplifies considerably,

$$\hat{H}_n = \begin{pmatrix} n\omega & g\sqrt{n} & g\sqrt{n} & \\ g\sqrt{n} & n\omega & & g\sqrt{n} \\ g\sqrt{n} & & n\omega & g\sqrt{n} \\ & g\sqrt{n} & g\sqrt{n} & n\omega \end{pmatrix} ,$$

the eigenvalues can be calculated and the time evolution matrix becomes, using the abbreviation $\varphi \equiv gt\sqrt{n}$,

$$\boxed{e^{-\imath\hat{H}_n t} = e^{-\imath\hat{H}_n^{A1} t} e^{-\imath\hat{H}_n^{A2} t} = \begin{pmatrix} \cos^2\varphi & \imath\sin\varphi\cos\varphi & \imath\sin\varphi\cos\varphi & -\sin^2\varphi \\ \imath\sin\varphi\cos\varphi & \cos^2\varphi & -\sin^2\varphi & \imath\sin\varphi\cos\varphi \\ \imath\sin\varphi\cos\varphi & -\sin^2\varphi & \cos^2\varphi & \imath\sin\varphi\cos\varphi \\ -\sin^2\varphi & \imath\sin\varphi\cos\varphi & \imath\sin\varphi\cos\varphi & \cos^2\varphi \end{pmatrix}} . \tag{24.43}$$

For a π-pulse, we get,

$$e^{-\imath\hat{H}_n t} \xrightarrow{\pi/2} \frac{1}{2}\begin{pmatrix} 1 & \imath & \imath & -1 \\ \imath & 1 & -1 & \imath \\ \imath & -1 & 1 & \imath \\ -1 & \imath & \imath & 1 \end{pmatrix} . \tag{24.44}$$

It is interesting to note that some superposition states completely separate from the optical mode,

$$e^{-\imath\hat{H}_n t}\begin{pmatrix} 0 \\ 1 \\ -1 \\ 0 \end{pmatrix} = \begin{pmatrix} 0 \\ 1 \\ -1 \\ 0 \end{pmatrix} \quad \text{and} \quad e^{-\imath\hat{H}_n t}\begin{pmatrix} 1 \\ 0 \\ 0 \\ -1 \end{pmatrix} = \begin{pmatrix} 1 \\ 0 \\ 0 \\ -1 \end{pmatrix} . \tag{24.45}$$

24.2.1.3 Dispersive excitation

In the dispersive limit, $\Delta_i \gg n^{1/2} g_i$, the dynamic evolution can be evaluated from a first order perturbative approach, analogous to the one already made for the standard JCM model. In this approach, the off-diagonal matrix elements (24.41) generate a light-shift of the energy levels appearing on the diagonal of the approximated matrix. Using the abbreviation $\Lambda_i \equiv g_i^2/\Delta_i$, the temporal evolution matrix $e^{-\imath\hat{H}_n t}$ can now be evaluated from,

$$\hat{H}_n = -\frac{\Delta_1 + \Delta_2}{2}\mathbb{I}_4 + \begin{pmatrix} n\Lambda_1 + n\Lambda_2 & & & \\ & -n\Lambda_1 + (n+1)\Lambda_2 & & \\ & & (n+1)\Lambda_1 - n\Lambda_2 & \\ & & & -(n+1)\Lambda_1 - (n+1)\Lambda_2 \end{pmatrix} . \tag{24.46}$$

We now assume that the light field only interacts with the upper level, as in the case of the dual resonance configuration studied in Exc. 17.2.5.4. This can be taken into account, neglecting those terms in the matrix (24.45) rotating with a positive Rabi frequency. Letting, moreover, $\Delta_1 = \Delta_2$ and $\Omega_1 = \Omega_2$, we obtain,

$$\hat{H}_n^{(1)} = \begin{pmatrix} 0 & & & \\ & -n\Lambda & & \\ & & -n\Lambda & \\ & & & -2(n+1)\Lambda \end{pmatrix} . \tag{24.47}$$

Thus, the temporal evolution is,

$$\boxed{e^{-\imath \hat{H}_n t} = \begin{pmatrix} 1 & & & \\ & e^{-n\Lambda} & & \\ & & e^{-n\Lambda} & \\ & & & e^{-2(n+1)\Lambda} \end{pmatrix}} . \tag{24.48}$$

For $\Lambda = \pi$,

$$e^{-\imath \hat{H}_n t} \xrightarrow{\pi} \begin{pmatrix} 1 & & & \\ & -1 & & \\ & & -1 & \\ & & & 1 \end{pmatrix} . \tag{24.49}$$

24.2.1.4 Bloch vector and the Q-function in the JC model with 2 atoms

Despite the more complex structure of the Hilbert space, the Bloch vectors of the individual atoms and the Q-function can be evaluated in analogy to Sec. 17.2.2. The Bloch vector is,

$$\vec{\rho}_{A1} = \tfrac{1}{\sqrt{2}} \begin{pmatrix} \sqrt{2}\, \mathfrak{Re}\, \rho_{12(A1)} \\ \sqrt{2}\, \mathfrak{Im}\, \rho_{12(A1)} \\ \rho_{22(A1)} - \rho_{11(A1)} \end{pmatrix} \qquad \text{where} \qquad \rho_{ij(A1)} = \mathrm{Tr}\ |i\rangle_1\langle j|\psi\rangle\langle\psi| \ . \tag{24.50}$$

In particular we have,

$$\begin{aligned} \rho_{22(A1)} &= \sum_{i,j,n} {}_2\langle j|_1\langle i|\langle n|1\rangle_1\langle 2|\psi\rangle\langle\psi|n\rangle|i\rangle_1|j\rangle_2 \qquad (24.51) \\ &= \sum_{j,n} {}_2\langle j|_1\langle 2|\langle n|\psi\rangle\langle\psi|n\rangle|1\rangle_1|j\rangle_2 \\ &= \sum_{n,m,m'} \langle n| \left(c_{2,1,m}|m\rangle\langle m'+1|c^*_{1,1,m'+1} + c_{2,2,m}|m'-1\rangle\langle m'|c^*_{1,2,m'}\rangle \right) |n\rangle \\ &= \sum_n (c^*_{1,1,n} c_{2,1,n} + c^*_{1,2,n} c_{2,2,n}) \ . \end{aligned}$$

Summarizing,

$$\begin{array}{rcl} \rho_{12(Ai\neq Aj)} & = & \sum_n (c^*_{1,1,n} c_{j,i,n} + c^*_{i,j,n} c_{2,2,n}) \\ \rho_{11(Ai\neq Aj)} & = & \sum_n (|c_{1,1,n}|^2 + |c_{i,j,n}|^2) \\ \rho_{22(Ai\neq Aj)} & = & \sum_n (|c_{j,i,n}|^2 + |c_{2,2,n}|^2) \end{array} \ . \tag{24.52}$$

The function $Q(\alpha)$ for the JC dynamics of 2 atoms is,

$$
\begin{aligned}
Q(\alpha) &= \tfrac{1}{\pi}\langle\alpha|\hat{\rho}_{field}|\alpha\rangle = \tfrac{1}{\pi}\langle\alpha|\sum_{i,j}\ {}_2\langle j|_1\langle i|\psi\rangle\langle\psi|i\rangle_1|j\rangle_2|\alpha\rangle \qquad (24.53)\\
&= \tfrac{1}{\pi}\langle\alpha|\sum_{m,n}(c^*_{2,2,m-1}c_{2,2,n-1}|n-1\rangle\langle m-1| + c^*_{1,2,m}c_{1,2,n}|n\rangle\langle m|\\
&+ c^*_{2,1,m}c_{2,1,n}|n\rangle\langle m| + c^*_{1,1,m+1}c_{1,1,n+1}|n+1\rangle\langle m+1|)|n\rangle|\alpha\rangle\\
&= e^{-|\alpha|^2}\left[\left|\sum_n c_{2,2,n-1}\frac{\alpha^n}{\sqrt{n!}}\right|^2 + \left|\sum_n c_{1,2,n}\frac{\alpha^n}{\sqrt{n!}}\right|^2 + \left|\sum_n c_{2,1,n}\frac{\alpha^n}{\sqrt{n!}}\right|^2 + \left|\sum_n c_{2,2,n+1}\frac{\alpha^n}{\sqrt{n!}}\right|^2\right] .
\end{aligned}
$$

24.2.1.5 Correlating 2 atoms in the JC model

The investigations of the last section can be applied to describe the transfer of quantum coherence from one atom to another. The size of our system is now increased by the additional degrees of freedom, provided by internal states of the second atom. A suitable basis was defined in equation (1.223). Now, we imagine the following Gedankenexperiment: Starting from the initial condition that two adjacent atoms are in their respective electronic ground states, we assume a microwave $\pi/2$-pulse to create *simultaneously, but independently* on both atoms, a superposition of the HFS levels. Then, a non-resonant optical π-pulse interacts with the upper HFS level of the first atom $|1\rangle_{A1}$, and afterward the second atom $|2\rangle_{A2}$. Instead of reducing the atomic states and preparing a Schrödinger cat state in the optical field, (as we did in Sec. 17.2), we now project the field state onto the coherent state $|\beta\rangle$ and leave the atoms in a correlated state. The total procedure can be resumed by tracing the evolution of the whole state in the following suggestive way [38, 319]:

$$
\begin{pmatrix}|\beta\rangle\\0\\0\\0\end{pmatrix}
\overset{\pi/2\text{ microwave}}{\curvearrowright}
\tfrac{1}{4}\begin{pmatrix}1\\ \imath\\ \imath\\ -1\end{pmatrix}|\beta\rangle
\overset{\pi\text{ opt+atom1}}{\curvearrowright}
\tfrac{1}{4}\begin{pmatrix}|\beta\rangle\\ -\imath|-\beta\rangle\\ \imath|\beta\rangle\\ |-\beta\rangle\end{pmatrix}
\overset{\pi\text{ opt+atom2}}{\curvearrowright}
\tfrac{1}{4}\begin{pmatrix}|\beta\rangle\\ -\imath|-\beta\rangle\\ -\imath|-\beta\rangle\\ -|\beta\rangle\end{pmatrix}
$$

$$
\overset{\pi/2\text{ microwave}}{\curvearrowright}
\tfrac{1}{4}\begin{pmatrix}1\\0\\0\\1\end{pmatrix}|\beta\rangle + \frac{1}{4}\begin{pmatrix}1\\0\\0\\-1\end{pmatrix}|-\beta\rangle
\overset{\text{reduction}}{\curvearrowright}
\tfrac{1}{2}\begin{pmatrix}1\\0\\0\\-1\end{pmatrix}|\beta\rangle\ . \qquad (24.54)
$$

If this procedure is extended to an arbitrary number of atoms, obviously all atoms being excited by the same optical mode before its projection in a coherent state $|\beta\rangle$ are included in the entangled state,

$$
|\psi\rangle = \tfrac{1}{4}\begin{pmatrix}1\\:\\1\end{pmatrix}|\beta\rangle + \tfrac{1}{4}\begin{pmatrix}1\\:\\-1\end{pmatrix}|-\beta\rangle\ . \qquad (24.55)
$$

Finally, the correlation of the spin orientation of the atoms must be probed with additional laser light fields, which are selectively irradiated onto the atoms and resonantly tuned to a rapidly decaying optical transition. The states correlated in this

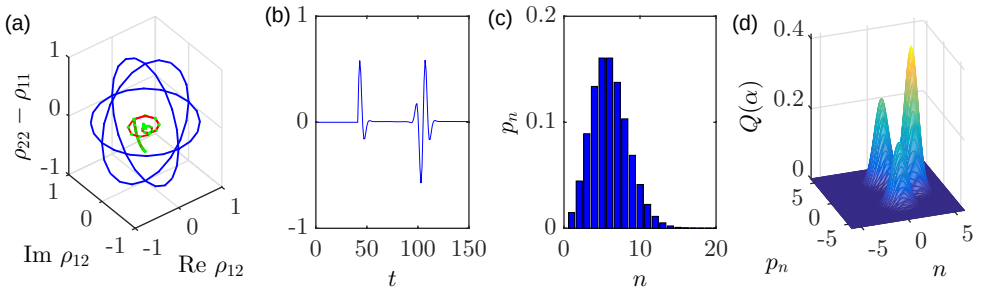

Figure 24.5: (code) Evolution of the state during a Jaynes-Cummings interaction with 2 atoms: (a) Bloch vector for the two atoms, (b) time evolution of the coherence ρ_{12} showing the phenomenon of collapse and revival, (c) distribution of photons, and (d) $Q(\alpha)$-function.

way show a relatively low order entanglement, the von Neumann information entropy only being $S' = -\langle \log_2 \rho \rangle = N - 1$.

In a matricial notation the entangling gate can be expressed defining the state,

$$\begin{aligned} \langle\psi| &= \begin{pmatrix} c_{+\beta 11} & c_{+\beta 12} & c_{+\beta 21} & c_{+\beta 22} & c_{-\beta 11} & c_{-\beta 12} & c_{-\beta 21} & c_{-\beta 22} \end{pmatrix} \\ &= \langle\beta| \otimes \langle \text{atom}_1| \otimes \langle \text{atom}_2| \ . \end{aligned} \tag{24.56}$$

In this basis, the dispersive π-pulse is represented by,

$$\mathcal{U}_{\text{disp}} \equiv \begin{pmatrix} 1 & & & & & & & \\ & & & & -1 & & & \\ & & & & & -1 & & \\ & & & 1 & & & & \\ & & & & 1 & & & \\ & -1 & & & & & & \\ & & -1 & & & & & \\ & & & & & & & 1 \end{pmatrix} . \tag{24.57}$$

A resonant $\pi/2$-pulse acting on the *both atoms simultaneously* does,

$$\mathcal{U}_{\text{reson}} \equiv \mathbb{I} \otimes \mathcal{U}^{(2)}_{\pi/2} \otimes \mathbb{I} = \tfrac{1}{\sqrt{2}} \begin{pmatrix} 1 & \imath & \imath & -1 & & & & \\ \imath & 1 & -1 & \imath & & & & \\ \imath & -1 & 1 & \imath & & & & \\ -1 & \imath & \imath & 1 & & & & \\ & & & & 1 & \imath & \imath & -1 \\ & & & & \imath & 1 & -1 & \imath \\ & & & & \imath & -1 & 1 & \imath \\ & & & & -1 & \imath & \imath & 1 \end{pmatrix} . \tag{24.58}$$

Now, concatenating and projecting on the Glauber state $|\beta\rangle$ we obtain, a posteriori,

a unitary entangling gate,

$$\mathcal{U}_{\rm entangl} \equiv {\rm Tr}_\beta\ |\beta\rangle\langle\beta|\mathcal{U}_{\rm reson}\mathcal{U}_{\rm disp}\mathcal{U}_{\rm reson}|\beta\rangle\langle\beta| = \tfrac{1}{\sqrt{2}}\begin{pmatrix} 1 & 0 & 0 & -1 \\ 0 & -1 & -1 & 0 \\ 0 & -1 & -1 & 0 \\ -1 & 0 & 0 & 1 \end{pmatrix} \tag{24.59}$$

$$\text{such that} \quad \begin{pmatrix} 1 \\ 0 \\ 0 \\ -1 \end{pmatrix} = \mathcal{U}_{\rm entangl}\begin{pmatrix} 1 \\ 0 \\ 0 \\ 0 \end{pmatrix} .$$

24.2.2 Phononic quantum gate

The normal mode coupling can be used to create *quantum entanglement*. A suggested procedure to correlate two atoms '1' and '2' is shown in Fig. 24.6 [159, 383]. The atoms are regarded as qubits with the possible states of excitation $|g\rangle$ and $|e\rangle$. Additionally, the atoms are trapped (either they are ions in a linear ion trap or atoms in standing light wave sustained by a ring cavity). The are assumed to be cooled to the vibrational ground state $|0\rangle$, from which they can be coherently excited to the second collective vibrational mode $|1\rangle$ by means of a Raman transition, as illustrated in Fig. 24.6.

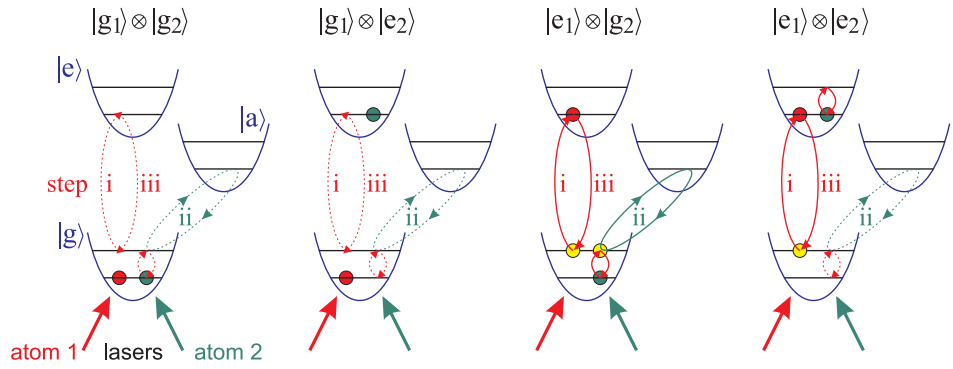

Figure 24.6: Scheme for an XOR-gate in an ion trap or a ring-cavity (see text for explanation). The four possible initial collective states respond differently to a predefined laser pulse sequence. Possible transitions are represented by solid lines, impossible transitions by dashed lines. $|a\rangle$ is an auxiliary excited level.

The sequence reads,

$$\begin{array}{llllll} |g_1\rangle|g_2\rangle|0\rangle & & |g_1\rangle|g_2\rangle|0\rangle & & |g_1\rangle|g_2\rangle|0\rangle & & |g_1\rangle|g_2\rangle|0\rangle \\ |g_1\rangle|e_2\rangle|0\rangle & \overset{\text{step 1}}{\curvearrowright} & |g_1\rangle|e_2\rangle|0\rangle & \overset{\text{step 2}}{\curvearrowright} & |g_1\rangle|e_2\rangle|0\rangle & \overset{\text{step 3}}{\curvearrowright} & |g_1\rangle|e_2\rangle|0\rangle \\ |e_1\rangle|g_2\rangle|0\rangle & & -\imath|g_1\rangle|g_2\rangle|1\rangle & & +\imath|g_1\rangle|g_2\rangle|1\rangle & & |e_1\rangle|g_2\rangle|0\rangle \\ |e_1\rangle|e_2\rangle|0\rangle & & -\imath|g_1\rangle|e_2\rangle|1\rangle & & -\imath|g_1\rangle|e_2\rangle|1\rangle & & -|e_1\rangle|e_2\rangle|0\rangle \end{array} . \tag{24.60}$$

Using the tensor notation $|\psi\rangle \otimes |\psi\rangle \equiv |\psi_1\rangle|\psi_2\rangle$ and introducing a matrix notation by

defining a basis as,

$$|g\rangle\otimes|g\rangle=\begin{pmatrix}1\\0\\0\\0\end{pmatrix}\ ,\ |g\rangle\otimes|e\rangle=\begin{pmatrix}0\\1\\0\\0\end{pmatrix}\ ,\ |e\rangle\otimes|g\rangle=\begin{pmatrix}0\\0\\1\\0\end{pmatrix}\ ,\ |e\rangle\otimes|e\rangle=\begin{pmatrix}0\\0\\0\\1\end{pmatrix}\ , \tag{24.61}$$

we can set up the truth table for this gate, also known as Cirac-Zoller gate, as,

$\|\psi\rangle$	$\|\psi\rangle$	$\|\psi\rangle\otimes\|\psi\rangle$	
$\|g\rangle$	$\|g\rangle$	$\|g\rangle\otimes\|g\rangle$	1
$\|g\rangle$	$\|e\rangle$	$\|g\rangle\otimes\|e\rangle$	1
$\|e\rangle$	$\|g\rangle$	$\|e\rangle\otimes\|g\rangle$	1
$\|e\rangle$	$\|e\rangle$	$-\|e\rangle\otimes\|e\rangle$	-1

$$\Longrightarrow\qquad U_{\rm CiZo}=\begin{pmatrix}1&0&0&0\\0&1&0&0\\0&0&1&0\\0&0&0&-1\end{pmatrix}\ . \tag{24.62}$$

We now define a new basis for the second atom only via $|a_2\rangle=\frac{1}{\sqrt{2}}(|g_2\rangle+|e_2\rangle)$ and $|b_2\rangle=\frac{1}{\sqrt{2}}(|g_2\rangle-|e_2\rangle)$. The basis transform corresponds to,

$$\begin{pmatrix}|g\rangle\otimes|a\rangle\\|g\rangle\otimes|b\rangle\\|g\rangle\otimes|a\rangle\\|g\rangle\otimes|b\rangle\end{pmatrix}=\tfrac{1}{\sqrt{2}}\mathbb{I}\otimes H\begin{pmatrix}|g\rangle\otimes|g\rangle\\|g\rangle\otimes|e\rangle\\|g\rangle\otimes|g\rangle\\|g\rangle\otimes|e\rangle\end{pmatrix}\quad\text{where}\quad\mathbb{I}\otimes H=\tfrac{1}{\sqrt{2}}\begin{pmatrix}1&1&0&0\\1&-1&0&0\\0&0&1&1\\0&0&1&-1\end{pmatrix} \tag{24.63}$$

is the Hadamard gate applied to the second qubit. Finally, we obtain the *controlled NOT* gate,

$$\mathcal{U}_{\tt XOR}=(\mathbb{I}\otimes H)\mathcal{U}_{\rm CiZo}(\mathbb{I}\otimes H)^{-1}=\begin{pmatrix}1&0&0&0\\0&1&0&0\\0&0&0&1\\0&0&1&0\end{pmatrix}\ . \tag{24.64}$$

In particular, if $|\psi_1\rangle$ is initially in a superposition state, the states $|\psi_1\rangle$ and $|\psi_2\rangle$ end up entangled,

$$\mathcal{U}_{\tt XOR}(|g\rangle+|e\rangle)\otimes\mathbb{I}=\tfrac{1}{\sqrt{2}}(|g\rangle\otimes|g\rangle+|e\rangle\otimes|e\rangle)\ . \tag{24.65}$$

24.2.3 Quantum gates via controlled collisions

The proposed conditional quantum operation is based on a conditional collisional phase shift, the condition being that the atoms are in a particular state of excitation. In a suggestive notation for the Bloch vector of a particle subject to a resonant radiation pulse, the interaction is described by,

$$|\downarrow\rangle\xrightarrow{\pi/2}|\downarrow\rangle+\imath|\uparrow\rangle\xrightarrow{\pi/2}|\uparrow\rangle\xrightarrow{\pi/2}|\downarrow\rangle-\imath|\uparrow\rangle\xrightarrow{\pi/2}|\downarrow\rangle\ . \tag{24.66}$$

Jaksch demonstrated the following *phase gate*,

$$\begin{matrix}\downarrow\downarrow\\\uparrow\downarrow\\\downarrow\uparrow\\\uparrow\uparrow\end{matrix}\longrightarrow\begin{matrix}\downarrow\downarrow\\-\downarrow\uparrow\\\uparrow\downarrow\\\uparrow\uparrow\end{matrix}\ . \tag{24.67}$$

This gate is equivalent to the *XOR* port for the qubits defined by $\downarrow$ and $\downarrow \pm \uparrow$, since,

$$\begin{array}{l} \downarrow (\downarrow \pm \uparrow) \\ \uparrow (\downarrow \pm \uparrow) \end{array} \longrightarrow \begin{array}{l} \downarrow (\downarrow \mp \uparrow) \\ \uparrow (\downarrow \pm \uparrow) \end{array} . \tag{24.68}$$

24.2.4 Exercises

24.2.4.1 Ex: Generating a Bell state

Show that the operation $\overset{c}{X}_{01}(H \otimes \mathbb{I})$, where H is the Hadamard gate acting on the first qu-bit and $\overset{c}{X}_{01}$ the controlled NOT acting on the second qubit, applied to the 2-qubit ground state generates *Bell* type entanglement.

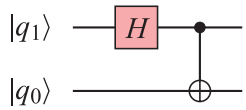

Figure 24.7: Quantum circuit generating Bell type entanglement.

24.3 Quantum gates

In *quantum information* we use the notions introduced in the preceding sections and formalize the calculation. In this section, we present a brief formal introduction to the field of *quantum computation with qubit matrices*. The formalism is abstract, but we may keep in mind a chain of entangled ions confined in a linear Paul trap. We will show how the electronic states of the ions are correlated to form a single collective state, and how quantum gates can be realized on such correlated particles. With three ions, an arbitrary quantum gate can be implemented, which includes and generalizes the three-bit Toffoli gate.

To construct a quantum gate, we need at least two qubits spanning a 4-dimensional Hilbert space, since $\mathbb{H}^2 \otimes \mathbb{H}^2$ and $\mathbb{H}^1 \otimes \mathbb{H}^4$ are isomorph, that is,

$$\begin{aligned} |\varepsilon\rangle_0|\mu\rangle_1 &= (|0\rangle_0 + \imath|1\rangle_0)(|0\rangle_1 + \imath|1\rangle_1) &&= \begin{pmatrix} |0\rangle_0|0\rangle_1 \\ \imath|0\rangle_0|1\rangle_1 \\ \imath|1\rangle_0|0\rangle_1 \\ -|1\rangle_0|1\rangle_1 \end{pmatrix} \\ \triangleq \quad |0\rangle_0|\varepsilon\mu\rangle_1 &= |00\rangle_1 + \imath|01\rangle_1 + \imath|10\rangle_1 - |11\rangle_1 &&= \begin{pmatrix} |00\rangle_1 \\ \imath|01\rangle_1 \\ \imath|10\rangle_1 \\ -|11\rangle_1 \end{pmatrix} . \end{aligned} \tag{24.69}$$

A presentation on the subject is available at (watch talk). See also the websites IBM Circuit Composer, Qiskit, Cirq, and Pennylane.

24.3.1 The qubit

The general state of a qubit is a quantum superposition in the Hilbert space $\mathbb{H}^2$,

$$|\varepsilon\rangle = \alpha|0\rangle + \imath\beta|1\rangle = \begin{pmatrix} \alpha \\ \imath\beta \end{pmatrix} \ . \tag{24.70}$$

and can be represented by a point on the Bloch sphere.

The possible outcomes of a *measurement* of its state are represented by a classical truth table,

$$\frac{|q_0\rangle}{\begin{matrix}|0\rangle \\ |1\rangle\end{matrix}} \quad , \qquad \text{for example} \qquad |1\rangle = \begin{pmatrix} 0 \\ 1 \end{pmatrix} \ . \tag{24.71}$$

While the possible values of a measurement are restricted to the binaries 0 or 1, but the probability with which one of the two results is encountered depends on the position of the Bloch vector at the time the measurement was performed.

As we have seen earlier, the two principle ways a light mode acts on a two-level system are the resonant interaction and the dispersive interaction. From the Jaynes-Cummings model (17.35) and (17.42),

$$\begin{aligned} R(\tau) &\equiv \begin{pmatrix} \cos\frac{\pi}{2}\tau & \imath\sin\frac{\pi}{2}\tau \\ \imath\sin\frac{\pi}{2}\tau & \cos\frac{\pi}{2}\tau \end{pmatrix} \overset{\tau\to 1}{\longrightarrow} \begin{pmatrix} & \imath \\ \imath & \end{pmatrix} \ , \\ D(\tau) &\equiv \begin{pmatrix} e^{\imath\pi\tau} & 0 \\ 0 & 1 \end{pmatrix} \qquad\qquad \overset{\tau\to 1}{\longrightarrow} \begin{pmatrix} -1 & \\ & 1 \end{pmatrix} \ . \end{aligned} \tag{24.72}$$

Both interactions lead to unitary evolutions of the qubit's state.

The two gates (24.72) are particular cases of the most fundamental single qubit quantum gate, which can be written as,

$$\boxed{\mathcal{U}_3(\vartheta,\varphi,\lambda) = \begin{pmatrix} \cos\frac{\vartheta}{2} & -e^{\imath\lambda}\sin\frac{\vartheta}{2} \\ e^{\imath\varphi}\sin\frac{\vartheta}{2} & e^{\imath\lambda+\imath\varphi}\cos\frac{\vartheta}{2} \end{pmatrix}} \ , \tag{24.73}$$

which is a unitary operation since $\det\mathcal{U}_3(\vartheta,\varphi,\lambda) = e^{\imath(\lambda+\varphi)}$. Special cases are the *Hadamard gate*,

$$H \equiv \mathcal{U}_3(\tfrac{\pi}{2},0,\pi) = \tfrac{1}{\sqrt{2}}\begin{pmatrix} 1 & 1 \\ 1 & -1 \end{pmatrix} \ , \tag{24.74}$$

and the *phase gate*,

$$\mathcal{U}_1(\varphi) \equiv \mathcal{U}_3(0,\varphi,0) = \begin{pmatrix} 1 & 0 \\ 0 & e^{\imath\varphi} \end{pmatrix} \ . \tag{24.75}$$

Phase rotations about particular angles receive specific names. For example,

$$\boxed{Z \equiv -\hat{\sigma}_z = \mathcal{U}_1(\pi)} = |-q_0\rangle\langle q_0| \ , \tag{24.76}$$

is simply the negative Pauli z-matrix defined in (1.154). The *negation* in the Hilbert space $\mathbb{H}^2$,

$$\boxed{X \equiv \hat{\sigma}_x = \mathcal{U}_3(\pi, 0, \pi) = |\bar{q}_0\rangle\langle q_0|} \,, \tag{24.77}$$

is simply the Pauli x-matrix.

Analogously to classical logic circuits, which can be represented by concatenated symbols, quantum circuits can be composed by concatenations of unitary operations. Fig. 24.8(b) lists fundamental quantum logic gates together with their classical counterparts shown in Fig. 24.8(a).

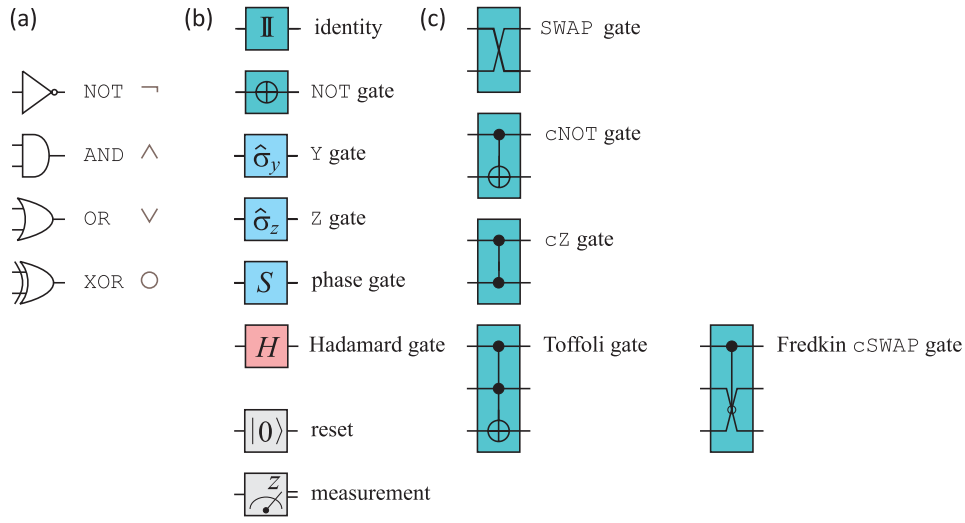

Figure 24.8: (a) Common symbols for fundamental classical gates, (b) for single qubit quantum gates, and (c) for three qubit quantum gates.

24.3.2 Quantum gates of 2 qubits

We can generalize the single-qubit algebra to arbitrary registers using the *direct* sum and the *external product* defined in (1.223) and (1.225),

$$\begin{array}{c} |q_1, q_0\rangle \\ \hline |0,0\rangle \\ |0,1\rangle \\ |1,0\rangle \\ |1,1\rangle \end{array} \quad , \qquad \text{for example} \qquad |0,1\rangle = \begin{pmatrix} 0 \\ 1 \\ 0 \\ 0 \end{pmatrix} \,. \tag{24.78}$$

24.3.2.1 Single qubit gates in $\mathbb{H}^4$

Single qubit gates can be embedded in multi-qubit registers. For example, the *negation* of 'NOT' gate in $\mathbb{H}^4$ can be applied either to the first or the second qubit [7],

$$\boxed{\begin{array}{l} X_0 \hat{=} \mathbb{I} \otimes \hat{X} = |q_1, \bar{q_0}\rangle\langle q_1, q_0| \\ X_1 \hat{=} \hat{X} \otimes \mathbb{I} = |\bar{q_1}, q_0\rangle\langle q_1, q_0| \end{array}} \ . \tag{24.79}$$

Example 164 (*Negation gates*): The classical truth table for the negation of qubit q_1 reads,

$\|q_1, q_0\rangle \curvearrowright$	$\|\bar{q}_1, q_0\rangle$
$\|0,0\rangle$	$\|0,1\rangle$
$\|0,1\rangle$	$\|0,0\rangle$
$\|1,0\rangle$	$\|1,1\rangle$
$\|1,1\rangle$	$\|1,0\rangle$

(24.80)

In the quantum language the relations (24.79) are executed by multiplying the unitary transform describing the negation gate with the truth table representation (24.78) of the input state $|q_1, q_0\rangle$,

$$X \otimes \mathbb{I}|q_1, q_0\rangle = \begin{pmatrix} 0 & 0 & 1 & 0 \\ 0 & 0 & 0 & 1 \\ 1 & 0 & 0 & 0 \\ 0 & 1 & 0 & 0 \end{pmatrix} \begin{pmatrix} 0 & 0 \\ 0 & 1 \\ 1 & 0 \\ 1 & 1 \end{pmatrix} = |\bar{q}_1, q_0\rangle \ . \tag{24.81}$$

Analogously, Hadamard and other rotation gates $\mathcal{U}$ are applied to specific qubits of a register via $\mathbb{I} \otimes ... \otimes \mathcal{U} \otimes ... \otimes \mathbb{I}$.

24.3.2.2 Parallel and serial operations

In order to execute unitary operations U_k on different qubits q_k of a quantum register in parallel, the complete Hilbert space must be spanned first before the individual operation can be described by matrix multiplication,

$$U = U_1 \otimes U_0 = (U_1 \otimes \mathbb{I}) \ (\mathbb{I} \otimes U_0) \ . \tag{24.82}$$

Consecutive operations U, V on the quantum register can be concatenated, $U \ V$.

24.3.2.3 The controlled NOT gate

The most interesting two-qubit quantum gate is the 'controlled NOT' gate or *antivalence*, which we will now discuss in detail. This gate is originally defined on $\mathbb{H}^2 \otimes \mathbb{H}^2$. The quantum operation is implemented by first going to the Hilbert space $\mathbb{H}^1 \otimes \mathbb{H}^4$, applying the unitary transform,

$$\mathbb{I} \triangleright X = \begin{pmatrix} \mathbb{I}_2 & \\ & X \end{pmatrix} \ , \tag{24.83}$$

[7] Note that we call 'first' the rightmost qubit.

where X has been defined in Eq. (24.77), and finally returning to $\mathbb{H}^2 \otimes \mathbb{H}^2$:

$$
\begin{array}{ccccc}
|\varepsilon\rangle_0|\mu\rangle_1 & \triangleq |0\rangle_0|\varepsilon\mu\rangle_1 & \xrightarrow{\hat{N}} \delta_{\varepsilon=0}|\varepsilon\rangle_0|\mu\rangle_1 + \delta_{\varepsilon=1}|\varepsilon\rangle_1 \begin{pmatrix} 1 & \imath \\ \imath & 1 \end{pmatrix}^2 |\mu\rangle_1 & \triangleq |\varepsilon\rangle_0|\varepsilon \oplus \mu\rangle_1 \\
\begin{pmatrix} |0\rangle_0|0\rangle_1 \\ \imath|0\rangle_0|1\rangle_1 \\ \imath|1\rangle_0|0\rangle_1 \\ -|1\rangle_0|1\rangle_1 \end{pmatrix} & \triangleq \begin{pmatrix} |00\rangle_1 \\ \imath|01\rangle_1 \\ \imath|10\rangle_1 \\ -|11\rangle_1 \end{pmatrix} & \xrightarrow{\hat{N}} \begin{pmatrix} |00\rangle_1 \\ \imath|01\rangle_1 \\ \imath|11\rangle_1 \\ -|10\rangle_1 \end{pmatrix} & & \triangleq \begin{pmatrix} |0\rangle_0|0\rangle_1 \\ \imath|0\rangle_0|1\rangle_1 \\ \imath|1\rangle_0|1\rangle_1 \\ -|1\rangle_0|0\rangle_1 \end{pmatrix}
\end{array} . \tag{24.84}
$$

The short-hand notation of the 'controlled NOT' operation on $\mathbb{H}^4$ can be written as,

$$
\boxed{\begin{array}{lll}
\overset{c}{X}_{10} & \hat{=}\ \mathbb{I} \triangleright X & = |q_1, q_1 \oplus q_0\rangle\langle q_1, q_0| \\
\overset{c}{X}_{01} & \hat{=}\ X \triangleleft \mathbb{I} = \mathbb{S}(\mathbb{I} \triangleright X)\mathbb{S} & = |q_0 \oplus q_1, q_0\rangle\langle q_1, q_0|
\end{array}} . \tag{24.85}
$$

where the 'SWAP' operator $\mathbb{S}$ has been defined in (1.229). When the qubits addressed by a gate are not identified from their position in the tensor product, an index at the gate symbol indicates which qubits are involved. For example, X_0 inverts the first qubit q_0, and $\overset{c}{X}_{0\to 1} = \overset{c}{X}_{01}$ controls the state of the second qubit q_1 by the first one.

Example 165 (*Controlled NOT gates*): We can easily verify,

$$
\begin{aligned}
\overset{c}{X}_{10} &= |0\rangle\langle 0| \otimes \mathbb{I} + |1\rangle\langle 1| \otimes X \\
&= \begin{pmatrix} 1 & 0 \\ 0 & 0 \end{pmatrix} \otimes \begin{pmatrix} 1 & 0 \\ 0 & 1 \end{pmatrix} + \begin{pmatrix} 0 & 0 \\ 0 & 1 \end{pmatrix} \otimes \begin{pmatrix} 0 & 1 \\ 1 & 0 \end{pmatrix} = \begin{pmatrix} \mathbb{I} & 0 \\ 0 & X \end{pmatrix} ,
\end{aligned} \tag{24.86}
$$

and

$$
\begin{aligned}
\overset{c}{X}_{01} &= \mathbb{I}| \otimes |0\rangle\langle 0| + X \otimes |1\rangle\langle 1| \\
&= \begin{pmatrix} 1 & 0 \\ 0 & 1 \end{pmatrix} \otimes \begin{pmatrix} 1 & 0 \\ 0 & 0 \end{pmatrix} + \begin{pmatrix} 0 & 1 \\ 1 & 0 \end{pmatrix} \otimes \begin{pmatrix} 0 & 0 \\ 0 & 1 \end{pmatrix} = \mathbb{S}\overset{c}{X}_{10}\mathbb{S} .
\end{aligned} \tag{24.87}
$$

The SWAP gate itself can be generated from cNOT gates, as will be shown in Exc. 24.3.7.1. Do the Excs. 24.3.7.2 to 24.3.7.3.

24.3.3 Boolean versus linear algebra

It is now time to work out the fundamental difference between classical and quantum computing. The mathematical formalism underlying *classical computing* is the *Boolean algebra*, while the formalism underlying *quantum computing* is the *linear algebra*.

Example 166 (*Controlled NOT gates*): We illustrate the difference between classical and quantum computing at the example of the XOR gate represented by

the classical truth table,

$$\begin{array}{cc} |q_1, q_0\rangle \curvearrowright & |q_1, q_1 \oplus q_0\rangle \\ \hline |0,0\rangle & |0,0\rangle \\ |0,1\rangle & |0,1\rangle \\ |1,0\rangle & |1,1\rangle \\ |1,1\rangle & |1,0\rangle \end{array} \tag{24.88}$$

The operation can be realized via unitary transform,

$$\mathbb{I} \triangleright X|q_1, q_0\rangle = \texttt{XOR}_1|q_1, q_0\rangle = \begin{pmatrix} 1 & 0 & 0 & 0 \\ 0 & 1 & 0 & 0 \\ 0 & 0 & 0 & 1 \\ 0 & 0 & 1 & 0 \end{pmatrix} \begin{pmatrix} 0 & 0 \\ 0 & 1 \\ 1 & 0 \\ 1 & 1 \end{pmatrix} = \begin{pmatrix} 0 & 0 \\ 0 & 1 \\ 1 & 1 \\ 1 & 0 \end{pmatrix} = |q_1, q_1 \oplus q_0\rangle \ . \tag{24.89}$$

The unitary transform allows not only to propagate specific states $|q_1, q_0\rangle$ of the basis through the circuit, but also linear combinations, such as for example the state $|0,0\rangle + |1,0\rangle$.

Quantum superpositions are not permitted in classical computing, which is to say that the only permitted input states are the eigenstates of the product basis. Consequently, gate operations inducing superpositions, such as the Hadamard gate are not allowed. Only gate operations transforming an eigenstate into another eigenstate are possible, such as the `NOT` or the `NAND` gate.

It is important to stress that *everything you can do on a classical computer, you can do on a quantum computer, and vice versa.* The question is simply whether you can do it in due time. The first part of the statement is obvious by the fact that quantum computing is described by unitary transformations on a large but discrete and finite Hilbert space. The transformations are represented by matrices, which can be processed on a classical computer. The second part of the statement is a bit more tricky, because the fundamental gates of classical computing are `AND` and `OR` operations, which are not unitary. So see this, we set up the classical truth table for the `AND` gate,

$$\begin{array}{cc} |q_1, q_0\rangle \curvearrowright & |q_1, q_1 \wedge q_0\rangle \\ \hline |0,0\rangle & |0,0\rangle \\ |0,1\rangle & |0,0\rangle \\ |1,0\rangle & |1,0\rangle \\ |1,1\rangle & |1,1\rangle \end{array} \tag{24.90}$$

and the corresponding transform,

$$\texttt{AND}_1|q_1, q_0\rangle = \begin{pmatrix} 1 & 0 & 0 & 0 \\ 0 & 0 & 0 & 0 \\ 0 & 0 & 1 & 0 \\ 0 & 0 & 0 & 1 \end{pmatrix} \begin{pmatrix} 0 & 0 \\ 0 & 1 \\ 1 & 0 \\ 1 & 1 \end{pmatrix} = \begin{pmatrix} 0 & 0 \\ 0 & 0 \\ 1 & 0 \\ 1 & 1 \end{pmatrix} = |q_1, q_1 \wedge q_0\rangle \ . \tag{24.91}$$

Hence, the fundamental gates of classical computing cannot be constructed only from unitary `XOR` and `NOT` gates. Another way to see this is by noticing that the result $|0,0\rangle$ of the truth table (24.90) can be obtained from two different input states, which

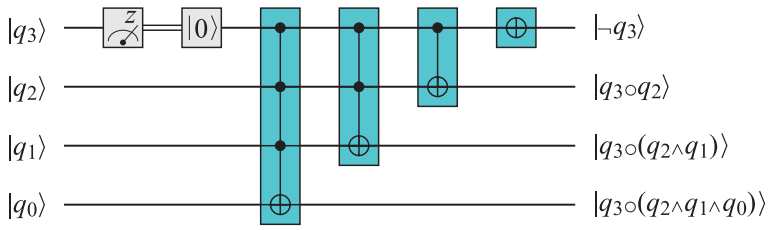

Figure 24.9: Quantum circuit realizing logical gates. While the `NOT` and `XOR` gates can be made reversible, the `AND` and `OR` gates require projection of some qubits.

means that the classical operation is not reversible. Do the Excs. 24.3.7.4 to 24.3.7.5.

In Exc. 24.3.7.10 we will show how to embed `AND` and `OR` into more general three-bit quantum gates, which then can be projected into non-unitary `AND` and `OR` gates.

24.3.4 Fundamental and universal quantum gates of 3 qubits and more

We now consider three qubits in $\mathbb{H}^8 \equiv \mathbb{H}^2 \otimes \mathbb{H}^2 \otimes \mathbb{H}^2$. The *truth table* has the shape,

$$\begin{array}{c} |q_2, q_1, q_0\rangle \\ \hline |0,0,0\rangle \\ |0,0,1\rangle \\ |0,1,0\rangle \\ |0,1,1\rangle \\ |1,0,0\rangle \\ |1,0,1\rangle \\ |1,1,0\rangle \\ |1,1,1\rangle \end{array} \quad , \quad \text{for example} \quad |0,1,0\rangle = \begin{pmatrix} 0 \\ 0 \\ 1 \\ 0 \\ 0 \\ 0 \\ 0 \\ 0 \end{pmatrix} . \tag{24.92}$$

We choose $\mathbb{I}_8$ as the basis of $\mathbb{H}^8$. We assume that the number represented by the state $|q_2, q_1, q_0\rangle$ is $[q_2 q_1 q_0]_{binary} = [2^2 q_2 + 2^1 q_1 + 2^0 q_0]_{decimal}$.

The unitary transform implemented by a quantum gate can be understood as a permutation of the basis vectors in the truth table. We can generalize the permutation rules (1.229) to 3D Hilbert spaces $\mathbb{H}^2 \otimes \mathbb{H}^2 \otimes \mathbb{H}^2$, where $M \otimes N \otimes R = \mathbb{S}_{01}(N \otimes M \otimes R)\mathbb{S}_{01} = \mathbb{S}_{12}(M \otimes R \otimes N)\mathbb{S}_{12} = \mathbb{S}_{01}(R \otimes N \otimes M)\mathbb{S}_{02}$, with the transformation matrices,

$$\mathbb{S}_{01} = \mathbb{I} \otimes \mathbb{S} \quad , \quad \mathbb{S}_{12} = \mathbb{S} \otimes \mathbb{I} \quad , \quad \mathbb{S}_{02} = \mathbb{S}_{01}\mathbb{S}_{12}\mathbb{S}_{01} \ , \tag{24.93}$$

where the operator $\mathbb{S}$ has again been taken from (1.229). In Exc. 24.3.7.7 we derive the explicit matricial forms of $\mathbb{S}_{ij}$.

Examples of fundamental three-qubits gates are, in short notation, the *negation* in $\mathbb{H}^8$,

$$\begin{aligned} X_0 &\hat{=} \mathbb{I} \otimes \mathbb{I} \otimes X = |q_2, q_1, \bar{q_0}\rangle\langle q_2, q_1, q_0| \\ X_1 &\hat{=} \mathbb{I} \otimes X \otimes \mathbb{I} = |q_2, \bar{q_1}, q_0\rangle\langle q_2, q_1, q_0| \\ X_2 &\hat{=} X \otimes \mathbb{I} \otimes \mathbb{I} = |\bar{q_2}, q_1, q_0\rangle\langle q_2, q_1, q_0| \ , \end{aligned} \tag{24.94}$$

the *antivalence*,

$$\begin{aligned}
\overset{c}{X}_{10} &\equiv \mathbb{I}\otimes(\mathbb{I}\rhd X) &&= |q_2,q_1,q_1\oplus q_0\rangle\langle q_2,q_1,q_0| \\
\overset{c}{X}_{01} &\equiv \mathbb{S}_{01}\overset{c}{X}_{10}\mathbb{S}_{01} &&= |q_2,q_0\oplus q_1,q_0\rangle\langle q_2,q_1,q_0| \\
\overset{c}{X}_{02} &\equiv \mathbb{S}_{12}\overset{c}{X}_{01}\mathbb{S}_{12} &&= |q_0\oplus q_2,q_1,q_0\rangle\langle q_2,q_1,q_0| \\
\overset{c}{X}_{20} &\equiv \mathbb{S}_{02}\overset{c}{X}_{02}\mathbb{S}_{02} &&= |q_2,q_1,q_2\oplus q_0\rangle\langle q_2,q_1,q_0| \\
\overset{c}{X}_{21} &\equiv \mathbb{S}_{02}\overset{c}{X}_{01}\mathbb{S}_{02} &&= |q_2,q_2\oplus q_1,q_0\rangle\langle q_2,q_1,q_0| \\
\overset{c}{X}_{12} &\equiv \mathbb{S}_{12}\overset{c}{X}_{21}\mathbb{S}_{12} &&= |q_1\oplus q_2,q_1,q_0\rangle\langle q_2,q_1,q_0| \ ,
\end{aligned} \tag{24.95}$$

from which we get explicitly, as verified in Exc. 24.3.7.8,

$$\overset{c}{X}_{10} = \begin{pmatrix} \mathbb{I} & & & \\ & X & & \\ & & \mathbb{I} & \\ & & & X \end{pmatrix} \quad , \quad \overset{c}{X}_{20} = \begin{pmatrix} \mathbb{I} & & & \\ & \mathbb{I} & & \\ & & X & \\ & & & X \end{pmatrix} \quad , \quad \overset{c}{X}_{21} = \begin{pmatrix} \mathbb{I} & & & \\ & \mathbb{I} & & \\ & & & X\otimes\mathbb{I} \end{pmatrix} . \tag{24.96}$$

It is possible to show that all quantum logic gates can be reduced to a universal so-called *Toffoli gate* [55],

$$\begin{aligned}
\mathbb{H}^8 &\xrightarrow{\mathcal{U}} \mathbb{H}^8 \\
|q_2,q_1,q_0\rangle &\xrightarrow{\mathcal{U}} |q_2,q_1,(q_2\wedge q_1)\oplus q_0\rangle \\
\mathbb{I}_8 &\xrightarrow{\mathcal{U}} \mathcal{U} \ ,
\end{aligned} \tag{24.97}$$

or in short-hand notation,

$$\boxed{\overset{cc}{X}_{210} = \mathbb{I}\rhd\mathbb{I}\rhd X = |q_2,q_1,(q_2\wedge q_1)\oplus q_0\rangle\langle q_2,q_1,q_0| = \begin{pmatrix} \mathbb{I}_6 & \\ & \hat{\sigma}_x \end{pmatrix}} \ , \tag{24.98}$$

as will be shown in Exc. 24.3.7.9 and 24.3.7.10.

Obviously, to perform quantum calculations, we need at least two qubits and operations acting simultaneous on both. Do the Excs. 24.3.7.11 to 24.3.7.12.

The extension of the formalism to more than three qubits is straightforward, and the implementation of a quantum algorithm on a classical computer is quite simple, the difficulty mainly being the size of the Hilbert space, which rapidly explodes with increasing numbers of qubits.

In practice, the task often consists in breaking down a problem into a sequence of operations on a binary quantum register. As we have shown in Sec. 24.3.3 every irreversible classical algorithm can be mapped to a corresponding reversible quantum algorithm. This brute force 'quantization' is, however, very inefficient since it uses as many (and even more) qubits than the classical algorithm.

Until now, we restricted to pure states $|\psi_f\rangle = \bigotimes_k[\alpha_k|0\rangle_k + \beta_k|1\rangle_k]$ generated from an initial eigenstate $|\psi_i\rangle = \bigotimes_k |0\rangle_k$ by reversible quantum computing. The density

Table 24.1: Symbols and definitions of common quantum gates.

gate	symbol	matrix
identity	$\mathbb{I}$	$\mathcal{U}_3(0,0,0)$
inversion	$X = \texttt{NOT}$	$\hat{\sigma}_x = \mathcal{U}_3(\pi,0,\pi)$
Pauli Y	Y	$\hat{\sigma}_y = \mathcal{U}_3(\pi,\frac{\pi}{2},\frac{\pi}{2})$
Pauli Z	Z	$\hat{\sigma}_z = \mathcal{U}_1(\pi)$
S gate	S	$\hat{\sigma}_z = \mathcal{U}_1(\frac{\pi}{2})$
T gate	T	$\hat{\sigma}_z = \mathcal{U}_1(\frac{\pi}{4})$
Hadamard gate	H	$\mathcal{U}_3(\frac{\pi}{2},0,\pi)$
swap gate	$\mathbb{S} = \texttt{SWAP}$	$\begin{pmatrix} 1 & 0 & 0 & 0 \\ 0 & 0 & 1 & 0 \\ 0 & 1 & 0 & 0 \\ 0 & 0 & 0 & 1 \end{pmatrix}$
controlled X	$\overset{c}{X} = \texttt{cX}$	$\mathbb{I} \rhd \hat{\sigma}_x = \begin{pmatrix} \mathbb{I}_2 & 0 \\ 0 & \hat{\sigma}_x \end{pmatrix}$
controlled Z	$\overset{c}{Z} = \texttt{cZ}$	$\mathbb{I} \rhd \hat{\sigma}_z = \begin{pmatrix} \mathbb{I}_2 & 0 \\ 0 & \hat{\sigma}_z \end{pmatrix}$
controlled H	$\overset{c}{H} = \texttt{cH}$	$\mathbb{I} \rhd H = \begin{pmatrix} \mathbb{I}_2 & 0 \\ 0 & H \end{pmatrix}$
Toffoli	$\overset{cc}{X} = \texttt{ccX}$	$\mathbb{I} \rhd \mathbb{I} \rhd \hat{\sigma}_x = \begin{pmatrix} \mathbb{I}_6 & \\ & \hat{\sigma}_x \end{pmatrix}$

operator can then be written,

$$\boxed{\hat{\rho} = |\psi_f\rangle\langle\psi_f| = \mathcal{U}|\psi_i\rangle\langle\psi_i|\mathcal{U}^\dagger} \,. \tag{24.99}$$

In the next section, following up on Sec. 14.2.3, we will discuss how projective measurements introduce irreversibility into the evolution of the density operator.

24.3.5 State propagation and projective measurements

The measurement of a qubit projects the Hilbert space on its two possible outcomes. For example, measuring the first out of three qubits means,

$$\mathbb{H} \otimes \mathbb{H} \otimes \mathbb{H} \overset{measure}{\longrightarrow} \begin{cases} |0\rangle \otimes \mathbb{H} \otimes \mathbb{H} \\ |1\rangle \otimes \mathbb{H} \otimes \mathbb{H} \end{cases} . \tag{24.100}$$

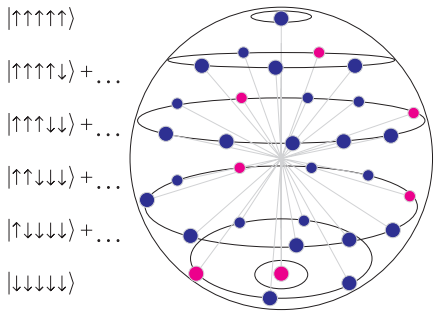

Figure 24.10: Illustration of the possible states of a 5-qubit system.

We consider a density matrix $\hat{\rho}$ operating on the entire Hilbert space and define projectors,

$$\hat{P}_j^{(n)} = \mathbb{I} \otimes ... \otimes |n\rangle_j\langle n| \otimes ... \otimes \mathbb{I} \qquad \text{with} \qquad n = 0, 1 \; . \tag{24.101}$$

that, applied to a specific qubit q_j, project its state onto the eigenstate $|0\rangle$ or $|1\rangle$, respectively. A projective measurement of the j-th qubit with two possible outcomes $|q_j\rangle = |0\rangle, |1\rangle$ with the respective probabilities $p_j^{(0)}, p_j^{(1)}$, generates the mixed states reduced density operator,

$$\boxed{\hat{\rho}_j^{\text{red}} = \sum_{n=0,1} p_j^{(n)} \frac{\hat{P}_j^{(n)} \hat{\rho} \hat{P}_j^{(n)}}{\text{Tr } \hat{\rho} \hat{P}_j^{(n)}}} \; . \tag{24.102}$$

Note that, a priori, $\hat{\rho}_j^{\text{red}}$ has the same rank as $\hat{\rho}$, but a more diagonal structure, since some coherences have been traced out.

24.3.5.1 Quantum state tomography

Any density operator of a pure or mixed state of an individual qubit can be expanded as,

$$\hat{\rho}_j = \tfrac{1}{2} \left(\mathbb{I} + a_j \hat{\sigma}_j^x + b_j \hat{\sigma}_j^y + c_j \hat{\sigma}_j^z \right) = \tfrac{1}{2} \begin{pmatrix} 1 + c_j & a_j - \imath b_j \\ a_j + \imath b_j & 1 - c_j \end{pmatrix} \; , \tag{24.103}$$

where,

$$\hat{\sigma}_j^k = \mathbb{I} \otimes ... \otimes \hat{\sigma}^k \otimes ... \otimes \mathbb{I} \; , \tag{24.104}$$

and $\hat{\sigma}^k$ are the Pauli matrices. The parameters a_j, b_j, and c_j can be determined by measurements,

$$\boxed{\langle \hat{\vec{\sigma}}_j \rangle = \text{Tr } \hat{\rho} \hat{\vec{\sigma}}_j = \begin{pmatrix} a_j \\ b_j \\ c_j \end{pmatrix}} \; , \tag{24.105}$$

where $\hat{\rho}$ is the density matrix of the whole system.

24.3.5.2 Measurements on a single qubit

A single qubit $|\psi\rangle = \alpha|0\rangle + \beta|1\rangle$, normalized as $|\alpha|^2 + |\beta|^2 = 1$, is described by the density operator,

$$\hat{\rho} = \begin{pmatrix} \rho_{00} & \rho_{01} \\ \rho_{10} & \rho_{11} \end{pmatrix} = |\psi\rangle\langle\psi| = \begin{pmatrix} |\alpha|^2 & \alpha\beta^* \\ \alpha^*\beta & |\beta|^2 \end{pmatrix} \ . \tag{24.106}$$

A projective measurement of the qubit with two possible outcomes, $|q\rangle = |0\rangle, |1\rangle$ with the respective probabilities $p^{(0)} = |\alpha|^2$ and $p^{(1)} = |\beta|^2$, generates the mixed states reduced density operator,

$$\hat{\rho}^{\rm red} = p^{(0)} \frac{|0\rangle\langle 0|\hat{\rho}|0\rangle\langle 0|}{{\rm Tr}\ \hat{\rho}|0\rangle\langle 0|} + p^{(1)} \frac{|1\rangle\langle 1|\hat{\rho}|1\rangle\langle 1|}{{\rm Tr}\ \hat{\rho}|1\rangle\langle 1|} = |\alpha|^2|0\rangle\langle 0| + |\beta|^2|1\rangle\langle 1| \ . \tag{24.107}$$

Some physical processes may not only project the density operator onto a specific basis, but onto a particular eigenstate,

$$\hat{\rho} \longrightarrow \hat{\rho}^{\rm prj} = |0\rangle\langle 0|\hat{\rho}|0\rangle\langle 0| \ . \tag{24.108}$$

Example 167 (*Quantum Zeno effect on a single qubit*): As an example, let us express the quantum Zeno effect in quantum computing language. Starting from a two-level system in its ground state,

$$\hat{\rho}^{in} = \begin{pmatrix} 1 & 0 \\ 0 & 0 \end{pmatrix} \quad , \quad \mathcal{U}_3(\vartheta, 0, 0) = \begin{pmatrix} \cos\vartheta & -\sin\vartheta \\ \sin\vartheta & \cos\vartheta \end{pmatrix} \ ,$$

we perform small rotations,

$$\hat{\rho}^{rot} = \mathcal{U}_3(\vartheta,0,0)\hat{\rho}^{in}\mathcal{U}_3(\vartheta,0,0)^\dagger = \begin{pmatrix} \cos^2\vartheta & \cos\vartheta\sin\vartheta \\ \cos\vartheta\sin\vartheta & \sin^2\vartheta \end{pmatrix} \begin{pmatrix} 1 & 0 \\ 0 & 0 \end{pmatrix} \ ,$$

before measuring the system,

$$\hat{\rho}^{\rm red} = \cos^2\vartheta \frac{|0\rangle\langle 0|\hat{\rho}^{rot}|0\rangle\langle 0|}{{\rm Tr}\ \hat{\rho}^{rot}|0\rangle\langle 0|} + \sin^2\vartheta \frac{|1\rangle\langle 1|\hat{\rho}^{rot}|1\rangle\langle 1|}{{\rm Tr}\ \hat{\rho}^{rot}|1\rangle\langle 1|} = \begin{pmatrix} \cos^2\vartheta & 0 \\ 0 & \sin^2\vartheta \end{pmatrix} \ .$$

Discarding the possibility that the system be excited, we project it system onto the ground state,

$$\hat{\rho}^{fin} = |0\rangle\langle 0|\hat{\rho}^{\rm red}|0\rangle\langle 0| = |0\rangle\langle 0|\mathcal{U}_3(\vartheta,0,0)\hat{\rho}^{in}\mathcal{U}_3(\vartheta,0,0)^\dagger|0\rangle\langle 0| = \begin{pmatrix} \cos^2\vartheta & 0 \\ 0 & 0 \end{pmatrix} \ .$$

On the other hand, repeating the procedure n times with $\vartheta = \frac{\pi}{2n}$ and $n \to \infty$, we find,

$$\hat{\rho}^{fin} = \lim_{n\to\infty} \left(|0\rangle\langle 0|\mathcal{U}_3(\tfrac{\pi}{2n},0,0)\hat{\rho}^{in}\mathcal{U}_3(\tfrac{\pi}{2n},0,0)^\dagger|0\rangle\langle 0| \right)^n = \begin{pmatrix} \lim_{n\to\infty}\cos^{2n}\frac{\pi}{2n} & 0 \\ 0 & 0 \end{pmatrix} = \hat{\rho}^{in} \ .$$

That is, the evolution of the system is frozen by too many measurements.

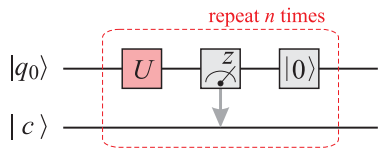

Figure 24.11: Quantum Zeno effect on a single qubit.

24.3.5.3 Measurements in two qubit systems

Let us now consider a two-qubit system $q_1 \otimes q_0$ described by the initial density matrix,

$$\hat{\rho} = \hat{\rho}_1 \otimes \hat{\rho}_0 = \begin{pmatrix} |\alpha_1|^2 & \alpha_1\beta_1^* \\ \alpha_1^*\beta_1 & |\beta_1|^2 \end{pmatrix} \otimes \begin{pmatrix} |\alpha_0|^2 & \alpha_0\beta_0^* \\ \alpha_0^*\beta_0 & |\beta_0|^2 \end{pmatrix} \tag{24.109}$$

$$= \begin{pmatrix} (\rho_1)_{00} & (\rho_1)_{01} \\ (\rho_1)_{10} & (\rho_1)_1 \end{pmatrix} \otimes \begin{pmatrix} (\rho_0)_{00} & (\rho_0)_{01} \\ (\rho_0)_{10} & (\rho_0)_1 \end{pmatrix} = \begin{pmatrix} \rho_{00\otimes 00} & \rho_{00\otimes 01} & \rho_{10\otimes 00} & \rho_{01\otimes 01} \\ \rho_{00\otimes 10} & \rho_{00\otimes 11} & \rho_{01\otimes 10} & \rho_{01\otimes 11} \\ \rho_{10\otimes 00} & \rho_{10\otimes 01} & \rho_{11\otimes 00} & \rho_{11\otimes 01} \\ \rho_{10\otimes 10} & \rho_{10\otimes 11} & \rho_{11\otimes 10} & \rho_{11\otimes 11} \end{pmatrix},$$

where we defined $\rho_{kl\otimes mn} \equiv (\rho_1)_{kl}(\rho_0)_{mn}$. Projective measurements of qubit q_1 with two possible outcomes, $|q_1\rangle = |0\rangle, |1\rangle$, with the respective probabilities $p^{(0)} = |\alpha_1|^2$ and $p^{(1)} = |\beta_1|^2$, yields the reduced density operator,

$$\hat{\rho}_1^{\rm red} = p^{(0)} \frac{[|0\rangle\langle 0| \otimes \mathbb{I}]\hat{\rho}[|0\rangle\langle 0| \otimes \mathbb{I}]}{\mathrm{Tr}\ \hat{\rho}[|0\rangle\langle 0| \otimes \mathbb{I}]} + p^{(1)} \frac{[|1\rangle\langle 1| \otimes \mathbb{I}]\hat{\rho}[|1\rangle\langle 1| \otimes \mathbb{I}]}{\mathrm{Tr}\ \hat{\rho}[|1\rangle\langle 1| \otimes \mathbb{I}]} \tag{24.110}$$

$$= \frac{|\alpha_1|^2}{\rho_{00\otimes 00} + \rho_{01\otimes 01}} \begin{pmatrix} \rho_{00\otimes 00} & \rho_{00\otimes 01} & 0 & 0 \\ \rho_{01\otimes 00} & \rho_{01\otimes 01} & 0 & 0 \\ 0 & 0 & 0 & 0 \\ 0 & 0 & 0 & 0 \end{pmatrix} + \frac{|\beta_1|^2}{\rho_{10,10} + \rho_{11,11}} \begin{pmatrix} 0 & 0 & 0 & 0 \\ 0 & 0 & 0 & 0 \\ 0 & 0 & \rho_{10\otimes 10} & \rho_{10\otimes 11} \\ 0 & 0 & \rho_{11\otimes 10} & \rho_{11\otimes 11} \end{pmatrix}.$$

The inversion of qubit q_1 is,

$$\langle \hat{\sigma}_1^z \rangle = \mathrm{Tr}\ \hat{\rho}\,[\hat{\sigma}^z \otimes \mathbb{I}] = \rho_{00,00} + \rho_{01,01} - \rho_{10,10} - \rho_{11,11}\ . \tag{24.111}$$

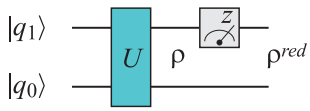

Figure 24.12: Projective measurement. After an operation U, two qubits remain in an entangled state $\hat{\rho}$. Measurement of qubit q_1 reduces the state to $\hat{\rho}^{\rm red}$, while transferring the information to a classical channel c.

Example 168 (*Measurements on disentangled qubits*): As a particular case, let us first consider two disentangled qubits $|\psi\rangle = |q_1\rangle \otimes |q_0\rangle = [\alpha_1|0\rangle +$

$\beta_1|1\rangle] \otimes [\alpha_0|0\rangle + \beta_0|1\rangle]$, such that,

$$\hat{\rho} = \begin{pmatrix} \alpha_1\alpha_0 \\ \alpha_1\beta_0 \\ \beta_1\alpha_0 \\ \beta_1\beta_0 \end{pmatrix} \begin{pmatrix} \alpha_1^*\alpha_0^* & \alpha_1^*\beta_0^* & \beta_1^*\alpha_0^* & \beta_1^*\beta_0^* \end{pmatrix} \tag{24.112}$$

$$= \begin{pmatrix} |\alpha_1|^2|\alpha_0|^2 & |\alpha_1|\alpha_0^*\beta_0^* & \alpha_1\beta_1^*|\alpha_0|^2 & \alpha_1\beta_1^*\alpha_0\beta_0^* \\ |\alpha_1|^2\alpha_0^*\beta_0 & |\alpha_1|^2|\beta_0|^2 & \alpha_1\beta_1^*\alpha_0^*\beta_0 & \alpha_1\beta_1^*|\beta_0|^2 \\ \alpha_1^*\beta_1|\alpha_0|^2 & \beta_1\alpha_1^*\alpha_0\beta_0^* & |\beta_1|^2|\alpha_0|^2 & |\beta_1|^2\alpha_0\beta_0^* \\ \alpha_1^*\beta_1\alpha_0^*\beta_0 & \alpha_1^*\beta_1|\beta_0|^2 & |\beta_1|^2\alpha_0^*\beta_0 & |\beta_1|^2|\beta_0|^2 \end{pmatrix} .$$

A projective measurements of qubit q_1 with two possible outcomes, $|q_1\rangle = |0\rangle_1, |1\rangle_1$ with the respective probabilities $p_0 = |\alpha_1|^2$ and $p_1 = |\beta_1|^2$, yields the reduced density operator,

$$\hat{\rho}_1^{\rm red} = p^{(0)} \frac{[|0\rangle\langle 0| \otimes \mathbb{I}]\hat{\rho}[|0\rangle\langle 0| \otimes \mathbb{I}]}{\text{Tr } \hat{\rho}[|0\rangle\langle 0| \otimes \mathbb{I}]} + p^{(1)} \frac{[|1\rangle\langle 1| \otimes \mathbb{I}]\hat{\rho}[|1\rangle\langle 1| \otimes \mathbb{I}]}{\text{Tr } \hat{\rho}[|1\rangle\langle 1| \otimes \mathbb{I}]} \tag{24.113}$$

$$= |\alpha_1|^2 \begin{pmatrix} |\alpha_0|^2 & \alpha_0\beta_0^* & 0 & 0 \\ \alpha_0^*\beta_0 & |\beta_0|^2 & 0 & 0 \\ 0 & 0 & 0 & 0 \\ 0 & 0 & 0 & 0 \end{pmatrix} + |\beta_1|^2 \begin{pmatrix} 0 & 0 & 0 & 0 \\ 0 & 0 & 0 & 0 \\ 0 & 0 & |\alpha_0|^2 & \alpha_0\beta_0^* \\ 0 & 0 & \alpha_0^*\beta_0 & |\beta_0|^2 \end{pmatrix}$$

$$= [|\alpha_1|^2|0\rangle\langle 0| + |\beta_1|^2|1\rangle\langle 1|] \otimes \hat{\rho}_0 .$$

The inversion of qubit q_1 is,

$$\langle \hat{\sigma}_1^z \rangle = |\alpha_1|^2 - |\beta_1|^2 . \tag{24.114}$$

That is, we are left with a mixture of two product states, $|0\rangle \otimes [\alpha_0|0\rangle + \beta_0|1\rangle]$ or $|1\rangle \otimes [\alpha_0|0\rangle + \beta_0|1\rangle]$. Analogically, a projective measurements of qubit q_0 yields,

$$\hat{\rho}_0^{\rm red} = |\alpha_0|^2\hat{\rho}_1 \otimes |0\rangle\langle 0| + |\beta_0|^2\hat{\rho}_1 \otimes |1\rangle\langle 1| \tag{24.115}$$

and $\langle \hat{\sigma}_0^z \rangle = |\alpha_0|^2 - |\beta_0|^2$.

Example 169 (*Measurements on entangled qubits*): Now, we consider two entangled qubits $|\psi\rangle = \alpha[|0\rangle \otimes |0\rangle] + \beta[|1\rangle \otimes |1\rangle]$, with $|\alpha|^2 + |\beta|^2 = 1$, such that,

$$\hat{\rho} = \begin{pmatrix} \alpha \\ 0 \\ 0 \\ \beta \end{pmatrix} \begin{pmatrix} \alpha^* & 0 & 0 & \beta^* \end{pmatrix} = \begin{pmatrix} |\alpha|^2 & 0 & 0 & \alpha\beta^* \\ 0 & 0 & 0 & 0 \\ 0 & 0 & 0 & 0 \\ \alpha^*\beta & 0 & 0 & |\beta|^2 \end{pmatrix} . \tag{24.116}$$

Projective measurements of qubit q_1 with two possible outcomes yields in both of the two cases, $|q_1\rangle = |0\rangle, |1\rangle$, the reduced density operator,

$$\hat{\rho}_1^{\rm red} = p^{(0)} \frac{[|0\rangle\langle 0| \otimes \mathbb{I}]\,\hat{\rho}\,[|0\rangle\langle 0| \otimes \mathbb{I}]}{\text{Tr } \hat{\rho}[|0\rangle\langle 0| \otimes \mathbb{I}]} + p_1 \frac{[|1\rangle\langle 1| \otimes \mathbb{I}]\hat{\rho}[|1\rangle\langle 1| \otimes \mathbb{I}]}{\text{Tr } \hat{\rho}[|1\rangle\langle 1| \otimes \mathbb{I}]} \tag{24.117}$$

$$= \begin{pmatrix} |\alpha|^2 & 0 & 0 & 0 \\ 0 & 0 & 0 & 0 \\ 0 & 0 & 0 & 0 \\ 0 & 0 & 0 & |\beta|^2 \end{pmatrix} = |\alpha|^2[|0\rangle\langle 0| \otimes |0\rangle\langle 0|] + |\beta|^2[|1\rangle\langle 1| \otimes |1\rangle\langle 1|] .$$

A projective measurements of qubit q_1 would yield exactly the same result.

24.3.6 The field of quantum information

The possibility to experimentally control, manipulate and read out individual qubits gave birth to a new field of physics in the past two decades now called *quantum information*. This fields includes the more specific areas of *quantum processing* (which itself splits into the subareas of *quantum computing* and *quantum simulation*), *quantum communication*, and *quantum sensing* (see Sec. 24.4).

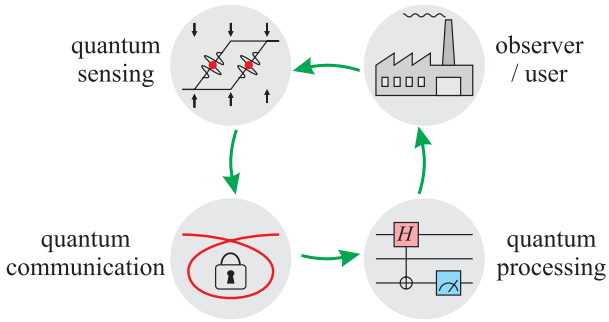

Figure 24.13: Key technologies of the second quantum revolution.

The fundamental epitomic systems on which the quantum information technologies are based are listed in the table below. Although the correspondence is oversimplified, it gives a coarse idea of the involved areas of quantum mechanics. Technological revolutions have often been triggered by paradigmatic 'paradoxes' which, in fact, were mostly dramatized juxtapositions of classical and innovative concepts and stop being paradoxical, once they have been resolved by a more complete theory. The table also lists the cornerstone paradoxes of quantum information technologies.

area	quantum computing	communication	sensing
system	two-level atom / spin	harmonic oscillator	propagation of free atom
device	qubit	photon	interferometer
phenomenon	quantum entanglement		superposition & measurement
paradox	EPR paradox		Schrödinger cat

24.3.6.1 Physical implementation of quantum computers

Quantum entanglement and information processing protocols for quantum computing have been implemented with various technologies (see table below for a non-exhaustive list), some of them pursued by private companies. Every approach has its advantages and disadvantages, the main figures of merit being the *qubit number*, the *qubit connectivity*, and the *gate fidelity*. Other important factors are *scalability*, *qubit homogeneity*, and *ease of fabrication and use*.

physical system	description	companies	publications
ions	trapped ion array	IonQ, AQT	[596, 546]
neutral atoms	optical lattice	-	[17]
transmons	superconducting JJ arrays	IBM, Google, ...	[27]
molecules	NMR on bonds in molecules	-	[885]
NV centers	color centers in diamond	-	[652]
quantum dots	quantum dots arrays	diraq	[529]
photons	polarization or timing	-	[797]

Example 170 (*Quantum volume of perfect processor*): The *quantum volume* of an N-qubit quantum processor is a metric invented by IBM that characterizes the largest random quantum circuit that the device can efficiently simulate. The formula for quantum volume is given by:

$$\text{quantum volume} = N^2 \times \text{maximal depth} \ . \tag{24.118}$$

In the case of a perfect N-qubit processor, the maximal depth is equal to N since each gate can be applied in parallel on all qubits, and there are N such layers. Therefore, the quantum volume of a perfect N-qubit processor is quantum volume $= N^3$. This means that a perfect N-qubit quantum processor can efficiently simulate random quantum circuits of up to N^3 gates. However, in reality, quantum processors suffer from errors due to various sources such as decoherence and imperfect gate operations, and as a result, their quantum volume is typically much lower than this theoretical limit.

24.3.6.2 Quantum sensing 2.0

Many sensors are based on interferometry, as explained in Sec. 24.4.2. The circuit exhibited in Fig. 24.14 visualizes the basic principle of an interferometer. The two Hadamard gates correspond to Ramsey pulses, and the controlled U gate realizes the interaction, which transfers information from the U gate to the sensing qubit.

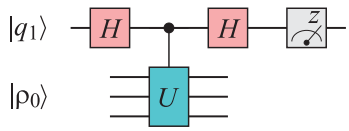

Figure 24.14: Quantum interferometry.

As mentioned in Sec. 18.2.2 and in Sec. 23.1.5, the sensitivity of interferometers can be enhanced when correlated particles are used. In Exc. 24.3.7.16 we show how the interferometer of Fig. 24.14 can be modified in order to benefit from correlated particles.

24.3.6.3 Continuous variable quantum information

Continuous variable quantum information is the area of quantum information science that makes use of physical observables with continuous spectra, like the strength of an electromagnetic field. Continuous-variable quantum computation is performed on infinite-dimensional Hilbert spaces and may be called 'analog', while qubit quantum

computation is performed on finite-dimensional Hilbert spaces (2^N with N the number of qubits) and may be called 'digital'.

Bosonic modes are examples of systems being studied for the implementation of continuous-variable quantum information. By modeling each mode of the electromagnetic field as a quantum harmonic oscillator with its associated field operators, one defines a canonically conjugate pair of variables for each mode, the so-called *quadratures*, which span a phase space on which Wigner quasi-probability distributions can be defined. Quantum measurements on such a system can be performed using homodyne and heterodyne detectors. Interestingly, qubits can be encoded into a continuous variable [332]. The procedure is easily understood at the example of a two-level atom dispersively interacting with a cavity mode studied within the Jaynes-Cummings model in Sec. 17.2.2 and in the Exc. 17.2.5.6. See also Sec. 24.2.1.

In all approaches to quantum computing, it is important to know whether a task under consideration can be carried out efficiently by a classical computer. An algorithm might be described in the language of quantum mechanics, but upon closer analysis, reveals to be implementable using only classical resources [331], even if making use of quantum entanglement. When the Wigner quasi-probability representations of all the quantities (states, time evolutions and measurements) involved in a computation are non-negative, then they can be interpreted as ordinary probability distributions, indicating that the computation can be modeled as an essentially classical one [570].

24.3.6.4 Quantum Fourier transform

The *quantum Fourier transform* (QFT) is a linear transformation on qubits and the quantum analogue of the inverse discrete Fourier transform. The quantum Fourier transform is a part of many quantum algorithms, notably Shor's algorithm for factoring and computing the discrete logarithm or the quantum phase estimation algorithm for estimating the eigenvalues of a unitary operator.

The quantum Fourier transform can be performed efficiently on a quantum computer, with a particular decomposition into a product of simpler unitary matrices. Using a simple decomposition, the discrete Fourier transform on 2^n amplitudes can be implemented as a quantum circuit consisting of only $O(n^2)$ Hadamard gates and controlled phase shift gates, where n is the number of qubits. This can be compared with the classical discrete Fourier transform, which takes $O(2^n)$ gates, which is exponentially more than in the classical case. However, the quantum Fourier transform acts on a quantum state, whereas the classical Fourier transform acts on a vector, so not every task that uses the classical Fourier transform can take advantage of this exponential speedup.

The quantum Fourier transform is the classical discrete Fourier transform applied to the vector of amplitudes of a quantum state, where we usually consider vectors of length $N = 2^n$. The classical Fourier transform acts on a vector $(x_0, x_1, \ldots, x_{N-1}) \in \mathbb{C}^N$ and maps it to the vector $(y_0, y_1, \ldots, y_{N-1}) \in \mathbb{C}^N$ according to the formula:

$$\boxed{y_k = \frac{1}{\sqrt{N}} \sum_{n=0}^{N-1} x_n \omega_N^{\mp kn}} \,, \tag{24.119}$$

where $k = 0, 1, \ldots, N-1$ and $\omega_N = e^{2\pi\imath/N}$ and ω_N^n is an N^{th} root of unity. The lower sign holds for the *inverse* FT.

Similarly, the quantum Fourier transform acts on a quantum state $|x\rangle = \sum_{i=0}^{N-1} x_i|i\rangle$ and maps it to a quantum state $\sum_{i=0}^{N-1} y_i|i\rangle$ according to the same formula (24.119). In case that $|x\rangle$ is a basis state, the quantum Fourier Transform can also be expressed as the map,

$$|x\rangle \mapsto \frac{1}{\sqrt{N}} \sum_{k=0}^{N-1} \omega_n^{xk} |k\rangle \ . \tag{24.120}$$

Equivalently, the quantum Fourier transform can be viewed as a unitary matrix (or a quantum gate, similar to a Boolean logic gate for classical computers) acting on quantum state vectors, where the unitary matrix is given by,

$$F_N = \frac{1}{\sqrt{N}} \begin{pmatrix} 1 & 1 & 1 & 1 & \cdots & 1 \\ 1 & \omega & \omega^2 & \omega^3 & \cdots & \omega^{N-1} \\ 1 & \omega^2 & \omega^4 & \omega^6 & \cdots & \omega^{2(N-1)} \\ 1 & \omega^3 & \omega^6 & \omega^9 & \cdots & \omega^{3(N-1)} \\ \vdots & \vdots & \vdots & \vdots & & \vdots \\ 1 & \omega^{N-1} & \omega^{2(N-1)} & \omega^{3(N-1)} & \ldots & \omega^{(N-1)(N-1)} \end{pmatrix} \tag{24.121}$$

where $\omega = \omega_N$. Do the Excs. 24.3.7.13 and 24.3.7.14.

The QFT is unitary,

$$\boxed{FF^\dagger = \mathbb{I}\,,} \tag{24.122}$$

and can be efficiently performed on a quantum computer. The quantum gates used in the circuit are the Hadamard gate and the controlled phase gate R_m,

$$H = \tfrac{1}{\sqrt{2}} \begin{pmatrix} 1 & 1 \\ 1 & -1 \end{pmatrix} \qquad \text{and} \qquad R_m = \begin{pmatrix} 1 & 0 \\ 0 & e^{2\pi\imath/2^m} \end{pmatrix} \ , \tag{24.123}$$

with $e^{2\pi\imath/2^m} = \omega_{(2^m)}$ the primitive 2^m-th root of unity. The circuit is composed of H gates and the controlled version of R_m.

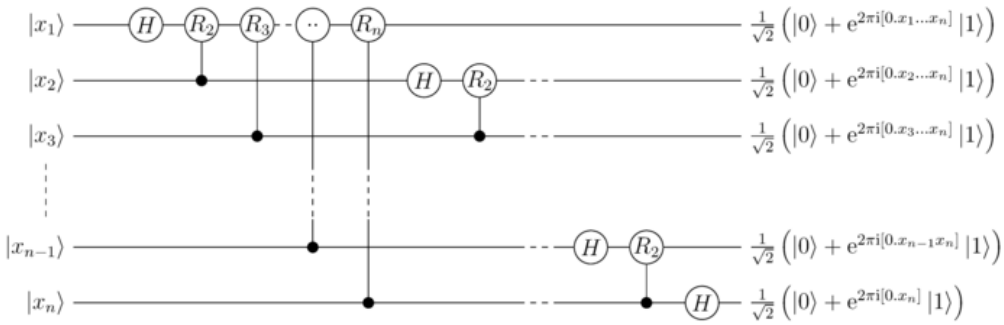

Figure 24.15: Quantum circuit for QFT with n qubits (without rearranging the order of output states).

All quantum operations must be linear, so it suffices to describe the function on each one of the basis states and let the mixed states be defined by linearity. This is in contrast to how Fourier transforms are usually described. We normally describe Fourier transforms in terms of how the components of the results are calculated on an arbitrary input. This is how you would calculate the path integral or show BQP is in PP. But it is much simpler here (and in many cases) to just explain what happens to a specific arbitrary basis state, and the total result can be found by linearity.

The quantum Fourier transform can be approximately implemented for any N; however, the implementation for the case where N is a power of 2 is much simpler. As already stated, we assume $N = 2^n$. We have the orthonormal basis consisting of the vectors $|0\rangle, \ldots, |2^n - 1\rangle$. The basis states enumerate all the possible states of the qubits, $|x\rangle = |x_1 x_2 \ldots x_n\rangle = |x_1\rangle \otimes |x_2\rangle \otimes \cdots \otimes |x_n\rangle$, where $|x_j\rangle$ indicates that qubit j is in state x_j, with x_j either 0 or 1. By convention, the basis state index x orders the possible states of the qubits lexicographically, i.e. by converting from binary to decimal in this way:

$$x = x_1 2^{n-1} + x_2 2^{n-2} + \cdots + x_n 2^0 \ . \tag{24.124}$$

It is also useful to borrow fractional binary notation:

$$[0.x_1 \ldots x_m] = \sum_{k=1}^{m} x_k 2^{-k} \ . \tag{24.125}$$

For instance, $[0.x_1] = \frac{x_1}{2}$ and $[0.x_1 x_2] = \frac{x_1}{2} + \frac{x_2}{2^2}$. With this notation, the action of the quantum Fourier transform can be expressed in a compact manner:

$$\begin{aligned} \mathrm{QFT}(|x_1 x_2 \ldots x_n\rangle) = \frac{1}{\sqrt{N}} \left(|0\rangle + e^{2\pi\imath\ [0.x_n]}|1\rangle\right) \otimes \left(|0\rangle + e^{2\pi\imath\ [0.x_{n-1}x_n]}|1\rangle\right) \otimes \cdots \\ \otimes \left(|0\rangle + e^{2\pi\imath\ [0.x_1 x_2 \ldots x_n]}|1\rangle\right) \ , \end{aligned} \tag{24.126}$$

where we have used $[0.x_1 x_2 ... x_m] = [x_1 x_2 ... x_n]/2^m$. This can be seen by rewriting the formula for the Fourier transform in the binary expansion:

$$\mathrm{QFT}(|x\rangle) = \frac{1}{\sqrt{N}} \sum_{k=0}^{2^n-1} \omega_n^{xk} |k\rangle = ... = \frac{1}{\sqrt{N}} \bigotimes_{j=1}^{n} \left(|0\rangle + \omega_n^{x2^{n-j}}|1\rangle\right) \ . \tag{24.127}$$

Now, we have $\omega_n^{x2^{n-j}} = e^{\frac{2\pi\imath}{2^n} x 2^{n-j}} = e^{2\pi\imath(x2^{-j})}$. Let,

$$\begin{aligned} f(j) = x2^{-j} = 2^{-j} \sum_{r=1}^{n} x_r 2^{n-r} = \sum_{r=1}^{n} x_r 2^{n-j-r} \\ = \sum_{r=1}^{n-j} x_r 2^{n-j-r} + \sum_{r=n-j+1}^{n} x_r 2^{n-j-r} = a(j) + b(j) \ . \end{aligned} \tag{24.128}$$

then $a(j) \in \mathbb{N}_0$, because $2^{n-j-r} \geq 0$, for $n-j-r \geq 0$, and $b(j) = 0.x_{n-j+1} x_{n-j+2} \ldots x_n$, thus the (2) becomes:

$$e^{2\pi\imath f(j)} = e^{2\pi\imath(a(j)+b(j))} = e^{2\pi\imath a(j)} \cdot e^{2\pi\imath b(j)} = e^{2\pi\imath[0.x_{n-j+1}x_{n-j+2}\cdots x_n]} \ , \tag{24.129}$$

since $e^{2\pi\imath a(j)} = 1$ for all j. Then we can write:

$$\mathrm{QFT}(|x_1 x_2 \dots x_n\rangle) = \frac{1}{\sqrt{N}} \bigotimes_{j=1}^{n} \left(|0\rangle + \omega_n^{x 2^{n-j}} |1\rangle\right) \tag{24.130}$$

$$= \frac{1}{\sqrt{N}} \bigotimes_{j=1}^{n} \left(|0\rangle + e^{2\pi\imath [0.x_{n-j+1} x_{n-j+2} \dots x_n]} |1\rangle\right)$$

$$= \frac{1}{\sqrt{N}} \left(|0\rangle + e^{2\pi\imath [0.x_n]} |1\rangle\right) \otimes \left(|0\rangle + e^{2\pi\imath [0.x_{n-1} x_n]} |1\rangle\right) \otimes \cdots \otimes \left(|0\rangle + e^{2\pi\imath [0.x_1 x_2 \dots x_n]} |1\rangle\right) \ .$$

To obtain this state from the circuit depicted above, a swap operations of the qubits must be performed to reverse their order. After the reversal, the n-th output qubit will be in a superposition state of $|0\rangle$ and $e^{2\pi\imath\ [0.x_1 \dots x_n]}|1\rangle$, and similarly the other qubits before that (take a second look at the sketch of the circuit above).

In other words, the discrete Fourier transform, an operation on n qubits, can be factored into the tensor product of n single-qubit operations, suggesting it is easily represented as a quantum circuit (up to an order reversal of the output). In fact, each of those single-qubit operations can be implemented efficiently using a Hadamard gate and controlled phase gates. The first term requires one Hadamard gate and $(n-1)$ controlled phase gates, the next one requires a Hadamard gate and $(n-2)$ controlled phase gate, and each following term requires one fewer controlled phase gate. Summing up the number of gates, excluding the ones needed for the output reversal, gives $n + (n-1) + \cdots + 1 = n(n+1)/2 = O(n^2)$ gates, which is quadratic polynomial in the number of qubits.

The QFT is useful in the simulation of Hamiltonian evolution governed by conjugate variables,

$$e^{-\hat{H}t/\hbar} \qquad \text{where} \qquad \hat{H} = \frac{\hat{p}}{2m} + \frac{m}{2}\omega^2 \hat{x}^2 \ , \tag{24.131}$$

where, similar to the *time-splitting spectral algorithm*, we may replace differential operators,

$$\hat{p} = F^{-1}\ \hat{x}\ F \ . \tag{24.132}$$

24.3.7 Exercises

24.3.7.1 Ex: Two-bit `SWAP` gate

Represent the two-qubit `SWAP` gate by a succession of three `CNOT` gates.

24.3.7.2 Ex: Quantum computing code for spin-squeezing

Express spin-squeezing of 2, respectively, 3 qubits by a quantum circuit. See also Exc. 23.1.9.13!

24.3.7.3 Ex: Controlled `Z`-gate

Check that the Cirac-Zoller `cZ` gate is invariant under spin exchange. This fact justifies the symmetry of the symbol with respect to the two coupled qubits.

24.3.7.4 Ex: Boolean logic

Write an algorithm encoding a decimal integer A_0 into a binary,

$$D = \sum_{k=0}^{k_{\max}} 2^k a_k \ .$$

24.3.7.5 Ex: Boolean logic

a. Design a classical logic circuit only based on `NAND` gates for the increment by 1 of a number encoded in a n-bit register.
b. Design a classical logic circuit only based on `NAND` gates for the addition of two numbers.

24.3.7.6 Ex: Fredkin cSWAP gate

a. Write down the truth table for the *Fredkin gate* defined by the protocol that the qubits q_1 and q_0 are swapped only if the state of qubit q_2 is 1.
b. Write down the matrix realizing the Fredkin gate.
c. Check that the quantum circuit sketched in Fig. 24.16, which only envolves two-qubit quantum gates, realizes a Fredkin gate.

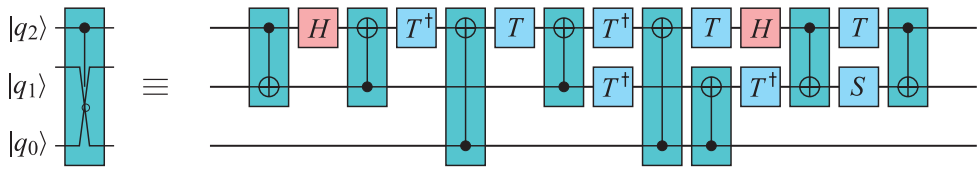

Figure 24.16: Quantum circuit realizing a Fredkin gate $\overset{cc}{X}_{012}$.

24.3.7.7 Ex: Three-bit SWAP gate

a. Convince yourself that the SWAP gates defined by (24.93) have the explicit matrix form,

$$\mathbb{S}_{ij}(k, k_{ij}) \equiv 1 \qquad \text{where} \qquad \begin{cases} k = [0, ..., 7] \\ k_{12} = [0, 1, 4, 5, 2, 3, 6, 7] \\ k_{01} = [0, 2, 1, 3, 4, 6, 5, 7] \\ k_{02} = [0, 4, 2, 6, 1, 5, 3, 7] \end{cases} ,$$

the index k indicating the column and k_{ij} the row where the matrix has an entry.
b. Verify,

$$\mathbb{S}^{-1} = \mathbb{S} \quad , \quad \mathbb{S}_{ij}^{-1} = \mathbb{S}_{ij} \ .$$

24.3.7.8 Ex: Quantum gates

Verify the formulae (24.95).

24.3.7.9 Ex: Toffoli gate

a. Write down the truth table for the *Toffoli gate*.
b. Write down the matrix realizing the Toffoli gate.
c. Check that the quantum circuit sketched in Fig. 24.17, which only envolves two-qubit quantum gates realizes a *Toffoli gate*.

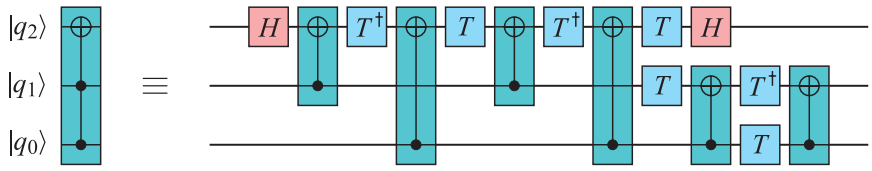

Figure 24.17: Quantum circuit realizing a Toffoli gate $\overset{cc}{X}_{012}$.

24.3.7.10 Ex: Classical and quantum logic

a. Verify $\neg(A \vee B) = \neg A \wedge \neg B$ and $A \oplus B = (\neg A \wedge B) \vee (A \wedge \neg B)$.
b. How would you realize the classical logical operations `AND`, `OR`, and `XOR` on a quantum computer?

24.3.7.11 Ex: Quantum composer

Show that the following diagrams describe identical unitary operations:

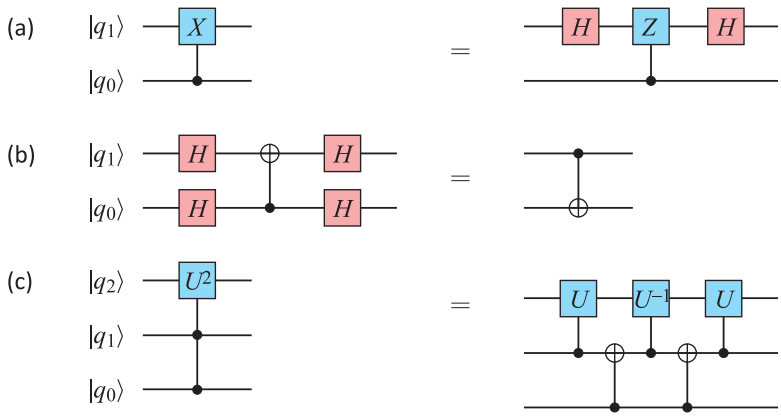

Figure 24.18: Quantum composer.

24.3.7.12 Ex: Classical addition of two qubits

Design a quantum algorithm for the classical addition of up to 8 qubits.

24.3.7.13 Ex: CARL simulation on a quantum computer

Try to recast the so-called CARL Hamiltonian,

$$\hat{H} = U_0(\hat{a}_+^\dagger \hat{a}_- e^{-\imath k\hat{r}} + \hat{a}_+ \hat{a}_-^\dagger e^{\imath k\hat{r}})$$

such that it can be simulated by a sequence of quantum gates.

24.3.7.14 Ex: Quantum Fourier transform on a quantum computer

Write down the QF transformation matrix for the case of $N = 4 = 2^2$ and phase $\omega = \imath$.

24.3.7.15 Ex: Three entangled qubits

a. Imagine a three-qubit quantum gate or a sequence of gates generating from the ground state the three partite states [253]:

$$|\text{GHZ}\rangle \equiv \tfrac{1}{\sqrt{2}}(|000\rangle + |111\rangle \qquad \text{and} \qquad |\text{W}\rangle \equiv \tfrac{1}{\sqrt{3}}(|001\rangle + |010\rangle + |100\rangle) \ .$$

b. Show how the procedure for the generation of the $|\text{GHZ}\rangle$ state can be easily extended to N entangled particles.

24.3.7.16 Ex: Scattering circuit

a. Consider the controlled $\mathcal{U}$ gate given by,

$$\overset{c}{\mathcal{U}}_{10} = |0\rangle\langle 0| \otimes \mathbb{I} + |1\rangle\langle 1| \otimes \mathcal{U} \ ,$$

where U is an arbitrary unitary operation, and the quantum circuit given by,

$$M = [H \otimes \mathbb{I}]\overset{c}{\mathcal{U}}_{10}[H \otimes \mathbb{I}]$$

and depicted in Fig. 24.14. Starting from an initial state $|0\rangle\langle 0| \otimes \hat{\rho}_0$, show, that a measurement of the first qubit $|q_1\rangle$ of the final state,

$$\hat{\rho}_f = M[|0\rangle\langle 0| \otimes \hat{\rho}_0]M^\dagger$$

yields,

$$\langle \hat{\sigma}_1^z \rangle = \mathfrak{Re}\left[\text{Tr}_0\ \hat{\rho}_0 \mathcal{U}\right] \qquad \text{and} \qquad \langle \hat{\sigma}_1^y \rangle = \mathfrak{Im}\left[\text{Tr}_0\ \hat{\rho}_0 \mathcal{U}\right] \ .$$

b. Calculate $\langle \vec{\hat{\sigma}}_1 \rangle$ for the case that $\mathcal{U}$ is a one-qubit phase gate given by (24.75).
c. Calculate $\langle \vec{\hat{\sigma}}_1 \rangle$ for the case that $\mathcal{U} = X$ is a one-qubit NOT gate given by (24.77).

24.3.7.17 Ex: Heisenberg-limited quantum sensing

This exercise aims at showing that entangled qubits allow for phase measurements beyond the standard quantum limit. Proceed as follows:
a. Express standard Ramsey interferometry for a single qubit as a sequence of quantum gates and calculate the uncertainty of the final Bloch vector component $\Delta\hat{S}_z/||\hat{S}_z||$.
b. Repeat (a) with a product state of two qubits.
c. Plot the relative uncertainty of the inversion $(\Delta\hat{S}_z^2/\langle\hat{S}_z^2\rangle)^{1/2}$ after the Ramsey cycle as a function of the precession phase for the cases (a) and (b), as well as the spin squeezing parameter $\sqrt{N}\langle\Delta\hat{S}_y\rangle/|\langle\hat{S}_z\rangle|$ [869, 209].
d. Repeat (b) with two entangled qubits and interpret your observations.

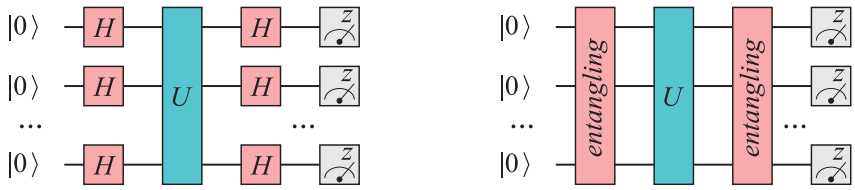

Figure 24.19: Scheme for Heisenberg-limited quantum sensing.

24.4 Metrology and quantum sensing

We have seen at the end of the last section how to perform projective measurements in entangled systems. In the following we will now show that such systems have the potential of improving the sensitivity of measurements. The field of research dealing with this, called *quantum sensing*, represents an extension of the field of metrology into the quantum regime. Before discussing the stakes of quantum information science in metrology, let us review in a comprehensible way what metrology and sensing is about.

24.4.1 Atomic clocks

Metrology is the art of sensing, and sensing is simply the activity of measuring a physical quantity as accurately as possible. The most fundamental quantities to measure are time and space. However, *absolute space and time do not exist*. According to the restricted and the general theory of relativity they are interconnected by velocity and additionally depend on the presence of masses exerting gravitational forces.

Hence, before talking about clocks, we need to spend a few words on the physical quantity they are supposed to measure: *time*. In the same way as it is meaningless to talk about space with nothing in it, time is only there, because things are happening. Space is the distance between things and time is nothing else than the distance between events.

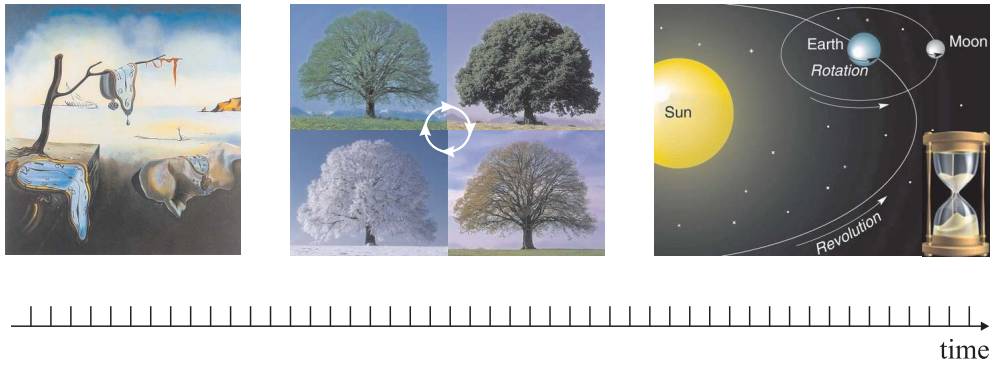

Figure 24.20: (left) 'Time persistence' by Salvatore Dali. (center) Recurrent events. (right) Periodic astronomical cycles.

In our current physical understanding of the universe the most elementary events

are collisions between (real or virtual) particles. Obviously, our universe is full of time. In order to bring any succession of such events into a logical and causal order, a reference time line is needed. It allows for historical book keeping of sequences of events, that we may call *histories*. And in order to facilitate a comparison between different histories, this reference time line should follow a simple deterministic rule, e.g. be periodic or exponentially decaying. In fact, both types of processes are currently used for time measurements. E.g. exponential processes, such as radioactive decay is commonly used in radioactive dating.

The most common practical approach to the measurement of time, however, is based on the observation of recurrent phenomena that we think of being periodic, such as a day on Earth, the dripping of a water pipe, or the oscillation of a pendulum or of an atomic excitation. Assuming the time intervals separating the recurrent phenomena as being all the same, we build a ruler for time which we call *clock*.

But now comes a tricky question: How do we know whether a clock is really periodic? In fact, we never know for sure whether the time intervals are really all the same. We only know that some clocks deserve a greater degree of confidence based on the fact that *more care has been taken in their design and construction*, or based on the observation that clocks built in a certain manner tend to deviate less from each other than clocks built in a different manner. The other approach would be to compare several totally *independent* clocks and to give preference to those who deviate less from each other.

An important criterion for a useful clock concerns its duty cycle. The shorter the cycling time, the faster we can extract information from the clock, and the higher is the accuracy we can reach in a given integration time. Ancient time standards had been link to the periodic motion of celestial bodies, e.g. the revolution time of the Earth around the sun. Therefore, clocks with smaller duty cycles have been engineered, such as the clepsydra or the hour glass. But their calibration to periodical astronomical cycles remained tedious and slow. Historically, the development of ever precise clocks has been motivated by navigation. Indeed, 1 minute of inaccuracy in the clock generates an uncertainty of 28 km in global positioning. And this motivation still prevails nowadays, although, meanwhile, atomic clocks are reaching uncertainties of below 10^{-18} and extremely short duty cycles on the order of femto-seconds.

The left part of Fig. 24.21 shows the basic idea of any human-made clock, which consists in locking an oscillating mechanism, whose time constant can be manipulated, for instance a pendulum or a laser, by a very precise periodic process, that we call *resonance*. This resonance can be an astronomic period or the transition of an atomic between two states of excitation. Expressing the stability of a clock that can be obtained in a given integration time as,

$$\sigma = \frac{\Gamma_{\rm nat} + \Gamma_{\rm pert}}{\omega} \frac{1}{S/N_{\rm noise}} \ , \tag{24.133}$$

we see that we better look for oscillators and resonances operating at high frequencies ω, having very narrow widths $\Gamma_{\rm nat}$, being subject to very weak perturbations and line broadenings $\Gamma_{\rm pert}$, and delivering a good signal-to-noise ratio. The right part of Fig. 24.21 shows the concept of a cesium beam *atomic clock*. A microwave oscillator operating at $\omega/2\pi = 9.1\,\text{GHz}$ excites cesium atoms passing through a microwave cavity thus generating in a detector a frequency-dependent error signal which can be

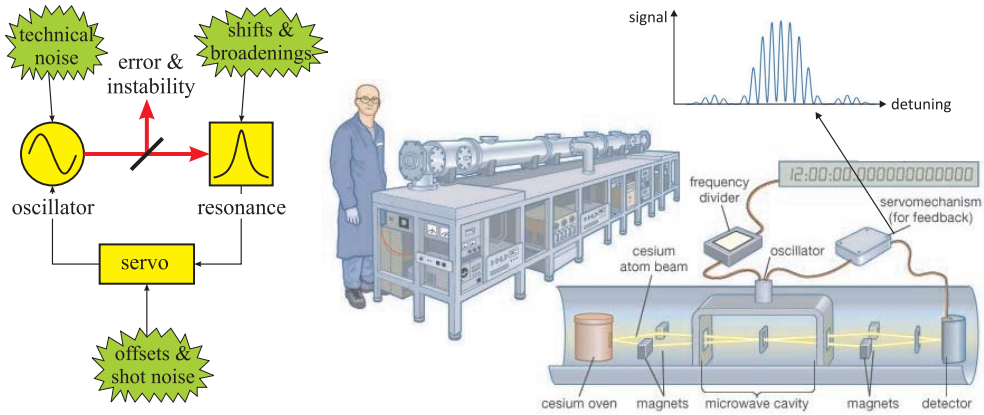

Figure 24.21: (left) Principle of any clock and possible perturbations. (right) Cesium beam atomic clock and Ramsey interference fringes.

used to correct the oscillator frequency.

24.4.1.1 Gravitational red-shift

Clocks and gravimeters are intrinsically related the gravitational redshift. The *gravitational red-shift* is that phenomenon in which electromagnetic waves or photons traveling out of a gravitational well (seem to) lose energy. This loss of energy corresponds to a decrease in the wave frequency and increase in the wavelength. Gravitational redshift can be interpreted (i) as a consequence of the *equivalence principle* stating that gravity and acceleration are equivalent and the redshift is caused by the Doppler effect. It can also be understood (ii) as a consequence of the mass-energy equivalence stating that 'falling' photons gain energy (though there are numerous subtleties that complicate a rigorous derivation). Finally, it can be understood (iii) in terms of gravitational time dilation at the source of the radiation: an oscillator (producing electromagnetic radiation) will seem to 'tick' faster when exposed to a stronger gravitational potential.

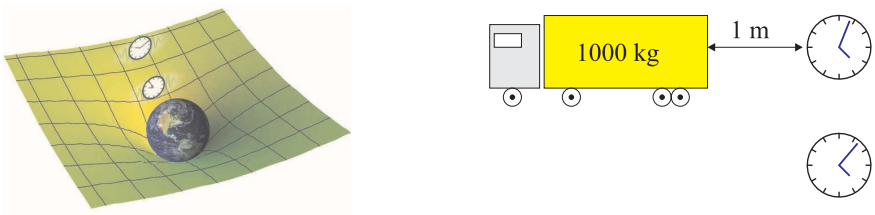

Figure 24.22: Gravitational redshift is due to the dilation of time near heavy masses.

To first approximation, the gravitational redshift is proportional to the difference in gravitational potential. In a homogeneous field,

$$\frac{\Delta\nu}{\nu} = \frac{\Delta\lambda}{\lambda} \simeq \frac{g\Delta z}{c^2} \ , \tag{24.134}$$

where Δz is the change in height. Accounting for the accompanying gravitational time dilation affecting the atomic clock in the satellite is crucially important for accurate navigation. For this reason, *metrology* of time and *gravimetry* are closely interrelated. Do the Exc. 24.4.6.1.

Example 171 (*Prediction by the equivalence principle and general relativity for a uniform gravitational field or acceleration*): Einstein's theory of general relativity incorporates the equivalence principle, which can be stated in various different ways. One such statement is that gravitational effects are locally undetectable for a free-falling observer. Therefore, in a laboratory experiment at the surface of the earth, all gravitational effects should be equivalent to the effects that would have been observed if the laboratory had been accelerating through outer space at g. One consequence is a gravitational Doppler effect. If a light pulse is emitted at the floor of the laboratory, then a free-falling observer says that by the time it reaches the ceiling, the ceiling has accelerated away from it, and therefore when observed by a detector fixed to the ceiling, it will be observed to have been Doppler shifted toward the red end of the spectrum. This shift, which the free-falling observer considers to be a kinematic Doppler shift, is thought of by the laboratory observer as a gravitational redshift. Such an effect was verified in the 1959 Pound-Rebka experiment. Since this prediction arises directly from the equivalence principle, it does not require any of the mathematical apparatus of general relativity, and its verification does not specifically support general relativity over any other theory that incorporates the equivalence principle.

24.4.2 Quantum sensing

Let us first define what we mean by a *sensor* in general before discussing what quantum mechanics has to do with it. A *sensor* is a device, module, machine, or subsystem whose purpose is to detect events or changes in its environment and send the information to other electronics, frequently a computer processor. Progress in engineering, science, medicine, and other disciplines is unavoidably conditioned to sensing: What you cannot measure, you cannot improve! In many areas of applications, however, conventional sensing techniques have met fundamental limitations, and novel disruptive approaches are required in order to reach higher sensitivity and precision.

In many cases, limitations are imposed by the macroscopic, i.e. *classical*, nature of the sensor, and much can be gained by using microscopic sensors. These however, follow different rules of physics given by *quantum mechanics*. Nuclear magnetic resonance spectroscopy (NMR), magnetic resonance imaging, and the development of transistors, LEDs, solar panels, and lasers are examples of technologies developed during the first so-called quantum revolution in the 20th century, which was based on the exploitation of the particle-wave duality. However, the full potential of quantum mechanics goes much further. Today *quantum sensing* is, together with quantum computation and quantum communication (see Sec. 24.3.6), one of the key technologies anticipated to drive the quantum revolution 2.0. However, unlike quantum sensing with light, which is on the verge of turning into mature 2.0 technologies, with applications e.g. in quantum imaging, quantum sensing applications with matter waves are nowadays exclusively on the 1.0 level.

Let us discuss the disruptive role of quantum mechanics at the example of an *atom*, which is a paradigmatic example for a sensor subject to quantum laws. The reasons for this are numerous: (i) Because all atoms of a given species are strictly identical (that is, indistinguishable in the quantum statistical sense) they can be used in different sensing devices, places and countries. We do not need to duplicate reference standards, such as the Original Meter or the Original Kilogram safely kept in Paris. We simply recommend to people wishing to construct their own clock standard to gather cesium atoms (wherever you can find them) and try to excite the 9.1 GHz hyperfine transition (with whatever technique you prefer). In the end, you just need to prove that your clock is sufficiently good. (ii) Some atomic species have ultra-narrow transitions outperforming any imaginable artificial device by many orders of magnitude, which makes them ideal candidates for clock resonances. (iii) Atoms can easily be moved in space with extremely high precision, which makes them suitable for matter wave interferometers, which are useful for the measurement of distances and the sensing of forces.

The main reason, however, for the superiority of atoms (and other quantum devices, such as SQUIDs, quantum dots or nitrogen-vacancy (NV) centers in diamond) with respect to classical objects in sensing applications is, that they can exist in superposition states (of their internal excitation or of their center-of-mass motion) whose evolution delicately depends on external parameters, such as forces. We can now define a *quantum sensor* as a measurement device exploiting quantum correlations in order to enhance sensitivity and resolution, f.ex. quantum superpositions or entanglement [209]. Typically its core is a single atomic two-level system (or any other kind of qubit), whose superposition states (i) are sensitive to some environment parameter, (ii) can be manipulated in a controlled way, and (iii) can be read out.

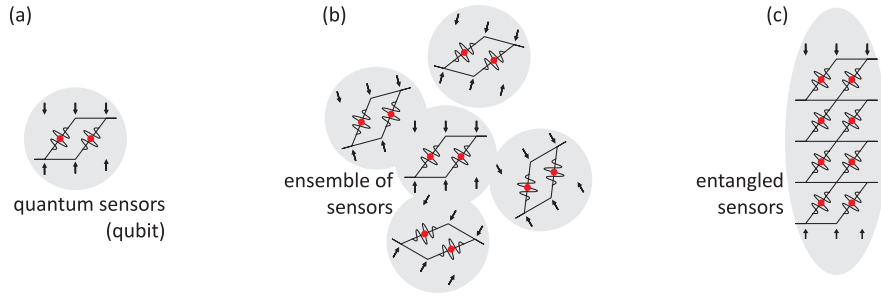

Figure 24.23: (left) Single qu-bit. (center) Larger signals can be observed using ensemble of qu-bits. (right) Collective manipulations on entangled qu-bits allow precisions beyond the standard quantum limit.

In fact, quantum sensors already exist since the invention of atomic clocks and matter wave interferometers, which build on the control and detection of quantum states in individual qubits, even though in practice, most of these device are operated with large incoherent ensembles of qubits. Even if perturbations related to uncontrolled inter-qubit interactions (collisions, thermal excitations, etc.) can be avoided, the sensitivity that can be reached with such ensembles is bound to the standard quantum limit imposed by quantum projection noise (see Secs. 18.2.2 and 23.1.5).

Novel approaches investigate the possibilities of overcoming these limits via the creation of strong interparticle correlations via entanglement, spin-squeezing [869], or superradiant lasing [644]. Such correlations have been created with atoms, which therefore qualify as building blocks of quantum computers or sensing devices capable of overruling the standard quantum limit.

Example 172 (*'Quantumness' of atomic quantum sensors*): The question we want to address here is: What is actually 'quantum' in an atomic quantum sensors?
A possible answer could be: Not much!
OK, atoms have discrete energy levels. But a coin also does and shows the same projection noise features as atoms!
Then, one can point out the role of coherence: Atoms can be in a superposition of two states. But Ramsey fringes can be obtained with classical light beams. The fact that Ramsey fringes can be observed with atoms is simply due to the fact that electrons behave like waves (matter) waves, which is indeed a quantum 1.0 feature. On the other hand, an atom can be described as a classical spinning top and its interaction with light as a torque exerted on the rotor.
The good news is that you do things with atoms that are difficult to do with coins. Atoms are strictly identical and can be sensitive to electric or magnetic fields and gravity in a very reproducible way. Another very important feature is that atoms can be entangled, which you can't do with atoms. But here we are going beyond 1.0 technology.
Important for gravimeter: use neutral particle matter waves, e.g. atoms, not electronic excitation states!

24.4.2.1 Working principle of a quantum sensor

As mentioned above, in order to measure a weak force it is not sufficient to sense it, one also has to read the result. In the field of atom optics, this can conveniently be done with light fields taking the information from an atom isolated in a vacuum chamber to the macroscopic world. In order not to loose information already at the level of the light-atom interaction, one generally tries to avoid dissipation and keep the interaction coherent [8].

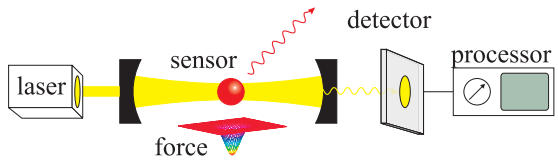

Figure 24.24: Taking information from the sensor to the detector.

A typical quantum sensor can be described by the generic Hamiltonian [209],

$$\hat{H}(t) = \hat{H}_{\rm qbit} + \hat{H}_{\rm cntrl}(t) + \hat{H}_{\rm int}(t) \ , \tag{24.135}$$

[8] E.g. by using two-level systems not subject to motion, collisions, spontaneous emission, etc.. Sometimes spontaneous emission can be controlled by confining both, the atom and the interrogating light field, in a cavity.

composed of a (known) internal Hamiltonian $\hat{H}_{\rm qbit}$, a control Hamiltonian $\hat{H}_{\rm cntrl}$ allowing to manipulate or tune the sensor, and a signal Hamiltonian $\hat{H}_{\rm int}$ allowing to pass information about the state of the system to the outside world.

Typically, the internal Hamiltonian is static and defines the energy eigenstates $|0\rangle$ and $|1\rangle$,

$$\hat{H}_{\rm qbit} = E_0|0\rangle\langle 0| + E_1|1\rangle\langle 1| \ . \tag{24.136}$$

The qubit internal Hamiltonian may contain additional interactions, such as couplings to other qubits or time-dependent stochastic terms due to interactions with an environment.

Many quantum sensing protocols require to manipulate the qubit either before, during, or after the sensing process. This is achieved via a control Hamiltonian, which allows implementing a sequence of appropriate quantum gates, such as the Hadamard gate or Pauli X and Y gates. These gates are nothing else than what, in the language of atom interferometry is known as $\pi/2$ or π-pulses around different axes. Advanced sensing schemes employing more than one sensor qubit may further require conditional gates, especially controlled-NOT gates to generate entanglement, swap gates to exploit memory qubits, and controlled phase shifts in quantum phase estimation (see Sec. 24.3). Finally, the control Hamiltonian can include control fields for systematically tuning the transition frequency $\hbar\omega_0 = E_1 - E_2$.

Finally, the signal Hamiltonian represents the coupling between the sensor qubit and a signal $V(t)$ to be measured. When the signal is weak (which is assumed here) $\hat{H}_{\rm int}$ adds a small perturbation to the internal Hamiltonian. The signal Hamiltonian can then be separated into two qualitatively different contributions,

$$\hat{H}_{\rm int} = \hat{H}_{{\rm int},\parallel} + \hat{H}_{{\rm int},\perp} \ , \tag{24.137}$$

where $\hat{H}_{{\rm int},\parallel}$ is the parallel (commuting) and $\hat{H}_{{\rm int},\perp}$ the transverse (non-commuting) components, respectively. The two components can quite generally be captured by,

$$\begin{aligned} \hat{H}_{{\rm int},\parallel} &= \tfrac{\gamma}{2} V_\parallel(t)[|1\rangle\langle 1| - |0\rangle\langle 0|] \\ \hat{H}_{{\rm int},\perp} &= \tfrac{\gamma}{2}[V_\perp(t)|1\rangle\langle 0| + V_\perp^\dagger(t)|0\rangle\langle 1|] \ , \end{aligned} \tag{24.138}$$

where γ is the coupling or transduction parameter of the qubit to the signal $V(t)$. We verify,

$$\begin{aligned} [\hat{H}_{\rm qbit}, \hat{H}_{{\rm int},\parallel}] &= 0 \\ [\hat{H}_{\rm qbit}, \hat{H}_{{\rm int},\perp}] &= \tfrac{\gamma}{2} V_\perp(E_0 - E_1)(|0\rangle\langle 1| - |1\rangle\langle 0) \ . \end{aligned} \tag{24.139}$$

Examples of coupling parameters include the Zeeman shift parameter or the Stark shift parameter of electric dipoles in an electric field. The parallel and transverse components of a signal have distinctly different effects on the quantum sensor. A commuting perturbation $\hat{H}_{{\rm int},\parallel}$ leads to shifts of the energy levels and an associated change of the transition frequency ω_0. A non-commuting perturbation $\hat{H}_{{\rm int},\perp}$, by contrast, can induce transitions between levels, manifesting through an increased transition rate. Most often, this requires the signal to be time-dependent (resonant with the transition) in order to have an appreciable effect on the quantum sensor.

An important class of signals are vector signal $\mathbf{V}(t)$, in particular, those provided by electric or magnetic fields. The interaction between a vector signal and a qubit can be described by the signal Hamiltonian,

$$\hat{H}_{\rm int} = \gamma \mathbf{V}(t) \cdot \hat{\vec{\sigma}} \ , \tag{24.140}$$

where $\hat{\vec{\sigma}}$ is the vector of Pauli matrices (1.153). For a vector signal, the two signal functions $V_\parallel(t)$ and $V_\perp(t)$ are,

$$\begin{aligned} V_\parallel(t) &= V_z(t) \\ V_\perp(t) &= V_x(t) + \imath V_y(t) \ , \end{aligned} \tag{24.141}$$

where the z-direction is defined by the qubit's quantization axis. The corresponding signal Hamiltonian,

$$\hat{H}_V(t) = \gamma \hat{\sigma}_x \mathfrak{Re}\, V_\perp(t) + \gamma \hat{\sigma}_y \mathfrak{Im}\, V_\perp(t) + \gamma \hat{\sigma}_z V_\parallel(t) \ , \tag{24.142}$$

is just the one of the Rabi model extensively discussed in Sec. 16.3.

24.4.2.2 Sensing forces by matter wave interferometry

Matter wave interferometry is ideal for sensing weak forces or sensing strong forces with high precision. Many interferometers employ the Ramsey scheme, which consists in sandwiching the sensing Hamiltonian between two $\pi/2$-control Hamiltonian pulses $\hat{H}_{\rm cntrl}$ preparing and reading out the atomic coherence. Between the pulses (or interaction zones), the atomic coherence is influenced by the parallel part of the sensing Hamiltonian $\hat{H}_{{\rm int},\parallel}$.

The basic idea is the following: One takes a matter wave and lets it fall in the Earth's gravitational field. But before that, apply a laser pulse separating the matter wave into two parts taking different paths. Thus, the Broglie waves of the two parts will accumulate different phases, which results in an interference pattern when the waves are superimposed again. As illustrated in Fig. 24.25, the matter wave interferometry works similarly to the Ramsey method used in atomic clocks with the difference that in the former the trajectories of the atomic center-of-mass motion must be separated in real space as much as possible (see Sec. 16.3.6 on Ramsey pulses and NMR, Sec. 2.1.3 on gravity with Excs. 1.7.6.2 and 1.7.6.3, Sec. 29.2.2 on Bragg interferometry and photon echos with Excs. 29.2.4.1) [9].

A particularly smart way to do matter wave interferometry is via the observation of Bloch oscillations of matter waves in a periodic lattice (see Sec. 4.2.2). The Bloch oscillations can be understood in the following picture: A resting atom has infinite de Broglie wavelength. Being constantly accelerated by gravity, the matter wave reduces its de Broglie wavelength from ∞ to a value, where it becomes commensurate with the periodicity of the standing light wave potential. At this moment Bragg scattering comes into play, reflecting the atomic motion back into upward direction, and the process starts over again. The atoms evolve like jumping on a trampoline with a frequency given,

$$\nu_{\rm blo} = \frac{mg}{2\hbar k_{\rm lat}} \ . \tag{24.143}$$

[9] See also Sec. 32.5 and 33.5 on interferometric and spectroscopic techniques.

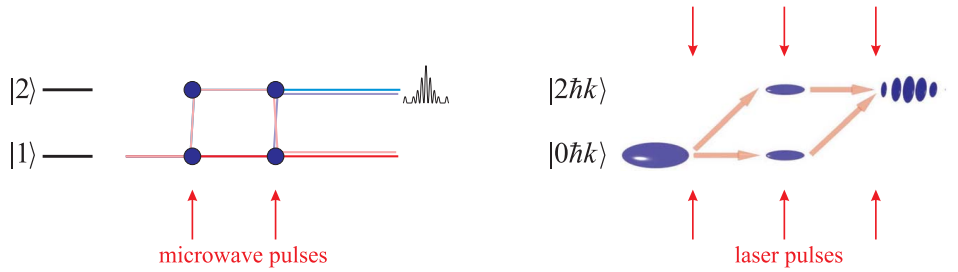

Figure 24.25: Difference between clocks and interferometers. (left) Ramsey-type clock. (right) Ramsey-Bordé interferometer. A movie can be seen at (watch movie).

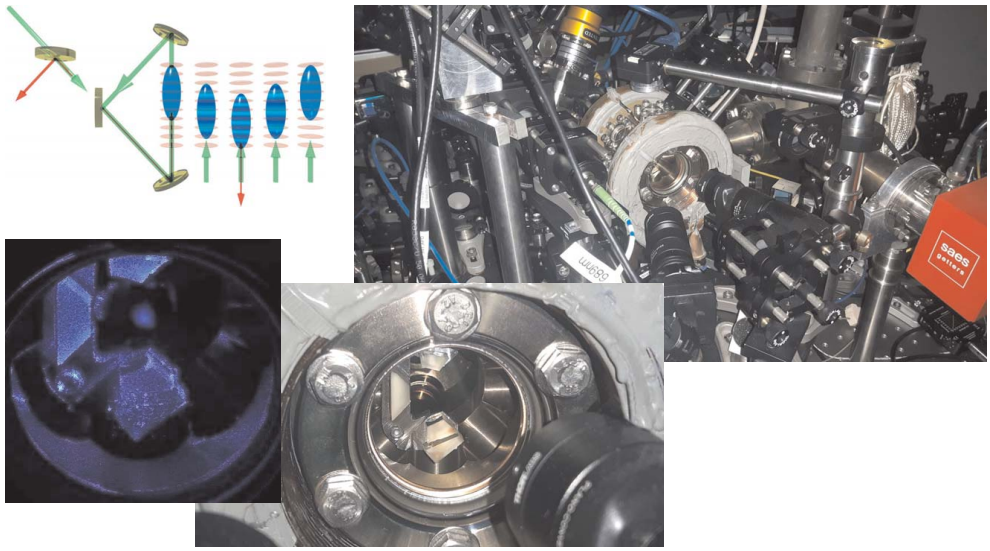

Figure 24.26: Working principle and pictures of the Sr Bloch oscillation interferometer constructed at the IFSC, USP.

24.4.3 Parameter estimation from measurements

The purpose of metrology is the design of technical devices capable of measuring physical quantities with high precision. This obviously necessitates a high degree of correlation between the physical parameter on which we want to obtain information and the observable that is really measured by the device. This is not always easy to achieve and depends on the engineer's skills and inventiveness. A paradigmatic example is Ramsey's idea to sense phase shifts in atom interferometers by measuring atomic internal state populations.

Finding the most likely value for a parameter by measurement is relatively straightforward. It is, however, as important to evaluate the precision of a measurement, and this can be much more complicated. Technically, we may get an idea of the precision by comparing measurements produced by different devices. But it is also interesting to be able to evaluate the precision upfront, before the device has been constructed,

as this may serve as a guidance for the design of the best possible device, at least for idealized conditions.

In practice, the experimentalist will design an apparatus aiming at measuring the dependence (or independence) on a particular observable, say $\hat{M}$, from a parameter, say θ [10]. To increase the confidence in the measurement outcome, the experimentalist will repeat the measurement many times. As any measurement is subject to technical (classical) noise and intrinsic (quantum) noise, the repetitions will generate a distribution of results, which are commonly represented as a histogram. The relevant question in any such measurement is now, how much the outcome probability distribution $P(\theta)$ depends on the experimental parameter θ. We purpose of this section is to introduce quantities, such as the *fidelity* and the *Fisher information*, quantifying this dependency. The greater these figures of merit are, the greater the dependency of $P(\theta)$ on θ and the higher the sensitivity of the measurement apparatus.

24.4.3.1 Repeated measurements

Let us call $p(\mu|\theta)$ the conditional probability of measuring a result μ given that the experimental control parameter is θ. The combined probability to observe the sequence of results $\vec{\mu} = \{\mu_1, .., \mu_N\}$ in N independent measurements is then,

$$P(\vec{\mu}|\theta) = \prod_{i=1}^{N} p(\mu_i|\theta) \ . \tag{24.144}$$

The statistical mean value and variance are,

$$\boxed{1 = \sum_{\vec{\mu}} P(\vec{\mu}|\theta) \quad , \quad \bar{\theta} = \sum_{\vec{\mu}} P(\vec{\mu}|\theta)\theta \quad , \quad (\Delta\theta)^2 = \sum_{\vec{\mu}} P(\vec{\mu}|\theta)(\theta - \bar{\theta})^2} \tag{24.145}$$

the sum extending over all possible sequences of N measurement results.

> **Example 173 (*Bernoulli trial*):** As a first simple example, let us consider the experiment of tossing a coin (also called *Bernoulli trial*) with faces called $\pm$. At the end of the flight we grab the coin, read the upper face, and acknowledge one of two possible results, $\mu = \pm$. The experimental control parameter θ could be related to the symmetry of the coin: If it is evenly distributed, the coin will be unbiased, and we expect the probability of finding the $+$-side to be
>
> $$p(\mu|\theta) = p(+|\theta) = \tfrac{1}{2} \ . \tag{24.146}$$
>
> When we repeat the experiment N times, there are 2^N possible combinations $\vec{\mu}$, such that,
>
> $$p(\mu_i|\theta) = p(\pm|\theta) = \tfrac{1}{2} \quad \Rightarrow \quad P(\vec{\mu}|\theta) = \tfrac{1}{2^N} \quad \Rightarrow \quad \sum_{\vec{\mu}} P(\vec{\mu}|\theta) = 1 \ . \tag{24.147}$$
>
> Solve Exc. 24.4.6.2.

[10] Sometimes we will be interested in the dependence of several observables $\hat{\mathbf{A}}$ from a set of various parameters $\vec{\theta}$.

Example 174 (*Ramsey interferometer*): Another example where the value of the control parameter influences the result of the measurement is the Ramsey experiment with a two-level system (see Excs. 16.3.7.6 and 16.3.7.7). Reading out the population of the upper state $\mu = +$ we find,

$$p(+|\theta) = \cos^2 \tfrac{\theta}{2} = \tfrac{1}{2} + \tfrac{1}{2}\cos\Delta\tau \quad \text{and} \quad p(-|\theta) = \sin^2 \tfrac{\theta}{2} \ . \tag{24.148}$$

The precision of the estimation of a parameter ϑ from a measurement of an observable $\hat{A}$ which depends on that parameter is obtained from error propagation [825],

$$(\Delta\vartheta)^2 = \frac{\langle\Delta\hat{A}\rangle^2}{|\partial_\vartheta\langle\hat{A}\rangle|^2} = \frac{\langle\hat{A}^2\rangle - \langle\hat{A}\rangle^2}{|\partial_\vartheta\langle\hat{A}\rangle|^2} \ . \tag{24.149}$$

At the example of the Rabi experiment illustrated in Fig. 24.27, it simply means

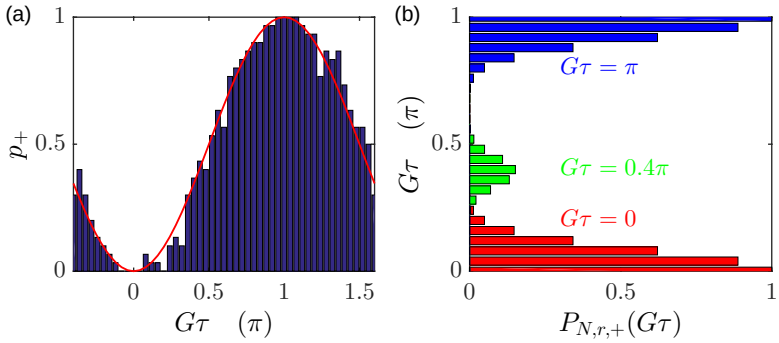

Figure 24.27: (code) (a) Simulation of a Rabi experiment where the pulse area is varied. At each value of the pulse area $N = 30$ excitation trials are done and the ratio of successful trials p_+/N is plotted. Obviously, the precision with which a specific pulse area can be measured increases with the number of trials. (b) Histogram of measurement results obtained for three different pulse areas. The question here is, given an excitation is observed, how likely is it due to the parameter being tuned to exactly the right position.

that an experimental parameter (here, the pulse area) can be determined with lower imprecision $\Delta\vartheta$ when the slope of the error signal $|\partial_\vartheta\langle\hat{A}\rangle|$ is steep (here, at mid height of the Rabi fringe). Additionally, the noise of the measured variable $\Delta\hat{A}$ should be small (here, at the top and bottom of the Rabi fringe). Interestingly, in Exc. 23.1.9.23 we show that $\Delta\vartheta_z^2 = \frac{\langle\Delta\hat{S}_z\rangle^2}{|\partial_\vartheta\langle\hat{S}_z\rangle|^2} = \frac{1}{N}$ does not dependent on the parameter.

24.4.3.2 Classical Fisher information

Let us assume two distributions $P(\vec{\mu}|\theta)$ and $P(\vec{\mu}|\theta')$ differing from each other by the fact that they belong to slightly different parameters θ and $\theta' = \theta + \vartheta$. The fidelity between two distributions can be defined as [524],

$$d_{\rm f}(\theta,\theta') = \left(\sum_{\vec{\mu}} \sqrt{P(\vec{\mu}|\theta)P(\vec{\mu}|\theta')}\right)^2 \stackrel{\theta=\theta'}{\longrightarrow} 1 \ . \tag{24.150}$$

With the boundary conditions,

$$1 = \sum_{\vec{\mu}'} P(\vec{\mu}'|\theta+\vartheta) \qquad \text{and therefore} \qquad 0 = \sum_{\vec{\mu}} \partial_\vartheta P(\vec{\mu}|\theta+\vartheta)\ , \tag{24.151}$$

we may derive the *Fisher information* [115, 270],

$$\begin{aligned} F_{\rm c}(\theta) &= -4\,\frac{\partial^2 d_{\rm f}(\theta,\theta+\vartheta)}{\partial\vartheta^2}\bigg|_{\vartheta=0} \qquad (24.152)\\ &= -4\,\frac{\partial}{\partial\vartheta}\left(\sum_{\vec{\mu}'}\sqrt{P(\vec{\mu}'|\theta)P(\vec{\mu}'|\theta+\vartheta)}\sum_{\vec{\mu}}\frac{\sqrt{P(\vec{\mu}|\theta)}}{2\sqrt{P(\vec{\mu}|\theta+\vartheta)}}\frac{\partial P(\vec{\mu}|\theta+\vartheta)}{\partial\vartheta}\right)\bigg|_{\vartheta=0}\\ &= -4\sum_{\vec{\mu}'}\frac{\partial\sqrt{P(\vec{\mu}'|\theta)P(\vec{\mu}'|\theta+\vartheta)}}{\partial\vartheta}\overset{0}{\cancel{}}\sum_{\vec{\mu}}\frac{\sqrt{P(\vec{\mu}|\theta)}}{2\sqrt{P(\vec{\mu}|\theta+\vartheta)}}\frac{\partial P(\vec{\mu}|\theta+\vartheta)}{\partial\vartheta}\overset{0}{\cancel{}} -\\ &\quad -4\cancel{\textstyle\sum_{\vec{\mu}'}\sqrt{P(\vec{\mu}'|\theta)P(\vec{\mu}'|\theta+\vartheta)}}\overset{1}{\cancel{}}\sum_{\vec{\mu}}\frac{\partial}{\partial\vartheta}\left(\frac{\sqrt{P(\vec{\mu}|\theta)}}{2\sqrt{P(\vec{\mu}|\theta+\vartheta)}}\frac{\partial P(\vec{\mu}|\theta+\vartheta)}{\partial\vartheta}\right)\bigg|_{\vartheta=0}\\ &= -4\sum_{\vec{\mu}}\frac{\partial P(\vec{\mu}|\theta+\vartheta)}{\partial\vartheta}\frac{\partial}{\partial\vartheta}\frac{\sqrt{P(\vec{\mu}|\theta)}}{2\sqrt{P(\vec{\mu}|\theta+\vartheta)}}\\ &= \sum_{\vec{\mu}}\frac{1}{P(\vec{\mu}|\theta)}\left(\frac{\partial P(\vec{\mu}|\theta)}{\partial\vartheta}\right)^2\ . \end{aligned}$$

Hence, the (classical) Fisher information can be calculated from,

$$\boxed{F_{\rm c}(\theta) = \sum_{\vec{\mu}}\frac{1}{P(\vec{\mu}|\theta)}\left(\frac{\partial P(\vec{\mu}|\theta)}{\partial\theta}\right)^2 = \sum_{\vec{\mu}} P(\vec{\mu}|\theta)\left(\frac{\partial\ln P(\vec{\mu}|\theta)}{\partial\theta}\right)^2}\ . \tag{24.153}$$

The *Cramér-Rao* bound gives a lower bound for the variance,

$$\boxed{\Delta\theta \geq \Delta\theta_{\rm CR} \equiv \frac{1}{\sqrt{F(\theta)}}}\ . \tag{24.154}$$

Example 175 (*Meaning of the Fisher information*): The formulation of the Fisher information in terms of the second derivative of the fidelity lends itself to an intuitive graphical interpretation. The Fisher information measures how fast a probability or quasi-probability distribution changes towards a recognizably different distribution when a particular parameter is modified. Let us for example consider a harmonic oscillator in a coherent state $|\beta\rangle = |re^{\imath\varphi}\rangle$ represented by the Husimi distribution $Q_{|\beta\rangle}(\alpha)$, as plotted in Fig. 14.2. The question is, how much do we have to change the amplitude r, or the phase φ, or a quadrature component $r\cos\varphi$ or $r\sin\varphi$ in order to get a noticeably different Husimi distribution, and how does this change depend on the photon number $n = |\alpha|$? This change is what is called Fisher information.
The width of the Husimi distribution of a coherent in the Glauber plane is independent on its amplitude, that is, the states $|r_1e^{\imath\varphi_1}\rangle$ and $|r_2e^{\imath\varphi_2}\rangle$ both have the same width [see Fig. 2.14 or 24.28(a)], since,

$$\Delta\hat{x} = \langle(\hat{a}+\hat{a}^\dagger)^2\rangle - \langle\hat{a}+\hat{a}^\dagger\rangle^2 = 1 \tag{24.155}$$

$$\Delta\hat{p} = \langle(\imath\hat{a}-\imath\hat{a}^\dagger)^2\rangle - \langle\imath\hat{a}-\imath\hat{a}^\dagger\rangle^2 = 1\ . \tag{24.156}$$

Now, assuming $r_1 = r_2 \equiv r$, the distance of the two states is approximately the arc between them, $a = r(\varphi_2 - \varphi_1)$. Hence, the phase difference is inversely proportional to the amplitude $r = |\alpha| = \sqrt{n}$,

$$\Delta\varphi \propto \frac{1}{\sqrt{n}} \,. \tag{24.157}$$

While the Husimi distribution works well for coherent states, it fails to represent non-classical features, such as quantum interferences. These are better viewed in the Wigner distribution, where they appear as very narrow structures, whose widths rapidly decrease with the amplitude of the harmonic oscillation. Obviously, quantum interferences are extremely sensitive to parameter changes, provided the change occurs in a direction perpendicular to the fringes. Fig. 24.28 illustrates this at the example of a Schrödinger cat state. The distribution obviously changes much faster upon shifts along the p_α than along the $\_\alpha$ direction.

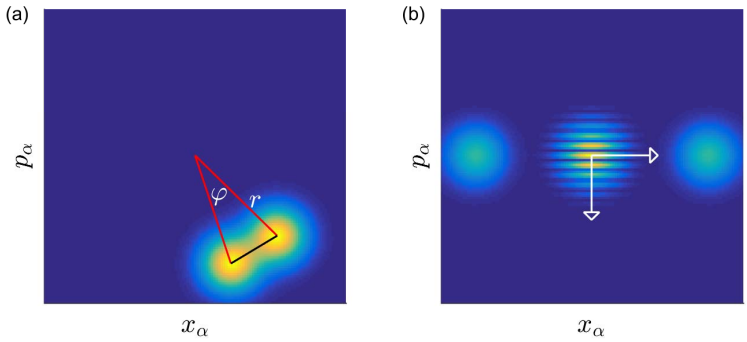

Figure 24.28: (code) (a) Wigner distribution of two coherent states separated by a small angle φ. (b) Wigner distribution of a cat state exhibiting quantum interferences.

24.4.4 Quantum Fisher information

The previously introduced quantifiers for parameter estimation can be extended to quantum mechanics with the definition of a *quantum Fisher information* and a *quantum Cramér-Rao bound*. Quantum parameter estimation aims at measuring the value of a continuous parameter θ that is encoded in the state of a quantum system characterized by the density operator $\hat{\rho}_\theta$, via its interaction with the external force that we want to characterize. The estimation process consists of two steps: in the first step, the state of the system (i.e. the measurement apparatus) $\hat{\rho}_\theta$ is measured; in the second step, the estimate of θ is determined by data processing the measurement outcomes.

In quantum mechanics $\vec{\mu}$ is just the eigenvalue spectrum. The big advantage in using quantum systems is, that the exigency that the measurements be independent can be overcome, via the use of entangled atoms. In the best case this can lead to a more favorable scaling of the Cramér-Rao bound like $1/N$, leading to a considerable *metrological gain*. The following sections are devoted to developing the notions of quantum parameter estimation.

The quantum Fisher information can be regarded as a generalization of the variance concept. Via the Cramér-Rao bound, it gives similar information but it can be extended to several parameters, in which case it corresponds to the covariance matrix, and to mixed states.

24.4.4.1 Quantum Fisher information for a pure state depending on a single parameter

As a first example, we will study the sensitivity of a pure state on changes of a single parameter. Let us consider a small deviation of a parameter θ by ϑ and expand the wavefunction [574],

$$|\psi(\theta+\vartheta)\rangle = |\psi(\theta)\rangle + \vartheta \tfrac{\partial}{\partial\vartheta}|\psi(\theta)\rangle \equiv |\psi\rangle + \vartheta\partial_\vartheta|\psi\rangle \ , \tag{24.158}$$

where in the last expression we drop the argument θ for readability. The fidelity is given by,

$$\begin{aligned} |\langle\psi(\theta)|\psi(\theta+\vartheta)\rangle|^2 &= |1+\vartheta\langle\psi|\partial_\vartheta\psi\rangle|^2 \\ &= 1+\vartheta\langle\psi|\partial_\vartheta\psi\rangle + \vartheta\langle\partial_\vartheta\psi|\psi\rangle + \vartheta^2\langle\partial_\vartheta\psi|\psi\rangle\langle\psi|\partial_\vartheta\psi\rangle \ . \end{aligned} \tag{24.159}$$

On the other hand,

$$\begin{aligned} 1 &= \langle\psi(\theta+\vartheta)|\psi(\theta+\vartheta)\rangle \\ &= 1+\vartheta\langle\psi|\partial_\vartheta\psi\rangle + \vartheta\langle\partial_\vartheta\psi|\psi\rangle + \vartheta^2\langle\partial_\vartheta\psi|\partial_\vartheta\psi\rangle \ . \end{aligned} \tag{24.160}$$

Substituting this result into the fidelity, we get,

$$|\langle\psi(\theta)|\psi(\theta+\vartheta)\rangle|^2 = 1-\vartheta^2\langle\partial_\vartheta\psi|\partial_\vartheta\psi\rangle + \vartheta^2\langle\partial_\vartheta\psi|\psi\rangle\langle\psi|\partial_\vartheta\psi\rangle \ . \tag{24.161}$$

The so called *Bures distance* is defined as,

$$d_{\rm f}(\theta,\theta') \equiv 2-2|\langle\psi(\theta)|\psi(\theta')\rangle|^2 \ , \tag{24.162}$$

where the factor 2 is just convention and serves to meet the classical formulas. Hence,

$$\begin{aligned} d_{\rm f}(\theta,\theta+\vartheta) &\equiv 2-2|\langle\psi(\theta)|\psi(\theta+\vartheta)\rangle|^2 \\ &= 2\vartheta^2\langle\partial_\vartheta\psi|\partial_\vartheta\psi\rangle - 2\vartheta^2\langle\partial_\vartheta\psi|\psi\rangle\langle\psi|\partial_\vartheta\psi\rangle \ . \end{aligned} \tag{24.163}$$

The *Fisher information* is defined as,

$$F_{\rm q}(\theta) \equiv \frac{\partial^2}{\partial\vartheta^2} d_{\rm f}(\theta,\theta+\vartheta)\Big|_{\vartheta=0} \ , \tag{24.164}$$

so that we finally get,

$$\boxed{F_{\rm q}(\theta) = 4\left(\langle\partial_\vartheta\psi|\partial_\vartheta\psi\rangle - \langle\partial_\vartheta\psi|\psi\rangle\langle\psi|\partial_\vartheta\psi\rangle\right) \ .} \tag{24.165}$$

In Exc. 24.4.6.5 we derive the quantum Fisher information for separable states.

Example 176 (*Generalization to multi-parameter metrology*): The quantum Fisher information can be generalized to several parameters. Let us consider a small deviation of a set of parameters $\vec{\theta}$ by $\vec{\vartheta}$ and expand the wavefunction [574],

$$|\psi(\vec{\theta}+\vec{\vartheta})\rangle = |\psi(\vec{\theta})\rangle + \sum_\alpha \tfrac{\partial}{\partial\vartheta_\alpha}\psi(\vec{\theta}+\vec{\vartheta})\rangle\Big|_{\vec{\vartheta}=0}\vartheta_\alpha \equiv |\psi\rangle + \sum_\alpha \vartheta_\alpha|\partial_\alpha\psi\rangle \ , \quad (24.166)$$

where in the last expression we drop the argument $\vec{\theta}$ for readability. The *fidelity* is given by,

$$\begin{aligned}|\langle\psi(\vec{\theta})|\psi(\vec{\theta}+\vec{\vartheta})\rangle|^2 &= |1+\sum_\alpha \vartheta_\alpha\langle\psi|\partial_\alpha\psi\rangle|^2 \qquad (24.167)\\ &= 1+\sum_\alpha\vartheta_\alpha\langle\psi|\partial_\alpha\psi\rangle + \sum_\beta\vartheta_\beta\langle\partial_\beta\psi|\psi\rangle + \sum_{\mu,\nu}\vartheta_\alpha\vartheta_\beta\langle\partial_\alpha\psi|\psi\rangle\langle\psi|\partial_\beta\psi\rangle \ .\end{aligned}$$

On the other hand,

$$\begin{aligned}1 = \langle\psi(\vec{\theta}+\vec{\vartheta})|\psi(\vec{\theta}+\vec{\vartheta})\rangle &= \left(\langle\psi| + \sum_\alpha\vartheta_\alpha\langle\partial_\alpha\psi|\right)\left(|\psi\rangle + \sum_\alpha\vartheta_\alpha|\partial_\alpha\psi\rangle\right) \qquad (24.168)\\ &= 1+\sum_\alpha\vartheta_\alpha\langle\psi|\partial_\alpha\psi\rangle + \sum_\alpha\vartheta_\alpha\langle\partial_\alpha\psi|\psi\rangle + \sum_{\alpha,\beta}\vartheta_\alpha\vartheta_\beta\langle\partial_\alpha\psi|\partial_\beta\psi\rangle \ .\end{aligned}$$

Substituting this result into the fidelity, we get,

$$|\langle\psi(\vec{\theta})|\psi(\vec{\theta}+\vec{\vartheta})\rangle|^2 = 1 - \sum_{\alpha,\beta}\vartheta_\alpha\vartheta_\beta\langle\partial_\alpha\psi|\partial_\beta\psi\rangle + \sum_{i,j}\vartheta_\alpha\vartheta_\beta\langle\partial_\alpha\psi|\psi\rangle\langle\psi|\partial_\beta\psi\rangle \ . \quad (24.169)$$

The so called Bures distance is defined as,

$$d_{\rm f}(\vec{\theta},\vec{\theta}') \equiv 2 - 2|\langle\psi(\vec{\theta})|\psi(\vec{\theta}')\rangle|^2 \ . \quad (24.170)$$

Hence,

$$\begin{aligned}d_{\rm f}(\vec{\theta},\vec{\theta}+\vec{\vartheta}) &= 2-2|\langle\psi(\vec{\theta})|\psi(\vec{\theta}+\vec{\vartheta})\rangle|^2 \qquad (24.171)\\ &= 2\sum_{\alpha,\beta}\vartheta_\alpha\vartheta_\beta\langle\partial_\alpha\psi|\partial_\beta\psi\rangle - 2\sum_{\alpha,\beta}\vartheta_\alpha\vartheta_\beta\langle\partial_\alpha\psi|\psi\rangle\langle\psi|\partial_\beta\psi\rangle \ .\end{aligned}$$

The Fisher information is now a matrix,

$$\begin{aligned}F_{\rm q}^{(\mu\nu)}(\vec{\theta}) &= \frac{\partial^2}{\partial\vartheta_\mu\partial\vartheta_\nu}d_{\rm f}(\vec{\theta},\vec{\theta}+\vec{\vartheta})\Big|_{\vec{\vartheta}=0} \qquad (24.172)\\ &= 2\frac{\partial}{\partial\vartheta_\mu}\sum_{\alpha,\beta}\frac{\partial\vartheta_\alpha\vartheta_\beta}{\partial\vartheta_\nu}\left(\langle\partial_\alpha\psi|\partial_\beta\psi\rangle - \langle\partial_\alpha\psi|\psi\rangle\langle\psi|\partial_\beta\psi\rangle\right)\\ &= 2\frac{\partial}{\partial\vartheta_\mu}\sum_\alpha\left(\vartheta_\alpha\langle\partial_\alpha\psi|\partial_\nu\psi\rangle - \langle\partial_\alpha\psi|\psi\rangle\langle\psi|\partial_\nu\psi\rangle + \vartheta_\alpha\langle\partial_\nu\psi|\partial_\alpha\psi\rangle - \langle\partial_\nu\psi|\psi\rangle\langle\psi|\partial_\alpha\psi\rangle\right)\\ &= 2\left(\langle\partial_\mu\psi|\partial_\nu\psi\rangle - \langle\partial_\mu\psi|\psi\rangle\langle\psi|\partial_\nu\psi\rangle + \langle\partial_\nu\psi|\partial_\mu\psi\rangle - \langle\partial_\nu\psi|\psi\rangle\langle\psi|\partial_\mu\psi\rangle\right) \ .\end{aligned}$$

We finally get [11],

$$\boxed{F_{\rm q}^{(\mu\nu)}(\vec{\theta}) = 4\mathfrak{Re}\left(\langle\partial_\mu\psi|\partial_\nu\psi\rangle - \langle\partial_\mu\psi|\psi\rangle\langle\psi|\partial_\nu\psi\rangle\right)\ .} \tag{24.173}$$

24.4.4.2 Quantum Fisher information via generators

In Eq. (24.165) we calculated the Fisher information from derivatives of wavefunctions. The derivatives represent operations, for instance angular momentum, $\hat{G}_\varphi \equiv \hat{S}_z \propto \partial_\varphi$, called *generators*. With these operations the dependence of pure states on parameters can be formulated as Heisenberg-type equations,

$$\frac{\partial\hat{\rho}_\theta}{\partial\theta} \equiv \imath(\hat{\rho}_\theta\hat{G}_\theta - \hat{G}_\theta\hat{\rho}_\theta) \qquad \text{with the solution} \qquad \hat{\rho}_\theta = e^{-\imath\theta\hat{G}_\theta}\hat{\rho}_0 e^{\imath\theta\hat{G}_\theta}\ . \tag{24.174}$$

Interestingly, those equations can always be rewritten as,

$$\frac{\partial\hat{\rho}_\theta}{\partial\theta} \equiv \tfrac{1}{2}(\hat{L}_\theta\hat{\rho}_\theta + \hat{\rho}_\theta\hat{L}_\theta)\ , \tag{24.175}$$

where we defined the *symmetric logarithmic derivative*,

$$\boxed{\hat{L}_\theta = 2\imath(\hat{\rho}_\theta\hat{G}_\theta - \hat{G}_\theta\hat{\rho}_\theta)\ .} \tag{24.176}$$

The equivalence of (24.174) and (24.175) is easy to check substituting $\hat{L}_\theta$ and using the pure state condition, $\hat{\rho}_\theta^2 = \hat{\rho}_\theta = |\psi_\theta\rangle\langle\psi_\theta|$. The advantage of expression (24.187) is that, without using the pure state condition, the quantum Fisher information can now we written as,

$$\begin{array}{lll} F_{\rm q}(\theta) & = \mathrm{Tr}\,\hat{\rho}_\theta\hat{L}_\theta^2 & = 4\mathrm{Tr}\,\hat{\rho}_\theta(\hat{G}_\theta^2 - \hat{G}_\theta\hat{\rho}_\theta\hat{G}_\theta) \\ & = \langle\psi_\theta|\hat{L}_\theta^2|\psi_\theta\rangle & = 4(\langle\hat{G}_\theta\psi_\theta|\hat{G}_\theta\psi_\theta\rangle - \langle\hat{G}_\theta\psi_\theta|\psi_\theta\rangle\langle\psi_\theta|\hat{G}_\theta\psi_\theta\rangle) \end{array} \tag{24.177}$$

which coincides with (24.165) when we set the generator $\hat{G}_\theta \equiv \partial_\theta$.

24.4.4.3 Quantum Fisher information for pure light states

Common systems for quantum sensing are light fields or ensembles of atoms on which we will focus in the following. The procedure will be (i) to identify the parameters θ for which we want to calculate the Fisher information, (ii) to formulate the corresponding generators $\hat{G}_\theta$ and the symmetric logarithmic derivatives, and (iii) evaluate the Fisher information by tracing in the Fock or Dicke basis.

[11] Note that for pure states, the quantum Fisher information is deeply connected to the symmetric *covariance matrix*, which for a set of operators $\hat{G}_\mu$ is defined as,

$$\mathbf{C} = \mathrm{cov}[\hat{G}_\mu, \hat{G}_\nu] = \langle(\hat{G}_\mu - \langle\hat{G}_\mu\rangle)(\hat{G}_\nu - \langle\hat{G}_\nu\rangle)\rangle = \tfrac{1}{2}\langle\hat{G}_\mu\hat{G}_\nu + \hat{G}_\nu\hat{G}_\mu\rangle - \langle\hat{G}_\mu\rangle\langle\hat{G}_\nu\rangle\ .$$

The most basic operations we may perform with states of light are displacements and rotations in the Glauber plane applying the unitary transformations for harmonic oscillator states (2.120), respectively, (2.130), which we may write as,

$$\mathcal{D}(r) = e^{\imath r(\imath e^{-\imath\varphi}\hat{a} - \imath e^{\imath\varphi}\hat{a}^\dagger)} \qquad \text{and} \qquad \mathcal{R}(\varphi) = e^{\imath\varphi\hat{a}^\dagger\hat{a}} \ . \tag{24.178}$$

Indeed, fixing the angle φ, the free parameter will be $\theta \equiv r$, and the operator $\mathcal{D}(r)$ describes radial displacement by an amount r,

$$|\alpha\rangle \equiv |\alpha_0 + \beta\rangle = \mathcal{D}(r)|\alpha_0\rangle = e^{\beta\hat{a}^\dagger - \beta^*\hat{a}}|\alpha_0\rangle \tag{24.179}$$

where we have set $\beta \equiv re^{\imath\varphi}$. We may now write the density operator for Glauber states,

$$\hat{\rho}_r = |\alpha\rangle\langle\alpha| = \mathcal{D}(\beta)|\alpha_0\rangle\langle\alpha_0|\mathcal{D}^\dagger(\beta) = e^{-\imath r\hat{G}_r}|\alpha_0\rangle\langle\alpha_0|e^{\imath r\hat{G}_r} \ , \tag{24.180}$$

introducing the displacement generating operator,

$$\boxed{\hat{G}_r \equiv \imath e^{\imath\varphi}\hat{a}^\dagger - \imath e^{-\imath\varphi}\hat{a}} \ . \tag{24.181}$$

Hence, the radial quantum Fisher information (24.177) is equal to the variance of the rotated quadrature field components, $F_{\rm q}(r) = 4\langle\hat{n}^2\rangle - 4\langle\hat{n}\rangle^2$.

On the other hand, fixing the radius r, the free parameter will be $\theta \equiv \varphi$, and the operator $\mathcal{R}$ describes rotation by an amount φ,

$$|\alpha\rangle \equiv |e^{\imath\varphi}\alpha_0\rangle = \mathcal{R}(\varphi)|\alpha_0\rangle = e^{\imath\varphi\hat{a}^\dagger\hat{a}}|\alpha_0\rangle \ . \tag{24.182}$$

We may now write the density operator for Glauber states,

$$\hat{\rho}_\varphi = |\alpha\rangle\langle\alpha| = \mathcal{R}(\varphi)|\alpha_0\rangle\langle\alpha_0|\mathcal{R}^\dagger(\varphi) = e^{-\imath\varphi\hat{G}_\varphi}|\alpha_0\rangle\langle\alpha_0|e^{\imath\varphi\hat{G}_\varphi} \ , \tag{24.183}$$

introducing the rotation (or phase shift) generating operator,

$$\boxed{\hat{G}_\varphi \equiv -\hat{a}^\dagger\hat{a}} \ . \tag{24.184}$$

Hence, the azimuthal quantum Fisher information is equal to the photon number variance, $F_{\rm q}(\varphi) = 4\langle\hat{n}^2\rangle - 4\langle\hat{n}\rangle^2$.

The expectation values of these generating operators $\langle\psi_\theta|\hat{G}_\theta|\psi_\theta\rangle$ and $\langle\psi_\theta|\hat{G}_\theta^2|\psi_\theta\rangle$ with $\theta \equiv r, \varphi$ permit us now calculate the quantum Fisher information for specific pure states of light $|\psi_\theta\rangle$. In Exc. 24.4.6.6 we calculate the quantum Fisher information for some paradigmatic single mode light fields. The results are summarized in Tab. 24.2.

It is interesting to discuss the results in the light of Figs. 14.2. The quantum Fisher information is always largest along the degree of freedom, at which the Wigner function exhibits the finest structure. For example, it is large for coherent states for rotations in the Glauber plane, for Fock states for radial displacements, and for squeezed states along the quadratures.

It seems that, while some of the considered states may have quantum Fisher information exceeding the classical *shot noise* limit, none of them exhibits Heisenberg scaling. Of course the hottest candidate, which would be the squeezed coherent state, was not considered, yet.

Table 24.2: Quantum Fisher information for various light states.

state	basis	Fisher information	Fisher information
Glauber	$\|\alpha\rangle$	$F_{\rm q}^{(\varphi)} = 4\|\alpha\|^2$	$F_{\rm q}^{(r)} = 4$
Fock	$\|n\rangle$	$F_{\rm q}^{(\varphi)} = 0$	$F_{\rm q}^{(r)} = 4 + 8n$
squeezed vacuum	$\|0,\xi\rangle$	$F_{\rm q}^{(\varphi)} = 2\sinh^2 2\|\xi\|^2$	$F_{\rm q}^{(r)} = 0$
cat	$\|\alpha\rangle + \|-\alpha\rangle$	$F_{\rm q}^{(x)} = 4(1 + e^{-2\|\alpha\|^2})$	$F_{\rm q}^{(y)} = 4(1 + 4\alpha^2)(1 + e^{-2\|\alpha\|^2})$
thermal	$\sum_n \frac{\bar{n}^n \|n\rangle\langle n\|}{(1+\bar{n})^{1+n}}$	$F_{\rm q}^{(\varphi)} = 0$	$F_{\rm q}^{(r)} = \sum_{k,m} \frac{2(\lambda_k - \lambda_m)^2}{\lambda_k + \lambda_m} \|\langle k\|\hat{G}_r\|m\rangle\|^2$

24.4.4.4 Quantum Fisher information for pure collective spin states

The most basic operations we may perform with collective atomic spin states are rotations about different axis on the Bloch sphere. We consider two cases, rotations about the y-axis by an angle ϑ and rotations about the z-axis by an φ described by the expression (23.38),

$$R_y(\vartheta)\hat{\mathbf{S}} = e^{\imath\vartheta\hat{S}_y}\hat{\mathbf{S}}e^{-\imath\vartheta\hat{S}_y} \qquad \text{and} \qquad R_z(\varphi)\hat{\mathbf{S}} = e^{\imath\varphi\hat{S}_z}\hat{\mathbf{S}}e^{-\imath\varphi\hat{S}_z} \ . \tag{24.185}$$

The collective spin states transform like,

$$|\psi\rangle = e^{-\imath\vartheta\hat{S}_y}|\psi_0\rangle \qquad \text{and} \qquad |\psi\rangle = e^{-\imath\varphi\hat{S}_z}|\psi_0\rangle \ . \tag{24.186}$$

We may now write the density operators,

$$\hat{\rho}_\vartheta = |\psi\rangle\langle\psi| = e^{-\imath\vartheta\hat{S}_y}|\psi_0\rangle\langle\psi_0|e^{\imath\vartheta\hat{S}_y} \qquad \text{and} \qquad \hat{\rho}_\varphi = |\psi\rangle\langle\psi| = e^{-\imath\varphi\hat{S}_z}|\psi_0\rangle\langle\psi_0|e^{\imath\varphi\hat{S}_z} \ , \tag{24.187}$$

introducing the generating operations

$$\boxed{\hat{G}_\vartheta = \hat{S}_y = \tfrac{1}{2\imath}(\hat{S}_- - \hat{S}_+) \qquad \text{and} \qquad \hat{G}_\varphi = \hat{S}_z \ .} \tag{24.188}$$

Again, the expectation values of these generating operators $\langle\psi_\theta|\hat{G}_\theta|\psi_\theta\rangle$ and $\langle\psi_\theta|\hat{G}_\theta^2|\psi_\theta\rangle$ with $\theta \equiv \vartheta, \varphi$ permit us now calculate the quantum Fisher information for specific pure collective spin $|\psi_\theta\rangle$. In Exc. 24.4.6.7 we calculate the quantum Fisher information for some paradigmatic collective spin states introduced in Sec. 23.1. The results are summarized in Tab. 24.3.

It is interesting to discuss the results in the light of Figs. 23.8. Apparently, *coherent spin states* are bounded by the *standard quantum limit*. The sensitivity is highest for rotations along great circles around the Bloch sphere.

Any *Fock spin state* is azimuthally symmetric, which explains $F_{\rm q}(\varphi) = 0$. We also note,

$$F_{{\rm q},|S,0\rangle}(\vartheta) = \tfrac{N^2}{2} + N \qquad \text{and} \qquad F_{{\rm q},|S,\pm S\rangle}(\vartheta) = N \ , \tag{24.189}$$

which means, that Fock states are sensitive to rotations within sagittal planes. While near the poles the quantum Fisher information scales linearly with the particle number, close to the equatorial plane it approaches the Heisenberg limit [110].

Table 24.3: Quantum Fisher information for various collective spin states.

state	basis	Fisher information	Fisher information
coherent	$\|\vartheta,\varphi\rangle^{\otimes N}$	$F_{\mathrm{q}}^{(\vartheta)} = N\sin\vartheta$	$F_{\mathrm{q}}^{(\varphi)} = N$
Fock	$\|S,M\rangle$	$F_{\mathrm{q}}^{(\vartheta)} = \frac{N^2}{2} + N - 2M^2$	$F_{\mathrm{q}}^{(\varphi)} = 0$
W	$\|S,S-1\rangle$	$F_{\mathrm{q}}^{(\vartheta)} = 3N - 2$	$F_{\mathrm{q}}^{(\varphi)} = 0$
cat	$\cos\frac{\vartheta}{2}\|S,S\rangle + e^{\imath\varphi}\sin\frac{\vartheta}{2}\|S,-S\rangle$	$F_{\mathrm{q}}^{(\vartheta)} = N$	$F_{\mathrm{q}}^{(\varphi)} = N^2(1-\cos\vartheta)$
GHZ	$\frac{1}{\sqrt{2}}(\|S,S\rangle + \|S,-S\rangle)$	$F_{\mathrm{q}}^{(\vartheta)} = N$	$F_{\mathrm{q}}^{(\varphi)} = N^2$
NOON	$\frac{1}{\sqrt{2}}(\|S,S\rangle + e^{\imath 2S\vartheta}\|S,-S\rangle)$	$F_{\mathrm{q}}^{(\vartheta)} = N$	$F_{\mathrm{q}}^{(\varphi)} = N^2$
squeezed	$e^{-\imath\zeta\hat{S}_z^2/2}\|\frac{\pi}{2},0\rangle^N$	$\simeq \frac{N^2}{2}(1-2\cos^{2N-2}\zeta+...)$	

In contrast, *cat states* allow for Heisenberg-scaling only for rotations in the equatorial plane. For rotations within sagittal planes the quantum Fisher information scales linearly with N. Hence, differently from Fock states, cat states permit azimuthal sensing without Ramsey sequence. Particular cat states are the NOON and the GHZ states.

Cat states are extremely difficult to generate and to preserve from decoherence. They cannot be generated from Glauber states via unitary transforms. *Spin-squeezed states* are much more robust and better suited for Heisenberg-limited sensing.

Fig. 23.8 illustrates that the uncertainty distribution depends on the type of collective states. This is obviously interesting for metrological applications based on interferometric phase measurements, as discussed in Sec. 18.2.2. A *metrological gain* in the signal-to-noise ratio beyond the *standard quantum limit* depends on the type of entanglement generated.

24.4.4.5 Quantum Fisher information for mixed states

The advantage of the symmetric logarithmic derivative formulation is, that it can be generalized to mixed states. We express the density matrix expanded in an eigenstate basis as [825],

$$\hat{\rho}_\theta = \sum_k \lambda_k |k\rangle\langle k| \qquad \text{with} \qquad \mathbb{I} = \sum_k |k\rangle\langle k| \ . \tag{24.190}$$

In this case, a comparison between the expressions (24.174) and (24.175) yields,

$$\hat{L}_\theta \sum_k \lambda_k |k\rangle\langle k| + \sum_k \lambda_k |k\rangle\langle k|\hat{L}_\theta = 2\imath \sum_k \lambda_k |k\rangle\langle k|\hat{G}_\theta - 2\imath\hat{G}_\theta \sum_k \lambda_k |k\rangle\langle k| \tag{24.191}$$

$$\Leftrightarrow \quad \sum_{k,m}(\lambda_k+\lambda_m)|k\rangle\langle k|\hat{L}_\theta|m\rangle\langle m| = 2\imath\sum_{k,m}(\lambda_k-\lambda_m)|k\rangle\langle k|\hat{G}_\theta|m\rangle\langle m|$$

$$\Leftrightarrow \quad (\lambda_k+\lambda_m)\langle k|\hat{L}_\theta|m\rangle = 2\imath(\lambda_k-\lambda_m)\langle k|\hat{G}_\theta|m\rangle \qquad \forall k,m \ .$$

Hence,

$$\boxed{\hat{L}_\theta = 2\imath\sum_{k,m}\frac{\lambda_k-\lambda_m}{\lambda_k+\lambda_m}|k\rangle\langle k|\hat{G}_\theta|m\rangle\langle m| \ .} \tag{24.192}$$

Note that the pure state symmetric logarithmic derivative [Eq. (24.187) with $\hat{\rho}_\theta = |\psi\rangle\langle\psi| = |k\rangle\langle k|$] is recovered by setting $\lambda_k = \delta_{k,\psi}$ and $\lambda_m = \delta_{m,\psi}$.

The quantum Fisher information is now,

$$F_{\rm q}(\theta) = {\rm Tr}\,(\hat{\rho}_\theta \hat{L}_\theta^2) = \sum_n \langle n|\hat{\rho}_\theta \hat{L}_\theta^2|n\rangle \ . \tag{24.193}$$

Inserting the expressions (24.190) and (24.192), we get,

$$\begin{aligned} F_{\rm q}(\theta) &= \sum_n \langle n| \left(\sum_{n'} \lambda_{n'} |n'\rangle\langle n'| \right) \left(2\imath \sum_{k,m} \frac{\lambda_k - \lambda_m}{\lambda_k + \lambda_m} |k\rangle\langle k|\hat{G}_\theta|m\rangle\langle m| \right) \times \\ &\qquad \times \left(2\imath \sum_{k',m'} \frac{\lambda_{k'} - \lambda_{m'}}{\lambda_{k'} + \lambda_{m'}} |k'\rangle\langle k'|\hat{G}_\theta|m'\rangle\langle m'| \right) |n\rangle \\ &= 4 \sum_{k,m} \frac{(\lambda_k - \lambda_m)^2}{\lambda_k + \lambda_m} \frac{\lambda_k}{\lambda_m + \lambda_k} |\langle k|\hat{G}_\theta|m\rangle|^2 \ . \end{aligned} \tag{24.194}$$

Hence,

$$\boxed{F_{\rm q}(\theta) = 2 \sum_{k,m} \frac{(\lambda_k - \lambda_m)^2}{\lambda_k + \lambda_m} |\langle k|\hat{G}_\theta|m\rangle|^2 \ .} \tag{24.195}$$

An alternative expression for the quantum Fisher information can be derived as follows,

$$F_{\rm q}(\theta) = 2 \sum_{k,m} \frac{(\lambda_k - \lambda_m)^2}{\lambda_k + \lambda_m} |\langle k|\hat{G}_\theta|m\rangle|^2 = 2 \sum_{k,m} \frac{(\lambda_k + \lambda_m)^2 - 4\lambda_k\lambda_m}{\lambda_k + \lambda_m} |\langle k|\hat{G}_\theta|m\rangle|^2 \tag{24.196}$$

$$\begin{aligned} &= 4 \sum_{k,m} \lambda_k |\langle k|\hat{G}_\theta|m\rangle|^2 - \sum_{k,m} \frac{8\lambda_k\lambda_m}{\lambda_k + \lambda_m} |\langle k|\hat{G}_\theta|m\rangle|^2 \\ &= 4 \sum_{k,m} \lambda_k \langle k|\hat{G}_\theta|m\rangle\langle m|\hat{G}_\theta|k\rangle - \sum_{k,m} \frac{8\lambda_k\lambda_m}{\lambda_k + \lambda_m} |\langle k|\hat{G}_\theta|m\rangle|^2 \\ &= 4{\rm Tr}\,\hat{\rho}\hat{G}_\theta^2 - \sum_{k,m} \frac{8\lambda_k\lambda_m}{\lambda_k + \lambda_m} |\langle k|\hat{G}_\theta|m\rangle|^2 \ . \end{aligned}$$

In Exc. 24.4.6.6(e) we calculate the quantum Fisher information for a thermal state of light.

The Cramér-Rao bound defines the achievable largest precision of parameter estimation, however, it is not clear what has to be measured to reach this precision bound. An optimal measurement can be carried out if we measure in the eigenbasis of the $\hat{L}_\theta$ [115, 116]. This operator is defined such that it can be used to describe the quantum dynamics of the system with the equation [825].

24.4.4.6 Quantum Fisher information for multi-parameter metrology

For a mixed state

$$\hat{\rho}_\theta = \sum_i \lambda_i |\lambda_i\rangle\langle\lambda_i| \tag{24.197}$$

the quantum Fisher information becomes [524, 525],

$$F_{\rm q}^{(\mu\nu)}(\vec{\theta}) = \sum_{\substack{i,j \\ \lambda_i \neq -\lambda_j}} \frac{\mathfrak{Re}\left(\langle\lambda_i|\partial_\mu\hat{\rho}_\theta|\lambda_j\rangle\langle\lambda_j|\partial_\nu\hat{\rho}_\theta|\lambda_i\rangle\right)}{\lambda_i+\lambda_j} \tag{24.198}$$

$$= \sum_{\substack{i \\ \lambda_i \neq 0}} \frac{(\partial_\mu\lambda_i)(\partial_\nu\lambda_i)}{\lambda_i} + 4\lambda_i\mathfrak{Re}\,\langle\partial_\mu|\lambda_i|\partial_\nu\lambda_i\rangle - \sum_{\substack{i,j \\ \lambda_i \neq -\lambda_j}} \frac{8\lambda_i\lambda_j}{\lambda_i+\lambda_j}\mathfrak{Re}\left(\langle\partial_\mu\lambda_i|\lambda_j\rangle\langle\lambda_j|\partial_\nu\lambda_i\rangle\right) .$$

Using the symmetric logarithmic derivative (24.174) the Fisher information can also be written [689],

$$F_{\rm q}^{(\mu\nu)}(\vec{\theta}) = \sum_{\substack{i,j \\ \lambda_i \neq -\lambda_j}} \frac{2\mathfrak{Re}\left(\langle\lambda_i|[\hat{G}_\mu,\hat{\rho}_\theta]|\lambda_j\rangle\langle\lambda_j|[\hat{\rho}_\theta,\hat{G}_\nu]|\lambda_i\rangle\right)}{\lambda_i+\lambda_j} . \tag{24.199}$$

Example 177 (*Fisher information on the Bloch sphere*): As an example we may consider the Fisher information matrix whose components are calculated with the collective spin components $\hat{S}_{x,y,z}$ as generators,

$$F_{\rm q}^{(\mu\nu)}(\vec{\theta}) = \sum_{\substack{i,j \\ \lambda_i \neq -\lambda_j}} \frac{2\mathfrak{Re}\left(\langle\lambda_i|[\hat{S}_\mu,\hat{\rho}_\theta]|\lambda_j\rangle\langle\lambda_j|[\hat{\rho}_\theta,\hat{S}_\nu]|\lambda_i\rangle\right)}{\lambda_i+\lambda_j} . \tag{24.200}$$

Its eigenvalues are nothing else than the quantum Fisher informations with respect to particular generators already calculated in Tab. 24.3. Setting up the complete matrix facilitates the identification of optimal squeezing protocols [689].

24.4.5 Quantum Fisher information for coupled systems

We have seen that it is quite straightforward to calculate the quantum Fisher information for single mode systems in pure states. In quantum systems where different degrees of freedom are coupled a measurement is generally performed only one of them. As shown in the context of the Jaynes-Cummings model in Sec. 17.2.3, the partial measurement leaves the system in a mixed states, which makes the calculation of the quantum Fisher information more involved. In the following, we will calculate for the Jaynes-Cummings model the evolution of the quantum Fisher information during quantum collapse and revival and for the Dicke model the dependence of the quantum Fisher information on the atom-field coupling strength [853].

24.4.5.1 Quantum Fisher information in the Jaynes-Cummings model

In the Jaynes-Cummings model the quantum Fisher information can be calculated analytically. As we are interested not only in quantum superpositions of the atomic

excitation state, but also in quantum correlations (such as squeezing) in the light mode, we need to expand the field mode in a Fock basis,

$$\hat{\rho} = \sum_{n,j} |n\rangle\langle n| \otimes |j\rangle\langle j| \ , \tag{24.201}$$

which considerably increases the dimension of the Hilbert space. The time dependence of the system is obtained from the propagator (17.30), leading to (17.46),

$$|\psi(t)\rangle = e^{-\imath \hat{H}_n t}|\psi(0)\rangle = \sum_n (c_{1,n}|1,n\rangle + c_{2,n-1}|2,n-1\rangle) \ . \tag{24.202}$$

Starting from the total density matrix $\hat{\rho}(t) = |\psi\rangle\langle\psi|$, tracing over the field mode as done in (17.55) allows us to calculate the Fisher information for the atomic degrees of freedom,

$$\hat{\rho}_{\rm at} = {\rm Tr}_{\rm li}\, \hat{\rho} = \sum_{j=1,2} \langle j|\hat{\rho}|j\rangle = \sum_n (c_{1,n}|1\rangle + c_{2,n}|2\rangle)(c^*_{1,n}\langle 1| + c^*_{2,n}\langle 2|)$$
$$F_{\rm q,at}(\theta) = 4{\rm Tr}\, \hat{\rho}_{\rm at}(\hat{G}^2_{\theta,{\rm at}} - \hat{G}_{\theta,{\rm at}}\hat{\rho}_{\rm at}\hat{G}_{\theta,{\rm at}}) \ , \tag{24.203}$$

where

$$\hat{G}_{y,{\rm at}} = \tfrac{1}{2}\hat{\sigma}_y \qquad \text{and} \qquad \hat{G}_{z,{\rm at}} = \tfrac{1}{2}\hat{\sigma}_z \ . \tag{24.204}$$

are the relevant generators (24.181) and (24.184) for the light field. Tracing over the atomic degrees of freedom as done in (17.54) allows us to calculate the Fisher information for the field mode,

$$\hat{\rho}_{\rm li} = {\rm Tr}_{\rm at}\, \hat{\rho} = \sum_{n=0}^{\infty} \langle n|\hat{\rho}|n\rangle = \sum_{n,m} (c^*_{1,m}c_{1,n}|n\rangle\langle m| + c^*_{2,m-1}c_{2,n-1}|n-1\rangle\langle m-1|) \tag{24.205}$$
$$F_{q,{\rm li}}(\theta) = 4{\rm Tr}\, \hat{\rho}_{\rm li}(\hat{G}^2_{\theta,{\rm li}} - \hat{G}_{\theta,{\rm li}}\hat{\rho}_{\rm li}\hat{G}_{\theta,{\rm li}}) \ ,$$

where

$$\hat{G}_{\varphi,{\rm li}} = -\hat{a}^\dagger\hat{a} \qquad \text{and} \qquad \hat{G}_{r,{\rm li}} = \imath(e^{\imath\varphi}\hat{a}^\dagger - e^{-\imath\varphi}\hat{a}) \tag{24.206}$$

are the relevant generators (24.188) for the atom.

The time evolution of the quantum Fisher information, calculated in Exc. 24.4.6.9 and plotted in Fig. 24.29, has a simple interpretation. The atomic Fisher informations stay below the classical limit of 1, because there is only a single atom. The nutational information $F_{\rm q,at}(y)$ depends on the orientation of the atomic coherence while it rotates in the equatorial plane, and it vanishes during the quantum collapse period. The precessional information $F_{\rm q,at}(z)$ drops to 0 only during the Ramsey pulses at the beginning and end of the evolution. In contrast, the light field Fisher informations can exceed the classical limit of 1. The azimuthal information $F_{\rm q,at}(\varphi)$ is largest during quantum collapse, when the coherence is stored in the light fields, which is due to the fact that the light field is then in a Schrödinger cat state. The radial information $F_{\rm q,at}(r)$ oscillates with the relative phase shift between the two coherent states composing the Schrödinger cat.

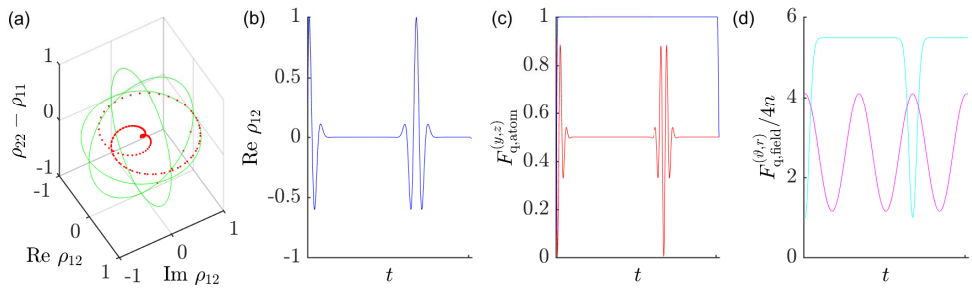

Figure 24.29: (code) (a) Evolution of the atomic state represented on the Bloch sphere. Evolutions of (b) the atomic coherence, (c) the quantum Fisher informations for the atom (red) $F_{\mathrm{q,at}}(y)$ and (blue) $F_{\mathrm{q,at}}(z)$, and (d) for the field mode (cyan) $F_{\mathrm{q,at}}(\varphi)$ and (magenta) $F_{\mathrm{q,at}}(r)$.

24.4.5.2 Scaling with particle number

The Jaynes-Cummings model discussed above considers an arbitrary number of photons, but only a single atom, which limited the Fisher information to below 1.

We found that in the 'classical' cases the quantum Fisher information is bounded by the numbers of (quasi-)particles, $F_{\mathrm{q},|\alpha\rangle} \leq 4n$, respectively, $F_{\mathrm{q},|\vartheta,\varphi\rangle^{\otimes N}} \leq N$. For other 'non-classical' states, however, this limitation can be surpassed. Quantum advantage is reached when $N^2 > F_{\mathrm{q}}/N > 1$, that is, the Cramér-Rao bound scales with $1/N$ called Heisenberg limit rather than $1/\sqrt{N}$ called shot-noise limit.

The quantum Fisher information is always larger than the classical Fisher information,

$$F_{\mathrm{c}}(\theta) \leq F_{\mathrm{q}}(\theta) \ . \tag{24.207}$$

If $F_{\mathrm{c}}(\theta) = F_{\mathrm{q}}(\theta)$ locally optimal at θ,

$$\mathrm{Var}[\hat{\theta}] \geq \frac{1}{NF_{\mathrm{c}}(\theta)} \geq \frac{1}{NF_{\mathrm{q}}(\theta)} \ . \tag{24.208}$$

Let us now turn our attention to the case of several atoms.

24.4.5.3 Quantum Fisher information in the Dicke model

The calculation of the quantum Fisher information for a single mode light field coupling to *several atoms* is even more complicated, as the dimension of the Hilbert space increases with the number of atoms. Nevertheless, it remains feasible within the Dicke model [853] treating the atomic cloud as a collective spin state, while the field mode is still expanded in a Fock basis,

$$\hat{\rho} = \sum_{n,M} |n\rangle\langle n| \otimes |S,M\rangle\langle S,M| \ , \tag{24.209}$$

with the Hamiltonian,

$$\hat{H} = \Delta_{\mathrm{c}}\hat{a}^\dagger\hat{a} + \Delta_{\mathrm{a}}\hat{S}_z + (\hat{a}^\dagger + \hat{a})(\hat{S}_+ + \hat{S}_-) \ . \tag{24.210}$$

Apart from the different basis used to describe the atomic state, the procedure is the same as for the Jaynes-Cummings model. Again, the system is described by a density operator $\hat{\rho} = \hat{\rho}_{\rm at} \otimes \hat{\rho}_{\rm li}$, such that the density operators of the subsystems $\hat{\rho}_{\rm at} = {\rm Tr}_{\rm li}\hat{\rho}$ and $\hat{\rho}_{\rm li} = {\rm Tr}_{\rm at}\hat{\rho}$ are necessarily mixed,

$$\hat{\rho}_{\rm li} = {\rm Tr}_{\rm at}\,\hat{\rho} = \sum_{M=-S}^{S} \langle S, M|\hat{\rho}|S, M\rangle \quad , \quad \hat{\rho}_{\rm at} = {\rm Tr}_{\rm li}\,\hat{\rho} = \sum_{n=0}^{\infty} \langle n|\hat{\rho}|n\rangle \ , \tag{24.211}$$

and the relevant generators for the atomic cloud must now be formulated with the collective spin operators,

$$\hat{G}_{y,{\rm at}} = \hat{S}_y \quad \text{and} \quad \hat{G}_{z,{\rm at}} = \hat{S}_z \ . \tag{24.212}$$

The Fisher informations are again calculated from the formulas (24.204) and (24.205), respectively.

Here, we are particularly interested in analyzing beyond mean field solutions in steady state [853].

24.4.5.4 Saturability of the quantum Cramér-Rao bound in multi-parameter systems

The saturability of the quantum Cramér-Rao bound in collective measurements, i.e. joint measurements over many copies of the quantum state, can be measured via strong commutativity $[L_i, L_j] = 0$ or weak commutativity $\langle [L_i, L_j] \rangle = 0$ [626].

24.4.6 Exercises

24.4.6.1 Ex: Red-shift of sun light and on Earth

a. Calculate the gravitational redshift of light escaping from the sun.
b. Calculate the blue-shift of navigational signals from GPS satellites orbiting at 20000 km altitude with respect to the surface of Earth. Compare it to the Doppler shift resulting from their orbital velocity.
c. In astronomy, the magnitude of a gravitational redshift is often expressed as the velocity that would create an equivalent shift through the relativistic Doppler effect. Calculate the sunlight redshift and the GPS signal blue-shift in terms of this velocity.

24.4.6.2 Ex: Scaling with the number of measurements

Imagine you have a coin which you suspect to be manipulated so that, when tossed, it doesn't provide a 50% chance to show the face side. Assuming that all flip trials are independent, how many trials are necessary to prove that the probability for 'face' is 60%? How many for 51%? What would be necessary to obtain a more favorable scaling with the number of trials?

24.4.6.3 Ex: Fisher information and Cramér-Rao bound for a Gaussian distribution

Calculate the Fisher information and Cramér-Rao bound for a Gaussian distribution in a Ramsey experiment.

24.4.6.4 Ex: Superresolution for two incoherent light sources

In this exercise we review the classical and quantum theory of *superresolution* for incoherent point sources of light [831, 830]. The goal is to determine from the intensity distribution in the image plane $\Lambda(x)$ the unknown positions X_s with $s = 1, 2$ of the point sources in the object plane.
a. Express $\Lambda(x)$ assuming Gaussian or pinhole point-spread functions $\langle x|\psi_s\rangle = \langle x - X_s|\psi\rangle$.
b. Generalize the classical Fisher information for continuous variables and multi-parameter systems and express it for the intensity distribution $\Lambda(x)$ choosing the parameters,

$$\theta_\mu = \tfrac{1}{2}(X_1 + X_2) \qquad \text{and} \qquad \theta_\nu = X_2 - X_1 \ . \tag{24.213}$$

24.4.6.5 Ex: Quantum Fisher information for separable states

Show that for a pure separable N-particle state depending on a single parameter the quantum Fisher information (24.165) scales as $F_\mathrm{q} \propto N$.

24.4.6.6 Ex: Fisher information for common light states

a. Using the expression (24.173) calculate the quantum Fisher information for a Glauber state.
b. Now, use the expression (24.177) to calculate the quantum Fisher information for a Glauber state,
c. a Fock state,
d. a squeezed state, and
e. a cat state.
f. Using the expression (24.195) calculate the quantum Fisher information for a thermal state of light with respect to amplitude and phase [853].

24.4.6.7 Ex: Fisher information for common collective spin states

a. Using the expression (24.173) calculate the quantum Fisher information for coherent spin states with respect to variations of the polar and azimuthal angles ϑ and φ.
b. Calculate the logarithmic derivatives for a coherent spin state with respect to variations of the polar and azimuthal angles and use the expression (24.188) to calculate the quantum Fisher information.
c. Calculate the quantum Fisher information for the collective spin states $|\mathrm{Fock}\rangle$ and $|\mathrm{W}\rangle$, as well as for
d. the states $|\mathrm{cat}\rangle$, $|\mathrm{GHZ}\rangle$, and $|\mathrm{NOON}\rangle$, and finally for
e. a spin-squeezed state $|\mathrm{squeezed}\rangle$.

24.4.6.8 Ex: Symmetric logarithmic derivative in a Ramsey experiment

a. For a single two-level atom initially in its ground state $\hat{\rho}_0 = |0\rangle\langle 0|$ determine the state $\hat{\rho}_1$ reached by a rotation by 90° about the y-axis [522, 825].
b. Show that for this state holds, $\imath(\hat{\rho}_1\hat{\sigma}_z - \hat{\sigma}_z\hat{\rho}_1) = \hat{\rho}_1\hat{\sigma}_y + \hat{\sigma}_y\hat{\rho}_1$.
c. Generalize to collective spin states for many atoms.
d. Expand $\hat{\rho}_1$ for small precessions.
e. Determine the logarithmic derivative and the quantum Fisher information for the precession.

24.4.6.9 Ex: Quantum Fisher information in the Jaynes-Cummings model

Calculate for the Jaynes-Cummings model the quantum Fisher information for the atomic and light degrees of freedom with respect to the relevant generators.

24.4.6.10 Ex: Transmission estimation

A common task in quantum sensing is the estimation of the intensity transmission of light through a lossy device (absorber or beam splitter) [876]. Here, we estimate the quantum Cramér-Rao bound for such a measurement for different (quantum) states of light.

24.5 Further reading

24.5.1 on entanglement

A. Einstein et al., *Can quantum-mechanical description of physical reality be considered complete* [DOI]

J.S. Bell et al., *On the Einstein-Podolsky-Rosen paradox* [DOI]

A. Aspect, *Experimental Test of Bell's Inequality Using Time-Varying Analyzers* [DOI]

S.J. van Enk, *Single-particle entanglement* [DOI]

K. Gietka et al., *Quantum-enhanced interferometry with cavity QED-generated nonclassical light* [DOI]

24.5.2 on quantum information

S. Aaronson et al., *The computational complexity of linear optics* [DOI]

H. Azuma, *Quantum computation with the Jaynes-Cummings model* [DOI]

S.D. Bartlett et al., *Efficient Classical Simulation of Continuous Variable Quantum Information Processes* [DOI]

M. Bindhani et al., *Quantum simulation of Jaynes-Cummings model on IBM Q-system* [DOI]

V.K. Jain et al., *Quantum Simulation of Discretized Harmonic Oscillator on IBM Quantum Computer* [DOI]

S. Sefi et al., *How to Decompose Arbitrary Continuous-Variable Quantum Operations* [DOI]

P. Sundsoy et al., *Quantum Computing, Linear optics implementations* [DOI]

IBM, *Quantum computing* [http]

Wikipedia, *Quantum Fourier transform* [http]

C.S. Hamilton et al., *Gaussian boson sampling* [DOI]

N. Quesada et al., *Gaussian boson sampling using threshold detectors* [DOI]

Han-Sen Zhong et al., *Quantum computational advantage using photons* [DOI]

24.5.3 on quantum computing

I. Pogorelov et al., *Compact Ion-Trap Quantum Computing Demonstrator* [DOI]

T. Manovitz et al., *Trapped-Ion Quantum Computer with Robust Entangling Gates and Quantum Coherent Feedback* [DOI]

24.5.4 on quantum sensing

B. Yurke et al., *SU(2) and SU(1,1) interferometers* [DOI]

A.D. Cronin et al., *Optics and interferometry with atoms and molecules* [DOI]

L. Pezzè et al., *Quantum metrology with nonclassical states of atomic ensembles* [DOI]

D. Braun et al., *Quantum-enhanced measurements without entanglement* [DOI]

J. Kitching et al., *Atomic sensors - A review* [DOI]

C.L. Degen et al., *Quantum sensing* [DOI]

24.5.5 on Fisher information

S.L. Braunstein et al., *Statistical Distance and the Geometry of Quantum States* [DOI]

S.L. Braunstein et al., *Generalized Uncertainty Relations: Theory, Examples, and Lorentz Invariance* [DOI]

C. Emary et al., *Chaos and the quantum phase transition in the Dicke model* [DOI]

J. Rehacek et al., *Uncertainty relations from Fisher information* [DOI]

B.M. Escher et al., *General framework for estimating the ultimate precision limit in noisy quantum-enhanced metrology* [DOI]

G. Tóth et al., *Quantum metrology from a quantum information science perspective* [DOI]

T.-L. Wang et al., *Quantum Fisher information as a signature of the superradiant quantum phase transition* [DOI]

J. Liu et al., *Fidelity susceptibility and quantum Fisher information for density operators with arbitrary ranks* [DOI]

B. Liu et al., *Quantum Fisher information width in quantum metrology* [DOI]

J. Liu et al., *Quantum Fisher information matrix and multiparameter estimation* [DOI]

J.J. Meyer, *Fisher Information in Noisy Intermediate-Scale Quantum Applications* [DOI]

J. Wang et al., *Quantum advantage of time-reversed ancilla-based metrology of absorption parameters* [DOI]

K. Gietka et al., *Understanding and Improving Critical Metrology. Quenching Superradiant Light-Matter Systems Beyond the Critical Point* [DOI]

T.J. Volkoff et al., *Saturating the one-axis twisting quantum Cramér-Rao bound with a total spin readout* [DOI]

J.T. Reilly et al., *Speeding up squeezing with a periodically driven Dicke model* [DOI]

Chapter 25

Atomic motion in optical cavities

In the preceding chapter we concentrated on the dynamics of the field modes of laser-pumped cavities. We devoted a particular attention to the role of scatterers, e.g. atoms, located in the mode volume and coupling the dynamics of counterpropagating modes. We assumed the atoms to be fixed in space, or at most subject to an external force constraining their motion. We have also seen that the coupling of counterpropagating modes critically depends on the position of the atom. Now, the cavity fields are expected to exert light forces on the atoms eventually leading to their displacement. As we will see in the following, this fact can have enormous impact on the coupling dynamics and even induce macroscopic instabilities.

We devote Sec. 25.1 to the derivation of the complete equations of motion for the case of a single atom, allowing for all degrees of freedom to be treated as quantized: the atomic excitation, the motion of its center of mass, and the radiation field in the cavity. We will provide a simple recipe for finding the suitable equations of motion depending on which degree of freedom s to be treated as quantized and which dissipation process to be taken into account. We will also show how and under which circumstances the atomic excitation may be adiabatically eliminated.

In Sec. 25.2 we generalize the equations of motion of many atoms, but treating all degrees of freedom as classical. This leads us to the paradigmatic Collective Atomic Recoil Laser (CARL), a self-organization phenomenon whose relationship to other such instabilities will be discussed in Sec. 25.3.

Finally, in Secs. 25.4 and 25.5 we will treat the light field, respectively, the atomic motion quantum mechanically and show in which sense the obtained dynamics are different.

25.1 Cavity interacting with a single atom

Here, we consider atoms interacting with the modes of an optical cavity pumped by lasers. As we saw in the previous chapter, the density of the modes in a cavity is concentrated around the optical axis, such that a scatterer located within the mode emits preferentially within the cavity, where the light is recycled. Therefore, we can in many situations treat the system as one-dimensional.

In free space, as discussed in Chp. 20, the force of light has two components: the radiation pressure, which scatters photons isotropically into space, and the dipole

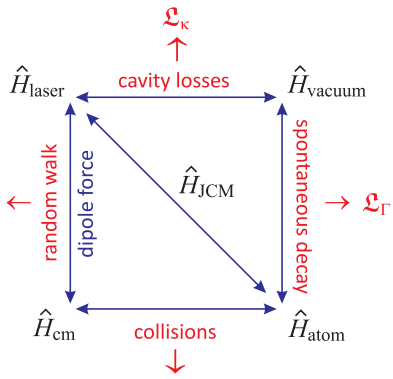

Figure 25.1: Hamiltonian in quantum optics.

force, which can be interpreted in terms of a redistribution of photons between light modes. In cavities, where the isotropic scattering is much reduced, radiative pressure can often be neglected. In contrast, if light is tuned away from atomic resonances, the atom will feel a dipole force originating from the backscattering of photons between counterpropagating modes.

25.1.1 Linear and ring cavities

We must distinguish two types of cavities with very different behaviors: The linear cavity or (*Fabry-Pérot etalon*), where counterpropagating modes form a single mode, and the ring cavity, where counterpropagating modes have independent photon budgets.

For a *linear cavity*, boundary conditions imposed by the surfaces of the cavity mirrors determine the possible spatial mode functions, which are necessarily standing waves. The amplitudes of the electric field are in second quantization (14.8),

$$\hat{\mathcal{E}}(z,t) = \hat{\mathcal{E}}^+(z,t)e^{-\imath\omega t} + \hat{\mathcal{E}}^-(z,t)e^{\imath\omega t} \qquad (25.1)$$
$$\text{with} \quad \hat{\mathcal{E}}^+(z,t) = \hat{\mathcal{E}}_1\hat{a}(t)e^{\imath kz} = (\hat{\mathcal{E}}^-(z,t))^\dagger \ .$$

with $[\hat{a},\hat{a}^\dagger] = 1$. With this we obtain, for a single atom coupled to the mode of the cavity pumped by a laser, within the dipolar approximation and the RWA [1], the following relevant contributions to the Hamiltonian ($\hbar = 1$),

$$\begin{aligned}
\hat{H}_{\rm atom} &= -\Delta_a\hat{\sigma}^+\hat{\sigma}^- + \tfrac{\hat{p}^2}{2m} \qquad (25.2)\\
\hat{H}_{\rm cav} &= -\Delta_c\hat{a}^\dagger\hat{a}\\
\hat{H}_{\rm atom:cav} &= g\hat{a}^\dagger\hat{\sigma}^- e^{-\imath k\hat{z}} + h.c.\\
\hat{H}_{\rm laser:cav} &= \imath\eta\hat{a}^\dagger + h.c. \ ,
\end{aligned}$$

neglecting the dynamics of the pump field, which is supposed to be classical, $\eta = \delta_{fsr}\langle\hat{a}_{in}^\dagger\rangle$. Note that the propagator $e^{-\imath\hat{H}_{\rm laser:cav}t}$ corresponds to a coherent state

[1] For the transformation into the rotating frame see the derivation of Sec. 16.3.1.

displacement operator. Δ_a is the detuning between the light and the atomic resonance, Δ_c between the light and cavity resonance and g is the light-atom coupling force, also called the single-photon Rabi frequency. Neglecting the kinetic energy term $\hat{p}^2/2m$, the photonic recoil $e^{-\imath k v \hat{z}}$, and the pumping η we recover the *Jaynes-Cummings model*. Do the Excs. 25.1.7.1 and 25.1.7.2.

For a *ring cavity*, we must distinguish the counterpropagating modes $\hat{a}_\pm$,

$$\hat{\mathcal{E}}^+(z,t) = \hat{\mathcal{E}}_1 \hat{a}_+(t) e^{\imath k z} + \hat{\mathcal{E}}_1 \hat{a}_-(t) e^{-\imath k z} = (\hat{\mathcal{E}}^-(z,t))^\dagger \ . \tag{25.3}$$

such that the total Hamiltonian $\hat{H}$ consists of the following parts [2],

$$\boxed{\begin{aligned} \hat{H}_{\text{atom}} &= \hat{H}_{\text{electron}} + \hat{H}_{\text{motion}} = -\Delta_a \hat{\sigma}^+ \hat{\sigma}^- + \frac{\hat{p}^2}{2m} \\ \hat{H}_{\text{cav}} &= -\Delta_c \hat{a}_+^\dagger \hat{a}_+ - \Delta_c \hat{a}_-^\dagger \hat{a}_- \\ \hat{H}_{\text{atom:cav}} &= g \hat{a}_+^\dagger \hat{\sigma}^- e^{-\imath k \hat{z}} + h.c. + g \hat{a}_-^\dagger \hat{\sigma}^- e^{\imath k \hat{z}} + h.c. \\ \hat{H}_{\text{laser:cav}} &= -\imath \eta_+ (\hat{a}_+ - \hat{a}_+^\dagger) - \imath \eta_- (\hat{a}_- - \hat{a}_-^\dagger) \end{aligned}} \ . \tag{25.4}$$

We identify the degrees of freedom of the system through the quantum observables appearing in the Hamiltonian: the counterpropagating modes of light with the amplitudes ($\hat{a}_\pm$), the internal degrees of freedom ($\hat{\sigma}^z, \hat{\sigma}^\pm$), and the spatial coordinates of the atom ($\hat{z}, \hat{p}$).

In contrast to linear cavities, ring cavities have the following particularities: 1. The phase of the standing wave is free to move; 2. the counterpropagating modes of the cavity have independent photon budgets, each backscattering event conserves momentum; 3. the backscattering acts on the phase of the standing wave. Atoms can be trapped by the dipole force within the cavity mode volume. The dipole force corresponds to a backscattering of photons between modes.

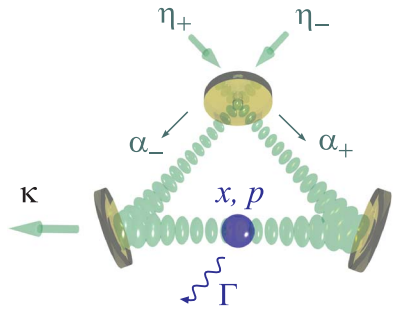

Figure 25.2: Scheme of an atom interacting with a ring cavity showing the relevant degrees of freedom ($\hat{x}$, $\hat{p}$, $\hat{a}_\pm$) and the possible decay processes (κ, Γ) for the derivation of the field equations.

[2] Throughout this chapter we will sometimes emphasize the motional degree of freedom in green color, photonic states in blue, electronic excitation states in pink.

25.1.2 Eliminating spontaneous emission and cavity decay

In fact, there are more degrees of freedom involved in the dynamics of atoms moving in a laser-pumped ring cavity, because of the atoms may scatter light into directions other than the cavity modes by spontaneous emission, and the cavity modes may decay by transmission through the mirrors. Therefore, we need to treat the respective vacuum field modes receiving the photons, $\hat{a}_{\mathbf{k}}$ and $\hat{a}_{\omega}$, quantum mechanically and include the respective Hamiltonians,

$$\begin{aligned} \hat{H}_{\text{atom:vacuum}} &= \sum_{\mathbf{k}} g_{\text{atom:vacuum}} \hat{a}^{\dagger}_{\mathbf{k}} \hat{\sigma}^{-} e^{-\imath \mathbf{k}\cdot\hat{\mathbf{r}}} + h.c. \\ \hat{H}_{\text{cav:bath}} &= \sum_{\omega} g_{\text{cav:bath}} \hat{a}^{\dagger}_{\omega} \hat{a}_{+} + g_{\text{cav:bath}} \hat{a}^{\dagger}_{\omega} \hat{a}_{-} + h.c. \ , \end{aligned} \tag{25.5}$$

in the description of the coupled dynamics. Here, $g_{\text{atom:vacuum}}$ denotes the vacuum Rabi frequency, that is, the coupling strength between the atomic dipole and the electromagnetic vacuum into which spontaneously emitted photons may escape. On the other hand, $g_{\text{cav:bath}}$ denotes the coupling strength between the cavity mode and the spectrum of electromagnetic modes into which cavity photons can escape and which we will from now on call *heat bath* to facilitate its semantic distinction from the spontaneous vacuum. The total density operator, the Hamiltonian and the equation of motion are, consequently,

$$\begin{aligned} \bar{\rho} &= \hat{\rho}_{\text{atom}} \otimes \hat{\rho}_{\text{electron}} \otimes \hat{\rho}_{\text{cav}} \otimes \hat{\rho}_{\text{vacuum}} \otimes \hat{\rho}_{\text{bath}} \\ \bar{H} &= \hat{H}_{\text{motion}} + \hat{H}_{\text{electron}} + \hat{H}_{\text{cav}} + \hat{H}_{\text{atom:cav}} + \hat{H}_{\text{laser:cav}} + \hat{H}_{\text{atom:vacuum}} + \hat{H}_{\text{cav:bath}} \\ \dot{\bar{\rho}} &= -\imath[\bar{H}, \bar{\rho}] \ . \end{aligned} \tag{25.6}$$

With the inclusion of the vacuum field modes $\hat{a}_{\omega}$ and $\hat{a}_{\mathbf{k}}$ the number of degrees of freedom to be treated literally explodes, and we have to find a way to eliminate them from the equation of motion. We do this by partially tracing the density operator over the vacuum field modes using the Weisskopf-Wigner theory,

$$\tilde{\rho} \equiv \text{Tr}_{\text{vacuum}} \ \text{Tr}_{\text{bath}} \ \bar{\rho} = \hat{\rho}_{\text{atom}} \otimes \hat{\rho}_{\text{electron}} \otimes \hat{\rho}_{\text{cav}} \ . \tag{25.7}$$

This allows us to reduce the Hamiltonian $\hat{H} = \bar{H} - \hat{H}_{\text{atom:vacuum}} - \hat{H}_{\text{cav:bath}}$. The price to pay is, that the equation of motion for this receives dissipative terms: The Liouville equation turns into a *master equation* with the following form,

$$\boxed{\begin{aligned} \dot{\hat{\rho}} = -\imath[\hat{H}, \hat{\rho}] \quad &+ \quad \mathcal{L}_{\text{atom:vacuum}} + \mathcal{L}_{\text{cav:vacuum,+}} + \mathcal{L}_{\text{cav:vacuum,-}} \\ \mathcal{L}_{\text{atom:vacuum}} \hat{\rho}(t) \quad &= \quad -\gamma\{\hat{\sigma}^{+}\hat{\sigma}^{-}\hat{\rho}(t) - 2\hat{\sigma}^{-}\hat{\rho}(t)\hat{\sigma}^{+} + \hat{\rho}(t)\hat{\sigma}^{+}\hat{\sigma}^{-}\} \\ \mathcal{L}_{\text{cav:bath},\pm} \hat{\rho}(t) \quad &= \quad -\kappa\{\hat{a}^{\dagger}_{\pm}\hat{a}_{\pm}\hat{\rho}(t) - 2\hat{a}_{\pm}\hat{\rho}(t)\hat{a}^{\dagger}_{\pm} + \hat{\rho}(t)\hat{a}^{\dagger}_{\pm}\hat{a}_{\pm}\} \end{aligned}} \ , \tag{25.8}$$

where $\hat{H}$ is the Hamiltonian from (25.4). We see that each degree of freedom has its own loss mechanism. κ for the finite transmission of the resonator mirrors [169, 304] [3], Γ for the spontaneous emission, and γ_{frc}, when we exert a frictional force on the atoms.

[3] Here, we only consider cavity decay into a zero temperature reservoir without quantum phase fluctuations.

25.1.2.1 The problem with spontaneous emission in cavities

The above treatment still is incomplete, if we regard $\hat{\rho}$ as the atomic Bloch vector. The reason is that we know what the dissipative Lindblad terms $\mathcal{L}_{\text{vacuum}}\tilde{\rho}$ generated by spontaneous emission look like for the atomic excitation $\hat{\rho}_{\text{atom}}$, but the Hamiltonian $\hat{H}_{\text{atom:vacuum}}$ also *contains the motional degree of freedom* $e^{-\imath\mathbf{k}\cdot\hat{\mathbf{r}}}$, which is intrinsically three-dimensional. That is, the dissipative terms also need to describe, how the motion diffuses in momentum space.

The inclusion of dissipative terms, however, is difficult, because unavoidable photonic recoil violates the supposed one-dimensionality of the atomic motion along the optical axis. Omnidirectional photonic recoil is also incompatible with the assumption that the momentum is quantized in multiples of $2\hbar k$ in the direction of the optical axis. And finally, if we consider degenerate matter waves, photonic recoil will eject atoms from a BEC. Even if, neglecting the emission process, we only consider absorption, we would need a quantization in multiples of $1\hbar k$ instead of $2\hbar k$. In the following, in order to keep the problem 1D, we will neglect momentum diffusion, i.e. we consider the simplified Hamiltonian $\tilde{H}$ and discard motional terms from the term $\mathcal{L}_{\text{vacuum}}\hat{\rho}$.

25.1.2.2 Quantum derivation of the CARL equations

To obtain the equations of motion we insert the Hamiltonian (25.4) into the equations for the field operators, for which the following commutation rules hold, $[\hat{a}_\pm, \hat{a}_\pm^\dagger] = 1$ and $[\hat{a}_\pm, \hat{a}_\mp^\dagger] = 0 = [\hat{a}_\pm, \hat{a}_\pm]$,

$$\begin{aligned}\dot{\hat{a}}_+ &= \imath[\hat{H}, \hat{a}_+] - \kappa\hat{a}_+ \\ &= -\imath\Delta_c[\hat{a}_+^\dagger\hat{a}_+, \hat{a}_+] + \imath g e^{-\imath k\hat{z}}\hat{\sigma}^-[\hat{a}_+^\dagger, \hat{a}_+] + \imath g e^{\imath k\hat{z}}\hat{\sigma}^+[\hat{a}_+, \hat{a}_+] + \eta_+[\hat{a}_+ - \hat{a}_+^\dagger, \hat{a}_+] - \kappa\hat{a}_+ \\ &= (-\kappa + \imath\Delta_c)\hat{a}_+ - \imath g\hat{\sigma}^- e^{-\imath kx} + \eta_+ \ ,\end{aligned} \tag{25.9}$$

and similarly for $\hat{a}_-$. For the Pauli deexcitation matrix, using the usual commutation rules for the *Pauli spin matrices* (1.154), that is $[\hat{\sigma}^+, \hat{\sigma}^-] = \hat{\sigma}_z$, $\hat{\sigma}_z\hat{\sigma}^\pm = \pm\hat{\sigma}^\pm$, and $[\hat{\sigma}^-, \hat{\sigma}^-] = 0$, we calculate,

$$\begin{aligned}\dot{\hat{\sigma}}^- &= \imath[\hat{H}, \hat{\sigma}^-] - \gamma\hat{\sigma}^- \\ &= -\imath\Delta_a[\hat{\sigma}^+\hat{\sigma}^-, \hat{\sigma}^-] + \imath g e^{\imath k\hat{z}}\hat{a}_+[\hat{\sigma}^+, \sigma^-] + \imath g e^{-\imath k\hat{z}}\hat{a}_-[\hat{\sigma}^+, \sigma^-] - \gamma\hat{\sigma}^- \\ &= (-\gamma + \imath\Delta_a)\hat{\sigma}^- + \imath g e^{\imath k\hat{z}}\hat{a}_+\hat{\sigma}_z + \imath g e^{-\imath k\hat{z}}\hat{a}_-\hat{\sigma}_z \ .\end{aligned} \tag{25.10}$$

For the Pauli inversion matrix, using the following commutation rules, $[\hat{\sigma}_z, \hat{\sigma}^+\hat{\sigma}^+] = 0$ and $[\hat{\sigma}_z, \hat{\sigma}^\pm] = \pm 2\hat{\sigma}^\pm$, we calculate,

$$\begin{aligned}\dot{\hat{\sigma}}_z &= \imath[\hat{H}, \hat{\sigma}_z] - 2\gamma - 2\gamma\hat{\sigma}_z \\ &= \imath g e^{-\imath k\hat{z}}\hat{a}_+^\dagger[\hat{\sigma}^-, \hat{\sigma}_z] + \imath g e^{\imath k\hat{z}}\hat{a}_-^\dagger[\hat{\sigma}^-, \hat{\sigma}_z] + \imath g e^{\imath k\hat{z}}\hat{a}_+[\hat{\sigma}^+, \hat{\sigma}_z] + \imath g e^{-\imath k\hat{z}}\hat{a}_-[\hat{\sigma}^+, \hat{\sigma}_z] - 2\gamma\hat{\sigma}_z \\ &= -2\gamma - 2\gamma\hat{\sigma}_z + 2\imath g e^{-\imath k\hat{z}}\hat{a}_+^\dagger\hat{\sigma}^- + 2\imath g e^{\imath k\hat{z}}\hat{a}_-^\dagger\hat{\sigma}^- - 2\imath g e^{\imath k\hat{z}}\hat{a}_+\hat{\sigma}^+ - 2\imath g e^{-\imath k\hat{z}}\hat{a}_-\hat{\sigma}^+ \ .\end{aligned} \tag{25.11}$$

Finally, we need to derive the equations governing the motion of atoms. For the position we obtain,

$$\dot{\hat{z}} = \imath[\hat{H}, \hat{z}] = \imath[\tfrac{\hat{p}^2}{2m}, \hat{z}] = \tfrac{1}{m}\hat{p} \ . \tag{25.12}$$

In order to calculate the momentum, we need to do a small auxiliary calculation. With the commutator $[\hat{z},\hat{p}] = \imath$ we derive,

$$[\hat{z}^n,\hat{p}] = \imath\frac{\delta\hat{z}^n}{\delta\hat{z}} = \imath n\hat{z}^{n-1} \tag{25.13}$$
$$[e^{\imath k\hat{z}},\hat{p}] = \sum_{n=0}^{\infty}\frac{(\imath k)^n}{n!}[\hat{z}^n,\hat{p}] = -k\sum_{n=0}^{\infty}\frac{(\imath k)^{n-1}}{(n-1)!}\hat{z}^{n-1} = -ke^{\imath k\hat{z}} \ ,$$

and with this result,

$$\begin{aligned}\dot{\hat{p}} &= \imath[\hat{H},\hat{p}] \\ &= \imath g\hat{a}_+^\dagger\hat{\sigma}^-[e^{-\imath k\hat{z}},\hat{p}] + c.c. + \imath g\hat{a}_-^\dagger\hat{\sigma}^-[e^{\imath k\hat{z}},\hat{p}] + c.c. \\ &= -\imath gk\hat{a}_+^\dagger\hat{\sigma}^-e^{-\imath k\hat{z}} + c.c. + \imath gk\hat{a}_-^\dagger\hat{\sigma}^-e^{\imath k\hat{z}} + c.c. \ .\end{aligned} \tag{25.14}$$

The *quantum Langevin equations* [169] describing the dynamics of the internal and external degrees of freedom of the atom and the field are coupled,

$$\boxed{\begin{aligned}\dot{\hat{a}}_\pm &= (-\kappa+\imath\Delta_c)\hat{a}_\pm - \imath g\hat{\sigma}^-e^{\mp\imath k\hat{z}} + \eta_\pm \\ \dot{\hat{\sigma}}^- &= (-\gamma+\imath\Delta_a)\hat{\sigma}^- + \imath g(e^{\imath k\hat{z}}\hat{a}_+ + e^{-\imath kz}\hat{a}_-)\hat{\sigma}_z \\ \dot{\hat{\sigma}}_z &= -2\gamma\hat{\sigma}_z + 2\imath g(e^{-\imath k\hat{z}}\hat{a}_+^\dagger + e^{\imath k\hat{z}}\hat{a}_-^\dagger)\hat{\sigma}^- - 2\imath g(e^{\imath k\hat{z}}\hat{a}_+ + e^{-\imath k\hat{z}}\hat{a}_-)\hat{\sigma}^+ \\ \dot{\hat{z}} &= \hat{p}/m \\ \dot{\hat{p}} &= \imath g\hbar k\hat{\sigma}^-(\hat{a}_+^\dagger e^{-\imath k\hat{z}} - \hat{a}_-^\dagger e^{\imath k\hat{z}}) + c.c.\end{aligned}} \ . \tag{25.15}$$

We may also verify,

$$\begin{aligned}\dot{\hat{n}}_+ &= \imath[\hat{H},\hat{n}_+] \\ &= \imath[-\Delta_c\hat{a}_+^\dagger\hat{a}_+ + g\hat{a}_+^\dagger\hat{\sigma}^-e^{-\imath k\hat{z}} + g\hat{a}_+\hat{\sigma}^+e^{\imath k\hat{z}} - \imath\eta_+(\hat{a}_+ - \hat{a}_+^\dagger),\hat{a}_+^\dagger\hat{a}_+] \\ &= (\eta_+ - \imath ge^{-\imath k\hat{z}}\hat{\sigma}^-)\hat{a}_+^\dagger + (\eta_+ + \imath g\hat{\sigma}^+e^{\imath k\hat{z}})\hat{a}_+ \ ,\end{aligned} \tag{25.16}$$

and hence conservation of momentum,

$$[\hat{H},\hbar k(\hat{n}_+ - \hat{n}_-) - \hat{p}] = \hbar k\eta_+(\hat{a}_+^\dagger + \hat{a}_+) - \hbar k\eta_-(\hat{a}_-^\dagger + \hat{a}_-) \ , \tag{25.17}$$

in the absence of pumping, $\eta_+ = 0 = \eta_-$.

25.1.3 Adiabatic elimination of the excited state

Under certain conditions, however, the internal and external dynamics occur at very different time scales, which allows a decoupling of the differential equations [4]. When the light fields are very detuned from atomic resonances, $\Delta_a \gg \Gamma$, the internal dynamics of the atoms is very fast, that is, the internal state adapts very rapidly to the boundary conditions defined by the external state and the state of the light field.

[4] In good cavity the limit the degrees of freedom of atomic excitation $\hat{\sigma}^\pm$ drop out of the dynamics, in the bad cavity limit, the fields $\hat{a}^\pm$ drop out of the dynamics.

Therefore, the internal state has no separate dynamics of its own, and we can adiabatically eliminate the internal degrees of freedom. Thus, we can neglect correlations between degrees of freedom, $\langle \hat{a}_\pm \hat{\sigma}^\pm \rangle = \langle \hat{a}_\pm \rangle \langle \hat{\sigma}^\pm \rangle$ etc. [648, 300]. The adiabatic elimination of the excited state comes down to treating the atom as a classical antenna.

We obtain the stationary solutions for $t \to \infty$ in the same way as for the optical Bloch equations [see Eq. (16.151)], assuming in Eq. (25.15),

$$\dot{\hat{\sigma}}^- = 0 = \dot{\hat{\sigma}}_z \tag{25.18}$$

where $\langle \hat{\sigma}^- \rangle = \rho_{21}$. Introducing the position-dependent Rabi frequency of the atom in the standing wave [5],

$$\hat{\Omega}(z) = 2g(e^{\imath k\hat{z}}\hat{a}_+ + e^{-\imath k\hat{z}}\hat{a}_-) \ , \tag{25.19}$$

we write,

$$\begin{aligned} 0 &= (-\gamma + \imath\Delta_a)\hat{\sigma}^- + \tfrac{1}{2}\imath\hat{\Omega}\hat{\sigma}_z \\ 0 &= -2\gamma - 2\gamma\hat{\sigma}_z + \imath\hat{\Omega}^\dagger\hat{\sigma}^- - \imath\hat{\Omega}\hat{\sigma}^+ \ . \end{aligned} \tag{25.20}$$

These equations are solved by,

$$\begin{aligned} \hat{\sigma}_z(\infty) &= \frac{-2(\gamma^2 + \Delta_a^2)}{2(\gamma^2 + \Delta_a^2) + \hat{\Omega}^\dagger\hat{\Omega}} \\ \text{and} \quad \hat{\sigma}^-(\infty) &= \frac{-\imath(\gamma + \imath\Delta_a)\hat{\Omega}}{2(\gamma^2 + \Delta_a^2) + \hat{\Omega}^\dagger\hat{\Omega}} \simeq \frac{-\imath(\gamma + \imath\Delta_a)}{2\Delta_a^2}\hat{\Omega} \ . \end{aligned} \tag{25.21}$$

Inserting the approximated expression for $\hat{\sigma}^-(\infty)$ into the equation of motion (25.15) for the light modes,

$$\begin{aligned} \dot{\hat{a}}_\pm &= (-\kappa + \imath\Delta_c)\hat{a}_\pm - \imath g\hat{\sigma}^-(\infty)e^{\mp\imath k\hat{z}} + \eta_\pm \\ &= \left(-\kappa + \imath\Delta_c - \frac{g^2\gamma}{\Delta_a^2} - \frac{\imath g^2}{\Delta_a}\right)\hat{a}_\pm - \left(\frac{g^2\gamma}{\Delta_a^2} + \frac{\imath g^2}{\Delta_a}\right)e^{\mp 2\imath k\hat{z}}\hat{a}_\mp + \eta_\pm \ , \end{aligned} \tag{25.22}$$

and for the atomic momentum,

$$\begin{aligned} \dot{\hat{p}} &= \imath g\hbar k\hat{\sigma}^-(\infty)(\hat{a}_+^\dagger e^{-\imath k\hat{z}} - \hat{a}_-^\dagger e^{\imath k\hat{z}}) - \imath g\hbar k\hat{\sigma}^+(\infty)(\hat{a}_+ e^{\imath k\hat{z}} - \hat{a}_- e^{-\imath k\hat{z}}) \\ &= \frac{2\hbar k\gamma g^2}{\Delta_a^2}(\hat{a}_+^\dagger\hat{a}_+ - \hat{a}_-^\dagger\hat{a}_-) - \frac{2\imath\hbar k g^2}{\Delta_a}(e^{2\imath k\hat{z}}\hat{a}_+\hat{a}_-^\dagger - e^{-2\imath k\hat{z}}\hat{a}_+^\dagger\hat{a}_-) \ . \end{aligned} \tag{25.23}$$

Defining the light-shift U_0 caused by only one photon and the scattering rate γ_0 by,

$$U_0 \equiv \frac{g^2}{\Delta_a} \qquad \text{and} \qquad \gamma_0 \equiv \frac{\Gamma g^2}{\Delta_a^2} \ , \tag{25.24}$$

with $\Gamma = 2\gamma$, we finally get a set of equations, where the internal degree of freedom of the atom has been eliminated,

$$\boxed{\begin{aligned} \dot{\hat{a}}_\pm &= (-\kappa - \gamma_0 + \imath\Delta_c - \imath U_0)\hat{a}_\pm - (\gamma_0 + \imath U_0)e^{\mp 2\imath k\hat{z}}\hat{a}_\mp + \eta_\pm \\ \dot{\hat{p}} &= 2\hbar k\gamma_0(\hat{a}_+^\dagger\hat{a}_+ - \hat{a}_-^\dagger\hat{a}_-) + 2\imath\hbar k U_0(e^{-2\imath k\hat{z}}\hat{a}_+^\dagger\hat{a}_- - e^{2\imath k\hat{z}}\hat{a}_+\hat{a}_-^\dagger) \end{aligned}} \ . \tag{25.25}$$

[5] Note that the factor of 2 ensure consistency with previous definitions of the Rabi frequency, such as in (17.21). Note also, that $[\hat{\Omega}, \hat{\Omega}^\dagger] = 8g^2 \neq 0$, but this is negligible when the fields are large enough to be considered as classical. On the other hand the quadratic terms $\Omega^\dagger\Omega$ are negligible when they are small compared to γ^2 or Δ_a^2.

25.1.3.1 Radiation pressure and the adiabatically approximated Hamiltonian

The impact of radiation pressure should be considered when the pumping laser is close to a resonance. Then $\gamma_0 \ll U_0$ is no longer satisfied [300], and we get one more term from the equation for the atomic force: $\propto \hbar\gamma_0(|\alpha_+|^2 - |\alpha_-|^2)$.

For the adiabatically approximated Hamiltonian we get immediately from (25.4) [567],

$$\boxed{\begin{aligned}\hat{H} = \frac{\hat{p}^2}{2m} &+ \sum_{\pm}(U_0 - \Delta_c)\hat{a}_\pm^\dagger\hat{a}_\pm \\ &+ U_0(e^{-2\imath k\hat{z}}\hat{a}_+^\dagger\hat{a}_- + e^{2\imath k\hat{z}}\hat{a}_+\hat{a}_-^\dagger) - \imath\sum_{\pm}\eta_\pm(\hat{a}_\pm - \hat{a}_\pm^\dagger)\end{aligned}} \quad , \tag{25.26}$$

as shown in Exc. 25.1.7.3. Note that dissipative terms are (naturally) absent from this Hamiltonian, so that it shall not be used for the description of radiation pressure. On the other hand, all coherent terms of the equations of motion can be derived from this Hamiltonian (25.26), and we can verify momentum conservation (25.17) and deduce transformation properties. Solve the Exc. 25.1.7.4.

These equations, which we will call CARL equations for reasons that we will become clear in Sec. 25.2, describe the coupled dynamics of atoms being accelerated by the *kick* $e^{\imath k\hat{z}}$ imparted by the photonic recoil received upon scattering a photon from one mode into the counterpropagating one. In the same time, the backscattering *annihilates* a photon $\hat{a}_\pm$ in one mode and *creates* a photon $\hat{a}_\mp^\dagger$ in the counterpropagating mode. From now on we will exclusively use the CARL equations.

Finally, let us summarize, how the operators act on states and observables of the coupled system, noting that the same transformation rules as for free and trapped atoms (2.143) also hold for the optical lattice,

$$\boxed{\begin{array}{rclcrcl} e^{\imath k\hat{z}}|z\rangle &=& |z\rangle & , & e^{-\imath k\hat{z}}\hat{z}e^{\imath k\hat{z}} &=& \hat{z} \\ e^{\imath k\hat{z}}|p\rangle &=& |p+\hbar k\rangle & , & e^{-\imath k\hat{z}}\hat{p}e^{\imath k\hat{z}} &=& \hat{p}+\hbar k \\ \hat{a}_\pm|n\rangle &=& \sqrt{n}|n-1\rangle & , & e^{-\imath k\hat{z}}\hat{H}(\hat{z},\hat{p})e^{\imath k\hat{z}} &=& \hat{H}(\hat{z},\hat{p}-\hbar k) \\ \hat{a}_\pm^\dagger|n\rangle &=& \sqrt{n+1}|n+1\rangle & , & e^{\imath a\hat{p}/\hbar}\hat{H}(\hat{z},\hat{p})e^{-\imath a\hat{p}/\hbar} &=& \hat{H}(\hat{z}-a,\hat{p}) \end{array}} \quad . \tag{25.27}$$

For $ka = \pi$ the phase shift vanishes: $[e^{\imath\pi\hat{p}/\hbar k}, \hat{H}(\hat{z},\hat{p})] = 0$.

The dynamics is given by the time evolutions,

$$e^{-(\imath/\hbar)\hat{H}t}\hat{z}(0)e^{(\imath/\hbar)\hat{H}t} \quad , \quad e^{-(\imath/\hbar)\hat{H}t}\hat{p}(0)e^{(\imath/\hbar)\hat{H}t} \quad , \quad e^{-(\imath/\hbar)\hat{H}t}\hat{n}(0)e^{(\imath/\hbar)\hat{H}t} \; . \tag{25.28}$$

In Exc. 25.1.7.5 we calculate the photon number superposition state resulting from a kick $e^{\imath k_{kck}\hat{z}}$.

25.1.4 Adiabatic elimination of the cavity modes

We have seen in Sec. 25.1.3 how to eliminate the internal atomic degrees of freedom, once the condition $|\Delta_a| \gg \Gamma$ is satisfied. We may try an analogous treatment accounting for the limit $|\Delta_c| \gg \kappa$. In this case, the cavity fields evolve on a fast time

scale, adiabatically following the evolution of the other degrees of freedom. Hence, we set,

$$\dot{\hat{a}}_{\pm} = 0 \ , \tag{25.29}$$

and obtain from the first Heisenberg equation (25.15),

$$\hat{a}_{\pm}(\infty) = \frac{\imath g \hat{\sigma}^{-} e^{\mp \imath k \hat{z}} - \eta_{\pm}}{-\kappa + \imath \Delta_c} \ . \tag{25.30}$$

Defining,

$$U_c \equiv \frac{g^2 \Delta_c}{\kappa^2 + \Delta_c^2} \qquad \text{and} \qquad \kappa_c \equiv \frac{g^2 \kappa}{\kappa^2 + \Delta_c^2} \ , \tag{25.31}$$

we can write the position-dependent Rabi frequency (25.19) as,

$$\begin{aligned} \Omega(z) = 2g(e^{\imath k \hat{z}} \hat{a}_{+} + e^{-\imath k \hat{z}} \hat{a}_{-}) \quad &= 2(\kappa_c + \imath U_c) \left(\frac{\eta_{+} e^{\imath k \hat{z}} + \eta_{-} e^{-\imath k \hat{z}}}{g} - 2\imath \hat{\sigma}^{-} \right) \\ &\overset{\eta_{\pm}=0}{\longrightarrow} -4\imath(\kappa_c + \imath U_c)\hat{\sigma}^{-} \ , \end{aligned} \tag{25.32}$$

in the limit of no pumping $\eta_{\pm} = 0$. Inserting this into the other Heisenberg equations (25.15), we immediately get,

$$\dot{\hat{\sigma}}^{-} = (-\gamma + \imath \Delta_a)\hat{\sigma}^{-} + \tfrac{\imath}{2}\Omega(z)\hat{\sigma}_z \overset{\eta_{\pm}=0}{\longrightarrow} (-\gamma + \imath \Delta_a)\hat{\sigma}^{-} + 2(\kappa_c + \imath U_c)\hat{\sigma}^{-}\hat{\sigma}_z \ , \tag{25.33}$$

and

$$\dot{\hat{\sigma}}_z = -2\gamma \hat{\sigma}_z + \imath \Omega^{\dagger}(z)\hat{\sigma}^{-} - \imath \hat{\sigma}^{+}\Omega(z) \overset{\eta_{\pm}=0}{\longrightarrow} -2\gamma \hat{\sigma}_z - 4\kappa_c \hat{\mathbb{I}} \ , \tag{25.34}$$

as well as, $\dot{\hat{z}} = \hat{p}/m$ and

$$\dot{\hat{p}} = \imath g \hbar k \hat{\sigma}^{-}(e^{-\imath k \hat{z}} \hat{a}_{+}^{\dagger} - e^{\imath k \hat{z}} \hat{a}_{-}^{\dagger}) - \imath g \hbar k \hat{\sigma}^{+}(e^{\imath k \hat{z}} \hat{a}_{+} - e^{-\imath k \hat{z}} \hat{a}_{-}) \overset{\eta_{\pm}=0}{\longrightarrow} 0 \ . \tag{25.35}$$

That is, in summary,

$$\boxed{\begin{aligned} \dot{\hat{\sigma}}^{-} &= (-\gamma - 2\kappa_c + \imath \Delta_a - 2\imath U_c)\hat{\sigma}^{-} \\ \dot{\hat{\sigma}}_z &= -2\gamma \hat{\sigma}_z - 4\kappa_c \hat{\mathbb{I}} \\ \dot{\hat{p}} &= 0 \end{aligned}} \ . \tag{25.36}$$

Alternatively, the coherent part of these equations can be derived by insert $\hat{a}_{\pm}(\infty)$ directly in the Hamiltonian (25.4). This will be done in Exc. 25.1.7.6. The equations (25.36) tell us that, in the absence of cavity decay and spontaneous emission, the atomic population will not undergo nutation, but the dipole moment will rotate with a velocity which depends on the inversion. The dynamics becomes interesting in the presence of several atoms, as studied in 23.4.2.

25.1.5 General rules for deriving equations of motion

We have, in the previous sections, derived Heisenberg equations (25.15), respectively (25.25) which, together with the Schrödinger equation for the system's state $|\psi(t)\rangle$ or the master equation for the density operator $\hat{\rho}(t)$ form an *over-complete* set. This

section aims at providing a general recipe for choosing the right set of equations depending on two basic criteria for the nature of the degrees of freedom involved in the dynamics: (i) Do judge it necessary to treat the degree of freedom as quantum or may a classical description be sufficient; and (ii) Is the degree of freedom subject to dissipation (e.g. spontaneous emission of the electronic excitation, cavity decay of the field mode, or collisions messing up the center-of-mass motion), or not. The procedure, which will be applied throughout the remaining part of this chapter, leads to very different descriptions of the system depending on the specific parameter regime.

1. The procedure is generally applicable to coupled systems: We first need to *identify all relevant degrees of freedom and set up the Hamiltonian*, possibly eliminating irrelevant degrees of freedom, e.g. via adiabatic elimination or by tracing over them, if they contribute to dissipation. In the context of atoms coupled to a ring cavity, we assume our system to be in some state [6],

$$|\psi(t)\rangle = |\mathbf{r}\rangle \otimes |\alpha_+\rangle \otimes |\alpha_-\rangle \otimes |i\rangle \ , \tag{25.37}$$

   coupling the atomic motion, the light fields and the electronic excitation, although the electronic excitation $|i\rangle$ is often eliminated adiabatically. The dissipative degrees of freedom related to vacuum modes leading to spontaneous emission and cavity decay, as well as collisions between moving atoms are traced away, but may be considered in the master equation for the density operator and in the Heisenberg equations, where the corresponding decay rates are added phenomenologically.

   This first item has already been solved in the previous sections and led us to the Hamiltonian (25.4) and the corresponding Heisenberg equations (25.15), or the adiabatically approximated Hamiltonian (25.26) and the corresponding Heisenberg equations (25.25).

2. Now, we must decide which degrees of freedom B can be treated as *classical*. Typically, those are highly excited degrees of freedom (e.g. fast velocities of many photons in a mode). The corresponding operators can be substituted by their expectation value. Purely classical energy terms in the Hamiltonian can be ignored and removed. For the degrees of freedom $\hat{A}$ we want to treat as *quantum*, we chose an appropriate common basis, which can be discrete $\{|m\rangle\}$ where m is a complete set of quantum numbers. It can also be continuous $\{|\mathbf{r}\rangle\}$ or a combination of both $\{|\mathbf{r}, m\rangle\}$. Now, we need to expand all operators on the chosen basis.

3. For the quantized degrees of freedom must now decide, whether they all evolve coherently or whether they are subject to dissipation. In the first case, perform steps A4 to A7, in the second case, perform steps B4 to B7.

A4. In the case of coherent dynamics, we *expand the state* of the system $|\psi(t)\rangle$ on the whole basis. For example, expanded on a partially continuous basis, the

[6] Throughout this chapter we will denote momentum states by the Greek letters $|\mu\rangle$ or $\nu\rangle$. Photonic states will be labeled by the Latin letters $|n\rangle$ or $|m\rangle$. Electronic excitation states will be labeled by the Latin letters $|i\rangle$ or $|j\rangle$. Finally, expansion coefficients c_{ν,i,n_+,n_-} of the state or of the density matrix elements will sometimes be emphasized in red.

coupled atom-ring cavity state may read,

$$|\psi(t)\rangle = \sum_{n_+,n_-,i} \int d^3r \; c_{n_+,n_-,i}(\mathbf{r},t)|\mathbf{r}\rangle \otimes |n_+\rangle \otimes |n_-\rangle \otimes |i\rangle \; , \tag{25.38}$$

where $\langle \mathbf{r}, \alpha_+, \alpha_-, i|\psi(t)\rangle = c_{n_+,n_-,i}(\mathbf{r},t)$ are the expansion coefficients depending on photon numbers $n_\pm$ in the counterpropagating light modes, the electronic excitation state i, and the atomic position $\mathbf{r}$ treated in terms of a continuous wavefunction in space [7]. When we want to treat the atomic motion as being quantized in discrete momentum states labeled by some integer number μ, we adopt the notation,

$$|\psi(t)\rangle = \sum_{\nu,n_+,n_-,i} c_{\nu,n_+,n_-,i}(t)|\nu\rangle \otimes |n_+\rangle \otimes |n_-\rangle \otimes |i\rangle \; , \tag{25.39}$$

where $\langle \nu, \alpha_+, \alpha_-, i|\psi(t)\rangle = c_{\nu,n_+,n_-,i}(t)$ are the new expansion coefficients.

A5. Next, we write down the *Schrödinger equation* for the state $|\psi(t)\rangle$, insert the expansion on the basis, and we derive a linear set of equation of motion for the expansion coefficients $\dot{c}_{\{m\}}(\mathbf{r})$. This set governs the dynamics of the quantum degrees of freedom.

A6. The dynamics of the classical degrees of freedom B is obtained by taking the expectation values of the *Heisenberg equations*. Here, we need to take care that the quantum degrees of freedom appearing in the Heisenberg equations are expressed by their expansions.

A7. The coupled set of equations for the expectation values of projectors of the system into a particular state, that is, $\dot{c}_{\{m\}}$ (respectively, $\dot{c}_{\{m\}}(\mathbf{r})$), and of observables B really represents all we need to describe the system dynamics and to simulate it numerically. Hack everything into your PC, pronto!

B4. In the case of dissipative dynamics, derive the master equation obeying commutation rules for all quantized degrees of freedom including the Lindbladt terms and expand every quantized degrees of freedom on the common basis, we do the same expansions, but,

$$\hat{\rho}(t) = |\psi(t)\rangle\langle\psi(t)| \; . \tag{25.40}$$

B5. Derive the linear set of equation of motion for the matrix elements $\dot{\rho}_{\{m\},\{n\}}$.

B6. Take the expectation values $\mathrm{Tr}\, \hat{\rho}\hat{B}$ of the Heisenberg equations for all degrees of freedom to be handled classical as expanding the quantized degrees of freedom on their basis.

B7. The coupled set of equations for $\dot{\rho}_{\{m\},\{n\}}$ and $\dot{B}$ is sufficient to describe the dynamics of the system, hack everything into your PC, pronto!

[7] Note that, in the absence of other quantum numbers, we rather use to write $c(\mathbf{r}) = \psi(\mathbf{r})$.

Let us apply the procedure to the simplest case that the electronic excitation has been adiabatically eliminated and *all* remaining degrees of freedom can be treated classical. Then we do not require a Hamiltonian, nor the Schrödinger equation. We just take the expectation value of the Heisenberg equations (25.25) for all degrees of freedom which is easy to do, because there is no quantum state to be expanded: we just can replace the operators by c-numbers,

$$\boxed{\begin{aligned} \dot{\alpha}_\pm &= (-\kappa + \imath\Delta_c - \imath U_0)\alpha_\pm - \imath U_0 e^{\mp 2\imath k z}\alpha_\mp + \eta_\pm \\ \dot{p} &= 2\imath\hbar k U_0(e^{-2\imath k z}\alpha_+^\dagger\alpha_- - e^{2\imath k z}\alpha_+\alpha_-^\dagger) \end{aligned}} \,. \tag{25.41}$$

These *totally classical* equations, called CARL equations, will be studied in the subsequent sections, while a thorough discussion of partially quantized equations of motion is postponed to Sec. 25.4.

25.1.5.1 CARL as a beam splitter

Neglecting spontaneous emission, $\gamma_0 = 0$, cavity pumping, $\eta = 0$, cavity decay, $\kappa = 0$, and cavity detuning, $\Delta_c = 0$, the CARL equations in the adiabatic approximation can be derived from the following Hamiltonian,

$$\hat{H} = \frac{\hat{p}^2}{2m} + \sum_\pm U_0\hat{a}_\pm^\dagger\hat{a}_\pm + U_0(e^{-2\imath k\hat{z}}\hat{a}_+^\dagger\hat{a}_- + e^{2\imath k\hat{z}}\hat{a}_+\hat{a}_-^\dagger) \,, \tag{25.42}$$

and read,

$$\begin{aligned} \dot{\hat{a}}_\pm &= -\imath U_0\hat{a}_\pm - \imath U_0 e^{\mp 2\imath k\hat{z}}\hat{a}_\mp \\ \dot{\hat{p}} &= 2\imath\hbar k U_0(e^{-2\imath k\hat{z}}\hat{a}_+^\dagger\hat{a}_- - e^{2\imath k\hat{z}}\hat{a}_+\hat{a}_-^\dagger) \,, \end{aligned} \tag{25.43}$$

or with the substitution $\hat{b}_\pm \equiv \hat{a}_\pm e^{\imath U_0 t}$,

$$\begin{aligned} \dot{\hat{b}}_\pm &= -\imath U_0 e^{\mp 2\imath k\hat{z}}\hat{b}_\mp \\ \ddot{\hat{b}}_\pm &= -U_0^2\hat{b}_\pm - 2k\dot{z}U_0 e^{\mp 2\imath k\hat{z}}\hat{b}_\mp \,, \end{aligned} \tag{25.44}$$

we see that, if the motion weren't a dynamic variable, $\dot{\hat{z}} = 0$, the field amplitudes would just perform harmonic oscillations.

On the other hand, with the substitution $\hat{c} \equiv \hat{a}_+ e^{\imath k\hat{z}} + \hat{a}_- e^{-\imath k\hat{z}}$ [8], the complete Hamiltonian rephrased as,

$$\boxed{\hat{H} = \frac{\hat{p}^2}{2m} + U_0\hat{c}^\dagger\hat{c}} \,. \tag{25.45}$$

Here, we see that, if the motion described by $(\hat{z}, \hat{p})$ weren't a dynamic variable, our system would simply be a harmonic oscillator vibrating with the frequency U_0.

[8] Provided we are allowed to commute the operators $\hat{z}$ and $\hat{a}_\pm$.

25.1.5.2 Classical limit of the equations of motion

For atoms much hotter than the recoil limit and macroscopic light intensities we may replace the quantum operators by complex numbers $z \equiv \hat{z}$, $\alpha_\pm \equiv \hat{a}_\pm$ and $\rho_{21} = \hat{\sigma}^-$. The classical equations of motion (25.41) for the coupled system of a single atom confined at the position $r = z$ of the dipolar potential of a ring cavity can be cast into the form,

$$\boxed{\begin{aligned}\begin{pmatrix}\dot{\alpha}_+\\ \dot{\alpha}_-\end{pmatrix} &= \begin{pmatrix}-\kappa-\gamma_0+\imath(\Delta_c-U_0) & -(\gamma_0+\imath U_0)e^{-2\imath kz}\\ -(\gamma_0+\imath U_0)e^{2\imath kz} & -\kappa-\gamma_0+\imath(\Delta_c-U_0)\end{pmatrix}\begin{pmatrix}\alpha_+\\ \alpha_-\end{pmatrix}+\begin{pmatrix}\eta_+\\ \eta_-\end{pmatrix}\\ \dot{p} &= 2\hbar k\gamma_0(\alpha_+\alpha_+^*-\alpha_-\alpha_-^*)+2\imath\hbar kU_0(\alpha_+^*\alpha_-e^{-2\imath kz}-\alpha_+\alpha_-^*e^{2\imath kz})\end{aligned}} \,. \tag{25.46}$$

Recalling that $\alpha_\pm^*\alpha_\pm$ is the number of photons in the respective mode, we can interpret this equation as a rate equation: The number of photons in a mode α_+ changes by photon losses at a rate κ from resonator, or by gain due to backscattering from the counterpropagating mode, or by pumping with an external incident light field at rate η_+.

The equations (25.46) completely describe our coupled atom-cavity system. They are totally classical and work for both, atoms and macroscopic particles.

25.1.6 Cumulant expansion for CARL

The dynamics of quantum correlations such as $\hat{a}_+^\dagger\hat{a}_-$ or $\hat{a}_+\sigma^+$ can be derived from Heisenberg equations, as well. As an example, let us consider the adiabatically eliminated Hamiltonian (25.26) and ignore the quantized nature of the atomic motion, the relevant first-order field-field correlations are then $\hat{a}_+^2$, $\hat{a}_+^\dagger\hat{a}_+$, $\hat{a}_+^{\dagger 2}$, $\hat{a}_-^2$, $\hat{a}_-^\dagger\hat{a}_-$, $\hat{a}_-^{\dagger 2}$, $\hat{a}_+\hat{a}_-$, $\hat{a}_+\hat{a}_-^\dagger$, $\hat{a}_+^\dagger\hat{a}_-$, $\hat{a}_+^\dagger\hat{a}_-^\dagger$. From the Heisenberg equation we get, for instance,

$$\begin{aligned}\frac{d}{dt}\hat{a}_+^2 &= \imath[\hat{H},\hat{a}_+^2] \\ &= -2\imath(U_0-\Delta_c)\hat{a}_+^2+2U_0\left(e^{2\imath k\hat{z}}\hat{a}_+\hat{a}_-^\dagger-e^{-2\imath k\hat{z}}\hat{a}_+\hat{a}_-\right)-2\imath\eta_+\hat{a}_+ \,.\end{aligned} \tag{25.47}$$

This is the lowest order *cumulant expansion*. The expectation values form a system of 10 linear first order differential equations [135] from which we can calculate the steady-state of the system.

The correlation functions and spectra are obtained directly from the CARL equation for the cavity fields (25.25) using the Wiener-Khinchin theorem (17.81) and the quantum regression theorem (17.137). With the substitutions, $t \to 0$, $\hat{B} \to 1$, $\hat{A} \to d\hat{A}_k/d\tau$, and $\xi_i(\tau)\hat{A}_i(0) \to \zeta_i\hat{A}_i(\tau)$, the quantum regression theorem can be written in the form,

$$\boxed{\frac{d}{d\tau}\langle\hat{A}_k(\tau)\rangle = \sum_i \zeta_i\langle\hat{A}_i(\tau)\rangle \qquad \Longrightarrow \qquad \frac{d}{d\tau}\langle\hat{A}_k(\tau)\hat{C}(0)\rangle = \sum_i \zeta_i\langle\hat{A}_i(\tau)\hat{C}(0)\rangle} \,. \tag{25.48}$$

Applied, for example, to the correlation function (25.47), we obtain from the CARL equation (25.25), with $\gamma_0 = 0$ and $\Delta_c = 0$,

$$\frac{d}{d\tau}\langle\hat{a}_+(\tau)\hat{a}_+(0)\rangle = (-\kappa - \imath U_0)\langle\hat{a}_+(\tau)\hat{a}_+(0)\rangle - \imath U_0 e^{-2\imath k\hat{z}}\langle\hat{a}_-(0)\hat{a}_+(0)\rangle + \eta_+\langle\hat{a}_+(0)\rangle \ . \tag{25.49}$$

Repeating this calculation for the other first-order correlations functions we obtain a system of 10 linear first order differential equations, which can be solved via Laplace transform.

25.1.7 Exercises

25.1.7.1 Ex: Origin of quantum correlations

Derive the Hamiltonian (25.2) from the JCM Hamiltonian (17.21) transforming it into the co-rotating frame.

25.1.7.2 Ex: Linear pumping of a cavity mode

Study how the Hamiltonian $\hat{H}_{pmp} = \imath\eta^*\hat{a} - \imath\eta\hat{a}^\dagger$, describing linear pumping of a cavity mode, fills the cavity with photons in the absence of dissipation (see also (15.29)).

25.1.7.3 Ex: The adiabatically approximated Hamiltonian

a. Derive the adiabatically approximated Hamiltonian (25.26) from the total Hamiltonian (25.4).
b. Derive the CARL equations (25.25) directly from the adiabatically approximated Hamiltonian.
c. Show that, in the absence of pumping, the energy stored in the light fields is conserved separately from the mechanical energy of the atom.
d. Verify momentum conservation.

25.1.7.4 Ex: Hamiltonian after adiabatic elimination of internal states for a linear cavity including counter-rotating terms

Repeat the adiabatic elimination of Sec. 25.1.4 for a linear cavity including counter-rotating terms.

25.1.7.5 Ex: Periodicity of a lattice

Assume a symmetrically pumped ring cavity in equilibrium with an atom initially at rest. What photonic states are generated in the counterpropagating light modes, when the atom is kicked by an external force imparting a sudden recoil of $\hbar k_{kck}$.

25.1.7.6 Ex: Adiabatic elimination of the cavity modes

Derive the coherent part of the equations of motion (25.36) directly from the Hamiltonian (25.4) in the absence of pumping, $\eta_\pm = 0$, and in the limit of large cavity detunings, $|\Delta_c| \gg \kappa$.

25.2 CARL: The collective atomic recoil laser

The *collective atomic recoil laser* (*CARL*) was first predicted in 1994 [101] as an atomic analog of FEL. The idea consists of a monochromatic homogeneous beam of moving two-level atoms (all atoms have the same velocity), a strong counterpropagating pump laser beam, and a weak copropagating probe beam tuned to the blue side of the resonance. The lasers form a standing light wave that moves in the same direction as the atoms. Atoms that are faster than the velocity of the standing wave are rejected by the maxima of the dipolar potential created by the standing wave and feel a repulsive force. Atoms that are slower than the standing wave velocity are pushed by the dipole potential maxima and feel an accelerating force. These forces can be interpreted as backscattering of photons from the pump wave into the probe wave. This redistribution of energy amplifies the contrast of the stationary wave, which in turn amplifies the backscattering efficiency, etc. Therefore, the CARL converts kinetic energy into coherent radiation (or more precisely, into an increase of the energy difference between probe and pump) mediated by atomic bunching. It is a self-amplifying mechanism. The CARL signature is a transient exponential amplification for the incident probe, which defines the frequency of the 'CARL laser'. The first experimental realization of CARL used a ring cavity [490].

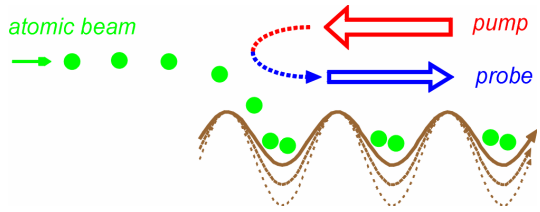

Figure 25.3: Collective atomic recoil laser.

25.2.1 Classical CARL equations for many mobile atoms

The preceding sections dealt with a single atom in a ring cavity. More interesting dynamics, however, emerge in the presence of several atoms, because their motion can be become correlated via their simultaneous interaction with the same two counter-propagating modes of the cavity, as illustrated in the following movie (watch movie). A talk on CARL can be assisted at (watch talk).

To describe experiments dealing with many atoms, we have to extend the equations of motion (25.26) to N atoms via $z \longrightarrow z_j$ and $p \longrightarrow p_j$, where $j = 1, N$,

$$\boxed{\begin{aligned} \dot{\alpha}_\pm &= (-\kappa - \imath N U_0)\alpha_\pm - \imath U_0 \sum_{j=1}^{N} e^{\mp 2\imath k z_j}\alpha_\mp + \eta_\pm \\ \dot{p}_j &= -2\imath\hbar k U_0(\alpha_+\alpha_-^* e^{2\imath k z_j} - \alpha_-\alpha_+^* e^{-2\imath k z_j}) \end{aligned}} \,. \tag{25.50}$$

with the kinetic and potential energies [9],

$$E_{kin} = \sum_j \frac{p_j^2}{2m} \quad , \quad E_{pot} = \sum_j U_0 |\alpha_+ e^{\imath k z_j} + \alpha_- e^{-\imath k z_j}|^2 \ . \tag{25.51}$$

If the atomic density distribution is homogeneous, the phases of randomly scattered photons destructively interfere and the quantity,

$$b \equiv \tfrac{1}{N} \sum_j e^{-2\imath k z_j} \ , \tag{25.52}$$

called *bunching parameter*, vanishes. That is, the impact of the scatterers on the light modes cancels out, as we will see in Exc. 25.2.5.1 for the case of two atoms. If on the other hand, atoms accumulate in the antinodes of the standing wave, it increases the contrast of it can spread more efficiently collectively by Bragg scattering. The particularity of the CARL is that during the temporal evolution the bunching process can amplify itself leading to an exponential growth of the counterpropagating mode, accompanied by an increasingly pronounced self-bunching.

In general, the equations can not be solved analytically, especially when the pump varies over time. A first approach consists in iterating them numerically,

$$\begin{aligned} \alpha_\pm(t+dt) &= \alpha_\pm(t) + dt \ [-(\kappa + \imath N U_0 - \imath \Delta_c)\alpha_\pm - \imath N U_0 b \alpha_\mp + \eta_\pm(t)] \\ z_j(t+dt) &= z_j + dt \ \tfrac{1}{m} p_j \\ p_j(t+dt) &= p_j - dt \ 2\imath\hbar k U_0 (\alpha_+ \alpha_-^* e^{2\imath k z_j} - \alpha_- \alpha_+^* e^{-2\imath k z_j}) \ . \end{aligned} \tag{25.53}$$

In Exc. 25.2.5.2 we will extend the equations (25.50) to the presence of two atomic species, and in Exc. 25.2.5.3 we will use them to describe the response of the light fields to an inertially moving atom supposing that is does not feel the CARL force.

25.2.1.1 Locking of the pump laser

In practice the resonant frequency of a cavity fluctuates due to ambient noise. Hence, it is easier, experimentally, to lock the pump laser on a cavity mode, e.g. using the Pound-Drever-Hall method. This means,

$$\alpha_+ = \frac{\eta_+}{\kappa} \ . \tag{25.54}$$

In the presence of atoms, however, the resonant frequency can be shifted due to the refractive index of the atomic cloud [264]. Moreover, the shift depends on the atomic bunching and consequently varies during the dynamics of the CARL. The way the locking circuit works, is to continuously adjust the detuning between the laser and the cavity Δ_c (defined for the empty cavity) such as to maximize the amplitude of the field $|\alpha_+|$ and, hence, the transmission of the cavity filled with atoms. The dynamics of the detuning must be incorporated by an additional equation modeling the action of locking. Now that we know the effect, which an ideal lock should have, we can

[9] Note, that there is also a radial motion of the atom coupled to the axial movement. The coupling happens, because the axial motion influences the number of intracavity photons of the radiation field which, in turn, determines the depth of the dipole potential.

apply the boundary condition (25.54) and eliminate the pump mode α_+ from the dynamics of the system. That is, the following equations are usually sufficient to describe the CARL:

$$\boxed{\begin{array}{rcl} \dot{\alpha}_- & = & (-\kappa + \imath\Delta_c - \imath U_0)\alpha_- - \imath U_0 e^{-2\imath kz}\alpha_+ + \eta_- \\ m\ddot{z} & = & 2\imath\hbar k U_0 \alpha_+ (\alpha_- e^{-2\imath kz} - \alpha_-^* e^{2\imath kz}) \end{array}} \quad . \tag{25.55}$$

The frequency offset of the cavity resonances caused by the atom, U_0, can exceed the width of the cavity κ. From equation (22.67) we know,

$$|\alpha_+(\infty)|^2 = \frac{\chi\chi^*}{(\chi^2 + U_0^2)(\chi^{*2} + U_0^2)}\eta_+^2 \ .$$

The maxima of $|\alpha_+(\infty)|^2$ as a function of Δ_c give the shifted resonances of the modes.

Example 178 (*Locking on transverse modes*): We already mentioned that as the CARL accelerates, the frequency of the light which is backscattered to the probe shifts to the red until it escapes from the resonant mode. What happens if we provide another resonant mode that can receive photons? We will show in the following calculation, that CARL simply picks up the closest mode to dump the photons. The starting point is generalized CARL equations to accommodate a second reverse mode labeled β_-,

$$\begin{aligned} \dot{\alpha}_+ &= -(\kappa - \imath\Delta_c)\alpha_+ - \imath U_0(u_+^* u_+\alpha_+ + u_+^* u_-\alpha_- + u_+^* u_\beta\beta_-) + \eta_+ \\ \dot{\alpha}_- &= -(\kappa - \imath\Delta_c)\alpha_- - \imath U_0(u_-^* u_-\alpha_- + u_-^* u_+\alpha_+ + u_-^* u_\beta\beta_-) \\ \dot{\beta}_- &= -(\kappa - \imath\Delta_\beta)\beta_- - \imath U_0(u_\beta^* u_\beta\beta_- + u_\beta^* u_+\alpha_+ + u_\beta^* u_-\alpha_-) \\ m\ddot{x} &= -U_0\nabla|\alpha_+ u_+ + \alpha_- u_- + \beta_- u_\beta|^2 \ , \end{aligned} \tag{25.56}$$

com $u_\pm = e^{\pm\imath kz}$ and $u_\beta = e^{-\imath k_\beta x}$. We obtain,

$$\begin{aligned} \dot{\alpha}_+ &= -(\kappa - \imath\Delta_c + \imath N U_0)\alpha_+ - \imath U_0 e^{-2\imath kz}\alpha_- - \imath U_1 e^{-\imath(k+k_\beta)x}\beta_- + \eta_+ \\ \dot{\alpha}_- &= -(\kappa - \imath\Delta_c + \imath N U_0)\alpha_- - \imath U_0 e^{2\imath kz}\alpha_+ - \imath U_1 e^{\imath(k-k_\beta)x}\beta_- \\ \dot{\beta}_- &= -(\kappa - \imath\Delta_\beta + \imath N U_1)\beta_- - \imath U_1 e^{\imath(k+k_\beta)x}\alpha_+ - \imath U_1 e^{-\imath(k-k_\beta)x}\beta_- \\ m\ddot{x} &= -U_0(2\imath k e^{2\imath kz}\alpha_-^*\alpha_+ - 2\imath k e^{-2\imath kz}\alpha_+^*\alpha_-) \\ &\quad - U_1(\imath(k+k_\beta)e^{\imath(k+k_\beta)x}\beta_-^*\alpha_+ - \imath(k+k_\beta)e^{-\imath(k+k_\beta)x}\alpha_+^*\beta_-) \\ &\quad - U_1(\imath(k-k_\beta)e^{\imath(k-k_\beta)x}\alpha_-^*\beta_- - \imath(k-k_\beta)e^{-\imath(k-k_\beta)x}\beta_-^*\alpha_-) \ . \end{aligned} \tag{25.57}$$

Note that $k - k_\beta \approx 0$ and $k + k_\beta \approx 2k$. The result of the simulation is displayed in Fig. 25.4.

25.2.1.2 Analytic approximations for one-sided pumping and perfect bunching

Here, we will assume for simplicity, that the atoms are perfectly bunched, $z_j = z$ and $p_j = p$, i.e. they have *zero temperature*. This means that we only need to consider a single equation of motion for the atoms. However, their coupling to the cavity modes is N times stronger, which means that we have to substitute $U_0 \longrightarrow U_N \equiv NU_0$ in the equation of motion for the cavity fields.

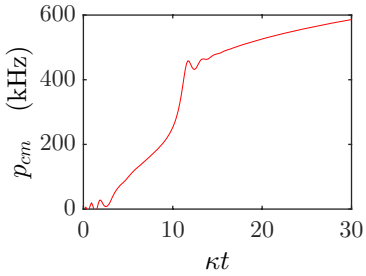

Figure 25.4: (code) The CARL locks to other modes of the cavity.

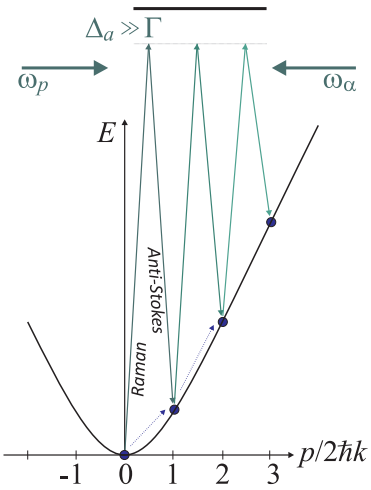

Figure 25.5: In the momentum picture the CARL acceleration process occurs as Raman-anti-Stokes processes along the free-particle dispersion relation.

When only one atom is in the cavity or when the atoms are perfectly bunched together, it is possible to derive analytical solutions. Particularly interesting is the following situation: We pump the cavity from one side. The pump is supposed to be dominant and locked to a resonance, such that we can neglect the feedback of the system on the pump, that is, we can assume, $\alpha_+ = \eta/\kappa$. Using the abbreviations $\chi \equiv \kappa + \imath U_0 - \imath\Delta_c$ and the photon recoil shift [300],

$$\omega_{\rm rec} \equiv \frac{\hbar k^2}{2m} \ , \tag{25.58}$$

the equations (25.26) then become,

$$\boxed{\begin{array}{rcl} \dot{\alpha}_- &=& -\chi\alpha_- - \imath U_N \alpha_+ e^{2\imath kz} \\ k\dot{v} &=& 4\omega_{\rm rec}\imath U_0 \alpha_+ (\alpha_- e^{-2\imath kz} - \alpha_-^* e^{2\imath kz}) \end{array}} \ . \tag{25.59}$$

We consider the stationary case (25.26). Doing the ansatz,

$$\alpha_- \equiv \beta e^{2\imath kx} \qquad \text{where} \qquad \dot{\beta} = 0 \tag{25.60}$$

we assume that the atom and the standing wave have the same velocity, that is, they move in phase. We obtain as solution,

$$\beta = \frac{-\imath U_N \alpha_+}{\kappa + 2\imath k v} \quad , \quad k\dot{v} = 8\omega_{\rm rec} U_0^2 \alpha_+^2 \frac{2\kappa}{\kappa^2 + 4k^2 v^2} \ . \tag{25.61}$$

If $\kappa \ll 2kv$, then the differential equation is approximately solved by,

$$(kv)^3 = 3\varepsilon\kappa U_0^2 \alpha_+^2 t \ . \tag{25.62}$$

This means that the CARL frequency, that is, the frequency difference between the emitted probe wave and the incident light, increases temporarily. The frequency corresponds to the double Doppler shift. As the frequency of the probe light gradually shifts away from the cavity resonance, the probe light finally stops being amplified, and the amplitude of the probe field decreases: CARL is only a transient phenomenon. In fact, the behavior described by the equation (25.61) was observed in experiments [490].

Example 179 (*Universal scaling*): Our formula describing CARL,

$$\begin{aligned} \dot{\alpha}_- &= -\frac{\imath U_0 \eta_+}{\chi} \sum\nolimits_j e^{2\imath k z_j} - \chi \alpha_- \\ k\dot{v}_j &= -4\omega_{\rm rec} \imath U_0 \eta_+ \left(\frac{\alpha_-}{\chi^*} e^{-2\imath k z_j} - \frac{\alpha_-^*}{\chi} e^{2\imath k z_j} \right) - \gamma_{\rm frc} k v_j \ , \end{aligned} \tag{25.63}$$

where $\chi = \kappa + \imath N U_0 - \imath \Delta_c$, can be rewritten in terms of a universal 'scaling' if we define,

$$\begin{aligned} \tau &= 4\omega_{\rm rec}\rho t \quad \text{and} \quad \bar{\gamma} = \frac{\gamma_{\rm frc}}{4\omega_{\rm rec}\rho} \\ \theta_j &= 2kz_j \quad \text{and} \quad P_j = \frac{2kv_j}{4\omega_{\rm rec}\rho} \\ A &= \frac{\imath|\chi|}{\chi^*\sqrt{\rho N}}\alpha_- \quad \text{and} \quad \bar{\chi} = \frac{\chi}{4\omega_{\rm rec}\rho} \ . \end{aligned} \tag{25.64}$$

We obtain,

$$\begin{aligned} \dot{A} &= \frac{1}{N}\sum\nolimits_j e^{\imath\theta_j} - \bar{\chi} A \\ \dot{\theta} &= P_j \\ \dot{P}_j &= -2(A^* e^{-\imath\theta_j} + A e^{\imath\theta_j}) - \bar{\gamma} P_j \ . \end{aligned} \tag{25.65}$$

provided that the universal scaling parameter ρ is set to,

$$\rho \equiv \left(\frac{N U_0^2 \eta_+^2}{8\omega_{\rm rec}^2 |\chi|^2} \right)^{1/3} \ . \tag{25.66}$$

The meaning of the ρ parameter can be gathered by rewriting it in terms of the number of photons of the pump $|\alpha_+|^2 = \eta_+^2/\kappa^2$ and the depth of the dipolar potential $U_d = U_0|\alpha_+|^2$,

$$\rho^3 = \frac{N}{\alpha_+^2} \frac{U_d^2}{8\omega_{\rm rec}^2} \ . \tag{25.67}$$

The ρ parameter therefore indicates the number of atoms per photon and the ratio between the depth of the dipolar trap and the photonic recoil energy.

25.2.2 Observation of CARL in ring cavities

The first observation of CARL was achieved with a cloud of 100 μK cold rubidium atoms interacting with a high finesse ring cavity [490]. In a thermal cloud the atomic motion prevents bunching, i.e. $b = 0$ so that according to Eq. (25.50) the cavity fields do not couple to the atoms. Density fluctuations that could seed CARL dynamics are rapidly washed out by thermal motion.

This problem can be circumvented by applying a robust *pre-bunching*, which can be done by subjecting the atoms to a periodic potential, e.g. via a standing wave formed by two counterpropagating cavity modes. The atoms then arrange themselves into a periodic lattice, so that the bunching parameter is initially $b \simeq 1$. If one cavity is then extinguished, a CARL dynamics can take place, until thermal motion succeeds in washing out the periodic lattice. This dynamics is illustrated in the simulation exhibited in Fig. 25.6 for the case of strontium atoms. The finite temperature of the cloud is accounted for via an initial density and momentum distribution for the atoms given by,

$$p_{0,j} = \sqrt{m k_B T}\ \zeta_j \qquad \text{and} \qquad z_{0,j} = \frac{\sqrt{2}}{k}\sqrt{\frac{k_B T}{U_0}}\ \zeta_j\ , \tag{25.68}$$

where ζ_j is a normally distributed random variable.

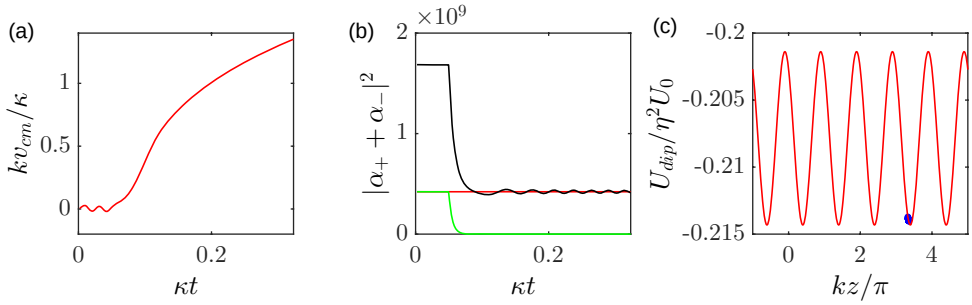

Figure 25.6: (code) Simulation for $N = 10^5$ strontium atoms at $T = 10\,\mu\text{K}$ temperature interacting via their $\Gamma = (2\pi)$ kHz narrow intercombination line at $\lambda = 689\,\text{nm}$ with a ring cavity (decay rate $\kappa = (2\pi)\ 1.7\,\text{MHz}$ and waist $w_0 = 68.4\,\mu\text{m}$). CARL dynamics is triggered by switching off one of two pump lasers whose intracavity power is $P = 1\,\text{W}$. (a) Doppler shift of the CARL-accelerated atoms, (b) interference signal between the two cavity light modes, and (c) atomic distribution in the standing wave potential.

Example 180 (*Curiosities: Atomic transport around mirrors*): Displacement of the atomic cloud in a unidirectionally pumped ring-cavity. The left and right image in Fig. 25.7 are taken for different pumping directions α. The upper cloud shows atoms trapped in the main focus of the ring-cavity. The lower traces stem from atoms transported from the focus passed the mirrors T_1 and T_2 towards the incoupling mirror located at the place where the lower traces intersect. The lower trace are imaged twice, because the imaging beam is reflected from the incoupling mirror surface, before it is sent to a photodiode.

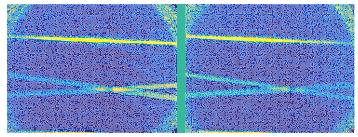

Figure 25.7: Displacement of the atomic cloud in a unidirectionally pumped ring-cavity. The left and right figures are taken for different pumping directions α. The upper cloud shows atoms trapped in the main focus of the ring-cavity. The lower traces stem from atoms transported from the focus passed the mirrors T_1 and T_2 towards the incoupling mirror located at the place where the lower traces intersect. The lower trace are imaged twice, because the imaging beam is reflected from the incoupling mirror surface, before it is sent to a photodiode.

25.2.2.1 CARL in the presence of friction forces

A feature of CARL, as it has been detected in Fig. 25.6 is, that it does not lead to a stationary state: the atoms are monotonically accelerated and the Doppler-shift of the backscattered probe light increases at the same pace. After a while, the frequency of the probe light runs out of the cavity resonance, so that the CARL dynamics starts to be suppressed. This led to a reduction of the oscillation amplitude of the interference signal observed in Fig. 25.6(b).

In order to maintain CARL strong we can think of limiting the acceleration by a friction force. How this works is illustrated in Fig. 25.8, where by subject the atoms to an optical molasses switched on at time $\kappa t = 0.3$. The friction can be incorporated into the CARl equations (25.50) via an additional force,

$$F_{\rm frc} = -\beta_{\rm frc} p \ . \tag{25.69}$$

We observe that the frequency shift of the backscattered light stabilizes at a lower value and that the oscillation amplitude of the interference signal is stronger than without molasses [843].

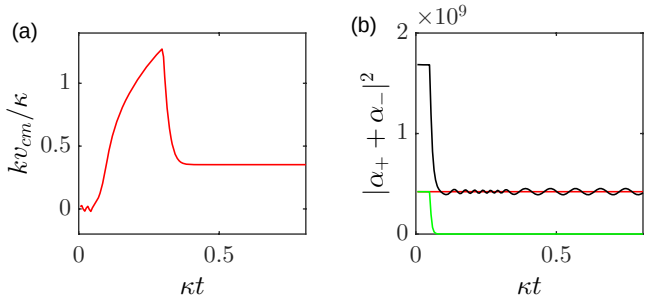

Figure 25.8: (code) Influence of an external friction force (switched on at $\kappa t = 0.3$) proportional to $\beta_{\rm frc} = 3.8 \cdot 10^6\,{\rm s}^{-1}$. Other parameters are the same as in Fig. 25.6.

Let us note that, while provide a nice intuition, the description of the impact of an optical molasses force is incomplete, because it disregards heating effects caused by random photon scattering processes. The temperature of the atomic cloud is given

by an equilibrium between friction and heating processes. The correct inclusion of optical molasses in the CARL dynamics will be studied in Sec. 25.6.1.

25.2.2.2 CARL in the presence of injected probe light

It is also interesting to study the impact of a weak injected probe light on the CARL dynamics. This light may have the same frequency as the pump light, $\eta_-/|\eta_-| = \eta_+/|\eta_+|$. This is for example the case, when light is backscattered from imperfection of the cavity mirror surfaces. Or may have a different frequency (provided the probe frequency is resonant to a cavity mode),

$$\eta_- = e^{\imath \Delta\nu t} \ . \tag{25.70}$$

The injected light fields η_+ and η_- create a standing light wave potential, in which the atoms move as being subject to an array of hurdles. The CARL force is too weak, the atoms will get stuck. We study this in Exc. 25.2.5.4. In Exc. 25.2.5.5 we study CARL dynamics for the case that the atoms are subject to an additional harmonic potential.

25.2.2.3 Impact of radiation pressure on CARL

CARL is a coherent force resulting from a coupling of only two counterpropagating modes of the cavity. As such, it can be derived from a potential. However, photons may also be scattered out of the cavity and get lost for the system. These processes give rise to an additional radiation pressure force, which has been given in Eq. (25.46),

$$F_{\rm rp} = 2\hbar k \gamma_0 (\alpha_+ \alpha_-^* - \alpha_- \alpha_+^*) \ . \tag{25.71}$$

But this force is weak when the laser is tuned far enough from the atomic resonance.

Fig. 25.9 shows a simulation of the impact of radiation pressure for the same system as in Fig. 25.6. For clarity the radiation pressure force has been exaggerated by a factor of 100.

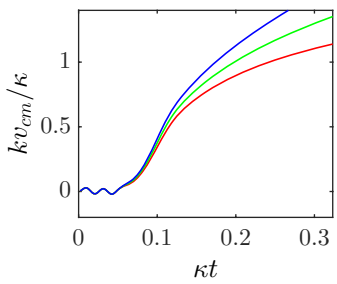

Figure 25.9: (code) Influence of radiation pressure on CARL.

25.2.3 Optical instability in ring cavities

We have until now concentrated on the regime of weak coupling, $NU_0 < 1$. If the pump laser is tuned closer to resonance, or if the number of atoms is increased, so that $NU_0 > 1$, we observe instabilities in the coupled atom-field dynamics, which critically depend on the pump intensities [615]. Imagine a sample of atoms trapped in an optical lattice formed by a symmetrically pumped ring cavity, $\eta_+ = \eta_-$. The system is stationary, the atoms are confined at the antinodes of the standing wave, the light fields are equal in strength, $\alpha_+ = \alpha_-$. At time $t = 0$ we suddenly reduce the pump rate η_- of the non-stabilized mode by only a few percent. The response of the system observed in experiment [615] is to completely break down the field α_-. The disappearance of the standing wave ejects most atoms and reduces NU_0, until the coupling gets so weak that the dynamics is essentially governed by the injected fields. The system recovers a stationary state, with much less atoms.

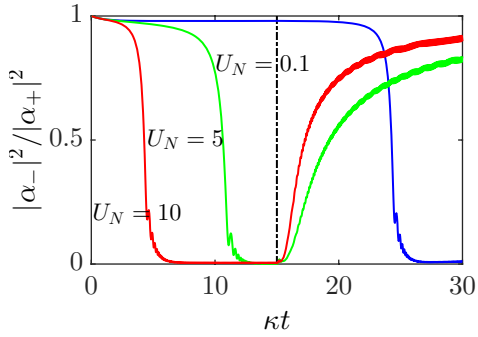

Figure 25.10: (code) Dynamics simulated with equations (25.46). At time $\kappa t = 0$ the pump rate η_- is reduced by 1%. After a certain time that depends on NU_0, the standing wave breaks down ejecting atoms from the mode volume. Here, we simulate this via an artificial linear trap loss process setting in at time $\kappa t = 15$. As a result of the diminishing NU_0 the standing wave recovers.

The physical explanation for the instability is reminiscent to the CARL behavior described in previous sections. Because atom-field coupling is strong, a small imbalance of the injected beam intensities is sufficient to displace the atoms to a location, where the light which they scatter into the reverse direction interferes destructively with the injected light. A simple argument explains, why the standing wave is attracted towards a position where it gets unstable. We treat the imbalance $\eta_+ > \eta_-$ as if it was due to a scatterer fixed in space inside the mode volume sitting on an edge of the standing wave (corresponding to a $\pi/4$ phase shift), such that it only scatters light from α_+ into α_-, but not the other way round. Whether the phase of the standing wave adjusts itself to that of pump field or such that the scatterer sits at the bottom of the potential well depends on the ratio of the coupling to the external field (given by κ) and to the scatterer (given by U_0). If U_0 is stronger, the field is pulled towards the scatterer dragging along the atoms which are free to move. The stationary situation is therefore a displacement of the standing wave and the atoms by $\lambda/4$, which is just the position where the cavity field α_- and the injected field

$\alpha_-^{(in)}$ are out of phase. The injected light is not transmitted through the cavity any more.

Note that the instability occurs in a plane wave situation, there is no need to consider the transversal motion. Furthermore, it is a single-atom effect, since we assume perfect bunching. We may therefore consider a single atom strongly coupled to the cavity and use the set of equations (25.46). In the *undepleted pump approximation* we assume $\dot{\alpha}_+ = 0$, and if the atom adiabatically follows the dynamics of the potential valley, $\ddot{x} = 0$, so that,

$$0 = -\chi\alpha_+ - \imath U_0\sqrt{\frac{\alpha_+\alpha_-^*}{\alpha_+^*\alpha_-}}\alpha_- + \eta_+ \ , \tag{25.72}$$

$$\dot{\alpha}_- = -\chi\alpha_- - \imath U_0\sqrt{\frac{\alpha_+^*\alpha_-}{\alpha_+\alpha_-^*}}\alpha_+ + \eta_- \ .$$

The first equation yields,

$$\alpha_+ = \frac{\eta_+}{\chi + \imath U_0\frac{|\alpha_-|}{|\alpha_+|}} \ , \tag{25.73}$$

$$|\alpha_+| \approx \frac{\eta_+}{\chi}\left(1 - \frac{U_0^2}{2\eta_+^2}|\alpha_-|^2\right) \ .$$

Plugging this result into the second equation and assuming the laser on resonance, $\Delta_c = NU_0$, so that we may replace χ by κ, we get,

$$\dot{\alpha}_- \approx -\kappa\alpha_- - \frac{\imath U_0\eta_+}{\kappa}\frac{\alpha_-}{|\alpha_-|} + \frac{\imath U_0^3}{2\kappa\eta_+}|\alpha_-|\alpha_- + \eta_- \ . \tag{25.74}$$

This equation describes *optical bistability*.

25.2.4 Phononic coupling of atoms mediated by a ring cavity

Phonons can be understood as vibrational excitations of quantum particles (atoms) in quantized traps. When atoms are interconnected in vibrational lattices, phonons can be transferred and shared between atoms [10]. Due to the particularity of the ring cavity of conserving the photonic momentum at each backscattering event, the photonic momentum can be understood as a phononic excitation, propagating in one dimension along the optical axis of the cavity.

We now consider a symmetrically pumped ring cavity [301]. The atoms are very cold and deep in the Lamb-Dicke regime. Using blue-detuned light the atoms will be trapped at the nodes of the standing wave, $kz_j = \pi/2 + kZ_j$, where Z_j are small displacements. Hence, we may expand,

$$e^{\mp 2\imath kz_j} \simeq -(1 \mp 2\imath kZ_j) \ . \tag{25.75}$$

With the abbreviation $\chi \equiv \kappa - \imath(\Delta_c - NU_0)$ and defining the center-of-mass of the small displacements, $Z_{cm} = \frac{1}{N}\sum_j Z_j$, the equation for the two field modes are,

$$\dot{\alpha}_\pm \simeq -\chi\alpha_\pm + \imath NU_0(\mp 2\imath kZ_{cm})\alpha_\mp + \eta \ . \tag{25.76}$$

[10] This is similar to the situation in micromasers, where several atoms can share a single photon.

Neglecting the impact of the atom on the amplitudes of the fields, we may derive the steady-state solution,

$$\alpha_\pm = \eta \frac{\chi + \imath N U_0 (1 \mp 2\imath k Z_{cm})}{\chi^2 + N^2 U_0^2} \ . \tag{25.77}$$

As shown in (25.28) the normalized field intensity can be written as,

$$\tfrac{1}{2\varepsilon_0 c E_1^2} I(z,t) = |\alpha_+|^2 + |\alpha_-|^2 + 2|\alpha_+||\alpha_-| \cos(2kz + 2\theta) \ , \tag{25.78}$$

provided the field amplitudes are expressed by,

$$\alpha_\pm = |\alpha_\pm| e^{\pm \imath\theta} \quad \text{such that} \quad \alpha_+ \alpha_-^* = |\alpha_+||\alpha_-| e^{2\imath\theta} \quad \text{and} \quad \tan 2\theta = \frac{\mathfrak{Im}\, \alpha_+ \alpha_-^*}{\mathfrak{Re}\, \alpha_+ \alpha_-^*} \ . \tag{25.79}$$

Now,

$$\begin{aligned} \tan 2\theta &= \frac{\mathfrak{Im}\, [\chi + \imath N U_0 (1 - 2\imath k Z_{cm})][\chi^* - \imath N U_0 (1 - 2\imath k Z_{cm})]}{\mathfrak{Re}\, [\chi + \imath N U_0 (1 - 2\imath k Z_{cm})][\chi^* - \imath N U_0 (1 - 2\imath k Z_{cm})]} \\ &= 4 N U_0 k Z_{cm} \frac{-\Delta_c + 2 N U_0}{-\kappa^2 - \Delta_c^2 + 4 \Delta_c N U_0 - 4 N^2 U_0^2 + 4 N^2 U_0^2 (k Z_{cm})^2} \\ &\simeq \frac{4 N U_0 (\Delta_c - 2 N U_0)}{\kappa^2 + (\Delta_c - 2 N U_0)^2} k Z_{cm} \ . \end{aligned} \tag{25.80}$$

An individual atom in this optical potential feels the dipolar force,

$$\begin{aligned} m \ddot{z}_j &= [-\hbar U_0 \partial_z I]_{z=z_j} = 4 \hbar k U_0 |\alpha_+||\alpha_-| \sin(2kz_j + 2\theta) \\ &= 4 \hbar k U_0 \eta^2 \frac{|(\chi + i N U_0)^2 - 4 N^2 U_0^2 (k Z_{cm})^2|}{|\chi^2 + N^2 U_0^2|^2} \sin\left(2kz_j + \frac{2 N U_0 (\Delta_c - 2 N U_0)}{\kappa^2 + (\Delta_c - 2 N U_0)^2} 2 k Z_{cm} \right) \\ &\simeq \frac{4 \hbar k U_0 \eta^2}{\kappa^2 + \Delta_c^2} \sin\left(2kz_j + \frac{2 N U_0 (\Delta_c - 2 N U_0)}{\kappa^2 + (\Delta_c - 2 N U_0)^2} 2 k Z_{cm} \right) \equiv \frac{m}{2k} \omega_0^2 \sin(2kz_j - 2\mu_j k Z_{cm}) \ , \end{aligned} \tag{25.81}$$

where,

$$m \omega_0^2 \equiv \frac{8 \hbar k^2 U_0 \eta^2}{\kappa^2 + 4 U_0^2} \qquad \text{and} \qquad \mu_j \equiv \frac{2 N U_0 |2 N U_0 - \Delta_c|}{\kappa^2 + (2 N U_0 - \Delta_c)^2} \ . \tag{25.82}$$

Expanding this equation around the nodes we readily obtain,

$$\boxed{k \ddot{Z}_j + \omega_0^2 \mu_j \simeq \mu_j k Z_{cm} = \frac{\mu_j}{N} \sum_j k Z_j} \ , \tag{25.83}$$

which describes the force on a single atom. Note that the harmonic force, $\omega_0^2 k Z_j$, on the atom is continuously fed by the center-of-mass force, $\omega_0^2 \mu_j k Z_{cm}$. The above equation can be rewritten as,

$$\begin{pmatrix} k\ddot{Z}_1 \\ k\dot{Z}_1 \\ k\ddot{Z}_2 \\ k\dot{Z}_2 \\ . \end{pmatrix} = \begin{pmatrix} 0 & -\omega_0^2 (1 - \frac{\mu_j}{N}) & 0 & -\omega_0^2 \frac{\mu_j}{N} & . \\ 1 & 0 & 0 & 0 & . \\ 0 & -\omega_0^2 \frac{\mu_j}{N} & 0 & -\omega_0^2 (1 - \frac{\mu_j}{N}) & . \\ 0 & 0 & 1 & 0 & . \\ . & . & . & . & . \end{pmatrix} \begin{pmatrix} k\dot{Z}_1 \\ k Z_1 \\ k\dot{Z}_2 \\ k Z_2 \\ . \end{pmatrix} \ . \tag{25.84}$$

The eigenvalues of the matrix are $e = \imath\omega_0, \imath\omega_0\sqrt{1-\mu_j}$. Therefore, we expect, in addition to the secular frequency ω_0, a second oscillation frequency,

$$\omega_{cm} = \omega_0\sqrt{1-\mu_j} \ . \tag{25.85}$$

We find splitting in the strong coupling regime, $g > \Gamma$, but we consider the weak coupling regime, $g < \Gamma$, to implement the phononic coupling.

Example 181 (*Two-coupled atoms*): Here we rewrite the field equations for two atoms in center-of-mass coordinates,

$$Z = \frac{z_1 + z_2}{2} \qquad \text{and} \qquad z = z_2 - z_1 \ ,$$

finding,

$$\dot{\alpha}_\pm = (-\kappa + \imath\Delta_c - 2\imath U_0)\alpha_\pm - 2\imath U_0\alpha_\mp e^{\mp 2\imath kZ}\cos kz + \eta \ .$$

25.2.4.1 Probing the phonon spectrum

To probe the phonon spectrum, we can measure (or simulate) the oscillation of a single atom $z_j(t)$ in the presence of several atoms. The Fourier spectrum of the oscillation should reveal the frequency components of the center-of-mass motion $Z(t)$ and the relative motion.

An experimental method for observing normal modes consists in parametrically exciting the atomic motion at a modulation frequency ω_ϕ and watch out for a resonant enhancement of the vibration amplitude near the secular frequency ω and the collective frequency ω_{cm} both defined in (25.82). In practice, the atomic vibration can be excited by an external force, for example, a Bragg spectroscopic setup as it is used for driving recoil-induced resonances (RIR),

$$\dot{p}_j = 2\imath\hbar k U_0(\alpha_+^*\alpha_- e^{-2\imath kz_j} - \alpha_+\alpha_-^* e^{2\imath kz_j}) + F_{rir}\sin\omega_\phi t \ . \tag{25.86}$$

Alternatively, we may shake the intracavity standing wave by modulating the phase of the pump field,

$$\eta_\pm(t) = \eta e^{\pm\imath\phi_0\sin\omega_\phi t} \ . \tag{25.87}$$

Fig. 25.11 shows typical resonance curves obtained by simulating the CARL equations (25.50) together with the modulation term (25.87). Being shaken for a while, the atoms suffer parametric heating visible as a noticeable increase of their kinetic energy, as seen in Fig. 25.11(a). The atomic motion, in turn, acts back on the intracavity field fields leading to a modulated photon imbalance between both.

Note, that the phase modulation frequency should not exceed the cavity decay time, $\omega_\phi < \kappa$. Otherwise, even in the absence of atoms, we expect a low-pass behavior as discussed in Sec. 15.2.2, impeding that the applied phase modulation be transformed into an efficient shaking of the phase θ of the intracavity standing wave.

25.2.5 Exercises

25.2.5.1 Ex: Anticorrelated atoms

Study the CARL equations (25.50) for the case of two fixed atoms sitting at positions $kz_1 = kz_2 - \pi$.

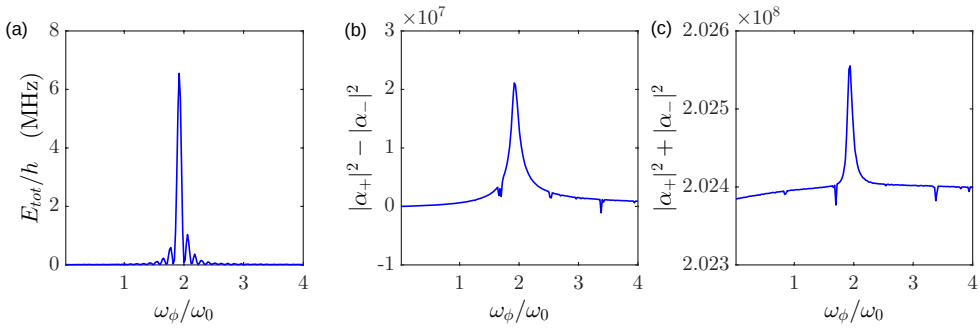

Figure 25.11: (code) Response of the cavity field to a phase modulation of the pump light. (a) Kinetic energy, (b) photon imbalance, and (c) total photon number. The simulation assumes $N = 10^6$ strontium atoms initially at $T = 1\,\mu\text{K}$ driven on the $\lambda = 689\,\text{nm}$ line and $\kappa/2\pi = 3.4\,\text{MHz}$, $\Delta_c = 2U_0$, $\eta = 10^4\kappa$, $NU_0/\kappa = -.02$, $\phi_0 = 0.01$. The calculated secular frequencies are $\omega_0 = 0.35\kappa$ and $\omega_0\sqrt{1-\mu_N} = 0.32\kappa$.

25.2.5.2 Ex: Coupled motion of Rb and Cs atoms in a ring-cavity

Find out by simulation of the classical CARL equation, whether the motion of a Rb atom and a Cs atom can be coupled to the same mode of a ring cavity.

25.2.5.3 Ex: Inertially moving atom in a ring-cavity

Illustrate by simulation of the classical CARL equation, how an inertially moving single atom pushes the wave formed by two counterpropagating modes of a ring cavity.

25.2.5.4 Ex: CARL in a harmonic potential

Extend the CARL dynamics by an additional harmonic potential for the atoms and study the steady state gain as a function of cavity detuning Δ_c.

25.2.5.5 Ex: Impact of potential barriers on CARL

Illustrate by simulation of the classical CARL equations how (a) mirror backscattering and (b) an external harmonic trapping potential influence the dynamics of an atom interacting with two counterpropagating modes of a ring cavity.

25.2.5.6 Ex: CARL without cavity

Discuss whether CARL can be observed without a ring-cavity.

25.2.5.7 Ex: Cavity cooling in a ring cavity

Study cavity cooling in a ring cavity as a function of (a) friction and (b) detuning.

25.2.5.8 Ex: Motion of atoms in a ring-cavity including internal states

Motion of atoms in a ring-cavity, including internal states.

25.3 Phenomena related to CARL

The *collective atomic recoil laser* (CARL) unifies the principles of the FEL and LWI. Assume two-level atoms in their ground state moving against the pump beam $\mathbf{k}_2$. An (at first) weak probe beam k_1 which is blue detuned with respect to $\mathbf{k}_2$ builds a together with $\mathbf{k}_2$ a standing wave fraction moving in direction $\mathbf{v}$. This fraction gives rise to a moving dipole potential $V(\mathbf{r})$ and a light force on the atoms. If the moving standing wave is slower than the atoms (and the light frequency detuning from the atomic resonance is suitable), the atoms fall into the potential valleys by rescattering photons from the pump into the probe wave. This way they amplify the probe (they push the ponderomotive wave like the FEL), deepen the light potential valleys, are therefore further focused, etc.. We get a self-amplifying avalanche and feedback. In this process, the kinetic energy of the atoms is transformed into laser light. Or to resume: Collective recoil with self-bundeling produced by cooperative Compton-scattering generates coherent laser light [101].

The following notes first discuss the basic equations of motion in the limit of very far detuning, where the internal dynamics can be adiabatically eliminated. Then we turn our attention to some characteristic features of CARL.

25.3.1 Recoil-induced resonances

The *recoil-induced resonances* (RIR) can be explained in two complementary pictures [181]. In the Raman picture, an atomic transition stimulates Raman transitions between momentum states of the free atom without influencing the atomic excitation (the atom remains in a dark state) $\rho_{\text{atom}} \otimes |\mathbf{p}\rangle\langle\mathbf{p} + 2\hbar\mathbf{k}|$. Absorption $\Delta > 0$ or amplification $\Delta > 0$ of the probe field $\mathbf{k}_s$ by the pump field $\mathbf{k}_p$ is a result of the population imbalance. However, it is not an excitation imbalance (compare LWI) $\rho_{\text{atom}} \otimes |\mathbf{p} + 2\hbar\mathbf{k}\rangle\langle\mathbf{p} + 2\hbar\mathbf{k}| - \rho_{\text{atom}} \otimes |\mathbf{p}\rangle\langle\mathbf{p}|$. In the Rayleigh picture the RIRs are an effect of coherent backward *Bragg scattering* of the probe wave at the phase-lag between the induced light-shift grating and the atomic density grating resulting from the periodic optical potential.

25.3.1.1 RIR-spectroscopy

Two laser beams 1 and 2 having each two different frequencies $\omega - \Delta\omega/2$ and $\omega + \Delta\omega/2$ are irradiated from two different directions enclosing a small angle θ into the atomic trap,

$$\begin{aligned} \mathcal{E}(\mathbf{r}, t) &= \mathcal{E}_1 + \mathcal{E}_2 \\ &= \mathcal{E}^{(0)} \left[\cos\left(\mathbf{k}_1 \cdot \mathbf{r} - (\omega - \tfrac{1}{2}\Delta\omega)t\right) + \cos(\mathbf{k}_2 \cdot \mathbf{r} - \left(\omega + \tfrac{1}{2}\Delta\omega\right)t)\right] \\ &\approx 2\mathcal{E}^{(0)} \cos\left(\mathbf{K} \cdot \mathbf{r} - \omega t\right) \cos\left(\tfrac{1}{2}\mathbf{q} \cdot \mathbf{r} - \tfrac{1}{2}\Delta\omega t\right) , \end{aligned} \tag{25.88}$$

where $\mathbf{q} \equiv \mathbf{k}_2 - \mathbf{k}_1$ and $\mathbf{k} \equiv \frac{1}{2}(\mathbf{k}_2 + \mathbf{k}_1)$. The cycle-averaged intensities are $I_i(t) = 2\varepsilon_0 c|\mathcal{E}_i|^2 = 4\varepsilon_0 c\mathcal{E}^{(0)} \cos\left(\frac{1}{2}\mathbf{q} \cdot \mathbf{r} - \frac{1}{2}\Delta\omega t\right)$. Atoms coherently interacting with the light

fields (which are tuned far from any atomic resonance) can redistribute the photons between the optical modes in a *nearly-degenerate* four-wave mixing process (4WM) thus modifying the amplitudes $\mathcal{E}_i^{(0)}$ so that a signal occurs.

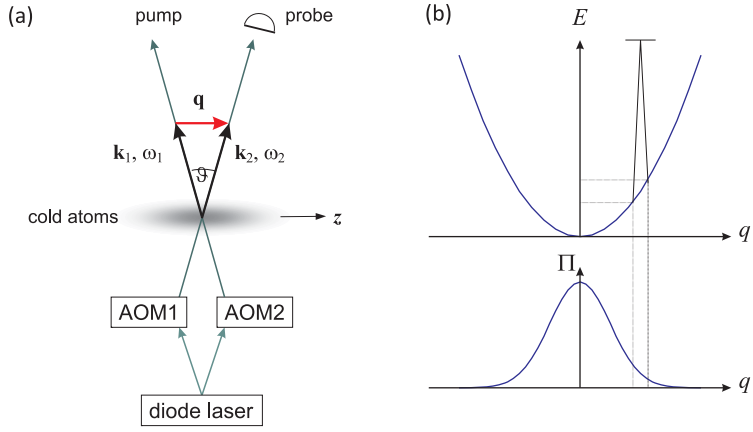

Figure 25.12: Principle scheme for RIR spectroscopy.

From symmetry considerations, it is easy to see that a homogeneous density distribution (along $\mathbf{q}$) of the motionless atoms does not give rise to a signal, neither. So let us assume that the atoms be bunched inside an optical grating according to some periodic distribution $n(z) = n_0 \sin^2 k_\lambda z$, but disregard their kinetics. The signals then generalize to,

$$\begin{aligned}\mathcal{E}_1(z,t) &= \mathcal{E}_1 + \beta n(z)\chi^{(3)}(\mathcal{E}_1+\mathcal{E}_2)\mathcal{E}_1\mathcal{E}_2\mathcal{E}_1 + \beta n(z)\chi^{(3)}(\mathcal{E}_1+\mathcal{E}_2)\mathcal{E}_1\mathcal{E}_2\mathcal{E}_1 \\ &= \mathcal{E}_1 + \beta n(z)\chi^{(3)}\left(2\mathcal{E}^{(0)}\cos\left(\tfrac{1}{2}qz - \tfrac{1}{2}\Delta\omega t\right)\right)\mathcal{E}_1\mathcal{E}_2\mathcal{E}_1\end{aligned} \tag{25.89}$$

and analogous for $\mathcal{E}_2(z,t)$. Or following Lambert-Beer [485],

$$\begin{aligned}I_1(x,z,t) &= |\mathcal{E}_1|^2 \exp\left(2\imath\frac{\pi}{\lambda}\int \chi^{(3)}\left(2E^{(0)}\cos\left(\tfrac{1}{2}qz - \tfrac{1}{2}\Delta\omega t\right)\right)dy\right) \\ &= |\mathcal{E}_1|^2 \exp\left(2\imath\frac{\pi}{\lambda}\int n(x,y,z)...dy\right) \\ &= |\mathcal{E}_1|^2 \exp\left(2\imath\frac{\pi}{\lambda}n_0\sin^2 k_\lambda z\int ...dy\right) \\ I_1(t) &= \int I_1(x,z,t)dxdz\ .\end{aligned} \tag{25.90}$$

Regarding the momentum transfer, the 4WM process can be interpreted as Bragg scattering af the atoms at one of the two counterpropagating standing waves. We develop the theory if Bragg scattering in Sec. 29.2.

25.3.1.2 Temperature measurements via RIR

Temperature measurement are usually carried out by the time-of-flight method followed by absorption imaging. Alternatively, one can perform spectroscopy of RIR

resonances. In the latter case, we detect intensity variations in a probe laser beam, i.e. the polarisation of the sample under the influence of *all* irradiated laser beams. We have seen that $\alpha \propto \mathfrak{Im}\,\chi \propto \mathfrak{Im}\,\mathcal{P} \propto \mathfrak{Im}\,\rho_{12}$. It is thus sufficient to calculate the atomic coherences, if necessary including the motional states of the atoms. Calculated by [353]

$$W(t) = \frac{\pi}{2}\frac{\Omega_1\Omega_2}{\Delta}\sqrt{\frac{mv}{k_{\mathrm{B}}T}}\left[\frac{\partial}{\partial v}e^{-mv^2/2k_{\mathrm{B}}T}\right]_{v=\Delta\omega(t)/q} . \tag{25.91}$$

25.3.1.3 RIR-spectroscopy on trapped atoms

In the case of free particles, the Raman beams interact for every detuning with a different velocity class of atoms. The atoms are almost not disturbed. In the case of trapped atoms, a coherence can be excited, and since the atoms periodically change their velocity, be read out or reexcited at a later time. The same atom can thus interact with the Raman beams at different times/detunings. If the trap is a standing wave, the situation is complicated by the fact that there are two overlapping gratings: The standing wave and the Raman grating. However, if the trap is much deeper than the Raman grating the atoms can be considered as localized.

The signature of atomic oscillation is a modulation in the RIR signal with the periodicity of the secular frequency [484, 678].

Let us consider a standing-wave dipole-trap with $\omega_z = 2\pi \times 700\,\mathrm{kHz}$, $\omega_r = 2\pi \times 1\,\mathrm{kHz}$ and $U_{dip} = h \times 30\,\mathrm{MHz} \;= 4000 \times 2\varepsilon = 45\omega_z = 2100\omega_z$. The $100\,\mu\mathrm{K}$ cold atoms are therefore deep inside at the bottom of trap. This implies that the atomic energy levels are sharp and equally distant, and that the transitions are degenerate upon coupling by Raman-beams. If we apply a scan of $\pm 2\pi \times 300\,\mathrm{kHz}$, we will not excite the longitudinal motion. But the radial motion can be excited. As seen earlier the absorption signal is $\alpha \propto \mathfrak{Im}\,\rho_{12}$. What happens to the coherence, if the radiation is swept across a resonance depends on the scanning speed. If the scan is slow, we expect $\alpha \propto \mathfrak{Im}\,\rho_{12}(\infty)$. We should be able to resolve the resonances [353, 355, 354] as peaks at $\pm\omega_r, \pm 2\omega_r, \ldots$ In contrast, if the scan is fast, as long as Δ_c is far from resonance, the population of the excited level ρ_{22} is just too small and nothing happens. When Δ_c passes through 0, the coherence ρ_{12} is excited, and can now be driven by the laser even when Δ_c is tuned far away. The coherence precesses faster and faster.

Let us compare to the situation of a laser swept across an electric dipole resonance. In analogy to the cavity response in reflection to a laser scanned across an eigenfrequency, we might expect a ringing coming from interference of the radiating electric dipole (which has been induced while the laser was close to resonance) with the original laser frequency. The radiated electric field is proportional to the excited state population. If we allow for a change of the input field, for example $\Delta_c(t)$, the Bloch-equations must be numerically integrated,

$$\rho(t + dt) = \rho(t) + dt\; M\rho(t) \; . \tag{25.92}$$

It is already clear that we should expect a ringing with exactly the time-dependent frequency $\Delta_c(t)$. Fig. 25.13 shows

This simple mathematical model only assumes a resonance with a given width and a frequency-scanned oscillator. The physical nature of the resonance and the level splitting are not specified and the formalism should be applicable to a variety of

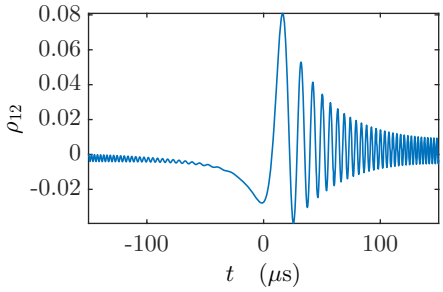

Figure 25.13: (code) Time-evolution of the atomic coherence as the driving laser frequency is swept across resonance. The parameters are $\Gamma = 2\pi \times 8\,\mathrm{kHz}$, $\Omega = 0.2\Gamma$, $\Delta = -50\Gamma..50\Gamma$ and $t = -150..150\,\mu\mathrm{s}$.

situations. A ringing is, in fact, observed for RIR scans, if the scanning speed is too fast, in particular for atoms trapped in optical lattices. Ringing can also be generated in classical harmonic oscillators and laser-driven two-level systems as we will see in Exc. 29.5.4.1.

25.3.1.4 RIR versus CARL

The dynamics is characterized by backaction of the atomic motion onto the cavity field. In this respect there is a connection to RIR resonances in the limit investigated by [485]. While normal RIR is the action of the atomic motion on light fields, they demonstrate that in the same time the Raman-lattice influences the atomic motion. The coherence is limited by the time the photon spends in the sample (similar to the limitation of superradiant Rayleigh scattering, without photonic recycling by a ring-cavity). Real backaction in the sense of coherent interdependence of the photonic and the kinetic degrees of freedom requires recycling of the photons.

25.3.2 FEL: the free electron laser

Normal lasers work by an inversion in the internal degrees of freedom, that is, bound electrons are excited to energetically higher orbitals, from where they can decay by emitting monochromatic light of well-defined frequency. Because, the *free electron laser* (*FEL*) works with beams of *free* electrons, they are tunable over wide frequency ranges. They have much higher efficiencies above 65%.

The principle is the following: Relativistic electrons are guided through an *undulator*, which is a device producing a magnetic field with periodically alternating polarization. Here, the electrons are subjected to a Lorentz force, $\mathbf{F} = -e\mathbf{v} \times \mathbf{B}$, forcing the electrons to oscillate with the periodicity of the undulator field. This corresponds to a dipole moment interacting with the incident light field. The transverse velocity of the electrons within the magnetic field of an incident light produces a Lorentz force in the axial direction called *ponderomotive force*. This force accelerates the electrons when they are a bit slower than the ponderomotive wave. Otherwise the electrons are decelerated. In the second case, the energy of the electrons is transmitted to the light field, which leads to a *bunching* of the atoms. Because it is a parametric

process, there is a continuous energy flow between the field and the motion of the e^- (analogous to parametric Raman cooling). Thus, the FEL converts the kinetic energy of the electron beam into laser radiation. The inversion in a FEL can be interpreted as a relative displacement of the probability distributions for absorption and emission of photons in momentum space,

$$W_{abs}(\Delta) = \text{sinc}^2 \tfrac{1}{2}(\Delta + \varepsilon/2) \qquad (25.93)$$
$$W_{abs}(\Delta) = \text{sinc}^2 \tfrac{1}{2}(\Delta - \varepsilon/2) \ ,$$

where $\varepsilon = \hbar k^2/2m_e$. The gain is a convolution of the difference of the above distribution with the momentum distribution of the electrons [744].

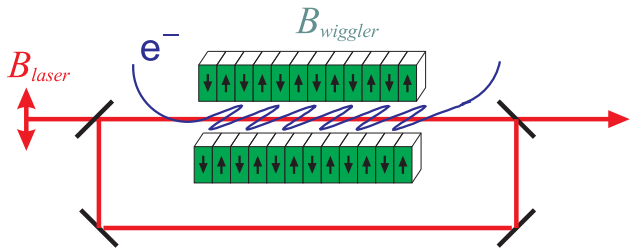

Figure 25.14: Free electron laser.

There various kinds of FELs. In stimulated Compton FELs, described by the shown Feyman graphs, the electrons are scattered by virtual (momentum transfer without energy transfer) photons of the wiggler. In Bremsstrahlungs FEL, the electrons are scattered at a static field. Virtual photons of the static field are scattered at the electrons, who then emit Bremsstrahlung an change their propagation direction. In Raman FELs very dense electron beams produce charge density oscillations, which provides an additional effect. Free Electron Lasers already have a wide range of application ranging from biology and medicine to lithography and material science.

25.3.3 CARL in an ion storage ring

Bonifacio *et al.* [102] suggested to study collective atomic recoil lasing (CARL) with relativistic atoms. They found that using very fast atoms it should, in principle, be possible to get large CARL frequency shifts and much higher power enhancement factors than observed in free-electron lasers (FEL). Relativistic atomic velocities can be achieved in heavy ion accelerators such as the GSI heavy ion accelerator in Darmstadt and TSR ion storage ring in Heidelberg. Therefore the question arises, if CARL could be an alternative way to produce very energetic and intense UV radiation in concurrence to the FEL. In fact, CARL-based systems may prove more powerful and versatile as their electronic counterparts: Cooling techniques based on electron beams or on hybrid optical-radiofrequency friction forces are able to cool the ionic beams down to mK temperatures.

The CARL which has been predicted ten years ago by Bonifacio *et al.* [101], has recently been observed with cold atoms stored in a high-finesse ring cavity [490, 843]. This proof of principle, now may motivate a deeper study of the figure of merit of a

relativistic CARL. This short note, however, shows that a relativistic CARL is still, in my opinion, far from being realizable.

25.3.4 Matter wave superradiance

There is a close relationship between CARL and the phenomenon of *matter wave superradiance* (or *superradiant Rayleigh scattering*) [100, 719], which will be discussed in the following sections.

In 1999 the group of W. Ketterle at the MIT made a surprising observation, when it illuminated an elongated Bose-Einstein condensate with a short linearly polarized laser pulse traversing the condensate perpendicularly to the long axis [416]. Instead of producing radiation with a dipole pattern, as we might expect for a polarized atomic cloud undergoing Rayleigh scattering, they observed emission of directional light bursts along the symmetry axis of the condensate. They also observed that some of the atoms were accelerated at angles of 45°. And these atoms could emit other generations of atoms at angles of 45°.

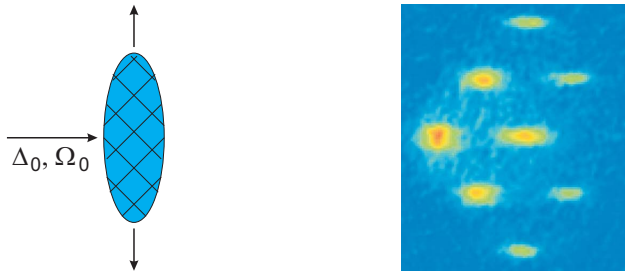

Figure 25.15: (code) Flight-of-time measurement of the atomic momentum distribution after matter wave superradiance.

The phenomenon was explained as follows. Let us imagine a first photon scattered by an atom into the direction of the long axis of the condensate. This atom will be accelerated by the photonic recoil in a direction of 135° with respect to the direction of the photon, and it will interfere with the rest of the condensate thus generating a standing matter wave of oriented in such a way, that the following photons are scattered into the same direction as the first one via Bragg scattering. This reinforces the contrast of the matter wave, etc.. We obtain an exponential gain of photons in the mode defined by the first scattered photon, as well as of the mode receiving the scattered matter wave. As the path of the gain is longer along the long axis of the condensate, this mode is favored. That is, the condensate can be considered as a cavity embracing the solid angle $\Omega_{\rm sol}$.

The Rayleigh scattering rate for a single atom is,

$$R_1 = \sin^2\theta\sigma(\Delta_a)\frac{I}{\hbar\omega}\frac{3\Omega_{\rm sol}}{8\pi}\ , \tag{25.94}$$

where $\theta$is the angle between the polarization of the incident laser (intensity I) and the direction into which the light is scattered. The cross-section is $\sigma(\Delta_a) = \sigma_0\frac{\Gamma^2}{4\Delta^2+2\Omega^2+\Gamma^2}$, where $\sigma_0 = 3\frac{\lambda^2}{2\pi}$. Now, for the set of atoms, the superradiant scattering rate is not

only amplified by the number of condensed atoms, N, but also by the number of atoms, N_r, already being in the mode receiving scattered atoms,

$$R_{sr} = R_1 N \frac{N_r + 1}{2} \ . \tag{25.95}$$

This is the *superradiance matter wave*.

25.3.5 Exercises

25.3.5.1 Ex: Good and bad cavity regime

What are the characteristics distinguishing the good from the bad cavity limit.

25.3.5.2 Ex: Ringing in resonant systems

In this exercise we study ringing in (a) an excited classical harmonic oscillator and (b) in a laser-driven two-level system.

25.4 Quantization of the atomic motion in cavities

At the beginning of this chapter we set up the complete Hamiltonian of the coupled atom-cavity system. Then tracing over dissipative degrees of freedom, we derived the master equation or derived the Heisenberg equations for the operators appearing in the remaining Hamiltonian quantum mechanically. But then for CARL we restricted to a classical treatment of the motion, as well as of the cavity modes.

Resuming the discussion started in Sec. 25.1.5 we will, in the remaining sections of this chapter, analyze effects due to the *quantization* of degrees of freedom represented by operators. The present section will (i) on a quantum description of the motion (with and without adiabatic elimination of the internal atomic dynamics and (ii) on issues arising from the presence of many atoms.

25.4.1 Quantum description of the motion

Concretely, let us analyze again the situation of a single atom interacting with a ring cavity. We assume validity of the adiabatic elimination of the internal atomic excitation and want to treat the light fields as classical. In contrast, the atomic motion is considered as quantum:

$$|\psi\rangle = |z\rangle_{\rm motion} \otimes \cancelto{\text{classical}}{|\alpha_+\rangle \otimes |\alpha_-\rangle} \otimes \cancelto{\text{adiab.elim.}}{|i\rangle_{\rm electron}} \to |z\rangle \ . \tag{25.96}$$

Since the motion, being the only quantum degree of freedom, is not subject to dissipation, we may use the Schrödinger equation in addition to Heisenberg equations for the light fields. Then, following the procedure outlined in Sec. 25.1.5, with z being the only quantum number, we find that the system is completely described by the dynamics of the expansion coefficients,

$$\begin{aligned} \imath\hbar \frac{d}{dt} \langle z|\psi(t)\rangle &= \langle z|\hat{H}|\psi(t)\rangle \\ \dot{\alpha}_\pm &= \langle z|\tfrac{\imath}{\hbar}[\hat{H}, \hat{a}_\pm] - \kappa \hat{a}_\pm|z\rangle \ . \end{aligned} \tag{25.97}$$

Plugging in the Hamiltonian (25.26), we obtain the Schrödinger equation for the particle's motional wavefunction [11],

$$\imath\hbar\frac{d}{dt}\langle z|\psi(t)\rangle = \frac{p^2}{2m}\langle z|\psi(t)\rangle + U_0\langle z|\hat{a}_+^\dagger\hat{a}_- e^{-2\imath k\hat{z}} + \hat{a}_+\hat{a}_-^\dagger e^{2\imath k\hat{z}}|\psi(t)\rangle \ , \tag{25.98}$$

and the Heisenberg equations for the light fields,

$$\begin{aligned}\dot{\alpha}_\pm &= \langle z|(-\kappa+\imath\Delta_c-\imath U_0)\hat{a}_\pm + \imath U_0 e^{\mp 2\imath k\hat{z}}\hat{a}_\mp + \eta_\pm|z\rangle \\ &= (-\kappa+\imath\Delta_c-\imath U_0)\alpha_\pm + \imath U_0\alpha_\mp\langle z|\int dz|\psi(t)\rangle\langle\psi(t)|e^{\mp 2\imath k\hat{z}}|z\rangle + \eta_\pm \\ &= (-\kappa+\imath\Delta_c-\imath U_0)\alpha_\pm + \imath U_0\alpha_\mp\int dz|\psi(z,t)|^2 e^{\mp 2\imath kz} + \eta_\pm \ .\end{aligned} \tag{25.99}$$

In summary,

$$\boxed{\begin{aligned}\dot{\psi}(z) &= \frac{\imath\hbar}{2m}\frac{d^2}{dz^2}\psi(z) - \imath U_0\left(\alpha_+^\dagger\alpha_- e^{-2\imath kz} + \alpha_+\alpha_-{}^\dagger e^{2\imath kz}\right)\psi(z) \\ \dot{\alpha}_\pm &= (-\kappa+\imath\Delta_c-\imath U_0)\alpha_\pm + \imath U_0\alpha_\mp\int dz|\psi(z)|^2 e^{\mp 2\imath kz} + \eta_\pm\end{aligned}} \ . \tag{25.100}$$

These are the new CARL equations that should be used in cases when the particle is *slower than the recoil velocity*, in which its motion must be described as a propagating matter wave. Note, that under this form, the equations can easily be generalized to apply to macroscopic wavefunctions such as a Bose-Einstein condensate.

The expectation value of the particle's position is then calculated via,

$$\begin{aligned}z(t) &= \langle\psi(0)|\hat{z}(t)|\psi(0)\rangle = \langle\psi(0)e^{-\imath\hat{H}t}|\hat{z}|e^{\imath\hat{H}t}\psi(0)\rangle \\ &= \langle\psi(t)|\hat{z}|\psi(t)\rangle = \int\langle\psi(t)|z\rangle\langle z|\hat{z}|z'\rangle\langle z'|\psi(t)\rangle dzdz' = \int z|\psi(t,z)|^2 dz \ .\end{aligned} \tag{25.101}$$

We can verify that the expectation value of the particle's position satisfies the classical equation of motion,

$$\begin{aligned}m\ddot{z} &= \langle\psi(t)|m\ddot{\hat{z}}|\psi(t)\rangle = 2\imath\hbar kU_0\left(\hat{a}_+^\dagger\hat{a}_-\langle\psi(t)|e^{-2\imath k\hat{z}}|\psi(t)\rangle - \hat{a}_+\hat{a}_-^\dagger\langle\psi(t)|e^{2\imath k\hat{z}}|\psi(t)\rangle\right) \\ &= 2\imath\hbar kU_0\left(\hat{a}_+^\dagger\hat{a}_- e^{-2\imath k\langle\psi(t)|\hat{z}|\psi(t)\rangle} - \hat{a}_+\hat{a}_-^\dagger e^{2\imath k\langle\psi(t)|\hat{z}|\psi(t)\rangle}\right) \\ &= 2\imath\hbar kU_0\left(\hat{a}_+^\dagger\hat{a}_- e^{-2\imath kz} - \hat{a}_+\hat{a}_-^\dagger e^{2\imath kz}\right) \ .\end{aligned} \tag{25.102}$$

25.4.1.1 About the origin of quantized motion

The quantization of the light field into photons is, as discussed in Chp. 17, an intrinsic property of light. In contrast, the quantization of atomic motion is less obvious, because the atoms are not confined in a trapping potential. The reason for it lies in

[11] Terms of the Hamiltonian (25.26) which do not depend on z or p have been ignored, as they can be removed form the Schrödinger equation by a simple unitary transformation. Note that this can be done even though these terms depend on the field amplitudes $\alpha_\pm$.

the monochromaticity of the driving laser fields and the one-dimensional geometry of the system, which allow us to write the recoil operator (1.294) or (2.143) as,

$$\boxed{e^{2\imath k\hat{z}} = \int |p + 2\hbar k\rangle\langle p| dp} \ . \tag{25.103}$$

Inserting it into the interaction part of the CARL Hamiltonian,

$$\hat{H}_{int} = U_0(e^{-2\imath k\hat{z}}\hat{a}_+^\dagger\hat{a}_- + e^{2\imath k\hat{z}}\hat{a}_+\hat{a}_-^\dagger) \ , \tag{25.104}$$

the Schrödinger equation for the expanded wavefunction

$$|\psi\rangle = \int c(p)|p\rangle dp \tag{25.105}$$

yields,

$$\begin{aligned} \imath\hbar\frac{d}{dt}\langle p|\psi\rangle &= U_0\hat{a}_+^\dagger\hat{a}_-\langle p|e^{-2\imath k\hat{z}}|\psi\rangle + U_0\hat{a}_+\hat{a}_-^\dagger\langle p|e^{2\imath k\hat{z}}|\psi\rangle \\ = \imath\hbar\frac{d}{dt}c(p) &= U_0[\hat{a}_+^\dagger\hat{a}_-c(p+2\hbar k) + \hat{a}_+\hat{a}_-^\dagger c(p-2\hbar k)] \ . \end{aligned} \tag{25.106}$$

That is, if the initial momentum distribution is narrow, $\Delta p \ll 2\hbar k$, and if CARL-induced recoil due to backscattering of photons between counterpropagating modes is the only force acting on the atoms, the momentum of the atoms can only adopt discrete values in units of $2\hbar k$, *as if the atomic velocity were quantized.* That is, the quantization of the field is, in some way, imprinted on the distribution of the atomic moment, so that we may as well use a discrete notation,

$$|\psi\rangle = \sum_\nu c_\nu|\nu\rangle \ , \tag{25.107}$$

such that [12],

$$\imath\hbar\frac{d}{dt}c_\nu = U_0\hat{a}_+^\dagger\hat{a}_-c_{\nu+1} + U_0\hat{a}_+\hat{a}_-^\dagger c_{\nu-1} \ . \tag{25.108}$$

Example 182 (*Analogy to the Bose-Hubbard Hamiltonian*): Interestingly the CARL Hamiltonian with quantized motion (25.104) has, in momentum space, a similar shape as the 1D Bose-Hubbard Hamiltonian in position space,

$$\begin{aligned} \hat{H} &= \sum_\nu \hbar\omega_{\rm rec}\nu^2 + U_0\sum_\nu\left(|\nu-1\rangle\langle\nu|\hat{a}_+^\dagger\hat{a}_- + |\nu-1\rangle\langle\nu|\hat{a}_+\hat{a}_-^\dagger\right) \\ &= \hbar\omega_{\rm rec}\sum_\nu\nu^2 + U_0\hat{a}_+^\dagger\hat{a}_-\sum_\nu\hat{A}_{\nu-1}^\dagger\hat{A}_\nu + U_0\hat{a}_+\hat{a}_-^\dagger\sum_\nu\hat{A}_{\nu+1}^\dagger\hat{A}_\nu \ . \end{aligned}$$

[12] Note that, instead of expanding the state $|\psi\rangle$, we could expand the motional wavefunction into plane waves,

$$\langle z|\tilde{\psi}\rangle = \tilde{\psi}(z) = \tfrac{1}{\sqrt{2\pi}}\sum_n c_n(t)e^{2\imath nkz} \qquad \text{normalized as} \qquad \int dz|\tilde{\psi}(z)|^2 = 1 = \sum_n |c_n(t)|^2 \ .$$

Insertion of this expansion into the quantized CARL equations (25.100) yields the same results.

Now, it is important to understand that the statement that *photonic recoil is quantized does not mean that the dipolar optical force can only be transmitted in units of* $2\hbar k$, as if the force needed to accumulate a certain amount of energy before it makes a sudden transition to a different momentum state. Rather, the probability to find an initially resting atom subject to a force in the momentum state $2\hbar k$ gradually increases with time. The atom gradually evolves into a coherent superposition of states $|0\rangle + |2\hbar k\rangle + |4\hbar k\rangle + ..$, and only when we *measure* the momentum distribution will it have to decide in which state it ended up. The expectation value of the center-of-mass momentum linearly, as long as the force is constant. A slide show on the quantized CARL can be viewed at (watch talk).

25.4.2 Discretization of the momentum states

We will now assume that, for the physical reasons described above, the motional state of the atom can only exist with momenta corresponding to multiples of twice the photonic recoil.

25.4.2.1 Schrödinger equation approach

We basically repeat the treatment of Sec. 25.4.1, but now expanding the motion on a discrete basis of momenta labeled by an integer number ν,

$$|\psi\rangle = |\nu\rangle_{\rm motion} \otimes \cancelto{\text{classical}}{|\alpha_+\rangle \otimes |\alpha_-\rangle} \otimes \cancelto{\text{adiab.elim.}}{|i\rangle_{\rm electron}} \to |\nu\rangle \ . \tag{25.109}$$

Applying the recipe detailed at the beginning of Sec. 25.4, we write down the same Schrödinger equation as in (25.98) [13], but now projecting on $\langle\nu|$ rather than on $\langle z|$ and inserting the expansion (25.107) and,

$$e^{2\imath k\hat{z}} = \sum_\nu |\nu+1\rangle\langle\nu| \qquad \text{and} \qquad \hat{p} = \sum_\nu \nu 2\hbar k|\nu\rangle\langle\nu| \ . \tag{25.110}$$

We get,

$$\langle\nu|\imath\hbar\frac{d}{dt}\sum_{\nu''} c_{\nu''}|\nu''\rangle = \langle\nu|\sum_{\nu'}\frac{(\nu' 2\hbar k)^2}{2m}|\nu'\rangle\langle\nu'| \tag{25.111}$$
$$+ U_0\left(\sum_{\nu'}|\nu'-1\rangle\langle\nu'|\hat{a}_+^\dagger\hat{a}_- + \sum_{\nu'}|\nu'+1\rangle\langle\nu'|\hat{a}_+\hat{a}_-^\dagger\right) \ .$$

And from the Heisenberg equation (25.15) for light modes,

$$\langle\psi|\dot{\hat{a}}_\pm|\psi\rangle = \langle\psi|(-\kappa+\imath\Delta_c-\imath U_0)\hat{a}_\pm - \imath U_0 e^{\mp\imath 2k\hat{z}}\hat{a}_\mp + \eta_\pm|\psi\rangle \ , \tag{25.112}$$

we get,

$$\sum_{\nu',\nu''}\langle\nu'|c_\nu^*\dot{\hat{a}}_\pm c_{\nu''}|\nu''\rangle = \sum_{\nu,\nu',\nu''}\langle\nu'|c_{\nu'}^*\left[(-\kappa+\imath\Delta_c-\imath U_0)\hat{a}_\pm - \imath U_0|\nu\mp 1\rangle\langle\nu|\hat{a}_\mp + \eta_\pm\right]c_{\nu''}|\nu''\rangle \ . \tag{25.113}$$

[13] Here again, as done in Sec. 25.4.1, we ignore terms of the Hamiltonian (25.26) which do not depend on z or p.

Finally,

$$\boxed{\begin{aligned}\dot{c}_\nu &= -4\imath\omega_{\rm rec}\nu^2 c_\nu - \imath U_0\left(\alpha_+^*\alpha_- c_{\nu+1} + \alpha_+\alpha_-^* c_{\nu-1}\right)\\ \dot{\alpha}_\pm &= (-\kappa + \imath\Delta_c - \imath U_0)\alpha_\pm - \imath U_0\alpha_\mp\sum_\nu c^*_{\nu\mp1}c_\nu + \eta_\pm\end{aligned}}\ . \tag{25.114}$$

In Exc. 25.4.7.1 and 25.4.7.2 we study the equations (25.114) in the presence of a constant external force.

25.4.2.2 Master equation approach

As in the situation under study the motion is the only quantum degree of freedom and not subject to dissipation, a master equation approach is useless, and we will show it here only for completeness.

In 25.4.7.3 we show a derivation obtained by directly inserting the adiabatically simplified Hamiltonian (25.26) into the Liouville equation (25.8). The result is,

$$\boxed{\begin{aligned}\dot{\rho}_{\mu,\nu} &= \imath(\nu-\mu)\left[(\nu+\mu)\omega_{\rm rec} - \Delta_c\right]\rho_{\mu,\nu}\\ &\quad +\imath U_0\left[\alpha_+^*\alpha_-(\rho_{\mu,\nu-1} - \rho_{\mu+1,\nu}) + \alpha_-^*\alpha_+(\rho_{\mu,\nu+1} - \rho_{\mu-1,\nu})\right]\\ \dot{\alpha}_\pm &= (-\kappa + \imath\Delta_c - \imath U_0)\alpha_\pm - \imath U_0\alpha_\mp\sum_\nu \rho_{\nu,\nu\mp1} + \eta_\pm\end{aligned}}\ . \tag{25.115}$$

25.4.3 Quantization of atomic motion without adiabatic elimination

So far we have discussed the quantization of the atomic motion in the CARL equations, which were obtained by adiabatic elimination of the electronically excited state. In the following, we will quantize the motion directly in the equations of motion (25.15) for the observables and in the Liouville equation for the density operator. We quantize the atomic motion along the optical z-axis simply by assuming that, in this direction, the momentum only exists in multiples of $\hbar k$, and organize up the Hilbert space like this,

$$|\psi\rangle = |\nu\rangle_{\rm motion}\otimes|i\rangle_{\rm electron}\otimes\cancel{|n\rangle_+\otimes|m\rangle_-}^{\rm classical} \to |\nu, i\rangle\ , \tag{25.116}$$

that is, skipping the quantum number counting the photons, we will treat the light fields classically, $\hat{a}_\pm = \alpha_\pm$,

$$\begin{aligned}\hat{p} &= \sum_\nu \nu\hbar k|\nu\hbar k\rangle\langle\nu\hbar k|\otimes\mathbb{I}\\ e^{-\imath k\hat{z}} &= \sum_\nu |\nu\hbar k - \hbar k\rangle\langle\nu\hbar k|\otimes\mathbb{I}\\ \hat{\sigma}^+ &= \mathbb{I}\otimes|2\rangle\langle1|\\ \hat{\rho} &= |\psi\rangle\langle\psi| = \sum_{\mu,\nu,i,j} c^*_{\mu,i}c_{\nu,j}|\mu\rangle\langle\nu|\otimes|i\rangle\langle j|\end{aligned}\ , \tag{25.117}$$

where in the last equation we defined $c_{\nu,j} = \langle p, j|\psi(t)\rangle = \langle \nu\hbar k, j|\psi(t)\rangle = \langle \nu, j|\psi(t)\rangle$, such that,

$$\rho_{\mu,\nu;i,j} \equiv \langle \mu, i|\hat{\rho}|\nu, j\rangle = c^*_{\mu,i}c_{\nu,j} \ . \tag{25.118}$$

Adopting the short notation $|\nu\rangle \equiv |\nu\hbar k\rangle$ we can write the state of the system,

$$\begin{aligned}
|\psi(t)\rangle &= \sum_\nu c_{\nu,1}|\nu\hbar k, 1\rangle + c_{\nu,2}|\nu\hbar k, 2\rangle \qquad (25.119)\\
\langle\psi(t)|\hat{p}|\psi(t)\rangle &= \hbar k \sum_\nu \nu(|c_{\nu,1}|^2 + |c_{\nu,2}|^2)\\
\langle\psi(t)|e^{\pm \imath k\hat{z}}|\psi(t)\rangle &= \sum_\nu (c^*_{\nu\pm1,1}c_{\nu,1} + c^*_{\nu\pm1,2}c_{\nu,2})\\
\langle\psi(t)|\hat{a}|\psi(t)\rangle &= \alpha \sum_\nu (|c_{\nu,1}|^2 + |c_{\nu,2}|^2) = \alpha\\
\langle\psi(t)|\hat{\sigma}^-|\psi(t)\rangle &= \sum_\nu c^*_{\nu,1}c_{\nu,2}\\
\langle\psi(t)|\hat{\sigma}_z|\psi(t)\rangle &= \sum_\nu (|c_{\nu,2}|^2 - |c_{\nu,1}|^2) \ .
\end{aligned}$$

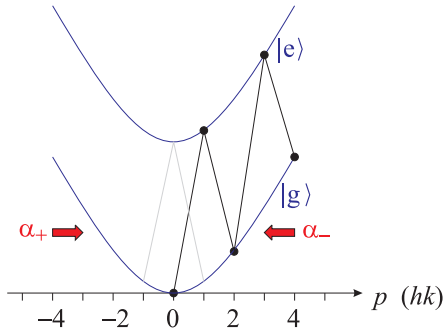

Figure 25.16: Illustration of the quantized motion.

To describe the dynamics of the system we could use the Schrödinger equation, but the Hamiltonian (25.4) does not contain spontaneous emission nor cavity decay. So, let us employ the equations of motion (25.15), which were derived from a master equation. The equation of motion for the field yields,

$$\begin{aligned}
\dot{\alpha}_\pm &= \langle\psi(t)|\dot{\hat{a}}_\pm|\psi(t)\rangle = \langle\psi(t)|(-\kappa + \imath\Delta_c)\hat{a}_\pm - \imath g\hat{\sigma}^- e^{\mp\imath k\hat{z}} + \eta_\pm|\psi(t)\rangle \qquad (25.120)\\
&= (-\kappa + \imath\Delta_c)\alpha_\pm + \eta_\pm - \imath g\sum_\nu c^*_{\nu\mp1,1}c_{\nu,2}\\
&= (-\kappa + \imath\Delta_c)\alpha_\pm + \eta_\pm - \imath g\sum_\nu \rho_{\nu\mp1,\nu;1,2} \ .
\end{aligned}$$

For the atomic motion we get,

$$\dot{x} = \langle\psi(t)|\dot{\hat{x}}|\psi(t)\rangle = \frac{1}{m}\langle\psi(t)|\hat{p}|\psi(t)\rangle = \frac{\nu\hbar k}{m} \ , \tag{25.121}$$

and

$$\begin{aligned}\dot{p} &= \langle\psi(t)|\dot{\hat{p}}|\psi(t)\rangle \qquad (25.122)\\ &= \langle\psi(t)|\imath g\hbar k\hat{\sigma}^-\left(\hat{a}_+^\dagger e^{-\imath kz}-\hat{a}_-^\dagger e^{\imath kz}\right)-\imath g\hbar k\hat{\sigma}^+\left(\hat{a}_+e^{\imath kz}-\hat{a}_-e^{-\imath kz}\right)|\psi(t)\rangle\\ &= \sum_\nu \imath g\hbar k\left(\alpha_+^*c_{\nu-1,1}^*c_{\nu,2}-\alpha_-^*c_{\nu+1,1}^*c_{\nu,2}-\alpha_+c_{\nu+1,1}c_{\nu,2}^*+\alpha_-c_{\nu-1,1}c_{\nu,2}^*\right)\\ &= \sum_\nu \imath g\hbar k(\alpha_+^*\rho_{\nu-1,\nu;1,2}-\alpha_-^*\rho_{\nu+1,\nu;1,2}-\alpha_+\rho_{\nu,\nu+1;2,1}-\alpha_-\rho_{\nu,\nu-1;2,1})\ .\end{aligned}$$

25.4.3.1 Maxwell-Bloch equations without adiabatic elimination

Analogously to the treatment in Sec. 16.3.2, we will now derive the master equation without adiabatic elimination of the excited state (in this case called *Maxwell-Bloch equations* from the Liouville equation [first line of Eq. (25.8)] using the Hamiltonian (25.4). The coherent part is,

$$\begin{aligned}\dot{\rho}_{\mu,\nu;i,j} &\equiv \langle\mu,i|\dot{\hat{\rho}}|\nu,j\rangle = -\imath\langle\mu,i|[\hat{H},\hat{\rho}]|\nu,j\rangle \qquad (25.123)\\ &= -\imath\sum_{p,u}\langle\mu,i|\hat{H}|p,u\rangle\rho_{p,\nu;u,j}+\imath\sum_{p,u}\rho_{\mu,q;i,v}\langle p,u|\hat{H}|\nu,j\rangle\\ &= -\imath\left[\frac{(\mu\hbar k)^2}{2m}-\Delta_a\delta_{i2}-\Delta_c(|\alpha_+|^2+|\alpha_-|^2)-\imath\eta_+(\alpha_+-\alpha_+^*)-\imath\eta_-(\alpha_--\alpha_-^*)\right]\rho_{\mu,\nu;i,j}\\ &\quad-\imath g\left[\alpha_+^*\delta_{i1}\rho_{\mu+1,\nu;2,j}+\alpha_+\delta_{i2}\rho_{\mu-1,\nu;1,j}+\alpha_-^*\delta_{i1}\rho_{\mu-1,\nu;2,j}+\alpha_-\delta_{i2}\rho_{\mu+1,\nu;1,j}\right]\\ &\quad+\imath\left[\frac{(\nu\hbar k)^2}{2m}-\Delta_a\delta_{j2}-\Delta_c\left(|\alpha_+|^2+|\alpha_-|^2\right)-\imath\eta_+(\alpha_+-\alpha_+^*)-\imath\eta_-(\alpha_--\alpha_-^*)\right]\rho_{\mu,\nu;i,j}\\ &\quad+\imath g\left[\alpha_+^*\delta_{j2}\rho_{\mu,\nu-1;i,1}+\alpha_+\delta_{j1}\rho_{\mu,\nu+1;i,2}+\alpha_-^*\delta_{j2}\rho_{\mu,\nu+1;i,1}+\alpha_-\delta_{j1}\rho_{\mu,\nu-1;i,2}\right]\\ &= \left[\imath\frac{(\nu^2-\mu^2)(\hbar k)^2}{2m}+\imath\Delta_a(\delta_{i2}-\delta_{j2})\right]\rho_{\mu,\nu;i,j}\\ &\quad+\imath g\left[\alpha_+^*\left(\delta_{j2}\rho_{\mu,\nu-1;i,1}-\delta_{i1}\rho_{\mu+1,\nu;2,j}\right)+\alpha_+\left(\delta_{j1}\rho_{\mu,\nu+1;i,2}-\delta_{i2}\rho_{\mu-1,\nu;1,j}\right)\right.\\ &\qquad\left.+\left(\alpha_-^*\delta_{j2}\rho_{\mu,\nu+1;i,1}-\delta_{i1}\rho_{\mu-1,\nu;2,j}\right)+\alpha_-\left(\delta_{j1}\rho_{\mu,\nu-1;i,2}-\delta_{i2}\rho_{\mu+1,\nu;1,j}\right)\right]\ .\end{aligned}$$

The incoherent part comprises the spontaneous decay [second line of Eq. (25.8)],

$$\begin{aligned}\langle\mu,i|\mathcal{L}_{atom-vac}\hat{\rho}|\nu,j\rangle &= -\gamma\langle\mu,i|\left[\hat{\sigma}^+\hat{\sigma}^-\hat{\rho}-2\hat{\sigma}^-\hat{\rho}\hat{\sigma}^++\hat{\rho}\hat{\sigma}^+\hat{\sigma}^-\right]|\nu,j\rangle \qquad (25.124)\\ &= -\gamma\sum_{p,u}\langle\mu,i|\hat{\sigma}^+\hat{\sigma}^-|p,u\rangle\rho_{p,\nu;u,j}+2\gamma\sum_{p,u,q,v}\langle\mu,i|\hat{\sigma}^-|p,u\rangle\rho_{p,q;u,v}\langle q,v|\hat{\sigma}^+|\nu,j\rangle.\\ &\quad-\gamma\sum_{p,u}\rho_{\mu,p;i,u}\langle p,u|\hat{\sigma}^+\hat{\sigma}^-|\nu,j\rangle\\ &= -\gamma\left[\delta_{i2}\rho_{\mu,\nu;i,j}-2\delta_{i1}\delta_{j1}\rho_{\mu,\nu;2,2}+\delta_{j2}\rho_{\mu,\nu;i,j}\right]\end{aligned}$$

and the cavity decay [third line of Eq. (25.8)],

$$\langle\mu,i|\mathcal{L}_{cavity-vac,\pm}\hat{\rho}|\nu,j\rangle = -\kappa\langle\mu,i|\hat{a}_\pm^\dagger\hat{a}_\pm\hat{\rho}-2\hat{a}_\pm\hat{\rho}\hat{a}_\pm^\dagger+\hat{\rho}\hat{a}_\pm^\dagger\hat{a}_\pm|\nu,j\rangle = 0\ . \qquad (25.125)$$

Finally, using the definition of the recoil shift $\omega_{\rm rec} = \hbar k^2/2m$ we get,

$$\boxed{\begin{aligned}
\dot\rho_{\mu,\nu;1,1} &= \imath(\nu^2-\mu^2)\omega_{\rm rec}\rho_{\mu,\nu;1,1} + 2\gamma\rho_{\mu,\nu;2,2} \\
&+ \imath\hbar g\left[-\alpha_+^*\rho_{\mu+1,\nu;2,1} + \alpha_+\rho_{\mu,\nu+1;1,2} - \alpha_-^*\rho_{\mu-1,\nu;2,1} + \alpha_-\rho_{\mu,\nu-1;2,1}\right] \\
\dot\rho_{\mu,\nu;1,2} &= \left[\imath(\nu^2-\mu^2)\omega_{\rm rec} - \imath\hbar\Delta_a\right]\rho_{\mu,\nu;1,2} - \gamma\rho_{\mu,\nu;1,2} \\
&+ \imath\hbar g\left[\alpha_+^*\rho_{\mu,\nu-1;1,1} - \alpha_+^*\rho_{\mu+1,\nu;2,2} + \alpha_-^*\rho_{\mu,\nu+1;1,1} - \alpha_-^*\rho_{\mu-1,\nu;2,2}\right] \\
\dot\rho_{\mu,\nu;2,1} &= \left[\imath(\nu^2-\mu^2)\omega_{\rm rec} + \imath\hbar\Delta_a\right]\rho_{\mu,\nu;2,1} - \gamma\rho_{\mu,\nu;2,1} \\
&- \imath\hbar g\left[\alpha_+\rho_{\mu-1,\nu;1,1} - \alpha_+\rho_{\mu,\nu+1;2,2} + \alpha_-\rho_{\mu+1,\nu;1,1} - \alpha_-\rho_{\mu,\nu-1;2,2}\right] \\
\dot\rho_{\mu,\nu;2,2} &= \imath(\nu^2-\mu^2)\omega_{\rm rec}\rho_{\mu,\nu;2,2} - 2\gamma\rho_{\mu,\nu;2,2} \\
&+ \imath\hbar g\left[\alpha_+^*\rho_{\mu,\nu-1;2,1} - \alpha_+\rho_{\mu-1,\nu;1,2} + \alpha_-^*\rho_{\mu,\nu+1;2,1} - \alpha_-\rho_{\mu+1,\nu;1,2}\right] \\
\dot\alpha_\pm &= (-\kappa + \imath\Delta_c - \imath U_0)\alpha_\pm + \eta_\pm - \imath g\sum_\nu \rho_{\nu\mp1,\nu;1,2}
\end{aligned}} \quad . \tag{25.126}$$

We note $\hat\rho_{\mu,\nu;2,1} = \hat\rho^*_{\nu,\mu;1,2}$.

The equations (25.126) form a set a equations to describe the quantized CARL without adiabatic elimination. And as shown in the derivation of the CARL equations (25.25), they contain radiation pressure. In Exc. 25.4.7.4 we study the quantized CARL Maxwell-Bloch equations without adiabatic elimination of the excited state for a three-level system.

25.4.4 Quantized motion with many particles

The Hamiltonian (25.98) holds for a single atom. If clouds of thermal atoms are considered, we may switch to a classical description of the motion, as done in (25.46). In the case of very cold (below the recoil limit) but still independent atoms, we may assume that they all are coherently distributed over the same momentum states. We may then apply a unique momentum state expansion for all atoms, as shown in the subsequent section.

If on the other hand quantum statistics play a role, then we need to replace the wavefunction in the Schrödinger equation (25.98) by field operators, as done in Sec. 29.5. In the following sections, we will restrict to single atoms that can be in a coherent superposition of momentum states or many atoms in a matter wave that can be treated as a c-number, e.g. a Bose-condensate without fluctuations.

25.4.4.1 Modal expansion of the motion of many independent atoms in the adiabatic approximation for one-sided pumping

Our starting point is the quantum version of the CARL equations (25.25), where we neglect spontaneous emission, $\gamma_0 = 0$. Setting $\alpha_+ = \eta_+/\kappa$ and $\eta_- = 0$ we get,

$$\boxed{\begin{aligned}
\dot{\hat a}_- &= (-\kappa + \imath\Delta_c - \imath U_0)\hat a_- - \imath U_0\tfrac{\eta_+}{\kappa}e^{-2\imath k\hat z_j} \\
m\ddot{\hat z}_j &= 2\imath\hbar k U_0(\hat a_+^\dagger\hat a_- e^{-2\imath k\hat z_j} - \hat a_+\hat a_-^\dagger e^{2\imath k\hat z_j})
\end{aligned}} \quad , \tag{25.127}$$

where the index j runs over all atoms. For this case, the total momentum is a constant of motion for N atoms is,

$$[\hat{H}, 2\hbar k\hat{a}_-^\dagger \hat{a}_- + \sum_{j=1}^{N} \hat{p}_j] = 0 \ . \tag{25.128}$$

where the Hamiltonian is obtained from (25.26) by eliminating the mode α_+ and summing over all atoms,

$$\hat{H} = \sum_j \left[\frac{\hat{p}_j^2}{2m} + \frac{\eta_+}{\kappa} U_0 \left(e^{-2\imath k\hat{z}_j} \hat{a}_- + e^{2\imath k\hat{z}_j} \hat{a}_-^\dagger \right) \right] + (U_0 - \Delta_c)\hat{a}_-^\dagger \hat{a}_- \ . \tag{25.129}$$

To treat the motion as being quantized we define a base $|\nu\rangle_j$,

$$\hat{p}_j|\nu\rangle_j = 2\hbar k\nu|\nu\rangle_j \qquad \text{and} \qquad |\psi(z_j)\rangle = \sum_\nu c_{j,\nu}|\nu\rangle_j \ , \tag{25.130}$$

and calculate the expected value of the equations (25.127) regarding the atomic motion,

$$\begin{aligned} \frac{d\hat{a}_-}{dt} &= (-\kappa - \imath\Delta_c)\hat{a}_- - \imath U_0 \tfrac{\eta_+}{\kappa} \sum_j \langle\psi(z_j)|e^{-2\imath k\hat{z}_j}|\psi(z_j)\rangle \\ &= (-\kappa + \imath\Delta_c - \imath U_0)\hat{a}_- - \imath U_0 \tfrac{\eta_+}{\kappa} \sum_{j,\mu,\nu} c_{j,\mu}^* c_{j,\nu\, j} \langle\mu|e^{-2\imath k z_j}|\nu\rangle_j \\ &= (-\kappa + \imath\Delta_c - \imath U_0)\hat{a}_- - \imath U_0 \tfrac{\eta_+}{\kappa} \sum_{j,\nu} c_{j,\nu}^* c_{j,\nu+1} \ . \end{aligned} \tag{25.131}$$

We do not use the second equation (25.127), but instead we use the Schrödinger equation $\imath\hbar\frac{d|\psi(z_j\rangle}{dt} = \hat{H}|\psi(z_j)\rangle$, which yields,

$$\begin{aligned} \imath\hbar \sum_\nu \frac{dc_{j,\nu}}{dt}|\nu\rangle_j = \sum_\nu \frac{1}{2m} p_j^2 c_{j,\nu}|\nu\rangle_j + \hbar\Delta_c \hat{a}_-^\dagger \hat{a}_- \sum_\nu c_j(\nu)|\nu\rangle_j \\ + \hbar U_0 \eta \sum_\nu (\hat{a}_-^\dagger e^{-2\imath k z_j} + \hat{a}_- e^{2\imath k z_j}) c_{j,\nu}|\nu\rangle_j \ . \end{aligned} \tag{25.132}$$

Projecting on ${}_j\langle\mu|$, we obtain [165],

$$\boxed{\begin{aligned} \dot{c}_{j,\mu} &= -4\imath\omega_{\rm rec}\mu^2 c_{j,\mu} - \imath\Delta_c \hat{a}_-^\dagger \hat{a}_- c_{j,\mu} - \imath U_0 \eta [\hat{a}_-^\dagger c_{j,\mu+1} + a_- c_{j,\mu-1}] \\ \dot{\hat{a}}_- &= -(\kappa + \imath\Delta_c)\hat{a} + N U_0 \eta \sum_\nu c_{j,\nu}^* c_{j,\nu+1} \end{aligned}} \ , \tag{25.133}$$

where we took the expectation value of Eq. (25.131). The equations (25.133) can be used for numerical simulations [696].

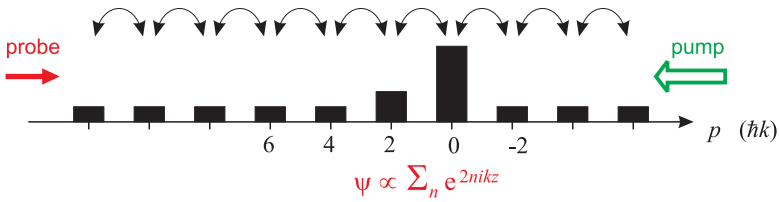

Figure 25.17: Probe light and 'bunching' when the temperature is raised.

25.4.4.2 Equations for the density matrix

The equations (25.133) allow to calculate the derivatives of the density matrix given by,

$$\varrho_{\mu,\nu} \equiv e^{-\imath(\mu-\nu)\Delta_c t}\frac{1}{N}\sum_j c_j^*(\mu)c_j(\nu)\ , \tag{25.134}$$

yielding,

$$\begin{aligned}\frac{d\varrho_{\mu,\nu}}{dt} &= e^{-\imath(\mu-\nu)\Delta_a t}N^{-1}\sum_j\left(\dot{c}^*_{j,\mu}c_{j,\nu}+c^*_{j,\mu}\dot{c}_{j,\nu}-\Delta_c c^*_{j,\mu}c_{j,\nu}\imath(\mu-\nu)\right) \\ &= e^{-\imath(\mu-\nu)\Delta_a t}N^{-1}\sum_j[\imath\omega_r(\mu^2-\nu^2)-\Delta_c\imath(\mu-\nu)]c^*_{j,\mu}c_{j,\nu}+ \\ &\quad +\imath U_0\eta\left[ac^*_{j,\mu+1}c_{j,\nu}-ac^*_{j,\mu}c_{j,\nu-1}+\hat{a}^\dagger c^*_{j,\mu-1}c_{j,\nu}-\hat{a}^\dagger c^*_{j,\mu}c_{j,\nu+1}\right]\ .\end{aligned} \tag{25.135}$$

Introducing $\tilde{a}\equiv ae^{\imath\Delta_c t}$ we finally obtain,

$$\boxed{\begin{aligned}\frac{d\varrho_{\mu,\nu}}{dt} &= \imath(\mu-\nu)[\omega_r(\mu+\nu)-\Delta_c]\varrho_{\mu,\nu} \\ &+ \imath U_0\eta\left[\tilde{a}(\varrho_{\mu+1,\nu}-\varrho_{\mu,\nu-1})+\tilde{a}^\dagger(\varrho_{\mu-1,\nu}-\varrho_{\mu,\nu+1})\right] \\ \frac{d\tilde{a}}{dt} &= -\kappa\tilde{a}-\imath NU_0\eta\sum_\nu\varrho_{\nu,\nu+1}\end{aligned}}\ . \tag{25.136}$$

These are the CARL equations for the density matrix. In 25.4.7.3 we show an alternative derivation obtained by directly inserting the adiabatically simplified Hamiltonian (25.26) into the Liouville equation (25.8).

We note, that $\sum_\nu \varrho_{\nu,\nu+1}$ is the 'bunching' and that $\varrho^*_{\mu,\nu}=\varrho_{\nu,\mu}$. The average moment is given by $\langle p\rangle=\sum_\nu \nu\varrho_{\nu,\nu}$. In the Figs. 25.18 and 25.19 we show simulations in the semi-classical regimes $\rho\gg 1$ in the 'bad-cavity' limit, $\kappa>1$, and the 'good-cavity' limit $\kappa\ll 1$.

Here are some movies illustrating the quantum CARL dynamics, simulated using the momentum state expansion (watch movie) and (watch movie). The following dynamics were calculated via direct integration of the Schrödinger equation without momentum state expansion: Bloch oscillations (watch movie), CARL dynamics (watch movie), and joint Bloch and CARL dynamics (watch movie). See also (watch talk).

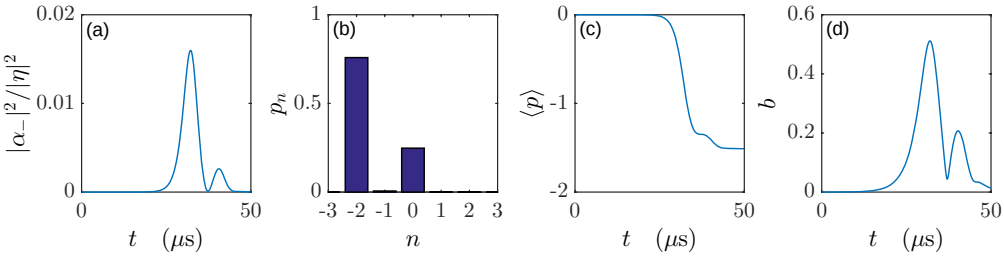

Figure 25.18: (code) Simulation of the CARL equation (25.133) in the superradiant, semi-classical, 'bad-cavity' regime for $\kappa_c = 4$, $\rho = 4$, $\Delta_c = 0$.

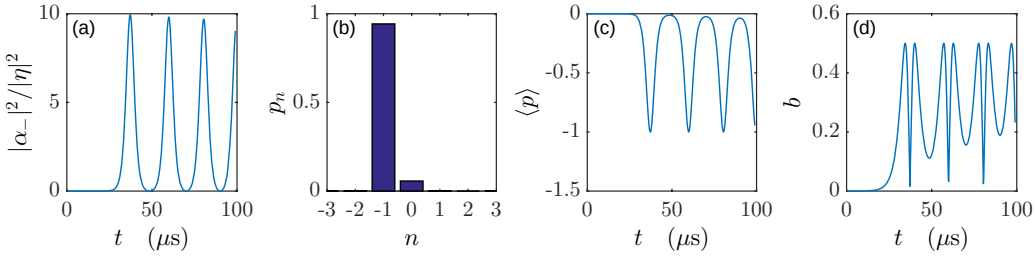

Figure 25.19: (code) Simulation of the CARL equation (25.133) in the superradiant, semi-classical, 'good-cavity' regime for $\kappa_c = 0.02$, $\rho = 4$, $\Delta_c = 0$.

25.4.5 Approximation for a bimodal momentum distribution

We observe that in the quantum regime the momentum distribution of the matter wave is bimodal, that is, only two momentum states are simultaneously populated. This justifies a simplification of the equations (25.136), assuming that at a given time, atoms must either be in a specific state $|\mu\rangle_j$ or in a superposition of this state is an adjacent state $|\mu-1\rangle_j$. Hence,

$$\begin{aligned}
\frac{d\varrho_{\mu,\mu}}{dt} &= -\imath U_0\eta(\tilde{a}\varrho_{\mu,\mu-1} - \tilde{a}^\dagger\varrho_{\mu-1,\mu}) = -\frac{d\varrho_{\mu-1,\mu-1}}{dt} \\
\frac{d\varrho_{\mu-1,\mu}}{dt} &= -\imath[(2\mu-1)\omega_r - \Delta_c]\varrho_{\mu-1,\mu} + \imath U_0\eta\tilde{a}(\varrho_{\mu,\mu} - \varrho_{\mu-1,\mu-1}) \\
\frac{d\tilde{a}}{dt} &= -\imath N U_\mu\eta\varrho_{\mu-1,\mu} - \kappa_c\tilde{a}\ .
\end{aligned} \tag{25.137}$$

Introducing the coherence $S_\mu = \varrho_{\mu-1,\mu}$ and the inversion $W_\mu = \varrho_{\mu,\mu} - \varrho_{\mu-1,\mu-1}$ and postulating the normalization $1 = \varrho_{\mu,\mu} + \varrho_{\mu-1,\mu-1}$,

$$\begin{aligned}
\frac{dW_\mu}{dt} &= -2\imath U_0\eta(\tilde{a}S_\mu^* - \tilde{a}^\dagger S_\mu) \\
\frac{dS_\mu}{dt} &= -\imath[(2\mu-1)\omega_r - \Delta_c]S_\mu + \imath U_0\eta\tilde{n}aW_\mu \\
\frac{d\tilde{a}}{dt} &= -\imath N U_0\eta S_\mu - \kappa_c\tilde{a}\ .
\end{aligned} \tag{25.138}$$

25.4.5.1 Linearization and stability analysis

We assume that the atoms are initially 'bunched' in a specific state $|\mu\rangle_j$. Only adjacent momentum states are coupled,

$$\begin{aligned}
\frac{d\varrho_{\mu+1,\mu}}{dt} &= \imath[\omega_r(2\mu+1)-\Delta_c]\varrho_{\mu+1,\mu} + \imath U_0\eta\tilde{a}^\dagger(\varrho_{\mu,\mu}-\varrho_{\mu+1,\mu+1}) \\
\frac{d\varrho_{\mu-1,\mu}}{dt} &= -\imath[\omega_r(2\mu-1)-\Delta_c]\varrho_{\mu-1,\mu} + \imath U_0\eta\tilde{a}(\varrho_{\mu,\mu}-\varrho_{\mu-1,\mu-1}) \\
\frac{d\tilde{a}}{dt} &= -\imath NU_0\eta(\varrho_{\mu,\mu+1}+\varrho_{\mu-1,\mu}) - \kappa_c\tilde{a}\ .
\end{aligned} \tag{25.139}$$

Conjugate the upper equation and build the sum and difference, $B_\mu \equiv \varrho_{\mu,\mu+1}+\varrho_{\mu-1,\mu}$ and $D_\mu \equiv \varrho_{\mu,\mu+1}-\varrho_{\mu-1,\mu}$,

$$\begin{aligned}
\frac{dB_\mu}{dt} &= \imath(\Delta_c-2\mu\omega_r)B_\mu - \imath\omega_\mu D_\mu + \imath U_0\eta\tilde{a}(\varrho_{\mu+1,\mu+1}-\varrho_{\mu-1,\mu-1}) \\
\frac{dD_\mu}{dt} &= \imath(\Delta_c-2\mu\omega_r)D_\mu - \imath\omega_r B_\mu - 2\imath U_0\eta\tilde{a} + \imath U_0\eta\tilde{a}(\varrho_{\mu+1,\mu+1}-2\varrho_{\mu,\mu}+\varrho_{\mu-1,\mu-1}) \\
\frac{d\tilde{a}}{dt} &= -\imath NU_0\eta B_\mu - \kappa_c\tilde{a}\ .
\end{aligned} \tag{25.140}$$

Use $\varrho_{\mu,\mu} \simeq 1$ and abbreviate $\delta_\mu \equiv 2r\omega_\mu - \Delta_c$,

$$\begin{aligned}
\frac{dB_\mu}{dt} &= -\imath\delta_\mu B_\mu - \imath\omega_r D_\mu \\
\frac{dD_\mu}{dt} &= -\imath\omega_r B_\mu - \imath\delta_r D_\mu - 2\imath U_0\eta\tilde{a} \\
\frac{d\tilde{a}}{dt} &= -\imath NU_0\eta B_\mu - \kappa_c\tilde{a}\ .
\end{aligned} \tag{25.141}$$

Seeking solution proportional to $x \equiv \bar{x}e^{\imath(\lambda-\delta_\mu)t}$,

$$\begin{aligned}
\imath\lambda\bar{B}_\mu &= -\imath\omega_\mu\bar{D}_\mu \\
\imath\lambda\bar{D}_\mu &= -\imath\omega_\mu\bar{B}_\mu - 2\imath U_\mu\eta\bar{a} \\
\imath(\lambda-\delta_\mu)\bar{a} &= -\imath NU_0\eta\bar{B}_\mu - \kappa_c\bar{a}\ .
\end{aligned} \tag{25.142}$$

Abbreviating $\Lambda_m \equiv \delta_m + \imath\kappa_c$, the characteristic equation is,

$$\det\begin{pmatrix} \lambda & \omega_r & 0 \\ \omega_r & \lambda & 2U_0\eta \\ NU_0\eta & 0 & \lambda-\Lambda_\mu \end{pmatrix} = \lambda^3 - \Lambda_\mu\lambda^2 - \omega_r^2\lambda + \omega_r^2\Lambda_\mu + 2NU_0^2\eta^2\omega_r = 0\ . \tag{25.143}$$

The gain is given by the imaginary part of λ. We have exponential amplification if $\mathrm{Im}\,\lambda < 0$. Hence, we search for solution with the lowest imaginary value.

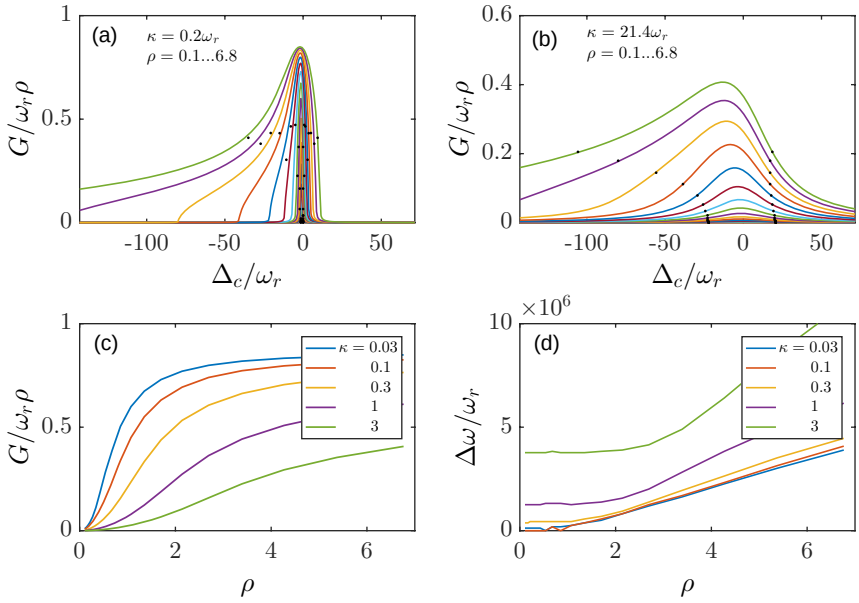

Figure 25.20: (code) Gain dependence on ρ and κ.

25.4.5.2 Universal scaling

To simplify the formulae simplify, we rescale them. We start from Eq. (25.136) and use the substitution for universal scaling,

$$\begin{aligned} \theta_j \equiv 2kz_j \quad &\text{and} \quad \bar{p}_j \equiv 2kv_j/\rho\omega_r \\ \tau \equiv \rho\omega_r t \quad &\text{and} \quad \kappa \equiv \kappa_c/\omega_r\rho \\ \bar{\lambda} \equiv \lambda/\omega_r\rho \quad &\text{and} \quad \bar{\delta}_\mu \equiv \delta_\mu/\omega_r\rho = 2\mu/\rho + \Delta_c/\omega_r\rho \\ \bar{A} \equiv (2/N\rho)^{1/2}\bar{a} \quad &\text{and} \quad \eta U_\mu \equiv \sqrt{\rho^3\omega_r^2/2N}\ . \end{aligned} \tag{25.144}$$

This reproduces the Bonifacio notation,

$$\begin{aligned} \bar{\lambda}\bar{B}_\mu + \rho^{-1}\bar{D}_\mu &= 0 \\ \bar{\lambda}\bar{D}_\mu + \rho^{-1}\bar{B}_\mu + \rho\bar{A} &= 0 \\ (\bar{\lambda} - \bar{\delta}_\mu - \imath\kappa)\bar{A} + \bar{B}_\mu &= 0\ . \end{aligned} \tag{25.145}$$

Skipping the bars, the characteristic equation reads,

$$\det \begin{pmatrix} \lambda & \rho^{-1} & 0 \\ \rho^{-1} & \lambda & \rho \\ 1 & 0 & \lambda - \delta_\mu - \imath\kappa \end{pmatrix} = (\lambda - \delta_\mu - \imath\kappa)(\lambda^2 - \rho^{-2}) + 1 = 0\ . \tag{25.146}$$

Let us first discuss the semiclassical limit, $\rho \gg 1$. In the good-cavity regime, $\kappa \simeq 0$, we may neglect the recoil shift, $2m\omega_r \to 0$, so that $\Lambda = \Delta_c$. The gain is largest

when $\Delta_c \to 0$. The characteristic equation reduces to $\lambda^3 = -1$, yielding the solutions $\lambda = 1, \frac{1}{2}(1 \pm \imath\sqrt{3})$. Hence, the gain $G = -\mathfrak{Im}\,\lambda$, is

$$\begin{aligned} G &= \tfrac{1}{2}\omega_r\rho\sqrt{3} \\ \Delta\omega_G &\simeq \omega_r\rho \gg \kappa_c, \omega_r \ . \end{aligned} \tag{25.147}$$

The gain bandwidth $\Delta\omega_G$ being much larger than the recoil frequency, the Bragg condition for scattering between different momentum states is approximately fulfilled for a large number of initial momenta. I.e. although the momentum transfer is quantized, $\Delta_c = n\omega_r$, the atoms can be accelerated to high velocities. From Eq. (25.140)(a) we see $|\bar{D}_\mu/\bar{B}_\mu| = \rho|\bar{\lambda}| \gg 1$, i.e. $\varrho_{\mu,\mu+1} \simeq \varrho_{\mu-1,\mu}$.

In the superradiant regime, $\kappa > 1$, of the semiclassical limit the characteristic equation reduces to $\lambda^2 = -\imath/\kappa$, i.e. $\lambda = \pm(1-\imath)/\sqrt{2\kappa}$.[14] Hence, the gain is,

$$\begin{aligned} G &= \tfrac{1}{2}\omega_r\rho\sqrt{2/\kappa} \\ \Delta\omega_G &\simeq \kappa_c = \omega_r\rho\kappa \gg \omega_r \ . \end{aligned} \tag{25.148}$$

In fact, the relative gain bandwidth is on the order of $\Delta\omega_G/\omega_r \simeq \rho \propto \left(nNU_0^2\right)^{1/3}$. Since recoil can be neglected we can have absorption or emission. The gain results from the difference bewteen the average rates of both.

Now we turn to the quantum limit, $\rho < 1$. In the good-cavity regime, $\kappa \simeq 0$, $\lambda = \rho^{-1} + \frac{1}{2}(\delta_m - \rho^{-1}) - \frac{1}{2}\sqrt{(\delta_m - \rho^{-1})^2 - 2\rho}$. Hence, the gain is,

$$\begin{aligned} G &= \tfrac{1}{2}\omega_r\rho\mathfrak{Im}\,\sqrt{(\delta_m - \rho^{-1})^2 - 2\rho} \simeq \tfrac{1}{2}\omega_r\rho\sqrt{2\rho} \\ \Delta\omega_G &= \omega_r\rho^{3/2} < \omega_r \ . \end{aligned} \tag{25.149}$$

In fact, the relative gain bandwidth is on the order of $\Delta\omega_G/\omega_r \simeq \rho^{3/2} \propto \sqrt{nNU_0^2}$. Here recoil plays a role so that we have emission without absorption. Gain results exclusively from emission. From Eq. ((25.140)a) we see $|\bar{D}_m/\bar{B}_m| = \rho|\bar{\lambda}| \simeq 1$, i.e. $\varrho_{m,m+1} \ll \varrho_{m-1,m}$.

In the superradiant regime, $\kappa > 1$, of the quantum limit, $\lambda = \rho^{-1} + \frac{\rho}{2}[(\delta_m - \rho^{-1}) + \imath\kappa]^{-1}$. Hence,

$$\begin{aligned} G &= \tfrac{1}{2}\omega_r\rho\frac{\rho\kappa}{(\delta_m - \rho^{-1})^2 + \kappa^2} \simeq \tfrac{1}{2}\frac{\omega_r\rho^2}{\kappa} \\ \Delta\omega_G &= \kappa_c > \omega_r\rho \ . \end{aligned} \tag{25.150}$$

The various regimes may be summarized in the following phase diagram. We will see later, that each region produces qualitatively different solutions of the full (non-linearized) equations.

[14] The assertion $\mathfrak{Re}\,\lambda \ll \kappa$ used to simplify the characteristic equation is compatible with the solution.

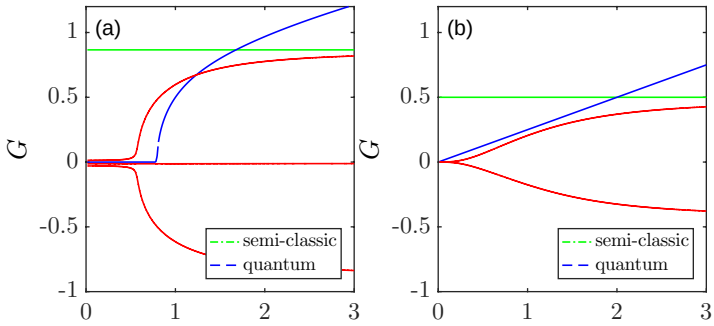

Figure 25.21: (code) Analytical approximations of the characteristic equation for the various regimes in the good-cavity limit $\kappa = 0.03$ (a) and the superradiant limit $\kappa = 2$ (b).

25.4.6 Simulation of random quantum trajectories

Spontaneous emission can induce a random walk of the atoms, which be accounted for by a proper master equation. We write the master equation for the density operator of a dissipative system, as shown in (23.116) [138, 904],

$$\boxed{\dot{\hat{\rho}} = \imath[\hat{\rho}, \hat{H}] - \tfrac{1}{2}\sum_{\mu}\{\hat{\rho}, \hat{L}_\mu^\dagger \hat{L}_\mu\} + \sum_{\mu} \hat{L}_\mu \hat{\rho} \hat{L}_\mu^\dagger} \ . \tag{25.151}$$

The first term describes the coherent part, the second part dissipation, and the third quantum jumps. The dissipative operators $\hat{L}_\mu$ appearing in the Lindblad terms model the impact of the environment. An alternative to solving the master equation consists in simulating single trajectories of the system with a Schrödinger equation, accounting for dissipation by a non-Hermitian effective Hamiltonian and for quantum fluctuations by a stochastic noise term.

As an example, let us consider the Hamiltonian for an atom interacting with a standing wave potential,

$$\hat{H} = \frac{\hat{p}^2}{2m} + U \cos k\hat{x} \ , \tag{25.152}$$

where $\hat{p} = \hbar q \hat{\nu} = -\imath\hbar d/dx$. We define a momentum basis $|\phi(\tau_0)\rangle = \sum_\nu c_\nu |\nu\rangle$ with $\sum_\nu |c_\nu|^2 = 1$. In this basis, the momentum and the position operator can be expanded as usual,

$$\hat{p} = \hbar q \sum_{\nu=-\infty}^{\infty} \nu |\nu\rangle\langle\nu| \quad \text{and} \quad \cos k\hat{x} = \tfrac{1}{2} \sum_{\nu=-\infty}^{\infty} (|\nu+1\rangle\langle\nu| + |\nu-1\rangle\langle\nu|) \ , \tag{25.153}$$

where $\hbar q$ is the momentum transferred upon a kick. The expectation value for the momentum and the position are then,

$$\langle\hat{p}\rangle = \sum_\nu \hbar q \nu |c_\nu|^2 \qquad \text{and} \qquad \langle \cos k\hat{x}\rangle = \tfrac{1}{2}\sum_\nu (c_\nu^* c_{\nu-1} + c_\nu^* c_{\nu+1}) \ . \tag{25.154}$$

The Lindblad operators describe deceleration of the rotor. With $\mu = \pm$, we get,

$$\hat{L}_\pm = g \sum_{\nu=0}^{\infty} \sqrt{\nu+1} |\pm\nu\rangle\langle\pm\nu \pm 1| \ , \tag{25.155}$$

such that,

$$\hat{L}_\pm^\dagger \hat{L}_\pm = g^2 \sum_{\nu=0}^{\infty} \nu |\pm\nu\rangle\langle\pm\nu| \quad \text{and} \quad \hat{L}_+^\dagger \hat{L}_+ + \hat{L}_-^\dagger \hat{L}_- = g^2 \sum_{\nu=-\infty}^{\infty} |\nu|\, |\nu\rangle\langle\nu| \ . \tag{25.156}$$

Now, as we have seen in Sec. 16.4.3, we may treat the first part of the Lindblad terms in (25.151) as the dissipative part of an an *effective Hamiltonian*,

$$\boxed{\hat{H}_{eff} = \hat{H} - \tfrac{\imath}{2} \sum_\mu \hat{L}_\mu^\dagger \hat{L}_\pm} \ . \tag{25.157}$$

That is, we can attempt a *quantum Monte Carlo wavefunction simulation* of an effective Schrödinger equation.

We define the quantity $dp_\pm \equiv \langle\phi(\tau_0)|\hat{L}_\pm^\dagger \hat{L}_\pm|\phi(\tau_0)\rangle d\tau$,

$$\frac{dp_+}{d\tau} = g^2 \sum_\nu |c_\nu|^2 \quad \text{and} \quad \frac{dp_-}{d\tau} = g^2 \sum_\nu |c_{-\nu}|^2 \ . \tag{25.158}$$

To perform simulations, we start with $|\phi(\tau_0)\rangle$. After a time $d\tau$, we generate a uniform random number ζ. After infinitesimal time, we compare the random number to the accumulated probability. If $\zeta > dp_\mu$, we say that a quantum jump occurred. The new wavefunction is,

$$|\phi(\tau_0)\rangle \to \frac{\hat{L}_\pm|\phi(\tau_0)\rangle}{\|\hat{L}_\pm|\phi(\tau_0)\rangle\|} = \frac{\sum_{\nu\geq 0}\sqrt{\nu+1}c_{\pm\nu\pm1}|\nu\rangle}{\sqrt{\sum_{\nu\geq 0}\nu|c_{\pm\nu}|^2}} \ . \tag{25.159}$$

If in contrast, $\zeta < 1 - \sum_\mu dp_\mu$, then the system continues to evolve slowly. However, dissipation losses have to be compensated by renormalization,

$$|\phi(\tau_0)\rangle \to \frac{(1 - \frac{\imath}{\hbar}\hat{H}_{eff}dt)|\phi(\tau_0)\rangle}{\sqrt{1 - \sum_k dp_k}} \ , \tag{25.160}$$

where the evolution is

$$\begin{aligned}
(|\phi(dt)\rangle &= 1 - \imath\hat{H}_{eff}dt/\hbar)|\phi(\tau_0)\rangle \qquad (25.161)\\
&= \left(1 - \tfrac{\imath}{\hbar}dt\frac{\hat{p}^2}{2m} - \tfrac{\imath}{\hbar}dtU\cos k\hat{x} - \tfrac{1}{2\hbar}dt\sum_\pm \hat{L}_\pm^\dagger\hat{L}_\pm\right)\sum_\nu c_\nu|\nu\rangle\\
&= \sum_\nu c_\nu|\nu\rangle - \tfrac{\imath}{\hbar}dt\tfrac{1}{2}\sum_\nu c_\nu\hbar^2\nu^2|\nu\rangle - \tfrac{\imath}{\hbar}dt\tfrac{1}{2}\sum_\nu c_\nu U(|\nu+1\rangle + |\nu-1\rangle)\\
&\quad - \frac{g^2}{2\hbar}dt\sum_{\nu\geq 0}\nu(c_\nu|\nu\rangle + c_{-\nu}|-\nu\rangle)\\
&= |\phi(\tau_0)\rangle - \frac{\imath}{2\hbar}dt\sum_\nu c_\nu\left[\nu(\hbar^2\nu - \imath g^2)|\nu\rangle + U|\nu+1\rangle + U|\nu-1\rangle\right] \ .
\end{aligned}$$

With this we can now follow the evolution of observables, such as $\langle\phi(t)|\nu\rangle\langle\nu|\phi(t)\rangle$, $\langle\phi(t)|\hat{p}|\phi(t)\rangle$, and $\langle\phi(t)|\cos k\hat{x}|\phi(t)\rangle$, in time.

25.4.7 Exercises

25.4.7.1 Ex: Quantized CARL equations in the presence of a constant external force

a. Generalize the quantized CARL equations (25.100), respectively, (25.114) for the presence of a constant external force.
b. Now, we consider a unidirectionally pumped ring cavity, with the pump laser locked to a cavity mode, in the presence of an external periodic potential. Show that this system is equivalent to CARL in a ring cavity pumped from both sides.

25.4.7.2 Ex: Competition between CARL and Bloch oscillations

Reproduce the simulations of [721].

25.4.7.3 Ex: Alternative derivation of the Maxwell-Bloch with adiabatic elimination

Derive the directly from the Liouville equation (25.8) using the Hamiltonian (25.26) in adiabatic elimination.

25.4.7.4 Ex: Maxwell-Bloch equations without adiabatic elimination

Derive the Maxwell-Bloch equations for a three-level system coupled to a ring cavity without adiabatic elimination, but with quantized motion.

25.4.7.5 Ex: Linearized quantum CARL

Analyze the quantum CARL according to [660].

25.5 Quantized light interacting with atoms moving in cavities

Cavity QED has been studied extensively in the context of the Jaynes-Cummings model in Sec. 17.2 and of cooperative scattering in Sec. 22.1, however, without addressing the issue of atomic motion which, via photonic recoil, inevitably influences the dynamics. We also started a discussion on the role of photonic recoil in Sec. 20.3, which will be continued in the following sections in the context of ring cavities,

$$\begin{aligned} \dot{c}_{n_+,n_-,i} &= \frac{d}{dt}\langle \mathbf{r}, \alpha_+, \alpha_-, i|\psi(t)\rangle = \langle \mathbf{r}, \alpha_+, \alpha_-, i|\frac{-\imath}{\hbar}\hat{H}|\psi(t)\rangle \\ \dot{\alpha}_\pm &= \langle\psi(t)|\dot{a}_\pm|\psi(t)\rangle = \langle\psi(t)|\tfrac{\imath}{\hbar}[\hat{H},\hat{a}_\pm] - \kappa\hat{a}_\pm|\psi(t)\rangle \ . \end{aligned} \tag{25.162}$$

Concretely, we will be using the Hamiltonian (25.26), obtained after adiabatic elimination of the excited state.

25.5.1 QED in ring cavities

Macroscopic high-finesse ring cavities interacting with a cloud of cold atoms allowed to enter the regime of strong collective coupling. However, new interesting aspects arise from the regime of strong coupling on the level of individual atoms.

Todays research projects on cold atoms in cavities are essential divided into two classes, each class realizing an opposite regime: Cavity quantum electrodynamics (CQED) experiments as they are done by the groups of Rempe [492] and Kimble use microcavities having mode volumes so small that few photons give rise to macroscopic field strength. In such cavities the atom-field coupling is made to exceed all other decay rates. The other regime is that of cavity-cooling mainly investigated by Vuletic at the MIT and, in the case of ring cavities, of the collective atomic recoil laser (CARL) realized in the Tübingen research group. In this second regime the cavities are so large that the light fields can be considered as classical.

An interesting question is, whether the two regimes can be married to realize a system, where collective effects and entanglement between optical and atomic modes can be observed. The central idea is not to increase the coupling strength by reducing the mode volume, but to reduce the decay rates, in particular the natural linewidth of the atomic transition by choosing an atomic species that can be laser-cooled on a narrow intercombination line.

Example 183 (*CQED by reducing the ring cavity mode volume*): Technically a ring cavity design with $(w, L, F) = (30\,\mu\text{m}, 4\,\text{cm}, 200000)$ is feasible. This is enough to get below the critical atom number, but this is not sufficient to get into the CQED regime. Reducing Γ seems unavoidable.
The isotope ^{88}Sr posses a narrow transition which can be used for optical cooling. The following table compares the various systems, i.e. a CQED example taken from Rempe, the macroscopic ring cavity with rubidium used in our Tübingen CARL experiments and a cavity tuned close to the strontium intercombination line.

experiment	Rempe, Rb	Tübingen, Rb	São Carlos, Sr
Γ	$(2\pi)6$ MHz	$(2\pi)6$ MHz	$(2\pi)7.6$ kHz
F	440000	80000	200000
κ	$(2\pi)0.7$ MHz	$(2\pi)22$ kHz	$(2\pi)19$ kHz
w	29 µm	100 µm	30 µm
L	500 µm	8.5 cm	4 cm
g	$(2\pi)4$ MHz	$(2\pi)88$ kHz	$(2\pi)13$ kHz
N_{crit}	0.5	34	1.6
n_{sat}	1.1	2312	0.16

With $N = 10^4$ the cooperativity parameter N/N_{crit} is in all cases well above 1.

25.5.2 Description of quantized light fields in cavities

In order to calculate the evolution of photon distributions in the counter-propagating modes $\hat{a}_\pm$ of a ring cavity, we develop CARL in a Fock basis. For simplicity, we first consider the *motion of a single atom as classical* and fixed (i.e. not as a degree of freedom), and we apply the adiabatic approximation. I.e. we have only two quantized

degrees of freedom, which we organize like,

$$|\psi\rangle = \cancel{|\nu\rangle_{\text{motion}}}^{\text{classical}} \otimes \cancel{|i\rangle_{\text{electron}}}^{\text{adiab.elim.}} \otimes |n\rangle_+ \otimes |n\rangle_- \to |n_+, n_-\rangle \ , \quad (25.163)$$

Expanding the fields into Fock states,

$$\boxed{|\psi\rangle = \sum_{n_+,n_-} c_{n_+,n_-} |n_+, n_-\rangle} \ , \quad (25.164)$$

the field operators and the density matrix read,

$$\hat{a}_+ = \sum_{n_+} \sqrt{n_+} |n_+ - 1\rangle\langle n_+| \otimes \mathbb{I} = \sum_{n_+,n_-} \sqrt{n_+} |n_+ - 1, n_-\rangle\langle n_+, n_-| \quad (25.165)$$

$$\hat{a}_- = \mathbb{I} \otimes \sum_{n_-} \sqrt{n_-} |n_- - 1\rangle\langle n_-| = \sum_{n_+,n_-} \sqrt{n_+} |n_+ - 1, n_-\rangle\langle n_+, n_-|$$

$$\hat{\rho} = |\psi\rangle\langle\psi| = \sum_{m_+,m_-,n_+,n_-} c^*_{m_+,m_-} c_{n_+,n_-} |m_+, m_-\rangle\langle n_+, n_-| \ .$$

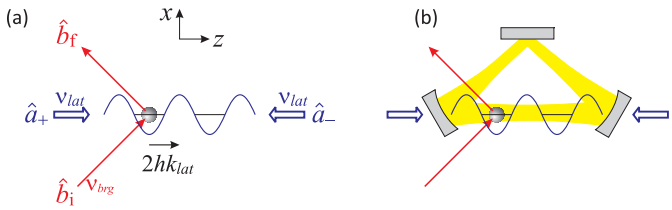

Figure 25.22: (a) Bragg scattering at a 1D optical lattice. (b) Same as in (a), but now the optical lattice is generated by the mode of an optical ring cavity.

Note that the master equation using the Lindbladt operator traces over the reservoir. Hence, the master equation only treats the cavity modes, but does not allow predictions on the quantum behavior of outcoupled fields. In order to describe e.g. quantum correlations in output field, one needs an input-output theory [169, 304].

In the case of classical motion quantum light fields,

$$\boxed{\begin{aligned}
\dot{c}_{n_+,n_-} &= \imath(\Delta_c - U_0)(n_+ + n_-)\, c_{n_+,n_-} \\
&- \imath U_0 \left(e^{-2\imath kz} \sqrt{n_+(n_- + 1)}\, c_{n_+-1,n_-+1} - e^{2\imath kz} \sqrt{(n_+ + 1)n_-}\, c_{n_++1,n_--1} \right) \\
&- \eta_+ \left(\sqrt{n_+ + 1}\, c_{n_++1,n_-} - \sqrt{n_+}\, c_{n_+-1,n_-} \right) \\
&- \eta_- \left(\sqrt{n_- + 1}\, c_{n_+,n_-+1} - \sqrt{n_-}\, c_{n_+,n_--1} \right) \\
\dot{z} &= 2\imath\hbar k U_0 \sum_{n_+,n_-} \left(e^{-2\imath kz} \sqrt{(n_+ + 1)n_-}\, c^*_{n_++1,n_--1} c_{n_+,n_-} \right. \\
&\qquad \left. - e^{2\imath kz} \sqrt{n_+(n_- + 1)}\, c^*_{n_+-1,n_-+1} c_{n_+,n_-} \right)
\end{aligned}} \ . \quad (25.166)$$

25.5.3 Photon backscattering for fixed atomic position

To tackle the problem of quantized light field we first assume an atom fixed in space, that is, we completely *disregard the motional degree of freedom* by setting $\hat{p} = 0$ and restricting to the Hamiltonian,

$$\hat{H} = \sum_{\pm} \omega_{\pm} \hat{a}_{\pm}^{\dagger} \hat{a}_{\pm} - \imath\eta_{\pm}(\hat{a}_{\pm} - \hat{a}_{\pm}^{\dagger}) + U_0(\hat{a}_{+}^{\dagger}\hat{a}_{-}e^{-2\imath k\hat{z}} + \hat{a}_{-}^{\dagger}\hat{a}_{+}e^{2\imath k\hat{z}}) \ . \tag{25.167}$$

In Exc. 25.5.7.1 we show how to cast the Hamiltonian into a matrix form using an appropriate basis already used in the discussion of the beam splitter in the photon representation in Sec. 14.5.1.

In Exc. 25.5.7.2(a) we derive the equations of motion for the components c_{n_+,n_-} of the state vector from the Schrödinger equation cavity decay. In Exc. 25.5.7.3(a) we derive the equations of motion for the components $\rho_{m_+,n_+;m_-n_-} = \langle m_+, m_-|\hat{\rho}|n_+, n_-\rangle$ of the density operator. Simulations performed based on these equations of motion are shown in Fig. 25.23).

The simulations reveal a number of interesting facts:

- The field amplitudes $|\alpha_{\pm}|^2$ execute oscillations due to CARL coupling, but with preserved Poissonian shape of the photon number distributions.
- When simulations are done with initial Fock states, they eventually relax to a Glauber state.
- The mean photon numbers and the atomic coordinates evolve in a continuous way.

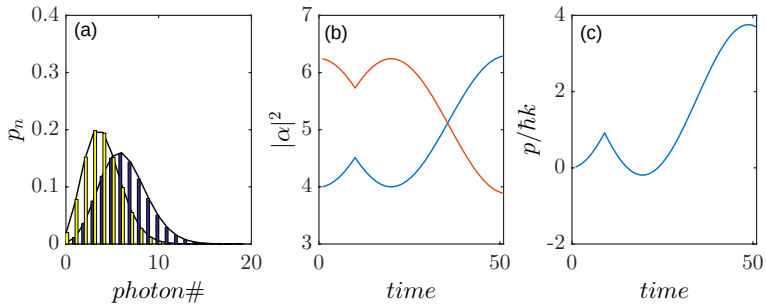

Figure 25.23: (code) Time-evolution of CARL with one classical atom and two quantized field modes. (a) Photon number distributions of two modes after some evolution time t. (b) Time-evolution of the mean photon number; at time $t = 10$, the atom is suddenly displaced. (c) Time-evolution of the (classical) atomic trajectory.

These observations are not surprising, once we understood the backscattering as a linear coupling between the modes being mediated by a beam splitter Hamiltonian of type (14.136) [15],

$$\hat{H}_{int} = U_0(\hat{a}_{+}^{\dagger}\hat{a}_{-}e^{-2\imath kz} + \hat{a}_{+}\hat{a}_{-}^{\dagger}e^{2\imath kz}) \ , \tag{25.168}$$

[15] Which itself represents a generalized displacement operator,

$$\hat{H}_{int} \simeq U_0(\alpha_{+}^{*}e^{-2\imath kz}\hat{a}_{-} + \alpha_{+}e^{2\imath kz}\hat{a}_{-}^{\dagger}) \equiv \imath\hbar\beta^{*}\hat{a}_{-} - \imath\hbar\beta\hat{a}_{-}^{\dagger} \ ,$$

for which we found the relationship (14.137),

$$\boxed{e^{-\imath\hat{H}_{int}t}\hat{a}_{\pm}e^{\imath\hat{H}_{int}t} = \hat{a}_{\pm}\cos U_0 t \pm \hat{a}_{\mp}e^{\mp 2\imath kz}\sin U_0 t} \ . \tag{25.169}$$

This means, that we expect (for a fixed location z of the atom) an oscillatory behavior of the field amplitudes $|\alpha_{\pm}|^2$ and also of the phase (encoded in $\alpha_+^*\alpha_-$), but no modification of the coherent photon statistics. On the contrary, as shown in Sec. 14.5.1, a beam splitter tends to transform sub-Poissonian states into Poissonian ones. In fact, *CARL is nothing else than a movable beam splitter.*

Non-linearity may come into play, if photonic recoil is included, i.e. if the *atomic motion itself becomes a degree of freedom.* This is the next step of our problem, that needs to be solved.

25.5.4 Quantized light fields and quantized recoil

The simulations of the preceding section show that the CARL Hamiltonian (25.168), despite the appearance of photon creation and annihilation operator, does not request recoil to be quantized: If an arbitrary momentum kick of the atom can be absorbed by the light fields, then an arbitrary dipole force can be transmitted to the atomic momentum! The momentum conservation law (25.17) does not imply quantization of photonic recoil. The question is now, how to conceal this fact with the observation of discrete momentum sidemodes [765]. We have seen earlier, that the quantization of the motion is transferred from the quantized photon fields via the operator (25.103) to the atom: An initially resting atom can only adopt motional states with momenta equal to a multiple of $2\hbar k$.

We will now take the quantization of the atomic momentum for granted and study quantized light modes coupled by *recoiling atoms*, we extend our Hilbert space like,

$$|\psi\rangle = |\nu\rangle_{\text{motion}} \otimes \cancel{|i\rangle_{\text{electron}}} \overset{\text{adiab.elim.}}{\longrightarrow} \otimes\, |n\rangle_+ \otimes |n\rangle_- \to |\nu, n_+, n_-\rangle \ , \tag{25.170}$$

Expanding the motion and fields [16],

$$\boxed{|\psi\rangle = \sum_{\nu,n_+,n_-} c_{\nu,n_+,n_-}|\nu, n_+, n_-\rangle} \ , \tag{25.171}$$

the momentum kick operator reads,

$$e^{-2\imath k\hat{z}} \otimes \mathbb{I} \otimes \mathbb{I} = \sum_{\nu} |\nu\hbar k - 2\hbar k, n_+, n_-\rangle\langle \nu\hbar k, n_+, n_-| \ . \tag{25.172}$$

since defining $\beta \equiv \frac{\imath U_0}{\hbar}\alpha_+ e^{2\imath kz}$, we find,

$$B(\beta t) = e^{-\imath\hat{H}_{int}t/\hbar} = e^{\beta^* t\hat{a}_- - \beta t\hat{a}_-^\dagger} \ .$$

[16] Note the fact, which is important for computation, that the dimension of the Hilbert space increases a lot, that is like dim $\nu \cdot$ dim $n_+ \cdot$ dim n_-, where $\nu, n_\pm$ are the numbers of states considered.

The equations of motions derived in Exc. 25.5.7.2 from the Schrödinger equation are now generalized to,

$$\boxed{\begin{aligned}\dot{c}_{\nu,n_+,n_-} &= \imath(\Delta_c - U_0)(n_+ + n_-)c_{\nu,n_+,n_-} \\ &- \imath U_0\left(\sqrt{n_+(n_- + 1)}c_{\nu-1,n_+-1,n_-+1} - \sqrt{(n_+ + 1)n_-}c_{\nu+1,n_++1,m_--1}\right) \\ &- \eta_+\left(\sqrt{n_+ + 1}c_{\nu,n_++1,n_-} + \sqrt{n_+}c_{\nu,n_+-1,n_-}\right) \\ &- \eta_-\left(\sqrt{n_- + 1}c_{\nu,n_+,n_-+1} + \sqrt{n_-}c_{\nu,n_+,n_--1}\right)\end{aligned}} \; . \tag{25.173}$$

Note that the general shape of fully quantized Schrödinger equations looks like,

$$\dot{c}_{\nu',n'_+,n'_-} = \begin{pmatrix} \ddots & \vdots & \\ \cdots & \mathcal{B}_{\{\nu',n'_+,n'_-\};\{\nu,n_+,n_-\}} & \cdots \\ & \vdots & \ddots \end{pmatrix} c_{\nu,n_+,n_-} \tag{25.174}$$

and for fully quantized master equations,

$$\begin{aligned}&\dot{\rho}_{\{\mu',m'_+,m'_-\};\{\nu',n'_+,n'_-\}} \\ &= \begin{pmatrix} \ddots & \vdots & \\ \cdots & \mathcal{L}_{\{\mu',m'_+,m'_-;\nu',n'_+,n'_-\};\{\mu,m_+,m_-;\nu,n_+,n_-\}} & \cdots \\ & \vdots & \ddots \end{pmatrix} \rho_{\{\mu,m_+,m_-\};\{\nu,n_+,n_-\}} \; .\end{aligned} \tag{25.175}$$

However, the mere inclusion of a third degree of freedom coupled to the other two degrees in the same linear fashion will modify the behavior of the system, which will continue to oscillate as it did before, now just involving the atomic motion in this dynamics. This behavior can only change, when we additionally consider the force equation,

$$\dot{\hat{p}} = 2\hbar k U_0(\hat{a}^\dagger_+\hat{a}_- e^{-2\imath kz} - \hat{a}_+\hat{a}^\dagger_- e^{2\imath kz}) \; , \tag{25.176}$$

which will lead to feedback. Inserting the expansion (25.171),

$$\dot{c}_{\nu,n_+,n_-} = 2\hbar k U_0\left(c_{\nu,n_+,n_-}\sqrt{n_+(n_- + 1)} - c_{\nu,n_+,n_-}\sqrt{n_+(n_- + 1)}\right) \; . \tag{25.177}$$

Note that, in contrast to CARL equations, the fully quantized equations (25.173) *are linear*. That is, it is the 'classization' [17] of the degrees of freedom which introduces the non-linearities, which are typical for CARL, e.g. the feedback introduced by classical light fields. The process of 'classization' corresponds to *tracing* over degrees of freedom, which we want to treat classically and thus remove from the Hamiltonian.

25.5.4.1 Calculation of observables

Once the time evolution of the coefficients $c_{\nu,n_+,n_-}(t)$ has been determined by solving the differential equation (25.173) we can calculate the observables in the following

[17] As opposed to the term quantization.

way. The probability distribution for photon numbers in the mode α_+ is given by,

$$\begin{aligned} P_{n_+}(t) &= \langle\psi(t)|\mathbb{I}\otimes|n_+\rangle\langle n_+|\otimes\mathbb{I}|\psi(t)\rangle \\ &= \sum_{\nu,n_-}\langle\nu,n_+,n_-|\nu,n_+,n_-\rangle = \sum_{\nu,n_-}|c_{\nu,n_+,n_-}(t)|^2 \ , \end{aligned} \tag{25.178}$$

the mean photon number by,

$$\langle\hat{n}_+(t)\rangle = |\alpha_+(t)|^2 = \sum_{n_+} n_+ P_{n_+}(t) = \sum_{\nu,n_+,n_-} n_+|c_{\nu,n_+,n_-}(t)|^2 \ , \tag{25.179}$$

and similarly for α_-. The probability distribution for momentum states is given by,

$$P_\nu(t) = \sum_{n_+,n_-}|c_{\nu,n_+,n_-}(t)|^2 \ , \tag{25.180}$$

the mean momentum by,

$$\langle\hat{p}(t)\rangle = \sum_{\nu,n_+,n_-}\nu\hbar k|c_{\nu,n_+,n_-}(t)|^2 \ , \tag{25.181}$$

the mechanical kinetic energy by,

$$\begin{aligned} E_{kin}(t) = \frac{\langle\hat{p}^2\rangle}{2m} &= \sum_{\nu,n_+,n_-}\frac{(\nu\hbar k)^2}{2m}|c_{\nu,n_+,n_-}(t)|^2 \\ &= \sum_{\nu,n_+,n_-}\nu^2\hbar\omega_{\rm rec}|c_{\nu,n_+,n_-}(t)|^2 \ , \end{aligned} \tag{25.182}$$

and the potential energy by,

$$\begin{aligned} E_{pot}(t) &= \hbar U_0\langle e^{-2\imath k\hat{z}}\hat{a}_+^\dagger\hat{a}_- + e^{2\imath k\hat{z}}\hat{a}_+\hat{a}_-^\dagger\rangle \\ &= \hbar U_0\sum_{\nu,n_+,n_-}\Big(c^*_{\nu+1,n_++1,n_--1}c_{\nu,n_+,n_-}\sqrt{(n_++1)n_-} \\ &\qquad + c^*_{\nu-1,n_+-1,n_-+1}c_{\nu,n_+,n_-}\sqrt{n_+(n_-+1)}\Big) \ . \end{aligned} \tag{25.183}$$

With this we can check conservation of the total photon number,

$$\langle\hat{n}_+(t)\rangle + \langle\hat{n}_-(t)\rangle = const \ , \tag{25.184}$$

of the mechanical energy,

$$E_{kin}(t) + E_{pot}(t) = const \ , \tag{25.185}$$

and of total linear momentum,

$$\hbar k[\langle\hat{n}_+(t)\rangle - \langle\hat{n}_-(t)\rangle] - \langle\hat{p}(t)\rangle = const \ . \tag{25.186}$$

25.5.4.2 Master equation for CQED with atomic recoil in the adiabatic approximation

Using the Hamiltonian (25.26) or (25.98), the expansion of the recoil operator (25.103), the expansion of the photon field operators (25.165), and the matrix representation of the density operator (14.20), that is,

$$\hat{\rho} = \sum_{\mu,\nu;m_+,n_+;m_-,n_-} |\mu, m_+, m_-\rangle \rho_{\mu,\nu;m_+,n_+;m_-,n_-} \langle \nu, n_+, n_-| \ , \tag{25.187}$$

the master equation (25.8) becomes,

$$\boxed{\langle \mu, m_+, m_-|\dot{\hat{\rho}}|\nu, n_+, n_-\rangle = -\imath\langle \mu, m_+, m_-|[\hat{H}, \hat{\rho}]|\nu, n_+, n_-\rangle + \mathcal{L}_{cavity-vac,\pm}\hat{\rho}} \ , \tag{25.188}$$

with the coherent contributions,

$$\begin{aligned}
&\langle \mu, m_+, m_-|[\tfrac{\hat{p}^2}{2m}, \hat{\rho}]|\nu, n_+, n_-\rangle = \omega_{\rm rec}(\mu^2 - \nu^2)\rho_{\mu,\nu;m_+,n_+;m_-,n_-} \qquad (25.189)\\
&\langle \mu, m_+, m_-|[(U_0 - \Delta_c)\hat{a}_\pm^\dagger \hat{a}_\pm, \hat{\rho}]|\nu, n_+, n_-\rangle = (U_0 - \Delta_c) n_\pm \rho_{\mu,\nu;m_+,n_+;m_-,n_-}\\
&\langle \mu, m_+, m_-|[-\imath\eta_+(\hat{a}_+ - \hat{a}_+^\dagger), \hat{\rho}]|\nu, n_+, n_-\rangle\\
&= -\imath\eta_+ \Big(\sqrt{m_+}\rho_{\mu,\nu;m_+-1,n_+;m_-,n_-} - \sqrt{m_+ + 1}\rho_{\mu,\nu;m_++1,n_+;m_-,n_-}\\
&\qquad + \sqrt{n_+}\rho_{\mu,\nu;m_+,n_+-1;m_-,n_-} - \sqrt{n_+ + 1}\rho_{\mu,\nu;m_+,n_++1;m_-,n_-} \Big)\\
&\langle \mu, m_+, m_-|[-\imath\eta_-(\hat{a}_- - \hat{a}_-^\dagger), \hat{\rho}]|\nu, n_+, n_-\rangle\\
&= -\imath\eta_- \Big(\sqrt{m_-}\rho_{\mu,\nu;m_+,n_+;m_- -',n_-} - \sqrt{m_- + 1}\rho_{\mu,\nu;m_+,n_+;m_-+1,n_-}\\
&\qquad + \sqrt{n_-}\rho_{\mu,\nu;m_+,n_+;m_-,n_- -1} - \sqrt{n_- + 1}\rho_{\mu,\nu;m_+,n_+;m_-,n_-+1} \Big)\\
&\langle \mu, m_+, m_-|[U_0 e^{-2\imath k\hat{z}}\hat{a}_+^\dagger \hat{a}_-, \hat{\rho}]|\nu, n_+, n_-\rangle\\
&= U_0 \Big(\sqrt{m_+(m_- + 1)}\rho_{\mu+1,\nu;m_+-1,n_+;m_-+1,n_-} + \sqrt{(m_+ + 1)m_-}\rho_{\mu-1,\nu;m_++1,n_+;m_- -1,n_-} \Big)\\
&\langle \mu, m_+, m_-|[U_0 e^{2\imath k\hat{z}}\hat{a}_+\hat{a}_-^\dagger, \hat{\rho}]|\nu, n_+, n_-\rangle\\
&= U_0 \Big(\sqrt{(n_+ + 1)n_-}\rho_{\mu,\nu-1;m_+,n_++1m_-,n_- -1} + \sqrt{n_+(n_- + 1)}\rho_{\mu,\nu+1;m_+,n_+-1;m_-,n_-+1} \Big) \ ,
\end{aligned}$$

and the incoherent contributions,

$$\begin{aligned}
&\langle \mu, m_+, m_-| - \kappa[\hat{a}_+^\dagger \hat{a}_+ \hat{\rho} - 2\hat{a}_+ \hat{\rho}\hat{a}_+^\dagger + \hat{\rho}\hat{a}_+^\dagger \hat{a}_+]|\nu, n_+, n_-\rangle \qquad (25.190)\\
&\qquad = -\kappa \big(m_+\rho_{\mu,\nu;m_+,n_+;m_-,n_-} + n_+\rho_{\mu,\nu;m_+,n_+;m_-,n_-}\\
&\qquad\qquad -2\sqrt{(m_+ + 1)(n_+ + 1)}\rho_{\mu,\nu;m_++1,n_++1;m_-,n_-} \big)\\
&\langle \mu, m_+, m_-| - \kappa[\hat{a}_-^\dagger \hat{a}_- \hat{\rho} - 2\hat{a}_- \hat{\rho}\hat{a}_-^\dagger + \hat{\rho}\hat{a}_-^\dagger \hat{a}_-]|\nu, n_+, n_-\rangle\\
&\qquad = -\kappa \big(m_-\rho_{\mu,\nu;m_+,n_+;m_-,n_-} + n_-\rho_{\mu,\nu;m_+,n_+;m_-,n_-}\\
&\qquad\qquad -2\sqrt{(m_- + 1)(n_- + 1)}\rho_{\mu,\nu;m_+,n_+;m_-+1,n_-+1} \big) \ .
\end{aligned}$$

25.5.5 Kicking and forcing an atom in a ring cavity

The question we want to elucidate here is, how a coupled atom-ring cavity system reacts to a kick transferring an arbitrary amount of momentum to the atom. We stud-

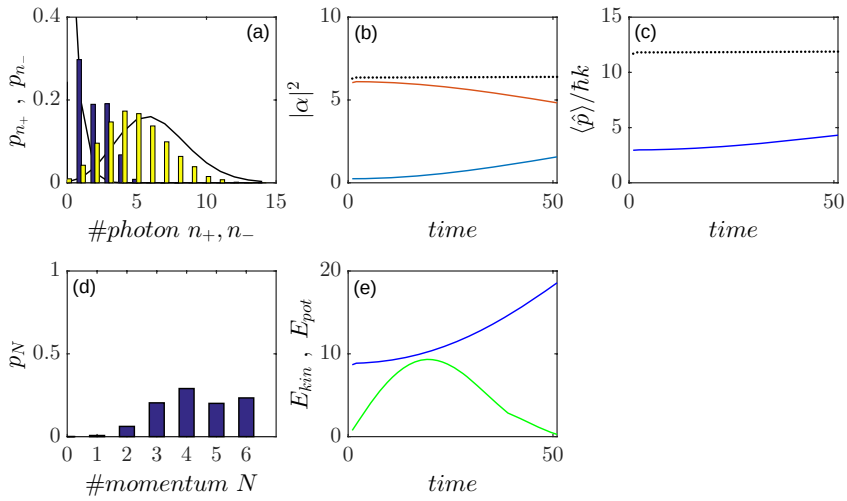

Figure 25.24: (code) Time-evolution of CARL with one classical atom and two quantized field modes. (a) Photon number distributions of two modes after some evolution time t. (b) Time-evolution of the mean photon number; at time $t = 10$, the atom is suddenly displaced. (c) Time-evolution of the (classical) atomic trajectory.

ied a similar question when studying the kicking of a harmonic oscillator in Sec. 2.6.2, however, the situation is quite different now because, in contrast to the harmonic oscillator, the motion of an atom subject to CARL dynamics is not localized and, hence, *not quantized*. That is, an arbitrarily kicked atom is not bound to join one of those momentum states it would populate when kicked by photonic recoil. Hence, a momentum state expansion like (25.107) is not appropriate, so that we have to go a step back and consider the Hamiltonian (25.26) again. See also (watch talk).

25.5.5.1 Kicking

Let us first describe the kick as an incoherent disruptive one time event transforming operators, the Hamiltonian and the system's state like,

$$\hat{A} \longrightarrow e^{-\imath q\hat{z}}\hat{A}e^{\imath q\hat{z}} \quad , \quad |\psi\rangle \longrightarrow e^{\imath q\hat{z}}|\psi\rangle \tag{25.191}$$

and in particular,

$$\hat{H} \longrightarrow e^{-\imath q\hat{z}}\hat{H}e^{\imath q\hat{z}} = \hat{H}(\hat{z}, \hat{p} - \hbar q) \quad , \quad \langle p|\psi\rangle \longrightarrow \langle p|e^{\imath q\hat{z}}|\psi\rangle = \langle p - \hbar q|\psi\rangle \ . \tag{25.192}$$

The Schrödinger equation tells us the system's evolution after the kick,

$$\imath\hbar\frac{d}{dt}\langle p|\psi\rangle = \frac{p^2}{2m}\langle p|\psi\rangle + U_0\left(\langle p|e^{-2\imath k\hat{z}}|\psi\rangle\hat{a}_+^\dagger\hat{a}_- + \langle p|e^{2\imath k\hat{z}}|\psi\rangle\hat{a}_+\hat{a}_-^\dagger\right) \ . \tag{25.193}$$

We remind that this equations contains CARL feedback via the simultaneous presence of $\hat{z}$ and $\hat{p}$. If we want to disregard the CARL force (assuming, for example, that the motion is totally imposed by an external force, as done in Sec. 22.1.8 in order to focus on the behavior of the light fields), we must not project the Schrödinger equation on $\langle p|$ but treat the motional degree of freedom as classical.

25.5.5.2 Forcing

Let us now describe the kick as a force $F(t) = mg\theta(t)$ being switched on at a given time, but being constant afterward,

$$\hat{H} = \frac{\hat{p}^2}{2m} + U_0 \left(e^{-2\imath k\hat{z}} \hat{a}_+^\dagger \hat{a}_- + e^{2\imath k\hat{z}} \hat{a}_+ \hat{a}_-^\dagger \right) + mg\hat{z} \ . \tag{25.194}$$

We note that with (1.267) the Hamiltonian transformed into the accelerated frame reads,

$$\begin{aligned} \hat{H} &\longrightarrow e^{-\imath mg\hat{z}t/\hbar} \hat{H} e^{\imath mg\hat{z}t/\hbar} + \imath\hbar \left(\frac{d}{dt} e^{\imath mg\hat{z}t/\hbar} \right)^\dagger e^{\imath mg\hat{z}t/\hbar} = \hat{H}(\hat{z}, \hat{p} - mgt) - mg\hat{z} \\ &= \frac{(\hat{p} - mgt)^2}{2m} + U_0 \left(e^{-2\imath k\hat{z}} \hat{a}_+^\dagger \hat{a}_- + e^{2\imath k\hat{z}} \hat{a}_+ \hat{a}_-^\dagger \right) \ . \end{aligned} \tag{25.195}$$

The Schrödinger equation for the transformed wavefunction $|\psi\rangle = |\tilde{\psi}\rangle e^{\imath mg\hat{z}t/\hbar}$, which tells us the system's evolution during the force,

$$\imath\hbar \frac{d}{dt} \langle p|\tilde{\psi}\rangle = \frac{(p - mgt)^2}{2m} \langle p|\tilde{\psi}\rangle + U_0 \left(\langle p|e^{-2\imath k\hat{z}}|\tilde{\psi}\rangle \hat{a}_+^\dagger \hat{a}_- + \langle p|e^{2\imath k\hat{z}}|\tilde{\psi}\rangle \hat{a}_+ \hat{a}_-^\dagger \right) \ , \tag{25.196}$$

has a similar shape to Eq. (25.193).

25.5.5.3 Vibrating

Another option might be to additionally confine the atom in a harmonic potential [891],

$$\begin{aligned} \hat{H} &= \frac{\hat{p}^2}{2m} + U_0 \left(e^{-2\imath k\hat{z}} \hat{a}_+^\dagger \hat{a}_- + e^{2\imath k\hat{z}} \hat{a}_+ \hat{a}_-^\dagger \right) + \frac{m}{2} \omega^2 \hat{z}^2 \\ &= \hbar\omega (\hat{A}^\dagger \hat{A} + \tfrac{1}{2}) + U_0 \left[D^\dagger(\alpha) \hat{a}_+^\dagger \hat{a}_- + D(\alpha) \hat{a}_+ \hat{a}_-^\dagger \right] \ , \end{aligned} \tag{25.197}$$

where $D(\alpha) \equiv e^{\alpha \hat{A}^\dagger - \alpha^* \hat{A}}$ with $\alpha \equiv \frac{2\imath k a_{ho}}{\sqrt{2}}$.

25.5.5.4 Quantized equations of motion

In both cases, 'kicking' and 'forcing', we may discretize momentum space, although in the latter case we need to transform back into the lab frame after having solved the Schrödinger equation (25.173).

25.5.6 Quantum correlations

Superradiant or CARL scattering exist due to a correlation of subsequent scattering events. In the quantum regime, the emergence of quantum correlations, such as entanglement and squeezing is to be expected as a consequence of CARL dynamics [598, 658, 675, 667, 668, 836, 166, 167, 168]. The advantage of doing CARL with BECs is the possibility to exploit the instability in the good-cavity regime to parametrically

amplify optical and matter waves, manipulate matter wave coherence properties and generate entanglement.

For the description of the dynamics of the fields, i.e. the momentum sidemodes and the cavity modes, a first-quantized treatment of the atomic motion [660] would be sufficient. All information can be extracted from a numerical simulation of the quantum CARL equations. However, here we are also interested in quantum correlations. Hence, in a first-quantized treatment of the atomic motion, the coefficients $\hat{c}_n$ must be treated as field operators. Alternatively, we derive the basic equations rigorously from a second-quantized treatment.

25.5.6.1 Generation of squeezing and entanglement via CARL

An experiment by [679] produces squeezing in transmission of a cavity resonantly interacting with single atoms. The effect was induced by vacuum Rabi-splitting. In our case we have a ring cavity, we operate far from equilibrium, we have classical Stark splitting. Hence, we may expect squeezing and entanglement from the CARL dynamics.

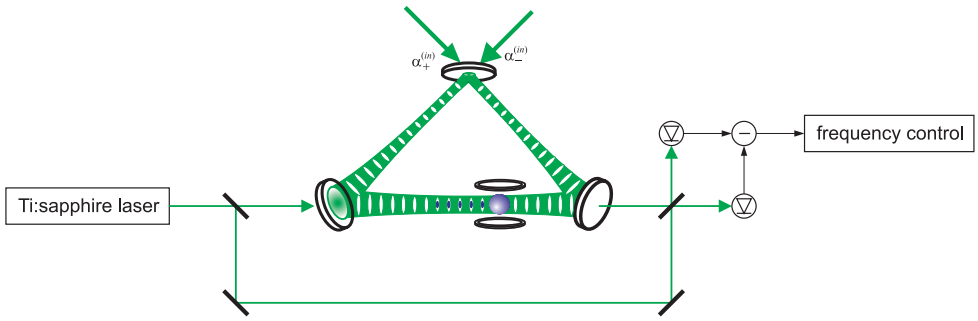

Figure 25.25: Production and detection of squeezing.

Differences between entanglement and correlation (correlations involve time or space coordinates $g(\tau)$, particles correlate across space and time, coherence).

Bragg scattering of light at an atomic grating (or simply the splitting of light at a beam splitter) is an irreversible process (see Sec. 14.5). CARL can be interpreted in terms of Bragg scattering of light at an atomic grating, which is generated itself by the Bragg scattering. Hence, the scattering of early photons influences the scattering of late photons, i.e. the scattering processes get correlated, the dynamics gets a history. The correlation between subsequent scattering processes is what preserves the coherence in CARL and superradiant Rayleigh scattering.

It is now interesting to ask how this classical correlations will behave in the quantum regime, i.e. upon 1. quantization of the motion of individual atoms and upon 2. quantization of atomic particle field. Following [598, 597, 600, 599, 658, 659, 667, 668], non-classical correlations such as entanglement of matter wave modes, and entanglement between matter-wave and optical modes is expected.

25.5.6.2 Quantum non demolition measurements with CARL

According to [668], a ring cavity could lend itself to quantum non demolition measurements. They consider our ring cavity being pumped from both sides through an incoupling mirror. A so-called pump mode is injected with a p-polarized light field, and a probe mode with a s-polarized light field. The light of the probe mode leaking through a mirror gives information about the atoms (e.g. via the refraction index). The counterpropagating pump light gives access to higher-order moments of the atom distribution.

The problem is that the effect is based on photon exchange between the modes, and those are orthogonally polarized. Even more problematic is that, in practice, the modes have different frequencies. Other work on this subject has been done by [43, 258, 567, 568, 146].

25.5.7 Exercises

25.5.7.1 Ex: Analogy between CARL and two-atom Dicke states

a. Write the Hamiltonian (25.167) in matrix form using the basis,

$$\psi_k = \{|0,0\rangle, |0,1\rangle, |1,0\rangle, |0,2\rangle, |1,1\rangle, |2,0\rangle, ...\} \ .$$

b. Now restrict to the finite number of states $\psi_k = \{|0,0\rangle, |0,1\rangle, |1,0\rangle, |1,1\rangle\}$ and discuss the analogy between CARL and two-atom Dicke states.

25.5.7.2 Ex: Cavity QED with Schrödinger equation

Assume a symmetrically pumped ring cavity in equilibrium with an atom at a fixed position.
a. Derive the equations of motion for the components for the probability amplitudes in a Fock state basis.
b. Express the possible initial states $|\alpha_+, \alpha_-\rangle$, $|\alpha_+, n_-\rangle$, and $|n_+, n_-\rangle$ in the Fock state basis. How to calculate the photon distribution p_{n_+}, the amplitudes of field modes $\alpha_\pm$, and the atom's position and momentum at later times of the evolution?

25.5.7.3 Ex: Cavity QED with density matrix

Assume a symmetrically pumped ring cavity in equilibrium with an atom at a fixed position.
a. Derive the equations of motion for the components of the density operator.
b. Write down the density operator describing two decoupled Glauber states? How to retrieve the Fock state populations from the density operator?
c. Now, assume that the atom can move. What will be the evolution of the motional state?

25.5.7.4 Ex: Photon number and momentum conservation

a. Calculate the evolution under CARL interaction, $e^{-\imath \hat{H}_{carl} t} \hat{n}_\pm e^{\imath \hat{H}_{carl} t}$, of the photon numbers in each mode and show that the total photon number is conserved.

b. Assuming conservation of total momentum calculate the evolution of the atomic momentum.

25.5.7.5 Ex: Self-synchronization of Bloch oscillations

Study the Bloch-CARL dynamics for the case of a sinusoidally modulated CARL pump light intensity. Choose as the modulation frequency the expected Bloch oscillation frequency and a variable phase delay.

25.6 Atomic self-organization in light fields

The CARL phenomenon introduced in the previous chapter raises a variety of questions, such as: How does it compare to an ordinary laser? Is there a phase transition? Of what kind would be this transition (in the Ehrenfest or Landau classification scheme)? What are the coherence properties (measured by correlation functions)? How do these properties depend on the random motion (temperature) of the atoms? These issues will be addressed in this chapter and in the later chapter within the models of *Langevin*, *Fokker*-Planck, *Vlasov*Vlasov, and *Kuramoto*.

25.6.1 The Langevin model

25.6.1.1 CARL with damping

We saw in the previous chapter that CARL is a transient phenomenon, the atoms and the phase of the light wave being continuously accelerated. However, it is possible to force stationary behavior by providing additional friction for the atoms. Such friction can be carried out by an *optical molasses* (see Sec. 26.2.1) characterized by a friction coefficient $\gamma_{\rm frc}$. The friction force can be added to the CARL equations of motion (25.69),

$$\begin{aligned} \dot{\alpha}_- &= -\kappa\alpha_- - \imath U_0\alpha_+ \sum_m e^{2\imath k z_m} \\ k\dot{v}_n &= 4i\omega_{\rm rec}U_0\alpha_+(\alpha_- e^{-2\imath k z_n} - \alpha_-^* e^{2\imath k z_n}) - \gamma_{\rm frc} k v_n \ . \end{aligned} \tag{25.198}$$

Now, the balance of forces happens at a well-defined atomic velocity, which incidentally corresponds to a well-defined CARL frequency. Assuming perfect 'bunching' $e^{2\imath k z_m} = e^{2\imath k z}$, and balanced forces, $\dot{v}_m = 0$ e $\alpha_- = \beta e^{2\imath k z}$ with $\dot{\beta} = 0$, we obtain for $\kappa \ll 2kv$,

$$\begin{aligned} \alpha_- &= \tfrac{-\imath N U_0 \alpha_+}{\kappa + 2\imath k v} e^{2\imath k z} \\ (kv)^3 &= \frac{2\omega_{\rm rec}\kappa N U_0^2 \alpha_+^2}{\gamma_{\rm frc}} \ . \end{aligned} \tag{25.199}$$

This result will be derived in Exc. 25.6.7.1.

Optical molasses obviously are subject to a cooling limit coming from the random scattering of photons. As a consequence, atoms follow a *random walk* in the momentum space, which leads to the diffusion and heating of atoms and impedes the

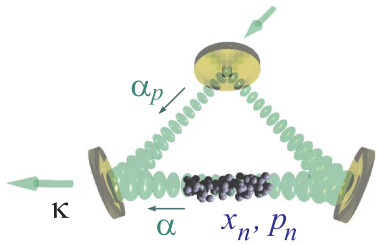

Figure 25.26: Scheme of the ring cavity.

bunching of atoms. It also turns out that a minimal grouping is required to initialize CARL. Therefore, there is a threshold behavior as a function of the equilibrium temperature of the molasses,

$$\boxed{\begin{aligned} \dot{\alpha}_- &= -\kappa\alpha_- - \imath U_0 \alpha_+ \textstyle\sum_m e^{2\imath k z_m} \\ k\dot{v}_n &= 4\imath\omega_{\rm rec} U_0 \alpha_+ (\alpha_- e^{-2\imath k z_n} - \alpha_-^* e^{2\imath k z_n}) - \gamma_{\rm frc} k v_n + \xi_n(t) \end{aligned}} \quad . \tag{25.200}$$

The equation corresponds to a *Langevin equation*, where the stochastic term $\xi_n(t)$ describes white noise. We can simulate this equation by a Runge-Kutta method, where the atoms are continually exposed to random momentum changes. For N atoms we need to solve $2N + 2$ Langevin equations to describe the dynamics of all degrees of freedom. The Langevin equations are associated to so-called *Fokker-Planck equations* [843, 698, 430, 842]. These describe the temporal evolution of the atomic density along the optical x-axis. With these equations we replace the $2N$ trajectories of individual particles by a one-dimensional field $P(x, t)$. The *Vlasov equation* represents a different approach: Here we assume that the equilibrium between cooling and heating is achieved by a continuous thermalization process described by a single rate γ_{th} [18].

25.6.1.2 Characterization of an optical molasses

Optical molasses is discussed in Sec. 26.2.1. In Exc. 26.2.5.1 we will show how, through a linearization of the radiative pressure force, we arrive at the following approximation,

$$\mathbf{F} = -\gamma_{\rm frc}\mathbf{v} \qquad \text{with} \qquad \gamma_{\rm frc} \simeq -\sqrt{3}\hbar k^2 s(1+s)^{-3/2} \ , \tag{25.201}$$

where $s = I/I_s$ is the saturation parameter. This formula estimates the maximum friction force, when the lasers are tuned close to an atomic resonance [19].

A more fundamental problem is the interdependence of the molasses friction and the CARL. In fact, because the dipole potential influences the detuning of the molasses

[18] Through a linearization of the CARL equations, the cavity dissipation itself is found to exert a friction force to the atoms [373, 301]. This implies the existence of diffusion and a finite equilibrium temperature even at if the atoms are initially at $T = 0$.

[19] We note that atomic species exhibiting a hyperfine structure in the ground state are subject to cooling phenomena called 'polarization gradient cooling', which can cause much higher friction coefficients.
We also note that, when the molasses is applied to atoms confined to a potential, the atomic levels can be displaced (e.g., by light-shift or the Zeeman effect). This causes an inhomogeneous effective detuning of the laser beams generating the molasses.

beams by light-shifting the D_2 line, the γ_{th} coefficient depends on Δ_a and η_+ (the reverse field $|\alpha_-|$ may be neglected). The threshold equations must then be solved in a self consistent way. It might however be possible to determine γ_{th} only slightly above threshold, where the modification is small, $\gamma_{th} \approx \gamma_{th}^{(thresh)}$.

25.6.1.3 Fluctuation-dissipation theorem

Trajectories of ensembles of particles subject to friction and stochastic forces can be described by *Langevin equations*. The friction and the diffusion forces are related by the *fluctuation-dissipation theorem*. This theorem states that, for a thermal sample of atoms whose coordinates θ_n follow,

$$\ddot{\theta}_n = -\gamma_{\rm frc}\dot{\theta}_n + \xi_n(t) \ , \tag{25.202}$$

the Langevin force $\xi(t)$ fluctuates stochastically with,

$$\langle \xi_n(t) \rangle = 0 \qquad \text{and} \qquad \langle \xi_n(t)\xi_m(t+\tau) \rangle = 2\gamma_{\rm frc}^2 D_T \delta_{mn}\delta(\tau) \ . \tag{25.203}$$

Here, the *diffusion coefficient*,

$$D_T = \frac{\sigma^2}{\gamma_{\rm frc}} \tag{25.204}$$

is related to the width of the Maxwell-Boltzmann velocity distribution,

$$\sigma = 2k\sqrt{\frac{k_{\rm B}T}{m}} \ . \tag{25.205}$$

25.6.1.4 Langevin simulations

The Langevin equations of CARL can be simulated, including the random term of the Langevin force, using the *Runge-Kutta method* [405]. The procedure consists in propagating a general first order differential equation,

$$\boxed{\dot{x} = f(x) + g(t)} \ , \tag{25.206}$$

subject to a deterministic force f and a stochastic noise g satisfying,

$$\langle g(t) \rangle = 0 \qquad \text{and} \qquad \langle g(t)g(t') \rangle = 2D\delta(t-t') \tag{25.207}$$

as follows,

$$\boxed{\begin{array}{rcl} x(dt) & = & x_0 + \frac{1}{2}dt[f(x_0) + f(\tilde{x})] + \zeta(2Ddt)^{1/2} \\ \text{with} \quad \tilde{x} & \equiv & x_0 + f(x_0)dt + \zeta(2Ddt)^{1/2} \end{array}} \ , \tag{25.208}$$

where ζ is a random variable distributed according to a normal (Gaussian) distribution normalized as [20],

$$\langle \zeta \rangle = 0 \qquad \text{and} \qquad \langle \zeta^2 \rangle = 1 \ . \tag{25.209}$$

[20] The MATLAB random number generator satisfies this requirement: $\langle \zeta_n \rangle \triangleq sum(randn(1,N))/N = 0$ and $\langle \zeta_n^2 \rangle \triangleq sum(randn(1,N).\wedge 2)/N = 1$.

25.6.1.5 Langevin simulation in the adiabatic approximation

Now, we apply this method to the CARL subject to an optical molasses. Making the adiabatic approximation $\ddot{\theta}_n = 0$, the starting point is,

$$\boxed{\begin{array}{rcll} \dot{\alpha}_- &=& -\kappa\alpha_- - \imath U_0 \alpha_+ \sum_m e^{\imath\theta_m} & \equiv B(\alpha_-, \theta_n) \\ \dot{\theta}_n &=& \frac{8i\omega_{\rm rec} U_0 \alpha_+}{\gamma_{\rm frc}} (\alpha_- e^{-\imath\theta_n} - \alpha_-^* e^{\imath\theta_n}) + \frac{\xi_n(t)}{\gamma_{\rm frc}} & \equiv F(\alpha_-, \theta_n) + \frac{\xi_n(t)}{\gamma_{\rm frc}} \end{array}} \,. \tag{25.210}$$

In order to apply the Runge-Kutta method (25.208), we identify the variables and functions,

$$x(t) \equiv \begin{pmatrix} \alpha_-(t) \\ \theta_n(t) \end{pmatrix} \quad , \quad f(x) \equiv \begin{pmatrix} B(\alpha_-, \theta_n) \\ F(\alpha_-, \theta_n) \end{pmatrix} \quad , \quad g(t) \equiv \begin{pmatrix} 0 \\ \xi_n(t)/\gamma_{\rm frc} \end{pmatrix} \,, \tag{25.211}$$

such that,

$$\tilde{x} = \begin{pmatrix} \tilde{\alpha}_- \\ \tilde{\theta}_n \end{pmatrix} = \begin{pmatrix} \alpha_-(0) \\ \theta_n(0) \end{pmatrix} + dt \begin{pmatrix} B(\alpha_-(0), \theta_n(0)) \\ F(\alpha_-(0), \theta_n(0)) \end{pmatrix} + \begin{pmatrix} 0 \\ \zeta_n \sqrt{2 D_T dt} \end{pmatrix} \tag{25.212}$$

and

$$\begin{aligned} x(dt) &= \begin{pmatrix} \alpha_-(dt) \\ \theta_n(dt) \end{pmatrix} \\ &= \begin{pmatrix} \alpha_-(0) \\ \theta_n(0) \end{pmatrix} + \frac{dt}{2} \left[\begin{pmatrix} B(\alpha_-(0), \theta_n(0)) \\ F(\alpha_-(0), \theta_n(0)) \end{pmatrix} + \begin{pmatrix} B(\tilde{\alpha}_-, \tilde{\theta}_n) \\ F(\tilde{\alpha}_-, \tilde{\theta}_n) \end{pmatrix} \right] + \begin{pmatrix} 0 \\ \zeta_n \sqrt{2 D_T dt} \end{pmatrix} \,. \end{aligned} \tag{25.213}$$

The Langevin equation can be used to simulate the temporal evolution of CARL. Fig. 25.27 shows a simulation of the frequency and amplitude of the CARL based on prescription (25.208).

25.6.1.6 Langevin simulation of the full dynamics

Without adiabatic approximation, the starting point is,

$$\boxed{\begin{array}{rcll} \dot{\alpha}_- &=& \kappa\alpha_- - \imath U_0 \alpha_+ \sum_m e^{\imath\theta_m} & \equiv B(\alpha_-, \theta_n) \\ \dot{\theta}_n &=& V_n & \\ \dot{V}_n &=& 8i\omega_{\rm rec} U_0 \alpha_+ (\alpha_- e^{-\imath\theta_n} - \alpha_-^* e^{\imath\theta_n}) - \gamma_{\rm frc} V_n + \xi_n(t) & \equiv F(\alpha_-, \theta_n, V_n) + \xi_n(t) \end{array}} \,. \tag{25.214}$$

In order to apply the Runge-Kutta method (25.208), we identify the variables and functions,

$$x(t) \equiv \begin{pmatrix} \alpha_-(t) \\ \theta_n(t) \\ V_n(t) \end{pmatrix} \quad , \quad f(x) \equiv \begin{pmatrix} B(\alpha_-, \theta_n) \\ V_n \\ F(\alpha_-, \theta_n, V_n) \end{pmatrix} \quad , \quad g(t) \equiv \begin{pmatrix} 0 \\ 0 \\ \xi_n(t) \end{pmatrix} \,, \tag{25.215}$$

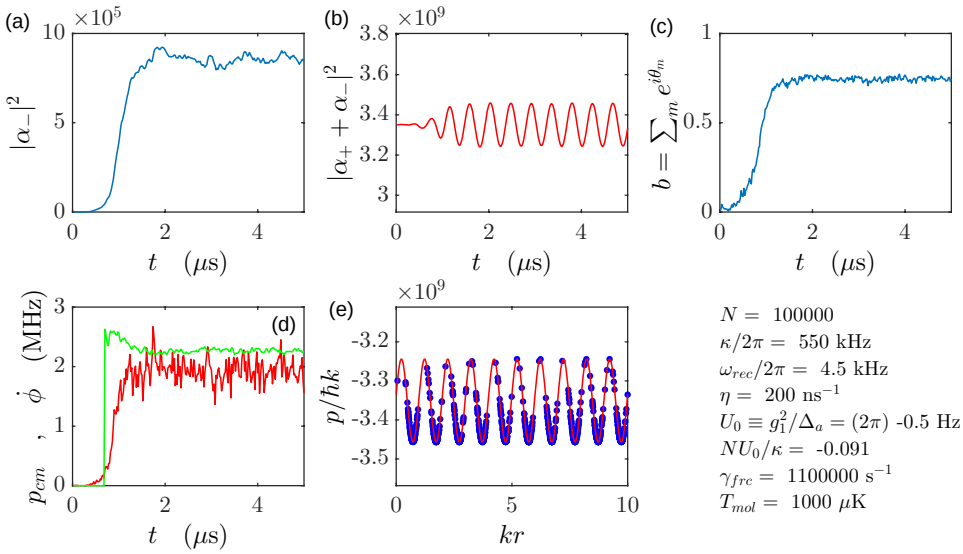

Figure 25.27: (code) Time evolution with phase transition of the viscous CARL in the adiabatic approximation. Shown are (a) the number of photons in the probe mode, (b) the beat signal, (c) the bunching, (d) the phase of the standing wave and the position of the center-of-mass of the cloud, and (e) the dipole potential calculated from (25.21) with the atomic distribution.

such that,

$$\tilde{x} = \begin{pmatrix} \tilde{\alpha}_- \\ \tilde{\theta}_n \\ \tilde{V}_n \end{pmatrix} \equiv \begin{pmatrix} \alpha_-(0) \\ \theta_n(0) \\ V_n(0) \end{pmatrix} + dt \begin{pmatrix} B\left(\alpha_-(0), \theta_n(0)\right) \\ V_n(0) \\ F\left(\alpha_-(0), \theta_n(0), V_n(0)\right) \end{pmatrix} + \begin{pmatrix} 0 \\ 0 \\ \zeta_n \sqrt{2\gamma_{\rm frc}^2 D_T dt} \end{pmatrix} \tag{25.216}$$

and

$$x(dt) = \begin{pmatrix} \alpha_-(dt) \\ \theta_n(dt) \\ V_n(dt) \end{pmatrix} = \begin{pmatrix} \alpha_-(0) \\ \theta_n(0) \\ V_n(0) \end{pmatrix} + \frac{dt}{2} \left[\begin{pmatrix} B\left(\alpha_-(0), \theta_n(0)\right) \\ V_n(0) \\ F\left(\alpha_-(0), \theta_n(0), V_n(0)\right) \end{pmatrix} + \begin{pmatrix} B(\tilde{\alpha}_-, \tilde{\theta}_n) \\ \tilde{V}_n \\ F(\tilde{\alpha}_-, \tilde{\theta}_n, \tilde{V}_n) \end{pmatrix} \right] + \begin{pmatrix} 0 \\ 0 \\ \zeta_n \sqrt{2\gamma_{\rm frc}^2 D_T dt} \end{pmatrix} . \tag{25.217}$$

25.6.2 The Fokker-Planck and the Vlasov model

The *Fokker-Planck equation* for a density distribution $Q(\mathbf{r}, t)$,

$$\frac{dQ}{dt} + Q\nabla \cdot \mathbf{v} = D\nabla^2 Q \ , \tag{25.218}$$

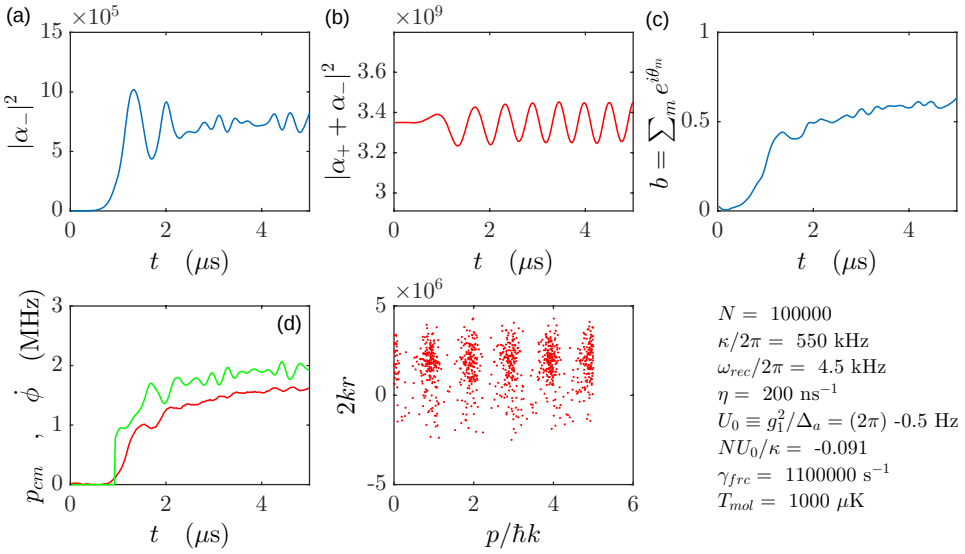

Figure 25.28: (code) Time evolution of the complete dynamics of the viscous CARL with phase transition. Same parameters as in Fig. 25.27. Shown are (a) the number of photons in the probe mode, (b) the beat signal, (c) the bunching, (d) the phase of the standing wave and the position of the center-of-mass of the cloud, and (e) the dipole potential calculated from (25.21) with the atomic distribution.

represents a generalization of the *continuity equation*, since with $\frac{d}{dt} \equiv \frac{\partial}{\partial t} + \mathbf{v} \cdot \nabla$, we obtain,

$$\frac{\partial Q}{\partial t} = -\nabla \cdot (\mathbf{v} Q) + D \nabla^2 Q \ . \tag{25.219}$$

If ρ is a local density, it the continuity equation reads,

$$\frac{d\rho}{dt} + \rho \nabla \cdot \mathbf{v} = 0 \ . \tag{25.220}$$

Knowing,

$$\frac{d}{dt} \equiv \frac{\partial}{\partial t} + \mathbf{v} \cdot \nabla \ , \tag{25.221}$$

we obtain,

$$\frac{\partial \rho}{\partial t} = -\nabla \cdot (\rho \mathbf{v}) \ . \tag{25.222}$$

The Fokker-Planck equation is just a generalization to include a diffusion process,

$$\frac{d\rho}{dt} + \rho \nabla \mathbf{v} = D_x \frac{\partial^2 \rho}{\partial x^2} \ , \tag{25.223}$$

or

$$\frac{\partial \rho}{\partial t} = -\nabla \cdot (\rho \mathbf{v}) + D_x \frac{\partial^2 \rho}{\partial x^2} \ . \tag{25.224}$$

25.6.2.1 Thermalization in the Fokker-Planck equation

We now apply the Fokker-Planck equation to the density distribution (25.210) of an atomic cloud subjected to the CARL force [843, 698]. As CARL is a one-dimensional process, we can use $\nabla \to \partial\theta$ and replace the velocity field $\mathbf{v} \to \dot{\theta}$:

$$\boxed{\begin{aligned} \dot{\alpha}_- &= -\kappa\alpha_- - \imath N U_0 \alpha_+ b \\ \frac{\partial Q}{\partial t} &= \frac{8\imath\omega_{\rm rec} U_0 \alpha_+}{\gamma_{\rm frc}} \frac{\partial}{\partial\theta}\left[(\alpha_- e^{-\imath\theta} - \alpha_-^* e^{\imath\theta})Q\right] + D_\theta \frac{\partial^2 Q}{\partial\theta^2} \end{aligned}} \ . \tag{25.225}$$

The position diffusion coefficient can be estimated by,

$$D_\theta = \frac{\langle k^2 v^2 \rangle}{\gamma_{\rm frc}} \ . \tag{25.226}$$

The normalization and the 'bunching' $|b|$ are given by,

$$1 = \int_0^{2\pi} Q(\theta,t) d\theta \quad , \quad b \equiv \int_0^{2\pi} Q(\theta,t) e^{-\imath\theta} d\theta \ . \tag{25.227}$$

To simulate the equations (25.225) we expand the distribution function in spatial harmonics [698],

$$Q(\theta,t) \equiv \sum_\nu Q_\nu(t) e^{\imath\nu\theta} \ . \tag{25.228}$$

In this expansion the normalization and the bunching become,

$$Q_0 = 1/2\pi \quad , \quad |b| = 2\pi |Q_1| \ , \tag{25.229}$$

and the equations (25.225) immediately yield,

$$\boxed{\begin{aligned} \dot{\alpha}_- &= -2\pi\imath N U_0 \alpha_+ Q_1 - \kappa\alpha_- \\ \frac{dQ_\nu}{dt} &= \frac{8\omega_{\rm rec} U_0 \alpha_+}{\gamma_{\rm frc}} \nu \left(\alpha_- Q_{\nu+1} + \alpha_-^* Q_{\nu-1}\right) - \nu^2 D_\theta Q_\nu \end{aligned}} \ . \tag{25.230}$$

We will derive the results (25.229) and (25.230) in Exc. 25.6.7.3. Also,

$$kv = \frac{d}{dt} \arctan \frac{\mathfrak{Im}\, \alpha_-}{\mathfrak{Re}\, \alpha_-} \ , \tag{25.231}$$

and,

$$\begin{aligned} \langle \dot{\theta} \rangle &\equiv \int_0^{2\pi} \dot{Q}(\theta,t) d\theta = \sum_\nu \dot{Q}_\nu(t) \int_0^{2\pi} e^{\imath\nu\theta} d\theta \\ &= \sum_\nu \frac{8\omega_{\rm rec} U_0 \alpha_+}{\gamma_{\rm frc}} \nu \left(\alpha_- Q_{\nu+1} \alpha_-^* Q_{\nu-1}\right) \delta_{\nu 0} = \frac{16\omega_{\rm rec} U_0 \alpha_+}{\gamma_{\rm frc}} \mathfrak{Re}\left(\alpha_- Q_1^*\right) \ . \end{aligned} \tag{25.232}$$

These equations can be easily simulated.

Matlab simulations of the Fokker-Planck equation, shown in Fig. 25.29, reproduce quantitatively the curves previously obtained by simulations of the Langevin equations.

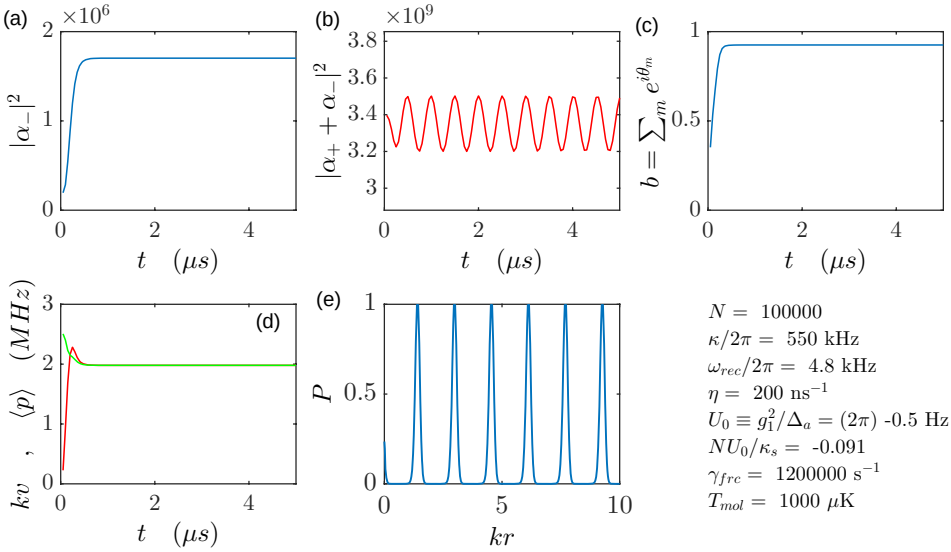

Figure 25.29: (code) Temporal evolution of the complete dynamics with phase transition of the viscous CARL. The same parameters as in Fig. 25.27. Shown are (a) the number of photons in the probe mode, (b) the beat signal, (c) the bunching, (d) the phase of the standing wave and the position of the center-of-mass of the cloud, and (e) the atomic density distribution.

25.6.2.2 Bistability and instability of the viscous CARL

The threshold can be found by simulating the Fokker-Planck equation while varying a control parameter (pumping power, temperature, number of atoms) sufficiently slowly, that the system always remains in a steady state. Fig. 25.30 shows the behavior of the CARL, while the pump power is linearly reduced and then linearly increased at different velocities. We observe a bistability that slightly depends on the speed of the ramp. The behavior of the mass-center velocity kv_{cm} and the phase of the standing wave, $\dot{\phi}$, are different [697] [21].

25.6.3 Thermalization in the Vlasov equation

The basic equations describing our ring-cavity filled with atoms are [490],

$$\boxed{\begin{aligned} \dot{\alpha}_- &= \kappa\alpha_- - \imath U_0 \alpha_+ \sum_m e^{\imath\theta_m} \\ \dot{\theta}_n &= V_n \\ \dot{V}_n &= 8\imath\omega_{\rm rec} U_0 \alpha_+ (\alpha_- e^{-\imath\theta_n} - \alpha_-^* e^{\imath\theta_n}) - \gamma_{\rm frc}(V_n - V_n^{(0)}) \end{aligned}}\,, \qquad (25.233)$$

[21] We can expect a second phase transition when the pump power exceeds a critical value, because for $NU_0 > \kappa$, the CARL becomes unstable again: It will unlock from the self-determined frequency and start to oscillate strongly. However, this effect is not described by the equations used for the simulation, which suppose an adiabatic elimination of the inertia.

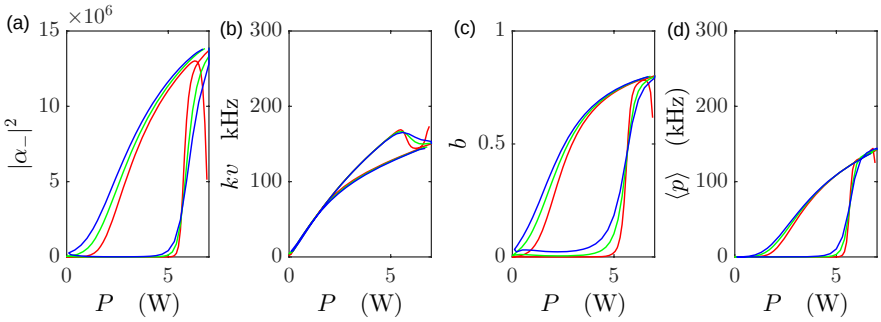

Figure 25.30: (code) Bistability of CARL near the threshold when the power is ramped at different paces.

if we assume the pump mode to be stationary $\alpha_+ = \eta_+/\kappa^{-1}$ and define the atomic bunching parameter by $b = \frac{1}{N}\sum_j e^{2ikx_j}$. A non-zero steady-state temperature is reached, if we allow the steady-state velocities of the atoms $v_j^{(0)}$ to be *different* for all atoms and distributed according to a Maxwell-Gaussian velocity distribution. The assumption of a common steady-state velocity for all atoms obviously results in perfect bunching and cooling to $T = 0$.

Let us introduce a local phase space density of the atomic cloud $Q(x, p, t)$ as a two-dimensional field in phase space. The time-evolution of this quantity is given by the so-called *Vlasov equation* (or collisionless Boltzmann equation),

$$0 = \partial_t Q + v\partial_x Q + F\partial_p Q + \gamma_{th}(Q - Q_0) \ , \tag{25.234}$$

where v and F are the center-of-mass velocity and force taken from equation (25.233) without the friction term. According to this equation the atomic cloud tends to a stationary distribution Q_0 as time goes on. Following Bonifacio *et al.* [103] and Javaloyes [431, 432, 433], we replace the friction term by an additional (Vlasov) equation:

$$\boxed{\begin{aligned} \dot\alpha_- &= -\imath N U_0 \alpha_+ b - \kappa\alpha_- \\ \dot\theta &= \omega_{\rm rec} V \\ \dot V &= \imath U_0 \alpha_+ (\alpha_- e^{-\imath\theta} - \alpha_-^* e^{\imath\theta}) \\ 0 &= \partial_t Q + \dot\theta\partial_\theta Q + \dot\varrho\partial_\varrho Q + \gamma_{\rm frc}(Q - Q_0) \end{aligned}} \ . \tag{25.235}$$

The bunching parameter can now be rewritten in terms of

$$b = \int_0^{2\pi} d\theta \int_{-\infty}^{\infty} d\varrho \ Q(\theta, \varrho, t) \ e^{2\imath\theta} \ . \tag{25.236}$$

The equilibrium distribution is chosen to be a homogeneous cloud with a Maxwell-Boltzmann velocity distribution,

$$Q_0 = \frac{1}{2\pi}\sqrt{\frac{\sigma}{\pi}} e^{-\sigma\varrho^2} \ , \tag{25.237}$$

where $\sigma \equiv \hbar\omega_{\rm rec}/k_{\rm B}T$ with $\omega_{\rm rec} \equiv \hbar k^2/2m$ such that $\int_0^{2\pi} d\theta \int_{-\infty}^{\infty} Q_0 d\varrho = 1$. We now perform a linear stability analysis. We expand Q around the steady state, $Q(\theta,\varrho,t) = Q_0(\varrho) + Q_1(\theta,\varrho,t)$ and retain to first order,

$$0 = \partial_t Q_1 + \dot\theta\partial_\theta Q_1 + \dot\varrho\partial_\varrho Q_0 + \gamma_{th} Q_1 \ . \tag{25.238}$$

Now we look for a time-dependent particular solution by inserting the ansatz,

$$\begin{aligned} \alpha_-(t) &= \beta_- e^{\imath\lambda t} \qquad \text{with} \qquad \dot\beta_- = 0 \\ Q_1(\theta,\varrho,t) &= H_1(\varrho) e^{-2\imath\theta} e^{\imath\lambda t} + c.c. \ , \end{aligned} \tag{25.239}$$

where $i\lambda \equiv \lambda_g + i\lambda_\omega$ into the field equation (25.235)a, the first order expansion of the Vlasov equation (25.238) (only retaining co-rotating terms) and into the expression for bunching (25.236). This ansatz accounts for the fact that, in steady state, we expect a fixed CARL frequency ν and a spatially modulated density distribution of the atoms. The set of equations becomes,

$$\begin{aligned} qi\lambda\beta_- &= -\kappa\beta_- - \imath N U_0 \tilde\eta_+ b e^{-\imath\lambda t} \\ 0 &= \imath\lambda H_1(\varrho) - 4\imath\omega_{\rm rec}\varrho H_1(\varrho) + \imath U_0\tilde\eta_+\beta_-\partial_\varrho Q_0 + \gamma_{th} H_1(\varrho) \\ b &= \int_0^{2\pi} d\theta \int_{-\infty}^{\infty} d\varrho \ H_1(\varrho) e^{\imath\lambda t} \ . \end{aligned} \tag{25.240}$$

With the definition,

$$\begin{aligned} \Gamma(\sigma,\gamma_{th},\imath\lambda) &\equiv \int_{-\infty}^{\infty} \frac{d\varrho \ \partial_\varrho Q_0}{\imath\lambda - 4\imath\omega_{\rm rec}\varrho + \gamma_{th}} \\ &= -\int_{-\infty}^{\infty} \frac{d\varrho \ 4\imath\omega_{\rm rec} Q_0}{(\imath\lambda - 4\imath\omega_{\rm rec}\varrho + \gamma_{th})^2} \ , \end{aligned} \tag{25.241}$$

the solution of the above set of equations is,

$$\begin{aligned} H_1(\varrho) &= \frac{-\imath U_0\tilde\eta_+\beta_-\partial_\varrho Q_0}{\imath\xi - 4\imath\omega_{\rm rec}\varrho + \gamma_{th}} \\ b &= -e^{\imath\xi t}\imath U_0\tilde\eta_+\beta_- 2\pi\Gamma(\sigma,\gamma_{th},\imath\lambda) \\ 0 &= \left[\kappa + \imath\lambda + N U_0^2\tilde\eta_+^2 \ 2\pi\Gamma(\sigma,\gamma_{th},\imath\lambda)\right] \ \beta_- \ . \end{aligned} \tag{25.242}$$

25.6.3.1 Calculation of the threshold

The bifurcation where the reverse field crosses the threshold to lasing occurs at $\lambda_g = 0$. We divide the field equation in real and imaginary parts,

$$\begin{aligned} \kappa + N U_0^2\tilde\eta_+^2 \ 2\pi\mathfrak{Re}\,\Gamma(\sigma,\gamma,\imath\lambda_\omega) &= 0 \\ \nu + N U_0^2\tilde\eta_+^2 \ 2\pi\mathfrak{Im}\,\Gamma(\sigma,\gamma,\imath\lambda_\omega) &= 0 \ . \end{aligned} \tag{25.243}$$

Now the condition $\lambda_\omega \mathfrak{Re}\,\Gamma(\sigma,\gamma_{th},\imath\lambda_\omega) = \kappa\mathfrak{Im}\,\Gamma(\sigma,\gamma_{th},\imath\lambda_\omega)$ leads to,

$$\int_{-\infty}^{\infty} \frac{d\varrho \ \varrho e^{-\sigma\varrho^2}(\kappa\lambda_\omega - 2\kappa\varepsilon\varrho + \lambda_\omega\gamma_{th})}{(\lambda_\omega - 2\varepsilon\varrho)^2 + \gamma_{th}^2} = 0 \ . \tag{25.244}$$

The values λ_ω where this integral is zero are inserted into one of the equations (25.243). Finally,

$$\tilde{\eta}_+^2 = \frac{-1}{N\tilde{U}_0^2\ 2\pi\mathfrak{Re}\,\kappa\Gamma(\sigma,\gamma_{th},\imath\lambda_\omega)}\ , \tag{25.245}$$

is the expression for the pump power threshold as a function of temperature σ, friction γ_{th}, cavity damping κ and coupling constant U_0. The intracavity CARL power is,

$$P_+ = \hbar\omega\delta\ \tilde{\eta}_+^2\ . \tag{25.246}$$

λ_ω is the associated CARL frequency, i.e. the frequency difference between probe and pump.

The final equations show that the threshold power drops as NU_0^2 increases. To see the dependencies of the threshold power on T and γ_{th}, we have to evaluation of the integral (25.244). Fig. 25.31 shows a numerical evaluation of Eqs. (25.244),(25.245) and (25.246) for finite T and γ_{th}.

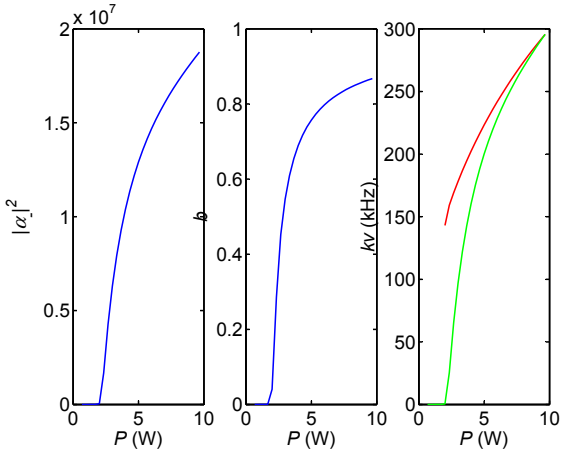

Figure 25.31: (code) Intracavity threshold power as a function of temperature and friction coefficient. The coupling strength is set to $\tilde{U}_0 = -10^{-7}$, the atom number is $N = 10^6$.

Apparently, the threshold pump power drops with vanishing friction and with low temperatures. For typical experimental situations, $T \approx 100\ \mu$K and $\gamma_{th} \approx 10\kappa$, we expect threshold powers on the order of about $P_+ = 1$ W, corresponding to $P_+^{(out)} = 4\ \mu$W leaking out of the cavity.

25.6.4 The Kuramoto model

Ripples on a dusty street driven by cars, rapids in a river arising spontaneously or behind an obstacle, wind blowing over a water surface spontaneously creating waves. Imagine a photon wind blowing over an atomic sea. Just like for water waves friction hinders boundless acceleration. The analogies are wind-molasses-friction, water-atoms, wind-acceleration-field, gravitation-dipole-force. The phenomenon is closely related to the *dissipative structure*. See also (watch talk) and (watch talk).

Our system has the advantage over macroscopic systems, that the hypothesis of uniform coupling is exactly satisfied, because the coupling medium, i.e. the light fields are delocalized within the cavity mode. In contrast, rapids develop exclusively behind the perturbation. There are no delay times effects and no spatial constraints due to a finite size of the individual oscillators.

The viscous CARL system is representative for of the vast class of *Kuramoto systems* [801]. This can be seen most appropriately by rewriting the CARL equations in terms of phase and amplitude of individual atoms. Another approach is via the Fokker-Planck equation, for which there already exists a Kuramoto equivalence.

Why is it interesting to investigate yet another coupled oscillator system? Our CARL is fully classical, although we deal with microscopic particle, such as atoms and photons. However, our system bears the possibility of being transferred to quantum situations, and thus to study the coupling of large ensembles of quantum oscillators. Furthermore, the coupling mechanism is well understood and controlable by experiment. Because the coupling goes through the standing wave fraction, it depends on the atom number and the coupling strength independently. Furthermore, the tunable friction force (temperature) corresponds to a variable width of the distribution of the oscillator frequencies, which we can manipulate in-situ and on-line.

Another realization of the Kuramoto model would be atoms in a ring cavity standing wave. Cold trapped atoms have the same oscillation frequencies. And thus do not need to synchronize. For hot atoms, however, the oscillation period depends on their kinetic energy.

The equation for the phases of the atoms is similar to the Kuramoto model [433],

$$\boxed{\dot{\theta}_n = \frac{K}{N}\sum_m \sin(\theta_n - \theta_m) - \xi_n(t)} \ . \tag{25.247}$$

The CARL equations which describes the dynamics of an ensemble of mean-field coupled oscillators, belong to the class of Kuramoto systems [432]. The main differences are: a Dirac-like distribution of eigenfrequencies and a mean-field self-consistently provided by a dynamical equation. Hence, in contrast to the original Kuramoto model, where the collective oscillation frequency is just the mean of the individual frequencies, the CARL frequency is self-determined and depends also on control parameters. This phenomenon is known from other systems like rhythmic applause, which only takes place by a reduction of the individual frequencies of clapping hands, towards a resonance. For this to happen the mean-field must self-adjust while the individual oscillators synchronize, e.g. the noise produce by the audience must adjust to the average desire of the audience to produce a satisfying level of noise.

In [864] is stated: 'The essence of the problem is the competition between the intrinsic disorder (i.e. noise and diffusion) and the dynamical coupling strength. In the Kuramoto model, the disorder enters via the distribution of natural frequencies, while the effective coupling strength is set by the parameter combination $K\cos\alpha_j$.'

25.6.4.1 Phase formalism of CARL

The starting point is the CARL equations (25.50). We make ansatz,

$$\alpha_+ \equiv \alpha_1 \quad , \quad \alpha_- \equiv \alpha_2\, e^{\imath\phi} \quad , \quad \eta_+ \equiv \eta_1 \quad , \quad \eta_- \equiv \eta_2\, e^{\imath\Delta} \ , \tag{25.248}$$

where the quantities with numeric suffixes are real, such that,

$$|\alpha_+ + \alpha_-|^2 = \alpha_1^2 + \alpha_2^2 + 2\alpha_1\alpha_2 \ \cos\phi \ . \tag{25.249}$$

By this ansatz we assume that a pumping laser is locked to the mode α_+ of the ring cavity, such that the phases of the fields α_+ and η_+ are equal and, without loss of generality, zero. On the other hand, the phase ϕ of the probe mode is a dynamic variable. Inserting the ansatz into the equations (25.50) we obtain,

$$\begin{aligned}
\dot\alpha_1 &= -(\kappa + \imath NU_0 - \imath\Delta_c)\alpha_1 - \imath U_0 \sum_n e^{-\imath\theta_n + \imath\phi}\alpha_2 + \eta_1 \ , \qquad (25.250)\\
\dot\alpha_2 + \imath\dot\phi\alpha_2 &= -(\kappa + \imath NU_0 - \imath\Delta_c)\alpha_2 - \imath U_0 \sum_n e^{\imath\theta_n - \imath\phi}\alpha_1 + \eta_2 e^{\imath\Delta - \imath\phi} \ ,\\
\ddot\theta_n &= 16\omega_{\rm rec}U_0\alpha_1\alpha_2\sin(\theta_n - \phi) \ .
\end{aligned}$$

The first two equations, which describe the dynamics of the fields, can be separated into real and imaginary parts,

$$\begin{aligned}
\dot\alpha_1 &= -\kappa\alpha_1 - U_0\sum_n \sin(\theta_n - \phi)\alpha_2 + \eta_1 \qquad (25.251)\\
\dot\alpha_2 &= -\kappa\alpha_2 + U_0\sum_n \sin(\theta_n - \phi)\alpha_1 + \eta_2\cos(\phi - \Delta) \ ,\\
\Delta_c &= NU_0\left(1 + N^{-1}\sum_n \cos(\theta_n - \phi)\frac{\alpha_2}{\alpha_1}\right) \ ,\\
\dot\phi &= \Delta_c - NU_0\left(1 + N^{-1}\sum_n \cos(\theta_n - \phi)\frac{\alpha_1}{\alpha_2}\right) - \frac{\eta_2}{\alpha_2}\sin(\phi - \Delta) \ .
\end{aligned}$$

Eliminating Δ_c, we can substitute the third and fourth equations for,

$$\dot\phi = U_0\left(\frac{\alpha_2}{\alpha_1} - \frac{\alpha_1}{\alpha_2}\right)\sum_n \cos(\theta_n - \phi) - \frac{\eta_2}{\alpha_2}\sin(\phi - \Delta) \ . \tag{25.252}$$

Defining the 'bunching' parameter,

$$b \equiv |b|e^{\imath\psi} \equiv N^{-1}\sum_n e^{\imath\theta_n} \ , \tag{25.253}$$

we finally obtain, in the presence of friction and dissipation,

$$\boxed{\begin{aligned}
\dot\alpha_1 &= -\kappa\alpha_1 - NU_0\alpha_2|b|\sin(\psi - \phi) + \eta_1\\
\dot\alpha_2 &= -\kappa\alpha_2 + NU_0\alpha_1|b|\sin(\psi - \phi) + \eta_2\cos(\phi - \Delta)\\
\dot\phi &= NU_0\left(\tfrac{\alpha_2}{\alpha_1} - \tfrac{\alpha_1}{\alpha_2}\right)|b|\cos(\psi - \phi) - \tfrac{\eta_2}{\alpha_2}\sin(\phi - \Delta)\\
\ddot\theta_n &= 16\omega_{\rm rec}U_0\alpha_1\alpha_2\sin(\theta_n - \phi) - \gamma_{\rm frc}\dot\theta_n + \xi_n
\end{aligned}} \ . \tag{25.254}$$

A particularly interesting case is that of unidirectional pumping, $\eta_2 = 0$. Assuming that the pump mode be not affected,$\dot\alpha_1 = 0$, and that the probe mode be weak,

$\alpha_1 \gg \alpha_2$, and making the adiabatic approximation, $\ddot{\theta}_n = 0$, of the atomic motion, we obtain,

$$\boxed{\begin{aligned} \dot{\alpha}_2 &= -\kappa\alpha_2 + NU_0\alpha_1|b|\sin(\psi-\phi) \\ \dot{\phi} &\simeq -\frac{NU_0\alpha_1}{\alpha_2}|b|\cos(\psi-\phi) \\ \dot{\theta}_n &= \frac{\xi_n}{\gamma_{\rm frc}} + \frac{16\omega_{\rm rec}U_0\alpha_1\alpha_2}{\gamma_{\rm frc}}\sin(\theta_n-\phi) \end{aligned}} \ . \tag{25.255}$$

We note that the equation for the phases of the atoms is similar to the Kuramoto equation (25.247).

25.6.4.2 Relationship between CARL and Kuramoto

The viscous CARL described by the formulas (25.255) corresponds to the Kuramoto model [801]. Defining $\theta_n \equiv 2kx_n$ as the position of the n^{th} atom, we assume the pump laser to be in resonance and write $\alpha_+ \equiv \eta_+/\kappa$ [490]. The diffusion in the momentum space is a process that limits the temperature in optical molasses.

We start from the Langevin equations (25.210). In addition, we assume that the standing wave propagates at a constant velocity, which is to say that for a strong viscous damping, the system quickly finds a steady state. This condition is formulated by $d_t|\alpha_-| = 0$ and $\dot{\alpha}_- = i\omega_{ca}\alpha_-$ with constant velocity ω_{ca}, which may be different from the velocity of the center of mass kv. We note that this assumption can introduce a considerable error, when used to describe temporal phase transitions, since, as shown by simulations of the complete dynamics (25.214), the mode α_- exhibits a transient behavior, as well. We obtain from the first Eq. (25.210),

$$\alpha_- = -\frac{\imath U_0\alpha_+}{\imath\omega_{ca}+\kappa}\sum_m e^{\imath\theta_m} \ . \tag{25.256}$$

Substituting Eq. (25.256) into the second equation (25.210),

$$\begin{aligned} \dot{\theta}_n &= \frac{\xi_n}{\gamma_{fr}} + \frac{8\omega_{\rm rec}NU_0^2\alpha_+^2}{\gamma_{fr}}\frac{1}{N}\sum_m\left(\frac{e^{\imath\theta_m-\imath\theta_n}}{\imath\omega_{ca}+\kappa} + \frac{e^{-\imath\theta_m+\imath\theta_n}}{-\imath\omega_{ca}+\kappa}\right) \\ &= \frac{\xi_n}{\gamma_{fr}} + \frac{16\omega_{\rm rec}NU_0^2\alpha_+^2}{\gamma_{fr}(\omega_{ca}^2+\kappa^2)}\frac{1}{N}\sum_m\left[\kappa\cos(\theta_m-\theta_n)+\omega_{ca}\sin(\theta_m-\theta_n)\right] \ . \end{aligned} \tag{25.257}$$

Defining the *order parameter*,

$$b \equiv |b|e^{\imath\psi} \equiv \frac{1}{N}\sum_m e^{\imath\theta_m} \ , \tag{25.258}$$

which also implies,

$$|b|\sin(\psi-\theta_n) = \frac{1}{N}\sum_m \sin(\theta_m-\theta_n) \ , \tag{25.259}$$

we can write Eq. (25.259) as,

$$\dot{\theta}_n = \frac{\xi_n}{\gamma_{fr}} + \frac{8\varepsilon NU_0^2\alpha_+^2\kappa}{\gamma_{fr}(\omega_{ca}^2+\kappa^2)}|b|\left[\cos(\psi-\theta_n)+\frac{\omega_{ca}}{\kappa}\sin(\psi-\theta_n)\right] \ . \tag{25.260}$$

In the 'good cavity' limit, $\kappa \ll \omega$, using $(2kv)^3 = 8\varepsilon N U_0^2 \alpha_+^2 \kappa/\gamma_{fr}$ and additionally assuming small amplitude oscillations, $\psi \approx \theta_n$, that is, good 'bunching',

$$\dot{\theta}_n \approx \frac{\xi_n}{\gamma_{fr}} + \frac{(2kv)^3}{\omega_{ca}^2}|b| + \frac{(2kv)^3}{\kappa\omega_{ca}}|b|\sin(\psi - \theta_n) \; . \tag{25.261}$$

This shows that in the limit of perfect 'bunching' $\omega_{ca} = 2kv$ must be satisfied. If really $\kappa \ll \omega$ is valid, we can despise the cosine. Introducing the Kuramoto coupling constant,

$$K \equiv \frac{16\omega_{\rm rec} N U_0^2 \alpha_+^2 \omega_{ca}}{\gamma_{fr}(\omega_{ca}^2 + \kappa^2)} \approx \frac{1}{\kappa}\left(\frac{16\omega_{\rm rec} N U_0^2 \alpha_+^2 \kappa}{\gamma_{fr}}\right)^{2/3} = (4\omega_{\rm rec}\rho)^2 \left(\frac{4}{\kappa\gamma_{fr}^2}\right)^{1/3} , \tag{25.262}$$

using $2\varepsilon\rho = (4\varepsilon N U_0^2 \alpha_+^2)^{1/3}$, Eq. (25.260) is precisely the one used by the *Kuramoto model* of N coupled harmonic oscillators synchronizing over time,

$$\boxed{\dot{\theta}_n \approx \frac{\xi_n}{\gamma_{fr}} + \frac{\kappa K}{\omega_{ca}}|b| + K|b|\sin(\psi - \theta_n)} \; . \tag{25.263}$$

Oscillators with $\omega_n \leq K|b|$ are locked. For a reasonable 'bunching' this is satisfied in the 'good cavity' limit.

25.6.4.3 Kuramoto model with inertial effects

It is possible to incorporate inertial effects into the Kuramoto model [2]: allowing for $\ddot{\theta}_n \neq 0$, but still assuming $d_t|\alpha_-| = 0$ and $\dot{\alpha}_- = i\omega\alpha_-$, the equation (25.257) becomes,

$$\ddot{\theta}_n = -\gamma_{fr}\dot{\theta}_n + \xi_n + \frac{16\omega_{\rm rec} N U_0^2 \alpha_+^2}{\omega^2 + \kappa^2}\frac{1}{N}\sum_m \left[\kappa\cos(\theta_m - \theta_n) + \omega\sin(\theta_m - \theta_n)\right] \tag{25.264}$$

$$= -\gamma_{fr}\dot{\theta}_n + \xi_n + \frac{\kappa}{\omega}K|b|\cos(\psi - \theta_n) + K|b|\sin(\psi - \theta_n) \; .$$

25.6.4.4 Fokker-Planck equation

Let us write the *Kuramoto equation* including stochastic noise,

$$\dot{\theta}_n = \omega + K|b|\sin(\psi - \theta_n) + \xi_n(t) \; , \tag{25.265}$$

define the order parameter,

$$b = |b|e^{\imath\psi} \; , \tag{25.266}$$

and the Langevin-force $\langle\xi_n(t)\rangle = 0$ and $\langle\xi_n(t)\xi_m(\tau)\rangle = 2D\delta_{ij}\delta(t-\tau)$.

The Fokker-Planck equation associated to Eq. (25.265) reads,

$$\frac{\partial\rho}{\partial t} = -\frac{\partial\rho\;\left[\omega + K|b|\sin(\psi - \theta)\right]}{\partial\theta} + D\frac{\partial^2\rho}{\partial\theta^2} \; , \tag{25.267}$$

where $D = \sigma^2/\gamma_{fr}$. Inserting $\rho(\theta, t) \equiv \sum_\nu \rho_\nu(t)e^{\imath\nu\theta}$,

$$\frac{\partial\rho_\nu}{\partial t} = -(\nu^2 D + \imath\nu\omega)\rho_\nu + \tfrac{1}{2}\nu K\left(b^*\rho_{\nu-1} - b\rho_{\nu+1}\right) \; , \tag{25.268}$$

especially,

$$\int_0^{2\pi} \rho(\theta,t)d\theta = 1 \qquad \Longrightarrow \qquad \rho_0 = \tfrac{1}{2\pi} \ , \tag{25.269}$$

and we defined the bunching as $|b|$, where,

$$b \equiv \int_0^{2\pi} \rho(\theta,t)e^{-i\theta}d\theta \qquad \Longrightarrow \qquad b \equiv 2\pi\rho_1 \ . \tag{25.270}$$

25.6.4.5 Laser-type equation for CARL

Defining the displacement of the n^{th} atomic oscillator as,

$$E_n \equiv e^{\imath\theta_n} \ , \tag{25.271}$$

we can rewrite the second equation (25.210) as,

$$\dot{E}_n = \frac{\imath\xi_n}{\gamma_{fr}}E_n - \frac{8\omega_{\rm rec}U_0\alpha_+}{\gamma_{fr}}(\alpha_- - \alpha_-^* E_n^2) \ . \tag{25.272}$$

Substituting α_- by the integral of the first equation (25.210),

$$\dot{E}_n = \frac{\imath\xi_n}{\gamma_{fr}}E_n + \frac{8\omega_{\rm rec}\imath NU_0^2\alpha_+^2}{\gamma_{fr}}\left(\int be^{-\kappa(t-t')}dt' + E_n^2\int b^* e^{-\kappa(t-t')}dt'\right) \ . \tag{25.273}$$

In the limit $e^{-\kappa(t-t')} = \kappa^{-1}\delta(t-t')$ we obtain an equation similar to that of an ordinary laser,

$$\begin{aligned}\dot{E}_n &= \frac{\imath\xi_n}{\gamma_{fr}}E_n + \frac{8\omega_{\rm rec}\imath NU_0^2\alpha_+^2}{\gamma_{fr}\kappa}(b + b^* E_n^2) \\ &= \frac{\imath\xi_n}{\gamma_{fr}}E_n + \frac{8\omega_{\rm rec}\imath NU_0^2\alpha_+^2}{\gamma_{fr}\kappa}\left(\sum_m E_m + \sum_m E_m^* E_n^2\right) \ .\end{aligned} \tag{25.274}$$

25.6.5 Thermodynamics of the CARL process

There is an analogy between the laser threshold and a second-order phase transition [749], p. 341 *ff*: '... The usual treatment of laser behavior is a self-consistent field theory. In the laser analysis each atom develops a radiating dipole in an electromagnetic field due to (i.e. emitted by) all the other atoms. The radiation field produced by an ensemble of radiating atoms is then calculated in a self-consistent fashion. (...This) suggests the identification of the laser electric field as the variable corresponding to the (...) order parameter and the atomic population inversion as that corresponding to the temperature.'

Note that numerical simulations revealed that in certain regimes the CARL corresponds to a first-order phase transition: At high temperatures the probe to pump power diagram shows bistability [431] and [697].

The correspondence between CARL and a common laser is illustrated by the table below. A number of questions arise from the analogy:

The CARL being a laser without inversion, what is the equilibrium parameter? Is it the temperature of the atomic cloud? How to calculate the density of states?

	ferromagnet	laser
control parameter	external magnetic field H	pump intensity $\mathcal{S}$
equilibrium parameter	temperature T	population inversion σ
order parameter	magnetization $\langle M\rangle = \begin{cases} 0 & T > T_c \\ c\sqrt{\frac{T_c - T}{T}} & T < T_c \end{cases}$	electric field $\langle E\rangle = \begin{cases} 0 & \sigma > \sigma_c \\ c\sqrt{\frac{\sigma_c - \sigma}{\sigma}} & \sigma < \sigma_c \end{cases}$
probability density	$P(M) \propto e^{-F(M)/k_{\mathrm{B}}T}$	P-representation $P(x,y) \propto e^{-G(x,y)/K\sigma}$
thermodyn. free energy	$F = F(T,H)$	$G(x,y)$
heat capacity	$C(T) = \frac{\partial E(T)}{\partial T}$	?

	CARL atoms	CARL light
control parameter	pump intensity η	pump intensity η
equilibrium parameter	temperature T	?
order parameter	bunching $b = \begin{cases} 0 & T > T_c \\ ? & T < T_c \end{cases}$	electric field $\langle\alpha\rangle = \begin{cases} 0 \\ ? \end{cases}$
probability density	?	?
thermody. free energy	?	?
heat capacity	?	?

25.6.6 CARL as a laser

Why is CARL a laser? What is the basic difference between CARL and an AOM or a moving Bragg mirror? CARL is essentially based on exponential self-amplification. This self-amplification is in fact observed in our switch-off experiment [490]. But a laser is normally understood as a steady-state system. For CARL to find to a steady-state we have to insert friction forces.

Gordon rewrites the CARL as a common laser: He generalizes the linear stability analysis (previous Sec.) and retains the lowest-order nonlinearity. The Fokker-Planck equations read:

$$\begin{aligned} \frac{dB_n}{d\tau} &= \imath n(aB_{n-1} + a^* B_{n+1}) - n^2 D B_n \\ \frac{da}{d\tau} &= B_1 - \kappa a \ , \end{aligned} \tag{25.275}$$

with $B_0 = 1$ and $B_{-n} = B_n^*$. Linearization means $B_{n>1} = 0$,

$$\begin{aligned} \frac{dB_1}{d\tau} &= \imath a - D B_1 \\ \frac{da}{d\tau} &= B_1 - \kappa a \end{aligned} \tag{25.276}$$

or,

$$\frac{d^2a}{d\tau^2} + (\kappa + D)\frac{da}{d\tau} + (\kappa D - \imath)a = 0 \tag{25.277}$$
$$\frac{d^2B_1}{d\tau^2} + (\kappa + D)\frac{dB_1}{d\tau} + (\kappa D - \imath)B_1 = 0$$

The determinant is,

$$\det \begin{pmatrix} -D-\lambda & \imath \\ 1 & -\kappa-\lambda \end{pmatrix} = (D+\lambda)(\kappa+\lambda) - \imath = 0 \tag{25.278}$$

Including the lowest-order nonlinear term means $B_{n>2} = 0$,

$$\frac{dB_2}{d\tau} = 2\imath a B_1 - 4DB_2 \tag{25.279}$$
$$\frac{dB_1}{d\tau} = \imath a + \imath a^* B_2 - DB_1$$
$$\frac{da}{d\tau} = B_1 - \kappa a$$

Assuming $dB_2/d\tau = 0$,

$$\frac{dB_1}{d\tau} = \imath a - \left(\frac{|a|^2}{2D} + D\right) B_1 \tag{25.280}$$
$$\frac{da}{d\tau} = B_1 - \kappa a$$

or,

$$\frac{d^2B_1}{d\tau^2} + (\kappa + D)\frac{dB_1}{d\tau} + (\kappa D - \imath)B_1 = -\frac{1}{2D}\left(\frac{d}{d\tau} + \kappa\right)|a|^2 B_1 \tag{25.281}$$
$$= -(K_1|a|^2 - K_2|a|^4)B_1$$
$$\frac{d^2a}{d\tau^2} + (\kappa + D)\frac{da}{d\tau} + (\kappa D - i)a = -\frac{|a|^2}{2D}\left(\frac{d}{d\tau} + \kappa\right)a$$

substitute $a(\tau) = A(\tau)e^{\lambda\tau}$ and Eq. (xx),

$$e^{\lambda\tau}\left(\frac{d^2}{d\tau^2} + 2\lambda\frac{d}{d\tau} + \lambda^2\right)A + e^{\lambda\tau}\left((\kappa + D)\frac{d}{d\tau} + (\kappa + D)\lambda\right)A - (\lambda^2 + D\lambda + \kappa\lambda)e^{\lambda\tau}A \tag{25.282}$$
$$= -\frac{|e^{\lambda\tau}A|^2}{2D}\left(e^{\lambda\tau}\frac{dA}{d\tau} + \lambda e^{\lambda\tau}A + \kappa e^{\lambda\tau}A\right)$$

neglect $d^2A/d\tau^2$and $|A|^2 dA/d\tau$,

$$e^{\lambda\tau}2\lambda\frac{dA}{d\tau} + e^{\lambda\tau}(\kappa + D)\frac{dA}{d\tau} = -\frac{|e^{\lambda\tau}A|^2}{2D}\left(\lambda e^{\lambda\tau}A + \kappa e^{\lambda\tau}A\right) \tag{25.283}$$

substitute back $a(\tau) = A(\tau)e^{\lambda\tau}$,

$$\begin{aligned}\frac{da}{d\tau} &= \lambda a - \frac{\lambda+\kappa}{2D(2\lambda+\kappa+D)}|a|^2 a \\ &= \lambda a - C|a|^2 a\end{aligned} \tag{25.284}$$

or,

$$\frac{d|a|^2}{d\tau} = 2|a|^2 \mathfrak{Re}\,\lambda - 2|a|^4 \mathfrak{Re}\,C \tag{25.285}$$

in steady-state,

$$0 = \lambda a - C|a|^2 a\ . \tag{25.286}$$

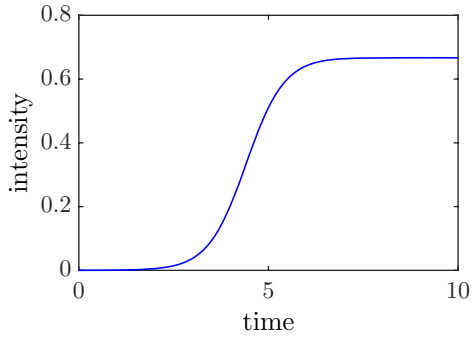

Figure 25.32: (code) Laser crossing the threshold.

According to A. Politi a general laser theory exists, there is no point in repeating this for CARL. The analogy is there and evident.

25.6.6.1 CARL as a ferromagnet

A similar treatment with $a(\tau) = A(\tau)e^{\lambda\tau}$ and $B_1(\tau) = \beta(\tau)e^{\lambda\tau}$ and $d^2\beta/d\tau^2 = 0$ and $|A|^2 d\beta/d\tau = 0$ and $\beta d|A|^2/d\tau = 0$ results in,

$$\begin{aligned}\frac{dB_1}{d\tau} &= \lambda B_1 - \frac{2\lambda+\lambda^*+\kappa}{2D(2\lambda+\kappa+D)}|a|^2 B_1 \\ &= \lambda B_1 - \tilde{C}|a|^2 B_1\ ,\end{aligned} \tag{25.287}$$

i.e. the instability comes from the field and it drives the bunching.

25.6.6.2 Out-of-equilibrium thermodynamics

Strictly speaking the above analogy is flawed. In particular the analogy between CARL bunching and ferromagnetic ordering is not good. While the ferromagnetic ordering occurs as a thermodynamic phase transition, the CARL bunching is driven by a dissipative force, which triggers spatio-temporal instabilities. Therefore viscous

CARL occurs far from thermodynamic equilibrium. This may point towards an interpretation of CARL bunching as a *dissipative structure* along the lines traced by Prigogine, who showed that *non-equilibrium may be a source of order*.

On the other hand, the laser itself is a system operating far from thermal equilibrium, since it requires a pump to emit steady-state radiation. Perhaps a comparison with *estruturas de Bénard* is better than with ferromagnets. Bénard structures occur as spontaneous breaking of translational symmetry, just like CARL. One could say that the periodicity of CARL is predefined by the pump laser wavelength, and thus not surprising. However, the size of the periodic structures is always fixed by boundary conditions in a more or less complicated way. For example, the size of the Bénard structures is fixed by the viscosity, the provided amount of heat, etc., the wavelength of surface waves can be calculated from first principles, i.e. the Navier-Stokes equations and the continuity equation for given boundary conditions. The symmetry breaking resides in the exact *place*, where the Bénard structure develops. It is the *phase*, which is broken, just like for CARL.

The Kuramoto model and the Weiss model of ferromagnetism are both mean field theories [756]. Despite the fundamental difference that ferromagnetism is a thermodynamic feature and Kuramoto a nonequilibrium phenomenon, they are far-reaching analogies. The role of temperature in ferromagnetism is played by external noise in Kuramoto. CARL is clearly a dissipative structure: *It survives only as long as energy is fed to the system.*

25.6.6.3 Finite and infinite temperature reservoirs

The phase transition is ruled by a competition of dissipation and diffusion. If the reservoir has zero temperature $\gamma_{\rm frc} \neq 0$ but $D = \sigma^2/\gamma_{\rm frc} = 0$, i.e. we have dissipation without diffusion. In this case, we do not expect a threshold behavior. The Lindtbladt operator for coupling to a finite-temperature reservoir is something like $\mathcal{L} \approx \kappa(\bar{n}+1)\{...emission...\} + \kappa\bar{n}\{...absorption...\} + \eta\{...phase\ noise...\}$, where $\bar{n}$ is the mean photon number at thermal equilibrium with a given temperature $T \propto \bar{n}/(\bar{n}+1)$. The interpretation in terms of dissipation without diffusion is correct according to A. Buchleitner. There are three kinds of noises: 0 temperature noise for $\bar{n} \to 0$, ∞ temperature noise for $\bar{n} \approx \bar{n}+1$ and phase noise. Thus for $T = 0$ the energy flux goes only from the system to the reservoir. At $T > 0$ entropy may go from the reservoir to the system. The system reaches its cooling limit when the temperatures of the system and the reservoir are balanced.

But how to explain Doppler cooling or cavity-cooling? The electromagnetic vacuum is an effective $T = 0$ reservoir, but the cooling is nevertheless limited by the spontaneous decay width or the cavity linewidth, resp.. Why does coupling to a zero-temperature reservoir not cool down to zero? Apparently, the coupling is afflicted by vacuum noise. This permits coupling of degrees of freedom having different temperatures without reaching a temperature equilibrium. Examples are the limit of cavity-cooling to the cavity decay width or simply Doppler-cooling by spontaneous emission.

Interprete damping as scattering into continuum!

25.6.7 Exercises

25.6.7.1 Ex: Viscous CARL

Assuming a perfect 'bunching', $e^{2\imath kz_m} = e^{2\imath kz}$, e $\alpha_- \equiv \beta e^{2\imath kz}$ with $\dot{\beta} = 0$ and $\ddot{z} = 0$ derive the equations (25.199).

25.6.7.2 Ex: Langevin simulations

Langevin simulations

25.6.7.3 Ex: Fokker-Planck equations

Derive the equations (25.229) and (25.230) from (25.227) and (25.225) applying the expansion (25.228).

25.6.7.4 Ex: Kuramoto simulations

Implement the Kuramoto model with pendulum clocks.

25.7 Coherent properties of CARL

In Sec. 25.6.1 we have demonstrated collective interaction of atoms with light fields and how the application of friction via optical molasses can lead to stationary CARL radiation at a self-determined frequency [489]. We have demonstrated that the molasses also lead to diffusion resulting in a threshold behavior and in atomic self-organization at finite temperatures [698, 843]. An interesting question is whether the temperature not only determines the collective behavior, but also the deviation from it. The temperature being related to the amount of random walk on top of the center-of-mass motion, we may wonder whether the viscous CARL radiation bears a signature of the atomic temperature not only in the self-determined CARL frequency, but also in the laser emission bandwidth. It is conceivable that the autocorrelation functions and the emission spectrum of the CARL are influenced by the fact that the atoms experience a random walk in momentum space due to the diffusion in the optical molasses.

In this section, we will attempt an analytical approach, present numerical simulations and discuss how to access to the informations experimentally. The Fokker-Planck approach described in Refs. [698, 843] is particularly well adapted to calculating collective variables. In contrast the simulation of the Langevin equation conveniently gives access to the noise properties.

25.7.1 Analytical derivation of the coherence

Our starting point are the Langevin equations (25.210) [698, 843] in the adiabatic limit, $\ddot{\theta}_n = 0$. The Langevin noise force is uncorrelated,

$$\langle \xi_n^*(t)\xi_m(t+\tau)\rangle \equiv \lim_{T\to\infty} \frac{1}{T}\int_0^T \xi_n^*(t)\xi_m(t+\tau)d\tau = 2D_{\dot{\theta}}\delta_{mn}\delta(\tau)\ , \tag{25.288}$$

where the momentum diffusion coefficient $D_{\dot\theta} = \gamma_{fr}\sigma^2$ is proportional to the atoms' equilibrium temperature, which is related to the Maxwell-Gaussian velocity spread by $\sigma \equiv 2k\sqrt{k_{\rm B}T/m}$. In contrast, the trajectories of the atoms are not, because all atoms are motionally coupled by the fields, so that the noise imparted to one atom is sensed by all others. Therefore the relationship (25.289) certainly does not hold for the atomic positions,

$$\langle\theta_n^*(t)\theta_m(t+\tau)\rangle \nsim \delta_{mn}\delta(\tau)\ . \tag{25.289}$$

25.7.1.1 Single atom

So, let us first concentrate on a single atom coupled to the cavity fields. If its velocity only fluctuates a little around a mean value ω_{ca}, we may write $\theta(t) \equiv \omega_{ca}t+\varphi(t)$. The randomized position has a Gaussian statistics leading to a Brownian motion described by a Wiener-Levy stochastic process: $\langle\varphi(t)\rangle = 0$ and $\langle\varphi(t)\varphi(t+\tau)\rangle = D_\theta(2t+\tau-|\tau|)$ ([749], p. 344),

$$R_{\dot\theta}(\tau) = \langle[\omega_{ca}+\dot\varphi(t)][\omega_{ca}+\dot\varphi(t+\tau)]\rangle = \langle\dot\varphi(t)\dot\varphi(t+\tau)\rangle = 2D_\theta\delta(\tau)\ , \tag{25.290}$$

where $D_\theta = \sigma^2/\gamma_{fr}$ is the position diffusion coefficient. Note that deterministic parts are removed from the function in order to satisfy $\langle\dot\varphi(t)\rangle = 0$. In that case the *spectral density of fluctuations of the atomic phase* is constant,

$$S_{\dot\theta}(f) = \int_{-\infty}^{\infty} R_{\dot\theta}(\tau)e^{-2\pi\imath f\tau}d\tau = 2D_\theta\ . \tag{25.291}$$

Note that $S_{\dot\theta}(f) = f^2S_\theta(f)$. The *variance of the fluctuations* for white noise is or,

$$\sigma_{\dot\theta}^2(\tau) = \langle\dot\varphi(t)^2\rangle = \frac{D_\theta}{\tau}\ . \tag{25.292}$$

Under the assumption $\dot\alpha_- = \imath\omega_{ca}\alpha_-$ and introducing the abbreviation $\alpha_0 \equiv -\imath U_0\alpha_+/(\kappa+\imath\omega_{ca})$, the first equation (25.210) takes the form $\alpha_- = \alpha_0 e^{\imath\theta}$ such that the *autocorrelation function of the field amplitude* reads,

$$\begin{aligned} R_\alpha(\tau) &\equiv \langle\alpha_-^*(t)\alpha_-(t+\tau)\rangle \\ &= |\alpha_0|^2\langle e^{\imath[\theta(t+\tau)-\theta(t)]}\rangle \\ &= |\alpha_0|^2 e^{\imath\omega_{ca}\tau}\langle e^{\imath[\varphi(t+\tau)-\varphi(t)]}\rangle = |\alpha_0|^2 e^{\imath\omega_{ca}\tau}\langle e^{\imath\tau\dot\varphi(t)}\rangle\ . \end{aligned} \tag{25.293}$$

In the case of a Gaussian distribution for the noise amplitude with $\dot\varphi(t) = \dot\varphi(-t)$, we have $\langle\dot\varphi^{2k-1}\rangle/(2k-1)! = 0$ and $\langle\dot\varphi^{2k}\rangle/(2k)! = \langle\frac{1}{2}\dot\varphi^2\rangle^k/k!$ [198, **?**, 263],

$$\begin{aligned} \langle e^{\imath\tau\dot\varphi(t)}\rangle &= \sum_k \frac{\imath^k\langle\tau^k\dot\varphi(t)^k\rangle}{k!} = \sum_k \frac{\imath^{2k}\langle\tau^{2k}\dot\varphi(t)^{2k}\rangle}{(2k)!} \\ &= \sum_k \frac{\langle-\frac{1}{2}\tau^2\dot\varphi(t)^2\rangle^k}{k!} = e^{-\frac{1}{2}\tau^2\langle\dot\varphi(t)^2\rangle}\ . \end{aligned} \tag{25.294}$$

Apparently, noise mainly affects the field's phase and not its amplitude. Note that the *first-order coherence* is just the normalized autocorrelation $g^{(1)}(\tau) \equiv R_\alpha(\tau)/R_\alpha(0)$,

$$\begin{aligned} g^{(1)}(\tau) &= e^{\imath\omega_{ca}\tau}e^{-\omega_{ca}^2\tau^2\sigma_v^2/2} \\ &= e^{\imath\omega_{ca}\tau}e^{-D_\theta|\tau|/2}\ . \end{aligned} \tag{25.295}$$

The *power spectral density* is a Lorentzian,

$$S_\alpha(\omega) = |\alpha_0|^2 \int_{-\infty}^{\infty} R_\alpha(\tau) e^{-\imath\omega\tau} d\tau \qquad (25.296)$$
$$= \frac{|\alpha_0|^2 D_\theta^2}{(\omega-\omega_{ca})^2 + D_\theta^2} \ .$$

The CARL *emission bandwidth* is thus $\frac{1}{2}D_\theta$. The above results show that the CARL laser bandwidth increases linearly with temperature and reduces with the friction force. In our experiment we have $\gamma_{fr} = 5\kappa$ and $\sigma = 10\kappa$, so that $D_\theta = \sigma^2/\gamma_{fr} = 20\kappa$. The CARL bandwidth is extremely large as compared to the CARL frequency $\omega_{ca} = 5\kappa$. The reason is that we only considered a single atom. The impact of several atoms will partially compensate and reduce the linewidth.

25.7.1.2 Many atoms, hand-waving

In order to account for the combined effect of many atoms, we reconsider the Eq. (25.210). If $\dot{\alpha}_- = \imath\omega_{ca}\alpha_-$, we may write it like,

$$\alpha_- = \alpha_0 \sum_m e^{\imath\theta_m} \ , \qquad (25.297)$$
$$\dot{\theta_n} = \frac{4\varepsilon\imath U_0 \alpha_+ \alpha_0}{\gamma_{fr}} \sum_m \left(e^{\imath\theta_m - \imath\theta_n} + e^{-\imath\theta_m + \imath\theta_n} \right) + \frac{\xi_n}{\gamma_{fr}} \ .$$

The light mode α_- appears to be a superposition of coherent waves having the same frequencies, $\alpha_m(t) = \alpha_0 e^{i\omega_{ca}t + i\varphi_m(t)}$, but interrupted by random phase jumps. We may thus try an analogous argumentation as for pressure broadening,

$$\langle \alpha_-^*(t)\alpha_-(t+\tau)\rangle = |\alpha_0|^2 \int \sum_n e^{-\imath\omega_{ca}t - \imath\varphi_n(t)} \sum_m e^{\imath\omega_{ca}t + \imath\omega_{ca}\tau + \imath\varphi_n(t+\tau)} dt$$
$$= |\alpha_0|^2 e^{\imath\omega_{ca}\tau} \sum_{n,m} \int e^{\imath\varphi_m(t+\tau) - \imath\varphi_n(t)} dt = N\langle \alpha_n^*(t)\alpha_m(t+\tau)\rangle \delta_{nm} \ .$$

Cross-terms vanish, the autocorrelation function is just the sum of the single-atom components. However, while we may view the noise impact of the atoms as coming from a single atom, the rate of the phase jumps is much higher, than for a single atom. For one atom the probability density for encountering a coherent interval of length τ is given by $p_1(\tau)d\tau = \frac{1}{2}D_\theta e^{-D_\theta|\tau|/2}d\tau$ [530]. Thus,

$$\langle \alpha_1^*(t)\alpha_1(t+\tau)\rangle = |\alpha_0|^2 e^{\imath\omega_{ca}\tau} e^{-D_\theta|\tau|/2} = |\alpha_0|^2 e^{\imath\omega_{ca}\tau} \int_\tau^\infty p_1(\tau')d\tau' \ . \qquad (25.298)$$

For N atoms we expect a probability density for encountering a coherent intervall of length τ,

$$p_N(\tau)d\tau = p_1(\tau/N)d\tau = \frac{D_\theta}{2\sqrt{N}} e^{-D_\theta|\tau|/2\sqrt{N}} d\tau \ , \qquad (25.299)$$

such that $\int_0^\infty p_N(\tau')d\tau' = 1$. However this remains to prove. Thus,

$$g_N^{(1)}(\tau) = e^{\imath\omega_{ca}\tau} \int_\tau^\infty p_N(\tau')d\tau' = e^{\imath\omega_{ca}\tau - D_\theta|\tau|/2\sqrt{N}} \ . \qquad (25.300)$$

The second-order correlation function is,

$$g_N^{(2)}(\tau) = 1 + |g_N^{(1)}(\tau)|^2 \ . \tag{25.301}$$

The laser bandwidth is accordingly reduced by,

$$D_N = \frac{D_\theta}{\sqrt{N}} \ . \tag{25.302}$$

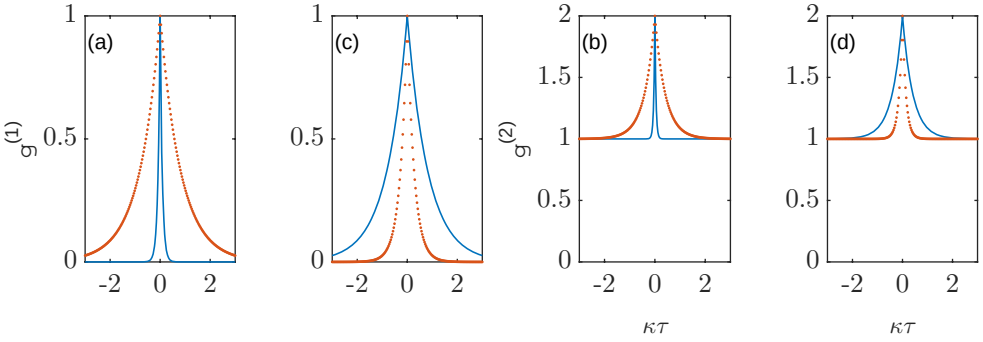

Figure 25.33: (code) First and second-order correlation functions. The solid and dotted lines in (a) and (b) are calculated for $N = 1$ and $N = 100$, resp.. The solid and dotted lines in (c) and (d) are calculated for $T = 100\,\mu\text{K}$ and $T = 300\,\mu\text{K}$, resp..

Fig. 25.33 shows the dependencies of the correlation functions on N and T. For $N = 10^6$ atoms the CARL bandwidth becomes $\beta_N = 0.01\kappa$, which is already well below any mechanical noise. The linewidth reduction with increasing atom numbers is quantitatively supported by numerical simulations (see below).

25.7.1.3 Many atoms, formal

In order to account for the combined effect of many atoms, we reconsider the Eq. (25.210). If $\dot{\alpha}_- = \imath\omega_{ca}\alpha_-$, we get,

$$\alpha_- = -\frac{\imath U_0 \alpha_+}{\kappa + \imath\omega_{ca}} \sum_m e^{\imath\theta_m} \ , \tag{25.303}$$

$$\dot{\theta_n} = \frac{4\varepsilon U_0^2 \alpha_+^2}{\gamma_{fr}\,(\kappa + \imath\omega_{ca})} \sum\nolimits_m \left(e^{\imath\theta_m - \imath\theta_n} + e^{-\imath\theta_m + \imath\theta_n}\right) + \frac{\xi_n}{\gamma_{fr}} \ .$$

The autocorrelation is then,

$$R_\alpha(\tau) \equiv \langle \alpha_-^*(t)\alpha_-(t+\tau)\rangle = \frac{U_0^2\alpha_+^2}{\kappa^2 + \omega_{ca}^2} \sum_{n,m} \langle e^{\imath\theta_n(t+\tau) - \imath\theta_m(t)}\rangle \tag{25.304}$$

$$= |\alpha_0|^2 e^{\imath\omega_{ca}\tau} \sum\nolimits_{n,m} \langle e^{\imath\varphi_n(t+\tau) - \imath\varphi_m(t)}\rangle = |\alpha_0|^2 e^{\imath\omega_{ca}\tau} \sum\nolimits_{n,m,k} \frac{\imath^k}{k!} \langle [\varphi_n(t+\tau) - \varphi_m(t)]^k\rangle$$

$$= |\alpha_0|^2 e^{\imath\omega_{ca}\tau} \sum\nolimits_{n,m,k} \frac{\imath^k}{k!} \sum\nolimits_{j=0}^{k} (-1)^j \binom{k}{j} \langle \varphi_n(t+\tau)^j \varphi_m(t)^{k-j}\rangle \ .$$

The main role of cavity-induced interparticle correlations is to self-consistently establish a constant center-of-mass motion ω_{ca}. We may, to first order, neglect the possibility that the coupling correlates the noise, since the noise is imprinted from the outside, i.e. the molasses. Therefore, $\langle\varphi_n(t+\tau)\varphi_m(t)\rangle \propto \delta_{nm}$,

$$\begin{aligned}\langle\varphi_n(t+\tau)^j\varphi_m(t)^{k-j}\rangle &= \sum\nolimits_{\text{all pairs}}\langle\varphi_n(t+\tau)^2\rangle^{j/2}\langle\varphi_m(t)^2\rangle^{k/2-j/2} \\ &= \frac{j!}{2^{j/2}(j/2)!}\frac{(k-j)!}{2^{(k-j)/2}(k/2-j/2)!}\langle\varphi_n(t+\tau)^2\rangle^{j/2}\langle\varphi_m(t)^2\rangle^{k/2-j/2}\end{aligned} \tag{25.305}$$

so that,

$$R_\alpha(\tau) = |\alpha_0|^2 e^{\imath\omega_{ca}\tau}\sum_{n,m,k}\frac{\imath^k}{k!}\sum_{j=0}^{k}\binom{k}{j}\frac{j!}{2^{j/2}(j/2)!}\frac{(k-j)!}{2^{(k-j)/2}(k/2-j/2)!}\langle\varphi_n(t+\tau)^2\rangle^{j/2}\langle\varphi_m(t)^2\rangle^{k/2-j/2}\ , \tag{25.306}$$

where j and k are even,

$$\begin{aligned}R_\alpha(\tau) &= |\alpha_0|^2 e^{\imath\omega_{ca}\tau}\sum\nolimits_{n,m,k}\frac{\imath^k}{2^{k/2}(k/2)!}\sum_{j=0}^{k}\binom{k/2}{j/2}\langle\varphi_n(t+\tau)^2\rangle^{j/2}\langle\varphi_m(t)^2\rangle^{k/2-j/2} \\ &= |\alpha_0|^2 e^{\imath\omega_{ca}\tau}\sum_{n,m,k}\frac{1}{(k/2)!}\left(-\frac{1}{2}\langle\varphi_n(t+\tau)^2\rangle - \frac{1}{2}\langle\varphi_m(t)^2\rangle\right)^{k/2} \\ &= |\alpha_0|^2 e^{\imath\omega_{ca}\tau}\sum_n e^{-\frac{1}{2}\langle\varphi_n(t+\tau)^2\rangle}\sum\nolimits_m e^{-\frac{1}{2}\langle\varphi_m(t)^2\rangle} = |\alpha_0|^2 N^2 e^{\imath\omega_{ca}\tau}e^{-\frac{1}{2}\langle\varphi_n(t+\tau)^2\rangle}e^{-\frac{1}{2}\langle\varphi_n(t)^2\rangle}\ .\end{aligned} \tag{25.307}$$

25.7.1.4 Memory effects

Relax adiabaticity, $\dot\alpha_- \neq \imath\omega_{ca}\alpha_-$, substitute $\beta = e^{\kappa t}\alpha_-$,

$$\begin{aligned}\dot\theta &= \frac{4\varepsilon\imath U_0\alpha_+}{\gamma_{fr}}\left(\beta e^{-\imath\theta-\kappa t} - \beta^* e^{\imath\theta-\kappa t}\right) + \frac{\xi}{\gamma_{fr}}\ , \\ \beta &= -\imath U_0\alpha_+\int^t e^{\imath\theta+\kappa t'}dt'\ .\end{aligned} \tag{25.308}$$

so that,

$$\begin{aligned}R_\alpha(\tau) &\equiv \langle\alpha_-^*(t)\alpha_-(t+\tau)\rangle = \langle e^{-\kappa t}\beta^*(t)e^{-\kappa t-\kappa\tau}\beta(t+\tau)\rangle \\ &= e^{-\kappa\tau}\langle e^{-2\kappa t}\beta^*(t)\beta(t+\tau)\rangle \\ &= U_0^2\alpha_+^2 e^{-\kappa\tau}\int\int^t\int^{t+\tau} e^{\imath\theta(t'')-\imath\theta(t')+\kappa t'+\kappa t''-2\kappa t}dt''dt'dt \\ &= U_0^2\alpha_+^2 e^{-\kappa\tau}\int\int^t\int^{t+\tau} e^{\imath\omega_{ca}t''-\imath\omega_{ca}t'+\imath\varphi(t'')-\imath\varphi(t')+\kappa t'+\kappa t''-2\kappa t}dt''dt'dt\ .\end{aligned} \tag{25.309}$$

Using the representation of half the δ-distribution $\int^t e^{(\imath\omega_{ca}+\kappa)t'}dt' = \delta_{1/2} = \lim_{\kappa\to 0}\frac{1}{\kappa+\imath\omega_{ca}}$.

25.7.1.5 Schawlow-Townes limit for CARL

The ultimate limit for the spectral purity of a perfectly stable laser oscillator is the *Schawlow-Townes limit* [730]. The origin of this limitation is the discrete nature of the light field. Similarly to quantum projection noise, which is caused by the discretisation of atomic energy levels, the optical *shot-noise* registered in photodetectors arises from the discrete repartition of electromagnetic energy in photons. With a laser power P, a cavity bandwidth κ and an interrogation time τ, the Allan variance [**?**] and the linewidth of a Schawlow-Townes limited laser are given by,

$$\sigma_{\mathrm{ST}}(\tau) = \frac{1}{\omega/\kappa}\frac{1}{\sqrt{(P/\hbar\omega)\tau}} , \qquad (25.310)$$
$$\beta = \kappa^2\frac{\hbar\omega}{P} .$$

In the case of CARL, using $P = \delta\hbar\omega|\alpha_-|^2$ the variance is $\sigma^2_{\mathrm{ST}}(\tau) = \kappa/\tau\omega\delta|\alpha_-|^2 \approx 10^{-20}\ \mathrm{s}/\tau$. The shot-noise which limits the CARL is not the one of the CARL light itself, but the random momentum kicks imparted by molasses-cooled atoms. The CARL linewidth is $\beta = \kappa^2/\delta|\alpha_-|^2 = 10^{-14}\kappa$.

The time-lap between two scattering events for a single atom be distributed according to $p_1(\tau)d\tau = \gamma e^{-\gamma\tau}d\tau$. What is the waiting time distribution for two atoms [733]? Schenzle related the waiting time distribution to the autocorrelation function $g^{(2)}(\tau)$.

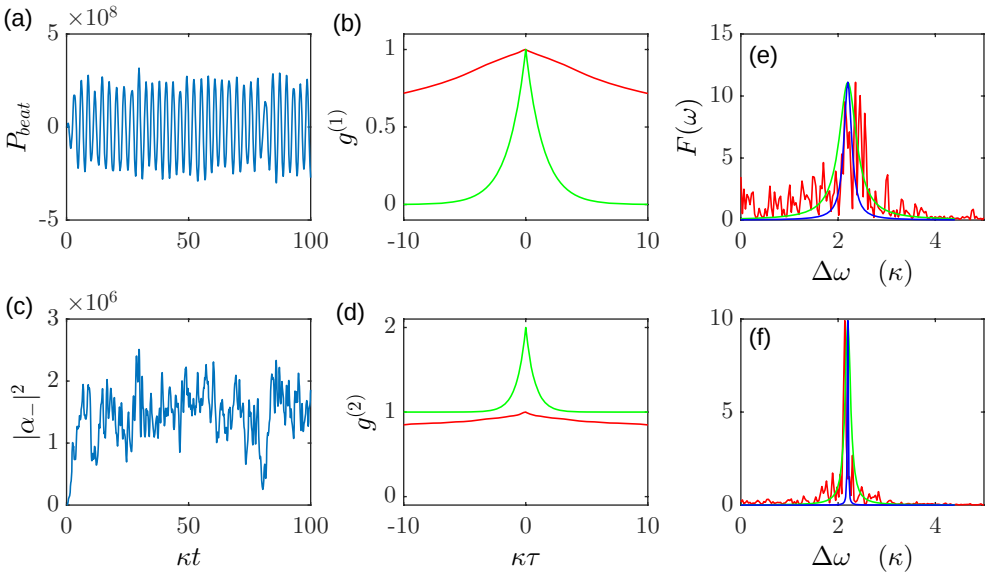

Figure 25.34: Simulated time-dependence of the (a) beat and the (b) intensity signals. Calculated (c) first and second-order correlation functions. The temperature was set to $T = 100\,\mu\mathrm{K}$ and the atom number to $N = 40$. (e-f) Spectra of the CARL laser for (e) 4 and (f) 40 atoms. The total coupling constant NU_0 has been held constant, only the number of atoms whose trajectories are simulated is varied.

Fig. 25.34(e-f) shows spectra of the CARL frequency obtained by Fourier-transforming the autocorrelation function of a Langevin-simulated trajectory of the CARL frequency. The width results from thermal fluctuations in the atomic motion induced by momentum diffusion in the molasses. It is clearly visible that the width is reduced when the atom number is increased, thus confirming Eq. (25.302).

25.7.2 Measuring the coherence properties

We may also attempt to verify the predictions in experiment. Our signals are the beams transmitted through the cavity mirrors.

25.7.2.1 Homodyne signal

Ideally in order to get the full information on the the first-order coherence, we should record both the in-phase and the quadrature component of the field $\alpha_- = \mathfrak{Re}\,\alpha_- + i\mathfrak{Im}\,\alpha_-$ by homodyning it with the local oscillator α_+. Thus we need to use both ports of the beamsplitter: For the in-phase component we get,

$$\begin{aligned} P^{(\mathrm{ph})}_{\mathrm{hody}} &\propto b^\dagger b - c^\dagger c \\ &= |\alpha_+\sqrt{\eta} + \alpha_-\sqrt{1-\eta}|^2 - |\alpha_+\sqrt{1-\eta} - \alpha_-\sqrt{\eta}|^2 \\ &= (1-2\eta)(|\alpha_-|^2 - |\alpha_+|^2) + 4\sqrt{\eta-\eta^2}\alpha_+\mathfrak{Re}\,\alpha_- \ . \end{aligned} \tag{25.311}$$

For a 50% beamsplitter the offsets disappear, $P^{(\mathrm{ph})}_{\mathrm{hody}} \propto= 2\alpha_+\mathfrak{Re}\,\alpha_-$, which means that the homodyne signal is insensitive to intensity noise in the individual ports. Similarly we obtain for the quadrature component,

$$\begin{aligned} P^{(qu)}_{\mathrm{hody}} &\propto |\alpha_+\sqrt{\eta} + \imath\alpha_-\sqrt{1-\eta}|^2 - |\alpha_+\sqrt{1-\eta} - \imath\alpha_-\sqrt{\eta}|^2 \\ &= -2\alpha_+\mathfrak{Im}\,\alpha_-. \end{aligned} \tag{25.312}$$

By mounting a piezo on one of the mirrors in the homodyne loop, we can influence which quadrature component to map. Is there a way how to get $\mathfrak{Im}\,\alpha_-$ and $\mathfrak{Re}\,\alpha_-$ simultaneously?

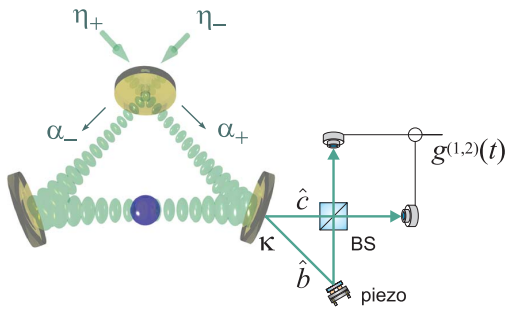

Figure 25.35: Homodyning the counterpropagating beams.

Knowing α_- we can calculate the *first order coherence*,

$$g^{(1)}(\tau) \equiv \frac{\langle\alpha^*(t)\alpha(t+\tau)\rangle}{\langle\alpha^*(t)\alpha(t)\rangle} = \frac{\int\alpha^*(t)\alpha(t+\tau)dt}{\int\alpha(t)^2dt}\ , \tag{25.313}$$

the *second-order coherence*,

$$g^{(2)}(\tau) \equiv \frac{\langle \alpha^*(t)\alpha^*(t+\tau)\alpha(t+\tau)\alpha(t)\rangle}{\langle \alpha^*(t)\alpha(t)\rangle^2} = \frac{\int P_-(t)P_-(t+\tau)dt}{\int P_-(t)dt} , \tag{25.314}$$

and the *emission spectrum* (power spectral density),

$$F(\omega) = \frac{1}{\pi}\mathfrak{Re}\int g^{(1)}(\tau)e^{\imath\omega\tau}d\tau . \tag{25.315}$$

All these quantities can be evaluated from numerical simulations of the Langevin equations.

Example 184 (*Real Signals*): What is recorded in experiment is the probe field power P_{probe} and only one quadrature component of the beat between the probe and the pump. The probe signal is simply,

$$P_- \propto |\alpha_-|^2 . \tag{25.316}$$

So it may be used directly for the $g^{(2)}(\tau)$ intensity correlation function (25.314) analogous to the *Hanbury-Brown-Twiss* experiment.
In contrast, the beat signal is obtained in a *Young* type experiment,

$$P_{beat} \propto |\alpha_+ \pm \alpha_-|^2 = |\alpha_+|^2 + |\alpha_-|^2 \pm 2\alpha_+ \mathfrak{Re}\,\alpha_- , \tag{25.317}$$

because we may assume α_+ real. Obviously, the beat signal oscillates between the limits $\pm 2\alpha_+|\alpha_-|$. Using only one port of the beamsplitter, we miss information on the other quadrature phase. The question arises now, how to calculate the spectrum if only the real part of the field $\mathfrak{Re}\,\alpha$ is known. The interesting quantity is $|g^{(1)}(\tau)|$, because it contains the information on the photon statistics. This function is smooth (it does not oscillate) and should in our case describe an exponential decay (25.295). Fortunately, from numerical calculation it seems that $|g^{(1)}(\tau)|$ is just the convolution of $\langle \mathfrak{Re}\,\alpha(t)\mathfrak{Re}\,\alpha(t+\tau)\rangle / \langle \mathfrak{Re}^{\,2}\alpha(t)\rangle$, so that we may recover the informations. For the spectrum, which is calculated from the complex quantity $g^{(1)}(\tau)$ the question is more delicate. It comes down to asking if,

$$F(\omega) \propto \mathfrak{Re}\int \langle \mathfrak{Re}\,\alpha(t)\mathfrak{Re}\,\alpha(t+\tau)\rangle\; e^{\imath\omega\tau}d\tau \tag{25.318}$$

gives the correct spectrum (25.315).

25.7.2.2 Impact of finite time window

Technical noise may overrule the thermal noise just like in ordinary lasers. This situation may change if atom numbers are low, so that we have bad statistics, or if the collective force is strong enough to correlate the noise.

The spectral width may also be limited by the finite time window $t \in [-\frac{1}{2}t_0, \frac{1}{2}t_0]$, which is taken for computing the spectrum. Even a perfect harmonic oscillation $\alpha_-(t) = \alpha_- e^{\imath\omega_{ca}t}$ will then have a finite bandwidth,

$$\begin{aligned}\mathcal{F}_{a_-}(\omega) &= \mathcal{F}[\alpha_- e^{\imath\omega_{ca}t}] \star \mathcal{F}[\chi_{[-t_0/2,t_0/2]}(t)] \\ &= \alpha_-\delta(\omega-\omega_{ca}) \star \sqrt{\frac{2}{\pi}}\frac{\sin\frac{1}{2}\omega t_0}{\omega} = \alpha_-\sqrt{\frac{2}{\pi}}\frac{\sin\frac{1}{2}(\omega-\omega_{ca})t_0}{(\omega-\omega_{ca})} .\end{aligned} \tag{25.319}$$

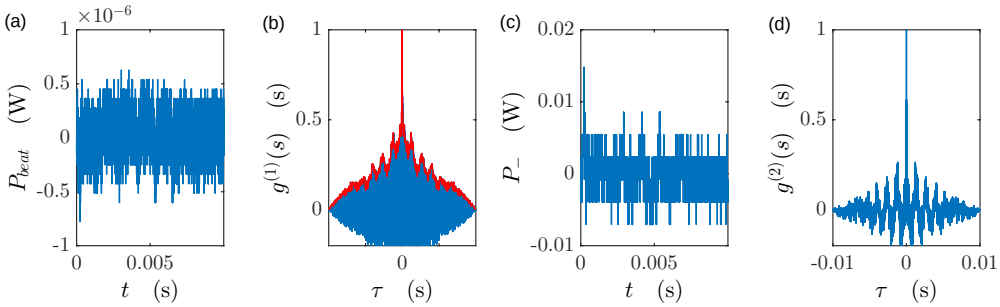

Figure 25.36: (code) Measured trajectories (a) and (b) and correlation functions (c) and (d) of the CARL laser. The coupling constant was $NU_0 = -0.1$.

The spectrum $S_{\alpha_-}(\omega) = |\mathcal{F}_{a_-}(\omega)|^2$ has a bandwidth of $\beta = 5.6/t_0$. For example an oscillation observed for a period 100 times longer than the cavity decay time, $t_0 = 100/\kappa$, the bandwidth will be $\beta = 0.056\kappa$. Simulations are based on the Langevin equation.

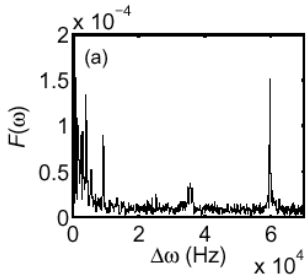

Figure 25.37: Spectrum of the CARL calculated from the first-order correlation function in Fig. 25.36(c). The coupling constant was $NU_0 = -0.1\kappa$.

25.7.3 Exercises

25.7.3.1 Ex: Autocorrelation functions

25.7.3.2 Ex: Signal-to-noise ratio of Bloch oscillations

You want to evaluate the stability of a noisy periodic signal. How many noisy oscillations do you have to observe in order to evaluate the oscillation period with a given S/N ratio [888].

25.8 Further reading

J. Guo et al., *Recoil-induced Resonances in Non-linear Spectroscopy* [DOI]

J.-Y. Courtois et al., *Recoil-induced Resonances in Cesium: An Atomic Analog to the Free Electron Laser* [DOI]

P. R. Hemmer et al., *Self-Organization, Broken Symmetry, and Lasing in an Atomic Vapor: The Interdependence of Gratings and Gain* [DOI]

G.-L. Lippi et al., *Spontaneous Generation of a Longitudinal Atomic Density Grating in Sodium Vapor* [DOI]

D.R. Meacher et al., *Method for Velocimetry of Cold Atoms* [DOI]

P. Verkerk et al., *Comment on "Spontaneous Generation of a Longitudinal Atomic Density Grating in Sodium Vapor"* [DOI]

S. Barbay et al., *Pump-probe spectroscopy of the sodium D line and the question of recoil-induced gratings in hot vapors* [DOI]

P.R. Berman, *Comparison of recoil-induced resonances and the collective atomic recoil laser* [DOI]

M. Vengalattore et al., *Optical bistability at low light level due to collective atomic recoil* [DOI]

V. Vuletic et al., *Three-dimensional cavity Doppler cooling and cavity sideband cooling by coherent scattering* [DOI]

M. Gangl et al., *Cold atoms in a high-Q ring cavity* [DOI]

S. Ostermann et al., *Atomic self-ordering in a ring cavity with counterpropagating pump fields* [DOI]

S.C. Schuster et al., *Supersolid properties of a Bose-Einstein condensate in a ring resonator* [DOI]

J. Léonard et al., *Supersolid formation in a quantum gas breaking continuous translational symmetry* [DOI]

J.K. Asbóth et al., *Optomechanical coupling in a one-dimensional optical lattice* [DOI]

G.R.M. Robb, *Dispersive optical bistability in cold atomic vapours* [DOI]

R. Culver et al., *Collective strong coupling of cold potassium atoms in a ring cavity* [DOI]

S. Bux et al., *Cavity-controlled matter wave superradiance at the recoil limit* [DOI]

R.J. Schulze et al., *Optomechanical approach to cooling of small polarizable particles in a strongly pumped ring cavity* [DOI]

25.8.1 on CARL

R. Bonifacio et al., *The self-consistent pendulum picture of the free electron laser revised* [DOI]

R. Bonifacio et al., *Collective atomic recoil laser (CARL) optical gain without inversion by collective atomic recoil and self-bunching of two-level atoms* [DOI]

R. Bonifacio et al., *A quantum model for collective recoil lasing* [DOI]

S. Gupta et al., *Cavity Nonlinear Optics at Low Photon Numbers from Collective Atomic Motion* [DOI]

M.S. Shahriar et al., *Ultrahigh enhancement in absolute and relative rotation sensing using fast and slow light* [DOI]

F. Zimmer et al., *Sagnac Interferometry Based on Ultraslow Polaritons in Cold Atomic Vapors* [DOI]

G.E. Stedman et al., *Ring-laser tests of fundamental physics and geophysics* [DOI]

Shanchao Zhang et al., *A dark-line two-dimensional magneto-optical trap of 85Rb atoms with high optical depth* [DOI]

25.8.2 on self-organization

J. Javaloyes et al., *Reduced Model for the Description of Radiation-Matter Interaction Including Atomic Recoil* [DOI]

J. Javaloyes et al., *Self-Generated Cooperative Light Emission Induced by Atomic Recoil* [DOI]

T. Griesser et al., *A Vlasov approach to bunching and selfordering of particles in optical resonators* [DOI]

Part VII

Degenerate Interacting Bose and Fermi Gases

Preface to the part *AtomOptics*

The field of *atom optics* deals with the motion of atoms and its control by technical tools. At high velocities with no external forces, the atoms follow straight paths, similar to light beams in *classical optics*. At low speeds, they propagate as waves, similarly to wave optics in Maxwell's theory of *electrodynamics*. The term *atom optics* emphasizes the analogy and the duality in the behavior of microscopic particles.

The *duality principle* is one of the fundamental ideas of quantum mechanics. The appearance of an object as a wave or as a particle depends on the situation in which it is observed. While the wave nature of light was well established in classical physics since a long time, Louis de Broglie was the first in 1924 to apply the duality principle also to massive particles and to predict that particles, under certain conditions, behave like waves whose wavelengths increase as their velocity decreases. Each particle (or sample of particles) is delocalized along a distance corresponding to the 'de Broglie wavelength'. This feature of the matter was soon discovered experimentally in electron beams and is still used today in commercial devices, for example in electron microscopes.

The laser was discovered in 1956. In a laser, light particles are forced to oscillate synchronously, that is, coherently. By analogy, we can raise the question whether a similar phenomenon can occur with massive particles, and whether it is possible to construct an *atom laser*. Such a device would emit coherent matter waves just as the laser emits coherent light. When a gas is cooled to very low temperatures, the Broglie waves of the atoms become very long and, if the gas is sufficiently dense, eventually overlap. If the gas consists of a single species of bosonic particles with all atoms being in the same quantum state, their Broglie waves interfere constructively thus and form a huge wave of coherent matter. This matter wave is described by a single wavefunction exhibiting long range order and having a single phase. If this wavefunction is formed inside a trap, all atoms accumulate in its ground state. Thus, we obtain a pure quantum state of many bodies in the kinetic degree of freedom [22]. The transition of a gas from individual atoms to a degenerate mesoscopic many-body quantum state occurs as a phase transition named *Bose-Einstein condensation* (BEC) as a homage to Bose and Einstein who predicted the effect already in 1924 [107, 259].

In chapter 26 we review experimental techniques which are essential for the preparation and study of ultracold atomic clouds of atoms. In Chp. 27 we study properties of quantum-degenerate gases. In Chp. 28 we concentrate on superfluid features of Bose-condensates. In Chp. 29 we focus on the interaction of Bose-condensates with radiation fields.

[22] In particular, for very cold atoms whose internal excitation occurs on a very different energy scale, the corresponding degree freedom is frozen and does not influence the kinetics.

Chapter 26

Manipulation of atomic gases

The course begins in this chapter with a presentation of the most important experimental techniques for cooling, trapping, manipulating and detecting atomic gases. The knowledge of these techniques will allow for a better understanding of how it is possible to generate and analyze all the effects mentioned above. Chp. ?? sets the foundations for the theoretical description of many-body fields with particular attention to issues arising from quantum statistics. Chp. 27 introduces the phenomenon of Bose-Einstein condensation, and the subsequent chapters focus on the thermodynamic, superfluid, coherent and dielectric properties of condensates.

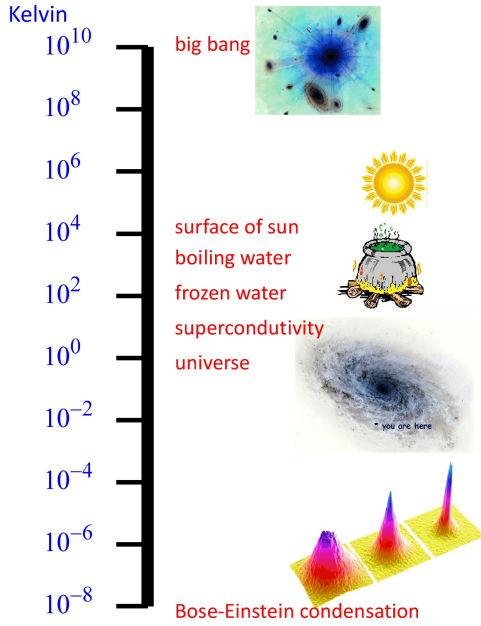

Figure 26.1: Temperature scale.

The incomparable success of atomic optics has been rewarded with 20 nobel prices in the last 25 years (Dehmelt, Paul, Ramsey, Cohen-Tannoudji, Chu, Phillips, Cornell, Wieman, Ketterle, Hänsch, Glauber, Hall, Wineland, Haroche, Ahskin) plus several indirectly related noble prices (De Gennes, Leggett, Thouless, Haldane, Kosterlitz). For review articles on BEC see [641, 192, 175, 322, 710, 780], [459] or check in internet

sites *http://amo.phy.gasou.edu/bec.html* and *http://jila.edu/bec.html*.

In this chapter we review the basic techniques of *Atomic Optics*, emphasizing the cooling, trapping and measurement of cold atomic gases. See also (watch talk) and (watch talk).

26.1 The atomic motion

26.1.1 The atom as a matter wave

We have already emphasized that atomic optics deals with the motion of atoms in a gas, that is, we are interested only in the external degrees of freedom of the atoms. To describe the motion of a free massive particle in one dimension, we write the Hamiltonian,

$$\hat{H} = -\frac{\hbar^2}{2m}\frac{d^2}{dx^2} \ . \tag{26.1}$$

Therefore, the general solution of the stationary Schrödinger equation,

$$\hat{H}\psi(x) = E\psi(x) \ , \tag{26.2}$$

is,

$$\psi(x) = Ae^{\imath kx} + Be^{-\imath kx} \qquad \text{with} \qquad k = \sqrt{\frac{2mE}{\hbar^2}} \ . \tag{26.3}$$

Note, that the wavefunctions $e^{\imath kx}$ are not quadratically integrable. On the other hand, they do not represent real physical systems. In practice, we need to consider wavepackets or specify a finite volume for the particle.

Note also that the eigenvalue spectrum of is continuous. To warrant the interpretation of the wavefunction as a probability density we will require quadratic integrability, $\int |\psi|^2 d^3r = 1$. This means that the wavefunction can not be infinite in a finite volume, but it can be infinite in an infinitely small volume.

The description of the atomic motion by a wave equation emphasizes the fact that microscopic particles have wave properties with each atom corresponding to a velocity-dependent *de Broglie wave*,

$$\boxed{\lambda_{\rm dB} = \frac{h}{p}} \ , \tag{26.4}$$

which describes the coherence length of the atom.

26.1.1.1 Characteristic velocities

The behavior of an atom described by the Schrödinger equation depends very much on its kinetic energy. At high velocities (or short de Broglie waves), it will behave like a classical particle with a well-defined trajectory. At low velocities (or long de Broglie waves), it will propagate like a wave and exhibit phenomena such as diffraction and interference. Therefore, it is important to highlight some characteristic velocity regimes.

Most optical cooling techniques are based on the removal of kinetic energy upon light scattering on electronic transitions. It is, therefore, interesting to compare the kinetic energy (or temperature) of an ensemble of atoms with the width Γ of the transition. The *Doppler limit* is given by (see Exc. 26.1.3.1),

$$k_{\rm B}T_{\rm D} = \frac{\hbar}{2}\Gamma \ . \tag{26.5}$$

We can also compare the kinetic energy with the energy transferred to an atom by the absorption of a single photon. The *photonic recoil* energy is given by,

$$k_{\rm B}T_{\rm rec} = \frac{\hbar^2 k^2}{2m} \ . \tag{26.6}$$

Atomic clouds with temperatures around $T \simeq T_{\rm D} = 10..1000\,\mu{\rm K}$ are called *cold*. Clouds with temperatures around and below $T \lesssim T_{\rm rec} = 0.1..10\,\mu{\rm K}$ are called *ultra-cold*.

In most atomic optical experiments we do not work with individual atoms (or ions), but with relatively dilute ensembles of atoms, called *clouds*. In general, clouds can not be described by a single wavefunction. Either we describe every atom by a separate and independent wavefunction (which only works when the atoms do not interact), or we describe the cloud by probability distributions (such as the 'density matrix'). Let us now consider a thermal cloud. The *Maxwell-Boltzmann distribution* of velocities is,

$$g(\mathbf{v}) = \sqrt{\frac{m}{2\pi k_{\rm B}T}}^{3} e^{-m\mathbf{v}^2/2k_{\rm B}T} \ . \tag{26.7}$$

This distribution is normalized, $\int g(\mathbf{v})d^3\mathbf{v} = \int_0^\infty 4\pi v^2 g(v)dv = 1$. Average velocity is now

$$\bar{v} = \int v g(v)dv = \sqrt{\frac{k_{\rm B}T}{m}} \ . \tag{26.8}$$

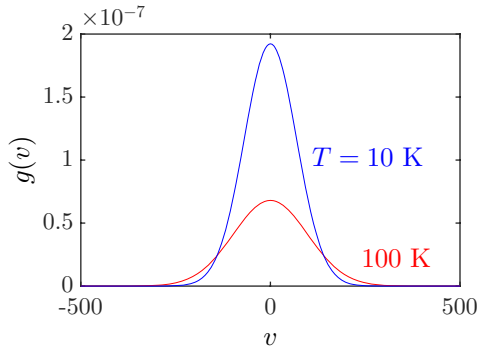

Figure 26.2: (code) Maxwell-Boltzmann distribution.

Maxwell-Boltzmann's law was experimentally proven by Otto Stern in 1920, using a primitive atomic beam and a simple time-of-flight technique based on a rotating drum for selecting atomic velocities. With the advent of laser spectroscopy, the MB

law and its limitations can be tested with highly improved accuracy. This law describes well the behavior of weakly interacting hot atoms. Deviations from this law are insignificant until, at low temperatures, quantum effects come into play. For this to happen the temperature must be so low that the atomic Broglie wavelengths become comparable to the average distance between particles. For a gas in thermal equilibrium the characteristic wavelength, called *thermal de Broglie wavelength*, is,

$$\boxed{\lambda_{\rm therm} \equiv \frac{h}{m\bar{v}} = \sqrt{\frac{2\pi\hbar^2}{mk_{\rm B}T}}} \ . \tag{26.9}$$

It represents an average over the de Broglie wavelengths of all atoms of the sample. When a dense gas is sufficiently dense, so that this quantity exceeds the average distance between atoms,

$$\rho \equiv n\lambda_{\rm therm}^3 > 1 \ , \tag{26.10}$$

where n is the atomic density, we enter a new regime, where the *Maxwell-Boltzmann law* ceases to be valid. Since $\lambda_{\rm therm} \propto T^{-1/2}$, this regime corresponds to low temperatures. The quantity ρ is called *phase space density*. A phase space density approaching 1 means an increased probability of finding *more than one atom per elementary phase space cell*. We then enter the regime of quantum degeneracy, where the Boltzmann statistics must be replaced by the Bose-Einstein statistics, in the case of bosons, or the Fermi-Dirac statistics, in the case of fermions. From the condition $n\lambda_{\rm therm}^3 \simeq 1$, we obtain

$$k_{\rm B}T_{\rm c} = \frac{1}{m}\left(\frac{2\pi\hbar}{\lambda_{\rm therm}}\right)^2 = \frac{(2\pi\hbar)^2 n^{2/3}}{m} \ . \tag{26.11}$$

For example, an atomic gas with density $n \sim 10^{16}\,{\rm cm}^{-3}$ and temperature 900 K is certainly in the classical regime, since $n^{-1/3} \sim 10^6\,{\rm cm} \ \gg \lambda_{\rm dB} = 10^{-9}\,{\rm cm}$. To observe quantum effects, we need relatively dense and cold clouds of atoms. In most gases, lowering the temperature or increasing the density promotes the system to liquidity before the quantum regime is reached. Well-known exceptions are spin-polarized hydrogen (H↑), which does not become liquid and helium, which exhibits quantum degeneracy effects in the liquid phase, although these effects are quite complex due to strong interparticle forces.

We have already seen that all particles in the quantum world are either *bosons* with integer spin or *fermions* with semi-integer spin. Fermions do not share a quantum state, because they must follow the *Pauli's exclusion principle*. They obey a quantum statistical distribution called *Fermi-Dirac distribution* (FD). In contrast, bosons enjoy to share a quantum state and even encourage other bosons to join them in a process called *bosonic stimulation*. Bosons obey a quantum statistical distribution called *Bose-Einstein distribution* (BE). The basic difference between the MB-statistics on one hand and the BE- or FD-quantum statistics on the other is that the former applies to identical particles which, however, are distinguishable from each other, while the second describes identical indistinguishable particles. For the BE/FD statistics one can derive [469] the occupancy number (7.91) for a non-degenerate quantum state having the energy ε when the system is kept at temperature T,

$$\boxed{w_{T,\mu} = \frac{1}{e^{\beta(\varepsilon-\mu)} \mp 1}} \ , \tag{26.12}$$

where we used the abbreviation $\beta \equiv 1/k_{\rm B}T$. The upper sign refers to the BE statistics, the lower sign to the FD statistics. The chemical potential μ is an important system parameter, which helps to normalize the distribution (26.12) to the total number of particles,

$$N = \sum_{\varepsilon} w_{T,\mu}(\varepsilon) \ . \tag{26.13}$$

Similarly, the total energy of the system is given by,

$$E = \sum_{\varepsilon} \varepsilon w_{T,\mu}(\varepsilon) \ . \tag{26.14}$$

A very remarkable effect occurs in a bosonic gas at a certain characteristic *critical temperature* $T_{\rm c}$: below this temperature a substantial fraction of the total number of particles occupies the lowest energy state, while all other states are occupied by a negligible number of particles. Above the transition temperature the macroscopic observables of the gas, such as pressure, heat capacity, etc., receive contributions of all states with a certain statistical weight, but without favoring the state of lower energy. Below the transition temperature, the observables are altered by a macroscopic occupation of the ground state, which results in dramatic changes of the thermodynamic properties. The phase transition is named after Shandrasekar Bose [107] and Albert Einstein [259] *Bose-Einstein condensation* (BEC).

26.1.2 Bose-Einstein condensation

The first hint, that Bose-Einstein condensation was more than just a theoretical fantasy came from London [528], who linked the newly discovered phenomenon of superfluidity in ^{4}He to BEC. However, the interpretation of the λ-point in terms of BEC was not obvious, because strong interactions between particles concealed the role of quantum statistics, and the thermodynamic potentials exhibited divergences at the critical temperature instead of discontinuities, as expected for an ideal gas BEC. These uncertainties triggered an intense search for other systems. In 1954, Schafroth pointed out that electron pairs can be seen as composite bosons and may form Bose-Einstein condensates at low temperatures [729]. In 1957, Bardeen, Cooper and Schrieffer developed the microscopic theory of superconductivity [54], after other researchers, including Blutt, Schaffrot, Fröhlich and Bogolubov, had suggested a relationship of this phenomenon to Bose condensation of electron pairs (nowadays called Cooper pairs).

Motivated by the need to test the concept of condensation of composite particles in weakly interacting systems, in 1962 *Blatt et al.* proposed the investigation of the BEC in gases of *excitons* [85]. Excitons are bound electron-hole pairs that can form a weakly interacting gas in certain non-metallic crystals. They are interesting because their small mass allows BEC at high temperatures and gas density can be controlled over a wide range, by only modifying the intensity of the optical excitation. Being *quasi-particles*, excitons can be created and annihilated, that is their number is not conserved. Excitons were discovered in 1968, and the first evidence for Bose-Einstein of biexciton molecules in a CuCl crystal dates back to 1979 [145].

The laser as coherence phenomenon between photons shares many analogies with condensates. However, photons are quasi-particles as well, and again their number

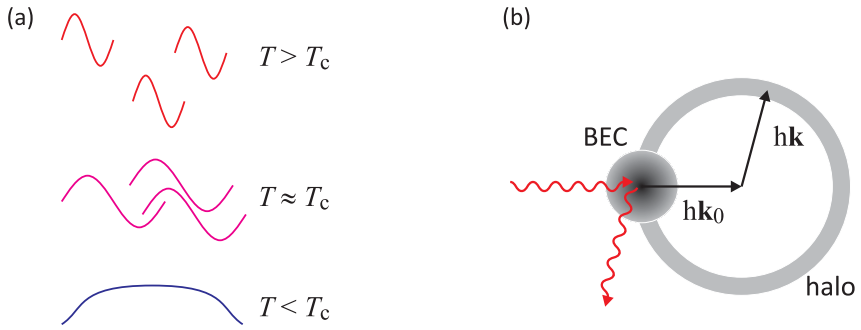

Figure 26.3: (a) Illustration of atomic Broglie waves at different temperatures with respect to the critical temperature. (b) Illustration of the recoil temperature: An atom recoiled by the momentum imparted by absorption of a single photon is ejected from the BEC.

is not conserved [1]. Hence, there is no phase transition: When an optical cavity containing photonic modes is cooled, the photons prefer to disappear in the walls of the cavity instead of condensing.

Hecht [375] suggested in 1959, followed by Stwalley and Nosanow [802] in 1976, that an atomic hydrogen gas with polarized spins would be an appropriate candidate for BEC. The advantage of this system is that interactions between atoms are weak and only give rise to a negligible quantum depletion below 1%. In 1978 Greytak and Kleppner started at the MIT intensive efforts to generate BECs in dilute hydrogen gases. In the 1990s, important advances in the cooling of atoms using laser light allowed to reach very low temperatures, and the invention of the magneto-optical trap (MOT) for neutral atoms permitted their spatial confinement and the compression of their density. These successes boosted efforts to try to create BEC in alkaline gases, which have electronic level schemes that lend themselves to optical cooling. Later, it was discovered that the phase space density in MOTs is limited by radiation trapping effects. As a solution to this problem, scientists had to learn how to trap atoms without the use of light in conservative traps, e.g. by their magnetic dipole moment, and to replace optical cooling with *evaporative cooling*. This was the crucial step that finally permitted to reach BEC in alkaline gases in 1995. Later, the hydrogen experiment, which initially stimulated the alkaline experiments, now taking advantage of their success, has been taken to BEC as well [291].

Why did it take so long to reach Bose-Einstein condensation, seven decades after its prediction by Bose and Einstein? How can we *see* when we have a condensate? What are the characteristics of a BEC accessible to observation and how to measure them? These are the answers that we will answer in the following sections. Solve Exc. 26.1.3.2.

[1] The chemical potential of photons is $\mu = 0$.

26.1.3 Exercises

26.1.3.1 Ex: Fundamental temperature limits

Calculate the Doppler limit, the recoil limit, and the threshold to quantum degeneracy for an atomic cloud of density $n = 10^{14}\,\mathrm{cm}^{-3}$ for the sodium $D2$ transition ($\lambda = 590\,\mathrm{nm}$, $\Gamma/2\pi = 10\,\mathrm{MHz}$) and the rubidium $D2$ transition ($\lambda = 780\,\mathrm{nm}$, $\Gamma/2\pi = 6\,\mathrm{MHz}$).

26.1.3.2 Ex: Boson or fermion?

Whether an atom is a fermion or boson solely depends on its total spin. Half-integer spin particles are fermions, integer spin particles are bosons. For example, Rb atoms have in the ground state $J = 1/2, I = 7/2$ and F integer, and therefore are bosons. Ca^+ ions have $J = 1/2$ and no hyperfine structure, and thus are fermions. ^{6}Li has the half-integer F and is a boson.
Decide on the bosonic or fermionic nature of the following atoms/molecules:
^{85}Rb with $I = 3/2$ in the state $^2S_{1/2}$
^{88}Sr with $I = 0$ in the state $^1S_0$
^{88}Sr with $I = 0$ in the state $^3P_2$
^{87}Sr with $I = 9/2$ in the state $^1S_0$
$^{172}Yb^+$ with $I = 0$ in the state $^2S_{1/2}$
$^{171}Yb^+$ with $I = 1/2$ in the state $^2S_{1/2}$

26.2 Optical cooling

As discussed in Sec. 20.2, the force exerted by a light field on an atom can be of two types: a dissipative force arising called *radiation pressure*, which is often used for optical cooling purposes, and a conservative *dipolar force* which often serves for the engineering of optical trapping potentials. Both applications of optical forces will be detailed in the following sections.

26.2.1 Optical molasses

In the *Doppler cooling* model, we treat the phenomenology of optical forces quantitatively by considering the amplitude, phase and frequency of a classical field interacting with the dipole of an atomic transition in a two-level atom. From Eq. (20.25) and previous definitions of Ω and Ω_{sat}, and with the intensity $I \propto \mathcal{E}^2$, we can write the *saturation parameter*,

$$s = \frac{I}{I_{\mathrm{sat}}} = \frac{\Omega^2}{\Omega_{\mathrm{sat}}^2} = \frac{\Omega^2}{\Gamma^2/2} \ , \tag{26.15}$$

and

$$\mathbf{F}_{\mathrm{rp}} = \frac{\hbar \mathbf{k} \Gamma}{2} \frac{s}{(2\Delta/\Gamma)^2 + 1 + s} \ . \tag{26.16}$$

Now, if we consider an atom propagating in $\mp z$ direction with the velocity v_z counterpropagating to a light wave detuned by Δ from the resonance, the total detuning will be

$$\Delta \longrightarrow \Delta \mp k v_z \ . \tag{26.17}$$

where the term kv_z is the Doppler shift. The force $F_\pm$ acting on the atom will be in the direction opposite to the motion,

$$\mathbf{F}_\pm = \pm\frac{\hbar\mathbf{k}\Gamma}{2}\frac{s}{(2(\Delta \mp kv_z)/\Gamma)^2 + 1 + s} \ . \tag{26.18}$$

Supposing now, that we have two light fields propagating in directions $\pm z$, the total force will be $\mathbf{F} = \mathbf{F}_+ + \mathbf{F}_-$. If kv_z is small compared to Γ and Δ, we find through a Taylor expansion,

$$F_z \simeq 4\hbar k s \frac{kv_z(2\Delta/\Gamma)}{[1 + s + (2\Delta/\Gamma)^2]^2} \ . \tag{26.19}$$

This expression shows that, if the detuning Δ is negative (that is, on the red side of the resonance), then the cooling force will oppose the motion and be proportional to the atomic velocity. Fig. 26.4 shows this decelerating dissipative force as a function of v_z at a detuning $\Delta = -\Gamma$ with $I = I_{\rm sat}/2$. The one-dimensional motion of the atom is thus behaving like being subject to a friction force which is proportional to the atomic velocity,

$$F_z \simeq \alpha_{\rm d} v_z \qquad \text{with} \qquad \alpha_{\rm d} = s\frac{-4k^2(2\Delta/\Gamma)}{1 + s + (2\Delta/\Gamma)^2} \ . \tag{26.20}$$

The proportionality factor, is just the *friction coefficient*.

However, the atom will not cool down indefinitely. At some point, the Doppler cooling rate will be balanced by the heating rate coming from the momentum fluctuations of the atom absorbing and remitting photons. The *Doppler cooling limit* is given by,

$$k_{\rm B}T = \hbar\frac{\Gamma}{2} \ , \tag{26.21}$$

as we will see in Exc. 26.2.5.1. This limit is generally, for alkaline atoms, on the order of dozens of micro-Kelvin. In the early years of cooling and trapping, the Doppler limit was thought to be a real physical barrier. But in 1988, several groups have shown that, in fact, atoms could be cooled well below the Doppler limit. The effect arises in atoms, whose ground state exhibits a hyperfine structure. We will show simplified one-dimensional models for sub-Doppler cooling in the next section. Resolve the Exc. 26.2.5.2.

26.2.2 Sub-Doppler cooling

It turns out that atoms with a hyperfine structure in the ground state can be cooled below the Doppler limit (26.5). To explain this unexpected observation, models involving a slow motion of the atoms in polarization gradients of a standing light wave have been invoked. The phenomenon is now known as *polarization gradient cooling*.

Two principal mechanisms for cooling atoms to temperatures below the Doppler limit are based on spatial polarization gradients. These two mechanisms, however, invoke very different physical processes and are distinct by the spatial dependence of the light polarization. A key point is that these sub-Doppler mechanisms only work on atoms with multiple ground state levels. Two parameters, the friction coefficient and the capture velocity, determine the importance of these cooling processes. In this

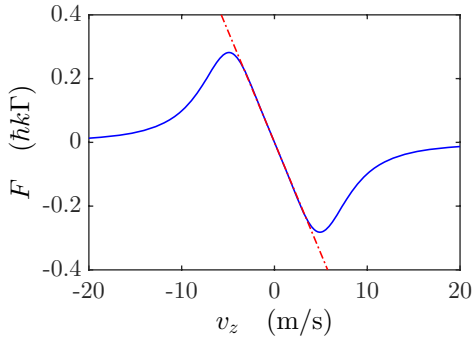

Figure 26.4: (code) Doppler force due to one-dimensional radiative pressure as a function of atomic velocity along the z-axis for red detuning $\Delta = -\Gamma$ at a light intensity of $I = 2I_{\rm sat}$. The solid line shows the exact expression for the restoring force [Eq (26.18)]. The broken line shows the approximate linear expression of the velocity dependence according to Eq. (26.19).

section we compare the expressions for these quantities in the sub-Doppler regime to those found by the conventional one-dimensional Doppler cooling model for optical molasses.

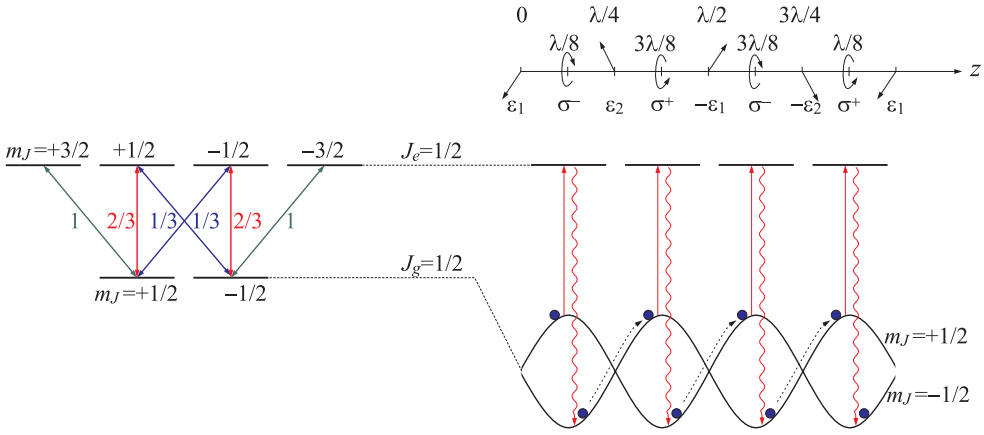

Figure 26.5: The upper line shows, how the polarization changes as a function of position (in units of a wavelength) for the 'lin-perp-lin' standing wave configuration. The figure below shows a simplified picture of the Sisyphus cooling mechanism for an atom with two levels, $J_g \leftrightarrow J_e$.

26.2.2.1 Lin ⊥ lin molasses

In the first case, two counterpropagating light waves with orthogonal linear polarizations form a standing wave. This configuration is familiarly called lin-perp-lin. Fig. 26.5 illustrates the change of polarization every period of $\lambda/8$ from linear to circular to linear again, but rotated by 90°, and so on [196]. Along the same distance, the light-atom coupling produces a periodic energy shift (light-shift) of the ground

state Zeeman levels. To illustrate the cooling mechanism, we assume the simplest case, a transition $J_g = \frac{1}{2} \longrightarrow J_e = \frac{3}{2}$. As shown in Fig. 26.5 an atom moving through the region $z \simeq \lambda/8$, where the polarization is σ_-, will see its population pumped to $J_g = -\frac{1}{2}$. In addition, the Clebsch-Gordan coefficients that control the dipolar coupling of the $J_e = \frac{3}{2}$ require that the $J_g = -\frac{1}{2}$ couples to σ_- with a force three times larger than the $J_g = +\frac{1}{2}$ does. The difference of the coupling forces leads to the light-shift between the two fundamental states shown in Fig. 26.5. As the atom continues to move toward $+z$, the relative coupling forces are reversed near $3\lambda/8$, where the polarization is essentially σ_+. Thus, the relative energy levels of the two hyperfine fundamental states oscillate 'out of phase' when the atom moves through the standing wave.

The fundamental idea is that the optical pumping rate, which always redistributes population to the lower hyperfine level, delays the light-shift of the atom moving through the field. The result is a 'Sisyphus effect', where the atom spends most of its time in sub-levels climbing a potential hill and thus converting kinetic energy into potential energy. This accumulated potential energy is subsequently dissipated by spontaneous emission to the electromagnetic modes of the vacuum. Simultaneously, the spontaneous emission transfers the population back to the lower one of two ground state levels. The lower diagram of Fig. 26.5 illustrates the phase delay of optical pumping. For this cooling mechanism to work, the optical pumping time, which is controlled by the intensity of the light, must be sufficiently slow to give the atom enough time to climb a noticeable part of the light-shift potential. This time essentially depends on the speed of the atom. As the atom is moving slowly, having previously been cooled by the Doppler mechanism, the light field must be weak in order to decrease the optical pumping rate. Interestingly, this physical picture combines the conservative dipole optical force, whose spatial integral gives rise to the mounts and valleys of the potential on which the atom moves, and the irreversible dissipation of energy by spontaneous emission, which is necessary for any type of cooling.

We can obtain simple expressions for the friction coefficient and the capture velocity after some definitions. As in the Doppler cooling model we define the friction coefficient $\alpha_{\rm lpl}$ as the proportionality constant between the force F and the atomic velocity v,

$$F = -\alpha_{\rm lpl} v \ . \tag{26.22}$$

We assume that the light field is tuned to the red of the transition J_g - J_e,

$$\Delta = \omega - \omega_0 \ , \tag{26.23}$$

and we denote the light-shifts of the levels $J_g = \pm\frac{1}{2}$ as $\Delta_\pm$, respectively. At the position $z = \lambda/8$, we find $\Delta_- = 3\Delta_+$ and at $z = 3\lambda/8$, $\Delta_+ = 3\Delta_-$. As the applied field is tuned to red, all $\Delta_\pm$ have negative values. Now, for the cooling mechanism to be efficient, the optical pumping time $\tau_{\rm p}$ should be similar to the time needed for an atom with velocity v to move from the bottom to the top of the potential, $\frac{\lambda/4}{v}$,

$$\tau_{\rm p} = \frac{\lambda/4}{v} \tag{26.24}$$

or

$$\Gamma' \simeq kv \ , \tag{26.25}$$

where $\Gamma' = 1/\tau_{\rm p}$ and $\lambda/4 \simeq 1/k$. Now, the energy W dissipated during a cycle of escalation and spontaneous emission is essentially the average energy difference between the light-shifted ground states, $\Delta_{\rm ls} \equiv \Delta_+ + \Delta_-$, that is $W \simeq -\hbar\Delta_{\rm ls}$. Therefore, the rate for energy dissipation is,

$$\frac{dW}{dt} = \Gamma'\hbar\Delta_{\rm ls} \ . \tag{26.26}$$

At the same time, every temporal energy change of a system can always be expressed as $\frac{dW}{dt} = \mathbf{F}\cdot\mathbf{v}$. Therefore, in this one-dimensional model, considering Eq. (26.23), we can write,

$$\frac{dW}{dt} = -\alpha_{\rm lpl}v^2 = -\Gamma'\hbar\Delta_{\rm ls} \ , \tag{26.27}$$

such that with (26.25),

$$\alpha_{\rm lpl} = -\frac{\Gamma'\hbar\Delta_{\rm ls}}{v^2} \simeq -kv\frac{\hbar\Delta_{\rm ls}}{v^2} \simeq -\frac{\hbar k^2\Delta_{\rm ls}}{\Gamma'} \ . \tag{26.28}$$

Note that since $\Delta < 0$, $\alpha_{\rm lpl}$ is a positive quantity. Also note, that for large detunings, ($\Delta \gg \Gamma$) Eq. (20.24) gives,

$$\frac{U}{\hbar} = \frac{\Delta_{\rm ls}}{4} = \frac{\Omega^2}{4\Delta} \ . \tag{26.29}$$

It is also true that for light-shifts, which are large compared to the natural width of ground state ($\Delta_{\rm ls} \gg \Gamma'$), and for large red detunings ($\Delta \gtrsim 4\Gamma$),

$$\frac{\Gamma}{\Gamma'} \simeq \frac{\Delta^2}{4\Omega^2} \ . \tag{26.30}$$

Therefore, the sub-Doppler friction coefficient can also be written,

$$\alpha_{\rm lpl} = -\frac{\hbar k^2\Delta}{4\Gamma} \tag{26.31}$$

Eq. (26.31) makes two remarkable predictions: Firstly, in the 'lin-perp-lin' configuration the sub-Doppler friction coefficient can be a large number in comparison to $\alpha_{\rm d}$. Note that from Eq. (26.20), with $I \lesssim I_{\rm sat}$ and $\Delta \gg \Gamma$,

$$\alpha_{\rm d} \simeq \hbar k^2 \left(\frac{\Gamma}{\Delta}\right)^3 \ , \tag{26.32}$$

and

$$\frac{\alpha_{\rm lpl}}{\alpha_{\rm d}} \simeq \left(\frac{\Delta}{\Gamma}\right)^4 \ . \tag{26.33}$$

Secondly, $\alpha_{\rm lpl}$ is independent of the intensity of the applied field. This last result is different from the friction coefficient, which is proportional to the field intensity up to until saturation (see Eq. (26.20)). However, although $\alpha_{\rm lpl}$ seems impressive, the range of atomic velocities where it can operate is constrained by the condition,

$$\Gamma' \simeq kv \ . \tag{26.34}$$

The ratio of the capture velocities for sub-Doppler versus Doppler cooling is therefore only,

$$\frac{v_{\rm lpl}}{v_{\rm d}} \simeq \frac{4\Delta_{\rm ls}}{\Delta} \ . \tag{26.35}$$

Fig. 26.6 graphically illustrates the comparison between the Doppler and the 'lin-perp-lin' sub-Doppler cooling mechanisms. The dramatic difference of the capture ranges is evident. Note also that the slopes of the curves give the friction coefficients and that, within the capture range, the slope is much steeper for the sub-Doppler mechanism.

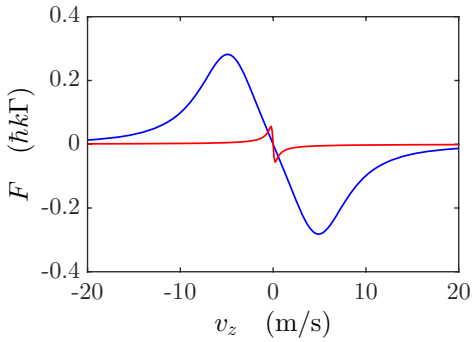

Figure 26.6: (code) Comparison of slopes, amplitudes, and capture ranges for Doppler and Sisyphus cooling.

26.2.2.2 σ^+-σ^- molasses

The second mechanism operates with two counterpropagating light beams, which are circularly polarized in opposite directions. When the two counterpropagating beams have the same amplitude, the resulting polarization is always linear and orthogonal to the propagation axis, but the tip of the polarization vector traces a helix with a periodicity of λ [see Fig. 26.7(b)]. The physics of this sub-Doppler mechanism *does not involve hill-climbing nor spontaneous emission*, but an imbalance of the photon scattering rates by the two counterpropagating light waves as the atom moves along the z-axis. This imbalance leads to a velocity-dependent force counteracting the atomic displacement. The essential factor leading to the different scattering rates is the creation of a population orientation along the z-axis between the sub-levels of the atomic ground state. The more populated sub-levels scatter more photons. Now, considering the energy level diagram (see Fig. 26.5) and the symmetry of the Clebsch-Gordan coefficients, it is evident that transitions $J_g = \frac{1}{2} \leftrightarrow J_e = \frac{3}{2}$ coupled by linearly polarized light can not produce an orientation of the population in the ground state. In fact, the simplest system exhibiting this effect is $J_g = 1 \leftrightarrow J_e = 2$. A measure for this orientation is the magnitude of the matrix element $\langle J_z \rangle$ between the sublevels $J_{g_z} = \pm 1$. For an atom at rest at the position $z = 0$ interacting with the light polarized along the y-direction, the light-shifts Δ_0 and $\Delta_\pm$ of the three sub-levels of the ground state would be,

$$\Delta_{+1} = \Delta_{-1} = \tfrac{3}{4}\Delta_0 \ , \tag{26.36}$$

and the stationary populations would be 4/17, 4/17 e 9/17, respectively. Obviously, linearly polarized light does not produce a stationary orientation, $\langle J_z \rangle_s = 0$. But when the atom begins to move along the z-axis with velocity v, it sees a linear polarization precessing about the axis of propagation at an angle $\varphi = kz = -kvt$. This precession gives rise to a new term in the Hamiltonian, $V = kvJ_z$. Furthermore, when we transform to a rotating coordinate system, the eigenfunctions of the Hamiltonian of the atom moving in this new 'inertial' system become linear combinations of the basis functions of the resting atom. The expectation value of the stationary orientation operator J_z, is now zero in the inertial system [196],

$$\langle J_z \rangle = \frac{40}{17} \frac{\hbar k v}{\Delta_0} = \hbar(\Pi_+ - \Pi_-) \ . \tag{26.37}$$

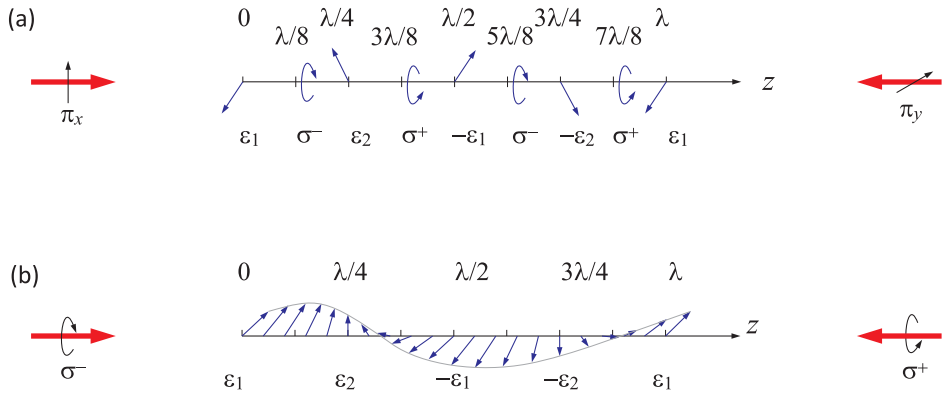

Figure 26.7: Polarization as a function of position (in units of a wavelength) for the σ^+-σ^- standing wave configuration.

Note that, as the expectation value of the orientation is nonzero only when the atom moves. In Eq. (26.37) we denote the populations of the sub-levels $|\pm>$ as $\Pi_\pm$, and we interpret nonzero matrix elements as a direct measure of the population difference between the ground state levels $|\pm>$. Note that, since Δ_0 is negative (red tuning), the Eq. (26.37) tells us, that the population Π_- is larger than Π_+. Now, when an atom traveling in $+z$ direction is exposed to two light waves with polarizations $\sigma_\mp$ propagating in the $\mp z$ directions, the preponderance of population in the state $|-\rangle$ will result in a higher scattering rate from the wave propagating in $-z$ direction. Therefore, the atom will be subject to a total force opposite to its movement and proportional to its velocity. The differential scattering rate is,

$$\frac{40}{17} \frac{kv}{\Delta_0} \Gamma' \ . \tag{26.38}$$

With a quantized momentum of $\hbar k$ transferred at each scattering event, the total force is,

$$F = \frac{40}{17} \frac{\hbar k^2 v \Gamma'}{\Delta_0} \ . \tag{26.39}$$

The friction coefficient $\alpha_{\rm cp}$ is,

$$\alpha_{\rm cp} = -\frac{40}{17}\hbar k^2 \frac{\Gamma'}{\Delta_0} \ , \tag{26.40}$$

which is a positive quantity, since Δ_0 is negative for red detuning. Comparing α_{cp} with $\alpha_{\rm lpl}$ we see, that α_{cp} must be much smaller, because we always assumed that the light shifts Δ are much larger than the linewidths Γ'. However, the heating rate due to fluctuations of the recoil is also much lower. Thus, the minimum temperatures that can be reached with the two sub-Doppler mechanisms are comparable.

Although the Doppler cooling mechanism also depends on an imbalance of scattering from counterpropagating light waves, in this case the imbalance comes from the fact that the Doppler shift experienced by the moving atoms leads to different probabilities for photon scattering. For the sub-Doppler mechanism the scattering probabilities from the two light waves are the same, but the ground state populations are not. The state with the largest population suffers the highest scattering rate.

26.2.3 Raman cooling

26.2.3.1 Optical cooling of confined particles

It is also possible to cool ions confined in a trap [870]. The direction of their motion and their velocity change periodically with the secular frequencies ζ_r und ζ_z. For optical cooling it is sufficient to irradiate a single red-detuned running-wave light field: In a real ion trap the cylindrical symmetry cannot be realized with absolute precision so that we get different secular frequencies $\zeta_x \neq \zeta_y \neq \zeta_z$ and a coupling of the degrees of freedom for all directions of space. The cooling of the ionic motion in a single direction results in a cooling of the motion in the other directions.

In the rest system of an ion oscillating in a harmonic trap the Doppler-shift of the laser frequency changes periodically: $\mathbf{v}(t) = \mathbf{v}_0 \cos \zeta_{r,z} t$. The ion absorbs therefore in its rest system the light on a withb of sidebands whose distance and strength depend on the oscillation frequency and amplitude. The absorption profile of a transition in such a harmonically vibrating ion follows as a convolution of the Lorentz profile $\mathcal{L}_\Gamma$, describing the naturally broadened resonance, with a function $\mathcal{S}$, describing the splitting of the absorption profile into sidebands [421]:

$$\mathcal{A}(\Delta) = (\mathcal{L}_\Gamma \star \mathcal{S})(\Delta) \quad , \quad \mathcal{S}(\Delta) = \sum_n \mathcal{J}_n(\mathbf{k}\cdot\mathbf{v}_0/\zeta_{r,z})^2 \delta(\Delta - n\zeta_{r,z}) \ . \tag{26.41}$$

$\mathcal{J}_n$ denotes the Bessel function of n^{th} order. In essence, the system is governed by three time-constants: The natural decay width of the cooling transition Γ is a measure for the inneratomic time scale, since it determines the average duration of absorption-emissions cycles. The secular frequencies $\zeta_{r,z}$ determine the time scales for changes in the external degrees of freedom, i.e. for changes of the ion's location and velocity. The Doppler-shift kv_0 of the resonance frequency in the return point of the ion motion finally, is a measure for the kinetic energy of the ion.

The relative importance of these three characteristic frequencies reveal the state of the ion in the trap. The modulation index $\mathbf{k}\mathbf{v}_0/\zeta_{r,z}$ decides on the height and the number of sidebands in the excitation spectrum. The better the ion has been cooled,

the smaller the modulation index and the smaller the height and number of sidebands. The kinetic energy of the ion is,

$$E_{\text{kin}} = \frac{1}{2}mv_0^2 = \frac{1}{2}m\zeta_{r,z}^2 x_0^2 \ . \tag{26.42}$$

The modulation index $\mathbf{kv}_0/\zeta_{r,z} = kx_0 = 2\pi x_0/\lambda$ is also called *Lamb-Dicke parameter*. By cooling the Lamb-Dicke parameter is so much reduced and the ion is so well localized that its motional sidebands are smaller than the wavelength of the exciting light. It then is in the so-called Lamb-Dicke regime $x_0 \ll \lambda$ [**?**] and has so small motional sidebands that they do not contribute to the line shape and do not influence the line width. Therefore the linear Doppler effect vanishes.

The quantity $\zeta_{r,z}/\Gamma$ defines the *resolution* of the sidebands. If the resolution is poor, we talk about weak confinement, else about strong confinement. Therefore the same ion can be weakly confined with respect to an allowed transition and strongly confined with respect to a forbidden transition. The cooling processes in the two cases of strong and weak trapping must be described differently. At weak confinement the oscillation frequency $\zeta_{r,z}$ is so slow that many absorption-emission cycles with the time constant Γ^{-1} can occur during one oscillation period. Cooling process and cooling limit are approximately the same as for free particles and are described by Doppler cooling.

26.2.3.2 Raman sideband cooling

In the case of strong confinement for the description of the cooling process we must consider the quantization of the motional energy in the harmonic potential. The two levels coupled by the narrow transition split into vibrational sublevels $|n_{r,z}\rangle$, which are populated in thermal equilibrium according to the Bose-Einstein distribution and have the kinetic energies E_{kin},

$$n_{r,z} = \frac{1}{e^{\hbar\zeta_{r,z}/k_{\text{B}}T} - 1} \qquad \text{and} \qquad E_{\text{kin}} = \hbar\zeta_{r,z}(n_{r,z} + \tfrac{1}{2}) \ . \tag{26.43}$$

To perform the so-called optical cooling *sideband cooling* [870] the laser is tuned to the first lower sideband. The laser light is then scattered in a Raman-Anti-Stokes process at the excited electronic state with a vibrational quantumnumber lower by 1 $|e, n_{r,z} - 1\rangle$. The subsequent spontaneous decay occurs most probably to the same vibrational substate of the ground state $|g, n_{r,z} - 1\rangle$. The net effect of such a scattering process therefore is a transition to the next lower vibrational quantum number. The zero point energy of the ion in the trapping potential cannot be underscored by cooling, $E_{\text{kin}} > \frac{1}{2}\hbar\zeta_{r,z}$ (for the Yb^+ ion it is $E_{\text{kin}} > 2\,\text{neV}$). However, the uncertainty of the kinetic energy, and the temperature T given by (26.43) have no lower limit [230].

At every absorption process, free particles carry away the momentum of the photons $\hbar k$. The recoil of a free Yb^+ ion corresponds to the frequency shift $\varepsilon/2\pi = 5.3\,\text{kHz}$. On a narrow transition, it yields a resonance at the frequency ε. For trapped ions, this is not the case, because the momentum is absorbed by the whole trap (see analogy to the *Mößbauer effect*).

26.2.3.3 Stimulated Raman sideband cooling

We may use two lasers detuned far from resonance to couple two vibrational states. However, additional dissipation by optical pumping is still required.

Numerous schemes have been tested to cool neutral atoms in optical lattices. For the schemes to work, the ion should be already in the Lamb-Dicke regime. Otherwise, transitions with transfer of higher vibrational quantum numbers $n_{r,z}$ are possible during spontaneous emission. The Lamb-Dicke limit is set by $kr < 1$, or,

$$\langle n \rangle = \frac{m\omega_{\rm trp}}{2\hbar k^2} \ . \tag{26.44}$$

This means that higher trap frequencies ease the required temperature at which sideband cooling can start to work.

26.2.4 Adiabatic cooling of an optical lattice

Adiabatic cooling by [454] in 1D. Defining the lattice constant Q_0, the Boltzmann factor $f_{\rm B} \equiv e^{-\hbar\omega/k_{\rm B}T}$, the initial thermal population $\pi_n = (1-f_{\rm B})f_{\rm B}^n$, the recoil energy $E_{\rm rec} \equiv \frac{\hbar^2 k^2}{2m}$,

$$\frac{k_{\rm B}T}{2} = \sum_n \frac{\pi_n}{\hbar Q_0} \int_{(n+1)^{th}\text{Bloch band}} \frac{p^2}{2m} dp = 2\sum_n \frac{\pi_n}{\hbar Q_0} \int_{n\hbar Q_0/2}^{(n+1)\hbar Q_0/2} \frac{p^2}{2m} dp \tag{26.45}$$

$$= 2E_{\rm rec}\left(\frac{Q_0}{k}\right)^2 \sum_{n=0}^{\infty} \pi_n \frac{3n^2+3n+1}{24} = E_{\rm rec}\left(\frac{Q_0}{k}\right)^2 \frac{1+4f_{\rm B}+f_{\rm B}^2}{12(1-f_{\rm B})^2} \ . \tag{26.46}$$

Furthermore,

$$f_{\rm B} = \frac{\bar{n}}{1+\bar{n}} \qquad \Longleftrightarrow \qquad \bar{n} = \frac{f_{\rm B}}{1-f_{\rm B}} \ .$$

26.2.5 Exercises

26.2.5.1 Ex: Optical molasses

Optical molasses are created (in one dimension) by two beams counterpropaganting lasers tuned to red of an atomic transition. Each of the laser beams exerts on the atoms the radiative pressure force $F_\pm = \hbar k \frac{\Gamma}{2} \frac{s}{[2(\Delta \pm k\nu)/\Gamma]^2+1+s}$. Δ is the detuning of the laser, ν is the velocity of an atom.

a. Show that for small velocities ($|kv| \ll \Gamma$ and $\Delta \leq \Gamma$) the optical molasses can be understood as a friction force and calculate the friction coefficient.

b. Heating processes caused by spontaneous emission limit the minimum temperature that can be reached in optical molasses. Calculate the laser tuning, where the temperature reaches its minimum value and specify the cooling limit.

Help: Suppose a one-dimensional molasses and assume, that the spontaneous emission only happens along this dimension. The heating rate follows from the scattering rate R through $\left(\frac{dE}{dt}\right)_{\rm heat} = \frac{d}{dt}\frac{\langle p^2\rangle}{2m} = \frac{\hbar^2k^2}{2m}2R$, the cooling rate follows from $\left(\frac{dE}{dt}\right)_{\rm cool} = Fv$.

26.2.5.2 Ex: Atomic fountain

In atomic fountains atoms are accelerated upward by a 'moving optical molasses'. After the molasses has been switched off, they perform a ballistic flight in the Earth gravitational field. The moving molasses is generated by two pairs of counterpropagating laser beams intersecting at right angle and oriented both at an angle of 45° with respect to gravity. The upgoing beams are tuned to the blue, and the counterpropagating downgoing beams have the same detuning to the red side of the atomic resonance ($\lambda = 780\,\mathrm{nm}$). Supposing that the resonator is close to the position of the molasses and has with negligible length, what should be the detuning in order to achieve 1 s time period between the two passages of the atoms through the microwave resonator?

26.3 Optical and magneto-optical traps

26.3.1 The magneto-optical trap

An apparently fatal obstacle to the confinement of particles by optical forces is Earnshaw's optical theorem. This theorem states that, if a force is proportional to the light intensity, its divergence must be zero because the divergence of the Poynting vector expressing the directional flux of intensity is zero inside a volume without sources nor sinks of radiation. The absence of divergence precludes the possibility of a restoring force to the interior at all places of a closed surface [29]. However, Earnshaw's optical theorem can be bypassed by a clever trick. The internal degrees of freedom of the atom (i.e., its electronic energy levels) can change the proportionality between the force and the Poynting vector in a position-dependent manner, such that the optical Earnshaw's theorem does not apply. Spatial confinement is then possible using the radiative pressure force generated by counterpropagating light beams. The most common trap configuration is based on a radial magnetic field gradient produced by a quadrupolar field and three pairs of counterpropagating circularly polarized laser beams tuned to the red of an atomic transition and intersecting at right angles at the point where the field is zero. This *magneto-optical trap* (*MOT*) uses the position-dependent Zeeman shift of the electronic levels as the atom moves in the radially increasing magnetic field. The use of circularly polarized light which is red-detuned by about Γ results in a spatially varying transition probability, whose effect is to produce a restoring force that pulls the atom back to the origin. To understand better how the trapping scheme works, we consider a two-level atom with a transition $J = 0 \to J = 1$ moving along the z-direction. We apply a magnetic field $\mathcal{B}(z)$ growing linearly with the distance from the origin. The Zeeman shifts of the electronic levels depend on the position,

$$\Delta_{\mathcal{B}} = \frac{\mu_{\mathrm{B}} g_F m_F}{\hbar} \frac{d\mathcal{B}}{dz} z \equiv \partial_z \omega_{\mathrm{Zeem}} \ , \tag{26.47}$$

see Fig. 26.8. We also apply counterpropagating laser beams along the directions $\pm z$ with circular polarizations of opposite signs and tuned to the red of the atomic transition. It is clear from Fig. 26.8 that an atom moving in $\pm z$ direction will scatter $\sigma_{\mp}$ type photons at a faster rate than $\sigma_{\pm}$ type photons, because the Zeeman effect

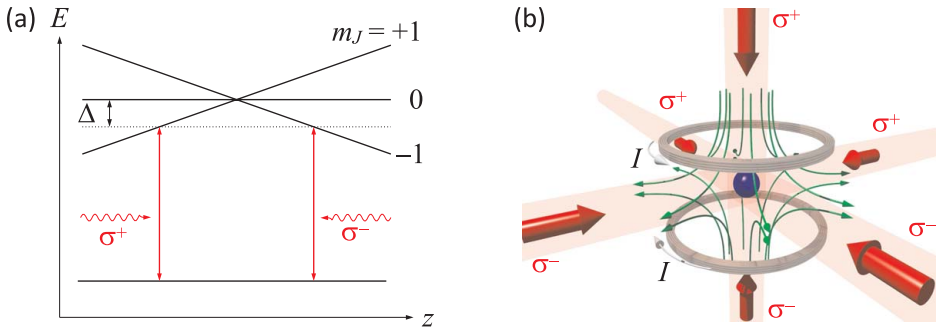

Figure 26.8: Left: Diagram of the energy level shift in an MOT, when an atom moves out of the center of the trap. A restoring force is observed around the indicated resonance positions. Right: Scheme of a typical MOT set up showing the six laser beams and the current-carrying coils in anti-Helmholtz configuration producing the quadrupolar magnetic field.

will pull the $\Delta m_J = \mp 1$ transition closer to the laser frequency. The expression for the radiation pressure force extends Eq. (26.18) to include the Doppler effect kv_z and the Zeeman effect,

$$F_{\pm z} = -\frac{\hbar k}{2}\Gamma \frac{2\Omega^2}{4(\Delta \pm kv_z \pm z\partial_z \omega_{\text{Zeem}})^2 + 2\Omega^2 + \Gamma^2} \ . \tag{26.48}$$

The atom will, therefore, feel a restoring force which pushes it back to the origin. If the laser beams are red-detuned by an amount $\Delta = -\Gamma$, the Doppler shift of the atomic motion introduces velocity-depending term to the restoring force, such that for small displacements and velocities the total restoring force can be expressed by the sum of a term which is linear in the velocity and a term which is linear in the displacement,

$$F_{\text{MOT}} = F_{1z} + F_{2z} = -\alpha \dot{z} - \kappa z \ , \tag{26.49}$$

as we will study in Exc. 26.3.3.1. From Eq. (26.49) we can derive the equation of motion of a damped harmonic oscillator with mass m,

$$\ddot{z} + \frac{2\alpha}{m}\dot{z} + \frac{\kappa}{m} z = 0 \ . \tag{26.50}$$

The damping constant α and the spring constant κ can be written compactly in terms of atomic parameters and the field as,

$$\kappa = \frac{16\hbar k \Gamma \Omega^2 \Delta \partial_z \omega_{\text{Zeem}}}{4\Delta^2 + 2 \cdot 6\Omega^2 + \Gamma^2} \ . \tag{26.51}$$

and

$$\alpha = \kappa \frac{k}{\partial_z \omega_{\text{Zeem}}} \ . \tag{26.52}$$

Typical conditions for MOT are $\Omega = \Gamma/2$, $\Delta = -\Gamma$. For typical MOTs,

$$\alpha \simeq 2 \cdot 10^{-22}\,\text{Ns/m} \qquad \text{and} \qquad \kappa \simeq 3.7 \cdot 10^{-19}\,\text{N/m} \ . \tag{26.53}$$

We can also estimate the curvature of the MOT,

$$\omega = \sqrt{\frac{\kappa}{m}} \simeq (2\pi)\ 200\,\mathrm{Hz}\ . \tag{26.54}$$

Solve Exc. 26.3.3.2.

Figure 26.9: Picture of a strontium MOT operated at 461 nm. The atomic cloud, which consists of about 10^6 atoms at 5 mK temperature is visible as a diffuse spot located inside a three-mirror ring cavity.

MOTs are realized with current-carrying coils in anti-Helmholtz configuration which generates a quadrupolar geometry potential. Near the center, the magnetic field and its absolute value are well approximated by,

$$\vec{\mathcal{B}} = q \begin{pmatrix} x \\ y \\ -2z \end{pmatrix} \qquad \text{and} \qquad |\vec{\mathcal{B}}| = q\mathcal{B}\sqrt{r^2 + 4z^2}\ , \tag{26.55}$$

with $r^2 = x^2 + y^2$ and the gradient $q \equiv \partial_r B$ is a constant, which depends only on the geometry of the coils and the current in them. Thus, the extension of the above results to three dimensions is simple if we consider the fact that the gradient of the quadrupolar field in the z-direction is twice the gradient in the radial directions x and y, such that $\kappa_z = 2\kappa_x = 2\kappa_y$.The damping term, which proportional to the velocity, implies that the kinetic energy E is dissipated from the atom (or a cloud of atoms) as,

$$E/E_0 = e^{-2\alpha t/m}\ , \tag{26.56}$$

where m is the atomic mass and E_0 the kinetic energy at the beginning of the cooling process. Therefore, the dissipative force term cools the atomic cloud and, at the same time, combines with the position-dependent term to confine it. The time constant for the damping,

$$\tau = \frac{m}{2\alpha} \tag{26.57}$$

is typically dozens of microseconds. It is important to keep in mind that a MOT is anisotropic, since the restoring force is proportional to the anisotropic field gradients. Because of its dissipative non-conservative nature, it is is more accurate to characterize a MOT by the maximum capture rate, rather than by a 'potential depth'.

In early experiments MOTs were loaded from a decelerated atomic beam. Later it was shown, that the low-velocity tail of the Maxwell-Boltzmann distribution provides a sufficient amount of atoms that can be captured by a MOT, so that it can be loaded directly from an atomic vapor at room temperature. Now many groups in the world use these assemblies for applications ranging from precision spectroscopy to the optical control of reactive collisions; the MOT has become the working horse of atom optics.

26.3.1.1 Density in a MOT

A typical MOT captures up to a billion atoms in a volume of a few $1\,\mathrm{mm}^3$ resulting in densities of $\sim 10^{10}\,\mathrm{cm}^{-3}$. Although a MOT works as a versatile and robust 'reaction cell' for many applications, the frequencies of the light beams must be tuned close to atomic transitions, which bears the disadvantage that a considerable fraction of atoms remains in excited states. This fact is at the origin of two processes limiting the density of a MOT: (1) losses of trapped atoms by collisions and (2) repulsive forces between the atoms caused by reabsorption of photons scattered within the cloud. Collisional losses arise from two sources: (i) hot atoms of the residual gas inside the chamber can elastically collide with cold atoms and kick them out of the MOT, and (ii) cold atoms in excited states can undergo inelastic binary collisions. 'Photon-induced repulsion' or *radiation trapping* arises when a trapped atom spontaneously emits a photon, which is then reabsorbed by other atoms. If the optical density of the cloud is high, it can take a long time for the photon to find its way out [2]. Since any photon exchange between two atoms will increase their relative momentum by $2\hbar k$, this leads to a repulsive force, which is proportional to the absorption cross section for the incident light beam. When this repulsive force balances the confining force exerted by the MOT, any increase in the number of trapped atoms augments its size, but its density.

26.3.1.2 Dark SPOT

In order to overcome the 'radiation trapping' effect, the atoms can be optically pumped into a 'dark' hyperfine level of the ground state that does not interact with the MOT light. In a conventional MOT one usually employs an auxiliary light beam called 'repumper', copropagating with the MOT beams, but tuned to another transition between hyperfine levels of the ground and excited states. The repumper recycles the population leaking out of the (not perfectly) cyclic MOT transition. As an example, Fig. 26.10 shows the MOT and repumper transitions for sodium.

In contrast to this conventional MOT, the scheme known as the *dark spontaneous force optical trap* (dark SPOT), passes the repumping beam through a glass plate the center of which is obstructed by a small circular disk. The shadow of this disk is projected into the center of the trap in such a way that the atoms in the center are

[2] E.g. a photon at the center of the sun will take thousands of years to get out.

not repumped back into the cyclic transition, but spend most of their time ($\sim 99\%$) in 'dark' hyperfine levels. While the cooling and confinement force continue to operate on the periphery of MOT, its center does not feel any radiation pressure. Dark SPOTs are able to increase the density of a trapped cloud by almost *two orders* of magnitude.

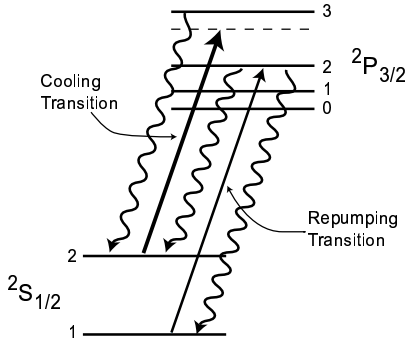

Figure 26.10: Hyperfine structure in sodium atoms showing the usual cooling, pumping, and repumping transitions.

26.3.2 Optical dipole traps

When temporal variations are to be applied to a confinement potential, magnetic fields are not the best choice, because they are slow and of limited spatial resolution. On the other side, laser beams can be varied quickly and in localized well. The dipole force exerted by a far-detuned laser beam can be derived from the gradient of the Rabi frequency $\mathbf{F} = -\nabla(\mathbf{d}\cdot\vec{\mathcal{E}})$. Hence, it can be derived from an optical potential, which can be used for trapping. The force may be attractive (toward the intensity maximum) or repulsive.

Compared to MOTs, optical traps (*far off-resonance optical trap*, FORT) are tuned far away from resonances, where the population in excited states is insignificant and spontaneous forces are absent. Note from Eq. (20.22), that spontaneous forces fall off with the square of the detuning while the potential derived from the dipolar force only decreases linearly with the detuning. The off-resonant optical density is negligible, so that radiation trapping is not an issue. The most simple FORT consists of a single focussed, linearly polarized gaussian laser beam tuned far to the red of an atomic resonance. For large detunings and strong field gradients the Eqs. (20.24) and Eqs. (20.25) become [345],

$$\boxed{U(\mathbf{r}) \simeq \frac{\hbar\Omega(\mathbf{r})^2}{4\Delta} = \frac{3\pi c^2}{2\omega_0^3}\frac{\Gamma}{\Delta}I(\mathbf{r}) \quad \text{and} \quad \hbar\gamma_{\rm sct}(\mathbf{r}) \simeq \sigma_a(\Delta)\frac{I(\mathbf{r})}{\omega} = \frac{3\pi c^2}{2\omega_0^3}\left(\frac{\Gamma}{\Delta}\right)^2 I(\mathbf{r})}\,, \tag{26.58}$$

using the Rabi frequency $\hbar\Omega = d_{12}\mathcal{E}$, the dipole moment $d_{12} = \sqrt{3\pi\varepsilon_0\hbar\Gamma/k^3}$, and the intensity $I = \frac{\varepsilon_0}{2}c|\mathcal{E}|^2$. This shows that the potential becomes directly proportional to the light intensity and inversely proportional to the detuning. Therefore, at large

detuning but very high intensity, the depth of the FORT can be maintained, although the atoms do not absorb photons. Important advantages of FORTs as compared to MOTs are: (1) high densities ($\sim 10^{12}\,\mathrm{cm}^{-3}$) and (2) a well-defined polarization axis along which the atoms can be aligned or oriented (polarization of the spins).

Since lasers beams can easily be manipulated in position, intensity, and frequency, they can realize a large wide variety of possible geometries. For example, with a focused laser beam, one may influence the local density of a condensate and stir it around by moving the position of the laser beam. Strongly focused laser beams are often used for transporting or manipulating microscopic objects in arrangements called *optical tweezers*. And with standing light waves, it is possible to form periodic optical lattices in one, two or three dimensions (see Sec. 28.4.2).

26.3.2.1 Spin relaxation

When the atomic ground state has a hyperfine structure, another relaxation mechanism can be observed: Near-resonance Raman scattering can induce transitions between hyperfine states causing a population redistribution of between Zeeman substates called *spin relaxation*. In magnetic traps, this can lead to losses, because not all Zeeman substates are trapped.

The rate of an arbitrary scattering process starting from an initial state $|F, m\rangle$ through several possible excited states $|F'_j, m'_j\rangle$ to a final state $|F''m''\rangle$ is, according to the formula of Kramers-Heisenberg [581],

$$\gamma_{Fm\to F'm'} \propto \left| \sum_j \frac{\alpha^{(F'_j m'_j)}_{Fm\to F'm'}}{\Delta_{F'_j m'_j}} \right|^2 . \tag{26.59}$$

Far from resonance the scattering decreases as Δ^2 for Rayleigh scattering, $Fm = F'm'$. Raman scattering, $Fm \neq F'm'$, is further suppressed by destructive interference of the different scattering paths.

In the case of rubidium, we calculate,

$$\gamma_{\mathrm{spin}} = \frac{3c^2\omega^4}{8\pi}\frac{70}{81}\Gamma^2 \left| \left(\frac{1}{\omega_{D1}}\right)^3 \frac{1}{\Delta_{D1}} - \left(\frac{1}{\omega_{D2}}\right)^3 \frac{1}{\Delta_{D2}} \right|^2 \frac{I_0}{\hbar\omega} . \tag{26.60}$$

26.3.2.2 Potential of a Gaussian beam

The *far-off resonance optical trap* (FORT) is an example of an optical trap based on dipole forces [345]. The intensity distribution of a gaussian beam with a diameter of w_0 at its waist is [3],

$$I(\mathbf{r}) = \frac{2P}{\pi w_0^2} e^{(-2x^2-2y^2)/w_0^2} e^{-z^2/z_R^2} , \tag{26.61}$$

where P is the total power of the beam and $z_R \equiv \pi w_0^2/\lambda$ the *Rayleigh length* at a given wavelength λ. The dipolar potential is given by (26.58). Using the potential depth,

$$\boxed{U_0 \equiv \frac{3\pi c^2}{2\omega_0^3}\frac{\Gamma}{\Delta}\frac{2P}{\pi w_0^2}} , \tag{26.62}$$

[3] See script on *Electrodynamics: Electricity, Magnetism and Radiation* (2025).

which is $U_0 < 0$ for red-detuned light, we can approach the potential near its center, that is, near the optical axis, $r \ll \frac{1}{2}w_0$, and within the range of the Rayleigh length, $z \ll \pi w_0^2/\lambda$, by a harmonic potential [4],

$$U(\mathbf{r}) \simeq U_0 e^{(-2x^2-2y^2)/w_0^2} e^{-z^2/z_R^2} \simeq U_0 \left(1 - \frac{2x^2+2y^2}{w_0^2} - \frac{z^2}{z_R^2}\right) \tag{26.63}$$
$$\equiv U_0 + \frac{m}{2}\omega_r^2 r^2 + \frac{m}{2}\omega_z^2 z^2 \equiv k_B T \left(\frac{U_0}{k_B T} + \frac{r^2}{2\bar{r}^2} + \frac{z^2}{2\bar{z}^2}\right) .$$

This leads to the equivalences,

$$\boxed{\begin{array}{rclcrcl} \omega_r &=& \frac{2}{w_0}\sqrt{\frac{U_0}{m}} &,& \omega_z &=& \frac{1}{z_R}\sqrt{\frac{2U_0}{m}} \\ \bar{r} &=& \frac{w_0}{2}\sqrt{\frac{k_B T}{U_0}} &,& \bar{z} &=& z_R\sqrt{\frac{k_B T}{2U_0}} \end{array}} . \tag{26.64}$$

Solve Excs. 26.3.3.3 and 26.3.3.4.

Example 185 (*Dipole trap for rubidium*): The formulas (26.58) hold for a two-level system. In case of the $D1$- and $D2$-lines of rubidium, we must consider all contributions weighted by the respective detunings,

$$U_0 \equiv \sigma_0 \frac{\hbar\Gamma}{4}\left(\frac{1}{\Delta_{D1}} + \frac{g_{D2}/g_{D1}}{\Delta_{D2}}\right)\frac{I_0}{\hbar\omega} \simeq \frac{3\hbar\pi c^2}{2\omega^2}\frac{\Gamma}{\Delta}\frac{I_0}{\hbar\omega} ,$$

where $g_{D2}/g_{D1} = 2$.
Similarly, the spontaneous emission rate is,

$$\gamma_{\rm sct} \simeq \frac{\pi c^2 \Gamma^2}{2\omega^2}\left(\frac{1}{\Delta_{D1}^2} + \frac{g_{D2}/g_{D1}}{\Delta_{D2}^2}\right)\frac{I_0}{\hbar\omega} .$$

The spontaneous emission rate decays faster with detuning than the potential depth. Thus, heating can be avoided by working at large detunings and providing higher laser intensities. Defining the recoil temperature by,

$$T_{\rm rec} = \frac{\hbar^2 k^2}{k_B m} ,$$

the *heating rate* is [345],

$$\dot{T} = \frac{1}{3} T_{\rm rec}\gamma_{\rm sct} = \frac{\hbar^2 k^2}{3mk_B}\gamma_{\rm sct} .$$

[4] The diameter of a Gaussian beam can be characterized in several ways,

$$\bar{r}_{1/\sqrt{e}\text{-radius}} = \frac{\bar{r}_{1/e^2\text{-radius}}}{\sqrt{2}} = \sqrt{2}\,\bar{r}_{1/e^2\text{-radius}} = \frac{\bar{r}_{1/2\text{-radius}}}{2\ln 2} ,$$

and $\bar{r}_{\text{-rms}} \equiv \bar{r}_{1/\sqrt{e}\text{-diam}}$ and $\bar{r}_{\text{-hwhm}} \equiv \bar{r}_{1/2\text{-diam}}$ and $\bar{r}_{\text{-diam}} = 2\bar{r}_{\text{-radius}}$.

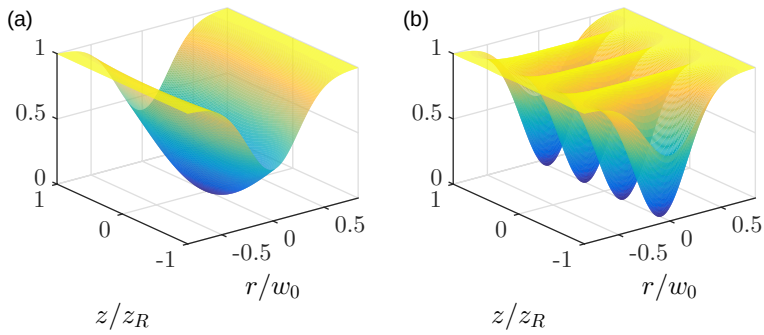

Figure 26.11: (code) (left) Dipole potential created by a Gaussian beam. (right) Dipole potential created by a stationary light wave.

26.3.2.3 Trapping in standing light waves

If both counterpropagating modes are pumped at different powers, $P_\pm$, the intensity distribution is,

$$I(\mathbf{r}) = \frac{2}{\pi w_0^2} e^{(-2x^2-2y^2)/w_0^2} e^{-z^2/z_R^2} \left| \sqrt{P_+} e^{\imath kz} + \sqrt{P_-} e^{-\imath kz} \right|^2 . \tag{26.65}$$

Defining the contrast of the standing wave as,

$$C_{sw} \equiv \frac{4\sqrt{P_+P_-}}{(\sqrt{P_+}+\sqrt{P_-})^2} , \tag{26.66}$$

we can express the potential depth by,

$$\boxed{U_0 = \frac{3\pi c^2}{2\omega_0^3}\frac{\Gamma}{\Delta}\frac{2(\sqrt{P_+}+\sqrt{P_-})^2}{\pi w_0^2} = \frac{3\pi c^2}{2\omega_0^3}\frac{\Gamma}{\Delta}\frac{8(\sqrt{P_+P_-})^2}{\pi w_0^2 C_{sw}}} . \tag{26.67}$$

Therefore, within the Rayleigh length, the potential is,

$$\begin{aligned} U(\mathbf{r}) &\simeq U_0 e^{(-2x^2-2y^2)/w_0^2} e^{-z^2/z_R^2} \frac{P_+ + P_- + 2\sqrt{P_+P_-}\cos kz}{P_+ + P_- + 2\sqrt{P_+P_-}} \\ &\simeq C_{sw} U_0 e^{-2\rho^2/w_0^2} \frac{P_+ + P_- + 2\sqrt{P_+P_-}\cos kz}{4\sqrt{P_+P_-}} . \end{aligned} \tag{26.68}$$

Neglecting terms containing higher powers of the coordinates than squared, we can also write,

$$U(\mathbf{r}) \simeq U_0 \left(1 - \frac{2x^2}{w_0^2} - \frac{2y^2}{w_0^2} - \frac{\sqrt{P_+P_-}}{(\sqrt{P_+}+\sqrt{P_-})^2} k^2 z^2 + ... \right) . \tag{26.69}$$

This leads to the identities,

$$\boxed{\begin{array}{rclcrcrcl} \omega_r &=& \frac{2}{w_0}\sqrt{\frac{U_0}{m}} &,& \omega_z &=& \frac{1}{z_R}\sqrt{\frac{2U_0}{m}} &,& \omega_{lat} = k\sqrt{\frac{C_{sw}U_0}{2m}} \\ \bar{r} &=& \frac{w_0}{2}\sqrt{\frac{k_B T}{U_0}} &,& \bar{z} &=& \frac{\sqrt{2}}{k}\sqrt{\frac{k_B T}{U_0}} & & \end{array}} . \tag{26.70}$$

Solve the Excs. 26.3.3.5, 26.3.3.6, and 26.3.3.7.

26.3.3 Exercises

26.3.3.1 Ex: Linearization of the MOT

Derive the friction coefficient and the spring constant for a MOT.

26.3.3.2 Ex: Design of a Zeeman slower

In this exercise we will design a 'decreasing field *Zeeman slower*' for strontium (see also Exc. 16.5.6.3).
a. Calculate the mean velocity of atoms in a strontium gas heated to 500° C. What is the Doppler shift for an atom moving at this velocity at the cooling transition at $\lambda = 461\,\text{nm}$ (linewidth 30.5 MHz)?
b. Assuming you want to decelerate a fraction of 20% of the atoms flying in a

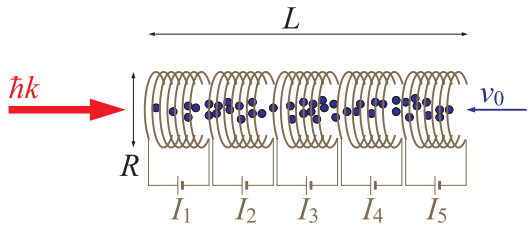

Figure 26.12: Design of a Zeeman slower.

particular direction, to what frequency should a counterpropagating laser (intensity $I = 20\,\text{mW/cm}^2$) be tuned in order to slow down the atoms?
c. Suppose the strontium atoms were always in resonance with the counterpropagating laser light while being decelerated. What would be the evolution of their Doppler shift along their trajectory (supposed to be on a straight line antiparallel to the laser beam).
d. In order to maintain the laser always in resonance we need to compensate for the diminishing Doppler shift along the atomic trajectory. This can be done exploiting the Zeeman shift induced by a magnetic field. We will now design a magnetic field generating an appropriate Zeeman shift. For simplicity, let us assume 5 identical radial solenoids distributed over $L = 30\,\text{cm}$ as sketched in Fig. 26.12, the only adjustable parameters being the currents in all solenoids, which need to be optimized such as to compensate the Doppler shift along the atom's trajectory.
e. Simulate the 1D trajectory of an atom cooled by the Zeeman slower.

26.3.3.3 Ex: Dipole trap near an intercombination line

a. Strontium has a strong transition ($\Gamma_{461} = (2\pi)\ 30.5\,\text{kHz}$) at 461 nm and a weak intercombination resonance ($\Gamma_{689} = (2\pi)\ 7.6\,\text{kHz}$) at 689 nm. A Gaussian laser beam with the power $P = 10\,\text{mW}$ focused to a waist of $w_0 = 100\,\mu\text{m}$ is tuned $\Delta_{689} = -(2\pi)\ 10\,\text{GHz}$ below the intercombination transition. Calculate the potential depth and the vibration frequencies for atoms trapped by this laser beam considering both resonances. What is the scattering rate on the two transitions.

b. Supposes that the trapped atomic cloud consists of $N = 10^8$ atoms at the temperature $T = 10\,\mu\text{K}$. Calculate the atomic density n_0 in the center of the cloud.

26.3.3.4 Ex: Dipole trap with a focused beam

a. Calculate the vibration frequencies of ^{87}Rb atoms confined in an optical trap consisting of a focused laser beam with the power $P = 10\,\text{W}$ and the beam diameter $w_0 = 100\,\mu\text{m}$. The laser beam is tuned 5 nm to the red side of the rubidium $D1$ resonance located at $\lambda = 795\,\text{nm}$.
b. Assume that the trapped atomic cloud consists of $N = 10^8$ atoms at the temperature $T = 100\,\mu\text{K}$. Calculate the atomic density n_0 in the center of the cloud.
c. The cross section for elastic collisions is $\sigma = 10^{-12}\,\text{cm}^2$. How many times do atoms meet on average?

26.3.3.5 Ex: Optical lattice

A laser beam with wavelength $\lambda_{\text{dip}} = 1064\,\text{nm}$, power $P = 2\,\text{W}$, and diameter $w_0 = 50\,\mu\text{m}$ is subdivided into three retroreflected beams intersecting at right angles. With this configuration we form a cubic optical lattice for strontium atoms, whose relevant transition lies at $\lambda_{Sr} = 461\,\text{nm}$ and has a decay width of $\Gamma_{Sr} = (2\pi)\,32\,\text{MHz}$. Calculate the potential depth and the secular frequencies.

26.3.3.6 Ex: Minimum optical lattice depth

Estimate the minimum required intensity of two counterpropagating laser beams tuned 7 GHz to the red of the strontium intercombination transition at 689 nm necessary to sustain an optical lattice exhibiting a single vibrational level.

26.3.3.7 Ex: Ring shaped optical potential

An interesting system is the $1D$ array of annular optical potentials realized in a standing wave formed by red-detuned Gaussian beam and a counterpropagating blue-detuned doonat-mode. In general, the tight longitudinal confinement freezes out the axial motion by *quantum confinement*. It can be readily shown [877] that in the far-off resonance case and if the potential is approximate by a harmonic potential around its minimum the eigenenergy spectrum is given by,

$$E_{pq} = U_0 + \hbar\omega(q + \tfrac{1}{2}) + \frac{\hbar^2 p^2}{2mR_0^2} \ .$$

It thus reproduces the ro-vibrational spectrum of a $2D$ artificial molecule and gives rise to two normal motions. In its ground state, we have the atom optical analog of a $2D$ rigid rotator. Gravity plays formally the same role as static electric fields for molecules. Such systems might be interesting for investigating the selection rules for transitions between ro-vibrational states involving conservation of total angular momentum of light and atoms and yield insight into the concept of orbital angular momentum of light fields.

26.3.3.8 Ex: Time-averaged trap

For sufficiently fast periodic displacements of a far-detuned laser beam it is possible to engineer effective more complicated trapping potential. What are the conditions for modulation speed? Simulate the effective trapping potential generated by a vibrating laser beam.

26.4 Magnetic traps

Purely magnetic traps are widely used in atom optics, where they served, e.g., for the first realizations of Bose-Einstein condensation (BEC). The most important feature that distinguishes magnetic traps is, that they do not need light to confine atoms. Hence, they are free of heating effects caused by photonic absorption, which turned out to be necessary condition for reaching BEC. Magnetic traps rely on the interaction of atomic spins with magnetic fields and gradients designed to contain the atoms. Depending on the sign of U and $\mathbf{F}$, atoms in states whose energy increases or decreases with the magnetic field are called 'low-field seekers' or 'high-field seekers', respectively. One might think, that it should be possible to trap atoms in any of these states, generating either a magnetic field minimum or a maximum. Unfortunately, only low-field seekers can be trapped in static magnetic fields, because in free space magnetic fields can not form maxima. Even though low-field seekers are not in the energetically lowest hyperfine levels, they can still be trapped because the rate of spontaneous emission through the magnetic dipole is $\sim 10^{-10}\,\mathrm{s}^{-1}$, and hence completely negligible. However, spin changing collisions can induce losses and limit the maximum densities. Solve Exc. 26.4.5.1.

The most basic static magnetic trap for neutral atoms is generated by a pair of current-carrying coils in anti-Helmholtz configuration (similar to the geometry used for a MOT), producing an axially symmetric qudrupolar magnetic field. Since this field configuration always has a central point, where the magnetic field disappears, non-adiabatic Majorana transitions can occur when the atom passes through the zero point. The transitions transfers population from a low-field seeking state to a high-field seeker, which consecutively is expelled from the trap. This problem can be overcome by using a different magnetic field geometries. One example is the so-called *magnetic bottle* also called the *Ioffe-Pritchard trap*, where the minimum field amplitude has a finite value different from zero. Other methods to eliminate the zero-field point are time-varying potentials, such as the time-orbiting potential (TOP) trap, or the application of an 'optical plug', which consist in an intense dipolar optical laser beam, tuned to the blue of an atomic transition, focused into the center of a quadrupole trap where the magnetic field is zero, and repelling the atoms from this area.

26.4.1 Quadrupolar traps and Majorana spin-flips

The most basic static magnetic trap for neutral atoms is generated by a pair of current-carrying coils in anti-Helmholtz configuration producing an axially symmetric quadrupolar magnetic field, as shown in Fig. 26.13.

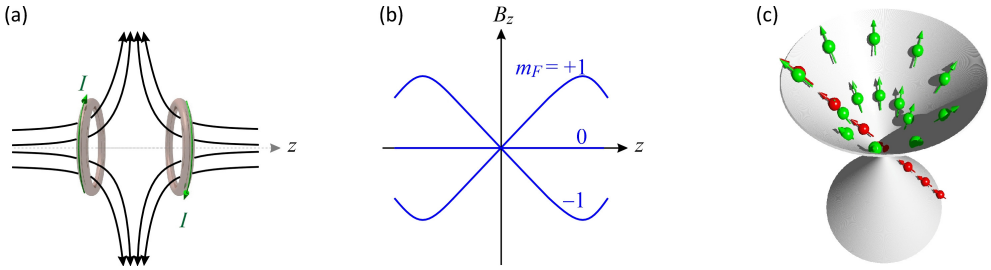

Figure 26.13: (a) Quadrupolar magnetic trap generated by a pair of current-carrying wires in anti-Helmholtz configuration. (b) Ground state energy levels of ^{23}Na, $^2S_{1/2}$, $F = 1$ as a function of axial distance from the trap center. (c) Illustration of Majorana spin-flips: The red atom passes through the hole, while the green one moves adiabatically avoiding the hole.

Close to the trap center an expansion of the magnetic field generated by anti-Helmholtz coils yields,

$$\vec{\mathcal{B}} = \begin{pmatrix} x \\ y \\ -2z \end{pmatrix} \partial_r \mathcal{B} \ , \tag{26.71}$$

where the field gradient $\partial_r B$ along radial direction $r^2 \equiv x^2 + y^2$ in the trap center depends on the applied current and the geometry of the coils. However, the 1:2 aspect ratio is generic for all quadrupolar potentials, as we will see in Exc. 26.4.5.2. We easily verify that,

$$\nabla \cdot \vec{\mathcal{B}} = 0 \qquad \text{but} \qquad \nabla |\vec{\mathcal{B}}| = \frac{\partial_r \mathcal{B}}{\sqrt{r^2 + 4z^2}} \begin{pmatrix} x \\ y \\ 4z \end{pmatrix} \ . \tag{26.72}$$

Thus, the quadrupolar magnetic potential is linear in the spatial coordinates,

$$\boxed{U(\mathbf{r}) = -|\vec{\mu}||\vec{\mathcal{B}}| = \mu_{\rm B} g_J m_J \ \partial_r \mathcal{B} \ \sqrt{r^2 + 4z^2}} \ , \tag{26.73}$$

where $2\partial_r \mathcal{B} = \partial_z \mathcal{B}$.

To calculate the *rms*-radius $\bar{r}$ of a cloud of temperature T confined to this potential, we set,

$$k_{\rm B} T \equiv U(\bar{r}, 0) = \mu_{\rm B} \bar{r} \partial_r \mathcal{B} \ , \tag{26.74}$$

and obtain the density distribution,

$$n(\mathbf{r}) = n_0 e^{-U(\mathbf{r})/k_{\rm B}T} = n_0 e^{-\sqrt{r^2+4z^2}/\bar{r}} \ . \tag{26.75}$$

Normalization requires,

$$\begin{aligned} N &= \int_{R^3} n(\mathbf{r}) \ d^3r = n_0 \int_{-\infty}^{\infty} \int_0^{\infty} e^{-\sqrt{r^2+4z^2}/\bar{r}} 2\pi r \ dr dz \qquad (26.76) \\ &= n_0 2\pi \bar{r}^2 \int_{-\infty}^{\infty} \int_{2|z|/\bar{r}}^{\infty} \xi e^{-\xi} d\xi dz = n_0 2\pi \bar{r}^2 \int_{-\infty}^{\infty} e^{-\frac{2|z|}{\bar{r}}} \left(1 + \tfrac{2|z|}{\bar{r}}\right) \ dz \\ &= n_0 2\pi \bar{r}^3 \int_0^{\infty} e^{-\zeta} (1 + \zeta) \ d\zeta = n_0 4\pi \bar{r}^3 \ . \end{aligned}$$

Therefore, the effective volume is, $V_{\rm eff} = 4\pi\bar{r}^3$. In application example is discussed in Exc. 26.4.5.3.

26.4.1.1 Majorana spin-flips

The quadrupolar trap is the simplest one that can be technically realized. Unfortunately, this trap is not stable because of the phenomenon of *Majorana spin-flips*, which expel atoms from the trapped cloud. Since this field configuration always has a central point, where the magnetic field disappears, non-adiabatic Majorana transitions can occur when the atom passes through the zero point [see Fig. 26.13(c)]. The disappearance of the field leaves the atoms disoriented, that is, ready to reorient their spins. The transitions transfer population from a low-field seeking state to a high-field seeker, which consecutively is expelled from the trap. This problem is particularly severe for hydrogen, where it can induce a so-called *relaxation explosion* [394].

From (26.74) we get the *rms*-radius,

$$\bar{r} = \frac{k_{\rm B}T}{\mu_{\rm B}\partial_r\mathcal{B}} \ . \tag{26.77}$$

The average velocity of an atom is,

$$\bar{v} = \sqrt{\frac{k_{\rm B}T}{m}} \ . \tag{26.78}$$

In order for the atomic motion in the magnetic potential to be adiabatic [so that Eq. (26.73) applies], the *local Larmor frequency*,

$$\omega_{\rm Larmor}(\mathbf{r}) = \frac{\mu_{\rm B}}{\hbar}\sqrt{r^2+4z^2}\partial_r\mathcal{B} \tag{26.79}$$

must be faster, than any change the atom might experience due to its motion with velocity $\mathbf{v}$. I.e. we need [650],

$$\omega_{\rm Larmor}(\mathbf{r}) > \frac{\mathbf{v}\cdot\nabla|\vec{\mathcal{B}}|}{|\vec{\mathcal{B}}|} \ . \tag{26.80}$$

For a quadrupolar trap, this can not be satisfied within a certain volume located at the trap center, since the expression (26.80) divergence near the center. This ellipsoidal volume is delimited by $\mathbf{r}_{\rm sf}$ given by the condition,

$$\omega_{\rm Larmor}(\mathbf{r}_{\rm sf}) \equiv \frac{\mathbf{v}\cdot\nabla|\vec{\mathcal{B}}|}{|\vec{\mathcal{B}}|} \ . \tag{26.81}$$

For our quadrupole trap,

$$\frac{\mathbf{v}\cdot\nabla|\vec{\mathcal{B}}|}{|\vec{\mathcal{B}}|} = \frac{\mathbf{v}\cdot\frac{\partial_r\mathcal{B}}{\sqrt{r_{\rm sf}^2+4z_{\rm sf}^2}}}{\partial_r\mathcal{B}\sqrt{r_{\rm sf}^2+4z_{\rm sf}^2}}\begin{pmatrix}x_{\rm sf}\\ y_{\rm sf}\\ 4z_{\rm sf}\end{pmatrix} = \frac{x_{\rm sf}v_x + y_{\rm sf}v_y + 4z_{\rm sf}v_z}{r_{\rm sf}^2+4z_{\rm sf}^2} \ . \tag{26.82}$$

Considering for simplicity only radial motion, $\mathbf{v} = v\hat{\mathbf{e}}_r$, then by equating (26.79) and (26.81),

$$\frac{\mu_{\rm B}}{\hbar}r_{\rm sf}\partial_r\mathcal{B} = \omega_{\rm Larmor}(r_{\rm sf}) = \frac{v}{r_{\rm sf}} \ , \tag{26.83}$$

that is, the spin-flip volume is on the order of,

$$r_{\rm sf} = \sqrt{\frac{\hbar v}{\mu_{\rm B}\partial_r \mathcal{B}}} \ . \tag{26.84}$$

Let us now estimate the spin relaxation rate from the flow of atoms through the volume,

$$\frac{1}{\tau_{\rm sf}} = N\frac{r_{\rm sf}^3}{V_{\rm eff}}\frac{\bar{v}}{r_{\rm sf}} \ , \tag{26.85}$$

where $r_{\rm sf}^3/V_{\rm eff}$ is simply the fraction of the cloud's volume overlapping with the spin-flip volume. Then,

$$\begin{aligned}\frac{1}{\tau_{\rm sf}} &= \frac{N}{4\pi\bar{r}^3} r_{\rm sf}^2 \bar{v} = \frac{N}{4\pi\left(\frac{k_{\rm B}T}{\mu_{\rm B}\partial_r\mathcal{B}}\right)^3}\frac{\hbar\bar{v}}{\mu_{\rm B}\partial_r\mathcal{B}}\bar{v} \\ &= \frac{N\hbar}{4\pi(k_{\rm B}T)^3}(\mu_{\rm B}\partial_r\mathcal{B})^2\frac{k_{\rm B}T}{m} = \frac{N\hbar(\mu_{\rm B}\partial_r\mathcal{B})^2}{4\pi m(k_{\rm B}T)^2} \ .\end{aligned} \tag{26.86}$$

That is, the problem gets worse when the cloud is cooled to low temperatures.

26.4.2 Magnetic Ioffe-type traps

The spin-flip problem can be overcome by using a different magnetic field geometries. One example is the so-called *magnetic bottle*, also called the *Ioffe-Pritchard trap* illustrated in Fig. 26.14(a), where the minimum field amplitude has a finite value different from zero. Other methods to eliminate the zero-field point are time-varying potentials, such as the time-orbiting potential (TOP) trap illustrated in Fig. 26.14(b) and discussed in Exc. 26.4.5.4 [267, 367], or the application of an 'optical plug', which consist in an intense dipolar optical laser beam, tuned to the blue of an atomic transition, focused into the center of a quadrupole trap where the magnetic field is zero, and repelling the atoms from this area (see Fig. 26.22). The advantage of Ioffe-Pritchard-type traps is that they are always harmonic sufficiently close to the trap center, which simplifies the theoretical treatment in many respects, as shown in Exc. 26.4.5.5.

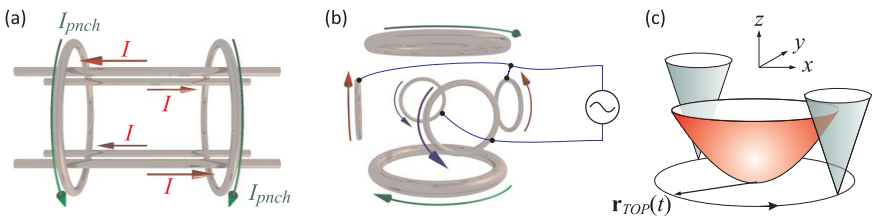

Figure 26.14: (a) Magnetic trap in Ioffe-Pritchard configuration. (b) Time-Orbiting Potential (TOP) trap. (c) Death-circle in a TOP trap.

Close to the trap center Ioffe-Pritchard-type traps are described by,

$$\boxed{U(\mathbf{r}) = \mu_{\rm B} g_F m_F \sqrt{\mathcal{B}_0^2 + (r\partial_r\mathcal{B})^2 + (z\partial_z\mathcal{B})^2}} \ , \tag{26.87}$$

and this magnetic trapping potential can be harmonically approximated by,

$$U(\mathbf{r}) \simeq \mu_{\rm B} g_F m_F \left(\mathcal{B}_0 + \frac{(r\partial_r \mathcal{B})^2}{2B_0} + \frac{(z\partial_z \mathcal{B})^2}{2B_0} \right) \tag{26.88}$$
$$\equiv const + \frac{m}{2}\omega_r^2 r^2 + \frac{m}{2}\omega_z^2 z^2 \equiv k_{\rm B} T \left(const + \frac{r^2}{2\bar{r}^2} + \frac{z^2}{2\bar{z}^2} \right) ,$$

where the *rms*-radius $\bar{r} = \omega_r^{-1}\sqrt{k_{\rm B}T/m}$ follow from the normalization of the density $n(\mathbf{r}) = n_0 e^{-U(\mathbf{r})/k_{\rm B}T}$ to the number of atoms,

$$N = \int n(\mathbf{r}) d^3 r = n_0 \int_0^\infty e^{-r^2/2\bar{r}^2} 2\pi dr \int_{-\infty}^\infty e^{-z^2/2\bar{z}^2} dz = n_0 (2\pi)^{3/2} \bar{r}^2 \bar{z} \equiv n_0 V_{\rm eff} . \tag{26.89}$$

The trap frequencies can be calculated as,

$$\omega_{r,z} = \sqrt{\frac{\mu_{\rm B}(\partial_r \mathcal{B}_{r,z})^2}{m\mathcal{B}_0}} . \tag{26.90}$$

The Earth's gravitational field deforms the trapping potential and, in the case of a harmonic potential, causes a gravitational sag without changing the secular frequencies of the potential. Assuming the potential to be given by,

$$U = \frac{m}{2}\omega_r^2 r^2 + \frac{m}{2}\omega_z^2 z^2 - mgz = \frac{m}{2}\omega_r^2 r^2 + \frac{m}{2}\omega_z^2 (z - g/\omega_z^2)^2 - \frac{m}{2} g^2/\omega_z^2 , \tag{26.91}$$

the atoms sag to a height of g/ω_z^2. In time-dependent traps, gravity causes a more complex behavior [362]. Important works have been done by [151, 654, 269, 349, 3, 199, 504, 507, 224]. We study the impact of gravitation in Exc. 26.4.5.6.

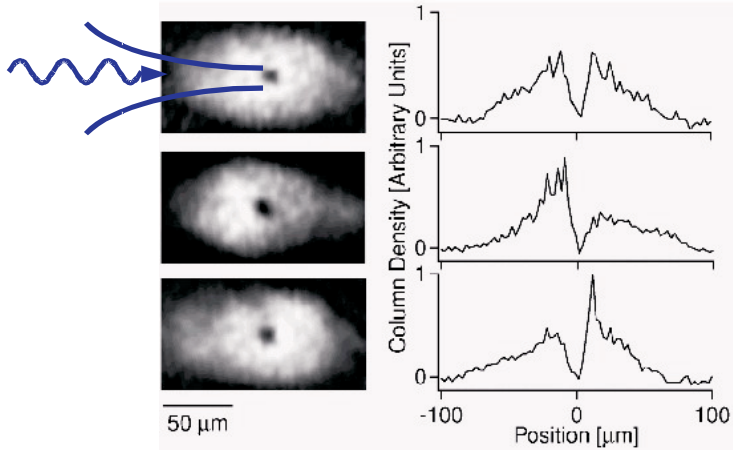

Figure 26.15: Creation of a repulsive hole by light tuned to the blue of an atomic transition.

26.4.2.1 Characterization of Ioffe-type traps

The 'time-of-flight' density distribution is,

$$r_{\rm ToF} = \sqrt{\bar{r}^2 + \bar{v}^2 t_{\rm ToF}^2} = \sqrt{\frac{k_{\rm B}T}{m}}\sqrt{\frac{1}{\omega_r^2} + t_{\rm ToF}^2} \simeq t_{\rm ToF}\sqrt{\frac{k_{\rm B}T}{m}} \ . \tag{26.92}$$

The *phase space density* is,

$$\rho = n_0\lambda_{\rm dB}^3 = \frac{N}{(2\pi)^{3/2}\bar{r}^2\bar{z}}\left(\frac{2\pi\hbar^2}{mk_{\rm B}T}\right)^{3/2} = N\omega_r^2\omega_z\left(\frac{\hbar}{k_{\rm B}T}\right)^3 = \zeta(3)\left(\frac{T_{\rm c}}{T}\right)^3 \ . \tag{26.93}$$

where $\zeta(3) = 1.202$ and

$$k_{\rm B}T_{\rm c} = \hbar\left(\frac{N\omega_r^2\omega_z}{\zeta(3)}\right)^{1/3} \tag{26.94}$$

is called 'critical temperature'. The *maximum collision rate* is,

$$\gamma_{\rm coll} = n_0\sigma\bar{v} = n_0 4\pi a_s^2\sqrt{\frac{k_{\rm B}T}{m}} \ , \tag{26.95}$$

The average collision rate can be obtained from,

$$\bar{\gamma}_{\rm coll}N = \frac{1}{N}\int \gamma_{\rm coll}(\mathbf{r})n(\mathbf{r})d^3r = \frac{\int \sigma\bar{v}n^2(\mathbf{r})d^3\mathbf{r}}{\int n(\mathbf{r})d^3r} \ . \tag{26.96}$$

26.4.3 Radiative coupling and evaporative cooling

As we saw in the last section, optical cooling becomes ineffective when the density of the gas is high. Hence, we need another dissipation mechanism to cool trapped atoms. A method called *evaporation* has been proposed by Hess [392] for spin-polarized hydrogen (H↑) and was observed by Masuhara et al. [556]. Later, evaporation was used on alkali metals [3, 650, 202]. A detailed review of the subject was published by Ketterle and van Druten [458].

Another collision-based cooling mechanism is *sympathetic cooling*. The technique was originally used in ion traps. Later it was applied to neutral atoms confined in magnetic traps. The idea is to get the cloud under study into thermal contact with a cold buffer gas. In some cases, the buffer gas may be optically or evaporatively cooled. Sympathetic cooling has been used in magnetic traps to create double condensates [613] and to cool fermions until the regime of quantum degeneracy [214].

26.4.3.1 Evaporative cooling

Evaporation always occurs when energetic particles abandon a system with finite bonding energy, removing more than their share of average energy per particle. Here, we consider the case of a finite-sized trapping potential, that is, the potential has an edge or a beak through which hot atoms, with sufficient kinetic energy to reach that region, may leave the trap. In the ideal case, this will lead to a complete truncation of the hot tail of the equilibrium Maxwell-Boltzmann velocity distribution. If the remaining system finds back to thermal equilibrium, it will do at a lower temperature. The redistribution of kinetic energy between atoms leading to *thermalization* occurs through elastic collisions.

Figure 26.16: The basic idea of evaporation consists in removing hot particles from the sample.

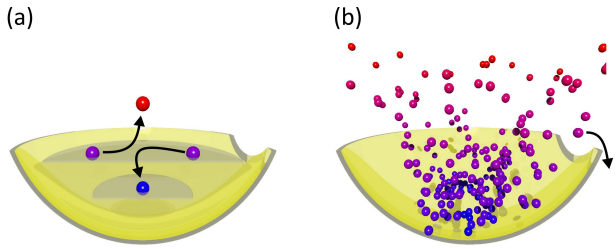

Figure 26.17: Principle of (a) rethermalization due to elastic collisions and (b) evaporation.

26.4.3.2 Truncating the Boltzmann distribution

Let us first explain how the truncation leads to colder temperatures [202].

The objective is to calculate the Boltzmann distribution in a particular trap for a given atom number N and temperature T. The first step is to obtain the density-of-states. For an isotropic harmonic trap $\varepsilon = \frac{p^2}{2m} + V(r)$ with $V(r) = \frac{m}{2}\omega^2 r^2$, it is,

$$\eta(\varepsilon)d\varepsilon = \frac{1}{(2\pi)^3}\int_V d^3r d^3k = \frac{2\pi(2m)^{3/2}}{h^3}\int_V \sqrt{\varepsilon - V(r)}d^3r d\varepsilon = \frac{\varepsilon^2 d\varepsilon}{2(\hbar\omega)^3} \ . \quad (26.97)$$

The atom density is,

$$n(\varepsilon) = e^{(\mu-\varepsilon)/k_B T} = w_{T,\mu}(\varepsilon) = Ze^{-\varepsilon/k_B T} \ . \quad (26.98)$$

From these expressions we obtain the atom number,

$$N = \int_0^\infty n(\varepsilon)\eta(\varepsilon)d\varepsilon = \int_0^\infty e^{(\mu-\varepsilon)/k_{\rm B}T}\frac{\varepsilon^2}{2(\hbar\omega)^3}d\varepsilon = Z\frac{(k_{\rm B}T)^3}{(\hbar\omega)^3}\ , \tag{26.99}$$

which we may now use to calibrate the fugacity via

$$Z = N\frac{(\hbar\omega)^3}{(k_{\rm B}T)^3}\ , \tag{26.100}$$

which finally allows us to calculate the total energy,

$$E = \int_0^\infty \varepsilon n(\varepsilon)\eta(\varepsilon)d\varepsilon = \int_0^\infty \varepsilon e^{(\mu-\varepsilon)/k_{\rm B}T}\frac{\varepsilon^2}{2(\hbar\omega)^3}d\varepsilon = 3Z\frac{(k_{\rm B}T)^4}{(\hbar\omega)^3} = 3Nk_{\rm B}T\ . \tag{26.101}$$

The evaporation consists in truncating the distribution function $n(\varepsilon)$ at some energy $\hbar\omega_{\rm rf}$. We get with $\beta \equiv (k_{\rm B}T)^{-1}$,

$$\tilde{N} = \int_0^{\hbar\omega_{\rm rf}} n(\varepsilon)\eta(\varepsilon)d\varepsilon = N\left(1 - \frac{2 + 2\beta\hbar\omega_{\rm rf} + (\beta\hbar\omega_{\rm rf})^2}{2e^{\beta\hbar\omega_{\rm rf}}}\right) \tag{26.102}$$

and

$$\tilde{E} = \int_0^{\hbar\omega_{\rm rf}} \varepsilon n(\varepsilon)\eta(\varepsilon)d\varepsilon = E\left(1 - \frac{6 + 6\beta\hbar\omega_{\rm rf} + 3(\beta\hbar\omega_{\rm rf})^2 + (\beta\hbar\omega_{\rm rf})^3}{6e^{\beta\hbar\omega_{\rm rf}}}\right)\ . \tag{26.103}$$

As the truncation removes the hottest atoms from the cloud, we loose atom number and energy. Assuming the existence of some rethermalization mechanism, we may now use the new values for N and T to calculate the new equilibrium Boltzmann distribution starting all over from Eq. (26.98),

$$N \longleftarrow \tilde{N} \qquad \text{and} \qquad T \longleftarrow \frac{\tilde{E}}{3Nk_{\rm B}} \tag{26.104}$$

Repeating this over and over the temperature will gradually reduce. The cooling process can be speed up by readjusting the truncation frequency to the actual temperature. This is called forced evaporation (see Fig. 26.18).

Example 186 (*Truncating in a quadrupole potential*): The formulas (26.102) and (26.102) were derived for a harmonic trap. An analogous calculation for a quadrupole potential yields, with the abbreviation $\varkappa \equiv \beta\hbar\omega_{\rm rf}$,

$$N(\varkappa) \approx -2\sqrt{Z}\frac{105 + 70\varkappa + 28\varkappa^2 + 8\varkappa^3}{\sqrt{\pi}105e^{\varkappa}} + \mathrm{erf}(\sqrt{\varkappa}) \tag{26.105}$$

$$E(\varkappa) \approx -\frac{2}{9}\sqrt{Z}\frac{945 + 630\varkappa + 252\varkappa^2 + 72\varkappa^3 + 16\varkappa^4}{\sqrt{\pi}105e^{\varkappa}} + \frac{9}{2}\mathrm{erf}(\sqrt{\varkappa})\ .$$

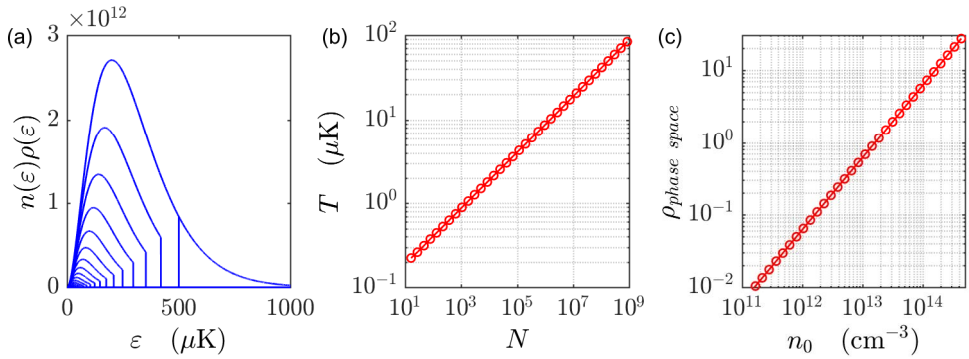

Figure 26.18: (code) (a) Forced evaporation by truncating the Boltzmann distribution over and over again. (b) Evolution of the temperature and (c) of the phase space density with number of remaining atoms.

26.4.3.3 Rethermalization

As already mentioned, rethermalization occurs due to elastic collisions. It needs more or less three collisions per atom to rethermalize a cloud [595, 882], so that the collision rate determines the speed of the evaporation process. A large collision rate is desirable to keep the evaporation process faster than trap loss processes. Evaporation ramps between several seconds and a minute are typical.

The maximum rate of elastic collisions between trapped atoms (in the trap center) is,

$$\gamma_{\rm coll} = n_0 \sigma_{\rm el} \bar{v} \sqrt{2} \propto \rho^3 N^{2/3} \ , \tag{26.106}$$

where n_0 is the peak density,

$$\sigma_{\rm el} = 8\pi a_s^2 \ , \tag{26.107}$$

is the cross-section for elastic collisions and, $\bar{v}$ being the average thermal velocity of the cloud, $\sqrt{2}\bar{v}$ is the average relative velocity between two of its atoms [457]. This formula gives the average collision rate at the *center of the cloud*, where the density is highest. To calculate the total collision rate, we need to integrate over the entire volume of the cloud,

$$\bar{\gamma}_{\rm coll} = \tfrac{1}{N} \int \gamma_{\rm coll}(\mathbf{r}) n(\mathbf{r}) d^3 r = \frac{\int \sigma_{\rm el} \bar{v} n^2(\mathbf{r}) d^3 r}{\int n(\mathbf{r}) d^3 r} \ . \tag{26.108}$$

For harmonic potential we find an average rate reduced by $2\sqrt{2}$, for linear potentials by 8. We verify this in Exc. 26.4.5.7. Finally, the rate for collision events is two times smaller, as it involves two atoms at a time.

Obviously, the evaporation process slows down when the cloud cools more, unless the edge of the potential is lowered, such that the hotter atoms of the colder cloud can be evaporated. By continually lowering the edge of the potential, while the atomic cloud keeps on rethermalizing (this procedure is called *forced evaporation*) very low temperatures in the nano-Kelvin regime can be achieved, and the phase space density can be increased by many orders of magnitude (between a MOT and a BEC there are 6 orders of magnitude) up to the threshold of Bose-Einstein condensation. Of course,

this is only possible by sacrificing many hot atoms. Even with a well optimized evaporation ramp (i.e., a controlled lowering of the potential edge), usually only some 0.1% of the atoms reach the condensation phase after about 500 collisions per atom.

Two aspects should be mentioned regarding the optimization of the evaporation ramp. The first aspect is, that elastic collisions with atoms from the residual background vapor of the vacuum chamber limit the lifetime of the trap. Therefore, the evaporation must be sufficiently fast, which requires either a high rate of elastic collisions or a good vacuum. A compromise must be found between a slow but efficient evaporative cooling and a minimization of the losses, which come into play when the evaporation takes too long. The second aspect is, that the dimensionality of the evaporation surface determines the effectiveness of the cooling. In the first demonstration of evaporation, H↑ atoms of a hot cloud were ejected over a saddle point. The saddle was located a small region away from the trap center, and only atoms with sufficient kinetic energy *along a certain direction*, $E_z > U_{\rm edge}$, could leave the trap. In such cases, evaporation is called one-dimensional. Even though ergodic redistribution due to anharmonicities of the potential will drive, sooner or later, all the atoms to this region, this effect becomes less pronounced when the cloud cools down, because the atoms accumulate at the bottom of the approximately harmonic (and therefore separable) potential. This fact has inhibited efficient evaporation of H↑ below 120 μK [291].

A second evaporative technique has been demonstrated in traps called *time-orbiting potential* (TOP) [650]. It is a feature of TOP traps to display a spatial region called a 'death-circle', where passing atoms are ejected from the trap. This fatal circle can act as a 2-dimensional evaporation surface, provided the radius of the circle is large enough [367]. However, under the influence of gravity the dimensionality is further reduced to 1D [457].

The most successful evaporation technique implemented so far is based on a radiative coupling of confined and free states. We discuss this technique in the following sections. Publications on *evaporative cooling* are [532, 579, 650, 672, 72, 572, 595, 268, 272, 380, 620, 392, 556, 202, 458, 881, 368, 551, 244, 394]. See ([175], Sec. 3.1.4) for an overview.

26.4.3.4 Adiabatic (de-)compression

The condition for *adiabatic decompression* of a trapping potential is,

$$\frac{|\dot{\omega}_{\rm trp}|}{\omega_{\rm trp}} \ll \omega_{\rm trp} \ . \tag{26.109}$$

The population of the quantized levels should not change under adiabatic decompression, $e^{\hbar\omega_i/k_{\rm B}T_i} = e^{\hbar\omega_f/k_{\rm B}T_f}$, and the phase space density remains unchanged, $n_i\lambda_{{\rm dB},i} = n_f\lambda_{{\rm dB},f}$. If this is true, then the temperature and density change as,

$$\frac{\omega_f}{\omega_i} = \frac{T_f}{T_i} = \left(\frac{n_f}{n_i}\right)^{3/2} \ . \tag{26.110}$$

Solve Exc. 26.4.5.8.

26.4.3.5 Radiative coupling of internal state

The most successful evaporation technique implemented so far is based on a radiative coupling of confined and free states. We discuss this technique in the following sections. See ([175], Sec. 3.1.4) for an overview.

The radiative coupling technique originates from an idea proposed by Pritchard et al. [368], who have already had some experience with radiofrequency spectroscopy in magnetically trapped neutral atoms [551, 380]. The spatial dependence of the Zeeman splitting is an intrinsic feature of magnetic traps. Irradiation of a radio wave at a certain frequency couples trapped and untrapped Zeeman substates at a well-defined distance from the trap center. This gives rise to a 3D evaporation surface, where the passing atoms can undergo Landau-Zener transitions and be expelled from the trap. The technical advantages of this technique are substantial: The magnetic trapping potential does not have to be manipulated, for example, by the creation of a nozzle, and the potential edges can be easily controlled by the radiofrequency. If evaporation is forced via a continuous reduction of the radiofrequency and if the evaporation ramp is optimized, the density will increase as well as the collision rate. Rethermalization will accelerate and initiate a self-accelerated evaporation process (*run-away evaporation*). Rf-evaporation was first demonstrated by Ketterle and colleagues [202]. Solve Exc. 26.4.5.9.

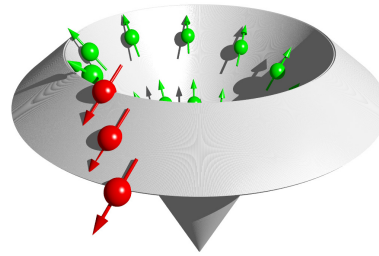

Figure 26.19: Illustration of evaporative truncation.

26.4.3.6 Adiabatic and diabatic limits of rf-induced evaporation

Rf-induced evaporation can be described within the formalism of the dressed atom [164], where the different states m_F of an atom with spin F are coupled to an rf-field [5], which we assume to be linearly polarized:

$$\mathcal{B}(t) = \mathcal{B}\hat{\mathbf{e}}_{\rm rf} \cos\omega t \ . \tag{26.111}$$

The element of the coupling matrix between the levels, $|F, m_F\rangle$ and $|F, m_F \pm 1\rangle$ is,

$$\Omega = \frac{\mu_{\rm B} g}{4\hbar} \left| \vec{\mathcal{B}}_{\rm rf} \times \hat{\mathbf{e}}_B \right| \sqrt{F(F+1) - m_F(m_F+1)} \ , \tag{26.112}$$

where g is the atomic g-factor and $\hat{\mathbf{e}}_B$ the orientation of the local static magnetic field.

The adiabatic potentials $U(r)$ are obtained through the eigenvalues of the atomic states dressed by the local magnetic field $\mathcal{B}(r)$. In the dressed atom picture, we consider the total energy of the atom plus the field of N radiofrequency photons. Without coupling, this simply means that $N\hbar\omega$ is added to the atomic Zeeman energies, resulting in a Zeeman pattern being vertically shifted by $N\hbar\omega$ for $N = 0, \pm 1, ...$ At positions where the rf-field is in resonance, curves with $\Delta N = 1$ intersect. Here, the coupling develops an *avoided crossing*, which determines the pattern of adiabatic energy levels [see Fig. 26.20(b)].

[5] Alternatively, a *microwave* frequency may be used to couple *different hyperfine levels*.

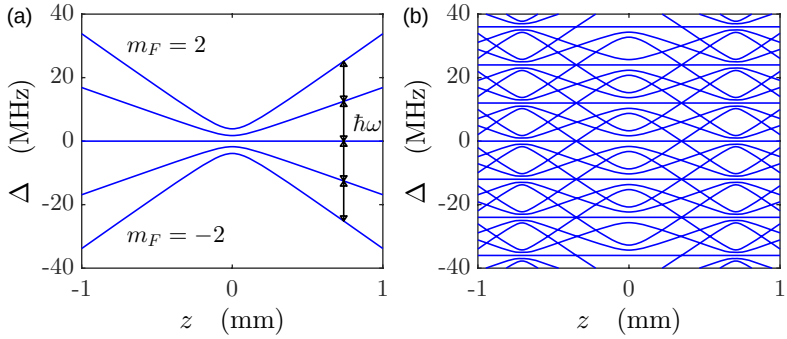

Figure 26.20: (code) (Left) Potentials due to the Zeeman structure of an atom in the ground state with $F = 1$. (Right) Adiabatic potentials resulting from the coupling of Zeeman levels via radiofrequency radiation being resonant with the difference of Zeeman levels at the position 0.7.

A slowly moving atom remains on the curve of an *adiabatic potential*. As an example, let us assume an atom in the hyperfine state $|F, F\rangle$ moving away from the center of the trap. When it comes close to resonance, the rf-field blends this state with other m_F-states, from the $|F, F-1\rangle$ down to the $|F, -F\rangle$ state, which changes the slope of the potential curve. Beyond the resonance point, the atomic state is adiabatically transformed into an untrapped high-field seeking state, and the atom is repelled from the trap. Thus, while passing the avoided crossing, the atom has emitted $2F$ rf-photons in a stimulated manner and inverted the orientation of both the electron and the nuclear spin.

In this way the radiofrequency generates an adiabatic potential surface with a depth of approximately $|m_F|\hbar(\omega - \omega_0)$, where ω_0 is the resonant rf-frequency at the center of the trap. The evaporation process corresponds, then, to the removal of the most energetic atoms out of the trap.

For this adiabatic picture to be valid, an adiabaticity condition must be fulfilled. This condition requires that the energy difference at the avoided crossover be larger than the energy uncertainty related to the limited time that an atom with velocity v spends in the resonance region. For a two-level system coupled by a matrix element V_{12} and an atom moving with velocity v along the z-axis, the transition probability P between the adiabatic curves is given by the *Landau-Zener formula* [707],

$$P = 1 - e^{-\xi} \quad \text{with} \quad \xi = \frac{2\pi|V_{12}|^2}{\hbar g \mu_B \partial_z \mathcal{B} v} \,. \tag{26.113}$$

The Landau-Zener theory is strictly valid only for a two-level system, which we use here only for a qualitative discussion of two following limiting cases.

For a weak rf-field, $\xi \ll 1$, P is much smaller than 1, i.e., the atoms remain predominantly on the diabatic surface shown in Fig. 26.20(a). The probability for a *spin flip* transition is, $P \approx t$, which describes the diabatic limit of rf-induced evaporative cooling: The atomic energy levels are almost unperturbed, the atoms often spill across the resonance surface, and only after $1/P$ oscillations, they spin-flip from the hyperfine state $|F, F\rangle$ to the $|F, F-1\rangle$.

The adiabatic limit is clearly the ideal situation for evaporative cooling. However, the evaporation process in a trap (with oscillation time T_{osc}) saturates at a lower rf-power. The condition for saturation is $P \approx T_{osc}/\tau_{\rm el}$, where $\tau_{\rm el}$ is the average time between two collisions. This means that an energetic atom is evaporated before it collides again.

Only the component of the magnetic field of the rf-radiation which is *perpendicular* to the magnetic trapping field induces spin-flips. In certain geometries of the confinement potential, for example the quadrupole trap, the magnetic field covers the entire solid angle. Consequently, there are two points where the trapping field and the rf-field are parallel and the elements of the transition matrix consequently zero. Within an area around these points, the coupling is diabatic. In practice however, the rf-transition can be sufficiently saturated that this area is small and does not strongly affect the evaporation efficiency.

Note also that gravitation deforms the equipotential surfaces of the confinement potential, which can reduce the evaporation efficiency [457]. Solve Exc. 26.4.5.10.

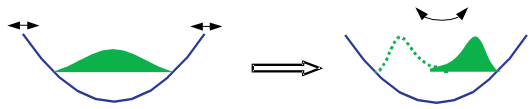

Figure 26.21: Effective potential due to a rapid modulation of the trap's location.

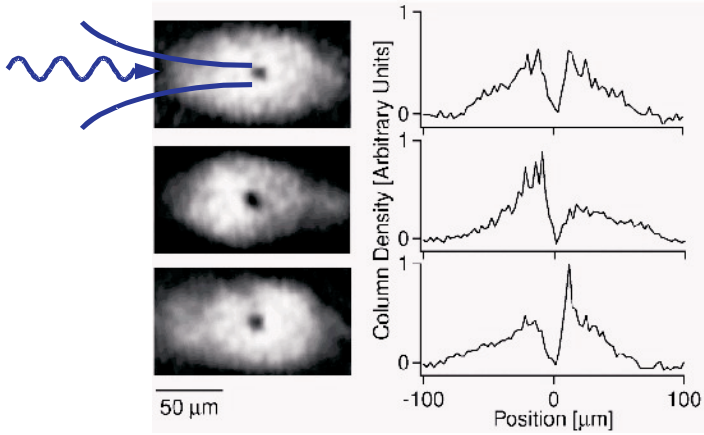

Figure 26.22: Creation of a repulsive hole by light tuned to the blue of an atomic transition.

26.4.4 Sympathetic cooling

The efficiency of evaporative cooling depends on the rate of interatomic collisions. However, there are atomic species with unfavorable, that is, small or even negative scattering lengths. Also, while at low temperatures only s-wave collisions occur (higher partial waves being frozen behind the centrifugal barrier), such collisions are prohibited for fermionic gases. Fermions or species with unfavorable scattering lengths

can not be cooled by evaporation. There is, however, another technique called *sympathetic cooling* by thermal contact with another species. The additional species is, in general, actively cooled (e.g., by evaporation), while the species of interest is passively cooled via elastic collisions with atoms of the additional species. Of course, for this scheme to work the *interspecies scattering length* and the mass ratio must be adequate to ensure adequate thermal coupling.

Following [611] the transfer of kinetic energy between two colliding atoms is reduced by a factor depending on the their mass difference,

$$\xi = \frac{4m_1m_2}{(m_1+m_2)^2} \ . \tag{26.114}$$

Around $3/\xi$ collisions per atom on average are required for complete thermalization of a gas. For example, for the Rb-Li mixture, we have $3/\xi = 12.4$. The collision rate is,

$$\Gamma_{\rm coll} = \sigma_{12}\bar{v}\int n_1(\mathbf{r})n_2(\mathbf{r})d^3r \ , \tag{26.115}$$

where the average thermal velocity is,

$$\bar{v} = \sqrt{\frac{8k_{\rm B}}{\pi}\left(\frac{T_1}{m_1}+\frac{T_2}{m_2}\right)} \ . \tag{26.116}$$

The instantaneous temperature is calculated by,

$$\gamma_{\rm therm} = -\frac{1}{\Delta T}\frac{d\Delta T}{dt} \ , \tag{26.117}$$

or via simulations: $\Delta T(t+dt) = \Delta T(t) - \Delta T(t)\gamma_{\rm therm}dt$. Following [213] the rethermalization rate is connected to the collision rate via,

$$\boxed{\gamma_{\rm therm} = \frac{\xi}{3}\left(\frac{\Delta E_{1\to2}}{N_1k_{\rm B}\Delta T}+\frac{\Delta E_{2\to1}}{N_2k_{\rm B}\Delta T}\right) = \frac{\xi}{3}\left(\frac{\Gamma_{\rm coll}}{N_1}+\frac{\Gamma_{\rm coll}}{N_2}\right)} \ . \tag{26.118}$$

Analytic solutions can be derived for harmonic traps. This will be studied in Excs. 26.4.5.11 and Exc. 26.4.5.12.

26.4.5 Exercises

26.4.5.1 Ex: Lack of trapping potentials for strong field seekers

Show that it is not possible to create magnetic trapping potentials for atoms in low-field seeking Zeeman states.

26.4.5.2 Ex: Quadrupolar potential

Show that for a quadrupolar trap always holds $2\partial_r\mathcal{B}_{\rm qua} = \partial_z\mathcal{B}_{\rm qua}$.

26.4.5.3 Ex: Magnetic quadrupole trap

a. Consider ^{87}Rb atoms confined in a magnetic trap with $\vec{\mathcal{B}}(x,y,z) = x \quad y \quad -2z \times 200\,\mathrm{G/cm}$. The atoms are in the state $|F=1, m_F=-1\rangle$ with the g-factor $g_F = 1/2$. Check whether it is reasonable to assume constant vibration frequencies for such traps.
b. Assume that the trapped atomic cloud consists of $N = 10^8$ atoms at temperature $T = 100\,\mathrm{K}$. Calculate the atomic density n_0 at the center of the cloud.
c. The cross section for elastic collisions is $\sigma = 10^{-12}\,\mathrm{cm}^2$. How many times do atoms meet in the middle of the trap?

26.4.5.4 Ex: TOP trap

The TOP trap (time-orbiting potential) was the first design to allow for Bose-Einstein condensation in 1995. It consists of the superposition of a quadrupolar magnetic field, with the radial and axial gradients $2\partial_r \mathcal{B}_{\mathrm{qua}} = \partial_z \mathcal{B}_{\mathrm{qua}}$), and a homogeneous magnetic field $\mathcal{B}_{\mathrm{top}}$ rotating in the symmetry plane of the quadrupole field. Atoms which oscillate with an amplitude beyond a given radius r_{d}, called the 'circle of death', undergo Majorana transitions and are expelled from the trap.
a. Calculate the radius of the death circle.
b. Plot the time-averaged 'effective' trapping potential.

26.4.5.5 Ex: Harmonic trap

Calculate the vibration frequencies of ^{87}Rb atoms trapped in a harmonic trap, when the atoms are in the $|F=1, m_F=-1\rangle$ hyperfine level of the ground state.

26.4.5.6 Ex: Gravitational sag in a trap

Consider (a) a quadrupolar trap and (b) an isotropic harmonic trap. What is the gradient, respectively the curvature of the trapping potential required to suspend a cloud of rubidium subject to gravitation? What is the sag of the cloud in the potential due to gravitation?

26.4.5.7 Ex: Mean collision rate

Assuming that the peak collision rate γ_{coll} is known, calculate the average collision rate (a) in a quadrupolar and (b) in a harmonic trap.

26.4.5.8 Ex: Adiabatic compression

How does temperature change upon adiabatic compression of (a) a quadrupole trap and (b) a harmonic trap. How do density, phase space density, and elastic collision rate vary. **Help:** Define the compression for quadrupole trap as $\eta \equiv \partial_r \mathcal{B}_{r,final}/\partial_r \mathcal{B}_{r,initial}$ and for harmonic trap as $\eta \equiv \omega_{r,final}/\omega_{r,initial}$.

26.4.5.9 Ex: RF-antenna for radiative coupling

Calculate the Rabi frequency that can be generated by an rf-antenna consisting of a single square loop with side length $L = 2\,\mathrm{cm}$ on a cloud of trapped ^{87}Rb atoms

located in the center of the loop on transitions between magnetic sublevels of the $F = 1$ ground state hyperfine structure. Assume the antenna to carry an ac-current with $I = 1\,\mathrm{A}$ amplitude.

26.4.5.10 Ex: Landau-Zener transitions

Consider a rubidium-88 cloud in its ground state $^2S_{1/2}, F = 1, m_F = -1$ confined in an isotropic quadrupolar potential with the gradient $200\,\mathrm{G/cm}$. To initiate an efficient radiofrequency evaporation, you want atoms crossing the region where the radiofrequency couples the Zeeman states to make a transition to the untrapped Zeeman state $m_F = 0$ with 95% probability. What is the amplitude of the required magnetic field.

26.4.5.11 Ex: Damping in mixtures of species

From Eq. (26.118) derive the interspecies thermalization rate for harmonic potentials.

26.4.5.12 Ex: Damping in mixtures of species

Describe the damping in mixtures of species, and show how to use a measurement of the damping time for a determination of the interspecies the scattering length.

26.5 Other traps

26.5.1 Ion traps

The electric charge of ions allow for their efficient manipulation and control by electric and magnetic fields exploiting the Coulomb-Lorentz force. In fact, the control is so good, that it is possible to isolate and store individual ions or even arrays of quantum entangled ions and to perform coherent operations on them, which qualifies them as quantum registers. Two different types of traps have been investigated. In *Penning trap*s [647], electrically charged particles are subjected to a radially attractive quadrupolar electrostatic field superimposed to an axial magnetostatic field forcing the particles into closed circular orbitals [6]. In the so-called *radiofrequency trap* or *Paul trap* –*Wolfgang Paul* received the Nobel Prize in 1989 together with Hans Dehmelt and Norman Ramsey– charged particles subjected to an alternating electric field with quadrupolar symmetry. Hyperboloidal electrode configurations produce saddle-shaped potentials, as shown in Fig. 26.24, which are, at any instant of time, parabolically repulsive in the one direction (axial or radial) and parabolically attractive in the other (radial or axial). The alternating electric field causes a periodic reorientation of the Coulomb force, which leads to a time-averaged parabolic quasi-potential $\Phi(\mathbf{r}, t)$. In this potential the particles perform harmonic oscillations at characteristic frequencies, which are independent of the oscillation amplitude [642]:

$$\Phi(r, z) = \Phi_0(t)(r^2 - 2z^2) \quad , \quad r^2 = x^2 + y^2 \ , \tag{26.119}$$

[6] Note that purely electrostatic fields do not lend themselves to trapping, since the necessary condition for the existence of minima in a potential, $\partial_i \partial_j \phi < 0$, does not obey the Laplace equation.

where the polarity is alternated at a radiofrequency Ω_a,

$$\Phi_0(t) = \Phi_{\rm dc} + \Phi_{\rm ac}\cos(\Omega_a t) \ . \tag{26.120}$$

$\Phi_{\rm dc}$ denotes the amplitude of the *dc* part of the voltage, $\Phi_{\rm ac}$ the amplitude of the *ac* part. The potential $\Phi(r,z,t)$ exerts, in the temporal average, a central force on the ion, if the radiofrequency field satisfies specific conditions.

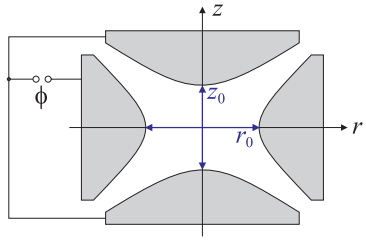

Figure 26.23: Geometry of the Paul trap.

26.5.1.1 Evaluation of the stability diagram

Paul traps do not have to have perfect quadrupolar geometry. To determine the secular frequencies of the pseudo-potential for an arbitrary geometry, we expand the potential around the position $\mathbf{r}_0$ of the potential minimum, which depends on the geometry of the electrodes and the applied voltages,

$$\begin{aligned}\Phi(\mathbf{r}) &= \Phi_a + (\mathbf{r}-\mathbf{r}_0)\nabla\Phi(\mathbf{r}_0) + \tfrac{1}{2}[(\mathbf{r}-\mathbf{r}_0)\nabla]^2\Phi(\mathbf{r}_0) + ... \\ &\equiv \Phi_a[1 + b_r(r-r_0)^2 + b_z(z-z_0)^2] \ .\end{aligned} \tag{26.121}$$

In the last step, we assume that the potential has an almost cylindrical shape. For a given geometry, the curvatures $b_{z,r}$ can be extracted from numerical simulations. From the continuity equation, we find $b_z = -2b_r$. The polarity of the electrodes is modulated with frequency Ω,

$$\Phi(\mathbf{r},t) = \Phi(\mathbf{r})(\zeta - \cos\Omega t) \ . \tag{26.122}$$

The equations of motion are derived from $m\ddot{\mathbf{r}} = -e\nabla\phi(\mathbf{r},t)$,

$$m\ddot{r}_j + 2e\Phi_a b_j(\zeta - \cos\Omega t)r_j = 0 \ . \tag{26.123}$$

Introducing the parameters a and q,

$$a_z = \frac{8e\phi_a b_z \zeta}{m\Omega^2} = -2a_r \qquad \text{and} \qquad q_z = \frac{4e\Phi_a b_z}{m\Omega^2} = -2q_r \ , \tag{26.124}$$

we arrive at the so-called *Mathieu equation* [566, 279],

$$\ddot{r}_j + \tfrac{1}{4}\Omega^2(a_j - 2q_j\zeta\cos\Omega t)r_j = 0 \ . \tag{26.125}$$

These equations predict stable orbits, provided that the parameters a and q are within the so-called stability diagram shown in Fig. 26.25.

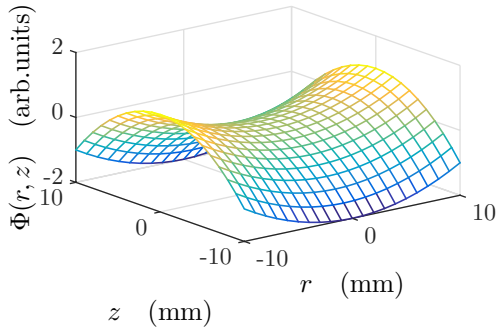

Figure 26.24: (code) Two-dimensional illustration of time-dependent potential: at each instant of time the potential has the form of a saddle. The potential rotates around the vertical axis at an appropriate pace.

According to these equations, the ion goes through oscillatory motions that are defined by the trap parameters a_i and q_i. For the motion of the ion to be finite, its oscillation amplitude may not exceed the boundaries defined by the electrodes. This condition imposes an allowed regime for the trap parameters called *stability diagram* [566].

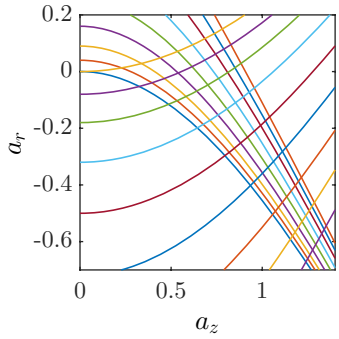

Figure 26.25: (code) Stability diagram.

In the limit $|a_i|, q_i \ll 1$ the ion travels only a short distance $s \ll r_0$ during one modulation period Ω_a. Then the ion undergoes a slow periodic motion called *macromotion* within the trapping potential with the secular frequency ζ_i. This motion is modulated by a rapid oscillation called *micromotion*, which is excited by the modulation field Ω_a. Without *dc* voltage applied between the ring and the endcaps, $a_i = 0$, the motion of the ion is described by the following simple equation:

$$r_i(t) = r_i^0 \left(1 - \tfrac{1}{2} q_i \cos \Omega_a t\right) \cos \zeta_i t \quad , \quad \zeta_i = \tfrac{1}{\sqrt{8}} q_i \Omega_a \quad , \quad i = r, z \ . \qquad (26.126)$$

The orbit of the ion is confined to the inner region of the trap, if its kinetic energy is less than $m\zeta_r^2 r_0^2 + M\zeta_z^2 z_0^2$. Since the trap is, at any instant of time, focusing in some directions and defocusing others, it is not a conservative potential. The oscillatory

motion (disregarding micromotion) of the ion, however suggests a model, where the trap is described by a pseudo-potential [279, 86] whose depth is,

$$D_z = \tfrac{q_z}{8} e V_{\rm ac} = 2D_r \qquad \text{if} \qquad a_i = 0 \ . \tag{26.127}$$

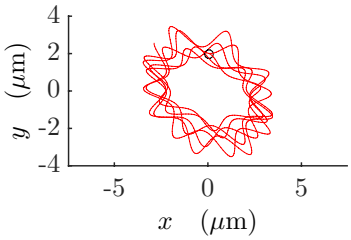

Figure 26.26: (code) Simulated micro- and macromotion of an ion.

Other geometries, deviating from the perfect quadrupole, are possible for the electrodes. These traps are also well described by equation (26.119), as long as the ion is near the trap center. For example, higher order multipolar traps have been used for trapping ion clouds [852], as well as Paul-Straubl traps [740] and storage rings [846]. Particularly important for the storage of arrays of cooled ions with applications in quantum computing is the *linear Paul trap* [670, 282, 669], where immobilized ions are aligned on a linear chain. The advantage of the linear trap, as compared to other traps designed for many ions, is the easier optical access to individual ions by focused laser beams and the possibility of canceling the micromotion.

26.5.2 Micromotion

The motion of an ion in a Paul trap is a superposition of two vibrations with the respective oscillation frequencies Ω_a (modulation frequency) and $\zeta_{r,z}$ (secular frequencies for radial and axial direction vibrations). For an ion in thermal equilibrium (i.e., without active cooling), the mean kinetic energies of the micro- and macromotion are equal [87].

The macromotion can be reduced by cooling, in contrast to the micromotion, which is constantly excited by the modulation of the applied electric field [157]. On the other hand, the amplitude of the micromotion decreases with the distance of the ion from the trap center and, in the minimum of the pseudo potential, disappears completely. Therefore, to suppress the micromotion, it is imperative to cool the macromotion and push the ion to the trap center, if necessary, using additional static electric fields. Since the frequency of the micromotion is much higher than that of the macromotion, the dynamic sidebands can be resolved on a sufficiently narrow optical transition. When the modulation frequency Ω_a is very high, the secular frequencies of the macromotion are also high, so that even large optical transitions are able to resolve the macromotional sidebands. This is called the *strong coupling* regime.

Because of Coulomb repulsion, only a single atom can be at the center of a Paul trap, such that it is difficult to zero micromovement. One solution is to use a linear trap, where the center is smeared out over a straight line. Solve Exc. 26.5.4.1.

Example 187 (*Numerical calculation of the electric field created by a charged surface*): To calculate the trapping potential for a charged particle held on top of a planar microtrap structure, we proceed as follows. The energy of a charge in an electric field is $H = -e\Phi$. The electrostatic potential is given by Coulomb's law,

$$\Phi(\mathbf{r}) = \frac{1}{4\pi\epsilon_0}\sum_n \int_{V_n} \frac{\rho(\mathbf{r}')}{|\mathbf{r}-\mathbf{r}'|}dV' - \frac{1}{4\pi}\sum_n \int_{S_n} \Phi_n \frac{\mathbf{r}-\mathbf{r}'}{|\mathbf{r}-\mathbf{r}'|^3}d\mathbf{f}' + \frac{1}{4\pi}\sum_n \int_{S_n} \frac{\vec{\mathcal{E}}(\mathbf{r}')}{|\mathbf{r}-\mathbf{r}'|}\cdot d\mathbf{f}' \ ,$$

where ϕ_n is the voltage applied to the n-th boundary. In practice, electric fields are generated by electrodes set to specific voltages. Using the Dirichlet boundary conditions, we only retain the second term. Furthermore, to account for the planar geometry of the chip electrodes, we only consider surface boundaries in the $y' = 0$ plane,

$$\Phi(\mathbf{r}) = -\frac{1}{4\pi}\sum_n \Phi_n \int_{S_n} \frac{y dx' dz'}{\sqrt{(x-x')^2 + y^2 + (z-z')^2}^3} \ .$$

This implies that the field lines cross the chip surface orthogonally, which in reality is only true if the chip electrodes cover the whole area. Therefore, we

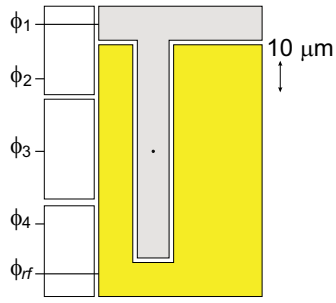

Figure 26.27: Possible design for a microchip ion trap. Φ_n are static potentials except for Φ_0, which is alternates sign with radio frequency.

only consider small gaps between the electrodes. We digitize the integral by dividing every electrode Φ_n into a number of identical surface elements Δf_m,

$$\Phi(\mathbf{r}) = -\frac{1}{4\pi}\sum_{n,m} \Phi_n \frac{y\Delta f_m}{\sqrt{(x-x_m)^2 + y^2 + (z-z_m)^2}^3} \ .$$

This formula can easily be evaluated numerically. A concrete example for a microchip ion trap is shown in Fig. 26.27.

Example 188 (*Numerical calculation of the magnetic field created by a current wire*): Current-carrying wires may exert Lorentz forces on the ions. The magnetostatic field is given by the Biot-Savart law,

$$\vec{\mathcal{B}}(\mathbf{r}) = \frac{\mu_0}{4\pi}\int_V \frac{(\mathbf{r}-\mathbf{r}')\times\mathbf{j}}{|\mathbf{r}-\mathbf{r}'|^3}dV' \ .$$

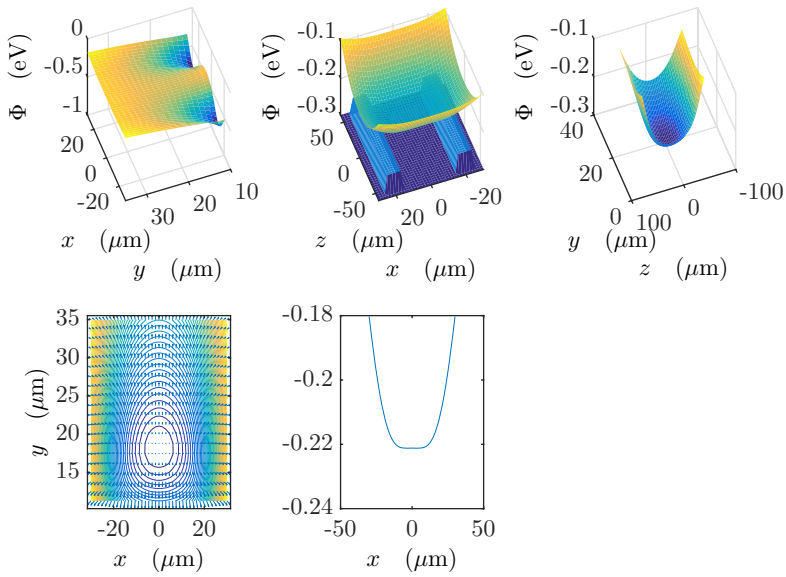

Figure 26.28: (code) Two-dimensional cuts through the electric potential generated by the microchip shown in Fig. 26.27 for $\Phi_{\rm rf} = 100$ V and $\Phi_j = 0$.

In practice magnetic fields are created by current-carrying wires. Those can be parametrized by one-dimensional currents, $\mathbf{j} = I\delta^2 d\mathbf{s}$, so that,

$$\vec{\mathcal{B}}(\mathbf{r}) = \frac{\mu_0 I}{4\pi}\int_C \frac{d\mathbf{s}' \times (\mathbf{r}-\mathbf{r}')}{|\mathbf{r}-\mathbf{r}'|^3}$$

$$|\vec{\mathcal{B}}(\mathbf{r})| = \frac{\mu_0 I}{4\pi}\sum_n \frac{\sqrt{ds_{y,n}^2(z-z_n)^2 + ds_{z,n}^2(x-x_n)^2 + ds_{x,n}^2(y-y_n)^2}}{\sqrt{(x-x_n)^2+(y-y_n)^2+(z-z_n)^2}^3} .$$

can immediately be numerically solved.

26.5.2.1 Electronic detection of ions

The presence of ions in the trap can be probed through the damping that they induce a coupled electronic resonance circuit [851, 857].

26.5.3 QUEST

Homonuclear atoms and dimers do not have a permanent electrical dipole moment, but they may have a permanent magnetic dipole moment. Therefore, homonuclear dimers must be confined by magnetic field gradients, or else an electric dipole moment must be *induced* by an oscillating electromagnetic field. In the optical regime, this was demonstrated with the quasi-electrostatic trap (*QUEST*).

In contrast, heteronuclear dimers are polar molecules with a permanent electric dipole moment, which can be quite large if the molecules are deeply bound. According to Earnshaw's theorem, there is no static magnetic field maximum in free space. Thus, no 'high-field seeking' state can be trapped. In principle, QUEST-type dipolar optical

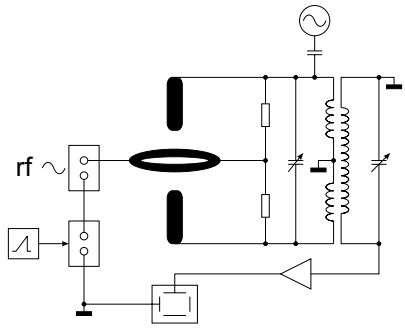

Figure 26.29: Resonance circuit for electronic ion detection. The trap is operated by a radiofrequency, while a DC voltage is scanned across the stability diagram. Simultaneously, an oscillating field is tuned near one of the trap's secular frequencies. When the stability point is such, that the secular frequency coincides with the frequency of the oscillating field, the motion of the ions is parametrically excited and the resonance circuit is damped. This damping is detected by a narrow-band amplifier.

traps can also be used for heteronuclear dimers. The problem is, however, that in contrast to homonuclear molecules, transitions between the vibrational ground state levels are possible. Thus, the light generating the QUEST also induces transitions leading to a redistribution of the population over all vibrational states.

Very far from resonance,

$$U_{\rm dip}(\mathbf{r}) = -\alpha_{\rm stat}\frac{I(\mathbf{r})}{2\varepsilon_0 c}\ . \tag{26.128}$$

Loosely bound homonuclear molecules are subject to the sum of the restoring forces exerted by magnetic traps on the individual atoms, $\mu_m = 2\mu_a$ and $d_m = 2d_a$. This is also true for heteronuclear molecules as long as the trapping potential is much weaker than the binding energy.

Example 189 (*Permanent electric dipole moment of LiRb*): The interaction energy of two dipoles is,

$$\hat{H}_{\rm int} = \frac{1}{4\pi\varepsilon_0}\frac{\mathbf{p}_1\cdot\mathbf{p}_2 - 3(\mathbf{p}_1\cdot\hat{\mathbf{r}})(\mathbf{p}_2\cdot\hat{\mathbf{r}})}{r^3}\ .$$

Thus, two identical dipoles with 1 Debye $= 10^{-27}/2.998\,\mathrm{Cm} = 10^{-19}/c\,\mathrm{Cm}^2\,/\,\mathrm{s} = 39.36\ ea_{\rm B}$ parallel oriented at a distance $r = 1\,\mu\mathrm{m}$ have the energy,

$$\hat{H}_{\rm int} = \frac{1}{4\pi\varepsilon_0}\frac{p^2}{r^3} \approx h \times 1.5\,\mathrm{MHz} \approx k_{\rm B} \times 73\,\mu\mathrm{K}\ .$$

For example, LiRb has an electrical dipole moment of between -2 and -4.2 Debye depending on the vibrational state of the molecule.

26.5.4 Exercises

26.5.4.1 Ex: Coulomb repulsion in linear Paul trap

Coulombian repulsion prevents that two ions confined in a linear Paul trap be simultaneously in the ground state. Determine the spatial extent of the ground state

and the depth of the potential in the pseudo-potential approximation. What is the equilibrium distance of the ions?

26.5.4.2 Ex: Motion of ions in a surface Paul trap

Programs on the motion of ions in a surface Paul trap.

26.6 Analysing techniques

To analyze the kinetic state of an atomic gas and, for example, to identify the presence of a Bose-Einstein condensate, it is necessary to measure its spatial or momentum distributions. However, the only way to gather information from the atoms is to throw some kind of particles into them and to detect, where these particles are scattered. The most suitable particle to penetrate an ultra-high vacuum chamber surely is the *photon*. Therefore, apart from few exceptions where electron beams are used, all information on ultra-cold gases has been obtained so far through their reactions to incident laser beams [401, 142, 22, 434, 335].

26.6.1 Time-of-flight imaging

The most common imaging techniques measure the absorption of a laser beam by an atomic cloud after a *time-of-flight* or the dispersion of a laser beam induced by a trapped cloud. The amplitude $\mathcal{E}_0$ of a light wave traversing an atomic cloud of diameter L and characterized by the refractive index η is modified by a factor $e^{\imath\omega L\eta/c}$. For an inhomogeneous cloud, we have,

$$\mathcal{E} = \mathcal{E}_0 e^{\imath\omega L/c} \exp\left(\imath\frac{\omega}{c}\int_{-\infty}^{\infty}(\eta(\mathbf{r})-1)dz\right) . \tag{26.129}$$

We can approximate the refractive index by the atomic susceptibility,

$$\eta = \sqrt{1+\chi} \simeq 1+\frac{\chi}{2} \qquad \text{with} \qquad \chi = -\frac{4\pi n(\mathbf{r})}{k^3(2\Delta/\Gamma+\imath)} . \tag{26.130}$$

where $n(\mathbf{r})$ is the density distribution of the cloud. The imaginary part of the susceptibility is related to the *absorption coefficient* α and the real part to the *dispersion coefficient* δ,

$$\mathfrak{Im}\,\chi = \frac{\alpha}{\omega/c} \qquad \text{and} \qquad \mathfrak{Re}\,\chi = \frac{2\delta}{\omega/c} . \tag{26.131}$$

Now, the absorption and dispersion coefficients can be related to the optical cross-section $\sigma(\Delta)$ defined in (1.102) [530], where Δ is the detuning of light frequency from an atomic resonance, whose linewidth is Γ. This result is called the *optical theorem*,

$$\alpha = n\sigma(\Delta) \qquad \text{and} \qquad \delta = n\sigma(\Delta)\frac{\Delta}{\Gamma} , \tag{26.132}$$

Finally, we obtain the *Lambert-Beer law*,

$$\boxed{\mathcal{E} = \mathcal{E}_0 e^{\imath\omega L/c} \exp\left[\imath\sigma(\Delta)\left(\frac{\imath}{2}-\frac{\Delta}{\Gamma}\right)\int_{-\infty}^{\infty} n(\mathbf{r})dz\right] \equiv \mathcal{E}_0 e^{\imath\omega L/c} e^{-b/2} e^{\imath\varphi}} . \tag{26.133}$$

For the intensity, $I \propto |\mathcal{E}|^2$, we get,

$$\frac{I}{I_0} = \exp\left[-\sigma(\Delta)\int_{-\infty}^{\infty} n(\mathbf{r})dz\right] \equiv e^{-b} \ . \tag{26.134}$$

The *absorption* b describes the loss of intensity for the laser beam due to scattering by the (disordered) atoms. It is strong near resonance, but diminished quadratically with the detuning Δ. The scattering is necessarily accompanied by radiation pressure accelerating and heating the atoms. The *dispersion* φ describes the refraction of the laser beam by the atomic density distribution (which for this purpose can be considered as continuous) [176, 286]. It disappears in resonance and diminishes slowly with increased detuning ($\propto \Delta$). It is connected to the dipole force and, thus, does not heat the atomic cloud. The coefficient φ describes the phase shift of the electromagnetic wave transmitted through the atomic cloud.

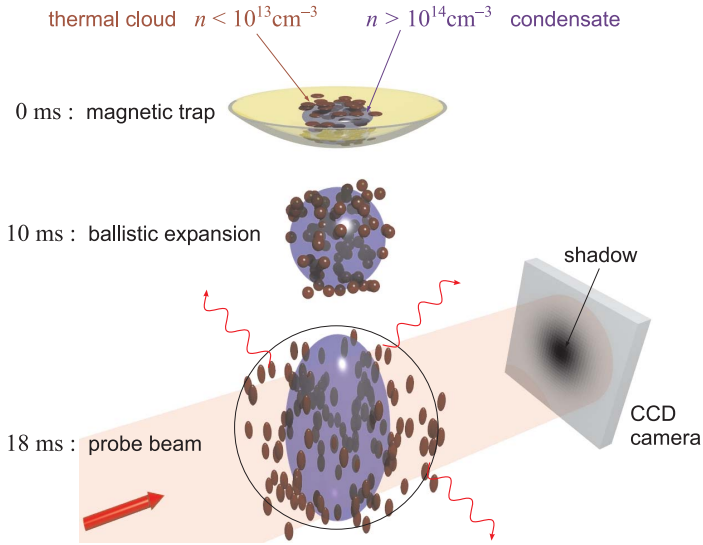

Figure 26.30: Sequence of a typical time-of-flight experiment: As soon as the trapping potential is suddenly switched off, the atomic cloud ballistically expands for 18 ms, before it is illuminated by a short resonant laser pulse. The shadow printed by the cloud onto the beam is photographed by a CCD camera.

26.6.2 Absorption imaging

Let us now detail the experimental process of *absorption imaging* (see Fig. 26.31): The trap confining the atomic cloud is suddenly turned off, thus letting the atoms, accelerated by the Earth's gravitation, fall for a flight time of a few ms. Then a pulse of a resonant laser light, whose diameter is much larger than the size of the cloud, is irradiated. The local attenuation of the beam intensity $I \sim |\mathcal{E}|^2$ can be related through the absorption b (also called *optical density* or *optical depth*) to the atomic density via,

$$-\ln\frac{I(x,y)}{I_0} = b(x,y) = \sigma(\Delta)\int n(\mathbf{r})dz \ . \tag{26.135}$$

The shadow printed by the atomic cloud on the transverse profile of the laser beam is recorded by a CCD camera.

We have already noted that the absorption is accompanied by radiative pressure. After some scattering events, due to the photonic recoil, the atoms have accumulated a sufficiently large velocity, and therefore a sufficiently large Doppler shift, to be out of resonance with the laser beam. Subsequent photons are no longer scattered by the atoms and only contribute to increase the illumination of the CCD camera without carrying any information about the presence of atoms. Consequently, it is advantageous to use very short laser pulses. In addition, the intensity of the laser beam should not saturate the transition in order to guarantee an optical cross-section, which is independent of the intensity, and hence to guarantee the validity of the Lambert-Beer law. Finally, the laser frequency must be tuned perfectly to resonance, $\Delta = 0$. Otherwise, the interaction between the laser beam and the atomic cloud becomes partially dispersive, which leads to a focusing or defocusing of the laser beam by refraction and a distortion of the image making it impossible to estimate the size of the cloud.

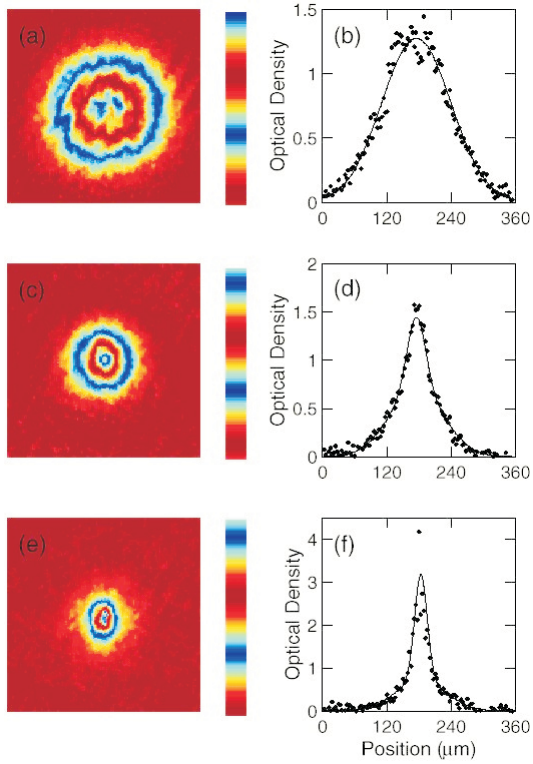

Figure 26.31: Absorption images after a time-of-flight allow to identify the presence of a Bose-condensate through its characteristic momentum distribution. Shown are images (a,b) above, (c,d) slightly below, and (e,f) well below the critical temperature for a Bose-Einstein phase transition (figures [367]).

Fig. 26.31 shows examples of absorption images of an atomic cloud taken at differ-

ent stages of the evaporation process. Fig. 26.31(a,b) was taken at a temperature of 320 nK; the cloud is large and isotropic and therefore purely thermal. At 250 nK [see Fig. 26.31(c,d)] an elliptically shaped part appears in the center of the thermal cloud. And at 180 nK [see Fig. 26.31(e,f)] the thermal cloud almost completely disappeared for the benefit of the condensate. A quantitative evaluation of the condensed fraction is given in Sec. 7.3.2. Solve the Excs. 26.6.6.2 and 26.6.6.1.

26.6.3 Dispersive imaging

The absorption imaging technique is destructive, because of the involved ballistic expansion and also because of the radiative pressure exerted by the resonant imaging beam, which accelerates and heats the atomic cloud. That is, the measurement process messes up the distributions of the cloud, such that a second image taken after the first one will give different results. However, there is a non-destructive imaging technique called *dispersive imaging* or *phase contrast imaging*. In this technique, the laser light is tuned sufficiently far from resonance, $|\Delta| \gg \Gamma$, for spontaneous emission and heating induced by random photonic recoil to be negligible [22]. This permits to take a series of consecutive images and create a *movie* of the temporal evolution of the cloud. Another advantage of this technique is the low off-resonant optical density, which allows to take pictures of very dense clouds *in situ*, that is, *while they are confined in a trap*.

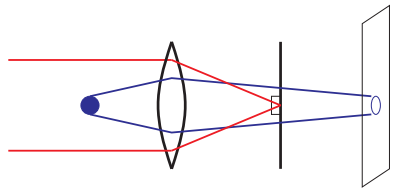

Figure 26.32: Scheme for dispersive images.

The physical quantity which is measured by this method is the local phase shift of the wavefront of the probe laser. Wavefront distortions are difficult to measure. To transform the phase profile into an intensity profile, a method known from classical optics called *Schlieren method* is used. It is based on the interference of the probe beam with its distorted wavefront and a reference plane wave. In practice, there are several possibilities. For *dark-ground imaging*, the part of the incident beam not having interacted with the atoms is blocked behind the interaction zone (see Fig. 26.32)

$$\bar{I}_{\mathrm{dg}} = \tfrac{1}{2}|\mathcal{E} - \mathcal{E}_0|^2 = I_0|e^{-b/2+\imath\varphi} - 1|^2 \qquad (26.136)$$
$$\xrightarrow{b\to 0} I_0\varphi^2 = I_0 b\frac{\Delta^2}{\Gamma^2} \ .$$

The intensity signal $\bar{I}_{\mathrm{dg}}$ is quadratic in optical density b.

For *phase contrast imaging*, the part of the beam not having interacted with the atoms receives a phase shift of $\lambda/4$ with respect to the part of the beam having

interacted with the atoms:

$$\bar{I}_{\rm pc} = \tfrac{1}{2}|\mathcal{E} - \mathcal{E}_0 + \mathcal{E}_0 e^{\pm \imath\pi/2}|^2 = I_0|e^{-b/2+\imath\varphi} - 1 + e^{\pm\imath\pi/2}|^2 \overset{b\to 0}{\longrightarrow} I_0(\pm 1+\varphi)^2 \simeq I_0\left(1 \pm b\frac{\Delta}{\Gamma}\right) . \tag{26.137}$$

The intensity $\bar{I}_{\rm pc}$ is linear in b and, consequently, more sensitive to weak signals. Finally, a third technique, called *polarization contrast imaging*, detects the local birefringence of the atomic cloud [113, 712].

The imaging techniques shown so far only allow to visualize the instantaneous density distribution of the atomic cloud $n(\mathbf{r})$. If we are interested in other quantities, we have to conceive the experiment in such a way, that the desired information leaves its signatures in the density distribution. For example, to measure the excitation frequencies of a condensate, which can perturb its shape and observe the subsequent time evolution of $n(\mathbf{r}, t)$ via dispersive imaging [438, 573, 23, 459].

26.6.4 Reconstruction of column-integrated absorption images

Assume cylindrical symmetry $n(\mathbf{r}) = n(r, z)$, with $r = \sqrt{x^2 + y^2}$. Absorption images are *column-integrated*, i.e. they are taken by integration along the x-axis,

$$\frac{I(y,z)}{I_0(y,z)} = e^{-\sigma \int n(r,z)dx} = e^{-\sigma f(y,z)} . \tag{26.138}$$

The radial density can be recovered by tomography [208, 246, 640],

$$n(r,z) = \frac{1}{(2\pi)^2}\int (\mathcal{F}_y f)(\kappa_y, z) J_0(\kappa_y r) d\kappa_y . \tag{26.139}$$

This is called *image reconstruction* or *Fourier reconstruction* or *inverse Abel transform* and will we studied in Exc. 26.6.6.3.

26.6.5 Condensable atomic species

Early work on BEC has been done by [729, 54, 85, 145, 520]. Proposals for atomic gases withe from [375, 802, 798]. An appropriate BEC candidate must fulfill a few conditions: The transition wavelengths must be *accessible by laser light*, the level scheme should exhibit a *closed cycling transition* for laser cooling and have a reasonable pressure in gas phase. Furthermore, it is desirable to have a large HFS, metastable electronic state, no trapping state, large positive scattering length, Feshbach resonances. For sympathetic cooling it may be nice to have several isotopes of the same element.

The most common elements are alkalis, alkali earths and noble gases. The following gases have already been condensed ^{1}H, ^{1}He*, ^{7}Li, ^{23}Na, ^{85}Rb, and ^{87}Rb [20, 201, 114, 113, 713, 179, 367, 371]. Investigations in ^{1}Ne*, ^{39}K, ^{133}Cs, ^{x}Sr, ^{x}Cr and ^{40}Ca are underway [771, 350, 476, 671, 758, 64, 291].

26.6.6 Exercises

26.6.6.1 Ex: Lensing by cold clouds

The interaction of light with two-level atoms generates a susceptibility which gives rise to a refraction index,

$$\eta(\mathbf{r}) = \sqrt{1 - \frac{4\pi n(\mathbf{r})}{k^3(2\Delta/\Gamma + \imath)}} \ ,$$

where $n(\mathbf{r})$ is the cloud's density distribution and $\Gamma/2\pi = 30.5\,\mathrm{MHz}$ for strontium.
a. Calculate the phase-shift suffered by a light beam crossing an ultracold atomic cloud ($N = 10^5$, $T = 1\,\mu\mathrm{K}$) confined in an isotropic harmonic trap ($\omega_{trp} = (2\pi)\ 100\,\mathrm{Hz}$) as a function of detuning.
b. Estimate the focal distance of the cloud for $\Delta = -\Gamma$.

26.6.6.2 Ex: Optical density

A cloud of $N = 10^6$ ^{87}Rb atoms is prepared in a cylindrical harmonic trap characterized by the axial vibration frequencies $\omega_z = (2\pi)\ 50\,\mathrm{Hz}$ and the radial one $\omega_r = (2\pi)\ 200\,\mathrm{Hz}$. The experimenter takes the absorption image after 18 ms time-of-flight, as shown in Fig. 26.31(a). A pixel of the CCD camera corresponds to 5 µm in real space.
a. At what temperature is the phase transition to Bose-Einstein condensate to be expected?
b. Determine the temperature of the sample.
c. Evaluate its density distribution.
d. Evaluate the resonant optical density for the $D2$-transition at 780 nm along the symmetry axis of the trapped cloud.

26.6.6.3 Ex: Inverse Abel transformation

Calculate the inverse Abel transform using Bessel of an arbitrary function in 2D.

26.7 Further reading

Ph.W. Courteille et al., *Bose-Einstein condensation of trapped atomic gases* [DOI]

H.J. Metcalf and P. van der Straaten, *Laser cooling and trapping* [ISBN]

Y.B. Ovchinnikov et al., *A Zeeman slower based on magnetic dipoles* [DOI]

S.C. Bell et al., *A slow atom source using a collimated effusive oven and a single-layer variable pitch coil Zeeman slower* [DOI]

R.A. Cline et al., *Spin relaxation of optically trapped atoms by light scattering* [DOI]

M. Defrise et al., *Three-dimensional image reconstruction from complete projections* [DOI]

V. Dribinski et al., *Reconstruction of Abel-transformable images: The Gaussian basis-set expansion Abel transform method* [DOI]

P.A. Vicharelli et al., *Iterative method for computing the inverse Abel transform* [DOI]

Y. Castin et al., *Limit of Doppler cooling* [DOI]

D.A. Steck et al., *Rubidium-87 D Line Data* [DOI]

D.A. Steck et al., *Rubidium-85 D Line Data* [DOI]

M.G. Raizen et al., *Stochastic cooling of atoms using lasers* [DOI]

Jiazhong Hu et al., *Creation of a Bose-condensed gas of* ^{87}*Rb by laser cooling* [DOI]

26.7.1 on gravimetry

S. Abend et al., *Atom-chip fountain gravimeter* [DOI]

G. Ferrari et al., *Long-Lived Bloch Oscillations with Bosonic Sr Atoms and Application to Gravity Measurement* [DOI]

K. Gietka et al., *A supersolid-based gravimeter in a ring cavity* [DOI]

26.7.2 on strontium (metrology)

D.S. Barker et al., *Enhanced magnetic trap loading for atomic strontium* [DOI]

Y. Bidel et al., *Coherent light transport in a cold strontium cloud* [DOI]

I. Courtillot et al., *Efficient cooling and trapping of strontium atoms* [DOI]

E.M. Bridge et al., *A vapor cell based on dispensers for laser spectroscopy* [DOI]

A. Brusch et al., *Hyperpolarizability Effects in a Sr Optical Lattice Clock* [DOI]

D.E. Chang et al., *Controlling dipole-dipole frequency shifts in a lattice-based optical atomic clock* [DOI]

L. Couturier et al., *Measurement of the strontium triplet Rydberg series by depletion spectroscopy of ultracold atoms* [DOI]

A. Derevianko et al., *Colloquium: Physics of optical lattice clocks* [DOI]

G. Ferrari et al., *Precision frequency measurement of visible intercombination lines of strontium* [DOI]

G. Ferrari et al., *Cooling of Sr to high phase-space density by laser and sympathetic cooling in isotopic mixtures* [DOI]

T. Fukuhara et al., *Degenerate Fermi Gases of Ytterbium* [DOI]

T. Fukuhara et al., *Mott insulator of ultracold alkaline-earth-metal-like atoms* [DOI]

S.M. Heider et al., *Hyperfine structure of ^{87}Sr in the $^3P_2$ metastable state* [DOI]

Fachao Hu et al., *Analyzing a single-laser repumping scheme for efficient loading of a strontium magneto-optical trap* [DOI]

T. Ido et al., *Optical clocks based on ultracold neutral strontium atoms* [DOI]

C. Javaux et al., *Modulation-free pump-probe spectroscopy of strontium atoms* [DOI]

H. Katori et al., *Magneto-optical trapping and cooling of strontium atoms down to the photon recoil temperature* [DOI]

T.H. Loftus et al., *Magnetic trapping of ytterbium and the alkaline-earth metals* [DOI]

T.H. Loftus et al., *Narrow line cooling and momentum-space crystals* [DOI]

T.H. Loftus et al., *Narrow line cooling finite photon recoil dynamics* [DOI]

A.D. Ludlow et al., *Ultracold strontium clock: Applications to the measurement of fundamental constant variations* [DOI]

Y.N. Martinez de Escobar et al., *Two-photon photoassociative spectroscopy of ultracold ^{88}Sr* [DOI]

P.G. Mickelson et al., *Repumping and spectroscopy of laser-cooled Sr atoms using the $(5s5p)^3P_2$-$(5s4d)^3D_2$ transition* [DOI]

N.V. Morrow, *Feedback Control of Atomic Motion in an Optical Lattice* [DOI]

T. Mukaiyama et al., *Recoil-Limited Laser Cooling of ^{87}Sr Atoms Near the Fermi Temperature* [DOI]

S.B. Nagel et al., *Magnetic trapping of metastable $^3P_2$ atomic strontium* [DOI]

M.A. Norcia et al., *Narrow-line laser cooling by adiabatic transfer* [DOI]

I. Nosske et al., *Two-dimensional magneto-optical trap as a source for cold strontium atoms* [DOI]

Y.B. Ovchinnikov et al., *A permanent Zeeman slower for Sr atomic clock* [DOI]

J.E. Sansonetti et al., *Wavelengths, transition probabilities, and energy levels for the spectrum of neutral strontium* [DOI]

R. Santra et al., *High-accuracy optical clock via three-level coherence in neutral bosonic ^{88}Sr* [DOI]

S. Snigirev et al., *Fast and dense magneto-optical traps for strontium* [DOI]

F. Sorrentino et al., *Laser cooling and trapping of atomic strontium for ultracold atoms physics, high-precision spectroscopy and quantum sensors* [DOI]

S. Stellmer et al., *Detection and manipulation of nuclear spin states in fermionic strontium* [DOI]

S. Stellmer et al., *Reservoir spectroscopy of 5s5p $^3P_2$-5snd $^3D_{1,2,3}$ transitions in strontium* [DOI]

A.V. Taichenachev et al., *Magnetic field-induced spectroscopy of forbidden optical transitions with application to lattice-based optical atomic clocks* [DOI]

Z.W. Barber et al., *Direct excitation of the forbidden clock transition in neutral ^{174}Yb atoms confined to an optical lattice* [DOI]

A. Traverso et al., *Inelastic and elastic collision rates for triplet states of ultracold strontium* [DOI]

M. Yasuda et al., *Lifetime Measurement of the $^3P_2$ Metastable State of Strontium Atoms* [DOI]

G. Verma et al., *A compact atomic beam based system for Doppler-free laser spectroscopy of Strontium atoms* [DOI]

Xinye Xu et al., *Cooling and trapping of atomic strontium* [DOI]

T. Zelevinsky et al., *Optical clock and ultracold collisions with trapped strontium atoms* [DOI]

26.7.3 on strontium (quantum degeneracy)

B.J. DeSalvo et al., *Degenerate Fermi gas of ^{87}Sr* [DOI]

Y.N. Martinez de Escobar et al., *Bose-Einstein Condensation of ^{84}Sr resonance at large detuning* [DOI]

Meng Khoon Tey et al., *Double-degenerate Bose-Fermi mixture of strontium* [DOI]

P.G. Mickelson et al., *Bose-Einstein Condensation of ^{88}Sr Through Sympathetic Cooling with ^{87}Sr* [DOI]

S. Stellmer et al., *Bose-Einstein condensation of strontium* [DOI]

S. Stellmer et al., *Bose-Einstein condensation of ^{86}Sr* [DOI]

S. Stellmer et al., *Creation of Ultracold Sr_2 Molecules in the Electronic Ground State* [DOI]

S. Stellmer et al., *Laser Cooling to Quantum Degeneracy* [DOI]

Chapter 27

Bose-Einstein condensation

The experimental verification of Bose and Einstein's prediction was for a long time a cherished dream of many physicists. On the one hand, several phenomena have been related to BEC in the past, for example, the phenomenon of superfluidity in liquid helium and superconductivity. On the other hand, these strongly interacting systems are not pure enough to clearly identify the role of BEC. In 1995, however, Bose-Einstein condensation of weakly interacting confined atomic gases was achieved in several laboratories [20, 203, 114, 367]. This success gave rise to a revolution in atom optics documented in an enormous amount of theoretical and experimental work. While initial work focused on the equilibrium thermodynamics of condensates near the phase transition, very soon the dynamic response of condensates to perturbations was the subject of in-depth investigations, followed by the study of superfluid characteristics, quantum transport phenomena, the interaction of condensates with light, of condensed gas mixtures [613, 792], and the behavior of condensates in periodic potentials. To name only a few landmarks, we mention the creation of vortices [557, 541] and quantum turbulence [386], the realization of various types of atom lasers [571, 19, 90, 360] and atom interferometers with condensates [363, 483], the coherent amplification of matter waves [416, 486, 418, 221], the creation of the Mott insulating states in optical lattices [337], the study of condensates in reduced dimensions [603], the Anderson localization of atomic matter waves [144, 695], the observation of Feshbach type collision resonances [178, 415, 845] and Efimov states [487, 58], the creation of homonuclear molecular [338, 440, 184, 908, 886, 388] and heteronuclear condensates [637] and degenerate Fermi gases [214], the observation of BCS type pairing [398, 339], the observation of matter wave superradiance [416] and the interaction of condensates with optical cavities [765, 132] and with surfaces [68].

It is clearly unthinkable to discuss all matters in this course. Let us, however, give a basic and practical introduction to atomic optics with condensates.

27.1 Bose-Einstein condensation of dilute gases

The challenge of the experimental realization of Bose-Einstein condensation is the preparation of a very dense sample of very cold atoms. In practice, the first step consists in providing an atomic gas, for example, of an alkali metal. This is done by heating the metal in an oven (or sometimes in a dispenser). The atoms being ejected from the metal and forming a hot gas are then forced through a nozzle out of the oven, where they form a hot atomic beam. Some experiments employ a *Zeeman*

slower, which is a device that decelerates the fast atoms of the beam by means of a counterpropagating laser exerting a radiative pressure force. A position-dependent magnetic field applied along the trajectory of the atoms is calculated in order to compensate for the Doppler decreasing shift of the decelerated atoms and to ensure that the laser always stays in resonance with an atomic transition (see Exc. 16.5.6.3). Velocities around 30 m/s are realistic and low enough to allow the capture of the atoms by a magneto-optical (MOT) trap. Usually, some 10^9 atoms are captured in a few seconds.

MOTs do not only trap atoms, but simultaneously cool them down to the Doppler limit of typically some 10 μK. Quasi-resonant optical traps, such as MOT, are afflicted by the problem of radiation trapping (see Sec. 26.3.1), which limits the densities of atomic clouds to typically $10^{11}\,\mathrm{cm}^3$. This corresponds (at temperatures close to the Doppler limit) to phase space densities several orders of magnitude away from the threshold to Bose-Einstein condensation. For this reason, the atoms are transferred from the MOT to a potential exempt of radiative pressure force, for example, an optical dipole potential or a magnetic trap.

Once the atoms are confined in such a conservative potential, all the light beams are turned off, and the technique of evaporative cooling is activated (see Sec. 26.4.3). That is, the effective potential is deformed (for example, by an irradiated radiofrequency) in a way to skim out hot atoms and leave behind a cooler sample. This however supposes that the atomic cloud finds back to thermal equilibrium afterwards. As the rethermalization happens by elastic collisions, a high atomic density is necessary, which is often achieved via a compression of the trapping potential. In general, 99.9% of the atoms must be sacrificed to condense the rest. Finally, the momentum distribution is imaged after a time of free expansion. This is done by irradiation of a probe laser pulse (see Fig. 26.31). The entire process of producing a condensed cloud usually takes between 10 s and 60 s.

27.1.1 Condensate of alkaline gases

The first experimental observation of Bose-Einstein condensation was done with a dilute rubidium gas by Cornell and Wieman at the Joint Institute for Laboratory Astrophysics (JILA) [20]. A group from the University of Texas [367, 179] used rubidium as well. A group led by Ketterle from the Massachusetts Institute of Technology (MIT) created the first sodium condensate. And a group led by Hulet from Rice University opted for lithium [114, 112], which has a slightly negative scattering length, $a = -27.3a_\mathrm{B}$. In this situation, only small condensates are expected to be stable [710, 799], which explains the observation of a limited number of about 1400 condensed lithium atoms. Meanwhile, Bose-Einstein condensation has been achieved with many other species, such as ^{1}H [291], ^{85}Rb [173], ^{4}He* [699], ^{133}Cs [771], ^{39}K [671], ^{4}Ne [64], ^{88}Sr [789], or even molecules [884].

27.1.2 Condensation of hydrogen

Hydrogen is a very interesting element to study condensation, because its short scattering length, $a \approx 1.23a_\mathrm{B}$, makes it an almost ideal gas. Consequently, the three-body collision rate causing losses is weak, even at very high densities. Since the mass of

hydrogen is small, the critical temperature is high. The simplicity of its electronic structure allows precise calculations of the interaction potentials based on fundamental principles, which can thus be tested experimentally.

Twenty years after having started the project of condensing dilute hydrogen gases, Greytak and Kleppner [291] crossed the phase transition at a temperature of 50 μK with an atomic density of $5 \times 10^{15}\,\mathrm{cm}^{-3}$. The number of condensed atoms was 10^9, which corresponds to a condensed fraction below 10% [1]. The condensed cloud had a needle-like shape of 15 μm diameter and 5 mm length. It was detected by an *in situ* measurement technique of the atomic velocity distribution.

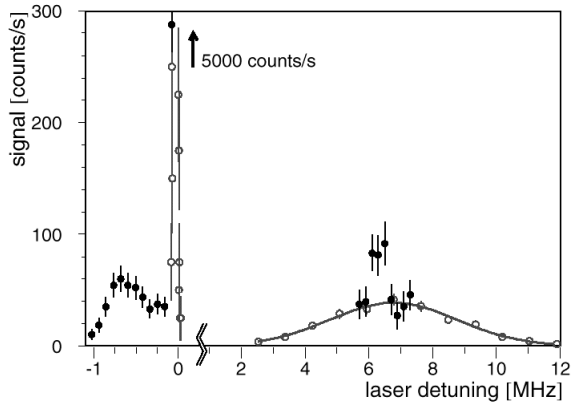

Figure 27.1: Spectrum of condensed hydrogen.

27.1.3 Recognizing Bose-Einstein condensates

'How to recognize the presence of a condensate, what are its signatures?' We have already seen in Sec. 7.3.3 that, trapped inside a confinement potential, an ultracold ideal Bose-gas has a modified density distribution when Bose-Einstein statistics come into play. Below the critical temperature the density distribution is well described by a superposition of a condensed cloud concentrated in the trap's ground state and a thermal cloud distributed over several vibrationally excited states. We thus expect distinct distribution functions for both clouds, and the same is true for the momentum distribution. The splitting of the distribution functions in two fractions occurs abruptly during the phase transition to quantum degeneracy. In a real gas, however, the interatomic collisions have a drastic influence on the distribution functions and the behavior of the gas at the phase transition, and we are obliged to develop a more general theory in order to quantitatively understand the thermodynamic properties (temperature, critical point, heat capacity, ...) through the measured static quantities (density, number of atoms, condensed fraction, ...).

'What observables can be measured in the laboratory?' In fact, with few exceptions, the only accessible quantity is the *spatial density distribution* of the atomic cloud

[1] When the condensed fraction and the density are too high, losses induced by dipolar spin-flip processes predominate over the gain due to evaporative cooling of the thermal cloud [394].

$n(\mathbf{r})$ measured after a time of ballistic expansion. Information on non-trivial properties of the condensate, for example, its dynamic behavior (excitations, superfluidity, turbulence, ...) or its coherent features (phase, correlations, ...), can only be gathered through an observation of the condensate's response to applied perturbations. Solve the Excs. 27.1.5.1 and 27.1.5.2.

27.1.4 Photon condensation

An interesting question is that of the possibility of *photon condensation* and its relationship to the laser. The relationship is not that obvious because, on one hand atomic condensates are produced by evaporating a ensemble in constant thermal equilibrium, while on the other hand the photonic laser requires inversion, which is a highly non-equilibrium situation. And under the constraint of having to reduce its energy, a photon gas trapped in an optical cavity has the simpler alternative to let photons escape into the void by annihilating them on the cavity walls, as it happens for black-body radiation. Since the number of photons in a cavity is not conserved, the chemical potential disappears, $\mu = 0$. The density of states can be written,

$$u(\nu) = \frac{8\pi V}{c^3} \frac{\epsilon^2 d\epsilon}{h^2} \ . \tag{27.1}$$

It is the same as in the Debye model. Planck's formula now follows from,

$$u(\epsilon)d\epsilon = \frac{1}{V}\epsilon f_{\mathrm{BE}}(\epsilon)\rho(\epsilon)d\epsilon \ , \tag{27.2}$$

where f_{BE} is the Bose-Einstein distribution. Hence, the treatment of the photons as indistinguishable particles following the Bose-Einstein distribution is equivalent to assuming a Boltzmann distribution for waves with quantized energies.

Nevertheless, one can imagine a photonic gas in thermal equilibrium with an atomic gas through Compton scattering [459]. In fact, photon condensation was observed experimentally [470]. Also, there are theories about superfluid photon gases [148] [2].

[2] Bose-Einstein condensation occurs in thermal equilibrium when entropy is maximized by putting a macroscopic population of atoms into the ground state of the system. It might appear counter-intuitive that an apparently highly ordered state as the Bose condensate maximizes entropy. However, only the particles in excited states contribute to the entropy. Their contribution is maximized at a given total energy by forming a Bose condensate in the ground state and distributing the remaining atoms among higher energy states. A macroscopic population of atoms in the ground state of the system is achieved simply by lowering the temperature of the sample. This is in contrast to the optical laser where a non-equilibrium process is necessary to place a macroscopic population of photons in a single mode of the electromagnetic field. This is due to the fact that, unlike photons, the number of atoms is conserved. For bosonic atoms, the lowest entropy state below a certain temperature includes a macroscopic population of the ground state. In contrast, when one cools down a blackbody cavity, the cavity empties. Photons do not Bose condense into the ground state of the cavity, but are absorbed by the walls. The absorbed energy leads to a larger entropy than forming a Bose condensate. The laser phenomenon requires inversion of the active medium characterized by a 'negative' temperature. In that sense, 'lasing' of atoms is a simpler phenomenon than lasing of light –all you need to do is cool a gas! However, if a photon gas would thermalize while the number of photons is conserved, it would be described by a Bose-Einstein distribution with non-zero chemical potential and could form a Bose condensate. Thermalization with number conservation is possible, for example, by Compton scattering with a thermal electron gas [459].

27.1.5 Exercises

27.1.5.1 Ex: Condensation of ions

Discuss the possibility of creating Bose-Einstein condensates from ionic clouds.

27.1.5.2 Ex: Isobaric impurities

Discuss the possibility of creating Bose-Einstein condensates with isobaric species.

27.2 Quantum theory

As detailed above, interatomic interactions strongly influence the properties of Bose-Einstein condensates, even their density and momentum distributions. For a correct interpretation of the experimental measurements a theoretical many-body treatment taking care of these interactions is compulsory. This is done through a description of the atomic distribution as a *scalar field of matter* called *second quantization*, where the atoms are treated as delocalized Broglie waves. For an introduction to this formalism see [850].

27.2.1 Description of the atom as a scalar field

In position space a state with n particles can be described in a canonically quantized way by a *field operator*,

$$\hat{\Psi}(\mathbf{r}_1, ..., \mathbf{r}_n, t) = \hat{\psi}^\dagger(\mathbf{r}_1, t) \cdot ... \cdot \hat{\psi}^\dagger(\mathbf{r}_n, t)\hat{\Psi}_0 \quad , \quad \hat{\psi}(\mathbf{r})\hat{\Psi}_0 = 0 \ , \tag{27.3}$$

where $\hat{\Psi}_0$ is the vacuum state, i.e. the state without atoms. The field operators $\hat{\psi}(\mathbf{r}, t)$ and $\hat{\psi}^\dagger(\mathbf{r}, t)$ annihilate, respectively create, an atom at position $\mathbf{r}$ and time t. This state represents a *bosonic Fock state* and can be generated from the empty state by a sequence of individual particle creation operators. Applying the notions and rules developed for the harmonic oscillator in Sec. 2.6.1, we can define a coherent state of bosonic matter as,

$$|\hat{\Phi}(t)\rangle = \sum_{n=0}^{\infty} \frac{N^{n/2}}{\sqrt{n!}} |\hat{\Psi}(\mathbf{r}_1, ..., \mathbf{r}_n, t)\rangle \ . \tag{27.4}$$

The field operators for particle creation and annihilation are normalized to the number of atoms and satisfy the following commutation rules,

$$
\begin{array}{lrcl}
\text{(i)} & [\hat{\psi}(\mathbf{r}), \hat{\psi}(\mathbf{r}')]_- & = & 0 \\
\text{(ii)} & [\hat{\psi}(\mathbf{r}), \hat{\psi}^\dagger(\mathbf{r}')]_- & = & \delta^3(\mathbf{r}-\mathbf{r}') \quad , \quad \hat{\psi}^\dagger(\mathbf{r}) = \int d^3r' \hat{\psi}^\dagger(\mathbf{r}')\delta^3(\mathbf{r}-\mathbf{r}') \\
\text{(iii)} & [\hat{\psi}(\mathbf{r}), \hat{N}]_- & = & \hat{\psi}(\mathbf{r}) \quad , \quad \hat{N} = \int d^3r' \hat{\psi}^\dagger(\mathbf{r}')\hat{\psi}(\mathbf{r}') \\
\text{(iv)} & [\hat{\psi}(\mathbf{r}), \hat{\mathbf{p}}]_- & = & \frac{\hbar}{\imath}\nabla\hat{\psi}(\mathbf{r}) \quad , \quad \hat{\mathbf{p}} = \int d^3r' \hat{\psi}^\dagger(\mathbf{r}')(\tfrac{\hbar}{\imath}\nabla')\hat{\psi}(\mathbf{r}') \\
\text{(v)} & [\hat{\psi}(\mathbf{r}), \hat{H}]_- & = & \imath\hbar\frac{\partial}{\partial t}\hat{\psi}(\mathbf{r})
\end{array}
\tag{27.5}
$$

The last equation is the Heisenberg equation of motion and describes the dynamics of a system whose *many-body Hamiltonian* $\hat{H} \equiv \hat{H}_{\rm cm} + \hat{H}_{\rm self}$ for N bosons interacting within an external potential $V_{\rm trp}$ in second quantization is defined by [3],

$$
\boxed{
\begin{aligned}
\hat{H}_{\rm cm} &\equiv \int d^3r \hat{\psi}^\dagger(\mathbf{r}) \left(-\frac{\hbar^2}{2m}\nabla^2 + V_{\rm trp}(\mathbf{r},t) \right) \hat{\psi}(\mathbf{r}) \\
\hat{H}_{\rm self} &\equiv \int d^3r \int d^3r' \hat{\psi}^\dagger(\mathbf{r})\hat{\psi}^\dagger(\mathbf{r}')V_{\rm coll}(\mathbf{r}-\mathbf{r}')\hat{\psi}(\mathbf{r}')\hat{\psi}(\mathbf{r})
\end{aligned}
}
\quad . \tag{27.6}
$$

The equations (27.5) and (27.6) represent the foundation of the theory of ultracold bosonic gases. However, to solve the equations, we will need to apply some simplifications, which will be discussed in the following sections. For example, we will generally assume that the temperature of the sample is $T = 0$, and that all atoms are condensed. Also, in a first time, we will neglect quantum fluctuations, replacing field operators with complex numbers. And finally, we will need to handle the nonlinear term appearing in $\hat{H}_{\rm self}$ and which signs responsible for collisions between atoms.

27.2.2 Quantum scattering at low temperatures

To simplify the term $\hat{H}_{\rm self}$, we have to go back to Secs. 13.2.5 (and following) and study the phenomenon of the elastic collisions in the ultracold regime. For simplicity, we consider two particles without internal degrees of freedom with masses m_1 and m_2 approaching each other along the z-axis [163, 858]. Neglecting spin-spin and spin-orbit interactions, the Schrödinger equation in the inertial center-of-mass system is given by (13.115),

$$
\left(-\frac{\hbar^2}{2m^*}\nabla^2 + V_{\rm coll}(r) \right) \hat{\psi}(\mathbf{r}) = E\hat{\psi}(\mathbf{r}) \ , \tag{27.7}
$$

where $\mathbf{r} = \mathbf{r}_1 - \mathbf{r}_2$ is the momentary interatomic separation, $r = |\mathbf{r}|$, and $m_r \equiv m_1 m_2/(m_1+m_2)$ is the reduced mass of atomic collision partners. We assume that the interatomic potential, $V_{\rm coll}(r)$, is spherically symmetrical. In the asymptotic limit of large separations [4], and in the Born-approximation (13.135), the solution of Eq. (27.7)

[3] Sometimes the Landau potential is used for canonical and macrocanonic ensembles. It defined by, $\hat{\Omega} = \hat{H}_{\rm cm} + \hat{H}_{\rm self} - \int d^3r \hat{\psi}^\dagger(\mathbf{r})\mu\hat{\psi}(\mathbf{r})$, where μ is the chemical potential.

[4] This means, $r \gg r_0$, where r_0 is the range of potential $V(r)$.

can be seen as the sum of an incident plane wave and a scattered spherical wave modulated with a certain amplitude $f(\theta)$,

$$\psi(\mathbf{r}) = e^{\imath kz} + f(\theta)\frac{e^{\imath kr}}{r} \ , \tag{27.8}$$

where $k = \sqrt{2m_r E/\hbar^2}$ is the amplitude of the wavevector of the incident and scattered waves and θ the angle between r and z. The function $f(\theta)$ is called *scattering amplitude* and determines the scattering cross-section for s-wave collision through the expression [see (13.123)],

$$\frac{d\sigma}{d\Omega} = |f(\theta)|^2 \ . \tag{27.9}$$

where $d\Omega = \sin\theta d\theta d\phi$ is an element of the solid angle. To calculate the scattering amplitude, we expand the wavefunction (27.8) into spherical partial waves of orders ℓ of the angular momentum, as done in (13.136),

$$f_k(\theta) = \frac{1}{k}\sum_{\ell=0}^{\infty}(2\ell+1)P_\ell(\cos\theta)e^{\imath\delta_\ell}\sin\delta_\ell \ . \tag{27.10}$$

The collision cross section has been shown in (13.148) to be given by,

$$\sigma = \frac{4\pi}{k^2}\sum_{\ell=0}^{\infty}(2\ell+1)\sin^2\delta_\ell \ . \tag{27.11}$$

For a potential with finite range, that is, a potential falling faster than r^{-3} with the distance (interatomic potentials usually fall as r^{-6} or r^{-7}), the phase shift satisfies,

$$\delta_\ell \propto k^{2\ell+1} \tag{27.12}$$

for small k. In ultra-cold gases, the collision energy is very low and $k \to 0$. Thus the scattering will be dominated by terms with $\ell = 0$. This is the so-called limit of *s-wave scattering*. In this limit the Eqs. (27.10) can be approximated as,

$$f_k(\theta) = \frac{1}{k}e^{\imath\delta_0}\sin\delta_0 \ . \tag{27.13}$$

27.2.3 Scattering length

For $\ell = 0$, taking the limit $k \to 0$, we define the *scattering length* a_s via,

$$\frac{\mathfrak{Im}\, f_k(\theta)}{\mathfrak{Re}\, f_k(\theta)} = \tan\delta_0 \equiv -\tan ka_s \ . \tag{27.14}$$

Therefore, the scattering length defined by (27.14) and the cross section (27.11) are given at very low temperatures at the asymptotic boundary by,

$$\boxed{a_s = -\frac{\delta_0}{k} \qquad \text{and} \qquad \sigma = 4\pi a_s^2} \ . \tag{27.15}$$

The scattering process can be interpreted as follows: During a collision, the system's wavefunction undergoes a phase shift, δ_0, which may be positive or negative, depending on the sign of a_s. If $a_s < 0$, the phase is 'delayed' by the collision. This corresponds to an attractive interaction. In contrast, if $a_s > 0$, the phase is 'advanced' and the interaction is repulsive, as illustrated in Fig. 13.16. Of course, the intensity of the interaction is proportional to the value of $|a_s|$. The expression for σ in Eq. (27.15) indicates, that the atoms behave like *hard spheres* with radius $|a_s|$. The specific value of a_s will depend on the interaction potential, however, the details of the potential are unimportant, as all information about the collision is already contained in a_s. Consequently, in the low-energy limit, we can assume that the collision is mediated by an effective potential $V_{\text{eff}}(\mathbf{r})$, which has the particularity,

$$\int V_{\text{coll}}(\mathbf{r}) d^3r = \frac{4\pi\hbar^2}{m} a_s \equiv g \ . \tag{27.16}$$

This has been shown in Sec. 13.1.2. Consequently, the effective interaction between two particles at positions $\mathbf{r}$ and $\mathbf{r}'$ can be considered as contact interaction given by [5],

$$V_{\text{coll}}(\mathbf{r}, \mathbf{r}') = \frac{g}{2} \delta(\mathbf{r} - \mathbf{r}') \ . \tag{27.17}$$

The factor $\frac{1}{2}$ comes from the reduced mass introduced when converting the collision potential $V_{\text{coll}}(\mathbf{r})$ specified in center-of-mass coordinates back into an interaction energy $V_{\text{coll}}(\mathbf{r}, \mathbf{r}')$ needed in lab coordinates.

The interatomic interaction potential decides on the value of the scattering length a_s: A repulsive potential corresponds to a positive a_s. For a purely attractive potential that does not support bound states a_s is negative, and for an attractive potential that supports bound states a_s may be positive or negative depending on the proximity of the last bound vibrational state of the interaction potential below the dissociation limit.

27.2.4 The mean field approximation

The *mean-field theory* (MFT) or *local density approximation* (LDA) is based on the assumption of *hard sphere collisions* between atoms (as described by the potential (27.17)) propagating through a locally homogeneous mean-field potential, $\frac{g}{2}|\hat{\psi}(\mathbf{r})|^2$. The procedure is also called *regularization of the interaction*.

Thus, the mean-field energy of a condensate is proportional to the density of the gas n and to a single atomic constant, which is the scattering length a_s. Its presence in the Gross-Pitaevskii equation emphasizes its impact on shape, dynamic stability and many other properties of the condensate. For example, the mean-field interaction contributes to the broadening of a condensed wavepacket, and consequently contracts its momentum distribution in comparison with an ideal gas. Homogeneous condensates with a negative scattering length are unstable, because the attempt of such a

[5] The *Hartree-Fock-Bogolubov method* (HFB) for the mean-field theory disregards corrections of higher orders, for example, due to the renormalization of the scattering length. It also neglects quantum depletion due to the correlation effects of the order of $N_{\text{out}}/N = \frac{5}{8}\sqrt{\pi}\sqrt{a^3 n_0}$. The theory mean-field supposes the validity of the *Born approximation*, that is, two-body correlations are neglected, $\hat{\psi}(\mathbf{r}') \approx \hat{\psi}(\mathbf{r})$ and $\int d^3R V_{\text{coll}}(\mathbf{R}) = \frac{g}{2}$.

condensate to lower its self-energy by increasing its density also increases the rate of inelastic three-body collisions until the condensate collapses.

27.2.5 Gross-Pitaevskii equation

The Heisenberg equation [last line of (27.5)] is equivalent to the *variational principle*, as stated by the Ehrenfest theorem,

$$\imath\hbar\frac{d\hat{\psi}}{dt} = \frac{\delta\mathcal{H}}{\delta\hat{\psi}^\dagger} \ . \tag{27.18}$$

This facilitates the derivation of the equation of motion for the atomic field. With the Hamiltonian (27.6) in the mean-field approximation,

$$\mathcal{H}_{\rm atom} \equiv \mathcal{H}_{\rm cm} + \mathcal{H}_{\rm mf} \qquad \text{with} \qquad \mathcal{H}_{\rm mf} \equiv \int d^3r\hat{\psi}^\dagger(\mathbf{r},t)\frac{g}{2}|\hat{\psi}(\mathbf{r},t)|^2\hat{\psi}(\mathbf{r},t) \ , \tag{27.19}$$

we find the *non-linear Schrödinger equation*,

$$\left[-\frac{\hbar^2}{2m}\nabla^2 + V_{\rm trp}(\mathbf{r},t) + g|\hat{\psi}(\mathbf{r},t)|^2\right]\hat{\psi}(\mathbf{r},t) = \imath\hbar\frac{\partial}{\partial t}\hat{\psi}(\mathbf{r},t) \ . \tag{27.20}$$

Remember that, despite their symbol $\hat{\psi}$, which usually is associated to wavefunctions, and the fact that they satisfy a non-linear Schrödinger equation the field operators are represented by matrices acting of many-body states. That is, Eq. (27.20) also represents a Heisenberg equation for the field operators.

A common approximation is the *Bogolubov prescription*, where the field operators describing the condensate and its fluctuations are decomposed into a complex function, $\psi_0(\mathbf{r}) \equiv \langle\hat{\psi}(\mathbf{r})\rangle$ called *condensed wavefunction*, which can be chosen as the *order parameter* of the system, and a small perturbation, $\delta\hat{\psi}(\mathbf{r}) \equiv \hat{\psi}(\mathbf{r}) - \psi_0(\mathbf{r})$ describing *thermal excitations*. At zero temperature, we can neglect the excitations [61], and our system is completely described by a single wavefunction, $\psi_0(\mathbf{r},t)$, obeying the famous *Gross-Pitaevskii equation* (*GPE*),

$$\left[\frac{-\hbar^2}{2m}\nabla^2 + V_{\rm trp}(\mathbf{r},t) + g|\psi_0(\mathbf{r},t)|^2\right]\psi_0(\mathbf{r},t) = \imath\hbar\frac{\partial}{\partial t}\psi_0(\mathbf{r},t) \ . \tag{27.21}$$

27.2.5.1 Spontaneous breaking of gauge symmetry

The description of a condensate by a single macroscopic wavefunction means that we attribute a well-defined phase to it. However, the GPE does not allow us to predict, which phase between 0 and 2π this will be, and we have to assume, that the BEC chooses its phase spontaneously when it undergoes the phase transition to quantum degeneracy. This principle is called *spontaneous breaking of gauge symmetry* [6]. In Exc. 27.2.6.2 we study the relation between the fact of having exactly N atoms in a condensate and a well-defined phase φ, knowing that these two quantities are conjugate variables having to satisfy a Heisenberg uncertainty relation.

[6] An alternative way of modeling the development of a BEC phase is based on measurement theory. See also (14.86) for an analogy to the correct state of a laser.

27.2.6 Exercises

27.2.6.1 Ex: Derivation of the non-linear Schrödinger equation

Derive the non-linear Schrödinger equation using (a) the commutator relation (27.5)(v) and (b) the variational expression (27.18).

27.2.6.2 Ex: Spontaneous breaking of gauge symmetry

One of the primary characteristics of a condensate is its phase coherence. Now, consider a condensate with exactly N atoms. The exact knowledge of the atom number implies a totally uncertain phase of the condensate, according to Heisenberg's uncertainty relation. Explain this contradiction!

27.3 Approximate solutions of the Gross-Pitaevskii equation

27.3.1 Stationary GPE

In cases where the external potential is stationary, $V_{\rm trp}(\mathbf{r},t) = V_{\rm trp}(\mathbf{r})$, the temporal dependency of the GPE can be removed by the ansatz,

$$\psi_0(\mathbf{r},t) = \psi_0(\mathbf{r}) e^{-\imath\mu t/\hbar} \ . \tag{27.22}$$

This gives the stationary Gross-Pitaevskii equation,

$$\boxed{\left[\frac{-\hbar^2}{2m}\nabla^2 + V_{\rm trp}(\mathbf{r}) + g|\psi_0(\mathbf{r})|^2\right]\psi_0(\mathbf{r}) = \mu\psi_0(\mathbf{r})} \ , \tag{27.23}$$

where μ is called the *chemical potential*. Solve Exc. 27.3.4.1.

27.3.2 Trapped condensates and the Thomas-Fermi limit

27.3.2.1 Free particles

The wavefunction of free particles, $V(\mathbf{r}) = 0$, can be described by a plane wave,

$$\psi(\mathbf{r}) = \sqrt{n} e^{\imath \mathbf{k}\cdot\mathbf{r}} \ , \tag{27.24}$$

also called the Hartree solution. Inserted it into the equation of Gross-Pitaevskii equation,

$$E(k) = \frac{\hbar^2 k^2}{2m} + gn \ , \tag{27.25}$$

we observe a *gap* in the energy spectrum due to the interaction.

27.3.2.2 Ideal gas in a harmonic potential

Most experiments apply non-isotropic (often cylindrical) potentials, which are additionally distorted by the mean-field. Hence, the non-linear term of the GPE is important, and the spatial coordinates can not be separated. However, assuming an ideal gas and a harmonic potential, the dimensions could be separated, as demonstrated in Sec. 2.5.5, even when the potential is not isotropic. It is then sufficient to consider one-dimensional problems with $g = 0$,

$$\left[-\frac{\hbar^2}{2m}\frac{\partial^2}{\partial x^2} + \frac{m}{2}\omega_x^2\hat{x}^2\right]\psi_n = \mu_n\psi_n \ . \tag{27.26}$$

In this limit, the GPE is nothing more than the usual Schrödinger equation, which has the well-known spectrum (2.119) and the solutions (2.118).

27.3.2.3 Ideal gas in an isotropic potential

In the case of an ideal gas trapped in a spherically symmetric potential, as shown in (3.34), the Schrödinger equation can be reduced to its radial component,

$$\left[\frac{\partial^2}{\partial r^2} + \frac{2}{r}\frac{\partial}{\partial r} - \frac{l(l+1)}{r^2} + V_{\rm trp}(r)\right] f_{nlm}(r) = \mu_{nl} f_{nlm}(r) \ , \tag{27.27}$$

with the solution (3.18),

$$\psi_n(r,\vartheta,\varphi) = \sum_{l,m} f_{nlm}(r) Y_{lm}(\vartheta,\varphi) \tag{27.28}$$

The differential equation (27.27) can be solved numerically by Runge-Kutta type methods,

$$\begin{pmatrix} f'' \\ f' \end{pmatrix} = \begin{pmatrix} \frac{2}{r} & \mu + \frac{l(l+1)}{r^2} - V_{\rm trp}(r) \\ 1 & 0 \end{pmatrix} \begin{pmatrix} f' \\ f \end{pmatrix} \ . \tag{27.29}$$

27.3.2.4 Thomas-Fermi limit for strong interactions

In the case of strong interactions, the kinetic energy term can be neglected, at least in the center of the cloud, where the mean-field energy is stronger. For this case, called *Thomas-Fermi limit*, the GPE solution is easy,

$$|\psi_0(\mathbf{r})|^2 = \frac{\mu - V_{\rm trp}}{g} \ . \tag{27.30}$$

The chemical potential follows from the normalization condition,

$$N = \int_{n(\mathbf{r})>0} n(\mathbf{r}) d^3\mathbf{r} \ . \tag{27.31}$$

In the case of an cylindrical harmonic oscillator potential, $V_{\rm trp}(r,z) = \frac{m}{2}(\omega_r^2 r^2 + \omega_z^2 z^2)$, the chemical potential is,

$$\mu = \left(\frac{15Ng}{8\pi}\right)^{2/5} \left(\frac{m}{2}(\omega_r^2\omega_z)^{2/3}\right)^{3/5} \ . \tag{27.32}$$

The radial size σ of the condensate follows from $n(r_{\rm hw},0)=\frac{n(0,0)}{2}$,

$$r_{\rm hw}=\sqrt{\frac{\mu}{m\omega_r^2}}\ . \tag{27.33}$$

Solve the Excs. 27.3.4.2 and 27.3.4.3.

27.3.3 Variational treatment of the GPE

The many-body Hamiltonian (27.19) can be used as an *energy functional*,

$$E[\psi_0]\equiv\langle\mathcal{H}[\psi_0]\rangle=\int d^3r\left[\frac{\hbar^2}{2m}|\nabla\psi_0|^2+V_{\rm trp}(\mathbf{r})|\psi_0|^2+\frac{g}{2}|\psi_0|^4\right]\ , \tag{27.34}$$

from which, using the variational condition (27.18), we have derived the Gross-Pitaevskii equation (27.21). Hence, the wavefunction ψ_0 minimizes the functional [237]. By inserting an ansatz for the wavefunction with adjustable parameters, the functional provides conditions to optimize these parameters.

The *variational method* is useful e.g. for finding the ground state wavefunction of a condensate in an arbitrarily shaped trap or to perform a stability analysis of a condensate with attractive interatomic forces.

27.3.3.1 Finding the fundamental state of the GPE

This problem of finding the ground state wavefunction of a condensate consists in finding the ψ for which the energy $\mathcal{H}[\psi]$ goes to a minimum. In general, the functional has the form $\mathcal{H}[\psi]=\int f[\psi,\nabla\psi]d^3r$. The fastest way to the minimum is to reduce the energy by varying ψ in that direction, where the gradient $\delta\mathcal{H}/\delta\psi^*$ is largest, that is,

$$\begin{aligned}\mathcal{H}&\to\mathcal{H}[\psi+\tau\ \tfrac{\delta\mathcal{H}}{\delta\psi^*}]\\ \psi&\to\psi+\tau\tfrac{\delta\mathcal{H}}{\delta\psi^*}\ ,\end{aligned} \tag{27.35}$$

with the boundary condition, that the normalization must be preserved. Formally, this problem is similar to a time-dependent Gross-Pitaevskii equation, but with *imaginary time*. Physically, the procedure, called the *steepest descent method*, can be interpreted as applying a heavily 'overdamped' friction force,

$$\frac{\partial\psi}{\partial\tau}=\frac{\delta\mathcal{H}}{\delta\psi^*}\ . \tag{27.36}$$

In practice, the procedure is as follows: we start with a trial wavefunction, for example, the exact solution of the interaction-free case. This function is now propagated in imaginary time, using the complete Hamiltonian including the non-linear term, and then renormalized:

$$\hbar\frac{\partial}{\partial t}\psi(\mathbf{r},t)=\mathcal{H}(\mathbf{r})\psi(\mathbf{r},t)\ . \tag{27.37}$$

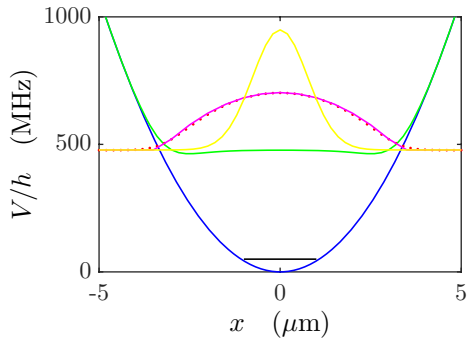

Figure 27.2: (code) Calculation of the BEC wavefunction by the steepest descent method (red dots). Also shown are the ideal gas approximation (yellow line) and the Thomas-Fermi approximation (magenta line), as well as the ground state energy (black line) and the chemical potential (green line).

Substituting the imaginary unit i in the time-dependent Gross-Pitaevskii equation (27.21) by -1, we obtain,

$$\psi(\mathbf{r}, t + dt) = [1 - \hbar^{-1}\mathcal{H}(\mathbf{r})dt]\psi(\mathbf{r}, t) \tag{27.38}$$
$$\psi'(\mathbf{r}, t) \equiv \frac{\psi(\mathbf{r}, t + dt)}{|\psi(\mathbf{r}, t + dt)|} \to \psi(\mathbf{r}, t) \ .$$

This procedure is repeated until the function converges. Since this method is derived from a variational principle, it only serves to find the ground state of the trapping potential. It can not be used for excited states (with the exception of vortex states, where in cylindrical coordinates the Hamiltonian differs by an additional centrifugal term).

27.3.3.2 Collapse and stabilization of condensates with attractive interactions

Attractive interactions destabilize a Bose-Einstein condensate. Since the interaction energy, $4\pi\hbar^2 a_s n/m$, of a condensate with negative scattering length decreased with increasing density n, the condensate attempts to lower its interaction energy by increasing its density until it succumbs to inelastic two-body spin-changing collisions of to three-body collisions leading to the formation of molecules [799]. Strictly speaking, this only holds true for homogeneous condensates. In the presence of a trapping potential, however, the zero-point energy exerts a kinetic pressure, which counteracts the *condensate collapse* to a certain extent, such that small condensates are stabilized. This can be verified by inserting a Gaussian wavefunction $\psi_0 \propto e^{-r^2/2\bar{r}^2}$ into the energy functional (27.34). Varying the radius $\bar{r}$ of the condensate, we find a local minimum where the condensate is stable. Calculations for spherical traps predict [710, 192],

$$N_{\min} \simeq 0.575 \frac{a_{\rm trp}}{|a_s|} \ , \tag{27.39}$$

where $a_{\rm trp} = \sqrt{\hbar/m\omega_{\rm trp}}$.

The atomic species ^{7}Li has a slightly negative scattering length $a_s = -27.3a_{\rm B}$. As can be seen in Fig. 27.3, small condensates can survive in a confining trap, since the energy functional has a local minimum [114, 112, 711]. Solve Exc. 27.3.4.4.

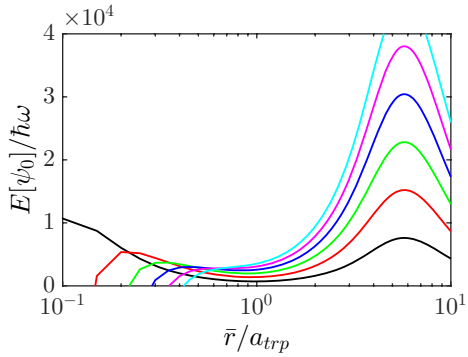

Figure 27.3: (code) Energy of a ^{7}Li condensate in a harmonic isotropic potential with $\omega_{\rm trp} = (2\pi)$ 50 Hz with $N = 500$ atoms (linha inferior) up to $N = 3000$ (linha superior) when the radius $\bar{r}$ of the condensate is varied.

27.3.4 Exercises

27.3.4.1 Ex: GPE in dimensionless units

Use the following abbreviations to rewrite the Gross-Pitaevskii equation and its solution for a harmonic isotropic potential in dimensionless units,

$$\begin{array}{llll} V_1 & \equiv V_{\rm trp}/\hbar\omega_{\rm trp} & V_{\rm trp} & = \frac{m}{2}\omega_{\rm trp}^2 r^2 \\ \mathbf{r}_1 & \equiv \mathbf{r}/a_{\rm trp} & a_{\rm trp} & = \sqrt{\hbar/m\omega_{\rm trp}} \\ \mu_1 & \equiv \mu/\hbar\omega_{\rm trp} & T_1 & \equiv k_{\rm B}T/\hbar\omega_{\rm trp} \\ \psi_1 & \equiv \psi/a_{\rm trp}^{3/2} & p_1 & \equiv a_{\rm trp}p/\hbar \\ g & \equiv 4\pi\hbar^2 a/m & g_1 & \equiv 8\pi N_0 a/a_{\rm trp} \end{array}$$

27.3.4.2 Ex: Interacting gas in an isotropic potential

Consider the potential $V(\mathbf{r}) = V(r)$, such that the wavefunction will have radial symmetry, $\psi(\mathbf{r}) = \frac{\phi(r)}{r}$. Rewrite the Gross-Pitaevskii equation for the function ϕ [401].

27.3.4.3 Ex: Interacting gas in a cylindrical potential

Consider the potential $V(\mathbf{r}) = V(\rho, z)$, such that the wavefunction will have rotational symmetry, $\psi(\rho, z, \varphi) = \frac{\phi(\rho,z)}{\rho}$. Rewrite the Gross-Pitaevskii equation for the function ϕ [401].

27.3.4.4 Ex: Collapse of condensate with attractive interactions

A Bose-Einstein condensate of ^{7}Li may become unstable due to attractive interatomic forces, the scattering length being $a_s = -27.3a_\mathrm{B}$. Consider the radial Gross-Pitaevskii Hamiltonian with an external harmonic potential with the oscillation frequency $\omega_\mathrm{trp}/(2\pi) = 50$ Hz. Using the variational method, determine the maximum number of atoms allowing for a stable condensate. (Note that the derived minimization condition must be evaluated numerically.)

27.4 Elementary excitations

The dynamics of Bose-Einstein condensates is usually studied by observing the change of their shape in response to temporal variations in the trapping potential. The simplest variation surely consists in suddenly removing the trapping potential altogether. Consequently, the first experiment performed with a BEC was the study of its ballistic expansion [20, 268, 142] (see Sec. 27.7.1).

On the other hand, the temporal variation of the potential can also be a small oscillatory or pulsed perturbation, for example, a small modification of the amplitude of the trapping field, a displacement or a local anisotropy induced by the dipole force of a laser beam tuned far away from resonance. It is even conceivable to manipulate the self-energy of the condensate or to irradiate electromagnetic waves, which couples internal atomic excitation levels or states of the atomic motion [61, 21, 783, 438, 573, 761, 256, 800, 439, 632, 782, 313]. The response of the condensate to such small perturbations can be understood by a linearized model of the Gross-Pitaevskii equation, which we will present in the following sections.

27.4.1 Bogolubov spectrum of excitations

To analyze the spectrum of a condensate's response to small perturbations, let us follow Bogolubov's treatment of the time-dependent Gross-Pitaevskii equation [780]. We start by substituting Eq. (27.20) [255],

$$\hat{\psi}(\mathbf{r},t) \longrightarrow \hat{\psi}(\mathbf{r},t)e^{-\imath\mu t/\hbar} \,, \tag{27.40}$$

which gives us,

$$\left[-\frac{\hbar^2}{2m}\nabla^2 + V_\mathrm{trp}(\mathbf{r}) + g|\hat{\psi}(\mathbf{r},t)|^2\right]\hat{\psi}(\mathbf{r},t) = \left[\mu + \imath\hbar\frac{\partial}{\partial t}\right]\hat{\psi}(\mathbf{r},t) \,. \tag{27.41}$$

The *Bogolubov prescription* now consists in approximating the field operators of the condensate by a sum of the equilibrium wavefunction, which is interpreted as a complex number, and a small perturbation, which conserves its operator character,

$$\hat{\psi}(\mathbf{r},t) \simeq \psi_0(\mathbf{r}) + \delta\hat{\psi}(\mathbf{r},t) \,. \tag{27.42}$$

This treatment assumes that most atoms are condensed, $N - N_0 \ll N_0$, and only a few thermal atoms are left out.

Applying the *Bogolubov transform*,

$$\boxed{\delta\hat{\psi}(\mathbf{r},t) \equiv \sum_{\mathbf{k}} u_{\mathbf{k}}(\mathbf{r})\hat{a}_{\mathbf{k}}(t) + v^*_{\mathbf{k}}(\mathbf{r})\hat{a}_{\mathbf{k}}(t)^\dagger} \ , \tag{27.43}$$

the perturbation is expressed as a superposition of amplitudes for annihilation and creation of non-interacting *quasi-particles*. By inserting this ansatz into the Gross-Pitaevskii equation, we obtain a linear system of equations called *Bogolubov-de Gennes equations*.

27.4.1.1 Semi-classical approximation

To simplify the equations, let us neglect the operator character of the quasi-particle by doing the substitutions,

$$\hat{a}_{\mathbf{k}} \to e^{-\imath\omega_{\mathbf{k}}t} \qquad \text{and} \qquad \hat{a}^\dagger_{\mathbf{k}} \to e^{\imath\omega_{\mathbf{k}}t} \ . \tag{27.44}$$

That is, we insert the ansatz (27.42) with,

$$\delta\hat{\psi}(\mathbf{r},t) \equiv u_{\mathbf{k}}(\mathbf{r})e^{-\imath\omega_{\mathbf{k}}t} + v^*_{\mathbf{k}}(\mathbf{r})e^{\imath\omega_{\mathbf{k}}t} \ , \tag{27.45}$$

into the Gross-Pitaevskii equation (27.41), we look for the lowest order,

$$\left(-\frac{\hbar^2}{2m}\nabla^2 + V_{\rm trp} + g|\psi_0|^2\right)\psi_0 = \mu\psi_0 \ , \tag{27.46}$$

and we collect the terms of first order in $e^{\pm\imath\omega_{\mathbf{k}}t}$, neglecting terms of order $u^2_{\mathbf{k}}, v^{*2}_{\mathbf{k}}$ or higher,

$$\begin{aligned} -\frac{\hbar^2}{2m}\nabla^2 u_{\mathbf{k}} + V_{\rm trp}u_{\mathbf{k}} + 2g\psi_0^2 u_{\mathbf{k}} - g\psi_0^2 v^*_{\mathbf{k}} &= \mu u_{\mathbf{k}} + \hbar\omega_{\mathbf{k}}u_{\mathbf{k}} \\ \frac{\hbar^2}{2m}\nabla^2 v_{\mathbf{k}} - V_{\rm trp}v_{\mathbf{k}} - 2g\psi_0^2 v_{\mathbf{k}} + g\psi_0^2 u^*_{\mathbf{k}} &= -\mu v_{\mathbf{k}} + \hbar\omega_{\mathbf{k}}v_{\mathbf{k}} \ . \end{aligned} \tag{27.47}$$

Introducing the abbreviations $n = \psi_0^2$ and,

$$\mathcal{L} \equiv \frac{-\hbar^2\nabla^2}{2m} + V_{\rm trp} + 2gn - \mu \ , \tag{27.48}$$

we can write

$$\begin{pmatrix} \mathcal{L} - \hbar\omega_{\mathbf{k}} & gn \\ gn & \mathcal{L} + \hbar\omega_{\mathbf{k}} \end{pmatrix}\begin{pmatrix} u_{\mathbf{k}} \\ v_{\mathbf{k}} \end{pmatrix} = \left[\begin{pmatrix} \mathcal{L} & gn \\ gn & \mathcal{L} \end{pmatrix} - \hbar\omega_{\mathbf{k}}\hat{\sigma}_z\right]\phi_k = 0 \ , \tag{27.49}$$

with $\hat{\sigma}_z$ being the third Pauli matrix. The solution of Eq. (27.49) is given by the requirement, that the determinant of the matrix be 0,

$$\hbar\omega_{\mathbf{k}} = \sqrt{\mathcal{L}^2 - (gn)^2} \ . \tag{27.50}$$

The object

$$\phi_{\mathbf{k}} \equiv \begin{pmatrix} u_{\mathbf{k}}(\mathbf{r}) \\ v_{\mathbf{k}}(\mathbf{r}) \end{pmatrix} \tag{27.51}$$

is called a *normal mode* of the condensate. The normal modes (27.50) are orthonormal,

$$\langle \phi_{\mathbf{k}} | \phi_{\mathbf{k}'} \rangle = \int d\mathbf{r} \phi^\dagger_{\mathbf{k}}(\mathbf{r}) \hat{\sigma}_z \phi_{\mathbf{k}'}(\mathbf{r}) = \delta_{\mathbf{k},\mathbf{k}'} \ , \tag{27.52}$$

which means that *the modes do not interact*, that is, the quasi-particles *do not collide*.

For homogeneous systems or at the interior of a large condensate with strong interactions, we can assume that the potential is approximately constant, $V_{\rm trp} \to 0$, and kinetic energy negligible compared to the self-energy, and Eq. (27.41) shows us, $\mu \to gn$. Assuming plane waves,

$$u_{\mathbf{k}}(\mathbf{r}) \equiv u e^{\imath \mathbf{k}\cdot\mathbf{r}} \qquad \text{and} \qquad v_{\mathbf{k}}(\mathbf{r}) \equiv v e^{\imath \mathbf{k}\cdot\mathbf{r}} \ , \tag{27.53}$$

we obtain the *Bogolubov spectrum* of elementary excitations,

$$\boxed{\hbar\omega_{\mathbf{k}} = \sqrt{\frac{\hbar^2\mathbf{k}^2}{2m}\left(\frac{\hbar^2\mathbf{k}^2}{2m} + 2\mu\right)}} \ . \tag{27.54}$$

which corresponds to a *dispersion relation* for Bose-Einstein condensates. For an interacting gas, the collective modes are distortions of the condensate, caused by restoring forces originating in the finite compressibility of the gas.

27.4.1.2 Phonon- and particle-like excitations

The coefficients u and v describe the annihilation and u^* and v^* the creation of *quasi-particles* called *phonons* or *elementary excitations*. Two limits are interesting. In the low energy limit, $\frac{\hbar^2\mathbf{k}^2}{2m} \ll gn(\mathbf{r})$, we create *phonon-like excitations*. The Bogolubov spectrum becomes,

$$\hbar\omega^{\rm ph}_{\mathbf{k}} \simeq c_{\rm s}\hbar k \qquad \text{with} \qquad c_{\rm s} \equiv \sqrt{\frac{ng}{m}} \ . \tag{27.55}$$

Here is $c_{\rm s}$ the *sound velocity* inside the condensate. The fact that, comparing (27.54) and (27.55), we find,

$$\hbar\omega_{\mathbf{k}} > \hbar\omega^{\rm ph}_{\mathbf{k}} \tag{27.56}$$

for all $\mathbf{k}$ is the *Landau criterion* for the superfluidity of the condensate. It means that, for an object being dragged through the condensate with a velocity less than $c_{\rm s}$, it does not become energetically favorable to produce excitations, see Fig. 27.4. Therefore, the object will move without dissipation, which is an important characteristic of superfluids. Experiments demonstrated this manifestation of superfluidity by slowly stirring a strongly focused blue-detuned laser through a condensate. We will come back to this in Sec. 28.1.1.

In the high energy limit, $\frac{\hbar^2\mathbf{k}^2}{2m} \gg gn(\mathbf{r})$, we create *particle-like excitations*. The Bogolubov spectrum becomes,

$$\hbar\omega^{\rm pa}_{\mathbf{k}} = \frac{\hbar^2\mathbf{k}^2}{2m} \ . \tag{27.57}$$

In this limit, we recover the quadratic dispersion relation of free particles, as seen in Fig. 27.4.

Experimentally, the complete Bogolubov spectrum (27.54) can be measured by Bragg spectroscopy [791, 781] (see Sec. 29.2). Solve Exc. 27.4.3.1.

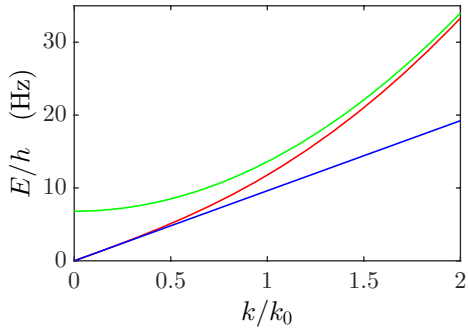

Figure 27.4: (code) Bogolubov spectrum (red), phonon limit (blue line) and particle limit (green line).

27.4.2 Excitation of normal modes

In the simplest case, we generate a perturbation as a weak additional potential in the Gross-Pitaevskii equation (27.41),

$$\left[\mathcal{L} - gn + f_+(\mathbf{r})e^{-\imath\omega_p t} + f_-(\mathbf{r})e^{\imath\omega_p t}\right]\hat{\psi} = \imath\hbar\frac{\partial}{\partial t}\hat{\psi}(\mathbf{r},t)\ . \tag{27.58}$$

After the Bogolubov transform (27.45) we now have,

$$\left[\begin{pmatrix}\mathcal{L} & gn\\ gn & \mathcal{L}\end{pmatrix} - \hbar\omega_{\mathbf{k}}\sigma_3\right]\begin{pmatrix}u(\mathbf{r})\\ v(\mathbf{r})\end{pmatrix} = -\begin{pmatrix}f_+(\mathbf{r})\psi_0(\mathbf{r})\\ f_-^*(\mathbf{r})\psi_0^*(\mathbf{r})\end{pmatrix}\ . \tag{27.59}$$

The solution of this equation is found by expanding the amplitudes $u(\mathbf{r})$ and $v(\mathbf{r})$ into normal modes,

$$\begin{pmatrix}u(\mathbf{r})\\ v(\mathbf{r})\end{pmatrix} = \sum_{\mathbf{k}} c_{\mathbf{k}}\phi_{\mathbf{k}}(\mathbf{r}) \qquad \text{and} \qquad \begin{pmatrix}f_+(\mathbf{r})\psi_0(\mathbf{r})\\ f_-^*(\mathbf{r})\psi_0^*(\mathbf{r})\end{pmatrix} = \sum_{\mathbf{k}} g_{\mathbf{k}}\phi_{\mathbf{k}}(\mathbf{r})\ , \tag{27.60}$$

where $g_{\mathbf{k}}$ is given by the overlap integral,

$$g_{\mathbf{k}} = \int d\mathbf{r}\phi_{\mathbf{k}}^\dagger(\mathbf{r})\sigma_3\begin{pmatrix}f_+(\mathbf{r})\psi_0(\mathbf{r})\\ f_-^*(\mathbf{r})\psi_0^*(\mathbf{r})\end{pmatrix}\ . \tag{27.61}$$

To calculate the response of the condensate to a given perturbation $f_\pm(\mathbf{r})$, we must first calculate the normal mode spectrum $\phi_{\mathbf{k}}(\mathbf{r})$ from the Bogolubov equation (27.49). After that, we can calculate the coefficients (27.61). Inserting the expansions into the Eq. (27.59), we obtain the response of the condensate,

$$\begin{pmatrix}u(\mathbf{r})\\ v(\mathbf{r})\end{pmatrix} = -\sum_{\mathbf{k}}\frac{g_{\mathbf{k}}/\hbar}{\omega_{\mathbf{k}} - \omega}\phi_{\mathbf{k}}\ . \tag{27.62}$$

The deviation, which is observed for resonant excitation, is due to the neglected losses and non-linear effects.

27.4.2.1 Classification of normal modes

BECs often have cylindrical symmetry, $\psi(\mathbf{r}) = \psi_0(r, z)$. In this case, similar calculations to those shown above, result in analytical expressions for the frequencies of the elementary excitations. These frequencies were derived by [191] [7]. The modes can be classified by their main quantum numbers n_r and by their multipolar moment ℓ. Examples are the *surface excitation* or *shape oscillation* ($n_r = 0$) and the *compression oscillation* ($n_r \neq 0$). Special cases are called *shaking mode*, *breathing mode* ($n_r = 1, \ell = 0$), and *swirling mode*. In the case of cylindrical symmetry, the projection of the angular momentum onto the symmetry axis m is the relevant quantum number. The dispersion relations are,

$$
\begin{aligned}
&\omega(\ell, \mp m = \ell) = |m|\omega_r^2 \\
&\omega(\ell, \mp m = \ell - 1) = |m|\omega_r^2 + \omega_z^2 \\
&\omega(\ell, \mp m = \ell - 2) = \omega_r^2 \left[2|m| + 2 + \tfrac{3}{2}\lambda^2 \mp \sqrt{(|m| + 2 - \tfrac{3}{2}\lambda^2)^2 + 2\lambda^2(|m| + 1)}\right] \\
&\omega(\ell, \mp m = \ell - 3) = \omega_r^2 \left[2|m| + 2 + \tfrac{7}{2}\lambda^2 \mp \sqrt{(|m| + 2 - \tfrac{5}{2}\lambda^2)^2 + 6\lambda^2(|m| + 1)}\right] ,
\end{aligned}
\tag{27.63}
$$

where λ is the aspect ratio $\lambda = \omega_z/\omega_r$. Obviously, higher excitation orders depend on the trap geometry. Moreover, we can easily see, that occasional degeneracies must arise for specific aspect ratios. For example, when $\omega_+(2, 0) = 2\omega(2, 2)$, we derive from (27.63) the condition $\lambda = \sqrt{16/7}$, and when $\omega_+(2, 0) = 2\omega_-(2, 0)$, we derive $\lambda = \frac{1}{6}\sqrt{77 + 5\sqrt{145}}$.

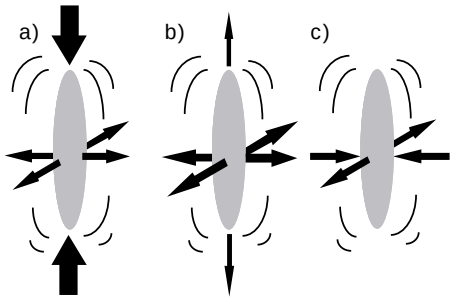

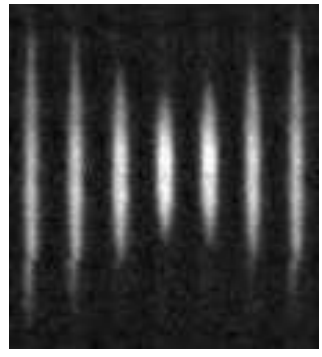

(d)

Figure 27.5: Normal modes of a BEC. (a) Shape oscillation, (b) breathing oscillation, and (c) quadrupole oscillation. (d) Non-destructive measurements of quadrupolar vibrations of a BEC [782].

[7] It is worth mentioning that the linearized theory applies to *small perturbations*. Strong disturbances render the dynamics chaotic, since the energy is coupled to many modes of excitation.

27.4.2.2 Quantum depletion

Following Bogolubov's theory the *quantum depletion* is given by,

$$\frac{\delta N}{N} = \frac{1}{N}\sum_{\mathbf{k}} \int d^3r |v_{\mathbf{k}}(\mathbf{r})|^2 \ . \tag{27.64}$$

27.4.2.3 Fluctuations in BECs

Fluctuations in condensates are reduced as compared to thermal ensembles. Non-linearities are always very sensitive to fluctuations (see the laser). Therefore, we have to look at closer at collisions. For 3-body decay in a thermal source, $\langle \rho(\mathbf{r})^3 \rangle \sim 6\langle \rho(\mathbf{r}) \rangle^3$, and in a coherent source: $\langle \rho(\mathbf{r})^3 \rangle \sim \langle \rho(\mathbf{r}) \rangle^3$ [128, 771].

27.4.3 Exercises

27.4.3.1 Ex: Sound velocity in the Thomas-Fermi regime

Consider a condensate of $N = 10^5$ ^{87}Rb atoms confined to an isotropic harmonic potential with secular frequency $\omega_{\rm trp} = (2\pi)$ 50 Hz. Remember $a_s = 110 a_{\rm B}$ and use the Thomas-Fermi approximation.
a. Evaluate the chemical potential.
b. Calculate the sound velocity at the center of the condensate.

27.5 Hydrodynamics and the propagation of sound

The question arises how the elementary excitations relate to the phenomenon of *sound*, well known from the hydrodynamic theory of superfluid ^{4}He proposed by Landau [499]. The *hydrodynamic regime* is characterized by the dominance of collisions [8]. On the other hand, Bogolubov's theory describes elementary excitations in the *collisionless regime*, where *quasi-particles* do not interact [9]. There is, therefore, a great motivation to study excitations with condensates in a very dense regime, where one can expect to recover predictions of hydrodynamic theory.

The hydrodynamic regime is reached, when the *free path* of the particles is smaller than the wavelength of the sound, that is [10],

$$l_{\rm mfp} < \lambda/2\pi \ . \tag{27.65}$$

27.5.1 Zero, first and second sound

The occurrence of several types of sound was related by Tisza and London to the existence of superfluid and normal components in ^{4}He [622]. The *second sound* is a quantum phenomenon, where the heat transfer occurs as an *wave-like motion* instead

[8] Collisions prevent condensation, because they localize the particles. This is the reason for the large quantum depletion, which in ^{4}He is of the order of 10% and hides effects of quantum statistics. Quantum depletion prevents any form of long-range order, as this requires delocalization.

[9] Bogolubov's theory assumes that the only impact of collisions is to deform the dispersion relationship, keeping the collective modes orthogonal.

[10] Note the similarity to the Ioffe-Regel criterion.

of being diffusive. Heat takes the place of pressure in normal sound waves called *first sound*. This induces a very high thermal conductivity. At temperatures below the λ-point, ^{4}He has the highest known conductivity of all materials (a few hundred times higher than copper).

The *zero sound* was introduced by Landau to name quantum vibrations in Fermi quantum liquids. This sound can not be seen as a simple wave of compression and rarefaction. In gaseous condensates, the zero sound corresponds to the elementary excitation called *phonon-like*.

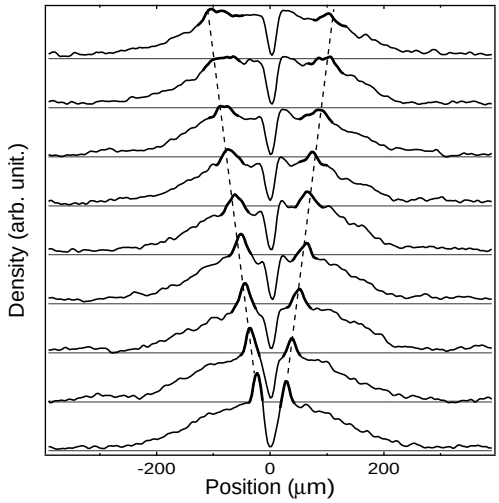

Figure 27.6: (code) Consecutive measurements of the BEC density profile showing the propagation of zero sound. The sound was excited by a blue-detuned laser tuned focused into the middle of the BEC (lower curve). The other curves show how the perturbation propagates towards the edges of the BEC.

Finally, the excitation called *particle-like* or *ballistic*, observed in gaseous condensates has no correspondence in dense superfluids, since the mean free path there is too short. The various regimes accessible in condensed gasses are listed in the following table [21, 23, 343, 456, 755, 783, 782, 283]:

regime	range scale	energy range	condensate	thermal cloud
collision-less	$k^{-1} < \xi < l_{\rm mfp}$	$\frac{\hbar^2}{2ml^2_{\rm mfp}} < gn_0 < \frac{\hbar^2k^2}{2m}$	ballistic	ballistic
collision-less	$\xi < k^{-1} < l_{\rm mfp}$	$\frac{\hbar^2}{2ml^2_{\rm mfp}} < \frac{\hbar^2k^2}{2m} < gn_0$	zero sound	ballistic
hydrodynamic	$\xi < l_{\rm mfp} < k^{-1}$	$\frac{\hbar^2k^2}{2m} < \frac{\hbar^2}{2ml^2_{\rm mfp}} < gn_0$	second sound	first sound

(27.66)

normal modes			$qR \ll 1$
macroscopic			$qa \ll 1$
beyond Bogolubov			$qa > 1$
superfluid (TF limit, LDA)	$E_{\rm self} \gg E_{\rm kin}$	$8\pi N a \gg a_{\rm ho}$	$a_{\rm ho} \gg \xi$
???	$E_{\rm self} \ll E_{\rm kin}$	$8\pi N a \ll a_{\rm ho}$	$a_{\rm ho} \ll \xi$
collision-less	$\gamma_{\rm coll} \ll \frac{\hbar q^2}{2m}$		$q l_{\rm mfp} \ll 1$
hydrodynamic	$\gamma_{\rm coll} > \frac{\hbar q^2}{2m}$		$q l_{\rm mfp} > 1$

(27.67)

With $l_{\rm mfp} \simeq 1/n_{\rm therm}\sigma$. Typical values are,

$$\begin{aligned}
&a = 0..1000 a_{\rm B} && = 0..50\,{\rm nm} \\
&n^{-1/3} && = 20..200\,\mu{\rm m} \\
&2\pi/q && = 0.2..\infty\,\mu{\rm m} \\
&\xi = \sqrt{8\pi n a}^{-1} && = 0.03..30\,\mu{\rm m} \\
&a_{\rm ho} = \sqrt{\hbar/m\omega_{\rm trp}} && = 0.1..3\,\mu{\rm m} \\
&2\pi/k_F = 2\pi a_{\rm ho}(48N)^{-1/6} && = 30..70\,\mu{\rm m}
\end{aligned} \tag{27.68}$$

The various regimes of sound are distinguished by frequency shifts and damping rates of the collective modes, which depend on the density (determining the mean-field energy and the mean free path) and the temperature (controlling the ratio between condensed and normal fraction). The quantity

$$\xi \equiv \frac{1}{\sqrt{8\pi a_s n}} \,, \tag{27.69}$$

is called *healing length*.

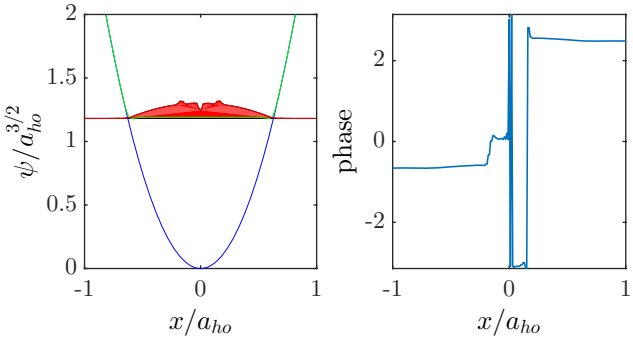

Figure 27.7: Simulation of the propagation of sound toward the edges of the condensate.

27.6 Momentum representation

We showed in Sec. 1.5.7, that the wavefunctions can be represented in the spatial or the momentum domain. These notions can be extended to the second quantization procedure by generalizing the equations (1.214),

$$\boxed{\hat{a}_{\mathbf{k}} \equiv \frac{1}{\sqrt{(2\pi)^3 V}} \int \hat{\psi}(\mathbf{r}) e^{-\imath \mathbf{k}\cdot\mathbf{r}} d^3 r \quad , \quad \hat{\psi}(\mathbf{r}) \equiv \sqrt{\frac{V}{(2\pi)^3}} \int \hat{a}_{\mathbf{k}} e^{\imath \mathbf{k}\cdot\mathbf{r}} d^3 k} \ . \tag{27.70}$$

Differently from (1.214) we chose here a normalization, which leaves the field operators $a_{\mathbf{k}}$ without unit.

27.6.1 Confined particles

In the case of confined atoms, $\mathcal{H} = \mathcal{H}_{\rm cm} + V_{\rm trp}(\mathbf{r}) + \mathcal{H}_{\rm self}$, we get sharp eigenvalues,

$$\hat{a}_{\mathbf{k}} = \frac{1}{V} \sum_{\mathbf{k}'} \hat{a}_{\mathbf{k}'} \delta^{(3)}(\mathbf{k} - \mathbf{k}') \ . \tag{27.71}$$

We insert this in equation (27.70),

$$\begin{aligned} \hat{\psi}(\mathbf{r}) &= \sqrt{\tfrac{1}{(2\pi)^3 V}} \sum_{\mathbf{k}'} \hat{a}_{\mathbf{k}'} \int \delta^{(3)}(\mathbf{k} - \mathbf{k}') e^{\imath \mathbf{k}\cdot\mathbf{r}} d^3 k \\ &= \sqrt{\tfrac{1}{(2\pi)^3 V}} \sum_{\mathbf{k}'} \hat{a}_{\mathbf{k}} e^{\imath \mathbf{k}\cdot\mathbf{r}} = \sum_{\mathbf{k}} u_{\mathbf{k}}(\mathbf{r}) \hat{a}_{\mathbf{k}} \ , \end{aligned} \tag{27.72}$$

thus making an expansion of the condensate into plane waves,

$$u_{\mathbf{k}}(\mathbf{r}) = \tfrac{1}{\sqrt{(2\pi)^3 V}} e^{\imath \mathbf{k}\cdot\mathbf{r}} \ , \tag{27.73}$$

which is particularly adapted to the 3D box potential, $V_{\rm trp}(\mathbf{r}) \equiv \infty$ se $r > R$. Also, we calculate,

$$\hat{a}_{\mathbf{k}} = \sqrt{\tfrac{1}{(2\pi)^3 V}} \int \hat{\psi}(\mathbf{r}) e^{-\imath \mathbf{k}\cdot\mathbf{r}} d^3 r = \int \hat{\psi}(\mathbf{r}) u^*_{\mathbf{k}}(\mathbf{r}) d^3 \mathbf{r} \ . \tag{27.74}$$

We obtain the observable commutation rules from (27.5),

$$[\hat{a}_{\mathbf{k}}, \hat{a}^\dagger_{\mathbf{k}'}] = \delta_{\mathbf{k}\mathbf{k}'} \quad , \quad [\hat{a}_{\mathbf{k}}, \hat{a}_{\mathbf{k}'}] = 0 \quad , \quad \hat{N} = \sum_{\mathbf{k}} \hat{a}^\dagger_{\mathbf{k}} \hat{a}_{\mathbf{k}} \ . \tag{27.75}$$

Using the following mathematical relationships,

$$\tfrac{1}{(2\pi)^3 V} \sum_{\mathbf{k}} e^{-\imath \mathbf{k}\cdot(\mathbf{r}-\mathbf{r}')} = \delta^3(\mathbf{r} - \mathbf{r}') \quad \text{and} \quad \tfrac{1}{(2\pi)^3 V} \int d^3\mathbf{r} e^{\imath(\mathbf{k}'-\mathbf{k})\cdot\mathbf{r}} = \delta_{\mathbf{k},\mathbf{k}'} \ , \tag{27.76}$$

and easy to show for plane waves,

$$\sum_{\mathbf{k}} u^*_{\mathbf{k}}(\mathbf{r}) u_{\mathbf{k}}(\mathbf{r}') = \delta^3(\mathbf{r} - \mathbf{r}') \quad \text{and} \quad \int u^*_{\mathbf{k}}(\mathbf{r}) u_{\mathbf{k}'}(\mathbf{r}) d^3\mathbf{r} = \delta_{\mathbf{k}\mathbf{k}'} \ . \tag{27.77}$$

In Exc. 27.6.4.1 we will check the validity of the commutation rules (27.75), and in Exc. 27.6.4.2 we derive the following representation of the Hamiltonian:

$$\boxed{\begin{aligned}\mathcal{H} &= \int d^3r\hat{\psi}^\dagger(\mathbf{r})\left(-\frac{\hbar^2}{2m}\nabla^2+V_{\rm trp}(\mathbf{r})\right)\hat{\psi}(\mathbf{r}) \\ &\quad +\frac{g}{2}\int d^3r\int d^3r'\hat{\psi}^\dagger(\mathbf{r})\hat{\psi}^\dagger(\mathbf{r}')\delta(\mathbf{r}-\mathbf{r}')\hat{\psi}(\mathbf{r}')\hat{\psi}(\mathbf{r}) \\ &= \sum_{\mathbf{k}}\frac{\hbar^2\mathbf{k}^2}{2m}\hat{a}^\dagger_{\mathbf{k}}\hat{a}_{\mathbf{k}}+\sum_{\mathbf{k},\mathbf{k}'}\hat{a}^\dagger_{\mathbf{k}}V_{\mathbf{k},\mathbf{k}'}\hat{a}_{\mathbf{k}'}+\frac{g}{2}\sum_{\mathbf{k},\mathbf{k}',\mathbf{k}''}\hat{a}^\dagger_{\mathbf{k}}\hat{a}^\dagger_{\mathbf{k}'}\hat{a}_{\mathbf{k}''}\hat{a}_{\mathbf{k}+\mathbf{k}'-\mathbf{k}''}\end{aligned}} \quad , \tag{27.78}$$

with the abbreviation,

$$V_{\mathbf{k},\mathbf{k}'}=\int u^*_{\mathbf{k}}(\mathbf{r})V_{\rm trp}(\mathbf{r})u_{\mathbf{k}'}(\mathbf{r})d^3\mathbf{r}=\tfrac{1}{(2\pi)^3}\int V_{\rm trp}(\mathbf{r})e^{\imath(\mathbf{k}'-\mathbf{k})\mathbf{r}}d^3\mathbf{r}\ . \tag{27.79}$$

The equation of motion for the momentum wavefunction now becomes,

$$\imath\hbar\frac{\partial}{\partial t}\hat{a}_{\mathbf{k}}=[\hat{a}_{\mathbf{k}},\mathcal{H}]=\frac{\hbar^2\mathbf{k}^2}{2m}\hat{a}_{\mathbf{k}}+\sum_{\mathbf{k}'}V_{\mathbf{k},\mathbf{k}'}\hat{a}_{\mathbf{k}'}+g\sum_{\mathbf{k}',\mathbf{k}''}\hat{a}^\dagger_{\mathbf{k}'}\hat{a}_{\mathbf{k}''}\hat{a}_{\mathbf{k}+\mathbf{k}'-\mathbf{k}''}\ . \tag{27.80}$$

27.6.1.1 Harmonically confined particles

In harmonic traps, $V_{\rm trp}(r)=\frac{m}{2}\omega^2_{\rm trp}r^2$, the motion can be canonically quantized,

$$\hat{a}=\frac{1}{\sqrt{2}}\left(\frac{\hat{r}}{a_{\rm trp}}\mp\imath a_{\rm trp}\hat{p}\right)\quad,\quad \mathcal{H}_{\rm cm}=\sum_{\mathbf{k}}\hbar\omega_{\rm trp}\hat{a}^\dagger_{\mathbf{k}}\hat{a}_{\mathbf{k}}\ , \tag{27.81}$$

with the size of the ground state,

$$a_{\rm trp}\equiv\sqrt{\frac{\hbar}{m\omega_{\rm trp}}}\ . \tag{27.82}$$

As an alternative notation we could introduce,

$$|\mathbf{r}\rangle\equiv\hat{\psi}^\dagger(\mathbf{r})\quad\text{and}\quad|\mathbf{k}\rangle\equiv\hat{a}^\dagger_{\mathbf{k}}\ . \tag{27.83}$$

Hence, just considering the ground state of the trap, that is, assuming that the atomic motion be frozen, our Hamiltonian becomes:

$$\mathcal{H}_{\rm cm}+\mathcal{H}_{\rm self}=\hbar\omega_{\rm trp}\hat{a}^\dagger\hat{a}+\frac{g}{2}\hat{a}^\dagger\hat{a}^\dagger\hat{a}\hat{a}\ . \tag{27.84}$$

27.6.2 Thomas-Fermi limit

In the limit of negligible kinetic energy (that is, in the middle of a large condensate) with the analytical form of the condensate wavefunction,

$$\hat{\psi}(\mathbf{r})\propto\sqrt{n_0}\left(1-\frac{\mathbf{r}^2}{\mathbf{r}_0^2}\right)\ , \tag{27.85}$$

the transformation (27.70) allows us to derive an expression for the momentum distribution,

$$|a(\mathbf{k})|\propto\frac{J_1(\mathbf{k}\cdot\mathbf{r}_0)}{(\mathbf{k}\cdot\mathbf{r}_0)^2}\ . \tag{27.86}$$

27.6.2.1 Width of the momentum distribution

It is interesting to compare the size of an ideal gas condensate with the size of an interacting condensate. We can express the Thomas-Fermi radius as,

$$\Delta r_{\rm TF} = a_{\rm trp}\sqrt{\frac{\mu}{\hbar\omega_{\rm trp}}}\ . \tag{27.87}$$

The Heisenberg limit requires,

$$\Delta p_{\rm TF} = \frac{\hbar}{\Delta r_{\rm TF}}\ . \tag{27.88}$$

Since $\sqrt{\mu/\hbar\omega_{\rm trp}} > 1$, the interaction increases the volume of the condensate, but restricts the distribution of its velocities. For a hypothetical thermal Boltzmann gas having the same temperature,

$$\Delta r_{\rm therm} = a_{\rm trp}\sqrt{\frac{k_{\rm B}T}{\hbar\omega_{\rm trp}}} \qquad \text{and} \qquad \Delta p_{\rm therm} = \frac{\hbar}{a_{\rm trp}}\sqrt{\frac{k_{\rm B}T}{\hbar\omega_{\rm trp}}}\ . \tag{27.89}$$

The thermal cloud *is not at the Heisenberg limit*, because $\sqrt{k_{\rm B}T/\hbar\omega_{\rm trp}} > 1$.

These relationships were experimentally confirmed [791] by measurements of the velocity distributions of condensates using a Bragg spectroscopy technique (see Sec. 29.2). It is interesting to note that the measured widths of velocity distributions were *lower than the photonic recoil limit*, $\hbar k/m \simeq 30$ mm/s for ^{87}Rb.

27.6.3 Master equation approach

The Hamiltonian that describes a BEC in second quantization in an orthonormal set of energy eigenfunctions reads:

$$\begin{aligned}
\mathcal{H} &= \sum\nolimits_{i,j} \mathcal{H}^{(ij)}_{\rm atom}\hat{a}^\dagger_i\hat{a}_j + \sum_{i,j,k,l}\tfrac{1}{2}W^{(ijkl)}\hat{a}^\dagger_i\hat{a}^\dagger_j\hat{a}_k\hat{a}_l \qquad (27.90)\\
\mathcal{H}^{(ij)}_{\rm atom} &= \langle\phi_i|\tfrac{1}{2m}\mathbf{p}^2 + V_{\rm trp}(\mathbf{r})|\phi_j\rangle\\
W^{(ijkl)} &= g\int \phi_i(\mathbf{r})\phi_j(\mathbf{r})\phi_k(\mathbf{r})\phi_l(\mathbf{r})d^3r\ .
\end{aligned}$$

The inclusion of spontaneous processes (one-body-loss, dephasing) requires a master equation including a *Lindblad term* within a density matrix formalism. The von Neumann equation for the density operator reads:

$$\begin{aligned}
\frac{d}{dt}\hat{\rho} &= -\imath[V,\hat{\rho}] + \mathcal{L}\hat{\rho} \qquad (27.91)\\
\mathcal{L}_{\text{one-body loss}} &\equiv \kappa(2\hat{a}\hat{\rho}\hat{a}^\dagger - \hat{a}^\dagger\hat{a}\hat{\rho} - \hat{\rho}\hat{a}^\dagger\hat{a})\\
\mathcal{L}_{\text{one-body feeding}} &\equiv \kappa(2 + 2\hat{a}^\dagger\hat{\rho}\hat{a} - \hat{a}\hat{a}^\dagger\hat{\rho} - \hat{\rho}\hat{a}\hat{a}^\dagger)\\
\mathcal{L}_{\text{two-body loss}} &\equiv \kappa\left(2\hat{a}^2\hat{\rho}\hat{a}^{\dagger 2} - \hat{a}^{\dagger 2}\hat{a}^2\hat{\rho} - \hat{\rho}\hat{a}^{\dagger 2}\hat{a}^2\right)\ .
\end{aligned}$$

27.6.4 Exercises

27.6.4.1 Ex: Commutators in momentum space

Demonstrate the validity of the commutation rules (27.75).

27.6.4.2 Ex: Commutators in momentum space

Derive the representation (27.78) of the Hamiltonian.

27.7 Condensates at finite temperature

27.7.1 Ballistic expansion of a bosonic gas

As discussed in Sec. 26.6, the atomic density distributions are revealed through their interaction with a laser beam. The problem with imaging a confined condensate is, on the one hand, its very high optical density, which inhibits the penetration of resonant light and, on the other hand, its very small size, which is often below the diffraction limit and prevents its optical resolution. As discussed in Sec. 26.6, both problems can be avoided by the time-of-flight imaging technique, which consists in quickly switching off the trap and dropping the atomic cloud (see Fig. 26.30). If the switching-off process is fast enough, the potential energy is lost, but in the course of ballistic expansion, the self-energy is transformed into kinetic energy. Both the self-energy transformed to kinetic energy and the inherent initial kinetic energy contribute to blow up the size of the atomic cloud, so that the density rapidly decreases. After a few 10 ms, when the optical density is sufficiently low (on the order of 1), the cloud can be imaged via its absorption of a resonant laser beam. The condensate, which is about 10 times denser than the thermal cloud, has a much larger repulsive self-energy. When the condensate is suddenly released from its trap, its explosion is accelerated by this self-energy, and the acceleration is faster in those directions, where the confining potential was stronger [401, 142]. Therefore, the aspect ratio of the condensate's shape is inverted during the flight time [459, 142]. In contrast, the self-energy of the thermal cloud is relatively insignificant. Therefore, its spatial density after a time of free expansion reflects the pure velocity distribution of the atomic cloud while it was trapped. This allows the interpretation of the spatial distribution of the expanded cloud in terms of a *temperature* of the trapped cloud.

27.7.1.1 Popov approximation

The Popov decomposition separates the condensed part, described by a c-number $\phi \equiv \langle \hat{\psi} \rangle$ and normalized to the number of condensed atoms N_0 from the thermal part

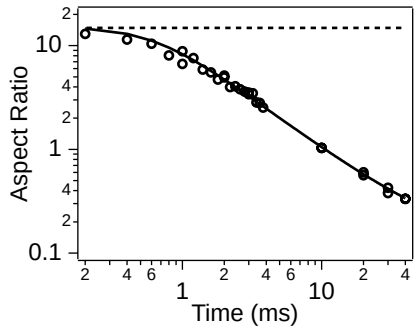

Figure 27.8: Inversion of aspect ratio during time-of-flight. The frequencies of the harmonic trap were $\omega_r = (2\pi) \cdot 248$ Hz and $\omega_r = (2\pi) \cdot 16$ Hz [459].

$\tilde{\psi} \equiv \hat{\psi} - \phi$, which keeps track of the quantum nature of the Bose-gas [239],

$$\begin{aligned}
\mathcal{K} &= \mathcal{K}_0 + \mathcal{K}_1 + \mathcal{K}_1^\dagger + \mathcal{K}_2 \qquad (27.92)\\
\mathcal{K}_0 &= \int d^3\mathbf{r}\phi^*(\mathbf{r}) \left(-\frac{\hbar^2}{2m}\nabla^2 + V_{\rm trp}(\mathbf{r}) + \frac{g}{2}|\phi|^2 - \mu \right) \phi(\mathbf{r})\\
\mathcal{K}_1 &= 0 \qquad \text{if} \qquad [\mathcal{L} - gn_0(\mathbf{r})]\phi(\mathbf{r}) = 0\\
\mathcal{K}_2 &= \int d^3r \left[\tilde{\psi}^+(\mathbf{r})\mathcal{L}\tilde{\psi}(\mathbf{r}) + \frac{g}{2}\left(\phi(\mathbf{r})^2\tilde{\psi}^+(\mathbf{r})\tilde{\psi}^+(\mathbf{r}) + \phi^*(\mathbf{r})^2\tilde{\psi} + (\mathbf{r})\tilde{\psi}(\mathbf{r}) \right) \right]\\
\mathcal{L} &\equiv -\frac{\hbar^2}{2m}\nabla^2 + V_{\rm trp}(\mathbf{r}) - \mu + 2gn(\mathbf{r})\\
n(\mathbf{r}) &= n_0(\mathbf{r}) + n_T(\mathbf{r}) = |\phi(\mathbf{r})|^2 + \langle \tilde{\psi}^\dagger(\mathbf{r})\tilde{\psi}(\mathbf{r}) \rangle \ .
\end{aligned}$$

We perform the Bogolubov transform to the diagonalized Hamiltonian,

$$\begin{aligned}
\mathcal{K}_{Popov} &= \mathcal{K}_0 + \sum\nolimits_j \varepsilon_j \hat{b}_j^+ \hat{b}_j \qquad (27.93)\\
\tilde{\psi}(\mathbf{r}) &= \sum\nolimits_j u_j(\mathbf{r})\hat{b}_j - v_j^*(\mathbf{r})\hat{b}_j^+\\
\delta_{jk} &= \int d^3r \left(u_j u_k^* - v_j v_k^* \right)\\
\delta_{jk} &= [\hat{b}_j, \hat{b}_k^+] \ .
\end{aligned}$$

This yields a set of equations for elementary excitations (quasi-particle excitations in a diagonalized energy space),

$$\begin{aligned}
N_j &= [\exp(\varepsilon_j/k_{\rm B}T) - 1]^{-1} \qquad (27.94)\\
n_T(\mathbf{r}) &= \sum\nolimits_j \left[\left(|u_j|^2 + |v_j|^2 \right) N_j + |v_j|^2 \right]\\
\mathcal{L}u_j(\mathbf{r}) - gn_0(\mathbf{r})v_j(\mathbf{r}) &= \varepsilon_j u_j(\mathbf{r}) \ ,\\
\mathcal{L}v_j(\mathbf{r}) - gn_0(\mathbf{r})u_j(\mathbf{r}) &= -\varepsilon_j v_j(\mathbf{r}) \ .
\end{aligned}$$

The quantum depletion at $T = 0$ [last term in the density $n(\mathbf{r})$] may be neglected. In this zero-temperature limit, the equations simplify to yield the Gross-Pitaevskii

equation. We may separate these equations using auxiliary functions [413],

$$\begin{aligned} \tilde{\psi}_j^{(\pm)}(\mathbf{r}) &\equiv u_j(\mathbf{r}) \pm v_j(\mathbf{r}) \\ \hat{h}_0 &\equiv \mathcal{L} - gn_0(\mathbf{r}) \\ \hat{h}_0\tilde{\psi}_j^{(+)}(\mathbf{r}) &= E_j\tilde{\psi}_j^{(-)}(\mathbf{r}) \ . \end{aligned} \tag{27.95}$$

The eigenvalue equations that one gets after substituting (III.2.5) into (III.2.4) may be solved by expanding in a set of eigenfunctions of $\hat{h}_0$:

$$\begin{aligned} \tilde{\psi}_j^{(\pm)}(\mathbf{r}) &\equiv \sum\nolimits_\alpha c_\alpha^{(j)}\phi_\alpha(\mathbf{r}) \\ \hat{h}_0\phi_\alpha(\mathbf{r}) &\equiv \varepsilon_\alpha\phi_\alpha(\mathbf{r}) \\ \sum\nolimits_\beta (M_{\alpha\beta} + \varepsilon_\alpha\delta_{\alpha\beta})\varepsilon_\beta c_\alpha^{(j)} &= E_j^2 c_\alpha^{(j)} \\ M_{\alpha\beta} &= 2g\int \phi_\alpha^*(\mathbf{r})n_0(\mathbf{r})\phi_\beta(\mathbf{r})d^3r \ . \end{aligned} \tag{27.96}$$

27.7.2 Hartree-Fock approach

27.7.2.1 Two-gas model for $T > 0$

The two phases of a condensate above $T = 0$ have a specific interdependence, which makes it possible to treat the problem with an approximation, where only the condensed part influences the non-condensed and not vice versa [238]. The HFB equation is solved for the condensed part alone, assuming $n_{\rm therm} = 0$. The condensate wavefunction and the chemical potential are derived from that, f.e. using numerical methods like the method of steepest descent. The effective potential for the thermal cloud in the presence of a condensate is:

$$V_{1,\rm eff}(\mathbf{r}_1) = V_{1,\rm trap}(\mathbf{r}_1) + g_1|\psi_1(\mathbf{r}_1)|^2 \ . \tag{27.97}$$

Next, we diagonalize the Schrödinger equation:

$$[-\nabla_1^2 + V_{1,\rm eff}(\mathbf{r}_1)]\psi_{1,j}(\mathbf{r}_1) = 2E_{1,j}\psi_{1,j}(\mathbf{r}_1) \ , \tag{27.98}$$

maintaining the normalization,

$$1 = \int |\psi_{1,j}(\mathbf{r}_1)|^2 d^3\mathbf{r}_1 \ . \tag{27.99}$$

This provides us with the energy eigenvalues of the excited trap states and their eigenfunctions. One can f.e. guess an eigenvalue and numerically solve the Schrödinger equation using Runge-Kutta integration routines. The eigenfunction will probably diverge. In this case, we vary the eigenvalue until the solution converges.

Finally, we can calculate the thermal density distribution:,

$$\begin{aligned} N_j &\equiv [\exp((E_{1,j} - \mu_1)/k_{\rm B}T_1) - 1]^{-1} \\ n_{\rm therm}(\mathbf{r}_1) &= \sum\nolimits_j N_j|\psi_{1,j}(\mathbf{r}_1)|^2 \ , \end{aligned} \tag{27.100}$$

and all thermodynamic potentials, as shown in Sec. 7.3.2.

A more sophisticated method uses self-consistent recursion [413]. Here, the thermal density is plugged back into the HFB equation, and the whole procedure is repeated until it converges.

27.7.2.2 Hartree-Fock approximation

We have already seen that, inside a trap the condensate occupies the lowest vibrational level, whereas the atoms of the thermal gas are distributed among all levels. The trapping potential is often harmonic, $U_{\rm trp}(\mathbf{r}) = \frac{m}{2}\omega_r^2 r^2$, with secular frequencies ω_r typically on the order of several tens or hundreds of Hz. The spatial (radial) extent of the vibration levels varies a lot with their quantum number, $r_j = \sqrt{(2j+1)\hbar/m\omega_r}$. This naturally produces a *separation of the thermal (or normal) and condensate fractions* at $T > 0$, which does not exist for a homogeneous gas and which allows (up to a certain degree) an individual treatment of the two fractions. The details of the interaction between the two fractions are very complicated and are still under intense theoretical investigation. However, to understand the shape of a trapped atomic cloud and other characteristics, we can use a simple approximate model [**?**, 413], assuming that the condensate is only weakly disturbed by the thermal cloud. In contrast, the presence of the condensate dramatically modifies the potential for the thermal atoms. Therefore, we must *first* calculate the density of the condensate $n_0(\mathbf{r})$, *before* calculating that of the thermal cloud. If this procedure is applied iteratively, it is called *Hartree-Fock method*:

i. We start with $n_{\rm therm}(\mathbf{r}) = 0$;

ii. we solve the GPE $\left(-\frac{\hbar^2}{2m}\Delta + V_{\rm trp}(\mathbf{r}) - \mu + g\left[|\psi(\mathbf{r})|^2 + n_{\rm therm}(\mathbf{r})\right]\right)\psi(\mathbf{r})$ numerically with the steepest descent method, we derive μ and ψ, and also $n(\mathbf{r}) = |\psi(\mathbf{r})|^2 + n_{\rm therm}(\mathbf{r})$;

iii. assuming that collisions between atoms of the thermal cloud, the density of which is weak, can be neglected, we can view the cloud as an ideal gas in a potential modified by the strongly anharmonic mean field of the condensate, $V_{\rm trp}(\mathbf{r}) + 2gn(\mathbf{r})$, we calculate the thermal density $n'_{\rm therm}(\mathbf{r}) = \lambda_{\rm dB}^{-3} g_{3/2}\left(\exp\frac{V_{\rm trp}(\mathbf{r})-\mu+2gn(\mathbf{r})}{k_{\rm B}T}\right)$;

iv. we start over at (ii) using the new thermal density.

We can now calculate the total energy,

$$U = \int d^3r \left(\psi(\mathbf{r})\tfrac{-\hbar^2\nabla^2}{2m}\psi(\mathbf{r}) + V_{\rm trp}(\mathbf{r})n(\mathbf{r}) + \tfrac{g}{2}[2n(\mathbf{r})^2 - n_0(\mathbf{r})] - \tfrac{1}{h^3}\int d^3k\,\tfrac{\hbar^2k^2}{2m}n(\mathbf{r},\mathbf{k})\right) \tag{27.101}$$

$$= \int d^3\mathbf{r}\left(\psi(\mathbf{r})\tfrac{-\hbar^2\nabla^2}{2m}\psi(\mathbf{r}) + V_{\rm trp}(\mathbf{r})n(\mathbf{r}) + \tfrac{g}{2}[2n(\mathbf{r})^2 - n_0(\mathbf{r})] + \tfrac{3k_{\rm B}T}{2\lambda_{\rm dB}^3}g_{3/2}\left[\exp\tfrac{V_{\rm trp}(\mathbf{r})-\mu+2gn(\mathbf{r})}{k_{\rm B}T}\right]\right)$$

and other thermodynamic quantities.

27.7.3 Ideal gas limit

Consider the ideal gas in an isotropic harmonic potential. The excitation spectrum then takes the form:

$$f(\mathbf{k},\mathbf{r}) = n(\mathbf{k},\mathbf{r}) \tag{27.102}$$

$$\varepsilon_{\rm HF}(\mathbf{k},\mathbf{r}) = \mathcal{L}(\mathbf{k},\mathbf{r}) = \frac{\hbar^2\mathbf{k}^2}{2m} + V(\mathbf{r}) - \mu\ .$$

We can immediately calculate:

$$
\begin{aligned}
g &\longrightarrow 0 \\
\mu &\xrightarrow{g\to 0} \tfrac{3}{2}\hbar\omega \\
\phi(\mathbf{r}) &\xrightarrow{g\to 0} \frac{\sqrt{N_0}}{\pi^{3/4}a_{\rm trp}^{3/2}}\exp(-\frac{\mathbf{r}^2}{2a_{\rm trp}^2}) \\
E_{\rm kin} &= \int \phi(\mathbf{r})\frac{-\hbar^2\Delta}{2m}\phi(\mathbf{r})d^3r = -\tfrac{9}{4}N_0\hbar\omega \\
n_{\rm therm}(\mathbf{r}) &\xrightarrow{g\to 0} \int f(\mathbf{r}\cdot\mathbf{k})d^3\mathbf{k} = \frac{1}{\lambda_{\rm dB}^3}g_{3/2}\left[\exp\left(\tfrac{V_{\rm trp}(\mathbf{r})-\mu}{k_{\rm B}T}\right)\right] \\
N_{\rm therm} &\xrightarrow{g\to 0} \int n_{\rm therm}(\mathbf{r})d^3\mathbf{r} = \left(\frac{k_{\rm B}T}{\hbar\omega}\right)^3 g_3\left[\exp\left(\tfrac{\mu}{k_{\rm B}T}\right)\right] \\
U &\xrightarrow{g\to 0} \int \varepsilon_{HF} f(\mathbf{r}\cdot\mathbf{k})d^3\mathbf{r}\cdot\mathbf{d}^3k = 3k_{\rm B}T\left(\frac{k_{\rm B}T}{\hbar\omega}\right)^3 g_4\left[\exp\left(\tfrac{\mu}{k_{\rm B}T}\right)\right] .
\end{aligned}
\tag{27.103}
$$

27.7.4 Exercises

27.7.4.1 Ex: Ballistic expansion of a condensate

Calculate the ballistic expansion of a ^{87}Rb BEC initially confined in a cylindrically symmetric trap with secular frequencies $\omega_z = 20\,\text{Hz}$ and $\omega_r = 100\,\text{Hz}$.

27.8 Numerical simulations of the Gross-Pitaevskii equation

To simulate the one-dimensional evolution of a wavepacket following the Gross-Pitaevskii equation,

$$
\imath\hbar\frac{\partial}{\partial t}\psi(z,t) = \left[\frac{-\hbar^2}{2m}\frac{d^2}{dz^2} + V_{\rm trp}(z) + |\psi(z,t)|^2\right]\psi(z,t) \; . \tag{27.104}
$$

we solve iteratively [664],

$$
\psi(z,t+dt) = \psi(z,t) + dt\dot{\psi}(z,t) \; . \tag{27.105}
$$

As initial state we choose, $\psi(z,0) = e^{-z^2/2\bar{z}^2}e^{\imath kz}$, where $k \equiv \sqrt{2mE}/\hbar$ is the wavevector.

The numerical propagation is conveniently performed using the *time-splitting spectral algorithm* [52, 51, 50, 302], which can be easily extended to two dimensions.

27.8.1 Crank-Nicholson-Crout algorithm

27.8.1.1 Crank-Nicholson-Crout algorithm for the time-dependent Schrödinger equation

The *Crank-Nicholson algorithm* goes as follows. The time-dependent Schrödinger equation in one dimension,

$$\frac{\partial}{\partial t}\psi(x,t) = \frac{\imath\hbar}{2m}\frac{\partial^2}{\partial x^2}\psi(x,t) - \frac{\imath V(x)}{\hbar}\psi(x,t) \tag{27.106}$$

is a parabolic partial differential equation. We usually seek a solution on an interval $x \in [a,b]$ and $t > 0$. The solution is uniquely determined from boundary conditions: $\psi(a,t) = \psi(b,t) = 0$ and $\psi(x,0) = g(x)$. One method for numerical solution solves for the values of the wavefunction on a regular grid of dimension $h = (b-a)/N_x$ in x and τ in t:,

$$\psi_j^k = \psi(a + jh, k\tau) \ . \tag{27.107}$$

The derivatives are replaced by simple finite differences. The r.h.s. of the equation at the grid point (i,j) is then,

$$\frac{\imath\hbar}{2mh^2}\left(\psi_{j+1}^k - 2\psi_j^k + \psi_{j-1}^k\right) - \frac{\imath V(a+jh)}{\hbar}\psi_j^k = \sum_{m=0}^{N} \imath H_{jm}\psi_j^k \ , \tag{27.108}$$

where H is a real symmetric tridiagonal matrix (provided $V(x)$ is real). The l.h.s. of the equation can be replaced either by a forward or backward difference,

$$\frac{\psi_j^{k+1} - \psi_j^k}{\tau} \qquad \text{or} \qquad \frac{\psi_j^k - \psi_j^{k-1}}{\tau} \ , \tag{27.109}$$

which, when combined with the r.h.s. gives the explicit algorithm,

$$\psi^{k+1} = (1 + \imath H\tau)\psi^k \qquad \text{or} \qquad \psi^k = (1 - \imath H\tau)\psi^{k+1} \ . \tag{27.110}$$

The Crank Nicholson Algorithm averages both,

$$(1 - \imath H\tau/2)\psi^{k+1} = (1 + \imath H\tau/2)\psi^k \ . \tag{27.111}$$

This method is a second order algorithm in t, i.e. the discretization error decreases as τ^2. The finite difference representation of the second derivative d^2/dx^2 is also good to second order in h^2. The Crank-Nicholson Algorithm also gives a unitary evolution in time. That is especially useful for quantum mechanics where unitarity assures that the normalization of the wavefunction is unchanged over time. The algorithm steps the solution forward in time by one time unit, starting from the initial wavefunction at $t = 0$. According to the Crank-Nicholson scheme, the time stepping process is half explicit and half implicit. The implicit part involves solving a tridiagonal system. That solution is accomplished by Crout reduction, a direct method related to Gaussian elimination and LU decomposition.

To simplify the algorithm we have chosen units in which the Planck constant $\hbar = 1$, time step $\tau = 1$ and the spatial separation $h = 1$. This can always be arranged by an appropriate redefinition of mass and potential: $m = m_{SI}\ h^2/\tau\hbar$ and $V = V_{SI}\ \tau/h$.

27.8.1.2 Crank-Nicholson algorithm for the time-dependent Gross-Pitaevskii equation

The Crank-Nicholson algorithm [6],

$$\frac{\imath\left(\varphi_j^{n+1}-\varphi_j^n\right)}{\Delta} = -\frac{\varphi_{j+1}^{n+1}-2\varphi_j^{n+1}+\varphi_{j-1}^{n+1}+\varphi_{j+1}^n-2\varphi_j^n+\varphi_{j-1}^n}{2h^2} + \frac{1}{2}\left(\frac{c(x_j)^2}{4}+n\frac{|\varphi_j^n|^2}{(x_j)^2}\right)\left(\varphi_j^{n+1}+\varphi_j^n\right) . \tag{27.112}$$

Introducing abbreviations,

$$B(\varphi_j^{n+1}-\varphi_j^n) = -A\left(\varphi_{j+1}^{n+1}-2\varphi_j^{n+1}+\varphi_{j-1}^{n+1}+\varphi_{j+1}^n-2\varphi_j^n+\varphi_{j-1}^n\right)+C_j^n\left(\varphi_j^{n+1}+\varphi_j^n\right) . \tag{27.113}$$

Can be rewritten as,

$$A\varphi_{j+1}^{n+1}+\left(-2A+B-C_j^n\right)\varphi_j^{n+1}+A\varphi_{j-1}^{n+1} = -A\varphi_{j+1}^n+\left(2A+B+C_j^n\right)\varphi_j^n-A\varphi_{j-1}^n = X_j^n . \tag{27.114}$$

The set of equations,

$$\begin{pmatrix} -2A-B-C_1^n & A & 0 & \cdots & 0 \\ A & -2A-B-C_2^n & A & \cdots & 0 \\ 0 & A & -2A-B-C_3^n & \ddots & 0 \\ \vdots & \vdots & \ddots & \ddots & \vdots \\ 0 & 0 & \cdots & A & -2A-B-C_j^n \end{pmatrix} \begin{pmatrix} \varphi_1^{n+1} \\ \varphi_2^{n+1} \\ \varphi_3^{n+1} \\ \vdots \\ \varphi_j^{n+1} \end{pmatrix} = \begin{pmatrix} X_1^n \\ X_2^n \\ X_3^n \\ \vdots \\ X_j^n \end{pmatrix} \tag{27.115}$$

can be solved by inverting tridiagonal matrix. Set $\varphi_0^{n+1} = \varphi_{J+1}^{n+1} = 0$. Run a loop $j = 1, .., J$. Assume given $\varphi_1^{n+1} = \varphi_j^{n+1}$,

$$\varphi_{j+1}^{n+1} = \frac{X_j^n}{A} + \frac{2A-B+C_j^n}{A}\varphi_j^{n+1} - \varphi_{j-1}^{n+1} . \tag{27.116}$$

27.8.2 Time-splitting spectral algorithm: Coherent propagation

We write the one-dimensional GPE in the form,

$$\imath\hbar\frac{\partial\psi(x,t)}{\partial t} = -\frac{\hbar^2}{2m}\nabla^2\psi(x,t)+V(x)\psi(x,t)+\frac{4\pi\hbar^2 a_s}{m(2r_h)^2}|\psi(x,t)|^2\psi(x,t) \tag{27.117}$$

for $a < x < b$. Choose periodic boundary conditions, $\psi(a,t) = \psi(b,t)$ and $\psi_x(a,t) = \psi_x(b,t)$. Various methods are known to solve the GPE numerically, such as the *Crank-Nicholson algorithm*. The *time-splitting spectral algorithm* (TSSA) consists in solving the first and the second of the following equations in two distinct steps [52, 51, 50, 302],

$$\begin{aligned} \frac{\partial\psi(x,t)}{\partial t} &= -\imath\frac{V(x)}{\hbar}\psi(x,t)-\imath\frac{g_{1D}}{\hbar}|\psi(x,t)|^2\psi(x,t) \\ \frac{\partial\psi(x,t)}{\partial t} &= i\frac{\hbar}{2m}\psi_{xx}(x,t) , \end{aligned} \tag{27.118}$$

i.e. we discretize in space using $x = a + j(b-a)/M$ and $k = 2\pi l/(b-a)$ such that $k\,(x-a) = 2\pi lj/M$. We propagate half the way, $\Delta t/2$, in time,

$$\varphi_x \equiv e^{-\frac{\imath}{\hbar}(V(x)+g_{1D}|\psi(x,t)|^2)\frac{\Delta t}{2}}\psi(x,t) \tag{27.119}$$

for $j = 0, .., M-1$. Now we propagate the spectral components, $(\mathcal{F}\varphi)_k \equiv \sum_{j=0}^{M-1}\varphi_x e^{-2\pi\imath lj/M}$, in momentum space and transform back, $(\mathcal{F}^{-1}\varphi)_x \equiv M^{-1}\sum_{l=-M/2}^{M/2-1}\varphi_k e^{2\pi\imath lj/M}$,

$$\phi_x \equiv \mathcal{F}^{-1}\left[e^{\imath\frac{\hbar}{2m}k^2\Delta t}(\mathcal{F}\varphi)_k\right]\ . \tag{27.120}$$

for $l = -M/2, .., M/2-1$. Finally, we propagate the remaining time, $\Delta t/2$,

$$\psi(x, t+dt) = e^{-\frac{\imath}{\hbar}(V(x)+g_{1D}|\phi_x|^2)\frac{\Delta t}{2}}\phi_x\ . \tag{27.121}$$

Compared to the Crank-Nicholson algorithm time-splitting spectral algorithm has several advantages:

- TSSA is much much faster, especially, for large arrays;
- No divergence, perfect reversibility;
- Imaginary version yields same density shape as steepest descent.

But there are problems:

- The coherent version changes shape, maybe it's due to ifft(fft(x))!=x;
- The imaginary version mixes up real and imag parts;
- Don't know how to generalize to coupled GPEs.

27.8.2.1 Time-splitting spectral algorithm for coupled GPEs

Write the one-dimensional GPE in the form,

$$\begin{aligned}
\imath\hbar\frac{\partial\psi_1(x,t)}{\partial t} &= -\frac{\hbar^2}{2m}\nabla^2\psi_1(x,t) + V(x)\psi_1(x,t) + \frac{4\pi\hbar^2 a_s}{m(2r_h)^2}|\psi_1(x,t)|^2\psi_1(x,t) \\
&\quad + \frac{\hbar}{2}\Omega_{\rm mw}\psi_2(x,t) + \hbar\Delta_{\rm mw}\psi_1(x,t) \\
\imath\hbar\frac{\partial\psi_2(x,t)}{\partial t} &= -\frac{\hbar^2}{2m}\nabla^2\psi_2(x,t) + V(x)\psi_2(x,t) + \frac{4\pi\hbar^2 a_s}{m(2r_h)^2}|\psi_2(x,t)|^2\psi_2(x,t) \\
&\quad + \frac{\hbar}{2}\Omega_{\rm mw}\psi_1(x,t)
\end{aligned} \tag{27.122}$$

for $a < x < b$. Choose periodic boundary conditions, $\psi(a,t) = \psi(b,t)$ and $\psi_x(a,t) = \psi_x(b,t)$. We generalize the *time-splitting spectral algorithm*,

$$\begin{aligned}
\frac{\partial\psi_1(x,t)}{\partial t} &= -\frac{\imath}{\hbar}V(x)\psi_1(x,t) - \frac{\imath}{\hbar}g_{1D}|\psi_1(x,t)|^2\psi_1(x,t) - \imath\Delta_{\rm mw}\psi_1(x,t) - \frac{\imath}{2}\Omega_{\rm mw}\psi_2(x,t) \\
\frac{\partial\psi_2(x,t)}{\partial t} &= -\frac{\imath}{\hbar}V(x)\psi_2(x,t) - \frac{\imath}{\hbar}g_{1D}|\psi_2(x,t)|^2\psi_2(x,t) - \frac{\imath}{2}\Omega_{\rm mw}\psi_1(x,t) \\
\frac{\partial\psi_1(x,t)}{\partial t} &= \imath\frac{\hbar}{2m}\psi_{xx1}(x,t) \\
\frac{\partial\psi_2(x,t)}{\partial t} &= \imath\frac{\hbar}{2m}\psi_{xx2}(x,t) \ ,
\end{aligned} \tag{27.123}$$

i.e. we discretize in space and propagate half the way, $\Delta t/2$, in time,

$$\begin{aligned}
\varphi_{x1} &\equiv \psi_1(x,t) - \left[\left(\frac{\imath}{\hbar}V(x) + \frac{\imath}{\hbar}g_{1D}|\psi_1(x,t)|^2 + i\Delta_{\rm mw}\right)\psi_1(x,t) - \frac{\imath}{2}\Omega_{\rm mw}\psi_2(x,t)\right]\frac{\Delta t}{2} \\
\varphi_{x2} &\equiv \psi_1(x,t) - \left[\left(\frac{\imath}{\hbar}V(x) + \frac{\imath}{\hbar}g_{1D}|\psi_2(x,t)|^2\right)\psi_2(x,t) - \frac{\imath}{2}\Omega_{\rm mw}\psi_1(x,t)\right]\frac{\Delta t}{2} \ .
\end{aligned} \tag{27.124}$$

Since we here use the first order Taylor expansion of the exponential function, we introduce an error that we have to keep low by renormalizing the wavefunction after each step. Now we propagate the spectral components in momentum space and transform back,

$$\begin{aligned}
\phi_{x1} &\equiv \mathcal{F}^{-1}\left[e^{\imath\frac{\hbar}{2m}k^2\Delta t}(\mathcal{F}\varphi_{x1})_k\right] \\
\phi_{x2} &\equiv \mathcal{F}^{-1}\left[e^{\imath\frac{\hbar}{2m}k^2\Delta t}(\mathcal{F}\varphi_{x2})_k\right] \ ,
\end{aligned} \tag{27.125}$$

for $l = -M/2, .., M/2-1$. Finally, we propagate the remaining time, $\Delta t/2$,

$$\begin{aligned}
\psi_1(x,t+dt) &= \phi_{x1} - \left[\left(\frac{\imath}{\hbar}V(x) + \frac{\imath}{\hbar}g_{1D}|\phi_{x1}|^2 + \frac{\imath}{2}\Delta_{\rm mw}\right)\phi_{x1} - \frac{\imath}{2}\Omega_{\rm mw}\phi_{x2}\right]\frac{\Delta t}{2} \\
\psi_2(x,t+dt) &= \phi_{x1} - \left[\left(\frac{\imath}{\hbar}V(x) + \frac{\imath}{\hbar}g_{1D}|\phi_{x2}|^2\right)\phi_{x2} - \frac{\imath}{2}\Omega_{\rm mw}\phi_{x1}\right]\frac{\Delta t}{2} \ .
\end{aligned} \tag{27.126}$$

27.8.2.2 Spinor notation

It may be possible to simplify the notation by writing the wavefunction as a spinor, $\vec{\psi} \equiv \begin{pmatrix}\psi_1 \\ \psi_2\end{pmatrix}$. Now the non-kinetic part of the coupled GPE can be written,

$$\frac{\partial\vec{\psi}(x,t)}{\partial t} = M\vec{\psi}(x,t) \ , \tag{27.127}$$

with the matrix,

$$M = \begin{pmatrix} -\frac{\imath}{\hbar}V(x) - \frac{\imath}{\hbar}g_{1D}|\psi_1(x,t)|^2 - \imath\Delta_{\rm mw} & -\frac{\imath}{2}\Omega_{\rm mw} \\ -\frac{\imath}{2}\Omega_{\rm mw} & -\frac{\imath}{\hbar}V(x) - \frac{\imath}{\hbar}g_{1D}|\psi_2(x,t)|^2 \end{pmatrix} \ , \tag{27.128}$$

and the solution,

$$\vec{\psi}(x,t) = e^{Mt}\vec{\psi}(x,0) \ . \tag{27.129}$$

Let us now abbreviate the matrix by,

$$M = \begin{pmatrix} A & B \\ B & D \end{pmatrix} \ . \tag{27.130}$$

The matrix is diagonalized with the unitary transforms,

$$\mathcal{U} = \frac{1}{\sqrt{2\Delta}} \begin{pmatrix} \frac{A-D}{2B} + \Delta & \frac{A-D}{2B} - \Delta \\ 1 & 1 \end{pmatrix} \quad \text{and} \quad \mathcal{U}^{-1} = \frac{1}{\sqrt{2\Delta}} \begin{pmatrix} 1 & -\frac{A-D}{2B} + \Delta \\ -1 & \frac{A-D}{2B} + \Delta \end{pmatrix} \ . \tag{27.131}$$

The eigenvalue matrix is,

$$\mathcal{U}^{-1} M \mathcal{U} = \begin{pmatrix} E_1 & 0 \\ 0 & E_2 \end{pmatrix} \tag{27.132}$$

with $E_{1,2} = \frac{1}{2}A + \frac{1}{2}D \pm B\Delta$. Here we used the abbreviation $\Delta = \sqrt{\left(\frac{D-A}{2B}\right)^2 + 1}$. The formal solution now reads,

$$\vec{\psi}(x,t) = \exp\left[\mathcal{U}\begin{pmatrix} E_1 & 0 \\ 0 & E_2 \end{pmatrix}\mathcal{U}^{-1}t\right]\vec{\psi} = \mathcal{U}\begin{pmatrix} e^{E_1 t} & 0 \\ 0 & e^{E_2 t} \end{pmatrix}\mathcal{U}^{-1}\vec{\psi}(x,0) \ . \tag{27.133}$$

This formula can easily be computed, because the block matrices of transform U are diagonal in x.

27.8.3 Wavepacket propagation

27.8.3.1 1D simulations

We want to describe the one-dimensional evolution of an atomic wavepacket according to the Schrödinger equation. The problem is fully described by [664],

$$\imath\hbar\frac{\partial}{\partial t}\psi(z,t) = \frac{-\hbar^2}{2m}\frac{d^2}{dz^2}\psi(z,t) + V(z)\psi(z,t) \ . \tag{27.134}$$

Numerically the Schrödinger equation is integrated via,

$$\psi(z, t+dt) = \psi(z,t) + dt\,\dot{\psi}(z,t) \ . \tag{27.135}$$

The initial state of the wavepacket is set to $\psi(z,0) = e^{-z^2/2\bar{z}^2}e^{\imath kz}$, where $k \equiv \sqrt{2mE}/\hbar$ is its wavevector.

The numerical propagation is conveniently done with the time-splitting spectral algorithm [52, 51, 50, 302].

The flux is,

$$\psi\nabla\psi = 0 \ . \tag{27.136}$$

27.8.3.2 2D simulations

We want to describe the two-dimensional evolution of an atomic wavepacket according to the Schrödinger equation. The problem is fully described by,

$$\frac{-\hbar^2}{2m}\left(\frac{d^2}{dx^2}+\frac{d^2}{dz^2}\right)\Psi(x,z,t)+V(x,z)\Psi(x,z,t)=\imath\hbar\frac{\partial}{\partial t}\Psi(x,z,t)\ . \tag{27.137}$$

Since the potential is conservative, we separate the time-evolution,

$$\Psi(x,z,t)=\psi(x,z)e^{-\imath Et/\hbar} \tag{27.138}$$

The initial shape of the wavefunction moving along the y coordinate could be a Gaussian,

$$\psi(x,z)=\psi_x(x,0)\psi_z(0,z)=(2\pi\sigma_x\sigma_z)^{-1/2}\,e^{-x^2/4\sigma_x^2-z^2/4\sigma_y^2}\ . \tag{27.139}$$

We can assume $\sigma_z\gg\sigma_x$ and obtain an effectively one-dimensional model, $E=E_{kz}$. Set,

$$\psi(x,z,0)=\phi(x,z)e^{-\imath k_z z} \tag{27.140}$$

and,

$$-\frac{d^2}{dz^2}\phi(x,z)+2\imath k_z\frac{d}{dz}\phi(x,z)=\frac{d^2}{dx^2}\phi(x,z)+\left[\frac{2m}{\hbar^2}E_{kz}-\frac{2m}{\hbar^2}V(x,z)-k_z^2\right]\phi(x,z)\ , \tag{27.141}$$

and,

$$\frac{d}{dz}\phi(x,z)=\frac{d^2}{dx^2}\phi(x,z)-\frac{2m}{\hbar^2}V(x,z)\phi(x,z) \tag{27.142}$$

$$\frac{d}{dz}\phi(x,z)=\frac{1}{2\imath k_z}\frac{1}{dx^2}[\phi(x-dx,z)-2\phi(x,z)+\phi(x+dx,z)]-\frac{m}{\imath k_z\hbar^2}V(x,z)\phi(x,z)\ .$$

Discretize in steps dz.

27.8.3.3 Reflection from a potential barrier

Now we allow for a change of direction. We assume that a matter wave with wavevector $\mathbf{k}_0=k_{0x}\hat{\mathbf{e}}_x+k_{0y}\hat{\mathbf{e}}_y=k_0\hat{\mathbf{e}}_x\sin\alpha+k_{0y}\hat{\mathbf{e}}_y\cos\alpha$, runs towards a potential step. If the step is sharp, $V(x)=V_1\theta(-x)+V_2\theta(x)$, the following ansatz is reasonable,

$$\begin{aligned}\psi_0(x,y)&=e^{\imath xk_x+\imath yk_y}\\ \psi_1(x,y)&=re^{-\imath xk_x+\imath yk_y}\\ \psi_2(x,y)&=te^{\imath xk'_x+\imath yk_y}\end{aligned} \tag{27.143}$$

and we have to solve the equations,

$$\begin{aligned}\frac{-\hbar^2}{2m}\left(\frac{d^2}{dx^2}+\frac{d^2}{dy^2}\right)(\psi_0+\psi_1)&=(E-V_1)(\psi_0+\psi_1)\\ \frac{-\hbar^2}{2m}\left(\frac{d^2}{dx^2}+\frac{d^2}{dy^2}\right)\psi_2&=(E-V_2)\psi_2\ .\end{aligned} \tag{27.144}$$

In the step is smooth, $V(x\to-\infty)=V_1<V_2=V(x\to\infty)$, the situation is more complicated. Let us set $V(x)=(V_1-V_2)\frac{1}{\pi}\arctan x+\frac{1}{2}(V_1+V_2)$.

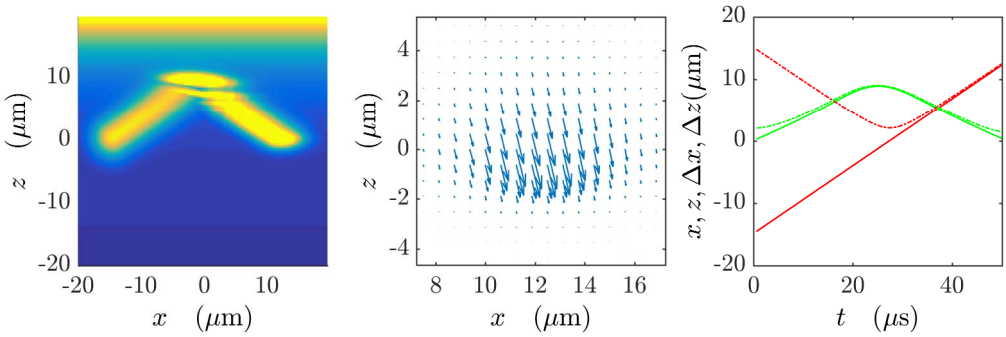

Figure 27.9: (code) Reflection of a wavepacket at a potential barrier. Do evanescent matter waves propagate along the barrier? Is there an atomic analogue to the Goos-Hänchen shift?

27.8.4 Exercises

27.8.4.1 Ex: Propagation of wavefunctions

Programs on the propagation of wavefunctions.

27.8.4.2 Ex: Programs on wavepackets reflected from potential barriers

Programs on wavepackets reflected from potential barriers.

27.9 Further reading

E.A. Cornell, *Very Cold Indeed: The Nanokelvin Physics of Bose-Einstein Condensation* [DOI]

F. Dalfovo et al., *Theory of Bose-Condensation in Trapped Gases* [DOI]

Ph.W. Courteille et al., *Bose-Einstein Condensation of Trapped Atomic Gases* [DOI]

A.J. Leggett, *Bose-Einstein condensation in the alkali gases Some fundamental concepts* [DOI]

C.J. Myatt et al., *Production of Two Overlapping Bose-Einstein Condensates by Sympathetic Cooling* [DOI]

W. Ketterle et al., *Making, probing and understanding Bose-Einstein condensates* [DOI]

Chapter 28

Superfluid and coherent properties of Bose-Einstein condensates

Superfluid liquids or gases are distinguished by their ability to sustain flow without dissipation, i.e. flow which is free of viscous damping. The phenomenon of superfluidity is a well-known property of liquid ^{4}He, but the relationship between superfluidity and Bose-Einstein condensation in this strongly interacting system is not trivial. The situation is much simpler in weakly interacting Bose gases, where the superfluid fraction is almost identical with the condensed fraction and the normal phase of the fluid with the thermal fraction. The availability of dilute gas Bose-Einstein condensates now offers the unique opportunity to study the complicated interdependence between superfluidity and condensation.

28.1 Superfluidity in quantum gases

The *superfluidity* of a gaseous condensate, which is one of its most apparent properties, is intrinsically linked to interatomic collisions. To characterize this phenomenon, it is useful to define some parameters. In the local-density approximation, the *homogeneity* of a gas of N atoms with the thermal de Broglie wavelength (26.9) confined inside a harmonic trap with the ground state size defined by (2.94), is characterized by,

$$\frac{k_B T}{\hbar\omega_{\rm trp}} = \frac{2\pi a_{\rm trp}^2}{\lambda_{\rm therm}^2} \ . \tag{28.1}$$

For a typical experimental situation, $k_B T/\hbar\omega_{\rm trp} \approx N^{1/3} \approx 100$. This shows that the assumption of a locally homogeneous gas is generally a good approximation. With the definition of the *healing length* (27.69), the degree of superfluidity of a condensate with density n can be cast into the form,

$$\frac{gn}{\hbar\omega_{\rm trp}} = \frac{a_{\rm trp}^2}{\xi^2} \ . \tag{28.2}$$

For a typical experimental situation, $a_{\rm trp}^2/\xi^2 \approx 100$. A parameter that well characterizes the importance of interatomic forces within a condensate is the gas *dilution*,

$$na_s^3 = \frac{a_s^2}{8\pi\xi^2} \ . \tag{28.3}$$

The typical numerical value $na_s^3 \approx 10^{-5}$ shows, that atomic gases are usually very dilute, although interatomic forces play an important role in the dynamics of condensates. In contrast, three-body collisions can be totally neglected, because the probability to have three atoms close to each other is even lower than the probability for two atoms.

There are several manifestations of phenomena linked to superfluidity, such as the behavior of collective elementary excitations, superfluid flow of non-circulating topological modes, quantized flux in vortices and matter wave solitons, which will be discussed in the following sections.

28.1.1 Landau's criterion for superfluidity

According to Landau, the phenomenon of superfluidity is rooted in the particular character of the Bogolubov spectrum of elementary excitations (27.54). Let us consider a bosonic fluid at a given temperature moving with velocity v. A macroscopic obstacle in the path of the superfluid can generate elementary excitations. That is, a fraction of the kinetic energy of the fluid is transferred to these excitations, thereby decelerating the fluid and causing *viscosity*. With the excitation energy $\mathcal{E}(p)$ and the momentum $\mathbf{p}$, the total energy of the fluid interacting with the obstacle is,

$$E = \mathcal{E}(p) + \frac{(\mathbf{p}+M\mathbf{v})^2}{2M} = \mathcal{E}(p) + \mathbf{p}\cdot\mathbf{v} + \tfrac{1}{2}Mv^2 + \frac{p^2}{2M} \simeq \mathcal{E}(p) + \mathbf{p}\cdot\mathbf{v} + \tfrac{1}{2}Mv^2 \ , \tag{28.4}$$

where M is the total mass of the superfluid. Since the term $Mv^2/2$ is the initial kinetic energy of the fluid, $\mathcal{E}(p) + \mathbf{p}\cdot\mathbf{v}$ represents the excitation energy. And since the kinetic energy of the superfluid can only be diminished by the excitation, we need $\mathcal{E}(p) + \mathbf{p}\cdot\mathbf{v} < 0$. Finally, as $\mathcal{E}(p)$ must be positive, the condition for generating elementary excitations is,

$$\mathcal{E}(p) \leq pv \ , \tag{28.5}$$

where $\mathbf{p}$ and $\mathbf{v}$ are antiparallel.

Therefore, there is a relative *minimum velocity* between the fluid and the obstacle, called *critical Landau velocity*, for creating excitations,

$$v_c = \min\left(\frac{\mathcal{E}(p)}{p}\right) \ . \tag{28.6}$$

For velocities below v_c, it is impossible to generate excitations, and there is no mechanism to decrease the kinetic energy of the fluid. As a result, the system becomes superfluid [499].

The spectrum of elementary excitations for a weakly interacting condensate, is the Bogolubov spectrum (27.54). The graph Fig. 28.1 shows, that for velocities below the sound velocity given by (27.56), $v < c_s$, the curve representing the propagation of

the perturbation does not cross the Bogolubov spectrum. That is, the perturbation can not be converted into excitations, which is only possible when $v > c_s$.

In an ideal condensate without interactions, $a_s = 0$, the Bogolubov spectrum reduces to the quadratic dispersion relation of free particles, which means that there is no critical velocity, $v_c = c_s$. Consequently, it is always possible to excite the condensate, that is, an ideal condensate can not be superfluid, and, as first pointed out by Landau: *superfluidity and Bose-Einstein condensation are different phenomena.*

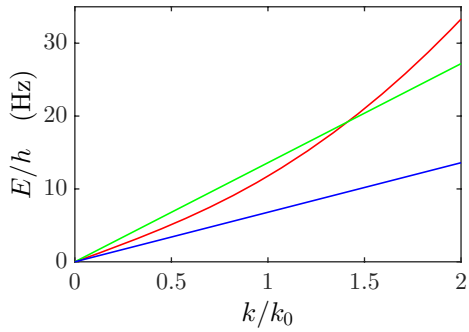

Figure 28.1: (code) Landau's criterion for superfluidity. Slow perturbations (blue line) do not cross the Bogolubov spectrum (red line) and do not generate excitations. Rapid perturbations (green line) cross the spectrum and can be dissipated.

28.1.2 Impurity scattering

A first hint for the superfluid nature of Bose-Einstein condensates is the fact that the hydrodynamic theory of superfluidity describes well the collective excitations (see Sec. 27.5). Moreover, several experiments provided direct evidence for the superfluid nature of condensates. For example, via a calorimetric measurement [680]: A condensate, stirred around by a rotating far blue-detuned laser beam, dissipated atoms to the thermal fraction of the atomic cloud, provided the stirring velocity exceed a certain *critical velocity* v_c: At lower velocities, the perturbation did not lead to dissipation. At higher velocities, phonons were excited and the cloud was heated. In a subsequent experiment, perturbation-induced density fluctuations were observed *in vivo* and *in situ* [633]. When the stirring speed was below the critical velocity, the density was almost homogeneous, thus indicating superfluid flow. When, however, the stirring speed exceeded v_c, atoms piled up in front of the stirring beam, and the resulting pressure gradients led to a turbulent flow around the perturbation and to dissipation.

The critical velocity v_c found in the stirring experiments was about ten times smaller than the local sound velocity c_s,

$$c_s \equiv \sqrt{\frac{gn}{m}} = \frac{\hbar}{\sqrt{2}m\xi} \,. \tag{28.7}$$

In fact, while the onset of dissipation is accelerated by turbulence around the *macroscopic object* traversing the superfluid, the local sound velocity (28.8) is derived for

a *microscopic object*. Puzzled by this discrepancy, Chikkatur *et al.* [149] studied the motion of microscopic atomic impurities through a condensate. The *impurity* was created by transferring a few atoms out of the original BEC from the trapped state $|F = 1, m_F = -1\rangle$ to the free state $|F = 1, m_F = 0\rangle$ via induced Raman transitions. The initial velocity was adjusted by the laser beams exciting the Raman transition (polarization, incident angle and relative detuning) to satisfy the Bragg condition (see Sec. 29.2). After the free impurity passed through the BEC, the trap was switched off, a Stern-Gerlach magnetic field gradient was pulsed to separate atoms in different Zeeman states, and finally the atoms were detected via time-of-flight imaging (see Sec. 26.6.1). When the initial velocity of the impurity was well above a critical value given by the local velocity of sound, ultracold s-wave collisions between impurity atoms and the stationary condensate distributed the momenta of the collision partners uniformly. In TOF images this appeared as a *circular halo* centered around the center-of-mass momentum of the collision partners (see Fig. 28.2). When, however, the initial velocity of the impurity was reduced, its collision rate with the stationary condensate was suppressed and the trajectory became superfluid.

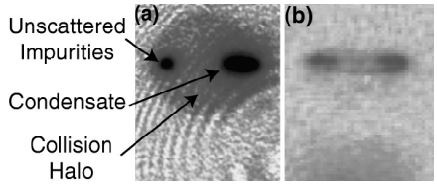

Figure 28.2: (a) Scattering of impurities at velocities above the critical velocity. The presence of a halo indicates the occurrence of collisions between the impurity and the condensate dissipating the relative kinetic energy. (b) For velocities below the critical velocity the halo disappears.

28.1.3 Hydrodynamic theory of superfluidity

For the description of superfluidity a hydrodynamic theory is adequate. Therefore, we will rewrite the time-dependent Gross-Pitaevskii equation (27.21). We consider the general case, in which the external potential $V_{\rm trp}(\mathbf{r}, t)$ depends on time. The wavefunction can be written by defining the density and the velocity fields,

$$\phi(\mathbf{r}, t) = \sqrt{n_0(\mathbf{r}, t)} e^{\imath\theta(\mathbf{r},t)} \tag{28.8}$$

$$\mathbf{v}_s(\mathbf{r}, t) = \frac{\mathbf{j}(\mathbf{r}, t)}{n_0(\mathbf{r}, t)} = \frac{1}{2\imath m} \frac{1}{n(\mathbf{r}, t)} \left[\phi^*(\mathbf{r}, t)\nabla\phi(\mathbf{r}, t) - \nabla\phi^*(\mathbf{r}, t)\phi(\mathbf{r}, t)\right] .$$

This gives,

$$\mathbf{v}_s(\mathbf{r}, t) = \tfrac{\hbar}{m}\nabla\theta(\mathbf{r}, t) . \tag{28.9}$$

From the GPE we derive the continuity and the Navier-Stokes equations:

$$\frac{\partial n}{\partial t} + \nabla(\mathbf{v}_s n) = 0 \tag{28.10}$$

$$m\frac{\partial \mathbf{v}_s}{\partial t} + \nabla\left(V_{\rm trp} + gn - \frac{\hbar^2 a}{2m\sqrt{n}}\nabla^2\sqrt{n} - \mu + \frac{m}{2}\mathbf{v}_s^2\right) = 0 .$$

We can see that the hydrodynamic behavior of a BEC depends greatly on the quantum phase θ. When the kinetic pressure is small compared to the mean-field energy,

$$m\frac{\partial \mathbf{v}_s}{\partial t} + \nabla\left(V_{\rm trp} + gn + \frac{m}{2}\mathbf{v}_s^2\right) = 0 \ . \tag{28.11}$$

This is the *Euler equation* for a fluid with a potential flow. This equation and the *continuity equation* have the typical structure of equations describing superfluids at $T = 0$. This is due 1. to the presence of a Bose-Einstein condensate allowing us to formulate an equation for a complex *order parameter*, and 2. to the presence of interactions, included via the pressure term in the Euler equation, which are necessary condition for superfluidity.

At zero temperature, the entire fluid is superfluid. Moreover, in the Gross-Pitaevskii approximation, the whole fluid is condensed. Therefore, $\mathbf{v}_s(\mathbf{r}, t)$ is the velocity flow of the superfluid [1].

28.2 Topological modes

Significant manifestations of superfluidity are associated with rotational phenomena. An example is the occurrence of *scissor modes* [351], which are excited, when an angular momentum is suddenly applied to a condensate confined in an anisotropic trap. This can be done via a sudden reorientation of the symmetry axis of the trap [548, 547]. The condensate responds to this perturbation by an oscillation of its inclination implemented by an *irrotational superfluid flow*. The excitation spectrum reflects the strong reduction of the inertial momentum for superfluids.

The most rigorous manifestation of superfluidity, however, is the occurrence of a quantized and persistent current, called *quantized vortex*. In contrast to the elementary excitations, which must be created by perturbations, the vortex is a *stationary* (or *topological mode*) solution of the Gross-Pitaevskii equation Eq. (27.21).

Work on vortices has been done by [558, 541, 680, 633, 149, 351, 548, 542, 147, 18, 704, 236, 424, 131, 901].

28.2.1 Vortices

From Eq. (28.9) it is easy to see, that the superfluid is non-rotational, that is,

$$\nabla \times \mathbf{v}_s(\mathbf{r}, t) = 0 \ . \tag{28.12}$$

This raises the question, how vortices are possible. The solution to this apparent contradiction is, that Eq. (28.12) does not apply, when the phase exhibits a singularity. Consider, for example, a closed loop C around the singularity. In a vortex, the superfluid current is pulled by the phase gradient, $\mathbf{v} = \frac{\hbar}{m}\nabla\theta$. For the condensate wavefunction to be well defined, the phase variation $\Delta\theta$ around the loop must be a multiple of 2π, that is,

$$\Delta\theta = \oint_C \nabla\theta \cdot d\mathbf{l} = 2\pi\ell \ . \tag{28.13}$$

[1] This is not the case for strongly interacting superfluids, such as superfluid helium, where the normal fluid fraction is considerable.

where ℓ is an integer. Therefore, we can calculate the *circulation* Γ around the closed loop, that is,

$$\Gamma = \oint_C \mathbf{v}_s(\mathbf{r},t)\cdot d\mathbf{l} = \frac{h}{m}\ell \ . \tag{28.14}$$

Apparently, the superfluid circulation is quantized in units of $\hbar/m$. The parameter ℓ is called *charge of the vortex* and measures, in unit of h, the quantized angular momentum of the vortex.

In addition, the flow must be persistent, because its circulation can only be changed in a discontinuous way, by overcoming a discrete energy barrier, which requires energy coming e.g. from thermal excitations. Clearly, the normal (thermal) fraction of a gas can also have a circular flow. However, the disordered microscopic motion of each individual particle causes a viscous drag that prevents the persistence of the flow in the absence of a torque. This is in contrast to superfluid flow, which persists even without external torque. The issues of vortex stability, formation, and topology were addressed in recent experiments [557, 541, 542, 147, 18]. Solve the Excs. 28.2.6.1 and 28.2.6.2.

The kinetic energy per unit vortex length can be estimated from a semi-classical approach. First, we define as the mass density ρ_m of the superfluid. If n is the particle density, $\rho_m = nm$. The kinetic energy of a flux line at the radius r is,

$$\mathcal{E}_{\rm kin} = \tfrac{1}{2}\rho_m v_s^2 = \frac{\hbar^2\ell^2}{2m}\frac{n}{r^2} \ . \tag{28.15}$$

To obtain the kinetic energy per unit length, we integrate the expression (28.21) over a plane perpendicular to the vortex axis. Note, however, that the velocity field is $v_s \propto r^{-1}$ and, therefore, can not be integrated from zero. Instead, we begin the integration at a radius given by the *healing length* ξ, which represents a measure of the vortex core size. Now, the kinetic energy per unit length is,

$$E_{\rm semi} = \int_0^{2\pi}\int_\xi^R \mathcal{E}_{\rm kin}(\mathbf{r}) r dr d\theta = \pi n \frac{\hbar^2\ell^2}{m}\ln\frac{R}{\xi} \ . \tag{28.16}$$

Note, that a multiply charged vortex carrying the entire angular momentum $\ell = \ell_0$ of the superfluid is energetically less favorable than an ensemble of ℓ_0 vortices with unit charge $\ell = 1$. Therefore, a multiply charged vortex is unstable and may decay to several single charge vortices.

To calculate exactly the energy of a vortex, we do the following ansatz,

$$\Phi_0(\mathbf{r}) = \phi(r,z)e^{\imath\ell\vartheta} \ , \tag{28.17}$$

we then solve the Gross-Piatevskii equation (27.21) numerically, and calculate the expectation value of the energy of the vortex through the expression,

$$\langle\Phi_0|\hat{H}|\Phi_0\rangle = \int d^3\mathbf{r}\left[\tfrac{\hbar^2}{2m}|\nabla\Phi_0(r,z)|^2 + V_{\rm trp}|\phi(r,z)|^2 + g|\phi(r,z)|^4\right] \ , \tag{28.18}$$

where $\hat{H}$ is the Gross-Pitaevskii Hamiltonian.

The calculation yields for energy per unit length of a single charge vortex in a uniform cylindrical condensate [649],

$$E_{\rm unif} = \pi n\tfrac{\hbar^2}{m}\ln\left(1.464\tfrac{R}{\xi}\right) \ , \tag{28.19}$$

which is very close to our semi-classical prediction. Although the wavefunction $|\phi(r,z)|$ has no analytic form, it can be shown by a variational approach, that the trial wavefunction,

$$|\phi(r,z)| = \frac{nr}{\sqrt{2\ell^2\xi^2 + r^2}} \tag{28.20}$$

is a good approximation [649]. Note that the healing length ξ characterizes the size of the vortex. For a superfluid, we can calculate the total energy of the vortex exactly, because the fluid is confined in all directions,

$$E_{\rm tot} = \tfrac{4\pi n_0}{3}\tfrac{\hbar}{m}\ln\left(0.671\tfrac{R_r}{\xi_0}\right) \ , \tag{28.21}$$

where n_0 and ξ_0 are, respectively, the density and healing length at the center of the fluid. R_z and R_r are, respectively, the extensions of the cloud along the axial and radial directions within the Thomas-Fermi approximation.

28.2.1.1 Creation and detection of vortices

The first superfluid vortex was observed 1979 in ^{4}He [894]. For gaseous condensates, two approaches have been employed to produce vortices. Either one stirs the atomic cloud in order to impart an angular momentum to it. This can be done by rotating the (anisotropic) trap during the process of forced evaporation with time-orbiting magnetic fields or with an optical spoon. The vortex state is formed when the critical temperature for condensation is crossed. An alternative method is to imprint a 2π circular phase gradient into a previously created condensate. Indeed, the local phase of a matter wave can be manipulated via a local modification of the potential depth, which can be achieved by a Stark shift induced by a far-detuned laser beam [236]. Focused into a tiny spot which is moved across the condensate, the laser beam will create a phase gradient, which in turn will cause a velocity flow. It is important to force the local density at the center of the vortex to zero, which can be achieved via a proper design of the trapping potential (e.g., a Mexican hat-shaped potential), and let the BEC then relax to the vortex state.

A variation of this method [867] avoids the need for relaxation processes. In this configuration the phase gradient is created through a *local* Raman coupling between two internal atomic states (for example, in ^{87}Rb the two trappable Zeeman states $|F, m_F\rangle = |1,-1\rangle$ to $|2,1\rangle$). At the spots, where the focused Raman beams hit the condensate, atoms were dynamically converted from the ground state to the excited state. The circular trajectory of the spots and the rotation speed were calculated such as to generate a toroidal topology for the adiabatic population transfer. The process was coherent and allowed to directly construct and shape the vortex wave function. We study this experiment in more detail in the Exc. 28.2.6.3.

In confined single-species condensates the diameter of the vortex core is on the order of the healing length, 2ξ. With typical values of $2\xi \approx 0.4$ μm it is thus way too small to be imaged *in situ*, and ballistic expansion times of several 10 ms are necessary. On the other hand, in double condensates formed by two repelling species (e.g. the two states $|2,1\rangle$ and $|1,-1\rangle$ in ^{87}Rb), one of the species can form a vortex around the second. In this case, the diameter of the vortex core, is determined by the diameter of the condensate of the second species and, hence, much larger. When

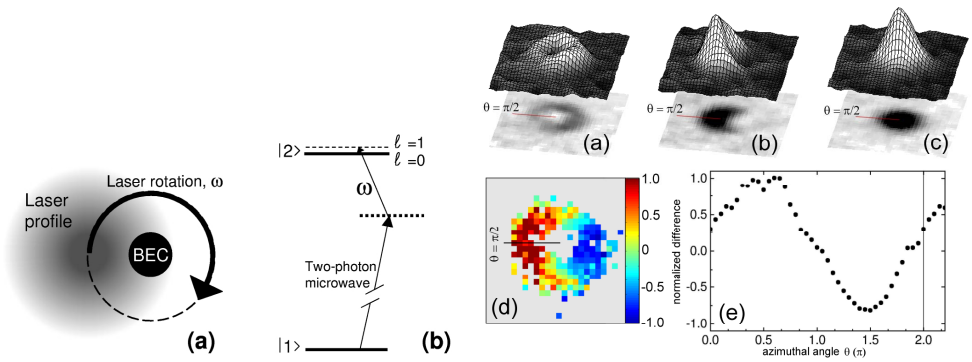

Figure 28.3: (Left) Scheme of the experiment [557]. (Medium) Level system used. (Right) Density distribution of a vortex state: (a) (the visible atoms are in the upper hyperfine state), (b) after a $\pi/2$-pulse and (c) after a π-pulse (the visible atoms are in the lower hyperfine state). The images (d) and (e) visualize the phase slip around the vortex.

the second species is selectively removed (e.g. by the radiative pressure exerted by a resonant laser), and the vortex in the first species can be studied by *in situ* imaging of the confined density distribution [558].

A particularly smart detection method for vortices is based on matter wave interferometry (see Sec. 28.3.3). Here, two matter waves, that is, the vortex state in $|2,1\rangle$ and a (reference) ground state BEC in $|1,-1\rangle$ are coherent mixed via a resonant two-photon radiofrequency $\pi/2$-pulse. The resulting matter wave interference patterns reveals the phase profile of the vortex (see Fig. 28.3).

28.2.1.2 Stability

In a topologically 'singly-connected' trap, for example a potential harmonic, vortices do not represent the lowest energy eigenstate, and they must decay to the ground state. If the mean-field energy of the condensate is weak compared to the kinetic energy, $gn_0/\hbar\omega_z \ll 1$, the healing length will exceed the size of the BEC, $\xi \gg a_{\rm trp}$, and the vortex rapidly decays by dissipating its excess energy to thermal excitation. Such BECs can not be considered superfluid. If the mean-field interaction is strong, the vortex spontaneously breaks azimuthal symmetry, moves away from the center and exits the condensate on a spiral-shaped trajectory [704]. Nevertheless, the decay time may be quite long.

On the other hand, a vortex can be the ground state of a 'multiply-connected' trap (for example, a toroidal potential). Such a potential can be realized as the temporal average of a harmonic potential with a small rotating anisotropy [541]. In such geometries vortices are extremely stable.

28.2.1.3 Vortex precession

A radial force acting on a vortex results in a radial displacement and a precession about the symmetry axis. The effect, known as *Magnus effect* [424], is due to pressure

imbalances on the vortex surface. A radial force naturally arises, when the core is displaced from the center, because local pressure gradients will force the vortex out of the center toward regions with lower densities. Experimentally, a slow precession ($\sim$ 1 Hz) spiraling the vortex toward the rim of the condensate has been observed [18] by taking a succession of nondestructive images.

28.2.2 Vortex lattices

Superfluid ^{4}He in a rotating bucket spontaneously develops symmetrically organized vortex patterns. Similar phenomena can be observed, when a dilute gas Bose-Einstein condensate is forced to rotate [131] at a given frequency Ω. The energy in the rotating system receives an additional contribution from the centrifugal term, $U_{rot}(\mathbf{r}) = U_{\rm trp}(\mathbf{r}) - \Omega L_z$, where $L_z = \hbar N l_z$, and $l_z = \imath(y\partial_x - x\partial_y)$ is the angular momentum of the individual atoms. If the rotation is slow, the energy ΩL_z is too small to force the condensed wavefunction to rotate. If the rotation frequency is beyond a critical value Ω_c, the *time-averaged* potential, $U_{rot}(\mathbf{r})$ eventually develops a local minimum in the center, thus adopting the toroidal shape. For non-interacting gases, the critical frequency coincides with the radial secular frequency, $\Omega_c = \omega_r$. Then the radial restoring force of the trap does not balance the centrifugal force, such that atoms can escape from the trap. However, for superfluid gases the critical frequency is reduced, $\Omega_c < \omega_r$. Between the rotation frequencies $\Omega = \Omega_c$ and $\Omega = \omega_r$, the state with the lowest energy in the toroidal potential is the vortex, whose filament is pinned to the symmetry axis. For even higher rotation frequencies, we could expect a single vortex with a larger winding number (more than the phase winding of 2π for a single turn). However, individual multiple-order vortices in harmonic traps are unstable. Instead, vortex lattices [131] called *Abricosov lattices* will form. For a given trapping potential and mean-field energy, the symmetry of the lattice and the number of vortices depend on the rotation frequency Ω. Counter-intuitively, the angular momentum of individual particles l_z *is not quantized*. When we vary Ω, regimes of forbidden l_z (i.e. when no vortex pattern is formed) alternate with allowed regimes. The discontinuous transition from one vortex pattern to another is a first-order phase transition, which spontaneously breaks one symmetry to form another. An upper limit for the rotation speed is given by the equilibrium between the centrifugal force and the radial restoring force of the trapping potential at $\Omega = \omega_r$.

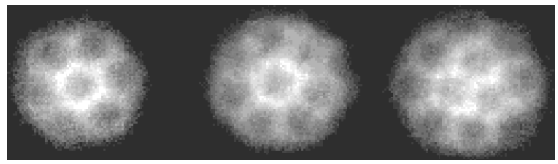

Figure 28.4: Abricosov vortex lattice.

These patterns of vortex lattices were observed in experiments using the *stirring method*, which consists in brushing a far-detuned focused laser ('optical spoon') around the rim of a condensate [541] at a certain frequency Ω. In this experiment, the ratio of the mean-field energy to the kinetic energy was $gn_0/\hbar\omega_z = a_{\rm trp}^2/2\xi^2 > 100$. Beyond a certain critical rotation frequency, $\Omega_c \approx 2\pi \times 150$ Hz, a single central vortex

was formed. At even higher frequency, a symmetrical vortex lattice appeared in a transverse plane (see Fig. 28.4). Finally, at rotation frequencies near the radial trap frequency ω_r, the condensate wavefunction became turbulent and finally disappeared. As soon as the optical spoon was removed, the vortex lattice gradually decayed losing the vortices one by one.

28.2.3 Solitons

Work on solitons has been done by [899, 866, 557, 867, 601, 690, 423, 612, 129, 42, 251, 124, 223].

28.2.3.1 Dark solitons

Solitons are non-singular solutions of any equation satisfying,

$$|\psi(\mathbf{r},t)| = |\psi(\mathbf{r}-\mathbf{v}t)| \ . \tag{28.22}$$

Solitons are well known to occur in non-linear optical media, for example in optical fibers, when dispersion is counterbalanced by self-phase modulation, such that optical signals propagate without spreading. The Gross-Pitaevskii equation is another example for a nonlinear wave equation supporting soliton-like solutions. States called *dark soliton* or *twisted state* with a dynamically stable density dip are expected in condensates with repulsive interactions [601, 690, 423, 612]. In contrast to topologically stable states, for example, vortices, dark solitons are pseudo-defects, the decay of which, even though it may be slow, is topologically trivial. Due of the greater freedom of movement of their wavefunctions, solitons can be distorted by complex deformations [129]. Soliton-like matter wave states were initially observed in superfluid ^{3}He-B [42]. In dilute gases, the size of the solitons is of the order of healing length.

The first dark solitons in dilute gases were created by applying an inhomogeneous phase shift to a condensate [124, 223]. One half of the condensate was irradiated by a far-detuned laser pulse (detuning Δ, Rabi frequency Ω, duration $\tau \ll \hbar/gn_0$) in order to advance the phase of this part of the condensate by $\varphi = \Omega^2\tau/4\Delta$. When the phase shift was set to π, an abrupt phase gradient developed at the boundary delimiting the two halves. The condensate reacted to the phase gradient by developing a deep density minimum all along the boundary corresponding to a soliton (see Fig. 28.5). The phase distribution can also be imaged by interferometric techniques based on Bragg diffraction (see Sec. 29.2). In one dimension, the density dip of the soliton corresponds to a node of the dipolar topological mode [867, 601, 612].

The abrupt phase gradient at the boundary plane exerts a force trying to increase the gap, while repulsive interactions work to heal it. At zero temperature, this balance ensures the dynamic stability of the soliton. While a perfect dark soliton should be stationary, experiments [124, 223] revealed that solitons with finite contrast propagate along the direction of the plane's normal vector with a velocity, which must always be less than the local sound velocity,

$$v_{\rm sol} = c_s\sqrt{\frac{n_{\rm sol}}{n}} \ , \tag{28.23}$$

where n is the peak density of the condensate and n_{sol} the density at the bottom of the dark soliton [690, 423]. Fig. 28.5 shows that the soliton develops a curvature when

it propagates. One reason for this is a slower sound velocity, $c_s = \sqrt{gn_0/m}$, on the edges of the condensate, where the density is lower. The second reason is, that the density in the dip, $n_{\rm sol}$, goes to zero at the edges. In the presence of a thermal cloud, dissipation reduces the contrast of the density dip and accelerates the soliton, until it reaches the sound velocity c_s and finally disappears.

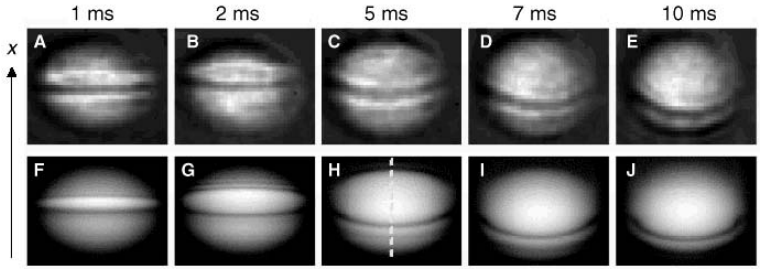

Figure 28.5: Solitons.

28.2.3.2 Bright solitons

In condensates with attractive interactions *bright solitons* have been observed, as well [462, 449].

28.2.4 Description of general topological modes

A coherent *topological mode* is a stationary solution of the *Gross-Pitaevskii equation*,

$$\left[-\frac{\hbar^2}{2m}\nabla^2 + U_{\rm trp}(\mathbf{r}) + \frac{4\pi\hbar^2 a_s}{m}N|\phi_n|^2\right]\phi_n(\mathbf{r}) = E_n\Phi(\mathbf{r}) \ . \tag{28.24}$$

These modes can be calculated using an *optimized perturbation theory* [175]. We separate the Hamiltonian into an unperturbed part and a perturbed part, $\hat{H} = \hat{H}_0 + \Delta\hat{H}$, where the unperturbed part now depends on variational parameters,

$$\hat{H} = \hat{H}_0(u, v, ..) + \Delta H \ . \tag{28.25}$$

As usual, the first-order energy correction is,

$$E_n^{(1)}(u, v, ..) = E_n^{(0)}(u, v, ..) + \langle\Phi_n^{(0)}|\Delta\hat{H}|\Phi_n^{(0)}\rangle \ , \tag{28.26}$$

where the $\Phi_n^{(0)} = \Phi_n^{(0)}(u, v, ..)$ are the solutions of the unperturbed Hamiltonian $\hat{H}_0$. Once the energies are found, we must minimize them in terms of the variational parameters,

$$\frac{\partial E_n}{\partial u} = 0 \quad , \quad \frac{\partial E_n}{\partial v} = 0... \ . \tag{28.27}$$

With these parameters, we obtain the energies and the wavefunctions [2].

[2] Excited modes can be understood stationary matter waves with the trap serving as a cavity.

28.2.4.1 Creation of topological modes

One possibility of creating topological modes is to apply a temporal modulation to the trapping potential [899]. The modulation frequency must be resonant with the energy difference between the excited mode and the ground state. Another possibility is to vary the interaction energy via a modulation of the scattering length in the vicinity of a *Feshbach resonance* [179].

The steady-state situation of a cloud in a stationary trap is *thermal equilibrium*, that is, inversion is not possible. At a time-dependent (e.g. shaking) potential however, for example, transitions to excited vibrational levels can be driven. These can generate inversion, provided collision-induced relaxation is not too fast [3].

28.2.5 Turbulence

The issue of turbulence is one of the most important problems of classical physics yet to be solved [278]. In superfluids, restrictions imposed by quantum mechanics constrain the emergence of turbulence, which is then called *quantum turbulence*. On the other hand, the study of quantum turbulence can improve our understanding of *classical turbulence* [243]. Recently, the study of the dynamics of a ensemble of vortices in a Bose-Einstein condensate allowed the identification of signatures of quantum turbulence [386, 370].

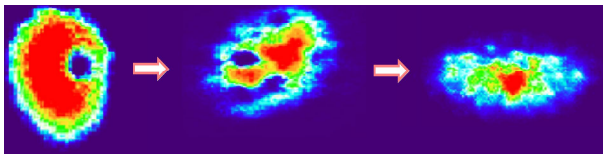

Figure 28.6: Turbulence.

28.2.6 Exercises

28.2.6.1 Ex: Comparison between the quantum and the classical vortex

Consider a vortex around a straight line along the z-axis at $r = 0$. Compare the radial velocity variation of a quantum vortex with that of a classical one.

28.2.6.2 Ex: Singularity in vortices

Show for the above simple example,

$$\nabla \times \mathbf{v}_s(\mathbf{r}, t) = \hat{\mathbf{z}} \frac{\ell h}{m} \delta(x)\delta(y) \ .$$

[3] The dynamics of atoms trapped in a harmonic potential is similar to the Jaynes-Cummings dynamics of an optical mode. However, the non-linear condensate self-interaction changes the situation and makes the collisions being collective.

28.2.6.3 Ex: Phase-engineering of a vortex state

The first vortex in a dilute gas was created at the JILA [558]. Study the paper and explain in detail, how the vortex was created.

28.3 Atom optics

Unlike the photons [497], there is no doubt about the fact that atoms are particles. On the other hand, the deep analogy between light and matter, resulting from the particle-wave duality, prompted de Broglie in 1924 to ascribe a *wave* to each massive particle, whose wavelength would be a function of the particle's momentum. Whether an atom behaves more like a particle or a wave depends on the specific experimental situation. For example, interferometers emphasize its wave nature: Atoms are able to interfere with *themselves*, when their Broglie wavelength is coherently split and then recombined. (Bosonic) atoms are able to interfere with other atoms, if their de Broglie wavelengths are greater than their distances. For this to happen, it requires high densities and very low temperatures, that is, high phase space densities. When the phase space densities are so high that the Broglie waves come into contact, effects of quantum statistics begin to influence the dynamics of the atoms, and fermions will behave differently from bosons.

Analogously to the distinction between classical and laser optics, we can separate the area of conventional atomic optics working with individual, mutually incoherent atoms, from the area of coherent atomic optics working with Bose-Einstein condensates. Unlike for the study of phenomena related to superfluidity, gases with weak interatomic interactions are generally more useful for the study of the coherent properties of condensates and for application in atomic optics. Nevertheless, interatomic collisions increase the complexity of the dynamics of matter waves interacting with atom optical devices, by introducing non-linarities analogous to those known from nonlinear optics and thus raising the field of *nonlinear atom optics*.

28.3.1 Atomic optical tools

The basic equipment of an atomic optics laboratory [588, 4, 656, 289, 674] comprises atomic beams, atom traps, lenses and waveguides, various types of mirrors and resonators, Stern-Gerlach type matter wave polarizers, de Broglie wave phase shifters based on Bragg diffraction, and a multitude of atomic beam gratings. Obviously, gratings allow the construction of atom interferometers, which are used in experiments and high precision devices, for example, atomic gyroscopes and gravimeters. Other applications for atomic beams controlled by atom optical elements are in atomic holography for the projection of complex pattern into integrated semiconductor circuits [602], in lithography [823], and in microscopy [235].

An important feature of atoms (as compared to light) is the existence of a rich internal structure providing a wealth of additional degrees of freedom, whose dynamics (of the Bloch vector) is frequently entangled with the motional dynamics (of the de Broglie wave). This allows to monitor (e.g. in matter wave interferometers) the evolution of the motional state of the matter wave via an observation of the internal

excitation. Moreover, in some interferometers, the de Broglie wave is not even split, and one does interferometry with completely immobile atoms or ions [411].

The epitome of a coherent light source is the laser, and we may ask whether there is a material analogue, which would be a source of coherent matter [874, 105, 777, 400, 609, 471] serving for *coherent atom optics*. In fact, we may already consider a trapped condensate as a stationary *atom laser* pulse with the trapping potential playing the role of the laser resonator. While most atom optical devices (including conventional atomic interferometers) do not require mutual coherence of atoms, certain applications take advantage of an intense, highly directional, monochromatic, and coherent atom source. In this respect, atom lasers are much superior to thermal atomic beams. While a thermal beam contains about 10^{-12} atoms per mode and a magneto-optical trap about 10^{-6}, a condensed mode may contain more than 10^6 atoms. Condensates offer the advantage of large de Broglie wave amplitudes and de Broglie wavelengths as long as their actual size (which can be much longer than optical wavelengths). And for an atom laser, the coherence length can even be longer than that of the condensate from which it emerged. This obviously has a major impact on the sensitivity and resolution of atom optical elements, in particular those, where atomic coherence is important, for example, atom interferometers. Without doubt atom lasers will replace conventional atomic beams in precision measurement of fundamental constants and tests of fundamental symmetries ([Phys. World (mar,97) p.43]). Finally, atom lasers are crucial for nonlinear optics.

Also of interest are the references [776, 602, 681, 502, 709, 48, 385, 247, 673, 222, 396, 692, 422, 734, 76, 235, 860].

28.3.2 The atom laser

A large number of techniques for making an *atom laser* has already been developed [571, 24, 578, 19, 90, 360, 552] and theories on atom lasers have been formulated [357, 607, 872, 848, 412]. The following sections are devoted to explaining, why the term atom laser is justified. For the reasoning we will let as guide by the optical laser.

We already mentioned the *trapping potential* (replacing the resonator in lasers) as a major ingredients of an atom laser [4]. Another necessary feature would be the availability of an *output coupling* mechanism, which we still need to discuss in the following. Apart from these more practical aspects, we need to prove, that atom lasers are indeed *phase-coherent*, and we have to clarify the role of *bosonic stimulation* and of *irreversibility* in the production process of a BEC.

28.3.2.1 Bosonic stimulation and irreversibility

The gain mechanism for optical lasers is photonic stimulation of atoms inciting them to emit other photons into the stimulating mode. The atomic laser operates in a similar way. Atoms trapped in a potential constitute a thermal reservoir. Binary collisions redistribute the atoms among the vibrational energy levels of the potential. If a vibrational level already contains an atomic population, Bose-Einstein quantum

[4] Coherent reflection of atom laser beams has been demonstrated [98, 26, **?**], and an atom laser cavity with efficient transverse focusing has been built [92]

statistics will encourage atoms involved in a collision process to join this level. Ultimately, this comes down to an irreversible pumping of a single level, where the atoms accumulate to build a single degenerate quantum state. Bose condensation is always the result of *bosonic stimulation*. However, the dynamics and time scale for the formation of a condensate have been controversially discussed, until some experiments [578] could directly visualize *in vivo* the process of nucleation and the exponential amplification at the center of a thermal cloud (see Fig. 28.7).

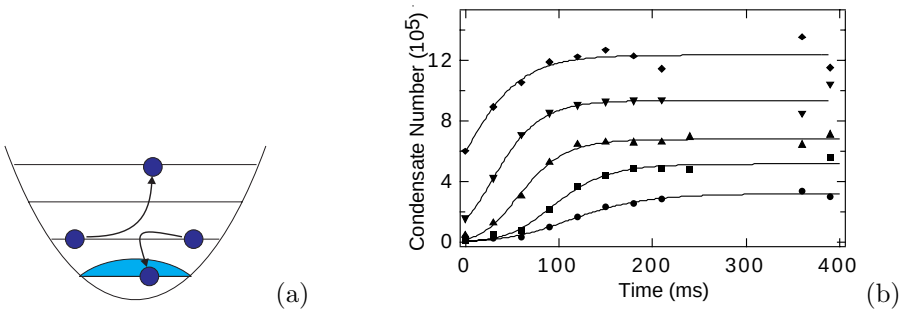

Figure 28.7: (a) Illustration of the idea of bosonic stimulation. (b) The curves show the growth of a condensate toward thermal equilibrium for different initial numbers of condensed atoms.

The very high concentration of population in a single phase space cell during the creation of a condensate represents a dramatic reduction of entropy. Since the total entropy can not decrease, the condensate must be coupled to a thermal reservoir receiving the excess entropy. This coupling is necessarily irreversible. In practice, the reservoir is the cloud of thermal atoms, whose energy is spread over many vibrational states. Irreversibility is introduced by collisions and the subsequent removal of the hottest atoms.

28.3.2.2 Phase of a condensate and first and higher-order coherences

First-order coherence and long-range order are necessary conditions for assigning a single global phase to the condensate. The existence of a single phase, and the possibility of measuring it, were questioned in the past. Certainly, the phase of a BEC is not observable *by itself*, but only *the relative phase* of two condensates.

The intrinsic phase-coherence of condensates has demonstrated in many experiments. An early example [364] employed internal state interferometry by splitting and remixing ^{87}Rb condensates trapped in the different Zeeman states $|F, m_F\rangle = |1, -1\rangle$ and $|2, 1\rangle$. They found that the phase was remembered for times longer than 150 ms. In another experiment [21, 459, 848], illustrated in Fig. 28.8, a condensate was spatially split in two halves and then recombined. The interpenetration of the two halves at a well-defined relative velocity gave rise to a clear matter wave interference pattern. This ability of ballistically expanding condensates to interfere demonstrated the absence of a random phase lag during the expansion process and that the preservation of the condensates' long range order. However, under the repulsive influence of the mean-field energy, the phase profile of a released condensate evolves in a non-uniform

but well-defined manner [760].

The homogeneity of the phase of a *confined* condensate was also confirmed experimentally [790, 359, 91] through interferometric techniques based on Bragg diffraction (see Sec. 29.2.2). The spatial coherence of an output coupled atom laser has been verified with a double-slit experiment [91]. And the temporal coherence of an atom laser beam was shown to be Fourier-limited by the finite output coupling time [**?**].

Similar to Young's double slit experiment in optics, the observation of matter wave interference only indicates first-order coherence, i.e. amplitude fluctuations in the matter field. Signatures for the presence of higher-order coherences in condensates were discovered in other experiments: The second-order correlation function, which represents a measure for intensity fluctuations (number of particles) in the matter field, was derived from measurements of the condensate's release energy [461]. And the third-order coherence can be deduced from a comparison of the three-body recombination rates for condensed and thermal clouds [128].

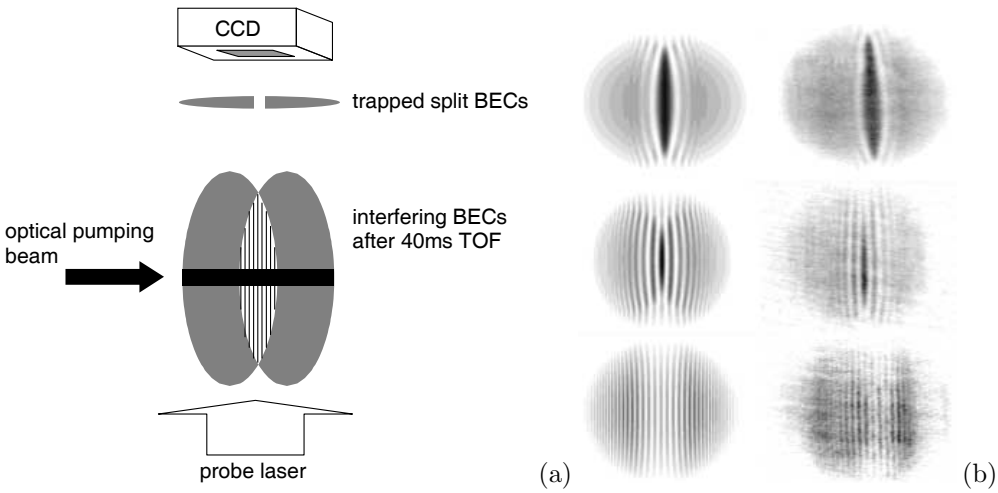

Figure 28.8: (a) Scheme for observation of matter wave interference. (b) Interference fringes.

A reliable characterization of atom number fluctuations and matter wave phase fluctuations in condensates is important for the simple reason, that these fluctuations will limit ultimately the resolution of atom interferometers, analogous to the *Schawlow-Townes limit* in lasers.

28.3.2.3 Output coupling

The *output coupler* for a trapped condensate plays a role similar to that of the partially reflecting mirror of a laser resonator. It transfers a fraction of condensed atoms out of the trapping potential through a coherent coupling to untrapped states. The coupling can be conveniently implemented via adiabatic potentials (see 20.1.3 and 26.4.3) generated by radiation (e.g. radiofrequency pulses [571] or continuous radiofrequency [90]). Also, pairs of laser beams in Raman configuration can create a coherent quasi-

continuous and well-collimated atomic beam [360] and tunneling can give rise to a pulsed mode-locked atom laser (*mode-locked laser*) [19].

A trapped condensate represents a *finite reservoir* from which an atom laser can be fed. For a really cw atom laser, an incoherent pumping mechanism, continuously feeding the BEC, while it delivers atoms to the atom laser, is still lacking [544].

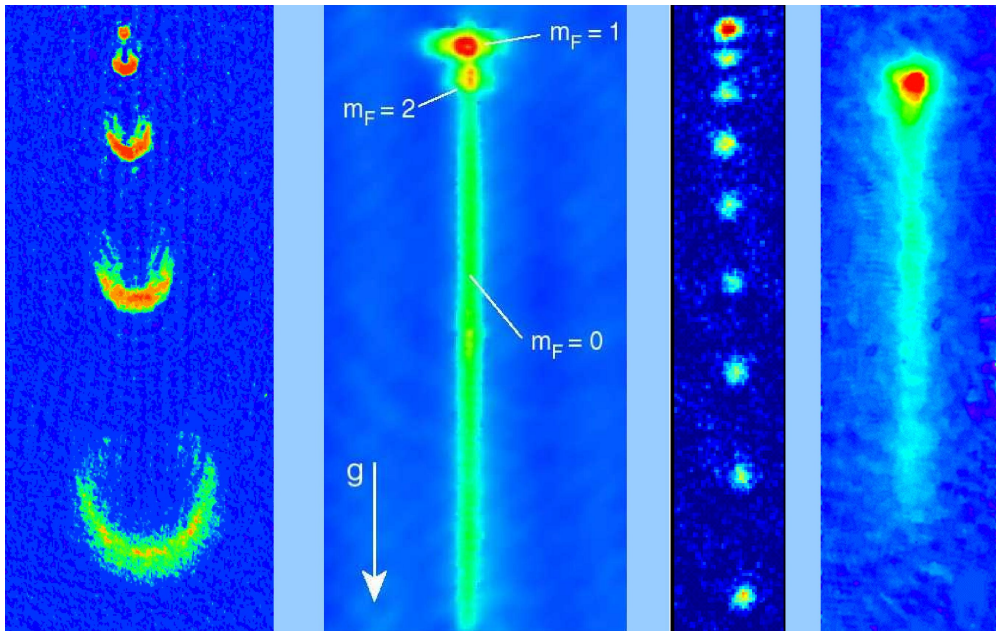

Figure 28.9: Several types of atomic lasers realized, from left to right at the MIT in 1997, in Munich in 1999, at Yale in 1998, and at NIST in 1999. The vertical sizes of the images are, from left to right: 5, 2, 0.5, and 1 mm.

28.3.3 Atomic interferometry with Bose-Einstein condensates

The most obvious use of an atom laser is within an atomic interferometer [791, 779, 99, 359, 91, 760, 461, 128, 639, 220, 585, 604]. Many types of interferometers have been developed over the years. First of all, we note that the interferometric idea can be realized in the spatial domain (e.g. an atomic beam passing through a light wave) or in the time domain (e.g. a trapped atomic cloud or an immobile trapped ion irradiated by a pulsed light) [104, 411, 682, 321].

Furthermore, depending on the involved degree of freedom (kinetic or internal excitation), we may distinguish two types of interferometers. Matter wave interferometers operating with the kinetic degree of freedom often use beam splitters based on Bragg diffraction [483, 639, 359, 760]. Matter wave interferometers involving internal degrees of freedom generally couple two species of condensates, that is, two condensates in different states of internal excitation, for example, in different Zeeman [792], hyperfine [613, 364, 585], or dressed states [506]. The phases of two BECs in different internal states, which we will call $|\pm\rangle$, evolve according to their respective chemical

potentials, $\varphi_{|\pm\rangle}(t) = \mu_{|\pm\rangle}t$. The accumulated phases are not directly observable, but their difference, $\Delta\varphi(t)$, can be measured by *Ramsey interferometry*.

28.3.4 Non-linear atomic optics

In classical nonlinear optics, the interaction between matter (e.g. dilute gases) and light is described by Maxwell's equations. The electromagnetic field $\mathbf{E}$ creates a macroscopic polarization,

$$\mathbf{P}(\mathbf{r},t) = \chi(\mathbf{E})\mathbf{E}(\mathbf{r},t) = \chi^{(1)}\cdot\mathbf{E} + \chi^{(3)} : \mathbf{EEE} + \dots \,. \tag{28.28}$$

which in turn acts back onto the field. Higher-order processes, such as *self-focusing*, *second-harmonic generation*, *four-wave mixing*, etc. are described by the non-linear susceptibility $\chi^{(3)}$. These processes require the presence of a non-linear medium (the vacuum polarization itself being too small [450, 348]).

The role of binary collisions in coherent matter wave optics, as described by the nonlinear term in the Gross-Pitaevskii equation (27.21), is very similar to the role of the third-order nonlinear susceptibility in quantum optics [509, 483, 221, 326, 828, 451, 372, 453, 511, 191, 374]. For example, if the atomic interaction is repulsive, the nonlinear term tries to increase the size of the condensate as much as possible within the limits imposed by the trapping potential. This behavior is analogous to the phenomenon of *self-defocusing* known in non-linear optics.

Small-amplitude elementary oscillations are well described by the *Bogolubov-de Gennes equations*, which are a linearized version of the Gross-Pitaevskii equation [175]. On the other hand, large-amplitude oscillations, which are sensitive to the nonlinear mean-field interaction [769], showed a splitting of the frequency for quasi-particle excitation, in analogy with the generation of the second-harmonic (*SHG*) in quantum optics [374].

Other phenomena, such as matter wave *phase conjugation* and four waves mixing (*4WM*) [326] have been observed in experiments [221]. The three matter wave modes for the nonlinear mixing were produced out of a single condensate by applying two short consecutive sequences of Bragg diffraction pulses. The condensates are created in the same spatial region, but at different times. The nonlinear mixing during the process of spatial separation was observed by time-of-flight images.

The geometry of the laser beams is shown in Fig. 28.10(a) in the laboratory system. A first standing wave light pulse is generated by lasers $\mathbf{k}_1$ and $\mathbf{k}_2$ detuned from each other by an amount, such that the Bragg condition is satisfied and the momentum $\mathbf{p}_2 = \hbar\mathbf{k}_1 - \hbar\mathbf{k}_2$ is transmitted to the diffracted atoms. Then, a second standing wave light pulse formed by lasers $\mathbf{k}_1$ and $\mathbf{k}_3 = -\mathbf{k}_1$ transmits to the diffracted atoms the momentum $\mathbf{p}_3 = 2\hbar\mathbf{k}_1$. The duration and intensity of the standing waves are adjusted such as to create an approximately equal distribution of N_j^0 atoms in all three condensate momentum modes, each mode having a different momentum, $\mathbf{p}_1 = 0$, $\mathbf{p}_2$, and p_3. Initially, the three wavepackets $\hat{\psi}_j \equiv \hat{\psi}_0(\mathbf{r})e^{i\mathbf{p}_j\mathbf{r}/\hbar}$ overlap. The nonlinear term in the Gross-Pitaevskii equation mixes the wavepackets while they separate to

form other wavepackets, $\hat{\psi}_4 \sim g\hat{\psi}_j^+\hat{\psi}_m\hat{\psi}_n e^{i\mathbf{p}_4\cdot\mathbf{r}/\hbar}$, where,

$$N_4 = -N_j + N_j^0 = N_m - N_m^0 = N_n - N_n^0 = \sum\nolimits_{\kappa=1}^{3}(N_\kappa^0 - N_\kappa) \qquad (28.29)$$
$$\mathbf{p}_4 = -\mathbf{p}_j + \mathbf{p}_m + \mathbf{p}_n$$
$$p_4^2 = -p_j^2 + p_m^2 + p_n^2 \ .$$

To produce the new momenta, $\mathbf{p}_4 \neq \mathbf{p}_1, \mathbf{p}_2, \mathbf{p}_3$, the corresponding wavepackets must gather atoms from all three initial packets $\mathbf{p}_1 \neq \mathbf{p}_2 \neq \mathbf{p}_3$.

The experimental observation of a newly emerging wavepacket $\hat{\psi}_4$ has two complementary interpretations: In the inertial system defined by $\mathbf{p}_1 = -\mathbf{p}_3$ [see Fig. 28.10(b)], the wavepackets $\hat{\psi}_1$ and $\hat{\psi}_3$ suffer elastic collisions. The direction in which the condensates are scattered is, a priori, isotropic. The injection of a third condensate $\hat{\psi}_2$ bosonically stimulates the formation of a forth one, $\hat{\psi}_4$, in a predefined direction $\mathbf{p}_4 = -\mathbf{p}_2$. The laws of conservation for the particle numbers, momenta, and energies (28.29) only allow processes, which can be interpreted as degenerate 4WM in this inertial system. Each of the wavepackets $\hat{\psi}_1$ and $\hat{\psi}_3$ sacrifice N_4 atoms to create a new wavepacket $\hat{\psi}_4$ and to amplify the wavepacket $\hat{\psi}_2$. The redistribution of atoms is a coherent process.

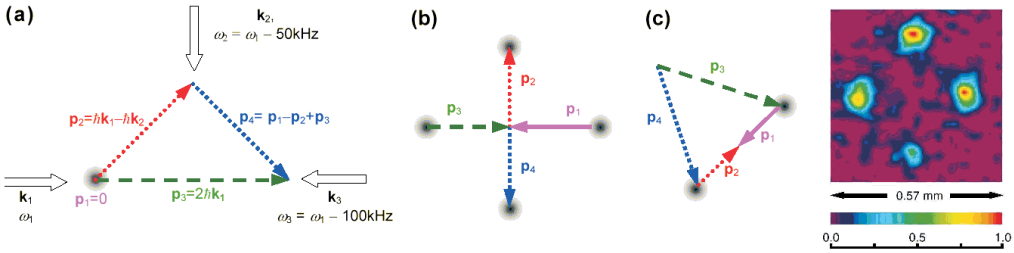

Figure 28.10: Matter wave 4WM can be illustrated (a) in the laboratory system, or (b) in the inertial system defined by $p_1 = -p_3$, or (c) in the system defined by $p_1 = -p_2$. In each system the process has a different physical interpretation (see text). The right image shows the experimental result.

The second interpretation becomes clear in the inertial system, in which $\mathbf{p}_1 = -\mathbf{p}_2$ [see Fig. 28.10(c)]. The conservation of energy only allows scattering products satisfying $p_4 = p_3$, that is, $\hat{\psi}_1^+\hat{\psi}_2\hat{\psi}_3$ and $\hat{\psi}_2^+\hat{\psi}_1\hat{\psi}_3$. In this system, the process can be interpreted as Bragg diffraction of the wavepacket $\hat{\psi}_3$ by the matter wave lattice formed by $\hat{\psi}_1$ and $\hat{\psi}_2$. The wavepacket $\hat{\psi}_4$ is nothing more than the first diffraction order. Unlike the Bragg diffraction in an optical lattice (see Sec. 29.2), the Bragg diffraction by a matter wave lattice requires nonlinear mixing through binary atomic collisions. Thus, the number of redistributed atoms depends on parameters such as the interatomic interaction strength, the size of the condensate, and the collision time between the wavepackets, i.e. the time that the wavepackets spend together before separating.

Despite the similarity with the optical counterpart, matter wave 4WM is fundamentally different: The number of particles must be conserved and the energy-momentum dispersion relation is not linear. Furthermore, while photons require the

presence of a nonlinear medium in order to participate in higher-order processes, atomic matter waves mix through binary collisions.

28.4 Quantum atom optics

When describing a condensate by the Gross-Pitaevskii equation, we specify a phase and an atom number. However, both are conjugate quantities, which can not be specified without uncertainty. So, what does the BEC really look like: a Glauber state or rather a Fock state? We need to be careful. Certainly, it makes no sense talking about the absolute phase of a single BEC. Only the *relative phase* between *two* BECs matters. The condition for interference is, that we do not know, from which condensate the interfering atom came $\Delta N \Delta\varphi \geq 1$. So, the relative atom number must be uncertain.

28.4.1 Quantum transport

Now, let us imagine two BECs in a double-well potential. Atoms may be move between the wells via *Josephson tunneling*, even if the height of the barrier is higher than the atomic energy. Hence, the motion is a type of *quantum transport*. Be $\psi(\mathbf{r},t) = \psi_1(\mathbf{r})e^{\imath\mu_1 t/\hbar} + \psi_2(\mathbf{r})e^{\imath\mu_2 t/\hbar}$. In elongated traps the Josephson current is obtained as the expectation value of the *flux operator*,

$$I(z,t) = \frac{\imath\hbar}{2m}\int\left(\psi(\mathbf{r},t)\frac{d}{dz}\psi^*(\mathbf{r},t) - c.c.\right)dxdy\ . \tag{28.30}$$

One obtains,

$$I(z,t) = \frac{\imath\hbar}{2m}\int\left(\psi_1\frac{d\psi_1^*}{dz} + \psi_2\frac{d\psi_2^*}{dz} + \psi_1\frac{d\psi_2^*}{dz}e^{\imath(\mu_1-\mu_2)t/\hbar} + \psi_2\frac{d\psi_1^*}{dz}e^{\imath(\mu_2-\mu_1)t/\hbar} - c.c.\right)dxdy\ . \tag{28.31}$$

Choosing the original phase of the two condensates equal to zero, the time-independent terms are real and cancel each other, leaving,

$$\begin{aligned} I(z,t) &= \frac{\imath\hbar}{2m}\int\left(\psi_1\frac{d\psi_2}{dz} - \psi_2\frac{d\psi_1}{dz}\right)2\imath\sin\tfrac{(\mu_1-\mu_2)t}{\hbar}dxdy \\ &\equiv I_0\sin\tfrac{(\mu_1-\mu_2)t}{\hbar}\ . \end{aligned} \tag{28.32}$$

This shows that the current oscillates in time. This feature is well-known for *Josephson junction* in superconductors.

The question is now, what will be the steady-state of the two BECs [636]. Experiments have shown, that the BECs will gradually evolve into a superposition of number states, until they are coherent. The time scale is set by Josephson tunneling. The same interference pattern would result from BECs initially having well-defined phases [5].

[5] If two Josephson-coupled BECs are initially in Fock-states, the current must initially be a quantum superposition of all currents corresponding to all possible atom number differences. This quantum superposition decoheres rapidly, leaving behind a semi-classical oscillation.

28.4.2 Optical lattices and the Mott insulator

We have already pointed out in Sec. 26.3.2, that laser beams tuned far away from resonances serve to construct trapping potentials for atoms. Laser beams incident on the atomic cloud under various angles allow the engineering of a large diversity of geometries for attractive potentials (with red tuned lasers) or repulsive potentials (with blue tuned lasers). Various cooling methods can be combined with dipolar traps, for example, Doppler cooling [414], Raman cooling [366], evaporative cooling [3], or gravitational Sisyphus cooling [620]. A particularly interesting geometry is that of are optical lattice, which we will discuss in the following sections.

28.4.2.1 Bloch bands with mean field interaction

The deformation of Bloch bands in the presence of mean field interaction has been discussed in [878, 880]. Under certain circumstances, the bands develop loops at the edges of a Brillouin zone. This is due to superfluidity overwhelming Bragg reflection.

28.4.2.2 The Hubbard model in 1D

The *Hubbard model* gives an approximate description of the physics of interacting *particles* in a lattice. Depending on the type of particle one distinguishes the *Bose-Hubbard model* from the *Fermi-Hubbard model* used in solid state physics for the description of superconducting systems and the hopping of electrons between the atoms of a solid crystalline lattice.

The foundations of the Hubbard model lie in the Bloch-Wannier formalism exposed in Sec. 4.2.3 for the case one-dimensional sinusoidal potentials. Although we already define particle creation and annihilation operator in both, the Bloch and the Wannier basis, there we restricted to individual particles, which dispensed us from taking into account symmetrization constraints and inter-particle interactions. The presence of many particles is best described in a second-quantized Fock state notation for Bloch and Wannier states,

$$|n,q\rangle \longrightarrow |N_{n,q}\rangle \qquad \text{respectively,} \qquad |n,j\rangle \longrightarrow |N_{n,j}\rangle \;, \tag{28.33}$$

where we drop the index n when it is clear that the particles stays in the n^{th} band. In the Wannier basis, the bosonic field operators must satisfy the commutation relation,

$$[\hat{w}_j, \hat{w}^\dagger_{j'}]_- = 1 \quad \text{with} \quad \begin{aligned} \hat{w}^\dagger_{j'}|N_j\rangle &= \sqrt{N_j+1}|N_j+1\rangle \\ \hat{w}_{j'}|N_j\rangle &= \sqrt{N_j}|N_j-1\rangle \end{aligned} \;, \tag{28.34}$$

while the fermionic field operators must satisfy,

$$[\hat{w}_j, \hat{w}^\dagger_{j'}]_+ = 0 \quad \text{with} \quad \begin{aligned} \hat{w}^\dagger_{j'}|N_j\rangle &= \sqrt{1-N_j}|N_j+1\rangle \\ \hat{w}_{j'}|N_j\rangle &= \sqrt{N_j}|N_j-1\rangle \end{aligned} \;. \tag{28.35}$$

In Sec. 4.2.3 we have derived the number operator and Hamiltonian for a given band n,

$$\hat{N}^{(n)}_j = \hat{w}^\dagger_j \hat{w}_j \qquad , \qquad \hat{H}^{(n)} = -\sum_{j,j'} \mathfrak{J}(\Delta j) \hat{w}^\dagger_j \hat{w}_{j'} \;, \tag{28.36}$$

where,

$$\begin{aligned}\mathfrak{J}(\Delta j) &= -\langle n, z_{j'}|\hat{H}^{(n)}|n, z_j\rangle \\ &= \int_{\mathbb{R}}\int_{\mathbb{R}} \langle n, z_{j'}|z'\rangle\langle z'|\left(\frac{\hbar^2}{2m}\frac{\partial^2}{\partial z^2} - V_0\cos^2 k_1\hat{z}\right)|z\rangle\langle z|n, z_j\rangle dz dz' \\ &= \int_{\mathbb{R}} \langle n, z_{j'}|z\rangle\left(\frac{\hbar^2}{2m}\frac{\partial^2}{\partial z^2} - V_0\cos^2 k_1\hat{z}\right)\langle z|n, z_j\rangle dz \ .\end{aligned} \tag{28.37}$$

In the tight-binding limit, we only consider tunneling between neighboring sites, $\mathfrak{J}(j-j') = \mathfrak{J}\,\delta_{j,j\pm1}$, setting $\mathfrak{J} = \mathfrak{J}(1)$.

Example 190 (*Link between particle field operators and Wannier states*): Many-particle field operators have been introduced in Sec. 27.2.1,

$$\hat{\psi}(z) = \sum_{n,j}\langle z|n, z_j\rangle\hat{w}_j^{(n)} \ .$$

We verify the commutator,

$$\begin{aligned}[\hat{\psi}(z), \hat{\psi}^\dagger(z')]_- &= \delta^{(3)}(z-z') = \sum_{n,j}\langle z|n, z_j\rangle\langle n, z_j|z'\rangle \\ &= \sum_{n,j,n',j'}\langle z|n, z_j\rangle\langle n', z_{j'}|z'\rangle\delta_{n,n'}\delta_{j,j'} = \sum_{n,j,n',j'}\langle z|n, z_j\rangle\langle n', z_{j'}|z'\rangle[\hat{w}_j, \hat{w}_{j'}^\dagger]_- \ ,\end{aligned}$$

the particle number operator,

$$\begin{aligned}\hat{N} &= \int \hat{\psi}^\dagger(z)\hat{\psi}(z)dz = \sum_{n,j,n',j'}\hat{w}_{j'}^\dagger\hat{w}_j\int\langle n', z_{j'}|z\rangle\langle z|n, z_j\rangle dz \\ &= \sum_{n,j,n',j'}\langle n', z_{j'}|n, z_j\rangle\hat{w}_{j'}^\dagger\hat{w}_j = \sum_{n,j}\hat{w}_j^\dagger\hat{w}_j \ ,\end{aligned}$$

and the Hamiltonian,

$$\begin{aligned}\hat{H} &= \int\hat{\psi}^\dagger(z)\left(-\frac{\hbar^2}{2m}\frac{\partial^2}{\partial z^2} + V_0\cos^2 k_1\hat{z}\right)\hat{\psi}(z)dz \\ &= \sum_{n,j,n',j'}\hat{w}_{j'}^\dagger\hat{w}_j\int\langle n', z_{j'}|z\rangle\left(-\frac{\hbar^2}{2m}\frac{\partial^2}{\partial z^2} + V_0\cos^2 k_1\hat{z}\right)\langle z|n, z_j\rangle dz = -\sum_{n,j,n',j'}J(\Delta j)\hat{w}_{j'}^\dagger\hat{w}_j \ .\end{aligned}$$

28.4.2.3 Additional trapping potential

The presence of an additional trapping potential can also be considered,

$$\begin{aligned}\hat{\mathcal{V}} &= \int\hat{\psi}^\dagger(z)V_{\rm trp}(z)\hat{\psi}(z)dz \\ &= \sum_{n_1,j_1,n_2,j_2}\hat{w}_{j_1}^\dagger\hat{w}_{j_2}\int V_{\rm trp}(z)\langle n_1, z_{j_1}|z\rangle\langle z|n_2, z_{j_2}\rangle dz \ .\end{aligned} \tag{28.38}$$

To simplify this expression, we assume that the potential depth of $V_{\rm trp}$ *does not vary much between adjacent sites*,

$$\hat{\mathcal{V}} \simeq \sum_j\hat{w}_j^\dagger\hat{w}_j\int V_{\rm trp}(z)|\langle z|0, z_j\rangle|^2dz \simeq \sum_j V_{\rm trp}(z_j)\hat{w}_j^\dagger\hat{w}_j \ . \tag{28.39}$$

28.4.2.4 *s*-wave collisions between bosons

The short-range interaction Hamiltonian (*s*-wave for bosons) reads, in the pseudo-potential approximation,

$$\hat{H}_{coll} = \frac{g}{2}\int \hat{\psi}^\dagger(z)\hat{\psi}^\dagger(z)\hat{\psi}(z)\hat{\psi}(z)dz \tag{28.40}$$
$$= \frac{g}{2}\sum_{n_1,j_1,n_2,j_2,n_3 j_3,n_4,j_4} \hat{w}^\dagger_{j_1}\hat{w}^\dagger_{j_2}\hat{w}_{j_3}\hat{w}_{j_4}\int \langle n_1, z_{j_1}|z\rangle\langle n_2, z_{j_2}|z\rangle\langle z|n_3, z_{j_3}\rangle\langle z|n_4, z_{j_4}\rangle dz \ .$$

To simplify this complicated expression, we assume (i) that the *energy of a collision be too low to excite interband transitions*, so that atoms being in the lowest band $n_\alpha = 0$ stay there. (ii) The lattice is so deep, that the *Wannier functions of adjacent sites do not overlap*, so that only on-site collisions contribute,

$$\hat{H}_{coll} \simeq \frac{g}{2}\sum_j \hat{w}^\dagger_j\hat{w}^\dagger_j\hat{w}_j\hat{w}_j\int |\langle z|0, z_j\rangle|^4 dz \tag{28.41}$$
$$= \frac{g}{2}\sum_j \hat{N}_j(\hat{N}_j - 1)\int |\langle z|0, z_j\rangle|^4 dz = \frac{U}{2}\sum_j \hat{N}_j(\hat{N}_j - 1) \ ,$$

where we defined,

$$U \equiv \frac{g}{2}\sum_j \int |\langle z|0, z_{j=0}\rangle|^4 dz \ . \tag{28.42}$$

In the limit of very deep lattices, when the Wannier function can be approximated by the ground state wavefunction of a harmonic oscillator, $\langle 0|0, z_{j=0}\rangle \simeq (\pi a_{\rm ho}^2)^{-1/4}e^{-z^2/2a_{\rm ho}^2}$, we find,

$$U = g\int \langle z|0, z_{j=0}\rangle^4 dz \simeq \frac{g}{\pi a_{\rm ho}^2}\int e^{-2z^2/a_{\rm ho}^2}dz = \frac{g}{\sqrt{2\pi}a_{\rm ho}} \ . \tag{28.43}$$

28.4.2.5 The Bose-Hubbard model in 3D

The Hubbard model in the tight-binding limit can readily be generalized to 3D [636, 337]. Collecting the Hamiltonian terms (28.36), (28.39), and (28.41), we arrive at,

$$\boxed{\hat{H} = -\mathfrak{J}\sum_{j,j'}\hat{w}^\dagger_j\hat{w}_{j'} + \sum_j \varepsilon_j\hat{N}_j + \frac{1}{2}U\sum_j \hat{N}_j(\hat{N}_j - 1)} \ , \tag{28.44}$$

where

$$\mathfrak{J} = \int d^3r \ w^*(\mathbf{r} - \mathbf{r}_j)\left[-\frac{\hbar}{2m}\nabla^2 + V_0(\mathbf{r})\right]w(\mathbf{r} - \mathbf{r}_j) \ . \tag{28.45}$$

and

$$U \equiv \frac{4\pi a_s\hbar^2}{m}\int |w^*(\mathbf{r})|^4 d^3r \ , \tag{28.46}$$

and in the presence of an additional external trap,

$$\varepsilon_j \equiv \int V_{\rm trp}(\mathbf{r})|w(\mathbf{r} - \mathbf{r}_j)|^2 d^3r \simeq V_{\rm trp}(\mathbf{r}_j) \ , \tag{28.47}$$

and $w(\mathbf{r}) = w(x)w(y)w(z)$ are the *Wannier functions* for an individual particle. We assume for the moment a homogeneous condensate.

The Hilbert space dimension of the Bose-Hubbard model grows exponentially with the number of atoms N and the number of sites L,

$$D_b = \binom{N_b + L - 1}{N_b} , \tag{28.48}$$

according to the partition function derived in quantum statistics. For the Fermi-Hubbard model, the Pauli exclusion principle leads to the Hilbert space dimension,

$$D_f = \binom{L}{N_f} . \tag{28.49}$$

In three dimensional lattices the Hilbert space grows even faster. Therefore, it is a difficult computational task to model or simulate such systems, and generally not possible for more than 20 atoms and 20 lattice sites.

28.4.2.6 The Mott insulator

At zero temperature, the Bose-Hubbard model (in the absence of disorder) predicts the atomic ensemble to be an a Mott insulating state (MI) when $\mathfrak{J} \ll U$, a superfluid state (SF) when $\mathfrak{J} \gg U$, or a *supersolid phase* (SS), where both solid and superfluid phases (diagonal and off-diagonal) coexist. Mott insulation phases are characterized by integer site occupation numbers, by the existence of an energy gap for particle-hole excitations, and zero compressibility. In the presence of disorder, a third phase, the *Bose glass* exists. This phase is insulation because of the Anderson localization effects. Bose glass is characterized by a finite compressibility, the absence of a gap, and an infinite superfluid susceptibility [281]. See also (watch talk).

In the Mott insulating state, the atoms are *localized* at individual sites of an optical lattice. On one hand, the localization impedes any phase relation between atoms at different sites, that is, at a given site the phase uncertainty $\Delta\phi$ is complete. But at the same time, there is a perfect correlation of the atom number at each site known as *spin squeezing* [6], because (in a homogeneous lattice) every site contains exactly the same number of atoms, that is, the atom number uncertainty ΔN tends to zero. At a given lattice site, the number of atoms and the phase of the wavefunction can not be simultaneously fixed: $\Delta N \Delta\phi > 1$.

The absence of relative coherence between different sites and of the ability to interfere prohibits the description of the system by a single global wavefunction and the use of the Gross-Pitaevskii equation. Nevertheless, the Mott insulating state is not equivalent to a completely randomized sample. On the contrary, the coherence only changes its character [7].

The *Mott transition* of a condensate from a superfluid state and to state of a *Mott insulator* occurs as a *quantum phase transition*, because it is driven by quantum fluc-

[6] The spin squeezing feature makes the Mott insulator interesting for spectroscopy at the *Heisenberg limit* and for quantum computation.

[7] Remember, that the Fock state is a complicated superposition of Glauber states. The disappearance and reappearance of coherence is reminiscent to the phenomenon of collapse and revival in the Jaynes-Cummings model.

tuations rather than of thermal noise. Therefore, it is a direct result of Heisenberg's uncertainty relation.

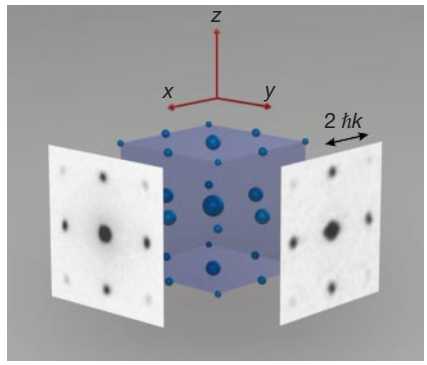

Figure 1 Schematic three-dimensional interference pattern with measured absorption images taken along two orthogonal directions. The absorption images were obtained after ballistic expansion from a lattice with a potential depth of $V_0 = 10E_r$ and a time of flight of 15 ms.

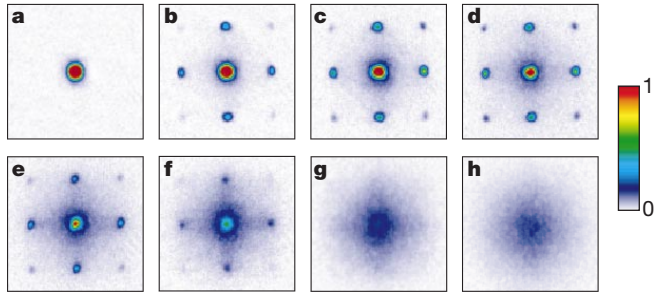

Figure 2 Absorption images of multiple matter wave interference patterns. These were obtained after suddenly releasing the atoms from an optical lattice potential with different potential depths V_0 after a time of flight of 15 ms. Values of V_0 were: **a**, 0 E_r; **b**, 3 E_r; **c**, 7 E_r; **d**, 10 E_r; **e**, 13 E_r; **f**, 14 E_r; **g**, 16 E_r; and **h**, 20 E_r.

Figure 28.11: Signature of the Mott phase.

In the limit of strong tunneling and weak interactions, $\mathfrak{J} \gg U$, the matter wave function looks like a *Bloch state*,

$$|\psi_{SF}\rangle \sim \left(\sum_{i=1}^{M} \hat{a}_i^\dagger\right)^N |0\rangle \ . \tag{28.50}$$

The variance of the number of particles per site is Poissonian, $\sigma_{SF} \sim \sqrt{N_i}$, that is, the wavefunction per lattice site is (quasi)-coherent. However, the total wavefunction is delocalized over all lattice sites, the local wavefunctions have a rigid phase relationship and no long-range coherence. Otherwise, the matter wave function is an independent

product of *Fock states*,

$$|\psi_{MI}\rangle \sim \prod_{i=1}^{M} (\hat{a}_i^\dagger)^n |0\rangle \ . \tag{28.51}$$

The momentum distribution in terms of Wannier functions is [352, 879],

$$n(\mathbf{k}) = |w(\mathbf{k})|^2 \sum_{i,j} e^{\imath \mathbf{k}(\mathbf{r}_i - \mathbf{r}_j)} \langle \hat{a}_i^\dagger \hat{a}_j \rangle \ . \tag{28.52}$$

The atoms are localized in individual sites and there is a perfect correlation of the particle number in each site, known as *spin-squeezed state*, i.e. the variance tends to zero, $\sigma_{MI} \to 0$. The Mott transition is characterized by $\sigma = \frac{1}{2}$. In a given site, the atom number and the phase of the wavefunction cannot be known simultaneously: $\Delta N \Delta\phi < 1$. Therefore, the on-site wavefunction loose their relative coherence and capability to interfere. They cannot be described by a single global wavefunction and do not follow the Gross-Pitaevskii equation. However, this state is not equivalent to a completely randomized ensemble. Rather the *coherence is transferred from inter-site correlations to inner-site correlations* (keep in mind that a Fock state is a complicated superposition of Glauber states). This is somehow analogous to collaps and revival in the Jaynes-Cummings model.

The Mott transition between the superfluid and the *Mott insulator* phase is a *quantum phase transition*, since it is driven by quantum fluctuations rather than themal noise. Thus it is a direct result of Heisenberg's incertainty relation.

These features make optical lattices in the Mott insulating phase interesting for spectroscopy at the *Heisenberg limit* and quantum computing.

> **Example 191 (*Practical Aspects*):** Normal MOT loaded $3D$ lattices have filling factors of $1/10$ per site. Sophisticated Raman-sideband cooling schemes are necessary to achieve higher factors. Alternatively, one may fill $1D$ or $3D$ lattices from a BEC, which offers low temperatures and high densities, so large filling factors, but quantum degeneracy is not a requirement (what matters is that only the lowest band is populated).
> We may go to $1D$ configurations. In order to get good signal contrast despite the small number of sites, large filling factors are necessary. Even though spin-squeezing is possible, the weak lateral confinement makes it hard to reach the Mott insulating regime. An improvement could be the use of $1D$ arrays of annular traps, because of the tighter lateral confinement. Alternatively, we may fill a $3D$ lattice with 1 to 3 atoms per site and some 150000 sites. Low atom numbers make it easier to resolve the Mott transition. Typical numbers are $\nu_{\text{trp}} \approx 50\,\text{Hz}$, $\nu_{Gauss} \approx 60\,\text{Hz}$, $\nu_{lattice} \approx 30\,\text{kHz} \ \approx 22 E_{rec}$.
> For quantum gate application, spin squeezing is important since the entangling
>
> pulse area depends on the on-site interaction energy $\frac{4\pi a_s \hbar^2}{m} n$, but it is not necessary to have only a single atom per site. What is the deeper relationship of the Mott spin-squeezing and the entanglement achievable by quantum gates [426]?
> Probing is simply done by free expansion and observation of the interference patterns as the image of the momentum space distribution. The periodic structure of the density distribution causes a periodic pattern in momentum space,

and since in the superfluid phase the ....
For inhomogeneous systems, superfluid and Mott insulating phases with different (integral atom number) populations may coexist. The Mott insulating phase is characterized by a gap in the excitation spectrum (precisely the one that inhibits the atomic mobility). This may be probed by applying potential gradients designed to overcome the gap.
The Mott insulating phase is not equivalent to random dephasing in the sites. The latter one causes a broadening of the interference patterns. If all atoms at all sites had the same phase (which is possible in a single realization, but highly unlikely, because such a state cannot be generated on purpose since this would violate the uncertainty principle) they could constructively interfere.
An important signature of is the *incompressibility of a Mott insulator*. This distinguishes it from a superfluid. Even more fundamental [314] is the fact that particle-hole pairs are localized. The $\mu - J/U$ phase diagram is most significant...

Example 192 (*Band insulator, Fermi-Hubbard model*): The Pauli principle gives rise to an energy gap in a Fermi gas and makes it a *band insulator* [475], *antiferromagnetic phases*. Transfer a pure Fermi gas in an optical lattice [399].

28.4.3 Schrödinger cat BECs

Ruostekoski *et al.* [708] proposed a double BEC system consisting of two momentum sidemodes and a far-off resonance laser beam that constantly spontaneously redistributes the atoms between the sidemodes. Homodyne detection of the scattered photons established *relative phase* information in such a way, that the relative number information is blurred in such a way that both sidemodes evolve into a simultaneous superposition of phase and number states. They disregard thermal excitations and two-body collisions. The cats are very sensitive to decoherence.

Cirac *et al.* [156] and Gordon *et al.* [327] consider Josephson double species condensates. The relative atom numbers Rabi flop. Mediated by the mean-field the systems may evolve into cats. The proposals have been reexamined by Dalvit *et al.* [197]. Other contributions come from [325, 393, 714, 683, 426]. First experiments on spin-squeezed states have been made by [636].

28.4.4 Exercises

28.4.4.1 Ex: Superfluid to Mott insulator transition

Consider a condensate trapped in a 3D *simple cubic* optical lattice with lattice spacing l. The Hamiltonian can be written as,

$$\hat{H} = -J \sum_{i,j} \delta_{ij}^{(1)} \hat{a}_i^\dagger \hat{a}_j + \tfrac{U}{2} \sum_i \hat{a}_i^\dagger \hat{a}_i^\dagger \hat{a}_i \hat{a}_i \ ,$$

where $\hat{a}_i$ ($\hat{a}_i^\dagger$) is the operator annihilating (creating) one boson in the lattice site i; $\delta_{ij}^{(1)} = 1$ only when i and j are nearest neighbors, otherwise it is zero. Assume a total

of $M \gg 1$ sites, periodic boundary conditions in the x, y, and z directions, and $U > 0$. On this lattice we consider the construction operator $\hat{b}_s^\dagger$ defined in the following way:

$$\hat{b}_s^\dagger = \tfrac{1}{\sqrt{M}} \sum_i \hat{a}_i^\dagger \ .$$

a. Describe the action of this construction operator.
b. Derive the commutation relation,

$$[\hat{a}_\alpha, \hat{b}_s^\dagger] = \tfrac{1}{\sqrt{M}} \ .$$

c. Derive the commutation relation,

$$[\hat{a}_\alpha, (\hat{b}_s^\dagger)^N] = \tfrac{N}{\sqrt{M}} (\hat{b}_s^\dagger)^{N-1} \ .$$

d. Suppose that the following N-atom state exists:

$$|N, SF\rangle \equiv \tfrac{1}{\sqrt{N!}} (\hat{b}_s^\dagger)^N |0\rangle \ ,$$

where SF stands for a name label (and not for quantum numbers). Show that for $N = M$ we have $\hat{a}_\alpha |N, SF\rangle = |N-1, SF\rangle$.
e. Define the density operator for the site i as $\hat{n}_i = \hat{a}_i^\dagger \hat{a}_i$. Calculate the density fluctuation,

$$\Delta n_i = \sqrt{\langle \hat{n}_i^2 \rangle - \langle \hat{n}_i \rangle^2}$$

of the state $|N, SF\rangle$ with $N = M$.
f. Calculate the total energy $\langle H \rangle$ with the state $|N, SF\rangle$.
g. Next consider the state,

$$|N, MI\rangle \equiv \prod_j \hat{a}_j^\dagger |0\rangle \ .$$

Calculate $\langle \hat{a}_i^\dagger \hat{a}_j \rangle$ and the density fluctuations Δn_i for this state.
h. Calculate the total energy $\langle H \rangle$ with the state $|N, MI\rangle$.
i. Discuss the energy for the states $|N, SF\rangle$ and $|N, MI\rangle$. Which one is the ground state? How to make a ground state change from $|N, SF\rangle$ to $|N, MI\rangle$?

28.5 Further reading

M.R. Matthews et al., *Vortices in a Bose-Einstein Condensate* [DOI]

K.M. Mertes et al., *Nonequilibrium Dynamics and Superfluid Ring Excitations in Binary Bose-Einstein Condensates* [DOI]

I. Bloch, *Ultracold quantum gases in optical lattices* [DOI]

J. Estève et al., *Squeezing and entanglement in a Bose-Einstein condensate* [DOI]

Chapter 29

Interaction of Bose-Einstein condensates with light

Light can essentially be used in two ways for the manipulation of matter waves: 1. Tuned *far from resonance*, light serves to create conservative optical dipole potentials (see Secs. 26.3.2 and 28.4.2). In such circumstances the states of internal atomic excitation can be adiabatically eliminated from the description of the center-of-mass dynamics. 2. *Close to resonance* the situation is quite different, but even then, the coherent excitation of internal states may allow for a controlled manipulation of the atomic motion. Among the examples discussed in the following sections are the adiabatic sweeps, the Raman output coupler, Bragg pulses, photoassociation, and matter wave superradiance (see Fig. 29.1).

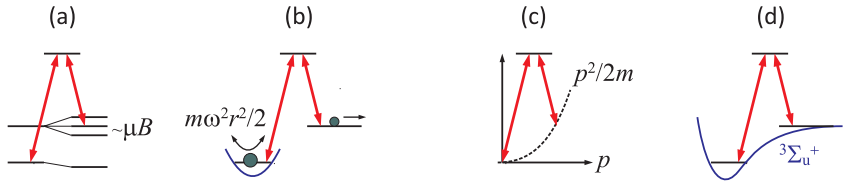

Figure 29.1: Different types of coherent coupling: (a) coherent coupling of hyperfine levels, (b) coupling from a confined state to the continuum of free states, (c) mutual coupling of different velocity states of an atom, and (d) coupling between a (collisional) state of two free atoms with a bound molecular state.

29.1 Scattering of light by degenerate gases

29.1.1 The structure factor for degenerate quantum gases

We introduced in Sec. 21.1.1 the notion of the structure factor, where it was used to characterize the scattering of light by thermal distributions of atoms. To characterize the scattering of matter waves, we must generalize the notion of the structure factor. We wrote in (21.3) the Fourier transform of the density distribution, which now becomes, after inserting $\hat{n}(\mathbf{r}) = \hat{\psi}^\dagger(\mathbf{r})\hat{\psi}(\mathbf{r})$ and the plane wave expansion (27.70),

$$\hat{\rho}^\dagger(\mathbf{q}) = \int \hat{\psi}^\dagger(\mathbf{r})\hat{\psi}(\mathbf{r})e^{\imath\mathbf{q}\cdot\mathbf{r}}d^3r = \tfrac{V}{(2\pi)^3}\iiint \hat{a}^\dagger_{\mathbf{k}'}\hat{a}_{\mathbf{k}}e^{\imath(\mathbf{k}-\mathbf{k}'+\mathbf{q})\cdot\mathbf{r}}d^3k'd^3kd^3r\ . \qquad (29.1)$$

With (27.76) and assuming sharp momenta (27.71),

$$\hat{\rho}^\dagger(\mathbf{q}) = V^2 \iint \hat{a}^\dagger_{\mathbf{k}'} \hat{a}_{\mathbf{k}} \delta_{\mathbf{k}',\mathbf{k}+\mathbf{q}} d^3k' d^3k = \sum_{\mathbf{k}',\mathbf{k}} \hat{a}^\dagger_{\mathbf{k}'} \hat{a}_{\mathbf{k}} \delta_{\mathbf{k}',\mathbf{k}+\mathbf{q}} \ . \tag{29.2}$$

Finally,

$$\boxed{\hat{\rho}^\dagger(\mathbf{q}) = \sum_{\mathbf{k}} \hat{a}^\dagger_{\mathbf{k}+\mathbf{q}} \hat{a}_{\mathbf{k}} = \sum_{\mathbf{k}} |\mathbf{k}+\mathbf{q}\rangle\langle\mathbf{k}|} \ . \tag{29.3}$$

Hence, $\hat{\rho}^\dagger(\mathbf{q})$ describes the scattering of an atom with the momentum $\mathbf{k}$ to $\mathbf{k}+\mathbf{q}$. We also find,

$$\hat{\rho}^\dagger(\mathbf{q}) = \hat{\rho}(-\mathbf{q}) \ . \tag{29.4}$$

Understanding the fundamental state $|g\rangle$ as the state without excitations, we define the *static structure factor* (21.5) now normalized to the number of particles [779],

$$\boxed{S(\mathbf{q}) \equiv \tfrac{1}{N}\langle g|\hat{\rho}(\mathbf{q})\hat{\rho}^\dagger(\mathbf{q})|g\rangle} \ , \tag{29.5}$$

as a generalization of the classical structure factor. The static structure factor describes the probability to excite a condensate by creating a quasi-particle with momentum $\mathbf{k}$. We will need these notions in the Sec. 29.2.3.

The *dynamic structure factor* is obtained from $S(\mathbf{q}) = \int S(\mathbf{q},\omega)d\omega$ and measures the density of correlations in the ground state with 0 momentum. The formula describes, how an atom probes its environment by scattering quasi-particles back and forth,

$$S(\mathbf{q},\omega) = \tfrac{1}{N}\sum_f \langle g|\hat{\rho}(\mathbf{q})|f\rangle\langle f|\hat{\rho}(\mathbf{q})|g\rangle \hbar\delta(\hbar\omega - E_f + E_g) \ . \tag{29.6}$$

Solve the Excs. 29.1.6.1 to 29.1.6.5.

Example 193 (*Spatial coherence and the correlation function*): The *spatial coherence* can be defined by [CCT & Aspect],

$$\boxed{F(\mathbf{x}) \equiv \int \langle \mathbf{r}|\hat{\rho}|\mathbf{r}+\mathbf{x}\rangle d^3r = \int e^{\imath\mathbf{k}\cdot\mathbf{x}}\langle\mathbf{k}|\hat{\rho}|\mathbf{k}\rangle d^3k} \ . \tag{29.7}$$

We will demonstrate this relationship in Exc. 29.1.6.6. The *coherence length* ξ is given by $F(\xi) = \frac{1}{e}F(0) = \frac{1}{e}$. A *second order correlation function* is defined by,

$$\boxed{\begin{aligned} g^{(2)}(\mathbf{r}_1,\mathbf{r}_2) &= \frac{\langle\hat{\psi}^\dagger(\mathbf{r}_1)\hat{\psi}^\dagger(\mathbf{r}_2)\hat{\psi}(\mathbf{r}_2)\hat{\psi}(\mathbf{r}_1)\rangle}{\langle\hat{n}(\mathbf{r}_1)\rangle\langle\hat{n}_2(\mathbf{r})\rangle} \\ g^{(2)}(\mathbf{r}) &\equiv g^{(2)}(\mathbf{r}_1,\mathbf{r}_1+\mathbf{r}) \end{aligned}} \ .$$

29.1.2 The structure factor in Bragg spectroscopy

29.1.2.1 The Hamiltonian of the Rayleigh scattering process

In Sec. 1.7.3 we saw the Galilei-boost (1.321),

$$|\mathbf{k}+\mathbf{q}\rangle = e^{\imath\mathbf{q}\cdot\hat{\mathbf{r}}}|\mathbf{k}\rangle \ . \tag{29.8}$$

In the second quantization we generalize to,

$$|\mathbf{k}+\mathbf{q}\rangle = \int \hat{\psi}^\dagger(\mathbf{r}) e^{\imath \mathbf{q}\cdot\mathbf{r}} \hat{\psi}(\mathbf{r}) d^3r |\mathbf{k}\rangle = \hat{\rho}^\dagger(\mathbf{q})|\mathbf{k}\rangle \ . \tag{29.9}$$

Thus, we can implement the second quantization by simply replacing $e^{\imath \mathbf{q}\cdot\mathbf{r}}$ by $\hat{\rho}^\dagger(\mathbf{q})$. Now, the Hamiltonian for the process of a photon absorption from the mode $\hat{c}_{\mathbf{k}_i}$, taking into account the photonic recoil, was introduced in (20.6),

$$\hat{H}_{int} = \hbar\Omega(\hat{\mathbf{r}}) e^{-\imath \mathbf{k}_i\cdot\hat{\mathbf{r}}} \hat{c}_{\mathbf{k}_i} \hat{\sigma}^+ + c.c. \ . \tag{29.10}$$

If the process is followed by the reemission of a photon to the mode $\hat{c}_{\mathbf{k}_f}$,

$$\boxed{\hat{H}_{int} = \hbar\Omega(\hat{\mathbf{r}}) e^{\imath(\mathbf{k}_f-\mathbf{k}_i)\cdot\mathbf{r}} \hat{c}^\dagger_{\mathbf{k}_f} \hat{c}_{\mathbf{k}_i}} \ . \tag{29.11}$$

Going to second quantization, as done in (29.9), and doing the Fourier transform [1],

$$\tilde{H}_{int} = C \sum_{\mathbf{p}_f,\mathbf{p}_i} \hat{c}^\dagger_{\mathbf{k}_f} \hat{c}_{\mathbf{k}_i} \hat{a}^\dagger_{\mathbf{p}_f} \hat{a}_{\mathbf{p}_i} \delta_{\mathbf{k}_f-\mathbf{k}_i+\mathbf{p}_f-\mathbf{p}_i} \ . \tag{29.12}$$

We assume here, that the light modes $\mathbf{k}_i$ and $\mathbf{k}_f$ are predefined, but the velocities $\mathbf{p}_i$ are distributed. Otherwise, in the expression (29.12), we must also sum over light modes [2],

$$\boxed{\tilde{H}_{int} = C \sum_{\mathbf{k}_i,\mathbf{k}_f,\mathbf{p}_i,\mathbf{p}_f} \hat{c}^\dagger_{\mathbf{k}_f} \hat{c}_{\mathbf{k}_i} \hat{a}^\dagger_{\mathbf{p}_f} \hat{a}_{\mathbf{p}_i} \delta_{\mathbf{k}_f-\mathbf{k}_i+\mathbf{p}_f-\mathbf{p}_i}} \ , \tag{29.13}$$

where C is a normalization constant. This Hamiltonian describes the elementary scattering process as a process of four wave mixing (4WM) [459, 780]. The light and the atoms are treated on equal footings as modes which can receive (quasi-)particle populations, and the scattering corresponds to a redistribution of populations between the modes [3].

The Hamiltonian (29.13) can be applied to various situations, such as spontaneous or stimulated Rayleigh scattering or Bragg scattering, depending on which ones of the modes $\mathbf{k}_f$, $\mathbf{k}_i$, $\mathbf{p}_f$, and $\mathbf{p}_i$ are populated or filtered by imposed boundary conditions.

Using momentum conservation $\mathbf{q} \equiv \mathbf{k}_f - \mathbf{p}_i = -\mathbf{p}_f + \mathbf{p}_i$, we obtain the cross section,

$$\left(\frac{d\sigma}{d\Omega}\right)_{\mathbf{k}_i\to\mathbf{k}_f} = C^2 \sum_f |\langle f|\hat{H}_{int}|i\rangle|^2 = C^2 \sum_f |\langle f| \sum_{\mathbf{p}_i} \hat{c}^\dagger_{\mathbf{k}_i+\mathbf{q}} \hat{c}_{\mathbf{k}_i} \hat{a}^\dagger_{\mathbf{p}_i-\mathbf{q}} \hat{a}_{\mathbf{p}_i} |i\rangle|^2 \ , \tag{29.14}$$

Example 194 (*Description of Bragg scattering via the structure factor*): In this example we irradiate two plane waves in directions $\mathbf{k}_1$ and $\mathbf{k}_2$ into a Bose-Einstein condensate. The total intensity will be,

$$I_{mod}(\mathbf{r},t) = I\cos(\mathbf{q}\cdot\mathbf{r}-\omega t) \qquad \text{with} \qquad \mathbf{q} = \mathbf{k}_1 - \mathbf{k}_2 \ . \tag{29.15}$$

[1] $\hat{a}_{\mathbf{p}}$ and $\hat{a}^\dagger_{\mathbf{p}}$ are the operators of the quantized atomic field, while $\hat{c}_{\mathbf{k}}$ and $\hat{c}^\dagger_{\mathbf{k}}$ are the operators of the light fields.

[2] Note the different form of this Hamiltonian as compared to (21.10).

[3] This is analogous to the way, in which a 'collision' redistributes atomic populations between momentum modes. We will discuss this general concept of 4WM in Secs. 29.3.4 and 28.3.4.

and the optical potential,

$$V_{mod} = \frac{\hbar\Gamma^2}{8\Delta} I \cos(\mathbf{q}\cdot\mathbf{r} - \omega t) = \frac{\hbar\Gamma^2}{8\Delta}\frac{I}{2I_{sat}}(e^{\imath\mathbf{q}\cdot\mathbf{r}-\imath\omega t} + e^{-\imath\mathbf{q}\cdot\mathbf{r}+\imath\omega t}) \qquad (29.16)$$
$$\rightarrow \hat{V}_{mod} = \frac{V}{2}[\hat{\rho}^\dagger(\mathbf{q})e^{-\imath\omega t} + \hat{\rho}^\dagger(-\mathbf{q})e^{\imath\omega t}] \ .$$

Now, the transition rate is [780],

$$\frac{W}{N} = 2\pi\Omega_R^2 S(\mathbf{q},\omega) = \frac{2\pi}{N\hbar}\left(\frac{V}{2}\right)^2 \sum_f |\langle f|\hat{\rho}^\dagger(\mathbf{q})|g\rangle|^2 \delta(\hbar\omega - (E_f - E_g)) \ , \ (29.17)$$

with $\frac{V}{2} = \hbar\Omega_R$.

Resolve Exc. 29.1.6.7.

29.1.3 Bosonic stimulation

We assume in the following weak light intensities (and hence a negligible contribution of the Mollow fluorescence spectrum). That is, without cooperative effects the light would be elastically scattered by Rayleigh scattering. Now, we adopt a notation labeling the multimodal state by the numbers of photons and atoms distributed over the available light and momentum modes. That is, the initial state consists of $n_{\mathbf{p}}$ atoms distributed over momentum atomic states $\mathbf{p}$ and $N_{\mathbf{k}}$ photons distributed over wave vector modes $\mathbf{k}$ denoted by $|...N_{\mathbf{k}}...\rangle_{rad} \otimes |...n_{\mathbf{p}}...\rangle_{at}$:

$$|i\rangle \equiv |...n_{\mathbf{p}_i}...n_{\mathbf{p}_f}...\rangle_{at} \ \otimes |...N_{\mathbf{k}_i}...N_{\mathbf{k}_f}...\rangle_{rad} \equiv \left|\begin{matrix}...n_{\mathbf{p}_i}...n_{\mathbf{p}_f}... \\ ...N_{\mathbf{k}_i}...N_{\mathbf{k}_f}...\end{matrix}\right\rangle \ , \qquad (29.18)$$

where we introduced the vector-like notation for notational compactness.

A particular scattering process can be treated like a 'collision' by redistributing the initial populations to final populations:

$$|f\rangle = \left|\begin{matrix}...n_{\mathbf{p}_i} - 1...n_{\mathbf{p}_f} + 1... \\ ...N_{\mathbf{k}_i} - 1...N_{\mathbf{k}_f} + 1...\end{matrix}\right\rangle \ . \qquad (29.19)$$

We write the matrix element,

$$\langle f|\hat{H}_{int}|i\rangle \propto \left\langle\begin{matrix}...n_{\mathbf{p}_i''}...n_{\mathbf{p}_f''}... \\ ...N_{\mathbf{k}_i''}...N_{\mathbf{k}_f''}...\end{matrix}\right| C \sum_{\mathbf{k}_i',\mathbf{k}_f',\mathbf{p}_i',\mathbf{p}_f'} \hat{c}^\dagger_{\mathbf{k}_f'}\hat{c}_{\mathbf{k}_i'}\hat{a}^\dagger_{\mathbf{p}_f'}\hat{a}_{\mathbf{p}_i'}\delta_{\mathbf{k}_f'-\mathbf{k}_i'+\mathbf{p}_f'-\mathbf{p}_i'} \left|\begin{matrix}...n_{\mathbf{p}_i}...n_{\mathbf{p}_f}... \\ ...N_{\mathbf{k}_i}...N_{\mathbf{k}_f}...\end{matrix}\right\rangle \ . \qquad (29.20)$$

Assuming that all modes are not degenerate, such that $[\hat{a}_{\mathbf{p}_f}, \hat{a}^\dagger_{\mathbf{p}_i}] = \delta_{\mathbf{p}_f,\mathbf{p}_i}$, that is, $\hat{a}^\dagger_{\mathbf{p}_f}$ and $\hat{a}_{\mathbf{p}_f}$ only act on the mode $|n_{\mathbf{p}_f}\rangle_{at}$, etc.,

$$\sum_{\mathbf{p}_i'} \hat{a}_{\mathbf{p}_i'}|...n_{\mathbf{p}_i}...\rangle_{at} = \sum_{\mathbf{p}_i} \sqrt{n_{\mathbf{p}_i}}|...n_{\mathbf{p}_i} - 1...\rangle_{at} \qquad (29.21)$$
$$\text{and} \quad \sum_{\mathbf{p}_f'} \hat{a}^\dagger_{\mathbf{p}_f'}|...n_{\mathbf{p}_f}...\rangle_{at} = \sum_{\mathbf{p}_f} \sqrt{n_{\mathbf{p}_f}+1}|...n_{\mathbf{p}_f}+1...\rangle_{at} \ ,$$

as well as,

$$\sum_{\mathbf{k}'_i} \hat{c}_{\mathbf{k}'_i} |...N_{\mathbf{k}_i}...\rangle_{rad} = \sum_{\mathbf{k}_i} \sqrt{N_{\mathbf{k}_i}} |...N_{\mathbf{k}_i} - 1...\rangle_{rad} \tag{29.22}$$

$$\text{and} \quad \sum_{\mathbf{k}'_f} \hat{c}^\dagger_{\mathbf{k}'_f} |...N_{\mathbf{k}_f}...\rangle_{rad} = \sum_{\mathbf{k}_f} \sqrt{N_{\mathbf{k}_f} + 1} |...N_{\mathbf{k}_f} + 1...\rangle_{rad} \ .$$

Let us now assume for a moment, that the photon is scattered to the vacuum, that is, the final mode of light is initially empty, $N_{\mathbf{k}_f} = 0$ [4],

$$\begin{aligned} &\langle f|\hat{H}_{int}|i\rangle_{inel} \qquad (29.23)\\ &\propto \left\langle \begin{matrix} ...n_{\mathbf{p}''_i}...n_{\mathbf{p}''_f}... \\ ...N_{\mathbf{k}''_i}...N_{\mathbf{k}''_f}... \end{matrix} \middle| \sum_{\mathbf{p}_f,\mathbf{p}_i,\mathbf{k}_f,\mathbf{k}_i} \sqrt{N_{\mathbf{k}_i}} \sqrt{n_{\mathbf{p}_f}+1} \sqrt{n_{\mathbf{p}_i}} \middle| \begin{matrix} ...n_{\mathbf{p}_i}-1...n_{\mathbf{p}_f}+1... \\ ...N_{\mathbf{k}_i}-1...1_{\mathbf{k}_f}... \end{matrix} \right\rangle \\ &= \sum_{\mathbf{p}_f,\mathbf{p}_i,\mathbf{k}_f,\mathbf{k}_i} \sqrt{N_{\mathbf{k}_i}} \sqrt{n_{\mathbf{p}_f}+1} \sqrt{n_{\mathbf{p}_i}} \delta_{N_{\mathbf{k}''_i},N_{\mathbf{k}_i}-1} \delta_{N_{\mathbf{k}''_f},N_{\mathbf{k}_f}+1} \delta_{n_{\mathbf{p}''_i},n_{\mathbf{p}_i}-1} \delta_{n_{\mathbf{p}''_f},n_{\mathbf{p}_f}+1} \\ &= \sqrt{N_{\mathbf{k}_i}} \sqrt{n_{\mathbf{p}_f}+1} \sqrt{n_{\mathbf{p}_i}} \ . \end{aligned}$$

Obviously, the differential scattering cross-section,

$$\boxed{\left(\frac{d\sigma}{d\Omega}\right)_{inel} \propto N_{\mathbf{k}_i}(n_{\mathbf{p}_f}+1)n_{\mathbf{p}_i}} \ . \tag{29.24}$$

depends, in addition to the numbers of provided photons $N_{\mathbf{k}_i}$ and atoms $n_{\mathbf{p}_i}$ in the initial mode, also on the *number of atoms in the final mode* $n_{\mathbf{p}_f}$. This amplification of the probability of the scattering process is called *bosonic stimulation*.

Now, we consider the degenerate case, where the initial atomic momentum mode coincides with the final mode, $n_{\mathbf{p}_f} = n_{\mathbf{p}_i}$. In this case,

$$\sum_{\mathbf{p}'_f=\mathbf{p}'_i} \hat{a}^\dagger_{\mathbf{p}'_f} \hat{a}_{\mathbf{p}'_i} |...n_{\mathbf{p}_i}...n_{\mathbf{p}_f}...\rangle_{at} = \sum_{\mathbf{p}'_i} \hat{a}^\dagger_{\mathbf{p}'_i} \hat{a}_{\mathbf{p}'_i} |...n_{\mathbf{p}_i}...n_{\mathbf{p}_i}...\rangle_{at} = \sum_{\mathbf{p}_i} n_{\mathbf{p}_i} |...n_{\mathbf{p}_i}...n_{\mathbf{p}_i}...\rangle_{at} \ , \tag{29.25}$$

and a calculus analogous to (29.23) yields,

$$\langle f|\hat{H}_{int}|i\rangle_{el} \propto \left\langle \begin{matrix} ...n_{\mathbf{p}''_i}...n_{\mathbf{p}''_f}... \\ ...N_{\mathbf{k}''_i}...N_{\mathbf{k}''_f}... \end{matrix} \middle| \sum_{\mathbf{p}_i,\mathbf{k}_f,\mathbf{k}_i} \sqrt{N_{\mathbf{k}_i}} n_{\mathbf{p}_i} \middle| \begin{matrix} ...n_{\mathbf{p}_i}...n_{\mathbf{p}_i}... \\ ...N_{\mathbf{k}_i}-1...1_{\mathbf{k}_f}... \end{matrix} \right\rangle \tag{29.26}$$

$$= \sum_{\mathbf{p}_i,\mathbf{k}_f,\mathbf{k}_i} \sqrt{N_{\mathbf{k}_i}} n_{\mathbf{p}_i} \ {}_{rad}\langle ...N_{\mathbf{k}''_i}...N_{\mathbf{k}''_f}...|...N_{\mathbf{k}_i}-1...1_{\mathbf{k}_f}...\rangle_{rad} \ {}_{at}\langle ...n_{\mathbf{p}''_i}...n_{\mathbf{p}''_f}...|...n_{\mathbf{p}_i}...n_{\mathbf{p}_i}...\rangle_{at}$$

$$= \sum_{\mathbf{p}_i,\mathbf{k}_f,\mathbf{k}_i} \sqrt{N_{\mathbf{k}_i}} n_{\mathbf{p}_i} \delta_{N_{\mathbf{k}''_i},N_{\mathbf{k}_i}-1} \delta_{N_{\mathbf{k}''_f},N_{\mathbf{k}_f}+1} \delta_{n_{\mathbf{p}''_i},n_{\mathbf{p}_i}} \delta_{n_{\mathbf{p}''_f},n_{\mathbf{p}_i}} = \sqrt{N_{\mathbf{k}_i}} n_{\mathbf{p}_i} \ .$$

Now, the differential scattering cross-section,

$$\boxed{\left(\frac{d\sigma}{d\Omega}\right)_{el} \propto N_{\mathbf{k}_i} n^2_{\mathbf{p}_i}} \ , \tag{29.27}$$

[4] We will discuss later the case, where the scattering is (bosonically) stimulated by the number of photons already present in the final mode prior to the scattering process.

only depends on the number of provided photons $N_{\mathbf{k}_i}$ and the number of atoms $n_{\mathbf{p}_i}$ in the initial mode.

29.1.3.1 Elastic and inelastic scattering

The interpretation of the result is the following: Light can be scattered in two ways: (i) with or (ii) without change of atomic moment distribution. The event of a photon scattering (29.19) then it consists of two terms (29.24) and (29.27) [662],

$$\frac{d\sigma}{d\Omega} = \left(\frac{d\sigma}{d\Omega}\right)_{el} + \left(\frac{d\sigma}{d\Omega}\right)_{inel} . \tag{29.28}$$

The first term of (29.28) occurs when the momentum of the scattering atom does not change, $\mathbf{p} = \mathbf{q}$, that is, when the populations of the momentum states $n_{\mathbf{p}}$ and $n_{\mathbf{q}}$ do not change. The corresponding term (29.27) describes elastic Rayleigh scattering. This process is coherent, that is, the phase relationship between the incident wave and the outgoing wave is fixed, because the photon emission is self-stimulated. I.e. it decays to the original mode via *forward scattering* within the angle defined by the *phase matching condition* $\vartheta < \lambda/d$, where d is the size of the atomic sample [459]. This contribution is dispersive, reversible, and conservative, and it is at the origin of the dipole force.

The second term of (29.28) is the inelastic part of Rayleigh scattering, where an atom with the initial momentum $n_{\mathbf{p}}$ is scattered to the momentum state $n_{\mathbf{q}}$. This term is absorptive, dissipative, and spontaneous. The frequency of the photons is shifted, a momentum is imparted to the atom, such that the process is incoherent. Hence, a suggestive way of expressing the differential scattering cross-section (29.19) is,

$$\frac{d\sigma}{d\Omega} \propto \left|\sum_i n_i \langle i|\hat{H}_{int}|i\rangle\right|^2 + \sum_{i\neq f} n_i(1+n_f)|\langle i|\hat{H}_{int}|f\rangle|^2 , \tag{29.29}$$

where $|i\rangle$ and $|f\rangle$ denote momentum states of the atomic sample.

The bosonic stimulation of inelastic Rayleigh scattering represents a way to overcome, on one hand the restrictive phase matching condition, and on the other the incoherence of the scattering into large angles. For non-interacting systems of localized bosons $S(\mathbf{q},\omega)$ can be expressed using single particle states $|i\rangle$ with energy E_i and population N_i [see (21.3) and (21.6)],

$$S(\mathbf{q},\omega) = N\left|\sum_i n_i \langle i|\hat{H}_{int}|i\rangle\right|^2 \delta(\omega) + N\sum_{i\neq f} |\langle f|\hat{H}_{int}|i\rangle|^2 n_i(n_f+1)\delta[\omega-(E_f-E_i)/\hbar] , \tag{29.30}$$

with $S_0(\mathbf{q}) = |\langle\hat{\rho}^\dagger(\mathbf{q})\rangle|^2 = \left|\sum_i n_i\langle i|\hat{H}_{int}|i\rangle\right|^2$.

29.1.4 Playing with bosonic and fermionic states

Here, we want to address the question, whether scattering processes are influenced by bosonic stimulation or cooperative enhancement. Let us consider the case of N atoms (bosons or fermions) generated from vacuum by operators $\hat{a}^\dagger_m(\mathbf{q})|0\rangle$, where m

indicates some additional quantum number (for example, the vibrational state of a loose trapping potential) helping us to enumerate fermionic states, and $\mathbf{q}$ indicates the momentum (considered independent from the trapping potential for short enough times). The operators respect the rules,

$$\begin{aligned} &[\hat{a}_m(\mathbf{0}), \hat{a}_n(\mathbf{q})]_\mp = 0 = [\hat{a}_m^\dagger(\mathbf{0}), \hat{a}_n^\dagger(\mathbf{q})]_\mp \\ \text{and} \quad &[\hat{a}_m(\mathbf{0}), \hat{a}_n^\dagger(\mathbf{q})]_\mp = \delta_{m,n}\delta_{\mathbf{0},\mathbf{q}} \quad \text{and} \quad \hat{a}_m(\mathbf{q})|0\rangle = 0 \ , \end{aligned} \tag{29.31}$$

where upper signs hold for bosons and lower signs for fermions. Initially the N atoms are in the bosonic, respectively, fermionic many-body state [599],

$$\boxed{|\Psi_b^{(N)}(\mathbf{0})\rangle = \tfrac{1}{\sqrt{N!}}\hat{a}_0^\dagger(\mathbf{0})^N|0\rangle \quad \text{resp.} \quad |\Psi_f^{(N)}(\mathbf{0})\rangle = \prod_{n=0}^{N-1}\hat{a}_n^\dagger(\mathbf{0})|0\rangle} \ . \tag{29.32}$$

Note that $|\Psi_b^{(N)}(\mathbf{0})\rangle = |N\rangle$ is a Fock state satisfying $\langle\Psi_b^{(N)}(\mathbf{0})|\Psi_b^{(N)}(\mathbf{0})\rangle = 1$, while $|\Psi_f^{(N)}(\mathbf{0})\rangle$ is a product state being normalized as well, $\langle\Psi_f^{(N)}(\mathbf{0})|\Psi_f^{(N)}(\mathbf{0})\rangle = 1$.

Probing the number of atoms in a many-body state is done by,

$$N = \langle\Psi|\hat{N}|\Psi\rangle \quad \text{where} \quad \hat{N} = \int \hat{\psi}^\dagger(\mathbf{r})\hat{\psi}(\mathbf{r})d^3r = \sum_{m,\mathbf{k}}\hat{a}_m^\dagger(\mathbf{k})\hat{a}_m(\mathbf{k}) \ , \tag{29.33}$$

or if we are only interested in a particular momentum state $\mathbf{k}$ and vibrational state m,

$$\langle\Psi|\hat{N}_m(\mathbf{k})|\Psi\rangle = \langle\Psi|\hat{a}_m^\dagger(\mathbf{k})\hat{a}_m(\mathbf{k})|\Psi\rangle = \|\hat{a}_m(\mathbf{k})|\Psi\rangle\|^2 \ . \tag{29.34}$$

Other possible many-body states are bosonic or fermionic product states,

$$\boxed{|\Psi^{(N_1)}(\mathbf{0})\rangle|\Psi^{(N_2)}(\mathbf{q})\rangle} \ . \tag{29.35}$$

We will see in 29.1.6.9 that product states are normalized if the partial states are normalized. Explicitly,

$$\begin{aligned} |\Psi_b^{(N_1)}(\mathbf{0})\rangle|\Psi_b^{(N_2)}(\mathbf{q})\rangle &= \frac{1}{\sqrt{N_1!N_2!}}\hat{a}_0^\dagger(\mathbf{0})^{N_1}\hat{a}_0^\dagger(\mathbf{q})^{N_2}|0\rangle \\ |\Psi_f^{(N_1)}(\mathbf{0})\rangle|\Psi_f^{(N_2)}(\mathbf{q})\rangle &= \prod_{n=0}^{N_1-1}\hat{a}_n^\dagger(\mathbf{0})\prod_{n=0}^{N_2-1}\hat{a}_n^\dagger(\mathbf{q})|0\rangle \ . \end{aligned} \tag{29.36}$$

Note, that product states in the same mode need renormalization when merged,

$$|\Psi_b^{(N_1)}(\mathbf{0})\Psi_b^{(N_2)}(\mathbf{0})\rangle = \frac{1}{\sqrt{N_1!N_2!}}\hat{a}_0^\dagger(\mathbf{0})^{N_1+N_2}|0\rangle = \sqrt{\binom{N_1+N_2}{N_1}}|\Psi_b^{(N_1+N_2)}(\mathbf{0})\rangle \ , \tag{29.37}$$

for example, $|\Psi_b^{(N)}(\mathbf{0})\Psi_b^{(1)}(\mathbf{0})\rangle = \sqrt{N+1}|\Psi_b^{(N+1)}(\mathbf{0})\rangle$.

A $\pi/2$-Bragg pulse has the faculty to transfer 50% of the atoms into a momentum mode $\mathbf{q}$, thus creating a new state where every single atom lives in a coherent

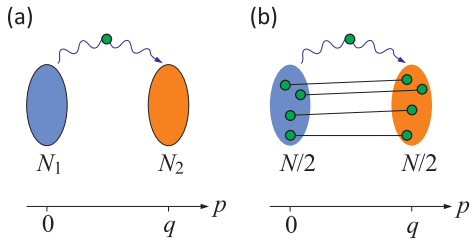

Figure 29.2: Cartoon of (a,b) bosonic stimulation and (c,d) cooperative enhancement.

superposition of two momenta,

$$\boxed{\begin{aligned} |\Psi_b^{(brgg,N)}(\mathbf{0},\mathbf{q})\rangle &= \frac{[\hat{a}_0^\dagger(\mathbf{0})+\hat{a}_0^\dagger(\mathbf{q})]^N}{\sqrt{2^N N!}}|0\rangle = \sum_{n=0}^{N}\binom{N}{n}\frac{\hat{a}_0^\dagger(\mathbf{0})^n\hat{a}_0^\dagger(\mathbf{q})^{N-n}}{\sqrt{2^N N!}}|0\rangle \\ |\Psi_f^{(brgg,N)}(\mathbf{0},\mathbf{q})\rangle &= \prod_{n=0}^{N-1}\frac{[\hat{a}_n^\dagger(\mathbf{0})+\hat{a}_n^\dagger(\mathbf{q})]}{\sqrt{2^N}}|0\rangle \end{aligned}} \quad . \tag{29.38}$$

In the following, we will study scattering processes, that is, fluctuations, in the presence of the states (29.35) or (29.38).

29.1.4.1 Bosonic stimulation versus cooperative enhancement by a Bragg grating

Now, we scatter a photon, whose fate is not of interest here, but which triggers possible transitions of an atom sitting together with N_1 atoms in the momentum state $\mathbf{0}|0\rangle$ towards another momentum state $\mathbf{q}|0\rangle$ initially populated with N_2 atoms via the operator,

$$\hat{H} = \sum_m \hat{a}_m^\dagger(\mathbf{k})\hat{a}_m(\mathbf{0}) \ , \tag{29.39}$$

which in fact is nothing else than the static structure factor. Applying this process to bosonic or fermionic clouds, as defined in (29.32), we find *bosonic stimulation* only in the case of bosons,

$$\boxed{\langle\Psi^{(N_1-1)}(\mathbf{0})\Psi^{(N_2)}(\mathbf{q})|\hat{H}|\Psi^{(N_1)}(\mathbf{0})\Psi^{(N_2-1)}(\mathbf{q})\rangle = \delta_{\mathbf{k},\mathbf{q}}\begin{cases}\sqrt{N_1 N_2} & \text{for bosons}\\ 1 & \text{for fermions}\end{cases}} \ , \tag{29.40}$$

as will be shown in Exc. 29.1.6.10(a). The transition probabilities are then,

$$\frac{d\sigma}{d\Omega} = |\langle f|\hat{H}|i\rangle|^2 = \delta_{\mathbf{k},\mathbf{q}}\begin{cases}N_1 N_2 & \text{for bosons}\\ 1 & \text{for fermions}\end{cases} \ . \tag{29.41}$$

Note, that these results does not change in the presence of a Bragg grating not participating in the dynamics:

$$\langle\Psi_b^{(M-1)}(\mathbf{0})\Psi_b^{(brgg,N+1)}(\mathbf{0},\mathbf{q})|\hat{H}|\Psi_b^{(M)}(\mathbf{0})\Psi_b^{(brgg,N)}(\mathbf{0},\mathbf{q})\rangle = 1 \ . \tag{29.42}$$

However, applying the same scattering process between a BEC with M atoms and the Bragg state defined in (29.38) consisting of N atoms, we identify two interesting possibilities for which we find,

$$\boxed{\begin{array}{lcl}\langle\Psi_b^{(M-1)}(\mathbf{0})\Psi_b^{(brgg,N)}(\mathbf{0},\mathbf{q})|\hat{H}|\Psi_b^{(M)}(\mathbf{0})\Psi_b^{(brgg,N-1)}(\mathbf{0},\mathbf{q})\rangle & = & (\delta_{\mathbf{k},\mathbf{0}}+\delta_{\mathbf{k},\mathbf{q}})\sqrt{MN}\\ \langle\Psi_b^{(M)}(\mathbf{q})\Psi_b^{(brgg,N-1)}(\mathbf{0},\mathbf{q})|\hat{H}|\Psi_b^{(M-1)}(\mathbf{q})\Psi_b^{(brgg,N)}(\mathbf{0},\mathbf{q})\rangle & = & \delta_{\mathbf{k},\mathbf{q}}\sqrt{MN}\end{array}} \,. \tag{29.43}$$

Interestingly, we find the same expression for bosons and for fermions,

$$\boxed{\langle\Psi_{b,f}^{(brgg,N-1)}(\mathbf{0},\mathbf{q})\Psi_{b,f}^{(1)}(\mathbf{q})|\hat{H}|\Psi_{b,f}^{(brgg,N)}(\mathbf{0},\mathbf{q})\rangle = \sqrt{\tfrac{N}{2}}\left[\delta_{\mathbf{k},\mathbf{0}} \pm \tfrac{N-1}{2}(\delta_{\mathbf{k},\mathbf{0}}+\delta_{\mathbf{k},\mathbf{q}})\right]} \,. \tag{29.44}$$

as will be shown in Exc. 29.1.6.10(b). The transition probabilities are then for boson and for fermions,

$$\frac{d\sigma}{d\Omega} = |\langle f|\hat{H}|i\rangle|^2 = \delta_{\mathbf{k},\mathbf{q}}\frac{N}{2}\frac{(N-1)^2}{4} \,. \tag{29.45}$$

This means that, if $\mathbf{k}=\mathbf{0}$ or $\mathbf{k}=\mathbf{q}$, the scattering is subject to *cooperative enhancement* by a factor of $N/2$ (which is the number of atoms in each of the momentum state $\mathbf{0}$ and $\mathbf{q}$) independently on the quantum nature of the atom (boson or fermion). That is, the probability that the scattered atoms joins one of the two momentum goes, for large N, like N^2, but for $N=1$ there is no enhancement possible. Do Exc. 29.1.6.11.

29.1.4.2 Interpretation of bosonic stimulation as cooperative enhancement

The distinction between spontaneous and stimulated processes is not always obvious, as there is a whole world of cooperative processes in between those two concepts, for instance, superradiance, Bragg scattering, and enhanced spontaneous emission into a resonant cavity. All those processes have in common that they are amplified by fluctuations.

Example 195 (*Stimulated emission versus spontaneous emission: Cooperativity in a cavity*): Let us first discuss the case of a cavity. Vacuum fluctuations (VF) are structured by a cavity (finesse F) leading to a modified DOS becoming anisotropic and developing spectral resonances. In resonance the VFs are enhanced (we get a standing wave of VFs), while off resonance they are suppressed. Therefore, an excited atom placed inside a cavity will suffer 'spontaneous stimulation' to decay into the cavity mode. Alternatively, we may say that the atom not only reacts to the local VFs but to all VFs reflected F times by the cavity mirrors provided these VFs are in phase (which is the case when the cavity is resonant). That is, *cavity-enhanced VFs amplify scattering into cavity modes* and, as we argued in Sec. 15.3 the VFs are measured by the structure factor (15.98).
Note, that the presence of photons in the cavity does not stimulate 'additionally', because stimulated emission and absorption are reversible processes.

Example 196 (*Bragg scattering: Cooperativity in a lattice*):

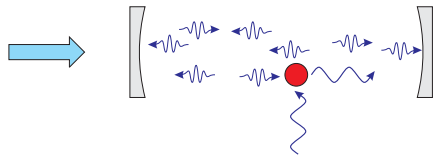

Figure 29.3: Cartoon of cooperative enhancement in a cavity.

Example 197 (*Matter wave superradiance and CARL: Cooperativity in a BEC*): We have seen that the stimulated processes mentioned above do not rely on quantum statistics, but rather on symmetry and coherence. Let us start with a naive picture of bosonic stimulation, a concept which can be applied to matter waves [460]. The physical process behind bosonically stimulated scattering is, that the presence of a macroscopically occupied state increases the density fluctuations of the system, and bosonically enhanced scattering is simply the diffraction of particles from these density fluctuations measured by $S(\mathbf{q},\omega)$.

29.1.5 Collective scattering for condensates with interactions

Until now we totally disregarded interactions between particles. Correlations are introduced in a BEC by interactions between the atoms. Therefore, collective scattering effects are influenced by interactions, while on the other hand an ideal gas ($gn \to 0$) scatters like an ultra-cool non-degenerate thermal cloud. In this sense, particle-like excitations ($\mathbf{p}^2/2m \gg gn$) in an interacting BEC behave like thermal atoms. The mean-field energy can be seen as resulting from excitations of phonon pairs. These pairwise excitations populate the momentum modes, which modify the scattering of light via bosonic stimulation. That is, an interacting condensate ($gn > 0$) gives a collective response to an incident light beam. Note that $\mu > 0$ is possible when $V(\mathbf{r}) \neq 0$ and $gn \neq 0$ even if $T \to 0$, which is the case here considered.

What is the nature of the collective behavior? 1. The Bogolubov spectrum is modified. In the phononic regime, the absence of dispersion allows the definition of a speed of sound. 2. The scattering of light can be suppressed by excitation of phonon pairs. This effect is anisotropic and more pronounced in forward direction. That is, the resonance at which the light is scattered is shifted and broadened. The latter effect is understood via destructive interference of two processes: Scattering from a BEC to the momentum mode $\mathbf{k}$ and from the momentum mode $-\mathbf{k}$ to a BEC.

It is important to be aware that the notion of *bosonic stimulation* $\sim n_i(1+n_f)$ and *fermionic inhibition* $\sim n_i(1-n_f)$ also has its limitations, when interatomic interactions are not negligible, that is, when the quantum depletion is remarkable [329, 561]. The effect of interatomic collisions can be taken into account as contributions of pair correlations to the ground state of the BEC,

$$|\psi_0, n_0\rangle = |n_0, 0, 0\rangle - \sum_{\mathbf{k}} (v_{\mathbf{k}}^2/u_{\mathbf{k}}^2)|n_0-2, 1, 1\rangle + \sum_{\mathbf{k}} (v_{\mathbf{k}}^2/u_{\mathbf{k}}^2)^2 |n_0-4, 2, 2\rangle - \dots\,, \quad (29.46)$$

where $|n_0, n_{\mathbf{k}}, n_{-\mathbf{k}}\rangle$ denotes the state with n_0 atoms in the trap's ground state and $n_{\pm\mathbf{k}}$ atoms in the momentum mode $\mathbf{k}$, where $v_{\mathbf{k}}^2$ is the average population of momentum

mode $\mathbf{k}$. The populated recoil modes result in a increase of spontaneous emission by a factor of $v_{\mathbf{k}}^2 = 1 + u_{\mathbf{k}}^2$. We can also understand the modification of the scattering rate as resulting from small scale inhomogeneities generated by pair correlations. The effect is strongest at small scattering angles, that is in forward direction.

29.1.6 Exercises

29.1.6.1 Ex: Sum rules for the dynamic structure factor

Derive the following sum rules for the norm, the kinetic energy, and the compressibility,

$$\begin{aligned} S(\mathbf{q}) &= \int S(\mathbf{q},\omega)d\omega \\ \frac{\hbar^2 q^2}{2m} &= \int \hbar\omega S(\mathbf{q},\omega)d\omega \\ \frac{\kappa^2}{2} &= \int \frac{S(\mathbf{q},\omega)}{\hbar\omega}d\omega\Big|_{\mathbf{q}\to 0} \end{aligned} .$$

29.1.6.2 Ex: Interaction energy of a condensate via spatial coherence

Show that the total energy of a condensate is given by $\langle U\rangle = \frac{1}{2}\int n(\mathbf{r}_1)U(\mathbf{r}_1 - \mathbf{r}_2)g^{(2)}(\mathbf{r}_1,\mathbf{r}_2)n(\mathbf{r}_2)d^3r_1 d^3r_2$.

29.1.6.3 Ex: Structure factor of a condensate in the local density approximation

Calculate the structure factor of a condensate in the local density approximation (LDA) [122, 779].

29.1.6.4 Ex: Structure structure of a Fermi gas

Calculate the structure factor for Bragg scattering on a Fermi gas.

29.1.6.5 Ex: Structure factor of a heteronuclear mixture

In this exercise we discuss the structure factor of a heteronuclear mixture (specifically contemplating ^{6}Li mixed with ^{87}Rb) generalizing the available theory for Li spin mixtures to heteronuclear mixtures [171, 295, 296, 838]. The total dynamic structure factor is,

$$S(q,\omega) = S_{87,87}(q,\omega) + S_{6,6}(q,\omega) + S_{6,87}(q,\omega) + S_{87,6}(q,\omega) \ .$$

Exciting the Bragg resonance for Li, the Rb cloud would stay unaffected,the such that around $\omega/2\pi = 295$ kHz, $S_{87,87}(q,\omega) = 0$, as well as, $S_{6,87}(q,\omega) = S_{87,6}(q,\omega) = 0$. For Fermi gas $S_{6,6}(q,\delta) \to 1$, except if Bose gas induces Li-Li correlations, as in the case of BCS-pairing of phonon-mediated Efimov states.
How does Rb influence the Bragg scattering of Li? Via a variation of the apparent

mass as a displacement of the Bragg resonance or as a second peak appearing at a specific detuning of the Bragg beams at $\omega_{6,6} * 6/(6+87)$?

29.1.6.6 Ex: Spatial coherence of a condensate

Derive the relationship (29.7).

29.1.6.7 Ex: Structure factor for Bragg scattering

Demonstrate the following relationships,

$$\frac{dp_{cm}(\mathbf{q},\omega)}{dt} = -m\omega_z^2 z_{cm} + \hbar q \frac{\Omega_{br}^2}{2} \int d\delta' [S(\mathbf{q},\omega') - S(-\mathbf{q},-\omega')] \frac{\sin(\omega-\omega')t_{br}}{\omega-\omega'}$$

$$\ddot{p}_{cm}(q,\omega) + \omega_z^2 p_{cm} = \hbar q \frac{\Omega_{br}^2}{2} \int d\omega' [S(\mathbf{q},\omega') - S(-\mathbf{q},-\omega')] \cos(\omega-\omega')t_{br} \longrightarrow 0 \ .$$

29.1.6.8 Ex: Commutation expressions for bosons and fermions

Verify the following useful commutation relations:
a. For bosons,

$$\hat{a}_m(\mathbf{k})\hat{a}_n^\dagger(\mathbf{q})^N = N\delta_{m,n}\delta_{\mathbf{k},\mathbf{q}}\hat{a}_n^\dagger(\mathbf{q})^{N-1} + \hat{a}_n^\dagger(\mathbf{q})^N \hat{a}_m(\mathbf{k}) \ , \tag{29.47}$$

which can be generalized to,

$$\begin{aligned} &\hat{a}_m(\mathbf{k})[\hat{a}_n^\dagger(\mathbf{q}_1) + \hat{a}_n^\dagger(\mathbf{q}_2)]^N \\ &\quad = N\delta_{m,n}\left(\delta_{\mathbf{k},\mathbf{q}_1} + \delta_{\mathbf{k},\mathbf{q}_2}\right)[\hat{a}_n^\dagger(\mathbf{q}_1) + \hat{a}_n^\dagger(\mathbf{q}_2)]^{N-1} + [\hat{a}_n^\dagger(\mathbf{q}_1) + \hat{a}_n^\dagger(\mathbf{q}_2)]^N \hat{a}_m(\mathbf{k}) \ . \end{aligned} \tag{29.48}$$

b. For fermions do not support macroscopic populations of the type $\hat{a}_n^\dagger(\mathbf{q})^N$. Performing a number P of permutations of the operators and assuming that one fermion of the product state is in the internal state n, we calculate,

$$\hat{a}_n(\mathbf{k}) \prod_{m=0}^{N-1} \hat{a}_m^\dagger(\mathbf{q}) = (-1)^P \left[\delta_{\mathbf{k},\mathbf{q}} \prod_{m\neq n}^{N-1} \hat{a}_m^\dagger(\mathbf{q}) - \prod_{m=0}^{N-1} \hat{a}_m^\dagger(\mathbf{q})\hat{a}_n(\mathbf{k}) \right] \ . \tag{29.49}$$

If none of the fermions of the product state is in state n the first part of the sum simply vanishes. This expression can also be generalized to,

$$\begin{aligned} \hat{a}_n(\mathbf{k}) \prod_{m=0}^{N-1} [\hat{a}_m^\dagger(\mathbf{q}_1) + \hat{a}_m^\dagger(\mathbf{q}_2)] &= (-1)^P \prod_{m\neq n}^{N-1} [\hat{a}_m^\dagger(\mathbf{q}_1) + \hat{a}_m^\dagger(\mathbf{q}_2)] \hat{a}_n(\mathbf{k}) [\hat{a}_n^\dagger(\mathbf{q}_1) + \hat{a}_n^\dagger(\mathbf{q}_2)] \\ &= (-1)^P \left[(\delta_{\mathbf{k},\mathbf{q}_1} + \delta_{\mathbf{k},\mathbf{q}_2}) \prod_{m\neq n}^{N-1} [\hat{a}_m^\dagger(\mathbf{q}_1) + \hat{a}_m^\dagger(\mathbf{q}_2)] - \prod_{m=0}^{N-1} [\hat{a}_m^\dagger(\mathbf{q}_1) + \hat{a}_m^\dagger(\mathbf{q}_2)] \hat{a}_n(\mathbf{k}) \right] \ . \end{aligned} \tag{29.50}$$

29.1.6.9 Ex: Extracting the atom number from many-body states

Verify the normalization of (a) the bosonic Fock state (29.32), (b) the fermionic product state (29.32), (c) the bosonic product state (29.35), (d) the bosonic Bragg grating state (29.37), and (e) the fermionic Bragg grating state (29.37). **Help:** Speed up the calculations by using the results of 29.1.6.8.

29.1.6.10 Ex: Bosonic stimulation and cooperative enhancement by lattices of bosons and fermions

Compare bosons and fermions with respect to (a) bosonic stimulation and (b) cooperative enhancement.

29.1.6.11 Ex: Cooperative enhancement versus bosonic stimulation

CARL amplification comes from cooperativity not from bosonic stimulation [599, 460, 739], that is, it should work for fermions and boltzons. To demonstrate this proceed as follows:
a. Set up the single-atom Hamiltonian for a 3D harmonic potential in which the atoms (bosons or fermions) are initially placed allowing for the possibility of momentum recoil by photon scattering. This disregards the trap's inhomogeneity, but is a good assumption for short times. What are the eigenfunction of this Hamiltonian? Calculate the expectation value for the density distribution. Express the field operators in momentum space. Express the lowest energy states for a bosonic/fermionic cloud in momentum representation.
b. Now apply a $\pi/2$-Bragg-pulse imparting the recoil $\mathbf{K}$ to the cloud. What is the resulting state? Recalculate the expectation value for the density distribution.
c. Now, assume the presence of another free (test) atom (or photon). Write down the Hamiltonian and the wavefunction for this atom. It is supposed to interact with the atomic cloud via the (perturbatively treated) interaction potential,

$$\hat{V} = \lambda \int d^3r \hat{\psi}_1^\dagger(\mathbf{r})\hat{\psi}_2^\dagger(\mathbf{r})\hat{\psi}_2(\mathbf{r})\hat{\psi}_1(\mathbf{r}) \ .$$

Calculate the probability that the atom is scattered at a particular wavevector, i.e. determine the cooperative enhancement factor.
d. Is cooperative enhancement possible with just one atom?
e. How about cooperative enhancement in a cavity, when cooperativity is ensured by a single atom plus all its mirror images?

29.2 Bragg diffraction

An important technique for manipulating the atomic motion is by *Bragg diffraction* [5]. It allows the coherent transfer of atoms to other states of motion or to superpositions of motional states, and is extremely useful for applications, such as the realization of

[5] The idea is analogous to the manipulation of the **k**-vector of light waves by acousto-optic modulators.

matter wave beamsplitters [483] and atomic lasers, or for the targeted excitation of quasi-particles [483, 790, 779].

To implement Bragg diffraction, we consider two laser pulses with different frequencies and propagation directions $\omega, \mathbf{k}_\omega$ and $\omega - \Delta\omega, \mathbf{k}_{\omega-\Delta\omega}$, detuned from an atomic resonance and intersecting at the position of atoms under an angle ϑ, as shown in Fig. 29.4(a). The superposition of the electric fields of the light beams,

$$E = E_0 e^{\imath(\mathbf{k}_\omega\cdot\mathbf{r}-\omega t)} + E_0 e^{\imath[\mathbf{k}_{\omega-\Delta\omega}\cdot\mathbf{r}-(\omega-\Delta\omega)t]} = E_0 e^{\imath(\mathbf{k}_\omega\cdot\mathbf{r}-\omega t)}\left(1 + e^{-\imath(\mathbf{q}\cdot\mathbf{r}-\Delta\omega t)}\right)$$
$$= 2E_0 e^{\imath(\mathbf{k}_\omega\cdot\mathbf{r}-\omega t)} e^{-\frac{\imath}{2}(\mathbf{q}\cdot\mathbf{r}-\Delta\omega t)} \cos\tfrac{\mathbf{q}\cdot\mathbf{r}-\Delta\omega t}{2} \ , \qquad (29.51)$$

where $\mathbf{q} \equiv \mathbf{k}_\omega - \mathbf{k}_{\omega-\Delta\omega}$, produces a standing light wave with an intensity proportional to,

$$|E|^2 = 4E_0^2 \cos^2\tfrac{\mathbf{q}\cdot\mathbf{r}-\Delta\omega t}{2} = 2E_0^2[1 + \cos(\mathbf{q}\cdot\mathbf{r} - \Delta\omega t) \ , \qquad (29.52)$$

with which the atoms interact.

The Bragg diffraction technique has proven extremely efficient: up to 100% of the atoms can be transferred to well-defined momentum sidemodes. In general, the components of a cloud with different momentum modes overlap during the time scale of the Bragg pulses. They only separate spatially after a ballistic flight time, which then allows their identification via absorption imaging.

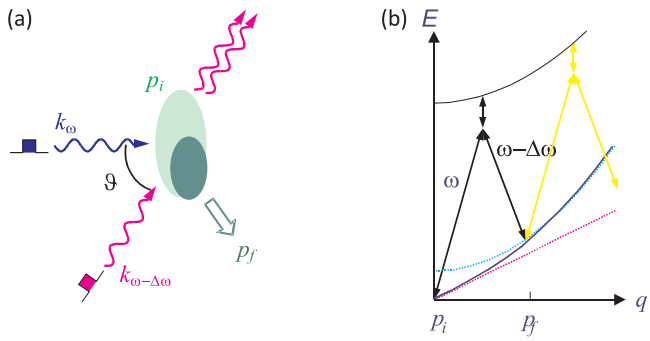

Figure 29.4: Bragg scattering of atoms at a standing light wave. (a) Geometric layout: Short pulses of two laser beams in Raman configuration enclosing an angle of ϑ and detuned from each other by $\Delta\omega$ are simultaneously irradiated into the cloud. (b) Bogolubov dispersion relation for interacting condensates (blue line). The quadratic dispersion relation (cyan) holds for free particles, and the linear dispersion relation (magenta) for phonon excitations.

29.2.1 Interpretations of the Bragg diffraction process

Bragg's diffraction can be treated within the formalism developed in Sec. 29.1.2, as will be shown later, in Sec. 29.2.3. But before that, let us present a simplified approach and several simple pictures illustrating the dynamics of Bragg diffraction.

29.2.1.1 Bragg diffraction picture

The *first interpretation* of this phenomenon is as *matter wave Bragg diffraction* at a standing light wave (i.e. an one-dimensional optical lattice) formed by two crossing

pulsed laser beams [6]. We consider atoms initially at rest exposed to the standing wave (29.51) with $\Delta\omega = 0$ and $\mathbf{q} \equiv q\hat{\mathbf{e}}_z$, such that the dipolar potential $U \propto |E|^2$ is, with (29.52),

$$U(z) = U_0 \cos^2 \tfrac{qz}{2} \ . \tag{29.53}$$

Assuming a given finite interaction time τ, the modulation of the local phase of the atoms becomes [7],

$$\boxed{\psi_\tau(z) = \psi_0(z) e^{\imath U(z)\tau/\hbar} = \psi_0(z) e^{\frac{\imath}{2\hbar} U_0 \tau(\cos qz + 1)} = \psi_0(z) e^{\imath U_0 \tau/2\hbar} \sum_n \imath^n J_n(\tfrac{U_0\tau}{2\hbar}) e^{\imath n q z}} \ , \tag{29.54}$$

where J_n are the Bessel functions of the first kind [8].

The condensed wavefunction evolves into a superposition of motional modes, which correspond to the diffraction orders of Bragg scattering and their amplitudes through the Bessel functions J_n. The diffraction efficiency increases with laser intensity and with time.

Now, we need to generalize this result to the propagating standing wave of the expression (29.52). The intensity generates a dipole potential,

$$U(z,t) \approx U_0 \cos^2 \tfrac{q_z z - \Delta\omega t}{2} \ , \tag{29.55}$$

so that the condensate now evolves according to,

$$\psi(z,t) = \psi_0(z) e^{\imath/\hbar \int_{t_0}^{t_0+\tau} U(z,t) dt} = \psi_0(z) e^{\imath/\hbar \int_{t_0}^{t_0+\tau} U_0 \cos^2 \frac{q_z z - \Delta\omega t}{2} dt} \ . \tag{29.56}$$

For short interaction times, $\tau \ll 2\pi/\Delta\omega$, ...

29.2.1.2 Compton scattering picture

The *second interpretation* is that of *Compton scattering*: Spontaneous Rayleigh scattering of a photon from a mode $\mathbf{k}_\omega$ into a solid angle around $\mathbf{k}_{\omega-\Delta\omega}$ leaves an atom with the recoil momentum $\hbar\mathbf{q} \equiv \mathbf{p}_f \cdot \mathbf{p}_i$. Of course, one can *stimulate* the Rayleigh scattering process by providing the laser mode $\mathbf{k}_\omega - \Delta\omega$ at the entrance. By replacing the spontaneous output mode with a stimulated input mode, we increase the probability for an atomic recoil in the momentum mode $\hbar\mathbf{q}$, which is thus pre-selected by the choice of $\mathbf{k}_{\omega-\Delta\omega}$. Since the elementary scattering process must conserve energy and total momentum,

$$\begin{aligned} \hbar\omega + \frac{p_i^2}{2m} &= \hbar(\omega - \Delta\omega) + \frac{p_f^2}{2m} \\ \hbar\mathbf{k}_i + \mathbf{p}_i &= \hbar\mathbf{k}_f + \mathbf{p}_f \ , \end{aligned} \tag{29.57}$$

we obtain the *Bragg condition*,

$$\boxed{E = \Delta\omega = \frac{p_f^2}{2m} - \frac{p_i^2}{2m} = \frac{(\mathbf{p}_f - \mathbf{p}_i)^2}{2m} + \frac{(\mathbf{p}_f - \mathbf{p}_i)\cdot\mathbf{p}_i}{m} = \frac{q^2}{2m} + \frac{\mathbf{q}\cdot\mathbf{p}_i}{m}} \ . \tag{29.58}$$

[6] Note, that the initial population of the recoil mode should be small. Otherwise, since Bragg diffraction is a coherent and thus reversible process, atoms initially in the recoil mode are transferred back to the original matter wave mode.

[7] Using the Jacobi-Anger expansion, $e^{\imath\beta\cos x} = \sum_n \imath^n J_n(\beta) e^{\imath n x}$.

[8] Andreas got $\psi_0(z) \sum_n J_n^2(U_0\tau/2\hbar) e^{\imath n q z/2}$.

Expressed by the Bragg angle, the condition reads,

$$q = \sqrt{(\mathbf{p}_f - \mathbf{p}_i)^2} = \sqrt{\hbar^2\mathbf{k}_i^2 + \hbar^2\mathbf{k}_f^2 - 2\hbar^2\mathbf{k}_i\mathbf{k}_f} \simeq \hbar\mathbf{k}_i\sqrt{2 - 2\cos\theta} = 2\hbar k_i \sin\vartheta/2 \ . \tag{29.59}$$

The efficiency for transferring atoms to the recoil mode depends on the fulfillment of this condition. The Bragg condition can be employed to select higher diffraction orders.

29.2.1.3 Stimulated Raman scattering picture

A *third interpretation* is as *stimulated Raman scattering* between two different kinetic states of the atom [see 29.4(b)]. In fact, the momentum modes $\mathbf{p}_i$ and $\mathbf{p}_f$ have different energies, which, for a condensate, are determined by the Bogolubov spectrum [322]. By varying the angle ϑ in the Bragg condition (29.58), we can choose the amount of energy to be transferred and thus probe the spectrum, i.e. measure the excitation energy $E(\mathbf{q}, \mu)$ as a function of the momentum $\mathbf{q}$ and the chemical potential μ in the particle regime $\mathbf{q}^2/2m \gg \mu$, as well as in the phonon regime $\mathbf{q}^2/2m \ll \mu$. On the other hand, varying the detuning $\Delta\omega$ in the Bragg condition (29.58), we selectively address different velocity classes of a gas or condensate, which allows us to probe its velocity distribution. This procedure is called spectroscopy of *recoil-induced resonances* (RIR) [181, 790]. RIR spectroscopy also provides detailed information on the mean-field energy and the (inhomogeneous) density distribution of a condensate. Note, finally, that Bragg scattering is closely related to *Kapitza-Dirac* scattering of atomic beams, well-known in conventional atom optics [448, 333].

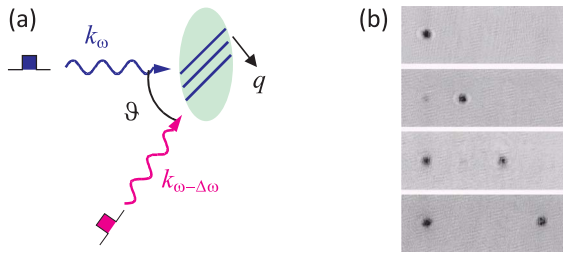

Figure 29.5: Bragg scattering of atomic clouds. (a) Geometric layout as in 29.4. Here, we assume $p_i = 0$. (b) Experiment showing coherent splitting by a Bragg pulse.

29.2.1.4 Coherent splitting

There is a general interest in the possibility of dividing phase space by coherent coupling of otherwise independent modes. We are talking, of course, about double slits or beamsplitters, which represent an essential tool of quantum mechanics. Bragg diffraction realizes a beamsplitter for atomic clouds analogous to the optical beamsplitter. In fact, Bragg diffraction has been used for the realization of output couplers for atom lasers and for atom interferometers. A suggestion that is sometimes made is the following: 'A condensate is a macroscopically populated momentum mode. The Bragg beamsplitter divides the phase space into two entangled output modes. Shouldn't it

be possible to generate a macroscopic superposition of two condensates, i.e. a really macroscopic Schrödinger cat?' of the type

$$(|\Psi_+\rangle + |\Psi_-\rangle) \ . \tag{29.60}$$

Their is an obvious fundamental interest to study such states and the mechanisms leading to their decoherence (see Sec. 18.1.1).

To clarify the situation, we first have to say, what we mean by *Schrödinger cat*. A Schrödinger cat is a quantum superposition of many-body states. A perfect cat made of N two-level atoms can be expressed as $|++...\rangle \pm |--...\rangle$. The Einstein-Podolsky-Rosen (EPR) and the Greenberger-Horne-Zeilinger states (GHz) belong to this category. The degree of entanglement of the cat is measured by the information entropy defined as $S = -\langle \log_2 \hat{\rho} \rangle$, where $\hat{\rho}$ is the density operator. The information entropy measures the amount of classical information that can be encoded in the quantum state. For example, the entropy of a perfect cat state is $S = 1$ bit, because if we find one of the atoms in the state $|+\rangle$, we know that all others are in the same state.

Second, we have to explain, what we mean by a *beamsplitter*. Subject to a beam splitting process, every individual atom has the choice between one of two output ports. However, if the process is coherent, every atom will evolve into a coherent superposition, but it does so independently from the other atoms. That is, we can write the state of the atomic cloud as a product state of *Schrödinger kittens* $(|+\rangle \pm |-\rangle)^N$, but no real cat. The information entropy is $S = N$ bit, as for independent atoms. *Clearly, the state (29.60) is NOT the state generated by a beamsplitter!* Nevertheless, the beamsplitter creates a certain correlation between the two modes (see Sec.14.5).

It may come as a surprise, that a condensate composed of totally delocalized atoms coherently interacting with a homogeneous light field (the photons of the Bragg beams are totally delocalized over the field mode including the condensate volume) increases its entropy from 1 to N bits. This argument, however, would be the same for a non-condensed *thermal* cloud being sufficiently cold that the thermal de Broglie wavelengths exceeds the size of the cloud. That is, even in condensates the photons are scattered by individual atoms. The interaction with the light *localizes* one atom in the condensate before removing it from there by recoil. Nevertheless, cooperative interaction of several atoms with a light mode is possible, e.g. in superradiance or when the photons are recycled by means of an optical cavity, as in the Jaynes-Cummings model.

29.2.2 Bragg interferometry of a thermal gas

Even above the critical temperature the momentum distribution of a dilute thermal gas is (slightly) modified by quantum statistics, i.e. by the classical, bosonic or fermionic nature of the gas. We have already emphasized that Bragg interferometry can be used to measure the momentum distribution of a gas via RIR spectroscopy, whether the gas is condensed or thermal. Now, let us discuss Bragg interferometry on a thermal gas, based on the articles [555] and [210].

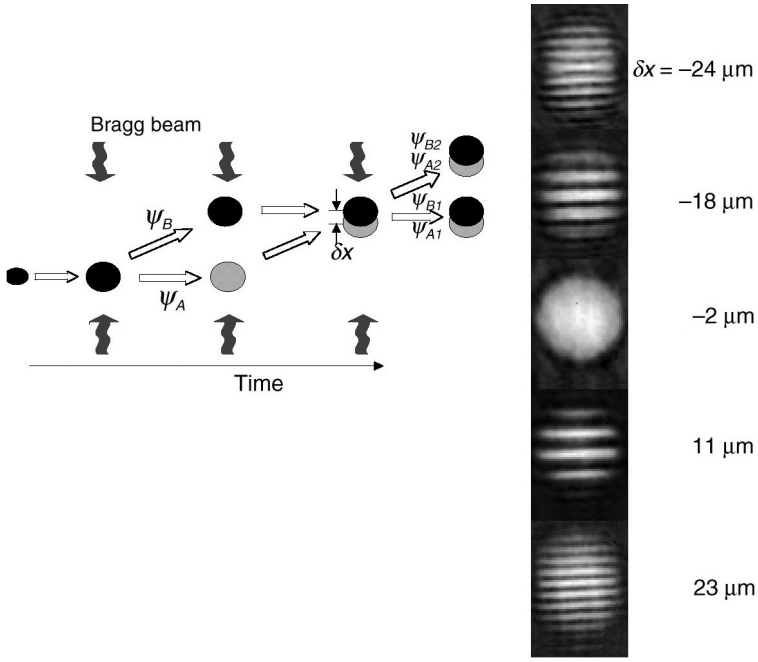

Figure 29.6: Bragg interferometer.

29.2.2.1 Free evolution of a thermal cloud

To describe the Bragg scattering process quantitatively, we interpret it as a *Raman transition between discrete atomic momentum states governed by a Schrödinger equation*. On the other hand, as long as no radiation is incident the atomic center-of-mass wavefunctions evolve freely or under the constraint of an external potential. That is, both processes concern the same motional degree of freedom. In order to derive a complete quantum model, let us first develop the formalism for the description of the free evolution of a thermal cloud, then we explain how a resonant radiation can be included.

We consider a thermal atomic cloud initially distributed over many momentum classes according to the Maxwell-Boltzmann velocity distribution,

$$D(k_z) = \frac{\hbar}{(2\pi m k_B T)^{1/2}} e^{-\hbar^2 k_z^2/2mk_BT} = \frac{e^{-\pi k_z^2/k_{therm}^2}}{k_{therm}} \ , \tag{29.61}$$

using $k_{therm} \equiv 2\pi/\lambda_{therm}$ and (26.9). Because of the inhomogeneity of the distribution, any evolution of atoms belonging to specific momentum classes caused by velocity-selective radiation pulses, must be calculated with individual atoms. The final momentum distribution (e.g. after a pulse sequence) can then be obtained by weighing with the individual evolution with the initial momentum distribution [9].

[9]The procedure neglects interatomic interactions, which is always a good presumption, for example, for an ultracold Fermi gas [214] or for ^{88}Sr atoms, which have a very small scattering length.

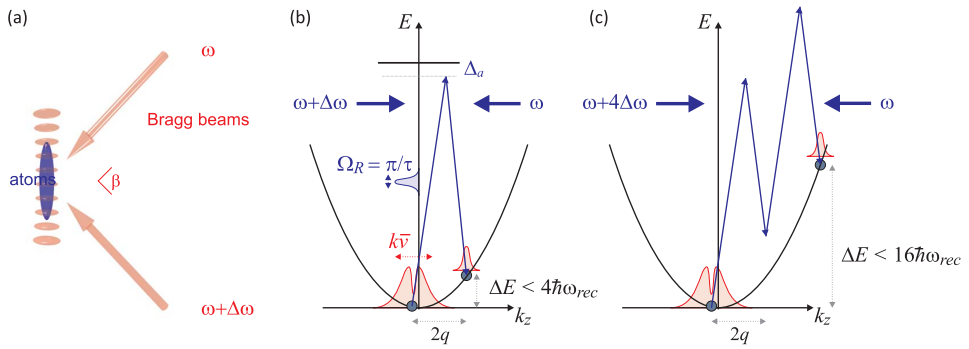

Figure 29.7: (a) Geometry for Bragg diffraction. (b) Illustration of a Raman transition between two points of the free-particle dispersion curve, when the atoms are initially thermally distributed. (c) Same as (a), but now the detuning $\Delta\omega$ is adjusted for second-order Bragg diffraction.

We describe the quantum state of a thermal atom $|\psi\rangle$ as a plane wave, $\langle z|\psi\rangle \propto e^{\imath k_z z}$, which in momentum space corresponds to a Dirac distribution, $\langle k_z|\psi\rangle \propto \delta(z - z_0)$. Without radiative coupling, we describe the evolution in momentum space by the solution of the Schrödinger equation (or propagator),

$$\langle k_z|\psi(t)\rangle = e^{\imath \hat{H} t/\hbar}\langle k_z|\psi(0)\rangle \ . \tag{29.62}$$

In free space, with the Hamiltonian $\hat{H}_{free} = \hbar^2 k_z^2/2m$, the wavefunction is obviously constant.

In order to couple two intervals of momentum distribution by resonant radiation, we first need to duplicate the Hilbert space,

$$a_{i,k_z}(t) \equiv \langle i|\psi_{k_z}(t)\rangle = \langle i|\langle k_z|\psi(t)\rangle \tag{29.63}$$

with $i = 1, 2$. Note that, in this case, the Hilbert spaces are not disjunct.

To obtain the atomic momentum distribution after the application of a pulse sequence, we calculate the evolution of the amplitudes a_{j,k_z} for a variety of initial momenta and weigh the final populations of the momentum states with the distribution function $D(k_z)$. The number of atoms expected in the zeroth and first Bragg diffraction order is, therefore,

$$N_j(t) = \int D(k_z)|a_{j,k_z}(t)|^2 dk_z \ . \tag{29.64}$$

29.2.2.2 Bragg scattering and RIR

For large momentum distributions, $T \gg T_{rec}$, the atomic cloud occupies many momentum states, such that the Bragg scattering produces a RIR-like signal. That is, the scattering probability is proportional to the *population difference* of the initial and final momentum states, as discussed in Sec. 25.3.1. The number of scattered atoms/photons is, therefore,

$$\dot{N}_{brg} \propto \Omega_R \left.\frac{\partial D(k_z)}{\partial k_z}\right|_{k_z = \hbar m \Delta\nu/q} \ . \tag{29.65}$$

where,

$$\Omega_R = \frac{\Omega_1\Omega_2}{2\Delta_a} = \frac{1}{\Delta_a}\frac{3\lambda^2}{4\pi}\frac{\Gamma}{\hbar\omega}\sqrt{I_1 I_2} = \frac{3\pi c^2 I}{\hbar\omega^3}\frac{\Gamma}{\Delta_a} \tag{29.66}$$

is the two-photon Rabi frequency. For very narrow momentum distributions, $T \ll T_{rec}$, we may assume the atomic cloud to occupy only a single momentum state,

$$\dot{N}_{brg} \propto \Omega_R D(k_z) \ . \tag{29.67}$$

The transition rate per atom is then given by [780],

$$\frac{W}{N} = \frac{2\pi\hbar}{N}\Omega_R^2 \sum_f |\langle f|\hat{\rho}^\dagger(\mathbf{k})|g\rangle|^2 \delta(\hbar\nu - E_f + E_g) \equiv 2\pi\Omega_R^2 S(\mathbf{k},\nu) \ . \tag{29.68}$$

As illustrated in Fig. 29.7, to scatter an atom with the initial wavevector k_z to the next higher momentum state $k_z + 2q$, the Bragg condition requires,

$$\Delta\nu_R = \nu_{R2} - \nu_{R1} = \frac{\hbar(k_z+2q)^2}{2m} - \frac{\hbar k_z^2}{2m} = \frac{2\hbar q}{m}(k_z + q) \ . \tag{29.69}$$

If we tune $\Delta\nu(\pm\Delta k_z)$ until the Bragg signal $\dot{N}_{brg}$ drops to $e^{-1/2}$,

$$\Delta\nu_R(\Delta k_z) - \Delta\nu_R(-\Delta k_z) = \frac{4\hbar\Delta k_z q}{m} = \frac{4\hbar q}{m}\frac{\sqrt{m k_B T}}{\hbar} = 4q\sqrt{\frac{k_B T}{m}} \ . \tag{29.70}$$

29.2.2.3 Bragg scattering by free atoms

Let us first assume that during the Bragg pulse only two discrete atomic momentum states $j = 0, 1$ are coupled [452, 84, 555, 210], and that trapping potentials are absent or can be neglected. This is justified for Bragg pulse sequences much shorter than an oscillation period of the trap. We denote the probability amplitudes for the two momentum states by momentum space wavefunctions a_{j,k_z}. They correspond to atoms with initial momenta $\hbar k_z$ that are coupled to states with momentum $\hbar k_z' = \hbar(k_z + 2q)$. The temporal evolution of the amplitudes under the action of the Bragg light is given by the solutions of the Schrödinger equation [555, 210],

$$\begin{pmatrix} a_{0,k_z}(t) \\ a_{1,k_z}(t) \end{pmatrix} = e^{-\imath\hat{H}_R t/\hbar} \begin{pmatrix} a_{0,k_z}(0) \\ a_{1,k_z}(0) \end{pmatrix} \ , \tag{29.71}$$

with the Hamiltonian,

$$\boxed{\hat{H}_R = \begin{pmatrix} \frac{\hbar^2}{2m}k_z^2 & \frac{\hbar}{2}\Omega_R \\ \frac{\hbar}{2}\Omega_R & \frac{\hbar^2}{2m}k_z'^2 - \hbar\delta \end{pmatrix}} \ , \tag{29.72}$$

where $\Delta = 2\hbar q^2/m - \delta$ is the detuning of the Bragg lasers from the recoil shift. When the Bragg light is switched off, the Hamiltonian simplifies to,

$$\hat{H}_{free} = \begin{pmatrix} \frac{\hbar^2}{2m}k_z^2 & 0 \\ 0 & \frac{\hbar^2}{2m}k_z'^2 - \hbar\delta \end{pmatrix} \ . \tag{29.73}$$

Concatenating temporal evolutions described by $e^{-\imath\hat{H}_R t/\hbar}$ and $e^{-\imath\hat{H}_{free}t/\hbar}$, the phase evolution of individual atoms in momentum state superpositions can be calculated for arbitrary sequences of pulses separated by intervals of free evolution, for example, Ramsey-type sequences.

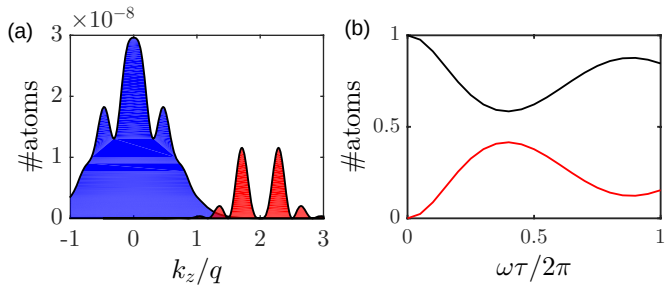

Figure 29.8: (code) (a) Distribution of momentum classes in the direction of k_z after irradiation of a 2π Bragg pulse. The width of the structure is determined by the power broadening of the Raman transition. (b) Temporal evolution of the populations of the momentum states 0 and $2q$.

29.2.2.4 Bragg scattering by trapped particles

When trapped atoms are considered, the problem arises that the Hilbert space of momentum states is simultaneously coupled by two interactions: a moving optical lattice (generated by the Bragg lasers) and the (harmonic) trap. However, the situation gets simpler if a separation of the scales is possible. In general, the duration of a pulse is very short, $\tau \ll 2\pi/\omega_z$. In contrast, the duration of a free evolution period Δt (e.g. in a Ramsey cycle) may be such, that it is no more negligible compared to a trap oscillation period, so that we need to account for the action of the trapping potential explicitly.

As the trap couples the atomic momenta with the atomic positions ($E_{kin} + E_{pot} = const$), the initial spatial distribution of the atoms must now be considered. For simplicity, we describe it as a thermal Gaussian, similarly to what has been done in Eq. (29.61) for the momentum distribution,

$$G(z) = \sqrt{\frac{m\omega_z^2}{2\pi k_B T}} e^{-m\omega_z^2 z^2/2k_B T} = \frac{e^{-\pi z^2/a_z^4 k_{therm}^2}}{a_z^2 k_{therm}} \ . \tag{29.74}$$

Beginning with the positions z and initial momenta k_z, after a diffraction pulse transferring the recoil $2q$ to part of the atoms and being short enough not to change their positions, the atoms follow classical trajectories. The atomic momenta (now depending on time) are simply the solution of the equation of motion $\hbar \dot{k}_z = -m\omega_z^2 z$ with the initial conditions $z(0) = z$ and $k_z(0) = k_z$, respectively, $k_z'(0) = k_z + 2q$,

$$\begin{aligned} \tilde{k}_z(t) &= k_z \cos\omega_z t - \frac{m\omega_z}{\hbar} z \sin\omega_z t \\ \tilde{k}_z'(t) &= (k_z + 2q)\cos\omega_z t - \frac{m\omega_z}{\hbar} z \sin\omega_z t \ , \end{aligned} \tag{29.75}$$

where the first expression holds for non-diffracted atoms and the second for diffracted atoms. These momenta are substituted for k_z and k_z', respectively, in the Hamiltonians (29.72) and (29.73). As the Bragg pulses are short compared to the oscillation period, $\tau \ll 2\pi/\omega_z$, the effect of the trapping potential may be neglected during Bragg scattering. This means that the Hamiltonian $\hat{H}_R$ depends on $\tilde{k}_z(t)$, but can be

treated as time-independent for the short intervals τ. In contrast, the Hamiltonian for free propagation $\hat{H}_{free}$ depends on the time, if Δt is long. In this case, the phase evolution of the atoms in both coupled states can be described by the time evolution operator as,

$$\boxed{e^{-\imath\hat{H}_{free}t/\hbar} = \begin{pmatrix} \exp\left(-\imath\int_0^t dt\,\frac{\hbar}{2m}\tilde{k}_z^2(t)\right) & 0 \\ 0 & \exp\left(-\imath\int_0^t dt\,\left[\frac{\hbar}{2m}\tilde{k}_z'^2(t)-\delta\right]\right) \end{pmatrix}} . \quad (29.76)$$

Since the amplitudes a_{j,z,k_z} now also depend on the initial atomic positions, the final populations of the momentum states must be additionally weighted with the initial spatial distribution. Therefore, the Eq. (29.64) for the expected the numbers of diffracted and non-diffracted atoms must be replaced by,

$$N_j(t) = \iint D(k_z)G(z)\left|a_{j,z,k_z}(t)\right|^2 dk_z dz\ . \quad (29.77)$$

In practice, however, it might be a good approximation to assume small displacements around a δ-shaped position distribution. Note, that the transformation (29.75) must be repeated for every free evolution pulse of a sequence.

Example 198 (*Approximation for small displacements*): In practice, we may neglect the displacements, $z \simeq 0$. Then the equations (29.75) simplify to,

$$\tilde{k}_z(t) = k_z\cos\omega_z t \quad \text{and} \quad \tilde{k}_z'(t) = (k_z+2q)\cos\omega_z t\ .$$

Inserting them in (29.76) we obtain for the propagator,

$$e^{-\imath\hat{H}_{free}t/\hbar}$$
$$= \exp\left(-\frac{\imath\hbar k_z^2}{4m\omega_z}(\cos\omega_z t\sin\omega_z t+\omega_z t)\right)\begin{pmatrix}1 & 0\\ 0 & \exp\left(-\frac{\imath\hbar q k_z}{2m\omega_z}(\cos\omega_z t\sin\omega_z t+\omega_z t)\right)\end{pmatrix}\ .$$

In Exc. 29.2.4.1 we will study the behavior of an ultracold atomic cloud subject to a gravitational potential during a Ramsey-Bordé sequence.

29.2.2.5 Bloch equations approach

Experimentally, we observe decoherence of the dynamics described above on a very slow time scale. This phenomenon can be included in a description based on Bloch equations,

$$\frac{d}{dt}\vec{\rho}_{k_z}(\tau) = M_j\vec{\rho}_{k_z}(\tau)\ , \quad (29.78)$$

with

$$\vec{\rho}_{k_z}(\tau) = \begin{pmatrix}\rho_{00,k_z}(\tau)\\ \rho_{01,k_z}(\tau)\\ \rho_{10,k_z}(\tau)\\ \rho_{11,k_z}(\tau)\end{pmatrix} \quad \text{and} \quad M_j = \begin{pmatrix} 0 & \Gamma & \frac{\imath}{2}\Omega_R & -\frac{\imath}{2}\Omega_R \\ 0 & -\Gamma & -\frac{\imath}{2}\Omega_R & \frac{\imath}{2}\Omega_R \\ \frac{\imath}{2}\Omega_R & -\frac{\imath}{2}\Omega_R & -\gamma-\imath\Delta_j & 0 \\ -\frac{\imath}{2}\Omega_R & \frac{\imath}{2}\Omega_R & 0 & -\gamma+\imath\Delta_j \end{pmatrix} \quad (29.79)$$

with the solution,

$$\vec{\rho}_{k_z}(\tau) = e^{M_3 t} e^{M_2 t} e^{M_1 t} \vec{\rho}_{k_z}(0) \tag{29.80}$$

with,

$$\Delta_1 = \frac{\hbar}{2m}(k_z + 2q)^2 - \Delta\nu - \frac{\hbar}{2m}k_z^2 \tag{29.81}$$
$$\Delta_3 = \frac{\hbar}{2m}\left[(k_z + 2q)\cos\omega_{tr}\tau\right]^2 - \frac{\hbar}{2m}\left[(k_z + 2q)\cos\omega_{tr}\tau - 2q\right]^2 - \Delta\nu \ .$$

We weigh populations with the initial momentum distribution,

$$N_j(\tau) \equiv \int D(k_z)\rho_{jj,k_z}(\tau)dk_z \ . \tag{29.82}$$

29.2.2.6 Kapitza-Dirac scattering

An atomic beam with longitudinal de Broglie wavelength $\lambda_{dB} = h/p$ diffracted by a solid periodic grating with a slit distance of d receives a transverse amplitude modulation. In the far field, this generates focuses at angles defined by $n\lambda_{dB}/d = \sin\vartheta$. Alternatively, the grating may consist of a standing light wave detuned from resonances. The standing wave will create a periodic optical potential, which imprints a transverse phase modulation on the atomic beam. In the far field, the result will be the same as for the solid grating. Each atom will evolve into a superposition of momentum sidemodes $\pm n2\hbar k$, without any momentum having been transferred to the atoms. The diffraction angle is again $\sin\vartheta = \pm n2\hbar k/p = \pm n\lambda_{dB}/(\lambda/2)$, where $\lambda/2 = d$ is the periodicity of the standing light wave. However, this is only true if the phase shift is much smaller than π. This scheme is called the *Raman-Nath regime* or the regime of *Kapitza-Dirac scattering*. An equivalent condition for this regime is, that the interaction time is less than a period of oscillation in the optical potential, $\tau \ll \sqrt{\hbar/\omega_{rec}/U}$, or $v_{trans}\tau \ll \lambda$.

The Raman-Nath regime is realized by a very focused optical standing wave. A wave that is not plane can be considered a superposition of many spatial modes. Since (off-resonant) scattering (absorption followed by induced emission) corresponds to a photon redistribution between spatial modes, in a tight waist the phase matching condition is somewhat relaxed and minor corrections to the energy balance are possible. In a certain sense, Kapitza-Dirac scattering is the inverse process of 'forward scattering' of a laser beam passing through an atomic cloud: the roles of light and atoms are exchanged. The requirement that the interaction time be short implies, that the light grating is 'optically dilute' for the atomic beam [10].

For larger Rabi frequencies,

$$\Omega_R \gg \frac{2\hbar q\sigma_{k_z}}{m} \ , \tag{29.83}$$

with $\sigma_{k_z} = \sqrt{mk_{\mathrm{B}}T/\hbar^2}$ being the width of the momentum distribution, the Doppler broadening is dominated by power broadening, meaning that Bragg diffraction occurs

[10] Note, that we usually employ the term of *optical diluteness* the other way round, i.e. an atomic cloud can be optically dilute (or dense) for a laser beam.

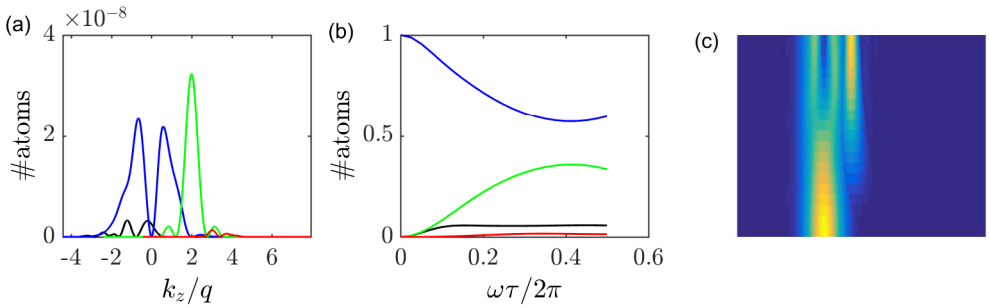

Figure 29.9: (code) (a) Distribution of momentum classes in the direction of k_z after irradiation of a π Bragg pulse. (b,c) Temporal evolution of the populations of the momentum states nq.

all over the atomic cloud. At some point, however, the Rabi frequency becomes comparable to the energy difference between adjacent momentum states, and Kapitza-Dirac scattering sets in. According to [84] the scattering will stay two-state like as long as the Rabi frequency fulfills the condition,

$$\Omega_R \ll \frac{\hbar}{m}(4q^2 - 2q\sigma_{k_z}) \; . \tag{29.84}$$

In the Kapitza-Dirac regime, the large energy uncertainty, connected with the fast coupling rate, allows several momentum states to be coupled simultaneously. In particular the Bragg Hamiltonian is replaced by,

$$\hat{H}_\tau = \begin{pmatrix} \ddots & \ddots & & & \\ \ddots & \frac{\hbar(k_z-2q)^2}{2m} + \delta & \frac{\Omega_R}{2} & & \\ & \frac{\Omega_R}{2} & \frac{\hbar k_z^2}{2m} & \frac{\Omega_R}{2} & \\ & & \frac{\Omega_R}{2} & \frac{\hbar(k_z+2q)^2}{2m} - \delta & \ddots \\ & & & \ddots & \ddots \end{pmatrix} . \tag{29.85}$$

The crossover from the Bragg-diffraction regime to Kapitza-Dirac scattering is a smooth transition. As we will see below, for intermediate Rabi frequencies (here $1\,\mathrm{MHz} > \Omega_R/2\pi > 100\,\mathrm{kHz}$) the neighboring diffraction states, corresponding to momentum shifts of $4\hbar q$ and $-2\hbar q$ (second and minus first order), are scarcely populated. For higher and higher Rabi frequencies, $\Omega_R/2\pi > 1\,\mathrm{MHz}$, the scattering populates more and more diffraction orders.

29.2.2.7 Higher-order Bragg scattering

Higher-order Bragg scattering is possible as well. Then the $2n$-photon Rabi frequency must be calculated and inserted in the second diagonal of (29.85).

29.2.3 Bragg spectroscopy of a condensate

To measure the Bogolubov spectrum, we need to excite perturbations in a condensate and study its reaction [780].

Let us now imagine that the potential has the form of a standing wave. Technically this can be done by two laser beams having the same frequency crossing at the position of the atoms,

$$V_{trap}(\mathbf{r},t) \equiv \tfrac{V}{2} e^{\imath \mathbf{q}_1\cdot\mathbf{r}-\imath\omega t} + \tfrac{V}{2} e^{\imath \mathbf{q}_2\cdot\mathbf{r}-\imath\omega t} \ . \tag{29.86}$$

Choosing the coordinate system such that, $\mathbf{q}_1 \equiv (k_x, 0, k_z)$ and $\mathbf{q}_1 \equiv (k_x, 0, -k_z)$,

$$V_{trap}(\mathbf{r},t) = \tfrac{V_x}{2} e^{\imath k_z z-\imath\omega t} + \tfrac{V_x}{2} e^{-\imath k_z z+\imath\omega t} \ , \tag{29.87}$$

with $V_x \equiv V e^{ik_x x}$. With this weak perturbation applied to the atoms, we make the ansatz,

$$\psi(\mathbf{r},t) = e^{-\imath\mu t/\hbar}\left(\psi_0(\mathbf{r},t) + u(t)e^{\imath k_z z-\imath\omega t} - v(t)e^{-\imath k_z z+\imath\omega t}\right) \ , \tag{29.88}$$

where the amplitudes of the perturbation, $u(t)$ and $v(t)$, only vary slowly in time. Assuming that ψ_0 is fairly homogeneous, i.e. $\langle\psi_0|\nabla_z|\psi_0\rangle \simeq 0$, the momentum transferred to the BEC is,

$$\langle\psi(\mathbf{r},t)| - \imath\hbar\nabla_z|\psi(\mathbf{r},t)\rangle = \hbar k_z(|u|^2 - |v|^2) \ . \tag{29.89}$$

We can now solve the Gross-Pitaevskii equation (27.20) in the same way as in Sec. 27.4.1 inserting the ansatz (29.88). The terms proportional to $e^{\imath k_z z-\imath\omega t}$ are,

$$\frac{\hbar^2\mathbf{k}_z^2}{2m}u + \frac{V}{2}\psi_0 + g\left(|\psi_0|^2 + |u|^2 + |v|^2\right)u + g\psi_0^2 v + g|v|^2 u + g|\psi_0|^2 u = \left(\imath\hbar\frac{\partial}{\partial t} + \hbar\omega + \mu\right)u \ , \tag{29.90}$$

and the analogously for $e^{-\imath k_z z+\imath\omega t}$. Using $\mu = gn = g|\psi_0|^2$ and assuming that the perturbation is weak, $|u|, |v| \ll |\psi_0|$, we obtain,

$$\begin{aligned} \left(\frac{\hbar^2k^2}{2m} + gn\right)u + \frac{V}{2}\psi_0 - gnv &= \left(\imath\hbar\frac{\partial}{\partial t} + \hbar\omega\right)u \\ -\left(\frac{\hbar^2k^2}{2m} + gn\right)v - \frac{V}{2}\psi_0 + gnu &= \left(-\imath\hbar\frac{\partial}{\partial t} + \hbar\omega\right)v \ . \end{aligned} \tag{29.91}$$

This effect is called *Bragg diffraction* of atoms by a standing light wave.

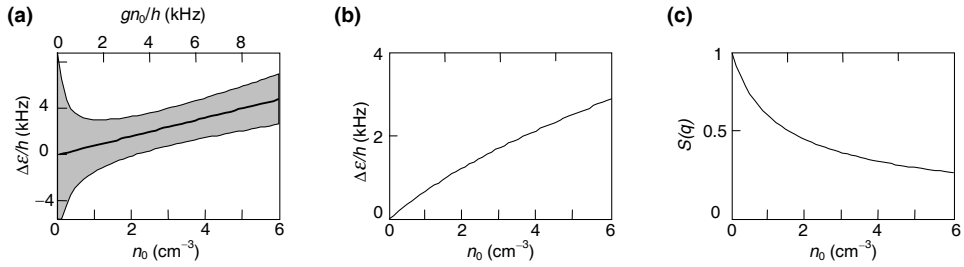

Figure 29.10: Spectrum of elementary excitations.

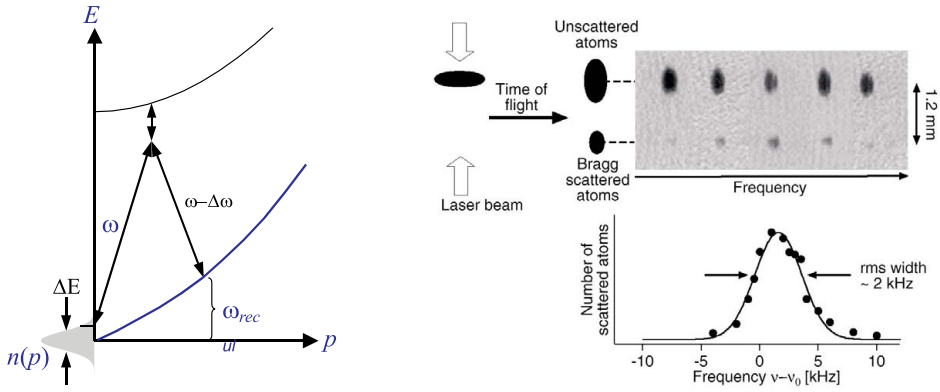

Figure 29.11: Spectrum of elementary excitations.

Using $\mathcal{L} \equiv \frac{\hbar^2\mathbf{k}^2}{2m} + V_{trap} + 2gn - \mu - \imath\hbar\frac{\partial}{\partial t}$, we can write,

$$\begin{pmatrix} \mathcal{L} - \hbar\omega_{\mathbf{k}} & -gn \\ -gn & \mathcal{L} + \hbar\omega_{\mathbf{k}} \end{pmatrix} \begin{pmatrix} u \\ v^* \end{pmatrix} = 0 \ . \tag{29.92}$$

These equations can be decoupled using the Bogolubov transform.

We calculate the momentum transferred to the BEC, assuming ψ_0 to be fairly homogeneous,

$$\langle\psi(\mathbf{r},t)| - \imath\hbar\nabla|\psi(\mathbf{r},t)\rangle = \hbar\mathbf{q}(|u|^2 - |v|^2) \ . \tag{29.93}$$

29.2.4 Exercises

29.2.4.1 Ex: Bragg diffraction in a Ramsey-Bordé interferometer

A Ramsey-Bordé interferometer consists of a $\frac{\pi}{2}$-π-$\frac{\pi}{2}$ laser pulse sequence of Bragg diffraction pulses leading to a splitting and recombination of an atomic wavefunction in momentum space. Simulate the behavior of a cold atomic cloud subject to a gravitational potential during a Ramsey-Bordé sequence using the formalism developed in Sec. 29.2.2. See also Excs. 1.7.6.2 and 1.7.6.3.

29.3 Matter wave superradiance

29.3.1 Classical superradiance

The Bragg beam splitter introduced in the last section does not give rise to collective scattering, even when the atoms are as strongly correlated as in a condensate. On the other hand, collective scattering is known to occur in a classical gas: When two atoms excited to an internal energy level, $\sim hc/\lambda$, are separated by a distance R too large to form a molecule, but smaller than the wavelength of the excited transition, $a_B \ll R \ll \lambda$, the atoms are coupled to the electromagnetic continuum by the same radiation that they emit (see Fig. 29.12). The dipole moments of the atoms stimulate each other to emit, and we observe a synchronized and accelerated relaxation, resulting in a coherent

and directional burst of radiation [229, 685]. The directionality of the radiation is due to a destructive interference of the dipolar radiation patterns emitted by the atoms in all directions except the direction chosen by the first emitted photon. This direction is random (except when bosonically stimulated). The atomic sample evolves, during this time, to a state of coherent superposition, until all the atoms are deexcited. This phenomenon is called *Dicke superradiance*. A similar effect exists for matter waves, and will be discussed in the following sections [416].

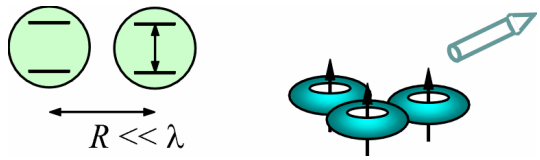

Figure 29.12: Superradiance assumes small interatomic distances compared to the wavelength of the excited dipole. Toroidal interference patterns interfering constructively in only one direction.

29.3.2 Matter wave superradiance & CARL

We consider the process of Rayleigh scattering from a condensate. The scattering rate obviously depends on the number of atoms and the laser intensity. The crucial point now is, that this rate can be stimulated by populations in the output modes, that is, the modes of scattered light and the atomic recoil modes. Matter and light participate in the scattering process as equal partners. In Sec. 29.2.1 we showed that Bragg scattering can be interpreted as *optical stimulation of matter wave scattering*. By analogy, it is possible to imagine a process of *wave matter stimulation of light scattering*. We will now discuss such a process, called *superradiant Rayleigh scattering* or *matter wave superradiance* (MWSR) [416], with the help of the small cartoon shown in Fig. 29.13. See also (watch talk).

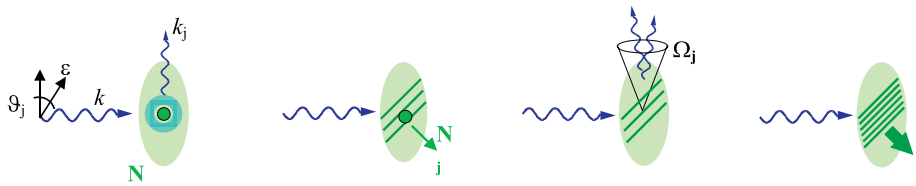

Figure 29.13: Cartoon for MWSR (see text).

Let us imagine an elongated condensate, subject to a magnetic field directed along its long axis and illuminated perpendicularly to the long axis by a linearly polarized laser beam. The scattered light is emitted into a (toroidal) dipolar radiation pattern. The fraction of the light scattered into the solid angle Ω_j, which is inclined by angle ϑ_j with respect to the polarization of the incident laser is $\Omega_j \sin^2 \vartheta_j/(8\pi/3)$. Of course, the number of scattered photons also depends on the optical cross section σ and the number of scattering atoms N_0. When an atom, recoiling due to the transfer of one unit of photonic momentum, moves with a speed of a few centimeters per second

through the condensate, it interferes with other atoms of the condensate, thus forming a wave matter grating. The grating, the lifetime of which is long in comparison to the scattering rate, now stimulates subsequent photons to follow the same path Ω_j and receives, in turn, the scattering atoms. In other words, the bosonic stimulation of the scattering process by the N_j atoms already populating the recoil mode amplifies the photon scattering rate by a factor of $N_j + 1$. The differential optical cross section (power P_j scattered into the direction Ω_j divided by the laser intensity I) is [416],

$$\frac{d\sigma}{d\Omega_j} = \frac{P_j}{I} = \frac{\Omega_j \sin^2 \vartheta_j}{8\pi/3} \sigma N_0 (N_j + 1) \ . \tag{29.94}$$

Each scattering event of a photon into the mode Ω_j transfers an atom to the recoil mode N_j:

$$\dot{N}_j = P_j/\hbar\omega \equiv G_j N_j \qquad \text{where} \qquad G_j = \frac{I}{\hbar\omega} \sigma \frac{\Omega_j \sin^2 \vartheta_j}{8\pi/3} N_0 \ . \tag{29.95}$$

The phase matching condition is satisfied for a solid angle of approximately $\Omega_j = \lambda^2/A_j$, where A_j is the cross-sectional area of the condensate. If l_j is the length of condensate, we can write,

$$G_j = \frac{I}{\hbar\omega} \sigma \frac{\sin^2 \vartheta_j}{8\pi/3} n_0 \lambda^2 l_j \ . \tag{29.96}$$

With the atomic density $n_0 = N_0/(A_j l_j)$, the factor $n_0 \lambda^2 l_j$ describes the optical density of the BEC in the direction of the scattering. Therefore, we obtain *exponential gain* for the atom number N_j, that is, the process is self-amplifying.

Using the terms of the *dressed atom* picture, we would say that the excited state of our system is formed by the BEC and the laser mode. This state relaxes to a state formed by the recoiled atoms and the scattered photons. The exponential gain occurs, when this system exhibits inversion. The inversion is maintained, until the BEC is completely transferred to the momentum recoil modes [11].

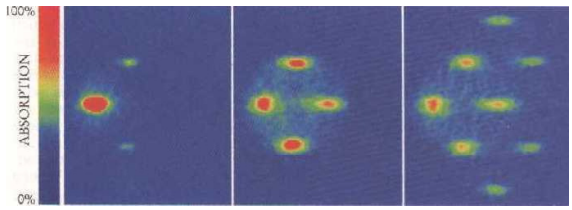

Figure 29.14: Observation of matter wave superradiance.

[11] Superradiant scattering is due to a nonlinear coupling between two matter waves and two optical waves in a *four-wave mixing* process (4WM) interpreted as scattering of light *from* a wave matter *stimulated* by a wave matter mode. The process does not require nonlinearity due to collisions, but it works with an ideal gas, $g \to 0$. This distinguishes it from the 4WM of four matter waves, studied in Sec. 28.3.4 and interpreted as a scattering of atoms by a matter wave stimulated by matter wave mode, and 4WM in quantum optics involving four photons. But in all cases bosonic stimulation is crucial.

It is instructive to compare Dicke superradiance and matter wave superradiance. Dicke superradiance is induced by an electronic coherence between adjacent atoms. It requires a sufficiently long coherence time for the atomic dipoles. On the other hand, MWSR is a coherence effect between two states of the atomic center-of-mass motion, i.e. the condensed state and a momentum sidemode. A long lifetime of this coherence is necessary to allow for correlations between successive scattering events. The coherence lifetime corresponds to a coherence length, which for a condensate is equal to its physical size, whereas for a thermal cloud, it only corresponds to its thermal Broglie wavelength. This explains why it is difficult to observe MWSR with non-condensed atomic clouds.

Since the scattered photons quickly leave the BEC, there is no feedback or bosonic stimulation by the optical output mode. This can be interpreted as a fast decaying cavity mode, and the regime is called the *bad cavity limit*. Let us now imagine, that the photons were recycled, for example, via an optical cavity constructed around the BEC and reflecting back the photons emitted in the solid angle Ω_j [12]. The mirrors of the cavity create reflection images of the radiating atoms, which increase the *density of states*, the scattering rate, and the gain G_j increase by a factor of $8F/\pi$. An interesting question now is, what happens in the limit $F \to \infty$. If the decay of the cavity mode, and therefore the removal of photons from the coherent interaction zone (which is precisely the volume occupied by the BEC) is slow, the MWSR process seems to be doubly stimulated, optically and atomically. However, in this case we also expect the inverse process, where photons are scattered back to the original mode, to occur and to be stimulated by the number of atoms N_0 in the condensate. We see that the simple picture of bosonic stimulation does not work in this case, and a more complete model including the possibility of Rabi oscillations amplified by stimulated emission is necessary [13].

29.3.3 Amplification of matter and light waves

The feedback-induced exponential gain giving rise to the phenomenon of MWSR can be used to construct a phase-coherent amplifier of matter and light waves. After all, the momentum side modes observed in the MWSR process [416] already represent amplified vacuum fluctuations. To experimentally realize a *coherent matter wave amplifier* [486, 418], it is sufficient to replace the vacuum fluctuations of the original MWSR experiment with a small *seed condensate*: $\sim 0.1\%$ of the 'mother condensate' proved sufficient to stimulate the matter wave amplifier. The seed condensate was created by Bragg diffraction transferring atoms from the mother BEC to another momentum state (see Sec. 29.2). The matter wave grating formed by interference of the seed condensate and the mother BEC was subsequently amplified by a MWSR pulse. The gain for the atom number in the seed condensate was 10 to 100 depending on the

[12] Alternatively, we may imagine a scheme decelerating of the group velocity of the light pulse.

[13] The phenomenon of the matter wave superradiance can be understood without quantization of the atomic motion [**?**] and, in particular, without quantum degeneracy. A cold and dense thermal cloud can show the phenomenon of MWSR [897]. The scattered light forms together with the pump light, a propagating standing light wave, from which the atoms are scattered by Bragg diffraction. Atoms are accelerated by the CARL effect [181, 101, 503, 598, 597, 486, 418, 417] through a coherent redistribution of photons between the pump and scattered modes. However, as was shown later-on, the different recoil modes of the condensate exhibit phase-coherence, which is not explained by a theories treating the atomic motion semi-classically.

intensity and duration of the MWSR pulse. Finally, the coherence of the amplification process was demonstrated by *active atom interferometry* using the Ramsey scheme: One of the interferometer arms consisted of the amplified seed condensate and the other of a reference condensate (local oscillator) especially created by Bragg diffraction from the mother condensate. The observation of interference between these two matter waves proved the coherence of the amplification process and the existence of a well-defined phase relationship between the input and the output of the matter wave amplifier.

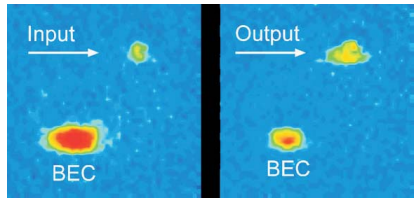

Figure 29.15: Matter wave amplification of a 'seed condensate' at the expense of a 'mother condensate'. Time-of-flight imaging visualizes the condensate's momentum distribution.

In analogy to electronics, we may consider the coherent matter wave amplifier as an *active device* complementing the atom optical toolbox of *passive device*s (see Sec. 28.3.1).

29.3.4 Four-wave mixing of optical and matter waves

We will now make an attempt to categorize the various scattering processes involving condensates. Let us first return to the radiation pressure [Fig. 29.16(a)], where an incident photon is spontaneously scattered into a random direction. The isotropy of the scattering process can, however, be broken when certain directions (i.e. spatial modes) are favored by bosonic stimulation. The symmetry of the roles of matter wave modes and light modes allows us to treat both on the same footing, for example, we can stimulate scattered modes either by matter of light waves.

Let us first have a look at stimulation by optical modes [Fig. 29.16(b) and (c)]. Fig. (b) describes optical four-wave mixing (4WM) in nonlinear optical media, i.e. *optically stimulated scattering of photons* from a standing light wave, which is a 4WM process of 4 photons. Fig. (c) describes Bragg scattering, i.e. an *optically stimulated scattering of atoms* by a standing light wave, which is a 4WM process of 2 photons and 2 atoms.

Similarly, a scattering process can also be stimulated by a macroscopic number of atoms in a recoil mode [Fig. 29.16(d) and (f)]. Fig. (d) describes superradiant Rayleigh scattering and matter wave amplification, i.e. scattering of photons *stimulated by a de Broglie wave*, which again corresponds to 4WM of 2 photons and two atoms. Fig. (e) describes amplification of a laser pulse by superradiant Rayleigh scattering, i.e. scattering of photons in a matter wave with *double stimulation by light waves and de Broglie waves*, which once again is a 4WM process of 2 photons and 2 atoms. Finally, Fig. (f) describes the basic process of nonlinear atom optics, i.e. the scattering of atoms by a matter wave *stimulated by de Broglie waves*, which is a 4WM process of 4 atoms.

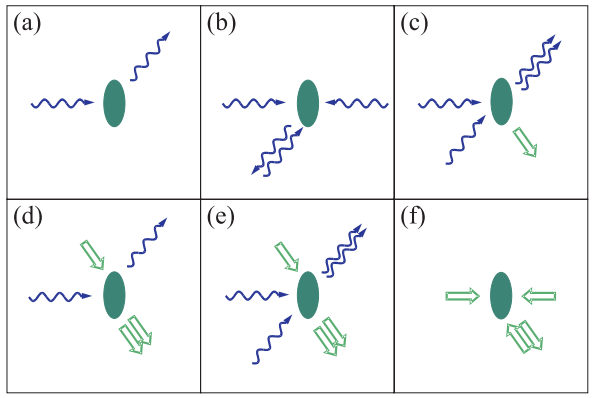

Figure 29.16: Schematic comparison of 4WM processes between light and matter wave modes. (a) Spontaneous emission, (b) classical 4WM of light modes, (c) Bragg scattering, (d) superradiant Rayleigh scattering, respectively, matter wave amplification, (e) optical amplification, and (f) 4WM of matter waves.

29.4 Condensates in electronically excited states

The interaction between condensates and light has, so far, been treated in the limit where the *population of excited states can be neglected or adiabatically eliminated.* An example was the coherent coupling of different kinetic states of an atom by a method called *Bragg diffraction* discussed in Sec. 29.2.

On the other hand, atoms can have metastable excited states, which can introduce new degrees of freedom, and a whole world of new problems emerges that need to be addressed: How do condensed atoms move, when they are in different states of internal excitation (or superposition of states), and how do atoms in different states interact with each other? We will now turn our attention to coherent coupling of internal states [14].

In Sec. 29.4.1 we will show how to generalize the second-quantized formalism introduced in 27.2.1 in order to deal with coupled condensates in different states of internal excitation.

In Sec. 29.4.2 we will discuss examples of how coherent coupling of two states can be accomplished either by radiofrequency/microwave radiation or by two laser beams in Raman configuration. In order to avoid spontaneous relaxation, we often choose state with low excitation energy, for example, within the hyperfine structure ($\hat{H} \sim \mathbf{I}\cdot\mathbf{J}$) or the Zeeman structure ($\hat{H} \sim \mu \cdot B$) of the electronic ground state. But one can also consider the coupling between different *kinetic states* of free atoms $\hat{H} \sim \mathbf{p}^2/2m$, or the *output coupling* of atoms confined to a trapping potential ($\hat{H} \sim \frac{m}{2}\omega^2\mathbf{r}^2$), or even a chemical coupling between a vibrational state of two atoms bound together to form

[14] We will disregard, for the moment, possible effects due to inhomogeneous broadening caused by the finite volume of the cloud inside the potential (Zeeman shift in magnetic traps or dynamic Stark shift optical traps) or effects due to interatomic interactions. But we have to keep in mind, that interatomic interaction can have a big impact on the dynamics, because the chemical potential of each condensate depends on its number of atoms. Thus, in view of the inhomogeneity of the trapping potential, the transfer of atoms can excite oscillations and sound waves in the condensates.

a molecular and a state, where the same two atoms are free and involved in an elastic collision.

Finally, in Sec. 29.4.3 we will show how to harness the forces induced by atom-light coupling in order to design new geometries of trapping potentials.

29.4.1 Theory of the interaction of condensates with light

Let us consider two Bose-Einstein condensates in the mean-field approximation consistent of atoms in two different internal excitation states, ψ_1 and ψ_2, separated by the energy $\hbar\omega_0$. We illuminate the BEC by a plane wave of monochromatic light with the frequency ω. The formal procedure consists of constructing the Hamiltonian of individual atoms, as done in Eq. (20.2), and then quantizing the field of matter [658],

$$\hat{H}_{atom} = |1\rangle\hat{H}^{(1)}_{cm}\langle 1| + |2\rangle(\hat{H}^{(2)}_{cm} + \hbar\omega_0)\langle 2| \qquad \text{where} \qquad \hat{H}^{(j)}_{cm} = \frac{\hat{\mathbf{p}}^2}{2m} + V^{(j)}_{trap}(\hat{\mathbf{r}}) \ , \tag{29.97}$$

where we allow for the fact that the trapping potentials can be different for the two excitation states. We assume that atoms in different states of excitation are distinguishable, such that their respective wavefunctions commute:

$$\hat{\psi}_j(\mathbf{r}) \equiv |j\rangle\langle j|\hat{\psi}(\mathbf{r}) \quad , \quad [\hat{\psi}_j(\mathbf{r}), \hat{\psi}_{j'}(\mathbf{r})] = \delta_{jj'}\delta^3(\mathbf{r}-\mathbf{r}') \ . \tag{29.98}$$

However, we need to consider interatomic collisions which, in the mean-field approximation (27.19) are described by,

$$\hat{H}^{(j)}_{mf} = \int \hat{\psi}^\dagger_j(\mathbf{r})\frac{2\pi\hbar^2 a_s}{m}\hat{\psi}_j(\mathbf{r})d^3r \ . \tag{29.99}$$

The total atomic Hamiltonian is then a generalization of the many-body Hamiltonian (27.6),

$$\boxed{\mathcal{H}_{atom} = \int \hat{\psi}^\dagger_1(\mathbf{r})\left(\hat{H}^{(1)}_{cm} + \hat{H}^{(1)}_{mf}\right)\hat{\psi}_1(\mathbf{r})d^3r + \int \hat{\psi}^\dagger_2(\mathbf{r})\left(\hat{H}^{(2)}_{cm} + \hat{H}^{(2)}_{mf} + \hbar\omega_0\right)\hat{\psi}_2(\mathbf{r})d^3r} \ . \tag{29.100}$$

29.4.1.1 Interaction with a single light mode

The normalized annihilation operator for a photon in mode $\mathbf{k}$ is,

$$\vec{\mathcal{E}}^+(\mathbf{r}) = \sqrt{\tfrac{\hbar\omega}{2\varepsilon_0 V}}\vec{\epsilon}\hat{a}e^{\imath\mathbf{k}\cdot\mathbf{r}} \ . \tag{29.101}$$

The semi-classical Hamiltonian (the light not being quantized) of individual particles is, in the rotating wave approximation,

$$\hat{H}_{field} = \hbar\omega\hat{a}^\dagger\hat{a} \qquad \text{and} \qquad \hat{H}_{int} = -\hat{\mathbf{d}}\cdot\hat{\vec{\mathcal{E}}} = -|2\rangle\hat{\mathbf{d}}^+\cdot\hat{\vec{\mathcal{E}}}^+\langle 1| - |1\rangle\hat{\mathbf{d}}^-\cdot\hat{\vec{\mathcal{E}}}^-\langle 2| \ . \tag{29.102}$$

For a condensate we still need to second-quantize the interaction part of the Hamiltonian which, disregarding collisions gives [15],

$$\boxed{\mathcal{H} = \hat{H}_{field} + \mathcal{H}_{atom} - \int \left(\hat{\mathbf{d}}^{+} \cdot \hat{\vec{\mathcal{E}}}^{+} \hat{\psi}_2^{\dagger}(\mathbf{r}) \hat{\psi}_1(\mathbf{r}) + \hat{\mathbf{d}}^{-} \cdot \hat{\vec{\mathcal{E}}}^{-} \hat{\psi}_1^{\dagger}(\mathbf{r}) \hat{\psi}_2(\mathbf{r}) \right) d^3 r} \ . \tag{29.103}$$

With the Hamiltonian (29.103) we derive the Heisenberg equations for the condensate respecting the commutation rules (29.98) [16],

$$\begin{aligned} \dot{\hat{\psi}}_2 &= -\tfrac{\imath}{\hbar}(\hat{H}_{cm} + \hbar\omega_0)\dot{\hat{\psi}}_2 + \tfrac{\imath}{\hbar}\hat{\mathbf{d}}^{+} \cdot \hat{\vec{\mathcal{E}}}^{+} \hat{\psi}_1 \\ \dot{\hat{\psi}}_1 &= -\tfrac{\imath}{\hbar}\hat{H}_{cm}\dot{\hat{\psi}}_1 + \tfrac{\imath}{\hbar}\hat{\mathbf{d}}^{-} \cdot \hat{\vec{\mathcal{E}}}^{-} \hat{\psi}_2 \ . \end{aligned} \tag{29.104}$$

We transform to the non-rotating coordinate system by $\tilde{\psi}_2 \equiv \psi_2 e^{\imath\omega t}$ and $\tilde{\vec{\mathcal{E}}}^{+} \equiv \hat{\vec{\mathcal{E}}}^{+} e^{\imath\omega t}$ introducing the detuning $\Delta \equiv \omega - \omega_0$:

$$\partial_t \tilde{\psi}_2 = \imath(\Delta - \tfrac{1}{\hbar}\hat{H}_{cm})\tilde{\psi}_2 + \tfrac{\imath}{\hbar}\hat{\mathbf{d}}^{+} \cdot \tilde{\vec{\mathcal{E}}}^{+} \tilde{\psi}_1 \ . \tag{29.105}$$

Making the adiabatic approximation $\partial_t \tilde{\psi}_2 = 0$ and disregarding the external degree of freedom, $\hat{H}_{cm} = 0$, we obtain,

$$\tilde{\psi}_2 = \frac{\imath \hat{\mathbf{d}}^{+} \cdot \tilde{\vec{\mathcal{E}}}^{+}}{\hbar\Delta} \tilde{\psi}_1 \ . \tag{29.106}$$

29.4.1.2 Heisenberg equation for the light field

Similarly, we can write the Heisenberg equation for the light mode,

$$\frac{d\hat{a}}{dt} = \frac{\imath}{\hbar}[\mathcal{H}, \hat{a}] = -\imath\omega\hat{a} + \imath\sqrt{\tfrac{\omega}{2\varepsilon_0 V}} \int \hat{\mathbf{e}}_{\mathbf{k}} e^{-\imath\mathbf{k}\cdot\mathbf{r}} \cdot \left(\hat{\mathbf{d}}^{+} \hat{\psi}_2^{\dagger} \hat{\psi}_1 + \hat{\mathbf{d}}^{+} \hat{\psi}_1^{\dagger} \hat{\psi}_2 \right) d^3 r \ . \tag{29.107}$$

The integration of this gives the distribution of the fields (incident and scattered), such that,

$$\tilde{\vec{\mathcal{E}}}^{+}(\mathbf{r}) = \tilde{\vec{\mathcal{E}}}_{in}^{+}(\mathbf{r}) + \int K(\mathbf{d}, \mathbf{r} - \mathbf{r}') \hat{\psi}_1^{+}(\mathbf{r}') \hat{\psi}_1(\mathbf{r}') d^3\mathbf{r}' \ , \tag{29.108}$$

with the kernel:

$$K(\mathbf{d}, \mathbf{r}) = \frac{1}{4\pi\varepsilon_0} \left[k^2 (\mathbf{R} \times \mathbf{d}) \times R \frac{e^{\imath kR}}{R} + [3\mathbf{R}(\mathbf{R} \cdot \mathbf{d} - \mathbf{d})] \left(\frac{1}{R^3} - \frac{\imath k}{R^2} \right) e^{\imath kR} \right] \ . \tag{29.109}$$

We focus on the first term dominating in the far-field, and neglect the second term by letting $R \approx r - \hat{\mathbf{e}}_R \cdot \mathbf{r}'$ and $\hat{R} \approx r$. We also define $\mathbf{k}_s \equiv k\hat{\mathbf{e}}_R$, and we only retain the term of order $1/R$. In this Born approximation for optically thin media, we obtain,

$$K(\mathbf{d}, \mathbf{r}) \simeq \frac{1}{4\pi\varepsilon_0} \frac{e^{ikR}}{r} k^2 (\mathbf{r} \times \mathbf{r}) \times \mathbf{d} e^{-\imath\mathbf{k}_s \mathbf{r}'} \ . \tag{29.110}$$

[15] Or, by defining the Rabi frequency g_1 generated by a single photon, $\mathcal{H}_{int} = -\imath\hbar g_1 \hat{a} \int d^3\mathbf{r} \hat{\psi}_2^{\dagger}(\mathbf{r}) e^{\imath\mathbf{k}\cdot\mathbf{r}} \hat{\psi}_1(\mathbf{r}) + h.c.$.

[16] In the first quantization, these equations would simply be the equations of motion for the amplitudes of the fundamental and excited states.

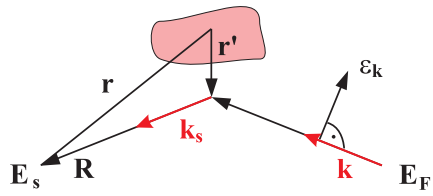

Figure 29.17: Scheme for the light scattering off a condensate.

29.4.1.3 Incident plane waves

When we now excite the condensate by a plane wave,

$$\hat{\vec{\mathcal{E}}}^{+}_{in}(\mathbf{r}) = \tfrac{1}{2}\vec{\epsilon}e^{\imath\mathbf{k}\cdot\mathbf{r}} \ , \tag{29.111}$$

we derive in the Born approximation of the equation (29.108):

$$\tilde{\vec{\mathcal{E}}}^{+}_{s}(\mathbf{r}) = \frac{1}{4\pi\varepsilon_0}\frac{e^{\imath kR}}{r}k^2\mathbf{r}\times(\mathbf{r}\times\hat{\mathbf{d}}^{-})\int e^{-\imath\mathbf{k}_s\mathbf{r}'}\hat{\psi}^{\dagger}_1(\mathbf{r}')\hat{\psi}_2(\mathbf{r}')d^3r' \ , \tag{29.112}$$

and from this the fluorescence spectrum.

29.4.2 STIRAP & adiabatic sweep

A frequent problem for experimenters is the need to transfer a magnetically trapped atomic cloud from one Zeeman or hyperfine state to another. We will present here two techniques called STImulated Raman Adiabatic Passage and *adiabatic sweep*.

29.4.2.1 Adiabatic sweep

To discuss the adiabatic sweep, we consider the example of a ^{87}Rb cloud trapped in the state $|F, m_F\rangle = |2, -2\rangle$. The application of resonant radiofrequency radiation to the transition $|2, -2\rangle$-$|2, -1\rangle$ also couples all other m_F states and causes a diffusion of the atomic populations toward an uncontrollable mixture of states. An alternative is the application of a ramp sweeping the radiofrequency from red to blue (or vice versa). Such a ramp is able to transfer the entire population toward the opposite Zeeman state $|2, +2\rangle$. To see this, we solve the Schrödinger equation, $|\psi(t + dt)\rangle = e^{\imath H\ dt}|\psi(t)\rangle$, iteratively,

$$H = \begin{pmatrix} 0 & \frac{1}{2}\Omega & 0 & 0 & 0 \\ \frac{1}{2}\Omega & -\Delta & \frac{1}{2}\Omega & 0 & 0 \\ 0 & \frac{1}{2}\Omega & -2\Delta & \frac{1}{2}\Omega & 0 \\ 0 & 0 & \frac{1}{2}\Omega & -3\Delta & \frac{1}{2}\Omega \\ 0 & 0 & 0 & \frac{1}{2}\Omega & -4\Delta \end{pmatrix} . \tag{29.113}$$

The initial population distribution is $|\psi(t)\rangle = \begin{pmatrix} 1 & 0 & 0 & 0 & 0 \end{pmatrix}^t$. Ω is the Rabi frequency generated by the radiofrequency, $\Delta(t)$ is the instantaneous detuning. The curves of Fig. 29.18 show the temporal evolution of populations $|\langle k|\psi(t)\rangle|^2$.

The disadvantage of this method is that only the external (fully stretched) states $|m_F| = F$ can be interconverted.

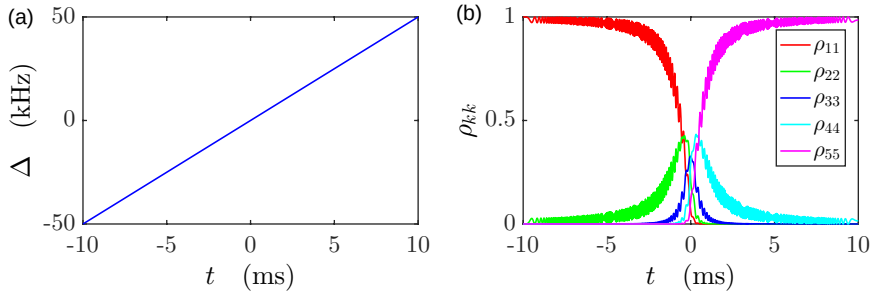

Figure 29.18: (code) Adiabatic sweep through the ground state ^{87}Rb $F = 2$. The Rabi frequency is $\Omega = (2\pi)8$ kHz. The frequency ramp is $\Delta(t) = \frac{t}{t_m}\,(2\pi)50$ kHz with $t_m = 10$ ms. The red line shows the evolution of the population in the state $|2,-2\rangle$, the green line of state $|2,+2\rangle$, and the blue line is the sum of the populations of all other states.

29.4.2.2 Sweep through a dark resonance

To discuss STIRAP, let us think of how to transfer atoms from the state $|1\rangle \equiv |2,2\rangle$ to $|2\rangle \equiv |2,1\rangle$. The general idea consists in applying two radiation fields with Rabi frequencies Ω_{13} and Ω_{23}, tuned a bit out of resonance with an intermediate state $|3\rangle$, $\Delta_{13} = \Delta_{23} \neq 0$, in a counterintuitive pulse sequence. That is, the field Ω_{23} is applied first and then adiabatically turned down, while the field Ω_{13} is ramped up. This method is capable of transferring all atoms.

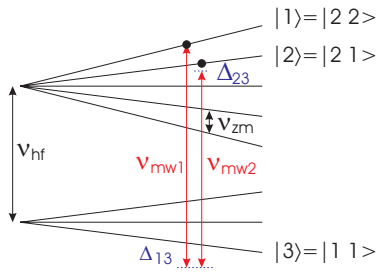

Figure 29.19: STIRAP.

Considering the example of the preceding section, we will discuss here another option (see Fig. 29.19). We consider continuous microwave fields with fixed tunings Δ_{13} to the red of the state $|3\rangle \equiv |1,1\rangle$ state. Now, we apply a ramp to the second microwave field Δ_{23}, such that the two radiation fields, at some point, cross the Raman resonance, for example,

$$\nu_{mw1} = \nu_{hf} + 3\nu_{zm} + \Delta_{13} \qquad \text{and} \qquad \nu_{mw2}(t) = \nu_{hf} + 2\nu_{zm} + \Delta_{23}(t)\ . \tag{29.114}$$

The evolution of the populations can be simulated by iterative solution of the Schrödinger

equation, $|\psi(t+dt)\rangle = e^{iH\ dt}|\psi(t)\rangle$ with,

$$\hat{H} = \begin{pmatrix} 0 & 0 & \frac{1}{2}\Omega_{13} \\ 0 & \Delta_{23} - \Delta_{12}(t) & \frac{1}{2}\Omega_{23} \\ \frac{1}{2}\Omega_{13} & \frac{1}{2}\Omega_{23} & \Delta_{23} \end{pmatrix} . \tag{29.115}$$

The initial population distribution is $|\psi(t)\rangle = \begin{pmatrix} 1 & 0 & 0 \end{pmatrix}^t$. The curves of Fig. 29.20 show the temporal evolution of the populations $|\langle k|\psi(t)\rangle|^2$.

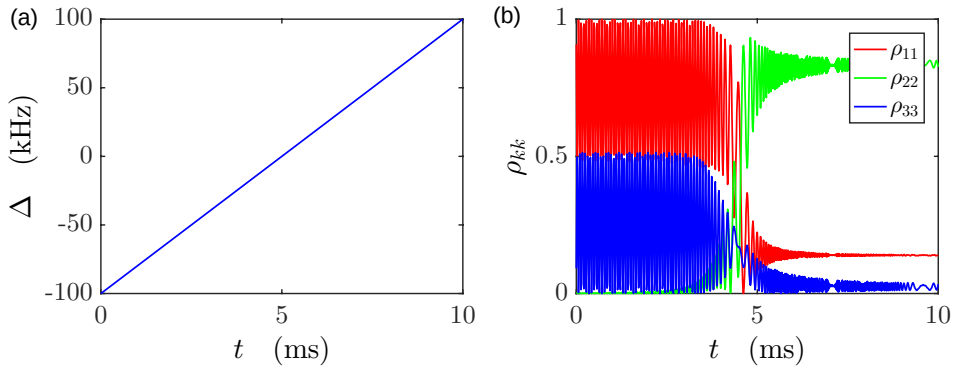

Figure 29.20: (code) STIRAP ramp through a dark resonance. Here, the Rabi frequencies are $\Omega_{13} = \Omega_{23} = 2\pi 10$ kHz. The frequency of the first microwave is $\Delta_{13} = (2\pi)10$ kHz and the frequency ramp of the second microwave is given by $\Delta_{23}(t) = \frac{2t-t_m}{t_m}\ (2\pi)100$ kHz, where $t_m = 10$ ms.

29.4.3 Condensate in adiabatic potentials

Adiabatic potentials have already been introduced in Secs. 20.1.3 and 26.4.3. Here, we will focus on the dynamics of condensed atoms in different states of electronic excitation, when these states are subject to different potentials and radiation fields that can induce transitions between the states. In particular, we consider paramagnetic atoms in different Zeeman states placed in inhomogeneous static magnetic fields and subject to single-mode or multi-mode radiofrequency radiation fields [177]. To simplify the problem, let us concentrate on two-level systems, e.g. a system with the total spin $F = \frac{1}{2}$ [906], and only consider the one-dimensional case.

29.4.3.1 Coupled Gross-Pitaevskii equations

For a single atom the Hamiltonian is the one given in (20.13),

$$\hat{H}(\mathbf{r}) = |1\rangle \left(\tfrac{1}{2}\mu_B g_F B(\mathbf{r}) - \tfrac{1}{2}\hbar\omega\right) \langle 1| + |2\rangle \left(-\tfrac{1}{2}\mu_B g_F B(\mathbf{r}) + \tfrac{1}{2}\hbar\omega\right) \langle 2| + |1\rangle \tfrac{1}{2}\hbar\Omega \langle 2| + |2\rangle \tfrac{1}{2}\hbar\Omega \langle 1| . \tag{29.116}$$

With the definition,

$$\hat{\psi}_k(\mathbf{r}) \equiv \langle k|\hat{\psi}(\mathbf{r})\rangle , \tag{29.117}$$

and the abbreviation $\hbar\Delta(\mathbf{r}) \equiv \mu_B g_F B(\mathbf{r}) - \hbar\omega(\mathbf{r})$ we proceed to the second quantization via,

$$\boxed{\begin{aligned}\mathcal{H} &= \sum_{k\neq m}\int d^3r\ \hat{\psi}_k^\dagger\left[\frac{-\hbar^2\nabla^2}{2m} + \tfrac{1}{2}u_{kk}\hat{\psi}_k^\dagger\hat{\psi}_k + \tfrac{1}{2}u_{k,m}\psi_m^\dagger\hat{\psi}_m\right]\hat{\psi}_k \\ &+ \left[(-1)^k\tfrac{\hbar}{2}\Delta(\mathbf{r})\hat{\psi}_k^\dagger\hat{\psi}_k + \tfrac{\hbar}{2}\Omega(\mathbf{r})(\hat{\psi}_k^\dagger\hat{\psi}_m + \psi_m^\dagger\hat{\psi}_k)\right]\end{aligned}} \ . \tag{29.118}$$

The total energy of the system is the sum of the energies of the individual condensates (kinetic, potential, and collisional interaction) *plus* the interspecies collisional interaction energy. The coefficients $u_{kl} = 4\pi\hbar^2 a_{kl}/m$ with the scattering lengths a_{kl} govern the impact of the collisions.

The interaction with the radiofrequency field leads to Rabi oscillations with frequency Ω [17] The tuning of the radiofrequency depends on the position, due to the non-homogeneous Zeeman shift Δ. Also, to simplify the model, we assume $u_{kl} = 0$ for $k \neq l$,

$$\hat{H} = \sum_{k\neq m}\int d^3r\ \hat{\psi}_k^\dagger\left[\frac{-\hbar^2\nabla^2}{2m} + \tfrac{1}{2}u_{kk}\hat{\psi}_k^\dagger\psi_k\right]\psi_k + \left[(-1)^k\tfrac{\hbar}{2}\Delta(\mathbf{r})\hat{\psi}_k^\dagger\hat{\psi}_k + \tfrac{\hbar}{2}\Omega\left(\hat{\psi}_k^\dagger\psi_m + \hat{\psi}_m^\dagger\hat{\psi}_k\right)\right] \ . \tag{29.119}$$

From the Heisenberg equations of motion for the field operators of the matter wave and the light, we obtain [906],

$$\imath\dot{\hat{\psi}}_1 = -\tfrac{1}{\hbar}[\hat{H},\hat{\psi}_1] = \frac{\delta\hat{H}}{\hbar\delta\hat{\psi}_1^\dagger} = \left(\frac{-\hbar^2\nabla^2}{2m} + u_{11}\hat{\psi}_1^\dagger\hat{\psi}_1 - \tfrac{\hbar}{2}\Delta(\mathbf{r})\right)\hat{\psi}_1 + \tfrac{\hbar}{2}\Omega\hat{\psi}_2 \tag{29.120}$$

$$\imath\dot{\hat{\psi}}_2 = -\tfrac{1}{\hbar}[\hat{H},\hat{\psi}_2] = \frac{\delta\hat{H}}{\hbar\delta\hat{\psi}_2^\dagger} = \left(\frac{-\hbar^2\nabla^2}{2m} + u_{22}\hat{\psi}_2^\dagger\hat{\psi}_2 + \tfrac{\hbar}{2}\Delta(\mathbf{r})\right)\hat{\psi}_2 + \tfrac{\hbar}{2}\Omega\hat{\psi}_1 \ .$$

The adiabatic potentials follow from a point-wise diagonalization of the Hamiltonian, assuming that the atomic movement evolves in sufficiently small steps.

29.4.3.2 One-dimensional case

The reduction of the dimensionality of the Gross-Pitaevskii equation is shown in Sec. ??. Applying this to our case, we consider a one-dimensional potential $V(\mathbf{r}) = V(z)$ and assume condensates being radially homogeneous within the radial diameter r_h. In this case, we can neglect the radial kinetic energy. As normalization then requires,

$$\int_{-r_h}^{r_h}\int_{-r_h}^{r_h}\int_{-\infty}^{\infty}|\hat{\psi}(\mathbf{r})|^2 d^3r = (2r_h)^2\int_{-\infty}^{\infty}|\hat{\psi}(z)|^2 dz = 1 \ , \tag{29.121}$$

replacing $\hat{\psi}(\mathbf{r}) = \frac{\hat{\phi}(z)}{2r_h}$ and $g_{kk} = \frac{u_{kk}}{(2r_h)^2}$, the Gross-Pitaevskii equation and the normalization condition adopt a particularly simple form,

$$\imath\hbar\frac{\partial}{\partial t}\hat{\phi}(z) = \left(-\frac{\hbar^2}{2m}\frac{\partial^2}{\partial z^2} + V_{trap}(z) + Ng_{1D}|\hat{\phi}(z)|^2\right)\hat{\phi}(z) \ . \tag{29.122}$$

[17] We are neglecting the possibility, that the coupling force may, in principle, be inhomogeneous, if the orientation of the magnetic field is not uniform.

The coupled equations are now,

$$\imath\dot{\hat{\phi}}_1 = \left(\frac{-\partial_z^2}{2m} + g_{11}\hat{\phi}_1^\dagger\hat{\phi}_1 - \frac{m}{4}\omega_z^2 z^2 - \tfrac{1}{2}\Delta_0\right)\hat{\phi}_1 + \tfrac{1}{2}\Omega\phi_2 \tag{29.123}$$
$$\imath\dot{\hat{\phi}}_2 = \left(\frac{-\partial_z^2}{2m} + g_{22}\hat{\phi}_2^\dagger\hat{\phi}_2 + \frac{m}{4}\omega_z^2 z^2 + \tfrac{1}{2}\Delta_0\right)\hat{\phi}_2 + \tfrac{1}{2}\Omega\hat{\phi}_1 \ .$$

with,

$$\int_{-\infty}^{\infty} |\hat{\phi}_1(z)|^2 + |\hat{\phi}_2(z)|^2 dz = 1 \ . \tag{29.124}$$

This set of equations can be solved numerically by first identifying the ground state using the 'steepest descent' method and then propagating it in real time while slowly varying $\Delta(\mathbf{r},t)$ or $\Omega(t)$.

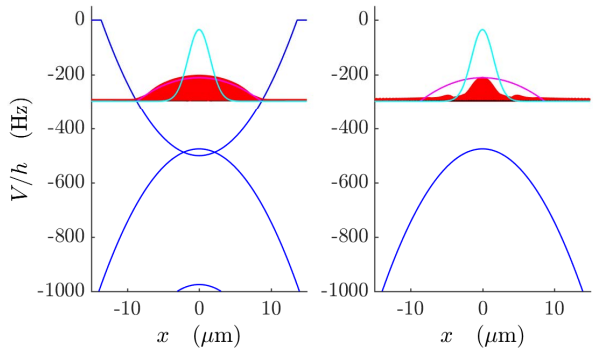

Figure 29.21: (code) Two coupled condensates.

29.4.3.3 Damping

A heuristic way of introducing damping could be as follows: We write down the condensate velocity field as,

$$m\mathbf{v}(\mathbf{r},t) = \hbar\frac{\hat{\phi}^*(\mathbf{r},t)\nabla\hat{\phi}(\mathbf{r},t) - \nabla\hat{\phi}^*(\mathbf{r},t)\hat{\phi}(\mathbf{r},t)}{2\imath n(\mathbf{r},t)} \ , \tag{29.125}$$

and subject it to a friction force,

$$E_{fr} = -\gamma r v \ . \tag{29.126}$$

The problem with the coupled GPE approach is that in the absence of damping any even small modification of the coupling triggers collective oscillations, so that the ground state is not found. A numerical method to minimize the total energy cannot be used, because the minimum is the untrapped state, so that all atoms are lost. It seems that a master equation approach is necessary to introduce damping. An alternative (but cheap) way is the following. The coupled GPEs were written in the dressed states basis. Thus, if the Rabi frequency is strong enough to completely

decouple the dressed states, the dressed states represent good quantum numbers, and the GPEs are appropriately written in a diagonal basis, i.e. the GPEs decouple on adiabatic potentials [18],

$$V_{ad,k}(z) = -(-1)^k \frac{1}{2}\sqrt{\hbar^2\Omega^2 + [\mu_B g_F B(z) - \hbar\omega]^2}\ , \tag{29.127}$$

and we obtain,

$$\imath\dot{\hat{\phi}}_k = \left(\frac{-\partial_z^2}{2m} + V_{ad,k}(z) + g_{kk}\hat{\phi}_k^\dagger\hat{\phi}_k\right)\hat{\phi}_k\ . \tag{29.128}$$

29.4.3.4 Ex: Multiple BECs coupled by radiation via GPEs

Programs on multiple BECs coupled by radiation via GPEs.

29.5 Interaction between condensates and optical cavities

In 29.4.1 we have set up the many-body Hamiltonian (29.103) describing the interaction of a matter wave (treated in mean-field approximation) with an incident light field. We emphasized the role of photonic recoil in (29.128). In the following sections we aim at applying this theory to the particular case of atoms interacting with two counterpropagating modes of an optical ring cavity. The system has already been studied in Chp. 25 in the context of CARL, where the atomic motion, as well as the light fields, have mostly been treated classically.

CARL is based on a coherent redistribution of photons between the two counterpropagating modes of a moving standing light wave mediated by atoms which are located in the mode volume. Cooperative Compton scattering induces a collective atomic recoil and a self-bunching of the atoms, which results in an exponential gain for the optical mode receiving the scattered photons. The recent observation of the MWSR [416] in a BEC raises the question about an ultra-cold version of CARL [598, 393]. In MWSR the long coherence time of a BEC establishes a strong correlation between subsequent elastic Rayleigh scattering events mediated by very stable quasi-particle excitations. The feedback of these excitations on the laser creates an *exponential* gain for the optical mode receiving the scattered photons [417, 181, 101, 503, 598, 597, 486, 418, 417].

We have discussed the classical CARL earlier in the superradiant as well as the good-cavity regime. We have also generalized the problem to the case of quantized atomic motion (see Sec. 25.4) and to quantized radiation fields (see Sec. 25.5). The internal states were always adiabatically eliminated. In the following, we will fully quantize the bosonic atomic particle field.

The advantages of this second quantization is that interatomic interactions, quantum fluctuations, and decoherence of the matter wave can be taken into account. Various proposals have been made focusing on either one of the above three aspects. Fundamental aspects of the BEC-in-a-cavity-system lead into two directions: 1. quantum synchronization and 2. quantum correlations.

[18] Gravitation can be included by $V_{ad,k}(z) \to V_{ad,k}(z) + mgz$.

The system under consideration is a BEC of two-level atoms with transition resonance frequency ω_0 trapped in an external magnetic trap, located inside the mode volume of a ring cavity and interacting with its light modes. The atomic field operators obey the commutation relations,

$$\begin{aligned}[\hat{\psi}_k(\mathbf{r}), \hat{\psi}_m^\dagger(\mathbf{r}')] &= \delta_{km}\delta^{(3)}(\mathbf{r}, \mathbf{r}') \\ [\hat{\psi}_k(\mathbf{r}), \hat{\psi}_m(\mathbf{r}')] &= 0 = [\hat{\psi}_k^\dagger(\mathbf{r}), \hat{\psi}_m^\dagger(\mathbf{r}')] \ ,\end{aligned} \tag{29.129}$$

where $k, m = 1, 2$ label the internal state of the atoms. In general, the light field consists of only *two* counterpropagating monochromatic modes with Rabi frequencies $2g\hat{a}_\pm^\dagger\hat{a}_\pm$. Choosing the coordinate system properly, we can set the wavevectors of the modes as $\mathbf{k}_+ \cdot \hat{\mathbf{e}}_r = k\hat{z} = -\mathbf{k}_- \cdot \hat{\mathbf{e}}_r$. The second-quantized Hamiltonian is a generalization of (25.4),

$$\mathcal{H} = \mathcal{H}_{atom} + \mathcal{H}_{atom-atom} + \mathcal{H}_{atom-cav} + \hat{H}_{cav} + \hat{H}_{laser-cav} \ , \tag{29.130}$$

where,

$$\boxed{\begin{aligned}
\mathcal{H}_{atom} &= \int d^3r\hat{\psi}_1^\dagger(\mathbf{r})\left(\frac{\hat{p}^2}{2m} + V_1(\mathbf{r})\right)\hat{\psi}_1(\mathbf{r}) \\
&\quad + \int d^3r\hat{\psi}_2^\dagger(\mathbf{r})\left(\frac{\hat{p}^2}{2m} + V_2(\mathbf{r}) - \Delta_a\right)\hat{\psi}_2(\mathbf{r}) \\
\mathcal{H}_{atom-atom} &= \textstyle\sum_{i=1,2}\int d^3r\hat{\psi}_i^\dagger(\mathbf{r})\hat{\psi}_i^\dagger(\mathbf{r})\frac{u_{ii}}{2}\hat{\psi}_i(\mathbf{r})\hat{\psi}_i(\mathbf{r}) \\
&\quad + \int d^3r\hat{\psi}_1^\dagger(\mathbf{r})\hat{\psi}_2^\dagger(\mathbf{r})\frac{u_{12}}{2}\hat{\psi}_2(\mathbf{r})\hat{\psi}_1(\mathbf{r}) \\
\mathcal{H}_{atom-cav} &= \textstyle\sum_\pm g\hat{a}_\pm\int d^3r\hat{\psi}_2^\dagger(\mathbf{r})e^{\pm\imath kz}\hat{\psi}_1(\mathbf{r}) + h.c. \\
\hat{H}_{cav} &= -\textstyle\sum_\pm \Delta_c\hat{a}_\pm^\dagger\hat{a}_\pm \\
\hat{H}_{laser-cav} &= -\textstyle\sum_\pm \imath\eta_\pm(\hat{a}_\pm - \hat{a}_\pm^\dagger)
\end{aligned}} \ , \tag{29.131}$$

with $u_{ij} \equiv 4\pi\hbar^2 a_{s,ij}/m$.

Various approximations can be made depending on the subject of interest. For example, if only one cavity mode, $\hat{a}_+$, is strongly pumped, such that the field becomes intense, we may remove the term $\hat{H}_{laser-cav}$ and describe the field mode classically by a Rabi frequency Ω. The interaction between the pump mode and the cavity is then, $\hat{H}_{atom-pump} = \frac{\hbar\Omega}{2}e^{-\imath\omega_2 t}\int d^3r\hat{\psi}_2^\dagger(\mathbf{r})e^{\imath k\hat{z}}\hat{\psi}_1(\mathbf{r}) + h.c.$.

A talk on this subject is available at (watch talk).

29.5.1 Ideal gas Hamiltonian after adiabatic elimination

Assuming the light fields to be tuned far from resonance we disregard spontaneous emission, as explained in Sec. 25.1.2, and adiabatically eliminate the internal states, as shown in Sec. 25.1.3 [668, 165]. On the other hand, we treat the light field and the atomic motion in second quantization. The canonical way to describe a BEC interacting with *two* optical modes $\hat{a}_\pm$ is to second-quantize the single-particle Hamiltonian

(25.26),

$$\boxed{\begin{aligned}\mathcal{H} &\simeq \int d^3r\hat{\psi}^\dagger(\mathbf{r})\left(\frac{\hat{\mathbf{p}}^2}{2m}+V_{trap}(\mathbf{r})+\frac{u}{2}\hat{N}(\mathbf{r})\right)\hat{\psi}(\mathbf{r})+(\hat{N}U_0-\Delta_c)\sum_{\pm}\hat{a}_\pm^\dagger\hat{a}_\pm \\ &+ U_0\hat{a}_+^\dagger\hat{a}_-\int d^3r\hat{\psi}^\dagger(\mathbf{r})e^{-2\imath kz}\hat{\psi}(\mathbf{r})+h.c.-\imath\sum_{\pm}\eta_\pm(\hat{a}_\pm-\hat{a}_\pm^\dagger)\end{aligned}}\ , \tag{29.132}$$

where $\hat{\psi}(\mathbf{r})$ is now the ground-state wave function of the matter wave, $u=4\pi\hbar^2a_s/m$ in the *mean-field approximation* and,

$$U_0=\frac{g^2}{\Delta_a}\ , \tag{29.133}$$

when the mode to mode coupling strength. This adiabatically approximated Hamiltonian looks very similar to (25.26).

29.5.2 Expansion into momentum states

It is useful to convert the Hamiltonian to momentum space via a plane wave expansion of the BEC according to (27.70),

$$\hat{\psi}(\mathbf{r})=\sqrt{\tfrac{V}{(2\pi)^3}}\int\hat{c}_\mathbf{q}e^{\imath\mathbf{q}\cdot\mathbf{r}}d^3q \qquad \text{with} \qquad [\hat{a}_\mathbf{q},\hat{a}_{\mathbf{q}'}]=\delta_{\mathbf{q},\mathbf{q}'}\ . \tag{29.134}$$

The conversion of that Hamiltonian part $\mathcal{H}_{bec}$ to momentum space has been demonstrated in (27.78),

$$\mathcal{H}_{bec}=\sum_\mathbf{q}\frac{\mathbf{q}}{2m}\hat{c}_\mathbf{q}^\dagger\hat{c}_\mathbf{q}+\sum_{\mathbf{q},\mathbf{q}'}\hat{c}_\mathbf{q}^{\prime\dagger}V_{\mathbf{q}',\mathbf{q}}\hat{c}_\mathbf{q}+\frac{u}{2}\sum_{\mathbf{q},\mathbf{q}',\mathbf{q}''}\hat{c}_\mathbf{q}^\dagger\hat{c}_\mathbf{q}^{\prime\dagger}\hat{c}_\mathbf{q}^{\prime\prime}\hat{c}_\mathbf{q}+\mathbf{q}'-\mathbf{q}''\ . \tag{29.135}$$

The light field part $\hat{H}_{cav}$ remains unchanged and the atom-light interaction becomes using (29.3),

$$\begin{aligned}\mathcal{H}_{bec-cav}&=U_0\int\hat{\psi}^\dagger(\mathbf{r})\hat{a}_+^\dagger\hat{a}_-e^{-\imath(\mathbf{k}_+-\mathbf{k}_-)\cdot\mathbf{r}}\hat{\psi}(\mathbf{r})d^3r+h.c. \qquad (29.136)\\ &=\imath\hbar U_0\hat{a}_+^\dagger\hat{a}_-V\int\int\hat{c}^\dagger(\mathbf{q}')\hat{c}(\mathbf{q})\delta^3(\mathbf{q}-\mathbf{q}'-2k\hat{\mathbf{e}}_z)d^3qd^3q'=U_0\hat{a}_+^\dagger\hat{a}_-\sum_\mathbf{q}\hat{c}_{\mathbf{q}-2\mathbf{k}}^\dagger\hat{c}_\mathbf{q}\ .\end{aligned}$$

All in all,

$$\boxed{\begin{aligned}\mathcal{H} &= \sum_\mathbf{q}\frac{\mathbf{q}^2}{2m}\hat{c}_\mathbf{q}^\dagger\hat{c}_\mathbf{q}+\sum_{\mathbf{q},\mathbf{q}'}\hat{c}_{\mathbf{q}'}^\dagger V_{\mathbf{q}',\mathbf{q}}\hat{c}_\mathbf{q}+\frac{u}{2}\sum_{\mathbf{q},\mathbf{q}',\mathbf{q}''}\hat{c}_\mathbf{q}^\dagger\hat{c}_{\mathbf{q}'}^\dagger\hat{c}_{\mathbf{q}''}\hat{c}_{\mathbf{q}+\mathbf{q}'-\mathbf{q}''} \\ &+ (\hat{N}U_0-\Delta_c)\sum_\pm\hat{a}_\pm^\dagger\hat{a}_\pm+U_0\hat{a}_+^\dagger\hat{a}_-\sum_\mathbf{q}\hat{c}_{\mathbf{q}-2\mathbf{k}}^\dagger\hat{c}_\mathbf{q}-\imath\sum_\pm\eta_\pm(\hat{a}_\pm-\hat{a}_\pm^\dagger)\end{aligned}}\ . \tag{29.137}$$

The BEC-CARL equations of motion are readily obtained from the Heisenberg equations,

$$\imath\frac{d\hat{c}_{\mathbf{p}}}{dt} = [\hat{c}_{\mathbf{p}},\mathcal{H}] = \frac{q^2}{2m}\hat{c}_{\mathbf{p}} + \sum_{\mathbf{q}} V_{\mathbf{p},\mathbf{q}}\hat{c}_{\mathbf{q}} + u\sum_{\mathbf{q},\mathbf{q}'}\hat{c}^\dagger_{\mathbf{q}}\hat{c}_{\mathbf{q}'}\hat{c}_{\mathbf{q}-\mathbf{q}'+\mathbf{p}} + U_0\hat{a}^\dagger_+\hat{a}_-\hat{c}_{\mathbf{p}+2\mathbf{k}} + h.c.$$
$$\imath\frac{d\hat{a}_\pm}{dt} = [\hat{a}_\pm,\mathcal{H}] = (\hat{N}U_0 - \Delta_c)\hat{a}_\pm + U_0\hat{a}_\mp\sum_{\mathbf{q}}\hat{c}^\dagger_{\mathbf{q}\mp 2\mathbf{k}}\hat{c}_{\mathbf{q}} + \imath\eta_\pm \ . \tag{29.138}$$

29.5.2.1 Discretization of the momentum space

Assuming the BEC to be initially at rest with 0 temperature, its momentum state can be written as $\hat{c}_{\mathbf{0}}$. And if the dynamics only involves the z-axis, then all momentum states are separated by multiples of $2\hbar k$, such that we may replace the labeling by integer numbers: $\hat{c}_{\mathbf{q}} \to \hat{c}_n$. We get,

$$\mathcal{H} = \sum_n \frac{n^2q^2}{2m}\hat{c}^\dagger_n\hat{c}_n + \sum_{n,n'}\hat{c}^\dagger_{n'}V_{n',n}\hat{c}_n + \frac{u}{2}\sum_{n,n',n''}\hat{c}^\dagger_n\hat{c}^\dagger_{n'}\hat{c}_{n''}\hat{c}_{n+n'-n''} \tag{29.139}$$
$$+\sum_\pm\left(\hat{N}U_0 - \Delta_c\right)\hat{a}^\dagger_\pm\hat{a}_\pm + U_0\hat{a}^\dagger_+\hat{a}_-\sum_n\hat{c}^\dagger_{n-1}\hat{c}_n + h.c. - \imath\eta_\pm(\hat{a}_\pm - \hat{a}^\dagger_\pm) \ .$$

Neglecting the external trapping potential and collisions the Heisenberg equations for the field and the atomic motion now read,

$$\frac{d\hat{c}_n}{dt} = -\imath[\hat{c}_n,\mathcal{H}] = -\imath\frac{n^2k^2}{2m}\hat{c}_n + U_0\hat{a}^\dagger_+\hat{a}_-\hat{c}_{n+1} + h.c. \tag{29.140}$$
$$\frac{d\hat{a}_\pm}{dt} = -\imath[\hat{a}_\pm,\mathcal{H}] = (\hat{N}U_0 - \Delta_c)\hat{a}_\pm + U_0\hat{a}_\mp\sum_n\hat{c}^\dagger_{n\mp1}\hat{c}_n + \imath\eta_\pm \ .$$

These equations look identical to those found in (25.114).

29.5.3 BECs in two internal states coupled by a cavity

A lossy cavity can act as an effective *zero temperature reservoir*. One possible implementation [428] realizes a three-level cycling scheme, with two BECs in two ground states $|g_1\rangle$ and $|g_2\rangle$ coherently coupled by a two-photon transition (Raman-lasers or microwave-radiofrequency combination). The ground states are additionally coupled by an irreversible Raman transition via an intermediate spontaneously decaying level $|e\rangle$. One transition is not driven but stimulated by a ring cavity mode $\hat{a}$.

The Hamiltonian consists of three parts, the BEC energy $\mathcal{H}_{bec}$, the interaction energy with the coherent coupling assumed to be classical $\mathcal{H}_{cpl}$ and the interaction with the mode of a ring cavity $\mathcal{H}_{cav}$ treated quantum mechanically ($\hbar = 1$),

$$\mathcal{H} = \mathcal{H}_{bec} + \mathcal{H}_{cpl} + \mathcal{H}_{cav} \tag{29.141}$$
$$= \int d^3r\ \hat{\psi}^\dagger_1\left(\tfrac{-\nabla^2}{2m} + V + \tfrac{u_{11}}{2}\hat{\psi}^\dagger_1\hat{\psi}_1 + \tfrac{u_{12}}{2}\hat{\psi}^\dagger_2\hat{\psi}_2\right)\hat{\psi}_1 +$$
$$+\int d^3r\ \hat{\psi}^\dagger_2\left(\tfrac{-\nabla^2}{2m} + V + \tfrac{u_{12}}{2}\hat{\psi}^\dagger_1\hat{\psi}_1 + \tfrac{u_{22}}{2}\hat{\psi}^\dagger_2\hat{\psi}_2\right)\hat{\psi}_2 +$$
$$+\int d^3r\ \left(-\Delta_{mw}\hat{\psi}^\dagger_1\hat{\psi}_1 + \tfrac{\Omega_{mw}}{2}\hat{\psi}^\dagger_1\hat{\psi}_2 + h.c.\right) + \int d^3r\ \left(g_{cv}\hat{a}\hat{\psi}^\dagger_1\hat{\psi}_2 + h.c.\right) - \Delta_{cv}\hat{a}^\dagger\hat{a} \ .$$

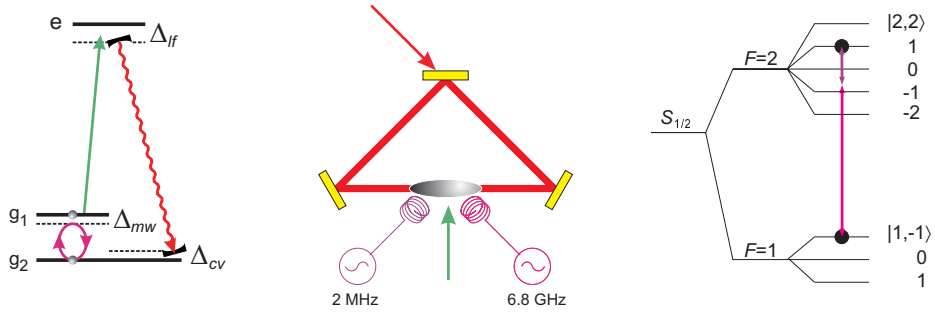

Figure 29.22: (code) (a) Level scheme with a microwave-driven hyperfine structure, a laser-driven optical transition, and a cavity-enhanced Raman deexcitation. (b) Ring cavity used for the experiment. (c) Scheme for coupling the Zeeman states $|2,1\rangle$ and $|1,-1\rangle$ with a two-photon transition in a magnetic trap.

The BEC energy consists of the two energies (kinetic, potential, self) of the individual BECs and the cross-species interaction proportional to $u_{kl} = 4\pi\hbar^2 a_{kl}/m$. The interaction energy with the classical microwave frequency (mostly we will assume $\Delta_{mw} = 0$) leads to Rabi flopping with frequency Ω_{mw}. Finally, the incident light field is treated classically with a Rabi frequency Ω_{lf} and a detuning Δ_{lf}, while the cavity field is treated quantum mechanically with a coupling constant Ω_{cv} and a detuning Δ_{cv}. The irreversible coupling leads to an energy contribution where $g_{cv} \equiv \Omega_{lf}\Omega_{cv}/2\Delta_{lf}$ is the two-photon Rabi-frequency if the auxiliary state is adiabatically eliminated. From the Heisenberg equations of motion for the matter wave and the optical field operators we obtain,

$$
\begin{aligned}
\dot{\hat{\psi}}_1 &= \imath[H,\hat{\psi}_1] = -\imath\frac{\delta H}{\delta\hat{\psi}_1^\dagger} \qquad (29.142)\\
&= -\imath\left(\frac{-\nabla^2}{2m} + V + u_{11}|\hat{\psi}_1|^2 + u_{12}|\hat{\psi}_2|^2\right)\hat{\psi}_1 - \imath\left(\tfrac{\Omega_{mw}}{2} + g_{cv}\hat{a}\right)\hat{\psi}_2 - \imath\Delta_{mw}\hat{\psi}_1 \ ,\\
\dot{\hat{\psi}}_2 &= \imath[\hat{H},\hat{\psi}_2] = -\imath\frac{\delta H}{\delta\hat{\psi}_2^\dagger}\\
&= -\imath\left(\frac{-\nabla^2}{2m} + V + u_{12}|\hat{\psi}_1|^2 + u_{22}|\hat{\psi}_2|^2\right)\hat{\psi}_2 - \imath\left(\tfrac{\Omega_{mw}}{2} + g_{cv}\hat{a}^\dagger\right)\hat{\psi}_1 \ ,\\
\dot{\hat{a}} &= \imath[\hat{H},\hat{a}] - \tfrac{\kappa}{2}\hat{a} = -\imath\frac{\delta H}{\delta\hat{a}^\dagger} - \tfrac{\kappa}{2}\hat{a}\\
&= -\imath\int d^3r\ g_{cv}\hat{\psi}_1\hat{\psi}_2^\dagger - \left(\imath\Delta_{cv} + \tfrac{\kappa}{2}\right)\hat{a} \ .
\end{aligned}
$$

Example 199 (*Single atoms in two states interacting with a cavity*): As a first example, we start from the matter wave Hamiltonian (29.141) for two coupled BECs and neglect the center-of-mass motion (and consequence the condensate part, i.e. self-interaction, kinetic energy and the external potential).

Furthermore, we assume $\hat{\psi}_i(\mathbf{r}) = \hat{c}_i \delta^3(\mathbf{r})$,

$$\begin{aligned} \mathcal{H} &= \mathcal{H}_{bec} + \mathcal{H}_{clp} + \mathcal{H}_{cav} \\ &= -\Delta_{mw}\hat{c}_1^\dagger \hat{c}_1 + \tfrac{\Omega_{mw}}{2}\hat{c}_1^\dagger \hat{c}_2 + g_{cv}\hat{a}\hat{c}_1^\dagger \hat{c}_2 + h.c. - \Delta_{cv}\hat{a}^\dagger \hat{a} \ . \end{aligned} \tag{29.143}$$

Consequently, the Heisenberg equations of motion are simply,

$$\begin{aligned} \dot{\hat{c}}_1 &= -\imath \left(\tfrac{\Omega_{mw}}{2} + g_{cv}\hat{a}\right)\hat{c}_2 - \imath\Delta_{mw}\hat{c}_1 \\ \dot{\hat{c}}_2 &= -\imath \left(\tfrac{\Omega_{mw}}{2} + g_{cv}\hat{a}^\dagger\right)\hat{c}_1 \\ \dot{\hat{a}} &= -\imath g_{cv}\hat{c}_1\hat{c}_2^\dagger - \left(\imath\Delta_{cv} + \tfrac{\kappa}{2}\right)\hat{a} \ . \end{aligned} \tag{29.144}$$

Obviously, since the matter wave degree of freedom is ignored, the dynamics only concerns the Bloch vector. Simulations of these equations are exhibited in Fig. 29.23 and in movies that can be watched under (watch movie) and (watch movie).

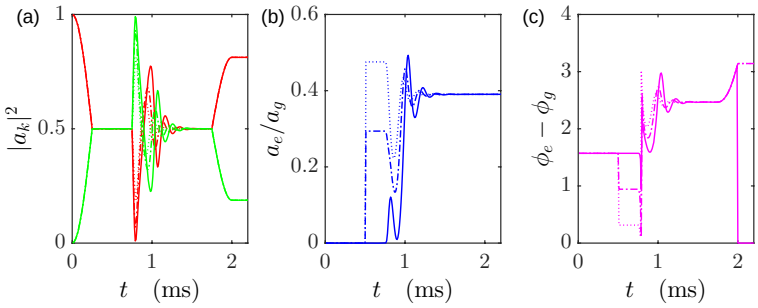

Figure 29.23: (code) Bloch vector phase stabilization in the cavity. (a) Populations and (b) coherences.

Example 200 (*Interpretation of the ultracold fusion via analogy with two-level system*): The chemical potential of the BECs in both states shifts the energy levels up depending on the inversion, $\mu_2 - \mu_1 \propto N_2 - N_1$. If the inversion oscillates the spontaneous Raman cycle periodically meets resonance, and takes place. Note that, since atomic motion is not considered, the energy gap due to the finite cavity detuning can only be bridged in resonance, $\mu_2 - \mu_1 = \kappa$. Oscillation simulates Doppler shift of thermal motion in Doppler cooling. Raman scattering takes the role of spontaneous emission in the cooling process. The only role of the cavity is to introduce irreversibility. Raman scattering is only supported in one direction: However, it is not relevant to have a ring cavity.

29.5.4 Exercises

29.5.4.1 Ex: BEC damping in cavities

Programs on BEC damping in cavities.

29.5.4.2 Ex: Second-quantized CARL equations

Calculate the commutators $[\hat{\psi}_j(\mathbf{r}), \mathcal{H}]$ and $[\hat{a}_\pm, \mathcal{H}]$, where $\mathcal{H}$ is the Hamiltonian (29.131) and $\hat{\psi}_1$ and $\hat{\psi}_2$ the ground and excited state wave functions, respectively.

29.5.4.3 Ex: Second-quantized adiabatically approximated CARL Hamiltonian

a. Derive the adiabatically approximated CARL Hamiltonian in second quantization.
b. Derive the CARL equations of motion from the adiabatically approximated Hamiltonian in second quantization.
c. Show that the derived Hamiltonian simplifies to (25.26) in the single atom limit.

29.5.4.4 Ex: BEC-CARL equations from the adiabatically approximated CARL Hamiltonian

Derive the BEC-CARL equations from the adiabatically approximated CARL Hamiltonian (29.134).

29.5.4.5 Ex: Origin of quantum correlations

The BEC-CARL Hamiltonian has been shown to generate quantum correlations between optical and matter wave modes [598, 658]. Discuss whether they are a many-body effect (bosonic stimulation) or just due to coherences between motional states of single atoms.

29.5.4.6 Ex: Ultracold fusion

Derive from Eqs. (29.144) using the definitions (??) and (??) the Eqs. (??).

29.6 Further reading

29.6.1 on Ramsey-Bordé interferometry

F. Riehle, *Optical Ramsey Spectroscopy in a Rotating Frame: Sagnac Effect in a Matter-Wave Interferometer* [DOI]

M. Kasevich et al., *Atomic Interferometry Using Stimulated Raman Transitions* [DOI]

M. Kasevich, *Measurement of the Gravitational Acceleration of an Atom with a Light-Pulse Atom Interferometer* [DOI]

29.6.2 on BEC-light interaction

H.D. Politzer, *Light incident on a Bose-condensed gas* [DOI]

A. Görlitz et al., *Enhancement and Suppression of Spontaneous Emission and Light Scattering by Quantum Degeneracy* [DOI]

P.C. Bons et al., *Quantum Enhancement of the Index of Refraction in a Bose-Einstein Condensate* [DOI]

O. Zobay et al., *Dynamics of matter-wave and optical fields in superradiant scattering from Bose-Einstein condensates* [DOI]

Y. Yoshikawa et al., *Observation of Superradiant Raman Scattering in a Bose-Einstein Condensate* [DOI]

Y. Yoshikawa et al., *Superradiant light scattering from thermal atomic vapors* [DOI]

M.M. Cola et al., *Theory of Collective Raman Scattering from a Bose-Einstein Condensate* [DOI]

M.M. Cola et al., *Robust Generation of Entanglement in Bose-Einstein Condensates by Collective Atomic Recoil* [DOI]

M.M. Cola et al., *A Condensate in a Lossy Cavity: Collective Atomic Recoil and Generation of Entanglement* [DOI]

M.M. Cola et al., *Entanglement in a Bose-Einstein condensate by collective atomic recoil* [DOI]

D.M. Stamper-Kurn et al., *Spinor Condensates and Light Scattering from Bose-Einstein Condensates* [DOI]

D. Schneble et al., *The Onset of Matter-Wave Amplification in a superradiant Bose-Einstein-Condensate* [DOI]

M.G. Moore et al., *Quantum optics of a Bose-Einstein condensate coupled to a quantized light field* [DOI]

M.G. Moore et al., *Atomic Four-Wave Mixing Fermions versus Bosons* [DOI]

M.G. Moore et al., *Optical control and entanglement of atomic Schroedinger fields* [DOI]

W. Ketterle et al., *Does Matter Wave Amplification Work for Fermions* [DOI]

N. Piovella et al., *Quantum fluctuations and entanglement in the collective atomic recoil laser using a Bose-condensate* [DOI]

D. Jaksch et al., *Uniting Bose-Einstein condensates in optical resonators* [DOI]

S. Ritter et al., *Dynamical Coupling between a Bose-Einstein Condensate and a Cavity Optical Lattice* [DOI]

D. Schneble et al., *Raman amplification of matter waves* [DOI]

G.A. Prataviera et al., *Trap environnement effects over quantum statistics and atom-photon correlations in the collective-atomic-recoil laser* [DOI]

S.A. Gardiner et al., *Cavity-assited quasiparticle damping in a Bose-Einstein Condensate* [DOI]

P. Horak et al., *Coherent Dynamics of Bose-Einstein Condensates in High-finesse Optical Cavities* [DOI]

P. Horak et al., *Dissipative Dynamics of Bose Condensates in Optical Cavities* [DOI]

W. Ketterle et al., *Collective Enhancement and Suppression in Bose-Einstein Condensates* [DOI]

W. Ketterle et al., *Does Matter Wave Amplification Work for Fermions?* [DOI]

W. Ketterle, *Comment on 'Electromagnetic Wave Dynamics in Matter-Wave Superradiant Scattering'* [DOI]

Part VIII

Instrumentation of a Quantum Optics Lab

Preface to the part

This part of the script is issued from a practical lab course in *Quantum Optics* given at São Carlos Physics Institute of the University of São Paulo in the years between 2010 and 2025. It treats part of the knowledge that any student working in a modern quantum optics laboratory needs with emphasis in electronics and optics. The topics are certainly not exhaustive. For instance, many labs work with ultrahigh vacuum, cryogenics, or advanced instrumentation and experimental hardware control, which are beyond the scope of this course.

In chapter 30 we set the show how to work with Gaussian laser beams. In Chp. 31 we review some basic knowledge of applied electronics useful for the lab. In Secs. 32 and 33 we discuss some basic applications and finally in Sec. 34 we give a very brief introduction into control theory.

1338

Chapter 30

Gaussian optics and the polarization of light

The objective of this part of the course is to introduce the student into the basics of *Gaussian optics* and *polarizations optics*. The student will learn how to transform the diameter and the divergence of a Gaussian beam using lenses and telescopes and to analyze and manipulate the polarization of a laser beam.

30.1 Some more basic notions

30.1.1 Definition of photometric quantities

The *radiant energy* W is the total energy emitted from a source. The *radiant power* P (or radiant flux) is the total energy emitted per second. The *radiance* $L(\Omega)$ is defined as the power radiated (emitted, reflected, transmitted or received) under an angle θ through a surface element $d\mathbf{A}$ into a solid angle element $d\Omega = \sin\theta d\theta d\phi$. It is a directional quantity indicating how much of the power will be received by an optical system looking at that surface from a specified angle of view,

$$\boxed{P = \int L(\Omega) dA_n d\Omega} \,. \tag{30.1}$$

Spectral densities are denoted by an index ν, e.g. $P = \int P_\nu(\nu) d\nu$. In (30.1), $dA_n \equiv \hat{\mathbf{n}} \cdot d\mathbf{A} = dA \cos\theta$ is the projection of the surface element onto the surface normal. The quantity,

$$I^* = \int L(\Omega) d\Omega \tag{30.2}$$

is called *radiant intensity*.

> **Example 201 (*Angular distribution of thermal radiation*):** In a blackbody in thermal equilibrium with its surroundings (e.g the walls of a cavity) the radiation is isotropic with a spectral energy distribution given by Planck's law. This means that at any point of the volume of the blackbody radiator an imaginary volume element radiates energy in all directions of space, such that the radiance into a specific solid angle element is,
>
> $$L(\Omega) = \bar{u} \frac{c}{4\pi} \,. \tag{30.3}$$

Radiation passing under an angle θ through a hole of size $dA = dA_n/\cos\theta$ into a specific solid angle element $d\Omega$ generates the radiance,

$$\frac{\partial^2 P}{\partial\Omega\partial A} = L(\Omega)\cos\theta \ . \tag{30.4}$$

In *any* direction we get,

$$\frac{\partial P_\nu}{\partial A} = \int_{\text{half sphere}} L_\nu(\Omega)\cos\theta d\Omega = \bar{u}\frac{c}{4\pi}\int_0^{2\pi} d\phi \int_0^{\pi/2} \cos\theta\sin\theta d\theta = \frac{c\bar{u}}{4} \ . \tag{30.5}$$

Summing up over all surface elements of a sphere of radius R,

$$P = \int \frac{\partial P}{\partial A} dA = \frac{c\bar{u}}{4} R^2 \int_0^{2\pi} d\phi \int_0^{\pi} \sin\theta d\theta = \pi R^2 c\bar{u} \ . \tag{30.6}$$

Accordingly, the spectral distribution is, using Planck's law,

$$P_\nu = P\frac{8\pi h\nu^3}{c^3}\frac{1}{e^{\beta\hbar\omega}-1} = \frac{8\pi^2 R^2 h\nu^3}{c^2}\frac{1}{e^{\beta\hbar\omega}-1} \ . \tag{30.7}$$

A detector covers itself a finite solid angle $d\Omega = \frac{dA'\cos\theta'}{r^2}$. The radiant flux for $r^2 \gg dA, dA'$ can then be expressed as,

$$d\Phi = L(\Omega)dA\cos\theta d\Omega = L(\Omega)dA\cos\theta\frac{dA'\cos\theta'}{r^2} \tag{30.8}$$

$$\text{that is} \qquad \Phi = \int_A\int_{A'} \frac{L(\Omega)}{r^2}\cos\theta\cos\theta' dA dA' \ .$$

Note that for isotropic sources (30.8) is symmetric upon interchanging emitter and detector with regard to θ and θ' or dA and dA'. Furthermore, the formula demonstrates that the radiant flux emitted into the unit solid angle is proportional to $\cos\theta$ (Lambert's law). An example for such a source is a hole with the area dA in a blackbody radiation cavity (see Fig. 30.1). Solve Excs. 30.1.2.1 and 30.1.2.2.

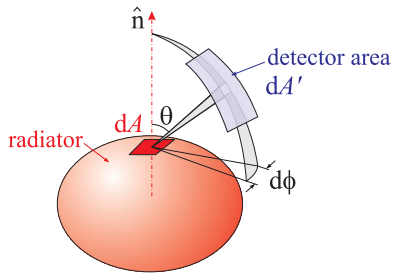

Figure 30.1: Illustration of the radiance.

Note that it is impossible to increase the radiance of a source by any sophisticated imaging optics [219]. This means that the image dA^* of a radiation source dA never has a larger radiance than the source itself. It is true that the flux density can be increased by focussing the radiation. The solid angle, however, into which radiation

from the image dA^* is emitted is also increased by the same factor. Therefore, the radiance does not increase. In fact, because of inevitable reflection, scattering, and absorption losses of the imaging optics, the radiance of the image dA^* is, in practice, always less than that of the source. A strictly parallel light beam would be emitted into the solid angle $d\Omega = 0$. With a finite radiant power this would imply an infinite radiance L, which is impossible. This illustrates that such a light beam cannot be realized. The radiation source for a strictly parallel beam anyway has to be a point source in the focal plane of a lens. Such a point source with zero surface cannot emit any power.

Example 202 (*Radiance of the sun*): An area $A = 1\,\mathrm{m}^2$ of the Earth's surface receives at normal incidence from the sun about $P/A = 1.35\,\mathrm{kW/m}^2$ of intensity. Since the sun covers an angle of $\theta = 0.53°$ seen from the Earth, we can estimate the sun's radiance as,

$$L = \frac{P}{A\Omega} = \frac{P}{A\int_0^{2\pi}\int_0^{\theta}\sin\theta d\theta d\phi} \simeq \frac{P}{A\pi\theta^2} \approx 2\cdot 10^4\,\mathrm{kW\,m^{-2}\,ster^{-1}}\ .$$

The total power received by the Earth is $\frac{P}{A}\pi R_{Earth}^2$. The total power emitted by the sun is $\frac{P}{A}4\pi d_{sun-Earth}^2$.

Example 203 (*Radiance of a HeNe laser*): We consider a HeNe laser emitting $P = 1\,\mathrm{mW}$ of power from a $w_0 = 1\,\mathrm{mm}$ beam waist into an angle of $2\theta = 0.067°$. With a typical emission bandwidth of $\Delta\nu = 1\,\mathrm{MHz}$ the spectral radiance is,

$$L_\nu = \frac{P_\nu}{A\Omega} \simeq \frac{P}{\pi w_0^2\,\pi\theta^2\,\Delta\nu} \approx 1\,\mathrm{kW\,s\,m^{-2}\,ster^{-1}}\ .$$

For comparison, the sun's radiance at it's surface ($T = 6000\,\mathrm{K}$) at the same wavelength as the HeNe laser is,

$$L_\nu = \frac{Lu_\nu}{\bar{u}} \approx 5\,\mathrm{nW\,s\,m^{-2}\,ster^{-1}}\ .$$

30.1.2 Exercises

30.1.2.1 Ex: Emission of an argon laser

The angular divergence of the output from a $P = 1\,\mathrm{W}$ argon laser is assumed to be $\alpha = 4\cdot 10^{-3}\,\mathrm{rad}$.
a. Calculate the radiance L and the radiant intensity I_1 of the laser beam and the irradiance I (intensity) at a surface 1 m away from the output mirror, when the laser beam diameter at the mirror is $2w_s = 2\,\mathrm{mm}$.
b. What is the spectral power density $u(\nu)$ if the laser bandwidth is 1 MHz?

30.1.2.2 Ex: Photosynthetically active radiation

The photon flux density and the photosynthetically active radiation (PAR) are defined as,

$$\eta_{photon} \equiv \frac{\int_{\lambda_1}^{\lambda_2} u(\lambda,T)\frac{\lambda}{\hbar c N_A}d\lambda}{\int_{\lambda_1}^{\lambda_2} u_{\mathrm{Pl}}(\lambda,T)d\lambda} \qquad \text{and} \qquad \eta_{\mathrm{PAR}} = \frac{\int_{\lambda_1}^{\lambda_2} u(\lambda,T)d\lambda}{\int_0^{\infty} u(\lambda,T)d\lambda}\ ,$$

where $\lambda_1 = 400\,\text{nm}$ and $\lambda_2 = 700\,\text{nm}$ delimit the range, where photosynthesis takes place. Calculate both quantities for a blackbody at $T = 5800\,\text{K}$ temperature. Plot them as a function of temperature in the range $T = 300..6000\,\text{K}$.

30.1.2.3 Ex: Power calibration of a Czerny-Turner spectrometer

Spectrometers are designed to measure power spectral densities $P_\lambda(\lambda)$, such that, integrated over a finite wavelength interval, one obtains the power, $P_{\text{tot}} = \int_{\lambda_1}^{\lambda_2} P_\lambda(\lambda) d\lambda$. Figure out how to calibrate the power spectral density measured by a spectrometer with finite resolution $\Delta\lambda_{\text{res}}$ using a HeNe laser with known power.

30.2 Introduction to Gaussian optics

30.2.1 Wave equation and beam parameters

At first sight, one might think that the propagation of laser light is well described by the laws of geometrical optics. On closer inspection it turns out, however, that laser beams behave in many respects more like plane waves with their energy is concentrated near an optical axis. The electro-magnetic fields satisfy the *wave equation*,

$$k^2 u + \nabla^2 u = 0 \ . \tag{30.9}$$

For waves propagating in z direction, $u = \psi(x, y, z)e^{-\imath kz}$, one obtains a Schrödinger-like equation [474],

$$2\imath k \frac{\partial \psi}{\partial z} - \frac{\partial^2 \psi}{\partial x^2} - \frac{\partial^2 \psi}{\partial y^2} = 0 \ , \tag{30.10}$$

where $\partial^2\psi/\partial z^2$ has been neglected.

To describe a *Gaussian beam*, we choose an exponential ansatz and introduce two parameters, which can vary along the propagation axis z: $P(z)$ is a complex phase shift and $q(z)$ a complex parameter, whose imaginary part describes the diameter of the beam. The ansatz,

$$\psi = e^{-\imath\left[P(z) + k(x^2+y^2)/2q(z)\right]} \tag{30.11}$$

leads to [1],

$$0 = (q' - 1)\frac{\imath k(x^2 + y^2)}{q^2} - 2\imath P' + \frac{2}{q} \ . \tag{30.12}$$

In order for Eq. (30.12) to hold for all x and y, we need $q' = 1$ and $P' = \frac{-\imath}{q}$. Integrating q', we find

$$q = q_0 + z \ . \tag{30.13}$$

It is useful to introduce real beam parameters,

$$\frac{1}{q} \equiv \frac{1}{R} - \imath\frac{\lambda}{\pi w^2} \ . \tag{30.14}$$

Inserting these into Eq. (30.10),

$$\psi = e^{-\imath P - \imath\frac{k(x^2+y^2)}{2R} - \frac{(x^2+y^2)}{w^2}} \ , \tag{30.15}$$

[1] See script on *Electrodynamics: Electricity, Magnetism and Radiation* (2025), Sec. 7.4.2..

it becomes clear that $R(z)$ is the radius of curvature and $w(z)$ the beam diameter. Evaluating q_0 at the position of the focus (waist of the beam), where $R = \infty$, we obtain from (30.13) and (30.14)

$$w^2(z) = w_0^2 \left[1 + \left(\frac{\lambda z}{\pi w_0^2}\right)^2\right] \quad \text{and} \quad R(z) = z \left[1 + \left(\frac{\pi w_0^2}{\lambda z}\right)^2\right] . \tag{30.16}$$

Normalizing the intensity to the total power, we may write the radial intensity distributions as,

$$I_z(x, y) = \frac{2P}{\pi w(z)^2} e^{-2(x^2+y^2)/w(z)^2} . \tag{30.17}$$

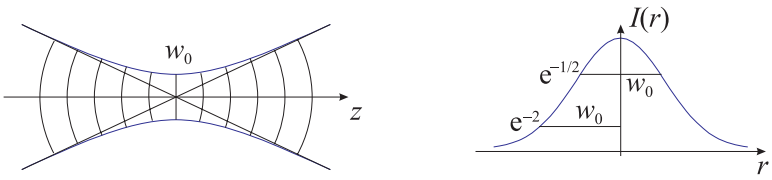

Figure 30.2: (Left) Propagation of the beam along the optical axis. (Right) Cross section of a Gaussian laser beam.

30.2.2 Transfer matrices

For the practical work with Gauss beams it is helpful to introduce transfer matrices, which describe the transformation of a Gauss beam through optical components along the optical axis. The matrix

$$\mathbf{M} = \begin{pmatrix} a & b \\ c & d \end{pmatrix} \tag{30.18}$$

transforms the beam parameter q in the following way:

$$q(z) = \frac{aq(0) + b}{cq(0) + d} . \tag{30.19}$$

Transfer matrices allow to calculate, how the parameters R and w transform along the optical axis across the optical elements or in free space. The most common optical elements are lenses, crystals, prisms, mirrors and cavities. For example, the matrix for propagation in free space of a beam over a distance d is,

$$\mathbf{M} = \begin{pmatrix} 1 & d \\ 0 & 1 \end{pmatrix} \tag{30.20}$$

and the matrix for transformation through a thin lens with focal distance f,

$$\mathbf{M} = \begin{pmatrix} 1 & 0 \\ -1/f & 1 \end{pmatrix} . \tag{30.21}$$

It is interesting to note that the transfer matrices are the same as those, which in classical beam optics transform the vector, whose components are the distance of the beam from the optical axis y and its divergence $y'(z)$:

$$\begin{pmatrix} y(z) \\ y'(z) \end{pmatrix} = \mathbf{M} \begin{pmatrix} y(0) \\ y'(0) \end{pmatrix} . \tag{30.22}$$

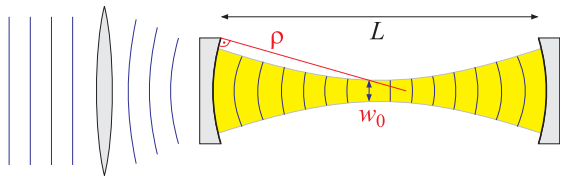

Figure 30.3: Coupling a Gaussian beam of light into cavity requires matching of the phase fronts.

Fig. 30.3 shows that coupling a Gaussian beam of light into a cavity requires matching of the phase fronts. Solve the Excs. 30.2.3.1 to 30.2.3.16 [219, 474, 859].

30.2.3 Exercises

30.2.3.1 Ex: Imaging through a thin lens

In classical ray optics the equations describing the focusing of a thin lens are given by,

$$\frac{1}{f} = \frac{1}{g} + \frac{1}{b} \qquad \text{and} \qquad \frac{b}{g} = \frac{B}{G} ,$$

where f is the focal distance of the lens, g the distance between the object and the lens, b the distance between the image and the lens, G the size of the object, and B the size of the image.
At what distance from an object of size $G = 1$ mm do you have to place a thin lens with focal distance $f = 100$ mm in order to obtain a ten times larger image? Test your result in practice.

30.2.3.2 Ex: Image of a convex lens

Show that with a convex lens of focal distance f the smallest distance between object and image should be $s = 4f$.

30.2.3.3 Ex: Telescope with ray optics

In classical optics the transfer matrix for the propagation of a beam through free space and through a thin lens are given, respectively, by

$$M_{\text{free}} = \begin{pmatrix} 1 & d \\ 0 & 1 \end{pmatrix} \qquad \text{and} \qquad M_{\text{lens}} = \begin{pmatrix} 1 & 0 \\ -1/f & 1 \end{pmatrix} .$$

The transfer between a point z_0 of the optical axis and a point z_1 is described by

$$\begin{pmatrix} y(z_1) \\ y'(z_1) \end{pmatrix} = M_{\text{free}} \begin{pmatrix} y(z_0) \\ y'(z_0) \end{pmatrix} .$$

Here, y is the distance of a beam ray from the optical axis and $y' = \frac{dy}{dx}$ its divergence. Use this formalism to design a 3 times magnifying telescope with two lenses have, respectively, the focal lengths $f_1 = 100\,\text{mm}$ and $f_2 = 300\,\text{mm}$.

30.2.3.4 Ex: Ray tracing

Simulate the trajectory of a ray of light traversing under an angle a layer of a material with a refraction index characterized by a Gaussian profile.

30.2.3.5 Ex: The eye

The effective distance between the cornea and the lens of the eye is 2.5 cm, and the lens is in contact with the eye. To resolve two very close points, their images on the retina must be on two non-adjacent cone cells (i.e. there must be at least one non-activated cone cell between the images). The cone cells are about 1 µm apart.
a. What is the smallest angle ϵ under which two points are still separately perceptible? Assume that the direct beams P, P' are not refracted.
b. How close can the two points P_1 and P_2 be, at a distance of 20 m from the eye, so that they are still separately perceptible?

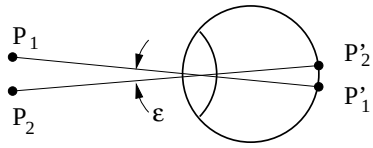

Figure 30.4: The eye.

30.2.3.6 Ex: Microscope

A simple homemade microscope consists of two convex lenses, each one with a diffractive power of 20 dpt, fixed at the extremities of a 30 cm long tube.
a. Wie groß ist die Tubuslänge dieses Mikroskops?
b. Wie groß ist der Abbildungsmaßstab des Mikroskops?
c. Welche Vergrößerung erreicht das Mikroskop? Gehen Sie davon aus, dass die deutliche Sehweite 25 cm beträgt.
d. Wie weit muss sich der Gegenstand vor dem Objektiv befinden, damit er im Auge des Betrachters scharf abgebildet wird?

30.2.3.7 Ex: Classical cloaking with four lenses

Can you design a system of four lenses (focal distances f_1, f_2, $f_3 = f_2$, and $f_4 = f_1$) separated by three distances $t_1 = f_1 + f_2$, t_2, and $t_3 = t_1$, such that the system appears to be invisible for an observer looking through the lenses [150]?

30.2.3.8 Ex: Diameter of a Gaussian beam

You are blocking part of a laser beam with a razor blade mounted on a translation stage allowing you to vary the horizontal position. At the same time, you observe the transmitted power P. You observe that, for varying the power between 16% and 84%, you need to vary the translation by 140 µm. What is the diameter of the Gaussian beam?

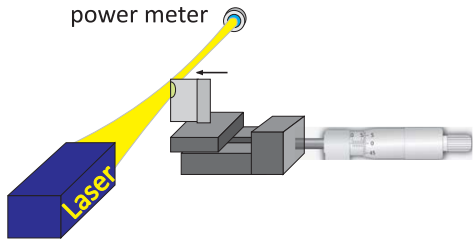

Figure 30.5: Diameter of a Gaussian beam.

30.2.3.9 Ex: Diffraction of a Gaussian beam at a slit

a. Determine the power loss suffered by a Gaussian beam passing through a one-dimensional slit, assuming that the beam hits the slit in its center.
b. Calculate the diffraction pattern produced by the slit.
c. A laser beam ($\lambda = 633\,\text{nm}$) looses 50% of its power after being passed through a slit. At a distance of $L = 1\,\text{m}$ behind the slit appear diffraction patterns exhibiting first minima at $\Delta x = 1\,\text{mm}$ to both sides of the central peak. Determine the diameter of the Gaussian beam.

30.2.3.10 Ex: Diffraction of a Gaussian beam at a pinhole

a. Determine the power loss suffered by a Gaussian beam passing through the center of a a pinhole of radius R.
b. A laser beam ($\lambda = 633\,\text{nm}$) looses 50% of its power after being passed through a slit. At a distance of $L = 1\,\text{m}$ behind the slit appear diffraction patterns exhibiting a first minimum at a distance $\Delta b = 1\,\text{mm}$ from the optical axis. Determine the diameter of the Gaussian beam. Help: The first ring of destructive interference occurs under an angle of $\sin\theta = 1.22\frac{\lambda}{2R}$.

30.2.3.11 Ex: Focusing a HeNe laser

The output beam from an HeNe laser with a confocal resonator ($\rho = L = 30\,\text{cm}$) is focused by a lens of $f = 30\,\text{cm}$, 50 cm away from the output mirror. Calculate the location of the focus, the Rayleigh length, and the beam waist in the focal plane.

30.2.3.12 Ex: Spatial filtering

A nearly parallel Gaussian beam with $\lambda = 500\,\text{nm}$ is expanded by a telescope with two lenses of focal lengths $f_1 = 1\,\text{cm}$ and $f_2 = 10\,\text{cm}$, illustrated in the figure. The

spot size at the entrance lens is $w = 1\,\text{mm}$.
a. Why does an aperture in the focal plane improve the quality of the wave fronts in the expanded beam by eliminating perturbations due to diffraction effects by dust and other imperfections on the lens surfaces?
b. What is the diameter of this aperture, if 95% of the intensity is transmitted?

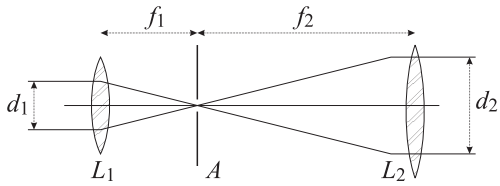

Figure 30.6: Beam-expanding telescope with an aperture in the focal plane.

30.2.3.13 Ex: Transverse mode selection in an Ar laser

An argon laser oscillating at $\lambda = 488\,\text{nm}$ with resonator length $d = 100\,\text{cm}$ and two mirrors with radius $R_1 = \infty$ and $R_2 = 400\,\text{cm}$ has an intracavity circular aperture close to the spherical mirror to prevent oscillation on transversal modes. Estimate the maximum diameter of the aperture that introduces losses $\gamma_{diffr} < 1\%$ for the TEM_{00} mode, but prevents oscillation of higher transverse modes, which without the aperture have a net gain of 10%.

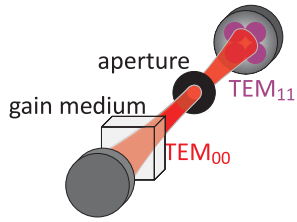

Figure 30.7: Transverse mode selection in an Ar laser.

30.2.3.14 Ex: Anamorphic prism

A prism can be used for expansion of a laser beam if the incident beam is nearly parallel to the prism surface. Calculate the angle of incidence α for which a laser beam transmitted through a rectangular glass prism with an $\varepsilon = 45°$ base angle is expanded tenfold.

30.2.3.15 Ex: Anamorphic prism pair

An *anamorphic prism* pair is a setup consisting of two prisms through which a laser beam is passed under specific angles. The angles can be chosen such as to change the beam diameter only in the p-plane.
a. Calculate, for a single prism with refractive index $n = 1.5$, the beam expansion for

an incidence angle of $\theta_1 = 57°$ and an exit angle of 0°. How large must the base angle β of the prism be for this to be possible?
b. How must the second prism be aligned in order for the beam transmitted to this second prism to remain parallel to the incident beam? Note, that an anamorphic

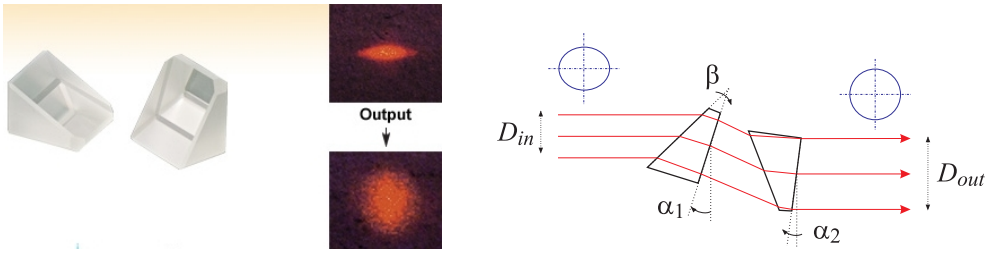

Figure 30.8: (Left) Anamorphic prisms (Thorlabs, PS870). (Right) Geometry of the beam transformation. The entrance side of a prism is often chosen close to the Brewster angle, while the exit side treated carries an anti-reflexion coating.

prism pair does not allow to correct for astigmatism. This requires cylindrical lenses.

30.2.3.16 Ex: Beam steering with two wedged substrates

The wavevector of a laser beam is generally aligned with one or more adjustable reflective mirrors. Alternatively, one may use a pair of rotatable transmissive wedged substrates. Calculate the wave vector of a laser beam after its transmission through two $\epsilon = 3°$ wedged, 2 mm thick, AR-coated substrates with the refraction index $n_{rfr} = 1.5134$ at 689 nm, each one rotated by $\theta_{1,2}$ from some normal position.

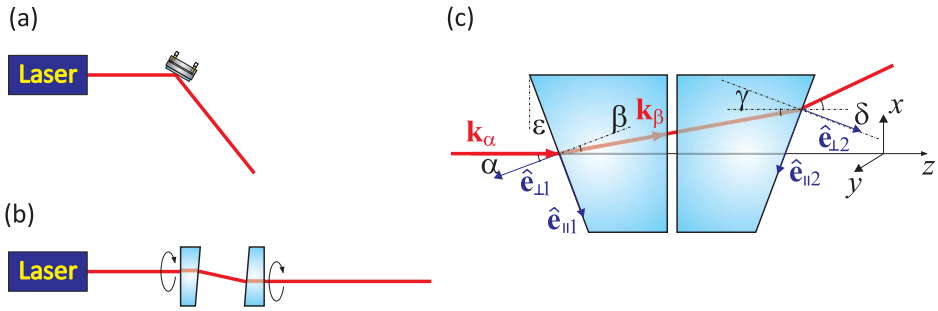

Figure 30.9: Beam steering with two rotatable wedged substrates (see Thorlabs, PS810).

30.2.4 *Experiment: Measuring the diameter of a Gaussian laser beam*

Most laser beams exhibit a Gaussian shape transverse intensity distribution, as we will study in this experiment.

1. Measure the phase profile of a helium-neon laser. To this end fix a razor blade on a translation stage and move it sideways into the beam. From the power of the partially blocked beam $\int_F I(x,y)dxdy$, where F is the cross section of the unblocked part of the beam, $w(z)$ can be determined (see Excs. 30.2.3.8 to 30.2.3.10).

30.2.5 *Experiment: Measuring the parameters of a Gaussian laser beam*

Once a Gaussian beam has been characterized at a given position z, the transfer matrix formalism allows us to calculate its shape at any position along the optical axis. In this experiment, we will study the propagation of a Gaussian beam through free space [see Eqs. (30.16)] and its transformation through a thin lens with focal distance f. For the latter one, we obtain directly after the lens,

$$\frac{1}{R(z \searrow 0)} = \frac{1}{R(z \nearrow 0)} - \frac{1}{f} \,. \tag{30.23}$$

1. Focus the beam with a lens. Measure the beam diameter at 3 different locations. Compare with the prediction of Gaussian optics.

2. Set up a 1:3 telescope and verify that the outgoing beam is collimated.

30.2.6 *Experiment: Spatial filtering with a pinhole*

Laser light emitted from diode lasers is often astigmatic and has an irregular beam profile. The beam profile can be purified by passing it through an optical fiber or a pinhole, however, at the price of losing power.

1. Focus the beam of a HeNe laser with a lens of $f = 100\,\text{mm}$ focal distance onto a pinhole. Observe the interference fringes and, from their distance from the optical axis, infer the diameter of the pinhole.

2. Remove the higher-order diffraction rings with an iris and compare the beam profile with that of a Gaussian beam. What are the divergence and the waist of the spatially filtered beam (see Exc. 30.2.3.10)?

30.3 Introduction to polarization optics

A laser usually has a well-defined polarization, e.g. , linear or circular. The polarizations can be transformed into one another through a *quarter waveplate* ($\lambda/4$) or a *half waveplate* ($\lambda/2$) by a Fresnel rhomb or other birefringent elements. Superpositions of polarizations can be separated by a *polarizing beam splitter*.

Waveplates consist of thin sheets of *birefringents crystal*s, which are transparent material characterized by anisotropic refraction indices. Cut in a particular way, a birefringent crystal can exhibit a polarization-dependent refraction index, allowing to control the retardation of a light beam as a function of its polarization. The thickness

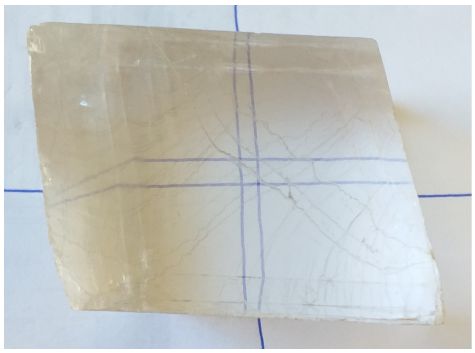

Figure 30.10: (Left) Transmission through a birefringent crystal. (Right) $\lambda/2$-waveplate mounted in a rotation stage.

of a waveplate determines the retardation of one polarization axis with respect to the other.

In practice, the degree of freedom of polarization is often used for separating counterpropagating light fields, e.g. in ring lasers, by means of elements called *optical diode* or *optical isolator*, which consist of a Faraday rotator and $\lambda/2$ waveplate. Another practical example is the use of $\lambda/4$ in double passage. An incoming beam can be separated from a returning beam by using a $\lambda/4$ waveplate and a polarizing beam splitter.

30.3.1 Jones matrices

The term *polarization* is defined in relation to a fixed coordinate system, while the term *helicity* denotes the direction of rotation of the polarization vector with respect to the direction of propagation of the light beam. The polarization of a beam propagating in z-direction can easily be expressed by a vector of complex amplitude,

$$\vec{\mathcal{E}}(\mathbf{r},t) = \begin{pmatrix} a \\ b \\ 0 \end{pmatrix} e^{\imath kz - \imath\omega t} = \begin{pmatrix} 1 \\ e^{-\imath\phi}|b|/|a| \\ 0 \end{pmatrix} |a| e^{\imath kz - \imath\omega t} \ . \tag{30.24}$$

The angle $\phi = \arctan \frac{\Im\mathfrak{m}\, ab^*}{\Re\mathfrak{e}\, ab^*}$ determines the polarization of the light beam. A polarization is linear when $\phi = 0$ and circular when $\phi = \pi/2$. $|b|/|a|$ is, hence, the degree of ellipticity. A polarization rotator for linearly polarized light (e.g., a sugar solution) is described by the following *Jones matrix* (we will restrict to the x-y-plane)

$$M_{\text{rotator}}(\phi) = \begin{pmatrix} \cos\phi & \sin\phi \\ -\sin\phi & \cos\phi \end{pmatrix} \ , \tag{30.25}$$

where ϕ is the rotation angle. For the Faraday rotator the sign of the rotation angle depends on the propagation direction of the laser beam. A *polarizer* projects the polarization onto a specific axis. In the case of the x-axis Jones matrix is,

$$M_{\text{polarizer}} = \begin{pmatrix} 1 & 0 \\ 0 & 0 \end{pmatrix} \ . \tag{30.26}$$

If the rotation angle is ϕ,

$$M_{\text{polarizer}}(\phi) = \begin{pmatrix} \cos\phi & \sin\phi \\ -\sin\phi & \cos\phi \end{pmatrix} \begin{pmatrix} 1 & 0 \\ 0 & 0 \end{pmatrix} \begin{pmatrix} \cos\phi & \sin\phi \\ -\sin\phi & \cos\phi \end{pmatrix}^{-1} . \tag{30.27}$$

Other components, such as electro-optical modulators or phase plates are birefringent crystals, which act only on one of the two optical axes. If only the y axis is optically active, the Jones' matrix is,

$$M_{\theta\text{-waveplate}} = \begin{pmatrix} 1 & 0 \\ 0 & e^{\imath\theta} \end{pmatrix} . \tag{30.28}$$

For $\theta = 2\pi/n$ we obtain a λ/n-waveplate. When we rotate the waveplate and therefore the optically inactive axis to an angle ϕ, the Jones matrices are,

$$\begin{aligned} M_{\theta\text{-waveplate}}(\phi) &= \begin{pmatrix} \cos\phi & \sin\phi \\ -\sin\phi & \cos\phi \end{pmatrix} \begin{pmatrix} 1 & 0 \\ 0 & e^{\imath\theta} \end{pmatrix} \begin{pmatrix} \cos\phi & \sin\phi \\ -\sin\phi & \cos\phi \end{pmatrix}^{-1} \\ &= \begin{pmatrix} \cos^2\phi + e^{\imath\theta}\sin^2\phi & -\sin\phi\cos\phi + e^{\imath\theta}\sin\phi\cos\phi \\ -\sin\phi\cos\phi + e^{\imath\theta}\sin\phi\cos\phi & \sin^2\phi + e^{\imath\theta}\cos^2\phi \end{pmatrix} . \end{aligned} \tag{30.29}$$

In most cases, we use quarter waveplates $\lambda/4$,

$$M_{\lambda/4}(\phi) = \begin{pmatrix} \cos^2\phi + \imath\sin^2\phi & (-1+\imath)\sin\phi\cos\phi \\ (-1+\imath)\sin\phi\cos\phi & \sin^2\phi + \imath\cos^2\phi \end{pmatrix} \tag{30.30}$$

and half waveplates $\lambda/2$,

$$M_{\lambda/2}(\phi) = \begin{pmatrix} \cos 2\phi & -\sin 2\phi \\ -\sin 2\phi & -\cos 2\phi \end{pmatrix} . \tag{30.31}$$

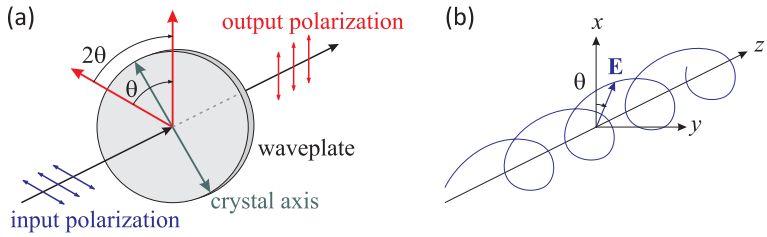

Figure 30.11: (a) Rotation of the polarization by a birefringent waveplate. (b) Illustration of a circularly polarized light wave.

Combinations of $\lambda/2$ waveplates and *Faraday rotator*s are used as *optical isolator*, also called *optical diode*.

30.3.2 Fresnel formulae

Reflection and transmission of a beam of light at a surface depend on the polarization of the light and the angle of incidence. They are described by the *Fresnel formula*:

$$\begin{aligned}
\left(\frac{I_{0t}}{I_{0i}}\right)_s &= T_s = \left(\frac{2\sin\theta_t\cos\theta_i}{\sin(\theta_i+\theta_t)}\right)^2 \\
\left(\frac{I_{0r}}{I_{0i}}\right)_s &= R_s = \left(-\frac{\sin(\theta_i-\theta_t)}{\sin(\theta_i+\theta_t)}\right)^2 \\
\left(\frac{I_{0t}}{I_{0i}}\right)_p &= T_p = \left(\frac{2\sin\theta_t\cos\theta_i}{\sin(\theta_i+\theta_t)\cos(\theta_i-\theta_t)}\right)^2 \\
\left(\frac{I_{0r}}{I_{0i}}\right)_p &= R_p = \left(\frac{\tan(\theta_i-\theta_t)}{\tan(\theta_i+\theta_t)}\right)^2 .
\end{aligned} \tag{30.32}$$

The angles of incidence and transmission are related by Snell's law: $n_1 \sin\theta_i = n_2 \sin\theta_t$.

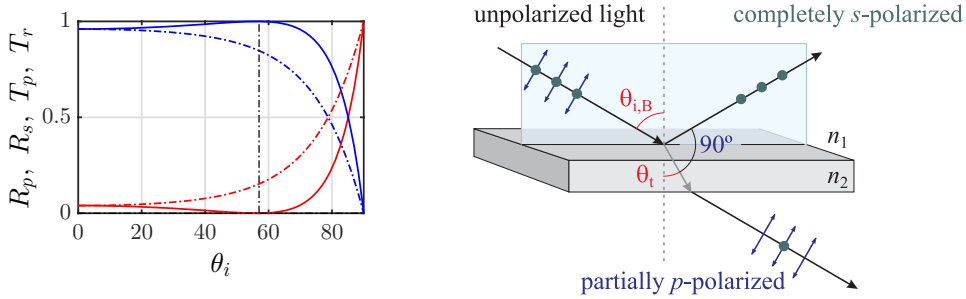

Figure 30.12: (code) (Left) Fresnel formulae showing the angular dependence of t_s (red solid), r_s (green dash-dotted), t_p (blue dashed), and r_p (cyan dotted) for reflection from and transmission through a piece of glass-air interface. (Right) Interfaces between optical media with different reflection indices can act like polarizers: Light reflected from a glas surface under the Brewster angle is completely s-polarized, while the transmitted light is partially p-polarized. The notation s comes from *senkrecht*, i.e. perpendicular to the plane spanned by the incident and reflected light beams, while p means *parallel* to this plane.

The *Brewster angle* $\theta_{i,B}$ is reached, when $\theta_{i,B} + \theta_t = 90°$, i.e., when following Snell's law,

$$n_1 \sin\theta_{i,B} = n_2 \sin(90° - \theta_{i,B}) = n_2 \cos\theta_{i,B} \ . \tag{30.33}$$

Hence, the Brewster angle is given by,

$$\tan\theta_{i,B} = \frac{n_2}{n_1} \ . \tag{30.34}$$

Resolve the exercises 30.3.4.1 to 30.3.4.5.

30.3.3 Stokes parameters

In quantum mechanics the *Stokes parameters* of a light beam with horizontal and vertical polarizations, $\hat{a}_h$ and $\hat{a}_v$, satisfying,

$$[\hat{a}_k, \hat{a}_m^\dagger] = \delta_{km} \ , \tag{30.35}$$

with $k, m = h, v$ are defined by,

$$\boxed{\begin{aligned} \hat{S}_0 &\equiv \hat{a}_h^\dagger \hat{a}_h + \hat{a}_v^\dagger \hat{a}_v \\ \hat{S}_1 &\equiv \hat{a}_h^\dagger \hat{a}_h - \hat{a}_v^\dagger \hat{a}_v \\ \hat{S}_2 &\equiv \hat{a}_h^\dagger \hat{a}_v e^{\imath\theta} + \hat{a}_v^\dagger \hat{a}_h e^{-\imath\theta} \\ \hat{S}_3 &\equiv -\imath(\hat{a}_h^\dagger \hat{a}_v e^{\imath\theta} - \hat{a}_v^\dagger \hat{a}_h e^{-\imath\theta}) \end{aligned}} \ . \tag{30.36}$$

The Stokes parameters exhaustively describe the polarization state of a light beam. It is interesting, that the vector $\hat{\mathbf{S}}$ with components S_j with $j = 1, 2, 3$ satisfies the SU(2) spin algebra,

$$[\hat{S}_k, \hat{S}_m] = 2\imath\epsilon_{kmn}\hat{S}_n \qquad \text{and} \qquad \hat{\mathbf{S}}^2 = \hat{S}_0^2 + 2\hat{S}_0 \ , \tag{30.37}$$

as will be shown in Exc. 30.3.4.6. It is conveniently pictured on a Poincaré sphere or as a polarization ellipse. In the classical limit we get,

$$\begin{aligned} \hat{S}_0 &= I \\ \hat{S}_1 &= Ip\cos 2\psi \cos 2\chi \\ \hat{S}_2 &= Ip\sin 2\psi \cos 2\chi \\ \hat{S}_3 &= Ip\sin 2\chi \ , \end{aligned} \tag{30.38}$$

with I the light intensity (eventually normalized to the single-photon light intensity), the degree of polarization p. Obviously,

$$\hat{S}_1^2 + \hat{S}_2^2 + \hat{S}_3^2 = p^2 \hat{S}_0^2 \ . \tag{30.39}$$

30.3.4 Exercises

30.3.4.1 Ex: Light power control using polarization optics

The power of a laser beam can be regulated by a combination of a half-wave plate and a polarizing beam splitter. By how many degrees do you have to rotate the waveplate in order to reduce the light power by a factor of 2? Use the Jones matrices to justify your response. **Advice:** Look up the Jones matrices (30.31) and (30.26). Test your result in practice.

30.3.4.2 Ex: Jones matrices

Consider a linearly polarized laser beam passing twice through a $\lambda/4$, first in direction of the optical axis, the second time in opposite direction. Calculate the final polarization.

30.3.4.3 Ex: Intensity transmitted through a polarizer

Unpolarized light of intensity I_0 is transmitted through a polarizer with thickness $d = 1\,\mathrm{mm}$. Calculate the transmitted intensity when the absorption coefficients for the two polarizations are $\alpha_{\parallel} = 100\,\mathrm{cm}^{-1}$ and $\alpha_{\perp} = 5\,\mathrm{cm}^{-1}$.

30.3.4.4 Ex: Thickness of a half-waveplate

A birefringent quartz crystal is characterized by different refraction indices of the ordinary beam $n_o = 1.544$ and the extraordinary beam $n_e = 1.553$. Calculate the necessary thickness of a quartz waveplate to be used as a $\lambda/2$ retarder at 633 nm. Choose an appropriate waveplate from the Thorlabs catalogue. How thick would a calcite waveplate ($n_o = 1.658$, $n_e = 1.486$)?

30.3.4.5 Ex: Faraday isolator

A Faraday rotator is a device exploiting the Faraday effect to rotate the polarization of a light beam according to the Jones matrix,

$$M_{Faraday}(\phi) = \begin{pmatrix} \cos\phi & -\mathbf{k}\cdot\hat{\mathbf{e}}_z \sin\phi \\ \mathbf{k}\cdot\hat{\mathbf{e}}_z \sin\phi & \cos\phi \end{pmatrix} , \tag{30.40}$$

where $\mathbf{k}$ is the wavevector of the light beam. An optical diode is composed by a $\phi = 45°$ Faraday rotor sandwiched between two polarizers rotated by $\phi = 45°$ with respect to each other.
a. How is the polarization of a light beam changed after a double passage (back and forth) through a Faraday rotator?
b. Calculate what happens to a light beam upon a single passage through a Faraday rotator in either direction $\mathbf{k}$ and $-\mathbf{k}$?

30.3.4.6 Ex: Stokes parameters

For the Stokes parameters defined in (30.42) prove the following relationships,

$$[\hat{S}_k, \hat{S}_m] = 2\imath\epsilon_{kmn}\hat{S}_n \qquad \text{and} \qquad \hat{\mathbf{S}}^2 = \hat{S}_0^2 \ .$$

30.3.5 *Experiment: Polarization of a helium-neon laser*

We will now analyze and manipulate the polarization of a laser beam in practice.

1. Pass the beam of a helium-neon laser through a polarizer and a quarter- resp. half-waveplate. Analyze the polarization using a rotatable second polarizer for various rotation angles of the waveplate. Sketch the transmitted intensity as a function of the rotation angle of the beamsplitter in a polar diagram. How good can you achieve linear and circular polarization?

2. Characterize the polarization of a helium-neon laser by sketching the transmitted intensity through a polarizing beamsplitter as a function of the rotation

angle of the beamsplitter in a polar diagram. Now couple the laser beam to a Fabry-Pérot interferometer. What do you observe? Place a quarter-waveplate at the output of the helium-neon laser and characterize again the polarization. What do you observe at the Fabry-Pérot interferometer?

3. Use a quarter-waveplate to separate a beam of light from a counterpropagating beam according to Fig. 30.13.

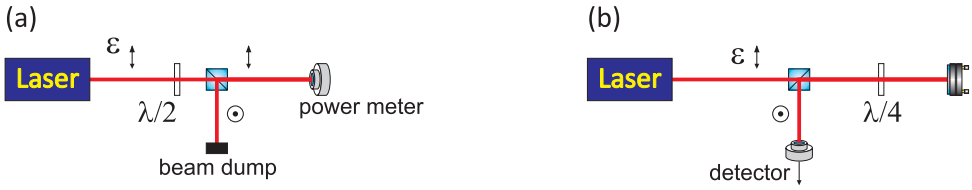

Figure 30.13: (a) Power control of a light beam and (b) separation of counterpropagating beams through polarization optics.

4. Characterize an optical insulator. Optimize its extinction.

30.3.6 *Experiment: Measuring the Brewster angle*

Any interface between two transparent materials with different refraction indices reflects a part of incident light depending on the polarization and the angle of incidence, as predicted by Fresnels formulae (30.32).

1. Measure the transmission by a glass plate as a function of the angle of incidence for two orthogonal polarizations and determine the Brewster angle.

2. Mirrors can change the polarization of a light beam and, for example, transform a linear polarization into elliptical. Determine the degree of ellipticity for a given mirror.

3. How does a mirror transform the polarization and the helicity of a reflected laser beam?

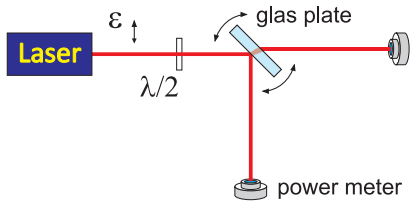

Figure 30.14: Measuring the Brewster angle by varying the tilt of a glas plate.

30.3.7 *Experiment: Pockels cell*

Pockels cells are birefringent crystals allowing to manipulate the polarization of a laser beam by application of a voltage.

1. Prepare a laser beam by passing it through a polarizer followed by a half-waveplate and a second polarizer. Observe the intensity transmitted and reflected through the last polarizer as a function of the rotation angle of the half-waveplate.

2. Use the EOM as a Pockels cell by placing it between the half-waveplate and the second polarizer. Supply a voltage between 0 V and 350 V to the EOM. Measures the intensity of reflected and transmitted light as a function of the supplied voltage and prepare a diagram. What do you observe when you rotate either the half-waveplate or the EOM?

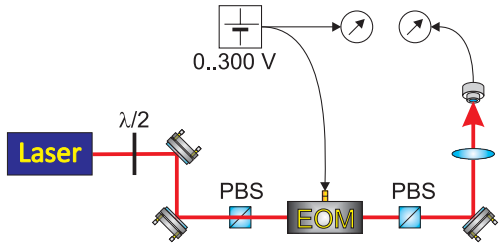

Figure 30.15: Scheme for using an EOM as a Pockels cell.

30.4 Laguerre-Gaussian light modes

Light beams not only possess polarization, but can also have orbital angular momentum. This property of light can impressively demonstrated at the so-called *Laguerre-Gaussian mode*s.

These modes can be produced by means of masks resembling *Fresnel zone plate*. Fresnel zone plates are masks consisting of concentric sequences of bright (transmitting) and dark (absorbing) rings. The diameters of the rings are selected in such a way that the diameters of the rings defined by the bright rings interfere constructively at a certain distance f_1 on the optical axis and form a 'focus' there. For this purpose, the distance d_n of the n^{th} ring must satisfy the condition,

$$d_n = \sqrt{(f_1 + n\lambda)^2 - f_1^2} \simeq \sqrt{2 f_1 n \lambda}\,. \tag{30.41}$$

For a given zone plate there are other focuses at smaller distances,

$$f_k = \frac{d_n^2 - k^2 n^2 \lambda^2}{2kn\lambda} \simeq \frac{d_n^2}{2kn\lambda} = \frac{f_1}{k}\,. \tag{30.42}$$

In order to separate the beams diffracted by the zone plate into a given focus from those diffracted into other focuses or not being diffracted at all, we pass the beam

through an iris diaphragm localized at the desired focus and recollimate the beam by means of a lens, as shown in Fig. 30.16.

The phase profile of the beam can be viewed interferometrically (see Fig. 30.16) by overlapping a plane wave laser beam. With a *neutral density filter* the intensities of the overlapping beams can be adjusted to maximize the contrast.

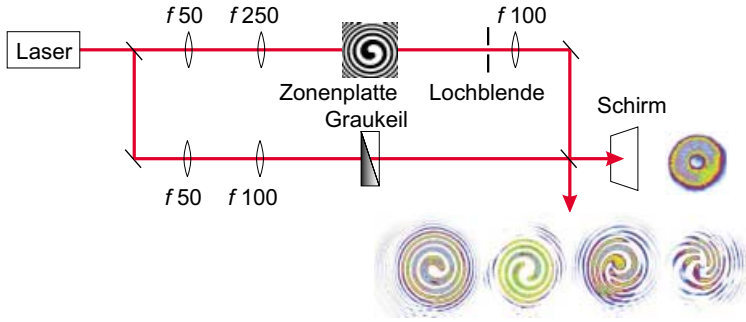

Figure 30.16: Creation of Laguerre-Gaussian modes.

Now, for realizing Laguerre-Gaussian light modes, we use Fresnel zone plates with spiral patterns, instead of concentric rings. In contrast to the Gaussian mode, the Laguerre-Gauß modes exhibit an intensity minimum on the optical axis (doonat mode). Their phase profiles can be viewed by interferometry [14].

30.4.1 *Experiment: Generating a Laguerre-Gaussian mode*

In this experiment, we will...

1. Construct the interferometer sketched in Fig. 30.16 using adequate Fresnel zone plates. What do you observe in the diffracted beam and in the interferogram, when instead of filtering the principal focus f_1 you filter a higher order focus?

2. Pass a Laguerre-Gauß laser beam through a $\lambda/2$ waveplate. How does the angular orbital momentum change when you change the rotation? What happens upon reflection from a mirror?

3. Slightly misalign the mode-matching between the Laguerre-Gauß beam and the Gaussian reference beam until you observe multiple fringes. What do you observe?

30.5 Further reading

M. Born, *Principles of Optics* [ISBN]

H. Kogelnik et al., *Laser Beams and Resonators* [DOI]

W. Demtröder, *Atoms, Molecules and Photons: An Introduction to Atomic, Molecular, and Quantum Physics* [ISBN]

J. Weiner et al., *Light-matter interaction, Fundamentals and applications* [DOI]

G.A. Fowles, *Introduction to Modern Optics* [ISBN]

J.S. Choi et al., *Paraxial ray optics cloaking* [DOI]

30.5.1 on Stokes parameters

W.P. Bowen et al., *Polarization Squeezing of Continuous Variable Stokes Parameters* [DOI]

30.5.2 on Laguerre-Gauss modes

L. Allen et al., *Orbital Angular Momentum of Light and the Transformation of Laguerre-Gaussian Laser Modes* [DOI]

Chapter 31

Electronics and radiofrequency

For the control and regulation of important quantum optical devices, such as EOMs, AOMs, laser diodes, photodiodes, piezos etc., *electronic circuit*s are necessary. The aim of this chapter is to provide practical know-how in the basics of electronics.

31.1 Introduction to electronic circuits

31.1.1 Passive electronic components

Electronic components which are characterized by a fixed impedance are called *passive*. The most common devices are resistors, capacitors, and inductances. For their handling, it is useful to be able to identify their impedance from their labeling.

The values of the resistances of resistors are generally codified by colored rings. The first ring to be considered is the one closest to a terminal. In case of 4 rings, the first two rings are to be considered as digits, the third ring gives the exponent 10. With five rings, the first three are digits and the forth gives the exponent of 10. The last ring, in both cases specifies the tolerance of the value of the resistance.

There are various types of capacitors depending on the employed materials for the dielectric medium (paper, ceramics, polyester, electrolyte made of aluminum and electrolyte made of tantalum). Electrolyte capacitors have a defined polarity, and an reversion of their voltage supply can result in their explosion. The value of the capacitance is generally written on their body, as well as their maximum allowed operating voltage. Also the polarity of electrolyte capacitors is always indicated (although there can be some confusion with regard to the physical and technical direction of the current flow). Ceramic and polyester capacitors can have their values either written in letters or color coded. The color code sequence is similar to that of resistors, with the first two digits devoted to the digits, the third to the multiplier exponent, the forth to the tolerance, and the fifth for the maximum voltage. In case of printed numbers, the first two numbers represent the first two digits, and the third one represents the numbers of 0 before the decimal point. In all cases (colors or digits), the value is given in picoFarads. With more modern serigraphic techniques, some capacitors have their values printed directly in Farads (micro, nano and pico). In these cases, the letter denoting the unit also serves to mark the decimal point. For example, 2n2 means 2.2 nF.

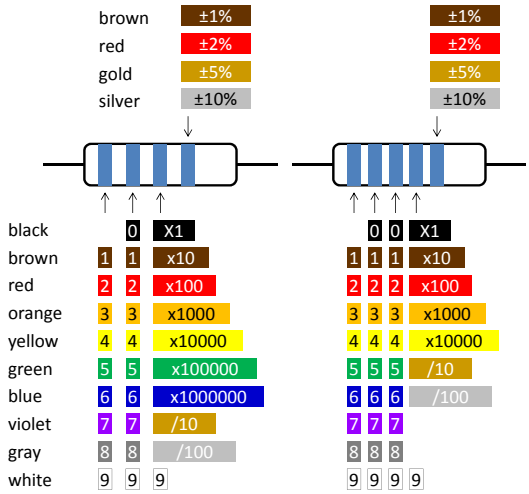

Figure 31.1: Color code for resistors with 4 and 5 rings.

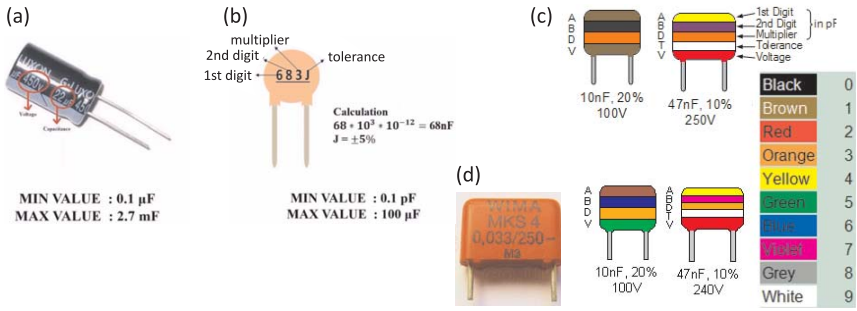

Figure 31.2: (Left) Electrolyte aluminum capacitors. (Center) Polyester capacitor and color code. (Right) Ceramic capacitor.

31.1.2 Active electronic components and the *pn*-junction

Diodes, transistors, photodiodes, operational amplifiers are called *active components*, because their current-to-voltage curve is non-linear, their response $I = I(U)$ cannot be described by a single constant value, but depends on the applied voltage.

During this course we will work a lot with *operational amplifiers* (OpAmp), which are integrated circuits designed to amplify input signals with characteristics that are entirely determined by external components. This feature makes them easy to use and extremely versatile.

OpAmps are generally found encapsulated in DIL type housings (dual in line), which means that they have two lines of 4 pins. The sequence of pins is numerated in counter-clockwise orientation, and they have a mark on the side of pin 1. It is always recommend to obtain the datasheet of the OpAmp since, despite a usual pin compatibility ensured by the various OpAmp manufacturers, deviations are frequent.

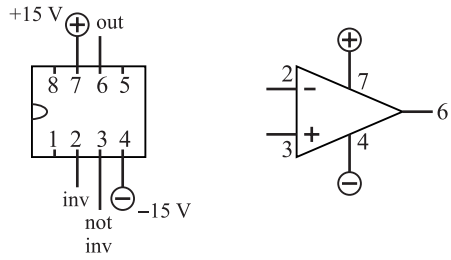

Figure 31.3: (Left) Schematic symbol of an OpAmp; (Right) Pin layout of a standard OpAmp.

31.1.3 Electronic circuits

Amplification or control circuits are nowadays mostly realized with *operational amplifiers* (*OpAmp*). The advantage of an OpAmp compared to circuits based on transistors is, that their properties are almost independent of their internal structure. Hence, their properties can be personalized via an external feedback realized with external components. The input of an OpAmp does not require current. OpAmps amplify the voltage difference between the non-inverting input (+) and the inverting (-). For most practical matters we can assume, that the OpAmp has infinite amplification and negligible input impedance.

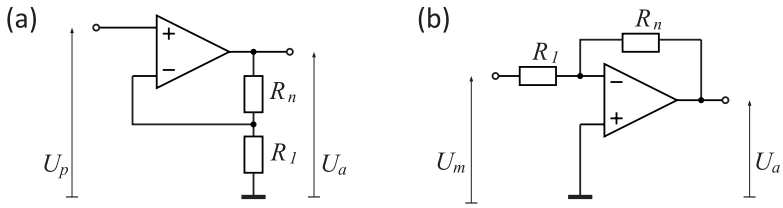

Figure 31.4: (Left) Principle scheme of a standard OpAmp. (Center) Non-inverting amplifier. (Right) Inverting amplifier.

OpAmps can be used as *inverting amplifiers* or *non-inverting amplifiers*. Using *Kirchhoff's rules* for the *loops* and *nodes* of the circuit, we find for a non-inverting amplifier,

$$\frac{U_e}{R_1} = -\frac{U_a}{R_1 + R_n} \quad , \quad G = 1 + \frac{R_n}{R_1} \; . \tag{31.1}$$

This becomes clear noting that, since no voltage is dropped between the inputs (+) and (-), the input voltage must be equal to the voltage drop at R_1. And since the non-inverting input does not deliver current, the currents traversing the resistances R_n and R_1 must be equal. For the inverting amplifier, we find,

$$\frac{U_a}{R_n} = -\frac{U_e}{R_1} \quad , \quad G = -\frac{R_n}{R_1} \; . \tag{31.2}$$

This becomes clear noting that, since the input (-) does not drag current, the currents traversing the resistances R_n and R_1 must cancel each other.

Changing the resistances R to inductances L or capacitances C, it becomes possible to influence the frequency response of the amplifying circuit. The impedance are,

$$Z_L = \imath L\omega \quad , \quad Z_C = \frac{1}{\imath C\omega} \ . \tag{31.3}$$

For the calculation of the amplification wit complex impedances, we just take the absolute value of the gain G.

31.1.4 The thermoelectric effect

31.1.4.1 Seebeck effect

The Seebeck effect is a classic example of an electromotive force (EMF) and leads to measurable currents or voltages in the same way as any other EMF. The local current density is given by,

$$\mathbf{J} = \sigma(-\nabla V + \mathbf{E}_{emf}) \ , \tag{31.4}$$

where V is the local voltage, and σ is the local conductivity. In general, the Seebeck effect is described locally by the creation of an electromotive field,

$$\mathbf{E}_{emf} = -S\nabla T \ , \tag{31.5}$$

where S is the Seebeck coefficient (also known as thermopower), a property of the local material, and ∇T is the temperature gradient.

The Seebeck coefficients generally vary as function of temperature and depend strongly on the composition of the conductor. For ordinary materials at room temperature, the Seebeck coefficient may range in value from $-100\,\mu\text{V/K}$ to $+1000\,\mu\text{V/K}$.

If the system reaches a steady state, where $\mathbf{J} = 0$, then the voltage gradient is given simply by the emf:

$$-V = S\Delta T \ . \tag{31.6}$$

This simple relationship, which does not depend on conductivity, is used in the thermocouple to measure a temperature difference; an absolute temperature may be found by performing the voltage measurement at a known reference temperature. A metal of unknown composition can be classified by its thermoelectric effect if a metallic probe of known composition is kept at a constant temperature and held in contact with the unknown sample that is locally heated to the probe temperature. It is used commercially to identify metal alloys. Thermocouples in series form a *thermopile*. Thermoelectric generators are used for creating power from heat differentials.

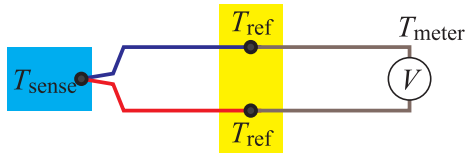

Figure 31.5:

31.1.4.2 Peltier effect

When an electric current is passed through a circuit of a thermocouple, heat is evolved at one junction and absorbed at the other junction. This is known as Peltier Effect and is named after a physicist. The Peltier effect is the presence of heating or cooling at an electrified junction of two different conductors. When a current is made to flow through a junction between two conductors, A and B, heat may be generated or removed at the junction. The Peltier heat generated at the junction per unit time is,

$$\dot{Q} = (\Pi_A - \Pi_B)I \ , \tag{31.7}$$

where Π_A and Π_B are the Peltier coefficients of conductors A and B, and I is the electric current (from A to B). The total heat generated is not determined by the Peltier effect alone, as it may also be influenced by Joule heating and thermal-gradient effects (see below).

The Peltier coefficients represent how much heat is carried per unit charge. Since charge current must be continuous across a junction, the associated heat flow will develop a discontinuity if Π_A and Π_B are different. The Peltier effect can be considered as the back-action counterpart to the Seebeck effect (analogous to the back-EMF in magnetic induction): if a simple thermoelectric circuit is closed, then the Seebeck effect will drive a current, which in turn (by the Peltier effect) will always transfer heat from the hot to the cold junction. The close relationship between Peltier and Seebeck effects can be seen in the direct connection between their coefficients [406, 822]:

$$\Pi = TS \ . \tag{31.8}$$

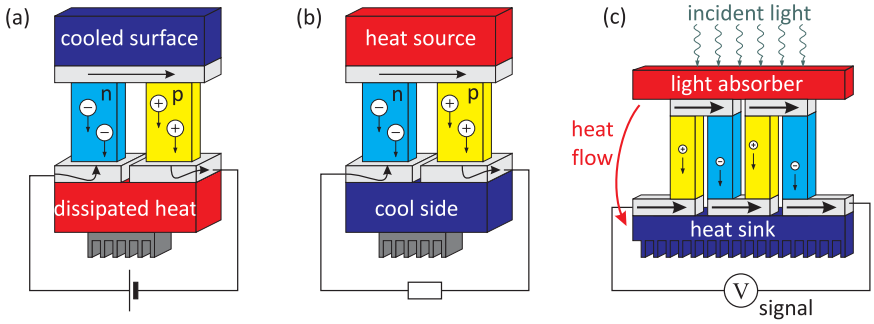

Figure 31.6: (a) Peltier cooler, (b) voltage generator or heat sensor, and (c) heat or radiation sensor with thermocouples connected in parallel.

31.1.5 Exercises

31.1.5.1 Ex: Integrator with operational amplifier

Based on the two golden rules for operational amplifiers, (1) $I_+ = I_- = 0$ A and (2) $U_+ = U_-$, show that the output voltage U_a at the integrated circuit shown in the figure is: $U_a = \frac{1}{RC} \int U_e dt$.

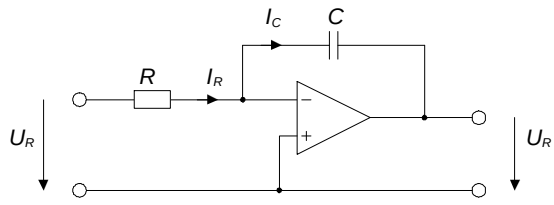

Figure 31.7: Integrator with operational amplifier.

31.1.5.2 Ex: Low-pass filter using an OpAmp

Using an inverting operational amplifier design a simple low-pass filter with a constant amplification of 10 at low frequencies and diminishing gain above 10 kHz. Calculate the Bode diagram (i.e. the frequency-dependent gain and phase-shift of your circuit. What is the gain reduction per octave?

31.1.6 *Experiment: Amplifiers and active filters*

Here, we will learn how to use OpAmps: We will start mounting a 10-fold inverting amplifier on a breadboard and then modify the external passive components, such as to build a low-pass filter.

1. Assemble on a breadboard a simple inverting amplifier using an OpAmp. Use 10 kΩ resistors at the input aim for an amplification factor of 10.

2. Test the circuit with a frequency generator and an oscilloscope.

3. Modify the circuit such as to obtain a low-pass filter with $f_g = 50$ kHz bandwidth and test the circuit again.

31.1.7 *Experiment: Peltier element and thermistor*

Here, we will learn how to use a Peltier element and a thermistor. A *thermistor* is nothing else than a well-calibrated resistor with temperature-dependent resistance (see Fig. 31.9).

1. Connect a Peltier element to a 1 A current source and bring one of the two surfaces of the Peltier element into thermal contact with a heat sink. What do you observe?

2. Bring a 10 kΩ thermistor in thermal contact with either of the two surfaces of the Peltier element and measure its resistance. What do you observe?

3. Can you imagine a feedback logic evaluating the measured resistance in order to control the current applied to the Peltier element such as to maintain constant the temperature of the surface not connected to the heat sink.

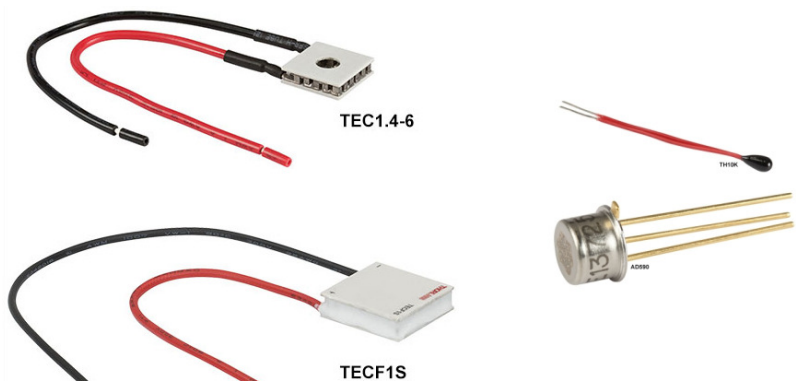

Figure 31.8: Pictures of Peltier elements, a thermistor, and an AD590 temperature transducer.

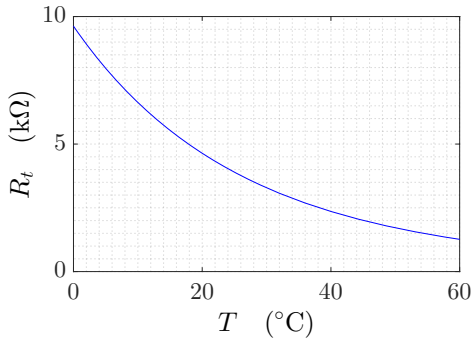

Figure 31.9: Calibration curve for a 10 kΩ thermistor from Thorlabs.

31.2 Detectors

31.2.1 Photodiodes

Most active components are many of *semiconductor* characterized by a relatively large band gap between the valence band and the conduction band. By appropriate doping of the material with donors (p-type) or acceptors (n-type) a semiconductor can be made conductive. The most basic semiconductor element, which is the *diode* consists of a junction of two types of semiconductors, as shown in Fig. 31.10.

Our first task will be to construct a *photo detector*. The central part of a photodetector is the photodiode. We have at our disposal silicium *pin*-photodiodes of the type C30822E of the company Perkin Elmer and of the type FFD100.

Photodiodes exploit an intrinsic photoeffect of semiconductor *pn*-junctions. In the transition region, free electrons of the n-type semiconductor and excess holes of the p-type semiconductor are drifting into the respective opposite semiconductor, where they recombine. The consequence is a transition zone with a charge carrier depletion, which acts as a barrier and has an intrinsic capacitance. The charge carrier imbalance

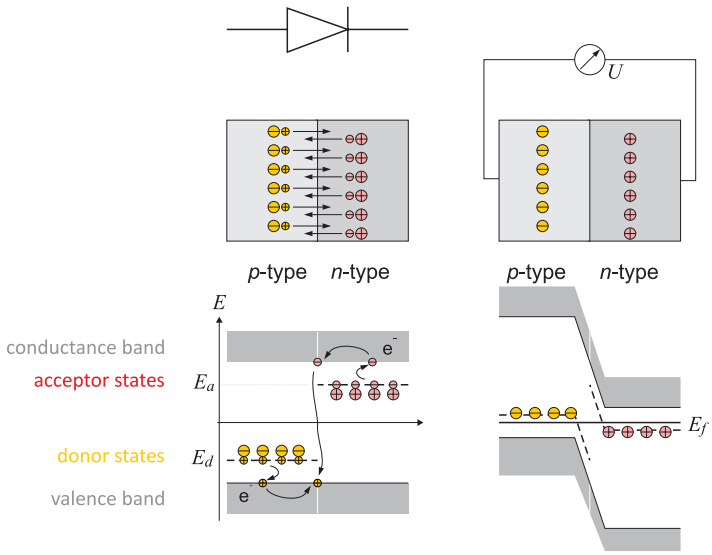

Figure 31.10: Joining a p-type and a n-type doped semiconductor (left) one observes a charge carrier redistribution across the pn transition (right).

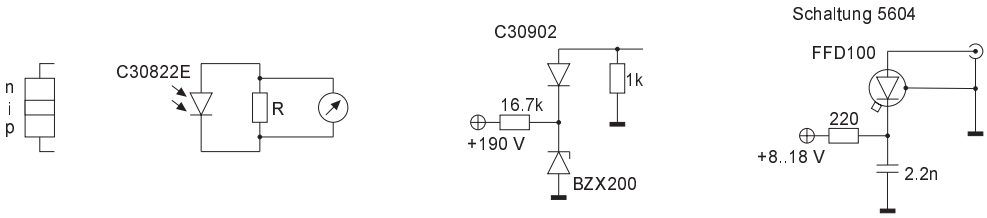

Figure 31.11: Circuit with photodiode.

gives rise to an electric field across the junction. The energy liberated during the recombination process can be dissipated via emission of light.

The reverse process is also possible: Via the intrinsic photoeffect, light irradiated into the pn-junction can lift electrons from the valence into the conduction band, thus generating pairs of charge carriers. Under the influence of the electric field across the junction, the holes flow to the edge of the p domain and the electrons flow to the n domain. This part of the current is called *drift current*. A smaller part, called the *diffusion current*, has its origin in the diffusion of the electron-hole pairs formed in the edge regions. Since these minority charge carriers have only a limited lifetime before they recombine, only the part of the current generated within a few units of the diffusion lengths near the charge carrier zone contributes. This results in an external photovoltaic voltage at the electrodes of the photodiode. If the photodiode is connected to a load, a photocurrent will flow, which is composed, as mentioned above, by the drift current of the charge carrier zone and the diffusion current from its edges.

The principal scheme of a pin diode is illustrated in Fig. 31.12(left): A weakly

doped intrinsic layer separates the p and the n conductor. This reduces the capacity of the barrier. The current at short circuit is proportional to the light power. A photodiode is always operated in blocking direction. A negative offset voltage reduces the capacity of the pn-junction.

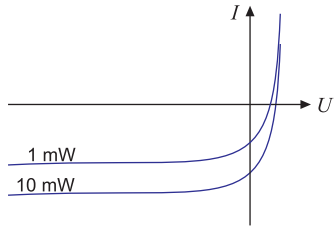

Figure 31.12: (code) U-I dependence of a photodiode.

Despite all measures the pn-junction capacity remains finite. One can model the impact of the pn-junction capacity via a replacement diagram. The voltage drop is

$$\frac{U(\omega)}{U_0} = \frac{R_L||\frac{1}{\imath\omega C}}{R_i + \left(R_L||\frac{1}{\imath\omega C}\right)} = \frac{\frac{R_i||R_L}{R_i}}{1+\imath\omega C(R_i||R_L)} \ . \tag{31.9}$$

For high load resistances the frequency response obviously becomes load-independent. For small loads, $R_L < R_i$, the band width of the photodiode is dramatically increased to $\omega_g = 1/R_L C$. In the same time, however, the amplification drops to $V = R_L/R_i$.

31.2.2 Exercises

31.2.2.1 Ex: Photomultiplier

The anode of a photomultiplier tube is connected by a resistor of $R = 1\,\mathrm{k}\Omega$ to ground. The stray capacitance is 10 pF, the current amplification 10^6, and the anode rise time 1.5 ns. What is the peak amplitude and the halfwidth of the anode output pulse produced by a single photoelectron? What is the dc output current produced by 10^{-12} W cw radiation at $\lambda = 500\,\mathrm{nm}$, if the quantum efficiency of the cathode is $\eta = 0.2$ and the anode resistor $R = 10^6\,\Omega$? Estimate the necessary voltage amplification of a preamplifier (a) to produce 1 V pulses for single-photon counting; and (b) to read 1 V on a dc meter of the cw radiation?

31.2.2.2 Ex: Optical image intensifier

A manufacturer of a two-stage optical image intensifier states that incident intensities of 10^{-17} W at $\lambda = 500\,\mathrm{nm}$ can still be 'seen' on the phosphor screen of the output state. Estimate the minimum intensity amplification, if the quantum efficiency of the cathodes and the conversion efficiency of the phosphor screens are both 0.2 and the collection efficiency of light emitted by the phosphor screens is 0.1. The human eye needs at least 20 photons/s to observe a signal.

31.2.2.3 Ex: Photovoltaic detector

Estimate the maximum output voltage of an open photovoltaic detector at room temperature under 10 µW irradiation when the photocurrent of the shortened output is 50 µA and the dark current is 50 nA.

31.2.3 *Experiment: Taking the response function of a photodiode*

In this part of the lab course, we will learn to solder and set up simple electronic circuits. We will also learn how to identify the connections of a photodiode and mount into a case with BNC connectors. Finally, we will characterize the photodiode for use in future applications. Initially, we will work without offset voltage, later we will apply a voltage and identify its impact [1].

1. Connect an LED to a function generator and make it blink at low frequencies adjusting the offset and the amplitude of the output voltage. Shine the light onto your photodiode and monitor the signal on an oscilloscope. Explain your observations.

2. Reduce the amplitude and adjust the offset until you observe a sinusoidal signal. Increase the frequency and explain your observations. (Note that the response of LEDs is extremely fast (MHz).) Determine the bandwidth of your detector.

3. Measure the current at short circuit. Connect a $R = 10\,\mathrm{k\Omega}$ resistive load in parallel to the photodiode output and measure the voltage drop into this load.

4. Characterize the photodetector with respect to its sensitivity (in A/W) by varying the load.

5. How is the frequency response of the photodiode modified by the load? Measure bandwidth as a function of the load. Adjust the load until the detector (circuit including photodiode and resistor) has a bandwidth of 10 kHz (which is sufficient for many applications).

6. Apply a 10 V voltage in reverse direction and analyze again the sensitivity and the bandwidth of your photodetector. Note that the blinking LED can be replaced by a rotating chopper wheel.

Example of a measured characterization of a photodiode.

31.3 Introduction to radiofrequency components

31.3.1 VCOs and the generation of rf-sidebands

Voltage-controlled oscillators (*VCO*) serve to generate variable radiofrequencies. They are the basis for most function generators. A useful particularity of VCOs is the

[1] Datasheet for the Photodiode FFD100 see appendix Fig. 35.21,
data sheet for the Photodiode C30822E see appendix Fig. 35.22.

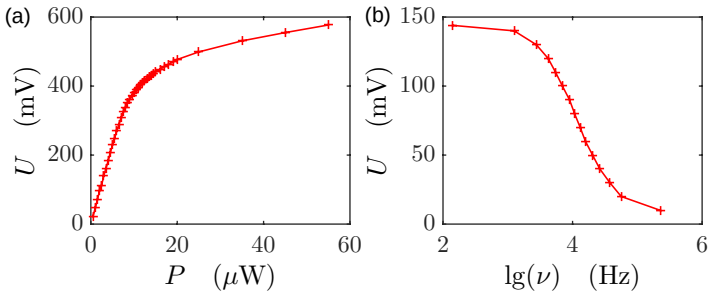

Figure 31.13: (a) Calibration of a photodiode, measured voltage as a function of the incident light power. (b) Low-pass behavior of a resistive charge of 90 kΩ.

possibility modulate the frequency and phase of an optical carrier wave by modulating the control voltage of a VCO at low frequency.

The modulation of the carrier wave generates sidebands. This can be seen by expanding the signal which carries the phase modulation into a Fourier series,

$$Ae^{\imath\omega t+\imath\beta\sin\Omega t} = Ae^{\imath\omega t}\sum_{k=-\infty}^{\infty} J_k(\beta)e^{\imath k\Omega t} \simeq Ae^{\imath\omega t} + J_1(\beta)Ae^{\imath\omega t+\imath\Omega t} + J_{-1}(\beta)Ae^{\imath\omega t-\imath\Omega t} \tag{31.10}$$

when the *modulation index* β is small. Here, $J_{-k}(\beta) = (-1)^k J_k(\beta)$ are the Bessel functions. This is in contrast to amplitude modulation, which is described by only two symmetric sidebands,

$$A(1+\beta\sin\Omega t)e^{\imath\omega t} = Ae^{\imath\omega t}\left(1+\frac{\beta}{2\imath}(e^{\imath\Omega t}-e^{-\imath\Omega t})\right) . \tag{31.11}$$

For *amplitude modulation* (*AM*) the beat signals between the carrier frequency and the two sidebands are in phase, i.e.,

$$\left|e^{\imath\omega t}+e^{\imath(\omega\pm\Omega)t}\right|^2 = 2+e^{\imath\Omega t}+e^{-\imath\Omega t} . \tag{31.12}$$

For *phase modulation* (*PM*) the beat signal are in counter-phase, i.e.,

$$\left|e^{\imath\omega t}+e^{\imath(\omega\pm\Omega)t+\imath\pi/2}\right|^2 = 2+\imath e^{\pm\imath\Omega t}-\imath e^{\mp\imath\Omega t} . \tag{31.13}$$

In the case of AM, the amplitude is blurred, but the phase at zero-crossing is well defined. In the case of PM, the amplitude in the antinode is sharp, but the phase of the zero-crossing is blurred.

It is not easy to transform AM into PM, and vice versa. In fact, the phase between carrier and sidebands can be varied, for example by adding an AC voltage, $\sqrt{2}e^{\imath\omega t+3\imath\pi/4}$ to the signal; however, it is not easy to transform synchronized phases into opposite phases.

As shown in Eq. (31.10), the spectrum of a signal with phase modulation (PM) consists of discrete lines, called sidebands, whose amplitudes are given by Bessel

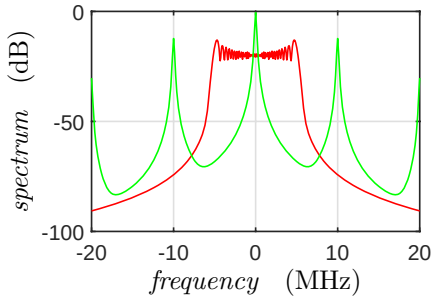

Figure 31.14: (code) Frequency spectra of a phase-modulated carrier frequency for $\Delta\omega = 5\,\mathrm{MHz}$ modulation excursion and (red) $\omega = 100$ kHz modulation frequency ($\beta = \frac{\Delta\omega}{\Omega} = 50$) and (green) $\omega = 10\,\mathrm{MHz}$ modulation frequency ($\beta = 0.5$). Furthermore, a $\gamma = 100\,\mathrm{kHz}$ resolution linewidth is assumed.

functions,

$$S(\omega) = \sum_{k=-\infty}^{\infty} |A\mathcal{J}_k(\beta)|^2 \delta(\omega + k\Omega) \ . \tag{31.14}$$

In real systems, the sidebands have finite widths γ due to frequency noise or the finite resolution of the detectors. In the case of Lorentzian line profiles, we have,

$$S(\omega) = \sum_{k=-\infty}^{\infty} |A\mathcal{J}_k(\beta)|^2 \frac{\beta^2}{(\omega - k\Omega)^2 + \beta^2} \ . \tag{31.15}$$

31.3.2 Mixers

A *frequency mixer* is a nonlinear electrical circuit that creates new frequencies from two input signals, e.g. the sum and difference of the input frequencies. A device that has a non-linear (e.g. exponential) characteristic can act as a mixer. Passive mixers use one or more diodes and rely on their non-linear relation between voltage and current. Active mixers use an amplifying device (such as a transistor) to increase the strength of the product signal.

Mixers may be classified by their topology: An unbalanced mixer, in addition to producing a product signal, allows both input signals to pass through and appear as components in the output. A single-balanced mixer is arranged with one of its inputs applied to a balanced (differential) circuit so that either the local oscillator (LO) or signal input (RF) is suppressed at the output, but not both. A double-balanced mixer has both its inputs applied to differential circuits, so that neither of the input signals and only the product signal appears at the output. Double balanced mixers are more complex and require higher drive levels than unbalanced and single-balanced designs.

In practice, mixers are widely used to shift signals from one frequency range to another, a process known as *heterodyning*, in order to facilitate signal transmission or further signal processing. Frequency mixers are also used to modulate a carrier signal in radio transmitters, as product detectors, phase detectors, or frequency multipliers.

31.3.2.1 Diode

The non-linearity (or non-Ohmic behavior) of a diode can be used to create a simple unbalanced mixer producing the original frequencies as well as their sum and their difference. The current I through an ideal diode as a function of the voltage U across it is given by an exponential function,

$$I = I_0(e^{qU/k_BT} - 1) \ . \tag{31.16}$$

The exponential can be expanded as $e^x - 1 \simeq x + \frac{x^2}{2}$. Suppose that the sum of the two input signals $U_1 + U_2$ is applied to a diode, and that an output voltage is generated that is proportional to the current through the diode [e.g. by providing the voltage that is present across a resistor in series with the diode, as shown in Fig. 31.15(a)]. Then, disregarding the constants in the diode equation, the output voltage will have the form,

$$\begin{aligned} U_0 &= (U_1 + U_2) + \tfrac{1}{2}(U_1 + U_2)^2 + ... \\ &= (U_1 + U_2) + \tfrac{1}{2}(U_1^2 + 2U_1U_2 + U_2^2) + ... \ . \end{aligned} \tag{31.17}$$

The ellipsis represents all the higher powers of the sum which we assume to be negligible for small signals.

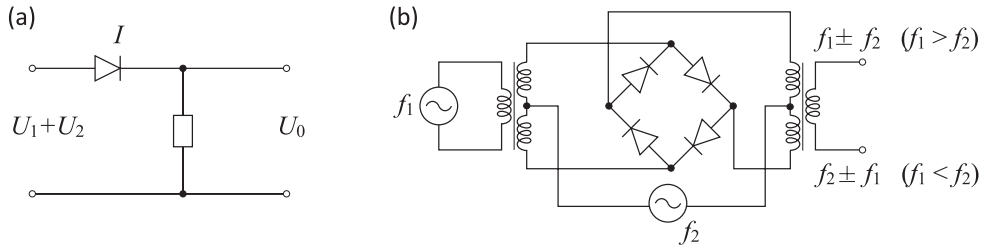

Figure 31.15: (a) Mixing two signal at a diode. (b) Schematic diagram of a double-balanced passive diode mixer (also known as a ring modulator). There is no output unless both f_1 and f_2 inputs are present, though f_2 (but not f_1) can be DC.

Suppose that two input sinusoids of different frequencies, $U_1 = \sin\omega_1 t$ and $U_2 = \sin\omega_2 t$ are fed into the diode. The signal U_0 becomes:

$$U_0 = (\sin\omega_1 t + \sin\omega_2 t) + \tfrac{1}{2}(\sin^2\omega_1 t + 2\sin\omega_1 t \sin\omega_2 t + \sin^2\omega_2 t) + ... \ . \tag{31.18}$$

Ignoring all terms except for the $\sin\omega_1 t \sin\omega_2 t$ term we get,

$$U_0 = 2\sin\omega_1 t \sin\omega_2 t + ... = \cos(\omega_1 t - \omega_2 t) - \cos(\omega_1 t + \omega_2 t) + ... \ , \tag{31.19}$$

demonstrating how new frequencies are created from the mixer.

31.3.2.2 Switching

Another form of mixer operates by switching, with the smaller input signal being passed inverted or non-inverted according to the phase of the local oscillator (LO).

This would be typical of the normal operating mode of a packaged double balanced mixer, with the local oscillator drive considerably higher than the signal amplitude.

The aim of a switching mixer is to achieve linear operation over the signal level by means of hard switching, driven by the local oscillator. Mathematically, the switching mixer is not much different from a multiplying mixer. Instead of the LO sine wave term, we would use the signum function. In the frequency domain, the switching mixer operation leads to the usual sum and difference frequencies, but also to further terms, e.g. $\pm 3f_{LO}$, $\pm 5f_{LO}$, etc.. The advantage of a switching mixer is that it can achieve (with the same effort) a lower noise figure and larger conversion gain. This is because the switching diodes or transistors act either like a small resistor (switch closed) or large resistor (switch open), and in both cases only a minimal noise is added. From the circuit perspective, many multiplying mixers can be used as switching mixers, just by increasing the LO amplitude.

31.3.2.3 Modulation and demodulation

Mixers are often used for modulation or demodulation purposes. Suppose we have on one hand a *carrier* signal, $U_{carrier} = \cos \omega t$, also called *local oscillator*. This may be a constant radiofrequency emitted by an antenna or a microwave. On the other hand, we have a reference signal which we want to transport somewhere else, $U_{ref} = \cos \Omega t$. Used as a modulator the mixer will simple multiply,

$$U_{mod} = U_{carrier} U_{ref} = \cos \omega t \cos \Omega t = \tfrac{1}{2} \cos[(\omega - \Omega)t] + \tfrac{1}{2} \cos[\omega + \Omega)t] \ . \quad (31.20)$$

Thus the mixer output contains two frequencies, the sum and the difference. Supposing that ω is a frequency in a range that can be radiated by antenna and Ω an acoustic frequency, both frequency components $\omega \pm \Omega \simeq \omega$ will be radiated.

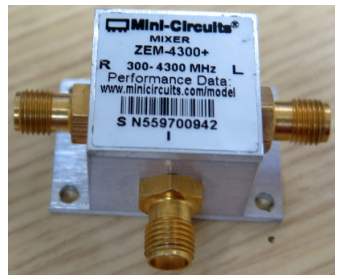

Figure 31.16: Picture of a radiofrequency mixer.

On the side of the receiver, who also has access to a synthesizer generating a signal $U_{carrier} = \cos \omega t$, we will use the mixer as a demodulator,

$$U_{demod} = U_{carrier} U_{mod} = \cos^2 \omega t \cos \Omega t = \tfrac{1}{2}(\cos 2\omega t + 1) \cos \Omega t \ . \quad (31.21)$$

If $\omega \gg \Omega$, the carrier oscillation can easily be removed by a low-pass filter,

$$U_{filtered} = \tfrac{1}{2} \cos \Omega t \propto U_{ref} \ . \quad (31.22)$$

That is, we recover the original information. And this holds even when the reference signal is (slowly) varying in amplitude or frequency, such as in the case of an acoustic signal [2]. Resolve Exc. 31.3.3.1.

31.3.2.4 Filtering with a mixer

Suppose we have a signal containing many frequency components (which may vary slowly in time), $U_{noisy}(t) = \sum_n A(\omega_n)e^{\imath\omega_n t}$ in complex notation, and that the signal we are interested in is an amplitude at a known particular frequency ω_0. By demodulating,

$$U_{sig}(t) = U_{noisy}(t)e^{-\imath\omega_0 t} = \sum_n A(\omega_n)e^{\imath\omega_n t}e^{-\imath\omega_0 t} = \sum_n A(\omega_n)e^{\imath(\omega_n-\omega_0)t} \ , \quad (31.23)$$

and low-pass filtering the lowest frequency component, i.e. $\omega_n - \omega_0 \simeq 0$,

$$U_{filtered} = A(\omega_0) \ . \quad (31.24)$$

This even holds for continuous noise spectra, $U_{noisy}(t) = \int A(\omega)e^{\imath\omega t}d\omega$, since,

$$U_{sig}(t) = U_{noisy}(t)e^{-\imath\omega_0 t} = \int_{-\infty}^{\infty} A(\omega)e^{\imath\omega t}e^{-\imath\omega_0 t}d\omega = \int_{-\infty}^{\infty} A(\omega+\omega_0)e^{\imath\omega t}d\omega \ , \quad (31.25)$$

and low-pass filtering with a filter bandwidth $\Delta\omega$,

$$U_{filtered} = \int_{-\Delta\omega}^{\Delta\omega} A(\omega+\omega_0)e^{\imath\omega t}d\omega \simeq A(\omega_0)2\Delta\omega \ . \quad (31.26)$$

Such techniques are widely used in lock-in amplifiers (see Sec. 31.4.3).

31.3.3 Exercises

31.3.3.1 Ex: Phase modulation

a. Show that it is not possible to construct a periodic phase modulation function such that the signal has only two sidebands.
b. Compare the spectra $\sum_{k=-\infty}^{\infty} J_k(M)e^{\imath k\Omega t} = e^{\imath M\sin\Omega t}$ and $\sum_{k=-\infty}^{\infty} |J_k(M)|e^{\imath k\Omega t}$. Can you detect phase modulation of a photodetector signal on a spectrum analyzer? How about amplitude modulation?

31.3.4 *Experiment: Creating sidebands on a radiofrequency*

In this exercise, we will understand the origin of sidebands as we'll see them emerge from a modulation spectrum when we gradually increase the modulation index [3].

1. Take a VCO, for example, ZOS-100+ from MiniCircuits. Study the datasheet and drive the VCO with an AC voltage. Vary the amplitude and the frequency of the voltage and observe the output signal of the VCO on a spectrum analyzer.

[2] In complex notation, $U_{in} = e^{\imath\omega t}$, $U_{mod} = U_{in}e^{\imath\Omega t} = e^{\imath(\omega+\Omega)t}$, $U_{demod} = U_{mod}e^{-\imath\omega t} = e^{\imath\Omega t}$.
[3] Datasheet for the VCO see appendix Fig. 35.16,
data sheet for the variable attenuator see appendix Fig. 35.17,
data sheet for the mixer see appendix data sheet Fig. 35.19.

2. Try to understand the spectrum observing the limiting cases $\Omega \gg \Delta\omega$ and $\Omega \ll \Delta\omega$. How can you read Ω and Δf from the spectra in both cases?

3. Write a MATLAB program to simulate the spectrum.

31.4 Measurement instrumentation

31.4.1 Sample-and-hold circuit

sample-and-hold circuit Solder on euroboard

31.4.2 Box-car integrator

box-car integrator Solder on euroboard

31.4.3 Lock-in amplifier

An *lock-in amplifier* (also called a phase-sensitive rectifier or *mixer*) is an amplifier that can measure a weak electrical signal by modulating the signal by a reference signal with a known frequency and phase. The device represents a bandpass filter with an extremely narrow bandwidth and, therefore, improves the signal-to-noise ratio (SNR). DC or AC noise components are efficiently filtered.

Download an illustration of the working principle of a *lock-in amplifier* here.

31.4.4 *Experiment: Building a lock-in amplifier*

Let's now build a lock-in amplifier. The principle is illustrated in Fig. 31.17(a). The sinusoidal signal discriminated at a non-linear line is switched on and off in the lock-in by a switch. At the same time, the inverted signal (i.e., phase shifted by 180°) is turned off and on. Both signals are combined and low-pass filtered. As Fig. 31.17(b) shows, the sign of the filtered signal depends on the phase between the discriminator and the TTL signal controlling the switch [4]

1. Create the circuit sketched in Fig. 31.17(a) on a circuit board and test it by varying the phase between the modulated output signal and the TTL signal provided by a function generator.

31.5 Further reading

P. Horowitz et al., *The art of electronics* [DOI]

U. Tietze et al., *Halbleiterschaltungstechnik* [DOI]

[4] Datasheets for the operational amplifier see appendix Fig. 35.24, data sheet for the switch see appendix Fig. 35.23.

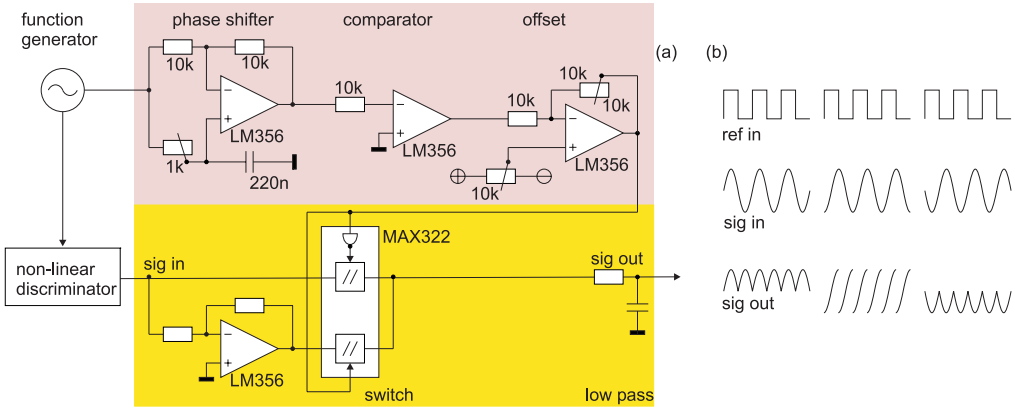

Figure 31.17: (a) Principal scheme of a lock-in amplifier. (b) Mode of operation.

Chapter 32

Quantum optics and optical interferometry

The objective of this chapter is to introduce the basics of optical *interferometry*. We will see, how to match the light modes in optical cavities and fibers, and to phase-match the wavefronts of two laser beams in order to detect their frequency beating with a photodetector. Furthermore, he will learn how to handle essential tools of *quantum electronics*, such as a piezo-electric transducer, an electro-optic modulator, and an acousto-optic modulator, used in interferometry, as discussed in Secs. 32.4.1 to 32.4. Interferometers have versatile applications such as 1. for the detection of very small length variations (as for example caused by gravitational waves), 2. as vibration and inertial sensors, or in 3. the transmission of information (radio).

32.1 Introduction to interferometry

32.1.1 Beam splitter in $\mathcal{S}$-representation

The essential component of any interferometer is the (non-polarizing) *beam splitter*.

We consider a classical lossless beam splitter with electric fields incident at both its inputs. The two output fields E_c and E_d are linearly related to the inputs through

$$\begin{pmatrix} \mathcal{E}_c \\ \mathcal{E}_d \end{pmatrix} = \begin{pmatrix} t_{ac} & r_{bc} \\ r_{ad} & t_{bd} \end{pmatrix} \begin{pmatrix} \mathcal{E}_a \\ \mathcal{E}_b \end{pmatrix} \ , \tag{32.1}$$

where the 2×2 element is the beam splitter matrix. r and t are the reflectance and transmittance along a particular path through the beam splitter, that path being indicated by the subscripts.

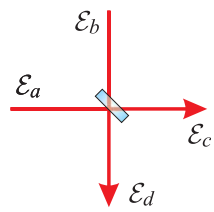

Figure 32.1: Beam splitter.

Assuming the beam splitter removes no energy from the light beams, the total output energy can be equated with the total input energy, reading

$$|\mathcal{E}_c|^2 + |\mathcal{E}_d|^2 = |t_{ac}\mathcal{E}_a + r_{bc}\mathcal{E}_b|^2 + |r_{ad}\mathcal{E}_a + t_{bd}\mathcal{E}_b|^2 = |\mathcal{E}_a|^2 + |\mathcal{E}_b|^2 \ . \tag{32.2}$$

Factorizing the expression in the center we obtain terms in $|\mathcal{E}_a|^2$, $|\mathcal{E}_b|^2$, $|\mathcal{E}_a\mathcal{E}_b^*|$, and $|\mathcal{E}_a^*\mathcal{E}_b|^2$. Comparing with the terms in the right-hand side expression we find that the equation can only be true for any field amplitudes, if the following relationships between reflectance and transmittance are satisfied,

$$\boxed{|t_{ac}|^2 + |r_{ad}|^2 = 1 = |t_{bd}|^2 + |r_{bc}|^2 \quad \text{and} \quad t_{ac}r_{bc}^* + r_{ad}t_{bd}^* = 0} \ . \tag{32.3}$$

We write each r and t as a complex number having an amplitude and phase factor accounting for possible phase shifts of a beam as it reflects or transmits at the beam splitting surface. From the second equation (32.3) we obtain,

$$t_{ac}r_{bc}^* + t_{bd}^*r_{ad} = |t_{ac}||r_{bc}|e^{\imath(\phi_{ac}-\phi_{bc})} + |t_{bd}||r_{ad}|e^{\imath(\phi_{ad}-\phi_{bd})} = 0 \ . \tag{32.4}$$

This expression can only be true if,

$$\phi_{ad} - \phi_{bd} + \phi_{bc} - \phi_{ac} = \pi \qquad \text{and} \qquad \frac{|r_{bc}|}{|t_{bd}|} = \frac{|r_{ad}|}{|t_{ac}|} \ . \tag{32.5}$$

Comparing the second equation (32.5) with the first two equations (32.3) we conclude,

$$|r_{ac}| = |r_{bd}| \equiv \sqrt{R} \qquad \text{and} \qquad |t_{ad}| = |t_{bc}| \equiv \sqrt{T} \ , \tag{32.6}$$

where we defined the reflection and the transmission of the beam splitter. It follows that

$$\boxed{R + T = 1} \ . \tag{32.7}$$

Without loss of generality, we may set $\phi_{bd} \equiv 0$, so that $\phi_{ac} = \phi_{ad} - \phi_{bc} - \pi$. Then,

$$\mathcal{S} = \begin{pmatrix} t_{ac} & r_{bc} \\ r_{ad} & t_{bd} \end{pmatrix} = \begin{pmatrix} -\sqrt{T}e^{\imath(\phi_{ad}-\phi_{bc})} & \sqrt{R}e^{\imath\phi_{bc}} \\ \sqrt{R}e^{\imath\phi_{ad}} & \sqrt{T} \end{pmatrix} \ . \tag{32.8}$$

Until, now the calculations were totally general, so that the above results hold for any type of beam splitting device. Let us now give a concrete example.

Example 204 (*Beam splitters*): For beam splitting at dielectric interfaces in particular we know that the electric field amplitude does not suffer phase shifts upon transmission, $\phi_{ac} \equiv 0$, implying $\phi_{ad} - \phi_{bc} = \pi$. Hence,

$$\mathcal{S} = \begin{pmatrix} \sqrt{T} & \sqrt{R}e^{\imath\phi_{bc}} \\ \sqrt{R}e^{\imath(\phi_{bc}+\pi)} & \sqrt{T} \end{pmatrix} \ . \tag{32.9}$$

Thus, the two off-diagonal elements are 180° out of phase. For the situation depicted in Fig. 32.1 one of the reflections occurs at an optical more dilute medium. For this reflection the phase shift is 0. But the other reflection occurs at an optical denser medium and therefore suffers a 180° phase shift. With this constraints the matrix describing a lossless beam splitter reads,

$$\boxed{\begin{pmatrix} \mathcal{E}_c \\ \mathcal{E}_d \end{pmatrix} = \begin{pmatrix} \sqrt{T} & \sqrt{R} \\ -\sqrt{R} & \sqrt{T} \end{pmatrix} \begin{pmatrix} \mathcal{E}_a \\ \mathcal{E}_b \end{pmatrix}} \ . \tag{32.10}$$

32.1.2 Piezo-electric actuator

The piezo-electricity effect describes the reciprocal action between mechanical pressure (from Greek: piézein - press) and electrical voltage in solids. It is based on the phenomenon that occurs in the regular deformation of certain piezoelectric materials: at the surface occur displacements of electric charges creating microscopic dipoles inside the unit cells. The sum over all the unit cells of the crystal leads to a macroscopically measurable electrical voltage. The deformation should be directed, which means, that the pressure is not applied from all sides on the crystal, but for example only on opposite sides.

On the other hand, by applying an electric voltage, a crystal (or piezo-ceramic element) may be deformed. Like any other solid body, piezo-electric crystals can execute mechanical vibrations. In a *piezo-electric actuator* (or piezo transducer PZT), these vibrations can be electrically excited. The frequency of the vibrations depend only on the speed of sound (which is a constant of the material) and the dimensions of the actuator. Therefore, actuators are also suitable for realizing oscillators (for example, quartz crystals). The piezo-electric effect can only occur in non-conductive materials (e.g., lead titanate zirconate).

When a voltage is applied to the piezo-ceramic in the direction of polarization, we observe an expansion in this direction and a perpendicular contraction. Depending on the employed material and the coefficient for piezo-electric strain d, stretches up to $\Delta l/l = 0.15\%$ can be obtained:

$$\Delta l = d\mathcal{E} l_0 \ , \tag{32.11}$$

where l_0 is the length of the actuator and $E = U/l_0$ the amplitude of the electric field. The elongation effect is therefore proportional to the field strength and the overall length of the actuator. To achieve large stretches with manageable electrical voltages, actuator discs are often stacked (mechanical circuit in series and electric circuit in parallel).

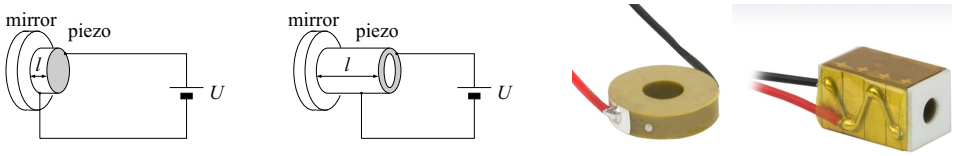

Figure 32.2: (Left) Scheme of mirrors mounted on a piezo actuator having the shape of a disc or a ring. (Right) Photos of a ring piezo and a piezo stack.

Negative voltages with respect to the orientation of the discs cause a contraction. However, negative voltages can also cause a change in the polarization state of the piezo and should therefore be avoided! In electrical circuits, piezoelectric actuators introduce a capacitance with a relative dielectric constant between 600 and 5000 and an internal resistance of about $10^8\ \Omega$ depending on the material. See Exc. 32.1.10.1.

32.1.3 Michelson and Mach-Zehnder interferometer

Interferometry is a technique exploiting the interference of waves coherently split and recombined by beam splitters. Sufficiently stable interferometers allow to visualize

variations of the path lengths of two or more partial waves following different pathways as an alteration of constructive and destructive interference.

The two most common types of interferometers are the *Michelson interferometer* and the *Mach-Zehnder interferometer* are depicted in Fig. 32.3. The advantages of the Michelson interferometer are an easy alignment and the need of only one beamsplitter. The advantage of the Mach-Zehnder interferometer is a direct optical access to both output ports of the interferometer. The following treatment applies to both types.

The field amplitude of a laser beam, $\mathcal{E}_i$, with frequency, $\omega = ck$, is divided by a beam splitter (reflectivity $\sqrt{R}$) into a transmitted $\mathcal{E}_t$ and a reflected beam $\mathcal{E}_r$,

$$\mathcal{E}_r = \sqrt{R_1}\mathcal{E}_i \qquad \text{and} \qquad \mathcal{E}_t = \sqrt{1-R_1}\mathcal{E}_i \ , \tag{32.12}$$

where we disregard possible phase-shifts upon reflection at optically dilute interface. The energy is obviously conserved, $|\mathcal{E}_r|^2 + |\mathcal{E}_t|^2 = \mathcal{E}_i^2$.

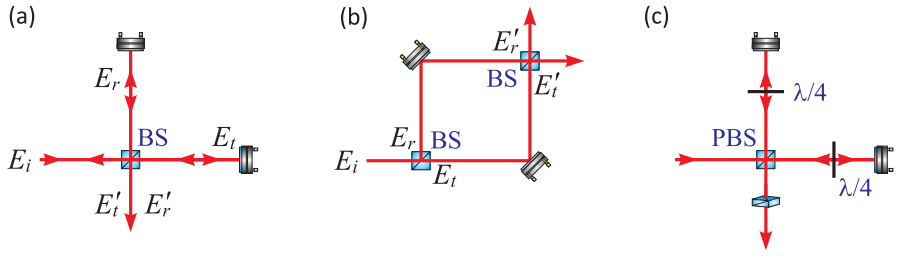

Figure 32.3: Principle of a two-beam interferometer: (a) Michelson interferometer and (b) Mach-Zehnder interferometer using non-polarizing beamsplitters. (c) Michelson interferometer using a polarizing beamsplitter.

We consider the Mach-Zehnder interferometer sketched in Fig. 32.3 with one arm of length L_r, which can be varied by a piezo, and the other arm of length L_t,

$$\mathcal{E}_r' = \mathcal{E}_r e^{2\imath k L_r} \qquad \text{and} \qquad \mathcal{E}_t' = \mathcal{E}_t e^{2\imath k L_t} \ . \tag{32.13}$$

The beams are recombined on a second beam splitter and sent to a photodetector, whose signal is,

$$\begin{aligned} I &\propto |\sqrt{R_2}\mathcal{E}_r' + \sqrt{1-R_2}\mathcal{E}_t'|^2 \\ &= |\sqrt{R_2}\sqrt{R_1}e^{2\imath k L_r} + \sqrt{1-R_2}\sqrt{1-R_1}e^{2\imath k L_t}|^2 \mathcal{E}_i^2 \ . \end{aligned} \tag{32.14}$$

Hence,

$$I \propto R_2 R_1 + (1-R_2)(1-R_1) + 2\sqrt{R_2}\sqrt{R_1}\sqrt{1-R_2}\sqrt{1-R_1}\cos[2k(L_t - L_r)] \ . \tag{32.15}$$

For reflectivities of $R_1 = R_2 = 50\%$, we get,

$$\boxed{I \propto \tfrac{1}{2} + \tfrac{1}{2}\cos[2k(L_t - L_r)]} \ . \tag{32.16}$$

It is important to realize that, while superpositions of light field amplitudes in the same mode interfere, *superpositions of light field amplitudes in different modes*

do not. For example, the superposition of two plane waves with equal frequency and polarization interferes,

$$\left|\begin{pmatrix}\mathcal{E}_1+\mathcal{E}_2\\0\end{pmatrix}\right|^2 = |\mathcal{E}_1+\mathcal{E}_2|^2 \ , \tag{32.17}$$

while the superposition of two plane waves with equal frequency but different polarizations does not,

$$\left|\begin{pmatrix}\mathcal{E}_1\\0\end{pmatrix}+\begin{pmatrix}0\\\mathcal{E}_2\end{pmatrix}\right|^2 = |\mathcal{E}_1|^2+|\mathcal{E}_2|^2 \ . \tag{32.18}$$

Solve the Excs. 32.1.10.2 to 32.1.10.4.

32.1.4 Coherence and spectrum of a light field

We have seen above that interferometers probe the electric field amplitude rather than the intensity. For this reason, they are suited to measure the first-order correlation function $g^{(1)}(\tau)$ and the emission spectrum, which are defined by,

$$g^{(1)}(\tau) \equiv \frac{\langle \mathcal{E}^-(t)\mathcal{E}^+(t+\tau)\rangle}{\langle \mathcal{E}^-(t)\mathcal{E}^+(t)\rangle} \qquad \text{and} \qquad S_{\mathcal{E}}(\omega) \equiv \mathcal{F}[g^{(1)}(\tau)] \ . \tag{32.19}$$

As an example, Fig. 32.4 shows the aurocorrelation function and spectrum of a simultaneously amplitude- and phase-modulated laser beam, $\mathcal{E}(t) = (1+n\cos\omega_n t)e^{\imath m \sin\omega_m t}$.

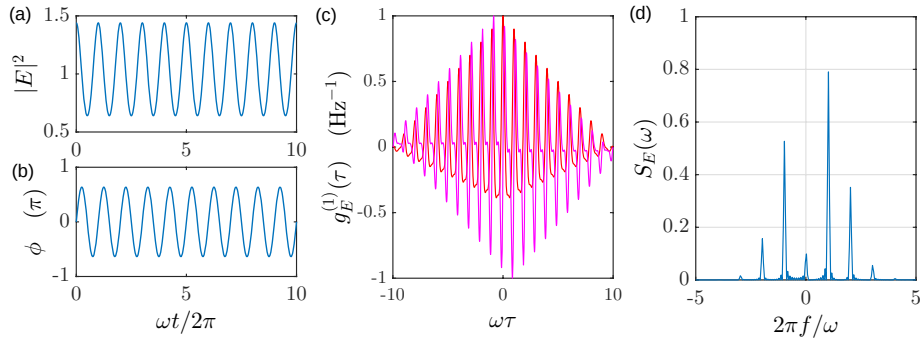

Figure 32.4: (code) (a) Amplitude and (b) phase of the electric field, with $n = 0.2$, $m = 1$, and $\omega_n = \omega_m = (2\pi)\ 1\,\mathrm{Hz}$. (c) Aurocorrelation function and (d) spectrum of the light field.

32.1.5 Birefringent interferometer

A *birefringent interferometer* or *Lyot filter* consists of one or more birefringent crystals mounted onto a rotation frame between two polarizers. Let n_o and $n_e = n_o + \Delta n$ be the refractive indices of the normal and the extraordinary axis, respectively. The corresponding Jones matrix is then,

$$\mathcal{M} = \begin{pmatrix}1&0\\0&0\end{pmatrix}\begin{pmatrix}\cos\phi&\sin\phi\\-\sin\phi&\cos\phi\end{pmatrix}\begin{pmatrix}e^{\imath k_0 L}&0\\0&e^{\imath k_e L}\end{pmatrix}\begin{pmatrix}\cos\phi&-\sin\phi\\\sin\phi&\cos\phi\end{pmatrix}\begin{pmatrix}1&0\\0&0\end{pmatrix} \ , \tag{32.20}$$

Such that,

$$\begin{pmatrix} \mathcal{E}_{out} \\ 0 \end{pmatrix} = \mathcal{M} \begin{pmatrix} \mathcal{E}_{in} \\ 0 \end{pmatrix} = \begin{pmatrix} \left(e^{\imath k_0 L} \cos^2 \phi + e^{\imath k_e L} \sin^2 \phi \right) \mathcal{E}_{in} \\ 0 \end{pmatrix} . \tag{32.21}$$

By trigonometric transformations it is possible to show, that the transmission $T \equiv |\mathcal{E}_{out}/\mathcal{E}_{in}|^2$ is,

$$\boxed{T(\lambda, \phi) = |e^{\imath k_0 L} \cos^2 \phi + e^{\imath k_e L} \sin^2 \phi|^2 = 1 - \sin^2 2\phi \sin^2 \tfrac{\pi L \Delta n}{\lambda}} . \tag{32.22}$$

For $\phi = 45°$ the transmission becomes simply,

$$T(\lambda, \tfrac{\pi}{4}) = \cos^2 \tfrac{\pi L \Delta n}{\lambda} . \tag{32.23}$$

In practice Lyot filters are often used, placed under the Brewster angle inside ring cavity lasers, as frequency selective elements. Frequently, birefringent plates of different thicknesses are stacked,

$$T(\lambda) = T_1(\lambda) T_2(\lambda) , \tag{32.24}$$

in order to increase the frequency selectivity. Furthermore, when the axis of the birefringent plates are rotated by fixed angles $\Delta\alpha$ with respect to each other,

$$T(\lambda, \alpha) = T_1(\lambda, \alpha) T_2(\lambda, \alpha + \Delta\alpha) , \tag{32.25}$$

the frequency of maximum transmission can be tuned by simply rotating the stack as a whole by an angle α. See 32.1.10.5.

A Lyot filter can be considered an interferometer, because it splits and recombines the polarization vector of a light beam in two parts following the ordinary and the extraordinary axis of the birefringent crystal. This is somewhat analogous to the Michelson interferometer depicted in Fig. 32.3(c).

32.1.6 Optical resonators

Optical cavities consist of an arrangement of mirrors reflecting the light beams in such a way, that they form a closed path. Since light that entered the cavity is performing there many round trips before it is transmitted again or absorbed, the light power is considerably enhanced, i.e. cavities can store light.

Light which is to resonate in the cavity must satisfy the boundary condition, that the mirror surfaces coincide with standing wave nodes. Therefore, in a cavity with length L only a discrete spectrum of wavelengths $N\frac{\lambda}{2} = L$ can be resonantly amplified, where N is a natural number. Because of this property, cavity are often used as frequency filters or optical spectrum analyzers: Only frequencies $\nu = N\delta_{fsr}$ are transmitted, where

$$\boxed{\delta_{fsr} = c/2L} \tag{32.26}$$

is the free spectral range of the cavity.

Cavities are characterized on one hand by their geometry, i.e. the curvature and the distance of their mirrors, and on the other hand by their finesse, which is given by the reflectivity of their mirrors. Let us first study the finesse. Regarding the cavity

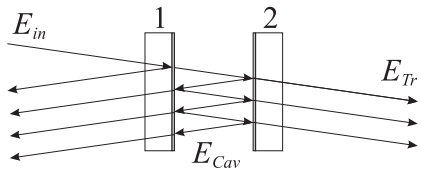

Figure 32.5: Multiple interference in an optical cavity.

as a multipass interferometer [218], we can derive expressions for the reflected and transmitted intensity as a function of frequency [1]. The so-called *Airy formula* for transmission and reflection are,

$$\frac{\mathcal{E}_{refl}}{\mathcal{E}_{in}} = r_1 - \frac{t_1^2 r_2 e^{2\imath kL}}{1 - r_1 r_2 e^{2\imath kL}} \qquad \text{and} \qquad \frac{\mathcal{E}_{trns}}{\mathcal{E}_{in}} = \frac{t_1 t_2 e^{\imath kL}}{1 - r_1 r_2 e^{2\imath kL}} \ . \tag{32.27}$$

In terms of intensity, assuming identical mirrors, $r_1 = r_2 = \sqrt{R}$ and $t_1 = t_2 = \sqrt{T}$, and neglecting possible absorptive losses, $A = 1 - R - T = 0$,

$$\boxed{\frac{I_{refl}}{I_{in}} = \frac{(\frac{2F}{\pi})^2 \sin^2 \frac{\Delta}{2\delta_{fsr}}}{1 + (\frac{2F}{\pi})^2 \sin^2 \frac{\Delta}{2\delta_{fsr}}} \qquad \text{and} \qquad \frac{I_{trns}}{I_{in}} = \frac{1}{1 + (\frac{2F}{\pi})^2 \sin^2 \frac{\Delta}{2\delta_{fsr}}}} \ , \tag{32.28}$$

where R is the reflectivity of a mirror and $\delta = 4\pi L/\lambda = 2\pi\nu/\delta_{fsr}$. The transmission curve of a cavity has a finite transmission bandwidth $\Delta\nu$, which depends on the reflectivity of the mirrors. The finesse of a cavity is defined by

$$\boxed{F \equiv \frac{2\pi\delta_{fsr}}{\kappa} = \frac{\pi\sqrt{R}}{1-R}} \ . \tag{32.29}$$

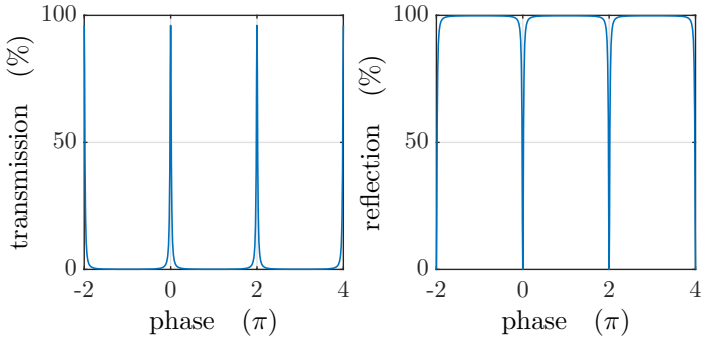

Figure 32.6: (code) Transmission and reflection through a resonator.

Note that factors others than the finite reflectivity may degrade the finesse of a cavity. For example, an imperfect mirror flatness (commonly specified as λ/F_{surf})

[1] See script on *Electrodynamics: Electricity, Magnetism and Radiation* (2025), Exc. 7.3.6.16.

reduces the finesse to [218],

$$F_{tot} = \left(\frac{1}{F} + \frac{1}{F_{surf}} \right)^{-1} . \tag{32.30}$$

.

The geometry of a cavity must satisfy certain conditions, in order to be stable [474]. Besides the main longitudinal modes a cavity possesses transverse modes of the order TEM_{mn}, whose frequencies are given by [2],

$$\nu/\delta_{fsr} = (q+1) + \frac{m+n+1}{\pi} \arccos \sqrt{\left(1 - \frac{L}{\rho_1}\right)\left(1 - \frac{L}{\rho_2}\right)} . \tag{32.31}$$

A *confocal cavity* with degenerate transverse modes, $\rho_1 = \rho_2 = L$, is particularly suited as optical spectrum analyzer.

The diameter of the beam waist in the cavity is,

$$w_0 = \sqrt[4]{\left(\frac{\lambda}{\pi}\right)^2 \frac{L(\rho_1 - L)(\rho_2 - L)(\rho_1 + \rho_2 - L)}{(\rho_1 + \rho_2 - 2L)^2}} . \tag{32.32}$$

For an optimal coupling of the light into the cavity the Gaussian laser beam must be matched to the cavity's geometry of the cavity, i.e. diameter and divergence of the laser beam must be adapted to the cavity mode with a suitable arrangement of lenses [219, 474]. See Excs. 32.1.10.6 to 32.1.10.11.

32.1.7 Dielectric mirrors and filters

Dielectric mirrors and filters are multiple beam interferometers in a similar sense as Fabry-Pérot cavities. They consist of stacks of thin dielectric layers with alternating refraction indices [3].

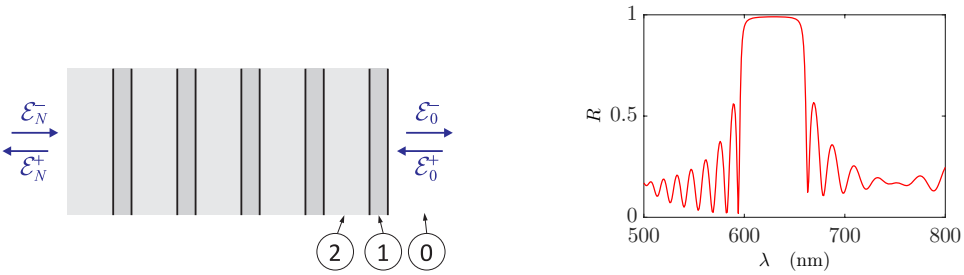

Figure 32.7: (code) Reflection by a high reflecting mirror made of 10 layers with $n_1 = 2.4$ and $\Delta z_1 = 80\,\mathrm{nm}$ alternating with 10 layers with $n_2 = 1.5$ and $\Delta z_2 = 500\,\mathrm{nm}$. The absorption coefficient for each layer is supposed to be $\alpha = 0.2\%$. The beam impinges from vacuum, $n_0 = 1$.

Reflections of $R = 99.999\%$ can be reached which, applied of superpolished mirrors, allow for the construction of cavities with finesse $F > 300000$. On the other

[2] See script on *Electrodynamics: Electricity, Magnetism and Radiation* (2025), Sec. 7.4.2.2.
[3] See script on *Electrodynamics: Electricity, Magnetism and Radiation* (2025), Sec. 7.1.7.

anti-reflection coatings can be applied to surfaces reducing their reflections to below $R = 0.1\%$. See Excs. 32.1.10.12 and 32.1.10.13 [219, 518].

32.1.8 Optical fibers

An *optical fiber* is a waveguide in which light is guided by internal total reflection. The total reflection occurs between layers with different refractive indices called *fiber core* and *fiber cladding*. The core is the central region of the optical fiber where the light is guided. In order to create guiding conditions, the refractive index of the core must be higher than the one of the cladding. The cladding diameter is typically 8 to 10 times the *mode field diameter* (MFD) of the fundamental mode. In general, MFD is greater than the physical diameter of the fiber core, which means that some optical power is always guided by the fiber cladding as an evanescent wave.

The *cut-off wavelength* λ_{co} of an optical fiber is the wavelength above which a guided mode of a waveguide ceases to exist. For wavelength longer than λ_{co} an optical fiber becomes single-mode. At wavelengths shorter than λ_{co} several optical modes may propagate and the fiber becomes multi-mode. The cut-off wavelength is directly related to the core diameter of the fiber $\lambda_{co} \propto \emptyset$. For

$$\frac{\lambda}{2} < \emptyset < \lambda \qquad \text{or equivalently} \qquad \emptyset < \lambda < 2\emptyset \tag{32.33}$$

the fiber is single-mode. For $\lambda > 2\emptyset$ no guided mode exists and for $\emptyset > \lambda$ the fiber becomes multimode.

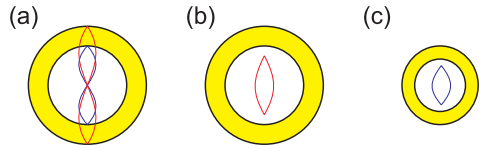

Figure 32.8: Mono-mode waveguiding by optical fibers.

The *numerical aperture* is a measure of the acceptance angle of the fiber. It is very important because it determines how strongly a fiber guides light, and so how resistant it is to bend-induced losses. The numerical aperture can be defined by the acceptance angle of the fiber, though as this is highly diverging in space it is rather complicated to reach a simple definition. It is most convenient to define the NA in terms of the relative indices of core and cladding glass forming the fiber waveguide:

$$NA = \sin\tfrac{\theta_a}{2} = \sqrt{n_{core}^2 - n_{clad}^2} \simeq \sqrt{2n_{core}^2 \delta n}\ , \tag{32.34}$$

where δn is the index difference between the core and cladding. An optical fiber with 'high' numerical aperture will confine light more strongly in the core, and so support guidance further above cut-off. This attribute has two important effects: (a) it will be single-mode over a greater range of wavelengths than is possible with a fiber with a 'low' numerical aperture fiber and (b) it will still guide a single-mode when coiled or bent to a smaller diameter.

32.1.8.1 Multi-mode, mono-mode, and polarization maintaining fibers

Many types of fibers are currently available for a large variety of applications.

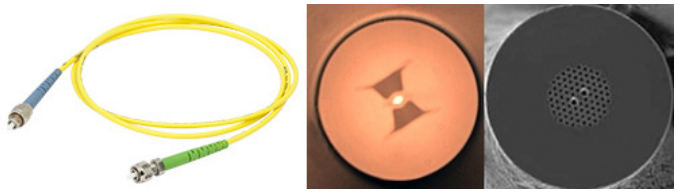

Figure 32.9: (Left) Fiber patch cord, (center) cross section of a bow-tie polarization maintaining fiber, and (right) cross section of a photonic crystal fiber.

32.1.9 Laser gyroscope and the Sagnac effect

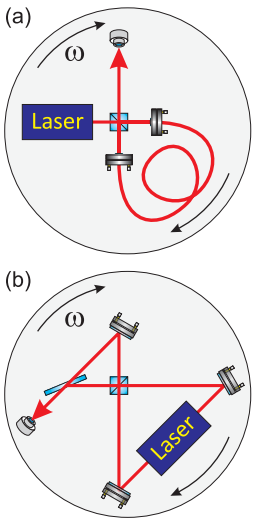

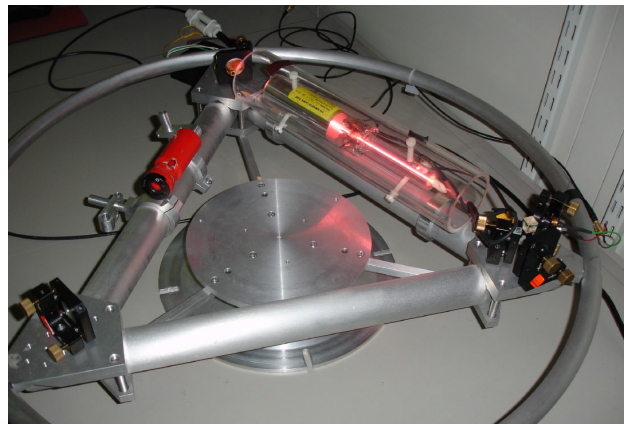

Figure 32.10: (a) Principle scheme of a fiber-based Sagnac interferometer. (b,c) Laser gyroscope realized with a HeNe gain tube.

Gyroscopes are based on the *Sagnac effect*. They are based on a ring cavity mounted on a rotating stage, as shown in Fig. 32.10(a). Let us, for simplicity first consider a circular path for the light beam (e.g. a fiber-based ring cavity) rotating at an angular velocity Ω. Then the time needed for the light beam to travel in either one of the two directions is,

$$t_\pm = \frac{(2\pi \pm \Omega t_\pm)r}{c} = \frac{2\pi r}{c \mp \Omega r} \ , \tag{32.35}$$

that is,

$$\Delta t \equiv t_+ - t_- = \frac{4\pi r^2 \Omega}{c^2 - \Omega^2 r^2} \simeq \frac{4\pi r^2 \Omega}{c^2} \equiv \frac{4A\Omega}{c^2} \ , \tag{32.36}$$

where A is the area enclosed by the path. This formula can be generalized to arbitrary paths.

For example, assuming an interferometer with $A = 1\,\mathrm{m}^2$ at rest in an Earth-based system, $\Omega \simeq 2\pi/24\,\mathrm{h}$, the time difference for light propagating along the two directions

is $\Delta t \approx 3 \cdot 10^{-21}$ s and the path difference $\Delta L = c\Delta t \approx 100$ fm. The frequency shift is,

$$\boxed{\Delta v = k(v_+ - v_-) = k(2\Omega r) = \frac{\sqrt{4\pi A}\Omega}{\lambda}} \,, \tag{32.37}$$

yielding for the given example of an Earth-based interferometer $\Delta\nu \approx 400$ Hz.

32.1.10 Exercises

32.1.10.1 Ex: Characterizing a piezo actuator

In order to characterize a recently purchased piezo actuator (Thorlabs, TA0505D024W) a Scientific Initiation student sets up a Michelson interferometer driven by a HeNe laser beam. Scanning the voltage applied to the piezo through the entire permitted range, he observes 8.8 oscillations of the interference fringes. What is the piezo displacement per volt?

32.1.10.2 Ex: Michelson interferometer

The figure 32.11 shows a Michelson interferometer containing in one arm an airtight 5 cm long cell with glass windows. Light with wavelength $\lambda = 500$ nm is used. After the cell has been evacuated, the interference pattern shifts by 60 fringes. Use this information to calculate the refractive index of air at atmospheric pressure. With what accuracy can you determine the refractive index with this method?

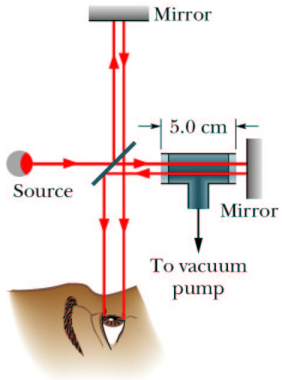

Figure 32.11:

32.1.10.3 Ex: Michelson interferometer

Assume that a signal-to-noise ratio of 50 has been achieved in measuring the fringe pattern of a Michelson interferometer with one continuously moving mirror. Estimate the minimum path length ΔL that the mirror has to travel in order to reach an accuracy of $\Delta\lambda = 10^{-4}$ nm in the measurement of a laser wavelength at $\lambda = 600$ nm.

32.1.10.4 Ex: Rotating the polarization with a Mach-Zehnder interferometer

Using the Jones matrix formalism demonstrate how to use the Mach-Zehnder interferometer setup sketched in the figure to rotate the polarization of a linearly polarized laser beam in an electronically controlled way using a piezo actuator mounted in ones of the interferometer arms.

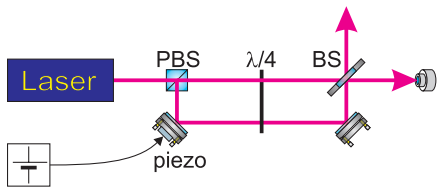

Figure 32.12:

32.1.10.5 Ex: Lyot filter

Consider a Lyot filter with two plates ($L_1 = 1\,\text{mm}$ and $L_2 = 4\,\text{mm}$) with the refraction indices $n_o = 1.40$ in the fast axis and $n_e = 1.45$ in the slow axis.
a. Calculate the transmission peaks of the Lyot filter as a function of λ for the rotation angle $\phi = 45°$.
b. Determine the transmitted intensity $I(\phi)$ as a function of the rotation angle ϕ for a fixed wavelength λ. What is the contrast of the transmitted intensity for arbitrary values of λ if the absorption losses are 2%?

32.1.10.6 Ex: Wedge-shaped etalon

A beam of light of wavelength $\lambda = 683\,\text{nm}$ with large diameter is incident perpendicularly on the first of two quadratic plates. Each plate has the edge length 120 mm; at the left edge the plates touch each other, at the right edge they are separated by a wire of $d_w = 0.048\,\text{mm}$ in diameter. The air between the plates acts as a thin layer.
a. How many interference fringes does an observer see from above this arrangement?
b. Now suppose that the incident light be white. Will the interference pattern at the far left be bright or dark?
c. Starting from the left edge there will be a series of interference minima, whose position depend on the wavelength of the light. For what light color (blue or red) will the minimum be closer to the edge?

32.1.10.7 Ex: Fabry-Perot interferometer

The dielectric coatings of each plate of a Fabry-Perot interferometer have the following specifications: $R = 98\%$, $A = 0.3\%$. The flatness of the surfaces is $\lambda/100$ at $\lambda = 500\,\text{nm}$.
a. Estimate the finesse from (32.27) and (32.30), the maximum transmission, and the spectral resolution of the FPI for a plate separation of 5 mm.

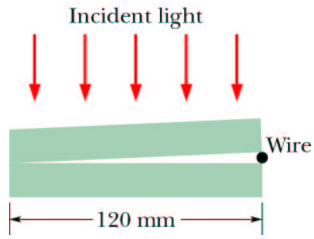

Figure 32.13:

b. Show that, for a given absorption, the transmitted intensity decreases with increasing reflectivity. Explain why. **Note:** A trade-off between high finesse and high transmission at a given absorption $A > 0$, called *impedance matching*, is reached by maximizing the intracavity intensity. For a symmetric cavity, it can be shown that impedance matching is reached for $A = T$.

32.1.10.8 Ex: Confocal and concentric cavities

a. Calculate the spectrum of longitudinal and transverse modes for (i) a confocal cavity ($\rho_a = \rho_b = L$) and (ii) a concentric cavity ($\rho_a = \rho_v = L/2$). Interpret the results.
b. Assuming radii of curvature $\rho_a = \rho_b = 5$ cm and a finesse of $F = 500$ for the cavity, how precise must the length of the cavity be adjusted in order to observe only longitudinal modes in the transmission spectrum?

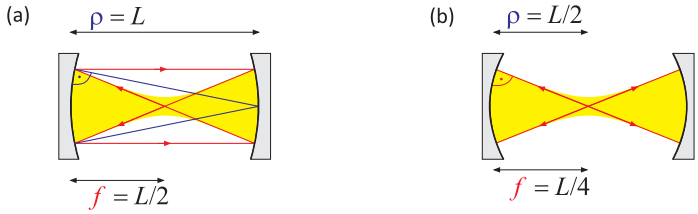

Figure 32.14: (a) Confocal cavity and (b) concentric cavity.

32.1.10.9 Ex: Thermal drift of a laser cavity

Estimate the frequency drift of a laser oscillating at $\lambda = 500\,\text{nm}$ because of thermal expansion of the resonator at a temperature drift of $1°\,\text{C/h}$, when the resonator mirrors are mounted on distance-holder rods a. made of invar and b. made of fused quartz.

32.1.10.10 Ex: Stability of a supercavity

Consider a non-confocal optical cavity of 10 cm length whose spacer is made of (i) aluminum, (ii) stainless steel, (iii) invar steel, (iv) fused quartz, (v) Zerodur, and (vi) ULE. The cavity is maintained at constant temperature with a precision of

0.001 C. What maximum drift do you estimate for its resonance frequency at 633 nm?

32.1.10.11 Ex: Fabry-Perot interferometer as optical spectrum analyzer

A confocal FPI shall be used as optical spectrum analyzer, with a free spectral range of $\delta_{fsr} = 3\,\text{GHz}$. Calculate the mirror separation L and the finesse that is necessary to resolve spectral features in the laser output within $\Delta\nu = 10\,\text{MHz}$. What is the minimum reflectivity R of the mirrors, if the surface finesse is $F_S = 500$?

32.1.10.12 Ex: Interference and colors filters

Strontium atoms resonantly driven by two lasers at 461 nm and 689 nm emit fluorescence light at both wavelengths. Because the red transition is 5000 times narrower than the blue one, the red fluorescence is much weaker and difficult to detect. Find a suitable low-pass filter in the Thorlabs® catalogue suppressing the blue light sufficiently to be sure that any fluorescence recorded after the filter must be resulting from the red transition. What signal ratios can you achieve with a single filter? Consider interference filters as well as color filters.

32.1.10.13 Ex: Interference filter

An interference filter shall be designed with peak transmission at $\lambda = 550\,\text{nm}$ and a bandwidth of 5 nm. Estimate the reflectivity R of the dielectric coatings and the thickness of the etalon, if no further transmission maximum is allowed between 350 and 750 nm.

32.1.10.14 Ex: Cut-off wavelength of a single-mode fiber

You want to transport 461 nm light via a polarization maintaining single-mode fiber. How do you need to choose the cut-off wavelength of the fiber? Assuming a 50% coupling efficiency, how much power can you get through the 5 nm long fiber? Choose a model from the Thorlabs catalog and justify your choice.

32.1.10.15 Ex: Exc Numerical aperture of a fiber

Calculate the numerical aperture of a step-index fiber with core refraction index n_{core} and cladding refraction index $n_{cladding}$ considering the scheme 32.15.

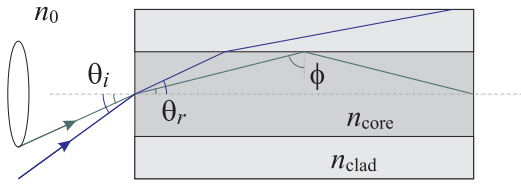

Figure 32.15:

32.1.10.16 Ex: Tuning by tilting an etalon

a. It is a common method to tune an etalon (or dielectric mirror or waveplate) to a certain transmission wavelength by tilting it as a whole with respect to the optical axis (without changing its intrinsic alignment. Does the tilt increase or decrease the wavelengths of the transmission peaks? Justify your answer. What is the implication for a dielectric mirror to be used under a non-normal angle of incidence?
b. A narrow band interference filter consisting of a glas plate coated on both surfaces has the following characteristics: thickness $L = 0.5\,\text{mm}$, refractive index $n_{rfr} = 1.45$, central wavelength $\lambda_{eff} = 706\,\text{nm}$, and bandwidth $\Delta\lambda = 0.3\,\text{nm}$. Considering the filter as Fabry-Pérot etalon, calculate its free spectral range, its finesse, and the reflectivity of its surfaces.
c. Assuming that the filter of part (b) can be tilted from normal incidence up to an angle $\theta_{max} = 35°$, how far will the center frequency shift. Prepare a graph showing λ_{eff} as a function of θ.

32.1.10.17 Ex: Double MZI as a model for Coherent Back-Scattering

Consider the setup shown in Fig. 32.16 and calculate the signal observed on the photodetector for arbitrary phase shifts ϕ and arbitrary rotation angles α by the $\lambda/2$-waveplate.

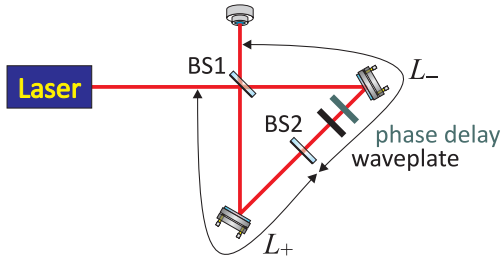

Figure 32.16: Double Mach-Zehnder interferometer.

32.1.11 *Experiment: Mach-Zehnder interferometer*

The Mach-Zehnder interferometer and the Michelson interferometer are the two most common two-beam interferometers. For the realization of the following project prior knowledge of 1. Gaussian beams (see Sec. 30.2), 2. photodetectors (see Sec. 31.2.1), and 3. piezo-electric transducers (see Sec. 32.1.2) is required.

1. Set up a Mach-Zehnder interferometer with a piezo in one of the arms according to Fig. 32.3(a). Optimize the phase matching of the two beams onto a photodetector and the rotation of the $\lambda/2$-waveplates until you obtain visible interference patterns.

2. Vary the length of one arm of the interferometer using the piezo. Measure the contrast of the interference fringes and discuss from which parameters it depends and how it can be maximized.

3. Rotate the first $\lambda/2$-waveplate (behind the laser). What do you observe? Explain the observation!

4. Remove the PBS in front of the photodetector. What do you observe? Explain the observation!

5. If a piezo is used, vary the voltage applied to the piezo-electric actuator and measure the voltage expansion coefficient d.

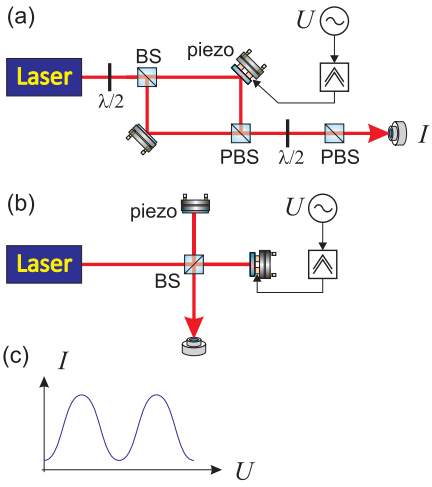

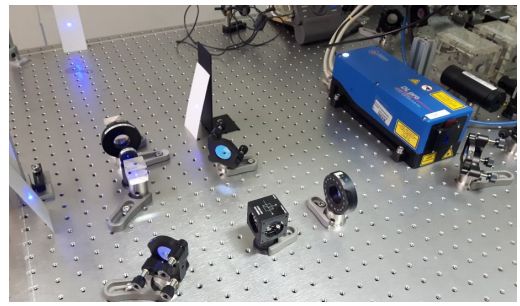

Figure 32.17: Setup for (a) a Mach-Zehnder interferometer or (b) a Michelson interferometer. (BS) non-polarizing beamsplitter, (PBS) polarizing beamsplitter. (c) Signal on the photodetector as a function of the length variation of an arm of the interferometer.

32.1.12 *Experiment: Fabry-Pérot cavity*

A Fabry-Pérot cavity is a typical multi-beam interferometer.

1. Set up a Fabry-Pérot cavity according to Fig. 32.18 and mode-match a laser beam into the cavity. Scan the cavity length using a piezo and observe the transmitted spectrum on an oscilloscope. What do you observe?

2. If an ECDL is used, vary the current and the temperature of the laser diode. What do you observe? Vary the frequency of the diode laser by scanning the piezo transducer of the laser cavity. Observe the mode spectrum of the laser in the transmission signal of the cavity. Measure its free spectral range, the transmission linewidth, and the finesse of the cavity.

Optical cavities are frequently used as *optical spectrum analyzers*. For this application, it is helpful to simplify the intrinsic mode spectrum of the cavity by using a confocal design, where all transerse modes are degenerated. We will now set up an optical cavity and characterize it by its free spectral range and its finesse. Then we will analyze its mode spectrum and modify its geometry to make it confocal.

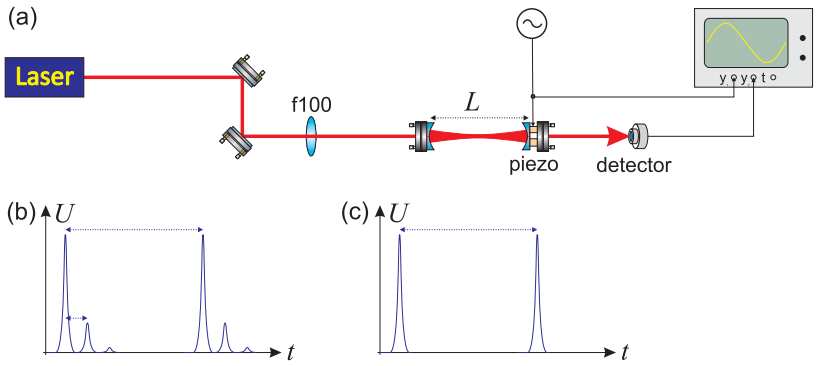

Figure 32.18: (a) Setup for aligning a confocal resonator. (b) Transmission spectrum of the cavity for non-confocal alignment. (c) Same as (b) but for the case of confocal alignment.

1. Couple a laser beam into a cavity as shown in Fig. 32.18. The cavity provided by this tinker course consists of a plane incoupler ($\rho_1 = \infty$, $R_1 = 98\%$) and a high reflector ($\rho_2 = 25\,\text{mm}$, $R_2 = 99.8\%$). Position the mirror at a distance L, where the cavity is stable. Calculate the free spectral range, the finesse, the diameter of the beam waist.

2. Optimize the phase-matching of the laser beam to the cavity. In order to do this, (a) measure the diameter of the diode laser beam, (b) determine the lens which can be used to focus down to the beam waist of the cavity. How does the transmission spectrum change upon the beam matching?

32.1.13 *Experiment: Fizeau interferometer*

A *Fizeau interferometer* is a device allowing to analyze the rugosity of surfaces.

1. Set up a Fizeau interferometer according to Fig. 32.18.

32.1.14 *Experiment: Coupling light into an optical fiber*

Coupling a laser beam into an optical fiber is a delicate task, requiring a good collimation optics and full control over the 6 degrees of freedom defining a laser beam: horizontal and vertical position, horizontal and vertical tilt, beam diameter and divergence.

1. Redirect the light of a HeNe laser via two adjustable mirrors into a fiber collimator in such a way that the beam is not deviated from the optical axis by the collimator.

2. Now connect (a) a multimode fiber and (b) a single mode fiber to the collimator. Optimize the coupling by walking the laser beam and by adjusting the focus of the fiber collimator. What differences do you observe for multi- and single mode fibers?

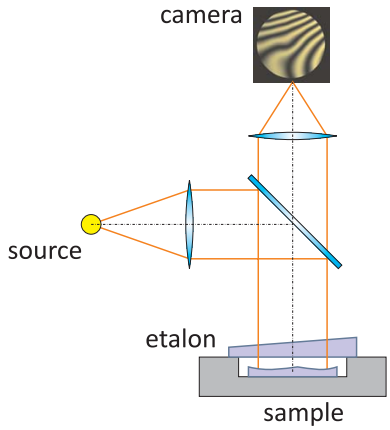

Figure 32.19: Principle of operation of a Fizeau interferometer.

32.2 Conventional light sources and lasers

For the first half of the 20-th century these assumptions matched the available light sources, usually incandescent, arc or plasma discharge lamps. After the invention of the laser in 1958, single mode and pulsed lasers quickly replaced the lamps as a source for optical excitation. These new light sources initiated a revolution in optical science, the consequence of which continue to reverberate through modern sciences and applied technologies. The characteristics of laser sources are far superior to the old lamps in all respects. They are intense, collimated, spectrally narrow and phase coherent. The laser gave rise to a multitude of new spectroscopic techniques and new disciplines, such as quantum electronics, the study of statistical properties of light in quantum optics, optical cooling and trapping of microscopic particles, the control of chemical reactivity, and new technologies for imaging and high resolution microscopy. The impact the laser had on technology is only comparable to that of to the invention of the transistor. See also (watch talk).

The laser produces light through an optical quantum amplification process based on the stimulated emission of electromagnetic radiation. The term 'laser' is an acronym for 'Light Amplification by Stimulated Emission of Radiation'. A laser differs from other light sources in that it emits *coherent* light. Its spatial coherence allows the light to be focused on a very tiny spot, where the concentration of energy is sufficient for applications such as laser cutting and lithography. The spatial coherence also allows it to collimate a laser beam over large distances, that is, the light forms a concentrated beam propagating in a straight line. Lasers can also have a very high temporal coherence, which corresponds to a very narrow spectrum, that is, lasers usually emit a single very well defined color of light. The extreme temporal coherence can be used to produce pulses of light as short as a femtosecond. In addition, laser light is polarized.

In 1917, Albert Einstein established the theoretical foundations of the laser in an article 'Zur Quantentheorie der Strahlung' through a rederivation of Max Planck's radiation law. He proposed a mechanism explaining how light is absorbed and emitted from atoms. The fundamental ingredient is that the photon can be emitted in two

different ways, by spontaneous emission, an indeterministic process that occurs without physical reason, or by stimulated emission. This latter emission process occurs because of stimulation by light, which is already present in the system and represents the fundamental mechanism of the laser. In the following decade German and American researchers experimentally confirmed the phenomena of stimulated emission and negative absorption, that is, gain. In 1950, Alfred Kastler (French physicist and Nobel Prize in Physics of 1966) proposed the method of optical pumping, confirmed experimentally two years later by other French physicists.

In 1953, Charles Townes produced the first microwave amplifier called *maser*, a device that operates similarly to the laser but amplifies microwave radiation instead of visible or infrared radiation. However, Townes' maser was unable to emit light continuously. In 1955, in the Soviet Union, Nikolay Basov and Aleksandr Prokhorov solved the problem of continuous operation using atoms with more than two energy levels. These level systems were able to sustain a permanent population inversion of an energetic level decaying to a less energetic system by releasing light via stimulated emission. Despite the fact that several prominent physicists, including Niels Bohr, John von Neumann, and Isidor Rabi, argued that the maser violates Heisenberg's uncertainty principle and therefore could not work, in 1964, Charles Townes, Nikolay Basov and Aleksandr Prokhorov shared the Nobel Prize in Physics for fundamental work in the field of quantum electronics that led to the realization of oscillators and amplifiers based on the maser principle.

In 1957, Charles Townes and Arthur Schawlow, from the Bell labs, began to seriously study feasibility of an 'optical maser'. In 1958, the Bell labs submitted a patent proposing a scheme for optical radiation, and Schawlow and Townes presented a scientific paper. Simultaneously, at the Columbia University, the PhD student Gordon Gould was working on the energy levels of excited thallium. In 1957-8, Gould and independently Prokhorov, Schawlow and Townes proposed the use of an open resonator, which later became an essential component of the laser. Gould also proposed several possible applications for a laser, such as spectrometry, interferometry, the radar, and nuclear fusion. He continued to develop the idea, and filed a patent application in April 1959. The United States Patent Office dismissed his application, and granted a patent to the Bell Labs in 1960. Gould won his first minor patent in 1977 after a 28-year fight, and it took him until 1987 to win his first significant process in the struggle, when a federal judge ordered the United States Patent Office to issue to Gould patents for optical pumping and the invention of a laser based on the principle of electrical gas discharge.

It was Theodore Maiman, who on May 16, 1960, operated the first working laser at the Hughes Research Laboratories, Malibu, California, evincing several other research teams, including the ones of Townes at Columbia University, of Schawlow at Bell Labs, and Gould at the company TRG (Technical Research Group). Maiman's laser used a synthetic solid-state ruby crystal pumped by a flash lamp to produce red laser light at 694 nm wavelength; however, the device was only capable of pulsed operation due to its three-level pumping scheme. Later in 1960, the first gas laser was built, using a helium-neon mixture, which was capable of continuous operation in the infrared spectrum. Basov and Javan proposed the concept of a semiconductor laser diode. In 1962, the first laser diode device, made of gallium arsenide, was realized emitting near-infrared light. Nowadays, laser diodes are available in various spectral regimes

up to the UV.

Figure 32.20: First suggested application in 1964 of a (left) HeNe laser and (right) a diode laser.

Interestingly, despite many attempts, it has not yet been possible to manufacture yellow or green laser diodes.

32.2.1 Features and operation of lasers

To understand how a laser operates, we consider the process of absorption and emission of light by an atom. Following Bohr's model an absorbed photon raises an electron from a lower orbit to a higher orbit, and when the electron returns back to the ground state, it re-emits a photon in an arbitrary direction.

When we illuminate a sample of N atoms, N_1 atoms of which are in the ground state, by a radiation field, the absorption rate depends on the field intensity $I(\nu)$ and a constant B_{12}, which is characteristic for the transition,

$$R_{abs} \propto B_{12} I(\nu) N_1 \ . \tag{32.38}$$

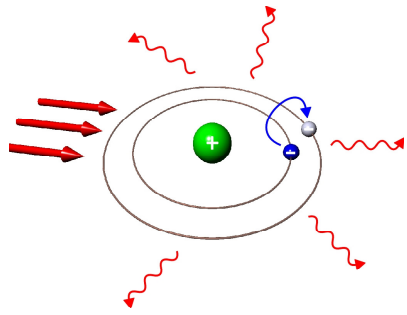

Figure 32.21: Bohr's model of photon absorption.

The emission rate depends on the number of atoms N_2 in the excited state, such that,

$$R_{sp} \propto A_{21} N_2 \ . \tag{32.39}$$

As the excited state has more energy, it can decay by itself (i.e. spontaneously) to a lower energy state. Einstein's brilliant idea now was to postulate a third process, which he called stimulated emission,

$$R_{st} \propto B_{21} I(\nu) N_2 \ . \tag{32.40}$$

In this process, an incident photon stimulates an excited atom to transfer the electron to a lower orbit. The released energy is then used to form a second photon, which is in all respects identical to the first. This process is necessary to ensure that, in thermal equilibrium, the population of the states follows Boltzmann's law.

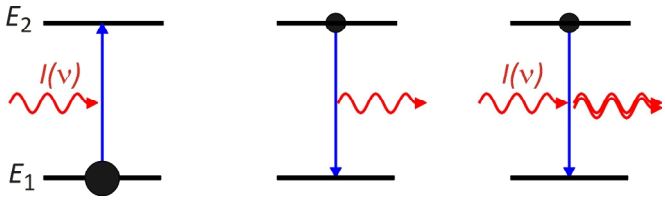

Figure 32.22: Einstein's model of absorption and spontaneous and stimulated emission.

Obviously, absorption decreases the intensity of a light beam crossing the atomic sample, while stimulated emission amplifies it. In order to amplify incident light, the gain in intensity must overcome the losses. Therefore, we need the absorption processes to be less frequent than the stimulated emission processes, i.e. the number of atoms in the excited state N_2 must exceed the number of atoms in the ground state $N_1 < N_2$.

We can easily write the rate equation,

$$\frac{dN_2}{dt} = -A_{21} N_2 - B_{21} I(\nu) N_2 + B_{21} I(\nu) N_1 = -\frac{dN_1}{dt} \ , \tag{32.41}$$

with $N = N_1 + N_2$. It is easy to solve this equation. The result is,

$$N_2 = \frac{I(\nu) B_{21} N}{A + 2 B_{21} I(\nu)} [1 - e^{-(A_{21} + 2 B_{21} I(\nu)) t}] < N_1 \ . \tag{32.42}$$

The graphical representation 32.23 shows the temporal behavior of the populations N_1 (in green in the figure) and N_2 (in blue), reaching a state of equilibrium after a certain time. By increasing the intensity of the incident light, we observe that the curves approach each other but never cross. That is, in a two-level system, we always get $N_1 > N_2$ and the populations are never inverted. Therefore, amplification of light as in the laser does not happen.

Fortunately, we can resort to a trick by inserting a third level. Ensuring that the decay rate of the (metastable) state E_3 is much slower than the optical pumping to this state via the driven transition $E_1 \to E_2$ followed by a rapid decay $E_2 \to E_3$, we can reach the situation $N_3 > N_1$. Now it is possible to amplify light, which is resonant with the transition $E_2 \to E_3$.

What are the minimum requirements for the realization of a laser? The first condition is that the *pumping cycle is irreversible* to ensure that the processes of

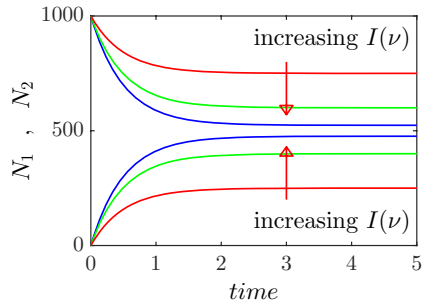

Figure 32.23: (code) Impossibility of achieving inversion in a two-level system.

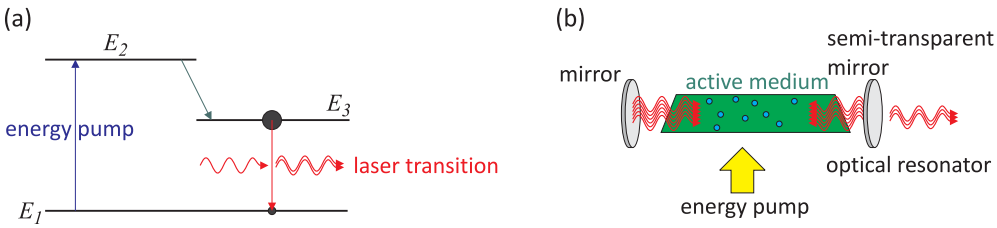

Figure 32.24: Basics of a laser: (a) Level system and (b) principle scheme.

stimulated emission and absorption do not compensate. Spontaneous emission is irreversible and can be incorporated into a three-level system.

The second condition is the existence of a *stimulated emission process*, because we want the amplified photon to be an exact copy of the incident photon.

The third requirement is a *feedback mechanism* that synchronizes the amplification processes by different atoms in a disordered environment, such as a gas. Mirrors are ideal because they increase the effective gain path, i.e. the distance within which inverted atoms can amplify light. Also, the mirrors define the phase of the light wave, since the standing wave formed by the counterpropagating light fields must have nodes on the surfaces of the mirrors.

32.2.1.1 Threshold condition

According to the *Lambert-Beer law* the intensity of a monochromatic laser beam evolves, on its way through a gas of two-level atoms with energies $E_2 - E_1 = \hbar\omega_0$ like,

$$I(z,\nu) = I(0,\nu)e^{-\alpha(\nu)z} \ , \tag{32.43}$$

where the frequency-dependent absorption coefficient,

$$\boxed{\alpha(\nu) = [N_1 - \tfrac{g_1}{g_2}N_2]\sigma(\nu)} \ , \tag{32.44}$$

is determined by the absorption cross section $\sigma(\nu)$ for the transition and by the inversion,

$$\Delta N \equiv \tfrac{g_1}{g_2}N_2 - N_1 \ , \tag{32.45}$$

which determines whether stimulated emission prevails or absorption: For $\Delta N > 0$, the absorption coefficient $\alpha(\nu)$ becomes negative and the incident wave is amplified instead of attenuated [218].

If the active medium is placed between two mirrors [Fig. 32.24(b)], the wave is reflected back and forth, and traverses the amplifying medium many times, which increases the total amplification. With the length L of the active medium the total gain factor per single round-trip without losses is,

$$G(\nu) = \frac{I(\nu, 2L)}{I(\nu, 0)} = e^{-2\alpha(\nu)L} \ . \tag{32.46}$$

A mirror with reflectivity R reflects only the fraction R of the incident intensity. The wave therefore suffers at each reflection a fractional reflection loss of $(1 - R)$. Furthermore, absorption in the windows of the cell containing the active medium, diffraction by apertures, and scattering due to dust particles in the beam path or due to imperfect surfaces introduce additional losses. When we summarize all these losses by a loss coefficient γ, which gives the fractional energy loss $\Delta W/W$ per round-trip time T, the intensity I decreases without an active medium per round-trip as,

$$I(2d, \nu) = I(0, \nu)e^{-\gamma} \ . \tag{32.47}$$

Including the amplification by the active medium with length L, we obtain for the intensity after a single round-trip through the resonator with length d, which may be larger than L:

$$I(2d, \nu) = I(0, \nu)e^{-2\alpha(\nu)L-\gamma} \ . \tag{32.48}$$

The wave is amplified if the gain overcomes the losses per round-trip. This implies that,

$$-2L\alpha(\nu) = 2L\Delta N\sigma(\nu) > \gamma \ , \tag{32.49}$$

which yields the threshold condition for the population difference,

$$\Delta N > \Delta N_{thr} = \frac{\gamma}{2L\sigma(\nu)} \ . \tag{32.50}$$

If the inverted population difference ΔN of the active medium is larger than ΔN_{thr}, a wave that is reflected back and forth between the mirrors will be amplified in spite of losses, therefore its intensity will increase.

The wave is initiated by spontaneous emission from the excited atoms in the active medium. Those spontaneously emitted photons that travel into the right direction (namely, parallel to the resonator axis) have the longest path through the active medium and therefore the greater chance of creating new photons by induced emission. Above the threshold they induce a photon avalanche, which grows until the depletion of the population inversion by stimulated emission just compensates the repopulation by the pump. Under steady-state conditions the inversion decreases to the threshold value ΔN_{thr}, the saturated net gain is zero, and the laser intensity limits itself to a finite value I_L. This laser intensity is determined by the pump power, the losses γ, and the gain coefficient $\alpha(\nu)$.

The frequency dependence of the gain coefficient $\alpha(\nu)$ is related to the line profile $g(\nu - \nu_0)$ of the amplifying transition. Without saturation effects (i.e. for small

intensities), $\alpha(\nu)$ directly reflects this line shape, for homogeneous as well as for inhomogeneous profiles. According to (32.44) and (??) we obtain with the Einstein coefficient B_{ik},

$$\alpha(\nu) = \Delta N \sigma(\nu) = -\Delta N (h\nu/c) B_{12}(\nu - \nu_0) \ , \tag{32.51}$$

which shows that the amplification is largest at the line center ν_0. For high intensities, saturation of the inversion occurs, which is different for homogeneous and for inhomogeneous line profiles.

The loss factor γ also depends on the frequency ν because the resonator losses are strongly dependent on ν. The frequency spectrum of the laser therefore depends on a number of parameters.

32.2.1.2 Applications of lasers in industry and fundamental research

Among their many applications, lasers are nowadays used in compact disc players, laser printers, and bar code scanners, optical fibers and optical communication, laser surgery and skin treatments, welding, cutting and machining, military devices, distance and velocity measurements, projectors, laser pointers, etc..

In fundamental research (in particular on atomic gases, metamaterials, etc.), the laser plays elementary roles in the areas of photonics, quantum computers, metrology, frequency combs, and atomic clocks (laser-based clocks are up to 1000 times more stable than the best state-of-the-art microwave clocks).

We all know that light is a wave. With the invention of the laser we found a process and a device to make this light coherent. On the other hand, since de Broglie's assertion we know that *matter is a wave, as well.* Is it conceivable to construct a matter laser? Yes, it is! The first coherent matter wave was in fact observed in 1995. This state of matter, also called Bose-Einstein condensate, was predicted by Bose and Einstein in 1924. To create a Bose-Einstein condensate, we need, similarly to the laser, that the matter waves interfere constructively in a way that they amplify each other. For this, the Broglie wavelength of the particles, which constitute the matter, must be longer than the distance between them. Assuming a typical average distance on the order of μm, this corresponds to an average velocity of the particles of mm/s or a temperature of some 100 nK.

32.2.2 HeNe laser

HeNe lasers are gas lasers, whose gain medium consists of a mixture of 90% helium and 10% neon at a total pressure of about 1 Torr excited by a small electrical discharge. The most widely used transition wavelength is at 632.8 nm.

Fig. 32.25(a) shows the principle scheme of a commercial HeNe laser. The distance between the high-reflecting mirror (R_{hr}) and the output coupler (R_{oc}) determines the free spectral range δ_{fsr}. Typically, a HeNe laser operates on two or three longitudinal modes separated by δ_{fsr}. As illustrated in Fig. 32.25(b), the numbers of lasing modes above threshold depends on the ratio of gain-to-loss. Fig. 32.25(c) shows the optical pumping scheme to reach inversion on three of the lasing transitions at 632.8 nm, 1.15 μm, and 3.39 μm.

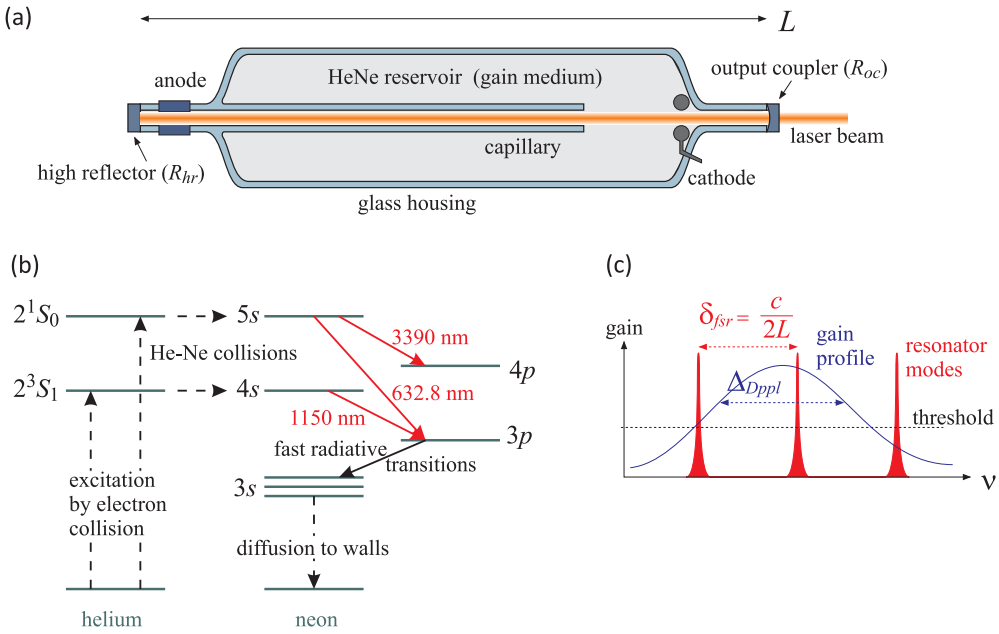

Figure 32.25: (a) Construction scheme of a HeNe laser. (b) Gain and emission profile. (c) Optical pumping scheme.

32.2.3 Diode laser

A laser diode is electrically a *pin*-diode. The active region of the laser diode is in the intrinsic (i) region, and the carriers (electrons and holes) are pumped into that depletion region from the n- and p-doped regions respectively. The depletion region, devoid of any charge carriers, forms as a result of the difference in electrical potential between n- and p-type semiconductors wherever they are in physical contact. Unlike a regular diode, the goal for a laser diode is to recombine all carriers in the i region, and produce light.

Figure 32.26: (Left) Laser diode with protective housing removed, e.g. using a can opener. (Right) Laser diode collimator.

32.2.3.1 Generation of light

Electrons and holes present in the same region may recombine or 'annihilate' by spontaneous emission of photons with energy equal to the difference between the electron's original state and hole's state (see Fig. 31.10). This is in contrast to a conventional semiconductor junction diode, where the energy released from the recombination is carried away as phonons, i.e. lattice vibrations. Spontaneous emission below the lasing threshold is the operating mode of an LED. While spontaneous emission is necessary to initiate laser oscillation, it contributes to reduce the efficiency of a laser operating above threshold.

One condition for lasing is that, in the absence of stimulated emission, electrons and holes may coexist in proximity to one another without recombining immediately. For typical diode laser materials the 'upper-state lifetime' or 'recombination time' is on the order of a nanosecond. A nearby photon with energy equal to the recombination energy can cause recombination by stimulated emission. This generates another photon of the same frequency, polarization, and phase, traveling in the same direction as the first photon. In this way stimulated emission will cause gain for an optical wave in the injection region, and the gain increases as the number of electrons and holes injected across the junction increases.

32.2.3.2 Optical cavity and laser modes

As in other lasers, the gain region needs to be surrounded by an optical cavity providing optical feedback. In its simplest form, a laser diode is made in the shape of a narrow optical waveguide on a the surface of a crystal. The two ends of the crystal are cleaved to form perfectly smooth, parallel edges, forming a Fabry-Pérot resonator. Emitted photons will travel along the waveguide, be amplified by stimulated emission and reflected several times from each end face before exiting. If the losses due to absorption and incomplete reflection from the end facets are smaller than the gain, the diode begins to 'lase'.

Important properties of laser diodes are determined by the geometry of the optical cavity. If the waveguide is thick compared to the wavelength of the light, it can support higher-order transverse optical modes. The laser is then called 'multi-mode'. These transversely multi-mode lasers are adequate for application where high power is needed, for example, in printing, activating chemicals, or pumping other types of lasers.

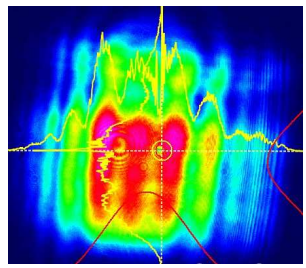

Figure 32.27: Typical beam profile of a multimode laser diode (Thorlabs, L450P1600MM.

For applications requesting small focused beams the waveguide must be made narrow, on the order of the optical wavelength, such that only a single transverse mode is supported, and one ends up with a diffraction-limited beam. Such single spatial mode devices are used for optical storage, laser pointers, and fiber optics. Note that these lasers may still support multiple longitudinal modes, and thus can lase simultaneously at multiple wavelengths. The wavelength emitted is a function of the band-gap of the semiconductor material and the modes of the optical cavity. In general, the maximum gain will occur for photons with energy slightly above the band-gap energy, and the modes nearest the peak of the gain curve will lase most strongly. The width of the gain curve will determine the number of additional 'side modes' that may also lase, depending on the operating conditions. Single spatial mode lasers that can support multiple longitudinal modes are called Fabry-Pérot (FP) lasers. A FP laser will lase at multiple cavity modes within the gain bandwidth of the lasing medium. The number of lasing modes in an FP laser is usually unstable, and can fluctuate due to changes in current or temperature.

Single spatial mode diode lasers can be designed so as to operate on a single longitudinal mode. These single frequency diode lasers exhibit a high degree of stability, and are used in spectroscopy and metrology, and as frequency references. Single frequency diode lasers are classed as either distributed feedback (DFB) lasers or distributed Bragg reflector (DBR) lasers.

Due to diffraction, the beam diverges (expands) rapidly after leaving the chip, typically at 30 degrees vertically by 10 degrees laterally. A lens must be used in order to form a collimated beam like that produced by a laser pointer. If a circular beam is required, cylindrical lenses and other optics are used. For single spatial mode lasers, using symmetrical lenses, the collimated beam ends up being elliptical in shape, due to the difference in the vertical and lateral divergences.

32.2.3.3 Distributed Bragg reflector lasers and distributed feedback lasers

The simple diode described above has been heavily modified in recent years to accommodate modern technology, resulting in a variety of types of laser diodes. One example is the distributed Bragg reflector laser (DBR). It consists of a monolithic single frequency laser diode, characterized by an optical cavity consisting of an electrically or optically pumped gain region between two mirrors to provide feedback. One of the mirrors is a broadband reflector and the other mirror is wavelength selective so that gain is favored on a single longitudinal mode, resulting in lasing at a single resonant frequency. The broadband mirror is usually coated with a low reflectivity coating to allow emission. The wavelength selective mirror is a periodically structured diffraction grating with high reflectivity. The diffraction grating is etched into the semiconductor within a non-pumped, or passive region of the cavity.

A distributed feedback laser (DFB) is a monolithic single frequency laser diode with a diffraction grating etched close to the *pn*-junction of the diode aiming at stabilizing the lasing wavelength. This grating acts like an optical filter, causing a single wavelength to be fed back to the gain region and lase. Since the grating provides the feedback that is required for lasing, reflection from the facets is not required. Thus, at least one facet of a DFB is anti-reflection coated. The DFB laser has a stable wavelength that is set during manufacturing by the pitch of the grating,

and can only be tuned slightly with temperature. DFB lasers are widely used in optical communication applications, where a precise and stable wavelength is critical.

32.2.3.4 ECDL

An *extended-cavity diode laser* (*ECDL*) is an optical setup based on a laser diode chip, which typically has one end anti-reflection (AR) coated, and the laser resonator is completed with a collimating lens and a mirror, as shown in Fig. 32.28(a). The extended external laser resonator introduces various new features and options: Compared to a standard laser diode, the longer resonator increases the damping time of the intracavity light according to Eq. (32.29), and thus allows for lower phase noise and a smaller emission linewidth (in single-frequency operation). Furthermore, it opens the way for inserting frequency-selective optical components into the extended laser resonator, such as narrow-band Fabry-Pérot etalons or diffraction gratings, which can further *reduce the linewidth* and even allow to *tune and control the frequency* of the laser.

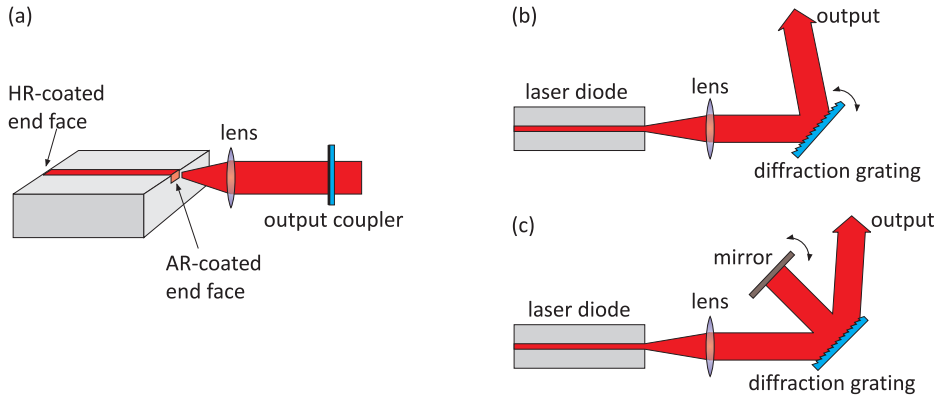

Figure 32.28: (a) ECDL with an AR-coated laser diode and an external mirror. (b) Littrow configuration. (c) Littmann configuration.

Tunable ECDLs based on diffraction grating as the wavelength-selective element are also called grating-stabilized diode lasers. The common Littrow configuration Fig. 32.28(b) generates optical feedback to the laser diode chip by retro-reflecting the first-order diffracted beam from the grating. The emission wavelength can be tuned by slightly tilting the diffraction grating. A disadvantage of this configuration is, that the tilt also changes the direction of the output beam, which is inconvenient for many applications.

In the Littman-Metcalf configuration Fig. 32.28(c), the grating angle is held fixed, and an additional mirror is used to reflect the first-order beam back into the laser diode. The wavelength can be tuned by rotating that mirror. This configuration offers a fixed direction of the output beam, and also tends to exhibit a smaller linewidth, as the wavelength selectivity is stronger, because the wavelength-dependent diffraction occurs twice per resonator round trip. A disadvantage is that the zero-order reflection of the beam reflected by the tuning mirror is lost, so that the output power is lower than that of a Littrow laser.

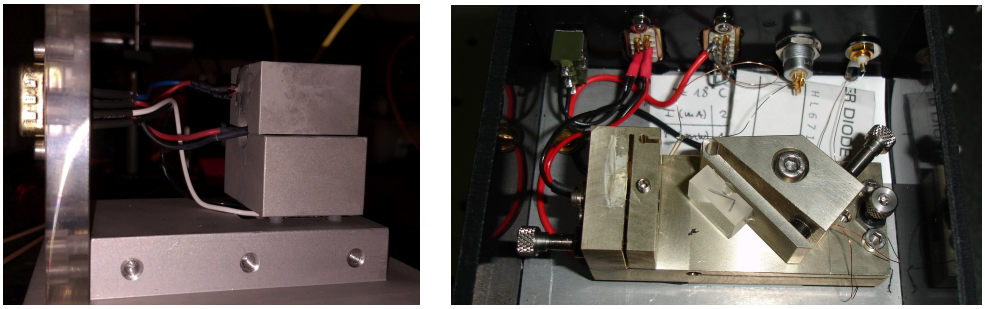

Figure 32.29: (Left) Side view of a 'free-running' laser diode mounted in a collimator (Thorlabs, LT110P-B) clamped in an aluminum block cooled by a Peltier element (Thorlabs, TEC3-6) and whose temperature is measured by a thermistor (Thorlabs, TH10K). (Right) Top view of a home-built ECDL laser in Littrow configuration. The diode collimator is clamped into the left mount. a holographic grating (Newport, 10HG2000-475-1) is glued to the right mount, whose angle can be adjusted mechanically and via a piezo. The whole setup is cooled by a Peltier element mounted on the bottom of the base plate.

New concepts have recently become popular, such as the so-called *cat-eye laser* [47, 320, 70], where the frequency-selective element is an extremely narrow-band (0.3 nm) optical filter [4].

By adjusting the tilt angle of a grating or a narrow-band filter by means of a piezo an extremely fine tuning of the emission frequency is possible, while coarse tuning of the frequency over a range of several nanometers is typically achieved by changing the temperature and the laser current. Typical linewidths of free-running ECDLs are well below 5 MHz. Controlling the laser temperature, current, and piezo voltage by active feedback circuits (e.g. within a Pound-Drever-Hall servo electronics) emission bandwidths in the milliHertz range have been achieved, which corresponds to quality factors of the laser oscillator of up to 10^{18}.

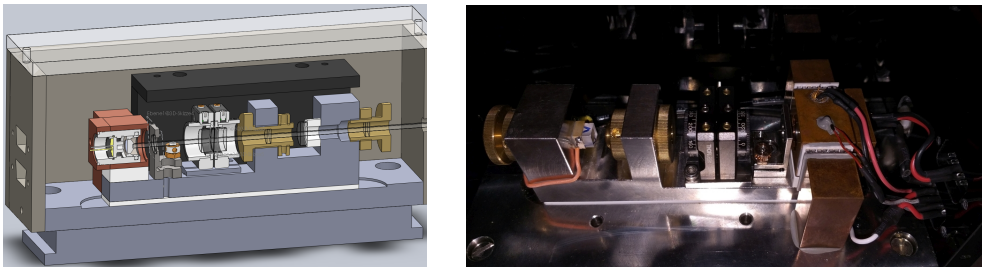

Figure 32.30: (Left) Construction plan of a home-built ECDL lasers in cat-eye configuration. (Right) Side view of the cat-eye laser.

In comparison to other laser types, a *diode laser* exhibits, the advantage of a very small size and a compact design. They are, in general, easy to handle and can be

[4] Available from Semrock or Laseroptik.

controlled conveniently via current and temperature. However, they also have the disadvantage of a large beam divergence and a broad emission spectrum. The beam divergence can be compensated by a collimation optics in front of the laser diode.

The temperature has an impact on the band structure of the *pn*-transition of the laser diode and hence on the frequency. Therefore, it is stabilized via a Peltier element, which is mounted underneath the laser diode holder. The degree of freedom is used for tuning the laser frequency in wide steps.

32.2.3.5 Pulsed diode lasers

Diode lasers can be used for generating ultrashort pulses either with various techniques of mode locking or with gain switching. Typically, pulses with durations between 0.5 and 5 ps and pulse repetition rates between 1 GHz and hundreds of giga-Hertz are generated with mode locking. In extreme cases, the repetition rate can even be above 1 THz. The main application of ultrafast diode lasers is in optical fiber communications systems, where such lasers function as pulse sources of fast data transmitters or for all-optical signal processing.

Common techniques for mode locking of diode lasers are active ore passive mode locking. Active mode locking can be accomplished with an optical modulator in the laser resonator. This is usually either an electro-absorption modulator in the form of an unpumped region with some modulated voltage, or an amplifying section where the drive current is modulated. Passive mode locking relies on a saturable absorber in the resonator. This can simply be an unpumped section of the device. It is common to apply an electrical bias for adjusting the absorber properties. However, the recovery time of that kind of absorber is fairly long. Shorter recovery times are achieved e.g. by implanting nitrogen (N^+ or N_2^+) ions from one facet. This introduces crystal defects, where carriers can recombine. The absorber is often placed at a resonator end, but it can also be placed somewhere within the resonator so that different pulses can meet in the absorber (colliding pulse mode locking).

For pulse repetition rates roughly below 10 GHz, an external cavity setup is usually required, as a monolithic device would become too long. The extended cavity may be an ECDL setup. Another technical approach is to incorporate the semiconductor chip into a ring laser resonator made of optical single-mode fiber. In the latter case, the resonator is typically much longer, and allows the use of fiber-optic components. The semiconductor device may then be a fiber-coupled semiconductor optical amplifier (SOA).

External-cavity lasers have various advantages: The pulse repetition rate can be chosen in a wide range, and can easily be tuned e.g. by moving the end mirror, or with a fiber resonator by stretching a piece of fiber with a piezo transducer. It is possible to insert an optical filter for fixing the emission wavelength, or use a diffraction grating as the end mirror (Littrow configuration; see the article on external-cavity diode lasers). Even for higher pulse repetition rates, where harmonic mode locking is required, external-cavity devices can be advantageous, because they have a potential for lower laser noise, e.g. in the form of timing jitter. Therefore, mode-locked external-cavity diode lasers sometimes compete with mode-locked fiber lasers in areas where monolithic laser diodes would not be suitable. On the other hand, a monolithic setup with fundamental mode locking can be very compact, much cheaper to manufacture,

and can exhibit very robust pulse emission.

On the other hand, mode-locked diode lasers are subject to various limitations, which do not allow them to reach the full performance potential of, e.g., mode-locked fiber lasers: The pulse energy is fairly limited often far below 1 pJ. Average output powers are often below 1 mW. Due to the short upper-state lifetime, ultrafast semiconductor lasers are generally not suitable for lower repetition rates of e.g. well below 1 GHz, except with synchronous pumping. Although the gain bandwidth of semiconductors would be compatible with pulse durations of a few tens of femtoseconds, the pulse durations achieved are usually much longer at least hundreds of femtoseconds, and often picoseconds. The pulse formation dynamics are relatively complicated, e.g. due to nonlinear phase changes associated with gain saturation, and difficult to optimize. The pulse quality is normally not as good as e.g. for mode-locked fiber lasers. In particular, there are often additional satellite pulses, caused e.g. by imperfections of the anti-reflection coating. Also, the pulses are often chirped, i.e. they are not bandwidth-limited. The timing jitter and the noise of other pulse parameters are higher than for other mode-locked lasers. This is partly a consequence of the low power level.

32.2.3.6 Tapered amplifiers and injection locking

Other ways to amplify a the power of a laser without altering its coherence properties are using a *tapered amplifier* or via *injection locking* also called *master-slave locking* [123, 527] (see Fig. 32.31).

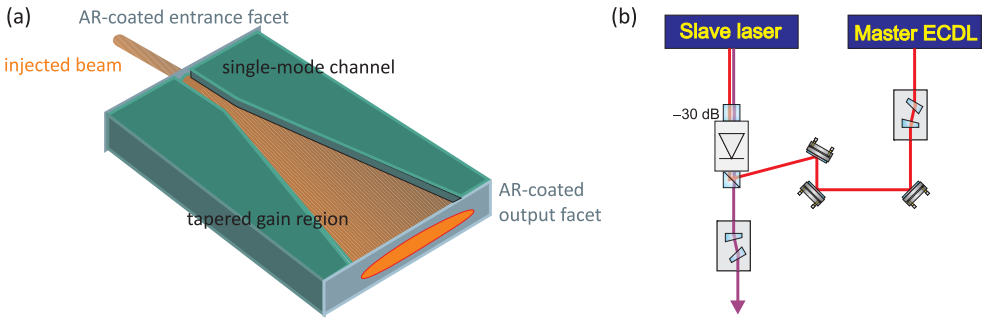

Figure 32.31: (a) Tapered amplifiers are available e.g. from Eagleyard. (b) Principle of injection locking.

The description presented here uses semi-classical laser rate equations [526]. Assuming that the master and the slave laser field are given by, respectively,

$$E_{\mathrm{inj}} = A_{\mathrm{inj}} e^{-\imath\omega_{\mathrm{inj}} t} e^{\imath\phi_{\mathrm{inj}}(t)} \qquad \text{and} \qquad E = A e^{-\imath\omega_s t} e^{\imath\phi_s(t)} \,, \tag{32.52}$$

The phase difference between the both fields is denoted by $\phi(t) = \phi_s(t) - \phi_m(t)$. Now, Considering the semi-classical laser rate equations we can describe the impact of the

master laser field in the slave laser,

$$\begin{aligned}\frac{dA(t)}{dt} &= \frac{1}{2}g[N(t)-N_{\text{th}}]A(t)+\kappa A_{\text{inj}}\cos\phi(t) \\ \frac{d\phi(t)}{dt} &= \frac{\alpha}{2}[N(t)-N_{\text{th}}]-\kappa\frac{A_{\text{inj}}}{A(t)}\sin\phi(t)-\Delta\omega \\ \frac{dN(t)}{dt} &= J-\gamma_N N(t)-[\gamma_p+g[N(t)-N_{\text{th}}]A(t)^2\ ,\end{aligned} \tag{32.53}$$

where $A(t)$ is the field amplitude normalized as $A^2(t)=S(t)$, and $S(t)$ is the photon number. $N(t)$ is the number of carriers in the slave laser, and the other parameters are g laser gain coefficient, N_{th} threshold carrier number, κ coupling coefficient, α linewidth enhancement factor, γ_p photon decay rate, N carrier recombination rate, J pump current normalized by electron charge, $\Delta\omega$ frequency difference between the master and the free running slave $\omega_m-\omega_s$. The parameter κ describes the rate at which the photons of the master laser enter into the slave laser cavity and is given in terms of the cavity quality factor,

$$\kappa=\frac{\omega_s}{2Q}\ . \tag{32.54}$$

From the steady state solutions of above equations, we can obtain the frequency locking range,

$$-\kappa\sqrt{(1+\alpha^2)}\sqrt{\frac{P_{\text{inj}}}{P_s}}<\Delta\omega<\kappa\sqrt{\frac{P_{\text{inj}}}{P_s}}\ , \tag{32.55}$$

where P_{inj}/P_s is the master laser fraction power used for the injection locking and P_s is the power of slave laser. From equation 4.25 we can see that the locking range is determined by the amplitude ratio between the fields and by the cavity quality factor since $\kappa\propto Q^{-1}$. Therefore, lasers with low Q are easier to lock. On the other hand, this leads to increased laser linewidth that reduces the phase noise performance of the injection locking systems. For higher injection ratio P_{inj}/P_s also results in a large locking range, which also makes the lock easier to achieve.

32.2.4 Exercises

32.2.4.1 Ex: Conventional light sources and lasers

Compare the properties of an incandescent light and a laser.

32.2.4.2 Ex: Threshold inversion for lasing 1

Calculate the necessary threshold inversion of a gas laser transition at $\lambda=500\,\text{nm}$ with the transition probability $A_{ik}=5{\cdot}10^7\,\text{s}^{-1}$ and a homogeneous linewidth $\Delta\nu_{hom}=20\,\text{MHz}$. The active length is $L=20\,\text{cm}$ and the resonator losses per round-trip are $\gamma=5\%$.

32.2.4.3 Ex: Threshold inversion for lasing 2

A laser medium has a Doppler-broadened gain profile of halfwidth $\delta\nu=2\,\text{GHz}$ and central wavelength $\lambda=633\,\text{nm}$. The homogeneous width is 50 MHz, and the transition

probability $A_{ik} = 10^8\,\mathrm{s}^{-1}$. Assume that one of the resonator modes ($L = 40\,\mathrm{cm}$) coincides with the center frequency ν_0 of the gain profile. What is the threshold inversion for the central mode, and at which inversion does oscillation start on the two adjacent longitudinal modes if the resonator losses are 10%?

32.2.4.4 Ex: Mode pulling in an active resonator

The frequency of a passive resonator mode ($L = 15\,\mathrm{cm}$) lies $0.5\Delta\nu_D$ away from the center of the Gaussian gain profile of a gas laser at $\lambda = 632.8\,\mathrm{nm}$. Estimate the mode pulling if the cavity resonance width is 2 MHz and $\Delta\nu_D = 1\,\mathrm{GHz}$.

32.2.4.5 Ex: Spatial hole-burning

Assume a laser transition with a homogeneous width of 100 MHz, while the inhomogeneous width of the gain profile is 1 GHz. The resonator length is $d = 200\,\mathrm{cm}$ and the active medium with length $L \ll d$ is placed $a = 20\,\mathrm{cm}$ from one end mirror. Estimate the spacing of the spatial hole-burning modes. How many modes can oscillate simultaneously if the unsaturated gain at the line center exceeds the losses by 10%?

32.2.4.6 Ex: Optimizing the transmission of laser output mirrors

Estimate the optimum transmission of the laser output mirror if the unsaturated gain per round trip is 2 and the internal resonator losses are 10%.

32.2.4.7 Ex: Mode selection in a HeNe laser

A HeNe laser with an unsaturated gain of $G(\nu_0) = 1.3$ per round trip at the center of the Gaussian gain profile with halfwidth $\Delta\nu_D = 1.5\,\mathrm{GHz}$ has a resonator length of $d = 50\,\mathrm{cm}$ and total losses of 4%. Single-mode operation at ν_0 is achieved with a coated tilted etalon inside the resonator. Design the optimum combination of etalon thickness and finesse.

32.2.4.8 Ex: Mode hopping in a HeNe laser

A single-mode HeNe laser with resonator length $L = 15\,\mathrm{cm}$ is tuned by moving a resonator mirror mounted on a piezo. Estimate the maximum tuning range before a mode hop will occur, assuming an unsaturated gain of 10% at the line center and resonator losses of 3%. What voltage has to be applied to the piezo (expansion 1 nm/V) for this tuning range?

32.2.4.9 Ex: Mode selection with an intracavity etalon

Mode selection in an argon laser is often accomplished with an intracavity etalon. What is the frequency drift of the transmission maximum
a. for a solid fused quartz etalon with thickness $d = 1\,\mathrm{cm}$ due to a temperature change of 2° C?
b. For an air-space etalon with $d = 1\,\mathrm{cm}$ due to an air pressure change of 4 mbar?
c. Estimate the average time between two mode hopes (cavity length $L = 100\,\mathrm{cm}$) for a temperature drift of 1° C/h or a pressure drift of 2 mbar/h.

32.2.4.10 Ex: Frequency and intensity noise of a laser

A single-mode laser is frequency stabilized onto the slope of the transmission maximum of an external reference Fabry-Perot interferometer made of invar with a free spectral range of 8 GHz. Estimate the frequency stability of the laser
a. against temperature drifts, if the FPI is temperature stabilized within 0.01°C,
b. against acoustic vibrations of the mirror distance L in the FPI with amplitudes of 100 nm.
c. Assume that the intensity fluctuations are compensated to 1% by a difference amplifier. Which frequency fluctuations are still caused by the residual intensity fluctuations, if a FPI with a free spectral range of 10 GHz and a finesse of 50 is used for frequency stabilization at the slope of the FPI transmission peak?

32.2.5 *Experiment: Analyzing the mode structure of a HeNe laser*

Here we will analyze the mode structure of a HeNe laser via (i) an optical spectrum analyzer and (ii) a radiofrequency spectrum analyzer. We will also try to unravel the polarization of the laser light.

1. Couple the light of a HeNe laser simultaneously into an optical spectrum analyzer and a radiofrequency spectrum analyzer. What do you observe when you slightly heat the laser housing? Calculate from your observations the length of the laser cavity.

2. Pass the light through a $\lambda/4$-plate and then through a polarizing beam splitter. What do you observe in the two output ports of the PBS?

32.2.6 *Experiment: Adjusting the threshold of an ECDL laser*

Here we will construct a diode laser in Littmann configuration.

1. Take a laser diode, a Peltier cooler, a thermistor, a piezo transducer, and a diffraction grating. Put everything together.

2. Optimize the threshold. Analyze the emission spectrum with an optical spectrum analyzer.

32.3 Introduction to optical phase and frequency modulation

32.3.1 Acousto-optic modulator

The *acousto-optic modulator AOM* permits fast frequency and amplitude variations of a laser beam. Because it does not incorporate mechanical parts, it works without fatigue. AOMs are used, for instance, in laser printers, where the gray tone of a pixel can be adjusted via the intensity of the laser beam, while its position (rows and

columns) is varied by a rotating mirror and the drum propagating the paper sheet. In quantum optics labs they are frequently used for fast (down to μs) switching on and off, intensity control, and super-fine frequency-tuning of laser beams. The angular deflection of the first-order diffracted beam upon frequency tuning, which is often perceived as an inconvenience, can be circumvented by double-passage through the AOM.

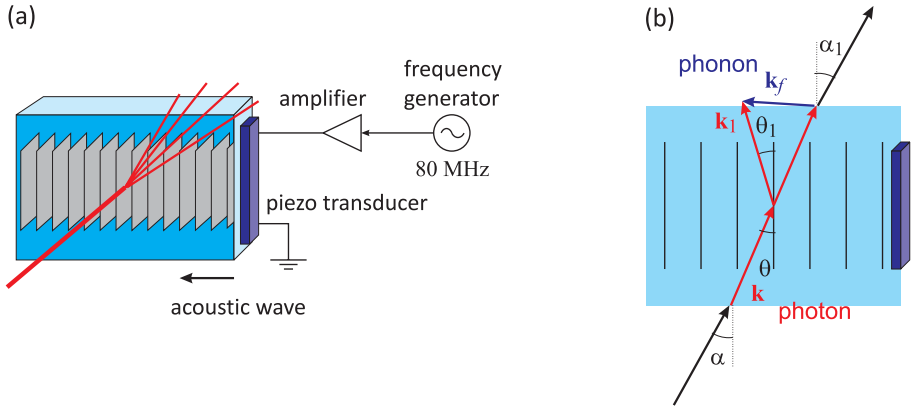

Figure 32.32: (a) Principle of the acousto-optic modulator. (b) Scheme of the diffraction in an acousto-optic modulator: A photon with wavevector k is scattered by a phonon with wavevector k_1 resulting in a photon with wavevector k_f.

The acousto-optic modulator consists of a piece of crystal (or glass) excited by an acoustic wave with frequency f produced by a piezo-electric transducer (see Sec. 32.3.1) mounted perpendicularly to propagation direction of the laser beam. The sound waves propagate through the crystal as density fluctuations periodically changing the refraction index n. The incident light is diffracted through Brillouin scattering at the spatial modulation of the refraction index. In a wave picture, the process can be interpreted as Bragg scattering of a light wave (with its wavelength inside the crystal $\lambda_n = 2\pi/k_n = c/n\nu$) from a density grating. c/n is the propagation velocity of light inside the crystal. Since phonons (with their wavelength $\lambda_f = 2\pi/k_f = c_f/f$, where c_f is the sound velocity in the crystal) are quantized and can only be emitted and absorbed entirely, the frequency of the first-order diffraction is $\nu_1 = \nu + f$. In case of an ideal adjustment of the Bragg angle, the *Bragg condition* results in $\theta_1 = \theta$ (see Fig. 32.32),

$$\sin\theta = \frac{k_f}{2k} = \frac{f\lambda_n}{2c_f} \ . \tag{32.56}$$

Since the laser beam is refracted when it enters the crystal, the relation between the incidence and exit angle is given by *Snell's law*, $\sin\alpha = n\sin\theta$. With this, the Bragg condition can be written,

$$\boxed{\sin\alpha = \frac{f\lambda}{2c_f}} \ . \tag{32.57}$$

The angle between the 0^{th} and the 1^{st} order is, hence, 2α.

In a corpuscular picture, the process can be understood as a *four-wave mixing* (*4WM*) between photons and phonons. The deflection of the laser beam is a consequence of momentum, $\mathbf{k}_1 = \mathbf{k} + \mathbf{k}_f$. The frequency shift corresponds exactly to the Doppler shift induced by the Brillouin scattering (absorption and reemission of a phonon in reverse direction), and we obtain a relationship that is equivalent to the Bragg condition,

$$f = \nu_1 - \nu = 2\nu \frac{c_f \sin\theta}{c/n} \ . \tag{32.58}$$

From the Bragg condition, knowing the deflection angle and the (fixed) frequency shift, we can calculate the sound velocity. A typical value is $c_f \simeq 4200$ m/s [5]

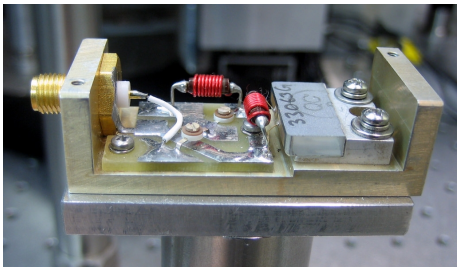

Figure 32.33: Image of an AOM without cover.

An AOM works best (highest diffraction efficiency in to the first Bragg order, which may reach more than 90%) at a specific radiofrequency, which typically is located somewhere in the range $f = 40...800$ MHz, the most common one being 80 MHz. Deviations from this 'center frequency' are possible within a range of typical $\pm 10\%$ of the center frequency.

32.3.2 Electro-optic modulator

An *electro-optic modulator* is an optical device with which, by an applied voltage, the phase, frequency, amplitude or direction of a light beam can be modulated. Modulation bandwidths in the GHz regime are possible. In the simplest case, the EOM consists of a crystal (e.g., lithium niobate), whose refractive index depends on the amplitude of the local electric field. That is, when a lithium niobate crystal is exposed to an electric field the speed of light propagation is reduced. One can thus control the phase of a light beam at the output of a crystal by inserting it into a plate capacitor and applying a voltage. The phase shift of the light depends linearly on the applied voltage.

EOMs are often used to generate sidebands in a monochromatic laser beam. They are also used as *Pockels cell*, i.e., as a voltage-controlled phase-plate. The Pockels

[5] The result (32.58) can be derived from conservations laws for energy $\omega_1 = \omega + \omega_f$ and momentum $\mathbf{k}_1 = \mathbf{k} + \mathbf{k}_f$. Defining $\omega \equiv 2\pi\nu$, $\omega_1 \equiv 2\pi\nu_1$ and $\omega_f \equiv 2\pi f$ we find,

$$\frac{\omega_f^2}{c_f} = \mathbf{k}_f^2 = (\mathbf{k}_1 - \mathbf{k})^2 = k_1^2 + k^2 - 2\mathbf{k}_1 \cdot \mathbf{k} = \frac{\omega_1^2}{c_n^2} + \frac{\omega^2}{c_n^2} - \frac{2\omega\omega_1}{c_n^2}\cos(2\theta) \simeq \frac{4\omega\omega_1}{c_n^2}\sin^2\theta \ .$$

With $\omega_1 \simeq \omega$ we reproduce the result [892, 893].

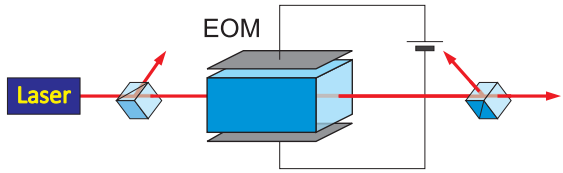

Figure 32.34: Electro optic modulator.

effect produces in a medium a *birefringence*, which depends linearly on the applied electric field. This is in contrast to the *Kerr effect*, in which the birefringence depends in a quadratic form of the electric field.

Suppose the optically inactive axis is x. In this case, the influence of EOM on the polarization of a laser beam is described by

$$\mathcal{M}_{EOM}(\theta) = \begin{pmatrix} 1 & 0 \\ 0 & e^{\imath\theta} \end{pmatrix} . \tag{32.59}$$

For operation as a Pockels cell, the EOM is inserted between two crossed polarizers oriented, e.g., along the x and y axis. The EOM itself is rotated by an angle ϕ,

$$\begin{aligned} \mathcal{M}_{Pockels}(\theta,\phi) &= \begin{pmatrix} 0 & 0 \\ 0 & 1 \end{pmatrix} \begin{pmatrix} \cos\phi & \sin\phi \\ -\sin\phi & \cos\phi \end{pmatrix} \begin{pmatrix} 1 & 0 \\ 0 & e^{\imath\theta} \end{pmatrix} \begin{pmatrix} \cos\phi & -\sin\phi \\ \sin\phi & \cos\phi \end{pmatrix} \begin{pmatrix} 1 & 0 \\ 0 & 0 \end{pmatrix} \\ &= 2\imath e^{\imath\theta/2} \sin\tfrac{\theta}{2} \sin\phi\cos\phi \begin{pmatrix} 0 & 0 \\ 1 & 0 \end{pmatrix} , \end{aligned} \tag{32.60}$$

For $\phi = \pi/4$ we get,

$$\mathcal{M}_{Pockels}(\theta, \tfrac{\pi}{4}) = \imath e^{\imath\theta/2} \sin\tfrac{\theta}{2} \begin{pmatrix} 0 & 0 \\ 1 & 0 \end{pmatrix} . \tag{32.61}$$

That is, an incident beam of light, $\mathbf{E} = E\hat{\mathbf{e}}_x$, linearly polarized in x-direction is rotated into the y-direction and, depending on the phase shift θ, it is completely blocked or transmitted through the Pockels cell [see Fig. 32.35(a)],

$$I_{tr} = I_0 \sin^2\tfrac{\theta}{2} . \tag{32.62}$$

32.3.3 Optical phase modulation

The frequency and the phase of a laser beam can be influenced and modulated similarly to radiofrequency signals. We can therefore use the calculation of Sec. 31.3.1 completely, only changing the carrier frequency to be the frequency of the light: The Fourier expansion of a complex-valued periodic function $s(x)$ into a series is defined as,

$$s_N(x) = \sum_{k=-N}^{N} c_k e^{\imath kx} \qquad \text{where} \qquad c_k = \frac{1}{2\pi}\int_{2\pi} s(x) e^{-\imath kx} dx . \tag{32.63}$$

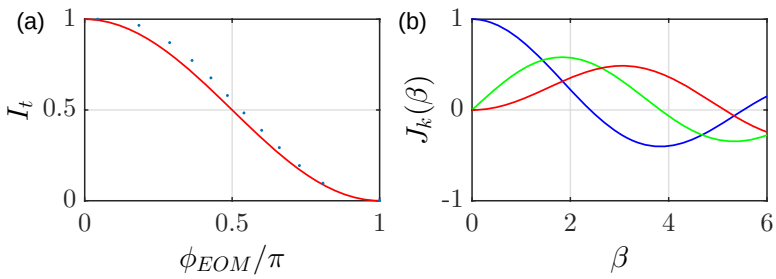

Figure 32.35: (code) (a) Effect of a Pockels cell. The solid line was calculated with the Eq. (32.60), the dotted was measured experimentally. (b) Lowest-order Bessel functions.

Applying this to the modulated phase shift factor $s(\Omega t) = e^{\imath\theta(t)}$ with $\theta(t) \equiv \beta \sin \Omega t$, we get,

$$s_N(\Omega t) = \sum_{k=-\infty}^{\infty} c_k e^{\imath k \Omega t} \qquad \text{where} \qquad c_k = \frac{1}{2\pi} \int_{-\pi}^{\pi} e^{\imath\beta \sin \Omega t} e^{-\imath k \Omega t} d\Omega t \ , \tag{32.64}$$

but the Fourier coefficients are nothing else than the integral definition of the k-th order Bessel function,

$$J_k(\beta) \equiv \frac{1}{2\pi} \int_{-\pi}^{\pi} e^{\imath(\beta \sin \tau - k\tau)} d\tau \ , \tag{32.65}$$

where $J_{-k}(\beta) = -J_k(\beta)$. Hence, we may write the electric field,

$$\boxed{\begin{aligned} E(t) &= e^{\imath[kz - \omega t + \imath\theta(t)]} = e^{\imath(kz-\omega t)} \sum_{k=-\infty}^{\infty} J_k(\beta) e^{\imath k \Omega t} \\ &\simeq J_0(\beta) e^{\imath\omega t} + J_1(\beta) e^{\imath\omega t + \imath\Omega t} + J_{-1}(\beta) e^{\imath\omega t - \imath\Omega t} \end{aligned}} \ . \tag{32.66}$$

For small modulation indices β only the lowest-order Bessel function contribute noticeable amplitudes, as illustrated in Fig. 32.35(b).

The interpretation of this is, that *phase modulation* imprints sidebands onto a monochromatic laser beam. These sidebands are independent modes which can be resolved, e.g. with an optical spectrum analyzer, as illustrated in Fig. 32.36.

Technically the phase can be modulated by means of an electro-optical modulator, as shown in Fig. 32.37(b). Alternatively, one may apply a periodic modulation of the current which controls a diode laser, as shown in Fig. 32.37(a), which can be done e.g. by inductive coupling using a *bias-T*.

From (32.66) we immediately see that phase modulation remains invisible for a photodetector measuring $|E(t)|^2$. Imagine, however, that the light passes through a frequency-selective absorber, as illustrated in Fig. 32.37(b), such that the sidebands suffer unequal losses. Then the photodetector will record (apart from a constant offset) a signal oscillating at the frequency Ω,

$$\begin{aligned} |E(t)|^2 &= \left| J_0(\beta) e^{\imath\omega t} + a J_1(\beta) e^{\imath\omega t + \imath\Omega t} + b J_{-1}(\beta) e^{\imath\omega t - \imath\Omega t} \right|^2 \\ &= J_0(\beta)^2 + (a+b) J_1(\beta)^2 + (a-b) J_0(\beta) J_1(\beta) 2 \cos \Omega t + \dots \ . \end{aligned} \tag{32.67}$$

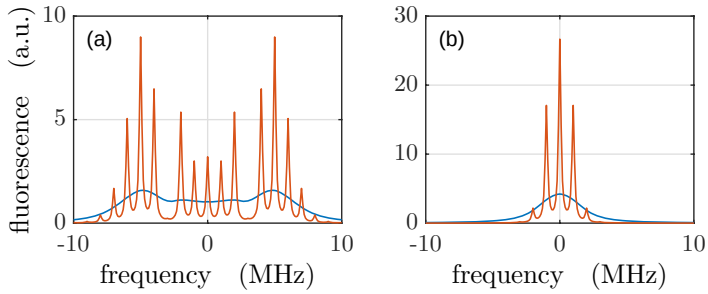

Figure 32.36: (code) Phase modulation sidebands with high (left) and low (right) modulation index resolved by a narrow (red) or broad (blue) filter.

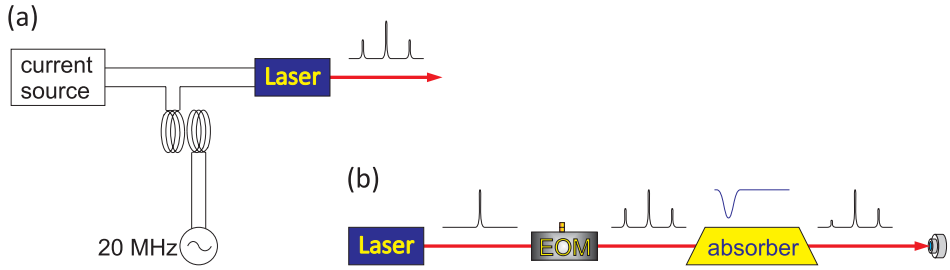

Figure 32.37: (a) Scheme for phase modulation of a diode laser by modulating the drive current. (b) Phase modulation with an external EOM followed by frequency-selective absorption of the lower sideband.

This idea is at the heart of powerful spectroscopic techniques, such as *frequency modulation spectroscopy*, *modulation transfer spectroscopy*, and the *Pound-Drever-Hall* frequency stabilization technique.

32.3.4 Exercises

32.3.4.1 Ex: Response time of an AOM

A beam of light at 689 nm focused to a waist of 100 µm passes through the crystal of an 80 MHz AOM, characterized by a sound velocity of $c_s = 4200\,\mathrm{m/s}$.
a. By how much the first diffraction order is deflected by the AOM? Regarding the beam divergence of the Gaussian beam, will it be possible to spatially separate the diffraction orders?
b. An experimentalist ramps the driving frequency between 70 and 90 MHz by means of a voltage-controlled oscillator. What is the range of diffraction angles covered?
c. Estimating the response time of the AOM by the time that the traveling sound wave needs to cover a distance corresponding to the focus of the light beam, how fast can the experimentalist switch off the light beam by suddenly interrupting the driving signal? What is the modulation bandwidth of the AOM?
d. The light beam passes through the AOM at a distance of $d = 2\,\mathrm{mm}$ from the piezo transducer generating the sound wave. How will this fact limit response time?

32.3.4.2 Ex: Intensity stabilization with a Pockels cell

Assume that the output power of a laser shows random fluctuations of about 5%. Intensity stabilization is accomplished by a Pockels cell with a halfwave voltage of 600 V. Estimate the ac output voltage of the amplifier driving the Pockels cell that is necessary to stabilize the transmitted intensity if the Pockels cell is operated around the maximum slope of the transmission curve.

32.3.4.3 Ex: Generating sidebands with an EOM

An EOM (e.g. Thorlabs, EO-PM-NR-C1) characterized by a half-wave voltage of $U_{hwv} = 230\,\mathrm{V}$ at 689 nm is to be used to generate optical sidebands at 20 MHz.
a. Estimate numerically, how much voltage amplitude at what frequency a frequency generator must provide in order to generate optical sidebands having half the light power as the carrier?
b. How high must the finesse of a 5 cm confocal Fabry-Pérot spectrum analyzer be in order to resolve the sidebands.

32.3.4.4 Ex: Reflection of a phase-modulated signal from an optical cavity

A phase-modulated light beam (modulation frequency $f = 20\,\mathrm{MHz}$) is reflected from an optical cavity and recorded by a fast photodetector, whose bandwidth is larger than f. Using the Airy formulae for the electric field of a light beam reflected from a cavity (32.27) calculate the reflection spectrum, that is, the intensity of reflected light as a function of detuning $\Delta = \omega - \omega_c$, where ω is the frequency of the light and ω_c a resonant frequency of the cavity. What frequency components does the photodetector signal contain.

32.3.4.5 Ex: Switching time for an EOM

a. Describe what happens to a laser beam passing through an EOM when its refraction index n is suddenly changed.
b. Estimate the transient time for the phase shift to take place.
c. For a length of the EOM crystal of $L = 1\,\mathrm{cm}$ and a laser wavelength of $\lambda = 689\,\mathrm{nm}$ estimate the change Δn required to achieve a phase shift of 180°.

32.3.5 *Experiment: Characterizing an AOM*

Fig. 32.38 illustrates the setup, use, and test of an AOM. It is recommended familiarizing with the operation principle of a *voltage-controlled oscillator* (*VCO*) (see Sec. 31.3.1) and a voltage-controlled *variable attenuator*. We will also learn how to use a spectrum analyzer [6].

1. Optimize a diffraction efficiency of the AOM. What are the impacts of the Bragg angle, the radiofrequency power, and the laser beam diameter.

[6] Data sheet for the VCO see appendix Fig. 35.16,
data sheet for the AOM see appendix Fig. 35.20

2. Measure the deflection angle as a function of the applied radiofrequency. Based on this result, calculate the sound velocity in the crystal.

3. Measure the diffraction efficiency as a function of the applied radiofrequency power at a fixed Bragg angle. Repeat the measurement optimizing the Bragg angle for every value of the radiofrequency.

4. Reduce the radiofrequency power using the variable voltage-controlled attenuator. Determine the diffraction efficiency as a function of radiofrequency power.

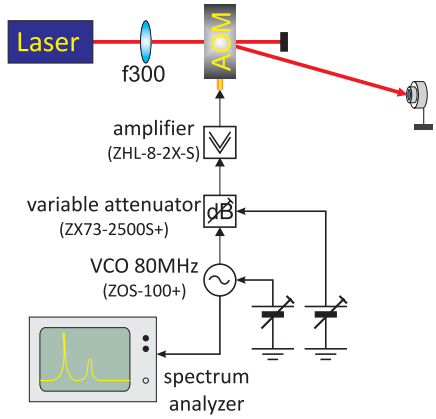

Figure 32.38: Setup for testing an acousto-optic modulator.

See Fig. 32.39.

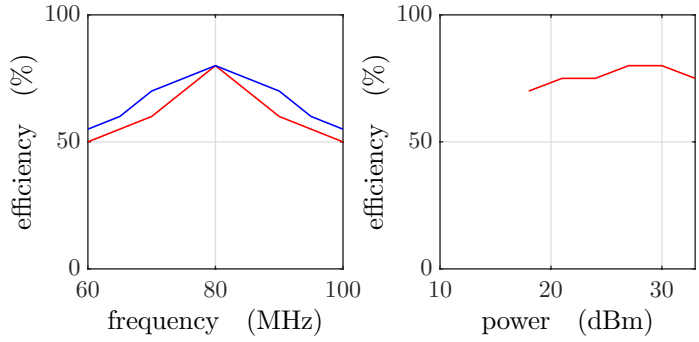

Figure 32.39: Example of measured efficiency curves.

32.3.6 *Experiment: EOM in a Mach-Zehnder interferometer*

Here we will learn to operate an EOM as Pockels cell and as phase modulator.

1. Align a laser beam through an electro-optic modulator. Supply a voltage between 0 V and 500 V to the EOM. Test its operation by beating the ordinary with the extraordinary beam. Modulate the supply voltage at a low frequency.

2. Set up a Mach-Zehnder interferometer by phase-matching the exit beam of the EOM with a part of the input beam.

3. The interferometer provides a mean to convert a phase modulation into an amplitude modulation. Describe this feature theoretically using the Eqs. (31.12) and (31.13).

4. Use the EOM as a Pockels cell. Rotate the EOM by 45° around the optical axis. Probe the polarization of the outgoing beam with a polarization filter.

5. Modulate the EOM and show that the light acquires sidebands.

32.3.7 *Experiment: Creating sidebands with an EOM*

EOMs can be used to generate optical sidebands [7].

1. Apply the required voltages to a VCO (MiniCircuits, ZOS100), until it generates a variable frequency between 40 and 60 MHz. Attenuate the power with a variable attenuator up to −20 dBm. Check the amplitude and frequency with a spectrum analyzer.

2. Add a bias-T to the power supply of a laser diode. Observe the transmission spectrum of a Fabry-Pérot cavity for various frequencies and modulation amplitudes. Determine the modulation index. Use the known distance of the sidebands to estimate the finesse of the Fabry-Pérot cavity.

32.4 Radiofrequency techniques and the transfer of information

It often happens that information is coded within a frequency band corresponding to wavelengths which are not easily transported to other locations. For example, audio frequencies (speech or music), ones they are converted to electromagnetic vibrations, correspond to wavelengths of hundreds of kilometers. Such waves are very difficult to radiate and are subject to diffraction.

For this reason, audio frequencies are often used to *modulate* so-called carriers, which in turn are chosen in frequency ranges which are easy to radiate by antennas. This is the basic idea of the radio, where the carrier frequencies are typically chosen in the MHz regime. But information can as well be encoded into laser beams, as illustrated in Fig. 32.40.

[7] Datasheet for the VCO see appendix Fig. 35.16,
data sheet for the power divider see appendix Fig. 35.18,
data sheet for the mixer see appendix Fig. 35.19

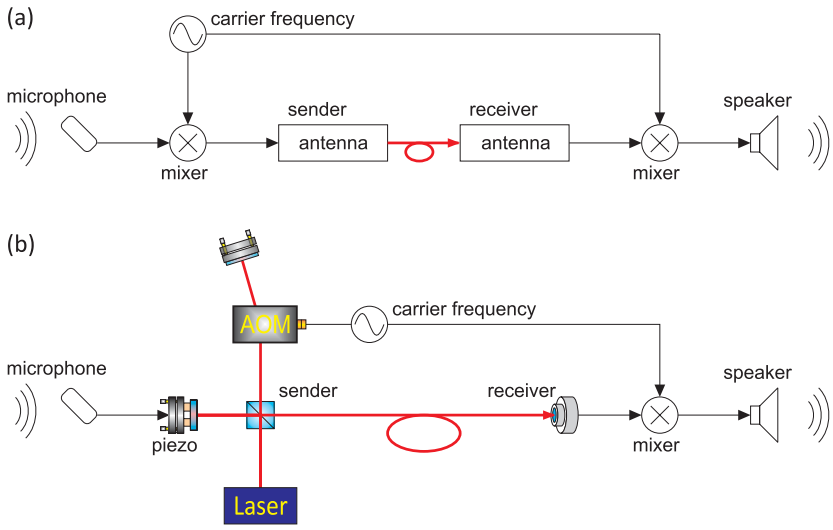

Figure 32.40: Analogy between radio transmission (a) and heterodyne techniques with a laser (b).

32.4.1 Measurement of a frequency beat

Interferometry is always based on the splitting and recombination of a wave, e.g., a laser beam or a matter wave. The recombination of laser beams is always a little technical challenge, as it requires a perfect phase matching of the Gaussian laser modes. Let us consider two plane waves $\mathcal{E}_1 = Ae^{\imath\omega_1 t}$ and $\mathcal{E}_2 = Ae^{\imath\omega_2 t}$ impinging on a photodiode. We suppose that they are phase-matched, such that their wavevectors are parallel. The photodiode then generates a *beat signal*,

$$\boxed{I = |\mathcal{E}_1 + \mathcal{E}_2|^2 = AB[2 + 2\cos(\omega_1 - \omega_2)t]} \ . \tag{32.68}$$

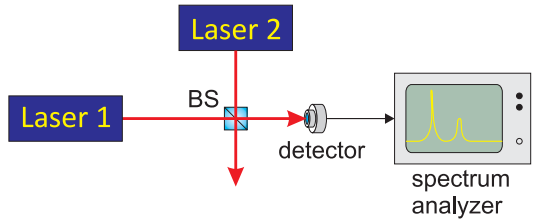

Figure 32.41: Principle of a beat frequency measurement.

In practice, laser beams are usually not plane waves, but have a finite diameter and radius of curvature. In order to get a high contrast signal, a good phase-matching of the beams is important in order to obtain a strong photodiode signal.

32.4.2 Homodyne method

For the *homodyne method* the field amplitude of a laser beam, E_i, with frequency, $\omega = ck$, is divided by a beam splitter (reflectivity $R = |\eta|^2 \simeq 50\%$) into a reference beam (reflection at an optically dilute medium) and a probe beam, exactly as we have done for the Michelson interferometer in Sec. 32.1.3, when we obtained the formula (32.16) [8],

$$I \propto 1 + \cos[k(L_t - L_r)] \ . \tag{32.69}$$

However, we will now modulate the path length of one interferometer arm, e.g. using an EOM, $L_r = L_r(t)$. The modulation can, but does not need to be sinusoidal. In fact it may be an arbitrary radiofrequency signal, e.g. generated by acoustic sound. Restricting to small modulation amplitudes, $kL_r \ll \pi$, and choosing the length of the interferometer arms such that,

$$\boxed{I(t) \propto \sin kL_r \simeq kL_r(t)} \ , \tag{32.70}$$

we see, that the photodetector signal will reproduce the modulation signal. In other words, we encoded information on a laser beam, which carries it (e.g. through an optical fiber) to another place.

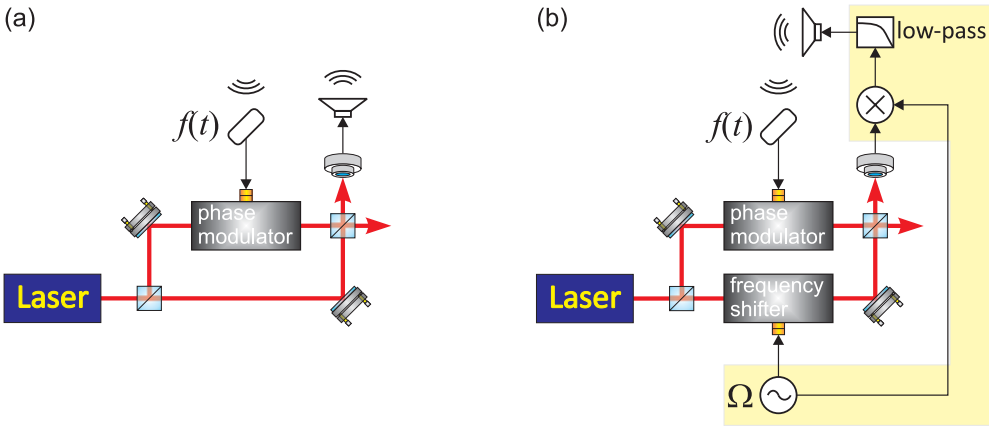

Figure 32.42: Principle scheme of the (a) homodyning and (b) heterodyning technique at the example of a Mach-Zehnder interferometer. The components in the yellow area of (b) constitute a Lock-In amplifier.

32.4.3 Heterodyne method

The *heterodyne method* is similar to the homodyne one, except that the probe beam is frequency-shifted (e.g., by the passage through an AOM operated at frequency Ω),

$$\mathcal{E}'_t = \mathcal{E}_t e^{\imath kL_t + \imath \Omega t} \ . \tag{32.71}$$

[8] Here, we call $L_{t,r}$ the total length of the interferometer arm (back and forth for Michelson, one-way for Mach-Zehnder).

The photodetector signal generated by the beams after their recombination at the beam splitter is,

$$\begin{aligned} I &\propto \left|(1-\eta)\mathcal{E}_r e^{\imath kL_r} + \eta\mathcal{E}_t e^{\imath kL_t+\imath\Omega t}\right|^2 \\ &= \left|-(1-\eta)\eta\mathcal{E}_i e^{\imath kL_r} + \eta(1-\eta)\mathcal{E}_i e^{\imath kL_t+\imath\Omega t}\right|^2 \\ &= \left|(1-\eta)\eta\mathcal{E}_i\right|^2 \left|-e^{2\imath kL_r} + e^{\imath kL_t+\imath\Omega t}\right|^2 \ . \end{aligned} \tag{32.72}$$

This signal is now demodulated with the AOM frequency,

$$Ie^{\imath\Omega t} \propto \left|-e^{\imath kL_r} + e^{\imath kL_t+\imath\Omega t}\right|^2 e^{i\Omega t} = e^{2\imath\Omega t} - e^{\imath k(L_t-L_r)+2\imath\Omega t} - e^{-\imath k(L_t-L_r)} \ . \tag{32.73}$$

A low-pass filter cuts all ac-components of the signal,

$$\boxed{I_{\text{filtered}}(t) \propto -e^{-\imath k(L_t-L_r)} \simeq -1 + \imath k[L_t - L_r(t)]} \ , \tag{32.74}$$

for small signal amplitudes $L_r(t)$.

32.4.4 Measuring the quadrature components of an electric field

Photodetectors measure intensities $I \propto |\vec{\mathcal{E}}|^2$. Sometimes, however, we are interested in the electric field itself, for example, when we want to get the correlation function $g^{(1)}(\tau)$ and the spectrum $S_\mathcal{E}(\omega)$ of a signal. A frequently used procedure consists in beating the signal of interest with a frequency-shifted local oscillator and demodulating the *quadrature components* of the beat signal.

Let us consider a signal of interest $\mathcal{E}_{\text{sig}}(t) = |\mathcal{E}_{\text{sig}}|e^{\imath\phi(t)}$ with information encoded in the temporal behavior of the phase $\phi(t)$. The first step consists in beating this signal on a photodetector with a frequency-shifted local oscillator $\mathcal{E}_{\text{lo}}(t) = |\mathcal{E}_{\text{lo}}|e^{\imath\omega_{\text{lo}}t}$, yielding a photocurrent,

$$S \propto |\mathcal{E}_{\text{sig}} + \mathcal{E}_{\text{lo}}|^2 = |\mathcal{E}_{\text{sig}}|^2 + |\mathcal{E}_{\text{lo}}|^2 + 2|\mathcal{E}_{\text{lo}}||\mathcal{E}_{\text{sig}}|\cos[\omega_{\text{lo}}t - \phi(t)] \ . \tag{32.75}$$

Now, demodulating this signal simultaneously with the local oscillator frequencies $\cos\omega_{\text{lo}}t$ and $\sin\omega_{\text{lo}}t$, we get,

$$\begin{aligned} U_c &= S\cos\omega_{\text{lo}}t = |\mathcal{E}_{\text{lo}}||\mathcal{E}_{\text{sig}}|\cos\phi(t) + \text{oscillating terms} \\ U_s &= S\sin\omega_{\text{lo}}t = |\mathcal{E}_{\text{lo}}||\mathcal{E}_{\text{sig}}|\sin\phi(t) + \text{oscillating terms} \ , \end{aligned} \tag{32.76}$$

where the oscillating terms can be removed by a low-pass filtering. Finally, we calculate,

$$|\mathcal{E}_{\text{sig}}| = \frac{\sqrt{U_c^2+U_s^2}}{|E_{\text{lo}}|} \qquad \text{and} \qquad \tan\phi(t) = \frac{U_s}{U_c} \ , \tag{32.77}$$

and obtain the electric field via,

$$\boxed{\mathcal{E}_{\text{sig}} = |\mathcal{E}_{\text{sig}}|e^{\imath\phi(t)} = \frac{\sqrt{U_c^2+U_s^2}}{|\mathcal{E}_{\text{lo}}|}e^{\imath\arctan\frac{U_s}{U_c}}} \ . \tag{32.78}$$

32.4.5 Exercises

32.4.5.1 Ex: Pound-Drever-Hall signal

Consider the photodetector signal of Exc. 32.3.4.4. What signal do you observe when demodulating the signal with an oscillation of frequency f? Calculate the derivative of the signal close to resonance; from which parameters does the slope depend, and how must you choose the modulation index to maximize it?

32.4.6 *Experiment: Beating two lasers*

In this exercise, we will ...

1. Take two independent lasers operating at nearly the same frequency (within $\sim 1\,\mathrm{GHz}$) and overlap them at a (non-polarizing) beam splitter.
2. Focus one of the ports of the beam splitter on a photodetector with large band width ($\sim 1\,\mathrm{GHz}$).
3. Analyze the beat signal on a spectrum analyzer.
4. Focus a helium-neon laser onto a fast photodetector and determine the free spectral range of the laser resonator.

32.4.7 *Experiment: Homo- and heterodyning with a Michelson interferometer*

In this exercise, we will ...

1. Set up a Michelson interferometer.

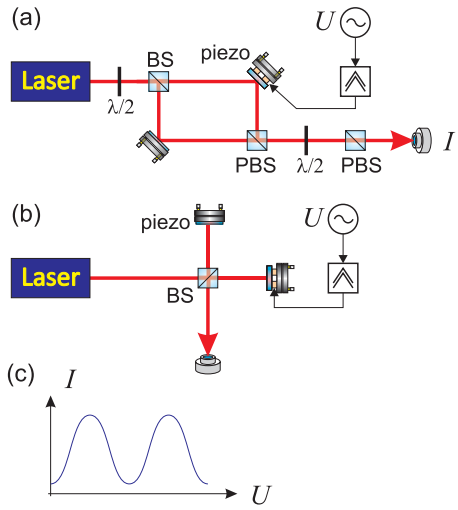

Figure 32.43: Homo- and heterodyning with a Michelson interferometer.

32.5 Further reading

C.J. Buczek et al., *Laser injection locking* [DOI]

Zhixin Liu et al., *Optical Injection Locking: From Principle to Applications* [DOI]

H. Kogelnik et al., *Laser Beams and Resonators* [DOI]

A. Yariv, *Quantum Electronics* [DOI]

A. Yariv et al., *Optical waves in crystals* [DOI]

W. Demtröder, *Atoms, Molecules and Photons: An Introduction to Atomic- Molecular- and Quantum Physics* [DOI]

W. Lichten, *Precise Wavelength Measurements and Optical Phase Shifts: I. General Theory* [DOI]

W.W. Chow, *The ring laser gyro* [DOI]

Chapter 33

Optical spectroscopy

Modern 'optics' is to be understood as 'physics of light-matter interaction' in the optical energy regime. In this sense, this area of physics comprises quantum optics, photonics, atomic physics, and atom optics. Since the invention of the laser the field of optics has seen a huge technological progress leading to the development of extremely powerful and precise tool for investigating and manipulating matter. The femtosecond laser, the frequency comb, atomic interferometers and clocks, and Bose-Einstein condensation are just a few examples.

Spectroscopy is the art of taking and interpreting spectra, i.e. frequency-dependent response functions. The variety of spectroscopic techniques is so overwhelming that a survey is hopeless. As the course also aims at familiarizing the student with applications, a major part of this course will concentrate on techniques employed and available in quantum optics labs. These techniques are mostly oriented toward ultra-high resolution spectroscopy and techniques of manipulating the motion of atoms.

In Sec. 33.1 to 33.4.3, we will try various spectroscopic techniques applied to atomic or cavity resonances.

33.1 Spectrometer and monochromator

Typical dispersive devices are *prisms* and *gratings*.

- lateral displacement as a function of λ
- spectral resolving power $R = |\lambda/\Delta\lambda| = |\nu/\Delta\nu|$
- Rayleigh criterion

33.1.1 Prism spectrometer

For a symmetrical arrangement ($\alpha_1 = \alpha_2 = \alpha$) it is easy to see from Fig. 33.1 that, $\beta = \frac{1}{2}\epsilon$ and $\theta = 2(\alpha - \beta)$. Snell's law the yields,

$$n = \frac{\sin\alpha}{\sin\beta} = \frac{\sin\frac{1}{2}(\theta+\epsilon)}{\sin\frac{1}{2}\epsilon} \ . \tag{33.1}$$

Hence,

$$\frac{dn}{d\theta} = \frac{1}{2}\frac{\cos\frac{1}{2}(\theta+\epsilon)}{\sin\frac{1}{2}\epsilon} \ , \tag{33.2}$$

or

$$\frac{d\theta}{dn} = \frac{\sin\frac{1}{2}\epsilon}{1 - n^2 \sin\frac{1}{2}\epsilon} \ . \tag{33.3}$$

The angular dispersion is therefore,

$$\frac{d\theta}{d\lambda} = \frac{\sin\frac{1}{2}\epsilon}{1 - n^2 \sin\frac{1}{2}\epsilon} \frac{dn}{d\lambda} \ . \tag{33.4}$$

The spectral dispersion of typical transparent materials is on the order of $-dn/d\lambda \approx 10^{-4}$.

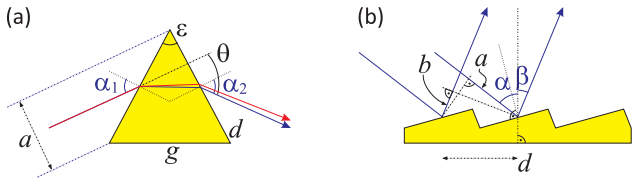

Figure 33.1: Illustration of (a) the prism spectrometer and (b) the grating spectrometer.

Example 205 (*Prism spectrometer*): We calculate the angular dispersion for an equilateral prism ($\sin\frac{1}{2}\epsilon = 0.5$) made of BK7 for two superposed wavelength $\lambda_1 = 461\,\text{nm}$ ($n_{\lambda_1} = 1.5243$) and $\lambda_2 = 633\,\text{nm}$ (with $n_{\lambda_2} = 1.5151$) to be,

$$d\theta = \frac{1}{\sqrt{1 - (n/2)^2}} dn \approx 0.8^\circ \ .$$

The resolving power can be calculated, once we have expressed the limiting aperture $a = d\cos\alpha$ where $d = g/(2\sin\frac{\epsilon}{2})$,

$$\left|\frac{\lambda}{\Delta\lambda}\right| = a\frac{d\theta}{d\lambda} = \frac{g\cos\alpha}{1 - n^2\sin\frac{1}{2}\epsilon}\frac{dn}{d\lambda} = g\frac{dn}{d\lambda} \ . \tag{33.5}$$

Solve Exc. 30.2.3.14.

33.1.2 Grating spectrometer

Destructive interference occurs for,

$$\Delta s = m\lambda = a - b = d\sin\alpha - d\sin\beta \ . \tag{33.6}$$

Frequently used is the so-called *Littrow configuration* for which $\alpha = -\beta$.

The grating represents a multiple beam interferometer, because the beams reflected from every groove of the grating are phase-shifted by amounts (setting $\alpha = 0$,

$$\delta = \tfrac{2\pi}{\lambda}\Delta s = -2\pi\frac{d}{\lambda}\sin\beta \ . \tag{33.7}$$

The sum of the reflections from N grooves of an incident plane wave $E_{in} = E_0 e^{\imath(\mathbf{k}\cdot\mathbf{r}-\omega t}$ is therefore,

$$\mathcal{E}_r = \sqrt{R}\mathcal{E}_0 \sum_{m=0}^{N} e^{\imath \mathbf{k}_r\cdot\mathbf{r}-\omega t} e^{im\delta} = \sqrt{R}E_0 e^{\imath \mathbf{k}_r\cdot\mathbf{r}-\omega t} \frac{1-e^{\imath N\delta}}{1-e^{\imath\delta}} \ . \tag{33.8}$$

Consequently, the intensity is,

$$I_r = RI_0 \frac{\sin^2 \frac{N}{2}\delta}{\sin^2 \frac{1}{2}\delta} \ . \tag{33.9}$$

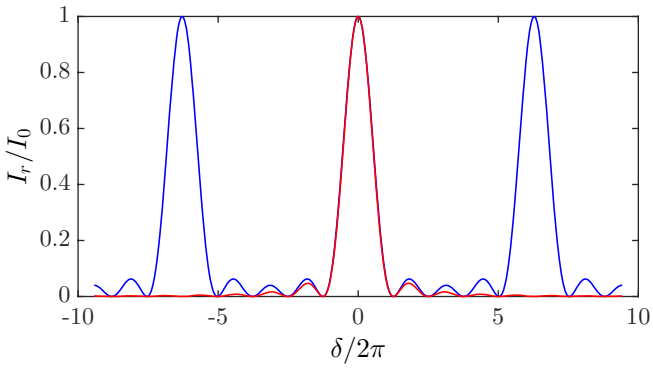

Figure 33.2: (code) Reflection curve of a diffraction grating.

The angular dispersion is, using Eqs. (33.7) and (33.6),

$$\frac{d\beta}{d\lambda} = \left(\frac{d\lambda}{d\beta}\right)^{-1} = -\frac{m}{d\cos\beta} = -\frac{\sin\alpha - \sin\beta}{\lambda\cos\beta} \ . \tag{33.10}$$

The resolving power is,

$$\left|\frac{\lambda}{\Delta\lambda}\right| = \frac{Nd(\sin\alpha - \sin\beta)}{\lambda} = mN \ . \tag{33.11}$$

Solve Exc. 33.1.3.1, 33.1.3.2, and 33.1.3.3.

33.1.3 Exercises

33.1.3.1 Ex: Resolution of a grating spectrometer

Calculate the spectral resolution of a grating spectrometer with an entrance slit width of 10 µm, focal lengths $f_1 = f_2 = 2$ m of the mirrors M1 and M2, a grating with 1800 grooves/mm and an angle of incidence $\alpha = 45°$. What is the useful minimum slit width if the size of grating is $100 \times 100\,\text{mm}^2$?

33.1.3.2 Ex: Grating spectrometer

The spectrometer in Exc. 33.1.3.1 shall be used in first order for a wavelength range around 500 nm. What is the optimum blaze angle, if the geometry of the spectrometer allows an angle of incidence α about 20°?

33.1.3.3 Ex: Littrow grating

Calculate the number of grooves/mm for a Littrow grating for a 25° incidence at $\lambda = 488\,\text{nm}$ (i.e., the first diffraction order is being reflected back into the incident beam at an angle $\alpha = 25°$ to the grating normal).

33.1.3.4 Ex: Combining spectrometers

A fluorescence spectrum shall be measured with a spectral resolution of 10^{-2} nm. The experimenter decides to use a crossed arrangement of grating spectrometer (linear dispersion: 0.5 nm/mm) and FPI of Exc. 32.1.10.7. Estimate the optimum combination of spectrometer slit width and FPI plate separation.

33.1.4 *Experiment: Separating bichromatic light by prisms and gratings*

In this experiment we will study the dispersive power of a prism and a grating.

1. Combine the beams of a helium-neon laser and a laser at 461 nm via a beam-splitter. Pass this combination through a prism and quantify the dispersion.
2. Calculate the minimum angle between the two beams.
3. Shine the combination onto a reflection grating and quantify the dispersion.

33.1.5 *Experiment: Thorlabs optical spectrum analyzer*

CCS175, characterization, Thorlabs ® tour.

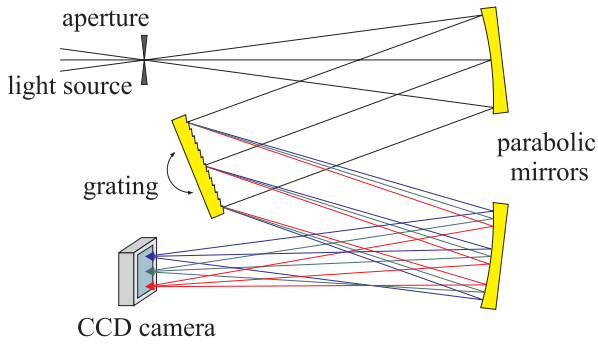

Figure 33.3: Principle of operation of a Czerny-Turner monochromator.

Czerny-Turner CCD spectrometer

1. Irradiate light on OSA and observe the spectrum.

33.1.6 *Experiment: HighFinesse wavemeter*

Wavemeters measure the wavelength of monochromatic light sources by interference. One type of wavemeter is based on a Michelson interferometer, where the length of one interferometer arm is uniformly increased while the interference fringes are counted. Counting the fringes of a known reference laser simultaneously and comparing the counts of the unknown and the reference laser, the wavelength of the unknown laser can be determined with high precision (down to 2 MHz resolution).

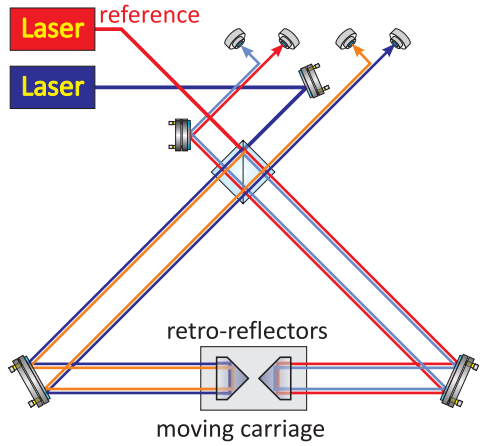

Figure 33.4: Principle of operation of a Michelson-type wavemeter.

1. HighFinesse WSU30, characterization.

33.2 Fluorescence, excitation, and absorption spectroscopy

Depending on the information we want to extract from a sample and on the available instrumentation various types of spectroscopic techniques are possible, which will be discussed on the following sections.

33.2.1 Classification of spectroscopic methods

It is important to distinguish *fluorescence spectra* from *excitation spectra*: Fluorescence spectra are taken by processing the light emitted from a radiator in a monochromator. That is, the light is shone onto a spectral band filter, which only transmits a narrow fraction of the fluorescence spectrum. The power of the transmitted light is measured with a detector. Upon changing the center frequency of the band filter,

different components of the fluorescence spectrum are measured, thus yielding a curve $u(\nu)$, which represents the spectral energy density of the radiator [see Fig. 33.5(a,d)].

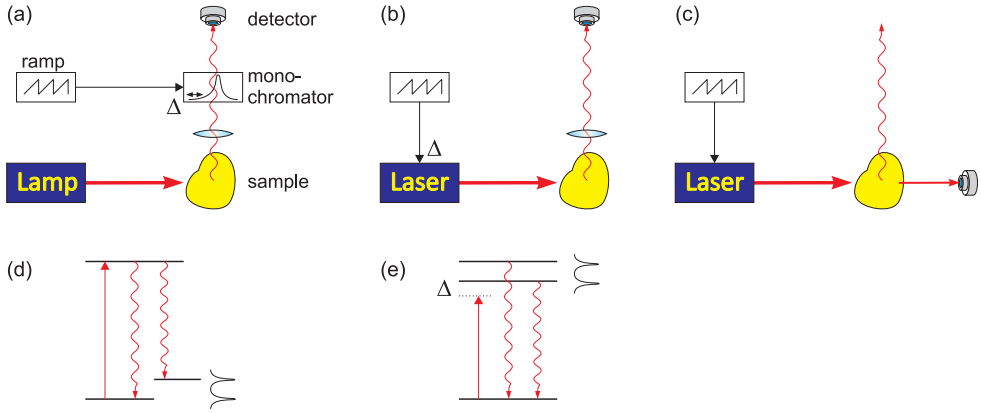

Figure 33.5: (a) Taking a fluorescence spectrum, (b) an excitation spectrum, and (c) an absorption spectrum. Typical level schemes for (d) fluorescence spectroscopy and (e) excitation or absorption spectroscopy.

In contrast to fluorescence spectroscopy, excitation or absorption spectra are taken by varying the frequency of the light exciting a sample. The reemitted light is then measured by a detector without discriminating its frequency components. Obviously, both method yield very different information about the scatterer [see Fig. 33.5(b,c,e)]. Depending on whether the scattered of the transmitted light is detected, we speak of excitation and absorption spectroscopy.

33.2.2 Saturated absorption spectroscopy

One of the most popular spectroscopic technique is *saturation spectroscopy*, as it is simple, robust, and allows to avoid Doppler-broadening. There are, however, many

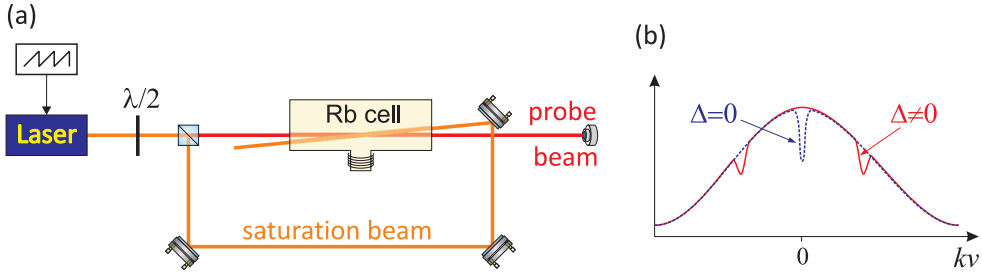

Figure 33.6: (a) Experimental scheme for saturated absorption spectroscopy. (b) Spectral hole burning by the counter-propagating saturation and probe beams for (red) detuned and (blue) resonant light.

possible implementations of saturation spectroscopy, f.ex. *frequency modulation spec-*

troscopy or *modulation transfer spectroscopy*, which we will present in the following.

33.2.2.1 Calculation of the Lamb-dip

The scheme known as *Lamb-dip spectroscopy* and which is illustrated in Fig. 33.6(a), consists in a cell filled with a gas [for example, atomic rubidium whose resonance frequency is $\omega_0 = ck = 2\pi c/780\,\text{nm}$ and decay rate is $\Gamma = (2\pi)\ 6\,\text{MHz}$] and two laser beams with the same frequency ω, but propagating in opposite directions. One is called the saturating beam, the other probe beam.

The basic idea is that, if the laser frequency is detuned from resonance, $\omega \neq \omega_0$, the counter-propagating beams will interact with different velocity classes (i.e. atomic velocities projected on the optical axis, $v = \mathbf{v}\cdot\hat{\mathbf{e}}_\mathbf{k}$), which results in two distinct 'holes' in the excitation profile [red curve in Fig. 33.6(b)]. Only for resonant light, $\omega = \omega_0$, will the counter-propagating beams interact with the same velocity class (i.e. atomic velocities with $v = 0$). The 'holes' in the excitation profile then overlap thus leading to a deeper depression called Lamb-dip [blue curve in Fig. 33.6(b)].

For a quantitative description of the Lamb-dip we consider Maxwell's one-dimensional and normalized velocity distribution,

$$\rho(v)dv = \sqrt{\frac{m}{2\pi k_B T}} e^{-mv^2/2k_B T} dv \ . \tag{33.12}$$

As an example, we consider a gas at $T = 300\,\text{K}$ temperature, where the partial pressure of rubidium is about $P = 10^{-1}\,\text{mbar}$, such that the particle density is,

$$n(T) = \frac{P}{k_B T} \ . \tag{33.13}$$

We also assume a cell length of $L = 10\,\text{cm}$.

The probe laser intensity is below saturation, such that the optical cross section for an atom moving with velocity v, isaccording to (??),

$$\sigma(v) = \frac{6\pi}{k^2} \frac{\Gamma^2}{4(\omega - \omega_0 - kv)^2 + \Gamma^2} \ , \tag{33.14}$$

where we considered the fact that the atoms moving with the velocity v along the optical axis perceive the probe laser beam as Doppler-shifted by an amount kv.

The saturating laser now has high intensity. Let us suppose here, $\Omega \equiv 10\Gamma$, where Ω is the Rabi frequency caused by the saturating laser. In this way, it creates a population of N_e atoms in the excited state. Since this population is missing in the ground state, $N_g = N - N_e$, the absorption is reduced for the probe beam by a factor,

$$\frac{N_e}{N} = \frac{\Omega^2}{4(\omega - \omega_0 + kv)^2 + 2\Omega^2 + \Gamma^2} \ . \tag{33.15}$$

In contrast to (33.14), we now have to consider saturation broadening, as shown in the derivation of (??).

We will now calculate the spectrum of the optical density for the probe laser, $O_D(\omega)$, and the light intensity transmitted through the cell, $\frac{I}{I_0} = e^{-O_D}$, according to the Lambert-Beer law(??).

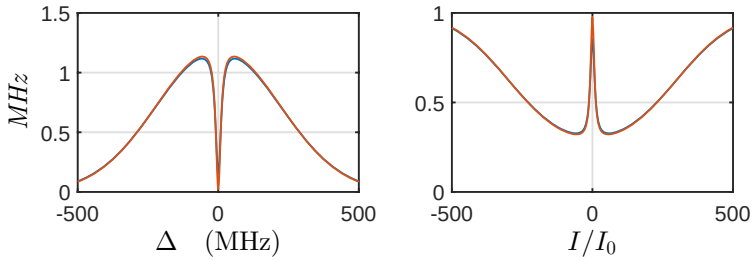

Figure 33.7: (code) (a) Optical density and (b) absorption. (Blue) Integral formula and (green) approximation for high temperature and high saturation.

The optical density with Doppler broadening is,

$$O_D(T,\omega) = Ln(T)\int_{-\infty}^{\infty} \tfrac{N_g - N_e}{N}\sigma(v)\rho(v)dv \tag{33.16}$$
$$= L\frac{P}{k_BT}\sqrt{\frac{m}{2\pi k_BT}}\frac{6\pi}{k^2}\int_{-\infty}^{\infty}\left(1 - \frac{2\Omega^2}{4(\Delta+kv)^2 + 2\Omega^2 + \Gamma^2}\right)\frac{\Gamma^2}{4(\Delta-kv)^2+\Gamma^2}e^{-mv^2/2k_BT}dv\ ,$$

with $\Delta \equiv \omega - \omega_0$ and substituting $N_g - N_e = N - 2N_e$. The widths of the three distribution functions are, respectively,

$$\begin{aligned}
\delta\nu_{sat} &= \sqrt{\tfrac{1}{2}\Omega^2 + \tfrac{1}{4}\Gamma^2} \approx (2\pi)\ 68\,\text{MHz} && \text{for the saturating beam}\\
\delta\nu_{Dpp} &= k\sqrt{\tfrac{k_BT}{m}} \approx (2\pi)\ 217\,\text{MHz} && \text{for the Doppler broadening}\\
\delta\nu_{prb} &= \tfrac{1}{2}\Gamma \approx (2\pi)\ 3\,\text{MHz} && \text{for the probe beam}
\end{aligned} \tag{33.17}$$

where $\bar{v} = \sqrt{k_BT/m}$ is the mean atomic velocity (or the *rms* width) of Maxwell's distribution. Since the spectral width of the probe laser spectrum is much smaller, we can replace it by a δ-function,

$$\frac{\Gamma^2}{4(\Delta-kv)^2+\Gamma^2} \longrightarrow \frac{\pi\Gamma}{2}\delta(\Delta - kv)\ , \tag{33.18}$$

which gives,

$$\begin{aligned}
O_D(T,\omega) \simeq L\frac{P}{k_BT}\sqrt{\frac{m}{2\pi k_BT}}\frac{6\pi}{k^3}\int_{-\infty}^{\infty}\left(1 - \frac{2\Omega^2}{4(\Delta+kv)^2+2\Omega^2+\Gamma^2}\right)\times \\
\times\frac{\pi\Gamma}{2}\delta(\Delta-kv)e^{-mv^2/2k_BT}dkv \\
= L\frac{P}{k_BT}\sqrt{\frac{m}{2\pi k_BT}}\frac{6\pi}{k^3}\frac{\pi\Gamma}{2}\left(1 - \frac{2\Omega^2}{8\Delta^2+2\Omega^2+\Gamma^2}\right)e^{-m(\Delta/k)^2/2k_BT}\ .
\end{aligned} \tag{33.19}$$

The *Lamb dip* is the narrow (Doppler-free) feature in the center of the the spectrum exhibited in Fig. 33.7. Lamb-dip spectra are commonly serve as frequency references for laser frequency stabilization schemes.

33.2.3 Frequency modulation and modulation transfer spectroscopy

Variations of the saturation spectroscopic idea are the *frequency modulation spectroscopy* (FMS) and the *modulation transfer spectroscopy* (MTS). The basic scheme of those techniques is shown in Fig. 33.8. As in saturation spectroscopy, two counterpropagating beams interact with the same atoms of a molecular gas, but now one of the beams is frequency-modulated (e.g. using an electro-optic modulator). In the FMS configuration, the probe beam is modulated, and the sidebands are discriminated at the spectral feature generated by the saturation beam in a very similar way as for the Pound-Drever-Hall technique. The profile of the FMS signal is calculated in Exc. 33.2.4.3 [514, 83, 365, 770, 447, 137, 249, 757, 732, 402, 540].

In the MTS configuration, the saturation beam is modulated, and the sidebands are transferred to the probe beam via nonlinear four-wave mixing processes. In both cases, the sidebands are demodulated with the local oscillator frequency driving the EOM.

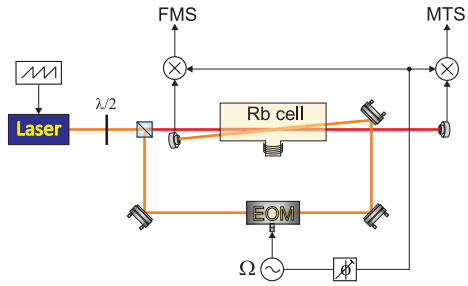

Figure 33.8: Schemes of frequency-modulation and modulation transfer spectroscopy.

The advantages of both techniques is, that they generate dispersive Doppler-free lineshapes. The FMS signal appears as a sharp feature on top of a large Doppler background (similarly to the Lamb-dip). In contrast, the MTS signal is free from Doppler background. The MTS signal recorded by the photodetector is given by,

$$I(\Delta) = \sum_{a,b} \frac{\mu_{ab}^2}{\gamma_j + \imath\delta} \left(\frac{1}{\gamma_{ab} + \imath(\Delta + \delta/2)} - \frac{1}{\gamma_{ab} + \imath(\Delta + \delta)} + \frac{1}{\gamma_{ab} - \imath(\Delta - \delta)} - \frac{1}{\gamma_{ab} - \imath(\Delta - \delta/2)} \right) , \tag{33.20}$$

where a and b denote the lower and upper levels, μ_{ab}^2 is the electric dipole moment, γ_{ab} is the optical relaxation rate, γ_j is the decay of the energy level j of the molecule, and δ is the modulation frequency. Behind the mixer we see the electric signal,

$$S(\Delta, \vartheta) = \mathrm{Re}\left[I(\Delta) e^{-\imath\varphi} \right] , \tag{33.21}$$

where ϑ is the demodulation phase [539]. The curves are shown in Fig. 33.8.

Example 206 (*Modulation transfer spectroscopy*): Modulation transfer spectroscopy is caused by four-wave mixing (4WM) processes, which have the

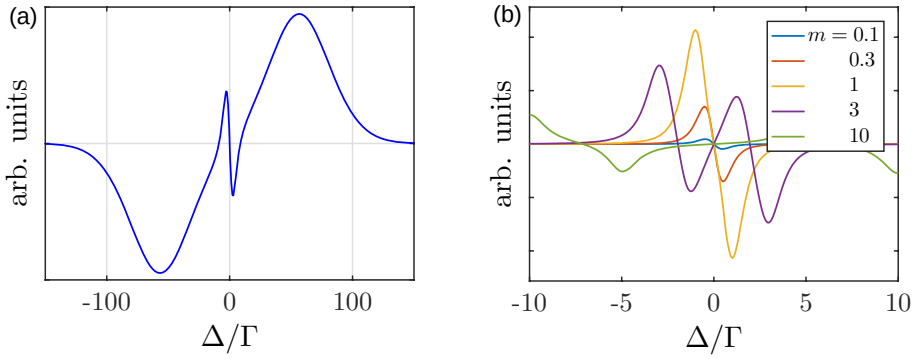

Figure 33.9: (code) (a) Calculated FMS signals and (b) MTS signals as a function of detuning for various modulation indices.

general form $P(\omega+\Omega) = \chi^{(3)}(\omega+\Omega)E_s(\omega_s)E_p(\omega_s)E_s^*(\omega_s-\Omega)$, or similar. When the beams ω and ω_s are counter-propagating, and the atoms are moving, their resonances shift toward $\omega \mp \mathbf{k}\cdot\mathbf{v}$, respectively in the atomic rest system. Resonant enhancement of 4WM occurs, when one of the intermediate levels coincides with ω_0:

$$\begin{aligned}
&\omega - \mathbf{k}\cdot\mathbf{v} = \omega_0 \\
&(\omega - \mathbf{k}\cdot\mathbf{v}) - (\omega + \mathbf{k}\cdot\mathbf{v} - \Omega) = 0 \\
&(\omega - \mathbf{k}\cdot\mathbf{v}) - (\omega + \mathbf{k}\cdot\mathbf{v} - \Omega) + (\omega + \mathbf{k}\cdot\mathbf{v}) = \omega_0 \\
&(\omega - \mathbf{k}\cdot\mathbf{v}) - (\omega + \mathbf{k}\cdot\mathbf{v} - \Omega) + (\omega + \mathbf{k}\cdot\mathbf{v}) - (\omega - \mathbf{k}\cdot\mathbf{v} + \Omega) = 0 \ .
\end{aligned}$$

Assuming $\omega = \omega_s = \omega - 0$, these resonances reduced to,

$$\mathbf{k}\cdot\mathbf{v} = 0, \pm\Omega \ ,$$

and similarly for the other 4WM processes. This means, that the saturation beam burns holes in the velocity distribution at $\mathbf{k}\cdot\mathbf{v} = 0, \pm\frac{1}{2}\Omega, \pm\Omega$, which modulate the probe beam.

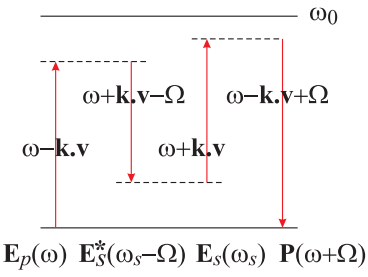

Figure 33.10: Levels involved in 4WM upon MTS.

33.2.4 Exercises

33.2.4.1 Ex: Width of the absorption band

The resonator of a dye laser with a large emission bandwidth additionally contains an absorbing (dense) gas. The absorption spectrum of the gas is Lorentzian with a width of 3 GHz, and the absorption coefficient has, in the middle of the absorption line (at 600 nm), the value of 0.2. What are the maximum and minimum relative spectral distances $\Delta f/\Delta f_0$ of the axial modes within the spectral range of the absorption, compared to the distances Δf_0 of the empty resonator?

33.2.4.2 Ex: Lorentz and Gaussian profiles

At which detuning is a Doppler-broadened line dominated by Lorentzian profile of the transition?

33.2.4.3 Ex: Frequency-modulation spectroscopy

Calculate the FMS spectrum for a rubidium gas (describing the atoms as a two-level system) under the conditions specified in Sec. 33.2.2 and assuming a modulation frequency of $f = 10\,\text{MHz}$ and a modulation index of $\beta = 1$.

33.2.5 *Experiment: Rubidium Lamb-dips*

In this exercise, we will spectroscopically identify the various lines of the rubidium D_2-transition of the isotopes ^{87}Rb and ^{85}Rb. The hyperfine splittings of the ground and excited states are reproduced in Fig. 33.11.

1. Set up the optics for a Lamb-dip spectroscopy as shown in Fig. 33.11.

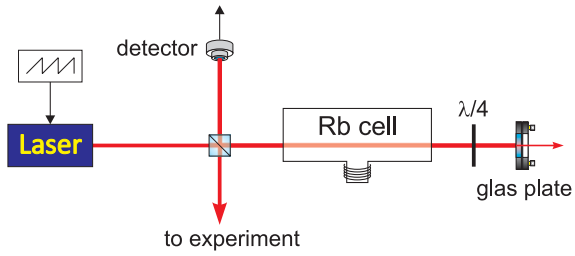

Figure 33.11: Saturation spectroscopy.

2. Fig. 33.12 shows a typical spectrum recorded with a rubidium gas cell. Find an interpretation for the various lines of the spectrum.

33.3 Polarization spectroscopy

The *Hänsch-Couillaud technique* uses the *birefringence* of certain materials, devices, or gases.

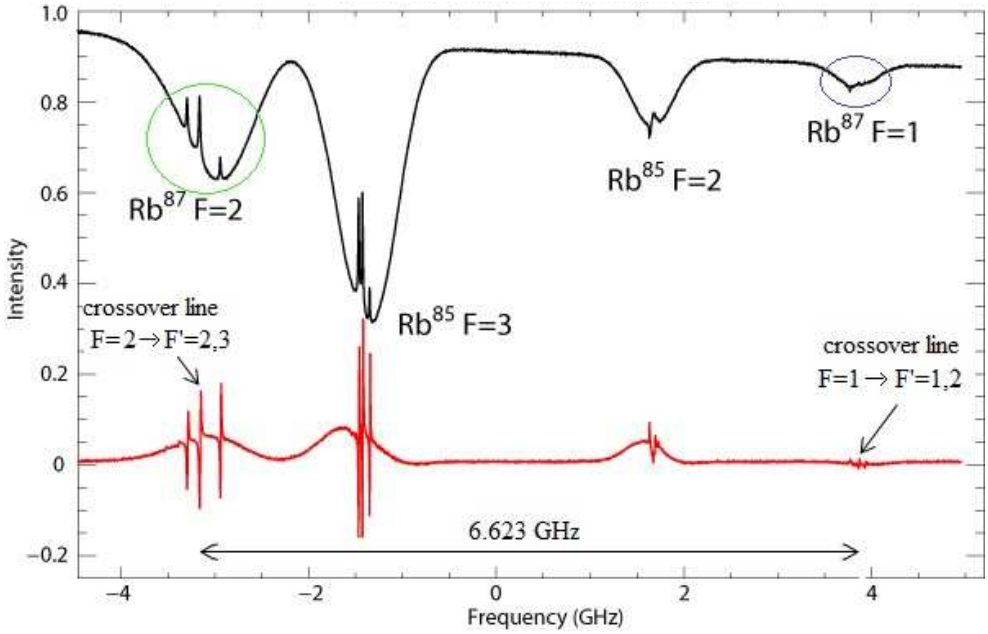

Figure 33.12: (Black) Lamb-dip spectroscopy of a rubidium gas (natural isotope mixture of ^{85}Rb and ^{87}Rb) showing the hyperfine structure transitions of the D2-line. (Red) Derivative of the spectrum in (a).

33.3.1 Birefringent cavity

We consider a birefringent cavity exhibiting slightly different path lengths for two axis that we will call, respectively, *ordinary* and *extraordinary*. Fig. 33.13(a) shows the optical setup. The detector signals may be calculated via a concatenation of the Jones matrices for a $\lambda/2$-plate, the transmissive response of the cavity, another $\lambda/2$-plate, and finally a polarizing beam splitter,

$$\begin{pmatrix} E_o \\ E_e \end{pmatrix} = M \begin{pmatrix} 1 \\ 0 \end{pmatrix} \qquad with \tag{33.22}$$

$$M \equiv \begin{pmatrix} \cos\beta & \sin\beta \\ -\sin\beta & \cos\beta \end{pmatrix} \begin{pmatrix} \frac{T}{1-Re^{2ik_oL}} & 0 \\ 0 & \frac{T}{1-Re^{2ik_eL}} \end{pmatrix} \begin{pmatrix} \cos\alpha & \sin\alpha \\ -\sin\alpha & \cos\alpha \end{pmatrix} . \tag{33.23}$$

For the particular polarization angles $\alpha = \frac{\pi}{4}$ and $\beta = 0$, we derive the difference of the photodetector signals,

$$\Delta I = |E_o|^2 - |E_e|^2 = \tfrac{T^2}{2} \left[\frac{1}{1 - R^2 - 2R\cos 2k_oL} - \frac{1}{1 - R^2 - 2R\cos 2k_eL} \right] . \tag{33.24}$$

As Fig. 33.13(b) demonstrates, the spectra corresponding to the axis, obtained by ramping the laser frequency are slightly shifted with respect to each other. Their subtraction leads to a dispersive lineshape that suits for laser locking purposes in the so-called *Hänsch-Couillaud* stabilization.

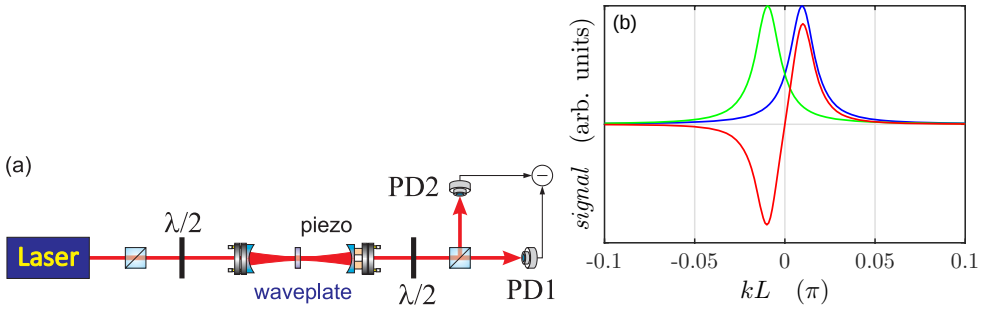

Figure 33.13: (code) (a) Generating a Hänsch-Couillaud error signal by transmission of a birefringent linear cavity. (b) Signals recorded by the two photodetectors (blue and green) and their difference (red).

33.3.2 *Experiment: Birefringence of a ring cavity*

Birefringence automatically occurs in a ring cavities. In this exercise, we will analyze the birefringence observed in reflection of a such a ring cavity. In a *ring cavity*, the resonance frequencies of the s-polarized and the p-polarized modes are slightly shifted from one another due to the different penetration depth of the s- and p-polarized light modes into the layers of the dielectric mirrors. For a moderate finesse of the cavity (say $\mathcal{F} = 2000$), the modes actually overlap. This leads to a birefringence used in the

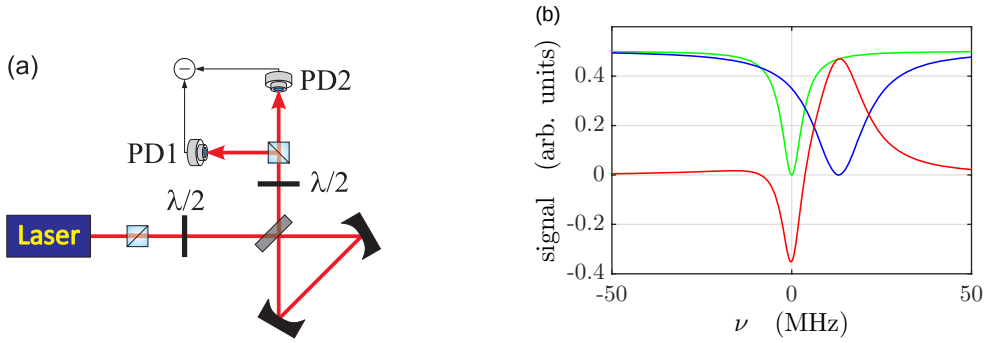

Figure 33.14: (code) (a) Generating a Hänsch-Couillaud error signal by (a) reflection from a ring cavity and (b) transmission of a linear cavity containing a Brewster plate. (b) Signals recorded by the two photodetectors (blue and green) and their difference (red). (a) Reflection signals $|E_s|^2$ and $|E_p|^2$ from a birefringent cavity with $\delta_{fsr} = 8.2\,\text{GHz}$, $\varphi_s = 0$, $R_{hr,s} = 99.97\%$, $R_{ic,s} = 99.74\%$, $F_s = \pi(R_{hr,s}^2 R_{ic,s})^{1/6}/[1-(R_{hr,s}^2 R_{ic,s})^{1/3}]$, $\varphi_p = 0.01$, $R_{hr,p} = 99.92\%$, $R_{ic,p} = 99.34\%$, and $F_p = \pi(R_{hr,p}^2 R_{ic,p})^{1/6}/[1-(R_{hr,p}^2 R_{ic,p})^{1/3}]$. (b) Difference $|E_s|^2 - |E_p|^2$.

famous Hänsch-Couillaud locking scheme. The detector signal in the scheme shown in the figure may calculated via a concatenation of the Jones matrices for a $\lambda/2$-plate, the reflective response of the ring cavity, another $\lambda/2$-plate, and finally a polarizing

beam splitter,

$$\begin{pmatrix} E_s \\ E_p \end{pmatrix} = M \begin{pmatrix} 1 \\ 0 \end{pmatrix} \quad with \tag{33.25}$$

$$M \equiv \begin{pmatrix} \cos\beta & \sin\beta \\ -\sin\beta & \cos\beta \end{pmatrix} \begin{pmatrix} \frac{1-e^{-2\pi\imath\omega/\delta_{fsr}+\imath\phi_s}}{1-R_s e^{-2\pi\imath\omega/\delta+\imath\phi_s}} & 0 \\ 0 & \frac{1-e^{-2\pi\imath\omega/\delta_{fsr}+\imath\phi_p}}{1-R_p e^{-2\pi\imath\omega/\delta+\imath\phi_p}} \end{pmatrix} \begin{pmatrix} \cos\alpha & \sin\alpha \\ -\sin\alpha & \cos\alpha \end{pmatrix}.$$

Calculating $|E_s|^2$ and $|E_p|^2$ as a function of the laser frequency ω reproduces the curves plotted in Fig. 33.14(a).

1. x

33.4 Other spectroscopic techniques

33.4.1 Mode-locked femtosecond laser

Mode-locking is a technique in optics by which a laser can be made to produce pulses of light of extremely short duration, down to the order of femtoseconds. The basis of the technique is to induce a fixed-phase relationship between the longitudinal modes of the laser's resonant cavity. Constructive interference between these modes can cause the laser light to be produced as a train of pulses.

In a simple laser, each of these cavity modes amplified within the bandwidth of the gain medium oscillates independently, with no fixed relationship between each other. The individual phase of the light waves in each mode is not fixed, and may vary randomly due to such things as thermal changes in materials of the laser. In lasers with only a few oscillating modes, interference between the modes can cause beating effects in the laser output, leading to fluctuations in intensity; in lasers with many thousands of modes, these interference effects tend to average to a near-constant output intensity.

If instead of oscillating independently, each mode operates with a fixed phase relation to the other modes. Instead of a random or constant output intensity, the modes of the laser will periodically constructively interfere with one another, producing an intense burst or pulse of light. Such a laser is said to be *mode-locked* or *phase-locked*. These pulses occur separated in time by $\tau = 2L/c$, where τ is the laser cavity round trip time and corresponds to the cavity's inverse free spectral range.

33.4.1.1 Active mode-locking

The most common active mode-locking technique places a standing wave electro-optic modulator (EOM) into the laser cavity. When driven with a sinusoidal electrical signal, this produces an amplitude modulation of the light in the cavity. Considering this in the frequency domain, if a mode has optical frequency ν, and is amplitude-modulated at a frequency f, the resulting signal has sidebands at optical frequencies $\nu \pm f$. The modulation frequency is now chosen to coincide with the cavity's free spectral range, $f = \delta_{fsr}$, and since the sidebands are driven in-phase, the central mode and the adjacent modes will be phase-locked together. Further operation of the

modulator on the sidebands produces phase-locking of the $\nu \pm 2f$ modes, and so on until all modes in the gain bandwidth are locked.

This process can also be considered in the time domain. The amplitude modulator acts as a weak 'shutter' to the light bouncing between the mirrors of the cavity, attenuating the light when it is 'closed', and letting it through when it is 'open'. If the modulation rate f is synchronized to the cavity round-trip time τ, then a single pulse of light will bounce back and forth in the cavity. The actual strength of the modulation does not have to be large; a modulator that attenuates 1% of the light when 'closed' will mode-lock a laser, since the same part of the light is repeatedly attenuated as it traverses the cavity.

Related to this amplitude modulation (AM), active mode-locking is frequency modulation (FM) mode-locking, which uses a modulator device based on the acousto-optic effect. This device, when placed in a laser cavity and driven with an electrical signal, induces a small, sinusoidally varying frequency shift in the light passing through it. If the frequency of modulation is matched to the round-trip time of the cavity, then some light in the cavity sees repeated upshifts in frequency, and some repeated downshifts. After many repetitions, the upshifted and downshifted light is swept out of the gain bandwidth of the laser. The only light which is unaffected is that which passes through the modulator when the induced frequency shift is zero, which forms a narrow pulse of light.

The third method of active mode-locking is synchronous mode-locking, or synchronous pumping. In this, the pump source (energy source) for the laser is itself modulated, effectively turning the laser on and off to produce pulses.

33.4.1.2 Passive mode-locking

Passive mode-locking techniques are those that do not require a signal external to the laser to produce pulses. Rather, they use the light in the cavity to cause a change in some intracavity element, which will then itself produce a change in the intracavity light. A commonly used device to achieve this is a saturable absorber.

A saturable absorber is an optical device that exhibits an intensity-dependent transmission. For passive mode-locking, ideally a saturable absorber will selectively absorb low-intensity light, and transmit light which is of sufficiently high intensity. When placed in a laser cavity, a saturable absorber will attenuate low-intensity constant wave light (pulse wings). However, because of the somewhat random intensity fluctuations experienced by an un-mode-locked laser, any random, intense spike will be transmitted preferentially by the saturable absorber. As the light in the cavity oscillates, this process repeats, leading to the selective amplification of the high-intensity spikes, and the absorption of the low-intensity light. After many round trips, this leads to a train of pulses and mode-locking of the laser.

Considering this in the frequency domain, if a mode has optical frequency ν, and is amplitude-modulated at a frequency nf, the resulting signal has sidebands at optical frequencies $\nu \pm nf$ and enables much stronger mode-locking for shorter pulses and more stability than active mode-locking, but has startup problems.

Saturable absorbers are commonly liquid organic dyes, but they can also be made from doped crystals and semiconductors. Semiconductor absorbers tend to exhibit very fast response times ($\sim$100 fs), which is one of the factors that determines the

final duration of the pulses in a passively mode-locked laser. In a colliding-pulse mode-locked laser the absorber steepens the leading edge while the lasing medium steepens the trailing edge of the pulse.

There are also passive mode-locking schemes that do not rely on materials that directly display an intensity dependent absorption. In these methods, nonlinear optical effects in intracavity components are used to provide a method of selectively amplifying high-intensity light in the cavity, and attenuation of low-intensity light. One of the most successful schemes is called Kerr-lens mode-locking (KLM), also sometimes called 'self mode-locking'. This uses a nonlinear optical process, the optical Kerr effect, which results in high-intensity light being focussed differently from low-intensity light. By careful arrangement of an aperture in the laser cavity, this effect can be exploited to produce the equivalent of an ultra-fast response time saturable absorber.

33.4.2 Frequency comb

In optics, a frequency comb is a laser source whose spectrum consists of a series of discrete, equally spaced frequency lines. Frequency combs can be generated by a number of mechanisms, including periodic modulation (in amplitude and/or phase) of a continuous-wave laser, four-wave mixing in nonlinear media, or stabilization of the pulse train generated by a mode-locked laser. The invention of the *frequency comb* represents a breakthrough in ultrahigh resolution spectroscopy, which was honored with the Nobel price attributed to Theodor Hänsch in 2005 [896, 441, 403, 404, 610, 8, 812].

The frequency domain representation of a perfect frequency comb is a series of delta functions spaced according to,

$$f_n = f_{ceo} + n f_{rep} \ , \tag{33.26}$$

where n is an integer, f_{rep} is the comb tooth spacing (equal to the mode-locked laser's repetition rate or, alternatively, the modulation frequency), and f_{ceo} is the carrier offset frequency, which is less than f_{rep}. Combs spanning an octave in frequency (i.e., a factor of two) can be used to directly measure (and correct for drifts in) f_{ceo}. Thus, octave-spanning combs can be used to steer a piezoelectric mirror within a carrier-envelope phase-correcting feedback loop. Any mechanism by which the combs' two degrees of freedom (f_{rep} and f_{ceo}) are stabilized generates a comb that is useful for mapping optical frequencies into the radio frequency for the direct measurement of optical frequency.

33.4.2.1 Spectrum of a frequency comb

The field emitted by a pulsed laser characterized by its pump laser frequency ν, the *repetition rate* f_{rep}, and the pulse width T, can be given as a temporal sequence of Gaussian shaped pulses. The repetition is mathematically described as a convolution of the Gaussian profile with a sum of temporal δ-functions displaced in time,

$$\boxed{E(t) = \cos 2\pi\nu t \left(\sum_n \delta(t - \tfrac{n}{f_{rep}}) \star e^{-t^2/T^2} \right) = \cos 2\pi\nu t \sum_n e^{-(t-\frac{n}{f_{rep}})^2/T^2}} \ . \tag{33.27}$$

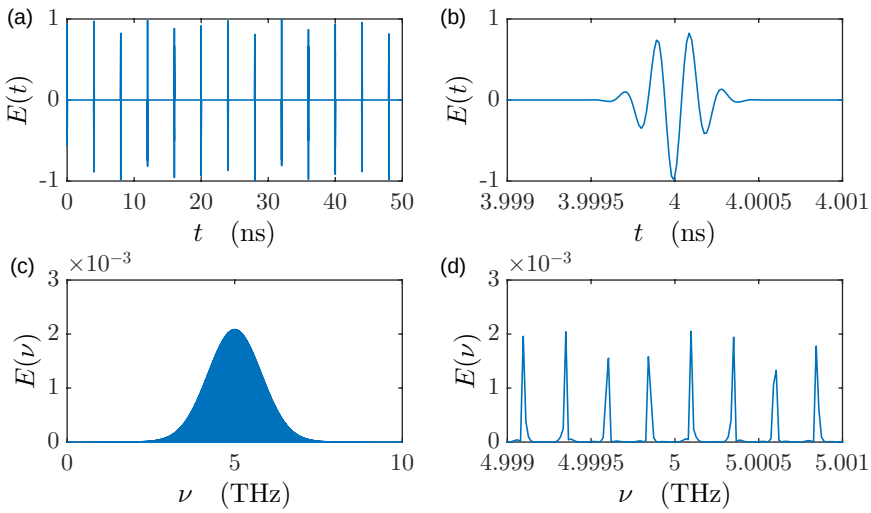

Figure 33.15: (code) Pulse train (a,b) and spectrum (b,c).

The carrier under each pulse is phase-shifted with respect to the adjacent pulse, except when the laser is mode-locked, that is, when,

$$\cos 2\pi\nu t = \cos 2\pi\nu(t + \tfrac{1}{f_{rep}}) \ . \tag{33.28}$$

The Fourier transform of the laser field (33.27) is,

$$\begin{aligned} \mathcal{F}[E(t)] &= \int_{-\infty}^{\infty} e^{-\imath\omega t} \cos 2\pi\nu t \sum_n e^{-(t-n/f_{rep})^2/T^2} dt \\ &= \tfrac{1}{2} \sum_n \int_{-\infty}^{\infty} e^{-\imath(\omega-2\pi\nu)t} e^{-(t-n/f_{rep})^2/T^2} dt \ , \end{aligned} \tag{33.29}$$

where neglect negative frequency components. Using the rules,

$$\mathcal{F}[f(t)e^{\imath\Omega t}] = \int_{-\infty}^{\infty} e^{-\imath\omega t} f(t) e^{\imath\Omega t} dt = (\mathcal{F}f)(\omega - \Omega) \tag{33.30}$$

$$\text{and} \qquad \mathcal{F}[f(t-T)] = \int_{-\infty}^{\infty} e^{-\imath\omega t} f(t-T) dt = e^{-\imath\omega T}(\mathcal{F}f)(\omega)$$

$$\text{and} \qquad \mathcal{F}[e^{-t^2/T^2}] = \int_{-\infty}^{\infty} e^{-\imath\omega t} e^{-t^2/T^2} dt = T\sqrt{\pi} e^{-T^2\omega^2/4}$$

we get,

$$E(\omega) = \mathcal{F}[E(t)] = \tfrac{1}{2} T\sqrt{\pi} e^{-T^2(\omega-2\pi\nu)^2/4} \sum_n e^{-\imath(\omega-2\pi\nu)n/f_{rep}} \ . \tag{33.31}$$

We now write the pump laser frequency as,

$$\nu \equiv m f_{rep} + f_{ceo} \ , \tag{33.32}$$

where we set $m \in \mathbb{N}$ and call $|f_{ceo}| < f_{rep}$ the *carrier envelope offset*. We also express the Fourier frequency by,

$$\omega \equiv 2\pi(\eta f_{rep} + f_{ceo}) \ , \tag{33.33}$$

firstly *without* specifying that η be an integer number. The spectrum is,

$$|E(\omega)|^2 = \tfrac{1}{4}\pi T e^{-T^2(\omega-2\pi\nu)^2/2} \left| \sum_n e^{-2\pi i n(\eta-m)} \right|^2 \ , \tag{33.34}$$

which only gives contributions for,

$$\eta = \frac{\omega - 2\pi f_{ceo}}{2\pi f_{rep}} \in \mathbb{N} \ . \tag{33.35}$$

I.e. the spectrum of comb frequencies is,

$$\boxed{|E(\omega)|^2 = \tfrac{1}{4}\pi T e^{-T^2(\omega-2\pi\nu)^2/2} \sum_n \delta[\omega - (n f_{rep} + f_{ceo})]} \ . \tag{33.36}$$

The δ-function comes from the fact that the sum of (33.35) over many oscillations $e^{-2\pi i n(\eta-m)}$ vanishes by destructive interference, except when they are *in phase*, which is just the case when $\omega = n f_{rep} + f_{ceo}$.

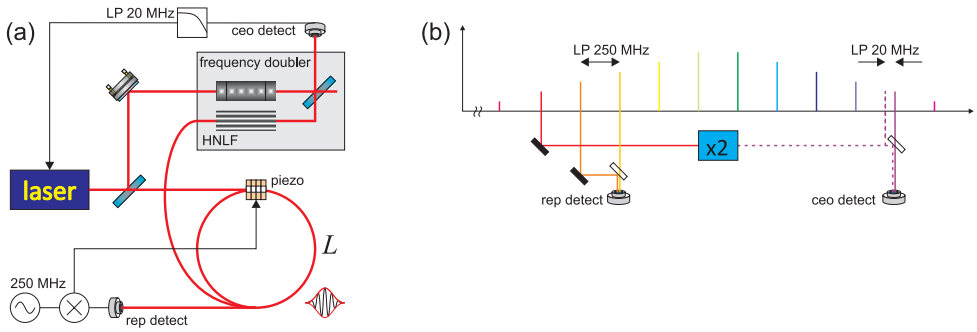

Figure 33.16: (a) Scheme and (b) operation principle of a frequency comb with control of the repetition rate and the carrier envelope offset.

33.4.2.2 Mode-locking of a frequency comb

From Eq. (33.28) we see that *mode-locking* is achieved when,

$$\frac{\nu}{f_{rep}} = m + \frac{f_{ceo}}{f_{rep}} \in \mathbb{N} \ , \tag{33.37}$$

which implies $f_{ceo} = 0$. Eq. (33.36) then becomes,

$$|E(\omega)|^2 = \frac{\pi T}{4} e^{-T^2(\omega-2\pi\nu)^2/2} \sum_n \delta(\omega - n f_{rep}) \ , \tag{33.38}$$

which means that all comb frequencies are locked.

33.4.2.3 Referencing radio and optical frequencies

In a frequency comb f_{rep} is easy to measure, as one just has to filter the beat of the comb light with a low pass filter cutting off frequency components higher than f_{rep}, as illustrated in Fig. 33.16. In contrast, measuring f_{ceo} is more complicated. Unless we have an octave spanning frequency comb, i.e. there are two frequencies in the comb,

$$\nu_1 = m_1 f_{rep} + f_{ceo} \quad \text{and} \quad \nu_2 = m_2 f_{rep} + f_{ceo} \ , \tag{33.39}$$

such that $\nu_2 = 2\nu_1 + \Delta\nu$ with $|\Delta\nu| < |f_{ceo}|$, i.e. $m_2 = 2m_1$. We get,

$$m_2 f_{rep} + f_{ceo} = 2m_1 f_{rep} + 2f_{ceo} + \Delta\nu \ , \tag{33.40}$$

or,

$$f_{ceo} = -\Delta\nu \ . \tag{33.41}$$

33.4.2.4 Dual comb spectroscopy

Optical sensors are based on the interaction of light with matter and are often implemented like some kind of spectrometer. The ideal sensor should detect a given substance with great sensitivity, identify it (especially in the presence of many other substances or a noisy background) and quantify it. Add to these features the ability to perform measurements in real time, if possible remotely, in a compact and easy-to-use assembly at affordable price, and we have an absolutely non-trivial problem. Broadband sources allow to detect multiple substances, but have limitations in resolution, calibration or acquisition time. Monochromatic sources allow good resolution, but in general have limitations on tunability and spectral coverage. The sensitivity can be increased by increasing the optical path of interaction, requiring multi-pass cells or resonant optical cavities, which augment the complexity of the setup. Finally, the detection method places limits on the acquisition rate and also on the sensitivity. Particularly the Fourier transform spectroscopy uses broadband incoherent light sources and the time of acquisition and resolution are limited by the speed of translation of a mechanical stage, as well as the range of its displacement. Here, the use of optical frequency combs replacing the incoherent sources, combined with *dual comb spectroscopy*, brings important advantages [839, 389].

33.4.3 Multi-photon spectroscopy

33.4.4 Raman spectroscopy

Raman spectroscopy is a spectroscopic technique typically used to determine vibrational modes of molecules, although rotational and other low-frequency modes of systems may also be observed. Raman spectroscopy is commonly used in chemistry to provide a structural fingerprint by which molecules can be identified. Raman spectroscopy relies upon inelastic scattering of photons, known as Raman scattering. A source of monochromatic light, usually from a laser in the visible, near infrared, or near ultraviolet range is used, although X-rays can also be used. The laser light interacts with molecular vibrations, phonons or other excitations in the system, resulting in the energy of the laser photons being shifted up or down. The shift in energy

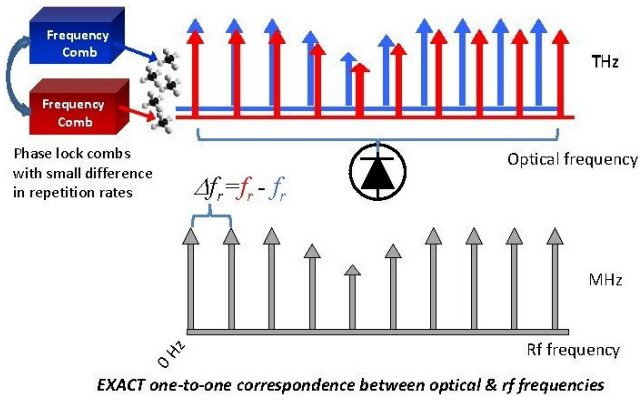

Figure 33.17: Principle of dual comb spectroscopy.

gives information about the vibrational modes in the system. Infrared spectroscopy typically yields similar, complementary, information.

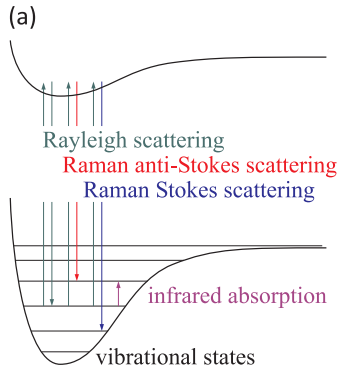

Figure 33.18: Energy-level diagram showing the states involved in Raman spectra.

Typically, a sample is illuminated with a laser beam. Electromagnetic radiation from the illuminated spot is collected with a lens and sent through a monochromator. Elastic scattered radiation at the wavelength corresponding to the laser line (Rayleigh scattering) is filtered out by either a notch filter, edge pass filter, or a band pass filter, while the rest of the collected light is dispersed onto a detector.

Spontaneous Raman scattering is typically very weak; as a result, for many years the main difficulty in collecting Raman spectra was separating the weak inelastically scattered light from the intense Rayleigh scattered laser light (referred to as 'laser rejection'). Historically, Raman spectrometers used holographic gratings and multiple dispersion stages to achieve a high degree of laser rejection. In the past, photomultipliers were the detectors of choice for dispersive Raman setups, which resulted in long acquisition times. However, modern instrumentation almost universally employs notch or edge filters for laser rejection. Dispersive single-stage spectrographs, for example Czerny-Turner (CT) monochromators (see Sec. 33.1.5), paired with CCD

detectors are common.

The name 'Raman spectroscopy' typically refers to vibrational Raman using laser wavelengths which are not absorbed by the sample. Raman spectroscopy is used in chemistry to identify molecules and study chemical bonding and intramolecular bonds. Because vibrational frequencies are specific to a molecule's chemical bonds and symmetry (the fingerprint region of organic molecules is in the wavenumber range $500 - 1500\,\mathrm{cm}^{-1}$, Raman provides a fingerprint to identify molecules.

In solid-state physics, Raman spectroscopy is used to characterize materials, measure temperature, and find the crystallographic orientation of a sample. As with single molecules, a solid material can be identified by characteristic phonon modes. Information on the population of a phonon mode is given by the ratio of the Stokes and anti-Stokes intensity of the spontaneous Raman signal. Raman spectroscopy can also be used to observe other low frequency excitations of a solid, such as plasmons, magnons, and superconducting gap excitations. Distributed temperature sensing (DTS) uses the Raman-shifted backscatter from laser pulses to determine the temperature along optical fibers.

33.4.5 Time-resolved spectroscopy

pump-probe spectroscopy

33.5 Further reading

G.C. Bjorklund, *Frequency-Modulation Spectroscopy: A new Method for Measuring Weak Absorptions and Dispersions* [DOI]

J.L. Hall et al., *Optical Heterodyne Saturation Spectroscopy* [DOI]

J.J. Snyder et al., [DOI]

R.K. Kaj et al., *High-Frequency Optically Heterodyned Saturation Spectroscopy via Resonant Degenerate Four-Wave Mixing* [DOI]

G. Camy et al., *Heterodyne Saturation Spectroscopy through Frequency Modulatiof the Saturating Beam* [DOI]

M. Ducloy et al., *Theory of Degenerate Four-Wave Mixing in Resonant Doppler-Broadened Media II* [DOI]

J.H. Shirley, *Modulation Transfer Processes in Optical Heterodyne Saturation Spectroscopy* [DOI]

A. Schenzle et al., *Phase Modulation Laser Spectroscopy* [DOI]

L. Hollberg et al., *Measurement of the shift of Rydberg energy levels incuded by blackbody radiation* [DOI]

L.S. Ma et al., *Optical Heterodyne Spectroscopy Enhanced by an External Optical Cavity: Toward Improved Working Standards* [DOI]

L.S. Ma et al., *Spectroscopy of Te2 with Modulation Transfer Reference Lines for Precision Spectroscopy in Yb* [DOI]

Chapter 34

Locking circuits

In a laboratory we are often confronted with the need to control the value of a physical parameter, f.ex., room temperature, currents and voltages, or the frequency and intensity of laser beams. The physical discipline dealing with the fundamental concepts of this field is called *control theory* and its application to development of automatic control systems is called *control engineering*.

In this chapter, after a brief introduction into *control theory*, we will design and construct a few automatic control systems, which are common in quantum optics labs.

34.1 Introduction to control theory

The minimum ingredients of a control system are 1. a *sensor* measuring the actual value of the parameter to be controlled (e.g., a thermometer), 2. an *actuator* capable of correcting the value (e.g., a heater or cooler), and 3. a suitable *controller* (*servo system*) linking sensor and actuator thus providing a feedback.

The controller comprises a *comparator* comparing the measured value with a reference and delivers the difference to a controller, which may be implemented electronically by proportional control, *PID control*, bistable hysteretic control, or programmable logic control. Older controller units have been mechanical, as in a carburetor. Finally, the value computed by the controller is delivered to an actuator, which manipulates and changes a variable in the controlled system (or *plant*).

34.1.1 Open- and closed-loop control

Fundamentally, there are two types of control loop: *open loop* control, and *closed loop* (feedback) control.

In open loop control, the control action from the controller is independent of the 'process output' (or 'controlled process variable'). An example of this is a central heating boiler controlled only by a timer, so that heat is applied for a constant time, regardless of the temperature of the building. The control action is the switching on/off of the boiler. The process output is the building temperature.

In closed loop control, the control action from the controller is dependent on the process output. In the case of the boiler analogy, this would include a thermostat to monitor the building temperature, and thereby feed back a signal to ensure the controller maintains the building at the temperature set on the thermostat. A closed loop controller therefore has a feedback loop which ensures the controller exerts a

control action to give a process output the same as the 'reference input' or 'set point'. For this reason, closed loop controllers are also called feedback controllers.

The definition of a closed loop control system is *a control system capable of canceling the deviation of a system variable from a reference value by means of a feedback signal computed from a measured value of the variable and used to act on the system in a controlled way* [787]. Automatic feedback control has revolutionized all areas of human activities.

To overcome the limitations of the open-loop controller, control theory introduces *feedback*. A closed-loop controller uses feedback to control states or outputs of a dynamical system. Its name comes from the information path in the system: process inputs (e.g. voltage applied to an electric motor) have an effect on the process outputs (e.g. speed or torque of the motor), which is measured with sensors and processed by the controller; the result (the control signal) is 'fed back' as input to the process, closing the loop.

Closed-loop controllers have the following advantages over open-loop controllers:

- disturbance rejection (such as hills in the cruise control example above)
- guaranteed performance even with model uncertainties, when the model structure does not match perfectly the real process and the model parameters are not exact
- unstable processes can be stabilized
- reduced sensitivity to parameter variations
- improved reference tracking performance

In some systems, closed-loop and open-loop control are used simultaneously. In such systems, the open-loop control is termed feedforward and serves to further improve reference tracking performance.

34.1.1.1 Closed-loop transfer function

Due to noise the variables of the system become time-dependent. The output of the system $y(t)$ is fed back through a sensor measurement F to a comparison with the reference value $r(t)$. The controller C then takes the error $e(t)$ (difference) between the reference and the output to change the inputs $u(t)$ to the system under control P. This is shown in the figure. This kind of controller is a closed-loop controller or feedback controller. We will restrain here to *single-input-single-output control* systems (SISO) disregarding the possibility of having multiple and interdependent inputs and outputs.

If we assume the controller C, the plant P, and the sensor F are linear and time-invariant (i.e. elements of their transfer function $C(s)$, $P(s)$, and $F(s)$ do not depend on time), the systems above can be analyzed using the Laplace transform on the variables, $U(s) = \mathcal{L}u(t)$, $Y(s) = \mathcal{L}y(t)$, and $R(s) = \mathcal{L}r(t)$. Here,

$$s \equiv \imath f \tag{34.1}$$

is an abbreviation for the imaginary Fourier frequency component f of the noise. In the following sections we will, however, characterize the transfer functions in terms

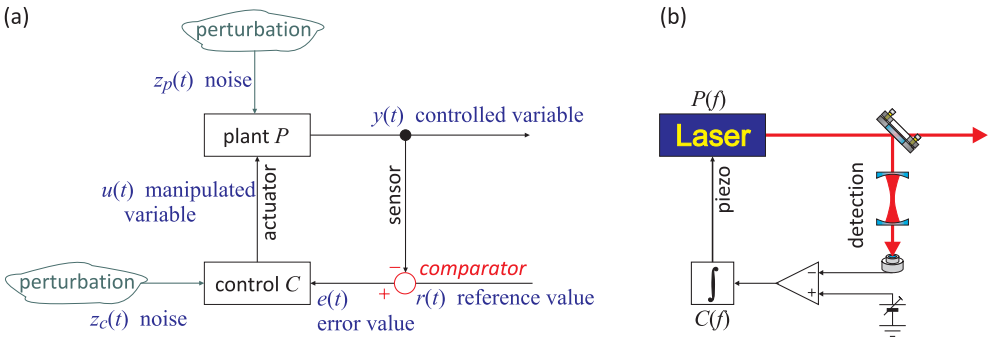

Figure 34.1: (a) General schematic diagram of a feedback loop. (b) Possible implementation for the frequency stabilization of a laser to a cavity resonance,

of real Fourier frequencies. The theoretical foundation of Linear Time-Independent (LTI) systems is outsourced to Sec. 35.2.

For a control to work, it needs to know in which direction to act and when the control point is reached. Therefore, each control needs a slope (*discriminator*) crossing zero. This can be implemented by comparing the signal $Y(f)$ delivered by the detector (for simplicity assumed to be frequency-independent) with a reference signal R. The error signal $E(f) = R(f) - Y(f)$ is then processed by a controller C, and the control signal $U(f)$ is passed, via an actuator (for simplicity assumed to be frequency-independent), to the controlled device P. The controlled device (and obviously all other components of the circuit) are subject to perturbations Z. The transfer functions form a closed control circuit described by the following relations:

$$Y(f) = P(f)U(f) \quad \text{and} \quad U(f) = C(f)E(f) \quad \text{and} \quad E(f) = R(f) - Y(f)\,. \tag{34.2}$$

Solving the system of equations (34.2) for $Y(f)$ in terms of $R(f)$ gives,

$$\boxed{Y(f) = \frac{P(f)C(f)}{1 + P(f)C(f)}\, R(f) \equiv H(f)R(f)}\,. \tag{34.3}$$

$H(s)$ is referred to as the closed-loop transfer function of the system. The numerator $V(f) \equiv P(f)C(f)$ is called the *forward gain* (*open-loop gain*) from R to Y, and the denominator is one plus the gain in going around the feedback loop, the so-called *loop gain*. If $|P(f)C(f)| \gg 1$, i.e. it has a large norm with each value of f, and then $Y(f) \simeq R(f)$ and the output closely tracks the reference input.

34.1.1.2 Noise reduction via feedback circuits

We have seen that the idea of *locking*, whether mechanical or electronic, is to bring a given physical signal Y to a predetermined value R and lock it there, which is the role of the control circuit or *regulator*. Now, considering a possible perturbation of the plant (see Fig. 34.1) by noise Z_p and also of the regulator by noise Z_c, the result (34.3) must be generalized,

$$Y(f) = \frac{P(f)C(f)}{1 + P(f)C(f)} R(f) + \frac{P(f)C(f)}{1 + P(f)C(f)} Z_c(f) + \frac{1}{1 + P(f)C(f)} Z_p(f)\,, \tag{34.4}$$

or,

$$\boxed{Y(f) = \frac{1}{1+V(f)^{-1}}[R(f)+Z_c(f)] + \frac{1}{1+V(f)}Z_p(f)} \,. \tag{34.5}$$

This shows that, provided the open loop gain is high enough, perturbations affecting the plant can be efficiently be neutralized. In contrast, noise entering via the control cannot be suppressed, and this fact is independent on the chosen controller transfer function: *Perturbations entering between the measurement point and the input of the regulator are not eliminated*! Consequently, the detector (which generally works with very low signals) should not introduce or let penetrate noise, because this affects the variable to be controlled: Any variation of the steering variable at the regulator will be transmitted 1 to 1.

In the following, we will discuss the most common controller called PID-servo.

34.1.2 PID feedback control

A *PID controller* continuously calculates an error value $e(t)$ as the difference between a desired setpoint and a measured process variable and applies a correction based on proportional, integral, and derivative terms. PID is an acronym for Proportional-Integral-Derivative, referring to the three terms operating on the error signal to produce a control signal.

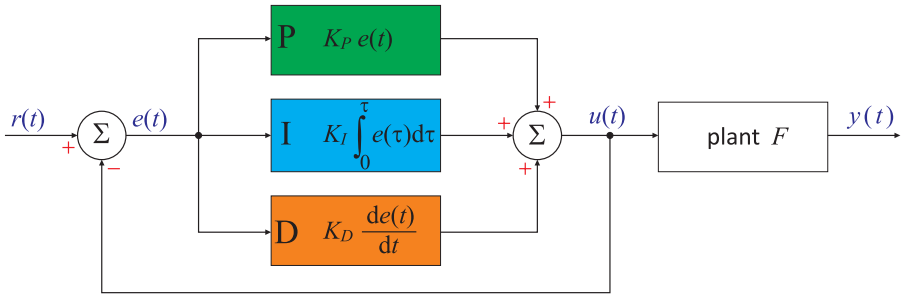

Figure 34.2: A block diagram of a PID controller in a feedback loop, $r(t)$ is the desired process value or 'set point', and $y(t)$ is the measured process value. A proportional-integral-derivative controller (PID controller) is a control loop feedback mechanism control technique widely used in control systems.

The theoretical understanding and application dates from the 1920s, and they are implemented in nearly all analogue control systems; originally in mechanical controllers, and then using discrete electronics and latterly in industrial process computers. The PID controller is probably the most-used feedback control design.

If $u(t)$ is the control signal sent to the system, $y(t)$ is the measured output and $r(t)$ is the desired output, and tracking error $e(t) = r(t) - y(t)$, a PID controller has the general form,

$$\boxed{u(t) = K_P e(t) + K_I \int e(\tau)d\tau + K_D \frac{de(t)}{dt}} \,. \tag{34.6}$$

The desired closed loop dynamics is obtained by adjusting the three parameters K_P, K_P, and K_I, often iteratively by 'tuning' and without specific knowledge of a plant model. Stability can often be ensured using only the proportional term. The integral term permits the rejection of a step disturbance (often a striking specification in process control). The derivative term is used to provide damping or shaping of the response [1].

Applying Laplace transformation results in the transformed PID controller equation,

$$\boxed{U(f) = \left(K_P + K_I \frac{1}{\imath f} + K_D \imath f\right) E(f) \equiv C(f)E(f)} \,, \tag{34.7}$$

defining the PID controller transfer function $C(f)$.

From equations (34.6) or (34.7) we immediately see that the PID transfer functions can readily be implement in electronic circuits using resistors (P), capacitors (I), and inductances (D).

Example 207 (*Comparing servo controllers*): We now assume a low-pass behavior for the plant,

$$P(f) = \frac{1}{1 + \imath f/f_c} \,,$$

and analyze the feedback circuit for four cases.

- The first one is that of a proportional servo, $C(f) = K_P$. Then, Eq. (34.5) reads,

$$Y = \frac{K_P}{1 + \imath f/f_c + K_P}(R + Z_c) + \frac{1 + \imath f/f_c}{1 + \imath f/f_c + K_P} Z_p$$
$$\begin{cases} \stackrel{s\to 0}{\longrightarrow} \frac{K_P}{1+K_P}(R + Z_c) + \frac{1}{1+K_P} Z_p \\ \stackrel{s\to\infty}{\longrightarrow} \frac{K_P f_c}{\imath f}(R + Z_c) + Z_p \end{cases} .$$

  We see that, for limited open-loop gain, noise affecting the plant Z_p is not eliminated at low frequencies. Additionally, at high frequencies, the gain for the error signal R drops like -6dB/oct.

- The second case is that of an integral servo $C(f) = K_I/\imath f$. Then Eq. (34.5) reads,

$$Y = \frac{K_I/\imath f}{1 + \imath f/f_c + K_I/\imath f}(R + Z_c) + \frac{1 + \imath f/f_c}{1 + \imath f/f_c + K_I/\imath f} Z_p$$
$$\begin{cases} \stackrel{f\to 0}{\longrightarrow} R + Z_c + \frac{\imath f}{K_I} Z_p \\ \stackrel{\to\infty}{\longrightarrow} \frac{K_I f_c}{(\imath f)^2}(R + Z_c) + Z_p \end{cases} .$$

  Apparently, the noise Z_p is now eliminated at low frequencies. However, the gain for R drops even faster at high frequencies.

[1] PID controllers are the most well established class of control systems: however, they cannot be used in several more complicated cases, especially if MIMO systems are considered.

- The third case is that of a PI-servo, $C(f) = K_P + K_I/\imath f$. Then Eq. (34.5) reads,

$$Y = \frac{K_P + K_I/\imath f}{1 + \imath f/f_c + K_P + K_I/\imath f}(R + Z_c) + \frac{1 + \imath f/f_c}{1 + \imath f/f_c + K_P + K_I/\imath f} Z_p$$
$$\begin{cases} \stackrel{f\to 0}{\longrightarrow} R + Z_c + \frac{\imath f}{K_I} Z_p \\ \stackrel{f\to\infty}{\longrightarrow} \frac{f_c K_P}{\imath f}(R + Z_c) + Z_p \end{cases},$$

  which represents a viable compromise, since it has the same low-frequency behavior as the I-servo, but at high frequencies the gain for R drops only like -6dB/oct.

- Finally, the forth case is that of a PID-servo, $C(f) = K_D \imath f + K_P + K_I/\imath f$. Then Eq. (34.5) reads,

$$Y = \frac{K_D \imath f + K_P + K_I/\imath f}{1 + \imath f/f_c + K_D \imath f + K_P + K_I/\imath f}(R + Z_c) + \frac{1 + \imath f/f_c}{1 + K_D \imath f + K_P + K_I/\imath f} Z_p$$
$$\begin{cases} \stackrel{f\to 0}{\longrightarrow} R + Z_c + \frac{\imath f}{K_I} Z_p \\ \stackrel{f\to\infty}{\longrightarrow} \frac{1}{1+1/f_c K_d}(R + Z_c) + \frac{1}{f_c K_D} Z_p \end{cases}.$$

  The low-frequency behavior remains still the same, but at high frequencies the gain for R stays constant.

A time domain analysis shows that P regulators have little phase lag, but the controlled variable can not be zeroed. On the other hand, I regulators have finite control bandwidth, but the controlled variable can be zeroed. PI regulators (parallel circuit of P and I regulators) have a reaction time $T_n = K_P/K_I$; that is, the jump response is advanced by T_n in comparison to the regulator I.

In the time domain we can summarize that regulators

- D are characterized by the absence of memory, but they are very fast,
- P have no idea of the strength of their impact,
- I increase their impact in time until the error disappears.

For practical PID controllers, a pure differentiator is neither physically realizable nor desirable due to amplification of noise and resonant modes in the system. Therefore, a phase-lead compensator type approach is used instead, or a differentiator with low-pass roll-off [406, 287, 288, 822]. See Excs. 34.2.3.1 and 34.2.3.2.

Like any real system, the controlled device behaves as a low-pass for manipulations or perturbations at high frequency. In other words, the device can only respond to external perturbations with finite speed. This delay of the response leads to a phase shift that can reverse the sign of the error signal $E(f)$ and transform a negative feedback into a positive feedback. Now, in the case that there are high frequency perturbations, for which the amplification of the closed control circuit is > 1, these perturbations can be amplified to form oscillations. These oscillations, which occur at the bandwidth of the closed loop gain are called *servo oscillations*.

Fig. 34.3 illustrates the necessity of optimizing the gain and the frequency response of the servo circuit: A proportional servo simply providing a frequency-independent gain $C(f) = K_P$ will lead to a forward gain $R(f) \propto P(f)$ exhibiting a low-pass behavior, i.e. a phase-shift $\phi = -\pi/2$ transforming negative to positive feedback. The gain at the frequency where this happens need to be lower than 1, otherwise the feedback servo will generate servo-oscillations, i.e. it will oscillate at the lowest Fourier frequencies where noise is amplified. A PI-servo alleviates this problem by a phase shift in opposite direction.

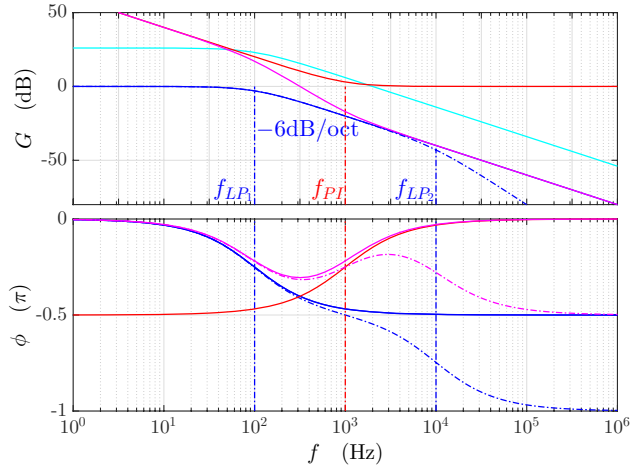

Figure 34.3: (code) Bode diagram for a plant subject to low-pass behavior and for a PI-servo. (blue solid) Low-pass filter with 100 Hz bandwidth; (blue dash-dotted) another low-pass filter at 100 kHz; (cyan) same as blue, but amplified by 20 dB; (red) PI-servo; (magenta) open-loop amplification.

34.1.3 Noise transfer in feedback loops

In order to develop a model for noise transfer we must understand what noise is and how it can be measured. This is not a simple task and we therefore outsourced a proper discussion to Sec. 35.3. Here, we will only use the information that noise affecting a signal $y(t)$ is quantified by a *spectral noise density* defined as the Fourier transform of the signal's autocorrelation function (35.59),

$$S_y(f) \equiv \mathcal{F}[\overline{y^*(t)y(t+\tau)}] \; . \tag{34.8}$$

Now, we can see how noise is transmitted through an LTI device $P(f)$:

$$\boxed{Y(f) = P(f)X(f) \quad \Rightarrow \quad S_y(f) = |P(f)|^2 S_x(f)} \; . \tag{34.9}$$

This result can be applied to our formula (34.5) describing a feedback loop,

$$\boxed{S_y(f) = \left|\frac{1}{1+V(f)^{-1}}\right|^2 S_c(f) + \left|\frac{1}{1+V(f)}\right|^2 S_p(f)} \; . \tag{34.10}$$

This formula describes how a servo control shapes the noise spectrum of a feedback-controlled variable $y(t)$.

Example 208 (*Noise reduction by feedback*): As an example, let us study the control circuit for stabilizing a laser to a cavity mode depicted in Fig. 34.1(b) using the following additional background information: The laser frequency ω be perturbed by $1/f$ noise described by the power spectral density,

$$S_p(f) \equiv 2 \cdot 10^{-24}/f \ .$$

This noise enters the feedback loop via the fluctuations $z_p(t)$ depicted in

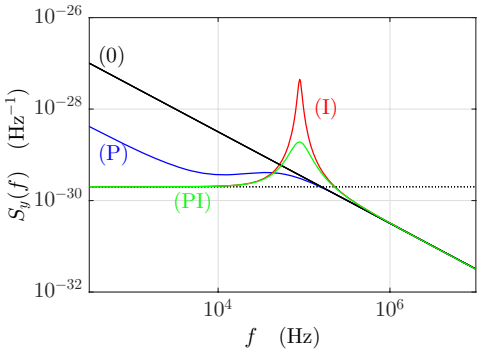

Figure 34.4: (code) Spectral density of frequency fluctuations of the servo system exhibited in Fig. 34.2. Shown is the spectral noise density $S_y(f)$ of the laser light for 4 different feedback gain curves: (black solid) no feedback control $C(f) = 0$, (blue) P-regulator with $C(f) = 4$, (red) I-regulator with $C(f) = 5 \cdot 10^6/\imath f$, and (green) PI-regulator $C(f) = 4 + 5 \cdot 10^6/\imath f$.

Fig. 34.1(a). The black solid line in Fig. 34.4 traces the noise spectrum $S_p(f)$, which is also the noise expected for the laser without feedback loop. Furthermore the optical cavity, which constitutes the essential part of the regulator, is itself afflicted by acoustic noise and thermal drifts which, for simplicity, we describe by a white Fourier frequency spectrum given by,

$$S_c(f) \equiv 2 \cdot 10^{-30}\,\mathrm{Hz}^{-1} \ ,$$

and represented by the black dotted line in Fig. 34.4. As we have seen, servos systems always have a finite bandwidth beyond which noise is fully coupled to the system. For example in laser frequency locks, the weakest point of a servo chain is often the small bandwidth of a piezo transducer used to correct the length of the laser cavity. We describe this behavior by a low-pass filter for the transfer function of the laser,

$$P(f) = \frac{1}{1 + \imath f/f_c}$$

with a bandwidth of $f_c = 10\,\mathrm{kHz}$.
Fig. 34.4 demonstrates how the $1/f$ noise $S_p(f)$ can be efficiently suppressed at frequencies below the low-pass filter cut-off f_c to a value limited by the white noise $S_c(f)$ entering through the regulator. As predicted by the formula (34.10), the suppression of the noise $S_p(f)$becomes all the better, as the open-loop gain

$V(f)$ gets higher. However, with the amplification of the controller, also the gain of the closed control circuit increases, and this necessarily causes phase shifts, which lead to (servo-)oscillations in the circuit appearing as a strong peak of strong noise around a certain Fourier frequency f_{bw} characterizing the bandwidth of the closed loop servo system. Note that high-frequency noise, to which the cavity might be subject, is not coupled to the laser, because it is filtered by the low-pass filter $P(f)$ to the same extend as the error signal itself.

The next example, exhibited in Fig. 34.5, shows the experimental characterization of a dye laser locked via the Pound-Drever-Hall technique (see Sec. 34.3.3) to an optical cavity.

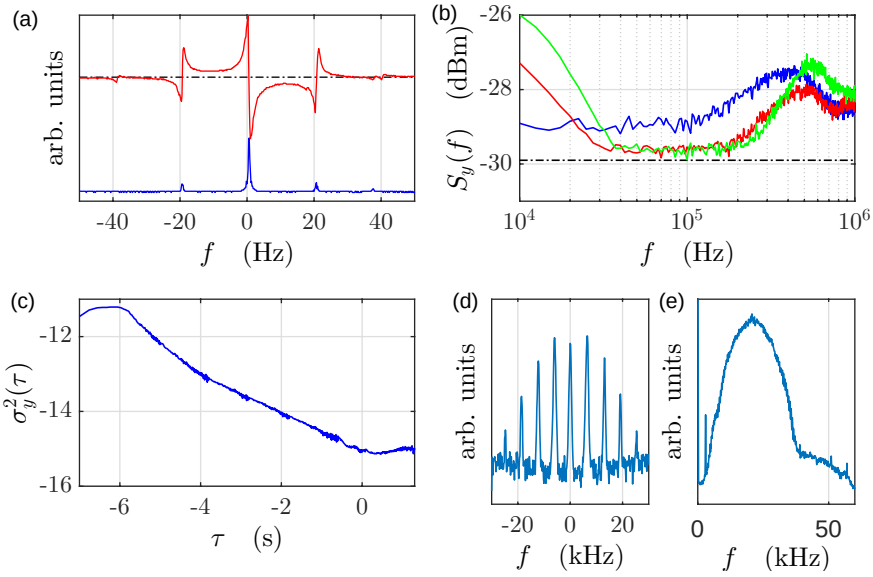

Figure 34.5: Characterization of a Pound-Drever-Hall stabilization of a dye laser. (a) PDH error signal (red) and cavity transmission signal (blue), (b) spectral density of frequency fluctuations, (c) Allan variance. (d-e) Beat signals of Mach-Zehnder interferometers. In (d) one interferometer arm is passed through an optical fiber attached to a piezo transducer to which a sinusoidal 5 kHz modulation of is applied. This demonstrates the sensitivity of optical fibers to acoustic noise. In (e) one interferometer arm is send to another optical table and back. This demonstrates how mechanical vibrations of optical components in the beam path can broaden the spectrum of a laser field.

34.2 Amplitude stabilization circuits

34.2.1 Laser intensity stabilization with an AOM

The light emitted from lasers is generally subject to *frequency fluctuations* and *intensity fluctuations*, which are unacceptable for many applications. In this section we will construct an *intensity stabilization* for a laser beam.

One way of stabilizing the light intensity of a laser beam consists in using the an acousto-optic modulator, as shown in Fig. 34.6. The first Bragg diffraction order (see Sec. 32.3.1) is focused onto a photodiode. Intensity fluctuations of the light recorded by the photodiode are converted into voltage fluctuations, processed by an electronic circuit fed back to the AOM. The intensity of light diffracted into the first order can be controlled via the power of the radiofrequency alimenting the AOM. The control circuit can now be conceived such as to neutralize the intensity fluctuations recorded by the photodiode.

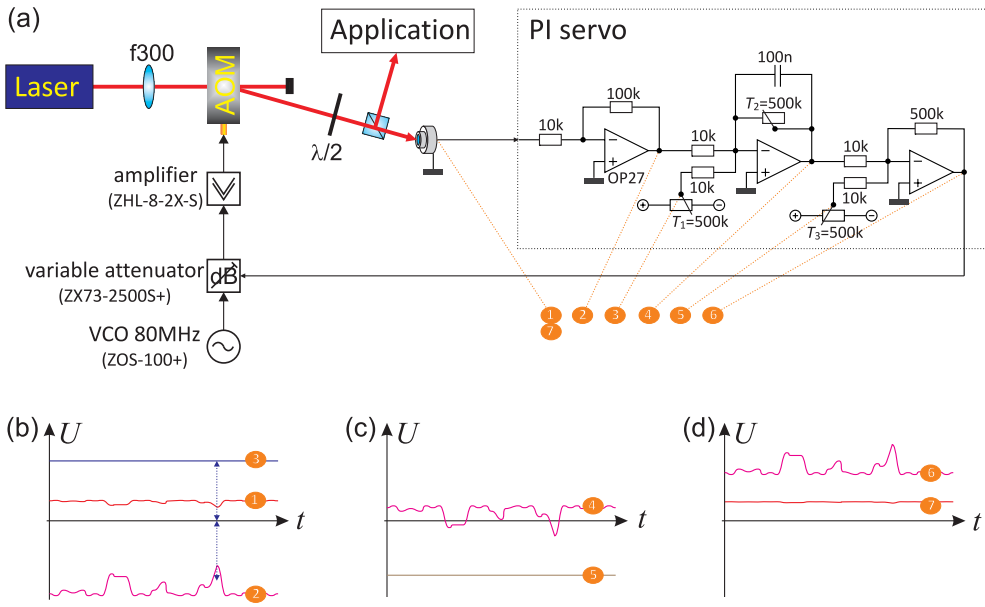

Figure 34.6: (a) Layout of the intensity control. The variable attenuator controls the amplitude of the radiofrequency driving the AOM: low voltage (0 V) increases the attenuation, high voltage (+16 V) reduces it. The sketched control circuit realizes a negative feedback, when the photodetector produces a positive signal. (b-d) Signals recorded at the test points of the circuits shown in (a). See text for explanations.

34.2.1.1 Operation principle and adjustment procedure

The idea of the intensity stabilization is illustrated in Fig. 34.6(b-d): The laser intensity scattered into the first diffraction order is recorded by a photodiode (test point 1 in the figure). The signal is then amplified (and inverted) by a first OpAmp (test point 2). The trimmer T_1 (test point 3) is now adjusted to a positive voltage compensating the DC part of the signal (2), i.e., the sum (2+3) after being inverted and amplified by the second OpAmp (test point 4), should be around zero DC. The signal (2+3) is called *error signal*, since it is this signal which tells us in which direction the control circuits has to work to counteract the power fluctuation. In the present design, the second OpAmp also incorporates the PI servo (see Sec. 34.1), which can be adjusted via the amplification of the trimmer T_2 and the capacity C.

It is now important to realize, that the variable attenuator works best around a given control voltage, which is provided by adding via the trimmer T_3 (test point 5) and a third OpAmp an appropriate offset. Furthermore, we note that variable attenuator reduces its attenuation with increasing control voltage. Thus, the control signal (test point 6) works to enhance the efficiency of the AOM, when the photodiode signals a power drop, and vice versa. As a result, the light power in the first diffraction order is stabilized, however, at a level inferior to the unstabilized power [822, 288].

The trimmers of the servo circuits can be adjusted using the following procedure:

1. Observe the light intensity and its fluctuations at test point (1), set test point (4) to ground (e.g. short-circuiting the trimmer T_2), and adjust trimmer T_3 until the light intensity level is at bit lower than the lowest fluctuations.
2. Reconnect test point (4) to the circuit and adjust trimmer T_1 until the voltage at test point (4) cancels to zero.

34.2.2 PI servo for a current stabilization

Many applications in quantum optics require very stable high currents, for instance, in coils generating magnetic field for atomic trapping potentials. Here, we will construct a *PI servo* to para realize a *current stabilization*.

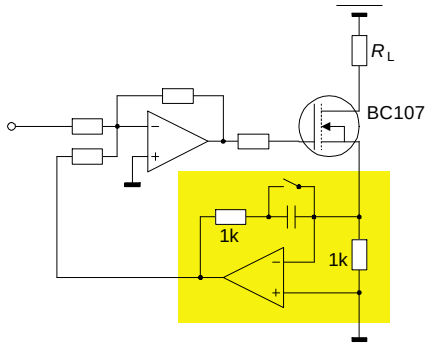

Figure 34.7: Current stabilization.

34.2.3 Exercises

34.2.3.1 Ex: Integrator

Determine the transfer function of the circuit depicted in Fig. 34.8. What kind of control circuit is it?

34.2.3.2 Ex: PID controller

Consider the PID controller transfer function in series,

$$C(f) = K\left(1 + \frac{1}{\imath f T_I}\right)(1 + \imath f T_D) \ ,$$

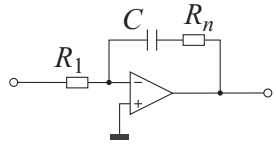

Figure 34.8:

a first-order low-pass filter in the feedback loop,

$$F(f) = \frac{1}{1 + \imath f T_F} \ ,$$

and a linear actuator with low-pass behavior,

$$P(f) = \frac{A}{1 + \imath f T_P} \ .$$

How do you have to choose the various time constants in order to let the closed-loop transfer function be $H(f) = 1$.

34.2.4 *Experiment: Development of an intensity stabilization*

We will now set up up an intensity stabilization. For the realization of the project prior knowledge of 1. photodetectors (see Sec. 31.2.1), 2. acousto-optic modulators (AOM) (see Sec. 32.3.1), 3. electronic circuits (see Sec. 31.1.3), and 4. control circuits (see Sec. 34.1) is required.

1. Realize the optical setup illustrated in Fig. 34.6. Optimize the alignment of the AOM (in particular, the focus and the Bragg angle) in order to maximize the efficiency of the AOM. Take care not to saturate the photodiode, if necessary adapt the load resistance (see Sec. 31.1.). Study the data sheet of the variable attenuator.

2. Derive and plot the transfer function for ac-signals of the electronic circuit. What kind of control circuit is it?

3. Set up the electronic circuit exhibited in Fig. 34.6. Test it by observing the signals at the six test points marked in the circuit diagram. Understand and interprete the roles of the three adjustable parameters: input offset, amplification, and output offset.

4. Incorporate the servo circuit into the optical setup as shown in Fig. 34.6. How to make sure the circuit is operating properly? [2].

[2] Datasheet for the VCO see appendix Fig. 35.16,
data sheet for the variable attenuator see appendix Fig. 35.17,
data sheet for the amplifier see appendix Fig. 35.15.

34.2.5 *Experiment: PI servo for a current stabilization*

How to control high currents? How to dramatically increase the switching speed despite inductive loads and eddy currents?

1. Connect a resistive charge to a voltage source. Insert a *MOSFET* into the circuit and a small resistor. Control the gate of the MOSFET with a voltage and measure the current of the circuit via the voltage drop at the small resistor as a function of the gate voltage.

2. Now control the gate voltage via the voltage measured at the small resistor and measure again the dependency voltage-to-current.

34.3 Frequency stabilization circuits

Although lasers are often monochromatic, they generally have a poor intrinsic frequency stability, that is, the frequency of the light field $E(t) = \sin \omega t$ drifts in time, $\omega = \omega(t)$ on a time scale, which is slow in comparison to the oscillation period $1/\omega$. The reasons for these drifts are typically acoustic noise or thermal drifts to which the laser device is subject and which are difficult to avoid.

Often it is much easier to guarantee the mechanical and thermal stability of a passive device exhibiting resonances, such as an optical cavity. Furthermore, nature provides intrinsically stable resonances, such as narrow atomic transitions. These resonances can be used to actively stabilize the frequency of lasers via feedback servo circuits. In the following sections we will present a few common techniques.

34.3.1 Side-of-fringe stabilization to/of a Fabry-Pérot cavity

Resonances are generally characterized by peaked profiles symmetrically centered about a resonance frequency ω_0. Excited by a laser field of frequency ω, they respond by an oscillation whose amplitude depends on the detuning $\omega - \omega_0$. Unfortunately, the amplitude of the response signal does not tell us, whether the detuning is positive or negative. We have to invent techniques allowing us to extract this information from the response signal and to generate a true error signal.

One of these techniques is the *side-of-fringe stabilization* technique illustrated in Fig. 34.9. Here, the laser tuned to one side of the optical resonance such that, when the laser frequency drifts, the response signal increases or decreases correspondingly. Technically, this is achieved by comparing (i.e. subtracting) the response signal with a stable reference signal.

34.3.2 Lock-in method for frequency stabilizing to/of a cavity

One method of stabilizing a laser on a resonator consists in modulating the frequency slightly and then demodulating the transmission signal of the resonator at the same frequency. This is the so-called *lock-in method*. Frequency modulation of the laser beam can be done by modulating the laser diode feed current, the piezo of the extended laser cavity or using an AOM. Fig. 34.10 shows the layout of the optical assembly.

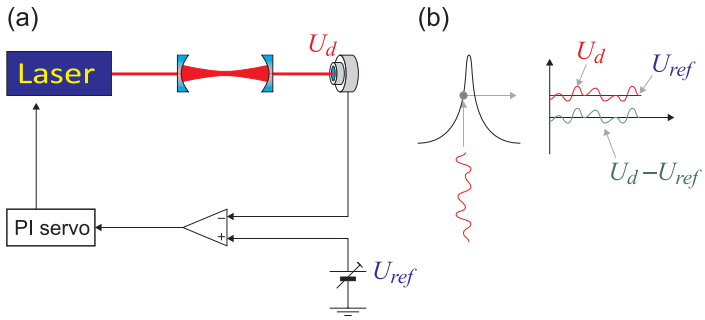

Figure 34.9: (a) Frequency stabilization to a cavity using the side-of-fringe method. (b) The laser is tuned to rising (or falling) slope of a transmission curve of a Fabry-Pérot cavity. The error signal is compared with reference voltage.

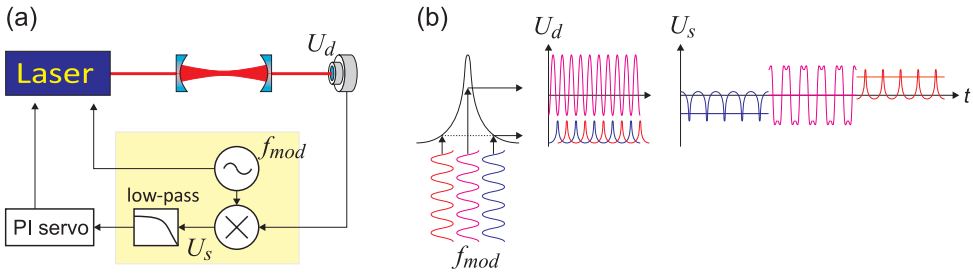

Figure 34.10: (a) Frequency stabilization to a cavity using the lock-in method. (b) Frequency-modulated signals applied to a resonance suffer a period doubling, when the signal frequency is close to resonance. By demodulating the signals discriminated at the resonance profile, we obtain, after averaging over a period, a DC voltage that is proportional to the frequency detuning. The yellow area denotes the components constituting the lock-in amplifier.

The principle of control through modulation is explained in Fig. 34.10(a). A laser beam passes twice (round-trip) through an *acousto-optic modulator* fed by a radiofrequency voltage with modulated frequency, $\omega(t) = \omega_c + M \cos ft$. Here, the modulation frequency is much lower than its amplitude (or frequency excursion), $f \ll M$. The laser beam is now injected into an optical cavity and the frequency of the laser tuned near a resonance of the cavity. The dependence of the transmission on the frequency is described in good approximation of the *Airy formula* by a Lorentzian,

$$I(\omega) = \frac{\gamma^2}{4(\omega - \omega_0)^2 + \gamma^2} \ . \tag{34.11}$$

The signal transmitted through the cavity [see Fig. 34.10(b)],

$$U_d(t) = I(\omega(t)) = \frac{\gamma^2}{4\left(\omega_c + M\cos ft - \omega_0\right)^2 + \gamma^2} \ , \tag{34.12}$$

is demodulated by a lock-in amplifier [see Fig. 34.10(c)],

$$U_s(t) = U_d(t)\cos(ft + \phi) \ , \tag{34.13}$$

integrated with a locking electronics [see Fig. 34.10(d)]

$$\bar{U}_s(t) = \frac{1}{T}\int_0^T U_s(t)dt \ . \tag{34.14}$$

and used to control the piezo of the laser's extended cavity.

34.3.3 Pound-Drever-Hall stabilization

When the frequency of a carrier wave ω is modulated by a frequency Ω [3], the spectrum consists of sidebands the frequencies and phases of which can be calculated from an expansion of the wave in Bessel functions. Let N be the modulation excursion and $J_k(x)$ the Bessel function of the order k. Higher-order sidebands $k > 1$ are usually dropped in the calculation,

$$e^{\imath(\omega t + N\sin\Omega t)} = e^{\imath\omega t}[-J_1(N)e^{\imath\Omega t} + J_0(N) + J_1(N)e^{-\imath\Omega t}] \ . \tag{34.15}$$

From the latter expression, it can be seen that the spectrum of sidebands is formed

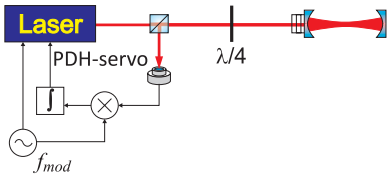

Figure 34.11: Frequency stabilization to a cavity using the Pound-Drever-Hall method.

by the frequencies ω and $\omega \pm \Omega$. A resonator responds to a field of incident light $E_0(\omega)$ oscillating with frequency ω by reflecting the field (R: reflectivity of mirrors, δ_{fsr}: free spectral range)

$$E_r(\omega) = E_0(\omega)\sqrt{R}\frac{1 - e^{-\imath\omega/\delta_{fsr}}}{1 - R\ e^{-\imath\omega/\delta_{fsr}}} \ , \tag{34.16}$$

where the amplitude and the phase of the reflected light field follow from the relation $E_r(\omega) = |E_r(\omega)|e^{\imath\phi(\omega)}$. Obviously the field of the reflected light is strong only, when the laser frequency is close to one mode of the resonator (when ω/δ is an integer number). By inserting Eq. (34.16) into Eq. (34.15), we obtain the response of the resonator to a field containing sidebands as a function of the frequency of light ω, of the modulation frequency Ω, and of the cavity finesse,

$$\begin{aligned} |E_{tot}|^2 &= |e^{\imath\omega t}[J_1(N)E_r(\omega+\Omega)e^{\imath\Omega t} + J_0(N)E_r(\omega) - J_1(N)E_r(\omega-\Omega)e^{-\imath\Omega t}]|^2 \\ &= J_0(N)J_1(N)E_r(\omega+\Omega)e^{\imath\Omega t} + J_0(N)J_1(N)E_r^*(\omega-\Omega)e^{\imath\Omega t} + ... + c.c. \ . \end{aligned} \tag{34.17}$$

The contributions of the reflected field to the current in the photodetector, $|E_r|^2$, oscillating with frequency Ω and extracted by the alternating current $e^{-i\Omega t + i\theta}$ (θ is

[3] Remember that we specify all frequencies except the free spectral range δ_{fsr} in radians.

an arbitrarily chosen phase angle), are

$$S_{PDH} = |E_{tot}|^2 e^{-i\Omega t + i\theta} \tag{34.18}$$
$$= J_0(N)J_1(N)\mathfrak{Re}\left\{e^{\imath\theta}[E_r^*(\omega)E_r(\omega+\Omega) - E_r(\omega)E_r^*(\omega-\Omega)]\right\} + \dots .$$

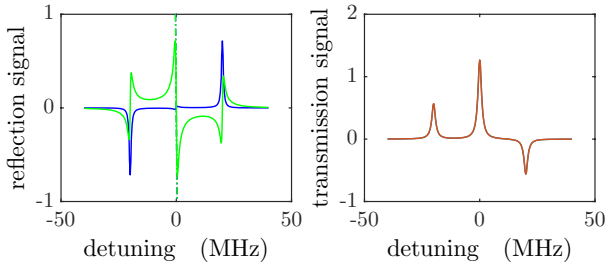

Figure 34.12: (code) (Left) Pound-Drever-Hall reflection signal for $\theta = 0, \pi/2$. (Right) Transmission signal.

By a suitable choice of the modulation index, the pre-factor containing Bessel functions (and therefore the signal amplitude) can be maximized. That is the case, for $M \simeq 1.1$ (see Exc. 32.4.5.1). Each of the two parts of the summation in the above equation is the result of a beating of the carrier $E_r(\omega)$ with one of the sidebands $E_r(\omega \pm \Omega)$. Only those optical sidebands being close to a mode of the resonator provide, along with the radiofrequency sidebands, contributions to the reflection signal

The dependence of the reflection signal S_{PDH} on the frequency ω is shown in Fig. 34.12(a). The antisymmetric shape and the zero-crossing slope are ideal for use as a discriminator generating an *error signal* for a frequency stabilization. This method is called *Pound-Drever-Hall method*.

34.3.4 Phase stabilization of standing waves

For the stabilization of the phase of a standing wave one can use the following scheme. It is similar to the homodyne method used with the Michelson interferometer with the difference that laser beam separation and recombination are done at different beam splitters.

34.3.5 Frequency-offset locking with phase-locked loops

Many application in spectroscopy require two stable lasers emitting at different but well-defined and tunable frequencies. Examples are stimulated Raman transitions, or the spectroscopy of atoms interacting with optical cavities [133]. In the following we will discuss and compare different approaches to locking one laser to another laser using a phase-locked loop (PLL). See also (watch talk).

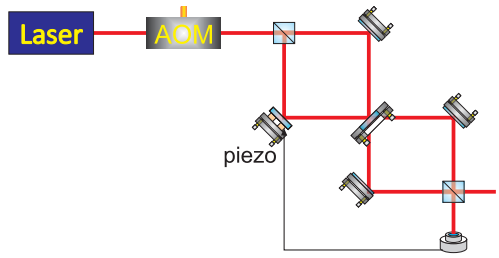

Figure 34.13: Phase stabilization.

34.3.5.1 VCO and mixing

In a *phase-locked loop* one tries to synchronize a self-sustained oscillator, in general realized by a VCO, with a local oscillator. The VCO generates an ac-voltage U_{rf}, whose frequency is tuned via a dc-control-voltage U_{ct} around a center frequency ω_0, as shown in Fig. 34.14(a). It can be modeled by,

$$\boxed{U_{rf}(t) = 2B\cos\phi(t) \qquad \text{with} \qquad \frac{d\phi}{dt} = \omega_0 + KU_{ct}(t)} \; . \tag{34.19}$$

The local oscillator produces an ac-voltage, $U_{lo}(t) = A\sin\phi_{lo}(t)$. A mixer multiplies both signals,

$$U_d(t) = AB\left(\sin[\phi_{lo}(t) - \phi(t)] + \sin[\phi_{lo}(t) + \phi(t)]\right) \; . \tag{34.20}$$

See also Exc. 34.3.7.1.

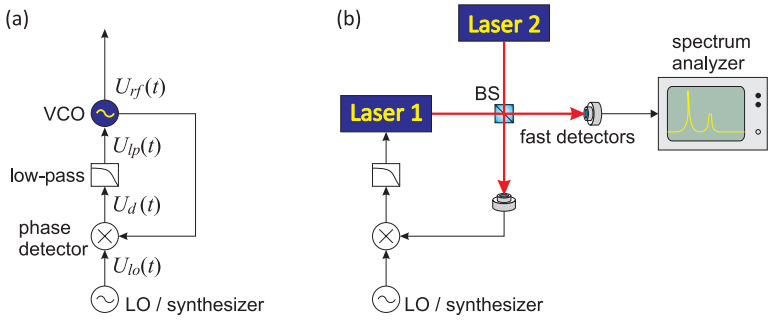

Figure 34.14: (a) PLL to lock a VCO to a reference oscillator LO. (b) PLL to lock the difference frequency of two lasers to a LO.

34.3.5.2 Low-pass filtering

The multiplied signal U_d contains all information about frequency deviations of the VCO from the LO. To extract them, we *low-pass filter* this signal, cutting off all high frequency components, i.e. apply the filter transfer function,

$$F(f) = (1 + sRC)^{-1} \; . \tag{34.21}$$

The signal of the filter is $U_{lp}(f) \equiv F(f)U_d(f)$. In time domain, which is obtained by a Laplace transform, $F(t) = (RC)^{-1}\theta(t)e^{-t/RC}$, such that

$$U_{lp}(t) = F \star U_d(t) = \int_{-\infty}^{\infty} F(t-\tau)U_d(\tau)d\tau = \frac{e^{-t/RC}}{RC}\int_{-\infty}^{t} e^{\tau/RC}U_d(\tau)d\tau \ . \quad (34.22)$$

The derivative is obviously,

$$\frac{dU_{lp}}{dt} + \frac{U_{lp}}{RC} = \frac{U_d(t)}{RC} = \frac{AB}{RC}\sin\left[\phi_{lo}(t) - \phi(t)\right] \ , \quad (34.23)$$

inserting the above expression for U_d. Note, that we would have obtained the same result using control theory (see Sec. 34.1).

34.3.5.3 Phase synchronization

The phase synchronization servo is closed by setting $U_{ct} = U_{lp}$. Thus we may substitute $U_{lp}(t)$ and define $\psi \equiv \phi - \phi_{lo}$,

$$\frac{d^2\psi}{dt^2} + \frac{1}{RC}\frac{d\psi}{dt} + \frac{KAB}{RC}\sin\psi = -\frac{d^2\phi_{lo}}{dt^2} - \frac{1}{RC}\left(\frac{d\phi_{lo}}{dt} - \omega_0\right) \ . \quad (34.24)$$

In most cases the LO frequency varies slowly, so that we may assume $\dot{\phi_{lo}} = \omega_{lo}$,

$$\frac{d^2\psi}{dt^2} + \frac{1}{RC}\frac{d\psi}{dt} + \frac{KAB}{RC}\sin\psi = -\frac{1}{RC}\left(\omega_{lo} - \omega_0\right) \ . \quad (34.25)$$

Hence, a PLL generates a signal $U_{rf}(t)$ having approximately the same (time-dependent) frequency as the local oscillator $U_{lo}(t)$. The equation is identical to that of an overdamped rotator or a resistively shunted Josephson junction [655].

We observe that the PLL is locking to servo oscillations. The spectrum of signal produced by the VCO exhibits sidebands as soon as the loop is closed. Their amplitude depends on the gain, their frequency varies with the offset voltage controlling the VCO.

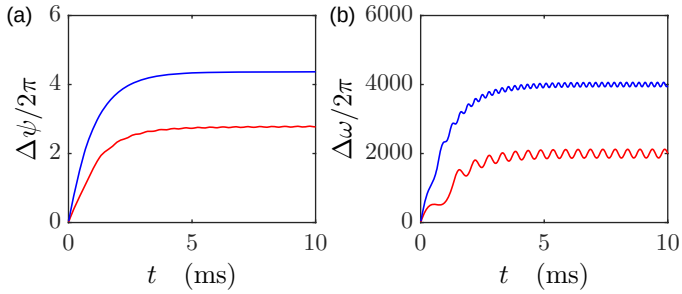

Figure 34.15: (code) Simulation of (a) the phase and (b) frequency difference in a PLL for (red) $\omega_{lo} - \omega_0 = (2\pi)$ 2 kHz and (blue) 4 kHz.

34.3.6 Frequency-offset locking using transfer cavities

Sometimes we want to take a ultra-high resolution spectrum in a frequency region, where there is no reference frequency available nearby. By nearby we mean frequency regimes which can be reached by PLLs based on frequency beats on fast photodetectors, as studied in Sec. 34.3.5. A possible method consists in the use of an optical *transfer cavity*.

Here, a reference laser stabilized to a known frequency ω_{ref}, e.g. via a saturation spectroscopy to an atomic transition, is used to lock a piezo-tunable optical cavity (called transfer cavity), as shown in Fig. 34.16. The cavity in turn is used to lock the spectroscopy laser $\omega_{blu-las}$, e.g. via the Pound-Drever-Hall method.

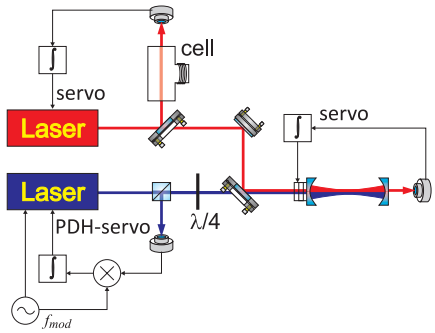

Figure 34.16: Schematic view of a transfer cavity locking system involving three cascaded servo systems for (i) the stabilization of the reference laser to a known frequency; (ii) of the transfer cavity to the reference laser, and (iii) of the spectroscopy laser to the transfer cavity.

Two issues need to be considered when using the transfer cavity scheme:

- The scheme does not permit tuning of the spectroscopy laser; this feature must be included using, e.g. AOMs (see Sec. 32.3.1) of PLL offset locks (see Sec. 34.3.5).
- The use of piezo in the transfer cavity is incompatible with its high-level thermal and mechanical stabilization. This means that special care must be taken in the design of the reference laser in order to avoid degradation of the stability of the transfer cavity via the servo lock.

The whole locking scheme consists of three cascaded servo loops (see Fig. 34.16). To model the transfer of stability from the reference to the spectroscopy laser, we write down the following relations,

$$\begin{aligned} \omega_{red-las} &= H_{sat}(f)\omega_{ref} \\ N_{red-trns}\delta_{fsr} &= H_{trns}(f)\omega_{red-las} \\ \omega_{blu-las} &= H_{pdh}(f)N_{blu-trans}\delta_{fsr} \ . \end{aligned} \tag{34.26}$$

In the absence of noise or for perfect servos, $H_x \to 1$, we get,

$$\omega_{blu-las} = \frac{N_{blu-trans}}{N_{red-trans}}\omega_{red-las} \ . \tag{34.27}$$

We assume specific transfer functions for the closed-loop gains of the three servos and describe the impact of noise by adding frequency deviations $\Delta\omega$ entering at various points.

34.3.7 Exercises

34.3.7.1 Ex: Schemes for laser tuning

Discuss the two PLL-setups shown in Fig. 34.17.

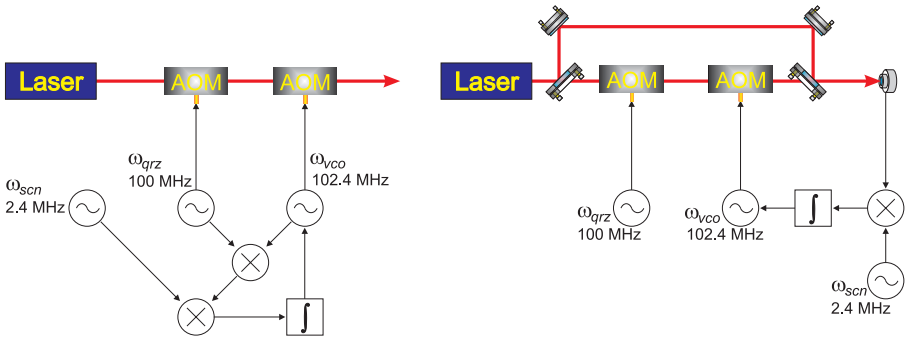

Figure 34.17: Two schemes for laser tuning.

34.3.8 *Experiment: Stabilizing a laser to a cavity*

Here is, how we are going to stabilize a laser to a cavity:

1. Stabilize a helium-neon laser to a Fabry-Pérot cavity, generating a frequency modulation by modulating the laser diode current or the piezo of the extended cavity. Choose a modulation frequency in the range of $f \simeq 1$ kHz and a modulation amplitude in the range of $M \simeq 5$ MHz. Adjust the reference voltage of the control electronics until the error signal is symmetrical.

2. If you do not have a lock-in amplifier available, construct one following the project Sec. 31.4.3.

3. Now, do the opposite, stabilizing the optical cavity to the laser frequency using the resonator piezo as control element.

4. Vary the optical setup now modulating the frequency using an AOM (see Fig. 34.18).

34.3.9 *Experiment: Pound-Drever-Hall locking*

Now we will stabilize a laser to a cavity using the Pound-Drever-Hall technique [106, 245]:

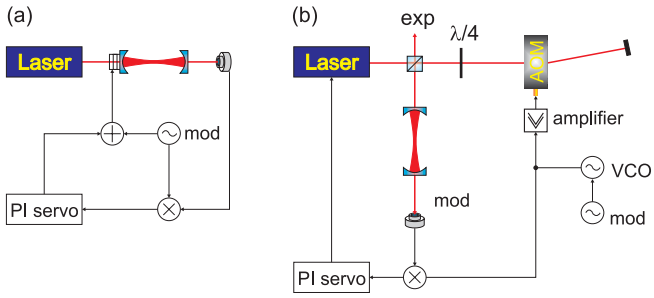

Figure 34.18: Variations on the same theme: (a) Frequency stabilization of a cavity to a laser frequency using the lock-in method. This method is often used for spectral filtering of a laser beam by a transmission etalon. (b) Frequency stabilization of a laser to a cavity using an AOM. The advantage of using an AOM compared to the scheme shown in Fig. 34.10 is, that only the beam injected into the cavity is modulated, but not the beam used for the main experiment.

1. Consider the reflected signal. To do this, separate the beam injected into the resonator from the reflected beam by means of a $\lambda/4$ waveplate and a polarizing beam splitter.

2. Now analyze the reflected signal with a fast photodetector at a spectrum analyzer.

3. Demodulate the signal with the modulation frequency. Vary the length of the cables. Optimize the slope of the error signal by a suitable choice of frequency and modulation excursion [4].

34.4 Further reading

34.4.1 on frequency noise description

D.W. Allan, *Statistics of atomic frequency standards* [DOI]

J.A. Barnes et al., *Characterization of frequency stability* [DOI]

J.L. Stewart, *The power spectrum of a carrier frequency modulated by Gaussian noise* [DOI]

D.S. Elliott et al., *Extracavity laser band-shape and bandwidth modification* [DOI]

L.S. Cutler, *Some Aspects of the Theorv and Measurement of Frequency Fluctuations in Frequency Standards* [DOI]

D.B. Sullivan et al., *Characterization of Clocks and Oscillators* [ISBN]

[4] Datasheet for the VCO see appendix Fig. 35.16,
data sheet for the power splitter see appendix Fig. 35.18,
data sheet for the mixer see appendix Fig. 35.19.

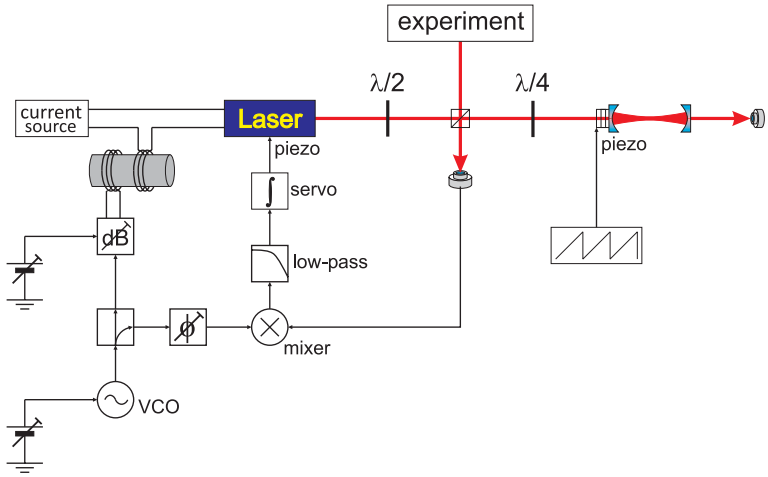

Figure 34.19: Setup of a frequency regulator following Pound-Drever-Hall. VCO: Voltage-Controlled Oscillator, LT: power splitter, dB: variable attenuator, LP: low-pass filter.

G. Di Domenico et al., *Simple approach to the relation between laser frequency noise and laser line shape* [DOI]

J. Appel et al., *A versatile digital GHz phase lock for external cavity diode lasers* [DOI]

L. Ricci et al., *A compact grating-stabilized diode laser system for atomic physics* [DOI]

G. Ritt et al., *Laser frequency offset locking using a side of filter technique* [DOI]

A.S. Arnold et al., *A simple extended-cavity diode laser* [DOI]

E.C. Cook et al., *High passive-stability diode-laser design for use in atomic-physics experiments* [DOI]

C.J. Hawthorn et al., *Littrow configuration tunable external cavity diode laser with fixed direction output beam* [DOI]

Huanqian Loh et al., *Influence of grating parameters on the linewidths of external-cavity diode lasers* [DOI]

Y. Shimada et al., *A simplified 461-nm laser system using blue laser diodes and a hollow cathode lamp for laser cooling of Sr* [DOI]

R.J. Steed, *Derivations of the Phase Noise Spectra of Lasers and of Lasers Passing Through Interferometers* [ISBN]

34.4.2 on laser stabilization

J. Alnis et al., *Stable diode lasers for hydrogen precision spectroscopy* [DOI]

J. Alnis et al., *Subhertz linewidth diode lasers by stabilization to vibrationally and thermally compensated ultralow-expansion glass Fabry-Pérot cavities* [DOI]

L. Couturier et al., *Laser frequency stabilization using a commercial wavelength meter* [DOI]

K. Huang et al., *Microcontroller-based locking in optics experiments* [DOI]

Shun Wu et al., *Direct fiber comb stabilization to a gas-filled hollow-core photonic crystal fiber* [DOI]

Y.N. Zhao et al., *Sub-Hertz frequency stabilization of a commercial diode laser* [DOI]

R.W.P. Drever et al., *Laser Phase and Frequency Stabilization Using an Optical Resonator* [DOI]

D. Budker et al., *Obtaining frequency markers of variable separation with a spherical mirror Fabry-Perot interferometer* [DOI]

34.4.3 on control theory

U. Tietze et al., *Halbleiterschaltungstechnik* [ISBN]

O. Föllinger et al., *Regelungstechnik: Einführung in die Methoden und ihre Anwendung* [ISBN]

Chapter 35

Appendices to 'Instrumentation of a Quantum Optics Lab'

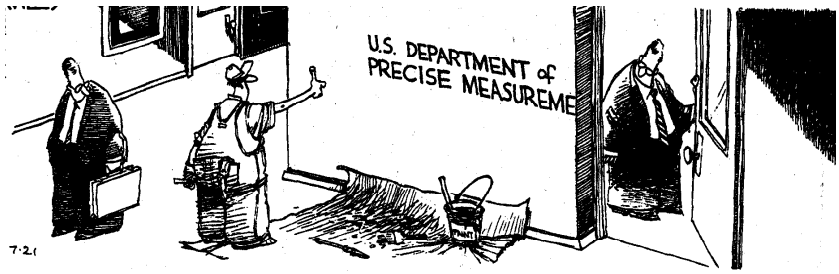

Figure 35.1: At the National Institute for Standards and Technology (NIST).

35.1 Calculating the uncertainty of measured quantities

35.1.1 Mean value and standard deviation

Mean value and *standard deviation* are defined by,

$$\bar{x} \equiv \frac{1}{N}\sum_k x_k \qquad \text{and} \qquad \sigma_{\bar{x}} \equiv \sqrt{\frac{1}{N-1}\sum_k (x_k - \bar{x})^2}\ . \tag{35.1}$$

The standard deviation can be weighed by a confidence parameter,

$$\bar{x} \equiv \frac{\sum_k w_k x_k}{\sum_k w_k} \qquad \text{and} \qquad \sigma_{\bar{x}} \equiv \frac{1}{\sqrt{\sum_k w_k}} \tag{35.2}$$

Weighing by individual standard deviation,

$$w_k \equiv \frac{1}{\sigma_k^2} \qquad \text{for} \qquad \sigma_k = \sigma_0 \tag{35.3}$$

gives,

$$\bar{x} \equiv \frac{\sum_k \frac{x_k}{\sigma_k^2}}{\sum_k \frac{1}{\sigma_k^2}} = \sigma_{\bar{x}}^2 \sum_k \frac{x_k}{\sigma_k^2} \overset{\sigma_k=\sigma_0}{\longrightarrow} \frac{1}{N}\sum_k x_k \quad \text{with} \quad \sigma_{\bar{x}} \equiv \frac{1}{\sqrt{\sum_k \frac{1}{\sigma_k^2}}} \overset{\sigma_k=\sigma_0}{\longrightarrow} \frac{\sigma_0}{\sqrt{N}} \tag{35.4}$$

or,

$$\hat{\sigma}_{\bar{x}} \equiv \sigma_{\bar{x}}\chi_v \overset{\sigma_k=\sigma_0}{\longrightarrow} \sqrt{\frac{1}{N-1}\sum_k (x_k-\bar{x})^2} \tag{35.5}$$

$$\chi_v = \sqrt{\frac{1}{N-1}\sum_k \frac{(x_k-\bar{x})^2}{\sigma_i^2}} \; .$$

From error propagation

$$\Delta\bar{x} \equiv \sqrt{\frac{1}{N}\sum_k \Delta x_k^2} \; . \tag{35.6}$$

35.1.1.1 χ^2-fit

The χ^2-fit of a constant of a function $y = f(x)$ to a measured data set (x_k, y_k) is,

$$\chi^2 = \frac{1}{N(N-1)}\sum_k [f(x_k) - y_k]^2 \; . \tag{35.7}$$

The above formula suggest that, increasing the number of measurements $N \to \infty$ we could pull the error to zero. This, however, is NOT TRUE. If the standard deviation is smaller than the precision Δ of the measurement tool, the error will be limited by Δ,

$$\bar{y} \pm \max(\sigma, \Delta) \; . \tag{35.8}$$

35.1.2 Error propagation

The *error propagation* for a function $f(x_1, x_2, ..)$ is given by,

$$\Delta f = \sqrt{\left(\frac{\partial f}{\partial x_1}\right)^2 \Delta x_1^2 + \left(\frac{\partial f}{\partial x_2}\right)^2 \Delta x_2^2 + ...} < \left|\frac{\partial f}{\partial x_1}\right| \Delta x_1 + \left|\frac{\partial f}{\partial x_2}\right| \Delta x_2 + ... \; . \tag{35.9}$$

Calculations can often be simplified by noting that the four fundamental operations, $f = x_1 \pm x_2$, $f = x_1 x_2$, and $f = \frac{x_1}{x_2}$ allow us to simply add the relative errors,

$$\frac{\Delta f}{f} = \frac{\Delta x_1}{x_1} + \frac{\Delta x_2}{x_2} \; . \tag{35.10}$$

Alternatively, we may use the following quick rules,

$$\begin{array}{rrcrl}
\textit{sum}: & f \pm \Delta f = & (x \pm \Delta x) + (y \pm \Delta y) & = & (x+y) \quad \pm (\Delta x + \Delta y) \\
\textit{subtraction}: & f \pm \Delta f = & (x \pm \Delta x) - (y \pm \Delta y) & = & (x-y) \quad \pm (\Delta x + \Delta y) \\
\textit{multiplication}: & f \pm \Delta f = & (x \pm \Delta x) \cdot (y \pm \Delta y) & = & (x \cdot y) \quad \pm (x\Delta y + y\Delta x) \\
\textit{division}: & f \pm \Delta f = & \frac{x \pm \Delta x}{y \pm \Delta y} & = & \frac{x}{y} \quad \pm \frac{1}{y^2}(x\Delta y + y\Delta x) \\
\textit{power}: & f \pm \Delta f = & (x \pm \Delta x)^n & = & x^n \quad \pm n x^{n-1}\Delta x
\end{array} \; . \tag{35.11}$$

Example 209 (*Error propagation*): Let us study the following example,

$$f = \frac{x_1}{x_2 + a}$$
$$\Longrightarrow \Delta f = f\frac{\Delta x_1}{x_1} + f\frac{\Delta(x_2+a)}{x_2+a} = f\frac{\Delta x_1}{x_1} + f\frac{\Delta x_2}{x_2+a} \ .$$

35.1.3 Fitting a curve

We start defining the following prescription to calculate mean values,

$$\bar{x} \equiv \frac{1}{N}\sum_{k=1}^{N} x_k \quad , \quad \overline{xy} \equiv \frac{1}{N}\sum_{k=1}^{N} x_k y_k \ . \tag{35.12}$$

For a *fit* of a *linear curve* $f(x) = ax + b$ to a data set $\{x_k, y_k\}_{k\in[1,N]}$, we calculate ,

$$\boxed{f(x) = ax + b \quad , \quad a = \frac{\overline{xy} - \bar{x}\,\bar{y}}{\overline{x^2} - \bar{x}^2} = \frac{\overline{(x-\bar{x})y}}{\overline{(x-\bar{x})^2}} \quad , \quad b = \frac{\bar{y}\,\overline{x^2} - \overline{xy}\,\bar{x}}{\overline{x^2} - \bar{x}^2} = \bar{y} - a\bar{x}} \ . \tag{35.13}$$

The uncertainties are obtained via,

$$\Delta y = \sqrt{\frac{N}{N-2}\overline{(ax+b-y)^2}} \quad , \quad \Delta a = \Delta y\sqrt{\frac{1}{N\,(\overline{x^2} - \bar{x}^2)}} = \frac{\Delta y}{\sqrt{N\,\overline{x-\bar{x}}}} \tag{35.14}$$
$$, \quad \Delta b = \Delta y\sqrt{\frac{\overline{x^2}}{N\,\overline{x^2} - \bar{x}^2}} = \Delta y\sqrt{\frac{\overline{x^2}}{N\,\overline{x-\bar{x}}}} \ .$$

To fit an *exponential curve* $f(x) = \beta e^{\alpha x}$, we simply convert the data set $\{x_k, v_k\} \equiv \{x_k, \lg y_k\}$, calculate the mean values of the decadal logarithm using the recipe (35.12), and fit a linear curve $\tilde{f}(x) = \lg f(x) = \frac{\alpha}{\ln 10}x + \lg\beta \equiv ax + b$ in a semi-logarithmic scale to the data set $\{x_k, v_k\}$. This gives,

$$\boxed{f(x) = \beta e^{\alpha x} \quad , \quad \frac{\alpha}{\ln 10} = a = \frac{\overline{x\lg y} - \bar{x}\,\overline{\lg y}}{\overline{x^2} - \bar{x}^2} \quad , \quad \lg\beta = b = \frac{\overline{\lg y}\,\overline{x^2} - \overline{x\lg y}\,\bar{x}}{\overline{x^2} - \bar{x}^2}} \ . \tag{35.15}$$

To fit a *power law curve* $f(x) = \beta x^{\alpha}$, we simply convert the data set $\{u_k, v_k\} \equiv \{\lg x_k, \lg y_k\}$, calculate the mean values of the decadal logarithm using the recipe (35.12), and fit the linear curve $\tilde{f}(x) = \lg f(x) = \alpha\lg x + \lg\beta \equiv ax + b$ in a double-logarithmic scale to the data set $\{u_k, v_k\}$. This gives,

$$\boxed{f(x) = \beta x^{\alpha} \quad , \quad \alpha = a = \frac{\overline{\lg x\lg y} - \overline{\lg x}\,\overline{\lg y}}{\overline{\lg x^2} - \overline{\lg x}^2} \quad , \quad \lg\beta = b = \frac{\overline{\lg y}\,\overline{\lg x^2} - \overline{\lg x\lg y}\,\overline{\lg x}}{\overline{\lg x^2} - \overline{\lg x}^2}} \ . \tag{35.16}$$

35.1.4 Probability density

Consider a function $P(x)$ having the meaning of a *probability* depending on a variable $x \in [-\infty, \infty]$. The *probability density* $\rho(x)$ is defined as its derivative, $\rho(x) = P'(x)$, such that,

$$P(x) = \int_{-\infty}^{\infty} \rho(t)dt \qquad \text{with} \qquad P(-\infty) = 0 \qquad \text{and} \qquad P(\infty) = 1 \ . \tag{35.17}$$

Every probability must have the same likeliness, i.e.,

$$P(x) = \zeta_n \ , \tag{35.18}$$

where $\zeta_n \in [0, 1]$ is a uniformly distributed *random variable*. In order to numerically generate a *stochastic distribution*, we have to invert the distribution function, i.e. when ζ_n is generated by a computer, then

$$\boxed{x_n = P^{-1}(\zeta_n)} \tag{35.19}$$

is the distribution of the random variable x_n. In other words, a histogram of x_n reproduces the probability density $\rho(x)$.

Let us, for example, consider the Boltzmann distribution,

$$P(x) \equiv 1 - e^{-\beta x} \ . \tag{35.20}$$

Probing the probability with a random number, as in (35.18), we obtain the random variable via (35.19),

$$x_n = P^{-1}(\zeta_n) = -\frac{1}{\beta} \ln(1 - \zeta_n) \ . \tag{35.21}$$

The histogram of this random variable x_n can directly be compared with the probability density $\rho(x)$ given by,

$$\rho(x) = P'(x) = \beta e^{-\beta x} \ . \tag{35.22}$$

This is illustrated in Fig. 35.2(a).

Example 210 (*Probability density of a Gaussian distribution*): Another example is the *error function* given by,

$$\mathrm{erf}(x) \equiv \frac{2}{\sqrt{\pi}} \int_0^x e^{-t^2} dt \ .$$

By define the probability function,

$$P(x) \equiv \frac{1}{2}[\mathrm{erf}(x) - \mathrm{erf}(-\infty)] = \frac{1}{\sqrt{\pi}} \int_{-\infty}^x e^{-t^2} dt \ .$$

Probing the probability with a random number, as in (35.18), we obtain the random variable via (35.19),

$$x_n = P^{-1}(\zeta_n) = \mathrm{erf}^{-1}(2\zeta_n - 1) \ .$$

The histogram of this random variable x_n can directly be compared with the probability density $\rho(x)$, which is nothing else than the Gauss function,

$$\rho(x) = P'(x) = \frac{1}{\sqrt{\pi}} e^{-x^2} = 2\mathrm{erf}'(x) \ .$$

This is illustrated in Fig. 35.2(b).

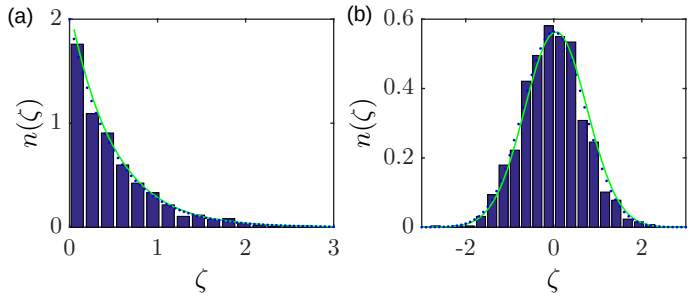

Figure 35.2: (code) (a) Boltzmann distribution simulated by random numbers (histogram). The numerical derivative of this distribution is shown as a blue dotted line, and the probability density as a green solid line. (b) Error function probability distribution simulated by random numbers (histogram). The numerical derivative of the error function is shown as a blue dotted line, and the Gauss function as a green solid line.

35.2 Deepening control theory

The variation of a physical quantity (e.g., a voltage or a temperature) in time is called *signal*. In a specific environment or technical device, such a variation may cause other physical quantities to change as well. For example, the rise in temperature of an optical cavity may modify its length and its resonance frequency, while the inverse is not true. This feature is illustrated by a block diagram as shown in Fig. 35.3, where $x(t)$ denotes the variation of a physical quantity (called *input*) that causes the variation of another quantity $y(t)$ (called *output*). The precise way how $y(t)$ depends on $x(t)$ depends on the particularities of the device, which is labeled by a symbol $\mathcal{T}$ called transfer function. $\mathcal{T}$ is in fact an operator acting on functions and transforming input signals into output signals.

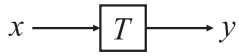

Figure 35.3: Transfer and modification of a time-dependent signal.

While we have described above the transfer of (time-varying) signals, the same feature can be treated in frequency domain via Fourier or Laplace-transforms. This script is not the right place to recapitulate the mathematics of these transforms, and we will restrict ourselves to reproducing some on the most fundamental results, as we may need them in the following.

35.2.1 Analysis techniques - frequency domain and time domain

Mathematical techniques for analyzing and designing control systems fall into two different categories:

Frequency domain: In this type the values of the state variables, the mathematical variables representing the system's input, output and feedback are represented

as functions of frequency. The input signal and the system's transfer function are converted from time functions to functions of frequency by a transform such as the Fourier transform, Laplace transform, or Z transform. The advantage of this technique is that it results in a simplification of the mathematics; the differential equations that represent the system are replaced by algebraic equations in the frequency domain which are much simpler to solve. However, frequency domain techniques can only be used with linear systems, as mentioned above.

Time-domain state space representation: In this type the values of the state variables are represented as functions of time. With this model the system being analyzed is represented by one or more differential equations. Since frequency domain techniques are limited to linear systems, time domain is widely used to analyze real-world nonlinear systems. Although these are more difficult to solve, modern computer simulation techniques such as simulation languages have made their analysis routine.

In contrast to the frequency domain analysis of the classical control theory, modern control theory utilizes the time-domain state space representation, a mathematical model of a physical system as a set of input, output and state variables related by first-order differential equations. To abstract from the number of inputs, outputs and states, the variables are expressed as vectors and the differential and algebraic equations are written in matrix form (the latter only being possible when the dynamical system is linear). The state space representation (also known as the 'time-domain approach') provides a convenient and compact way to model and analyze systems with multiple inputs and outputs. With inputs and outputs, we would otherwise have to write down Laplace transforms to encode all the information about a system. Unlike the frequency domain approach, the use of the state-space representation is not limited to systems with linear components and zero initial conditions. 'State space' refers to the space whose axes are the state variables. The state of the system can be represented as a point within that space.

35.2.1.1 Signal transfer through LTI systems without delay

For an operator $\mathcal{T}$ transforming a temporal signal $x(t)$ into a signal $y(t)$,

$$y(t) = \mathcal{T}x(t) \ , \tag{35.23}$$

to be *linear* and time-independent, we require,

$$\begin{aligned} \mathcal{T}[\alpha x_1(t) + \beta x_2(t)] &= \alpha\mathcal{T}[x_1(t)] + \beta\mathcal{T}[x_2(t)] \\ \mathcal{T}[x(t-\tau)] &= \mathcal{T}[x(t)] \star \delta(t-\tau) \ , \end{aligned} \tag{35.24}$$

where the $\star$ denotes a convolution,

$$(f \star g)(t) = \int_{-\infty}^{\infty} f(\tau)g(t-\tau)d\tau \ . \tag{35.25}$$

Such system are called *Linear Time-Independent LTI* systems [1].

[1] To be more general, also the derivative and integral of the output signal must be included (see later sections).

35.2.1.2 Laplace transform

We define the *Laplace transform* $\mathcal{L}$ as a linear operator acting on a signal $x(t)$ defined through,

$$\mathcal{L}... \equiv \int_{-\infty}^{0} ...e^{st}d\tau \ . \tag{35.26}$$

The frequency variable is denoted by the imaginary quantity $s = \imath f$. The question is now, what is the meaning of the Laplace operator?

To answer this question, we start introducing the pulse response $h(t)$ via

$$h(t) = \mathcal{T}[\delta(t)] \tag{35.27}$$

as the reaction of a system $\mathcal{T}$ to a pulse $\delta(t)$. Now, it is easy to see, that the operator $\mathcal{P}$ defined as,

$$\mathcal{P}... \equiv h(t) \star ... \ , \tag{35.28}$$

and which describes the convolution of an arbitrary input signal with the pulse response, satisfies the above linearity condition. Now calculating,

$$\mathcal{P}e^{st} = h(t) \star e^{st} = \int_{-\infty}^{0} h(\tau)e^{s(t-\tau)}d\tau = \mathcal{L}[h(t)] \cdot e^{st} = (\mathcal{L}h)(s) \cdot e^{st} \ , \tag{35.29}$$

we find that the functions e^{st} are eigenfunctions of the operator $\mathcal{P}$ with the eigenvalues $\mathcal{L}[h(t)]$, which are just the Laplace transforms of the pulse response.

We can now expand arbitrary functions $x(t)\theta(t)$ in a Laplace series and obtain,

$$\mathcal{L}[h(t) \star x(t)] = \int_{-\infty}^{0} h(t) \star e^{st} \ x(t)dt = (\mathcal{L}h)(s) \int_{-\infty}^{0} e^{st}x(t)dt = (\mathcal{L}h)(s) \cdot (\mathcal{L}x)(s) \ . \tag{35.30}$$

The convolution on the left-hand side is in time domain, while the product on the right-hand side is in frequency domain.

35.2.1.3 Pulse and jump response from a transfer function

The transmission of a signal by an element of a control loop can be described in the temporal or spectral domain [288, 308, 545], and we can switch from one representation to another via Laplace transformation. Operators of LTI systems $\mathcal{T}$ are represented by products with spectral functions in frequency-domain, $\tilde{F}(s)\cdot... = (\mathcal{L}F)(s)\cdot...$ or convolutions with time-varying functions in time-domain, $F(t) \star ...$,

$$\begin{aligned} y(t) &= \mathcal{T}x(t) \\ &\overset{Laplace}{\longrightarrow} \tilde{y}(s) = \tilde{F}(s) \cdot \tilde{x}(s) \\ &\overset{inverse\ Laplace}{\longrightarrow} y(t) = F(t) \star x(t) \ . \end{aligned} \tag{35.31}$$

In practice, the function $\tilde{F}(f)$ can be determined by feeding a sinusoidal signal with amplitude $x(s)$ into the system, measuring $y(s)$ (which is a complex number) [2],

[2] From now on, we will drop the tilde $\sim$ on transfer functions and amplitudes, when it is clear that we are in frequency-domain.

and calculating

$$F(s) = \frac{y(s)}{x(s)} \ . \tag{35.32}$$

The transitory behavior $F(t)$ can in practice be extracted via an adequate choice of the test function, f.ex., the response to a pulse:

$$\begin{aligned} x(t) &= \delta(t) \\ \overset{Laplace}{\longrightarrow} \quad y(s) &= F(s) \\ \overset{inverse\ Laplace}{\longrightarrow} \quad y(t) &= F(t) \ , \end{aligned} \tag{35.33}$$

or to a sudden jump:

$$\begin{aligned} x(t) &= \theta(t) \\ \overset{Laplace}{\longrightarrow} \quad y(s) &= F(s)/s \\ \overset{inverse\ Laplace}{\longrightarrow} \quad y(t) &= \int_0^t F(\tau) d\tau \ . \end{aligned} \tag{35.34}$$

Here, $\theta(t)$ denotes the Heavyside function, which is 1 for $t > 0$ and 0 else. The time-dependent function, which describes the pulse response is often used as a symbol for a specific control loop element.

The pulse response works in a similar way as the Green's function procedure: Wanting to know how a loop control element F transforms a given input signal $x(t)$ into an output signal $y(t)$, i.e., $y(t) = F(t) \star x(t)$, we produce a rapid pulse leading to the output,

$$y_\delta(t) = F(t) \star \delta(t) = F(t) \ . \tag{35.35}$$

Now, once we know $F(t)$, the response to arbitrary input signals can be computed via,

$$y(t) = y_\delta(t) \star x(t) \ . \tag{35.36}$$

35.2.1.4 Bode diagram and polar diagram

The *Bode diagram* illustrates the transfer function in the spectral domain on a bilogarithmic scale separating the amplitude spectrum from the phase spectrum [see Fig. 35.4(a-b)]. Frequency regions, where $|F(s)|$ or $\varphi(s)$ vary particularly strongly are nicely emphasized in the polar representation [see Fig. 35.4(c-d)].

For LTI systems $F(s)$ is always a rational function and can, hence, be represented by its poles and zeros in the complex plane,

$$F(s) = A \frac{(s-a_1)(s-a_2)...(s-a_n)}{(s-b_1)(s-b_2)...(s-b_n)} \ . \tag{35.37}$$

With this, $F(s)$ is analytical and conform, i.e., multiple curves in the s-plane are represented in an isogonal way in the $F(s)$-plane. In order to avoid that the eigenfunctions e^{st} oscillate and diverge, it is necessary that all the poles and zeros are in the left halfplane.

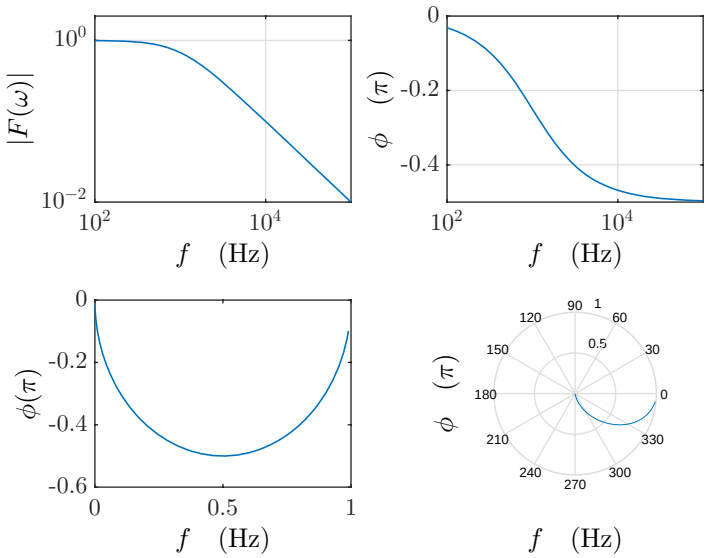

Figure 35.4: (code) Bode diagram.

35.2.2 Algebra of transfer circuits

A technical realization of a signal transfer circuit is illustrated by a signal flux diagram, which itself corresponds to the formalism of linear operators. As shown in Fig. 35.5, signals can be

- (a) added $(f_1 + f_2)(t) \equiv f_1(t) + f_2(t)$,
- (b) multiplied $(f_1 \cdot f_2)(t) \equiv f_1(t) \cdot f_2(t)$,
- (c) combined $f_1(t) = f_2(t)$,
- (d) transformed $f_2(t) = F[f_1](t) \equiv F(f_1(t))$,
- (e) connected in parallel $(F_1 + F_2)[f(t)] \equiv F_1[f(t)] + F_2[f(t)]$,
- (f) connected in series $(F_1 \circ F_2)[f(t)] \equiv F_1[F_2[f(t)]]$,

Mathematically, the functions $f(t)$ form a *vector space* and the operators $F[f]$ a *ring*. The linear operators generally are defined implicitly by a system of differential equations. The particular case of linear systems is considerably simpler. The general circuit shown in Fig. 35.5(g) corresponds to the differential equation,

$$0 = F[x_1, .., x_k, \partial_t x_1, .., \partial_t x_k, y_1, .., y_j] \ . \tag{35.38}$$

The linearity $F[\lambda f_1 + \mu f_2] = \lambda F[f_1] + \mu F[f_2]$ warrants that this equation becomes,

$$0 = [1 + \partial_t + ... + \int dt + ...]y_k = [1 + \partial_t + ... + \int dt + ...]x_j \ . \tag{35.39}$$

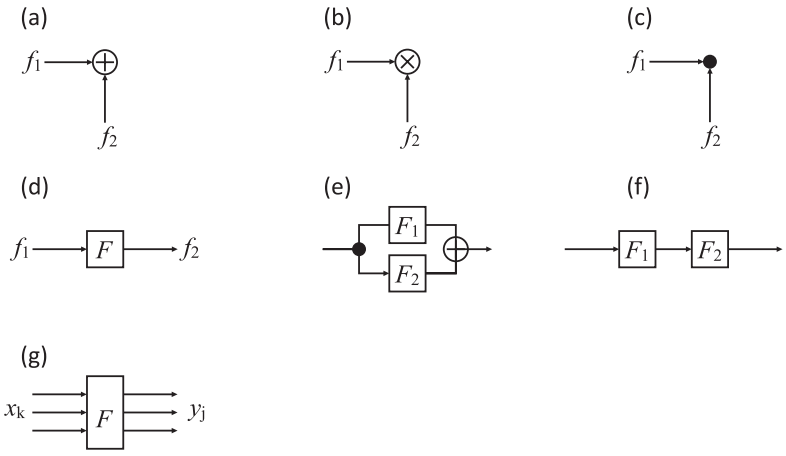

Figure 35.5: LTI circuits.

Note that the multiplication, the derivation, and the integration are linear operators in the same sense as the Fourier and the Laplace transformation.

Linear differential equations can be Laplace transformed. The corresponding transfer function is,

$$F(s) = F(-\delta + \imath\omega) \equiv \frac{\mathcal{L}y(t)}{\mathcal{L}x(t)} \ . \tag{35.40}$$

In the Laplace-transformed space the operations multiplication, derivation, and integration are all replaced by multiplications:

$$\mathcal{L}[\lambda + \partial_t + ... + \int dt + ...] = \lambda + s + ... + \frac{1}{s} \ . \tag{35.41}$$

With this, the control loop elements and the additive nodes can be used to completely represent a control circuit.

The characteristic responses of components are frequently non-linear (e.g. transistor). For small signal amplitudes, these response functions, and also multiplication points (e.g. mixers) can be linearized by Taylor expansion up to first order,

$$\begin{aligned} y_0 + \Delta y &= F[x_{01} + \Delta x_1, ..., x_{0k} + \Delta x_k] \\ &= F[x_{01}, ..., x_{0k}] + \left(\frac{\partial F}{\partial x_1}\right)_0 \Delta x_1 + ... + \left(\frac{\partial F}{\partial x_k}\right)_0 \Delta x_k \ , \end{aligned} \tag{35.42}$$

with $y_0 = 0 = F[x_{01}, ..., x_{0k}]$ giving,

$$\Delta y = \left(\frac{\partial F}{\partial x_1}\right)_0 \Delta x_1 + ... + \left(\frac{\partial F}{\partial x_k}\right)_0 \Delta x_k \ . \tag{35.43}$$

For example for a multiplication point,

$$\Delta y = K_1 \Delta x_1 + K_2 \Delta x_2 \ . \tag{35.44}$$

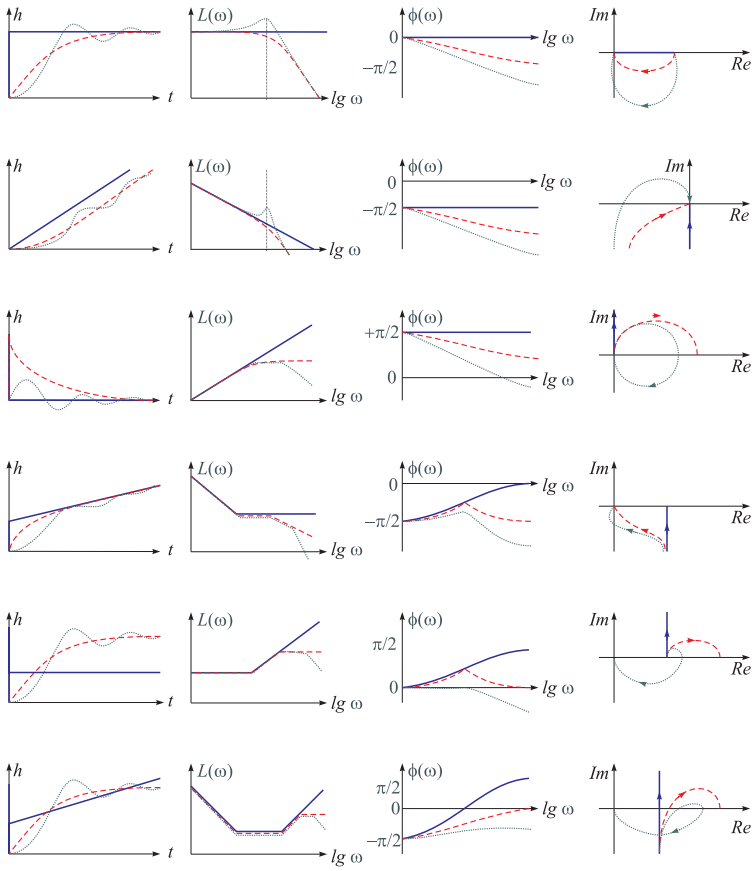

Figure 35.6: Transfer function $h(t) = \frac{y(t)}{x_w}$, Bode diagram amplitude $L(\omega) = 20 \lg |F_R|$ and phase $\varphi = \arctan \frac{\Im \mathfrak{m}\ F_R}{\Re \mathfrak{e}\ F_R}$, and polar representation $F(i\omega) = \Re \mathfrak{e}\, F_R + i \Im \mathfrak{m}\, F_R$ of the most common regulators. With delay time (—), $T_2 = T_1 = 0$, first order with delay time (- - -), $T_2 = 0 \neq T_1$, and second order $(\cdots)$, $T_2 \neq 0 \neq T_1$. From top to bottom, the diagrams show the regulators P, I, D, PI, PD, and PID, described by the equations (35.45) and (35.46).

35.2.2.1 Regulators

For many circuits, it is sufficient to restrict to combinations of resistive (proportional), capacitive (integral), and inductive (differential) circuits. Then, the general case of a control regulator is that of a $PID - T_1 ... T_n$-element, meaning that:

$$T_2^2 \ddot{y} + T_1 \dot{y} + y = K_D \dot{x} + K_P x + K_I \int dt x = K_P \left(x + T_v \dot{x} + \frac{1}{T_n} \int dt x \right) \ , \quad (35.45)$$

corresponding to the transfer function,

$$F(s) = \frac{K_D s + K_P + K_I/s}{1 + T_1 s + T_2^2 s^2} = \frac{(1 + T_v s + 1/T_n s)}{1 + T_1 s + T_2^2 s^2} \ . \quad (35.46)$$

In literature, two notations are used for the constants. They are linked via: $K_D \equiv K_P T_v$ and $K_I \equiv K_P / T_n$. The stationary behavior is obtained setting the delays to

zero: $T_n \equiv 0$.

Example 211 (*PID regulators*): For example, for a *proportional regulator*, we have,

$$y = K_P x_w \qquad \text{and} \qquad F_R = K_P \ , \tag{35.47}$$

for an *integral regulator* with time delay T_1, we have,

$$T_1 \dot{y} + y = K_I \int x_w dt \qquad \text{and} \qquad F_R = \frac{K_I}{s(1+sT_1)} \ , \tag{35.48}$$

or for a *PID regulator* without delay, we have,

$$y = K_P x_w + K_D \dot{x}_w + K_I \int x_w dt \qquad \text{and} \qquad F_R = K_P + \frac{K_I}{s} + K_D s \ . \tag{35.49}$$

Since there are three basic operations (multiplication with 1, s and $1/s$), in the end, all rational circuit elements can be reduced to an addition and concatenation of proportional $F(s) = K_P$, integral $F(s) = K_I/s$, and differentials elements, $F(s) = K_D s$. In particular, $PID{-}T_1 ... T_n$ circuits can be constructed by putting in parallel P, I, and D regulators concatenated with delay elements T_1. The possibility of feedback opens other possibilities [see Fig. 35.7(a)].

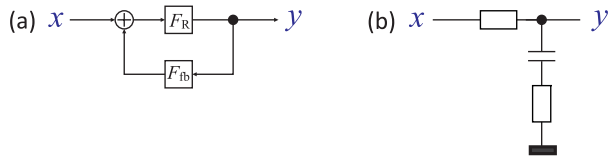

Figure 35.7: (a) Circuit with feedback, (b) low-pass filter circuit.

Example 212 (*Low-pass filter and time delays*): We consider the example of a low-pass filter exhibited in Fig. 35.7(b) and described by the equation,

$$F(\imath\omega) = \frac{R + \imath\omega L + 1/\imath\omega C}{R_i + R + \imath\omega L + 1/\imath\omega C} \ . \tag{35.50}$$

I.e., we have a $PID - T_1 T_2$ circuit.
Another example, is the dead time circuit,

$$y(t) = x(t - T_t) \quad \text{and} \quad F(s) = e^{-sT_t} \ . \tag{35.51}$$

We have,

$$F(\imath\omega) = e^{-\imath\omega T_t} F_0 \quad \text{and} \quad |F(\imath\omega)| = F_0 \quad \text{and} \quad \varphi(\imath\omega) = -\omega T_t \ . \tag{35.52}$$

Hence, dead time circuits produce phase shifts, which are proportional to the dead time interval T_t.

35.2.2.2 Heuristic rules for the Bode diagram

Any deviation of the amplitude spectrum from $n \cdot 6$dB/octave to $(n+1) \cdot 6$dB/octave causes a retardation in the phase spectrum of 90°. At the cut-off frequency, where the inclination changes its behavior, the phase shift is just 45°. A deviation to higher/lower inclinations shifts the phase by ±90°. (This does not hold for some phase-shifting circuits).

35.2.2.3 Transfer function of feedback circuits

Fig. 35.7 shows the idea underlying the feedback,

$$F(s) = \frac{1}{1/F_R - F_{fb}} \ . \tag{35.53}$$

For example, for $F_R = 1/T_1 s$ and $F_{fb} = -1$ we have,

$$F(s) = \frac{1}{1 + T_1 s} \ , \tag{35.54}$$

which corresponds to a delay element (or high-pass filter).

For F_r being a proportional element, we say that the feedback rigid, for F_r being differential, the feedback is anticipating, and for F_r being integral, the feedback is delaying.

35.2.3 Stability of feedback circuits

As discussed above, the transfer function of the feedback circuit is,

$$H(s) = \frac{F(s)}{1 + F(s)F_{fb}(s)} \ . \tag{35.55}$$

The *open loop gain* is $V(s) = F(s)F_{fb}(s)$. The circuit is stable, when for all the eigenfunctions e^{st}, that do not decay with $Re\ s \geq 0$, the transfer function of the feedback circuit is finite, $H(s) < \infty$.

An equivalent criterion is the *Nyquist criterion*: *The curve $V(\imath\omega)$ to $\omega \in [0; \infty[$ must always bypass the point of instability at $Re\ s = -1$ leaving it on the left side. That is, considering negative frequencies, the curve should not circle this point.* Fig. 35.9 shows an example.

35.2.4 Further topics in control theory

35.2.4.1 Nonlinear control theory

Linear control theory applies to systems made of devices which obey the superposition principle, which means roughly that the output is proportional to the input. They are governed by linear differential equations. A major subclass is systems which in addition have parameters which do not change with time, called linear time invariant (LTI) systems. These systems are amenable to powerful frequency domain mathematical techniques of great generality, such as the Laplace transform, Fourier transform, Z transform, Bode plot, root locus, and Nyquist stability criterion. These lead to a description of the system using terms like bandwidth, frequency response, eigenvalues, gain, resonant frequencies, poles, and zeros, which give solutions for system response and design techniques for most systems of interest.

Nonlinear control theory covers a wider class of systems that do not obey the superposition principle, and applies to more real-world systems, because all real control systems are nonlinear. These systems are often governed by nonlinear differential equations. If only solutions near a stable point are of interest, nonlinear systems can often be linearized by approximating them by a linear system using perturbation theory, and linear techniques can be used.

P-servo with rigid feedback	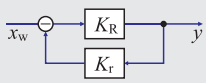	*P*	$K_P = \frac{K_R}{1+K_r K_R} \xrightarrow{K_P \to \infty} \frac{1}{K_r}$
P-servo with yielding feedback	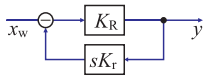	*P*-T_1	$K_P = K_R \quad , \quad T_1 = K_R K_r \quad \text{for} \quad K_R \ll \infty$
		I	$K_I = K_r^{-1} \quad \text{for} \quad K_R \to \infty$
P-servo with yielding feedback	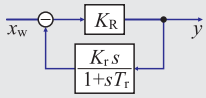	*PD*-T_1	$K_P = K_R \quad , \quad T_v = T_r \quad , \quad T_1 = T_r + K_r K_R \quad \text{for} \quad K_R \ll \infty$
		PI	$K_P = T_r/K_r \quad , \quad T_n = T_r \quad \text{for} \quad K_R \to \infty$
P-servo with delayed feedback	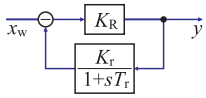	*PD*-T_1	$K_P = \frac{K_R}{1+K_r K_R} \quad , \quad T_v = T_r \quad , \quad T_1 = \frac{T_r}{1+K_r K_R} \quad \text{for} \quad K_R \ll \infty$
		PD	$K_P = 1/K_r \quad , \quad T_v = T_r \quad \text{for} \quad K_R \to \infty$
P-servo with delayed yielding feedback	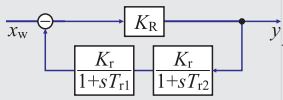	*PID*	$K_P = \frac{T_{r1}+T_{r2}}{K_{r1}K_{r2}} \quad , \quad T_v = \frac{T_{r1}T_{r2}}{T_{r1}+T_{r2}} \quad , \quad T_n = T_{r1}+T_{r2} \quad \text{for} \quad K_R \to \infty$
P-servo with two delay circuits in the feedback	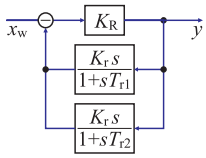	*PID*	$K_P = \frac{T_{r1}+T_{r2}}{K_{r1}(T_{r1}-T_{r2})} \quad , \quad T_v = \frac{T_{r1}T_{r2}}{T_{r1}+T_{r2}} \quad , \quad T_n = T_{r1}+T_{r2} \quad \text{for} \quad K_R \to \infty \quad \text{and} \quad T_{r1} > T_{r2}$
I-servo with rigid feedback	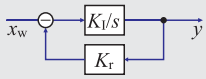	*P*-T_1	$K_P = \frac{1}{K_r} \quad , \quad T_1 = \frac{1}{K_I K_r}$
I-servo with yielding feedback	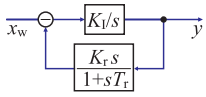	*PI*-T_1	$K_P = \frac{K_I T_r}{1+K_I K_r} \quad , \quad T_n = T_r \quad , \quad T_1 = \frac{T_r}{1+K_I K_r}$

Figure 35.8: Some examples for feedback regulators. The columns show from left to right: the nomenclature, the circuit diagram, the behavior, and the constants of the LTI system.

35.2.4.2 MIMO control systems

In this script we restrict to *single-input single-output control systems* (*SISO*), which is the simplest and most common type, in which one output is controlled by one control signal. Examples are the temperature control or an audio system, in which the control input is the input audio signal and the output is the sound waves from the speaker.

In contrast, *multiple-input multiple-output control systems* (*MIMO*) are found in more complicated systems. For example, modern large telescopes such as the Keck and MMT have mirrors composed of many separate segments each controlled by an actuator. The shape of the entire mirror is constantly adjusted by a MIMO active optics control system using input from multiple sensors at the focal plane, to compensate for changes in the mirror shape due to thermal expansion, contraction, stresses as it is rotated and distortion of the wavefront due to turbulence in the atmosphere.

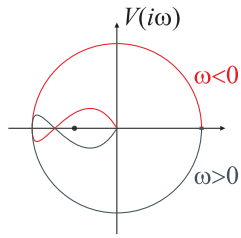

Figure 35.9: Illustration of the Nyquist criterion.

Another example are ultra-stable laser systems stabilized by combinations of fast actuators with low dynamic range and slow actuators with large dynamic range.

35.2.5 Exercises

35.2.5.1 Ex: Step response

Calculate the step response of a low-pass filter using the Laplace transform formalism.

35.3 Characterization of stability

The quality factor of a resonance measured with an oscillator in its function as a measuring apparatus for the resonance frequency is named *precision*. The precision also includes the perturbations to which the controlled oscillator is exposed and can be understood as the standard deviation of the frequency realized by the standard. The temporal or spectral behavior of precision, i.e. the stability can e.g. measured directly by comparing similar but independent standards. The reciprocal of the spread of the frequency realizations of an ensemble of similar standards is called *reproducibility*. The term reproducibility is also used to compare the frequencies of an individual standard before and after readjustment of all its technical parameters.

The *accuracy* is defined as the degree of agreement between the frequency realized by the standard and the defined standard frequency, i.e. the frequency that would be displayed in the fault-free ideal case [3]. The accuracy is always less than the quality of the resonance and the certainty of it center frequency. It includes the precision and limits the reproducibility [13]. The fact that the accuracy is related to the ideal case of absent errors implies that it cannot be measured directly. It must be inferred indirectly through model assumptions regarding the measuring apparatus estimating the probability for presumed or possible errors. We then speak of the *uncertainty* of the measured value [162].

The temporal or spectral behavior of *accuracy* is called *stability*. It is measurable and is quantified in the frequency domain by the *spectral density of fluctuations* and in the time domain best by the *Allan variance*. The noise is now the physical phenomenon that manifests itself as a deviation from the optimal stability.

[3] For example, when a measurement apparatus for the constant π provided the value $x = 3.141\ 59\ (12)$, then the accuracy is $x - \pi$ and the precision 0.000 12.

The stability that an ideal frequency standard can achieve in principle is proportional to quality factor of the resonance $\omega/(\Delta\omega_{nat}+\Delta\omega_{broaden})$ and the signal-to-noise ratio of the control signal S/N. Hence, the stability can be optimized by choosing atomic transitions with small spontaneous decay rates $\Delta\omega_{nat}$. Appropriate techniques for the experimental preparation of the resonance limit the influence of line broadening mechanisms $\Delta\omega$. According to the Fourier theorem, the resolution of narrow lines requires long observation times. Now, the control signal of a feedback regulator can only be determined after a whole observation period. This means that the apparatus already must have an intrinsic stability good enough that the frequency does not leave the control range during a period of observation. Furthermore, a better signal-to-noise ratio can improve the precision with which the line center of the resonance can be determined.

Ultimately, the most promising way to increase the accuracy of a frequency standard seems to be to choose the highest possible transition frequencies ω, provided that the oscillations can still be counted electronically, or be linked in a phase-coherent way to oscillators generating countable oscillations, e.g. using frequency combs. The requirement of phase coherence at optical frequencies puts the laser in the focus of interest in metrology.

35.3.1 Quantifying frequency fluctuations

The following sections deal with perturbation-induced fluctuations of the laser frequency, i.e. frequency noise. To characterize the behavior of an oscillator (especially when used as a frequency standard), it is necessary to introduce some concepts that allow the quantitative description of the noise. The most important are reproducibility, stability, spectral density of fluctuations, Allan variance, and emission bandwidth. The basic work on this has been carried out at the National Bureau of Standards (NBS) in Boulder, Co, USA [12, 13, 56, 188].

35.3.1.1 Stability in the frequency domain, spectral fluctuation density

The instantaneous amplitude of an oscillator, e.g. the electric field of a laser radiation, can be written,

$$\mathcal{E}(t) = \mathcal{E}_0(t)e^{\imath\phi(t)} \ . \tag{35.56}$$

noise afflicts phase and amplitude. In the following we will neglect amplitude noise, $\mathcal{E}_0(t) = \mathcal{E}_0$, and if the frequency fluctuations only deviate slightly from a mean value, $\omega_0 \gg |\dot{\varphi}(t)|$, we may write,

$$\phi(t) \equiv \omega_0 t + \varphi(t) \ . \tag{35.57}$$

In the following, we will often consider normalized frequency fluctuations,

$$y(t) = \dot{\varphi}(t)/\omega_0 \ . \tag{35.58}$$

When measuring stability, one must differentiate between *deterministic fluctuations* and *stochastic noise*. Deterministic fluctuations are usually due to inadequate control of equipment parameters. They generate systematic errors and slow drifts $y_{sys}(t)$ which, if one recognizes them as such in time domain measurements (measure for sufficiently long times!), can be subtracted and disregarded. Stochastic noise,

however, is stationary:

$$\overline{y_{sto}(t)} = \overline{y(t) - y_{sys}(t)} = 0 \qquad \text{defining} \qquad \overline{y(t)} \equiv \lim_{T\to\infty} \frac{1}{T} \int_0^T y(t)dt \tag{35.59}$$

as the time average. In the following only stationary stochastic fluctuations are considered.

Let us take a look at the *autocorrelation function* of the phase defined as,

$$\boxed{R_y(\tau) \equiv \overline{y^*(t)y(t+\tau)} = \lim_{T\to\infty} \frac{1}{T} \int_0^T y^*(t)y(t+\tau)\rangle d\tau} \tag{35.60}$$

and the *spectral density of phase fluctuations* which, according to the *Wiener-Khintchine theorem*, can be obtained as the Fourier transform of the autocorrelation function,

$$\boxed{S_y(f) \equiv \mathcal{F}R_y(\tau) = \int_{-\infty}^{\infty} R_y(\tau)e^{-2\pi\imath f\tau}d\tau} \ . \tag{35.61}$$

The normalized density of frequency fluctuations $S_y(f)$ is a spectral quantity with the unit 1/Hz. Frequency and phase fluctuations are linked by:

$$S_{\dot{x}}(f) = f^2 S_x(f) \ , \tag{35.62}$$

as will be shown in Exc. 35.3.3.1. Also,

$$S_{ax}(f) = a^2 S_x(f) \ , \tag{35.63}$$

If the integral of the spectral fluctuation density is finite it corresponds, according to the definition (35.62), to the noise power or the mean square deviation of a measured variable:

$$\int_0^\infty S_y(f)df = R_y(0) = \overline{|y(t)|^2} < \infty \ . \tag{35.64}$$

35.3.1.2 Model of noise

Measurements seem to confirm today that stochastic fluctuations in frequency standards can be traced back to a few additive noise processes with different physical origins and different frequency responses [12]:

$$\boxed{S_y(f) = \sum_{\beta=-2}^{2} h_\beta f^\beta} \ . \tag{35.65}$$

The table below lists the most common ones.

This noise model is based on the assumption that the noise processes it describes operate in all Fourier frequency ranges, which violates the requirement (35.64). The dilemma does not arise in experiment, since the integration over an unlimited Fourier frequency range is not a realistic concept in that each measurement only takes a finite time τ, so that very low frequencies below a cut-off frequency $f_{min} = 2\pi/\tau$ are not

noise type	$S_x(f)$	$S_y(f)$	$\sigma_y^2(\tau)$
white phase noise	h_2	$h_2 f^2$	$\propto \frac{h_2}{\tau^2}$
flicker phase noise	$h_1 f^{-1}$	$h_1 f^1$	$\propto \frac{h_1}{\tau^2}$
white frequency noise	$h_0 f^{-2}$	$h_0 f^0$	$\frac{h_0}{2\tau}$
flicker frequency noise	$h_{-1} f^{-3}$	$h_{-1} f^{-1}$	$h_{-1} 2 \ln 2$
random walk frequency drifts	$h_{-2} f^{-4}$	$h_{-2} f^{-2}$	$h_{-2} \frac{(2\pi)^2}{6} \tau$

Table 35.1: *Spectral fluctuation density and Allan-variance for common noise processes [56].*

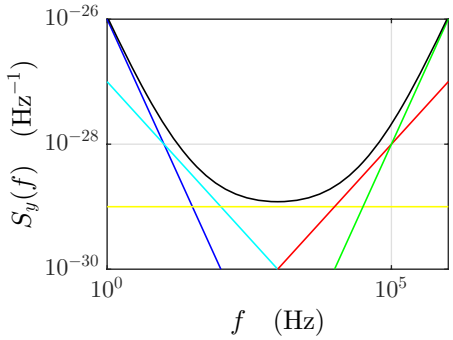

Figure 35.10: Noise model according to (35.65).

perceived. In addition, every real data acquisition system has a low-pass behavior with a cut-off frequency f_{max}, so that high frequencies also do not contribute to the integral. These bandwidth constraints enforce the condition (35.64) for the five noise processes assumed by (35.65) [513]. The measure for the noise power in any case has the form: $\int_{f_{min}}^{f_{max}} S_y(f) df$.

35.3.1.3 Description of stability in the time domain, Allan variance

Temporal frequency fluctuations of an oscillator can be measured by *discriminating the frequency fluctuations at the dispersive profile of a resonance* (or error signal) and convert it into voltage fluctuations. It is just the curve exhibited by a spectrum analyzer to which the error signal is fed, as illustrated by the left setup of Fig. 35.12.

Like any physical quantity, frequency fluctuations can only be measured as an average over an *integration time interval* τ imposed by the measuring apparatus. The k-th measurement of the quantity y at the time t_k results in the measured value:

$$y_k(\tau) = \frac{1}{\tau} \int_{t_k}^{t_k+\tau} y(t) dt \ . \tag{35.66}$$

Assuming that the dead time of the measuring apparatus is negligible (if necessary, technical precautions must be taken to meet this requirement approximately), the

variance of stochastic noise can be expressed as follows:

$$\sigma_y^2(\tau) = \frac{1}{N-1}\sum_{k=1}^{N} y_k^2 \qquad \text{where} \qquad \overline{y_k} = 0 \ . \tag{35.67}$$

The variance is a direct measure of the stability of an oscillator in time domain. It is measured from a discrimination of the error signal in a similar way as the fluctuation density $S_y(f)$. However, as illustrated by the left setup of Fig. 35.12, the discriminated signal is recorded in time domain, e.g. by an oscilloscope.

The variance can be linked to the spectral density of frequency fluctuations in frequency domain by Fourier transformation. With the Heaviside step function Θ the following relationship can be given [188, 12, 36],

$$\sigma_y^2(\tau) = \int_0^\infty S_y(f)|\mathcal{F}\zeta_1(f)|^2 df \qquad \text{where} \qquad \zeta_1(t) = \frac{1}{\tau}\Theta_{[-\tau,0]}(t) \ , \tag{35.68}$$

is the area-normalized jump function, which models the duration of the integration time τ. Its Fourier-transform is the transfer function of the equivalent filter.

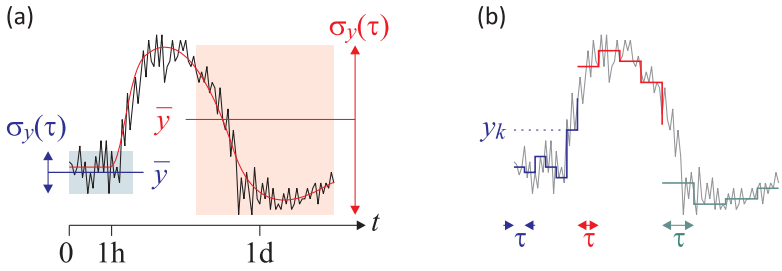

Figure 35.11: (a) Noise can exhibit very different short and long time behavior. (b) Any measurement needs a minimum integration time.

It turns out that the variance for $1/f$ noise and for stochastic drifts ($1/f^2$ noise) diverges at the lower limit, i.e. this variance is not useful for practical applications. The divergence comes from the fact that for longer and longer measurements ($N \to \infty$), respectively, smaller and smaller Fourier frequencies ($f \to 0$), longer and longer periodic fluctuations can be identified as such, while for shorter measurements they appear as linear drifts. One way out is to calculate the variance for a limited number k of measurement data and to average the variances of M of such data sets of length k. This variance converges for a larger number of noise processes. This so-called pair variance ($k = 2$) or *Allan variance* is widely used:

$$\boxed{\sigma_y^2(\tau) = \frac{1}{2M}\sum_{j=1}^{M}(y_{2j} - y_{2j-1})^2} \ . \tag{35.69}$$

Like the normal variance, the Allan variance can also be related to the spectral density of frequency fluctuations:

$$\sigma_y^2(\tau) = \int_0^\infty S_y(f)|\mathcal{F}\zeta_2(f)|^2 df \qquad \text{where} \qquad \zeta_2(t) \equiv \tfrac{1}{\sqrt{2}}[\zeta_1(t) - \zeta_1(-t)] \ . \tag{35.70}$$

The Fourier transforms of the step functions $\zeta_1(t)$ and $\zeta_2(t)$ will be calculated in Exc. 35.3.3.2, as well as the variances for white noise.

35.3.2 Power spectral density

It is important not to confuse the spectral density of frequency fluctuations with the power spectral density of the oscillator defined via the *autocorrelation function of the field amplitude* [4],

$$\boxed{R_{\mathcal{E}}(\tau) \equiv \langle \mathcal{E}^*(t)\mathcal{E}(t+\tau)\rangle = \mathcal{E}_0^2 \langle e^{\imath[\phi(t+\tau)-\phi(t)]}\rangle = \mathcal{E}_0^2 e^{\imath\omega_0\tau}\langle e^{\imath[\varphi(t+\tau)-\varphi(t)]}\rangle} \ , \quad (35.71)$$

as its Fourier transform,

$$\boxed{S_{\mathcal{E}}(\omega) = \mathcal{F}R_{\mathcal{E}}(\tau)} \ . \quad (35.72)$$

The power spectral density is typically measured as the beat frequency of two independent oscillators. It is just the curve exhibited by a spectrum analyzer to which the beat signal is fed, as illustrated in the right setup of Fig. 35.12.

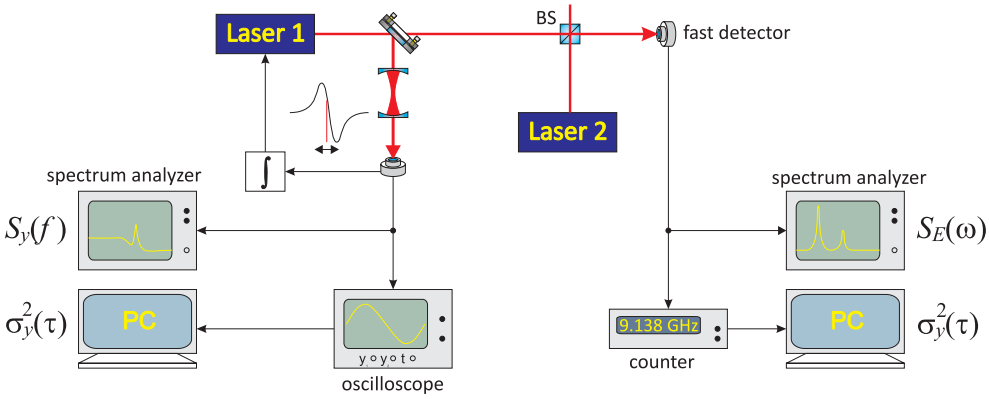

Figure 35.12: (left) Setup for measuring the spectral density of frequency fluctuations $S_y(f)$ and the Allan variance $\sigma_y^2(\tau)$ of laser 1 discriminating it at the slope of transmission signal of an optical cavity. (right) The power spectral density $S_{\mathcal{E}}(\omega)$ can be found as the beat signal between two lasers and either be exhibited on a spectrum analyzer $S_{\mathcal{E}}(\omega)$ or counted and processed to an Allan variance $\sigma_y^2(\tau)$.

The beat spectrum is the convolution of the emission bandwidth of the two oscillators,

$$S_{\mathcal{E}}(\omega) = S_{\mathcal{E},laser1}(\omega) * S_{\mathcal{E},laser2}(\omega) \ . \quad (35.73)$$

In particular, for the case that we have good reasons to believe that one laser is much narrower than the other, the power spectral density $S_{\mathcal{E}}(\omega)$ will reflect the emission spectrum of just the broader laser. Note that the power spectral density derived

[4] Note that the *first-order coherence* is just the normalized autocorrelation,

$$g^{(1)}(\tau) \equiv \frac{\langle \mathcal{E}^*(t)\mathcal{E}(t+\tau)\rangle}{\langle \mathcal{E}^*(t)\mathcal{E}(t)\rangle} = \frac{R_{\mathcal{E}}(\tau)}{R_{\mathcal{E}}(0)} \ .$$

.

from a beat of two independent (uncorrelated) oscillators gives us information on their true emission bandwidths, which is relevant e.g. for resolving narrow atomic transitions. On the other hand, the stability measures $S_y(f)$ and $\sigma_y^2(\tau)$ derived from a discriminated error signal (left setup in Fig. 35.12) only tell us the stability of an oscillator with respect to the reference from which the error signal was derived, e.g. the transmission slope of an optical cavity.

35.3.2.1 Spectral noise power density in the case of white noise

The spectral noise power density $S_{\mathcal{E}}(\omega)$ of the field $\mathcal{E}(t)$ of an oscillator can, in the case of white frequency noise, be related to the spectral density of its frequency fluctuations. In the case of a laser oscillator, the half-width half maximum of the spectral noise power density, i.e. the emission bandwidth, is often specified. We will, in the following, derive the emission spectrum for the case of white Gaussian noise [794, 263, 240].

In Exc. 35.3.3.3 we show that for a *Gaussian noise process* holds [198, 263],

$$\left\langle e^{-\imath[\varphi(t)-\varphi(t+\tau)]} \right\rangle = e^{-\left\langle[\varphi(t)-\varphi(t+\tau)]^2\right\rangle/2} \,. \tag{35.74}$$

Now we set $\varphi(t) = \omega_0 \int_0^t y(t')dt'$ using (35.58) and obtain,

$$\begin{aligned} \left\langle[\varphi(t)-\varphi(t+\tau)]^2\right\rangle &= \left\langle \omega_0^2 \left[\int_0^\tau y(t')dt'\right]^2 \right\rangle = \omega_0^2 \int_0^\tau \int_0^\tau \langle y(t')y(t'')\rangle \, dt'dt'' \\ &= \omega_0^2 \int_0^\tau \int_0^\tau R_y(t'-t'')dt'dt'' = 2\omega_0^2 \int_0^\tau (\tau - t) R_y(t)dt \,. \end{aligned} \tag{35.75}$$

Using (35.61), we now substitute the autocorrelation function by its Fourier transform, the spectral fluctuation density, $R_y(t) = \int_0^\infty S_y(f) e^{2\pi\imath f t} df$:

$$\begin{aligned} \left\langle[\varphi(t)-\varphi(t+\tau)]^2\right\rangle &= 2\omega_0^2 \int_0^\infty S_y(f) \int_0^\tau (\tau - t) e^{2\pi\imath f t} dt df \\ &= 2\omega_0^2 \int_0^\infty S_y(f) \left(\frac{\sin \pi f \tau}{2\pi f}\right)^2 df + \text{imaginary part} \,. \end{aligned} \tag{35.76}$$

We neglect the imaginary part.

For Markovian white noise the phase fluctuations are δ-distributed, which means,

$$R_y \equiv \langle y^*(t)y(t+\tau)\rangle = h_0\delta(\tau) \qquad \text{and} \qquad S_y(f) = h_0 = const. \tag{35.77}$$

I.e. the so-called *white noise* is characterized by a constant spectral density of phase fluctuations. Carrying on the calculation (35.76) for the case of white frequency noise we get,

$$\left\langle[\varphi(t)-\varphi(t+\tau)]^2\right\rangle = \frac{h_0\omega_0^2|\tau|}{\pi} \int_0^\infty \left(\frac{\sin x}{x}\right)^2 dx = \frac{h_0\omega_0^2|\tau|}{2} \,. \tag{35.78}$$

With this result, we can undertake to calculate the autocorrelation function of the field amplitude (35.71),

$$R_{\mathcal{E}}(\tau) = \mathcal{E}_0^2 e^{\omega_0\tau} e^{-h_0\omega_0^2|\tau|/2} \,. \tag{35.79}$$

The resulting *power spectral density* (35.72) is [5]:

$$\boxed{S_{\mathcal{E}}(\omega) = \mathcal{E}_0^2 \int_{-\infty}^{\infty} R_{\mathcal{E}}(\tau) e^{-\imath(\omega-\omega_0)\tau} d\tau = \frac{2h_0\omega_0^2}{4\Delta^2 + (h_0\omega_0^2/2)^2}} \,, \tag{35.80}$$

where $\Delta \equiv \omega - \omega_0$ is the deviation of the oscillator frequency from the center frequency ω_0. Thus, the the emission spectrum for the case of white Gaussian noise is a Lorentzian profile with the *laser emission bandwidth*,

$$\boxed{\beta = \tfrac{1}{2} h_0 \omega_0^2} \,. \tag{35.81}$$

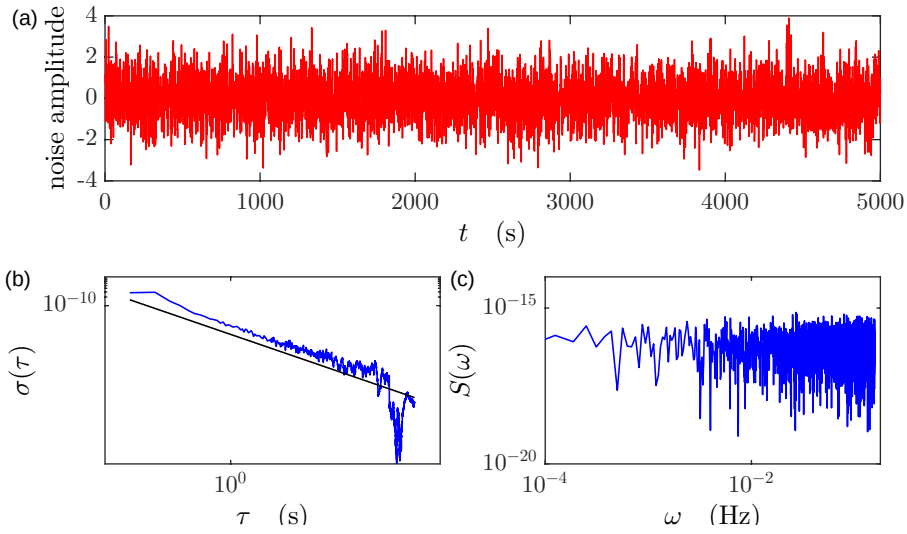

Figure 35.13: (code) Allan variance (b) and spectral density of frequency fluctuations (c) calculated from a randomly generated data set (a).

The Lorentz shape of the emission profile of an oscillator or a resonance always indicates white noise of the underlying frequency fluctuation density. In this sense, the Lorentz form of the natural broadening of an atomic resonance can also be traced back to the white noise of the vacuum fluctuations. Here, the emission bandwidth has to be replaced by the natural linewidth. The Allan variance in this case is:

$$\sigma_y^2(\tau) = \frac{h_0}{2\tau} = \frac{1}{Q^2}\frac{1}{\Gamma}\frac{1}{\tau} \,. \tag{35.82}$$

with the linewidth (FWHM) $\Gamma = h_0\omega_0^2/2$ and $Q = \omega_0/\Gamma$ and indicates the maximum achievable stability for a frequency standard that is coupled to the resonance ω_0.

[5] Using $\mathcal{F}[e^{-a|x|}] = \int_{-\infty}^{\infty} e^{-a|t|} e^{-\imath\omega t} dt = \frac{2a}{a^2+\omega^2}$.

35.3.2.2 Spectral noise power density in case of periodic phase perturbation

The momentary deflection of the oscillator can be described in the case of a harmonic phase disturbance by equation (35.60) with the additional condition: $\phi(t) = N \sin \Omega t$. The frequency fluctuation density and the Allan variance are obtained in this case:

$$S_y(f) = \left(\frac{fN}{2\omega_0}\right)^2 \delta(f - \Omega) \qquad \text{resp.} \qquad \sigma_y^2(\tau) = \left(\frac{\Omega N}{2\omega_0}\right)^2 \frac{\sin^2 \Omega\tau/2}{\Omega\tau/2} \ . \tag{35.83}$$

The spectral noise power density consists of a discrete spectrum of sidebands, the number and height of which is given by the modulation index N:

$$\boxed{S_{\mathcal{E}}(\omega) = \sum_{n=-\infty}^{\infty} |J_n(N)|^2 \delta(\omega - \omega_0 - \Omega)} \ . \tag{35.84}$$

A full width at half maximum of the spectral noise power density cannot be specified. However, as a measure of the emission bandwidth of the oscillator, the frequency spacing of the sideband of the highest order can be understood, the height of which corresponds to at least half the height of the carrier frequency ω_0.

35.3.3 Exercises

35.3.3.1 Ex: Spectral density of frequency fluctuations

Prove the relationship $S_{\dot{x}}(f) = f^2 S_x(f)$.

35.3.3.2 Ex: Allan variance for white noise

a. Calculate the Fourier transform of step function $\zeta_1(t)$ and the one-point variance for white noise from its definition (35.68).
b. Repeat the calculation for the step function $\zeta_2(t)$ and the Allan variance as defined in (35.70).

35.3.3.3 Ex: Gaussian noise process

Prove the relationship (35.75) for a *Gaussian noise process* characterized by,

$$\frac{\langle A^{2n} \rangle}{(2n)!} = \frac{\langle A^2 \rangle^n}{2^n n!} \qquad \text{and} \qquad \langle A^{2n-1} \rangle = 0 \ .$$

35.4 Data sheets

The following pages contain the data sheets of the main components used in this course.

HL6722G

AlGaInP Laser Diode

opnext
Powered by HITACHI

ODE-208-220E (Z)

Rev.5
Mar. 2005

Description

The HL6722G is a 0.67 µm band AlGaInP index-guided laser diode with a multi-quantum well (MQW) structure. It is suitable as a light source for bercode scanner, and various other types of optical equipment. Hermetic sealing of the package assures high reliability.

Features

- Visible light output at wavelengths up to 680 nm
- Single longitudinal mode
- Continuous operating output: 5 mW CW
- Low voltage operation: 2.7 V Max
- Low current operation: 32 mA Typ
- Built-in monitor photodiode

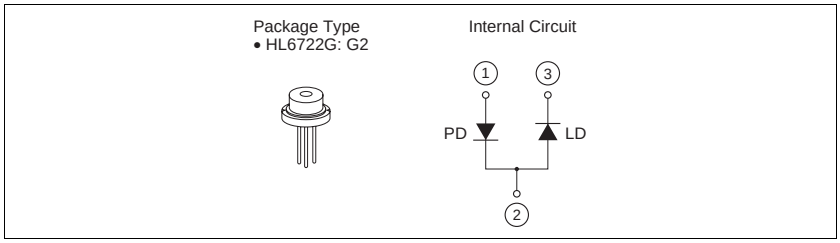

opnext
Powered by HITACHI

Figure 35.14: Data sheet for the diode laser from Thorlabs, model Hitachi HL6722G.

Coaxial

Amplifier

ZHL-2-8

50Ω Medium High Power 10 to 1000 MHz

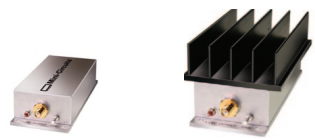

ZHL-2-8X ZHL-2-8

SMA version shown

Features

- wideband, 10 to 1000 MHz
- high IP3, +38 dBm typ.
- medium high power, 29 dBm min.

Applications

- VHF/UHF
- test equipment
- cellular
- instrumentation
- laboratory

CASE STYLE: T34

Connectors	Model	Price	Qty.
BNC	ZHL-2-8	$525.00 ea.	(1-9)
BNC	ZHL-2-8X	$515.00 ea.	(1-9)
SMA	ZHL-2-8-S	$535.00 ea.	(1-9)
SMA	ZHL-2-8X-S	$525.00 ea.	(1-9)

Electrical Specifications

MODEL NO.	FREQ. (MHz)		GAIN (dB)			MAXIMUM POWER OUTPUT (dBm)		DYNAMIC RANGE		VSWR (:1) Max.		DC POWER	
	f_L	f_U	Min.	Typ.	Flatness Max.	(1 dB Compr.) Min.	Input (no damage)	NF (dB) Typ.	IP3 (dBm) Typ.	In	Out	Volt (V) Nom.	Current (A) Max.
ZHL-2-8	10	1000	31	35	±1.0	+29	+5	10.0	+38	2.0	2.0	24	0.6
ZHL-2-8X*	10	1000	31	35	±1.0	+29	+5	10.0	+38	2.0	2.0	24	0.6

* Heat sink not included
Open load is not recommended, potentially can cause damage.
With no load derate max input power by 20 dB

To order without heat sink, add suffix X to model number. Alternative heat sinking and heat removal must be provided by the user to limit maximum temperature to 65°C, in order to ensure proper performance. For reference, this requires thermal resistance of user's external heat sink to be 1.35°C/W Max.

Maximum Ratings

Operating Temperature	-20°C to 65°C
Storage Temperature	-55°C to 100°C
DC Voltage	+25V Max.

Permanent damage may occur if any of these limits are exceeded.

Outline Drawing

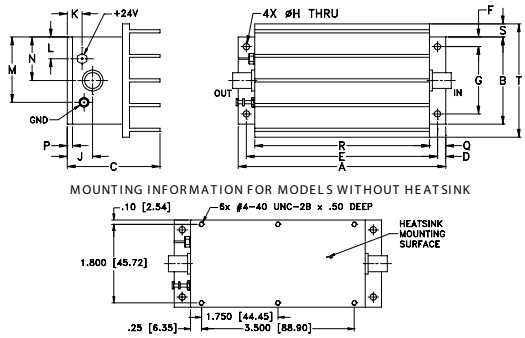

Figure 35.15: Data sheet for the rf-amplifier from MiniCircuits, model ZHL-2-8.

Coaxial

Voltage Controlled Oscillator ZOS-100+

Dual Output 50 to 100 MHz

CASE STYLE: BR386

Connectors	Model	Price	Qty.
SMA	ZOS-100+	$119.95	(1-9)

+ RoHS compliant in accordance with EU Directive (2002/95/EC)

The +Suffix has been added in order to identify RoHS Compliance. See our web site for RoHS Compliance methodologies and qualifications.

Features

- octave bandwidth
- linear tuning, 4.5 MHz/V typ.
- excellent harmonic suppression, -29 dBc typ.
- rugged shielded case
- protected by US Patent, 6,943,629

Applications

- auxiliary output freq. monitoring
- load insensitive source

Electrical Specifications

FREQUENCY (MHz)		POWER OUTPUT (dBm) Typ.		TUNING VOLTAGE (V)		PHASE NOISE (dBc/Hz) SSB at offset frequencies: Typ.			PULLING (MHz) pk-pk (open/short)	PUSHING (MHz/V)	TUNING SENSITIVITY (MHz/V)	HARMONICS (dBc)		3 dB MODULATION BANDWIDTH (MHz)	DC OPERATING POWER	
Min.	Max.	Main	Aux.	Min.	Max.	10 kHz	100 kHz	1 MHz	Typ.	Typ.	Typ.	Typ.	Max.	Typ.	Vcc (volts)	Current (mA) Max.
50	100	+9	-12	1	16	-111	-131	-143	0.026	0.25	4.5	-29	-20	0.1	12	140

Maximum Ratings

Operating Temperature	-55°C to 85°C
Storage Temperature	-55°C to 100°C
Absolute Max. Supply Voltage (Vcc)	+16V
Absolute Max. Tuning Voltage (Vtune)	+18V

all specifications: 50 ohm system
Permanent damage may occur if any of these limits are exceeded.

electrical schematic

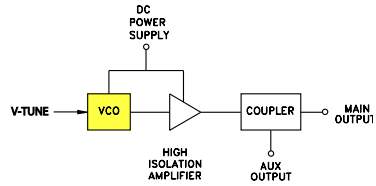

Outline Drawing

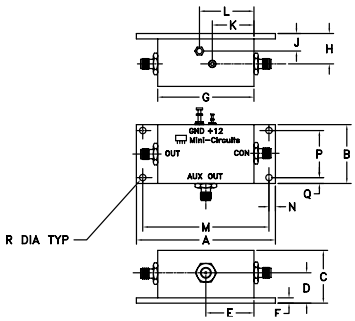

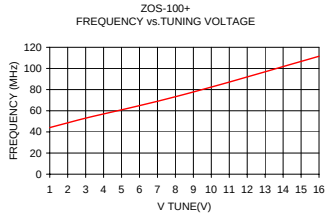

Outline Dimensions (inch / mm)

A	B	C	D	E	F	G	H	J	K	L	M	N	P	Q	R	wt
3.25	1.38	1.25	.71	1.13	.125	2.25	.71	.41	.98	1.28	2.950	.15	1.100	.14	.150	grams
82.55	35.05	31.75	18.03	28.70	3.18	57.15	18.03	10.41	24.89	32.51	74.93	3.81	27.94	3.56	3.81	180

Figure 35.16: Data sheet for the Voltage-Controlled Oscillator (VCO) from Minicircuits, model ZOS-100+.

Coaxial

Voltage Variable Attenuator

ZX73-2500+

50Ω 10 to 2500 MHz

FEMALE SMA shown

CASE STYLE: GD958

SMA	Connectors	Model	Price	Qty.	Case
INPUT	**OUTPUT**				
FEMALE	**FEMALE**	ZX73-2500-S+	$49.95	(1-9)	GD958
MALE	**FEMALE**	ZX73-2500M-S+	$49.95	(1-9)	GD1163

+ RoHS compliant in accordance with EU Directive (2002/95/EC)

The +Suffix has been added in order to identify RoHS Compliance. See our web site for RoHS Compliance methodologies and qualifications.

Maximum Ratings

Operating Temperature	-55°C to 85°C
Storage Temperature	-55°C to 85°C
Absolute Max. Supply Voltage (V+)	12V
Absolute Max. Control Voltage (Vcrtl)	20V
Absolute Max. RF Input Level	+20 dBm

Permanent damage may occur if any of these limits are exceeded.

Features

- Broadband, 10-2500 MHz
- IP3, +43 dBm typ.
- 40 dB attenuation @ 1500 MHz
- Good VSWR at in /out ports over attenuation range
- No external bias and RF matching network required
- Shielded case
- Protected by US Patent 6,790,049

Applications

- Variable gain amplifier
- Power level control
- Feed-forward amplifiers
- ALC circuits

Outline Drawing (GD958)

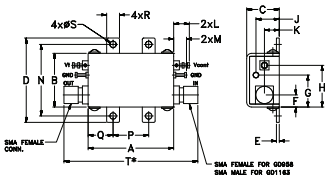

Outline Dimensions (inch / mm)

A	B	C	D	E	F	G	H	J
1.20	**.75**	**.46**	**1.18**	**.04**	**.17**	**.45**	**.59**	**.33**
30.48	19.05	11.68	29.97	1.02	4.32	11.43	14.99	8.38

K	L	M	N	P	Q	R	S	T	wt.
.21	**.22**	**.18**	**1.00**	**.50**	**.35**	**.18**	**.106**	**1.88**	**grams**
5.33	5.59	4.57	25.40	12.70	8.89	4.57	2.69	47.75	35.0

Note:

* T dimension is 2.05 inch (52.07 mm) for GD1163 Case Style.

Electrical Specifications (T_{AMB}= 25°C)

FREQ. (MHz)		MIN. INSERTION LOSS, dB (+15V)		MAX. ATTENUATION dB (0V)		INPUT POWER (dBm)	CONTROL Voltage (V)	CONTROL Current (mA)	IP3 (dBm)	RETURN LOSS[1] (dB)	POWER SUPPLY Voltage (V)	POWER SUPPLY Current (mA)
Min.	Max.	Typ.	Max.	Typ.	Min.	Max.		Max.	Typ.	Typ.		Max.
10	500	3.0	4.6	55	41	+20	0 - 17	30	43	20	+3 to +5	5
500	1500	3.3	5.0	40	30	+20	0 - 17	30	43	20	+3 to +5	5
1500	2500	4.0	6.2	37	25	+20	0 - 17	30	44	20	+3 to +5	5

Notes:
Rise/Fall time: 14μSec/25μSec Typ.
Switching Time, turn on/off: 14μSec/25μSec Typ.
[1] Improved R. Loss in/out performance can be achieved at certain frequencies by choosing a V+ between +3V to +5V

Equivalent Schematic

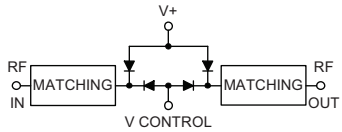

ZX73-2500+
TYPICAL ATTENUATION AT 1000MHz

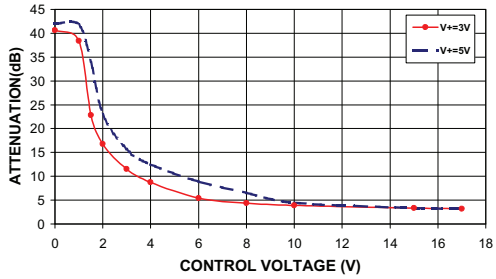

Figure 35.17: Data sheet for the voltage-controlled variable attenuator from Minicircuits, model ZX73-2500+.

Plug-In

Power Splitter/Combiner

PSC-2-1+
PSC-2-1

2 Way-0° 50Ω 0.1 to 400 MHz

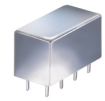

CASE STYLE: A01
PRICE: $14.20 ea. QTY. (1-9)

+ RoHS compliant in accordance with EU Directive (2002/95/EC)

The +Suffix identifies RoHS Compliance. See our web site for RoHS Compliance methodologies and qualifications.

Maximum Ratings

Operating Temperature	-55°C to 100°C
Storage Temperature	-55°C to 100°C
Power Input (as a splitter)	1W max.
Internal Dissipation	0.125W max.

Pin Connections

SUM PORT	1
PORT 1	5
PORT 2	6
GROUND	2,3,4,7,8
CASE GROUND	2,3,4,7,8

Features

- wideband, 0.1 to 400 MHz
- low insertion loss, 0.4 dB typ.
- rugged welded construction

Applications

- VHF/UHF
- federal & defense communications

Outline Drawing

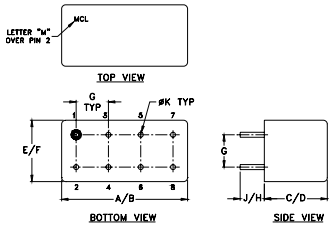

Outline Dimensions (inch / mm)

A	B	C	D	E	F
.770	.800	.385	.400	.370	.400
19.56	20.32	9.78	10.16	9.40	10.16
G	H	J	K		wt
.200	.20	.14	.031		grams
5.08	5.08	3.56	0.79		5.2

Electrical Specifications

FREQ. RANGE (MHz)	ISOLATION (dB)						INSERTION LOSS (dB) ABOVE 3.0 dB						PHASE UNBALANCE (Degrees)			AMPLITUDE UNBALANCE (dB)		
	L		M		U		L		M		U		L	M	U	L	M	U
f_L-f_U	Typ.	Min	Typ.	Min	Typ.	Min	Typ.	Max.	Typ.	Max.	Typ.	Max.	Max.	Max.	Max.	Max.	Max.	Max.
0.1-400	20	15	25	20	25	20	0.2	0.6	0.4	0.75	0.6	1.0	2.0	3.0	4.0	0.15	0.2	0.3

L = low range [f_L to 10 f_L] M = mid range [10 f_L to f_U/2] U= upper range [f_U/2 to f_U]

Typical Performance Data

Frequency (MHz)	Insertion Loss (dB)		Amplitude Unbalance (dB)	Isolation (dB)	Phase Unbalance (deg.)	VSWR S	VSWR 1	VSWR 2
	S-1	S-2						
0.10	3.23	3.23	0.00	24.82	0.01	1.16	1.37	1.37
5.00	3.14	3.14	0.00	35.64	0.01	1.10	1.11	1.11
20.00	3.18	3.17	0.00	35.33	0.03	1.11	1.10	1.10
40.00	3.18	3.18	0.00	34.39	0.02	1.12	1.10	1.10
60.00	3.22	3.22	0.00	33.16	0.02	1.12	1.09	1.09
80.00	3.24	3.24	0.00	31.85	0.04	1.13	1.09	1.09
100.00	3.24	3.24	0.00	30.68	0.05	1.13	1.09	1.09
150.00	3.28	3.27	0.00	28.37	0.04	1.14	1.08	1.08
175.00	3.31	3.30	0.01	27.46	0.07	1.14	1.07	1.07
200.00	3.32	3.31	0.01	26.72	0.05	1.15	1.07	1.07
225.00	3.32	3.31	0.01	26.14	0.02	1.15	1.06	1.06
250.00	3.37	3.36	0.01	25.65	0.05	1.15	1.06	1.06
300.00	3.41	3.38	0.03	24.88	0.10	1.15	1.06	1.06
350.00	3.47	3.44	0.03	24.40	0.06	1.16	1.08	1.07
400.00	3.50	3.46	0.04	23.86	0.05	1.18	1.10	1.09

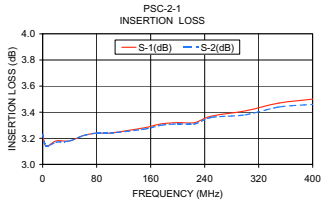

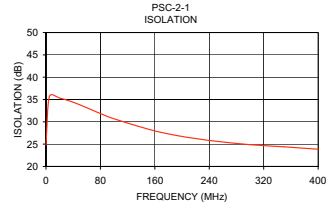

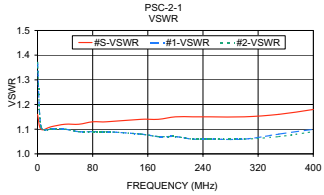

electrical schematic

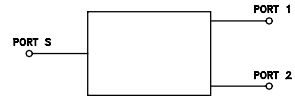

Mini-Circuits®
ISO 9001 ISO 14001 CERTIFIED

ALL NEW minicircuits.com

REV. A
M98898
PSC-2-1
HY/TD/CP
070202

P.O. Box 350166, Brooklyn, New York 11235-0003 (718) 934-4500 Fax (718) 332-4661 For detailed performance specs & shopping online see Mini-Circuits web site

The Design Engineers Search Engine Provides ACTUAL Data Instantly From MINI-CIRCUITS At: www.minicircuits.com

RF/IF MICROWAVE COMPONENTS

Figure 35.18: Data sheet for the power divider from Minicircuits, model PSC-2-1.

Plug-In

Frequency Mixer

SRA-2CM+

Level 7 (LO Power +7 dBm) 5 to 1000 MHz

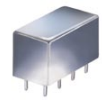

CASE STYLE: A01
PRICE: $18.20 ea. QTY (1-9)

+ RoHS compliant in accordance with EU Directive (2002/95/EC)

The +Suffix has been added in order to identify RoHS Compliance. See our web site for RoHS Compliance methodologies and qualifications.

Maximum Ratings

Operating Temperature	-55°C to 100°C
Storage Temperature	-55°C to 100°C
RF Power	50mW
IF Current	40mA

Pin Connections

LO	8
RF	1
IF	3,4^
GROUND	2,5,6,7
CASE GROUND	2,5,6,7

^ *pins must be connected together externally*

Features

- excellent conversion loss, 5.27 dB typ.
- good L-R isolation, 35 dB typ. L-I isolation, 30 dB typ.
- rugged welded construction
- hermetic

Applications

- VHF/UHF
- cellular
- defense & federal communications
- ISM/GSM

Outline Drawing

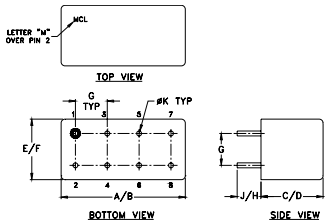

Outline Dimensions (inch / mm)

A	B	C	D	E	F
.770	.800	.385	.400	.370	.400
19.56	20.32	9.78	10.16	9.40	10.16
G	H	J	K		wt
.200	.20	.14	.031		grams
5.08	5.08	3.56	0.79		5.2

Electrical Specifications

FREQUENCY (MHz)		CONVERSION LOSS (dB)				LO-RF ISOLATION (dB)						LO-IF ISOLATION (dB)					
		Mid-Band m			Total Range	L		M		U		L		M		U	
LO/RF f_L-f_U	IF	$\bar{X}$	σ	Max.	Max.	Typ.	Min.	Typ.	Min.	Typ.	Min.	Typ.	Min.	Typ.	Min.	Typ.	Min.
5-1000	DC-1000	5.27	.04	7.0	8.5	60	50	35	30	30	25	50	45	30	25	25	20

1 dB COMP.: +1 dBm typ.

L = low range [f_L to 10 f_L] m= mid band [2f_L to f_U/2] M = mid range [10 f_L to f_U/2] U = upper range [f_U/2 to f_U]

Typical Performance Data

Frequency (MHz)		Conversion Loss (dB)	Isolation L-R (dB)	Isolation L-I (dB)	VSWR RF Port (:1)	VSWR LO Port (:1)
RF	LO	LO +7dBm	LO +7dBm	LO +7dBm	LO +7dBm	LO +7dBm
5.00	35.00	7.36	67.00	67.00	5.03	4.09
38.13	68.13	5.59	54.82	53.34	1.40	3.04
71.27	41.27	5.30	49.15	48.13	1.31	2.99
137.53	107.53	5.33	46.10	45.22	1.27	2.83
200.00	170.00	5.35	42.68	41.91	1.24	2.82
236.93	206.93	5.27	41.09	40.29	1.24	2.72
303.20	273.20	5.28	39.42	38.94	1.24	2.76
336.33	306.33	5.42	39.72	36.88	1.26	2.77
402.60	372.60	5.63	38.13	35.49	1.30	2.85
468.86	438.86	5.62	37.15	35.09	1.37	2.84
535.13	505.13	5.87	35.49	32.57	1.45	2.97
568.26	538.26	6.01	35.26	31.27	1.50	2.96
634.53	604.53	6.17	36.03	29.46	1.61	3.10
700.79	670.79	6.68	38.00	30.29	1.70	3.21
767.06	737.06	6.49	38.00	29.92	1.85	3.09
800.19	770.19	6.11	39.26	28.34	2.01	3.03
833.33	803.33	6.37	39.87	27.52	2.08	3.08
899.59	869.59	6.80	40.23	26.99	2.32	3.39
965.86	935.86	6.86	42.61	25.65	2.53	3.58
1000.00	969.00	7.10	44.90	24.17	2.76	3.76

Electrical Schematic

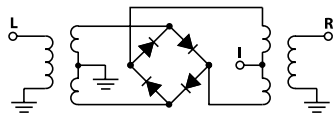

Figure 35.19: Data sheet for the mixer from Minicircuits, model SRA-2CM+.

SPECIFICATIONS				
AO Medium				TeO2
Acoustic Velocity				4.2 mm/µs
Active Aperture*	2.5	mm 'L' X	1	mm 'H'
Center Frequency (Fc)				80 MHz
RF Bandwidth	20 MHz @	-10 dB	Return Loss	
Input Impedance				50 Ohms Nominal
VSWR @ Fc				1.3 :1 Max
Wavelength				442-633 nm
Insertion Loss				4 % Max
Reflectivity per Surface				1 % Max
Anti-Reflection Coating				MIL-C-48497
Optical Power Density				250 W/mm^2
Contrast Ratio				1000 :1 Min
Polarization				90 ° To Mounting Plane

PERFORMANCE VS WAVELENGTH				
Wavelength (nm)	**442**	**488**	**515**	**633**
Saturation RF Power (W)	0.27	0.33	0.36	0.55
Bragg Angle (mr)	4.2	4.6	4.9	6
Beam Separation (mr)	8.4	9.2	9.8	12

PERFORMANCE VS BEAM DIAMETER			
Beam Diameter (µm)	**200**	**300**	**500**
at Wavelength (nm)	633	633	633
Diffraction Efficiency (%)	80	83	85
Rise Time (nsec)	34	49	80
	15.9	10.6	6.3
	10	5	1

Figure 35.20: Data sheet for the acousto-optic modulator (AOM) from Crystal Technologies, model AOMO 3080-120.

Silicon PIN Photodiodes - Large Area, Fast Response Time – 400 nm to 1100 nm

The FFD series devices are high-quality, large-area, high-speed, N-type Si PIN photodiodes in hermetically sealed TO packages designed for the 400 nm to 1100 nm wavelength range. The FND-100Q has a quartz window to enhance UV responsivity.

Preamplifiers

Preamplifier modules incorporating these photodiodes are available on a custom basis.

Si PINs – Large Area, Fast Response

Typical Characteristics @ T = 22º C

Part #	Standard Package	Photo Sens. Diam. (mm)	Resp. @ 900 nm (A/W)	Dark Current Id (nA)	Spect. Noise Curr. Dens. In (fW/√Hz)	Cap. @ 100 kHz Cd (pF)	Response Time tr (ns)	NEP @ 900 nm (fW/√Hz)	Bias Volt (V)
FFD-040B	Y	1	0.58	1	18	1.8	2	31	15
FFD-100	B	2.5	0.58	2	25	8.5	3.5	44	15
FFD-200	C3	5.1	0.58	4	36	30	5	62	15
FND-100Q	B	2.5	0.58	10	60	8.5	2	100	90

Typical Applications

Laser detection systems, fast pulse detection, instrumentation, and high-speed switching.

Figure 35.21: Data sheet for the photo diode from Perkin Elmers FDD100.

Detectors

Silicon Epitaxial PIN Photodiodes - High Speed – 400 nm to 1100 nm

The C30736 series of high-speed epitaxial silicon PIN photodetectors provide fast response and good quantum efficiency in the spectral range between 400 nm and 1100 nm. These devices are optimized for high-speed, high volume and low cost applications. Standard sizes include 0.25 mm, 0.5 mm, 1.0 mm, 1.5 x 1.5 mm, and custom sizes can be accomodated depending on volume required. Available in plastic surface mount packages and in chip form.

Silicon Epitaxial PIN Photodiodes

Typical Characteristics @ T = 22º C

Part #	Standard Package	Photo Sens. Diam. (mm)	Resp. @ 870 nm (A/W)	Dark Current @2V Id (nA)	Spect. Noise Curr. Dens. In (fW/√Hz)	Cap. @ 100 kHz Cd (pF)	Response Time tr (ns)	NEP @ 870 nm (fW/√Hz)	Bias Volt (V)
C30736-1	Chip form	0.20	0.55	0.05	6	0.75	0.3	11	2
C30736-2	Chip form	0.50	0.55	0.10	10	1.5	0.5	18	2
C30736-3	Chip form	1.5 x 1.5	0.55	0.50	50	14	0.3	91	2

Silicon PIN Photodiodes - Standard N-Type – 400 nm to 1100 nm

The C308XX series devices are high-quality N-type Si PIN photodiodes in hermetically sealed TO packages designed for the 400 nm to 1100 nm wavelength region.

Si PINs – Standard N-Type

Typical Characteristics @ T = 22º C

Part #	Standard Package	Photo Sens. Diam. (mm)	Resp. @ 900 nm (A/W)	Dark Current Id (nA)	Spect. Noise Curr. Dens. (fA/√Hz)	Cap. @ 100 kHz Cd (pF)	Response Time tr (ns)	NEP @ 900 nm (fW/√Hz)	Bias Volt (V)
C30807E	A	1	0.6	1	18	2.5	3	30	45
C30808E	B	2.5	0.6	3	31	6	5	52	45
C30822E	C	5	0.6	5	40	17	7	67	45
C30809E	C3	8	0.6	7	47	35	10	79	45
C30810E	D	11.4	0.6	30	98	70	12	163	45

Typical Applications

Laser detection systems, photometry, data transmission, instrumentation, and high-speed switching.

Silicon PIN Photodiodes - Large Area, Fast Response Time – 400 nm to 1100 nm

The FFD series devices are high-quality, large-area, high-speed, N-type Si PIN photodiodes in hermetically sealed TO packages designed for the 400 nm to 1100 nm wavelength range. The FND-100Q has a quartz window to enhance UV responsivity.

Preamplifiers

Preamplifier modules incorporating these photodiodes are available on a custom basis.

Si PINs – Large Area, Fast Response

Typical Characteristics @ T = 22º C

Part #	Standard Package	Photo Sens. Diam. (mm)	Resp. @ 900 nm (A/W)	Dark Current Id (nA)	Spect. Noise Curr. Dens. In (fW/√Hz)	Cap. @ 100 kHz Cd (pF)	Response Time tr (ns)	NEP @ 900 nm (fW/√Hz)	Bias Volt (V)
FFD-040B	Y	1	0.58	1	18	1.8	2	31	15
FFD-100	B	2.5	0.58	2	25	8.5	3.5	44	15
FFD-200	C3	5.1	0.58	4	36	30	5	62	15
FND-100Q	B	2.5	0.58	10	60	8.5	2	100	90

Typical Applications

Laser detection systems, fast pulse detection, instrumentation, and high-speed switching.

6

Figure 35.22: Data sheet for the photo diode from Perkin Elmers C30822E.

19-0350; Rev 0; 12/94

MAXIM

Precision, Dual-Supply, SPST Analog Switches

General Description

The MAX320/MAX321/MAX322 are precision, dual, SPST analog switches designed to operate from ±3V to ±8V dual supplies. The MAX320 has two normally open (NO) switches and the MAX321 has two normally closed (NC) switches. The MAX322 has one NO and one NC switch. Low power consumption (1.25mW) makes these parts ideal for battery-powered equipment. They offer low leakage currents (100pA max) and fast switching speeds (t_{ON} = 150ns max, t_{OFF} = 100ns max).

The MAX320 series, powered from ±5V supplies, offers 35Ω max on-resistance (R_{ON}), 2Ω max matching between channels, and 4Ω max R_{ON} flatness.

These switches also offer 5pC max charge injection and a minimum of 2000V ESD protection per Method 3015.7.

For equivalent devices specified for single-supply operation, see the MAX323/MAX324/MAX325 data sheet. For quad versions of these switches, see the MAX391/MAX392/MAX393 data sheet.

Applications

Battery-Operated Systems	Sample-and-Hold Circuits
Heads-Up Displays	Guidance and Control Systems
Audio and Video Switching	Military Radios
Test Equipment	Communications Systems
±5V DACs and ADCs	PBX, PABX

Features

- **Low On-Resistance, 35Ω max (16Ω typical)**
- **R_{ON} Matching Between Channels <2Ω**
- **R_{ON} Flatness <4Ω**
- **Guaranteed Charge Injection <5pC**
- **Bipolar Supply Operation (±3V to ±8V)**
- **Low Power Consumption, <1.25mW**
- **Low Leakage Current Over Temperature, <2.5nA at +85°C**
- **Fast Switching, t_{ON} <150ns, t_{OFF} <100ns**
- **Guaranteed Break-Before-Make (MAX322 only)**

Ordering Information

PART	TEMP. RANGE	PIN-PACKAGE
MAX320CPA	0°C to +70°C	8 Plastic DIP
MAX320CSA	0°C to +70°C	8 SO
MAX320CUA	0°C to +70°C	8 µMAX
MAX320C/D	0°C to +70°C	Dice*
MAX320EPA	-40°C to +85°C	8 Plastic DIP
MAX320ESA	-40°C to +85°C	8 SO
MAX320EJA	-40°C to +85°C	8 CERDIP**
MAX320MJA	-55°C to +125°C	8 CERDIP**

Ordering Information continued at end of data sheet.

** Contact factory for dice specifications.*
*** Contact factory for availability.*

Pin Configurations/Functional Diagrams/Truth Tables

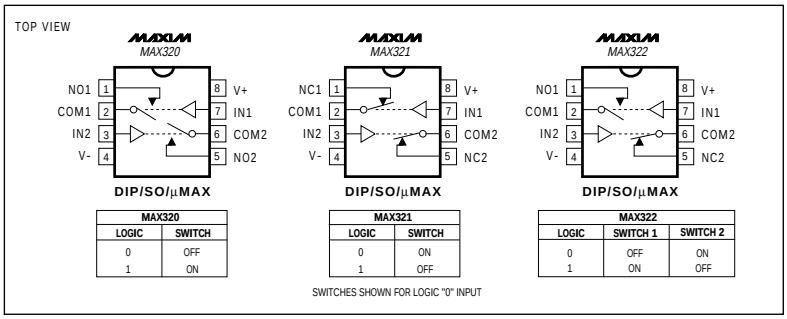

MAX320	
LOGIC	SWITCH
0	OFF
1	ON

MAX321	
LOGIC	SWITCH
0	ON
1	OFF

MAX322		
LOGIC	SWITCH 1	SWITCH 2
0	OFF	ON
1	ON	OFF

SWITCHES SHOWN FOR LOGIC "0" INPUT

Figure 35.23: Data sheet for the digital switch MAX322 from Maxim.

National Semiconductor

August 2000

LM741
Operational Amplifier

General Description

The LM741 series are general purpose operational amplifiers which feature improved performance over industry standards like the LM709. They are direct, plug-in replacements for the 709C, LM201, MC1439 and 748 in most applications.

The amplifiers offer many features which make their application nearly foolproof: overload protection on the input and output, no latch-up when the common mode range is exceeded, as well as freedom from oscillations.

The LM741C is identical to the LM741/LM741A except that the LM741C has their performance guaranteed over a 0˚C to +70˚C temperature range, instead of −55˚C to +125˚C.

Features

Connection Diagrams

Metal Can Package

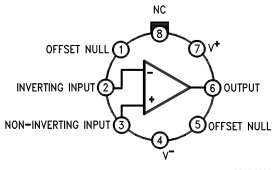

Note 1: LM741H is available per JM38510/10101

Order Number LM741H, LM741H/883 (Note 1), **LM741AH/883 or LM741CH**
See NS Package Number H08C

Dual-In-Line or S.O. Package

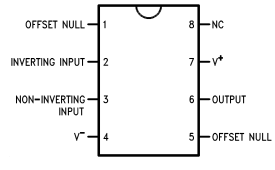

Order Number LM741J, LM741J/883, LM741CN
See NS Package Number J08A, M08A or N08E

Ceramic Flatpak

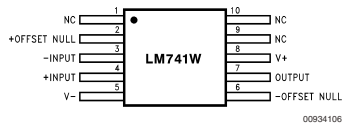

Order Number LM741W/883
See NS Package Number W10A

Typical Application

Offset Nulling Circuit

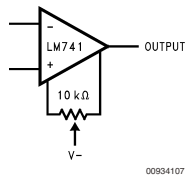

 DS009341

Figure 35.24: Data sheet for the operational amplifier LM741 from National Semiconductor.

ANALOG DEVICES

Low-Noise, Precision Operational Amplifier

OP27

FEATURES

Low Noise: 80 nV p-p (0.1 Hz to 10 Hz), 3 nV/√Hz
Low Drift: 0.2 μV/°C
High Speed: 2.8 V/μs Slew Rate, 8 MHz Gain Bandwidth
Low V_{OS}: 10 μV
Excellent CMRR: 126 dB at V_{CM} of ±11 V
High Open-Loop Gain: 1.8 Million
Fits 725, OP07, 5534A Sockets
Available in Die Form

GENERAL DESCRIPTION

The OP27 precision operational amplifier combines the low offset and drift of the OP07 with both high speed and low noise. Offsets down to 25 μV and drift of 0.6 μV/°C maximum make the OP27 ideal for precision instrumentation applications. Exceptionally low noise, e_n = 3.5 nV/√Hz, at 10 Hz, a low 1/f noise corner frequency of 2.7 Hz, and high gain (1.8 million), allow accurate high-gain amplification of low-level signals. A gain-bandwidth product of 8 MHz and a 2.8 V/μsec slew rate provides excellent dynamic accuracy in high-speed, data-acquisition systems.

A low input bias current of ±10 nA is achieved by use of a bias-current-cancellation circuit. Over the military temperature range, this circuit typically holds I_B and I_{OS} to ±20 nA and 15 nA, respectively.

The output stage has good load driving capability. A guaranteed swing of ±10 V into 600 Ω and low output distortion make the OP27 an excellent choice for professional audio applications.

(Continued on page 7)

PIN CONNECTIONS

TO-99
(J-Suffix)

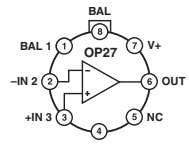

8-Pin Hermetic DIP
(Z-Suffix)
Epoxy Mini-DIP
(P-Suffix)
8-Pin SO
(S-Suffix)

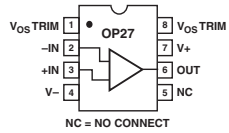

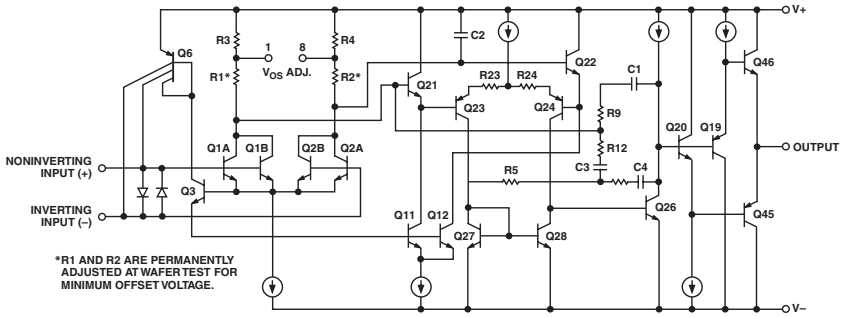

Figure 1. Simplified Schematic

Figure 35.25: Data sheet for the operational amplifier OP27 from Analog Devices.

Bibliography

[1] M. Sebawe Abdalla, S. S. Hassan, and A.-S. F. Obada, *Multiphoton transition in the tavis-cmmmings model*, Phys. Rev. A **34** (1986), 4869, DOI.

[2] J. A. Acebrón, L. L. Bonilla, and R. Spigler, *Synchronization in populations of globally coupled oscillators with inertial effects*, Phys. Rev. E **62** (2000), 3437, DOI.

[3] C. S. Adams, H. J. Lee, N. Davidson, M. Kasevich, and S. Chu, *Evaporative cooling in a crossed dipole trap*, Phys. Rev. Lett. **74** (1995), 3577, .

[4] C. S. Adams, M. Sigel, and J. Mlynek, *Atom optics*, Phys. Rep. **240** (1994), 143.

[5] G. Adesso, F. Dell'Anno, S. De Siena, F. Illuminati, and L. A. M. Souza, *Optimal estimation of losses at the ultimate quantum limit with non-gaussian states*, Phys. Rev. A **79** (2009), 040305(R), DOI.

[6] S. K. Adhikari, *Coupled Bose-Einstein condensate: Collapse for attractive interaction*, Phys. Rev. A **63** (2001), 043611, .

[7] G. S. Agarwal, *Vacuum-field Rabi splitting in a microwave absorption by Rydberg atoms in a cavity*, Phys. Rev. Lett. **53** (1984), 1732, .

[8] B. Agate, B. Stormont, A. J. Kemp, C. T. A. Brown, U. Keller, and W. Sibbett, *Simplified cavity designs for efficient and compact femtosecond cr:lisaf lasers*, Opt. Comm. **205** (2002), 207.

[9] Y. Aharonov, D. Falkoff, E. Lerner, and H. Pendleton, *A quantum characterization of classical radiation*, Ann. Phys. (N.Y.) **39** (1966), 498.

[10] F. Albarelli, A. Ferraro, M. Paternostro, and M. G. A. Paris, *Nonlinearity as a resource for nonclassicality in anharmonic systems*, Phys. Rev. A **93** (2016), 032112.

[11] R. Alicki, *The markov master equations and the Fermi golden rule*, International journal of Theoretical Physics (1977).

[12] D. W. Allan, *Statistics of atomic frequency standards*, Proc. of the IEEE **54** (1966), 221.

[13] D. W. Allan, J. H. Shoaf, and D. Halford, *Statistics of time and frequency data analysis*, NBS Monographs **140** (1974), 151.

[14] L. Allen, M. W. Beijersbergen, R. J. C. Spreeuw, and J. P. Woerdman, *Orbital angular momentum of light and the transformation of laguerre-gaussian laser modes*, Phys. Rev. A **45** (1992), 8185, .

[15] C. Altafini, *Commuting multiparty quantum observables and local compatibility*, Opt. Comm. **72** (2005), 012112, DOI.

[16] T. P. Altenmüller and A. Schenzle, Phys. Rev. A **49** (1994), 2016.

[17] M. Anderlini, P. J. Lee, B. L. Brown, J. Sebby-Strabley, W. D. Phillips, and J. V. Porto, *Controlled exchange interaction between pairs of neutral atoms in an optical lattice*, Nature **448** (2007), 452, DOI.

[18] B. P. Anderson, P. C. Haljan, C. E. Wieman, and E. A. Cornell, *Vortex precession in Bose-Einstein condensates: Observations with filled and empty cores*, Phys. Rev. Lett. **85** (2000), 2857, .

[19] B. P. Anderson and M. A. Kasevich, *Macroscopic quantum interference from atomic tunnel arrays*, Science **282** (1998), 1686, .

[20] M. H. Anderson, J. R. Ensher, M. R. Matthews, C. E. Wieman, and E. A. Cornell, *Observation of Bose-Einstein condensation in a dilute atomic vapor*, Science **269** (1995), 198, .

[21] M. R. Andrews, D. M. Kurn, H.-J. Miesner, D. S. Durfee, C. G. Townsend, S. Inouye, and W. Ketterle, *Propagation of sound in a Bose-Einstein condensate*, Phys. Rev. Lett. **79** (1997), 0553, .

[22] M. R. Andrews, M. O. Mewes, N. J. Van Druten, D. S. Durfee, D. M. Kurn, and W. Ketterle, *Direct, non-destructive observation of a bose condensate*, Science **273** (1996), 84.

[23] M. R. Andrews, D. M. Stamper-Kurn, H. J. Miesner, D. S. Durfee, C. G. Townsend, S. Inouye, and W. Ketterle, *Erratum: Propagation of sound in a Bose-Einstein condensate*, Phys. Rev. Lett. **80** (1997), 2967.

[24] M. R. Andrews, C. G. Townsend, H.-J. Miesner, D. S. Durfee, D. M. Kurn, and W. Ketterle, *Observation of interference between two bose condensates*, Science **275** (1997), 637, .

[25] M. Antezza and Y. Castin, *Fano-hopfield model and photonic band gaps for an arbitrary atomic lattice*, Phys. Rev. A **80** (2009), 013816, DOI.

[26] A. S. Arnold, C. MacCormick, and M. G. Boshier, *An adaptive inelastic magnetic mirror for Bose-Einstein condensates*, ePrints (2001), cond–mat/0103586, .

[27] F. Arute, K. Arya, R. Babbush, D. Bacon, and et al., *Quantum supremacy using a programmable superconducting processor*, Nature **574** (2019), 505.

[28] J. K. Asbóth, P. Domokos, H. Ritsch, and A. Vukics, *Self-organization in a cavity field: Threshold, bistability, and scaling laws*, Phys. Rev. A **72** (2005), 053417, DOI.

[29] A. Ashkin and J. P. Gordon, *Stability of radiation-pressure particle traps: an optical earnshaw theorem*, Opt. Lett. **8** (1978), 511, DOI.

[30] N. W. Ashkroft and D. N. Mermin, *Solid state physics*, Hartcourt College publishers, 1976, ISBN.

[31] A. Aspect, Ph. Grangier, and G. Roger, *Experimental realization of Einstein-podolski-rosen-bohm gedankenexperiment: A new violation of bell's inequalities*, Phys. Rev. Lett. **49** (1982), 91, .

[32] Alain Aspect, J. Dalibard, and J. Roger, *Experimental test of bell's inequality using time-varying analyzers*, Phys. Rev. Lett. **49** (1982), 1804, .

[33] Alain Aspect, P. Grangier, and G. Roger, Opt. Lett. **8** (1981), 511.

[34] S. Asselie, A. Cipris, and W. Guerin, *Optical interpretation of linear-optics superradiance and subradiance*, Phys. Rev. A **106** (2022), 063712, DOI.

[35] P. W. Atkins and R. S. Friedman, *Molecular quantum mechanics*, Oxford University Press, 1997, ISBN.

[36] C. Audoin, *Frequency metrology*, Rendiconti della Scuola Intern. di Fisica ?Enrico Fermi? **LIVIII or LXVIII** (1980), 169.

[37] M. Aymar and O. Dulieu, *Calculation of accurate permanent dipole moments of the lowest $^{1,3}s^+$ states of heteronuclear alkali dimers using extended basis sets*, J. Chem. Phys. **122** (2005), 204302, .

[38] H. Azuma, *Quantum computation with the Jaynes-Cummings model*, Progr. Theor. Phys. **126** (2008), 369.

[39] R. Bachelard, H. Bender, Ph. W. Courteille, N. Piovella, C. Stehle, C. Zimmermann, and S. Slama, *Role of mie scattering in the seeding of matter-wave superradiance*, Phys. Rev. A **86** (2012), 043605.

[40] R. Bachelard, Ph. W. Courteille, R. Kaiser, and N. Piovella, *Resonances in mie scattering by an inhomogeneous atomic cloud*, Europhys. Lett. **97** (2012), 14004.

[41] R. Bachelard, N. Piovella, W. Guerin, and R. Kaiser, *Collective effects in the radiation pressure force*, Phys. Rev. A **94** (2016), 033836.

[42] S. Backhaus, S. Pereverzev, R. W. Simmonds, A. Loshak, J. C. Davis, and R. E. Packard, *Discovery of a metastable pi-state in a superfluid he-3 weak link*, Nature **392** (1998), 687.

[43] S. N. Bagayev, V. S. Egorov, I. B. Mekhov, P. V. Moroshkin, I. A. Chekhonin, E. M. Davliatchine, and E. Kindel, *Resonant nonstationary amplification of polychromatic laser pulses and conical emission in an optically dense ensemble of neon metastable atoms*, Phys. Rev. A **68** (2003), 043812, .

[44] V. S. Bagnato, G. P. Lafyatis, A. G. Martin, E. L. Raab, R. N. Ahmad-Bitar, and D. E. Pritchard, *Continuous stopping and trapping of neutral atoms*, Phys. Rev. Lett. **58** (1987), 2194.

[45] V. S. Bagnato, D. E. Pritchard, and D. Kleppner, *Bose-Einstein condensation in an external potential*, Phys. Rev. A **35** (1987), 4354, DOI.

[46] Vanderlei S. Bagnato, *Simple calculation of the spatial evolution of atoms in a trap during occurance of Bose-Einstein condensation*, Phys. Rev. A **54** (1996), 1726, DOI.

[47] X. Baillard, A. Gauguet, S. Bize, P. Lemonde, Ph. Laurent, A. Clairon, and P. Rosenbusch, *Interference-filter-stabilized external-cavity diode lasers*, Opt. Commun. **266** (2006), 609, .

[48] V. I. Balykin, V. S. Letokhov, Yu. B. Ovchinnikov, and A. I. Sidorov, *Quantum-state selective mirror reflection of atoms by laser light*, Phys. Rev. Lett. **60** (1988), 2137, .

[49] A. Bambini and S. Geltman, *Feshbach resonances in cold collisions of potassium atoms*, Phys. Rev. A **65** (2002), 062704, .

[50] Weizhu Bao and Qiang Du, *Computing the ground state solution of a Bose-Einstein condensates by a normalized gradient flow*, SIAM J. Sci. Comput. **25** (2004), 1674, .

[51] Weizhu Bao, D. Jaksch, and P. A. Markowich, *Numerical solution of the Gross-Pitaevskii equation for Bose-Einstein condensation*, J. Comp. Phys. **187** (2003), 318, .

[52] Weizhu Bao, Shi Jin, and P. A. Markowich, *On time-splitting spectral approximations for the schrödinger equation in the semiclassical regime*, J. Comp. Phys. **175** (2002), 487, .

[53] A. Barchielli, L. Lanz, and G. M. Prosperi, *A model for the macroscopic description and continual observations in quantum mechanics*, Il Nuovo Cimento **72** (1982), 79.

[54] J. Bardeen, L. N. Cooper, and J. R. Schrieffer, *Microscopic theory of superconductivity*, Phys. Rev. **106** (1957), L162, .

[55] A. Barenco, C. H. Bennett, R. Cleve, D. P. DiVincenzo, N. Margolus, P. Shor, T. Sleator, J. A. Smolin, and H. Weinfurter, *Elementary gates for quantum computation*, Phys. Rev. A **52** (1995), 3457.

[56] J. A. Barnes, L. S. Cutler, and et al., *Characterization of frequency stability*, IEEE Trans. Instr. Meas. **20** (1971), 105.

[57] S. M. Barnett and S. J. D. Phoenix, *Information theory, squeezing and quantum correlations*, Phys. Rev. A **44** (1991), 535, .

[58] G. Barontini, C. Weber, F. Rabatti, J. Catani, G. Thalhammer, M. Inguscio, and F. Minardi, *Observation of heteronuclear atomic Efimov resonances*, ePrints **09014584** (2009), .

[59] G. R. Barwood and et al., *Frequency measurements on optically narrowed rb-stabilized laser diodes at 780 nm and 795 nm*, Appl. Phys. B **53** (1991), 142, .

[60] K. Baumann, C. Guerlin, F. Brennecke, and T. Esslinger, *Dicke quantum phase transition with a superfluid gas in an optical cavity*, Nature **464** (2010), 1301, DOI.

[61] G. Baym and C. J. Pethick, *Ground-state properties of magnetically trapped Bose-condensed rubidium gas*, Phys. Rev. Lett. **76** (1996), 6, .

[62] Q. Beaufils, G. Tackmann, X. Wang, B. Pelle, S. Pelisson, P. Wolf, and F. Pereira dos Santos, *Laser controlled tunneling in a vertical optical lattice*, Phys. Rev. Lett. **106** (2011), 213002, DOI.

[63] A. Beige and G. C. Hegerfeldt, *Projection postulate and atomic quantum zeno effect*, Phys. Rev. A **53** (1996), 53.

[64] H. C. W. Beijerinck, E. D. J. Vredenbregt, R. J. W. Stas, M. R. Doery, and J. G. C. Tempelaars, *Prospects for Bose-Einstein condensation of metastable neon atoms*, Phys. Rev. A **61** (2000).

[65] J. S. Bell, *On the Einstein-podolsky-rosen paradox*, Physics Physique Fizika **1** (1964), 195, DOI.

[66] C. M. Bender, S. Boettcher, and P. N. Meisinger, *Pt-symmetric quantum mechanics*, J. Math. Phys. **40** (1999), 2201, .

[67] C. M. Bender, Brody, and P. N. Jones, *Complex extension of quantum mechanics*, Phys. Rev. Lett. **89** (2002), 270401, .

[68] H. Bender, Ph.W. Courteille, C. Marzok, C. Zimmermann, and S. Slama, *Direct measurement of intermediate-range casimir-polder potentials*, Phys. Rev. Lett. **104** (2010), 083201.

[69] C. H. Bennett, *Quantum information and quantum computation*, Phys. Today Okt 1995 (1995), 25.

[70] Sh. Bennetts, G. D. McDonald, K. S. Hardman, J. E. Debs, C. C. N. Kuhn, J. D. Close, and N. P. Robins, *External cavity diode lasers with 5khz and 200nm tuning range at 1.55 um and for linewidth measurement*, Opt. Exp. **22** (2014), 10642.

[71] M. J. Berg, C. M. Sorensen, and A. Chakrabarti, *Patterns in mie scattering: evolution when normalized by the Rayleigh cross section*, Appl. Opt. **44** (2005), 7487, .

[72] T. Bergeman, G. Erez, and H. J. Metcalf, *Magneto-static trapping fields for neutral atoms*, Phys. Rev. A **35** (1987), 1535, DOI.

[73] T. Bergeman, A. J. Kerman, J. Sage, S. Sainis, and D. DeMille, *Prospects for production of ultracold $x^1\sigma^+$ rbcs molecules*, Eur. Phys. J. D **31** (2004), 179, .

[74] T. Bergeman, M. G. Moore, and M. Olshanii, *Atom-atom scattering under cylindrical harmonic confinement: Numerical and analytic studies of the confinement induced resonance*, Phys. Rev. Lett. **91** (2003), 163201.

[75] J. Bergquist, R. G. Hulet, W. M. Itano, and D. J. Wineland, *Observation of quantum jumps in a single atom*, Phys. Rev. Lett. **57** (1986), 1699.

[76] S. Bernet, M. K. Oberthaler, R. Abfalterer, J. Schmiedmayer, and A. Zeilinger, *Coherent frequency shift of atomic matter waves*, Phys. Rev. Lett. **77** (1996), 5160.

[77] M. V. Berry, *Quantal phase factors accompanying adiabatic changes*, Proc. R. Soc. Lond. A **392** (1984), 45, DOI.

[78] M. J. Bhaseen, J. Mayoh, B. D. Simons, and J. Keeling, *Dynamics of nonequilibrium Dicke models*, Phys. Rev. A **85** (2012), 013817, DOI.

[79] T. Bienaimé, R. Bachelard, J. Chabé, M. T. Rouabah, L. Bellando, Ph. W. Courteille, N. Piovella, and R. Kaiser, *Interplay between radiation pressure force and scattered light intensity in the cooperative scattering by cold atoms*, J. Mod. Opt. **61** (2014), 18.

[80] T. Bienaimé, S. Bux, E. Lucioni, Ph. W. Courteille, N. Piovella, and R. Kaiser, *Observation of cooperative radiation pressure in presence of disorder*, Phys. Rev. Lett. **104** (2010), 183602.

[81] M. Bindhani, B. K. Behera, and P. K. Panigrahi, *Quantum simulation of Jaynes-Cummings model on ibm q-system*, (2020), .

[82] G. Birkl, M. Gatzke, I. H. Deutsch, S. L. Rolston, and W. D. Phillips, *Bragg sccattering from atoms in optical lattices*, Phys. Rev. Lett. **75** (1995), 2823, .

[83] G. C. Bjorklund, *Frequency-modulation spectroscopy: A new method for measuring weak absorptions and dispersions*, Opt. Lett. **5** (1980), 15.

[84] P. B. Blakie and R. J. Ballagh, *Mean-field treatment of Bragg scattering from a Bose-Einstein condensate*, J. Phys. B **33** (2000), 3961, .

[85] M. Blatt, K.W. Boër, and W. Brandt, *Bose-Einstein condensation of excitons*, Phys. Rev. **126** (1962), 1691.

[86] R. Blatt, *über den einfluß der atombewegung auf die messung atomarer resonanzen*, Habilitation Hamburg (1987).

[87] R. Blatt, P. Zoller, G. Holzmüller, and I. Siemers, *Brownian motion of a parametric oscillator: A model for ion confinement in radio frequency traps*, Z. Phys. D **4** (1986), 121.

[88] G. Blatter, *Quantenmechanik*, http://www.itp.phys.ethz.ch/research/condmat/vortex/lectur
Zürich, 2005.

[89] I. Bloch, *Ultracold quantum gases in optical lattices*, Nature Physics **1** (2005), 23, .

[90] I. Bloch, T. W. Hänsch, and T. Esslinger, *Atom laser with a cw output coupler*, Phys. Rev. Lett. **82** (1999), 3008, .

[91] I. Bloch, Th. W. Hänsch, and T. Esslinger, *Measurement of the spatial coherence of a trapped Bose-gas at the phase transition*, Nature **403** (2000), 166, .

[92] I. Bloch, M. Köhl, M. Greiner, T. W. Hänsch, and T. Esslinger, *Optics with an atom laser beam*, Phys. Rev. Lett. **87** (2001), 030401, .

[93] C. A. Blockley, D. F. Walls, and H. Risken, *Quantum collapses and revivals in a quantized trap*, Europhys. Lett. **17** (1992), 509.

[94] J. L. Bohn and P. S. Julienne, *Prospects for influencing scattering lengths with far-off-resonance light*, Phys. Rev. A **56** (1997), 1486, .

[95] J. G. Bohnet, K. C. Cox, M. A. Norcia, J. M. Weiner, Z. Chen, and J. K. Thompson, *Reduced spin measurement back-action for a phase sensitivity ten times beyond the standard quantum limit*, Nature Phot. **8** (2014), 731, DOI.

[96] C. F. Bohren and D. R. Huffman, *Absorption and scattering of light by small particles*, John Wiley and Sons, New York, 1981, ISBN.

[97] J. J. Bollinger, W. M. Itano, D. J. Wineland, and D.J.Heinzen, *Optimal frequency measurements with maximally correlated states*, Phys. Rev. A **54** (1996), 4649, .

[98] K. Bongs, S. Burger, G. Birkl, K. Sengstock, W. Ertmer, K. Rzazewski, A. Sanpera, and M. Lewenstein, *Coherent evolution of bouncing Bose-Einstein condensates*, Phys. Rev. Lett. **83** (1999), 3577, .

[99] K. Bongs, S. Burger, S. Dettmer, J. Arlt, W. Ertmer, and K. Sengstock, *A waveguide for Bose-Einstein condensates*, Phys. Rev. Lett. **63** (2000), 031602, .

[100] R. Bonifacio, F. S. Cataliotti, M. Cola, L. Fallani, C. Fort, N. Piovella, and M. Inguscio, *Superradiant light scattering from a moving Bose-Einstein condensate*, Opt. Comm. **233** (2004), 155, .

[101] R. Bonifacio and L. De Salvo, *Collective atomic recoil laser (carl) optical gain without inversion by collective atomic recoil and self-bunching of two-level atoms*, Nucl. Instrum. Methods A **341** (1994), 360, DOI.

[102] R. Bonifacio, L. De Salvo, and W. A. Barletta, *Relativistic theory of the collective atomic recoil laser*, Nucl. Instr. Methods in Phys. Research A **384** (1997), 337, .

[103] R. Bonifacio and Ph. Verkerk, Opt. Commun. **124** (1996), 469, .

[104] Ch. J. Bordé, *Atom interferometry with internal state labeling*, Phys. Lett. A **140** (1989), 10, .

[105] ———, *Amplification of atomic fields by stimulated emission of atoms*, Phys. Lett. A **204** (1995), 217, .

[106] M. Born, 1980, ISBN.

[107] Satyendra N. Bose, *Plancks Gesetz und Lichtquantenhypothese*, Z. Phys. **26** (1924), 178.

[108] T. Bourdel, J. Cubizolles, L. Khaykovich, K. M. F. Magalhaes, S. J. J. M. F. Kokkelmans, G. V. Shlyapnikov, and C. Salomon, *Measurement of the interaction energy near a Feshbach resonance in a ^{6}li Fermi gas*, Phys. Rev. Lett. **91** (2003), 020402, .

[109] N. Boutassetta, A. R. Allouche, and M. Aubert-Frécon, *Theoretical study of the electronic structure of the Sr2 molecule*, Phys. Rev. A **53** (1996), 3845, DOI.

[110] Ph. Bouyer and M. A. Kasevich, *Heisenberg-limited spectroscopy with degenerate Bose-Einstein gases*, Phys. Rev. A **56** (1997), R1083, DOI.

[111] E. Braaten and H.-W. Hammer, *Universality in few-body systems with large negative scattering length*, Phys. Rep. **428** (2006), 259, .

[112] C. C. Bradley, C. A. Sackett, and R. G. Hulet, *Analysis of in situ images of Bose-Einstein condensates of lithium*, Phys. Rev. A **55** (1997), 3951, .

[113] ———, *Bose-Einstein condensation of lithium: Observation of limited condensate number*, Phys. Rev. Lett. **78** (1997), 985, .

[114] C. C. Bradley, C. A. Sackett, J. J. Tolett, and R. G. Hulet, *Evidence of Bose-Einstein condensation in an atomic gas with attractive interactions*, Phys. Rev. Lett. **75** (1995), 1687, .

[115] S. L. Braunstein and C. M. Caves, *Statistical distance and the geometry of quantum states*, Phys. Rev. Lett. **72** (1994), 3439, DOI.

[116] S. L. Braunstein, C. M. Caves, and G. J. Milburn, *Generalized uncertainty relations: Theory, examples, and lorentz invariance*, Annals Phys. **247** (1996), 135, DOI.

[117] F. Brennecke, T. Donner, S. Ritter, T. Bourdel, M. Köhl, and T. Esslinger, *Cavity QED with a Bose-Einstein condensate*, Nature **250** (2007), 268, .

[118] G. K. Brennen, C. M. Caves, P. S. Jessen, and I. H. Deutsch, *Quantum logic gates in optical lattices*, Phys. Rev. Lett. **82** (1999), 1060, .

[119] Léon Brillouin, *La mécanique ondulatoire de schrödinger: une méthode générale de resolution par approximations successives*, Comptes Rendus de l'Academie des Sciences **183** (1926), 24.

[120] I. N. Bronstein and K. A. Semandjajew, *Taschenbuch der mathematik*, Thun und Franfurt, Main, 1978, ISBN.

[121] M. Brune, S. Haroche, V. Lefevre, J. M. Raimond, and N. Zagury, *Quantum nondemolition measurement of small atom numbers by Rydberg atom phase-sensitive detection*, Phys. Rev. Lett. **65** (1990), 0976, .

[122] A. Brunello, F. Dalfovo, L. Pitaevskii, S. Stringari, and F. Zambelli, *Momentum transferred to a trapped Bose-Einstein condensate by stimulated light scattering*, **64** (2001), 063614, .

[123] C. J. Buczek, R. J. Freiberg, and M. L. Skolnic, *Laser injection locking*, Proc. IEEE **61** (1973), 1411.

[124] S. Burger, K. Bongs, S. Dettmer, W. Ertmer, K. Sengstock, A. Sanpera, G. V. Shlyapnikov, and M. Lewenstein, *Dark solitons in Bose-Einstein condensates*, Phys. Rev. Lett. **83** (1999), 5198, .

[125] J. P. Jr. Burke, *Theoretical investigation of cold slkali atom collisions*, PhD thesis (1999).

[126] J. P. Jr. Burke, J. L. Bohn, B. D. Esry, and C. H. Greene, *Prospects of mixed-isotope Bose-Einstein condensates in rubidium*, Phys. Rev. Lett. **80** (1998), 2097, .

[127] K. Burnett, *An intimate gathering of bosons*, Science **267** (1996), 0182, .

[128] E. A. Burt, R. W. Ghrist, C. J. Myatt, M. J. Holland, E. A. Cornell, and C. E. Wieman, *Coherence, correlations, and collisions: What one learns about Bose-Einstein condensates from their decay*, Phys. Rev. Lett. **79** (1997), 337, .

[129] Th. Busch and J. R. Anglin, *Wave-function monopoles in Bose-Einstein condensates*, Phys. Rev. A **60** (1999), 2669, .

[130] D. A. Butts and D. S. Rokhsar, *Trapped Fermi gases*, Phys. Rev. A **55** (1997), 4346, DOI.

[131] _____, *Predicted signatures of rotating Bose-Einstein condensates*, Nature **397** (1999), 327, .

[132] S. Bux, Ch. Gnahm, R. A. Maier, C. Zimmermann, and Ph. W. Courteille, *Cavity-controlled matter wave superradiance at the recoil limit*, Phys. Rev. Lett. **106** (2011), 203601.

[133] S. Bux, G. Krenz, S. Slama, C. Zimmermann, and Ph.W. Courteille, *Ultra-cold atoms in an optical cavity: Two-mode laser locking avoiding radiation pressure*, Appl. Phys. B **89** (2007), 181.

[134] S. Bux, E. Lucioni, H. Bender, T. Bienaimé, K. Lauber, C. Stehle, C. Zimmermann, S. Slama, Ph. W. Courteille, N. Piovella, and R. Kaiser, *Cooperative scattering by cold atoms*, J. Mod. Opt. **57** (2010), 1841.

[135] A. Bychek, Ch. Hotter, D. Plankensteiner, and H. Ritsch, *Superradiant lasing in inhomogeneously broadened ensembles with spatially varying coupling*, ePrints (2021), arXiv2105.11023, DOI.

[136] K. E. Cahill and R. J. Glauber, *Density operators and quasiprobability distributions*, Phys. Rev. **177** (1969), 1882.

[137] G. Camy, Ch. J. Bordé, and M. Ducloy, *Heterodyne saturation spectroscopy through frequency modulation the saturating beam*, Opt. Comm. **41** (1982), 325, .

[138] G. G. Carlo, G. Benenti, and D. L. Shepelyansky, *Dissipative quantum chaos: Transition from wave packet collapse to explosion*, Phys. Rev. Lett. **95** (2005), 164101, .

[139] H. J. Carmichael, *Analytical and numerical results for the steady state in cooperative resonance fluorescence*, J. Phys. B **13** (1980), 3551, DOI.

[140] R. Carminati, A. Cazé, D. Cao, F. Peragut, V. Krachmalnicoff, R. Pierrat, and Y. De Wilde, *Electromagnetic density of states in complex plasmonic systems*, Surf. Sci. Rep. **70** (2015), 1, DOI.

[141] L. D. Carr and et al., *Cold and ultracold molecules: science, technology and applications*, New J. Phys. **11** (2009), 055009, .

[142] Y. Castin and R. Dum, *Bose-Einstein condensates in time dependent traps*, Phys. Rev. Lett. **77** (1996), 5315, .

[143] C. M. Caves and G. J. Milburn, *Quantum mechanics of measurements distributed in time II*, Phys. Rev. A **36** (1987), 5543.

[144] J. Chabé, G. Lemarie, B. Grémaud, D. Delande, P. Szriftgiser, and J. C. Garreau, *Experimental observation of the anderson metal-insulator transition with atomic matter waves*, Phys. Rev. Lett. **101** (2008), 255702, .

[145] L. L. Chase, N. Peyghambarian, G. Grynberg, and A. Mysyrowicz, *Evidence for Bose-Einstein condensation of biexcitons in CuCl*, Phys. Rev. Lett. **42** (1979), 1231.

[146] W. Chen, D. Meiser, and P. Meystre, *Cavity QED determination of atomic number statistics in optical lattices*, Phys. Rev. A **75** (2007), 23812, DOI.

[147] F. Chevy, K. Madison, and J. Dalibard, *Measurement of the angular momentum of a rotating Bose-Einstein condensate*, Phys. Rev. Lett. **85** (2000), 2223, .

[148] R. Y. Chiao and J. Boyce, *Bogoliubov dispersion relation and the possibility of superfluidity for weakly-interacting photons in a 2d photon fluid*, Phys. Rev. A (1999), quant-ph/9905001.

[149] A. P. Chikkatur, A. Görlitz, D. M. Stamper-Kurn, S. Inouye, S. Gupta, and W. Ketterle, *Suppression and enhancement of impurity scattering in a Bose-Einstein condensate*, Phys. Rev. Lett. **85** (2000), 483, .

[150] J. S. Choi and J. C. Howell, *Paraxial ray optics cloaking*, Opt. Exp. **22** (2014), 29465, DOI.

[151] Steve Chu, J. E. Bjorkholm, A. Ashkin, and A. Cable, *Experimental observation of optically trapped atoms*, Phys. Rev. Lett. **57** (1986), 314.

[152] A. Cipris, *Long-lived collective modes of light in cold atoms: Experimental and numerical studies on subradiance and anderson localization*, Ph.D. thesis, Université Côte d'Azur, Nice, 2022.

[153] A. Cipris, R. Bachelard, R. Kaiser, and W. Guerin, *van der waals dephasing for Dicke subradiance in cold atomic clouds*, Phys. Rev. A **103** (2021), 033714.

[154] A. Cipris, N. A. Moreira, T. S. do Espirito Santo, P. Weiss, C. J. Villas-Boas, R. Kaiser, W. Guerin, and R. Bachelard, *Subradiance with saturated atoms: Population enhancement of the long-lived states*, Phys. Rev. Lett. **126** (2021), 103604, DOI.

[155] J. I. Cirac, R. Blatt, P. Zoller, and W. D. Phillips, *Laser cooling of trapped ions in a standing wave*, Phys. Rev. A **46** (1992), 2668, .

[156] J. I. Cirac, M. Lewenstein, K. Molmer, and P. Zoller, *Quantum superpositions states of Bose-Einstein condensates*, Phys. Rev. A **57** (1998), 1208.

[157] J. I. Cirac, M. Lewenstein, and P. Zoller, *Quantum dynamics of a laser-cooled ideal gas*, Phys. Rev. A **50** (1994), 3409, .

[158] J. I. Cirac and P. Zoller, *Decoherence, continuous observation, and quantum computing: A cavity QED model*, Phys. Rev. Lett. **75** (1995), 3788, .

[159] ———, *Quantum computation with cold trapped atoms*, Phys. Rev. Lett. **74** (1995), 4091, DOI.

[160] N. V. Cohan, D. Pugh, and R. H. Tredgold, *Band structure of diamond*, Proc. Phys. Soc. **82** (1963), 65, .

[161] E. Cohen, H. Larocque, F. Bouchard, F. Nejadsattari, Y. Gefen, and E. Karimi, *Geometric phase from aharonov-bohm to pancharatnam-berry and beyond*, Nature Rev. **1** (2019), 437, DOI.

[162] E. R. Cohen, *Uncertainty and error in physical measurements*, Rendiconti della Scuola Intern. di Fisica 'Enrico Fermi' **CX** (1992), 11.

[163] C. Cohen-Tannoudji, B. Diu, and F. Lao, *Quantum mechanics*, 1, vol. 1 & 2, 1977, ISBN.

[164] C. Cohen-Tannoudji, J. Dupont-Roc, and G. Grynberg, *Photons and atoms: Introduction to quantum electrodynamics*, John Wiley and Sons New York, 1992, ISBN.

[165] M. M. Cola, *Collective atomic recoil in ultracold atoms: Advances and applications*, Dissertation Milano (2003).

[166] M. M. Cola, M. G. A. Paris, and N. Piovella, *Robust generation of entanglement in Bose-Einstein condensates by collective atomic recoil*, Phys. Rev. A **70** (2004), 43809, DOI.

[167] M. M. Cola, M. G. A. Paris, N. Piovella, and R. Bonifacio, *A condensate in a lossy cavity: Collective atomic recoil and generation of entanglement*, J. Mod. Opt. **51** (2004), 1043, DOI.

[168] _____, *Entanglement in a Bose-Einstein condensate by collective atomic recoil*, J. Phys. B **37** (2004), S187, DOI.

[169] M. J. Collett and C. W. Gardiner, *Squeezing of intracavity and travelling-wave light fields produced in parametric amplification*, Phys. Rev. A **30** (1984), 1386, .

[170] Y. Colombe, T. Steinmetz, G. Dubois, F. Linke, D. Hunger, and J. Reichel, *Strong atom field coupling for bose Einstein condensates in an optical cavity on a chip*, Nature **250** (2005), 272, .

[171] R. Combescot, S. Giorgini, and S. Stringari, *Molecular signatures in the structure factor of an interacting Fermi gas*, Europhys. Lett. **75** (2006), 695, .

[172] E. A. Cornell, *Very cold indeed: The nanokelvin physics of Bose-Einstein condensation*, J. Res. Natl. Inst. Stand. Tech. **101** (1996), 419.

[173] S. L. Cornish, N. R. Claussen, J. L. Roberts, E. A. Cornell, and C. E. Wieman, *Stable 85rb Bose-Einstein condensates with widely tunable interactions*, Phys. Rev. Lett. **85** (2000), 1795, .

[174] R. Côté, B. Segev, and M. G. Raizen, *Retardation effects on quantum reflection from an evanescent-wave atomic mirror*, Phys. Rev. A **58** (1998), 3999, .

[175] Ph. W. Courteille, V. S. Bagnato, and V. I. Yukalov, *Bose-Einstein condensation of trapped atomic gases*, Laser Phys. **11** (2001), 659–800.

[176] Ph. W. Courteille, S. Bux, E. Lucioni, K. Lauber, T. Bienaimé, R. Kaiser, and N. Piovella, *Modification of radiation pressure due to cooperative scattering of light*, Euro. Phys. J. D **58** (2010), 69.

[177] Ph. W. Courteille, B. Deh, J. Fortágh, A. Günther, S. Kraft, C. Marzok, S. Slama, and C. Zimmermann, *Highly versatile atomic micro traps generated by multifrequency magnetic field modulation*, J. Phys. B **39** (2006), 1055.

[178] Ph. W. Courteille, R. S. Freeland, D. J. Heinzen, F. A. van Abeelen, and B. J. Verhaar, *Observation of a Feshbach resonance in cold atom scattering*, Phys. Rev. Lett. **81** (1998), 69.

[179] Ph. W. Courteille, D. J. Han, R. H. Wynar, and D. J. Heinzen, *New observation of Bose-Einstein condensation of ^{87}rb atoms in a magnetic top trap*, Proc. of SPIE **3270** (1998), 116.

[180] Ph. W. Courteille, D. Rivero, G. H. de FrançÃ§a, C. A. Pessoa Jr, A. Cipris, M. N´ unez Portela, R. C. Teixeira, and S. Slama, *Photonic bands and normal mode splitting in optical lattices interacting with cavities*, Phys. Rev. A **111** (2024), 013310, DOI.

[181] J.-Y. Courtois, G. Grynberg, B. Lounis, and P. Verkerk, *Recoil-induced resonances in cesium: An atomic analog to the free electron laser*, Phys. Rev. Lett. **72** (1994), 3017, .

[182] J. M. Cowley, *Diffraction physics*, 1981, ISBN.

[183] K. C. Cox, G. P. Greve, J. M. Weiner, and J. K. Thompson, *Deterministic squeezed states with collective measurements and feedback*, Phys. Rev. Lett. **116** (2016), 093602, DOI.

[184] J. Cubizolles, T. Bourdel, S. J. J. M. F. Kokkelmans, G. V. Shlyapnikov, and C. Salomon, *Production of long-lived ultracold li_2 molecules from a Fermi gas*, Phys. Rev. Lett. **91** (2003), 240401, .

[185] F. J. P. Cuevas, *Aspects of hybrid confinement for a Bose-Einstein condensate: Global pressure and compressibility*, Ph.D. thesis, Universidade de São Paulo, 2013, .

[186] R. Culver, A. Lampis, B. Megyeri, K. Pahwa, L. Mudarikwa, M. Holynski, Ph. W. Courteille, and J. Goldwin, *Collective strong coupling of cold potassium atoms in a ring cavity*, New J. Phys. **18** (2016), 113043.

[187] M. O. Terra Cunha, J. A. Dunningham, and V. Vedral, *Entanglement in single-particle systems*, Proc. R. Soc. **463** (2007), 2277, DOI.

[188] L. S. Cutler and C.L. Searle, *Some aspects of the theory and measurement of frequency fluctuations in frequency standards*, Proc. of the IEEE **54** (1966), 136.

[189] M. Ben Dahan, E. Peik, Y. Castin, and C. Salomon, *Bloch oscillations of atoms in an optical potential*, Phys. Rev. Lett. **76** (1996), 4508, .

[190] J. P. Dahl and M. Springborg, *The morse oscillator in position space, momentum space, and phase space*, J. Chem. Phys. **88** (1988), 4535.

[191] F. Dalfovo, S. Giorgini, M. Guillemas, L. Pitaevski, and S. Stringari, *Collective and single particle excitations of a trapped Bose-Einstein condensate*, Phys. Rev. A **56** (1997), 3840, .

[192] F. Dalfovo, S. Giorgini, L. P. Pitaevskii, and S. Stringari, *Theory of Bose-condensation in trapped gases*, Rev. Mod. Phys. **71** (1999), 463, cond-mat/9806038.

[193] J. Dalibard, *Optical traps and optical lattices*, 2013, ⊙Lecture.

[194] J. Dalibard, Y. Castin, and K. Molmer, *Wave-function approach to dissipative processes in quantum optics*, Phys. Rev. Lett. **68** (1992), 580, DOI.

[195] J. Dalibard and C. Cohen-Tannoudji, *Dressed-atom approach to atomic motion in laser light: The dipole force revisited*, J. Opt. Soc. Am. B **2** (1985), 1707.

[196] ———, *Laser cooling below the doppler limit by polarization gradients: Simple theoretical studies*, J. Opt. Soc. Am. B **6** (1989), 2023.

[197] D. A. R. Dalvit, J. Dziarmaga, and W. H. Zurek, *Decoherence in Bose-Einstein condensates: Towards bigger and better schroedinger cats*, Phys. Rev. A **62** (2000), 13607, .

[198] W. B. Davenport and W. L. Root, *An introduction to the theory of random signals and noise*, 1958, ISBN.

[199] N. Davidson, H. J. Lee, C. S. Adams, M. Kasevich, and S. Chu, *Long atomic coherence times in an optical dipole trap*, Phys. Rev. Lett. **74** (1995).

[200] J. Davis, M. Kumari, R. B. Mann, and S. Ghose, *Wigner negativity in spin- j systems*, Phys. Rev. Res. **3** (2021), 033134, DOI.

[201] K. B. Davis, M.-O. Mewes, M. R. Andrews, N. J. van Druten, D. S. Durfee, D.M. Kurn, and W. Ketterle, *Bose-Einstein condensation in an gas of sodium atoms*, Phys. Rev. Lett. **75** (1995), 3969, .

[202] K. B. Davis, M.-O. Mewes, M. A. Joffe, M. R. Andrews, and W. Ketterle, *Evaporative cooling of sodium atoms*, Phys. Rev. Lett. **74** (1995), 5202, .

[203] K. B. Davis, M.-O. Mewes, and W. Ketterle, *An analytical model for evaporative cooling of atoms*, Appl. Phys. B **60** (1995), 155, .

[204] Y. N. Martinez de Escobar, P. G. Mickelson, P. Pellegrini, S. B. Nagel, A. Traverso, M. Yan, R. Côté, and T. C. Killian, *Two-photon photoassociative spectroscopy of ultracold 88sr*, Phys. Rev. A **78** (2008), 062708, DOI.

[205] S. R. de Groot, G. J. Hooyman, and C. A. Ten Deldam, Proc. R. Soc. Lond. A **203** (1950), 266.

[206] F. A. de Oliveira, M. S. Kim, and P. L. Knight, *Properties of displaced number states*, Phys. Rev. A **41** (1990), 2645, .

[207] K. Debnath, Y. Zhang, and K. Mølmer, *Lasing in the superradiant crossover regime*, Phys. Rev. A **98** (2018), 063837, DOI.

[208] M. Defrise, D. W. Townsend, and R. Clack, *Three-dimensional image reconstruction from complete projections*, Phys. Med. Biol. **34** (1989), 573, DOI.

[209] C. L. Degen, F. Reinhard, and P. Cappellaro, *Quantum sensing*, Rev. Mod. Phys. **89** (2017), 035002, DOI.

[210] B. Deh, C. Marzok, S. Slama, C. Zimmermann, and Ph. W. Courteille, *Bragg spectroscopy and Ramsey interferometry with an ultracold Fermi gas*, Appl. Phys. B **97** (2009), 387, DOI.

[211] B. Deh, C. Marzok, C. Zimmermann, and Ph. W. Courteille, *Feshbach resonances in mixtures of quantum degenerate ^{6}Li and ^{87}Rb gases*, Phys. Rev. A **77** (2008), 010701(R), DOI.

[212] R. DeHoff, *Thermodynamics in material science*, Taylor Francis, 2006, ISBN.

[213] G. Delannoy, S. G. Murdoch, V. Boyer, V. Josse, P. Bouyer, and A. Aspect, *Understanding the production of dual Bose-Einstein condensation with sympathetic cooling*, Phys. Rev. A **63** (2001), 051602, .

[214] B. DeMarco and D. S. Jin, *Onset of fermi-degeneracy in a trapped atomic gas*, Science **285** (1999), 1703, DOI.

[215] B. DeMarco, S. B. Papp, and D. S. Jin, *Pauli blocking of collisions in a quantum degenerate atomic Fermi gas*, Phys. Rev. Lett. **86** (2001), 5409, DOI.

[216] D. DeMille, *Quantum computation with trapped polar molecules*, Phys. Rev. Lett. **88** (2002), 067901, .

[217] D. Demille, *Using molecules to measure nuclear spin-dependent parity violation*, Phys. Rev. Lett. **100** (2008), 023003, .

[218] W. Demtröder, *Laser spectroscopy*, 1988, ISBN.

[219] ———, *Atoms, molecules and photons: An introduction to atomic- molecular- and quantum physics*, Springer, 2006.

[220] L. Deng, E. W. Hagley, J. Denschlag, J. E. Simsarian, M. Edwards, C. W. Clark, K. Helmerson, S. L. Rolston, and W. D. Phillips, *Temporal matter-wave-dispersion talbot effect*, Phys. Rev. Lett. **83** (1999), 5407.

[221] L. Deng, E. W. Hagley, J. Wen, M. Trippenbach, Y. Band, P. S. Julienne, J. E. Simsarian, K. Helmerson, S. L. Rolston, and W. D. Phillips, *Four-wave mixing with matter waves*, Nature **398** (1999), 218, .

[222] J. Denschlag, D. Cassettari, and J. Schmiedmayer, *Guiding neutral atoms with a wire*, Phys. Rev. Lett. **82** (1999), 201.

[223] J. Denschlag, J. E. Simsarian, D. L. Feder, Charles W. Clark, L. A. Collins, J. Cubizolles, L. Deng, E. W. Hagley, K. Helmerson, W. P. Reinhardt, S. L. Rolston, B. I. Schneider, and W. D. Phillips, *Generating solitons by phase engineering of a Bose-Einstein condensate*, Science **287** (2000), 97.

[224] M. T. DePue, C. McCormick, S. L. Winoto, S. Oliver, and D. S. Weiss, *Unity occupation of sites in a 3d optical lattice*, Phys. Rev. Lett. **82** (1999), 2262, DOI.

[225] I. H. Deutsch and P. S. Jessen, *Quantum state control in optical lattices*, Phys. Rev. A **57** (1995), 1972, .

[226] I. H. Deutsch, R. J. C. Spreeuw, S. L. Rolston, and W. D. Phillips, *Photonic band gaps in optical lattices*, Phys. Rev. A **52** (1995), 1394, DOI.

[227] R. G. DeVoe and R. G. Brewer, *Observation and superradiant and subradiant spontaneous emission of two trapped ions*, Phys. Rev. Lett. **76** (1996), 2049, DOI.

[228] P. G. S. Dias, M. Frometa, P. H. N. Magnani, K. R. B. Theophilo, M. Hugbart, Ph. W. Courteille, and R. C. Teixeira, *Mirror-assisted backscattering interferometry to measure the first-order correlation function of the light emitted by quantum scatterers*, Phys. Rev. A **104** (2021), 053716, DOI.

[229] R. H. Dicke, *Coherence in spontaneous radiation processes*, Phys. Rev. **93** (1954), 99, DOI.

[230] F. Diedrich, J.C. Bergquist, W.I. Itano, and D.J. Wineland, *Laser cooling to the zero-point energy of motion*, Phys. Rev. Lett. **62** (1989), 403, .

[231] C. M. Tokarsky Dieguez, L. V. Montanheiro, L. Berbeka Cleto, M. J. C. Bonfim, and C. A. Dartora, *Os fundamentos quânticos da ressonância magnética nuclear*, Rev. Bras. Ens. Fís. **40** (2018), e1310, DOI.

[232] P. A. M. Dirac, *Quantized singularities in the electromagnetic field*, Proc. Roy. Soc. A **133** (1931), 60.

[233] ———, *The cosmological constants*, Nature **139** (1937), 323.

[234] ———, *The principles of quantum mechanics*, Oxford University Press, 4th ed., 1947, ISBN.

[235] R. B. Doak, R. E. Grisenti, D. S. Rehbein, G. Schmahl, J. P. Toennies, and Ch. W"oll, *Towards realization of an atomic de broglie microscope: Helium atoms focussing using fresnel zone plates*, Phys. Rev. Lett. **83** (1999), Atom Optics.

[236] L. Dobrek, M. Gajda, M. Lewenstein, K. Sengstock, G. Birkl, and W. Ertmer, *Optical generation of vortices in trapped Bose-Einstein condensates*, Phys. Rev. A **60** (1999), 3381, .

[237] R. J. Dodd, *Approximate solutions of the nonlinear schrödinger equation for ground and excited states of Bose-Einstein condensates*, J. Res. Natl. Inst. Stand. Tech. **101** (1996), 545.

[238] R. J. Dodd, M. Edwards, and C. W. Clark, *Two-gas description of dilute Bose-Einstein condensates at finite temperature*, J. Phys. B: At. Mol. Opt. Phys. **32** (1999), 4107, DOI.

[239] R. J. Dodd, M. Edwards, C. W. Clark, and K. Burnett, *Collective excitations of Bose-Einstein condensed gases at finite temperatures*, Phys. Rev. A **57** (1998), R32, .

[240] G. Di Domenico, St. Schilt, and P. Thomann, *Simple approach to the relation between laser frequency noise and laser line shape*, Appl. Opt. **49** (2010), 4801, DOI.

[241] P. Domokles, J. M. Raimond, M. Brune, and S. Haroche, Phys. Rev. A **52** (1995), 3554.

[242] P. Domokos and H. Ritsch, *Collective cooling and self-organization of atoms in a cavity*, Phys. Rev. Lett. **89** (2002), 253003, DOI.

[243] R. Donelly and C. Swanson, *Quantum turbulence*, J. Fluid Mech. **173** (1986), 387, .

[244] J. M. Doyle, B. Friederich, J. Kim, and D. Patterson, *Buffer-gas loading of atoms and molecules into a magnetic trap*, Phys. Rev. A **52** (1995), .

[245] R. W. P. Drever, J. L. Hall, F. V. Kowalski, J. Hough, G. M. Ford, A. J. Munley, and H. W. Ward, *Laser phase and frequency stabilization using an optical resonator*, Appl. Phys. B **31** (1983), 97, .

[246] V. Dribinski, A. Ossadtchi, V. A. Mandelshtam, and H. Reislera, *Reconstruction of abel-transformable images: The gaussian basis-set expansion abel transform method*, Rev. Sci. Instrum. **73** (2002), 2634, DOI.

[247] M. Drndic, W. D. Phillips, A. Aspect, and et al., *Properties of microelectromagnet mirrors as reflectors of cold rb atoms*, Phys. Rev. A **60** (1999), 4012, .

[248] P. D. Drummond and H. J. Carmichael, *Volterra cycle and the cooperative fluorescence critical point*, Opt. Commun. **27** (1978), 160, DOI.

[249] M. Ducloy and D. Bloch, *Theory of degenerate four-wave mixing in resonant doppler-broadened media II*, J. Physique **43** (1982), 57.

[250] O. Dulieu and P. S. Julienne, *Coupled channel bound states calculations for alkali dimers using the Fourier grid method*, J. Chem. Phys. **103** (1995), 60, .

[251] R. Dum, A. Sanpera, K.-A. Suominen, M. Brewczyk, M. Kus, K. Rzazewski, and M. Lewenstein, *Wave packet dynamics with Bose-Einstein condensates*, Phys. Rev. Lett. **80** (1998), 3899, .

[252] Ho Trung Dung, L. Knöll, and D.-G. Welsch, *Intermolecular energy transfer in the presence of dispersing and absorbing media*, Phys. Rev. A **65** (2002), 043813, DOI.

[253] W. Dür, G. Vidal, and J. I. Cirac, *Three qubits can be entangled in two inequivalent ways*, Phys. Rev. A **62** (2000), 062314, DOI.

[254] J. H. Eberly, *Emission of one photon in an electric dipole transition of one among n atoms*, J. Phys. B: At. Mol. Opt. Phys. **39** (2006), DOI.

[255] M. Edwards, R. J. Dodd, C. W. Clark, and K. Burnett, *Zero-temperature, mean-field theory of atomic Bose-Einstein condensates*, J. Res. Natl. Inst. Stand. Tech. **101** (1996), 553.

[256] M. Edwards, P. A. Ruprecht, K. Burnett, R. J. Dodd, and C. W. Clark, *Collective excitations of atomic Bose-Einstein condensates*, Phys. Rev. Lett. **77** (1996), 1671, .

[257] V. Efimov, *Energy levels arising from resonant two-body forces in a three-body system*, Phys. Lett. B **33** (1970), 563, .

[258] V. S. Egorov, V. N. Lebedev, I. B. Mekhov, P. V. Moroshkin, I. A. Chekhonin, and S. N. Bagayev, *Coherent interaction of laser pulses in a resonant optically dense extended medium under the regime of strong field-matter coupling*, Phys. Rev. A **69** (2004), 033804, .

[259] A. Einstein, *Quantentheorie des einatomigen idealen gases*, S. B. Kgl. Preuss. Akad. Wiss. **35** (1924).

[260] A. Einstein, B. Podolsky, and N. Rosen, *Can quantum-mechnical description of physical reality be considered complete?*, Phys. Rev. **47** (1935), 777, .

[261] J. Eiselt and H. Risken, *Quasiprobability distributions for the Jaynes-Cummings model with cavity damping*, Phys. Rev. A **43** (1991), 346.

[262] A. C. Elitzur and L. Vaidman, *Quantum mechanical interaction-free measurements*, Found. Phys. **23** (1993), 987, DOI.

[263] D. S. Elliott, Rajarshi Roy, and S. J. Smith, *Extracavity laser bandshape and bandwidth modification*, Phys. Rev. A **26** (1982), 12, .

[264] Th. Elsässer, B. Nagorny, and A. Hemmerich, *Collective sideband cooling in an optical ring cavity*, Phys. Rev. A **67** (2003), 051401(R), .

[265] C. Emary and T. Brandes, *Quantum chaos triggered by precursors of a quantum phase transition: The Dicke model*, Phys. Rev. Lett. **90** (2003), 044101, DOI.

[266] K. Enomoto, M. Kitagawa, K. Kasa, S. Tojo, and Y. Takahashi, *Determination of the s-wave scattering length and the c6 van der waals coefficient of ^{174}yb via photoassociation spectroscopy*, Phys. Rev. Lett. **98** (2007), 203201, DOI.

[267] J. R. Ensher, D. S. Jin, M. R. Matthews, C. E. Wieman, and E. A. Cornell, *Bose-Einstein condensation in a dilute gas: Measurement of energy and ground-state occupation*, Phys. Rev. Lett. **77** (1996), 4984, .

[268] U. Ernst, A. Marte, F. Schreck, J. Schuster, and G. Rempe, *Bose-Einstein condensation in a pure ioffe-pritchard field configuration*, Europhys. Lett. **41** (1997), 1, .

[269] W. Ertmer, R. Blatt, J. L. Hall, and M. Zhu, *Laser manipulation of atomic beam velocities: Demonstration of stopped atoms and velocity reversal*, Phys. Rev. Lett. **54** (1985), 996.

[270] B. M. Escher, R. L. de Matos Filho, and L. Davidovich, *General framework for estimating the ultimate precision limit in noisy quantum-enhanced metrology*, Nature Phys. **7** (2011), 406, DOI.

[271] B. D. Esry, Ch. H. Greene, and H. Suno, *Threshold laws for three-body recombination*, Phys. Rev. A **65** (2001), 10705(R), .

[272] T. Esslinger, I. Bloch, and T. W. Hänsch, *Bose-Einstein condensation in a quadrupople-ioffe configuration trap*, Phys. Rev. A **58** (1998), R2664.

[273] L. E. Estes, Th. H. Keil, and L. M. Narducci, *Quantum-mechanical description of two coupled harmonic oscillators*, Phys. Rev. **175** (1968), 286, DOI.

[274] P. O. Fedichev, Yu Kagan, G. V. Shlyapnokov, and J. T. M. Walraven, *Influence of nearly resonant light on the scattering length in low-temperature atomic gases*, Phys. Rev. Lett. **77** (1996), 2913, .

[275] G. Ferioli, I. Ferrier-Barbut, and A. Browaeys, *Emergence of second-order coherence in the superradiant emission from a free-space atomic ensemble*, ePrints (2024), arXiv2410.08652, DOI.

[276] E. Fermi, *Motion of neutrons in hydrogenous substances*, Ricerca Scientifica **7** (1936), 13.

[277] H. Feshbach, *Unified theory of nuclear reactions*, Annals of Physics **5** (1958), 357.

[278] R. P. Feynman, *Application of quantum mechanics to liquid helium*, Prog. Low Temp. Phys. **1** (1955), 17.

[279] E. Fischer, *Dreidimensionale stabilisierung von ladungsträger in einem vierpolfeld*, Z. Phys. **156** (1959), 1.

[280] W. Fischer and I. Lieb, *Funktionentheorie*, Vieweg Studium, Aufbaukurs Mathematik, 1983.

[281] M. P. A. Fisher, P. B. Weichman, G. Grinstein, and D. S. Fisher, *Boson localization and the superfluid-insulator transition*, Phys. Rev. B **40** (1989), 546.

[282] P. T. Fisk, M. A. Lawn, and C. Coles, *Laser cooling of 171yb+ ions a linear paul trap*, Appl. Phys. B **57** (1993), 287.

[283] M. Fliesser and R. Graham, *Hidden symmetry of collisionless sound of bose condensates in anisotropic traps*, Phys. Rev. A **59** (1999), R27, .

[284] H. M. Flórez, *Espectroscopia de correlação em condição de transparência eletromagneticamente induzida: regime dinâmico e ressonâncias das bandas laterais em átomos frios*, Ph.D. thesis, Universidade de Sã Paulo, 2016.

[285] DOIV. S. Bagnato and D. Kleppner, *Bose-Einstein condensation in low-dimensional traps*, Phys. Rev. A **44** (1991), 7439, .

[286] DOIR. Bachelard and N. Piovella and Ph. W. Courteille, *Cooperative scattering and radiation pressure force in dense atomic clouds*, Phys. Rev. A **84** (2011), 013821.

[287] O. Föllinger, *Regelungstechnik*, 1985.

[288] ———, *Regelungstechnik: Einführung in die methoden und ihre anwendung*, Hütig, 2008.

[289] C. J. Foot, H. Wu, E. Arimondo, and G. Morigi, *Optical elements for interferometry of atoms with j-greater-than-1*, J. de Physique **4** (1993), 1913.

[290] R. S. Freeland, *Photoassociation spectroscopy of ultracold and Bose-condensed atomic gases*, PhD thesis (2001).

[291] D. G. Fried, T. C. Killian, L. Willmann, D. Landhuis, S. C. Moss, D. Kleppner, and T. J. Greytak, *Bose-Einstein condensation of atomic hydrogen*, Phys. Rev. Lett. **81** (1998), 3811, .

[292] R. Friedberg and J. T. Manassah, *Effects of including the counterrotating term and virtual photons on the eigenfunctions and eigenvalues of a scalar photon collective emission theory*, Phys. Lett. A **372** (2008), 2514, DOI.

[293] _____, *Reply to: Comment on: Effects of including the counterrotating term and virtual photons on the eigenfunctions and eigenvalues of a scalar photon collective emission theory; phys. lett. a 372 (2008) 2514; phys. lett. a 372 (2008) 5732*, Phys. Lett. A **372** (2008), 5734, DOI.

[294] H. Friedrich, *Theoretische atomphysik*, Springer, 1990, ISBN.

[295] J. Fuchs, G. J. Duffy, G. Veeravalli, P. Dyke, M. Bartenstein, C. J. Vale, P. Hannaford, and W. J. Rowlands, *Molecular Bose-Einstein condensation in a versatile low power crossed dipole trap*, J. Phys. B **40** (2007), 4109, .

[296] J. Fuchs, C. Ticknor, P. Dyke, G. Veeravalli, E. Kuhnle, W. Rowlands, P. Hannaford, and C. J. Vale, *Binding energies of 6 li p-wave Feshbach molecules*, Phys. Rev. A **77** (2008), 053616, .

[297] S. Fuchs and S. Y. Buhmann, *Purcell-dicke effect for an atomic ensemble near a surface*, Europhys. Lett. **124** (2018), 34003, DOI.

[298] S. Gammelmark and K. Molmer, *Phase transitions and Heisenberg limited metrology in an ising chain interacting with a single-mode cavity field*, New J. Phys. **13** (2011), 053035, DOI.

[299] _____, *Interacting spins in a cavity: Finite-size effects and symmetry-breaking dynamics*, Phys. Rev. A **85** (2012), 042114, DOI.

[300] M. Gangl and H. Ritsch, *3d dissipative motion of atoms in a strongly coupled driven cavity*, Eur. Phys. J. D **8** (2000), 29, .

[301] _____, *Cold atoms in a high-q ring cavity*, Phys. Rev. A **61** (2000), 043405, .

[302] J. J. García-Ripoll and V. M. Pérez-García, *Optimizing schrödinger functionals using sobolev gradients: Application to quantum mechanics and nonlinear optics*, SIAM J. Sci. Comput. **23** (2001), 1316, .

[303] C. W. Gardiner, *Quantum noise*, Springer-Verlag, Berlin, 1991, ISBN.

[304] C. W. Gardiner and M. J. Collett, *Input and output in damped quantum systems: Quantum stochastic differential equations and the master equation*, Phys. Rev. A **31** (1985), 3761, .

[305] J. R. Gardner, R. A. Cline, J. D. Miller, D. J. Heinzen, H. M. J. M. Boesten, and B. J. Verhaar, *Collisions of doubly spin-polarized ultracold 85 rb atoms*, Phys. Rev. Lett. **74** (1995), 3764, .

[306] B. M. Garraway, *The Dicke model in quantum optics: Dicke model revisited*, Phil. Trans. R. Soc. A **369** (2011), 1137, DOI.

[307] B. M. Garraway, P. L. Knight, and J. Steinbach, *Dissipation of quantum superpositions*, Appl. Phys. B **60** (1995), 63.

[308] J. D. Gaskill, *Linear systems, fourier transforms and optics*, John Wiley & sons, 1978, ISBN.

[309] S. Gasparinetti, J.-C. Besse, M. Pechal, R. D. Buijs, Ch. Eichler, H. J. Carmichael, and A. Wallraff, *Two-photon resonance fluorescence of a ladder-type atomic system*, Phys. Rev. A **100** (2019), 033802, DOI.

[310] M. Gegg, A. Carmele, A. Knorr, and M. Richter, *Superradiant to subradiant phase transition in the open system Dicke model: dark state cascades*, New J. Phys. **20** (2018), 013006, DOI.

[311] J. Gelhausen, M. Buchhold, A. Rosch, and P. Strack, *Quantum-optical magnets with competing short- and long-range interactions: Rydberg-dressed spin lattice in an optical cavity*, SciPost Phys. **1** (2016), 004, DOI.

[312] M. Gell-Mann and J. B. Hartle, *Decoherent histories quantum mechanics and copenhagen quantum mechanics*, ePrints (2021), .

[313] S. D. Gensemer and D. S. Jin, *Transition from collisionless to hydrodynamic behavior in an ultracold atomic gas*, Phys. Rev. Lett. **87** (2001), 173201, .

[314] F. Gerbier, A. Widera, S. Fölling, O. Mandel, T. Gericke, and I. Bloch, *Phase coherence of an atomic mott insulator*, Phys. Rev. Lett. **95** (2005), 050404, .

[315] R. Gerritsma, G. Kirchmair, F. Zähringer, E. Solano, R. Blatt, and C. F. Roos, *Quantum simulation of the dirac equation*, Nature Lett. **463** (2010), 68, .

[316] C. C. Gerry and P. L. Knight, *Introductory quantum optics*, Cambridge, 2005, ISBN.

[317] H. Gießen, J. D. Berger, G. Mohs, P. Meystre, and S. F. Yelin, *Cavity-modified spontaneous emission: From Rabi oscillations to exponential decay*, Phys. Rev. A **53** (1996), 2816.

[318] K. Gietka, L. Ruks, and Th. Busch, *Understanding and improving critical metrology. quenching superradiant light-matter systems beyond the critical point*, Quantum **6** (2022), 700, DOI.

[319] K. Gietka, T. Wasak, J. Chwedeńczuk, F. Piazza, and H. Ritsch, *Quantum-enhanced interferometry with cavity QED-generated non-classical light*, Eur. J. Phys. D **71** (2017), 0273, DOI.

[320] M. Gilowski, Ch. Schubert, M. Zaiser, W. Herr, T. Wuebena, T. Wendrich, T. Mueller, E. M. Rasel, and W. Ertmer, *Narrow bandwidth interference filter-stabilized diode laser systems for the manipulation of neutral atoms*, Opt. Commun. **280** (2007), 443.

[321] D.M. Giltner, Phys. Rev. Lett. **75** (1995), 2638.

[322] S. Giorgini, L.P. Pitaevskii, and S. Stringari, *Thermodynamics of a trapped Bose-condensed gas*, J. Low Temp. Phys. **109** (1997), 309, .

[323] S. Giovanazzi, A. Görlitz, and T. Pfau, *Tuning the dipolar interaction in quantum gases*, Phys. Rev. Lett. **89** (2002), 130401, .

[324] S. Giovanazzi, D. O'Dell, and G. Kurizki, *Density modulations of Bose-Einstein condensates via laser-induced interactions*, Phys. Rev. Lett. **88** (2002), 130402, .

[325] E. V. Goldstein, M. G. Moore, and P. Meystre, *Non-linear manipulation and control of matter waves*, Laser Phys. (1999), quant-ph/9906088.

[326] E. V. Goldstein, K. Plättner, and P. Meystre, *Atomic phase-conjugation from a bose condensate*, J. Res. Natl. Inst. Stand. Technol. **101** (1996), 583.

[327] D. Gordon and C. M. Savage, *Creating macroscopic superpositions with Bose-Einstein condensates*, Phys. Rev. A **59** (1999), 4623, .

[328] J. P. Gordon and A. Ashkin, *Motion of atoms in a radiation trap*, Phys. Rev. A **21** (1980), 1606, DOI.

[329] A. Görlitz, A. P. Chikkatur, and W. Ketterle, *Enhancement and suppression of spontaneous emission and light scattering by quantum degeneracy*, Phys. Rev. A **63** (2001), R041601, DOI.

[330] B. Goss-Levi, *Ultra-cold fermionic atoms team up as molecules: Can they form cooper pairs as well*, Phys. Today (2004), .

[331] D. Gottesman, *The heisenberg representation of quantum computers*, ePrints **arXiv:quant-ph/9807006** (1998), .

[332] D. Gottesman, A. Kitaev, and J. Preskill, *Encoding a qubit in an oscillator*, Phys. Rev. A **64** (2001), 012310, DOI.

[333] P. L. Gould, G. A. Ruff, and D. E. Pritchard, *Diffraction of atoms by light: The near-resonant kapitza-dirac effect*, Phys. Rev. Lett. **56** (1986), 827.

[334] I. S. Gradshteyn and I.M. Ryzhik, *Table of integrals, series, and products*, Elsevier, 2007, ISBN.

[335] R. Graham and D. Walls, *Spectrum of light scattered from a weakly interacting Bose-Einstein condensed gas*, Phys. Rev. Lett. **76** (1996), 1774.

[336] D. M. Greenberger, M. A. Horne, A. Shimony, and A. Zeilinger, *Bell's theorem without inequalities*, Am. J. Phys. **58** (1990), 1131.

[337] M. Greiner, O. Mandel, T. Esslinger, T. W. Hänsch, and I. Bloch, *Quantum phase transition from a superfluid to a mott insulator in a gas of ultracold atoms*, Nature **415** (2002), 39, .

[338] M. Greiner, C. A. Regal, and D. S. Jin, *Emergence of a molecular Bose-Einstein condensate from a Fermi gas*, Nature **426** (2003), 537, .

[339] _____, *Probing the excitation spectrum of a Fermi gas in the BCS-BEC crossover regime*, Phys. Rev. Lett. **94** (2005), 070403, .

[340] M. Greiner, C. A. Regal, C. Ticknor, J. L. Bohn, and D. S. Jin, *Detection of spatial correlations in an ultracold gas of fermions*, Phys. Rev. Lett. **92** (2004), 150405, .

[341] W. Greiner, *Relativistic quantum mechanics: Wave equations*, Springer, 2nd ed., 1987, ISBN.

[342] G. F. Gribakin and V. V. Flambaum, *Calculation of the scattering length in atomic collisions using the semiclassical approximation*, Phys. Rev. A **48** (1993), 546, .

[343] A. Griffin and E. Zaremba, *First and second sound in a uniform bose gas*, Phys. Rev. A **56** (1997), 4839, .

[344] D. J. Griffiths, *Introduction to quantum mechanics*, Pearson Prentice Hall, New Jersey, 2005, ISBN.

[345] R. Grimm, M. Weidemüller, and Y. B. Ovchinnikov, *Optical dipole traps for neutral atoms*, Adv. At. Mol. Opt. Phys. **42** (2000), 95, .

[346] F. Gross, *Relativistic quantum mechanics and field theory*, Wiley, 2nd ed., 1999, ISBN.

[347] S. Grossmann and M. Holthaus, *On Bose-Einstein condensation in harmonic traps*, Phys. Lett. A **208** (1995), 188, .

[348] G. Grynberg and J.-Y. Courtois, *Sur la possibilité d'observer la non-linéarité du vide par conjugaison de phase optique*, C.R. Acacd. Sci. Paris **311** (1990), 1149.

[349] G. Grynberg, B. Lounis, P. Verkerk, J.-Y. Courtois, and C. Salomon, *Quantized motion of cold cesium atoms in two- and three-dimensional optical potentials*, Phys. Rev. Lett. **70** (1993), 2249, .

[350] D. Guéry-Odelin, J. Söding, P. Desbiolles, and J. Dalibard, *Is Bose-Einstein condensation of atomic cesium possible?*, Europhys. Lett. **44** (1998), 25.

[351] D. Guéry-Odelin and S. Stringari, *Scissors mode and superfluidity of a trapped Bose-Einstein condensed gas*, Phys. Rev. Lett. **83** (1999), 4452, .

[352] L. Guidoni and P. Verkerk, *Optical lattices: Cold atoms ordered by light*, J. Opt. B: Quantum Semiclass. Opt. **1** (1999), R23, DOI.

[353] J. Guo, P. R. Berman, H. Dubetsky, and G. Grynberg, *Recoil-induced resonances in non-linear spectroscopy*, Phys. Rev. A **46** (1992), 1426, .

[354] Jun Guo, *Contribution of energy continuum states to probe absorption signal of atoms in one-dimensional optical molasses*, Phys. Rev. A **49** (1994), 3934, DOI.

[355] Jun Guo and P. R. Berman, *Recoil-induced resonances in pump-probe spectroscopy*, Phys. Rev. A **47** (1993), 4128.

[356] S. Gupta, Z. Hadzibabic, M. W. Zwierlein, B. J. Verhaar, and W. Ketterle, *Radio-frequency spectroscopy of ultracold fermions*, Sciencexpress (2003), 1, .

[357] A. M. Guzman, M. Moore, and P. Meystre, *Theory of a coherent atomic-beam generator*, Phys. Rev. A **53** (1996), 977.

[358] Z. Hadzibabic, S. Gupta, C. A. Stan, C. H. Schunck, M. W. Zwierlein, K. Dieckmann, and W. Ketterle, *Fiftyfold improvement in the number of quantum degenerate fermionic atoms*, Phys. Rev. Lett. **91** (2003), 160401, .

[359] E. W. Hagley, L. Deng, M. Kozuma, M. Trippenbach, Y. B. Band, M. Edwards, M. Doery, P. S. Julienne, K. Helmerson, S. L. Rolston, and W. D. Phillips, *Measurement of the coherence of a Bose-Einstein condensate*, Phys. Rev. Lett. **83** (1999), 3112, .

[360] E. W. Hagley, L. Deng, M. Kozuma, J. Wen, K. Helmerson, S. L. Rolston, and W. D. Phillips, *A well-collimated quasi-continuous atom laser*, Science **283** (1999), 1706, .

[361] J. Hald, J. L. Sorensen, C. Schori, and E. S. Polzik, *Spin squeezed atoms: A macroscopic entangled ensemble created by light*, Phys. Rev. Lett. **83** (1999), 1319, .

[362] D. S. Hall, J. R. Ensher, D. S. Jin, and et al., *Recent experiments with Bose-condensed gases at JILA*, Proc. SPIE **3270** (1998), 98, cond-mat/9903459.

[363] D. S. Hall, M. R. Matthews, J. R. Ensher, C. E. Wieman, and E. A. Cornell, *Dynamics of component separation in a binary mixture of Bose-Einstein condensates*, Phys. Rev. Lett. **81** (1998), 1539, .

[364] D. S. Hall, M. R. Matthews, C. E. Wieman, and E. A. Cornell, *Measurements of relative phase of two-component Bose-Einstein condensates*, Phys. Rev. Lett. **81** (1998), 1543, .

[365] J. L. Hall, L. Hollberg, T. Baer, and H. G. Robinson, *Optical heterodyne saturation spectroscopy*, Appl. Phys. Lett. **39** (1981), 680.

[366] D.-J. Han, S. Wolf, S. Oliver, C. McCormick, M. T. DePue, and D. S. Weiss, *3d Raman sideband cooling of cesium atoms at high density*, Phys. Rev. Lett. **85** (2000), 724, .

[367] D. J. Han, R. H. Wynar, Ph. W. Courteille, and D. J. Heinzen, *Bose-Einstein condensation of large numbers of atoms in a magnetic time-averaged orbiting potential trap*, Phys. Rev. A **57** (1998), R4114.

[368] S. Haroche, J. C. Gay, and G. Grynberg (eds.), *Atom traps*, World Scientific, 1989.

[369] T. Hartmann, F. Keck, H. J. Korsch, and S. Mossmann, *Dynamics of Bloch oscillations*, New J. Phys. **6** (2004), 2, DOI.

[370] J. A. Seman Harutiniam, *Study of excitations in a Bose-Einstein condensate*, Ph.D. thesis, Universidade de São Paulo, 2011.

[371] L. V. Hau, B. D. Busch, Ch. Liu, Z. Dutton, M. M. Burns, and J. A. Golovchenko, *Near-resonant spatial images of a confined Bose-Einstein condensates in a 4-dee magnetic bottle*, Phys. Rev. A **58** (1998), R54, .

[372] L. V. Hau, S. E. Harris, Z. Dutton, and C. H. Behroozi, *Light speed reduction to 17 metres per second in an ultracold atomic gas*, Nature **397** (1999), 594, DOI.

[373] G. Hechenblaikner, M. Gangl, P. Horak, and H. Ritsch, *Cooling an atom in a weakly driven high-q cavity*, Phys. Rev. A **58** (1998), 3030.

[374] G. Hechenblaikner, O. M. Maragò, E. Hodby, J. Arlt, S. Hopkins, and C. J. Foot, *Observation of harmonic generation and nonlinear coupling in the collective dynamics of a Bose-Einstein condensate*, Phys. Rev. Lett. **85** (2000), 692, .

[375] C. E. Hecht, *The possible superfluid behaviour of hydrogen atom gases and liquids*, Physica **25** (1959), 1159.

[376] D. J. Heinzen, J. J. Childs, J. E. Thomas, and M. S. Feld, *Enhanced and inhibited visible spontaneous emission by atoms in a confocal resonator*, Phys. Rev. Lett. **58** (1987), 1320, DOI.

[377] ———, *Errata*, Phys. Rev. Lett. **58** (1987), 2153, DOI.

[378] D. J. Heinzen and M. S. Feld, *Vacuum radiative level shift and spontaneous-emission linewidth of an atom in an optical resonator*, Phys. Rev. Lett. **59** (1987), 2623, DOI.

[379] W. Heisenberg, *Physik und philosophie*, S. Hirzel Verlag, 6. Auflage, Stuttgart, 2000, ISBN.

[380] K. Helmerson, A. Martin, and D. E. Pritchard, *Laser and rf spectroscopy of magnetically trapped neutral atoms*, J. Opt. Soc. Am. B **9** (1992), 483.

[381] A. Hemmerich, Phys. Rev. Lett. **68** (1992).

[382] ———, Phys. Rev. Lett. **72** (1994).

[383] ———, *Quantum entanglement in dilute optical lattices*, Phys. Rev. A **60** (1999), 943, .

[384] A. Hemmerich and T. W. Hänsch, *Two-dimensional atomic crystal bound by light*, Phys. Rev. Lett. **70** (1993).

[385] C. Henkel, C. I. Westbrook, and A. Aspect, *Quantum reflection: Atomic matter wave optics in an attractive exponential potential*, J. Opt. Soc. Am. B **13** (1996), 233, .

[386] E. A. L. Henn, J. A. Seman, G. Roati, K. M. F. Magalh aes, and V. S. Bagnato, *Emergence of turbulence in an oscillating Bose-Einstein condensate*, Phys. Rev. Lett. **103** (2009), 045301, .

[387] K. Hepp and E. Lieb, *On the superradiant phase transition for molecules in a quantized radiation field: the Dicke maser model*, Annals of Phys. **76** (1973), 360, DOI.

[388] J. Herbig, T. Kraemer, M. Mark, T. Weber C. Chin, H.-C. Nägerl, and R. Grimm, *Preparation of a pure molecular quantum gas*, Science **301** (2003), 1510, .

[389] D. I. Herman, C. Weerasekara, L. C. Hutcherson, F. R. Giorgetta, and K. C. Coss, *Precise multispecies agricultural gas flux determined using broadband open-path dual-comb spectroscopy*, Science Advances **7** (2021), eabe9765.

[390] G. Herzberg, *Molecular spectra and molecular structure. i - spectra of diatomic molecules*, Springer, 1950, ISBN.

[391] C. Herzog and M. Olshanii, *Trapped bose gas: The canonical versus grand canonical statistics*, Phys. Rev. A **55** (1997), 3254, .

[392] H. F. Hess, *Evaporative cooling of magnetically trapped spin-polarized hydrogen*, Phys. Rev. B **34** (1986), 3476.

[393] J. Heurich, M. G. Moore, and P. Meystre, *Cavity atom optics and the 'free atom laser'*, Opt. Commun. **179** (2000), 549, .

[394] T. W. Hijmans, Yu. Kagan, and G. V. Shlyapnikov, *Bose condensation and relaxation explosion in magnetically trapped atomic hydrogen*, Phys. Rev. B **48** (1993), 12886, .

[395] L. Hilico, C. Fabre, S. Reynaud, and E. Giacobino, *Linear input-output method for quantum fiuctuations in optical bistability with two-level atoms*, Phys. Rev. A **46** (2002), 4397, DOI.

[396] E. A. Hinds, M. G. Boshier, and I. G. Hughes, *Magnetic waveguide for trapping cold atom gases in two dimensions*, Phys. Rev. Lett. **80** (1998), 645, .

[397] Tin-Lun Ho and E. J. Mueller, *High temperature expansion applied to fermions near Feshbach resonance*, Phys. Rev. Lett. **92** (2004), 160404, .

[398] E. Hodby, S. T. Thompson, C. A. Regal, M. Greiner, A. C. Wilson, D. S. Jin, E. A. Cornell, and C. E. Wieman, *Production efficiency of ultracold Feshbach molecules in bosonic and fermionic systems*, Phys. Rev. Lett. **94** (2005), 120402, .

[399] W. Hofstetter, J. I. Cirac, P. Zoller, E. Demler, and M. D. Lukin, *High-temperature superfluidity of fermionic atoms in optical lattices*, Phys. Rev. Lett. **89** (2002), 220407, .

[400] M. J. Holland and J. Cooper, *Expansion of a Bose-Einstein condensate in a harmonic potential*, Phys. Rev. A **53** (1996), R1954, .

[401] M. J. Holland, D. S. Jin, M. L. Ciafalo, and J. Cooper, *Emergence of interaction effects in Bose-Einstein condensation*, Phys. Rev. Lett. **78** (1997), 3801, .

[402] L. Hollberg, L. S. Ma, M. Hohenstatt, and J. L. Hall, *Precision measurement by optical heterodyne techniques*, Proc. SPIE **426** (1983), 91.

[403] R. Holzwarth, Th. Udem, T. W. Hänsch, J. C. Knight, W. J. Wadsworth, and P. St. J. Russell, *Optical frequency synthesizer for precision spectroscopy*, Phys. Rev. Lett. **85** (2000), 2264.

[404] R. Holzwarth, M. Zimmermann, Th. Udem, T. W. Hänsch, P. Russbüldt, K. Gäbel, R. Poprawe, J. C. Knight, W. J. Wadsworth, and P. St. J. Russell, *White-light frequency comb generation with a diode-pumped cr:lisaf laser*, Opt. Lett. **26** (2000), 1376.

[405] Rebecca L. Honeycutt, *Stochastic runge-kutta algorithms, i. white noise*, Phys. Rev. A **45** (1992), 600, .

[406] P. Horowitz and W. Hill, *The art of electronics*, Cambridge Universty Press, 2001, ISBN.

[407] O. Hosten, R. Krishnakumar, J. Engelsenand, and M. A. Kasevich, *Quantum phase magnification*, Science **352** (2016), 1552.

[408] Ch. Hotter, D. Plankensteiner, and H. Ritsch, *Continuous narrowband lasing with coherently driven v-level atoms*, New J. Phys. **22** (2020), 113021, DOI.

[409] M. Houbiers, H. T. C. Stoof, W. I. McAlexander, and R. G. Hulet, *Elastic and inelastic collisions of li-6 atoms in magnetic and optical traps*, Phys. Rev. A **57** (1998), R1497, .

[410] K. Huang, *Statistical mechanics*, John Wiley and Sons, 1987, ISBN.

[411] R. Huesmann, Ch. Balzer, Ph. W. Courteille, W. Neuhauser, and P. E. Toschek, *Single-atom interferometry*, Phys. Rev. Lett. **82** (1999), 1611.

[412] D. A. W. Hutchinson, *Self-consistent effects of continuous wave output coupling of atoms from a Bose-Einstein condensate*, Phys. Rev. Lett. **82** (1999), 6, .

[413] D. A. W. Hutchinson, E. Zaremba, and A. Griffin, *Finite temperature excitations of a trapped bose gas*, Phys. Rev. Lett. **78** (1997), 1842, .

[414] Tetsuya Ido, Yoshitomo Isoya, and Hidetoshi Katori, *Optical-dipole trapping of sr atoms at a high phase-space density*, Phys. Rev. A **61** (2000), 061403(R), .

[415] S. Inouye, M. R. Andrews, J. Stenger, H.-J. Miesner, D. M. Stamper-Kurn, and W. Ketterle, *Observation of Feshbach resonances in a Bose-Einstein condensate*, Nature **392** (1998), 151, DOI.

[416] S. Inouye, A. P. Chikkatur, D. M. Stamper-Kurn, J. Stenger, D. E. Pritchard, and W. Ketterle, *Superradiant Rayleigh scattering from a Bose-Einstein condensate*, Science **285** (1999), 571, DOI.

[417] S. Inouye, R. F. Löw, S. Gupta, T. Pfau, A. Görlitz, T. L. Gustavson, D. E. Pritchard, and W. Ketterle, *Amplification of light and atoms in a Bose-Einstein condensate*, Phys. Rev. Lett. **85** (2000), 4225, .

[418] S. Inouye, T. Pfau, S. Gupta, A. P. Chikkatur, A. Görlitz, D. E. Pritchard, and W. Ketterle, *Phase-coherent amplification of atomic matter-waves*, Nature **402** (1999), 641, DOI.

[419] W. M. Itano, J. C. Bergquist, J. J. Bollinger, J. M. Gilli-Gans, D. J. Heinzen, F. L. Moore, M. G. Raizen, and D. J. Wineland, *Quantum projection noise: Population fluctuations in two-level systems*, Phys. Rev. A **47** (1993), 3554, DOI.

[420] W. M. Itano, J. J. Bollinger, and D. J. Wineland, *Quantum zeno effect*, Phys. Rev. A **41** (1990), 2295, .

[421] W. M. Itano and D. J. Wineland, *Laser cooling of ions stored in harmonic and penning traps*, Phys. Rev. A **25** (1982), 35, .

[422] H. Ito, T. Nakata, K.Sakaki, M. Ohtsu, K. I. Lee, and W. Jhe, *Laser-spectroscopy of atoms guided by evanescent waves in micron-sized hollow optical fibers*, Phys. Rev. Lett. **76** (1996), 4500.

[423] A. D. Jackson, G. M. Kavoulakis, and C. J. Pethick, *Solitary waves in clouds of Bose-Einstein condensates*, Phys. Rev. A **58** (1998), 2417, .

[424] B. Jackson, J. F. McCann, and C. S. Adams, *Vortex line and ring dynamics in trapped Bose-Einstein condensates*, Phys. Rev. A **61** (2000), 013604.

[425] J. D. Jackson, *Classical electrodynamics*, John Wiley and Sons, 1999, ISBN.

[426] D. Jaksch, J.-J. Briegel, J. I. Cirac, C. W. Gardiner, and P. Zoller, *Entanglement of atoms via cold controlled collisions*, Phys. Rev. Lett. **82** (1998), 1975, .

[427] D. Jaksch, J. I. Cirac, P. Zoller, S. L. Rolston, R. Côté, and M. D. Lukin, *Fast quantum gates for neutral atoms*, Phys. Rev. Lett. **85** (2000), 2208, .

[428] D. Jaksch, S. A. Gardiner, K. Schluze, J. I. Cirac, and P. Zoller, *Uniting Bose-Einstein condensates in optical resonators*, Phys. Rev. Lett. **86** (2001), 4733, .

[429] J. Janszky, P. Domokos, and P. Adam, *Coherent states on a circle and quantum interference*, Phys. Rev. A **48** (1993), 2213, DOI.

[430] J. Javaloyes, Ph. W. Courteille, M. Perrin, G.-L. Lippi, and A. Politi, *Spontaneous ordering in cold atomic clouds*, Opt. Phot. News **16, (12) and 22 (2005)** (2005).

[431] J. Javaloyes, G. L. Lippi, and A. Politi, *Reduced model for the description of radiation-matter interaction including atomic recoil*, Phys. Rev. A **68** (2003), 033405, .

[432] J. Javaloyes, M. Perrin, G.-L. Lippi, and A. Politi, *Self-generated cooperative light emission induced by atomic recoil*, Phys. Rev. A **70** (2004), 23405, .

[433] J. Javaloyes, M. Perrin, and A. Politi, *Collective atomic recoil laser as a synchronization transition*, Phys. Rev. E **78** (2008), 11108, .

[434] J. Javanainen and J. Ruostekoski, *Off-resonance light scattering from low-temperature bose and Fermi gases*, Phys. Rev. A **52** (1995), 3033, .

[435] E. T. Jaynes, *The gibbs paradox*, (1992), 1–22, .

[436] E. T. Jaynes and F. W. Cummings, *Comparison of quantum and semiclassical radiation theories with application to the beam maser*, Proc. IEEE **51** (1963), 89.

[437] P. S. Jessen and I. H. Deutsch, *Optical lattices*, Adv. At. Mol. Opt. Phys. **37** (1996), 95, .

[438] D. S. Jin, J. R. Ensher, M. R. Matthews, C. E. Wieman, and E. A. Cornell, *Collective excitations of a Bose-Einstein condensate in a dilute gas*, Phys. Rev. Lett. **77** (1996), 420, .

[439] D. S. Jin, M. R. Matthews, J. R. Ensher, C. E. Wieman, and E. A. Cornell, *Temperature-dependent damping and frequency shifts in collective excitations of a dilute Bose-Einstein condensate*, Phys. Rev. Lett. **78** (1997), 764, .

[440] S. Jochim, M. Bartenstein, A. Altmeyer, G. Hendl, C. Chin, J. Hecker Denschlag, and R. Grimm, *Pure gas of optically trapped molecules created from fermionic atoms*, Phys. Rev. Lett. **91** (2003), 240402, .

[441] D. J. Jones, S. A. Diddams, J. K. Ranka, A. Stentz, R. S. Windeler, J. L. Hall, and S. T. Cundiff, *Carrier-envelope phase control of femtosecond mode-locked lasers and direct optical frequency synthesis*, Science **288** (2000), 635.

[442] R. Jones, J. A. Needham, I. Lesanovsky, F. Intravaia, and B. Olmos, *Modified dipole-dipole interaction and dissipation in an atomic ensemble near surfaces*, Phys. Rev. A **97** (2018), 053841, DOI.

[443] B. Juisgaard, A. Kozhekin, and E. S. Polzik, *Experimental long-lived entanglement of two macroscopic objects*, Nature **413** (2001), 400, .

[444] P. S. Julienne, *Cold binary atomic collisions in a light field*, J. Res. Natl. Inst. Stand. Tech. **101** (1996), 487, DOI.

[445] P. S. Julienne, K. Burnett, Y. B. Band, and W.C. Stwalley, *Stimulated Raman molecule production in Bose-Einstein condensates*, Phys. Rev. A **58** (1998), R797, .

[446] R. Kaiser, *Quantum multiple scattering*, J. Mod. Opt. **56** (2009), 2082, DOI.

[447] R. K. Kaj, D. Bloch, J. J. Snyder, G. Camy, and M. Ducloy, *High-frequency optically heterodyned saturation spectroscopy via resonant degenerate four-wave mixing*, Phys. Rev. Lett. **44** (1982), 1251.

[448] P. L. Kapitza and P. A. M. Dirac, *The deflection of electrons from standing light waves*, Proc. Roy. Soc. Lond. (1933), 297.

[449] T. Karpiuk, M. Brewczyk, S. Ospelkaus-Schwarzer, K. Bongs, M. Gajda, and K. Rzazÿewski, *Soliton trains in Bose-Fermi mixtures*, Phys. Rev. Lett. **93** (2004), 100401, .

[450] R. Karplus and M. Neumann, *The scattering of light by light*, Phys. Rev. **83** (1950), 776.

[451] A. Kasapi, M. Jain, G. Y. Jin, and S. E. Harris, *Electromagnetically induced transparency: Propagation dynamics*, Phys. Rev. Lett. **74** (1995), 2447, .

[452] M. Kasevich and S. Chu, *Measurement of the gravitational acceleration of an atom with a light-pulse atom interferometer*, Appl. Phys. B **54** (1992), 321, DOI.

[453] M. M. Kash, V. A. Sautenkov, A. S. Zibrov, L. Hollberg, G. R. Welch, M. D. Lukin, Y. Rostovtsev, E. S. Fry, and M. O. Scully, *Ultraslow group velocity and enhanced nonlinear optical effects in a coherently driven hot atomic gas*, Phys. Rev. Lett. **82** (1999), 5229, .

[454] A. Kastberg, W. D. Phillips, S. L. Rolston, R. J. C. Spreeuw, and P. S. Jessen, *Adiabatic cooling of cesium to 700nk in an optical lattice*, Phys. Rev. Lett. **74** (1995), 1542, .

[455] G. W. Kattawar and G. N. Plass, *Electromagnetic scattering from absorbing spheres*, Appl. Opt. **6** (1967), 1377, .

[456] G. M. Kavoulakis and C. J. Pethick, *Quasi-one-dimensional character of sound propagation in elongated Bose-Einstein condensed clouds*, Phys. Rev. A **58** (1998), 1563.

[457] W. Ketterle and N. J. Van Druten, *Bose-Einstein condensation of a finite number of particles trapped in one or three dimensions*, Phys. Rev. A **54** (1996), 656.

[458] _____, *Evaporative cooling of trapped atoms*, Adv. At. Mol. Opt. Phys. **37** (1996), 181, .

[459] W. Ketterle, D. S. Durfee, and D. M. Stamper-Kurn, *Making, probing and understanding Bose-Einstein condensates*, Proc. Int. School of Phys. Enrico Fermi **CXL** (1999), 67, .

[460] W. Ketterle and Shin Inouye, *Does matter wave amplification work for fermions?*, Phys. Rev. Lett. **86** (2001), 4203, DOI.

[461] W. Ketterle and H.-J. Miesner, *Coherence properties of bose condensates and atom lasers*, Phys. Rev. A **56** (1997), 3291, .

[462] A. Kevin, E. Strecker, Guthrie, B. Partridge, Andrew, G. Truscott, and Randall G. Hulet, *Formation and propagation of matter-wave soliton trains*, Nature **417** (2002), 150.

[463] W. F. Kielhorn, *A technique for measurement of vector and tensor polarization in solid spin one polarized targets*, Ph.D. thesis, University of Texas at Austin, 1991, DOI.

[464] A. H. Kiilerich and et al., Phys. Rev. A **92** (2015), 032124.

[465] K. Kirsten and D. J. Toms, *Bose-Einstein condensation of atomic gases in a general harmonic-oscillator confining potential trap*, Phys. Rev. A **54** (1996), 4188.

[466] P. Kirton, M. M. Roses, J. Keeling, and E. G. Dalla Torre, *Introduction to the Dicke model: From equilibrium to nonequilibrium, and vice versa*, Adv. Quantum Technol. **2** (2019), 1800043, DOI.

[467] M. Kitagawa, K. Enomoto, K. Kasa, Y. Takahashi, R. Ciurylo, P. Naidon, and P. S. Julienne, *Two-color photoassociation spectroscopy of ytterbium atoms and the precise determinations of s-wave scattering lengths*, Phys. Rev. A **77** (2008), 012719, DOI.

[468] M. Kitagawa and M. Ueda, *Squeezed spin states*, Phys. Rev. A **47** (1993), 5138, DOI.

[469] C. Kittel, *Elementary statistical physics*, John Wiley and Sons, 1976, ISBN.

[470] J. Klaers, J.Schmitt, F. Vewinger, and M. Weitz, *Bose-Einstein condensation of photons in an optical microcavity*, eprints **1007.4088** (1999), .

[471] B. Kneer, T. Wong, K. Vogel, W. P. Schleich, and D. F. Walls, *Generic model of an atom laser*, Phys. Rev. A **58** (1998), 4841, .

[472] B. Koczor, R. Zeier, and S. J. Glaser, *Continuous phase-space representations for finite-dimensional quantum states and their tomography*, Phys. Rev. A **101** (2020), 022318, DOI.

[473] A. F. Koenderink and W. L. Vos, *Light exiting from real photonic band gap crystals is diffuse and strongly directional*, Phys. Rev. Lett. **91** (2003), 213902.

[474] H. Kogelnik and X. Y. Li, *Laser beams and resonators*, Appl. Opt. **5** (1966), 1550, DOI.

[475] M. Köhl, H. Moritz, T. Stöferle, K. Günter, and T. Esslinger, *Fermionic atoms in a three dimensional optical lattice: Observing Fermi surfaces, dynamics, and interactions*, Phys. Rev. Lett. **94** (2005), 080403, .

[476] S. J. J. M. F. Kokkelmans, B. J. Verhaar, and K. Gibble, *Prospects for Bose-Einstein condensation in cesium*, Phys. Rev. Lett. **81** (1998), 951, .

[477] V. Kokoouline, O. Dulieu, R. Kosloff, and F. Masnou-Seeuws, *Mapped fourier methods for long-range molecules: Application to perturbations in the $Rb_2(0_u^+)$ photoassociation spectrum*, J. Chem. Phys. **110** (1999), 9865, .

[478] K. Kopitzky, *Einführung in die festkörperphysik*, Teubner, 1986, ISBN.

[479] S. A. Koppell, Y. Israel, A. J. Bowman, B. B. Klopfer, and M. A. Kasevich, *Transmission electron microscopy at the quantum limit*, Appl. Phys. Lett. **120** (2021), 190502, DOI.

[480] M. Korek, A. R. Allouche, M. Kobeissi, A. Chaalan, M. Dagher, K. Fakherddin, and M. Aubert-Frécon, Chem. Phys. **256** (2000), 1.

[481] S. Kotochigova, P. S. Julienne, and E. Tiesinga, *Ab initio calculation of the KRb dipole moments*, Phys. Rev. A **68** (2003), 022501.

[482] S. Kotochigova, E. Tiesinga, and P. S. Julienne, *Photoassociative formation of ultracold polar krb molecules*, Eur. Phys. J. D **31** (2004), 189, .

[483] M. Kozuma, L. Deng, E. W. Hagley, J. Wen, R. Lutwak, K. Helmerson, S. L. Rolston, and W. D. Phillips, *Coherent splitting of Bose-Einstein condensed atoms with optically induced Bragg diffraction*, Phys. Rev. Lett. **82** (1999), 871.

[484] M. Kozuma, Y. Imai, K. Nakagawa, and M. Ohtsu, *Observation of transient response of recoil-induced resonance: A method for the measurement of atomic motion in an optical standing wave*, Phys. Rev. A **52** (1995), R3421, .

[485] M. Kozuma, K. Nakagawa, W. Jhe, and M. Ohtsu, *Observation of temporal behavior of an atomic wavepacket localized in an optical potential*, Phys. Rev. Lett. **76** (1996), 2428, .

[486] M. Kozuma, Y. Suzuki, Y. Torii, T. Saguira, T. Kaga, E. W. Hagley, and L. Deng, *Phase-coherent amplification of matter-waves*, Science **286** (1999), 2309, .

[487] T. Kraemer, M. Mark, P. Waldburger, J. G. Danzl, C. Chin, B. Engeser, A. D. Lange, K. Pilch, A. Jaakkola, H.-C. Nägerl, and R. Grimm, *Evidence for Efimov quantum states in an ultracold gas of cesium atoms*, Nature **428** (2005), 155.

[488] Hendrik A. Kramers, *Wellenmechanik und halbzählige quantisierung*, Zeitschrift für Physik **39** (1926), 828.

[489] D. Kruse, M. Ruder, J. Benhelm, C. von Cube, C. Zimmermann, Ph. W. Courteille, B. Nagorny, Th. Elsässer, and A. Hemmerich, *Cold atoms in a high-q ring-cavity*, Phys. Rev. A **67** (2003), 051802(R).

[490] D. Kruse, C. von Cube, C. Zimmermann, and Ph. W. Courteille, *Observation of lasing mediated by collective atomic recoil*, Phys. Rev. Lett. **91** (2003), 183601.

[491] R. Kubo, *Generalized cumulant expansion method*, J. Phys. Soc. Jap. **17** (1962), 1100, DOI.

[492] A. Kuhn, M. Hennrich, and G. Rempe, *Deterministic single-photon source for distributed quantum networking*, Phys. Rev. Lett. **89** (2002), 067901.

[493] G. Kurizki and A. Z. Genack, *Suppression of molecular interactions in periodic dielectric structures*, Phys. Rev. Lett. **61** (1988), 2269.

[494] A. Kuzmich, L. Mandel, and N. P. Bigelow, *Generation of spin squeezing via continuous quantum nondemolition measurement*, Phys. Rev. Lett. **85** (2000), 1594, DOI.

[495] P. Kwiat, H. Weinfurter, Th. Herzog, A. Zeilinger, and M. A. Kasevich, *Interaction-free measurement*, Phys. Rev. Lett. **74** (1995), 4763, DOI.

[496] A. Lakhtakia, *Positive and negative Goos-Hänchen shifts and negative phase-velocity mediums (alias left-handed materials)*, ePrints:Physics0305133 (2003), .

[497] W. E. Jr. Lamb, *Anti-photon*, Appl. Phys. B **60** (1995), 77, DOI.

[498] A. Lambrecht, J.-M. Courty, and S. Reynaud, *Transverse effects on squeezing with atoms*, J. de Physique **36** (1996), 93, DOI.

[499] L. D. Landau, Butterworth-Heinemann, 1937, ISBN.

[500] G. T. Landi, *Quantum information and quantum noise*, unpublished, Rochester, 2018, ⊙Lecture notes.

[501] _____, 2019, ⊙Lecture notes.

[502] A. Landragin, G. Labeyrie, R. Kaiser, N. Vansteenkiste, C. I.Westbrook, and A. Aspect, *Specular versus diffuse reflection of atoms from an evanescent wave from mirror*, Opt. Lett. **21** (1996), 1591.

[503] C. K. Law and N. P. Bigelow, *Amplifying an atomic wave signal using a Bose-Einstein condensate*, Phys. Rev. A **58** (1998), 4791.

[504] J. Lawall, S. Kulin, B. Saubamea, N. Bigelow, M. Leduc, and C. Cohen-Tannoudji, *Three-dimensional laser cooling of helium beyond the single-photon recoil limit*, Phys. Rev. Lett. **75** (1995), 4194.

[505] L. J. LeBlanc, M. C. Beeler, K. Jiménez-García, A. R. Perry, S. Sugawa, R. A. Williams, and I. B. Spielman, *Direct observation of zitterbewegung in a Bose-Einstein condensate*, New. J. Phys. **15** (2013), 073011, .

[506] E. S. Lee, C. Geckeler, J. Heurich, A. Gupta, K.-I. Cheong, S. Secrest, and P. Meystre, *Dark states of dressed Bose-Einstein condensates*, Phys. Rev. A **60** (1999), 4006, .

[507] H. J. Lee, C. S. Adams, M. Kasevich, and S. Chu, *Raman cooling of atoms in an optical dipole trap*, Phys. Rev. Lett. **76** (1996), 2658, .

[508] P. J. Lee, M. Anderlini, B. L. Brown, J. Sebby-Strabley, W. D. Phillips, and J. V. Porto, *Sublattice addressing and spin-dependent motion of atoms in a double-well lattice*, Phys. Rev. Lett. **99** (2007), 020402, DOI.

[509] G. Lenz, P. Meystre, and E. M. Wright, *Non-linear atom optics*, Phys. Rev. Lett. **71** (1993), 3271, .

[510] U. Leonhardt and H. Paul, *Measuring the quantum state of light*, Prog. Quant. Electr. **19** (1995), 89, .

[511] U. Leonhardt and P. Piwnicki, *Relativistic effects of light in moving media with extremely low group velocity*, Phys. Rev. Lett. **85** (2000), 822, .

[512] N. Leppenen and E. Shahmoon, *Quantum bistability at the interplay between collective and individual decay*, ePrints **arXiv2404.0213** (2024), DOI.

[513] P. Lesage and C. Au doin, *Characterization and measurement of time and frequency stability*, Radio Science (1979).

[514] M. D. Levenson and G. L. Eesley, *Polarization selective optical heterodyne detection for dramatically improved sensitivity in laser spectroscopy*, Appl. Phys. **19** (1979), 1.

[515] M. Lewenstein and Juha Javanainen, *Cooperative quantum jumps with two atoms*, Phys. Rev. Lett. **59** (1987), 1289, .

[516] R. J. Lewis-Swan, M. A. Norcia, J. R. K. Cline, J. K. Thompson, and A. M. Rey, *Robust spin squeezing via photon-mediated interactions on an optical clock transition*, Phys. Lett. Lett. **121** (2018), 070403, 10.1103/PhysRevLett.121.070403.

[517] Mingzhe Li, Zijun Yan, Jincan Chen, Lixuan Chen, and Chuanhong Chen, *Thermodynamic properties of an ideal Fermi gas in an external potential with* $U = br^t$ *in any dimensional space*, Phys. Rev. A **58** (1998), 1445, .

[518] W. Lichten, *Precise wavelength measurements and optical phase shifts: I. general theory*, J. Opt. Soc. Am. A **2** (1985), 1869, .

[519] T. K. Lim, S. K. Duffy, and W. C. Damert, *Efimov states in the 4he trimer*, Phys. Rev. Lett. **38** (1977), 341, .

[520] Jia Ling Lin and J. P. Wolfe, *Bose-Einstein condensation of paraexcitons in stressed Cu2O*, Phys. Rev. Lett. **71** (1993), 1222, .

[521] Ch. Lisdat, O. Dulieu, H. Knöckel, and E. Tiemann, *Inversion analysis of k2 coupled electronic states with the fourier grid method*, Eur. Phys. J. D **17** (2001), 319, .

[522] Bo Liu, GuoLong Li, YanMing Che, Jie Chen, and XiaoGuang Wang, *Quantum fisher information width in quantum metrology*, Science China: Physics, Mechanics & Astronomy **62** (2019), 040301, DOI.

[523] Haonan Liu, S. B. Jäger, Xianquan Yu, S. Touzard, A. Shankar, M. J. Holland, and T. L. Nicholson, *Rugged mhz-linewidth superradiant laser driven by a hot atomic beam*, Phys. Rev. Lett. **125** (2020), 253602, DOI.

[524] Jing Liu and Xiaoguang Wang Heng-Na Xiongb, Fei Songa, *Fidelity susceptibility and quantum fisher information for density operators with arbitrary ranks*, Physica A **410** (2014), 167, DOI.

[525] Jing Liu, Haidong Yuan, Xiao-Ming Lu, and Xiaoguang Wang, *Quantum fisher information matrix and multiparameter estimation*, J. Phys. A: Math. Theor. **53** (2020), 023001, DOI.

[526] Zhixin Liu and R. Slávik, *Optical injection locking: From principle to applications*, J. Lightwave Techn. **38** (2020), 43.

[527] Zhixin Liu and Radan Slavík, *Optical injection locking: From principle to applications*, J. Lightwave Tech. **38** (2020), 43.

[528] F. London, *On the Bose-Einstein condensation*, Nature **54** (1938), 947.

[529] D. Loss and D. P. DiVincenzo, *Quantum computation with quantum dots*, Phys. Rev. A **57** (1998), 120, DOI.

[530] R. Loudon, *The quantum theory of light*, Clarendon Press Oxford, 1982, ISBN.

[531] R. Loudon and P. L. Knight, *Squeezed light*, J. Mod. Opt. **34** (1987), 709.

[532] R. V. E. Lovelace, C. Mehanian, T. J. Tommila, and D. M. Lee, *Magnetic confinement of a neutral gas*, Nature **318** (1985), 30.

[533] L. A. Lugiato, A. Gatti, and E. Brambilla, *Quantum imaging*, J. Opt. B: Quantum Semiclass. Opt. **4** (2002), S176.

[534] L. A. Lugiato and G. Strini, *On the squeezing obtainable in parametric oscillators and bistable absorption*, Opt. Comm. **41** (1981), 67, .

[535] _____, *On nonclassical effects in two-photon optical bistability and two-photon laser*, Opt. Comm. **41** (1982), 374, .

[536] M. D. Lukin and P. R. Hemmer, *Quantum entanglement via optical control of atom-atom interactions*, Phys. Rev. Lett. **84** (2000), 2818, .

[537] E. Lundh and M. Wallis, *Ratchet effect for cold atoms in an optical lattice*, Phys. Rev. Lett. **94** (2005), 110603, DOI.

[538] T. Luu and A. Schwenk, *Three-fermion problems in optical lattices*, Phys. Rev. Lett. **98** (2007), 103202, .

[539] L. S. Ma, Ph. W. Courteille, G. Ritter, W. Neuhauser, and R. Blatt, *Spectroscopy of te_2 with modulation transfer: Reference lines for precision spectroscopy in yb*, Appl. Phys. B **57** (1993), 159.

[540] L. S. Ma and J. L. Hall, *Optical heterodyne spectroscopy enhanced by an external optical cavity: Toward improved working standards*, IEEE J. Quant. Electr. **26** (1990), 2006.

[541] K. M. Madison, F. Chevy, W. Wohlleben, and J. Dalibard, *Vortex formation in a stirred Bose-Einstein condensate*, Phys. Rev. Lett. **84** (1999), 806, .

[542] _____, *Vortex lattices in a stirred Bose-Einstein condensate*, (1999), cond-mat/0004037.

[543] Th. Maier, S. Kraemer, L. Ostermann, and H. Ritsch, *A superradiant clock laser on a magic wavelength optical lattice*, Opt. Exp. **22** (2014), 13269, DOI.

[544] E. Mandonnet, R. Dum, A. Minguzzi, I. Carusotto, Y. Castin, and J. Dalibard, *Evaporative cooling of an atomic beam*, Eur. Phys. J. D **10** (2000), 9.

[545] H. Mann, H. Schiffelgen, and R. Froriep, *Einführung in die regelungstechnik*, Hanser-Verlag München, 2009, ISBN.

[546] T. Manovitz, Yotam Shapira, Lior Gazit, Nitzan Akerman, and Roee Ozeri, *Trapped-ion quantum computer with robust entangling gates and quantum coherent feedback*, Phys. Rev. X Quantum **3** (2022), 010347, DOI.

[547] O. M. Maragò, G. Hechenblaikner, E. Hodby, and C. J. Foot, *Temperature dependence of damping and frequency shifts of the scissors mode of a trapped Bose-Einstein condensate*, Phys. Rev. Lett. **86** (2001), 3938, .

[548] O. M. Maragò, S. A. Hopkins, J. Arlt, E. Hodby, G. Hechenblaikner, and C. J. Foot, *Observation of the scissors mode and evidence for superfluidity of a trapped Bose-Einstein condensed gas*, Phys. Rev. Lett. **84** (2000), 2056, .

[549] M. Marinescu, *Computation of the scattering length and effective range in molecular physics*, Phys. Rev. A **50** (1994), 3177, .

[550] C. Clay Marston and G. G. Balint-Kurti, *The Fourier grid hamiltonian method for bound state eigenvalues and eigenfunctions*, J. Chem. Phys. **91** (1989), 3571, .

[551] A. G. Martin, K. Helmerson, V. S. Bagnato, G. P. Lafyatis, and D. E. Pritchard, *Rf spectroscopy of trapped neutral atoms*, Phys. Rev. Lett. **61** (1988), 2431, .

[552] J. L. Martin, C. R. McKenzie, N. R. Thomas, J. C. Sharpe, D. M. Warrington, P. J. Manson, W. J. Snadle, and A. C. Wilson, *Output coupling of a Bose-Einstein condensate formed in a top trap*, J. Phys. B. **32** (1999), 3065.

[553] N. Marzari, A. A. Mostofi, J. R. Yates, I. Souza, and D. Vanderbilt, *Maximally localized wannier functions: Theory and applications*, Rev. Mod. Phys. **84** (2012), 1419, DOI.

[554] K.-P. Marzlin, Weiping Zhang, and Barry C. Sanders, *Creation of skyrmions in a spinor Bose-Einstein condensate*, Phys. Rev. A **62** (2000), 13602, .

[555] C. Marzok, B. Deh, S. Slama, C. Zimmermann, and Ph. W. Courteille, *In situ Ramsey interferometry and diffraction echo with an ultracold Fermi gas*, Phys. Rev. A **78** (2008), 021602(R), DOI.

[556] N. Masuhara, J. M. Doyle, J. C. Sandberg, D. Kleppner, T. J. Greytak, H. F. Hess, and G. P. Kochanski, *Evaporative cooling of spin-polarized atomic hydrogen*, Phys. Rev. Lett. **61** (1988).

[557] M. R. Matthews, B. P. Anderson, P. C. Haljan, D. S. Hall, M. J. Holland, J. E. Williams, C. E. Wieman, and E. A. Cornell, *Watching a superfluid untwisting itself*, Phys. Rev. Lett. **83** (1999), 3358, .

[558] M. R. Matthews, B. P. Anderson, P. C. Haljan, D. S. Hall, C. E. Wieman, and E.A. Cornell, *Vortices in a Bose-Einstein condensate*, Phys. Rev. Lett. **83** (1999), 2498, .

[559] C. E. Máximo, N. Piovella, Ph. W. Courteille, R. Kaiser, and R. Bachelard, *Spatial and temporal localization of light in two dimensions*, Phys. Rev. A **92** (2015), 062702.

[560] T. Mayer-Kuckuk, *Atomphysik*, Teubner Studienbücher, 1985, ISBN.

[561] I. E. Mazets, *Incoherent scattering of light by a Bose-Einstein condensate of interacting atoms*, (2000), quant-ph/0003126.

[562] A. R. McGurn, K. T. Christensen, F. M. Mueller, and A. A. Maradudin, *Anderson localization in one-dimensional randomly disordered optical systems that are periodic on average*, Phys. Rev. B **47** (1993), 13120, .

[563] D. M. Meekhof, C. Monroe, B. E. King, W. M. Itano, and D. J. Wineland, *Generation of nonclassical motional states of a trapped atom*, Phys. Rev. Lett. **76** (1996), 1797, .

[564] S. Y. T. Meerakker and et. al., *Direct measurement of the radiative lifetime of vibrationally excited oh radicals*, Phys. Rev. Lett. **95** (2005), 013003, .

[565] D. Meiser, Jun Ye, D. R. Carlson, and M. J. Holland, *Prospects for a millihertz-linewidth laser*, Phys. Rev. Lett. **102** (2009), 163601, DOI.

[566] J. Meixner and F.W. Schäfke, *Mathieu'sche funktionen und sphäroidfunktionen*, Springer-Verlag Berlin (1954).

[567] I. B. Mekhov, V. S. Egorov, V. N. Lebedev, P. V. Moroshkin, I. A. Chekhonin, and S. N. Bagayev, *Strong light-matter coupling: parametric interactions in a cavity and free-space*, quant-ph/0607033 (2006), .

[568] I. V. Mekhov, C. Maschler, and H. Ritsch, *Light scattering from ultracold atoms in optical lattices as an optical probe of quantum statistics*, Phys. Rev. A **76** (2007), 053618, DOI.

[569] C. R. Menegatti, *Trap loss in a rubidium crossed dipole trap by short-range photoassociation*, Phys. Rev. A **87** (2013), 053404, .

[570] N. C. Menicucci, P. van Loock, M. Gu, C. Weedbrook, T. C. Ralph, and M. A. Nielsen, *Universal quantum computation with continuous-variable cluster states*, Phys. Rev. Lett. **97** (2006), 110501, DOI.

[571] M.-O. Mewes, M. R. Andrews, D. M. Kurn, D. S. Durfee, C. G. Townsend, and W. Ketterle, *Output coupler for Bose-Einstein condensed atoms*, Phys. Rev. Lett. **78** (1997), 582, .

[572] M.-O. Mewes, M. R. Andrews, N. J. van Druten, D. M. Kurn, D. S. Durfee, and W. Ketterle, *Bose-Einstein condensation in a tightly confining dc magnetic trap*, Phys. Rev. Lett. **77** (1996), 416, .

[573] M.-O. Mewes, M. R. Andrews, N. J. van Druten, D. M. Kurn, D. S. Durfee, C. G. Townsend, and W. Ketterle, *Collective excitations of a Bose-Einstein condensation in a magnetic trap*, Phys. Rev. Lett. **77** (1996), 988, .

[574] J. J. Meyer, *Fisher information in noisy intermediate-scale quantum applications*, Quantum **4** (2021), 539, DOI.

[575] R. Meyer, *Trigonometric interpolation method for one-dimensional quantum-mechanical problems*, J. Chem. Phys. **52** (1969), 2053.

[576] V. Meyer, M. A. Rowe, D. Kielpinski, C. A. Sackett, W. M. Itano, C. Monroe, and D. J. Wineland, *Experimental demonstration of entanglement-enhanced rotation angle estimation using trapped ions*, Phys. Rev. Lett. **86** (2001), 5870, .

[577] F. H. Mies, C. J. Williams, P. S. Julienne, and M. Krauss, *Estimating bounds on collisional relaxation rates of spin-polarized ^{87}Rb atoms at ultracold temperatures*, J. Res. Natl. Inst. Stand. Tech. **101** (1996), 521.

[578] H.-J. Miesner, D. M. Stamper-Kurn, M. R. Andrews, D. S. Durfee, S. Inouye, and W. Ketterle, *Bosonic stimulation in the formation of a Bose-Einstein condensate*, Science **279** (1998), 1005, .

[579] A. L. Migdall, J. V. Prodan, W. D. Phillips, T. H. Bergman, and H. J. Metcalf, *First observation of magnetically trapped neutral atoms*, Phys. Rev. Lett. **54** (1985), 2596.

[580] G. Milburn, *Intrinsic decoherence in quantum mechanics*, Phys. Rev. A **44** (1991), 5401, .

[581] J. D. Miller, R. A. Cline, and D. J. Heinzen, *Far-off-resonance optical trapping of atoms*, Phys. Rev. A **47** (1993), R4567, .

[582] Randell L. Mills, *The grand unified theory of classical quantum mechanics*, ISBN.

[583] P. W. Milonni, *The quantum vacuum: An introduction to quantum electrodynamics*, Academic, San Diego, 1994, ISBN.

[584] P. W. Milonni and R. W. Boyd, *Momentum of light in a dielectric medium*, Adv. Opt. Phot. **2** (2010), 519, .

[585] F. Minardi, C. Fort, P. Maddaloni, M. Modugno, and M. Inguscio, *Time-domain atom interferometry across the threshold for Bose-Einstein condensation*, ePrints (2001), cond–mat/0103602, .

[586] Z. K. Minev, S. O. Mundhada, S. Shankar, P. Reinhold, R. Gutiérrez-JÃ¡uregui, R. J. Schoelkopf, M. Mirrahimi, H. J. Carmichael, and M. H. Devoret, *To catch and reverse a quantum jump mid-flight*, Nature **570** (2019), 200, DOI.

[587] B. Misra and E. C. G. Sudarshan, *The zeno paradox in quantum theory*, J. Math. Phys. **18** (1977), 756.

[588] J. Mlynek, V. Balykn, and P. Meystre, *"topical review"*, Appl. Phys. B **54** (1992).

[589] A. J. Moerdijk, B. J. Verhaar, and A. Axelsson, *Resonances in ultracold collisions of 6li, 7li, and 23na*, Phys. Rev. A **51** (1995), 4852, .

[590] A. J. Moerdijk, B. J. Verhaar, and T. M. Nagtegaal, *Collisions of dressed ground-state atoms*, Phys. Rev. A **53** (1996), 4343, .

[591] M. Mohammad, Eunjong Kim, Xueyue Zhang, A. Sipahigil, P. B. Dieterle, A. J. Keller, A. Asenjo-Garcia, D. E. Chang, and O. Painter, *Cavity quantum electrodynamics with atom-like mirrors*, Nature **569** (2019), 692, DOI.

[592] B. R. Mollow, *Stimulated emission and absorption near resonance for driven systems*, Phys. Rev. A **5** (1972), 2217.

[593] _____, *Pure-state analysis of resonant light scattering: Radiative damping, saturation, and multiphoton effects*, Phys. Rev. A **12** (1975), 1919.

[594] K. Mølmer, Y. Castin, and J. Dalibard, *Monte-carlo wave-function method in quantum optics*, J. Opt. Soc. Am. B **10** (1993), 524, DOI.

[595] C. Monroe, E. A. Cornell, C. A. Sackett, C. J. Myatt, and C. E. Wieman, *Measurement of cs-cs elastic scattering at t=30uk*, Phys. Rev. Lett. **70** (1993), 414, .

[596] Th. Monz, Ph. Schindler, J. T. Barreiro, M. Chwalla, D. Nigg, W. A. Coish, M. Harlander, W. Hänsel, M. Hennrich, and R. Blatt, *14-qubit entanglement: Creation and coherence*, Phys. Rev. Lett. **106** (2011), 130506, DOI.

[597] M. G. Moore and P. Meystre, *Optical control and entanglement of atomic schrödinger fields*, Phys. Rev. A **59** (1999), 1754, DOI.

[598] _____, *Theory of superradiant scattering of laser light from Bose-Einstein condensates*, Phys. Rev. Lett. **83** (1999), 5202, .

[599] _____, *Atomic four-wave mixing: Fermions versus bosons*, Phys. Rev. Lett. **86** (2001), 4199, DOI.

[600] M. G. Moore, O. Zobay, and P. Meystre, *Quantum optics of a Bose-Einstein condensate coupled to a quantized light field*, Phys. Rev. A **60** (1999), 1491, DOI.

[601] S. A. Morgan, R. J. Ballagh, and K. Burnett, *Solitary-wave solutions to nonlinear schrödinger equations*, Phys. Rev. A **55** (1997), 4338, .

[602] M. Morinaga, M. Yasuda, T. Kishimoto, F. Shimizu, J.-I. Fujita, and S. Matsui, *Holographic manipulation of a cold atom beam*, Phys. Rev. Lett. **77** (1996), 802, .

[603] H. Moritz, T. Stöferle, K. Günter, M. Köhl, and T. Esslinger, *Confinement induced molecules in a 1d Fermi gas*, Phys. Rev. Lett. **94** (2005), 210401, .

[604] O. Morsch, J. H. Müller, M. Cristiani, and E. Arimondo, *Coherent acceleration and Landau-Zener tunneling of Bose-Einstein condensates in 1-d optical lattices*, ePrints (2001), cond–mat/0103466, .

[605] N.F. Mott and H. S. W. Massey, *The atomic theory of atomic collisions i and ii*, Oxford Scientific Publications at the Clarendon Press, 1965, ISBN.

[606] M. Movre and G. Pichler, *Resonance interaction and self-broadening of alkali resonance lines i. adiabatic potential curves*, J. Phys. B **10** (1977), 2631, .

[607] G. M. Moy, J. J. Hope, and C. M. Savage, *Atom laser based on Raman transitions*, Phys. Rev. A **55** (1997), 3631.

[608] _____, *Born and markov approximations for atom lasers*, Phys. Rev. A **59** (1999), 667.

[609] G. M. Moy and C. M. Savage, *Output coupling for an atom laser by state change*, Phys. Rev. A **56** (1997), R1087.

[610] O. D. Mücke, R. Ell, A. Winter, Jung-Won Kim, J. R. Birge, L. Matos, and F. X. Kärtner, *Self-referenced 200 mhz octave-spanning ti:sapphire laser with 50 attosecond carrier-envelope phase jitter*, Opt. Exp. **13** (2005), 5163, .

[611] M. Mudrich, S. Kraft, K. Singer, R. Grimm, A. Mosk, and M. Weidemüller, *Sympathetic cooling with two atomic species in an optical trap*, Phys. Rev. Lett. **88** (2002), 253001.

[612] A. E. Muryshev, H. B. Van Linden Van Den Heuvell, and G. V. Shlyapnikov, *Stability of standing matter waves in a trap*, Phys. Rev. A **60** (1999), 2665, .

[613] C. J. Myatt, E. A. Burt, R. W. Ghrist, E. A. Cornell, and C. E. Wieman, *Production of two overlapping Bose-Einstein condensates by sympathetic cooling*, Phys. Rev. Lett. **78** (1997), 586, DOI.

[614] S. B. Nagel, P. G. Mickelson, A. D. Saenz, Y. N. Martinez, Y. C. Chen, T. C. Killian, P. Pellegrini, and R. Côte, *Photoassociative spectroscopy at long range in ultracold strontium*, Phys. Rev. Lett. **94** (2005), 083004, DOI.

[615] B. Nagorny, Th. Elsässer, and A. Hemmerich, *Collective atomic motion in an optical lattice formed inside a high finesse cavity*, Phys. Rev. Lett. **91** (2003), 153003, .

[616] W. Nagourney, J. Sandberg, and H. G. Dehmelt, *Shelved optical electron amplifier: Observation of quantum jumps*, Phys. Rev. Lett. **56** (1986), 2797.

[617] R. Napolitano, J. De Luca, V. S. Bagnato, and G. C. Marques, *Effect of finite numbers in the Bose-Einstein condensation of a trapped gas*, Phys. Rev. A **55** (1997), R3954, .

[618] A. Narayanaswamy and G. Chen, *Dyadic green's functions and electromagnetic local density of states*, J. Quant. Spectr. Rad. Transfer **111** (2009), 12, DOI.

[619] L. M. Narducci, H. M. Doss, P. Ru, M. O. Scully, S. Y. Zhu, and C. Keitel, *A simple model of a laser without inversion*, Opt. Comm. **81** (1991), 379, .

[620] N. R. Newbury, C. J. Myatt, E. A. Cornell, and C. E. Wieman, *Gravitational sisyphus cooling of 87rb in a magnetic trap*, Phys. Rev. Lett. **74** (1995), 2196, .

[621] Hyunchul Nha, Young-Tak Chough, and Kyungwon An, *A high phase-space-density gas of polar molecules*, Phys. Rev. A **62** (2000), 021801(R), DOI.

[622] T. Nikuni and A. Griffin, *Landau-khalatnikov two-fluid hydrodynamics of a trapped bose gas*, Phys. Rev. A **63** (2001), 033608.

[623] M. A. Norcia, R. J. Lewis-Swan, J. R. K. Cline, Bihui Zhu, A. M. Rey, and J. K. Thompson, *Cavity-mediated collective spin-exchange interactions in a strontium superradiant laser*, Science **361** (2018), 259, DOI.

[624] M. A. Norcia and J. K. Thompson, *Cold-strontium laser in the superradiant crossover regime*, Phys. Rev. X **6** (2016), 011025, DOI.

[625] M. A. Norcia, M. N. Winchester, J. R. K. Cline, and J. K. Thompson, *Superradiance on the millihertz linewidth strontium clock transition*, Sci. Adv. **2** (2016), e:1601231, DOI.

[626] H. I. Nurdin, *Saturability of the quantum cramér-rao bound in multiparameter quantum estimation at the single-copy level*, IEEE Control Systems Lett. **8** (2024), 376, DOI.

[627] N. Nygaard and K. Mølmer, *Component separation in harmonically trapped boson-fermion mixtures*, Phys. Rev. A **59** (1999), 2974, .

[628] K. M. OHara, S. R. Granade, M. E. Gehm, T. A. Savard, S. Bali, C. Freed, and J. E. Thomas, *Ultrastable co_2 laser trapping of lithium fermions*, Phys. Rev. Lett. **82** (1999), 4204.

[629] K. M. OHara, S. L. Hemmer, M. E. Gehm, S. R. Granade, and J. E. Thomas, *Observation of a strongly interacting degenerate Fermi gas of atoms*, Science **298** (2002), 2179, .

[630] M. Ö. Oktel and Ö. E. Müstecaplýoglu, *Electromagnetically induced left-handedness in a dense gas of three-level atoms*, Phys. Rev. A **70** (2004), 053806, DOI.

[631] B. Olmos, D. Yu, Y. Singh, F. Schreck, K. Bongs, and I. Lesanovsky, *Long-range interacting many-body systems with alkaline-earth-metal atoms*, Phys. Rev. Lett. **110** (2013), 143602, DOI.

[632] R. Onofrio, D. S. Durfee, C. Raman, M. Köhl, C. E. Kuklewicz, and W. Ketterle, *Surface excitations in a Bose-Einstein condensate*, Phys. Rev. Lett. **84** (2000), 810, .

[633] R. Onofrio, C. Raman, J. M. Vogels, J. Abo-Shaeer, A. P. Chikkatur, and W. Ketterle, *Observation of superfluid flow in a Bose-Einstein condensed gas*, Phys. Rev. Lett. **85** (2000), 2228, .

[634] L. Ortiz-Gutiérrez, R. C. Teixeira, A. Eloy, D. Ferreira da Silva, R. Kaiser, R. Bachelard, and M. Fouché, *Mollow triplet in cold atoms*, New J. Phys. **21** (2019), 093019, DOI.

[635] ———, *Mollow triplet in cold atoms*, New J. Phys. **21** (2019), 093019, DOI.

[636] C. Orzel, A. K. Tuchman, M. L. Fenselau, M. Yasuda, and M. A. Kasevich, *Squeezed states in a Bose-Einstein condensate*, Science **291** (2001), 2386, .

[637] S. Ospelkaus, A. Pe'er, K.-K. Ni, J. J. Zirbel, and B. Neyenhuis, *Ultracold dense gas of deeply bound heteronuclear molecules*, ePrints (2003), 0802.1093, .

[638] H. Ouerdane and M. J. Jamieson, *Scattering parameters for cold lirb and narb collisions derived from variable phase theory*, Phys. Rev. A **70** (2004), 022712, .

[639] Yu. B. Ovchinnikov, J. H. Müller, M. R. Doery, M. J. R. Vredenbregt, K. Helmerson, S. L. Rolston, and W. D. Phillips, *Diffraction of a released Bose-Einstein condensate by a pulsed standing light wave*, Phys. Rev. Lett. **83** (1999), 284, .

[640] R. Ozeri, J. Steinhauer, N. Katz, and N. Davidson, *Direct observation of the phonon energy in a Bose-Einstein condensate by tomographic imaging*, Phys. Rev. Lett. **88** (2002), 220401, .

[641] A. S. Parkins and D. F. Walls, *The physics of trapped dilute gas Bose-Einstein condensates*, Phys. Rep. **303** (1998), 1.

[642] W. Paul, O. Osberghaus, and E. Fischer, *Ein Ionenkäfig*, Forschungsberichte des Wirtschafts- und Verkehrsministerium Nordrhein-Westfalen, Westdeutscher Verlag Köln-Opladen (1958).

[643] J. P. Paz and W. H. Zurek, *Environnement-induced decoherence and the transition from quantum to classical*, Lect. notes in Phys. **587** (2002), 77, .

[644] B. M. Peden, D. Meiser, M. L. Chiofalo, and M. J. Holland, *Nondestructive cavity QED probe of Bloch oscillations in a gas of ultracold atoms*, Phys. Rev. A **80** (2009), 043803, DOI.

[645] E. Peik, M. Ben Dahan, I. Bouchoule, Y. Castin, and C. Salomon, *Bloch oscillations of atoms, adiabatic rapid passage, and monokinetic atomic beams*, Phys. Rev. A **55** (1997), 2989, DOI.

[646] T. Pellizzari, S. A. Gardiner, J. I. Cirac, and P. Zoller, Phys. Rev. Lett. **75** (1995), 3788.

[647] F. M. Penning, *Die glimmentladung bei niedrigem druck zwischen koaxialen zylindern in einem axialen magnetfeld*, Physica **3** (1936), 873.

[648] M. Perrin, G.-L. Lippi, and A. Politi, *Phase-transition in a radiation-matter interaction with recoil and collisions*, Phys. Rev. Lett. **86** (2001), 4520, .

[649] C. Pethick and H. Smith, *Bose-Einstein condensation in dilute gases*, Cambridge University Press, 2002, ISBN.

[650] W. Petrich, M. H. Anderson, J. R. Ensher, and E. A. Cornell, *Stable, tightly confining trap for evaporative cooling of neutral atoms*, Phys. Rev. Lett. **74** (1995), 3352, .

[651] D. S. Petrov, *Three-boson problem near a narrow Feshbach resonance*, Phys. Rev. Lett. **93** (2004), 143201, .

[652] S. Pezzagna and J. Meijera, *Quantum computer based on color centers in diamond*, Appl. Phys. Rev. **8** (2021), 011308, DOI.

[653] L. Pezze, A. Smerzi, M. K. Oberthaler, R. Schmied, and Ph. Treutlein, *Quantum metrology with nonclassical states of atomic ensembles*, Rev. Mod. Phys. **90** (2018), 035005, DOI.

[654] William D. Phillips and Harold Metcalf, *Laser deceleration of an atomic beam*, Physical Review Letters **48** (1982), 596.

[655] A. Pikovsky, M. Rosenblum, and J. Kurths, *Synchronization: A universal concept in nonlinear sciences*, Cambridge, University press (2001).

[656] Pierre Pillet Ed., *Optics and interferometry with atoms*, J. Physique II **4** (1994), 1877.

[657] N. Piovella, R. Bachelard, and Ph. W. Courteille, *Fluid description of the cooperative scattering of light by spherical atomic clouds*, J. Plasma Phys. **79** (2013), 413.

[658] N. Piovella, M. Cola, and R. Bonifacio, *Quantum fluctuations and entanglement in the collective atomic recoil laser using a Bose-Einstein condensate*, Phys. Rev. A **67** (2003), 013817, .

[659] ———, *Classical and quantum regimes in the collective atomic recoil laser from a Bose-Einstein condensate*, J. Mod. Opt. **51** (2004), 1019.

[660] N. Piovella, M. Gatelli, and R. Bonifacio, *Quantum effects in the collective light scattering by coherent atomic recoil in a Bose-Einstein condensate*, Opt. Commun. **194** (2001), 167, .

[661] D. Plankensteiner, Ch. Hotter, and H. Ritsch, *Quantumcumulants.jl: A julia framework for generalized mean-field equations in open quantum systems*, Quantum **6** (2021), 617, DOI.

[662] H. D. Politzer, *Bose-stimulated scattering off a cold atom trap*, Phys. Rev. A **55** (1997), 1140, .

[663] S. G. Porsev and A. Derevianko, *High-accuracy calculations of dipole, quadrupole, and octupole electric dynamic polarizabilities and van der waals coefficients c_6, c_8, and c_{10} for alkaline-earth dimers*, J. Exp. Theor. Phys. **102** (2006), 195, DOI.

[664] U. V. Poulsen and K. Mølmer, *Atomic reflection from a magnetic mirror: Beyond the adiabatic approximation*, Eur. Phys. J. D **11** (2000), 151, .

[665] E. A. Power, *Effect on the lifetime of an atom undergoing a dipole transition due to the presence of a resonating atom*, J. Chem. Phys. **46** (1967), 4297, .

[666] S. Prasad and R. J. Glauber, *Coherent radiation by a spherical medium of resonant atoms*, Phys. Rev. A **82** (2010), 063805, DOI.

[667] G. A. Prataviera, *Trap environnement effects over quantum statistics and atom-photon correlations in the collective-atomic-recoil laser*, Phys. Rev. A **67** (2003), 045602, .

[668] G. A. Prataviera and M. C. de Oliveira, *Continuous measurement of atom-number moments of a Bose-Einstein condensate by photodetection*, Phys. Rev. A **70** (2004), 011602(R), DOI.

[669] J. D. Prestage, G. J. Dick, and L. Maleki, *New ion trap for frequency standard applications*, J. Appl. Phys. **66** (1989), 1013.

[670] J. D. Prestage, R. L. Tjoelker, R. T. Wang, G. J. Dick, and L. Maleki, *Hg+ trapped ion standard with the superconducting cavity maser oscillator*, IEEE Trans. Instr. and Meas. **42** (1993), 200.

[671] M. Prevedelli, F. S. Cataliotti, E. A. Cornell, J. R. Ensher, C. Fort, L. Ricci, G. M. Tino, and M. Inguscio, *Trapping and cooling of potassium isotopes in a double-magneto-optical-trap apparatus*, Phys. Rev. A **59** (1999), 886, .

[672] D. E. Pritchard, *Cooling neutral atoms in a magnetic trap for precision spectroscopy*, Phys. Rev. Lett. **51** (1983), 1336, .

[673] D. E. Pritchard, R. A. Rubenstein, A. Dhirani, D. A. Kokorowski, E. T. Smith, T. D. Hammond, and B. Rohwedder, *Longitudinal atom optics using localized oscillating fields: A fully quantum-mechanical treatment*, Phys. Rev. A **59** (1999), 4641.

[674] A. M. Eds. Prokhorov et al., *Laser cooling and trapping*, Laser Physics **4** (1994), 829.

[675] Han Pu, Weiping Zhang, and P. Meystre, *Wave mixing of optical pulses and Bose-Einstein condensates*, Phys. Rev. Lett. **91** (2003), 150407, .

[676] R. R. Puri and S. V. Lawande, *Exact steady-state density operator for a collective atomic system in an external field*, Phys. Lett. A **72** (1979), 200.

[677] Ravinder Puri, *Mathematical methods of quantum optics*, Springer Series in Optical Sciences (2000).

[678] G. Raithel, G. Birkl, W. D. Phillips, and S. L. Rolston, *Compression and parametric driving of atoms in optical lattices*, Phys. Rev. Lett. **78** (1997), 2928, .

[679] M. G. Raizen, R. J. Thompson, R. J. Brecha, H. J. Kimble, and H. J. Carmichael, *Normal-mode splitting and linewidth averaging for two-state atoms in an optical cavity*, Phys. Rev. Lett. **63** (1989), 240.

[680] C. Raman, M. Köhl, R. Onofrio, D. S. Durfee, C. E. Kuklewicz, Z. Hadzibabic, and W. Ketterle, *Evidence for a critical velocity in a Bose-Einstein condensed gas*, Phys. Rev. Lett. **83** (1999), 2502, .

[681] N. Ramsey, *A new molecular beam method*, Phys. Rev. **76** (1949), 996.

[682] E. M. Rasel, M. K. Oberthaler, H. Batelaan, J. Schmiedmayer, and A. Zeilinger, *Atom wave interferometry with diffraction gratings of light*, Phys. Rev. Lett. **75** (1995), 2633.

[683] A. Rauschenbeutel, G. Nogues, S. Osnaghi, P. Bertet, M. Brune, J.-M. Raimond, and S. Haroche, *Step-by-step engineering of multiparticle entanglement*, Science **288** (2000), 2024.

[684] C. A. Regal, C. Ticknor, J. L. Bohn, and D. S. Jin, *Tuning p-wave interactions in an ultracold Fermi gas of atoms*, Phys. Rev. Lett. **90** (2003), 053201, .

[685] N. E. Rehler and J. H. Eberly, Phys. Rev. A **3** (1971), 1735, DOI.

[686] M. Reich, U. Sterr, and W. Ertmer, *Scheme for measuring a berry-phase in an atom interferometer*, Phys. Rev. A **47** (1993), 2518, .

[687] M. D. Reid, *Quantum theory of optical bistability without adiabatic elimination*, Phys. Rev. A **37** (1988), 4792, .

[688] ———, *Demonstration of the Einstein-podolsky-rosen paradox using nondegenerate parametric amplification*, Phys. Rev. A **40** (1989), 913.

[689] J. T. Reilly, S. B. Jäger, J. D. Wilson, J. Cooper, S. Eggert, and M. J. Holland, *Speeding up squeezing with a periodically driven dicke model*, Phys. Rev. Research **6** (2024), 033090, DOI.

[690] W. P. Reinhardt and C. W. Clark, *Soliton dynamics in the collisions of Bose-Einstein condensates: An analogue of the josephson effect*, J. Phys. B **30** (1997), L785.

[691] M. Reitz, Ch. Sommer, and C. Genes, *Cooperative quantum phenomena in light-matter platforms*, Phys. Rev. X **3** (2022), 010201, DOI.

[692] M. J. Renn, D. Montgomery, O. Vdovin, D. Z. Anderson, C. E. Wieman, and E. A. Cornell, *Laser-guided atoms in hollow optical fibers*, Phys. Rev. Lett. **75** (1995), 3253.

[693] H. Ritsch, P. Domokos, F. Brennecke, and T. Esslinger, *Cold atoms in cavity-generated dynamical optical potentials*, Rev. Mod. Phys. **85** (2013), 553, DOI.

[694] D. Rivero, C. A. Pessoa Jr., G. H. de França, R. C. Teixeira, S. Slama, and Ph. W. Courteille, *Quantum resonant optical bistability with a narrow atomic transition: bistability phase diagram in the bad cavity regime*, New J. Phys. **25** (2023), 093053, DOI.

[695] G. Roati, C. D'Errico, L. Fallani, M. Fattori, C. Fort, M. Zaccanti, G. Modugno, M. Modugno, and M. Inguscio, *Anderson localization of a non-interacting Bose-Einstein condensate*, Nature **453** (2008), 0895, .

[696] G. R. M. Robb and B. W. J. McNeil, *Four-wave mixing with self-phase matching due to collective atomic recoil*, Phys. Rev. Lett. **94** (2005), 023901, .

[697] G. R. M. Robb, B. W. J. McNeil, R. Bonifacio, and N. Piovella, *Dispersive optical bistability in cold atomic vapours*, Opt. Commun. **194** (2001), 151.

[698] G. R. M. Robb, N. Piovella, A. Ferraro, R. Bonifacio, Ph. W. Courteille, and C. Zimmermann, *Collective atomic recoil lasing including friction and diffusion effects*, Phys. Rev. A **69** (2004), 041403(R).

[699] A. Robert, O. Sirjean, A. Browaeys, J. Poupard, S. Nowak, D. Boiron, C. I. Westbrook, and A. Aspect, *A Bose-Einstein condensate of metastable atoms*, Science **292** (2001), 461.

[700] J. L. Roberts, N. R. Claussen, J. P. Jr. Burke, C. H. Greene, E. A. Cornell, and C. E. Wieman, *Resonant magnetic field control of elastic scattering in cold 85rb*, Phys. Rev. Lett. **81** (1998), 5109, .

[701] J. L. Roberts, N. R. Claussen, S. L. Cornish, E. A. Donley, E. A. Cornell, and C. E. Wieman, *Controlled collapse of a Bose-Einstein condensate*, ePrints (2001), cond–mat/0102116, .

[702] F. Robicheaux and J. V. Hernández, *Many-body wave function in a dipole blockade configuration*, Phys. Rev. A **72** (2005), 063403, DOI.

[703] H. Rohde, J. Eschner, F. Schmidt-Kaler, and R. Blatt, *Optical decay from a fabry-perot cavity faster than the decay time*, J. Opt. Soc. Am. B **19** (2002), 1425, .

[704] D. S. Rokhsar, *Vortex stability and persistent currents in trapped bose gases*, Phys. Rev. Lett. **79** (1997), 2164, .

[705] O. Romero-Isart and J. J. García-Ripoll, *Quantum ratchets for quantum communication with optical superlattices*, Phys. Rev. A **76** (2007), 052304, DOI.

[706] P. Rosario, A. C. Santos, N. Piovella, R. Kaiser, A. Cidrim, and R. Bachelard, *Detecting entanglement from macroscopic measurements of the electric field and its fluctuations*, Phys. Rev. Lett. **133** (2024), 050203, DOI.

[707] J. R. Rubbmark, M. M. Kash, M. G. Littman, and D. Kleppner, *Dynamical effects at avoided level crossings: A study of the Landau-Zener effect using Rydberg atoms*, Phys. Rev. A **23** (1981), 3107.

[708] J. Ruostekoski and D. F. Walls, *Bose-Einstein condensate in a double-well potential as an open quantum system*, Phys. Rev. A **58** (1998), R50, .

[709] P. A. Ruprecht, M. J. Holland, and K. Burnett, *Dynamical effects in atom optics*, Phys. Rev. A **49** (1994), 4726.

[710] P. A. Ruprecht, M. J. Holland, K. Burnett, and M. Edwards, *Time-dependent solutions of the nonlinear schrödinger equation for Bose-condensed trapped neutral atoms*, Phys. Rev. A **51** (1995), 4704.

[711] C. A. Sackett, C. C. Bradley, and R. G. Hulet, *Bose-Einstein condensation in lithium*, Appl. Phys. B **65** (1997), 433.

[712] C. A. Sackett, C. C. Bradley, M. Welling, and R. G. Hulet, *Bose-Einstein condensation of lithium*, Bra. J. Phys. **27** (1997), 154, .

[713] C. A. Sackett, J. M. Gerton, M. Welling, and R. G. Hulet, *Measurements of collective collapse in a Bose-Einstein condensate with attractive interactions*, Phys. Rev. Lett. **82** (1999), 876, .

[714] S. A. Sackett, D. Kielpinski, B. E. King, C. Langer, V. Meyer, C. J. Myatt, M. Rowe, Q. A. Turchette, W. M. Itano, D. J. Wineland, and C. Monroe, *Experimental entanglement of four particles*, Nature **404** (2000), 256.

[715] J. D. Sakurai and J. J. Napolitano, *Modern quantum mechanics*, John Wiley and Sons, 1999, ISBN.

[716] P. L. Saldanha, *Quantum analysis of the direct measurement of light waves*, New J. of Phys. **16** (2014), 013021.

[717] P. L. Saldanha and C. H. Monken, *Interaction between light and matter: a photon wave function approach*, New J. of Phys. **13** (2011), 073015, DOI.

[718] L. Salvi, N. Poli, V. Vuletić, and G. M. Tino, *Squeezing on momentum states for atom interferometry*, Phys. Rev. Lett. **120** (2018), 033601, DOI.

[719] L. De Salvo, R. Saers, S. Bartalini, F.S. Cataliotti, L. Fallani, C. Fort, I. Herrera, and M. Inguscio, *From superradiant Rayleigh scattering to Bragg scattering*, Eur. Phys. J. D (2004), .

[720] M. Samoylova, N. Piovella, R. Bachelard, and Ph. W. Courteille, *Microscopic theory of photonic bandgaps in optical lattices*, Opt. Comm. **312** (2014), 94.

[721] M. Samoylova, N. Piovella, M. Holynski, Ph.W. Courteille, and R. Bachelard, *One-dimensional photonic band gaps in optical lattices*, Annual Review of Cold Atoms and Molecules **2** (2014), 193.

[722] M. Samoylova, N. Piovella, G. Robb, R. Bachelard, and Ph. W. Courteille, *Synchronisation of Bloch oscillations by a ring cavity*, Opt. Exp **23** (2015), 14823.

[723] M. Sánchez-Barquilla, R. E. F. Silva, and J. Feist, *Cumulant expansion for the treatment of light-matter interactions in arbitrary material structures*, J. Chem. Phys. **152** (2020), 034108, DOI.

[724] L. Sanchez-Mondragon, N. B. Narozhny, and J. H. Eberly, *Theory of spontaneous emission line shape in an ideal cavity*, Phys. Rev. Lett. **51** (1983), 550, .

[725] G. Santarelli, Ph. Laurent, P. Lemonde, A. Clairon, A. G. Mann, S. Chang, A. N. Luiten, and C. Salomon, *Quantum projection noise in an atomic fountain: A high stability cesium frequency standard*, Phys. Rev. Lett. **82** (1999), 4619, .

[726] W. Saslow, T. K. Bergstresser, and M. L. Cohen, *Band structure and optical properties of diamond*, Phys. Rev. Lett. **16** (1966), 0354, .

[727] Th. Sauter, R. Blatt, W. Neuhauser, and P.E. Toschek, *Observation of quantum jumps*, Phys. Rev. Lett. **57** (1986), 1696, .

[728] _____, *Quantum jumps observed in the fluorescence of a single ion*, Opt. Comm. **60** (1986), 287, .

[729] M. R. Schafroth, *Theory of superconductivity*, Phys. Rev. **96** (1954), 1442.

[730] A. L. Schawlow and C.H. Townes, *Infrared and optical masers*, Phys. Rev. **112** (1958), 1940.

[731] S. Scheel and S. Y. Buhmann, *Macroscopic quantum electrodynamics - concepts and applications*, Acta Physcia Slovaca **5** (2008), 675, DOI.

[732] A. Schenzle, R. G. Devoe, and R. G. Brewer, *Phase modulation laser spectroscopy*, Phys. Rev. A **25** (1982), 2606, .

[733] A. Schenzle, R. G. DeVoe, and R. G. Brewer, *Possibility of quantum jumps*, Phys. Rev. A **33** (1986), 2127, .

[734] M. Schiffer, M. Rauner, S. Kuppens, M. Zinner, K. Sengstock, and W. Ertmer, *Guiding, focusing, and cooling of atoms in a strong dipole potential*, Appl. Phys. B **67** (1998), 705.

[735] A. Schilke, C. Zimmermann, Ph. W. Courteille, and W. Guerin, *Optical parametric oscillation with distributed feedback in cold atoms*, Nature Phot. **6** (2012), 101 letter.

[736] S. Schiller, *Hydrogenlike highly charged ions for tests of the time independence of fundamental constants*, Phys. Rev. Lett. **98** (2007), 180801, .

[737] W. Schleich, *Quantum optics in phase space*, Wiley-VCH, 2001, ISBN.

[738] U. Schlöder, T. Deuschle, C. Silber, and C. Zimmermann, *Autler-townes splitting in two-color photoassociation of 6 li*, Phys. Rev. A **68** (2003), 051403.

[739] D. Schneble, Y. Torii, M. Boyd, E. W. Streed, D. Pritchard, and W. Ketterle, *The onset of matter-wave amplification in a superradiant Bose-Einstein condensate*, Science **300** (2003), 475, .

[740] C. A. Schrama, E. Peik, W. W. Smith, and H. Walther, *Novel miniature ion traps*, Opt. Comm. **101** (1993), 32.

[741] E. Schrödinger, Brit. Journ. f. the Philos. of Science III (1952).

[742] M. Schubert, I. Siemers, and R. Blatt, *Line shape of three-level ions in paul traps*, Phys. Rev. A **39** (1989), 5098.

[743] A. S. Schumovsky, R. Taras, and Tram Quang, *Collective jumps in a system of three-level atoms*, Opt. Comm. **64** (1987), 45.

[744] M. O. Scully, *Fel*, Phys. Rev. Lett. **70** (1993), 1433.

[745] ———, *Condensation of n bosons and the laser phase transition analogy*, Phys. Rev. Lett. **82** (1999), 3927, .

[746] M. O. Scully, E. S. Fry, C. H. Raymond Ooi, and K. Wodkiewicz, *Directed spontaneous emission from an extended ensemble of n atoms: Timing is everything*, Phys. Rev. Lett. **96** (2006), 010501, DOI.

[747] ———, *The effects of the n atom collective lamb shift on single photon superradiance*, Phys. Lett. A **373** (2009), 1283, DOI.

[748] M. O. Scully and A. A. Svidzinsky, *The super of superradiance*, Science **325** (2009), 1510, DOI.

[749] M. O. Scully and M. S. Zubairy, *Quantum optics*, Cambridge University Press, 1997, ISBN.

[750] J. Seke, *The counter-rotating terms in the superradiance*, Il Nuove Cimente **7** (1986), 447, .

[751] Jian Qi Shen, *Negatively refracting atomic vapour*, J. Mod. Opt. **53** (2006), 2195, .

[752] Jian Qi Shen, J. Almlöf, and S. He, *Negative permeability in a λ-type three level atomic vapor*, Appl. Phys. A **87** (2006), 291, DOI.

[753] Jian-Qi Shen, Zhi-Chao Ruan, and Sailing He, *How to realize a negative refractive index material at the atomic level in an optical frequency range*, J. Zhejiang University SCIENCE **5** (2004), 1322, DOI.

[754] Jiteng Sheng, Yuanxi Chao, Santosh Kumar, Haoquan Fan, J. Sedlacek, and J. P. Shaffer, *Intracavity Rydberg-atom electromagnetically induced transparency using a high-finesse optical cavity*, Phys. Rev. A **96** (2017), 033813, DOI.

[755] V. B. Shenoy and Tin-Lun Ho, *First and second sound modes of a Bose-Einstein condensate in a harmonic trap*, Phys. Rev. Lett. **80** (1998), 3895.

[756] Masatoshi Shiino, *Dynamic behavior of of stochastic systems of infinitely many coupled nonlinear oscillators exhibiting phase transitions of mean-field-type: H theorem on asymptotic approach to equilibrium and critical slowing down of order parameter*, Phys. Rev. A **36** (1987), 2393, .

[757] J. H. Shirley, *Modulation transfer processes in optical heterodyne saturation spectroscopy*, Opt. Lett. **7** (1982), 537.

[758] G. V. Shlyapnikov, J. T. M. Walraven, U. M. Rahmanov, and M. W. Reynolds, *Decay-kinetics and Bose-condensation in a gas of spin-polarized triplett helium*, Phys. Rev. Lett. **73** (1994), 3247.

[759] A. Simoni, F. Ferlaino, G. Roati, G. Modugno, and M. Inguscio, *Magnetic control of the interaction in ultracold k-rb mixtures*, Phys. Rev. Lett. **90** (2003), 163202, .

[760] J. E. Simsarian, J. Denschlag, M. Edwards, C. W. Clark, L. Deng, E. W. Hagley, K. Helmerson, S. L. Rolston, and W. D. Phillips, *Imaging the phase of an evolving Bose-Einstein condensate wavefunction*, Phys. Rev. Lett. **85** (2000), 2040, .

[761] K. G. Singh and D. S. Rokshar, *Collective excitations of a confined Bose-Einstein condensate*, Phys. Rev. Lett. **77** (1996), 1667, .

[762] K. Sinha, B. Prasanna Venkatesh, and P. Meystre, *Collective effects in casimir-polder forces*, Phys. Rev. Lett. **121** (2018), 183605.

[763] S. E. Skipetrov and I. M. Sokolov, *Magnetic-field-driven localization of light in a cold-atom gas*, Phys. Rev. Lett. **114** (2015), 053902, .

[764] S. E. Skipetrov and I.M. Sokolov, *Absence of anderson localization of light in a random ensemble of point scatterers*, Phys. Rev. Lett. **112** (2014), 023905, DOI.

[765] S. Slama, S. Bux, G. Krenz, C. Zimmermann, and Ph. W. Courteille, *Superradiant Rayleigh scattering and collective atomic recoil lasing in a ring cavity*, Phys. Rev. Lett. **98** (2007), 053603.

[766] S. Slama, C. von Cube, B. Deh, A. Ludewig, C. Zimmermann, and Ph. W. Courteille, *Phase-sensitive detection of Bragg-scattering at 1d optical lattices*, Phys. Rev. Lett. **94** (2005), 193901.

[767] S. Slama, C. von Cube, M. Kohler, C. Zimmermann, and Ph. W. Courteille, *Multiple reflections and diffuse scattering in Bragg scattering at optical lattices*, Phys. Rev. A **73** (2006), 023424.

[768] S. Slama, C. von Cube, A. Ludewig, M. Kohler, C. Zimmermann, and Ph. W. Courteille, *Dimensional crossover in Bragg scattering from optical lattices*, Phys. Rev. A **72** (2005), 031402(R).

[769] A. Smerzi and S. Fantoni, *Large amplitude oscillations of a bose condensate*, Phys. Rev. Lett. **78** (1997), 3589, .

[770] J. J. Snyder, R. K. Kaj, D. Bloch, and M. Ducloy, *High-sensitivity nonlinear spectrocopy using a frequency-offset pump*, Opt. Lett. **5** (1980), 163.

[771] J. Söding, D. Guéry-Odelin, P. Desbiolles, F. Chevy, H. Inamori, and J. Dalibard, *Three-body decay of a rubidium Bose-Einstein condensate*, Appl. Phys. B **69** (1999), 257, .

[772] O. Somech and E. Shahmoon, *Quantum entangled states of a classically radiating macroscopic spin*, Phys. Rev. X Quantum **5** (2024), 010349, DOI.

[773] E. Y. Song, D. Barberena, D. J. Young, E. Chaparro, A. Chu, S. Agarwal, Z. Niu, J. T. Young, A. M. Rey, and J. K. Thompson, *A dissipation-induced superradiant transition in a strontium cavity-qed system*, Science Adv. **11** (2025), eadu5799, DOI.

[774] A. Sørensen and K. Mølmer, *Entanglement and quantum computation with ions in thermal motion*, Phys. Rev. A **62** (2000), 022311, DOI.

[775] C. M. Sorensen and D. J. Fischbach, *Patterns in mie scattering*, Opt. Comm. **173** (2000), 145, .

[776] A. V. Soroko, *Creation of an intended atomic wave using laser radiation*, J. Phys. B **30** (1997), 5621.

[777] R. J. C. Spreeuw, T. Pfau, U. Janicke, and M. Wilkens, *Laser-like scheme for atomic-matter waves*, Europhys. Lett. **32** (1995), 469.

[778] Y. Stalgies, I. Siemers, B. Appasamy, T. Altevogt, and P. E. Toschek, *The spectrum of single-atom resonance fluorescence*, Europhys. Lett. **35** (1996), 259, DOI.

[779] D. M. Stamper-Kurn, A. P. Chikkatur, A. Görlitz, S. Inouye, S. Gupta, D. E. Pritchard, and W. Ketterle, *Excitation of phonons in a Bose-Einstein condensate by light scattering*, Phys. Rev. Lett. **83** (1999), 2876, .

[780] D. M. Stamper-Kurn and W. Ketterle, *Spinor condensates and light scattering from Bose-Einstein condensates*, Proc. Les Houches Summer School, Session LXXII (2000), .

[781] D. M. Stamper-Kurn, H.-J. Miesner, A. P. Chikkatur, S. Inouye, J. Stenger, and W. Ketterle, *Quantum tunneling across spin domains in a BEC*, Phys. Rev. Lett. **83** (1999), 661, .

[782] D. M. Stamper-Kurn, H.-J. Miesner, S. Inouye, M. R. Andrews, and W. Ketterle, *Collisionless and hydrodynamic excitations of a Bose-Einstein condensate*, Phys. Rev. Lett. **81** (1998), 500, .

[783] ———, *Excitations of a Bose-Einstein condensate at non-zero temperature: A study of zero, first, and second sound*, ePrints: cond-mat/9801262 (1998), .

[784] J. Stanojevic and R. Côté, *Many-body Rabi oscillations of Rydberg excitation in small mesoscopic samples*, Phys. Rev. A **80** (2009), 033418, DOI.

[785] J. Stare and G. G. Balint-Kurti, *Fourier grid hamiltonian method for solving the vibrational Schrödinger equation in internal coordinates: Theory and test applications*, J. Phys. Chem. A **107** (2003), 7204, .

[786] D. A. Steck, *Rubidium 87 d line data*, unpublished (2003), .

[787] J. J. Di Steffano, A. R. Stubberud, and I. J. Williams, *Feedback and control systems*, Schaums outline series, McGraw-Hill, 1967.

[788] A. Stein, H. Knöckel, and E. Tiemann, *Fourier-transform spectroscopy of Sr2 and revised ground-state potential*, Phys. Rev. A **78** (2008), 042508, DOI.

[789] S. Stellmer, M. K. Tey, Bo Huang, R. Grimm, and F. Schreck, *Bose-Einstein condensation of strontium*, Phys. Rev. Lett. **103** (2009), 200402, DOI.

[790] J. Stenger, S. Inouye, M. R. Andrews, H.-J. Miesner, D. M. Stamper-Kurn, and W. Ketterle, *Strongly enhanced inelastic collisions in a Bose-Einstein condensate near Feshbach resonances*, Phys. Rev. Lett. **82** (1999), 2422, .

[791] J. Stenger, S. Inouye, A. P. Chikkatur, D. M. Stamper-Kurn, D. E. Pritchard, and W. Ketterle, *Bragg spectroscopy of a Bose-Einstein condensate*, Phys. Rev. Lett. **82** (1999), 4569, .

[792] J. Stenger, S. Inouye, D. M. Stamper-Kurn, H.-J. Miesner, A. P. Chikkatur, and W. Ketterle, *Spin domains in ground state spinor Bose-Einstein condensates*, Nature **396** (1998), 345.

[793] S. Stenholm, *The semiclassical theory of laser cooling*, Rev. Mod. Phys. **58** (1986), 699, .

[794] J. L. Stewart, *The power spectrum of a carrier frequency modulated by gaussian noise*, Proc. of the IRE **42** (1954), 1539.

[795] D. Stoler, *Equivalence class of minimum uncertainty wavepackets*, Phys. Rev. D **1** (2006), 3217, .

[796] M. Stoll and T. K?hler, *Production of three-body Efimov molecules in an optical lattice*, Phys. Rev. A **72** (2005), 022714, .

[797] Th. Stolz, H. Hegels, M. Winter, B. Röhr, Ya-Fen Hsiao, L. Husel, G. Rempe, and S. Dürr, *Quantum-logic gate between two optical photons with an average efficiency above 40%*, Phys. Rev. X **12** (2022), 021035, DOI.

[798] H. T. C. Stoof, *Atomic bose gas with a negative scattering length*, Phys. Rev. A **49** (1995), 3824, .

[799] H. T. C. Stoof and M. Bijlsma, *Degeneracy effects on the relaxation and recombination of adsorbed doubly polarized atomic hydrogen*, Phys. Rev. B **49** (1994), 422.

[800] S. Stringari, *Collective excitations of a trapped Bose-condensate gas*, Phys. Rev. Lett. **77** (1996), 2360, .

[801] S. H. Strogatz, *From kuramoto to crawford: Exploring the onset of synchronization in populations of coupled oscillators*, Physica D **143** (2000), 1, .

[802] W. C. Stwalley and L. H. Nosanow, *Possible new quantum systems*, Phys. Rev. Lett. **36** (1976), 910.

[803] P. Sundsoy and E. Fjeldberg, *Quantum computing, linear optics implementations*, ePrints: arXiv **1607.03935** (2016), .

[804] A. A. Svidzinsky and Jun-Tao Chang, *Comment on: Effects of including the counterrotating term and virtual photons on the eigenfunctions and eigenvalues of a scalar photon collective emission theory; phys. lett. a 372 (2008) 2514*, Phys. Lett. **372** (2008), 5732, .

[805] _____, *Cooperative spontaneous emission as a many-body eigenvalue problem*, Phys. Rev. A **77** (2008), 043833, DOI.

[806] A. A. Svidzinsky, Jun-Tao Chang, and M. O. Scully, *Dynamical evolution of correlated spontaneous emission of a from a uniformly excited cloud of atoms*, Phys. Rev. Lett. **100** (2008), 160504, DOI.

[807] A. A. Svidzinsky and M. O. Scully, *Evolution of collective n atom states in single photon superradiance: Effect of virtual lamb shift processes*, Opt. Comm. **282** (2009), 2894, DOI.

[808] J. Szczepkowski, M. Gronowski, A. Grochola, W. Jastrzebski, M. Tomza, and P. Kowalczyk, *Excited electronic states of sr_2: Ab initio predictions and experimental observation of the $2^1\Sigma_u^+$ state*, J. Chem. Phys. **127** (2010), 4473, DOI.

[809] Y. Takasu, K. Komori, K. Honda, M. Kumakura, T. Yabuzaki, and Y. Takahashi, *Photoassociation spectroscopy of laser-cooled ytterbium atoms*, Phys. Rev. Lett. **93** (2004), 123202, DOI.

[810] M. Tanifuji, *Polarization phenomena in physics*, World Scientific, 2018, DOIISBN.

[811] M. Tavis and F. W. Cummings, *Exact solution for an n-molecule-radiation-field hamiltonian*, Phys. Rev. **170** (1998), 379, .

[812] H. R. Telle, B. Lipphardt, and J. Stenger, *Kerr-lens, mode-locked lasers as transfer oscillators for optical frequency measurements*, Appl. Phys. B **74** (2002), 1.

[813] W. R. Theis, *Grundzüge der Quantentheorie*, Teubner Studienbücher, 1985, ISBN.

[814] L. H. Thomas, Nature **117** (1926), 514, .

[815] R. J. Thompson, G. Rempe, and H. J. Kimble, *Observation of normal mode splitting for an atom in an optical cavity*, Phys. Rev. Lett. **68** (1992), 1132, .

[816] H. R. Thorsheim, J. Weiner, and P. S. Julienne, *Laser-induced photoassociation of ultracold sodium atoms*, Phys. Rev. Lett. **58** (1987), 2420.

[817] J. H. Thywissen, *Ultracold atoms in lattices*, 2023, ⊙ICTP-SAIFR Lecture.

[818] E. Tiesinga, A. J. Moerdijk, B. J. Verhaar, and H. T. C. Stoof, *Conditions for Bose-Einstein condensation in magnetically trapped atomic cesium*, Phys. Rev. A **46** (1992), R1167, .

[819] E. Tiesinga, B.J. Verhaar, and H. T. C. Stoof, *Threshold and resonance phenomena in ultracold ground-state collisions*, Phys. Rev. A **47** (1993), 4114, .

[820] E. Tiesinga, C. J. Williams, and P. S. Julienne, *Photoassociative spectroscopy of highly excited vibrational levels of alkali dimers: Green's function approach for eigenvalue solvers*, Phys. Rev. A **57** (1998), 4257, [Tiesinga98].

[821] E. Tiesinga, C. J. Williams, P. S. Julienne, K. M. Jones, P. D. Lett, and W. D. Phillips, *A spectroscopic determination of scattering lengths for sodium atom collisions*, J. Res. Natl. Inst. Stand. Tech. **101** (1996), 505.

[822] U. Tietze and Ch. Schenk, *Halbleiterschaltungstechnik*, ISBN.

[823] G. Timp, R. E. Behringer, D. M. Tennant, J. E. Cunningham, M. Prentiss, and K. K. Berggren, *Using light as a lens for submicron, neutral-atom lithography*, Phys. Rev. Lett. **69** (1992), 1636, .

[824] S. Tojo, M. Kitagawa, K. Enomoto, Y. Kato, Y. Takasu, M. Kumakura, and Y. Takahashi, *High-resolution photoassociation spectroscopy of ultracold ytterbium atoms by using the intercombination transition*, Phys. Rev. Lett. **96** (2006), 153201, DOI.

[825] G. Tóth and I. Apellaniz, *Quantum metrology from a quantum information science perspective*, J. Phys. A **47** (2014), 424006, DOI.

[826] G. Tóth, C. Knapp, O. Gühne, and H. J. Briegel, *Optimal spin squeezing inequalities detect bound entanglement in spin models*, Phys. Rev. Lett. **99** (2007), 250405, DOI.

[827] ———, *Spin squeezing and entanglement*, Phys. Rev. A **79** (2009), 042334, DOI.

[828] M. Trippenbach, Y. B. Band, and P. S. Julienne, *Four wave mixing in the scattering of Bose-Einstein condensates*, Opt. Exp. **3** (1999), 530.

[829] A. G. Truscott, K. E. Strecker, W., I. McAlexander, Guthrie, B. Partridge, and R. G. Hulet, *Observation of Fermi pressure in a gas of trapped atoms*, Science **291** (2001), 2570, .

[830] Mankei Tsang, *Resolving starlight: a quantum perspective*, Contemp. Phys. **60** (2020), 279, DOI.

[831] Mankei Tsang, R. Nair, and Xiao-Ming Lu, *Quantum theory of superresolution for two incoherent optical point sources*, Phys. Rev. X **6** (2016), 031033, DOI.

[832] Q. A. Turchette, C. J. Hood, W. Lange, H. Mabuchi, and H. J. Kimble, *Measurement of conditional phase shifts for quantum logic*, Phys. Rev. Lett. **75** (1995), 4710, .

[833] M. Uria, P. Solano, and C. Hermann-Avigliano, *Deterministic generation of large fock states*, Phys. Rev. Lett. **125** (1992), 093603, DOI.

[834] L. Vaidman, *On the realization of interaction-free measurements*, Quantum Opt. **6** (1994), 119, DOI.

[835] D. V. van Coevorden, R. Sprik, A. Tip, and A. Lagendijk, *Photonic band gap structure of atomic lattices*, Phys. Rev. Lett. **77** (1996), 2412, .

[836] R. van der Stam, *Superradiant scattering of laser light from a Bose-Einstein condensater*, Dissertation (2006).

[837] J. Vanier and C. Au doin, *The quantum physics of atomic frequency standards*, Adam Hilger, Bristol and Philadelphia, 1989, ISBN.

[838] G. Veeravalli, E. Kuhnle, P. Dyke, and C. J. Vale, *Bragg spectroscopy of a strongly interacting Fermi gas*, ePrints **08092145** (2008), .

[839] F. S. Vieira, F. C. Cruz, D. F. Plusquellic, and S. A. Diddams, *Tunable resolution terahertz dual frequency comb spectrometer*, Opt. Exp. **24** (2016), 30100, DOI.

[840] J. M. Vogels, R. S. Freeland, C. C. Tsai, B. J. Verhaar, and D. J. Heinzen, *Coupled singlet-triplet analysis of two-color cold-atom photoassociation spectra*, Phys. Rev. A **61** (2000), 043407, .

[841] J. M. Vogels, C. C. Tsai, R. S. Freeland, S. J. J. M. F. Kokkelmans, B. J. Verhaar, and D. J. Heinzen, *Prediction of Feshbach resonances in collisions of ultracold rubidium atoms*, Phys. Rev. A **56** (1997), R1067, .

[842] C. von Cube, S. Slama, M. Kohler, C. Zimmermann, and Ph. W. Courteille, *Creating and probing long-range order in atomic clouds*, Fortschr. Phys. **54** (2006), 726.

[843] C. von Cube, S. Slama, D. Kruse, C. Zimmermann, Ph. W. Courteille, G. R. M. Robb, N. Piovella, and R. Bonifacio, *Self-synchronization and dissipation-induced threshold in collective atomic recoil lasing*, Phys. Rev. Lett. **93** (2004), 083601.

[844] J. von Neumann, *Mathematical foundations of quantum mechanics*, Princeton University Press, 1955, ISBN.

[845] V. Vuletic, A. J. Kerman, Cheng Chin, and S. Chu, *Observation of low-field Feshbach resonances in collisions of cesium atoms*, Phys. Rev. Lett. **82** (1999), 1406, .

[846] I. Waki, S. Kassner, G. Birkl, and H. Walther, *Observation of ordered structures of laser-cooled ions in a quadrupole storage ring*, Phys. Rev. Lett. **68** (1993), 2007.

[847] S. Wallentowitz and W. Vogel, *Reconstruction of the quantum mechanical state of a trapped ion*, Phys. Rev. Lett. **75** (1995), 2932.

[848] H. Wallis and H. Steck, *Inseparable time evolution of anisotropic Bose-Einstein condensates*, Europhys. Lett. **41** (1998), 477, .

[849] J. Walraven, *Atomic physics*, unpublished, Amsterdam, 2018, ⊙.

[850] ———, *Quantum gases*, unpublished, Amsterdam, 2019, ⊙.

[851] J. Walz, (1991).

[852] J. Walz, I. Siemers, M. Schubert, W. Neuhauser, and R. Blatt, *Motional stability of a nonlinear parametric oscillator: Ion storage in the rf octupole trap*, Europhys. Lett. **21** (1993), 183.

[853] Teng-Long Wang, Ling-Na Wu, Wen Yang, Guang-Ri Jin, N. Lambert, and F. Nori, *Quantum fisher information as a signature of the superradiant quantum phase transition*, New. J. Phys. **16** (2014), 063039, DOI.

[854] Tun Wang, S. F. Yelin, R. Côté, E. E. Eyler, S. M. Farooqi, P. L. Gould, M. Kostrun, D. Tong, and D. Vrinceanu, *Superradiance in ultracold Rydberg gases*, Phys. Rev. A **75** (2007), 033802, DOI.

[855] M. Weidemüller, A. Görlitz, Th. W. Hänsch, and A. Hemmerich, *Local and global properties of light-bound atomic lattices investigated by Bragg diffraction*, Phys. Rev. A **58** (1998), 4647, .

[856] M. Weidemüller, A. Hemmerich, A. Görlitz, T. Esslinger, and Th. W. Hänsch, *Bragg diffraction in an atomic lattice bound by light*, Phys. Rev. Lett. **75** (1995), 4583, .

[857] C. J. Weiner, J. J. Bollinger, F. L. Moore, and D. J. Wineland, *Electrostatic modes as a diagnostic*, Phys, Rev. A **49** (1994), 3842.

[858] J. Weiner, V. S. Bagnato, S. Zilio, and P. S. Julienne, *Experiments and theory in cold and ultracold collisions*, Rev. Mod. Phys. **71** (1999), 1.

[859] J. Weiner and P.-T. Ho, *Light-matter interaction, fundamentals and applications*, John Wiley & Sons, Hokoken, New Jersey, 2003, ISBN.

[860] D. S. Weiss, B.C. Young, and S. Chu, *Precision measurement of h/mcs based on photon recoil using laser-cooled atoms and atomic interferometry*, Appl. Phys. B **59** (1994), 217.

[861] S. B. Weiss, M. Bhattacharya, and N. P. Bigelow, *Calculation of the interspecies s-wave scattering length in an ultracold na-rb vapor*, Phys. Rev. A **68** (2003), 042708, .

[862] M. Weissbluth, *Atoms and molecules*, Students Edition Academic Press, San Diego, 1978, ISBN.

[863] G. Wentzel, *Eine verallgemeinerung der quantenbedingungen für die zwecke der wellenmechanik*, Zeitschrift für Physik **38** (1926), 518.

[864] K. Wiesenfeld, P. Colet, and S. H. Strogatz, *Frequency locking in josephson arrays: Connection with the kuramoto model*, Phys. Rev. E **57** (1998), 1563, .

[865] E. P. Wigner, *On the behavior of cross sections near thresholds*, Phys. Rev. **73** (1948), 1002.

[866] J. Williams, R. Walser, J. Cooper, E. Cornell, and M. Holland, *Nonlinear josephson-type oscillations of a driven, two-component Bose-Einstein condensate*, Phys. Rev. A **59** (1999), R31, .

[867] J. E. Williams and J. E. Holland, *Preparing topological states of a Bose-Einstein condensate*, Nature **401** (1999), 568, .

[868] M. N. Winchester, M. A. Norcia, J. R. K. Cline, and J. K. Thompson, *Magnetically induced optical transparency on a forbidden transition in strontium for cavity-enhanced spectroscopy*, Phys. Rev. Lett. **118** (2017), 263601.

[869] D. J. Wineland, J. J. Bollinger, W. M. Itano, and D. J. Heinzen, *Squeezed atomic states and projection noise in spectroscopy*, Phys. Rev. A **50** (1994), 67, DOI.

[870] D. J. Wineland and H. G. Dehmelt, *Proposed* $10^{14}\delta n < n$ *laser fluorescence spectroscopy on* Tl^{+} *mono-ion oscillator*, Bull. Am. Phys. Soc. **20** (1975), 637.

[871] D. J. Wineland and W. M. Itano, *Laser cooling of atoms*, Phys. Rev. A **20** (1979), 1521, DOI.

[872] H. M. Wiseman, *Defining the (atom) laser*, Phys. Rev. A **56** (1997), 2068.

[873] _____, *Light amplification without stimulated emission: Beyond the standard quantum limit to the laser linewidth*, Phys. Rev. A **60** (1999), 4083, DOI.

[874] H. M. Wiseman and M. J. Collett, *An atom laser based on dark-state cooling*, Phys. Lett. A **202** (1995), 246, .

[875] M. Woldeyohannes and S. John, *Coherent control of spontaneous emission near a photonic band edge*, J. Opt. B **5** (2003), R43, .

[876] T. S. Woodworth, Kam Wai Clifford Chan, C. Hermann-Avigliano, and A. M. Marino, *Transmission estimation at the cramÃ©r-rao bound for squeezed states of light in the presence of loss and imperfect detection*, Phys. Rev. A **102** (2020), 052603, DOI.

[877] E. M. Wright and D. F. Walls, *Collapses and revivals of Bose-Einstein condensates formed in small atomic samples*, Phys. Rev. Lett. **77** (1996), 2158, .

[878] Biao Wu, R. B. Diener, and Qian Niu, *Bloch waves and Bloch bands of Bose-Einstein condensates in optical lattices*, Phys. Rev. A **65** (2002), 025601, .

[879] Biao Wu and Qian Niu, *Nonlinear Landau-Zener tunneling*, Phys. Rev. A **61** (2000), 023402, DOI.

[880] _____, *Superfluidity of Bose-Einstein condensate in an optical lattice: Landau-Zener tunnelling and dynamical instability*, New J. Phys. **5** (2003), 104, .

[881] Huang Wu, E. Arimondo, and C. J. Foot, *Dynamics of evaporative cooling for Bose-Einstein condensation*, Phys. Rev. A **56** (1997), 560.

[882] Huang Wu and Ch. J. Foot, *Direct simulation of evaporative cooling*, J. Phys. B **29** (1996), L321, .

[883] Jin-Hui Wu, M. Artoni, and G. C. La Rocca, *Controlling the photonic band structure of optically driven cold atoms*, J. Opt. Soc. Am. B **25** (2008), 1840, DOI.

[884] R. Wynar, R. S. Freeland, D. J. Han, C. Ryu, and D. J. Heinzen, *Molecules in a Bose-Einstein condensate*, Science **287** (2000), 1016.

[885] Tao Xin, Bi-Xue Wang, Ke-Ren Li, Xiang-Yu Kong, Shi-Jie Wei, Tao Wang, Dong Ruan, and Gui-Lu Long, *Nuclear magnetic resonance for quantum computing: Techniques and recent achievements*, Chinese Physics B **27** (2018), 020308, DOI.

[886] K. Xu, T. Mukaiyama, J. R. Abo-Shaeer, J. K. Chin, D. E. Miller, and W. Ketterle, *Formation of quantum-degenerate sodium molecules*, Phys. Rev. Lett. **91** (2003), 210402, .

[887] Minghui Xu, S. B. Jäger, S. Schütz, J. Cooper, G. Morigi, and M. J. Holland, *Supercooling of atoms in an optical resonator*, Phys. Rev. Lett. **116** (2016), 153002, DOI.

[888] Victoria Xu, M. Jaffe, C. D. Panda, S. L. Kristensen, L. W. Clark, and H. Müller, *Probing gravity by holding atoms for 20 seconds*, Science **366** (2019), 745.

[889] N. Yamamoto, *Parametrization of the feedback hamiltonian realizing a pure steady state*, Phys. Rev. A **72** (2005), 024104, DOI.

[890] Ziyun Yan, *Bose-Einstein condensation of a trapped gas in n dimensions*, Phys. Rev. A **59** (1999), 4657, .

[891] G. J. Yang, L. Zhang, and W. Shu, *Light amplification through collective atomic recoil motion modified by a harmonic potential*, Phys. Rev. A **68** (2003), 063802, .

[892] Amnon Yariv, *Quantum electronics*, 1967, ISBN.

[893] Amnon Yariv and P. Yeh, *Optical waves in crystals*, 2002, ISBN.

[894] E. J. Yarmchuk, M. J. V. Gordon, and R. E. Packard, *Observation of stationary vortex arrays in rotating superfluid helium*, Phys. Rev. Lett. **43** (1979), 214, .

[895] M. Yasuda, T. Kishimoto, M. Takamoto, and H. Katori, *Photoassociation spectroscopy of 88sr: Reconstruction of the wave function near the last node*, Phys. Rev. A **73** (2006), 011403(R), DOI.

[896] Jun Ye, H. Schnatz, and L. W. Hollberg, *Optical frequency combs: From frequency metrology to optical phase control*, IEEE J. Sel. Top. QE **9** (2003), 1041.

[897] Yutaka Yoshikawa, Yoshio Torii, and Takahiro Kuga, *Superradiant light scattering from thermal atomic vapors*, Phys. Rev. Lett. **94** (2005), 083602, .

[898] Deshui Yu, *Photonic band structure of the three-dimensional ^{88}Sr atomic lattice*, Phys. Rev. A **84** (2011), 043833, DOI.

[899] V. I. Yukalov, E. P. Yukalova, and V. S. Bagnato, *Non-ground-state Bose-Einstein condensates of trapped atoms*, Phys. Rev. A **56** (1997), 4845, .

[900] N. A. Zaitsev, I. V. Matyushkin, and D. V. Shamonov, *Numerical solution of the thomas-Fermi equation for the centrally symmetric atom*, Russian Microelectronics, Translated from Mikroelektronika, Vol.33, Pag.372 **33** (2004), 303, DOI.

[901] Francesca Zambelli and Sandro Stringari, *Quantized vortices and collective oscillations of a trapped Bose-Einstein condensate*, Phys. Rev. Lett. **81** (1998), 1754, .

[902] Haoqing Zhang, A. Chu, C. Luo, J. K. Thompson, and A. M. Rey, *Control and amplification of bloch oscillations via photon-mediated interactions*, Phys. Rev. Res. **5** (2023), L032039, DOI.

[903] Yuan Zhang, Yu-Xiang Zhang, and K. Mølmer, *Monte-carlo simulations of superradiant lasing*, New J. Phys. **20** (2018), 112001, DOI.

[904] O. V. Zhirov and D. L. Shepelyansky, *Quantum synchronization*, Eur. Phys. J. D **38** (2006), 375, .

[905] Bihui Zhu, J. Marino, N. Y. Yao, M. D. Lukin, and E. A. Demler, *Dicke time crystals in driven-dissipative quantum many-body systems*, Phys. Rev. Lett. **21** (2019), 073028, DOI.

[906] O. Zobay and B. M. Garraway, *Atom trapping and two-dimensional Bose-Einstein condensates in field-induced adiabatic potentials*, Phys. Rev. A **69** (2004), 023605, .

[907] P. Zoller, M. Marte, and D. F. Walls, *Quantum jumps in atomic systems*, Phys. Rev. A **35** (1987), 198, .

[908] M. W. Zwierlein, C. A. Stan, C. H. Schunck, S. M. F. Raupach, S. Gupta, Z. Hadzibabic, and W. Ketterle, *Observation of Bose-Einstein condensation of molecules*, Phys. Rev. Lett. **91** (2003), 250401, .

Index